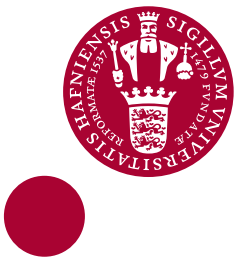

Magnetic Properties Results from Martian Surface Landers and Rovers

Goetz, Walter; Hviid, Stubbe; Madsen, Morten Bo; Kinch, Kjartan Münster

Published in:
The Martian Surface:

Publication date:
2008

Document version
Publisher's PDF, also known as Version of record

The Martian Surface

Composition, Mineralogy, and Physical Properties

Phenomenal new observations from Earth-based telescopes and Mars-based orbiters, landers, and rovers have dramatically advanced our understanding of the past environments on Mars. These include the first global-scale infrared and reflectance spectroscopic maps of the surface, leading to the discovery of key minerals indicative of specific past climate conditions; the discovery of large reservoirs of subsurface water ice; and the detailed *in situ* roving investigations of three new landing sites, which give us firm evidence for the presence of liquid water on the surface or in the shallow subsurface in the distant past.

This important, comprehensive book provides an overview of the latest Mars compositional and mineralogic discoveries since the last major review of this topic was published in 1992. It is an essential resource for researchers and students in planetary science, astronomy, space exploration, planetary geology, and planetary geochemistry. Specialized terms are defined throughout, so the material will be easily understood by researchers entering this field. Color figures can be found at www.cambridge.org/9780521866989.

JIM BELL is Associate Professor in the Department of Astronomy at Cornell University. He is the Lead Scientist for the Pancam color imaging system on the NASA Mars Exploration Rovers *Spirit* and *Opportunity*, and is also a member of the science teams of the NASA Mars Pathfinder, Near Earth Asteroid Rendezvous (NEAR), Mars 2001 Odyssey Orbiter, Mars 2005 Reconnaissance Orbiter, and 2009 Mars Science Laboratory rover mission teams. He has authored or co-authored more than 150 peer-reviewed scientific papers on Mars, is an editor for *Icarus*, and has an asteroid named after him (8146 Jimbell) by the International Astronomical Union.

Cambridge Planetary Science

Series Editors:

Fran Bagenal, David Jewitt, Carl Murray, Jim Bell, Ralph Lorenz,
Francis Nimmo, Sara Russell

Books in the series:

1 Jupiter: The Planet, Satellites and Magnetosphere*
Edited by Bagenal, Dowling and McKinnon
9780521035453

2 Meteorites: A Petrologic, Chemical and Isotopic Synthesis*
Hutchison
9780521035392

3 The Origin of Chondrules and Chondrites
Sears
9780521836036

4 Planetary Rings
Esposito
9780521362221

5 The Geology of Mars
Edited by Chapman
9780521832922

6 The Surface of Mars
Carr
9780521872010

7 Volcanism on Io: A Comparison with Earth
Davies
9780521850032

8 Mars: An Introduction to its Interior, Surface and Atmosphere
Barlow
9780521852265

9 The Martian Surface: Composition, Mineralogy, and Physical Properties
Edited by Bell
9780521866989

*Issued as a paperback

THE MARTIAN SURFACE

Composition, Mineralogy, and Physical Properties

Edited by

JIM BELL

CAMBRIDGE
UNIVERSITY PRESS

CAMBRIDGE UNIVERSITY PRESS
Cambridge, New York, Melbourne, Madrid, Cape Town, Singapore, São Paulo, Delhi

Cambridge University Press
The Edinburgh Building, Cambridge CB2 8RU, UK

Published in the United States of America by Cambridge University Press, New York

www.cambridge.org
Information on this title: www.cambridge.org/9780521866989

First published 2008

Printed in the United Kingdom at the University Press, Cambridge

A catalog record for this publication is available from the British Library

Library of Congress Cataloging in Publication data
The Martian Surface : composition, mineralogy, and physical properties / Jim F. Bell, editor.
p. cm.
Includes index.
1. Mars (Planet) – Surface. 2. Mars (Planet) – Geology. I. Bell, Jim. II. Title.
QB641.M375 2008
559.9′23–dc22
2007046271

ISBN 978-0-521-86698-9 hardback

DEDICATION

There is a relatively small community of "Martians" living here on Earth who study the Red Planet from afar, using images and other data acquired from telescopes or sent back by robotic orbiters, landers, and rovers. Because we are a small community, the loss of a colleague is keenly and sadly felt in our field. This book is dedicated to those colleagues whom we have lost during the past 15 years or so, since the last major review book on this topic was published. Among the most prominent, prolific, and respected of these departed friends are the gentlemen pictured here in the following page: Roger G. Burns, Robert B. ("Rob") Hargraves, Larry A. Haskin, Norman H. Horowitz, Harold P. ("Chuck") Klein, Jens Martin Knudsen, Leonard J. Martin, Harold ("Hal") Masursky, Henry J. ("Hank") Moore, Vassily I. Moroz, James B. Pollack, David J. Roddy, Carl Sagan, David H. Scott, Eugene M. ("Gene") Shoemaker, and Gerald A. Soffen.

These colleagues played critical roles in the fundamental scientific, engineering, educational, and managerial work that led directly to today's spectacularly successful era of Mars exploration. The results, interpretations, and speculations about Mars described here in this book are a tribute to their pioneering work, and we honor their memories and accomplishments by continuing to try to unlock the mysteries of the Red Planet.


Roger G. Burns

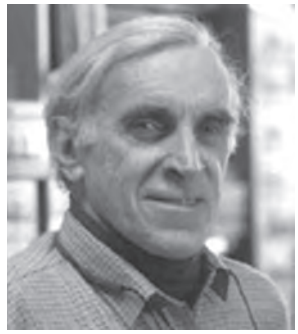
Robert B. Hargraves

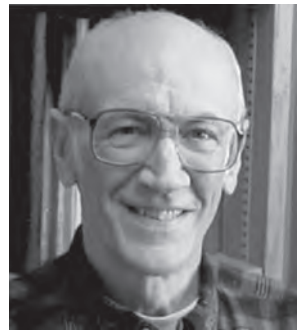
Larry A. Haskin


Norman H. Horowitz


Harold P. Klein


Jens Martin Knudsen


Leonard J. Martin


Harold Masursky


Henry J. Moore


Vassily I. Moroz


James B. Pollack


David J. Roddy

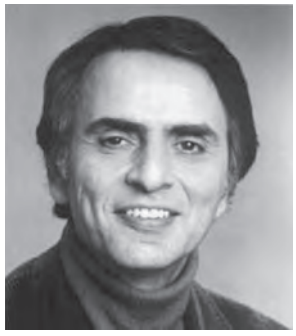
Carl Sagan


David H. Scott

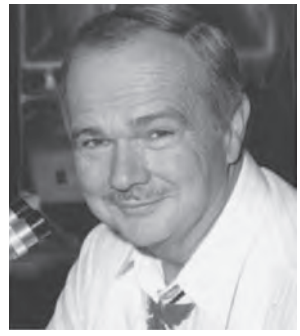
Eugene M. Shoemaker


Gerald A. Soffen

CONTENTS

The color plates are between pages 302 and 303

LIST OF CONTRIBUTORS

MARIO H. ACUÑA
NASA Goddard Space Flight Center
Laboratory for Extraterrestrial Physics
Code 695
Greenbelt, MD 20771
USA

RAY E. ARVIDSON
Earth & Planetary Science
Washington University
St Louis, MO 63130
USA

JOSHUA L. BANDFIELD
Arizona State University
MC 6305
Mars Space Flight Facility
Tempe, AZ
USA

JAMES F. BELL III
Cornell University
Department of Astronomy
402 Space Sciences Building
Ithaca, NY 14853-6801
USA

JEAN-PIERRE BIBRING
Institut d'Astrophysique Spatiale
Universite Paris Sud
Bat. 121
Orsay Cedex, F-91405
France

JANICE L. BISHOP
SETI Institute
515 N. Whisman Road
Mountain View, CA 94034
USA

DIANA L. BLANEY
JPL
MS 183-501
4800 Oak Grove Drive
Pasadena, CA 91109
USA

WILLIAM V. BOYNTON
Lunar and Planetary Laboratory
University of Arizona
Tuscon, AZ 85721
USA

JOHANNES BRÜCKNER
Geochemistry Department
Max Planck Institut für Chemie
PO Box 3060
Mainz D-55020
Germany

WENDY M. CALVIN
Department of Geological Science
MS 172
University of Nevada
Reno, NV 89557-0138
USA

BENTON C. CLARK
Planetary Sciences Laboratory
Lockheed Martin Aerospce
MS 8001, PO Box 179
Denver, CO 80201
USA

ROBERT N. CLAYTON
Enrico Fermi Institute
5640 S. Ellis Avenue, RI 440
Chicago, IL 60637
USA

PHILIP R. CHRISTENSEN
Planetary Exploration Laboratory
Arizona State University
Moeur Building 110D
Tempe, AZ 85287
USA

JOHN E. P. CONNERNEY
NASA Goddard Space Flight Center
Code 691
Greenbelt, MD
USA

DAVID J. DES MARAIS
NASA Ames Research Center
MS 239-4
Moffett Field, CA 94035-1000
USA

GERLIND DREIBUS
Cosmochemistry Deparment
Max Planck Institut für Chemie
PO Box 3060
Mainz D-55020
Germany

THANASIS E. ECONOMOU
Laboratory for Astrophysics & Space Res.
University of Chicago
933 East 56th Street
Chicago, IL 60637
USA

WILLIAM H. FARRAND
Space Science Institute
4750 Walnut Street, # 205
Boulder, CO 80301
USA

WILLIAM C. FELDMAN
Los Alamos National Laboratory
MS D466
Space & Atmospheric Science
Los Alamos, NM 87545
USA

ROBIN L. FERGASON
School of Earth & Space Exploration
Arizona State University
PO Box 876305
Tempe, AZ 85287-6305
USA

C. NICOLE FOLEY
Department of Terrestrial Magnetism
Carnegie Institute of Washington
5241 Broad Branch Road, NW
Washington, DC 20015-1305
USA

OLIVIER GASNAULT
Laboratoire d'Astrophysique
14 Avenue Belin
Toulouse, 31400
France

PAUL GEISSLER
US Geological Survey
2255 N. Gemini Drive
Flagstaff, AZ 86001
USA

RALF GELLERT
Department of Physics
University of Guelph
Guelph, ON
N1G 2W1
Canada

TIMOTHY D. GLOTCH
Department of Geosciences
SUNY at Stony Brook
Stony Brook, NY 11794
USA

WALTER GOETZ
Max Planck Institute for Solar System Research
Max Planck Str. 2
Katlenburg-Lindau, 37191
Germany

MATT P. GOLOMBEK
JPL
MS 183-501
4800 Oak Grove Drive
Pasadena, CA 91109
USA

STEVEN GOREVAN
Honeybee Robotics Spacecraft Mechanisms Corporation
460 W. 34th Street
New York, NY 10001
USA

RONALD GREELEY
Planetary Geology Group
Arizona State University
Tempe, AZ 85287-1404
USA

JOHN P. GROTZINGER
Geology & Planetary Sciences
California Institute of Technology
MC 170-25
1200 E. California Blvd.
Pasendena, CA 91125
USA

WILLIAM M. GRUNDY
Lowell Observatory
1400 W. Mars Hill Road
Flagstaff, AZ 86001
USA

EDWARD A. GUINNESS
Washington University
Campus Box 1169
St Louis, MO 63130
USA

ALBERT F. C. HALDEMANN
JPL
4800 Oak Grove Drive
Pasadena, CA 91109
USA

VICTORIA E. HAMILTON
Hawaii Institute of Geophysics & Planetology
University of Hawaii
1680 East-West Road
Honolulu, HI 96822
USA

KEN E. HERKENHOFF
U.S. Geological Survey
Astrogeology Team
2255 N. Gemini Drive
Flagstaff, AZ 86001-1698
USA

STUBBE F. HVIID
Max Planck Institute for Solar System Research
Max Planck Str. 2
Katlenburg-Lindau, 37191
Germany

BRIAN M. HYNEK
Department of Geological Sciences
Laboratory for Atmospheric and Space Physics
392 UCB
University of Colorado
Boulder, CO 80309
USA

BRUCE M. JAKOSKY
University of Colorado, Boulder
LASP/Campus Box 392
Boulder, CO 80309-0392
USA

JERRY B. JOHNSON
Cold Regions Research & Engineering Laboratory
Alaska Office
PO Box 35170
Ft. Wainwright, AK 99703
USA

JEFFREY R. JOHNSON
US Geological Survey
Astrogeology Team
2255 N. Gemini Drive
Flagstaff, AZ 86001-1698
USA

BRADLEY JOLLIFF
Washington University
Campus Box 1169
One Bookings Drive
St Louis, MO 63130
USA

SUNITI KARUNATILLAKE
Cornell University
514 Space Sciences Building
Ithaca, NY 14853-6801
USA

JOHN M. KELLER
University of Arizona
1629 E. University Blvd.
Tuscon, AZ 85721
USA

HUGH H. KIEFFER
Celestial Reasonings
2256 Christmas Tree Lane
Carson City, NV 89703
USA

KJARTAN M. KINCH
CRSR Cornell University
408 Space Sciences Building
Ithaca, NY 13853
USA

GUNTHER KLETETSCHKA
NASA Goddard Space Flight Center
Code 691
Greenbelt, MD
USA

GÖSTAR KLINGELHÖFER
Institut für Anorganische Chemie und Analytische Chemie
University of Mainz
Mainz, 55099
Germany

ALASTAIR KUSACK
Honeybee Robotics Spacecraft Mechanisms Corporation
460 W. 34th Street
New York, NY 10001
USA

YVES LANGEVIN
Institut d'Astrophysique Spatiale
91405 Orsay
France

RACHEL C. F. LENTZ
University of Hawai'i at Manoa
Hawai'i Institute of Geophysics and Planetology
1680 East-West Road, POST 602
Honolulu, HI 96822
USA

MORTEN B. MADSEN
Niels Bohr Institute for Astronomy
University of Copenhagen
Universitetsparken 5
Copenhagen, DK-2100
Denmark

SYLVESTRE MAURICE
Centre d'Etude Spatiale des Rayonnements
9 Avenue du Colonel Roche
BP 24346
Toulouse Cedex 4
France

TIMOTHY McCONNOCHIE
NASA Goddard Space Flight Center
Mailstop 693.0
Greenbelt, MD 20771
USA

TOM McCORD
Space Science Institute
4750 Walnut Street, Suite 205
Boulder
Colorado 80301
USA

ALFRED McEWEN
Lunar & Planetary Laboratory
University of Arizona
1541 E. University Blvd.
Tuscon, AZ 85721-0063
USA

SCOTT M. McLENNAN
Department of Geosciences
SUNY Stony Brook
Stony Brook, NY 11794-2100
USA

HARRY Y. McSWEEN JR.
Department of Earth & Planetary Science
University of Tennessee
Knoxville, TN 37996-1410
USA

MICHAEL T. MELLON
Laboratory for Atmospheric & Space Physics
University of Colorado
Boulder, CO 80309-0392
USA

DOUGLAS W. MING
NASA/JSC
Code KX, Building 31, Room 120
2101 NASA Road 1
Houston, TX 77058
USA

JEFFERY E. MOERSCH
Department of Earth & Planetary Science
University of Tennessee
1412 Circle Drive, Room 306
Knoxville, TN 37996
USA

RICHARD V. MORRIS
NASA/JSC
Code KR, Building 31, Room 120
2101 NASA Road 1
Houston, TX 77058
USA

PATRICK C. PINET
UMR 5562/CNRS
Observatoire Midi-Pyrenees
14 Avenue Edouard Belin
Toulouse, 31400
France

THOMAS H. PRETTYMAN
Los Alamos National Laboratory
MS D466
Space and Atmospheric Science
Los Alamos, NM 87545
USA

NATHANIEL E. PUTZIG
Laboratory for Atmospheric & Space Physics
University of Colorado
Campus Box 392
Boulder, CO 80309
USA

ROBERT C. REEDY
Institute of Meteoritics
University of New Mexico
MSC03-2050
Albuquerque, NM 87131
USA

L. RICHTER
German Aerospace Center (DLR)
Institute of Space Simulation
Linder Hoehe
Cologne, D-51170
Germany

RUDOLF RIEDER
Cosmochemistry Deparment
Max Planck Institut für Chemie
PO Box 3060
Mainz D-55020
Germany

A. DEANNE ROGERS
Department of Geosciences
SUNY at Stony Brook
Stony Brook, NY 11794
USA

STEVEN W. RUFF
Mars Space Flight Facility
Arizona State University
Moeur Building, Room 131
Tempe, AZ 85287-6305
USA

RICHARD A. SIMPSON
Stanford University
David Packard #332
350 Serra Mall
Stanford, CA 94305-9515
USA

JASON SODERBLOM
Lunar and Planetary Laboratory
University of Arizona
1629 E. University Blvd.
Tucson, AZ 85721
USA

LAURENCE A. SODERBLOM
US Geological Survey
2255 North Gemini Drive
Flagstaff, AZ 86001
USA

STEVE W. SQUYRES
Department of Astronomy
Cornell University
428 Space Sciences Building
Ithaca, NY 14853
USA

ROBERT J. SULLIVAN
CRSR
Cornell University
308 Space Sciences Building
Ithaca, NY 14853
USA

G. JEFFREY TAYLOR
Hawaii Institute of Geophysics & Planetology
1680 East-West Road
Post 504
Honolulu, HI 96822
USA

SHANE THOMPSON
Arizona State University
School of Earth and Space Exploration
Box 871404
Tempe, AZ 85287
USA

TIM N. TITUS
US Geological Survey
Astrogeology Team
2255 N. Gemini Drive
Flagstaff, AZ 86001-1698
USA

ALIAN WANG
Department of Earth & Planetary Sciences
Washington University
Campus Box 1196
1 Bookings Drive
St Louis, MO 63130-4862
USA

HEINRICH WÄNKE
Abteilung Kosmochemie
Max Planck Institut für Chemie
PO Box 3060
Mainz D-55020
Germany

CATHY WEITZ
Planetary Science Institute
NASA
1700 East Fort Lowell
Suite 106
Tuscon, AZ 85719
USA

MICHAEL B. WYATT
Brown University
Department of Geological Science
324 Brook Street
Providence, RI 02912-1846
USA

ALBERT YEN
JPL/Caltech
4800 Oak Grove Road
M/S 183-501
Pasadena, CA 91109-8099
USA

JUTTA ZIPFEL
Forschungsinstitut und Naturmuseum
Senckenberg
Frankfurt/Main, D-60325
Germany

FOREWORD

The concept of a *frontier* is a commonplace metaphor in the physical sciences, as well as in the history of exploration. Today, one of the most tangible and alluring of all such frontiers is represented by the surface of Mars. This is because of the literally phenomenal scientific progress that has resulted from the intensified robotic exploration of the Red Planet since 1996. In little more than a decade (1996–2007), scientific viewpoints have been altered more profoundly than in the previous 30+ years. Some would describe this radical alteration in thinking as a *scientific revolution*. A case for this perspective is made in a convincing fashion here in *The Martian Surface: Composition, Mineralogy, and Physical Properties*, edited by Jim Bell and written by him and 82 other colleagues who study Mars for a living. Indeed, since the dawn of the Space Age, now in its 50th year (1957–2007), thoughts have often drifted to the so-called "Martian frontier," with an ever-changing and sometimes disappointing scientific appreciation of what it might offer. This book puts the emerging "new Mars" into a modern scientific context on the basis of an ensemble of up-to-date scientific hypotheses and viewpoints. It brings Mars alive and promotes prospects for future scientific exploration that are certain to continue the revolution at hand.

The Mars that scientific exploration has come to witness today is vastly more dynamic and scientifically interesting than that which the Viking missions of the 1970s revealed. When the last full compilation of scientific thinking about Mars was captured in the early 1990s (The 1992 University of Arizona Press book *Mars*, edited by Hugh Kieffer, Bruce Jakosky, Conway Snyder, and Mildred Matthews), the planet was effectively viewed as a nearly static geological world with intriguing but enigmatic climate cycles and little prospect for what we describe today as "habitability" or "biological potential." In the post-Viking view of Mars, all the dynamics of the planet and its hydrologic cycles were relegated to the most distant past, with only lurking and ephemeral signatures in the geology and atmosphere visible today. While interesting as one variety of silicate planet, Mars was not viewed as a scientific "holy grail," with revolutionary potential. NASA's only plans post-Viking converged upon a mission initially described as the "Mars Geosciences and Climatology Orbiter" (MGCO), which was later renamed *Mars Observer* in the latter part of the 1980s. This comprehensive mission was to have investigated the Martian "system" in a fashion more akin to an Earth Observing System (EOS) than any traditional planetary remote-sensing mission, in order to understand what scientific steps were justifiable in the competitive scientific landscape of the time.

When Mars Observer failed in the early 1990s, the development of a more agile and distributed approach to Mars exploration was put in place, resulting in the reconnaissance observations of the Mars Global Surveyor (MGS). The MGS catalyzed the scientific revolution that began in 1996 when the ALH 84001 meteorite shocked the scientific and public communities into the renewed possibilities of life, or at least of primitive biological activity, on Mars. The measurements of MGS, however, provided the framework for quantifying and understanding a "new Mars." This framework, and the scientific impact of MGS as our views of the surface of Mars evolved from relative unknowns to well-measured systems, is articulated here by the authors of this book. For example, in June 2000 Mike Malin and Ken Edgett rocked the scientific community when they presented evidence for geologically recent runoff of liquid water on Mars, despite the current understanding of its stability. This explosive discovery was a first glimmer of the revolution that was at hand. In the words of Steven Jay Gould, the mainstream thinking of this exciting time had its equilibrium punctuated by revolutionary discoveries that allowed a new set of theories about the role of water and potentially life on Mars to take root. *The Martian Surface: Composition, Mineralogy, and Physical Properties* paints for the reader a first-hand impression of the impact of such discoveries on the web of geological, geochemical, and climatological processes that shape any planet's surface.

Perhaps most catalytic in the unfolding Martian scientific revolution has been the interplay of measurements from the armada of reconnaissance-oriented orbiters (MGS, Mars Odyssey, and ESA's Mars Express) and landed exploration via the Mars Exploration Rovers *Spirit* and *Opportunity*. Indeed, the authors of this missive bring to light, for the first time, the emerging view of Mars that has been gleaned from the ongoing "voyages" of the rovers. This new view challenges the old post-Viking thinking by bringing the role of water into focus in ways that were somewhat unimagined just 30 years ago. While Mars may appear to have been a static, forever-desiccated world, the discoveries that the *Spirit* and *Opportunity* rovers have made in their surface reconnaissance of the geochemical systems accessible on Mars today have painted a far different picture. From the ongoing work of the twin rovers to the just-commencing surveys of the Mars Reconnaissance Orbiter (MRO), it

now appears as if Mars is indeed a "water planet," or at least a silicate planet in which the impact of water has manifested itself in a broad variety of scales and signatures. Understanding the many roles water has played in the evolution of the surface of Mars and its relation ultimately to the habitability of the Red Planet is elegantly portrayed in this book. Yet there is so much more to be learned.

Mars has become a tangible scientific frontier, thanks to the integrated measurements, experiments, and syntheses of the past decade. Fitting the story together is fraught with challenges, but the colleagues who have contributed to this timely summary and review of the field manage to succeed in a dramatic fashion. Their concluding arguments present a case for continuing the scientific conquest of the Martian frontier in this new era of NASA's Vision for Space Exploration (VSE). Indeed, thanks to the pioneering efforts of the women and men around the world who are exploring Mars robotically (many of whom are coauthors of the chapters in this book), the path toward human exploration of Mars has been clarified and even accelerated. Mars is indeed a compelling scientific frontier; via the scientific framework presented here, we are closer to being there ourselves!

James B. Garvin
NASA Chief Scientist for Mars Exploration, 2000–2005
Goddard Space Flight Center, Greenbelt, MD

ACKNOWLEDGMENTS

Someone once said that editing a multiauthor academic treatise is like herding cats. That is probably an understatement; it is at least insulting to cats (who would never lower themselves to being "herded"). Anyway, I have no idea why anyone would have said that.

In 2004 I asked a number of colleagues who had been instrumental in pulling together the important and extremely useful 1992 University of Arizona Press *Mars* book if they knew if anyone was planning to update the part of that tome dealing with the composition, mineralogy, and physical properties of the Martian surface, given the major advances in those areas that had occurred in the decade-plus since then. No one knew of any such plans, but everyone acknowledged that it would be a challenge, given the continual arrival of new datasets and discoveries and the resulting rapid expansion and evolution of our state of knowledge. Still, perhaps foolishly, I decided that it would be better to at least gather a snapshot of our current view of this topic rather than wait for some "lull" in Mars exploration that would allow us all to catch our breath and just spend our time writing papers about what it all means. Indeed, many of us hope that such a lull (like the one from about 1982 through to 1997) never happens again (and thus we tacitly accept the challenge of having to write those papers breathlessly).

In that spirit, my first major acknowledgment is to the more than hundred colleagues who gave me early advice and encouragement or who are the lead authors or coauthors of the chapters in this book. These people are a sample of the community of planetary scientists who are on the "front lines" of Mars exploration, having conducted – and in many cases still actively conducting – the investigations, calibrations, experiments, and analyses that are daily modifying our understanding of the Red Planet. Most of these folks (indeed, most scientists nowadays) have frenetic schedules and have to balance huge responsibilities on many levels – mission operations, major laboratories, teaching, management, student mentoring, family. I am indebted to these colleagues for agreeing to take some precious time out of their busy lives to summarize and review recent major results in their areas of specialization. I am also grateful for their indelible patience in the face of what must often have seemed like incessant nagging from a pesky editor.

Secondly, all of us – editor, authors, readers – are indebted to the dozens of colleagues who provided independent external reviews for all of the chapters of this book. These people also are among the leading experts in Mars studies, and they, too, sacrificed significant time to perform an important community service: making sure that the results and other information in these chapters are accurate (or at least appropriately acknowledged as speculative), complete, and balanced. Specifically, I would like to thank Dave Agresti, Janice Bishop, Bonnie Buratti, David Catling, Ben Clark, Claude d'Uston, Vicky Hamilton, Jim Garvin, Gary Hansen, Lon Hood, Bruce Jakosky, Jeff Johnson, Hugh Kieffer, Melissa Lane, Scott McClennan, Hap McSween, Mike Mischna, Jeff Moersch, Jeff Moore, Dick Morris, Jack Mustard, Horton Newsom, Mike Ramsey, Ken Tanaka, Timothy Titus, Alan Treiman, Deanne Rogers, and Ted Roush for reviewing one or more chapters in this book. Your time and effort have substantially improved this summary and review, and will have hopefully made it a much more useful future resource for students and other researchers new to this field.

Many other people helped to pull this project together at many stages. I thank Karla Consroe at Cornell University for providing an enormous amount of administrative and editorial assistance. I am also grateful to Bobby Fogel and Marilyn Lindstrom at NASA Headquarters for their initial encouragement of this project, and for helping to secure a small NASA grant (NNX06AH45G) to support some of the administrative costs associated with editing this book. I also thank Helen Goldrein (Morris), Vince Higgs, and Susan Francis at Cambridge University Press for their constant helpful advice and patience, and for their support for including this book in Cambridge's prestigious Planetary Science series.

Finally, I would like to acknowledge the love and support from my wife Maureen and my children Erin and Dustin. This has been one of my "Sunday afternoon projects" for several years now, and it could not have been done without their indulgence and patience with my incessant tippity-tapping at the keyboard during random free moments at home.

On to Mars!

Jim Bell
Cornell University
Ithaca, NY

PART I

INTRODUCTION AND HISTORICAL PERSPECTIVE

1

Exploration of the Martian surface: 1992–2007

L. A. SODERBLOM AND J. F. BELL III

ABSTRACT

Following the demise of the 1992 Mars Observer mission, NASA and the planetary science community completely redefined the Mars exploration program. "Follow the Water" became the overarching scientific theme. The history and distribution of water is fundamental to an understanding of climate history, formation of the atmosphere, geologic evolution, and Mars' modern state. The strategy was to search for past or present, surface or subsurface, environments where liquid water, the fundamental prerequisite for life, existed or exists today. During the 1996–2007 time frame, seven richly successful orbital and landed missions have explored the Martian surface, including NASA's Mars Global Surveyor (MGS), Mars Pathfinder Lander and Sojourner Rover, Mars Odyssey Orbiter, Mars Exploration Rovers (*Spirit* and *Opportunity*), Mars Reconnaissance Orbiter, and ESA's Mars Express (MEx) orbiter. "Follow the Water" has borne fruit. Although the Martian surface is largely composed of unaltered basaltic rocks and sand, the Rovers discovered water-lain sediments, some minerals only formed in water, and aqueous alteration of chemically fragile igneous minerals. The geological records of early water-rich environment have shown hints of profuse and neutral-to-alkaline water that later evolved to sulfurous acidic conditions as aqueous activity waned. We now have a global inventory of near-surface water occurring as hydrated minerals and possibly ice and liquid in equatorial and mid latitudes and as masses of water ice making up an unknown but potentially large fraction of the polar regolith. Martian meteorites have provided new insights into the early formation of Mars' core and mantle. We now know that Mars possessed a magnetic dynamo early after its core formed and that the magnetic field disappeared very early, leaving the early atmosphere unprotected to erosion by the solar wind. Our view of Mars' geological evolution has been dramatically enriched by a wealth of new mineralogical and chemical information and new ideas. We stand well poised to pursue the major new scientific questions that have emerged.

1.1 MARS EXPLORATION PROGRAM, THE NEW ERA: 1992–2007

At the time of publication of the last comprehensive scientific compilation on Mars (Kieffer *et al.*, 1992), the exploration of the Red Planet by robotic spacecraft had been largely suspended for over a decade since the completion of the Viking project in 1982. Phobos-2 had achieved Mars orbit in 1988, contributed important new information, but survived only a few months. The next major successful missions, MGS and Mars Pathfinder (MPF), were not launched until 21 years after Viking. Even so, during this hiatus our understanding of Mars continued to expand rapidly owing to (a) continued analysis of the wealth of data returned by Mariners 4, 6, 7, and 9, Phobos-2, the two Viking orbiters, and the two Viking Landers (Kieffer *et al.*, 1992); (b) a rich collection of new Earth-based spectroscopic observations of Mars that capitalized on major advances in telescopic instrumentation (Chapter 2); and (c) laboratory analysis of the growing suite of Mars meteorites, many collected on the Antarctic blue-ice fields, that had an enormous impact on Mars science (Chapter 17).

In 1992 NASA had restarted the robotic Mars exploration program with the launch of the Mars Observer mission (Table 1.1). As an experiment to save money, NASA had elected to base the Mars Observer spacecraft, with its rich, ambitious scientific payload, on a line of earth-orbital communications satellites. Unfortunately, Mars Observer was lost just before reaching Mars orbit; the cause was surmised to be a rupture of the monomethyl hydrazine fuel pressurization system. Faced with the rapidly growing and renewed interest in Mars exploration by the scientific and public communities and the loss of Mars Observer, NASA, the National Academy of Sciences (NAS), and the scientific community were compelled to completely rethink the approach to Mars exploration.

In the 1993–6 time frame, NASA's Mars Expeditions Strategy Group (later evolved to become NASA's Mars Exploration Program Analysis Group or MEPAG), consisting of planetary scientists, mission managers, and program administrators, formulated a new Mars robotic exploration program that would include launches every 26 months (the cycle by which favorable, low-energy launch opportunities to Mars repeat). Ideally, at least two spacecraft would be launched in each opportunity to enhance program resilience to mission failure (see Table 1.1). This group also laid out a new set of scientific goals and rationale for Mars exploration (discussed in the next section) that formed the basis for planning the next decade. The explosion of new knowledge and scientific discoveries that resulted from the Mars exploration missions that followed, including both NASA and ESA Mars missions listed in Table 1.1, forms, in large part, the basis for this book.

The new NASA plan that emerged saw the launch of both the Mars Global Surveyor Orbiter and the Mars

The Martian Surface: Composition, Mineralogy, and Physical Properties, ed. J. F. Bell III. Published by Cambridge University Press.

Table 1.1. *Missions and investigations relevant to Mars surface science: 1988–2007*

Launch/status	Mission	Nation/ agency	Mission outcome/science investigations described in this volume[a]
1988	Phobos-1, Phobos-2	USSR	Phobos-1 failed; Phobos-2 reached Mars orbit and survived for several months; ISM
1992	Mars Observer	NASA	Failed: lost prior to Mars arrival
1996, mission ended 2006	Mars Global Surveyor (MGS)	NASA	MOC, TES, MAG/ER, MOLA
1996	Mars 96	USSR	Launch vehicle failed
1996, mission ended 1997	Mars Pathfinder (MPF)	NASA	IMP, Mars Pathfinder APXS, Magnetic Properties
1998	Nozomi	Japan	Failed: no orbit insertion
1998	Mars Climate Orbiter	NASA	Lost on arrival (human navigation error)
1999	Mars Polar Lander	NASA	Lost on arrival (crashed into Mars)
1999	Deep Space 2 Probes	NASA	Carried by MPL – failed; no signal after release
2001–current	Mars Odyssey Orbiter	NASA	GRS, NS, HEND, THEMIS
2003–current	Mars Express Orbiter	ESA	HRSC, MARSIS, OMEGA
2003	Beagle 2 Lander	ESA	Carried by Mars Express – failed landing
2003–current	Mars Exploration Rovers (MER)	NASA	Two Rovers (*Spirit* and *Opportunity*), each carrying Pancam, Mini-TES, MER APXS, MB, MI, RAT, Magnetic Properties
2005–current	Mars Reconnaissance Orbiter (MRO)	NASA	CRISM, HiRISE, CTX, MARCI, MCS, SHARAD

Note: [a]Investigations discussed in this book: CRISM (Compact Reconnaissance Imaging Spectrometer for: Mars), CTX (Context Camera); GRS (Gamma Ray Spectrometer); HEND (High-Energy Neutron Detector); HiRISE (High Resolution Imaging Science Experiment); HRSC (High Resolution Stereo Camera); IMP (Imager for Mars Pathfinder); ISM (Imaging Spectrometer for Mars); MAG/ER (Magnetometer and Electron Reflection); Mars Pathfinder APXS (Alpha Proton X-ray Spectrometer); MARCI (Mars Color Imager); MARSIS (Subsurface Sounding Radar/Altimeter), MB (Mössbauer Spectrometer); MCS (Mars Climate Sounder), MER APXS (Mars Exploration Rover Alpha Particle X-ray Spectrometer); MI (Microscopic Imager); Mini-TES (Miniature Thermal Emission Spectrometer); MOC (Mars Orbiter Camera); MOLA (Mars Orbiter Laser Altimeter); NS (Neutron Spectrometer); OMEGA (Observatoire pour la Minéralogie, l'Eau, les Glaces et l'Activité, Visible and Near-IR Imaging Spectrometer); Pancam (Panoramic Camera); RAT (Rock Abrasion Tool); SHARAD (Shallow Radar), TES (Thermal Emission Spectrometer); THEMIS (Thermal Emission Imaging System).

Pathfinder Lander/Sojourner Rover in the 1996 launch opportunity. Mars Global Surveyor re-flew much of the lost Mars Observer scientific payload (Magnetometer and Electron Reflection [MAG/ER], Mars Orbiter Camera [MOC], Mars Orbiter Laser Altimeter [MOLA], Thermal Emission Spectrometer [TES], Radio Science); two other key instruments (Gamma Ray Spectrometer [GRS] and Pressure Modulator Infrared Radiometer [PMIRR]) were reserved for subsequent opportunities. Mars Global Surveyor was tremendously productive, operating in orbit for about 10 years. It generated a wealth of new global datasets including an unprecedented global map of surface topography from MOLA that has had widespread scientific impact; extremely high-resolution MOC images (down to ~0.5 m/pixel) of a plethora of fluvial, polar, volcanic, and eolian features; TES global mineralogical maps using thermal infrared emission spectroscopy; MAG/ER discovery of an ancient magnetic dynamo, and high-order gravity maps from Radio Science (Chapters 9, 11, 21, 25). Today's active missions and the missions in development have all relied heavily on this rich collection of MGS data for their design and planning.

Mars Pathfinder had both strong scientific and engineering motives. EDL (Entry, Descent, and Landing) at Mars is quite a difficult feat (see Muirhead and Simon, 1999; Mishkin, 2003). Unlike the atmospheres of the Earth, Venus, or Titan, the Martian atmosphere is too thin for use of a parachute alone as the final stage in descent and landing. Pathfinder engineered and demonstrated a novel approach: after descending by parachute to ~50 m above the surface, a cluster of rocket motors was fired to stop the descent, airbags were inflated to encase the vehicle, and it then did a free-fall and bounced to rest at the surface. This approach allows safe landing on rough rock-strewn sites, like the flood plain that Pathfinder was sent to in the hope of accessing a broad collection of rock types. Soon after landing, Pathfinder deployed its second major engineering achievement: the Sojourner rover, the first successful rover on the Martian surface. A modification of this proven air-bag approach was later adopted for the two Mars Exploration Rovers. Mars Pathfinder made key scientific findings, including characterizing the chemical and physical properties of soils and rocks (see Chapters 3, 12, 17, 19, 20, and 21).

A series of other missions was launched by several nations in the 1996 and 1998 Mars opportunities; all of these met failure in different forms (Table 1.1), reinforcing the historic difficulty in successfully conducting Mars missions (of 38 Mars missions attempted since 1960, only 17 were fully

or partially successful; see http://mars.jpl.nasa.gov/missions/log/). In 2000 NASA commissioned an external committee (the Mars Program Independent Assessment Team, chaired by A. Thomas Young) to conduct a major review of the failures of Mars Polar Lander (MPL), Mars Climate Orbiter (MCO), and Deep Space 2 (DS2); the general conclusion was that the projects had been under-funded and had lacked sufficient resources for adequate testing and quality control. The committee tied the low-funding levels to excessive zeal for NASA's new "faster, better, cheaper" philosophy. It strongly urged NASA to restore funding for high-risk planetary exploration missions to an appropriate level, to insure a more realistic chance of success. It also recommended cancellation of the soon-to-be-launched Mars Surveyor 2001 Lander, a derivative of the failed 1998 MPL. As a result, only one mission, the Mars Odyssey Orbiter, was launched in the 2001 opportunity. NASA did ultimately follow many of the Assessment Team's recommendations, including requesting increased levels of funding and invoking requirements for increased mission robustness for the restructured Mars exploration program that we enjoy today.

Mars Global Surveyor had re-flown all but two of the key instruments that were on the original Mars Observer science payload. The PMIRR was re-flown on Mars Climate Orbiter and thus was lost a second time. Owing to obsolescence and unavailability of parts, the PMIRR design was discontinued as a further flight option. In its place, NASA eventually selected Mars Climate Sounder (MCS, a modern version of PMIRR) for flight on the current Mars Reconnaissance Orbiter. For Mars Odyssey 2001, the final remnant of the Mars Observer payload, the GRS package, was upgraded to include the Neutron Spectrometer (NS) and Russian High-Energy Neutron Detector (HEND). With the addition of a newly selected visible and thermal-emission imager Thermal Emission Imaging System (THEMIS-VIS and THEMIS-IR), the continuing Mars Odyssey Mission has been extremely productive, making major advances in global mapping of the physical and chemical properties of the Martian surface (Chapters 5, 6, 10, 18) and also serving as a relay satellite for more than 95% of the down-linked data from the *Spirit* and *Opportunity* rovers. Noteworthy among the many Mars Odyssey results are the discovery and mapping of near-surface reservoirs of hydrogen, most likely occurring as water ice at the poles and as hydrated minerals near the equator (Chapters 5, 6).

Four more spacecraft were launched to Mars in the 2003 opportunity: two by ESA (Mars Express/Beagle 2) and two by NASA (the Mars Exploration Rovers *Spirit*, MER-A, and *Opportunity*, MER-B). The MEx Orbiter approached Mars in late December 2003, released the Beagle 2 Lander, and successfully entered orbit. For reasons unknown, Beagle failed during landing as radio communication was never established. Mars Express has now been operating in orbit for over three years and has produced a wealth of scientific data, including stereo and color images from HRSC and global maps of composition from OMEGA, a French-led visible-to-near-IR imaging spectrometer (Chapters 7, 8). Noteworthy among the MEx results is the suggestion from OMEGA data that alteration of surface materials changed from neutral-pH or slightly alkaline conditions (e.g., phyllosilicates as a dominant weathering product) early in Mars' history to acidic alteration (e.g., sulfates as a dominant weathering product) in a later era (Chapter 7).

The two NASA Mars Exploration Rovers landed on Mars in early 2004: *Spirit* in Gusev crater on January 4 and *Opportunity* in Meridiani Planum on January 24. These robotic field geologists have enjoyed more than 3 years of successful operation on Mars at the time of this writing, roving and exploring the Martian surface over a combined distance >16 km. They have exceeded their nominal mission lifetimes and distance goals by more than tenfold. Each rover carries a potent payload of remote sensing instruments (Pancam and MiniTES) and a suite of *in situ* instruments mounted on a robotic arm (Microscopic Imager [MI], Alpha Particle X-ray Spectrometer [APXS], Mössbauer Spectrometer [MB], and Rock Abrasion Tool [RAT]). The scientific results and achievements of these prolific missions in exploring and characterizing the geology, geochemistry, and mineralogy of the Martian surface are a major feature of this book and the principal subjects of Chapters 4, 13, 15, 16, 18, 19, 20, 21, 22, 23, 24, and 26.

In 2005, NASA launched the Mars Reconnaissance Orbiter, and the spacecraft successfully achieved orbit and commenced mapping the surface in 2006. At the time of this writing, MRO results from Compact Reconnaissance Imaging Spectrometer for Mars (CRISM), MCS, and Shallow Radar (SHARAD) are just emerging; early results from the High Resolution Imaging Science Experiment (HiRISE) instrument, which has begun spectral imaging in the visible with an unprecedented aerial-photo-scale resolution of 30 cm/pixel, are discussed in Chapter 8.

As a final note, during the bountiful 1996–2007 period of Mars spacecraft missions and resultant new knowledge about Mars, Earth-based telescopic observations and continuing analysis of pre-1992 mission imaging and spectroscopy datasets continued to add valuable new information about the Martian surface chemistry, mineralogy, physical properties, weather systems, dust storms, and migration of atmospheric volatiles. These include new observations from ground-based telescopes and the Earth-orbiting Hubble Space Telescope (Chapters 2, 8); new analyses of Phobos-2 Imaging Spectrometer for Mars (ISM) visible-to-near-IR reflectance spectra of the part of the Martian surface covered before that mission failed (Chapters 2, 7); new analyses of Mariner 6 and 7 Infrared Spectrometer (IRS) measurements of small regions of Mars studied during those 1969 flyby missions (Chapter 2); and a broad spectrum of new insights gained from continued investigation of the growing collection of Martian meteorites (Chapters 17, 22).

1.2 SCIENTIFIC RATIONALE AND GOALS FOR MARS EXPLORATION: FOLLOW THE WATER

The US Planetary Exploration Program has been traditionally recommended, reviewed, and evaluated for NASA

by two sets of science advisory bodies: (1) one internal to NASA that includes standing committees of the NASA Advisory Council (NAC) and ad hoc committees such as the MEPAG that was set up to advise the NASA Mars Program Office; and (2) an independent set of National Academy of Science committees (e.g., the Space Studies Board or SSB, the Committee on Lunar and Planetary Exploration or COMPLEX). All of these committees rely heavily on participation of the planetary research community. The severely felt loss of the ambitious Mars Observer Mission in 1993, after such a long hiatus in Martian exploration after the Viking missions, caused NASA and these advisory bodies to lay out an aggressive new exploration program with launches to Mars every 26 months.

Throughout Mars exploration a recurrent theme has been the search for evidence of past or present life: Did life ever evolve on Mars and if not, why not? A goal of the Viking Program was to search for extant life, a task that proved to be extremely difficult. Although there was general consensus that the combined results of Viking's life-detection experiments were negative (e.g., Klein *et al*., 1992; Chapter 26), the results of one of those experiments (Viking Labeled Release Experiment) remain in debate with continuing claims that the data are consistent with extant Martian life (see Levin, 2004). The NASA Mars Expeditions Strategy Group (precursor to MEPAG) laid out a new crosscutting theme for the program – focus on the role, history, and occurrence of water (McCleese *et al*., 1996). Considered to be the fundamental prerequisite for life as we know it, the strategy was to search for past or present, surface or subsurface, environments where liquid water existed or exists today. This approach would then yield a set of sites on Mars for detailed *in situ* study and the eventual return of samples to the Earth that would have the best chance of confirming the presence or absence of past or present life. This early 1996 strategy was cast into a set of goals centered on *Life, Climate, and Resources* with the crosscutting theme of "follow the water."

In its review of the new plan, COMPLEX (1996) was highly supportive but felt that the strategy needed to be more clearly spelled out as relating to understanding the geology of Mars (in which water has played a major role throughout Martian evolution) and the search for resources (water, extractable oxygen, minerals) to support eventual human exploration. MEPAG (2006) broadened this set of goals to be *Life, Climate, Geology, and Preparation for Human Exploration*. Water, as the crosscutting core of the scientific goals and objectives of the program, was and remains a key feature of the Mars program, and is an important part of planning future missions. A strong component in the evaluation of missions and science payloads for selection became their ability to search for the evidence of current or past water. The NASA Mars Phoenix Mission, scheduled for launch in August 2007, continues to "follow the water"; it is intended to land at a high northern latitude site where water ice is presumed to be close enough to the surface to be probed and analyzed.

Mars Sample Return (MSR) to Earth has remained among the highest scientific priorities in the Mars Exploration Program, dating back to the Viking era. The long-term Mars exploration strategies laid out by the NASA and NAS committees in the late 1990s included ambitious plans to begin MSR missions during the decade to follow. As Mars exploration unfolded over the next few years, however, it became clear that sample return before 2010 was programmatically unrealistic, given the pace and funding of the program and the occurrences of dramatic failures that caused significant program restructuring. Although congressional funding for NASA's Mars program was increased (based partly on the recommendations of the Mars Program Independent Assessment Team's analysis of the MCO, MPL, and DS2 failures), any potential increases that could be funneled into MSR were largely consumed in restoring the recommended program robustness. The estimated costs for MSR itself also rose, not only because of its inherent complexity and difficulty, but also from increasing requirements on higher mission reliability.

In 2002 the National Academy of Sciences Space Studies Board published a landmark set of recommended priorities for NASA's planetary science program from 2003 to 2013 that was based on a comprehensive decadal survey conducted within the planetary science community (NAS Space Studies Board, 2003). The report reinforced MSR as of highest priority for Mars exploration and called for NASA to begin preparations for sample return in the 2013 time frame or soon thereafter. COMPLEX (2003), in assessment of NASA's Mars program plan, recommended that MSR be launched in 2011. However NASA's current Mars plan recognizes the prudence of conducting more extensive surface and orbital investigations to identify optimum sample return sites before the costly investment of MSR is made. Recently published Mars exploration strategic planning documents that cover the period from 2007 to 2016 now call for the first MSR mission sometime in the time frame beyond 2020 (Beaty *et al*., 2006; McCleese *et al*., 2006; MEPAG, 2006). To move MSR earlier, as the scientific community has repeatedly urged, will require a national imperative and a much greater level of funding than NASA's Mars Exploration Program now enjoys. In the meantime, NASA's next robotic Mars rover mission, the Mars Science Laboratory (MSL), is now being built for launch in September–October 2009 (http://mars.jpl.nasa.gov/missions/future/msl.html). MSL will take the *in situ* search for chemical clues of life to a new level with its capabilities to detect multiple organic compounds, study isotopic chemistry, and search for traces of subsurface water.

The Mars missions of the last decade listed in Table 1.1 (that are largely the subjects covered in this book) have made enormous strides in our understanding of the composition, mineralogy, and physical properties of the surface and in the crosscutting theme of understanding the evolution, role, and current disposition of water on Mars. Every chapter in this book touches on (most of them very directly) the role of water in the planet's early evolution and its subsequent geologic processes and history. Each chapter also helps to reveal that "follow the water" has been a remarkably effective strategy for further expanding on the Viking-era discovery that Mars has undergone significant climatic changes over the course of time.

1.3 SCOPE, ORGANIZATION, AUDIENCE, AND GOALS OF THE BOOK

It has been 15 years since the last major research-level summary book about Mars was written (Kieffer *et al*., 1992), and more than 14 years since the last major research-level book containing a few chapters summarizing what was known of Mars composition and mineralogy was published (Pieters and Englert, 1993). Those works summarized the Viking and telescopic-era view of Mars at the time. As described above, since then, however, our view of the composition, mineralogy, and physical properties of the surface of Mars has changed dramatically because of new data from Hubble Space Telescope and other telescopes, and the Phobos-2, MGS, Mars Odyssey, Mars Pathfinder, MEx, the twin Mars Exploration Rover missions, and Mars Reconnaissance Orbiter missions. Magnificent new datasets are now available that have, in some cases, completely changed our worldview of the Red Planet. These new missions have provided quantitative, unambiguous evidence for the presence of liquid water on the Martian surface in the distant past, and for the presence of water ice in the subsurface of the polar regions today. Water has played a more important role in the geologic and geochemical evolution of the surface than many scientists thought based on previously available data. Even though new data are still streaming in and new discoveries are still being made, it is time for a scholarly update of the state of knowledge of this important and exciting field. This book is intended to be that update.

However, it is important to point out that this book is not intended to be a complete review and summary of all of Mars science, as the University of Arizona *Mars* book was in 1992. The explosion in data and knowledge about Mars during the last decade has made it impossible to adequately write such a book again as a single volume work (even the 1992 *Mars* book was nearly 1500 pages long, after all). Therefore, this book concentrates on just one aspect of this far-reaching field: the composition, mineralogy, and physical properties of the Martian surface. The intention is to treat that topic thoroughly using contributions from some of the leading active researchers working in this area. Other recent books have been written that focus on our expanded understanding of Martian geology (e.g., Carr, 2007; Chapman, 2007), and other excellent book chapters and review papers have been written covering new data and results in Martian geology and geophysics (e.g., Head *et al*., 2001; Nimmo and Tanaka, 2005; Solomon *et al*., 2005) and atmospheric sciences (Encrenaz, 2001; Greeley *et al*., 2001). This book should complement, not duplicate, those other works, for researchers looking to get a more complete and current "snapshot" of the state of Mars science.

This book is part of the Cambridge University Press *Planetary Science* series, and as such is intended to be a thorough reference for researchers and teachers covering this field. The intended audience for this book is researchers, upper-level undergraduates, and graduate students in planetary science, astronomy, space exploration, planetary geology, and planetary geochemistry. Contributed chapters are primarily technical in nature, at a reading and content level comparable to research articles in journals like the *Journal of Geophysical Research* or *Icarus*, where many planetary science peer-reviewed results are published. However, throughout the book, there has been a concerted effort to minimize (and at least define and where possible, reference) esoteric terms, acronyms, and other jargon to make sure that the information presented here is accessible to students, new researchers, and other novices just entering this field. The hope is that this book will become the definitive resource and review of Mars surface composition, mineralogy, and physical properties issues for students and researchers for the next decade, just as the Arizona *Mars* book was for the previous decade. In addition, it is hoped that the book will be used as the basis for or as a resource in university courses being taught on Mars, planetary remote sensing, or planetary geochemistry.

1.4 INTRODUCING MARS' GLOBAL GEOLOGICAL EVOLUTION

To provide context for the discussions that follow in this and other chapters, we give a general description of Mars' physiographic provinces, their nomenclature, the geological sequence of their formation, and our best understanding of their ages. Mars exhibits a global dichotomy in its crustal structure and ages of geologic units (see Nimmo and Tanaka, 2005) whose origin is still largely a mystery. This is dramatically exhibited in one of the premier MGS datasets, a map of global topography (Figure 1.1) acquired by the Mars Orbiter Laser Altimeter (MOLA) carried by the Mars Global Surveyor (Zuber *et al*., 2000).

The boundary dividing the dichotomy in Mars' global physiography follows approximately a great circle that is tilted ~30° to the equator and with highest and lowest latitudes at ~50° E and ~230° E. (Note: Planetary scientists studying Mars use both West [°W]- and East [°E]-based longitude definition systems to describe the cartographic locations of features on the surface. West longitude is preferred by those who favor a convention of increasing sub-solar longitude as the planet rotates. East longitude is preferred by those more comfortable with right-handed spherical coordinate systems. Both systems are recognized by the International Astronomical Union as valid.) South of this boundary are heavily cratered ancient terrains of higher-than-average elevation; the large impact basins, Hellas and Argyre, stand out in the topographic map from their depressed floors. To the north of the boundary are younger units that vary in elevation. They consist of (1) vast, smooth, mixed sedimentary and volcanic plains that are generally lower than average Mars; and (2) the Tharsis volcanic region of high plateaus and ridges centered near 240° E, where several enormous volcanoes including the largest, Olympus Mons, are found. A tectonic rift valley, the 4000-km-long Valles Marineris, opens to the east of Tharsis and ends in channels and flow features reaching to the north into the low plains. Superposed on these two global units are a plethora of younger erosional and

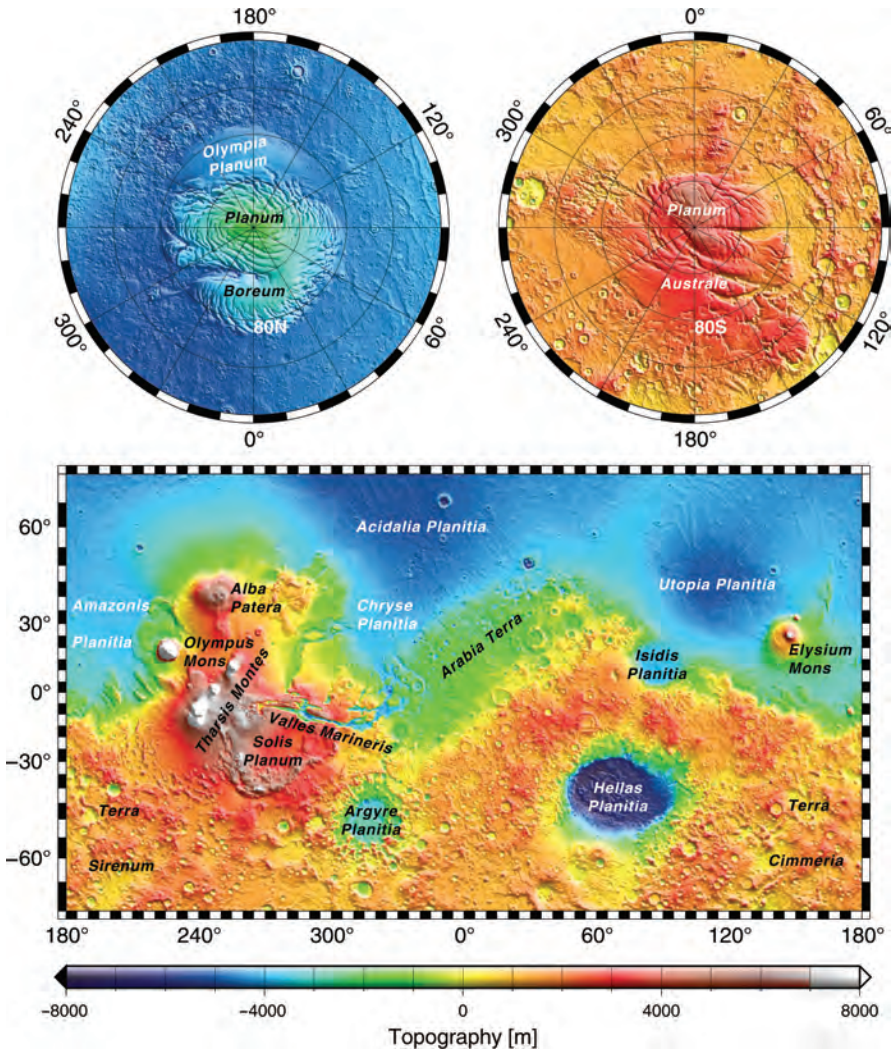

Figure 1.1. Global topography of Mars from the MGS MOLA experiment. (Credit: NASA and the Mars Global Surveyor Mars Orbiter Laser Altimeter Team.) (For a color version of this figure, please refer to the color plate section or to the e-Book version of this chapter.)

depositional features of volcanic, fluvial, lacustrine, glacial, and eolian origin. At both poles, geologically young sequences of layered strata consisting of water ice, carbon dioxide ice, and dust are covered by active veneers of perennial and seasonal water and carbon dioxide ice caps.

Beginning with Scott and Carr (1978), the distribution and sequence of Mars' global geologic units has been extensively worked out using photogeological methods applied to the now vast collection of images acquired by cameras aboard orbital spacecraft (see Scott *et al.*, 1986–7; Tanaka, 1986; Chapters 8, 10). Terrain units are mapped based on geomorphic textures, depositional or stratigraphic superposition relationships, crosscutting relationships (tectonic patterns, erosive features, impact craters), and the relative abundance of superposed impact crater populations. Chronological order is deduced from a combination of the superposition and transection relationships and the number-density of superposed impact craters. Three major geologic periods have been defined, from oldest to youngest: Noachian, Hesperian, and Amazonian. Their general distribution and the type localities for the major periods (Noachis Terra, Hesperia Planum, and Amazonis Planitia) are shown in the geologic map of Figure 1.2. This map further illustrates the global dichotomy. The ancient Noachian units reside primarily in the higher elevation, heavily cratered southern highlands. The Amazonian units are mostly located in the lower northern plains, in the Tharsis and Elysium volcanic plateaus, and in the polar layered complexes. The Hesperian units lie mostly along the margins between the Noachian and the Amazonian, although numerous occurrences of Hesperian terrains are found within both the older and younger units.

The sequence of evolution of the geologic features and units in Figure 1.2, based on superposition, crosscutting features, and the relative numbers of impact craters formed on exposed surfaces, provides a relative chronologic sequence. A next major step in understanding Mars' geologic evolution is to develop an absolute timescale. We know that the terrestrial planets accreted about 4.5 Ga (billion years ago). We know from studies of the lunar highlands and analyses of lunar samples that a period of intense late heavy bombardment, accompanying the last stages of accretion, ended ~3.85 Ga (Strom *et al.*, 2005). There is a reasonably firm basis that the Martian crust and the heavily cratered earliest Noachian terrains date to the cessation of heavy bombardment estimated for the Moon. Consequently, the age of Mars' earliest crust is reasonably well constrained.

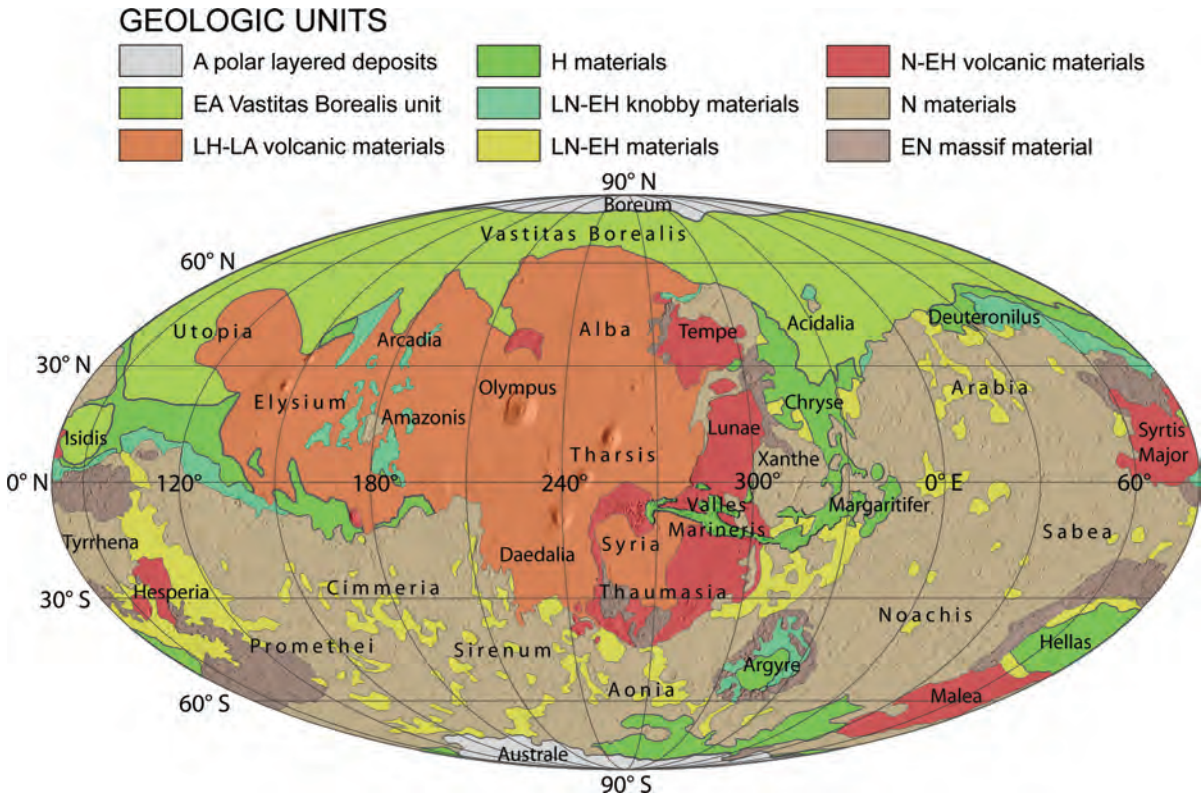

Figure 1.2. Generalized global geologic map. Symbols: Early and Late (E and L) Noachian, Hesperian, and Amazonian (N, H, and A). (Credit: Nimmo and Tanaka, 2005, Reprinted, with permission, from the *Annual Review of Earth and Planetary Sciences*, Volume 33; © 2005 by Annual Reviews; www.annualreviews.org.) (For a color version of this figure, please refer to the color plate section or to the e-Book version of this chapter.)

To model absolute ages of younger terrains requires knowledge of the production rate of impact craters through time. One model in wide use today was derived largely from extrapolation of the lunar cratering rate to Mars and from the observed populations of Mars-crossing asteroids (Hartmann and Neukum, 2001; Hartmann, 2005). Table 1.2 summarizes Hartmann's recent absolute timescale for Martian evolution. Our knowledge of the fluxes of impacting bodies through time is likely inaccurate by a factor of 2 or more (Hartmann and Neukum, 2001; Nimmo and Tanaka, 2005). Still, because the age of the accretion and formation of the Martian core and mantle (~4.5 Ga) are well documented from isotopic studies of Martian meteorites (see Chapters 17 and 22), the earliest part of the timescale is reasonably well-constrained. However, the time of the end of the Hesperian and onset of the Amazonian is uncertain by 1–2 Ga.

Based on this timescale, the Noachian covered roughly the first Ga after Mars accreted. When the crust formed, early in this period, the enigmatic global dichotomy of lowlands–highlands was created. This is evidenced by relics of large ancient impact craters and basins that can be identified in the MGS MOLA topography throughout the northern plains (e.g., Frey, 2004). Younger volcanics later filled these plains and largely masked the old structures. The origin of the dichotomy remains a mystery, but formation of lowlands by enormous impact basins (see Wilhelms and Squyres, 1984) and long-wavelength mantle convection (see Zuber *et al.*, 2000; Nimmo and Tanaka, 2005) have been suggested. The Hellas and Argyre impact basins were formed as heavy bombardment tapered off in the middle of the Noachian. Throughout this era, rates of volcanism appear to have been 10–100 times higher than in the Amazonian (Hartmann and Neukum, 2001). Such volcanism pervasively flooded the inter-crater areas and crater floors in the ancient highlands. Mars' atmosphere was apparently exsolved in the early Noachian during magmatic overturn of the mantle. An early warm water–rich environment is evidenced by pervasive dendritic channels formed in the Middle-to-Late Noachian (see Carr, 1996, 2007; Head *et al.*, 2001).

By the onset of the Hesperian, impact bombardment had dramatically slowed. Although rates of volcanism began to fall as well, large towering volcanic constructs were built on the Tharsis and Elysium plateaus as the crust cooled and strengthened. Major tectonic activity continued as well, opening the vast extensional rift in Valles Marineris. Large outflow channels developed in many locales, along the margins of the highland–lowland boundary, and winding northward out of Valles Marineris (Figures 1.1 and 1.2). This history of the Hesperian is supported by recent geologic mapping by Tanaka *et al.* (2003, 2005), who used MOLA topography (Figure 1.1) and meter-scale-resolution MOC images to identify the Vastitas Borealis formation (Figure 1.2), interpreted to be sediments debouched by outflow channels into vast regions of the low northern plains that extend as far as the north polar basin (Figure 1.2).

Table 1.2. *Toward a Martian chronology, generalized from Hartmann (2005)*

Estimated age, 10^6 yrs.	Geomorphic feature, Martian period or geological process
<10–50	Youngest lava flows, Elysium–Cerberus, Amazonis, Olympus Mons
170	Basaltic lava flows, unknown locations; 5 basaltic shergottites
100–1000	Background lava flows in Elysium, Amazonis, Cerberus, Olympus Mons
300–500	Basaltic lava flows, unknown locations; 2 basaltic shergottites
200–600	*Late/Mid Amazonian boundary*
≤670	Transient water exposure in the nakhlite Lafayette, unknown location
~1000–2000	*Mid/Early Amazonian boundary*
1300	Igneous rock-forming episodes, unknown locations from the Nakhlites
2000–3200	*Amazonian/Hesperian boundary*
3000–3500	Many outflow channels
~3200–3600?	*Late/Early Hesperian boundary*
3000–3500	Oldest <2 km-scale craters
~3500–3700?	*Hesperian/Noachian boundary*
3700–4500	Resurfacing rates 10X–100X higher than in Amazonian
3700–4500	Oldest >20 km craters
~3600–3900?	*Late/Mid Noachian boundary*
~3800–4100?	*Mid/Early Noachian boundary*
~3970	Carbonates in ALH 84001
~4510	Formation of Martian crust and ALH 84001

During the Amazonian period, volcanic, tectonic, and fluvial processes rapidly waned (e.g., Head *et al.*, 2001; Hartmann, 2005). Evidence for channeling of the surface by water or glacial ice is only rarely found in Middle and Late Amazonian terrains. By the Middle Amazonian, tectonism had virtually ceased even in the active Tharsis and Elysium volcanic regions. Although volcanic eruption rates also fell dramatically, extremely young volcanic flows (ages <50 million years old (50 Ma) based on sparse impact craters) do occur in a few regions (e.g., near Olympus Mons). It is likely that active volcanism continues to this day at a quiescent level; it is improbable that Martian volcanism ended 98% of the way through geologic time. The polar layered deposits (PLD) are of Late Amazonian age; the exposed layers may record Mars' climatic history as far back as 10–100 Ma. Active polar processes continue today, as the polar deposits are continually formed and eroded by dust and volatiles migrating in and out of the polar regions over timescales ranging from seasonal to long-term (10^6–10^7 yrs) and driven by changes in obliquity (e.g., Touma and Wisdom, 1993; Laskar *et al.*, 2004). By the Late Amazonian, Mars became the arctic desert planet that we see today. Eolian processes came to dominate, scouring the surface, moving massive dune fields like the north circumpolar erg, and stirring storms of bright reddish-brown dust across the globe.

1.5 OUR CURRENT UNDERSTANDING OF THE MARTIAN SURFACE

Since 1992 when the comprehensive work *Mars* (Kieffer *et al.*, 1992) was published, our understanding of the nature and evolution of the Martian surface has undergone a revolutionary expansion. The dictum "follow the water" has truly paid off scientifically. We have examined the geological processes and chemical details of Mars' watery past both from orbit and at the surface. We have followed the chemical evolution of Mars' water through time to learn how its surface environment changed. Although the bulk of the surface materials consists of weakly altered basaltic minerals, we see extensive alteration in local environments. We have direct evidence for water-lain sediments and extensive interaction of subsurface water with chemically-fragile igneous minerals. We see suggestions of early more profuse and more alkaline waters, later evolving to become highly acidic as aqueous activity waned. Martian meteorites have given up many isotopic secrets about the early formation of Mars' core, mantle and crust, and the varieties of magma sources from which they were derived. We now know Mars possessed an early magnetic dynamo and think that it disappeared very early, leaving the atmosphere unprotected to loss by the scavenging processes of the solar wind. We have an inventory of near-surface water, occurring as ice or in hydrated minerals across the globe and as high concentrations of water ice in the polar regolith. Our view of Mars' geological evolution has been dramatically enriched by a wealth of new mineralogical and chemical information and new ideas. Here we summarize the current understanding of the physical character, chemistry, mineralogy, and evolution of the Martian surface that is expanded in detail in the chapters that follow.

1.5.1 Fundamentally a basaltic planet

Mars' dark regions have long been inferred to be basaltic from telescopic observations, reinforced by Phobos-2 ISM's identification of LCP (low-Ca) and HCP (high-Ca) pyroxenes (Chapter 2). MGS/TES (Chapter 9), Mars Odyssey THEMIS (Chapter 10), and MEx OMEGA (Chapter 7) provide global maps of many mineralogical components and have confirmed the general basaltic nature of Mars' surface. Collectively, they reveal a great variety in the igneous lithologies exposed in the dark regions that are mostly unaltered or only weakly so. Thus, even with the wide variety of secondary minerals and phases (e.g., oxides, glasses, sulfates, and clays) discovered on Mars and described throughout this volume, the fundamental makeup of the surface is still basaltic, with typically only a weak degree of alteration (Chapters 22, 23, 24, 26).

TES, THEMIS, and OMEGA are highly complementary investigations. For example, TES and THEMIS data provide evidence for plagioclase feldspar, silica glasses, quartz-rich phases, and dacite, none of which could be detected by OMEGA. In contrast, TES and THEMIS are not particularly sensitive to sulfates or phyllosilicates like those that OMEGA has identified. Olivine is a key

rock-forming mineral on terrestrial planets that is very vulnerable to aqueous alteration. TES, THEMIS, and OMEGA all confirm olivine-bearing basalts to be common throughout dark regions, and all have identified local areas of high-olivine concentration (Chapters 7, 9, 10). These investigations have also extensively mapped pyroxenes, another class of key rock-forming minerals, showing them to be diverse and widespread on Mars. TES finds highly variable HCP/LCP ratios throughout Hesperian and Noachian units, pointing to great diversity in magma chemistry. OMEGA results suggest LCP is enriched in some Noachian areas and HCP is more abundant in younger volcanic shields. One interpretation is that because enstatite (LCP) melts at higher temperature than diopside (HCP), the increased LCP concentration might signal higher temperatures in the early magmas (Chapter 7).

TES distinguished two global-scale volcanic units (TES Surface Type 1 [or ST1] and Surface Type 2 [or ST2]; Chapters 5, 9, 17, 22). ST1 is older, is concentrated in Noachian regions, and consists of unaltered plagioclase-rich and clinopyroxene-rich basalt (Chapter 9). Surface Type 2 occurs in Amazonian-Hesperian northern plains, is higher in silica-rich phases, and has been suggested to be more andesitic (Chapter 9). Mars Pathfinder APXS measurements also suggested the presence of soil-free rocks (SFR) similar in composition to andesitic basalts (Chapter 3). Alternatively, ST2 and SFR surfaces may be coated with secondary phases (silica glass, zeolites, clays) and/or dust (Chapters 3, 9, 12, 17, 19, 22). Interestingly, Mars Odyssey GRS measurements found no detectable difference in Si content or K/Th ratio between TES Types 1 and 2, although it did show K to be ~30% higher in Type 2 (Chapter 5). Regardless, it is still possible that ST1 and ST2 represent different magma sources. Adding to the diversity, TES and THEMIS data suggest local exposures of high-silica rocks, possibly quartz- and plagioclase-rich granitoids and dacites (Chapters 9, 10), and GRS detected very low-Si rocks west of Tharsis. In summary, orbital data have revealed diverse igneous rocks ranging from ultramafic high-olivine basalts to silicic dacites and granitoids, rivaling the diversity found in the Earth's crust.

The mafic components of typical Martian soils studied at the landing sites also reveal the presence of weakly altered basalts. The elemental composition of the sandy-to-cloddy soils at all sites was found to be chemically similar (Chapters 3, 4, 12) and MER Mössbauer (MB) observations directly characterized the soil mineralogy (Chapter 15). Mössbauer shows that soils on the Meridiani and Gusev plains and within the geologically complex Columbia Hills are virtually identical in terms of their iron-bearing mineralogy, with the exception of the unique sulfur-rich "Paso Robles" soil in Gusev. It is remarkable that in almost all of these soils, from diverse geologic settings on opposite hemispheres, MB analyses show 33%–34% olivine, 6%–8% magnetite, and 33%–37% pyroxene; the mafic component of average Martian soil is clearly olivine basalt (Chapter 15). Further, the observed APXS correlation between Ti and Fe in the soils implies that the magnetite is most likely titanium bearing (titanomagnetite; Chapter 4). Mössbauer measurements and the results of the MER and MPF Magnetic Properties experiments (Chapter 16) indicate that almost all fine-grained dust and soil particles on Mars are magnetic, and that the magnetic component of the soil is a relatively unaltered igneous mineral rather than an alteration product such as maghemite. Clearly, the globally uniform "Laguna Class" soils do not appear to have been exposed to significant aqueous alteration (Chapters 15, 16). This finding represents a significant paradigm shift from a decade ago, when it was widely assumed that the presence of fine-grained ferric oxides and oxyhydroxides indicated that typical Martian dust and soil was a heavily weathered secondary alteration product. Apparently, the altered (ferric) phases in the dust and soil represent only a minor weathered veneer and are not representative of the bulk volumetric properties of Martian soil grains.

Analyses of Martian meteorites (shergottites, nakhlites, and chassignites; SNCs) further point to the principally basaltic nature of the Martian crust (Chapters 17, 22). All SNCs are lavas or cumulates derived from a wide variety of basaltic magmas. As representative members of these classes contain gases matching the atmosphere isotopic chemistry measured by Viking, the evidence is convincing that they are from Mars (Chapter 17). Their ejection ages cluster, indicating that groups were ejected in single impacts. Some groups exhibit wide ranges in crystallization age (up to 400 Ma), indicating long-lived local volcanic activity. It is not understood why the crystallization ages of most meteorites are extremely young (95% $\leq$1.3 Gyr). This is apparently inconsistent with chronological models that suggest that half of the surface is >2 Gyr old and raises a serious open issue. Nevertheless, even with the young crystallization ages, the SNC isotopic chemistry shows that the magma sources from which they were derived are ancient; these magmas formed very early (~4.5 Ga), around the time of formation of the core, mantle, and crust, and have remained unchanged and intact for billions of years (Chapters 17, 22).

SNC meteorites were evidently derived from heterogeneous mantle magma sources (Chapters 17, 22), consistent with the variable igneous mineralogies mapped by TES, THEMIS, OMEGA, and GRS. Although SNCs and rocks analyzed at the surface and from orbit are somewhat different (Chapters 4, 5, 14, 15, 17, 22), all exhibit a common mineralogic inventory (ferroan olivine and pyroxenes and sodic plagioclase) that distinguishes them from terrestrial basalts. For example, the pristine Gusev basalts are similar to olivine-phyric shergottites, and Bounce Rock, believed to be a Meridani erratic derived from the subsurface by a distant impact, is virtually identical to basaltic shergottite meteorites (Chapters 4, 17, 22). With the exception of the single ancient meteorite ALH 84001 that exhibits significant secondary carbonate minerals (Chapters 17, 22, 23, 26), aqueous alteration of SNC meteorites is very mild, although ubiquitous. Evidently, subsurface aqueous alteration on Mars, at least in the regions sampled by the SNC meteorites, was limited in intensity and duration.

In summary, the bulk of the Martian surface and crust consists of minimally altered igneous rocks. This seems inconsistent with ample evidence presented throughout this

volume (and summarized in the next section) that a variety of styles of aqueous alteration have occurred in many locales. The picture that emerges is that the globally integrated intensity, duration, available water, and other factors controlling the degree of aqueous alteration must have been far less than that required to affect a significant fraction of Mars' igneous crust and mantle overall.

1.5.2 Mars' altered surface, dominated by acid-sulfate processes

It is important to ask, to what degree have the basaltic surface materials on Mars been altered? Sulfur-containing soils and sulfate-bearing rocks were found at the Viking, Pathfinder, and MER landing sites and point to possible low-pH aqueous conditions resulting from acid-sulfate alteration. However, most of the observed altered materials are still fundamentally basaltic in their overall chemistry (see Figure 23.2 in Chapter 23 and Figure 24.4 in Chapter 24). In contrast to the apparent ubiquity of S-bearing soils and rocks, no surface exposures of carbonates (beyond traces seen in dust by TES and Miniature Thermal Emission Spectrometer [Mini-TES], see Chapters 9, 14) have been found by *in situ* or orbital techniques, and only minor amounts are found in many young ($\leq$1.3 Ga) SNC meteorites (Chapters 17, 22). The only direct evidence for the presence of ancient carbonates is from the single old ($\sim$4.5 Ga crystallization age) meteorite ALH 84001. The carbonates in ALH 84001 appear to have been formed around 3.9 Ga. Evidence for other rare alteration products (clays and aluminous phases) that form under near-neutral pH conditions have also been found by OMEGA and MER (Chapters 7, 23, 26). Along with the carbonates in ALH 84001, these secondary minerals may be much older than the sulfates, possibly recording earlier ancient non-acidic aqueous conditions.

As far back as the 1930s the reddish-brown color of the dust in bright regions and dust storms was conjectured to arise from iron oxide (Chapter 2). By the 1960s, oxidized basalt became the leading candidate for the origin of the dust. Viking soils were estimated to contain $\sim$18% FeO, and subsequent telescopic work suggested that the dust contained extremely fine-grained (nm-sized grains or nanophase) crystalline "red" hematite (Fe_2O_3) and/or other poorly crystalline iron oxides/oxyhydroxides (Chapters 2, 23). OMEGA has mapped the ubiquitous ferric oxides but has only revealed the presence of anhydrous ferric phases (Chapter 7).

Discovery by TES of small concentrations of coarse-grained, crystalline "gray" hematite, potentially formed in liquid water, was a key new finding in the search for alteration minerals on Mars; eventually, it led to the decision to land the *Opportunity* rover in Meridiani Planum. In one scenario for the formation of gray hematite, goethite (FeOOH) precipitates in water, is buried, and re-crystallizes to hematite. MER data have provided conclusive evidence that liquid water was involved in forming the Meridiani hematite (Chapters 4, 13, 14, 15, 23, 24, 26). MER mineralogical analyses (MB, Mini-TES, Pancam) have confirmed the existence of coarse-grained anhydrous ferric oxide (hematite) and oxyhydroxide (goethite) in specific locations and samples at the landing sites. MER data also confirm the presence of the ubiquitous nanophase ferric oxide and/or oxyhydroxide phase inferred from earlier telescopic and orbital observations, although the MER data cannot distinguish between hematite, goethite, ferrihydrite, or perhaps other minerals as the nanophase material (Chapters 2, 13, 14, 15, 16).

Viking soils exhibited surprisingly high levels of S and Cl, and similarly high levels were also found in Pathfinder and MER soils (Chapters 3, 4, 23). GRS also mapped high levels of Cl in some regions (Chapter 5). The observed correlation between Mg and S abundances in APXS data and the high concentration of S in soil clods have been interpreted to indicate the presence of Mg-sulfate cements. Such high-relative abundances of S and Cl in the soils led to the realization that low-pH acid-sulfate weathering was a major alteration pathway on Mars (Chapters 3, 4, 23, 24, 26). In Eagle crater on Meridiani Planum, *Opportunity* discovered sedimentary outcrops (the Burns formation) made up of jarosite [$(K,Na,H_3O)Fe_3(SO_4)_2(OH)_6$], hematite, Mg- and Ca-sulfates, and siliciclastic materials derived from altered basaltic sand (Chapters 4, 14, 15, 23, 24). The hematite occurs in spherules (and their weathered lags); evidently, these now-famous "blueberries" are concretions (hard, compact aggregates of mineral matter formed by precipitation from an aqueous solution) formed by later stage fluids (Chapter 24). Some strata in the Noachian-Hesperian Burns formation appear to be eolian but others exhibit textural features strongly indicative of formation in shallow flowing surface water. These observations have led to the interpretation of Meridiani Planum outcrops as "dirty" evaporites (Chapters 23, 24, 26). This interpretation has been challenged by suggestions that base surges from impact events or volcanic explosion could produce the observed textures and chemical observations (Chapters 24, 26). Identification of jarosite in the sedimentary rock is of signal importance, however, as this mineral only forms by aqueous processes under low-pH conditions; clearly, aqueous acid-sulfate alteration was involved. Although telescopic and OMEGA observations have not detected jarosite (Chapters 7, 8), OMEGA has mapped a variety of other hydrated sulfates in stratified terrains, including kieserite (monohydrated $MgSO_4$), gypsum (dihydrated $CaSO_4$), and polyhydrated sulfates of unknown mineralogy (Chapter 7).

Spirit landed in Gusev, a 150-km Noachian crater, whose rim was breached by Ma'adim Vallis, an ancient channel system that left sediments on the crater floor resembling deltas (Chapter 26). The landing site is on a Hesperian plain, mantled by typical soil (basalt sand mixed with ferric oxide dust, ubiquitous at all sites) and with minimally altered basalts scattered about. Only minor evidence for aqueous activity was found on the Gusev plains: small, possibly mineralized veins in some rocks; light-toned, possibly cemented dust coatings on other rocks. However, after *Spirit* drove $\sim$3 km to the Columbia Hills, highly altered soils and rocks emerged. While scrambling uphill, *Spirit* excavated bright reddish and yellowish soils at a location

known as Paso Robles (Chapter 13); these soils exhibit the highest sulfur content (~30 wt.%) measured so far by APXS (Chapter 4). The mineralogy of these soils has been modeled as containing Fe-, Mg-, and Ca- sulfates, Ca-phosphates, hematite, halite, allophane, and amorphous silica (Chapters 4, 13, 23). Mössbauer measurements showed Paso Robles to be rich in ferric-sulfates that Mini-TES data showed to be hydrated (perhaps ferrihydrite; Chapters 14, 15). Acid-sulfate aqueous alteration is again implicated, as Paso Robles soil might be an evaporite deposit formed from solutions rich in Fe, Mg, Ca, S, P, and Si (Chapters 23, 24). Unlike the weakly altered Gusev plains basalts that were difficult to grind with the MER RAT (Chapters 20, 21), most altered rocks found in the Columbia Hills were very soft – evidence (though not unique) of exposure to highly acidic sulfurous conditions. Many of the Columbia Hills rocks have rudimentary sedimentary textures; they may be of both volcaniclastic and impact derivation. Others, like the Peace outcrops, appear to be well-sorted (eolian?) mafic basaltic sand cemented by Mg- and Ca-sulfates (Chapters 23, 24). An important MB discovery is that many of these rocks contain goethite, a hydroxylated iron oxide that only forms in water (Chapter 15). As in Meridiani Planum, these kinds of discoveries provide conclusive evidence that at least some putatively Noachian rocks of the Columbia Hills may have been altered under *aqueous* acid-sulfate conditions (Chapters 4, 14, 15, 23, 24, 26).

There is some evidence for altered materials on the Martian surface that appear to have been produced in neutral-pH or slightly alkaline conditions. For example, the Independence Class rocks of the Columbia Hills are among the very few rocks that appear to have undergone substantial leaching of their original basaltic elemental character, leading to major Al-enrichment. They may well contain various aluminous phases including phyllosilicate clays such as montmorillonite or other smectite phases (such as nontronite). The evidence for the presence of clays in these rocks supports a model of their formation near-neutral pH conditions (see Figure 23.4, Chapter 23). An exciting and important discovery by OMEGA is of isolated Noachian units that exhibit spectral absorption features in the 2.2–2.4-μm region that are diagnostic of phyllosilicates and arise from Fe-OH, Mg-OH, and Al-OH vibrations in clays such as nontronite, chamosite, and montmorillonite (Chapter 7). If these observations and their interpretation are correct, they provide strong supporting evidence for an early epoch, prior to the period of pervasive acid-sulfate conditions, when an alkaline or neutral-pH water-rich environment existed on Mars.

Telescopic spectra from the 1960s and later Mariner 6 and 7 IRS and Phobos-2 ISM spectra showed the surface to contain bound water at the 1%–10% level. However, exactly how the water was bound (i.e., as ice, adsorbed water, structural hydrate or hydroxyl groups, etc.; see Chapter 2) was unknown. Odyssey GRS and NS have mapped hydrogen concentrations in the upper meter of the Martian regolith, estimating the global distribution of water-equivalent-hydrogen (WEH) with high precision (Chapters 5, 6) and OMEGA has mapped hydrated sulfates and hydrated phyllosilicates at high-spatial resolution (Chapter 7). GRS and NS data provide an estimate of an average of 7 wt.% WEH in the upper meter at Meridiani Planum. Because the Meridiani sulfate sediments appear mantled by only a few cm of soil, this estimate may closely correspond to the water abundance in the upper meter of the Burns formation. The estimated range of crystal-bound water in these sediments is 6–22 wt.% derived from the measured mineralogy (stoichiometrically) and modeled mineralogy (range of specific candidate hydrous minerals) of the sediments (Chapter 23). Comparison with the GRS/NS value of 7 wt.% suggests that at this site the water is mostly held in hydrated and hydroxylated minerals (Chapter 23).

Where are the carbonates on Mars? This remains a mystery. Like the Earth and Venus, Mars must have outgassed significant amounts of carbon dioxide into its early atmosphere. Coupled with evidence of plentiful water in the earliest period of Martian geologic history, carbonates should have formed (Chapters 24, 26). Other than trace amounts of carbonate detected in the fine Martian surface dust by TES and Mini-TES (Chapters 9, 14), though, convincing evidence for surface carbonate deposits has yet to be found. Both TES and OMEGA should have easily detected any substantial carbonate exposures if they existed. The only evidence for *ancient* carbonates comes from the meteorite ALH 84001, which is known for the (now generally discounted) possibility that it contains relicts of ancient Martian life (Chapters 17, 26). This is the only Noachian Martian meteorite, with a crystallization age of 4.5 Ga (all other SNCs are Amazonian). Its Fe–Mg–Ca carbonate globules date to 3.9 Ga and could have formed in hydrothermal precipitation in CO_2-rich fluids (Chapters 17, 23). Perhaps crustal waters were then alkaline, allowing carbonates to precipitate, and then later when conditions became more acidic surface carbonates were destroyed (Chapters 7, 23). Alternatively, the early alkaline waters in which the ALH 84001 carbonates precipitated may have existed in the subsurface, isolated from an early contemporaneous acidic surface environment. Such a surface–subsurface isolation has been proposed for formation of the carbonates in the nakhilites during the Amazonian (see Figure 24.6, Chapter 24).

Most of the SNCs are very young by Martian standards. One-third of them have crystallization ages <0.2 Ga, two-thirds are <0.6 Ga and the remainder are ~1.3 Ga (Chapter 17). All display some degree of alteration, but none is pervasively altered. Secondary phases include sulfates, carbonates, iron oxides, sulfides, and poorly crystalline silicates or aluminosilicates. The variety of minor Fe-, Ca-, and Mg-rich carbonates that exist in these young samples of the Martian crust suggest a wide range of conditions (e.g., variable pH) in the subsurface, perhaps even today (Chapters 17, 22, 23).

1.5.3 Martian evolution: accretion through Hesperian

The accreted bulk chemistry of Mars is better constrained by recent evidence from (1) improved moment of inertia estimates (0.3662 for Mars compared to 0.3315 for Earth; Folkner *et al.*, 1997), leading to better refined core and

mantle density structure (Bertka and Fei, 1998); (2) elemental and isotopic chemistry of Martian meteorites (Chapters 17, 22); (3) GRS orbital elemental abundance data (Chapter 5); and (4) MPF and MER APXS surface elemental composition data (Chapters 3, 4). The estimated uncompressed density of Mars (3.8–3.9 g cm^{-3}) is lower than that of Earth (4.4–4.5 g cm^{-3}), whereas the Martian mantle is likely denser (~3.5 g cm^{-3}) than Earth's (3.34 g cm^{-3}). Mars' lower bulk density is consistent with the available chemistry data in that (1) moderately volatile elements (e.g., K, P, S, Cl) are more abundant in meteorites and *in situ* measurements on the Martian surface (Chapters 4, 17) and (2) GRS measurements that show the surface K/Th ratio to be twice that of Earth's crust (Chapter 5). With respect to the higher mantle density, although the bulk Fe/Si must be lower for Mars, FeO is much more abundant (~18%) in both Martian meteorites and in the surface as measured by GRS and APXS. This probably arises because a larger fraction of the planet's Fe was oxidized and occurs as FeO in its mantle, with correspondingly less in the core as Fe^0. It may be that Mars' metallic Fe was oxidized by water or as a result of its higher oxygen abundance during accretion. The relatively large difference in bulk composition between Mars and Earth suggests that thorough mixing across accretional source regions in the inner Solar System did not occur (Chapters 4, 17, 22).

The 4.5 Ga age of ALH 84001 shows that Martian igneous processes began soon after accretion. Martian meteorite isotope systematics constrain the time of differentiation of the interior into a core and mantle to have largely completed within the first few $\times 10^7$ years; the core might have existed only ~12 Ma after accretion (Chapter 22). Mars may have possessed a magma ocean at this early time, from which the early crust crystallized. Martian meteorites other than ALH 84001 have very young (<1.3 Ga, Amazonian) crystallization ages; still, isotopic data show that their parent magma sources evolved early, perhaps within the first few $\times 10^7$ years after accretion. Although they are all generally basaltic, these younger meteorites exhibit substantial diversity (e.g., in Ca/Si and Mg/Si, Chapter 17). Their ancient magma sources must have remained intact and segregated for several Ga, until partial melting occurred and the young meteorites in our collection crystallized during the Amazonian (Chapters 17, 22).

MGS MAG/ER discovered regions of strong remnant magnetization concentrated in the southern Noachian highlands, showing that Mars possessed a magnetic dynamo very early in its history (Chapter 11). The younger northern Amazonian plains show only weak magnetic signatures. Earlier modeling had suggested that such a dynamo, driven by thermal convection, might have lasted for the first billion years (Chapter 11 and references therein). We now know that the dynamo ceased very early, probably <0.5 Ga after accretion. Impacts that created the Hellas and Argyre basins demagnetized large regions of the ancient crust. Thus, by the time these impacts occurred, the dynamo had expired. The estimated age of Argyre and Hellas are 4.1 ± 0.1 Ga, near the end of heavy bombardment (Hartmann and Neukum, 2001; Frey, 2004; Strom *et al.*, 2005).

The global hemispheric dichotomy in the crust also appears to have emerged during this early period. Its origin remains a major debate, ranging between thinning of the northern crust by late basin-scale impacts and/or by short-lived early convection (Nimmo and Tanaka, 2005; Solomon *et al.*, 2005). Evidently, evolution of the dichotomy was largely completed before the end of late heavy bombardment but overlapped with the period of the planet's active magnetic dynamo. This is evidenced by (1) the lack of significant remnant magnetic signatures in the northern lowlands (Chapter 11); and (2) numerous subtle relicts of large impacts that underlie the Amazonian deposits in the northern lowlands (Chapter 22). The smooth northern plains lie ~5 km lower than the ancient highland terrains and the Tharsis volcanic plateau. MGS topography and gravity data are best fit by a lower density crust (typically 2.5–3.0 g cm^{-3}) of highly variable thickness (30–100 km) overlying a denser (typically 3.0–3.5 g cm^{-3}) mantle (see Zuber *et al.*, 2000; Neumann *et al.*, 2004). The thinner crust under the northern plains was later overlain by veneers of younger sediments and basaltic lavas (from which most of the SNC meteorites appear to have been derived). Thicker crust underlies and supports the Tharsis volcanic plateau. The petrology of the less dense crust is unknown; no samples are evident in the meteorites (including ALH 84001, with a density of 3.41 g cm^{-3}). This also remains an outstanding puzzle.

During the Noachian, volatile-rich magmas transported water, carbon dioxide, and other volatiles from the mantle to the surface, helping to form the atmosphere. There are several lines of evidence that Mars' early atmosphere was dense and wet (Chapters 9, 22, 24, 26). Foremost, the Noachian terrains exhibit ubiquitous valley networks (including Ma'adim Vallis that flowed into Gusev crater) suggesting an early fluvial, if not pluvial, environment. Compared to Earth, Mars' lower bulk density is evidence for the accretion of a higher fraction of volatiles. For example, geophysical models suggest Mars' magma ocean could have had 2 wt.% water, and recent simulations of accretion suggest abundant water could have been present from late-arriving water-rich planetary embryos (Chapter 22). If only a few percent of this inventory devolved from the interior, ample surface water would have been available to carve valley networks, produce playa evaporites, and leave layered sandstones cemented by subsurface fluids. Additionally, the early atmosphere might have contained up to several bars of CO_2 that could have generated an effective greenhouse, keeping the surface water liquid (Chapter 26). Although volcanically active up to the recent era (e.g., possible lava flows <50 Ma; Table 1.2), the Tharsis plateau is ancient; the bulk of its development was largely completed by the end of the Noachian (Phillips *et al.*, 2001). It is generally agreed that the high levels of Tharsis volcanism and tectonism played a pivotal role in the Noachian period, with massive outgassing of CO_2 and H_2O to the atmosphere leading to a warmer and wetter early environment (Nimmo and Tanaka 2005; Solomon *et al.*, 2005).

If abundant carbonates ever did form at the Martian surface, it would have been in just such an early warmer and wetter environment, probably under a denser CO_2

atmosphere. In fact, our only sample of the early Martian crust (ALH 84001, crystallization age 4.5 Ga) contains secondary carbonate globules that formed ~4 Ga (Chapters 17, 23) at the time of the hypothesized Noachian warmer, wetter environment. Carbonates require a slightly alkaline environment both to form and to survive (see Figure 22.4 of Chapter 22). MER results indicate that by the Late Noachian and Early Hesperian the aqueous alteration environments had become acidic at two sites on opposite hemispheres (Chapters 23, 24). It seems straightforward, then, to speculate that most near-surface carbonates were destroyed by these later pervasive acidic fluids. A reaction product of Ca-carbonate with sulfuric acid is gypsum ($CaSO_4 \cdot 2H_2O$), a mineral that OMEGA has in fact identified in a few locations (Chapter 7). OMEGA's discovery of isolated occurrences of phyllosilicates in Noachian terrains further adds to this picture. Phyllosilicates are stable in near-neutral Eh and pH environments (see Figure 23.4 of Chapter 23). The picture that emerges is that during the latter half of the Noachian, the chemistry of near-surface waters gradually shifted from alkaline to near-neutral conditions to acidic conditions, and stable species shifted from carbonates, to phyllosilicates, to sulfates (Chapters 7, 9, 23, 24, 26).

As the thermal convection in the core tapered off and the magnetic dynamo disappeared in the Early Noachian, escape of Mars' early dense atmosphere was accelerated. No longer shielded by a magnetic field, the atmosphere was exposed to scavenging by the solar wind (Chapters 11, 26). Viking results showed that the current atmospheric D/H is 5 times that of Earth, testifying to the long-term sputtering of the atmosphere by the solar wind and the thermal escape of H (Chapter 22). The shift from early alkaline to later acidic conditions may have been the result of a combination of factors: the gradual fall in atmospheric pressure, the collapse of the greenhouse, the gradual loss of water as hydrogen escaped or ice was sequestered to the polar regions and the subsurface, and the long-term injection of sulfurous volcanic vapors into the environment by Tharsis and by other centers of early intense volcanism. The Independence Class rocks in the Columbia Hills may record the earlier slightly alkaline or neutral pH environment, but all other altered rocks and soils investigated in the Hills appear to have been altered by later acid-sulfate aqueous conditions, probably with low water-rock ratios (Chapters 23, 24). Likewise, the sulfate-rich sediments and hematite concretions of the Meridiani Planum Burns formations (cemented eolian sandstones likely derived from so-called "dirty" playa evaporites) date to the episode of Late Noachian sulfurous acidic waters (Chapters 4, 9, 14, 15, 23, 24, 26).

By the beginning of the Hesperian (estimated ~3.5–3.7 Ga; Table 1.2), the formation of valley networks by pluvial activity appears to have largely ceased. It is thought that as Mars continued to cool much of the water was trapped as ice in the upper kilometer or so. Episodic catastrophic outflow channels continued to burst forth throughout the Hesperian period (Chapter 26), possibly triggered by volcanic magmas interacting with the water ice stored in the crust. Through the Hesperian, volcanic and fluvial activity dramatically waned, but isolated major events continued. The basaltic lava plains where the *Spirit* rover landed in the floor of Gusev crater are thought to date to the Hesperian. The Adirondack Class basalts on that plain exhibit minimal aqueous alteration (Chapters 4, 14, 15, 23) and resemble the young basaltic shergottite meteorites (Chapters 17, 22). Clearly, very little aqueous activity has occurred since these Hesperian basaltic plains were emplaced (Chapter 21).

1.5.4 The Amazonian and active processes today

The end of the Hesperian is estimated by Hartmann (2005) to be in the range 2.0–3.2 Ga (Table 1.2). By this estimate the Amazonian has lasted for ~60% of Mars' entire geologic history. There is some evidence for fluvial activity during the Early and Middle Amazonian but it is extremely sparse in contrast to the dense valley networks of the warmer, wetter Noachian or to the significant outflow channels of the less wet Hesperian (Chapter 26). During the Amazonian, the Martian surface appears to have evolved into the arctic desert that we see today. The Early Amazonian is marked by widespread volcanism throughout Amazonis Planitia that extends from Tharsis to Elysium (Figure 1.2). Tectonism also continued in these regions but at a lower level than in the Hesperian; by the Middle Amazonian it had effectively ceased (see Head *et al.*, 2001). Although volcanism in Amazonis Planitia declined throughout the Amazonian, what appear to be extremely young (10–50 Ma) lava flows are found near Olympus Mons and in southern Elysium Planitia. It seems improbable that Mars' volcanic lava eruptions stopped after 98% of Martian geologic time; episodic, quiescent volcanic activity in these regions probably continues through today.

With the single exception of ancient ALH 84001, all available Martian meteorites crystallized after 1.3 Ga and are Amazonian (Chapters 17, 22). As two-thirds are younger than 600 Ma and one-third are younger than 200 Ma, they appear fairly uniformly scattered throughout the Amazonian in age. Why the meteorite ages are skewed toward younger (Amazonian) ages, given that more than half of Mars' surface is Noachian and Hesperian, is largely a mystery. It has been suggested that perhaps only these young rocks are sufficiently resilient to survive the impact-driven transport to Earth (Chapter 17). Although the Amazonian meteorites are only weakly altered, they display small amounts of secondary aqueous minerals, including carbonates, clays, sulfates, and halite, indicating that subsurface aqueous fluids likely permeated these young rocks after crystallization (Chapters 17, 23). Perhaps some of these fluids came into contact with isolated subsurface deposits of ancient carbonates that had been sealed off from the surface environment and which thus survived the Late Noachian– to Early Hesperian–pervasive period of acid-sulfate alteration.

The Martian surface appears to have experienced very little aqueous activity since the Hesperian. Basaltic rocks of Hesperian age are found ubiquitously at all landing sites except at Meridiani Planum (although the Meridiani soil contains unaltered basaltic sand of unknown source;

Chapters 15, 20, 21). These basaltic rocks show minimal alteration, although many have surfaces that suggest weak leaching, silica glass coatings, eolian polish, and/or dust (Chapters 3, 4, 8, 12, 13, 14, 19). RAT grindings from the interiors of the fresh Hesperian basalts of the Gusev crater plain (Adirondack Class) show little to no trace of ferric iron (Chapter 13). The soils at all five landing sites appear quite similar. Mössbauer data show that the ubiquitous Laguna Class soils found in the Gusev crater plains, in the Columbia Hills, and on Meridiani Planum (on opposite hemispheres) are nearly identical both in content of primary igneous minerals and of the globally uniform ferric-rich clay-sized dust (Chapters 2, 4, 8, 9, 13, 14, 15). Evidently, basaltic sand has been homogenized by eons of saltation on a global scale or else the parental basalts are globally quite uniform. Unaltered olivine and magnetite show that these soils have not been exposed to liquid water for any appreciable length of time since the Hesperian (Chapters 15, 16). Eolian processes and occasional impacts dominate the Amazonian. In fact, MGS MOC observed the appearance of a number of small impact craters over the 10-year span of MGS observations (Malin *et al.*, 2006). MER made many direct observations regarding the role of current winds in mixing and shaping these deposits, including time-lapse movies of dust devils and microscopic observations of basaltic sand grain sizes that are optimal for transport by saltation (Chapter 20).

While variable amounts of H_2O and/or OH^- exist today in the equatorial soils and rocks, ranging from a few-to-several percent (from Odyssey GRS/NS, Chapters 5, 6) to tens of percent (for Paso Robles soil and the Meridiani outcrop; Chapter 23), most of this water is likely tied up in hydrated or hydroxylated minerals. Water ice is not stable at latitudes $<45^\circ$ unless buried by a largely impermeable layer (Chapter 6). However, modern gullies were discovered by MGS MOC at latitudes between 30° and 50° in both northern and southern hemispheres. Although dry landslides and discharge of subsurface liquid CO_2 have been proposed, most of the suggestions for gully formation involve liquid water in some form, either discharged from aquifers intercepting slopes or by a variety of models involving melting of ground ice or snow (Chapters 8, 9, 26). Recently, Malin *et al.* (2006) have discovered some gullies that have changed albedo (brightened) over several-year spans, which they ascribe to the action of liquid water released from subsurface aquifers or other sources. Although the evidence is inconclusive, these gullies offer the tantalizing possibility that liquid water occasionally issues from the subsurface today.

The most active processes on Mars today occur in the polar regions (Chapters 5, 6, 7, 8, 9, 10, 18, 25, 26). Roughly, a quarter of the entire atmosphere annually cycles into and out of the seasonal CO_2 polar caps; on the order of a meter of CO_2 condenses and snows onto the surface during the polar winters. After the seasonal CO_2 deposit (that extends to $\sim\pm55^\circ$ latitudes) sublimes in the polar spring, Mars' permanent north polar and south polar residual caps (NPRC and SPRC) emerge. The polar regions contain most of the near-surface (upper meter) concentration of water ice, both in the permanent caps and cold-trapped in the near-surface ice in the regolith (Chapters 5, 6, 25). Since the Viking Missions, the NPRC has been known to be composed of water ice, as it warms rapidly after the seasonal CO_2 disappears. By contrast, the surface of the SPRC was known to be CO_2 ice as its temperature remains near the CO_2 frost point after the seasonal cap is gone. Observations from recent missions show that the SPRC may actually be largely a permanent water-ice cap, but one that is covered by a 1–10 m veneer of CO_2 ice (Chapters 5, 6, 7, 25). Carved in the top of this CO_2 veneer are a series of smooth-walled, quasi-circular pits that form an exotic terrain dubbed "Swiss Cheese." The pits bottom out on a flat resilient layer that is probably the top of the permanent residual water-ice cap. Monitoring of the size and shape of the pits with MGS MOC over periods of years reveals that they are expanding at 2–4 m/yr, indicating that they must reside in subliming layers of CO_2 ice and not of water ice (Chapter 25).

The residual ice caps (SPRC and NPRC) are stratigraphically the uppermost layers of the PLD. These vast complexes are concentrated north and south of roughly $\pm 80^\circ$ latitudes (Figure 1.1). The PLD were discovered in the 1960s with Mariner 7. They exhibit hundreds of flat-lying layers up to tens of meters thick; each PLD complex covers $\sim 10^6\,km^2$. In the north, the NPRC covers most of the PLD; in the south, the SPRC covers only a small central region ($\sim 10^5\,km^2$) of PLD. Evidently, formation of the PLD is directly coupled to the residual water-ice caps, and thus they likely contain records of past climates, perhaps extending back more than 10 Ma.

The polar CO_2 cycle exerts major control over the climate and responds to changes in orbital and obliquity (tilt of the rotation axis) variations (Chapter 26). Change in obliquity is the most important driver of climate change (e.g., Touma and Wisdom, 1993; Laskar *et al.*, 2004). During periods of low obliquity, the polar regions become colder, trap more water and CO_2, and cause the atmospheric pressure to fall. During periods of high obliquity, the poles are exposed to more insolation during polar summers and lose water to the equatorial regions. In extreme cases, most of the polar water ice could flow to lower latitudes, covering the surface globally with up to tens of meters of ice. Such ice flows could produce glaciers; evidence for their existence has indeed been observed (e.g., Lucchitta, 1981; Kargel *et al.*, 1995; Head *et al.*, 2005). At high obliquity, polar temperatures could rise to the melting point of ice, possibly generating liquid water in the polar regions (Chapter 26).

An area of anomalous behavior within the south polar seasonal CO_2 deposit has become known as the "cryptic" region (Chapters 7, 25). During retreat of the seasonal cap in the southern mid spring, this region becomes dark in visible-light images, first suggesting that the CO_2 had sublimed and that the region should begin to warm. However, thermal-IR measurements reveal that the cryptic region remains cold, near the frost temperature of CO_2. Two possible explanations are that either the CO_2 deposit is a coarse-grained slab (Chapters 9, 25) or that it is dirty CO_2 snow (Chapter 7). This anomalous region also exhibits bizarre features known as "black spiders," seasonal albedo features appearing as dark round spots with halos and

fans. A model proposed for their formation (Kieffer *et al.*, 2006) involves CO_2 forming as a slab that may have embedded dust. As sunlight heats the dust grains, they migrate downward, effectively cleaning the slab; holes in the slab anneal behind them. Sunlight can then penetrate through the clean slab to a dark substrate, subliming CO_2 at the base. As CO_2 gas flows toward regions where it can vent, it scours the substrate and entrains dark dust that is finally jetted onto the surface. The physics of the model for this active Martian polar process is remarkably similar to a model invoked to explain active dark plumes observed erupting from the surface of Triton's nitrogen ice cap (Soderblom *et al.*, 1990).

1.6 OUTSTANDING QUESTIONS AND FUTURE CHALLENGES

As in any field of scientific exploration and research, the more we learn about the Martian surface, the deeper and more focused our questions become. Here we summarize some of the major outstanding questions relevant to the study of the composition, mineralogy, and physical properties of the Martian surface. These include old questions that have remained unanswered since the days of the Viking Missions, as well as some new ones that have emerged from the rich new knowledge gained over the last decade of Martian exploration.

1.6.1 Character of the Martian crust

The nature of the global dichotomy remains in debate, and is argued to be organized by early low-order mantle convection or by early large impacts into the northern plains. The existence of relic basin-scale impact features beneath the Amazonian sedimentary/volcanic plains suggests that the northern lowland crust may be as ancient as the southern cratered highlands. That the southern highland terrains stand several kilometers above the northern lowlands shows the crust to vary in thickness roughly between 30 km and 100 km and to be less dense than the mantle. What is the nature of this density contrast? Is it analogous to the lunar crust? Rocks of higher silica content such as andesitic basalts have been suggested as a component of the crust. If true, does this provide evidence for broad-scale early fractional crystallization of the crust? More detailed investigations of the ancient magnetized crust will certainly shed more light on the nature of the crust overall. Higher spatial resolution will help elucidate the depth of magnetization, the crustal thickness, early thermal profiles, and the basal structures of Tharsis and Elysium volcanic constructs and of large impact basins such as Hellas and Argyre.

1.6.2 Early aqueous chemistry

Did Mars' aqueous surface environment evolve from earlier alkaline or neutral-pH conditions to later very acidic conditions during the Middle-to-Late Noachian? Isolated evidence of phyllosilicates (clays) that require near-neutral pH to form appears in some older Noachian terrains; products of sulfuric acid alteration abound in younger Noachian rocks at the MER landing sites. If this transition did occur, what caused the change from alkaline to acidic? Was early long-lived volcanism in Tharsis and Elysium a key factor? How profuse was early surface water, and when and how did it decline in abundance? Were the ephemeral shallow seas like those found in Meridiani Planum, evidenced by the acidic siliciclastic evaporites and festoon cross-bedding textures of the Burns formation, ubiquitous across the Martian surface or were they rare, even unique to that region? Perhaps the high-regional concentration of hematite suggests the latter. Did an even more alkaline environment predate the phyllosilicates, and were significant abundances of carbonates ever deposited at the surface? Did subsequent highly acidic conditions then erase virtually all surface traces of carbonates and most traces of clays? Or did alkaline and acidic conditions coexist during this early epoch, with the alkaline conditions in the subsurface sealed off from the acidic conditions at the surface? Because we find both sulfate and carbonate secondary alteration minerals in young Amazonian meteorites, this latter scenario remains a realistic possibility.

1.6.3 Survival of primitive basaltic minerals

Although we have substantial evidence that acid-sulfate alteration was commonplace, perhaps even pervasive, across the Martian surface during the Late Noachian, it had to be quite limited in total effect. Other than the globally uniform bright red ferric-bearing dust, on average the surface rocks and soils are only weakly altered basalts. Chemically fragile minerals like olivine are mapped ubiquitously in low-albedo regions of the Noachian highlands. Basalt rocks on the Gusev crater floor have been exposed throughout the Amazonian and during much of the Hesperian (perhaps >3.5 Ga) and exhibit very minimal aqueous alteration. Ubiquitous runoff channels in the Late Noachian also seem inconsistent with widespread ancient exposures of olivine. How did primitive igneous minerals survive the early wet period? Clearly, surface water cannot have been around but for a fraction of time after these primitive minerals were exposed at the surface. Surface water must have been geologically short-lived, locally concentrated, and/or limited in volume. Only a small fraction of the Burns formation is consistent with deposition and evaporation of open shallow water; most of it consists of eolian dune deposits. Further, if the extent of the Burns formation is marked by the concentration of hematite mapped from orbit, it was also limited in region as well as duration. Was it simply that the combined volume and duration of liquid water at the near surface was too small to affect but a fraction of the bulk of the igneous crust? Was the limited nature and early decline of surface water tied to the loss of the atmosphere or to long-lived Tharsis/Elysium volcanism?

1.6.4 Martian meteorite enigmas

A number of major issues also remain in the interpretation of the SNCs. The first deals with their typically young crystallization ages. Given that more than half of Mars' surface terrains are Hesperian and Noachian (greater than about

3.5 Ga), why are 95% of the meteorite crystallization ages <1.3 Ga? Suggestions that this skewed age distribution arises because only young igneous rocks are sufficiently resilient to survive the cataclysmic journey to Earth or that thick debris mantles overly most of the ancient rocks are less than satisfying explanations. That a number of SNCs have very young Amazonian crystallization ages (<200 Ma) is exciting because it supports the notion that low-level, quiescent volcanism must continue through today, consistent with extremely sparse crater populations on some (estimated 10–50 Ma) volcanic flows. Where are these active volcanic regions and what are their modern eruption rates? The SNCs exhibit minor secondary alteration minerals, including carbonates and sulfates. Evidently, a variety of aqueous fluids have percolated through the subsurface in recent Amazonian time. What are these fluids and what are their sources? Distinct from terrestrial basalts, SNCs and Martian surface materials share basic characteristics (ferroan olivine and pyroxenes and sodic plagioclase) but they differ geochemically in other ways. For example, why do Gusev basalts and Bounce Rock (that closely resembles basaltic shergottites) exhibit higher K, higher Al/Si, and lower Mg/Si than do any of the SNC meteorites? Additionally, meteorites have much lower K than seen in surface materials. Have processes concentrated such volatile elements at the surface? Is the crust stratified with respect to such compositions?

1.6.5 Polar phenomena and climate change

In situ exploration of the deep polar regions remains a fundamental goal for future lander and rover missions. Observations from the surface of polar geologic processes and records, of the physics of active phenomena in the polar volatiles, and of atmospheric phenomena that control global weather systems, all offer a rich set of scientific opportunities. Direct investigation of active CO_2 ice layers, the "Swiss cheese" and "cryptic region," are key targets for surface exploration. Most of the known inventory of water now resides in the upper meter of the polar regolith. But how much water is locked up in the upper few kilometers of the polar crust? What climatological records are held in the hundreds of strata in the polar layered terrains? How far back in time do they extend? Understanding the role of Mars' changing eccentricity and obliquity in controlling the modern climate is of paramount importance for understanding the global migration of water. Does water episodically migrate from the polar regions to the equatorial areas where infrequent volcanism continues in Tharsis and Elysium? Is there occasional (10–100 Ma) interaction between volcanic eruptions and temporary equatorial water ice, perhaps resulting in rare aqueous environments even in the current geologic epoch? Are such events recorded in the polar layered terrains?

1.6.6 The search for life goes on

During 1996–2007, seven major NASA and ESA planetary spacecraft successfully achieved Mars orbit or landed on the surface (Table 1.1). These missions have been scientifically prolific and, coupled with continuing analyses of Martian meteorites, have generated an enormous wealth of new information that permits us to sharpen and refocus our search for evidence of Martian life. We have "followed the water" and have begun to assemble a clearer picture of the chemical conditions in Mars' early aqueous environment. We suspect that both slightly alkaline and extremely acidic aqueous environments existed in the Noachian. It is likely that alkaline conditions preceded acidic conditions, but perhaps they coexisted, isolated from one another regionally or as surface versus subsurface conditions. Ancient outcrops of clay minerals formed in less acidic conditions may be more likely to have harbored ancient evidence for life. Ancient carbonates were formed in ALH 84001 some 3.9 Ga. Around this time period there must have been conditions conducive for carbonate formation, but whether or not these conditions were only in the subsurface we do not yet know. Continued searches by orbiting spectrometers for clays, silica, carbonates, and other aqueous alteration minerals remain critical for potentially revealing ancient habitats. Modern habitable environments are most likely restricted to those containing subsurface liquid water. Carbonates and sulfates found in SNCs testify to the existence of subsurface briny liquids during the Middle and Late Amazonian. Climatic changes driven by oscillating obliquity could episodically generate conditions for surface water even during the current geological epoch. Search for such sites by orbiters is an essential task. Evidence suggested for liquid water in the formation of modern gullies is tantalizing. In our search for Martian life, ultimately, the return of carefully selected samples for analysis by the most sophisticated laboratory techniques will be required. Currently, an MSR mission is beyond at least the next decade in NASA's planning horizon. But discovery of compelling surface or subsurface geological evidence of benign aqueous environments could certainly accelerate that schedule.

REFERENCES

Beaty, D. W., M. A. Meyer, and the Mars Advance Planning Group, 2006 Update to "Robotic Mars Exploration Strategy 2007–2016," Unpublished white paper, posted November 2006 by the Mars Exploration Program Analysis Group (MEPAG), http://mepag.jpl.nasa.gov/reports/index.html, 24pp., 2006.

Bertka, C. M. and Y. Fei, Implications of Mars Pathfinder data for the accretion history of the terrestrial planets, *Science* **281**, 1838–40, 1998.

Carr, M. H., *Water on Mars*, Oxford University Press, 1996.

Carr, M. H., *The Surface of Mars*, Cambridge University Press, 2007.

Chapman, M. (ed.), *The Geology of Mars: Evidence from Earth-based Analogs*, Cambridge University Press, 472pp., 2007.

COMPLEX, *On NASA Mars Sample-Return Mission Options*, Washington, D.C.: National Academy of Sciences, 1996.

COMPLEX, *Assessment of Mars Science and Mission Priorities*, Washington, D.C.: National Academy Press, 2003.

Encrenaz, T., The atmosphere of Mars as constrained by remote sensing, *Space Sci. Rev.* **96**, 411–24, 2001.

Folkner, W. M., C. F. Yoder, D. N. Yuan, E. M. Standish, and R. A. Preston, Interior structure and seasonal mass redistribution of Mars from radio tracking of Mars Pathfinder, *Science* **278**, 1749–52, 1997.

Frey, H. V., A timescale for major events in early Mars crustal evolution. *Lunar Planet. Sci. Conf.* **XXXV**, Abstr. 1382, 2004.

Greeley, R., R. O. Kuzmin, and R. M. Haberle, Aeolian processes and the effects on understanding the chronology of Mars, *Space Sci. Rev.* **96**, 393–404, 2001.

Hartmann, W. K., Martian cratering 8: isochron refinement and the chronology of Mars, *Icarus* **174**, 294–320, 2005.

Hartmann, W. K. and G. Neukum, Cratering chronology and evolution of Mars. In *Composition and Origin of Cometary Materials* (ed. K. Altwegg, P. Ehrenfreund, J. Geiss, and W. F. Huebner), Netherlands: Kluwer Academic, pp. 165–94, 2001.

Head, J. W., R. Greeley, M. P. Golombek, *et al.*, Geological processes and evolution, *Space Sci. Rev.* **96**, 263–92, 2001.

Head, J. W., G. Neukum, R. Jaumann, *et al.*, Tropical to mid-latitude snow and ice accumulation, flow and glaciation on Mars, *Nature* **434**, 346–51, 2005.

Kargel, J. S., V. R. Baker, J. E. Beget, *et al.*, Evidence of ancient continental glaciation in the Martian northern plains, *J. Geophys. Res.* **100**, 5351–68, 1995.

Kieffer, H. H., P. R. Christensen, and T. N. Titus, CO_2 jets formed by sublimation beneath translucent slab ice in Mars' seasonal south polar ice cap, *Nature* **442**, 793–6, 2006.

Kieffer, H., B. Jakosky, C. Snyder, and M. Matthews (eds.), *Mars*, Tucson: University of Arizona Press, 1498pp., 1992.

Klein, H. P., N. H. Horowitz, and K. Biemann, The search for extant life on Mars. In *Mars* (ed. H. H. Kieffer, B. M. Jakosky, C. W. Snyder, and M. S. Matthews), Tucson: University of Arizona Press, pp. 1221–33, 1992.

Laskar, J., A. C. M. Corrieia, M. Gastineau, *et al.*, Long term evolution and chaotic diffusion of the insolation quantities of Mars, *Icarus* **170**, 343–54, 2004.

Levin, G. V., Interpretation of new results from Mars with respect to life. In *Instruments, Methods, and Missions for Astrobiology VIII* (ed. R. B. Hoover, G. V. Levin, and A. Y. Rozanov), *Proc. SPIE* **5555**, pp. 126–38, 2004.

Lucchitta, B. K., Mars and Earth: comparison of cold-climate features, *Icarus* **45**, 264–302, 1981.

Malin, M. C., K. S. Edgett, L. V. Posiolova, S. M. McColley, and E. Z. N. Dobrea, Present-day impact cratering rate and contemporary gully activity on Mars, *Science* **314**, 1573–7, 2006.

McCleese, D. J. and the Mars Advance Planning Group, *Mars Exploration Strategy 2007–2016*, NASA, Jet Propulsion Laboratory, Pasadena, California, http://mepag.jpl.nasa.gov/reports/index.html, 2006.

McCleese, D. J. and the Mars Expeditions Strategy Group, *The Search for Life on Mars*, NASA, Jet Propulsion Laboratory, Pasadena, California, http://mepag.jpl.nasa.gov/reports/index.html, 2001 [written in 1996].

MEPAG, the Mars Exploration Program Analysis Group, *Mars Scientific Goals, Objectives, Investigations, and Priorities* (ed. J. Grant), http://mepag.jpl.nasa.gov/reports/index.html, 31pp., 2006.

Mishkin, A., *Sojourner: An Insider's View of the Mars Pathfinder Mission*, Berkley, CA, 352pp., 2003.

Muirhead, B. K. and W. L. Simon, *High Velocity Leadership*, New York: Harper Business, 1999.

National Research Council Space Studies Board, *New Frontiers in the Solar System, An Integrated Exploration Strategy*, Washington, D.C.: National Academy of Sciences, 2003.

Neumann, G. A., M. T. Zuber, M. A. Wieczorek, *et al.*, Crustal structure of Mars from gravity and topography, *J. Geophys. Res.* **109**, E8:E08002, pp. 1–18, 2004.

Nimmo, F. and K. L. Tanaka, Early crustal evolution of Mars, *Ann. Rev. Earth Planet Sci.* **33**, doi:10.1146/annurev.earth.1133.092203.122637, 2005.

Phillips, R. J., M. T. Zuber, S. C. Solomon, *et al.*, Ancient geodynamics and global-scale hydrology on Mars, *Science* **291**, 2587–91, 2001.

Pieters, C. M. and P. A. J. Englert (eds.), *Remote Geochemical Analysis: Elemental and Mineralogical Composition*, Cambridge University Press, 594pp., 1993.

Scott, D. H. and M. H. Carr, Geologic map of Mars. *USGS Misc. Inv. Ser. Map*, I-1083, 1978.

Scott, D. H., K. L. Tanaka, R. Greeley, and J. E. Guest, Geologic maps of the western and eastern equatorial and polar regions of Mars. *USGS Misc. Inv. Ser. Map*, I1802-A, B, C, 1986–7.

Soderblom, L. A., T. L. Becker, S. W. Kieffer, *et al.*, Triton's geyser-like plumes: discovery and basic characterization, *Science* **250**, 410–15, 1990.

Solomon, S. C., O. Aharonson, J. M. Aurnou, *et al.*, New perspectives on ancient Mars, *Science* **307**, 1214–20, 2005.

Strom, R. G., R. Malhotra, T. Ito, F. Yoshida, and D. A. Kring, The origin of planetary impactors in the inner solar system, *Science* **309**, 1847–50, 2005.

Tanaka, K. L., The stratigraphy of Mars, *J. Geophys. Res.* **91**, E139–58, 1986.

Tanaka, K. L., J. A. Skinner, and T. M. Hare, Geologic map of the northern plains of Mars, *USGS Sci. Inv. Map*, 2888, 2005.

Tanaka, K. L., J. A. Skinner, T. M. Hare, T. Joyal, and A. Wenker, Resurfacing history of the northern plains of Mars based on geologic mapping of Mars global surveyor data, *J. Geophys. Res.* **108**, E4:8043, 24-1–24-32, 2003.

Touma, J. and J. Wisdom, The chaotic obliquity of Mars, *Science* **259**, 1294–7, 1993.

Wilhelms, D. E. and S. W. Squyres, The Martian hemispheric dichotomy may be due to a giant impact, *Nature* **309**, 138–40, 1984.

Zuber, M. T., S. C. Solomon, R. J. Phillips, *et al.*, Internal structure and early thermal evolution of Mars from Mars global surveyor topography and gravity, *Science* **287**, 1788–93, 2000.

2

Historical context: the pre-MGS view of Mars' surface composition

W. M. CALVIN AND J. F. BELL III

ABSTRACT

This chapter summarizes the state of understanding of Mars surface composition in the decade before the arrival of Mars Global Surveyor and Mars Pathfinder (about 1987–1997), updating earlier historical reviews on this topic by Soderblom (1992) and Roush *et al.* (1993). Here we summarize analyses of telescopic and spacecraft spectroscopic data sets with reference to relevant terrestrial analog studies, laboratory measurements, and modeling work. The chapter is organized around a synthesis of surface mineralogy types that have been identified and searched for: unaltered mafic volcanic minerals; alteration products including oxidized iron, hydrated minerals, and phyllosilicates; the search for carbonates; early, if equivocal evidence of sulfates; and finally, polar deposits. We highlight the way that these precursor studies have influenced the design, selection, and implementation of the current generation of science investigations focused on unraveling the composition and mineralogy of the surface of Mars.

2.1 INTRODUCTION

Mars has been the object of detailed spectroscopic observations since the early 1960s. Initial telescopic work was followed by spatially resolved observations from the Mariner 6, 7 and 9 spacecraft, and multispectral optical and infrared observations with Viking both on the surface and from orbit. Early researchers were able to identify the strong bound water feature beyond 3 μm, the preponderance of oxidized iron contributing to the visible spectral shape, the presence of relatively unoxidized mafic, presumably volcanic minerals based on features near 1 and 2 μm, and that the seasonal polar cap was dominated by CO_2 ice and the residual north cap was made of water ice (e.g., Larson and Fink, 1972; Houck *et al.*, 1973; Pimentel *et al.*, 1974; Singer *et al.*, 1979; Clark and McCord, 1982). These early observations were summarized by Soderblom (1992), in the University of Arizona Press book, *Mars* (known by some as the "Mars bible") and also by Roush *et al.* (1993). In the years preceding the launch and loss (just three days before orbit insertion) of the NASA Mars Observer orbiter in 1993, and the subsequent successes of NASA's Mars Global Surveyor (MGS) orbiter and Mars Pathfinder (MPF) lander/rover in 1997, knowledge of the surface composition and mineralogy was advanced by acquisition and analysis of data from the French Imaging Spectrometer for Mars (ISM) instrument on the Soviet Phobos 2 orbiter, by new ground- and space-based telescopic observations from the visible through the infrared, by new analyses of previous Mariner and Viking spacecraft data, and by theoretical modeling and laboratory studies of Mars analog materials.

This chapter briefly summarizes the progress in our understanding of surface material compositions from the late 1980s to the turn of the new millennium and prior to the advent of global mineral and compositional maps and interpretations from the MGS Thermal Emission Spectrometer (see Chapter 9), the Mars Odyssey GRS, NS, and THEMIS instruments (see Chapters 5, 6, and 10, respectively), and the European Space Agency (ESA) Mars Express orbiter OMEGA instrument (see Chapter 7), whose results are summarized elsewhere in this book. In keeping with other summaries and reviews (e.g., Soderblom, 1992; Roush *et al.*, 1993; Bell, 1996) surface composition is discussed according to mineralogical class. These classes are somewhat further subdivided by the wavelength range used to uncover their characteristics. We first present the best spectral profiles from the visible through the thermal infrared that were available at the end of this time frame, and then discuss spectral features in terms of primary mafic mineralogy, oxidative alteration products, and minerals suggesting more substantial alteration such as hydrated silicates, sulfates, and carbonates. The measured composition of polar volatiles are treated separately, followed by a brief synopsis of the state of knowledge regarding Martian surface composition and mineralogy prior to the advent of this last decade's phenomenal explosion of new global- and regional-scale orbiter, lander, and rover compositional and mineralogic measurements.

2.2 TYPICAL SPECTRAL PROFILES

By the time of the arrival of MGS in orbit (1997), very good spectral profiles of typical Martian terrains from the visible through to the thermal infrared had been derived from the synthesis of data from multiple instruments and data sets. Mustard and Bell (1994) generated typical bright and dark region composite spectra by merging the then-best available ground-based telescopic and ISM measurements. Figure 2.1 shows spectra from Erard and Calvin (1997), who synthesized the Mustard and Bell (1994) data with that from the Mariner 6/7 Infrared Spectrometer (IRS) instruments.

The Martian Surface: Composition, Mineralogy, and Physical Properties, ed. J. F. Bell III. Published by Cambridge University Press.

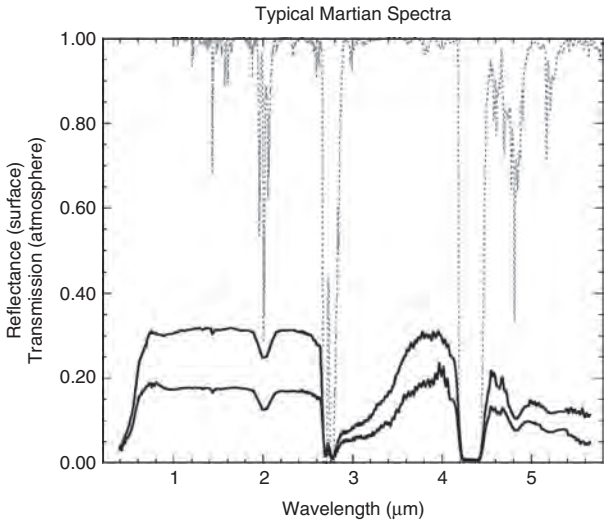

Figure 2.1. Surface reflectance spectra from 0.4 to 5.6 μm given by Erard and Calvin (1997). Data were synthesized using ground-based telescopic data from Mustard and Bell (1994) and space-based spectra from Phobos-2 ISM and Mariner 6/7 IRS data. Beyond approximately 3.5 μm, surface thermal emission begins to contribute to the measured signal; these spectra were corrected to reflectance using Kirchoff's law (reflectance = 1 – emissivity) and assuming Lambertian (cosine solar incidence angle) surface scattering behavior. A calculated transmission spectrum for the Martian atmosphere containing CO_2, H_2O, O_3, and CO from Crisp (1990) is shown as the gray dashed line.

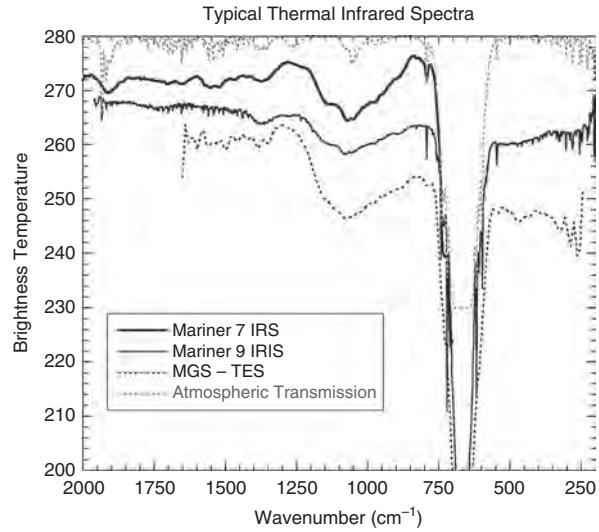

Figure 2.2. Typical thermal infrared spectra of Mars. The Mariner 7 IRS spectrum is an average of five spectra over Meridiani Sinus (M7 99:104). The Mariner 9 IRIS spectrum is an average of 1700 spectra acquired after orbit 100 (largely clear atmosphere). A typical TES spectrum from early in the mission is also shown. A calculated transmission spectrum for the Martian atmosphere multiplied by 50 and offset by 230 K is shown as the gray dashed line (Crisp, 1990).

Quite evident in these spectra are the strong red slope from 0.3 to 0.7 μm in both bright and dark regions, attributed to ferric minerals (likely iron oxides and hydroxides), the variable strength and position of an absorption feature near 0.9 μm caused by ferric minerals in bright regions and/or ferrous minerals in unaltered mafic materials in dark regions (likely volcanic rocks, sand, and dust high in Mg and Fe and moderately low in Si), and the strong, broad, and ubiquitous absorption feature beyond 3 μm from bound water and/or OH^- trapped in surface materials. Differences in the shape and center of the spectral peak near 0.8 μm were noted as well as variations in slope in the near-infrared (flat for bright regions, downward trending for dark regions). Weak features near 2.3 μm were observed first in telescopic data (McCord *et al.*, 1982) and subsequently explored both in ISM data (Murchie *et al.*, 2000) and higher resolution telescopic spectra (Clark *et al.*, 1990; Bell *et al.*, 1994); interpretations will be discussed later in this chapter. Early data also suggested absorption features near 1.9 μm, but these data were equivocal given the potential contribution from water in either the Martian or terrestrial atmospheres and the proximity to atmospheric CO_2 bands. In addition, scattering by atmospheric dust was found to contribute strongly to the spectral slopes of dark regions, but less so to bright regions (Erard *et al.*, 1994).

Also evident in Figure 2.1 are multiple strong absorptions by the intervening Martian atmosphere. The figure shows a calculated model of the Mars atmosphere from Crisp (1990) including nominal abundances of carbon dioxide, water, ozone, and carbon monoxide. The strongest CO_2 features occur near 1.4, 2.0, 2.7, from 4.2 to 4.4, from 4.6 to 5, and at 5.2 μm. Numerous other weak features occur from other minor constituents, as described in detail by Crisp (1990).

Figure 2.2 shows typical thermal-infrared spectra of Mars from the Mariner 7 IRS, the Mariner 9 Infrared Imaging Spectrometer (IRIS), and MGS/TES in the spectral range from 2000 to 200 cm^{-1} (5 to 50 μm) (Cimino and Calvin, 1997; Christensen *et al.*, 2000). When Mariner 9 arrived at Mars in 1971, the planet was in the midst of a large global dust storm. The spectral profile exhibited a strong 10-μm silicate signature and occasional structure from water ice in clouds, and water vapor (e.g., Hanel *et al.*, 1992). The Mariner 9 spectrum in Figure 2.2 is an average from IRIS data having emission angles $<60°$, brightness temperature at 1300 $cm^{-1} > 260$ K, and orbit numbers >100 (meaning that the dust had largely settled from the atmosphere).

Clear atmosphere Mariner 9 spectra were combined with broadband emissivity from the Infrared Thermal Mapper (IRTM) of the Viking to show that there were spatial variations in surface infrared emissions (Christensen, 1998), a fact exploited successfully in follow-on observations from later Mars orbital infrared instrumentation. Mariner 7 IRS data were acquired during a clear atmospheric period at higher spatial resolution than IRIS, but with limited spatial coverage and with unavoidably strong variation in emission angle among the spectra, because the mission was a flyby not an orbiter. Those spectra were acquired only up to the strong atmospheric absorption at 700 cm^{-1} (14 μm) and show a broad and strong silicate envelope from 1250 to 850 cm^{-1}, and CO_2 "hot bands" at 1050 cm^{-1}, also seen with IRIS (Maguire, 1977; and Figure 2.2). Due to the strongly varying atmospheric component, only limited surface interpretations

of these IRS thermal-infrared spectra were attempted. However, the silicate band strength was shown to correlate at least in part with atmospheric pathlength, consistent with a contribution from atmospheric dust (Cimino and Calvin, 1997) and some IRS spectra were interpreted to be consistent with the presence of goethite (α-FeOOH), particularly in the Hellas region (Kirkland and Herr, 2000). Figure 2.2 again shows that numerous absorptions due to the Martian atmosphere contribute to observed spectra in the thermal infrared.

2.3 MAFIC MINERALOGY

Early in the history of Martian observations it was recognized that low-albedo regions had spectral shapes consistent with basaltic compositions, with some contribution from oxidized materials mixed at large spatial scales or as surface coatings (see reviews by Soderblom, 1992; and Roush *et al.*, 1993). In Martian dark region spectra the location of the reflectance peak at 0.75 μm is more distinct than in bright regions, there is a well-defined absorption centered near 1.0 μm, and there is a general downward slope in reflectance toward longer wavelengths. All of these characteristics are consistent with near-infrared spectra of terrestrial basalts, and the implied presence of basaltic compositions in these spectra is consistent with spacecraft morphologic evidence of volcanic landforms and analysis of the basaltic SNC meteorites and their varying compositions (see Chapter 17). The presence of a red spectral slope in the visible, even in the dark regions, argued that the telescopic spectra of these regions were either being mixed with spectra of bright, dusty regions or that the basaltic minerals that compose the dark regions are covered or coated by variable amounts of brighter, ferric-rich dust. The bright regions are spectrally similar to some altered basaltic materials (e.g., Singer *et al.*, 1979; Singer, 1982), further strengthening the case for the presence of relatively unaltered mafic components in the dark regions.

A number of factors conspired to make the detailed identification and mapping of mafic minerals like olivine and pyroxene on Mars difficult using telescopic or spacecraft measurements prior to the 1990s. These factors included the low-spatial resolution of many of the measurements (and the subsequent dilution of small-scale spectrally unique signatures), the difficulty in quantitatively modeling mineral abundances from visible to near-IR spectra because of the confounding effects of particle size and multiple overlapping ferric and ferrous mineral absorption features, and even the effects of subtle variations in band shape, especially on the long wavelength side of the 1-μm feature, due to temperature effects. For example, Hinrichs and Lucey (2002) have shown that band edge shifts up to 0.05 μm can occur for 40-K variations in surface temperature, a range that is routinely encountered on the Martian surface during the daytime.

With data from the Phobos-2 ISM instrument (Bibring *et al.*, 1990), detailed spatial variability in the spectral shape between 0.76 and 3.16 μm was observed at high-spatial resolution for the first time. In particular, detailed definition

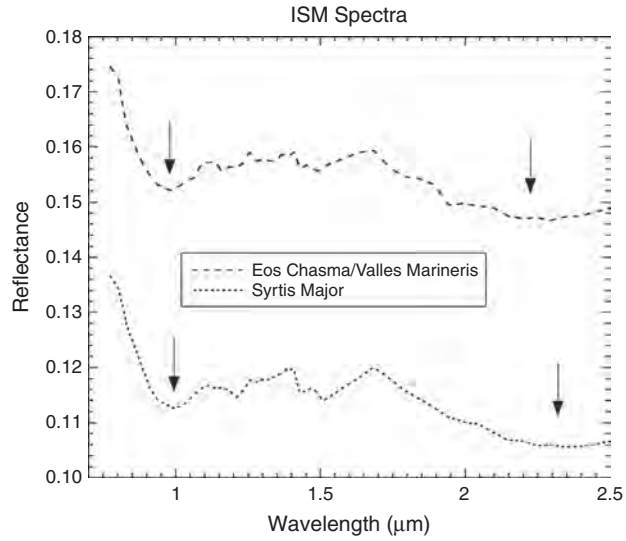

Figure 2.3. Representative Phobos-2 ISM spectra showing variations in the broad mafic absorption features near 1 and 2 μm.

of the "2-μm" pyroxene feature was possible. The "2-μm" band is a broad envelope centered between 2.0 and 2.3 μm in pyroxenes, and typically occurs at longer wavelengths in ISM spectra. In addition, subtle differences in band centers near 1 μm were observed (e.g., Mustard *et al.*, 1997; Murchie *et al.*, 2000; Figure 2.3). Models of band center shifts of both the 1-μm and the 2-μm features were used to fit these spectra with combinations of low- and high-Ca pyroxenes (e.g., Mustard and Sunshine, 1995; Mustard *et al.*, 1997). This 2-pyroxene mineralogy dominated by low-calcium pyroxene is uncommon on Earth, but characteristic of SNC meteorites and has implications both for mantle composition and evolution (see Chapter 17).

Parts of Lunae Planum and Syrtis Major were found to lack a 2-μm band (Murchie *et al.*, 2000) and Nili Patera was found to need a contribution from a feature near 1.2-μm to best match the spectrum (Mustard and Sunshine, 1995). While the potential for olivine to contribute to the shape of the 1-μm absorption feature was suggested in the late 1970s, this interpretation was considered inconclusive given the poor spatial resolution of the data and the calibration challenges of observing through the Earth's (and Martian) atmosphere (see the discussion in Roush *et al.*, 1993). In order to fit the ISM spectra of Nili Patera, it was noted that the additional absorption near 1.2 μm was likely due to a combination of low- and high-Ca pyroxenes, rather than other mineral phases that have features in this region such as plagioclase or olivine. While Mustard and Sunshine (1995) considered the inclusion of olivine, it was below the detection limits of their models. In retrospect, given the identification of abundant olivine in Nili Fossae by MGS-TES (Hoefen *et al.*, 2003) and its subsequent widespread identification in higher resolution orbital and, eventually, surface rover data (e.g., Morris *et al.*, 2004; Bibring *et al.*, 2005; Hamilton and Christensen, 2005), it seems plausible that olivine may also contribute to the shape of the near-infrared spectra at this location.

SNC meteorites represent samples of the primary igneous mineralogy of Mars (see Chapter 17). During this era, a number of researchers measured the spectra of SNC meteorites in an effort to correlate remotely sensed spectra of Mars with these samples. For example, Sunshine *et al.* (1993) applied the Modified Gaussian Model (MGM) to interpret the spectrum of Elephant Moraine A79001 in terms of calcic pyroxene variations associated with two different basaltic lithologies observed in the meteorite. Additional studies of SNCs using the MGM method to assess pyroxene components include Schade and Wäsch (1999) to quantify pigeonite and augite in Zagami and Nakhla and McFadden and Cline (2005) who fit 9 SNCs for olivine, pyroxene, and augite. Bishop *et al.* (1998) measured ALH 84001, particularly for weak features from minor organics and carbonates. Hamilton *et al.* (1997) measured samples from the three major SNC lithologies in thermal emission in order to correlate with spectra from TES. All of these studies showed strong links between laboratory-derived meteorite spectra and the best available Mars remote sensing data sets, across a wide range of wavelengths, and all ultimately provided further support for what was then still a controversial hypothesis that the SNCs were from Mars.

2.4 IRON OXIDES AND HYDROXIDES

Mars is reddish brown because of the absorption of ultraviolet to blue (and to a lesser extent green) light by iron-bearing minerals on its surface. Many telescopic observations of Mars have been performed during the past century with the explicit goal of identifying and quantifying the composition of the iron-bearing minerals on the surface and in the airborne dust (see, for example, the review by Bell, 1996). Fundamental to understanding the history and evolution of Martian weathering processes is determining to what extent physical, chemical, and/or photo-oxidative weathering contribute to or control alteration of the primary basaltic materials. The amount of water involved in dissolution and hydrolysis of mafic minerals is key to determining if the surface environment was more clement at an earlier time (e.g., Gooding *et al.*, 1992). To within a few percent, the overall shape of the mean visible to near-IR spectral reflectance curve of Mars has been known since the late 1960s. More recent telescopic and spacecraft observations and reinterpretations of previous data sets have concentrated on providing more specific information on band centers, band depths, and the spatial distribution of observed spectral features, in order to further constrain the specific iron oxide and oxyhydroxide components that may contribute to the visible spectral shape.

Telescopic spectra showed that absorption band positions in most bright regions on Mars are consistent with the presence of a small amount (less than 5%) of well-crystalline "red" hematite (submicron- to several micron-sized grains of α-Fe_2O_3) (e.g., Morris *et al.*, 1989; Bell *et al.*, 1990). Further, the relative weakness of the red hematite absorption features combined with the flat near-IR character and intense but smooth reflectance drop-off from the visible down to the near UV in typical Mars spectra argued for the presence of a matrix of much more poorly crystalline or nanophase ferric-bearing materials (e.g., Morris *et al.*, 1989, 1993; see Bell, 1996, for a thorough review). Differences in the red hematite abundance and distribution between and among bright and dark regions have been inferred from higher resolution multispectral imaging and imaging spectroscopic observations from HST, ISM, and even Viking Orbiter measurements (e.g., Geissler *et al.*, 1993; Mustard and Bell, 1994; Bell *et al.*, 1997).

Significant effort has also been expended exploring the spectral properties of other Fe^{3+}-bearing materials that could be consistent with the available data. These minerals include palagonite, ferrihydrite, iron-substituted montmorillonites, lepidocrocite, and iron-bearing hydrated sulfates such as jarosite and schwertmannite (Singer, 1982; Burns, 1987; Banin *et al.*, 1992; Bishop *et al.*, 1993; Morris *et al.*, 1993, 1996; Bishop and Murad, 1996; Table 2.1). Exploration of these terrestrial materials supports the contribution of iron oxide and oxyhydroxide components to the visible wavelength spectral shape of Mars, even though the spatial resolution and fidelity of the available Mars data prior to the 1990s, combined with confounding effects like particle size, overlapping absorption features, and the pigmentary nature of fine-grained iron oxides, did not allow the identification of other specific ferric phases.

In the mid infrared, early studies suggested that the spectra from Mariner 9 IRIS were most consistent with at most a thin surface patina or staining of iron oxide on underlying silicates (Hunt *et al.*, 1973; Toon *et al.*, 1977). Bell *et al.* (1995) and Roush and Bell (1995) compared modern laboratory measurements of iron oxides, hydroxides, and palagonitic material with Mariner 7, Mariner 9, and telescopic mid infrared data. They showed that nanophase ferric oxide components have different spectra than crystalline forms. These components should be identified based on well-resolved features at longer wavelengths (lower wavenumbers) but they concluded identification would require both high signal-to-noise and improved spatial resolution.

Ultimately, detailed orbital studies and *in situ* studies have proven that there are indeed many diverse kinds of ferrous iron-bearing silicates (olivine, pyroxene, ilmenite, magnetite) and ferric iron-bearing oxides, oxyhydroxides, and oxyhydroxy-sulfates (hematite – both "red" and coarse-grained "gray" varieties, goethite, magnetite, nontronite, jarosite, and other as-yet unidentified ferric sulfates) that occur on Mars. These discoveries, outlined in more detail in other chapters throughout this book (see, for example, Chapters 9, 14, 15, and 16), have vindicated the original telescopic and early spacecraft searches for these climatically diagnostic mineral species. However, the isolated and sometimes rare spatial occurrence of the most interesting iron oxide and hydroxide phases amidst a virtual sea of globally homogenized nanophase ferric oxide dust grains in the surface soils and the atmospheric aerosols have also pointed out the critical need for extremely high-spatial resolution to enable their detection.

Table 2.1. *Minerals detected, inferred, or sought in historical Mars observations*

Mineral or material	Notes, results	Example references
Carbonates: e.g., Calcite ($CaCO_3$); Siderite ($FeCO_3$); Magnesite ($MgCO_3$); Scapolite ($Ca_4[Al_6Si_6O_{24}]CO_3$) Hydrous carbonates: e.g., Artinite ($Mg_2CO_3(OH)_2 \cdot 3H_2O$); Hydromagnesite ($Mg_5(CO_3)_4(OH)_2 \cdot 4H_2O$)	Simple carbonate phases not detected in significant abundances; minor amounts possible in dust and in some spectra, hydrated forms lack strong carbonate features. Telescopic evidence for surface bicarbonate anions, but specific identification uncertain.	McKay and Nedell (1988); Clark *et al.* (1990); Pollack *et al.* (1990); Bell *et al.* (1994); Calvin *et al.* (1994)
Sulfates: e.g., Kieserite ($MgSO_4 \cdot H_2O$); Gypsum ($CaSO_4 \cdot 2H_2O$); "Polyhydrated sulfate" [$(Fe,Mg,Ca) \cdot nH_2O$]; Anhydrite ($CaSO_4$); Jarosite [$(K,Na)Fe_3(SO_4)_2(OH)_6$)]	Telescopic evidence for SO_4^{2-} anionic group absorptions but specific identification of any of these phases was uncertain. Specific sulfate identifications ultimately came from later MER and OMEGA measurements (see Chapters 7 and 15).	Burns (1987); Pollack *et al.* (1990); Blaney and McCord (1995); Bell (1996)
"Red" hematite: (α-Fe_2O_3, μm-sized particles)	Identified in telescopic and ISM spectra from crystalline ferric bands near 0.65 and 0.9 μm.	Bell *et al.* (1990); Murchie *et al.* (1993)
"Nanophase" ferric oxides: e.g. (α-Fe_2O_3, nm-sized particles)	Inferred from telescopic, spectral analog studies as the strongly pigmenting material responsible for the visible color of Mars, but lacking crystalline ferric absorptions in the near-IR.	Morris *et al.* (1989, 1990, 1993)
Goethite: (α-FeOOH)	Inferred from analysis of some Mariner IRS and Viking orbiter multispectral images; definitive identification uncertain.	Geissler *et al.* (1993); Kirkland and Herr (2000)
Palagonite	Field term for altered basaltic tephra; many are visible to near-IR spectral analogs to Mars, probably as a result of the presence of nanophase hematite.	Singer *et al.* (1979); Singer (1982); Roush *et al.* (1993); Morris *et al.* (1993); Clancy *et al.* (1995)
Phyllosilicates: e.g., Montmorillonite (Al,Mg smectite); Nontronite (Fe smectite); Greenalite, Chamosite, Cronstedtite (Fe serpentines)	Weak bands in the 2.0 to 2.5 μm range detected in some telescopic and ISM spectra, but specific layer silicate identification equivocal.	Hunt *et al.* (1973); Toon *et al.* (1977); McCord *et al.* (1978); Singer *et al.* (1979); Bell and Crisp (1993); Murchie *et al.* (1993); Calvin (1998)
Pyroxene: e.g., Low-Ca (LCP): Enstatite ($Mg_2Si_2O_6$); Pigeonite ($[Mg,Fe,Ca]Si_2O_6$); High-Ca (HCP): Diopside ($[Ca,Mg,Fe]Si_2O_6$); Augite ($[Ca,Na,Mg,Fe](Si,Al)_2O_6$)	Identified in telescopic and ISM spectra from distinctive 1- and 2-μm absorption features. Both LCP and HCP detected and mapped based on band center variations tied to laboratory pyroxene spectral studies.	McCord *et al.* (1978, 1982); Roush *et al.* (1993); Mustard and Sunshine (1995); Mustard *et al.* (1997); Murchie *et al.* (2000)
Olivine: Forsterite (Mg_2SiO_4); Fayalite (Fe_2SiO_4)	Inferred from analysis of some telescopic studies from weak absorption near 1.2 to 1.5 μm, but definitive identification uncertain.	Huguenin (1987); Roush *et al.* (1993)
"Hydrated minerals"	Detected telescopically and by IRS at the 1–3 wt.% level based on ubiquitous presence of 3-μm band, but specific hydrated mineral identification uncertain.	Sinton (1967); Houck *et al.* (1973); Pimentel *et al.* (1974); Murchie *et al.* (1993, 2000); Calvin (1997); Erard and Calvin (1997)
Other ferric oxides, oxyhydroxides, or oxyhydroxysulfates: e.g., Lepidocrocite (γ–FeOOH); Ferrihydrite ($\sim Fe_2O_3 \cdot nH_2O$); Schwertmannite ($\sim Fe_8O_8(OH)_6SO_4$);	Inferred from analysis of some telescopic studies from visible color and ferric absorption band near 0.9 μm, but definitive identification uncertain.	Burns (1987); Banin *et al.* (1992); Bishop and Murad (1996); Morris *et al.* (1996)
CO_2 ice	Detected in both seasonal polar caps.	Herr and Pimentel (1969); Larson and Fink (1972)
H_2O ice	Detected in north residual polar cap and as an enhancement in the edge of the seasonal cap.	Clark and McCord (1982); Calvin and Martin (1994)

2.4.1 Aqueous alteration minerals

The first spectral indications of aqueous alteration of Martian surface materials came from the identification of bound water from a large, broad absorption feature beyond 3 μm (Sinton, 1967; Houck *et al*., 1973). This band was observed by both IRS and ISM, and simple band ratios suggested variations in band strength with either latitude (Pimentel *et al*., 1974) or geographic location (Murchie *et al*., 1993). Murchie *et al*. (2000) noted that small regions of both bright and dark areas observed by ISM showed anomalous behavior with stronger 3-μm band depth. They suggested hydrated ferric minerals and/or sulfates, but the data could not provide evidence for specific phases. Both Calvin (1997) and Baldridge and Calvin (2004) found hydration increases over both Aram Chaos and Meridiani, the largest coarse-grained hematite locations identified from orbit by TES (Christensen *et al*., 2001). This was interpreted as evidence for other hydrated minerals at these sites, and supported an aqueous formation model for the bulk hematite. Calvin (1998) proposed that low-albedo phyllosilicate minerals might be responsible for the increased hydration in dark regions. In retrospect, it appears likely that IRS was sensitive to the hydrated sulfates now known to be a substantial component of outcrop rocks in Meridiani (e.g., Squyres *et al*., 2004). Data from IRS and ISM only overlap in Ganges and Eos Chasmae, and the spatial resolution and viewing geometry are different between the two instruments. Yet there is agreement in areas that are mapped as slightly more hydrated than average by both instruments in the region of overlap. Milliken and Mustard (2005) have developed a normalized optical path length that uses this 3-μm feature to quantify water content and which appears promising for its application on Mars, especially as hydrated minerals may make some contribution to the water-equivalent-hydrogen signal observed by the Mars Odyssey Gamma Ray and Neutron Spectrometers (e.g., Fialips *et al*., 2005; see Chapters 5 and 6).

Weak but distinct absorption features in the spectral range from 2 to 2.5 μm were observed in the earliest telescopic data sets and subject to additional high-spectral resolution observations over time (e.g., McCord *et al*., 1978; Singer *et al*., 1979; Clark *et al*., 1990; Bell and Crisp, 1993; Bell *et al*., 1994). Initial interpretations focused on phyllosilicate minerals, which have known metal-OH overtone features in this wavelength range. Bicarbonate (HCO_3) and bisulfate (HSO_4) anions in framework silicates (i.e., scapolite) were proposed by Clark *et al*. (1990), though this was viewed skeptically at the time. High-spectral resolution observations and models clearly show contributions from carbon monoxide in the Martian atmosphere in this spectral range and some features appear to originate from telluric, Martian, or solar atmospheric absorption features (Bell *et al*., 1994). Both Clark *et al*. (1990) and Bell *et al*. (1994) showed that at least some of the narrow, weak features seen in Mars spectra in the 2.0- to 2.5-μm region were due to surface mineralogy, however. Calvin *et al*. (1994) modeled this spectral range in IRS data with hydrous carbonate minerals and Murchie *et al*. (2000) interpreted ISM absorptions in these wavelengths as resulting from metal-OH overtone vibrations in poorly crystalline clay minerals.

Spectroscopic observations by the Mariner 9 IRIS instrument detected spectral features near 9.0-μm in the atmospheric dust that were interpreted to be most consistent with montmorillonite (Hunt *et al*., 1973) or a basalt–montmorillonite mixture (Toon *et al*., 1977). More recent re-analyses of the IRIS measurements have shown that poorly crystalline weathering products like palagonite may in fact be more consistent with the data than smectite clay, however, based on improved knowledge of the optical constants of palagonites and on the scattering properties of atmospheric dust particles (e.g., Roush *et al*., 1993; Clancy *et al*., 1995). Modeling of Martian aerosols using Infrared Space Observatory data showed narrow features in the 2.7-μm region, suggesting a phyllosilicate composition of the dust (Fedorova *et al*., 2002), and optical properties of dust aerosols determined from the surface by the Imager for Mars Pathfinder also suggested platy (clay) grains (Markiewicz *et al*., 1999).

There have been many spectroscopic searches for sulfate and carbonate minerals on Mars in order to try to quantitatively substantiate numerous theoretical and indirect arguments for the occurrence of these phases. Most analyses during this era were inconclusive because of poor spatial resolution or calibration challenges related to difficult ground-based telescopic observations. The most convincing results, though still largely viewed as equivocal, are those of Blaney and McCord (1995) and Pollack *et al*. (1990). Blaney and McCord (1995) detected an absorption feature near 4.5-μm in telescopic spectra from Mauna Kea that was interpreted as an SO_4^{2-} overtone band in sulfates in the Martian surface and/or airborne dust. Careful atmospheric modeling revealed that this feature is probably not due to any known species in the Martian atmosphere; however, the specific mineralogy responsible could not be identified. Pollack *et al*. (1990) used the Kuiper Airborne Observatory to obtain high-quality spectra from 5.4 to 10.5 μm. These data showed evidence for spectral features due to carbonate (near 6.7 μm) and sulfate (near 8.7 and 9.8 μm) anionic complexes in the airborne dust. Again, however, specific mineralogies could not be identified. Lellouch *et al*. (2000) used the Infrared Space Observatory (ISO) to obtain globally averaged spectra at extremely high-spectral resolution. They identified several absorption features at 5.7, 6.3, 7.2, and 11.1 μm in addition to the silicate envelope from 8 to 12 μm. They interpreted the features at 7.2 and 11.1 μm as consistent with carbonates, but found no precise match among existing library spectra, and could not determine if the possible carbonate occurred either on the surface or in the airborne dust due to the disk-integrated nature of the observations.

2.4.2 Polar volatiles

Spectroscopic observations have established that both seasonal ice caps primarily consist of CO_2 ice (e.g., Herr and Pimentel, 1969; Larson and Fink, 1972) and that the north residual cap is primarily composed of water ice (e.g., Clark

and McCord, 1982). Summertime temperature measurements and atmospheric water vapor abundance mapping support these observations for the north residual cap (Farmer *et al*., 1976; Kieffer *et al*., 1976) and show that the upper surface of the southern residual cap is primarily CO_2 (Kieffer, 1979; Davis and Wanio, 1981). While small amounts of CO_2 may exist in the interior of the residual caps as ice mixed with water and dust, or in clathrate form (CO_2 molecules physically enclosed within the crystal structure of H_2O ice), thermal modeling and the rheology of CO_2 ice do not support substantial CO_2 in the interiors of either the northern or southern ice sheets (Mellon, 1996; Nye *et al*., 2000). Extensive summaries of the relevant historical work on the polar layered deposits and volatile caps have been published by Thomas *et al*. (1992), James *et al*. (1992), and Jakosky and Haberle (1992).

A large number of polar studies occurred in the decade before the arrival of MGS, and the discussion here focuses on compositional rather than geologic, morphologic, or stratigraphic analyses. Efforts to understand the volatile content and the physical properties of the seasonal and residual ice caps emphasized new laboratory studies, particularly of carbon dioxide ices, data mining of Viking and Mariner data sets for thermal modeling, seasonal variations, and compositional constraints, and new observations with HST and other telescopes.

Hansen (1997) determined the optical constants of solid CO_2 using clear crystals. Calvin and Martin (1994) analyzed Mariner 7 data of the seasonal cap, showing an enhancement of water ice at the receding cap edge, strong spatial heterogeneity in the retreating cap spectra, and models that suggested the late seasonal cap was "more like glacier ice with cracks and bubbles" rather than a fine snow pack or frost. Figure 2.4 shows the spectrum of this late seasonal cap observed by Mariner 7 compared with models of water and carbon dioxide frosts based on Hapke (1993) and using modern optical constants (Warren, 1984; Hansen, 1997). The temperature dependence of the spectrum of water ice is well known (e.g., Fink and Sill, 1982; Grundy and Schmitt, 1998) and particularly at colder temperatures the development of a narrow feature at 1.65 μm will be observed, in addition to changes in band shapes between amorphous and crystalline water ice.

Paige *et al*. (1994) and Paige and Keegan (1994) mapped the thermal inertia (a measure of a material's resistance to changes in temperature) and albedo of the north and south residual caps, respectively, using Viking Orbiter data. They noted that much of the north polar layered deposits appear underlain by solid ice or ice-cemented soils, in contrast to those in the south. They also noted that atmospheric conditions have a significant effect on derived albedo and thermal inertia, in particular atmospheric dust contributed to anomalously low-observed thermal emission from the southern residual cap in the Viking data. Paige *et al*. (1994) also noted frost cover variations between Mariner 9 and Viking that were further explored by Bass *et al*. (2000) and Bass and Paige (2000). Bass *et al*. (2000) modeled the northern residual cap composition and found that less dust is required for their model to match the observations if the water ice is coarse-grained, and more if it is fine-grained, consistent with earlier results from Kieffer (1990). The amount of dust within the residual water ice remained largely unconstrained, however, because good estimates of the ice grain size are not possible with optical data alone.

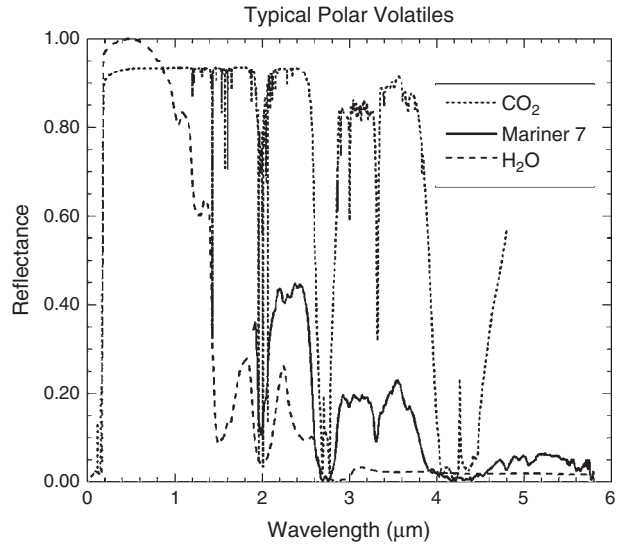

Figure 2.4. Polar volatiles. Calculated spectra for water (200 μm) and carbon dioxide (100 μm) frosts compared with a Mariner 7 spectrum of the receding seasonal cap. Strong features at 2.28 and 2.34 μm in the Mariner data are consistent with large pathlengths in ice and suppression of the level beyond 3 μm is attributed to minor amounts of water ice.

Finally, James *et al*. (1996) and Cantor *et al*. (1998) reported on the style and rate of seasonal ice cap recession as observed by HST, in the south and north, respectively. Cantor *et al*. (1998) were able to observe and model the increase in albedo and decrease in the red/violet color ratio as the north seasonal CO_2 ice cap sublimes and exposes the residual H_2O-ice layer.

2.5 SUMMARY: POISED FOR A NEW ERA

In the decade of Mars exploration prior to the start of global high-resolution geologic and mineral mapping by the MGS mission, telescopic, laboratory, and precursor spacecraft data coupled with novel modeling approaches improved our understanding of the compositional variability of the surface of Mars, the planet's ferric and mafic mineralogy, and the relationship between SNC meteorites and remotely sensed data. Pyroxene was known to be a major component of the low-albedo terrains from telescopic studies and Phobos-2 ISM measurements, and equivocal evidence for olivine had been found. Telescopic detection of iron oxide minerals and refined interpretations of color data from the Viking and Mars Pathfinder missions showed that crystalline iron oxides are not a major component of the soils. Rather, nanophase ferric oxides dominate the visible to near-IR spectral properties of the bright regions. While numerous models and observations suggested the possible

presence of phyllosilicates, carbonates, and sulfates, there was no consensus on the interpretation of weak spectral features and no "smoking gun" that uniquely identified specific alteration minerals. In retrospect, this appears to have been mostly a manifestation of the low-spatial resolution of the early spectroscopic searches, combined with what has turned out to be the very small-scale, spatially restricted occurrences of the most interesting mineral phases on Mars. The 3-μm water of hydration feature was found to be ubiquitous, but initial focused studies showed evidence for regional variations in hydration band strength that proved to be correlated with areas later identified as keys to the aqueous history of the planet.

Seasonal polar caps were shown to be ice "sheets" rather than frost or snow deposits, and seasonal and interannual variability were identified and characterized. Models demonstrated that the south perennial cap could not be solid CO_2 ice. Major open questions included the nature and occurrence of specific alteration minerals associated with polar volatiles and the amount of dust in the seasonal and residual ice caps.

This early work set the stage for new observations and interpretations from instruments onboard the Mars Global Surveyor, Mars Odyssey, and Mars Express orbiters. TES has now globally mapped the planet's mafic and primary silicate mineralogy at spatial scales of a few kilometers (e.g., Christensen *et al.*, 2000; Bandfield, 2002; see Chapter 9). New observations are also beginning to constrain polar deposits and alteration minerals. The residual and seasonal ice caps have shown to be host to numerous enigmatic properties and processes (Thomas *et al.*, 2000, 2005), and water ice has been observed in the south polar residual cap (Bibring *et al.*, 2004; Titus, 2005). As described in later chapters, Mars Express OMEGA spectrometer observations are found to be consistent with the presence of phyllosilicates and sulfates (Gendrin *et al.*, 2005; Langevin *et al.*, 2005; Poulet *et al.*, 2005; see Chapter 7). While no large-scale carbonate deposits have yet been identified on the surface at the scale of the available orbital (or surface lander, rover) measurements, recent models of TES data suggest a small carbonate component in the atmospheric dust (Bandfield *et al.*, 2003). Other terrestrial analog studies and focused regional studies with TES data have been interpreted as indicating evidence for hydrated sulfates, small amounts of carbonates, and possibly clays (e.g., Bishop *et al.*, 2004; Noe Dobrea *et al.*, 2006).

Evidence for specific sulfates widely distributed on Mars is convincing, thanks to *in situ* "ground truth" surface data sets from the Mars rovers *Spirit* and *Opportunity* (see Chapters 4, 13, 14, and 15 for details). Evidence for phyllosilicate minerals appears to be emerging from both surface and orbital observations (see Chapters 4, 7, and 23 for details). However, definitive identification of specific carbonate species from multiple wavelengths and instruments, and community consensus surrounding any carbonate identification, remains elusive. With evidence mounting that Mars once had warmer and wetter epochs, and presumably a thicker CO_2-rich atmosphere, the question "Where are the carbonates?" remains as vexing today as it was when it was first posed by the Mars community more than 25 years ago (e.g., Pollack *et al.*, 1987; Fanale *et al.*, 1982, 1992; Burns, 1993).

The decade since the arrival of Mars Pathfinder and Mars Global Surveyor has been one of tremendous growth in our knowledge of the composition and history of the Martian surface. While previous advances had been made in our understanding of the surface mineralogy and composition and their spatial distribution, the onslaught of new instruments and techniques are now allowing us to view Mars in a wholly new light.

ACKNOWLEDGMENTS

We thank John Pearl for providing the Mariner 9 IRIS spectrum in Figure 2.2, and Jack Mustard for providing the Phobos-2 ISM spectra in Figure 2.3. This work was supported by NASA's Planetary Geology and Geophysics Program and Mars Data Analysis Program in separate grants to both JFB and WMC.

REFERENCES

Baldridge, A. M., and W. M. Calvin, Hydration state of the Martian coarse-grained hematite exposures: implications for the origin and evolution, *J. Geophys. Res., E, Planets* **109.4,** 2004.

Bandfield, J. L., Global mineral distributions on Mars, *J. Geophys. Res.* **107**, 9–1, CiteID 5042, doi:10.1029/2001JE001510, 2002.

Bandfield, J. L., T. D. Glotch, and P. R. Christensen, Spectroscopic identification of carbonate minerals in the Martian dust, *Science* **301**, 1084–7, 2003.

Banin, A., B. C. Clark, and H. Wänke, Surface chemistry and mineralogy. In *Mars* (ed. H. H. Kieffer *et al.*), Tucson: University of Arizona Press, pp. 594–625, 1992.

Bass, D. S. and D. A. Paige, Variability of Mars' north polar water ice cap – II. Analysis of Viking IRTM and MAWD data, *Icarus* **144**, 397–409, 2000.

Bass, D. S., K. E. Herkenhoff, and D. A. Paige, Variability of Mars' north polar water ice cap – I. Analysis of Mariner 9 and Viking Orbiter imaging data, *Icarus* **144**, 382–96, 2000.

Bell III, J. F., Iron, sulfate, carbonate, and hydrated minerals on Mars. In *Mineral Spectroscopy: A Tribute to Roger G. Burns*. (ed. M. D. Dyer, C. McCammon, and M. W. Schaefer), Geochem. Soc. Spec. Pub. No. **5**, Houston, 359–80, 1996.

Bell III, J. F. and D. Crisp, Groundbased imaging spectroscopy of Mars in the near-infrared – Preliminary-results, *Icarus* **104**, 2–19, 1993.

Bell III, J. F., T. B. McCord, and P. D. Owensby, Observational evidence of crystalline iron-oxides on Mars, *J. Geophys. Res.* **95**, 14447–61, 1990.

Bell III, J. F., J. B. Pollack, T. R. Geballe, D. P. Cruikshank, and R. Freedman, Spectroscopy of Mars from 2.04 to 2.44 μm during the 1993 opposition: absolute calibration and atmospheric vs. mineralogic origin of narrow absorption features, *Icarus* **111**, 106–23, 1994.

Bell III, J. F., T. L. Roush, and R. V. Morris, Mid-infrared transmission spectra of crystalline and nanophase iron

oxides/oxyhydroxides and implications for remote sensing of Mars, *J. Geophys. Res.* **100**(E3), 5297–307, 1995.

Bell III, J. F., M. J. Wolff, P. B. James, *et al.*, Mars surface mineralogy from Hubble Space Telescope imaging during 1994–1995: observations, calibration, and initial results, *J. Geophys. Res.* **102**, 9109–23, 1997.

Bibring, J.-P., M. Combes, Y. Langevin, *et al.*, ISM observations of Mars and Phobos: first results, *Proc. Lunar Planet. Sci. Conf. 20th*, 461–71, 1990.

Bibring, J.-P., Y. Langevin, F. Poulet, *et al.*, Perennial water ice identified in the south polar cap of Mars, *Nature* **428**, 627–30, 2004.

Bibring, J.-P., Y. Langevin, A. Gendrin, *et al.*, Mars surface diversity as revealed by the OMEGA/Mars express observations, *Science* **307**, 1576–81, 2005.

Bishop, J. L. and E. Murad, Schwertmannite on Mars? Spectroscopic analyses of schwertmannite, its relationship to other ferric minerals, and its possible presence in the surface materials on Mars. In *Mineral Spectroscopy: A Tribute to Roger G. Burns* (ed. M. D. Dyer, C. McCammon, and M. W. Schaefer), Geochem. Soc. Spec. Pub. No. 5, Houston, 337–58, 1996.

Bishop, J. L., C. M. Pieters, and R. G. Burns, Reflectance and Mössbauer spectroscopy of ferrihydrite-montmorillonite assemblages as Mars soil analog materials, *Geochim. Cosmochim. Acta* **57**, 4583–95, 1993.

Bishop, J. L., C. M. Pieters, T. Hiroi, and J. F. Mustard, Spectroscopic analysis of martian meteorite Allan Hills 84001 powder and applications for spectral identification of minerals and other soil components on Mars, *Meteorit. Planet. Sci.* **33**(4), 699–707, 1998.

Bishop, J. L., M. D. Dyar, M. D. Lane, and J. F. Banfield, Spectral identification of hydrated sulfates on Mars and comparison with acidic environments on Earth, *Int. J. Astrobiol.* **3**(4), 275–85, 2004.

Blaney, D. L. and T. B. McCord, Indications of sulfate minerals in the Martian soil from earthbased spectroscopy, *J. Geophys. Res.-Planets* **100**, 14433–41, 1995.

Burns, R. G., Ferric sulfates on Mars, *J. Geophys. Res.* **92**(B4), E570–4, 1987.

Burns, R. G., Rates and mechanisms of chemical weathering of ferromagnesian silicate minerals on Mars, *Geochim. Cosmochim. Acta* **57**, 4555–74, 1993.

Calvin, W. M., Variation of the 3-μm absorption feature on Mars: observations over eastern Valles Marineris by the Mariner 6 infrared spectrometer, *J. Geophys. Res. – Planets* **102**, 9097–107, 1997.

Calvin, W. M., Could Mars be dark and altered? *Geophys. Res. Lett.* **25**, 1597–600, 1998.

Calvin, W. M. and T. Z. Martin, Spatial variability in the seasonal south polar-cap of Mars, *J. Geophys. Res. – Planets* **99**, 21143–52, 1994.

Calvin, W. M., T. V. V. King, and R. N. Clark, Hydrous carbonates on Mars: evidence from Mariner 6/7 infrared spectrometer and ground-based telescopic spectra, *J. Geophys. Res. – Planets* **99**, 14659–75, 1994.

Cantor, B. A., M. J. Wolff, P. James, and E. Higgs, Regression of Martian north polar cap: 1990–1997 Hubble Space Telescope observations, *Icarus* **136**, 175–91, 1998.

Christensen, P. R., Variations in Martian surface composition and cloud occurrence determined from thermal infrared spectroscopy: analysis of Viking and Mariner 9 data, *J. Geophys. Res. – Planets* **103**, 1733–46, 1998.

Christensen, P. R., J. L. Bandfield, M. D. Smith, V. E. Hamilton, and R. N. Clark, Identification of a basaltic component on the Martian surface from thermal emission spectrometer data, *J. Geophys. Res.* **105**, 9609–22, 2000.

Christensen, P. R., R. V. Morris, M. D. Lane, J. L. Bandfield, and M. C. Malin, Global mapping of Martian hematite mineral deposits: remnants of water-driven processes on early Mars, *J. Geophys. Res. – Planets* **106**, 23873–85, 2001.

Cimino, G. and W. M. Calvin, The Mariner 7 infrared spectra: calibration and a preview for TES (abstract), *28th LPSC*, 231–2, 1997.

Clancy, R. T., S. W. Lee, G. R. Gladstone, W. W. McMillan, and T. Roush, A new model for Mars atmospheric dust based upon analysis of ultraviolet through infrared observations from Mariner-9, Viking, and Phobos, *J. Geophys. Res. – Planets* **100**, 5251–63, 1995.

Clark, R. N. and T. B. McCord, Mars residual north polar cap: Earth-based spectroscopic confirmation of water ice as a major constituent and evidence for hydrated minerals, *J. Geophys. Res.* **87**, 367–70, 1982.

Clark, R. N., G. A. Swayze, R. B. Singer, and J. B. Pollack, High-resolution reflectance spectra of Mars in the 2.3-μm region: evidence for the mineral scapolite, *J. Geophys. Res.* **95**, 14463–80, 1990.

Crisp, D., Infrared radiative-transfer in the dust-free martian atmosphere, *J. Geophys. Res.* **95**, 14577–88, 1990.

Davis, D. W. and L. A. Wanio, Measurements of water vapor in Mars' Antarctic, *Icarus* **45**, 216–30, 1981.

Erard, S. and W. Calvin, New composite spectra of Mars, 0.4–5.7 μm, *Icarus* **130**, 449–60, 1997.

Erard, S., J. Mustard, S. Murchie, *et al.*, Martian aerosols: near-infrared spectral properties and effects on the observation of the surface, *Icarus* **111**, 317–37, 1994.

Fanale, F. P., J. R. Salvail, W. B. Banerdt, and R. S. Saunders, Mars: the regolith-atmosphere-cap system and climate change, *Icarus* **50**, 381, 1982.

Fanale, F. P., S. E. Postawko, J. B. Pollack, M. H. Carr, and R. O. Pepin, Mars: epochal climate change and volatile history. In *Mars* (ed. H. H. Kieffer, B. M. Jakosky, C. W. Snyder, and M. S. Matthews), Tucson: University of Arizona Press, pp. 1135–79, 1992.

Farmer, C. B., D. W. Davies, and D. D. Laporte, Mars: northern summer ice cap – water-vapor observations from Viking 2, *Science* **194**, 1339–41, 1976.

Fedorova, A. A., E. Lellouch, D. V. Titov, T. de Graauw, and H. Feuchtgruber, Remote sounding of the Martian dust from ISO spectroscopy in the 2.7 μm CO_2 bands, *Planet. Space Sci.* **50**, 3–9, 2002.

Fialips, C. I., J. W. Carey, D. T. Vaniman, *et al.*, Hydration state of zeolites, clays, and hydrated salts under present-day Martian surface conditions: can hydrous minerals account for Mars Odyssey observations of near-equatorial water-equivalent hydrogen?, *Icarus* **178**, 74–83, 2005.

Fink, U. and G. T. Sill, The infrared spectral properties of frozen volatiles. In *Comets* (ed. L. L. Wilkening), Tucson: University of Arizona Press, pp. 164–202, 1982.

Gendrin, A., N. Mangold, J.-P. Bibring, *et al.*, Sulfates in Martian layered terrains: the OMEGA/Mars Express view, *Science* **307**, 1587–91, 2005.

Gooding, J. L., R. E. Arvidson, and M. Y. Zolotov, Physical and chemical weathering. In *Mars* (ed. H. H. Kieffer, B. M. Jakosky, C. W. Snyder, and M. S. Matthews), Tucson: University of Arizona Press, pp. 626–51, 1992.

Geissler, P. E., R. B. Singer, G. Komatsu, S. Murchie, and J. Mustard, An unusual spectral unit in West Candor Chasma: evidence for aqueous or hydrothermal alteration in the Martian canyons, *Icarus* **106**, 380–91, 1993.

Grundy, W. M. and B. Schmitt, The temperature-dependent near-infrared absorption spectrum of hexagonal H_2O ice, *J. Geophys. Res.* **103**(E11), 25809–22, 1998.

Hamilton, V. E. and P. R. Christensen, Evidence for extensive, olivine-rich bedrock on Mars, *Geology* **33**, 433–6, 2005.

Hamilton, V. E., P. R. Christensen, and H. Y. McSween, Determination of Martian meteorite lithologies and mineralogies using vibrational spectroscopy, *J. Geophys. Res. – Planets* **102**, 25593–603, 1997.

Hanel, R. A., B. J. Conrath, D. E. Jennings, and R. E. Samuelson, The measured radiation field, Chapter 6, *Exploration of the Solar System by Infrared Remote Sensing*. Cambridge: Cambridge University Press, 1992.

Hansen, G. B., The infrared absorption spectrum of carbon dioxide ice from 1.8 to 333 μm, *J. Geophys. Res. – Planets* **102**, 21569–87, 1997.

Hapke, B., *Theory of Reflectance and Emittance Spectroscopy*, New York, NY: Cambridge University Press, 455pp., 1993.

Herr, K. C. and G. C. Pimentel, Infrared absorptions near 3 microns recorded over the polar cap of Mars, *Science* **166**, 496–9, 1969.

Hinrichs, J. L. and P. G. Lucey, Temperature-dependent near-infrared spectral properties of minerals, meteorites, and lunar soil, *Icarus* **155**, 169–80, 2002.

Hoefen, Todd M., R. N. Clark, J. L. Bandfield, *et al*., Discovery of olivine in the Nili Fossae region of Mars, *Science* **302**(5645), 627–30, 2003.

Houck, J. R., J. B. Pollack, C. Sagan, D. Schaack, and J. Decker, High altitude infrared spectroscopic evidence for bound water on Mars, *Icarus* **18**, 470–80, 1973.

Huguenin, R. L., The silicate component of martian dust, *Icarus* **70**, 162–8, 1987.

Hunt, G. R., L. M. Logan, and J. W. Salisbury, Mars: components of infrared spectra and composition of the dust cloud, *Icarus* **18**, 459–69, 1973.

Jakosky, B. M. and R. M. Haberle, The seasonal behavior of water on Mars. In *Mars* (ed. H. H. Kieffer, *et al*.), Tucson: University of Arizona Press, pp. 969–1016, 1992.

James, P. B., H. H. Kieffer, and D. A. Paige, The seasonal cycle of carbon dioxide on Mars. In *Mars* (ed. H. H. Kieffer *et al*.), Tucson: University of Arizona Press, pp. 934–68, 1992.

James, P. B., R. T. Clancy, S. W. Lee, and L. J. Martin, Seasonal recession of Martian south polar cap: 1992 HST observations, *Icarus* **123**, 87–100, 1996.

Kieffer, H. H., Mars south polar spring and summer temperatures: residual CO_2 frost, *J. Geophys. Res.* **84**, 8263–88, 1979.

Kieffer, H. H., H_2O grain-size and the amount of dust in Mars residual north polar-cap, *J. Geophys. Res. – Solid Earth and Planets* **95**, 1481–93, 1990.

Kieffer, H. H., S. C. Chase, T. Z. Martin, E. D. Miner, and F. D. Palluconi, Martian north pole summer temperatures: dirty water ice, *Science* **194**, 1341–4, 1976.

Kirkland, L. E. and K. C. Herr, Spectral anomalies in the 11 and 12 μm region from the Mariner Mars 7 infrared spectrometer, *J. Geophys. Res.* **105**(9), 22507–15, 2000.

Langevin, Y., F. Poulet, J.-P. Bibring, and B. Gondet, Sulfates in the north polar region of Mars detected by OMEGA/Mars Express, *Science* **307**, 1584–6, 2005.

Larson, H. P. and U. Fink, Identification of carbon dioxide on the Martian polar caps, *Astrophys. J.* **171**, L91–5, 1972.

Lellouch, E., T. Encrenaz, T. de Graauw, *et al*., The 2.4–45 μm spectrum of Mars observed with the infrared space observatory, *Planet. Space Sci.* **48**, 1393–405, 2000.

Maguire, W. C., Martian isotopic ratios and upper limits for possible minor constituents as derived from Mariner 9 infrared spectrometer data, *Icarus* **32**, 85–97, 1977.

Markiewicz, W. J., R. M. Sablotny, H. U. Keller, *et al*., Optical properties of the Martian aerosols as derived from Imager for Mars Pathfinder midday sky brightness data, *J. Geophys. Res. – Planets* **104**, 9009–17, 1999.

McCord, T. B., R. N. Clark, and R. L. Huguenin, Mars: near-infrared spectral reflectance and compositional implications, *J. Geophys. Res.* **83**(B11), 5433–41, 1978.

McCord, T. B., R. N. Clark, and R. B. Singer, Mars: near-infrared spectral reflectance of surface regions and compositional implications, *J. Geophys. Res.* **87**(B4), 3021–32, 1982.

McFadden, L. A. and T. P. Cline, Spectral reflectance of Martian meteorites: spectral signatures as a template for locating source region on Mars, *Meteorit. Planet. Sci.* **40**, 151–72, 2005.

McKay, C. P. and S. S. Nedell, Are there carbonate deposits in the Valles Marineris, Mars?, *Icarus* **73**, 142–8, 1988.

Mellon, M. T., Limits on the CO_2 content of the Martian polar deposits, *Icarus* **124**, 268–79, 1996.

Milliken, R. E. and J. F. Mustard, Quantifying absolute water content of minerals using near-infrared reflectance spectroscopy, *J. Geophys. Res. – Planets* **110**, 2005.

Morris, R. V., D. G. Agresti, H. V. Lauer Jr., *et al*., Evidence for pigmentary hematite on Mars based on optical, magnetic, and Mössbauer studies of superparamagnetic (nanocrystalline) hematite, *J. Geophys. Res.* **94**, 2760–78, 1989.

Morris, R. V., J. L. Gooding, H. V. Lauer Jr., and R. B. Singer, Origins of Marslike spectral and magnetic properties of a Hawaiian palagonitic soil, *J. Geophys. Res.* **95**, 14427–34, 1990.

Morris, R. V., D. C. Golden, J. F. Bell III, H. V. Lauer Jr., and J. B. Adams, Pigmenting agents in Martian soils: inferences from spectral, Mossbauer, and magnetic properties of nanophase and other iron oxides in Hawaiian palagonitic soil PN-9, *Geochim. Cosmochim. Acta* **57**, 4597–609, 1993.

Morris, R. V., D. W. Ming, D. C. Golden, and J. F. Bell III, An occurrence of jarositic tephra on Mauna Kea, Hawaii: implications for the ferric mineralogy of the Martian surface. In *Mineral Spectroscopy: A Tribute to Roger G. Burns* (ed. M. D. Dyer, C. McCammon, and M. W. Schaefer), Geochem. Soc. Spec. Pub. No. 5, Houston, 327–36, 1996.

Morris, R. V., G. Klingelhöfer, B. Bernhardt, *et al*., Mineralogy at Gusev crater from the Mössbauer spectrometer on the spirit rover, *Science* **305**, 833–6, 2004.

Murchie, S., L. Kirkland, S. Erard, J. Mustard, and M. Robinson, Near-infrared spectral variations of Martian surface materials from ISM imaging spectrometer data, *Icarus* **147**, 444–71, 2000.

Murchie, S., J. Mustard, J. Bishop, *et al*., Spatial variations in the spectral properties of bright regions on Mars, *Icarus* **105**, 454–68, 1993.

Mustard, J. F. and J. F. Bell III, New composite reflectance spectra of Mars from 0.4 to 3.14 μm, *Geophys. Res. Lett.* **21**, 353–6, 1994.

Mustard, J. F. and J. M. Sunshine, Seeing through the dust: Martian crustal heterogeneity and links to the SNC meteorites, *Science* **267**(5204), 1623–6, 1995.

Mustard, J. F., S. Murchie, S. Erard, and J. M. Sunshine, In situ compositions of Martian volcanics: implications for the mantle, *J. Geophys. Res.* **102**, 25605–15, 1997.

Noe Dobrea, E. Z., J. F. Bell III, T. H. McConnochie, and M. Malin, Analysis of a spectrally unique deposit in the dissected Noachian terrain of Mars, *J. Geophys. Res.* **111**, E6, 2006.

Nye, J. F., W. B. Durham, P. M. Schenk, and J. M. Moore, The instability of a south polar cap on Mars composed of carbon dioxide, *Icarus* **144**, 449–55, 2000.

Paige, D. A., and K. D. Keegan, Thermal and albedo mapping of the polar-regions of Mars using Viking thermal mapper observations: 2. South polar-region, *J. Geophys. Res. – Planets* **99**, 25993–26013, 1994.

Paige, D. A., J. E. Bachman, and K. D. Keegan, Thermal and albedo mapping of the polar-regions of Mars using Viking thermal mapper observations: 1. North polar-region, *J. Geophys. Res. – Planets* **99**, 25959–91, 1994.

Pimentel, G. C., P. B. Forney, and K. C. Herr, Evidence about hydrate and solid water in the Martian surface from the 1969 Mariner infrared spectrometer, *J. Geophys. Res.* **79**, 1623–34, 1974.

Pollack, J. B., J. F. Kasting, S. M. Richardson, and K. Poliakoff, The case for a wet, warm climate on Mars, *Icarus* **71**, 203–24, 1987.

Pollack, J. B., T. Roush, F. Witteborn, *et al.*, Thermal emission-spectra of Mars (5.4–10.5-μm): evidence for sulfates, carbonates, and hydrates, *J. Geophys. Res. – Solid Earth and Planets* **95**, 14595–627, 1990.

Poulet, F., J. P. Bibring, J. F. Mustard, *et al.*, Phyllosilicates on Mars and implications for early martian climate, *Nature* **438**, 623–7, 2005.

Roush, T. L. and J. F. Bell III, Thermal emission measurements 2000–400 cm^{-1} (5–25 μm) of Hawaiian palagonitic soils and their implications for Mars, *J. Geophys. Res.* **100**(E3), 5309–17, 1995.

Roush, T. L., D. L. Blaney, and R. B. Singer, The surface composition of Mars as inferred from spectroscopic observations. In *Remote Geochemical Analysis: Elemental and Mineralogical Composition* (ed. C. Pieters and P. Englert), Cambridge University Press, pp. 367–93, 1993.

Schade, U. and R. Wäsch, Near-infrared reflectance spectra from bulk samples of the two Martian meteorites Zagami and Nakhla, *Meteorit. Planet. Sci.* **34**, 417–24, 1999.

Singer, R. B., Spectral evidence for the mineralogy of high-albedo soils and dust on Mars, *J. Geophys. Res.* **87**(B12), 10159–68, 1982.

Singer, R. B., T. B. McCord, R. N. Clark, J. B. Adams, and R. L. Huguenin, Mars surface composition from reflectance spectroscopy: a summary, *J. Geophys. Res.* **84**, 8415–26, 1979.

Sinton, W. M., On the composition of Martian surface materials, *Icarus* **6**, 222–8, 1967.

Soderblom, L. A., The composition and mineralogy of the Martian surface from spectroscopic observations: 0.3 μm to 50 μm. In *Mars* (ed. H. H. Kieffer, B. M. Jakosky, C. W. Snyder, and M. S. Matthews), Tucson: University of Arizona Press, pp. 557–97, 1992.

Squyres, S. W., R. E. Arvidson, J. F. Bell III, *et al.*, The opportunity rover's Athena science investigation at Meridiani Planum, Mars, *Science* **306**, 1698–703, 2004.

Sunshine, J. M., L. A. McFadden, and C. M. Pieters, Reflectance spectra of the Elephant Moraine-A79001 meteorite: implications for remote-sensing of planetary bodies, *Icarus* **105**, 79–91, 1993.

Thomas, P., S. Squyres, K. Herkenhoff, A. Howard, and B. Murray, Polar deposits of Mars. In *Mars* (ed. H. H. Kieffer *et al.*), Tucson: University of Arizona Press, pp. 767–95, 1992.

Thomas, P. C., M. C. Malin, K. S. Edgett, *et al.*, North-south geological differences between the residual polar caps on Mars, *Nature* **404**, 161–4, 2000.

Thomas, P. C., M. C. Malin, P. B. James, *et al.*, South polar residual cap of Mars: features, stratigraphy, and changes, *Icarus* **174**, 535–59, 2005.

Titus, T. N., Thermal infrared and visual observations of a water ice lag in the Mars southern summer, *Geophys. Res. Lett.* **32**, 2005.

Toon, O. B., J. B. Pollack, and C. Sagan, Physical properties of the particles composing the martian dust storm of 1971–1972, *Icarus* **30**, 663–96, 1977.

Warren, S. G., Optical constants of ice from the ultraviolet to the microwave, *Appl. Opt.* **23**, 1206–25, 1984.

PART II

ELEMENTAL COMPOSITION: ORBITAL AND *IN SITU* SURFACE MEASUREMENTS

PART II.A

Results and Interpretations from New *in situ* APXS Measurements

3

Martian surface chemistry: APXS results from the Pathfinder landing site

C. N. FOLEY, T. E. ECONOMOU, R. N. CLAYTON, J. BRÜCKNER, G. DREIBUS, R. RIEDER, AND H. WÄNKE

ABSTRACT

The Mars Pathfinder Alpha Proton X-ray Spectrometer (APXS) was utilized to determine the major and minor elemental abundances of rocks and soils at the 1997 landing site in Ares Vallis. The determined abundances suggest that: (1) the rocks are covered with various amounts of soil; (2) the Soil-Free Rock (SFR) chemistry is similar to that of an evolved SNC-like (SNC – Shergottite, Nakhlite, and Chassignite) igneous tholeiitic basalt-andesite to andesite that is minimally altered (possibly similar to Type 2 TES material); (3) the carbon content is below detection limits for all samples, implying <5% as $MgCO_3$ (Brückner *et al.*, 1999); (4) the α-mode oxygen abundance indicates that mineral-bound water, above the value for igneous rocks, is present in some rocks and is therefore indicative of some nonigneous alteration and therefore possibly rock-rinds that obscure the petrology of the SFR; and (5) the Pathfinder soils are similar to the Viking fines and may be composed of mafic igneous material like the SNC meteorites and of volatiles deposited from volcanic emissions, as previously suggested by Clark (1993) for the Viking soils.

3.1 INTRODUCTION

The Mars Pathfinder mission to Ares Vallis in July 1997, the first lander mission since those of the Viking missions, was the first equipped with a robotic rover to extend the chemical analyses of the Martian surface beyond that immediately proximal to the lander. While the Viking missions were the first to analyze the chemistry of soils on the Martian surface, the Pathfinder mission was the first to make *in situ* measurements of both the rocks and the soils (and in particular, to make measurements of the soils without presorting or sifting them).

The Pathfinder lander was equipped with an atmospheric structure instrument (ASI), a multispectral imager (IMP), a rover camera, and the APXS. The main scientific objective of the mission was to unveil the geochemistry of the Pathfinder landing site. In particular, the goals were to understand the role that volatiles (such as water, carbon dioxide, and sulfur) may have had, to understand the major element chemistry of the rocks, and to put these measurements into a greater context through comparison with other Martian remote-sensing measurements as well as with the Martian meteorites (SNCs; see Chapter 17). Because the Pathfinder APXS was capable of measuring concentrations of all major and minor rock-forming elements ranging from carbon through nickel in atomic number, it was utilized to determine the geochemistry and infer the petrology of the rocks and soils at the landing site, as described in detail in Section 3.4.

3.1.1 Landing site description

The Pathfinder landing site (Figure 3.1a and b) is possibly a floodplain created from waters catastrophically emanating from southern Ares and Tiu channels (Golombek *et al.*, 1997a). Geomorphic features such as streamlined islands, undulating ground, and strewn angular boulders at the site support this floodplain hypothesis (Golombek *et al.*, 1997a). Ejecta from nearby impacts may also be present at the landing site (Golombek *et al.*, 1997a).

Ares and Tiu Valles are two of the many channels emanating from chaos regions south of the channels in the Xanthe Terra region of Mars. Chaos regions are interpreted to be potential watersheds from which groundwater was catastrophically released during the Hesperian period, between 3.1 and 1.8 Ga ago (Nelson and Greeley, 1999). Another potential watershed for flooding through the Ares and Tiu channels includes the eastern portion of Valles Marineris (Nelson and Greeley, 1999). The initiation of these flooding and channel formation events may be linked to the uplift and volcanic development of the Tharsis region in the late Noachian (~3.5 Ga), possibly concurrent with the formation of the giant rift, Valles Marineris, along with other ridged plains in the Chryse Planitia (Nelson and Greeley, 1999 and references therein). Furthermore, continued volcanism in the Tharsis region and the proximal eruption of the Lunae Planum flood basalts to Xanthe Terra may also have provided geothermal heat to release frozen groundwater during the Hesperian (Baker *et al.*, 1991). The Xanthe Terra region, through which Ares and Tiu Valles cut, is inferred to be Noachian, as old as ~4.5 Ga based on crater densities, cut by channel materials that are Hesperian, as young as ~1.8 Ga (Tanaka *et al.*, 1992). The Mars Pathfinder landing site is located approximately 800 km from the channel mouths of Ares and Tiu, within the mid fan of the channels (Nelson and Greeley, 1999 and references therein). Using terrestrial liquid water flood analogs, sand-sized particles from the channel walls are expected to have been delivered to and past the Pathfinder landing site. Larger clasts may have been delivered to the Pathfinder landing site as ice-rafted debris (Nelson and Greeley, 1999

The Martian Surface: Composition, Mineralogy, and Physical Properties, ed. J. F. Bell III. Published by Cambridge University Press.

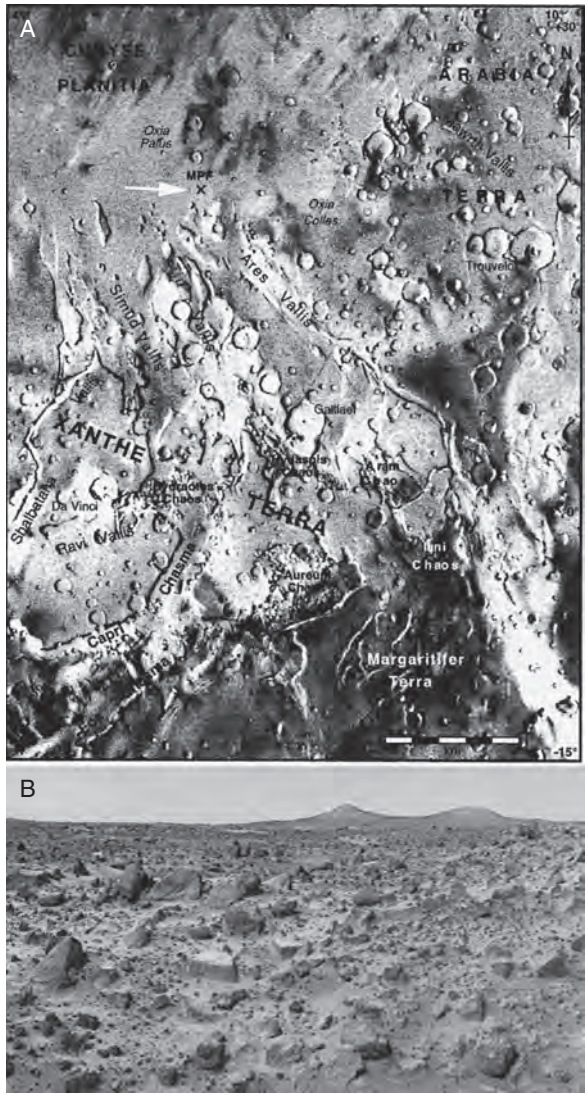

Figure 3.1. (a) The Mars Pathfinder landing site (MPF) located mid-fan from the mouths of Ares and Tiu Valles. As shown, both channels emanate from chaos regions located south of the mouths of the channels within Xanthe Terra. Figure is from Nelson and Greeley (1999). (b) Pathfinder image of the landing site.

and references therein) or by debris flows consisting of a mixture of water, ice, gas, and rock debris moving downslope (Tanaka, 1999). Thus, the surface sediments and boulders at the Mars Pathfinder landing site may therefore be Noachian- to Hesperian-aged highland plain material with reworked sediments from repeated flooding and impacting occurring over billions of years.

The scientific rationale for choosing this landing site was that, as floodplain material, it may contain a variety of rock types from the surrounding region and possibly even from the ancient southern highlands (Golombek *et al.*, 1997b). The anticipated diverse group of rocks in Ares Vallis was optimal because it had the potential to provide a plethora of information from one landing site. Igneous rocks found could reveal the type of volcanic and/or plutonic processes occurring locally and possibly more globally. Sedimentary rocks found could reveal the magnitude of weathering involving liquid water on the surface of Mars. Metamorphic rocks, if found, would indicate a significant rock cycle occurring on Mars involving burial and exhumation of earlier igneous or sedimentary rocks.

3.1.2 Instrument description

The Pathfinder APXS design is a result of many years of development of α-scattering instruments designed for remote-sensing missions. The first such α-scattering instrument was developed at the University of Chicago by Turkevich (1961). That instrument was used to analyze lunar samples *in situ* on the Surveyor V, VI, and VII missions (Turkevich *et al.*, 1969; Franzgrote *et al.*, 1970; Patterson *et al.*, 1970). A modified α-scattering instrument, the Mini-Alpha, was designed and tested for potential Mars missions by Economou *et al.* (1973) and is further described by Economou and Turkevich (1976). This Mini-Alpha design was further modified for a potential mission to Phobos by Dieter Hovestadt at the Max-Planck-Institut für Extraterrestriche Physik in Garching, Germany (Hovestadt *et al.*, 1990). The Pathfinder APXS is a derivative of the Mini-Alpha and Phobos APXS, but was jointly redesigned to be less massive and to consume less power by Rudolf Rieder at the Max-Planck-Institut für Chemie in Mainz, Thanasis Economou at the University of Chicago, Lev Mukhin at the Space Research Institute in Moscow, and Slava Ryadchenko at the All Union Research Institute for Atomic Reactors in Dimitrovgrad. The Pathfinder APXS was originally designed and flown on the Russian Mars 1996 mission, which failed to reach Mars. The instrument is also described in further detail by Rieder *et al.* (1997a).

The instrument sensor head, which is cylindrical having dimensions of 52 mm in diameter and 70 mm in height, contains a ring of nine radioactive ^{244}Cm alpha sources surrounding a ring of six collimators for the alpha sources, a central collimator for the alpha and proton detectors, and an X-ray detector as shown in Figure 3.2a and b. The α and proton detectors are situated in a telescoping fashion at the end of these collimators because the α particles stop in the first detector while the protons, having higher energy, pass through the α detector and are stopped and detected in the proton detector behind it. The X-ray detector, a Si-PIN, is located to the side of the sensor head.

The instrument relies on the α decay of ^{244}Cm, located within the instrument sensor head, to generate sample signals. The decay of ^{244}Cm, which has a half-life of 18.1 years (Parrington *et al.*, 1996), releases α particles and ^{244}Pu X-rays. These α particles and X-rays produce α, proton, and characteristic X-ray signals from samples due to elastic α scattering, (α, p) reactions, and α-Particle Induced X-ray Emission (α-PIXE) and X-ray fluorescence (XRF), respectively. With the calibration and Martian data analyses, the α-mode was capable of independently measuring C, O, Si, Ca, and Fe abundances in Pathfinder samples. The proton-mode enabled measurement of Na, Mg, Al, Si, S, and N. The X-ray mode enabled measurement of abundances of elements which have X-ray signals ranging from 1 to

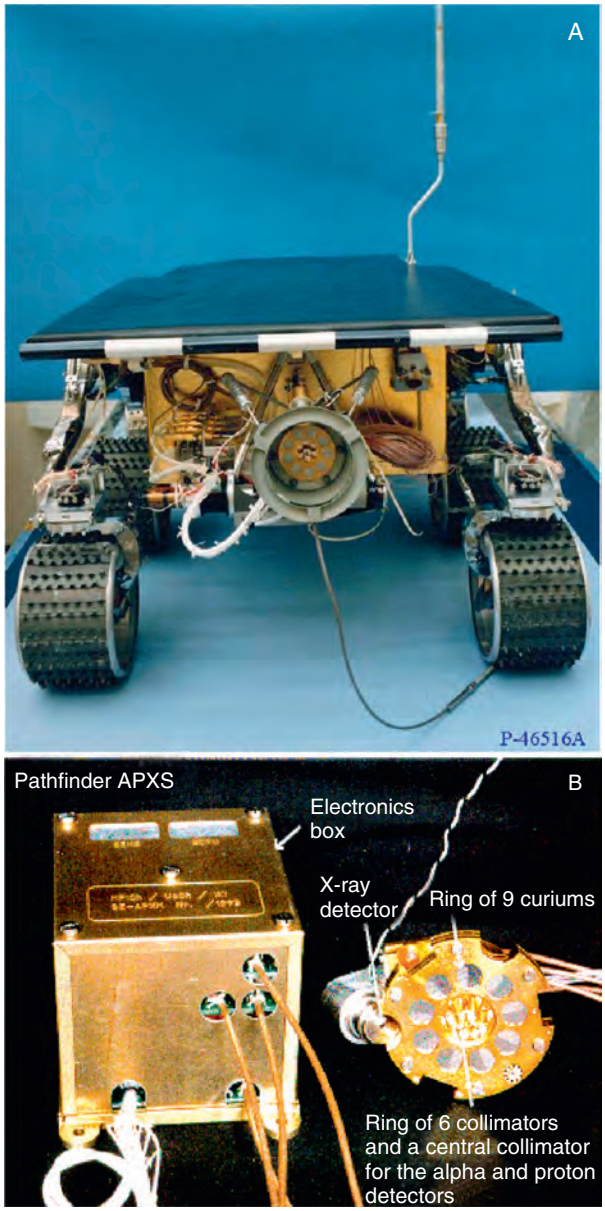

Figure 3.2. (a) The APXS on the Sojourner rover. (b) The APXS Pathfinder instrument. The sensor head consists of a ring of nine curium sources surrounding a central detector which has seven collimators for the telescoping α and proton central detectors, as shown on the right. The cylinder, which is 42 mm long and is attached to the sensor head to position the APXS against analyzed samples, is not shown here. The diameter of the circular gold-coated sensor head is 52 mm. The X-ray detector is located on the side of the instrument head. The electronics box for the APXS is also shown on the left in this figure. (For a color version of this figure, please refer to the color plate section or to the e-Book version of this chapter.)

15 KeV. Thus all major and minor rock-forming elements ranging from Na through Ni in atomic number were measured in the Pathfinder samples. The three systems can be used independently but it is the combination of all three modes, providing in some cases complementary and in other cases redundant information, that results in an accurate and complete chemical analysis.

The physics of elastic scattering from target atoms was described in detail by Rutherford *et al.* (1930), who first used α-scattering experimental data from Geiger and Marsden (1909) to determine the size of atomic nuclei (Rutherford, 1911) using Coulomb scattering principles. As derived by Rutherford from the conservation of angular momentum and energy, the energy of the scattered α depends upon both the scattering angle and the atomic mass of the target atom. Thus, with the scattering angles constrained to be near 180°, the maximal energy of the scattered α particles from the sample surface is purely a function of the atomic mass.

The intensity of elastically scattered α particles is determined by the Rutherford cross-section as well as by the sample composition. The cross-section for α backscattering, which determines the relative probability of scattering for different elements at various angles, has also been described by Rutherford *et al.* (1930). This relationship shows that elastic scattering from higher Z elements is more probable than that from lower Z elements for the same scattering angle. As a result, the α mode is more sensitive for higher Z element measurements. With the cross-sections well understood, the sample composition as a function of element intensities can be determined.

Inelastic α scattering also occurs particularly from lower Z elements, most significantly carbon and oxygen, as noted by Bittner and Moffat (1954) and Ferguson and Walker (1940), respectively. The cross-sections for inelastic scattering are more variable with scattering angle than those for elastic scattering. The intensities from inelastic scattering have been experimentally determined in order to evaluate sample compositions.

The equations relating the elastic and inelastic scattering of the α particles as well as the resulting intensity of scattered α particles are discussed in detail by Patterson *et al.* (1965) and Foley (2002). In summary, the intensity of a measured element is proportional to the abundance of that element, while the energy at which this intensity is measured is proportional to the atomic mass of the element. For an infinitely thin sample, α particles will lose no energy traversing through the sample. Therefore, the α spectrum of intensity versus energy for a measured element will look like a vertical line. For a thick target, α particles from the surface as well as from depths $\sim$<10 μm backscatter to the detector. The actual maximum depth from which α particles return from can be estimated from previous experimental data compiled by Ziegler (1977). Alpha particles scattering from deeper in the sample lose energy traversing through the sample. Therefore, the α spectrum of intensity versus energy for an element within a homogeneous thick target is rectangular in shape, as shown in Figure 3.3. Equations which describe energy loss of α particles with depth are given by Patterson *et al.* (1965).

Some nuclei (particularly low-Z nuclei) will undergo (α, p) reactions upon being bombarded with the α particles from the decay of ^{244}Cm, and thus release protons and sometimes gamma rays from their nuclei. This nuclear reaction can occur when the kinetic energy of the α particle exceeds the Q value, for which the general nuclear reaction is described by Tipler (1987). Furthermore, some elements have multiple energies at which (α, p) reactions will occur. Since the α

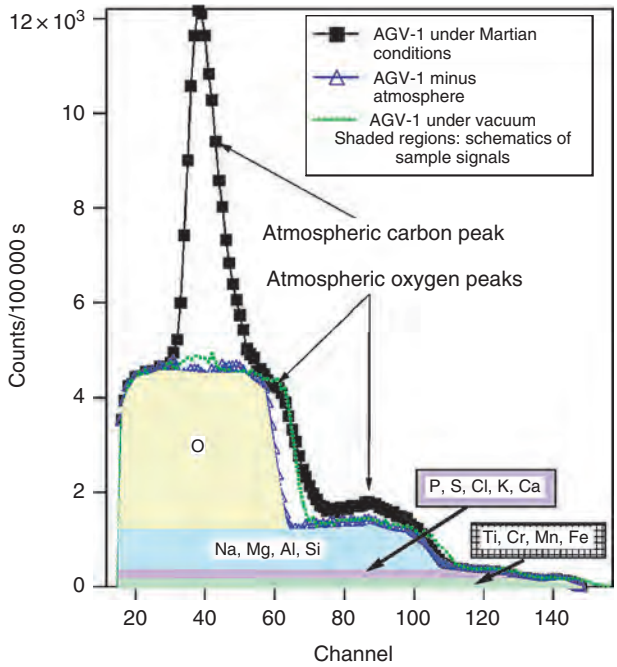

Figure 3.3. Alpha-mode laboratory spectrum of an andesite standard, AGV-1, under Martian conditions. The atmospheric signals from the carbon and oxygen of carbon dioxide form peaks within the AGV-1 sample run. The carbon atmospheric peak is centered at approximately channel 39, while the oxygen atmospheric peaks are centered at approximately channel 60 and 88. Using the atmospheric subtraction technique described within Foley *et al.* (2003a), the atmosphere-free spectrum for AGV-1 has been computed and is plotted here as well. The α spectrum for AGV-1 under vacuum is also shown for comparison. Sample signals for each element are shaded. (For a color version of this figure, please refer to the color plate section or to the e-Book version of this chapter.)

particles lose energy as they traverse through the sample, some of these proton reactions occur within the sample, rather than at the sample surface. The elements within the Pafthfinder samples that produce significant proton signals for the APXS include nitrogen, sodium, magnesium, aluminum, silicon, and sulfur, whose laboratory standard spectra are shown in Figure 3.4. The intensities of the proton signals from a given element vary as a function of mean sample composition and concentration of the element with approximately the same intensity dependence as that for the α particles.

Incident α particles and X-rays from the ^{244}Cm cause sample atoms to emit characteristic X-rays. X-rays from the lower Z elements from sodium through calcium are predominantly generated by α particle bombardment, while those from the higher Z elements are predominantly generated by X-ray bombardment. Characteristic X-rays are generated from depths up to approximately 80 μm by α and XRF. However, the average sampling depth by the X-rays varies with atomic number due to absorption of outgoing X-rays within the sample. In particular, lower Z X-rays, such as those from sodium and silicon, come from the top few micrometers while higher Z X-rays, such as those from iron, come from depths of up to 18 μm for samples having approximately basaltic compositions.

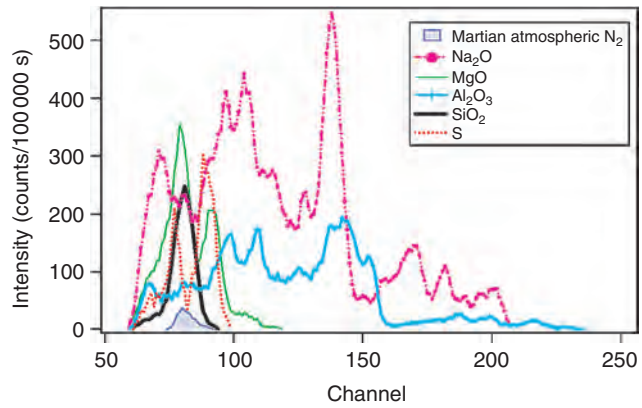

Figure 3.4. Proton-mode laboratory spectra. The multiple spectral signals at different channels, proportional to energies, are due to proton release from sample nuclei (and Martian atmosphere in the case of nitrogen) from (α, p) reactions. The Na_2O curve was calculated from measurement of NaCl. (For a color version of this figure, please refer to the color plate section or to the e-Book version of this chapter.)

3.2 APXS CALIBRATION

Due to time constraints to deliver the flight instrument for launch, the calibration of the Pathfinder APXS was accomplished by two separate calibration teams using two duplicate laboratory instruments at the University of Chicago (Foley *et al.*, 2003a,b) and at the Max-Planck-Institut für Chemie (Brückner *et al.*, 2003). During both calibrations, numerous powdered standards of oxides, pure elements, and geostandards were analyzed to derive routines to determine the compositions of the unknowns at the Pathfinder landing site. Rocks which were approximately homogeneous in surface composition on a millimeter scale, having various surface textures, were also analyzed. While Brückner *et al.* (2003) calibrated the X-ray mode of the APXS, Foley *et al.* (2003a) calibrated all three instrument modes. Both laboratories, however, utilized the α mode of the instrument to determine the concentration of sample carbon in the Pathfinder samples. The extremely similar results from the independent X-ray calibrations and carbon determinations illustrate the accuracy of both laboratories and techniques.

For each laboratory, the instrument was operated inside a stainless steel vacuum chamber that has two compartments. The upper compartment houses the APXS instrument and has an intake and exhaust valve that can regulate the pressure and introduce gas into the chamber. The lower chamber can be sealed off from the upper one providing a means to pressurize the lower chamber without affecting the upper one and hence use the lower chamber to change samples. Samples may be loaded into the lower chamber onto a sample stage that can be raised to the cylindrical base of the APXS.

3.2.1 The X-ray mode

The X-ray calibration of Brückner *et al.* (2003) utilized calibration curves derived from analyses of numerous geostandards to determine the composition of the Pathfinder samples. In contrast, the calibration of Foley *et al.* (2003a)

utilized theoretically predicted X-ray generation and matrix effects verified by analyses of laboratory geostandards to calculate the Pathfinder compositions.

The characteristic X-ray spectral peaks are nearly gaussian with small low-energy tails caused by incomplete charge collection within the X-ray detector. The X-ray peak shapes, areas, and backgrounds were analyzed using two different techniques. A least-squares fitting technique using laboratory-derived peak shapes for each element was applied by Brückner *et al.* (2003) to take into account the small non-gaussian low-energy shoulder of the peaks. Each X-ray spectrum was split in three spectral regions, which were fit separately. In contrast, Foley *et al.* (2003a) used a least-squares fitting technique with gaussian peak fitting, which deconvolves overlapping peaks and compensates for non-gaussian tails on an adjustable order polynomial background on the entire spectrum. The parameters of the peaks, such as the peak center positions and the full width at half maximum (FWHM), vary as a function of resolution and are therefore determined for each spectrum. For both techniques, care was taken to assure comparable laboratory conditions to those on the Martian surface. The Martian resolution was fairly constant as discussed by Brückner *et al.* (2003) which was important for measurement during times when temperatures varied from +9 to −75 °C. Both calibration teams corrected for all escape and K_β peaks, as described in detail by Brückner *et al.* (2003) for laboratory and Pathfinder samples. Collected X-ray spectra were, thus, first analyzed in the ways described above to remove the spectral background and to compute the peak areas for each element. These areas were then utilized to compute the sample concentrations.

Foley *et al.* (2003a,b) determined the concentrations within samples using software written by O. F. Prilutsky, from the Space Research Institute of the Russian Academy of Sciences. This program takes into account the excitation from both the α particles and the X-rays from ^{244}Cm radioactive source as well as X-ray absorption within the sample. The program, therefore, makes ZAF (ZAF-atomic number [Z], Absorption, and Fluorescence) corrections like modern EDSs (Electron Density Systems) and electron probes. In order to calculate elemental abundances, this program needs values for X-ray intensities from standards. These intensities, normalized to the same collection time, for characteristic X-ray peaks from standards were experimentally determined during the calibration. These standards were fine-powdered oxides or fine-powdered pure elements having greater than 99.9% chemical purity and uniform grain size. The standards used to measure the respective elements within parentheses include NaCl (Na, Cl), $MgCO_3$ (Mg), Al_2O_3 (Al), SiO_2 (Si), $CaHPO_4$ (Ca, P), S (S), K_2CO_3 (K), TiO_2 (Ti), Cr (Cr), MnO_2 (Mn), and $FeSO_4$ (Fe). The proportionality of the count rate to the concentration of each element in the standard, instrument geometry, as well as experimentally determined outgoing X-ray matrix effects were then used to measure the composition of the samples being analyzed. A certain oxidation state for each element was assumed, and therefore oxygen was calculated using stoichiometry. As fore mentioned, this technique is very similar to that used conventionally in analytical electron microscopy. It differs by its incorporation of the fraction of characteristic X-rays generated by α particles and X-rays within a given volume of sample, and the unique geometry parameters of the APXS described by Rieder *et al.* (1997b).

By measuring the compositions of a number of powder geostandards under Martian conditions, the accuracy of the Foley *et al.* (2003a) calibration method for the X-ray mode was determined. The geostandards analyzed include AGV-1 (andesite), BCR-1 (basalt), G-1 (granite), G-2 (granodiorite), DTS-1 (dunite), BCS-301 (iron-rich sediment), PCC-1 (dunite), and OTB-1 (basalt) (with only the first five analyzed under simulated Martian conditions). The meteorites analyzed include ALH 84001 (Martian orthopyroxenite), ALH 77005 (shergottite), EET 79001 (shergottite), Bruderheim (L6 ordinary chondrite), Murchison (CM2 carbonaceous chondrite), and Allende (CV3 carbonaceous chondrite) in vacuum. The analyses of BCS-301, PCC-1, and the meteorites were particularly useful to infer the accuracy of the calibration technique for elements such as excess O (in mineral-bound water for PCC-1 and Murchison), C, P, S, Cr, and Mn (as described further by Foley, 2002). The assigned analytical uncertainties of measurements for the Pathfinder samples are determined by combining the laboratory errors from the calibrations (Foley *et al.*, 2003a) with the statistical errors for each sample.

Rigorous calibration curves were determined for compositions within a comparable range to the Pathfinder samples through analyses of various geostandards by Brückner *et al.* (2003). Calibration geostandards include AN-G (andesite), BE-N (basalt), Mica-Fe, Millbillillie (eucrite), Murchison (CM2), and SSK1.1 (andesite) under Martian simulated conditions. Since these samples span the composition range of the Pathfinder samples, the calibration curves eliminate the need for additional corrections for matrix effects within the Pathfinder samples. Based upon the element signal as a function of atomic number for the calibration curves, only P, Cl, and Mn appear to be outliers in terms of the expected count rate for a given element. Thus, some systematic errors for these elements resulting from use of this calibration are possible (Brückner *et al.*, 2003). Average errors for each element were computed using the calibration curve and the statistical errors for each measured element. Although the average errors are not listed by Brückner *et al.* (2003), the accuracy is comparable as verified by the similar bulk chemical Pathfinder results by the two groups.

3.2.2 The alpha-proton mode

Foley *et al.* (2003a) calibrated the α-proton combined mode to measure C, N, O, Na, Mg, Al, Si, (S, P, Cl as a group), (K, Ca as a group), Ti, and (Mn, Cr, Fe, Ni as a group) for the Pathfinder analyses. The α-proton mode relied on the X-ray mode for Mg/Si, S/Si, P/Si, Cl/Si, K/Ca, Mn/Fe, and Cr/Fe ratios. With these ratios from the X-ray mode, the α-proton mode then gives the abundances of the remaining measurable elements. This results in independent α-proton mode measurements of C, N, O, Na, Al, Si, (K, Ca), Ti, and (Mn, Cr, Fe, Ni). Like the X-ray mode, the α and proton

modes rely on spectra of fine-grained oxide standards for their calibration libraries.

Unlike the X-ray mode, the α and proton spectra contain atmospheric signals from the carbon and oxygen in the Martian atmospheric CO_2 and from atmospheric nitrogen, respectively, which must first be removed before sample analyses. Once the atmospheric contributions are removed, the α and proton signals are analyzed by a least-squares fit to yield a result which is partially dependent on the X-ray mode. However, the α mode accuracy is more strongly affected by changes in measurement distance and sample texture, which is less the case for the X-ray mode. The correction for atmospheric effects, sample distance, and sample texture, as well as the resulting accuracy of the α-proton combined mode are described in detail by Foley *et al*. (2003a).

In brief, sample texture and distance differences cause some deviation from the expected rectangular shape of the α spectra for elements having resonant scattering of the α particles at some energies. Textural effects were overcome by analyzing standards having textures similar to those of the analyzed samples. Since the resonant features are in the calibration library as well as the analyzed samples, correction is not a problem if the approximate texture of the analyzed sample is known. Resonant features are subdued in powdered samples and are more pronounced in polished samples and rocks, perhaps because of increased energy scattering and loss in powdered samples which have grain sizes similar to the typical penetration depth of the α particles. These effects are minor for resonant features in sodium, aluminum, and magnesium alpha spectra. However, there is a significant effect for silicon, due to its high abundance in samples analyzed. Thus rocks are more accurately analyzed with the polished standard for silica, while soils are more accurately analyzed with the fine powder standard.

The Pathfinder measurement distance exceeded the laboratory calibration distance by 4–15 mm. This distance change affects the computed α-mode abundances alone (Foley, 2002). Distance effects were overcome by computing the sample distance utilizing the iron signal of the α mode and adjusting both the oxygen and silicon standards by an experimentally and theoretically predicted amount to compensate for the distance change (Foley, 2002). The distance change has a maximum effect on the silicon and oxygen abundances of 7 and 12 relative percent (which are smaller than the measurement errors), respectively, which were corrected for during analyses. Sample texture and distance also affect the carbon signal. However, since Pathfinder sample carbon was determined to be below the detection limit (as discussed in the following section), this is not pertinent.

The effects of the Martian atmosphere on the α and proton spectra were determined using a simulated Martian gas mix, identical to measured Martian atmosphere, of 95.32% CO_2, 2.7% N_2, and 1.6% Ar (Owen *et al*., 1997; Owen, 1992). There are two general effects on the α spectra. The first effect is a shift in the energy of returned α particle energy from a given element due to the energy loss in the gas before and after scattering from the sample. The second effect is the contribution to the α spectra predominantly from carbon and oxygen of the carbon dioxide gas, with only a negligible α signal from nitrogen gas and no detected α signal from argon. The atmospheric α contributions are three thin-sample peaks, due to the low density of the atmosphere, and are within the spectrum collected under Martian conditions. As shown in Figure 3.3, only the carbon atmospheric peak is clearly discernible for sample spectra. The two lowest-energy peaks are due predominantly to α particles resonantly scattered from atmospheric carbon and oxygen nuclei, respectively. The highest-energy peak is due to low-angle resonant scattering from oxygen nuclei close to the alpha detector. The amplitudes, centers, and widths of the carbon and oxygen peaks vary linearly with number density. Since the carbon peak is the only directly measurable atmospheric peak in the α spectra of laboratory geostandards as well as Pathfinder samples, it was used to infer the parameters of the other two atmospheric peaks. Most of the atmosphere parameters can be computed from the measurable parameters of the carbon peak. The high-energy oxygen width, however, is approximately constant with change in number density.

The proton spectra have several peaks due to (α, p) reactions occurring within samples at different energies for each proton-producing element. The only significant effect of the Martian atmosphere on the proton spectra is to introduce a small contribution from the atmospheric nitrogen. This nitrogen contribution was measured by pointing the APXS toward the sky to measure only atmosphere during a period of atmospheric number density comparable to that of the Pathfinder sample measurements. This modeled atmospheric contribution is shown in Figure 3.4 along with the computed and/or measured values for the proton library spectra including those of Na_2O, MgO, Al_2O_3, SiO_2, and S. This proton library consists of the collected intensities from analyzing standards of chemically pure and homogeneous fine-grained simple compounds (NaCl, MgO, Al_2O_3, and SiO_2) and elemental sulfur. There is no proton signal from the oxygen within these oxides. The proton intensity is proportional to the concentration of the proton emitters: Na, Mg, Al, Si, and S.

In the Foley *et al*. (2003a) calibration, the α and proton data were merged and analyzed as one set of data and therefore we refer to their results as coming from the α-proton mode. The two modes are merged because some elements have lower and less distinctive intensities in the α mode and higher and/or more distinctive intensities in the proton mode and vice versa. For example, the sodium signal for the α mode is typically difficult to decipher from the large silicon signal in basaltic to andesitic samples, but is easily seen in the proton mode. Because of this, the accuracy of sodium measurement is better for the proton mode than for the α mode. The other element contributing to the sodium region of the protons is aluminum. In order to assure that sodium was calculated accurately from the proton mode, the Al/Si ratio in the alpha-proton mode was set from the X-ray data. The merging of the α and proton spectra was done for each calibration standard as well as each analyzed sample. A least-squares program was then used to calculate the

abundances in the unknown using the library, consisting of merged α and proton spectra from homogeneous fine-powdered oxides and/or elements. The least-squares program fits the analyzed spectrum with the intensities measured from the standards and converts the measured intensities to sample concentrations using equations given by Foley (2002). Alpha-proton mode error bars for the Foley *et al.* (2003b) Pathfinder analyses are computed from average relative percent deviations determined in the laboratory calibration and the counting statistical errors for each sample.

The raw α spectra for geostandards were compared with calculated α spectra assuming stoichiometric oxygen excluding mineral-bound water from their individual references. Also, the raw α spectra were compared with the α spectral fit from the α-proton program including all measured elements. This was done to observe the magnitude of the oxygen signal due to mineral-bound water in geostandards. Figure 3.5a shows the raw laboratory spectrum for BCR-1, minus atmosphere, compared with the α spectrum assuming stoichiometric oxygen (Govindaraju, 1994) excluding water. Because BCR-1 contains less than 1 wt.% water, the raw and the synthetic spectra for BCR-1 are very similar. Figure 3.5b shows the raw and synthetic spectra for PCC-1. Because PCC-1 contains 4.71 wt.% water (Govindaraju, 1994), the raw spectrum for PCC-1 is much higher in the oxygen region than the calculated α spectrum excluding water. A calculated spectrum including water matches the raw spectrum well.

The α-mode oxygen measurements, shown in Figure 3.6, yield an accuracy of 1 relative percent (1σ) both for geostandards containing <1 wt.% water and for samples containing abundant water, as described in detail by Foley (2002). Hydrogen is the only rock-forming element that cannot be detected directly by the APXS. However, its

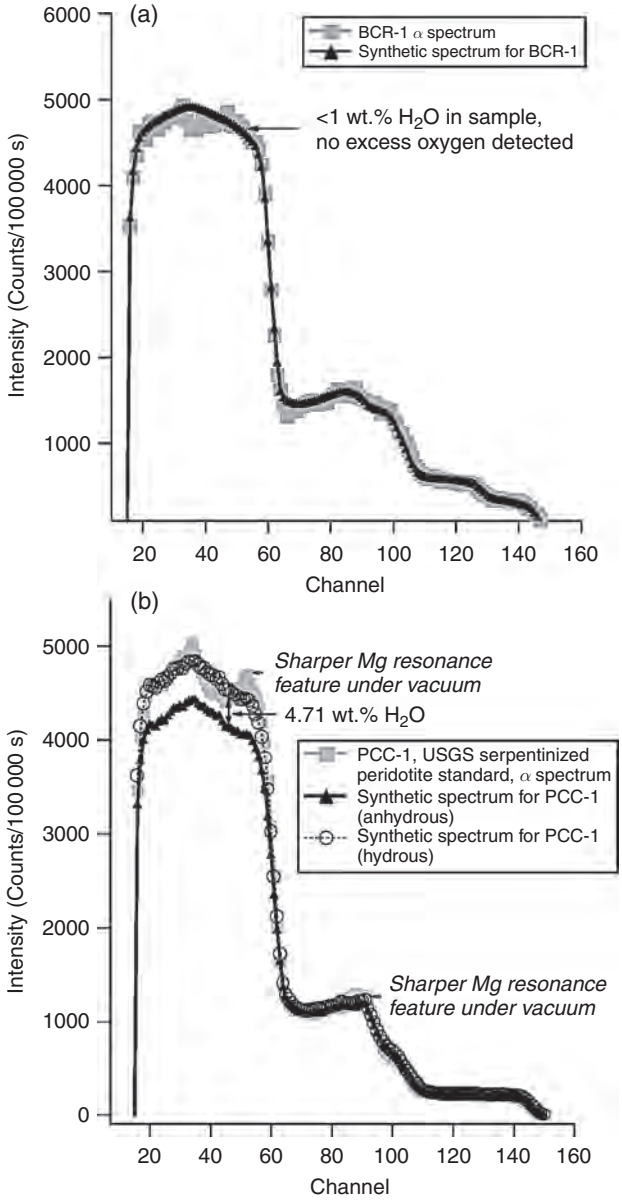

Figure 3.5. Series of α-mode laboratory spectra showing the detection of excess oxygen, present in samples having greater than 1 wt.% water. (a) The raw spectrum minus atmospheric signals for a basalt standard, BCR-1, and a spectral fit using the α program with the library calibration values assuming the oxidation states as listed in Govindaraju (1994). No excess oxygen was detected. (b) (1) The raw spectrum for a serpentinized peridotite standard, PCC-1; (2) the synthetic anhydrous spectrum from the α program with the library calibration values also assuming oxidation states as listed in Govindaraju (1994); (3) the α program fit which includes oxygen bound as water. There is a significant excess of oxygen signal when sample water is present.

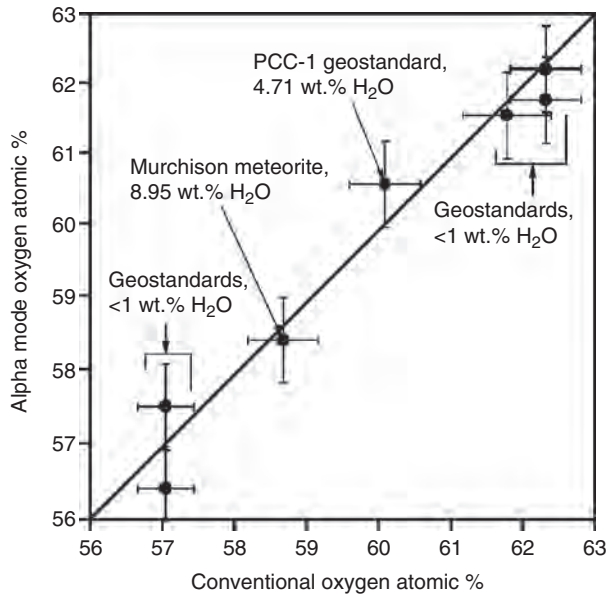

Figure 3.6. Laboratory α-mode bulk oxygen accuracy for geostandards and Murchison meteorite. Atomic percent of the α mode is plotted versus the atomic percent of the conventional oxygen concentration on hydrogen-free basis (because the alpha-mode cannot measure hydrogen). This plot shows geostandards containing <1 wt.% water including AGV-1, BCR-1, G-1, G-2, and DTS-1 all measured under Martian conditions, and samples containing water, as labeled, were measured under vacuum. The bulk oxygen measurement by the α-mode has a relative 1σ error of one relative percent calculated from the analyses of multiple geostandards. The errors for conventional values are average errors for total oxygen calculated by propagating the reported errors for each oxide and converting it into the total oxygen error.

Table 3.1. *Foley* et al. *(2003b) X-ray mode results (± 1σ)*

Soils	Na_2O*	MgO	Al_2O_3	SiO_2	P_2O_5	SO_3	Cl	K_2O	CaO	TiO_2	Cr_2O_3	MnO	Fe_2O_3
A-2 Deploy	3.2 ± 0.7	8.7 ± 2.0	10.4 ± 0.8	40.9 ± 0.8	0.9 ± 0.2	6.0 ± 1.2	0.7 ± 0.2	0.50 ± 0.04	6.1 ± 0.4	0.7 ± 0.2	0.3 ± 0.1	0.5 ± 0.1	21.2 ± 0.9
A-4 Next to Yogi	3.2 ± 0.7	8.0 ± 1.9	10.6 ± 0.8	41.0 ± 0.9	1.2 ± 0.2	6.9 ± 1.4	0.8 ± 0.2	0.50 ± 0.07	5.6 ± 0.4	1.0 ± 0.3	0.4 ± 0.1	0.4 ± 0.1	20.4 ± 0.8
A-5 Dark Next to Yogi	3.2 ± 0.6	7.1 ± 1.7	10.4 ± 0.8	40.7 ± 0.9	0.6 ± 0.1	5.7 ± 1.1	0.8 ± 0.2	0.50 ± 0.05	6.1 ± 0.4	0.6 ± 0.1	0.5 ± 0.1	0.20 ± 0.06	23.7 ± 1.0
A-9 Disturbed Soil by Scooby	2.6 ± 2.4	6.4 ± 1.6	10.2 ± 0.9	41.7 ± 0.9	0.8 ± 0.2	6.6 ± 1.4	1.2 ± 0.3	0.70 ± 0.09	6.4 ± 0.5	0.8 ± 0.2	0.2 ± 0.1	0.1 ± 0.1	22.2 ± 1.0
A-10 Lamb	1.8 ± 0.7	7.5 ± 1.7	9.8 ± 0.7	41.3 ± 0.9	0.6 ± 0.1	6.4 ± 1.3	0.8 ± 0.2	0.40 ± 0.04	6.0 ± 0.4	0.8 ± 0.2	0.3 ± 0.1	0.4 ± 0.1	24.0 ± 1.0
A-15 Mermaid	2.7 ± 0.8	6.7 ± 1.6	9.9 ± 0.8	43.2 ± 1.0	0.6 ± 0.1	5.2 ± 1.1	0.8 ± 0.2	0.70 ± 0.07	5.5 ± 0.4	0.8 ± 0.2	0.3 ± 0.1	0.3 ± 0.1	23.2 ± 1.0
Indurated soil													
A-8 Scooby Doo	3.1 ± 0.8	6.4 ± 1.5	10.5 ± 0.8	45.0 ± 1.0	0.5 ± 0.1	5.5 ± 1.1	0.9 ± 0.2	0.80 ± 0.06	7.0 ± 0.5	0.7 ± 0.2	0.1 ± 0.1	0.3 ± 0.1	19.1 ± 0.8
Rocks	**Na_2O***	**MgO**	**Al_2O_3**	**SiO_2**	**P_2O_5**	**SO_3**	**Cl**	**K_2O**	**CaO**	**TiO_2**	**Cr_2O_3**	**MnO**	**FeO**
A-3 Barnacle	3.2 ± 0.5	2.1 ± 0.5	12.8 ± 0.9	54.1 ± 1.1	0.7 ± 0.1	2.0 ± 0.4	0.5 ± 0.1	1.1 ± 0.07	5.7 ± 0.4	0.6 ± 0.1	0.10 ± 0.04	0.3 ± 0.1	16.7 ± 0.7
A-7 Yogi	4.9 ± 0.8	5.2 ± 1.2	11.2 ± 0.9	47.4 ± 1.1	0.5 ± 0.1	4.4 ± 0.9	0.8 ± 0.2	0.70 ± 0.06	6.6 ± 0.5	0.7 ± 0.2	0.10 ± 0.1	0.4 ± 0.1	17.1 ± 0.7
A-16 Wedge	4.9 ± 0.9	4.1 ± 1.0	11.5 ± 0.8	48.0 ± 1.1	0.6 ± 0.1	3.0 ± 0.6	0.6 ± 0.1	0.80 ± 0.07	6.9 ± 0.5	0.7 ± 0.2	0.00 ± 0.04	0.3 ± 0.1	18.6 ± 0.8
A-17 Shark	3.6 ± 0.8	3.9 ± 1.0	10.7 ± 0.8	53.9 ± 1.2	0.5 ± 0.1	1.7 ± 0.4	0.5 ± 0.1	0.80 ± 0.09	7.7 ± 0.6	0.5 ± 0.2	0.10 ± 0.1	0.4 ± 0.1	15.8 ± 0.7
A-18 Half Dome	4.0 ± 0.7	3.4 ± 0.8	12.3 ± 0.9	50.0 ± 1.1	0.6 ± 0.1	3.0 ± 0.6	0.7 ± 0.2	1.0 ± 0.08	6.0 ± 0.5	0.7 ± 0.2	0.10 ± 0.1	0.4 ± 0.1	17.9 ± 0.7

Key: All X-ray Na_2O* values are calculated from α-proton mode Na_2O/SiO_2 values except for A-9, disturbed soil by Scooby Doo, which is derived from X-ray. Errors are the statistical and laboratory combined error, at the 1σ level. Sulfur is assumed to have +6 oxidation state because of its high abundance, and because of the Viking soil analyses which support this oxidation state (Toulmin *et al.*, 1977). Fe is assumed to have +3 oxidation state in the soils and +2 oxidation state in the rocks based on IMP (Imager for Mars Pathfinder) red/blue ratios which indicate more oxidized iron in the soils than the rocks (McSween *et al.*, 1999).

Table 3.2. *Brückner* et al. *(2003) X-ray mode results*

Soils	Na_2O	MgO	Al_2O_3	SiO_2	P_2O_5	SO_3	Cl	K_2O	CaO	TiO_2	Cr_2O_3	MnO	Fe_2O_3
A-2 Deploy							Not reported						
A-4 Next to Yogi	1.00	9.95	8.22	42.5	1.89	7.58	0.57	0.60	6.09	1.08	0.2	0.76	19.6
A-5 Dark Next to Yogi	1.05	9.20	8.71	41.0	1.55	6.38	0.55	0.51	6.63	0.75	0.4	0.34	23.0
A-9 Disturbed Soil by Scooby							Not reported						
A-10 Lamb	1.32	8.16	7.41	41.8	0.95	7.09	0.53	0.45	6.86	1.02	0.3	0.51	23.6
A-15 Mermaid	0.97	7.46	7.59	44.0	1.01	6.09	0.54	0.87	6.56	1.20	0.3	0.46	23.0
Indurated soil													
A-8 Scooby Doo	1.56	7.24	9.09	45.6	0.61	6.18	0.55	0.78	8.07	1.09	—	0.52	18.7
Rocks	**Na_2O**	**MgO**	**Al_2O_3**	**SiO_2**	**P_2O_5**	**SO_3**	**Cl**	**K_2O**	**CaO**	**TiO_2**	**Cr_2O_3**	**MnO**	**FeO**
A-3 Barnacle	1.69	3.20	11.02	53.8	1.42	2.77	0.41	1.29	6.03	0.92	0.1	—	16.2
A-7 Yogi	1.19	6.71	9.68	49.7	0.99	4.89	0.50	0.87	7.35	0.91	—	0.47	16.7
A-16 Wedge	2.30	4.58	10.24	48.6	1.00	3.29	0.41	0.96	8.14	0.95	—	0.65	18.9
A-17 Shark	2.03	3.50	10.03	55.2	0.98	1.88	0.38	1.14	8.80	0.65	0.05	0.49	14.8
A-18 Half Dome	1.78	3.91	10.94	51.8	0.97	3.11	0.37	1.10	6.62	0.82	—	0.52	18.1
Ave. error (rel.%)	40	10	7	10	20	20	15	10	10	20	50	25	5

presence is inferred by excess oxygen above that which can be bound with all other detected elements in their highest oxidation states. Thus, one may infer the water content in samples for which the oxidation states of sample elements are known to within a resulting error of ~1 wt.% water.

Also important for understanding the volatile content of the Martian soils and rocks is measurement of sample carbon. Carbon is detectable by the α mode only if present above 0.3–0.8 wt.% (Foley *et al.*, 2003a,b and Brückner *et al.*, 2003, respectively). Under Martian conditions carbon, if present, will appear in channels 15–32 as a rectangle-like feature on top of the rest of the spectrum. Since no sample carbon was detected, it is assumed to be <0.3–0.8 wt.% and therefore the accuracy of sample carbon measurement was not further quantified.

3.2.3 Application of calibration to Pathfinder data

In order to apply the fore mentioned calibration routines to the Pathfinder dataset, one difference between the laboratory and flight instruments (which are otherwise identical) had to be addressed. This difference is the presence of a thin alumina/VYNS (~1200 Å alumina/organic polymer) film held by a stainless steel grid in the laboratory instruments between the sources and the sample. This protective grid is used in the laboratory as a barrier to protect the instrument chamber and samples from curium contamination. The steel grid is thicker than the range of the α particles and it therefore prevents some α particles from reaching the sample, but causes an insignificant absorption of the 14–18 KeV X-rays from the curium sources. Therefore, relatively fewer α particles will scatter or undergo (α, p) in the presence of the protective grid. Absorption by the grid causes the α and proton spectral signals for laboratory standards to be relatively lower than those in the Pathfinder samples. Because all the standard intensities are reduced by the same relative amount, this does not affect the calculation of the absolute sample abundances for the α and proton modes. The X-ray mode Pathfinder abundances, however, are affected by the change in the proportion of α particles and X-rays striking the sample. Characteristic X-rays from the sample are excited by both α particles and X-rays from the curium sources, as previously discussed. With a decreased α beam, there is less characteristic X-ray production from the sample. The proportion of generation of sample X-rays by α particles and X-rays has been determined experimentally with the laboratory APXS by analyzing pure oxide targets with and without a 28 μm mylar foil over the curium sources. This mylar absorbs all of the α particles, and thus prevents them from interacting with the sample. By comparing the laboratory X-ray yield with and without the mylar foil, the ratios of the X-ray produced by α particles and the X-rays from the ^{244}Cm source were measured for many elements and inferred for others (Figure 3.7). The standard library utilized by Foley *et al.* (2003a), which contains the intensities corresponding to a certain atomic percent of each element, and the calibration curves of Brückner *et al.* (2003) were corrected to compensate for this instrument difference. The fraction of characteristic

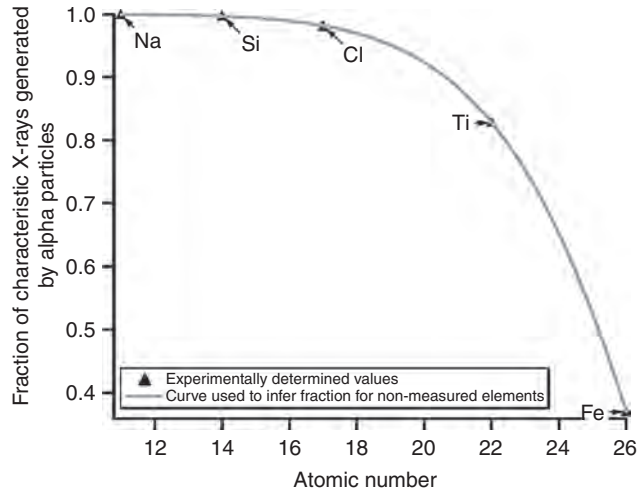

Figure 3.7. Fraction of sample characteristic X-rays generated by alphas for different atomic numbers. The plot shows that elements lower than manganese in atomic number have more of their characteristic X-rays generated by α particles, while elements higher than manganese in atomic number have more generated by X-rays. The curve used to infer the fraction for non-measured elements is an exponential fit to the data points.

X-rays generated by α bombardment was used to increase the reference library values and the calibration curve results by an appropriate amount. Since the steel grid reduces the intensity of α particles by 15% (its surface area) it reduces the amount of X-ray generation by α particles by 15%. The new library values and the calibration curve results are therefore increased by 15% of the fraction of characteristic X-rays produced by α particles for the Pathfinder sample analyses.

The initial Pathfinder data analyses (Rieder *et al.*, 1997b) were performed only with the X-ray mode of the instrument uncorrected for the absence of the protective grid on the flight instrument. This is the reason for the differences in the abundances computed by the earlier study by Rieder *et al.* (1997b) and those completed later by Brückner *et al.* (2003) and Foley *et al.* (2003b). All of the abundances in the X-ray mode are different from those initially derived. In particular, the differences are large enough that the inferred Pathfinder SFR composition was re-classified as basalt-andesitic to tholeiitic andesite (with a silica content of ~57%) rather than purely andesitic (with a silica content of ~62 wt.%), which has significant implications for the understanding of the petrology of the Pathfinder rocks, as discussed in the following sections.

3.3 CHEMICAL RESULTS

Using the newly tested X-ray library modified for instrumental differences, the data from five rocks and seven soils at the Pathfinder site were re-analyzed with results given in Tables 3.1 (Foley *et al.*, 2003b) and 3.2 (Brückner *et al.*, 2003). The most prominent differences between these results and those of Rieder *et al.* (1997b) are lower abundances of

Table 3.3. *Na_2O abundances for X-ray and alpha-proton modes*

Soils	Na_2O X-ray abundances (wt.%) $\pm 1\sigma$	Na_2O α-proton abundances (wt.%) $\pm 1\sigma$
A-2 Deploy	5.5 ± 0.4	3.2 ± 0.7
A-4 Next to Yogi	4.8 ± 1.0	3.2 ± 0.7
A-5 Dark Next to Yogi	3.2 ± 0.9	3.2 ± 0.6
A-9 Disturbed Soil by Scooby	2.6 ± 2.4	2.6 ± 2.4
A-10 Lamb	2.0 ± 0.6	1.8 ± 0.7
A-15 Mermaid	1.8 ± 1.4	2.7 ± 0.8
Indurated soil		
A-8 Scooby Doo	2.6 ± 0.8	3.1 ± 0.8
Rocks		
A-3 Barnacle Bill	2.8 ± 1.6	3.2 ± 0.5
A-7 Yogi	2.2 ± 2.5	4.9 ± 0.8
A-16 Wedge	3.8 ± 1.0	4.9 ± 0.9
A-17 Shark	3.9 ± 1.9	3.6 ± 0.8
A-18 Half Dome	4.0 ± 0.8	4.0 ± 0.7

Source: Foley *et al.* (2003b).

silica and higher abundances of iron as well as new measurements of P_2O_5, Cr_2O_3, and MnO. The reasons for these differences between the preliminary Rieder *et al.* (1997a) results and these final X-ray results were described in Section 3.2.

All X-ray abundances in Table 3.1 from Foley *et al.* (2003b) were independently measured by the X-ray mode with the exception of Na_2O, which was measured by the α-proton mode. The α-proton mode values are more accurate than X-ray values for Na_2O because of larger counting statistical uncertainties and background uncertainties due to a light leak in the x-ray mode (as discussed further by Brückner *et al.*, 2003). Even with the higher statistical error, the X-ray results for Na_2O from Foley *et al.* (2003b) are within 1σ of the α-proton results given here (Table 3.3).

All of the chemical results from Brückner *et al.* (2003) (Table 3.2) were derived from the X-ray mode alone. A comparison of the X-ray results from Foley *et al.* (2003b) and Brückner *et al.* (2003) is shown in Figure 3.8. They agree within 1σ for MgO, SiO_2, SO_3, Cl, K_2O, some CaO, TiO_2, Cr_2O_3, and Fe_2O_3. The Brückner *et al.* (2003) results for Na_2O are significantly lower than the X-ray or α-proton mode X-ray values from Foley *et al.* (2003b). This may be due to the difficulty in subtracting the background from the sodium region for the X-ray sodium region, and hence the higher possibility of systematic errors in the X-ray Na_2O values. The Brückner *et al.* (2003) abundances for P_2O_5 and MnO are both systematically higher than the abundances of Foley *et al.* (2003b) by ~ 1–2σ. These differences may be due to uncertainties in the calibration curves for these elements, which were uncorrected for matrix effects, as discussed by Brückner *et al.* (2003). Specifically, these abundance differences may be due to differences in the handling of the asymmetrical X-ray peak contributions from the neighboring sulfur and iron. The Brückner *et al.* (2003) aluminum values are all systematically lower by approximately 2σ, while the values of calcium are higher for all Pathfinder samples than the X-ray results of Foley *et al.* (2003b). These differences are due to systematic differences in the calibration routines near the accuracy level of the measurements. All differences between the two calibration routines are within 1–2σ and these differences do not alter the bulk chemistry of the average soils or of the SFR (discussed later) enough to change the interpretations of their petrology.

The α-proton abundances for C, O, Na, Si, (K, Ca as a group), and Fe for the Martian rocks and soils have been obtained independent of the X-ray mode. Elements measured by the α-proton and X-ray modes are in agreement with one another, within error, verifying the accuracy of the measured abundances (Foley *et al.*, 2003b). The additional contribution of the α-proton mode is the determination of the concentrations of sample carbon and oxygen, which the X-ray mode cannot measure. Sample carbon was not detected in any of the Pathfinder APXS analyses, implying that the carbon concentration is below 0.3–0.8 wt.% (Foley *et al.*, 2003b and Brückner *et al.*, 2003, respectively), the approximate detection limits for carbon, in both the rocks and soils at the Pathfinder site. The bulk oxygen determination from the α mode has yielded some excess oxygen in some of the rocks, above that which may be accounted for by stoichiometric relationships with measured major elements. It is probable that this excess oxygen is bound to hydrogen, which is the only major rock-forming element not measured with the APXS. The absolute amount of excess oxygen is dependent on the choice of stoichiometry for both iron and sulfur, the only measured major elements which may have varying oxidation states which are not well-constrained. Using the abundances measured from the α mode, the amount of excess oxygen detected can be converted to an amount of mineral-bound water possibly present in the samples with different assumptions of the oxidation states of iron and sulfur. Table 3.4 lists the variation in inferred water content with assumptions of oxidation state. The probable range of water content for the soils, based on these analyses and visible and near-infrared spectra (McSween *et al.*, 1999; Bell *et al.*, 2000; Bridges *et al.*, 2001), is between -1.4 ± 1.7 and 1.0 ± 1.6 wt.%; none of which is significantly different from zero. The probable range of water content for the rocks based on the same assumptions is between 0.1 ± 1.3 and 4.3 ± 1.3 wt.%. The bulk α-proton abundances and the variation in the potential water content with oxidation state are discussed further by Foley *et al.* (2003b).

Since the X-ray mode is the most independent of the three modes, its elemental abundances are used with the sodium content from the α-proton joint mode to yield bulk sample abundances on a dry basis from the Foley *et al.* (2003b) analyses which may then be compared with other chemical analyses of the Martian surface to determine the petrology of the Pathfinder rocks and soils. Use of the Brückner *et al.* (2003) X-ray values yields comparable interpretations.

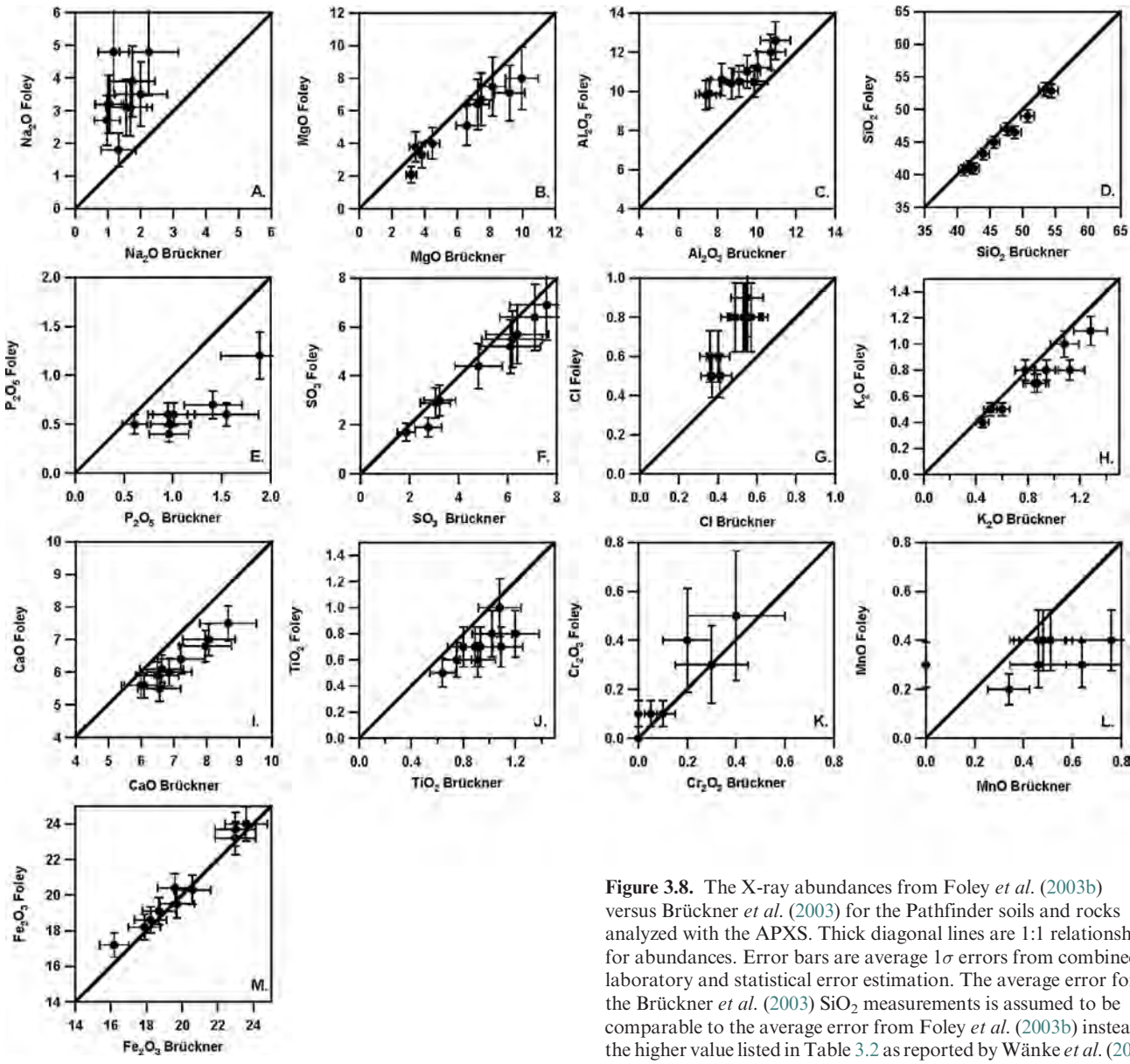

Figure 3.8. The X-ray abundances from Foley *et al.* (2003b) versus Brückner *et al.* (2003) for the Pathfinder soils and rocks analyzed with the APXS. Thick diagonal lines are 1:1 relationship for abundances. Error bars are average 1σ errors from combined laboratory and statistical error estimation. The average error for the Brückner *et al.* (2003) SiO_2 measurements is assumed to be comparable to the average error from Foley *et al.* (2003b) instead of the higher value listed in Table 3.2 as reported by Wänke *et al.* (2001).

3.4 PETROLOGY OF THE PATHFINDER SOILS AND ROCKS

3.4.1 Soils

The Pathfinder soils appear to be products of chemical alteration of original mafic material by fluids or gases rich in sulfur and chlorine. The lack of detection of carbon implies the absence of carbonate. If carbonates were once present in surface materials, they may have been dissolved by acidic weathering conditions during more recent epochs, as hypothesized by Wänke and Dreibus (1994) and Clark (1999). They have argued that carbonates should not be expected at the surface of Mars because of the high abundance of SO_3. Shergottites, the most abundant group of Martian meteorites, contain mantle-derived concentrations of ~200 ppm H_2O, ~100 ppm CO_2, and between 1200 and 5600 ppm SO_2. Terrestrial MORBs contain ~200 ppm H_2O and similar concentrations of SO_2 and CO_2. On Mars, which is poorer in H_2O and CO_2 but similar or richer in SO_2, it is expected that SO_2 dominates the volcanic gases (as inferred from the meteorite volatile abundances summarized by Wänke and Dreibus, 1994). At least part of the SO_2 quickly transformed to SO_3 will together with water vapor produce sulfuric acid, which in turn will decompose carbonates and return CO_2 to the atmosphere. The sulfuric acid will also decompose olivine and form $MgSO_4$ and $FeSO_4$. Large deposits of sulfates have been observed by the Mars Exploration Rover (MER) missions *Spirit* (Gusev crater) and *Opportunity* (Meridiani Planum) at the equatorial regions of Mars (Gellert *et al.*, 2004; Rieder *et al.*, 2004).

Alteration of the Pathfinder soils is supported by the high FeO/MnO weight ratios of some soils and the high abundances of S and Cl in all soils. The average Pathfinder soil FeO/MnO weight ratio is 68 ± 15, which overlaps the SNC values. Yet, some Pathfinder soils, like A-5, have FeO/MnO

Table 3.4. *Inferred Pathfinder water abundances ±1σ*

Soils	[H_2O wt.%][a]	[H_2O wt.%][b]	[H_2O wt.%][c]
A-2	n.d.	1.6 ± 1.7	−0.6 ± 1.7*
A-4	n.d.	1.2 ± 1.7	−1.0 ± 1.7*
A-5	n.d.	−1.4 ± 1.7*	−3.7 ± 1.7*
A-10	n.d.	2.5 ± 1.7	0.3 ± 1.7*
A-15	n.d.	1.0 ± 1.6*	−1.2 ± 1.6*
Rocks			
A-3	2.0 ± 1.3	0.3 ± 1.3*	−1.9 ± 1.3
A-7	7.1 ± 1.4	3.4 ± 1.4*	1.3 ± 1.4*
A-8†	—	2.9 ± 1.6	1.0 ± 1.6*
A-16	4.2 ± 1.3	1.5 ± 1.5*	−0.8 ± 1.4
A-17	5.7 ± 1.3	4.3 ± 1.3*	2.2 ± 1.3
A-18	2.7 ± 1.3	0.1 ± 1.3*	−2.0 ± 1.3

Key: The different columns are for varying assumed oxidation states of sulfur and iron.
[a] S^{2-} and Fe^{2+},
[b] S^{6+} and Fe^{2+},
[c] S^{6+} and Fe^{3+}.
Errors are calculated from statistical error and laboratory accuracy. n.d. means not determined; † indurated soil; * probable oxidation state based on IMP data (McSween *et al.*, 1999; Bell *et al.*, 2000; Bridges and Crisp, 2000). Some samples have * labels on both columns (3) and (4) because red/blue ratios from different IMP analyses yield contradictory results and may therefore be less reliable.

values as high as 135 ± 30 (obtained by the Chicago calibration, only). The Mainz group found at Meridiani Planum several soil samples with high FeO/MnO ratios of around 100 (Rieder *et al.*, 2004) that also contained high contents of the mineral hematite as determined by the Mössbauer Spectrometer (Klingelhöfer *et al.*, 2004). This FeO/MnO deviation for the Pathfinder soils may indicate that some of the Pathfinder soil is not derived by physical weathering of igneous rocks. This is further supported by the prevalence of correlated MgO, SO_3, and Cl, indicative of the presence of salts that may have resulted from weathering. Some ideas for the formation of Martian soil include chemical weathering of basaltic starting materials in a warmer and wetter ancient (3–4 Ga) climate (Banin *et al.*, 1992; Gooding, 1992; Burns, 1993), sporadic weathering of basalt at high temperatures during shock events (Morris *et al.*, 1995), or thermal alteration of palagonitic tephra by heating during penetration or emplacement of hot lava (Bell *et al.*, 1993).

The Martian Pathfinder soil appears to consist of nanophase iron oxides, silicate mineraloids (amorphous materials), and salts (Banin *et al.*, 1997 and references therein). Bell *et al.* (2000) and Morris *et al.* (2000) claim that these materials match the chemistry, near-infrared to visible spectroscopy data and the magnetic experiment data (Madsen *et al.*, 1999; Hargraves *et al.*, 2000) most consistently. The Imager for Mars Pathfinder (IMP) visible and near-infrared Pathfinder imager operated in the 400–1000 nm range and observed the Pathfinder soils and rocks (Bell *et al.*, 2000 and references therein). The soil IMP data are most consistent with palagonitic weathering of SNC-like basaltic glasses (Bell *et al.*, 2000; Morris *et al.*, 2000). Morris *et al.* (2000) further suggest that glassy protoliths on Mars may be produced by volcanic fire fountaining and/or impact processes (with later enrichment in S and Cl). Comparison with rates of lunar glass production supports this as a viable possible source for the Martian soils (Morris *et al.*, 2000).

As summarized by Banin (2005), the Martian soil appears to be a product of the slow chemical and physical alteration involving gaseous and aqueous species within the Martian atmosphere and/or hydrosphere with Martian rocks. The soil compositional results from the Viking, Pathfinder, *Spirit*, and *Opportunity* missions have all been utilized to infer possible widespread processes affecting the Martian surface which include acid-fog reactions of volcanic emissions with bedrock (Banin *et al.*, 1997; Tosca *et al.*, 2004), and/or precipitation of salts from the evaporation of shallow seas (Squyres *et al.*, 2004) or seeping-up acidic groundwater (Burns and Fisher, 1990).

Some of these soil formation hypotheses may be tested through analyses of how such processes will affect the soils' chemistry. For example, changes in abundances due to acid-fog reactions for Shergotty were calculated by Bell *et al.* (2000), using the experimental data of Banin *et al.* (1997). In particular, acid-fog reactions leach out Ti, Fe, Al, and Mg and add volatiles (such as sulfur and chlorine) contained in the original acid-fog. However, there is no measurable difference between the Viking 1 soils, Pathfinder soils, and Shergotty Mg/Si or Ti/Fe values. This indicates that if weathering and/or acid-fog reactions were widespread on the Martian surface, then the starting material must have been more mafic than Shergotty (a typical Martian basalt). In support of some chemical alteration process, the IMP soil spectral data (based primarily on iron absorptions) independent of the APXS chemical composition are similar to spectra of Hawaiian tephra that have been aqueously and thermally altered (Bell *et al.*, 2000).

An additional model, proposed by Brückner *et al.* (1999), of major soil formation purports the mechanical mixing of Martian meteorites, Pathfinder SFR, and volcanic emissions. The Martian soils show a considerable Mg concentration from which it was inferred, based on Viking data, that the crust of Mars is mafic (Clark, 1993). The Martian meteorites also have mafic to ultramafic composition (see Chapter 17). In contrast, the rocks at Ares Vallis represent highly fractionated crustal material, rich in Si and K, but low in Mg, which holds regardless of the nature of these rocks, that is, igneous or sedimentary. The compositional difference between soils and rocks cannot simply be explained by physical weathering of these rocks, even considering weathering and interaction with volcanic gases SO_2 and HCl (Wänke *et al.*, 2001). Addition of material richer in Mg and Fe, but poorer in K and Cr as observed by the Martian meteorites, seems unavoidable. Taking the almost identical soil composition at the three landing sites (Viking 1 and 2 and Pathfinder) as representative for the whole

surface soil of Mars, Brückner *et al.* (1999) have shown that all elements fit into a two-component mixing model with the Pathfinder rocks (high K, low Mg contents) as one component and the Martian meteorites as the other component. Hence, it was concluded that large geologic units of Pathfinder rock composition as well as of basaltic (Martian meteorites) composition must exist on Mars and these units cover about equal areas. This hypothesis is consistent with the orbital Thermal Emission Spectrometer (TES) data (Bandfield *et al.*, 2000). The admixture of a Pathfinder type rock component is needed to especially account for the high K content of the soils.

3.4.2 Rocks

The full suite of X-ray, proton-mode, and alpha-mode measurements (including water abundance modeling) need to be evaluated to interpret the petrology of the Pathfinder rocks. Although the α-proton mode and the X-ray mode yield similar chemical abundances for the Pathfinder rocks on a volatile-free basis, the potential presence and abundance of water in some of the rocks brings into question the hypothesis that they are unaltered igneous rocks. If the Pathfinder rocks are indeed igneous, then their bulk chemistry must first be examined on an anhydrous basis, as is done for terrestrial igneous rocks (Philpotts, 1990). However, the amount of water estimated to be present in the Pathfinder rocks A-7 and A-17 is higher than that of any unaltered terrestrial mafic igneous rocks or SNC meteorites. A-7 and A-17 may instead be metamorphic or sedimentary rocks. Therefore, various petrogeneses of the Pathfinder rocks will be considered.

The Pathfinder rocks analyzed with the APXS were also examined with the rover and lander cameras having spatial resolutions of 0.7–1 mm per pixel at closest range (McSween *et al.*, 1999). Used in tandem, the two instruments may be able to determine the lithology of the rocks examined. However, the rocks have ambiguous textures. Some have lineations and/or flutes while some are bumpy and/or pitted (McSween *et al.*, 1999). The texture of some rocks resembles volcanic vesicles. However, these vesicles may also have been formed by chemical etching of the rocks to produce a pitted texture. A chemical etching process was described by Campbell and Claridge (1987) for some rocks in Antarctica. Furthermore, vesicles can also be produced by honeycomb weathering which commonly forms in sandstones by a combination of chemical salt weathering reactions and physical weathering (Robinson and Williams, 1994). The rocks also have abundant ventifacts (facets and polished fragments from sandblasting), which obscure the original rock texture (Bridges *et al.*, 1999). Thus, the textural observations from the rover camera images do not unequivocally determine the lithology of the rocks.

The rock images and the chemical analyses both support various amounts of soil cover on the rocks. Since the soil contains significantly more sulfur, the sulfur content was utilized to infer the composition of the Pathfinder SFR using linear regressions (Figure 3.9) as done previously (Rieder *et al.*, 1997b; McSween *et al.*, 1999). This SFR composition may then be utilized to infer the potential lithology of the Pathfinder rocks.

Images from the Pathfinder landing site suggest that some of the Pathfinder rocks may be conglomerates, resulting from and indicative of intense fluvial weathering of the Martian surface (Rover Team, 1997; Ward *et al.*, 1999). One possibility is that the Pathfinder rocks are graywackes as suggested by McSween *et al.* (1999). Pettijohn (1975, p. 212) describes graywackes as dark gray sandstones with a significant matrix content in which either lithic fragments (lithic graywackes) or feldspars (feldspathic graywackes) dominate. Graywackes form one-fifth to one-fourth of all (terrestrial) sandstones, and are most common in Paleozoic and earlier orogenic belts. They are absent in undeformed sequences deposited on stable cratonic or shield areas. They are generally marine, and in many terrestrial samples are believed to be turbidite sands (Pettijohn, 1975, p. 230). As a note of caution, however, sandstones are normally classified on the basis of their texture and modal (visual mineral abundance) mineralogical composition (Pettijohn, 1975, p. 210). With only the normative (inferred mineral abundance from bulk chemistry) mineralogical composition and a rover view of the surface of the rock, classification of the Pathfinder SFR as sedimentary is problematic.

It is unlikely that some chemical weathering process or conglomeration of sediments produced abundances which are so consistent with an evolved igneous rock from an SNC parent composition (as illustrated by the work of Minitti and Rutherford [2000] described later on within this section). Furthermore, some Pathfinder rocks (e.g., Barnacle Bill, A-3, which has the lowest inferred water content) have spectral properties which match those of fresh basalt to basalt-andesite (Smith *et al.*, 1997; Ward *et al.*, 1999), and others (e.g., Shark, A-17, which has the highest inferred water content) which match those of weathered basalt or basalt-andesite (Smith *et al.*, 1997). The water content of some Pathfinder rocks, which is the only chemical data bringing into question the rocks' igneous origin, may thus be due to weathering of original evolved igneous rocks (basalt-andesites) involving little to no major chemical changes except for the addition of water and oxidation of iron. Mössbauer detection of ferric oxyhydroxides (hematites) and oxyhydroxysulfates (jarosites) at the Meridiani Planum *Opportunity* landing site as well as its detection of weakly and pervasively altered olivine within the plains and Columbia Hills of the *Spirit* landing site, respectively, support such a hypothesis (Klingelhöfer *et al.*, 2004; Morris *et al.*, 2006).

An important caveat of these interpretations is that all of these comparisons of the Pathfinder SFR assume that its composition may be accurately deduced using the linear regressions. However, there are four observations bringing into question the determination of the SFR chemistry in this fashion. First, while many oxides show good linear regressions against sulfate, some major elements such as calcium and aluminum show considerable scatter among the rock data. This implies that there is some chemical heterogeneity among the rocks. Second, the plot of the sodium versus sulfate shows that the rock trend with sulfate is different

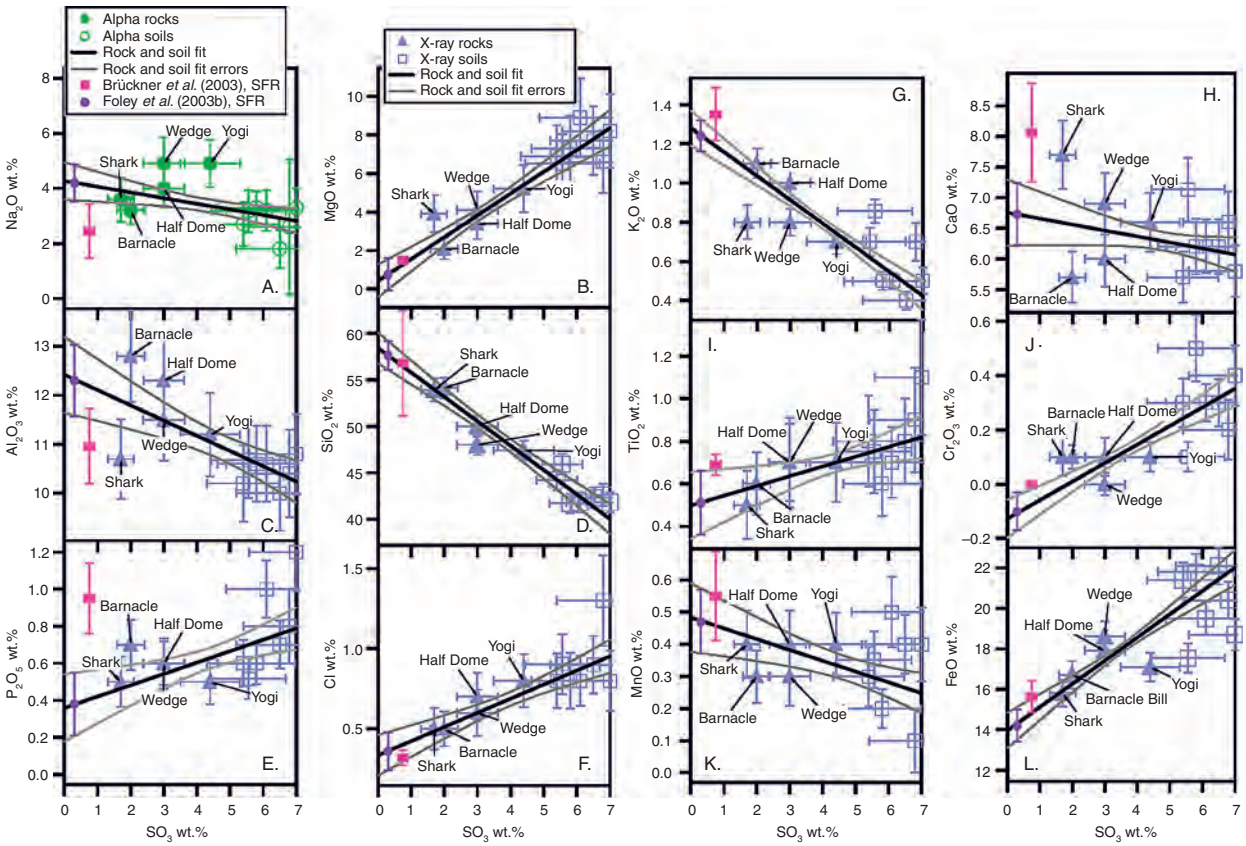

Figure 3.9. Linear regressions for oxide and element contents, calculated from data in Table 3.1, versus sulfate content for Pathfinder rocks and soils. All of the rocks have considerably less sulfur than the soils and linear trends to no sulfur are made showing that some soil-like component appears to cover the rocks by varying degrees. The linear regressions enable computation of the soil-free rock composition (SFR) and were computed using the technique of Williamson (1968) which takes into account the errors in both the ordinate and the abscissa for each oxide-sulfate pair. Some oxides, such as MgO and SiO_2, show good linear trends to low sulfate content in the rocks. However, other oxides such as Al_2O_3 and CaO, indicate some chemical heterogeneity among the rocks, and the FeO plot illustrates some chemical heterogeneity among the soils. (For a color version of this figure, please refer to the color plate section or to the e-Book version of this chapter.)

from the linear regression trend acquired with both rock and soil data. Specifically, the concentration of Na_2O in rocks increases with sulfate. This increase of Na_2O in the rocks with increasing sulfate may imply some sort of alteration trend (i.e., as the remnant of the evaporation of a fluid containing such salts rich in both sodium and sulfur). If so, then the SFR Na_2O abundance may be 2.4 wt.% attained from linear regression of the rocks alone. Third, there is chemical heterogeneity among the soils' iron content. While A-5, A-10, and A-15 are all high in iron content, A-2, A-4, and A-8 are substantially lower in iron content. This implies that the linear regression for the iron content of the rocks may be inappropriate. Fourth, the observation from the α-proton joint mode that the A-17 Pathfinder rock, which is also least covered with soil, contains 3.3 ± 1.3 wt.% water, assuming a 50/50 mixture of FeO and Fe_2O_3, is inconsistent with the interpretation that all the rocks are completely unaltered igneous rocks. Hence, some linear regression trends as well as the water content of the rocks bring into question the validity of linear regression analyses to determine an SFR composition. There are, therefore, some significant differences from an ideal mix of purely unaltered igneous rocks with sulfate-rich more mafic soils. They are not, however, as evident as the overall patterns of good linear regressions for most oxides. Therefore, the deviations (from the linear fit and among the water contents) probably indicate some minor weathering reactions occurring on the rock surfaces that do not appear to drastically affect the derived composition of the Pathfinder SFR (as inferred from the quality of the linear fits, or the r^2 values, which are utilized to determine the error bars for the SFR composition in addition to the individual error measurements).

To derive the SFR composition, Brückner *et al.* (2003) fitted only the rock data and extrapolated the linear regression line to higher sulfur values. For all elements, except for Al, the soil data scatter around the rock regression line (Brückner *et al.*, 2003). This observation indicates that there is adhering soil on the surface of the rocks, however, not sufficient to cover the rock surfaces completely. A-17, the one rock with the lowest S content, comes close to the derived SFR composition. This implies that A-17 has the lowest soil coverage of all rocks. If A-17 had an alteration rind, then all other rocks would have the same type of rind, otherwise they would scatter much more. However, the existence of some type of alteration rind cannot be excluded. Keeping in mind the low penetration depth of alphas and

X-rays, this rind could be rather thin (less than ca. 50 μm) and in the worst case contiguous. It would mean only an altered surface composition was obtained by the APXS measurements and the composition of the underlying rock is not known. A-17's water content should be almost the same as the water content of the pure rind or rock, while the soils should have less water than the rocks, otherwise more water would have been found on those rocks with higher soil coverage. From Table 3.4, it appears that the detected water contents of the rocks are somewhat inconsistent with the coverage of soil implying a more complex scenario. Based on these observations, it is possible that the rind (if present) covered the rock surfaces only partly. Saltating dust grains could have polished fractions of the surface area over eons. Furthermore, it is possible that this partial rind contains only water which has not chemically altered the original rock composition. In this scenario, the SFR composition resembles a water-poor silicon-rich igneous rock.

If the Pathfinder rocks are igneous, then they may contain up to 0.13 wt.% sulfur (the maximum sulfur content measured in SNC meteorites, such as Zagami) as FeS or FeS_2, the two iron sulfide phases found in SNC meteorites. The data from both the rocks and the soils may be used for the linear regressions (Figure 3.9) to 0.1 – 0.3 wt.% (Foley *et al*., 2003b and Brückner *et al*., 2003, respectively) sulfur to compute the SFR composition (Table 3.5). Although most X-ray abundances from this study and the Brückner *et al*. (2003) abundances are similar, those of Brückner *et al*. (2003) were computed from the rock data alone and extrapolated to 0.3 wt.% sulfur. This different treatment therefore yields different results for some elements. In particular, the soil-free values for CaO and Na_2O are affected by this difference. In contrast, the differences in P_2O_5 are due to differences in the asymmetrical peak corrections, as described previously in the calibration section. All other SFR values are the same within the measurement errors.

This SFR chemical composition may then be used to compute a normative mineral composition, with the assumption that the SFR is igneous, by the same technique typically used for terrestrial fine-grained igneous rocks for classification purposes (Philpotts, 1990). The linear regressions to 0–0.3 wt.% sulfate under the assumption that the rocks are igneous, yield an SFR that is a tholeiitic andesite to basalt-andesite (the composition lies on the 57% silica content border between andesites and basalt-andesites) using the classification scheme for volcanic rocks based on total alkalis, silica, FeO, and MgO content as described by Le Bas *et al*. (1986) and Irvine and Baragar (1971).

While the new and previous Pathfinder SFR compositions are similar to terrestrial anorogenic tholeiitic andesite from Galapagos, this similarity does not necessarily explain the actual Martian petrogenesis. As described by Minitti and Rutherford (2000), the source material for the Galapagos andesite (Juster *et al*., 1989) is iron-rich and aluminum-poor relative to other terrestrial magmas. However, it is not as iron-rich and aluminum-poor as the estimated parent magmas typical of SNCs like that of Chassigny, a Martian dunite (Johnson *et al*., 1991), and of Shergotty, a Martian basalt (Hale *et al*., 1997).

Table 3.5. *The abundances for the soil-free rock (SFR)*

Oxide or element	Foley SFR	Brückner SFR
Na_2O	4.2 ± 0.6	2.46 ± 1.00
MgO	0.8 ± 0.8	1.51 ± 0.15
Al_2O_3	12.3 ± 0.7	11.0 ± 0.8
SiO_2	57.7 ± 1.5	57.0 ± 1.5
P_2O_5	0.4 ± 0.2	0.95 ± 0.20
S	0.10 + 0.04	0.30 + 0.06
Cl	0.4 ± 0.1	0.32 ± 0.05
K_2O	1.20 ± 0.08	1.36 ± 0.13
CaO	6.7 ± 0.5	8.09 ± 0.80
TiO_2	0.50 ± 0.15	0.69 ± 0.14
Cr_2O_3	—	—
MnO	0.5 ± 0.1	0.55 ± 0.14
FeO	14.2 + 0.8	15.7 + 0.8

Key: Error bars for the Foley *et al*. (2003b) Pathfinder SRF are derived using the errors in both the oxide or element and sulfur in the linear regression. Error bars listed for SFR of Brückner *et al*. (2003) results are approximate errors for their regression based on their average reported errors and assuming that their silica error is comparable to that of Foley *et al*. (2003b).
Source: From Foley *et al*. (2003b) and Brückner *et al*. (2003).

Minitti and Rutherford (2000) showed experimentally that the Pathfinder sulfur-free rock can be formed using the estimated Chassigny parent magma (Johnson *et al*., 1991). The experimental results of Minitti and Rutherford (2000) with a hydrated Chassigny parent magma are similar to the preliminary chemical abundances for the SFR from Rieder *et al*. (1997a). However, the newly computed Pathfinder SFR composition is numerically closer for some major oxides, like SiO_2 and FeO, to a highly evolved product from the dry Chassigny parent magma. Some results of the water-bearing experiments do appear to match the Pathfinder SFR chemistry as well as, or better than, the results of the dry experiments (Figure 3.10). Nevertheless, the proximity of most oxides to the anhydrous lines of descent (as visualized by following the trend of the anhydrous samples to the lower MgO values) brings into question the need to invoke a hydrous source magma to form the Pathfinder SFRs, and demonstrates that the final Pathfinder SFR chemistry can be obtained in an igneous fashion from the Chassigny source magma.

The Pathfinder SFR represents the most fractionated material measured on Mars so far. The K concentrations of 1.1 wt.% compared to the estimated abundance of 305 ppm K in the Martian mantle (Wänke and Dreibus, 1994) lead to an enrichment factor of 36. Assuming a simple one-stage process for the generation of these rocks, this means a rather small degree of partial melting on the order of 3%.

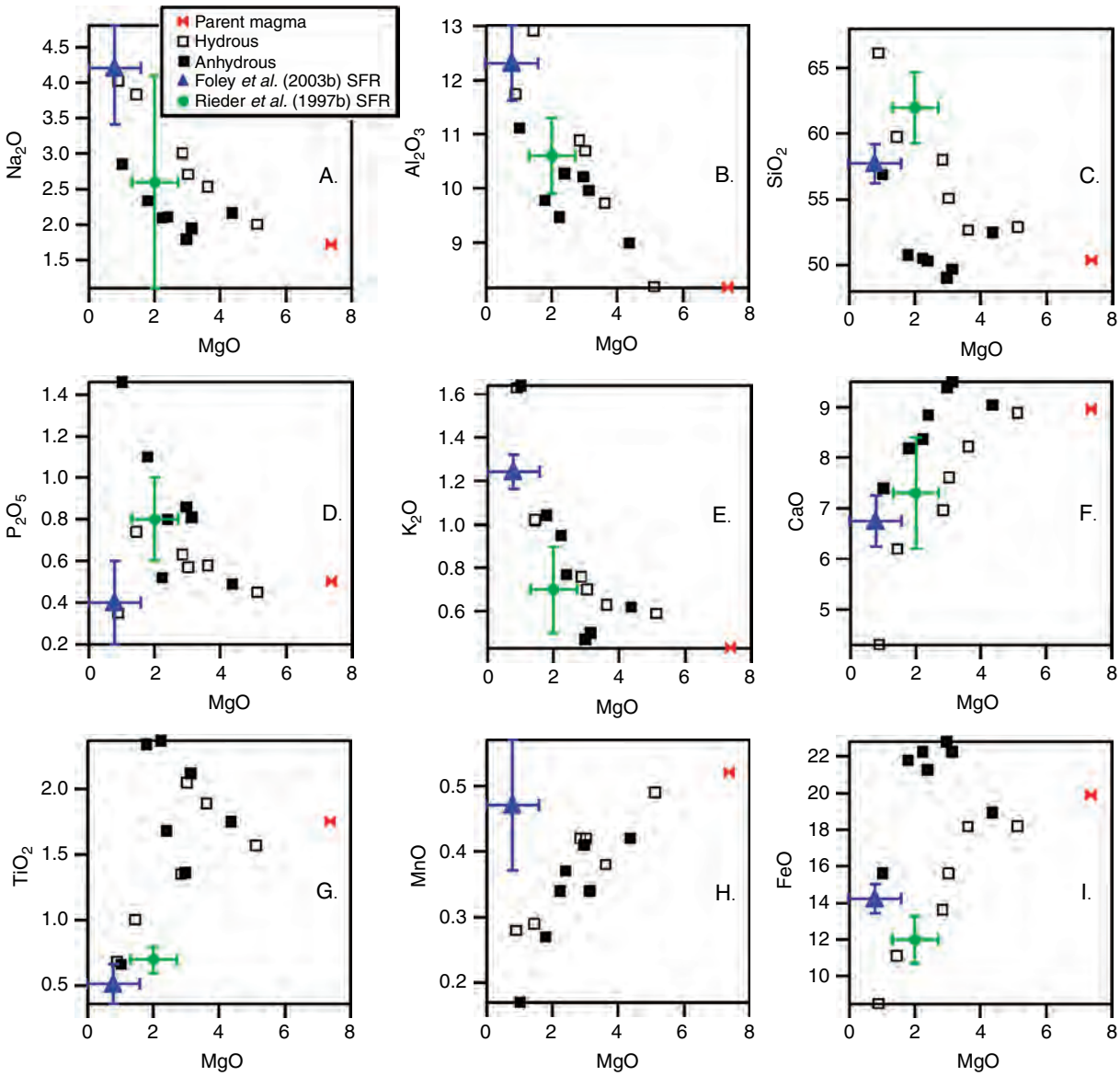

Figure 3.10. Experimental data for wt.% oxides plotted versus MgO wt.% from Minitti and Rutherford (2000) for dry (solid squares) and hydrated (open squares) crystallization experiments from a Chassigny parent magma composition compared with the Pathfinder SFR compositions. Error bars for Minitti and Rutherford (2000) data are small, as shown graphically within their oxide plots, but are not given numerically and are therefore not plotted here. Abundances are plotted against MgO wt.% as an indicator of the degree of crystallization due to olivine and pyroxene formation. For many elements, the new Pathfinder SFR composition appears to be consistent with both the hydrous and the anhydrous results. However, for the major oxides SiO_2 and FeO, it is most similar to the experimental results of the dry crystallization from the Chassigny parent magma by Minitti and Rutherford (2000). (For a color version of this figure, please refer to the color plate section or to the e-Book version of this chapter.)

Another useful way of comparing the Pathfinder and SNC chemistries is to compare element ratios. In particular, element ratios such as Mg/Si versus Al/Si and FeO/MnO of igneous rocks have been observed to be distinct for different parent bodies (Jagoutz *et al.*, 1979 and Wänke *et al.*, 1986; Wänke and Dreibus, 1988 and Drake *et al.*, 1989, respectively). Furthermore, element ratios Ca/Si versus Fe/Si are informative of SNC igneous rock types (see Chapter 17).

For the Mg/Si versus Al/Si relation, rocks having higher Mg/Si and lower Al/Si are more mafic and hence more representative of the mantle, while samples which have lower Mg/Si and higher Al/Si have more plagioclase and are more representative of the crust. The Pathfinder SFR plots at the lowest Mg/Si and the highest Al/Si value along the inferred SNC fractionation line from Wänke *et al.* (1986), corresponding to that expected for rock that is more evolved than an SNC basalt. The bulk igneous FeO/MnO, which does not fractionate during igneous processes (Laul and Schmitt, 1973), represents the mantle value after the original FeO/MnO attained by the planetary body from accretion and after planetary differentiation with core formation (Wänke and Dreibus, 1988; Drake *et al.*, 1989). The FeO/MnO for the SFR of 30 ± 9 is similar to the average SNC value of 40, which supports a Martian igneous, as

opposed to sedimentary, origin. Furthermore, the low values for Ca/Si and Fe/Si (lower than all SNCs) of the Pathfinder SFR reinforce its geochemically evolved nature, reflected by its relatively high silicon content. In comparison, terrestrial tholeiitic basalt-andesites also have lower Ca/Si and Fe/Si than terrestrial basalts.

Recently, our understanding of the use of ratio trends of Mg/Si versus Al/Si to distinguish between Martian and terrestrial mantle fractionation processes has been broadened with new chemical analyses of primitive basalts at the Gusev landing site (McSween *et al*., 2004) and the newly found Yamato 980459 (Greshake *et al*., 2004), as well as TES Types 1 and 2 inferred compositions (McSween *et al*., 2003), all of which fall along the terrestrial fractionation line. This implies that there may be more similarities in bulk planetary chemistry between Earth and Mars than previously inferred. Furthermore, the other currently known SNCs all of which are significantly below the terrestrial fractionation line may be more similar to terrestrial intraplate magmatic suites in composition and petrology (Nekvasil *et al*., 2004). The similarity of the Pathfinder SFR chemistry to that expected for an evolved SNC implies that the Pathfinder rocks are likely to be igneous rocks which have not been significantly affected by chemical erosional processes, but may contain minor weathering products.

3.5 COMPARISONS WITH OTHER MARTIAN MATERIALS

The bulk chemical abundances from the Pathfinder data enable the comparison with the Viking 1 and 2 XRF MER APXS, TES, and SNC abundances. This comparison serves to broaden and deepen our understanding of the potential petrogenesis of the Pathfinder samples.

3.5.1 Pathfinder versus Viking and MER analyses

In order to compare soils from the Pathfinder with those of the Viking and MER missions, the chemical abundances for soils from the Viking 1 and 2 XRF (Clark *et al*., 1982) measurements were normalized to 100% with certain assumptions. Because the Viking XRF instruments did not measure Na_2O, P_2O_5, Cr_2O_3, or MnO and possibly because of particle size effects (Clark *et al*., 1982), the Viking abundances did not total to 100%. In order to compare the Viking values directly with the Pathfinder values, average Na_2O/SiO_2, P_2O_5/SiO_2, Cr_2O_3/Fe_2O_3, and MnO/Fe_2O_3 Pathfinder values were assumed for the Viking soils, and then the Viking soils were re-normalized to 100%. Sulfur and iron are computed as SO_3 and Fe_2O_3 because of the Viking soil measurements (Toulmin *et al*., 1977) which support the presence of sulfur as SO_3, and because of the redness of the Martian soils that support the presence of iron as Fe_2O_3.

The soil abundances from the Viking and Pathfinder analyses have some similarities and differences. The Pathfinder and Viking soils contain similar concentrations of all elements measured, within the measurement errors. However, the potassium content of the Pathfinder soils is significantly higher than those of the Viking soils, which are below the Viking detection limit of 0.12 wt.% K (Clark *et al*., 1982). The Viking abundances of both Al_2O_3 and Fe_2O_3 are systematically lower, while both SiO_2 and SO_3 abundances are systematically higher than the Pathfinder results. More variability for the Cl abundances was detected by the Viking XRF instruments. The Viking and Pathfinder abundances of MgO, CaO, and TiO_2 show no systematic differences. The observed systematic differences may be due to differences in contributions from local rocks, particle sizes measured, and soil depth analyzed by the different instruments. The Viking landers scooped soil into the XRF instrument from soil depths of 0–22 cm (Clark *et al*., 1982). Also, many of the Viking soils were sieved before analyses, leading to the predominant measurement of fines having diameters less than 2 mm (Clark *et al*., 1982). In contrast, the Pathfinder APXS was placed against *in situ* soil and therefore measured soil surfaces, which consisted of fines mixed with pebbles and/or clods (Bell *et al*., 2000). The differences in Cl may be due to the sampling depth difference between the Viking and Pathfinder instrument. For example, two of the Viking soils (U-6 and U-7) have the lowest Cl content and are from depths of 6 and 12 cm, respectively. In contrast, the Viking and Pathfinder abundance differences for SiO_2, Al_2O_3, K_2O, and Fe_2O_3, may be explained by the differences in rock content and abundances within the analyzed soils.

The Pathfinder and Viking soils are very similar to the MER soils at the Gusev crater landing site and to some soils at the Meridiani landing site (Gellert *et al*., 2004 and Rieder *et al*., 2004, respectively). This is most likely the result of global mixing and distribution by dust storms (Gellert *et al*., 2004). However, the soils at the Pathfinder, Gusev crater, and Meridiani landing sites also show distinctive contributions from local rocks analyzed by the APXS. There is more basalt-andesitic or weathered basalt material at the Pathfinder site, more primitive basaltic component at the Gusev plains, and more evaporite rock components at the Meridiani site. There is more definitive evidence of aqueous alteration at both the Gusev and Meridiani landing sites than at the Pathfinder landing site because of improvements in the APXS, rock preparation tools which enabled the grinding of the MER rocks, and the additional information gathered from the Mini-TES (Mini-TES – Miniature Thermal Emission Spectrometer), Mössbauer, and Microscopic Imager instruments. The MER APXS, which has better X-ray energy resolution and higher signal-to-noise ratios (because of improvements in the detector), has the ability to measure bromine and zinc at levels indicative of aqueous alteration in the soils at both Gusev and Meridiani (Gellert *et al*., 2004; Rieder *et al*., 2004). The soil at both Gusev and Meridiani coats the rocks to varying degrees with ferric-iron-rich dust (Bell *et al*., 2004a,b; Christensen *et al*., 2004a,b; Morris *et al*., 2004). There is evidence of rock rinds possibly different in chemistry from the soils which are apparent from the rock–soil trends investigated by McSween *et al*. (2004). Some rock–soil trends

investigated by McSween *et al.* (2004) even imply that some of the soils at the MER sites were created by chemical weathering of the local rocks. The Mini-TES measurement of minor carbonates and bound water at the Gusev site, hematite-rich soils at the Meridiani site, rock rinds indicative of chemical weathering on some rocks at the Gusev site, and evaporite-rich soils and rocks at the Meridiani landing site are all indicative of aqueous alteration at both sites. The Gusev site underwent less intense aqueous alteration and has apparently been dominated by physical weathering for some time, as indicated by the prevalence of pyroxene and olivine in the soils (Bell *et al.*, 2004a; Christensen *et al.*, 2004a; Morris *et al.*, 2004). In contrast, from all of the rover remote-sensing instruments as well as from textural evidence as discussed by Squyres *et al.* (2004), the Meridiani site appears to have undergone long-term episodic alteration by inundation followed by evaporation of water.

Thus, in contrast to the Pathfinder SFR, the MER APXS analyses, acquired from two distinct landing sites from many kilometers of explored terrain (as described by in Chapter 4), yield rock compositions ranging from basaltic, similar in bulk chemistry to the SNC meteorite Shergotty, to basalts more primitive than any SNCs. Some rocks are covered with wind-blown soil and others with weathered rock rinds at the Gusev landing site (Christensen *et al.*, 2004a; Gellert *et al.*, 2004; McSween *et al.*, 2004). Basaltic and evaporite-rich rocks occur at the Meridiani landing site (Christensen *et al.*, 2004b; Rieder *et al.*, 2004).

3.5.2 Pathfinder rocks versus TES surface types and SNCs

As noted in the previous section, the MER results have shown that there are several types of igneous and/or altered rocks that may be difficult to separate from the TES classification. Hence, the MER results have revealed that the local geology and geochemistry are far more complicated than hinted at the regional scale by remote sensing.

Nevertheless, Mars appears to have two distinct end-member types of igneous rocks on its surface. This is inferred from the observation that the large compositional difference between soil and rocks at the Pathfinder landing site cannot be explained by physical weathering of these rocks even considering strong weathering and interaction with volcanic gases rich in SO_2 and HCl (Brückner *et al.*, 1999; Wänke *et al.*, 2001). Addition of material richer in Mg and Fe, but poorer in K and Cr (as compared to local rocks) is a definite necessity. Such a material is in fact known from the composition of Martian meteorites. In particular, the Pathfinder soil can be explained as a two-component mixture of physically broken down soil-free local rocks as one component and the mean composition of Martian meteorites as the other component (Wänke *et al.*, 2001). A close inspection of the mixing model revealed that in addition to these two major components an iron-rich component is required, too. Areas rich in hematite have been observed at the surface of Mars (Christensen *et al.*, 2000); hence, addition of Fe from the hematite deposits is plausible. However, one should bear in mind that hematite and Mg were originally supplied by weathering of basaltic material, for example, decomposition of olivine, which dissolves easily in slightly acidified liquids.

The Mainz group concluded from their Pathfinder data and their mixing model that large geological units of Pathfinder SFR composition as well as basaltic (Martian meteorite) composition must exist on Mars and cover about equal areas (Wänke *et al.*, 2001; Brückner *et al.*, 2003). That is exactly what has been inferred by Bandfield *et al.* (2000) from two types of TES surface spectra of Mars. These two TES surface spectra are called Type 1, which is prevalent in the southern highlands, and appears to be basalt (Bandfield *et al.*, 2000; Boynton *et al.*, 2003), and Type 2, which is prevalent in the northern lowlands, and appears to be either andesite (Bandfield *et al.*, 2000) or weathered basalt (Wyatt and McSween, 2002).

The mineral abundances inferred from TES Types 1 and 2 both contain up to 15% sheet silicates (Bandfield *et al.*, 2000) implying that both surfaces may have been altered by aqueous processes. The volumetric mineral abundances of Type 1 and Type 2 TES compositions (Bandfield *et al.*, 2000; Wyatt and McSween, 2002), the normative mineral abundances for the Pathfinder SFR, and two SNC meteorite modal mineralogies are listed in Table 3.6. Los Angeles and QUE 94201 are the only SNC meteorites listed in Table 3.6 because they are most similar (for the known SNCs) to the mineralogies of the Pathfinder SFR and the TES surface spectra. As shown, the inferred mineral content for the SFR does not match either Type 1 or 2 well, but is overall more similar to Type 1. This may be due to the inability to acquire an accurate mineral norm for the SFR in this fashion (due to the potential presence of nonigneous minerals such as clays) or it may imply that the Pathfinder rocks are indeed a local unique type of igneous rock which is not similar to Type 1 or 2 (the former is thought to be more probable based upon reasons described in the following paragraph).

In contrast, comparison of the major-element composition of the Pathfinder SFR with the composition inferred from the TES data (Hamilton *et al.*, 2001; McSween *et al.*, 2003) shows a close correspondence with TES Type 2, with the exception of magnesium, which is much lower in the SFR. The TES-derived abundance of about 15–30% phyllosilicates implies a water content of 2–4 wt.%, assuming 12 wt.% water in the clay minerals. This is consistent with the APXS measurement on rock A-17. Furthermore, as pointed out by Brückner *et al.* (2003), the Mars Odyssey orbiter Gamma Ray Spectrometer data also detect higher abundances of silica and potassium in the Type 2 materials (Boynton *et al.*, 2003) implying that this unit may indeed be basalt-andesitic and that if it is altered material, it must be on the order of centimeters deep (due to the penetration depth of the gamma rays). That in turn would mean that the Pathfinder rocks (if representative of Type 2 surface material) that are several tens of centimeters in height should almost entirely consist of altered material, which cannot be excluded, but is not likely given the major and minor element ratios matches with those expected of an evolved igneous SNC rock.

Table 3.6. *Mineral abundances for Pathfinder SFR, SNCs Los Angeles and Que94201, and TES Types 1 and 2 martian surfaces*

SFR norm mineral comp.	Los Angeles mineral mode	QUE 94201 mineral mode	Type 1*	Type 2*	Type 1**	Type 2**
49.7% Feldspar; $An_{20}Or_{19}$	~43% Feldspar, ($An_{41}Or_4$ to $An_{58}Or_1$)	~46% Plag. ($An_{52–66}$)	50% Plag	35% Plag.	33% Plag.	25% Plag.
18.3% Cpx and 17.3% Opx	~38% Cpx	~44% Cpx	25% High-Ca Pyx	10% Cpx	41% Low- and High-Ca Pyx	16% High-Ca Pyx
9.5% Qtz or silica-rich glass			15% Sheet silicates	15% Sheet silicates	14% Clay/sheet silicates	31% Clay
				25% K-rich glass		14% K-feldspar

Key: All Type 1 and 2 TES measurements have errors of approximately 10–15 absolute % (Bandfield *et al*., 2000). Bandfield *et al*. (2000) results are Type 1* and Type 2*. Wyatt and McSween (2002) results are Type 1** and Type 2**. Minerals less abundant than 5% are not listed.

3.6 CONCLUSIONS

The new chemical analyses of Foley *et al*. (2003b) and Brückner *et al*. (2003) yield similar bulk abundances which differ somewhat from the preliminary X-ray analyses of Rieder *et al*. (1997b). The results indicate that the Pathfinder rocks are more silica-rich and iron-poor than the Pathfinder soils and appear to be covered with various amounts of wind-blown soil and possibly an optically thick (for the APXS) weathering rind. These final analyses also include minor element abundances for P, Cr, and Mn (from the X-ray mode) and an upper limit on carbon abundance (from the α-mode detection limits) which are roughly in agreement with one another. Furthermore, the α-proton mode calibration of Foley *et al*. (2003a) yields refined sodium abundances and bulk oxygen abundances indicative of mineral-bound water of $\sim 4.3 \pm 1.3$ wt.% in some of the Pathfinder SFRs.

The inferred chemical composition of the SFRs is more silica-rich and iron-poor than any SNC meteorite. The compositions of the SFRs are consistent with evolved (relative to typical SNC basalt) SNC-like igneous rocks that are minimally altered, as indicated by the elemental ratio trends and crystallization trends as well as the presence of mineral-bound water. The Pathfinder SFR compositions are similar to basalt-andesites that form by crystallization of a dry Chassigny magma parent source (Minitti and Rutherford, 2000). The matches of the element and oxide ratios of Mg/Si, Al/Si, Ca/Si, Fe/Si, and FeO/MnO with the expected values for an evolved SNC also support this interpretation.

The Pathfinder SFR may be ancient highland material from the Xanthe Terra, delivered to the mouth of Ares and Tiu Vallis during one of the many debris flows in the Hesperian period. This highland material, being rich in feldspars relative to pyroxene (Bandfield *et al*., 2000), may have formed during an early magma ocean phase on Mars analogous to the formation of the lunar anorthositic highland materials. One observation supporting the possibility of a Martian magma ocean includes the Noachian heavily cratered unit which appears to cover most of the southern highlands and to underlie the northern lowlands (Frey *et al*., 2001). Alternatively, perhaps these highly evolved Martian igneous rocks were formed during episodes of flood basalt eruption through the ancient highland materials. Ascent through the thick crust typical of the southern hemisphere of up to ~70 km (Zuber *et al*., 2000) may have enabled sufficient evolution of the magma.

The Martian soils appear to be mixtures of mafic igneous material like the SNC meteorites and the volatiles deposited from volcanic emissions (Clark, 1993). In particular, the prevalence of abundant sulfur and chlorine in both the Viking and Pathfinder soils indicates that they are not simply created by the physical erosion of basalt, but that they also contain salts from the addition of such volatiles by a yet-to-be-determined chemical process such as precipitation from an evaporating fluid, condensation on aerosol dust particles, or some other yet hypothesized process.

Similarities and differences between the Pathfinder, Viking, and MER soils reveal significant information about the Martian surface. Frequent global dust storms, common on Mars, may have delivered and removed a significant portion of the soil at the Pathfinder landing site (Golombek *et al*., 1997a). Aeolian deposition of the soils is estimated to contribute particles of ~500–2300 μm based on the thermal inertia studies of Christensen and Moore (1992) and Christensen and Malin (1993). However, the Pathfinder soils analyzed with the APXS consisted of mixtures of fines, clods, and pebbles within the centimeter-size range (Bell *et al*., 2000). Some of the Pathfinder soils may be from the same debris-flow and/or flooding events that may have delivered many of the Pathfinder rocks to the mid-fan section of the Ares and Tiu Vallis (Nelson and Greeley, 1999), and some of the Pathfinder soils may be from the Xanthe Terra highly cratered ancient unit (3.8–1.8 Ga). This may explain why some of the fragments within the Pathfinder soil are more mafic than the Viking fines. The similarity of the Pathfinder soil to the Viking 1 and 2 soils, which are

thousands of kilometers apart, imply that the fines in the northern hemisphere may be well mixed and may represent an average composition of either the northern hemisphere or perhaps even most of the Martian surface as also inferred by Bell *et al*. (2000). However, there is some indication of local rock contribution to the soil, as evident in the case of Pathfinder landing site which has rocks with rather high potassium that is also reflected in the soil composition. Although carbonate may reside in the subsurface, the lack of carbonates and the high abundances of S and Cl in the surface soils imply that a dominant surface process during the more recent epochs is the destruction of surficial carbonate (if once present) and the release of CO_2 (Wänke and Dreibus, 1994; Clark, 1999).

REFERENCES

Baker, V. R., R. G. Strom, V. C. Gulick, *et al*., Ancient oceans, ice sheets, and the hydrologic cycle on Mars, *Nature* **352**, 589–94, 1991.

Bandfield, J. L., V. E. Hamilton, and P. R. Christensen, A global view of martian surface compositions from MGS-TES, *Science* **287**, 1626–30, 2000.

Banin, A., The enigma of the martian soil, *Science* **309**, 888–90, 2005.

Banin, A., B. C. Clark, and H. Wänke, Surface chemistry and mineralogy. In *Mars* (ed. H. H. Keiffer, B. M. Jakosky, C. W. Snyder, and M. S. Matthews), Tuscon: University of Arizona Press, pp. 594–625, 1992.

Banin, A., F. X. Han, I. Kan, and A. Cicelsky, Acidic volatiles and the Mars soil, *J. Geophys. Res.* **102**, 13341–56, 1997.

Bell III, J. F., R. V. Morris, and J. B. Adams, Thermally altered palagonitic tephra: a spectral and process analogue to the soil and dust of Mars, *J. Geophys. Res.* **98**, 3373–85, 1993.

Bell, J. F. H. Y. McSween, J. A. Crisp, *et al*., Mineralogical and compositional properties of martian soil and dust: results from Mars Pathfinder, *J. Geophys. Res.* **105**(E1), 1721–55, 2000.

Bell III, J. F., S. W. Squyres, R. E. Arvidson, *et al*., Pancam multispectral imaging results from the Spirit rover at Gusev crater, *Science* **305**, 800–6, 2004a.

Bell III, J. F., S. W. Squyres, R. E. Arvidson, *et al*., Pancam multispectral imaging results from the Opportunity rover at Meridiani Planum, *Science* **306**, 1703–9, 2004b.

Bittner, J. W. and R. D. Moffat, Elastic scattering of α particles by carbon, *Phys. Rev.* **96**, 347–77, 1954.

Boynton, W. V., G. J. Taylor, D. Hamara, *et al*., Compositional diversity of the martian crust: preliminary data from the Mars Odyssey gamma-ray spectrometer: In *Lunar Planet. Sci. XXXIV*, Houston, TX: Lunar and Planetary Institute, Abstract 2108 (CD-ROM), 2003.

Bridges, N. T. and J. A. Crisp, The Mars Pathfinder APXS sites: new insights from improved IMP calibration and image analysis, *Lunar Planet. Sci. XXXI*, Houston, TX: Lunar and Planetary Institute, Abstract #1740 (CD-ROM), 2000.

Bridges, N. T., R. Greeley, A. F. C. Haldemann, *et al*., Ventifacts at the Pathfinder landing site, *J. Geophys. Res.* **104**(E4), 8595–615, 1999.

Bridges, N. T., J. A. Crisp, and J. F. Bell III, Characteristics of the Pathfinder APXS sites: implications for the composition of Martian rocks and soils, *J. Geophys. Res.* **106**, 14621–65, 2001.

Brückner, J., G. Dreibus, G. W. Lugmair, *et al*., Chemical composition of the martian surface as derived from Pathfinder, Viking, and martian meteorite data, *Lunar and Planetary Science XXX*, Houston, TX: Lunar and Planetary Institute, Abstract #1250 (CD-ROM), 1999.

Brückner, J., G. Dreibus, R. Rieder, and H. Wänke, Refined data of Alpha Proton X-ray analyses of soils and rocks at the Mars Pathfinder site: implications for surface chemistry, *J. Geophys. Res.* **108**(E12), ROV 35-1 through 35-18, 2003.

Burns, R. G., Rates and mechanisms of chemical weathering of ferromagnesian silicate minerals on Mars, *Geochim. Cosmochim. Acta* **57**, 4555–74, 1993.

Burns, R. G. and D. S. Fisher, Iron-sulfur mineralogy of Mars: magmatic evolution and chemical weathering products, *J. Geophys. Res.* **95**(B9), 14415–21, 1990.

Campbell, I. B. and G. G. C. Claridge, *Antarctica: Soils, Weathering Processes, and Environment, Developments in Soil Science* 16, New York: Elsevier Science Publishing Co. Inc., 368pp., 1987.

Christensen, P. R. and M. Malin, A simple model of clastic sediments on Mars (abstract), *Lunar Planet. Sci. XXIV*, **285**, 1993.

Christensen, P. R. and H. Moore, The martian surface layer. In *Mars* (ed. H. H. Kieffer *et al*.), Tucson: University of Arizona Press, pp. 687–729, 1992.

Christensen, P. R., J. L. Bandfield, R. N. Clark, *et al*., Detection of crystalline hematite mineralization on Mars by the Thermal Emission Spectrometer: evidence for near-surface water, *J. Geophys. Res.* **105**(E4), 9623–42, 2000.

Christensen, P. R., S. W. Ruff, R. L. Fergason, *et al*., Initial results from the Mini-TES experiment in Gusev crater from the Spirit rover, *Science* **305**, 837–42, 2004a.

Christensen, P. R., M. B. Wyatt, T. D. Glotch, *et al*., Mineralogy at Meridiani Planum from the Mini-TES experiment on the Opportunity rover, *Science* **306**, 1733–9, 2004b.

Clark, B. C., Geochemical components in martian soil, *Geochim. Cosmochim. Acta* **57**, 4575–81, 1993.

Clark, B. C., On the non-observability of carbonates on Mars, *5th Int. Conf. Mars*, LPI Contribution No. 972, Houston, TX: Lunar and Planetary Institute, Abstract #6214 (CD-ROM), 1999.

Clark, B. C., A. K. Baird, R. J. Weldon, *et al*., Chemical composition of martian fines, *J. Geophys. Res.* **87**, 10059–67, 1982.

Drake, M. J., H. E. Newsom, and C. J. Capobianco, V, Cr, Mn in the Earth, Moon, EPB, and SPB, and the origin of the Moon: experimental studies, *Geochim. Cosmochim. Acta* **53**, 2101–11, 1989.

Economou, T. E. and A. L. Turkevich, An alpha particle instrument with alpha, proton, and X-ray modes for planetary chemical analyses, *Nucl. Instrum. Meth.* **134**, 391, 1976.

Economou, T. E. A. L. Turkevich, and J. H. Patterson, An alpha particle experiment for chemical analysis of the martian surface and atmosphere, *J. Geophys. Res.* **78**, 781–91, 1973.

Ferguson, A. J. and L. R. Walker, The scattering of alpha particles by carbon and oxygen, *Phys. Rev.* **58**, 666–71, 1940.

Foley, C. N., Mars Pathfinder APXS analyses and interpretations, Ph.D. dissertation, The University of Chicago, Chicago, IL, 2002.

Foley, C. N., T. E. Economou, R. N. Clayton, and W. Dietrich, Calibration of the Mars Pathfinder alpha proton X-ray spectrometer, *J. Geophys. Res.* **108**(E12), ROV 36-1 through 36-22, 2003a.

Foley, C. N., T. E. Economou, and R. N. Clayton, Final chemical results from the Mars Pathfinder alpha proton X-ray spectrometer, *J. Geophys. Res.* **108**(E12), ROV 37-1 through 37-21, 2003b.

Franzgrote, E. J., J. H. Patterson, A. L. Turkevich, T. E. Economou, and K. P. Sowinski, Chemical composition of the lunar surface in Sinus Medii, *Science* **167**, 376–9, 1970.

Frey, H., K. M. Shockey, E. L. Frey, J. H. Roark, and S. E. H. Sakimoto, A very large population of likely buried impact basins in the northern lowlands of Mars revealed by MOLA data, *Lunar Planet. Sci. XXXII*, Houston, TX: Lunar and Planetary Institute, Abstract #1680 (CD-ROM), 2001.

Geiger, H. and E. Marsden, On a diffuse reflection of the α-particles, *Proc. R. Soc.* **A82**, 495–500, 1909.

Gellert, R., R. Rieder, R. C. Anderson, *et al.*, Chemistry of rocks and soils in Gusev crater from the Alpha Particle X-ray Spectrometer, *Science* **305**, 829–32, 2004.

Golombek, M. P., R. A. Cook, T. Economou, *et al.*, Overview of the Mars Pathfinder mission and assessment of landing site predictions, *Science* **278**, 1743–8, 1997a.

Golombek, M. P., R. A. Cook, H. J. Moore, and T. Parker, Selection of the Mars Pathfinder landing site, *J. Geophys. Res.* **102**, 3967–88, 1997b.

Gooding, J. L., Soil mineralogy and chemistry on Mars: possible clues from salts and clays in SNC meteorites, *Icarus* **99**, 28–41, 1992.

Govindaraju, K., Compilation of working values and sample description for 383 geostandards, *Geostand. Newsl.* **18**, 1–158, 1994.

Greshake, A., J. Fritz, and D. Stöffler, Petrology and shock metamorphism of the olivine-phyric shergottite Yamato 980459: evidence for a two-stage cooling and a single-stage ejection history, *Geochim. Cosmochim. Acta* **68**, 2359–77, 2004.

Hale, V. P. S., H. Y. McSween Jr., and G. A. McKay, Cumulus pyroxene in Shergotty: the discrepancy between experimental and observational studies, *Lunar Planet. Sci. XVIII*, Houston, TX: Lunar and Planetary Institute, Abstract #1363 (CD-ROM), 1997.

Hamilton, V. E., M. B. Wyatt, H. Y. McSween Jr., and P. R. Christensen, Analysis of terrestrial and martian volcanic compositions using thermal emission spectroscopy: 2. Application to martian surface spectra from MGS TES, *J. Geophys. Res.* **106**, 14733–46, 2001.

Hargraves, R. B., J. M. Knudsen, P. Bertelsen, *et al.*, Magnetic enhancement on the surface of Mars?, *J. Geophys. Res.* **105**, 1819–27, 2000.

Hovestadt, D., B. Andreychikov, B. Akhmetshin, *et al.*, Measurement of the surface composition of the Mars moon Phobos: the ALPHA-X experiment on the Phobos mission, *Adv. Space Res.* **10**(3–4), (3)53–(3)56, 1990.

Irvine, T. N. and W. R. A. Baragar, A guide to the chemical classification of the common volcanic rocks, *Can. J. Earth Sci.* **8**, 525–48, 1971.

Jagoutz, E., H. Palme, H. Baddenhausen, *et al.*, The abundances of major, minor, and trace elements in the earth's mantle as derived from primitive ultramafic nodules, *Proc. Lunar Planet. Sci. Conf. X*, 2031–50, 1979.

Johnson, M. C., M. J. Rutherford, and P. C. Hess, Chassigny petrogenesis: melt compositions, intensive parameters, and water contents of martian (?) magmas, *Geochim. Cosmochim. Acta* **55**, 349–66, 1991.

Juster, T. C., T. L. Grove, and M. R. Perfit, Experimental constraints on the generation of FeTi basalts, andesites, and rhyodacites at the Galapagos spreading center, 85° W and 95° W, *J. Geophys. Res.* **94**(B7), 9251–74, 1989.

Klingelhöfer, G., R. V. Morris, B. Bernhardt, *et al.*, Jarosite and hematite at Meridiani Planum from Opportunity's Mössbauer Spectrometer, *Science* **306**, 1740–5, 2004.

Laul, J. C., and R. A. Schmitt, Chemical composition of Apollo 15, 16, and 17 samples, *Proc. Lunar Sci. Conf. X, Geochim. Cosmochim. Acta* **2** (Suppl. 4), 1349–67, 1973.

Le Bas, M. J., R. W. Le Maitre, A. Streckeissen, and B. Zanettin, A chemical classification of volcanic rocks based on the total alkali-silica diagram, *J. Petrol.* **27**, 745–50, 1986.

Madsen, M. B., S. F. Hviid, H. P. Gunnlaugsson, *et al.*, The magnetic properties experiments on Mars Pathfinder, *J. Geophys. Res.* **104**, 8761–79, 1999.

McSween Jr., H. Y., S. L. Murchie, J. A. Crisp, *et al.*, Chemical, multispectral, and textural constraints on the composition and origin of rocks at the Mars Pathfinder landing site, *J. Geophys. Res.* **104**(E4), 8679–715, 1999.

McSween Jr., H. Y., T. L. Grove, and M. B. Wyatt, Constraints on the composition and petrogenesis of the martian crust, *J. Geophys. Res.* **108**(E12), 5135, doi:10.1029/2003JE002175, 2003.

McSween Jr., H. Y., R. E. Arvidson, J. F. Bell III, *et al.*, Basaltic rocks analyzed by the Spirit rover in Gusev crater, *Science* **305**, 842–5, 2004.

Minitti, M. E., and M. J. Rutherford, Genesis of the Mars Pathfinder "sulfur-free" rock from SNC parental liquids, *Geochim. Cosmochim. Acta* **64**(14), 2535–47, 2000.

Morris, R. V., D. C. Golden, J. F. Bell III, and H. V. Lauer Jr., Hematite, pyroxene, and phyllosilicates on Mars: implications from oxidized impact melt rocks from Manicouagan crater, Quebec, Canada, *J. Geophys. Res.* **100**, 5319–28, 1995.

Morris, R. V., D. C. Golden, J. F. Bell III, *et al.*, Mineralogy, composition, and alteration of Mars Pathfinder rocks and soils: evidence from multispectral, elemental, and magnetic data on terrestrial analogue, SNC meteorite, and Pathfinder samples, *J. Geophys. Res.* **105**, 1757–817, 2000.

Morris, R. V., G. Klingelhöfer, B. Bernhardt, *et al.*, Mineralogy at Gusev crater from the Mössbauer Spectrometer on the Spirit Rover, *Science* **305**, 833–6, 2004.

Morris, R. V., G. Klingelhöfer, C. Schröder, *et al.*, Mössbauer mineralogy of rock, soil, and dust at Gusev crater, Mars: Spirit's journey through weakly altered olivine basalt on the plains and pervasively altered basalt in the Columbia Hills, *J. Geophys. Res.* **111**, E02S13, 2006.

Nekvasil, H., A. Dondolini, J. Horn, *et al.*, The origin and evolution of silica-saturated alkalic suites: an experimental study, *J. Petrol.* **45**, 693–721, 2004.

Nelson, D. M. and R. Greeley, Geology of Xanthe Terra outflow channels and the Mars Pathfinder landing site, *J. Geophys. Res.* **104**, 8653–69, 1999.

Owen, T., The composition and early history of the atmosphere of Mars. In *Mars.* (ed. H. H. Kieffer, B. M. Jakosky, C. W. Snyder, and M. S. Matthews), Tucson, AZ: University of Arizona Press, pp. 818–34, 1992.

Owen, T., K. Biemann, D. R. Rushneck, *et al.*, The composition of the atmosphere at the surface of Mars, *J. Geophys. Res.* **82**, 4635–9, 1997.

Parrington, J. R., H. D. Knox, S. L. Breneman, E. M. Baum, and F. Feiner, *Nuclides and Isotopes*, San Jose, CA: General Electric, 1996.

Patterson, J. H., A. L. Turkevich, and E. Franzgrote, Chemical analyses of surfaces using alpha particles, *J. Geophys. Res.* **70**(6), 1311–27, 1965.

Patterson, J. H., A. L. Turkevich, E. J. Franzgrote, T. E. Economou, and K. P. Sowinski, Chemical composition of a lunar surface in a terra region near the crater Tycho, *Science* **8**, 825–8, 1970.

Pettijohn, F. J., *Sedimentary Rocks*, 3rd edn. New York: Harper & Row, 628pp., 1975.

Philpotts, A. R., *Principles of Igneous and Metamorphic Petrology*, New Jersey: Prentice Hall; Simon & Schuster, 498pp., 1990.

Rieder, R., H. Wänke, T. Economou, and A. Turkevich, Determination of the chemical composition of martian soil and rocks: the alpha proton X-ray spectrometer, *J. Geophys. Res.* **102**(E2), 4027–44, 1997a.

Rieder, R., T. Economou, H. Wänke, *et al.*, The chemical composition of the martian soil and rocks returned by the mobile alpha proton X-ray spectrometer: preliminary results from the X-ray mode, *Science* **278**, 1771–4, 1997b.

Rieder, R., R. Gellert, R. C. Anderson, *et al.*, Chemistry of rocks and soils at Meridiani Planum from the Alpha Particle X-ray Spectrometer, *Science* **306**, 1746–9, 2004.

Robinson, D. A. and R. B. G. Williams, *Rock Weathering and Landform Evolution*, Chichester, England: John Wiley & Sons, 519pp., 1994.

Rover Team, Characterization of the Martian surface deposits by the Mars Pathfinder rover, Sojourner, *Science* **278**, 1765–8, 1997.

Rutherford, E., The scattering of α and β particles by matter and the structure of the atom, *Philos. Mag.*, Series 6, **21**, 669–88, 1911.

Rutherford, E., J. Chadwick, and C. D. Ellis, *Radiations from Radioactive Substances*, London, England: Cambridge University Press, 1930.

Smith, P. H., J. F. Bell, N. T. Bridges, *et al.*, Results from the Mars Pathfinder camera, *Science* **278**, 1758–65, 1997.

Squyres, S. W., J. P. Grotzinger, R. E. Arvidson, *et al.*, In situ evidence for an ancient aqueous environment at Meridiani Planum, Mars, *Science* **306**, 1709–14, 2004.

Tanaka, K. L., Debris-flow origin for the Simud/Tiu deposit on Mars, *J. Geophys. Res.* **104**, 8637–52, 1999.

Tanaka, K. L., D. H. Scott, and R. Greeley, Global stratigraphy. In *Mars* (ed. H. H. Kieffer *et al.*), Tucson, AZ: University of Arizona Press, pp. 345–82, 1992.

Tipler, P. A., *Modern Physics*, New York: Worth Publishers, 1987.

Tosca, N. J., S. M. McLennan, D. H. Lindsley, and M. A. A. Schoonen, Acid-sulfate weathering of synthetic martian basalt: the acid fog model revisited, *J. Geophys. Res.* **109**, E05003, doi:10.1029/2003JE002218, 2004.

Toulmin III, P., A. K. Baird, B. C. Clark, *et al.*, Geochemical and mineralogical interpretation of the Viking inorganic chemical results, *J. Geophys. Res.* **82**, 4625–34, 1977.

Turkevich, A. L., Chemical analysis of surfaces by use of large-angle scattering of heavy charged particles, *Science* **134**, 672–4, 1961.

Turkevich, A. L., E. F. Franzgrote, and J. H. Patterson, Chemical composition of lunar surface in Mare Tranquillitatis, *Science* **165**, 277–9, 1969.

Wänke, H. and G. Dreibus, Chemical composition and accretion history of terrestrial planets, *Philos. Trans. R. Soc. Lond.* **A325**, 545–57, 1988.

Wänke, H. and G. Dreibus, Chemistry and accretion history of Mars, *Philos. Trans. R. Soc. Lond.*, Ser. **A349**, 285–93, 1994.

Wänke, H., G. Dreibus, E. Jagoutz, *et al.*, ALHA 77005 and the chemistry of the Shergotty parent body (Mars) (abstract) *Lunar Planet. Sci. XVII*, 919–20, 1986.

Wänke, H., J. Brückner, G. Dreibus, R. Rieder, and I. Ryabchikov, Chemical composition of rocks and soils at the Pathfinder site, *Space Sci. Rev.* **96**, 317–30, 2001.

Ward, A. W., L. R. Gaddis, R. L. Kirk, *et al.*, General geology and geomorphology of the Mars Pathfinder landing site. *J. Geophys. Res.* **104**(E4), 8555–71, 1999.

Williamson, J. H., Least-squares fitting of a straight line, *Can. J. Phys.* **46**, 1845–7, 1968.

Wyatt, M. B. and H. Y. McSween Jr., Spectral evidence for weathered basalt as an alternative to andesite in the northern lowlands of Mars, *Nature* **417**, 263–6, 2002.

Ziegler, J. F., The electronic and nuclear stopping of energetic ions, *Appl. Phys. Lett.* **31**, 544–6, 1977.

Zuber, M. T., S. C. Solomon, R. J. Phillips, *et al.*, Internal structure and early evolution of Mars from Mars Global Surveyor topography and gravity, *Science* **287**, 1788–93, 2000.

4

Mars Exploration Rovers: chemical composition by the APXS

J. BRÜCKNER, G. DREIBUS, R. GELLERT, S. W. SQUYRES, H. WÄNKE, A. YEN, AND J. ZIPFEL

ABSTRACT

The Alpha Particle X-Ray Spectrometers (APXSs) on board the Mars Exploration Rovers (MERs) determine the elemental compositions of Martian samples. Improvements to the version of the instrument flown on the Mars Pathfinder (MPF) mission allow, for the first time, *in situ* detection and quantification of trace elements such as nickel, zinc, and bromine. The APXS measurements are performed by placing the sensor head against or immediately above the sample surface. A wealth of compositional diversity has been discovered at the two MER landing sites. At Gusev crater, fresh rock surfaces in the plains resemble primitive basalts, while rocks in the Columbia Hills are significantly weathered and enriched in mobile elements such as phosphorus, sulfur, chlorine, and bromine. Sandstones cemented by sulfates as well as evidence for clay formation have also been found in the Columbia Hills. At Meridiani Planum, the layered sedimentary rocks were found to consist primarily of sulfates mixed with siliciclastic debris. Iron-rich spherules and their fragments, confirmed to be hematitic by the Mössbauer spectrometer (MB), are found armoring the soil bedforms as well as embedded in the outcrop rocks. A variety of unusual objects, including an iron-nickel meteorite and a likely ejecta fragment similar to a Martian meteorite, have also been discovered. The elemental compositions of soils analyzed at both sites are remarkably similar, indicative of global-scale homogenization or the similarity of the soil precursors. The APXS *in situ* data together with those from Martian meteorites imply an ancient basaltic Martian crust enriched with incompatible elements (potassium) and volatile elements (sulfur and chlorine). Compared to the Earth's mantle, the Martian mantle contains higher amounts of iron and volatile elements like potassium, and higher concentrations of phosphorus.

4.1 INTRODUCTION

In 1976, the Viking 1 and Viking 2 stationary landers started their successful missions at Chryse Planitia (22° N, 48° W) and Utopia Planitia (48° N, 134° E) respectively. Each lander carried a surface sampler (a 3-m retractable boom-and-scoop assembly) that delivered soil samples to the X-ray spectrometer (Clark and Baird, 1973) mounted at the deck of the lander. Thus for the first time, the elemental composition of Martian soils was determined. The soil compositions at both landing sites, more than 7000 km apart, showed remarkable similarities, suggesting Mars is covered with a material of relatively uniform composition, even down to depths of several centimeters (Banin *et al.*, 1992). The high Fe and low K/Ca ratio pointed to a mafic source material, but, the high S and Cl contents of the soils could result from enrichments with salt precipitates (Toulmin *et al.*, 1977), or from a Martian crust that is inherently high in S (Clark and Baird, 1979a,b), or from condensates of volcanic exhalations (Baird and Clark, 1981). Assuming the latter scenario, the silicate fraction of Viking soils matches the composition of shergottites (a class of Martian meteorites) (Baird and Clark, 1981). As shown below, the soil compositions of all landing sites are very similar, suggesting a global homogenization mechanism.

Based on the experience with the Viking scoops, where small rocks were just out of reach, a different approach to elemental analyses was taken by the following landed missions. Rovers provided the necessary mobility for exploration of larger areas. To date, three APXSs have been carried and deployed by rovers to determine the chemical composition of rocks and soils encountered along the rovers' traverses.

In 1997, MPF carried the first mobile platform to Mars, Rover Sojourner, to explore a landing site at Ares Vallis (19° N, 34° W) (Golombek *et al.*, 1999). The MPF APXS sensor head was attached to a deployment device on board Sojourner. The instrument had three measurement modes: the alpha mode, where back-scattered alpha particles, emitted by the curium sources (Cm-244), were measured by a central alpha detector; the proton mode, where alpha-induced protons were measured by a charged particle detector; and the X-ray mode, where induced X-rays were measured by an off-axis mounted solid-state X-ray detector (Rieder *et al.*, 1997a).

The different modes of the APXS method have both advantages and disadvantages. The alpha mode is sensitive to carbon and oxygen and, to a lesser extent, elements with higher Z (atomic number) in vacuum; however, in the CO_2 atmosphere of Mars, the sensitivity for C and O contained in a sample is strongly reduced (Brückner *et al.*, 2003; Foley *et al.*, 2003a). The proton mode supports the alpha mode for analyses of elements such as magnesium and aluminum (Foley *et al.*, 2003a). The X-ray mode uses two mechanisms to excite X-rays inside a sample: alpha Particle Induced X-ray Emission (PIXE) and X-Ray Fluorescence (XRF) resulting from the X-ray emission of plutonium (Pu-240, a decay product of Cm-244). The combination of these two excitation

The Martian Surface: Composition, Mineralogy, and Physical Properties, ed. J. F. Bell III. Published by Cambridge University Press.

modes provides good sensitivities for low-Z elements due to PIXE and high-Z elements due to XRF. As a result, all elements between sodium and iron (with the exceptions of Sc and V) have been detected by the MPF APXS. Additional details of the APXS technique can be found in Section 4.2.

The results of MPF APXS analyses of Martian soils confirmed the mafic nature of the soils as initially inferred by Viking (Rieder *et al*., 1997b). For the first time, however, several rocks on the Martian surface were analyzed. After conversion to a soil-free rock composition (Wänke *et al*., 2001), these rocks exhibit high Si and K and low Mg and Fe compared to the soil and may represent not basaltic but felsic compositions. The alpha mode enabled (1) the determination of oxygen abundances, (2) confirmation of carbon abundances below the detection limit in all samples, and (3) the potential presence of H_2O in some samples (Brückner *et al*., 2003; Foley *et al*., 2003b). A detailed description of the MPF APXS and analytical results can be found in Chapter 3.

In 2004, the two MERs started their long journeys: Rover *Spirit* at Gusev crater (15° S, 175° E) and Rover *Opportunity* at Meridiani Planum (2° S, 6° W). The MER APXS together with the MB, the Microscopic Imager (MI), and the Rock Abrasion Tool (RAT) are mounted on the turret of the five degree-of-freedom robotic Instrument Deployment Device (IDD), permitting precise positioning of the sensor heads and the tool (Squyres *et al*., 2003).

The MER APXS is based on "lessons learned" during the MPF mission. For the X-ray mode, the major differences from the MPF instrument are as follows (Rieder *et al*., 2003): A collimated, central, high-resolution X-ray detector, a preamplifier mounted close to the detector (for noise reduction), increased X-ray sensitivity for Ni, Cu, Br, and other high-Z trace elements, a coaxial arrangement of the alpha sources, a reduced source to sample distance (geometry), and titanium foils covering the alpha sources for ease of handling (avoiding possible radioactive contamination). The focus of the new design was to obtain high-quality X-ray data with low detection limits, which unfortunately reduced the sensitivity of the alpha mode relative to the MPF instrument. The proton mode was eliminated from the design because the energy resolution of the X-ray detector permits easy determination of Mg and Al. As a result, the name of the APXS was changed from Alpha Proton X-Ray Spectrometer to Alpha Particle X-Ray Spectrometer to reflect the change but to keep the same acronym APXS.

Several measures were taken to improve the design and the sensitivity of the MER APXS. The distance between source and sample was reduced from 50 mm (MPF) to 30 mm. For MER the X-ray detector was placed in the favorable center of the ring sources. This location was taken by the alpha detector in the Pathfinder instrument where the X-ray detector was attached on the side. The new symmetric design with a central X-ray detector collimator resulted in a circular sample diameter of 25 mm (versus 50 mm for MPF). The radial acceptance function of the detector (contribution of unit areas to the total signal as a function of distance from the center of the field of view) can be described as follows: 95% of the X-ray signal comes from a diameter of 25 mm, while 50% of the signal from a diameter of 14 mm. If an object that is much smaller than the field of view (fov) is positioned in the center of the fov, it contributes more to the total signal than an object lying off center, for example outside of the 14-mm diameter circle.

Although only two-thirds of the MPF radioactive material was utilized, the MER sensitivity increased by more than a factor of 10 due to the new geometry. The energy resolution of the advanced MER X-ray detector was improved by about a factor of 2 compared to MPF (Rieder *et al*., 2003). As a result of all these improvements in the MER APXS design, the integration times to obtain statistically meaningful data were reduced compared to MPF operations. For example, several tens of minutes are sufficient for determination of the major element compositions (Si, Fe, Ca, etc.) compared to several hours for MPF. Because the emphasis of most APXS analyses was on minor and trace element compositions, however, typical APXS integrations times were set to several hours.

In the current architecture for NASA's Mars Exploration Program, an even more advanced APXS with higher sensitivity and shorter counting times will be on board the Mars Science Laboratory rover planned for a 2009 launch.

4.2 THE MER ALPHA PARTICLE X-RAY SPECTROMETERS

The MER APXSs are *in situ* instruments that determine the elemental compositions of soils and rocks by X-ray spectroscopy. Each instrument consists of a main avionics box residing inside the rover and a sensor head mounted on the IDD (Figure 4.1). The main constituents of the sensor head are the high-resolution X-ray detector with its supporting electronics and the radioactive Curium-244 sources (Figure 4.2). The sensor head is brought into contact or into a hovering position above the sample by the IDD, and

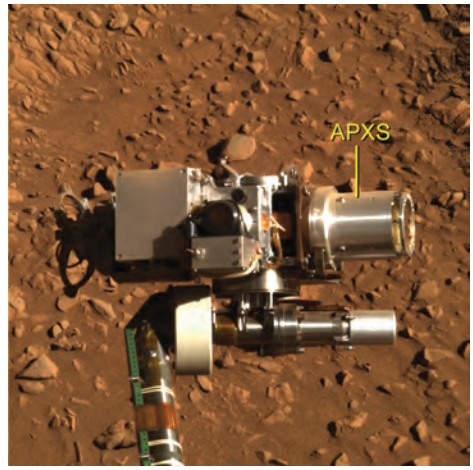

Figure 4.1. MER Alpha Particle X-ray Spectrometer (APXS). Sensor head (label) is mounted on the turret (lower part), which is attached to the instrument deployment device (arm on the bottom). (Picture taken at Gusev crater on sol 287 by Pancam [NASA/JPL, Cornell].) (For a color version of this figure, please refer to the color plate section or to the e-Book version of this chapter.)

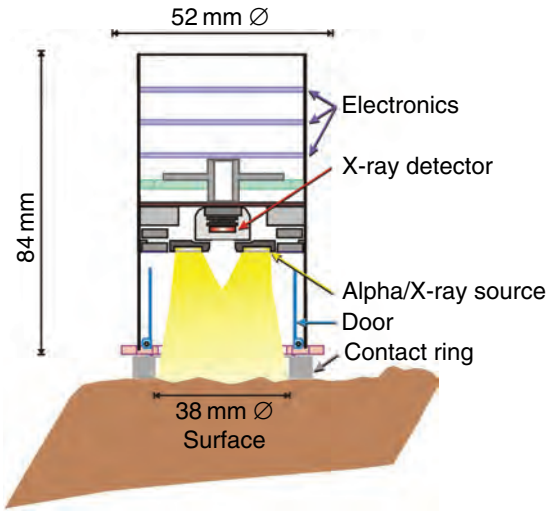

Figure 4.2. MER Alpha Particle X-ray Spectrometer sensor head. (For a color version of this figure, please refer to the color plate section or to the e-Book version of this chapter.)

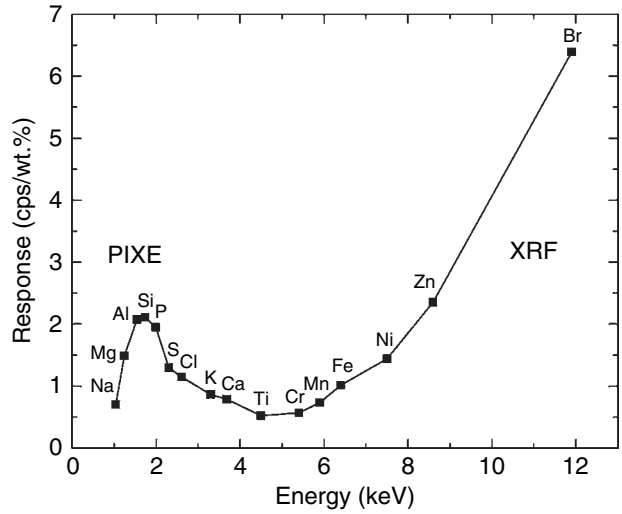

Figure 4.3. Sensitivity (or response) for elements measured by the Alpha Particle X-ray Spectrometer.

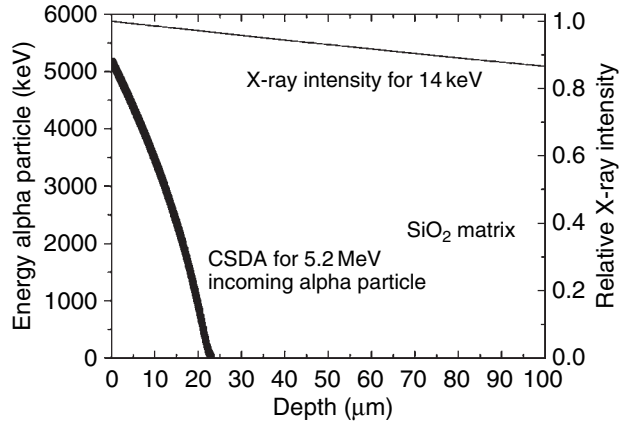

Figure 4.4. Average penetration depth (μm) of alpha particles having an incoming energy of 5.2 MeV using the continuous slowing down approximation (CSDA) and the relative intensity of X-rays with an incoming energy of 14 keV as a function of depth, both for a SiO_2 composition.

the APXS is subsequently commanded "ON" to collect the X-ray spectrum of the sample. Six curium pellets, arranged in a ring structure around the X-ray detector, irradiate the sample with alpha particles and X-rays. The excitation is followed by emission of X-rays that are characteristic for each element.

4.2.1 Fundamental principles

The APXS method incorporates two well-established methods for chemical analysis, PIXE and XRF, using curium. The curium sources emit alpha particles as well as X-rays (as already mentioned). This provides a well-balanced sensitivity for all elements from Na up to Br (increasing atomic number, Z). Lower Z elements are efficiently excited only by alpha particles while elements heavier than Ti are mainly excited by X-rays (Figure 4.3). The X-ray spectrum is recorded from 900 eV to 17 keV, which allows measurement of the K-lines of elements Na to Zr as well as L-lines of elements with higher Z. The novel X-ray detector has a favorable energy resolution of 160 eV at the Fe Kα-line (6.4 keV) when exposed to "advantageous" temperatures below −40 °C, which allows unambiguous determination of the elemental constituents. Based on peak areas, the abundances of these elements are determined.

To well understand the APXS method, its sensitivity, and depth dependence, one has to focus on the microscopic processes in the sample. The measured APXS X-ray spectrum is a complex combination of various processes that involve the penetration of the source radiation into the sample, ejection of inner shell electrons from the sample atoms, and subsequent emission of characteristic X-rays from these atoms, which finally pass through the sample toward the detector. The different processes are described in the following paragraphs.

Primary radiation spectrum of the source

The Cm-244 source covered with 2.5 μm thin Ti foils emits alpha particles of approximately 5.2 MeV and X-rays from the daughter nucleus Pu-240. Per 100 emitted alpha particles, only approximately 10 X-rays are emitted that are distributed over several L-lines of Pu. The main lines are at 14.29 and 18.29 keV. The half-life of Cm-244 is relatively long – 18.11 years – which is very favorable for long-term missions.

Penetration depth of radiation within sample

Alpha particles penetrating the sample undergo numerous scatter events causing change of direction and a loss of energy leading to a so-called random walk. Since the scatter direction is very much peaked in the forward direction and each discrete energy loss is small compared to the energy of the alpha particle, one can use the empirical stopping power (energy loss per path length) to retrieve an energy of the alpha particle in a certain depth of the sample. Figure 4.4 shows that the alpha particles penetrate the sample less than

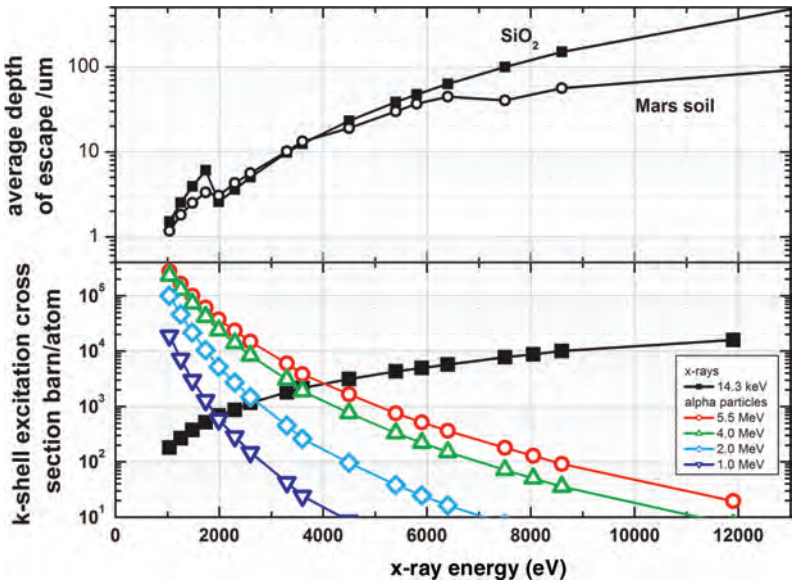

Figure 4.5. Bottom: K-shell excitation cross-section (barn/atom) for 14 keV X-rays and alpha particles (energy range of 1–5.5 MeV). Top: Average depth (μm) of escaping X-rays as a function of energy (eV) for two types of samples (quartz soil and Martian soil). (For a color version of this figure, please refer to the color plate section or to the e-Book version of this chapter.)

about 25 μm deep. The stopping power can be separated into two parts. First, there is the nuclear stopping power, caused by Coulomb scattering of the alpha particles with the nucleus. This process produces backscattered alpha particles that can be measured in the Rutherford backscattering mode, as used by the MPF APXS (alpha mode) (Brückner *et al*., 2003). The second interaction is the electronic stopping power where alpha particles interact with the electrons of the sample. The latter is by far responsible for most of the energy loss of the alpha particles within the sample and creates inner shell electron ejection. Alpha particles lose their energy in small discrete increments, so an alpha particle can excite many atoms along its path until it has lost its kinetic energy.

X-rays penetrate the sample differently. The main process of energy loss is the photoelectric effect. Here the X-ray interacts with the bound electrons of the nucleus and transfers all its energy to the electron of a given shell. The electron is ejected from the shell and leaves an unoccupied state within the shell. This "hole" in the shell is filled by an outer shell electron that either emits characteristic X-rays or Auger electrons. If an electron of the lowest shell was ejected, a Kα or Kβ X-ray line is produced that is diagnostic for the elements detected by the APXS.

The penetration depth of alpha particles and X-rays emitted by the Cm-244 source can be seen in Figure 4.4. The incoming alpha particles lose all their energy within the first 25 μm of the sample (exposed to vacuum), while the X-rays reach depths far greater than 100 μm.

Excitation cross sections

The cross sections for inner shell excitation due to interactions with alpha particles and X-rays are shown in Figure 4.5. The cross sections for alpha particles are highest for low-Z elements and decrease by orders of magnitude as a function of higher Z. As the alpha particle loses its energy while penetrating the sample, the cross sections also decrease. In contrast, the cross sections for X-rays are increasing with increasing Z.

Whenever an inner shell hole is generated, two competing processes can occur. For low-Z elements Auger electron emission is the most probable (only 2% fluorescence yield for Na). For higher Z elements the emission of the characteristic X-ray becomes more probable (e.g., Fe has a 35% fluorescence yield).

Escape of X-rays

When a characteristic X-ray is produced in the sample it has to reach the surface of the sample and advance in the direction of the detector to be measured by the APXS. In general, higher characteristic energies correspond to a larger range through the sample for these X-rays. Figure 4.5 shows the average escape depth of characteristic X-rays calculated for SiO_2 and for a typical Martian soil. The calculation assumes an emission along the surface normal.

In both excitation processes (by alpha particles and by X-rays) the range of incoming radiation is larger than the range of the emitted characteristic X-rays. Thus, Figure 4.5 provides a good estimate for the average "information depth" of the APXS method for each element. The signal of low-Z elements typically stems from the topmost micrometers while Fe has an average information depth of ~40 μm in Martian soils.

These facts explain the well-balanced sensitivity of the APXS for all elements between Na and Br. Low-Z elements have high excitation cross sections for alpha particles and are well sampled due to the high alpha to X-ray ratio of the curium source. High-Z elements have a higher fluorescence yield and both the incoming and outgoing radiation has a

larger range, resulting in more sample volume contributing to the signal.

The values for radiation penetration depth, cross sections, and escape depth described above can be used to calculate the expected signal for a given sample composition. Such a radiative transfer model can be developed by approximating the sample by a series of layers. For each layer the intensity of the incoming radiation is multiplied by the cross section for inner shell excitation for each element. In the case of alpha particles, the cross sections have to account for their energies in this respective depth. Weighted with the fluorescence yield for X-ray emission and the probability of reaching the surface, the signal at the boundary of this layer is determined. Summing over all layers, the intensity for all elements in the given sample is obtained. These calculated intensities could have been used to calibrate the APXS spectra – i.e. to transform spectral peak areas into weight abundance. Nevertheless, the simpler, empirical approach of calibrating the APXS with certified standards was utilized. The calibration results (sensitivity per abundance) contain the physical constants such as excitation cross sections and fluorescence yields. It is important to mention that both calibration methods assume that the sample is homogeneous with depth.

Figure 4.5 also illustrates several effects that have to be taken into account during interpretation and analysis of APXS spectra. The intensity of certain X-rays depends also on the sample composition. Figure 4.5 shows the average escape depth for each element in a SiO_2 matrix. This depth typically increases with higher energy. However, for phosphorus at ~2 keV, there is a decrease in depth because the phosphorus radiation is just above the binding energy of the inner Si electron. Therefore, characteristic X-rays of phosphorous can be absorbed efficiently by silicon reducing their depth of analysis. Another example are nickel X-rays (7.5 keV) which can easily be absorbed by iron atoms that make up ~20% of Martian soil by weight. Compensation for these matrix effects are considered in the data processing algorithms (as discussed below).

Another implication of Figure 4.5 is that the APXS results are sensitive to heterogeneity with depth or layering. For example, a sodium salt layer several micrometers thick above the typical Martian soil would produce a large Na signal from this layer plus most of the higher Z signals from underlying material that penetrate the top Na salt layer. On the other hand, several micrometers of Fe oxide on the surface would attenuate the signals from the underlying material (especially those of low-Z elements). In addition, the Fe signal in this case would not be representative of the abundance in this layer because the volume of this layer (in the field of view) is significantly smaller than the normal sample volume that contributes to the Fe signal. In other words, each element needs an "infinite" thick layer (or volume) to produce a full signal. For Na, the infinite layer is only a few micrometers thick, while for Fe more than 40 μm are required.

The large variety of samples measured on both rovers and especially the sample preparation provided by the RAT showed that such hypothetical thin layering in the micrometer region was not encountered on Mars. Since the analysis depth increases gradually from Na onward, layering would have a definite effect on the major rock-forming elements from Na to Si that would significantly show up in elemental compositions as "strange" enrichments.

In order to avoid these problems in XRF and PIXE measurements in terrestrial laboratories, the sample is usually "homogenized" either by melting finely ground powder into glass pellets or by averaging results taken with a high spatial resolution particle beam across the sample. Such techniques are obviously not viable for APXS analyses on Mars, and errors associated with heterogeneities of the sample could contribute in an unknown manner to the absolute accuracies in the elemental determinations.

4.2.2 X-ray spectra

A typical APXS X-ray spectrum obtained at Gusev crater is shown in Figure 4.6. The spectrum is a histogram that records the number of counts per channel where the channel numbers represent the X-ray energy. Because all processes for absorption and emission are of a statistical nature, the number of counts in each channel has a corresponding statistical uncertainty. The statistical error of the total X-ray peak is simply the square root of its peak area, which is affected by the background and potential interferences of other peaks. The spectral fit program takes all these components into account and delivers an overall statistical error (for more on statistical errors and precision, see Gellert *et al*., 2006). Consequently, the data acquisition requires a certain time to get sufficient statistics, short times for large peaks from major elements and longer times for weak peaks from minor and trace elements.

The X-ray spectrum of Figure 4.6 visualizes the strength of the APXS method, where the characteristic peaks can clearly be separated. The spectrum shows some elements, which mainly come from the background of the instrument structure itself, namely Cu at 8.05 keV and Zr at 15.78 keV. Also argon, which makes up 1.5% of the 10-mbar thin Martian atmosphere, is detected at 2.95 keV.

The logarithmic scale reveals the excellent peak to background ratio of the APXS method. The strongest photon radiation after the decay of Cm-244 is the well-known L-line of Pu-240 at 14.8 keV (emission probability 0.08 per disintegration), while higher energy X- and gamma-rays are several orders of magnitude weaker. The very low intensity of high-energy radiation emitted by Cm-244 as well as good shielding of the nearby high-intensity Co-57 of the MB provides a low background at energies beyond 8 keV. Any high-energy radiation would produce (via the Compton Effect in the sample or the detector material) a much higher background in the spectrum than encountered for the APXS. The low background made it possible to detect for the first time Ni, Zn, and Br on the surface of Mars. Besides these elements, which were usually detected for all samples, trace elements like Cu, Pb, Sr, Y, Ga, or Ge could be clearly detected in some samples, where their abundance was unusually high.

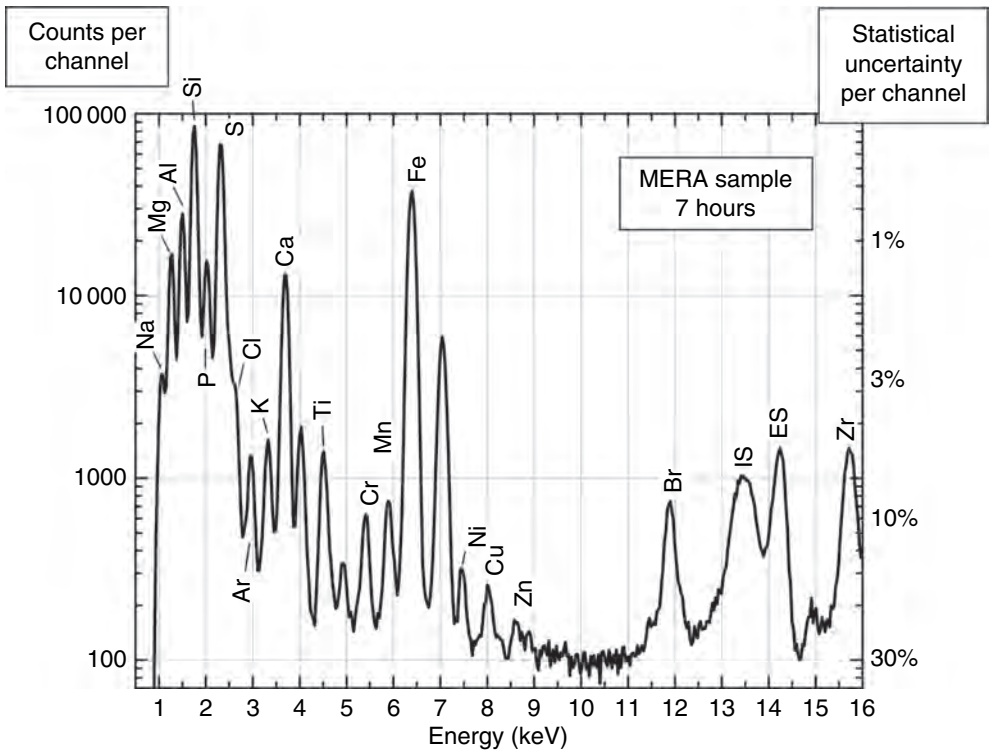

Figure 4.6. X-ray spectrum of a typical sample taken by the Alpha Particle X-ray Spectrometer at Gusev crater. The counts per channel are plotted versus the corresponding X-ray energy (keV). The main elemental peaks (Kα-lines) are labeled, while Kβ-lines are unlabeled. Signals from elastic scattering (ES) and inelastic scattering (IS) of the incoming Pu X-rays are indicated. Cupper and Zr peaks mainly result from instrument background, while argon is from the atmosphere. Also shown is the average statistical uncertainty as a function of counts on the right *y*-axis (%) (see Section 4.2.2).

4.2.3 Peak fit analysis

The first step of the analysis of the APXS data consists of a least square fit analysis of the spectrum to extract peak areas for each element. A model spectrum is generated with Gaussian peaks plus small exponential tails at their theoretically well-known energies (Gellert *et al.*, 2006). For each element all significant peaks were taken into account with fixed intensity ratios, for example Kα to Kβ peaks. Then several parameters are varied, such as peak height, energy calibration, peak width (full-width-at-half-maximum), and background height, until the deviation of the calculated data with the measured data is minimized. The deviation (chi^2) is measured as the summed square of the difference between model and spectrum content divided by the square root of the channel content as statistical error (Gellert *et al.*, 2006). The given statistical error bars of the peak areas are extracted using this chi^2.

4.2.4 Concentration evaluation

The transfer of derived peak areas to concentration values is done using the calibration of the instrument before launch with a number of certified geological standard specimens. The response curve, plotted in Figure 4.3, derived from approximately 50 samples (see list of calibration samples in Gellert *et al.*, 2006), represents the sensitivity of each element for the APXS method. Sensitivity (or response) is expressed as peak area in counts per second and per weight percent of the element. This is the first step of the transformation of peak area into abundance.

Since the APXS cannot measure light elements like oxygen, elements are converted to their typical oxides, like Si as SiO_2. For multivalent elements, most importantly sulfur and iron, we always assumed FeO and SO_3. Iron was by default assigned to FeO; although from Mössbauer spectroscopy (Morris *et al.*, 2006) it is known that between 10% and 50% of iron is present in the form of Fe^{3+}. However, the resulting effect on normalization and matrix correction is usually less than 1% and can easily be corrected if a Fe^{3+}/Fe_{total} ratio is available for the sample. The assignment of sulfur as SO_3 has greater implications to the normalization of the results and also to the matrix effects. Elemental sulfur or compounds like pyrite or sulfides would significantly change the results especially for the high sulfur-bearing soils at Gusev and outcrops at Meridiani. However, APXS mass balance considerations and mineralogical results by the MB strongly support the assumption of sulfate being the predominant oxide of sulfur.

The normalization furthermore assumes the absence of completely invisible compounds like carbonate and water. The sum of the calculated oxide abundances is normalized to 100% to compensate for the different distances between sample surface and detector that mainly affect the absolute height of all peaks simultaneously. Calibration measurements and one experiment performed on the rock "Temples (sol 266–268)" revealed the validity of this procedure. The results of 4 measurements at distances from close contact to 2 cm standoff agreed within the statistical errors.

4.2.5 Matrix effects

The intensity of the detected peaks is influenced by the composition of the sample itself as the emitted radiation can be re-absorbed on the way to the sample surface. This so-called "matrix effect" is taken into account in the APXS analysis. On the basis of the first derived composition

(retrieved with absorption cross sections of an average matrix) an updated set of absorption cross sections is calculated and the composition is corrected for this. The process is iteratively repeated until the composition converges. This analysis method of taking into account matrix effects, which was developed and tested during calibration, significantly improved the accuracy of the derived composition (Gellert *et al*., 2006).

More details on the MER APXS instrument and measurement and analysis methods can be found in Rieder *et al*. (2003) and Gellert *et al*. (2006). Chapter 3 also provides additional relevant background information related to the MER APXS' precursor instrument, the MPF APXS.

4.2.6 Operations

Almost all APXS operations were carried out during the cold Martian nights, when temperatures were below −40 °C, allowing the X-ray detector to achieve its highest energy resolution. These nightly integrations are feasible because the APXS has a moderate power consumption of only 2.5 W. Once the instrument is switched "ON," it operates on its own as a stand-alone unit. Usually, the rover was "woken up" during the night, the APXS integration was started, and then the rover was commanded to "sleep" again.

The APXS integration times lasted typically from several to about 10 hours. To ensure good data quality over such long periods, the total integration time was subdivided in up to 12 separate intervals, with a duration specified by a ground command. This allowed checking the repeatability of the spectra after they had been acquired. It also enabled selection of spectra with good energy resolution taken during low temperatures (mostly nightly hours) compared to data taken at higher temperatures (morning hours with different sun incident angles on the sensor head). The selected spectra were summed to improve the signal-to-noise ratio of small peaks. Trace elements like Ni, Zn, and Br could be detected, which had concentration ranges down to 100 ppm with statistical errors of ~20%. Accepting larger errors, very low concentrations down to detections limits could be determined (e.g., 30 ppm for Br). In contrast, major and minor elements were typically measured with peak area uncertainties of a few percent.

Occasionally, quick APXS spectra were taken for 30 minutes during the morning when appropriate temperatures allowed a sufficiently good energy resolution. These so-called "touch-and-go" integrations served as a fast means to check the chemical composition of a sample, usually soils. The abundance uncertainties obtained by these short-term spectra are higher compared to the nightly integrations, but still the major elemental composition could be derived very well.

4.2.7 Samples

The typical APXS data analysis presumes a homogeneous sample within the 2.5 cm diameter field of view as described above. Nevertheless, the possibility of horizontal and vertical sample heterogeneity has to be taken into account. Visual inspection of the samples by either the rover cameras and/or the MI is helpful to obtain information on potential heterogeneities on the centimeter to millimeter scale. For example, two types of samples with obviously heterogeneous composition were found on Meridiani Planum: the iron nickel meteorite "Heatshield Rock" and the iron-rich concretions (spherules) found in many soil samples and some sedimentary rocks. Also, certain exposed subsurface samples found on Gusev revealed light and dark components. In all these cases, the "average" chemical composition obtained by the APXS analysis has to be taken with great care.

After the rover was positioned close to a designated target, a spot in the work volume of the IDD was selected using the stereo front Hazard Avoidance Cameras (Hazcam). The IDD was deployed for *in situ* work and several measurements of a given target were carried out using the IDD instruments, typically with a tool-change from one instrument to another. The natural (undisturbed) surface of soils and rocks was measured by the APXS and the other IDD instruments. As rocks have a layering due to wind-blown dust and weathering, most times additional treatment was applied. Specifically, the RAT was used to brush the rock target to remove dust coatings and another set of IDD measurements was carried out. Then, often times, the same spot was abraded by the RAT to expose material with less or no weathering and more IDD measurements were done (Arvidson *et al*., 2006). The sequential analytical approach provided important data of the investigated rock samples as described below.

4.3 CHEMISTRY OF GUSEV CRATER

The mobility of the *Spirit* rover (also known as MER-A) allowed *in situ* studies of rocks and soils over a large area on Mars. Within the first 160 sols of the mission, *Spirit* explored the surroundings of the Columbia Memorial Station (landing site) and drove over Gusev plains while passing several impact craters (e.g., "Bonneville crater") (Squyres *et al*., 2004a). Then, she reached the Columbia Hills, which rise about 100 m above the surrounding volcanic plains, about 2.6 km to the southeast of her landing site. For approximately 540 sols, the rover investigated samples on these hills ("West Spur" and "Husband Hill"). Afterward, *Spirit* drove downhill south into the "Inner Basin," where she discovered more remarkable samples. Details of *Spirit*'s trek are described in Arvidson *et al*. (2006) and Golombek *et al*. (2006).

Names have been assigned to geographic features, soils, and rocks by the Athena Science Team (the group of scientists and mission operations staffers who guide the rovers on Mars) for planning and operations purposes. These names are not formally recognized by the International Astronomical Union. To better identify targets investigated by different instruments, the sol number of the APXS measurement is often indicated in the measurement name. The APXS sol number is the sol of the end of the integration, as many measurements were started before midnight and finished the next morning.

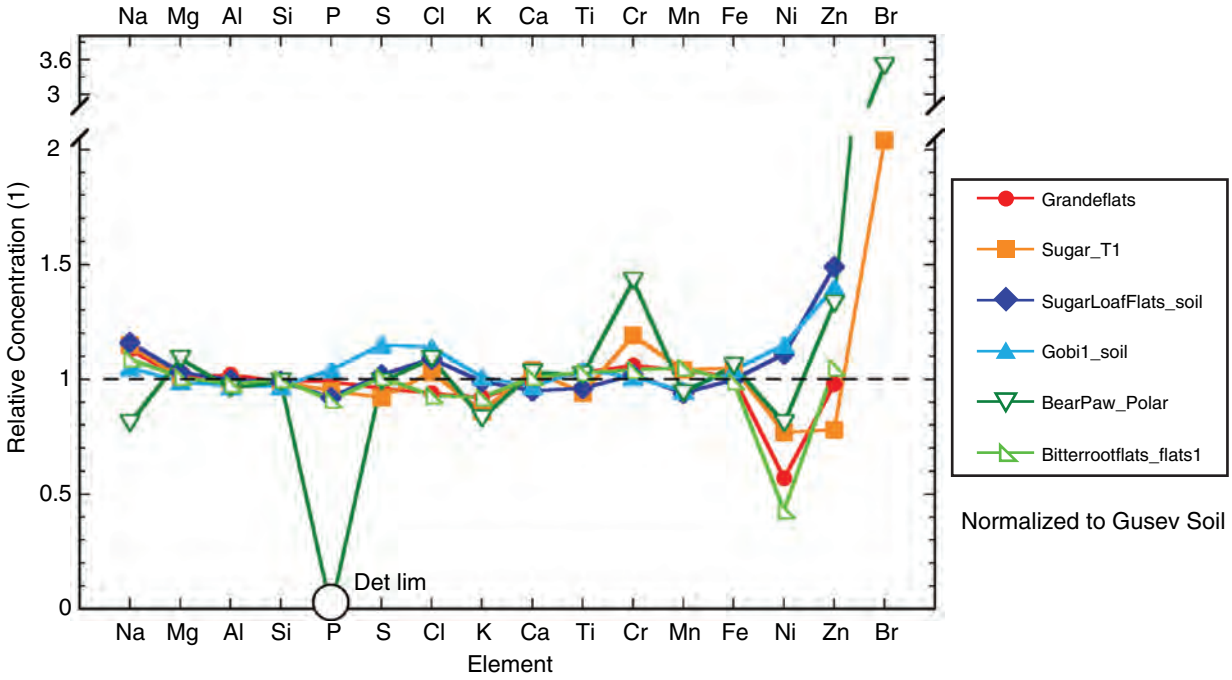

Figure 4.7. Undisturbed Gusev soil concentrations relative to "Gusev Soil (sol 14)." Notes: Long APXS integration times for soils "Grandeflats (sol 47)" and "Gobi1_soil (sol 71)"; short integration times (<1 hour) for soils "Sugar_T1 (sol 52)," "SugarLoafFlats_soil (sol 71)," "BearPaw (sol 74)," and "Bitterrootflats_flats1 (sol 105)." The sol number denotes the elapsed number of Martian days after landing, sol 14 means that the APXS data recording was stopped on day 14. The *y*-axis is linear with a break to cover the full range of data. Key: Det Lim = Concentration is below detection limit. (For a color version of this figure, please refer to the color plate section or to the e-Book version of this chapter.)

4.3.1 Gusev plains

The composition of soils, trenches, and rocks analyzed during the primary and extended missions are shown in Table 4.1 (Gellert *et al.*, 2006).

Samples measured by the APXS can be generally classified as soils or rocks. The term "soil" is used here to denote any loose, unconsolidated material that can be distinguished from rocks, bedrock or strongly cohesive sediments. No implication of the presence or absence of organic materials or living matter is intended.

Gusev plains soils

In general, the major element compositions of the soils at the Viking 1, Viking 2, MPF, and Gusev landing sites are very similar. This supports the hypothesis of a globally mixed soil component, most likely driven by dust storms (Clark *et al.*, 1982; Wänke *et al.*, 2001).

Soil surfaces were measured occasionally by the APXS along the rover traverse at Gusev crater. The so-called "undisturbed soil" consisted of the uppermost layer, not touched by the rover's wheel. Most undisturbed soils exhibit rather similar chemical compositions comparable to the undisturbed soil "Gusev Soil (sol 14)" (Figure 4.7). As the integration time of "Gusev Soil" was rather long (13 hours), resulting in very good counting statistics (Gellert *et al.*, 2006), this soil is used for normalization of other soil compositions to facilitate comparisons. It turned out that the composition of "Gusev Soil" is rather typical (close to the mean soil composition). On the other hand, the chemical soil composition differed markedly from rock compositions encountered along the traverse. The soils have enrichments in the elements P, S, Cl, K, Ti, Ni, and Zn and depletions in Mg, Cr, Mn, and Fe when compared to typical Gusev plains basalts such as rock "Humphrey" (see below).

The Ni content of about 500 ppm in the undisturbed soils is about three to four times higher compared to its concentration in the primitive Gusev basalts (discussed below). Nickel in the soil is apparently derived from weathered basalt and a meteoritic component (Gellert *et al.*, 2006). In the primitive basalts Ni correlates with Mg. Assuming the Mg/Ni ratio of 400 found in basalts to be valid for the basaltic portion in the soil, the "basaltic" Ni content can be estimated: The mean Mg content of about 5% of the soils corresponds to a Ni content of 125 ppm. The difference between the total Ni content of 500 ppm of the soil and the 125 ppm Ni from the basaltic component provides a possible meteoritic Ni abundance. Assuming carbonaceous chondrite material of type CI (a "primitive" class of meteorites) a meteoritic component of about 3% can be estimated, or only 0.4 wt.% assuming an iron meteorite composition with higher Ni concentrations (Gellert *et al.*, 2006).

Significant compositional variations are observed for certain undisturbed soil surfaces in the Columbia Hills. A soil dubbed "Crumble (sol 457)" shows larger compositional variations in P, S, Ti, Cr, Ni, Zn, and Br and higher Al/Si and lower Fe/Si ratios compared to most Gusev plains soils (Figure 4.8). Lithic fragments observed in the "Crumble" soil target could indicate that this soil has an admixture of nearby Wishstone Class rocks. Also "Goldfinger Jaws (sol

Table 4.1. *Compositions of all Gusev samples from sol 14 to 633*

Sol	Type	Sample	N	T	Na_2O	SE	MgO	SE	Al_2O_3	SE	SiO_2	SE	P_2O_5	SE	SO_3	SE	Cl	SE	K_2O	SE
A014	SU	Gusev_Soil	45	13.5	2.76	0.23	8.34	0.12	9.89	0.14	46.3	0.44	0.87	0.08	6.61	0.08	0.78	0.02	0.48	0.06
A018	RU	Adirondack_asis	126	0.1	2.32	1.64	9.09	0.50	10.93	0.46	45.6	1.04	0.72	0.37	3.47	0.27	0.43	0.06	0.14	0.15
A033	RB	Adirondack_brush	129	11.2	2.78	0.18	9.51	0.10	11.35	0.11	45.7	0.37	0.57	0.06	2.16	0.03	0.36	0.01	0.12	0.05
A034	RR	Adirondack_RAT	123	5.5	2.41	0.20	10.83	0.12	10.87	0.12	45.7	0.41	0.52	0.07	1.23	0.03	0.20	0.01	0.07	0.05
A041	SC	Crest_morning	76	0.7	2.80	0.93	8.67	0.27	10.02	0.29	46.0	0.71	0.80	0.26	5.26	0.17	0.69	0.04	0.43	0.15
A042	RU	Mimi	95	4.5	2.94	0.22	8.39	0.12	10.04	0.13	45.0	0.43	0.85	0.08	5.50	0.08	0.74	0.02	0.49	0.06
A043	SD	Track	72	2.4	2.88	0.27	8.45	0.15	10.30	0.17	46.8	0.53	0.81	0.09	5.00	0.10	0.60	0.02	0.45	0.06
A044	SF	Rampflats	68	0.3	2.54	1.25	8.69	0.37	10.23	0.38	46.3	0.92	0.87	0.32	6.06	0.26	0.71	0.06	0.43	0.17
A045	SC	Angelflats	59	0.5	3.09	1.79	8.59	0.47	9.96	0.36	45.5	0.64	0.78	0.28	6.19	0.21	0.78	0.05	0.48	0.16
A047	SU	Grandeflats	70	4.5	3.13	0.21	8.41	0.11	10.05	0.11	46.0	0.33	0.86	0.08	6.33	0.09	0.73	0.02	0.44	0.06
A049	ST	Road Cut_Floor3_	57	6.5	2.44	0.25	8.90	0.13	9.83	0.14	46.2	0.47	0.68	0.08	6.11	0.09	0.69	0.02	0.38	0.06
A050	ST	Road Cut_WallMIonl	62	7.6	2.65	0.24	8.77	0.13	9.96	0.16	46.1	0.47	0.73	0.08	5.69	0.08	0.77	0.02	0.37	0.06
A052	SU	Sugar_T1	74	0.5	3.18	0.96	8.47	0.28	9.67	0.29	45.6	0.77	0.83	0.26	6.10	0.21	0.80	0.05	0.41	0.15
A055	RU	Humphrey_Ashley_asis	131	0.3	3.00	0.86	8.76	0.23	10.66	0.23	45.9	0.64	0.65	0.22	3.53	0.13	0.58	0.04	0.19	0.13
A057	RU	Humphrey_Heyworth_asis	129	0.6	2.92	1.23	8.69	0.33	11.13	0.27	45.7	0.63	0.63	0.21	3.24	0.11	0.54	0.03	0.19	0.12
A058	RB	Humphrey_brush	134	3.4	2.95	0.21	8.82	0.12	11.20	0.14	45.9	0.43	0.62	0.07	2.63	0.05	0.49	0.01	0.18	0.06
A059	RR	Humphrey_RAT1	128	5.0	2.76	0.21	9.49	0.12	10.78	0.15	46.3	0.42	0.57	0.07	1.09	0.03	0.32	0.01	0.13	0.05
A060	RR	Humphrey_RAT2	125	5.0	2.54	0.28	10.41	0.14	10.68	0.13	45.9	0.43	0.56	0.07	1.28	0.03	0.26	0.01	0.10	0.05
A063	RU	Plank_Asis	113	0.4	3.04	0.79	8.27	0.24	9.72	0.26	44.0	0.69	0.75	0.23	5.85	0.18	0.72	0.04	0.33	0.14
A065	SU	SugarLoafFlats_soi	70	0.5	3.20	1.03	8.57	0.30	9.86	0.28	45.9	0.75	0.81	0.26	6.76	0.23	0.84	0.05	0.47	0.16
A071	SU	Gobi1_soil	58	2.9	2.91	0.29	8.25	0.15	9.56	0.16	45.0	0.52	0.91	0.09	7.61	0.13	0.88	0.03	0.49	0.07
A074a	SD	Serpent_Scuffed	71	4.0	2.89	0.25	8.86	0.14	10.12	0.15	46.7	0.48	0.66	0.08	4.39	0.08	0.54	0.02	0.40	0.06
A074b	SU	BearPaw	86	0.6	2.23	1.07	9.06	0.24	9.54	0.31	46.0	0.47	0.15	0.34	6.56	0.17	0.85	0.05	0.40	0.15
A081a	RB	Mazatzal_NewYork_Brush	110	1.8	2.54	0.25	7.70	0.14	8.50	0.16	44.5	0.50	1.19	0.09	7.62	0.12	1.28	0.03	0.54	0.06
A081b	RU	Mazatzal_Texas_asis	114	2.5	3.10	0.24	8.23	0.13	9.15	0.13	43.7	0.45	0.97	0.08	7.62	0.11	0.99	0.02	0.45	0.06
A082	RR	Mazatzal_NewYork_RAT1	107	4.6	2.74	0.21	9.02	0.12	9.92	0.13	45.7	0.43	0.82	0.07	3.33	0.05	0.54	0.01	0.29	0.06
A083	RU	Mazatzal_Oregon_Asis	101	2.7	2.83	0.24	8.09	0.13	8.94	0.13	44.5	0.46	1.03	0.08	7.77	0.11	1.11	0.02	0.51	0.06
A086	RR	Mazatzal_Brooklyn_RAT2	107	6.4	2.78	0.20	9.72	0.11	10.70	0.12	45.8	0.41	0.65	0.07	1.48	0.03	0.23	0.01	0.16	0.05
A100	RB	Route66_brushed	132	6.0	2.88	0.20	8.67	0.11	10.78	0.14	44.8	0.39	0.74	0.07	4.20	0.05	0.55	0.01	0.23	0.05
A105	SU	Bitterrootflats_flats1	48	0.6	3.01	1.19	8.43	0.34	9.68	0.31	46.3	0.82	0.79	0.29	6.67	0.25	0.72	0.05	0.44	0.17
A113	SU	Bighole_Mayfly_surface	69	0.6	3.10	1.23	8.39	0.33	9.92	0.26	46.1	0.64	0.88	0.24	6.37	0.18	0.79	0.04	0.47	0.15
A114	ST	Bighole_RS2	84	9.9	2.51	0.21	9.19	0.11	9.06	0.13	43.7	0.40	0.80	0.08	9.13	0.10	1.00	0.02	0.35	0.06
A115	ST	Bighole_Trico	67	4.0	2.47	0.25	9.04	0.14	9.08	0.14	44.2	0.47	0.74	0.08	8.37	0.12	1.00	0.02	0.34	0.06

Sol	Type	Sample	CaO	SE	TiO_2	SE	Cr_2O_3	SE	MnO	SE	FeO	SE	Ni	SE	Zn	SE	Br	SE
A014	SU	Gusev_Soil	6.36	0.05	0.86	0.07	0.31	0.03	0.33	0.01	16.0	0.11	556	51	293	18	31	17
A018	RU	Adirondack_asis	7.52	0.23	0.71	0.23	0.69	0.11	0.40	0.14	18.0	0.39	241	171	242	100	nd	
A033	RB	Adirondack_brush	7.84	0.05	0.49	0.06	0.63	0.03	0.39	0.01	18.0	0.10	149	33	80	8	nd	
A034	RR	Adirondack_RAT	7.75	0.05	0.48	0.06	0.61	0.03	0.41	0.01	18.8	0.12	165	39	81	11	14	15
A041	SC	Crest_morning	6.98	0.12	0.72	0.20	0.49	0.06	0.36	0.06	16.6	0.21	341	100	329	51	112	30
A042	RU	Mimi	7.07	0.06	0.68	0.07	0.55	0.04	0.40	0.01	17.3	0.12	249	45	182	16	53	17
A043	SD	Track	6.52	0.07	0.91	0.08	0.41	0.04	0.36	0.02	16.5	0.15	364	65	257	27	56	21
A044	SF	Rampflats	6.58	0.16	0.77	0.23	0.26	0.07	0.29	0.09	16.2	0.29	287	138	246	74	38	39
A045	SC	Angelflats	6.69	0.14	0.68	0.15	0.38	0.07	0.30	0.07	16.5	0.18	551	135	211	63	69	37
A047	SU	Grandeflats	6.32	0.05	0.89	0.07	0.33	0.03	0.34	0.01	16.1	0.08	318	51	288	20	nd	
A049	ST	Road Cut_Floor3_	6.14	0.06	1.00	0.08	0.43	0.04	0.34	0.01	16.8	0.12	443	61	318	26	61	21
A050	ST	Road Cut_WallMIonl	6.24	0.05	1.02	0.07	0.40	0.04	0.35	0.01	16.8	0.12	592	56	255	20	65	18
A052	SU	Sugar_T1	6.60	0.13	0.81	0.18	0.37	0.06	0.34	0.07	16.7	0.24	429	112	229	53	63	34
A055	RU	Humphrey_Ashley_asis	7.53	0.12	0.48	0.12	0.57	0.06	0.40	0.06	17.7	0.19	151	85	159	42	49	26
A057	RU	Humphrey_Heyworth_asis	7.54	0.11	0.53	0.11	0.61	0.06	0.39	0.05	17.9	0.20	105	70	72	30	39	26
A058	RB	Humphrey_brush	7.76	0.06	0.54	0.06	0.60	0.04	0.39	0.01	17.9	0.12	158	41	95	13	37	16
A059	RR	Humphrey_RAT1	8.19	0.06	0.58	0.06	0.68	0.03	0.41	0.01	18.6	0.12	202	39	117	11	49	16
A060	RR	Humphrey_RAT2	7.84	0.05	0.55	0.06	0.60	0.03	0.41	0.01	18.8	0.12	164	39	112	11	52	16
A063	RU	Plank_Asis	6.81	0.12	0.57	0.13	0.57	0.06	0.42	0.07	18.9	0.24	27	81	134	43	42	31
A065	SU	SugarLoafFlats_soi	6.04	0.13	0.83	0.16	0.31	0.06	0.31	0.07	15.9	0.24	620	131	435	67	nd	
A071	SU	Gobi1_soil	6.17	0.07	0.89	0.08	0.31	0.04	0.31	0.02	16.5	0.15	641	73	409	32	30	22
A074a	SD	Serpent_Scuffed	6.57	0.06	0.94	0.07	0.46	0.04	0.36	0.01	17.0	0.13	475	60	210	22	53	19
A074b	SU	BearPaw	6.57	0.11	0.88	0.14	0.44	0.06	0.31	0.07	16.9	0.15	450	113	391	53	108	30
A081a	RB	Mazatzal_NewYork_Brush	6.63	0.07	0.84	0.08	0.26	0.04	0.32	0.02	17.9	0.15	553	63	457	28	100	21
A081b	RU	Mazatzal_Texas_asis	6.23	0.06	0.81	0.07	0.35	0.04	0.33	0.01	18.0	0.14	471	54	391	23	37	18
A082	RR	Mazatzal_NewYork_RAT1	7.57	0.06	0.69	0.07	0.45	0.03	0.40	0.01	18.4	0.12	342	46	222	16	144	18
A083	RU	Mazatzal_Oregon_Asis	6.35	0.06	0.77	0.07	0.21	0.03	0.33	0.01	17.4	0.13	607	58	579	26	64	20
A086	RR	Mazatzal_Brooklyn_RAT2	8.02	0.06	0.59	0.06	0.54	0.03	0.42	0.01	18.9	0.12	132	39	75	11	161	17
A100	RB	Route66_brushed	7.83	0.05	0.59	0.06	0.53	0.03	0.39	0.01	17.7	0.11	181	37	125	10	46	15
A105	SU	Bitterrootflats_flats1	6.45	0.15	0.89	0.18	0.32	0.07	0.34	0.08	15.8	0.25	237	129	308	74	nd	
A113	SU	Bighole_Mayfly_surface	6.07	0.11	1.00	0.16	0.37	0.06	0.31	0.06	16.1	0.19	467	108	192	50	32	31
A114	ST	Bighole_RS2	5.74	0.04	0.87	0.07	0.36	0.03	0.34	0.01	16.8	0.10	466	45	460	17	64	16
A115	ST	Bighole_Trico	5.86	0.06	0.89	0.07	0.43	0.04	0.34	0.02	17.1	0.14	466	64	382	28	47	21

Table 4.1. (*cont*.)

Sol	Type	Sample	N	T	Na_2O	SE	MgO	SE	Al_2O_3	SE	SiO_2	SE	P_2O_5	SE	SO_3	SE	Cl	SE	K_2O	SE
A122	SD	Owens_soil_Track	83	0.5	3.07	1.00	8.41	0.29	10.65	0.27	47.0	0.71	0.95	0.26	5.45	0.19	0.63	0.04	0.47	0.15
A126	SU	Accelerator_Soil	47	0.6	3.06	1.65	8.15	0.46	10.02	0.40	46.3	0.83	0.83	0.30	6.40	0.24	0.77	0.05	0.45	0.17
A135	SD	Santa_Anita_trench_surface	91	0.6	3.04	1.67	8.73	0.46	10.71	0.37	47.0	0.69	0.77	0.27	4.67	0.16	0.54	0.03	0.42	0.15
A140	ST	Boroughs_Mills_bottom	76	8.3	2.36	0.21	9.82	0.13	8.47	0.13	41.4	0.39	0.71	0.08	11.19	0.12	0.68	0.01	0.35	0.06
A141	ST	Boroughs_Hellskitchen_side	83	4.0	2.53	0.24	10.48	0.14	7.85	0.12	39.2	0.40	0.80	0.08	14.06	0.16	0.73	0.02	0.36	0.06
A150a	RU	Mojave_Joshua_Asis	127	0.4	3.07	0.98	9.38	0.29	10.36	0.29	44.8	0.69	0.53	0.25	3.47	0.14	0.57	0.04	0.20	0.13
A158	SD	Shredded_dark4_soil	89	0.5	3.25	0.85	8.73	0.26	11.29	0.26	47.8	0.70	0.75	0.23	4.10	0.15	0.52	0.03	0.45	0.15
A164	RU	Goldklumpen_Asis	94	4.5	3.09	0.22	8.89	0.12	10.32	0.13	45.0	0.43	1.12	0.08	8.36	0.10	0.83	0.02	0.31	0.06
A167	SU	Goldfinger_Jaws_soil	92	0.5	3.31	1.17	9.84	0.36	10.08	0.41	46.3	0.78	0.80	0.26	5.26	0.18	0.62	0.04	0.41	0.15
A170	RU	Fools_gold_Asis	92	3.0	2.64	0.30	9.37	0.16	10.86	0.15	44.2	0.47	1.14	0.08	9.71	0.13	0.68	0.02	0.18	0.06
A172	RR	Pot_of_Gold_RAT	89	5.0	3.03	0.21	9.91	0.13	10.32	0.13	42.9	0.41	1.08	0.08	7.96	0.10	0.57	0.01	0.20	0.06
A176	RU	Breadbox_Sourdough	56	4.0	3.01	0.25	8.56	0.12	10.17	0.12	46.0	0.38	1.06	0.08	7.12	0.10	0.76	0.02	0.40	0.06
A178	RU	String_of_pearls_Perlx	70	4.0	2.91	0.24	8.95	0.14	9.89	0.14	43.4	0.45	1.09	0.08	8.34	0.12	0.67	0.02	0.34	0.06
A195	RU	WoolyPatch_Sabre_asis	100	5.8	3.41	0.20	8.54	0.11	9.68	0.12	44.8	0.41	0.96	0.07	7.33	0.09	1.08	0.02	0.40	0.06
A197	RR	WoolyPatch_Sabre_RAT	86	5.7	3.33	0.22	10.92	0.14	12.60	0.17	46.8	0.44	1.24	0.08	2.87	0.05	0.78	0.02	0.07	0.05
A199	RR	Woolypatch_Mastodon_RAT	99	5.6	2.92	0.20	11.62	0.13	10.34	0.12	46.4	0.43	1.20	0.08	2.41	0.04	1.03	0.02	0.04	0.05
A214	RU	Clovis_Plano_asis	105	5.3	3.46	0.21	8.80	0.11	9.66	0.12	44.9	0.42	1.02	0.08	7.77	0.09	1.23	0.02	0.42	0.06
A216	RB	Clovis_Plano_Brush	90	4.7	3.55	0.23	10.79	0.14	9.34	0.13	43.4	0.42	1.13	0.08	7.98	0.10	1.88	0.03	0.35	0.06
A218	RR	Clovis_Plano_RAT	72	4.7	3.64	0.23	11.52	0.13	8.95	0.10	42.2	0.38	1.05	0.08	7.53	0.10	1.63	0.03	0.35	0.06
A225	RB	Clovis_BrushMosaic	90	0.8	3.02	1.11	11.46	0.30	8.85	0.27	42.6	0.52	0.81	0.36	9.29	0.25	1.74	0.06	0.45	0.15
A227	SU	Kilmary_soil	74	0.7	2.77	0.90	8.42	0.26	9.59	0.26	45.7	0.68	0.87	0.25	7.50	0.20	0.94	0.04	0.49	0.15
A228	RU	Ebenezer_TinyTim	123	0.5	2.87	0.75	11.16	0.25	10.71	0.24	47.4	0.67	0.94	0.21	4.67	0.14	1.33	0.05	0.36	0.14
A229	RU	Ebenezer_Cratchit_asis	120	5.3	3.20	0.20	10.89	0.13	10.40	0.12	46.8	0.42	1.00	0.07	5.18	0.07	1.32	0.02	0.35	0.06
A231	RB	Ebenezer_brushed	95	6.0	2.59	0.21	13.57	0.15	9.93	0.12	47.5	0.43	0.97	0.07	3.81	0.06	1.54	0.02	0.32	0.06
A232	RR	Ebenezer_RAT	72	6.0	2.32	0.22	14.82	0.17	9.28	0.13	47.4	0.45	0.97	0.08	3.20	0.06	1.46	0.02	0.33	0.06
A235	RF	Ebenezer_Fritz_RATgrindings	103	0.6	3.01	0.81	13.49	0.28	10.18	0.24	45.3	0.64	0.94	0.22	3.01	0.12	1.38	0.05	0.30	0.13
A240	SU	Greeneyes_soilTG	78	0.7	2.91	0.85	8.39	0.25	9.85	0.23	45.8	0.62	0.95	0.24	7.44	0.19	0.85	0.04	0.44	0.15
A259	SD	Disturbance_soil	84	4.7	3.21	0.23	8.42	0.12	10.13	0.14	46.4	0.45	0.90	0.08	6.65	0.09	0.76	0.02	0.46	0.06
A266	RU	Temples_dwarf_asis	99	7.7	3.27	0.20	9.06	0.11	9.47	0.11	45.3	0.40	0.98	0.07	7.37	0.08	1.33	0.02	0.41	0.06
A274	RU	Tetl_clumb_asis	70	6.3	3.31	0.22	9.49	0.11	10.10	0.11	46.4	0.40	0.91	0.08	6.52	0.08	1.42	0.02	0.43	0.06
A280	SD	Coffee_disturbed_soil	73	6.5	3.17	0.21	8.94	0.12	9.80	0.12	45.0	0.43	1.02	0.08	6.48	0.08	0.87	0.02	0.42	0.06
A284	RU	Uchban_Koolik_asis	76	6.1	3.21	0.22	9.14	0.12	9.74	0.12	45.1	0.43	0.98	0.08	7.38	0.09	1.32	0.02	0.43	0.06
A287	RR	Uchben_Koolik_RAT	90	8.3	2.44	0.20	14.28	0.13	9.52	0.10	45.6	0.35	0.94	0.07	5.26	0.06	1.85	0.02	0.35	0.06
A291	RB	Uchben_Chiikbes_brush	86	6.5	2.82	0.22	12.14	0.14	9.96	0.12	45.4	0.42	1.04	0.08	5.92	0.08	2.62	0.03	0.40	0.06

Sol	Type	Sample	CaO	SE	TiO_2	SE	Cr_2O_3	SE	MnO	SE	FeO	SE	Ni	SE	Zn	SE	Br	SE
A122	SD	Owens_soil_Track	6.38	0.12	0.88	0.16	0.33	0.06	0.28	0.07	15.4	0.21	391	100	239	48	31	31
A126	SU	Accelerator_Soil	6.50	0.14	0.96	0.19	0.29	0.07	0.32	0.08	15.9	0.25	641	141	402	73	nd	
A135	SD	Santa_Anita_trench_surface	6.27	0.11	0.89	0.20	0.42	0.06	0.34	0.06	16.1	0.20	483	95	291	45	19	26
A140	ST	Boroughs_Mills_bottom	5.77	0.05	0.90	0.07	0.39	0.03	0.36	0.01	17.5	0.11	507	49	285	17	162	19
A141	ST	Boroughs_Hellskitchen_side	5.76	0.05	0.85	0.08	0.39	0.04	0.34	0.01	16.5	0.12	438	54	253	20	205	21
A150a	RU	Mojave_Joshua_Asis	7.39	0.12	0.57	0.12	0.53	0.06	0.37	0.07	18.7	0.22	97	80	159	39	89	28
A158	SD	Shredded_dark4_soil	6.31	0.12	0.67	0.16	0.36	0.06	0.33	0.06	15.3	0.21	536	102	200	45	36	29
A164	RU	Goldklumpen_Asis	5.26	0.05	0.72	0.07	0.21	0.03	0.20	0.01	15.6	0.11	737	51	97	13	73	18
A167	SU	Goldfinger_Jaws_soil	5.90	0.12	0.73	0.14	0.27	0.06	0.32	0.06	16.0	0.21	854	118	110	42	36	27
A170	RU	Fools_gold_Asis	5.13	0.05	0.60	0.07	0.19	0.03	0.17	0.01	15.1	0.12	777	57	80	15	73	18
A172	RR	Pot_of_Gold_RAT	5.86	0.05	0.77	0.07	0.27	0.03	0.24	0.01	16.7	0.12	894	52	112	13	77	17
A176	RU	Breadbox_Sourdough	6.04	0.06	0.85	0.07	0.31	0.04	0.28	0.01	15.3	0.09	704	63	150	21	34	18
A178	RU	String_of_pearls_Perlx	6.37	0.06	0.76	0.07	0.23	0.03	0.29	0.01	16.6	0.13	533	56	201	19	69	18
A195	RU	WoolyPatch_Sabre_asis	5.62	0.04	0.89	0.07	0.24	0.03	0.20	0.01	16.7	0.11	516	44	193	13	185	17
A197	RR	WoolyPatch_Sabre_RAT	3.64	0.04	0.94	0.07	0.27	0.03	0.10	0.01	16.3	0.11	607	47	89	12	318	20
A199	RR	Woolypatch_Mastodon_RAT	3.44	0.03	0.91	0.07	0.18	0.03	0.13	0.01	19.2	0.12	553	46	54	11	493	21
A214	RU	Clovis_Plano_asis	6.15	0.05	0.85	0.07	0.19	0.03	0.27	0.01	15.0	0.10	562	44	175	12	908	24
A216	RB	Clovis_Plano_Brush	5.86	0.05	0.75	0.07	0.18	0.03	0.27	0.01	14.3	0.10	538	47	107	13	901	26
A218	RR	Clovis_Plano_RAT	6.04	0.05	0.84	0.07	0.17	0.03	0.30	0.01	15.6	0.08	735	55	118	16	239	20
A225	RB	Clovis_BrushMosaic	5.39	0.09	0.84	0.14	0.18	0.05	0.23	0.06	14.9	0.15	670	94	99	33	993	45
A227	SU	Kilmary_soil	5.88	0.10	0.84	0.14	0.28	0.05	0.31	0.06	16.3	0.20	533	100	264	44	263	37
A228	RU	Ebenezer_TinyTim	4.24	0.08	0.79	0.13	0.14	0.04	0.21	0.04	15.1	0.18	453	80	146	32	193	29
A229	RU	Ebenezer_Cratchit_asis	4.31	0.04	0.78	0.06	0.17	0.03	0.17	0.01	15.3	0.10	478	41	92	9	267	17
A231	RB	Ebenezer_brushed	3.63	0.03	0.76	0.06	0.16	0.03	0.15	0.01	15.0	0.10	497	43	72	10	293	18
A232	RR	Ebenezer_RAT	3.44	0.04	0.79	0.07	0.16	0.03	0.16	0.01	15.6	0.11	523	47	99	13	222	19
A235	RF	Ebenezer_Fritz_RATgrindings	3.93	0.08	0.90	0.14	0.18	0.05	0.18	0.04	17.1	0.20	731	93	56	29	352	36
A240	SU	Greeneyes_soilTG	6.17	0.11	0.82	0.14	0.21	0.05	0.29	0.05	15.8	0.19	548	95	285	42	nd	
A259	SD	Disturbance_soil	6.22	0.05	0.84	0.07	0.29	0.03	0.30	0.01	15.3	0.11	467	48	293	17	24	16
A266	RU	Temples_dwarf_asis	5.75	0.04	0.85	0.06	0.19	0.03	0.35	0.01	15.4	0.10	568	42	175	11	1543	28
A274	RU	Tetl_clumb_asis	5.18	0.04	0.86	0.07	0.20	0.03	0.28	0.01	14.7	0.08	558	48	204	15	694	23
A280	SD	Coffee_disturbed_soil	6.36	0.05	0.88	0.07	0.34	0.03	0.34	0.01	16.2	0.11	469	47	252	15	101	17
A284	RU	Uchban_Koolik_asis	5.90	0.05	0.86	0.07	0.19	0.03	0.30	0.01	15.2	0.11	564	47	206	14	735	24
A287	RR	Uchben_Koolik_RAT	4.48	0.03	0.80	0.06	0.15	0.03	0.25	0.01	13.9	0.06	593	41	118	9	674	20
A291	RB	Uchben_Chiikbes_brush	4.39	0.04	0.80	0.07	0.16	0.03	0.23	0.01	13.9	0.10	547	44	158	12	903	24

Table 4.1. (*cont.*)

Sol	Type	Sample	N	T	Na_2O	SE	MgO	SE	Al_2O_3	SE	SiO_2	SE	P_2O_5	SE	SO_3	SE	Cl	SE	K_2O	SE
A300	RB	Lutefisk_flatfish_Brushed	95	7.3	2.56	0.20	14.34	0.15	10.29	0.12	46.0	0.41	0.95	0.07	3.44	0.05	2.02	0.02	0.29	0.06
A304	RB	Lutefisk_RATRoe_brushed	88	5.5	2.45	0.22	15.12	0.17	10.17	0.13	45.5	0.43	1.04	0.08	3.05	0.05	2.47	0.03	0.24	0.06
A315	SD	Tofurkey_disturbedsoil	100	2.7	3.37	0.31	8.68	0.16	10.31	0.16	46.9	0.50	0.88	0.08	5.82	0.09	0.68	0.02	0.43	0.06
A334	RB	Wishstone_chisel_brush	102	2.7	5.12	0.28	4.94	0.14	15.64	0.24	46.3	0.49	2.63	0.11	3.47	0.07	0.59	0.02	0.54	0.06
A335	RR	Wishstone_chisel_RAT	97	3.3	4.98	0.25	4.50	0.10	15.03	0.17	43.8	0.44	5.19	0.13	2.20	0.05	0.35	0.01	0.57	0.06
A342	SD	Penny_dist_soil	101	3.3	3.45	0.23	9.42	0.13	10.63	0.14	46.7	0.46	0.84	0.08	4.80	0.08	0.57	0.01	0.40	0.06
A349	RU	dreaming_asis	76	2.5	4.48	0.29	5.64	0.13	14.68	0.21	47.0	0.52	1.74	0.10	4.10	0.09	0.71	0.02	0.56	0.06
A353	RU	champagne_asis	73	3.3	4.20	0.23	6.15	0.10	13.48	0.15	46.4	0.36	1.79	0.09	4.40	0.08	0.72	0.02	0.53	0.06
A355	RB	champagne_brush	129	9.0	5.30	0.21	4.56	0.07	15.75	0.15	45.8	0.38	2.64	0.08	2.50	0.04	0.62	0.01	0.51	0.06
A356	RR	champagne_RAT1	53	9.0	5.04	0.25	3.94	0.09	14.86	0.17	43.4	0.42	5.07	0.12	1.94	0.04	0.60	0.01	0.53	0.06
A357	RR2	champagne_RAT2	53	9.0	5.02	0.23	3.98	0.08	14.83	0.14	43.5	0.32	5.05	0.11	1.96	0.04	0.60	0.01	0.53	0.06
A374	RB	Peace_brushed	81	4.7	2.28	0.20	14.20	0.14	6.29	0.08	41.6	0.32	0.99	0.08	7.86	0.09	0.92	0.02	0.16	0.05
A377	RR1	Peace_RAT1	90	4.7	0.37	0.37	19.75	0.23	2.80	0.10	37.1	0.41	0.59	0.08	12.88	0.15	0.89	0.02	0.01	0.05
A380	RR2	Peace_RAT2	43	4.7	0.00	0.37	21.53	0.27	2.24	0.06	37.3	0.40	0.49	0.08	10.64	0.15	0.72	0.02	0.00	0.05
A380b	RU	Alligator_APXSspot_TG	86	0.4	3.27	0.86	11.24	0.28	7.78	0.25	42.7	0.54	0.75	0.27	7.81	0.21	1.33	0.06	0.27	0.14
A381	RU	Alligator_APXSspot_long	86	4.7	3.00	0.21	10.90	0.14	7.81	0.11	42.5	0.41	0.86	0.08	7.71	0.10	1.37	0.02	0.27	0.06
A385b	RB	Alligator_scale_brushed	77	0.2	1.59	1.50	16.27	0.41	5.49	0.33	41.8	0.60	0.29	0.83	8.48	0.52	1.26	0.08	0.19	0.15
A401	SD	PasoRobles_disturbed soil	88	2.7	1.64	0.21	5.53	0.09	4.13	0.07	21.8	0.24	5.61	0.14	31.72	0.30	0.55	0.02	0.19	0.06
A416	RB	Watchtower_Joker_Brush	78	2.7	2.78	0.27	10.10	0.16	12.22	0.19	44.1	0.48	2.72	0.11	4.70	0.08	1.14	0.03	0.76	0.07
A417	RR	Watchtower_Joker_RAT	85	5.3	2.67	0.23	10.00	0.13	12.33	0.15	42.4	0.41	4.50	0.11	3.43	0.06	0.80	0.02	0.74	0.06
A427	SD	Paso_light	85	6.5	1.42	0.18	5.19	0.08	6.27	0.08	24.9	0.22	4.69	0.11	31.62	0.25	0.73	0.02	0.40	0.06
A428	SD	Paso_dark	88	6.1	3.24	0.21	8.74	0.11	10.44	0.13	46.1	0.43	0.96	0.07	5.68	0.07	0.55	0.01	0.39	0.06
A429b	RB	BensClod_brushed	73	8.2	3.29	0.23	5.11	0.09	15.12	0.15	49.8	0.42	4.66	0.11	5.02	0.06	0.85	0.02	0.65	0.06
A430	SD	Paso_DarkLight	84	9.3	3.02	0.26	8.64	0.12	9.72	0.11	43.2	0.40	1.38	0.08	7.73	0.08	0.58	0.01	0.38	0.06
A457	SU	Crumble	78	10.0	3.40	0.19	8.73	0.09	11.83	0.11	47.1	0.30	1.39	0.07	4.02	0.05	0.60	0.01	0.41	0.06
A469	RU	Methuselah_Keystone	72	5.8	3.32	0.23	8.38	0.11	12.44	0.13	47.0	0.37	1.23	0.08	4.95	0.07	0.92	0.02	0.51	0.06
A470	RB	Methuselah_Haunch	76	8.9	3.44	0.21	8.48	0.09	13.61	0.12	46.9	0.34	2.41	0.09	4.15	0.05	1.23	0.02	0.56	0.06
A475	RB	Methuselah_Pittsburg	72	2.8	3.32	0.28	8.30	0.13	12.49	0.15	44.6	0.38	3.17	0.11	4.73	0.09	1.36	0.03	0.45	0.06
A477	SU	Liberty_Bell	80	4.5	3.09	0.31	8.58	0.15	10.78	0.15	47.7	0.49	0.83	0.08	4.75	0.08	0.55	0.01	0.43	0.06
A481	RU	Reef	64	10.5	3.48	0.23	8.16	0.11	12.52	0.14	46.3	0.42	2.62	0.09	4.92	0.07	1.06	0.02	0.40	0.06
A484	RB	Jibsheet	84	10.2	3.60	0.22	8.64	0.11	12.07	0.13	45.2	0.40	2.51	0.09	6.43	0.07	1.28	0.02	0.37	0.06
A491	RU	Paros	79	7.5	3.42	0.23	7.91	0.11	13.73	0.15	46.8	0.43	2.31	0.09	4.97	0.07	1.05	0.02	0.37	0.06
A495	RU	Pequod_Ahab	76	10.0	3.42	0.22	7.82	0.11	13.37	0.15	46.4	0.41	2.68	0.09	4.33	0.06	0.96	0.02	0.39	0.06
A496	RB	Pequod_Ahab_brushed	81	8.9	3.48	0.22	8.42	0.11	13.10	0.14	46.0	0.41	2.83	0.09	4.29	0.06	0.98	0.02	0.38	0.06

Sol	Type	Sample	CaO	SE	TiO_2	SE	Cr_2O_3	SE	MnO	SE	FeO	SE	Ni	SE	Zn	SE	Br	SE
A300	RB	Lutefisk_flatfish_Brushed	4.59	0.04	0.80	0.06	0.16	0.03	0.17	0.01	14.2	0.09	629	42	103	10	581	20
A304	RB	Lutefisk_RATRoe_brushed	4.62	0.04	0.78	0.07	0.16	0.03	0.18	0.01	14.1	0.10	605	46	112	12	339	19
A315	SD	Tofurkey_disturbedsoil	6.24	0.06	0.84	0.07	0.31	0.04	0.32	0.01	15.1	0.12	412	51	237	18	nd	
A334	RB	Wishstone_chisel_brush	6.86	0.07	2.16	0.09	0.01	0.03	0.22	0.01	11.5	0.10	99	41	96	14	nd	
A335	RR	Wishstone_chisel_RAT	8.89	0.07	2.59	0.10	0.00	0.02	0.22	0.01	11.6	0.10	67	40	64	13	nd	
A342	SD	Penny_dist_soil	6.20	0.06	0.70	0.07	0.33	0.03	0.31	0.01	15.5	0.12	679	52	162	15	37	17
A349	RU	dreaming_asis	6.62	0.07	1.86	0.10	0.03	0.03	0.25	0.01	12.2	0.11	57	48	122	19	58	19
A353	RU	champagne_asis	6.67	0.06	1.97	0.09	0.04	0.03	0.25	0.01	13.3	0.08	86	44	105	15	54	18
A355	RB	champagne_brush	6.59	0.04	2.84	0.08	0.00	0.02	0.22	0.01	12.6	0.08	41	30	71	7	38	13
A356	RR	champagne_RAT1	8.78	0.07	2.99	0.10	0.00	0.02	0.24	0.01	12.5	0.09	24	40	81	13	72	18
A357	RR	champagne_RAT2	8.75	0.06	2.96	0.09	0.00	0.02	0.25	0.01	12.5	0.08	45	41	58	13	68	16
A374	RB	Peace_brushed	4.85	0.04	0.71	0.07	0.57	0.04	0.41	0.01	19.1	0.09	603	52	138	15	160	18
A377	RR1	Peace_RAT1	5.44	0.05	0.41	0.06	0.59	0.04	0.42	0.01	18.7	0.13	540	49	94	13	181	19
A380	RR	Peace_RAT2	4.90	0.06	0.45	0.07	0.75	0.05	0.47	0.02	20.4	0.16	774	72	64	22	71	22
A380b	RU	Alligator_APXSspot_TG	4.83	0.10	0.57	0.13	0.54	0.06	0.40	0.08	18.4	0.18	498	113	287	55	237	37
A381	RU	Alligator_APXSspot_long	4.98	0.05	0.68	0.07	0.57	0.04	0.40	0.01	18.8	0.13	565	49	225	15	244	19
A385b	RB	Alligator_scale_brushed	4.72	0.13	0.53	0.16	0.63	0.09	0.33	0.10	18.3	0.23	506	171	205	78	217	47
A401	SD	PasoRobles_disturbed soil	6.84	0.06	0.62	0.07	0.04	0.03	0.25	0.01	21.0	0.12	109	49	98	18	494	26
A416	RB	Watchtower_Joker_Brush	6.06	0.06	1.89	0.09	0.00	0.03	0.22	0.01	13.3	0.11	58	45	132	17	262	21
A417	RR	Watchtower_Joker_RAT	7.44	0.06	2.21	0.08	0.00	0.02	0.22	0.01	13.2	0.10	67	37	140	12	251	19
A427	SD	Paso_light	6.94	0.05	0.88	0.07	0.35	0.03	0.30	0.01	16.1	0.09	561	46	116	12	478	20
A428	SD	Paso_dark	6.25	0.05	0.89	0.07	0.38	0.03	0.33	0.01	15.9	0.11	414	43	209	13	52	15
A429b	RB	BensClod_brushed	7.62	0.05	1.40	0.07	0.47	0.03	0.16	0.01	5.6	0.04	592	40	58	8	65	14
A430	SD	Paso_DarkLight	6.39	0.05	0.99	0.07	0.37	0.03	0.34	0.01	17.2	0.11	395	40	235	12	69	15
A457	SU	Crumble	6.53	0.04	1.02	0.07	0.23	0.03	0.30	0.01	14.4	0.06	424	39	123	9	52	14
A469	RU	Methuselah_Keystone	5.75	0.05	2.21	0.08	0.11	0.03	0.31	0.01	12.8	0.07	155	40	117	13	232	18
A470	RB	Methuselah_Haunch	6.36	0.04	1.96	0.07	0.05	0.03	0.27	0.01	10.5	0.05	92	34	81	9	204	16
A475	RB	Methuselah_Pittsburg	7.40	0.07	1.90	0.09	0.05	0.03	0.21	0.01	12.0	0.08	147	47	100	17	460	24
A477	SU	Liberty_Bell	6.37	0.06	0.83	0.07	0.34	0.03	0.33	0.01	15.3	0.11	427	47	228	16	32	16
A481	RU	Reef	7.02	0.05	1.52	0.08	0.13	0.03	0.24	0.01	11.5	0.08	184	37	97	10	208	17
A484	RB	Jibsheet	6.71	0.05	1.94	0.08	0.04	0.03	0.22	0.01	10.9	0.07	83	32	89	8	302	17
A491	RU	Paros	6.45	0.05	1.37	0.07	0.02	0.03	0.17	0.01	11.4	0.08	74	35	76	9	151	17
A495	RU	Pequod_Ahab	7.15	0.05	1.99	0.08	0.06	0.03	0.19	0.01	11.1	0.08	114	34	88	9	243	17
A496	RB	Pequod_Ahab_brushed	7.13	0.05	1.92	0.07	0.05	0.03	0.20	0.01	11.1	0.08	94	34	80	9	250	17

Table 4.1. (*cont*.)

Sol	Type	Sample	N	T	Na_2O	SE	MgO	SE	Al_2O_3	SE	SiO_2	SE	P_2O_5	SE	SO_3	SE	Cl	SE	K_2O	SE
A499	RB	Pequod_MobyDick	78	8.5	3.45	0.22	7.98	0.11	12.62	0.14	45.8	0.41	2.56	0.09	4.81	0.06	1.02	0.02	0.43	0.06
A502	SU	Pequod_Doubloon_TG	91	0.2	2.48	2.09	8.44	0.57	11.80	0.58	45.7	0.71	2.20	0.76	5.32	0.25	0.67	0.06	0.50	0.20
A511	RB	Backstay_Scuppers	94	9.0	4.15	0.21	8.31	0.10	13.25	0.14	49.5	0.43	1.39	0.08	1.52	0.03	0.35	0.01	1.07	0.06
A512	RU	Backstay_Scurvy	87	8.8	3.83	0.21	8.28	0.10	12.89	0.14	49.4	0.44	1.29	0.08	2.12	0.04	0.44	0.01	0.96	0.06
A532	RU	Independence_Jefferson	59	8.8	2.61	0.24	5.20	0.09	13.33	0.14	53.5	0.45	3.23	0.10	5.08	0.06	0.72	0.01	0.97	0.06
A533	RB	Independence brushed	80	8.8	3.05	0.24	5.60	0.11	12.93	0.17	52.6	0.48	2.31	0.09	6.16	0.08	0.61	0.01	0.60	0.06
A542	RB	Independence_Penn2_Scuffed	89	8.7	3.18	0.24	3.38	0.09	18.69	0.18	54.9	0.47	3.48	0.10	2.20	0.04	0.30	0.01	0.52	0.06
A552	RU	Descartes_Discourse	83	8.9	3.14	0.19	9.35	0.09	9.93	0.10	45.3	0.29	1.38	0.08	7.64	0.08	1.30	0.02	0.61	0.06
A553	RB	Descartes_Discourse_brush	84	9.0	3.15	0.19	9.67	0.10	9.82	0.10	45.2	0.31	1.40	0.08	7.59	0.08	1.39	0.02	0.64	0.06
A557	RU	Bourgeosie_Chic.	75	8.9	3.92	0.24	5.44	0.10	12.26	0.17	48.4	0.44	3.24	0.10	3.50	0.05	0.83	0.01	1.47	0.07
A560	RB	Bourgeosie_Matrice.	83	7.4	3.41	0.22	9.33	0.12	10.89	0.13	46.3	0.42	1.50	0.08	6.90	0.08	1.07	0.02	0.77	0.06
A563	RU	Bourgeosie_Haussman	73	9.0	3.11	0.23	9.12	0.12	10.91	0.13	47.5	0.43	1.39	0.08	7.93	0.09	1.09	0.02	0.52	0.06
A566	RU	Assemblee_Gruyere	67	8.9	1.70	0.17	8.21	0.09	17.39	0.15	51.0	0.33	1.60	0.08	4.03	0.05	0.92	0.02	0.93	0.06
A571	RU	Assemblee_APXS	64	8.9	1.88	0.24	7.53	0.12	16.62	0.19	50.4	0.47	1.85	0.09	4.22	0.06	0.96	0.02	1.00	0.06
A587	SU	Whymper	89	8.0	3.18	0.28	8.61	0.13	9.79	0.12	45.4	0.42	0.93	0.07	7.42	0.08	0.83	0.01	0.45	0.06
A588	SD	Lambert_Couzy_mod	86	9.5	3.17	0.20	8.84	0.10	9.86	0.11	45.6	0.40	0.93	0.07	6.95	0.08	0.76	0.01	0.43	0.06
A600	RU	Irvine	86	10.9	2.68	0.26	10.63	0.12	8.29	0.09	47.0	0.34	0.97	0.07	2.37	0.03	0.45	0.01	0.68	0.06
A607	SD	LandsEnd	92	10.4	3.48	0.20	8.13	0.10	11.38	0.12	47.0	0.40	1.11	0.07	5.28	0.06	0.60	0.01	0.46	0.06
A611	SU	HangTwo	88	9.7	3.60	0.21	7.24	0.10	12.34	0.13	47.7	0.42	2.10	0.08	6.16	0.07	0.78	0.01	0.51	0.06
A630	RU	Hillary_Khumjung	59	6.8	4.00	0.25	7.90	0.11	13.37	0.15	46.8	0.44	2.35	0.09	4.55	0.07	1.17	0.02	0.54	0.06
A633	RU	Hillary_NamcheBazaar	76	9.0	4.06	0.20	6.98	0.08	13.69	0.12	46.5	0.30	2.79	0.09	4.22	0.05	1.18	0.02	0.52	0.06

Sol	Type	Sample	CaO	SE	TiO_2	SE	Cr_2O_3	SE	MnO	SE	FeO	SE	Ni	SE	Zn	SE	Br	SE
A499	RB	Pequod_MobyDick	7.03	0.05	1.83	0.08	0.08	0.03	0.21	0.01	12.1	0.08	137	35	96	9	197	17
A502	SU	Pequod_Doubloon_TG	7.03	0.16	1.90	0.27	0.21	0.08	0.22	0.14	13.4	0.19	390	148	106	63	80	39
A511	RB	Backstay_Scuppers	6.04	0.04	0.93	0.06	0.15	0.03	0.24	0.01	13.0	0.08	191	34	269	11	nd	
A512	RU	Backstay_Scurvy	6.04	0.04	0.92	0.07	0.17	0.03	0.25	0.01	13.4	0.09	228	36	274	12	nd	
A532	RU	Independence_Jefferson	5.64	0.04	1.24	0.07	0.09	0.03	0.15	0.01	8.1	0.06	578	43	116	10	90	16
A533	RB	Independence brushed	6.60	0.05	1.58	0.08	0.19	0.03	0.12	0.01	7.3	0.05	2086	54	96	8	70	14
A542	RB	Independence_Penn2_Scuffed	7.28	0.05	1.88	0.08	0.04	0.03	0.08	0.00	3.9	0.03	444	35	667	13	nd	
A552	RU	Descartes_Discourse	5.56	0.04	0.97	0.07	0.17	0.03	0.24	0.01	14.3	0.06	436	39	209	10	155	15
A553	RB	Descartes_Discourse_brush	5.41	0.04	1.00	0.07	0.18	0.03	0.26	0.01	14.2	0.06	450	39	236	11	159	15
A557	RU	Bourgeosie_Chic.	8.01	0.06	2.38	0.09	0.05	0.03	0.21	0.01	10.2	0.07	239	37	132	10	61	15
A560	RB	Bourgeosie_Matrice.	5.19	0.04	0.91	0.07	0.13	0.03	0.20	0.01	13.3	0.09	409	40	133	10	142	16
A563	RU	Bourgeosie_Haussman	5.67	0.04	1.02	0.07	0.16	0.03	0.19	0.01	11.2	0.08	344	38	280	12	190	16
A566	RU	Assemblee_Gruyere	3.77	0.03	0.79	0.06	2.86	0.05	0.15	0.01	6.4	0.04	1248	47	244	11	65	14
A571	RU	Assemblee_APXS	4.70	0.04	1.05	0.07	2.69	0.05	0.15	0.01	6.7	0.05	1174	48	247	12	64	15
A587	SU	Whymper	6.08	0.04	0.86	0.06	0.26	0.03	0.31	0.01	15.7	0.10	433	40	411	14	31	15
A588	SD	Lambert_Couzy_mod	6.10	0.04	0.87	0.06	0.28	0.03	0.31	0.01	15.8	0.10	460	39	367	12	48	15
A600	RU	Irvine	6.03	0.04	1.06	0.06	0.20	0.03	0.36	0.01	19.2	0.08	289	37	230	11	nd	
A607	SD	LandsEnd	6.33	0.04	1.17	0.07	0.28	0.03	0.28	0.01	14.4	0.09	313	36	248	10	60	14
A611	SU	HangTwo	7.13	0.05	1.20	0.07	0.13	0.03	0.22	0.01	10.8	0.07	168	33	155	9	104	15
A630	RU	Hillary_Khumjung	5.93	0.05	1.91	0.08	0.02	0.03	0.21	0.01	11.2	0.08	51	37	121	12	262	18
A633	RU	Hillary_NamcheBazaar	6.19	0.04	2.24	0.08	0.01	0.03	0.19	0.01	11.4	0.05	53	33	113	9	342	17

Notes: Concentration in weight % of oxides and Cl or parts per million by weight for Ni, Zn, and Br. Keys: N = Geometric norm (sum of oxides; norm is a relative indicator for distance between detector and sample surface); T = Total integration time [hours]; SE = Absolute statistical error (2 sigma error for the precision of this value); RB = Rock brushed; RR = Rock "ratted" (abraded); RU = Rock undisturbed (as is); RF = abraded fines; SD = Soil disturbed; ST = Soil trench; SU = Soil undisturbed, nd = not detected.

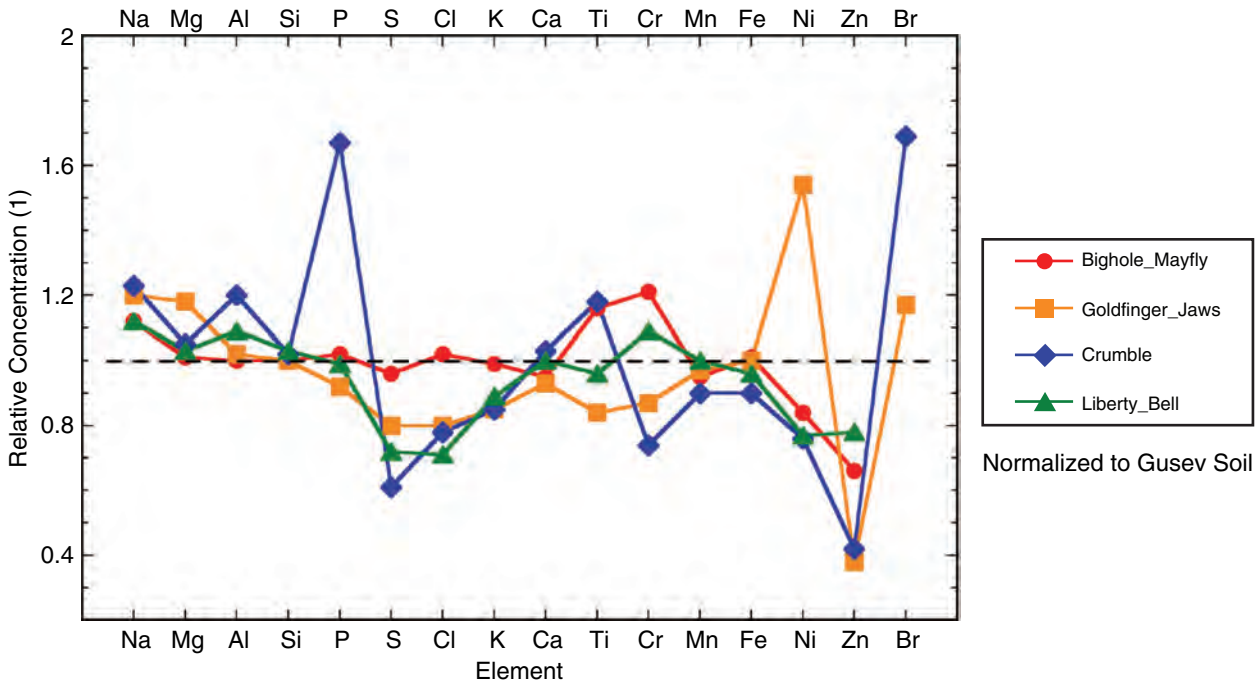

Figure 4.8. Undisturbed Gusev soil (SU) contents relative to "Gusev Soil (sol 14)." Soils have larger concentrations variations than those of Figure 4.7. Soils are "Bighole (sol 113)," "Goldfinger_Jaws (sol 167)," "Crumble (sol 457)," and "Liberty Bell (sol 477)." (For a color version of this figure, please refer to the color plate section or to the e-Book version of this chapter.)

167)" exhibits some large variations in Mg, P, Ti, Ni, and Zn, but no lithic fragments have been observed.

The Mg/Si weight percent ratio of almost all soil types is very constant. For undisturbed soils the mean ratio was 0.236 ± 0.004, and it was 0.242 ± 0.010 for disturbed surfaces. Exceptions for undisturbed soils were "Goldfinger Jaws (sol 167)," "Hang Two (sol 611)," and "El Dorado Scuff Shadow (sol 709)" (note: samples with sol numbers above 640 are not listed in Table 4.1); for disturbed soils the exceptions were "Paso Robles (sol 401)," "Paso Robles Light (sol 427)," "El Dorado Scuff Edgar (sol 710)," and "Dead Sea Samra (sol 723)," which are described below. Higher Mg/Si ratios of 0.31 and 0.35 due to higher fractions of Mg salts were also measured in the floor ("The Boroughs Mills, sol 140") and wall ("The Boroughs Hells Kitchen, sol 141") of the trench "The Boroughs," respectively, as discussed later. This constancy of the Mg/Si ratio, except for the quoted samples, is a further indication of a globally mixed soil component in the upper soils layers, undisturbed and disturbed. It also highlights the capability of the APXS to detect local anomalies in the soil that can point to possible aqueous activity.

The mean Fe/Mn weight percent ratio of all undisturbed soils is 50.8 ± 3.4, and the mean Fe/Mn ratio of basaltic Gusev rocks is 45.7 ± 0.5. The similarities in Fe/Mn ratios between undisturbed soils and rocks imply that the source material for the soil was not substantially altered by oxidation–reduction weathering processes. Furthermore, this ratio matches the Fe/Mn ratio for the estimated Mars mantle composition by Wänke and Dreibus (1988), implying that during magmatic processes FeO was not fractionated from MnO.

While S and Cl are among the most variable elements in soils, a nearly constant Cl/S ratio of 0.30 was found, except for the above-mentioned trench "The Boroughs" and disturbed soils in the Paso Robles and El Dorado areas as discussed below. In general, elemental variations among undisturbed soil surfaces are small except for the trace elements Ni, Zn, and Br, where variations by a factor of 2 or more have been observed. This may be related to the mobility of the chemical compounds these elements form, and/or the local environment. For example, bromine salts are known to be more soluble than Cl and S compounds. A reasonable hypothesis for the homogeneous soil composition at all Martian landing sites (Tables 4.1 and 4.2) is that global dust storms and local dust devils could be effective soil homogenization processes that have occurred over millions to billions of years (Gellert *et al.*, 2004).

Phosphorus concentrations of undisturbed soils have a well-defined mean value of 0.37 ± 0.02 wt.%, which is also observed for many disturbed soil samples. As the small error of the mean P concentration of undisturbed soils indicates, P is an element that exhibited a very small overall compositional variation along *Spirit*'s traverse. Assuming that most P is hosted in Ca-phosphate minerals, the easy dissolution of these phosphates from rocks exposed to weakly acidic water, accompanied by the sorption of dissolved Ca-phosphates by rocks upon desiccation, could provide an explanation for such an even distribution (Dreibus *et al.*, 1996; Dreibus and Haubold, 2004). Three undisturbed soils, "Crumble (sol 457)," "Pequod Doubloon (sol 502)" also a Touch-and-Go measurement, and "Hang Two (sol 611)," exhibited higher P concentrations of up to 1.0 wt.%, which may represent a local soil component derived from P-rich rocks in the neighborhood.

Table 4.2. *Compositions of all Meridiani samples from sol 14 to 638*

Sol	Type	Sample	N	T	Na_2O	SE	MgO	SE	Al_2O_3	SE	SiO_2	SE	P_2O_5	SE	SO_3	SE	Cl	SE	K_2O	SE
B011	SU	Tarmac	50	7.5	1.83	0.28	7.58	0.12	9.26	0.13	46.3	0.47	0.83	0.08	4.99	0.08	0.63	0.02	0.47	0.06
B015	RU	Robert.E	93	1.4	1.56	0.88	8.29	0.21	7.46	0.18	39.6	0.49	0.97	0.19	19.42	0.28	0.81	0.03	0.57	0.07
B023	SU	Hematite_Slope_Hema2	62	5.0	2.12	0.26	7.50	0.12	8.59	0.13	42.7	0.45	0.81	0.08	4.77	0.08	0.68	0.02	0.43	0.06
B025	ST	Trench_floor (Big Dig)	68	5.0	2.03	0.24	7.49	0.11	9.21	0.12	45.9	0.38	0.80	0.08	6.96	0.09	0.70	0.02	0.49	0.06
B026	ST	Trench_sidewall (Big Dig)	58	5.1	1.92	0.30	7.42	0.13	9.05	0.14	45.3	0.48	0.75	0.08	5.69	0.09	0.59	0.02	0.45	0.06
B029	RU	McKittrick_asis	95	5.0	2.28	0.25	8.14	0.12	8.39	0.12	43.1	0.41	0.97	0.08	12.73	0.14	0.87	0.02	0.53	0.06
B030	RU	Guadalupe_asis	75	3.4	1.88	0.30	7.95	0.14	7.26	0.12	40.3	0.44	1.01	0.09	18.75	0.22	0.87	0.02	0.58	0.06
B031	RR	McKittrick_RAT	81	4.4	1.67	0.27	8.00	0.13	6.20	0.12	38.3	0.40	0.99	0.09	21.31	0.22	0.60	0.02	0.56	0.06
B036	RR	Guadalupe_RAT	100	3.9	1.66	0.26	8.45	0.12	5.85	0.10	36.2	0.37	0.97	0.09	24.91	0.25	0.50	0.01	0.53	0.06
B040	RU	Last_Chance_Makar_asis	94	6.5	2.09	0.23	7.65	0.10	7.06	0.09	38.4	0.36	1.00	0.08	18.91	0.18	0.90	0.02	0.56	0.06
B041	RU	Dells_HiHo_asis	86	0.5	2.40	1.36	8.10	0.35	8.75	0.35	43.9	0.76	0.97	0.30	11.42	0.31	0.84	0.05	0.55	0.08
B043	RU	Mojo2_asis	91	4.3	2.26	0.25	7.82	0.12	8.39	0.12	43.0	0.43	0.98	0.08	12.97	0.15	0.86	0.02	0.56	0.06
B045	RR	Mojo2_RAT	86	3.9	1.64	0.27	8.38	0.13	6.18	0.10	36.3	0.38	1.01	0.09	23.61	0.24	0.54	0.02	0.59	0.06
B046b	RU	BerryBowl_Rubel_Full	93	13.0	2.29	0.21	6.82	0.09	8.02	0.12	39.5	0.34	0.76	0.07	5.60	0.06	0.72	0.01	0.38	0.06
B048	RU	BerryBowl_Empty	91	3.7	2.11	0.27	7.86	0.13	8.12	0.12	42.7	0.44	0.97	0.08	14.08	0.16	0.99	0.02	0.56	0.06
B049	RU	RasperryNewton	91	0.3	2.29	1.06	8.41	0.31	8.34	0.27	41.4	0.65	1.01	0.25	15.19	0.37	0.93	0.06	0.61	0.08
B051	RU	RealSharksTooth_enamel1	97	3.3	2.16	0.25	8.16	0.13	6.99	0.11	38.3	0.40	0.99	0.08	18.70	0.20	0.85	0.02	0.52	0.06
B060	SU	MontBlanc_LeHauches	67	12.8	2.24	0.19	7.63	0.08	9.22	0.09	45.3	0.29	0.94	0.07	7.34	0.07	0.79	0.01	0.48	0.06
B066	RU	BounceRock_Glanz	53	4.0	1.97	0.32	6.56	0.14	9.68	0.16	48.5	0.50	0.99	0.09	3.66	0.08	0.57	0.02	0.27	0.06
B068	RR	BounceRock_Case_Rat	89	4.3	1.66	0.25	6.84	0.11	10.48	0.14	51.6	0.51	0.92	0.08	0.56	0.03	0.10	0.01	0.11	0.05
B070	RU	BounceRock_Maggie	104	4.5	2.16	0.25	7.65	0.12	10.74	0.16	47.5	0.45	0.88	0.08	4.63	0.07	0.94	0.02	0.27	0.06
B080	SU	JackRussel_SoilBesi	64	2.7	2.21	0.27	6.81	0.13	7.66	0.13	38.6	0.47	0.77	0.08	4.90	0.10	0.68	0.02	0.37	0.06
B081	ST	BeagleBurrow_Trench	66	4.0	2.34	0.29	7.59	0.14	9.88	0.15	47.1	0.50	0.74	0.08	4.57	0.08	0.49	0.02	0.41	0.06
B087	RR	Golf_Post_RAT_FRAM	71	10.4	1.50	0.22	8.63	0.11	5.82	0.08	34.7	0.33	0.97	0.08	25.21	0.22	0.66	0.01	0.50	0.06
B090	SD	Scuff_Nougat	90	8.7	2.35	0.23	7.78	0.11	9.25	0.14	45.6	0.41	0.86	0.07	5.81	0.07	0.60	0.01	0.44	0.06
B091	SU	Fred_Ripple_soil	94	4.0	2.34	0.23	7.27	0.11	7.67	0.11	38.8	0.39	0.82	0.08	4.83	0.08	0.70	0.02	0.34	0.06
B100	SU	Leahs_Choice	81	5.1	2.44	0.23	6.89	0.11	7.82	0.11	39.2	0.39	0.82	0.08	5.95	0.08	0.77	0.02	0.38	0.06
B106	RU	LionStone_Leo_asis	95	5.0	1.98	0.25	8.03	0.12	7.21	0.11	39.7	0.39	0.98	0.08	18.80	0.19	1.00	0.02	0.57	0.06
B108	RR	LionStone_Numa_RAT	73	5.0	1.72	0.32	8.80	0.15	6.22	0.11	37.2	0.39	1.01	0.09	22.84	0.24	0.91	0.02	0.58	0.06
B122	RU	FigTree_Barberton	67	2.4	1.76	0.34	14.79	0.23	6.20	0.18	44.3	0.51	0.66	0.09	5.56	0.11	0.60	0.02	0.29	0.06
B123	SU	HillTop_Wilson	81	2.6	2.38	0.30	7.61	0.15	9.21	0.16	45.3	0.50	0.87	0.09	7.12	0.12	0.84	0.02	0.51	0.06
B139	RR	Tennessee_RAT	60	11.7	1.36	0.24	8.38	0.11	5.87	0.11	35.0	0.33	1.03	0.08	24.94	0.22	0.65	0.01	0.58	0.06
B142	RU	Kentucky_asis	87	0.4	0.88	2.77	8.04	0.49	7.89	0.48	43.2	0.95	0.80	0.49	13.41	0.36	0.83	0.07	0.53	0.09

Table 4.2. (*cont.*)

Sol	Type	Sample	CaO	SE	TiO_2	SE	Cr_2O_3	SE	MnO	SE	FeO	SE	Ni	SE	Zn	SE	Br	SE
B011	SU	Tarmac	7.31	0.06	1.04	0.07	0.45	0.04	0.37	0.01	18.8	0.13	423	57	241	20	32	17
B015	RU	Robert.E	5.03	0.07	0.74	0.12	0.19	0.04	0.28	0.04	15.0	0.14	597	72	569	34	nd	
B023	SU	Hematite_Slope_Hema2	6.13	0.06	0.78	0.07	0.30	0.04	0.31	0.01	24.8	0.17	633	64	312	24	37	19
B025	ST	Trench_floor (Big Dig)	6.69	0.06	1.13	0.08	0.40	0.04	0.35	0.01	17.7	0.11	634	61	428	24	159	21
B026	ST	Trench_sidewall (Big Dig)	6.72	0.06	1.24	0.08	0.46	0.04	0.36	0.02	19.9	0.15	631	69	348	28	130	21
B029	RU	McKittrick_asis	5.72	0.05	0.87	0.07	0.26	0.03	0.30	0.01	15.7	0.11	588	49	295	16	211	18
B030	RU	Guadalupe_asis	4.92	0.05	0.84	0.08	0.17	0.04	0.30	0.01	15.1	0.12	657	60	373	23	43	19
B031	RR	McKittrick_RAT	4.42	0.05	0.81	0.08	0.19	0.03	0.30	0.01	16.5	0.12	735	56	279	19	342	21
B036	RR	Guadalupe_RAT	4.91	0.05	0.65	0.07	0.17	0.03	0.30	0.01	14.8	0.11	589	50	324	17	30	16
B040	RU	Last_Chance_Makar_asis	4.84	0.04	0.70	0.06	0.16	0.03	0.30	0.01	17.4	0.11	686	48	397	16	32	15
B041	RU	Dells_HiHo_asis	5.70	0.11	0.94	0.24	0.29	0.06	0.33	0.08	15.6	0.21	625	109	292	49	346	39
B043	RU	Mojo2_asis	5.98	0.05	0.88	0.07	0.23	0.03	0.29	0.01	15.6	0.11	633	52	414	19	90	17
B045	RR	Mojo2_RAT	5.19	0.05	0.74	0.07	0.20	0.03	0.26	0.01	15.3	0.12	656	54	427	21	105	19
B046b	RU	BerryBowl_Rubel_Full	5.24	0.04	0.70	0.06	0.27	0.03	0.27	0.01	29.3	0.15	801	45	331	13	41	15
B048	RU	BerryBowl_Empty	5.51	0.05	0.84	0.07	0.20	0.03	0.34	0.01	15.6	0.12	607	53	426	21	103	19
B049	RU	RasperryNewton	5.29	0.12	0.84	0.22	0.16	0.06	0.27	0.07	15.1	0.21	553	119	460	63	177	36
B051	RU	RealSharksTooth_enamel1	4.37	0.05	0.67	0.07	0.17	0.03	0.24	0.01	17.7	0.13	653	55	388	21	100	18
B060	SU	MontBlanc_LeHauches	6.59	0.04	1.02	0.07	0.33	0.03	0.34	0.01	17.6	0.07	470	42	404	14	nd	
B066	RU	BounceRock_Glanz	10.93	0.10	0.83	0.09	0.10	0.04	0.42	0.02	15.5	0.11	153	63	110	25	41	21
B068	RR	BounceRock_Case_Rat	12.09	0.09	0.74	0.07	0.11	0.03	0.40	0.01	14.4	0.11	81	42	38	12	39	17
B070	RU	BounceRock_Maggie	9.83	0.07	0.69	0.07	0.12	0.03	0.37	0.01	14.2	0.10	162	40	145	12	33	15
B080	SU	JackRussel_SoilBesi	5.10	0.06	0.68	0.07	0.30	0.04	0.27	0.02	31.5	0.24	882	84	304	31	35	23
B081	ST	BeagleBurrow_Trench	6.73	0.07	1.23	0.08	0.48	0.04	0.36	0.02	17.9	0.14	592	66	256	25	40	21
B087	RR	Golf_Post_RAT_FRAM	4.82	0.04	0.76	0.06	0.19	0.03	0.36	0.01	15.7	0.10	634	45	526	16	33	15
B090	SD	Scuff_Nougat	6.70	0.05	1.09	0.07	0.46	0.03	0.38	0.01	18.5	0.11	456	43	320	14	232	17
B091	SU	Fred_Ripple_soil	4.93	0.05	0.70	0.07	0.28	0.03	0.28	0.01	30.9	0.20	1089	66	361	22	53	19
B100	SU	Leahs_Choice	5.14	0.05	0.72	0.07	0.25	0.03	0.28	0.01	29.2	0.18	773	60	331	20	46	19
B106	RU	LionStone_Leo_asis	5.11	0.04	0.78	0.07	0.19	0.03	0.29	0.01	15.3	0.11	573	48	389	17	76	16
B108	RR	LionStone_Numa_RAT	5.03	0.05	0.77	0.08	0.18	0.03	0.29	0.01	14.3	0.11	572	52	415	19	268	20
B122	RU	FigTree_Barberton	4.42	0.06	0.51	0.07	0.50	0.04	0.36	0.02	19.8	0.17	1639	89	207	25	47	21
B123	SU	HillTop_Wilson	6.73	0.07	0.97	0.08	0.36	0.04	0.37	0.02	17.6	0.14	503	62	376	26	35	19
B139	RR	Tennessee_RAT	5.03	0.04	0.79	0.07	0.20	0.03	0.32	0.01	15.7	0.10	679	47	533	17	35	15
B142	RU	Kentucky_asis	6.34	0.14	0.92	0.24	0.24	0.07	0.24	0.11	16.5	0.23	652	127	439	62	139	35

Sol	Type	Sample	N	T	Na_2O	SE	MgO	SE	Al_2O_3	SE	SiO_2	SE	P_2O_5	SE	SO_3	SE	Cl	SE	K_2O	SE
B145	RR	Kentucky_Cubble_Hill2_RAT	76	4.0	1.54	0.39	9.20	0.17	5.90	0.12	35.9	0.39	1.05	0.09	24.38	0.26	0.65	0.02	0.57	0.06
B147	RR	Virginia_RAT	71	4.0	1.83	0.29	9.00	0.14	6.32	0.11	36.9	0.40	1.07	0.09	22.09	0.24	0.60	0.02	0.60	0.06
B149	RR	Ontario_London_RAT	87	3.0	1.64	0.28	9.14	0.15	5.99	0.11	36.4	0.40	1.11	0.09	23.71	0.26	0.72	0.02	0.57	0.06
B153	RR	Grindstone_RAT	82	4.0	1.70	0.28	8.38	0.13	6.36	0.11	38.0	0.39	1.07	0.09	21.50	0.23	1.45	0.03	0.58	0.06
B155	RR	Kettlestone_RAT	69	4.0	1.45	0.31	8.63	0.15	5.85	0.11	36.2	0.39	1.03	0.09	23.03	0.26	1.75	0.03	0.55	0.06
B162	RR	Millstone_Dramensfjord_RAT	66	4.0	1.58	0.29	7.41	0.13	6.20	0.11	37.6	0.41	1.17	0.09	21.11	0.24	1.98	0.04	0.59	0.06
B166	SU	Soil_Millstone_Dahlia	77	4.0	2.40	0.28	7.14	0.13	10.04	0.15	47.7	0.49	0.81	0.08	5.19	0.09	0.64	0.02	0.55	0.06
B175	RU	Hoghead_ArnoldZiffel_Asis	82	5.0	2.11	0.25	8.29	0.13	7.89	0.13	41.5	0.42	0.99	0.08	14.76	0.16	1.26	0.02	0.56	0.06
B178	RR	Diamond_Jenness_Holman3 RAT1	76	4.0	1.72	0.23	6.47	0.10	6.71	0.10	40.6	0.34	1.05	0.08	19.62	0.19	1.37	0.03	0.63	0.06
B180	RR	Diamond_Jenness_Holman3 RAT2	60	4.0	1.71	0.31	6.49	0.14	6.70	0.13	40.1	0.44	1.06	0.09	19.64	0.23	1.64	0.03	0.63	0.06
B184	RR	MacKenzie_Campell_RAT	64	4.0	1.93	0.31	5.43	0.13	7.27	0.13	43.0	0.46	1.15	0.09	17.01	0.21	1.90	0.03	0.69	0.06
B187	RR	Inuvik_Toruyuktuk_RAT	53	3.8	1.79	0.25	5.45	0.11	7.17	0.11	39.9	0.37	1.11	0.09	18.17	0.20	1.67	0.03	0.67	0.07
B195	RR	Bylot_RAT	63	4.0	1.86	0.29	6.81	0.13	6.52	0.12	37.9	0.42	1.01	0.09	19.33	0.23	1.69	0.03	0.60	0.06
B199	RU	Sermilik_vein_asis	62	4.0	2.11	0.31	7.87	0.15	7.83	0.14	42.2	0.46	0.96	0.09	14.03	0.18	0.94	0.02	0.55	0.06
B214	RU	Escher_Kirchner_Asis	73	5.0	2.63	0.27	7.67	0.13	7.81	0.12	41.9	0.41	1.01	0.08	14.42	0.16	1.67	0.03	0.59	0.06
B216	RB	Escher_Kirchner_brushed	67	4.0	2.46	0.20	7.57	0.08	7.59	0.08	41.5	0.25	1.00	0.07	15.61	0.13	1.72	0.02	0.61	0.06
B217	RU	Escher_Nolde_dirty	80	4.6	2.21	0.26	7.83	0.12	9.32	0.12	45.8	0.45	0.86	0.08	5.49	0.08	0.62	0.02	0.43	0.06
B218	RB	Escher_Nolde_brushed	72	8.0	2.22	0.24	7.65	0.11	8.11	0.13	42.9	0.41	1.06	0.08	10.53	0.12	1.26	0.02	0.52	0.06
B220	RR	Escher_Kirchner_RAT	74	4.0	1.63	0.28	8.37	0.13	6.06	0.11	36.5	0.39	1.01	0.09	23.03	0.25	0.78	0.02	0.57	0.06
B237a	SD	Auk_RAT	70	7.0	2.39	0.24	6.90	0.11	10.41	0.13	48.8	0.47	0.84	0.07	4.56	0.07	0.58	0.01	0.59	0.06
B237b	SU	Aukling_soil_TG	71	0.3	1.79	4.78	8.41	0.86	9.58	0.84	47.2	1.40	0.23	0.87	4.82	0.29	0.61	0.09	0.45	0.11
B240	RU	Ellesmere_NoCoating	70	2.0	1.85	0.50	8.03	0.23	7.27	0.18	40.4	0.50	1.00	0.10	18.01	0.25	1.26	0.03	0.60	0.07
B241	RU	Ellesmere_Barbeau	53	3.3	2.09	0.32	7.47	0.16	7.39	0.16	41.5	0.49	0.97	0.10	14.99	0.21	1.18	0.03	0.59	0.07
B249	SU	Rocknest_void_soil	80	3.3	2.39	0.22	7.65	0.10	9.59	0.11	46.7	0.35	0.85	0.08	4.62	0.07	0.59	0.01	0.48	0.06
B260	RU	Wopmay_Otter	61	1.0	1.92	0.83	7.67	0.23	7.31	0.20	40.4	0.61	1.04	0.19	18.29	0.33	1.07	0.05	0.62	0.08
B261	RU	Wopmay_Otter_b	60	3.0	2.01	0.31	7.67	0.15	7.27	0.13	40.5	0.47	1.06	0.09	18.32	0.23	1.03	0.03	0.60	0.07
B283	RU	Wanganui	40	3.3	1.95	0.35	7.43	0.17	8.47	0.17	43.5	0.53	0.95	0.10	11.93	0.19	0.96	0.03	0.59	0.07
B306	RB	Paikia_brushed	81	4.0	1.74	0.27	8.08	0.13	6.45	0.14	38.7	0.41	1.09	0.09	21.47	0.23	1.10	0.02	0.54	0.06
B307	RR	Paikia_RAT	63	3.0	1.84	0.31	7.86	0.15	6.36	0.12	37.7	0.44	1.13	0.09	21.35	0.26	1.42	0.03	0.57	0.06
B308	RB	Wharenhui_RAT_stalled	72	4.0	1.68	0.27	9.38	0.14	6.28	0.11	37.0	0.40	1.02	0.09	21.55	0.24	1.07	0.02	0.54	0.06
B311	RU	Pohutu_asis	75	3.5	2.55	0.28	7.86	0.14	8.63	0.17	42.6	0.45	0.91	0.09	11.14	0.15	0.84	0.02	0.50	0.06
B312	RR	Wharenhui_RAT	71	4.0	1.83	0.27	9.11	0.14	6.43	0.11	37.5	0.40	1.08	0.09	21.33	0.23	1.49	0.03	0.56	0.06
B368	ST	Left_of_peanut_TrenchFloor	78	3.0	2.20	0.22	7.13	0.11	8.98	0.13	44.6	0.47	0.84	0.08	6.58	0.10	0.50	0.02	0.45	0.06
B369	SU	Crest_RippleCrest	80	4.0	2.13	0.20	6.39	0.10	7.36	0.13	37.4	0.37	0.87	0.08	4.64	0.08	0.71	0.02	0.33	0.06

Table 4.2. (*cont*.)

Sol	Type	Sample	CaO	SE	TiO_2	SE	Cr_2O_3	SE	MnO	SE	FeO	SE	Ni	SE	Zn	SE	Br	SE
B145	RR	Kentucky_Cubble_Hill2_RAT	4.72	0.05	0.71	0.07	0.18	0.03	0.33	0.01	14.7	0.12	618	55	371	20	54	17
B147	RR	Virginia_RAT	4.43	0.05	0.84	0.07	0.21	0.03	0.39	0.01	15.5	0.12	664	58	381	22	74	18
B149	RR	Ontario_London_RAT	4.85	0.05	0.74	0.07	0.20	0.03	0.31	0.01	14.5	0.12	638	57	357	21	27	18
B153	RR	Grindstone_RAT	4.64	0.05	0.83	0.07	0.19	0.03	0.33	0.01	14.8	0.11	604	53	319	18	39	17
B155	RR	Kettlestone_RAT	4.85	0.05	0.80	0.08	0.20	0.04	0.33	0.01	15.2	0.12	644	59	346	22	nd	
B162	RR	Millstone_Dramensfjord_RAT	5.11	0.05	0.75	0.08	0.21	0.04	0.31	0.01	15.8	0.13	616	59	437	24	nd	
B166	SU	Soil_Millstone_Dahlia	7.32	0.06	0.85	0.08	0.34	0.04	0.39	0.01	16.6	0.13	339	52	226	19	25	17
B175	RU	Hoghead_ArnoldZiffel_Asis	5.45	0.05	0.83	0.07	0.22	0.03	0.25	0.01	15.7	0.11	465	48	388	18	108	17
B178	RR	Diamond_Jenness_Holman3 RAT1	5.09	0.05	0.79	0.07	0.17	0.03	0.33	0.01	15.4	0.09	531	52	444	20	nd	
B180	RR	Diamond_Jenness_Holman3 RAT2	5.03	0.06	0.81	0.07	0.22	0.04	0.31	0.01	15.5	0.13	611	61	486	26	nd	
B184	RR	MacKenzie_Campell_RAT	4.60	0.05	0.86	0.08	0.20	0.04	0.32	0.01	15.6	0.12	546	58	447	24	nd	
B187	RR	Inuvik_Toruyuktuk_RAT	5.48	0.06	0.86	0.08	0.22	0.04	0.36	0.01	17.1	0.12	606	64	489	27	nd	
B195	RR	Bylot_RAT	5.01	0.05	0.77	0.07	0.23	0.04	0.37	0.02	17.7	0.14	933	67	499	26	nd	
B199	RU	Sermilik_vein_asis	5.84	0.06	0.91	0.07	0.29	0.04	0.34	0.01	16.0	0.13	540	59	380	23	187	20
B214	RU	Escher_Kirchner_Asis	5.72	0.05	0.81	0.07	0.25	0.03	0.27	0.01	15.1	0.11	435	50	352	18	607	24
B216	RB	Escher_Kirchner_brushed	5.66	0.04	0.79	0.07	0.21	0.03	0.28	0.01	14.8	0.06	449	44	287	14	608	21
B217	RU	Escher_Nolde_dirty	6.88	0.06	1.11	0.07	0.50	0.04	0.41	0.01	18.5	0.13	395	50	281	18	69	18
B218	RB	Escher_Nolde_brushed	7.03	0.05	0.94	0.07	0.28	0.03	0.31	0.01	17.0	0.11	547	47	435	17	238	18
B220	RR	Escher_Kirchner_RAT	5.00	0.05	0.75	0.07	0.18	0.03	0.24	0.01	15.7	0.12	564	55	314	19	425	24
B237a	SD	Auk_RAT	7.38	0.06	0.85	0.07	0.28	0.03	0.35	0.01	15.9	0.11	323	46	178	14	nd	
B237b	SU	Aukling_soil_TG	7.25	0.20	1.08	0.29	0.42	0.10	0.27	0.17	17.8	0.30	233	151	194	70	nd	
B240	RU	Ellesmere_NoCoating	5.26	0.07	0.76	0.08	0.20	0.04	0.25	0.02	15.0	0.14	509	66	380	28	395	26
B241	RU	Ellesmere_Barbeau	5.79	0.07	0.81	0.08	0.23	0.04	0.39	0.02	16.3	0.14	528	70	453	31	1232	38
B249	SU	Rocknest_void_soil	7.30	0.06	0.91	0.07	0.45	0.04	0.40	0.01	18.0	0.10	344	48	184	15	nd	
B260	RU	Wopmay_Otter	5.22	0.09	0.81	0.18	0.19	0.05	0.20	0.05	15.1	0.19	519	92	394	45	368	34
B261	RU	Wopmay_Otter_b	5.25	0.06	0.69	0.08	0.18	0.04	0.20	0.01	15.1	0.13	510	62	363	25	424	26
B283	RU	Wanganui	6.79	0.08	0.89	0.08	0.29	0.04	0.33	0.02	15.8	0.15	417	74	391	33	nd	
B306	RB	Paikia_brushed	4.49	0.05	0.76	0.08	0.18	0.03	0.27	0.01	14.9	0.11	564	51	624	22	147	18
B307	RR	Paikia_RAT	4.59	0.06	0.77	0.07	0.16	0.04	0.33	0.02	15.7	0.14	571	62	628	29	nd	
B308	RB	Wharenhui_RAT_stalled	4.27	0.05	0.76	0.07	0.21	0.03	0.29	0.01	15.8	0.12	804	58	301	19	103	18
B311	RU	Pohutu_asis	6.33	0.06	0.77	0.07	0.24	0.03	0.28	0.01	17.3	0.13	466	55	273	20	44	18
B312	RR	Wharenhui_RAT	4.10	0.05	0.81	0.07	0.20	0.03	0.32	0.01	15.1	0.12	605	55	259	18	38	18
B368	ST	Left_of_peanut_TrenchFloor	6.75	0.07	1.17	0.09	0.46	0.04	0.39	0.02	19.9	0.15	449	61	409	26	70	20
B369	SU	Crest_RippleCrest	4.88	0.05	0.67	0.07	0.27	0.04	0.29	0.01	33.8	0.22	1292	73	357	23	101	21

Sol	Type	Sample	N	T	Na_2O	SE	MgO	SE	Al_2O_3	SE	SiO_2	SE	P_2O_5	SE	SO_3	SE	Cl	SE	K_2O	SE
B370	SU	Caviar_undisturbedSoil	80	6.0	2.17	0.22	6.61	0.10	7.83	0.10	39.8	0.40	0.82	0.07	5.05	0.07	0.68	0.01	0.40	0.06
B373	SD	Scuff_Srcuffy	67	6.0	2.11	0.20	7.20	0.10	9.10	0.14	45.3	0.44	0.88	0.08	6.06	0.08	0.52	0.01	0.44	0.06
B381	RU	Russett_Cobble	64	6.0	1.84	0.20	7.15	0.10	6.81	0.10	38.5	0.36	1.05	0.08	20.82	0.21	0.94	0.02	0.57	0.06
B393	RU	Omaha as is	78	3.0	2.00	0.22	7.39	0.12	7.10	0.14	39.4	0.42	1.01	0.09	19.81	0.23	0.89	0.02	0.56	0.06
B400	RU	Gagarin_asis	70	3.9	2.00	0.28	7.19	0.13	7.54	0.12	41.0	0.43	1.04	0.09	16.51	0.19	0.98	0.02	0.56	0.06
B401	RB	Gagarin_brush	78	3.5	1.79	0.28	7.25	0.13	6.71	0.12	38.3	0.40	1.03	0.09	21.46	0.23	0.92	0.02	0.57	0.06
B403	RR	Gagarin_RAT	69	4.0	1.35	0.20	7.33	0.10	4.90	0.08	32.6	0.32	1.07	0.09	28.62	0.28	0.61	0.02	0.51	0.06
B416	SU	Mobarek_undist_soil	81	3.0	2.21	0.26	6.75	0.13	8.19	0.13	41.5	0.36	0.86	0.08	5.21	0.08	0.67	0.02	0.42	0.06
B420	SU	RippleCrest_NoRooz	86	3.6	2.11	0.30	6.67	0.14	7.72	0.12	39.5	0.41	0.88	0.08	5.90	0.09	0.72	0.02	0.39	0.06
B420b	SU	RippleCrest_MayNoRooz	84	3.0	2.19	0.20	6.61	0.10	7.76	0.11	39.0	0.41	0.84	0.08	5.15	0.09	0.70	0.02	0.36	0.06
B443	SU	Recovery_Cure	52	3.8	2.01	0.20	6.43	0.09	7.78	0.11	40.0	0.42	0.83	0.08	5.54	0.09	0.72	0.02	0.43	0.06
B499	SD	NorthDune_New_Track	72	1.0	2.32	0.28	7.05	0.17	8.74	0.20	44.8	0.60	0.91	0.11	6.59	0.16	0.72	0.03	0.47	0.07
B505	SU	Purgatrough_ThroughPlain	84	3.8	2.15	0.18	6.54	0.09	7.80	0.10	39.3	0.38	0.82	0.07	5.24	0.07	0.65	0.02	0.39	0.06
B507	SD	Purgatory_Track2	76	3.8	2.13	0.22	7.02	0.12	8.70	0.17	44.1	0.44	0.94	0.08	7.36	0.11	0.76	0.02	0.50	0.06
B509	SU	Purgatory_Flank1	85	3.6	2.18	0.18	6.37	0.08	7.94	0.09	39.9	0.29	0.80	0.07	5.07	0.07	0.66	0.02	0.42	0.06
B548	RR	IceCream_RAT	59	13.5	1.74	0.18	7.31	0.08	5.91	0.07	36.2	0.25	1.04	0.07	23.81	0.17	0.64	0.01	0.58	0.06
B552	RU	Cobble_Arkansas	54	12.1	1.96	0.16	7.90	0.08	8.23	0.08	42.6	0.28	1.27	0.07	9.90	0.10	1.31	0.02	0.55	0.06
B554	RU	Cobble_Perseverance	26	12.2	1.50	0.19	7.12	0.10	8.83	0.11	44.0	0.38	1.21	0.08	6.91	0.09	0.95	0.02	0.55	0.06
B556	RB	LemonRind	69	12.0	2.22	0.16	7.07	0.07	7.49	0.07	40.2	0.25	1.07	0.07	15.30	0.12	1.49	0.02	0.55	0.06
B558	RR	Fruitbasket_Strawberry	79	12.1	1.57	0.17	8.09	0.09	5.72	0.07	32.8	0.29	0.99	0.07	27.39	0.22	0.57	0.01	0.50	0.06
B560	RR	LemonRind_RAT	77	10.6	2.02	0.22	7.83	0.10	6.17	0.08	35.1	0.32	1.05	0.08	23.12	0.20	1.54	0.02	0.54	0.06
B593	RB	Elephant	59	2.7	1.84	0.24	7.37	0.13	6.84	0.13	38.8	0.44	1.08	0.10	19.53	0.25	0.90	0.03	0.61	0.07
B594	RU	Desception	56	10.3	1.79	0.17	7.45	0.09	6.63	0.08	38.5	0.30	1.05	0.07	19.83	0.16	0.74	0.01	0.58	0.06
B634	RR	Olympia_Kalavrita	71	10.4	1.78	0.22	7.39	0.10	6.52	0.09	37.5	0.35	0.98	0.08	20.72	0.18	0.56	0.01	0.55	0.06
B638	RB	Olympia_Ziakas	77	12.0	1.73	0.16	7.36	0.07	6.26	0.06	36.9	0.23	1.02	0.07	23.00	0.16	0.84	0.01	0.55	0.06

Table 4.2. (*cont.*)

Sol	Type	Sample	CaO	SE	TiO_2	SE	Cr_2O_3	SE	MnO	SE	FeO	SE	Ni	SE	Zn	SE	Br	SE
B370	SU	Caviar_undisturbedSoil	5.67	0.05	0.78	0.07	0.32	0.03	0.29	0.01	29.4	0.18	750	56	300	18	47	17
B373	SD	Scuff_Srcuffy	6.87	0.06	1.25	0.07	0.46	0.04	0.39	0.01	19.3	0.13	386	51	351	19	94	19
B381	RU	Russett_Cobble	5.47	0.05	0.80	0.07	0.20	0.03	0.30	0.01	15.4	0.11	628	51	585	21	60	16
B393	RU	Omaha as is	5.16	0.06	0.83	0.07	0.20	0.03	0.30	0.01	15.3	0.13	634	58	441	23	53	18
B400	RU	Gagarin_asis	5.46	0.06	0.89	0.08	0.20	0.03	0.34	0.01	16.2	0.13	543	56	450	23	73	19
B401	RB	Gagarin_brush	5.36	0.05	0.78	0.07	0.17	0.03	0.31	0.01	15.2	0.12	574	55	405	21	67	18
B403	RR	Gagarin_RAT	5.78	0.06	0.68	0.08	0.17	0.03	0.35	0.01	15.9	0.11	585	56	436	22	54	17
B416	SU	Mobarek_undist_soil	6.17	0.06	0.85	0.07	0.33	0.04	0.33	0.01	26.3	0.15	608	63	282	22	39	17
B420	SU	RippleCrest_NoRooz	5.30	0.05	0.80	0.07	0.28	0.04	0.29	0.01	29.3	0.19	850	63	371	22	73	19
B420b	SU	RippleCrest_MayNoRooz	5.27	0.05	0.78	0.07	0.27	0.04	0.29	0.01	30.6	0.21	965	71	348	25	96	21
B443	SU	Recovery_Cure	5.69	0.06	0.79	0.07	0.32	0.04	0.32	0.02	29.0	0.20	729	75	354	28	48	20
B499	SD	NorthDune_New_Track	7.06	0.10	1.02	0.09	0.41	0.05	0.39	0.03	19.4	0.21	445	87	298	40	130	27
B505	SU	Purgatrough_ThroughPlain	5.39	0.05	0.75	0.07	0.32	0.03	0.28	0.01	30.2	0.19	743	61	331	20	48	17
B507	SD	Purgatory_Track2	6.75	0.06	1.05	0.07	0.35	0.04	0.37	0.01	19.8	0.15	463	55	452	23	121	21
B509	SU	Purgatory_Flank1	5.54	0.05	0.73	0.07	0.29	0.03	0.26	0.01	29.7	0.13	865	64	328	21	45	17
B548	RR	IceCream_RAT	5.49	0.04	0.78	0.06	0.21	0.03	0.31	0.01	15.8	0.07	449	41	480	14	109	15
B552	RU	Cobble_Arkansas	7.24	0.05	0.95	0.07	0.26	0.03	0.33	0.01	17.4	0.07	539	45	418	15	110	16
B554	RU	Cobble_Perseverance	6.84	0.06	0.93	0.07	0.23	0.04	0.31	0.01	20.5	0.12	508	65	327	24	79	19
B556	RB	LemonRind	6.07	0.04	0.89	0.06	0.24	0.03	0.37	0.01	17.0	0.06	525	41	474	14	67	14
B558	RR	Fruitbasket_Strawberry	5.13	0.04	0.72	0.06	0.19	0.03	0.39	0.01	15.8	0.10	504	39	563	14	84	15
B560	RR	LemonRind_RAT	5.20	0.04	0.75	0.06	0.19	0.03	0.38	0.01	16.0	0.10	508	41	457	14	67	15
B593	RB	Elephant	5.49	0.07	0.79	0.09	0.22	0.04	0.28	0.02	16.1	0.14	576	66	450	29	294	24
B594	RU	Desception	5.06	0.04	0.80	0.07	0.19	0.03	0.23	0.01	17.0	0.09	515	46	423	16	103	16
B634	RR	Olympia_Kalavrita	5.84	0.04	0.79	0.07	0.25	0.03	0.33	0.01	16.6	0.10	496	42	394	14	67	15
B638	RB	Olympia_Ziakas	5.12	0.03	0.76	0.06	0.18	0.03	0.31	0.01	15.8	0.06	544	39	559	13	74	14

Notes: Concentration in weight % of oxides and Cl or parts per million by weight for Ni, Zn, and Br. Keys: N = Geometric norm (sum of oxides; norm is a relative indicator for distance between detector and sample surface); T = Total integration time (hours); SE = Absolute statistical error (2 sigma error for the precision of this value); RB = Rock brushed; RR = Rock "ratted" (abraded); RU = Rock undisturbed (as is); RF = abraded fines; SD = Soil disturbed; ST = Soil trench; SU = Soil undisturbed, nd = not detected.

Disturbed soil is material that was scuffed, trenched, or otherwise exposed by the rover wheels. Depending on their motion history, either slightly stirred material by simple wheel rotations or deeply churned material by scuffing/trenching was accessible. Several disturbed soil samples (e.g., "Mimi Tracks (sol 43)," "Disturbance (sol 259)," "Tofurkey (sol 315)," and "Penny (sol 342)" in Husband Hill), showed only small compositional variations compared to the undisturbed soil "Gusev Soil (sol 14)."

Gusev plains trenches

Trenches, excavated by the rover wheels, have a depth of up to ~10 cm and provided unique subsurface samples for analyses by the rover science instruments. Three trenches had been excavated at the time of writing (e.g., Arvidson *et al.*, 2006). Measurements were made on floor targets and/or one wall target within each trench, as well as on undisturbed soil close to the trench. There are subtle and apparent differences in elemental compositions (Gellert *et al.*, 2006; Wang *et al.*, 2006). Measurements of the "Road Cut" Trench (sols 47–50), which is located within a depression called "Laguna Hollow," consisted of surface, floor, and wall targets. Their chemical compositions are very similar, except for Cr and Br abundances at floor and wall, which are enriched compared to the "Gusev Soil" target.

Measurements of "Big Hole" trench (sols 113–115), which was located about 600 m southeast of Bonneville crater and between "Missoula" and "Lahontan" craters, consisted of one undisturbed surface target and two floor targets. Enrichments of S, Cl, Cr, and Br were discovered in the materials analyzed on the trench floor. However, the S/Cl ratio remained the same as for other soils: about 3.6 (Figure 4.9). K and P contents were depleted in the floors. These findings provided initial hints that water played some role in subsurface processes at Gusev crater.

The third trench, called "The Boroughs (sols 135 to 141)," was located at about two-thirds of the way from Bonneville crater to the Columbia Hills. The surface ("Santa Anita"), floor ("Boroughs Mills"), and wall ("Boroughs Hellskitchen") of the trench were measured with the APXS. Sulfur concentrations were substantially enriched in the wall and floor compared to its undisturbed surface value: an S to Cl ratio of about 20 was found compared to 3.6 for most soils (note: in Figure 4.9 the reverse ratio of Cl to S is shown). The most striking features were the high S, Br abundances of the wall (the wall target revealed the highest S content – 14 wt.% SO_3 – measured up to sol 141), which were even higher than on the floor, even though the Cl concentrations were in the range of Gusev soils. The concentration of the other elements was very similar for the wall and floor. The correlated increase of Mg and S and an enrichment of Br that appears to have occurred in a several centimeters thick subsurface layer points to the possibility of salts deposited by groundwater (Haskin *et al.*, 2005; Wang *et al.*, 2006). This discovery of a possible subsurface layer enriched in salts provided one of the first strong pieces of evidence that water had once played a role in the evolution of surface materials in Gusev crater.

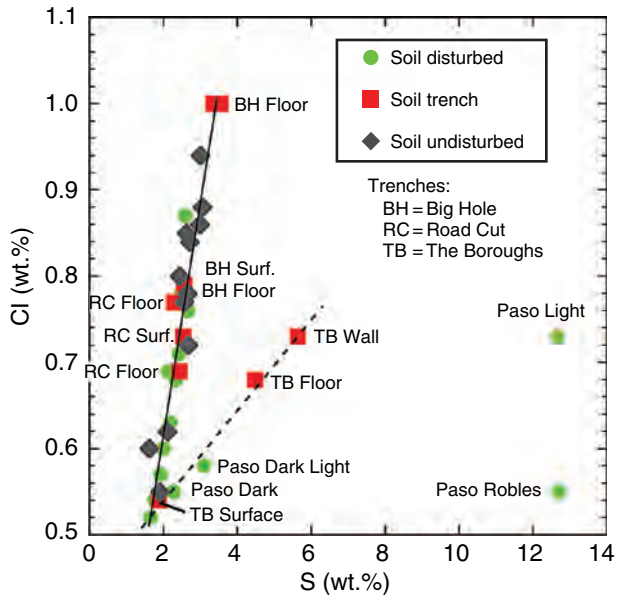

Figure 4.9. Chlorine versus sulfur concentrations for disturbed soils, undisturbed soils, and trenches. Most samples have a constant Cl/S ratio of about 0.28, while samples of the trench "The Boroughs" show a ratio of 0.14, which means an enrichment of S (up to 6 wt.%) compared to Cl. Some "Paso Robles" soils have even higher enrichments of S (up to 12.7 wt.%). (For a color version of this figure, please refer to the color plate section or to the e-Book version of this chapter.)

To find out which elements are associated with the large amounts of SO_3 observed in the subsurface samples of The Boroughs trench, the mineralogy of the samples was estimated from the observed elemental composition. To consider the oxidation state of iron the Fe^{3+}/Fe_{total} ratios measured in the trench by the MB were used (Morris *et al.*, 2004, 2006). All MgO in the subsurface, which was not residing in silicates, was attributed to $MgSO_4$. A good correlation of the calculated amounts of MgO with SO_3 in the three trench samples was found (Gellert *et al.*, 2006). However, only 70% of the measured SO_3 content was found to be related to MgO. Therefore, ferric sulfates were assumed for the remaining 30% SO_3 as a suitable compound, based on Mössbauer data of the (np-Ox) component that might be associated with Fe^{3+} sulfates (Morris *et al.*, 2006). For the missing sulfur compound, 3–4 mol.% of $Fe_2(SO_4)_3$ could be consistent with the subsurface samples of The Boroughs trench measured by the APXS (Gellert *et al.*, 2006).

The observed high sulfur content in two of the Gusev trenches could be taken as an indication of an even larger regional occurrence. Starting with the Laguna Hollow trench near the landing site, the amount of subsurface S content was increasing while approaching the Columbia Hills. However, since there were only three trenches, no definitive conclusion on the spatial distribution of subsurface material can be drawn. The increased S content could be either purely coincidental, or typical for most of the Gusev plains floor. It is noteworthy, however, that several indicators for aqueous interaction found in the APXS data occur simultaneously in the third trench: increased sulfur correlated with Mg,

decoupling of the otherwise constant S/Cl ratio, and the first high abundance of bromine that occurs as very soluble salts.

Gusev plains rocks

To investigate rocks with the APXS the RAT was often used to brush and/or grind surfaces. *In situ* measurements were carried out on (a) undisturbed (natural or as is) rock surfaces, (b) brushed rock surfaces, and/or (c) abraded rock surfaces. Mean elemental compositions are provided in Table 4.3. To better compare the different rock compositions, their concentrations were normalized to one Gusev reference rock, the basaltic rock "Humphrey RAT2 (sol 60)" (Gellert *et al*., 2006). After having entered the Columbia Hills it became apparent that the rocks were very diverse compared to the plains. Therefore, the rocks had to be split into two major groups: the plains basalts and the Columbia Hills rocks, which had to be subdivided, further.

APXS measurements of rocks were usually first performed on their undisturbed surface. Due to the ubiquitous airborne dust, the natural surfaces of rocks are variably covered with this fine material. Whenever possible, vertical surfaces were selected for *in situ* measurements, to minimize the amount of adhering airborne dust (which we expect to be present on any undisturbed rock surface). To visualize the amount of soil on the rock surface, the elemental concentrations of several undisturbed soils were normalized to the rock "Humphrey RAT2." These relative concentrations show a distinctive "M-shaped" pattern for the elements from Si to Ca (Gellert *et al*., 2006). A similar pattern was found for all undisturbed plains rocks, suggesting that all of their surfaces were covered with some soil or airfall dust. However, rocks in the Columbia Hills revealed a different elemental pattern, which indicated that either their soil/dust coverage is less, their composition is much different than the rock Humphrey, or both (Gellert *et al*., 2006).

The abundance of bromine seems to be randomly distributed among rocks and soils, except in trenches, as noted earlier. However, the generally highest Br contents were observed on the natural and brushed surfaces of some rocks. It has been speculated that very soluble Br salts precipitate at some rock surfaces, even under current Martian climate conditions in Gusev crater (Yen *et al*., 2005).

Brushing of the rock surfaces by the RAT removes some of the adhering soil and exposes an underlying layer, which may be different from both the natural surface and the subsurface abraded by a RAT grind operation (see example images and other information in Chapter 13). Brushed Gusev plains rocks exhibited the familiar M-shaped enrichment pattern of elements from Si to Ca as described above, suggesting that some soil is adhering to the brushed surface. The brushed surface of the rock dubbed "Mazatzal New York Brush (sol 81)" has a large enrichment of Ni, Zn, and Br pointing to Br salts and possibly other mobile compounds on this rock surface. Mazatzal's brushed surface has a dark-toned coating, while the underlying abraded basalt layer is grayish and the top natural surface is either a reddish dust cover or a light-toned yellowish coating depending on the location (Haskin *et al*., 2005). The APXS data and other remote sensing and *in situ* studies of Mazatzal imply a complex weathering history at the rock's surface, possibly related to multiple layers of either adhering materials and/or weathering rinds (Gellert *et al*., 2004; Haskin *et al*., 2005).

The RAT can grind several millimeters into a rock depending on its hardness, and hence, provide a surface that may best represent the composition of its interior. Inside the boreholes that were ground into the rocks either fresh material was exposed or a deeper, weathered layer encountered.

The three abraded rocks, "Adirondack (sol 34)," "Humphrey (sol 60)," and "Mazatzal (sol 86)," which were located in the area around the Columbia Memorial Station and at the rim of Bonneville crater were classified as primitive basalts (Gellert *et al*., 2004; McSween *et al*., 2004). Other smaller rocks within the Bonneville ejecta blanket were analyzed only as undisturbed or brushed: "Mimi (sol 42) *undisturbed*," "Plank (sol 63) *undisturbed*," "Route 66 (sol 100) *brushed*," and "Mohave Joshua Asis (sol 150a) *undisturbed*." For additional details, see the traverse map and in-depth discussion of all plains rocks in McSween *et al*. (2006a) and Arvidson *et al*. (2006).

Concentrations of S and Cl of the three basaltic rocks, Adirondack, Humphrey, and Mazatzal, are high in their undisturbed surfaces (1.3–3.1 wt.% S and 0.4–1.1 wt.% Cl), and even their abraded surfaces contain some S and Cl; i.e., ~0.5 wt.% S and ~0.3 wt.% Cl. These chlorine contents for abraded rocks are high compared to typical basaltic shergottites (one group of the Martian meteorites), whose contents range from 0.006 to 0.014 wt.% for Cl (Meyer, 2006). Thus, these Cl contents may suggest that the surfaces were either still contaminated by some debris left behind by the RAT brushes during the grinding operation, or that S and Cl are present in this material as the result of some process, perhaps aqueous alteration. For the MPF mission, a similar Cl content was found for the derived soil-free rock composition of Ares Vallis (Brückner *et al*., 2003; Foley *et al*., 2003b; see also Chapter 3).

Basaltic shergottites contain up to 0.3 wt.% S (e.g., Banin *et al*., 1992; see also Chapter 17). Although the measured concentrations of S in abraded Gusev basalts may be considered as not highly above other intrinsic rock values, the higher Cl abundances in the Gusev rocks could indicate the presence of trace amounts of salts. In general, the concentration patterns of all elements in the three primitive basalts at Gusev are very similar, with the exception of K and Br, which are higher in "Mazatzal" (Table 4.1). Based on this observation and the assumption that these materials are rather "clean" basaltic rocks, the composition of other rocks was normalized using the rock "Humphrey RAT2." All three normalized basaltic rock interiors become essentially identical, indicating the excellent repeatability of the APXS analysis and that these rocks likely have the same volcanic origin.

4.3.2 Gusev Columbia Hills

Hills soils

A significant variation in the elemental concentration of the soil was detected at a location on Husband Hill called "Paso

Table 4.3. *Mean elemental composition of rock classes at Gusev crater*

Sol	Class/Sample/Mean	Type	Na	Mg	Al	Si	P	S	Cl	K	Ca	Ti	Cr	Mn	Fe	Ni	Zn	Br
	Adirondack Class (samples selected)		wt.%													ppm		
34	Adirondack_RAT	RR	1.79	6.53	5.75	21.4	0.23	0.49	0.200	0.060	5.54	0.289	0.419	0.320	14.6	165	81	nd
60	Humphrey_RAT2	RR	1.89	6.28	5.65	21.5	0.25	0.51	0.258	0.083	5.60	0.329	0.414	0.316	14.6	164	112	52
86	Mazatzal_Brooklyn_RAT2	RR	2.06	5.86	5.66	21.4	0.28	0.59	0.233	0.136	5.73	0.353	0.372	0.323	14.7	132	75	161
	Mean	**RR**	**1.91**	**6.23**	**5.69**	**21.4**	**0.25**	**0.53**	**0.23**	**0.09**	**5.62**	**0.324**	**0.401**	**0.319**	**14.6**	**153**	**89**	**—**
	Standard Deviation %	RR	7.3	5.5	1.0	0.2	11	10	13	42	1.7	10	6.4	1.1	0.1	12	23	—
	Mininum	RR	1.79	5.86	5.65	21.4	0.23	0.49	0.20	0.06	5.54	0.289	0.372	0.316	14.6	132	75	52
	Maximum	RR	2.06	6.53	5.75	21.5	0.28	0.59	0.26	0.14	5.73	0.353	0.419	0.323	14.7	165	112	161
	Clovis (selected)																	
197	WoolyPatch_Sabre_RAT	RR	2.47	6.59	6.67	21.9	0.54	1.15	0.779	0.056	2.60	0.565	0.19	0.079	12.7	607	89	318
199	Woolypatch_Mastodon_RAT	RR	2.16	7.01	5.47	21.7	0.52	0.96	1.03	0.033	2.46	0.547	0.12	0.103	14.9	553	54	493
218	Clovis_Plano_RAT	RR	2.70	6.95	4.74	19.7	0.46	3.02	1.63	0.291	4.32	0.505	0.11	0.234	12.2	735	118	239
232	Ebenezer_RAT	RR	1.72	8.94	4.91	22.2	0.42	1.28	1.46	0.278	2.46	0.472	0.11	0.122	12.1	523	99	222
287	Uchben_Koolik_RAT	RR	1.81	8.61	5.04	21.3	0.41	2.11	1.85	0.294	3.20	0.481	0.10	0.193	10.8	593	118	674
	Mean	**RR**	**2.17**	**7.62**	**5.37**	**21.4**	**0.47**	**1.70**	**1.35**	**—**	**3.01**	**0.514**	**0.13**	**0.15**	**12.5**	**602**	**95**	**389**
	Standard Deviation %	RR	19	14	14	4.5	13	50	32	—	26	7.9	27	45	12	13	28	49
	Mininum	RR	1.72	6.59	4.74	19.7	0.41	0.96	0.78	0.03	2.46	0.472	0.10	0.08	10.8	523	54	222
	Maximum	RR	2.70	8.94	6.67	22.2	0.54	3.02	1.85	0.29	4.32	0.565	0.19	0.23	14.9	735	118	674
	Wishstone Class (selected)																	
335	Wishstone_chisel_RAT	RR	3.70	2.71	7.96	20.5	2.27	0.88	0.35	0.475	6.36	1.56	nd	0.170	9.0	67	64	nd
356	Champagne_RAT1	RR	3.74	2.37	7.86	20.3	2.21	0.78	0.60	0.437	6.27	1.79	nd	0.189	9.7	24	81	72
357	Champagne_RAT2	RR	3.72	2.40	7.85	20.3	2.20	0.79	0.60	0.438	6.25	1.78	nd	0.196	9.7	45	58	68
	Mean	**RR**	**3.72**	**2.50**	**7.89**	**20.4**	**2.23**	**0.81**	**0.52**	**0.45**	**6.29**	**1.71**	**nd**	**0.185**	**9.50**	**45**	**68**	**70**
	Standard Deviation %	RR	0.6	7.5	0.7	0.4	1.5	7.0	27	4.8	0.9	7.7		7.3	4.2	47	18	4.2
	Mininum	RR	3.70	2.37	7.85	20.3	2.20	0.78	0.35	0.44	6.25	1.56	nd	0.170	9.04	24	58	68
	Maximum	RR	3.74	2.71	7.96	20.5	2.27	0.88	0.60	0.47	6.36	1.79	nd	0.196	9.75	67	81	72
	Peace Class (selected)																	
377	Peace_RAT1	RR	0.27	11.9	1.48	17.3	0.26	5.16	0.889	nd	3.89	0.245	0.404	0.321	14.5	540	94	181
380	Peace_RAT2	RR	nd	13.0	1.18	17.4	0.21	4.26	0.720	nd	3.50	0.272	0.513	0.360	15.9	774	64	71
	Mean	**RR**	**0.27**	**12.4**	**1.33**	**17.4**	**0.23**	**4.71**	**0.80**	**nd**	**3.70**	**0.259**	**0.459**	**0.341**	**15.2**	**657**	**79**	**—**
	Standard Deviation %	RR		6.1	16	0.3	14	13	15		7.4	7.4	17	8.1	6.4	25	27	—
	Mininum	RR	0.27	11.9	1.18	17.3	0.21	4.26	0.72	nd	3.50	0.245	0.404	0.321	14.5	540	64	71
	Maximum	RR	0.27	13.0	1.48	17.4	0.26	5.16	0.89	nd	3.89	0.272	0.513	0.360	15.9	774	94	181
	Watchtower Class (all)																	
417	Watchtower_Joker_RAT	RR	1.98	6.03	6.52	19.8	1.97	1.37	0.80	0.617	5.31	1.33	nd	0.171	10.3	67	140	251
416	Watchtower_Joker_Brush	RB	2.06	6.09	6.47	20.6	1.19	1.88	1.14	0.632	4.33	1.13	nd	0.173	10.3	58	132	262
470	Methuselah_Haunch	RB	2.55	5.12	7.20	21.9	1.05	1.66	1.23	0.469	4.54	1.17	0.031	0.210	8.2	92	81	204
475	Methuselah_Pittsburg	RB	2.47	5.01	6.61	20.8	1.38	1.89	1.36	0.376	5.29	1.14	0.035	0.165	9.3	147	100	460
484	Jibsheet	RB	2.67	5.21	6.39	21.1	1.10	2.58	1.28	0.309	4.79	1.16	0.028	0.170	8.5	83	89	302

Table 4.3. (*cont*.)

Sol	Class/Sample/Mean	Type	Na	Mg	Al	Si	P	S	Cl	K	Ca	Ti	Cr	Mn	Fe	Ni	Zn	Br
			wt.%													ppm		
496	Pequod_Ahab_brushed	RB	2.58	5.08	6.93	21.5	1.23	1.72	0.98	0.319	5.09	1.15	0.031	0.153	8.6	94	80	250
499	Pequod_MobyDick	RB	2.56	4.81	6.68	21.4	1.12	1.93	1.02	0.353	5.03	1.10	0.054	0.162	9.4	137	96	197
	Mean	**RR-RB**	**2.41**	**5.34**	**6.69**	**21.0**	**1.29**	**1.86**	**1.12**	**0.44**	**4.91**	**1.17**	**0.036**	**0.17**	**9.22**	**97**	**103**	**275**
	Standard Deviation %	RR-RB	11	10	4.3	3.3	25	20	17	31	7.6	6.3	29	11	9.2	34	24	32
	Mininum	RR-RB	1.98	4.81	6.39	19.8	1.05	1.37	0.80	0.31	4.33	1.10	0.028	0.15	8.17	58	80	197
	Maximum	RR-RB	2.67	6.09	7.20	21.9	1.97	2.58	1.36	0.63	5.31	1.33	0.054	0.21	10.3	147	140	460
	Backstay Class																	
511	Backstay_Scuppers	RB	**3.08**	**5.02**	**7.01**	**23.1**	**0.61**	**0.61**	**0.35**	**0.89**	**4.31**	**0.56**	**0.10**	**0.19**	**10.1**	**191**	**269**	**nd**
	Independence Class (all)																	
533	Independence brushed	RB	2.26	3.38	6.84	24.6	1.01	2.47	0.613	0.499	4.72	0.95	0.128	0.096	5.7	2086	96	70
542	Independence_Penn2_Scuffed	RB	2.36	2.04	9.89	25.7	1.52	0.88	0.301	0.428	5.21	1.13	0.031	0.065	3.0	444	667	nd
532	Independence_Jefferson	RU	1.94	3.14	7.06	25.0	1.411	2.04	0.720	0.808	4.03	0.74	0.062	0.116	6.3	578	116	90
	Mean	**RB-RU**	**2.19**	**2.85**	**7.93**	**25.1**	**1.31**	**1.79**	**0.54**	**0.58**	**4.65**	**0.94**	**—**	**0.09**	**4.98**	**—**	**—**	**80**
	Standard Deviation %	RB-RU	10	25	21	2.2	20	46	40	35	13	21	—	28	35	—	—	18
	Mininum	RB-RU	1.94	2.04	6.84	24.6	1.01	0.88	0.30	0.43	4.03	0.74	0.03	0.07	2.99	444	96	70
	Maximum	RB-RU	2.36	3.38	9.89	25.7	1.52	2.47	0.72	0.81	5.21	1.13	0.13	0.12	6.29	2086	667	90

Notes: Preference was given to abraded samples, and then brushed samples and one undisturbed sample were used. Data are from Table 1. Key: nd = not detected, RR= Abraded rock, RB= brushed rock, RU= undisturbed rock.

Robles." Four different targets were measured there by the APXS: "Paso Robles (sol 401)," "Paso Light (sol 427)," "Paso Dark (sol 428)," and "Paso Dark-Light (sol 430)." Two of these disturbed soil targets (Paso Robles and Paso Light) consisted of light-colored material with S contents that were nearly 5 times higher than Gusev soil. The absolute sulfur concentration in Paso Robles was 12.7 wt.%, which was the highest S measured to that date in Gusev crater. The sulfur concentrations of these three Gusev soils are even higher than that of the sulfur-rich outcrops in Meridiani Planum (Rieder *et al.*, 2004). The high S content of Paso Robles is accompanied by a high Fe content (16.3 wt.%), consistent with the identification of ferric sulfate as the main iron-bearing mineral at Paso Robles by the MB (Morris *et al.*, 2006). Most other element concentrations were lower in Paso Robles compared to Gusev soil, likely due to dilution by the huge amount of over 30% SO_3. Exceptions are the elements P, Ca, Fe, and Br. The phosphorus abundance of 2.4 wt.% in Paso Robles was the highest P content ever observed in any kind of soil, and is 6 times higher than the mean 0.4 wt.% of other soils. Similarly, the Br concentrations of about 500 ppm of the two bright Paso Robles soils are 5 times higher than that of other soils.

Dark disturbed soils ("Paso Dark" and "Paso Dark-Light") adjacent to the bright material of Paso Robles may have been mixed into the bright material by the rover wheels. The composition of the dark samples was rather similar to Gusev soil except for depletion of Cl and enrichment of Br, which can be explained by a small admixture of bright Paso Robles material.

Paso Robles soil is extensively altered (Ming *et al.*, 2006). MB measurements show hematite (Fe_2O_3) contents (relative to total Fe content) of 20% for Paso Robles, and only 7% and 2% for Paso Light and Paso Dark, respectively. The corresponding Fe^{3+}/Fe_{total} ratios are 0.86, 0.79, and 0.27, respectively. Also, as mentioned above, the presence of a ferric sulfate is suggested (Morris *et al.*, 2006). It is likely that S exists in sulfate form because the soil is highly oxidized as shown by the high Fe^{3+}/Fe_{total}. Using the APXS data, a Fe^{3+}-sulfate content of 49 wt.% can be derived. If we assume apatite (a calcium, fluoride sulfate: $Ca_5F(PO_4)_3$) as a major carrier of P, the contents of 2.5 wt.% P and 4.8 wt.% Ca in "Paso Robles" would correspond to 14 wt.% apatite, i.e., phosphate would be the main host mineral for Ca (Gellert *et al.*, 2006). Assuming brushite (a hydrated calcium phosphate: $CaHPO_4 \cdot 2H_2O$) as the main phosphate mineral, however, only 3.2 wt.% Ca could satisfy P in the soil (Ming *et al.*, 2006). The remaining Al- and Si-bearing phases, after having extracted the sulfate and phosphate bearing phases, account for 14% to 18% (Ming *et al.*, 2006). The mineralogy and chemistry of Paso Robles soil very strongly indicate aqueous alteration processes. It has been suggested that Paso Robles is an evaporite deposit that formed from solutions rich in Fe, Mg, Ca, S, P, and Si (Ming *et al.*, 2006). It is not clear, however, if Paso Robles type soils occur only locally or in more widespread deposits that are undetected in subsurface layers. The APXS data are consistent with sulfur occurring as sulfate, therefore pure sulfur deposits as resulting from subsurface fumaroles are rather unlikely.

Columbia Hills rocks

The second part of *Spirit*'s journey took the rover into the scenic Columbia Hills. She ascended the so-called "West Spur," passed the Cumberland Ridge to reach the summit of Husband Hill (Arvidson *et al.*, 2006), and descended into the Inner Basin (where she is parked for the winter at the time of this writing). A substantial change in rock composition was encountered in the hills compared to the plains basalts. Based on major-element chemistry as measured by the APXS, a rock classification was established following the convention for terrestrial rocks. Each defined Class is named for a prominent rock belonging to the Class. There are six established classes (Squyres *et al.*, 2006a): (1) Adirondack Class, (2) Clovis Class, (3) Wishstone Class, (4) Peace Class, (5) Watchtower Class, and (6) Backstay Class, and the proposed class – Independence. Mean elemental composition of the classes are given in Table 4.3 and normalized to "Humphrey RAT2" compositions in Figure 4.10. The six established classes are described in detail using data from all instruments on board the rover *Spirit* by Squyres *et al.* (2006a). Except for the Adirondack Class, the other rock classes show various degrees of alteration due to aqueous activities during formation, as detailed mineralogical investigations illustrate (Ming *et al.*, 2006). Here, we review the general aspects of their chemical composition.

Some rocks have a heavily weathered appearance, such as "Pot of Gold (sol 172)," which was covered with small nodular protrusions, or the rock "Breadbox (sol 176)," where only thin rocky walls of material were remaining, possibly as a result of cavernous weathering. Most of the rocks studied with the APXS nearby show a similar chemical concentration pattern normalized to "Humphrey Rat2," except for potassium. Other examples were "Goldklumpen (sol 164)," "Fools Gold (sol 170)," and "String of Pearls (sol 178)." Pot of Gold was logged as "abraded," but images showed that the grind was incomplete and only some brushing occurred. APXS data of these weathered rocks were basically obtained from undisturbed surfaces, whose composition is very similar to normal soils indicating a rather thick soil layer covering these surfaces.

Brushed rocks in the Hills show different enrichment patterns compared to the plains basalts. Many rock surfaces are enriched in P, S, Cl, K, Ti, Ni, and Br compared to "Humphrey RAT2" (Gellert *et al.*, 2006). The phosphorus content of brushed Hills rocks is higher by up to a factor of 5 compared to brushed rock Humphrey. Exceptions are a peculiar rock called "Ben's Clod brushed (sol 429b)," which is enriched in P by a factor of 7 compared to Humphrey brushed, and conversely, an outcrop target "Alligator brushed (sol 385b)," which has a P content of only 0.13 wt.%, below that of Humphrey brushed (0.27 wt.%).

For many rocks, only brushed surface analyses are available, either because insufficient time or power was available to perform the grinding, or because the grind heads on the RAT had become too worn to use (while rock Watchtower was being abraded, the diamond-impregnated grind heads wore away). However, brushing of rock surfaces has still remained feasible. The investigations to date, however, reveal that many of the compositional features characteristic of abraded rocks

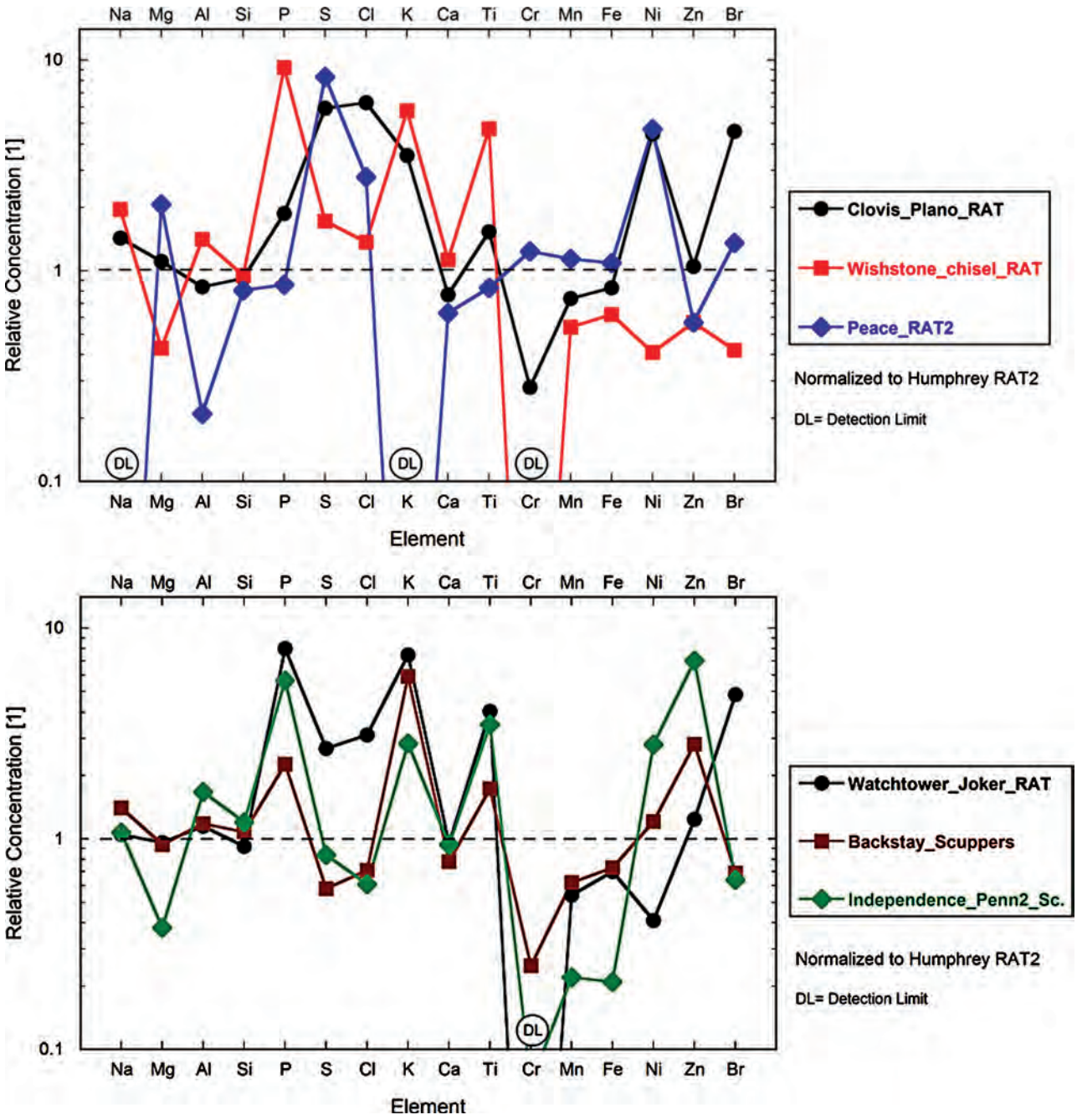

Figure 4.10. Typical compositions of Columbia Hills rock classes. The concentrations are normalized to Adirondack Class rock "Humphrey RAT2 (sol 60)." Top: Examples for Clovis Class, Wishstone Class, and Peace Class (all abraded surfaces). Bottom: Examples for Watchtower Class (abraded), Backstay Class (abraded), and Independence Class (brushed surface). Key: RAT = abraded surface. (For a color version of this figure, please refer to the color plate section or to the e-Book version of this chapter.)

can be seen already in the undisturbed and brushed surfaces. However, while brushed surfaces can be used for diagnostic purposes, it is more difficult to unravel the underlying rock type. For example, the brushed (but not abraded) outcrop "Methuselah (sol 475)" has a very similar enrichment pattern as brushed (and subsequently abraded) "Watchtower (sol 416)," suggesting that both are part of an extended outcrop of similar material despite the fact that they are located at opposite ends of an outcrop on Cumberland Ridge.

Clovis Class rocks. Clovis Class rocks are located in the West Spur of the Columbia Hills and include "Clovis," "Wooly Patch," "Ebenezer," "Tetl," "Uchben," and "Lutefisk." Comparing the three surface types of rock Clovis (undisturbed, brushed, and abraded), the major and minor element contents are similar except for Mg and Cl, which are lower for the undisturbed surface (Table 4.3). This is in contrast to plains basalts, where brushed and undisturbed surfaces had similar concentration patterns, while abraded surfaces revealed different concentrations. This provides evidence that

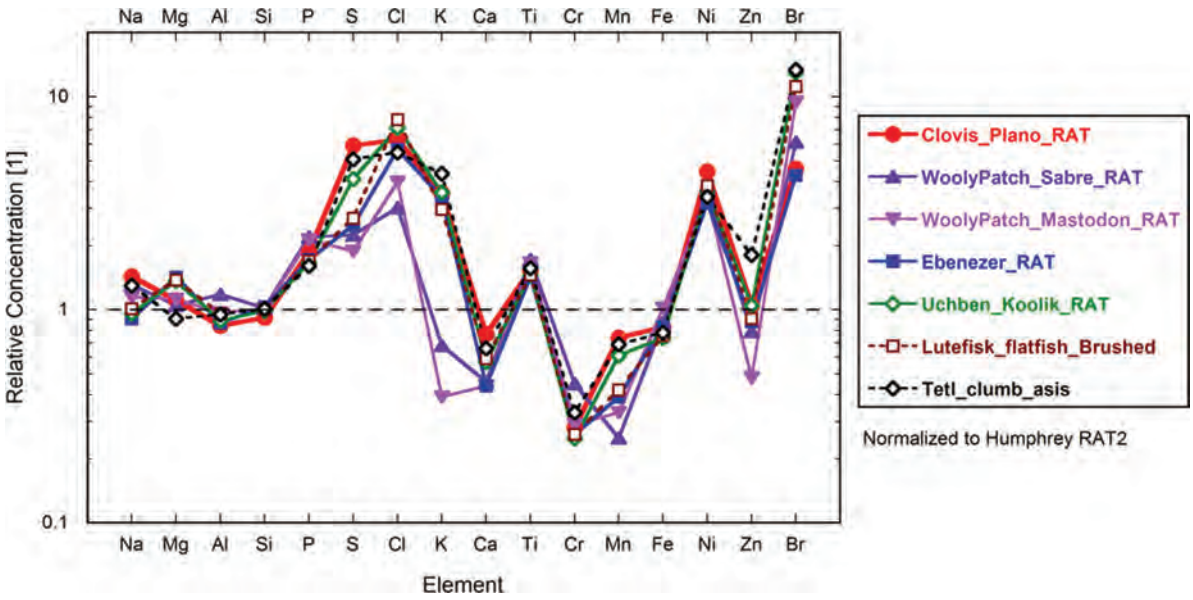

Figure 4.11. Members of the Clovis Class rocks normalized to Humphrey RAT2: "Wooly Patch Sabre RAT (sol 197)," "Wooly Patch Mastodon RAT (sol 199)," "Clovis Plano (sol 218)," "Ebenezer RAT (sol 232)," "Uchben Koolik RAT (sol 287)," "Lutefisk RAT Roe brushed (sol 304)," and "Tetl Clumb as is (sol 274)." Note the lower S, Cl, and K contents of the two Wooly Patch samples compared to the other rocks. Key: RAT = abraded surface, asis = undisturbed surface. (For a color version of this figure, please refer to the color plate section or to the e-Book version of this chapter.)

at least in some cases, brushed-only rocks can be used for classification as well. The rock compositions of three abraded Clovis rocks, "Clovis Plano (sol 218)," "Ebenezer (sol 232)," and "Uchben (sol 287)," normalized to "Humphrey RAT2," revealed enrichments of P, S, Cl, Ti, Ni, and Br, while Ca and Cr were depleted (Figure 4.11). The highest Br content (675 ppm) of all abraded rocks in Gusev crater was found in the rock Uchben, while the lowest Ca contents of about 2.5 wt.% were found for both Ebenezer and Wooly Patch. Brushed rock "Lutefisk (sol 304)" and even undisturbed rock "Tetl (sol 274)" both show concentration patterns very similar to the rock Clovis. Abraded "Wooly Patch Sabre (sol 197)" and "Wooly Patch Mastodon (sol 199)" also show related concentration patterns to the rock Clovis; however, S, Cl, and K contents are lower than other Clovis rocks. The high S, Cl, K, and Br contents of Clovis Class rocks compared to Humphrey even in the abraded surfaces suggest that these rocks were formed in an aqueous environment. Furthermore, it should be noted that MB detected the mineral goethite (α-FeOOH) in Clovis, a mineral that only forms as a product of aqueous activity (Morris *et al.*, 2006). In contrast, the rather high Ni contents in Clovis Class rocks could point to a large meteoritic impact (meteorites have high Ni concentrations), which released enormous amounts of heat and perhaps water at the time of impact. However, such a model still does not exclude the infiltration of water after the catastrophic event.

Wishstone and Watchtower Class rocks. Wishstone Class includes the well-investigated rocks "Wishstone (sol 335)" and "Champagne (sol 357)" (Table 4.3). These are examples of what geologists would call "float" rocks (pieces of rock that have been separated from their parent vein, strata, or outcrop by impact or weathering processes), which dominate the Husband Hills. No outcrops of Wishstone Class material have been found. They show the highest concentrations in Na, Al, and Ti (up to 3.7 wt.% Na, 8 wt.% Al, and 1.8 wt.% Ti) of all abraded rocks in Gusev crater and known Martian meteorites. MB identified about 1% ilmenite in these rocks, which is (together with the rock "Watchtower") one of the highest ilmenite contents at Gusev. Calcium is also very high (up to 6.4 wt.% Ca) in Wishstone Class. The lowest concentrations in Mg, Fe, and Ni (2.4 wt.% Mg, 9.0 wt.% Fe, and 50 ppm Ni) are found in Wishstone Class compared to abraded Gusev rocks except for brushed rock Independence (3 wt.% Fe).

Comparing Wishstone with the rock "Watchtower (sol 417)," similarities in concentration for most elements above Si, and also differences for Na to Al when normalized to Humphrey RAT2, are found (Figure 4.12). These differences, considered distinct enough, pointed to a new class of rocks. Hence, Watchtower was classified as a separate class.

Watchtower and Wishstone Class both have highly enriched P, K, and Ti contents (up to 2.3 wt.% P, 0.5 wt.% K, and 1.8 wt.% Ti), while Cr falls below the detection limit. The chemistry of Watchtower Class rocks could be explained by linear mixing of an endmember similar to Wishstone with lesser amount of another (unidentified) endmember that is richer in ferromagnesian material (Squyres *et al.*, 2006a).

The chemical compositions of brushed and abraded surfaces of the three phosphorus-rich rocks Wishstone, Champagne, and Watchtower are consistent with the brushed samples (compared to the abraded samples) exhibiting a loss of Ca phosphates and no loss of feldspars (Gellert *et al.*, 2006). This could be explained by an acidic weathering environment: In Martian meteorites phosphates dissolve readily in dilute acids, whereas plagioclase is stable (Dreibus *et al.*, 1996). Sulfate- and chloride-rich acidic

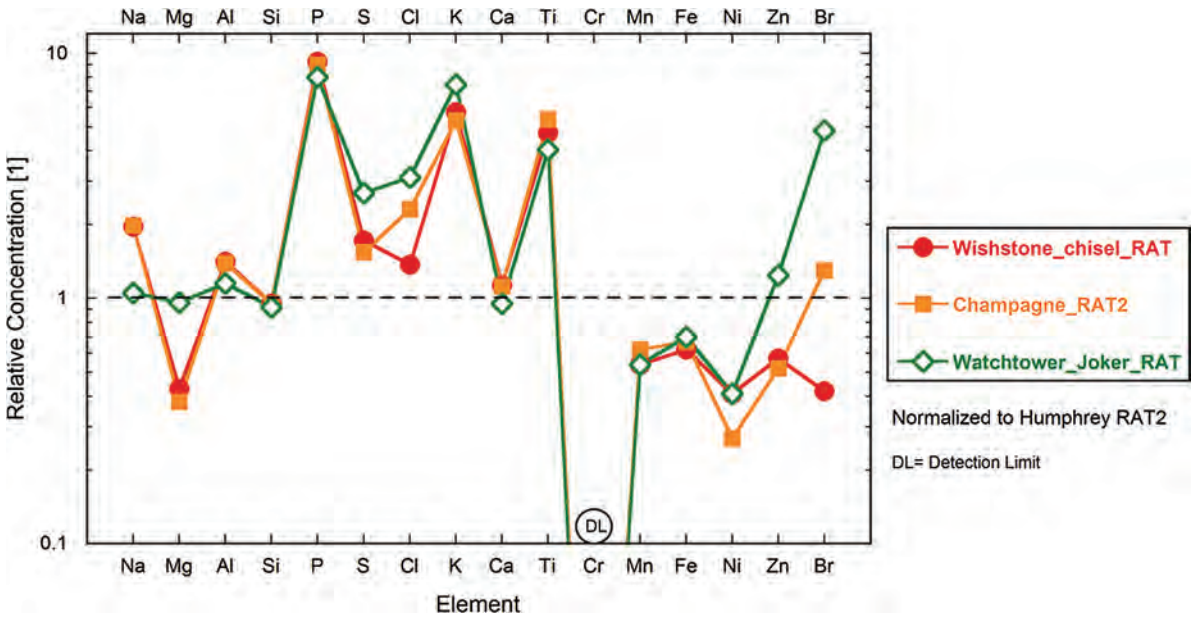

Figure 4.12. Concentrations normalized to Humphrey RAT2 of abraded rocks of Wishstone Class, Wishstone (sol 335) and Champagne (sol 357) and Watchtower Class (consisting only of one sample rock). (For a color version of this figure, please refer to the color plate section or to the e-Book version of this chapter.)

water could easily leach the phosphates from the rock surfaces, yet not weather the feldspar component.

The X-ray spectrum of the rock Wishstone revealed a signal that was identified unambiguously as lead (Pb) by its Lα and Lβ lines, even after taking a small instrument background into account. This is the first time Pb has been detected on Mars. A preliminary Pb calibration resulted in 100 ± 50 ppm and 75 ± 50 ppm Pb for the abraded and brushed surfaces of Wishstone, respectively. Since the Kα peak of arsenic may partially interfere with the Pb Lβ peak, a rather large concentration error had to be assigned to the Pb content in Wishstone (Gellert *et al.*, 2006).

Peace Class rocks. Peace Class rocks located at the Cumberland Ridge are distinct from any other rocks found in the Columbia Hills (Figure 4.13 and Table 4.3). The abraded surface of Peace has the highest Mg and S contents (up to 13 wt.% Mg and 5.2 wt.% S) and the lowest Al and Si contents (down to 1.5 wt.% Al and 17.5 wt.% Si) of all rocks found in Gusev crater so far. The low-Al concentration, along with the near-total lack of alkali elements (e.g., K is below the detection limit), is consistent with a low feldspar content. A modal calculation based on MB and APXS data was carried out for Peace (Ming *et al.*, 2006). The calculation included high Mg and Ca sulfates and low feldspar, as well as olivine, Mg-rich pyroxenes, magnetite, and SiO_2 polymorphs. This unusual occurrence of olivine and SiO_2 polymorphs could be explained by partial weathering of olivine in a mildly acidic environment (Ming *et al.*, 2006).

Nickel concentrations show a large variety among the Martian rocks (Figure 4.14). Adirondack, Wishstone, Watchtower, and Backstay Class rocks have Ni contents below 200 ppm. In contrast, Clovis and Independence Class rocks reveal very high Ni concentrations of more than 400 ppm (up to 2090 ppm for "Independence brushed"). Most soils have Ni contents above 400 ppm, which can be attributed to a meteoritic Ni-rich component (see above). Almost all Martian meteorites show Ni contents in the range of 45–340 ppm, except for Chassigny (480 ppm). It should be noted that basaltic Adirondack Class and the alterated Wishstone and Watchtower Class rocks fall in the low-Ni–Mg field of the Shergottite, Nakhlite, and Chassignite (SNC) meteorites (Figure 4.14). Adirondack and Wishstone Class rocks even have the same Ni/Mg ratio of 0.0024 as olivine-rich SNCs (olivine-phyric shergottites and the dunite Chassigny). The abraded outcrops of Clovis and Peace Class have Ni concentrations of above 500 ppm that exceed most soil contents requiring a Ni enrichment during the time of their formation. Asteroidal impact material can be a good candidate for a Ni source. During alteration, such surface Ni could be incorporated in sedimentary material.

The ratio of chlorine to bromine is always lower than the carbonaceous chondrite (type CI) ratio of 270, which means that Br is enriched compared to Cl, if a chondritic ratio is assumed to exist in the rocks. Since Br salts are more soluble than Cl salts, aqueous environments could explain the ubiquitous enrichment of Br (Yen *et al.*, 2005).

Backstay Class rock. At the crest of Cumberland Ridge a unique rock called "Backstay" was discovered that seemed different from the local outcrops based on Miniature Thermal Emission Spectrometer (Mini-TES) spectra (see, for example, Chapter 14). As the grinding teeth of the RAT were worn away, Backstay could only be brushed and then analyzed by the APXS (Table 4.3). Brushed rock "Backstay (sol 511)" was measured to have the highest K content (0.89 wt.%) of all rocks and the lowest S (0.6 wt.%) of all brushed ones. Compared to plains basalts, Backstay has lower Fe, Mn, and Cr contents. Backstay appears to be a loose piece of float basalt of unknown origin, similar to Adirondack Class rocks, but with lesser alteration

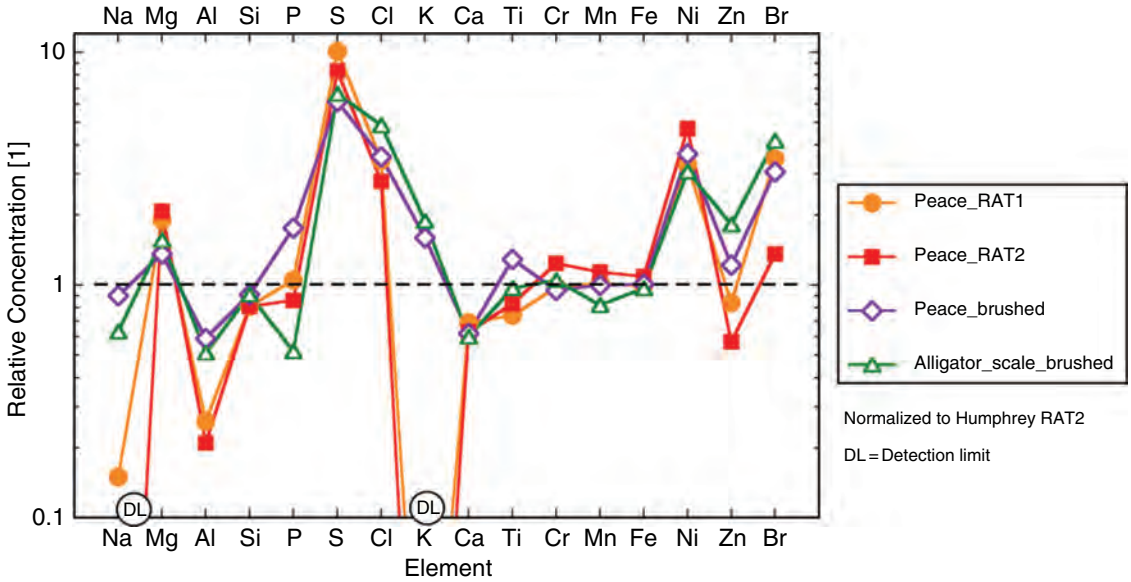

Figure 4.13. Relative concentrations of Peace Class rocks (abraded and brushed surfaces). Rock "Peace" is shown for two sequential RAT holes: first hole is sample "Peace RAT1" and second hole is deeper "Peace RAT2." (For a color version of this figure, please refer to the color plate section or to the e-Book version of this chapter.)

as indicated by lower S, Cl, and Br contents. Despite the fact that Backstay was the only rock observed to have these kinds of elemental characteristics, its important differences from Adirondack Class rocks and the presence of other rocks with similar Mini-TES and Pancam spectral signatures observed in the distance (but never inspected closely by the APXS or MB) (McSween *et al.*, 2006b; Squyres *et al.*, 2006a) support the creation of a new Backstay Class. A comparison with basaltic shergottites (Martian meteorites; see Chapter 17) is not consistent with a compositional match but reveals a probable higher concentration of feldspar (Figure 4.15). Although Backstay's smooth surface could be successfully brushed, some surface alteration related to some residual rind or coating material cannot be ruled out.

Independence Class rocks. On sol 528 the *Spirit* rover encountered a horizontal outcrop of light-toned, rough material, named "Independence," followed by the "Voltaire" outcrop. Several samples of the outcrop were analyzed by the APXS, both undisturbed and brushed (Table 4.3). Like the brushed clod "Bens Clod" near Paso Robles, a region 12 m lower in elevation and 150 m to the north-northeast, the Independence outcrop has high Al (up to 10 wt.%) and very low Fe contents (~6 wt.%). After having used a wheel scuff to expose more fresh surface, the APXS analyses showed an additional decrease in Fe, S, Cl, K, and Ni, indicating a further removal of contaminating dust. Sample "Independence Penn2 Scuff" revealed with 3.0 wt.% Fe the lowest Fe concentration measured in all Martian samples (*in situ*) including Martian meteorites (for Gusev Fe values, see Figure 4.10). Based on MB measurements, one-third of this Fe content is bound in ilmenite (Morris *et al.*, 2006). Also, the undisturbed rock sample "Assemblee" belongs to the low-iron rocks, but has an

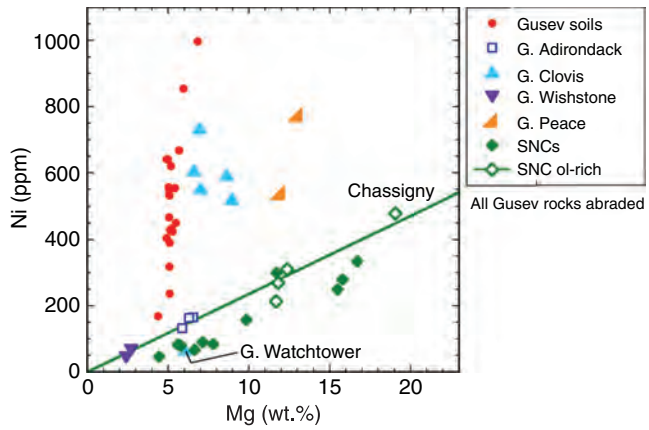

Figure 4.14. Nickel versus magnesium concentrations for various Martian rocks, including Martian meteorites. Regression line of SNC olivine-rich data points (3 olivine-phyric shergottites and the dunite Chassigny) was forced through zero. Note that Adirondack and Wishstone Class rocks lie on regression line. Key: G. = Gusev, SNC ol-rich = SNC olivine-rich. *Note:* some Ni-rich soils plotted here are not listed in Table 4.1. (For a color version of this figure, please refer to the color plate section or to the e-Book version of this chapter.)

anomalously high-Cr content of 1.9 wt.%. These low-Fe rocks with high Al/Si ratios were labeled Independence Class. Their compositional profile is similar to montmorillonite, a member of the smectite group (Clark *et al.*, 2007). Terrestrial montmorillonites often contain enrichments of minor or trace elements. This clay mineral is a typical aqueous alteration product of basalts. Most prominent in the Independence Class rocks, the APXS found varying and unusual high enrichments in minor and trace elements like Cr, Ni, Cu, Zn, Ga, and Y. There is also evidence for abundant Co and Ba in some members of this rock class.

Most rocks in Columbia Hills have been subjected to intermediate levels of aqueous alteration and especially the Independence Class (Clark *et al.*, 2007). About 5% by mass of montmorillonite is structural H_2O. But it can reversibly adsorb an additional 2–17 wt.% of water, even in a cold climate of Mars (Clark, 1978). If the occurrence of

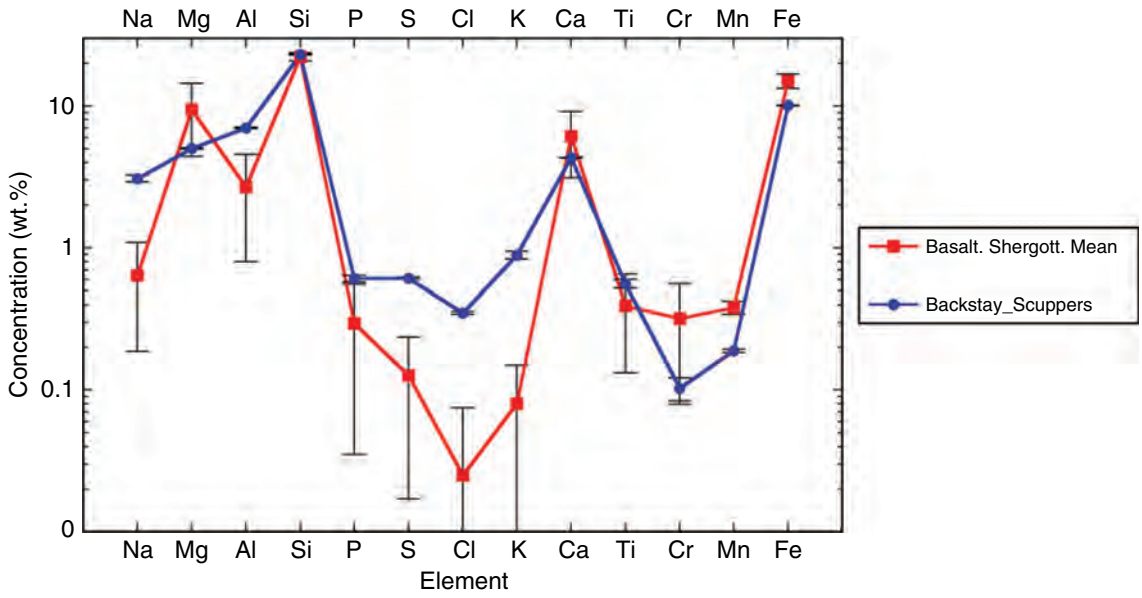

Figure 4.15. Concentration of "Backstay (sol 511)" in comparison with mean basaltic shergottites. Errors bars show the standard deviation of the mean of basaltic shergottites and the measurement error of Backstay. (For a color version of this figure, please refer to the color plate section or to the e-Book version of this chapter.)

smectites is widespread at shallow depths at Gusev crater, this hydrated mineral could contribute to the rather high concentrations of 7–10 wt.% water equivalent hydrogen detected by the Mars Odyssey Gamma-Ray Spectrometer (GRS) instrument suite (Feldman *et al.*, 2004; and in Chapters 5 and 6).

4.4 CHEMISTRY OF MERIDIANI PLANUM

The landing site of the *Opportunity* rover at Meridiani Planum is about 180° E of Gusev crater. Signatures of coarse-grained gray hematite found in orbit by the Thermal Emission Spectrometer (TES) of the Mars Global Surveyor spacecraft triggered the selection of the *Opportunity* landing site (Christensen *et al.*, 2000, 2001). On Earth, hematite can be formed by aqueous processes, weathering processes, or in some cases without water. At Meridiani, hematite was discovered all along the rover's traverse in the form of small spherules (dubbed "blueberries"), or in the form of fine particles in outcrops. The landscape along the rover's traverse can be briefly characterized as "sandy" plains with rolling dunes, otherwise nearly devoid of significant topographic features except for impact craters. Some craters have bright reddish rock outcrops exposed in their walls and ejecta deposits, and some of the outcrops are covered by a layer of dispersed spherules. Squyres *et al.* (2004b, 2006b) provide an overview of the *Opportunity* landing site and the rover's major initial findings.

The Meridiani samples studied by the APXS can be divided into several groups with distinct chemistry that are described below: basaltic and/or dusty soils, sulfur-rich outcrops, iron-rich spherules, and a few unusual objects. Chemical compositions of the soils, rocks, and spherules are provided in Table 4.2; more details are given by Gellert *et al.* (2008).

4.4.1 Meridiani soils

A small number of undisturbed soils free of spherules were measured by the APXS as of this writing (*Opportunity* sol 640). As in the case of undisturbed Gusev soils, the undisturbed Meridiani soils show a large homogeneity (Table 4.4). Gusev and Meridiani mean soil elemental compositions are remarkably similar for almost all elements (Figure 4.16). The largest differences between Meridiani and Gusev soils are lower Na and higher Fe in Meridiani. The higher Fe may be the result of admixture of dispersed hematite powder in the top-most Meridiani soils. The overall similarity in the Meridiani and Gusev soil chemistries provides further support for the idea of a globally mixed soil component.

4.4.2 Meridiani rocks

On sol 15, the APXS was placed against a rocky sample, called "Stone Mountain, Robert E. (sol 15)," located at the right side of the light-toned outcrop found at the "Eagle crater" wall (Bell *et al.*, 2004). The analysis of this sample surface, measured "as is," showed a sulfur concentration of 7.8 wt.% (or 19.4 wt.% SO_3), much higher than observed on Mars previously. In fact, this S content was more than a factor of 3 higher than typical soil contents at the Viking 1 (Chryse Planitia), Viking 2 (Utopia Planitia), MPF (Ares Vallis), and Gusev crater landing sites (Clark *et al.*, 1982; Brückner *et al.*, 2003; Gellert *et al.*, 2006) (Table 4.4). However, a corresponding increase in Cl was not observed in this outcrop. Typical concentration variations of Cl in soils are within a range of 0.3 to 1 wt.% and are correlated with S, as seen at Gusev. During the next weeks several APXS measurements were performed on various outcrop locations. Typically, the same spot was analyzed before (surface as is) and after brushing and/or grinding by the RAT. At a location referred to as "McKittrick (sols 29 and 31)" on the outcrop "El Capitan," the observed S concentration increased from

Table 4.4. *Comparison of Mars and Earth chemistry showing mean basaltic soil data of MER-A (Gusev crater), MER-B (Meridiani Planum), and MPF (Mars Pathfinder, Ares Vallis), concentration of basaltic Martian meteorites and Earth Continental crust*

Oxide [wt.%]	MER-A Gusev Mean Soil[a]	MER-B Meridiani Mean Soil[b]	MER-A Mean Soil S & Cl− free	MER-B Mean Soil S & Cl− free	MPF Mean Soil[c] S & Cl− free	Basaltic Martian Meteorites[d]	Earth Continental Crust[e]	Mars Mantle + Crust[f]
Na_2O	3.02	2.17	3.25	2.32	1.2	1.0–2.2	3.2	0.50
MgO	8.49	7.64	9.14	8.16	9.4	3.7–11.0	3.7	30.2
Al_2O_3	10.2	9.39	11.0	10.0	8.6	4.8–12.0	15.0	3.02
SiO_2	46.2	46.2	49.7	49.3	45.7	49.0–51.4	61.6	44.4
P_2O_5	1.01	0.85	1.09	0.91	1.1	0.6–1.5	0.2	0.16
SO_3	6.32	5.57	0	0	0	0.33–0.80	0.2	0
Cl	0.76	0.67	0	0	0	0.005–0.013	0.1	0.004
K_2O	0.46	0.48	0.49	0.51	0.7	0.06–0.25	2.6	0.037
CaO	6.37	7.15	6.85	7.63	7.1	10.0–11.0	5.4	2.45
TiO_2	0.95	0.97	1.02	1.03	1.1	0.8–1.8	0.7	0.14
Cr_2O_3	0.29	0.41	0.31	0.44	0.3	0.014–0.30	0.02	0.76
MnO	0.31	0.37	0.33	0.40	0.6	0.45–0.53	0.1	0.46
FeO	15.6	18.0	16.8	19.2	21.7	17.7–21.4	5.6	17.9
NiO	0.06	0.05	0.06	0.05		0.004–0.0083	0.007	0.051

Ref.:
[a] Gellert *et al.*, 2006;
[b] Rieder *et al.*, 2004; Gellert *et al.*, 2008;
[c] Brückner *et al.*, 2003;
[d] Banin *et al.*, 1992, Dreibus priv. com.;
[e] Wedepohl, 1995,
[f] Wänke and Dreibus, 1988, 1994.

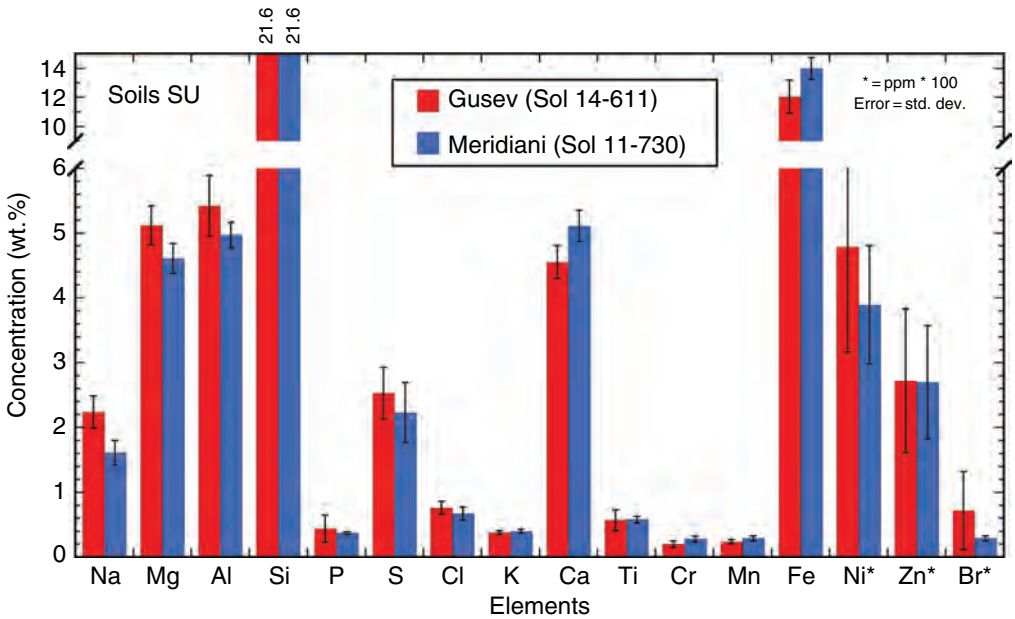

Figure 4.16. Comparison of Meridiani and Gusev mean soils. *Note: y*-axis is split by break with two different scales. (For a color version of this figure, please refer to the color plate section or to the e-Book version of this chapter.)

5.1 wt.% in the "as is" sample to 8.5 wt.% (or 21.3 wt.% SO_3) in the abraded sample. An increase in S after surface removal was a common observation on the outcrop of Eagle crater and later on other outcrop samples along the rover's traverse.

Analyses before and after abrading of McKittrick showed Br concentrations of 211 and 342 ppm, respectively. When compared with the observed chlorine concentrations, these concentrations are unusually high in comparison to most Martian meteorites, where the chlorine/bromine ratio is close to the ratio 270 of carbonaceous chondrites type CI (Palme and Beer, 1993) (Figure 4.17). The Br concentrations of

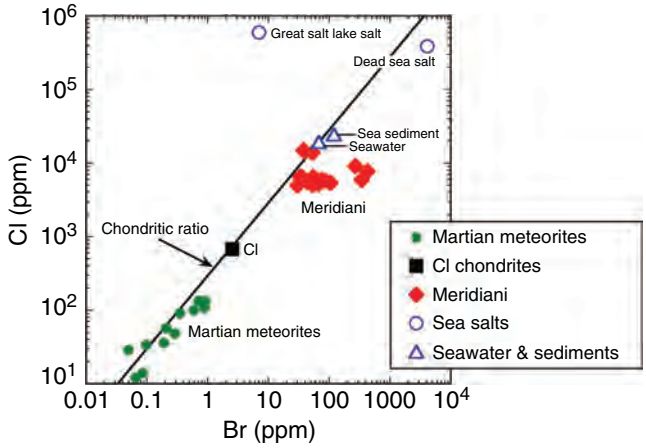

Figure 4.17. Chlorine versus bromine for Martian meteorites, carbonaceous chondrites type CI, Meridiani samples, and terrestrial sea salts, seawater, and sea sediments. (For a color version of this figure, please refer to the color plate section or to the e-Book version of this chapter.)

Martian meteorites are less than 1 ppm, which is far below the APXS detection limit of 30 ppm for Br.

Therefore, no detection of Br was expected before the mission. The observed Cl/Br ratio of 17.5 in the "McKittrick RAT (sol 31)" sample corresponds to an enrichment of Br over chlorine relative to CI-chondrite by a factor of 15. Another sample called "Guadalupe RAT (sol 36)," also on the El Capitan outcrop, was even richer in S (10 wt.%) than McKittrick but showed a Br content just at the detection limit of 30 ppm, which corresponds to a small enrichment of 1.6 of Br relative to chlorine (0.5 wt.%). Thus, Br concentrations varied by more than an order of magnitude depending on the position within the outcrop. However, no systematic vertical or horizontal variations of Br within the outcrop were found.

After the investigations of Eagle crater, *Opportunity* continued to drive along the path that the scientists together with the rover engineers had established on a day-by-day basis. Light-toned layered outcrops, first discovered in Eagle crater, were also found in other craters, as well as along the rover's traverse in the plains to Endurance and "Erebus" craters and beyond. The sulfur-rich outcrop rocks exhibit large-scale occurrences in Meridiani; over more than 8 km of route so far these outcrops have had similar elemental compositions (Squyres *et al.*, 2006b). Abraded outcrop samples exhibited very high sulfur contents all along this traverse with S concentration ranging from 6.8 wt.% ("MacKenzie Campbell RAT [sol 184]") in Endurance crater to 11.5 wt.% ("Gagarin RAT [sol 403]") near crater Vostok.

The rover's ingress into Endurance crater provided vertically (stratigraphically) and horizontally spaced samples that were measured by the APXS. Sample "MacKenzie Campbell RAT (sol 184)," located as deep inside the Endurance crater as the rover could descend, that is about 8–10 m stratigraphically below the crater's rim (Grotzinger *et al.*, 2005), shows the lowest S content of all abraded rocks. In fact, a continuous decrease of S content as a function of depth in the crater was observed. This decrease is accompanied by a decrease of Mg content, suggesting that $MgSO_4$ is depleted with depth in Endurance crater (Figure 4.18). On the other hand, the Cl contents show almost the opposite effect in Endurance: the lower the S content, the higher the Cl content, which is not the case for "MacKenzie Campbell RAT." While S and Mg contents are decreasing by 30%, Cl contents increase by a factor of 3 deep inside the crater. In general, Cl contents vary significantly along the whole traverse. Except for local anti-correlations (as in Endurance), no correlations with S, Na, or Br can be observed on larger scale (Table 4.4; Figure 4.19).

In situ and remote-sensing analyses of the different layers of Endurance provide evidence of episodes during which temperature, acidity, and water underwent significant changes (e.g., Squyres *et al.*, 2004b; Grotzinger *et al.*, 2005). However, survival of soluble salts on the outcrops points to a dry history of Meridiani since the time of the last watery period (e.g., Clark *et al.*, 2005).

Since S concentrations are markedly high in all measured outcrops, the concentration of major elements can provide constraints on the composition and the relative proportion of sulfur compounds in the outcrops. For example, in Figure 4.20, the relationship of Si versus S content is shown for different kinds of measured samples (disturbed and undisturbed soils, soils containing spherules, trenches, cobbles, and undisturbed, brushed and abraded rocks). A good correlation between Si and S is seen, except for soils containing spherules (these samples have a high Fe content, as described below). In a simple two-component mixing model it could be assumed that one component, which may be of basaltic or siliciclastic nature, contains almost all of the Si-bearing minerals, while the other component, consisting of minerals that likely precipitated from brines, contains most of the S. The most Si-rich sample in Figure 4.20 is an unusual rock for *Opportunity*'s traverse in Meridiani ("Bounce Rock," described below). Mixing these two components in various ratios, the amount of silicon-bearing phase is diluted by the sulfur-bearing phase. Similar dilution of Al as a function of S was observed, except again for spherule-rich soils. However, within small variations, the Mg content is independent of the S content (except for samples within Endurance, as noted above and below); that is there is no general dilution of Mg by S. This implies that the sulfur-bearing phase is also adding Mg. Indeed, the fact that abraded outcrop rocks in Endurance show a very good correlation of Mg and S suggests that $MgSO_4$ is a major component of the outcrop. Calcium and iron are not diluted by sulfur either. Assuming all SO_3 is bound to Mg and Ca sulfates and, according to MB data (Klingelhöfer *et al.*, 2004), to ferric sulfates, these rocks must contain about 40 wt.% sulfates. More details on derived outcrop mineral compounds are given by Morris *et al.* (2004), Clark *et al.* (2005), and in Chapters 15 and 23.

4.4.3 Meridiani spherules

The landing site and observable areas along the traverse are covered with soils that consist of fine-grained basaltic sand and a surface lag of spherules, spherule fragments, and other granules. These spherules have become known informally as Blueberries, although their color is gray rather than blue

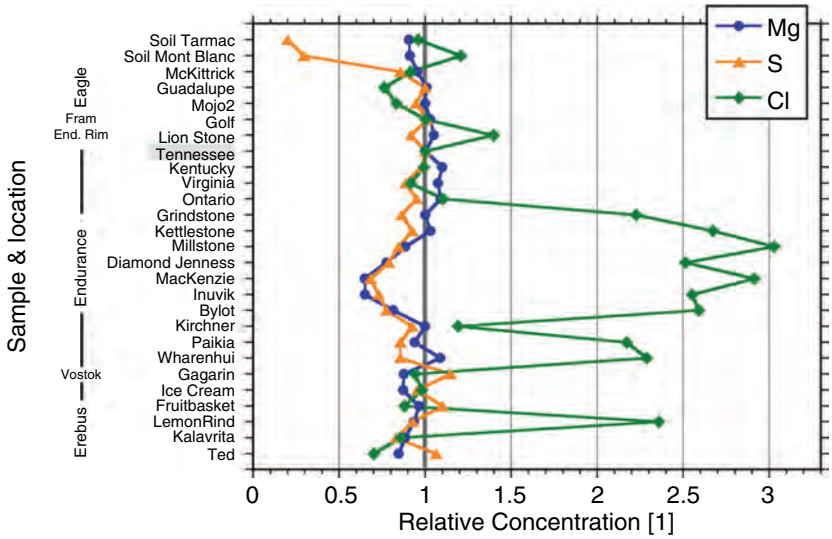

Figure 4.18. Concentrations (wt.%) relative to sample "Tennessee (sol 139)" of magnesium, sulfur, and chlorine for Meridiani outcrop and soil samples at different locations, such as Eagle crater, Fram crater, Endurance rim, Endurance crater, Vostok crater, and Erebus crater. (For a color version of this figure, please refer to the color plate section or to the e-Book version of this chapter.)

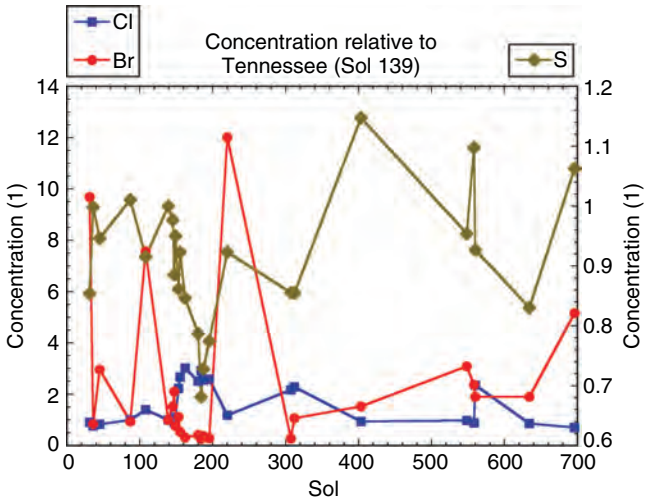

Figure 4.19. Concentrations (wt.%) relative to sample "Tennessee (sol 139)" of sulfur, chlorine, and bromine for abraded samples along the rover's traverse, listed by sol number. Note different scales for chlorine and sulfur. (For a color version of this figure, please refer to the color plate section or to the e-Book version of this chapter.)

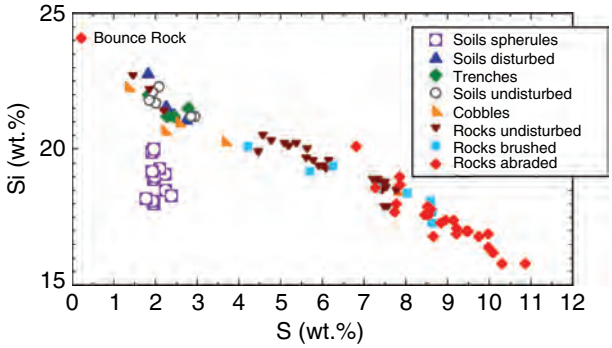

Figure 4.20. Silicon versus sulfur contents for different Meridiani samples including erratic sample "Bounce Rock." (For a color version of this figure, please refer to the color plate section or to the e-Book version of this chapter.)

(Squyres *et al.*, 2004b). Because the spherules are much smaller than the fields of view of the APXS and Mössbauer instruments, it is not possible to isolate individual spherules for detailed compositional analysis by these instruments. However, several independent observations demonstrate that their composition is dominated by hematite or high iron content (Squyres *et al.*, 2004c). First, Mini-TES observations of spherules that lie atop Meridiani soil show that the concentration of hematite correlates with the fraction of its field of view filled by spherules (Christensen *et al.*, 2004). Second, a Mössbauer measurement was made on an accumulation of loose spherules in a local depression in an outcrop named "Berry Bowl" inside of Eagle crater. This measurement showed a strong hematite signal, while an adjacent spherule-free sample produced a low hematite signal (Klingelhöfer *et al.*, 2004).

Third, an APXS analysis was made on the same outcrop called Berry Bowl. One half of this rock had a flat surface, sample "Berry Bowl empty (sol 48)," that revealed concentrations similar to the adjacent outcrop McKittrick (before grinding) with a high SO_3 content of 14.1 wt.% (Gellert *et al.*, 2008). However, the analysis of the other half of Berry Bowl, where the spherules were accumulated, sample "Berry Bowl full (sol 46b)," showed an unusually high Fe content of 22.8 wt.% (29.3 wt.% FeO-equivalent) and a low SO_3 content of 5.6 wt.%, which is similar to a nearby soil called "Hematite Slope (sol 23)." Berry Bowl full contained both spherules outcrop material and a detritus of dark sand (possibly basaltic grains) because the spherules do not completely fill the area of the bowl. The Fe/Mn ratios of Berry Bowl full (Fe/Mn = 108) and of the soil Hematite Slope (Fe/Mn = 80) are higher than the ratios measured in other soils and outcrops (Fe/Mn ~50). As Mn^{2+} has similar chemical characteristics as Fe^{2+}, Fe/Mn ratios are rather constant on a planetary surface. A high Fe/Mn ratio can result from the presence of Fe^{3+}-bearing minerals, such as hematite. The Fe/Mn ratios are high only in spherule-rich soils (Fe/Mn ~ 80–120), while they are low in a nearby excavated trench "Big Dig (sols 25 and 26)" (Fe/Mn ~40–60) or in

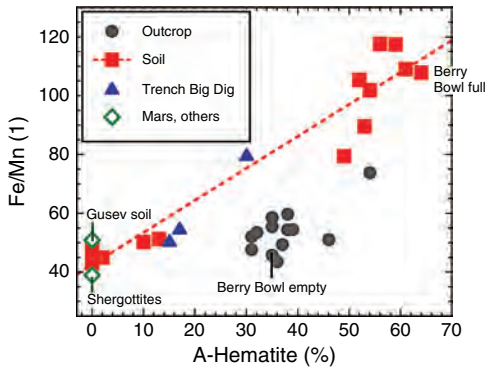

Figure 4.21. Iron–manganese ratio versus A-Hematite (percentage of total Fe in mineral hematite [Morris *et al.*, 2004]) from different Meridiani samples: as outcrops, soils (low and high Fe/Mn ratios), trench samples (top, bottom, and wall), and mean of shergottites and mean Gusev soil. The dashed line shows the good regression of 0.97 between Fe/Mn and A-Hematite for the soil samples. However, in outcrop samples the Fe/Mn is low while the A-Hematite is between 30% and 50%. This fact points to a fine-grained Hematite component. (For a color version of this figure, please refer to the color plate section or to the e-Book version of this chapter.)

abraded outcrops, where spherules are rare (Figure 4.21). These APXS results support the findings from other instruments that the spherules are the carrier of hematite.

Pancam spectra of spherules are consistent with (but do not uniquely identify) hematite (Bell *et al.*, 2004), and spherules sectioned with the RAT show consistent Pancam spectral properties throughout their interiors, indicating that the hematite is not simply present in coatings. Indeed, the spherules, which are strewn across most soils at the *Opportunity* landing site (Soderblom *et al.*, 2004), both inside Eagle crater and on the surrounding plains, appear to be the primary carriers of the coarse-grained gray hematite (Squyres *et al.*, 2004c) that was detected from orbit (Christensen *et al.*, 2000). The MB also detected hematite in spherule-free outcrops (Klingelhöfer *et al.*, 2004), although at lower concentrations than in the spherules (Figure 4.21). Measurements of spherule-free outcrops by the Mini-TES and Pancam instruments were also consistent with the presence of a finely dispersed hematite component (Bell *et al.*, 2004; Christensen *et al.*, 2004). Small quantities of hematite-rich spherules (2 vol.%) were found in rock exposures in Eagle crater and were interpreted as concretions (Squyres *et al.*, 2004c). Erosion of the soft sulfate-rich sedimentary rocks may be responsible for the accumulation of vast amounts of hematite-rich spherules and fragments just on top of the surface (Soderblom *et al.*, 2004).

Images by the MI show that spherules cut by the RAT have no internal structure besides minor traces resulting from the movement of the grinding teeth (e.g., MI images of sol 34; see Chapter 20). There is one example of a naturally broken spherule (acquired on sol 28) that shows concentric banding (Herkenhoff *et al.*, 2004). Thus, the question arises: Are the spherules made of pure hematite? The penetration depth of the radiation that is used by either the APXS or the MB to detect Fe-bearing minerals is about 40 µm (for the 6.4 keV Fe line, Figure 4.5) and up to 100 µm, respectively. Since the 1–6 mm sized spherules do not fill homogeneously the field of view of the APXS sensor head, the surface of the round objects have a mean distance from the ground and hence produce a stronger X-ray signal compared to the background material. In contrast to the APXS calibration samples that had flat surfaces and homogeneous compositions, the spherule-covered samples have irregular surfaces and inhomogeneous composition and hence are very difficult to evaluate. In addition, a thin dust coating on the surface of the spherules cannot be excluded. Indeed, airborne dust deposition on some of the spherules is consistent with Pancam images and spectra that reveal different "clean" and "dusty" spherule populations (Bell *et al.*, 2004). The mixed signal from spherules, background outcrop or soil material, and adhering dust cannot be sufficiently unraveled to derive a unique spherule signal in the APXS data. However, the assumption that most of the Fe detected by APXS in the spherules is from pure hematite is consistent with compositional modeling (Gellert *et al.*, 2008) and other MER datasets, most notably from the MB (Morris *et al.*, 2004, 2006).

4.4.4 Unusual Meridiani rocks

Two unusual rocks (for Meridiani), "Bounce Rock" and "Meridiani Planum," the latter is better known under the synonym "Heatshield Rock," were encountered on the plains of Meridiani Planum. Both are between 30 and 40 cm in diameter. These rocks are considerably larger than another class of unusual rocky materials encountered by *Opportunity*: centimeter-sized cobbles that are frequently found scattered among the soil-dominated landscapes of Meridiani Planum.

Bounce Rock

Bounce Rock was so named because it was found close to a bounce mark made by the airbag-encompassed lander just before it rolled into Eagle crater (see Chapter 13). Detailed MI images reveal a structure characterized by striations reminiscent of those of shatter cones which are typically caused by shock waves during impact (Herkenhoff *et al.*, 2004). The low force required by the RAT to grind into Bounce Rock (Squyres *et al.*, 2004b) gives further evidence for the relative softness of the rock compared, for example, to harder Gusev plains basalts. Data from the whole instrument suite on board the rover demonstrate that Bounce Rock is closely related to basaltic shergottites, a subgroup of the Martian meteorites (see Chapter 17). Multispectral images taken by the Pancam are consistent with Bounce Rock containing pyroxene and/or olivine, but parts of it are covered with dust and soil (Bell *et al.*, 2004). A similar mineralogy is inferred from spectra taken by the Mini-TES (Christensen *et al.*, 2004). Evaluation of Mini-TES spectra after subtracting hematite soil results in a modal mineralogy of a rock dominated by pyroxene (~55% clinopyroxene and ~5% orthopyroxene), and plagioclase (~20%) with minor constituents, comprising 5% olivine and 10% oxides (Christensen *et al.*, 2004). Mössbauer spectra were taken from one abraded surface and from eight different target spots of the undisturbed, dust-covered, and potentially coated surface of the rock. Only two surface spectra show

Table 4.5. *Chemical composition of abraded rock sample "Bounce Rock Case"*

Oxide wt.%	*s.d.*	Bounce Rock Case (RAT)	EETA 79001 Lithology B L 98	QUE 94201 L 98
SiO_2	*3.5*	51.6	49.4	47.9
TiO_2	*20*	0.74	1.18	1.84
Al_2O_3	*7*	10.5	11.2	11.0
Cr_2O_3	*20*	0.11	0.17	0.14
FeO	*6*	14.4	17.4	18.5
MnO	*8*	0.40	0.43	0.45
CaO	*8*	12.1	10.8	11.4
MgO	*17*	6.84	6.57	6.25
Na_2O	*8.5*	1.66	1.74	1.58
K_2O	*15*	<0.1	0.075	0.045
P_2O_5	*17*	0.92	1.28	
*Sum**		99.96	100.08	
S	*15*	0.22	0.193	
Cl	*12*	0.10	0.0048	0.0091
ppm				
Ni	*20*	<100	28	<20
Zn	*12*	<50	91	110
Br		<30	0.025	0.35

Notes: Keys: s.d. = standard deviation in rel. %, includes calibration accuracy; * = Bounce Rock composition sum includes sulfur as SO_3 in wt.%.

minor amounts of ferric Fe. Otherwise, Fe is exclusively distributed between pyroxene phases. There is no evidence for the presence of hematite or olivine in MB spectra. The absence of olivine is unique in dark Martian rocks measured by the MER rovers when compared to Mössbauer spectra acquired of basaltic rocks and soils encountered in the plains of Gusev crater and also to basaltic soils at Meridiani Planum (Klingelhöfer *et al.*, 2004; Morris *et al.*, 2004).

The Mössbauer parameters of pyroxene phases in Bounce Rock fall within the range of pyroxenes found in basaltic shergottites. The best match comes from pyroxene parameters reported for the meteorite QUE 94201 (Dyar, 2003), which are consistent with the presence of augite and pigeonite. The observation that parts of Bounce Rock are covered by soil/dust also is evident from APXS surface analyses on "Bounce Rock, Maggie (sol 70)" and "Bounce Rock, Glanz2 (sol 66)," two targets on the undisturbed surface (Zipfel *et al.*, 2004). Elements typically enriched in soil (e.g., S, Cl, Zn, and K) are significantly higher than for the post-RAT target "Bounce Rock, Case RAT (sol 68)." The chemical composition of Case (Table 4.5), e.g., SiO_2, MgO, P_2O_5, and Cr_2O_3, is close to the compositions of basaltic shergottites and, within this group of meteorites in particular, to lithology B of EETA 79001 and QUE 94201 (Figure 4.22). Average soils from Meridiani Planum and Gusev crater and Gusev plains basalt have significantly higher Cr_2O_3 concentrations than basaltic shergottites. However, Gusev basalts and Bounce Rock have Fe/Mn ratios and absolute MnO concentrations typical for Martian meteorites (average Fe/Mn atomic ratio of basaltic shergottites = 40, see Figure 4.23). Igneous basaltic rocks on Earth are not as

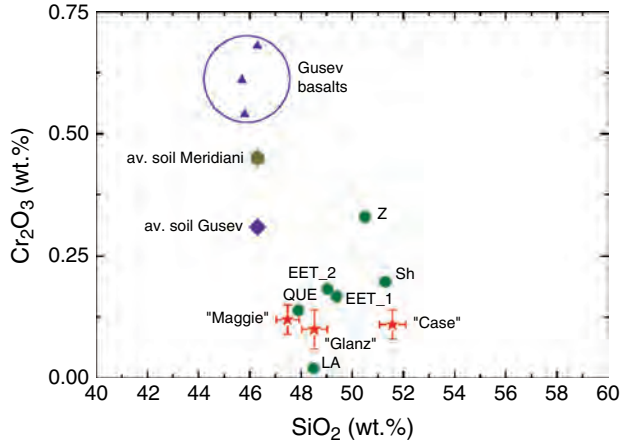

Figure 4.22. Element variation diagram of Cr_2O_3 (wt.%) versus SiO_2 (wt.%) of all Bounce Rock analyses (Glanz, Case, and Maggie), Gusev basalts, average Gusev soil, average Meridiani soil, and selected basaltic shergottites. Keys: LA = Los Angeles, QUE = QUE 94201 (Lodders, 1998), EET_1 = EETA 79001 lithology B (Lodders, 1998), EET_2 = EETA 79001 lithology B (Banin *et al.*, 1992), Sh = Shergotty (Lodders, 1998), Z = Zagami (Lodders, 1998). (For a color version of this figure, please refer to the color plate section or to the e-Book version of this chapter.)

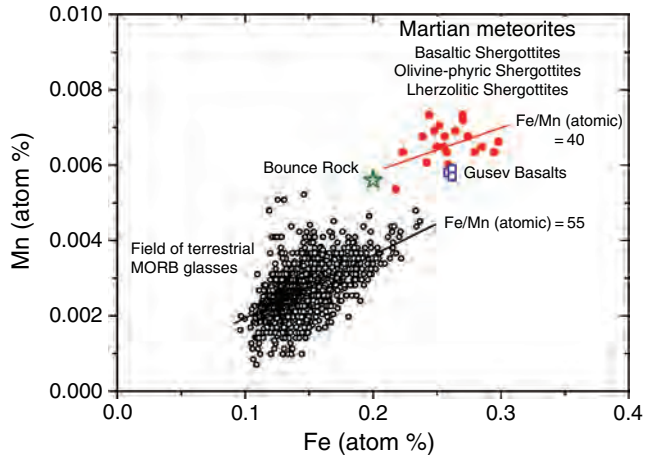

Figure 4.23. Relationship of Mn versus Fe (atomic) of Bounce Rock, selected Martian meteorites (data sources are the same as in Figure 4.22) and terrestrial glass compositions from Mid-Ocean Ridge basalts (MORB) from the Mid-Atlantic Ridge and East Pacific Rise (GEOROC, MPCh). (For a color version of this figure, please refer to the color plate section or to the e-Book version of this chapter.)

rich in Fe and Mn as comparable rocks on Mars as reflected by the composition of glasses in Mid-Ocean Ridge basalts from the Mid-Atlantic Ridge and East Pacific Rise (average Fe/Mn atomic ratio = 55). Over a range of compositions Fe and Mn remain nearly unfractionated during melting and are therefore excellent markers of the source composition, e.g., Earth versus Mars. In addition, mineral norm calculations of Case are consistent with a pyroxene-normative composition in accordance with Mössbauer results and basaltic shergottite properties. The MER analyses of Bounce Rock provide further evidence that Martian meteorites are indeed derived from Mars.

The chemistry of Bounce Rock is very distinct from all other samples in Meridiani, e.g. high SiO_2, Al_2O_3, CaO and lower FeO and Cr_2O_3, Ni and Zn. The abraded spot Case reveals with 0.1% the lowest S content so far measured with the APXS on Mars. This indicates that there is no cross-contamination of materials by the RAT. The isolated occurrence of Bounce Rock on the hematite-rich plains and the lack of any obvious lava flows or volcanic source regions in this part of Meridiani (e.g., Arvidson *et al*., 2003) indicate that it was possibly ejected from a nearby impact crater but never left the gravity field of Mars. Its location on the extension of continuous impact ejecta that originate from a crater 25 km in diameter positioned 75 km to the southwest makes this crater a possible candidate (Squyres *et al*., 2004b) for the source crater of Bounce Rock, although other craters in the Meridiani region and perhaps even beyond could also be the source.

Heatshield Rock

"Heatshield Rock (sol 349)," officially named "Meridiani Planum" by the Nomenclature Committee of the Meteoritical Society (Connolly *et al*., 2006), was found while exploring the crash site and remnants of the rover landing system's heat shield on the plains south of Endurance crater. Images taken by the Pancam (see Chapter 13) showed an object with a maximum dimension of 31 cm across with a smooth, shiny rock surface covered by depressions, partly reminiscent of so-called "regmaglypts," which are thumbprint-like pits formed by turbulent hypervelocity airstreams as iron meteorites ablates in a planetary atmosphere. Preferential melting of low melting point minerals, such as troilite (FeS), which causes similar surface structures, cannot be excluded. Spectra obtained by the Mini-TES on sol 339 and 342 show a thermal emissivity of 0.35, which is consistent with a metallic object like an iron meteorite. Analyses by the MB and APXS confirmed the metallic nature and meteoritic origin of the rock, and allowed the classification of the object as an iron meteorite. MB spectra reveal that ~94% of the Fe content of the brushed surface is bound in kamacite, the α –(FeNi) typically found in iron meteorites.

APXS X-ray spectra of Heatshield Rock showed high iron and nickel peaks together with a weaker typical soil spectrum stemming from dust on the surface. To extract the rock composition the X-ray spectra were analyzed only at energies above 6 keV. This is applicable as thin dust coverage neither affects the high energy signals from the rock, nor adds significant Fe or Ni to the spectrum (see above). For this unusual sample, Fe and Ni were assumed to occur as metals. The lower energy part of the spectrum did not show any significant enrichment in S or Cr compared to soil. The special concentration evaluation revealed that Heatshield Rock consists of about ~93 wt.% Fe and ~7 wt.% Ni. In addition, minor and trace elements were discovered that usually do not show up in X-ray spectra: ~300 ppm Ge and 70 ppm Ga (an upper limit). These concentrations are consistent with a classification of Heatshield Rock as an iron meteorite, particularly an IAB iron (e.g., Wasson and Kallemeyn, 2002).

Cobbles and fragments

In comparison to the Gusev plains which are covered largely by fragments of basaltic rocks, larger rock fragments are exceptionally rare at the Meridiani Planum landing site. Mostly centimeter-sized cobbles are found. The small sizes of these cobbles (>1cm) make it difficult to analyze them. This is mainly because the brush of the RAT cannot be applied to remove possible adhering soil/dust. Three cobble targets, "FigTree Barberton (sol 122)," "Arkansas (sol 552)," and "Perseverance (sol 554)," were studied by MB and APXS. Preliminary results of MB spectra indicate that Fig Tree Barberton contains minor amounts of kamacite. APXS analyses show exceptionally high concentrations of Ni and MgO in comparison to other targets in the vicinity. Thus FigTree Barberton is potentially a fragment of a stony or stony-iron meteorite (Schröder *et al*., 2006). APXS analyses of the other two targets, Arkansas and Perseverance, mainly reflect soil compositions and are therefore not conclusive as to the nature of the two cobbles.

The entry speed of meteoroids (small fragments of debris of the Solar System) on the Martian atmosphere is at average ~10 km s^{-1}. Based on a model that assumes that fragmentation of larger bodies in the atmosphere does not occur, Bland and Smith (2000) calculated that only small masses (10–50 g) can be sufficiently decelerated to survivable speeds in the thin Martian atmosphere. This is consistent with the finding of cobble FigTree Barberton to be a potential meteorite. It also allows speculation that some or most cobbles found at Meridiani Planum are potentially meteorite debris of stony or stony irons. It is not surprising that the only larger object recognized as a meteorite is an iron. The high internal strength of irons will allow survival upon impact without becoming disaggregated into centimeter-sized pieces. This also is consistent with the finding of two large neighboring rock fragments "Allan Hills" and "Zhong Shan" in the Columbia Hills, which were characterized as potential iron meteorites based on Mini-TES spectra and Pancam multispectral imaging and morphology (see Chapters 13 and 14).

4.5 CHEMICAL COMPOSITION OF THE CRUST AND MANTLE

The Martian surface has preserved a large number of impact craters, whose spatial distribution and frequency can provide information on relative ages of the different surface areas (e.g., Hartmann and Neukum, 2001). The absence of large-scale recycling of the crust and whole rock Rb-Sr isotopic compositions of the Martian meteorites (Jagoutz, 1991) suggest strongly that the crust was a product of an ancient planetary global differentiation process about 4.5 Ga.

Comparable chemical composition of the soils at the different landing sites between 50° N and 15° S indicates a thorough mixing of surface material on a global scale by airborne soil (see above). On the other hand, the global elemental maps of the GRS of the Mars Odyssey mission indicate deviations from the observed *in situ* trend: lower

Si and Fe contents in the Tharsis region and lower Fe in most of the southern highlands compared to the northern lowlands (Boynton *et al.*, 2007; see also Chapter 5). In the highlands, the surface could consist of rocks (with low Fe content) probably covered by a thin layer of "normal" airborne soil or a checkerboard pattern of rocks and soil. As the GRS samples the surface down to several tens of centimeters, the gamma-ray signal is composed of rock and soil components resulting in overall lower Fe concentrations. Based on GRS elemental maps some concentration variations are observable; on the other hand, the airborne soil component is representing a global mixture of weathering products of different geological provinces, a process probably going on over the last billions of years.

Sedimentary processes may well homogenize upper crustal Martian rocks, like they do on Earth (e.g., Taylor and McLennan, 1981). As a first approach, the average soil composition of Mars may be a reasonable estimate of the overall bulk crustal composition (Dreibus *et al.*, 2003; McLennan, 2001, 2003). Neglecting the extremely high average S (2.4 wt.%) and Cl (0.8 wt.%) concentrations of the soil, which may have originated from volcanic exhalations (Clark, 1993), the similarity of the average chemical composition of the soil and the basaltic shergottites is remarkable (Table 4.4).

Assuming that the mean soil composition may be representative of the entire Martian crust, a considerable difference to Earth's continental crust exists. The Martian crust contains higher Mg and lower Al and Si, and is thus more mafic in composition compared to Earth. The high FeO content of about 19.2 wt.% is consistent with the predicted Fe-rich Martian mantle (Dreibus and Wänke, 1987; Wänke and Dreibus, 1988, 1994). The estimation of the FeO content of the Martian mantle is based on the correlation of FeO with MnO in Martian meteorites, with the assumption of a carbonaceous chondrite, type CI, abundance of MnO in bulk Mars. Although the Martian soil has an average Fe^{3+}/Fe_{total} of 0.37 (Klingelhöfer *et al.*, 2004; Morris *et al.*, 2006) and is more oxidized than the basaltic shergottites, its mean FeO/MnO ratio of 44 is comparable to the value of 40 ± 4 in the basaltic shergottites. Because Mn^{2+} has chemical characteristics similar to Fe^{2+}, this small increase of the FeO/MnO ratio of Martian soils may reflect the presence of Fe^{3+}-bearing minerals in the soils (Figure 4.21).

Compared to Earth, the Martian crust is phosphorus-rich (Table 4.4). The high phosphate concentration in the Martian surface (about 1.0 wt.% P_2O_5, measured at Ares Vallis as well at Gusev and Meridiani) is consistent with a P-rich mantle as estimated by Dreibus and Wänke (1987) and Wänke and Dreibus (1988, 1994). An additional link between Martian meteorites and Martian crust is the correlation between Al and P for most Martian meteorites and Pathfinder rocks and soils (Figure 4.24). The correlation line of Figure 4.24 is only calculated for the meteorite samples, which show a considerable scattering. In these meteorites the content of the phosphates follows that of feldspar. The deviation of certain aliquots of the same meteorite from the correlation line may be a sampling effect due to inhomogeneous distribution of unusually large feldspar grains in small aliquots. The rock and soil samples of Ares Vallis, Gusev, and Meridiani scatter

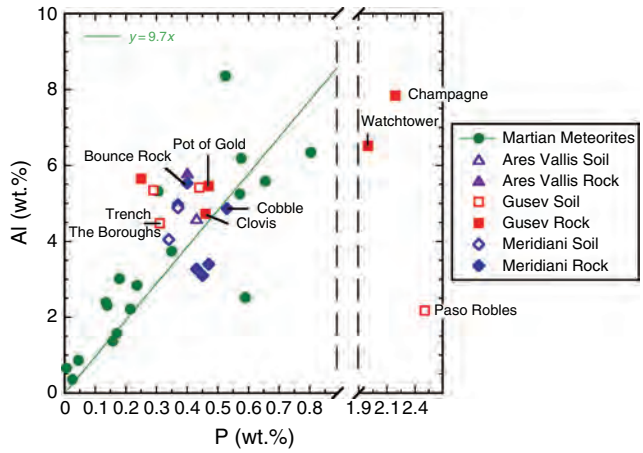

Figure 4.24. Aluminum versus phosphorus content for different Martian samples. Note the break in the *x*-axis. (For a color version of this figure, please refer to the color plate section or to the e-Book version of this chapter.)

around the correlation line. Even "Bounce Rock," a rock similar in composition to basaltic shergottites (see above), shows a P depletion relative to the average Martian meteorites. The opposite is found for the sedimentary rocks of Meridiani Planum. As shown in Figure 4.24, the extreme phosphate- and sulfate-rich rocks, as well as the disturbed soil Paso Robles (in the Columbia Hills with a P content of about 2 wt.%, but normal Al content), are the exceptions. The origin of these more evolved rocks is not clear; however, assuming an igneous origin, the high P contents would be close to the saturation limit of crystalline phosphates (Harrison and Watson, 1984; Tollari *et al.*, 2006).

Potassium is the exception to the similarity of the postulated Martian crustal composition and the basaltic shergottites (Brückner *et al.*, 2003; Dreibus *et al.*, 2003; McLennan, 2003). The mean K content (0.4 wt.%) of the basaltic soils in Gusev crater and Meridiani Planum (Table 4.4) is consistent with K values of other surface measurements. The K concentration map obtained from the Mars Odyssey GRS ranges from 0.2 to 0.5 wt.% (Boynton *et al.*, 2007; see also Chapter 5). The equatorial GRS data from the Soviet Phobos mission yielded 0.3 wt.% K (Surkov *et al.*, 1989, 1994; Trombka *et al.*, 1992). The Pathfinder mean soil has 0.5 wt.% K (Wänke *et al.*, 2001; Brückner *et al.*, 2003). All these K values are by a factor of 2–10 higher than those in Martian meteorites.

However, compared to the Earth's upper continental crust, with 2.8 wt.% K (Taylor and McLennan, 1995), the Martian surface has a small K inventory. From the good correlation of the highly incompatible K with Rb, Sr, and Nd in Martian meteorites, the inventory of such large ion lithophile (LIL) elements in the Martian crust was calculated. The higher K concentration on the Martian surface compared to the Martian meteorites might also suggest an enrichment of Rb in the crust, which should result in more radiogenic Sr in the Martian crust – consistent with Sr measurements in the shergottites (Jagoutz, 1991). From the Rb–Sr isotope systematic in Martian meteorites a crustal age of 4.3 ± 0.2 Ga was derived (Jagoutz, 1991).

As a consequence, the LIL elements can be inferred to have resided in the crust for more than 4 Gyr.

Values of the crustal thickness derived from geophysical data determined by Mars Global Surveyor are in the range of 30–100 km (Nimmo and Stevenson, 2001), ~50 km (Zuber *et al*., 2000), and 60 ± 24 km (Wieczorek and Zuber, 2002). From the mean crustal K content of 0.4 wt.% and the ratios of K/Rb = 200, K/Sr = 27, and K/Nd = 308 obtained from Martian meteorites (Brückner *et al*., 2003; Dreibus *et al*., 2003), the following abundances can be estimated for the Martian crust: 20 ppm Rb, 150 ppm Sr, and 13 ppm Nd. Assuming an average crustal thickness of 50 km, 55% of K, 56% of Rb, 38% of Sr, and 59% of Nd would reside in the crust compared to the Martian bulk composition, as estimated by Dreibus and Wänke (1984) and Wänke and Dreibus (1988, 1994).

Several estimates of the composition of the Martian mantle have been published within the last 30 years (e.g., Anderson, 1972; Morgan and Anders, 1979; Longhi *et al*., 1992; Lodders and Fegley, 1997; Halliday *et al*., 2001). Among these, the model of Dreibus and Wänke (1984), based on high precision analytical data of SNC meteorites, appears to have been validated by orbital and *in situ* data. For example, very recently, the K/Th ratio was measured from orbit with the Mars Odyssey GRS yielding a mean value of 5330 over the entire surface of Mars (Taylor *et al*., 2006; see also Chapter 5). This value is very close to 5450 estimated by the model of Wänke and Dreibus (1988, 1994). A global surface K/Th ratio of 5330 and 0.4 wt.% K in the crust corresponds to 0.75 ppm Th in the crust. This estimated crustal Th concentration means that 56 wt.% of the total bulk Th resides in a 50-km crust. Similar enrichment could be expected for uranium. K, Th, and U are responsible for internal planetary heat production. Our estimated crustal composition of 0.4 wt.% K and 0.75 ppm Th provides a similar distribution of heat-producing elements in the crust and mantle of Mars as is found in the Earth (Brückner *et al*., 2003).

The Wänke and Dreibus model postulated a high FeO abundance (17.9 wt.%) for the Martian mantle compared to Earth. This value comes close to the average FeO concentration measured by GRS over the whole Martian surface (Boynton *et al*., 2007; see also Chapter 5). The analyses of Martian surface rocks by the APXS also confirm high FeO concentrations (Wänke *et al*., 2001; Rieder *et al*., 2004; Gellert *et al*., 2006) and consequently imply similarly high FeO contents in the Martian mantle. Most profoundly, the high abundance of phosphorous in the rocks analyzed by APXS gives an important proof of the quality and precision of the data on the composition of the Martian mantle not only for major elements (Fe), but also for minor and trace elements (P and K) in the Wänke and Dreibus model.

4.6 CONCLUSIONS

In situ analyses of surface rocks and soils at three landing sites near the equator with the APXS method provide data about the chemical composition of the Martian surface and, by modeling and inference, also of the crust and mantle. APXS data indicate a huge compositional difference between soils and rocks at the landing sites, whereas most soils including those measured by the Viking Landers at Chryse Planitia and Utopia Planitia are chemically similar. The soils are basaltic in character, although there is a significant amount of S (mean 2.5 wt.%) and Cl (mean 0.8 wt.%). For the first time on Mars, trace elements, such as Ni, Zn, and Br, and Cu, Pb, Sr, Y, Ga, and Ge, could be clearly detected by the MER APXS depending on their concentrations. The enhanced Ni contents of the soils compared to primitive basalts in Gusev crater are consistent with the presence of a meteoritic component.

Two geological regions were encountered along the rover *Spirit*'s initial traverse at Gusev crater: the Gusev plains and the Columbia Hills. Fresh rock surfaces in the plains resemble primitive basalts. In contrast, disturbed soils and rocks located in the Columbia Hills revealed different elemental compositions. Several rock classes were recognized in the Columbia Hills. These rocks are significantly weathered and enriched in mobile elements, such as P, S, Cl, and Br. Even abraded rock surfaces of the Hills – samples of relatively dust-free rock interiors – have high Br concentrations.

The rocks at Meridiani Planum are light-toned, reddish-layered outcrops. Most of the abraded rocks showed high S contents and MB measurements revealed the mineral jarosite. High concentrations of Br were also discovered in abraded surfaces. The rocks in Meridiani Planum are salt-rich silicic sediments.

The undisturbed soil composition at Meridiani resembles that of Gusev crater and other landing sites; however, the Meridiani Fe, Ni, and Cr contents are higher, and the feldspathic elements Na and Al are lower. The enrichment of Fe likely results from admixed hematite as determined by MB.

One of the most intriguing features of Meridiani Planum is the large number of spherules that are mainly found on top of soils and outcrops. Smaller quantities of the spherules were also discovered inside the outcrops. In Eagle crater, some of the spherules appeared to be freshly eroded or about to erode from inside the outcrop rocks. APXS and MB measurements confirmed that the spherules contain high iron concentrations mainly present as hematite. Hematite-rich samples were discovered all along the rover's traverse, consistent with orbital measurements.

Erosional processes of the sulfate-rich rocks may be responsible for the lag-like accumulation of hematite-rich spherules and fragments on the surface. The formation of hematite is typically, but not exclusively, an indicator for aqueous activities under oxidizing conditions. The high Fe/Mn ratio of about 110 measured in the hematite-rich spherules is twice that of mean Martian rocks and soils where the Fe is divalent and chemically related to divalent Mn.

In situ measurements of samples at the Martian surface with APXS and MB point to a variety of sedimentary processes, such as evaporation in Meridiani Planum and various types of alteration in Gusev crater. The two MER landing sites provide clear evidence of ancient aqueous

environments, though the extent of the alterations appears to have been less at Gusev than at Meridiani.

The APXS data from the Pathfinder, *Spirit*, and *Opportunity* landing sites provide a basis for a global estimation of the Martian surface and crustal composition. The combination of *in situ* measurements and element correlations of the Martian meteorites implies an ancient basaltic crust with high abundances of incompatible (K, Rb, Nd, U, Th) and volatile (S, Cl) elements. Compared to the Earth's mantle, the Martian mantle contains about twice as much FeO, is richer in moderately volatile elements like potassium, and has a much higher abundance of phosphorus.

ACKNOWLEDGMENT

The APXS was mainly funded by the Max-Planck-Society and, in part, by the German Space Agency (DLR) (grant No. 50QM0014 and 50QM0005). Part of the work was supported under INTAS contract no. 001-348. Funding for Athena science team members was provided by NASA contracts through Cornell and JPL. A portion of this work was conducted at the Jet Propulsion Laboratory, California Institute of Technology, under a contract with NASA. We acknowledge the unwavering support of JPL engineering and MER operations staff.

REFERENCES

Anderson, D. L., The internal composition of Mars, *J. Geophys. Res.* **77**, 789–95, 1972.

Arvidson, R. E., F. P. Seelos, K. Deal, *et al.*, Mantled and exhumed terrains in Terra Meridiani, Mars, *J. Geophys. Res.* **108**(E12), ROV 14–1, CiteID 8073, doi:10.1029/2002JE001982, 2003.

Arvidson, R. E., S. W. Squyres, R. C. Anderson, *et al.*, Overview of the Spirit Mars Exploration Rover Mission to Gusev crater: landing site to Backstay Rock in the Columbia Hills, *J. Geophys. Res. – Planet* **111**, E02S01, doi:10.1029/2005JE002499, 2006.

Baird, A. K. and B. C. Clark, On the original igneous source of Martian fines, *Icarus* **45**, 113–23, 1981.

Banin, A., B. C. Clark, and H. Wänke, Surface chemistry and mineralogy. In *Mars* (ed. H. H. Kieffer, B. M. Jakosky, C. W. Snyder, and M. S. Matthews), Tucson: The University of Arizona Press, pp. 594–625, 1992.

Bell III, J. F., S. W. Squyres, R. E. Arvidson, *et al.*, Pancam multispectral imaging results from the Opportunity Rover at Meridiani Planum, *Science* **306**, 1703–9, 2004.

Bland, P. A. and T. B. Smith, Meteorite accumulation on Mars, *Icarus* **144**, 21–6, 2000.

Boynton, W. V., G. J. Taylor, L. G. Evans, *et al.*, Concentration of H, Si, Cl, K, Fe, and Th in the low- and mid-latitude regions of Mars, *J. Geophys. Res.* **112**, E12S99, doi:10.1029/2007JE002887, 2007.

Brückner, J., G. Dreibus, R. Rieder, and H. Wänke, Refined data of APXS analyses of soils and rocks at the Mars Pathfinder site: implications for surface chemistry, *J. Geophys. Res.* **108**(E12), 8094, doi:10.1029/2003JE002060, 2003.

Christensen, P. R., J. L. Bandfield, R. N. Clark, *et al.*, Detection of crystalline hematite mineralization on Mars by the Thermal Emission Spectrometer: evidence for near-surface water, *J. Geophys. Res.* **105**(E4), 9623–42, 2000.

Christensen, P. R., R. V. Morris, M. D. Lane, J. L. Bandfield, and M. C. Malin, Global mapping of Martian hematite mineral deposits: remnants of water-driven processes on early Mars, *J. Geophys. Res. – Planets* **106**(E10), 23873–85, doi:2000JE001415, 2001.

Christensen, P. R., M. B. Wyatt, T. D. Glotch, *et al.*, Mineralogy at Meridiani Planum from the Mini-TES experiment on the Opportunity Rover, *Science* **306**, 1733–9, 2004.

Clark, B. C., Implications of abundant hygroscopic minerals in the Martian regolith, *Icarus* **34**, 645–65, 1978.

Clark, B. C., Geochemical components in Martian soil, *Geochim. Cosmochim. Acta* **57**, 4575–81, 1993.

Clark, B. C. and A. K. Baird, Martian regolith X-ray analyzer; Test results of geochemical performance, *Geology* **1**, 15–18, 1973.

Clark, B. C. and A. K. Baird, Volatiles in the Martian regolith, *Geophys. Res. Lett.* **6**, 811–14, 1979a.

Clark, B. C. and A. K. Baird, Is the Martian lithospheree sulfur rich?, *J. Geophys. Res.* **84**, 8395–403, 1979b.

Clark, B. C., A. K. Baird, R. J. Weldon, *et al.*, Chemical composition of Martian fines, *J. Geophys. Res.* **87**(B12), 10059–67, 1982.

Clark, B. C., R. V. Morris, S. M. McLennan, *et al.*, Chemistry and mineralogy of outcrops at Meridiani Planum, *Earth Planet. Sci. Lett.* **240**, 73–94, 2005.

Clark, B. C., R. E. Arvidson, R. Gellert, *et al.*, Evidence for montmorillonite or its compositional equivalent in Columbia Hills, Mars, *J. Geophys. Res.* **112**, CiteID E06S01, doi:10.1029/2006JE002756, 2007.

Connolly Jr., H. C., J. Zipfel, J. N. Grossman, *et al.*, The Meteoritical Bulletin Number, No. 90, 2006, *Meteorit. Planet. Sci.* **41**(9), 1271–419, 2006.

Dreibus, G. and R. Haubold, Phosphorus sorption by terrestrial basalt and granite and implications for the martian mantle, *Icarus* **167**, 166–9, 2004.

Dreibus, G. and H. Wänke, Accretion of the earth and the inner planets, *Proc. 27th Int. Geol. Conf. Moskau*: Vol. 11, *Geochemistry and Cosmochemistry*, Utrecht: VNU Science Press, pp. 1–20, 1984.

Dreibus, G. and H. Wänke, Volatiles on Earth and Mars: a comparison, *Icarus* **71**, 225–40, 1987.

Dreibus, G., E. Jagoutz, B. Spettel, and H. Wänke, Phosphate-mobilization on Mars? Implication from leach experiments on SNC's, *Lunar Planet. Sci. XXVII*, Houston: Lunar and Planetary Institute, pp. 323–4, Extended Abstract, 1996.

Dreibus, G., J. Brückner, and W. V. Boynton, Evolution of the Martian crust as derived from surface measurements by Mars Odyssey, other space missions, and Martian meteorites, *6th Int. Conf. Mars 2003*, Pasadena, CA, USA, Abstract #3088, 2003.

Dyar, D. M., Ferric iron in SNC meteorites as determined by Mössbauer spectroscopy: implications for martian landers and martian oxygen fugacity, *Meteorit. Planet. Sci.* **38**, 1733–52, 2003.

Feldman, W. C., T. H. Prettyman, S. Maurice, *et al.*, Global distribution of near-surface hydrogen on Mars, *J. Geophys. Res.* **109**(E9), E09006, doi:10.1029/2003JE002160, 2004.

Foley, C. N., T. E. Economou, R. N. Clayton, and W. Dietrich, Calibration of the Mars Pathfinder alpha proton X-ray spectrometer, *J. Geophys. Res. – Planet* **108**(E12), 8095, doi:10.1029/2002JE002018, 2003a.

Foley, C. N., T. Economou, and R. N. Clayton, Final chemical results from the Mars Pathfinder alpha proton X-ray

spectrometer, *J. Geophys. Res. – Planets* **108**(E12), 8096, doi:10.1029/2002JE002019, 2003b.

Gellert, R., R. Rieder, R. C. Anderson, *et al.*, Chemistry of rocks and soils in Gusev crater from the alpha particle X-ray spectrometer, *Science* **305**, 829–32, 2004.

Gellert, R., R. Rieder, J. Brückner, *et al.*, The Alpha Particle X-Ray Spectrometer (APXS): results from Gusev crater and calibration report, *J. Geophys. Res. – Planets* **111**, E02S05, doi:10.1029/2005JE002555, 2006.

Gellert, R., R. Rieder, R. C. Anderson, *et al.*, In-situ chemistry along the traverse of Opportunity at Meridiani Planum: sulfate rich outcrops, iron rich spherules, global soils and various erratics, *J. Geophys. Res.* submitted, 2008.

GEOROC, Geochemistry of Rocks of the Oceans and Continents – Database, Max-Planck-Institut fuer Chemie, Mainz, Germany, URL: http://georoc.mpch-mainz.gwdg.de/georoc/.

Golombek, M. P., R. C. Anderson, J. R. Barnes, *et al.*, Overview of the Mars Pathfinder mission: launch through landing, surface operations, data sets, and science results, *J. Geophys. Res.* **104**, 8523–53, 1999.

Golombek, M. P., L. S. Crumpler, J. A. Grant, *et al.*, Geology of the Gusev cratered plains from the Spirit rover transverse, *J. Geophys. Res. – Planets* **111**, E02S07, doi:10.1029/2005JE002503, 2006.

Grotzinger, J. P., R. E. Arvidson, J. F. Bell III, *et al.*, Stratigraphy and sedimentology of a dry to wet eolian depositional system, Burns formation, Meridiani Planum, Mars, *Earth Planet. Sci. Lett.* **240**, 11–72, doi:10.1016/j.epsl.2005.09.039, 2005.

Halliday, A. N., H. Wänke, J. L. Birk, and R. N. Clayton, The accretion, composition, and early differentiation of Mars, *Space Sci. Rev.* **96**, 197–230, 2001.

Harrison, T. M. and E. B. Watson, The behavior of apatite during crustal anatexis: equilibrium and kinetic considerations, *Geochim. Cosmochim. Acta* **48**, 1467–77, 1984.

Hartmann, W. K. and G. Neukum, Cratering chronology and the evolution of Mars, *Space Sci. Rev.* **96**, 165–94, 2001.

Haskin, L. A., A. Wang, B. L. Jolliff, *et al.*, Water alteration of rocks and soils on Mars at the Spirit rover site in Gusev crater, *Nature* **436**, 66–9, doi:10.1038/nature03640, 2005.

Herkenhoff, K. E., S. W. Squyres, R. Arvidson, *et al.*, Evidence from Opportunity's microscopic imager for water on Meridiani Planum, *Science* **306**, 1727–30, 2004.

Jagoutz, E., Chronology of SNC meteorites, *Space Sci. Rev.* **56**, 13–22, 1991.

Klingelhöfer, G., R. V. Morris, B. Bernhardt, *et al.*, Jarosite and Hematite at Meridiani Planum from Opportunity's Mössbauer Spectrometer, *Science* **306**, 1740–5, 2004.

Lodders, K., A survey of shergottite, nakhlite and chassigny meteorites whole-rock compositions, *Meteorit. Planet. Sci.* **33**, A183–90, 1998.

Lodders, K. and B. Fegley Jr., An oxygen isotope model for the composition of Mars, *Icarus* **126**, 373–94, 1997.

Longhi, J., E. Knittle, J. R. Holloway, and H. Wänke, The bulk composition, mineralogy and internal structure of Mars. In *Mars* (ed. H. H. Kieffer, B. M. Jakosky, C. W. Snyder, and M. S. Matthews), Tucson: The University of Arizona Press, pp. 184–208, 1992.

McLennan, S. M., Crustal heat production and the thermal evolution of Mars, *Lunar Planet. Sci. XXXII*, Houston: Lunar and Planetary Institute, Abstract #1349 (CD-ROM), 2001.

McLennan, S. M., Composition and chemical evolution of the martian crust and mantle: integrating the data from missions and meteorites, *6th Int. Conf. Mars 2003*, Houston, TX: Lunar and Planetary Institute, Abstract #3099, 2003.

McSween, H. Y., R. E. Arvidson, J. F. Bell III, *et al.*, Basaltic rocks analyzed by the Spirit Rover in Gusev crater, *Science* **305**, 842–5, 2004.

McSween, H. Y., M. B. Wyatt, R. Gellert, *et al.*, Characterization and petrologic interpretation of olivine-rich basalts at Gusev crater, Mars, *J. Geophys. Res. – Planets* **111**, E02S10, doi:10.1029/2005JE002477, 2006a.

McSween, H. Y., S. W. Ruff, R. V. Morris, *et al.* Alkaline volcanic rocks from the Columbia Hills, Gusev crater, Mars, *J. Geophys. Res.* **111**, E09S91, doi:10.1029/2006JE002698, 2006b.

Meyer, C., The Mars Meteorite Compendium, *Astromaterials Research & Exploration Science (ARES)*, (JSC #27672 Revision C), Houston, Texas: Lyndon B. Johnson Space Center, URL: www-curator.jsc.nasa.gov/antmet/mmc, 2006.

Ming, D. W., D. W. Mittlefehldt, R. V. Morris, *et al.*, Geochemical and mineralogical indicators for aqueous processes in the Columbia Hills of Gusev crater, Mars, *J. Geophys. Res.* **111**, E02S12, doi:10.1029/2005JE002560, 2006.

Morgan, J. W. and E. Anders, Chemical composition of Mars, *Geochim. Cosmochim. Acta* **43**, 1601–10, 1979.

Morris, R. V., G. Klingelhöfer, B. Bernhardt, *et al.*, Mineralogy at Gusev crater from the Mössbauer Spectrometer on the Spirit Rover, *Science* **305**, 833–6, 2004.

Morris, R. V., G. Klingelhöfer, C. Schröder, *et al.*, Mössbauer mineralogy of rock, soil, and dust at Gusev crater, Mars: Spirit's journey through weakly altered olivine basalt on the plains and pervasively altered basalt in the Columbia Hills, *J. Geophys. Res.* **111**, E02S13, doi:10.1029/2005JE002584, 2006.

Nimmo, F. and D. J. Stevenson, Estimates of Martian crustal thickness from viscous relaxation of topography, *J. Geophys. Res.* **106**, 5085–98, 2001.

Palme, H. and H. Beer, Abundances of the elements in the solar system, *Landolt-Börnstein, Group VI: Astronomy and Astrophysics*, New Series VI/3a, Berlin: Springer Verlag, pp. 196–221, 1993.

Rieder, R., H. Wänke, T. Economou, and A. Turkevich, Determination of the chemical composition of Martian soil and rocks: the alpha proton X ray spectrometer, *J. Geophys. Res. – Planets* **102**(E2), 4027–44, 1997a.

Rieder, R., T. Economou, H. Wänke, *et al.*, The chemical composition of Martian soil and rocks returned by the mobile alpha proton X-ray spectrometer: preliminary results from the X-ray mode, *Science* **278**, 1771–4, 1997b.

Rieder, R., R. Gellert, J. Brückner, *et al.*, The new Athena alpha particle X-ray spectrometer for the Mars Exploration Rovers, *J. Geophys. Res.* **108**(E12), 8066, doi:10.1029/2003JE002150, 2003.

Rieder, R., R. Gellert, R. C. Anderson, *et al.*, Chemistry of rocks and soils at Meridiani Planum from the alpha particle X-ray spectrometer, *Science* **306**, 1746–9, 2004.

Schröder, C., R. Gellert, B. L. Jolliff, *et al.*, A stony meteorite discovered by the Mars Exploration Rover Opportunity on Meridiani Planum, Mars, *Meteorit. Planet. Sci.* **41**, 5285, 2006.

Soderblom, L. A., R. C. Anderson, and R. E. Arvidson, Soils of Eagle crater and Meridiani Planum at the Opportunity Rover landing site, *Science* **306**, 1723–6, 2004.

Squyres, S. W., E. Arvidson, E. T. Baumgartner, *et al.*, The Athena Mars Rover science investigation, *J. Geophys. Res.* **108**(E12), 8062, doi:10.1029/2003JE002121, 2003.

Squyres, S. W., R. E. Arvidson, J. F. Bell III, *et al.*, The Spirit Rover's Athena Science Investigation at Gusev crater, Mars, *Science* **305**, 794–9, 2004a.

Squyres, S. W., R. E. Arvidson, J. F. Bell III, *et al.*, The Opportunity Rover's Athena Science Investigation at Meridiani Planum, Mars, *Science* **306**, 1698–703, 2004b.

Squyres, S. W., J. P. Grotzinger, R. E. Arvidson, *et al*., In situ evidence for an ancient aqueous environment at Meridiani Planum, Mars, *Science* **306**, 1709–14, 2004c.

Squyres, S. W., R. E. Arvidson, D. L. Blaney, *et al*., Rocks of the Columbia Hills, *J. Geophys. Res. – Planets* **111**, E02S11, doi:10.1029/2005JE002562, 2006a.

Squyres, S. W., R. E. Arvidson, D. Bollen, *et al*., Overview of the Opportunity Mars Exploration Rover Mission to Meridiani Planum: Eagle crater to Purgatory Ripple, *J. Geophys. Res.* **111**, E12S12, doi:10.1029/2006JE002771, 2006b.

Surkov, Yu. A., V. L. Barsukov, L. P. Moskaleva, *et al*., Determination of the elemental composition of martian rocks from Phobos 2, *Nature* **341**, 595–8, 1989.

Surkov, Yu. A., L. P. Moskaleva, M. Yu. Zolotov, *et al*., Phobos-2 data on Martian surface geochemistry, *Geochem. Int*. **31**, 50–8, 1994.

Taylor, G. J., L. M. V. Martel, and W. V. Boynton, Mapping Mars geochemically, *Lunar Planet. Sci. XXXVIII*, Houston: Lunar and Planetary Institute, Abstract #1981 (CD-ROM), 2006.

Taylor, S. R. and S. M. McLennan, The composition and evolution of the continental crust: rare earth element evidence from sedimentary rocks, *Philos. Trans. R. Soc. Lond.* **A 301**, 381–99, 1981.

Taylor, S. R. and S. M. McLennan, The geochemical evolution of the continental crust, *Rev. Geophys.* **33**, 241–65, 1995.

Tollari, N., M. J. Toplis, and S.-J. Barnes, Predicting phosphate saturation in silicate magmas: an experimental study of the effects of melt composition and temperature, *Geochim. Cosmochim. Acta* **70**, 1518–36, doi:10.1016/j.gca.2005.11.024, 2006.

Toulmin III, P., H. J. Rose, Jr., R. P. Christian, *et al*., Geochemical and mineralogical interpretation of the Viking inorganic chemical results, *J. Geophys. Res.* **82**, 4625–34, 1977.

Trombka, J. I., L. G. Evans, R. Starr, *et al*., Analysis of the Phobos mission gamma-ray spectra from Mars, *Proc. Lunar Planet. Sci. XXII*, Houston: Lunar and Planetary Institute, pp. 23–9, 1992.

Wang, A., L. A. Haskin, S. W. Squyres, *et al*., Sulfate deposition in subsurface regolith in Gusev crater, Mars, *J. Geophys. Res.* **111**, E02S17, doi:10.1029/2005JE002513, 2006.

Wänke, H. and G. Dreibus, Chemical composition and accretion history of terrestrial planets, *Philos. Trans. R. Soc. Lond.* **A 325**, 545–57, 1988.

Wänke, H. and G. Dreibus, Chemistry and accretion history of Mars, *Philos. Trans. R. Soc. Lond.* **A 349**, 285–93, 1994.

Wänke, H., J. Brückner, G. Dreibus, R. Rieder, and I. Ryabchikov, Chemical composition of rocks and soils at the Pathfinder site, *Space Sci. Rev.* **96**, 317–30, 2001.

Wasson, J. T. and G. W. Kallemeyn, The IAB iron-meteorite complex: a group, five subgroups, numerous grouplets, closely related, mainly formed by crystal segregation in rapidly cooling melts. *Geochim. Cosmochim. Acta* **66**, 2445–73, 2002.

Wedepohl, K. H., The composition of the continental crust, *Geochim. Cosmochim. Acta* **59**, 1217–32, 1995.

Wieczorek, M. A. and M. T. Zuber, The thickness of the Martian crust as inferred from geoid-to-topography ratios, *Lunar Planet. Sci. XXXIII*, Houston: Lunar and Planetary Institute, Abstract #1390 (CD-ROM), 2002.

Yen, A. S., R. Gellert, C. Schröder, *et al*., An integrated view of the chemistry and mineralogy of martian soils, *Nature* **436**, 49–54, doi:10.1038/nature03637, 2005.

Zipfel, J., R. Anderson, J. Brückner, *et al*., APXS analyses of bounce rock: the first shergottite on Mars, *Meteorit. Planet. Sci.* **39** (Suppl. S), A118–A118, 2004.

Zuber, M. T., S. C. Solomon, R. J. Phillips, *et al*., Internal structure and early thermal evolution of Mars from Mars Global Surveyor topography and gravity, *Science* **287**, 1788–93, 2000.

PART II.B

Results and Interpretations from New Orbital Elemental Measurements

5

Elemental abundances determined via the Mars Odyssey GRS

W. V. BOYNTON, G. J. TAYLOR, S. KARUNATILLAKE, R. C. REEDY, AND J. M. KELLER

ABSTRACT

The Gamma Ray Spectrometer (GRS) onboard the Odyssey spacecraft has made the first global measurements of the elemental composition of the Martian surface using gamma rays measured from polar orbit. We report results for Si, Fe, K, Th, Cl, and H. The nominal spatial resolution is 450 km in diameter. Gamma Ray Spectrometer data show that the Martian surface is chemically heterogeneous. Elemental concentrations vary across the surface, including variations within high-albedo areas that are presumably covered with dust. Fe concentrations are uniformly high, in accord with the compositions of Martian meteorites and most rock samples analyzed *in situ*. K/Th is variable, but 95% of the surface has a weight ratio between 4000 and 7000. The mean (5300) is double that in terrestrial crustal rocks and in the inferred bulk silicate Earth. Cl varies substantially, with the highest values in the region west of the Tharsis Montes. Surface Types 1 and 2 (ST1 and ST2), identified from the Thermal Emission Spectrometer (TES) on Mars Global Surveyor (MGS), are indistinguishable except in the amount of K and Th they contain: ST2 is enriched in both elements by about 30% relative to ST1, while both types have similar K/Th ratios. The H_2O mass fraction (stoichiometrically derived from the H content) in equatorial regions ranges from about 1.5%–7%, indicative of the presence of hydrous minerals. H_2O content is very high in polar regions ($>60^\circ$ latitude north and south) and is consistent with the presence of ice mixed with variable amounts of dust and other regolith materials. H concentrations determined by the GRS are consistent within analytical uncertainty with those determined by the Mars Odyssey Neutron Spectrometer and the High-Energy Neutron Detector (discussed in Chapter 6).

5.1 INTRODUCTION

The Mars Odyssey GRS has given us our first look at the global chemical composition of the Martian surface. Analyses of Martian meteorites provide detailed chemical and isotopic compositions (see Chapter 17). However, all but one is relatively young (180–1300 Ma old) and their source regions on Mars remain unidentified. Chemical composition has been inferred from spectral measurements by the TES onboard MGS (e.g., Christensen *et al.*, 2001; Bandfield *et al.*, 2002; Wyatt *et al.*, 2004). However, the translation to chemical composition depends on occasionally nonunique spectral deconvolutions of minerals. Furthermore, TES does not provide complete mineralogical information in dusty regions. Thus, the GRS provides a unique dataset for use in unraveling the formation and evolution of the Martian crust.

Gamma Ray Spectrometer data clearly show that the surface of Mars is not uniform in composition. The concentrations of K, Th, Cl, H (expressed as equivalent H_2O), and Fe vary by a factor of 2 or more for regions larger than ~500 km in radius. Si varies less, but significantly. As discussed below, our multivariate analysis shows that these elements do not co-vary in any simple way, except for strong correlation between K and Th. This gives a complicated, yet rich, picture of a crust formed by igneous and modified by sedimentary processes. The elements fall into useful geochemical groups. K and Th are incompatible lithophile elements (e.g., Winter, 2001), so likely preserve the record of their mantle abundances. Fe and Si are major rock-forming elements. Cl and H can be greatly affected by aqueous alteration and transport (although the other elements can also be affected by aqueous processes and Cl is emitted with volcanic gases).

The elemental concentrations allow us to test hypotheses for the origin of ST1 and ST2 derived from Mars Global Surveyor TES (MGS-TES) data (e.g., Bandfield *et al.*, 2000; Wyatt and McSween, 2002), test models for the bulk composition of Mars, and assess the effects that aqueous processes may have had on the distribution of elements in the Martian crust. In this chapter we describe the methodology used to extract element concentrations from gamma-ray spectra and give an overview of the results of the observations. We then discuss some of the interesting problems in Martian geochemistry that GRS data allow us to address. These are the origins of ST1 and ST2, causes of the variability in Cl concentration, the bulk composition of Mars, the cause of the high H_2O content in the polar regions, variations in the thicknesses of seasonal CO_2 polar caps, and insights from Ar concentrations in the atmosphere over polar regions. Detailed discussions of the GRS data on surface compositions can be found in Boynton *et al.* (2007), Karunatillake *et al.* (2006, 2007), Keller *et al.* (2006), Newsom *et al.* (2007), and Taylor *et al.* (2006a, 2006b).

The Martian Surface: Composition, Mineralogy, and Physical Properties, ed. J. F. Bell III. Published by Cambridge University Press.

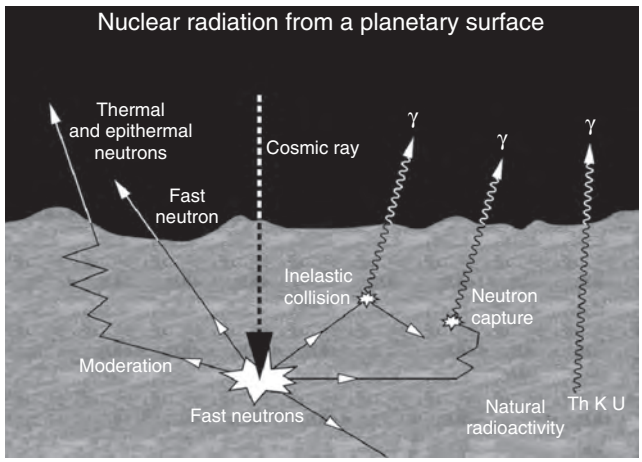

Figure 5.1. Schematic of how gamma rays are produced in the Martian surface. The radioactive isotope ^{40}K and elements Th and U (and their daughter isotopes) produce gamma rays when they decay. The interaction of high-energy (~1–10 GeV) cosmic-ray particles with nuclei in the surface materials produces energetic (fast) neutrons with typical energies of ~1–20 MeV. These fast neutrons can excite elemental nuclei by inelastic-scattering reactions, producing gamma rays. These fast neutrons are moderated by H and other elements, producing slow (thermal, ~0.02 eV) neutrons that can be captured by nuclei and result in the release of gamma rays of specific energies.

5.2 DATA ACQUISITION, PROCESSING, AND ANALYSIS

5.2.1 Data acquisition

The gamma rays measured by the Mars Odyssey GRS are made mainly by two processes, the decay of long-lived naturally occurring radiogenic elements (the isotope ^{40}K and the elements U and Th with their daughter isotopes) and by the interactions of cosmic ray particles, as shown schematically in Figure 5.1. Most cosmic-ray-produced gamma rays used to determine elemental abundances are made by the scattering of fast (energies of ~1–20 MeV) neutrons from a nucleus or by the capture of neutrons at or near thermal (~0.02 eV) energies. The production and transport of neutrons are discussed in Chapter 6. The use of gamma rays to determine the composition of a planetary body is reviewed in Evans *et al*. (1993) and references therein. Gamma-ray spectroscopy at Mars is complicated by the Martian atmosphere and by variable amounts of water in the surface (see Masarik and Reedy, 1996). The measured gamma rays are made in the top few tens of centimeters of the surface. The amount of any dust or water in the atmosphere is too thin to produce a detectable flux of gamma rays. A few gamma-ray spectra were measured by Soviet spacecraft at Mars, but the spectral and spatial resolutions were poor (e.g., Trombka *et al*., 1992).

The Mars Odyssey GRS is a high-purity germanium crystal with associated electronics and cooling system (Boynton *et al*., 2004). Gamma rays with energies between about 0.1 and 10 MeV are measured. The detection system has no collimation or focusing system, so gamma rays from all directions are recorded. Of the gamma rays from the surface, about 50% are from within a radius of 200–300 km from nadir (Boynton *et al*., 2004). The data reported in this chapter were acquired from June 2002 until April 2005. The Mars Odyssey spacecraft is in a nearly polar orbit and passes over 1° of latitude in ~20 s. To get good spatial resolution on the Martian surface, gamma-ray spectra are collected for every degree of latitude by dividing each orbit into 360 equal time intervals.

Although the typical count rate is ~200 s^{-1}, only less than 4% of these counts are measured in discrete line peaks, and only ~5%–10% of the counts in peaks are for gamma rays coming from Mars (Evans *et al*., 2006). Most counts are in a continuum, and most peaks are backgrounds from the material around the detector, such as Ge, Ti, and Mg. A spectrum from 0 to 8000 keV measured from Martian orbit is shown in Figure 5.2, with details for the spectrum from 1800 to 3000 keV shown in an insert. To get enough counts for analysis, long collection times (usually many days) are required (Boynton *et al*., 2004).

The gamma-ray spectra are stored by the spacecraft and periodically transmitted to Earth. Many steps are needed to process these spectra (Evans *et al*., 2006). Each spectrum is examined to check that there is nothing missing due to transmission errors. Spectra taken while the instrument and its electronics were unstable, while the instrument was not nadir pointing, or when the Sun was emitting high fluxes of energetic particles or X-rays were identified and flagged as unsuitable for routine analysis. Corrections are applied to the counts in every channel of a spectrum using measured temperatures in the spectrometer. Many consecutive spectra are summed, and the gain and offset needed to convert a channel number to an energy assuming a linear function are determined using 10 strong peaks. Using a temporal series of such gains and offsets, all individual spectra are adjusted so that the average gain is 0.625 keV/channel without an offset. These adjusted spectra are then stored in a database, from which summed spectra for specified times or locations on Mars can be generated.

5.2.2 Data processing

Using various long sums, over 330 peaks or features in the spectra have been observed. The sources of almost all of these peaks and features have been identified. The gain for peaks in these spectra is not perfectly linear and minor corrections, to convert a channel number to an exact energy, have been determined (Evans *et al*., 2006).

Determination of elemental abundances begins by selecting relatively intense gamma-ray peaks with minimal background interferences for the elements of interest. Spectra accumulated over long time periods are used to convert the counts for the channels in and around a peak into the net counts in the peak. The total number of counts in a peak is determined as an arithmetic sum, or as a least-squares fit to the counts in a peak, or in several closely-spaced peaks, using known peak shapes. The number of counts in the continuum underlying the peak is determined and used to get the net number of counts from the gamma ray of interest.

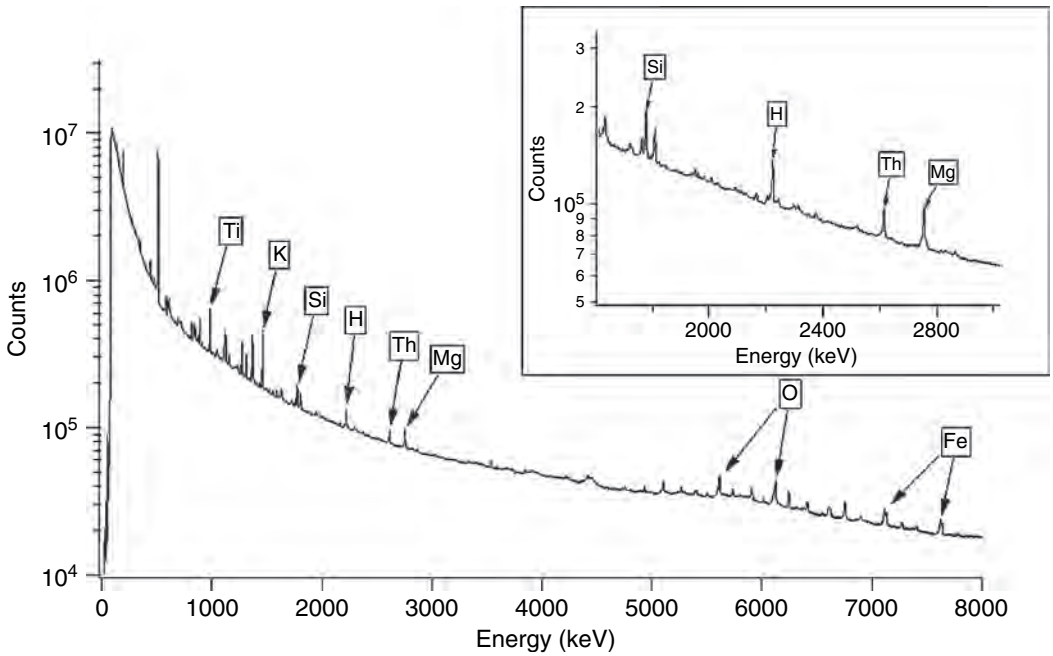

Figure 5.2. Gamma-ray spectrum up to 8000 keV produced by summing measurements for the equatorial band of Mars obtained during a 16-month period. Although they appear atop a broad featureless background, most peaks are sharp. The insert shows a close view of the energy region from 1600 to 3000 keV. Most peaks have little interference from other peaks. The Ti and Mg peaks are caused mainly by materials composing the material around the gamma-ray detector and do not reflect the Ti and Mg abundances on the Martian surface.

Backgrounds in a peak are separately determined, and their contributions to the counts in a peak are removed.

A forward calculation is used to convert the counts in a peak of interest to a value proportional to an elemental abundance (Boynton *et al.*, 2007). The forward calculation determines the count rate expected at the detector for each peak of interest for each ~20 s accumulation interval. The procedure also corrects for variation in the flux of gamma rays at the instrument as the thickness and composition of the Martian atmosphere changes with time. The well-tested NASA Ames Research Center Martian General Circulation Model (Haberle *et al.*, 1999) is used to predict the atmospheric thickness as a function of time and location. The forward calculation uses an assumed surface composition and topography of the Martian surface for all 0.5° by 0.5° cells within a 17° arc-radius from the spacecraft nadir. This radius was selected because over 99% of the detected gamma rays originate within it.

For the middle latitudes, the surface was assumed to be homogeneous with depth (at least for the top few tens of centimeters from which almost all gamma-ray-producing neutrons are made) and to have an adjusted mean soil composition measured by the Mars Pathfinder Alpha Proton X-ray Spectrometer (APXS) (Wänke *et al.*, 2001; Brückner *et al.*, 2003; Foley *et al.*, 2003). The adjustments consist of renormalization for an H_2O mass fraction of 3% and for rare-earth elements (REE) by assuming a chondritic ratio of REE/Th and a presumed Th content (Boynton *et al.*, 2007).

For each individual spectrum and each surface cell, the angle from the surface to the spacecraft is calculated. The gamma-ray flux emitted in that direction is then determined from a table generated by using calculated reaction rates in the surface for the atmospheric thickness at that time. The flux is also corrected for attenuation of the gamma rays as they are transported to the surface. Only gamma rays that have not undergone any change in energy are used. Neutron fluxes are calculated using the Monte Carlo N Particle eXtended code (MCNPX) (e.g., McKinney *et al.*, 2006). The rate of making gamma photons at each depth is determined from these neutron fluxes and all relevant nuclear reactions (Kim *et al.*, 2006). The flux of gamma rays escaping the surface is then attenuated using the atmospheric thickness to get the flux at the spacecraft. The efficiency for detecting gamma rays of a given energy is then used to get the expected count rate. These values are relative as an absolute flux of incident cosmic-ray particles was not assumed. For gamma rays from the decay of the naturally radioactive elements U and Th and the isotope ^{40}K, only assumed abundances are needed to get their fluxes at the Martian surface. Because of low counting rates, abundances for U have not yet been well determined.

When a spectrum is summed, all forward calculations for spatially overlapping ~20 s intervals are summed. A relative elemental abundance is determined by scaling the assumed abundance used for the forward calculations by the ratio of the observed to calculated count rates. For U, Th, and K, the result is the final abundance. For the other gamma rays, which are made by cosmic rays, additional corrections are needed. Although most gamma rays are made by neutrons, the neutrons measured by the neutron spectrometers on Mars Odyssey were not used because the fast- and thermal-neutron fluxes in the top tens of centimeters of the surface are needed, and the fluxes of these neutrons can change significantly in passing through the Martian atmosphere.

Silicon is mapped using the 1779 keV gamma ray made by neutron inelastic-scatter reactions with the main Si isotope, ^{28}Si. The neutrons making this gamma ray have energies above 1.8 MeV and are collectively called "fast neutrons." The flux of these fast neutrons varies in Mars with the flux of energetic cosmic-ray particles incident on Mars and with the composition of the surface. The counts in the highest-energy channels of the gamma-ray spectrometer are used to track and correct for relative changes in gamma-ray fluxes due to changes in cosmic-ray fluxes. Two elements cause most of the variations in fast-neutron fluxes: Fe and H. Iron is important because it generates more fast neutrons per cosmic-ray particle interaction than lighter elements. Hydrogen is very effective in slowing down neutrons and reduces the fast-neutron fluxes. The abundances of Fe and H as determined from gamma rays and results of MCNPX calculations are used to correct the Si abundance determined using the 1779 keV gamma ray (e.g., Boynton *et al*., 2007).

The reported mass fraction of Si is determined by normalizing the estimated mass fraction at the Mars Pathfinder landing site bin to the mean Si content of the Pathfinder APXS measurements. The normalization factor was used as a constant scale factor across the entire mid latitudes of Mars. The Pathfinder APXS has the benefit of sampling regolith within a landing ellipse of less geological heterogeneity than those of the Mars Exploration Rovers (MERs). It also analyzed rocks, a feat that the Vikings could not achieve. In spite of less geological heterogeneity at Pathfinder, the difference in spatial resolution between the GRS and the APXS is enormous. We accounted for this by computing a weighted mean of soil-free rock (13% areal fraction) and soil (87%) compositions. The former consists of fragments and outcrop >0.1 m in size. The rest is taken to be soil, which is typically unconsolidated material including those classified by *in situ* missions as soil, dust, drift, bedform armor, clasts, concretions, sand, etc. While MER and Viking mission compositional data were not used for the Si normalization, GRS-derived compositions were compared with mean compositions at both MER sites and the Viking 1 site. With the exception of Fe mass fractions, the GRS and mean *in situ* compositions were in agreement within net uncertainties (1 s_m, net uncertainty of the mean). Karunatillake *et al*. (2007) discuss estimating mean *in situ* compositions in detail, for comparison with and normalization of the GRS data.

Hydrogen, chlorine, and iron are determined using gamma rays made by the capture of neutrons at or near thermal (~0.02 eV) energies. The fluxes of thermal neutrons on Mars are affected mainly by H and by elements like Fe and Cl with high cross sections for absorbing thermal neutrons. Hydrogen can both increase the fluxes of thermal neutrons by the slowing down of faster neutrons and decrease thermal-neutron fluxes by absorbing thermal neutrons. The correction factor for gamma rays made by thermal neutrons is the ratio of Si gamma-ray fluxes made by thermal neutrons to those made by fast neutrons. All absolute capture-derived element concentrations (to date, Fe, Cl, and H) are consequently affected by the uncertainties in the Si abundance.

The GRS team is working on deriving abundances for other elements, especially Ca, Al, and S. These elements have weaker signals and so the results will have higher uncertainties and/or poorer spatial resolution. Oxygen has a good signal, but some of its gamma ray is made in the atmosphere, complicating its analysis. Other elements have weak gamma rays or strong interferences, so it will be much harder to determine their abundances.

For smaller bins ($< 10^\circ \times 10^\circ$ in latitude–longitude extent), the number of counts in the peak of interest is small, causing a fairly large uncertainty in the peak area. To reduce the uncertainties for such bins, the postcorrection bins are subject to a constant arc-radius mean filter, replacing the mass fraction of the central bin with the mean of those within the filter window. The radius of the smoothing window is the smallest for K (5°), which has the highest count rate, and increases for elements that have weaker gamma rays (10° for Cl, Fe, H, and Th; 15° for Si).

5.2.3 Data analysis and mapping

The region within which about 50% of the gamma-ray signal originates is between 450 and 600 km in diameter (roughly 8°–10° measured at the equator) depending upon energy. Thus, the spatial resolution varies for each element. Our data processing procedure takes this into account by summing spectra from within this region and accounting for atmospheric attenuation and detector efficiency (Boynton *et al*., 2007). Due to low counting statistics, however, smoothing as described above is required to reduce the noise in the maps presented in Figures 5.3–5.5. Thus, adjacent gamma-ray bins on the maps or on $5^\circ \times 5^\circ$ grids are spatially autocorrelated leading to information redundancy.

For Fe, Si, H, and Cl data, we report only those spatial resolution elements (these can be loosely called "bins") in regions where H contents are low enough to not interfere in the determination of each element's concentration. Hydrogen has a high cross section for capturing thermal neutrons, so it can significantly affect the flux of thermal neutrons in the upper ~30 cm of the Martian surface. To account for the effect of H, we use a correction procedure that involves both the measured fluxes of gamma rays from H, Fe, and Si, and the fluxes calculated from a neutron transport–gamma ray production model (Boynton *et al*., 2007). This approach results in reasonable values at equatorial latitudes. Because the corrections are inaccurate at higher polar latitudes where the influence of hydrogen dominates elemental signatures, the results presented here are constrained using a mask based upon H concentration values and described by Boynton *et al*. (2007). The H-mask corresponds to roughly ±45° of latitude from the equator. K and Th are not subject to the H-mask because they are naturally radioactive and the effect of H on neutron flux is not relevant. However, the data are most reliable between 75° S and 75° N latitude. At higher latitudes the concentrations of K and Th are diluted by very high water contents, so count rates are low and uncertainties high. The typical relative root-mean-square measurement uncertainties stemming from counting statistics for an average smoothed bin, s_{rms}, are Cl: 10%, Fe: 8%, H: 11%, K: 7%, Si: 2%, and Th: 10%.

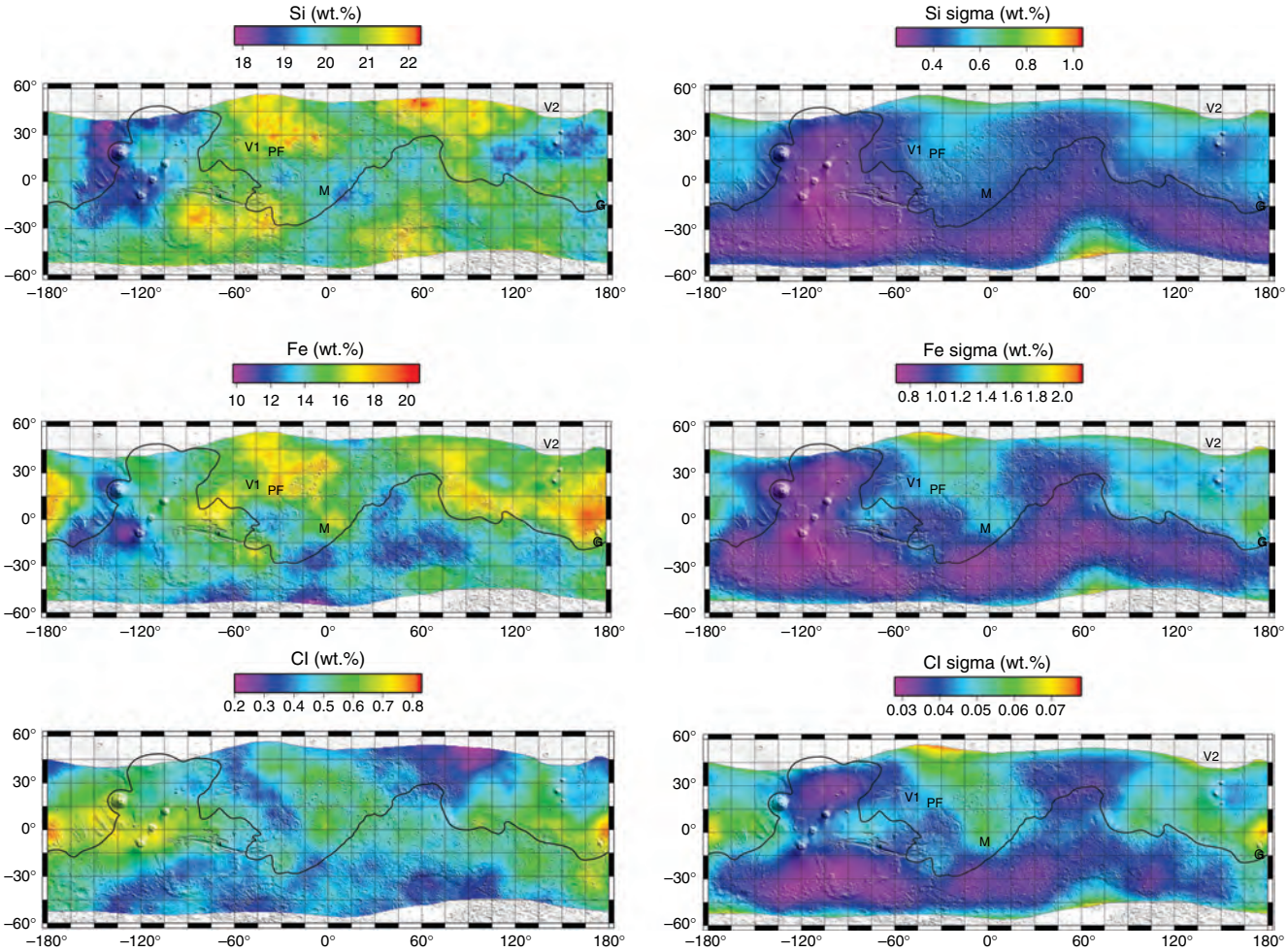

Figure 5.3. Maps of the Si, Fe, and Cl mass fractions (left) and of the $1s_m$ (right) variation at each point on Mars, in the equatorial zone where H concentrations are low enough to allow for ready calculation of elemental abundances. s_m is basically the instrumental uncertainty at each point (as an absolute, not relative, mass fraction) and consequently unrelated to the standard deviation of the sample population. Data have been smoothed using a mean filter. The data are displayed over a shaded relief map of Mars, with mission landing sites indicated (V1: Viking 1 in Chryse Planitia; V2: Viking 2 in Utopia Planitia; PF: Pathfinder in Ares Vallis; M: *Opportunity* in Meridiani Planum; G: *Spirit* in Gusev crater). The black outline is the 0 km contour, which roughly corresponds to the boundary between the southern highlands and northern lowlands. (For a color version of this figure, please refer to the color plate section or to the e-Book version of this chapter.)

In this chapter we present three products made from data collected through April 2005. First, we provide maps of the concentrations of Si, Fe, Cl, H_2O (derived from H concentration), K, Th, and K/Th. These maps are derived from a 0.5° base maps that have been smoothed with mean filters as mentioned in Section 5.2.2. They are useful for showing global (within the H-mask) variations in concentration. Second, we rebin the smoothed data at $5^\circ \times 5^\circ$ for bivariate scatter plots and multivariate correlations. Multivariate correlations reveal the unique interdependences among variables. Each partial correlation coefficient (r_i) quantifies this as the interdependence between the response variable and the *i*th predictor variable when all other predictors are held constant. This offers a major advantage over Peason's simple (i.e., bivariate or zero-order) correlation coefficients which are often driven by a covarying third variable (e.g., Cohen and Cohen, 1983). The effectiveness of the fit, as represented by the optimal correlation between the observed and modeled response values, is given by the multiple correlation coefficient, R. The square of this quantity, R^2, is known as the "coefficient of determination" and represents the variability of the response variable accounted for by the set of predictors. For example, $R^2 = 0.2$ would indicate that the set of predictors contribute 20% of the response variable variance. The magnitude of R^2 or of a partial correlation coefficient does not in itself represent statistical significance. We estimate the statistical significance of these correlation parameters with Fisher-Snedecor (for R^2), Student's-*t*, and standard normal distribution (for partial correlations) one-tail probability estimates.

Our multivariate correlation algorithm was based on distinct linear regression methods: least squares with heteroscedastic weighting (heteroscedastic least squares, HLS) (Rawlings *et al.*, 1998) and spatial autocorrelation (SA) (Upton and Fingleton, 1985). We also implemented hierarchical modeling to eliminate redundant predictor variables and generate a limited set that would correlate significantly with each response variable.

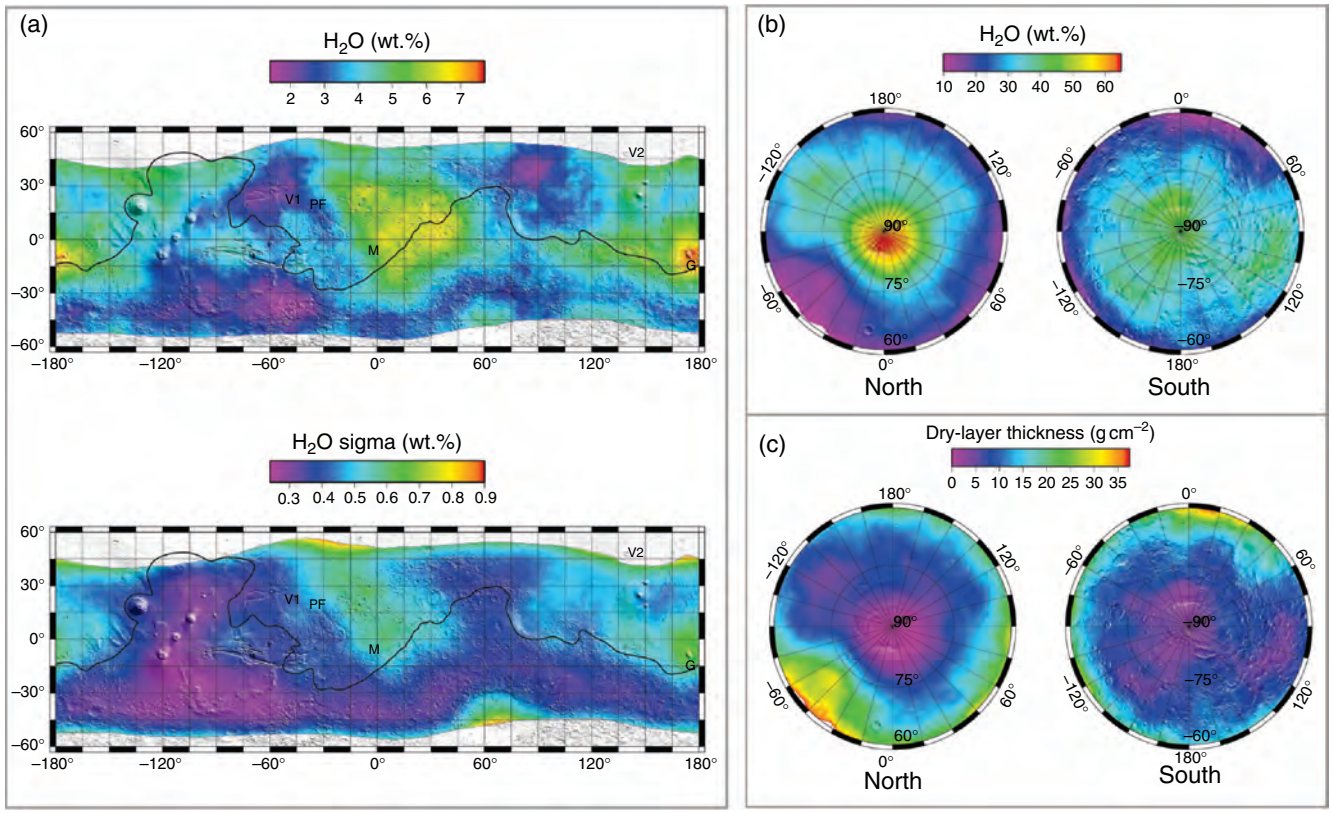

Figure 5.4. (a) Map of the mass fraction (%) of H_2O (stoichiometrically determined from H content) and the $1s_m$ in the equatorial region of Mars. The black outline and letters are as in Figure 5.3. (b) Lower-limit H_2O content in the polar regions based on models shown in Figure 5.7 with the assumption that there is no dry layer, that is, that the H_2O is homogeneously distributed. The high H_2O contents suggest that the ice was deposited on the surface of the soil with modest amounts of dust mixed into the ice as it was being deposited. (c) Map of the maximum dry-layer thickness in the polar regions based on models shown in Figure 5.7, but in this case the assumption is made that the lower layer is actually pure ice, 100% H_2O. (For a color version of this figure, please refer to the color plate section or to the e-Book version of this chapter.)

While a multiple-step iterative process, in essence it utilized comparative Student's-*t* and standard normal one-tail probabilities at >95% confidence levels to select predictor subsets. The results, all statistically significant in excess of 95% confidence, are presented in Table 5.1, and our methodology described in detail by Karunatillake *et al.* (2006).

For modeling purposes, the mass fraction of a given element was considered the response variable. Mass fractions of remaining elements, albedo (Christensen, 1988), rock areal fraction (Christensen, 1986), ST1 areal fraction, ST2 areal fraction (e.g., Bandfield *et al.*, 2000), and thermal inertia (Christensen and Malin, 1988) were considered the set of all predictors. Each variable of the final subset of predictors is statistically significant in excess of 95% confidence and identified by a partial correlation value. The partial correlation coefficients and the coefficient of determination (denoted by "R^2") are evaluated as means of HLS and SA analyses.

Third, we use summed spectra to compute mean element concentrations in the entire surface within the H-mask. These spectra involve large counting times ($>3 \times 10^7$ s), and correspondingly low instrumental uncertainties (relative uncertainties are Cl, Fe, and H: 6%; K: 0.3%, Si: 2%; Th: 4%) since counting uncertainties decrease as the inverse square root of accumulation time.

5.3 RESULTS

Maps of the distribution of Si, Fe, Cl, H_2O, K, Th, and K/Th (Figures 5.3–5.5) clearly show that the Martian surface is significantly heterogeneous, with statistically significant, though complex, covariances. We used multivariate analysis to examine correlations among element abundances and other properties. Results of that analysis are summarized in Table 5.1. Mean global concentrations are given in Table 5.2, within the H-mask for Fe, Si, Cl, and H (as water-equivalent H_2O); and between 75° S and 75° N for K and Th. We summarize the observations in this section and discuss the significance in Section 5.4. Uncertainties for the GRS data in Table 5.2 are instrumental uncertainties of the mean values and are consequently unrelated to compositional variability across the surface.

5.3.1 Iron

Fe concentrations (Figure 5.3) in the northern plains are higher than in the southern highlands, generally at the level of 1*s* (standard deviation of mass fractions). Concentrations are almost everywhere higher than in typical terrestrial basalts

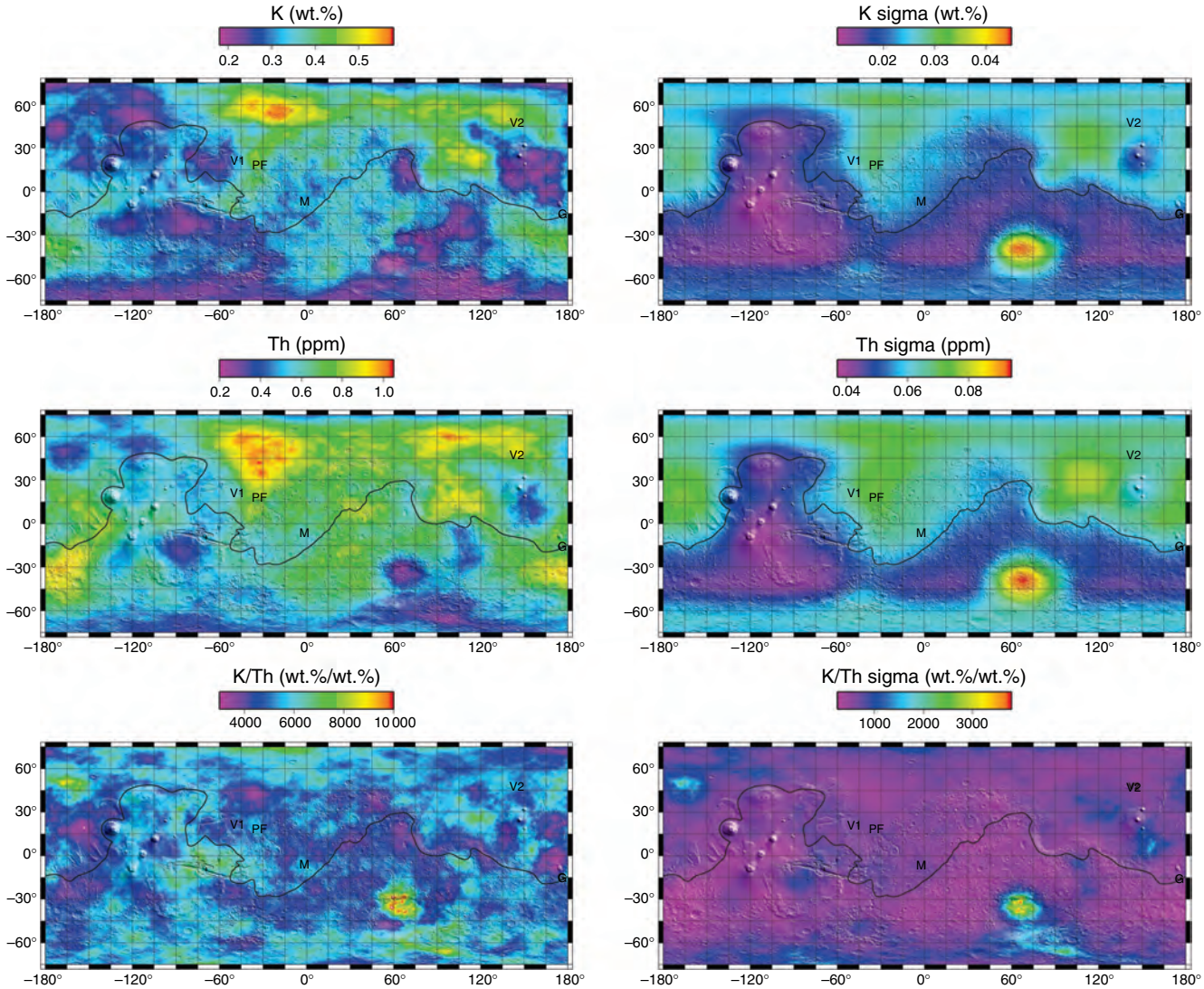

Figure 5.5. Maps (left) of the mass fraction of K (as %), Th (as mg/kg), and K/Th ratio (as ratio of mass fractions) and of the $1s_m$ variation at each point on Mars (right), in the region from 75° S to 75° N, where H concentrations are low enough to allow for ready calculation of elemental abundances; uncertainties are basically the instrumental uncertainty at each point and consequently unrelated to the standard deviation of the sample population. Data have been smoothed using a mean filter. The data are displayed over a shaded relief map of Mars, with mission landing sites indicated (V1: Viking 1 in Chryse Planities; V2: Viking 2 in Utopia Planitia; PF: Pathfinder in Ares Vallis; M: *Opportunity* in Meridiani Planum; G: *Spirit* in Gusev crater). The black outlines are as in Figure 5.3. (For a color version of this figure, please refer to the color plate section or to the e-Book version of this chapter.)

and generally consistent with the high Fe contents of Martian meteorites and rocks and soils at the Viking, Pathfinder, *Spirit*, and *Opportunity* landing sites (in spite of being consistently higher than mean compositions at Lander sites). Fe appears to be higher in a region extending from Amazonis to part of Elysium Planitia, a region north of Apollinaris Patera (north of the Gusev landing site), and in Chryse Planitia. It appears to be low west of the Tharsis Montes. The $5° \times 5°$ bin data (Figure 5.6) show that there is a clear peak between FeO mass fractions, w(FeO), of 18% and 21%. (The FeO mass fractions are calculated by multiplying the Fe concentration by the ratio of the molecular weight of FeO to the atomic weight of Fe; the calculation assumes all the iron is ferrous.) Higher values for Fe are confined to the northern lowlands and lower values occur in the southern highlands (Figure 5.3). The global average w(Fe) (using the H mask) is 14.3%, corresponding to w(FeO) of 18.4%. The GRS data are very similar to those for Shergottite, Nakhlite, and Chassignite (SNC) meteorites and surface samples (Figure 5.6). The distribution of Fe correlates with both Si (partial correlation, $r = 0.3$) and ST1 ($r = -0.3$), with the two contributing ~30% of the variability of Fe across the surface (Table 5.1).

5.3.2 Silicon

Si mass fractions vary from 18% to 23% (equivalent to $w(SiO_2)$ of 39%–50%), as shown in Figure 5.3. Most values are from $20\% < w(SiO_2) < 43\%$, roughly in the range typical of basalts. This suggests that much of the Martian surface is basaltic, in agreement with TES data (the issue of ST1 and ST2 is discussed below) and analyses of rocks at the Pathfinder and MER

Table 5.1. *Hierarchical multivariate correlation results for each element with variables of interest*

Response variable	R^2	Cl	Fe	H	K	Th	Si	Albedo	Rock abundance	ST1 abundance	ST2 abundance	Thermal inertia
Cl	0.4			0.2			−0.2					
Fe	0.3						0.3			−0.3		
H	0.2	0.3										
K	0.6					0.5				−0.2	0.2	
Th	0.6				0.5					−0.1	0.2	
Si	0.5	−0.3	0.3								0.2	0.2

Table 5.2. *GRS-derived mean element concentrations* in the Martian crust as mass fractions, with net uncertainties in parentheses*

Element	Global mean	ST1	ST2	Viking 1	Viking 2	Pathfinder	*Spirit*	*Opportunity*
Si	20.6 (0.3)	20.9 (0.3)	21.4 (0.7)	20.9 (0.5)	NA	21.0 (0.5)	19.6 (0.5)	19.8 (0.5)
Fe	14.3 (0.06)	13.5 (0.8)	16.0 (1.3)	15.4 (1.2)	NA	17.3 (1.3)	15.7 (1.2)	15.4 (1.3)
H_2O	3.9 (0.03)	3.4 (0.2)	3.7 (0.4)	2.5 (0.4)	NA	2.9 (0.5)	7.4 (0.6)	5.4 (0.6)
Cl	0.49 (0.03)	0.46 (0.03)	0.42 (0.04)	0.37 (0.04)	NA	0.37 (0.05)	0.68 (0.06)	0.59 (0.06)
K	0.330 (0.001)	0.320 (0.001)	0.433 (0.008)	0.32 (0.03)	0.48 (0.03)	0.42 (0.03)	0.33 (0.02)	0.32 (0.02)
Th	0.62 (0.02) mg/kg	0.63 (0.02)	0.94 (0.05)	0.60 (0.07)	0.83 (0.07)	0.80 (0.07)	0.65 (0.06)	0.61 (0.06)
K/Th	5330 (220)	5050 (180)	4600 (300)	5300 (800)	5800 (600)	5300 (600)	5100 (500)	5200 (700)
Cl/K	1.5 (0.09)	1.4 (0.09)	0.97 (0.09)	1.16 (0.17)	NA	0.88 (0.12)	2.06 (0.22)	1.84 (0.22)

*Mass fractions as % with the exception of Th. Uncertainties for mass fractions quoted as $1s_m$, the net uncertainty of the regional mean or of the estimate at lander coordinates. Consequently, they do not represent the variability of mass fractions across the surface. The global mean uses the global summed spectrum (total of 2.4×10^7 s counting time for global average) for K and Th, and the summed spectra within the H-mask for other elements. Uncertainty in the K/Th is calculated as $(m_K/m_{Th})[(s_{m,K}/K)^2 + (s_{m,Th}/Th)^2]^{1/2}$, where m_K and m_{Th} are mean concentration of K and Th (rows 5 and 6). An analogous formula was used for Cl/K. Note that only radiogenic elemental data are available for Viking 2, since it is located beyond the H-mask.

landing sites (see Chapters 3 and 4). The area around and to the west of the Tharsis Montes and Olympus Mons is distinctly low in Si, averaging between 18% and 19% ($w(SiO_2)$ 39%–41%). The standard deviation (s) in Si as a mass fraction is about 0.7% (Figure 5.3), so this region is significantly different from adjacent areas containing $w(Si) > 20\%$, but not at the $2s$ level. Nevertheless, this large region of apparently low Si is intriguing and may reflect a distinctive composition for relatively recent lava flows in this region of Mars. There is no evidence for large regions rich in Si that would indicate evolved rocks such as granite, though regions smaller than the nominal GRS spatial resolution of 450 km cannot be ruled out, and have indeed been identified in a few small regions by the MGS/TES instrument (e.g., Christensen *et al*., 2005). It is also possible that the spatial correlation (Table 5.1) of Si with Cl ($r = -0.3$) may be a consequence of this region, which also contains a high abundance of Cl. However, the correlations with thermal inertia ($r = 0.2$) and Fe ($r = 0.3$), with Cl, Fe, and thermal inertia collectively contributing 50% of spatial variability in Si, suggest additional complexities.

5.3.3 Chlorine

A factor of 4 variation (mass fractions 0.2%–0.8%) exists between regions of high and low Cl concentration over geographically large areas; the root-mean-square instrumental uncertainty as a mass fraction is only 0.05% (Figure 5.3). Smoothing reduces the range in concentrations, so this factor of 4 is a lower estimate of the variation on the Martian surface. This points to substantial and real variations in the Cl concentration. The most notable feature on the map is a region of extreme enrichment in Cl west of the Tharsis Montes shield volcanoes. This region of highest Cl is centered over the Medusae Fossae Formation along the highland–lowland boundary west of the giant shield volcanoes of Tharsis Montes (Scott and Tanaka, 1986), including the northwestern slope valleys (NSV) region (Dohm *et al*., 2001a,b, 2004). This region extends from 15° S to 15° N latitude and 120° W–160° E longitude and includes parts of Amazonia Planitia, an area south of Gusev crater into Terra Cimmeria, and west into Elysium Planitia. A triangular-shaped region of decidedly low Cl is centered at 45° N latitude and 70° E longitude northward of Syrtis Major extending up toward Utopia Planitia and Vastitas Borealis. Another region of low Cl is located in a band extending from southeast to northwest through Chryse Planitia and Tempe Terra. Other regions of low Cl occupy the southern highlands, such as those to the east and northwest of Hellas Planitia, east of Terra Sirenum, and a region including and extending west of the Argyre basin.

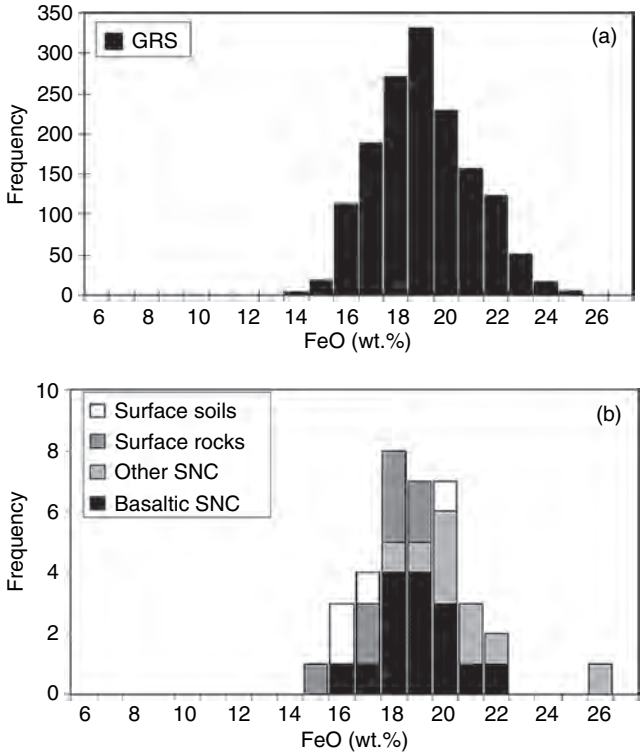

Figure 5.6. GRS 5° × 5° smoothed dataset for Fe mass fraction (converted to FeO). (a) shows a broad peak between w(FeO) of 18% and 21%. Data for Martian meteorites, Viking, Pathfinder, and *Spirit* landing sites (b) are similar. The data are consistent with Mars having significantly more FeO in its mantle than does Earth. Data sources: SNC meteorites from Lodders (1998) and Meyer (2003) and references therein; Viking from Clark *et al.* (1982); Pathfinder from Brückner *et al.* (2003); *Spirit* data from Gellert *et al.* (2004); *Opportunity* data from Rieder *et al.* (2004). Recalibrated APXS FeO estimates for *Spirit* (Gellert *et al.*, 2006) and *Opportunity* do not alter these observations. For the MER sites, only samples abraded with the Rock Abrasion Tool are included for rock analyses.

Surface Cl concentrations are consistent with those measured at landing sites, w(Cl) 0.3%–1.2% (Clark *et al.*, 1982; Wänke *et al.*, 2001; Brückner *et al.*, 2003; Foley *et al.*, 2003; Gellert *et al.*, 2004, 2006; Rieder *et al.*, 2004), and in inferred Martian brines (e.g., Rao *et al.*, 2005), implying that the surface is rich in Cl. Martian meteorites contain much less Cl than the surface materials, $w(\mathrm{Cl}) < 0.12\%$ (Lodders, 1998). The estimated bulk Cl mass fraction of Mars is 0.0038% (Dreibus and Wänke, 1984). It seems clear that Cl has been enriched in the surface materials on Mars. We discuss mechanisms for this enrichment in Section 5.4.2. Additional insight into the variability of Cl is given by its correlation with H ($r = 0.3$), Si ($r = -0.3$), and thermal inertia ($r = -0.1$), collectively accounting for 40% of the spatial variability (Table 5.1). The negative correlation with thermal inertia in particular suggests that at a global level, Cl is significantly affected by the mobile regolith component.

5.3.4 Hydrogen/H_2O in equatorial regions

The determination of the H concentration in equatorial regions is relatively straightforward. Its high concentration in polar regions leads to ambiguities in its concentration because of its moderating effect on thermal neutrons. Hence, we discuss them separately.

Hydrogen (expressed as H_2O) in equatorial regions (Figure 5.4) ranges from $w(H_2O)$ 2%–7%. Measurement uncertainties as mass fractions are only 0.2%–0.7%, so these variations certainly reflect variations on the surface of Mars. This is further supported by the spatial correlation of H with Cl ($r = 0.3$), contributing 20% of the variability in H in the mid latitudes (Table 5.1). The highest values are found in a large region centered on Arabia Planitia, northeast of the Meridiani landing site. It is also elevated in a band west of the Tharsis Montes extending all the way to the highlands north of Tyrrhena Patera. This generally enriched area contains a relatively small patch (about 15° × 30°) extending from the Gusev landing site and Apollinaris Patera east to Medusae Fossae. There are areas with significantly low H in the southern highlands around and west of the Argyre basin, at the highlands–lowlands boundary where large channels debauch into Chryse Planitia, and in the northern plains west of Utopia Planitia. The GRS detects gamma rays from the hydrogen nucleus, so we cannot determine if it is in the form of elemental hydrogen (though the concentration is too high for that to be likely), bound in minerals as H_2O or OH^-, adsorbed on grain surfaces, or as ice buried near the surface. It has been shown that under current Mars conditions it is possible for ice to be thermodynamically stable beneath the surface (Farmer and Doms, 1979; Mellon and Jakosky, 1993; Paige and Keegan, 1994). Summertime temperatures are too warm for ice to be stable at the surface over much of Mars, but the polar regions, down to about 60° latitude can have stable ice beneath the surface where it is protected from the warm summer temperatures by an insulating layer of dry soil. Feldman *et al.* (2004) and Chapter 6 suggest that hydrated minerals may be stable in the mid latitudes. Recent analysis of MER data indicate a significant presence of H in the form of chemically bound H_2O and OH^- as well. For example, Clark *et al.* (2005) suggest that hydrated minerals may contribute up to $w(H_2O) = 22\%$ in the Meridiani Planum outcrops. Morris *et al.* (2006), Ming *et al.* (2006), and Squyres *et al.* (2006) confirm the presence of goethite, a carrier of OH^-, in the Columbia Hills rocks, while raising the possibility of hydrous sulfates.

Our results are in general agreement with those presented in Chapter 6. Regions containing less than $w(H_2O)$ of 5% are slightly lower than that cited by Feldman *et al.* (2004) and Chapter 6, but are within 1s, hence within analytical uncertainty. At higher values of $w(H_2O)$, such as the Arabia region, the discrepancy exceeds 1s, but is within 2s. These differences may be caused by different approaches to data reduction, such as the extent and composition of a relatively dry layer above a wetter layer. The important point is that the results from neutron spectrometry and GRS are qualitatively the same: the highest values, such as in Arabia, in one dataset correspond to the highest values in the other.

5.3.5 Hydrogen in high latitudes (>60°)

We collected data over both poles only during times when the region was free of the seasonal CO_2 frost (Boynton *et al.*,

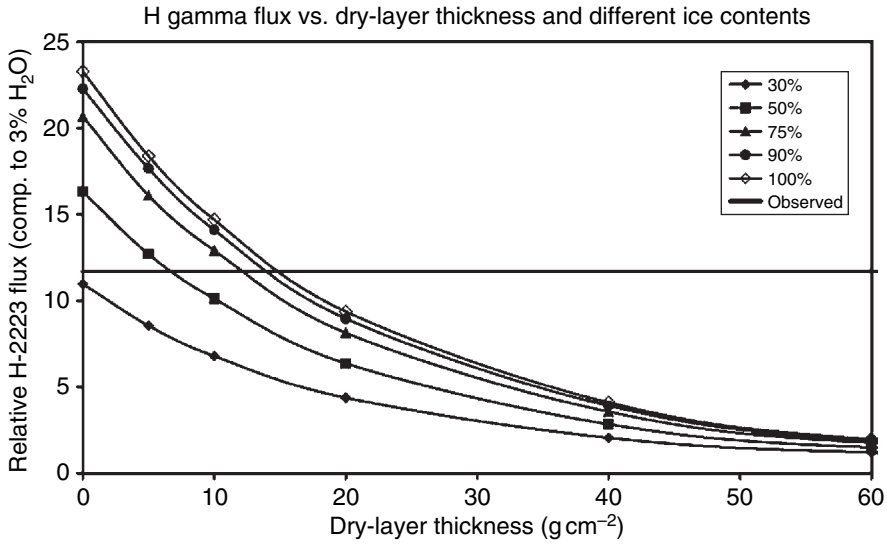

Figure 5.7. Model calculations of H gamma-ray flux versus dry-layer thickness and different H_2O contents in the lower layer. Shown also is a typical value found in the northern polar region (horizontal line). This observed value can be interpreted as $w(H_2O) = 32\%$ with no dry layer above it, or it can be interpreted as 100% H_2O buried beneath a dry layer with a thickness of $15\,g\,cm^{-2}$. Other values in between these are permitted, but the ice-rich material cannot be buried any deeper than $15\,g\,cm^{-2}$ nor can it be any lower in $w(H_2O)$ than about 32%. These curves define the limiting values mapped in Figure 5.4. The dry-layer thickness units could be converted to linear dimensions by dividing by the density of the surface if it were known.

2002). These times are determined when the flux of H gamma rays is at its maximum; during other times, the presence of the frost attenuates the gamma-ray flux coming from the surface. It is not possible to directly convert the instrument response into H_2O content, so we calculate the expected flux of gamma rays using many different models of H_2O distribution and compare the observations to these model calculations. We model the surface as two layers: an upper dry layer of various thicknesses having $w(H_2O) = 3\%$ and a semi-infinite lower ice-rich layer of various H_2O contents. The effects of different atmospheric thicknesses are also included in the models. The Martian atmosphere varies from place to place due to topography and from time to time due to seasonal frost formation. The atmosphere affects both the distribution of neutrons and the attenuation of gamma rays coming from the surface.

Figure 5.7 shows one set of such calculations. The family of curves shows that for a fixed ice content in the lower layer, the flux of H gamma rays increases as the upper dry layer gets thinner. It also shows that for a fixed thickness of the dry layer, the H gamma flux increases with increasing ice content. Both of these observations are just as expected. The curves are not linear for two reasons: the attenuation of the gamma rays due to the dry layer is an exponential function of its thickness, and the flux of thermal neutrons, which is the excitation source of the H gamma rays, is a complex function of the distribution of H in the surface.

We also show in Figure 5.7 a value for the observed flux in a typical location in the north polar region. This value is plotted as a line because we do not know the thickness of the dry layer at this location. This line of constant H flux crosses the family of curves and suggests that the H_2O mass fraction in the lower layer can range from somewhat more than 30%–100%, for dry-layer thicknesses of 0–$15\,g\,cm^{-2}$, respectively. (Neutron and gamma-ray absorption depend on the total mass of material per unit area through which the particles move, so physicists use the mass of column of unit thickness, hence $g\,cm^{-2}$. For a typical regolith density of $1.5\,g\,cm^{-3}$, $15\,g\,cm^{-2}$ corresponds to a thickness of 10 cm.)

Two things should be obvious from the figure. Under the constraints of the two-layer model, the $w(H_2O)$ cannot be lower than about 32%, and the dry-layer thickness cannot be greater than $15\,g\,cm^{-2}$. Any dry-layer thickness between 0 and $15\,g\,cm^{-2}$ is consistent with the observed H gamma ray and the corresponding ice content in the lower layer. Using only the H gamma-ray flux, we cannot determine the ice content any better than that because we have two unknowns and only one equation.

In principle, it is possible to devise another equation that can be used to address the question of the vertical distribution of H. In Figure 5.8 we plot a family of curves similar to those shown in Figure 5.7, except that in this case it is the flux of Si gamma rays that come from thermal-neutron capture. The curve for $w(H_2O) = 100\%$ in the lower layer is an endmember case. When the dry-layer thickness is zero, i.e. when only a pure ice layer exists, the flux of Si gamma rays is zero because there is no Si in pure ice. As the ice is buried with more dry soil, the Si flux increases, almost in direct proportion. What is surprising is that for some lesser H_2O contents in the lower layer, the Si flux is almost independent of the thickness of the dry layer. For example, when the lower layer has only $w(H_2O) = 30\%$, the Si flux actually decreases slightly as the dry layer gets thicker, then levels off starting with a thickness of about $30\,g\,cm^{-2}$. In this case, the higher H content in the lower layer is reducing the thermal-neutron flux in the layer above it. Because the mass of the H nucleus is similar to that of the neutron, the neutrons coming into the H_2O-rich layer from the dry layer are forward scattered deeper into the lower, H-rich layer. Once in this layer, the large capture cross section of H makes it difficult for the thermal neutrons to diffuse back out of the H-rich layer into the upper, Si-rich dry layer. This reduces the flux in the upper layer compared to what it would be without an H-rich layer below. In other words, the thermal-neutron flux in both layers is changing in a way that just balances the addition of more Si in the upper layer. As the dry layer gets much thicker, the H-flux converges to 1.0 for all ice contents, but it requires over $150\,g\,cm^{-2}$ ($\sim$1 m) of the dry layer.

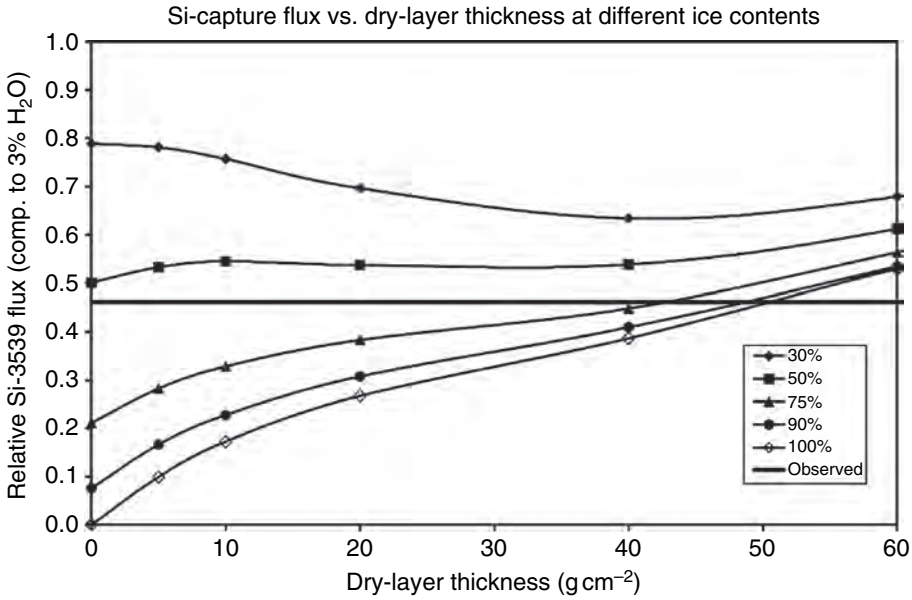

Figure 5.8. Model calculations of the Si neutron-capture 3539 keV gamma-ray flux versus dry-layer thickness and different H_2O contents in the lower layer. Shown also is a typical value found in the northern polar region. These curves show the combined effect of both different amounts of Si and different distributions of thermal neutrons in the upper few tens of centimeters. With pure ice at the surface, there is obviously no Si to generate corresponding gamma rays. As more dry layer is added, the Si flux goes up. An interesting effect is seen around 30%–50% $w(H_2O)$ in the lower layer; as more Si is added in the form of a thicker dry layer, the neutron flux drops a comparable amount so that the Si flux is nearly independent of dry-layer thickness. By combining the data in Figures 5.7 and 5.8, it is possible to determine both the dry-layer thickness and the H_2O content of the lower layer.

Based on Figure 5.7 we learned that for our typical location in the north the dry-layer thickness must be between 0 and 15 g cm^{-2}. With this constraint, Figure 5.8 tells us that $w(H_2O)$ of the lower layer must be between about 52% for 0 g cm^{-2} and 65% for 15 g cm^{-2} (the observed value of the Si-3539 flux for 15 g cm^{-2} lies between the curves for 50% and 75% H_2O). We can then go back to Figure 5.7 and see that with this constraint from Figure 5.8, the dry-layer thickness must be around 10 g cm^{-2}.

Figure 5.4 shows the lower limit H_2O content in the two polar regions. This lower limit is calculated by assuming zero thickness of the dry layer (see Figure 5.7). The north polar region shows a high H_2O content over the residual polar cap. On the basis of its low optical geometric albedo, the cap is thought to be largely H_2O ice. It may be disconcerting that the GRS-derived H_2O mass fractions shown over the polar cap are no higher than about 73%. The reason for the apparent low value over the residual cap is that the GRS has a large footprint. The size of the circle from which 50% of the signal comes is ~450 km in diameter, and for 75% of the signal it is 600 km (7.6° and 10.1° of arc on the surface, respectively). Because of this finite spot size, the instrument integrates over a large area, and some of the signal from the dry soil beyond the edge of the residual cap gets included when the spacecraft is directly over the residual cap. We have modeled the expected equivalent H_2O content over the residual cap using the known response function of the instrument (assuming 100% H_2O for the residual cap and $w(H_2O)$ = 75% buried under 10 g cm^{-2} of dry soil elsewhere), and we find a value within a few percent of what is observed. Thus the technique provides a good quantitative measure of the H content of the surface. It is important to remember, however, that a value read off the map at any particular point is not necessarily the H_2O content at that point; it is the value averaged over a large region that is centered at that point.

Minimum values for $w(H_2O)$ range from 25% to 40% over much of the north polar region away from the residual cap. There are a few places where the limiting mass fractions may reach 45%. The region around 45° W longitude, however, shows a substantially lower H_2O content. It is not clear why this region has less apparent H_2O than other longitudes. This area is near the mouth of Chasma Boreale, which may be a source of dry air in the form of Katabatic winds off the top of the polar cap. If so, it may be that the lower apparent H_2O content is really due to a thicker dry layer above the ice-rich layer. (The limiting values in Figure 5.4 may be due to a low H_2O content or may be due to a high H_2O content with a thicker dry layer.) In the south we find a 25%–40% range in limiting H_2O values as well, but without the higher values associated with the north residual cap. The spatial extent of the elevated H_2O content is also more uniform with respect to longitude in the south.

Figure 5.4 also shows a map of the maximum thickness of the dry layer made by assuming it covers pure H_2O ice as discussed above. Except for the color differences, the map looks similar to the one showing minimum H_2O content. This is expected because the H gamma flux is the same for both figures; it is only the algorithms to convert the H gamma flux into maps that differ. The maximum thicknesses are similar in the two polar regions. For most of the north polar region, the maximum thickness of the dry layer is between 15 and 25 g cm^{-2}; exceptions occur over the polar cap and in the area around 45° W longitude. The true thickness of the dry layer over the northern residual cap is presumably zero, but because of the finite spatial resolution of the GRS, some signal from the material surrounding the cap contributes to yield an apparent thickness around 5 g/cm^2. In the south, most of the polar region shows a maximum thickness within the range of 15–25 g cm^{-2} seen in the north.

When we consider in a qualitative sense the constraints provided by combining the Si and H data, we find that the estimates (rather than the limits) for the dry layer thicknesses are more on the order of 5–10 g cm^{-2}. The corresponding H_2O mass fractions in the lower layer range from about 40%–80%. This high concentration must reflect the

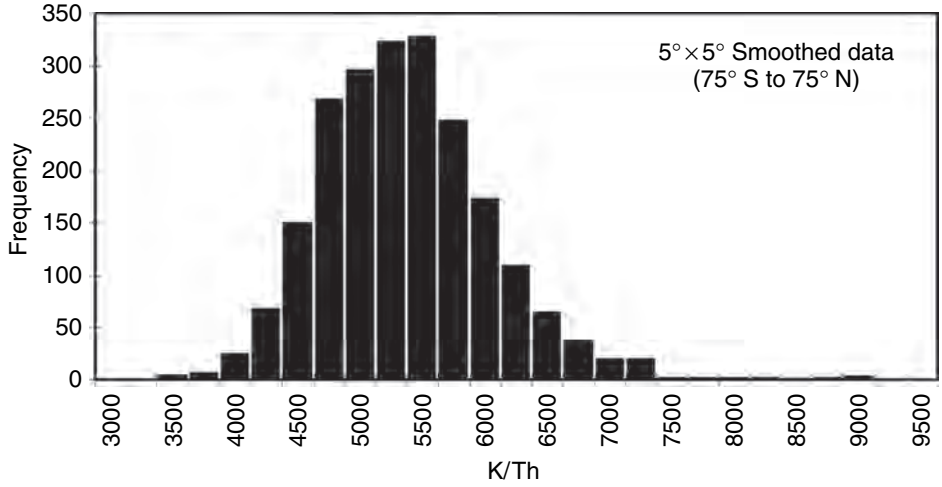

Figure 5.9. Distribution of K/Th values on Mars. Data are for 5° × 5° smoothed bins between 75° S and 75° N latitude, using data through March 2005. There is a clear peak in the distribution at about 5300.

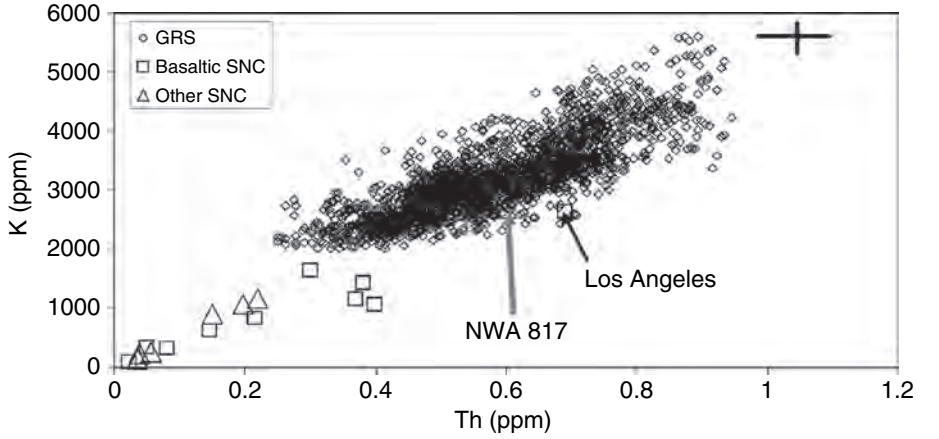

Figure 5.10. K and Th mass fractions (mg/kg) in 5° × 5° smoothed pixels from Mars Odyssey GRS data compared to basaltic (includes olivine phyric) SNC and other SNC meteorites. GRS data collected through March 2005. Uncertainty is shown for a typical GRS data point. SNC data are from Lodders (1998) and Meyer (2003) and references therein. Note that all but two meteorites (basaltic shergottite Los Angeles and nahklite NWA 817) plot substantially below GRS data, implying that the meteorites are not representative of typical Martian surface materials.

presence of ice. It is much too large to be contained in hydrous minerals.

5.3.6 Potassium and Thorium

K and Th are not uniformly distributed on Mars as evident both visually (Figure 5.5) and in their multivariate correlations (Table 5.1). The northern plains from about 60° W–180° E are rich in both, though the higher-than-average Th region extends much further south into the highlands. Both are generally medium to low over Tharsis. There is distinctly higher K and Th in the highlands in the region 15° S–45° S, and extending from 150° W to 165° E, encompassing a portion of Terra Cimmeria. The region west of Hellas contains average K, but has relatively high Th. The K/Th ratio varies by somewhat over a factor of 2, but about 95% of the surface area is between 4000 and 7000 (Figures 5.5 and 5.9). It is distinctly low west of Olympus Mons in Amazonis Planitia, in the region where Kasei Valles meets Chryse Planitia, in western Arabia Terra, and in Syrtis Major Planum. K/Th is high in Valles Marineris and surrounding region, Terra Cimmeria, and in the Hellas basin. These modest variations (most are within 1*s* of the mean) may reflect a combination of bulk Martian K and Th concentrations, igneous processes, and aqueous-related processes, including alteration, erosion, and deposition. However, the instrumental uncertainties in the K/Th measurements make these apparent differences statistically uncertain (Figure 5.5). For example, Hellas appears to have elevated K/Th with values up to 10 000, but the instrumental uncertainty, $1s_m$, is over 3000. On the other hand, other areas appear to be distinctly higher or lower, such as the high region in and south of Valles Marineris, at least at the 1*s* level (see Taylor *et al.*, 2006b, for a detailed discussion of the possible significance of these larger than $1s_m$ deviations from mean, and for a review of how K and Th are fractionated by igneous and aqueous alteration processes).

SNC meteorites in general have much lower K and Th contents than does the Martian surface (Figure 5.10). All but two SNC meteorites (shergottite Los Angeles and nakhlite NWA 817) have lower K than any GRS data points, and about half have lower Th. The average surface is clearly higher in Th and K than the average SNC meteorite. Overall, it appears that the Martian meteorites are not representative of the Martian crust, as also reported by analysis of data from the TES onboard Mars Global Surveyor (Hamilton *et al.*, 2003). The source areas for SNC meteorites must be either small relative to the GRS resolution, or covered with enough dust (altered and mobile surface material) to mask their chemical signatures, or buried beneath thin deposits of other surface materials. This requires only a

few tens of centimeters of dust. If the pervasive dust and soil are enriched in K and Th, then concentrations of K and Th in surface rocks might be lower than the values we observe in the GRS dataset.

5.3.7 Element correlations

K and Th show the most striking multivariate spatial correlations (Table 5.1 and Figure 5.10). As discussed in previous sections, and presented in Table 5.1, other elements that show statistically significant, but weak, correlations in multivariate analyses are Cl with H and Si, Fe with Si, H with Cl, and Si with Cl and Fe (Karunatillake *et al.*, 2006; Keller *et al.*, 2006). The strong correlation between K and Th is not surprising. K and Th have similar geochemical behavior (except under certain conditions of aqueous alteration). K and Th have very similar geochemical behavior in igneous systems, as shown by their similar, and very low ($<<1$), crystal-melt distribution coefficients (Beattie, 1993; Hauri *et al.*, 1994; Borg and Draper, 2003). Both elements are incompatible (i.e., they concentrate in magma rather than major silicate minerals) and their concentrations in magmas are not greatly affected by source rock composition or crystallizing phase, even when garnet is involved. Although there are interesting exceptions (e.g., phosphate minerals [Jones, 1995], phlogopite [Halliday *et al.*, 1995] and amphibole [Halliday *et al.*, 1995], in general, K/Th in a lava flow reflects the ratio in its mantle source region. Aqueous systems are another matter. As reviewed in detail by Taylor *et al.* (2006b), K and Th can be fractionated from each other, but the behavior is complicated and depends on water chemistry, pH, and mineral dissolution kinetics. The correlation of K and Th suggests that their variability is dominated by igneous processes. Other elements differ in their behavior during both igneous processing and aqueous alteration, leading to smaller or no correlations.

5.4 DISCUSSION

5.4.1 Surface Types 1 and 2

Mid infrared spectra from the MGS TES instrument indicated two distinct mineralogical units concentrated respectively in northern and southern low-albedo regions of Mars (Bandfield *et al.*, 2000). Material comprising ST1, found primarily in the southern hemisphere, has been interpreted to be dominated by minimally weathered basalt (Bandfield *et al.*, 2000). However, spectral comparisons with terrestrial mineral mixtures have not yielded a unique composition for the material concentrated within northern low-albedo regions, collectively named ST2. Bandfield *et al.* (2000) concluded that the spectral signature was consistent with a basaltic andesite to andesite composition, with the key feature being the possible presence of high-silica phases. In contrast, Wyatt and McSween (2002) argued that the spectra were equally consistent with ST2 being composed of weathered basalt. Our GRS data can be used to independently test these hypotheses for the nature of ST2 (see Karunatillake *et al.*, 2006, for details). In order to avoid complications due to large amounts of ice, regions corresponding to the polar H_2O ice regime were identified and excluded from both hemispheres using the "H-mask" described in Section 5.2.3.

We processed GRS data in two distinct ways to address the ST1–ST2 problem. First, we determined the mean element concentrations in regions dominated by ST1 and ST2, both smoothed with a 10° arc-radius circular median filter to remove noise, enabling a direct compositional comparison between the two units. These H-masked regions for ST1 and ST2 are "Region Type 1" (RT1: ST1 areal fraction > 17%) and "Region Type 2" (RT2: ST2 areal fraction > 36%) respectively. Mean compositions are given in Table 5.2. We computed RT2/RT1 ratios of mean concentrations of elements using cumulative gamma-ray spectra that originated from within region boundaries (Figure 5.11). In the second

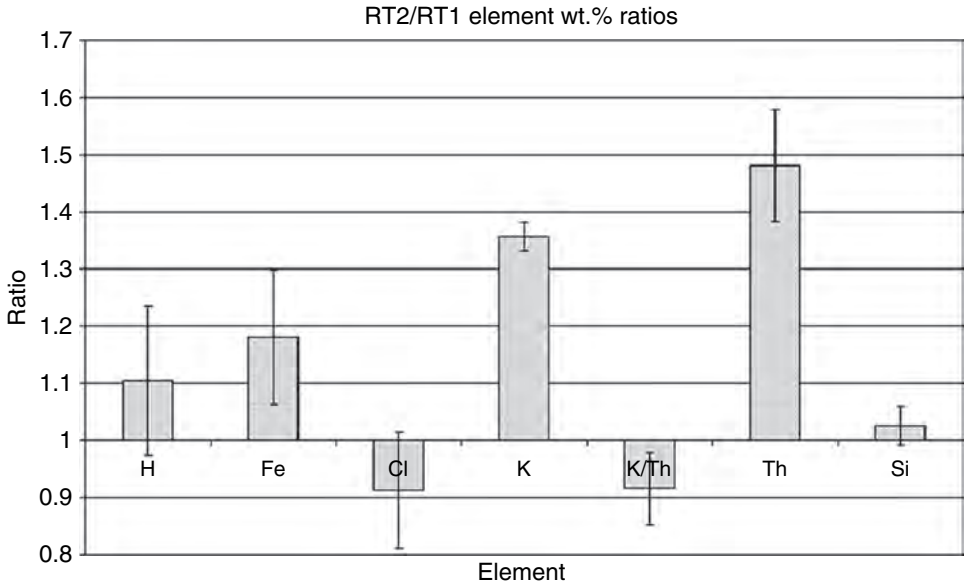

Figure 5.11. Ratios of mean element concentrations in Region Type 2 (RT2) to those in Region Type 1 (RT1). K/Th is the K/Th ratio in RT2 as a ratio to that in RT1. Each $1s_m$ error bar represents the net propagated instrumental uncertainty of the mean value ratio. K and Th are distinctly higher in ST2; Fe is slightly higher in ST2, but not at the $2s_m$ level.

form of data processing, we determined unique correlations among mean-smoothed mass fractions of various elements, median-smoothed areal fractions of ST1 and ST2, and other attributes of interest. An important result of our analysis is that RT2 is enriched in both K and Th by more than 30% relative to RT1, while the K/Th ratio is similar in the two regions (Figure 5.11). Furthermore, RT2 does not seem to be significantly enriched in Si relative to RT1. Among the most striking of our multivariate analysis results (Table 5.1) is that the spatial distribution of K correlates (at 95% and greater confidence) with only Th mass fraction ($r = 0.5$), ST2 areal fraction ($r = 0.2$), and ST1 areal fraction ($r = -0.2$). Similarly, the statistically most significant variables for the spatial distribution of Th are K ($r = 0.5$), ST2 ($r = 0.2$), and ST1 ($r = -0.1$). There appears to be an enrichment of Fe in ST2 (Table 5.2), although this correlation is not confirmed by multivariate analysis (Table 5.1).

One factor that must be considered when interpreting any observed spatial variability in element concentrations on Mars is that the Martian surface is a mix of rock and soil of differing compositions. Physical processes like impact gardening and wind transport that vary the soil/rock ratio could then account for variations in bulk elemental composition. Our regression analyses test this idea by the use of (optical geometric) albedo (Christensen, 1988), thermal inertia (Christensen and Malin, 1988), and rock abundance (Christensen, 1986) as predictor variables. All of these physical attributes might reasonably be expected to vary with soil/rock ratio over the depth range relevant to the GS. However, most of the elements, including K, do not show statistically significant (at 95% and greater confidence) variation with these variables (Table 5.1). We conclude, therefore, that a suitable model for ST2 must explain K and Th enrichment relative to the basalts of ST1 (Figure 5.11) on the basis of rock composition rather than variations in soil/rock ratio.

Among the models for ST2, the leading candidates are basalts altered by aqueous processes (e.g., Wyatt and McSween, 2002) and unaltered basaltic andesite (e.g., Bandfield *et al.*, 2000). We discuss each possibility below. We do not include H and Cl in our interpretation, since the former may be affected by the presence of subsurface ice and an unknown amount of bound water, while the latter may be influenced by the mobile component of the regolith (see Section 5.4.2). The similar K/Th ratio is particularly important in evaluating alternative interpretations for the origin of RT1 and RT2.

Alteration by water

Taylor *et al.* (2006b) discuss in detail how aqueous processes affect the K/Th ratio of planetary materials. Terrestrial analogs of subaerial neutral-pH and moderate-to-high water:rock aqueous alteration (e.g., Patino *et al.*, 2003) and subaqueous alteration (e.g., Staudigel *et al.*, 1996) suggest that K would fractionate from Th under either scenario. Analyses of MER data suggest low-pH alteration at Gusev and Meridiani (Hurowitz *et al.*, 2006). Depending on the duration of weathering, low pH might fractionate K from Th more effectively than at neutral pH (Taylor *et al.*, 2006b). However, we do not observe significant fractionation of K from Th, as evident in the clear coupling of K and Th distributions with each other and ST2 (Table 5.1) and the similarity of K/Th ratios between the two region types (Figure 5.11). Other weathering models such as silica-coated basalt (McLennan, 2003) and oxidized basalt (Minitti *et al.*, 2002) do not account in any simple way for the enrichment of K and Th in RT2.

Igneous processes

One igneous mechanism that could enrich K and Th in ST2 is fractional crystallization of basaltic magma. However, this would lead to a Si-enriched magma ($w(SiO_2) \sim 55\%$), although the details of Si enrichment depend on water content and oxygen fugacity (Minitti and Rutherford, 2000). There is no evidence for Si enrichment in RT2 within $1s_m$ error bars (Figure 5.11), which is contrary to the expectation from TES (e.g., Bandfield *et al.*, 2000). The disparity may in part be a consequence of sampling depth differences between the two instruments, since the GRS sampling depth of tens of centimeters is dramatically greater than the few hundred micrometers sampling depth of TES. In any event, testing the feasibility of enriching K and Th by fractional crystallization requires knowing the Si content in the parent magma, which we do not know with sufficient certainty.

An alternative model, subduction zone magmatism, fractionates K from Th because K concentrates in the aqueous fluid driven off the subducted slab, so K/Th is high in arc magmas (e.g., Hawkesworth *et al.*, 1997; Grove *et al.*, 2002). But the K/Th ratio for RT2, with a value of 4600, is typical for the Martian surface (Table 5.1). Therefore, decisive evidence for widespread formation of calc-alkaline basaltic andesite or andesite is lacking within ST2. Should ST2 material contain calc-alkaline andesites, it would probably be at spatial scales less than the GRS's ~450 km diameter footprint.

An alternative to both localized fractional crystallization and plate subduction mechanisms is initial bulk differentiation processes on Mars producing compositionally distinct magma source regions in the mantle. If that were true, and if the present crustal dichotomy generally follows the source regions, northern and southern basaltic provinces of distinct trace element compositions, including K and Th, could be produced. Isotopic, trace element abundances, oxygen fugacities, and wide range of Sr and Nd isotopic compositions in SNC meteorites favor distinct magma sources (Borg *et al.*, 2003). These differences might have arisen during magma ocean crystallization and subsequent overturn (Borg and Draper, 2003; Elkins-Tanton *et al.*, 2003, 2005). Although current simulations predict differences in Si content, the difference in K and Th content between RT2 and RT1 is generally consistent with magma ocean models. It is feasible that ST1 and ST2 are made predominately from igneous rocks derived from compositionally distinct mantle sources, as opposed to other igneous or aqueous alteration processes. The difference in Fe concentration between ST1 and ST2 (Table 5.2) is consistent with derivation from two

distinct mantle sources or depths of melting (Elkins-Tanton *et al.*, 2005).

5.4.2 Possible causes of Cl variability

Potassium and chlorine are uncorrelated. K does not emerge as a key predictor variable for Cl in multivariate analyses as shown in Table 5.1, while the bivariate correlation with Cl contributes only 0.2% of the spatial variability in K ($R^2 = 0.002$). Both are incompatible elements during partial melting, so the lack of correlation indicates that they have been affected by other processes. These include preferential release of Cl gases from magmas near the surface or during eruption, and aqueous alteration of surface deposits. In spite of the lack of correlation, the global average of the Cl/K ratio (1.5 ± 0.1) is not far from chondritic (1.24; McDonough and Sun, 1995). The uncertainty in Cl/K of 0.1 is the standard deviation, consequently reflecting the variation across the surface, not the uncertainty of the mean. The roughly chondritic Cl/K may reflect the bulk planetary Cl/K because both are moderately volatile elements. It also suggests that the crust is overall a closed system in which K and especially Cl have moved around but not been lost by recycling back into the mantle.

Formation of magma by partial melting transfers Cl (and other incompatible elements) to the crust from the mantle. It is lost with other volcanic gases when magma stalls in magma chambers at relatively shallow depths and when lava erupts. As it leaves magma in water-rich fluids, it will react with wall rocks surrounding magma chambers or dikes and with surface materials surrounding volcanic vents. These reactions will concentrate the Cl in those locations, at least until it is remobilized by circulating hydrothermal fluids or surface waters. These aqueous episodes redistribute the Cl. Thus, Cl concentrations reflect magmatic abundances, loss from magmas, and redistribution by aqueous fluids. The role of water in Cl redistribution is supported by the positive correlation between Cl and H_2O (Table 5.1).

Cl is heterogeneously distributed and varies by a factor of ~4 even after smoothing of data with a 10°-arc-radius mean filter (Figure 5.3). Several contiguous, geographically large (>20°) regions of high and low Cl concentrations are present. In particular, a region centered over the Medusae Fossae Formation west of Tharsis shows significantly elevated Cl. A large region north of Syrtis Major extending into Utopia Planitia in the northern hemisphere shows the lowest Cl concentrations. Based upon hierarchical multivariate correlations (as summarized in Section 3.7 and Table 5.1), Cl is positively associated with H while negatively associated with Si and thermal inertia (Figure 5.3). There are four likely geologic mechanisms that may have affected the Cl distribution seen by GRS: aeolian, volcanic, aqueous, and hydrothermal. While some of the distribution may be due to Cl-rich dust deposits transported by aeolian processes (as suggested by the correlation between Cl and thermal inertia in Table 5.1), this mechanism does not appear to account for all of the observed variability. We propose that reactions with volcanic exhalations may have been important for enriching Cl in Medusae Fossae Formation material, perhaps supplemented by hydrothermal activity in this region. Considering the obvious role water has played in shaping the Martian surface, the overall distribution of Cl may have been influenced by solution and precipitation from solutions. Cl concentration everywhere on Mars is elevated compared to Martian meteorites, perhaps suggesting that we are observing a mixture of Cl-rich fine materials and local rocks (Newsom *et al.*, 2007). The complex variations in elemental concentrations (Figures 5.3–5.5) suggest variations in local rock compositions. The abundances of Cl, K, and Th in the least dusty areas (e.g., Syrtis Major) may be explained by mixing between a soil with higher concentrations of Cl, K, and Th, and crustal rocks containing lower abundances of these elements, similar to Martian meteorites (Newsom *et al.*, 2007). Deconvolving the effects of dust and rocks to determine rock compositions is an important task for future research.

Gamma Ray Spectrometer results for Cl are consistent with lander measurements and observations, which also show elevated Cl concentrations varying between 0.3 and 1.2 wt.% Cl both locally and regionally (Clark *et al.*, 1982; Brückner *et al.*, 2003; Foley *et al.*, 2003; Rieder *et al.*, 2004; Gellert *et al.*, 2006). Reported values are also similar to previous estimates of 0.3 wt.% Cl within the upper hundred meters of the surface based upon isotopic excesses of ^{36}Ar and ^{81}Kr (neutron capture products involving Cl and Br) measured in Martian meteorites (Rao *et al.*, 2002). Mixing of local rocks with a global fine component rich in Cl and S has been widely discussed in explanations of soils found at the Viking and Pathfinder landing sites (e.g., Clark, 1993; Bell *et al.*, 2000; McSween and Keil, 2000) and in modeling of "soil-free rock" at Pathfinder (McSween *et al.*, 1999; Wänke *et al.*, 2001). Acid–fog reactions along with additional aqueous processing have been implicated for Cl enrichments found in soils and rock coatings found at Gusev crater (Arvidson *et al.*, 2004, 2006; Haskin *et al.*, 2005; Rao *et al.*, 2005; Yen *et al.*, 2005; Squyres *et al.*, 2006). At Meridiani, variations in Cl and related observations provide strong evidence for episodic liquid water and probable evaporitic conditions (Kargel, 2004; Rieder *et al.*, 2004; Clark *et al.*, 2005; McLennan *et al.*, 2005). These surface processes involving aeolian mixing of dust with a diversity of rock types, aqueous alteration, and interactions with volcanic exhalations likely account for much of the variation in Cl observed globally by GRS.

5.4.3 Martian bulk composition

The mean K/Th in the crust most likely reflects the bulk planetary K/Th (Taylor *et al.*, 2006a), so we can use it to test models for the bulk composition of Mars. This is a cosmochemically useful parameter as it is the ratio of a moderately volatile to a refractory element. The high FeO on the Martian surface may also reflect the bulk composition of the Martian mantle.

We discuss three prominent models for the bulk composition of Mars, each derived by a different method. Dreibus and Wänke (1984), Wänke and Dreibus (1988, 1994), and Longhi *et al.* (1992) estimate the bulk composition from

element correlations in SNC meteorites, with the assumption that refractory elements are present in chondritic abundances. This model is directly tied to Mars through element abundances in SNC meteorites. The Wänke–Dreibus model predicts that K/Th in bulk Mars is 5450. As shown in Table 5.1, global K/Th is 5300, consistent with the Wänke–Dreibus model. This is about twice the K/Th ratio in the bulk silicate Earth (e.g., Jagoutz *et al*., 1979; Taylor and McLennan, 1985; McDonough and Sun, 1995).

Ganapathy and Anders (1974) and Morgan and Anders (1979) modeled Mars as a mixture of chondritic materials that had been modified by the same limited set of processes that affected chondrites, such as variations in condensation temperature and fractionation of metal from silicate. They propose that there are three primary condensates from the solar nebula: a high-temperature, refractory-rich condensate; Fe–Ni metal; and magnesian silicates. Morgan and Anders (1979) define a fourth component, FeS and FeO, which they postulate formed by reaction of Fe metal with H_2S and H_2O respectively. Morgan and Anders (1979) point out that elements of similar volatility do not fractionate during nebular processes, allowing them to use four "index" elements (U, Fe, K, and Tl or ^{36}Ar) to calculate the abundances of 83 elements in the planet. They defined the concentrations of the index elements in Mars, using gamma-ray data from the Soviet orbiter Mars 5, thermal models available at the time, the density of the mantle and the Martian moment of inertia, and volatile elements present in the atmosphere. Morgan and Anders (1979) predicted a value of 620 for K/Th in bulk Mars, much lower than our surface value of 5300. However, this does not negate the general approach used for estimating planetary bulk compositions. Updated compositional data for Martian surface might allow a more reasonable estimate using their approach.

Lodders and Fegley (1997) focused on fitting the oxygen isotopic composition of Mars, known from SNC meteorites, to mixtures of chondritic meteorites. Their calculations estimate that Mars was constructed from a mixture of 85% H-chondrites, 11% CV-chondrites, and 4% CI-chondrites. Lodders and Fegley (1997) predicted a value of 16 000 for K/Th in bulk Mars, much higher than our data indicate. They recognized that the abundance of alkalis was higher in their model than in the Wänke–Dreibus model and in Martian meteorites. They suggested that aqueous leaching in the mantle and hydrothermal activity led to the preferential deposition of K and other alkalis, as well as halogens, in the Martian crust. This might be consistent with the roughly chondritic Cl/K ratio we observe (Table 5.2). However, the K/Th ratio does not vary greatly (Figure 5.10), so if K is enriched by aqueous transport, it is enriched everywhere on the surface by roughly the same amount, along with Th. K and Th behave similarly during igneous processing, but very differently in aqueous environments, so leaching as proposed by Lodders and Fegley (1997) would probably have fractionated K from Th much more than observed.

There is a clear peak between *w*(FeO) of 18% and 21% (Figure 5.6). The global average (using the H-mask) *w*(Fe) is 14.3%, corresponding to *w*(FeO) of 18.4%. Most importantly, the GRS-derived Fe content is almost everywhere higher than in common terrestrial basalts. Mid-Ocean Ridge basalts, for example, have an average *w*(FeO) of 10.5% (Melson *et al*., 1976). Thus, the GRS results appear to confirm the inference from meteorites that Mars is enriched in FeO compared to Earth. The Wänke and Dreibus (1988, 1994) estimate of *w*(FeO) of 17.9% is close to our crustal average and consistent with the Martian moment of inertia (Bertka and Fei, 1998a,b). However, the geophysical data allow the value to be slightly lower (12%–14%), as suggested by high-pressure experiments on chondritic meteorites by Agee and Draper (2004) and supported by geochemical modeling (Borg and Draper, 2003; Draper *et al*., 2005).

There is a clear difference in the abundance of moderately volatile elements and FeO in Mars compared to Earth. K/Th is almost double that in Earth. This implies that on average Mars accreted from materials that were richer in moderately volatile elements and on average more oxidized than the average of the materials that formed the Earth. In turn, this suggests that mixing among planetesimals was not extensive during the formation of the two planets, as argued on different grounds by Drake and Righter (2002). They show that the Earth's composition is unique – it is different from known chondrites and other planets, for example in Mg/Si and oxygen isotopic compositions. Drake and Righter (2002) conclude that there was not widespread mixing of material throughout the inner Solar System during accretion and that accretion zones were relatively narrow. This conclusion contrasts with calculations of the dynamics of planet formation, which suggest that there was considerable mixing of planetary embryos during the final stage of accretion (Wetherill and Stewart, 1993; Wetherill, 1994; Chambers, 2001).

5.4.4 H_2O in polar regions

The H_2O mass fraction in the polar regions is very high (Figure 5.4). The concentrations are so great that at least some of the H has to be present as solid H_2O. Furthermore, the high H-content regions overlap with those where ice is predicted to be thermodynamically stable beneath the surface under current conditions (Mellon and Jakosky, 1993; Mellon *et al*., 2004; Schörghofer and Aharonson, 2005). These results are similar within analytical uncertainty to those measured by the Odyssey neutron spectrometer and high-energy neutron detector (see Chapter 6). These observations strongly argue that the high H content the GRS observed in the polar regions is mostly due to ice mixed with soil. The high H regions begin north and south of the locations of the dissected terrain mapped by Mustard *et al*. (2001), which may be lag deposits formed by the sublimation of H_2O from ice-rich regolith. It is instructive to convert the H_2O mass fractions to volume fractions. These values are shown in Table 5.3. It can be seen that even the minimum H_2O contents correspond to volume fractions of about 50%. This much ice, which is a minimum amount assuming there is no dry layer above it, is more than can be reasonably accommodated by simply filling the pore space in preexisting

Table 5.3. *Conversion of $H_2O(s)$ mass fraction to volume fraction (as %)**

Mass fraction	Volume fraction
25	48
30	54
40	65
50	73
60	80

*Conversion assumes an average soil mineral density of $2.5\,g\,cm^{-3}$.

soil. The high ice contents inferred here suggest that the ice was emplaced on top of soil with small amounts of dust mixing in as the ice accumulated.

The correspondence of the places predicted by Mellon and Jakosky (1993) for ice stability and our observed high ice-content regions argues strongly that the observed distribution of ice is at or close to diffusive equilibrium with the atmosphere. It is tempting to argue that the ice was simply emplaced by diffusion of water vapor down into the soil until it reached a depth where the temperatures were below the frost point. As noted, however, the high H_2O contents are too great to be accommodated by any reasonable amount of soil porosity. We suggest the high ice contents require that the ice was deposited on the surface in the form of ice or frost under past climatic conditions where surface ice would have been stable. Levrard *et al.* (2004) and Mischna and Richardson (2005) have shown that as the obliquity of Mars changes from higher values to the current obliquity, ice will sublimate from equatorial latitudes and deposit at polar latitudes. This surface deposit, presumably mixed with dust as it forms, can account for the GRS observations reported here. As the climate changed to conditions more like the current climate, the near-surface ice would sublime away leaving a lag deposit behind that could account for the dry layer implied by the GRS data.

5.4.5 Thicknesses of seasonal carbon dioxide polar caps

Up to about a quarter of the mass of the Martian atmosphere can be removed as solid CO_2 near the poles (James *et al.*, 1992; Kieffer *et al.*, 1992). CO_2 frost forms when a region is permanently in the dark and sublimes after that region again receives sunlight. The thicknesses of these CO_2 deposits have been determined by the removal of gamma rays made in the surface below the CO_2 cap. The 2223 keV gamma ray from the capture of thermal neutrons by hydrogen is used (Kelly *et al.*, 2006). A gamma-ray spectrum is accumulated for a given location and period of time. A gamma-ray spectrum for that location for frost-free conditions is used to determine the distribution of H making the 2223 keV line. The attenuation of this gamma ray, with corrections for its flux under the CO_2 cap and for backgrounds from H near the instrument, is used to estimate the thickness of the CO_2 cap in units of $g\,cm^{-2}$. This unit is used, as the actual density of the CO_2 frost at the poles is not well known (but is probably about $1\,g\,cm^{-3}$). These columnar thickness and mass results have been determined for latitudes including $\pm 60^\circ$ and poleward. The maximum CO_2 thickness is about $100\,g\,cm^{-2}$ near the South Pole and about $80\,g\,cm^{-2}$ at the North Pole. Results as a function of time and location are in good agreement with those from the NASA Ames Research Center Martian General Circulation Model (Haberle *et al.*, 1999). There were small variations in cap thicknesses for different winter seasons.

5.4.6 Argon over the Martian polar regions

As the seasonal CO_2 polar caps form, additional atmosphere is transported to the regions where the CO_2 in the atmosphere is forming frost that settles to produce the caps. However, the volume fraction of CO_2 in the Martian atmosphere is 95.3%, with the remaining gases mainly N_2 and Ar. Neither N_2 nor Ar condenses when the CO_2 deposits, and both gases remain in the atmosphere. Measurements of these gases are of interest to planetary scientists, particularly those modeling its atmosphere, because knowing their seasonal and global distribution both provides quantitative constraints on wind vector fields and other transport parameters for Mars General Circulation Models. The 1294 keV gamma ray from the capture of thermal neutrons by ^{40}Ar has been used to study the fate of Ar in the polar atmospheres. By comparing the flux of this gamma ray with that expected for each location and period of time, the abundance of Ar can be determined. There was a factor of 6 enhancement in Ar measured for 75° S–90° S for 2 consecutive Mars years occurring near the onset of southern winter (Sprague *et al.*, 2007), but then the Ar enhancement quickly subsided. The enhancement near the North Pole is harder to determine because the atmosphere there is thicker and because the seasonal cap is not as thick. However, an enhancement of roughly a factor of 3 has been estimated from the Ar gamma-ray data. The results for the second winter at each pole were slightly different from those for the first winter.

5.5 SUMMARY AND CONCLUSIONS

Gamma Ray Spectrometer data show that the Martian surface is chemically heterogeneous. Elemental concentrations vary across the surface, including variations within high-albedo areas that are presumably covered with soil, including large regions (like Arabia) that are mantled with dust to depths of meters (Newsom *et al.*, 2007). Fe concentrations are uniformly high compared to terrestrial rock compositions, in accord with the compositions of Martian meteorites and most rock samples analyzed *in situ*. The K/Th ratio is variable, but 95% of the surface has a ratio between 4000 and 7000. The mean (5300) is double that in terrestrial crustal rocks and in the inferred bulk silicate Earth. Cl varies

substantially, with the highest values being associated with the region west of the Tharsis Montes. Surface Types 1 and 2 are indistinguishable except in the amount of K, Th, and Fe they contain: ST2 is enriched by about 30% (relative) in K and Th, but a small difference in the K/Th ratio is not statistically significant. These chemical differences suggest that ST1 and ST2 are composed of igneous rocks that formed from distinct mantle source regions. The H_2O mass fraction (stoichiometrically derived from the H concentration) in equatorial regions ranges from about 1.5%–7%, indicative of the presence of hydrous minerals. H_2O content is very high in polar regions ($>60^\circ$ latitude north and south) and is consistent with the presence of ice mixed with variable amounts of dust.

REFERENCES

Agee, C. B. and D. S. Draper, Experimental constraints on the origin of Martian meteorites and the composition of the Martian mantle, *Earth Planet. Sci. Lett.* **224**, 415–29, 2004.

Arvidson, R. E., R. C. Anderson, P. Bartlett, *et al.*, Localization and physical property experiments conducted by Opportunity at Meridiani Planum, *Science* **306**, 1730–3, 2004.

Arvidson, R. E., S. W. Squyres, R. C. Anderson, *et al.*, Overview of the Spirit Mars Exploration Rover Mission to Gusev crater: landing site to Backstay Rock in the Columbia Hills, *J. Geophys. Res. – Planets* **111**, doi:10.1029/2005JE002499, 2006.

Bandfield, J. L., Global mineral distributions on Mars, *J. Geophys. Res.* **107**(E6), CiteID 5042, doi:10.1029/2001JE001510, 2002.

Bandfield, J. L., V. E. Hamilton, and P. R. Christensen, A global view of Martian surface compositions from MGS-TES, *Science* **287**, 1626–30, 2000.

Beattie, P., The generation of uranium series disequilibria by partial melting of spinel peridotite: constraints from partitioning studies, *Earth Planet. Sci. Lett.* **117**, 379–91, 1993.

Bell III, J. F., H. Y. McSween Jr., J. A. Crisp, *et al.*, Mineralogic and compositional properties of Martian soil and dust: results from Mars Pathfinder, *J. Geophys. Res.* **105**, 1721–55, 2000.

Bertka, C. M. and Y. Fei, Density profile of an SNC model Martian interior and the moment-of-inertia factor of Mars, *Earth Planet. Sci. Lett.* **157**, 79–88, 1998a.

Bertka, C. M. and Y. Fei, Implications of Mars Pathfinder data for the accretion history of the terrestrial planets, *Science* **281**, 1838–40, 1998b.

Borg, L. E. and D. S. Draper, A petrogenetic model for the origin and compositional variation of the martian basaltic meteorites, *Meteorit. Planet. Sci.* **38**, 1713–31, 2003.

Borg, L. E., L. E. Nyquist, H. Weissman, C.-Y. Shih, and Y. Reese, The age of Dar al Gani 476 and the differentiation history of the martian meteorites inferred from their radiogenic isotopic systematics, *Geochim. Cosmochim. Acta* **67**, 3519–36, 2003.

Boynton, W. V., W. C. Feldman, S. W. Squyres, *et al.*, Distribution of hydrogen in the near surface of Mars: evidence for subsurface ice deposits, *Science* **297**, 81–5, 2002.

Boynton, W. V., W. C. Feldman, I. G. Mitrofanov, *et al.*, The Mars Odyssey Gamma-Ray Spectrometer Instrument Suite, *Space Sci. Rev.* **110**, 37–83, 2004.

Boynton, W. V., G. J. Taylor, L. G. Evans, *et al.*, Concentration of H, Si, Cl, K, Fe, and Th in the low- and mid-latitude regions of Mars. *J. Geophys. Res.* **112**, E12S99, doi:10.1029/2007JE002887, 2007.

Brückner, J., G. Dreibus, R. Rieder, and H. Wänke, Refined data of Alpha Proton X-ray Spectrometer analyses of soils and rocks at the Mars Pathfinder site: implications for surface chemistry, *J. Geophys. Res.* **108**(E12), doi:10.1029/2003JE002060, 2003.

Chambers, J. E., Making more terrestrial planets, *Icarus* **152**, 205–24, 2001.

Christensen, P. R., The spatial-distribution of rocks on Mars, *Icarus* **68**(2), 217–38, doi:10.1016/0019-1035(86)90020-5, 1986.

Christensen, P. R., Global albedo variations on Mars: implications for active aeolian transport, deposition, and erosion, *J. Geophys. Res. B Solid Earth Planets* **93**(B7), 7611–24, 1988.

Christensen, P. R. and M. C. Malin, High resolution thermal imaging of Mars, *Lunar Planet. Sci.* **19**, 180–1, 1988.

Christensen, P. R., J. L. Bandfield, V. E. Hamilton, *et al.*, Mars Global Surveyor Thermal Emission Spectrometer experiment: investigation description and surface science results, *J. Geophys. Res.* **106**, 23823–72, 2001.

Christensen, P. R., H. Y. McSween, J. L. Bandfield, *et al.*, Evidence for magmatic evolution and diversity on Mars from infrared observations, *Nature* **436**, 504–9, 2005.

Clark, B. C., Geochemical components in Martian soil, *Geochim. Cosmochim. Acta* **57**, 4575, 1993.

Clark, B. C., A. K. Baird, R. J. Weldon, *et al.*, Chemical composition of Martian fines, *J. Geophys. Res.* **87**, 10059–67, 1982.

Clark, B. C., R. V. Morris, S. M. McLennan, *et al.*, Chemistry and mineralogy of outcrops at Meridiani Planum. *Earth Planet. Sci. Lett.* **240**, 73–94, http://dx.doi.org/10.1016/j.epsl.2005.09.040, 2005.

Cohen, J. and P. Cohen, *Applied Multiple Regression/Correlation Analysis for the Behavioral Sciences*, London, England: L. Erlbaum Associates, 1983.

Dohm, J. M., R. R. Casavant, R. G. Strom, J. R. Zimbelman, and D. H. Scott, Latent outflow activity for western Tharsis, Mars: significant flood record exposed. *J. Geophys. Res.* **106**, 12301–14, 2001a.

Dohm, J. M., J. C. Ferris, V. R. Baker, *et al.*, Ancient drainage basin of the Tharsis region, Mars: potential source for outflow channel systems and putative oceans or Paleolakes, *J. Geophys. Res.* **106**, 32943–58, 2001b.

Dohm, J. M., J. C. Ferris, N. G. Barlow, *et al.*, The northwestern slope valleys (NSVs) region, Mars: a prime candidate site for the future exploration of Mars, *Planet. Space Sci.* **52**, 189–98, 2004.

Drake, M. J. and K. Righter, Determining the composition of the Earth, *Nature* **416**, 39–44, 2002.

Draper, D. S., L. E. Borg, and C. B. Agee, Crystallization of a Martian magma ocean and the formation of shergottites source regions: a less Fe-rich Mars?, *Lunar Planet. Sci. XXXVI*, Houston: Lunar and Planetary Institute, Abstract #1429, 2005.

Dreibus, G. and H. Wänke, Accretion of the Earth and the inner planets. *Proc. 27th Int. Geol. Conf.* **11**, 1–20, 1984.

Elkins-Tanton, L. T., E. M. Parmentier, and P. C. Hess, Magma ocean fractional crystallization and cumulate overturn in terrestrial planets: implications for Mars, *Meteorit. Planet. Sci.* **38**, 1753–71, 2003.

Elkins-Tanton, L. T., S. E. Zaranek, E. M. Parmentier, and P. C. Hess, Early magnetic field and magmatic activity on Mars from magma ocean cumulate overturn, *Earth Planet. Sci. Lett.* **236**, 1–12, 2005.

Evans, L. G., R. C. Reedy, and J. I. Trombka, Introduction to planetary remote sensing gamma ray spectroscopy. In *Remote*

Geochemical Analyses: Elemental and Mineralogical Composition (ed. C. M. Pieters and P. A. J. Englert), New York: Cambridge University Press, pp. 167–98, 1993.

Evans, L. G., R. C. Reedy, R. D. Starr, K. E. Kerry, and W. V. Boynton, Analysis of gamma-ray spectra measured by Mars Odyssey, *J. Geophys. Res. – Planets* **111**(E3), 2006.

Farmer, C. B. and P. E. Doms, Global seasonal variation of water vapor on Mars and the implications of permafrost on Mars, *J. Geophys. Res.* **84**, 2881–8, 1979.

Feldman, W. C., M. T. Mellon, S. Maurice, *et al.*, Hydrated states of $MgSO_4$ at equatorial latitudes on Mars, *Geophys. Res. Lett.* **31**, L16702, http://dx.doi.org/10.1029/2004GL020181, 2004.

Foley, C. N., T. Economou, and R. N. Clayton, Final chemical results from the Mars Pathfinder alpha proton X-ray spectrometer, *J. Geophys. Res.* **108**(E12), 8096, doi:10.1029/2002JE002019, 2003.

Ganapathy, R. and E. Anders, Bulk compositions of the Moon and Earth, estimated from meteorites, *Proc. Lunar Sci. Conf.* V, 1181–206, 1974.

Gellert, R., R. Rieder, R. C. Anderson, *et al.*, Chemistry of rocks and soils in Gusev crater from the alpha particle X-ray spectrometer, *Science* **305**, 829–32, 2004.

Gellert, R., R. Rieder, J. Brückner, *et al.*, The Alpha Particle X-Ray Spectrometer (APXS): results from Gusev crater and calibration report, *J. Geophys. Res.* **111**, E02S05, doi:10.1029/2005JE002555, 2006.

Grove, T. L., S. W. Parman, S. A. Bowring, R. C. Price, and M. B. Baker, The role of an H_2O-rich fluid component in the generation of primitive basaltic andesites and andesites from the Mt. Shasta region, N California, *Contrib. Mineral. Petrol.* **142**, 375–96, 2002.

Haberle, R. M., M. M. Joshi, J. R. Murphy, *et al.*, General circulation model simulations of the Mars Pathfinder atmospheric structure investigation/meteorology data, *J. Geophys. Res.* **104** (E4), 8957–74, doi:10.1029/1998JE900040, 1999.

Halliday, A. N., D.-C. Lee, S. Tommasini, *et al.*, Incompatible trace elements in OIB and MORB and source enrichment in the sub-oceanic mantle, *Earth Planet. Sci. Lett.* **133**, 379–95, 1995.

Hamilton, V. E., P. R. Christensen, H. Y. McSween Jr., and J. L. Bandfield, Searching for the source regions of Martian meteorites using MGS TES: integrating Martian meteorites into the global distribution of volcanic materials on Mars, *Meteorit. Planet. Sci.* **38**, 871–86, 2003.

Haskin, L. A., A. Wang, B. L. Jolliff, *et al.*, Water alteration of rocks and soils on Mars at the Spirit rover site in Gusev crater, *Nature* **436**, 66–9, 2005.

Hauri, E. H., T. P. Wagner, and T. L. Grove, Experimental and natural partitioning of Th, U, Pb, and other trace elements between garnet, clinopyroxene, and basaltic melts, *Chem. Geol.* **117**, 149–66, 1994.

Hawkesworth, C., S. Turner, D. Peate, F. McDermott, and P. vanCalsteren, Elemental U and Th variations in island arc rocks: implications for U-series isotopes, *Chem. Geol.* **139**, 207–21, 1997.

Hurowitz, J. A., S. M. McLennan, N. J. Tosca, *et al.*, In-situ and experimental evidence for acidic weathering of rocks and soils on Mars, *J. Geophys. Res. – Planets* **111**(E2), doi:10.1029/2005JE002515, 2006.

Jagoutz, E., H. Palme, H. Baddenhausen, *et al.*, The abundances of major, minor, and trace elements in the earth's mantle as derived from primitive ultramafic nodules, *Proc. Lunar Planet. Sci. Conf. X*, 2031–50, 1979.

James, P. B., H. H. Kieffer, and D. A. Paige, The seasonal cycles of carbon dioxide on Mars. In *Mars* (ed. H. H. Kieffer *et al.*), Tucson: University of Arizona Press, pp. 934–68, 1992.

Jones, J. H., Experimental trace element partitioning, *A Handbook of Physical Constants: Rock Physics and Phase Relations*, Washington, DC: American Geophysical Union, pp. 73–104, 1995.

Kargel, J. S., Proof for water, hints of life?, *Nature* **436**, 66–99, 2004.

Karunatillake, S., S. W. Squyres, G. J. Taylor, *et al.*, Composition of northern low-albedo regions of Mars: insights from the Mars Odyssey Gamma Ray Spectrometer, *J. Geophys. Res.* **111**, E03S05, doi:10.1029/2006JE002675, 2006.

Karunatillake, S., S. W. Squyres, W. V. Boynton, *et al.*, Chemical compositions at Mars landing sites subject to Mars Odyssey Gamma Ray Spectrometer constraints, *J. Geophys. Res.* **112**, E08S90, doi:10.1029/2006JE002859, 2007.

Keller, J. M., W. V. Boynton, S. Karuntillake, *et al.*, Equatorial and midlatitude distribution of chlorine measured by Mars Odyssey GRS, *J. Geophys. Res.* **111**, E03S08, doi:10.1029/2006JE002679, 2006.

Kelly, N. J., W. V. Boynton, K. Kerry, *et al.*, Seasonal polar carbon dioxide frost on Mars: CO_2 mass and columnar thickness distribution, *J. Geophys. Res. – Planets* **111**(E3), 2006.

Kieffer, H. H., B. M. Jakosky, and C. W. Snyder, The planet Mars: from antiquity to the present. In *Mars* (ed. H. H. Kieffer *et al.*), Tucson: University of Arizona Press, pp. 1–33, 1992.

Kim, K. J., D. M. Drake, R. C. Reedy, R. M. S. Williams, and W. V. Boynton, Theoretical fluxes of gamma rays from the martian surface, *J. Geophys. Res. – Planets* **111**(E3), 2006.

Levrard, B., F. Forget, F. Montmessin, and J. Laskar, Recent ice-rich deposits formed at high latitudes on Mars by sublimation of unstable equatorial ice during low obliquity, *Nature* **431**, 1072–5, 2004.

Lodders, K., A survey of shergottites, nahklite and chassigny meteorites whole-rock compositions, *Meteorit. Planet. Sci.* **33**, A183–90, 1998.

Lodders, K. and B. Fegley, Jr., An oxygen isotope model for the composition of Mars, *Icarus* **126**, 373–94, 1997.

Longhi, J., E. Knittle, J. R. Holloway, and H. Wänke, The bulk composition, mineralogy, and internal structure of Mars. In *Mars* (ed. H. H. Kieffer, B. M. Jakosky, C. W. Snyder, and M. S. Matthews), Tucson: University of Arizona Press, pp. 184–208, 1992.

Masarik, J. and R. C. Reedy, Gamma ray production and transport in Mars, *J. Geophys. Res.* **101**, 18891–912, 1996.

McDonough, W. F. and S.-S. Sun, The composition of the Earth, *Chem. Geol.* **120**, 223–53, 1995.

McKinney, G. W., D. J. Lawrence, T. H. Prettyman, *et al.*, MCNPX benchmark for cosmic ray interactions with the Moon, *J. Geophys. Res.* **111**, E06004, doi:10.1029/2005JE9002551, 2006.

McLennan, S. M., Sedimentary silica on Mars, *Geology* **31**, 315–18, 2003.

McLennan, S. M., J. F. Bell III, W. M. Calvin, *et al.*, Provenance and diagenesis of the evaporite-bearing Burns formation, Meridiani Planum, Mars, *Earth Planet. Sci. Lett.* **240**, 95–121, 2005.

McSween, H. Y., and K. Keil, Mixing relationships in the Martian regolith and the composition of globally homogeneous dust, *Geochim. Cosmochim. Acta* **64**, 2155–66, 2000.

McSween, H. Y., S. L. Murchie, J. Crisp, *et al.*, Chemical, multispectral, and textural constraints on the composition and origin of rocks at the Mars Pathfinder landing site, *J. Geophys. Res.* **104**, 8679–716, 1999.

Mellon, M. T. and B. M. Jakosky, Geographic variations in the thermal and diffusive stability of ground ice on Mars, *J. Geophys. Res.* **98**, 3345–64, 1993.

Mellon, M. T., W. C. Feldman, and T. H. Prettyman, The presence and stability of ground ice in the southern hemisphere of Mars, *Icarus* **169**, 324–40, doi:10.1016/j.icarus.2003.10.022, 2004.

Melson, W. G., T. Vallier, T. L. Wright, G. Byerly, and J. Nelen, Chemical diversity of abyssal volcanic glass erupted along Pacific, Atlantic, and Indian Ocean sea-floor spreading centers. In *The Geophysics of the Pacific Ocean Basin and Its Margins* (ed. G. H. Sutton, M. H. Manghnani, and R. Moberly), Washington, DC: American Geophysical Union, pp. 351–67, 1976.

Meyer, Jr. C., *Mars Meteorite Compendium*, NASA Johnson Space Center, JSC#27672 Revision (B), online: http://curator.jsc.nasa.gov/antmet/mmc/mmc.htm, 2003.

Ming, D. W., D. W. Mittlefehldt, R. V. Morris, *et al.*, Geochemical and mineralogical indicators for aqueous processes in the Columbia Hills of Gusev crater, Mars, *J. Geophys. Res.* **111**, E02S12, doi:10.1029/2005JE002560, 2006.

Minitti, M. E. and M. J. Rutherford, Genesis of the Mars Pathfinder "sulfur-free" rock from SNC parental liquids, *Geochim. Cosmochim. Acta* **64**, 2535–47, 2000.

Minitti, M. E., J. F. Mustard, and M. J. Rutherford, Effects of glass content and oxidation on the spectra of SNC-like basalts: applications to Mars remote sensing, *J. Geophys. Res. – Planets* **107**(E5), doi:10.1029/2001JE001518, 2002.

Mischna, M. A. and M. I. Richardson, A reanalysis of water abundances in the Martian atmosphere at high obliquity, *Geophys. Res. Lett.* **32**, L03201, doi:10.1029/2004GL021865, 2005.

Morgan, J. W. and E. Anders, Chemical composition of Mars. *Geochim. Cosmochim. Acta* **43**, 1601–10, 1979.

Morris, R. V., G. Klingelhöfer, C. Schröder, *et al.*, Mössbauer mineralogy of rock, soil, and dust at Gusev crater, Mars: Spirit's journey through weakly altered olivine basalt on the plains and pervasively altered basalt in the Columbia Hills, *J. Geophys. Res.* **111**, E02S13, doi:10.1029/2005JE002584, 2006.

Mustard, J. F., C. D. Cooper, and M. K. Rifkin, Evidence for recent climate change on Mars from the identification of youthful near-surface ground ice, *Nature* **412**, 411–14, 2001.

Newsom, H. E., L. S. Crumpler, R. C. Reedy, *et al.*, Geochemistry of Martian soil and bedrock in mantled and less mantled terrains with gamma ray data from Mars Odyssey, *J. Geophys. Res.* **112**(E3), 2007.

Paige, D. A. and K. D. Keegan, Thermal and albedo mapping of the polar regions of Mars using Viking thermal mapper observations: 2. South polar region, *J. Geophys. Res.* **99**, 25993–26013, 1994.

Patino, L. C., M. A. Velbel, J. R. Price, and J. A. Wade, Trace element mobility during spheroidal weathering of basalts and andesites in Hawaii and Guatemala, *Chem. Geol.* **202**, 343–64, 2003.

Rao, M. N., D. D. Bogard, L. E. Nyquist, D. S. McKay, and J. Masarik, Neutron capture isotopes in the Martian regolith and implications for Martian atmospheric noble gases, *Icarus* **156**, 352–72, 2002.

Rao, M. N., S. R. Sutton, D. S. McKay, and G. Dreibus, Clues to Martian brines based on halogens in salts from Nakhlites and MER samples, *J. Geophys. Res.* **110**(E12), E12S06, 2005.

Rawlings, J. O., S. G. Pantula, and D. A. Dickey, *Applied Regression Analysis: A Research Tool*, 2nd edn., New York: Springer, 1998.

Rieder, R., R. Gellert, R. C. Anderson, *et al.*, Chemistry of rocks and soils at Meridiani Planum from the Alpha Particle X-ray Spectrometer, *Science* **306**, 1746–9, 2004.

Schörghofer, N. and O. Aharonson, Stability and exchange of subsurface ice on Mars, *J. Geophys. Res. E.* **110**(E5), E05003, doi:10.1029/2004JE002350, 2005.

Scott, D. H. and K. L. Tanaka, Geologic map of the western equatorial region of Mars, *USGS Misc. Inv. Ser. Map*, I-1802-A (1:15,000,000), 1986.

Sprague, A. L., W. V. Boynton, K. E. Kerry, *et al.*, Mars' atmospheric argon: tracer for understanding Martian atmospheric circulation and dynamics. *J. Geophys. Res.* **112**, E03S02, doi:10.1029/2005JE002597, 2007.

Squyres, S. W., R. E. Arvidson, D. L. Blaney, *et al.*, Rocks of the Columbia Hills, *J. Geophys. Res. – Planets* **111**(E2), E02S11, doi:10.1029/2005JE002562, 2006.

Staudigel, H., T. Plank, B. White, and H. U. Schmincke, Geochemical fluxes during seafloor alteration of the basaltic upper crust: DSDP Sites 417 and 418. In *Subduction: Top to Bottom, Geophysical Monograph 96* (ed. G. E. Bebout *et al.*), Washington, DC: American Geophysical Union, pp. 19–38, 1996.

Taylor, G. J., W. Boynton, J. Brückner, *et al.*, Bulk composition and early differentiation of Mars, *J. Geophys. Res.* **111**, E03S10, doi:10.1029/2005JE002645, 2006a.

Taylor, G. J., J. D. Stopar, W. V. Boynton, *et al.*, Variations in K/Th on Mars, *J. Geophys. Res.* **111**, E03S06, doi:10.1029/2006JE002676, 2006b.

Taylor, S. R. and S. M. McLennan, *The Continental Crust: Its Composition and Evolution*, Oxford: Blackwell Scientific Publications, 312pp., 1985.

Trombka, J. I., L. G. Evans, R. Starr, *et al.*, Analysis of Phobos gamma-ray spectra from the Phobos mission at Mars. *Proc. Lunar Planet. Sci. Conf.* **22**, 23–29, 1992.

Upton, G. J. G. and B. Fingleton, *Spatial Data Analysis by Example: Point Pattern and Quantitative Data*. New York: J. Wiley, 1985.

Wänke, H. and G. Dreibus, Chemical composition and accretion history of the terrestrial planets. *Philos. Trans. R. Soc. Lond.* **A 325**, 545–57, 1988.

Wänke, H. and G. Dreibus, Chemistry and accretion history of Mars, *Philos. Trans. R. Soc. Lond.* **A349**, 285–93, 1994.

Wänke, H., J. Brückner, G. Dreibus, R. Rieder, and I. Ryabchikov, Chemical composition of rocks and soils at the Pathfinder site, *Space Sci. Rev.* **96**, 317–30, 2001.

Wetherill, G. W., The provenance of the terrestrial planets, *Geochem. Cosmochem. Acta* **58**, 4513–20, 1994.

Wetherill, G. W. and G. R. Stewart, Formation of planetary embryos: effects of fragmentation, low relative velocity, and independent variation of eccentricity and inclination, *Icarus* **106**, 190–209, 1993.

Winter, John D., *An Introduction to Igneous and Metamorphic Petrology*, New York: Prentice Hall, 2001.

Wyatt, M. and H. Y. McSween Jr., Spectral evidence for weathered basalt as an alternative to andesite in the northern lowlands of Mars, *Nature* **417**, 263–6, 2002.

Wyatt, M., H. Y. McSween Jr., K. L. Tanaka, and J. W. Head III, Global geologic context for rock types and surface alteration on Mars, *Geology* **32**, 645–8, 2004.

Yen, A. S., R. Gellert, C. Schröder, *et al.*, An integrated view of the chemistry and mineralogy of martian soils, *Nature* **436**, 49–54, 2005.

6

Volatiles on Mars: scientific results from the Mars Odyssey Neutron Spectrometer

W. C. FELDMAN, M. T. MELLON, O. GASNAULT, S. MAURICE, AND T. H. PRETTYMAN

ABSTRACT

The Mars Odyssey Neutron Spectrometer (MONS) is described and its capabilities to detect and quantify deposits of H and CO_2 ice within about 1 m of the surface are presented. After two Martian years in mapping orbit about Mars, two distinct domains of hydrogen deposits have been delimited. High-latitude domains in both hemispheres contain large, generally buried deposits of hydrogen and a near-equatorial domain contains more modest, yet significant, deposits. All observations are specified in units of water-equivalent hydrogen (WEH) and are compared with other observations of near-surface deposits of H_2O and OH. They are also discussed in terms of theoretical models of volatile exchange between different water reservoirs through the atmosphere or through a system of aquifers. The CO_2 ice cover of the residual cap near the South Pole is modeled and found not to be a significant part of the CO_2 inventory of Mars.

6.1 INTRODUCTION

The volatile inventory of a planet provides essential information regarding its formation and evolution. For example, the elemental composition of the feeding zones of the different terrestrial planets is expected to become increasingly rich in volatiles as the distance from the Sun increases (Lewis, 1972; Ciesla and Cuzzi, 2006). Exceptions to this rule provide important evidence for the occurrence of catastrophic events, such as what likely differentiated the Moon from the Earth (Cameron, 1988).

Other important roles that volatiles play are to control the mineralogy of near-surface material, the type of volcanism, and the genesis and support of life. Volatiles also play an important role in shaping the surface of a planet through physical alteration from water and ice flows and through chemical alteration through aqueous geochemistry. Lastly, volatiles regulate seasonal weather and longer-term climate variations.

The two most important volatiles on Mars are H_2O and CO_2. Both of these have clear, but very different signatures in planetary leakage neutron spectra. Observation of these spectra can therefore provide a very sensitive measure of the abundance and stratigraphy of hydrogen within the upper meter of the surface, and the time and spatial dependence of CO_2 ice deposition onto, and sublimation from, high-latitude terrain. The purpose of this chapter is to summarize the results to date obtained from data measured using the MONS. These data have provided global maps and their time variations of leakage neutron currents within three ranges of kinetic energy, K: thermal ($0 < K < 0.3$ eV), epithermal (0.3 eV$< K < 700$ keV), and fast ($K > 700$ keV). These maps were then used to generate maps of the hydrogen abundance (parameterized in terms of water-equivalent hydrogen, WEH) and its burial depth beneath a relatively hydrogen-free overburden. Water-equivalent hydrogen is determined as the mass fraction of water consistent with the neutron flux, assuming the water is uniformly distributed with depth.

6.2 THE MONS EXPERIMENT

Prime scientific objectives of MONS are to identify the major reservoirs of hydrogen on Mars, determine their relative contributions to the total water inventory of Mars, and estimate that portion of the current inventory that is near the surface and how it exchanges with the atmosphere. A second, but no less important objective is to map the seasonal variation of CO_2 frost and atmospheric composition, and place limits on the amount of CO_2 locked up in the veneer of CO_2 ice that covers the residual water-ice cap at high southern latitudes.

The MONS experiment makes use of the fact that all matter in the Solar System is exposed continuously to bombardment by galactic cosmic rays (GCRs) (see, e.g., discussion in Feldman *et al.*, 1993b). The longest-lived products of these collisions that remain within the regolith are neutrons. These neutrons are initially produced over a broad range of energies having maximum intensity between 5 and 10 MeV. After production, they moderate in energy to lower values through inelastic and elastic collisions with surrounding material, until they are either absorbed by the nuclear constituents of surface material or escape to space.

The distribution in energy of these escaping neutrons reflects the composition of near-surface material. The element that is most important in shaping neutron energy distributions is hydrogen because the neutron–proton elastic scattering collision cross-section is very high and the mass of a proton and neutron are nearly equal, thereby yielding the greatest energy loss per elastic collision. Mars Odyssey Neutron Spectrometer was designed to detect and discriminate the shape of the energy spectrum of outward leaking neutrons from Mars in order to characterize the distribution

The Martian Surface: Composition, Mineralogy, and Physical Properties, ed. J. F. Bell III. Published by Cambridge University Press.

of volatiles near the Martian surface, as described next. The sequence of neutron–nucleus interactions that shape the leakage neutron-flux energy distributions and thereby provide information about the elemental composition of near-surface material is provided in Section 6.3.

The sensor element of MONS is a segmented cubical block of borated plastic scintillator as shown in Figure 6.1 (Feldman *et al.*, 2002a; Boynton *et al.*, 2004). Different types of ionizing radiation interact with the sensor in characteristic ways. Gamma rays scatter by electrons, depositing part of their energy in a single, Compton scattering event, as illustrated schematically in the top scintillator element in Figure 6.1. Most neutrons undergo the same type of collision with protons in the scintillator, and energetic particles lose energy continuously until they either stop in the scintillator or penetrate through and escape to the outside. Energy losses for all of these events produce a continuum of energy depositions in single-interaction events that result in a smooth background in histograms of counts versus channel. These channels give the energy loss calibrated in equivalent-electron energy. In contrast, most thermal and epithermal neutrons, and a small fraction of fast neutrons will lose all of their energy in the scintillators, thereby producing a characteristic neutron capture reaction with the ^{10}B nuclei that are contained in the scintillators. The energy loss spectrum in these reactions is dominated by a single energy that corresponds to the Q value (the difference in internal energy between the initial and the final states of any reaction) of the capture reaction.

Because of the nonlinearity of plastic scintillators, this energy appears in the form of a monoenergetic electron of 93 keV. This reaction forms ^{7}Li in its first excited state 94% of the time, which then quickly decays to the ground state of ^{7}Li yielding a 478 keV gamma ray. Detection of this gamma ray by the scintillator occurs for only a fraction of the gamma rays produced so that the 93-keV charged particle peak sits on top of a very low-level Compton continuum, which is difficult (but not impossible) to see. This type of reaction is shown schematically in the lowest scintillator prism in Figure 6.1. If the energy of the incident neutron is sufficiently large, the slowing down process produces enough light in the scintillator to be separately observable, thereby producing two time-ordered, and for most such events, time-resolved interactions in the plastic. In this type of double-interaction event, the light output from the first interaction marks the total energy loss of the incident neutron, thereby providing information about its energy. The second interaction is the same neutron capture reaction as produced by a thermal and epithermal neutron. Identification and separation of double-interaction events thereby allow operation of the sensor as a capture-gated neutron energy spectrometer, from which an energy spectrum can be derived (see, e.g., Feldman *et al.*, 1993b, 2002a).

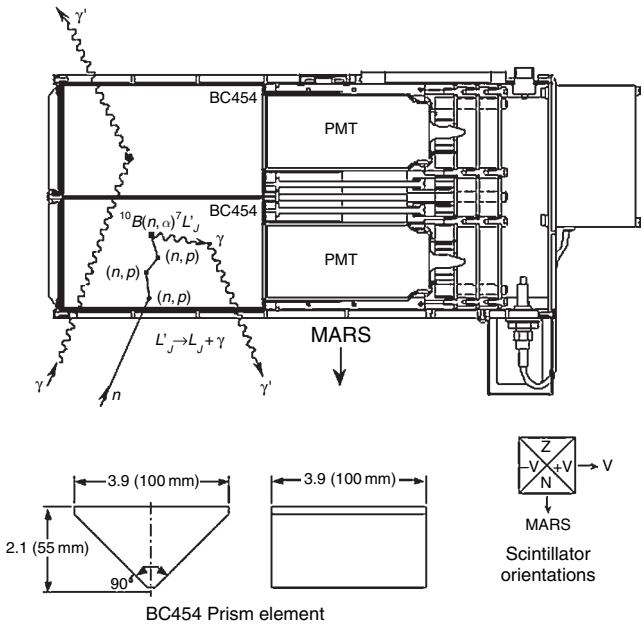

Figure 6.1. A line drawing of the sensor element of MONS showing the different kinds of neutron and gamma-ray interactions.

The Mars Odyssey spacecraft orbits Mars such that the outward face of the same prism always faces downward toward Mars (along the nadir, N, direction, which will be called Prism 1 throughout this chapter), one faces upward away from Mars (along the zenith, Z, direction, Prism 3), one faces forward along the velocity vector of the spacecraft parallel to the surface of Mars (+V, Prism 2), and one faces backward (−V, Prism 4). Because the velocity of the spacecraft in near-circular orbit about Mars is 3.39 km s^{-1}, which is higher than that of a thermal neutron (1.89 km s^{-1} at a temperature of 220 K), the forward-facing scintillator element scoops up thermal neutrons like a snow plow, and the backward-facing element outruns them (Feldman and Drake, 1986). Higher energy neutrons from Mars are less and less affected by this process the higher energy they have. Neutrons from the spacecraft are not affected at all because their place of origin travels with the same speed as the sensor. The difference in counting rate between the forward- and the backward-facing sensors therefore provides a sensitive measure of the thermal-neutron flux from Mars.

A 0.68 mm thick Cd sheet covers both of the end triangular faces of all four scintillator elements and a separate sheet covers the nadir face of Prism 1. Because Cd has a very large absorption cross section below about 0.3 eV, these sheets significantly reduce the contribution from thermal neutrons coming from these directions. Prism 1 therefore serves as a stand-alone epithermal-neutron sensor. Results of laboratory calibration of the sensor, along with its simulated response function, are given in Feldman *et al.* (2002a). Absolute calibration of the sensor as mounted on the spacecraft while in mapping orbit was made by equating thermal- and epithermal-counting rates measured poleward of +85° (Feldman *et al.*, 2003) to those determined from simulations of these rates using the Monte Carlo Neutral Particle eXtended computer code (MCNPX) fitted with a special planetary patch developed for Mars (Prettyman *et al.*, 2004). The second and third steps in this simulation process involve propagating these leakage fluxes to the orbit of Mars Odyssey using Liouville's theorem (Feldman *et al.*, 1989) and then folding them into the response function of the spectrometer.

An example of this procedure for epithermal neutrons is given in Figure 6.2. The sequence of steps used to

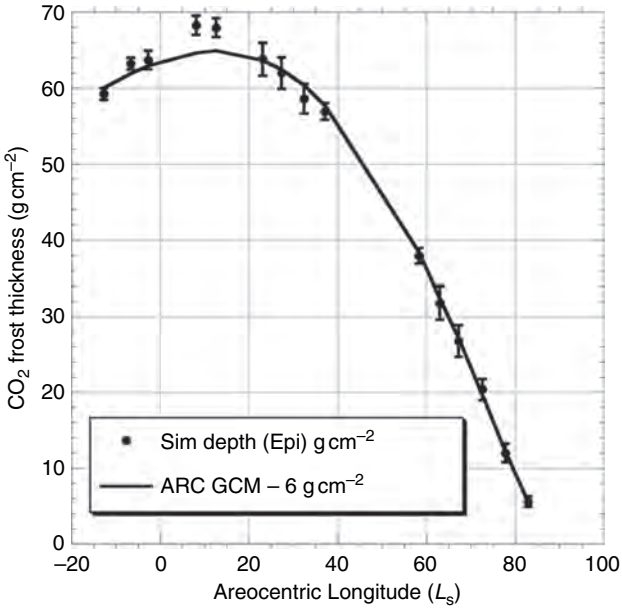

Figure 6.2. Comparison between the CO_2 frost thickness as a function of season poleward of +85° latitude and the calibrated simulation of those thicknesses using measured epithermal neutron counting rates.

implement this calibration is to first calibrate the thickness of seasonally deposited CO_2 ice simulated using the Ames Mars General Circulation Model (MGCM) (Haberle *et al*., 1999; Nelli *et al*., 2006) to those inferred from the measured time-dependent attenuation of hydrogen-capture 2.23 MeV gamma rays (measured using the GRS instrument aboard Mars Odyssey) poleward of 85° N. An offset of 6 g cm^{-2} was found necessary to obtain the best fit. These thicknesses were then used in a 1D layered simulation of epithermal-neutron counting rates for a layer of CO_2 ice above a thick deposit of 100% H_2O (Feldman *et al*., 2003). A multiplicative calibration factor for these simulated counting rates was then found that best fits the rates measured by MONS. As can be seen in Figure 6.2, the fit is excellent. This calibration factor, along with another one estimated using the same procedure for measured thermal-neutron currents, is used for all simulations of regolith compositions, hydrogen abundances, and stratigraphy for comparison with all thermal- and epithermal-neutron currents measured during the mission. The absolute calibration for fast-neutron currents was obtained poleward of 85° S latitude using the observed saturation of fast-neutron counting rates when the CO_2 ice is sufficiently thick during local winter (Prettyman *et al*., 2004). The calibrated fast-neutron model was then used to determine the thickness of CO_2 poleward of 85° N during northern winter, which was found to be consistent with the GCM, thus confirming the calibration assumptions for the thermal and epithermal neutrons.

The range of counting-rate histograms measured using the downward-facing sensor (Prism 1) is illustrated in Figure 6.3. An average of 600–20 s spectra is given in Figure 6.3a for times during northern summer poleward of 85° N. An average of the same number of spectra for times during northern winter is shown in Figure 6.3b. The solid lines in each spectrum give fits to a power-law continuum

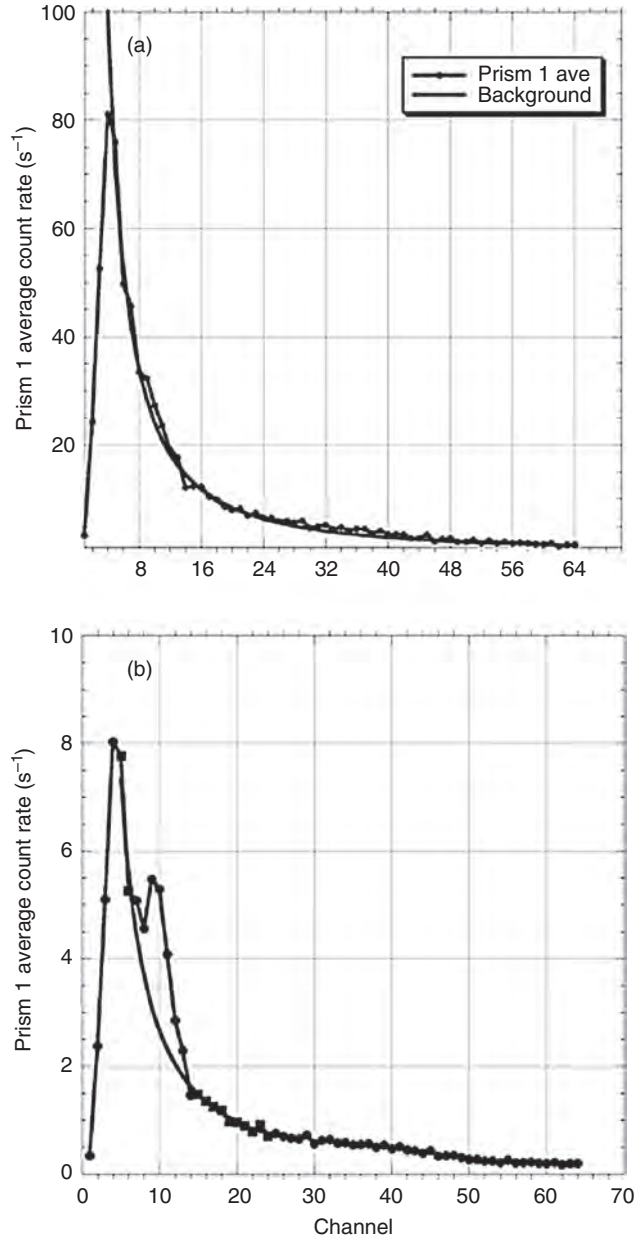

Figure 6.3. (a) The Prism 1 counting rate spectrum summed over 600, 20 s histograms measured while MONS was poleward of +85° during northern summer when there was no CO_2 ice on the ground. (b) The same counting rate histogram summed over conditions of maximum CO_2 ground cover during northern winter. The channels correspond to the electron-equivalent energies deposited in the scintillators by any ionizing radiation.

background that comes mostly from galactic and planetary gamma rays that lose energy in the scintillators. Inspection of the wintertime spectrum, which corresponds to a thick layer of CO_2 ice, and which is close to, but less intense than, an average spectrum measured above near-equatorial latitudes, shows that counting rates within the peak are determined quite well. The signal to continuum background ratio is seen to be very good, thereby lending confidence (and also relatively high accuracy) to our absolute calibration of measured MONS epithermal counting rates. This condition does not hold equally for measurements made during northern

summer at high northern latitudes where the groundwater ice content is high. This fact is seen by the very small area of the counts between the "peak" and the continuum background in Figure 6.3a. For these conditions, the signal to continuum background ratio is low, and systematic errors due to our choice of data-reduction procedure prevents an accuracy better than about ±10% (Feldman *et al.*, 2004a). As of September 2005, sufficient data have been accumulated that our statistical uncertainties in measured epithermal counting rates are of order ±1% at latitudes equatorward of about ±75° during local summer, and at high latitudes during local winter. Our estimate of systematic uncertainties for counting rates at all latitudes was made by comparing the results from three separate data-reduction codes (Tokar *et al.*, 2002; Prettyman *et al.*, 2004; Maurice *et al.*, 2007), each using a different algorithm for determining and subtracting the continuum background from measured counting-rate histograms.

All of the data that will be presented in this chapter use our latest code (Maurice *et al.*, 2007). This latest dataset extends from the start of mapping orbit on February 19, 2002, to the beginning of September 2005, just past the second summer at northerly latitudes. It is organized into two parts. The first consists of thermal-, epithermal-, and fast-neutron counting rates measured only during those parts of the year when there is no seasonal CO_2 ground frost cover. Only neutron energies nominally between about 700 keV and 2 MeV (actually, a small number of higher energy neutrons also contribute to the response in this range) were used for the fast-neutron rates. All counting rates are corrected to a constant atmospheric thickness of 16 g cm^{-2} and binned into a $2^\circ \times 2^\circ$ latitude–longitude cylindrical grid (Maurice *et al.*, 2007). This set is used for studies of the distribution of WEH. The second set consists of a time series of all measured counting rates, which is used for studies of the seasonal variation of CO_2 frost.

6.3 INFORMATION CONTENT OF NEUTRON DATA PACKETS

As mentioned in the previous section, neutrons are initially produced over a broad range of energies through interactions between GCRs and the nuclear constituents of planetary material. After production, these neutrons scatter down in energy to produce a final energy distribution of neutron flux (neutron flux is the neutron density times its speed) that is in equilibrium with the neutron production rate at high energies. Because of this equilibrium, the average rate of neutron energy loss across any energy boundary in an infinite medium must be constant, equal to the neutron production rate. Ultimately, these rates must equal the rate of energy loss to nonelastic collisions, primarily neutron absorption at thermal energies. For a hydrogen-rich medium, the neutron flux is low in the epithermal energy range because the energy loss rate due to elastic scattering is high. The neutron signature of hydrogen is therefore a very low neutron flux intensity in the epithermal-neutron energy range to balance the very large energy-loss rate at these intermediate energies. In contrast, the signature of pure CO_2 is very different. Here, the atomic masses of carbon and oxygen are intermediate between that of hydrogen and those of the major rock-forming elements that make up most of the regolith (e.g., Mg, Al, Si, Ca, Fe), thereby resulting in an intermediate energy-loss rate in the epithermal energy range. The flux intensity in this range is therefore intermediate between that of a hydrogen-rich and a hydrogen-poor soil. In contrast, both carbon and oxygen have extremely low thermal-neutron absorption cross sections, thereby yielding a very large neutron flux at thermal-neutron energies to attain equilibrium between neutron production and loss rates. Indeed, MCNPX simulations show that a pure, thick CO_2 layer yields a thermal-neutron counting rate that is about 30 times higher than that of a feldspathic, hydrogen-poor regolith.

As for most remote-sensing experiments, MONS returns counting-rate data that require a model to interpret in terms of physical reality. Although it is possible to convert measured neutron leakage currents into the abundance and stratigraphy of hydrogen and its time-varying CO_2 frost cover with the use of spatial models, the fact that there are only three measurables (thermal-, epithermal-, and fast-neutron currents) dictates that these models need to be extremely simple. Accordingly, a 1-D model is essential, which consists of two layers that are spatially infinite in surface area. The unknowns of this model include the abundance of hydrogen in the upper layer (Y%), the thickness of this layer (D in g cm^{-2}), and the abundance of hydrogen in the lower layer (X%), which is assumed to be infinitely thick. The thickness, D, can be translated to a physical depth, d, if the structure of the soil is known. In the absence of rocks, dividing D in g cm^{-2} by the density of the soil, ρ, in g cm^{-3}, yields the depth, d, in cm. For example, $D = 10$ g cm^{-2} is equivalent to about $d = 6$ cm if the density is about 1.65 g cm^{-3} as found at the Viking landing sites (Arvidson *et al.*, 1989). However, translation of D to d in the presence of rocks depends on the physical size of the rocks, their density, and their surface abundance.

The 2-layer model, while simple, is also grounded in reality. Theoretical models have suggested that dry soil should overlie ice-rich soil on Mars based on the basic physics of molecular diffusion and phase partitioning of water in soils (e.g., Mellon and Jakosky, 1993). In addition, terrestrial analogs of Martian permafrost in polar desert environments exhibit exactly this sort of stratigraphy (e.g., McKay *et al.*, 1998).

For the sake of simplicity, all hydrogen abundances in this chapter are specified in units of mass percent of WEH, even though neutrons cannot discriminate between the various possible molecular associations of hydrogen. For the case of a CO_2 upper layer, it is assumed to be CO_2 containing a variable mass fraction of dust and having a thickness, D.

The elemental composition of the top (100%–Y%) and bottom (100%–X%) layers needs to be either chosen a priori, or determined by some other means. Conveniently, the dependence of epithermal- and fast-neutron leakage currents on composition other than hydrogen is small (Feldman *et al.*, 1991; Hodges, 2002; Prettyman *et al.*, 2004; Lawrence *et al.*, 2006). Differences in the responses to low and high Fe-containing basalts, and the Mars Pathfinder

composition (Wänke *et al.*, 2001) amount to a maximum of 4%–5%, for epithermal- and fast-neutron leakage currents, respectively (Prettyman *et al.*, 2004). This difference becomes smaller as the WEH content becomes larger. In contrast, thermal-neutron currents are very sensitive to composition, amounting to a maximum of 30% for these compositions (Prettyman *et al.*, 2004). In addition, epithermal- and fast-neutron currents are sensitive to the thickness of the atmosphere at the 4%–5% level, but the thermal-neutron currents are relatively insensitive (Prettyman *et al.*, 2004). This sensitivity depends on hydrogen content in a known way. Using this knowledge (from simulations), we have developed an iterative procedure to correct all measured epithermal- and fast-neutron counting rates due to time-dependent and spatially dependent atmospheric-thickness variations using the MOLA-derived topography (Smith *et al.*, 1999), and the seasonal and geographical variations in atmospheric thickness calculated using the Laboratoire de Météorologie Dynamique (LMD) MGCM (Forget *et al.*, 1999). The results are counting-rate matrices corrected to that of a constant 16 g cm^{-2} thick atmosphere (see Maurice *et al.*, 2007).

Real geologic surfaces on Mars are more complicated than the simple semi-infinite half space model assumed here for our WEH analyses. An example would be terrain observed at Meridiani Planum and Gusev crater by the Mars Exploration Rovers (MERs) (Clark *et al.*, 2005; Grotzinger *et al.*, 2005; McLennan *et al.*, 2005; Yen *et al.*, 2005; Wang *et al.*, 2006a). Meridiani Planum and Gusev crater contain evaporite layers of hydratable minerals some tens of centimeters or more thick, along with circular depressions that contain a variable-thickness dust cover above local ground rock and soil compositions. This situation no doubt also exists at high latitudes where, in addition, layers of water ice–rich sediments are stable very near to the surface (Leighton and Murray, 1966; Farmer and Doms, 1979; Fanale *et al.*, 1986; Zent *et al.*, 1986; Paige, 1992; Mellon and Jakosky, 1993; Mellon *et al.*, 2004). The difference is that whereas the mean-free path for energy-loss collisions within low-WEH content material found at low to mid latitudes is about 1 m along the broken path of a neutron, it drops to about 1 cm for water-rich material (Feldman *et al.*, 1993a,b). Such short scattering lengths result in thermal neutrons being trapped in spatially confined hydrogen-rich regolith below the surface until they are absorbed by hydrogen and other rock-forming elements within these deposits. At polar latitudes, thin layers of dust near the surface covered by relatively thin layers of water ice, which could then appear as relatively low-albedo soil, can strongly modify leakage neutron currents (as well as neutron fluxes within these layers) by up to a factor of 2 (Feldman *et al.*, 1993a). Such a stratigraphy may appear to be an anomalous, self-absorbing thermal-neutron medium when viewed from orbit because normally escaping thermal and epithermal neutrons are locked up spatially and then absorbed below the surface by the hydrogen-rich, subsurface deposits. And, of course, there is ample proof from visible images that significant structural layering exists at spatial scales much smaller than the resolution of MONS (which is about 600 km) (e.g., see Malin and Edgett, 2001).

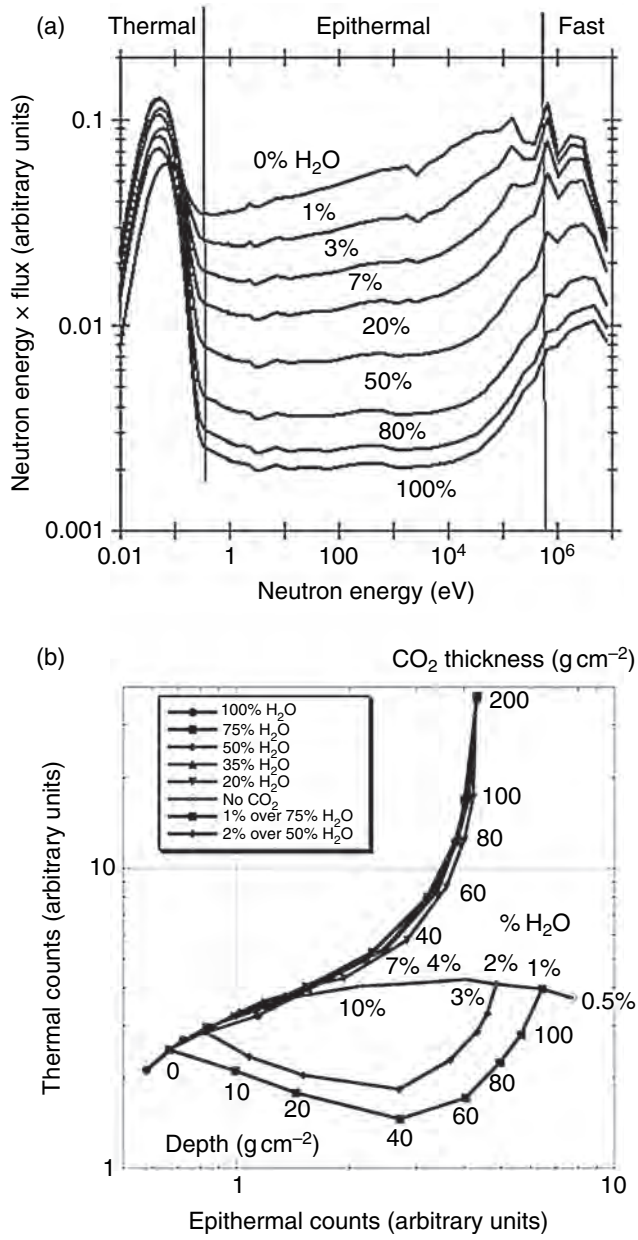

Figure 6.4. (a) Simulated neutron energy times flux spectra for a ferroan anorthosite composition loaded with various weight percents of H_2O. (b) Simulated thermal neutron (Prism 2 − Prism 4) and epithermal neutron (Prism 1) counting rates for a variety of surface compositions and stratigraphy. See the text for details.

A few examples of the expected variability of neutron counting rates for different surface conditions are shown next for purposes of illustration. Simulations of representative samples of neutron currents for a variety of one- and two-layered models are shown in Figure 6.4 (Feldman *et al.*, 2003). The spectra in Figure 6.4a assume a single, semi-infinite soil stratigraphy and have units of flux times neutron energy. These units are routinely chosen in nuclear physics for displaying energy spectra because neutron moderation theory (Fermi, 1950) predicts a $1/K$ dependence for energies in the epithermal energy range. Multiplication by K then yields a constant, as is evident for energies between 0.3 eV

and about 0.3×10^5 eV in Figure 6.4a. These spectra all assume a soil composition of Ferroan Anorthosite (FAN) loaded with various mass percentages of H_2O. A plot of the area beneath the thermal peaks at energies below about 0.4 eV as a function of regolith water content (not shown here but given in Figure 6.4b) shows that while the thermal neutrons first increase and then decrease with increasing H_2O content, they only span a factor of about 2 in intensity range. The initial increase occurs because the rate of thermalization increases with increasing H content, thereby confining the thermal neutrons to a smaller volume near the surface, which then increases their outward leakage rates. But eventually, thermal neutrons become trapped within this near-surface volume and are subsequently absorbed by hydrogen and the major rock-forming elements of the regolith. In contrast, the epithermal-neutron intensity varies over a range that spans a factor of 20, and the fast neutrons span a factor of about 8. This figure then demonstrates graphically that epithermal neutrons provide the most sensitive neutron measure of hydrogen while fast neutrons are a close second.

These simulations are expanded to two-layered models in Figure 6.4b (see also Feldman *et al.*, 1993a). Here, the neutron flux times energy type spectra shown in Figure 6.4a were converted to normalized counts per second for an assumed Pathfinder composition using a simulated model response function of the MONS calculated using MCNPX. For the purposes of this illustration, these rates are not calibrated in Figure 6.4b because the incident GCR intensity was normalized here to a constant current of one particle per cm^2 per second. The double-valued response of thermal-neutron rates to a single thick layer of Pathfinder soil composition containing various amounts of WEH is shown by the convex-upward horizontal line. Close inspection shows the thermal-neutron counting rates range between about 2 and 4 s^{-1}. Here, WEH increases from right to left, and therefore will be primarily determined by the epithermal counting rate. While the thermal neutron-counting rate for the single-layer stratigraphy (a homogeneous medium) first increases and then decreases as WEH increases, the opposite behavior occurs if this water-rich layer is buried beneath a relatively water-poor overburden. A different parameter is varying here (depth). At first the anomalous absorption in the water-rich layer dominates the escaping flux intensity, but eventually as the depth increases further, the escaping flux intensity approaches that of the homogeneous case dominated by the low water composition of the upper layer. The two concave-upward curves give 75% WEH beneath 1% WEH (lowest curve) and 50% WEH beneath 2% WEH (upper curve). This behavior reflects the effective anomalous absorption that is associated with any sharp, subsurface boundary between hydrogen-rich soil and hydrogen-poor soil that marks this type of stratigraphy, as just described.

In contrast, burial of a water-rich layer beneath a CO_2 layer of varying thickness yields the sharply upward-going curves that connect to the single WEH-rich Pathfinder soil curve at 20%, 35%, 50%, 75%, and 100% WEH. All curves bend upward to asymptote as a single vertical line having epithermal counting rates that are intermediate between that of hydrogen-rich and hydrogen-poor soils. The numbers next to these curves give the thickness of the CO_2 layer in g cm^{-2}. As can be seen, for CO_2 thicknesses greater than about 40 g cm^{-2}, the thermal-neutron counting rate no longer can be used to discriminate between the WEH content of the lower WEH-rich soil.

This range of possible counting rates is seen to closely resemble measured counting rates, shown in Figure 6.5 (note that the axes scales in Figure 6.4b are logarithmic and those in Figure 6.5 are linear). At the left are the counting rates for the whole planet and at the right, the highest latitudes ($\lambda < 70^\circ$ S and $\lambda > 80^\circ$ N) are excluded. The difference is seen most clearly in the scatter plot between thermal- and epithermal-neutron currents in the top two panels. The nearly vertical straight line at an epithermal-neutron counting rate of about 2 s^{-1} in Figure 6.5a (at the upper left) is for the latitude range between 70° S and 86.8° S, which includes the thick CO_2 veneer that covers most of the residual south polar cap. In contrast, the small downward- and leftward-angled straight line for epithermal rates between 1 and 2 s^{-1}, and the thermal rates between about 3.8 and 4.5 s^{-1} in Figure 6.5a at the lower left, is for the latitude range between 80° N and 86.8° N. These anomalies are visible for the fast-neutron counting rates by comparing the lower left-hand corners of Figures 5c and 5d, but are seen to be much subdued.

A complementary presentation showing the similarity between simulated and measured counting rates is shown in Figure 6.6 for three separate latitude ranges. These include the relatively WEH rich northern (panels 6 a,b) and southern (panels 6 e,f) high latitudes, and the relatively WEH poor near-equatorial latitudes (panels 6 c,d). In each of the fast versus epithermal counting rate maps on the left, labels for the WEH abundance of the assumed, single-layer ($D = 0$) semi-infinite simulations are shown below the lowest curved line, and lines for the series of simulations for 0, 10, and 20 g cm^{-2} thick layers containing 1% WEH are labeled using arrows. The same labeling scheme for the thermal versus epithermal counting rates is shown on the uppermost plot on the right, which is extended to include thicknesses as large as 60 g cm^{-2}. Here, the single, semi-infinite, unburied, water-rich layer is the topmost curve. We will return to a discussion of these data in the next section. However, we note here that although a scatter plot between fast and epithermal neutrons can discriminate WEH abundance from burial depth below a relatively desiccated overburden, the effect of burial depth is relatively small, comparable to that expected for different elemental compositions (~5%) and the current measurement uncertainties for fast neutrons (~15%) (Feldman *et al.*, 2004a). In addition, separation of various burial depths becomes very small beyond depths of about 20 g cm^{-2}. In contrast, discrimination between WEH abundance and burial depth in scatter plots of thermal- and epithermal-neutron currents is readily apparent down to about 60 g cm^{-2} if the composition is known. Unfortunately, the scatter plot between thermal- and epithermal-neutron counting rates in the middle panel of Figure 6.6 shows that this assumption is violated for at least some of the terrain at low to mid equatorial latitudes (45° S $< \lambda <$ 45° N). Here, thermal-neutron counting rates larger than the maximum allowed for a semi-infinite deposit of an average of Pathfinder and both Viking

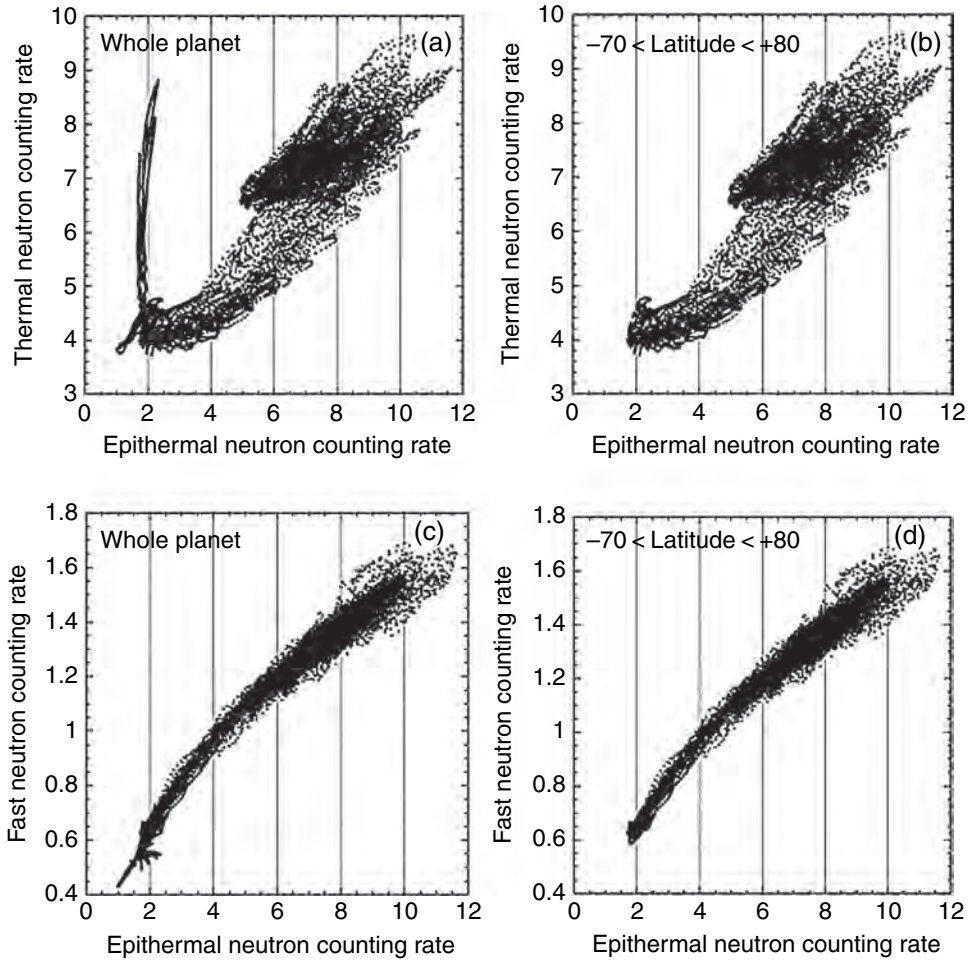

Figure 6.5. Scatter plots of measured thermal (Prism 2 – Prism 4), fast (energies between 0.7 and 2 MeV using Prism 1), and epithermal (Prism 1) neutron counting rates, in each $2^{o} \times 2^{o}$ cylindrical latitude × longitude surface elements on Mars. See the text for details.

soils containing no WEH are observed, yet should not be allowable. Because of the poor spatial resolution of MONS observations, any measured counting rate will actually be the average of counting rates from all samples within about a 600 km diameter spot size (Prettyman *et al.*, 2004). Therefore, every measured rate should be contained within the outermost boundaries of the simulations because they are convex outward (they form a convex set). Large regions of the Martian surface must therefore have compositions containing much less thermal neutron–absorbing elements such as Fe and/or Cl than do the Pathfinder and Viking soils (Prettyman *et al.*, 2004). This same conclusion must also hold for the upper boundary of the scatter plot between fast and epithermal neutrons because it is convex outward. Although there appears to be a violation of this rule for near-equatorial latitudes in Figure 6.6, it turns out that another contour for moderate WEH abundant soils beneath 0% WEH Pathfinder soil cradles these measurements from above (not shown in Figure 6.6).

Nevertheless, if the composition of surface soils is known, the thermal–epithermal counting-rate plots in the right-hand panels of Figure 6.6 can be interpreted readily in terms of WEH content of the lower layer and the thickness, D, of the upper layer. This fact was used by Feldman *et al.* (2006) to estimate these quantities within the Vastitas Borealis formation at high northerly latitudes. This formation contains a thick mantle that is derived from the outflow channels that pass near the Pathfinder and Viking landing sites (Head *et al.*, 2002; Kreslavsky *et al.*, 2002). Because the plots in Figure 6.6 were derived from simulations that used an average of the Pathfinder and both Viking compositions (Wänke *et al.*, 2001), the scatter plot in Figure 6.6b shows that for latitudes between 55° N and 75° N the WEH of the lower layer ranges between about 5% and 60% by mass, and the depth ranges between about 5 and 20 g cm^{-2}. These two ranges are very similar to those derived for soils at high-southerly latitudes (Prettyman *et al.*, 2004). Although not shown explicitly in Figure 6.6, a detailed look at the data shows that the maximum burial depth occurs at about 60° N latitude.

Another source of information regarding composition can be derived from the macroscopic absorption and energy-loss cross sections of surface material (Fermi, 1950). These are the only two parameters that control the energy distribution of neutron flux in equilibrium with surface soils:

$$\sum\nolimits_{\mathrm{a}} = \sum_{i=1}^{n} \sigma_{\mathrm{a}i} w_i \, A_{\mathrm{o}}/A_i \quad \mathrm{cm}^2\,\mathrm{g}^{-1} \tag{6.1}$$

and

$$\sum\nolimits_{\mathrm{el}} = \sum_{i=1}^{n} \zeta_i \, \sigma_{\mathrm{s}i} w_i \, A_{\mathrm{o}}/A_i \quad \mathrm{cm}^2\,\mathrm{g}^{-1}, \tag{6.2}$$

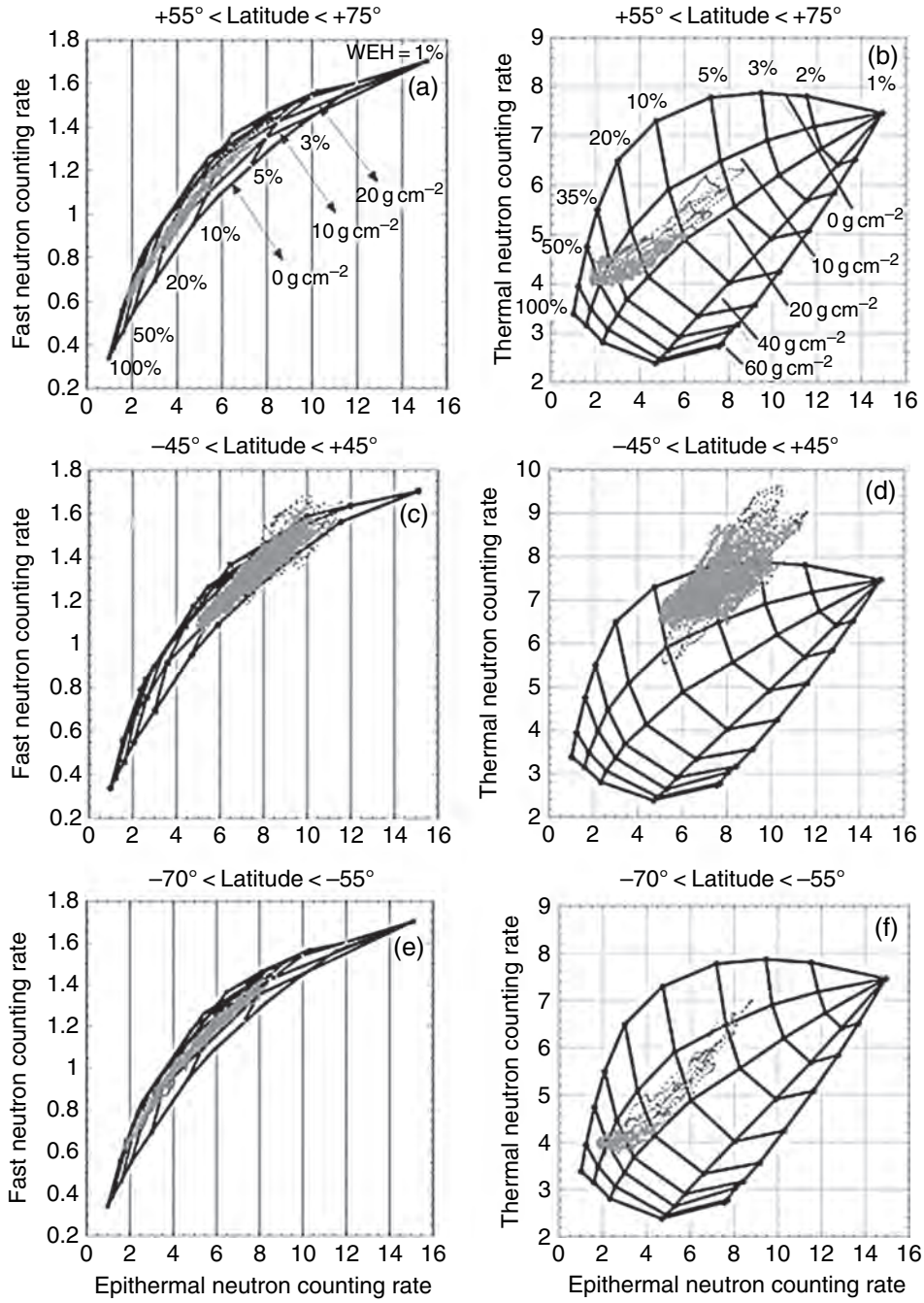

Figure 6.6. Scatter plots of measured thermal (Prism 2 – Prism 4), fast (energies between 0.7 and 2 MeV using Prism 1), and epithermal (Prism 1) neutron counting rates, in each $2^{o} \times 2^{o}$ cylindrical latitude x longitude surface elements on Mars overlayed on 2D matrices showing WEH abundance and depth beneath a surface layer containing 1 wt.% WEH. See the text for details.

respectively. Here σ_{ai} and σ_{si} are the elemental (i) absorption and elastic-scattering cross sections, ζ_i is the fractional neutron energy loss during elastic-scattering collisions, w_i is the weight fraction of element, i, having atomic mass, A_i, and A_o is Avagadro's number.

Strictly speaking, this derivation applies only for compositionally homogeneous terrain. Vertical layering such as that found at Meridiani Planum and Gusev crater (Clark *et al.*, 2005; Grotzinger *et al.*, 2005; McLennan *et al.*, 2005; Yen *et al.*, 2005; Wang *et al.*, 2006a) and inferred from optical imagery at many other locales (Malin and Edgett, 2001) would violate this assumption. Regardless, adoption of this assumption is the best we can do with the limited data available. These two cross sections are then proportional to the ratios of fast-to-epithermal-neutron currents (F/E) and fast-to-thermal-neutron currents (F/T) respectively (Feldman *et al.*, 1993b, 2000; Prettyman *et al.*, 2003). Global maps of these two ratios are shown in Figure 6.7. For the purpose of this display, the measured counting rates in each of the energy ranges were first normalized to unity before ratios were calculated in order to make the resulting maps as independent as possible to the sensitivities of the instrumentation. Because the mass of a proton is very close to that of a neutron, and is much smaller than that of its nearest, significantly abundant element, oxygen, the macroscopic energy-loss cross section (which is proportional asymptotically to $2/A_i$, where A_i is the atomic mass of element i [Fermi, 1950])

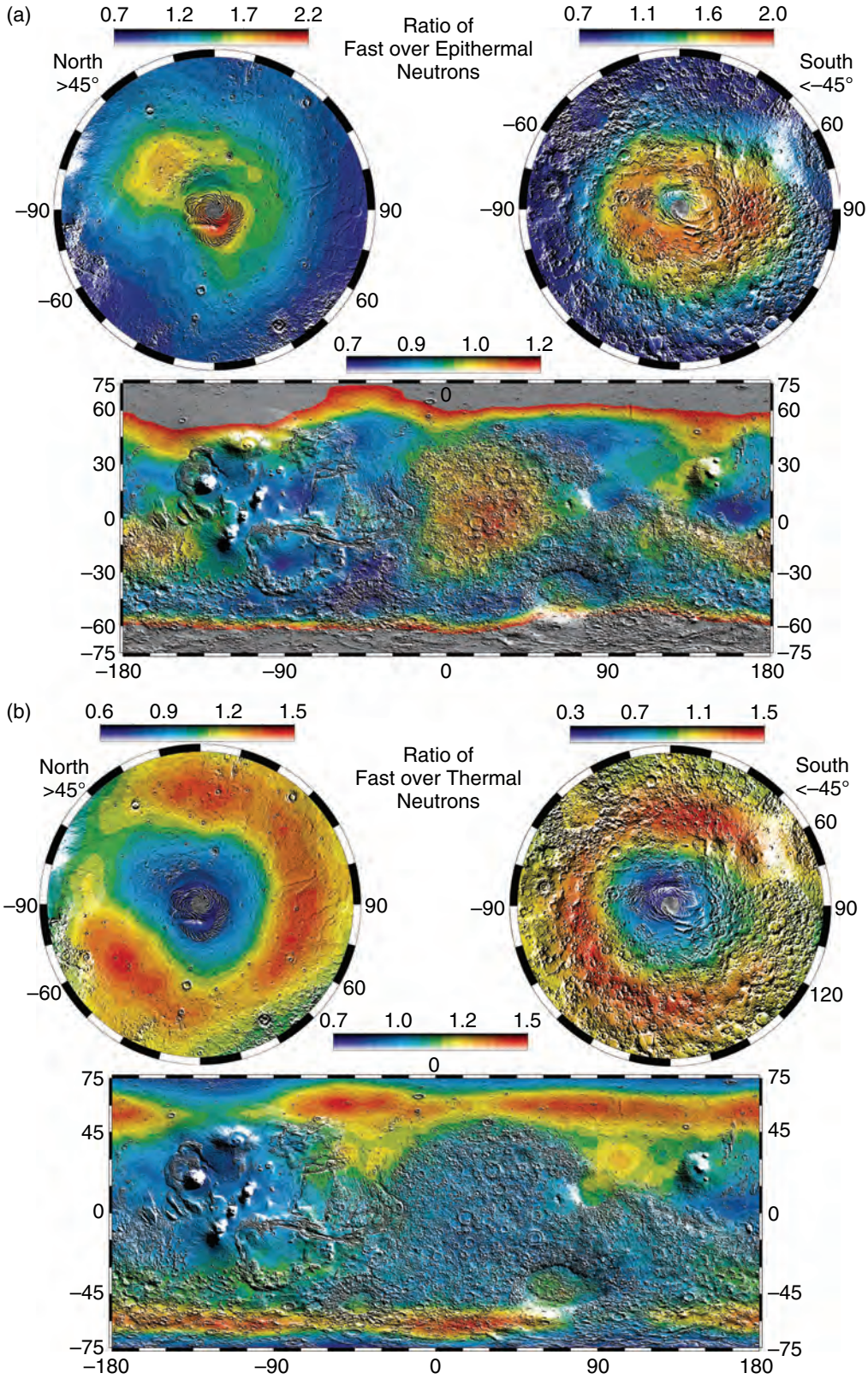

contains information that is dominated by hydrogen. We note though, that although construction of the ratio of fast-to-epithermal-neutron counting rates reduces its dependence on composition through the dependence of both fast and epithermal neutrons to the average atomic mass (Maurice *et al.*, 2000; Gasnault *et al.*, 2001), the

Figure 6.7. Maps of the ratios of fast over epithermal (a) and fast over thermal (b) neutron counting rates overlayed on shaded relief maps of Mars. In each set, the top maps are stereographic projections north of +45° latitudes (left) and south of –45° latitudes (right). The bottom maps are cylindrical projections between ±75° latitude. (For a color version of this figure, please refer to the color plate section or to the e-Book version of this chapter.)

Table 6.1 *Maximum/minimum ratio of lunar and Martian neutron counting rates*

Moon		Mars		Mars	
Thermal	3.0	Thermal	2.59	Fast/thermal	4.2
Epithermal	1.12	Epithermal	11.5	Fast/epithermal	3.1
Fast	1.30	Fast	3.95	Epithermal/thermal	5.88

epithermal neutrons by themselves provide a relatively unique proxy for the WEH abundance because the effect is so large (Feldman *et al.*, 1991, 2000; Lawrence *et al.*, 2006).

These measured counting rates can be placed into perspective by comparing them with those measured on the Moon (Feldman *et al.*, 2002b). The ratios of maximum to minimum thermal-, epithermal-, and fast-neutron counting rates for both the Moon and Mars during CO_2 frost-free conditions are compiled in Table 6.1. We note that although the range of thermal counting rates is the same for both planets (for different reasons), they are much larger for epithermal and fast neutrons for Mars then they are for the Moon. Whereas the maximum-to-minimum ratio of epithermal neutrons from the Moon (where water is virtually absent) is 1.12, it is 11.52 on Mars (which is very rich in water). The same comparison for fast-neutron counting rates yields similar results, although not quite as large a difference. We also note that while construction of the ratio of fast-to-epithermal-neutron counting rates (F/E) reduces its dependence on mass composition, it also reduces its dynamic range from 11.5 to 3.1. This difference needs to be compared with the relative effect on dynamic range caused by variations in elemental abundances for fast- and epithermal-neutron currents, which, by itself, is only a 5% effect.

Inspection of the north polar projection shows that the highest intensity comes from the residual water-ice deposit that covers the North Pole. Secondary maxima are centered on Scandia Colles in the north and a broad range of terrain at high southern latitudes. Note that the F/E ratio is a relative minimum above the south residual ice cap near the South Pole. Most of this cap is known to be covered by a thick veneer of CO_2 ice, in agreement with our interpretation that water ice is not exposed to the atmosphere above most of this cap.

The F/T maps show a different behavior. This map is not as easy to interpret because the thermal-neutron flux responds strongly both to composition and to burial depths of WEH. However, we note that the strongest features are relative zonal maxima between 50° and 60° latitude in both hemispheres. These maxima have spatial widths that are close to the full width at half maximum spatial response function of MONS. They therefore must reflect a relatively sharp latitudinal boundary between different compositional domains. A likely possibility is that these maxima reflect (although not uniquely) the onset of additional water ice–rich deposits poleward of 60° N and S latitudes that are buried beneath a relatively thick water-poor overburden at its lowest latitude boundary. More specifically, the ice-rich layer may be buried deeper than the detectability depth (~1 m) below a relatively dry overburden equatorward of about 60° N and S latitudes, and the depth shallows with increasing latitude such that it begins to be sensed by MONS poleward of this boundary. Such a stratigraphy is modeled by the two series of simulations that exhibit concave upward profiles in Figure 6.4b and is consistent with the fact just noted in Figures 5b and 5f that the maximum burial depth occurs at about 60° N and S latitudes. This behavior could then reflect a sharp latitudinal transition between WEH deposits that are associated with hydrous minerals alone equatorward of 50° N and S latitudes, to a prominent association with buried water ice in addition to water of hydration at more poleward latitudes (see, e.g., Figure 6.4 of Farmer and Doms, 1979). These buried water-ice deposits then quickly approach the surface at higher latitudes.

6.4 SCIENTIFIC RESULTS OF STUDIES TO DATE

6.4.1 The global distribution of WEH

The first determination of the global distribution of WEH on Mars was made using the neutron spectrometers aboard Mars Odyssey (Boynton *et al.*, 2002; Feldman *et al.*, 2002b; Mitrofanov *et al.*, 2002; Tokar *et al.*, 2002). Many theoretical studies of the stability of water ice on Mars conducted before then concluded that water ice should be stable just below the surface at high latitudes, but unstable at low to mid latitudes (Leighton and Murray, 1966; Farmer and Doms, 1979; Fanale *et al.*, 1986; Zent *et al.*, 1986; Paige, 1992; Mellon and Jakosky, 1993). The most comprehensive presentation of a lower bound to the global abundance of WEH inferred from epithermal-neutron counting rates alone was given in Feldman *et al.* (2004a) and illustrated over a shaded relief map of MOLA-generated topography (Smith *et al.*, 1999) in Figure 6.8. For this presentation, the epithermal-neutron counting rates averaged in individual $2° \times 2°$ latitude–longitude cylindrical-grid bins were first smoothed using a 2° radius Gaussian function before conversion to WEH using the algorithm given by Equation 1 in Feldman *et al.* (2004a). Inspection shows that although the dominant reservoirs of WEH in surface soils reside at high latitudes in both hemispheres as predicted, significant reservoirs also exist at near-equatorial latitudes. Different aspects of these observations are discussed next.

Similar maps of the global distribution of WEH were presented by Mitrofanov *et al.* (2002, 2003, 2004) from leakage neutron currents measured using the high energy neutron detector (HEND) experiment, also aboard Mars Odyssey. Their differences and their possible causes are presented in Appendix A. However, in the following review, we will concentrate on the data measured using MONS and their interpretations in terms of models of exchange between the various water reservoirs of Mars.

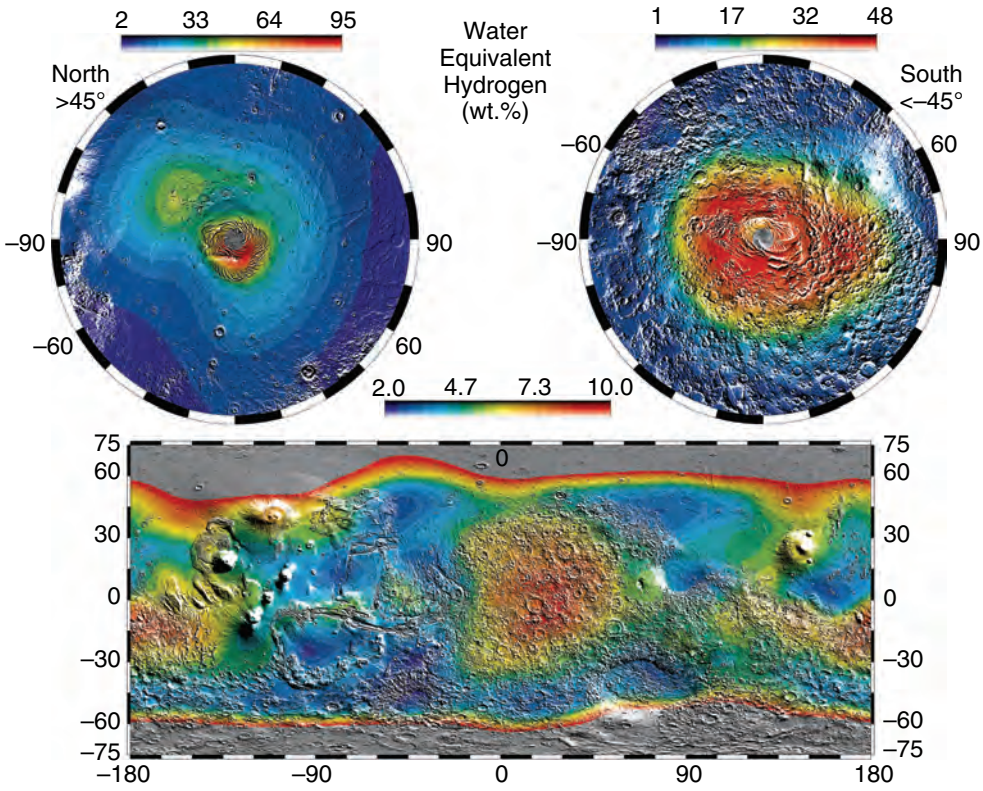

Figure 6.8. Maps of water-equivalent hydrogen overlaid on shaded relief maps of Mars. The top maps are stereographic projections north of +45° latitudes (left) and south of –45° latitudes (right). The bottom map is a cylindrical projection between ±75° latitude. (For a color version of this figure, please refer to the color plate section or to the e-Book version of this chapter.)

Starting first with the near-equatorial distribution of WEH, we see that it is concentrated in two longitudinal ranges south of the dichotomy boundary within highland terrain. The largest deposit is centered in southern Arabia Terra near the equator at about 30° E longitude. Translation of measured epithermal-neutron counting rates to WEH abundance assuming a single semi-infinite deposit of uniform Pathfinder composition yields a maximum abundance of $9.8 \pm 1.5\%$ by mass (Feldman *et al.*, 2004a). A secondary maximum occurs on the other side of the planet near Medusae Fossae at about 15° S and 175° W. It peaks at $8.8 \pm 1.3\%$ by mass. This deposit extends eastward until it intersects the meridional lane that skirts the western edge of Olympus Mons, which then connects to the much higher-abundance WEH deposit at high northern latitudes, where subsurface water ice is stable. It also extends westward until it connects with a second meridional lane that skirts the western side of Elysium Mons before connecting to the rich WEH deposit at high northern latitudes. Another prominent relative maximum occurs at Alba Patera (40° N and 110° W), amounting to $7.6 \pm 1.0\%$ by mass.

Equally important to note are the relative minima. Prominent minima occur along a broad meridional lane centered at about 60° W that connects through Solis Planum and Argyre on the south, through Echus Chasma and Chryse Planitia to Acidalia on the north. A second meridional lane of minimum WEH abundance at about 80° E connects the northeast corner of Hellas through the southeast corner of Isidis to Utopia basin on the north. A final prominent minimum is centered on Cerberus at 5° N and 165° E. All of the WEH-poor meridians cross a prominent zonal lane of relative minimum at about 45° S just north of the relative zonal maximum in F/T noted previously in Figure 6.7.

Water-equivalent hydrogen abundances within a selection of these locations are given in Table 6.2 (Feldman *et al.*, 2004a). Also included are estimates of the WEH abundances if they are assumed to be buried beneath a $10\,g\,cm^2$ layer containing 2% WEH. Such an assumption, with either a 2% or a 1% WEH-containing overburden, best fits the data within 45° of the equator, as seen in the middle left-hand panel of Figure 6.6 for WEH = 1% (Feldman *et al.*, 2004a). We note that the absolute minimum WEH abundance derived from epithermal-neutron counting rates assuming a semi-infinite stratigraphy is 2 wt.%.

At latitudes higher than about 50° N and S, WEH abundances are considerably higher. The peak abundance is observed over the north residual cap amounting to between 80% and 100% by mass. In contrast, the WEH abundance over the southern residual cap is a relative minimum, presumably because this cap is mostly covered by a thick veneer of CO_2 ice. A secondary maximum at northern latitudes covers a broad area centered on Scandia Colles at about 70° N and 130° W, amounting to about 50%–60% by mass. At high southern latitudes the WEH abundance is also high in a large area that has an equatorial extension at about 95° E. The maximum WEH abundances in the high southern latitude regions are between about 50% and 70% by mass (Prettyman *et al.*, 2004) as can also be seen in Figure 6.5f. Both WEH mass percentages are considerably larger than can fit into open pore spaces between regolith grains (Tokar *et al.*, 2002; Mitrofanov *et al.*, 2004; Prettyman *et al.*, 2004; Litvak *et al.*, 2006), thereby requiring a nondiffusive emplacement mechanism from the atmosphere and/or retention by

Table 6.2 *Lower-bound water-equivalent hydrogen abundances*

For selected sites ($5^o \times 5^o$ areas)			
		Mass % of H_2O	
Site	(Latitude, Longitude)	Semi-infinite	Below 10 g cm^{-2} 2% H_2O
Alba Patera	$+40^o$, -110^o	7.6 ± 1.0	
Arabia	-5^o, $+25^o$	9.8 ± 1.5	11.5 ± 1.7
Arabia Antipode	-15^o, -175^o	8.8 ± 1.3	10.2 ± 1.5
Argyre	-45^o, -45^o	2.0 ± 0.3	2.1 ± 0.3
Pathfinder	$+19.3^o$, -33.6^o	2.8 ± 0.4	3.0 ± 0.4
Sinus Meridiani	0.0^o, 0.0^o	7.7 ± 1.2	8.8 ± 1.3
Solis Planum	-25^o, -95^o	2.3 ± 0.3	2.4 ± 0.4
Viking 1	$+22.3^o$, -48.2^o	3.0 ± 0.4	3.2 ± 0.4
Viking 2	$+47.7^o$, $+134.1^o$	6.4 ± 1.0	7.2 ± 1.1

hydrogenous minerals. One example of a nondiffusive emplacement mechanism would be a relatively rapid airfall in the form of a mixture of dust and water ice as snow, driven by enhanced atmospheric water vapor that responds to changes in the Martian obliquity (Jakosky and Carr, 1985; Jakosky *et al.*, 1995; Head *et al.*, 2003; Mischna *et al.*, 2003a,b; Richardson *et al.*, 2003; Levrard *et al.*, 2004). This mechanism can be augmented by enhanced hydration of salts, zeolites, and/or clay minerals in the soil (Zent *et al.*, 1986). For example, more than 30% of the mass of smectite clays is expected from water of hydration poleward of 60° N and S latitude where, on average, the relative humidity is high (Zent *et al.*, 1986; Fialips *et al.*, 2005a). In this same latitude range, anhydrous $MgSO_4$ is predicted to be in the form of epsomite, which contains 51% of its mass in water molecules, and anhydrous $CaSO_4$ is predicted to be in the form of gypsum which contains 21% of its mass in water molecules (Fialips *et al.*, 2005a). Relative minima in the apparent water content of surface soils occur within northern Acidalia centered at about 55° W, at the mouth of Chasma Boreale, and within Olympia Undae, centered at about 80° N and 190° E.

In addition to preciptation and subsequent burial of snow, high concentrations of water ice may form naturally in Martian permafrost. Ice lenses and ice wedges are the most common forms of subsurface massive ice deposits on Earth (Williams and Smith, 1989). Ice lenses are stacks of alternating horizontal pure-ice layers millimeters to centimeters thick, within layers of ice-cemented soil that typically form when wet soils freeze (Miller, 1980). Terrestrial ice lenses are known to account for up to 75% of the volume of the upper meter of the ice-rich permafrost (Péwé, 1974). Ice wedges are vertical ice structures that form in polygonal fractured permafrost, as surface meltwater accumulates and freezes in the polygonal fractures (Lachenbruch, 1962; Black, 1976). Ice wedges can comprise as much as 50% of the volume of the top 3 m of soil (MacKay, 1972). On Mars, ice lenses and ice wedges may require at least small amounts of liquid water to be periodically present. However, the formation of these features could account for the observed high concentrations of ice, particularly in conjunction with pore-space ice and hydrated minerals.

As mentioned previously, orbital neutron spectroscopy is sensitive to WEH abundances only in the top meter of the surface, and the thickness of permafrost deposits can only be determined to depths of between 20 and 60 g cm^{-2}. Nevertheless, we can estimate a minimum thickness of a global equivalent layer (GEL) of water from the lower-limit water map shown in Figure 6.8. This estimate, T(GEL), was calculated from WEH abundances determined from epithermal-neutron counting rates by integrating zonal averages of the H_2O mass fraction, M_{H_2O},

$$T(\mathrm{GEL}) = \frac{\rho d \iint M_{H_2O}\, \mathrm{d}\,\Omega}{4\pi}, \tag{6.3}$$

within three contiguous latitude bands, $\lambda > 45°$ N, $45°$ S $< \lambda < 45°$ N, and $\lambda < 45°$ S. These bands were chosen to correspond roughly to where water ice may be stable at high northern and southern latitudes, and where it is predicted to be unstable at near-equatorial and mid latitudes. Here, T(GEL) is the equivalent thickness of H_2O assuming that it is distributed uniformly over the entire Martian surface, ρ is the density of soils near the surface, here chosen to be 1.65 g cm^{-3} (Arvidson *et al.*, 1989), d is an assumed thickness of the WEH deposits, and Ω is the latitude–longitude solid angle over the planet. Choosing $d = 1$ m, the total inventory of near-surface H_2O calculated as full-planet contributions from each zone amounts to 4.1 cm for latitudes south of 45° S, 5.6 cm for latitudes between 45° S and 45° N, and 4.4 cm for latitudes north of 45° N. Altogether these estimates yield about a 14 cm GEL on Mars. Of course, these estimates would be much larger if it were known that WEH abundances extend more deeply than can be sensed by neutron spectroscopy from orbit. However, the present estimate can be put in perspective when compared with the water estimated to be within the polar residual water-ice caps and their surrounding layered deposits, about 30 m (Carr, 1986; Smith *et al.*, 1999; Carr and Head, 2003), and to be contained in the atmosphere, which if deposited on the surface would cover Mars with a thin film of water about 10^{-5} m thick (Jakosky and Farmer, 1982).

An overview of the global distribution of WEH can be inferred from a calculation of zonal averages, as presented in Figure 6.9 (Feldman *et al.*, 2004a). Inspection shows immediately the dichotomy between high- and low-latitude WEH abundances. While the abundances are significant but low within about 50° of the equator, they rise abruptly at both higher northern and southern latitudes. In fact, an overlay of zonal averages of WEH abundances between 50° and 75° in each of the high-latitude regions shows they are closely equal. Whereas this abundance averages 23% between 50° S and 80° S latitude, it averages 18.5% between 50° N and 80° N latitude. Although we do not know the origin of the surprising north–south latitudinal symmetry derived from the MONS data, the large difference in topography between north and south (Smith *et al.*, 1999), the marked

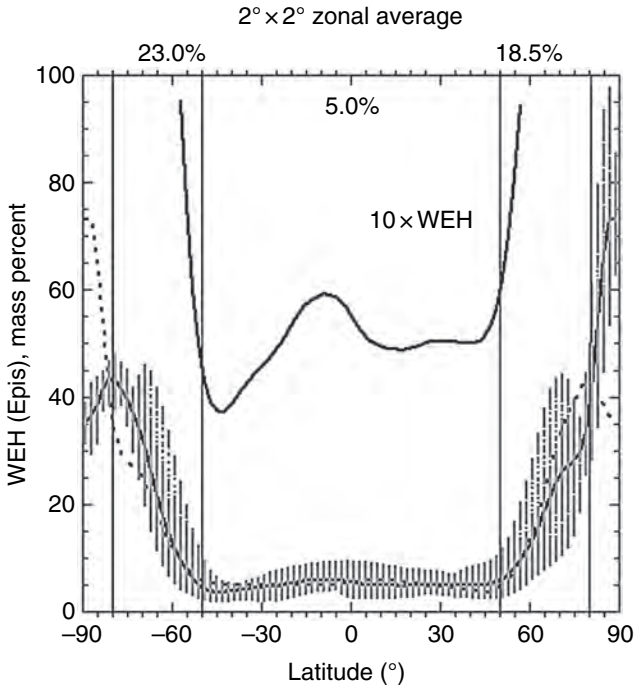

Figure 6.9. $2^{o} \times 2^{o}$ zonal averages of WEH abundance calculated using Prism 1 epithermal neutron counting rates. See the text for details.

differences in the geologic structure, and differences in aqueous history on geologic timescales of the northern and southern high-latitude terrains (Carr, 1996), suggest that none of these can be controlling factors in the present zonally averaged disposition of ground ice at high latitudes. Instead, the north–south symmetry in inferred ground ice and its strong latitude dependence suggest that the structure reflects the latitudinal dependence of soil temperature and the equilibrium with the long-term water-vapor content of the atmosphere (e.g., Leighton and Murray, 1966; Farmer and Doms, 1979). It is also predicted by MGCM simulations to result from ice deposition during periods of changing obliquity (Head *et al.*, 2003; Mischna *et al.*, 2003a,b; Richardson *et al.*, 2003; Levrard *et al.*, 2004) that are predicted by Laskar *et al.* (2002) during the last 5 Myr.

6.4.2 The present distribution of water ice and/or hydrous minerals near the equator

The special interest in near-equatorial abundances of WEH stems from the fact that water ice should not be stable anywhere within about 45° of the equator (Leighton and Murray, 1966; Farmer and Doms, 1979; Fanale *et al.*, 1986; Paige, 1992; Mellon and Jakosky, 1993; Mellon *et al.*, 2004; Schorghofer and Aharonson, 2005) unless it is isolated from the atmosphere by a low-permeability covering layer (e.g., Smoluchowski, 1968; Clifford and Hillel, 1983; Clifford, 1998), or unless past climate conditions were different than today, such as during a high-obliquity phase (Mellon and Jakosky, 1995). As presented in Section 4.1, a significant amount of WEH is observed at these latitudes. Alternative stratigraphy and/or molecular associations of the measured hydrogen abundance here are possible: (1) water ice buried beneath a low-permeability cover (e.g., Clifford, 1998), (2) water molecules adsorbed on the surfaces of soil grains (e.g., Fanale and Cannon, 1974; Zent *et al.*, 1986; Zent and Quinn, 1997; Tokano, 2003; Möhlmann, 2004), (3) structural OH and interlayer H_2O in clays (Zent *et al.*, 1986; Bish *et al.*, 2003a; Bibring *et al.*, 2005, 2006; Fialips *et al.*, 2005a; Poulet *et al.*, 2005; Jänchen *et al.*, 2006), (4) water associated with extra-framework cations in zeolites (Bish *et al.*, 2003a; Ruff, 2004; Fialips *et al.*, 2005a; Jänchen *et al.*, 2006), and (5) structural OH and H_2O in salt hydrates (Clark, 1978; Zolotov, 1989; Basilevsky *et al.*, 2003; Bish *et al.*, 2003a,b; Vaniman *et al.*, 2004; Feldman *et al.*, 2004b; Fialips *et al.*, 2005a; Navrotsky *et al.*, 2005; Jänchen *et al.*, 2006). Indeed, chemically and/or physically bound H_2O and/or OH has been found in infrared spectral reflectance data (Houck *et al.*, 1973; Pimental *et al.*, 1974; Calvin, 1997; Lane *et al.*, 2004), hydratable sulfates have been detected by, or inferred from, several of the experiments aboard the MER rovers at the Meridiani and Gusev landing site (Christensen *et al.*, 2004; Klingelhöfer *et al.*, 2004; Gellert *et al.*, 2006; Ming *et al.*, 2006; Morris *et al.*, 2006; Wang *et al.*, 2006a), and phyllosilicates and sulfates have been found by the OMEGA experiment aboard the Mars Express spacecraft (Bibring *et al.*, 2005, 2006; Gendrin *et al.*, 2005; Poulet *et al.*, 2005) and by MER at Gusev (Wang *et al.*, 2006b).

The zonal distribution of thermal and epithermal neutrons shown in Figures 6.7 and 6.9 strongly favor an interpretation of the observed WEH content of near-equatorial latitudes in terms of hydrated minerals. The sharp rise in WEH abundance at 50° N and S latitudes and the sharp enhancement in inferred burial depths at 60° N and S latitudes follow naturally from the addition of a distinct reservoir of buried water ice that first becomes detectable poleward of 60° N and S. At more equatorial latitudes, water ice is not stable within 1 m of the surface but migrates toward the surface as the latitudes increase. In addition, the area spanned by significant amounts of WEH near the equator of Mars is so large that it is difficult to believe that it is entirely due to water ice buried beneath a very low-permeability covering layer. Such low-permeability layers slow water-vapor diffusion but do not stop it. Given time, ice beneath a low-permeability layer will be lost unless there is some mechanism for recharge. For example, the longitudinal width of the deposit within Arabia having greater than 5% WEH abundance by mass spans a distance of about 3000 km. Much of it must therefore reflect deposits of hydratable minerals unless it was recharged within the last 5000 Martian years (see Section 6.4.4).

Can any one family of minerals, such as $MgSO_4$, dominate, as inferred from interpretations of elemental abundances measured at the Viking 1, Pathfinder, Meridiani Planum, and Gusev crater landing sites (Toulmin *et al.*, 1977; Clark and Van Hart, 1981; Wänke *et al.*, 2001; Christensen *et al.*, 2004; Rieder *et al.*, 2004; Gellert *et al.*, 2006; Ming *et al.*, 2006; Morris *et al.*, 2006; Wang *et al.*, 2006a)? If so, there must be as much as 10% of anhydrous $MgSO_4$ at many locations throughout the near-equatorial zone of Mars. The relative-humidity conditions for which the most likely

hydration states of $MgSO_4$ are stable were therefore studied (Bish *et al*., 2003a; Vaniman *et al*., 2004; Feldman *et al*., 2004b; Fialips *et al*., 2005a) to test this possibility. These states include kieserite (1 H_2O per molecule), hexahydrite (6 H_2O per molecule), epsomite (7 H_2O per molecule), and amorphous $MgSO_4$ (which has an H_2O abundance that is intermediate between that of kieserite and hexahydrite). Resulting maps of stability (Feldman *et al*., 2004b; Fialips *et al*., 2005a) based on a model of the physical temperature of surface soils (Mellon *et al*., 2004) show that this possibility cannot happen. Abundances of WEH above 5% by mass are observed both where hexahydrite and epsomite are stable and where they are not stable. Similarly, hexahydrite and epsomite are found to be stable where the WEH abundance is below 3% by mass.

Can any other single group of hydratable minerals account for the distribution of WEH that is observed? Thermodynamic stability boundaries were calculated from measurements for jarosite (Navrotsky *et al*., 2005) and a variety of zeolites and clays (Carey and Bish, 1996; Bish *et al*., 2003a; Fialips *et al*., 2005b; Jänchen *et al*., 2006), and the simple answer is "no" (Fialips *et al*., 2005a). However, mixtures of different hydrous minerals that correspond to a heterogeneous surface geology can account for the observations, and are indeed required to explain the distribution of WEH observed at near-equatorial latitudes in the absence of a sufficiently large-scale, low-permeability, low-WEH overburden (e.g., Smoluchowski, 1968; Clifford, 1998).

6.4.3 Correlations between the WEH distribution and the geomorphology of surface materials

Best estimates of the total inventory of water on Mars come from an analysis of geomorphic features such as rampart craters, collapsed chaotic terrain, massive outflow channels, and valley networks (Carr, 1986, 1996; Squyres, 1989; Baker, 2001; Jakosky and Phillips, 2001; Carr and Head, 2003). These analyses yield estimates that range between GELs of 100 and 500 m thick (Carr, 1986; Carr and Head, 2003). Measurements of the D/H ratio of the Martian atmosphere suggest that the estimated loss to space is 1–2 orders of magnitude less than the estimated GEL due to observations of geomorphic features (Yung *et al*., 1988; Carr, 1990; Jakosky, 1991; Luhman *et al*., 1992; Leshin, 2000). These estimates leave between 50 and 500 m of water unaccounted for. However, an estimate of the water contained in both residual water-ice caps and their surrounding layered deposits yields only 30 m (Carr, 1986; Smith *et al*., 1999; Carr and Head, 2003) and that contained in soils within 1 m of the surface yields only 14 cm (Feldman *et al*., 2004a). Is there any substantial evidence that the WEH distribution measured using MONS extends deeper than 1 m to account for the difference between the estimated and observed WEH reservoirs? Based on geomorphologic studies summarized next, the answer is "yes."

The first inter-comparison of epithermal-neutron counting rates measured using MONS and surface features interpreted from optical and laser altimeter observations showed (Tokar *et al*., 2002) that the boundary between high and low southern latitude WEH deposits fell just poleward of the locations of dissected and eroded terrain (Mustard *et al*., 2001). These features are interpreted as formerly water ice–rich deposits that have sublimated because of increasing solar insolation caused by a reduction in obliquity of the Martian spin axis. This sublimation then removed the support of a thinly cemented layer on the surface leading to its collapse and disaggregation by near-surface winds. The location of these disaggregated terrains also coincide with the boundary of mantled terrain having low sub kilometer-scale roughness and a strong prevalence of concave-upward topography (Head *et al*., 2002; Kreslavsky and Head, 2002). This roughness structure was inferred to result from an estimated 10 m thick sedimentary layer that is very rich in water ice and which mantles an underlying volcanic Hesperian-aged terrain. Also seen in the latitude zone between 30° and 60° are viscous flow features that are interpreted (Milliken *et al*., 2003) to require formerly ice-rich surface layers that are more than 10 m thick. Finally, hexagonal linear markings on surface layers between 50° N and 70° N latitude are interpreted as thermal stress–driven cracks in water ice–rich subsurface layers (Mellon *et al*., 1997; Kuzmin *et al*., 2004; Mangold *et al*., 2004).

6.4.4 Recharge/discharge mechanisms and their time scales

Theoretical analyses of the hydration state of near-surface soils have predicted that water can be supplied to surface material through several pathways. Liquid water from a source beneath the south polar residual water-ice cap may convect to equatorial latitudes as a fluid through a relatively deep aquifer (Clifford and Parker, 2001). Upward diffusion of water molecules driven by a planet-wide thermal gradient above this aquifer will then fill overlying pore space where they freeze out to form a water ice–rich cryosphere (Clifford, 1991). Sublimation from the top of the cryosphere can then continue upward to the atmosphere if the soil temperature is higher than the condensation point of atmospheric water vapor at ground level (Clifford, 1993; Mellon *et al*., 1997), and there is no low-permeability cover layer that could isolate lower layers from contact with the atmosphere (Smoluchowski, 1968; Clifford and Hillel, 1983; Clifford, 1998; Mischna *et al*., 2003b; Richardson *et al*., 2003; Feldman *et al*., 2004c; Mischna and Richardson, 2005). If ground ice is stable at a particular geographic location, the upward diffusion of water from an aquifer will be halted by the downward penetration of the seasonal thermal cycles, several meters to several tens of meters below the surface (Mellon *et al*., 1997). These deposits should therefore not be observable by an orbiting neutron spectrometer.

Alternatively, water molecules from the atmosphere will diffuse through near-surface soils from above to form subsurface water ice at depths where the mean soil temperature equals the atmospheric frost point (e.g., Zent *et al*., 1986; Mellon and Jakosky, 1993, 1995; Schorghofer and Aharonson, 2005). At all latitudes, water can be adsorbed on the surfaces of soil grains (Fanale and Cannon, 1974; Zent *et al*., 1986; Zent and Quinn, 1997; Tokano, 2003;

Möhlmann, 2004), perhaps forming a "liquid-like" layer (Möhlmann, 2005), and/or hydrate minerals that have sufficiently high enthalpies of hydration to be stable beneath the surface (Clark, 1978; Zolotov, 1989; Basilevsky *et al*., 2003; Bish *et al*., 2003a,b; Vaniman *et al*., 2004; Feldman *et al*., 2004b; Fialips *et al*., 2005a; Navrotsky *et al*., 2005; Jänchen *et al*., 2006). The zones of stability for retention by this delivery mechanism will be controlled by yearly averaged temperatures, surface topography, and atmospheric dynamics (Mellon and Jakosky, 1993; Mellon *et al*., 2004; Feldman *et al*., 2005; Schorghofer and Aharonson, 2005), and will require hundreds to thousands of years to fill (Mellon and Jakosky, 1993, 1995; Mellon *et al*., 2004).

The observed distribution of WEH generally favors the predictions of an atmospheric source over aquiferic circulation (Boynton *et al*., 2002; Feldman *et al*., 2002b; Mitrofanov *et al*., 2002; Tokar *et al*., 2002; Feldman *et al*., 2004a,c, 2005; Levrard *et al*., 2004; Mellon *et al*., 2004; Prettyman *et al*., 2004; Mellon and Feldman, 2006). The latitudinal boundary between high and low-WEH abundances at high southern latitudes is generally sharp (Boynton *et al*., 2002; Tokar *et al*., 2002; Prettyman *et al*., 2004) and agrees with that expected from an atmosphere that contains 20 precipitable microns (prm) of water vapor normalized to the zero-kilometer altitude datum (Mellon *et al*., 2004). This water-vapor content is very close to, but slightly higher than, the atmospheric hydration state that is presently observed (Jakosky and Farmer, 1982; Smith, 2002). The fit to the measured distribution in the north is similarly good and yields a similar atmospheric water abundance, but reveals two interesting longitudinal zones where the boundary does not match the theoretical distribution of the ice table (Mellon and Feldman, 2006). Poleward of this stability boundary the predicted depth distribution of the ice table (the transition between dry soil and ice-rich soil) is in excellent agreement with the neutron data, indicating that diffusive equilibrium with the atmosphere controls this depth over most of the high-latitude regions of Mars (Mellon *et al*., 2004; Mellon and Feldman, 2006). However, the abundance of WEH poleward of these boundaries is too large for its emplacement to be explained alone by diffusion into the regolith and direct vapor condensation as ice in the pore spaces within near-surface regolith (Tokar *et al*., 2002; Mitrofanov *et al*., 2004; Prettyman *et al*., 2004; Litvak *et al*., 2006). While the current ice table depth appears completely controlled by diffusive equilibrium with atmospheric water vapor, the emplacement of these deposits needs to be supplemented by another process, such as by water-ice sheets deposited directly onto the surface during past high-obliquity phases, by water of hydration held by salts, clays, or zeolites fed by diffusion into and through soil pore volumes from the atmosphere, or by the formation of periglacial deposits of massive ice (e.g., ice wedges or ice lenses).

High-latitude ground ice will also undergo secular and periodic change due to climate change and orbital oscillations (Mellon and Jakosky, 1995). In regions where ice is stable the diffusion process is expected to occur on a time scale of only hundreds to thousands of years depending on the mobility of water migrating through the soil (Mellon and Jakosky, 1993, 1995; Mellon *et al*., 2004). Orbital and axial oscillations such as obliquity are slow enough that the ice table is expected to track the stability conditions as water exchanges between ground ice and atmospheric reservoirs. Such cycles occur over 10^5 year time scales (Ward, 1974; Laskar, 1988; Laskar *et al*., 2002) and drive cycles of saturation and desiccation of the high-latitude regolith to depths of 1–2 m (Mellon and Jakosky, 1995). Therefore, subsurface ice detected by MONS is likely to be younger than the most recent obliquity cycle. On more recent time scales, secular climate changes could result in changes in the atmospheric hydration state that could shift the high-latitude ice table up or down slightly, however, a more pronounced effect would occur in more equatorial regions (Mellon *et al*., 2004).

At low and mid latitudes, if an increase in atmospheric hydration state occurred relatively recently, water ice that was stable during a previous enhanced humidity state would begin to sublimate back to the atmosphere thereby causing the upper level of the ice table to recede downward. Such a condition could have been induced by a recent climate change to warmer, dryer atmosphere and surface layer conditions. This possibility is inferred from visible imagery of a latitude band between 30° and 50° in both hemispheres of dissected terrain and viscous flow features (Mustard *et al*., 2001; Head *et al*., 2003; Milliken *et al*., 2003). This situation could also have been induced by a transient uncovering, and subsequent covering, of the south polar residual water-ice cap by the veneer of CO_2 ice that is presently in place (Jakosky *et al*., 2005; Thomas *et al*., 2005).

The distribution of WEH at low and mid latitudes inferred from epithermal-neutron counting rates measured using MONS was compared with models of water deposition and depletion of surface materials to gain insight. Starting first with a comparison of zonal averages of WEH with both the measured (Smith, 2002) and modeled (Mellon *et al*., 2004) water-vapor content of the atmosphere, we see in Figure 6.10 that the correspondence is poor (Feldman *et al*., 2005; Jakosky *et al*., 2005). Whereas the WEH distribution maximizes at about 10° S latitude, those of the atmospheric water-vapor content all maximize at about 25° N latitude (Smith, 2002; Mellon *et al*., 2004). The location of this latitude does not depend on whether the residual water ice deposit near the South Pole is mostly covered by a veneer of CO_2 or is uncovered. The only difference between the covered and uncovered conditions is that the average water-vapor content of the atmosphere nearly doubles for uncovered conditions. This lack of correspondence is hard to understand if the observed WEH is in the form of water ice that is in direct contact with the overlying atmosphere. Either there must be a very low-permeability cover layer that isolates the water vapor in sub-surface pore volumes from the atmosphere or the observed WEH reflects water of hydration of a heterogeneous mixture of different hydrous minerals (Feldman *et al*., 2004b; Fialips *et al*., 2005a) that are stable at many locations near the equator.

Another test of diffusive deposition directly from the atmosphere to equatorial sub-surface water ice is possible by comparing meridional transects through the WEH distribution with the albedo. The choice of 15° E longitude near

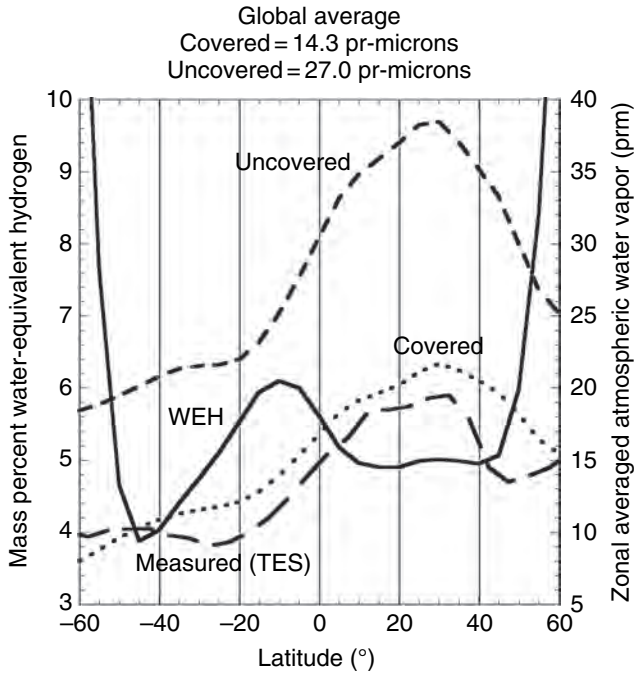

Figure 6.10. Comparison between zonal averages of measured WEH abundances and the atmospheric water-vapor content measured using TES and simulated using the Ames MGCM of conditions with the south polar residual water-ice cap covered, and uncovered by a thick veneer of CO_2 ice.

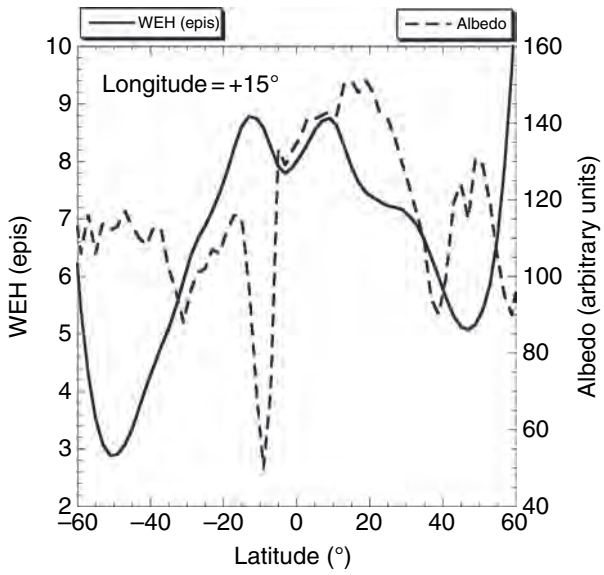

Figure 6.11. An overlay of meridional cuts through the WEH abundance and albedo maps at +15° E longitude. The scale of albedo is in arbitrary units spanning the range between 0 and 255.

the maximum of near-equatorial WEH deposits is shown in Figure 6.11 (Feldman *et al.*, 2005). The correlation is likewise poor (see also Jakosky *et al.*, 2005). Again, this result is difficult to understand if the deposit is in the form of water ice that is in close contact with the atmosphere because mean subsurface temperatures should be lowest beneath high-albedo surface layers, thereby making water ice more stable. In addition, if water ice was stable at some time in the recent past, the recession rate of the permafrost table should be largest where the temperature is highest, which should occur beneath terrain having low albedo. The opposite is observed at 10° S latitude where the albedo is a relative minimum and the WEH abundance is a relative maximum.

The correlation between WEH and elevation was studied next to see if atmospheric circulation patterns have any control on WEH deposition. The Ames MGCM was used for this purpose (Nelli *et al.*, 2006). This comparison is shown in Figure 6.12 for three meridional transects (Feldman *et al.*, 2005; Jakosky *et al.*, 2005). The transects at 15° E, 85° E, and 74° W longitude shown in Figures 6.12a,b, and c respectively were chosen to discriminate between a supply route through an aquifer that connects to the south polar residual water-ice cap (Clifford, 1987) or through the atmosphere. Whereas connection to the Arabia deposit at 15° E through an aquifer is possible because it is at an elevation lower than that of the South Pole without any intervening obstruction, the deposits along the 85° E meridian are disconnected from the South Pole by Hellas basin, and that just north of Ophir Chasma at about 5° W latitude and 74° W longitude, is cut off from the South Pole by Valles Marineris. There can be no aquifer supply from the north residual ice cap because its elevation is too low (Zuber *et al.*, 1998). Also there are problems with global connectedness of Clifford's aquifers. Such connected aquifers do not exist on Earth, and cannot be demonstrated to exist.

However, all examples shown in Figure 6.12 show a common correlation between relatively high elevations and north-facing topographic slopes south of the dichotomy boundary in the southern highlands. This result suggests that the large-scale Hadley circulation patterns control the deposition from the atmosphere onto the surface through precipitation, and subsequent vapor diffusion into and through surface soils (Feldman *et al.*, 2005). Such a two-step process is required to explain the lack of correlation between the observed distributions of equatorial WEH and atmospheric water vapor by itself. The pattern of WEH distribution is also consistent with MGCM simulations, which predict a wavenumber two longitudinal pattern of equatorial and subtropical water-ice precipitation on Mars. Predicted precipitation maxima in the vicinity of Arabia and Tharsis, and relative minima within meridional lanes that connect Acidalia, Chryse, and Argyre in the west and Utopia, Isidis, and Hellas in the east match very well maxima and minima in the observed WEH distribution (Feldman *et al.*, 2005; Jakosky *et al.*, 2005). It is important to note, though, that the presence of condensable water or precipitated water ice is not by itself sufficient to account for the observed spatial distribution of WEH. Retention of these surface H_2O deposits by hydratable minerals depends on the subsurface distribution of these minerals, which is presently not known. Nevertheless, an explanation in terms of retention of H_2O by hydrous minerals is also consistent with the lack of correlation between WEH abundances and albedo shown in Figure 6.11 because they are stable regardless.

A further test of the hypothesis that observed abundances of WEH at low to mid latitudes correspond to water ice that

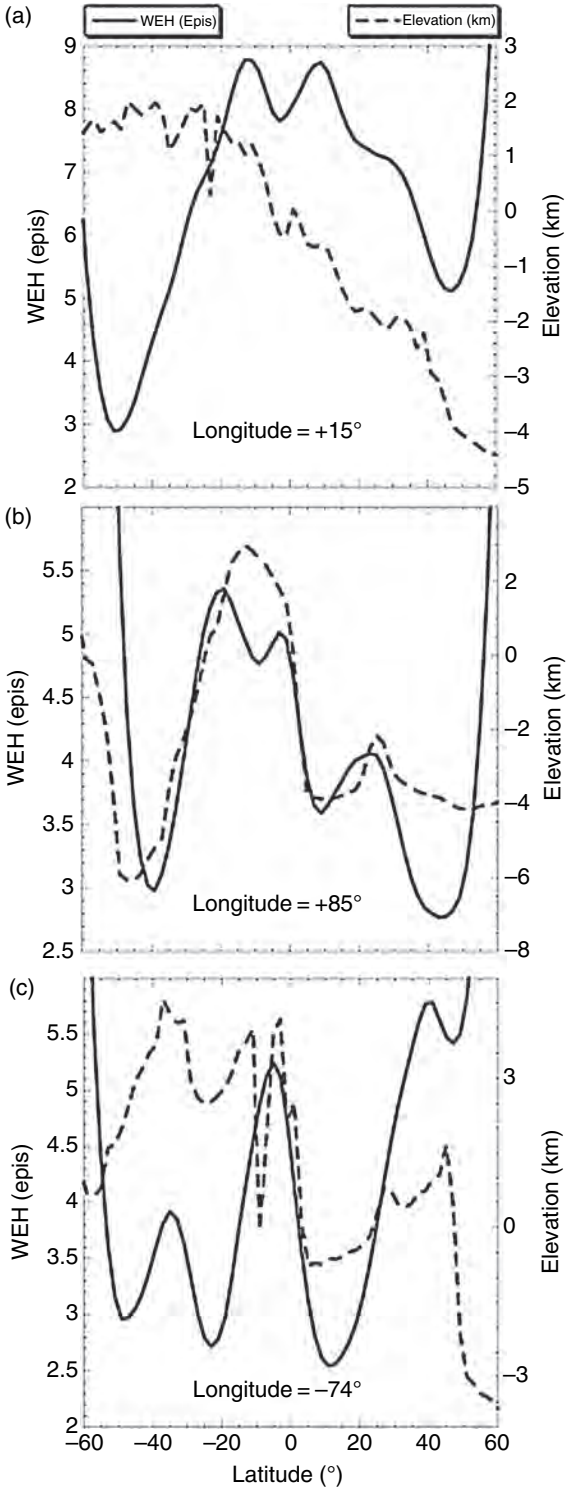

Figure 6.12. Overlays of meridional cuts through WEH abundance and ground elevation maps for east longitudes of (a) +15°, (b) +85°, and (c) –74°.

is in direct contact with the atmosphere was made recently (Feldman *et al.*, 2005). If water ice is present now, it must have been recharged sufficiently recently to prevent complete loss by sublimation to the atmosphere. If correct, then theoretical loss rates can be compared with WEH abundances to place limits on the time scale of a potential recent change in the climate of Mars. As before, if there has been no recent climate change, and/or a large area, near global low-permeability surface layer does not exist, then the observed WEH must be contained in hydrous minerals, which are stable over a wide range of longitudes at low latitudes (Fialips *et al.*, 2005a).

In order to place bounds on the occurrence of a recent climate change, it is assumed that at some time in the past, the CO_2 ice covering most of the residual south polar water-ice cap was lost, thereby enhancing the water-vapor content of the atmosphere (Jakosky *et al.*, 2005). Use of the Ames MGCM to simulate the resultant enhanced atmospheric hydration state after removal of the CO_2 cover yielded the zonal and global averaged atmospheric content shown in Figure 6.10. The theory of Mellon *et al.* (2004) was then used to calculate the locations of water ice stability within 1 cm of the surface at latitudes within 60° of the equator. The south cap was then assumed to be absent from CO_2 ice covering for a sufficiently long time to allow the complete filling of an assumed 40% regolith pore volume where ice would then be stable at the surface. A 40% pore volume was chosen to conform with estimates made by Arvidson *et al.* (1989) for the Viking landing sites. We then assume that at some time, t_i, in the past, the CO_2 covering reappeared, thereby destabilizing the mid-latitude water-ice deposits. The time since reappearance required to drop the water-ice table (subliming the ground ice away) in the places where surface water ice was newly stable, to depths such that the WEH abundance appears to be what it is seen now to be, can then be calculated in two steps. The first step requires fitting the simulations in Figure 6.5 of Mellon *et al.* (2004) to an analytical function to yield

$$dt_i/dD = C(T)D^2 \tag{6.4}$$

where t_i is the time since reappearance of the CO_2 cover to the present time in Mars years (1 Mars year = 1.88 Earth years), D is the time-dependent depth to the top of the receding permafrost table in g cm^{-2}, T is the temperature at the top of the permafrost layer, in K, which is assumed to be constant in time, and $C(T)$ is a constant function of T, given by

$$C(T) = 7.075 \times 10^{-14} \exp\left(\frac{6282.7}{T}\right). \tag{6.5}$$

Integration of Equation (6.1) then yields:

$$t_i = \frac{C(T)D^3}{3}. \tag{6.6}$$

The final step is to estimate the depth of the top of the present ice-rich permafrost table, D. This permafrost layer then consists of a totally filled pore space, which appears from orbit to be the observed WEH abundance. This step is accomplished using the simulations in Figure 6.13. Assuming a regolith grain density of 2.6 g cm^{-3}, a 40% pore volume translates to 19% water ice by mass, denoted by the vertical line in Figure 6.13. The simulations for various depths, D, to the permafrost table can then be interpolated to yield D as a function of the measured apparent present mass fraction of H_2O. Resultant times calculated using $t_i = C(T)\ D^3/3$ are presented in Figure 6.14.

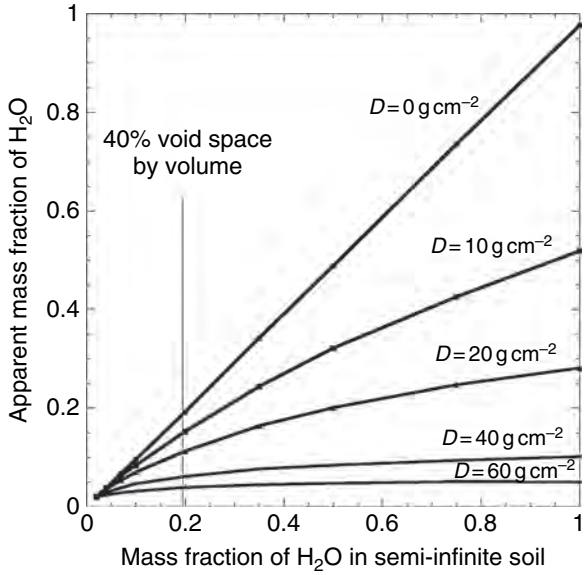

Figure 6.13. Simulations of the apparent mass fraction of H_2O calculated assuming a single semi-infinite stratigraphy as a function of the H_2O mass fraction of the permafrost layer buried at various depths, *D*.

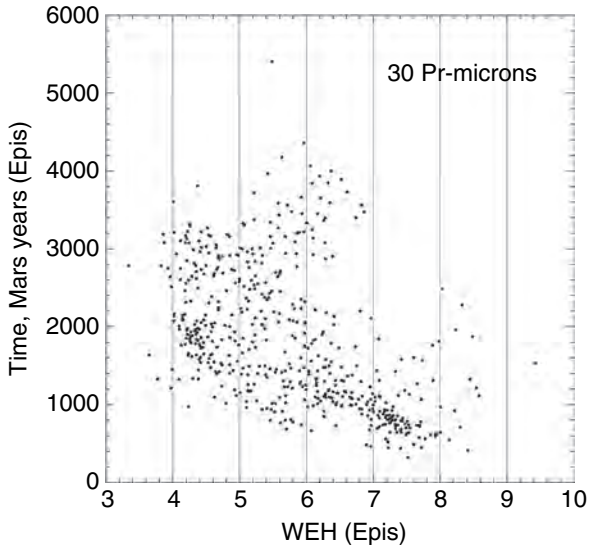

Figure 6.14. Scatter plot of calculated times (in Martian years) elapsed since the putative recovery of the residual water ice south polar cap by a thick veneer of CO_2 ice, using Equation 6.3. See the text for details.

All elapsed times are seen to be between about 400 and 5000 Mars years. In other words, WEH sensed by neutron spectroscopy from orbit can tell us little about long-term climate change that occurred in association with orbital variations of Mars (which are of order 10^5 years [Ward, 1974; Laskar, 1988]). Specifically, if there was a recent climate change on Mars, it would need to have happened during this 5000-year time period to agree with our assumptions. However, the lack of a clustering in elapsed time in Figure 6.14 since the putative recovery of the CO_2 ice veneer makes it unlikely that such an event happened recently. In addition, significant amounts of WEH are presently observed in large near-equatorial areas where water ice is not stable during CO_2 uncovered conditions. We therefore conclude that at least one of the assumptions made to make this calculation is wrong. Our previous results make it likely that near-equatorial WEH is presently stably bound and hence the observations of WEH by MONS are due to a heterogeneous mixture of hydrous minerals rather than water ice emplaced during a recent climate change event.

6.4.5 The inventory of surface CO_2 ice near the South Pole

We restrict the focus of this section to the CO_2-ice inventory of the south residual ice cap because the stage of analyses of seasonal cap variations is presently not sufficiently mature. Two independent approaches were followed to estimate the total mass of CO_2 ice that is contained in the relatively thin veneer that covers the residual water-ice cap near the South Pole. The first (Tokar *et al.*, 2003) concentrated on the counting rates measured using the forward-looking sensor (Prism 2), which primarily responds to thermal and epithermal neutrons. This analysis separated the portions of spacecraft trajectories that were approaching, and receding from the pole to get the best spatial resolution from the comparison between simulations and measurements. The need for this separation is driven by the asymmetric spatial response of the Neutron Spectrometer to thermal neutrons that is caused by the relatively high orbital speed of the Mars Odyssey spacecraft, which is larger than that of a thermal neutron.

Two models of the spatial structure of the residual cap needed to be assumed because the size of the cap is much smaller than the spatial resolution of the detector. The first used a uniform region centered at 87° S and 45° W with an area assumed to be 87 000 km^2, as inferred from MOC observations (Malin and Edgett, 2001). This area is assumed to be fully covered in variable-depth CO_2 over solid water-ice. The second is the "Swiss cheese" model of Thomas *et al.* (2000) and Malin and Edgett (2001) in which the area of the exposed water-ice substrate is variable and the thickness of CO_2 cover is chosen to be 8 m (Byrne and Ingersoll, 2003). Both models assume that the CO_2 ice cap is underlain by 100% by mass H_2O ice and is completely surrounded by soil that contains 50% H_2O by mass. For this last option, the area so determined was traded off with a variable dust loading. As the assumed dust content increases, the area containing CO_2 ice must also increase to get the same thermal- and epithermal-neutron counting rates.

In order to match measured counting rates, the uniformly covered, variable-depth model requires a thickness of $140 \pm 10\,g\,cm^{-2}$ of dust-free CO_2 ice having an area of 87 000 km^2. This yields a total mass of $1.2 \pm 0.1 \times 10^{17}$ g of residual CO_2 trapped in the cap. This mass is a lower limit because any residual dust should decrease thermal-neutron counting rates, which must be made up by an increasing thickness of CO_2.

If the CO_2 was 8 m thick as suggested by the "Swiss cheese" model, then the predicted thermal-neutron counting rates are saturated so that the only variable is the area of CO_2 cover with respect to the assumed total area of the cap

($87\,000\,km^2$). The best fit to a dust-free CO_2 cover requires that 60% of the $87\,000\,km^2$ cap area must be the exposed water-ice substrate. Assuming a CO_2 density of $1\,g\,cm^{-3}$ yields a total mass of 2.8×10^{17} g of CO_2.

A separate analysis by Prettyman *et al.* (2004) that used the epithermal-neutron counting rates returned by the downward-facing (Prism 1) sensor element determined that the fraction of exposed water-ice component of the cap was most likely 45% by area (assumed by Prettyman *et al.*, 2004, to be $98\,700\,km^2$ based on Viking imagery). In other words, 55% of the residual cap consists of thick CO_2 deposits and the remaining 45% consists of water ice–rich open area. If this percentage of open area is chosen instead of the foregoing 60% of $87\,000\,km^2$ estimate, then the dust content must amount to $28 \pm 7\%$ by mass to yield the same thermal counting rate. The resultant total dust mass is then $224\,g\,cm^{-2}$ if the CO_2 ice density is $1\,g\,cm^{-3}$. Both methods (Tokar *et al.*, 2003; Prettyman *et al.*, 2004) yield a total CO_2 mass on the cap that ranges between 1×10^{17} and 3×10^{17} g. This range translates to between 3% and 9% of the CO_2 that is seasonally cycled into and out of the atmosphere (Smith *et al.*, 2001). The cap can therefore not contribute importantly to the total CO_2 inventory of Mars, in agreement with the conclusions reached by Byrne and Ingersoll (2003).

Another byproduct of this analysis is that it allows a rough estimate of the time that the veneer of CO_2 ice has been in place. The dust deposition rate at the South Pole has been estimated by Thomas *et al.* (1992) to be $0.9 \times 10^{-3}\,g\,cm^{-2}/yr$. If the dust is uniformly loaded into the CO_2 ice that covers the residual water-ice cap, then it will take approximately 25 000 years to add up to $224\,g\,cm^{-2}$ (Tokar *et al.*, 2003). We note that this estimate is close to half the precession period of the spin axis of Mars (see, e.g., Laskar, 1988), which would tend to alternate the length and severity of the winter months between both poles.

6.5 SUMMARY AND CONCLUSIONS

Neutron data measured using the MONS have now spanned two full Martian years. An absolute calibration of resultant counting rates has allowed generation of a global map of minimum abundances of WEH and seasonal variations in the CO_2 ice cover of high-latitude terrain. A minimum estimate of the total water content of all WEH deposits observed using MONS amounts to a 14 cm thick global-equivalent layer of water. This amount is much lower than the 30 m contained within the residual polar ice caps and surrounding ice-rich terrain (Carr and Head, 2003), yet much larger than the 10^{-5} m contained in the atmosphere (Jakosky and Farmer, 1982).

Observed WEH deposits can be separated into two separate domains according to latitude. The domains at high northern and southern latitudes contain such high abundances of WEH that they likely correspond mostly to buried water ice because such deposits are stable at latitudes generally higher than (45°–55°) from the equator (e.g., Leighton and Murray, 1966). Water-equivalent hydrogen abundances between about 50° and 80° in both hemispheres average about 20% by mass. Deposits poleward of 60° S range up to $60\% \pm 10\%$ and are buried beneath a dry layer of $15 \pm 5\,g\,cm^{-2}$ at 60° S (Prettyman *et al.*, 2004). A similar study at high northern latitudes is consistent with WEH deposits that likewise range up to 60% by mass and burial depths that range between about 5 and $20\,g\,cm^{-2}$ (Feldman *et al.*, 2006). Both burial depths decrease with decreasing distance to the poles. Such large deposits consist of more ice than can be held as simple pore ice within volumes between regolith grains in a normal soil. If the observed WEH is entirely in the form of water ice, two possibilities are proposed: (1) it must have been deposited by multiple stages of precipitation during previous climate conditions driven by changes in the various elements of the Martian orbit; or (2) massive ice structures analogous to terrestrial ice lenses and ice wedges occur in abundance on Mars, the implication being that liquid water in at least trace amounts has played an important role in ice emplacement in recent times. However, these high-latitude WEH reservoirs possibly also contain large contributions from hydrous material such as clays, zeolites, and mineral salts.

The deposits closer than 45° from the equator are generally not stable if they correspond to water ice buried beneath a relatively dry layer that has sufficiently large permeability. The depth of this burial is found to average between about a few to $10\,g\,cm^{-2}$ of soil, which is assumed to contain 2% H_2O by mass (Feldman *et al.*, 2004a). If correct, then these deposits must either be emplaced by a recent climate change, or be in the form of hydrated minerals, which are stable at most longitudes close to the equator. Time scales for such a climate change must range between about 9000 and about 700 Earth years ago. Although all quantitative estimates such as these require a host of assumptions that can introduce significant uncertainties, it is unlikely that orbital neutron spectroscopy is sensitive to currently unstable water-ice deposits if they were emplaced during previous obliquity cycles of Mars.

If the molecular associations of the WEH deposits are in the form of hydrous minerals, then the observed WEH spatial distribution must correspond to the spatial distribution of these minerals near the surface. The close similarity between the spatial distribution of the observed WEH deposits with that predicted for precipitation of water ice by atmospheric circulation (Feldman *et al.*, 2005) suggests that the recharge mechanism of subsurface WEH near the equator requires the intermediate step of precipitation, rather than direct diffusion through the soil from a hydrated atmosphere alone.

In addition to what we have learned, it is also important to emphasize what cannot be learned from orbital neutron spectrometry. No evidence has yet been found in MONS data to unambiguously support the existence of a system of aquifers anywhere on Mars. The MONS experiment is sensitive to WEH deposits only if they exist within about 1 m of the surface, which puts it out of range to the aquifers. Additionally, it has poor spatial resolution (a FWHM diameter approximately equal to 600 km). An aquifer system could then indeed be present, but not be readily apparent in the existing MONS data.

APPENDIX A: COMPARISON BETWEEN MONS AND HEND RESULTS

The MONS and the HEND both measure leakage neutron currents from Mars. Whereas MONS is sensitive to 3 bands of energies spanning the range between 0 eV and about 8 MeV, HEND measures 4 bands that are sensitive to neutrons spanning the energy range between 0.3 eV and 15 MeV. Although a few aspects of the neutron counting-rate maps returned by HEND agree qualitatively with the maps presented in Figure 6.8, they differ significantly in both qualitative and quantitative details. For example, the HEND map of epithermal-neutron counting rates (Mitrofanov *et al.*, 2002; 2003, 2004) agrees qualitatively with those measured using MONS (Feldman *et al.*, 2004a; Prettyman *et al.*, 2004). In contrast, the HEND and MONS fast-neutron maps differ fundamentally. Whereas the MONS maps show similar reduced fast- and epithermal-neutron counting rates in Arabia (Feldman *et al.*, 2004a; Prettyman *et al.*, 2004), the HEND fast-neutron map shows no such reduction (Mitrofanov *et al.*, 2002). In addition, the HEND fast-neutron map shows much higher counting rates at high southerly latitudes than at high northerly latitudes, whereas the MONS fast-neutron maps show them to be nearly equal.

Although we do not know the cause of these discrepancies, we note that the HEND and MONS fast-neutron sensors are very different and have very different perspectives of the view of Mars from their spacecraft mounts. The MONS sensor is a capture-gated fast-neutron spectrometer and therefore accepts only those fast neutrons that lose all of their energy in the scintillator, thereby providing a known energy scale. This scale is continuously monitored using the well-defined peak at 93 keV equivalent electron energy generated by neutron capture by ^{10}B in the scintillators. Furthermore, MONS is mounted on the nadir face of the Mars Odyssey spacecraft and therefore has a clear field of view of all of Mars.

In contrast, the HEND sensor only measures the energy-loss spectrum, much like that returned for gamma rays by a Compton-scatter gamma-ray spectrometer (see, e.g., Verbinski *et al.*, 1968). The HEND energy channels must therefore be less than half of the actual incident neutron-energy scale. In addition, HEND is mounted midway up the spacecraft from the nadir face and views at least half of Mars through spacecraft structures that include the hydrazine fuel tank and THEMIS. The view through the hydrazine tank is especially problematic because it holds a significant charge of hydrogen-containing fluid that decreases discontinuously with time.

We do not understand the exact detection mechanism of HEND or the analysis procedures used by the HEND team that contributes to the lower abundance of WEH seen by HEND at high southern versus high northern latitudes. This difference in abundance no doubt leads to their estimate of non-zero burial depths of WEH at high southern latitudes and zero burial depths at high northern latitudes.

As was shown in this chapter, MONS sees comparable burial depths at both high northern and southern latitudes. These MONS results are consistent with interpretations of the thermal inertia of surface soils at high latitudes (Mellon *et al.*, 2000; Kreslavsky and Head, 2002; Sizemore and Mellon, 2006; Titus *et al.*, 2006); low-thermal inertias are observed at these latitudes, which are consistent with ice-free soils at the surface to depths of at least a few centimeters. For ice-cemented soils, the thermal inertia would be about a factor of ten times larger than is observed if pore-filling water ice extended to the surface. Even partial filling of the pore space with ice would also raise the thermal inertia significantly (Mellon *et al.*, 1997) to be above the observed values. In addition, analysis of the seasonal temperature cycles in the northern high latitudes (Titus *et al.*, 2006) indicates that an ice table depth of several centimeters is required, and that ice-rich soil extending to the surface is inconsistent with seasonal temperature data. Thus the HEND results are not consistent with the thermal observations and their analysis.

Another difference between the results of HEND and MONS is that no surface layer of thick CO_2 is seen by HEND to cover most of the south residual polar cap (Mitrofanov *et al.*, 2004), whereas it is strongly evident in MONS data (Tokar *et al.*, 2002; Prettyman *et al.*, 2004), as shown here in the fast/epithermal and WEH maps in the upper right-hand panels of Figures 6.7 and 6.8. Again, although we do not know the reason for this difference we note that the HEND sensors are positioned above the THEMIS detector on one side of the spacecraft. One of these spacecraft structures is the hydrazine fuel tank, whose contents are very effective in moderating neutrons and it expends its fuel load discontinuously with time.

ACKNOWLEDGMENTS

We wish to thank many of our colleagues for many enlightening discussions, most notably David Vaniman, Bruce Jakosky, Jim Murphy, Steven Nelli, and David Lawrence. We also owe Benedicte Diez a debt of gratitude for help in understanding the factors that limit our interpretations of thermal- and epithermal-neutron counting rates. Partial support of this work was provided by the DOE through Laboratory Directed Research and Development funds and by NASA. This research was conducted under the auspices of the DOE.

REFERENCES

Arvidson, R. E., J. L. Gooding, and H. J. Moore, The Martian surface as imaged, sampled, and analyzed by the Viking Landers, *Rev. Geophys.* **27**, 39–60, 1989.

Baker, V. R., Water and the Martian landscape, *Nature* **412**, 228–36, 2001.

Basilevsky, A. T., M. L. Litvak, I. G. Mitrofanov, *et al.*, Search for traces of chemically bound water in the Martian surface layer based on HEND measurements onboard the 2001 Mars Odyssey spacecraft, *Solar Syst. Res.* **37**, 387–96, 2003.

Bibring, J.-P., Y. Langevin, A. Gendrin, *et al*., Mars surface diversity as revealed by the OMEGA/Mars Express observations, *Science* **307**, 1576–81, 2005.

Bibring, J.-P., Y. Langevin, J. F. Mustard, *et al*., Global mineralogical and aqueous Mars history drived from OMEGA/Mars Express data, *Science* **312**, 400–4, 2006.

Bish, D. L., J. W. Carey, D. T. Vaniman, and S. J. Chipera, Stability of hydrous minerals on the martian surface, *Icarus* **164**, 96–103, 2003a.

Bish, D. L., D. T. Vaniman, C. Fialips, J. W. Carey, and W. C. Feldman, Can hydrous minerals account for the observed mid-latitude water on Mars?, *6th Int. Conf. Mars, July 20–25, Pasadena, California*, Houston, TX: Lunar and Planetary Institute, Abstract 3066, 2003b.

Black, R. F., Periglacial features indicative of permafrost: ice and soil wedges, *Quaternary Res.* **6**, 3–26, 1976.

Boynton, W. V., W. C. Feldman, S. W. Squyres, *et al*., Distribution of hydrogen in the near surface of Mars: evidence for subsurface ice deposits, *Science* **2907**, 81–5, 2002.

Boynton, W. V., W. C. Feldman, I. Mitrofanov, *et al*., The Mars Odyssey gamma-ray spectrometer instrument suite, *Space Sci. Rev.* **110**, 37–83, 2004.

Byrne, S. and A. P. Ingersoll, Martian climate events on timescales of centuries: evidence from feature morphology in the residual south polar ice cap, *Geophys. Res. Lett.* **30**, 1–4, 2003.

Calvin, W. M., Variation of the 3-μm absorption feature on Mars: observations over eastern Valles Marineris by the Mariner 6 infrared spectrometer, *J. Geophys. Res.* **102**, 9097–107, 1997.

Cameron, A. G. W., Origin of the solar system, *Annu. Rev. Astron. Astrophys.* **26**, 441–72, 1988.

Carey, J. W. and D. L. Bish, Equilibrium in the clinoptilolite-H_2O system. *Am. Mineral.* **81**, 952–62, 1996.

Carr, M. H., Mars: a water-rich planet?, *Icarus*, **68**, 187–216, 1986.

Carr, M. H., D/H on Mars: effects of floods, volcanism, impacts, and polar processes, *Icarus* **87**, 210–27, 1990.

Carr, M. H., *Water on Mars*, New York: Oxford University Press, 229pp., 1996.

Carr, M. H. and J. W. Head III, Oceans on Mars: an assessment of the observational evidence and possible fate, *J. Geophys. Res.* **108**(E5), 5042, doi:10.1029/2002JE001963, 2003.

Christensen, P. R., M. B. Wyatt, T. D. Glotch, *et al*., Mineralogy at Meridiani Planum from the Mini-TES experiment on the Opportunity Rover, *Science* **306**, 1733–9, 2004.

Ciesla, F. J. and J. N. Cuzzi, The evolution of the water distribution in a viscous protoplanetary disk, *Icarus* **181**, 178–204, 2006.

Clark, B. C., Implications of abundant hygroscopic minerals in the Martian regolith, *Icarus* **34**, 645–65, 1978.

Clark, B. C. and D. C. Van Hart, The salts of Mars, *Icarus* **45**, 370–8, 1981.

Clark, B. C., R. V. Morris, S. M. McLennan, *et al*., Chemistry and mineralogy of outcrops at Meridiani Planum, *Earth Planet. Sci. Lett.* **240**, 73–94, 2005.

Clifford, S. M., Polar basal melting on Mars, *J. Geophys. Res.* **92**, 9135–52, 1987.

Clifford, S. M., The role of thermal vapor diffusion in the subsurface hydrologic evolution of Mars, *Geophys. Res. Lett.* **18**, 2055–68, 1991.

Clifford, S. M., A model for the hydrological and climatic behavior of water on Mars, *J. Geophys. Res.* **98**, 10973–11016, 1993.

Clifford, S. M., Mars: the effect of stratigraphic variations in the regolith diffusive properties on the evolution and vertical distribution of equatorial ground ice, *Lunar Planet. Sci. Conf. XXIX*, Abstract #1922 (CD-ROM), 1998.

Clifford, S. M. and D. Hillel, The stability of ground ice in the equatorial region of Mars, *J. Geophys. Res.* **88**, 2456–74, 1983.

Clifford, S. M. and T. J. Parker, The evolution of the Martian hydrosphere: implications for the fate of a primordial ocean and the current state of the northern plains, *Icarus* **154**, 40–79, 2001.

Fanale, F. P. and W. A. Cannon, Exchange of adsorbed H_2O and CO_2 between the regolith and the atmosphere of Mars caused by changes in surface insolation, *J. Geophys. Res.* **79**, 3397–402, 1974.

Fanale, F. P., J. R. Salvail, A. P. Zent, and S. E. Postawko, Global distribution and migration of subsurface ice on Mars, *Icarus* **67**, 1–18, 1986.

Farmer, C. B. and P. E. Doms, Global seasonal variation of water vapor on Mars and the implications of permafrost, *J. Geophys. Res.* **84**, 2881–8, 1979.

Feldman, W. C. and D. M. Drake, A Doppler filter technique to measure the hydrogen content of planetary surfaces, *Nucl. Instr. Meth.* **A245**, 182–90, 1986.

Feldman, W. C., D. M. Drake, R. D. O'Dell, F. W. Brinkley Jr., and R. C. Anderson, Gravitational effects on planetary neutron flux spectra, *J. Geophys. Res.* **94**, 513–25, 1989.

Feldman, W. C., R. C. Reedy, and D. S. McKay, Lunar neutron leakage fluxes as a function of composition and hydrogen content, *Geophys. Res. Lett.* **18**, 2157–60, 1991.

Feldman, W. C., W. V. Boynton, B. M. Jakosky, and M. T. Mellon, Redistribution of subsurface neutrons caused by ground ice on Mars, *J. Geophys. Res.* **98**, 20855–70, 1993a.

Feldman, W. C., W. V. Boynton, D. M. Drake, Planetary neutron spectroscopy from Orbit. In *Remote Geochemical Analysis: Elemental and Mineralogical Composition* (ed. C. M. Pieters and P. J. Englert), Cambridge University press, pp. 213–34, 1993b.

Feldman, W. C., D. J. Lawrence, R. C. Elphic, *et al*., The chemical information content of lunar thermal and epithermal neutrons, *J. Geophys. Res. – Planets* **105**, 20347–63, 2000.

Feldman, W. C., T. H. Prettyman, R. L. Tokar, *et al*., Fast neutron flux spectrum aboard Mars Odyssey during cruise, *J. Geophys. Res.* **107**(A6), doi:10.1029/2001JA000295, 2002a.

Feldman, W. C., W. V. Boynton, R. L. Tokar, *et al*., Global distribution of neutrons from Mars: results from Mars Odyssey, *Science* **297**, 75–8, 2002b.

Feldman, W. C., T. H. Prettyman, W. V. Boynton, *et al*., CO_2 frost cap thickness on Mars during northern winter and spring, *J. Geophys. Res.* **108**(E9), 5103, doi:10.1029/2003JE002101, 2003.

Feldman, W. C., T. H. Prettyman, S. Maurice, *et al*., The global distribution of near-surface hydrogen on Mars, *J. Geophys. Res.* **109**, E09006, doi:10.1029/2003JE002160, 2004a.

Feldman, W. C., M. T. Mellon, S. Maurice, *et al*., Hydrated states of $MgSO_4$ at equatorial latitudes on Mars, *Geophys. Res. Lett.* **31**, L16702, doi:10.1029/2004GL020181, 2004b.

Feldman, W. C., J. W. Head, S. Maurice, *et al*., Recharge mechanism of near-equatorial hydrogen on Mars: atmospheric redistribution or sub-surface aquifer, *Geophys. Res. Lett.* **31**, L18701, doi:10.1029/2004GL020661, 2004c.

Feldman, W. C., T. H. Prettyman, S. Maurice, *et al*., Topographic control of hydrogen deposits at low to mid latitudes of Mars, *J. Geophys. Res.* **110**, E11009, doi:10.1029/2005JE002452, 2005.

Feldman, W. C., R. C. Elphic, O. Gasnault, *et al*., Stratigraphy of water-equivalent hydrogen at high northern latitudes on Mars,

Lunar Planet. Sci. Conf. XXXVII, Houston, TX: Lunar and Planetary Institute, Abstract #2246, 2006.

Fermi, E., *Nuclear Physics*, Chicago, IL: University of Chicago Press, 248pp., 1950.

Fialips, C. I., J. W. Carey, D. T. Vaniman, W. C. Feldman, and M. T. Mellon, Hydration state of zeolites, clays, and hydrated salts under present-day Martian surface conditions: can hydrous minerals account for Mars Odyssey observations of near equatorial water-equivalent hydrogen?, *Icarus* **178**, 74–83, 2005a.

Fialips, C. I., J. W. Carey, and D. L. Bish, Hydration-dehydration behavior and thermodynamics of chabazite, *Geochim. Cosmochim. Acta* **69**, 2293–308, 2005b.

Forget, F., F. Hourdin, R. Fournier, *et al.*, Improved general circulation models of the Martian atmosphere from the surface to above 80 km, *J. Geophys. Res. – Planets* **104**, 24155–76, 1999.

Gasnault, O., W. C. Feldman, S. Maurice, *et al.*, Composition from fast neutrons: application to the Moon, *Geophys. Res. Lett.* **28**, 3797–800, 2001.

Gellert, R., R. Rieder, J. Brückner, *et al.*, Alpha Particle X-Ray Spectrometer (APXS): results from Gusev crater and calibration report, *J. Geophys. Res.* **111**, E02S05, doi:10.1029/2005JE002555, 2006.

Gendrin, A., N. Mangold, J.-P. Bibring, *et al.*, Sulfates in Martian layered terrains: the OMEGA/Mars Express view, *Science* **307**, 1587–91, 2005.

Grotzinger, J. P., R. E. Arvidson, J. F. Bell III, *et al.*, Stratigraphy and sedimentology of a dry to wet eolian depositional system, Burns formation, Meridiani Planum, Mars, *Earth Planet. Sci. Lett.* **240**, 11–72, 2005.

Haberle, R. M., M. M. Joshi, J. R. Murphy, *et al.*, General circulation model simulations of the Mars Pathfinder atmospheric structure investigation/meteorology data, *J. Geophys. Res.* **104**, 8957–74, 1999.

Head III, J. W., M. A. Kreslavsky, and S. Pratt, Northern lowlands of Mars: evidence for widespread volcanic flooding and tectonic deformation in the Hesperian period, *J. Geophys. Res.* **107**(E1), doi:10.1029/2000JE001445, 2002.

Head, J. W., J. F. Mustard, M. A. Kreslavsky, R. E. Milliken, and D. R. Marchant, Recent ice ages on Mars, *Nature* **426**, 797–802, 2003.

Hodges, R. R., Reanalysis of lunar prospector neutron spectrometer observations over the lunar poles, *J. Geophys. Res.* **107**(E12), 5125, doi:10.1029/2000JE001483, 2002.

Houck, J. R., J. B. Pollack, C. Sagan, D. Schaack, and J. A. Decker Jr., High altitude infrared spectroscopic evidence for bound water on Mars, *Icarus* **18**, 470–80, 1973.

Jakosky, B. M., Mars volatile evolution: evidence from stable isotopes, *Icarus* **94**, 14–31, 1991.

Jakosky, B. M. and M. A. Carr, Possible precipitation of ice at low latitudes of Mars during periods of high obliquity, *Nature* **315**, 559–61, 1985.

Jakosky, B. M. and C. B. Farmer, The seasonal and global behavior of water vapor in the Mars atmosphere: complete global results of the Viking atmospheric water detector experiment, *J. Geophys. Res.* **87**, 2999–3019, 1982.

Jakosky, B. M. and R. J. Phillips, Mars' volatile and climate history, *Nature* **412**, 237–44, 2001.

Jakosky, B. M., B. G. Henderson, and M. T. Mellon, Chaotic obliquity and the nature of the Marian climate, *J. Geophys. Res.* **100**, 1579–84, 1995.

Jakosky, B. M., M. T. Mellon, E. S. Varnes, *et al.*, Mars low-latitude neutron distribution: possible remnant near-surface water ice and a mechanism for its recent emplacement, *Icarus* **175**, 58–67, 2005.

Jänchen, J., D. L. Bish, D. T. F. Möhlmann, and H. Stach, Investigation of the water sorption properties of Mars-relevant micro- and mesoporous minerals, *Icarus* **180**, 353–8, 2006.

Klingelhöfer, G., R. V. Morris, B. Bernhardt, *et al.*, Jarosite and hematite at Meridiani Planum from Opportunity's Mössbauer spectrometer, *Science* **306**, 1740–5, 2004.

Kreslavsky, M. A. and J. W. Head III, Mars: nature and evolution of young latitude-dependent water ice-rich mantle, *Geophys. Res. Lett.* **29**(15), 1719, doi:10.1029/2002GL015392, 2002.

Kuzmin, R. O., E. V. Zabalueva, I. G. Mitrofanov, *et al.*, Regions of potential existence of free water (ice) in the near surface Martian ground: results from the Mars Odyssey High-Energy Neutron Detector (HEND), *Solar Syst. Res.* **38**, 1–11, 2004.

Lachenbruch, A. H., Mechanics of thermal contraction cracks and ice-wedge polygons in permafrost, *Geol. Soc. Am. Spec. Paper* **70**, 69pp., 1962.

Lane, M. D., M. D. Dyar, and J. L. Bishop, Spectroscopic evidence for hydrous iron sulfate in the Martian soil, *Geophys. Res. Lett.* **31**, L19702, doi:10.1029/2004GL0212321, 2004.

Laskar, J. B., Secular evolution of the solar system over 10 million years, *Astron. Astrophys.* **198**, 341–62, 1988.

Laskar, J., B. Levrard, and J. Mustard, Orbital forcing of the Martian polar layered deposits, *Nature* **41**, 375–7, 2002.

Lawrence, D. J., W. C. Feldman, R. C. Elphic, *et al.*, Improved modeling of counting rates from the lunar prospector neutron spectrometer, *J. Geophys. Res. – Planets* **111**, CiteID E08001, doi:10.1029/2005JE002637, 2006.

Leighton, R. B. and B. C. Murray, Behavior of carbon dioxide and other volatiles on Mars, *Science* **153**, 136–44, 1966.

Leshin, L. A., Insights into Martian water reservoirs from analyses of Martian meteorite QUE94201, *Geophys. Res. Lett.* **27**, 2017–20, 2000.

Levrard, B., F. Forget, F. Montmessin, and J. Laskar, Recent ice-rich deposits formed at high latitudes on Mars by sublimation of unstable equatorial ice during low obliquity, *Nature* **431**, 1072–5, 2004.

Lewis, J. S., Metal/silicate fractionation in the solar system, *Earth Planet. Sci. Lett.* **15**, 286–90, 1972.

Litvak, M. L., I. G. Mitrofanov, A. S. Kozyrev, *et al.*, Comparison between polar regions of Mars from HEND/Odyssey data, *Icarus* **180**, 23–37, 2006.

Luhman, J. G., R. E. Johnson, and M. H. G. Zhang, Evolutionary impact of sputtering of the Martian atmosphere by O^+ pickup ions, *Geophys. Res. Lett.* **19**, 2151–4, 1992.

MacKay, J. R., The world of underground ice, *Ann. Assoc. Am. Geogr.* **62**, 1–22, 1972.

Malin, M. C. and K. S. Edgett, Mars Global Surveyor Mars Orbiter Camera: interplanetary cruise through primary mission, *J. Geophys. Res.* **106**, 23429–570, 2001.

Mangold, N., S. Maurice, W. C. Feldman, F. Costard, and F. Forget, Spatial relationships between patterned ground and ground ice detected by the Neutron Spectrometer on Mars, *J. Geophys. Res. – Planets* **109**, E08001, 2004.

Maurice, S., W. C. Feldman, D. J. Lawrence, *et al.*, High-energy neutrons from the Moon, *J. Geophys. Res.* **101**(E8), 20365–76, doi:10.1029/1999JE001151, 2000.

Maurice, S., W. C. Feldman, T. H. Prettyman, B. Diez, and O. Gasnault, Reduction of Mars Odyssey Data, *Lunar Planet. Sci. XXXVIII*, Houston, TX: Lunar and Planetary Institute, Abstract #2036, 2007.

McKay, C. P., M. T. Mellon, E. I. Friedman, Soil temperatures and stability of ice-cemented ground in the McMurdo Dry Valleys, Antarctica, *Antarct. Sci.* **10**, 31–8, 1998.

McLennan, S. M., J. F. Bell III, W. M. Calvin, *et al.*, Provenance and diagenesis of the evaporite-bearing Burns formation, Meridiani Planum, Mars, *Earth Planet. Sci. Lett.* **240**, 95–121, 2005.

Mellon, M. T. and B. M. Jakosky, Geographic variations in the thermal and diffusive stability of ground ice on Mars, *J. Geophys. Res.* **98**, 3345–64, 1993.

Mellon, M. T. and B. M. Jakosky, The distribution and behavior of Martian ground ice during past and present epochs, *J. Geophys. Res.* **100**, 11781–99, 1995.

Mellon, M. T. and W. C. Feldman, The global distribution of Martian subsurface ice and regional ice stability, *Lunar Planet. Sci. Conf. XXXVII*, Abstract #2246, 2006.

Mellon, M. T., B. M. Jakosky, and S. E. Postawko, The persistence of equatorial ground ice on Mars, *J. Geophys. Res.* **102**(E8), 19357–70, 1997.

Mellon, M. T., B. M. Jakosky, H. H. Kieffer, and P. R. Christensen, High-resolution thermal inertia mapping from the Mars Global Surveyor Thermal Emission Spectrometer, *Icarus* **148**, 437–55, 2000.

Mellon, M. T., W. C. Feldman, and T. H. Prettyman, The presence and stability of ground ice in the southern hemisphere of Mars, *Icarus* **169**, 324–40, 2004.

Miller, R. D., Freezing phenomena in soils. In *Applications of Soil Physics* (ed. D. Hillel), New York, NY: Academic Press, 1980.

Milliken, R. E., J. F. Mustard, and D. L. Goldsby, Viscous flow features on the surface of Mars: observations from high-resolution Mars Orbiter Camera (MOC) images, *J. Geophys. Res.* **108**(E6), 5057, doi:10.1029/2002JE002005, 2003.

Ming, D. W., D. W. Mittlefehldt, R. V. Morris, *et al.*, Geochemical and mineralogical indicators for aqueous processes in the Columbia Hills of Gusev crater, Mars, *J. Geophys. Res.* **111**, E02S12, doi:10.1029/2005JE002560, 2006.

Mischna, M. A., D. J. McCleese, M. I. Richardson, A. R. Vasavada, and R. J. Wilson, Volatile cycling and layering on Mars: observations, theory, and modeling, *6th Int. Conf. Mars, July 20–25, Pasadena, California*, Houston, TX: Lunar and Planetary Institute, Abstract #3145, 2003a.

Mischna, M. A., M. I. Richardson, R. J. Wilson, and D. J. McCleese, On the orbital forcing of Martian water and CO_2 cycles: a general circulation model study with simplified volatile schemes, *J. Geophys. Res.* **108**(E6), 5062, doi:10.1029/2003JE002051, 2003b.

Mischna, M. A. and M. I. Richardson, A reanalysis of water abundances in the Martian atmosphere at high obliquity, *Geophys. Res. Lett.* **32**, L03201, doi:10.1029/2004GL021865, 2005.

Mitrofanov, I. G., J. I. Trombka, C. d'Uston, *et al.*, Distribution of hydrogen in the near surface of Mars: evidence for subsurface ice deposits, *Science* **297**, 81–5, 2002.

Mitrofanov, I. G., M. L. Litvak, A. S. Kozyrev, *et al.*, Search for water in Martian soil using global neutron mapping by the Russian HEND instrument onboard the US 2001 Mars Odyssey spacecraft, *Solar Syst. Res.* **37**, 366–77, 2003.

Mitrofanov, I. G., M. L. Litvak, A. S. Kozyrev, *et al.*, Soil water content on Mars as estimated from neutron measurements by the HEND instrument onboard the 2001 Mars Odyssey spacecraft, *Solar Syst. Res.* **38**, 253–65, 2004.

Möhlmann, D. T. F., Water in the upper martian surface at mid- and low-latitudes: presence, state, and consequences, *Icarus* **168**, 318–23, 2004.

Möhlmann, D., Adsorption water-related potential chemical and biological processes in the upper Martian surface, *Astrobiology* **5**, 770–7, 2005.

Morris, R. V., G. Klingelhöfer, C. Schröder, *et al.*, Mössbauer mineralogy of rock, soil, and dust at Gusev crater, Mars: Spirit's journey through weakly altered olivine basalt on the plains and pervasively altered basalt in the Columbia Hills, *J. Geophys. Res.* **111**, E02S13, doi:10.1029/2005JE002584, 2006.

Mustard, J. F., C. D. Cooper, and M. K. Rifkin, Evidence for recent climate change on Mars from the identification of youthful near-surface ground ice, *Nature* **412**, 411–14, 2001.

Navrotsky, A., F. L. Forray, and C. Drouet, Jarosite stability on Mars, *Icarus* **176**, 250–3, 2005.

Nelli, S. M., J. R. Murphy, A. L. Sprague, *et al.*, Tracer transport in the NASA-Ames GCM, CNES/ESA 2006 Second Mars atmosphere modeling and observation workshop, *Conf. Proc. Feb. 27–Mar. 3*, Granada, Spain, 2006.

Paige, D. A., The thermal stability of near-surface ground ice on Mars, *Nature* **356**, 43–5, 1992.

Péwé, T. L., Geomorphic processes in polar deserts. In *Polar Deserts and Modern Man* (ed. T. L. Smiley and J. H. Zumberge), University of Arizona Press, 1974.

Pimental, G. C., P. B. Forney, and K. C. Herr, Evidence about hydrate and solid water in the Martian surface from the 1969 Mariner infrared spectrometer, *J. Geophys. Res.* **79**, 1623–34, 1974.

Poulet, F., J.-P. Bibring, J. F. Mustard, *et al.*, Phyllosilicates on Mars and implications for early Martian climate, *Nature* **438**, 623–7, 2005.

Prettyman, T. H., W. C. Feldman, R. C. Elphic, *et al.*, Mid-latitude composition of Mars from thermal and epithermal neutrons, *6th Int. Conf. Mars, July 20–25, Pasadena, California*, Houston, TX: Lunar and Planetary Institute, Abstract #3253, 2003.

Prettyman, T. H., W. C. Feldman, M. T. Mellon, *et al.*, Composition and structure of the Martian surface at high southern latitudes from neutron spectroscopy, *J. Geophys. Res.* **109**, E05001, doi:10.1029/2003JE002139, 2004.

Richardson, M. I., D. J. McCleese, M. Mischna, and A. R. Vasavada, Obliquity, ice sheets, and layered sediments on Mars: what spacecraft observations and climate models are telling us, *Lunar Planet. Sci. XXXIV*, Abstract #1281 (CD-ROM), 2003.

Rieder, R., R. Gellert, R. C. Anderson, *et al.*, Chemistry of rocks and soils at Meridiani Planum from the Alpha Particle X-Ray spectrometer, *Science* **306**, 1746–9, 2004.

Ruff, S. W., Spectral evidence for zeolite in the dust on Mars, *Icarus* **168**, 131–43, 2004.

Schorghofer, N. and O. Aharonson, Stability and exchange of subsurface ice on Mars, *J. Geophys. Res. – Planets* **110**, E05003, doi:10.1029/2004JE002350, 2005.

Sizemore, H. G. and M. T. Mellon, Effects of soil heterogeneity on Martian ground-ice stability and orbital estimates of ice table depth, *Icarus* **185**, 358–69, 2006.

Smith, D. E., M. T. Zuber, S. C. Solomon, *et al.*, The global topography of Mars and implications for surface evolution, *Science* **284**, 1495–507, 1999.

Smith, D. E., M. T. Zuber, and G. A. Neumann, Seasonal variations of snow depth on Mars, *Science* **294**, 2141–6, 2001.

Smith, M. D., The annual cycle of water vapor on Mars as observed by the Thermal Emission Spectrometer, *J. Geophys. Res.* **107**(E11), 5115, doi:10.1029/2001JE001522, 2002.

Smoluchowski, R., Mars: retention of ice, *Science* **159**, 1348–50, 1968.

Squyres, S. W., Water on Mars, *Icarus* **79**, 229–88, 1989.

Thomas, P., S. Squyres, K. Herkenhoff, A. Howard, and B. Murray, Polar deposits of Mars. In *Mars* (ed. H. H. Kieffer, B. M. Jakosky, C. W. Snyder, and M. S. Matthews), Tucson: University of Arizona Press, pp. 767–95, 1992.

Thomas, P. C., M. C. Malin, K. S. Edgett, *et al.*, North-south geological differences between the residual polar caps on Mars, *Nature* **404**, 161–4, 2000.

Thomas, P. C., M. C. Malin, P. B. James, *et al*., South polar residual cap of Mars: features, stratigraphy, and changes, *Icarus* **174**, 535–59, 2005.

Titus, T. N., T. H. Prettyman, and A. Colaprete, Thermal characterization of the three proposed Phoenix landing sites, *Lunar Planet. Sci. Conf. XXXVII*, Abstract #2161, 2006.

Tokano, T., Spatial inhomogeneity of the martian subsurface water distribution: implication from a global water cycle model, *Icarus* **164**, 50–78, 2003.

Tokar, R. L., W. C. Feldman, T. H. Prettyman, *et al*., Ice concentration and distribution near the south pole of Mars: synthesis of Odyssey and Global Surveyor analyses, *Geophys. Res. Lett.* **29**(19), 1904, doi:10.1029/2002GL015691, 2002.

Tokar, R. L., R. C. Elphic, W. C. Feldman, *et al*., Mars Odyssey neutron sensing of the south residual polar cap, *Geophys. Res. Lett.* **30**(13), 1677, doi:10.1029/2003GL017316, 2003.

Toulmin, P. I., A. K. Baird, B. C. Clark, *et al*., Geochemical and mineralogical interpretation of the Viking inorganic chemical results, *J. Geophys. Res.* **82**, 4625–34, 1977.

Vaniman, D. T., D. L. Bish, S. J. Chipera, *et al*., Magnesium sulfate salts and the history of water on Mars, *Nature* **431**, 663–5, 2004.

Wang, A., L. A. Haskin, S. W. Squyres, *et al*., Sulfate deposition in subsurface regolith in Gusev crater, Mars, *J. Geophys. Res.* **111**(E2), E02S17, doi:10.1029/2005JE002513, 2006a.

Wang, A., R. L. Korotev, B. L. Jolliff, *et al*., Evidence of phyllosilicates in Wooly Patch, an altered rock encountered at West Spur, Columbia Hills, by the Spirit rover in Gusev crater, Mars, *J. Geophys. Res.* **111**, E02S16, doi:10.1029/2005JE002516, 2006b.

Wänke, H., J. Bruckner, G. Dreibus, R. Rieder, and I. Ryabchikov, Chemical composition of rocks and soils at the Pathfinder site, *Space Sci. Rev.* **96**, 317–30, 2001.

Ward, W. R., Climate variations on Mars: 1. Astronomical theory of insolation, *J. Geophys. Res.* **79**, 3375–86, 1974.

Williams, P. J. and M. W. Smith, *The Frozen Earth*, Cambridge, UK: Cambridge University Press, 1989.

Verbinski, V. V., W. R. Burrus, T. A. Love, W. Zobel, and N. W. Hill, Calibration of an organic scintillator for neutron spectrometry, *Nucl. Instr. Meth.* **65**, 8–25, 1968.

Yen, A. S., R. Gellert, C. Schröder, *et al*., An integrated view of the chemistry and mineralogy of martian soils, *Nature* **436**, 49–54, 2005.

Yung, Y. L., J.-S. Wen, J. P. Pinto, *et al*., HDO in the Martian atmosphere: implications for the abundance of crustal water, *Icarus* **76**, 146–59, 1988.

Zent, A. P. and R. C. Quinn, Measurement of H_2O adsorption under Mars-like conditions: effects of adsorbent heterogeneity, *J. Geophys. Res.* **102**, 9085–95, 1997.

Zent, A. P., F. P. Fanale, J. R. Salvail, and S. E. Postawko, Distribution and state of H_2O in the high-latitude shallow subsurface of Mars, *Icarus* **67**, 19–36, 1986.

Zolotov, M. Yu., Water-bearing minerals in the Martian soil (thermodynamic prediction of stability), *Lunar Planet. Sci. Conf. XX*, 1257–8, 1989.

Zuber, M. T., D. E. Smith, S. C. Solomon, *et al*., Observations of the north polar region of Mars from the Mars Orbiter Laser Altimeter, *Science* **282**, 2053–60, 1998.

PART III

MINERALOGY AND REMOTE SENSING OF ROCKS, SOIL, DUST, AND ICES

PART III.A

Visible to Near-IR Telescopic and Orbital Measurements

7

Mineralogy of the Martian surface from Mars Express OMEGA observations

J.-P. BIBRING AND Y. LANGEVIN

ABSTRACT

In orbit on board the European Space Agency's (ESA) Mars Express spacecraft, the Observatoire pour la Minéralogie, l'Eau, les Glaces et l'Activité (OMEGA) visible to near-infrared spectral imager is acquiring a global compositional surface mapping dataset of Mars in order to reveal its major mineralogical and icy constituents. These data provide insights on the evolution of Mars on timescales ranging from seasonal variations to geological epochs. In particular, the identification and mapping of the spatial distribution of pristine magmatic rocks (including olivine, high-Ca pyroxene, and low-Ca pyroxene) and of three classes of altered minerals (hydrated phyllosilicates, hydrated sulfates, and anhydrous ferric oxides) in distinct areas has enabled the development of a new model for the evolution of the surface. The model includes three major eras spanning Martian history. The first era, during which phyllosilicates appear to have formed, was the most favorable to have hosted habitable conditions, with perennial and neutral to slightly alkaline pH surface liquid water. Mars then underwent a global environmental and climatic change, coupled to the formation of Tharsis and the release of large amounts of SO_2 and other volcanic gases, and the likely loss of most of its CO_2-rich atmosphere. This second era was characterized by low-pH (acidic) surface and subsurface groundwater, and the creation of large deposits of sulfate minerals. The third and most recent era in this model is dominated by atmospheric processes, leading primarily to the generation of anhydrous weathering products. OMEGA results attest to the huge potential of coupling geomorphological data to compositional measurements derived from visible and near-infrared observations, and provide important new data with which to infer the past history of Mars.

7.1 THE OMEGA INSTRUMENT ON BOARD THE MARS EXPRESS MISSION

Launched on a Soyouz-Fregat rocket from Baikonur (Kazakhstan) June 2, 2003, the ESA Mars Express (hereafter denoted as MEx) spacecraft (Chicarro *et al.*, 2004) was inserted into Mars orbit on December 25, 2003, and started its orbital mission in early January 2004. Its nominal duration of one Mars year was extended to a second one in September 2005. The MEx orbit is almost polar (inclination = 86.5°) and highly elliptical, with a periapsis of ~280 km and an apoapsis of ~11 000 km (orbital period ~6.5 hours). Its precession has been chosen to allow the periapsis to drift both in latitude and in longitude (~0.5°/day), so as to cover the Martian surface over one Mars year, and to enable global coverage by contiguous swaths. In addition, the Sun elevation at periapsis varies as a function of time, with sequential periods of night observations, favorable to subsurface radar sounding, and daylight observations, required for "optical" instruments analyzing solar reflected light to operate.

MEx has direct heritage from the Russian Mars-96 mission, which failed at launch on November 17, 1996. ESA approved MEx in 1997 as the first of a new type of "flexible missions," utilizing the spare units of five remote-sensing instruments originally developed for Mars-96. These instruments were designed to map the various Mars "envelopes": its exosphere (Analyzer of Space Plasmas and Energetic Atoms [ASPERA]), the atmosphere (Spectroscopic Investigation of the Characteristics of the Atmosphere of Mars [SPICAM], Planetary Fourier Spectrometer [PFS]), and the surface (Observatoire pour la Minéralogie, l'Eau, les Glaces et l'Activité [OMEGA], High Resolution Stereo Camera [HRSC]). A subsurface radar sounder was added (Mars Advanced Radar for Subsurface and Ionosphere Sounding [MARSIS]), as well as a surface landing station (Beagle 2). Unfortunately, Beagle 2 was lost after release from the Orbiter five days before Mars orbit insertion. Many more details about the MEx mission can be found in Chicarro *et al.* (2004).

The OMEGA instrument on board MEx is a visible to near-infrared hyperspectral imager, built under the responsibility of a Principal Investigator and Project Manager at Institut d'Astrophysique Spatiale (IAS) in Orsay, France, in cooperation with Laboratoire d'Etudes Spatiales et d'Instrumentation en Astrophysique (LESIA) in Meudon, France, Istituto di Fisica dello Spazio Interplanetario-Istituto Nazionale di AstroFisica (IFSI-INAF) in Roma, Italy, and the Space Research Institute (IKI) in Moscow, Russia (Bibring *et al.*, 2004a).

OMEGA couples an imaging capability (with an IFOV [instantaneous field of view] of 1.2 mrad) to a spectral capability by acquiring for each pixel the spectrum from 0.35 to 5.1 μm in 352 contiguous spectral channels ("spectels"). OMEGA includes three spectrometers, one for the visible to near-IR range (0.35–1.0 μm), and two to cover the near-infrared (NIR) range from 0.93 to 2.65 μm and 2.51 to 5.1 μm. The instrument has a spectral sampling of 7 nm, 13 nm and 20 nm in these spectral ranges, respectively. Two dedicated and

The Martian Surface: Composition, Mineralogy, and Physical Properties, ed. J. F. Bell III. Published by Cambridge University Press.

co-aligned telescopes are used to illuminate the visible to near-infrared and NIR subsystems separately. The visible to near-infrared subsystem operates in a "pushbroom" mode; it images a given line of Mars, perpendicular to the drift velocity of the spacecraft, along one direction of a bi-dimensional charge-coupled device (CCD) detector array, with the spectrum of each pixel spread over the other direction of the array by a concave holographic grating. The infrared subsystem operates in a "whiskbroom" mode: one pixel of Mars is imaged at a time, and its spectrum is acquired on two IR linear arrays, from 0.93 to 2.65 μm ("SWIR," for "Short Wavelength IR") and from 2.51 to 5.1 μm ("LWIR," for "Long Wavelength IR") respectively. A scanning mirror ahead of the NIR telescope enables contiguous pixel imaging in the crosstrack direction, perpendicular to the spacecraft drift velocity. For visible to near-infrared, SWIR, and LWIR, the second spatial dimension is provided by the movement of the spacecraft. With time, three-dimensional (two spatial and one spectral) image-cubes are built, which constitute the OMEGA dataset.

The imaging performance of OMEGA can be summarized as follows: with an IFOV of 1.2 mrad, the spatial sampling (crosstrack pixel size) is ~300 m/pixel when the observation is made close to periapsis, and up to 4.8 km/pixel from an altitude of 4000 km. OMEGA's prime goal is to acquire global coverage of Mars with a 1.5–4.8 km/pixel footprint, and to map selected areas amounting to ~5% of the surface at high resolution (footprint < 400 m). The instrument design allows a total field of view of 128 pixels crosstrack, or 8.8°, both for the visible to near-infrared pushbroom channel and the NIR whiskbroom channel. However, reconstruction of the images requires synchronizing the duration of a swath with the drift of the spacecraft in order to avoid both undersampling and oversampling. With an infrared integration time of typically 5 ms, chosen to enable a signal-to-noise ratio (SNR) >100 for typical Mars imaging conditions, the swath varies from 16 pixels when acquired at periapsis (high spacecraft orbital velocity, ~4 km s^{-1}) to 128 pixels when operating above 1500 km (slower spacecraft drift, <2 km s^{-1}). Thus, the high resolution mode data is made of strips some 5–8 km wide, and hundreds of kilometers long, while the global coverage data is made of strips 300–500 km in width, and thousands of kilometers long.

The nominal pointing mode is nadir. In order to target given units of interest, nadir pointing with a constant crosstrack offset angle are implemented. In addition, some observations have been made in inertial mode (3 axis stabilized), in particular to acquire limb profiles, and in a "spot pointing," or "EPF" (emission phase function) mode, to enhance the detection of atmospheric constituents. Due to severe mission resource constraints (mainly energy and downlink capability), a strict sharing with other investigations was imposed by ESA, assigning OMEGA an averaged data volume cap of 15% of the available downlink. This translated in OMEGA operating over less than 1 out of 4 MEx orbits on average, and for <60 minutes per orbit. As a consequence, during the first three Earth years of operations a large number of desired targets could not be imaged, and very little multiple coverage of the same area to monitor seasonal changes could be performed.

7.2 IDENTIFICATION OF SURFACE CONSTITUENTS

In order to retrieve the diagnostic signatures of surface constituents, several steps were followed, and a variety of data reduction techniques were used. The first steps consisted of removing the instrumental effects and the atmospheric contribution, dominated by the CO_2 bands. Then, the spectrum was divided by a synthetic solar reference spectrum. The resulting radiance factor or I/F spectral values (where I is the measured radiance and πF is the incident solar radiance at the top of the Martian atmosphere at the time of the observation) include all potential surface features.

Most features of interest can be enhanced by spectral band ratios, dividing the I/F at a wavelength position corresponding to the supposed maximum absorption (band center) to that of the nearby continuum. More sophisticated techniques are available, which search for coupled absorptions of a single component. For example, the Modified Gaussian Model (MGM; Sunshine and Pieters, 1993) is well suited to identify constituents such as pyroxene that exhibit absorption features that can be reproduced by a small number of Gaussians (see Section 7.5).

7.3 ISM/PHOBOS: PIONEERING RESULTS

The precursor to OMEGA in orbital hyperspectral NIR reflectance imaging of Mars was the Infrared Spectrometer for Mars (ISM), a first generation instrument built in France under the responsibility of IAS and Observatoire de Paris, Departement d'Espace (DESPA; Meudon, France) and carried on board the Soviet Phobos-1 and Phobos-2 missions launched in July 1988 (Bibring *et al.*, 1989). With an IFOV of 3.5 mrad, the footprint on the Martian surface from the circular equatorial orbit at the distance of the moon Phobos (6300 km) was ~22 km when nadir pointed. ISM was limited to the spectral range 0.76–3.16 μm due to technology transfer regulations. This spectral range was acquired simultaneously by 64 coregistered spectral measurements, on two linear arrays of 32 PbS detectors. Phobos-1 was lost en route to Mars, but Phobos-2 successfully operated from January to March 1989, until the premature end of its mission two months after Mars orbit insertion. ISM acquired ~40 000 spectra of Mars, primarily along 11 ground tracks (Figure 7.1), covering some 25% of the surface within the latitudes ±30°. Specific regions covered included Tharsis, Valles Marineris, Syrtis Major, and Arabia. Detailed discussion on data reduction and major results can be found in Erard *et al.* (1991), Mustard *et al.* (1993), Murchie *et al.* (1993), and Bibring and Erard (2001).

Five spectral indices were primarily used to characterize the spectral diversity of the units mapped on Mars by ISM. These indices were based on the ~1 μm and ~2.2 μm silicate (pyroxene) features, the ~3 μm hydration band, the slope of the continuum, and the NIR albedo. Low-albedo regions were found to be dominated by basalts with both low-calcium

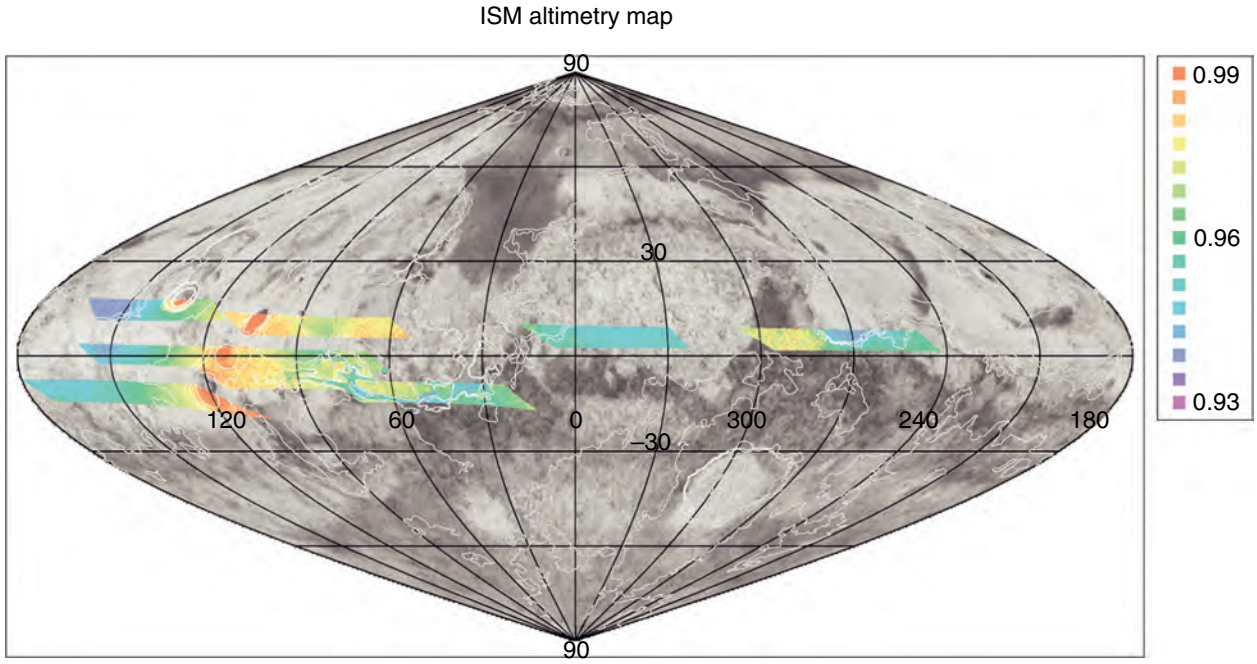

Figure 7.1. ISM coverage of Mars, superimposed on the Viking Mars Digital Image Model (MDIM; sinusoidal projection). The color scale indicates the depth of the 2.0 μm CO_2 absorption band (which corresponds to the elevation), from blue (the lowest) to red (the highest). (For a color version of this figure, please refer to the color plate section or to the e-Book version of this chapter.)

pyroxene (LCP) and high-calcium pyroxene (HCP), with regional differences in the LCP/HCP abundances. For example, the volcanic materials in Syrtis Major were found to be enriched in HCP relative to the floor of Valles Marineris, while the plateau plains of Ophir Planum were found to be intermediate in composition between these terrains. These results were interpreted as indicating a high depletion of Al in the early Martian mantle.

In the eastern part of Syrtis Major, the pyroxene features were reduced in contrast and the 1 μm absorption was elongated towards shorter wavelengths, indicating the presence of ferric oxides. The specific materials exposed were interpreted as dust cemented on a mafic substrate, possibly by a crystalline ferric phase.

The largest variations of the spectral parameters were found in Valles Marineris. Specifically, in the easternmost part of the canyon (in the chaotic terrains of Eos Chasma), a unique mixture of highly mafic and highly hydrated minerals was detected. In contrast, in the surrounding plateaus only homogeneously bright, hydrated, and soil-covered terrain was seen to the west (Tharsis), and darker, more anyhydrous material was exposed in to the northeast (Ophir Planum).

These results presented a somewhat puzzling picture of Mars. Were the pristine crustal rocks really as homogeneous as the ISM observations indicated, and if so, what did that imply for the evolution of the crust and mantle? The ~3 μm hydration feature is an ambiguous mineralogical indicator, for example, not discriminating between adsorbed water versus water/hydroxyl trapped in a mineral lattice. Thus, it was hard to know for sure if ISM had unambiguously detected any minerals that resulted from aqueous alteration. Would a

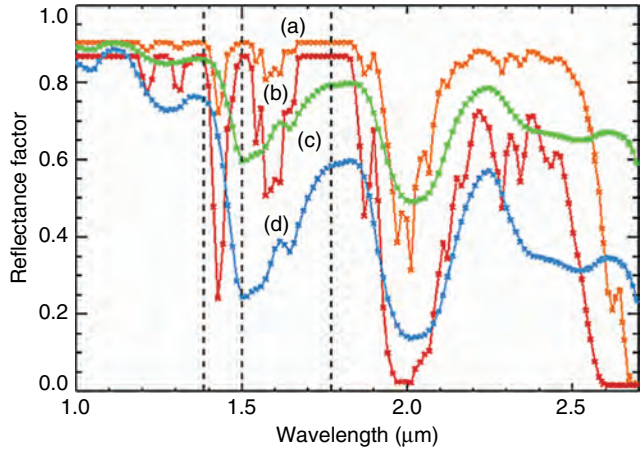

Figure 7.2. Model spectra of CO_2 ice with grains of (a) 1 mm (orange) and (b) 5 cm (red). Model spectra of H_2O ice with grains sizes of (c) 10 μm (green) and (d) 1000 μm (blue). The three dashed lines correspond to the OMEGA spectels at 1.38, 1.5, and 1.77 μm which are used for the determination of the strength of the H_2O ice absorption at 1.5 μm, as there are only weak CO_2 absorption at these wavelengths. (For a color version of this figure, please refer to the color plate section or to the e-Book version of this chapter.)

refined picture emerge from higher spatial resolution datasets, or was there a limitation in surface spectral diversity driven by the dust accumulating from global atmospheric circulation? ISM observations resulted in a host of new questions that motivated eventual OMEGA observations.

7.4 OMEGA OBSERVATIONS OF FROSTS AND ICES

OMEGA spectral characteristics and performance are very favorable for identifying H_2O and CO_2 ice and frost features in the SWIR channel, by the absorptions centered

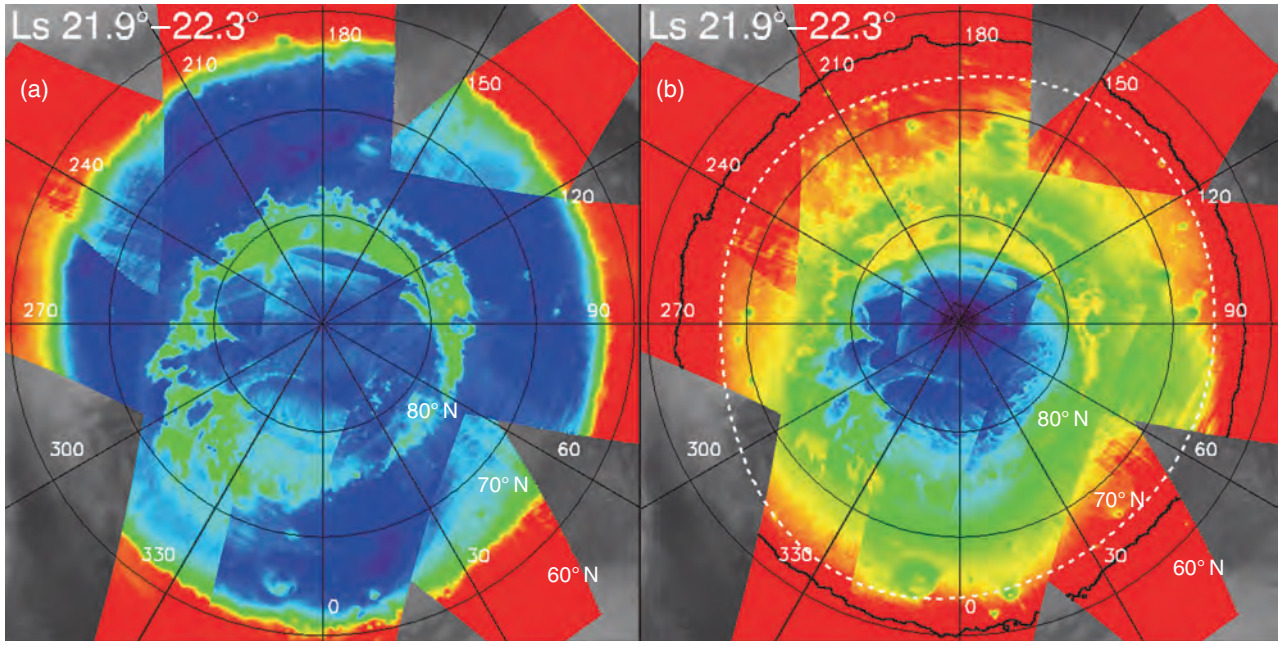

Figure 7.3. Seasonal evolution of the northern polar cap: spatial distribution of spectral signatures of H_2O ice and CO_2 ice observed by OMEGA in early northern spring ($L_s = 22°$, March 2006). (a) Band depth of the H_2O ice absorption feature at 1.5 μm. The rainbow scale covers the range from 60% (black) to 0% (red); (b) band depth of the CO_2 ice absorption feature at 1.43 μm, also from 60% (black) to 0% (red). The annulus observed by TES between the boundary of bright regions (black line on panel (b)) and that of regions at the equilibrium temperature of CO_2 ice (the so-called "crocus line," white dashes, from Titus *et al.*, 2003) is confirmed as being constituted of H_2O frost. At this season, the strongest CO_2 ice signatures (corresponding to large mean grain sizes) are observed over regions corresponding to the central parts of the north permanent cap. (For a color version of this figure, please refer to the color plate section or to the e-Book version of this chapter.)

near 1.25, 1.5, and 2 μm and 1.43 and 2 μm for H_2O and CO_2 ices, respectively. Moreover, the band shapes (width and depth) are direct indicators of the texture and mean size of the icy grains, which enable their qualitative assessment (Figure 7.2). Consequently, OMEGA has been able to monitor the seasonal evolution of both polar caps over one Martian year (Bibring *et al.*, 2005; Langevin *et al.*, 2005a; Douté *et al.*, 2007; see also Chapter 25). For example, Figure 7.3 illustrates the seasonal evolution of the north polar cap. Condensation of H_2O and that of CO_2 are roughly symmetrical in longitude, with H_2O frost observed down to 4° S of the CO_2 frost. When the spring sublimation is completed, all the CO_2 disappears, leaving a pure H_2O-ice-rich perennial cap.

Previous spacecraft observations in the visible (e.g., Benson and James, 2005) and in the thermal IR (Kieffer *et al.*, 2000) provided detailed information on the retreat of the southern seasonal cap. In mid spring, a cold and dark region (the so-called "cryptic region") develops over part of the cap (Kieffer *et al.*, 2000). OMEGA observations have demonstrated that the southern seasonal cap is almost free of water ice during most of the spring and summer, contrary to the northern seasonal cap. Furthermore, contrary to expectations, most of the cryptic region was shown to be dominated by dust contamination of the surface (Langevin *et al.*, 2006), with a possible link to a complex atmospheric circulation driven by the presence of Hellas basin.

The bright southern perennial cap consists of a thin veneer of annealed CO_2 ice, containing trace amounts (~0.03 wt.%) of dust and H_2O ice, probably trapped during the southern winter (Douté *et al.*, 2007). It covers an extended H_2O-rich glacier (Bibring *et al.*, 2004b). The water ice, unambiguously identified by OMEGA, is interpreted to be mixed with dust, which is why it does not show up in visible images.

As a consequence, the two perennial caps constitute a major reservoir of the presently known inventory of H_2O on Mars. Perennial CO_2 ice is apparently only a very minor constituent of the southern cap, and does not account for more than a small fraction of the present atmospheric mass of CO_2.

7.5 OMEGA OBSERVATIONS OF MAFIC MINERALS

The visible to near-infrared spectral range has long been recognized as very favorable for identifying diagnostic features of rock-forming minerals, such as Fe electronic crystal field transitions in olivines and pyroxenes (e.g., Adams and Filice, 1967; Soderblom, 1992 and references therein). Consequently, most olivine and pyroxene minerals can be identified from visible to near-infrared observations. Low-Fe silicates such as plagioclase feldspar, however, are nearly featureless in the visible to near-infrared and thus not readily identifiable with an instrument like OMEGA.

Pyroxenes [$(Ca,Fe,Mg)_2Si_2O_6$] are identified by the presence of two broad but distinct absorptions centered near 1 and 2 μm, with the band positions varying in a systematic pattern as a function of the pyroxene chemistry (Fe, Mg, and

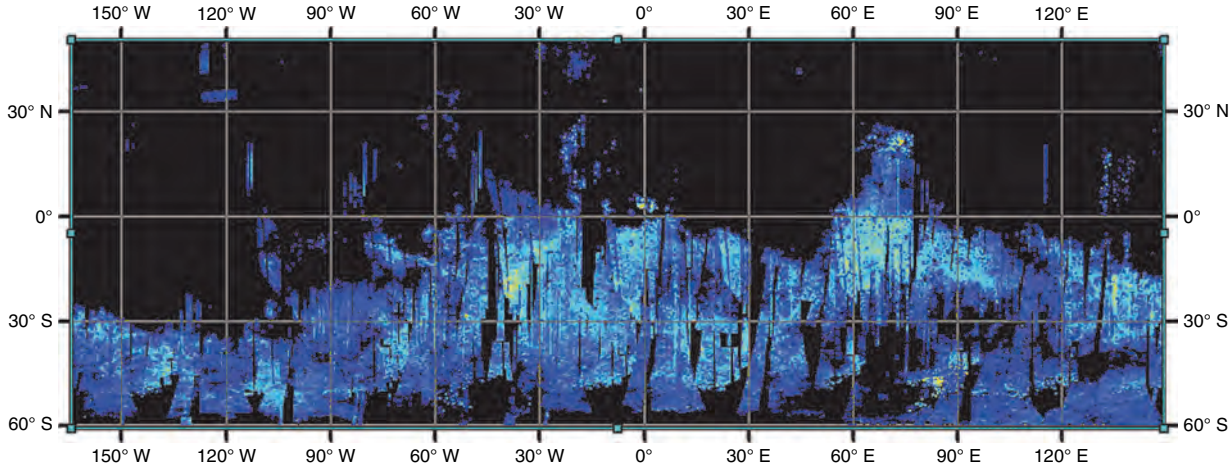

Figure 7.4 OMEGA global mapping of low-Ca pyroxene (LCP), for latitudes between −50° and +50°. (For a color version of this figure, please refer to the color plate section or to the e-Book version of this chapter.)

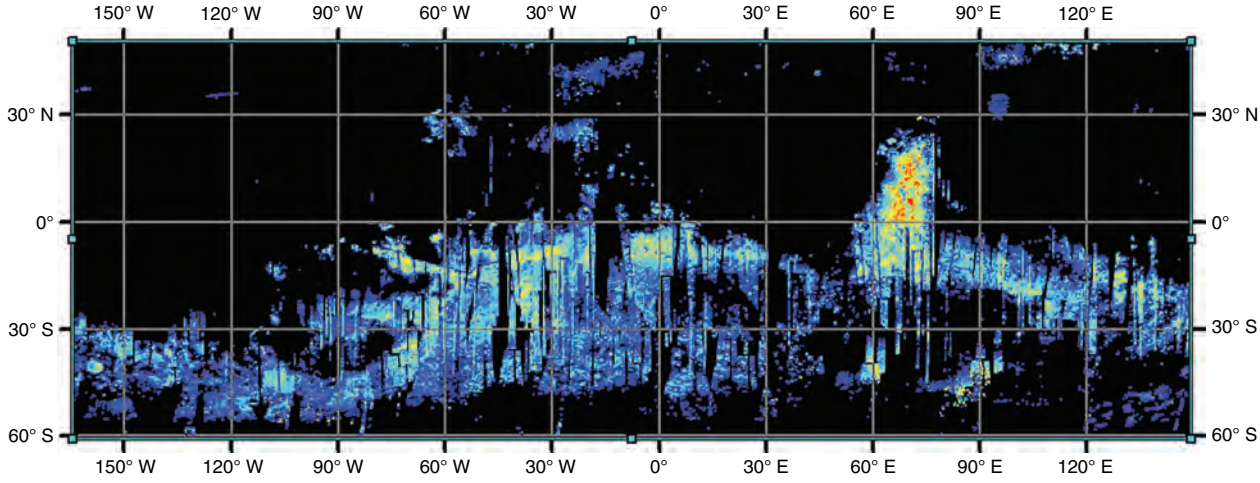

Figure 7.5 OMEGA global mapping of high-Ca pyroxene (HCP), for latitudes between −50° and +50°. (For a color version of this figure, please refer to the color plate section or to the e-Book version of this chapter.)

Ca abundance) and crystal structure: the band centers shift towards longer wavelengths with increasing calcium content. Low-calcium pyroxenes (e.g., orthopyroxene) have short wavelength band centers (~0.9 and ~1.85 μm) while high calcium pyroxenes (HCP; *e.g.*, clinopyroxene) have their band centers at longer wavelengths (~1.05 and ~2.3 μm). Because silicate rocks typical of terrestrial planet surfaces are mixtures of different minerals, the region around 1 μm can also exhibit absorption features that can originate from the presence of other minerals such as olivine (with a broad absorption centered at ~1.05 μm) and ferric oxides (with typical absorptions near ~0.9 μm). Most other minerals do not exhibit broad features near 2 μm, however. Therefore, it can be more definitive to detect pyroxenes through their ~2 μm features rather than their ~1 μm features.

Poulet *et al.* (2007) defined a spectral index based on band ratios, enabling the detection of pyroxenes independent of their Ca content. The resulting maps of this mineral at a global scale reveal the contrast between the units having preserved their pristine mafic composition (the heavily cratered highlands crust and volcanic outflows), and large areas such as the northern plains which have apparently been altered to or covered by pyroxene-free materials. In parallel, we have developed an algorithm based on the MGM, well suited to identify the pyroxene features, to discriminate between HCP and LCP, and to weight their relative abundance (Figures 7.4 and 7.5) (Sunshine and Pieters, 1993).

As a general trend, LCP is enriched in the older Noachian crust, while HCP is enriched in more recent lava flows (Mustard *et al.*, 2005). Figure 7.6 illustrates this pattern in the Syrtis Major region (Nili Fossae/Nili Patera areas), where the volcanic shield exhibits the highest HCP/LCP abundance ratio found at Mars. HCP-rich areas are darker, and generally appear more sandy (Figure 7.7). The HCP enrichment of the lava outflows might indicate partial melting or a low level of mixing within the magma chamber, since HCP (e.g., diopside) melts first, while LCP (e.g., enstatite) requires higher temperatures to

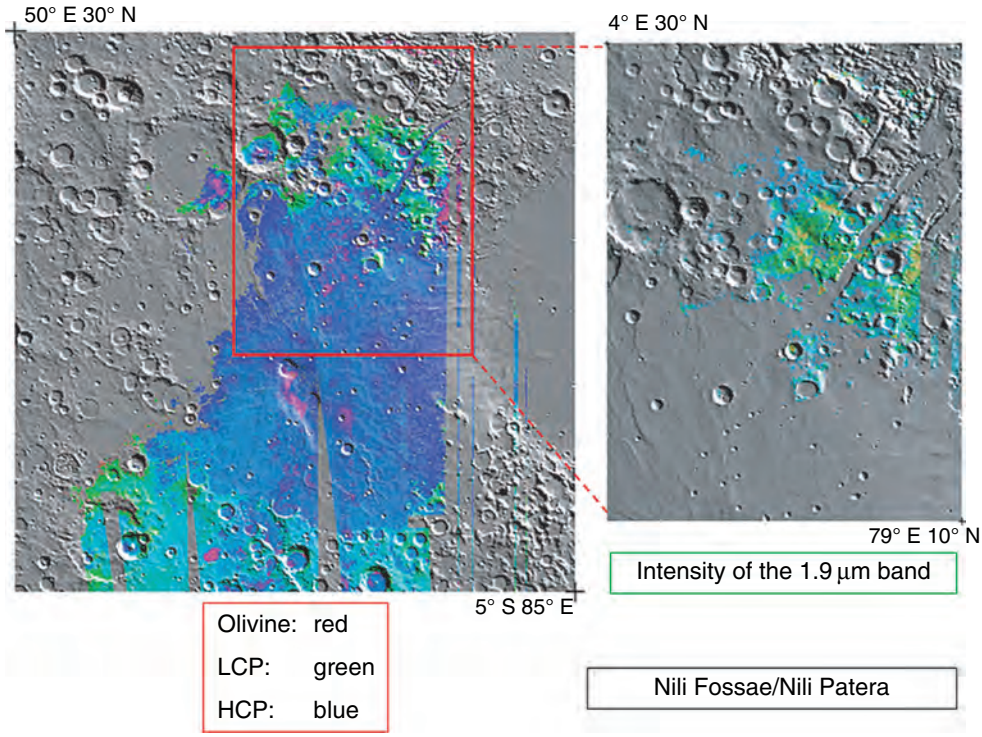

Figure 7.6 OMEGA mineralogical mapping of olivine, pyroxenes, and hydrated clays in the Syrtis Major area. The map at left reveals high-calcium pyroxene (HCP)-bearing lava outflows surrounded by the low-calcium pyroxene (LCP)-bearing Noachian crust and a number of smaller olivine-rich spots. The area in the red box is enlarged on the right and shows the intensity of the 1.93 μm absorption feature interpreted to indicate the location of hydrated clays, found in the ancient terrains and not buried by lava flows. (For a color version of this figure, please refer to the color plates section or to the e-Book version of this chapter.)

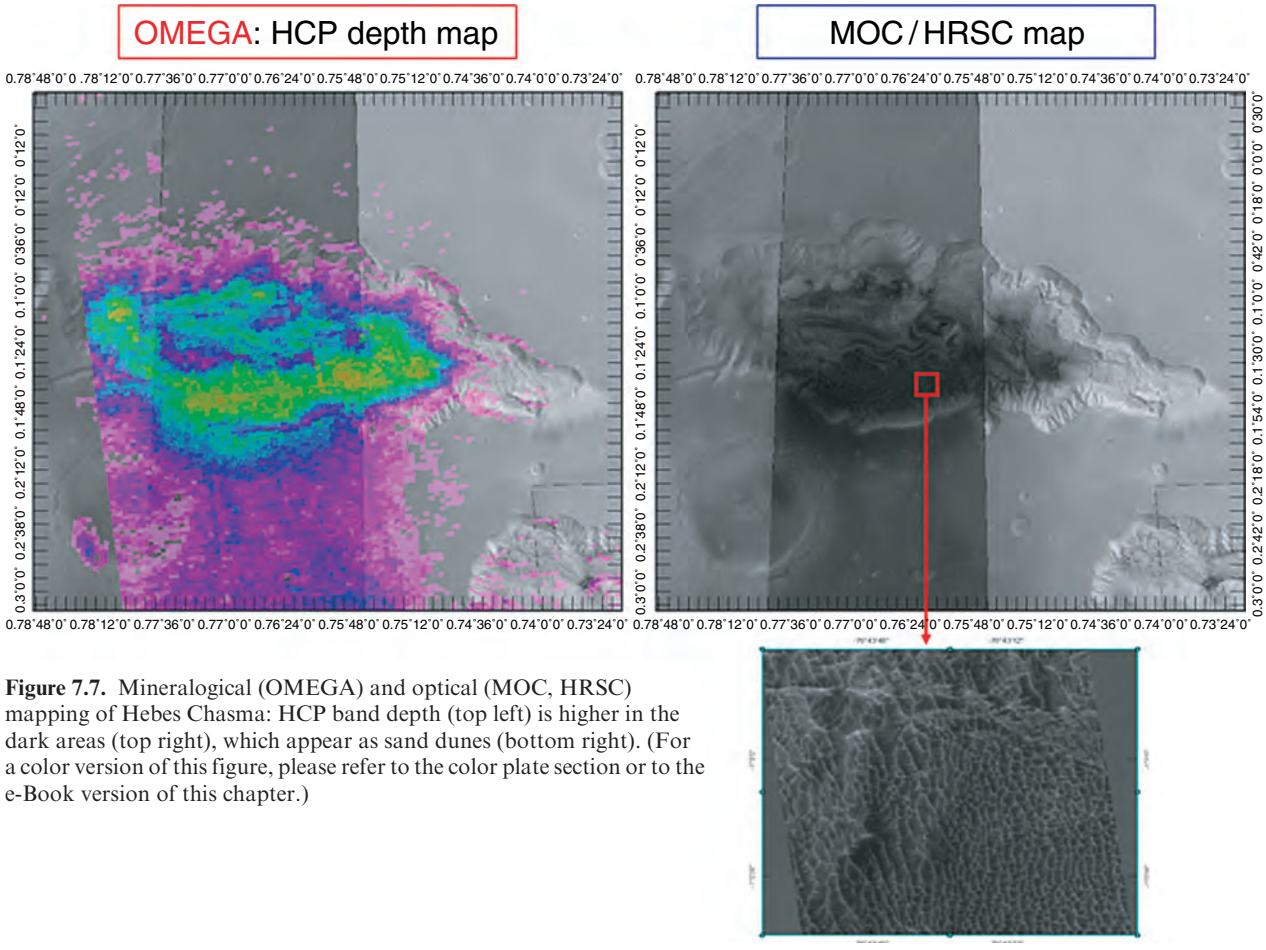

Figure 7.7. Mineralogical (OMEGA) and optical (MOC, HRSC) mapping of Hebes Chasma: HCP band depth (top left) is higher in the dark areas (top right), which appear as sand dunes (bottom right). (For a color version of this figure, please refer to the color plate section or to the e-Book version of this chapter.)

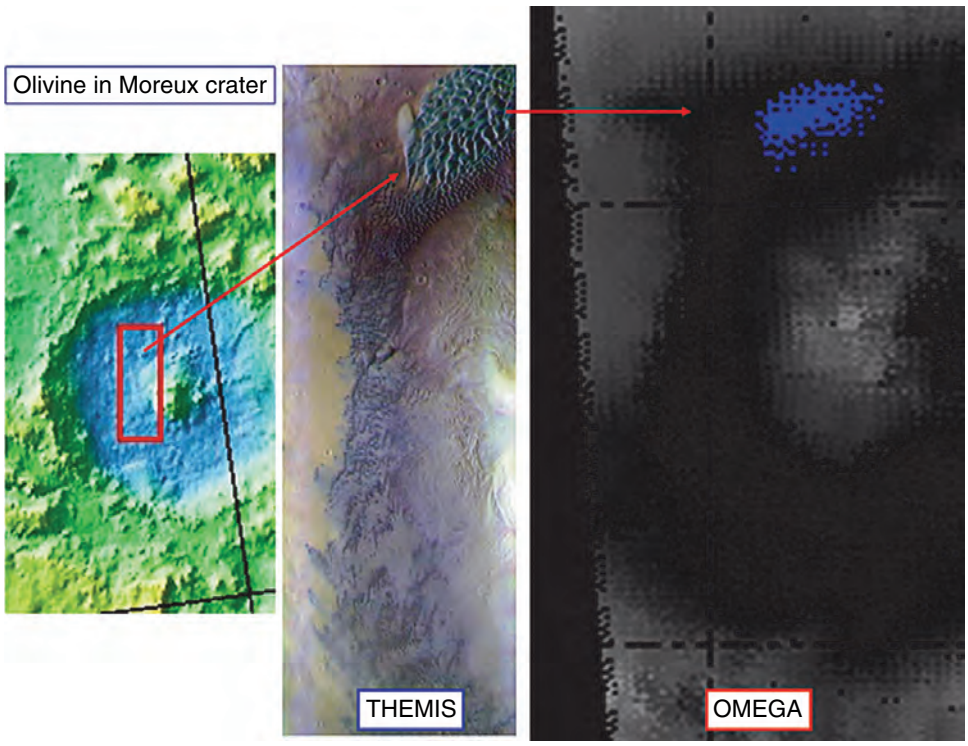

Figure 7.8. Olivine-rich dunes within Moreux crater, located at 41.5° N and 44.5° E, as identified by OMEGA (blue = olivine, right), in the MOLA (left) and THEMIS (middle) context. (For a color version of this figure, please refer to the color plate section or to the e-Book version of this chapter.)

melt. By contrast, the Noachian crust appears to have crystallized out of a fully melted magma, mixing LCP and HCP.

Olivine [$(Mg,Fe)_2SiO_4$] has a broad and complex absorption centered near 1 μm, which extends from 0.8 to 1.5 μm. This band complex broadens and deepens with increasing Fe content in the olivine, from forsterite [Mg_2SiO_4 (Fo_{100})] to fayalite [Fe_2SiO_4 (Fo_0)] (King and Ridley, 1987). For example, in USGS samples (Clark *et al.*, 1993), the absorption complex extends to about 1.55 μm for Fo_{89} and to 1.8 μm for Fo_{11}. In addition, there are systematic variations in the shape of the 1 μm absorption with grain size: increasing grain size broadens the bottom of the band and shifts the band towards longer wavelengths. One result is that forsterite with very large grains (>100 μm) and fayalite with smaller grains have similar spectra. Therefore, a precise olivine composition in terms of Mg/Fe ratio is difficult to assess from NIR spectral data only. Olivine has primarily been found by OMEGA in a variety of localized areas, including Nili Fossae and Terra Meridiani; in low-albedo regions such as Aonia Terra, Nereidum Montes, Terra Tyrrhena, and Oenotria Scopulus; in several unnamed and named craters: Gale, Herschel, Huygens, Schröter, Pollack, Schiaparelli, Herschel, and Moreux (Figure 7.8); and in Valles Marineris (Ius, Hebes, Capri, Melas, Ganges). Also, a large number of isolated olivine-rich spots have been detected around the rims of Isidis, Hellas, and Argyre (Figure 7.9). In addition to these olivine-rich areas, detailed radiative transfer modeling (Poulet *et al.*, 2007) indicates that olivine is likely present together with pyroxene in the large mafic areas, mainly as forsterite of small grain sizes (< tens of μm), possibly with concentrations of up to 20%.

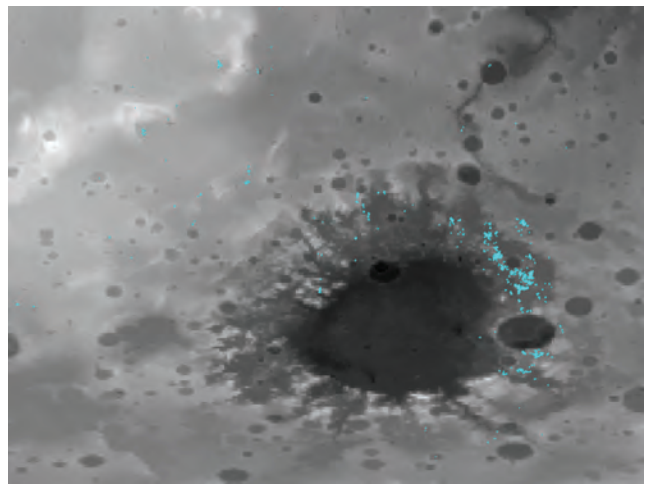

Figure 7.9. Olivine-rich spots surrounding the Argyre impact basin, centered at 50° S, 320° E), as identified by OMEGA (turquoise = olivine). (For a color version of this figure, please refer to the color plate section or to the e-Book version of this chapter.)

7.6 OMEGA OBSERVATIONS OF FERRIC OXIDES

Ferric-rich minerals can be detected through features in the visible and in the NIR (e.g., Burns, 1993): the electronic transitions of ferrous iron, which lead to absorption band centers from 0.95 to 1.05 μm depending on the composition, shift towards smaller wavelengths (from ~0.85 to 0.9 μm) when the oxidation state varies from ferrous to ferric. In addition, the spectrum of ferric-rich phases exhibits some specific features in the visible, in particular a shallow

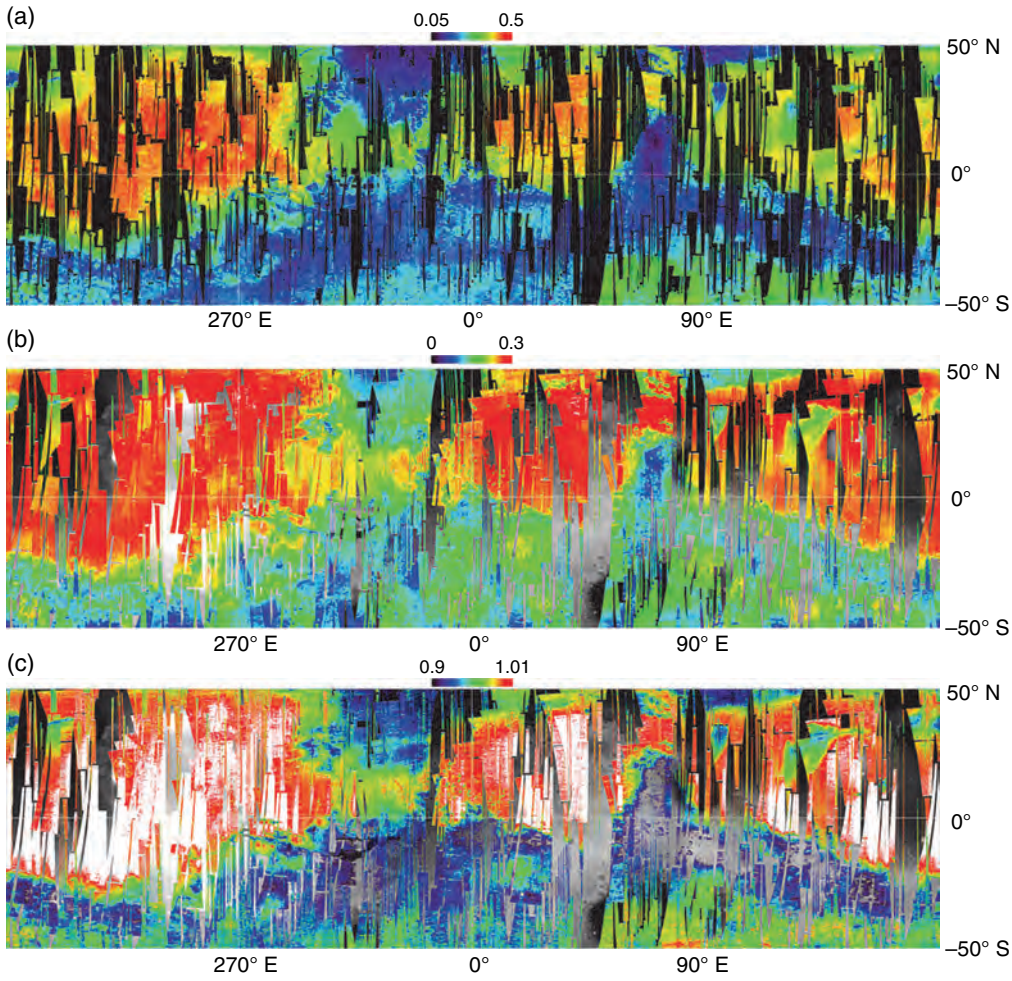

Figure 7.10. Global maps of (a) the NIR albedo; (b) crystalline ferric oxides, and (c) nanophase ferric oxides. (For a color version of this figure, please refer to the color plate section or to the e-Book version of this chapter.)

absorption band near ~0.6 μm and an absorption edge near ~0.53 μm. Several indexes have thus been defined to identify ferric minerals. However, they do not lead to identical maps, which indicates that the surface of Mars may contain a variety of ferric minerals that differ in composition, structure, crystallinity, and/or mean grain size, and that therefore may record possibly distinct formation processes.

The index based on the 0.53 μm absorption edge integrates all ferric-rich phases (e.g., Bell *et al.*, 1990; Morris *et al.*, 2000). The corresponding ferric mineral map (Figure 7.10b) shows a positive detection all over the Martian surface, with a high variation in intensity, well correlated to the NIR albedo (measured at 1.1 μm) (Figure 7.10a). Smaller concentrations are detected in the low-albedo mafic units, which could correspond to the presence of ferric minerals in the bulk of the crust.

Higher concentrations of ferric minerals appear to be found in the vast areas which do not exhibit mafic signatures: they may result from the alteration of these mafic regions, and appear as a bright reddish soil ("dust"). These areas correspond also to a positive detection when another spectral index, ratioing the reflectance at 0.98 to that at 0.8 μm, is used. This index is sensitive to the presence of so-called "nanophase hematite" (nanometer-sized particles of α-Fe_2O_3), as shown by Morris *et al.* (2000) (Figure 7.10c). The dust is subjected to atmospheric transport, resulting in the coverage of wide areas such as Olympus Mons and the

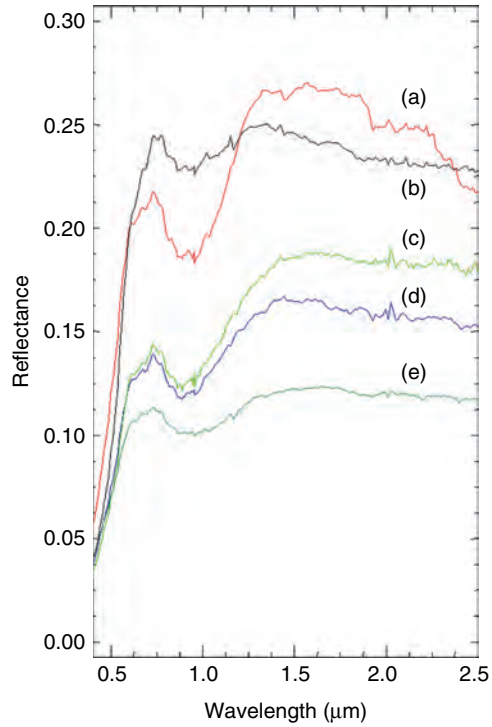

Figure 7.11. Typical OMEGA spectra of oxide-rich areas: (a) Aram Chaos (red); (b) Dust (black); (c) Candor Chasma (green); (d) and (e) Capri Chasma (blue, light green). (For a color version of this figure, please refer to the color plate section or to the e-Book version of this chapter.)

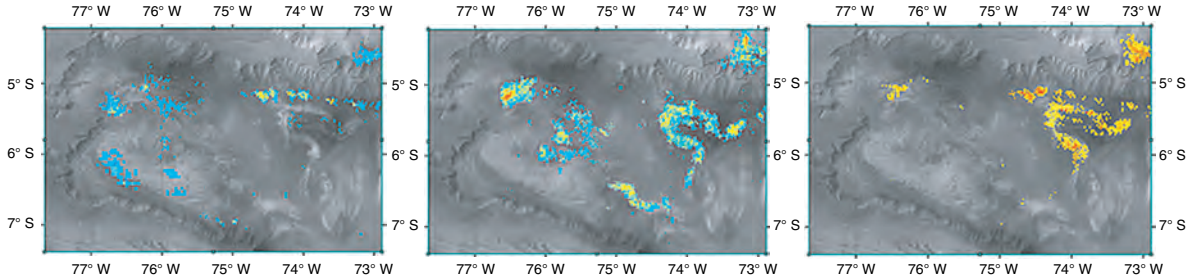

Figure 7.12. Spatial coupling of sulfates and oxides in Candor Chasma. Left: 1.9 μm band depth identified as polyhydrated sulfates (blue = 2%, red = 5% and above). Middle: 2.1 μm band depth, identified as kieserite (green = 2%, red = 5% and above). Right: oxide band depth, as modeled using the Modified Gaussian Model of Sunshine and Pieters (1993) (orange = 10%, red = 30% and above). (For a color version of this figure, please refer to the color plate section or to the e-Book version of this chapter.)

Tharsis volcanoes. However, this mobility does not affect the entire Martian surface, as demonstrated by the high mineralogical diversity still observed at all resolutions. An important observation made by OMEGA is that these ferric oxides, as shown in Section 7.7, are strictly anhydrous. On this basis, the OMEGA team has proposed that they may result from alteration by atmospheric peroxides rather than by liquid water (Bibring *et al.*, 2006).

A third and distinct class of ferric phases is detected by the occurrence of a deep 0.9 μm band and a strong reflectance increase to 1.3 μm (Figure 7.11). Such features are located in a few areas only, and appear coupled to the presence of hydrated minerals, mostly sulfates (discussed below). This class of ferric phases has been found in Terra Meridiani, Aram Chaos, and in association with layered deposits in Valles Marineris (Figure 7.12; Bibring *et al.*, 2007).

7.7 OMEGA DETECTIONS OF HYDRATED MINERALS

Minerals with water molecules either adsorbed or in their crystal structure exhibit relatively well-defined absorptions near 1.4, 1.9, and 3.0 μm, and are thus readily accessible to OMEGA detection (e.g., Bishop *et al.*, 1993, 1994; Roush *et al.*, 1993). O–H stretching, either symmetric (ν_1) or asymmetric (ν_3), has its fundamental absorption band at 2.9 μm, with overtones and combinations at 1.4 μm ($\nu_1 + \nu_3$). The H–O–H bending fundamental at ~6 μm (ν_2) has its first overtone at 3.1 μm, and a resulting combination feature ($\nu_2 + \nu_3$) at ~1.9 μm. These NIR features have been studied previously in lower spatial and spectral resolution Mars datasets (e.g., Houck *et al.*, 1973; Pimentel *et al.*, 1974; Calvin, 1997).

All hydrated phases exhibit a broad 3 μm band, which is thus not diagnostic of specific minerals. However, it can be used to evaluate the amount of water stored in the mineral structure (Jouglet *et al.*, 2007; Milliken *et al.*, 2007). Hydrated minerals are thus identified by features resulting from vibrations related to O–H and/or H_2O at ~1.4 and ~1.9 μm, together with those resulting from the coupling between OH and/or H_2O to metal (e.g., Al, Mg, Fe, Ca) or to anionic complexes such as SO_4^{2-}, and CO_3^{2-} (e.g., Clark *et al.*, 1990a,b; Swayze and Clark, 1990). Minerals containing hydroxyls exhibit the 1.4 μm band, as well as narrow absorptions between 2.0 and 2.4 μm which are typically combination overtones of an OH stretch and a metal–OH bend, and which can be very diagnostic of mineralogy (e.g., Bishop *et al.*, 1993, 1994; Roush *et al.*, 1993; Bell *et al.*, 1994). Hydrated sulfates have specific features resulting from the S–O stretches (fundamentals at ~10 μm), with overtones in the 2.2–2.5 μm region when in the presence of water (e.g., Crowley, 1991; Cloutis *et al.*, 2006). The precise position and shape of the sulfate NIR bands vary with composition, and for hydrated sulfates result in features at 2.2 and 2.4 μm. An important exception is that of monohydrated sulfates, such as kieserite ($MgSO_4 \cdot H_2O$), for which the 1.4 and 1.9 μm bands are shifted towards longer wavelengths at 1.6 and 2.1 μm respectively.

OMEGA has identified and mapped two classes of hydrated minerals: sulfates (Section 7.7.1) and phyllosilicates (Section 7.7.2). By contrast, carbonates (Section 7.7.3), which have two strong absorption features near ~3.5 and ~3.9 μm, have not been detected so far, above the detection limit of ~1%–2% in volume demonstrated by ground calibration.

One key outcome of OMEGA detection of hydrated species is that they are apparently found in only very localized areas (Figure 7.13). In particular, the ferric oxides that constitute the bright dust, which covers most of the northern plains and Tharsis, are strictly anhydrous (see Section 7.6).

7.7.1 Hydrated sulfates

Hydrated sulfates have so far been detected by OMEGA at the surface of Mars in three locations: in layered deposits of Valles Marineris (Gendrin *et al.*, 2005), in Terra Meridiani (Arvidson *et al.*, 2005), and in dark dunes of the northern polar cap (Langevin *et al.*, 2005b). In most cases, mixtures of sulfates appear to be present. In a few cases, however, due to their diagnostic signatures, specific sulfates have been identified with a high level of confidence: kieserite ($MgSO_4 \cdot H_2O$) and gypsum ($CaSO_4 \cdot 2H_2O$).

Gypsum exhibits in its 1.2–2.6 μm spectrum 6 unique spectral features (at 1.45, 1.75, 1.94, 2.22, 2.26, and 2.48 μm), which makes its potential for identification quite robust (Figure 7.14). On the basis of these six features, OMEGA has identified gypsum as the major constituent of the dark terrains of Olympia Planitia, intermixed with gypsum-free bright water-ice deposits (Figure 7.15) (Langevin *et al.*, 2005a).

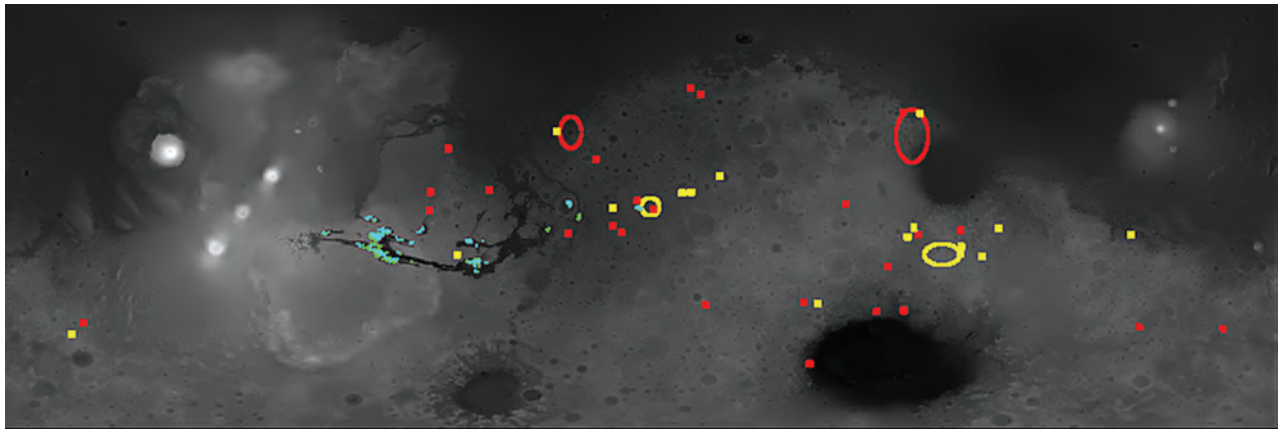

Figure 7.13. Distribution of all hydrated minerals detected so far by OMEGA at the surface of Mars, for latitude from −50° to +50°. Blue: monohydrated sulfates; green: polyhydrated sulfates; red: phyllosilicates; yellow: other hydrated minerals. (For a color version of this figure, please refer to the color plate section or to the e-Book version of this chapter.)

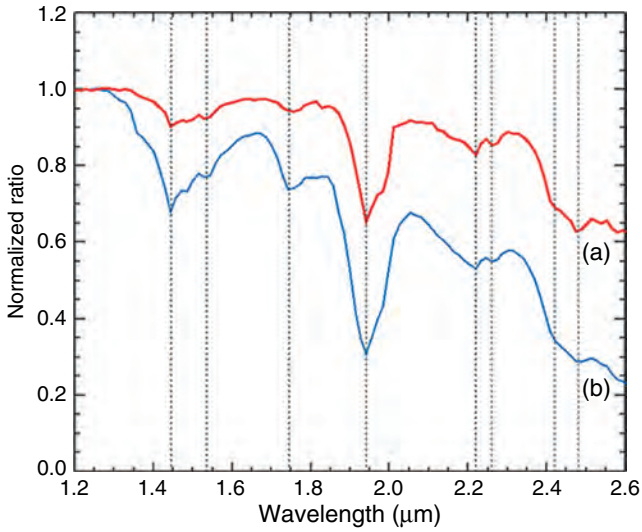

Figure 7.14. (a) OMEGA spectrum from 1.2 to 2.6 μm of a sulfate-rich region within the dark dunes of Olympia Planitia, within the northern polar cap, ratioed to a reference spectrum of a close-by dark area, and normalized to 1 at 1.25 μm. (b) Normalized ratio of two spectra obtained during ground calibration, that of a pure gypsum powder (<40 μm grain size) and that of an aluminum oxide powder, which is spectrally featureless in this wavelength range. Features are observed in both spectral ratios at 1.44, 1.53, 1.74, 1.94, 2.22, 2.26, 2.42, and 2.48 μm (dashed lines). (For a color version of this figure, please refer to the color plate section or to the e-Book version of this chapter.)

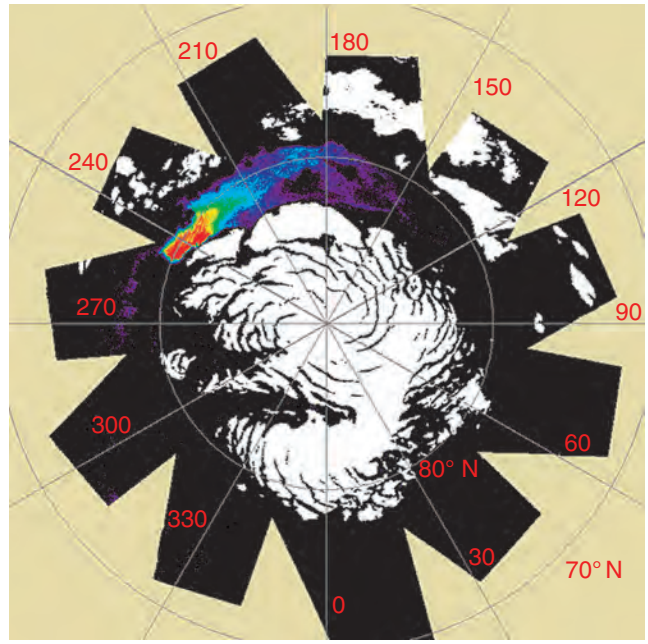

Figure 7.15. Area interpreted to be gypsum-rich within Olympia Planitia, illustrated by a false-color composite showing the distribution of the absorption at 1.93 μm relative to a continuum defined from 1.86 to 2.14 μm. The color code is a rainbow scale from black (<4% band depth) through blue, green, and yellow to red (>25% band depth). A strong absorption at 1.93 μm is observed on an extended dark area centered at 240° E, 80° N. White areas correspond to the regions with permanent water ice at the surface. (For a color version of this figure, please refer to the color plate section or to the e-Book version of this chapter.)

Kieserite also has specific absorption features in terms of position and shape, at 1.6, 2.1, and 2.4 μm (Figure 7.16). Its presence in a few locations at the surface of Mars is important, as this monohydrated mineral is known to be easily hydrated into epsomite ($MgSO_4 \cdot 7H_2O$), which can eventually dehydrate to hexahydrite ($MgSO_4 \cdot 6H_2O$) and amorphous Mg sulfate ($MgSO_4 \cdot 1.2H_2O$). Kieserite has been identified in several layered deposits within Valles Marineris (Figure 7.17), as well as in a small spot northeast of the Mars Exploration Rover (MER) *Opportunity* landing site, in Terra Meridiani (Figure 7.18).

Most of the hydrated sulfates detected by OMEGA appear to be polyhydrated, including possibly the amorphous Mg sulfate phase. Poulet *et al.* (2007) have shown that some of the sulfates detected in Terra Meridiani could be Fe-rich sulfates, for example, amarantite [$(Fe^{3+})(SO_4)(OH) \cdot 3(H_2O)$] or schwertmannite [$(Fe^{3+}{}_{16}O_{16}(OH)_{12}(SO_4)_2 \cdot nH_20)$]. However, jarosite [$(K,Na,H_3O)Fe_3(SO_4)_2(OH)_6$], detected by *Opportunity*, has a specific NIR spectrum which is not observed in OMEGA data.

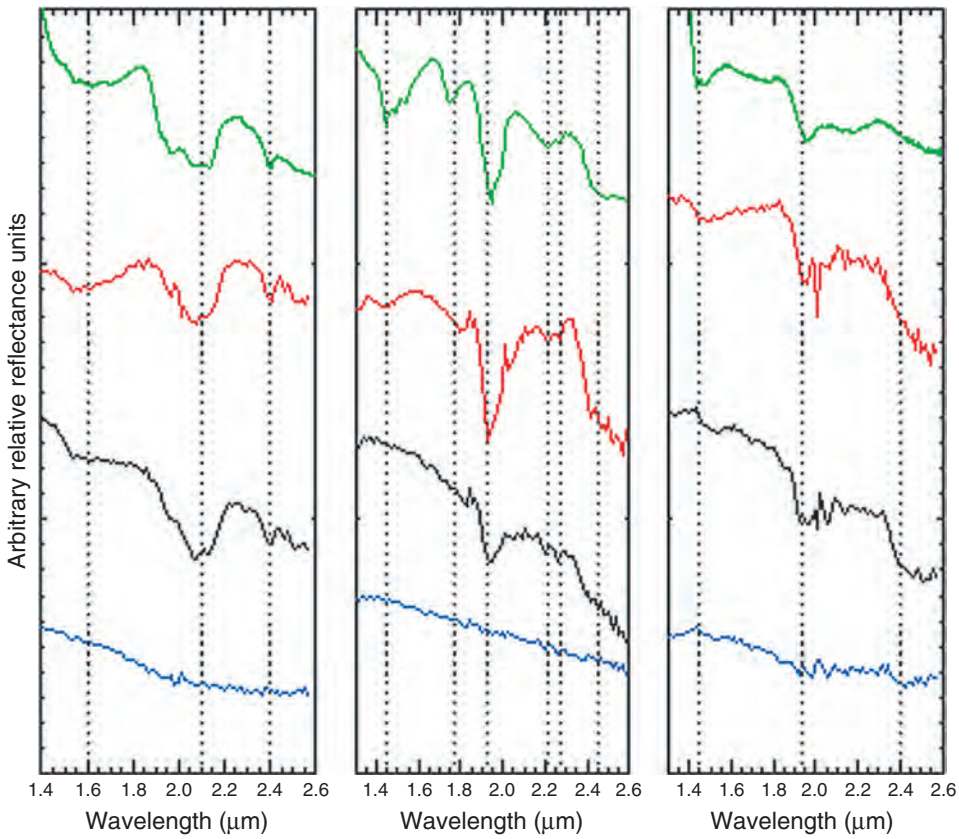

Figure 7.16. Hydrated sulfate spectra identified in the OMEGA observations. In each panel the bottom spectrum is a reference spectrum from a nonsulfate region. The next spectrum up is an OMEGA spectrum showing sulfate absorption features. The next spectrum up is a ratio of these sulfate/nonsulfate region spectra. Finally, at the top of each panel is a library sulfate mineral spectrum. Left panel: kieserite ($MgSO_4 \cdot H_2O$). Middle panel: gypsum ($CaSO_4 \cdot 2H_2O$). Right panel: polyhydrated sulfate; the library spectrum corresponds to epsomite ($MgSO_4 \cdot 7H_2O$) but other polyhydrated sulfates are also good spectral analogs. (For a color version of this figure, please refer to the color plate section or to the e-Book version of this chapter.)

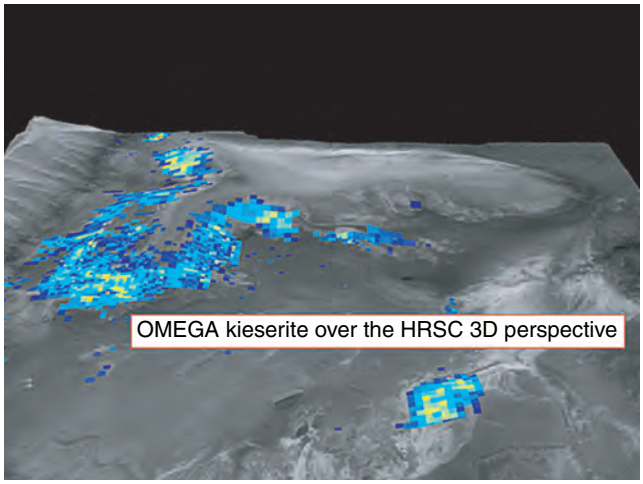

Figure 7.17. Spatial distribution of monohydrated sulfate (possibly kieserite), identified in OMEGA spectra, plotted over the HRSC three dimensional perspective model of Candor Chasma. (For a color version of this figure, please refer to the color plate section or to the e-Book version of this chapter.)

7.7.2 Hydrated phyllosilicates

As shown in Figure 7.13, OMEGA has detected a variety of phyllosilicates in localized areas, with the two largest areas located in the Nili Fossae and Mawrth Vallis areas (Poulet *et al.*, 2005). These detections constitute the best evidence that Mars once hosted liquid water over long durations, enabling the formation of these hydrated alteration phases.

The composition of the phyllosilicates is not identical in all locations (Figure 7.19). Mg/Fe smectites are always present, in particular as nontronite, and dominate in the Nili Fossae/Syrtis Major complex. Al-rich phyllosilicates, such as montmorillonite or chlorite, are also found, in particular in the Marwth Vallis area. However, kaolinite appears to be rare. This is an indication that the process responsible for the formation of the phyllosilicates, although it implies liquid water over long durations, may have been characterized by a rather low level of leaching (Chevrier *et al.*, 2007). With reference to conditions prevailing in terrestrial environments or during laboratory simulations when similar minerals are formed, the Martian fluids in which these smectites formed appear to have been neutral to alkaline, rather than acidic, at the time the aqueous alteration took place (Chevrier *et al.*, 2007).

The sites in which the phyllosilicates are mapped are all very ancient, exposed to the surface either by impact or by erosion. In the Nili Fossae area (Mangold *et al.*, 2007; Mustard *et al.*, 2007), the phyllosilicate-rich terrains all appear to predate the first lava flows from Nili Patera and Syrtis Major Planum, dated early Hesperian by crater counting. Phyllosilicate-rich sites include both ancient heavily crated terrains, which have not been buried by the lava flows, and recently excavated ones (Figure 7.6): apparently the impact process did not destroy or dehydrate these minerals, but might rather have triggered their formation. It is important to note that by contrast, the lobate ejecta craters within the Nili Patera caldera floor do not exhibit spectral evidence for hydrated minerals, which strongly indicates that this lava material was essentially dry.

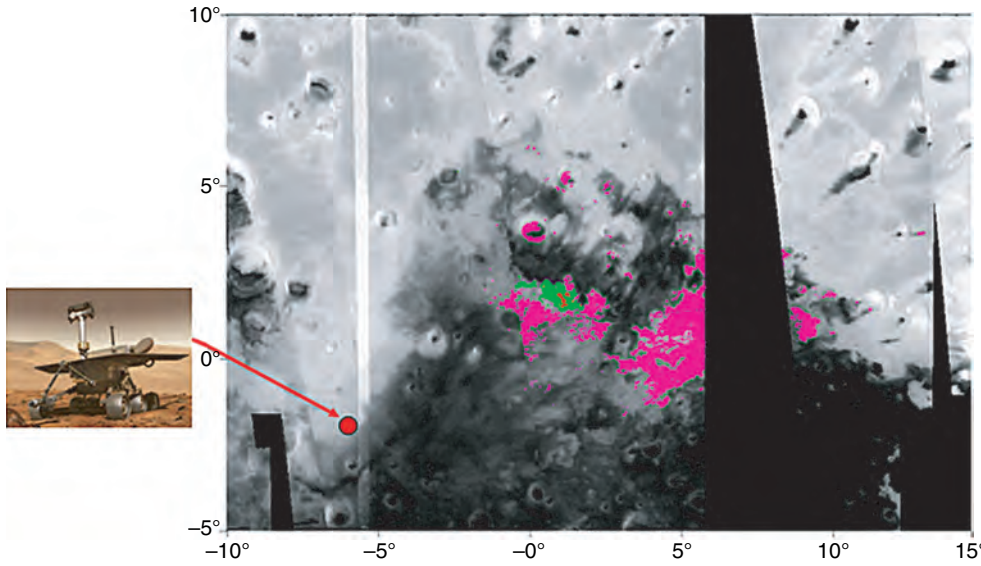

Figure 7.18. Distribution of kieserite (red), polyhydrated sulfates (green), and other hydrated minerals (pink) in Terra Meridiani. *Opportunity* site is shown. (For a color version of this figure, please refer to the color plate section or to the e-Book version of this chapter.)

In Mawrth Vallis (Poulet *et al.*, 2005; Loizeau *et al.*, 2007), as in all similar outflow channels, no hydrated minerals are found within the bed or the mouth of the channel (Figure 7.20). In contrast, hydrated minerals are found on the highly etched terrains along the flanks of the channel. One interpretation of this observation is that the phyllosilicates were formed prior to the outflow. The outflows themselves do not appear to have lasted long enough, nor to have constituted a sustained enough degree of fluvial activity, to form hydrated minerals such as clays. Rather, the outflow channels may result from transient episodes (e.g., Baker and Milton, 1974), violent enough to erode their flanks and to expose ancient materials which happen to have been processed by liquid water, in earlier times. Those earlier hydrated phyllosilicates then remained preserved as such until today.

7.7.3 Hydrated carbonates and other CO_2 sinks

We have searched the OMEGA data for carbonates in a wide variety of potential sites, all over the planet. In particular, we have performed a systematic characterization of the material related to impact craters within the northern plains, with the following rationale: If Mars once hosted a large ocean at a time when the atmosphere was dense enough for CO_2 to dissolve, ionize, and precipitate (as on the Earth), sedimentary layers of hydrated carbonates might have accumulated on the hypothetical ocean floor prior to these low altitude terrains draining, drying out, and filling with lava. Large enough impact craters could have reached down into these older layers and exposed in their ejecta some of their constitutive material. In fact, in their OMEGA spectra, most craters with diameter larger than ~20 km exhibit a clear signature of the crustal (mafic) bedrock (Bibring *et al.*, 2005). However, none of the ejecta, nor the central peaks, show the spectral signature of carbonates, nor even of any hydrated minerals. This is a strong indication that these terrains probably never hosted long-standing water bodies in the presence of a dense CO_2-rich atmosphere.

As described above (Section 7.4), OMEGA has shown that the two perennial polar caps are massive water ice glaciers, but do not constitute significant long-term CO_2 traps. With the lack of detection of abundant carbonates, it seems very likely that the atmosphere, although extremely tenuous, is the dominant CO_2 reservoir at present. This constitutes a major constraint in describing the long-term climatic evolution of Mars.

7.8 A DERIVED MARS MINERALOGICAL HISTORY

The identification and mapping of both primary igneous and secondary altered minerals, put into their geomorphological context, reveals some major features relevant to Mars history (Bibring *et al.*, 2006). Well-preserved mafic minerals are still observed on a wide scale in the oldest crust and in some spots in impact craters. By contrast, the northern lowlands are dominated by an alteration product characterized by anhydrous ferric oxide. Hydrated minerals have been detected in a restricted number of localized areas. They consist of two classes, phyllosilicates and sulfates, which are found in distinct terrains, formed by distinct processes, at distinct times. Phyllosilicates and sulfates can be thought to trace distinct eras, "phyllosian" and "theiikian," respectively, to reflect the names, in Greek, of their dominant minerals. Stratigraphic relationships suggest that the phyllosilicates have formed first, in a neutral to alkaline environment, followed by the sulfates, in an acidic environment. We are thus led to propose that in between the two eras, Mars underwent a global-scale climatic change. We attribute this major environmental evolution to the volcanic activity that led to the building of Tharsis and the filling of the northern plains (Figure 7.21).

Since phyllosilicates usually require water over a long duration to form, Mars likely hosted conditions sustaining liquid water on geological timescales in its very early history. This, in turn, requires there to have been abundant greenhouse gases, given the predicted low luminosity of the early Sun (e.g., Pollack *et al.*, 1987). However, like most young stars, the early Sun was likely an extreme ultraviolet emitter, with high ionizing efficiency, and with an intense solar wind:

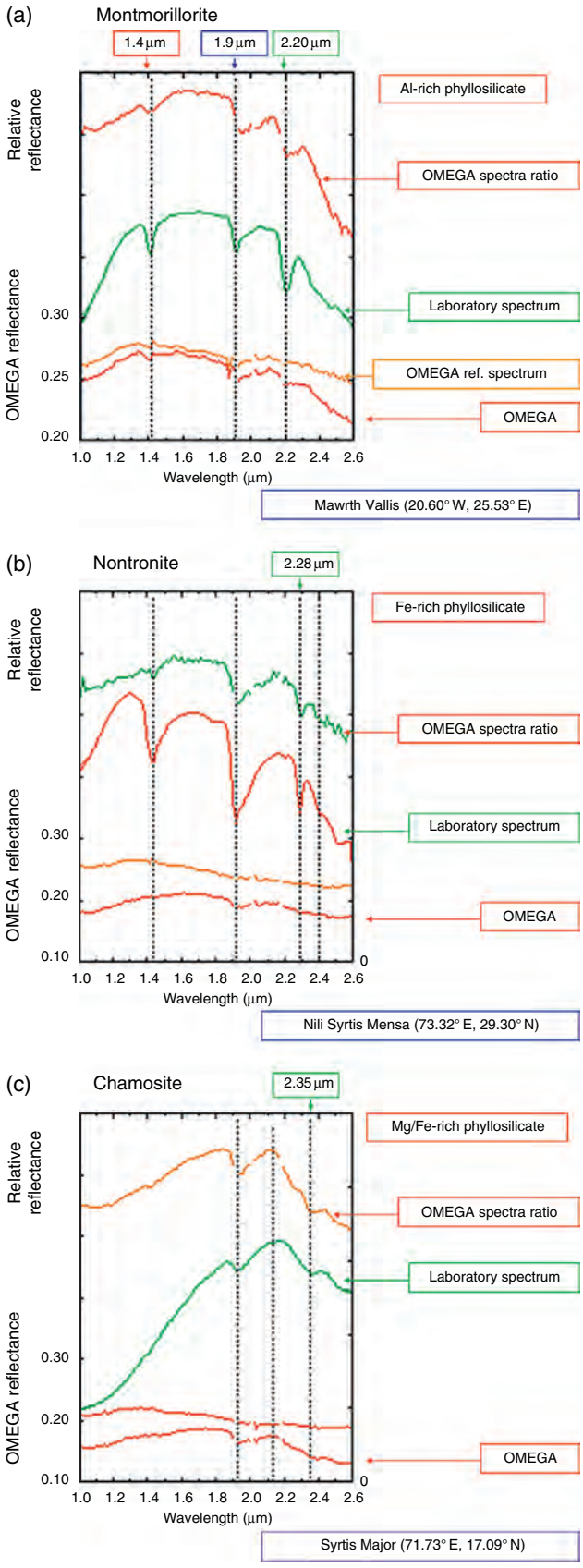

Figure 7.19. Spectra of hydrated phyllosilicates, as detected by OMEGA, compared to laboratory spectra, showing the diagnostic shift of the M-OH feature from 2.2 µm for Al-rich (a) to 2.28 µm Fe-rich (b) to 2.35 µm Mg/Fe-rich (c) species. (For a color version of this figure, please refer to the color plate section or to the e-Book version of this chapter.)

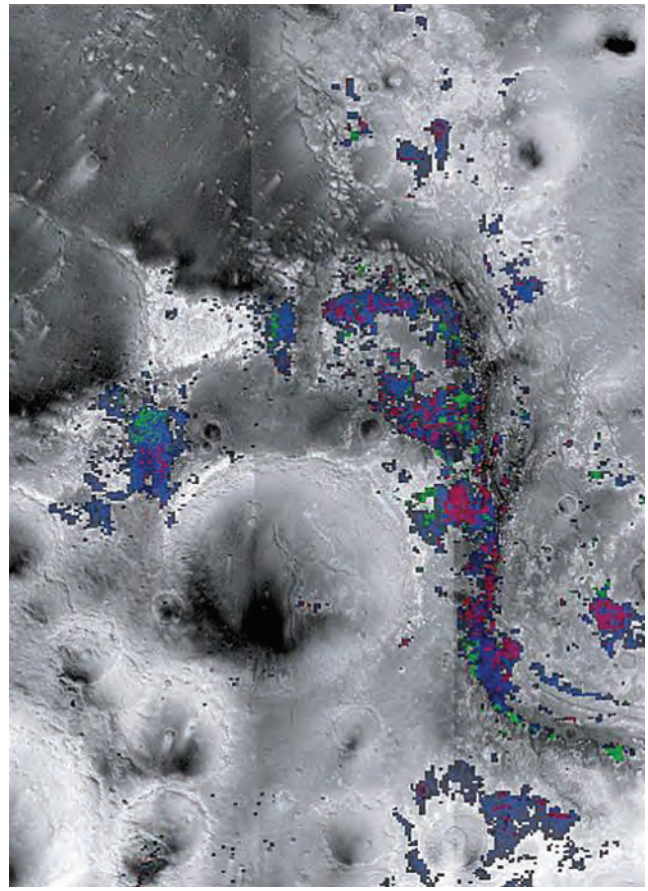

Figure 7.20. Clays in Mawrth Vallis. Distribution, over an HRSC mosaic (3 contiguous maps), of the minerals identified by OMEGA through their 1.93 µm (hydration, blue), 2.20 µm (montmorillonite, green), and 2.30 µm (Mg/Fe-rich smectites, red) features. (For a color version of this figure, please refer to the color plate section or to the e-Book version of this chapter.)

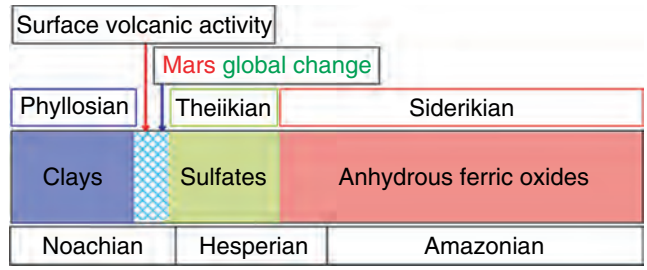

Figure 7.21. An OMEGA-derived Mars mineralogical history/timeline. (For a color version of this figure, please refer to the color plate section or to the e-Book version of this chapter.)

a planetary magnetic field was thus critical to protect against atmospheric loss. As demonstrated by the findings of remnant crustal magnetism by the MAG/ER investigation on Mars Global Surveyor (see Chapter 11), early Mars appears to have supported a global dynamo, which could have efficiently protected its atmosphere. The absence of magnetized minerals over Tharsis and in the northern plains is a strong indication that this dynamo shut off before the onset of the volcanism that raised Tharsis and filled the plains.

A possible explanation is that mantle convection could not sustain a sufficient temperature difference between the core and the mantle, required to maintain core convection, and

thus the dynamo and its associated magnetic field shut down. Cold plumes could have started to form, and to sink within the mantle and accumulate at the core/mantle boundary. This, in turn, could have triggered thermal instabilities, leading to the formation of hot plumes ascending to form Tharsis after some tens of millions years. In such a scheme, the formation of Tharsis would have happened long after the magnetic field had faded, and long after most of the atmosphere had been lost by solar wind erosion or other processes. In the tenuous resulting atmosphere, massive outgassing related to the volcanic activity could have injected S-rich compounds as dominant species, which then rapidly oxidized into sulfuric compounds, leading the environment (including any groundwater) to become highly acidic. These S-rich species precipitated widely over the planet, possibly in the form of nanophase S-rich grains, accounting for the large concentration of S detected by elemental APXS analyses at all rover and lander sites studied so far (see Chapters 3 and 4).

The present composition of the Martian atmosphere has an N_2/CO_2 value close to both the Venus value and that of the Earth (~3%), if one takes into account that most of the initial terrestrial CO_2 is presently trapped as carbonates. The N_2/CO_2 ratio is consistent with such an early physical loss mechanism. If the initial volatile reservoirs of Mars, Venus, and the Earth were similar, one would not expect massive depletion (more than 99.9%) of both CO_2 and N_2 with an identical efficiency, from two entirely different processes, if the CO_2 sequesters into carbonates whereas N_2 hardly condenses as a mineral. OMEGA data support a model in which most of the atmosphere escaped prior to the Theiikian; today's atmosphere would result from an equilibrium between the present (very limited) loss mechanisms, for example, as measured by MEx/ASPERA (Barabash *et al.*, 2007), and the supply of volatiles by residual internal activity.

In such a model, the Phyllosian era would have ended when the surface water could no longer remain stable as a liquid, instead evaporating and/or percolating and freezing as subsurface permafrost. Subsequent cratering would have buried most of the surface phyllosilicates with pristine crustal material. The large-scale tectonic effects that followed the building of Tharsis, such as the opening of Valles Marineris and the tilt of Terra Meridiani, as well as the localized rising of the geothermal water table, could have produced sequential supplies of liquid water to a variety of regions within these areas, for example cementing the S-rich nanophase grains into large sulfate deposits. This process would not necessarily require surface liquid water to be long-lasting, since sulfates can sediment even while water is evaporating. During this period, sulfate layers would have grown where surface water was supplied, in spatial and time relation with upwelling heat flow, such as in Tharsis. The Theiikian era would have ended rapidly, leading to a long era (Siderikian), lasting until the present, dominated by anhydrous surface oxidation and the creation of nanophase ferric oxides (siderikos in Greek) in a highly rarefied atmosphere. This oxidation likely results from a very slow process (timescales of Gyr) operating on the very superficial layers (sub-millimeter scale) of surface grains. During this era, a few volcanic or impact-related transient events could have brought water to the surface, forming "fluvial" or "valley" structures without necessarily adding a compositional imprint of hydrated minerals.

7.9 SUMMARY

Although one could have expected that the global circulation of dust would preclude identifying distinct units at the surface of Mars, the OMEGA investigation demonstrates a high degree of mineralogical diversity down to a subkilometer scale. Units of all ages, from the most ancient to the most recently processed ones, have been identified by their composition. In particular, the oldest units, although subjected to a longer period of potential weathering, still preserve their primary igneous content. In parallel, the detection and mapping of alteration products gives key clues to decipher the evolution of the Martian environment. Two classes of hydrated phases have been identified: placed in their geological context, and in relation with the *in situ* findings of the two NASA MERs, they enable a profoundly new model of the past Martian climate to be envisioned. Thirty years after the pioneering measurements of the Viking landers, the OMEGA orbital near-infrared survey indicates that Mars might indeed have hosted, once in its earlier past, conditions favoring liquid water to remain stable over long periods of time. The sites in which one might search for these potential habitats are not necessarily located where the optical images would have led us to consider; that is, primarily in relation with fluvial and other water-related landforms. OMEGA results so far suggest that the most favorable sites for preserving evidence of this early epoch are those that are characterized by a mineralogical signature of hydrated phyllosilicates. Most of these targets may have already been identified. A refined analysis by the Compact Reconnaissance Imaging Spectrometer for Mars instrument on the just-begun Mars Reconnaissance Orbiter mission, with similar spectral coverage but a ten-fold higher spatial sampling than OMEGA, will greatly enhance the characterization of these regions. It is our deep conviction that if ever life once emerged on Mars, these phyllosilicate-rich sites are the targets in which future *in situ* laboratories (e.g., the NASA Mars Science Laboratory and ESA/ExoMars missions) have the best chances of finding potential biorelics, at a microscopic scale.

REFERENCES

Adams, J. B. and A. L. Filice, Spectral reflectance 0.4 to 2.0 microns of silicate rock powders, *J. Geophys. Res.* **72**, 5705–15, 1967.

Arvidson, R. E., F. Poulet, J.-P. Bibring, *et al.*, Spectral reflectance and morphological correlations in eastern Terra Meridiani, Mars, *Science* **307**, 1591–4, 2005.

Baker, V. R. and J. D. Milton, Erosion by catastrophic floods on Mars and Earth, *Icarus* **23**, 27–41, 1974.

Barabash, S., A. Fedorov, R. Lundin, and J.-A. Sauvaud, Martian atmospheric erosion rates, *Science* **315**, 501–3, 2007.

Bell III, J. F., T. B. McCord, and P. D. Owensby, Observational evidence of crystalline iron oxides on Mars, *J. Geophys. Res.* **95**, 14447–61, 1990.

Bell III, J. F., J. B. Pollack, T. R. Geballe, D. P. Cruikshank, and R. Freedman, Spectroscopy of Mars from 2.04 to 2.44 μm during the 1993 opposition: absolute calibration and atmospheric vs. mineralogic origin of narrow absorption features, *Icarus* **111**, 106–23, 1994.

Benson, J. L. and P. B. James, Yearly comparisons of the Martian polar caps: 1999–2003 Mars Orbiter Camera observations, *Icarus* **174**, 513–23, 2005.

Bibring, J.-P. and S. Erard, The Martian surface, *Space Sci. Rev.* **96**(1–4), 293–316, 2001.

Bibring, J.-P., M. Combes, Y. Langevin, *et al.*, Results from the ISM experiment, *Nature* **341**, 591–3, 1989.

Bibring, J.-P., A. Soufflot, M. Berthé, *et al.*, OMEGA: observatoire pour la Minéralogie, l'Eau, les Glaces et l'Activité, *ESA SP* **1240**, 37–49, 2004a.

Bibring, J.-P., Y. Langevin, F. Poulet, *et al.*, Perennial water ice identified in the south polar cap of Mars, *Nature* **428**, 627–30, 2004b.

Bibring, J.-P., Y. Langevin, A. Gendrin, *et al.*, Mars surface diversity as revealed by the OMEGA/Mars Express Observations, *Science* **307**, 1591–4, 2005.

Bibring, J.-P., Y. Langevin, J. F. Mustard, *et al.*, Global mineralogical and aqueous Mars history derived from OMEGA/Mars Express data, *Science* **312**, 400–4, 2006.

Bibring, J.-P., R. E. Arvidson, A. Gendrin, *et al.*, Coupled ferric oxide and sulfates on the Martian surface, *Science* **317**, 1206–10, 2007.

Bishop, J. L., C. M. Pieters, and R. G. Burns, Reflectance and Mössbauer spectroscopy of ferrihydrite-montmorillonite assemblages as Mars soil analog materials, *Geochim. Cosmochim. Acta* **57**, 4583–95, 1993.

Bishop, J. L., C. M. Pieters, and J. O. Edwards, Infrared spectroscopic analyses on the nature of water in montmorillonite, *Clays Clay Miner.* **42**(6), 702–16, 1994.

Burns, R. G., *Mineralogical Applications of Crystal Field Theory*, Cambridge University Press, 1993.

Calvin, W. M., Variation of the 3-μm absorption features on Mars: observations over eastern Valles Marineris by the Mariner 6 infrared spectrometer, *J. Geophys. Res.* **1002**(E4), 9097–107, 1997.

Chevrier, V., F. Poulet, and J.-P. Bibring, Early geochemical environment of Mars as determined from thermodynamics of phyllosilicates, *Nature* **448**, 60–3, 2007.

Chicarro, A., P. Martin, and R. Trautner, The Mars Express mission: an overview, *ESA SP* **1240**, 3–13, 2004.

Clark, R. N., G. A. Swayze, R. B. Singer, and J. B. Pollack, High resolution reflectance spectra of Mars in the 2.3-μm region: evidence for the mineral scapolite, *J. Geophys. Res.* **95**, 14463–80, 1990a.

Clark, R. N., T. V. V. King, M. Klejwa, G. A. Swayze, and N. Vergo, High spectral resolution reflectance spectroscopy of minerals, *J. Geophys. Res.* **95**, 12653–80, 1990b.

Clark, R. N., G. A. Swayze, A. Gallagher, T. V. V. King, and W. M. Calvin, The USGS, Digital Spectral Library: Version 1 – 0.2 to 3.0 μm, USGS, *Open File Report 93–592*, 1993.

Cloutis, E. A., F. C. Hawthorne, S. A. Mertzman, *et al.*, Detection and discrimination of sulfate minerals using reflectance spectroscopy, *Icarus* **184**, 121–57, 2006.

Crowley, J. K., Visible and near-infrared (0.4–2.5 μm) reflectance spectra of playa evaporite minerals. *J. Geophys. Res.* **96**, 16231–40, 1991.

Douté, S., B. Schmitt, Y. Langevin, *et al.*, South pole of Mars: nature and composition of the icy terrains from Mars Express OMEGA observations, *Planet. Space Sci.* **55**, 113–33, 2007.

Erard, S., J.-P. Bibring, J. F. Mustard, *et al.*, Spatial variations in composition of the Valles Marineris and Isidis Planitia regions of Mars derived from the ISM data, *Proc. Lunar Planet. Sci. Conf. XXI*, 437–55, 1991.

Gendrin, A., N. Mangold, J.-P. Bibring, *et al.*, Sulfates in Martian layered terrains: the OMEGA/Mars Express view, *Science* **307**, 1587–91, 2005.

Houck, J. R., J. B. Pollack, C. Sagan, D. Schaack, and J. A. Decker Jr., High altitude infrared spectroscopic evidence for bound water on Mars, *Icarus* **18**, 470, 1973.

Jouglet, D., F. Poulet, R. E. Milliken, *et al.*, Hydration state of the Martian surface as seen by Mars Express OMEGA: 1. Analysis of the 3 μm hydration feature, *J. Geophys. Res.* **112**, E08S06, doi:10.1029/2006JE002846, 2007.

Kieffer, H. H., T. N. Titus, K. F. Mullins, and P. R. Christensen, Mars south polar spring and summer behavior observed by TES: seasonal cap evolution controlled by frost grain size, *J. Geophys. Res.* **105**, 9653–700, 2000.

King, T. V. V. and W. I. Ridley, Relation of the spectroscopic reflectance of olivine to mineral chemistry and some remote sensing implications, *J. Geophys. Res.* **92**, 11457–69, 1987.

Langevin, Y., F. Poulet, J.-P. Bibring, *et al.*, Summer evolution of the north polar cap of Mars as observed by the OMEGA/Mars Express observations, *Science* **307**, 1581–4, 2005a.

Langevin, Y., F. Poulet, J.-P. Bibring, and B. Gondet, Sulfates in the north polar region of Mars detected by the OMEGA/Mars Express observations, *Science* **307**, 1584–6, 2005b.

Langevin, Y., S. Douté, M. Vincendon, *et al.*, No signature of clear CO_2 ice from the "cryptic" regions in Mars' south seasonal polar cap, *Nature* **442**, 831–5, 2006.

Loizeau, D., N. Mangold, F. Poulet, *et al.*, Phyllosilicates in the Mawrth Vallis region of Mars, *J. Geophys. Res.* **112**, E08S08, doi:10.1029/2006JE002877, 2007.

Mangold, N., F. Poulet, J. F. Mustard, *et al.*, Mineralogy of the Nili Fossae region with OMEGA/Mars Express data: 2. Aqueous alteration of the crust, *J. Geophys. Res.* **112**, E08S04, doi: 10.1029/2006JE002835, 2007.

Milliken, R. E., J. F. Mustard, F. Poulet, *et al.*, Hydration state of the Martian surface as seen by Mars Express OMEGA: 2. H_2O content of the surface, *J. Geophys. Res.* **112**, E08S07, doi: 10.1029/2006JE002853, 2007.

Morris, R. V., D. C. Golden, J. F. Bell III, *et al.*, Mineralogy, composition, and alteration of Mars Pathfinder rocks and soils: evidence from multispectral, elemental, and magnetic data on terrestrial analogue, SNC meteorite, and Pathfinder samples, *J. Geophys. Res.* **105**, 1757–817, 2000.

Murchie, S. J., J. F. Mustard, J. Bishop, *et al.*, *Spatial variations in the spectral properties of bright regions on Mars*, *Icarus* **105**, 454–68, 1993.

Mustard, J. F., S. Erard, J.-P. Bibring, *et al.*, The surface of Syrtis Major: composition of the volcanic substrate and mixing with altered dust and soil, *J. Geophys. Res.* **98**, 3387–400, 1993.

Mustard, J. F., F. Poulet, A. Gendrin, *et al.*, Olivine and pyroxene diversity in the crust of Mars, *Science* **307**, 1594–7, 2005.

Mustard, J. F., F. Poulet, J. W. Head, *et al.*, Mineralogy of the Nili Fossae region with OMEGA/Mars Express data: 1. Ancient impact Melt in the Isidis basin and implication for the transition from the Noachian to Hesperian, *J. Geophys. Res.* **112**, E08S03, doi:10.1029/2006JE002834, 2007.

Pimentel, G. C., P. B. Forney, and K. C. Herr, Evidence about hydrate and solid water in the Martian surface from the 1969 Mariner infrared spectrometer, *J. Geophys. Res.* **79**, 1623–34, 1974.

Pollack, J. B., J. F. Kasting, S. M. Richardson, and K. Poliakoff, The case for a wet, warm climate on Mars, *Icarus* **71**, 203–24, 1987.

Poulet, F., J.-P. Bibring, J. F. Mustard, *et al*., Phyllosilicates on Mars and implications for early martian climate, *Nature* **438**, 623–8, 2005.

Poulet, F., C. Gomez, J.-P. Bibring, *et al*., Martian surface mineralogy from OMEGA/MEx: global mineral maps, *J. Geophys. Res*. **112**, E08S02, doi:10.1029/2006JE002840, 2007.

Roush, T. L., D. L. Blaney, and R. B. Singer, The surface composition of Mars as inferred from spectroscopic observations. In *Remote Geochemical Analysis: Elemental and Mineralogical Composition* (ed. C. M. Pieters and P. A. J. Englert), Cambridge, UK: Cambridge University Press, pp. 367–93, 1993.

Soderblom, L., The composition and mineralogy of the Martian surface from spectroscopic observations: 0.3 μm to 50 μm. In *Mars* (ed. H. Kieffer *et al*.), Tucson: University of Arizona Press, pp. 557–97, 1992.

Sunshine, J. M. and C. M. Pieters, Estimating modal abundances from the spectra of natural and laboratory pyroxene mixtures using the modified Gaussian model, *J. Geophys. Res*. **98**, 9075–87, 1993.

Swayze, G. A. and R. N. Clark, Infrared spectra and crystal chemistry of scapolites: implications for Martian mineralogy, *J. Geophys. Res*. **95**, 14481–95, 1990.

Titus, T. N., H. H. Kieffer, and P. R. Christensen, Exposed water ice discovered near the South Pole of Mars, *Science* **299**, 1048–51, 2003.

8

Visible to near-IR multispectral orbital observations of Mars

J. F. BELL III, T. D. GLOTCH, V. E. HAMILTON, T. McCONNOCHIE, T. McCORD, A. McEWEN, P. R. CHRISTENSEN, AND R. E. ARVIDSON

ABSTRACT

This chapter reviews observations and interpretations since the 1990s from orbital telescopic and spacecraft observations of Mars from the extended visible to short-wave near-IR (VNIR) wavelength range. Imaging and spectroscopic measurements from the Hubble Space Telescope (HST), Mars Global Surveyor Mars Orbiter Camera Wide Angle (MGS MOC/WA) instrument, Mars Odyssey Thermal Emission Imaging System Visible Subsystem (THEMIS-VIS), and Mars Express High Resolution Stereo Camera (MEx HRSC) and Observatoire pour la Minéralogie, l'Eau, les Glaces et l'Activité (OMEGA) have been acquired at spatial scales from global-scale ~1 to hundreds of kilometers resolution to regional-scale ~20–100 m resolution. Most high-albedo regions are homogeneous in color and thus, likely, composition, a supposition consistent with the long-held idea of the presence of a globally homogeneous aeolian dust unit covering much of the surface. Despite the presence and ubiquity of dust, these measurements still reveal the presence of significant VNIR spectral variability at a variety of spatial scales. For example, color variations and possibly mineralogic variations have been detected among small-scale (tens of meters) exposures of light-toned outcrop and layered materials in Meridiani Planum, Valles Marineris, and other areas. Within low-albedo regions, much of the observed color variability appears simply related to different amounts of covering or coating by nanophase ferric oxide-bearing dust and/or ferrous silicate-bearing sand. Some VNIR color units, however, in regions spanning the full range of observed surface albedos, correlate with geologic, topographic, or thermal inertia boundaries, suggesting that either composition/mineralogy or variations in physical properties (e.g., grain size, roughness, packing density) influence the observed color. Most recently, new visible wavelength multispectral observational campaigns from the Mars Reconnaissance Orbiter Mars Color Imager (MARCI) and the High Resolution Imaging Science Experiment (HiRISE) instruments have begun to obtain VNIR color images of the surface systematically at a global scale (MARCI) and locally at sub-meter per pixel resolution (HiRISE), further enhancing the role of multispectral color observations in the geologic, stratigraphic, and compositional interpretation of Martian surface processes.

8.1 INTRODUCTION

Mars has been observed at visual wavelengths since before recorded history, given its roughly bi-annual appearance as a prominent, reddish object in the night sky. Early naked eye and pretelescopic observations of Mars were instrumental in Kepler's validation of the Copernican heliocentric model of the Solar System. And of course, many early telescopic observers, first by eye and then photographically, proceeded to document fascinating seasonal and interannual changes in the bright and dark markings observed on the planet's surface. These visual wavelength observations allowed the planet's rotation period to be accurately derived, and the presence of seasonal cycles and an active atmosphere to be deduced. Excellent reviews and additional details regarding these earliest phases of Martian exploration can be found in Sheehan (1988), Kieffer *et al.* (1992a), and Martin *et al.* (1992).

Spectroscopic observations in the early part of the twentieth century (see reviews in Kuiper, 1952; de Vaucouleurs, 1954; Mutch *et al.*, 1976) were used to establish the thin nature and CO_2-dominated composition of the Martian atmosphere and to identify oxidized iron-bearing minerals as key mineralogic components of the high-albedo "continental" surfaces of the planet. Indeed, much of the history of visual wavelength (roughly defined as wavelengths from about 400 nm to about 750 nm) observations of Mars is closely coupled to the study of oxidized (Fe^{3+}-bearing or "ferric") and unoxidized (Fe^{2+}-bearing or "ferrous") iron minerals. This is because at these wavelengths iron is the most spectrally active of the cations that are found in the most common rock-forming minerals on silicate planetary surfaces (see Chapter 2). Ferric iron in the ubiquitous high-albedo regions gives Mars the distinctive reddish color that first drew the attention of the ancients, who saw a portent of blood (also reddish because of iron) in the sky and named the planet after their various gods of war. Conversely, it is ferrous iron that helps to give the low-albedo regions their distinctive dark tone, similar to the blacks to reddish browns often seen on relatively fresh, ferrous-rich volcanic lava plains and flows on the Earth.

More specifically, visible wavelength observations can be used to search for and map a variety of electronic, charge

The Martian Surface: Composition, Mineralogy, and Physical Properties, ed. J. F. Bell III. Published by Cambridge University Press.

transfer, and ligand field transitions (in minerals containing Fe^{2+}, Fe^{3+}, Fe^{3+}–Fe^{3+} or Fe^{3+}–Fe^{2+} pairs, and Fe^{3+}–O^{2-} bonds) that give different iron-bearing minerals their distinctive colors and which can provide remote-sensing information that is diagnostic of mineralogy (see reviews by Burns, 1970, 1993; Bell, 1992). It is often difficult or impossible to make quantitative estimates of mineral abundances from visible wavelength observations (or solar reflectance observations in general), however, because of the confounding effects that mineralogy, particle size, surface physical properties, and pigmenting or matrix effects all introduce when attempting to invert or spectrally "unmix" the observed solar spectral reflectance. Reviews and examples of the limitations of quantitative mineral abundance determination methods relevant to visible wavelength observations can be found in, for example, Clark and Roush (1984), Mustard and Pieters (1987), Morris and Lauer (1990), Roush *et al*. (1993), and Poulet and Erard (2004). Despite these limitations, visible wavelength observations of Mars can still provide qualitative assessments and some quantitative constraints on the relative abundance, particle size, and spatial extent of a variety of potential ferric and ferrous minerals that are relevant to studies of the planet's current and putative past geologic and climatic processes and regimes.

In addition to composition and mineralogy, visible wavelength observations, of course, also provide a substantial amount of information on the geology of the Martian surface. Review and interpretation of the geomorphology of Mars in general is beyond the scope of this book (see, instead, excellent reviews in Mutch *et al*., 1976; Kieffer *et al*., 1992b; Malin and Edgett, 2001; Carr, 2006); however, many aspects of the observed geology, morphology, and physical properties can be used to infer or in some cases directly derive compositional information about the surface. For example, properties of talus slopes on all scales can provide information on the strength of materials and their degree of sorting/packing (see, e.g., Chapter 20). The presence and detailed morphometric properties of channels and gullies can be used to infer properties of both the liquid that flowed through and created these landforms (possibly quite recently in some cases) as well as the substrate in which they were formed (e.g., Malin and Edgett, 2000a,b; Christensen, 2003; Heldmann *et al*., 2005). Even just measuring and mapping the wavelength-dependent albedo of the surface can provide constraints on the presence or absence of dust and ice. Albedo is also a key input parameter required for the accurate derivation of thermal inertia, which itself is partly governed by the surface composition (see Chapter 18).

In this chapter, we review major advances since the early 1990s in our understanding and knowledge of the surface composition, mineralogy, and physical properties of Mars as derived from high resolution visible wavelength orbital telescopic and spacecraft observations. These include results from investigations conducted using the Hubble Space Telescope (HST), the Mars Global Surveyor's Mars Orbiter Camera Wide Angle (MGS MOC/WA) instrument,the Mars Odyssey Orbiter's Thermal Emission Imaging System's Visible Imaging Subsystem (ODY THEMIS-VIS), the Mars Express High Resolution Stereo Camera (MEx HRSC) and Observatoire pour la Minéralogie, l'Eau, les Glaces et l'Activité (OMEGA) spectrometer, and the recently commenced Mars Reconnaissance Orbiter High Resolution Imaging Science Experiment and Mars Color Imager (MRO HiRISE and MARCI) instruments. Chapter 2 of this book and earlier reviews by Soderblom (1992) and Roush *et al*. (1993) provide additional summaries and details about earlier ground-based telescopic and Mariner 6, 7, 9 and Viking Orbiter 1 and 2 multispectral and spectroscopic observations of Mars and their implications for surface composition.

By their very nature, the measurements discussed here are actually "low resolution" observations when compared to remote sensing or *in situ* visible wavelength studies conducted by landers and rovers on Mars (see, e.g., Chapters 12, 13, 19, and 20). However, these observations have provided important new global context information on the uppermost surface layer and its variations with time, and improvements in instrumentation and space mission capabilities are allowing these observations to cover a significant fraction of the surface at resolutions ranging from synoptic (tens of kilometers) to regional (few kilometers to few hundred meters), to truly local-scale (tens of meters) – ultimately merging seamlessly with and augmenting "ground truth" visible wavelength studies at several Mars landing sites (e.g., Chapters 13 and 21, and Section 8.6).

8.1.1 HST multispectral and hyperspectral imaging

Instrumentation and observations

Hubble Space Telescope has observed Mars at UV, visible, and NIR wavelengths through eight oppositions (close passes of Earth and Mars) since 1990. Earth and Mars go through cycles of favorable and unfavorable oppositions (Earth–Mars closest approaches) because of the ~26 month synodic period of the planets and the significant eccentricity (0.09) of the Martian orbit (e.g., Martin *et al*., 1992; Bell, 2003). The HST's Wide Field and Planetary Camera 2 (WFPC2; Biretta, 2006), Advanced Camera for Surveys (ACS; Pavlovsky *et al*., 2006), and Near-Infrared Camera and Multi-Object Spectrograph (NICMOS; Barker *et al*., 2006) instruments have enabled global multispectral visible and NIR imaging of the planet at resolutions of typically 20–60 km/pixel at Martian equatorial latitudes. High resolution near-UV to NIR spectroscopy of the surface at similar resolutions has also been enabled by observations using the Space Telescope Imaging Spectrograph (STIS; Kim Quijano *et al*., 2003) instrument. The 2003 opposition was the closest approach of Mars to the Earth in nearly 60 000 years (and the closest until 2287), and HST was able to image the surface at an unprecedented (for Earth-based observations) 12 km/pixel resolution using WFPC2 and 6 km/pixel using ACS (Soderblom *et al*., 2006). These HST observations are among the highest spatial resolution global multispectral imaging data sets acquired at visible wavelengths, comparable in scale to the Viking approach red and violet imaging data analyzed by Soderblom *et al*.

(1978) and McCord *et al.* (1982), though not as high resolution as the red and blue MGS MOC/WA 2-color images, or the MARCI and HiRISE multispectral imaging observations that have been obtained by MRO since late 2006 (discussed in Sections 8.3 and 8.7).

Despite the fact that HST and its instruments are optimized for astrophysical (rather than planetary) observations, most of the multispectral images of Mars were acquired through narrow, medium, and wide-band filters that provided good sensitivity to atmospheric aerosols (UV, blue filters) or to variations in the physical and chemical properties of iron-bearing minerals (red, NIR filters). A subset of 11 filters (255, 336, 410, 502, 588, 631, 673, 763, 835, 953, 1042 nm) is common to almost all of the 1993–2005 WFPC2 Mars observations, providing a long baseline of consistent global-scale multispectral measurements of the planet. Imaging using the ACS camera in 2003 and 2005 sampled many of these same wavelengths (for consistency with the longer record of WFPC2 observations) but at a factor of two better spatial resolution. Near infrared images acquired with the NICMOS camera in 1997 and 2003 sampled 10 to 15 wavelengths from 950 to 2370 nm (a few overlapping with the WFPC2 images), many of which were chosen to provide sensitivity to hydrated mineral absorption features. More specific details on the circumstances, filters, calibration, and processing of HST images of Mars can be found in Bell (2003), Bell *et al.* (1997a), James *et al.* (1994, 1996), Noe Dobrea *et al.* (2003, 2008), Soderblom *et al.* (2006), and Wolff *et al.* (1997, 1999).

HST results: surface composition

James *et al.* (1994) studied 4-color visible to near-IR (VNIR) spectra of surface units from early HST/WFPC2 multispectral imaging observations of Mars. They found general agreement with previous ground-based telescopic spectra and hints of mineralogic variations associated with both high-albedo ferric regions and low-albedo ferrous regions. In a similar analysis, James *et al.* (1996) identified five distinct spectral units in red versus blue HST multispectral images and hypothesized that at least some of the observed variation could be due to mineralogic differences that could be discerned at these wavelengths for the first time because of HST's high spatial resolution (by ground-based standards) and synoptic-scale global coverage.

More detailed and spectrally extensive multispectral analyses from HST (Figure 8.1) were discussed by Bell *et al.* (1997a, 1999) and reviewed in Bell (2003). Average 10- to 12-color near-UV to NIR HST spectra of bright, dark, and polar ice surface units are consistent with previous ground-based spectra and confirm and extend the interpretation of high-albedo regions as ferric and low-albedo regions as ferrous. Specifically, spectra from HST confirmed the presence of weak ~530 nm and ~800–1000 nm absorption features in high and intermediate albedo regions that were interpreted by Bell *et al.* (1990) from ground-based spectra as evidence for crystalline ("red") hematite on Mars, and they confirmed the presence of a negative NIR slope and weak >900 nm absorption feature in low-albedo regions that were interpreted from ground-based data as evidence for pyroxene or perhaps other ferrous iron-bearing silicates by Singer *et al.* (1979 and references therein).

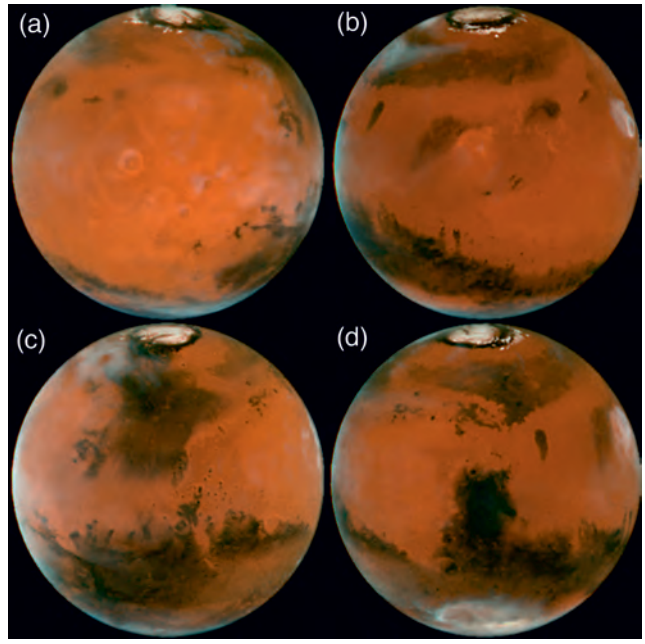

Figure 8.1. Color composite of HST WFPC2 images obtained during the 1999 opposition. Each image is an orthographic reprojection and color composite of images obtained at 410 nm (blue), 502 nm (green), and 673 nm (red). Images have been independently contrast enhanced to bring out additional cloud and ice details present primarily in the 410 nm images. (a) Images from April 28, 1999, with central meridian longitudes (CML) between 114° W and 124° W. (b) Images from May 6, 1999, with CML between 206° W and 216° W. (c) Images from April 27, 1999, with CML between 19° W and 30° W. (d) Images from May 1, 1999, with CML between 282° W and 294° W (Bell, 2003). (For a color version of this figure, please refer to the color plate section or to the e-Book version of this chapter.)

An intriguing small-scale example of spectral variability revealed by HST observations is the annulus of low-albedo sand dunes surrounding the north polar cap, which showed evidence for an extremely strong NIR ferrous absorption feature in HST spectra (e.g., Bell *et al.*, 1997b). Such a strong absorption band could result from the presence of well-sorted coarse-grained pyroxenes within the sand, a unique pyroxene (or other ferrous iron) mineralogy, some process that keeps polar dune sand grains much more dust-free than sand elsewhere on Mars, or some other as-yet uncharacterized atmospheric or photometric effect. Farrand *et al.* (2000) further examined small-scale spatial variations within HST multispectral images and reported initial results of spectral classification methods designed to constrain the surface mineralogy and its relationship to other global-scale parameters like albedo, thermal inertia, topography, and geology. Spectral parameters like the 835 and 953 nm band depth and the spectral slopes in the visible and NIR were used by Farrand *et al.* (2000) to identify and map unique spectral units. These units were hypothesized to correlate with regions of enhanced ferrous mineral abundances (low-albedo, deep 953 nm band), ferrous minerals with variable coverings

or coatings of nanophase ferric oxide dust (intermediate- to high-albedo regions with smoothly varying 953 nm absorptions and negative NIR spectral slopes), and both high-albedo and low-albedo regions that showed evidence of crystalline ferric oxide minerals (stronger 835 nm absorption band).

Morris *et al*. (2002) expanded this analysis by examining the relationship of these kinds of spectral parameters to lunar, Martian meteorite, and laboratory spectra and to the surface's thermal inertia and albedo derived from orbital observations. Low-albedo regions, for example, were shown to have a local reflectivity maximum near 763 nm and positive 953–1042 nm spectral slope consistent with the spectra of pigeonitic or orthopyroxenitic rocks like the basaltic Martian meteorites and ALH 84001 (see Chapter 17). The smooth transition of the HST surface spectra across low-albedo to high-albedo boundaries and the lack of a significant change in thermal inertia across these boundaries suggested to Morris *et al*. (2002) that variations in mobile dust cover, rather than induration, are responsible for the observed albedo differences. Interestingly, these authors also found that HST data do not reveal significant differences in the VNIR derived ferrous mineralogy of the low-albedo Type 1 and Type 2 spectral units derived from the MGS Thermal Emission Spectrometer (TES) infrared observations (e.g., Bandfield *et al*., 2000; see Chapter 9). Rather, at VNIR wavelengths, the difference between Type 1 (sometimes referred to as "basaltic") and Type 2 (sometimes referred to as "andesitic") surfaces appears to be consistent with an increase in the ferric dust component within Type 2 relative to Type 1. Visible wavelength observations thus appear less sensitive to intrinsic silicate mineralogy differences between Type 1 and Type 2 low-albedo materials than mid-IR observations.

Results from HST observations at longer NIR wavelengths using the NICMOS instrument in 1997 and 2003 have been reported by Noe Dobrea *et al*. (2003, 2008). Analysis of the 1997 NICMOS images focused on searching for and mapping the presence of hydrated minerals at key NIR wavelengths. Distinct spectral units were identified associated with low- and intermediate-albedo Acidalia terrains, southern hemisphere low-albedo terrains, and polar ices and clouds. Variations in H_2O- or OH-bearing minerals are inferred from these data within and around Acidalia. However, southern hemisphere low-albedo regions did not appear to exhibit significant hydrated mineral signatures. Analysis of the more recent, higher resolution, and more spatially extensive 2003 NICMOS observations revealed distinct NIR spectral endmembers associated with the south polar cap, the classic bright terrains Arabia and Tharsis/Olympus, northern Syrtis Major, southern Syrtis Major, Tyrrhena terra, and Acidalia Planitia. As in the 1997 data, the Acidalia endmember is distinct from the other dark terrain endmembers because it exhibits a strong negative NIR spectral slope, possibly resulting from thin dust coatings (e.g., Johnson and Grundy, 2001; Lichtenberg *et al*., 2007). While the sparse wavelength sampling of these NIR data did not allow unique constraints on the surface mineralogy to be derived, some of the observed spectral variations were consistent with variations in iron- and sulfur-bearing minerals, and the relatively strong negative spectral slope in the spectrum of Acidalia was consistent with the presence of hydrated alteration products. Intriguingly, comparison of NICMOS observations taken in 1997 and 2003 in Acidalia suggests seasonal variations in the presence of either adsorbed water or re-hydrated minerals in the Martian regolith (Noe Dobrea *et al*., 2008). This possibility clearly needs to be followed up with longer-timescale measurements from orbital spectroscopy experiments that are sensitive to hydrated minerals.

Finally, initial analysis of hyperspectral imaging spectroscopy observations of Mars using the STIS instrument has been reported by Bell *et al*. (2001) and Bell and Ansty (2007). The 0.25 nm spectral resolution of these observations provides the capability to spatially map subtle shifts in reflectance peaks and absorption band positions. However, analysis so far shows that the observed band shifts in STIS data from 1999 and 2003 are too small to be associated with specific changes in ferric or ferrous mineralogy like those studied in laboratory data by Morris *et al*. (2000). Rather, spectral differences between high- and low-albedo regions in STIS spectra are consistent with an increased crystalline ferric contribution in bright regions relative to dark regions, and the presence of low-Ca pyroxene or spectrally similar ferrous silicates in the dark regions. Searches for hydrated ferric sulfate minerals like jarosite in the STIS data (which span near-UV wavelengths that provide the potential to detect such phases, in abundances greater than about 10%) have so far been unsuccessful. While jarosite has been detected on Mars by the *Opportunity* rover (see Chapters 15, 23, and 24), the lack of evidence for this phase in the 20×80 km spatial resolution STIS data is entirely consistent with the relatively low fractional/areal abundance of this mineral as it has actually been observed on the surface. Most recently, analysis of STIS UV spectra acquired during the 2001 planet-encircling dust storm, when compared to data from the same instrument, wavelengths, and surface regions acquired during the clear 2003 opposition period, has allowed the derivation of new UV spectra of suspended atmospheric dust aerosols (Bell and Ansty, 2007). These data also enable new mineralogic constraints on iron-bearing mineral phases in the dust, as well as better-constrained optical constants and other inputs needed for radiative transfer models of dust and other atmospheric aerosols (e.g., Wolff *et al*., 1997, 1999).

HST results: albedo and photometry

Hubble Space Telescope images have also enabled detailed monitoring of surface albedo changes during part of the long gap between Viking-era orbital imaging and the start of routine MGS orbital imaging more than 15 years (nearly 8 Mars years) later. For example, Bell *et al*. (1999) generated an estimated global bolometric albedo map from HST images acquired in 1995 and 1997 and compared that map to Viking orbiter Infrared Thermal Mapper (IRTM)-derived bolometric albedo obtained from late 1970s/early 1980s (e.g., Pleskot and Miner, 1981). The difference in

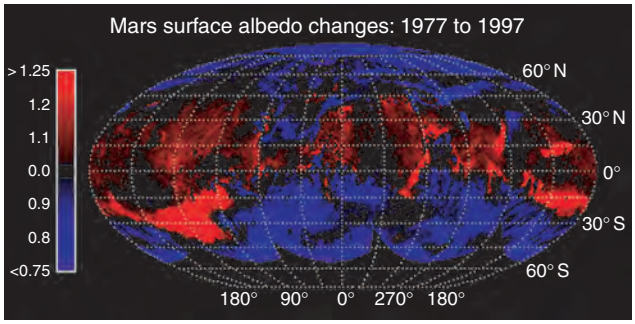

Figure 8.2. Global map of large-scale albedo changes on the Martian surface between the late 1970s and 1997, generated by differencing bolometric albedo maps generated from Viking Orbiter IRTM data (Pleskot and Miner, 1981) and HST (Bell *et al*., 1999). Redder areas here have brightened since the Viking era, and bluer areas here have darkened. The scale gives the ratio of the IRTM-derived Viking era bolometric albedo to the bolometric albedo from 1997 HST data estimated from 1042 nm global multispectral images (Bell *et al*., 1999). (For a color version of this figure, please refer to the color plate section or to the e-Book version of this chapter.)

albedo across this ~15-year time period (Figure 8.2) showed that large regional-scale changes in the surface reflectivity had occurred during that time span. For example, large portions of the southern highlands near 30° S and from 90° W to 160° W brightened dramatically since the Viking era, as did the boundaries of the classical low-albedo region Syrtis Major. Smaller-scale albedo variations were also noted in this and previous HST-Viking comparison studies by James *et al*. (1994, 1996). For example, the small classical dark region Cerberus near 15° N, 210° W essentially disappeared between the Viking and HST eras. More recent assessments of albedo variations have shown that these kinds of changes have continued to occur during the more recent era of orbital spacecraft exploration as well (Geissler, 2005). Aolian transport and redistribution of thin layers of ferric-iron-bearing dust appears to be the major surface modification process active in the present Martian environment. The winds are literally changing the map.

Hubble Space Telescope observations have also been used to study the photometric behavior of the Martian surface and atmosphere at a variety of phase angles and viewing geometries in order to constrain the physical properties of the surface and atmospheric aerosols (e.g., grain size, shape, single scattering albedo, etc.) and to provide inputs to surface and atmospheric radiative transfer models that require assumptions about physical properties and the phase function of the surface (e.g., Bell *et al*., 1999; Soderblom *et al*., 2006; see also Chapter 19). Hubble Space Telescope multispectral and photometric measurements have also been used to assist in the calibration and validation of multispectral data acquired by the Mars Odyssey THEMIS-VIS instrument (McConnochie *et al*., 2006; see below) and the Mars Exploration Rover Pancam instruments (e.g., Bell *et al*., 2005; see also Chapter 13).

Summary: HST

The HST data's broad wavelength coverage, superior spatial resolution compared to previous ground-based studies, and lack of terrestrial atmospheric interference enabled a unique new "window" into Mars surface compositional studies during the 1990s and early 2000s. Interestingly, despite the roughly order-of-magnitude improvement in spatial resolution compared to typical ground-based studies and improved spectral sampling compared to Viking orbiter observations, Mars surface spectra still appear to consist of significantly spatially mixed units even at the few tens of kilometer scale. Some of this mixing is due to atmospheric dust aerosols "contaminating" the surface signal, but even correcting for this effect and/or during extremely low dust opacity periods, even the lowest albedo surface units, presumably the most ferrous and "pristine" in terms of oxidation and weathering, appear to exhibit a reddish, ferric spectral overprint. Subsequent orbital and surface imaging and spectroscopy has shown that it is challenging, in many places and at *any* spatial resolution, to see through the ubiquitous and globally homogeneous ferric-bearing dust on Mars. Hubble Space Telescope imaging extended our view of the surface significantly, but the limitations still inherent in that dramatic new perspective became major factors in the design and planning of the next several generations of even higher spatial resolution Mars orbital multispectral imagers and spectrometers (see Chapters 7, 9, 10, and 19).

8.1.2 Mars Global Surveyor Mars Orbiter Camera Wide Angle (MOC/WA) multispectral imaging

The MOC on MGS has two WA cameras that obtain images at red (575–625 nm) and blue (400–450 nm) wavelengths from horizon to horizon at spatial resolutions of about 240 m/pixel to about 7.5 km/pixel (Malin *et al*., 1992). Most of the objectives and results derived from MOC/WA imaging observations have been related primarily to atmospheric studies, and so are beyond the scope of this chapter. Because the MOC/WA acquired images in two colors, however, there is a limited amount of surface-related compositional information derivable from the images. Color and morphology can be used together to distinguish between "clean" and "dusty" surfaces, surface ices, and atmospheric ice and dust aerosols. As discussed by James and Cantor (2001), absolute calibration of the MOC/WA cameras is accurate to within ~15%, which is adequate for general characterizations of gross regional albedo and color differences.

For example, Cantor *et al*. (2001) used MOC/WA images to chart and characterize the effects of more than 700 individual dust storms observed in 1999 alone. Follow-up studies (Cantor *et al*., 2002) reinforced the idea that local dust storms on Mars are ubiquitous throughout the Martian year and showed there to be an amazing repeatability from Mars year to Mars year in these and other Martian surface/meteorological phenomena. Other important surface-related uses for wide-angle orbital color observations have been monitoring of the growth and recession of the

planet's seasonal polar caps (e.g., James *et al.*, 2000, 2001; James and Cantor, 2001), and monitoring of the extent and opacity of diurnal and seasonal water-ice clouds, fogs, and hazes (e.g., Benson *et al.*, 2003) that form around the large volcanoes or within the canyons and chasms of Valles Marineris. Finally, most MOC/WA images show a dramatic "sun glint" or opposition surge from the planet's surface along the path of the Sun's specular reflection point. The intensity and width of this glint could potentially provide diagnostic information on the physical properties of the surface (single scattering albedo, average grain size, packing density, etc.; e.g., Thorpe, 1982; Hapke, 1993, 2002). Little effort has thus far been spent studying this effect, however, and thus inverting the enormous number of "zero phase" observations acquired from the MOC/WA during its more than four Mars years worth of imaging of the surface represents a largely untapped potential surface physical properties experimental data set.

8.1.3 Mars Odyssey THEMIS-VIS multispectral imaging

The NASA Mars Odyssey orbiter was placed into a ~400 km altitude, Sun-synchronous orbit inclined ~93° to the Martian equator and began routine observations of the planet in February 2002. The spacecraft crosses the equator on the dayside of the planet at local solar times varying between about 3:00 p.m. and about 5:30 p.m. over the course of the Odyssey mission. THEMIS-VIS is a fixed nadir-pointed Charge-Coupled Device (CCD) imaging camera with five narrowband filters bonded directly to the CCD (Christensen *et al.*, 2004a; McConnochie *et al.*, 2006). The filters are centered at 423, 540, 654, 749, and 860 nm and have a full width at half maximum intensity (FWHM) of ~50 nm. Each filter covers an approximately 1024 × 192 pixel region of the detector and allows only that specific wavelength to be imaged for those pixels. The filters are aligned such that multispectral coverage of the surface can be obtained using spacecraft groundtrack motion (traveling from north to south on the afternoon side of the orbit) to consecutively expose each surface region in view to each of the THEMIS-VIS filters. Instrumental scattered light issues severely degraded the utility of the 860 nm images (McConnochie *et al.*, 2006), such that it is no longer used for routine imaging. However, data through the four other color filters are well calibrated (based on previous and simultaneous telescopic, orbital, and surface cross calibration studies; McConnochie *et al.*, 2006; Figure 8.3) and useful for both morphologic and multispectral investigations. The imaging cadence and exposure durations are timed so that the desired region is covered by the desired filters with a small amount of spatial overlap. Images can be commanded to be acquired in 1 of 3 spatial resolution modes: 18, 36, and 72 m/pixel. Spacecraft and instrument resources dictate that spatial resolution, spectral coverage, and spatial coverage must all be traded off against each other for a given orbit's observations, and these parameters can also be traded against each other within broader observational campaigns over longer time periods focused on morphologic or color imaging.

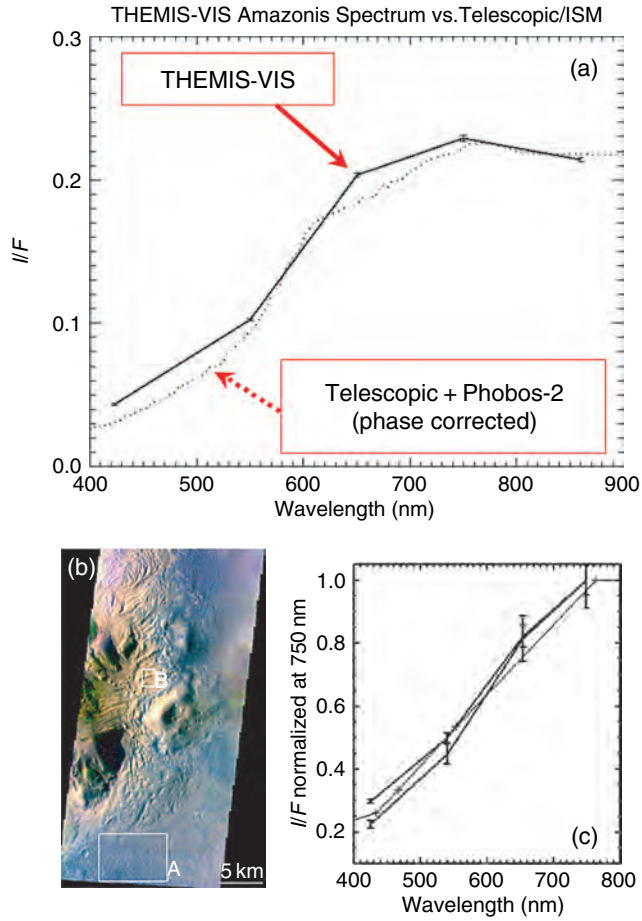

Figure 8.3. (a) Comparison between THEMIS-VIS average radiance factor (I/F) spectra in Amazonis Planitia compared directly to the average bright Amazonis spectrum from merged ground-based/Phobos-2 ISM data (Mustard and Bell, 1994). THEMIS-VIS filters are centered at 423, 540, 654, 749, and 860 nm and have an FWHM of ~50 nm; (b) False color view of THEMIS-VIS image V12518004, near 41.44° N, 44.66° E. (c) Spectra from regions A and B in (b). HST WFPC2 (thin line) and THEMIS-VIS (thick lines) spectra have been normalized at ~750 nm. (For a color version of this figure, please refer to the color plate section or to the e-Book version of this chapter.)

Here we describe as examples some initial results from three separate studies of Martian surface mineralogic variability utilizing THEMIS-VIS observations: a general assessment of visible-wavelength multispectral variability at the sub-100 m/pixel spatial scale within a large fraction of the THEMIS-VIS multispectral data set acquired to date; a study of olivine-rich terrains in the Syrtis Major and Valles Marineris regions; and a search for fine-scale alteration minerals within layered deposits in Aram, Aureum, and Iani Chaos.

THEMIS-VIS survey of visible-wavelength spectral variability at sub-100 m/pixel scales

THEMIS-VIS acquired approximately 48,773 image sequences between February 2002 and September 2005, a period that encompassed the primary mission and first year of the extended mission of the Mars Odyssey orbiter.

Of these, approximately 7923 were color image sequences (more than one VIS filter), and 6846 were acquired using at least 3 VIS filters. About 59% of these 3, 4, or 5 filter images were acquired using the 423, 540, 654, and 749 nm filters and 2 × summing, yielding a spatial resolution of 36 m/pixel. This "workhorse" color imaging mode was chosen as the best compromise between spatial and spectral coverage, given the limited data volume that could be stored within the instrument for each image. Approximately 18% and 8% of the 6846 images were acquired through these same filters but at 18 m/pixel and 72 m/pixel respectively. The remaining 15% of the 6846 images were acquired using other filter combinations, primarily 423, 540, 654 nm and 423, 540, 749 nm, and mostly using 4 × summing (72 m/pixel) for extended spatial coverage.

Bell *et al*. (2006) describe the calibration, map-projection, and initial analysis of these multispectral images based primarily on false-color RGB composites generated from 654, 540, and 423 nm images. These false-color images substantially enhance and exaggerate the color differences between different units in each scene. Examples of some of these false-color image products are shown in Figure 8.4. Many of the THEMIS-VIS multispectral images exhibit spectacular morphologic detail (see also Christensen *et al*., 2003), and most of them exhibit some sort of significant albedo or brightness contrasts (e.g., along shadows related to the late-afternoon viewing conditions or at the boundaries of polar ice deposits). However, a subset of the THEMIS-VIS multispectral images can be identified where the color variability appears correlated with morphologic and/or topographic features in the scene, is small-scale, and is not related to obvious instrumental or calibration artifacts (McConnochie *et al*., 2006). Constraining the data set this way rules out, for example, a large number of images in which variations in dust deposits with no obvious relationship to the underlying geology (other than the geology or topography providing occasional obstacles) can be seen, while still exploiting the fact that THEMIS-VIS was the first instrument to observe Mars from orbit in color at the ~100 m and smaller spatial scale.

Restricting the data set this way yielded a surprisingly small number of "interesting" images: only 633 of the 7923 THEMIS-VIS multispectral sequences acquired up to September 2005 (~8% of the total). Bell *et al*. (2006) classified these 633 "most interesting" color images into different categories using a qualitative (visual) classification scheme that included "blue" materials, layered terrains, craters, albedo contrasts, channels and valleys, canyonlands, highlands, etched terrains, dunes, wind- and slope-streaks and dust devil tracks, and atmospheric features. This relatively subjective classification scheme provides some general insight into what kinds of features/terrain display the greatest level of visual color variability, and thus potential compositional/mineralogic variability, at THEMIS-VIS sub-100 m spatial scales. Several of the most frequently occurring classes are discussed in more detail here.

For example, the largest class of anomalous color units are regions where the reflectance at 425 nm is much higher than the surroundings, and indeed much higher than the average (very low) blue reflectance of Mars. These regions are referred to as "blue" materials, even though their absolute color is still quite red, when viewed in approximate true color renderings generated from calibrated THEMIS-VIS images (e.g., Bell *et al*., 2003, 2006). Many such "blue" spots are found inside craters, but many are not. They may be indicators of the presence of dark basaltic sand dunes, ripples, or drift deposits that are unresolved at the scale of the VIS observations. Examples are shown in Figure 8.4a, and additional spectral details related to one of these regions in particular are described in Noe Dobrea *et al*. (2006).

Color variations within layered terrains form the next largest group of interesting sub-100 m resolution spectral anomalies at visible wavelengths (Bell *et al*., 2006). An impressive and representative example of color variations in the south polar layered deposits (e.g., Plaut *et al*., 2003) is shown in Figure 8.4b. One kind of layered material that has been the subject of intense study is the bright, reddish, cliff-forming deposits typical of that shown in Figure 8.4b from VIS sequence V04359003 in Ganges Chasma. The visible and infrared spectral properties of this class of material have also been studied by Ruff *et al*. (2001) (in the similar "White Rock" deposit in Pollack crater) and by Anderson and Hamilton (2005) in Ganges Chasma. The composition of many of these light-toned, reddish outcrops remains somewhat of a mystery. Ruff *et al*. (2001) did not find evidence for distinctive carbonate or sulfate absorptions based on infrared spectra, and they reported thermal inertias consistent with weakly cemented sediments, rather than bedrock. Visible wavelength observations are consistent with the presence of ferric oxides and/or oxyhydroxides in these materials at least as coloring/pigmenting agents, but as yet specific mineralogies have not been identified.

Finally, Figure 8.4c shows examples of some of the most interesting of the "etched terrain" class images defined by Bell *et al*. (2006). Perhaps not surprisingly, a large percentage of these images, and indeed a large percentage of the most interesting THEMIS-VIS images overall from the standpoint of color variability, come from the region in and around Meridiani Planum. This part of the planet has been shown in a number of remote-sensing studies to be a region of high thermal inertia and probably net erosion (in recent Martian history) (e.g., Arvidson *et al*., 2003; Edgett, 2005) and thus it is perhaps not surprising that the part of the planet with putatively the least amount of dust cover contains some of the most dramatic examples of surface color variations. Some of the variation appears related to the presence and small-scale variability of darker, bluer aeolian dune, drift, and sand sheet materials, but some may be related to compositional and/or mineralogic variations in small-scale layers or other deposits (as discussed below), revealed for the first time in color at these spatial scales.

Spectral characteristics of olivine-enriched terrains on Mars from THEMIS-VIS

Olivine is a mafic mineral of the general formula $(Mg,Fe)_2SiO_4$ and typically is found in mafic igneous rocks on Earth and Mars (and Martian meteorites), in some terrestrial metamorphic lithologies, and is a major constituent

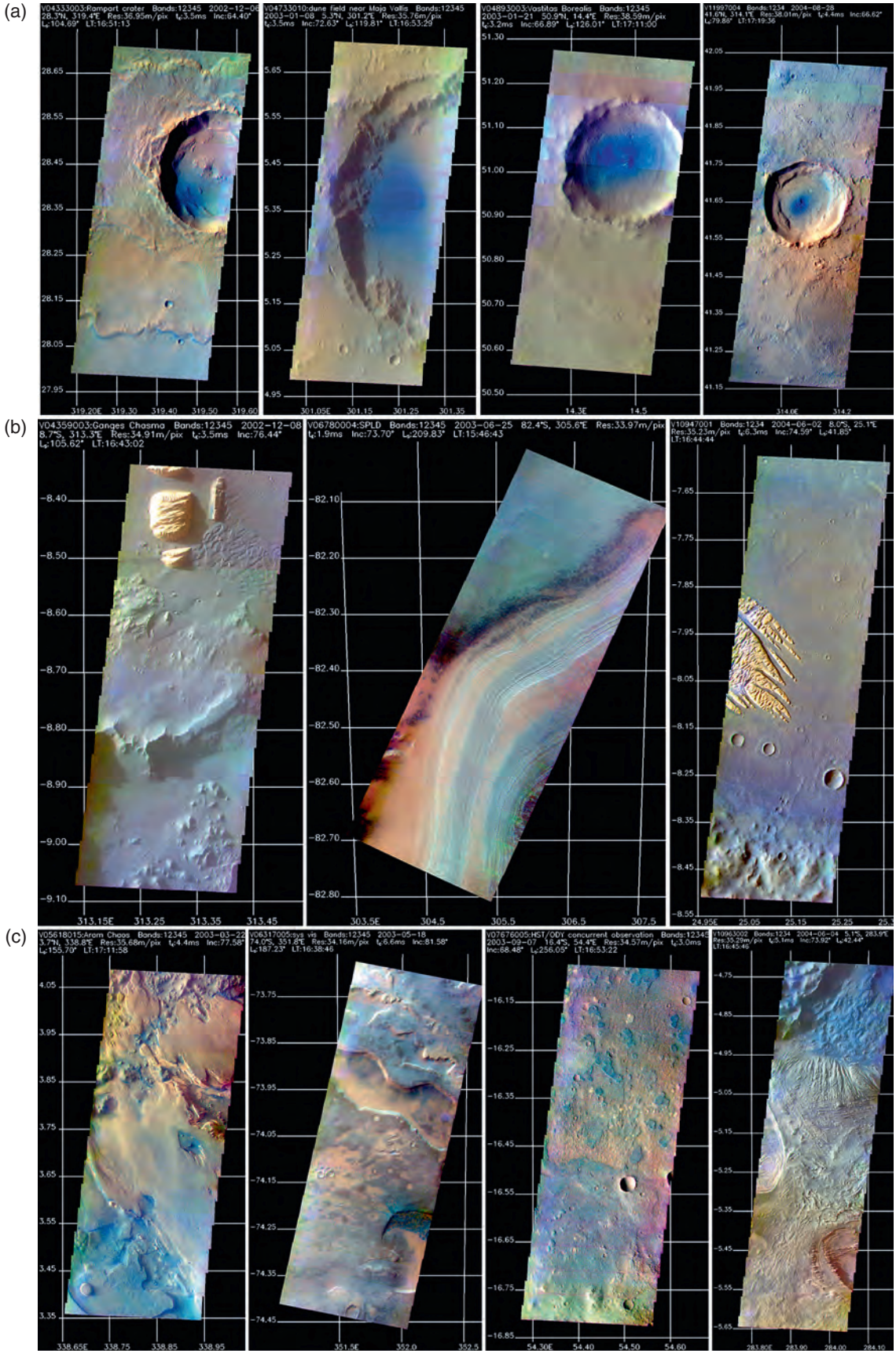
(a)
(b)
(c)

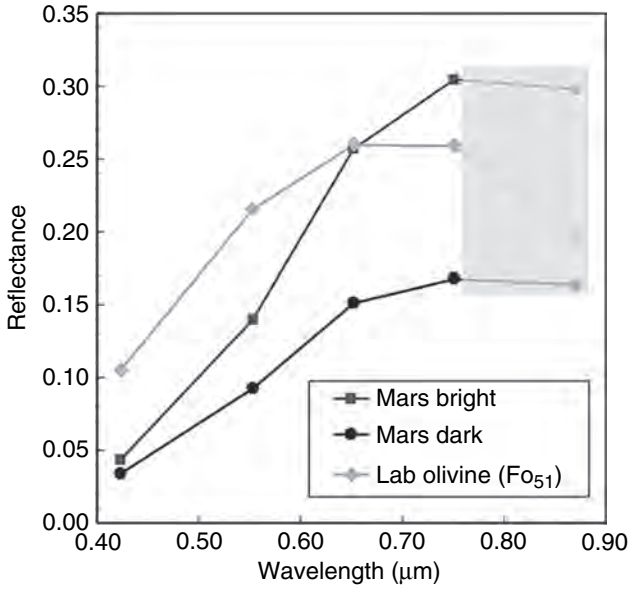

Figure 8.5. Mars bright and dark region spectra from Mustard and Bell (1994) and laboratory olivine spectrum convolved to THEMIS-VIS band passes. Shading indicates spectral region with considerable uncertainty because of scattered light in the 860 nm THEMIS-VIS data (McConnochie *et al*., 2006).

of the Earth's mantle and presumably that of Mars. Traditionally, olivine is considered a phase that is highly susceptible to alteration and/or dissolution in the presence of water, and its presence in ancient areas of Mars (see Chapters 7, 9, and 10) poses the question of whether or not its preservation indicates a largely cold, dry past climate for Mars. Data acquired by MGS/TES (Christensen *et al*., 1992, 2001) have been used to unequivocally identify localized enrichments of olivine on Mars at scales of tens to thousands of kilometers and to estimate the approximate solid solution composition ($\sim Fo_{65-70}$, where Fo# – "forsterite number" – is the percentage of Mg relative to total Mg + Fe) of the olivine (Hamilton *et al*., 2003; Hoefen *et al*., 2003). The 100 m scale distribution of olivine-enriched materials in many locations has been mapped by the thermal infrared subsystem of THEMIS (Hamilton and Christensen, 2005; see Chapter 10). THEMIS-VIS permits the multispectral investigation of these materials at even higher (~18 m/pixel) spatial resolution.

Magnesian olivines commonly exhibit a green color, and Hamilton and Christensen (2004) searched for an increase in reflectance in THEMIS visible spectra at 540 nm that might be present in areas with relatively greater abundances of olivine, such as the area surrounding the Nili Fossae and in areas in and around Ganges and Eos Chasmata. Such an increase in green reflectance is dependent on a variety of factors, including the particle size, Mg/Fe composition, abundance, and purity of the olivine, and may not produce a reliable spectral parameter in all cases. However, Figure 8.5 demonstrates that relative to typical Martian VNIR spectra, which exhibit a concave shape from 423 to 654 nm, olivine exhibits a convex shape in this region. This feature can be parameterized as the reflectance at 540 nm divided by the average reflectance at 423 and 654 nm. Values of this index greater than unity indicate increased green wavelength reflectance. In typical Martian spectra, this green reflectance index produces values less than unity because of the strong ferric absorption edge that dominates the visible part of the spectrum. Spectra from THEMIS-VIS images in the area of the Nili Fossae show few values of this index greater than unity, although increased values of the index generally are associated with olivine-bearing materials (Figure 8.6, Table 8.1). This result may be interpreted to mean that a green(er) material is present, but that its color is being suppressed by the strong ferric iron absorption, possibly by airborne dust, surface dust, or surface coatings. Olivine-bearing materials in Eos Chasma, Ganges Chasma, and craters in Aurorae Planum show values of this index greater than unity, but some of these values correlate with known artifacts of the VIS calibration, and a careful examination for correlation with spectral features in the THEMIS infrared data has not yet been performed.

In the NIR, Fe^{2+} produces 3 overlapping absorption features that are centered near 1000 nm. The position of the combined 1000 nm minimum can be diagnostic of the crystal chemistry of compositions in the olivine series (King and Ridley, 1987), although overlapping ~1000 nm bands from pyroxenes and ~800–900 nm bands in some iron oxides can frustrate or confuse the unique identification of olivine (e.g., Cloutis and Gaffey, 1991; Morris *et al*., 1995). Prior to the arrival at Mars of VNIR spectrometers on board the MEx and MRO spacecraft, the multispectral VIS subsystem of the THEMIS instrument offered the only opportunity to determine whether a discernable VNIR absorption attributable to olivine is apparent in the previously identified regions at the tens of meters scale. Ideally, a search for this feature would focus on the analysis of the longest wavelength VIS bands (749 and 860 nm respectively), but because of problems with the 860 nm data, it cannot be used and the relationship between 749 and 654 nm must be used instead. The 749 nm band is on the short wavelength side of the main 1000 nm olivine absorption feature, and should exhibit reduced reflectance in the presence of olivine, if the main olivine absorption feature is strong enough (however, what "strong enough" means in terms of relative signal strength or absolute abundance is not known a priori). Typical Martian spectra (e.g., Mustard and Bell, 1994), convolved to THEMIS-VIS spectral resolution, exhibit a positive slope from 654 to 749 nm, whereas the spectrum of an intermediate (Fo_{51}) composition laboratory olivine, also convolved to the

Caption for Figure 8.4.
(a) Examples of "Blue Crater Materials" observed in false-color THEMIS-VIS images. VIS imaging sequences V04333003, V04733010, V04893003, and V11997004. (b) Examples of "Layered Materials" observed in false color THEMIS-VIS images. VIS imaging sequences V04359003, V06780004, and V10947001. (c) Examples of "Etched Terrain" observed in false-color THEMIS-VIS images. VIS imaging sequences V05618015, V06317005, V07676005, V10963002. (For a color version of this figure, please refer to the color plate section or to the e-Book version of this chapter.)

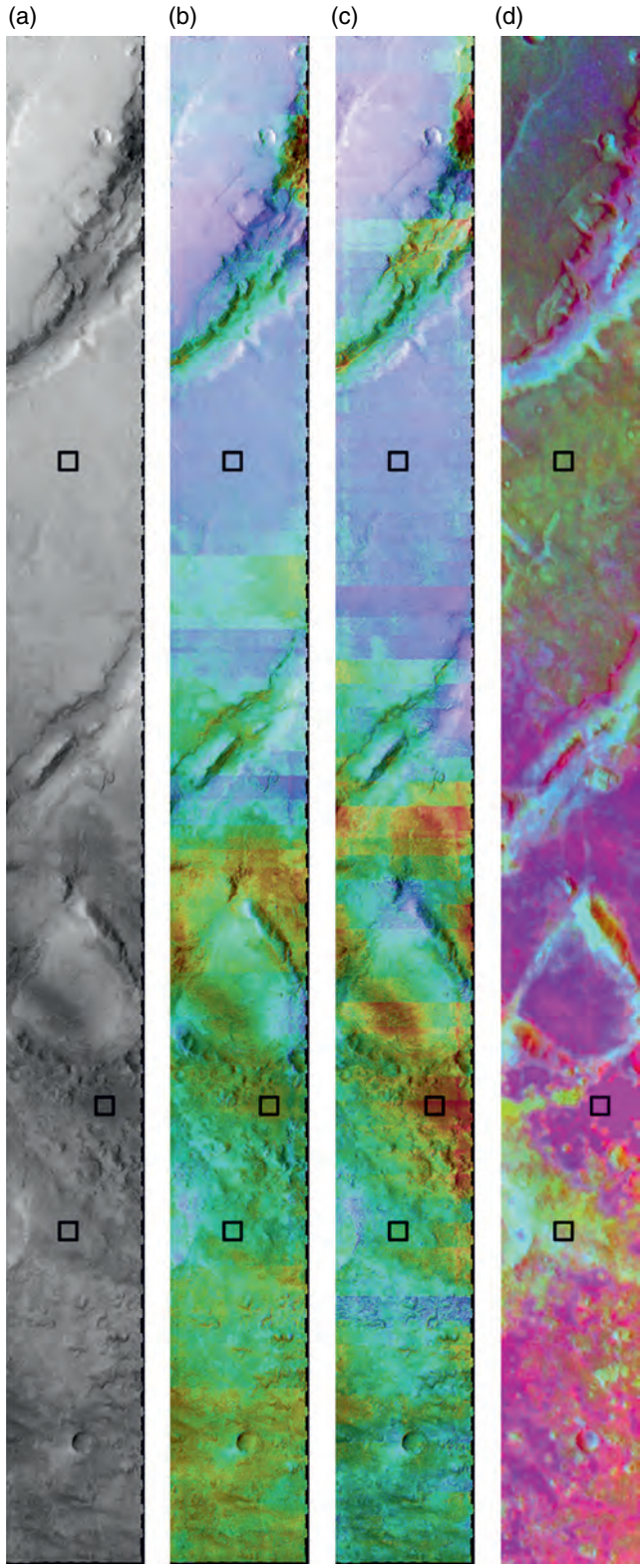

THEMIS-VIS band passes, displays a flat to slightly negative slope between 654 and 749 nm (Figure 8.5). Because the position of the ~1000 nm olivine feature shifts to shorter wavelengths with increasing Mg content, olivines with higher Fo# will exhibit increasingly negative 654–749 nm spectral slopes. Thus, if olivine of intermediate to magnesian composition is present in a given location on Mars at abundances greater than those represented by typical Martian spectra, the slope between these two bands may be nearly flat or negative. While not a unique interpretation given the confounding effects of pyroxenes and/or ferric oxide coatings, the attribution of such a slope to olivine could be strengthened by a direct correlation between the spatial distribution of the VIS-derived olivine parameter and the mapping of olivine spectral signatures from THEMIS or TES infrared data. Hamilton and Christensen (2004) also searched THEMIS-VNIR spectra for deviations from the positive 654 to 749 nm spectral slope typically observed in Martian dark regions. By subtracting 749 nm VIS images from their 654 nm counterparts, they identified negative 654–749 nm spectral slopes in the olivine-enriched units surrounding the Nili Fossae. Figure 8.6 shows a THEMIS-VIS ratio image of 654 nm radiance divided by 749 nm radiance, which highlights the 654–749 nm spectral slope. Indicated on the 654/749 nm ratio image are the locations of three regions: Region 2 exhibits ratio values greater than 1, indicative of a strong negative slope between 654 and 749 nm, whereas Regions 1 and 3 exhibit values indicative of positive slopes (Table 8.1). The average spectra of the three regions are shown in Figure 8.7 as compared to the typical Martian dark region spectrum from Figure 8.5. The average Region 2 spectrum shows an absorption at or beyond 749 nm and may be consistent with an increase in the local abundance of olivine. Comparison of the 654/749 nm ratio map to a decorrelation-stretched infrared image highlighting the distribution of olivine-enriched materials (Figure 8.6d) shows a positive correlation between flat to negative 654–749 nm spectral slopes (ratio values approaching or greater than 1) and the intensity of olivine-related features in the thermal infrared. This supports but does not prove the suggestion that the 654–749 nm spectral slope is indicative of an olivine absorption in the THEMIS-VIS data, and provides an example of a possible way to extend THEMIS-IR or TES lower spatial resolution results down to much smaller spatial scales. Further work is required to establish the

Figure 8.6. THEMIS-VIS (V02344006) and IR (I02344005) data from near the Nili Fossae. From left to right: (a) THEMIS band 3 (0.65 μm); (b) Band 3 image with colorized overlay of green reflectance index; values range from 0.025 (purple) to 1.187 (red); (c) Band 3 image with colorized overlay of B3–B4 slope; values range from 0.380 (purple) to 1.809 (red); and (d) THEMIS infrared decorrelation stretch (bands 9, 7, and 5 in RGB, respectively), with olivine-enriched materials in magenta. Images are ~19 km in width. Northernmost box in each is Region 1, central box is Region 2, southernmost box is Region 3. (For a color version of this figure, please refer to the color plate section or to the e-Book version of this chapter.)

Table 8.1. *Statistics of spectral analyses, V02344005*

Area	Avg. B3/B4 ratio value	Standard deviation (1σ)	Avg. green reflectance index value	Standard deviation (1σ)
Region 1	0.82	0.01	0.79	0.01
Region 2	1.05	0.03	0.92	0.01
Region 3	0.90	0.02	0.86	0.01
Whole image	0.89	0.07	0.86	0.07

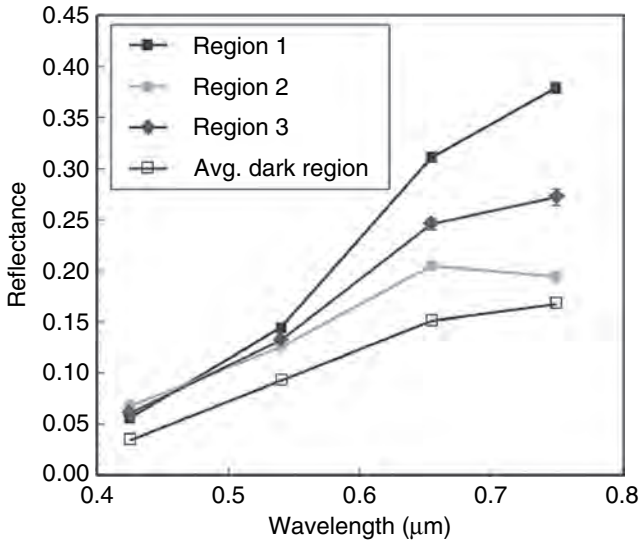

Figure 8.7. Average THEMIS-VNIR spectra (423–749 nm) of the three regions within Figure 8.6 as compared to the average spectrum of Martian dark regions (Mustard and Bell, 1994). Error bars on each region's spectrum represent 1σ standard deviation of averages (in some cases, error bars are smaller than symbols).

minimum abundance of olivine required for this feature to be observed in THEMIS-VIS data, however.

Fine-scale alteration minerals in layered deposits in Valles Marineris

THEMIS-VIS data have been used to distinguish and correlate layered units in Aram, Aureum, and Iani Chaos, large-scale depressions east of the broad Valles Marineris geologic province. These light-toned layered units are associated with hematite-rich deposits similar to those in Meridiani Planum (Catling and Moore, 2003; Glotch and Christensen, 2005; Glotch and Rogers, 2007), and those in Iani Chaos have been shown to be sulfate-rich by the MEx Orbiter's OMEGA visible/NIR imaging spectrometer (Gendrin *et al.*, 2005; see Chapter 7). Data from MGS TES indicate that these units, which appear light toned in THEMIS-VIS images, indeed have higher bolometric albedos (~0.18 versus ~0.12) than the surrounding chaotic terrains with which they are associated (Glotch and Christensen, 2005; Glotch and Rogers, 2007). In Aram and Aureum Chaos, the light-toned units are cliff-forming and generally lie stratigraphically above the hematite-rich unit, while the light-toned unit in Iani Chaos appears to be more friable and is coincident with the hematite-rich unit. In both regions, small exposures of light-toned material can also be seen within and below the chaotic terrain (Glotch and Christensen, 2005; Glotch and Rogers, 2007).

In addition to being significantly brighter, the layered units in these equatorial chaotic terrains also appear redder than the surrounding terrain in THEMIS-VIS color visible imagery. This increased redness is expressed in both false-color imagery and 540 nm band depth images (Figure 8.8). The increased redness may be due to an increased abundance of ferric iron relative to the surrounding basalt-dominated terrains. Another example of this kind of anomalous spectral unit is presented in Figure 8.9, from THEMIS-VIS data in Eos Chasma at the instrument's highest spatial resolution (18 m/pixel). Bright, reddish exposures on the chasma walls exhibit deeper absorption at 540 nm compared to other surrounding plains and chasma wall and floor materials, suggesting an increased abundance of crystalline ferric oxide, possibly hematite, in these exposures (Morris *et al.*, 2000; Bell *et al.*, 2006).

While THEMIS-VIS data do not prove an unambiguous relationship between layered outcrop units in places like Aram, Aureum, Iani, or Eos with outcrop rocks elsewhere on Mars, it is nonetheless interesting and perhaps informative that THEMIS-VIS observations in these places are consistent with Mars Exploratory Rover (MER)/Pancam multispectral measurements of bright, reddish outcrop rocks in Meridiani Planum. Meridiani outcrop rocks studied by the *Opportunity* rover show a strong reflectance increase from the near-UV to visible wavelengths consistent with the presence of nanophase ferric iron oxides, as well as evidence for weak absorptions near 535 nm and in the 800–1000 nm region that are consistent with the presence of crystalline ferric oxides like hematite (Bell *et al.*, 2004b; see also Chapter 13). *In situ* measurements at the MER *Opportunity* landing site in Eagle crater show that the bright, reddish outcrop has an average Fe^{3+}/Fe_{total} of 0.88, as opposed to an average Fe^{3+}/Fe_{total} of the basaltic soils of 0.37 (Klingelhöfer *et al.*, 2004).

8.1.4 Mars Express High Resolution Stereo Camera (HRSC) multispectral imaging

The HRSC (Neukum and Jaumann, 2004; Oberst *et al.*, 2004; Jaumann *et al.*, 2007) on the MEx spacecraft is delivering images of the Mars surface and atmosphere from its high-inclination, elliptical orbit that are intended to cover

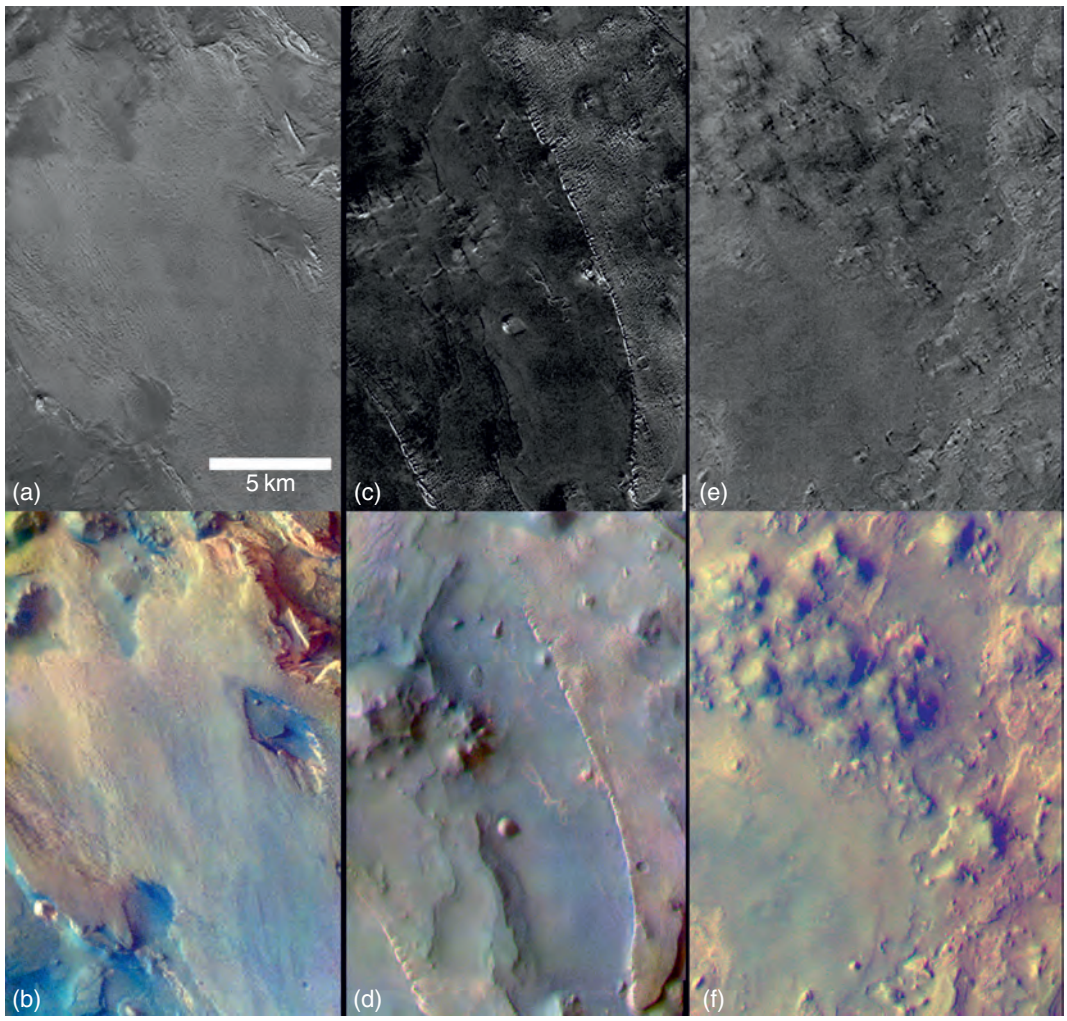

Figure 8.8. Examples of bright, reddish layered units in the equatorial chaotic terrains. Images are THEMIS-VIS 36 m/pixel false-color RGB composites using images at 654, 540, and 423 nm. (a) 540 nm band depth image V05618015 covering Aram Chaos. (b) False-color image V05618015. (c) 540 nm band depth image V10537001 covering Aureum Chaos. (d) False-color image V10537001. (e) 540 nm band depth image V10649001 covering Iani Chaos. (f) False-color image V10649001. (For a color version of this figure, please refer to the color plate section or to the e-Book version of this chapter.)

most of the Mars surface by the end of the mission. These are acquired in four specific narrow spectral passbands that sample the scene at different parts of the extended visual spectrum from near 400 nm to about 1000 nm and in five additional channels, four used for stereo and one nadir, that use a fifth (and wider) spectral passband (Table 8.2). These channels view from different angles and can be used for photometric and multispectral analysis. The HRSC has four basic capabilities: imaging, stereo, photometry, and color. These capabilities reveal landforms and clouds as well as topography, surface physical characteristics, and compositional units.

The HRSC focal plane consists of nine linear-array Si-CCD detectors, each consisting of 5184 pixels that view the scene, oriented perpendicular to the orbit track (Figure 8.10). An image is built up by repeatedly reading out each array as the spacecraft orbits over the surface and the scene sweeps across the camera focal plane. Each detector array views the scene at a different angle (Table 8.2) spread out from forward to aft of nadir so that each detector views a different line in the scene at any instant of time. The spacecraft is periodically rotated 180° so that the fore and aft positions are switched. The resolution at nadir and 250-km orbit altitude is nominally 10 m/pixel. The nominal data-acquisition mode is with the nadir channel at full spatial resolution. The color channels are normally operated in a macro-pixel mode of 2×2, 4×4, or 8×8 pixels summed on the spacecraft to reduce data volume.

Like all of the observations discussed in this chapter, the basic HRSC Mars observations record radiances as viewed from the top of the Mars atmosphere. Thus, both the atmosphere and the surface characteristics affect the measurements and each wavelength differently. These effects include gaseous and mineral absorption, scattering from aerosols out of the path (back on to the surface and back in to the instrument), the cosine solar illumination angle effect on surface brightness, the surface photometric scattering function, and shadows due to surface roughness at many different scales. These effects contribute to both the incident sunlight and the reflected light paths and are a function of location, time, and geometry of

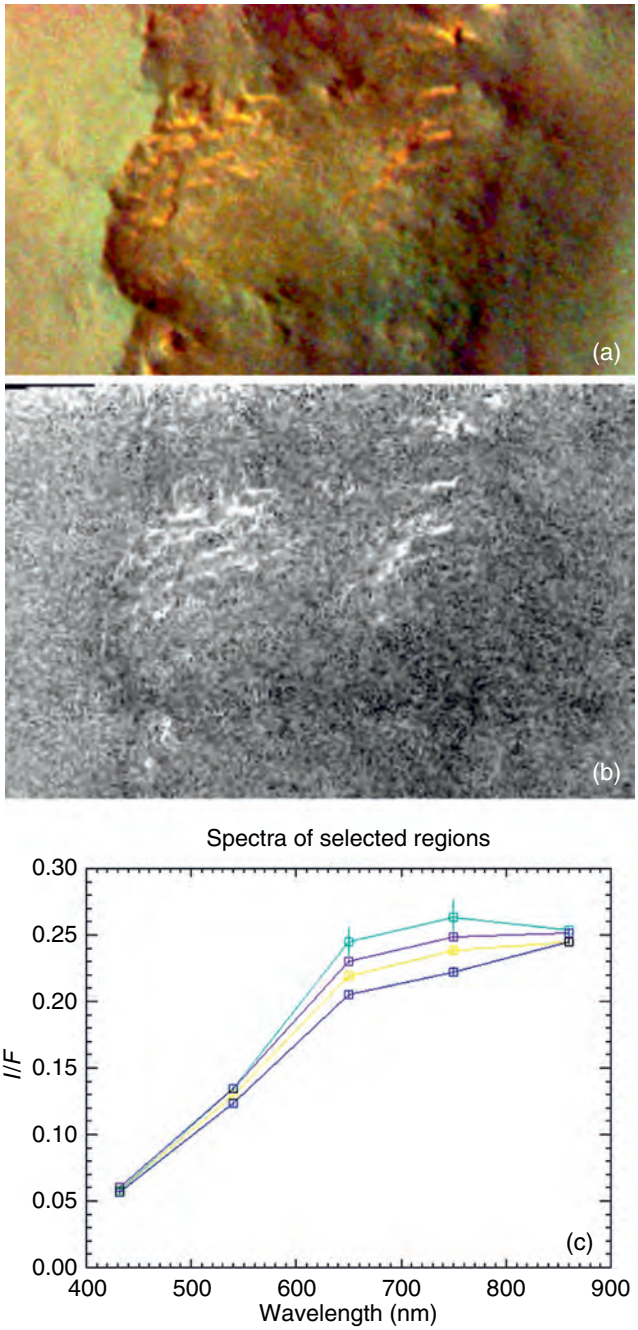

Figure 8.9. Example of bright, reddish layered wall units in Eos Chasma. (a) False-color RGB (654, 540, 423 nm) view of part of THEMIS-VIS image V01750002 at 18 m/pixel resolution; (b) 540 nm band depth map, interpreted to indicate that the bright, reddish materials in the chasma walls have a stronger crystalline ferric mineral (perhaps hematite) absorption feature; (c) Extracted 5-color THEMIS-VIS spectra of color units in this scene. The top spectrum is data from the bright, reddish, ferric-rich chasma wall materials that exhibit the deeper 540 nm absorption relative to surrounding terrains. Other spectra shown here are from "normal" surrounding plains, wall, and chasma floor materials. Analysis from Bell *et al.* (2006). The 860 nm data suffer from scattered light artifacts but are shown here for completeness. (For a color version of this figure, please refer to the color plate section or to the e-Book version of this chapter.)

Table 8.2. *The characteristics of the different HRSC instrument throughput. The nadir channel bandpass is also used for the four photometric/stereo channels, making a total of nine channels. See Neukum and Jaumann (2004) and Jaumann* et al. *(2007)*

Channel	Bandpass wavelenth (nm)	Viewing angle (°)
Nadir	675 ± 90	0
Blue	445 ± 40	−3
Green	540 ± 45	3
Red	750 ± 25	−16
Infrared	955 ± 40	16

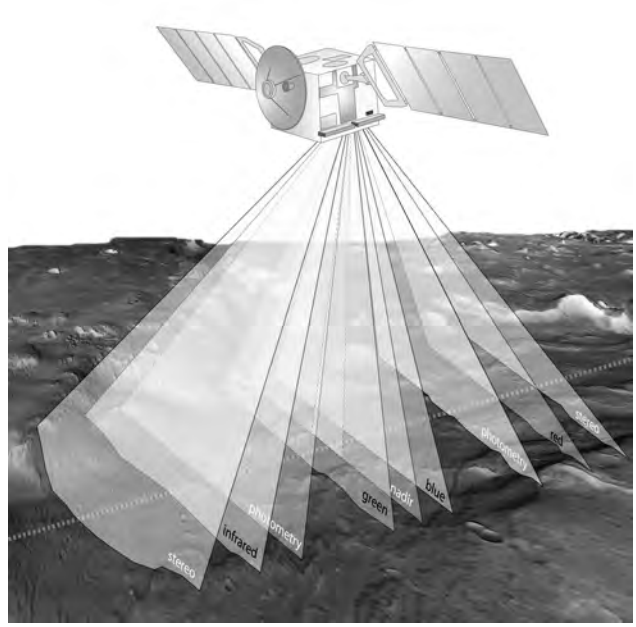

Figure 8.10. The Mars Express spacecraft is depicted orbiting above the Mars surface. The instantaneous viewing geometries of the nine HRSC linear detector arrays are shown. The nadir high-resolution channel is in the middle of the array of channels shown here. The viewing angles for each of the color channels are given in Table 8.2. Note that as the spacecraft orbit passes over the surface, each channel views the same surface location as the other channels, but at a different viewing angle and at a slightly different time.

illumination and emission of the surface element observed. The atmospheric scattering effects can be large (McCord *et al.*, 2007) depending on the lighting geometry (up to 25%–50% additional radiance for opacity approaching 1.0). Of course, the color capability of HRSC is also important for atmospheric studies. For example, cloud and dust structures in the atmosphere are more clearly defined when their color differences are used to map and describe them.

The I/F, or radiance factor at the geometry of observation and illumination (Hapke, 1993), for each pixel in each color can be calculated using the radiometric calibration files for the HRSC. Examples (McCord *et al.*, 2007) are shown for selected locations in scenes for the Valles Marineris region and the north polar region without and with the solar

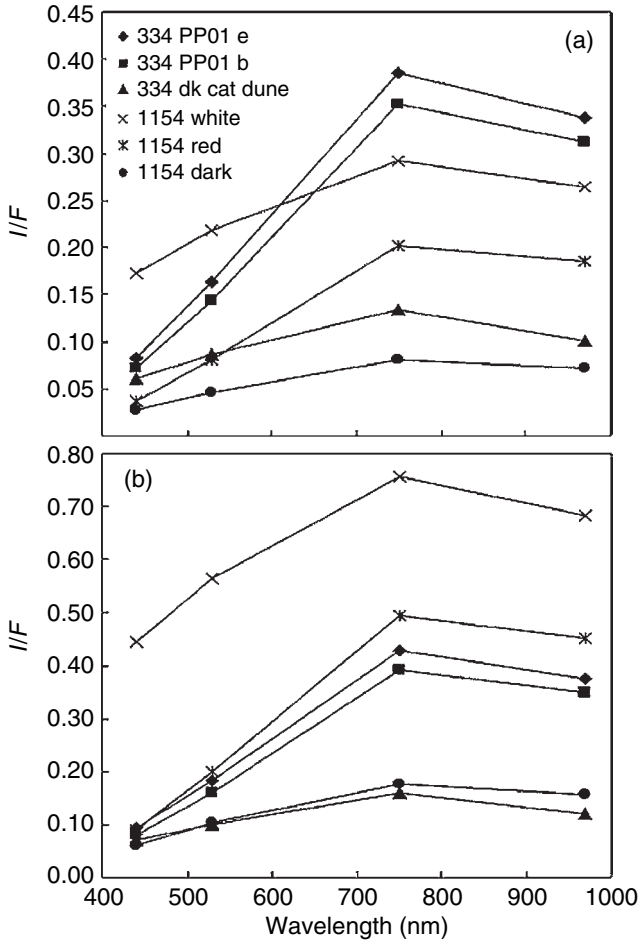

Figure 8.11. HRSC four-color spectra are plotted here for selected areas (McCord *et al.*, 2007) in several orbit image stripes, as designated in the Legend by orbit number and spot name. (a) Spectra as delivered by HRSC after radiometric calibration. (b) Spectra after correcting for solar illumination angle according to a cosine function.

illumination-angle cosine effect removed in Figure 8.11. By treating the HRSC color data as a four-space of vectors and searching this space for clusters of spectral types (see, Adams and Gillespie, 2006), McCord et al. (2007) found that selected polar and equatorial HRSC spectral images are dominated by bright red, dark red, and bright polar ice endmember materials. Ice is detected in the HRSC spectral data so far only in the polar images, and its spectra are consistent with previous observations that polar ice is contaminated by globally distributed "red" dust, although small areas (the brightest) show very little or no red dust effects and thus may be the freshest snow. McCord *et al.* (2007) used a simple linear mixing model with only bright and dark endmembers and a topographically controlled "shade" endmember to explore spectral variability within Valles Marineris (Figure 8.12). The derived fractional abundance maps show complex relationships between bright and dark materials at an unprecedented spatial scale and provide new information on the stratigraphic relationships among materials in the canyons. This initial study of the distribution of color units shows that HRSC data have potentially important implications for interpreting the geology of many places on Mars.

8.1.5 Mars Express OMEGA hyperspectral imaging and coordinated surface-orbital observations

The OMEGA VNIR spectrometer on MEx (Bibring *et al.*, 2004) has been acquiring hyperspectral imaging spectrometer observations of the Martian surface and atmosphere since 2004. OMEGA data sets consist of observations collected by the three components of the instrument: a pushbroom "V" channel spectrometer operating from 0.35 to 1.08 μm with 96 bands and 20 nm FWHM, an infrared whiskbroom "C" ("court") channel spectrometer operating from 0.98 to 2.6 μm with 128 bands and 20 nm FWHM, and an infrared whiskbroom "L" ("long") channel spectrometer operating from 2.5 to 5.08 μm with 128 bands and 30 nm FWHM (Bibring *et al.*, 2004). While complexities exist in the collection, reduction, and analysis of the OMEGA data (e.g., the three spectrometers have slightly different fields of view, and use of the longest wavelength portion of the L spectrometer has been problematical to date because of radiance calibration issues and the complex interplay of reflected solar radiation and surface emission that is characteristic of this part of the spectrum), the instrument has still yielded important new insights about the Martian surface. Details about many of the initial major scientific findings from OMEGA are provided in Chapters 7 and 25.

A different line of study using the OMEGA data has focused on the use of coordinated surface and atmospheric observations between OMEGA and instruments on the Mars Exploration Rovers, augmented with data from MGS and Mars Odyssey, to retrieve Lambert albedos and to place constraints on other physical and compositional properties derived from the OMEGA observations (Arvidson *et al.*, 2006; Lichtenberg *et al.*, 2007). Specifically, MER Pancam and Mini-TES observations of the surface and atmosphere from both the *Spirit* and *Opportunity* sites (Squyres *et al.*, 2003, 2004a,b; Bell *et al.*, 2004a,b; Smith *et al.*, 2004) have been acquired simultaneously with OMEGA orbital observations of the rovers' immediate surroundings in Gusev crater and Meridiani Planum as part of several coordinated observational campaigns. Here we briefly summarize the initial results from these observations.

Coordinated MER-OMEGA observations in Meridiani Planum

A number of OMEGA passes cover the *Opportunity* landing site and surrounding plains and cratered terrains. One of the highest spatial resolution passes was acquired on December 20, 2004, at ~09:11 local solar time, during MEx orbit 1183–5. This pass goes directly over the Meridiani plains, including the *Opportunity* rover traverse site and extends to the cratered terrain highlands to the south (Figure 8.13a). The data set has 32 pixels across track and thousands of pixels along track (roughly aligned in a north–south direction), with a spatial resolution of ~700 m/pixel along track and ~500 m/pixel across track.

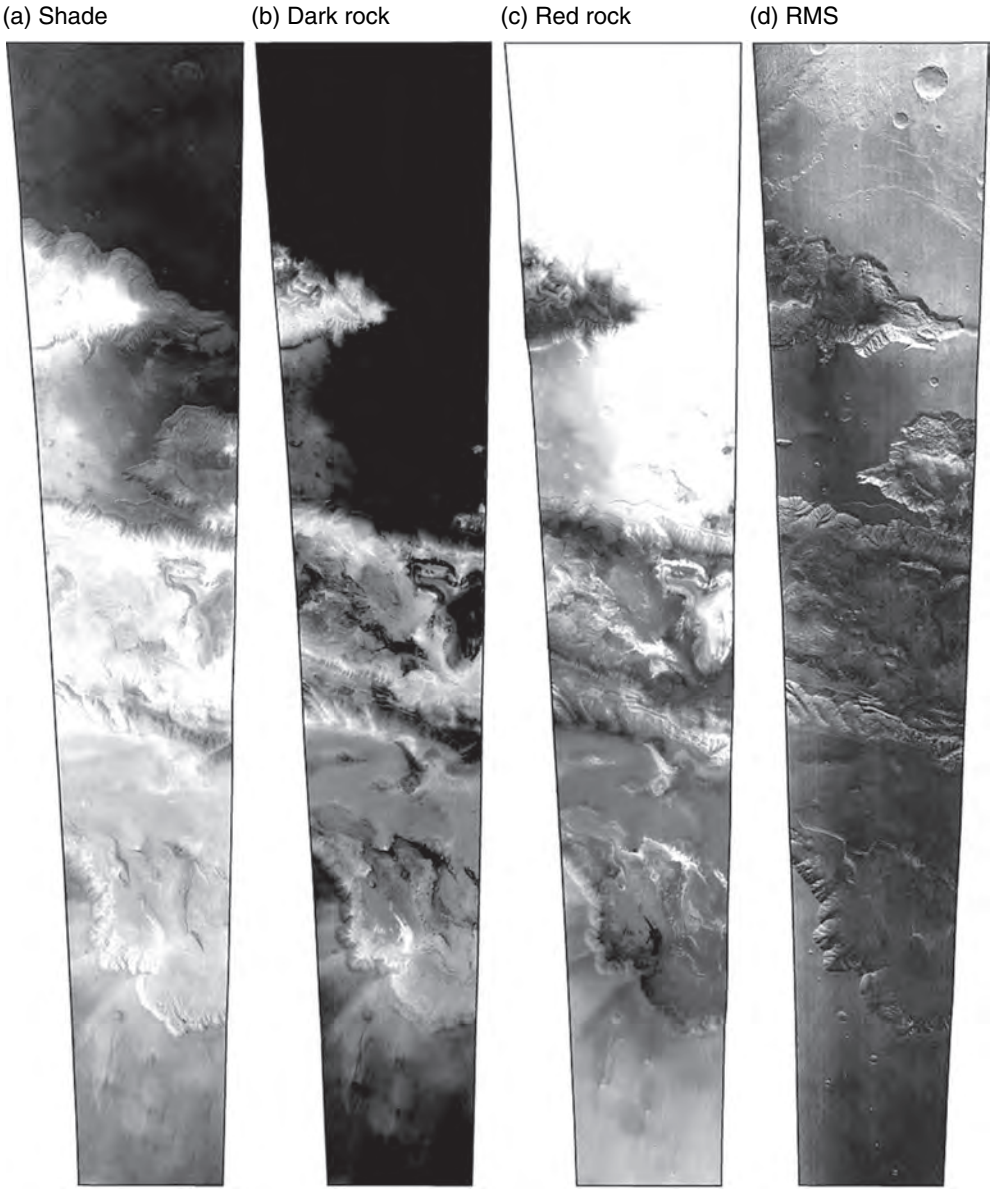

Figure 8.12. Endmember fractional abundance images from a linear spectral mixing model study of Mars Express HRSC data in Valles Marineris by McCord *et al*. (2007). (a) "Shade" fraction image, representing macroscopic or perhaps subpixel scale topography and roughness; (b) Dark red fraction image; (c) Bright red fraction image; (d) Root Mean Square (RMS) model residual image. The image is strongly contrast stretched and shows RMS errors on the order of 1%. The low overall residual error indicates that the simple linear model with bright, dark, and shade endmembers accounts well for the main spectral variability of the scene. Most of the high RMS pixels are associated with image misregistration or compression artifacts. A few areas of high RMS in the chasmata are possible candidates for materials that are spectrally different from the typical bright and dark endmembers. Lighter tones = higher fractional abundances or higher RMS error. Data from HRSC orbit 360 (McCord *et al.*, 2007).

OMEGA data for any given band are calibrated to radiance factor, i.e., I/F where I is the scene radiance on sensor and F is the solar irradiance divided by π (Hapke, 1993), using procedures described in detail by Arvidson *et al*. (2006). It is important to note that the observed I/F values include both atmospheric and surface contributions. To better understand the magnitude and effects of these contributions from atmospheric gases, dust, and ice aerosols, the data for OMEGA 1183–5 over the *Opportunity* site were modeled with the DISORT radiative transfer modeling code (Stamnes *et al*., 1988). DISORT models gas absorptions (CO_2, CO, H_2O), and scattering and absorption resulting from dust and ice aerosols, along with surface and atmospheric emission, and requires knowledge or assumptions about the atmospheric pressure and temperature profiles (e.g., from MGS/TES or MER/Mini-TES ([Smith, 2004]), the aerosol dust and ice physical properties and optical depths for the time and location of the observation (e.g., Wolff and Clancy, 2003; Clancy *et al*., 2003), the viewing geometries appropriate for the

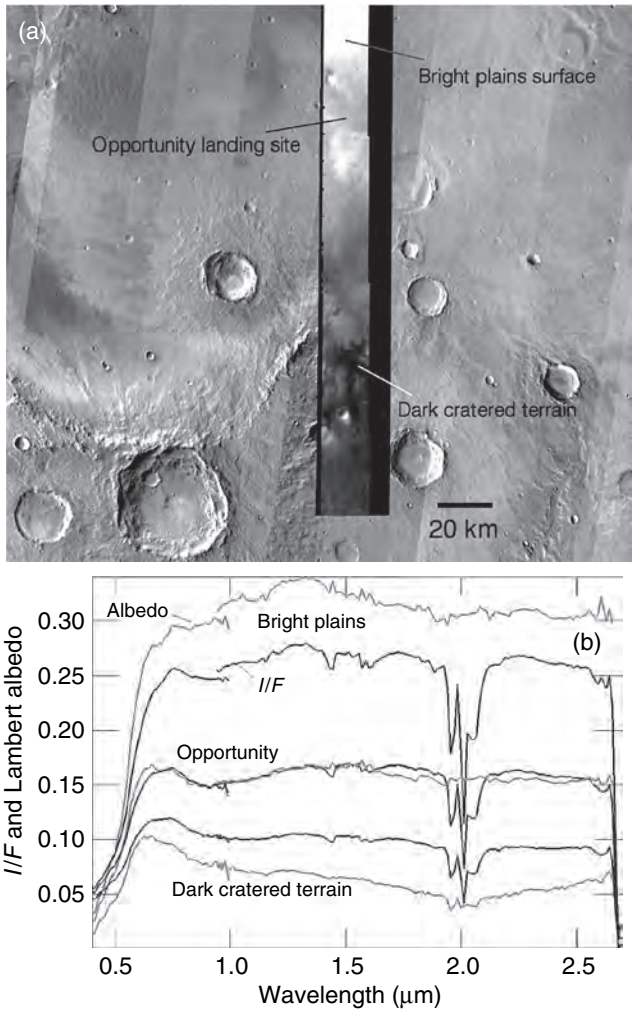

Figure 8.13. (a) Mosaic of THEMIS daytime IR-scaled brightness images overlain with grayscale IR version of OMEGA data from orbit 1183–5. Locations for which spectra were extracted for bright plains, the plains *Opportunity* site, and cratered terrain are shown. (b) I/F and retrieved Lambert Albedos for the sites shown in (a). Incidence angles in each case are ~33°. The emergence angle for the bright plains is ~8°, 18° for the *Opportunity* site, and ~33° for the cratered terrain site.

observations, the nominal passband centers and FWHM for the two OMEGA spectrometers, and surface reflectances along with an assumed surface phase function.

Examination of the DISORT model outputs shows that surface materials that are intrinsically spectrally "gray" still produce a red colored I/F spectrum in the visible to reflected infrared (to ~0.75 μm) and a weak absorption band at ~0.9 μm when observed from orbit, above the atmosphere (Arvidson *et al.*, 2006). This apparent reddening of the surface is a result of the presence of fine-grained, reddish, ferric-rich dust in the atmosphere, which, in the model, has a strong near-UV red spectral slope and a weak crystalline ferric absorption near ~0.9 μm similar to what has been observed in previous telescopic and spacecraft spectra of bright regions and airborne Martian dust (e.g., McCord *et al.*, 1971; Bell *et al.*, 1990, 2004a,b; Thomas *et al.*, 1999). The model spectra (Arvidson *et al.*, 2006) also show that the CO_2 gas bands dominate the spectrum from 1.4 to 2.6 μm, that the H_2O bands have only a minor impact on the spectra because of low H_2O concentrations (12 precipitable μm for model curves) in the typical Martian atmosphere, and that wavelengths longer than ~1 μm are not highly influenced by the presence of aerosols. Another important finding is that modeled radiance factors above low-albedo surfaces show I/F values that are higher than the intrinsic albedo of the surface itself, whereas modeled radiance factors over high-albedo surfaces show I/F values that are lower than the intrinsic albedo of the surface itself. This significant atmospheric control on the surface spectrum as observed from orbit is a consequence of the dominance of scattered skylight for the darker surfaces and attenuation of the radiance from the surface by the atmosphere for brighter surfaces (e.g., Clancy and Lee, 1991; Arvidson *et al.*, 2006).

The surface reflectances retrieved from the modeled OMEGA spectra for the *Opportunity* landing site (Figure 8.13b) show a surface that is still distinctly red in the visible to infrared as compared to the modeled input "gray" albedos. This observation is consistent with the presence of nanophase ferric oxides on the surface (e.g., Morris and Lauer, 1990; Bell *et al.*, 1993; Morris *et al.*, 2000), which has been confirmed by Pancam and Mössbauer measurements from *Opportunity* (e.g., Bell *et al.*, 2004b; Klingelhöfer *et al.*, 2004). The OMEGA spectrum for the *Opportunity* site also shows a subtle, broad reflectivity maximum near 1.5 μm, with an overall pattern consistent with a surface spectrum that has subtle, broad absorptions at ~1 and ~2 μm. The spectra are consistent with the presence of basaltic minerals like pyroxenes and possibly olivines, an inference also supported by surface measurements from *Opportunity* (Bell *et al.*, 2004b; Christensen *et al.*, 2004b; Klingelhöfer *et al.*, 2004). No obvious features are present between 2.1 and 2.5 μm, where OMEGA data for etched terrains to the north and northeast of the landing site show the presence of water-related absorption bands resulting from kieserite ($MgSO_4 \cdot H_2O$) and polyhydrated sulfates (e.g., $(Mg,Ca,Fe)SO_4 \cdot nH_2O$) (Arvidson *et al.*, 2005; Bibring *et al.*, 2005; Gendrin *et al.*, 2005; see Chapter 7). Rather, the 0.4–2.5 μm spectra for the *Opportunity* site appear to be primarily controlled by the broadly varying features associated with charge transfer and electronic transition features in anhydrous iron-bearing silicates and oxides. The lack of H_2O or metal-hydroxide vibrational features between 1 and 2.5 μm on the plains identified elsewhere on Mars using OMEGA data (e.g., Arvidson *et al.*, 2005; Bibring *et al.*, 2005; Gendrin *et al.*, 2005; Poulet *et al.*, 2005; see Chapter 7) argues against the presence of spectral contributions from hydrated sulfates or phyllosilicates. This inference is consistent with the relatively small percentage of surface exposure of sulfate-rich outcrops and the dominance of basaltic sands and hematitic concretions observed by *Opportunity* on the plains (e.g., Squyres *et al.*, 2004b,c; see Chapter 24) and is supported by examination of spectra normalized to nonplains spectra (e.g., cratered terrain exposures to the south) (Arvidson *et al.*, 2006).

Coordinated MER-OMEGA observations in Gusev crater

The OMEGA spectrometer acquired observations of Gusev crater within and surrounding the *Spirit* traverse path over the course of eight MEx orbits between January 2004 and October 2005. Lichtenberg *et al.* (2007) have analyzed observations associated with 3 of the highest spatial resolution OMEGA datasets (from orbits 24, 72, and 976), and have compared them with coordinated MER observations as well as morphologic and thermal inertia results from Mars Odyssey and other spacecraft measurements.

Lichtenberg *et al.* (2007) interpret the OMEGA results to indicate the presence of three major spectral-physical units in the *Spirit* traverse region at the several hundred meter per pixel spatial scale: bright, dusty plains material, dark plains material, and bright, crystalline hematite-bearing Columbia Hills material. These units are broadly consistent with "ground truth" Mini-TES and Pancam observations from MER (e.g., Bell *et al.*, 2004a; Christensen *et al.*, 2004c). OMEGA NIR spectral slope observations indicate that the bright dusty unit covering much of the Gusev plains must be quite thin, a result consistent with surface-derived MER albedo measurements of dust devil tracks, including new ones developed in "real time" during the mission (e.g., Bell *et al.*, 2004a; Greeley *et al.*, 2006; see also Chapter 13). MER *in situ* chemistry and mineralogy observations enable the detailed identification of the OMEGA dark plains materials as olivine-bearing basaltic rocks and sand, and confirm the presence of hematite in the Columbia Hills (e.g., Morris *et al.*, 2006).

Analysis of these kinds of coordinated orbital/surface multispectral observations is still in the early phases. Indeed, additional coordinated MER and OMEGA observations are still being performed on these active missions, and the future of such studies holds even more promise with the advent of additional coordinated surface-orbiter and orbiter-orbiter measurements from instruments on the MRO spacecraft.

8.1.6 Initial Mars Reconnaissance Orbiter multispectral imaging

Initial High Resolution Imaging Science Experiment (HiRISE) color imaging

The HiRISE on MRO includes broad-band color capability at high spatial resolution (McEwen *et al.*, 2007). The HiRISE Focal Plane contains 14 CCD detectors: 10 red-filter channels extending over the full swath width, and 4 additional CCDs over the central 20% of the swath that are covered with blue-green (BG) or NIR filters. The effective center wavelengths are 536 nm for the BG (similar to the Viking Orbiter green bandpass), 694 nm for the RED, and 874 nm for the NIR. Each CCD uses Time Delay and Integration (TDI) over 8, 32, 64, or 128 lines, which enables an adequate signal in spite of the 1 μrad instantaneous field of view (IFOV). Typical HiRISE color imaging scale is ~0.6 or ~1.2 m/pixel. Often the central RED images are acquired at full scale (~0.3 m/pixel) and are merged with the binned BG and NIR images to produce full-resolution merged color products. The swath width of each color observation is typically ~1.2 km, while the length can be up to 30 km or more. Color capability at high spatial resolution is a novel feature of HiRISE that will be used to assess possible compositional differences at small scales. The 3-color capability should detect color distinctions between compositional units, and will complement the mineralogic results from the Compact Reconnaissance Imaging Spectrometer (CRISM) (Murchie *et al.*, 2007) at up to 18 m/pixel scale. With the combined dataset it could be possible to pinpoint meter-scale outcrops of special interest to future exploration missions.

After orbital insertion on March 10, 2006, HiRISE acquired a few high-altitude Mars observations on March 23 and 25, before the start of the aerobraking phase. Four images were acquired on orbit 10 and another four images on orbit 11, all near the terminator at ~7:30 a.m. local time. The first images of each orbit provided the best illumination for color imaging, with the Sun ~11° above the horizon. Images with preliminary processing were evaluated during the six months of MRO aerobraking to develop, test, and refine calibration and image-processing techniques, including color registration. These early observations were of essentially random targets, and (not surprisingly) covered spectrally bland regions of Mars. Nevertheless, the high signal-to-noise ratio (SNR) of HiRISE enables enhancement of the very subtle color variations. The color image from orbit 10 is shown in McEwen *et al.* (2007). Of particular interest in that image was that all of the small (5–50 m diameter) fresh craters had ejecta with distinctive colors, providing information possibly useful for relative age determinations. Figure 8.14 shows a portion

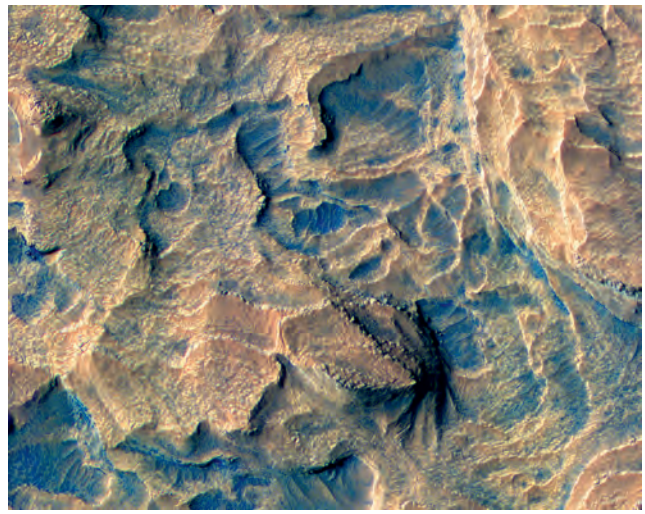

Figure 8.14. Portion of MRO HiRISE image TRA_000873_2015 of light-toned layered deposits on the floor of Bequerel crater. This enhanced RGB color composite was generated from BG, RED, and NIR filter observations (McEwen *et al.*, 2007) acquired on October 3, 2006. The complete image is centered at 21.4° N, 351.9° E, and the segment shown here is about 350 m wide and has a resolution of 25 cm/pixel. Rocky, perhaps dusty outcrop rock is reddish orange in this view, and less dusty, presumably basaltic sand, rocks, and boulders appear as varying shades of blue. Color in scenes like this at such remarkably high spatial resolutions can help establish relationships between geologic units, for example, relating boulders or debris falls back to specific layered units. (For a color version of this figure, please refer to the color plate section or to the e-Book version of this chapter.)

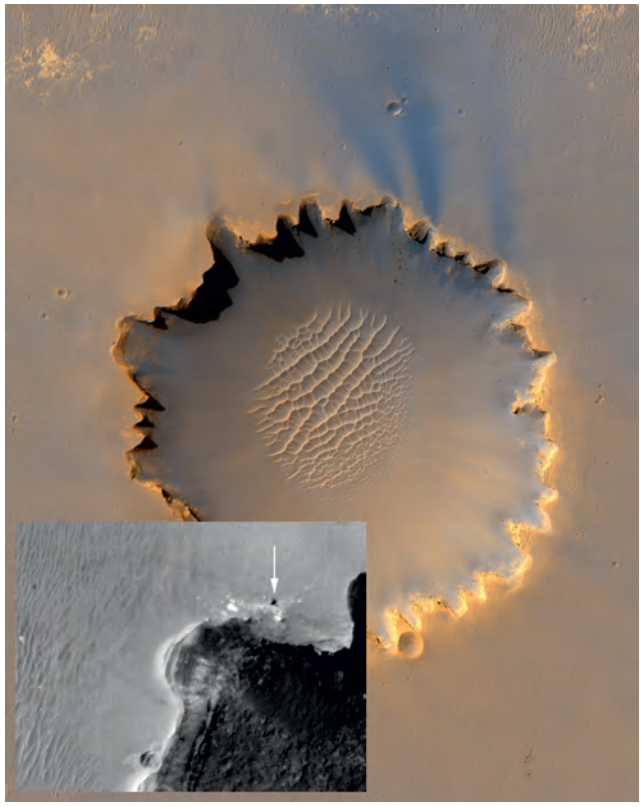

Figure 8.15. MRO HiRISE–enhanced color composite (generated from RED and BG filter observations; McEwen *et al.*, 2007) view of Victoria crater in Meridiani Planum. The crater is approximately 800 m in diameter. The inset shows part of the northwest rim of the crater; the small dark arrowed "rock" is the *Opportunity* rover, about 2 m across. The rover's tracks, looping around the adjacent alcove, can also be clearly seen in the images. (For a color version of this figure, please refer to the color plate section or to the e-Book version of this chapter.)

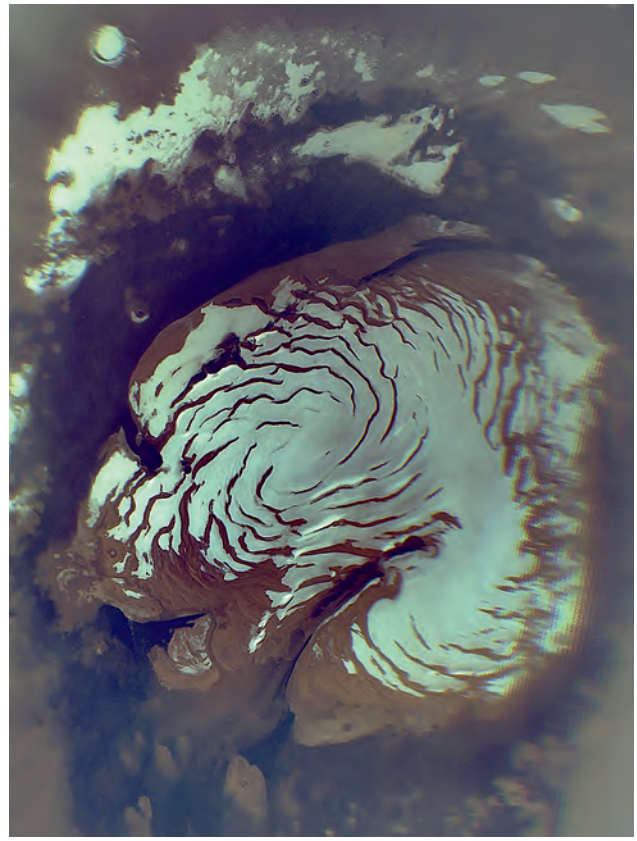

Figure 8.16. Initial MRO/MARCI 600, 550, 425 nm RGB color composite image of the north polar cap, acquired at the start of MRO orbital operations in late September 2006. The northern summer residual water ice cap seen here is about 1000 km in diameter. MARCI resolution is about 900 m/pixel. The resolution decrease on the right side of the field of view is an artifact of the map projection used here. (For a color version of this figure, please refer to the color plate section or to the e-Book version of this chapter.)

of the first image from orbit 11. The colors have been greatly enhanced – an image with a standard linear contrast stretch looks like a black and white image, with only extremely subtle color differences. The enlarged image sample reveals color differences associated with crater floors (perhaps trapped eolian materials), eroded and exposed crustal units, and ejecta from a small fresh crater (right center).

As of this writing, the MRO mission has just entered its primary mission phase. Initial checkout observations with HiRISE from MRO's final mapping orbit provide stunning demonstrations of the high resolution and multispectral capabilities of this new orbital imaging system (Figure 8.15). The HiRISE team expects to acquire binned color data with most images, even in regions where the color variations are expected to be very minor, because it requires only a few percent of the data volume and provides potentially unique and complementary information for assessing compositional or mineralogic variations.

Initial Mars Color Imager (MARCI) observations

Another visible-wavelength multispectral imaging system that is just beginning to acquire data on MRO is the Mars Color Imager (MARCI) instrument (Malin *et al.*, 2001; Schaeffer *et al.*, 2006). MARCI is a wide-angle multispectral imager with five visible and two UV filters that operates similarly to THEMIS-VIS by pushbrooming filter strips across the surface to build up color images in the spacecraft downtrack direction. The camera's 180° field of view provides limb-to-limb coverage and a nadir-looking spatial resolution of about 900 m/pixel. Initial observations acquired at the start of MRO mapping operations indicate excellent multispectral imaging performance and calibration, and provide a glimpse into the kinds of high-quality synoptic-scale surface color monitoring studies that will be enabled by the MARCI dataset (Figure 8.16).

8.1.7 Synthesis and implications

Despite some dramatic examples of visible-wavelength color variability at high spatial resolution in the THEMIS-VIS, HRSC, and HiRISE datasets, it nonetheless appears to be true that this kind of variability is extremely rare on Mars. One implication is that even at sub-100 m/pixel spatial resolution it is difficult to "see through the dust" using solar spectral reflectance observations in order to elucidate the

compositional and/or mineralogic nature of the surface bedrock/underlying substrate. Indeed, for many places on Mars, this appears to be true all the way down to the cm- to mm-scale resolution achievable using surface landers and rovers. For example, multispectral imaging results from the Viking Landers, Mars Pathfinder, and the *Spirit* rover in Gusev crater dominantly reveal dusty rocks and soils with spectral characteristics similar to the global average aeolian dust signature (e.g., Adams *et al.*, 1986; Guinness *et al.*, 1987; Bell *et al.*, 2000, 2004a). At the finest spatial resolutions, in the least dusty places, and/or in places where the dust has been brushed or ground away, significant spectral and compositional variations can be detected with multispectral reflectance observations (e.g., Smith *et al.*, 1997; McSween *et al.*, 1999, 2006; Bell *et al.*, 2002, 2004a,b). Indeed, at the sites known as Paso Robles, Arad, and Tyrone on the *Spirit* rover's traverse into the Columbia Hills region of Gusev crater, accidental disturbance of the dusty soils by the rover wheels revealed concentrations of spectrally and compositionally variable sulfate salts just below the (bland) visible surface (e.g., Johnson *et al.*, 2007; see also Chapter 13). Thus, at least some of the apparent spectral homogeneity of the Martian surface may only be skin deep.

Nonetheless, the observation that unambiguous compositionally or mineralogically interesting spectral variability at VNIR wavelengths is rare at *all* spatial scales appears to be a fact of life in observational studies of Mars. Thermal-infrared observations appear to be able to penetrate into the bedrock/underlying substrate to a greater degree (see Chapters 9 and 10), but even in that wavelength regime, discovery of "interesting" spectral variability is not the norm and appears mostly confined to the lowest albedo (least dusty) regions. One is left wondering what kinds of compositional/mineralogic variations are not being detected in the large fraction of the Martian surface that is covered or coated by aeolian dust, especially in dusty layered terrains or in the dusty ancient highlands; that bedrock may preserve the best evidence for very different past Martian climate regimes. An extended era of focused lander and rover studies, or a dramatic change in the way the winds blow the dust around, may be required to truly uncover the intrinsic compositional and mineralogic diversity of the surface on the global scale.

Still, such pessimism may be premature because only a small fraction of the Martian surface has been imaged in color at the hundreds-of-meters or less spatial scale. For example, as of late 2006, less than 4% of the Martian surface has been covered in color by the Mars Odyssey THEMIS-VIS camera at any spatial resolution ≤ 72 m/pixel. An even smaller fraction has been covered so far by HRSC on MEx at the tens of meters/pixel scale because of its highly elliptical orbit. And at the time of writing this chapter, HiRISE and CRISM on MRO had only just begun to image the surface in color at very fine spatial resolutions. While it may ultimately not be possible to increase high spatial resolution surface color imaging coverage by more than a few more percent even if these investigations continue successfully for years (because of onboard data storage and downlink data volume resource limitations), it is certainly possible that these investigations' planned sampling of a wide variety of geologic, topographic, albedo, and thermal inertia units could enable the sampling of a greater degree of compositional and/or mineralogic diversity as well.

8.2 SUMMARY

There have been a number of important VNIR imaging and spectroscopic studies of Mars conducted by telescopes and orbiting spacecraft since the 1990s. These include observations from HST and MGS, Mars Odyssey, MEx, and most recently, MRO spacecraft. These studies have defined the major classes of VNIR spectroscopic units on Mars at a variety of spatial scales, from global, tens to hundreds of kilometers/pixel resolution down to focused regional coverage at the sub-meter resolution being achieved by the newest orbital sensors.

High-albedo nonicy materials at all spatial scales are dominated spectrally at these wavelengths by the signature of poorly crystalline or nanophase ferric iron, an important component of the globally homogenized aeolian dust. However, there is evidence for spectral heterogeneity in high-albedo regions at finer spatial scales, for example in light-toned, presumably sulfate-rich outcrop (so-called "etched terrain") in places like Meridiani Planum and in light-toned, apparently more crystalline ferric-bearing layered materials in the walls and layers of some of the canyons and depressions in and around Valles Marineris.

Low-albedo materials display a wider range of VNIR spectral variability at all spatial scales that appears to be primarily related to varying degrees of ferric dust covering or coatings on dark, presumably basaltic substrates. The two major classes of low-albedo materials identified by infrared thermal emission spectroscopic observations (TES Surface Types 1 and 2) do not appear to be intrinsically compositionally distinct in VNIR observations to date; rather, the differences between these units in solar reflectance wavelengths appear to be primarily controlled by variable ferric dust cover (Type 2 more "dusty" than Type 1). Intrinsic variability in low-albedo material mineralogy from region to region has been reported in initial tens of kilometers resolution NIR spectroscopic studies (see Chapter 7) and has been interpreted to indicate variations in pyroxene and olivine chemistry and/or the olivine/pyroxene ratio of basaltic lava flows. While a number of VNIR ($\sim$400–1000 nm) multispectral imaging studies detect color differences in low-albedo terrains that correlate with geologic, topographic, thermal inertia, or other mapped physical parameters, such unique mineralogic interpretations are difficult or impossible to confirm from measurements at these wavelengths.

This is a research area that is changing rapidly because of the continuing infusion of new data. Specifically, continuing multispectral imaging observations at tens-of-meters scales from the Mars Odyssey THEMIS and MEx HRSC and new observations at sub-meter scales from the MRO HiRISE experiment are beginning to provide dramatic new examples of the power of color unit mapping for geologic and stratigraphic investigations. Perhaps the most exciting potential

for dramatic discoveries in compositional or mineralogic studies of Mars comes from the MRO CRISM instrument, which is beginning to acquire visible through mid-IR hyperspectral images at the hundreds of meters scale globally and at the tens of meters scale locally and will continue to do so over the next several years. The precursor lower spectral resolution multispectral investigations described in this chapter and precursor lower spatial resolution hyperspectral studies from the Phobos-2 ISM and Mars Express OMEGA instruments (see Chapter 7) indicate that there is a rich diversity of color *and* compositional units potentially detectable on Mars. Discovering, mapping, and interpreting that variability may be the key to untangling the enigmatic history of large-scale climate changes on Mars.

REFERENCES

Adams, J. B. and A. R. Gillespie, *Remote Sensing of Landscapes with Spectral Images: A Physical Modeling Approach*, Cambridge University Press, 362pp., 2006.

Adams, J. B., M. O. Smith, and P. E. Johnson, Spectral mixture modeling: a new analysis of rock and soil types at the Viking Lander I site, *J. Geophys. Res.* **91**, 8098–112, 1986.

Anderson, F. S. and V. E. Hamilton, A method for identifying mineralogical signatures in locales with large topography using atmospherically equalized THEMIS data, *Fall Meeting 2005*, American Geophysical Union, Abstract #P24A-05, 2005.

Arvidson, R. E., F. P. Seelos, K. Deal, *et al.*, Mantled and exhumed terrains in Terra Meridiani, Mars, *J. Geophys. Res.* **108**(E12), ROV 14–1, CiteID 8073, doi:10.1029/2002JE001982, 2003.

Arvidson, R. E., F. Poulet, J. P. Bibring, *et al.*, Spectral reflectance and morphologic correlations in eastern Terra Meridiani, Mars, *Science* **307**(5715), 1591–4, doi:10.1126/science.1109509, 2005

Arvidson, R. E., F. Poulet, R. V. Morris, *et al.*, Nature and origin of the hematite-bearing plains of Terra Meridiani based on analyses of orbital and Mars Exploration Rover data sets, *J. Geophys. Res.* **111**(E12), 2006.

Bandfield, J. L., V. E. Hamilton, and P. R. Christensen, A global view of martian volcanic compositions, *Science* **287**, 1626–30, 2000.

Barker, E., N. Pirzkal, K. Noll, *et al.*, *NICMOS Instrument Handbook*, Version 9.0, Baltimore: STScI, www.stsci.edu/hst/nicmos/documents/handbooks/current_NEW/cover.html, 2006.

Bell III, J. F., Charge-coupled device imaging spectroscopy of Mars: 2. Results and implications for martian ferric mineralogy, *Icarus* **100**, 575–97, 1992.

Bell III, J. F., HST studies of Mars. In *A Decade of Hubble Space Telescope Science* (ed. M. Livio, K. Noll, and M. Stiavelli), Cambridge University Press, pp. 1–24, 2003.

Bell III, J. F. and T. M. Ansty, High spectral resolution UV to near-IR observations of Mars during 1999, 2001, and 2003 using HST/STIS, *Icarus* **191**, 581–602, doi:10.1016/j.icarus.2007.05.019, 2007.

Bell III, J. F., T. B. McCord, and P. D. Owensby, Observational evidence of crystalline iron oxides on Mars, *J. Geophys. Res.* **95**, 14447–61, 1990.

Bell III, J. F., R. V. Morris, and J. B. Adams, Thermally altered palagonitic tephra: a spectral and process analog to the soil and dust of Mars, *J. Geophys. Res.* **98**(E02), 3373–85, 1993.

Bell III, J. F., M. J. Wolff, P. B. James, *et al.,* Mars surface mineralogy from Hubble Space Telescope imaging during 1994–1995: observations, calibration, and initial results, *J.Geophys. Res.* **102**, 9109–23, 1997a.

Bell III, J. F., M. J. Wolff, P. C. Thomas, P. B. James, and E. A. Cloutis, Mineralogy of unweathered Mars surface materials from HST multispectral imaging, Mars Telescopic Observations Workshop II, *LPI Technical Report 97-03*, 7–9, 1997b.

Bell III, J. F., M. J. Wolff, T. C. Daley, *et al.*, Near-infrared imaging of Mars from HST: surface reflectance, photometric properties, and implications for MOLA data, *Icarus* **138**, 25–35, 1999.

Bell III, J. F., H. Y. McSween Jr., J. A. Crisp, *et al.*, Mineralogic and compositional properties of martian soil and dust: results from Mars Pathfinder, *J. Geophys. Res.* **105**, 1721–55. 2000.

Bell III, J. F., M. J. Wolff, J. Sohl-Dickstein, and R. V. Morris, High resolution imaging spectroscopy of Mars using HST/STIS during 1999 and 2001, *Bull. Am. Astron. Soc.* **33**, 1127, 2001.

Bell III, J. F., W. H. Farrand, J. R. Johnson, and R. V. Morris, Low abundance materials at the Mars Pathfinder landing site: an investigation using spectral mixture analysis and related techniques, *Icarus* **158**, 56–71, 2002.

Bell III, J. F., T. H. McConnochie, M. J. Wolff, *et al.*, Visible color properties of Mars at sub-100 m resolutions from Mars Odyssey THEMIS-VIS, *Bull. Am. Astron. Soc.* **35**, 926, 2003.

Bell III, J. F., S. W. Squyres, R. E. Arvidson, *et al.*, Pancam multispectral imaging results from the Spirit rover at Gusev crater, *Science* **305**, 800–6, 2004a.

Bell III, J. F., S. W. Squyres, R. E. Arvidson, *et al.*, Pancam multispectral imaging results from the Opportunity rover at Meridiani Planum, *Science* **306**, 1703–9, 2004b.

Bell III, J. F., H. M. Arneson, W. H. Farrand, *et al.*, Large multispectral and albedo Panoramas acquired by the Pancam instruments on the Mars Exploration Rovers *Spirit and Opportunity*, *Lunar Planet. Sci. XXXVI*, Houston: Lunar and Planetary Institute, Abstract #1337 (CDROM), 2005.

Bell III, J. F., K. C. Bender, M. Caplinger, *et al.*, High spatial resolution visible wavelength orbital multispectral imaging of Mars from the *Mars Odyssey* THEMIS-VIS instrument, *Lunar Planet. Sci. Conf.* **37**, Abstract #1653, 2006.

Benson, J. L., B. P. Bonev, P. B. James, *et al.*, The seasonal behavior of water ice clouds in the Tharsis and Valles Marineris regions of Mars: Mars Orbiter Camera observations, *Icarus* **165**, 34–52, 2003.

Bibring, J.-P. A. Soufflot, M. Berthé, *et al.*, OMEGA: Observatoire pour la Mineralogie, l'Eau, les Glaces et l'Activité. In *Mars Express: The Scientific Payload*, ESA Special Publication 1240, Noordwijk: ESA Publications Division, pp. 37–49, 2004.

Bibring, J.-P., Y. Langevin, A. Gendrin, *et al.*, Mars surface diversity as revealed by the OMEGA/Mars Express observations, *Science* **307**(5715), 1576–81, doi:10.1126/science.1109509, 2005.

Biretta, J. A., *Wide Field and Planetary Camera 2 Instrument Handbook*, Version 9.2, Baltimore, MD: Space Telescope Science Institute Publication, STScI, www.stsci.edu/hst/wfpc2/documents/handbook/cycle16/cover.html, 2006.

Burns, R. G., *Mineralogical Applications of Crystal Field Theory*, New York: Cambridge University Press, 224pp., 1970.

Burns, R. G., Origin of electronic spectra of minerals in the visible-near infrared region. In *Remote Geochemical Analysis: Elemental and Mineralogical Composition* (ed. C. Pieters and P. Englert), Cambridge: Cambridge University Press, pp. 3–29, 1993.

Cantor, B. A., P. B. James, M. Caplinger, and M. J. Wolff, Martian dust storms: 1999 Mars Orbiter Camera observations, *J. Geophys. Res.* **106**, 23653–88, 2001.

Cantor, B. A., M. Malin, and K. S. Edgett, Multiyear Mars Orbiter Camera (MOC) observations of repeated martian weather phenomena during the northern summer season, *J. Geophys. Res.* **107**, 5014, doi:10.1029/2001JE001588, 2002.

Carr, M. H., *The Surface of Mars*, Cambridge University Press, 2006.

Catling, D. C. and J. M. Moore, The nature of coarse-grained crystalline hematite and its implications for the early environment of Mars, *Icarus* **165**, 277–300, 2003.

Christensen, P. R., Formation of recent martian gullies through melting of extensive water-rich snow deposits, *Nature* **422**, 45–8, 2003.

Christensen, P. R., D. L. Anderson, S. C. Chase, *et al.*, Thermal emission spectrometer experiment: the Mars observer mission, *J. Geophys. Res.* **97**, 7719–34, 1992.

Christensen, P. R., J. L. Bandfield, B. E. Halilton, *et al.*, Mars Global Surveyor Thermal Emission Spectrometer experiment: investigation description and surface science results, *J. Geophys. Res.* **106**, 23823–71, 2001.

Christensen, P. R., J. L. Bandfield, J. F. Bell III, *et al.*, Morphology and composition of the surface of Mars: Mars Odyssey THEMIS results, *Science* **300**, 2056–61, 2003.

Christensen, P. R., B. M. Jakosky, H. H. Kieffer, *et al.*, The Thermal Emission Imaging System (THEMIS) for the Mars 2001 Odyssey Mission, *Space Sci. Rev.* **110**, 37–83, 2004a.

Christensen, P. R., M. B. Wyatt, T. D. Glotch, *et al.*, Mineralogy at Meridiani Planum from the Mini-TES experiment on the Opportunity Rover, *Science* **306**, 1733–9, 2004b.

Christensen, P. R., S. W. Ruff, R. L. Fergason, *et al.*, Initial results from the Mini-TES experiment in Gusev crater from the Spirit Rover, *Science* **305**(5685), 837–42, 2004c.

Clancy, R. T. and S. W. Lee, A new look at dust and clouds in the Mars atmosphere: analysis of emission-phase-function sequences from global Viking IRTM observations, *Icarus* **93**, 135–58, 1991.

Clancy, R. T., M. J. Wolff, and P. R. Christensen, Mars aerosol studies with the MGS TES emission phase function observations: optical depths, particle sizes, and ice cloud types versus latitude and solar longitude, *J. Geophys. Res.* **108**(E9), 5098, doi:10.1029/2003JE002058, 2003.

Clark, R. N. and T. L. Roush, Reflectance spectroscopy: quantitative analysis techniques for remote sensing applications, *J. Geophys. Res.* **89**, 6329–40, 1984.

Cloutis, E. A. and M. J. Gaffey, Pyroxene spectroscopy revisited: spectral-compositional correlations and relationship to geothermometry, *J. Geophys. Res.* **96**, 22809–26, 1991.

de Vaucouleurs, G., *Physics of the Planet Mars*, London: Faber and Faber, 365pp., 1954.

Edgett, K. S., The sedimentary rocks of Sinus Meridiani: five key observations from data acquired by the Mars Global Surveyor and Mars Odyssey orbiters, *Mars* **1**, 5–58, 2005.

Farrand, W. H., J. F. Bell III, R. V. Morris, and M. J. Wolff, Global color units on Mars from 1999 HST/WFPC2 imaging data, *Bull. Am. Astron. Soc.* **32**, 1119, 2000.

Geissler, P. E., Three decades of martian surface changes, *J. Geophys. Res.* **110**, E02001, doi:10.1029/2004JE002345, 2005.

Gendrin, A., N. Mangold, J.-P. Bibring, *et al.*, Sulfates in martian layered terrains: the OMEGA/Mars Express view, *Science* **307**, 1587–90, 2005.

Glotch, T. D. and P. R. Christensen, Geologic and mineralogic mapping of Aram Chaos: evidence for a water-rich history, *J. Geophys. Res.* **110**, E09006, doi:10.1029/2004JE002389, 2005.

Glotch, T. D. and A. D. Rogers, Evidence for aqueous deposition of hematite- and sulfate-rich light-toned layered deposits in Aureum and Iani Chaos, Mars, *J. Geophys. Res.* **112**, E06001, doi:10.1029/2006JE002863, 2007.

Greeley, R., R. E. Arvidson, P. W. Barlett, *et al.*, Gusev crater: wind-related features and processes observed by the Mars Exploration Rover Spirit, *J. Geophys. Res.* **111**, E02S09, doi:10.1029/2005JE002491, 2006.

Guinness, E. A., R. E. Arvidson, M. A. Dale-Bannister, R. B. Singer, and E. A. Bruckenthal, On the spectral reflectance properties of materials exposed at the Viking landing sites. *J. Geophys. Res.* **92**, E575–87, 1987.

Hamilton, V. E. and P. R. Christensen, Green Mars: geologic characteristics of olivine-bearing terrains as observed by THEMIS, MOC, and MOLA, *Lunar Planet. Sci. XXXV*, Houston: Lunar and Planetary Institute, Abstract #2131 (CD-ROM), 2004.

Hamilton, V. E. and P. R. Christensen, Evidence for extensive, olivine-rich bedrock on Mars, *Geology* **33**, 433–6, doi: 410.1130/G21258.21251, 2005.

Hamilton, V. E., P. R. Christensen, H. Y. McSween Jr., and J. L. Bandfield, Searching for the source regions of martian meteorites using MGS TES: Integrating martian meteorites into the global distribution of volcanic materials on Mars, *Meteorit. Planet. Sci.* **38**, 871–85, 2003.

Hapke, B., *Theory of Reflectance and Emittance Spectroscopy*, New York: Cambridge University Press, 455pp., 1993.

Hapke, B., Bidirectional reflectance spectroscopy: 5. The coherent backscatter opposition effect and anisotropic scattering, *Icarus* **157**, 523–34, 2002.

Heldmann, J. L., O. B. Toon, W. H. Pollard, *et al.*, Formation of martian gullies by the action of liquid water flowing under current martian environmental conditions, *J. Geophys. Res.* **110**, CiteID E05004, 2005.

Hoefen, T. M., R. N. Clark, J. L. Bandfield, *et al.*, Discovery of olivine in the Nili Fossae region of Mars, *Science* **302**, 627–30, 2003.

James, P. B. and B. A. Cantor, Martian north polar cap recession: 2000 Mars Orbiter Camera observations, *Icarus* **154**, 131–44, 2001.

James, P. B., R. T. Clancy, S. Lee, *et al.*, Monitoring Mars with the Hubble Space Telescope: 1990–1991 observations, *Icarus* **109**, 79–101, 1994.

James, P. B., J. F. Bell III, R. T. Clancy, *et al.*, Global imaging of Mars by Hubble Space Telescope during the 1995 opposition, *J. Geophys. Res.* **101**, 18883–90, 1996.

James, P. B., B. A. Cantor, M. C. Malin, *et al.*, The 1997 spring regression of the martian south polar cap: Mars Orbiter Camera observations, *Icarus* **144**, 410–18, 2000.

James, P. B., B. A. Cantor, and S. Davis, Mars Orbiter Camera observations of the martian south polar cap in 1999–2000, *J. Geophys. Res.* **106**, 23635–52, 2001.

Jaumann, R., G. Neukum, T. Behnke, *et al.*, The High Resolution Stereo Camera (HRSC) experiment on Mars Express: instrument aspects and experiment conduct from interplanetary cruise through nominal mission, *Planet. Space Sci.* **55**, 928–52, 2007.

Johnson, J. R. and W. M. Grundy, Visible/near-infrared spectra and two-layer modeling of palagonite-coated basalts, *Geophys. Res. Lett.* **28**, 2101–4, 2001.

Johnson, J. R., J. F. Bell III, E. A. Cloutis, *et al.*, Mineralogic constraints on sulfur-rich soils from Pancam spectra at Gusev crater, Mars, *Geophys. Res. Lett.* **34**, L13202, doi:10.1029/2007GL029894, 2007.

Kieffer, H. H., B. M. Jakosky, and C. W. Snyder, The planet Mars: from antiquity to the present. In *Mars* (ed. H. H. Kieffer, B. M. Jakosky, C. W. Snyder, and M. S. Matthews), Tucson: University of Arizona Press, pp. 1–33, 1992a.

Kieffer, H. H., B. M. Jakosky, C. W. Snyder, and M. S. Matthews (eds.), *Mars*, Tucson: University of Arizona Press, 1498pp., 1992b.

Kim Quijano, J., T. Brown, I. Busko, *et al*., *STIS Instrument Handbook*, Version 7.0, Baltimore: Space Telescope Science Institute, www.stsci.edu/hst/stis/documents/handbooks/currentIHB/cover.html, 2003.

King, T. V. V. and W. I. Ridley, Relation of the spectroscopic reflectance of olivine to mineral chemistry and some remote sensing applications, *J. Geophys. Res.* **92**, 11457–69, 1987.

Klingelhöfer, G., R. V. Morris, B. Bernhardt, *et al*., Jarosite and hematite at Meridiani Planum from Opportunity's Mössbauer Spectrometer, *Science* **306**, 1740–5, 2004.

Kuiper, G. P., Planetary atmospheres and their origin. In *The Atmospheres of the Earth and Planets* (ed. G. P. Kuiper), University of Chicago Press, pp. 306–405, 1952.

Lichtenberg, K. A., R. E. Arvidson, F. Poulet, *et al*., Coordinated analyses of orbital and Spirit rover data to characterize surface materials on the cratered plains of Gusev Crater, Mars, *J. Geophys. Res.* **112,** E12S90, doi:10.1029/2006JE002850, 2007.

Malin, M. C. and K. S. Edgett, Evidence for recent groundwater seepage and surface runoff on Mars, *Science* **288**, 2330–5, 2000a.

Malin, M. C. and K. S. Edgett, Sedimentary rocks of early Mars, *Science* **290**, 1927–37, 2000b.

Malin, M. C. and K. S. Edgett, Mars Global Surveyor Mars Orbiter Camera: interplanetary cruise through primary mission, *J. Geophys. Res.* **106**, 23429–570, 2001.

Malin, M. C., G. E. Danielson, A. P. Ingersoll, *et al*., Mars Observer Camera, *J. Geophys. Res.* **97**, 7699–718, 1992.

Malin, M., J. F. Bell III, W. Calvin, *et al*., The Mars Color Imager (MARCI) on the Mars Climate Orbiter, *J. Geophys. Res.* **106**, 17651–72, 2001.

Martin, L. J., P. B. James, A. Dollfus, K. Iwasaki, and J. D. Beish, Telescopic observations: visual, photographic, polarimetric. In *Mars* (ed. H. H. Kieffer), Tucson: University of Arizona Press, pp. 34–70, 1992.

McConnochie, T. H., J. F. Bell III, D. Savransky, *et al*., Calibration and In-flight performance of the Mars Odyssey THEMIS Visible Imaging Subsystem (VIS) instrument, *J. Geophys. Res.* **111**, E06018, doi:10.1029/2005JE002568, 2006.

McCord, T. B., J. H. Elias, and J. A. Westphal, Mars: the spectral albedo (0.3–2.5 μm) of small bright and dark regions, *Icarus* **14**, 245–51, 1971.

McCord, T. B., R. B. Singer, B. R. Hawke, *et al*., Mars: definition and characterization of global surface units with emphasis on composition. *J. Geophys. Res.* **87**, 10129–48, 1982.

McCord, T. B., J. B. Adams, G. Bellucci, *et al*., Mars Express High Resolution Stereo Camera spectrophotometric data: characteristics and science analysis, *J. Geophys. Res.* **112**, E06004, doi:10.1029/2006JE002769, 2007.

McEwen, A. S., E. M. Eliason, J. W. Bergstrom, *et al*., MRO's High Resolution Imaging Science Experiment (HiRISE), *J. Geophys. Res.* **112**, CiteID E05S02, doi:10.1029/2005JE002605, 2007.

McSween Jr., H. Y., S. L. Murchie, J. Crisp, *et al*., Chemical, multispectral, and textural constraints on the composition and origin of rocks at the Mars Pathfinder landing site, *J. Geophys. Res.* **104**, 8679–716, 1999.

McSween, H. Y., M. B. Wyatt, R. Gellert, *et al*., Characterization and petrologic interpretation of olivine-rich basalts at Gusev crater, Mars, *J. Geophys. Res.* **111**, E02S10, doi:10.1029/2005JE002477, 2006.

Morris, R. V. and H. V. Lauer Jr., Matrix effects for reflectivity spectra of dispersed nanophase (superparamagnetic) hematite with application to martian spectral data. *J. Geophys. Res.* **95**, 5101–9, 1990.

Morris, R. V., D. C. Golden, J. F. Bell III, and H. V. Lauer Jr., Hematite, pyroxene, and phyllosilicates on Mars: implications from oxidized impact melt rocks from Manicougan crater, Quebec, Canada, *J. Geophys. Res.* **100**, 5319–29, 1995.

Morris, R. V., D. C. Golden, J. F. Bell III, *et al*., Mineralogy, composition, and alteration of Mars Pathfinder rocks and soils: evidence from multispectral, elemental, and magnetic data on terrestrial analogue, SNC meteorite, and Pathfinder samples, *J. Geophys. Res.* **105**, 1757–817, 2000.

Morris, R. V., J. F. Bell III, W. H. Farrand, and M. J. Wolff, Constraints on martian global surface mineralogical composition, albedo, and thermal inertia from Hubble Space Telescope extended-visible multispectral data, *Lunar Planet. Sci. XXXIII*, Houston: Lunar and Planetary Institute, Abstract #1913 (CD-ROM), 2002.

Morris, R. V., G. Klingelhöfer, C. Schröder, *et al*, Mössbauer mineralogy of rock, soil, and dust at Gusev crater, Mars: Spirit's journey through weakly altered olivine basalt on the plains and pervasively altered basalt in the Columbia Hills, *J. Geophys. Res.* **111**, E02S13, doi:10.1029/2005JE002584, 2006.

Murchie, S., R. Arvidson, P. Bedini, *et al*., Compact Reconnaissance Imaging Spectrometer for Mars (CRISM) on Mars Reconnaissance Orbiter (MRO), *J. Geophys. Res.* **112**, CiteID E05S03, doi:10.1029/2006JE002682, 2007.

Mustard, J. F. and J. F. Bell III, New composite reflectance spectra of Mars from 0.4 to 3.14 μm, *Geophys. Res. Lett.* **21**, 353–6, 1994.

Mustard, J. F. and C. M. Pieters, Quantitative abundance estimates from bidirectional reflectance measurements, *J. Geophys. Res.* **92**, E617–26, 1987.

Mutch, T. A., R. E. Arvidson, J. W. Head III, K. L. Jones, and R. S. Saunders, *The Geology of Mars*, Princeton, NJ: Princeton University Press, 400pp., 1976.

Neukum, G. and R. Jaumann, The high resolution stereo camera of Mars Express. In *Mars Express: The Scientific Payload* (ed. A. Wilson and A. Chicarro), *ESA SP-1240*, Noordwijk, Netherlands: ESA Publications Division, pp. 17–35, 2004.

Noe Dobrea, E. Z., J. F. Bell III, M. J. Wolff, and K. D. Gordon, H_2O- and OH-bearing minerals in the martian regolith: analysis of 1997 observations from HST/NICMOS, *Icarus* **166**, 1–20, 2003.

Noe Dobrea, E. Z., J. F. Bell III, T. H. McConnochie, and M. Malin, Analysis of a spectrally unique deposit in the dissected Noachian terrain of Mars, *J. Geophys. Res.* **111**, E06007, doi:10.1029/2005JE002431, 2006.

Noe Dobrea, E. Z., J. F. Bell III, M. J. Wolff, *et al*., Global-scale near infrared variability on Mars: analysis of 2003 Mars opposition observations from HST/NICMOS, *Icarus* **193**, 112–24, doi:10.1016/j.icarus.2007.07.026, 2008.

Oberst, J., T. Roatsch, B. Giese, *et al*., The mapping performance of the HRSC/SRC in Mars orbit, *Proc. IAU Commission IV, WG IV/9*, 2004.

Pavlovsky, C., *et al*., *Advanced Camera for Surveys Instrument Handbook for Cycle 16*, Version 7.1, Baltimore: STScI, www.stsci.edu/hst/acs/documents/handbooks/cycle16/cover.html, 2006.

Plaut, J. J., P. Christensen, K. Bender, *et al*., THEMIS visible imaging of the south polar layered deposits, Martian southern spring, *3rd Int. Conf. Mars Polar Sci. Exploration, October 13–17, 2003*, Alberta, Canada, Abstract #8130, 2003.

Pleskot, L. K. and Miner, E. D., Time variability of martian bolometric albedo, *Icarus* **45**, 179–201, 1981.

Poulet, F. and S. Erard, Nonlinear spectral mixing: quantitative analysis of laboratory mineral mixtures, *J. Geophys. Res.* **109**, E02009, 2004.

Poulet, F., J.-P. Bibring, J. F. Mustard, *et al*., Phyllosilicates on Mars and implications for early martian climate, *Nature* **438**(7068), 623–7, doi:10.1038/nature04274, 2005.

Roush, T. L., D. L. Blaney, and R. B. Singer, The surface composition of Mars as inferred from spectroscopic observations. In *Remote Geochemical Analysis: Elemental and Mineralogical Composition* (ed. C. Pieters and P. Englert), Cambridge: Cambridge University Press, pp. 367–93, 1993.

Ruff, S. W. P. R. Christensen, R. N. Clark, *et al*., Mars "White Rock" feature lacks evidence of an aqueous origin: results from Mars Global Surveyor, *J. Geophys. Res.* **106**, 23921–8, 2001.

Schaeffer, D., J. F. Bell III, M. Malin, *et al*., Calibration and validation of images from the Mars Reconnaissance Orbiter Mars Color Imager (MARCI) and Context Camera (CTX) instruments, *Bull. Am. Astron. Soc.* **38**, 604–5, Abstract #61.11, 2006.

Sheehan, W., *Planets and Perception: Telescopic Views and Interpretations, 1609–1909*, Tucson: University of Arizona Press, 324pp., 1988.

Singer, R. B., T. B. McCord, R. N. Clark, J. B. Adams, and R. L. Huguenin, Mars surface composition from reflectance spectroscopy: a summary, *J. Geophys. Res.* **84**, 8415–26, 1979.

Smith, M. D., Interannual variability in TES atmospheric observations of Mars during 1999–2003, *Icarus* **167**(1), 148–65, 2004.

Smith, M. D., M. J. Wolff, M. T. Lemmon, *et al*., First atmospheric science results from the Mars Exploration Rovers Mini-TES, *Science* **306**, 1750–3, 2004.

Smith, P. H., J. F. Bell III, N. T. Bridges, *et al*., First results from the Pathfinder camera, *Science* **278**, 1758–65, 1997.

Soderblom, J. M., J. F. Bell III, M. Y. H. Hubbard, and M. J. Wolff, Martian phase function: modeling the visible to near-infrared surface photometric function using HST-WFPC2 data, *Icarus* **184**, 401–23, doi:10.1016/j.icarus.2006.05.006, 2006.

Soderblom, L. A., The composition and mineralogy of the martian surface from spectroscopic observations: 0.3 μm to 50 μm. In *Mars* (ed. H. H. Kieffer, B. M. Jakosky, C. W. Snyder, and M. S. Matthews), Tucson: University of Arizona Press, pp. 557–97, 1992.

Soderblom, L. A., K. Edwards, E. M. Eliason, E. M. Sanchez, and M. P. Charette, Global color variations on the martian surface, *Icarus* **34**, 446–64, 1978.

Squyres, S. W., R. E. Arvidson, E. T. Baumgartner, *et al*., Athena Mars rover science investigation, *J. Geophys. Res.* **108**(E12), 8062, doi:10.1029/2003JE002121, 2003.

Squyres, S. W., R. E. Arvidson, J. F. Bell III, *et al*., The Spirit Rover's Athena science investigation at Gusev crater, Mars, *Science* **305**(5685), 794–9, doi:10.1126/science.1100194, 2004a.

Squyres, S. W., R. E. Arvidson, J. F. Bell III, *et al*., The Opportunity Rover's Athena science investigation at Meridiani Planum, Mars, *Science* **306**(5702), 1698–703, doi:10.1126/science.1106171, 2004b.

Squyres, S. W., J. P. Grotzinger, R. E. Arvidson, *et al*., In-situ evidence for an ancient aqueous environment on Mars, *Science* **306**, 1709–14, 2004c.

Stamnes, K., S. Tsay, W. Wiscombe, and K. Jayaweera, Numerically stable algorithm for discrete-ordinate-method radiative transfer in multiple scattering and emitting layered media, *Appl. Opt.* **27**, 2502–9, 1988.

Thomas, N., W. J. Markiewicz, R. M. Sablotny, *et al*., The color of the martian sky and its influence on the illumination of the martian surface, *J. Geophys. Res.* **104**, 8795–808, 1999.

Thorpe, T. E., Martian surface properties indicated by the opposition effect, *Icarus* **49**, 398–415, 1982.

Wolff, M. J. and R. T. Clancy, Constraints on the size of martian aerosols from TES spectral observations, *J. Geophys. Res.* **108**(E9), 5097, doi:10.1029/2003JE002057, 2003.

Wolff, M. J., S. W. Lee, R. T. Clancy, *et al*., 1995 observations of martian dust storms using the Hubble Space Telescope, *J. Geophys. Res.* **102**, 1679–92, 1997.

Wolff, M. J., J. F. Bell III, P. B. James, R. T. Clancy, and S. W. Lee, Hubble Space Telescope observations of the martian aphelion cloud belt prior to the Mars Pathfinder mission: water ice cloud and dust optical depths, *J. Geophys. Res.* **104**, 9027–42, 1999.

PART III.B

Mid-IR and Magnetic Orbital Measurements

9

Global mineralogy mapped from the Mars Global Surveyor Thermal Emission Spectrometer

P. R. CHRISTENSEN, J. L. BANDFIELD, A. D. ROGERS, T. D. GLOTCH, V. E. HAMILTON, S. W. RUFF, AND M. B. WYATT

ABSTRACT

The Thermal Emission Spectrometer (TES) on Mars Global Surveyor (MGS) mapped the surface, atmosphere, and polar caps of Mars from 1997 through 2006. TES provided the first global mineral maps of Mars, and showed that the surface is dominated by primary volcanic minerals (plagioclase feldspar, pyroxene, and olivine) along with high-silica, poorly crystalline materials. Differences in the abundances of these minerals were initially grouped into two broad compositional categories that correspond to basalt and basaltic andesite. Additional analysis has identified four surface compositional groups that are spatially coherent, revealing variations in the composition of the primary crust-forming magmas through time. In general, plagioclase, high-Ca clinopyroxene, and high-silica phases are the dominant mineral groups for most regions, with lesser amounts of orthopyroxene, olivine, and pigeonite. One of the fundamental results from the TES investigation was the identification of several large deposits of crystalline hematite, including those in Meridiani Planum, that were interpreted to indicate the presence of liquid water for extended periods of time. This interpretation led to the selection of Meridiani as the target for the *Opportunity* rover, the first time that a planetary landing site was selected on the basis of mineralogic information. Aqueous weathering may have formed some of the high-silica phases seen in TES spectra at high latitudes, and the Mars Express Observatoire pour la Minéralogie, l'Eau, les Glaces et l'Activité (OMEGA) spectrometer has detected phyllosilicates and sulfates, typically formed by aqueous weathering and deposition, in several locations. However, these minerals are not detected in TES spectra, indicating that they are present at abundances of less than 10%–15%. No carbonate outcrops have been detected at tens-of-kilometers scales anywhere on the planet. Carbonates have been inferred from TES spectra to be present in small (<5%) abundances in the Martian dust, possibly formed directly through interaction with atmospheric water vapor. Taken together, the presence of ancient primary volcanic minerals and the lack of abundant aqueous weathering products or precipitates suggests that Mars is a volcanic planet on which significant aqueous alteration has occurred only at limited times and in a limited number of locations. Mars does have a large inventory of water, but this water may have remained frozen throughout much of Mars history, resulting in little chemical weathering.

9.1 INTRODUCTION

At the time that the Thermal Emission Spectrometer (TES) instrument was proposed for the Mars Observer mission in 1986, remarkably little was known about the composition or mineralogy of the Martian surface. Telescopic near-infrared spectra had indicated the presence of some form of mineral-bound water (Moroz, 1964; McCord *et al.*, 1971; Sinton, 1971; Houck *et al.*, 1973) and suggested that pyroxenes were likely present and that olivine was not a dominant mineral phase (Adams, 1974; McCord *et al.*, 1978; Singer *et al.*, 1979; Singer and Roush, 1985). Phobos-2 ISM (ISM – Imaging Spectrometer for Mars) near-IR spectra in the 0.8–2.3 μm region were used to identify spectral units (Erard *et al.*, 1990; Mustard *et al.*, 1990; Mustard *et al.*, 1993), and to argue for the coexistence of both low- and high-Ca pyroxene (HCP) in several dark regions (Mustard and Sunshine, 1995; Mustard *et al.*, 1997). The red color of Mars and the subtle absorptions in the 0.6–0.8 μm region led to arguments for iron oxides as either crystalline or nanocrystalline phases (e.g., Soderblom, 1992; Bell, 1996; Erard and Calvin, 1997). Telescopic observations had provided some indication of the possible presence of sulfates and carbonates (Pollack *et al.*, 1990; Blaney and McCord, 1995). A handful of thermal infrared spectra were obtained of the surface by the Mariner 9 IRIS instrument after the global dust storms had cleared (Hanel *et al.*, 1972; Conrath *et al.*, 1973). The multispectral thermal-infrared data from the Viking Infrared Thermal Mapper (IRTM) (Kieffer *et al.*, 1977) revealed strong absorption features in the 9 and 20 μm IRTM bands (Christensen, 1982, 1998) whose depth correlated well with surface markings. When combined with the IRIS spectra these data suggested a basalt-like composition, but the difficulty in accurately modeling the atmosphere prevented a unique identification of the surface composition (Christensen, 1998). Finally, Earth-based telescopic thermal-IR observations acquired before TES successfully reached Mars also suggested a basaltic composition for dark regions in Acidalia Planitia that was consistent with the laboratory spectrum of an Antarctic basalt (Moersch *et al.*, 1997).

Taken together these early spectral observations made a case for the presence of volcanic rocks on the Martian surface. More importantly, these observations provided a strong rationale for sending visible and infrared spectrometers to Mars to explore the mineralogy of Martian surface materials in greater detail.

The Martian Surface: Composition, Mineralogy, and Physical Properties, ed. J. F. Bell III. Published by Cambridge University Press.

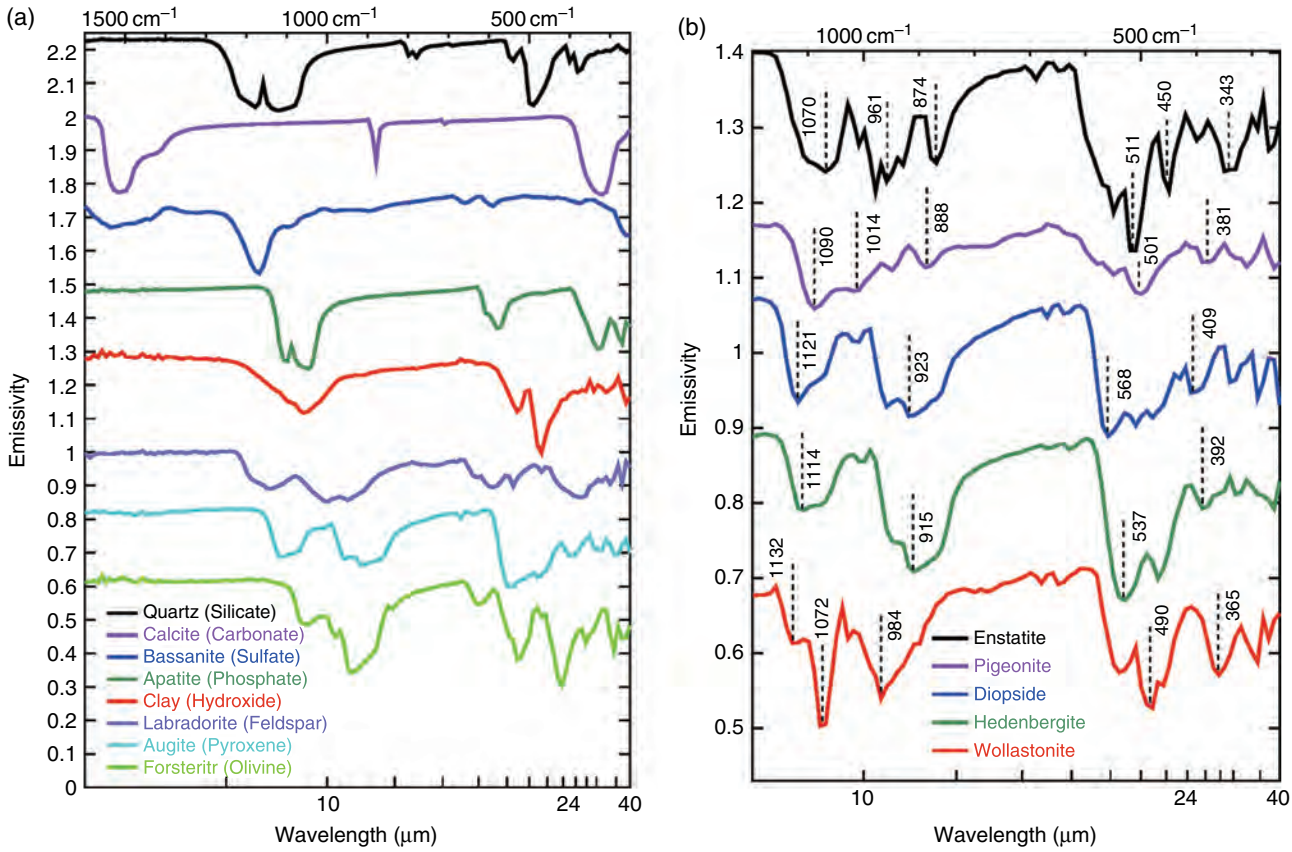

Figure 9.1. Infrared spectra of representative minerals. (a) Major mineral groups; (b) Pyroxene minerals. Band centers are indicated in cm^{-1}. (For a color version of this figure, please refer to the color plate section or to the e-Book version of this chapter.)

TES was initially developed for Mars Observer in order to study the composition and physical properties of the Martian surface, the composition and abundance of atmospheric aerosols and condensates, the 3D structure of the atmospheric temperature field, and the composition and evolution of polar ices (Christensen *et al.*, 1992). Because of the presence of vibrational features in the large majority of mineral groups in the infrared, it is possible to identify most of the minerals that may occur on the Martian surface using TES data. Important exceptions include the halide minerals that lack strong infrared absorptions. Using the minerals that can be identified, it is possible to investigate a broad spectrum of processes that could have occurred on the Martian surface, including primary rock-forming processes and subsequent alteration. Among the key questions regarding the composition of the surface of Mars that the TES investigation has addressed are: (1) the temporal and spatial variation in the composition of volcanic materials; (2) the existence of aqueous or hydrothermal deposits; (3) the existence and location of carbonates and other salts; (4) the composition and abundance of weathering products; (5) the relationship of SNC (SNC – Shergottite, Nakhlite, Chassigny) meteorites to regional composition; (6) the composition of unique surfaces such as "White Rock"; and (7) the composition and origin of Martian dust. The Mars Observer spacecraft failed three days before reaching Mars; however, TES was reflown successfully to Mars on the Mars Global Surveyor (MGS) spacecraft, reaching Mars in 1997 (Albee *et al.*, 2001).

9.2 BACKGROUND

9.2.1 Vibrational spectroscopy

Vibrational spectroscopy is based on the principle that vibrational motions occur within a crystal lattice at fundamental frequencies that are directly related to crystal structure and elemental composition – i.e., mineralogy (e.g., Wilson *et al.*, 1955; Farmer, 1974). The fundamental vibrational frequencies of these motions occur primarily within the thermal infrared (~5–100 μm) for geologic materials, and TES was specifically designed to observe these fundamental bands. Additional overtones and combination tones occur in the 1–5 μm region for many minerals, but these are typically weaker than the fundamental frequencies. The fundamental stretching vibrations vary significantly with different anion groups, such as CO_3, SO_4, PO_4, and SiO_4, producing unique, well-separated bands for carbonates, sulfates, phosphates, silicates, oxides, and hydroxides (Figure 9.1). The stretching and bending vibrational modes that typically occur at wavelengths greater than ~15 μm involve the major cations (e.g., Mg, Fe, Ca, and Na), and provide the means for uniquely identifying the individual minerals within these mineral groups (e.g., a "high-Ca augite" rather than simply "a pyroxene," Figure 9.1b) (e.g., Salisbury *et al.*, 1991; Salisbury, 1993; Lane and Christensen, 1997;

Christensen *et al.*, 2000a). Diagnostic metal-OH vibrations occur in the 2.2–2.4 μm range that are very well suited to studying phyllosilicates, zeolites, or palagonites (e.g., Hunt *et al.*, 1971). Examples of vibrational spectroscopy methods that are commonly used include IR emission and reflectance, near-IR reflectance, attenuated total reflectance (ATR), and Raman spectroscopy.

Extensive work over the past 40 years has demonstrated the utility of vibrational spectroscopy for the quantitative determination of mineral abundances in the mixtures found on planetary surfaces and within rocks (e.g., Lyon, 1962; Lazerev, 1972; Farmer, 1974; Hunt and Salisbury, 1976; Salisbury and Walter, 1989; Christensen and Harrison, 1993; Salisbury, 1993; Mustard and Hays, 1997; Lane and Christensen, 1998; Christensen *et al.*, 2000a; Hamilton and Christensen, 2000). Individual mineral components can be identified and rock types distinguished, allowing both the mineralogy and petrology to be determined (Walter and Salisbury, 1989; Feely and Christensen, 1999; Hamilton and Christensen, 2000). This work has included the development of quantitative models to predict and interpret vibrational spectra produced by emission from natural particulate surfaces (Conel, 1969; Salisbury and Eastes, 1985; Salisbury and Wald, 1992; Moersch and Christensen, 1995; Mustard and Hays, 1997; Ramsey and Christensen, 1998). Much use has been made of linear deconvolution methods to determine the abundances of the mineral components present in TES spectra (e.g., Adams *et al.*, 1986; Ramsey and Christensen, 1998), and this technique has been demonstrated to provide an accurate estimate of mineral abundances, both for mixtures of granular materials of a wide range of particle sizes (e.g., Johnson *et al.*, 1983; Mustard, 1993; Ramsey and Christensen, 1998) and for rocks of varying composition and grain size (Feely and Christensen, 1999; Hamilton and Christensen, 2000; Hamilton *et al.*, 2001; Wyatt *et al.*, 2001). Deconvolution of IR spectra has also been successful at determining the composition of specific phases in minerals, such as plagioclase, that occur in solid solution series (Milam *et al.*, 2004). The absolute errors in mineral determinations have been determined to be ±5–15% in both rock and granular mixtures (Ramsey and Christensen, 1998; Feely and Christensen, 1999; Hamilton and Christensen, 2000; Bandfield, 2002; Rogers and Christensen, 2007).

9.2.2 The TES instrument

The TES instrument contains an infrared (5.8–50 μm) spectrometer, along with broadband thermal (5.1–>100 μm) and visible/near-IR (VNIR) (0.3–2.9 μm) radiometers. The TES spectrometer is a Michelson interferometer that covers the 5.8–50 μm (1709–201 cm^{-1}) wavelength range at moderate (6 and 12 cm^{-1}) spectral resolution (Christensen *et al.*, 1992). The spectrometer portion of the instrument is the part that has the provided compositional information, and thus is the focus of this chapter. The radiometers have produced the temperature and reflectance measurements that have been used to study the thermophysical properties and the polar processes that are discussed and reviewed in Chapters 18 and 25. The TES spectrometer and radiometers have surface resolutions of $\sim 3 \times 6$ km, providing moderate resolution mapping of the entire planet.

The TES spectrometer used periodic views of an internal calibration target and of space to provide excellent, long-term calibration. The 1σ radiance noise level of an individual spectral sample in a single spectrum is $\sim 2.5 \times 10^{-8}$ W cm^{-2} sr^{-1}/cm^{-1} for wavenumbers from ~300 to 1400 cm^{-1}, increasing to $\sim 6 \times 10^{-8}$ and $\sim 4 \times 10^{-8}$ W cm^{-2} sr^{-1}/cm^{-1} at lower (250 cm^{-1}) and higher (1650 cm^{-1}) wavenumbers respectively (Christensen *et al.*, 2001a). The absolute accuracy of the TES spectra has been determined to be $\sim 4 \times 10^{-8}$ W cm^{-2} sr^{-1}/cm^{-1} from ~300 to 1400 cm^{-1} (Christensen *et al.*, 2001a). This uncertainty corresponds to an absolute temperature uncertainty of ~0.4 K for a surface temperature of 280 K, and ~1.5 K for a surface at 150 K. The emissivity spectra discussed throughout this chapter are derived by determining the brightness temperature at each wavenumber using the measured spectral radiance and assuming unit emissivity to solve for temperature in the Planck equation. The maximum brightness temperature is assumed to be the surface kinetic temperature, and the spectral radiance is divided by the radiance of a blackbody at this temperature to give the emissivity. This method explicitly assumes that the surface emissivity is unity at some wavelength. This assumption is supported by extensive laboratory measurements that show that virtually all minerals have an emissivity >0.99 at some wavelength between 5 and 50 μm (Salisbury *et al.*, 1992; Ruff *et al.*, 1997). The temperature uncertainty translates into a small, smoothly varying offset in the emissivity spectrum that varies from 0.001 at 400 cm^{-1}, to a maximum of 0.004 at 920 cm^{-1}, to essentially 0 at 1300 cm^{-1} (Christensen *et al.*, 2001a).

TES entered Mars orbit onboard MGS on September 11, 1997. Over the next 510 days the spacecraft completed a series of 1284 aerobraking and science phasing orbits in which the orbit was manipulated to achieve the desired mapping orbit with a 350 km altitude and a mean local time of 2 p.m. (Albee *et al.*, 2001). Since that time TES operated nearly continuously, acquiring over 206 million spectra. In February 2005 the second of two redundant neon lamps used to control the interferometer darkened to the point where it only had ~2 weeks of life remaining. At this time the TES spectrometer was turned off to conserve the remaining lifetime in the hopes of acquiring coincident observations with the Mars Climate Sounder on the Mars Reconnaissance Orbiter in the fall of 2006.

9.2.3 Surface–atmosphere separation

A key element of global mineral mapping using spectroscopy from orbit is the ability to accurately separate the surface and atmospheric components. These components have been uniquely identified and separated in TES spectra by using limb, emission phase function, and day–night observations (Bandfield *et al.*, 2000b; Smith *et al.*, 2000). Models using both radiative transfer and linear deconvolution methods have been developed for quantitatively separating the surface and atmospheric components of TES spectra (Smith *et al.*, 2000). These models, together with

atmospheric dust and water-ice cloud spectral properties, are used to separate the surface and atmospheric spectra. The atmospheric dust and water-ice spectra were determined using factor analysis, target transformation, and emission phase function techniques on TES spectra from a wide range of surfaces and atmospheric dust and loading (Bandfield *et al.*, 2000b; Bandfield and Smith, 2003).

The radiative transfer method uses a successive least-squares fitting to simultaneously model the spectral properties of atmospheric dust, atmospheric water ice, and surface emissivity and the derived atmospheric temperature gradient in each TES spectrum (Smith *et al.*, 2000). The deconvolution algorithm assumes that the TES spectra are linear combinations of atmosphere and surface spectral shapes and performs a linear least-squared fit with a library of dust, ice, and mineral spectra to determine the abundances of all components. The atmospheric components are then removed in accordance with their derived abundances to give a surface-only spectrum (Smith *et al.*, 2000).

The surface-only spectra derived from the radiative transfer and deconvolution algorithms were compared over a range of atmospheric dust opacities, water-ice abundances, and atmospheric temperatures. An estimate of the uncertainty in the surface emissivity spectra due to the combined instrumental and atmospheric modeling effects can be estimated by comparing the surface spectra derived from these two atmospheric-removal models. This emissivity uncertainty is typically less than ± 0.003 (Christensen *et al.*, 2000b), including all of the random and systematic instrumental uncertainties in the original spectra, as well as the uncertainties produced by the different atmospheric-removal models. In conditions of relatively low-infrared atmospheric dust opacity ($\tau < 0.5$), the atmospheric contribution depends nearly linearly on dust abundance. Once the spectral shape of this atmospheric contribution has been determined, the atmospheric effect can be modeled using linear addition of this spectral shape to the composite spectrum. This process is mathematically identical to treating the atmosphere as another component whose spectral contribution varies linearly with abundance, and the linear deconvolution method can model, and remove, the atmospheric contribution. The simpler linear deconvolution approach has typically been used for surface–atmosphere separation based on the close agreement between this method and the full radiative transfer approach. The best validation of the surface–atmosphere separation has been the good agreement between the surface mineralogy derived from orbital TES spectra with the *in situ* determination of the mineralogy at the Gusev and Meridiani rover sites (e.g., Christensen *et al.*, 2004a,b; Gellert *et al.*, 2004; McSween *et al.*, 2004; see also Chapter 14).

9.3 GLOBAL MINERAL MAPPING: MARS IS A VOLCANIC PLANET

9.3.1 Basalt

One of the key initial findings from the TES investigation was the identification of basalt as the major rock type on Mars (Christensen *et al.*, 2000b). Basalts were initially identified from TES spectra in equatorial dark regions, with Cimmeria and Syrtis Major being the type locales (Bandfield *et al.*, 2000a; Christensen *et al.*, 2000b). Surface spectra of the Cimmeria region derived using two different models to remove the atmospheric components provide an excellent match to the spectra of terrestrial basalts (Christensen *et al.*, 2000b; Smith *et al.*, 2000). Detailed modeling of the surface spectra shows that a mixture of plagioclase feldspar (45%), high-Ca clinopyroxene (augite and diopside) (25%), olivine (15%), and high-silica and other phases (15%) provides the best fit to the TES spectra (Figure 9.2). It is important to note that the spectral contrast of the TES spectra closely match the contrast observed in laboratory samples of basaltic sand; no scaling, contrast enhancement, or continuum removal is applied to the TES spectra. The TES spectra are consistent with what is expected for particulate materials on the surface, and no unusual particle size or other environmental effects are observed in these data. The match to sand-sized particles is also consistent with the thermal inertia and albedo values derived for dark regions, with dark regions typically composed of coarse-grained (100–500 μm) particles (Palluconi and Kieffer, 1981; Edgett and Christensen, 1991). Changes in spectral character with particle size effects, which can be important for particles less than ~65 μm in diameter (several times the wavelength) (Salisbury and Eastes, 1985; Ramsey and Christensen, 1998), affect both the band depth and the spectral shape. The close match in band depth and shape across the entire TES spectrum provides additional evidence that the particles on these surfaces are coarse enough (greater than ~65 μm) that particle size is not a factor, and that the surface components that are present at abundances greater than ~10% are likely to have been identified.

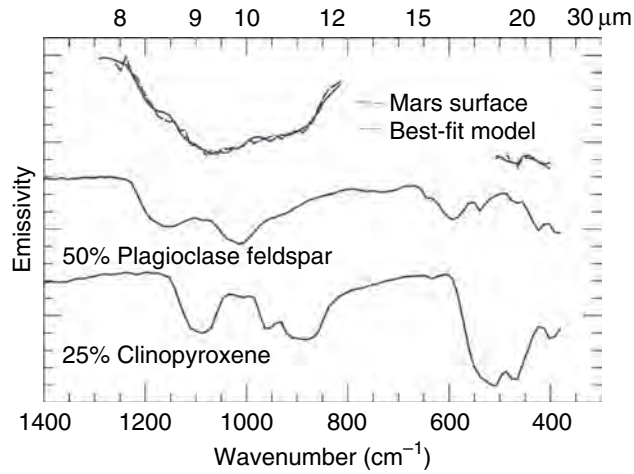

Figure 9.2. Deconvolution of TES basalt spectrum of Cimmeria. TES spectra from this region are well matched by plagioclase, pyroxene, and minor olivine and other phases. (Adapted from Christensen *et al.*, 2000b.) (For a color version of this figure, please refer to the color plate section or to the e-Book version of this chapter.)

The TES data provided the first detection and mapping of feldspar minerals on Mars (Christensen *et al.*, 2000b; Bandfield, 2002). The abundance of plagioclase feldspar derived from the TES data in Cimmeria is significantly

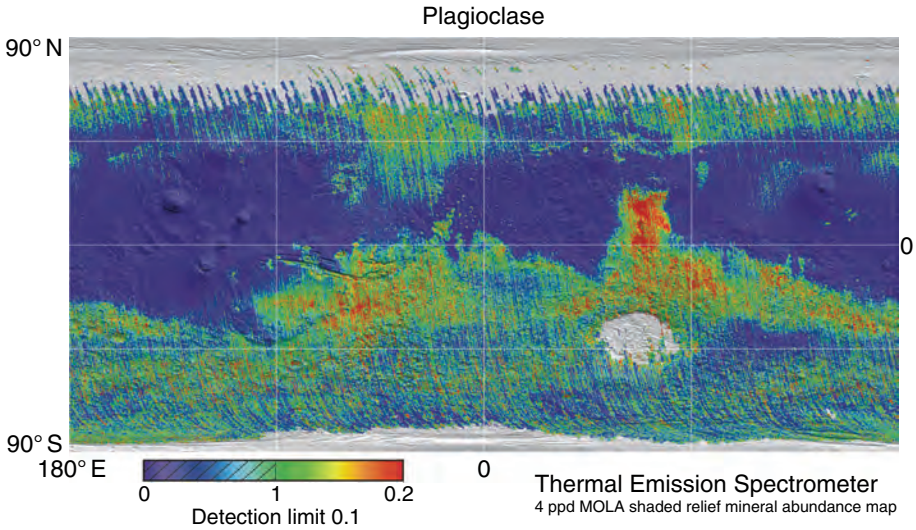

Figure 9.3. TES mineral map of plagioclase superimposed on the MOLA shaded relief map for location. (Based on Bandfield, 2002.) (For a color version of this figure, please refer to the color plate section or to the e-Book version of this chapter.)

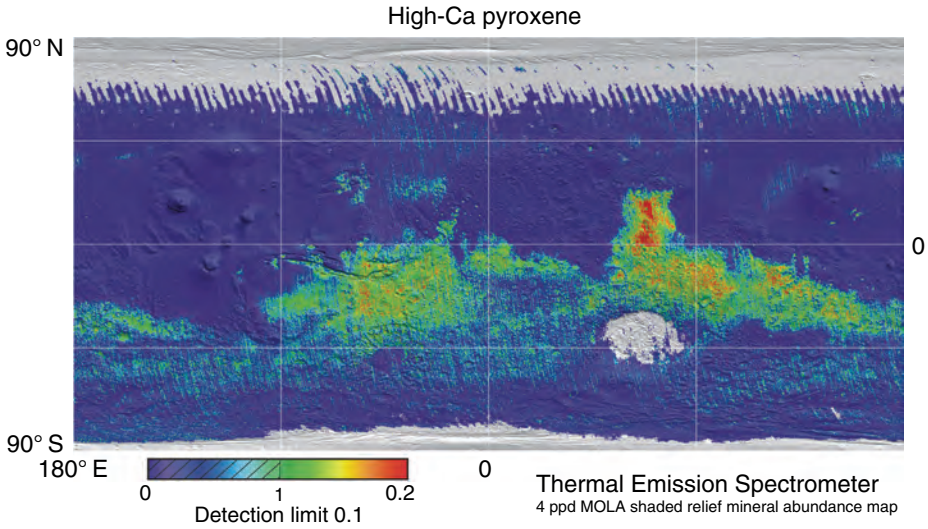

Figure 9.4. TES mineral map of high-Ca pyroxene superimposed on the MOLA shaded relief map for location. (Based on Bandfield, 2002.) (For a color version of this figure, please refer to the color plate section or to the e-Book version of this chapter.)

higher than that of pyroxene, with a plagioclase feldspar/pyroxene ratio of 1.8. The initial results suggested that the pyroxenes were predominately clinopyroxenes; subsequent analysis of TES data from the Cimmeria region indicates that the pyroxenes are a mixture of ortho- (low Ca) and clinopyroxenes (high Ca), with orthopyroxene making up ~1/3 of the total (Rogers and Christensen, 2007). Mustard and Sunshine (1995) and Mustard *et al.* (1997) also found both low-Ca pyroxenes (LCPs) and HCPs in dark regions in Syrtis Major and Eos Chasma using ISM data, although the TES results show that the abundance of orthopyroxene in Syrtis Major is only ~5% (Rogers and Christensen, 2007). Olivine was detected in the Cimmeria region, and has been found in many dark regions. The composition of the Cimmeria surface materials derived from these mineral abundances places these units in the range of basalt to basaltic andesite (Christensen *et al.*, 2000b).

Thermal Emission Spectrometer spectra from orbit show olivine- and pyroxene-bearing rocks and sands at the Gusev landing site of the Mars Exploration Rover (MER) *Spirit* (McSween *et al.*, 2006). *In situ* confirmation of these results has been provided by the *Spirit* Mössbauer, Mini-TES, and Alpha Particle X-ray spectrometer (APXS) instruments, which show the presence of olivine and pyroxene-bearing rocks (Christensen *et al.*, 2004a; Gellert *et al.*, 2004; McSween *et al.*, 2004; Morris *et al.*, 2004) that have not been subjected to significant water since early in their history (Golombek *et al.*, 2006; Morris *et al.*, 2006; see also Chapters 15 and 25).

9.3.2 Global mineral mapping

Following the initial identification of basalt as the primary rock type, the TES spectra have been analyzed to produce quantitative mineral abundance maps to search for other major mineral and rock types. Global mineral maps have been produced for 12 mineral groups using over 50 million atmospherically corrected TES spectra (Bandfield, 2002). These maps provided the first global mapping of the primary rock-forming minerals on Mars – e.g., feldspars, pyroxenes, and olivine, high-silica phases, carbonates, oxides, and phyllosilicates (Figures 9.3 and 9.4). Unfortunately, portions of the northern equatorial region are mantled by centimeters to meters of bright, fine-grained dust (e.g., Palluconi and

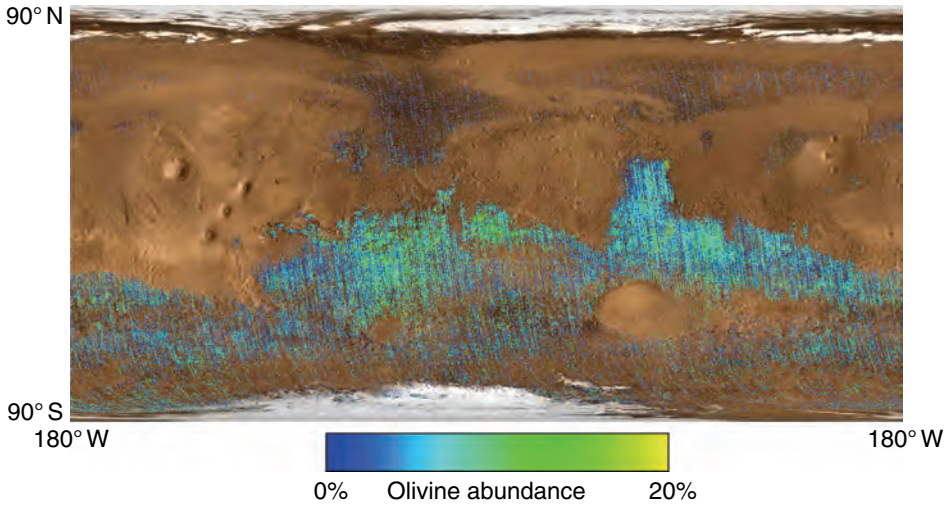

Figure 9.5. TES mineral map of olivine superimposed on the MOLA shaded relief map for location. (Based on McSween *et al.*, 2006.) (For a color version of this figure, please refer to the color plate section or to the e-Book version of this chapter.)

Kieffer, 1981; Christensen, 1985; Ruff and Christensen, 2002) that masks the spectral character of the underlying surface and prevents the remote determination of its mineralogy.

Global mapping by TES has confirmed that Mars is fundamentally a volcanic planet. The dark regions that are free of dust are dominated by primary volcanic minerals (plagioclase feldspar, HCPs, and olivine), with some areas containing low-Ca pyroxenes and higher abundances of glass or other high-silica phases (poorly crystalline to amorphous materials with Si/O ratios >0.35) (Bandfield, 2002; Rogers and Christensen, 2007). Feldspar is the dominant mineral phase in most locations (Figure 9.3). High-Ca clinopyroxenes are the most common pyroxene phase, although orthopyroxenes have been detected using TES (Hamilton *et al.*, 2003b; Rogers and Christensen, 2007), the Phobos-2 ISM (Mustard and Sunshine, 1995; Mustard *et al.*, 1997), and the Mars Express Observatoire pour la Minéralogie, l'Eau, les Glaces et l'Activité (OMEGA) spectrometers (Bibring *et al.*, 2005; Mustard *et al.*, 2005). Olivine is common, occurring at 5%–15% abundance in many regions (Figure 9.5) (Hamilton *et al.*, 2003b; Hoefen *et al.*, 2003; Bibring *et al.*, 2005; Mustard *et al.*, 2005; McSween *et al.*, 2006), with abundances of more than 25% in localized areas (Christensen *et al.*, 2003, 2005; Hamilton and Christensen, 2005; Rogers *et al.*, 2005).

What is significant from a global perspective is the ubiquitous presence of original volcanic mineral phases that are still present on Noachian aged (>2–3 Ga) surfaces. In addition, common aqueous weathering products, such as phyllosilicates, are not detected in TES spectra at abundance greater than ~10%, and could be absent in most regions. The rates of dissolution of olivine and pyroxene minerals in aqueous fluids can vary by several orders of magnitude under differing environmental conditions and are not well constrained for Mars (see summary by Tosca *et al.*, 2004). Despite these uncertainties, it seems unlikely that Martian rocks, with as much as 20% olivine, could have been exposed to significant volumes of water for geologic periods of time. This conclusion is supported by *in situ* observations of the rocks at Gusev crater, which show the presence of at most a thin (less than ~1 mm) alteration zone that is not chemically fractionated from the underlying rock interior, indicating that any alteration processes have had a low water to rock ratio (Hurowitz *et al.*, 2006). Taken together, the global TES observations suggest a scenario in which Mars has been dominated by cold, dry conditions with only relatively minor episodes of aqueous activity and alteration (Christensen *et al.*, 2003; Hoefen *et al.*, 2003; Christensen and Ruff, 2004).

Sulfates have been found by OMEGA in several locations (Bibring *et al.*, 2005; Gendrin *et al.*, 2005). Phyllosilicates have also been detected by OMEGA, but only in a very restricted number of areas that are commonly in association with dark deposits or eroded Noachian-aged outcrops (Bibring *et al.*, 2005; Poulet *et al.*, 2005). The phyllosilicate occurrences have been suggested to be consistent with an early hydrological system providing contact of igneous minerals with liquid water very early in Mars' history, followed by a more acidic environment in which sulfates formed (Bibring *et al.*, 2005, 2006; Gendrin *et al.*, 2005; Poulet *et al.*, 2005; see also Chapter 7). The lack of detection of sulfates and phyllosilicates at TES IR wavelengths suggests that they are present at abundances below the TES detection limit (10%–15%).

9.3.3 TES Types 1 and 2

One of the key findings of the TES experiment was the classification of the low-albedo surface materials into two global-scale units on the basis of the clustering of the mineral abundances into two major groupings that correspond to two basic thermal-IR spectral shapes (Bandfield *et al.*, 2000a). These surface types, which have come to be known as TES Type 1 and Type 2 (or, alternately Surface Type 1 [ST1] and Surface Type 2 [ST2] in some of the literature), differ primarily in the abundances of high-silica phases and pyroxene. Type 1 are plagioclase- and clinopyroxene-rich basalts found in the ancient cratered terrains, with characteristic locales in Cimmeria and Syrtis Major. Type 2 materials are commonly associated with the younger rocks of the northern lowlands, with some occurrences at high latitudes

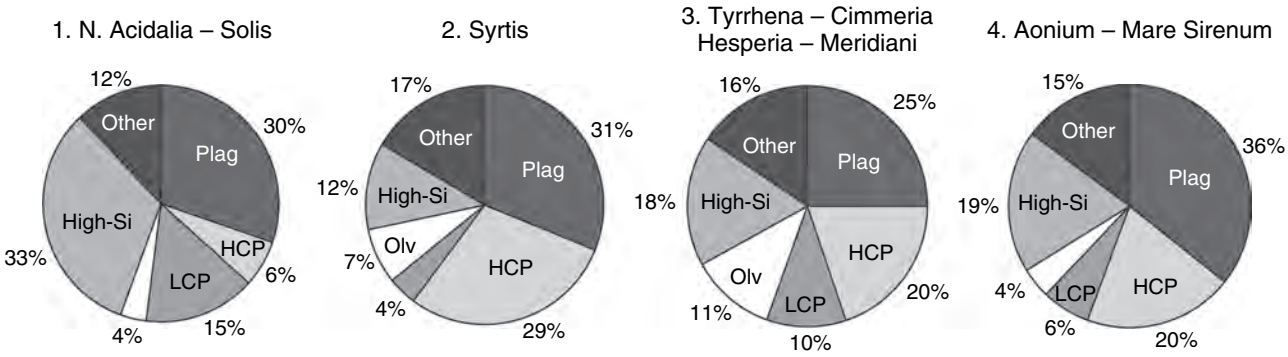

Figure 9.6. Pie charts of Groups 1–4 mineral abundances. (From Rogers *et al.*, 2007.)

in the southern highlands (Bandfield *et al.*, 2000a). These units are plagioclase-bearing with more silica-rich phases (glasses, secondary amorphous, or poorly crystalline high-silica materials with Si/O ratios >0.35 [Wyatt and McSween, 2002; Michalski *et al.*, 2005]) and fewer iron-bearing minerals than found in Type 1 rocks. These materials have the mineralogy and spectral character of basaltic andesites or andesites (Bandfield *et al.*, 2000a). The nature and origin of these high-silica materials has generated a good deal of discussion. One possibility is that the high-silica component in these rocks is primary volcanic glass, and that these rocks are true andesites. The possible existence of andesites on Mars is intriguing, perhaps implying more water in the mantle than on Earth, or suggesting differing temperatures or pressures at which melting occurred. However, several alternative hypotheses have been presented to explain the apparent andesitic character of the Type 2 spectrum. These include oxidation and recrystallization of an SNC-type basalt (Minitti *et al.*, 2002); alteration of basalt to produce clay minerals (phyllosilicates) (Wyatt and McSween, 2002) or zeolites (Ruff, 2004); silica or aluminous silica coating on basalt (Wyatt and McSween, 2002; Kraft *et al.*, 2003; Michalski *et al.*, 2005); and palagonitization of basalt (Morris *et al.*, 2003). While such explanations dispense with the need for large volumes of andesite or basaltic andesite on Mars, they require a process by which large regions of basaltic materials on Mars became altered (i.e., Type 2) while some remain relatively pristine (Type 1). This possibility was addressed by Wyatt *et al.* (2004) by suggesting that the high-latitude dominance of Type 2 materials is due to increased amounts of chemical weathering from basalt interactions with icy mantles at these latitudes. The dominance of igneous minerals measured by TES would still imply limited global chemical alteration on Mars, but with greater alteration occurring at high latitudes and in the low-lying northern plains (Wyatt *et al.*, 2004). The Dry Valleys of Antarctica may be the best terrestrial analogue for this kind of weathering on Mars because of the cold, hyper-arid environment, stable permafrost, and ground ice (Gibson *et al.*, 1983). Basalts in the Dry Valleys are dominated by plagioclase and pyroxene, with limited abundances of alteration phases similar to those proposed for Type 2 materials (palagonites, zeolites, smectites, and silica coatings). All of these secondary products can be produced on Mars by chemical weathering of basalt without an abundance of liquid water.

In some regions, such as in Nili Patera, high-silica glass phases are associated with steep-sided volcanic cones and stubby lava flows, and are clearly volcanic in origin (Christensen *et al.*, 2005). From these observations it appears that glasses have been capable of surviving billions of years on the Martian surface without having been completely weathered away. Therefore it is not unreasonable to suggest that volcanic glasses may indeed be contributing to the high-silica phases detected by TES.

Regardless of the origin of the high-silica materials, both the Type 1 and 2 surfaces, and thus the vast majority of exposed Martian rocks and sand, were initially volcanic in origin.

9.3.4 Regional volcanic variability

Subsequent detailed mapping using TES spectra has revealed important diversity in the volcanic composition from region to region (Rogers and Christensen, 2007; Rogers *et al.*, 2007). In general, plagioclase, high-Ca clinopyroxene, and high-silica phases are the dominant mineral groups for most regions, with lesser amounts of orthopyroxene, olivine, and pigeonite (Rogers and Christensen, 2007; Rogers *et al.*, 2007). These results have shown that some regions exhibit equal abundances of plagioclase and total pyroxene, and in some areas, total pyroxene abundance exceeds plagioclase abundance.

The mineral abundances of the major low-albedo regions cluster into four groups (Figure 9.6): (1) Northern Acidalia + Solis Planum; (2) Syrtis Major; (3) Tyrrhena Terra + Hesperia Planum + Cimmeria-Iapygia + Meridiani; and (4) Aonium-Phrixi + Mare Sirenum (Rogers and Christensen, 2007). These four classes are separated by ~10% or greater abundance differences in plagioclase, HCP, high-silica phases, olivine, and low-Ca pyroxene. Group 1 consists primarily of high-silica phases (30%–35%), plagioclase (~30%), and orthopyroxene (~15%). Group 2 surfaces consist primarily of high-Ca clinopyroxene (~30%), plagioclase (~30%), and high-silica phases (~10%). Group 3 surfaces consist primarily of plagioclase (~25%), high-Ca clinopyroxene (~20%), high-silica phases (15%–20%), low-Ca pyroxene (5%–15%), and olivine (10%–15%). Group 4 is characterized by 35%–40% plagioclase, ~20% HCP, 15%–20% high-silica

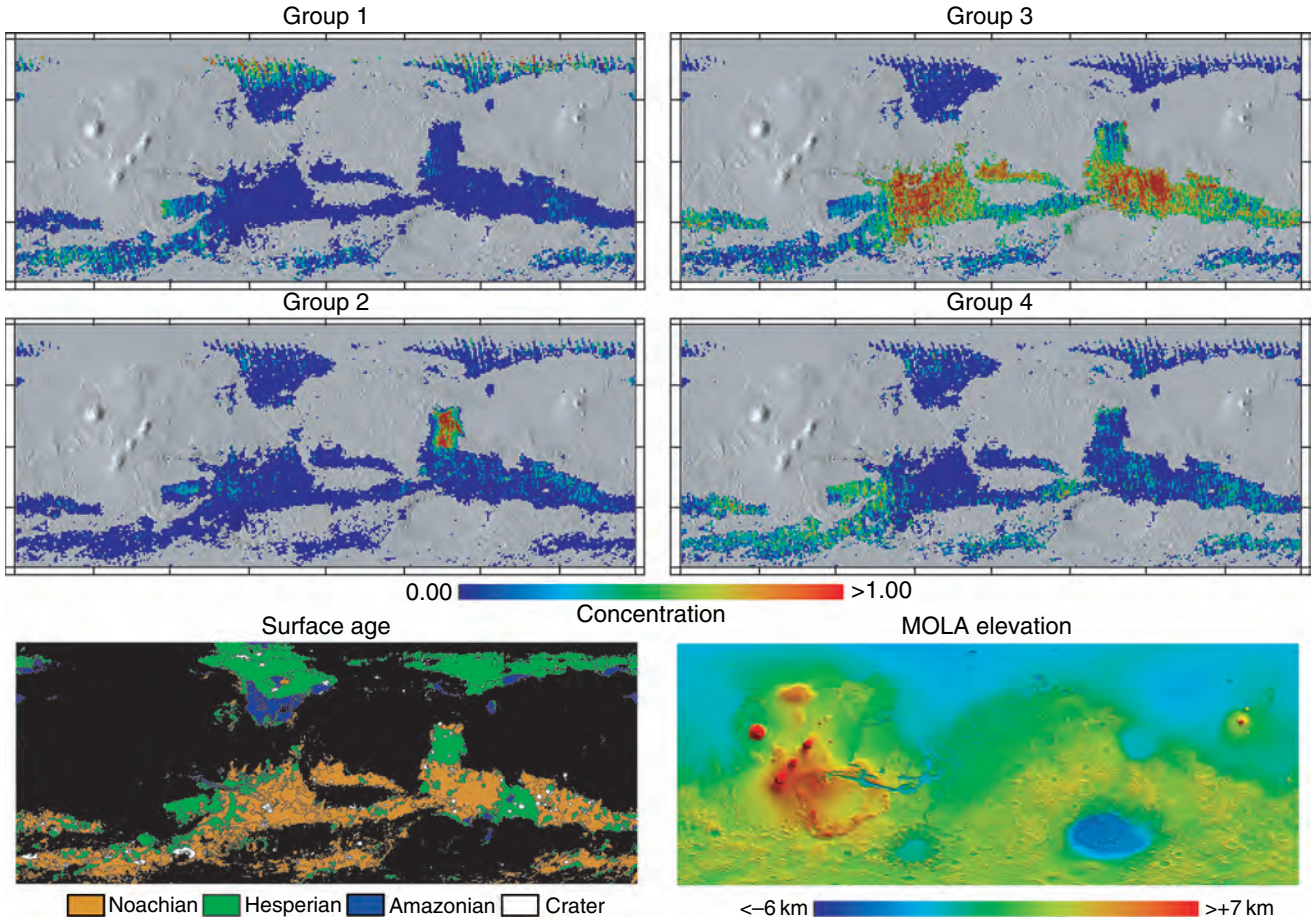

Figure 9.7. The spatial distribution of TES volcanic compositional Groups 1–4. The subtle compositional variations are spatially distinct, providing strong evidence that these volcanic terrains reflect differences in primary formation processes. (Based on Rogers *et al.*, 2007.) (For a color version of this figure, please refer to the color plate section or to the e-Book version of this chapter.)

phases and low (≤5%) abundances of olivine and low-Ca pyroxene (Rogers and Christensen, 2007).

The spectral differences between these four groups are subtle; however, they are comparable to spectral variations associated with terrestrial mafic and intermediate volcanic rocks. Given the previous evidence that Mars has probably experienced little crustal recycling (e.g., Zuber, 2001; Borg *et al.*, 2003; McSween *et al.*, 2003; Wieczorek and Zuber, 2004) and limited chemical weathering (e.g., Christensen *et al.*, 2001a; Christensen *et al.*, 2005; Goetz *et al.*, 2005; Hamilton *et al.*, 2005; Haskin *et al.*, 2005; Yen *et al.*, 2005), this lack of large compositional variations is not surprising.

Distributions for these spectral unit classes are shown in Figure 9.7. Surfaces with the highest abundance of high-silica phases (Group 1) are concentrated in the northern lowlands, Solis Planum, and scattered throughout the-southern mid- to high-latitude regions. Nearly all of the occurrences (~85%) of this group are located in Hesperian terrains and, with the exception of surfaces in Solis Planum, Group 1 is primarily found at latitudes poleward of ~45° N. Group 2 is located almost exclusively in Syrtis Major and is found on Hesperian-aged terrains. Group 3 is located exclusively in the southern highlands, and is the most widespread of the four units. Approximately 75% of the Group 3 surfaces are Noachian in age; the remaining 25% are Hesperian terrains. Group 4 is located primarily in the southern highlands, with the majority of occurrences in low-albedo terrains surrounding the Tharsis province (Figure 9.7). Group 4 occurrences are split nearly equally between Noachian and Hesperian terrains (Rogers and Christensen, 2007). Arranged by age, Group 3 is the oldest, followed by Groups 4 and 2, with Group 1 the youngest.

9.3.5 The degree of global surface alteration

A critical question concerns the degree to which the observed variations in the mineral composition observed by TES are due to the primary rock-forming processes or to subsequent weathering. A comparison of plagioclase, ferromagnesian silicates, and high-silica phases shows no trend toward increasing abundance of high-silica phases with a corresponding decrease in other phases (Rogers and Christensen, 2007). Furthermore, the compositional units exhibit moderate correlation with large-scale morphology and geographic/topographic province, suggesting control by primary bedrock units (Figure 9.7) (Rogers and Christensen, 2007). The abundance of high-silica phases in

Group 3 and that in Group 4 are similar, and the compositional differences are primarily with plagioclase, pyroxene, and olivine abundance; it is unlikely that a weathering scenario could produce the observed relative differences in high- and low-Ca pyroxene (Rogers and Christensen, 2007). Thus, the observed equatorial and mid-latitude mineral patterns cannot be attributed to weathering of feldspars and/or mafic minerals and subsequent formation of phyllosilicates or allophane/amorphous silica, but rather indicate true variability in primary volcanic compositions.

High-silica phases are present in varying amounts, and in some locations these may be secondary in origin. Those phases would likely be poorly crystalline aluminosilicates, amorphous silica or zeolites, all of which require only minimal water/rock ratios to form (Kraft *et al.*, 2003; Ruff, 2004). However, even if these phases are secondary, there is also strong evidence that the original unaltered substrates were different in composition than the average highlands (Rogers and Christensen, 2007). We therefore conclude that the mineralogic differences seen by TES in volcanic terrains, especially those throughout the equatorial and mid-latitude regions, are primarily due to differences in the original composition of crust-forming lavas.

9.3.6 Local compositional extremes

The combination of TES spectra and high-resolution infrared spectral mapping from the Mars Odyssey Thermal Emission Imaging System (THEMIS) and Mars Express OMEGA instruments has allowed compositional mapping at scales appropriate for local geologic processes, as well as the investigation of volcanic diversity at local and regional scales (see also Chapters 7 and 10). Martian igneous and sedimentary processes almost certainly resulted in diversity at kilometer scales, much like observed in terrestrial systems. Volcanic units are likely composed of materials formed by different degrees of partial melting and modified by fractional crystallization and interaction with crustal compositions during magma ascent and eruption. Similarly, sedimentary units presumably experienced mineral fractionation during fluvial or aeolian transport and deposition; erosion, tectonic activity, and impact may have excavated different subsurface materials at local scales.

Olivine basalts are observed in layers exposed at various heights in canyon walls up to 4.5 km beneath the surface (Christensen *et al.*, 2003). In Ganges Chasma (~10° S, 320° E) an ~100 m thick unit crops out over an area 30 by several 100 km in size (Christensen *et al.*, 2003). Olivine-rich units also occur on the floors, walls, and central peaks of numerous craters, such as those in Aurorae Planum (~10.5° S, 310° E) (Hamilton *et al.*, 2003c; Christensen *et al.*, 2005; Mustard *et al.*, 2005). In Ganges Chasma and Aurorae Planum, where olivine basalt layers are exposed within several hundred kilometers of each other, these layers occur at significantly different stratigraphic levels. These vertical differences suggest that olivine-rich basalts were erupted episodically at significantly different times throughout the formation of the Martian upper crust. Olivine basalts have also been identified on the floors of eroded channels such as Ares Valles (3° N, 342° E) (Rogers *et al.*, 2005) and in cratered terrains such as Nili Fossae (~23° N, 77° E) (Hamilton and Christensen, 2005; Mustard *et al.*, 2005). The *Spirit* rover in Gusev crater has also observed olivine-rich basalts *in situ* using IR, Mössbauer, and APXS spectra (Christensen *et al.*, 2004a; Gellert *et al.*, 2004; McSween *et al.*, 2004, 2006; Morris *et al.*, 2004; see also Chapters 4 and 15). These rocks likely represent less evolved lavas or contain higher abundances of cumulates or mantle xenoliths than typical basalts.

The growing inventory of olivine basalts suggests that ultramafic rocks may be a relatively common variant of Martian basalts.

High-silica volcanic rocks have also been detected using the combination of TES and THEMIS observations (see Chapter 10). For example, quartz and plagioclase granitoid rocks are exposed in crater central uplifts in two 30 km diameter craters on the northern flank of the Syrtis Major volcanic construct (Bandfield *et al.*, 2004). The association of these outcrops with central peaks suggests that these rocks were uplifted from depths of several kilometers by the impact process, and may be part of an unusual regional rock unit that is postulated to be a single granitoid pluton (Bandfield *et al.*, 2004). A likely process for their formation is partial melting of thick sequences of pre existing basaltic rocks at relatively low pressures to form high-silica trondhjemites and tonalites (Barker, 1979; Clark, 1992; Bandfield *et al.*, 2004).

Another example is a series of eruptive sequences observed in the Syrtis Major volcano that appear to have evolved in composition from basaltic to dacitic. This was the first demonstration from orbital observations that fractional crystallization occurs in Martian magma chambers (Christensen *et al.*, 2005). This diversity in composition is the result of igneous processes analogous to those found in large volcanic complexes on Earth.

Taken together, the TES, THEMIS, and OMEGA observations show that the Martian crust, while dominated by basalt, has produced a diversity of igneous materials whose range in composition from ultramafic high-olivine basalts to highly silicic dacites and granitoids rivals that found on the Earth.

9.4 THE ORIGIN OF VOLCANIC DIVERSITY

Despite its overall basaltic composition, Mars has experienced a variety of volcanic styles over an extensive period of time. These observations imply the existence of significant variations in magma composition that should be reflected in the complexity of its crustal evolution. Using the mineral mapping from TES it is possible to investigate the evolution of magma source regions in time and space by studying the composition of the derived lavas exposed at the surface. The TES data have shown that there is a substantial fraction of plagioclase (greater than ~25%) present in Noachian- and

Hesperian-aged terrains (Christensen *et al.*, 2000b; Bandfield, 2002; Hamilton *et al.*, 2003b; McSween *et al.*, 2003; Rogers and Christensen, 2007). The high plagioclase/pyroxene ratios derived for these terrains indicate that mantle source regions for these lavas could not have been already strongly depleted of their aluminous phases (Rogers and Christensen, 2007), as had been previously suggested (e.g., Mustard *et al.*, 1997, 2005). However, the formation of those ancient terrains may have contributed to the aluminum depletion event, as suggested by Hamilton *et al.* (2003b).

In a simple model of continued extraction of melt from reservoirs that had produced the earlier crustal materials, the modal proportions of plagioclase should decrease from Noachian to Hesperian terrains as Al is continuously removed from the mantle. However, no decrease in plagioclase abundance over time is observed (Rogers and Christensen, 2007). This indicates that the younger melts had a complex origin and were affected by additional processes. One possibility is that the younger lavas may have undergone increased fractionation of low-Ca pyroxene and olivine, relative to the older units. Alternatively, the younger magmas may have had a significant assimilated crustal component, offsetting the Al enrichment of the parent source. Finally, it is possible that Syrtis and other Hesperian lavas may have been derived by partial melting of the crust (Rogers and Christensen, 2007).

There are some spatial and temporal variations in the Noachian and Hesperian lavas, suggesting that variations in the degree of crystal fractionation, assimilation, and/or source region compositions have occurred. For example, areas in topographically high regions near the Tharsis Plateau (e.g., Thaumasia, Aonium Sinus, Phrixi Regio) exhibit lower abundances of olivine and greater plagioclase/pyroxene ratios than surrounding older highland terrains, suggesting that magmas in this region may have undergone increased olivine fractionation, possibly facilitated by a locally thicker crust (Rogers and Christensen, 2007).

Finally, the rocks in Northern Acidalia and Solis (Group 1) have abundant (>30%) high-silica phases. These rocks are found primarily at high latitudes (>45°), which suggest that these are alteration products (amorphous aluminous silica or zeolites), although a volcanic origin is also possible (Bandfield *et al.*, 2000a). As suggested by Wyatt *et al.* (2004) and Michalski *et al.* (2005), surface alteration at high latitudes is consistent with the availability of surface H_2O and is possibly linked to the locations of once-present snow deposits (Mustard *et al.*, 2001; Christensen, 2003; Milliken, 2003).

However, these materials have a slightly (~5%) higher plagioclase abundance and 10% less pyroxene than the typical basalts in the equatorial and mid-latitude regions. Thus, if the high-silica surfaces are simply altered average highlands basalt, then pyroxene would have had to have been preferentially weathered to produce high-silica phases without decreasing the plagioclase abundance (Rogers and Christensen, 2007).

A more plausible explanation is that the original rock mineralogy was different than that of the average highlands (Rogers and Christensen, 2007). These rocks would have had a higher plagioclase abundance than the average highlands composition, together with possibly higher glass and/or olivine abundance relative to pyroxene. This hypothesis is consistent with the model of volcanism proposed by Tanaka (2005), with extensive interaction with sub-surface ice resulting in rocks with early crystallized feldspar and abundant quenched glass. The original lithology of surfaces currently containing high-silica phases need not be the same for both the northern and southern high latitudes. For example, the northern plains of Acidalia may have contained a higher fraction of olivine or glass, while the southern high latitudes may have contained a higher fraction of plagioclase. The suggestion that the unaltered plains of northern Acidalia and other high-silica surfaces were different than the average highlands lithology is supported by the observed dominance of LCP in these areas. This mineralogy is unlike the highlands, where HCP is the dominant pyroxene.

Thus, as is the case for many long-debated questions, the competing hypotheses for the origin of "Type 2" material – namely a unique primary volcanic composition versus weathered basalt – may both be partially correct. These rocks appear to have a different initial volcanic mineralogy, with more feldspar and glass than typical basalts, and have also been subsequently slightly altered to form secondary silica phases (Wyatt *et al.*, 2004; Michalski *et al.*, 2005; Rogers and Christensen, 2007).

9.5 CARBONATES

9.5.1 Detection of carbonates

Carbonates in the regolith have long been proposed to play an important role in the CO_2 exchange cycle, possibly acting as a reservoir for sequestering large amounts of CO_2 from the ancient Martian atmosphere, and allowing long-term exchange between the surface and atmosphere (e.g., Booth and Kieffer, 1978; Fanale and Jakosky, 1982; Kahn, 1985; Fanale *et al.*, 1992). Specifically, carbonate minerals could form readily in a CO_2 atmosphere when water is present, and would provide an indicator of the presence of liquid water in the Martian past. Several Martian meteorites contain limited amounts of indigenous carbonate (McSween, 2003), suggesting that their formation has occurred on Mars. Alternative arguments have been made for CO_2 loss to space (e.g., Melosh and Vickery, 1989; Kass and Yung, 1995; Brain and Jakosky, 1998) or inhibition by specific water chemistries (e.g., Fairen *et al.*, 2004), which would suggest that large carbonate deposits might not exist. Finally, it is possible that Mars never had a thick CO_2 atmosphere. Thus, the presence, or absence, of carbonates has important implications for the evolution of the Martian atmosphere, placing constraints on the abundances, reaction chemistry, and history of H_2O and CO_2.

Carbonate minerals have unique absorptions throughout the infrared spectral region, with fundamental absorptions near 6.67 μm (1500 cm^{-1}), 28 μm (350 cm^{-1}), 11.25 μm

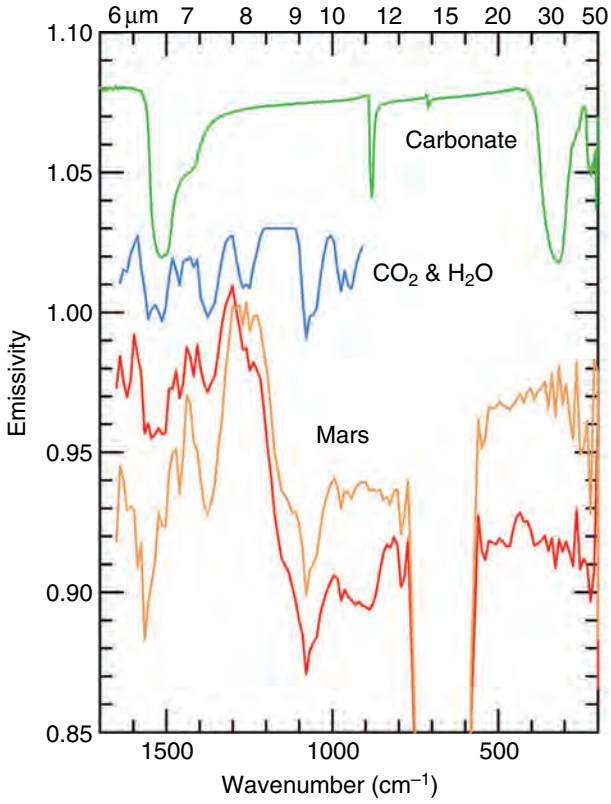

Figure 9.8. Comparison of TES bright and dark region spectra with the laboratory spectra of carbonates. The bright region spectrum is an average of TES spectra from Arabia (6.6° N to 10.7° N; 322.7° W); the dark region is from Syrtis Major (0° N to 1.7° N, 293° W). (From Christensen *et al.*, 2001a.) (For a color version of this figure, please refer to the color plate section or to the e-Book version of this chapter.)

($890\,cm^{-1}$), and overtone and combination bands at 2.35, 2.55, and 4.0 μm (Farmer, 1974; Salisbury *et al.*, 1992; Gaffey *et al.*, 1993; Lane and Christensen, 1997). Earth-based telescopic observations first suggested the presence of carbonates on Mars (Pollack *et al.*, 1990), but these observations required the use of spectral ratios in an attempt to remove atmospheric effects, making the identification of spectral features ambiguous. Searches for carbonates were conducted using the Mariner 6/7 spectrometer (McKay and Nedell 1988; Calvin *et al.*, 1994). Absorptions at 2.28 and 5.4 μm are consistent with hydrous carbonates in modest amounts (<10%–20%), but these identifications are tentative (Calvin *et al.*, 1994).

The TES wavelength range was chosen to include the carbonate fundamental vibrational bands at 6.67, 11.2, and 28 μm, with the specific goal of detecting carbonates (Christensen *et al.*, 1992). The OMEGA and Mars Reconnaissance Orbiter CRISM spectrometers cover the spectral range of the combination and overtone bands. Figure 9.8 shows representative mid-IR averaged spectra from bright and dark regions, together with spectra of CO_2, H_2O, and a scaled laboratory spectrum of calcite, corresponding to a surface abundance of ~10% (Lane, 1999). As illustrated in this representative spectrum, none of the spectral bands due to coarse-grained carbonates have been observed in the TES spectra, although it has been suggested that unique textural effects may subdue spectral band depths (Kirkland *et al.*, 2003).

A study of putative paleolacustrine basins using TES data found no evidence for carbonates (Stockstill *et al.*, 2005), and there is no other evidence for coarse-grained carbonates in the TES dataset. It is therefore possible to conclude that large-scale (> tens of kilometers sized) carbonate deposits are not currently exposed at the surface of Mars at abundances greater than ~5% (Christensen *et al.*, 2001a). The OMEGA instrument has subsequently seen no evidence for carbonates at abundances greater than several percent using the overtone vibrational bands in the 2–4 μm region (Bibring *et al.*, 2005). One cannot preclude burial of massive carbonates by younger units. However, the detection of aqueous hematite and sulfate units (discussed below) demonstrates that rare materials can be detected on the planet. Thus, either carbonate rock units are less common than hematite or sulfates, or the processes by which they remain "hidden" are more efficient.

Carbonates have, however, been inferred to be present in the fine-grained Martian dust using TES spectra (Bandfield *et al.*, 2003) and MER Mini-TES spectra (Christensen *et al.*, 2004a). The spectral region from 1300 to $1700\,cm^{-1}$ provides a unique opportunity to search for carbonates in fine-grained (<100 μm) materials due to the scattering properties of fine particulates. The spectral character in this region is sensitive to very small amounts (<1 wt.%) of highly absorbing materials, such as carbonates or bound water, that are mixed within the weakly absorbing silicates (Bandfield *et al.*, 2003). The observed spectral shape of Martian dust-covered surfaces (Figure 9.9) shows a broad emissivity maximum centered near $1480\,cm^{-1}$ (6.75 μm) and a second narrower maximum centered near $1640\,cm^{-1}$ (6.1 μm) that indicate the presence of materials that are strongly absorbing. The Mini-TES spectrometers on the *Spirit* and *Opportunity* rovers were able to improve the observations of these emission maxima due to the long integration times, short atmospheric path lengths, wider spectral range, and repetitive observations of the soil components at both landing sites (Christensen *et al.*, 2004a).

The $1480\,cm^{-1}$ band in fine-grained powders is unique to carbonate minerals; no other sample spectrum has been found that matches the Martian spectrum at these wavelengths (Bandfield *et al.*, 2003). The intensity of this band is sensitive to small quantities of carbonate minerals (>0.25 wt.%) intimately mixed with silicate minerals in fine-particulate materials (<63 μm) (Bandfield *et al.*, 2003). Its position shifts with the composition of the carbonate, with magnesite ($MgCO_3$) providing the best fit to the TES spectrum of Martian dust (Bandfield *et al.*, 2003). The spectral feature of dolomite ($CaMg(CO_3)_2$) is offset by $20\,cm^{-1}$ and calcite ($CaCO_3$) and dolomite are offset by $40\,cm^{-1}$ from the observed spectrum. Comparison with laboratory spectra indicates that the Martian dust contains 2–5 wt.% carbonate (Bandfield *et al.*, 2003). The $1640\,cm^{-1}$ feature is the expression of the fundamental bending mode of the H_2O molecule and represents bound or adsorbed water in the dust (Bandfield *et al.*, 2003; Christensen *et al.*, 2004a). Like the carbonate bands, the bound water feature is observed as a

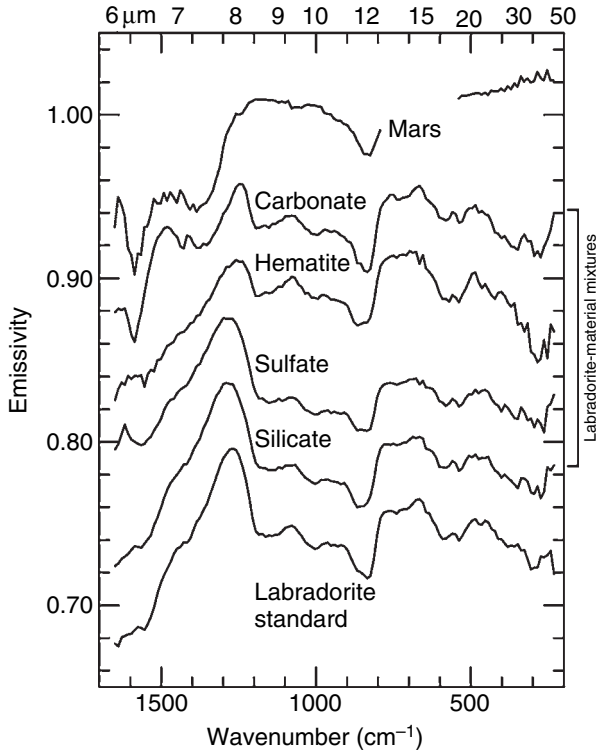

Figure 9.9. Mars dust, labradorite standard, and labradorite-material mixture spectra (offset). The spectral shape of labradorite is modified considerably with added carbonate at 1300 cm^{-1}, coincident with a fundamental carbonate absorption. The spectral shape outside this spectral region is not appreciably modified because strong silicate absorptions coincide with the other carbonate absorptions. Only the labradorite-carbonate mixture has a notable effect on the spectral shape, except for a peak present in the labradorite-sulfate mixture at 1640 cm^{-1} due to the bound water in gypsum. (From Bandfield, J. L., T. D. Glotch, and P. R. Christensen, Spectroscopic identification of carbonates in the Martian dust, *Science* **301**, 1084–87, 2003. Reprinted with permission from AAAS.)

peak in emission because of its high absorbance in this spectral region where silicates do not absorb strongly.

It has been suggested that the 1480 cm^{-1} spectral band is due to hydrous iron sulfates (Lane *et al.*, 2004). The spectra of hand samples ("walnut sized and friable") of hydrous iron sulfate have emission minima near 1400 and 1600 cm^{-1}, with an intervening emission maximum (Lane *et al.*, 2004). Significantly, however, the fine-grained (diameter $<63\,\mu m$) samples do not show the spectral features observed in the TES and Mini-TES spectra (Lane *et al.*, 2004). As discussed above, these features are unique to very fine-grained, highly absorbing materials mixed in a matrix of very fine grained, weakly absorbing silicates, and are only observed on Mars in the finest grained dust. This is the case both from orbit, where the 1480 and 1640 cm^{-1} features are only seen in very fine-grained (low thermal inertia) dust deposits (Bandfield *et al.*, 2003), and from the rovers, where they are only seen in localized dust coatings and hollows (Christensen *et al.*, 2004a). The lack of the emission maxima near 1480 cm^{-1} in the fine-grained hydrous iron sulfates is not consistent with these minerals being the source of the absorptions observed in Martian dust.

Both the carbonate and bound water features in the TES and Mini-TES spectra are only observed in the fine-grained soil components because the strongly absorbing carbonates and bound water are mixed within a matrix of weakly absorbing and scattering silicate materials. Unfortunately, there were no *in situ* instruments on the arm of the MERs that were capable of detecting carbon or carbonate minerals in order to better define the nature of the carbonates in the dust.

9.5.2 Carbonate formation

The lack of detectable carbonate rock outcrops suggests that the carbonate in the dust did not form by mechanical erosion and transport of carbonate rocks. Instead, it seems likely that the carbonates have formed directly in or on the dust through interactions with water vapor, perhaps in a mechanism similar to that simulated in a laboratory chamber by Booth and Kieffer (1978). Carbonate minerals may form under low-CO_2 pressure conditions in which liquid water is not stable but may be present in a transient state (Booth and Kieffer, 1978). It is unclear, however, how much, if any, water needs to be present for carbonate formation to take place. Mg and Ca carbonates and oxides should be common and thermodynamically stable weathering products in the present relatively dry and thin Martian atmosphere, whereas smectite clays and Ca carbonates would be present if weathering occurred under wetter conditions in a thicker CO_2 atmosphere (Gooding, 1978).

At present it is difficult to constrain the timing of carbonate formation in the Martian dust. Carbonate formation is dependent on a number of poorly known rates and factors under actual Martian conditions (e.g., Fanale *et al.*, 1992). Carbonates can form at a rapid rate when the Martian atmospheric conditions allow for liquid water in a transitory state (Kahn, 1985). Given the large surface area to volume ratio of the very small ($\leq 10\,\mu m$) dust particles, it is possible that carbonates are forming slowly today. Alternatively, carbonate formation could have become prohibitively slow under the current Martian surface pressure, and would only resume with an increase of atmospheric pressure (Kahn, 1985).

The wide distribution of dust containing 2–5 wt.% carbonate minerals may be a large sink of a thicker past Martian atmosphere. It is difficult to determine the total amount of CO_2 sequestered in Martian carbonates because the vertical extent of carbonate minerals is not constrained. However, a global regolith layer containing 2% carbonate that is 500 m thick could account for 0.5 bars of CO_2 (Fanale *et al.*, 1992; Bandfield *et al.*, 2003). Thus, the dust of Mars may provide the long-sought reservoir of a once-thicker (up to ~0.5 bar) CO_2 atmosphere.

9.6 AQUEOUS ROCKS AND PROCESSES

9.6.1 Hematite

Distribution, composition, and origin

Crystalline, coarse-grained, or "gray" hematite (α-Fe_2O_3) was identified from TES data and its occurrence has been

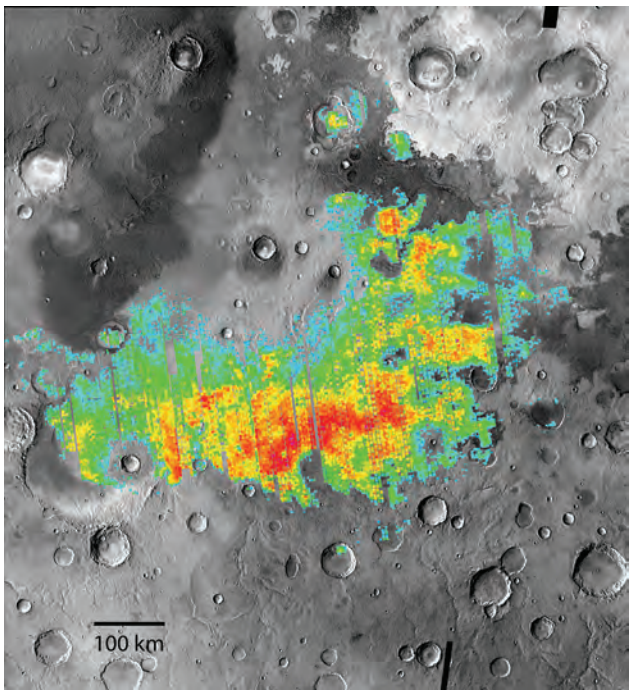

Figure 9.10. The spatial distribution of hematite in Meridiani Planum. The hematite abundance is shown in color, superimposed on a mosaic of THEMIS images of Meridiani Planum and the surrounding region. Red colors correspond to hematite abundances of 20%. (For a color version of this figure, please refer to the color plate section or to the e-Book version of this chapter.)

mapped globally (Christensen *et al.*, 2000c; Christensen *et al.*, 2001b; Christensen and Ruff, 2004). This mapping has revealed the presence of three major occurrences of crystalline hematite in the equatorial region. One, centered near 2° S latitude between 355° E and 360° E in Meridiani Planum, covers an area approximately 350 km by 750 km in size (Figure 9.10). The importance of this site for potential aqueous processes led directly to its selection as the target for the *Opportunity* MER mission. The second hematite occurrence is within Aram Chaos, a 300 km diameter ancient crater basin that has been filled with sediments and disrupted by subsequent chaos and outflow channel formation (Christensen *et al.*, 2001b; Glotch and Christensen, 2005). Similar deposits have been found in Aureum and Iani Chaos (Glotch and Rogers, 2007). These regions, like Aram Chaos, contain light-toned and hematite-bearing units that overlie chaotic terrain. Unlike Aram Chaos, the light-toned caprock units in Aureum and Iani Chaos have been shown to be sulfate-rich in OMEGA data (Gendrin *et al.*, 2005; Noe Dobrea *et al.*, 2006). The third region of hematite occurrence is in scattered locations throughout the Ophir/Candor region of Valles Marineris (Christensen *et al.*, 2001b; Knudson and Christensen, 2004).

Crystalline hematite is uniquely identified by the presence of fundamental vibrational absorption features centered near 300, 450, and $>525\,cm^{-1}$ (Christensen *et al.*, 2000c; Lane *et al.*, 2002; Glotch *et al.*, 2004). The depth and shape of the hematite fundamental bands showed that the hematite is crystalline and relatively coarse grained ($>10\,\mu m$) (Christensen *et al.*, 2000c; Christensen *et al.*, 2001b), and is distinct from the fine-grained (diameter <5–$10\,\mu m$), "red" crystalline hematite considered to be a minor spectral component in Martian bright regions (Morris *et al.*, 1997, 2000; Bell and Morris, 1999; see also Chapter 8). Laboratory thermal-emission measurements of hematite samples show variations in spectral properties for samples derived from different precursor minerals and by different processes (Glotch *et al.*, 2004). Hematites derived by lower-temperature (~300 °C) dehydroxylation of synthetic goethite, along with natural hematite samples derived from goethite precursors, are an excellent match to the TES spectra; hematites derived from high-temperature oxidation of magnetite provide a poor fit (Glotch *et al.*, 2004).

The Meridiani Planum materials are an in-place sedimentary unit that is regionally characterized by smooth, friable layers that are composed primarily of basaltic sediments with ~10%–15% crystalline gray hematite (Edgett and Parker, 1997; Christensen *et al.*, 2001b; Arvidson *et al.*, 2003; Christensen and Ruff, 2004). *In situ* observations from *Opportunity* strongly support an aqueous environment involving groundwater and evaporation (e.g., Squyres *et al.*, 2004; Grotzinger *et al.*, 2005; McLennan *et al.*, 2005). The hematite in Aram, Aureum, and Iani Chaos occurs in sedimentary layers that formed within these closed basins and appear to be closely associated in time (Hesperian) with the formation of the chaos and outflow terrains (Christensen *et al.*, 2001b; Glotch and Christensen, 2005; Glotch and Rogers, 2007). The Valles Marineris materials occur in small deposits (typically <50 km) that are associated with the interior layered deposits (Christensen *et al.*, 2001b; Knudson and Christensen, 2004). Many of these deposits have subsequently been shown to also contain sulfates (Bibring *et al.*, 2005; Gendrin *et al.*, 2005) suggesting similar formation process to those that formed the sulfate/hematite assembly in Meridiani Planum. Sub-surface water has been present in Aram, Aureum, and Iani Chaos and the hematite-bearing unit in Ophir/Candor is associated with layered, friable deposits that may be of aqueous origin (McCauley, 1978; Lucchitta, 1982; Nedell *et al.*, 1987; Glotch and Christensen, 2005; Gendrin *et al.*, 2005; Glotch and Rogers, 2007).

Formation modes for gray hematite can be grouped into two classes: (1) chemical precipitation and (2) thermal oxidation of magnetite-rich lavas. Chemical precipitation includes (a) precipitation of Fe oxides/oxyhydroxides at ambient temperatures from standing, oxygenated, Fe-rich water, followed by subsequent alteration to gray hematite (e.g., oxide iron formations), (b) precipitation from Fe-rich circulating fluids of hydrothermal or other origin, (c) low-temperature aqueous dissolution and leaching of iron-bearing silicates to form a residual precipitate rich in hematite (e.g., similar to a laterite), and (d) formation of hematitic surface coatings during weathering (Christensen *et al.*, 2000c; Christensen *et al.*, 2001b).

The regional geologic and mineralogic setting of all of these localities, together with the *in situ* observations by the *Opportunity* rover and the association in many regions with sulfates (Gendrin *et al.*, 2005), strongly favor models in which the deposits of crystalline gray hematite were formed

in an aqueous environment, either by chemical precipitation of hematite or an iron-oxide precursor from aqueous fluids under ambient or hydrothermal conditions.

Water at Meridiani Planum

The regional geologic context of Meridiani Planum provides additional constraints on the mode of formation of the layered rocks deposited there. The units that *Opportunity* landed on and explored are the uppermost layers in a ~200 m thick sequence of finely layered, friable sediments (e.g., Edgett and Parker, 1997; Arvidson *et al*., 2003; Christensen and Ruff, 2004; Edgett, 2005). The primary rock type present on the surface at Meridiani is basalt (Christensen *et al*., 2001b; Christensen and Ruff, 2004), currently occurring as wind-blown sand that was likely eroded from overlying basaltic layers. Sulfates are present in the near-surface layers explored by *Opportunity* (e.g., Squyres *et al*., 2004; Clark *et al*., 2005), but much of the underlying layers are basaltic sands that appear to have once been dunes (Grotzinger *et al*., 2005). The preponderance of basalt throughout Meridiani, including along the margins of the layered unit where the lower layers are exposed by erosion (Christensen and Ruff, 2004), suggests that much of this 200 m thick sequence is also primarily basaltic material. It is likely that much of the Meridiani layered units are composed of basaltic sands that were transported into a local basin by wind or water (Christensen and Ruff, 2004). Other hypotheses for the origin of these units include volcanic pyroclastic units (McCollom and Hynek, 2005) and impact base surge deposits (Knauth *et al*., 2005). The volcanic pyroclastic model suggests that the deposition of volcanic ash was followed by reaction with condensed sulfur-dioxide- and water-bearing vapors emitted from fumaroles (McCollom and Hynek, 2005). This model, however, would require both an implausible vertical compositional gradient within the primary volcanic deposits, and sulfur enrichment that correlates strongly with primary basalt composition (Squyres *et al*., 2006a). The observed geochemistry can be explained instead by a mixture of altered basalt and another component consisting of sulfates and hematite (Squyres *et al*., 2006a). The geologic setting, which includes the absence of nearby volcanic centers and a "wetting-upward" succession that records a progressive increase in the influence of groundwater and surface water in controlling depositional processes (Grotzinger *et al*., 2005; Glotch *et al*., 2006; Squyres *et al*., 2006a; Glotch and Rogers, 2007), is also closer to an aqueous environment than a volcanic one (see also discussion in Chapter 24). Arguments against an impact-generated base surge formation include (1) the thick (~200 m) sequence of layered rocks that make up the entire sequence of rocks in Meridiani; this sequence would require a massive impact (which is not observed) or a series of impacts that focused their deposits in Meridiani; (2) the lack of similar deposits elsewhere despite the ubiquitous occurrence of impact craters on Mars; and (3) the similar occurrence of hematite/sulfate mineral assemblages in layered rocks in Aram, Iani, and Aureum Chaos that appear to be associated with aqueous depositional environments (Christensen *et al*., 2001b; Gendrin *et al*., 2005; Glotch and Christensen, 2005; Glotch and Rogers, 2007).

An important constraint on the aqueous processes that formed the sulfates and hematite comes from the spatial distribution of hematite as mapped by TES. Insights into this question are found in two regions within the boundaries of the main hematite unit that have little or no hematite exposed on the surface. In both cases the hematite-free units are ~50 m thick and lie stratigraphically and topographically above the hematite-bearing unit (Christensen and Ruff, 2004). These units have similar morphology to the lower, hematite- and sulfate-bearing units, and may be basaltic sands that were not affected by the processes that formed sulfate and hematite in the lower units (Christensen and Ruff, 2004).

Another constraint comes from the spatial distribution of the layered materials themselves. The southern margin of the hematite unit appears to embay the high-standing terrain to the south, as originally noted by Edgett and Parker (1997) and discussed by subsequent authors (Christensen *et al*., 2000c; Hynek *et al*., 2002; Christensen and Ruff, 2004). This relationship suggests that the hematite-bearing unit was originally deposited in a dense, gravity-controlled fluid (Christensen and Ruff, 2004), rather than as a dispersed, air-fall layer (Hynek *et al*., 2002).

An important question today with regard to deposition within a basin is the nature of the topography surrounding the hematite deposit. Around 75% of its circumference, the hematite-bearing plains lie within a local trough, and in places where they are higher than their surroundings, this elevation difference is less than 50–100 m (Christensen and Ruff, 2004). A large amount of erosion has occurred in this region, as evidenced by etched plains and circular deposits that appear to have formed within now-eroded craters (Arvidson *et al*., 2003; Christensen and Ruff, 2004), making it unlikely that the remains of the original bounding topography of a closed basin would be preserved today.

Outliers of hematite-rich material to the north, west, and south are proposed to have been deposited within craters that formed separate closed basins (Christensen and Ruff, 2004). These outliers all occur within craters that are 20–40 km in diameter and are within 50 km of the margin. All of these occurrences appear to be eroded remnants of once-larger deposits. No hematite is observed on the inter-crater plains of the ancient cratered terrain, which vary in elevation from several hundred meters below to several hundred meters above the hematite-bearing unit. This lack of any detectable hematite on the plains units indicates either that hematite material was not deposited as a widely distributed unit, or that this material has been completely removed from the plains surfaces (Christensen and Ruff, 2004).

Based on the regional geologic context, it has been suggested that the layered, hematite- and sulfate-bearing units (called the Ph unit) were deposited within a series of local basins that were subsequently subjected to groundwater (Christensen and Ruff, 2004) and evaporation (Grotzinger *et al*., 2005; McLennan *et al*., 2005). The Ph unit lies on top of a distinctive etched unit (E) and on dissected ancient

cratered terrain (Arvidson *et al.*, 2003). Distinct differences in morphology, composition, and thermophysical properties indicate that units Ph and E were formed under dramatically different conditions, with unit E being originally lava plains (Arvidson *et al.*, 2003; Christensen and Ruff, 2004), and the relatively thin Ph units deposited as sediments and subjected to aqueous processes (Christensen and Ruff, 2004; Squyres *et al.*, 2004; Grotzinger *et al.*, 2005; Squyres and Knoll, 2005).

In this model of sedimentary deposition in closed basins followed by groundwater and evaporation, the environment changed from primarily aeolian deposition of basaltic sands to an aqueous groundwater/evaporation environment, and finally back to an aeolian environment in which the stratigraphically higher, hematite-free basaltic unit was deposited after the aqueous period was over. This model can account for: (1) the occurrence of a hematite-bearing (and presumably sulfate-bearing) unit over an area $\sim$150 000 km^2 in size with sharp upper and lower contacts; (2) spectral evidence for goethite, rather than high-temperature oxidation of magnetite, as the precursor to hematite; (3) the presence of a finely layered, friable texture on unit Ph in distinct contrast to the morphology of the Etched units on which it lies; (4) embayment relationships on the southern margin of unit Ph; (5) the occurrence of remnants of hematite-bearing units within isolated craters surrounding the main Ph unit, and the lack of these units on the intracrater plains; (6) the lack of other hydrothermal minerals; and (7) the presence of low-albedo, coarse-grained basaltic sand as the major component of unit Ph.

The formation of hematite-bearing material appears to have required a specific set of conditions that may have only occurred rarely through Mars history. The occurrence of unweathered olivine, pyroxene, and feldspar in basalts throughout the equatorial region provides strong evidence that extensive aqueous weathering has not occurred on Mars (Christensen *et al.*, 2000b, 2003; Hoefen *et al.*, 2003; Poulet *et al.*, 2005). Thus, the presence of a small number of bodies of ground and surface water appears to represent brief, localized phenomena set against the backdrop of a cold, frozen planet.

9.6.2 Phyllosilicates and other alteration products

Phyllosilicates (clays) and other alteration products have obvious implications for the role of water on Mars and have been sought in numerous spectroscopic studies (e.g., Singer *et al.*, 1985; Soderblom, 1992; Bell, 1996; Blaney *et al.*, 2003; Noe Dobrea *et al.*, 2003). Global mapping using TES has not shown unambiguous evidence for clays (Bandfield, 2002), primarily due to the fact that features diagnostic of clay minerals and some glassy or amorphous phases, both volcanic and authigenic (Wyatt and McSween, 2002), and some zeolites (Ruff, 2004) and palagonites (Morris *et al.*, 2003) have significant spectral overlap in the thermal IR wavelengths. Phyllosilicates have been identified using VNIR spectra from the Mars Express OMEGA instrument (Poulet *et al.*, 2005) in isolated occurrences on the Martian surface. Significantly, none of these occurrences is in Acidalia Planitia, the location of the greatest concentration of Type 2 material that may contain alteration products (Rogers and Christensen, 2007). This result is consistent with previous VNIR observations of Mars that have not provided definitive evidence of phyllosilicates in Acidalia Planitia at spatial scales observable using earth-based telescopes (e.g., Bell *et al.*, 1994; Blaney *et al.*, 2003; Noe Dobrea *et al.*, 2003).

While it may be impossible to differentiate unambiguously between all of these minerals because their spectral differences are so subtle, in some cases it may be more feasible (Koeppen and Hamilton, 2005). As was noted by Wyatt and McSween (2002) and Ruff (2004), some of the candidate clay minerals for Mars have distinguishing spectral characteristics in a portion of the thermal infrared (TIR) spectrum that has been excluded in atmospherically corrected TES spectra because of the absorption of atmospheric CO_2. The excluded region is wider than strictly necessary in an effort to avoid the confounding effects of CO_2 absorption in global mapping studies using spectral deconvolution. However, CO_2 opacity remains relatively low in the spectral region of the critical distinguishing feature between clay minerals and glasses, allowing for the possibility of identifying this specific feature in TES spectra. Work by Ruff and Christensen (2007) explores this possibility.

A simple spectral band ratio in the region near 530 cm^{-1}, where smectite clays and other minerals have absorptions, has been used to search for phyllosilicate (clay) minerals on the Martian surface (Ruff and Christensen, 2007). This band ratio, or spectral index, uses the ratio of the average of two TES bands at 518 and 529 cm^{-1} that are within a smectite clay absorption to the TES band at 560 cm^{-1}, which falls outside this absorption feature. This spectral index shows no evidence for phyllosilicate absorptions in the northern lowlands of Mars where the Type 2 spectral signature dominates (Ruff and Christensen, 2007). Olivine and other silicates do have absorptions near 530 cm^{-1} that would be detected by this index, and these absorptions are seen in the spectral index in some places on the planet. The absence of any absorption at these wavelengths in the low-albedo materials of the northern lowlands is remarkable, and suggests that only minerals lacking absorption in this spectral range (i.e., not phyllosilicates) are present. High-silica glasses, which were suggested by Bandfield *et al.* (2000a) to be major components of Type 2 material, do not have absorptions near 530 cm^{-1}, and are better candidates for the Type 2 spectral signature than phyllosilicates. However, this does not preclude the possibility that high-silica coatings on basaltic material, as some have suggested (Kraft *et al.*, 2003; Wyatt *et al.*, 2004; Michalski *et al.*, 2005), are present.

9.6.3 Sulfates

One of the key discoveries from the OMEGA experiment has been the detection of sulfates in several locations across the planet using vibrational absorption bands in the 3–4 μm region (Bibring *et al.*, 2005, 2006; Gendrin *et al.*, 2005; see also Chapter 7). Sulfates also have a fundamental vibrational feature near 8.7 μm (1150 cm^{-1}) that is covered by

TES. This feature is not observed in TES atmosphere-corrected surface spectra, and sulfates have not been detected at abundances greater than ~10% in deconvolution modeling of TES spectra (Bandfield *et al.*, 2000a; Christensen *et al.*, 2000b). Possible explanations for the lack of a TES detection are that sulfate abundances are below ~10%, or particle size or textural effects exist that may subdue the spectral band depth at longer wavelengths (Kirkland *et al.*, 2003). In addition, as discussed in Section 9.5, it has been suggested that hydrous iron sulfates are present in the Martian dust (Lane *et al.*, 2004).

A spectral inflection is present in the derived atmospheric dust spectrum (Bandfield *et al.*, 2000b; Smith *et al.*, 2000) whose position is consistent with sulfate. This observation is consistent with previous indications of sulfate from Earth-based telescopic near-IR spectra (Blaney and McCord, 1995). However, the relative depth of this feature does not vary with location, leading to the assumption that it is an atmospheric component (Bandfield *et al.*, 2000b; Smith *et al.*, 2000). If this is the case, then this feature does not pertain directly to the question of the nature of sulfur identified in lander observations (Clark and Baird, 1979; Reider *et al.*, 1997; McSween *et al.*, 1999; Bell *et al.*, 2000; Morris *et al.*, 2000). If this feature is present in the surface materials, then the lack of spatial variation in its depth implies that the abundance of sulfate is uniform everywhere on the planet. This implication does not appear plausible based on the geologic evidence for widespread variation in surface processes and the OMEGA results.

The TES results provide an estimate of the upper limit of sulfates of 10%–15%, even in regions where OMEGA has detected sulfate occurrence. This TES upper limit is consistent with the abundances measured at lander and rover sites. To date, the OMEGA observations have not been inverted to provide quantitative estimates of sulfate abundances.

The "White Rock" feature on Mars (within Pollack crater centered at ~8° S, 335° W) has long been viewed as a type example for a Martian playa deposit, largely due to its apparent high albedo along with its location in a closed impact crater basin. Playa deposits can host abundant sulfates and some carbonates, so White Rock was an important target for the TES investigation. A thorough analysis of this feature has been performed using albedo, thermal inertia, and spectral data from TES as well as high-resolution images from the Mars Orbiter Camera (Ruff *et al.*, 2001). These data demonstrate that White Rock is not anomalously bright relative to other Martian bright regions, reducing the significance of its supposedly high albedo and weakening the analogy to terrestrial playas. Its thermal inertia value indicates that it is not mantled by a layer of loose dust nor is it bedrock. Further, the thermal infrared spectrum of White Rock has little spectral contrast, with no obvious features of carbonates or sulfates. However, halite – a major evaporite playa mineral – has a flat spectrum and so can not be ruled out as a constituent of White Rock nor can small amounts (less than ~10%) of carbonates and sulfates. One explanation for the origin of White Rock consistent with the observations is that it is an eroded accumulation of compacted or weakly cemented aeolian sediment.

9.7 RELATIONSHIP TO MARTIAN METEORITES

For many years, and even today, our most detailed knowledge of the geochemistry and mineralogy of Mars has come from laboratory studies of meteorites ejected from the Martian surface (McSween, 1985, 1994, 2003; Treiman *et al.*, 2000; Nyquist *et al.*, 2001; see Chapter 17). These meteorites have been referred to as "SNC" meteorites for the three original classes: Shergottites, Nakhlites, and Chassigny. In more recent years, a fourth class has been identified from a single sample, ALH 84001. A more detailed summary of the mineralogy, petrology, and geochemistry of Martian meteorites can be found in Chapter 17, but in general, shergottites are basalts and ultramafic cumulates, nakhlites are clinopyroxenites, chassignites are dunites, and ALH 84001 is an orthopyroxenite. One of the most characteristic features of all of the meteorites is that they are dominated modally by pyroxene and/or olivine, with plagioclase feldspars occurring as a less abundant phase in most cases, including among most of the basaltic shergottites (which commonly contain subequal amounts of augite and pigeonite).

Broadly speaking, the prevalence of mafic (basaltic) lithologies among the Martian meteorites is consistent with the generally mafic character of the dust-free, dark regions of Mars observed telescopically and from orbit (e.g., Adams, 1968; McCord *et al.*, 1971; Mustard *et al.*, 1997; Bandfield *et al.*, 2000a; Christensen *et al.*, 2000b; Bibring *et al.*, 2005). However, in detail, there seem to be more differences than similarities between the mineralogies of the surface types that characterize the majority of Mars in TES data and those of the Martian meteorites. One of the most significant differences is that although mafic minerals are volumetrically dominant in the majority of meteorites, feldspars appear to dominate the primary mineralogies observed in TES data (Bandfield *et al.*, 2000a; Christensen *et al.*, 2000b) and the spectral signatures of ST1 and ST2 are not good matches to Martian meteorite spectra (Figure 9.11) (Hamilton *et al.*, 2003a). The composition of TES ST1 is basaltic, but is best modeled with plagioclase > pyroxene (and little pigeonite). TES ST2, regardless of whether it is interpreted as a primary basaltic andesite/andesite (Bandfield *et al.*, 2000a) or weathered basalt (Wyatt and McSween, 2002) lithology, has no equivalent among the meteorites. The TES spectrum of (high albedo) surface dust retrieved by Bandfield and Smith (2003) is low in contrast and relatively devoid of silicate spectral features in the reststrahlen region; it does, however, display a transparency feature characteristic of plagioclase feldspar, suggesting that phase may be dominant. The absolute abundances of other phases that might be present are poorly constrained at present. Although there are regional units with elevated abundances of olivine (Hoefen *et al.*, 2003), nearly equal amounts of plagioclase and high-Ca clinopyroxene, or rare cases with pyroxene > plagioclase (Rogers and Christensen, 2007), mineralogical mapping with TES data shows that there are no globally extensive areas characterized by

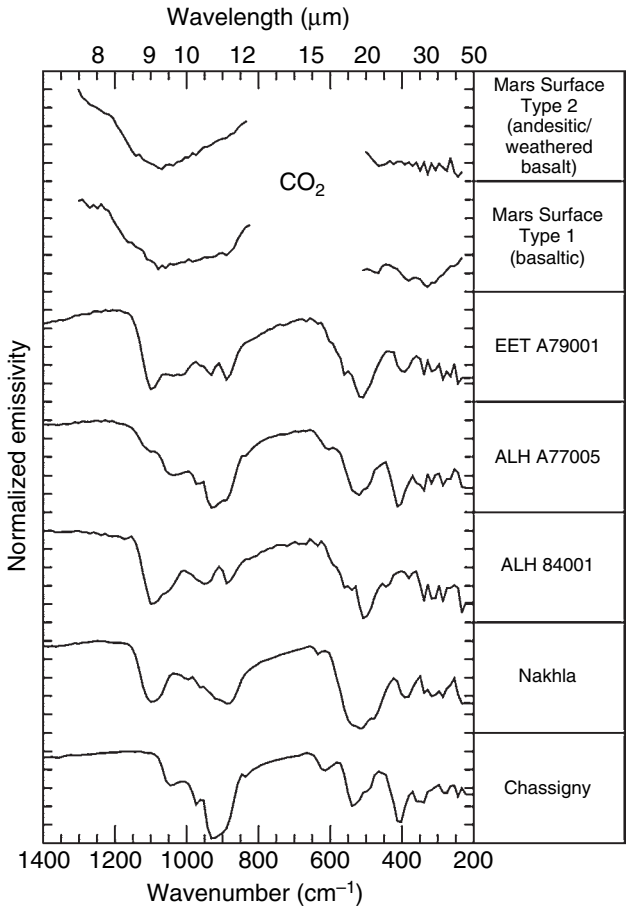

Figure 9.11. Comparison of spectra of TES Types 1 and 2 to Martian meteorite spectra.

ultramafic lithologies (e.g., clinopyroxenite, orthopyroxenite, dunite) (Bandfield, 2002).

Another way to compare Martian meteorite compositions to materials on Mars is to use thermal infrared laboratory spectra of the meteorites (Hamilton *et al.*, 1997) to identify TES spectra with similar signatures. Such an approach does not rely on spectral libraries, which may not contain mineral spectra representative of the exact compositions in Martian meteorites. A study by Hamilton *et al.* (2003b) used laboratory spectra of the major classes of Martian meteorites (along with Martian ST1, ST2, hematite, and atmospheric spectra) to linearly deconvolve (Ramsey and Christensen, 1998) the global TES dataset. In addition to searching for meteorite-like lithologies, a goal of this study was to constrain possible source regions of the meteorites, which could provide valuable contextual information, yield additional insight into the ejection process, and might allow crater count-derived ages of surface units to be directly linked to the absolute age of the meteorite(s), providing a means of anchoring the Martian geologic time scale. The study demonstrated that no spatially extensive (thousands of square kilometers) dark regions on Mars are dominated by thermal infrared spectral shapes resembling those of the Martian meteorites (Hamilton *et al.*, 2003b). However, in several local (tens to hundreds of kilometers) areas, concentrations of materials with meteorite-like spectra were identified at or above general TES detectability limits. The most notable occurrences, in terms of spatial extent and/or abundance of the meteorite-like component, are in the area around the Nili Fossae, in craters in Aurorae Planum, and in Eos Chasma. The spectra of olivine-rich meteorites Chassigny and ALHA 77005 were used in fits to data in all three locations in concentrations up to 20%. A spectral shape matching that of the orthopyroxenite ALH 84001 was identified in concentrations of up to 40% in Eos Chasma, in an area ~25–30 km in diameter, the largest spatial occurrence with such high abundances and the first unambiguous detection of an orthopyroxene component on the Martian surface. Nakhlite- and Shergottite-like spectral signatures were not identified in significant spatial or fractional abundances.

The identification of some Martian meteorite-like spectral signatures on Mars is promising, but cannot be interpreted uniquely as representing the source regions of the meteorites. It is nonetheless instructive to consider the locations in which these signatures have been identified in the context of a few of the known characteristics of the meteorites. Occurrences of Chassigny- and ALHA 77005-like spectral signatures in TES data are spread over sufficiently large areas that a large number of craters having the requisite dimensions to be considered candidates are present (as small as ~1.5–3 km [Head *et al.*, 2002; Beck *et al.*, 2005]). Nili Fossae may not be a good candidate source region because of the ancient age of the surface (Noachian, >3.0 Ga) relative to the much younger ages of the olivine-rich meteorites (< ~1.3 Ga). Furthermore, Chassigny and Nakhla appear to have been ejected in the same event (Nyquist *et al.*, 2001), but strong Nakhla-like signatures are not identified in the Nili Fossae region. Olivine-enriched materials in Aurorae Planum or in the Valles Marineris may be more age-appropriate, but the lack of strong Nakhla-like signatures poses the same problem for those locations. Studies of the likelihood of the Eos Chasma orthopyroxene-rich materials serving as the source of ALH 84001 are ongoing, and the location of these materials within a mass wasting deposit originating in the canyon wall may help explain why such an old rock (~4.52 Ga) would be found in an otherwise relatively young region (Hamilton *et al.*, 2003b).

Despite numerous analyses and various interpretations of TES data, the thermal emission spectra of the majority of dark surfaces on Mars generally are not consistent with Martian meteorite compositions, including the relatively common basaltic shergottites. Shergottite-like lithologies are distinguishable from other basalts observed in thermal infrared spectra of Mars, as demonstrated by the example of Mini-TES spectra of Bounce rock at the MER landing site in Meridiani Planum (Christensen *et al.*, 2004a; see Chapter 14). The lack of shergottite signatures at global scales suggests that shergottites are not characteristic of dark regions. This is in contrast to previous analyses based on VNIR data (e.g., Mustard and Sunshine, 1995), where the relative abundances of high- and low-Ca pyroxene were suggested to be consistent with the relative abundances of high- and low-Ca pyroxene in shergottites. However, these

relative abundances also are consistent with a wide range of absolute abundances that differ from those in shergottites, including those of the basaltic TES ST1 spectrum (Hamilton *et al.*, 2003b).

Global results from TES support the idea that the Martian meteorites are a biased sampling of the Martian crust. The dominance of plagioclase-rich basaltic compositions suggests that the bulk of the Martian crust in dark regions is not Al depleted; in fact, the formation of the crust may be responsible for the Al-depletion exhibited by the Martian meteorites, which represent a later period (or different style) of volcanism. The generally young ages of the meteorites have been used to infer that their sources are geologically young surfaces, such as portions of the Tharsis and Elysium regions. Indeed, recent work has suggested that long-rayed, young craters may be good candidates for some of the Martian meteorites (McEwen *et al.*, 2005; Tornabene *et al.*, 2006). Unfortunately, the ubiquitous dust covering these young volcanic regions may prevent mineralogical remote-sensing instruments from uniquely identifying them as potential SNC source regions.

9.8 HISTORY OF WATER

Many of the ancient terrains of Mars contain channels that were eroded by water (e.g., Carr, 1996). Analysis of the global distribution of these channels has shown that extensive fluvial activity occurred during a period of erosion early in Mars history that produced extensive infilling of craters, the development of local and regionally integrated drainage networks, and the formation of deltas and alluvial fan deposits (e.g., Gulick and Baker, 1989; Craddock and Maxwell, 1993; Grant, 2000; Hynek and Phillips, 2003; Malin and Edgett, 2003; Moore *et al.*, 2003; Forsberg-Taylor *et al.*, 2004; Mangold *et al.*, 2004; Howard *et al.*, 2005). The development of these drainage networks and depositional fans is suggestive of runoff from precipitation or rapid melting of snow, possibly aided by groundwater sapping (e.g., Gulick and Baker, 1989; Malin and Edgett, 2003; Hynek and Phillips, 2003; Mangold *et al.*, 2004; Howard *et al.*, 2005; Moore and Howard, 2005). It has also been proposed that Mars had extensive oceans on the basis of images and topographic data that suggest shorelines, smooth ocean floors, and glacial features (Parker *et al.*, 1993; Kargel *et al.*, 1995; Head *et al.*, 1999).

9.8.1 Evidence for a primarily cold, dry Mars

The results from global mineral mapping tend to show a different picture from what is seen in the Martian geomorphology. What has emerged from the mineralogy is an ancient surface whose original volcanic minerals are still generally preserved. The presence of original olivine, pyroxene, feldspar, and glass in ancient volcanic terrains indicates that, overall, Mars has undergone little alteration by water. Ancient pyroxene- and olivine-rich basalts are common; they are exposed more than 4.5 km below the surface in the walls of Valles Marineris and throughout the equatorial plains, including the floors of river channels cut by water (Christensen *et al.*, 2003; Hamilton *et al.*, 2003b; Hoefen *et al.*, 2003; Bibring *et al.*, 2005; Christensen *et al.*, 2005; Hamilton and Christensen, 2005; Mustard *et al.*, 2005; Rogers *et al.*, 2005). The old, glass-rich dacite flows on Syrtis Major are also highly susceptible to chemical weathering. The occurrence of these easily weathered minerals, both at the surface and deep beneath it, suggests that neither sub-surface hydrothermal activity nor surface aqueous weathering has significantly affected these very old rocks since they were emplaced. Evidence for aqueous minerals and aqueous alteration is certainly present, including phyllosilicates in limited locations (Bibring *et al.*, 2006) and the possible origin of Type 2 materials as an aqueous altered basalt (Wyatt and McSween, 2002). However, as discussed, above these regions represent relatively small areas, particularly in light of the better discrimination of truly Type 2 materials to limited portions of the Acidalia plains (Rogers and Christensen, 2007; Rogers *et al.*, 2007).

The *Spirit* rover at Gusev crater has provided additional mineralogic evidence for only limited aqueous weathering on Mars. The rocks on the crater floor are volcanic and extremely old, perhaps as much as 3 Gyr; yet the Mini-TES, Mössbauer, and APXS spectrometers and multispectral cameras on the rover clearly show the presence of olivine and pyroxene minerals that have been altered very little since these lavas first cooled (Christensen *et al.*, 2004a; Gellert *et al.*, 2004; McSween *et al.*, 2004; Morris *et al.*, 2004). These pristine volcanic rocks provide evidence that the Gusev plains have not been exposed to any significant amount of water since these lavas were erupted. They may have been "wetted," as evidenced by thin coatings on some rocks, but they have not been "soaked." Some rocks in the Columbia Hills observed by *Spirit* do show evidence for some degree of aqueous alteration (e.g., Gellert *et al.*, 2006; Ming *et al.*, 2006; Morris *et al.*, 2006; Squyres *et al.*, 2006b). However, it has been suggested based on Mini-TES data that some of these rocks are basaltic glasses that lack spectral evidence for phyllosilicates, despite indications for alteration from the other MER instruments (Ruff *et al.*, 2006). In any case, the Columbia Hills rocks appear to be older than the Gusev plains basalts, and may date to a very early episode of aqueous alteration.

It has been suggested that if Mars ever had a warm ocean then thick deposits of carbonates would have also formed through interactions with its CO_2 atmosphere (e.g., Booth and Kieffer, 1978; Fanale and Jakosky, 1982; Kahn, 1985; Fanale *et al.*, 1992). However, no evidence of carbonate rock layers has been found by the TES, THEMIS, or OMEGA instruments (Christensen *et al.*, 2001a; Bibring *et al.*, 2005), suggesting that if Mars ever had oceans, they were either too cold, too short lived, were covered by ice that limited interactions with the atmosphere, or had unique chemical conditions that prevented carbonates from forming. The inferred presence of small amounts of carbonate in the Martian dust and in Martian meteorites has shown that carbonates do form on Mars (Bandfield *et al.*, 2003; Christensen *et al.*, 2004a). However, these

minerals most likely formed by direct interaction with water vapor in the atmosphere or small amounts of fluid, rather than through erosion and transport of preexisting rock units formed in liquid. Clay minerals, which form primarily by aqueous weathering and are common on Earth, have also been shown by OMEGA and TES to be rare on Mars (Bibring *et al.*, 2005, 2006; Michalski *et al.*, 2005), again suggesting that Mars has experienced little aqueous alteration.

While lakes and drainage networks clearly suggest fluvial processes, the lack of extensive carbonates and clays, together with the presence of original olivine, pyroxene, feldspar, and glass, argues that fluvial processes were relatively short lived and occurred early in Mars' history. Thus, on a global scale, aqueous chemical weathering appears to have been a relatively minor process throughout much of Martian history.

9.8.2 A locally wet Mars

Clear evidence for liquid water has been found in the Meridiani Planum region explored by the *Opportunity* rover. Outcrops of layered sedimentary rocks were observed by *Opportunity*'s cameras, and the Mössbauer, APXS, and Mini-TES spectrometers show that these rocks contain high (30%–40%) abundances of sulfates (Christensen *et al.*, 2004b; Klingelhöfer *et al.*, 2004; Rieder *et al.*, 2005) formed by evaporation of sulfur-rich water (Squyres *et al.*, 2004; Grotzinger *et al.*, 2005; McLennan *et al.*, 2005). The presence of significant (25%) amorphous silica and no pyroxene or olivine in the outcrop (Glotch *et al.*, 2006) is also consistent with the view that the silicic precursor of the outcrop had been heavily weathered (Squyres *et al.*, 2004; Squyres and Knoll, 2005). The hematite is in 1–5 mm diameter spheres that occur within the rock layers (Bell *et al.*, 2004; Herkenhoff *et al.*, 2004), and were likely formed by fluids circulating through the sediments (e.g., Chan *et al.*, 2004; Squyres *et al.*, 2004). The coarsely layered rocks exposed at the base of Burns Cliff in Endurance crater appear to have been formed by migrating dunes, whereas the layers at the top of the cliff are made of sulfate-rich sediments deposited in water (Grotzinger *et al.*, 2005). These layers may record variations in climate from arid aeolian dunes, to wet evaporating playas where the sulfate salts were formed, to a groundwater system that formed the hematite spheres (Grotzinger *et al.*, 2005; McLennan *et al.*, 2005). This system may have persisted for thousands of years. The margins of this aqueous system may not have extended much beyond the current deposits of hematite seen from orbit, making this a large lake/groundwater system (Christensen and Ruff, 2004), rather than part of a global ocean (Hynek, 2005). Several nearby craters also have hematite-rich layered rocks, suggesting they may have held separate lakes.

Evidence for standing water is also seen at Aram Chaos, a 300 km diameter crater basin that is filled with layered rocks that contain hematite and sulfate and show evidence for a lake created by the release of massive amounts of subsurface water (Christensen *et al.*, 2001b; Catling and Moore, 2003; Gendrin *et al.*, 2005; Glotch and Christensen, 2005). Finely layered rocks that are easily eroded and contain hematite and sulfate are also found in the troughs of Valles Marineris (Christensen, *et al.*, 2001b; Knudson and Christensen, 2004; Gendrin *et al.*, 2005), suggesting that they were also deposited in standing water.

In addition, the occurrence of phyllosilicates in ancient terrains has been suggested to indicate an early hydrological system that put igneous minerals in contact with liquid water for extended periods of time very early in Mars' history (Bibring *et al.*, 2005, 2006; Gendrin *et al.*, 2005; Poulet *et al.*, 2005). This process may have occurred in only localized areas given the scarcity of phyllosilicate occurrences. This period of local alteration has been postulated to have then been followed by a more acidic environment in which sulfates formed (Bibring *et al.*, 2005, 2006; Gendrin *et al.*, 2005; Poulet *et al.*, 2005).

These occurrences provide strong evidence that water was stable in isolated regions for unconstrained periods of time. The prevailing environment during the early period of fluvial erosion may have been one of a cold, thin atmosphere with very limited mechanical erosion, punctuated by short periods of thicker atmosphere and greater erosion. These thicker atmospheres may have been produced by periodic orbitally forced climate changes (e.g., Ward, 1974; Pollack and Toon, 1982; Laskar *et al.*, 2004), or generated in the impact cratering process and lasting hundreds to thousands of years (Segura *et al.*, 2002). Fluvial erosion appears to have reached a climax in the late Noachian period (~3–3.5 Ga) (Howard *et al.*, 2005), with only limited activity since that time that is primarily associated with large catastrophic flood events (e.g., Carr, 1996), isolated channel formation (e.g., Gulick and Baker, 1990), and minor incision of small gullies (e.g., Malin and Edgett, 2000). What factors caused water to accumulate and allowed it to remain at these sites? The answer is unknown, but perhaps involves a combination of heat from sub-surface volcanic activity, high salt concentrations that lowered the freezing temperature, and/or a protective covering of ice over water released by catastrophic floods.

9.8.3 Modern snow and ice

There is growing evidence that Mars has a large inventory of water that is currently in the form of ice in the mid to high latitudes (Mustard *et al.*, 2001; Christensen, 2003; Head *et al.*, 2005; Shean *et al.*, 2005). Temperature measurements have demonstrated that the perennial north polar cap is water ice (Kieffer *et al.*, 1976). Recent measurements by Mars Orbiter Camera (MOC), THEMIS, and OMEGA have shown that windows of water ice are exposed within the south polar cap, indicating that water ice is present there beneath a thin layer of overlying CO_2 ice (Thomas *et al.*, 2000; Byrne and Ingersoll, 2003; Titus *et al.*, 2003; Bibring *et al.*, 2004). A substantial inventory of water ice was discovered using data from the Gamma Ray Spectrometer, Neutron Spectrometer, and the High-Energy Neutron Detector instruments on Mars Odyssey in the regions poleward of ~60° in both hemispheres (Boynton *et al.*, 2002;

Feldman *et al*., 2002; Mitrofanov *et al*., 2002; see also Chapters 5 and 6). Ice abundances are greater than ~80%, suggesting that the ice must have been deposited as a layer of snow or frost.

These high-latitude water reservoirs can migrate as the climate changes (e.g., Ward, 1974; Pollack and Toon, 1982; Jakosky and Carr, 1985; Jakosky *et al*., 1995; Haberle *et al*., 2001; Forget *et al*., 2006). Remnants of these ice deposits can be found in unusual landforms throughout the mid latitudes. One type is a "basketball-textured" terrain that only occurs between 30° and 50° latitude in both hemispheres and was suggested to form as soils cemented by ice deposited during the last "ice age" lose their ice and erode as the climate warms (Mustard *et al*., 2001). A second type of deposit occurs preferentially on cold, pole-facing slopes (Carr, 2001; Malin and Edgett, 2001; Christensen, 2003) as "pasted on" slope mantles up to ~10 m thick, often occurring in hollows; some have features suggestive of flow (Milliken, 2003). These characteristics suggest an ice-rich layer that was once more extensive but has been removed from all but the coldest, pole-facing slopes where it is protected against sublimation by a layer of desiccated dust/sediment. A third type of deposit is the inferred past presence of glaciers on the flanks of the large Tharsis volcanoes (e.g., Head *et al*., 2005), in locations that closely approximate those predicted by atmospheric circulation models (Forget *et al*., 2006).

Recent gullies also occur between ~30° and 50° latitude in both hemispheres (Malin and Edgett, 2000). These gullies have been proposed to form from discharge of liquid water from sub-surface aquifers (Malin and Edgett, 2000; Gaidos, 2001; Mellon and Phillips, 2001; Heldmann and Mellon, 2004; Malin *et al*., 2006), the rapid release of liquid CO_2 (Musselwhite *et al*., 2001), dry landslides (Treiman, 2003), the melting of ground ice that percolates to an impermeable layer (Gilmore and Phillips, 2002), the melting of pore ice that diffused inward from the atmosphere during periods of colder temperatures (Costard *et al*., 2002), or through melting of a snow layer deposited during periods of higher obliquity when surface ice was stable at these latitudes (Lee *et al*., 2001; Hartmann, 2002; Hecht, 2002; Christensen, 2003). Recent observations suggest that the gullies that show no clear association with mantles may have been active in the past decade (Malin *et al*., 2006). However, the nature of this activity and the source of fluid remain uncertain. Whatever their origin, the presence of gullies implies the occurrence of near-surface liquid water in the recent past.

9.9 SUMMARY

As seen from these results, there are large variations in the role water has had at different times and in different places on Mars. There is no question that Mars experienced periods of channel formation early in its history, yet those ancient rocks lack extensive carbonates and clays and contain minerals that quickly break down in a wet environment. The current climate is very dry and cold, yet the *Opportunity* rover landed on the floor of an ancient body of water. Finally, liquid water is not stable at the surface today, yet recent gullies emerge from modern aquifers or beneath modern snowpacks.

One possible means to reconcile these apparently conflicting views is that the erosional periods were too brief for extensive chemical weathering to have occurred (mechanical erosion of channels can proceed much more rapidly than chemical weathering). The erosional periods may have been caused by large impacts that produced very short-lived, thick atmospheres that allowed liquid water to persist (Segura *et al*., 2002). Thus, while Mars has a large inventory of water, it is likely that this water has remained frozen throughout much of Mars history, resulting in very little chemical weathering. Occasionally, this water was melted and released to form channels, lakes, and groundwater.

REFERENCES

Adams, J. B., Lunar and martian surfaces: petrologic significance of absorption bands in the near-infrared, *Science* **159**, 1453–5, 1968.

Adams, J. B., Visible and near-infrared diffuse reflectance spectra of pyroxenes as applied to remote sensing of solid objects in the solar system, *J. Geophys. Res.* **79**, 4829–36, 1974.

Adams, J. B., M. O. Smith, and P. E. Johnson, Spectral mixture modeling: a new analysis of rock and soil types at the Viking Lander 1 site, *J. Geophys. Res.* **91**, 8098–112, 1986.

Albee, A. L., R. E. Arvidson, F. Palluconi, and T. Thorpe, Overview of the Mars Global Surveyor Mission, *J. Geophys. Res.* **106**, 23291–316, 2001.

Arvidson, R. E., F. P. Seelos IV, K. S. Deal, *et al*., Mantled and exhumed terrains in Terra Meridiani, Mars, *J. Geophys. Res.* **108**(E12), 8073, doi:8010.1029/2002JE001982, 2003.

Bandfield, J. L., Global mineral distributions on Mars, *J. Geophys. Res.* **107**, doi:10.1029/2001JE001510, 2002.

Bandfield, J. L. and M. D. Smith, Multiple emission angle surface-atmosphere separations of Thermal Emission Spectrometer data, *Icarus* **161**, 47–65, 2003.

Bandfield, J. L., V. E. Hamilton, and P. R. Christensen, A global view of Martian volcanic compositions, *Science* **287**, 1626–30, 2000a.

Bandfield, J. L., M. D. Smith, and P. R. Christensen, Spectral data-set factor analysis and endmember recovery: application to analysis of martian atmospheric particulates, *J. Geophys. Res.* **105**, 9573–88, 2000b.

Bandfield, J. L., T. D. Glotch, and P. R. Christensen, Spectroscopic identification of carbonates in the Martian dust, *Science* **301**, 1084–87, 2003.

Bandfield, J. L., V. E. Hamilton, P. R. Christensen, and H. Y. McSween Jr., Identification of quartzofeldspathic materials on Mars, *J. Geophys. Res.* **109**, doi:10.1029/2004JE002290, 2004.

Barker, F., Trondhjemite: definition, environment, and hypothesis of origin. In *Trondhjemites, Dacites, and Related Rocks* (ed. F. Barker), New York: Elsevier, pp. 1–12, 1979.

Beck, P., P. Gillet, A. E. Goresy, and S. Mostefaoui, Timescales of shock processes in chondritic and Martian meteorites, *Nature* **435**, 1071–4, 2005.

Bell III, J. F., Iron, sulfate, carbonate, and hydrated minerals on Mars. In *Mineral Spectroscopy: A Tribute of Roger G. Burns*

(ed. M. D. Dyar *et al.*), The Geochemical Society, Special Publication No. 5, pp. 359–80, 1996.

Bell III, J. F. and R. V. Morris, Identification of hematite on Mars from HST, *Lunar Planet. Sci. XXX*, Abstract #1751, 1999.

Bell III, J. F., J. B. Pollack, T. R. Geballe, D. P. Cruikshank, and R. Freedman, Spectroscopy of Mars from 2.04 to 2.44 μm during the 1993 opposition: absolute calibration and atmospheric vs. mineralogic origin of narrow absorption features, *Icarus* **111**, 106–23, 1994.

Bell III, J. F., H. Y. McSween Jr., S. L. Murchie, *et al.*, Mineralogic and compositional properties of Martian soil and dust: results from Mars Pathfinder, *J. Geophys. Res.* **105**, 1721–55, 2000.

Bell III, J. F., S. W. Squyres, R. E. Arvidson, *et al.*, Pancam multispectral imaging results from the Opportunity Rover at Meridiani Planum, *Science* **306**, 1703–9, 2004.

Bibring, J.-P., Y. Langevin, F. Poulet, *et al.*, Perennial water ice identified in the south polar cap of Mars, *Nature* **428**, 627–30, 2004.

Bibring, J.-P., Y. Langevin, A. Gendrin, *et al.*, Mars surface diversity as revealed by the OMEGA/Mars Express observations, *Science* **307**, 1576–81, doi:1510.1126/science.1108806, 2005.

Bibring, J.-P., Y. Langevin, J. F. Mustard, *et al.*, Global mineralogical and aqueous Mars history derived from OMEGA/Mars Express data, *Science* **312**, 400–4, doi:410.1126/science.1122659, 2006.

Blaney, D. L. and T. B. McCord, Indications of sulfate minerals in the martian soil from Earth-based spectroscopy, *J. Geophys. Res.* **100**, 14433–41, 1995.

Blaney, D., D. Glenar, and G. Bjoraker, High spectral resolution spectroscopy of Mars from 2 to 4 μm: surface mineralogy and the atmosphere, *6th Int. Conf. Mars*, Pasadena, California, Abstract #3237 (CD-ROM), July 20–25, 2003.

Booth, M. C. and H. H. Kieffer, Carbonate formation in Marslike environments, *J. Geophys. Res.* **83**, 1809–15, 1978.

Borg, L. E., L. E. Nyquist, H. Weissman, C.-Y. Shih, and Y. Reese, The age of Dar al Gani 476 and the differentiation history of the martian meteorites inferred from their radiogenic isotopic systematics, *Geochim. Cosmochim. Acta* **67**, 3519–36, 2003.

Boynton, W. V., W. C. Feldman, W. Squyres, *et al.*, Distribution of hydrogen in the near surface of Mars: evidence for subsurface ice deposits, *Science* **297**, 81–5, 2002.

Brain, D. A. and B. M. Jakosky, Atmospheric loss since the onset of the Martian geologic record: combined role of impact erosion and sputtering, *J. Geophys. Res.* **103**, 22689–94, 1998.

Byrne, S. and A. P. Ingersoll, A sublimation model for martian south polar ice features, *Science* **299**, 1051–3, 2003.

Calvin, W. M., T. V. V. King, and R. N. Clark, Hydrous carbonates on Mars? Evidence from Mariner 6/7 Infrared Spectrometer and ground-based telescopic spectra, *J. Geophys. Res.* **99**, 14659–75, 1994.

Carr, M. H., *Water on Mars*, New York: Oxford University Press, 1996.

Carr, M. H., Mars Global Surveyor observations of fretted terrain, *J. Geophys. Res.* **106**, 23571–95, 2001.

Catling, D. C. and J. M. Moore, The nature of coarse-grained crystalline hematite and its implications for the early environment of Mars, *Icarus* **165**, 277–300, 2003.

Chan, M. A., B. Beitler, W. T. Parry, J. Ormo, and G. Komatsu, A possible terrestrial analogue for hematite concretions on Mars, *Nature* **429**, 731–4, 2004.

Christensen, P. R., Martian dust mantling and surface composition: interpretation of thermophysical properties, *J. Geophys. Res.* **87**, 9985–98, 1982.

Christensen, P. R., Regional dust deposits on mars: physical properties, age, and history, *J. Geophys. Res.* **91**, 3533–45, 1985.

Christensen, P. R., Variations in martian surface composition and cloud occurrence determined from thermal infrared spectroscopy: analysis of Viking and Mariner 9 data, *J. Geophys. Res.* **103**, 1733–46, 1998.

Christensen, P. R., Formation of recent martian gullies through melting of extensive water-rich snow deposits, *Nature* **422**, 45–8, doi:10.1038/nature01436, 2003.

Christensen, P. R. and S. T. Harrison, Thermal infrared emission spectroscopy of natural surfaces: application to desert varnish coatings on rocks, *J. Geophys. Res.* **98**, 19819–34, 1993.

Christensen, P. R. and S. W. Ruff, The formation of the hematite-bearing unit in Meridiani Planum: evidence for deposition in standing water, *J. Geophys. Res.* **109**, E08003, doi:08010.01029/02003JE002233, 2004.

Christensen, P. R., D. L. Anderson, S. C. Chase, *et al.*, Thermal Emission Spectrometer experiment: the Mars Observer mission, *J. Geophys. Res.* **97**, 7719–34, 1992.

Christensen, P. R., J. L. Bandfield, V. E. Hamilton, *et al.*, A thermal emission spectral library of rock forming minerals, *J. Geophys. Res.* **105**, 9735–8, 2000a.

Christensen, P. R., J. L. Bandfield, M. D. Smith, V. E. Hamilton, and R. N. Clark, Identification of a basaltic component on the martian surface from Thermal Emission Spectrometer data, *J. Geophys. Res.* **105**, 9609–22, 2000b.

Christensen, P. R., R. N. Clark, H. H. Kieffer, *et al.*, Detection of crystalline hematite mineralization on Mars by the Thermal Emission Spectrometer: evidence for near-surface water, *J. Geophys. Res.* **105**, 9623–42, 2000c.

Christensen, P. R., J. L. Bandfield, V. E. Hamilton, *et al.*, The Mars Global Surveyor Thermal Emission Spectrometer experiment: investigation description and surface science results, *J. Geophys. Res.* **106**, 23823–71, 2001a.

Christensen, P. R., R. V. Morris, M. D. Lane, J. L. Bandfield, and M. C. Malin, Global mapping of Martian hematite mineral deposits: remnants of water-driven processes on early Mars, *J. Geophys. Res.* **106**, 23873–85, 2001b.

Christensen, P. R., J. L. Bandfield, J. F. Bell III, *et al.*, Morphology and composition of the surface of Mars: Mars Odyssey THEMIS results, *Science* **300**, 2056–61, 2003.

Christensen, P. R., S. W. Ruff, R. L. Fergason, *et al.*, Initial results from the Miniature Thermal Emission Spectrometer experiment at the Spirit landing site at Gusev crater, *Science* **305**, 837–42, 2004a.

Christensen, P. R., M. B. Wyatt, T. D. Glotch, *et al.*, Mineralogy at Meridiani Planum from the Mini-TES Experiment on the Opportunity Rover, *Science* **306**, 1733–9, 2004b.

Christensen, P. R., H. Y. McSween Jr., J. L. Bandfield, *et al.*, Evidence for igneous diversity and magmatic evolution on Mars from infrared spectral observations, *Nature* **436**, doi:10.1038/nature03639, 2005.

Clark, B. C. and A. K. Baird, Is the martian lithosphere sulphur rich?, *J. Geophys. Res.* **84**, 8395–403, 1979.

Clark, B. C., R. V. Morris, S. M. McLennan, *et al.*, Chemistry and mineralogy of outcrops at Meridiani Planum, *Earth Planet. Sci. Lett.* **240**, 73–94, 2005.

Clark, D. B., *Granitoid Rocks*, New York: Chapman & Hall, 283 pp., 1992.

Conel, J. E., Infrared emissivities of silicates: experimental results and a cloudy atmosphere model of spectral emission from condensed particulate mediums, *J. Geophys. Res.* **74**, 1614–34, 1969.

Conrath, B., R. Curran, R. Hanel, *et al.*, Atmospheric and surface properties of Mars obtained by infrared spectroscopy on Mariner 9, *J. Geophys. Res.* **78**, 4267–78, 1973.

Costard, F., F. Forget, N. Mangold, and J. P. Peulvast, Formation of recent martian debris flows by melting of near-surface ground ice at high obliquity, *Science* **295**, 110–13, 2002.

Craddock, R. A. and T. A. Maxwell, Geomorphic evolution of the Martian highlands through ancient fluvial processes, *J. Geophys. Res.* **98**, 3453–68, 1993.

Edgett, K. S., The sedimentary rocks of Sinus Meridiani: five key observations from data acquired by the Mars Global Surveyor and Mars Odyssey orbiters, Mars, *Mars* **1**, 5–58, doi:10.1555/mars.2005.0002, 2005.

Edgett, K. S. and P. R. Christensen, The particle size of Martian aeolian dunes, *J. Geophys. Res.* **96**, 22765–76, 1991.

Edgett, K. S. and T. J. Parker, Water on early Mars: possible subaqueous sedimentary deposits covering ancient cratered terrain in western Arabia and Sinus Meridiani, *Geophys. Res. Lett.* **24**, 2897–900, 1997.

Erard, S. and W. Calvin, New composite spectra of Mars, 0.4–5.7 μm, *Icarus* **130**, 449–60, 1997.

Erard, S., J.-P. Bibring, and Y. Langevin, Determination of spectral units in the Syrtis Major-Isidis Planitia region from Phobos/ISM observations, *Lunar Planet. Sci. XX*, 327, 1990.

Fairen, A. G., D. Fernandez-Remolar, J. M. Dohm, V. R. Baker, and R. Amils, Inhibition of carbonate synthesis in acidic oceans on early Mars, *Nature* **431**, 423–6, 2004.

Fanale, F. P. and B. M. Jakosky, Regolith-atmosphere exchange of water and carbon dioxide on Mars: effects on atmospheric history and climate change, *Planet. Space Sci.* **30**, 819–31, 1982.

Fanale, F. P., S. E. Postawko, J. B. Pollack, M. H. Carr, and R. O. Pepin, Epochal climate change and volatile history. In *Mars* (ed. H. H. Kieffer *et al.*), Tucson, AZ: University of Arizona Press, 1992.

Farmer, V. C., *The Infrared Spectra of Minerals*, London: Mineralogical Society, 539pp., 1974.

Feely, K. C. and P. R. Christensen, Quantitative compositional analysis using thermal emission spectroscopy: application to igneous and metamorphic rocks, *J. Geophys. Res.* **104**, 24195–210, 1999.

Feldman, W. C., W. V. Boynton, R. L. Tokar, *et al.*, Global distribution of neutrons from Mars: results from Mars Odyssey, *Science* **297**, 75–8, 2002.

Forget, F., R. M. Haberle, F. Montmessin, B. Levrard, and J. W. Head, Formation of glaciers on Mars by atmospheric precipitation at high obliquity, *Science* **311**, 368–71, 2006.

Forsberg-Taylor, N. K., A. D. Howard, and R. A. Craddock, Crater degradation in the Martian highlands: morphometric analysis of the Sinus Sabaeus region and the simulation modeling suggest fluvial processes, *J. Geophys. Res.* **109**, E05002, doi:05010.01029/02004JE002242, 2004.

Gaffey, S. J., L. A. McFadden, D. Nash, and C. M. Pieters, Ultraviolet, visible, and near-infrared reflectance spectroscopy: laboratory spectra of geologic materials. In *Remote Geochemical Analysis: Elemental and Mineralogical Composition* (ed. C. M. Pieters and P. A. J. Englert), Cambridge: Cambridge University Press, pp. 43–78, 1993.

Gaidos, E. J., Cryovolcanism and the recent flow of liquid water on Mars, *Icarus* **153**, 218–23, 2001.

Gellert, R., R. Rieder, R. C. Anderson, *et al.*, Chemistry of rocks and soils at Gusev crater from the Alpha Particle X-ray Spectrometer, *Science* **305**, 829–32, 2004.

Gellert, R., R. Rieder, J. Brückner, *et al.*, Alpha Particle X-Ray Spectrometer (APXS): results from Gusev crater and calibration report, *J. Geophys. Res.* **111**, doi:10.1029/2005JE002555, 2006.

Gendrin, A., N. Mangold, J.-P. Bibring, *et al.*, Sulfates in martian layered terrains: the OMEGA/Mars Express view, *Science* **307**, 1587–90, 2005.

Gibson, E. K., S. J. Wentworth, and D. S. McKay, Chemical weathering and diagenesis of a cold desert soil from Wright Valley, Antarctica: an analog of martian weathering processes, *J. Geophys. Res.* **88**, A912–28, 1983.

Gilmore, M. S. and E. L. Phillips, The role of aquicludes in the formation of martian gullies, *Geology* **30**, 1107–10, 2002.

Glotch, T. D. and P. R. Christensen, Geologic and mineralogic mapping of Aram Chaos: evidence for a water-rich history, *J. Geophys. Res.* **110**, E09006, doi:09010.01029/02004JE02389, 2005.

Glotch, T. D. and A. D. Rogers, Evidence for aqueous deposition of hematite- and sulfate-rich light-toned layered deposits in Aureum and Iani Chaos, Mars, *J. Geophys. Res.* **112**, E06001, doi:10.1029/2006JE002863, 2007.

Glotch, T. D., R. V. Morris, P. R. Christensen, and T. G. Sharp, Effect of precursor mineralogy on the thermal infrared emission spectra of hematite: application to martian hematite mineralization, *J. Geophys. Res.* **109**, E07003, doi:07010.01029/02003JE002224, 2004.

Glotch, T. D., J. L. Bandfield, P. R. Christensen, *et al.*, The mineralogy of the light-toned outcrop at Meridiani Planum as seen by the Miniature Thermal Emission Spectrometer and implications for its formation, *J. Geophys. Res.* **111**, doi:10.1029/2005JE002672, 2006.

Goetz, W., P. Bertelsen, C. S. Binau, *et al.*, Indication of drier periods on Mars from the chemistry and mineralogy of atmospheric dust, *Nature* **436**, 62–5, 2005.

Golombek, M. P., J. A. Grant, L. S. Crumpler, *et al.*, Erosion rates at the Mars Exploration Rover landing sites and long-term climate change on Mars, *J. Geophys. Res.* **111**, doi:10.1029/JE002754, 2006.

Gooding, J. L., Chemical weathering on Mars, *Icarus* **33**, 483–513, 1978.

Grant, J. A., Valley formation in Margaritifer Sinus, Mars, by precipitation-recharged ground-water sapping, *Geology* **28**, 223–6, 2000.

Grotzinger, J., J. F. Bell III, W. Calvin, *et al.*, Stratigraphy, sedimentology and depositional environment of the Burns Formation, Meridiani Planum, Mars, *Earth Planet. Sci. Lett.* **240**, 11–72, 2005.

Gulick, V. C. and V. R. Baker, Fluvial valleys and martian palaeoclimates, *Nature* **341**, 514–16, 1989.

Gulick, V. C. and V. R. Baker, Origin and evolution of valleys on Martian volcanoes, *J. Geophys. Res.* **95**, 14325–44, 1990.

Haberle, R. M., C. P. McKay, J. Schaeffer, *et al.*, On the possibility of liquid water on present-day Mars, *J. Geophys. Res.* **106**, 23317–26, 2001.

Hamilton, V. E. and P. R. Christensen, Determining the modal mineralogy of mafic and ultramafic igneous rocks using thermal emission spectroscopy, *J. Geophys. Res.* **105**, 9717–34, 2000.

Hamilton, V. E. and P. R. Christensen, Evidence for extensive olivine-rich bedrock in Nili Fossae, Mars, *Geology* **33**, 433–6, 2005.

Hamilton, V. E., P. R. Christensen, and H. Y. McSween Jr., Determination of martian meteorite lithologies and mineralogies using vibrational spectroscopy, *J. Geophys. Res.* **102**, 25593–603, 1997.

Hamilton, V. E., M. B. Wyatt, H. Y. McSween Jr., and P. R. Christensen, Analysis of terrestrial and martian volcanic compositions using thermal emission spectroscopy: II. Application to martian surface spectra from MGS TES, *J. Geophys. Res.* **106**, 14733–47, 2001.

Hamilton, V. E., P. R. Christensen, and H. Y. McSween Jr., Determining the compositions of martian meteorites using thermal infrared emission spectroscopy: a precursor to martian surface spectroscopy, *Metorit. Planet. Sci.* **38**, 2003a.

Hamilton, V. E., P. R. Christensen, H. Y. McSween Jr., and J. L. Bandfield, Searching for the source regions of martian meteorites using MGS TES: integrating martian meteorites into the global distribution of igneous materials on Mars, *Meteorit. Planet. Sci.* **38**, 871–85, 2003b.

Hamilton, V. E., P. R. Christensen, and H. Y. McSween Jr., Global constraints on the source regions of martian meteorites from MGS TES data, *Meteorit. Planet. Sci.* **37**, 59, 2003c.

Hamilton, V. E., J. H. Y. McSween, and B. Hapke, Mineralogy of Martian atmospheric dust inferred from thermal infrared spectra of aerosols, *J. Geophys. Res.* **110**, doi:10.1029/2005JE002501, 2005.

Hanel, R. A., B. J. Conrath, W. A. Hovis, *et al.*, Infrared spectroscopy experiment on the Mariner 9 mission: preliminary results, *Science* **175**, 305–8, 1972.

Hartmann, W. K., Comparison of icelandic and martian hillside gullies, *Proc. Lunar Planet. Sci. XXXIII*, Abstract #1904, 2002.

Haskin, L. A., A. Wang, B. L. Jolliff, *et al.*, Water alteration of rocks and soils on Mars at the Spirit rover site in Gusev crater, *Nature* **436**, 66–9, doi:10.1038/nature03640, 2005.

Head, J. N., H. J. Melosh, and B. A. Ivanov, Martian meteorite launch: high-speed ejecta from small craters, *Science* **298**, 1752–6, 2002.

Head III, J. W., H. Hiesinger, M. A. Ivanov, and M. A. Kreslavsky, Possible ancient oceans on Mars: evidence from Mars Orbiter Laser altimeter data, *Science* **286**, 2134–7, 1999.

Head, J. W., G. Neukum, R. Jaumann, *et al.*, Tropical to mid-latitude snow and ice accumulation, flow and glaciation on Mars, *Nature* **434**, 346–51, 2005.

Hecht, M. H., Metastability of liquid water on mars, *Icarus* **156**, 373–86, 2002.

Heldmann, J. L. and M. T. Mellon, Observations of martian gullies and constraints on potential formation mechanisms, *Icarus* **168**, 285–304, 2004.

Herkenhoff, K. E., S. W. Squyres, R. Arvidson, *et al.*, Evidence from Opportunity's Microscopic Imager for water on Meridiani Planum, *Science* **306**, 1727–30, 2004.

Hoefen, T., R. N. Clark, J. L. Bandfield, *et al.*, Discovery of olivine in the Nili Fossae region of Mars, *Science* **302**, 627–30, 2003.

Houck, J. R., J. B. Pollack, C. Sagan, D. Schaack, and J. J. A. Decker, High altitude infrared spectroscopic evidence for bound water on Mars, *Icarus* **18**, 470–80, 1973.

Howard, A. D., J. M. Moore, and I. R. P. Irwin, An intense terminal epoch of widespread fluvial activity on early Mars: 1. Valley network incision and associated deposits, *J. Geophys. Res.* **110**, E12S14, doi:10.1029/2005JE002459, 2005.

Hunt, G. R. and J. W. Salisbury, Mid-infrared spectral behavior of metamorphic rocks, *Environ. Res. Paper* **543**-*AFCRL-TR-76–0003*, 67, 1976.

Hunt, G. R., J. W. Salisbury, and C. J. Lenhoff, Visible and near-infrared spectra of minerals and rocks: III. Oxides and hydroxides, *Mod. Geol.* **2**, 195–205, 1971.

Hurowitz, J. A., S. M. McLennan, N. J. Tosca, *et al.*, In situ and experimental evidence for acidic weathering of rocks and soils on Mars, *J. Geophys. Res.* **111**, doi:10.1029/2005JE002515, 2006.

Hynek, B. M., Implications for hydrologic processes on Mars from extensive bedrock outcrops throughout Terra Meridiani, *Nature* **431**, 156–9, 2005.

Hynek, B. M. and R. J. Phillips, New data reveal mature, integrated drainage systems on Mars indicative of past precipitation, *Geology* **31**, 757–60, 2003.

Hynek, B. M., R. E. Arvidson, and R. J. Phillips, Geologic setting and origin of Terra Meridiani hematite deposit on Mars, *J. Geophys. Res.* **107**, 5088, doi:5010.1029/2002E001891, 2002.

Jakosky, B. M. and M. A. Carr, Possible precipitation of ice at low latitudes of Mars during periods of high obliquity, *Nature* **315**, 559–61, 1985.

Jakosky, B. M., B. G. Henderson, and M. T. Mellon, Chaotic obliquity and the nature of the Martian climate, *J. Geophys. Res.* **100**, 1579–84, 1995.

Johnson, P. E., M. O. Smith, S. Taylor-George, and J. B. Adams, A semiempirical analysis of the reflectance spectra of binary mineral mixtures, *J. Geophys. Res.* **88**, 3557–61, 1983.

Kahn, R., The evolution of CO_2 on Mars, *Icarus* **62**, 175–90, 1985.

Kargel, J. S., V. R. Baker, J. E. Begét, *et al.*, Evidence of continental glaciation in the martian northern plains, *J. Geophys. Res.* **100**, 5351–68, 1995.

Kass, D. M. and Y. L. Yung, Loss of atmosphere from Mars due to solar wind-induced sputtering, *Science* **268**, 697–9, 1995.

Kieffer, H. H., J. S. C. Chase, T. Z. Martin, E. D. Miner, and F. D. Palluconi, Martian north pole summer temperatures: dirty water ice, *Science* **194**, 1341–4, 1976.

Kieffer, H. H., T. Z. Martin, A. R. Peterfreund, *et al.*, Thermal and albedo mapping of Mars during the Viking primary mission, *J. Geophys. Res.* **82**, 4249–92, 1977.

Kirkland, L. E., K. C. Herr, and P. M. Adams, Infrared stealthy surfaces: why TES and THEMIS may miss some substantial mineral deposits on Mars and implications for remote sensing of planetary surfaces, *J. Geophys. Res.* **198**, 5137, doi:5110.1029/2003JE002105, 2003.

Klingelhöfer, G., R. V. Morris, B. Bernhardt, *et al.*, Jarosite and hematite at Meridiani Planum from the Mössbauer spectrometer on the Opportunity rover, *Science* **306**, 1740–5, 2004.

Knauth, L. P., D. M. Burt, and K. H. Wohletz, Impact origin of sediments at the Opportunity landing site on Mars, *Nature* **438**, 1123–8, 2005.

Knudson, A. T. and P. R. Christensen, Hematite in Valles Marineris: context, composition, distribution, morphology, physical properties, and comparison to other Mars hematite deposits, *AGU Fall Meeting*, Abstract #P21A-0215, 2004.

Koeppen, W. C. and V. E. Hamilton, Discrimination of glass and phyllosilicate minerals in thermal infrared data, *J. Geophys. Res.* **110**, doi:10.1029/2005JE002474, 2005.

Kraft, M. D., J. R. Michalski, and T. G. Sharp, Effects of pure silica coatings on thermal emission spectra of basaltic rocks: considerations for Martian surface mineralogy, *Geophys. Res. Lett.* **30**, 2288, doi:2210.1029/2003GL018848, 2003.

Lane, M. D., Infrared optical constants of calcite and their relationship to particle size effects in thermal emission spectra of granular calcite, *J. Geophys. Res.* **104**, 14099–108, 1999.

Lane, M. D. and P. R. Christensen, Thermal infrared emission spectroscopy of anhydrous carbonates, *J. Geophys. Res.* **102**, 25581–92, 1997.

Lane, M. D. and P. R. Christensen, Thermal infrared emission spectroscopy of salt minerals predicted for Mars, *Icarus* **135**, 528–36, 1998.

Lane, M. D., R. V. Morris, S. A. Mertzman, and P. R. Christensen, Evidence for platy hematite grains in Sinus Meridiani, Mars, *J. Geophys. Res.* **107**, 5126, doi:5110.1029/2001JE001832, 2002.

Lane, M. D., M. D. Dyar, and J. L. Bishop, Spectroscopic evidence for hydrous iron sulfate in the Martian soil, *Geophys. Res. Lett.* **31**, doi:10.1029/2004GL021231, 2004.

Laskar, J. A., C. A. Correia, M. Gastineau, *et al.*, Long term evolution and chaotic diffusion of the insolation quantities of Mars, *Icarus* **170**, 343–64, 2004.

Lazerev, A. N., *Vibrational Spectra and Structure of Silicates*, New York: Consultants Bureau, 302pp., 1972.

Lee, P., C. S. Cockell, M. M. Marinova, C. P. McKay, and J. W. Rice, Snow and ice melt flow features in Devon Island, Nunavut, Arctic Canada as possible analogs for recent slope flow features on Mars, *Lunar Planet. Sci.* Abstract 1809 (CD-ROM), 2001.

Lucchitta, B. K., Ice sculpture in the Martian outflow channels, *J. Geophys. Res.* **87**, 9951–73, 1982.

Lyon, R. J. P., *Evaluation of Infrared Spectroscopy for Compositional Analysis of Lunar and Planetary Soils*, Stanford Research Institute, 1962.

Malin, M. C. and K. S. Edgett, Evidence for recent ground water seepage and surface runoff on Mars, *Science* **288**, 2330–5, 2000.

Malin, M. C. and K. S. Edgett, Mars Global Surveyor Mars Orbiter Camera: interplanetary cruise through primary mission, *J. Geophys. Res.* **106**, 23429–570, 2001.

Malin, M. C. and K. S. Edgett, Evidence for persistent flow and aqueous sedimentation on early Mars, *Science* **302**, 1931–4, 2003.

Malin, M. C., K. S. Edgett, L. V. Posiolova, S. M. McColley, and E. Z. Noe Dobrea, Present-day impact cratering rate and contemporary gully activity on Mars, *Science* **314**, 1573–7, 2006.

Mangold, N., C. Quantin, V. Ansan, C. Delacourt, and P. Allemand, Evidence for precipitation on Mars from dendritic valleys in the Valles Marineris area, *Science* **305**, 78–81, 2004.

McCauley, J. F., Geologic map of the coprates quandrangle of Mars, scale 1:5,000,000, *USGS Misc. Inv. Ser. Map*, I-897, 1978.

McCollom, T. M. and B. M. Hynek, A volcanic environment for bedrock diagenesis at Meridiani Planum on Mars, *Nature* **438**, 1129–31, doi:1110.1038/nature04390, 2005.

McCord, T. B., J. H. Elias, and J. A. Westphal, Mars: the spectral albedo (0.3–2.5?) of small bright and dark regions, *Icarus* **14**, 245–51, 1971.

McCord, T. B., R. Clark, and R. L. Huguenin, Mars: near-infrared reflectance and spectra of surface regions and compositional implications, *J. Geophys. Res.* **87**, 3021–32, 1978.

McEwen, A. S., B. S. Preblich, E. P. Turtle, *et al.*, The rayed crater Zunil and interpretations of small impact craters on Mars, *Icarus* **176**, 351–81, 2005.

McKay, C. P. and S. S. Nedell, Are there carbonate deposits in the Valles Marineris, Mars?, *Icarus* **73**, 142–8, 1988.

McLennan, S. M., J. F. Bell III, W. M. Calvin, *et al.*, Provenance and diagenesis of the evaporite-bearing Burns formation, Meridiani Planum, Mars, *Earth Planet. Sci. Lett.* **240**, 95–121, 2005.

McSween Jr., H. Y., SNC meteorites: clues to martian petrologic evolution, *Rev. Geophys.* **23**, 391–416, 1985.

McSween Jr., H. Y., What have we learned about Mars from SNC meteorites, *Meteoritics* **29**, 757–79, 1994.

McSween Jr., H. Y., Mars. In *Treatise on Geochemistry* Vol. 1 (ed. A. M. Davis *et al.*), Oxford, UK: Elsevier, pp. 601–21, 2003.

McSween Jr., H. Y., S. L. Murchie, J. A. Crisp, *et al.*, Chemical, multispectral, and textural constraints on the composition and origin of rocks at the Mars Pathfinder landing site, *J. Geophys. Res.* **104**, 8679–716, 1999.

McSween Jr., H. Y., T. L. Grove, and W. B. Wyatt, Constraints on the composition and petrogenesis of the martian crust, *J. Geophys. Res.* **108**(E12), 5135, doi:5110.1029/2003JE002175, 2003.

McSween Jr., H. Y., R. E. Arvidson, J. F. Bell III, *et al.*, Basaltic rocks analyzed by the Spirit rover in Gusev crater, *Science* **305**, 842–5, 2004.

McSween, H. Y., M. B. Wyatt, R. Gellert, *et al.*, Characterization and petrologic interpretation of olivine-rich basalts at Gusev crater, Mars, *J. Geophys. Res.* **111**, E02S10, doi:1029/2005JE002477, 2006.

Mellon, M. T. and R. J. Phillips, Recent gullies on Mars and the source of liquid water, *J. Geophys. Res.* **106**, 23165–80, 2001.

Melosh, H. J. and A. M. Vickery, Impact erosion of the primordial atmosphere of Mars, *Nature* **338**, 487–9, 1989.

Michalski, J. R., M. D. Kraft, T. G. Sharp, L. B. Williams, and P. R. Christensen, Mineralogical constraints on the high-silica Martian surface component observed by TES, *Icarus* **174**, 161–77, 2005.

Milam, K. A., H. Y. McSween Jr., V. E. Hamilton, J. M. Moersch, and P. R. Christensen, Accuracy of plagioclase compositions from laboratory and Mars spacecraft thermal emission spectra, *J. Geophys. Res.* **109**, E04001, doi:04010.01029/02003JE002097, 2004.

Milliken, R. E., Viscous flow features on the surface of Mars: observations from high-resolution MOC images, *J. Geophys. Res.* **108**, doi:10.1029/2002JE002005, 2003.

Ming, D. W., D. W. Mittlefehldt, R. V. Morris, *et al.*, Geochemical and mineralogical indicators for aqueous processes in the Columbia Hills of Gusev crater, Mars, *J. Geophys. Res.* **111**, doi:10.1029/2005JE002560, 2006.

Minitti, M. E., J. F. Mustard, and M. J. Rutherford, Effects of glass content and oxidation on the spectra of SNC-like basalts: applications to Mars remote sensing, *J. Geophys. Res.* **107**, doi:10.1029/2001JE001518, 2002.

Mitrofanov, I., D. Anfimov, A. Kozyrev, *et al.*, Maps of subsurface hydrogen from the high energy neutron detector, Mars Odyssey, *Science* **297**, 78–81, 2002.

Moersch, J. E. and P. R. Christensen, Thermal emission from particulate surfaces: a comparison of scattering models with measured spectra, *J. Geophys. Res.* **100**, 7465–77, 1995.

Moersch, J. E., T. Hayward, P. Nicholson, *et al.*, Identification of a 10 μm silicate absorption feature in the Acidalia region of Mars, *Icarus* **126**, 183–96, 1997.

Moore, J. M. and A. D. Howard, Large alluvial fans on Mars, *J. Geophys. Res.* **110**, E04005, doi:01029/02004JE002352, 2005.

Moore, J. M., A. D. Howard, W. E. Dietrich, and P. M. Schenk, Martian layered fluvial deposits: implications for Noachian climate scenarios, *Geophys. Res. Lett.* **30**, 2292, doi:2210.1029/2003GL019002, 2003.

Moroz, V. I., The infrared spectrum of Mars (1.1–4.1 μm), *Soviet Astron.* **8**, 273–81, 1964.

Morris, R. V., D. C. Golden, and J. F. Bell III, Low-temperature reflectivity spectra of red hematite and the color of Mars, *J. Geophys. Res.* **102**, 9125–33, 1997.

Morris, R. V., D. C. Golden, J. F. Bell III, *et al.*, Mineralogy, composition, and alteration of Mars Pathfinder rocks and soils: evidence from multispectral elemental, and magnetic data on terrestrial analogue, SNC meteorite, and Pathfinder samples, *J. Geophys. Res.* **105**, 1757–817, 2000.

Morris, R. V., T. G. Graff, S. A. Mertzman, M. D. Lane, and P. R. Christensen, Palagonitic (not andesitic) Mars: evidence from thermal emission and VNIR spectra of palagonitic

alteration rinds on basaltic rock, *6th Int. Conf. Mars*, Pasadena, California, Abstract #3211 (CD-ROM), July 20–25, 2003.

Morris, R. V., G. Klingelhöfer, B. Bernhardt, *et al*., Mineralogy at Gusev crater from the Mössbauer spectrometer on the Spirit Rover, *Science* **305**, 833–6, 2004.

Morris, R. V., G. Klingelhöfer, C. Schröder, *et al*., Mössbauer mineralogy of rock, soil, and dust at Gusev crater, Mars: Spirit's journey through weakly altered olivine basalt on the plains and pervasively altered basalt in the Columbia Hills, *J. Geophys. Res.* **111**, doi:10.1029/2005JE002584, 2006.

Musselwhite, D. S., T. D. Swindle, and J. I. Lunine, Liquid CO_2 breakout and the formation of recent small channels on Mars, *Geophys. Res. Lett.* **28**, 1283–5, 2001.

Mustard, J. F., Relationships of soil, grass, and bedrock over the Kaweah Serpentine Melange through spectral mixture analysis of AVIRIS data, *Remote Sens. Environ.* **44**, 293–308, 1993.

Mustard, J. F. and J. E. Hays, Effects of hyperfine particles on reflectance spectra from 0.3 to 25 μm, *Icarus*, **125**, 145–63, 1997.

Mustard, J. F. and J. M. Sunshine, Seeing through the dust: Martian crustal heterogeneity and links to the SNC meteorites, *Science* **267**, 1623–6, 1995.

Mustard, J. F., J.-P. Bibring, S. Erard, *et al*., Interpretation of spectral units of Isidis-Syrtis Major from ISM-Phobos 2 observations, *Lunar Planet. Sci. XXI*, 835–6, 1990.

Mustard, J. F., S. Erard, J.-P. Bibring, *et al*., The surface of Syrtis Major: composition of the volcanic substrate and mixing with altered dust and soil, *J. Geophys. Res.* **98**, 3387–400, 1993.

Mustard, J. F., S. Murchie, S. Erard, and J. M. Sunshine, In situ compositions of Martian volcanics: implications for the mantle, *J. Geophys. Res.* **102**, 25605–15, 1997.

Mustard, J. F., C. D. Cooper, and M. K. Rifkin, Evidence for recent climate change on Mars from the identification of youthful near-surface ground ice, *Nature* **412**, 411–14, 2001.

Mustard, J. F., F. Poulet, A. Gendrin, *et al*., Olivine and pyroxene diversity in the crust of Mars, *Science* **307**, 1594–7, 2005.

Nedell, S. S., S. W. Squyres, and D. W. Anderson, Origin and evolution of the layered deposits in the Valles Marineris, Mars, *Icarus* **70**, 409–41, 1987.

Noe Dobrea, E. Z., I. J. F. Bell, M. J. Wolff, and K. D. Gordon, H_2O- and OH-bearing minerals in the martian regolith: analysis of 1997 observations from HST/NICMOS, *Icarus* **166**, 1–20, 2003.

Noe Dobrea, E. Z., F. Poulet, and M. C. Malin, Omega analysis of light-toned outcrops in the chaotic terrain of the eastern Valles Marineris region, *Lunar Planet. Sci. XXXVII*, Abstract #2608, 2006.

Nyquist, L. E., D. D. Bogard, C.-Y. Shih, *et al*., Ages and geologic histories of martian meteorites, *Chronol. Evol. Mars* **96**, 105–64, 2001.

Palluconi, F. D. and H. H. Kieffer, Thermal inertia mapping of Mars from 60°S to 60°N, *Icarus* **45**, 415–26, 1981.

Parker, T. J., D. S. Gorsline, R. S. Saunders, D. C. Pieri, and D. M. Schneeberger, Coastal geomorphology of the martian northern plains, *J. Geophys. Res.* **98**, 11061–78, 1993.

Pollack, J. B. and O. B. Toon, Quasi-periodic climate changes on Mars: a review, *Icarus* **50**, 259–87, 1982.

Pollack, J. B., T. Roush, F. Witteborn, *et al*., Thermal emission spectra of Mars (5.4–10.5 μm): evidence for sulfates, carbonates, and hydrates, *J. Geophys. Res.* **95**, 14595–627, 1990.

Poulet, F., J.-P. Bibring, J. F. Mustard, *et al*., Phyllosilicates on Mars and implications for early martian climate, *Nature* **438**, 623–7, doi:610.1038/nature04274, 2005.

Ramsey, M. S. and P. R. Christensen, Mineral abundance determination: quantitative deconvolution of thermal emission spectra, *J. Geophys. Res.* **103**, 577–96, 1998.

Reider, R., T. Economou, H. Wanke, *et al*., The chemical composition of Martian soil and rocks returned by the mobile alpha proton X-ray spectrometer: preliminary results from the X-ray mode, *Science* **278**, 1771–4, 1997.

Rieder, R., R. Gellert, R. C. Anderson, *et al*., Chemistry of rocks and soils at Meridiani Planum from the Alpha Particle X-ray Spectrometer, *Science* **306**, 1746–9, 2005.

Rogers, A. D. and P. R. Christensen, Surface mineralogy of martian low-albedo regions from MGS TES data: implications for crustal evolution and surface alteration, *J. Geophys. Res.* **112**, E01003, doi:01010.01029/02006JE002727, 2007.

Rogers, A. D., P. R. Christensen, and J. L. Bandfield, Compositional heterogeneity of the ancient martian crust: analysis of Ares Vallis bedrock the THEMIS and TES data, *J. Geophys. Res.* **110**, doi:10.1029/2005JE002399, 2005.

Rogers, A. D., J. L. Bandfield, and P. R. Christensen, Global spectral classification of martian low-albedo regions with Mars Global Surveyor Thermal Emission Spectrometer (MGS-TES) data, *J. Geophys. Res.* **112**, E02004, doi:02010.01029/02006JE002726, 2007.

Ruff, S. W., Spectral evidence for zeolite in the dust on Mars, *Icarus* **168**, 131–43, 2004.

Ruff, S. W. and P. R. Christensen, Bright and dark regions on Mars: particle size and mineralogical characteristics based on Thermal Emission Spectrometer data, *J. Geophys. Res.* **107**, doi:10.1029/2001JE001580, 2002.

Ruff, S. W. and P. R. Christensen, Basaltic andesite, altered basalt, and a TES-based search for smectite clay minerals on Mars, *Geophys. Res. Lett.* **34**, CiteID L10204, doi:10.1029/2007GL029602, 2007.

Ruff, S. W., P. R. Christensen, P. W. Barbera, and D. L. Anderson, Quantitative thermal emission spectroscopy of minerals: a technique for measurement and calibration, *J. Geophys. Res.* **102**, 14899–913, 1997.

Ruff, S. W., P. R. Christensen, R. N. Clark, *et al*., Mars' "White Rock" feature lacks evidence of an aqueous origin: results from Mars global Surveyor, *J. Geophys. Res.* **106**, 23921–7, 2001.

Ruff, S. W., P. R. Christensen, D. L. Blaney, *et al*., The rocks of Gusev crater as viewed by the Mini-TES instrument, *J. Geophys. Res.* **111**, doi:10.1029/2006JE002747, 2006.

Salisbury, J. W., Mid-infrared spectroscopy: laboratory data, Chapter 4. In *Remote Geochemical Analysis: Elemental and Mineralogical Composition* (ed. C. Pieters and P. Englert), Cambridge: Cambridge University Press, 1993.

Salisbury, J. W. and J. W. Eastes, The effect of particle size and porosity on spectral contrast in the mid-infrared, *Icarus* **64**, 586–8, 1985.

Salisbury, J. W. and A. Wald, The role of volume scattering in reducing spectral contrast of reststrahlen bands in spectra of powdered minerals, *Icarus* **96**, 121–8, 1992.

Salisbury, J. W. and L. S. Walter, Thermal infrared (2.5–13.5 μm) spectroscopic remote sensing of igneous rock types on particulate planetary surfaces, *J. Geophys. Res.* **94**, 9192–202, 1989.

Salisbury, J. W., D. M. D'Aria, and E. Jarosewich, Mid-infrared (2.5–13.5 μm) reflectance spectra of powdered stony meteorites, *Icarus* **92**, 280–97, 1991.

Salisbury, J. W., L. S. Walter, N. Vergo, and D. M. D'Aria, *Infrared (2.1–25 μm) Spectra of Minerals*, Baltimore and London: The Johns Hopkins University Press, 267pp., 1992.

Segura, T. L., O. B. Toon, A. Colaprete, and K. Zahnle, Environmental effects of large impacts on Mars, *Science* **298**, 1977–80, 2002.

Shean, D. E., J. W. Head, and D. R. Marchant, Origin and evolution of a cold-based tropical mountain glacier on Mars: the Pavonis Mons fan-shaped deposit, *J. Geophys. Res.* **110**, E05001, doi:05010.01029/02004JE002360, 2005.

Singer, R. B. and T. L. Roush, Analysis of martian crustal petrology, *Bull. Am. Astron. Soc.* **17**, 737, 1985.

Singer, R. B., T. B. McCord, R. N. Clark, J. B. Adams, and R. L. Huguenin, Mars surface composition from reflectance spectroscopy: a summary, *J. Geophys. Res.* **84**, 8415–26, 1979.

Singer, R. B., P. D. Owensby, and R. N. Clark, Observed upper limits for clay minerals on Mars, *Lunar Planet. Sci. XVI*, 787–8, 1985.

Sinton, W. M., On the composition of martian surface materials, *Icarus* **6**, 222–8, 1971.

Smith, M. D., J. L. Bandfield, and P. R. Christensen, Separation of atmospheric and surface spectral features in Mars Global Surveyor Thermal Emission Spectrometer (TES) spectra: models and atmospheric properties, *J. Geophys. Res.* **105**, 9589–608, 2000.

Soderblom, L. A., The composition and mineralogy of the martian surface from spectroscopic observations: 0.3 μm to 50 μm. In *Mars* (ed. H. H. Kieffer *et al.*), Tucson: University of Arizona Press, pp. 557–93, 1992.

Squyres, S. W. and A. H. Knoll, Sedimentary rocks at Meridiani Planum: origin, diagenesis, and implications for life on Mars, *Earth Planet. Sci. Lett.* **240**, 1–10, 2005.

Squyres, S. W., J. P. Grotzinger, J. F. Bell, *et al.*, In-situ evidence for an ancient aqueous environment on Mars, *Science* **306**, 1709–14, 2004.

Squyres, S. W., O. Aharonson, R. E. Arvidson, *et al.*, Bedrock formation at Meridiani Planum, *Nature* **443**, doi:10.1038/nature05212, 2006a.

Squyres, S. W., R. E. Arvidson, D. L. Blaney, *et al.*, Rocks of the Columbia Hills, *J. Geophys. Res.* **111**, E02S11, doi:10.1029/2005JE002562, 2006b.

Stockstill, K. R., J. E. Moersch, S. W. Ruff, A. Baldridge, and J. Farmer, TES hyperspectral analyses of proposed paleolake basins on Mars: no evidence for in-place carbonates, *J. Geophys. Res.* **111**, E10, doi:10.1029/2005JE002353, 2005.

Tanaka, K. L., Geology and insolation-driven climatic history of Amazonian north polar materials on Mars, *Nature* **437**, doi:10.1038/nature04065, 2005.

Thomas, P. C., M. C. Malin, and K. S. Edgett, North-south geological differences between the residual polar caps on Mars, *Nature* **404**, 161–4, 2000.

Titus, T. N., H. H. Kieffer, and P. R. Christensen, Exposed water ice discovered near the south pole of Mars, *Science* **299**, 1048–51, 2003.

Tornabene, L. L., J. E. Moersch, H. Y. McSween, *et al.*, Identification of large (2–10 km) rayed craters on Mars in THEMIS thermal infrared images: implications for possible Martian meteorite source regions, *J. Geophys. Res.* **111**, doi:10.1029/2005JE002600, 2006.

Tosca, N. J., J. A. Hurowitz, L. Meltzer, S. M. McLennan, and M. A. A. Schoonen, Olivine weathering on Mars: getting back to basics, *Lunar Planet. Sci. XXXV*, Abstract #1043, 2004.

Treiman, A. H., Geologic settings of martian gullies: implications for their origins, *J. Geophys. Res.* **108**, doi:10.1029/2002JE001900, 2003.

Treiman, A. H., J. D. Gleason, and D. D. Bogard, The SNC meteorites are from Mars, *Planet. Space Sci.* **48**, 1212–30, 2000.

Walter, L. S. and J. W. Salisbury, Spectral characterization of igneous rocks in the 8–12 μm region, *J. Geophys. Res.* **94**, 9203–13, 1989.

Ward, W. R., Climatic variations on Mars: I. Astronomical theory of insolation, *J. Geophys. Res.* **79**, 3375–86, 1974.

Wieczorek, M. A. and M. T. Zuber, Thickness of the Martian crust: improved constraints from geoid-to-topography ratios, *J. Geophys. Res.* **109**, doi:10.1029/2003JE002153, 2004.

Wilson Jr., E. B., J. C. Decius, and P. C. Cross, *Molecular Vibrations: The Theory of Infrared and Raman Vibrational Spectra*, New York, NY: McGraw-Hill, 1955.

Wyatt, M. B. and H. Y. McSween Jr., Spectral evidence for weathered basalt as an alternative to andesite in the northern lowlands of Mars, *Nature* **417**, 263–6, 2002.

Wyatt, M. B., V. E. Hamilton, H. Y. McSween Jr., P. R. Christensen, and L. A. Taylor, Analysis of terrestrial and martian volcanic compositions using thermal emission spectroscopy: I. Determination of mineralogy, chemistry, and classification strategies, *J. Geophys. Res.* **106**, 14711–32, 2001.

Wyatt, M. B., H. Y. McSween Jr., K. L. Tanaka, and J. W. Head III, Global geologic context for rock types and surface alteration on Mars, *Geology* **32**, 645–8, doi:610.1130/G20527.20521, 2004.

Yen, A. S., R. Gellert, C. Schröder, *et al.*, An integrated view of the chemistry and mineralogy of martian soils, *Nature* **436**, 49–54, doi:10.1038/nature3637, 2005.

Zuber, M. T., The crust and mantle of Mars, *Nature* **412**, 220–7, 2001.

10

The compositional diversity and physical properties mapped from the Mars Odyssey Thermal Emission Imaging System

P. R. CHRISTENSEN, J. L. BANDFIELD, R. L. FERGASON,
V. E. HAMILTON, AND A. D. ROGERS

ABSTRACT

The Thermal Emission Imaging System (THEMIS) began mapping Mars in 2002 on the Mars Odyssey spacecraft. This instrument provides nine infrared and five visible surface-sensing and atmospheric bands, with spatial resolutions of 100 m in the IR and 18 m in the visible. THEMIS data have been used to investigate the composition and physical properties of the surface and polar ices, as well as to study atmospheric temperature, dust, and water vapor. THEMIS provides an excellent complement to the hyperspectral, 3–6 km spatial resolution Thermal Emission Spectrometer (TES) observations, and the two instruments have been used together to map the distribution of geologic units and to determine their detailed mineralogy. Among the major findings to date is the discovery of a diversity in volcanic compositions, from ultramafic olivine-rich basalts through basalts, dacite cones and flows, and granitic rocks uplifted by impact. These observations indicate that the Martian crust, while dominated by basalt, has undergone many of the processes of igneous differentiation that occur on Earth. THEMIS has not detected any carbonate outcrops at 100 m scales, suggesting that carbonate rocks have not formed on Mars and has also not detected any evidence for near-surface volcanic activity, liquid water, or ice that is close enough to the surface to produce a measurable thermal anomaly. THEMIS nighttime temperature measurements have shown the existence of exposed bedrock at 100 m to km scales, and layered materials of differing physical properties, with inferred differences in the processes that deposited or consolidated them. Rocky materials commonly occur on slopes, indicating that the production or exposure rate of blocks is greater than their rate of burial and/or erosion. Aeolian dunes, with grain sizes that differ from the surrounding terrain, are widespread. Finally, variations in the abundance of rocky materials in crater rays and ejecta occur that are consistent with rock breakdown over time. Taken together, the THEMIS data have shown that Mars is a compositionally diverse planet, with a complex geologic history that remains geologically active today.

10.1 INTRODUCTION

The THEMIS instrument on the NASA Mars Odyssey orbiter mission was designed to study surface composition, map the physical properties, investigate the composition, distribution, and temporal variability of polar ices, provide global maps of surface morphology at 18 m (visible) and 100 m (IR) spatial scales, and extend the long-term record of atmospheric temperature and dust and water-ice abundance (Christensen *et al.*, 2004a). THEMIS was specifically developed as a follow-on to the TES on Mars Global Surveyor (MGS), which has mapped Mars with 3–5 km spatial resolution at 5 and 10 cm^{-1} spectral resolution (286 and 143 bands) from 6 to 50 μm (e.g., Christensen *et al.*, 2001a; see Chapter 9). THEMIS complements TES observations with 100 m spatial resolution in eight surface-sensing bands ~1 μm wide, centered from 6.8 to 12.6 μm, and a single atmospheric band centered on the 15 μm CO_2 absorption (Christensen *et al.*, 2004a). In many cases the combination of TES and THEMIS data have proven to be highly effective in determining both the composition and the spatial distribution of different units that is necessary to interpret the geologic processes and history.

In this chapter we focus on the composition and physical property results from the THEMIS investigation. The properties of polar ices are discussed in Chapter 25, and the morphology and color results from the THEMIS visible camera are presented in Chapter 8. We make no attempt to review the substantial literature on surface processes that is derived from the THEMIS global IR mapping; excellent examples include the discovery of extensive dendritic channels and delta formations (e.g., Mangold *et al.*, 2004; Howard *et al.*, 2005), the processes of Martian landslides (Baloga and Bruno, 2005; Barnouin-Jha *et al.*, 2005), cold-based glaciers (Shean *et al.*, 2005), volcanic and tectonic landforms (Wyrick *et al.*, 2004; Mouginis-Mark and Christensen, 2005), cratering rates and processes (Lane *et al.*, 2003; Boyce *et al.*, 2005; McEwen *et al.*, 2005; Tornabene *et al.*, 2006), and the assessment of potential landing sites (Golombek *et al.*, 2003, 2005; Milam *et al.*, 2003; Pelkey *et al.*, 2003, 2004; Tanaka *et al.*, 2003; Weitz *et al.*, 2003; Christensen *et al.*, 2005b).

10.1.1 Major science questions

The key questions that THEMIS has investigated can be divided into three broad categories: (1) the search for aqueous environments, both ancient and active, that provide insight into biotic and prebiotic conditions; (2) the understanding of changes in environmental conditions, climate,

The Martian Surface: Composition, Mineralogy, and Physical Properties, ed. J. F. Bell III. Published by Cambridge University Press.

and geologic processes through time; and (3) the characterization of volcanic processes and their evolution in time. Specific topics include (1) evidence for aqueous mineralogies, with the emphasis on carbonate, sulfate, and phyllosilicate minerals; (2) the study of aqueous environments, focused on the morphologic evidence for liquid water, layered deposits, channels, and high deposition and erosion rates; (3) endogenic heating and the search for active "hot spots" and the mapping of recent volcanism; (4) evidence for hydrothermal activity through the search for silica and calcium carbonate deposits common in hydrothermal systems; (5) the use of impact craters and eroded channels as stratigraphic probes; and (6) the regional geologic mapping of volcanic flows, cones, and exposed intrusions.

The thermal-infrared spectral region was selected for mineral mapping because virtually all geologic materials, including carbonates, hydrothermal silica, sulfates, phosphates, hydroxides, and silicates have fundamental infrared absorption bands that are diagnostic of mineral composition. THEMIS has expanded upon the wealth of data from previous infrared experiments, including the Mariner 6/7 Infrared Spectrometer (Pimentel *et al.*, 1974), the Mariner 9 Infrared Interferometer Spectrometer (IRIS) (Hanel *et al.*, 1972b; Conrath *et al.*, 1973), the Viking Infrared Thermal Mapper (IRTM) (Kieffer *et al.*, 1977), the Phobos Termoscan (Selivanov *et al.*, 1989) and ISM (Bibring *et al.*, 1989), and the MGS/TES (Christensen *et al.*, 2001a). The TES instrument has collected hyperspectral images (143 and 286 spectral bands) of the entire Martian surface at wavelengths from 6 to 50 μm, providing an initial global reconnaissance of mineralogy and thermophysical properties (see Chapter 9). The Mars Express OMEGA (OMEGA – Observatiore pour la Minéralogie, l'Eau, les Glaces et l' Activité) experiment has extended this global mineral mapping using near-IR hyperspectral observations (Bibring *et al.*, 2005, 2006; Gendrin *et al.*, 2005; see Chapter 7).

THEMIS and TES both cover the 6.3–15.0 μm spectral region, allowing the combination of the high spectral resolution of TES with the high spatial resolution of THEMIS to achieve the goals of a global mineralogic inventory at the spatial scales necessary for detailed geologic studies within the Odyssey downlink capability. The Mars Exploration Rovers (MERs) contain miniature versions of the TES instrument (Christensen *et al.*, 2003b; see Chapter 14) that cover the THEMIS and TES spectral region, providing a powerful link from the meter scale viewed by Mini-TES to the 100 m scale of THEMIS to the global mineral mapping of MGS/TES. THEMIS-IR imaging has provided global coverage with higher resolution and clarity than Viking or the MGS Mars Orbiter Camera (MOC) wide-angle camera (Malin and Edgett, 2001). Visible imaging at 18 m spatial scale is intermediate between those of Viking and the detailed views from the MOC narrow-angle camera.

10.1.2 Instrument and mission overview

The THEMIS flight instrument consists of infrared and visible multispectral imagers that share optics and a housing, but have independent power and data interfaces to the spacecraft to provide system redundancy. The telescope is a three-mirror $f/1.6$ anastigmat design, with an effective aperture of 12 cm, a 20 cm effective focal length, and a 3.5° (downtrack) × 4.6° (crosstrack) field of view (Christensen *et al.*, 2004a). A calibration flag provides thermal calibration and is used to protect the detectors from direct illumination from the Sun. This calibration flag is stored against a side wall that maintains a known temperature of the flag for calibration purposes. The instrument weighs 11.2 kg, is 29 cm by 37 cm by 55 cm in size, and consumes an orbital average power of 14 W (*Christensen, et al.*, 2004a).

A major feature of the instrument is the use of an uncooled microbolometer array, which substantially reduces the instrument complexity. This array has 320 crosstrack pixels and 240 down-track pixels with an instantaneous field of view (IFOV) of 0.25 mrad (100 m from 400 km) and an image width of ~32 km. A small thermal electric cooler is used to stabilize the IR focal plane temperature to ±0.001 K. The IR imager has ten stripe filters that produce ten ~1 μm wide bands at nine separate wavelengths from 6.78 to 14.88 μm (Christensen *et al.*, 2004a).

The THEMIS visible imager (THEMIS-VIS) is a small (5.5 cm × 8.5 cm × 6.5 cm, <500 g) derivative of the Malin Space Science Systems (MSSS) Mars Polar Lander Mars Decent Imager (MARDI), with five color filters. This sensor has a 1024 × 1024 pixel focal plane with an 18 m IFOV that covers an 18.4 km wide swath bore-sighted with the IR imager through a beamsplitter (see Christensen *et al.*, 2004a; McConnochie *et al.*, 2006; and Chapter 8 for more instrument details on THEMIS-VIS).

For the THEMIS infrared imager, the measured noise equivalent delta temperature (NEΔT) for a reference surface temperature of 245 K varies from 1.5 K at 6.3 μm to 0.2 K at 11.0 μm; most of this variation is due to the variation in emitted energy for the 245 K reference temperature. The NEΔT in band 5 (9.3 μm) is 1 K at typical nighttime temperatures of 170 K. The signal-to-noise ratio for the visible imager, computed for a flat-lying, low-albedo (0.25) surface viewed at an incidence angle of 67.5° under aphelion conditions, varies from 200 to 400 (Christensen *et al.*, 2004a).

The Odyssey spacecraft is in a near-polar sun synchronous orbit with an equator-crossing local solar time that was ~3:30 p.m. at the beginning of the mission and has been between 5:00 p.m. and 6:00 p.m. during the primary mission and the first extended mission. Optimal observing conditions for IR mineralogic mapping occur during mission phases where the local true solar time is the earliest in the afternoon, and during the season when the atmosphere has the lowest dust and water-ice opacity. Optimal conditions for visible morphologic imaging occur when the incidence angles are between 60° and 80°. Nighttime infrared images are acquired during all phases of the mission. Polar observations are acquired throughout the Martian year to observe the autumn cap growth, winter night, and spring cap retreat.

10.2 VOLCANIC DIVERSITY AT GEOLOGIC SCALES

Spectral data from Earth-based telescopes and early spacecraft missions provided indications of compositional differences and the presence of iron-bearing minerals (e.g., McCord and Adams, 1969; Pimentel *et al.*, 1974; Hanel *et al.*, 1972a; Bibring *et al.*, 1989; Pollack *et al.*, 1990; Murchie *et al.*, 1993; Mustard *et al.*, 1993; Moersch *et al.*, 1997; Christensen, 1998). Global mineral mapping using TES and OMEGA infrared spectra has shown that Mars is fundamentally a volcanic planet, with dust-free rocks and sands dominated by primary volcanic minerals – plagioclase feldspars ($NaAlSi_3O_8$ to $CaAl_2Si_2O_8$), high- and low-Ca pyroxenes ($(Ca,Mg,Fe)_2Si_2O_6$), and olivine ($(Mg,Fe)_2SiO_4$), with some areas exhibiting higher abundances of glass or other high-silica phases (poorly crystalline to amorphous materials with Si/O ratios >0.35) (e.g., Bandfield *et al.*, 2000; Christensen *et al.*, 2000a, 2001b; Hamilton *et al.*, 2003a; Wyatt *et al.*, 2003; Bibring *et al.*, 2005; Mustard *et al.*, 2005; Rogers and Christensen, 2007). Feldspar is the dominant mineral phase in most locations. Olivine is common, occurring at 5%–15% abundance in many regions (Hamilton *et al.*, 2003a; Hoefen *et al.*, 2003; Bibring *et al.*, 2005; Mustard *et al.*, 2005; McSween *et al.*, 2006). The rocks in the ancient cratered terrains are basaltic in composition, whereas the younger rocks of the northern lowlands have more glass, more silica-rich minerals, and fewer iron-bearing pyroxene and olivine minerals (Bandfield *et al.*, 2000; Mustard *et al.*, 2005; Rogers and Christensen, 2007).

While the global reconnaissance from TES and OMEGA has revealed mineralogic variations between regional-scale units, Martian igneous processes almost certainly have produced much more diversity at the 100 m scales of individual flows, vents, and intrusions. For example, volcanic units are likely composed of materials formed by different degrees of partial melting and modified by fractional crystallization and interactions with crustal compositions during magma ascent and eruption. THEMIS multispectral observations, in conjunction with TES and OMEGA spectral data, have provided a highly effective means to investigate these geologic processes.

10.2.1 Olivine-rich basalt

The occurrence of olivine is significant because (1) it indicates silica undersaturation (a critical parameter in recognizing primitive, mantle-derived magmas); and (2) it weathers relatively rapidly under common aqueous conditions and thus can provide an indicator of environmental conditions in the time following rock emplacement.

Olivine-rich rocks have been identified from orbit at regional scales using TES data in several locations (Hamilton *et al.*, 2003a; Hoefen *et al.*, 2003). The combination of the high spatial resolution compositional maps derived from THEMIS data, together with the ability to determine the mineralogy from TES spectra, provides a powerful tool to map compositional units at geologically relevant scales. The THEMIS data show that these occurrences are common at localized (hundreds of meters) scales (Christensen *et al.*, 2003a; Hamilton and Christensen, 2003, 2005; Rogers *et al.*, 2005). Excellent examples of olivine-rich units are found in Nili Fossae (Hoefen and Clark, 2001; Hamilton and Christensen, 2005) (Figure 10.1). Spectral, thermal, visual, and topographic data demonstrate that the majority of olivine-rich material is in the form of in-place, layered rock units. Some high olivine concentrations are associated with spatially small areas dominated by loose sediments. These units most likely originated as olivine-rich basalt flows (Hamilton and Christensen, 2005).

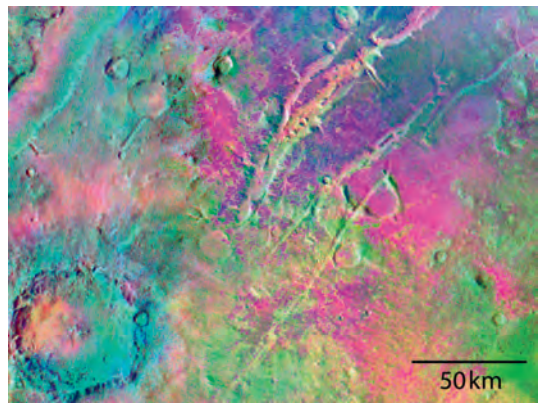

Figure 10.1. Olivine-rich basalts in Nili Fossae. Decorrelation-stretched (DCS) infrared mosaic of Nili Fossae region (20° N to 23.5° N, 75° E to 80° E). DCS bands 9 (12.57 μm), 7 (11.04 μm), and 5 (9.35 μm) are displayed as red, green, and blue, respectively. Olivine exposures are magenta to purple-blue in color. North is to the top in all images. North is up in all figures unless otherwise noted. (For a color version of this figure, please refer to the color plate section or to the e-Book version of this chapter.)

Olivine-rich basalts have also been found as individual units within sequences of layered rocks in an ever-increasing number of locations. Examples include an olivine basalt layer exposed in the walls of Ganges Chasma and olivine basalts exposed on the floor of Ares Valles (Rogers *et al.*, 2005). The Ganges unit is ~100 m thick and crops out over an area several hundred kilometers in size (Figure 10.2) (Christensen *et al.*, 2003a). The composition of this layer is basalt with greater than ~15% olivine with an Mg/(Mg + Fe) ratio of 0.60–0.70 (Fo60–70) (Christensen *et al.*, 2003a); the unit exposed below it on the floor of Ganges Chasma is determined from TES data to be basaltic.

An olivine-rich unit occurs on the floor of a 60 km diameter crater in Aurorae Planum immediately south of western Ganges Chasma (Hamilton *et al.*, 2003b; Hamilton and Christensen, 2003). This unit is mapped as a distinct spectral unit using THEMIS, and was positively identified as olivine-rich basalt using TES spectra. It is 10–12 K warmer than the surrounding terrain in nighttime THEMIS images, with a thermal inertia >800 $J\,m^{-2}\,K^{-1}\,s^{-1/2}$, indicating the presence of significant rocky material. This unit has been incised 15–20 m by channels, providing additional evidence that it is a competent layer. The olivine basalt forms the uppermost layer in a crater that is superimposed on the top of the thick sequence of layered rocks that comprise Aurorae Planum.

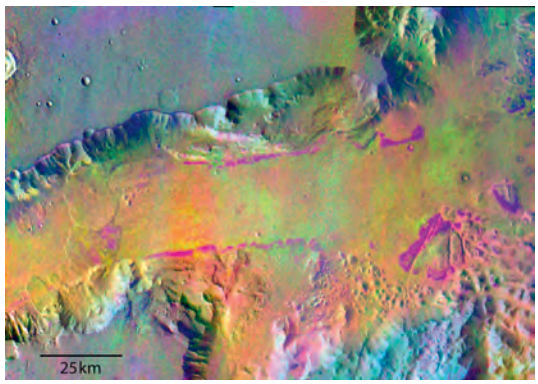

Figure 10.2. Olivine-rich basalt layers in Ganges Chasma. Multispectral IR mosaic created using a decorrelation (DCS) stretch of the calibrated radiance from bands 5 (centered at 9.35 μm), 7 (11.04 μm), and 8 (11.79 μm). Purple-colored bands trending E–W are olivine-rich basalt; yellow/orange-colored material on canyon floor is determined from TES to be basalt; blue-colored material on the plateaus is dust. (For a color version of this figure, please refer to the color plate section or to the e-Book version of this chapter.)

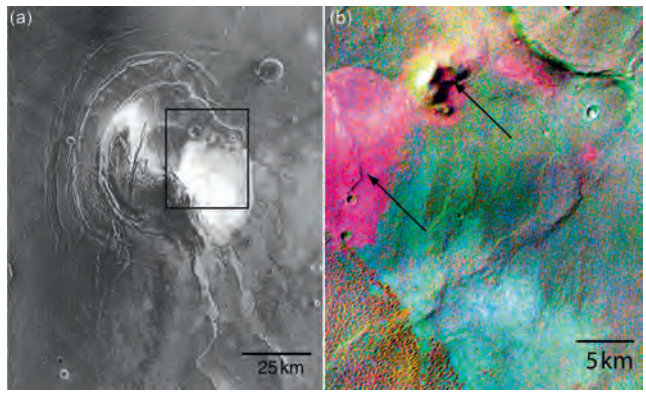

Figure 10.3. Nili Patera. (a) THEMIS nighttime temperature image showing the presence of bedrock, rocky dacite flows, and sand dunes. The bright (warm) surfaces have temperatures of up to 217 K. Box shows the location of Figure (b). (b) THEMIS 3-band multispectral IR DCS mosaic, showing the compositional units, including the dacite flow and cone (arrows), on the floor of the Nili Patera caldera. (For a color version of this figure, please refer to the color plate section or to the e-Book version of this chapter.)

Its position, composition, and morphology suggest that it was emplaced as a lava flow at a late stage in plains formation.

Olivine-rich basalts have also been observed *in situ* by the *Spirit* rover in Gusev crater using IR, Mössbauer, and Alpha Particle X-ray spectra (Christensen *et al.*, 2004b; Gellert *et al.*, 2004; McSween *et al.*, 2004, 2006; Morris *et al.*, 2004; see Chapters 4 and 15).

The widespread occurrence of olivine-rich basalts suggests that the formation of these rocks has been a common occurrence throughout Mars history. This growing inventory of olivine basalts suggests that mafic lithologies may be a relatively common variant of Martian basalts. They likely represent less-evolved lavas or contain higher abundances of cumulates or mantle xenoliths than typical basalts. In places, these units appear to have been erupted as lava flows; in other locations they may have been intruded as sills. The occurrence of the layers at significantly different stratigraphic levels within a single region suggests that olivine-rich basalts were erupted episodically at different times throughout the formation of the Martian plains.

10.2.2 Magma evolution in the Nili Patera Volcano

Nili Patera forms the northernmost caldera of a 400 by 200 km caldera complex at the summit of the ~1300 km diameter Hesperian-age Syrtis Major volcanic construct (Schaber, 1982; Hiesinger and Head, 2004). Nili Patera is ~50 km in diameter and lies ~1.8 km below the western caldera rim based on Mars Orbiter Laser Altimeter (MOLA) topography (Smith *et al.*, 2001). Approximately one-third of the floor material (~900 km^2) has unusually high nighttime temperatures (208–214 K; Figure 10.3a), which indicates the presence of bedrock or highly consolidated materials (Christensen *et al.*, 2003a). Barchan dunes, which form through sand transport across a hard surface where sand is limited, are seen on the western portion of these bedrock surfaces, suggesting that saltating sand may be the erosive agent that has scoured the upwind surface to bedrock (Christensen *et al.*, 2003a).

Compositional mapping with THEMIS multispectral and TES hyperspectral (Ruff and Hamilton, 2001) IR imaging shows distinct variations across the caldera floor and the surrounding flanks of the volcano (Figure 10.3b) (Christensen *et al.*, 2005a). Two primary floor units have been identified based on their mineralogy. The most extensive unit covers much of the eastern and western portions of the caldera floor. It is composed of 35% plagioclase, 25% high-Ca clinopyroxene, 10% orthopyroxene, 10% sulfate, and minor glass, olivine, and carbonate (Ruff and Christensen, 2003; Christensen *et al.*, 2005a). This unit is basalt that is similar in composition to the typical basalt (TES Surface Type 1; see Chapter 9) mapped using orbital TES data throughout much of the ancient cratered terrain (Bandfield *et al.*, 2000; Christensen *et al.*, 2000a; Rogers and Christensen, 2007).

The second unit occurs in an ~12 × 12 km^2 area on the central portion of the caldera floor with several nearby outliers (Figure 10.3b). Several 5–20 km sized flow units that are spectrally similar occur 50–60 km to the south along an arcuate trend. The composition of this unit, derived from low-resolution TES spectra, is much more silicic than the basalt, with 30% plagioclase, 30% high-Si glass, 15% clinopyroxene, and lesser sulfate and minor orthopyroxene (Christensen *et al.*, 2005a). The derived SiO_2 abundance (Hamilton and Christensen, 2000; Wyatt *et al.*, 2001; McSween *et al.*, 2003) of this unit is 60–63 wt.%. Given the contamination from the surrounding basaltic materials to the TES spectra, this derived SiO_2 abundance of the flow is a lower limit. Thus this unit is likely a dacite, making these rocks the most evolved rock composition of any volcanic unit yet found on Mars. The flow is lobate with steep margins, stands ~80 m above the floor, and has a surface morphology that is distinct from the surrounding floor materials (Figure 10.3). It surrounds a relatively steep-sided (~10°),

~300 m high cone, and postdates the basaltic floor materials based on its superposition across one of the grabens formed in the basalt (Figure 10.3). A high-viscosity glassy dacite composition is consistent with the occurrence of this unit as a relatively short and thick flow, its association with a steep-sided volcanic cone, and its distinct morphology.

THEMIS eight-point spectra closely match the TES spectra and can be analyzed to provide a quantitative measure of dacite abundance at 100 m scales (Christensen *et al.*, 2005a). The cone is dacitic (as are the spectrally distinct flows to the south), suggesting that the flow originated from the same source vent as the cone. Both the THEMIS and TES spectra suggest that the dunes are composed primarily of basalt, likely eroded from the upwind bedrock exposure. Along their western margin the dunes show subtle color and spectral variations that suggest an influx of dacitic sands (Christensen *et al.*, 2005a).

The geologic history inferred from the stratigraphic relationships indicates magma evolution occurred during the late stages of the formation of Syrtis Major, producing low-silica basalts followed by higher silica glassy dacites in cones and flows. Fractional crystallization of magma within a chamber commonly results in variations in the silica content of the erupted lavas over time. While evidence for this style of magma evolution is not common on Mars, the occurrence of basalts and dacites within Syrtis Major demonstrates that highly evolved lavas have been produced, at least locally, by magma evolution through fractional crystallization, and demonstrates that igneous processes analogous to those found in large volcanic complexes on Earth have also occurred on Mars.

10.2.3 Granitoid units

TES and THEMIS data have been used to identify Martian surface compositions dominated by quartz (SiO_2) and plagioclase feldspar (Bandfield *et al.*, 2004a; Bandfield, 2006). These materials have been identified near the central peaks of two craters ~95 km apart in northern Syrtis Major and in isolated locations near the southwest rim of Antoniadi crater (Figure 10.4). Two of the exposures occur in knobby terrains that are surrounded by the relatively flat surface of the crater interior. The other two exposures are located in two areas of heavily fractured terrain that lie near the boundary between the southeast rim of Antoniadi crater and an unnamed 75 km diameter crater. These exposures coincide with lower elevations in the region, but are relatively isolated and not ubiquitous. The spectrally unique exposures are near 61.8°–65.9° E longitude and 18.4°–20.5° N latitude; these coordinates cover a region of roughly 230 km by 125 km. The total areal extent of exposures with significant concentrations is 19 km^2.

All exposures have IR absorption features centered at shorter wavelengths than the surrounding plains. The emissivity of these surfaces is lower near 8.5 μm (THEMIS band 4) and higher from ~10 to 12 μm (bands 6–8, Figure 10.5) than the surrounding basaltic/basaltic andesite plains (Bandfield, 2002; Christensen *et al.*, 2005a). All of the exposures also have higher ~6.8 μm (bands 1/2) emissivity than the surrounding plains, indicating that there also is some absorption at 8 μm (band 3) relative to the plains.

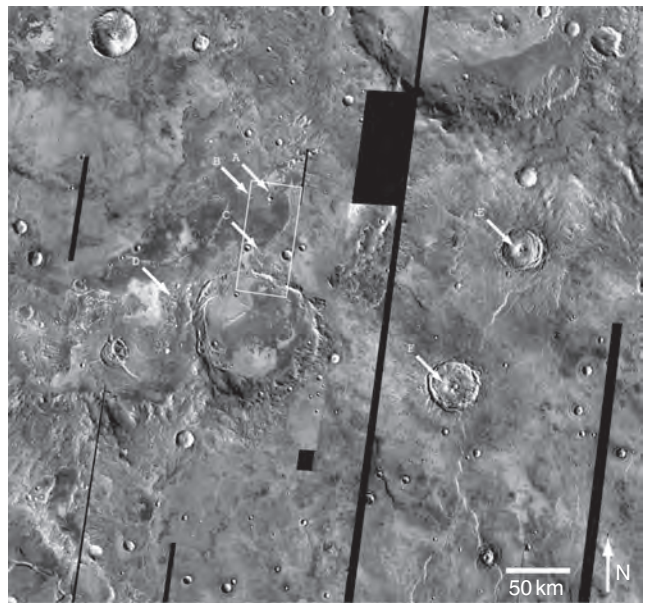

Figure 10.4. Granitic outcrops in the Syrtis Major region. Mosaic of THEMIS band 9 radiance images. Arrows denote approximate locations of quartzofeldspathic surfaces and the box indicates the area covered by shown in Figure 10.6. Letters correspond to the following locations: A – Large knobby terrain; B – Small knobby terrain; C – Eastern fractured terrain; D – Western fractured terrain; E – North crater; F – South crater. The mosaic covers approximately 60.1° E to 67.2° E and 16.3° N to 22.5° N.

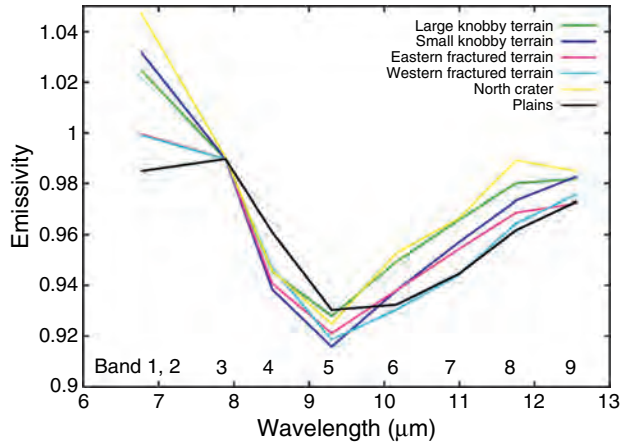

Figure 10.5. THEMIS surface emissivity spectra from surfaces exposed in the images shown in Figure 10.4. Basaltic plains (black) have higher emissivity in THEMIS bands 4 and 5 and lower emissivity in bands 6 to 8 relative to the quartz- and feldspar-rich surfaces (knobs, fractured terrains, and craters). Emissivities are above unity for many of these spectra because band 3 was used for surface temperature estimation even though there is lower emissivity at these wavelengths relative to bands 1 and 2 for quartz-rich surfaces. (For a color version of this figure, please refer to the color plate section or to the e-Book version of this chapter.)

Spectral unit concentration maps were produced by deconvolving bands 3 through 9 of each pixel of the atmospherically corrected data using the regional Mars surface spectrum derived from TES data, a laboratory spectrum of quartz monzonite, a water-ice cloud spectral shape, and a blackbody spectrum (Figure 10.6) (e.g., Ramsey and

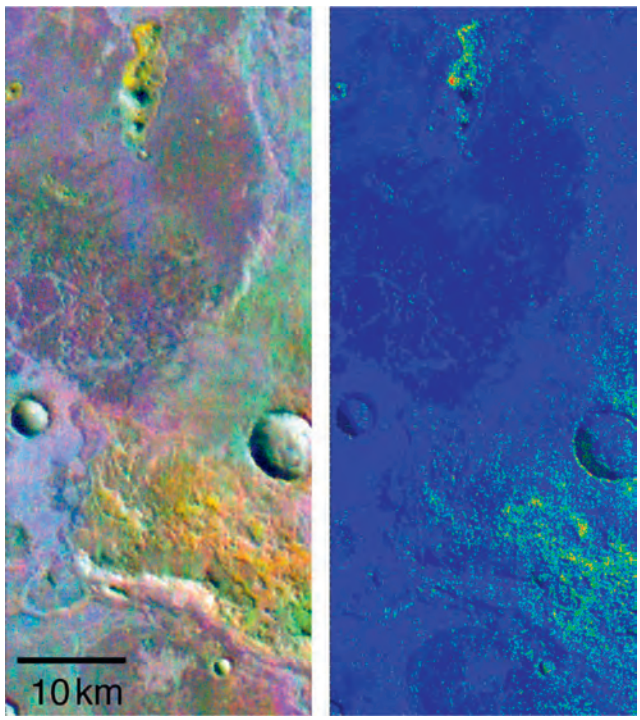

Figure 10.6. Granitoid abundances. THEMIS bands 8, 7, 5 DCS image (left), and THEMIS granitoid unit concentration map draped over surface temperature (right). Bands 8, 7, and 5 are displayed as red, green, and blue, respectively. Yellow colors coincide with higher band 8 and 7 and lower band 5 emissivities, consistent with surfaces that contain quartz and feldspar. Warmer colors in the concentration map indicate higher areal coverage of granitoid compositions. Red colors are nearly 100% coverage and blue indicates less than ~20% areal coverage. (For a color version of this figure, please refer to the color plate section or to the e-Book version of this chapter.)

Christensen, 1998; Bandfield *et al.*, 2004b). Root mean square errors are anti-correlated with surface temperature and are primarily due to random noise, indicating that no additional spectral endmembers are necessary to model the data. Retrieved concentrations of the quartz monzonite spectral endmember are highest in the central peak units and eastern knobby and fractured terrains (up to 40%), and are lower in the western knobby terrain (30%) and western fractured terrain (17%). The regional Mars surface endmember concentrations are anti-correlated with the quartz monzonite, ranging from ~20% to 100% for quartz monzonite concentrations of 40% to 0%, respectively.

The THEMIS spectra of five of the six granitoid composition surface units are identical within the uncertainties (Figure 10.5). The regional proximity of these surface units implies that they share a similar formation history and may be part of a single lithologic unit. The western fractured terrain exposure is not as prominent as the other exposures and appears to have a significant amount of the plains spectral signature contributing to its emissivity. However, it does have the same spectral trends as the other exposures and occurs in a similar surface morphology as the eastern fractured terrain exposure.

Nighttime THEMIS temperature data in the region are consistent with particulate surfaces rather than bedrock exposures. Particulate surfaces have roughly half the spectral contrast of broken rock surfaces (Ruff, 1998). Consequently, the areal coverage of the quartz monzonite endmember is roughly double the unit map concentrations (up to 70%–80%), consistent with the coincident low plains unit concentrations (0%–20%).

The granitoid composition surfaces cover a significant region. Though thermal-inertia values indicate that the surfaces are likely composed of loose particulate material, the association of granitoid surfaces with specific surface features and their localized nature suggest that the material has not been transported a significant distance from its source. It is impossible to determine if this composition is continuous in the subsurface where it is not exposed, or how much more extensive it may be. There are few surface features of similar morphology (e.g., central peak craters of similar size) as those that coincide with the exposures of quartz- and feldspar-rich surfaces within the region. It may be a continuous unit within the Martian subsurface, especially as the composition and context of the exposures suggest a subsurface formation. If the granitoid composition is not extensive at depth then it would be remarkable that it is largely confined to the localities that happen to be exposed. However, rock unit distributions can be more complex than a simple continuous body.

Syrtis Major is the only major volcanic construct on Mars that is not mantled with obscuring dust. This has enabled orbital remote sensing to gain insight into the variety of igneous compositions present at the surface in the region. The granitoid composition may be part of the ancient Noachian crust and could predate Syrtis Major, however. Antoniadi crater has been resurfaced by Hesperian age lava flows from Syrtis Major (Hiesinger and Head, 2004). The granitoid compositions had to be present and exposed prior to this resurfacing event. This association may disassociate the granitoid exposures from the Syrtis Major construct.

It is difficult to postulate on what the formation mechanisms may be outside the paradigm of plate tectonics, which is the dominant factor for producing differentiated magma compositions on Earth. However, large quantities of granitoid rocks were produced as trondhjemites on Earth by partial melting near the base of thick sequences of basaltic crust at 2.8–3.8 Ga, prior to the establishment of modern plate tectonics (Barker, 1979). Though such a formation mechanism is plausible on Mars, there is little evidence available at this time to either support or refute it (Bandfield *et al.*, 2004a; Bandfield, 2006).

These granitoid materials demonstrate that there are mechanisms on Mars that produce highly differentiated magmas. Though it is possible that the granitoid exposures add to the variety of igneous compositions associated with the Syrtis Major volcanic construct (Christensen *et al.*, 2005a), the geologic context of these exposures suggests a formation that predates Syrtis Major.

10.2.4 Spectrally distinct units

An initial assessment of spectral variety in a THEMIS image can be completed using decorrelation stretch (DCS) radiance images (Gillespie *et al.*, 1986), which enhance spectral variations present in the three spectral bands used to produce the image. This method provides a preliminary spectral analysis and reconnaissance of the spectral variety in the THEMIS dataset. Experience with the data has shown that three band (b) combinations – (1) b8, b7, b5; (2) b9, b6, b4; and (3) b6, b4,

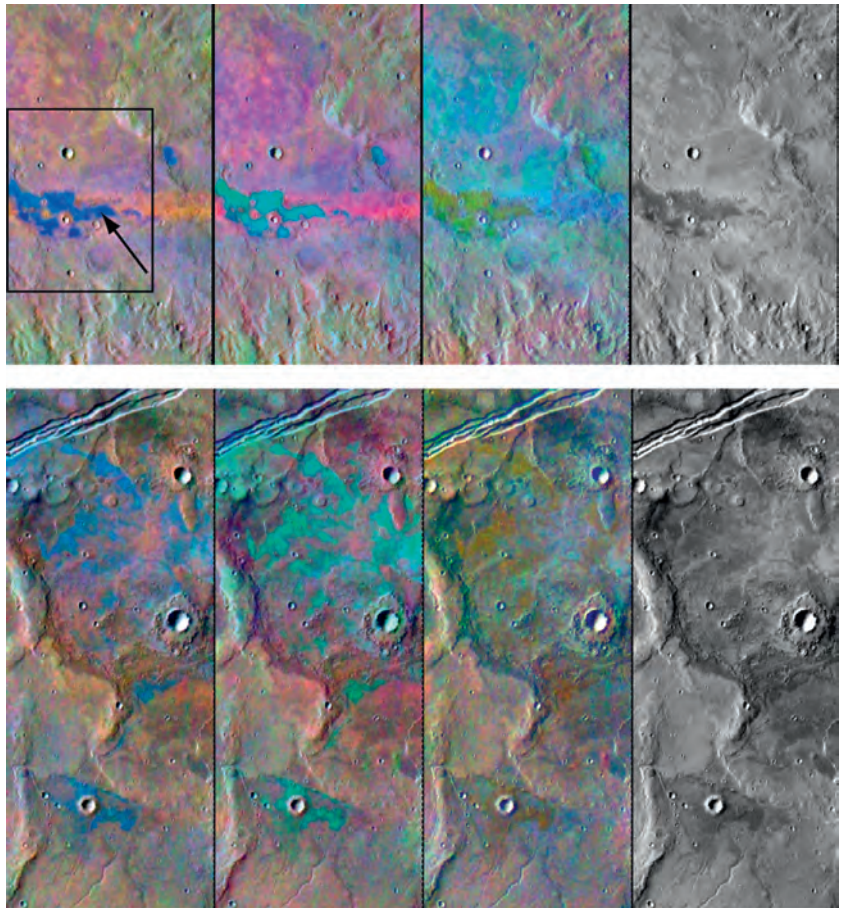

Figure 10.7. THEMIS DCS images for I08831002 (a) and I07734002 (b). The region of interest in these images is displayed as blue/teal/dirty-yellow (arrow) in the three DCS combinations described in the text. Each panel is 32 km wide. Box shows the location of the THEMIS image in Figure 10.8. (For a color version of this figure, please refer to the color plate section or to the e-Book version of this chapter.)

b2 (Figure 10.7) – provide a good representation of the spectral diversity. Other band combinations have been used for specific objectives and to search for specific mineral assemblages. For example, Hamilton and Christensen (2005) used bands 9, 7, and 5 to identify olivine-bearing rocks, and Stockstill *et al.* (2007) used bands 5, 8, and 7 to search for aqueous minerals.

The THEMIS DCS images display consistent patterns of spectral variability and unique spectral units, and led to the discovery of the volcanic diversity discussed above. The combined spatial and spectral information present in THEMIS data provides a bridge between more specialized datasets, such as low-spatial resolution spectrometers or dedicated imagers. Once a spectral unit is identified from imagery, a more detailed spectral analysis can be used to define the spectral response and ultimately the mineralogy of the surface. The spatial context from THEMIS has proven extremely valuable for understanding the surface mineralogy in the context of the local and regional surface morphology and thermophysical properties datasets (e.g., Bandfield *et al.*, 2004b; Christensen *et al.*, 2005a; Glotch and Christensen, 2005; Hamilton and Christensen, 2005; Rogers *et al.*, 2005; Bandfield, 2006). Spectrally unique units are commonly associated with distinct surface textures and morphologies as well as distinct albedo and thermophysical properties.

Example 1

Several THEMIS images in the southern highlands display a unique blue/teal/dirty-yellow color combination in the three standard DCS band combinations (Figure 10.7). These color combinations are consistent with a higher emissivity throughout the 8–12 μm spectral region. This spectral character can be similar to surface dust; however, the spatial distribution of the exposure, in particular the sharp boundaries that correlate with surface morphology, provides strong evidence that these are compositionally distinct geologic units.

Investigation of corresponding TES spectra confirms the uniqueness of this spectral unit. There is a strong slope present that results in extremely deep absorptions at long wavelengths compared to short wavelengths. Some of the surrounding area basaltic character is preserved, which is likely due to the inclusion of other components into the relatively large TES field of view (~3 km × 6 km).

This spectral character is highly unusual in the TES dataset. One possible cause of this spectral character is the presence of large amounts of oxides (particularly magnetite) that have prominent absorptions at wavelengths greater than ~15 μm. Alternatively, a spectrum with a sloped appearance could be caused by extreme anisothermality (more than ~50 K) within the field of view when the spectrum is converted to emissivity assuming a single surface temperature. However, if this were a cause of the spectral character, the magnitude is both remarkable and unique to these materials; most TES data, which often span sunlit and shaded boundaries, typically do not display this type of behavior. This spectral behavior is also not observed in THEMIS spectra of other materials, so a thermophysical explanation, i.e., mixtures of rocks and dust, would have to be unique to these materials.

Other datasets indicate that this is a relatively high albedo (but still <0.15) compared to the likely sandy surroundings (Figure 10.8). It is a highly scalloped unit that appears to be uncovered as the overlying terrain is stripped away. Nighttime THEMIS-IR data indicate that this is a relatively warm surface, indicating a higher thermal inertia than the surrounding terrain. The unit is likely not very thick because small (1–2 km), shallow (less than ~0.5 km depth) craters within the region of interest excavate through the unit and cover the surface with compositionally different ejecta.

There are a number of other regions that display similar, but more subtle, spectral characteristics. One example is friable deposits of the Medusa Fossae formation, which may be explained by (among other possibilities) volcanic air fall deposits associated with Apollonaris Patera (e.g., Bradley *et al.*, 2002).

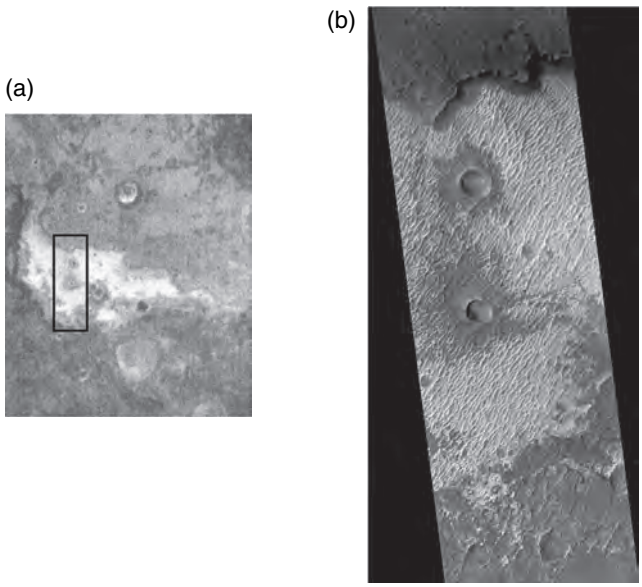

Figure 10.8. THEMIS nighttime image I06378009 (a) and MOC image M0701869 (b). Box on THEMIS image shows the location of the MOC image. The region of interest shown in Figure 10.7 is lighter in tone in the MOC image, but still a lower albedo surface than the surroundings. Relatively high nighttime temperatures indicate that the region of interest has a higher thermal inertia than the surrounding region. The MOC image is ~1.5 km across. The THEMIS image is ~32 km across.

Example 2

Many THEMIS images in the southern highlands display an association of yellow–orange with purple surface units in THEMIS band 8, 7, 5 DCS images (Figure 10.9). The THEMIS data indicate that there is more absorption at shorter wavelengths within the 8–12 μm region in the yellow-orange unit in THEMIS band 8, 7, 5 DCS images and is suggestive of differences in silica content between the units (e.g., Salisbury and Walter, 1989).

TES data display a distinct difference in spectral shape that is consistent with the THEMIS data, and spectral deconvolution results (e.g., Ramsey and Christensen, 1998) suggest that the purple surface unit contains slightly higher olivine concentrations and the yellow–orange unit contains slightly higher sheet silicate/glass/amorphous silica concentrations.

These types of compositions have been observed previously in TES data, but the subtle nature of the spectral differences and the lack of spatial context have made it difficult to interpret their origin. The clear spatial associations present in the THEMIS data demonstrate the geological relationship between these units and document their global occurrences. For example, the differences in mineralogy can be interpreted as either the effects of alteration of a mafic igneous composition or as two different igneous compositions. The relationships between the two compositions and the detailed morphology in THEMIS, MOC, and other imaging datasets can help to narrow the range of plausible interpretations.

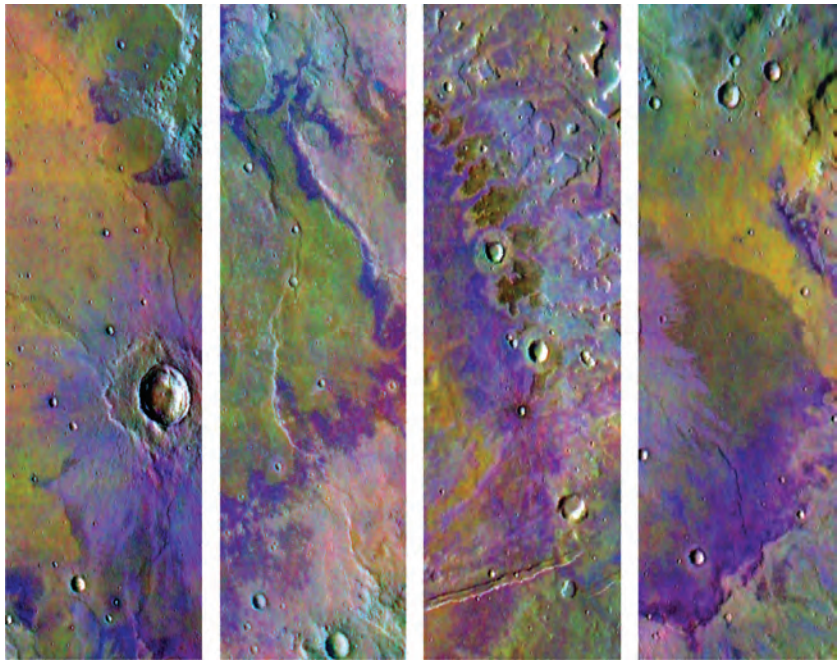

Figure 10.9. Examples of unique surface compositions found in the southern highlands. In THEMIS DCS images using bands 8, 7, 5, a pattern is observed in which a yellow-orange surface unit is often found in association with a purple unit. The purple unit has been determined from TES data to have slightly higher olivine concentrations and the yellow-orange unit contains slightly higher sheet silicate/glass/amorphous silica concentrations. Each panel represents a portion of a different THEMIS daytime IR image and is 32 km wide. (For a color version of this figure, please refer to the color plate section or to the e-Book version of this chapter.)

The examples shown here indicate that a large amount of spectral information is present in the THEMIS dataset. The spatial associations that often help to confirm the identification of the spectrally unique unit can greatly aid in identifying the geologic context. This links the mineralogy with the surface morphology for a more complete geologic picture.

10.2.5 What THEMIS has not found

In inventorying the global distribution of Martian rock types, it is important to consider what has not been observed. THEMIS is not capable of detecting the oxides, which absorb primarily at wavelengths >15 μm, nor directly detecting the halides, which are relatively transparent throughout the infrared. Of the minerals that THEMIS was designed to detect, carbonates (commonly $(Ca,Mg,Fe)CO_3$) are the most conspicuously absent. On Earth vast deposits of carbonate rocks have precipitated from warm oceans through interactions between CO_2 gas, water, and mineral grains. If Mars ever had a warm standing bodies of water, it has been suggested that extensive deposits of carbonates would have also formed through interactions with its CO_2 atmosphere. THEMIS bands 1 and 2 were specifically chosen to cover the ~6.5 μm fundamental C–O stretching absorption feature. However, no evidence of carbonate rock layers has been found by the THEMIS, TES, or OMEGA instruments (Christensen *et al.*, 2001a; Bibring *et al.*, 2005; Stockstill *et al.*, 2007), suggesting that if Mars ever had bodies of water, they were either too cold, too short lived, were covered by ice that limited interactions with the atmosphere, or had chemical conditions that prevented carbonates from forming. TES and the Mini-TES on the MERs have shown that small amounts of carbonates are present in the ubiquitous Martian dust (Bandfield *et al.*, 2003; Christensen *et al.*, 2004b). However, these minerals most likely formed by direct interaction with water vapor in the atmosphere. Phyllosilicate minerals, which form primarily by aqueous weathering, have been detected by OMEGA, but are relatively rare (Bibring *et al.*, 2005; Michalski *et al.*, 2005; Poulet *et al.*, 2005), consistent with the hypothesis that Mars has experienced little aqueous alteration.

While a variety of morphologic evidence clearly suggest that Mars has experienced fluvial processes, the lack of carbonates and extensive clay rock units, the presence of original olivine, pyroxene, and glass, and the inferred low surface erosion rates (e.g., Golombek *et al.*, 2006), all argue that fluvial processes were relatively short lived. Thus, on a global scale, aqueous chemical weathering appears to have been a relatively minor process throughout much of Martian history.

10.2.6 Implications for crustal formation and evolution

Multispectral IR imaging at 100 m scales has produced petrologic maps that are, for the first time, at scales appropriate for studying local geologic processes. At these scales we have identified rock units in basaltic terrains that have olivine abundances >20%, which on Earth would be classified as picrites. These rocks have been identified in eroded canyon walls and crater floors of ancient terrains in several areas, suggesting that they may be relatively common throughout the ancient Martian crust but remain unexposed in most locations. Local eruptive sequences are observed in the Syrtis Major region that appear to have evolved in composition from basaltic to dacitic, demonstrating that fractional crystallization occurs in Martian magma chambers. This diversity in composition is the result of igneous processes analogous to those found in large volcanic complexes on Earth. Rare occurrences of exposed quartz-bearing granitoid rocks have been discovered on Mars, suggesting the formation of highly evolved magmas. Taken together these observations show that the Martian crust, while dominated by basalt, has produced a diversity of igneous materials whose range in composition from ultramafic to highly silicic rivals that found on the Earth.

10.3 GEOLOGY HISTORY: A CASE STUDY IN MERIDIANI PLANUM

The Meridiani Planum region, centered near 0° N, 0° E, has received special attention following the discovery of coarse-grained, crystalline hematite (α-Fe_2O_3) using data from MGS/TES (Christensen *et al.*, 2000b, 2001b) and hence the subsequent selection of this site for investigation by the *Opportunity* rover (Morris *et al.*, 2000; Hynek *et al.*, 2002; Lane *et al.*, 2002, 2003; Arvidson *et al.*, 2003; Golombek *et al.*, 2003; Christensen and Ruff, 2004; Squyres *et al.*, 2004a). This irregularly shaped hematite deposit, centered at ~357° E and 2° S and spanning ~500 km in the E–W direction and ~300 km N–S, occurs in a primarily basaltic unit that is exposed at the top of a sequence of layered, easily eroded rocks that are stratigraphically above and postdate the ancient cratered terrain (Presley and Arvidson, 1988; Edgett and Parker, 1997; Christensen *et al.*, 2001b; Hynek *et al.*, 2002; Arvidson *et al.*, 2003; Newsom *et al.*, 2003). Hematite was proposed to have formed through aqueous processes (Christensen *et al.*, 2000b), although it was also suggested that this material may be an eroded volcanic ash deposit (Hynek *et al.*, 2002, 2003). The *in situ* observations by the *Opportunity* rover have revealed the presence of finely layered sulfate-bearing rocks and basaltic sandstones that strongly support the aqueous origin of these units (see Chapters 23 and 24), although alternative hypotheses involving volcanism (McCollom and Hynek, 2005) and impact base surge (Knauth *et al.*, 2005) have also been suggested. The interpretation of the physical properties, morphology, and composition from orbital observations allow the detailed *in situ* observations to be placed in the broader context of the regional geology, and provide strong constraints on the possible formation of the Meridiani units.

The abundance of hematite in the surface materials of the hematite-bearing unit (unit Ph of Arvidson *et al.*, 2003) (see also Figure 9.10 in Chapter 9) was determined to vary from ~5% to ~20% using linear deconvolutions of TES spectra (Bandfield, 2002; Christensen and Ruff, 2004). Laboratory thermal emission measurements of hematite samples show that hematites derived by low-temperature (~100–300 °C)

dehydroxylation of goethite are an excellent match to the TES spectra (Glotch *et al.*, 2004), and it is most likely that the hematite is formed in a low-temperature environment. Rover *in situ* observations have confirmed that the hematite was a postdepositional component formed at low temperatures by near-surface fluid–rock interactions (Chan *et al.*, 2004; Squyres *et al.*, 2004b; Grotzinger *et al.*, 2005; Squyres and Knoll, 2005; see Chapter 24).

TES spectra of the upper, hematite-bearing surface throughout the Meridiani region show abundances of plagioclase, pyroxene, and olivine that closely match typical Martian basalts; no other minerals besides hematite have been identified (Christensen and Ruff 2004; Glotch *et al.*, 2006). Sulfate minerals make up ~40% of the bright layer that was examined in detail by *Opportunity* and they appear to occur throughout the Meridiani region (Arvidson *et al.*, 2003; Christensen and Ruff, 2004; Hynek, 2005; Glotch *et al.*, 2006). While this layer, and the sulfates it contains, is an important component of the Ph layered sequence, sulfates have not been observed from orbit in Ph by OMEGA (Bibring *et al.*, 2005), TES, or THEMIS, and sulfate formation may be a relatively minor, possibly late-stage, component of the Ph sequence. The basaltic sands that are observed from orbit and exposed in the wall of Endurance crater (e.g., Grotzinger *et al.*, 2005) appear to be the dominant component of this sedimentary rock unit.

A key question to the origin of hematite and sulfate is their distribution within and above the sedimentary sequence of unit Ph. A 25 km wide, ~50 m high rise centered near 358.4° E, −0.2° S does not contain hematite, in contrast with the plains that surround it (Christensen and Ruff, 2004). The contact between the hematite-bearing and the hematite-poor units occurs at the base of this rise, suggesting that the material that comprises the rise is a stratigraphic unit that lies immediately above the hematite-bearing Ph unit. The crater age, morphology, and erosional style of this rise is similar to the hematite-bearing plains, suggesting that the two units were deposited under similar conditions and processes (Christensen and Ruff, 2004).

A similar example of an overlying, hematite-poor layer is observed in an eroded, 30 km wide, ~30 m high mesa centered at 358.5° E, 2.5° N near the northern margin of Ph (Figure 10.10), which appears to lie unconformably on top of dissected cratered terrain (Arvidson *et al.*, 2003; Christensen and Ruff, 2004). Hematite abundance varies across this mesa, decreasing significantly on the eastern and western margins. These changes are associated with changes in physical properties, with nighttime temperatures on the eastern and western hematite-free surfaces that are 6–12 K colder than the central hematite-rich surface (Figure 10.10). These temperature differences indicate that the hematite-bearing layer is physically different, and thus may have formed under a different set of processes or conditions than the other layers that make up the ~200 m thick sequence in Meridiani.

There are three occurrences of the hematite-bearing unit exposed south of the main Ph deposit (Christensen and Ruff, 2004) and several larger circular deposits to the northwest (Figure 10.11) (Christensen and Ruff, 2004). The southern

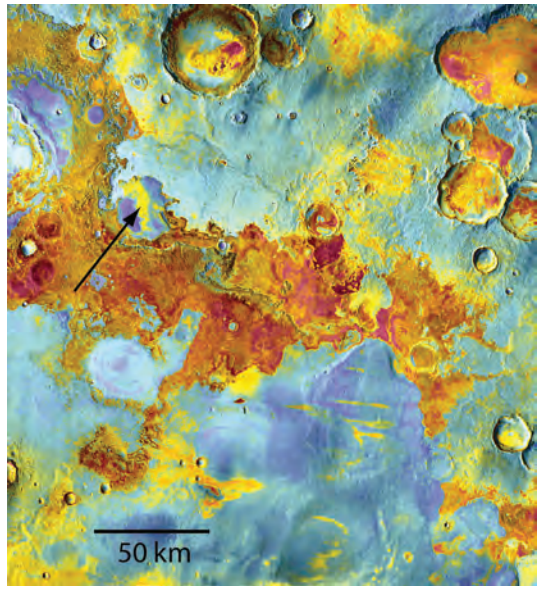

Figure 10.10. THEMIS day/night temperature mosaic of eastern Meridiani. The nighttime temperature data have been colorized and merged with the daytime temperature data. Fine-grained materials have low temperatures (170–190 K; blue) at night; coarser-grained materials are warmer (180–190 K; red). The mesa (arrow) has hematite in the central (yellow-colored) regions, with no hematite in the eastern and western portions. (For a color version of this figure, please refer to the color plate section or to the e-Book version of this chapter.)

examples occur within craters that are 20–40 km in diameter, are within 50 km of the southern margin, and appear to be eroded remnants of once-larger, intracrater deposits. No hematite is observed on the intercrater plains of the ancient cratered terrain south of Ph. In addition, the southern margin of the hematite unit appears to embay the high-standing terrain to the south (Edgett and Parker, 1997; Christensen *et al.*, 2000b; Hynek *et al.*, 2002; Christensen and Ruff, 2004). These relationships suggest that these hematite-bearing, layered units were originally deposited in a dense, gravity-controlled fluid, rather than as a widely dispersed, air-fall or impact generated layer. Unit Ph is also strikingly different from the underlying etched and dissected cratered terrain units (Arvidson *et al.*, 2003). It erodes in a significantly different manner, lacks the connected series of ridges found in the etched unit, shows clear evidence of layering that is unlike the lower units, and contains hematite. These observed differences in morphologic and thermophysical characteristics imply temporal changes in the processes or environments that formed them (Christensen *et al.*, 2003a).

Upon landing, *Opportunity*'s spectrometers and cameras confirmed the importance of water at Meridiani (e.g., Squyres *et al.*, 2004b). Outcrops of layered sedimentary rocks were observed by *Opportunity*'s cameras (see Chapter 13), and the Mössbauer, Alpha Particle X-Ray Spectrometer (APXS), and Mini-TES spectrometers found that these rocks contained high (30%–40%) abundances of sulfates formed by evaporation of sulfur-rich water (Christensen *et al.*, 2004c; Klingelhöfer *et al.*, 2004; Rieder *et al.*, 2005;

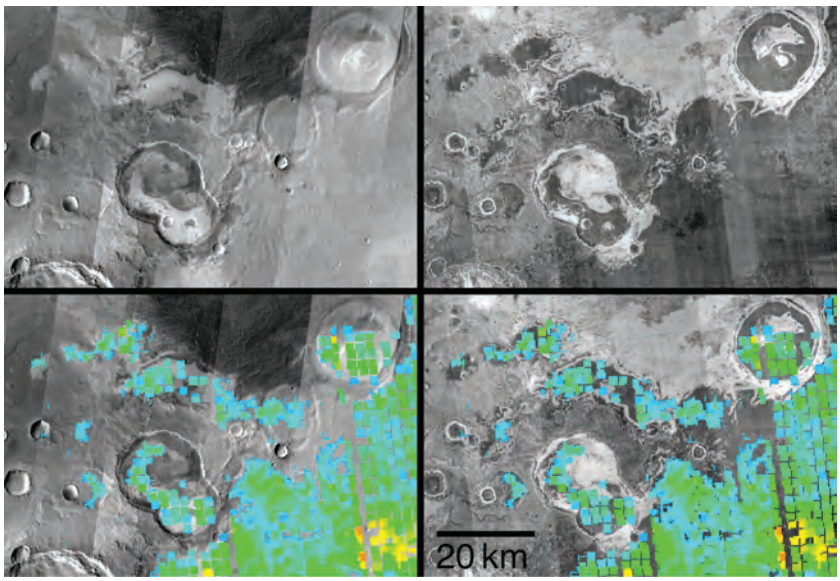

Figure 10.11. Hematite outliers in Meridiani northwest of the main hematite-bearing unit on which *Opportunity* landed. The hematite abundances were derived from TES and vary from ~5% (blue) to 20% (red). The TES data are superimposed on mosaics of day (left column) and night (right column) THEMIS infrared images. The hematite-bearing materials have similar thermal properties. Seen at THEMIS resolution, these materials occur only in the uppermost layer of the stack of layered materials that form these outliers of Ph. The two major outliers in this region occur within a double crater and on a circular mesa interpreted to be the remnant floor of a crater whose walls have been completely removed. (For a color version of this figure, please refer to the color plate section or to the e-Book version of this chapter.)

Glotch *et al.*, 2006; see Chapters 4, 14, and 15). The coarsely layered rocks exposed at the base of Burns Cliff in Endurance crater appear to have been formed by migrating dunes, whereas the layers at the top of the cliff are made of sulfate-rich sediments deposited in water (Grotzinger *et al.*, 2005). These layers may record variations in climate from arid aeolian dunes, to wet, evaporating playas where the sulfate salts were formed, to a groundwater system that formed the hematite spheres (e.g., Bandfield *et al.*, 2003; Chan *et al.*, 2004; Squyres *et al.*, 2004b; Grotzinger *et al.*, 2005).

Of the models that have been proposed for the broader Meridiani sequence, a model of deposition of sulfates and precursor Fe-oxyhydroxides in water and/or saturated sediments in a basin filled with basaltic sands accounts for (1) the occurrence of a thin hematite unit over an area ~150 000 km^2 in size with sharp upper (and possibly lower) contacts; (2) spectral evidence for goethite as a precursor to hematite; (3) the presence of a finely layered, friable texture on Ph in distinct contrast to the morphology of the etched units on which it lies; (4) embayment relationships on the southern margin of Ph; (5) the occurrence of remnants of hematite-bearing units within isolated craters surrounding the main Ph unit, and the lack of these units on the intercrater plains; (6) the lack of other hydrothermal minerals; (7) the presence of low-albedo, coarse-grained basalt, rather than ash, as the major component of the hematite-bearing unit; and (8) the differences in morphology between Ph and proposed ash units.

Crystalline hematite is also exposed in Aram Chaos (Catling and Moore, 2003; Glotch and Christensen, 2005), Aureum and Iani Chaos (Glotch and Rogers, 2007), and a few locations within Valles Mariners (Christensen *et al.*, 2001b). These locations typically have associated sulfates (Gendrin *et al.*, 2005) and friable, layered sequences, suggesting similar formation mechanisms. These deposits are, however, uncommon, implying a specific set of conditions that may have only occurred rarely through Mars history. The occurrence of unweathered olivine, pyroxene, and feldspar in basalts throughout the equatorial region provides strong evidence that extensive aqueous weathering has not occurred on Mars (Christensen *et al.*, 2000a, 2003a; Hoefen *et al.*, 2003; Bibring *et al.*, 2006). Thus, the presence of a small number of bodies of standing water appears to represent brief, localized phenomena set against the backdrop of a cold, frozen planet. What factors caused water to accumulate and allowed it to remain at these sites? The answer is unknown, but perhaps involved a combination of heat from sub-surface volcanic activity, high salt concentrations that lowered the freezing temperature, or a protective covering of ice over water released by catastrophic floods.

10.4 TEMPERATURE ANOMALIES

An important THEMIS objective is the search for temperature anomalies produced by surface cooling or heating due to near-surface liquid water or ice, or hydrothermal or volcanic activity respectively. The Odyssey early morning, late afternoon polar orbit is ideally suited for the detection of predawn temperature anomalies that are not produced by solar heating. Multispectral temperature maps with an NEΔT of 1 K have been produced for the entire planet.

THEMIS has mapped virtually all of Mars at night in the infrared at 100 m/pixel resolution, and has observed portions of the surface a second time up to one Mars year later. An automated analysis has been performed of all of these images to search for maximum temperatures greater than those expected from rocks or bedrock alone (220 K), and no example has been found in any image of a temperature that requires an internal heat source.

The THEMIS database has also been searched for spatial patterns that are potentially due to evaporative cooling associated with near-surface water, or to recent volcanic activity or hydrothermal heating. The THEMIS nighttime images exhibit very high spatial variability due to variations in surface properties such as rock layers, exposed bedrock, sand, and granular dunes. These thermal variations greatly

complicate the search for anomalous patterns associated with sub-surface water. Visual assessment of these data can allow identification of sites of active hydrothermal systems and potential near-surface igneous activity using the spatial distribution of temperature differences (e.g., along linear zones) to distinguish them from physical properties. Regions that have been manually analyzed for thermal anomalies have focused on young volcanic sites, where mobilization of ground ice would result from intrusive or extrusive volcanic activity.

A second technique to overcome the effects of surface temperature complexities has been a search for seasonal changes in surface temperature in order to isolate changes due to dynamic heating or cooling processes from those due to thermophysical properties. This process involved the use of histogram adjustments of the overlapping portions of two images to remove the additional complicating temperature changes produced by the two hour variation in local time of the spatially adjacent Odyssey orbits, and by the differences in season between the different observations. In addition, numerous image pairs have been converted to thermal inertia using the THEMIS Standard Thermal Model as a quantitative means to remove the time of day and seasonal effects (Fergason *et al.*, 2006; see also Chapter 18).

Based on the analysis to date, there is no evidence in the THEMIS thermal images for the existence of near-surface volcanic activity, liquid water, or ice that is close enough to the surface to be capable of producing measurable thermal anomalies. Repeat coverage will be emphasized in future observations and will improve the ability to use change detection algorithms, increasing the likelihood that thermal anomalies will be detected if any exist.

10.5 PHYSICAL PROPERTIES AND PROCESSES

10.5.1 THEMIS thermal inertia

THEMIS thermal inertia values are derived at a spatial resolution of 100 m/pixel, providing a significant improvement from previous mapping using TES data (e.g., Mellon *et al.*, 2000; Christensen *et al.*, 2001a; Putzig *et al.*, 2005). THEMIS data are used to calculate thermal inertia values of local regions (100 m scales), improving the interpretation of particle size distributions and material properties at geologic scales and the interpretation of the geologic history and processes that have affected the Martian surface (e.g., Christensen *et al.*, 2003a; Putzig *et al.*, 2004; Fergason *et al.*, 2006). Thermal inertia values are derived from THEMIS band 9 (12.57 μm) nighttime temperature data, which are converted to a thermal inertia by interpolation within a seven-dimensional look-up table using season, latitude, local solar time, thermal inertia, albedo, elevation, and atmospheric dust opacity as input parameters (Fergason *et al.*, 2006; see also Chapter 18). The effects of local slopes are not considered in the automated model, but can be determined by calculating THEMIS thermal inertia values in a nonautomated manner (Fergason *et al.*, 2006).

Surface albedo is a critical factor in controlling surface temperature. To date, the THEMIS visible imaging only covers a portion of the surface, and so TES albedo data, which are well calibrated and global, are typically used to estimate this parameter. Other model inputs, also at a coarser resolution than the THEMIS temperature data, are the TES atmospheric dust opacity and MOLA elevation values. Elevation (used to determine the atmospheric pressure) has a minor effect on the thermal inertia, and the atmospheric dust opacity does not vary significantly over the area of a THEMIS image. Sub-TES-pixel variations in albedo can affect the accuracy at which thermal inertia values can be calculated, and regions where albedo varies significantly (>0.1) over short distances (less than 3 km) should be interpreted with caution (Fergason *et al.*, 2006). The precision and absolute accuracy of the THEMIS thermal inertia values are 10%–15% and ~20%, respectively. These uncertainties are primarily due to (1) uncertainties in model input parameters, such as albedo, at the resolution of the THEMIS instrument; (2) instrument calibration; and (3) thermal model limitations (Fergason *et al.*, 2006).

10.5.2 Surface materials

Bedrock occurrences

THEMIS infrared images have revealed the occurrence of kilometer-scale outcrops of exposed bedrock. An example is shown in Figure 10.12 of exposed bedrock in the southern highlands. The Nili Patera caldera (9° N, 67° E) has nighttime surface brightness temperatures of 217–219 K

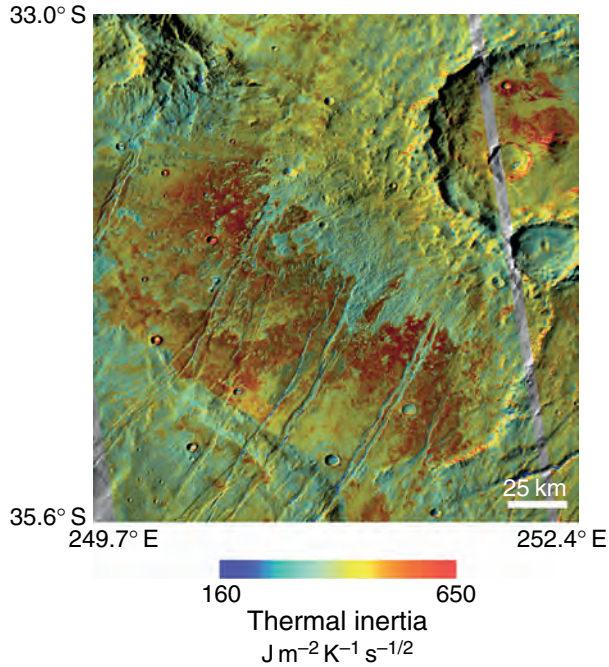

Figure 10.12. Exposed bedrock in the southern highlands. THEMIS thermal inertia mosaic (100 m/pixel resolution) overlaid onto a THEMIS daytime temperature mosaic, centered at 251.0° E, 34.3° S. (For a color version of this figure, please refer to the color plate section or to the e-Book version of this chapter.)

over an ~30 km^2 area (Figure 10.3a). Thermal models using the appropriate conditions predict temperatures of 220 K for a thermal inertia corresponding to solid rock (2200 J m^{-2} K^{-1} s$^{-1/2}$), indicating that portions of the caldera floor are exposed bedrock.

Bedrock surfaces are also observed within and near the mouth of Ares Valles (~22° N, ~324° E) (Rogers *et al.*, 2005), approximately 250 km downstream of the Pathfinder landing site. Two ~8 km diameter craters at this location have produced rays of ejecta that extend 2–3 crater diameters from their crater rims (Christensen *et al.*, 2003a). The nighttime temperatures of these deposits (191–193 K) show that they consist of disaggregated material with an average particle size of ≥ 1 mm. The preservation of the ejecta, including exquisitely detailed thermophysical patterns in individual rays that are superimposed on top of the bedrock, indicates a significant change in environmental conditions, with processes of erosion and stripping to bedrock occurring prior to crater formation, but not since.

Layered units

Layered materials are exposed in a variety of different environments and landforms on the Martian surface. Examples include the polar layered deposits (e.g., Thomas *et al.*, 1992; Herkenhoff and Plaut, 2000; Milkovich and Head, 2005), the walls of mesas and craters (e.g., Malin and Edgett, 2001; Pelkey *et al.*, 2004), channel deposits (e.g., Rogers *et al.*, 2005), and those within Valles Marineris (e.g., Nedell *et al.*, 1987; Komatsu *et al.*, 1993; McEwen *et al.*, 1999; Malin and Edgett, 2000; Weitz *et al.*, 2003; Beyer and McEwen, 2005; Quantin *et al.*, 2005) and in Meridiani Planum (e.g., Arvidson *et al.*, 2003; Christensen and Ruff, 2004). The presence of these layered materials indicates that each layer has distinct physical characteristics, causing differences in their resistance to erosion. These differences then imply a change in the depositional environment, and possibly the climate, under which each unit formed. Thus, knowledge of the physical and chemical properties of layers on Mars is an important step toward understanding the evolution of Martian environments and climates.

One example of layered materials is the interior layered deposits within Hebes Chasma. Hebes Chasma (centered at 284° E, ~1° N and ~310 km wide) is part of the Valles Marineris canyon system and contains a sequence of layered deposits that is ~5000 m in total thickness in its central plateau. Differences in thermophysical properties are observed in THEMIS images, and these correspond to different layers with different morphologic characteristics observed in MOC and THEMIS visible images. These correlated differences in thermophysical properties indicate that mobile sediment mantles are neither dominating nor obscuring the thermophysical properties, and high-resolution thermal inertia data can be used to determine and constrain the depositional environments.

Another example of layering occurs within a small (~1 km) crater in which basaltic layering exposed in the crater walls has been identified (Wright and Ramsey, 2006). The crater rim and ejecta blanket also have larger block sizes and a lower albedo than the surrounding ejecta-free plain, indicating a young impact age (Wright and Ramsey, 2006).

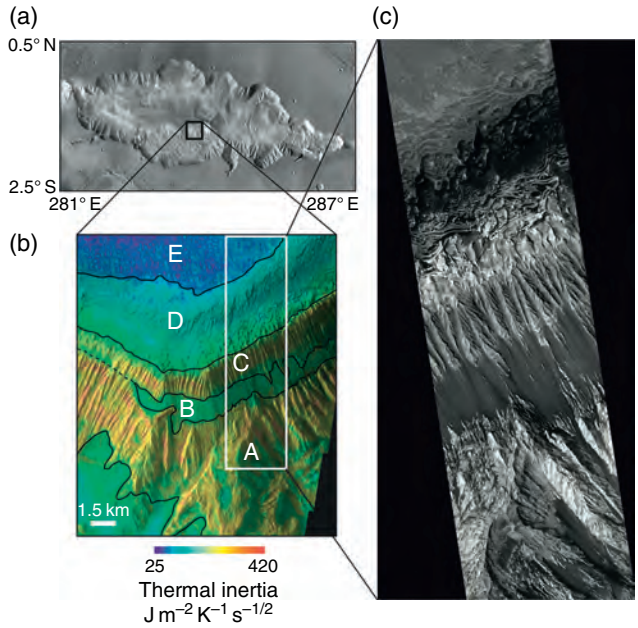

Figure 10.13. Hebes Chasma interior layered deposits. (a) THEMIS daytime temperature mosaic of Hebes Chasma. The black box indicates the location of the THEMIS thermal inertia mosaic; (b) THEMIS thermal inertia mosaic (100 m/pixel resolution) overlaid onto a THEMIS visible image V10052001 (18 m/pixel resolution) of Hebes Chasma, centered at 284° E, ~1° N; (c) Portion of MOC Narrow Angle image M0900284, courtesy of Malin Space Science Systems (MSSS/NASA/JPL). (For a color version of this figure, please refer to the color plate section or to the e-Book version of this chapter.)

Within the interior layered deposits of Valles Marineris, THEMIS images have shown the presence of layers of differing thermophysical properties. For example, in Hebes Chasma five different thermophysical/morphologic units can be seen (Figure 10.13) (Fergason *et al.*, 2006). At the base of the central plateau is a ~2400 m thick unit (A) with a thermal inertia of 290–420 J m^{-2} K^{-1} s$^{-1/2}$ (particle diameter of 780 μm [medium sand] and larger). This friable but competent unit erodes into a massive, fluted morphology resembling yardangs that may be the precursor to spur-and-gully-type terrain. Unit B is ~600 m thick that has a thermal inertia of 260–300 J m^{-2} K^{-1} s$^{-1/2}$ (490–900 μm particles; medium to coarse sand), consistent with mobile, unconsolidated sand eroded from layers above or below. Unit C is ~1000 m thick with a thermal inertia of 275–385 J m^{-2} K^{-1} s$^{-1/2}$ (620 μm particles [medium sand] and larger), and is eroding into a fluted morphology with narrower flutes than those in Unit A, suggesting it is less resistant to erosion than Unit A (Komatsu *et al.*, 1993). Unit D is ~800 m thick, with a thermal inertia of 190–250 J m^{-2} K^{-1} s$^{-1/2}$ (130–415 μm particles; fine to medium sand). The unit has a distinctive erosional pattern, forming a wavy, sinuous configuration suggestive of soft sediment deformation. The surface of the flat-lying central plateau (Unit E) has a thermal inertia ranging from 125 to 180 J m^{-2} K^{-1} s$^{-1/2}$, corresponding to ~100 μm diameter

particles (very fine sand), and is some of the lowest thermal inertia material in Hebes Chasma. This flat-lying material may have a higher thermal inertia substrate, but is dominated by air-fall dust (Fergason *et al.*, 2006).

The thermal inertia, together with an assessment of the morphology, can be used to constrain the processes that have formed the Hebes Chasma units (Fergason *et al.*, 2006). The thermal inertia of these deposits is $<420\,J\,m^{-2}\,K^{-1}\,s^{-1/2}$, which is too low to be consistent with lava flows. In addition, lava flows would likely be well lithified and would not erode in the fluted pattern observed in Units A and C. Emplacement of volcaniclastic materials or aeolian deposition of eroded basaltic sand followed by weak induration could be a potential mechanism for the formation of the interior layered deposits (Fergason *et al.*, 2006). A lacustrine emplacement of the layers has also been suggested for interior layered deposits observed in Hebes Chasma and other localities (e.g., Nedell *et al.*, 1987; Komatsu *et al.*, 1993; Lucchitta *et al.*, 1994; Malin and Edgett, 2000). However, Hebes Chasma does not appear to have a well-developed fluvial system by which materials were brought into the chasma, nor is there an observed outlet for removing water in the enclosed Hebes Chasma basin (e.g., Chapman and Tanaka, 2001). The wavy, sinuous erosional pattern of Unit D is suggestive of soft sediment deformation, and could be the result of plastic deformation of fluidized sediment rather than deposition in a lacustrine environment (Fergason *et al.*, 2006).

A friable volcanic ash deposit would account for the lower thermal inertia and the fluted erosion observed in Units A and C. Unit C has a lower thermal inertia and appears less resistive to erosion than Unit A, suggesting a less indurated material. Unit A could be a moderately welded tuff, with Unit C a less consolidated volcanic ash deposit (Hynek *et al.*, 2003; Fergason *et al.*, 2006).

Regardless of the formation process, the sharp thermophysical and morphologic boundaries between these layers suggests a transition of depositional environments or depositional mechanisms for each layer. Units A and C both erode in a fluted pattern, indicating that the material is weakly indurated yet resistive to erosion, and may have formed by a similar process. Unit D exhibits a unique erosional pattern that is strikingly different from Units A or C, suggesting a significant change in the depositional environment. This erosional pattern is suggestive of soft sediment deformation requiring some liquid medium. The scenario favored by Fergason *et al.* (2006) for the deposition of the layered deposits in Hebes Chasma includes multiple episodes of volcanic ash or aeolian sediment deposition followed by lithification, resulting in the formation of Units A and C. Then the deposition of additional material in a fluidized medium occurred, but did not necessarily include a standing body of water.

Talus and landslide materials

Nighttime IR images commonly show elevated temperatures on the slopes of canyons, craters, mesas, channels, and fissures (Figure 10.14). Slopes are typically 5–15 K warmer than their surroundings, independent of slope azimuth, and elevated temperatures occur on the walls of both closed and

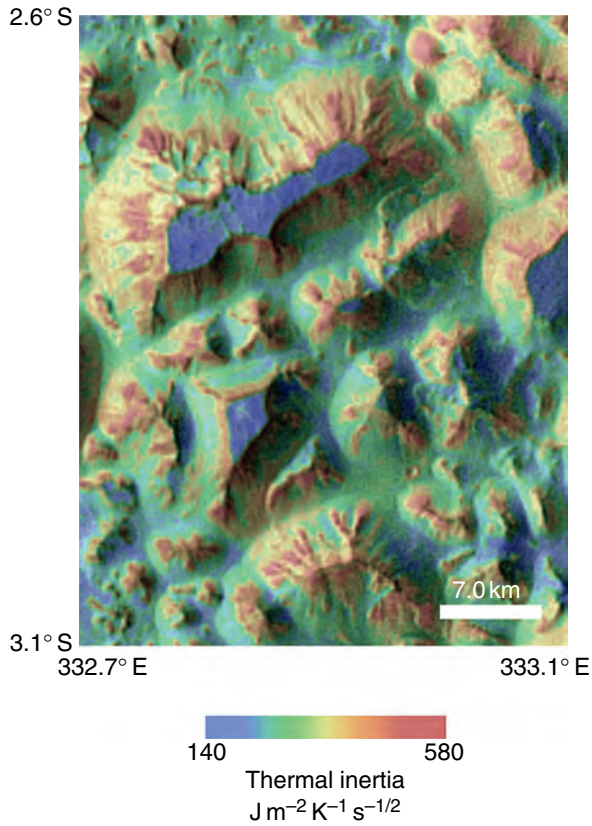

Figure 10.14. Rocks and talus on slopes. Rocks are warmer (red) than the colder (blue), dust-covered mesas and fine-sand (green) canyon floor. THEMIS nighttime temperature mosaic (100 m/pixel) overlaid onto THEMIS daytime temperature mosaic (100 m/pixel resolution), centered at 333.0° E, 2.9° S. (For a color version of this figure, please refer to the color plate section or to the e-Book version of this chapter.)

open depressions (Christensen *et al.*, 2003a). The higher slope temperatures appear to be due to a concentration of rocky (warm) material on slopes relative to the surrounding flat-lying surfaces, with concentrations of 10%–35% rocks required to produce the observed temperature differences.

The presence of rocky material on Martian slopes indicates that the production or exposure rate of blocks or *in situ* rock layers on slopes is greater than their rate of burial and/or weathering and erosion. Currently, the most prevalent form of burial on Mars is fallout of airborne dust. Several factors may reduce the amount of burial on slopes; dust may be removed in occasional catastrophic dust flows (Sullivan *et al.*, 2001; Aharonson *et al.*, 2003) or downslope movement of rocks, air turbulence over blocky material may prevent dust from settling, or, once settled, turbulence may enhance the remobilization of dust during periods of higher wind. Together, these processes prevent net dust accumulation to a thickness greater than the size of the blocky materials (greater than ~30 cm; Christensen *et al.*, 2003a).

Massive landslides have moved up to 8 km downslope from the walls throughout Valles Marineris, often exposing layers several hundred meters thick and ~0.5 km below the canyon rim that are warm (blocky) in nighttime IR images (Figure 10.15). Landslide deposits can have

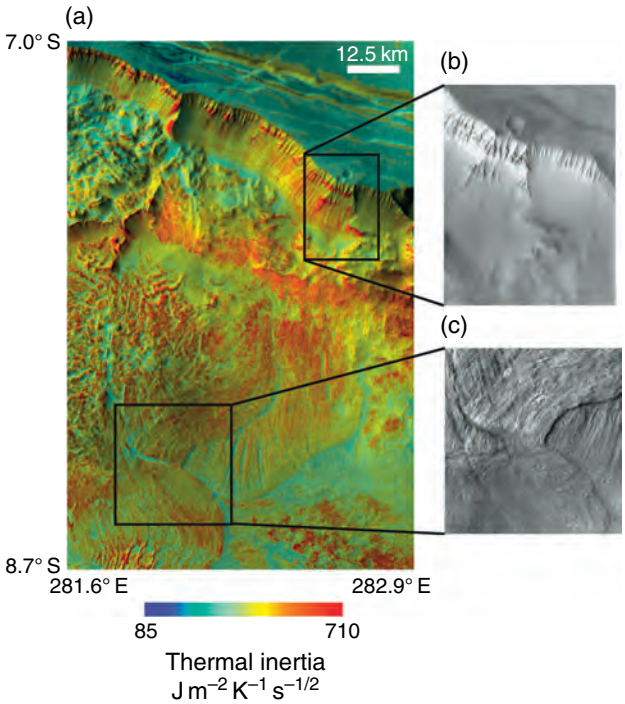

Figure 10.15. Landslide in western Melas Chasma, Valles Marineris. (a) THEMIS thermal inertia mosaic (100 m/pixel resolution) overlaid onto a THEMIS daytime temperature mosaic (100 m/pixel resolution), centered at 282.3° E, 7.9° S, illustrating multiple lobes of landslide deposits; (b) Portion of THEMIS visible image V16816003 (18 m/pixel resolution) of chasma wall material; (c) Portion of THEMIS visible image V02550002 (18 m/pixel resolution) of landslide flow boundaries. (For a color version of this figure, please refer to the color plate section or to the e-Book version of this chapter.)

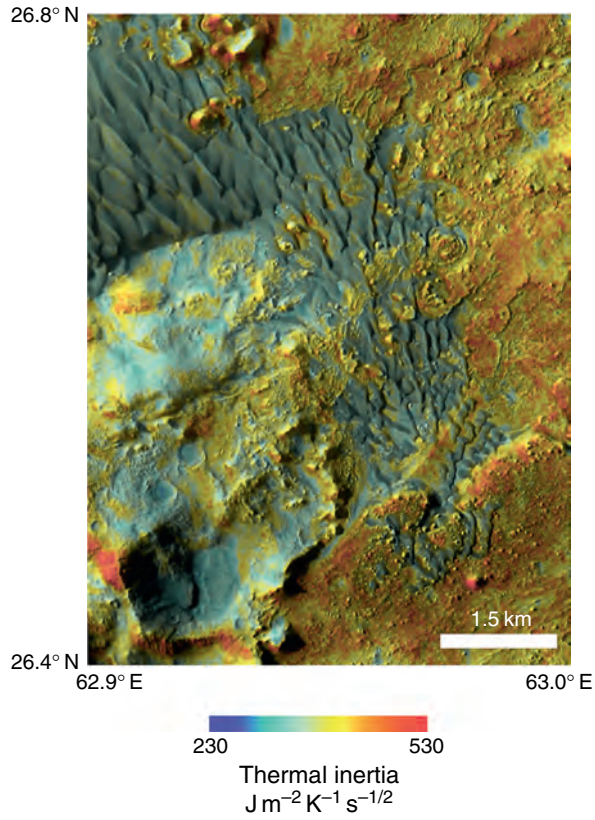

Figure 10.16. Sand dunes. Dunes in unnamed crater centered at ~63° E, 26.6° N. THEMIS thermal inertia (100 m/pixel resolution) overlaid onto THEMIS visible image mosaic (18 m/pixel resolution) showing surfaces that have eroded into mesas, knobs, ridges, and aeolian material. (For a color version of this figure, please refer to the color plate section or to the e-Book version of this chapter.)

temperature variations of 10–12 K between individual longitudinal and transverse ridges/grooves that are typically spaced 0.5–1.0 km apart and that formed during the landslide process. These temperature variations represent a factor of 3–5 difference in average particle size or a variation in surface rock abundance from 0% to 30% (Christensen *et al.*, 2003a).

Landslides in Valles Marineris have likely occurred throughout Martian history (between 3.5 Gyr and 50 Myr; Quantin *et al.*, 2004), and are a prominent gravity-driven process found throughout the Valles Marineris system. One landslide example is in western Melas Chasma (Figure 10.15). This example illustrates the typical size and morphologic features observed in landslides, and high-resolution THEMIS data can be used to improve the identification of morphologic features and the understanding of landslide processes and development on Mars in general. This landslide forms a broad, curved segment of chasma wall with slump blocks at the head of vast aprons of longitudinally ridged material, and is similar to landslide features observed elsewhere in Valles Marineris. Layers of high-inertia material visible in slump blocks match the location, thickness, and thermal inertia of similar materials in the wall rocks, suggesting that the original stratigraphy has been maintained in parts of the slide (Figure 10.15).

Landslides on Mars have been suggested to be more efficient at moving debris than those on Earth due to differences in gravity and resistance, and may be either large, wet debris flows (implying the intervention of water in order to explain the mobility ratio and morphologies), or dry rock avalanches (e.g., McEwen, 1989; Harrison and Grimm, 2003; Baloga and Bruno, 2005). Figure 10.15 shows examples of several flows originating from the same landslide scarp, suggesting multiple landslide events in a style that is common throughout Valles Marineris (e.g., Quantin *et al.*, 2004; Barnouin-Jha *et al.*, 2005; Chojnacki *et al.*, 2006).

Aeolian materials

Nighttime images of large dune fields can resolve individual dunes, revealing particle size differences between the dune and inter-dune surfaces and between the dune fields and the surrounding terrain (Figure 10.16). Inter-dune areas display temperature differences indicating particle size differences within the dune fields due to the accumulation of dust on inactive dunes or aeolian particle size sorting (Christensen *et al.*, 2003a; Fenton 2005; Fenton *et al.*, 2005; Fenton and Mellon, 2006).

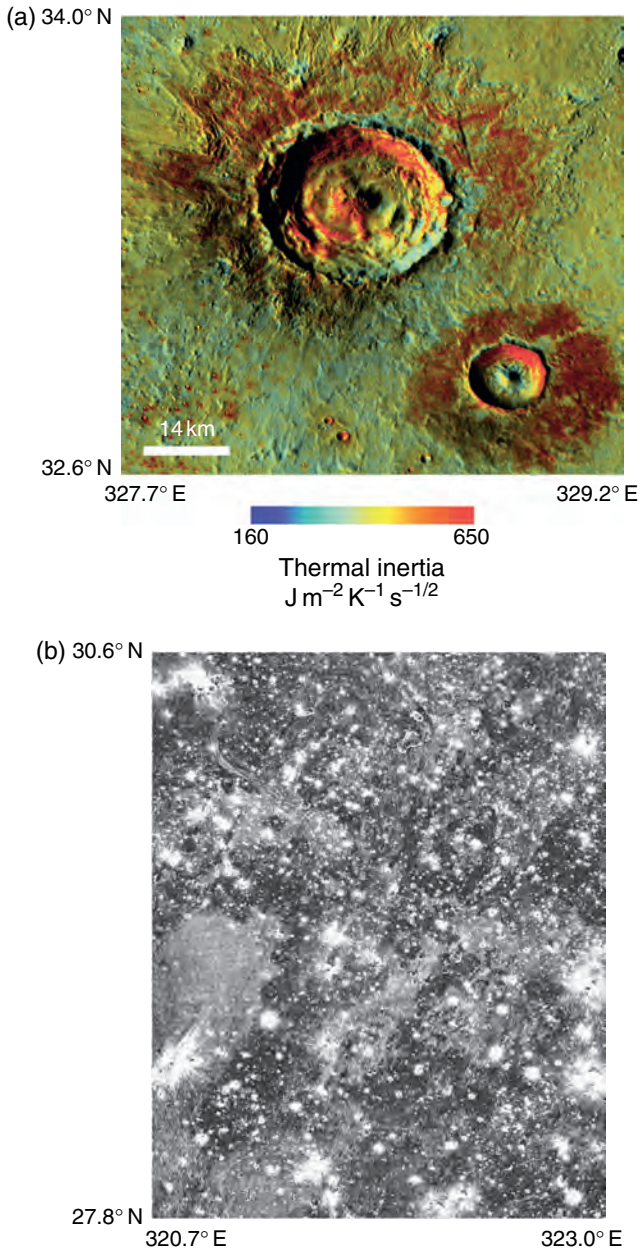

Figure 10.17. Craters. (a) Craters in Acidalia Planitia. THEMIS thermal inertia mosaic (100 m/pixel) overlaid onto a THEMIS daytime temperature mosaic (100 m/pixel resolution) of craters in Acidalia Planitia, centered at 328.5° E, 33.3° N. (b) Nighttime THEMIS temperature image showing rocky (warm) ejecta surrounding numerous small craters in Chryse Planitia. THEMIS nighttime temperature mosaic (100 m/pixel) of craters centered at 321.8° E, 29.2° N that has been stretched to emphasize crater ejecta. Black represents colder temperatures (minimum = 180 K) and white represents warmer temperatures (maximum = 195 K). (For a color version of this figure, please refer to the color plate section or to the e-Book version of this chapter.)

Extensive dust mantles exist within regions such as Tharsis and Arabia Terra. THEMIS nighttime IR images have shown that these dust mantles are remarkably continuous at 100 m/pixel scales, with virtually no evidence of rocky ridges or rubble covered flow boundaries protruding through the dust over thousands of square kilometers of lava flow fields.

Dark barchan dunes, which form through sand transport across a hard surface where a source of sand is limited, are seen superimposed on several bedrock surfaces, including the crater floor of an unnamed crater centered at ~63° E, 26.6° N (Figure 10.16). Sand transport across this region may have stripped away fines to expose the bedrock surface.

crater materials

Rocks are also detected in THEMIS infrared temperature images around numerous impact craters. Ejecta commonly have distinctive concentric temperature patterns and generally are relatively cool in daytime IR and warm in nighttime IR images (Figure 10.17). Coarse-grained ejecta are observed around craters varying in size from the limit of detection (~0.5 km diameter) to craters tens of kilometers in diameter. Observed patterns range from rays of blocky material radiating outward up to 8–10 crater diameters from the crater rim, to halos of coarse material extending 1–2 crater diameters. In some cases there is an outer annulus of material that is finer grained than the surrounding surface, which transitions to coarser material close to the crater rim. Flow-ejecta craters (e.g., Carr *et al.*, 1977; Mouginis-Mark, 1979; Barlow and Perez, 2003) can exhibit several distinct thermal inertia boundaries between different lobes, suggesting differences in the processes of ejecta emplacement or modification. Within a given region not all craters of similar size or degree of degradation have thermally distinct ejecta, nor is there a clear dependence of ejecta thermal pattern on crater size. These variations in the character of ejecta surfaces of similar-sized craters over short (kilometer-scale) distances are likely due to differences in crater age, and IR images provide a means to study crater age and surface modification rates using quantitative measurements of thermal inertia (Shorthill, 1973). In extreme examples, long crater rays extending up to hundreds of kilometers from 2 to 10 km diameter craters have been observed (McEwen *et al.*, 2005; Tornabene *et al.*, 2006). These relatively young long-rayed craters may be good candidates for some of the meteorites known to have originated on Mars (McEwen *et al.*, 2005; Tornabene *et al.*, 2006).

10.6 SUMMARY: INSIGHTS INTO MARTIAN GEOLOGIC PROCESSES

One of the primary objectives of the THEMIS investigation, and one of its main contributions to Mars science, is the insights that have been provided into the nature of the processes occurring on Mars at local geologic scales. Previous compositional studies using ground-based and spacecraft visible, near-IR, and thermal-IR spectroscopy had low (3–20 km) spatial resolution, and necessarily focused on regional units and processes. What the THEMIS data have revealed is that Mars has a compositional and textural diversity at 100 m spatial scales that can be associated with

specific impact, igneous, and sedimentary processes. These compositional and physical differences that THEMIS has found have been explored with TES and OMEGA data, and this combination of spatial and spectral coverage has proven exceedingly valuable in deciphering Mars' geologic history. In particular, THEMIS has revealed that small-scale igneous units occur and have a compositional diversity (shown to range from ultramafic basalts, through basaltic andesites, to dacites and granitoids) that rivals the diversity found on the Earth. While the abundance of some of these rock types is significantly lower than on Earth, their presence shows that many of the processes of igneous differentiation found on Earth also occur on Mars. Many of the compositional differences that have been identified are still not well explained.

The combination of THEMIS, TES, and OMEGA mapping has shown that carbonates, which the shortwave THEMIS infrared bands were specifically designed to detect, do not occur in outcrop at spatial scales of several hundred meters. While these observations cannot rule out the presence of carbonate rock layers at smaller scales or buried beneath younger rocks or dust, their complete absence at several hundred meter scales, especially in light of the discovery of small deposits of hematite, sulfates, and phyllosilicates (e.g., Christensen *et al*., 2001b; Gendrin *et al*., 2005; Bibring *et al*., 2006), suggests that they are not present. This finding places important constraints on models of Martian climate and environmental and chemical conditions through time.

One of the questions that the THEMIS investigation was focused on was the search for temperature anomalies associated with either near-surface heat sources or near-surface water. What was expected in the THEMIS nighttime temperature images, based on the relatively modest degree of spatial structure seen in the IRTM, Termoscan, and TES nighttime maps, was a relatively "bland" surface with little spatial diversity, on which thermal anomalies could be readily detected. What was found instead was a surface with a remarkable degree of spatial complexity. Still, no evidence has been found for any thermal anomaly that cannot be attributed to physical properties. However, the thermal structure seen in the THEMIS data significantly complicates the search, and much work remains to be done on these questions.

What the THEMIS temperature data have shown is that the surface retains the physical record of past geologic processes. The Martian surface has large areas of exposed bedrock outcrops as well as rocky layers in cliffs; these materials show significant variations in sediment size and/or rock-forming processes. Impact-generated ejecta patterns of rocks and fines are discernable in the thermophysical properties, as are landslide deposits and erosional bedforms. Among the implications from these results is the conclusion that in many regions the surface of Mars is not masked by mantles of mobile sand and dust. As a result, the thermally derived physical properties provide a means to study the physical evolution of the Martian surface by the processes of erosion and deposition.

Taken together, the THEMIS data have shown that Mars is a compositionally diverse and geologically active planet, whose complex geology is only beginning to be unraveled.

REFERENCES

Aharonson, O., N. Schorghofer, and M. F. Gerstell, Slope streak formation and dust deposition rates on Mars, *J. Geophys. Res.* **108**, 5138, doi:5110.1029/2003JE002123, 2003.

Arvidson, R. E., F. P. Seelos IV, K. S. Deal, *et al*., Mantled and exhumed terrains in Terra Meridiani, Mars, *J. Geophys. Res.* **108**(E12), 8073, doi:8010.1029/2002JE001982, 2003.

Baloga, S. M. and B. C. Bruno, Origin of transverse ridges on the surfaces of catastrophic mass flow deposits on the Earth and Mars, *J. Geophys. Res.* **110**, doi:10.1029/2004JE002381, 2005.

Bandfield, J. L., Global mineral distributions on Mars, *J. Geophys. Res.* **107**, doi:10.1029/2001JE001510, 2002.

Bandfield, J. L., Extended surface exposures of granitoid compositions in Syrtis Major, Mars, *Geophys. Res. Lett.* **33**, doi:10.1029/2005GL025559, 2006.

Bandfield, J. L., V. E. Hamilton, and P. R. Christensen, A global view of Martian volcanic compositions, *Science* **287**, 1626–30, 2000.

Bandfield, J. L., T. D. Glotch, and P. R. Christensen, Spectroscopic identification of carbonates in the Martian dust, *Science* **301** (1084), 1987, 2003.

Bandfield, J. L., V. E. Hamilton, P. R. Christensen, and H. Y. McSween Jr., Identification of quartzofeldspathic materials on Mars, *J. Geophys. Res.* **109**, doi:10.1029/2004JE002290, 2004a.

Bandfield, J. L., D. Rogers, M. D. Smith, and P. R. Christensen, Atmospheric correction and surface spectral unit mapping using Thermal Emission Imaging System data, *J. Geophys. Res.* **109**, E10008, doi:10010.11029/12004JE002289, 2004b.

Barker, F., Trondhjemite: definition, environment, and hypothesis of origin. In *Trondhjemites, Dacites, and Related Rocks* (ed. F. Barker), New York: Elsevier, pp. 1–12, 1979.

Barlow, N. G. and C. B. Perez, Martian impact crater ejecta morphologies as indicators of the distribution of subsurface volatiles, *J. Geophys. Res.* **108**, doi:10.1029/2002JE002036, 2003.

Barnouin-Jha, O. S., S. Baloga, and L. Glaze, Comparing landslides to fluidized crater ejecta on Mars, *J. Geophys. Res.* **110**, doi:10.1029/2003JE002214, 2005.

Beyer, R. A. and A. S. McEwen, Layering stratigraphy of eastern Corprates and northern Capri Chasmata, Mars, *Icarus* **179**, 1–23, doi:10.1016/j.icarus.2005.1006.1014, 2005.

Bibring, J.-P., M. Combes, Y. Langevin, *et al*., Results from the ISM experiment, *Nature* **341**, 591–3, 1989.

Bibring, J.-P., Y. Langevin, A. Gendrin, *et al*., Mars surface diversity as revealed by the OMEGA/Mars Express observations, *Science* **307**, 1576–81, doi:1510.1126/science.1108806, 2005.

Bibring, J.-P., Y. Langevin, J. F. Mustard, *et al*., Global mineralogical and aqueous Mars history derived from OMEGA/Mars Express data, *Science* **312**, 400–4, doi:410.1126/science.1122659, 2006.

Boyce, J. M., P. Mouginis-Mark, and H. Garbeil, Ancient oceans in the northern lowlands of Mars: evidence from impact crater depth/diameter relationships, *J. Geophys. Res.* **110**, E03008, doi:03010.01029/02004JE002328, 2005.

Bradley, B. A., S. E. H. Sakimoto, H. Frey, and J. R. Zimbelman, Medusa Fossae formation: new perspectives from Mars Global

Surveyor, *J. Geophys. Res.* **107**, doi:10.1029/2001JE001537, 2002.

Carr, M. H., L. S. Crumpler, J. A. Cutts, *et al.*, Martian impact craters and emplacement of ejecta by surface flow, *J. Geophys. Res.* **82**, 4055–65, 1977.

Catling, D. C. and J. M. Moore, The nature of coarse-grained crystalline hematite and its implications for the early environment of Mars, *Icarus* **165**, 277–300, 2003.

Chan, M. A., B. Beitler, W. T. Parry, J. Ormo, and G. Komatsu, A possible terrestrial analogue for hematite concretions on Mars, *Nature* **429**, 731–4, 2004.

Chapman, M. G. and K. L. Tanaka, Interior trough deposits on Mars: Subice volcanoes?, *J. Geophys. Res.* **106**, 10087–100, 2001.

Chojnacki, M., B. M. Jakosky, and B. M. Hynek, Surficial properties of landslides and surrounding units in Ophir Chasma, Mars, *J. Geophys. Res.* **111**, doi:10.1029/2005JE002601, 2006.

Christensen, P. R., Variations in Martian surface composition and cloud occurrence determined from thermal infrared spectroscopy: analysis of Viking and Mariner 9 data, *J. Geophys. Res.* **103**, 1733–46, 1998.

Christensen, P. R. and S. W. Ruff, The formation of the hematite-bearing unit in Meridiani Planum: evidence for deposition in standing water, *J. Geophys. Res.* **109**, E08003, doi:08010.01029/02003JE002233, 2004.

Christensen, P. R., J. L. Bandfield, M. D. Smith, V. E. Hamilton, and R. N. Clark, Identification of a basaltic component on the Martian surface from Thermal Emission Spectrometer data, *J. Geophys. Res.* **105**, 9609–22, 2000a.

Christensen, P. R., R. N. Clark, H. H. Kieffer, *et al.*, Detection of crystalline hematite mineralization on Mars by the Thermal Emission Spectrometer: evidence for near-surface water, *J. Geophys. Res.* **105**, 9623–42, 2000b.

Christensen, P. R., J. L. Bandfield, V. E. Hamilton, *et al.*, The Mars Global Surveyor Thermal Emission Spectrometer experiment: investigation description and surface science results, *J. Geophys. Res.* **106**, 23823–71, 2001a.

Christensen, P. R., R. V. Morris, M. D. Lane, J. L. Bandfield, and M. C. Malin, Global mapping of Martian hematite mineral deposits: remnants of water-driven processes on early Mars, *J. Geophys. Res.* **106**, 23873–85, 2001b.

Christensen, P. R., J. L. Bandfield, J. F. Bell III, *et al.*, Morphology and composition of the surface of Mars: Mars Odyssey THEMIS results, *Science* **300**, 2056–61, 2003a.

Christensen, P. R., G. L. Mehall, S. H. Silverman, *et al.*, The Miniature Thermal Emission Spectrometer for the Mars Exploration Rovers, *J. Geophys. Res.* **108**, 8064, doi:8010.1029/2003JE002117, 2003b.

Christensen, P. R., B. M. Jakosky, H. H. Kieffer, *et al.*, The Thermal Emission Imaging System (THEMIS) for the Mars 2001 Odyssey Mission, *Space Sci. Rev.* **110**, 85–130, 2004a.

Christensen, P. R., S. W. Ruff, R. L. Fergason, *et al.*, Initial results from the Miniature Thermal Emission Spectrometer experiment at the Spirit landing site at Gusev crater, *Science* **305**, 837–42, 2004b.

Christensen, P. R., M. B. Wyatt, T. D. Glotch, *et al.*, Mineralogy at Meridiani Planum from the Mini-TES Experiment on the Opportunity Rover, *Science* **306**, 1733–9, 2004c.

Christensen, P. R., H. Y. McSween Jr., J. L. Bandfield, *et al.*, Evidence for igneous diversity and magmatic evolution on Mars from infrared spectral observations, *Nature* **436**, doi:10.1038/nature03639, 2005a.

Christensen, P. R., S. W. Ruff, R. L. Fergason, *et al.*, Mars Exploration Rover candidate landing sites as viewed by THEMIS, *Icarus* **187**, 12–43, 2005b.

Conrath, B., R. Curran, R. Hanel, *et al.*, Atmospheric and surface properties of Mars obtained by infrared spectroscopy on Mariner 9, *J. Geophys. Res.* **78**, 4267–78, 1973.

Edgett, K. S. and T. J. Parker, Water on early Mars: possible subaqueous sedimentary deposits covering ancient cratered terrain in western Arabia and Sinus Meridiani, *Geophys. Res. Lett.* **24**, 2897–900, 1997.

Fenton, L. K., Potential sand sources for the dune fields in Noachis Terra, Mars, *J. Geophys. Res.* **110**, E11004, doi:11010.11029/12005JE002436, 2005.

Fenton, L. K. and M. T. Mellon, Thermal properties of sand from Thermal Emission Spectrometer (TES) and Thermal Emission Imaging System (THEMIS): spatial variations within the Proctor crater dune field on Mars, *J. Geophys. Res.* **111**, E06014, doi:06010.01029/02004JE002363, 2006.

Fenton, L. K., A. D. Toigo, and M. I. Richardson, Aeolian processes in Proctor crater on Mars: mesoscale modeling of dune-forming winds, *J. Geophys. Res.* **110**, doi:10.1029/2004JE002309, 2005.

Fergason, R. L., P. R. Christensen, and H. H. Kieffer, High resolution thermal inertia derived from THEMIS: thermal model and applications, *J. Geophys. Res.* **111**, E12004, doi:12010.11029/12006JE002735, 2006.

Gellert, R., R. Rieder, R. C. Anderson, *et al.*, Chemistry of rocks and soils at Gusev crater from the Alpha Particle X-ray Spectrometer, *Science* **305**, 829–32, 2004.

Gendrin, A., N. Mangold, J.-P. Bibring, *et al.*, Sulfates in martian layered terrains: the OMEGA/Mars Express view, *Science* **307**, 1587–90, 2005.

Gillespie, A. R., A. B. Kahle, and R. E. Walker, Color enhancement of highly correlated images: I. Decorrelation and HSI contrast stretches, *Remote Sens. Environ.* **20**, 209–35, 1986.

Glotch, T. D. and P. R. Christensen, Geologic and mineralogic mapping of Aram Chaos: evidence for a water-rich history, *J. Geophys. Res.* **110**, E09006, doi:09010.01029/02004JE02389, 2005.

Glotch, T. D. and A. D. Rogers, Evidence for aqueous deposition of hematite- and sulfate-rich light-toned layered deposits in Aureum and Iani Chaos, Mars, *J. Geophys. Res.* **112**, E06001, doi:10.1029/2006JE002863, 2007.

Glotch, T. D., R. V. Morris, P. R. Christensen, and T. G. Sharp, Effect of precursor mineralogy on the thermal infrared emission spectra of hematite: application to martian hematite mineralization, *J. Geophys. Res.* **109**, E07003, doi:07010.01029/02003JE002224, 2004.

Glotch, T. D., J. L. Bandfield, P. R. Christensen, *et al.*, The mineralogy of the light-toned outcrop at Meridiani Planum as seen by the Miniature Thermal Emission Spectrometer and implications for its formation, *J. Geophys. Res.* **111**, doi:10.1029/2005JE002672, 2006.

Golombek, M. P., J. A. Grant, T. J. Parker, *et al.*, Selection of the Mars Exploration Rover landing sites, *J. Geophys. Res.* **108**, 8072, doi:8010.1029/2003JE002074, 2003.

Golombek, M. P., R. E. Arvidson, J. F. Bell, *et al.*, Assessment of Mars Exploration Rover landing site predictions, *Nature* **436**, 44–8, doi:10.1038/nature03600, 2005.

Golombek, M. P., J. A. Grant, L. S. Crumpler, *et al.*, Erosion rates at the Mars Exploration Rover landing sites and long-term climate change on Mars, *J. Geophys. Res.* **111**, doi:10.1029/JE002754, 2006.

Grotzinger, J., J. F. Bell III, W. Calvin, *et al.*, Stratigraphy, sedimentology and depositional environment of the Burns Formation, Meridiani Planum, Mars, *Earth Planet. Sci. Lett.* **240**, 11–72, 2005.

Hamilton, V. E. and P. R. Christensen, Determining the modal mineralogy of mafic and ultramafic igneous rocks using thermal emission spectroscopy, *J. Geophys. Res.* **105**, 9717–34, 2000.

Hamilton, V. E. and P. R. Christensen, Detailed mineralogical analyses of Martian meteorite-like terrains using MGS TES and Odyssey THEMIS data, *Lunar Planet. Sci. XXXIV*, Abstract #1982 (CD-ROM), 2003.

Hamilton, V. E. and P. R. Christensen, Evidence for extensive olivine-rich bedrock in Nili Fossae, Mars, *Geology* **33**, 433–6, 2005.

Hamilton, V. E., P. R. Christensen, H. Y. McSween Jr., and J. L. Bandfield, Searching for the source regions of martian meteorites using MGS TES: integrating martian meteorites into the global distribution of igneous materials on Mars, *Meteorit. Planet. Sci.* **38**, 871–85, 2003a.

Hamilton, V. E., P. R. Christensen, and H. Y. McSween Jr., Global constraints on the source regions of martian meteorites from MGS TES data, *Meteorit. Planet. Sci.* **37**, 59, 2003b.

Hanel, R., B. Conrath, W. Hovis, *et al.*, Investigation of the martian environment by infrared spectroscopy on Mariner 9, *Icarus* **17**, 423–42, 1972a.

Hanel, R. A., B. J. Conrath, W. A. Hovis, *et al.*, Infrared spectroscopy experiment on the Mariner 9 mission: preliminary results, *Science* **175**, 305–8, 1972b.

Harrison, K. P. and R. E. Grimm, Rheological constraints on martian landslides, *Icarus* **163**, 347–62, 2003.

Herkenhoff, K. E. and J. J. Plaut, Surface ages and resurfacing rates of the polar layered deposits on Mars, *Icarus* **144**, 243–53, 2000.

Hiesinger, H. and J. W. Head III, The Syrtis Major volcanic province, Mars: synthesis from Mars Global Surveyor data, *J. Geophys. Res.* **109**, doi:10.1029/2003JE002143, 2004.

Hoefen, T. M. and R. N. Clark, Compositional variability of martian olivines using Mars Global Surveyor thermal emission spectra, *Lunar Planet. Sci. Conf. XXXII*, Abstract #2049 (CD-ROM), 2001.

Hoefen, T., R. N. Clark, J. L. Bandfield, *et al.*, Discovery of olivine in the Nili Fossae region of Mars, *Science* **302**, 627–30, 2003.

Howard, A. D., J. M. Moore, and I. R. P. Irwin, An intense terminal epoch of widespread fluvial activity on early Mars: 1. Valley network incision and associated deposits, *J. Geophys. Res.* **110**, E12S14, doi:10.1029/2005JE002459, 2005.

Hynek, B. M., Implications for hydrologic processes on Mars from extensive bedrock outcrops throughout Terra Meridiani, *Nature* **431**, 156–9, 2005.

Hynek, B. M., R. E. Arvidson, and R. J. Phillips, Geologic setting and origin of Terra Meridiani hematite deposit on Mars, *J. Geophys. Res.* **107**, 5088, doi:5010.1029/2002E001891, 2002.

Hynek, B. M., R. J. Phillips, and R. E. Arvidson, Explosive volcanism in the Tharsis region: Global evidence in the martian geologic record, *J. Geophys. Res.* **108**, 5111, doi:5110.1029/2003JE002062, 2003.

Kieffer, H. H., T. Z. Martin, A. R. Peterfreund, *et al.*, Thermal and albedo mapping of Mars during the Viking primary mission, *J. Geophys. Res.* **82**, 4249–92, 1977.

Klingelhöfer, G., R. V. Morris, B. Bernhardt, *et al.*, Jarosite and hematite at Meridiani Planum from the Mössbauer spectrometer on the Opportunity rover, *Science* **306**, 1740–5, 2004.

Knauth, L. P., D. M. Burt, and K. H. Wohletz, Impact origin of sediments at the Opportunity landing site on Mars, *Nature* **438**, 1123–8, 2005.

Komatsu, G., P. E. Geissler, R. G. Strom, and R. B. Singer, Stratigraphy and erosional landforms of layered deposits in Valles Marineris, Mars, *J. Geophys. Res.* **98**, 1993.

Lane, M. D., R. V. Morris, S. A. Mertzman, and P. R. Christensen, Evidence for platy hematite grains in Sinus Meridiani, Mars, *J. Geophys. Res.* **107**, 5126, doi:5110.1029/2001JE001832, 2002.

Lane, M. D., P. R. Christensen, and W. K. Hartmann, Utilization of the THEMIS visible and infrared imaging data for crater population studies in the Meridiani Planum landing site, *Geophys. Res. Lett.* **30**, 1770, doi:1710.1029/2003GL017183, 2003.

Lucchitta, B. K., N. K. Isbell, and A. Howington-Kraus, Topography of Valles Marineris: implications for erosional and structural history, *J. Geophys. Res.* **99**, 3783–98, 1994.

Malin, M. C. and K. S. Edgett, Sedimentary rocks of early Mars, *Science* **290**, 1927–37, 2000.

Malin, M. C. and K. S. Edgett, Mars Global Surveyor Mars Orbiter Camera: interplanetary cruise through primary mission, *J. Geophys. Res.* **106**, 23429–570, 2001.

Mangold, N., C. Quantin, V. Ansan, C. Delacourt, and P. Allemand, Evidence for precipitation on Mars from dendritic valleys in the Valles Marineris area, *Science* **305**, 78–81, 2004.

McCollom, T. M. and B. M. Hynek, A volcanic environment for bedrock diagenesis at Meridiani Planum on Mars, *Nature* **438**, 1129–31, doi:1110.1038/nature04390, 2005.

McConnochie, T. H., J. F. Bell III, D. Savransky, *et al.*, Calibration and in-flight performance of the Mars Odyssey THEMIS Visible Imaging Subsystem (VIS) Instrument, *J. Geophys. Res.* **111**, E06018, doi:10.1029/2005JE002568, 2006.

McCord, T. B. and J. B. Adams, Spectral reflectivity of Mars, *Science* **163**, 1058–60, 1969.

McEwen, A. S., Mobility of large rock avalanches; evidence from Valles Marineris, Mars, *Geology* **17**, 1111–14, 1989.

McEwen, A. S., M. C. Malin, M. H. Carr, and W. K. Hartmann, Voluminous volcanism on early Mars revealed in Valles Marineris, *Nature* **397**, 584–6, 1999.

McEwen, A. S., B. S. Preblich, E. P. Turtle, *et al.*, The rayed crater Zunil and interpretations of small impact craters on Mars, *Icarus* **176**, 351–81, 2005.

McSween Jr., H. Y., R. E. Arvidson, J. F. Bell III, *et al.*, Basaltic rocks analyzed by the Spirit rover in Gusev crater, *Science* **305**, 842–5, 2004.

McSween Jr., H. Y., T. L. Grove, and W. B. Wyatt, Constraints on the composition and petrogenesis of the martian crust, *J. Geophys. Res.* **108** (E12), 5135, doi:5110.1029/2003JE002175, 2003.

McSween, H. Y., M. B. Wyatt, R. Gellert, *et al.*, Characterization and petrologic interpretation of olivine-rich basalts at Gusev crater, Mars, *J. Geophys. Res.* **111**, E02S10, doi:1029/2005JE002477, 2006.

Mellon, M. T., B. M. Jakosky, H. H. Kieffer, and P. R. Christensen, High resolution thermal inertia mapping from the Mars Global Surveyor Thermal Emission Spectrometer, *Icarus* **148**, 437–55, 2000.

Michalski, J. R., M. D. Kraft, T. G. Sharp, L. B. Williams, and P. R. Christensen, Mineralogical constraints on the high-silica Martian surface component observed by TES, *Icarus* **174**, 161–77, 2005.

Milam, K. A., K. R. Stockstill, J. E. Moersch, *et al.*, THEMIS characterization of the MER Gusev crater landing site, *J. Geophys. Res.* **108**, 8078, doi:1029/2003JE002023, 2003.

Milkovich, S. M. and J. W. Head III, North polar cap of Mars: polar layered deposit characterization and identification of a fundamental climate signal, *J. Geophys. Res.* **110**, doi:10.1029/2004JE002349, 2005.

Moersch, J. E., T. Hayward, P. Nicholson, *et al.*, Identification of a 10 μm silicate absorption feature in the Acidalia region of Mars, *Icarus* **126**, 183–96, 1997.

Morris, R. V., M. D. Lane, S. Mertzman, T. D. Shelfer, and P. R. Christensen, Chemical and mineralogical purity of Sinus Meridiani hematite, *Lunar Planet. Sci. XXXI*, Abstract #1618 (CD-ROM), 2000.

Morris, R. V., G. Klingelhöfer, B. Bernhardt, *et al.*, Mineralogy at Gusev crater from the Mössbauer spectrometer on the Spirit Rover, *Science* **305**, 833–6, 2004.

Mouginis-Mark, P., Martian fluidized crater morphology: variations with crater size, latitude, altitude and target material, *J. Geophys. Res.* **84**, 8011–22, 1979.

Mouginis-Mark, P. J. and P. R. Christensen, New observations of volcanic features on Mars from the THEMIS instrument, *J. Geophys. Res.* **110**, doi:10.1029/2005JE002421, 2005.

Murchie, S., J. Mustard, J. Bishop, *et al.*, Spatial variations in the spectral properties of bright regions on Mars, *Icarus* **105**, 454–68, 1993.

Mustard, J. F., S. Erard, J.-P. Bibring, *et al.*, The surface of Syrtis Major: composition of the volcanic substrate and mixing with altered dust and soil, *J. Geophys. Res.* **98**, 3387–400, 1993.

Mustard, J. F., F. Poulet, A. Gendrin, *et al.*, Olivine and pyroxene diversity in the crust of Mars, *Science* **307**, 1594–7, 2005.

Nedell, S. S., S. W. Squyres, and D. W. Anderson, Origin and evolution of the layered deposits in the Valles Marineris, Mars, *Icarus* **70**, 409–41, 1987.

Newsom, H. E., C. A. Barber, T. M. Hare, *et al.*, Paleolakes and impact basins in southern Arabia Terra, including Meridiani Planum: implications for the formation of hematite deposits on Mars, *J. Geophys. Res.* **108**, 8075, doi:8010.1029/2002JE001993, 2003.

Pelkey, S. M., B. M. Jakosky, and P. R. Christensen, Surficial properties in Melas Chasma, Mars, from Mars Odyssey THEMIS data, *Icarus* **165**, 68–89, 2003.

Pelkey, S. M., B. M. Jakosky, and P. R. Christensen, Surficial properties in Gale crater, Mars, from Mars Odyssey THEMIS data, *Icarus* **167**, 244–70, doi:1016/j.icarus.2003.1009.1013, 2004.

Pimentel, G. C., P. B. Forney, and K. C. Herr, Evidence about hydrate and solid water in the martian surface from the 1969 Mariner infrared spectrometer, *J. Geophys. Res.* **79**, 1623–34, 1974.

Pollack, J. B., T. Roush, F. Witteborn, *et al.*, Thermal emission spectra of Mars (5.4–10.5μm): evidence for sulfates, carbonates, and hydrates, *J. Geophys. Res.* **95**, 14595–627, 1990.

Poulet, F., J.-P. Bibring, J. F. Mustard, *et al.*, Phyllosilicates on Mars and implications for early martian climate, *Nature* **438**, 623–7, doi:610.1038/nature04274, 2005.

Presley, M. A. and R. E. Arvidson, Nature and origin of materials exposed in the Oxia Palus-Western Arabia-Sinus Meridiani region, Mars, *Icarus* **75**, 499–517, 1988.

Putzig, N. E., M. T. Mellon, B. M. Jakosky, *et al.*, Mars thermal inertia from THEMIS data, *Lunar Planet. Sci. XXXV*, Abstract #1863 (CD-ROM), 2004.

Putzig, N. E., M. T. Mellon, K. A. Kretkea, and R. E. Arvidson, Global thermal inertia and surface properties of Mars from the MGS mapping mission, *Icarus* **173**, 325–41, 2005.

Quantin, C., P. Allemand, N. Mangold, and C. Delacourt, Ages of Valles Marineris (Mars) landslides and implications for canyon history, *Icarus* **172**, 555–72, 2004.

Quantin, C., P. Allemand, N. Mangold, G. Dromart, and C. Delacourt, Fluvial and lacustrine activity on layered deposits in Melas Chasma, Valles Marineris, Mars, *J. Geophys. Res.* **110**, E12S19, doi:10.1029/2005JE002440, 2005.

Ramsey, M. S. and P. R. Christensen, Mineral abundance determination: quantitative deconvolution of thermal emission spectra, *J. Geophys. Res.* **103**, 577–96, 1998.

Rieder, R., R. Gellert, R. C. Anderson, *et al.*, Chemistry of rocks and soils at Meridiani Planum from the Alpha Particle X-ray Spectrometer, *Science* **306**, 1746–9, 2005.

Rogers, A. D. and P. R. Christensen, Surface mineralogy of martian low-albedo regions from MGS TES data: implications for crustal evolution and surface alteration, *J. Geophys. Res.* **112**, E01003, doi:01010.01029/02006JE002727, 2007.

Rogers, A. D., P. R. Christensen, and J. L. Bandfield, Compositional heterogeneity of the ancient martian crust: analysis of Ares Vallis bedrock the THEMIS and TES data, *J. Geophys. Res.* **110**, doi:10.1029/2005JE002399, 2005.

Ruff, S. W., Quantitative thermal infrared emission spectroscopy applied to granitoid petrology, Ph.D. Dissertation thesis, 234pp., Arizona State University, 1998.

Ruff, S. W. and V. E. Hamilton, Mineralogical anomalies in Mars Nili Patera caldera observed with Thermal Emission Spectrometer data, *Lunar Planet. Sci. XXXII*, Abstract #2186 (CD-ROM), 2001.

Ruff, S. W. and P. R. Christensen, Identifying compositional heterogeneity in Mars' Nili Patera caldera using THEMIS and TES daa, *Lunar Planet. Sci. XXXIV*, Abstract # 2068 (CD-ROM), 2003.

Salisbury, J. W. and L. S. Walter, Thermal infrared (2.5–13.5 μm) spectroscopic remote sensing of igneous rock types on particulate planetary surfaces, *J. Geophys. Res.* **94**, 9192–202, 1989.

Schaber, G. G., Syrtis Major: a low-relief volcanic shield, *J. Geophys. Res.* **87**, 9852–66, 1982.

Selivanov, A. S., M. K. Naraeva, A. S. Panfilov, *et al.*, Thermal imaging of the surface of Mars, *Nature* **341**, 593–5, 1989.

Shean, D. E., J. W. Head, and D. R. Marchant, Origin and evolution of a cold-based tropical mountain glacier on Mars: the Pavonis Mons fan-shaped deposit, *J. Geophys. Res.* **110**, E05001, doi:05010.01029/02004JE002360, 2005.

Shorthill, R. W., Infrared atlas of the eclipsed Moon, *The Moon* **7**, 22–45, 1973.

Smith, D. E., M. T. Zuber, H. V. Frey, *et al.*, Mars Orbiter Laser Altimeter: experiment summary after the first year of global mapping of Mars, *J. Geophys. Res.* **106**, 23689–722, 2001.

Squyres, S. W., R. Arvidson, J. F. Bell III, *et al.*, The Opportunity Rover's Athena Science Investigation at Meridiani Planum, Mars, *Science* **306**, 1698–703, 2004a.

Squyres, S. W., J. P. Grotzinger, J. F. Bell, *et al.*, In-situ evidence for an ancient aqueous environment on Mars, *Science* **306**, 1709–14, 2004b.

Squyres, S. W. and A. H. Knoll, Sedimentary rocks at Meridiani Planum: origin, diagenesis, and implications for life on Mars, *Earth Planet. Sci. Lett.* **240**, 1–10, 2005.

Stockstill, K. R., J. E. Moersch, H. Y. McSween Jr., J. Piatek, and P. R. Christensen, TES and THEMIS study of proposed paleolake basins within the Aeolis quadrangle of Mars, *J. Geophys. Res.* **112**, 10.1029/2005JE002517, 2007.

Sullivan, R., P. Thomas, J. Veverka, M. Malin, and K. S. Edgett, Mass movement slope streaks imaged by the Mars Orbiter Camera, *J. Geophys. Res.* **106**, 23607–33, 2001.

Tanaka, K. L., M. H. Carr, J. A. Skinner, M. S. Gilmore, and T. M. Hare, Geology of the MER 2003 "Elysium" candidate landing site in southeastern Utopia Planitia, Mars, *J. Geophys. Res.* **108**, doi:10.1029/2003JE002054, 2003.

Thomas, P. C., S. Squyres, K. Herkenhoff, A. Howard, and B. Murray, Polar deposits of Mars. In *Mars* (ed. H. Kieffer, *et al.*), Tucson: University of Arizona Press, pp. 767–95, 1992.

Tornabene, L. L., J. E. Moersch, H. Y. McSween Jr., *et al.*, Identification of large (2–10 km) rayed craters on Mars in THEMIS thermal infrared images: implications for possible

Martian meteorite source regions, *J. Geophys. Res.* **111**, doi:10.1029/2005JE002600, 2006.

Weitz, C. M., T. J. Parker, M. H. Bulmer, F. S. Anderson, and J. A. Grant, Geology of the Melas Chasma landing site for the Mars Exploration Rover mission, *J. Geophys. Res.* **108**, doi:10.1029/2002JE002022, 2003.

Wright, S. P. and M. S. Ramsey, Thermal infrared data analyses of Meteor crater, Arizona: implications for Mars spaceborne data from the Thermal Emission Imaging System, *J. Geophys. Res.* **111**, doi:10.1029/2005JE002472, 2006.

Wyatt, M. B., V. E. Hamilton, H. Y. McSween Jr., P. R. Christensen, and L. A. Taylor, Analysis of terrestrial and martian volcanic compositions using thermal emission spectroscopy: I. Determination of mineralogy, chemistry, and classification strategies, *J. Geophys. Res.* **106**, 14711–32, 2001.

Wyatt, M. B., H. Y. McSween Jr., J. E. Moersch, and P. R. Christensen, Analysis of surface compositions in the Oxia Palus region on Mars from Mars Global Surveyor Thermal Emission Spectrometer observations, *J. Geophys. Res.* **108**, 5107, doi:5110.1029/2002JE001986, 2003.

Wyrick, D. Y., D. A. Ferrill, A. P. Morris, S. L. Colton, and D. W. Sims, Distribution, morphology and origins of Martian pit crater chains, *J. Geophys. Res.* **109**, E06005, doi: 06010.01029/02004JE002240, 2004.

11

Mars' crustal magnetization: a window into the past

M. H. ACUÑA, G. KLETETSCHKA, AND J. E. P. CONNERNEY

ABSTRACT

Mars Global Surveyor (MGS) discovered intense magnetization in the Mars crust. The planet, which today lacks a dynamo, somehow acquired a crust with at least 10, and perhaps as much as 100 times the volume magnetization intensity of Earth's crust. Interpretation of these data has provided a new and unique window into the origin and evolution of the planet. In this chapter we consider the implications of these discoveries for the understanding of processes that may have led to the minerals and geology that are observed on Mars' surface today. We also include relevant work associated with Earth's magnetic minerals and magnetic and mineralogical characteristics of SNC (SNC – Shergottite, Nakhlite, and Chassignite) meteorites. There is widespread agreement that the Martian dynamo ceased operation within $<$500 Myr of accretion and core formation, exposing the atmosphere to erosion by ion-pickup processes in the solar wind for $>$4 Gyr. This may constitute an important additional constraint on the minerals and geochemistry observed to date. There is less agreement on whether the magnetic record requires an early era of plate tectonics on Mars. A complete understanding of the crustal magnetic record remains as one of the most significant challenges in Martian geophysical research, one with great potential for understanding not only Mars' evolution but also many aspects of that of the terrestrial planets, asteroids, and the Moon.

11.1 INTRODUCTION

Establishing the existence of a magnetic field of internal origin associated with a Solar System body has long been recognized as a fundamental objective in planetary exploration. In addition to gravity, mapping a planetary magnetic field can provide unique and essential information about the state and composition of the planet's interior and its possible thermal history. No other observations from orbiting or flyby spacecraft are capable of yielding similar information with such profound and direct implications for the understanding of geology, tectonics, geochemistry, and thermal history. The discovery at Mars (and the Moon) of crustal fields that have been modified by impact and thermal processes that took place very early in the evolution of the solar system has added important new dimensions to our studies of planetary magnetism. The MGS spacecraft was able to observe strong remanent fields, ~20 times larger than those observed at Earth, uncontaminated by the mostly unresolved and confusing induction effects typically associated with crustal magnetic field studies at Earth or the interplanetary magnetic field (IMF) at the Moon. Thus, the discovery of Mars' strong crustal anomalies has provided not only a unique window into Mars' past, but also significant new impetus and views into our own understanding of terrestrial and lunar crustal magnetization. This chapter presents a summary of spacecraft and other observations conducted to date, their interpretation, and possible implications for the understanding of Mars' surface from a remanent magnetism point of view. It is not intended as a review of all the important work that has been carried out on Martian crustal magnetism, its origin, and implications for the thermal history and geologic evolution of the planet, but as an exploration of the possible relationship that may exist between crustal magnetism as observed today and surface processes. Where applicable, references to seminal studies of Mars magnetism, its origin and interpretation, are provided throughout the chapter for completeness.

11.1.1 Spacecraft measurements

Several missions launched to Mars in the early 1960s by the US and the former Soviet Union either failed outright or did not provide useful information about the Martian magnetic field environment (Connerney *et al.*, 2004). The first successful US mission to Mars was Mariner 4 and the spacecraft flew as close as 4 R_M (R_M = Martian radius) on July 15, 1965. The magnetic field measured onboard was indistinguishable from that of the undisturbed IMF and the investigators were only able to set an upper limit to the dipole moment of a possible present-day magnetic field of 3×10^{-4} M_e $\left(M_e = \text{Earth's dipole moment}, 8 \times 10^{15}\ \text{Tm}^3\right)$, equivalent to a Mars surface equatorial field of $<$100 nT (Smith *et al.*, 1965).

Despite numerous opportunities during the 32 years that elapsed until the arrival of MGS in 1997, no spacecraft instrumented to measure magnetic fields would pass close enough to the planet's surface to establish unambiguously the presence of an intrinsic magnetic field. The great interest in the question of Mars magnetism spawned much debate on the subject and an extensive body of literature. Based on the Soviet Phobos 2 orbiter observations in 1988 and earlier flybys, the magnetic field of Mars was estimated to be quite small based on the measured position of the Martian bow shock, and the debate

The Martian Surface: Composition, Mineralogy, and Physical Properties, ed. J. F. Bell III. Published by Cambridge University Press.

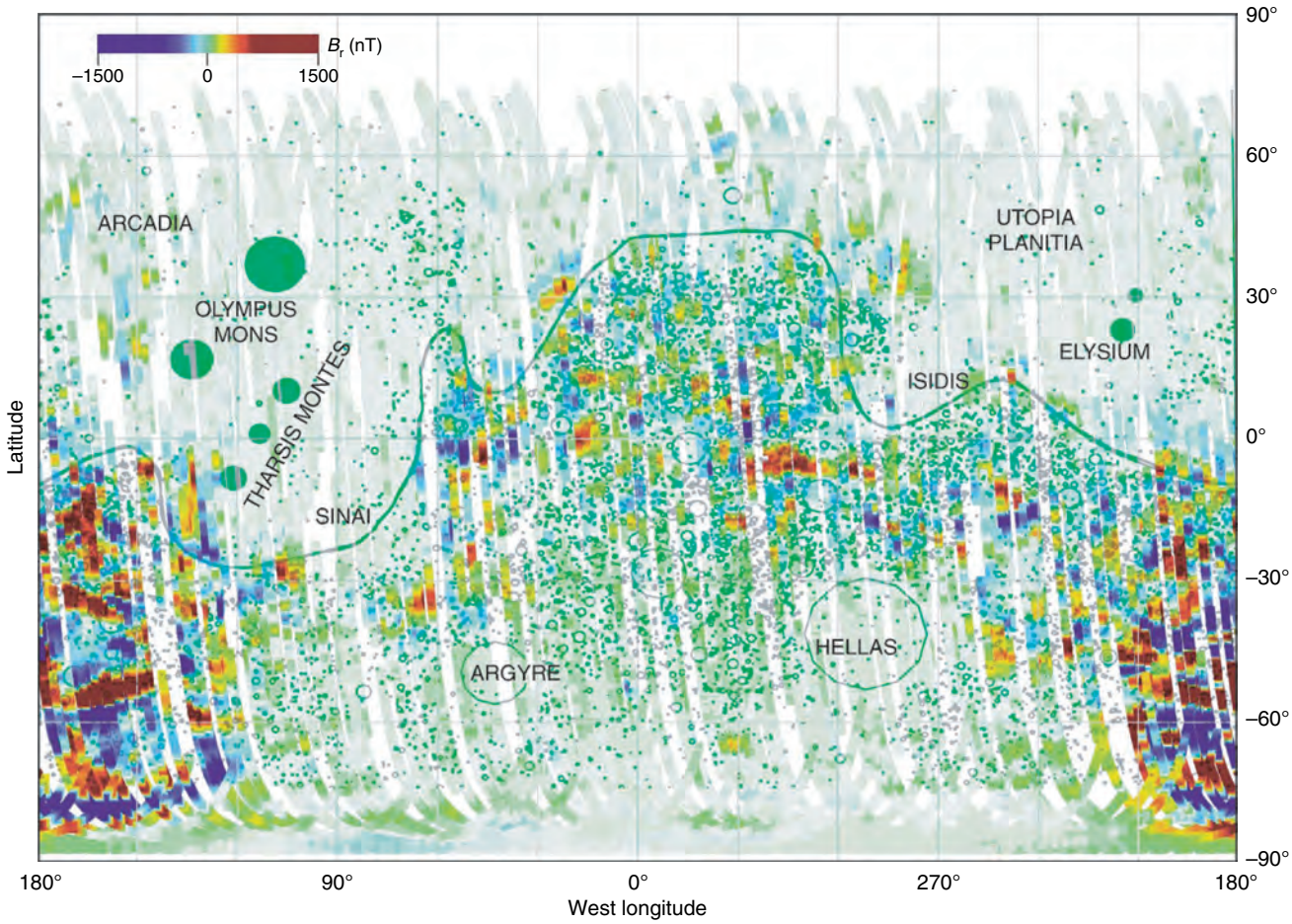

Figure 11.1. Map of the global distribution of Martian crustal magnetization. The intensity of the radial component of the measured magnetic field below 200 km altitude is plotted as a Mercator projection. Note that the majority of the magnetic sources lie south of the dichotomy boundary (solid green line) in the ancient Noachian terrain. The open circles represent craters with diameters >10 km (e.g., Barlow *et al.*, 2000); the solid circles represent the location and size of the Martian volcanoes. (For a color version of this figure, please refer to the color plate section or to the e-Book version of this chapter.)

centered primarily on the source responsible for the weak field: intrinsic (internal origin) or induced by the interaction of Mars' atmosphere with the solar wind (see, for example, Russell, 1978a,b; Ness, 1979; Slavin and Holzer, 1982; Riedler *et al.*, 1989; Dolginov and Zhuzgov, 1991; Mohlmann *et al.*, 1991; Slavin *et al.*, 1991; Gringauz *et al.*, 1993).

The MGS spacecraft arrived at Mars in September 1997, replacing Mars Observer (MO) that was lost on August 31, 1993, a few days before it was to be inserted into circular orbit around the planet. One of the MO/MGS Magnetic Field/Electron Reflectometer Investigation's (MAG/ER) primary science objectives was to "establish the nature of the magnetic field of Mars" to help answer the unresolved questions raised by previous missions. The high inclination, low-altitude orbits planned for the MO and MGS missions were ideal to obtain detailed global maps of the magnetic field, if one existed at all (Albee *et al.*, 1998, 2001). A significant advantage of the MGS over the MO mission in terms of magnetic field measurements was the use of aerobraking as a technique to reduce the spacecraft velocity without requiring fuel. The MGS orbit periapsis was designed to bring the spacecraft low enough into the Martian atmosphere (<150 km altitude) so that its solar panels could be used as drag surfaces or "flaps" to reduce spacecraft velocity. Although the initial mission plan called for only ~100 aerobraking orbits or ~30 days, a problem with a spacecraft solar panel caused the extension of the aerobraking phase to more than ~1600 orbits. This unexpected development resulted in the acquisition of low-altitude magnetic field data over a much greater range of Martian latitudes and longitudes than originally planned, yielding a surprising global map of the distribution of crustal magnetization (Acuña *et al.*, 1999, 2001) that is reproduced in Figure 11.1 for reference. It must be emphasized that this map illustrates only the *radial component* of the measured magnetic field *in situ*, since the tangential components were heavily contaminated by the fields induced on the dayside by the solar wind interaction with Mars. It is also clear that the magnetic field intensity indicated in the map does not reflect the intrinsic magnetization of the sources since their geometry and location are not precisely known. The map includes all measurements acquired below 200 km altitude down to ~90 km, the lowest periapsis covered by MGS, and hence blurs radial intensity variations over this range. For safety reasons the aerobraking orbit did not

provide coverage on the nightside of the planet except for a very short interval and as a result, low-altitude data over this region, free of solar wind induced effects, are not available. Details of MGS mission phases and the observations acquired by the MAG/ER during each phase can be found in Connerney *et al.* (2004). The final aerobraking phase was followed by the insertion of MGS into a circular mapping orbit at ~400 km altitude in the 2 a.m.–2 p.m. local time plane where it remained until communications with the spacecraft were lost in late 2006. This orbit provided almost complete latitude and longitude coverage of the planet at approximately constant altitude and hence was ideal for the development of potential models of the field. The MAG/ER investigation acquired data almost continuously during more than ~35 000 orbits, yielding an extensive and unique dataset. Global maps derived from nightside mapping orbit measurements as well as from combined datasets can be found in Connerney *et al.* (2001, 2005).

11.1.2 Instrumentation

The magnetic field instrumentation flown aboard MGS is the spare unit of the Mars Observer Magnetic Field Investigation and includes two redundant triaxial fluxgate magnetometers and an electron reflectometer (Acuña *et al.*, 1992). The vector magnetometers provided *in situ* sensing of the ambient magnetic field in the vicinity of the MGS spacecraft over the automatically selected full-scale ranges of ± 4 nT to $\pm 65\,536$ nT with a digital resolution of 12 bits. The electron reflectometer measured the local electron distribution function in the range of ~10 eV–20 KeV and remotely sensed the strength of the magnetic field down to the top of the Martian atmosphere using directional information provided by the vector magnetometer. Each magnetometer sensor was placed at the outer edge of articulated solar panels, ~5 m from the center of the spacecraft bus, while the electron reflectometer sensor was mounted directly on the spacecraft nadir panel. The instrumentation provided fast-vector measurements of the magnetic field (up to 16 vectors/second) over a dynamic range of 0.005–65 536 nT per axis. Full details of the MGS Magnetic Field Investigation are given in Acuña *et al.* (1992). This chapter concentrates almost exclusively on the results and interpretation of data obtained by the vector magnetometers and electron reflectometer, since they have the greatest relevance to possible surface processes at Mars, but it also includes a brief discussion of the results obtained by the Mars Exploration Rovers Magnetic Properties Experiment (Bertelsen *et al.*, 2004; see Chapter 16) for completeness.

11.2 MAGNETIC FIELD MAPS AND MODELS

The data acquired by MGS have been used by several investigators to develop models of the crustal field under a variety of constraints and assumptions. These, in turn, have been used to associate selected magnetic features derived from the models with topographic or geological features observed today on the surface, in attempts to reconstruct aspects of the thermal and geological history of Mars. The dayside, aerobraking orbit phase data provide the highest spatial resolution due to the low altitude of the periapses but were acquired over a range of altitudes, complicating their analytical representation. In addition, the strong perturbations associated with the solar wind interaction introduced large errors in the tangential components of the crustal field. Conversely, the nightside, mapping orbit data are largely free of solar wind induced disturbances and were acquired at almost constant altitude (~400 km) but this leads to lower spatial resolution as compared to the aerobraking phase data.

A number of methods for processing, mapping, modeling, and representing analytically the MGS magnetometer data have been used, each with its own assumptions, constraints, and resulting nonuniqueness. A detailed discussion of these methods and their advantages and limitations is outside the scope and objectives of this chapter but the following references can guide the reader to the appropriate publications. At least five such methods have been published: (1) binning and averaging of the radial field component (Acuña *et al.*, 1999, 2001; Connerney *et al.*, 2001); (2) spherical harmonic models (see below); (3) editing, detrending, and two-dimensional filtering of the 3 vector field components and the field magnitude at the mean spacecraft altitude (Hood and Zakharian, 2001; Hood *et al.*, 2005); (4) radial component variation along the orbit maps (Connerney *et al.*, 2005; see Figure 8); and (5) regional maps derived from the Electron Reflectometer data (Lillis *et al.*, 2004; see Figure 2).

Global, spherical harmonic models of the Martian magnetic field have been developed by Purucker *et al.* (2000), Arkani-Hamed (2001a, 2002a), Cain *et al.* (2002), Langlais *et al.* (2004), and others and are useful in providing a global view of the general distribution of crustal magnetization. However, their inherent nonuniqueness and limited resolution imply that extreme care must be exercised when the models are used to study possible associations of magnetic features with topography, geology, or small-scale (<200 km) surface features, or to predict weak field intensities where no measurements are available (Purucker *et al.*, 2000). It is also clear that in regions where the models disagree with the measurements the latter are not necessarily in error and the disagreement mostly reflects the limitations and assumptions associated with each model. A particularly interesting use of these techniques has been made by Hood and Zakharian (2001), Arkani-Hamed (2001b), Arkani-Hamed and Boutin (2004), and Frawley and Taylor (2004), examining the time evolution of the magnetic poles and paleo-equator of the ancient Martian dynamo and its possible association with polar wandering. Regional maps derived from Electron Reflectometer data have been obtained by Lillis *et al.* (2004) and Mitchell *et al.* (2007) and exhibit good agreement with those derived from the magnetometer measurements, but they do not provide directional information. These are illustrated in Figures 11.2a and 11.2b. The increased sensitivity provided by the electron reflectometer measurements reveals additional weak field features, particularly in the northern hemisphere, and these are discussed below.

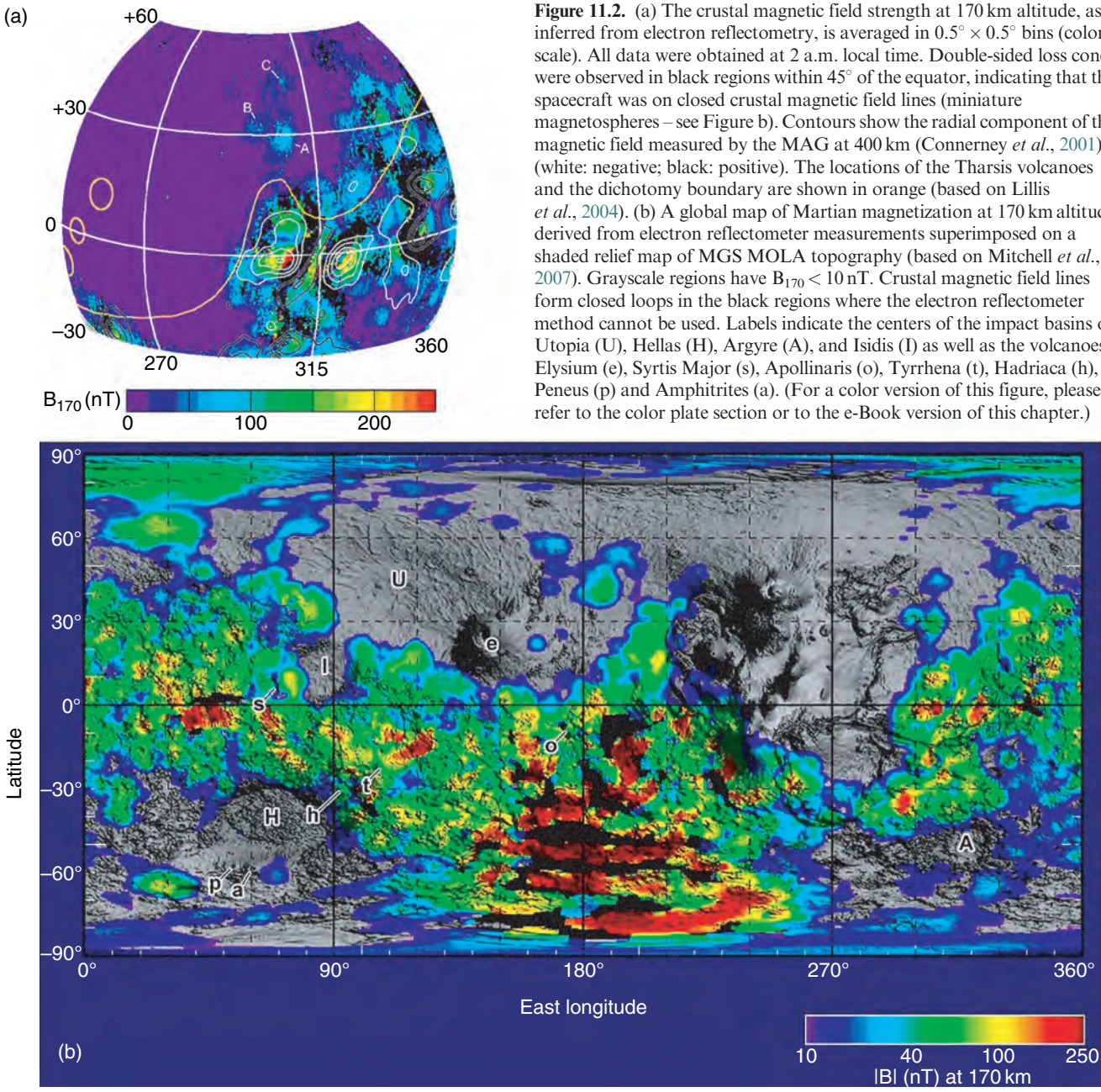

Figure 11.2. (a) The crustal magnetic field strength at 170 km altitude, as inferred from electron reflectometry, is averaged in $0.5^\circ \times 0.5^\circ$ bins (color scale). All data were obtained at 2 a.m. local time. Double-sided loss cones were observed in black regions within 45° of the equator, indicating that the spacecraft was on closed crustal magnetic field lines (miniature magnetospheres – see Figure b). Contours show the radial component of the magnetic field measured by the MAG at 400 km (Connerney *et al.*, 2001) (white: negative; black: positive). The locations of the Tharsis volcanoes and the dichotomy boundary are shown in orange (based on Lillis *et al.*, 2004). (b) A global map of Martian magnetization at 170 km altitude derived from electron reflectometer measurements superimposed on a shaded relief map of MGS MOLA topography (based on Mitchell *et al.*, 2007). Grayscale regions have $B_{170} < 10$ nT. Crustal magnetic field lines form closed loops in the black regions where the electron reflectometer method cannot be used. Labels indicate the centers of the impact basins of Utopia (U), Hellas (H), Argyre (A), and Isidis (I) as well as the volcanoes Elysium (e), Syrtis Major (s), Apollinaris (o), Tyrrhena (t), Hadriaca (h), Peneus (p) and Amphitrites (a). (For a color version of this figure, please refer to the color plate section or to the e-Book version of this chapter.)

11.3 SUMMARY OF PRINCIPAL MGS RESULTS

The MAG/ER investigation established conclusively that Mars does not currently possess a magnetic field of internal origin, but reported the unexpected discovery of strongly magnetized regions in its crust, closely associated with the ancient, heavily cratered terrain of the highlands south of the dichotomy boundary (Acuña *et al.*, 1998, 1999). Clearly, the discovery of intense magnetization in the crust implies that Mars possessed an Earth-like magnetic field of internal origin at some point in its past. As discussed by Spohn *et al.* (2001), evidence for a magnetic history of Mars was not entirely unexpected. Models of Mars' interior and thermal evolution (e.g., Stevenson *et al.*, 1983; Schubert and Spohn, 1990; Spohn, 1991; Spohn *et al.*, 1998) predicted the existence of a thermal convection–driven dynamo for at least the first billion years after accretion. Prior to the arrival of MGS at Mars the remnant magnetization of Martian meteorites had already suggested that the planet may have had in its past a surface magnetic field comparable in magnitude to that of the Earth (Curtis and Ness, 1988) and different regions of the Martian crust could have been magnetized with varying strengths and orientations representative of prior epochs of magnetic activity (Leweling and Spohn, 1997).

Spacecraft missions prior to MGS established that the present global magnetic field, if one existed at all, was

weak, with an estimated surface field strength of less than 50 nT. An improved estimate of the upper limit to the magnitude of any present Mars dipole moment was derived from the MGS data and yielded $\boldsymbol{M} = 2 \times 10^{17}\,\mathrm{A\,m^2}$, which corresponds to a surface equatorial field strength of 0.5 nT.

Complementing the discovery of crustal magnetism at Mars, the MGS MAG/ER experiment observed linear patterns of strikingly intense magnetization in the southern hemisphere (up to 1600 nT at $h = 100$ km), particularly over Terra Sirenum and Terra Cimmeria (Connerney *et al.*, 1999). These linear magnetic structures or "magnetic lineations" have been interpreted by some investigators (Connerney *et al.*, 1999, 2005; Sprenke and Baker, 2000) to result from processes similar to those associated with seafloor spreading at Earth. This association would imply that some form of plate tectonics and magnetic field reversals existed in Mars' early history. However, the sharp magnetization contrast required by the models of Connerney *et al.* (1999) and other authors suggests that alternative explanations involving the fracturing of a magnetized, thin crustal layer by tectonic stresses, perhaps associated with the Tharsis rise, should also be considered. We cannot claim that the magnetization pattern of the Martian crust and its implications for the thermal evolution of the planet are fully understood.

However, the MGS observations show that the majority of the crustal magnetic sources lie south of the dichotomy boundary on the ancient, densely cratered terrain of the highlands and extend ~60° S of this boundary. The relative weakness of crustal magnetization north of the dichotomy boundary, in spite of a widespread record of active volcanism and magmatic flows, suggests that dynamo action had ceased at this stage of crustal formation. The magnetization map derived from the sensitive measurements of the MGS Electron Reflectometer (Mitchell *et al.*, 2007) reveals numerous weak features in the northern hemisphere that suggest that in addition to impact demagnetization (discussed below), large-scale thermal demagnetization (also discussed below) took place, possibly in association with the Tharsis rise. The southernmost limit of the crustal magnetization region appears to be associated with the destruction or modification of the magnetized crust by the impacts that created the Argyre and Hellas basins. The magnetic field observations acquired over these and other impact basins indicate the presence of very weak fields most likely of external origin, also suggesting that the dynamo had ceased to operate when these basins were formed. It is estimated (e.g., Hartmann and Neukum, 2001, and references therein) that the Hellas and Argyre impacts took place less than ~300 Myr after Mars accretion was completed and therefore Mars dynamo cessation should coincide or predate this epoch if this interpretation is correct. The distribution of magnetization suggests that processes that took place after the cessation of dynamo action only modified the ancient, magnetized, relatively thin crust through deep impacts, magmatic flows, tectonics, or reheating above the minerals blocking temperatures (the temperature above which fluctuations of the magnetic moment stabilize and the original magnetic orientation of the particles is destroyed), or at least close to them, allowing viscous decay of magnetization.

Self-magnetization has also been considered as a viable mechanism to strengthen magnetic anomalies as the deep crust cooled below the blocking temperature of magnetic minerals. Modeling of magnetic crust of different thicknesses resulted in negligible magnetic contribution (Arkani-Hamed, 2005). However, when considering magnetic properties of minerals and their grain sizes it was shown that for certain concentrations of single domain (SD) magnetite and multidomain hematite (α-Fe_2O_3) this mechanism may contribute and play an important role in generating a magnetic signature (Kletetschka *et al.*, 2005). Weaker crustal magnetic sources detected in the northern hemisphere (Acuña *et al.*, 1999) are located in the younger, Amazonian plains, and dipole models (Acuña *et al.*, 1998; Ness *et al.*, 1999) tend to yield upper limits to source depths in excess of 100 km, close to the estimated depth to the Curie isotherm (the temperature level where magnetic materials lose their spontaneous magnetization) in this region (Smith *et al.*, 1999; Zuber *et al.*, 2000; Hood and Zakharian, 2001).

The above interpretation of the magnetic record of Mars was criticized by Schubert *et al.* (2000), who noted that impact into a homogeneously magnetized southern highlands crust should have left characteristic magnetic anomalies. While this is correct, it should be noted that the dissipation of impact energy might have resulted in heating and thermal demagnetization of a more extended region, with the effect that the expected anomaly pattern there would have been lost. With arguments similar to those used to explain the age distribution of the magnetization of lunar rocks, Schubert *et al.* (2000) suggested that the observations are also consistent with a late start of the dynamo. However, the extensive record of volcanism and unmagnetized magma flows throughout Martian history does not support this interpretation.

Relative ages across the dichotomy boundary have become less certain with the discovery of buried topographical features called "quasi-circular depressions" in both hemispheres (Frey, 2006a, b). If these are counted as vestigial remains of ancient craters, the underlying crust in the northern lowlands might be a great deal older than previously suggested (see also Mitchell *et al.*, 2007). Nevertheless, the origin of the crustal dichotomy remains a mystery, one that is fundamental to Mars evolution. It has been attributed to a large impact (Wilhelms and Squyres, 1984) or impacts (Frey and Schultz, 1988) and alternatively to tectonic processes (Wise *et al.*, 1979; Sleep, 1994). The similar apparent dichotomy in crustal magnetization gives some hope that the magnetic record, correctly deciphered, can help solve one of the most important outstanding questions of Mars evolution: the formation of the crust, its evolution, and the processes that led to the surface topology, geology, and geochemistry that we observe today. The possible crustal composition responsible for the Martian magnetic anomalies remains a significant challenge, since the derived magnetization per unit volume is ~20–30 times more intense than that observed at Earth. This topic is discussed below in connection with the study of possible rock-forming

minerals and the magnetization of SNC meteorites. The MGS measurements only provide information about the magnetic moment of the sources, not their precise extent depth-wise or the intensity of the magnetization per unit volume. Therefore, multiple interpretations are possible. However, thin layer models require such a large magnetization per unit volume that comparisons with Earth's crustal sources make them difficult to accept in terms of plausibility.

Figure 11.1 illustrates a distinct lack of magnetization associated with the major impact basins (Hellas, Argyre, Isidis, Utopia, Chryse) and volcanic provinces (Elysium, Olympus Mons, Tharsis Montes, Alba Patera). The former is attributed to the erasure of a preexisting magnetic imprint by large impacts (the so-called "impact demagnetization"); the latter is attributed to erasure by thermal events or formation after dynamo cessation. This map also shows extensive regions of the northern lowlands with a relatively weak magnetic imprint, but otherwise similar to that observed south of the dichotomy boundary, suggesting that much of the northern plains are underlain by older, weakly magnetized crust (Hood and Zakharian, 2001; Connerney *et al.*, 2005; Mitchell *et al.*, 2007).

This is particularly evident in Acidalia, Amazonis, Arcadia, and regions surrounding Chryse and Utopia. The smooth, flat, and relatively crater-free northern lowlands are thought to have experienced sedimentary or volcanic resurfacing in the Hesperian and Amazonian ages. The crustal magnetic fields mapped around the periphery of Olympus Mons suggest that the crust there has been "thermally demagnetized" by the emplacement of thick volcanic flows atop a previously magnetized crust (Mitchell *et al.*, 2007). Magnetic contours in Arcadia and Amazonis extend inward toward Olympus Mons no further than approximately the −2 km elevation contour, marking the extension of the aureole some 1000 km to the north and northwest. Similarly, magnetic contours mapped in the vicinity of Elysium Mons do not penetrate beyond the −2 km elevation contour that encircles the volcanic construct. Both of these constructs are massive enough to significantly load the lithosphere and both have emplaced volcanic flows, many kilometers thick, in their vicinity.

Volcanism on Mars is characterized by high rates of effusion (Greely and Spudis, 1981) that would be required to heat large volumes of crust beneath volcanic flows. However, significant magnetic fields are observed above volcanic provinces in the southern highlands (e.g., Syrtis Major west of the Isidis basin and Hesperia Planum to the northeast of Hellas). It is plausible that these flows have only partially demagnetized the underlying crust, in contrast to the flows of the northern lowlands. These low relief (∼0–1 km) flows are thin compared to those in Tharsis and Alba Patera. They are thought to be flood lavas extruded at extremely high rates, emplaced as a high volume, single-cooling unit of great extent (Greely and Spudis, 1981). The partial demagnetization associated with Hesperia, combined with the nearly complete demagnetization associated with Tharsis and its surrounding volcanism, suggests that crustal magnetization in this region could be borne in a layer a few kilometers thick (Connerney *et al.*, 2005). Likewise, the northern lowlands may have experienced a catastrophic volcanic flooding event in the Hesperian, burying the crust to a depth of ∼1 km or more (Head *et al.*, 2002). Such an event could appreciably diminish the magnetic signature of the underlying crust if the magnetized layer was relatively thin (few kilometers or less) and if the magnetic mineralogy of the carrier was susceptible to low-temperature remagnetization (e.g., as is magnetite). Over sufficiently long timescales (millions of years) thermal demagnetization of some crustal minerals (e.g., magnetite) requires temperatures of only ∼300 °C (Dunlop and Özdemir, 1997). Note that a succession of relatively thin flows cannot appreciably heat the crust below, as they cool too quickly. In order to heat an appreciable volume of crust, the flows must be emplaced as a single-cooling unit in a span of time that is short compared to the diffusive time constant of the layer(s). This is consistent with photogeologic and topographic analyses of these flows (e.g., Greeley and Spudis, 1981; Head *et al.*, 2002).

Lastly, the strong evidence for liquid water at the surface of Mars in its early history (e.g., Squyres *et al.*, 2004) also suggests that significant climate change has taken place. The fact that the Martian dynamo has not been active for more than 4 Gyr points to loss to space as being a significant, and perhaps the dominant mechanism (in addition to large impacts) responsible for atmospheric losses. In the absence of a magnetic field to stand off the solar wind, the Martian atmosphere is exposed directly to the scavenging effects of ion pick-up and sputtering, leading to significant losses of volatiles over its ∼4 Gyr history (Luhmann, 1991; Luhmann *et al.*, 1992; Brain and Jakosky, 1998; Mitchell *et al.*, 2001). How these mechanisms have affected surface processes remains to be studied in detail.

11.4 MAGNETIC MINERALOGY AND SNC METEORITES

Analyses of Martian meteorites and data from MGS have advanced our knowledge of the chemistry and structure of the Martian crust and mantle (e.g., Zuber, 2001). However, many fundamental questions remain to be answered. Among the unexplained problems is the nature of the highly magnetized crustal materials. Crustal magnetization on Mars is at least an order of magnitude greater than that on Earth, requiring large volumes of highly magnetized material in the Martian crust (Connerney *et al.*, 1999; Voorhies *et al.*, 2002). The source bodies may be quite thick, perhaps >50 km, and deep-seated (∼100 km; Nimmo and Gilmore, 2001; Arkani-Hamed, 2002b). However, as mentioned above, the thickness, magnetization intensity, and source depth are poorly constrained observationally (Connerney *et al.*, 2004).

Attempts were made to assess the nature of the magnetic minerals in the Martian soil by collecting small magnetic particles with strong magnets that were part of the

experiment packages on the Viking (Hargraves *et al.*, 1977) and Pathfinder (1997; Madsen *et al.*, 1999) landers, and the *Spirit* and *Opportunity* (2004; Madsen *et al.*, 2003) rover missions. This resulted in a list of potential magnetic mineral candidates being identified, notably metallic iron, magnetite ($Fe^{2+}Fe^{3+}{}_2O_4$) and/or titanomagnetite [$Fe^{2+}(Fe^{3+}, Ti^{4+})_2O_4$], maghemite ($\gamma$-$Fe_2O_3$), and monoclinic pyrrhotite [$Fe_{(1-x)}S$ ($x = 0$–0.17)], as well as spineloids and chromites (Weiss *et al.*, 2002c; Kontny *et al.*, 2004). The Viking Landers and the Mars Pathfinder Lander attracted materials using permanent magnets and concluded that the Martian soil must contain about 2% of magnetite or maghemite by volume. The modal amount was estimated based on the assumption of the existence of magnetite or maghemite content with saturation magnetization of 92 and 70 A m^2/kg, respectively. Magnets carried on the rovers ruled out hematite as a major carrier of induced magnetism (Bertelsen *et al.*, 2004; Goetz *et al.*, 2005; see also Chapter 16). However, the experiments established that virtually all of the Martian dust and silt grains contain induced magnetism carriers attracted by the permanent magnets.

Because the magnetic experiments on the landers and rovers were designed to investigate the induced magnetic properties of Martian soil, no direct connection can be drawn between the crustal magnetic anomalies on Mars (due to remanent magnetism) and the results from the magnetic properties experiments, however. Thus, the composition of the crustal sources of remanent magnetism does not necessarily represent the same spectrum of magnetic minerals sampled by the lander and rover magnet arrays. Magnets attract high-susceptibility minerals that may not have the potential to hold a stable remanence. None of these minerals yield information about remanence since low-susceptibility minerals such as hematite, goethite (α-FeOOH), SD magnetite, and pyrrhotite in silicates would not be attracted by the magnet arrays. Thus, the question remains about the identity of the magnetic minerals that may represent the sources of remanent magnetization in the anomalously large crustal sources detected from orbit by MGS MAG/ER.

11.4.1 Rock-forming minerals

Among the common rock-forming minerals only a few are capable of acquiring and retaining significant remanent magnetization (Kletetschka *et al.*, 2000a). These minerals are typically oxides and sulfides (Rochette *et al.*, 2001), which are commonly found on Earth. The available petrographic data for the SNC meteorites, inferences based on soil analyses, magnetic experiments on the Viking and Pathfinder missions, and inferences based on the Thermal Emission Spectrometer, suggest that magnetite, hematite, and pyrrhotite are the primary candidate magnetic minerals to be considered. Substitution minerals, such as low-Ti titanomagnetites and titanohematites ($Fe_{2-x}Ti_xO_3$, where $x < 0.2$), are similar to the magnetites and hematites, respectively, and need not be considered separately. Maghemite (an oxidized form of magnetite) has been considered based on earlier Pathfinder magnetic dust spectra (e.g., Bell *et al.*, 2000). Additionally, spinel solid solutions for relevant chemistry (e.g., Fe_2SiO_4–Fe_3O_4 and $(Fe,Mg)_2SiO_4$–Fe_3O_4; Kontny *et al.*, 2004) and chromites of certain composition ($Fe_{1.05}\ Cr_{1.31}\ Al_{0.35}\ Mg_{0.20}\ Ti_{0.06}\ O_{4.0}$; Curie temperature above 300 °C) may contribute to remanent magnetization (Kumar and Bhalla, 1984; Yu *et al.*, 2001). In summary, we believe that a total of eight magnetic minerals could contribute to the observed magnetic remanence: (1) pure iron, (2) iron nickel, (3) titanomagnetite, (4) titanohematite, (5) titanomaghemite, (6) pyrrhotite, (7) spinel, and (8) chromite.

11.4.2 Magnetizing mechanisms

Minerals contained within the cooling Martian crust were magnetized by the ambient magnetic field. There are two distinct mechanisms that allow homogeneous magnetizations of large volumes of rock within the crust at temperatures dependent on the particular mineral (commonly around 500 °C). The physical processes involved in these two mechanisms that allow locking of the magnetization are similar, however. Mechanism 1 is acquisition of thermo-remanent magnetization (TRM) by the magnetic minerals after cooling and the transitioning of magnetic grains through their mineral-specific blocking temperatures. Mechanism 2 is the acquisition of chemical remanent magnetization (CRM) – magnetization acquired during chemical changes of minerals in an external field (e.g., Dunlop and Özdemir, 1997) – which can also occur during cooling. However, in the case of CRM the magnetic minerals are formed in a superparamagnetic (nanometer-sized grains too small to have a stable magnetic moment) state as a result of the precipitation of new magnetic phases (e.g., during the phase exsolution processes). As the magnetic volume grows it reaches a size for which the magnetization becomes frozen (the superparamagnetic to SD state transition) and CRM is stable.

11.4.3 Rocks with maximum magnetization

The intense crustal magnetic sources detected in the Terra Sirenum region (120° W–210° W; 30° S–85° S) produce fields as strong as 1600 nT at 100 km altitude. This would correspond to a magnetic moment of some 1.6×10^9 Tm^3. Assuming a 30 km thick magnetized layer, this moment translates to a volume magnetization of ~20 A/m (see also Parker, 2003). It can be assumed that initially this magnetization was acquired through a TRM/CRM process because these are the only remanence acquisition mechanisms operating in the deep crustal rocks. Common values for remanent magnetizations acquired in the geomagnetic field by common terrestrial rocks are consistently near 1%–2% of their saturation remanence (see Table 11.1 in Kletetschka *et al.*, 2003, NRM column). Such data indicate that it is quite exceptional for terrestrial rocks to have magnetizations of the order of 20 A/m. Just as exceptional are the large crustal volumes required at Mars (30 km thick layer) with near-uniform magnetization.

The magnetization of hematite, magnetite, and pyrrhotite in their pure form changes according to grain size (see

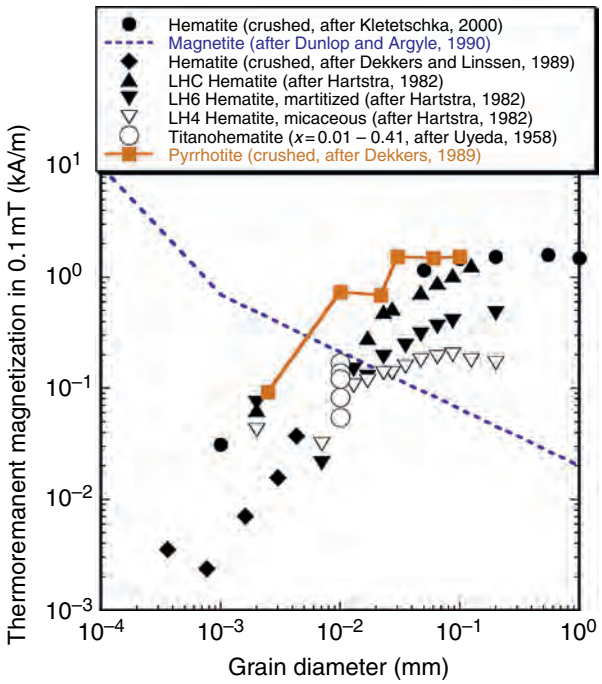

Figure 11.3. TRM magnetizations for the three main candidate minerals that could constitute the source of the magnetic anomalies on Mars. (For a color version of this figure, please refer to the color plate section or to the e-Book version of this chapter.)

Figure 11.3, and note that the unit is kA/m). The diagram, for an inducing field of 0.1 mT, indicates that the maximum possible TRM of large grains of hematite and pyrrhotite is slightly over 1000 A/m. Magnetization for small grains of magnetite is close to 10000 A/m. Both hematite and pyrrhotite can acquire strong magnetizations when the grain size is large. Thus, the maximum magnetization per unit volume of the rock formation occurs when hematite and pyrrhotite accumulate by coarse-grained ore-forming processes. In such a case the concentration of hematite and/or pyrrhotite can be >50% (by volume) and the magnetization of the entire rock can be greater than 500 A/m.

Magnetite can be more magnetic (by almost an order of magnitude) but only in small grain sizes that are able to produce single magnetic domains. In general, SD magnetites (submicrometer in size) do not crystallize from molten rock unless cooling is exceptionally rapid, as in the glassy, quenched margins of basalt flows (Brachfeld and Hammer, 2006). Another mechanism that can preserve the small grain size of magnetite in deep crustal rocks is exsolution from silicate minerals (Geissman *et al.*, 1988). Exsolution of fine-grained magnetite allows only about 0.5% (by volume) concentration due to problems associated with fitting magnetite in the host-phase crystal-lattice defects as well as changes from the phase hosting Fe that have to be compensated. This limits the maximum overall magnetization of rocks with magnetite (0.5% by volume) to about 50 A/m, an order of magnitude lower than the magnetizations of hematite and pyrrhotite. All three minerals, magnetite, hematite, and pyrrhotite can generate enough magnetization to produce the observed magnetic anomalies. However, a way must also be found to enhance the concentration of one or more of these minerals within large volumes of Martian crust while preserving the magnetizing direction. Ore deposits provide one possible way. The solution of this problem is directly connected to the early history of formation of the crust, and so determining the mineralogic origin of the crustal magnetization will have a major impact on the resulting inferred evolutionary path for the Martian crust. For example, the presence of hematite in the lower crust would imply high-oxidation levels. The occurrence of hematite-bearing lower crustal rocks on Earth is commonly attributed to the orogenic recycling of oxidized surface material (Frost, 1991), a process for which there is so far no clear evidence on Mars.

Both magnetite and pyrrhotite have been detected in SNC meteorites and suggest the possibility of large hydrothermal flows accumulating this mineral in a massive form. A lower crust with a large concentration of magnetite requires a special mechanism to disperse fine-grained material and/or to produce complex textures so that the magnetization can be stable and survive more than 4 Gyr. A pyrrhotite-rich crust would imply large-scale hydrothermal flows accumulating significant pyrrhotite concentrations in massive formations.

Titanohematite has both impact resistant remanence and sufficient magnetic intensity. A recently discovered empirical law (Kletetschka *et al.*, 2004a) further shows that the TRM intensity is particularly strong for minerals with low values of saturation magnetization. This might help to explain the strong magnetization of titanohematite without the need for "lamellar magnetism" (Robinson *et al.*, 2002) following regular TRM acquisition principles (Kletetschka, 2000; Kletetschka *et al.*, 2002). Titanohematite and/or hematite occurs frequently in the oxidized crust of the Earth, including the lower crustal rocks (Kletetschka and Stout, 1998; McEnroe *et al.*, 2001a, b; Kletetschka *et al.*, 2002). The crustal rocks can also be oxidized later as a result of hydrothermal activity, producing alteration zones with gradual decomposition of primary magnetite to hematite (Martinisation) (Just and Kontny, 2002). Postmagmatic pervasive alteration can take place during the early cooling history of the rock. This alteration is associated with retrograde P-T conditions and different paragenesis, implicating several episodes of fluid circulation. With the decrease of temperature the oxygen fugacity increases. The oxidation of magnetite can occur with a later stage of the pervasive alteration when biotite chloritizes within a temperature interval between 180 °C and 200 °C and pressures between 0.2 and 0.3 GPa (Jacquemont, 2002). However, because of the low-magnetic intensity of the altered minerals (Just, pers. comm.), and because this kind of alteration produces pure hematite as opposed to titanohematite exsolution, it is probably not a viable explanation for generating very intense magnetic anomalies on Mars.

Another potential magnetic source can be a metasedimentary high-grade rock which can contain intensely magnetic titanohematite (Kletetschka and Stout, 1998; Kletetschka *et al.*, 2000a). However, given the early time in Martian history proposed for the origin of these anomalies (Acuña *et al.*, 1999), this source appears to be unlikely because of the

large volume of rocks that would have to be formed, eroded, deposited, and deeply buried within a relatively short timescale. The magnetic source could consist of early oxide cumulates within the deep, initially very oxidized, igneous gabbro/norite rocks dominated by hemoilmenite (an ilmenite host with titanohematite lamellae; McEnroe *et al*., 2001b; Wilson *et al*., 1996). This requirement for an oxidized gabbro/norite type of rock would indicate the widespread occurrence of early highly oxidized magmas, either derived from the early highly oxidized composition of the planet, or from mixing with the early oxygen-rich fluids originating from a large body of water on the surface, possibly an early ocean on Mars. However, we have to state that our implications of a high-oxidation state are not supported by Mars meteorite analyses, perhaps indicating that the meteorites came from the crustal material that originated outside of the Terra Sirenum region as discussed below.

Another concept capable of significant magnetization increase over the southern highlands relates to thermal decomposition of iron-rich carbonates (Scott and Fuller, 2004). Water reacting with ancient Martian atmospheric carbon dioxide may have given rise to fluids that dissolved igneous rocks in the crust and precipitated iron-rich carbonates, as observed in some Martian meteorites (Golden *et al*., 2001; Barber and Scott, 2002, 2003). In the southern highlands, thermal decomposition of such iron-rich carbonates during metamorphism (French, 1971) could have given rise to enough SD magnetite to generate a strong source for the Martian crustal field. The lack of anomalies in the northern plains may result from higher water–rock ratios that prevented the formation or decomposition of iron-rich carbonates or the survival of SD magnetite. The Allan Hills 84001 meteorite is the only known Martian sample of Noachian age (Weiss *et al*., 2002b). Carbonate decomposition observed in this meteorite has, in general, very low-saturation remanence and, as such, is unlikely to represent a source of material that would contribute significantly to magnetic anomalies detected by MGS (Rochette *et al*., 2005).

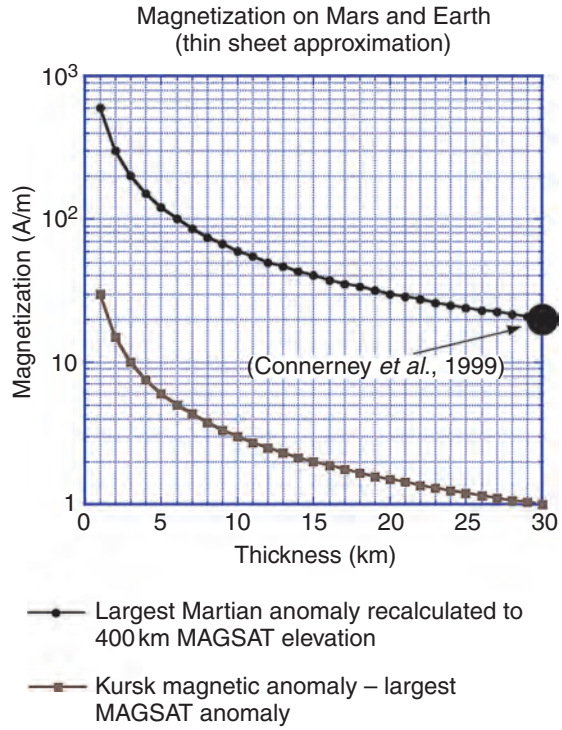

Figure 11.4. Homogeneous distribution of magnetization in a thin sheet of indicated thickness required to account for the 1500 nT anomaly considered by Connerney *et al*. (1999) is compared with the Kursk magnetic anomaly, the largest on Earth. (For a color version of this figure, please refer to the color plate section or to the e-Book version of this chapter.)

11.5 THE MAGNETISM OF SNC METEORITES

The SNC meteorites constitute an invaluable sample to study the possible magnetic properties of the Martian surface where they originated. As discussed above, one of the most likely mechanisms responsible for the observed crustal magnetization of Mars is TRM. The TRM values of the rock-forming minerals can be used to predict the concentration of these minerals required to generate the observed intense magnetic anomalies on Mars. These are upper limits, as we may expect the magnetic intensity to diminish with time due to viscous, shock, chemical, thermal, and randomizing effects (Collinson, 1997; Dunlop and Özdemir, 1997). The 4 ± 0.1 Gyr old Martian meteorite ALH 84001 is at present the oldest well-documented sample of Solar System material with remanent magnetization (Weiss *et al*., 2002a, b). The fact that this sample acquired its magnetization between 3.9 and 4.1 Ga is the main quantitative constraint that we have on the timing of the Martian core dynamo (Weiss *et al*., 2002c). It acquired its magnetization either in the dynamo field itself or in a strong crustal field after the dynamo died.

We compare the values required for homogeneous layer magnetization shown in Figure 11.4 (Kletetschka *et al*., 2000c) with the mineral-characteristic TRM values acquired in an Earth-like external magnetic field (Figures 11.5a and 11.5b). The data in Figure 11.5 represent pure mineral data and when diluted mathematically in non-magnetic unit volumes, we can use the thin-sheet approximation of Talwani (1965) and attempt to find a relation with the MGS-derived magnetization intensities as represented by Figure 11.4 to plot the individual mineral concentration curves required to generate the observed magnetic signatures (Figure 11.6).

The mineral concentrations with TRM acquired in an Earth-like magnetic field can be compared with concentrations of magnetic minerals found in SNC meteorites. In the following analysis, we attempt to find the most "magnetic" meteorite to constrain a maximum concentration estimate for the source. Concentrations can be deduced from measurements of the saturation magnetization (J_s) of SNC meteorites assuming magnetite as the sole mineral responsible for the magnetic signature. Hysteresis parameters for six of the SNC meteorites (ALH 77005, EETA 79001, Shergotty, Governador Valadares, Zagami, and Nahkla; see Cisowski, 1986) indicate that Nakhla and Governador Valadares have the largest J_s (0.46 A m^2 kg^{-1} and 0.38 A m^2 kg^{-1} respectively)

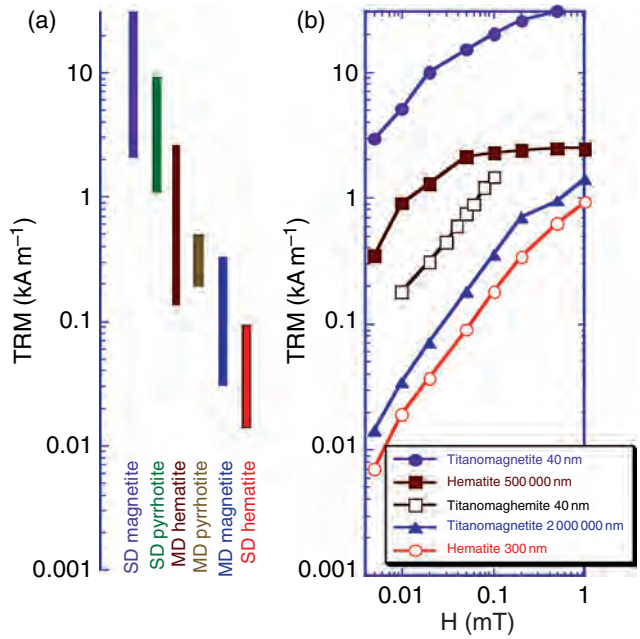

Figure 11.5. Summary of TRM acquisition in small magnetic fields. (a) Ranges of TRM intensities acquired in the geomagnetic field (~0.05 mT). (b) TRM acquisition trends for variable magnetizing field intensity: Single domain hematite and multidomain hematite (N115249 and N114078, respectively) were obtained from the Department of Mineral Sciences, NMNH, Smithsonian Institution, and are described in Kletetschka *et al.* (2000a). Single domain (SD) titanomaghemite data (40 nm) are from Özdemir and O'Reilly (1982). Ranges of TRM for magnetite, pyrrhotite, and hematite are from Clark (1983). Single domain (40 nm) and multidomain (MD) (2 mm) titanomagnetite curves are from Özdemir and O'Reilly (1982) and Tucker and O'Reilly (1980), respectively. (For a color version of this figure, please refer to the color plate section or to the e-Book version of this chapter.)

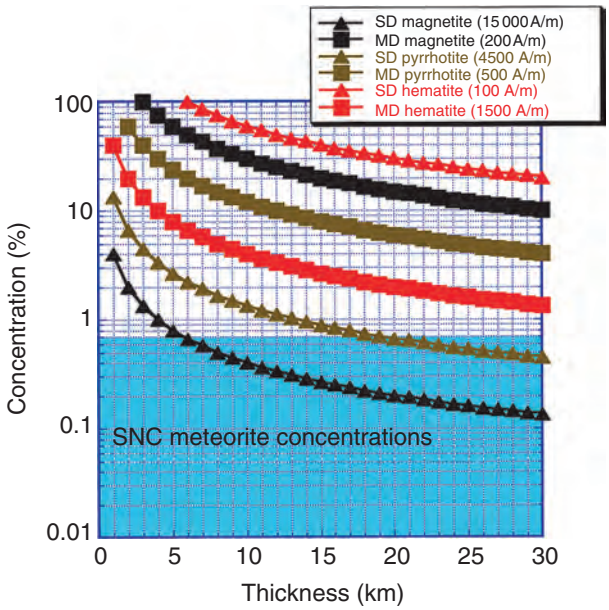

Figure 11.6. Concentrations of magnetic minerals with TRM in the indicated thickness required to account for the 1500 nT anomaly considered by Connerney *et al.* (1999). TRM values used for individual curves relate to Figure 11.5a and 11.5b. The concentration range of assumed SD titanomagnetite in SNC meteorites is also shown. (For a color version of this figure, please refer to the color plate section or to the e-Book version of this chapter.)

and would represent concentrations of 0.51% and 0.42% of pure magnetite ($J_s = 91$ A m^2 kg^{-1}; Hunt *et al.*, 1995). Collinson (1997) and McSween (1985) state that the magnetic carriers in Nakhla meteorites are titanomagnetites. The Ti component lowers the value of J_s ($J_s = 45$ A m^2 kg^{-1}; Hunt *et al.*, 1995) and therefore the maximum concentration estimate given above would increase to 0.8%–1.0% for TM 60 (titanomagnetite, 60% ulvospinel).

Observations of Nakhla thin sections (borrowed from Tim McCoy at the United States' Smithsonian Institution National Museum of Natural History [USNM], Smithsonian Institution, Washington DC) reveal the presence of large grains of titanomagnetite (less than about 0.3%, see Kletetschka *et al.*, 2000c). However, and as mentioned above, from the magnetic analysis of the Nakhla meteorite we may have a maximum concentration of titanomagnetite approaching 1%. This disagreement indicates that in the thin sections used for this study there is still <0.7% of TM 60 in very fine-grained form, which escaped the imaging technique. These grains would possibly overlap the SD range (<50 nm) and would have much larger coercivity of remanence. To resolve these issues we proceeded to measure magnetic acquisition and demagnetization curves for actual thin sections of SNC meteorites obtained from the USNM.

The thin sections were slices of Chassigny (USNM 6245), Nakhla (USNM 42616), and Shergotty (USNM 3213). Even though the SNC sections contained a very small volume of material, the magnetic signature from the magnetic minerals was detectable with a superconducting rock magnetometer in the laboratory. Isothermal remanent magnetization saturated after application of magnetic fields exceeding 0.3 T (Kletetschka *et al.*, 2000c). This large coercivity is characteristic of SD carriers and/or fine-scale microstructure in large grains. The crossover points between the acquisition curves and alternating field demagnetization curves indicate the presence of finely dispersed magnetic grains possibly overlapping the SD grain size range (Kletetschka *et al.*, 2000c).

In accordance with the observed TRM efficiency of titanomagnetites (see Figure 11.5), the multidomain titanomagnetite fraction (<0.3%) would contribute very little to the overall TRM signature. The remaining maximum amount of possible SD titanomagnetite (<0.7% – probably a mixture of pseudo-single domain and SD grains) would then contribute to the crustal magnetic signature. Following the thin sheet approximation of Talwani (1965), the minimum thickness of a layer of homogeneously magnetized crust containing SD titanomagnetite would have to exceed 5 km in order to generate the observed magnetic signal (see Figure 11.6).

The SNC meteorites' composition may not be representative of the materials in the magnetic anomaly regions discovered by MGS. In fact, since most SNC ages are less than ~2 Gyr and the Noachian terrain where the anomalies are found is generally considered to be >4 Gyr (Acuña *et al.*, 1999), we infer that most of the SNCs may have originated in the younger northern lowlands. Thus their magnetic properties may not accurately represent those applicable to the materials responsible for the crustal magnetic signatures found in the southern highlands.

11.6 STRESS AND TECTONICS: PLATE TECTONICS AT MARS?

The present-day state of magnetization of the Martian crust offers a unique *opportunity* to look into the past and constrain crustal formation and subsequent evolution. The largescale coherence of the crustal magnetic field first evident in the early MGS aerobraking observations (Acuña *et al.*, 1999; Connerney *et al.*, 1999) and later observed at mapping altitude (Connerney *et al.*, 2001, 2005) suggests that this magnetic imprint records a history of processes at the global scale. Early analysis of the intensely magnetized southern highlands introduced the intriguing possibility of plate tectonics and crustal spreading in the presence of a reversing dynamo having occurred early in Mars' evolution. The magnetic field observed over this region is organized in east–west-trending lineations, some extending over 2000 km in length. A remarkably good fit to the vector data acquired during several low-altitude (to 100 km) aerobraking passes over Terra Cimmeria and Terra Sirenum was obtained (Connerney *et al.*, 1999). The model consisted of 20 uniformly magnetized relatively thin (30 km) plates, 200 km in width, extending to infinity in the east–west direction (Figure 11.7). Plate magnetizations varied from approximately +20 A/m to –20 A/m, in a pattern reminiscent of the alternating magnetic polarities observed over mid-ocean ridges on Earth (e.g., Vine and Matthews, 1963).

Connerney *et al.* (1999) concluded that crustal magnetizations on Mars were at least an order of magnitude greater than those observed on Earth. This is a minimum because magnetization intensities cannot be constrained from orbit altitude (Connerney *et al.*, 1999). Intensities of tens of ampere per meter are required if one allows the maximum plausible thickness for the magnetic layer (30 km) as constrained by the possible depth to the Curie isotherm (Smith *et al.*, 2001). If the magnetized layer is thinner, say 3 km (Connerney *et al.*, 2005), one needs an additional order of magnitude magnetization intensity as mentioned above. Unfortunately, the observations constrain only the product of magnetization intensity and layer thickness. Parker (2003) and Voorhies *et al.* (2002) reached similar conclusions. Perhaps more controversial was the suggestion (Connerney *et al.*, 1999) that the observations could be fit with a pattern of magnetization like that found on Earth in association with crustal spreading in the presence of a reversing dynamo (see also Nimmo and Stevenson, 2000). The characteristic horizontal scale length of such features on Earth, determined by the crustal spreading rate and the characteristic time interval between dynamo reversals, is of order 10 km, a spatial scale well beyond the reach of orbiting spacecraft. Thus, many find it difficult to visualize how such variations might be mapped on Mars from orbital altitudes. However, variations of order 100 km width might result on Mars if the rate of spreading was greater and/or if dynamo reversals were less frequent, relative to Earth. Crustal spreading on Mars is expected to occur at a higher rate (Sleep, 1994), if at all, because of lower gravity (0.38 that of Earth) and the slightly greater density of the mantle. Little is known of dynamo reversals, except on Earth where the time between reversals of the magnetic field has varied greatly, with a few reversals per million years being typical.

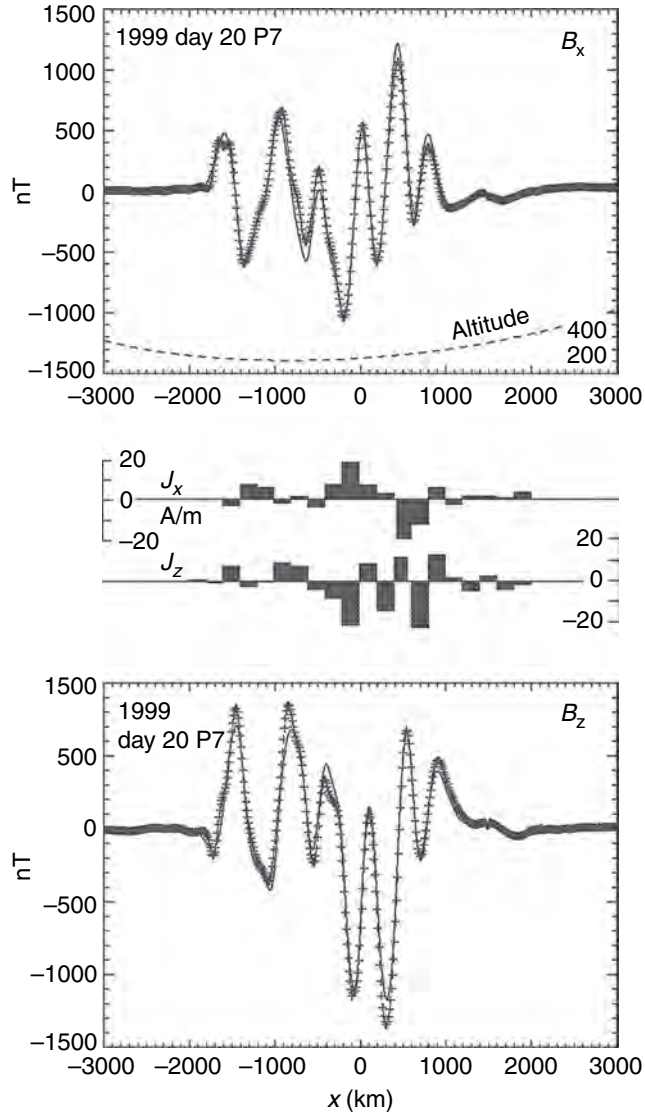

Figure 11.7. Vector magnetic field measured by MGS during aerobraking on calendar day 20, 1999. Periapsis occurred at 68.0° S, 181.2° W and 106 km altitude. The x (north) and z (down) components of the field sampled every 3 s (crosses) are compared with a model fit (solid line). Altitude variation (dashed line, in km) and observations are plotted as a function of distance x north and south of an origin at 53° S. Model consists of 20 uniformly magnetized slabs aligned with the y axis (east–west) and infinite in extent along y. The x and z components of the model crustal magnetization per unit volume (A m^{-1}) are indicated in the bar graphs between the two panels. (Figure from Connerney *et al.*, 1999.)

One virtue of the plate tectonic hypothesis is that this mechanism can produce, continuously, an efficiently magnetized crust with coherence over spatial scales that are very large – thousands of kilometers. On Mars, to explain the magnitude of the field observed at 100–400 km altitude,

we need a mechanism that is extremely efficient; one that produces coherence over spatial scales of 100 km (the MGS observations are sensitive to crustal magnetizations averaged over ~100 km scales) and one that magnetizes the maximum volume of crust (if we are to keep magnetization intensities within the realm of terrestrial experience). Of course, it is possible that even greater magnetization contrasts, over smaller spatial scales, are responsible for the variations observed by MGS. Observations at lower altitude will be required to explore this possibility. However, even greater magnetization intensities would then be required, since the average over 100 km needs to be very large.

Sprenke and Baker (2000) modeled the same observations under a variety of assumptions, and found that a crustal spreading model fit the observations well, particularly if a variation in magnetization intensity along the east–west direction was allowed. They too found magnetization intensities of tens of ampere per meter, assuming a 30 km thick crust. Their model allowed normal and reversed magnetization directions only, fixed in the direction of an assumed dipole. They also examined models with only one polarity (magnetic shell concept), creating a similar field by separation of many similarly magnetized slabs. Given the insensitivity of all such models to the addition or subtraction of a uniformly magnetized layer, the models differ little in practical terms; the distinction is in the mechanism of origin.

Nimmo (2000) proposed multiple giant dike swarms like the fragmented dike swarms observed on Earth (e.g., Ernst *et al.*, 2001) as a possible alternative to crustal spreading as an explanation for the lineations on Mars. The latter are abundant within the most ancient, Precambrian terrains on Earth, and coeval dikes can be traced from one continent to another after the continents are reconstructed by closure of the Atlantic Ocean. The formation of a series of suitable dikes on Mars is plausible (Nimmo, 2000), but even with very intense magnetization they would necessarily have to have been great in number and orders of magnitude wider than the 10 m widths typical of terrestrial dikes (Ernst *et al.*, 2001). Relatively few large dikes have been identified on Mars, compared with Earth and Venus; possible dikes identified in Terra Sirenum and Terra Cimmeria are not exactly oriented in the direction of the magnetic features and exhibit only few kilometer wide structures.

Fairen *et al.* (2002) proposed that the magnetic lineations on Mars were formed at a convergent plate margin through collision and accretion of terrains. In their model, the strongly magnetized southern highlands are "a jigsaw of continental and oceanic pieces" related to a past era of plate tectonics, formed by a process of crustal convergence rather than crustal generation. The crustal spreading proposal recently received additional support when an improved map of the crustal field became available (Connerney *et al.*, 2005). This map is a compilation of 2 Mars years of MGS MAG/ER observations from the nominal 400 km mapping altitude, using a new mapping method to further improve signal fidelity. This map offers very high spatial resolution for observations obtained at orbital altitude and reveals magnetic variations that appear in association with major known geologic features. The map is reproduced in Figure 11.8. This is a global map of ΔB_r, essentially a 360 by 180 pixel "image" of the filtered radial magnetic field, color-contoured over 2 orders of magnitude variation in signal amplitude. The map is superposed on the Mars Orbiter Laser Altimeter (MOLA) shaded topography map which appears where ΔB_r falls below a threshold value of ± 0.3 nT per degree latitude (5×10^{-3} nT/km) traversed by MGS. The threshold chosen for the minimum contour is set well above the noise level so that little noise appears in the map and to allow sufficient context imagery.

In this map Connerney *et al.* (2005) identified features that are, on Earth, uniquely associated with plate tectonics. In the Earth's case, crustal spreading in the presence of a reversing dynamo yields a pattern of magnetization with symmetry about the ridge axis and adjoining plates are bounded by a unique type of fault (called a "transform fault"). Transform faults may be identified in Earth's magnetic survey data by noting a discontinuous shift of the magnetic pattern ("stripes") along the fault (this has been traditionally the best way to identify transform faults). Transform faults are distinguished from simple strike slip faults by noting that for transform faults, the displacement along the fault reverses sign at a spreading center; one cannot align the magnetic pattern with a shift in one direction. A pair of putative transform faults, separated by approximately 1200 km, was identified in Meridiani. These parallel faults extend for thousands of kilometers and are consistent with relative plate motion on the surface of a sphere (small circles with a common axis of rotation). Likewise, a putative spreading center near 0° latitude was identified; the mapped field is consistent with symmetry about the spreading center. However, the limited spatial resolution available from orbit limits the power of this observation, and one would like more detailed observations (closer to the source) to unambiguously establish symmetry.

Nevertheless, the early plate tectonic hypothesis offers a familiar and interesting explanation for many notable Mars features. The Valles Marineris fault system appears much like a rift system, and is aligned in the direction consistent with the tensile forces implied by motion along the transform faults in Meridiani (Connerney *et al.*, 2005). The series of piecewise linear escarpments along much of the dichotomy boundary, originally identified as a series of ridge/transform fault segments by Sleep (1994), are likewise aligned in a consistent manner, though perhaps not as originally envisioned. The alignment of the large volcanic constructs of Tharsis (Arsia Mons, Pavonis Mons, Ascraeus Mons, extended to include Ceraunius Tholus, Uranius Patera, and the volcanic cones of Tempe Terra) along a great circle is suggestive of the alignment of volcanic island chains in the pacific (e.g., Hawaii-Emperor chain), thought to record the motion of a plate over a fixed mantle hotspot (Connerney *et al.*, 2005).

The consequences of an early era of plate tectonics are profound (Nimmo and Stevenson, 2000), if not easily reconciled with prevailing views of Mars evolution and the likelihood of mantle convection. The prevailing view of Mars evolution is dominated by the concept of stagnant lid convection (Schubert *et al.*, 1992; Hauck and Phillips, 2002), in which the planet cools slowly, inefficiently, by

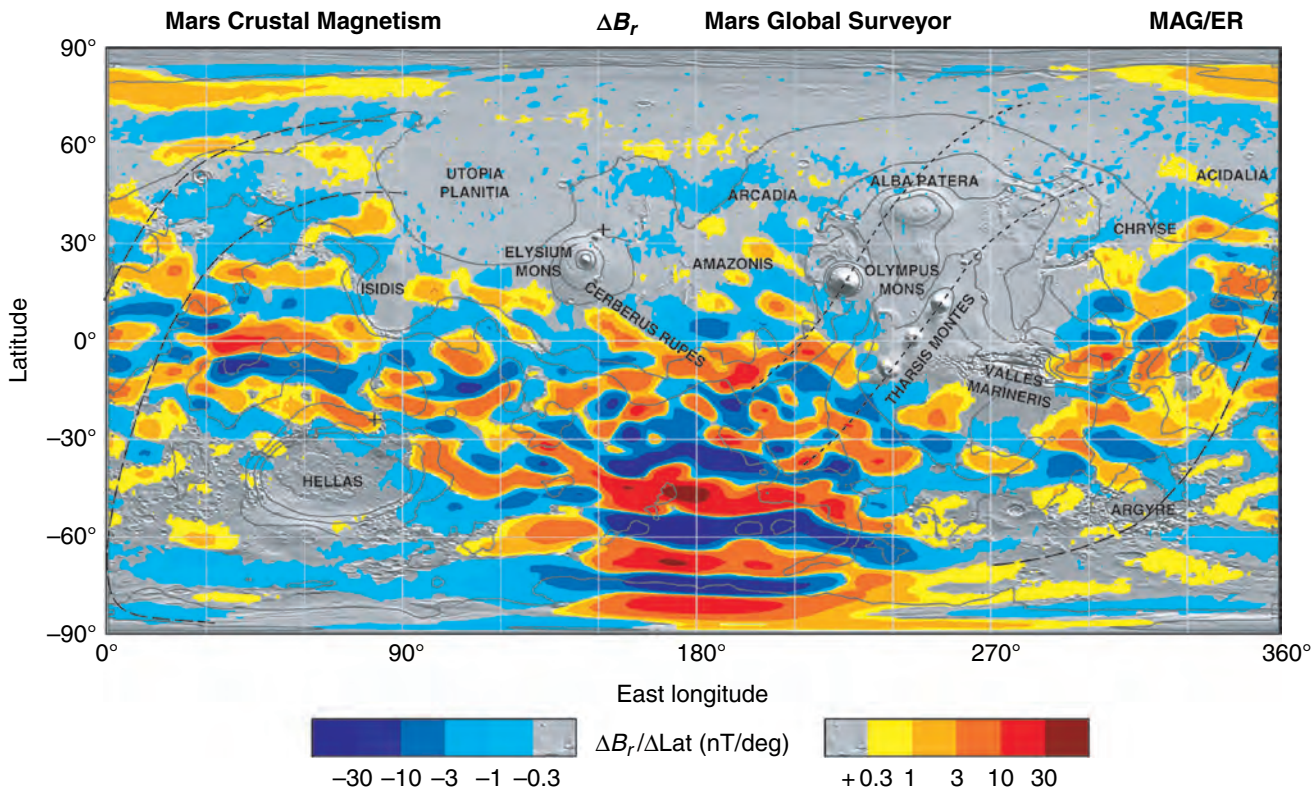

Figure 11.8. Map of the magnetic field of Mars observed by the Mars Global Surveyor satellite at a nominal 400 km altitude. Each pixel is colored according to the median value of the filtered radial magnetic field component observed within the 1° by 1° latitude/longitude range represented by the pixel. Colors are assigned in 12 steps spanning two orders of magnitude variation. Where the field falls below the minimum contour, a shaded MOLA topography relief map provides context. Contours of constant elevation (−4, −2, 0, 2, 4 km elevation) are superimposed, as are dashed lines representing rotations about common axes (short dashes – axis northeast of Elysium Mons; long dashes – axis northeast of Hellas). (For a color version of this figure, please refer to the color plate section or to the e-Book version of this chapter.)

conduction through a gradually thickening lithosphere. Plate tectonics cools the interior quickly, drives convection in the core, and encourages the generation of a planetary magnetic field by dynamo action. Indeed, the demise of the dynamo fairly early in Mars evolution may be related to the cessation of plate tectonics and its effects on heat transfer at the core.

11.7 IMPACT CRATERING AND DEMAGNETIZATION

The Martian crust has endured several large meteoroid impacts subsequent to the demise of an early global magnetic field. Shock pressures associated with these impacts appear to have demagnetized parts of the crust, to an extent determined by the shock resistance of the magnetic materials within it. Such demagnetization events have been characterized near large impact basins (Nimmo and Gilmore, 2001; Hood *et al.*, 2003; Kletetschka *et al.*, 2004b; Mohit and Arkani-Hamed, 2004). Impacts that form large basins generate pressures in excess of 1 GPa within a few crater radii of the impact site (e.g., Melosh, 1989). Crustal materials near the surface experience significantly reduced impact pressure, which varies with depth and distance from the impact point. Demagnetization experiments on magnetite, hematite, and titanohematite show that pressures of ~1 GPa magnitude are sufficient to partially demagnetize all of these minerals (e.g., Nagata, 1971; Pohl *et al.*, 1975; Halekas *et al.*, 2002; Rochette *et al.*, 2003a; Mohit and Arkani-Hamed, 2004; Artemieva *et al.*, 2005). The efficiency of demagnetization by impact pressure is proportional to the logarithm of the minerals' magnetic coercivity (e.g., Kletetschka *et al.*, 2004b). The impact pressure magnetic response from exsolved titanohematite samples is consistent with the magnetization decay near the Martian south polar Prometheus impact basin and may point to an oxidized igneous rock in the Terra Sirenum region at the time of acquisition of magnetic remanence. The remaining magnetic anomalies near large impact basins suggest moderate crustal coercivity, and would be consistent with titanomagnetite as a magnetic carrier and more reduced conditions during crustal formation. Alternatively, these weaker anomalies may be explained as a result of secondary impacts as discussed in more detail below.

Crustal remanence on Mars was likely acquired prior to the end of heavy bombardment (Acuña *et al.*, 1999), as evidenced by the lack of magnetization in the centers of impact basins. The shock wave generated by the impact produces high pressures that penetrate and demagnetize the crust well

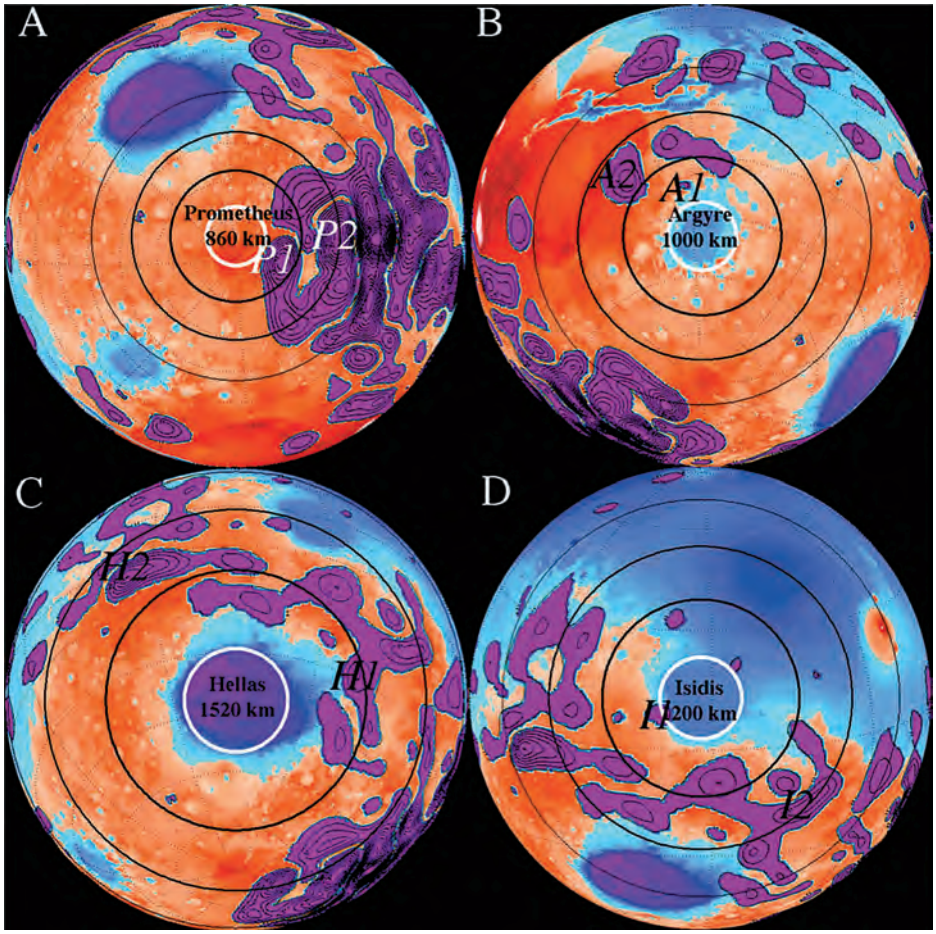

Figure 11.9. Topographic maps (MOLA – dark red is the highest and dark blue is the lowest altitude) compared with magnetic maps (MGS) across large impact basins (A: Prometheus, B: Argyre, C: Hellas, D: Isidis). Purple color indicates absolute values of radial magnetic signature exceeding 10 nT at night side and 400 km satellite altitude. Contour lines have contour interval 10 nT. Heavy white circle is the crater diameter. Circles of increasing diameters indicate the peak pressure exceeding 5, 2, and 1 GPa, respectively, during the impacts (estimated analytically; see text). (For a color version of this figure, please refer to the color plate section or to the e-Book version of this chapter.)

beyond the crater rim (Halekas *et al.*, 2002). If a large ambient magnetic field is present during the impact, the penetrating shock wave can induce a shock remanent magnetization (SRM) in low-coercivity minerals (Cisowski and Fuller, 1978). Impact sites are also sources of massive volumes of impact melt, which would normally upon cooling carry magnetic particles. These magnetic minerals would have a strong magnetic remanence if a significant global magnetic field were present when they cooled below their blocking temperatures. The absence of magnetic anomalies over these basins suggests that the cooling occurred most likely in the absence of a global magnetic field.

11.7.1 Impact model

Portions of the Mars crust were demagnetized by shocks associated with large impactors, in the absence of a dynamo. The temperatures achieved near the impact site would also have demagnetized the crust (Mohit and Arkani-Hamed, 2004). In analyzing the magnetic anomalies near the large impact basins, models for shock pressure propagation from the point of impact on Mars (Hood *et al.*, 2003) can be applied. Impact pressures can be readily estimated in four large Mars impact basins: Prometheus (Tanaka and Scott, 1987; Schenk and Moore, 2000; Milkovich *et al.*, 2002), Argyre, Hellas, and Isidis (Tanaka *et al.*, 1986). For details, see Kletetschka *et al.* (2004b).

Isobars for 1, 2, and 5 GPa pressures are plotted in Figure 11.9 for the large impact basins Prometheus, Argyre, Hellas, and Isidis (for crater location and calculated pressure diameters see Table 11.1). However, the pressure hemisphere does not extend to the surface because the pressure on the surface is by definition zero. The boundary condition (zero pressure) on the surface is accomplished by a rarefaction wave, equal in strength but opposite in sign to the shock wave, which propagates downward from the surface as soon as the shock wave arrives. The sum of the pressures in shock and rarefaction waves is always zero on the free surface and interference between the two waves occurs below the surface (see Figure 5.7 in Melosh, 1989). The maximum pressure experienced by the rock inside the interference zone increases more or less linearly with depth (see Figs. 5.7 and 5.8 in Melosh, 1989) until it reaches the maximum pressure predicted. Therefore, the pressures estimated from the Hugoniot equations (Hood *et al.*, 2003) are only valid at the bottom of the interference zone (for details, see Kletetschka *et al.*, 2004b). We estimate the depth at which the rock experiences pressures exceeding 1 GPa in Figure 11.10, allowing for approximately linear decrease in pressure toward the surface.

The association of crustal magnetic signatures at Mars with specific geological/topographic features is difficult and controversial. There is, as yet, no clear association between the magnetism of the Martian crust and surface morphology,

Table 11.1. *Mars basin data*

Basin	Latitude (°)	Longitude (°)	CD (km)	*I* (km)	ID (km)	PD1 (km)	PD2 (km)	PD5 (km)
Hellas	– 42	294	1520	6.7	520	9440	6530	4030
Isidis	13	273	1200	5.2	380	6970	4820	2970
Argyre	– 50	42	1000	4.3	300	5520	3820	2360
Prometheus	– 84	266	860	—	250	4550	3150	1940

Basin locations are determined by latitude and W longitude. CD is the basin diameter, *I* is the depth to the 1 GPa interference zone at distance CD, ID is the impactor's diameter calculated from CD using the impact scaling code developed by H. J. Melosh, available at http://www.lpl.arizona.edu/tekton/crater.html. PD1, PD2, and PD5 are the distances of peak pressure (1, 2, and 5 GPa) isolines estimated from the momentum conservation equations.

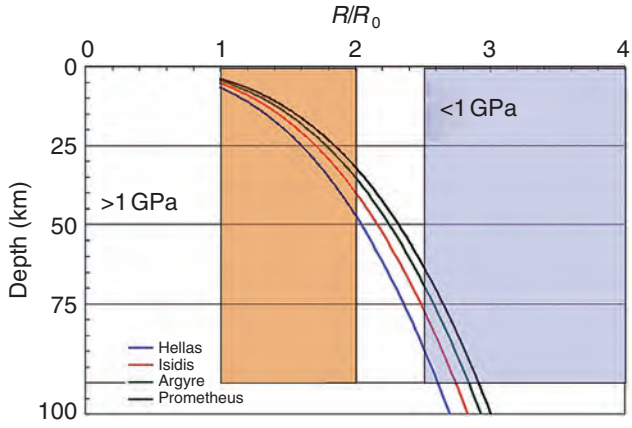

Figure 11.10. Plot of the distance from the center of impact versus depth where the maximum impact-pressure exposure exceeds 1 GPa. Hypothetical source of magnetic anomalies whose majority experienced the pressure exceeding 1 GPa is shown in brown and source affected by impact pressure less than 1 GPa is shown in light blue. (For a color version of this figure, please refer to the color plate section or to the e-Book version of this chapter.)

beyond the association with topography evidenced in the crustal dichotomy and the largest impact basins (Acuña *et al.*, 1999) and broad spatial correlation with the Martian valley networks (Harrison and Grimm, 2002). Of primary concern are crustal regions on Mars that contain magnetic sources, but we must also be concerned about how close to the center of the large (demagnetizing) impact basins these sources are. One analysis was done using contours of the radial magnetic field measured at 400 km altitude (Connerney *et al.*, 2001; see also Figure 11.8). A minimum contour value of 10 nT was chosen to eliminate spurious fields of external origin. Magnetic maps across major impact basins on Mars show a clear absence of magnetic field toward the centers of the impacts (Figure 11.9). However, the occurrence of magnetization close to the impact center would indicate the presence of magnetic minerals capable of retaining magnetization despite the shock event. Most of the static and impact experiments and observations on pressure demagnetization show that demagnetization effects increase with the magnetic coercivity (Hc) of the magnetic carrier (Nagata, 1971; Pohl *et al.*, 1975; Cisowski and Fuller, 1978; Pilkington and Grieve, 1992; Rochette *et al.*, 2003a).

11.7.2 Experiments

Kletetschka *et al.* (2004b) measured the saturation remanent magnetization of magnetic minerals, subjected them to a low-level impact pressure (1 GPa) in a weak magnetic field (~100 nT), and re-measured their magnetic remanence after the impact.

The samples had a broad spectrum of magnetic coercivity and thus were well chosen to show the effects of coercivity on impact pressure demagnetization reported previously (Nagata, 1971; Pohl *et al.*, 1975; Cisowski and Fuller, 1978; Pilkington and Grieve, 1992). Different minerals endured the impact with different resistance to demagnetization. Multi-Domain (MD) magnetite retained the least amount of magnetization ($12 \pm 3\%$) and had the lowest magnetic coercivity (1.8 mT). Both moderate coercivity minerals hematite and magnetite (13 mT and 19 mT for MD hematite and SD magnetite) retained $33 \pm 10\%$ and $33 \pm 8\%$ respectively. Titanohematite with exsolved lamellae had the largest coercivity (260 mT) and retained $75 \pm 11\%$ of its original remanent magnetization. The correlation between coercivity and pressure demagnetization, illustrated in Figure 11.11, indicates a proportionality relationship given by $M_{\%} \propto \log(H_c)$, where $M_{\%}$ is the percentage of remanent magnetization retained postimpact. This dependence is supported by experimental observations (Nagata, 1971; Pohl *et al.*, 1975; Cisowski and Fuller, 1978; Pilkington and Grieve, 1992). Our experiments on magnetic MD and SD magnetite are consistent with diamond anvil static pressure measurements on MD and SD magnetite (Gilder *et al.*, 2002), where the saturation magnetization of both MD and SD magnetite decreased by more than 50% after application of 3 GPa static pressure. Rochette *et al.* (2003b) found that pyrrhotite, another common rock-forming mineral, completely demagnetizes at 3 GPa at room temperature and retains less than 50% of its original magnetization between 1 and 2 GPa.

Impact demagnetization data can be compared with the major impact basins on Mars (Figure 11.9). Assuming that the magnetic sources are not deeper than 100 km, only the regions within ~2.5 crater radii of the impact basins can be

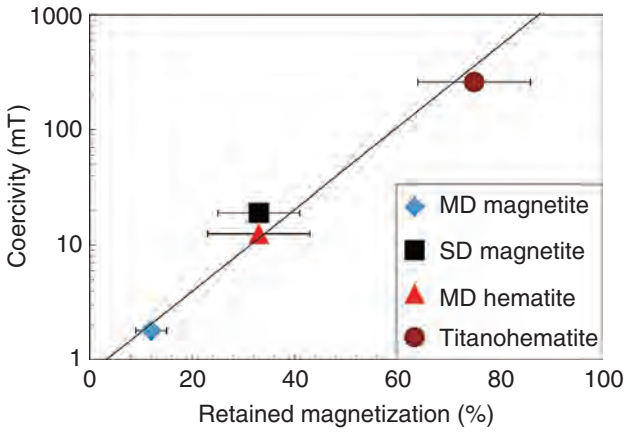

Figure 11.11. Magnetic coercivity of minerals is plotted against measurements of magnetic response to ~0.5–2.0 GPa shock pressure for various minerals. Error bars are based on 5 samples of MD magnetite, 3 samples of SD magnetite, 18 samples of MD hematite, and 16 samples of titanohematite with ilmenite exsolution. (For a color version of this figure, please refer to the color plate section or to the e-Book version of this chapter.)

significantly modified by the impact pressure. Most of the anomaly sources reside at depths less than 100 km (Acuña *et al.*, 1999; Connerney *et al.*, 1999; Nimmo and Gilmore, 2001; Arkani-Hamed, 2002b; Voorhies *et al.*, 2002; Hood *et al.*, 2003). Figure 11.10 shows that the pressure exceeds 1 GPa in most of the magnetic source volume occurring at distances less than 2 crater radii and shallower than 100 km. However, the magnetic source volumes that are farther away from the impact basin, from 2.5 to 4.0 radii, should be affected by pressures not exceeding 1 GPa (see Figure 11.10). For lack of more detailed information, we assume that the intensity of magnetization in the crust scales linearly with the amplitude of the magnetic field as measured from satellite altitudes. This would be the case, for example, if the field were due to a distribution of randomly oriented dipole sources in the crust. This estimate neglects potentially significant details of the source distribution, for example, the thickness of the magnetized layer, systematic variation in source geometry, and/or magnetization direction. We regard this estimate with caution and proceed with the assumption that this crustal magnetization can be crudely correlated to our experimental magnetic response of minerals (Figure 11.11).

The maxima in the magnetic anomalies, one located within the near region, 1.0–2.0 crater radii, and a second one within 2.5–4.0 crater radii, have a contrasting rate of decrease with respect to the proximity to the large impact basins. Beyond ~2.5 crater radii, the impact pressure should not exceed 1 GPa (Figure 11.10) and this crustal source volume is not significantly affected by the impact. The ratio of the largest anomaly in the near region divided by the largest magnetic anomaly in the far region (2.5–4.0 radii) should be indicative of the demagnetization efficiency. This procedure neglects important characteristics of source distribution and only crudely indicates the demagnetization effect of the original crustal magnetization. The observed decrease in crustal magnetization near the impact basins can then be related to experimentally derived responses to an impact pressure in terms of magnetic coercivity (Figure 11.11). The 60%–70% decrease in magnetization for Hellas, Argyre, and Isidis impact basins suggests that the magnetic anomalies near these basins are caused by magnetic minerals with moderate magnetic coercivity of ~10 mT (e.g., SD magnetite). The 10% decrease in magnetization observed for Prometheus can only be explained by magnetic minerals that have large magnetic coercivity (~1000 mT). This constraint on magnetic coercivity suggests either exsolved titanohematite or magnetite with very high aspect ratio as a magnetic carrier in this region.

The magnetic signatures observed around impact basins suggest the existence of three different types of sources in the crust. The first type contains magnetic minerals of intense remanence and large coercivity (e.g., titanohematite) and the distribution is suggested by an occurrence of large magnetic anomalies (Figure 11.1). The second type of magnetic crust contains magnetic minerals with moderate magnetic coercivity (e.g., SD magnetite) and is characterized by moderate magnetic anomalies. The third type has little or no magnetic signature and is either younger than the preexisting dynamo or the magnetic carriers were replaced later subsequent to disappearance of the dynamo. It is also conceivable that the magnetic source may have had very small magnetic coercivity (e.g., MD magnetite) and thus any magnetization it once had was unstable and decayed to a negligible value as a result of elevated temperatures in the deep crust.

The contrasting behavior of magnetic anomalies around Prometheus was discussed extensively by Langlais *et al.* (2004) in Figure 11.6. There are not many magnetic minerals with the large coercivity needed to explain the magnetic decay indicated near the Prometheus basin. In order to preserve large coercivity, magnetic minerals in general have large magnetic anisotropy, allowing an acquisition of magnetization only in certain directions. The most common rock-forming magnetic minerals of this nature are (titano-) hematite and pyrrhotite. The magnetization of hematite and pyrrhotite, in their pure form, changes according to grain size (Kletetschka *et al.*, 2003). The maximum possible TRM of large grains of hematite and pyrrhotite is more than 1000 A/m. Because both hematite and pyrrhotite can acquire strong magnetizations in large grain sizes, they could be part of large iron formations that may have evolved as a result of hydrothermal alteration early in the planet's history. In such cases the concentration of hematite and/or pyrrhotite could exceed 50% by volume and the intensity of magnetization of the bulk material could reach 500 A/m (Kletetschka *et al.*, 2000b).

These inferences about magnetic carriers in the Martian crust from impact demagnetization considerations may not be unique, however. Demagnetization of crustal materials by the primary impact shock wave at a given distance from the impact basin depends on the depth of the source region, which is poorly known, as well as the coercivity of the remanence carrier. It is possible, for example, that the anomaly sources in the Terra Sirenum region are simply at a shallower depth, where primary impact shock pressures were lower and demagnetization was less effective. Shallower sources would also be subject to basin-size-dependent demagnetization by secondary ejecta impacts (Artemieva *et al.*, 2005).

If local magnetic sources in the Martian crust are at shallow depths of a few kilometers (as suggested, for example, by Connerney *et al.*, 2005), then most of the shock demagnetization pattern outside the primary basins (>2.5 diameter, see Figure 11.10) would have been caused by secondary ejecta impacts (Artemieva *et al.*, 2005). The efficiency of secondary impact shock demagnetization is a very strong function of basin size and would be less effective for the smaller Prometheus basin. Basins with decreasing diameters are more effective in primary demagnetization of the near-surface layer (Figure 11.10) at a given number of basin radii from the center than other larger basins such as Hellas, Argyre, and Isidis. However, demagnetization by secondary impacts from these basins is more effective for primary basins with larger diameters (see Figure 11.2 in Artemieva *et al.*, 2005). Prometheus also has a weaker topographic signature than do the other larger basins, possibly suggesting that the impact is older. More likely is that the proximity of the basin to the polar ice caused more effective erosion due to numerous cyclings of the ice volume over the basin surface.

An alternate explanation (Hood *et al.*, 2003) for the greater strength of the anomalies in the Terra Sirenum region compared to those elsewhere in the southern highlands is that the Terra Sirenum region may be the only area in the southern highlands that escaped substantial shock demagnetization (and possibly also thermal demagnetization associated with Tharsis volcanism). This explanation considered demagnetization by the primary impact shock wave, which decays so rapidly with distance at depths less than 50 km (where the magnetization probably resides) that it may be difficult to reconcile quantitatively with the observations. However, if the magnetization exists mainly at shallow depths and if the magnetic carriers have the same basic properties everywhere on the planet, then consideration of secondary ejecta impact shock demagnetization (Artemieva *et al.*, 2005) may enable the mechanism proposed by Hood *et al.* (2003). Specifically, secondary ejecta demagnetization by Hellas, Argyre, and Isidis basin formation would have been effective out to a number of basin radii. The Terra Sirenum region could therefore still have escaped shock demagnetization even if remanence carriers there have the same properties as those elsewhere on Mars.

11.8 SUMMARY

The discovery of intense crustal magnetization at Mars has provided a new and unique window into the planet's past and its thermal evolution. The existence of "pure" magnetic anomalies, not contaminated by a strong magnetic field of deep internal origin, is providing a truly unique *opportunity* to study the crustal magnetization of a terrestrial planet, and has significant relevance for studies of the Moon, Mercury, and possibly the Earth as well. Moreover, the conclusion derived from impact demagnetization observations that the Martian dynamo ceased operation within less than ~500 Myr of accretion and core formation has significant implications not only for the interior but also for atmospheric evolution and its role in constraining the geochemistry and mineralogy that we observe on the Martian surface today. The large spatial scale, volume, and intensity of the Martian magnetic anomalies remain as significant interpretive challenges as we find ourselves limited to terrestrial analogs for models and possible processes. Unfortunately, deciphering of the Martian magnetic record is constrained to a very significant extent by the sparse coverage of the best available observations and the lack of very low-altitude data. Future missions involving airplanes, balloons, and surface vehicles carrying more sophisticated instruments than those utilized to date are needed to answer the fundamental questions raised by the MGS MAG/ER observations.

REFERENCES

Acuña, M. H., J. E. P. Connerney, P. Wasilewski, *et al.*, Mars Observer magnetic fields investigation, *J. Geophys. Res.* **97**, 7799–814, 1992.

Acuña, M. H., J. E. P. Connerney, P. Wasilewski, *et al.*, Magnetic field and plasma observations at Mars: initial results of the Mars Global Surveyor Mission, *Science* **279**, 1676–80, 1998.

Acuña, M. H., J. E. P. Connerney, N. F. Ness, *et al.*, Global distribution of crustal magnetism discovered by the Mars Global Surveyor MAG/ER Experiment, *Science* **284**, 790–3, 1999.

Acuña, M. H., J. E. P. Connerney, P. Wasilewski, *et al.*, The magnetic field of Mars: summary of results from the aerobraking and mapping orbits, *J. Geophys. Res.* **106**, 23403–17, 2001.

Albee, A. L., F. D. Palluconi, and R. E. Arvidson, Mars global surveyor mission: overview and status, *Science* **279**, 1671–2, 1998.

Albee, A. L., R. E. Arvidson, F. D. Palluconi, and T. Thorpe, Overview of the Mars Global Surveyor mission, *J. Geophys. Res.* **106**, 23291–316, 2001.

Arkani-Hamed, J., A 50-degree spherical harmonic model of the magnetic field of Mars, *J. Geophys. Res.* **106**(E10), 23197–208, 2001a.

Arkani-Hamed, J., Paleomagnetic pole positions and pole reversals on Mars, *Geophys. Res. Lett.* **28**(17), 3409–12, 2001b.

Arkani-Hamed, J., An improved 50-degree spherical harmonic model of the magnetic field of Mars derived from both high-altitude and low-altitude data, *J. Geophys. Res.* **107**(E5), doi:10.1029/2001JE001496, 2002a.

Arkani-Hamed, J., Magnetization of the Mars crust, *J. Geophys. Res.* **107**(E10), 5083, doi:10.1029/2001JE001835, 2002b.

Arkani-Hamed, J. and D. Boutin, Paleomagnetic poles of Mars: revisited, *J. Geophys. Res.* **109**(E03011), doi:10.1029/2003JE002229, 2004.

Arkani-Hamed, J., Magnetic crust of Mars. *J. Geophys. Res. – Planets* **110**(E8), 2005.

Artemieva, N., L. Hood, and B. A. Ivanov, Impact demagnetization of the martian crust: primaries versus secondaries, *Geophys. Res. Lett.* **32**, L22204, doi:10.1029/2005GL024385, 2005.

Barber, D. J. and E. R. D. Scott, Origin of supposedly biogenic magnetite in the martian meteorite Allan Hills 84001, *Proc. Nat. Acad. Sci. USA* **99**, 6556–61, 2002.

Barber, D. J. and E. R. D. Scott, Transmission electron microscopy of minerals in the martian meteorite Allan Hills 84001, *Meteorit. Planet. Sci.* **38**, 831–48, 2003.

Barlow, N. G., J. M. Boyce, F. M. Costard, *et al.*, Standardizing the nomenclature of Martian impact crater ejecta morphologies, *J. Geophys. Res.* **105**, 26733–8, 2000.

Bell, J. F., H. Y. McSween, J. A. Crisp, *et al.*, Mineralogic and compositional properties of martian soil and dust: results from Mars Pathfinder, *J. Geophys. Res. – Planets* **105**(E1), 1721–55, 2000.

Bertelsen, P., W. Goetz, M. B. Madsen, *et al.*, Magnetic properties experiments on the Mars exploration Rover Spirit at Gusev crater, *Science* **305**(5685), 827–9, 2004.

Brachfeld, S. A. and J. Hammer, Rock-magnetic and remanence properties of synthetic Fe-rich basalts: implications for Mars crustal anomalies, *Earth Planet. Sci. Lett.* **248**, 599–617, 2006.

Brain, D. A. and B. M. Jakosky, Atmospheric loss since the onset of the martian geologic record: the combined role of impact erosion and sputtering, *J. Geophys. Res.* **103**(E10), 22689–94, 1998.

Cain, J. C., B. Ferguson, and D. Mozzoni, An n = 90 internal potential function of the magnetic field of the martian crustal magnetic field, *J. Geophys. Res.* **107**(E10), doi:10.1029/2000JE001487, 2002.

Cisowski, S. M., Magnetic studies on Shergotty and other SNC meteorites, *Geochim. Cosmochim. Acta* **50**, 1043–8, 1986.

Cisowski, S. M. and M. Fuller, Effect of shock on magnetism of terrestrial rocks, *J. Geophys. Res.* **83**(NB7), 3441–58, 1978.

Clark, D. A., Comments of magnetic petrophysics, *Bull. Aust. Soc. Explor. Geophys.* **14**, 49–62, 1983.

Collinson, D. W., Magnetic properties of martian meteorites: implications for an ancient martian magnetic field, *Meteorit. Planet. Sci.* **32**(6), 803–11, 1997.

Connerney, J. E. P., M. H. Acuña, P. J. Wasilewski, *et al.*, Magnetic lineations in the ancient crust of Mars, *Science* **284**, 794–8, 1999.

Connerney, J. E. P., M. H. Acuña, P. J. Wasilewski, *et al.*, The global magnetic field of Mars and implications for crustal evolution, *Geophys. Res. Lett.* **28**, 4015–18, 2001.

Connerney, J. E. P., M. H. Acuña, N. F. Ness, T. Spohn, and G. Schubert, Mars crustal magnetism, *Space Sci. Rev.* **111**(1–2), 1–32, 2004.

Connerney, J. E. P., M. H. Acuña, N. F. Ness, *et al.*, Tectonic implications of Mars crustal magnetism, *Proc. Nat. Acad. Sci.* **102**(42), 14970–5, doi:10.1073/pnas.0507469102, 2005.

Curtis, S. A. and N. F. Ness, Remanent magnetism at Mars, *Geophys. Res. Lett.* **15**, 737, 1988.

Dekkers, M. J., Magnetic properties of natural pyrrhotite. II. High- and low-temperature behavior of Jrs and TRM as a function of grain size, *Phys. Earth Planet. Int.* **57**, 266–83, 1989.

Dekkers, M. J. and J. H. Linssen, Rockmagnetic properties of fine-grained natural low temperature haematite with reference to remanence acquisition mechanisms in red beds, *Geophys. J. Int.* **99**, 1–18, 1989.

Dolginov, Sh. Sh. and L. N. Zhuzgov, The magnetic field and magnetosphere of the planet Mars, *Planet. Space Sci.* **39**, 1493–510, 1991.

Dunlop, D. J. and K. S. Argyle, Thermoremanence and anhysteretic remanence of small multidomain magnetites, *J. Geophys. Res.*, **95**, 4561–77, 1990.

Dunlop, D. J. and Ö. Özdemir, *Rock Magnetism: Fundamentals and Frontiers*, Cambridge, UK: Cambridge University Press, 1997.

Ernst, R. E., E. B. Grosfils, and D. Mege, Giant dike swarms: Earth, Venus, and Mars, *Ann. Rev. Earth Planet. Sci.* **29**, 489–534, 2001.

Fairen, A. G., J. Ruiz, and F. Anguita, An origin for the linear magnetic anomalies on Mars through accretion of terranes: implications for dynamo timing, *Icarus* **160**, 220–3, 2002.

Frawley, J. J. and P. T. Taylor, Paleo-pole positions from martian magnetic anomaly data, *Icarus* **172**, 316–27, doi:10.1016/j.icarus.2004.07.025, 2004.

French, B. M., Stability relations of siderite ($FeCO_3$) in system Fe-C-O, *Am. J. Sci.* **271**, 37–78, 1971.

Frey, H., Impact constraints on the age and origin of the lowlands of Mars, *Geophys. Res. Lett.* **33**, L08S02, doi:10.129/2005GL024484, 2006a.

Frey, H., Impact constraints on, and a chronology for, major events in early Mars history, *J. Geophys. Res.* **111**, E08S91, doi:10.1029/2005JE002449, 2006b.

Frey, H. and R. A. Schultz, Large impact basins and the mega-impact origin for the crustal dichotomy on Mars, *Geophys. Res. Lett.* **15**, 229–32, 1988.

Frost, B. R., Stability of oxide minerals in metamorphic rocks. In *Oxides Minerals: Petrologic and Magnetic Significance* (ed. D. H. Lindsley), Blacksburg: Mineralogical Society of America, pp. 490–509, 1991.

Geissman, J. W., S. S. Harlan, and A. J. Brearley, The physical isolation and identification of carriers of geologically stable remanent magnetization: paleomagnetic and rock magnetic microanalysis and electron-microscopy, *Geophys. Res. Lett.* **15**, 479–82, 1988.

Gilder, S. A., M. LeGoff, J. Peyronneau, and J. Chervin, Novel high pressure magnetic measurements with application to magnetite, *Geophys. Res. Lett.* **29**(10), doi:10.1029/2001GL014227, 2002.

Goetz, W., P. Bertelsen, C. S. Binau, *et al.*, Chemistry and mineralogy of atmospheric dust at Gusev crater: indication of dryer periods on Mars, *Nature* **436**, 62–5, 2005.

Golden, D. C., D. W. Ming, C. S. Schwandt, *et al.*, A simple inorganic process for formation of carbonates, magnetite, and sulfides, in Martian Meteroite ALH84001, *Am. Mineral.* **86**, 370–5, 2001.

Greeley, R. and P. D. Spudis, Volcanism on Mars, *Rev. Geophys. Space Phys.* **19**(1), 13–41, 1981.

Gringauz, K. I., M. Verigin, J. Luhmann, C. T. Russell, and J. D. Mihalov, On the compressibility of the magnetic tails of Mars and Venus, *Plasma Environments of Non-magnetic Planets*, New York: Pergammon, pp. 265–70, 1993.

Halekas, J. S., D. L. Mitchell, R. P. Lin, *et al.*, Demagnetization signatures of lunar impact craters, *Geophys. Res. Lett.* **29**(13), 1645, 2002.

Hargraves, R. B., D. W. Collinson, R. E. Arvidson, and C. R. Spitzer, The Viking magnetic properties experiment: primary mission results, *J. Geophys. Res.* **82**, 4547–58, 1977.

Harrison, K. P. and R. E. Grimm, Controls on martian hydrothermal systems: application to valley network and magnetic anomaly formation, *J. Geophys. Res. – Planets* **107**(E5), art. no. 5025, 2002.

Hartmann, W. and G. Neukum, Chronology and evolution of Mars, *Space Sci. Rev.* **96**, 165–94, 2001.

Hartstra, R. L., Some rock magnetic parameters for natural iron-titanium oxides, Doctoral thesis, State University of Utrecht, 145pp., 1982.

Hauck, S. A. and R. J. Phillips, Thermal and crustal evolution of Mars, *J. Geophys. Res.* **107**(E7), doi:10.1029/2001JE001801, 2002.

Head III, J. W., M. A. Kreslavsky, and S. Pratt, Northern lowlands of Mars: evidence for widespread volcanic flooding and tectonic deformation in the Hesperian period, *J. Geophys. Res.* **107** (cite ID 5003), doi:10.1029/2000JE001445, 2002.

Hood, L. L. and A. Zakharian, Mapping and modeling of magnetic anomalies in the northern polar region of Mars, *J. Geophys. Res.* **106**, 14601–19, 2001.

Hood, L. L., N. C. Richmond, E. Pierazzo, and P. Rochette, Distribution of crustal magnetic anomalies on Mars: shock effects of basin-forming impacts, *Geophys. Res. Lett.* **30**(6), doi:10.1029/2002GL016657, 2003.

Hood, L. L., C. N. Young, N. C. Richmond, and K. P. Harrison, Modeling of major martian magnetic anomalies: further evidence for polar reorientations during the Noachian, *Icarus* **177**(1): 144–73, 2005.

Hunt, C. P., B. M. Moskowitz, and S. K. Banerjee, Magnetic properties of rocks and minerals. In *Rock Physics and Phase Relations: A Handbook of Physical Constants*, American Geophysical Union, pp. 189–203, 1995.

Jacquemont, B., *Etude des interactions eaux-roches dans le granite de Soultz-sous-Forêts. Quantification et modélisation des transferts de matière par les fluides*. Strasbourg: Université Luis Pasteur, 2002.

Just, J. and A. Kontny, The influence of hydrothermal activity on rock magnetic properties of granites from the EPS-1 drilling (Soultz-sous-Forêts, France), *European Geophysical Society Scientific Program*, EGS-A-04733, 2002.

Kletetschka, G., Intense remanence of hematite-ilmenite solid solution, *Geologica Carpathica* **51**(3), 187–187, 2000.

Kletetschka, G. and P. J. Wasilewski, Grain size limit for SD hematite, *Phys. Earth Planet. Inter.* **129**(1–2), 173–9, 2002.

Kletetschka, G. and J. H. Stout, The origin of magnetic anomalies in lower crustal rocks, Labrador, *Geophys. Res. Lett.* **25**(2), 199–202, 1998.

Kletetschka, G., P. J. Wasilewski, and P. T. Taylor, Hematite vs. magnetite as the signature for planetary magnetic anomalies?, *Phys. Earth Planet. Inter.* **119**(3–4), 259–67, 2000a.

Kletetschka, G., P. J. Wasilewski, and P. T. Taylor, Mineralogy of the sources for magnetic anomalies on Mars, *Meteorit. Planet. Sci.* **35**(5), 895–9, 2000b.

Kletetschka, G., P. J. Wasilewski, and P. T. Taylor, Unique thermoremanent magnetization of multidomain sized hematite: implications for magnetic anomalies, *Earth Planet. Sci. Lett.* **176**(3–4), 469–79, 2000c.

Kletetschka, G., P. J. Wasilewski, and P. T. Taylor, The role of hematite–ilmenite solid solution in the production of magnetic anomalies in ground and satellite based data, *Tectonophysics* **347**(1–3), 166–77, 2002.

Kletetschka, G., N. F. Ness, P. J. Wasilewski, J. E. P. Connerney, and M. H. Acuña, Possible mineral sources of magnetic anomalies on Mars, *The Leading Edge* **22**(8), 766–8, 2003.

Kletetschka, G., M. H. Acuña, T. Kohout, P. J. Wasilewski, and J. E. P. Connerney, An empirical scaling law for acquisition of thermoremanent magnetization, *Earth Planet. Sci. Lett.* **226**(3–4), 521–8, 2004a.

Kletetschka, G., J. E. P. Connerney, N. F. Ness, and M. H. Acuña, Pressure effects on martian crustal magnetization near large impact basins, *Meteorit. Planet. Sci.* **39**(11), 1839–48, 2004b.

Kletetschka, G., N. F. Ness, J. E. P. Connerney, M. H. Acuña, and P. J. Wasilewski, Grain size dependent potential for self generation of magnetic anomalies on Mars via thermoremanent magnetic acquisition and magnetic interaction of hematite and magnetite, *Phys. Earth Planet. Inter.* **148**(2–4), 149–56, 2005.

Kontny, A., A. B. Woodland, and M. Koch, Temperature-dependent magnetic susceptibility behaviour of spinelloid and spinel solid solutions in the systems Fe_2SiO_4-Fe_3O_4 and $(Fe, Mg)_2SiO_4$-Fe_3O_4, *Phys. Chem. Miner.* **31**(1), 28–40, 2004.

Kumar, A. and M. S. Bhalla, Source of stable remanence in chromite ores, *Geophys. Res. Lett.* **11**(3), 177–80, 1984.

Langlais, B., M. E. Purucker, and M. Mandea, Crustal magnetic field of Mars, *J. Geophys. Res.* **109**, E02008, doi:10.1029/2003JE002048, 2004.

Leweling, M. and T. Spohn, Mars: a magnetic field due to thermoremanence?, *Planet. Space Sci.* **45**, 1389–400, 1997.

Lillis, R. J., D. L. Mitchell, R. P. Lin, J. E. P. Connerney, and M. H. Acuña, Mapping crustal magnetic fields at Mars using electron reflectometry, *Geophys. Res. Lett.* **31**, l15702, doi:10.1029/2004gl020189, 2004.

Luhmann, J. G., The solar wind interaction with Venus and Mars: cometary analogies and contrasts, *Geophys. Monog. Ser.* **61**, 5, 1991.

Luhmann, J. G., R. E. Johnson, and M. H. G. Zhang, Evolutionary impact of sputtering of the martian atmosphere by O^+ pickup ions, *Geophys. Res. Lett.* **19**(21), 2151, 1992.

Madsen, M. B., S. F. Hviid, H. P. Gunnlaugsson, *et al.*, The magnetic properties experiments on Mars Pathfinder, *J. Geophys. Res. – Planets* **104**(E4), 8761–79, 1999.

Madsen, M. B., P. Bertelsen, W. Goetz, *et al.*, The magnetic properties experiments on the Mars Exploration Rover mission, *J. Geophys. Res.* **108**(E12), 8069, 2003.

McEnroe, S. A., R. J. Harrison, P. Robinson, U. Golla, and M. J. Jercinovic, Effect of fine-scale microstructures in titanohematite on the acquisition and stability of natural remanent magnetization in granulite facies metamorphic rocks, southwest Sweden: implication for crustal magnetism, *J. Geophys. Res.* **106**(B12), 30523–46, 2001a.

McEnroe, S. A., P. Robinson, and P. T. Panish, Aeromagnetic anomalies, magnetic petrology, and rock magnetism of hemo-ilmenite- and magnetite-rich cumulate rocks from the Sokndal Region, South Rogaland, Norway, *Am. Mineral.* **86**(11–12), 1447–68, 2001b.

McSween, H. Y., SNC meteorites: clues to Martian petrologic evolution, *Rev. Geophys.* **23**(4), 391–416, 1985.

Melosh, H. J., *Impact Cratering: A Geologic Process*, New York: Oxford University Press, p. 245, 1989.

Milkovich, S. M., J. W. Head, and S. Pratt, Meltback of Hesperian-aged ice-rich deposits near the south pole of Mars: evidence for drainage channels and lakes, *J. Geophys. Res. – Planets* **107**(E6), 2002.

Mitchell, D. L., R. P. Lin, C. Mazelle, *et al.*, Probing Mars' crustal magnetic field and ionosphere with the MGS Electron Reflectometer, *J. Geophys. Res.* **106**(E10), 23418–27, doi:10.1029/2000JE001435, 2001.

Mitchell, D. L., R. J. Lillis, R. P. Lin, J. E. P. Connerney, and M. H. Acuña, A global map of Mars' crustal magnetic field based on electron reflectometry, *J. Geophys. Res.* **112** (E01002), doi:10.1029/2005JE002564, 2007.

Mohit, P. S. and J. Arkani-Hamed, Impact demagnetization of the martian crust, *Icarus* **168**(2), 305–17, 2004.

Mohlmann, D., W. Riedler, J. Rustenbach, *et al.*, The question of an internal martian magnetic field, *Planet. Space Sci.* **39**, 83, 1991.

Nagata, T., Introductory notes on shock remanent magnetization and shock demagnetization of igneous rocks, *Pure Appl. Geophys.* **89**(6), 159–77, 1971.

Ness, N. F., The magnetic fields of Mercury, Mars and Moon, *Annu. Rev. Earth Planet Sci.* **7**, 248–88, 1979.

Ness, N. F., M. H. Acuña, J. Connerney, *et al*., MGS magnetic fields and electron reflectometer investigation: discovery of paleomagnetic fields due to crustal remanence, *Adv. Space Res*. **23**(11), 1879–86, 1999.

Nimmo, F., Dike intrusion as a possible cause of linear martian magnetic anomalies, *Geology* **28**, 391–4, 2000.

Nimmo, F. and M. S. Gilmore, Constraints on the depth of magnetized crust on Mars from impact craters, *J. Geophys. Res*. **106**, 12315–23, 2001.

Nimmo, F. and D. Stevenson, Influence of early plate tectonics on the thermal evolution and magnetic field of Mars, *J. Geophys. Res*. **105**, 11969–79, 2000.

Özdemir, Ö. and W. O'Reilly, An experimental study of thermoremanent magnetization acquired by synthetic monodomain titanomaghemites, *J. Geomag. Geoelec*. **34**, 467–78, 1982.

Parker, R. L., Ideal bodies for Mars magnetics, *J. Geophys. Res*. **108**(E1), 5006, doi:10.1029/2001JE001760, 2003.

Pilkington, M. and R. A. F. Grieve, The geophysical signature of terrestrial impact craters, *Rev. Geophys*. **30**(2), 161–81, 1992.

Pohl, J., U. Bleil, and U. Hornemann, Shock magnetization and demagnetization of basalt by transient stress up to 10 Kbar, *J. Geophys. – Zeitschrift Fur Geophysik* **41**(1), 23–41, 1975.

Purucker, M., D. Rauat, H. Frey, *et al*., An altitude-normalized magnetic map of Mars and its interpretation, *Geophys. Res. Lett*. **27**, 2449–52, 2000.

Riedler, W., D. Mohlmann, V. N. Oraeusky, *et al*., Magnetic fields near Mars: first results, *Nature* **341**, 604–7, 1989.

Robinson, P., R. J. Harrison, S. A. McEnroe, and R. B. Hargraves, Lamellar magnetism in the haematite-ilmenite series as an explanation for strong remanent magnetization, *Nature* **418**, 517–20, 2002.

Rochette, P., J. P. Lorand, G. Fillion, *et al*., Pyrrhotite and the remanent magnetization of SNC meteorites: a changing perspective on martian magnetism, *Earth Planet. Sci. Lett*. **190** (1–2), 1–12, 2001.

Rochette, P., G. Fillion, R. Ballou, *et al*., High pressure magnetic transition in pyrrhotite and impact demagnetization on Mars, *Geophys. Res. Lett*. **30**(13), 1683, doi:10.1029/2003GL017359, 2003a.

Rochette, P., G. Fillion, R. Ballou, *et al*., High pressure magnetic transition in monoclinic pyrrhotite, *Geophys. Res. Abs*. **30**, Abstract No. 01526, 2003b.

Rochette, P., J. Gattacceca, V. Cheurier, *et al*., Matching martian crustal magnetization and magnetic properties of martian meteorites, *Meteorit. Planet. Sci*. **40**, 529–40, 2005.

Russell, C. T., The magnetic field of Mars: Mars 3 evidence re-examined, *Geophys. Res. Lett*. **5**, 81–4, 1978a.

Russell, C. T., The magnetic field of Mars: Mars 5 evidence re-examined, *Geophys. Res. Lett*. **5**, 85–8, 1978b.

Schenk, P. M. and J. M. Moore, Stereo topography of the south polar region of Mars: volatile inventory and Mars Polar Lander landing site, *J. Geophys. Res. – Planets* **105**(E10), 24529–46, 2000.

Schubert, G. and T. Spohn, Thermal history of Mars and the sulfur content of its core, *J. Geophys. Res*. **95**, 14095–104, 1990.

Schubert, G., S. C. Solomon, D. L. Turcotte, M. J. Drake, and N. H. Sleep, Origin and thermal evolution of Mars. In *Mars* (ed. H. H. Kieffer, B. M. Jakosky, C. W. Snyder, and M. S. Matthews), Tucson, AZ: University of Arizona Press, pp. 147–83, 1992.

Schubert, G., C. T. Russell, and W. B. Moore, Geophysics: timing of the martian dynamo, *Nature* **408**, 666–7, 2000.

Scott, E. R. D. and M. Fuller, A possible source for the martian crustal magnetic field, *Earth Planet. Sci. Lett*. **220**, 83–90, 2004.

Slavin, J. A. and R. E. Holzer, The solar wind interaction with Mars revisited, *J. Geophys. Res*. **87**, 10285–96, 1982.

Slavin, J. A., K. Schwingenschuh, W. Riedler, and Y. Yeroshenko, The solar wind interaction with Mars: Mariner 4, Mars 2, Mars 3, Mars 5, and Phobos 2 observations of bow shock position and shape, *J. Geophys. Res*. **96**, 11235–41, 1991.

Sleep, N. H., Martian plate tectonics, *J. Geophys. Res*. **99**, 5639–55, 1994.

Smith, D. E., M. T. Zuber, S. C. Solomon, *et al*., The global topography of Mars and implications for surface evolution, *Science* **284**, 1495–503, 1999.

Smith, D. E., M. T. Zuber, and G. A. Neumann, Seasonal variations of snow depth on Mars, *Science* **294**(5549), 2141–6, 2001.

Smith, E. J., L. Davis Jr., P. J. Coleman, and D. E. Jones, Magnetic field measurements near Mars, *Science* **149**, 1241–2, 1965.

Spohn, T., Mantle differentiation and thermal evolution of Mars, Mercury, and Venus, *Icarus* **90**(2), 222–36, 1991.

Spohn, T., F. Sohl, and D. Breuer, Mars, *Astron. Astrophys. Rev*. **8**, 181–235, 1998.

Spohn, T., M. A. Acuña, D. Breuer, *et al*., Geophysical constraints on the evolution of Mars, *Space Sci. Rev*. **96**, 231–62, 2001.

Sprenke, K. F. and L. L. Baker, Magnetization, paleomagnetic poles, and polar wander on Mars, *Icarus* **147**, 26–34, 2000.

Squyres, S. W., J. P. Grotzinger, R. E. Arvidson, *et al*., In situ evidence for an ancient aqueous environment at Meridiani Planum, Mars, *Science* **306** (5702), 1709, 2004.

Stevenson, D. J., T. Spohn, and G. Schubert, Magnetism and thermal evolution of the terrestrial planets, *Icarus* **54**, 466–89, 1983.

Talwani, M., Computation with help of a digital computer of magnetic anomalies caused by bodies of arbitrary shape, *Geophysics* **30**, 797, 1965.

Tanaka, K. L. and D. H. Scott, *Geological Map of the Polar Regions of Mars*, Reston, VA: US Geological Survey, 1987.

Tanaka, K. L., R. Greeley, D. H. Scott, and J. E. Guest, New geologic map of Mars, *NASA Technical Memorandum* **88383**, 601–2, 1986.

Tucker, P. and W. O'Reilly, The laboratory simulation of deuteric oxidation of titanomagnetites: effect on magnetic properties and stability of thermoremanence, *Phys. Earth Planet. Int*. **23**, 112–33, 1980.

Uyeda, S., Thermo-remanent magnetism as medium of Paleomagnetism, with special reference to reverse thermo-remanent magnetism, *Jap. J. Geophys*., **2**, 1–23, 1958.

Vine, F. J. and D. H. Matthews, Magnetic anomalies over oceanic ridges, *Nature* **199**, 947–9, 1963.

Voorhies, C. V., T. J. Sabaka, and M. Purucker, On magnetic spectra of Earth and Mars, *J. Geophys. Res*. **107**(E6), doi:10.1029/2001JE001534, 2002.

Weiss, B. P., D. L. Shuster, and S. T. Stewart, Temperatures on Mars from $^{40}Ar/^{39}Ar$ thermochronology of ALH84001, *Earth Planet. Sci. Lett*. **201**, 465–72, 2002a.

Weiss, B. P., H. Vali, F. J. Baudenbacher, *et al*., Record of an ancient martian magnetic field in ALH84001. *Earth Planet. Sci. Lett*. **201**, 449–63, 2002b.

Weiss, B. P., H. Vali, F. J. Baudenbacher, *et al*., Records of an ancient martian magnetic field in ALH84001, *Earth Planet. Sci. Lett*. **201**(3–4), 449–63, 2002c.

Wilhelms, D. E. and S. W. Squyres, The martian hemispheric dichotomy may be due to a giant impact, *Nature* **309**, 138–40, 1984.

Wilson, J. R., B. Robins, F. M. Nielsen, J. C. Duchesne, and J. V. Auwera, The Bjerkreim-Sokndal Layered Intrusion, Southwest Norway. In *Layered Intrusions* (ed. R. G. Cawthorn), Amsterdam: Elsevier Science, pp. 231–55, 1996.

Wise, D. U., M. P. Golombek, and G. E. McGill, Tharsis province of Mars: geologic sequence, geometry, and a deformation mechanism, *Icarus* **38**, 456–72, 1979.

Yu, Y., D. J. Dunlop, Ö. Özdemir, *et al*., Magnetic properties of Kurokami pumices from Mt. Sakurajima, Japan, *Earth Planet. Sci. Lett*. **192**(3), 439–46, 2001.

Zuber, M. T., The crust and mantle of Mars, *Nature* **412**, 220–7, 2001.

Zuber, M. T., S. C. Solomon, R. J. Phillips, *et al*., Internal structure and early thermal evolution of Mars from Mars Global Surveyor topography and gravity, *Science* **287**, 1788–93, 2000.

PART III.C

Observations from Surface Landers/Rovers

12

Multispectral imaging from Mars Pathfinder

W. H. FARRAND, J. F. BELL III, J. R. JOHNSON,
J. L. BISHOP, AND R. V. MORRIS

ABSTRACT

The Imager for Mars Pathfinder (IMP) was a mast-mounted instrument on the Mars Pathfinder (MPF) lander which landed on Mars' Ares Vallis floodplain on July 4, 1997. During the 83 sols of MPF landed operations, the IMP collected over 16 600 images. Multispectral images were collected using 12 narrowband filters at wavelengths between 400 and 1000 nm in the visible and near-infrared (VNIR) range. The IMP provided VNIR spectra of the materials surrounding the lander including rocks, bright soils, dark soils, and atmospheric observations. During the primary mission, only a single primary rock spectral class, "Gray Rock," was recognized; since then, "Black Rock" has been identified. The Black Rock spectra have a stronger absorption at longer wavelengths than do Gray Rock spectra. A number of coated rocks have also been described, the Red and Maroon Rock classes, and perhaps indurated soils in the form of the Pink Rock class. A number of different soil types were also recognized with the primary ones being Bright Red Drift, Dark Soil, Brown Soil, and Disturbed Soil. Examination of spectral parameter plots indicated two trends which were interpreted as representing alteration products formed in at least two different environmental epochs of the Ares Vallis area. Subsequent analysis of the data and comparison with terrestrial analogs have supported the interpretation that the rock coatings provide evidence of earlier Martian environments. However, the presence of relatively uncoated examples of the Gray and Black Rock classes indicates that relatively unweathered materials can persist on the Martian surface.

12.1 INTRODUCTION

Between the success of the Viking landers in the late 1970s and the highly mobile Mars Exploration Rovers (MERs), *Spirit* and *Opportunity*, in the early 2000s, the MPF mission provided high quality VNIR (400–1000 nm) multispectral observations from a stationary platform and *in situ* rock and soil major element chemistry measurements from the spacecraft's Sojourner rover. The landing platform hosted the IMP stereo multispectral camera (Smith *et al*., 1997a) and the Sojourner rover was equipped with panchromatic wide-angle cameras and an Alpha Proton X-ray Spectrometer (APXS) (Rieder *et al*., 1997; Foley *et al*., 2003, see Chapter 3).

The targeted landing site for the MPF lander was chosen to satisfy engineering and safety constraints, such as being below 0 km elevation and having an acceptably flat surface with moderate rock abundance. It was also selected on the basis of its scientific interest as a floodplain site in Chryse Planitia that received effluent from the Ares, Simud, and Tiu Vallis outflow channels (Golombek *et al*., 1997a). These channels dissected Noachian-aged southern highlands and Hesperian-aged ridged plains and could have brought materials from these units into the landing ellipse. The floodplain that encompasses the landing site itself was mapped as Hesperian in age (Tanaka, 1997). Based on this geologic setting, a diversity of lithologies was expected at the landing site. Examination of Viking orbital color information prior to landing indicated that the landing site has a low red to violet ratio and an albedo intermediate between Martian bright and dark regions. Based on these color characteristics, it was expected that rock surfaces would be largely dust-free and unweathered (Golombek *et al*., 1997a). In postlanding studies, Wyatt *et al*. (2003) noted that the region is also intermediate between the basaltic "Surface Type 1" and, nominally, more andesitic and/or more weathered "Surface Type 2" spectral classes identified by the Mars Global Surveyor Thermal Emission Spectrometer (TES) (Bandfield *et al*., 2000; Wyatt and McSween, 2002; see also Chapter 9).

The spacecraft landed successfully on July 4, 1997, at approximately 19.13° N, 33.22° W. After landing, the MPF spacecraft was designated as the Sagan Memorial Station in honor of astronomer Carl Sagan. The spacecraft returned science data through 83 sols (a sol is a Martian day) of surface operations. It achieved its mission objectives both in terms of length of surface operations, collection of multispectral imagery, and *in situ* elemental analyses of rocks and soils by Sojourner's APXS instrument (Golombek *et al*., 1997b). The landscape observed by the IMP at the MPF landing site largely agreed with pre-landing expectations of a rock-strewn terrain, with drifts of bright eolian dust, linear dunes with darker surfaces, and scattered dark soils (Smith *et al*., 1997b). In its general appearance, the landscape was very similar to floodplains observed at the mouths of terrestrial examples of catastrophic flood channels (Golombek *et al*., 1999). While many of the rocks displayed surfaces coated with dust and/or indurated coatings, some rock faces and small cobbles appeared to be largely free of such coatings, allowing a more direct assessment of the primary rock mineralogy (e.g., McSween *et al*.,

The Martian Surface: Composition, Mineralogy, and Physical Properties, ed. J. F. Bell III. Published by Cambridge University Press.

1999; Morris *et al*., 2000; Murchie *et al*., 2000; Farrand *et al*., 2001; Bell *et al*., 2002).

The IMP was designed to accomplish a large number of tasks. These included VNIR multispectral measurements of rocks and soils in the vicinity of the lander, the collection of monochrome, color, and stereo panoramas of the landing site, observations of the lander's magnet experiment, imaging of the Sun in order to measure atmospheric opacity, general atmospheric observations documenting the presence or absence of clouds, observations of the lander's wind socks for wind characterization, and stereo range finding and morphologic studies of rocks and surface deposits (Smith *et al*., 1997a). The primary emphasis of this chapter is on IMP measurements of the multispectral reflectance properties of rocks and soils at the MPF landing site and on how the data have been used to provide key constraints on the mineralogy, origin, and evolution of the Ares Vallis region of Mars.

12.2 IMAGER FOR MARS PATHFINDER INSTRUMENT AND DATA

12.2.1 Rationale for multispectral remote sensing from Mars Pathfinder

The IMP built upon a heritage of VNIR remote sensing of the surface of Mars. Telescopic observations of Mars had been made in the same visible to near-infrared spectral range as well as at longer wavelengths (e.g., Singer *et al*., 1979; Singer, 1985; Chapter 2). These observations had revealed the strong influence of ferric iron absorptions in Martian bright region spectra, causing a steep absorption feature from the blue to red wavelengths with a relative reflectance maximum near 750 nm. This absorption edge was not as steep in the spectra of dark regions, and observations extending out to 2 μm and beyond indicated the presence of ferrous iron absorption bands which could be attributed to mafic silicate minerals such as pyroxene and potentially olivine (Roush *et al*., 1993). The Viking orbiters had provided three color information in the visible wavelengths (Klaasen *et al*., 1977) and the Viking landers had provided multispectral VNIR information (Huck *et al*., 1977). The IMP built on this heritage. Its multispectral capability was used to provide information on spectral parameters such as red/blue ratios which provide information on the relative level of oxidation of surface materials (recalling the steeper blue-to-red slope of Martian bright regions vis-à-vis those of the dark regions). Also, slope inflections in the blue to red region could also be used as a gauge of the relative level of oxidation of surface materials and this could be measured by the 530 nm band depth. The curvature of the spectrum in the 600 nm region could be indicative of the presence of other Fe^{3+}-bearing phases, such as goethite, which have a 660 nm absorption and thus the curvature can be assessed by the 600 nm band depth. Also, the presence of possible absorptions near 900 nm can be measured by calculation of the 900 nm band depth.

Table 12.1. *Band centers and full width half maximum (FWHM) bandwidths of the IMP multispectral filters. All values are in nanometers*

Left eye filters		Right eye filters	
Center	FWHM	Center	FWHM
443	26	443	26
671	20	480	27
802	21	531	30
858	34	600	21
898	41	671	20
931	27	752	19
968	31	967	30
1003	29		

12.2.2 IMP instrument characteristics

The IMP consisted of a mast-mounted CCD focal plane array with optics separated by 15 cm for stereoscopic imaging capability. It utilized a 512 × 512 CCD that was split in half to accommodate measurements from each "eye." Identical 248 × 256 pixel subarrays were allocated to each eye resulting in a 14.4° × 14.0° field of view. The optics' angular resolution of 1 mrad/pixel yielded a spatial resolution of approximately 1 mm/pixel to 1 cm/pixel for objects 1 to 10 m from the camera, respectively. Color information was provided in each eye by a filter wheel. Band centers and full width half maximum (FWHM) information for the resulting spectral channels are provided in Table 12.1. The 443 and 671 nm filters which are present in each eye provided blue and red stereo coverage, respectively. These two filters plus 10 more at 480, 531, 600, 752, 802, 858, 898, 931, 968, and 1003 nm constitute the 12 "geology bands" used for most multispectral assessments. Additional details about the IMP optics and electronics can be found in Smith *et al*. (1997a).

12.2.3 Data processing and calibration

The IMP was calibrated before launch with extensive characterization of its electronic and optical characteristics. The IMP data were calibrated based on preflight calibration coefficients and measurements made during surface operations of onboard calibration targets (Reid *et al*., 1999). The estimated radiometric accuracy of IMP data was >95% over all wavelengths (Reid *et al*., 1999). Calibration of the radiometric response of the IMP during surface operations was conducted using a calibration target consisting of three concentric rings of white, gray, and black (reflectance of approximately 0.05, 0.4, and 0.95), which were produced by embedding rutile and carbon black in varying percentages in a silicone matrix. Color targets were also provided to assess the IMP's spectral response. These consisted of chips with hematite (red), maghemite (brown), goethite (yellow), chrome dioxide (green), and cobalt (blue) pigments embedded in silicone. Surface measurements of the reflectance of the color chips provided excellent agreement with pre-flight measurements of their reflectance spectra (Reid *et al*., 1999).

Calibration during surface operations consisted of correction for instrumental sources of noise followed by comparison of the measured response from the gray level rings of the calibration target to the measured laboratory reflectance of the rings (Reid *et al*., 1999). Measurements of calibration target images acquired close in time to scene acquisition were used to convert the data at each band pass to apparent radiance factor. Radiance factor is defined by Hapke (1993, p. 262) as the ratio of the bidirectional reflectance of a surface to that of a perfectly diffuse surface illuminated at 0° incidence angle. As noted by Reid *et al*. (1999), the calculated radiance factor values did not strictly meet the Hapke (1993) definition of that quantity since the diffuse sky illumination was included in the calibration in addition to the direct solar illumination. Most of the work presented here utilized the quantity "relative reflectance" or R^*, which is the radiance factor divided by the cosine of the solar incidence angle (Reid *et al*., 1999; Bell *et al*., 2000). This is equivalent to the Hapke (1993) quantity of "reflectance factor," which is defined as the ratio of the reflectance of a surface to that of a perfectly diffuse surface under the same conditions of illumination and emittance angle. However, because different rock and soil surfaces in any measured scene are likely to deviate from the illumination and emission geometry of the calibration target, the values do not meet the strict Hapke (1993) definition of reflectance factor, thus the use of the term "relative reflectance."

12.2.4 Data collection

Over the course of the MPF mission, 16 661 images were returned from the IMP (Golombek *et al*.,1999). The types of data products are discussed next.

Panoramas

Five panoramas of landscape around the lander (Table 12.2) containing over 3500 component image frames were collected over the course of the MPF mission (Gaddis *et al*., 1999). On the first sol of the mission, before extension of the IMP's mast or deployment of the Sojourner rover, a partial "Mission Success" panorama in three right eye bands and one left eye band (for red stereo) was collected and transmitted to Earth with lossy compression. A losslessly compressed "Insurance" panorama was also acquired prior to mast deployment. The panorama was obtained with three right eye bands plus stereo coverage in blue filters (Herkenhoff *et al*., 2003). After mast deployment, the IMP acquired other panoramas with some gaps in spatial and spectral coverage, including the 3-color "Monster Pan" and "Gallery Pan" and the "Super Pan," which is a nearly comprehensive 360° view around the lander in all 12 geology filters, transmitted at an approximately 2:1 compression ratio (Gaddis *et al*., 1999). The Super Pan is composed of eight component octants, labeled S0181–S0188. Each octant is, in turn, composed of component segments. Because of the relatively small size of the IMP focal plane array, limited spacecraft memory, and limited downlink capacity, these component segments were collected piecemeal starting on sol 13 of the mission, with image acquisitions continuing until communication was lost with the spacecraft. The Super Pan was 83% complete at the time that communication was lost. Because of the long time of acquisition of the Super Pan, adjacent component segments were often collected under different solar and sky illumination conditions. Small amounts of airfall-deposited dust also accumulated on the IMP calibration target over the course of Super Pan acquisition, slightly affecting the resulting calibration to R^* (e.g., Johnson *et al*., 2003). A final version 3 calibration of the Super Pan image cube was carried out by Murchie *et al*. (2003) which included correction of registration errors and correlation of relative calibration for neighboring frames to the S0184 illumination conditions.

Multispectral spot collection

Over the course of the mission, 58 small spatial areas were imaged in all 12 geology filters in small 64 pixel × 64 pixel "multispectral spot" (MSS) observations. A full list of these observations was provided in Bell *et al*. (2000). The materials imaged in these MSS observations were characterized in terms of their overall 12 point spectra and in terms of spectral parameters derived from those spectra (Table 12.3). For convenience, we refer to the relative reflectance at a given wavelength as, for example, "R_{670}," for the R^* value at 670 nm. To be consistent, we

Table 12.2. *IMP Panoramas*

Pan name	Azimuthal coverage	Elevation coverage (# of tiers)	Bands used	Compression
Mission success	180° red stereo; 180° color	1	Right: 670, 530, 440 nm; Left: 670 nm	Lossy
Insurance	360°	3	Right: 750, 600, 530, 440 nm; Left: 440 nm	Lossless
Monster	360°	4	Right: 670 nm (all tiers), 930, 440 nm (middle two tiers); Left: 670 nm	Lossy
Gallery	360°	3	Right: 930, 670, 440 nm	Lossy
Super	360°	4	All geology filters	Lossless in red and blue stereo; lossy (2:1) in remaining bands

Table 12.3. *Relevant spectral parameters used in the characterization of IMP data that are referenced in this chapter*

Spectral parameter	Definition
Red/blue ratio	R_{670}/R_{440}
530 nm band depth	$1-[R_{530}/(0.609\times R_{440}+0.391\times R_{670})]$
600 nm band depth	$1-[R_{600}/(0.5\times R^{*}_{530}+0.5\times R_{670})]$
900 nm band depth	$1-[R_{900}/(0.5\times R_{800}+0.5\times R_{1000})]$

adopt this terminology in this chapter. More advanced processing techniques applied to the IMP multispectral data in more recent, postmission, studies are summarized below.

Other IMP observations

Other observations made by the IMP included atmospheric measurements (Smith and Lemmon, 1999 and references contained therein), wind sock observations (Sullivan *et al.*, 2000), astronomical observations (Murchie *et al.*, 1999; Thomas *et al.*, 1999), surface photometry observations (Johnson *et al.*, 1999), and observations of MPF's magnetic properties experiment (Madsen *et al.*, 1999).

12.3 IMP RESULTS

12.3.1 General results

As was noted above, the geologic setting observed by the IMP at the MPF landing site consisted of a rock-strewn landscape, with drifts of bright eolian dust, small linear eolian bedforms with darker surfaces, and scattered dark soils (Golombek *et al.*, 1999). Rocks observed by IMP exhibited red/blue color ratios consistent with varying degrees of dust coatings. Northeastern-facing rock surfaces often exhibited the lowest red/blue ratios and were thought to be the most dust-free because these rock surfaces face into the prevailing wind direction (McSween *et al.*, 1999). Downwind rock faces typically appeared dustier. The types of rock coatings observed by the IMP have since been used to draw inferences about past environments in the vicinity of the landing site (McSween *et al.*, 1999; Barnouin-Jha *et al.*, 2000; Bishop *et al.*, 2002).

12.3.2 Rocks

Gray Rock

Initial studies of rocks present at the MPF landing site (Smith *et al.*, 1997b; McSween *et al.*, 1999) described several spectral classes of rocks, some of which actually referred to rock coatings. Despite prelanding expectations that there might be an assemblage of different lithologies present at the landing site, the initial interpretation was that there was only a single spectral class that encompassed all those rock surfaces which were the least dusty. This was known as the

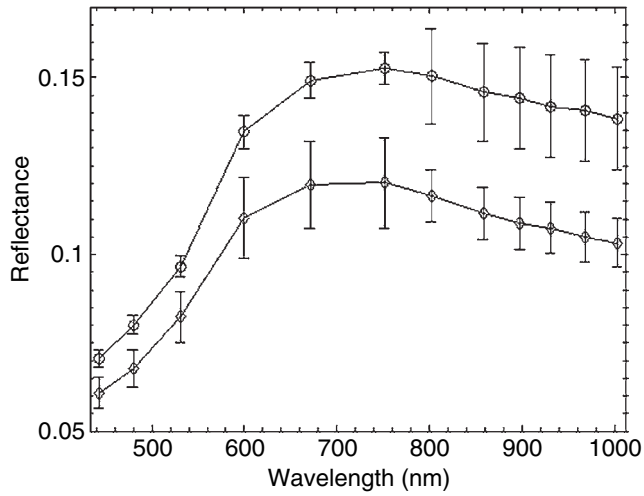

Figure 12.1. Example Gray Rock spectra averaged over tens of pixels from the rocks Shark (top) and rock in front of Moe (bottom). Error bars on this and subsequent spectral plots represent the standard deviation of the mean for the pixel spectra averaged.

"Gray Rock" spectral class. Brighter, presumably dustier coatings on downwind rock surfaces were characterized as "Red" and "Maroon" rock spectral classes. In addition, a "Pink" rock class was recognized which was characterized as either another form of coating or, quite possibly, an indurated soil (the Sojourner rover scuffed the surface of a Pink Rock and the results indicated that it was likely an indurated soil). In terms of Gray Rock's spectral properties, it was characterized by a low red/blue ratio and low 530 nm band depth. Both of these characteristics were interpreted as indicating the presence of predominantly ferrous iron mineral phases, based on previous multispectral image studies and laboratory analog investigations (e.g., Arvidson *et al.*, 1989; Bell *et al.*, 2000; Morris *et al.*, 2000). The peak reflectance in Gray Rock spectra is at 750 nm with a flat to negative sloping continuum at longer wavelengths. These spectral characteristics were interpreted as indicating either the lack of a mineral phase with an absorption in the 900–1000 nm range or the presence of a mineral phase whose band minimum occurs at, or longward of, the longest IMP band centered at 1003 nm. Named rocks representative of the Gray Rock spectral class were "Booboo," "Stimpy," and "Shark." Representative Gray Rock spectra are shown in Figure 12.1.

Morris *et al.* (2000) compared Gray Rock spectra to terrestrial analog materials and noted three possible explanations for the negative near-infrared (NIR) slope and lack of a well-defined long wavelength absorption. First, the rocks could contain high-Ca pyroxene and/or olivine, both of which have band minima at or beyond the IMP camera's sensitivity range near 1000 nm. Second, the rock surfaces could contain mechanical mixtures of nanophase ferric oxides in combination with a reflectance-lowering opaque phase such as magnetite (Morris and Neely, 1982). The third possibility was that the negative slope could be caused by a thin ferric oxide coating on a dark substrate (e.g., Fischer and Pieters, 1993; Johnson and Grundy, 2001). Murchie *et al.* (2003) suggested that Gray Rock might be a weathered basalt containing a significant fraction of

phyllosilicate minerals in its surficial weathering rind. This interpretation would mirror the interpretation by Wyatt and McSween (2002) of the so-called "Surface Type 2" lithology first identified by Bandfield *et al.* (2000) using data from the TES aboard Mars Global Surveyor. While Bandfield *et al.* (2000) had interpreted the Surface Type 2 spectrum as being caused by an andesitic lithology, Wyatt and McSween (2002) suggested that the spectrum is also consistent with a phyllosilicate-rich weathering rind on a more mafic basalt (although others have suggested alternative explanations; for example, Hamilton *et al.*, 2003). Phyllosilicates lack diagnostic spectral features in the wavelength range covered by IMP, thus they, possibly with accompanying opaque minerals, could act to mask a pyroxene band as was suggested by Murchie *et al.* (2003).

It has also been suggested from thermal infrared studies (Kraft *et al.*, 2003) that Gray Rocks' relatively high SiO_2 abundances may result from a coating of opaline silica. Such a silica coating could also mask a pyroxene absorption feature. Some dark-colored basaltic Hawaiian lava rocks with thin and shiny silica coatings exhibit reflectance maxima near 600–700 nm and negative NIR slopes; however, light-toned ceramic-like silica-coated Hawaiian rocks have a relative reflectance maximum at a shorter wavelength (near 600 nm; Bishop *et al.*, 2003b; Minitti *et al.*, 2002; Deal *et al.*, 2003), which is shorter than that observed in spectra of Gray Rocks.

Representative terrestrial analog spectra of several types of materials posited as being analogous to the Gray Rock surface are plotted in Figure 12.2. These include the clinopyroxenite SNC (SNC – Shergottite, Nakhlite, and Chassignite) meteorite Nakhla (Morris *et al.*, 2000), a silica coating (Bishop *et al.*, 2003a), and the <1 mm size fraction of palagonitic tephra HWHP 301 (Morris *et al.*, 2000). All of these materials have a negative slope in the NIR without a well-defined band minimum in the IMP wavelength range, but none, by themselves, represent an ideal match to the Gray Rock spectrum.

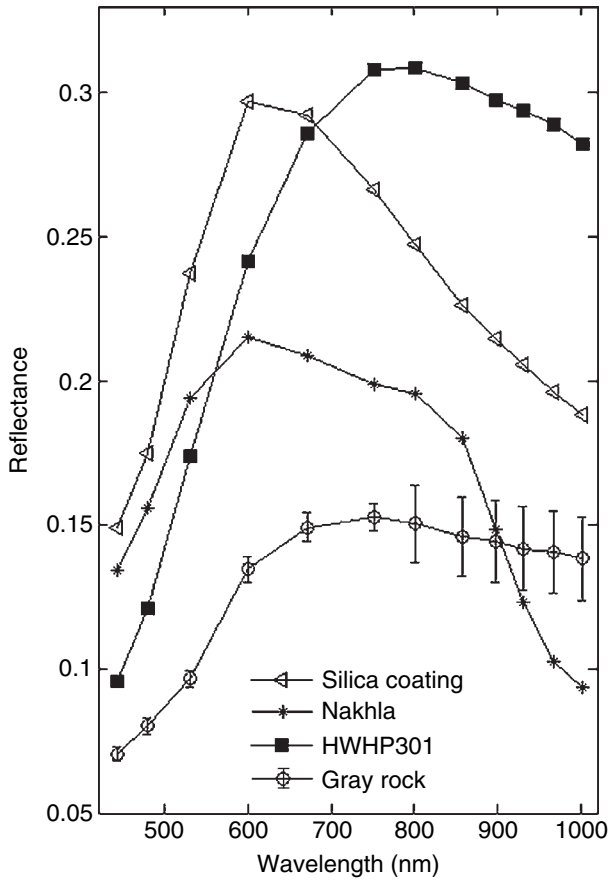

Figure 12.2. The IMP spectrum of the Gray Rock "Shark" compared against terrestrial analog materials which also display a negative NIR slope: a silica coating (Bishop *et al.*, 2003b), a palagonitic tephra, HWHP301 (Morris *et al.*, 2000), and the clinopyroxene-rich SNC meteorite Nakhla (Morris *et al.*, 2000).

Black Rock

Murchie *et al.* (2000) recognized several near-field examples of an additional rock spectral class that they named "Black Rock" and a single example of another rock spectral class referred to as "Orange Rock." Black Rock and Orange Rock spectra are shown in Figure 12.3. The Black Rock spectral class differs from the Gray Rock spectral class in that it has a relative reflectance maximum near 670 nm, versus Gray Rock's 750 nm reflectance peak, and a relatively strong long wavelength absorption band centered near 930 nm where the Gray Rock had a weak absorption at or longward of 1000 nm. Black Rock examples also have a very low red/blue ratio (<3.5). The Orange Rock spectrum has a 750 nm relative reflectance maximum and a long wavelength absorption band center near 900 nm. Murchie *et al.* (2000) posited that the Black Rock examples might contain more orthopyroxene or a combination of low-Ca clinopyroxene (possibly with olivine), or a ferric mineral in combination with a low-albedo lithology. Out of a set of SNC meteorite spectra,

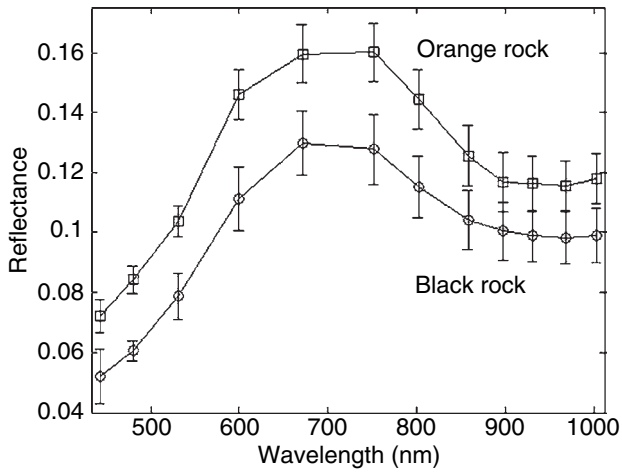

Figure 12.3. Orange and Black Rock spectra. Orange Rock spectrum from SuperPan octant S0188 referenced by Murchie *et al.* (2000). Black Rock spectrum from SuperPan octant S0184 (corresponds to Merényi *et al.* [2004] class O).

Wright *et al.* (2005) found the NIR Black Rock spectra to match well with that of the Dar al Gani (DaG) 735 meteorite. The DaG shergottites are mostly composed of pigeonite with a significant fraction (14%–20%) of Mg-rich olivine

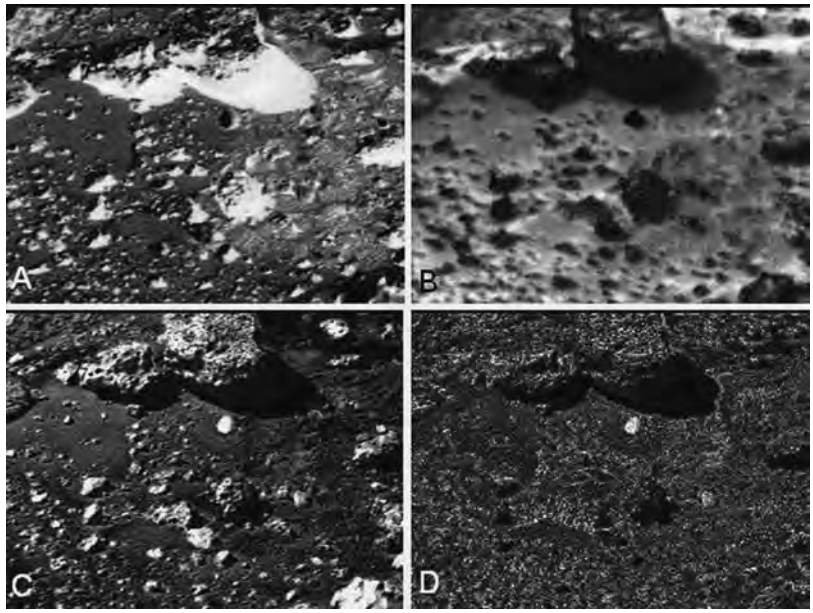

Figure 12.4. Fraction images and RMS error image from spectral mixture analysis of an MPF component left eye image segment from the S0185 SuperPan octant. (a)–(c) represent, respectively the shade, bright drift, and rock image endmembers. (d) is the RMS error image. The bright rock with the high RMS error image is a detection of the Black Rock spectral class.

megacrysts (Zipfel *et al*., 2000; Wadhwa *et al*., 2001). In contrast, the spectrum of Orange Rock is more consistent with a dust layer coating the rocks, as there is a maximum near 750 nm and a minimum near 920 nm, typical of many of the alteration materials suggested as constituents of coatings (e.g., McSween *et al*., 1999; Barnouin-Jha *et al*., 2000).

Spectrally distinct Black Rock spectral sub-classes were noted by Bell *et al*. (2002) and were detected through application of a spectral mixture analysis (SMA) methodology (e.g., Adams *et al*., 1986, 1993; Bell *et al*., 2002; Farrand *et al*., 2006). Spectral mixture analysis is an approach that models the measured signal from each spatial element as a linear combination of component "endmember" spectra. Only a small number of endmembers are needed to model each pixel spectrum and, by definition, the number of endmembers can be no more than one more than the number of image bands available. The relevant equation of SMA, in vector format is

$$R = a\mathbf{B} + e, \tag{12.1}$$

where R = the measured spectrum from the spatial element or pixel (in the Bell *et al*. (2002) study the values for each pixel were in R^*); $\boldsymbol{a}$ = a vector of fractions, one for each endmember used in the model; $\mathbf{B}$ = a matrix of endmember spectra; $\boldsymbol{e}$ = the vector of offset or residual values between the modeled, best-fit spectrum and the measured pixel spectrum. The end result of SMA is a series of "fraction" images, one for each endmember, and a root mean square (RMS) error image that encapsulates the error of the fit. The fraction images have values ideally between 0 and 1, where pixels with a value of 0 are devoid of the endmember material and pixels with a value of 1 are 100% filled with the endmember material. In the form of SMA applied in the Bell *et al*. (2002) study, the endmembers used were "image endmembers"; these are single pixel spectra or, more commonly, averages of a small number of pixel spectra that were taken to represent the best examples of each of the spectral endmembers. In the analysis of the Super Pan data, left and right eye data were analyzed separately and each image segment making up the Super Pan was analyzed individually. For both left and right eye data, there were generally three endmembers used: shade, bright dust, and rock. Shade is a non-material endmember that encompasses the effects of topographic shadowing and, to some extent, diffuse illumination, since shade pixels are extracted from the least illuminated, shadowed areas available in each scene. The residuals from each band can be captured in a single RMS error image which represents the goodness of fit of the modeled endmember to the data. Materials with spectra very different from those of the endmember spectra will have high RMS error values. Representative fraction images and an example of an RMS error image detection of a Black Rock occurrence are shown in Figure 12.4.

Larger (boulder-sized) occurrences of Black Rock in the far field of the Super Pan were noted by Murchie *et al*. (2003) and described in more detail by Farrand *et al*. (2004). Figure 12.5 shows examples of Black Rock boulders mapped by Farrand *et al*. (2004) through the application of a constrained energy minimization (CEM) (Farrand and Harsanyi, 1997) methodology. The CEM approach is related to the SMA approach in that it determines the fractional abundance of some endmember or target material. However, unlike SMA, not all endmember materials need be identified. Instead the scene is essentially decomposed in terms of a desired target spectrum and undesired background spectra. Pixels devoid of the target signature are constrained to be nulled to zero and those pixels that are identical to the target signature are constrained to equal one. Application of the CEM methodology in this instance was very useful, since the Black Rock occurrences represent an areally minor portion of the image scene and thus could not be well modeled as

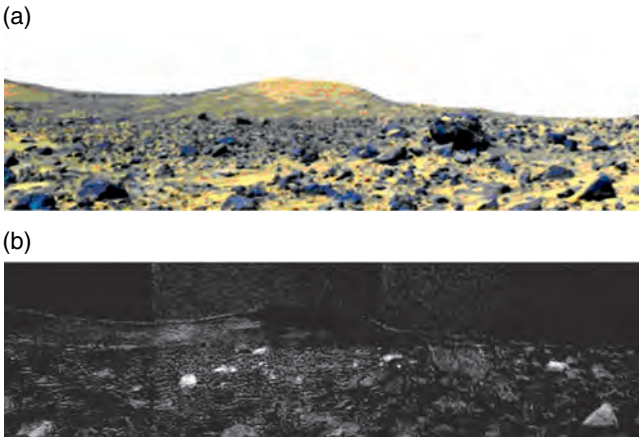

Figure 12.5. (a) 802, 671, and 443 nm composite of subset of octant S0183 centered on N. Twin Peak. (b) CEM fraction image highlighting occurences of Black Rock in far field of S0183 (see text). (For a color version of this figure, please refer to the color plate section or to the e-Book version of this chapter.)

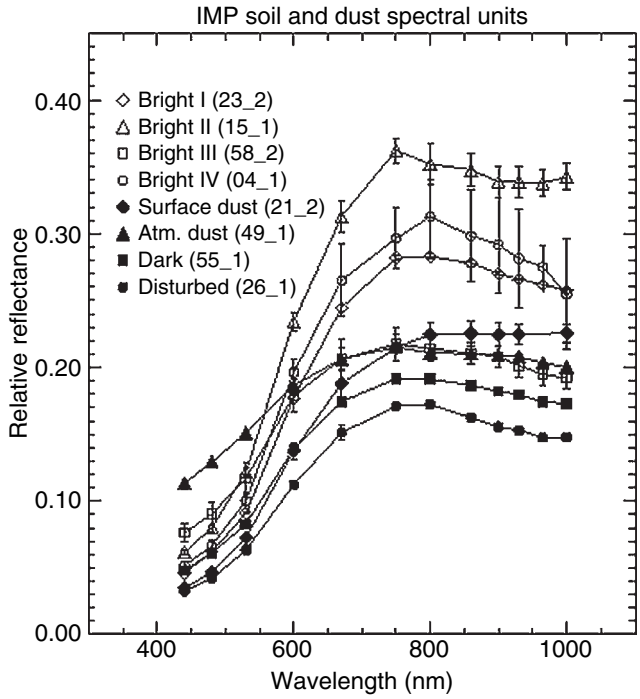

Figure 12.6. IMP soil and dust spectral units. (From Bell *et al.*, 2000.)

endmembers; that is, as materials that significantly contributed to the signal from pixels across the scene.

12.3.3 Soils

McSween *et al.* (1999) briefly discussed soils at the MPF landing site. Soils mentioned by these authors included "Bright Red Drift," which was characterized by a steep blue to red slope, a reflectance maximum at 750 nm and a lack of an NIR absorption feature. The other soil class mentioned by these authors was "Brown Soil" which has a lower albedo, a reflectance peak at 800 nm and a weak NIR absorption band. In the first comprehensive discussion of soil spectral properties at the MPF landing site, Bell *et al.* (2000) subdivided soils at the site into eight spectral classes. These classes were determined on the basis of partitioning clusters observed in 2D histograms of parameters derived from MSS observations. Spectra of these classes are shown in Figure 12.6. These classes include four different Bright Soil Classes: Surface Dust, Atmospheric Dust, Dark Soil, and Disturbed Soil.

The class with the widest spatial distribution and most closely linked to the McSween *et al.* (1999) "Bright Red Drift" is the "Bright I" class. It is characterized by a high red reflectance, a high red/blue ratio, and a flat to slightly negative NIR slope. Bright I soil spectra were interpreted as poorly crystalline Fe-rich dust and only minor amounts of mafic minerals. The "Bright II" class is somewhat less abundant, and is generally similar to the Bright I class except that it has a generally stronger long wavelength absorption between 800 and 1000 nm. The stronger NIR band in these soils was interpreted as indicating a greater abundance of crystalline ferric or ferrous minerals compared to Bright I soils. The "Bright III" and "Bright IV" classes are less abundant but are spectrally similar in that they have convex spectral shapes in the NIR with a relative reflectance maximum near 754 nm for the Bright III soils and near 800 nm for the Bright IV soils. Both Bright III and Bright IV soils were interpreted to consist of significant mafic minerals, perhaps mixed (Bright III) or coated (Bright IV) by Fe-rich dust or weathered coatings. The "Surface Dust" unit is also rare and is characterized by a positive slope from 800 to 1000 nm. This material was interpreted as almost "pure" nanophase ferric oxide dust, with no discernable mafic signature. The "Atmospheric Dust" unit is from a measurement of the sky, and exhibits a high blue reflectance and a low red/blue ratio, similar to the skylight spectrum described by Thomas *et al.* (1999). Like Surface Dust, Atmospheric Dust was not found to exhibit any discernable mafic spectral signature in IMP data.

The darker soil units described by Bell *et al.* (2000) were interpreted as being coarser-grained, compacted, and/or mixed with a larger amount of dark ferrous materials relative to bright materials. The set of dark soil units included "Dark Soil," and "Disturbed Soil." "Dark Soil" has a low reflectance in the red and NIR, a high reflectance in the blue (relative to the bright soil units described above), and a negative slope from 800 to 1000 nm. A NIR absorption feature is weak or absent. This material has been interpreted as being spectrally dominated at IMP wavelengths by coarser-grained ferric-rich material and perhaps a minor mafic component. The "Disturbed Soil" unit, exposed in places by the action of the rover wheels or lander airbags, is also low in its red and NIR reflectance but has a lower reflectance in the blue than does the "Dark Soil" unit. It also has a weak NIR absorption band. These characteristics lead to the interpretation of Disturbed Soil spectra as consistent with the presence of coarser-grained and/or more crystalline ferric or ferrous minerals compared to "normal" Bright I Soils and Dark

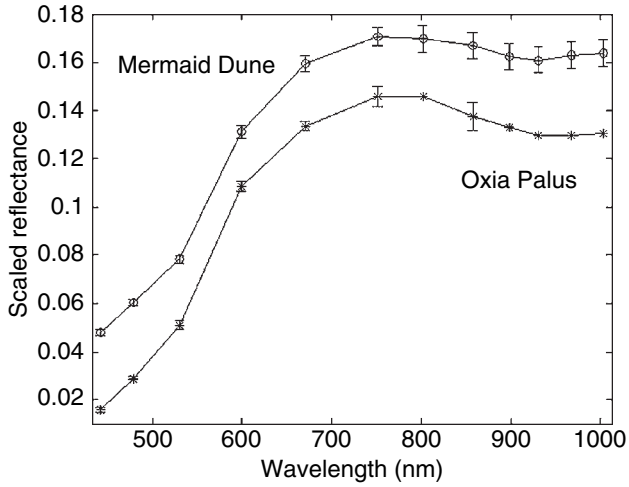

Figure 12.7. Comparison of Mermaid Dune spectrum to composite Oxia Palus spectrum. (From Morris *et al.*, 2000.)

Soils. The Disturbed Soil spectrum of Bell *et al.* (2000) is essentially the same as the Brown Soil noted by McSween *et al.* (1999) although occurences of Brown Soil include locations not disturbed by the lander airbags or rover activity.

Among the soils containing a discernable long wavelength absorption are dark soils coating linear aeolian bedforms such as "Mermaid" duneform. Morris *et al.* (2000) noted the similarity of the 930 band observed in spectra of Mermaid and related materials to that observed for the Oxia Palus region (Mustard *et al.*, 1997) and for orthopyroxene- and pigeonite-bearing SNC meteorite samples (Figure 12.7). This association suggested to Morris *et al.* (2000) that these soils might be spectrally dominated by low-Ca pyroxenes. Results from the Mars Express OMEGA (OMEGA – Observatoire pour la Minéralogie l'Eau les Glaces et l'Activité) imaging spectrometer have indicated higher fractions of low-Ca pyroxenes in the southern highlands of Mars (see Mustard *et al.*, 2005 and Chapter 7). Thus, it is possible that the materials coating Mermaid dune and similar features might be derived from rocks similar to those found in the southern highlands. The Sojourner rover lacked a microscopic imager to determine the grain size of the surface coating of aeolian bedforms such as Mermaid; however, Moore *et al.* (1999) suggested that the soils in Mermaid were poorly sorted mixtures that contained granules down to fine-grained dust. The examination of similar kinds of aeolian features by the *Spirit* rover (e.g., Greeley *et al.*, 2004; Farrand *et al.*, 2005) suggested that the Mermaid type of coating might similarly consist of an armoring of small basalt pebbles.

In SMA of component Super Pan scenes, Bell *et al.* (2002) noted that aprons of high relative fractional abundances of rock occurred in the soil around some rocks. These aprons were dubbed "Rock Soil" and were interpreted as the consequence of mechanical weathering of the rocks and the subsequent accumulation of small rock fragments in the soil nearby. This observation is consistent with an observation by Morris *et al.* (2000) that all the observed MPF soils have some contamination by ferrous oxide–rich rock

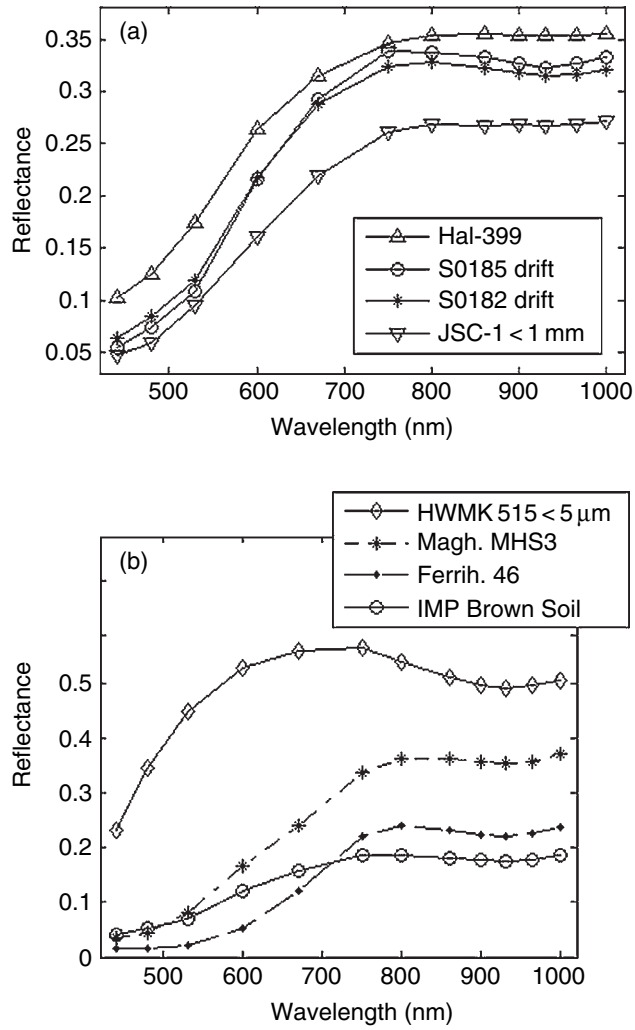

Figure 12.8. (a) Bright Drift spectra extracted from the S0182 and S0185 SuperPan octants compared with a Haleakala loose fines spectrum (Hal-399) and the JSC-1 Mars simulant (Allen *et al.*, 1998). (b) IMP Brown Soil spectrum from the S0186 SuperPan octant compared with terrestrial material that have a similar 930 nm band: a Mauna Kea jarositic tephra (the less than 5 µm fraction of HWMK 515; Morris *et al.*, 2000), a maghemite (MHS-3; Morris *et al.*, 2000), and a ferrihydrite (Ferrih. 46; Bishop *et al.*, 1998).

fragments and, likewise, that observed rocks were all contaminated by some ferric oxide–rich dust. These authors noted that MPF soils had R_{750}/R_{445} values >4.0 (average value of 5.7 ± 1.2) and rocks had R_{750}/R_{445} values <4.0 (average value of 2.9 ± 0.6). This red/blue ratio evidence is consistent with a highly oxidized, ferric iron–rich nature for the MPF soils and a more ferrous iron–rich nature for the MPF rocks. The contamination of rock surfaces by ferric oxide–rich dusts was illustrated by comparison to SNC meteorite samples, which do not display a significant ferric absorption edge and have a low R_{750}/R_{445} value of 1.3 ± 0.2 (Morris *et al.*, 2000).

Various terrestrial analogs and components have been proposed to account for the observed reflectance properties of soils observed by IMP. In Figure 12.8a, Bright Drift soil spectra from the S0182 and S0185 octants are compared with a soil from the summit of Haleakala volcano in Maui

(Hal-399; Bishop *et al.*, 2006) and the less than 1 mm fraction of the JSC-1 Mars analog spectrum (Allen *et al.*, 1998; Morris *et al.*, 2000). The spectrum of the altered Haleakala fines is about as bright as the Martian bright soils, but has less spectral character and similar behavior is observed in the JSC-1 spectrum. The Hal-399 sample is primarily composed of amorphous and poorly crystalline alteration products of volcanic glass and basaltic lava. Likewise, the JSC-1 sample is composed of ash particles with the majority of iron present as nanophase ferric oxides (Morris *et al.*, 2000). While the terrestrial analogs for the Bright Drift are fairly good matches, the nature of the Brown Soil material has more uncertainty. A number of materials with 930 nm band minima and band widths that resemble that in Brown Soil are shown in Figure 12.8b. These include a jarositic tephra from Mauna Kea (HWMK 515; Morris *et al.*, 2000), a maghemite sample (MHS-3; Morris *et al.*, 2000) and a ferrihydrite (Bishop *et al.*, 1998). The Brown Soil has been observed to have some spectral character in common with the "Maroon Rock" spectral class; the latter class and other rock coatings are discussed next.

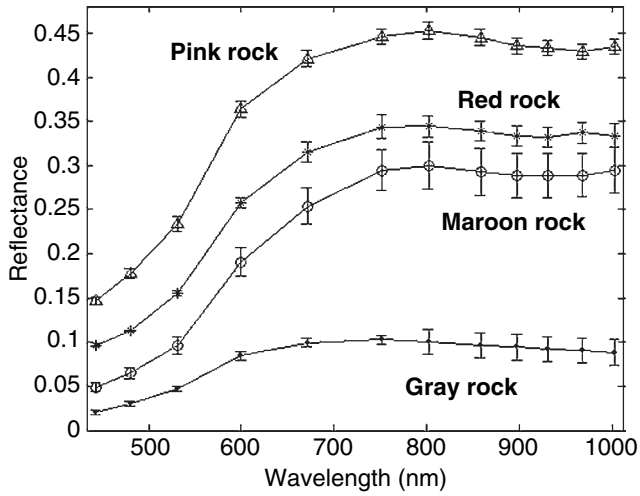

Figure 12.9. IMP spectra of Pink (Scooby Doo), Red (unnamed), Maroon, and Gray (Shark) Rock spectra. For purposes of clarity, Pink Rock has been offset upward by 0.05; Red Rock has been offset upward by 0.02; Gray Rock has been offset downward by 0.05.

12.3.4 Rock coatings

In addition to the Gray Rock spectral class, early studies of the IMP data noted additional classes of "Red Rock," "Maroon Rock," and "Pink Rock" (e.g., Smith *et al.*, 1997b; McSween *et al.*, 1999). The first two classes occur on rocks with "clean" Gray Rock faces and, thus, the "red" characteristics of these classes were interpreted as coatings (McSween *et al.*, 1999). Pink Rock was interpreted as either hardpan, encrusted drift materials, or indurated soil (McSween *et al.*, 1999; Moore *et al.*, 1999). Spectra of Maroon, Red, and Pink Rock examples are shown in Figure 12.9.

Red Rock surfaces have higher relative reflectance, higher red/blue ratios, and a stronger 530 nm band depth than Gray Rocks. Red Rocks have higher reflectances at short wavelengths than bright drifts and bright soils, but comparable reflectances and spectral properties in the NIR. Named rocks which have some surfaces with spectra representative of the Red Rock spectral class are "Half Dome," "Broken Wall," and "Wallace." Like the Red Rock faces, Maroon Rocks have high red/blue ratios and strong 535 nm band depths, but are lower in albedo than Red Rocks. Unlike Red Rocks and Gray Rocks, however, Maroon Rocks have a reflectance maximum at 800 nm and a weak absorption band at 900–930 nm. Named rocks representative of the Maroon Rock spectral class included the downwind side of "Yogi," "Flipper," and "Valentine." The type specimen for Pink Rock is the rock "Scooby Doo," which lies northeast of the MPF lander. While generally similar in spectral shape to bright drifts and soils, Pink Rocks have higher reflectance in all IMP bands. Pink Rocks can also be distinguished from bright drifts and soils by their higher reflectances at the shortest wavelengths.

Spectral parameter plots by McSween *et al.* (1999) revealed a primary and a secondary spectral trend between MPF rock classes. In Figure 12.10, 900 nm band depth versus red/blue ratio shows a primary trend of low red/blue ratio

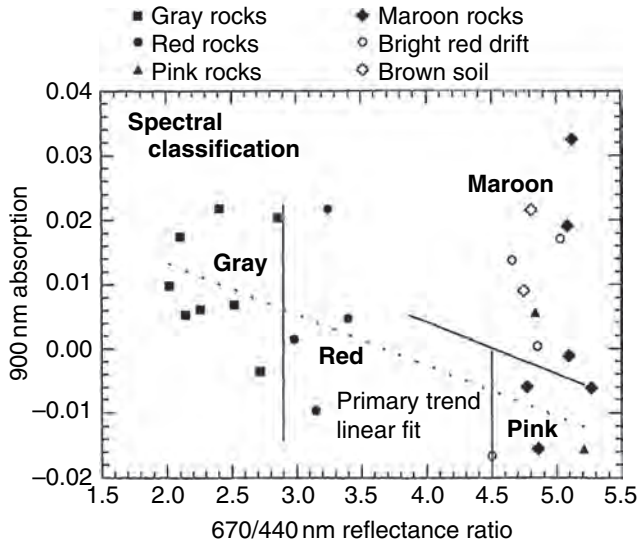

Figure 12.10. Spectral parameters used in the classification of Gray, Red, Maroon, and Pink Rock types. (Figure from McSween *et al.*, 1999.)

and high 900 nm band depth for Gray Rocks and Red Rock faces. A secondary trend, exhibiting a high red/blue ratio and low 900 nm band depth, was found for Pink Rocks, Maroon Rocks, and Brown Soils. The majority of rocks observed at the landing site follow the primary trend (McSween *et al.*, 1999). McSween *et al.* (1999) show additional spectral trends and interrelationships among rock classes in their plots of 900 nm band depth versus 530 nm band depth and of red/blue ratio versus 670 nm reflectance. The "primary trend" was interpreted as resulting from coatings of eolian dust on Gray Rock surfaces. The spectral behavior of the "secondary trend" materials has been interpreted by McSween *et al.* (1999) as resulting from the presence of a mineral phase not seen in the "primary trend" materials – possibly a ferrihydrite, maghemite, or composite

of ferric and ferrous phases such as those observed in impact melt rocks from Manicouagan crater (Morris *et al*., 1995).

A three-stage model was proposed by McSween *et al*. (1999) to explain the spectral classes of rocks and soils observed at the MPF landing site. In the first stage, an initial Brown Soil layer was overlain by large rocks which had, or in this stage developed, "Maroon" coatings. These rocks may have been from local volcanic sources, or may have been transported to the site during one of the catastrophic Ares Vallis flood events (e.g., Golombek *et al*., 1997a; Tanaka, 1997). In stage two, smaller, largely uncoated rocks and cobbles were emplaced, possibly as a result of impact events or mechanical weathering of larger, older rocks. During this stage, bright red drifts formed a relatively uniform surficial soil layer at the site. In stage three, the action of wind redistributed some of the red drift material into dunes and some of it coated rocks to form the Red Rock and possibly Pink Rock Classes. The wind action also partially removed the Maroon coatings, formed during the first stage, from the large rocks. This model accounts for the primary and secondary spectral trend differences of Red Rocks and Maroon Rocks by positing that the two different types of coatings, with different mineral constituents, were emplaced in different periods of time and, potentially, in different paleoenvironments.

The correlation of the spectral properties of coated rocks with APXS-determined chemistry was examined by Bridges *et al*. (2001), who found a roughly linear trend of red/blue ratio versus SO_3 for MPF rocks and soils. The reddest rock surface examined, A-7 on Yogi, had the most sulfur, and the bluest rock surface examined, A-17 (Shark) had the least sulfur. Because the sulfur content is assumed to be low in primary igneous rocks on Mars (e.g., McSween *et al*., 1999), this correlation was interpreted as being consistent with essentially all of the rock surfaces having varying degrees of "contamination" by ferric- and sulfur-bearing dust coverings and/or coatings. Barnouin-Jha *et al*. (2000) and Bridges *et al*. (2001) also noted that the rock surfaces facing toward the northeast, the direction from which the strongest winds originate, have lower red/blue ratios and, among those examined with the APXS, are lower in sulfur. These northeast-facing rocks were interpreted to have relatively thinner dusty/ferric coatings compared to other rocks. Observations by the MER *Spirit*'s APXS and Mössbauer spectrometers have shown that bright drift deposits at *Spirit*'s Gusev crater landing site have the most sulfur and Fe^{3+} of basaltic surface materials (Morris *et al*., 2006); thus the model of drift-coated rocks at the MPF site being more S-rich is a consistent observation.

Barnouin-Jha *et al*. (2000) noted that since the 530 nm band depth is lower for coated rocks than it is for bright drift with a comparable red/blue ratio, hematite might be more prevalent in the drifts and goethite might be more prevalent in the coated rocks with the strong 600 nm shoulder. Similarly, Murchie *et al*. (2001) interpreted the Maroon Rock coatings with the stronger 600 nm inflection as being bright red drift cemented to the rock surfaces with an additional ferric oxide phase, suggested to be goethite. However, neither the IMP nor other instruments on the MPF mission were able to provide definitive identification of specific ferric iron mineral phases.

Ward *et al*. (1999) and Murchie *et al*. (2001) categorized rocks at the landing site into shape classes (knobby, lobate, angular, equant, and tabular) and size classes (pebbles, cobbles, boulders). The knobby rocks were defined as rocks with rounded to angular protuberances and/or sockets. Lobate rocks were similar to the knobby rocks but with larger protuberances. Angular rocks had well-defined angular edges. Equant rocks were rounded to subangular. Tabular rocks were those with a high aspect ratio and a planar surface. Flat rocks were similar, but nearly buried. Pebbles were defined as those less than 6 cm in diameter and boulders were larger than surrounding rocks and sometimes elongated in shape. Cobbles are intermediate in size between pebbles and boulders and are usually, but not necessarily, rounded to subangular. Murchie *et al*. (2001) noted that tabular, angular, and equant rocks displayed a stronger 600 nm inflection than lobate and knobby rocks and pebbles. The latter were thus interpreted to be less coated. These authors also examined stratigraphic relations for these shape and size classes. Lobate, knobby, angular rocks, and pebbles were observed to lie on top of other rocks and to exhibit less of a 600 nm inflection, a lower red/blue ratio, and a lower 530 nm band depth than other rocks. All of this spectral evidence is consistent with these classes of rocks being the least coated among those studied at the MPF site. Murchie *et al*. (2001) concluded that tabular and angular rocks were emplaced first and developed coatings; lobate and knobby rocks were emplaced later, perhaps when the environment was not as conducive (drier, colder) to the formation of cementing mineral rock coatings. This model is consistent with the multistage model for coating and soil formation suggested by McSween *et al*. (1999).

A related model was developed by Bishop *et al*. (2002) using a combination of IMP spectral data, APXS chemical results, results from the MPF magnet experiment (Madsen *et al*., 1999), and laboratory studies of Martian analog materials to study the nature of the bright drifts, possibly cemented or indurated soils, and rock coatings observed at the MPF landing site. They suggested that mobile dust particles can account for the spectral and chemical properties of bright drifts observed at the MPF landing site and that this same dust, containing reactive sulfate and/or ferric oxyhydroxide phases, has also coated the rocks. Bishop *et al*. (2002) postulated that indurated soils and cemented coatings on rocks have formed in locations where these reactive components have interacted with soil or rock surfaces for the longest amount of time. In their model, iron oxyhydroxide minerals and sulfate salts, carried in the mobile dust, coat bare rock surfaces and form bonds (several types of bonds are possible: OH-cation, O-Si, or O-cation) with the rock surface to form an indurated coating. Chemical reaction or cementing of the dust/soil particles to the rock surfaces would also darken the spectra compared to rocks simply coated by a layer of dust/soil particles based on the results of lab experiments of cemented fines (Bishop *et al*., 2002). The laboratory samples prepared by Bishop *et al*. (2002) utilized mixtures of synthetic iron oxyhydroxide-montmorillonite

soils, natural sulfate-bearing volcanic soils, and hydrated magnesium sulfate in varying proportions. These mixtures had magnetic susceptibilities on the order of what was observed for the dust at the MPF site.

The spectral character of Maroon Rock resembles that of IMP soils and is believed to be a coating composed of soil-like materials. Like Brown Soil, the Maroon Rock spectral glass is a "secondary trend" material (McSween *et al.*, 1999) and could contain the same distinguishing mineralogic components discussed previously with regard to the nature of the secondary trend materials. The lower albedo of Maroon Rock spectra relative to that of Brown Soil could also be significant. As noted above, a chemically bound coating of volcanic fines would be expected to have a darker spectrum than that of the loose fines (Bishop *et al.*, 2002). Thus, the Maroon Rock spectrum is consistent with an optically thick coating of fines that has reacted with the rock surface to form a hardened coating akin to a desert varnish.

12.3.5 IMP photometric observations

As described in Chapter 19, the IMP was used during the MPF mission to acquire VNIR images of rocks and soils over a wide range of illumination geometries. Johnson *et al.* (1999) modeled these data using a Hapke radiative transfer model (Domingue *et al.*, 1997) to study the photometric and physical properties of materials at the landing site over phase angles from $\sim 0^\circ$ to $\sim 155^\circ$. Johnson *et al.* (1999) concluded that the photometric functions of the soils and dust-coated rocks were dominantly backscattering, with single-scattering albedos similar to those observed at the Viking Lander sites (e.g., Arvidson *et al.*, 1989; Guinness *et al.*, 1997). Mixture modeling using single-scattering albedos suggested that lighter-toned "Red" rock surfaces were a combination of dust, soil, and lower-albedo "Gray" rock types. This was consistent with the hypothesis noted previously that the Red Rock class represented Gray Rocks coated with dust and soil materials. The Gray Rocks also exhibited more forward-scattering signatures suggestive of surfaces more consistent with laboratory measurements of rough, clear spheres with few internal scatterers (McGuire and Hapke, 1995). This was consistent with qualitative comparisons of phase curves for the Gray Rocks, which indicated surfaces that were smooth on the centimeter to millimeter scale. The hypothesis advanced by Johnson *et al.* (1999) was that the surfaces of Gray Rocks were covered by a smooth coating similar to terrestrial varnished rock surfaces and/or a glassy rind. Bridges *et al.* (2001) noted that the forward scattering behavior of these rocks could also be consistent with an eolian polish on these rock surfaces. Ratios of reflectance spectra of the same rock surfaces acquired under different lighting conditions by Johnson *et al.* (1999) suggested that the major difference between spectra acquired at different times of day was in their overall reflectance values. However, subtle spectral differences at wavelengths <600 nm were thought to be the result of either residual atmospheric lighting effects or wavelength-dependent variations in the modeled photometric functions.

12.3.6 Classification of the IMP Super Pan

In order to obtain more comprehensive statistics on spectral classes contained in the IMP Super Pan and to search for potential new classes and obtain new perspectives on the distribution of known spectral classes, a number of octants in the Super Pan have been analyzed with a Self-Organizing Map (SOM) artificial neural network (ANN) classification approach (Farrand *et al.*, 2004, 2005; Merényi *et al.*, 2004). The ANN processing architecture used is a hybrid network, consisting of simple processing elements or neurons, structured into an input layer, an output layer, and one or more hidden layers, with each layer partially or fully connected to the next. The hidden layer in the architecture used by these workers was a two-dimensional SOM, modified from that originally developed by Kohonen (1997). The SOM hidden layer, whose function is clustering, was coupled with a categorization learning output layer, which was used to perform supervised classification. This approach for classification differs from previous studies which categorized the dataset in terms of spectral parameters (e.g., McSween *et al.*, 1999; Bell *et al.*, 2000) and those that had examined the spectral variability of the data through SMA (Bell *et al.*, 2002). Examination of spectral parameters was useful for relating the spectral properties of materials in the scene to known terrestrial analogs (e.g., Morris *et al.*, 2000) and determining spectral trends in the data (McSween *et al.*, 1999). Analysis through SMA was useful in determining the major and minor materials that contributed to the spectral variability of the dataset and for determining small-scale anomalous materials in the scene (such as the isolated occurrences of Black Rock). Application of the SOM ANN approach was used to produce class maps of the data where spectrally unique and mappable classes were determined and pixels in the Super Pan were assigned to these classes. This effort differs from previous studies in that, for example, examination of spectral parameter trends do not map out specific classes and the SMA fraction images map out only a small number of endmember classes. A larger number of classes with subtle spectral differences are mapped out in the SOM ANN classification. As noted earlier, such class maps can be used to gather improved statistics on major spectral surface units and to observe spatial trends in these classes.

Analysis of the S0184 octant (right eye class map shown in Figure 12.11) revealed several interesting trends, including the need for incorporating two Black Rock Classes to the models, each with distinct spectra. Several classes covered occurrences of Gray Rock as well; however, as noted above, there are several morphologic classes, each with the spectral designation of "Gray Rock." Several distinct soil classes were distinguished through the user-directed clustering approach. These included the broadly distributed bright red drift soils, the darker "rock soil" (Bell *et al.*, 2002), and other dark soils. Intriguingly, the classification hints at layering in the distant Twin Peaks. Figure 12.12b shows the left eye classification map that zooms in on South Twin Peak. There are three classes that are most abundant in the far field. Class M (purple) is associated with the top of North

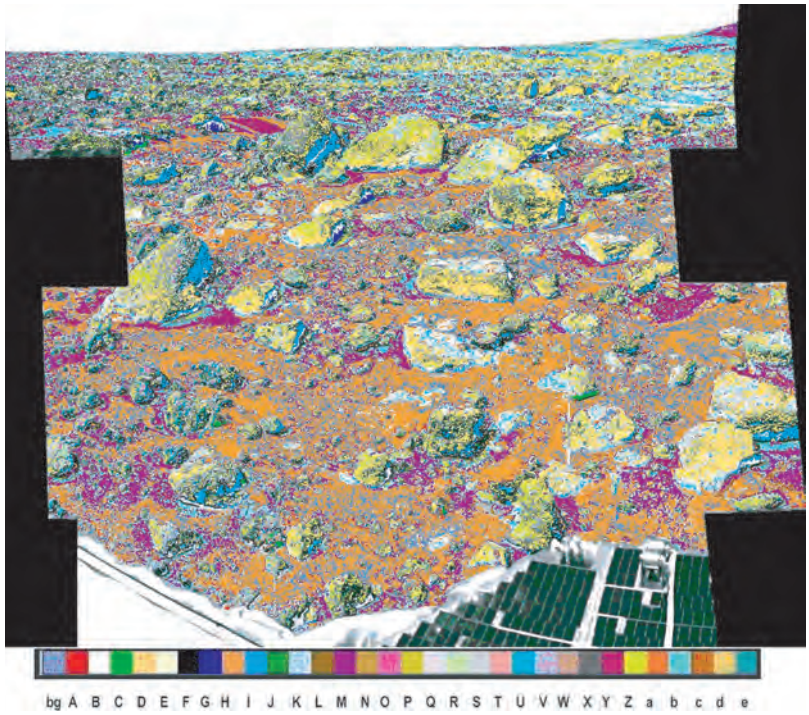

Figure 12.11. Classification map of the right-eye data from the S0184 octant of the SuperPan. Classification was obtained through application of the self-clustering approach of the SOM/ANN method described by Farrand *et al.* (2005) and Merényi *et al.* (2004). Color bar represents key to classes. (For a color version of this figure, please refer to the color plate section or to the e-Book version of this chapter.)

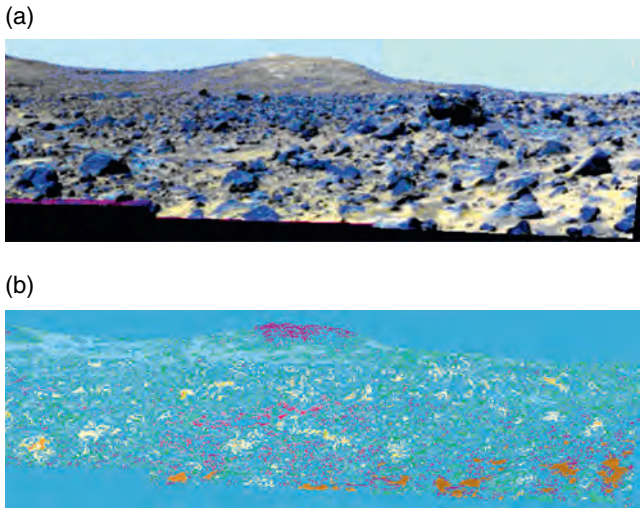

Figure 12.12. (a) Composite of left-eye bands 802, 671, and 443 nm for far field portion of octant S0183. (b) Class map for the far field of S0183 (left-eye data). Note the purple color (class M) associated with the top of North Twin Peak and prevalence of cyan colors of classes b and K in the far field. (For a color version of this figure, please refer to the color plate section or to the e-Book version of this chapter.)

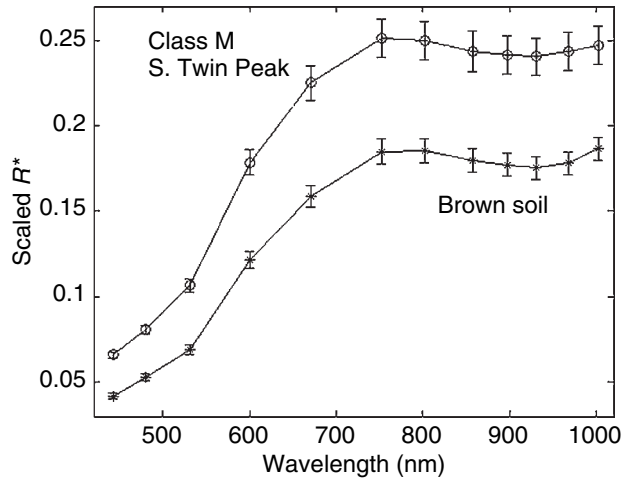

Figure 12.13. Comparison of the SOM/ANN class M spectrum averaged over the upper tiers of the Twin Peaks, compared to a near-field observation from the S0187 octant. Note similarity of the spectra in the 900–930 nm region and at the 530 nm kink and low curvature in the 600 nm region. The class M spectrum was offset upward by 0.05 for clarity.

and South Twin Peak and classes b (aquamarine) and K (cyan) cover much of the rest of the far field. Averages of these classes from the S0183 left scene indicate that class M has a shallow 900 nm absorption. Classes b and K are similar with b having a flatter NIR spectrum than K. In the near field, classes b and K can be associated with the "rock soil" class noted above and by Bell *et al.* (2002). The class M spectra, associated with the upper portion of the Twin Peaks, shares common spectral features with that of near-field examples of Brown Soil (Figure 12.13), with both having a pronounced kink at 530 nm and a broad long wavelength absorption centered at 930 nm. As was noted above, Brown Soil is a material on the "secondary" spectral trend along with Maroon Rocks, and these secondary trend materials have been suggested to contain a ferric-oxide phase absent from the "primary" trend materials. Possibilities include a ferrihydrite, maghemite, or hematite/pyroxene mixtures (McSween *et al.*, 1999) or goethite (Barnouin-Jha *et al.*, 2000; Murchie *et al.*, 2001). Thus, this distinguishing component from the secondary trend materials might also be a prominent constituent of the upper tiers of the Twin Peaks.

12.4 SUMMARY

The view that has emerged from analysis of the data provided by the MPF IMP and other MPF experiments is one of a field site generally similar to pre-landing expectations, but in detail consisting of unexpected features. Perhaps most important among the surprises was that the expectation that a "grab-bag" of rock types would be present was largely unfulfilled. All rocks examined by the APXS on board the Sojourner rover had similar chemical compositions, interpreted to be volcanic basalts or basaltic andesites (see Chapter 3). The IMP data were important in relating the spectral characteristics of the small number of rocks examined by the APXS to the vastly larger number of rocks observed at the site. Initial analysis of the IMP data indicated that all of the "cleanest" or minimally coated rock surfaces could be classified into a single "Gray Rock" spectral class. Gray Rocks all appear to have varying degrees of "contamination" by ferric oxide and sulfur-bearing dust coverings and/or coatings. Photometric models have suggested that the Gray Rock surfaces may have glassy rinds or eolian polished surfaces (Johnson *et al*., 1999; Bridges *et al*., 2001). However, postmission analysis of IMP Super Pan data (Murchie *et al*., 2000; Bell *et al*., 2002) revealed a small population of small rocks and rocky fragments/clasts (the "Black Rock" spectral class) that differ from the Gray Rock spectral class in that they exhibit a shorter wavelength relative reflectance maximum and a shorter wavelength NIR absorption band than the prevailing Gray Rock spectral class. These rare Black Rock materials may be endmembers that represent the least altered, least coated samples of "pristine" rock at the MPF site, or they could represent a distinct lithology transported to the field site by the catastrophic Ares Vallis flood. Unfortunately, the unique spectral character of these rocks was not recognized until after the mission had ended, and so they were never examined *in situ* by the APXS.

Soils at the landing site were originally classified in detail by Bell *et al*. (2000), but can be more generally grouped into 4 broad classes: Bright Red Drift, Brown Soil, Dark Soil, and Disturbed Soil. Analysis of the Bright Red Drift material by the APXS showed that it was chemically similar to the reddish drifts measured at the Viking landing sites (e.g., Clark *et al*., 1982), and it has since been shown to be chemically similar to the reddish drifts examined by the MERs (e.g., Rieder *et al*., 2004). IMP data indicated that this material lacked a well-defined absorption in the 900 nm region. However, Brown Soil, which was often associated with putatively indurated or more cohesive soil deposits (Bell *et al*., 2002), was observed to have a weak 900–930 nm absorption band. Some Dark Soil exposures, such as that seen on the eolian "Mermaid" duneform, were also observed to have a weak band with a 930 nm band minimum. The similarity between Dark Soil spectra and that of telescopic Martian dark region spectra such as Oxia Palus (e.g., Mustard and Bell, 1994) led Morris *et al*. (2000) to suggest that these Dark Soils might be spectrally dominated by low-Ca pyroxenes (orthopyroxene and/or pigeonite). By analogy with observation of similar bedforms studied by the *Spirit* rover, these could be surfaces armored by low-Ca, pyroxene-rich pebbles (e.g., Bell *et al*., 2004; Farrand *et al*., 2005). While the overall MPF landing site has been categorized as one that is of intermediate albedo and with characteristics intermediate between the TES Surface Type 1 and Surface Type 2 areas (Wyatt *et al*., 2003), the armored dune surfaces have spectral properties similar to larger dark regions to the south and thus provide some insight into what the nature of those larger dark regions might resemble. By analogy, larger dark regions could consist of broader expanses of coarse-grained basaltic clasts that form armored aeolian bedforms such as Mermaid. The Meridiani Planum dark region examined by the MER *Opportunity* has likewise been found to be a region with coarse-grained sands and armored duneforms (Soderblom *et al*., 2004; Squyres *et al*., 2004).

The MPF IMP results provide a view of a portion of the Martian surface directly affected by the catastrophic outflows that were important in shaping large expanses of Mars' northern hemisphere. The different types of rock coatings observed by the IMP can be explained in terms of there being environmentally distinct periods in Mars' past. The separation between the "primary" and "secondary" trend materials is indicative of different mineral constituents in each. This evidence, in combination with the observations that different shape classes of rocks have different spectral properties and that rocks with less of a 600 nm inflection are stratigraphically higher than those with more of a 600 nm inflection indicate that lobate and knobby rocks may have been emplaced later than tabular, angular, and equant rocks, and that the lack of a 600 nm inflection is consistent with a colder, drier climate less conducive to the formation of cementing mineral rock coatings. The presence of materials similar to the secondary trend materials on the upper tiers of the Twin Peaks might also indicate that the peaks represent older material. It can also be inferred that rocks that appear to have minimal to no coatings, primarily the Black Rock spectral class, have likely been in that type of state for some time. The persistence of such dry, dessicating conditions is consistent with observations by the MERs *Spirit* and *Opportunity* of abundant olivine and magnetite in the soils at both landing sites (Morris *et al*., 2004, 2006; Yen *et al*., 2005) and observations of crater degradation at the *Spirit* site that indicate low erosional rates (Golombek *et al*., 2006).

REFERENCES

Adams, J. B., M. O. Smith, and P. E. Johnson, Spectral mixture modeling: a new analysis of rock and soil types at the Viking Lander 1 site, *J. Geophys. Res.* **91** (B8), 8098–112, 1986.

Adams, J. B., M. O. Smith, and A. R. Gillespie, Imaging spectroscopy: interpretation based on spectral mixture analysis. In *Remote Geochemical Analysis: Elemental and Mineralogical Composition* (ed. C. M. Pieters and P. A. J. Englert), New York: Cambridge University Press, pp. 145–6, 1993.

Allen, C. C., R. V. Morris, K. M. Jager, *et al*., Martian regolith simulant JSC Mars-1, *Lunar Planet. Sci. Conf. XXIX*, Abstract #1690, 1998.

Arvidson, R. E., E. A. Guinness, M. A. Dale-Bannister, *et al.*, Nature and distribution of surficial deposits in Chryse Planitia and vicinity, Mars, *J. Geophys. Res.* **94**, 1573–87, 1989.

Bandfield, J. L., V. E. Hamilton, and P. R. Christensen, A global view of Martian surface compositions from MGS-TES, *Science* **287**, 1626–30, 2000.

Barnouin-Jha, O., S. Murchie, J. R. Johnson, J. F. Bell III, and R. V. Morris, Rock coatings at the Mars Pathfinder landing site, *Lunar Planet. Sci. XXXI*, Abstract #1267, 2000.

Bell III, J. F., H. Y. McSween Jr., S. L. Murchie, *et al.*, Mineralogic and compositional properties of Martian soil and dust: results from Mars Pathfinder, *J. Geophys. Res.* **105**, 1721–55, 2000.

Bell III, J. F., W. H. Farrand, J. R. Johnson, and R. V. Morris, Low abundance materials at the Mars Pathfinder landing site: an investigation using spectral mixture analysis and related techniques, *Icarus* **158**, 56–71, 2002.

Bell III, J. F., S. W. Squyres, R. E. Arvidson, *et al.*, Pancam multispectral imaging results from the Spirit rover at Gusev crater, *Science* **305**, 800–6, 2004.

Bishop, J. L., H. Froschl, and R. L. Mancinelli, Alteration processes in volcanic soils and identification of exobiologically important weathering products on Mars using remote sensing, *J. Geophys. Res.* **103**(31), 457–31, 456, 1998.

Bishop, J. L., A. Scheinost, J. F. Bell III, *et al.*, Ferrihydrite-Schwertmannite-Silicate mixtures as a model of Martian soils measured by Pathfinder, *Lunar Planet. Sci. 29th*, Abstract #1803, Lunar and Planetary Institute, Houston TX, 1998.

Bishop, J. L., S. L. Murchie, C. M. Pieters, and A. P. Zent, A model for formation of dust, soil, and rock coatings on Mars: physical and chemical processes on the Martian surface, *J. Geophys. Res.* **107**(E11), 5097, doi:10.1029/2001JE001581, 2002.

Bishop, J. L., M. Parente, and V. E. Hamilton, Identifying minerals on Mars through VNIR and mid-IR spectral deconvolution based on the Martian meteorites, *EOS Trans. AGU* **84**(46), Fall Meeting. Suppl., Abstract P21B-0045, 2003a.

Bishop, J. L., M. E. Minitti, M. D. Lane, and C. M. Weitz, The influence of glassy coatings on volcanic rocks from Mauna Iki, Hawaii and applications to rocks on Mars, *Lunar Planet. Sci. XXXIV*, Abstract #1516, 2003b.

Bishop, J. L., P. Schiffman, M. D. Dyar, *et al.*, Soil forming processes on Mars as determined by mineralogy: analysis of recent Martian spectral, chemical, and magnetic data and comparison with altered tephra from Haleakala, Maui, *Lunar Planet. Sci. XXXVII*, Abstract #1423, 2006.

Bridges, N. T., J. A. Crisp, and J. F. Bell III (2001) Characteristics of the Pathfinder APXS sites: implications for the composition of Martian rocks and soils, *J. Geophys.* **106**, 14621–66, 2001.

Clark, B. C., A. K. Baird, R. J. Weldon, *et al.*, Chemical composition of Martian fines, *J. Geophys. Res.* **87**, 10059–67, 1982.

Deal, K. S., R. E. Arvidson, and B. L. Jolliff, Remote mapping of the Ka'u Desert, Hawaii: silica in a Mars analog terrain, *Lunar Planet. Sci. XXXIV*, Abstract #1952, 2003.

Domingue, D., B. Harman, and A. Verbiscer, The scattering properties of natural terrestrial snows versus icy satellite surfaces, *Icarus* **128**, 28–48, 1997.

Farrand, W. H. and J. C. Harsanyi, Mapping the distribution of mine tailings in the Coeur d'Alene River Valley, Idaho through the use of a Constrained Energy Minimization technique, *Remote Sens. Environ.* **59**, 64–76, 1997.

Farrand, W. H., J. R. Johnson, and J. F. Bell III, N-Dimensional visualization and spectral mixture analysis applied to Imager for Mars Pathfinder data: detection and mapping of rocks and soils, *Lunar Planet. Sci. XXXII*, Abstract #1656, 2001.

Farrand, W. H., E. Merényi, S. Murchie, O. Barnouin-Jha, and J. Johnson, Mapping rock and soil units in the MPF Superpan using a Kohonen self-organizing map, *Lunar Planet. Sci. XXXV*, Abstract #1916, 2004.

Farrand, W. H., E. Merényi, S. Murchie, and O. S. Barnouin-Jha, Spectral class distinctions observed in the MPF IMP SuperPan using a self-organizing map, *Lunar Planet. Sci. XXXVI*, Abstract #2009, 2005.

Farrand, W. H., J. F. Bell III, J. R. Johnson, *et al.*, Spectral variability among rocks in visible and near infrared multispectral Pancam data collected at Gusev crater: examinations using spectral mixture analysis and related techniques, *J. Geophys. Res. – Planets* **111**, E02S15, doi:10.1029/2005JE002495, 2006.

Fischer, E. M., and C. M. Pieters, The continuum slope of Mars: Bi-directional reflectance investigations and applications to Olympus Mons, *Icarus* **102**, 185–202, 1993.

Foley, C. N., T. E. Economou, and R. N. Clayton, Final chemical results from the Mars Pathfinder alpha proton X-ray spectrometer, *J. Geophys. Res.* **108** (E12), doi:10.1029/2002JE002019, 2003.

Gaddis, L., R. Kirk, J. Johnson, *et al.*, Digital mapping of the Mars Pathfinder landing site: design, acquisition, and derivation of cartographic products for science applications, *J. Geophys. Res.* **104**, 8853–68, 1999.

Golombek, M. P., R. A. Cook, H. J. Moore, and T. J. Parker, Selection of the Mars Pathfinder landing site, *J. Geophys. Res.* **102**, 3967–88, 1997a.

Golombek, M. P., R. A. Cook, T. Economou, *et al.*, Overview of the Mars Pathfinder mission and assessment of landing site predictions, *Science* **278**, 1743–8, 1997b.

Golombek, M. P., H. J. Moore, A. F. C. Haldemann, T. J. Parker, and J. T. Schofield, Assessment of Mars Pathfinder landing site predictions, *J. Geophys. Res.* **104**, 8585–94, 1999.

Golombek, M. P., L. S. Crumpler, J. A. Grant, *et al.*, Geology of the Gusev cratered plains from the Spirit rover transverse, *J. Geophys. Res.* **111**, E02S07, doi:10.1029/2005JE002503, 2006.

Greeley, R., S. W. Squyres, R. E. Arvidson, *et al.*, Wind-Related Processes Detected by the Spirit Rover at Gusev crater, Mars, *Science* **305**, 810–21, 2004.

Guinness, E. A., R. E. Arvidson, I. H. D. Clark, and M. K. Shepard, Optical scattering properties of terrestrial varnished basalts compared with rocks and soils at the Viking Lander sites, *J. Geophys. Res.* **102**, 28687–703, 1997.

Hamilton, V. E., P. R. Christensen, and J. L. Bandfield, Volcanism or aqueous alteration on Mars? (Communication Arising), *Nature* **421**, 711–12, doi:10.1038/421711b, 2003.

Hapke, B., *Theory of Reflectance and Emittance Spectroscopy*, Cambridge University Press, 455pp., 1993.

Herkenhoff, K. E., J. R. Johnson, and L. A. Weller, The Imager for Mars Pathfinder Insurance Pan, *6th Int. Conf. Mars*, Abstract #3224, 2003.

Huck, F. O., D. J. Jobson, S. K. Park, *et al.*, Spectrophotometric and color estimates of the Viking lander sites, *J. Geophys. Res.* **82**, 4401–11, 1977.

Johnson, J. R. and W. M. Grundy, Visible/near-infrared spectra and two-layer modeling of palagonite-coated basalts, *Geophys. Res. Lett.* **28**, 2101–4, 2001.

Johnson, J. R., R. Kirk, L. A. Soderblom, *et al.*, Preliminary results on photometric properties of materials at the Sagan Memorial Station, Mars, *J. Geophys. Res.* **104**, 8809–30, 1999.

Johnson, J. R., W. M. Grundy, and M. T. Lemmon, Dust deposition at the Mars Pathfinder landing site: observations and

modeling of visible/near-infrared spectra, *Icarus* **163**, 330–46, 2003.

Klaasen, K. P., T. E. Thorpe, and L. A. Morabito, Inflight performance of the Viking visual imaging subsystem, *Appl. Opt*. **16**, 3158–70, 1977.

Kohonen, T., *Self-Organizing Maps*, in Springer Series in Information Sciences, vol. 30, Springer, Berlin, 1997.

Kraft, D., T. G. Sharp, and J. R. Michalski, Thermal emission spectra of silica-coated basalt and considerations for Martian surface morphology, *Lunar Planet. Sci. XXXIV*, Abstract #1420, 2003.

Madsen, M. B., S. F. Hviid, H. P. Gunnlaugsson, *et al*., The magnetic properties on Mars Pathfinder, *J. Geophys. Res*. **104**, 8761–94, 1999.

McGuire, A. F. and B. W. Hapke, An experimental study of light scattering by large, irregular particles, *Icarus* **113**, 134–55, 1995.

McSween Jr., H. Y., S. L. Murchie, J. A. Crisp, *et al*., Chemical, multispectral, and textural constraints on the composition and origin of rocks at the Mars Pathfinder landing site, *J. Geophys. Res*. **104**, 8679–716, 1999.

Merényi, E., A. Jain, and W. H. Farrand, Applications of SOM magnification to data mining. *WSEAS Trans. Syst*. **3**(5), 2122–8, 2004.

Minitti, M. E., J. F. Mustard, and M. J. Rutherford, Effects of glass content and oxidation on the spectra of SNC-like basalts: applications to Mars remote sensing, *J. Geophys. Res*. **107**(E5), doi:10.1029/2001JE001518, 2002.

Morris, R. V. and S. C. Neely, Optical properties of hematite-magnetite mixtures: implications for Mars, *Lunar Planet. Sci. XIII*, 548–9, 1982.

Moore, H. J., D. B. Bickler, J. A. Crisp, *et al*., Soil-like deposits observed by Sojourner, the Pathfinder rover, *J. Geophys. Res*. **104** (E4), 8729–46, 1999.

Morris, R. V., D. C. Golden, J. F. Bell III, and H. V. Lauer, Hematite, pyroxene, and phyllosilicates on Mars: implications from oxidized impact melt rocks from Manicouagan crater, Quebec, Canada, *J. Geophys. Res*. **100**, 5319–28, 1995.

Morris, R. V., D. C. Golden, J. F. Bell III, *et al*., Possible products of hydrolytic, hydrochloric, and sulfuric weathering at the Mars Pathfinder landing site: evidence from multispectral, elemental, and magnetic data on analogue and meteorite samples, *J. Geophys. Res*. **105**, 1757–817, 2000.

Morris, R. V., G. Klingelhöfer, B. Bernhardt, *et al*., Mössbauer mineralogy on Mars: first results from the *Spirit* landing site in Gusev crater, *Science* **305**, 833–6, 2004.

Morris, R. V., G. Klingelhöfer, C. Schröder, *et al*., Mössbauer mineralogy of rock, soil, and dust at Meridiani Planum, Mars: Opportunity's journey across sulfate-rich outcrop, basaltic sand and dust, and hematite lag deposits, *J. Geophys. Res*. **111**, E12S15, doi:10.1029/2006JE002791, 2006.

Murchie, S., N. Thomas, D. Britt, K. Herkenhoff, and J. F. Bell III, Mars Pathfinder spectral measurements of Phobos and Deimos: Comparisons with previous data, *J. Geophys. Res*. **104**, 9069–79, 1999.

Murchie, S., O. Barnouin-Jha, J. R. Johnson, *et al*., Diverse rock types at the Mars Pathfinder landing site, *Lunar Planet. Sci. XXXI*, Abstract #1267, 2000.

Murchie, S., O. Barnouin-Jha, J. Johnson, J. F. Bell III, and R. V. Morris, Spectral differences between shape classes of rocks at the Mars Pathfinder landing site, *Lunar Planet. Sci. XXXII*, Abstract #1825, 2001.

Murchie, S., O. Barnouin-Jha, K. Barnouin-Jha, *et al*., New insights into the geology of the Mars Pathfinder landing site from spectral and morphologic analysis of the 12-color Superpan panorama, *6th Int. Conf. Mars*, Abstract #3060, 2003.

Mustard, J. F. and J. F. Bell III, New composite reflectance spectra of Mars from 0.4 to 3.14 μm, *Geophys. Res. Lett*. **21**, 353–6, 1994.

Mustard, J. F., S. Murchie, S. Erard, and J. Sunshine, In situ compositions of Martian volcanics: implications for the mantle, *J. Geophys. Res*. **102**, 25605–15, 1997.

Mustard, J. F., F. Poulet, A. Gendrin, *et al*., Olivine and pyroxene diversity in the crust of Mars, *Science* **307**, 1594–7, 2005.

Reid, R. J., P. H. Smith, M. Lemmon, *et al*., Imager for Mars Pathfinder (IMP) image calibration. *J. Geophys. Res*. **104**, 8907–26, 1999.

Rieder, R., T. Economou, H. Wänke, *et al*., The chemical composition of martian soil and rocks returned by the mobile alpha proton X-ray spectrometer: preliminary results from the X-ray mode, *Science* **278**, 1771–4, 1997.

Rieder, R., R. Gellert, R. C. Anderson, *et al*., Chemistry of rocks and soils at Meridiani Planum from the Alpha Particle X-ray Spectrometer, *Science* **306**, 1746–9, 2004.

Roush, T. L., D. L. Blaney, and R. B. Singer, The surface composition of Mars as inferred from spectroscopic observations. In *Remote Geochemical Analysis: Elemental and Mineralogical Composition* (ed. C. M. Pieters and P. A. J. Englert), New York: Cambridge University Press, pp. 367–93, 1993.

Singer, R. B., Spectroscopic observations of Mars, *Adv. Space Res*. **5**, 59–68, 1985.

Singer, R. B., T. B. McCord, R. N. Clark, J. B. Adams, and R. L. Huguenin, Mars surface composition from reflectance spectroscopy: a summary. *J. Geophys. Res*. **84**, 8415–26, 1979.

Smith, P. H., M. G. Tomasko, D. Britt, *et al*., The Imager for Mars Pathfinder experiment, *J. Geophys. Res*. **102**, 4003–25, 1997a.

Smith, P. H., J. F. Bell III, N. T. Bridges, *et al*., Results from the Mars Pathfinder camera, *Science* **278**, 1758–65, 1997b.

Smith, P. H. and M. Lemmon, Opacity of the Martian atmosphere measured by the Imager for Mars Pathfinder, *J. Geophy. Res*. **104**, 8975–86, 1999.

Soderblom, L. A., R. C. Anderson, R. E. Arvidson, *et al*., Soils of Eagle crater and Meridiani Planum at the Opportunity landing site, *Science* **306**, 1723–6, 2004.

Squyres, S. W., R. E. Arvidson, J. F. Bell III, *et al*., The Opportunity Rover's Athena science investigation at Meridiani Planum, Mars, *Science* **306**, 1698–702, 2004.

Sullivan, R., R. Greeley, M. Kraft, *et al*., Results of the Imager for Mars Pathfinder windsock experiment, *J. Geophys. Res*. **105**, 24547–62, 2000.

Tanaka, K. L., Sedimentary history and mass flow structures of Chryse and Acidalia Planitiae, Mars, *J. Geophys. Res*. **102**, 4131–50, 1997.

Thomas, N., W. J. Markiewicz, R. M. Sablotny, *et al*., The color of the Martian sky and its influence on the illumination of the Martian surface, *J. Geophys. Res*. **104**, 8795–808, 1999.

Wadhwa, M., R. C. F. Lentz, H. Y. McSween Jr., and G. Crozaz, A petrologic and trace element study of Dar al Gani 476 and 489: twin meteorites with affinities to basaltic and lherzolitic shergottites, *Meteorit. Planet. Sci*. **36**, 195–208, 2001.

Ward, A., L. R. Gaddis, R. L. Kirk, *et al*., General geology and morphology of the Mars Pathfinder landing site, *J. Geophys. Res*. **104**, 8555–72, 1999.

Wright, S. P., W. H. Farrand, D. Rogers, and E. Merényi, The nature of the Mars Pathfinder "Black Rock" lithology: comparisons with SNC meteorites and OMEGA spectral images of Chryse Planitia, *EOS Trans. AGU*, **86**(52), Fall Meeting Suppl., Abstract P21B-0145, 2005.

Wyatt, M. B. and H. Y. McSween Jr., Spectral evidence for weathered basalt as an alternative to andesite in the northern lowlands of Mars, *Nature* **417**, 263–6, 2002.

Wyatt, M. B., H. Y. McSween, J. E. Moersch, and P. R. Christensen, Analysis of surface compositions in the Oxia Palus region on Mars from Mars Global Surveyor Thermal Emission Spectrometer observations, *J. Geophys. Res.* **108**(E9), 5107, doi:10.1029/2002JE001986, 2003.

Yen, A. S., R. Gellert, C. Schröder, *et al.*, An integrated view of the chemistry and mineralogy of martian soils, *Nature* **436**, doi:10.1038/nature03637, 2005.

Zipfel, J., P. Scherer, B. Spettel, G. Dreibus, and L. Schultz, Petrology and chemistry of the new shergottite Dar al Gani 476, *Meteorit. Planet. Sci.* **35**, 95–106, 2000.

13

Mars Exploration Rover Pancam multispectral imaging of rocks, soils, and dust at Gusev crater and Meridiani Planum

J. F. BELL III, W. M. CALVIN, W. H. FARRAND, R. GREELEY, J. R. JOHNSON, B. JOLLIFF, R. V. MORRIS, R. J. SULLIVAN, S. THOMPSON, A. WANG, C. WEITZ, AND S. W. SQUYRES

ABSTRACT

Multispectral imaging from the Panoramic Camera (Pancam) instruments on the Mars Exploration Rovers (MERs) *Spirit* and *Opportunity* has provided important new insights about the geology and geologic history of the rover landing sites and traverse locations in Gusev crater and Meridiani Planum. Pancam observations from near-UV to near-infrared (NIR) wavelengths provide limited compositional and mineralogic constraints on the presence, abundance, and physical properties of ferric- and ferrous-iron–bearing minerals in rocks, soils, and dust at both sites. High-resolution and stereo morphologic observations have also helped to infer some aspects of the composition of these materials at both sites. Perhaps most importantly, Pancam observations were often efficiently and effectively used to discover and select the relatively small number of places where *in situ* measurements were performed by the rover instruments, thus supporting and enabling the much more quantitative mineralogic discoveries made using elemental chemistry and mineralogy data. This chapter summarizes the major compositionally and mineralogically relevant results at Gusev and Meridiani derived from Pancam observations. Classes of materials encountered in Gusev crater include outcrop rocks, float rocks, cobbles, clasts, soils, dust, rock grindings, rock coatings, windblown drift deposits, and exhumed whitish/yellowish sulfur- and silica-rich soils. Materials studied in Meridiani Planum include sedimentary outcrop rocks, rock rinds, fracture fills, hematite spherules, cobbles, rock fragments, meteorites, soils, and windblown drift deposits. This chapter also previews the results of a number of coordinated observations between Pancam and other rover-based and Mars-orbital instruments that were designed to provide complementary new information and constraints on the mineralogy and physical properties of Martian surface materials.

13.1 INTRODUCTION

Multispectral imaging has been an important remote-sensing tool in Earth and planetary sciences for decades because of its ability to provide basic, essential information on geologic and/or atmospheric properties as well as its ability to provide secondary compositional or textural information that guides *in situ* analyses. Partly for this reason, multispectral imaging has been a key component of the scientific payloads of all five successful Mars surface lander/rover missions conducted to date. The cameras on the two Viking Landers (VL1: 1976–82; VL2: 1976–80; Huck *et al.*, 1975; Patterson *et al.*, 1977) acquired more than 1400 images of the detailed geomorphology, color, and photometric properties of surface soils and rocks and atmospheric aerosols, providing new information about the surface and atmosphere at the two landing sites (e.g., Mutch *et al.*, 1976; Pollack *et al.*, 1979; Carr, 1981; Sharp and Malin, 1984; Adams *et al.*, 1986; Arvidson *et al.*, 1989; Christensen and Moore, 1992). The Imager for Mars Pathfinder (IMP) multispectral camera (Smith *et al.*, 1997a) on the Mars Pathfinder lander collected more than 16 000 charge-coupled device (CCD) images of its landing site in Ares Valles. Like Viking, Pathfinder acquired important new information on the nature of the Martian surface via a combination of lander and rover imaging and other *in situ* elemental and meteorological measurements (e.g., Smith *et al.*, 1997b; Golombek *et al.*, 1999). Much more information on the compositional and mineralogic implications of IMP multispectral imaging is discussed in Chapter 12.

The most recent set of multispectral observations of the Martian surface were obtained by the Pancam investigations on the *Spirit* rover in Gusev crater and the *Opportunity* rover in Meridiani Planum. Pancam on each rover is a multispectral, panoramic, stereoscopic pair of 1024 × 1024 pixel CCD cameras separated by 30 cm and mounted on the rover mast 1.5 m above the surface. Multispectral images are acquired through a rotating set of narrowband filters placed in front of the optics. Thirteen of the 16 total filters between the 2 cameras were used to obtain images at 11 unique "geology" wavelengths between 430 and 1009 nm (Table 13.1). The other three filters provided the capabilities for broadband and direct solar imaging. Three of the "geology" wavelengths were chosen to be close to the peak red, green, and blue responses of the human color vision system, so that "true color" images of Martian scenery could be generated (e.g., Maki *et al.*, 1999; Bell *et al.*, 2006a). The other filters for Pancam were chosen to be sensitive to absorption features and the degree of crystallinity of several kinds of iron-bearing silicates and iron oxides/oxyhydroxides, and to be close to the filters used on the Pathfinder/IMP camera.

The Martian Surface: Composition, Mineralogy, and Physical Properties, ed. J. F. Bell III. Published by Cambridge University Press.

Table 13.1. *Pancam filter characteristics*

Name	λ_{eff}[a] (nm)	Bandpass (nm)	Comment
Left camera			
L1	739	338	EMPTY
L2	753	20	Red stereo L
L3	673	16	Geology
L4	601	17	Geology
L5	535	20	Geology
L6	482	30	Geology
L7	432	32	Blue stereo L
L8	440	20	Solar ND5
Right camera			
R1	436	37	Blue stereo R
R2	754	20	Red stereo R
R3	803	20	Geology
R4	864	17	Geology
R5	904	26	Geology
R6	934	25	Geology
R7	1009	38	Geology
R8	880	20	Solar ND5

[a] Effective wavelength of the band center, assuming sunlight is the source of the illumination.

Iron-bearing minerals had been known to be important components of the Martian surface based on telescopic and spacecraft remote-sensing studies (see, for example, reviews in Soderblom, 1992; Roush *et al*., 1993; Bell, 1996; Morris *et al*., 1985, 2000), and so Pancam filters were selected to sample the shape of the near-UV to visible ferric (Fe^{3+}) mineral absorption edge from ~440 to 750 nm, diagnostic crystalline ferric oxide absorption features centered near 650 nm and 860–900 nm (e.g., Sherman *et al*., 1982; Morris *et al*., 1985), and the short wavelength wing of the "1 micron" absorption band in ferrous (Fe^{2+}) silicates like pyroxene and olivine (e.g., Adams, 1974; Cloutis *et al*., 1986). Finally, left and right pairs of identical red and blue filters provide multispectral stereo imaging capability, with the red pair optimized for stereo imaging of Mars scenes with large albedo contrasts, and the blue pair optimized for scenes where topography and texture provide a larger source of scene contrast.

Pancam represents an important advance in the progression of Mars surface imaging investigations, as it possesses excellent multispectral and dynamic range capabilities similar to those of the Pathfinder/IMP camera, and roughly three times better spatial resolution compared to Pathfinder and Viking Lander cameras. Pancam was in fact designed so that it would directly help to fulfill the overall MER mission objectives of exploring two sites on the Martian surface where water may once have been present, and to assess past environmental conditions at those sites and their suitability for life (e.g., Squyres *et al*., 2003). Key Pancam investigation goals in support of these mission objectives included (1) assessing the high-resolution morphology, topography, and geologic context of each MER landing site; (2) obtaining color images to constrain the mineralogic, photometric, and physical properties of surface materials; and (3) determining dust and aerosol opacity and physical properties from direct imaging of the Sun and sky. In addition to directly addressing science goals of the MER mission, the Pancam investigation also provided supporting geology/albedo/color context measurements for the rovers' Mini-TES (Miniature Thermal Emission Spectrometer) infrared spectroscopy (see, for example, Chapter 14) and chemical, mineralogic, and Microscopic Imager (MI) measurements acquired by the *in situ* instruments on the rover's arm (see, for example, Chapters 4, 15, and 20). A much more detailed description of the objectives, design, testing, calibration, and preflight performance of the MER Pancams can be found in Bell *et al*. (2003), and details on the calibration and in-flight performance of the cameras on Mars can be found in Bell *et al*. (2006b).

The multispectral properties of the Martian surface are influenced by a wide variety of factors, including the composition and mineralogy of rocks and soils as well as their physical properties (surface textures, grain sizes, presence and nature of coatings, etc.). In this chapter we describe some of the major Martian surface multispectral and morphologic findings with relevance to composition and mineralogy that were obtained from MER/Pancam observations at both Gusev crater and Meridiani Planum. Discussed here are the visible to NIR (440–1009 nm) spectral properties of dust, bright and dark soils, spherules, rocky cobbles and clasts, and whole rock surfaces (natural, as well as brushed and abraded by the Rock Abrasion Tool or RAT). We discuss the Pancam remote-sensing findings in the broader context of surface and orbital remote sensing and *in situ* measurements of Martian surface materials presented in detail in many of the other chapters in this book. While some Pancam results relevant to surface physical properties are described here, significantly more detail on that topic can be found in Chapters 19 and 20.

13.2 MULTISPECTRAL AND MORPHOLOGIC PROPERTIES OF SURFACE MATERIALS AT GUSEV CRATER

13.2.1 Overview

As of *Spirit*'s Martian day (sol) 810 (April 14, 2006), the rover had traversed roughly 6876 m (odometry based on wheel turns) from her initial landing site (Figure 13.1). The traverse began in the Gusev cratered plains and included a visit to the rim and ejecta blanket of Bonneville crater, a ~3 km drive across the basaltic plains to the base of the Columbia Hills, a winter ascent of the West Spur and northwestern slopes of ~100 m high Husband Hill, and a summertime descent down the southeast slope into the Southern Basin, leading finally to the exploration of a layered, roughly circular, 80 m wide feature known as Home Plate not far from the basin's topographic low point. Details about much of this traverse and its geologic goals can be found in Squyres *et al*. (2004a) and Arvidson *et al*. (2006a). Starting in April 2006, *Spirit* spent

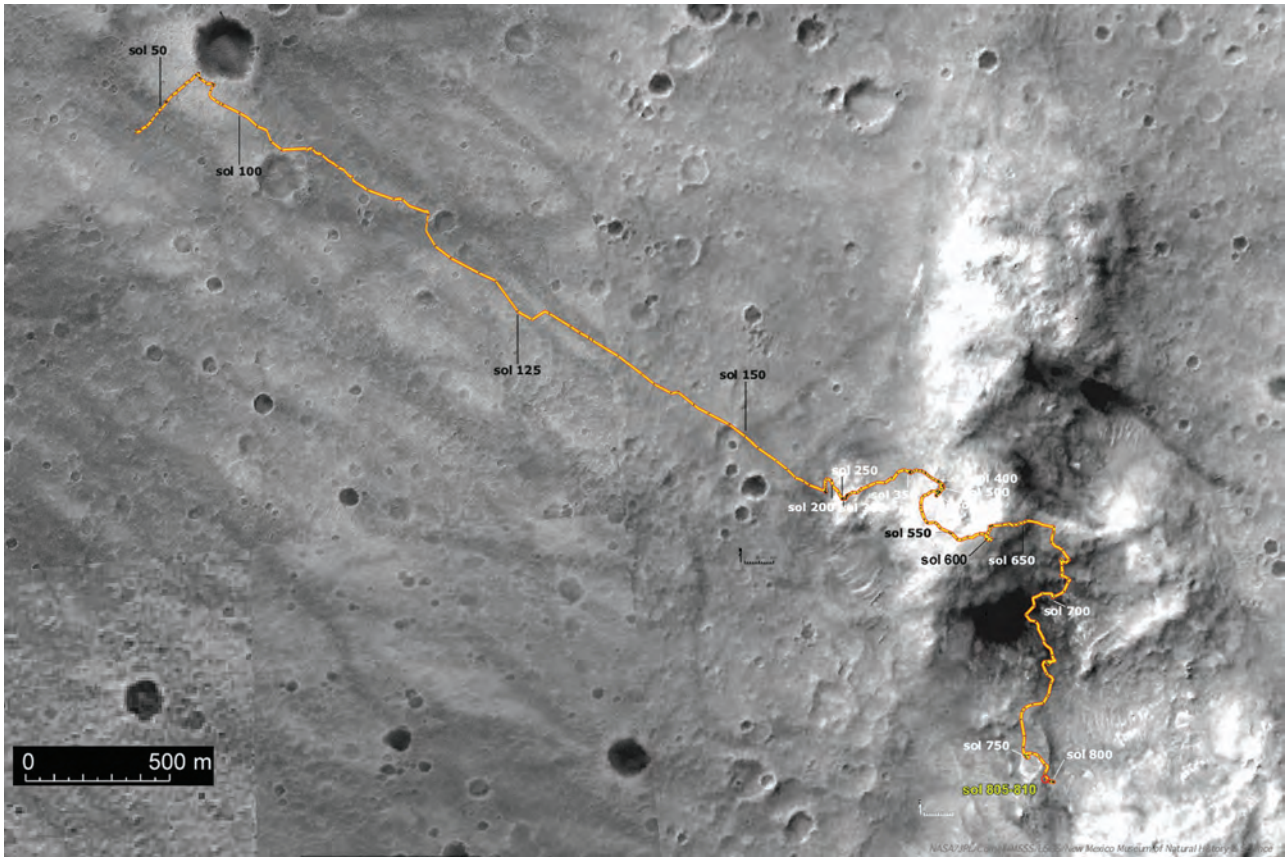

Figure 13.1. *Spirit's* traverse in Gusev crater as of sol 810 (April 14, 2006). (Base map from MGS/MOC [NASA/JPL/MSSS]. Traverse mapping by L. Crumpler, R. Li, and the MER/Athena Science Team.) (For a color version of this figure, please refer to the color plate section or to the e-Book version of this chapter.)

most of the rest of the year parked on a small ridge near Home Plate with her solar panels tilted toward the north in order to get enough solar power to survive her second Martian winter. As of this writing, *Spirit* has survived the winter and is beginning to explore in more detail exciting new science targets in the vicinity of Home Plate.

Here we describe the major classes of rocks, clasts, soils, and windblown drift deposits that were characterized by the Pancams along the Gusev crater traverse. Multispectral imaging can provide constraints on the composition and mineralogy of these materials that can be used to enhance, augment, or provide context for more diagnostic Mini-TES or *in situ* measurements of the composition and mineralogy. In some cases, though, even just monochromatic imaging at high resolution can provide constraints on the composition and origin of materials encountered, based on the geomorphology alone.

13.2.2 Outcrop rocks, float rocks, cobbles, and clasts

Geomorphology

A number of detailed studies of the geology and geomorphology of rocks and rocky materials of the Gusev cratered plains and the Columbia Hills have been published (e.g., Grant *et al.*, 2004; Squyres *et al.*, 2004a, 2006a; Crumpler *et al.*, 2005; Arvidson *et al.*, 2006a; Golombek *et al.*, 2006). While the details of the geology of the landing site presented in those papers are beyond the scope of this chapter, several kinds of morphologic features and properties have been observed during *Spirit*'s traverse that can help to provide constraints on the composition and physical properties of Gusev crater rocky materials (Figure 13.2).

For example, many of the "float" rocks and clasts (pieces of rock that have been separated from their parent vein, strata, or outcrop by impact or weathering processes) observed in the Gusev plains were observed to be extremely hard, based on the high-specific energies needed to grind into them with the RAT (Arvidson *et al.*, 2004). Their hardness, often angular to subangular appearance, and microscopic-scale textures (e.g., Herkenhoff *et al.*, 2004; see also Chapter 20) are all consistent with their identification as basaltic lava rocks, an inference confirmed by detailed *in situ* chemical and mineralogic measurements made on many of these rocks (see Chapters 4 and 15 for details). The relatively small number of rounded rocks observed on the plains and elsewhere in Gusev crater are generally darker and display signs of wind erosion rather than any unambiguous indications of a fluvial origin.

Another example of a morphologic indicator of composition is the identification of what appeared to be much softer, more friable, and platy or layered rocks (e.g., Bell *et al.*, 2004a; Arvidson *et al.*, 2006a). Some of the best examples of these were seen in the West Spur of Husband Hill, where many rocks were found to be softer based on RAT grinding energies. Chemical and mineralogical measurements on some of these kinds of rocks subsequently

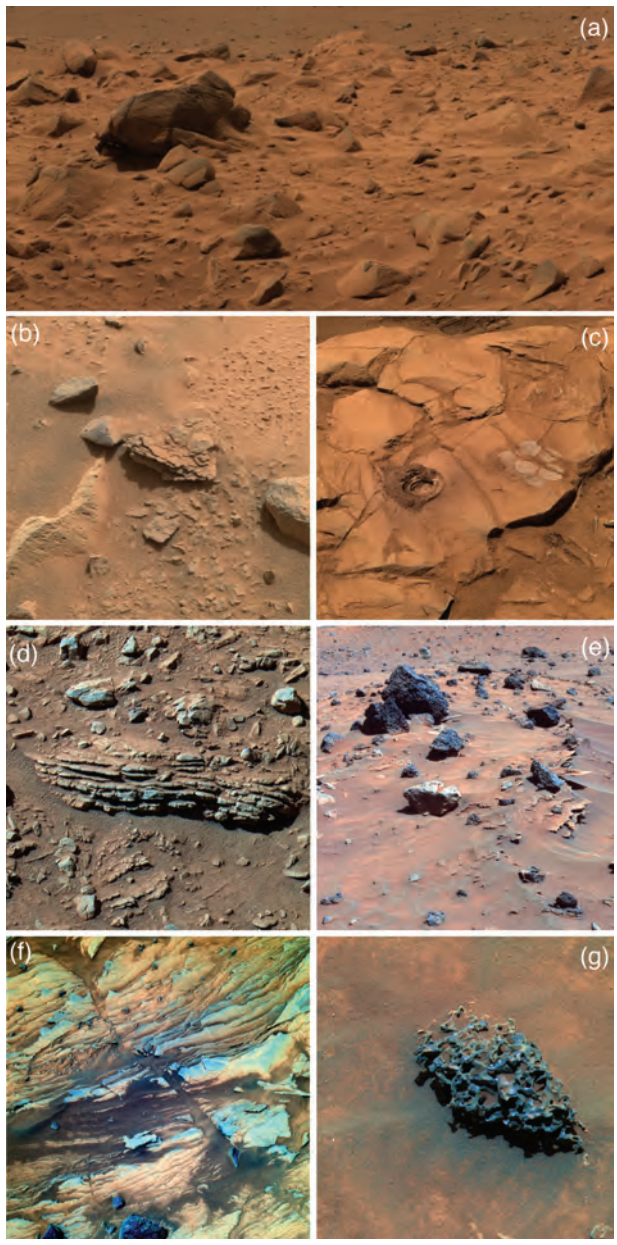

Figure 13.2. Examples of various morphologic classes/indicators that can be used to infer composition and/or physical properties of rocks at Gusev crater. (a) Angular Gusev plains rocks on the rim of Bonneville crater, subsequently identified as typical of the "Adirondack" class of hard, basaltic volcanic rocks that are ubiquitous on the plains. This is an approximate true color view of part of the sol 68–69 Pancam Bonneville crater panorama; (b) "Mimi," the first example of a friable, perhaps physically weathered rock observed in the Gusev crater plains. Pancam sol 40 sequence P2598 approximate true color view; (c) Example of a deep RAT hole (left) and "brush flower" spot (right) on the rock Clovis in the West Spur of Husband Hill. Pancam sol 226 sequence P2569 approximate true color view. (d) The small West Spur rock Tetl, one of the first examples of layered rocks encountered in Gusev crater. Pancam sol 264 false color view from sequence P2598. (e) Examples of vesicular and platy rocks at "Winter Haven" on Low Ridge, near Home Plate. The rock just left of center ("Allan Hills") may be an iron meteorite based on its morphology and extremely low Mini-TES infrared emissivity (see Ruff [2006] and Chapter 14). Pancam sol 809 false-color image from sequence P2535. (f) Finely layered outcrop rocks along the edge of Home Plate. Pancam sol 773 false color image from sequence P2456. (g) Pancam image of small, vesicular, wind-scoured rock ("Gong Gong") found near Home Plate. Approximate true color view from sol 736 sequence P2562. (For a color version of this figure, please refer to the color plate section or to the e-Book version of this chapter.)

showed an increased ferric to ferrous iron ratio, implying more altered compositions. Indeed, both hematite (α-Fe_2O_3) and goethite (α-FeOOH) were identified in some rocks, suggesting significant water-related alteration of parent basaltic compositions (e.g., Morris *et al.*, 2006a; see also Chapters 15 and 23).

A final example of morphology providing compositional clues for Gusev rocks is the identification of some rocks that appear pitted or vesicular (e.g., Bell *et al.*, 2004a; McSween *et al.*, 2004; Golombek *et al.*, 2006; see Figures 13.2e, 13.2g). The observed morphology of many of these rocks is consistent with outgassing of volatile-rich lavas (e.g., Crumpler *et al.*, 2007), most likely with some expansion of the pits and vesicles by subsequent aeolian erosion. These rocks are dark (except where covered by airfall dust) and have a relatively low ratio of ferric iron to total iron (Fe^{3+}/Fe_T), suggesting little chemical alteration since their eruption/emplacement (Morris *et al.*, 2006a). Two of these pitted rocks, Allan Hills and Zhong Shan near Home Plate, appeared somewhat more rounded than typical; based on their distinctive Mini-TES spectral features they have been interpreted as possible meteorites (see Ruff [2006] and Chapter 14 for more details).

Multispectral properties

Several distinct spectral classes of rocks have been identified from Pancam observations during *Spirit*'s traverse. These spectral classes generally correspond to those defined from APXS measured elemental chemistry (e.g., Gellert *et al.*, 2004; Squyres *et al.*, 2006a). There are more spectral classes than there are chemical classes, however, because some of the mineralogic variations (which Pancam is sensitive to) are apparently isochemical (see Chapters 15 and 23; Morris *et al.*, 2006a). For example, in some instances iron-bearing minerals have apparently changed from Fe^{2+}-bearing silicates like olivine and pyroxene to Fe^{3+}-bearing oxides and oxyhydroxides via weathering processes.

Farrand *et al.* (2006) made use of spectral mixture analysis techniques to identify the most spectrally "pure" rock surfaces; that is, those having the least contamination by dust. The spectral variability of the scenes that were examined was modeled as linear combinations of the so-called "endmember pixels" (typically "rock," "soil," and "shade") chosen directly from the images (e.g., Adams *et al.*, 1986). These simple 3-endmember models were valid for the vast majority of scenes imaged during *Spirit*'s traverse across the Gusev crater plains. In the Columbia Hills, lithologic diversity was greater and some scenes were found to contain more than one rock endmember or more than one soil endmember. Figure 13.3 is an example Gusev crater scene showing distinct Pancam spectral classes.

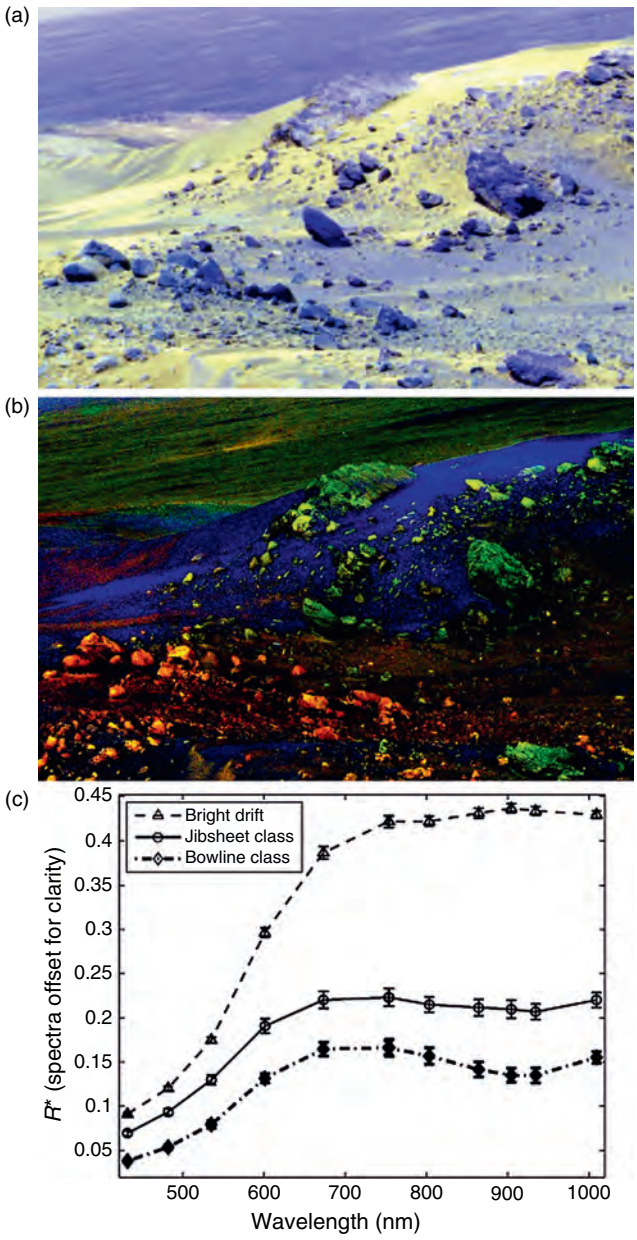

Figure 13.3. (a) False-color composite (red= 673 nm, green= 535 nm, blue= 432 nm) of the sol 608 P2582 Whittaker/Bowline scene. (b) Composite of endmember fraction images of spectrally distinct rock and soil components (red=Bowline type rocks; green=Whittaker/Hillary [Jibsheet class] type rocks; blue=bright drift soil). (c) Spectra of materials mapped out in the fraction image composite image. *R** is the radiance factor normalized by the solar elevation angle (Bell *et al.*, 2006b). (For a color version of this figure, please refer to the color plate section or to the e-Book version of this chapter.)

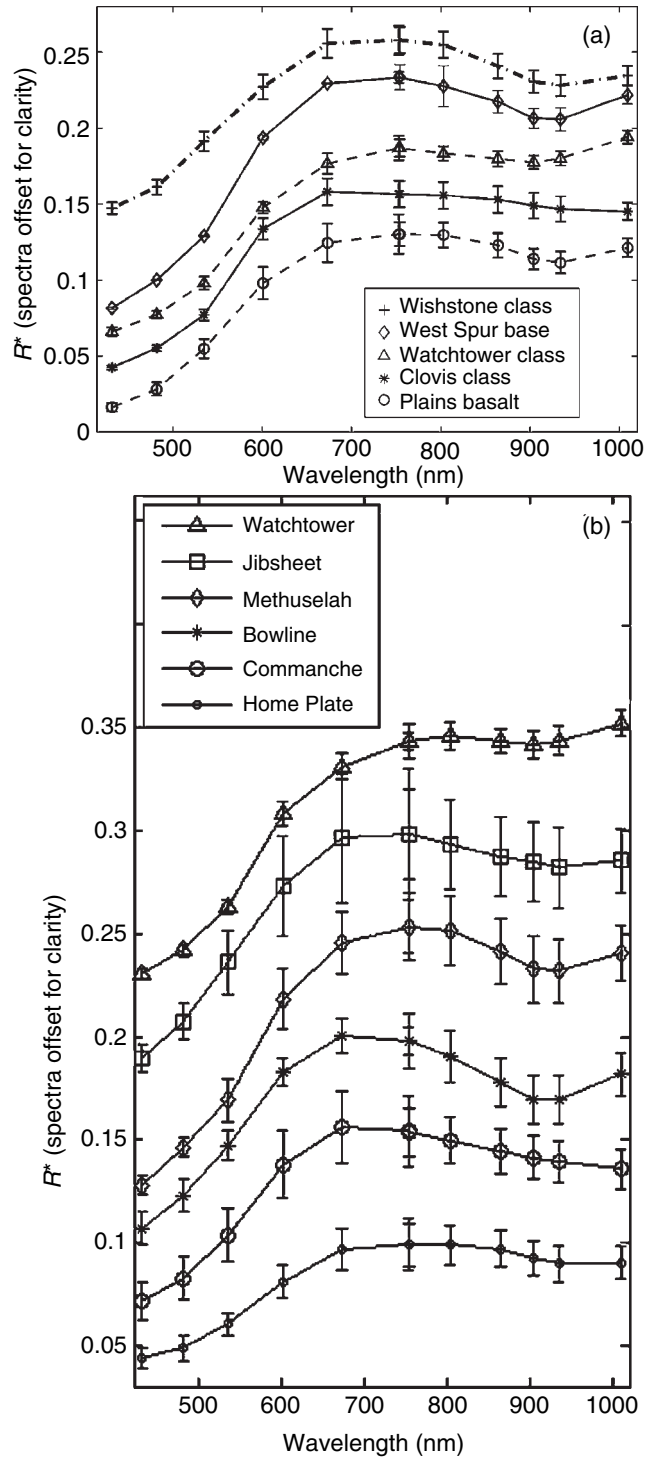

Figure 13.4 (a) Representative spectra of rock spectral classes described by Farrand *et al.* (2006). Peace class is not shown, but dark clasts from the Peace RAT grind were spectrally similar to the basalt spectral class. (b) Representative spectra of rock spectral classes observed after sol 419 (Farrand *et al.*, 2007b). Although observed at Husband Hill summit, the Bowline spectrum is similar to rocks observed at the Methuselah outcrop. *R** is the radiance factor normalized by the solar elevation angle (Bell *et al.*, 2006b).

The rock classes identified by Farrand *et al.* (2006) through *Spirit* sol 419 were: (1) Gusev plains basalts (equivalent to the Adirondack Class of Squyres *et al.*, 2006a); (2) Lower West Spur rocks (exemplified by the rocks "Pot of Gold" and "Wooly Patch"); (3) West Spur or Clovis Class; (4) Wishstone Class; (5) Peace Class; and (6) Watchtower Class. Figure 13.4a shows representative spectra of these six spectral classes (Farrand *et al.*, 2006). These classes were

defined on the basis of a set of spectral parameters, most notably the 535 nm band depth (the ratio of the reflectance at 535 nm to the "continuum" reflectance defined by a linear fit between nearby wavelengths; Clark and Roush, 1984), the 904 nm band depth, the 803/904 nm ratio, the 754–864 nm spectral slope, and the 754–1009 nm spectral slope. The first of these parameters is a measure of the degree of oxidation and crystallinity of the iron-bearing minerals on the surface; the others are measures of the relative abundance of crystalline ferrous silicate and/or ferric oxide phases (e.g., Bell *et al.*, 2000; Morris *et al.*, 2000; Farrand *et al.*, 2006).

Additional Pancam-based spectral classes of rocks have been identified since the initial study by Farrand *et al.* (2006). These new classes correspond to the Larry's Outcrop, Jibsheet, and Methuselah outcrop rocks near the summit of Husband Hill, the olivine-rich "Algonquin Class" rocks (e.g., see Chapter 14), which were observed at several outcrops on the eastern slopes of Husband Hill, and one or more classes associated with the circular "Home Plate" feature on the floor of the basin south of Husband Hill. Figure 13.4b shows representative spectra of some of these more recent, distinctive spectral classes.

Rocks such as Watchtower are interpreted as being highly altered. They have positive 754–1009 nm spectral slopes and significant 535 nm band depths. As seen in Figure 13.5, the 535 nm band depth correlates with high Fe^{3+}/Fe_T ratios as measured by *Spirit*'s Mössbauer spectrometer (e.g., Farrand *et al.*, 2006; Morris *et al.*, 2006a; Chapter 15). Less altered rocks with lower 535 nm band depths and a significant long wavelength (ferrous?) absorption feature centered near 904–934 nm were examined *in situ* at the Methuselah outcrop near the Husband Hill summit. Rocks at the Jibsheet outcrop have properties intermediate between those of Watchtower and Methuselah. Some rocks examined on the eastern slope of Husband Hill, exemplified in Figure 13.4b by the Larry's Bench spectrum, show a low 535 nm band depth, a comparatively short relative reflectance maximum at 673 nm, and an NIR reflectance decrease consistent with the presence of olivine. Pancam spectra alone cannot uniquely identify olivine, but in some cases the inferred presence of olivine from Pancam spectra has been confirmed by more definitive Mini-TES and Mössbauer mineralogical detections (see, e.g., Chapters 14 and 15), thus supporting the inferred presence of this mineral in some regions not measured by Mini-TES or the rover's *in situ* instruments.

Pancam multispectral imaging of Home Plate outcrops (Figure 13.6) demonstrates that natural rock surfaces with minimal dust coatings and RAT-brushed rock surfaces have low albedo and exhibit ~930 nm band absorptions consistent with the presence of low-calcium pyroxene and/or possibly ferric oxyhydroxides. Such absorptions are similar to those observed in relatively clean (or RAT-cleaned) rock surfaces on the West Spur of Husband Hill (Farrand *et al.*, 2006). The spectral similarity of Home Plate and West Spur rocks was also noted in Mini-TES thermal infrared spectral observations (deconvolution of thermal infrared spectra indicated high-glass abundances in both; e.g., Chapter 14). In Figure 13.6, redder, dustier surfaces gradually lose the 930 nm absorption

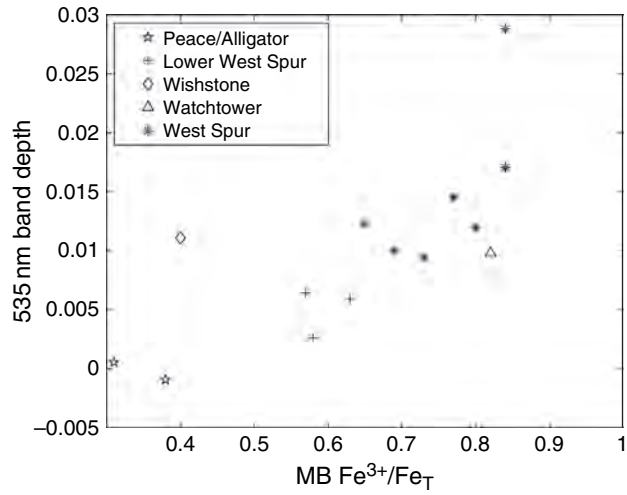

Figure 13.5. Plot of Fe^{3+}/Fe_T as measured by *Spirit*'s Mössbauer spectrometer (MB) versus 535 nm band depth for areas in the Columbia Hills that were subjected to *in situ* examinations.

band and display deeper 535 nm absorptions, apparently indicating the presence of nanophase and/or relatively more crystalline ferric oxides present in the dust covering or coating these rocks (e.g., Bell *et al.*, 2000, 2004a; Morris *et al.*, 2000; Farrand *et al.*, 2007a). Reflectance spectra of nearby vesicular, dark (minimally dusty), "float" rocks are similar to the spectra of RAT-brushed Home Plate rocks. Portions of the brushed region on the float rock Posey at the base of the Home Plate rim also exhibit the 930 nm band, although the average spectrum from the entire brushed region exhibits lower reflectance at 1009 nm than the brushed regions of the Home Plate outcrops (Figure 13.6). This is potentially the result of wavelength-dependent scattering effects such as enhanced specular reflections at the illumination/viewing geometry for Posey. Spectra of higher albedo portions of the Hilton Smith outcrop located on the northeastern rim of Home Plate exhibit a downturn toward 1009 nm that also was observed from the top of Husband Hill and found to be spatially distinctive across the eastern and southern Home Plate rims. While there is insufficient information for unambiguous determination of the origin of this feature at this time, this surface may represent a different type of coating (perhaps older and/or more indurated) than normal airfall dust.

13.2.3 Soils and windblown drift deposits

Definitions

The term "soil" has become commonly used in planetary science to describe the fine-grained, porous, uppermost layers of a regolith, despite the common terrestrial soil science viewpoint that the term applies only to material formed by or in the presence of organic compounds (e.g., Johnson, 1968; Markewitz, 1997). A useful generic definition of soil is "unconsolidated mineral matter that may differ chemically, physically, morphologically, or biologically from the material from which it is derived" (Soil Science Society of America, 1984). Martian soil in particular has been described as the excited "skin" of the part of the Martian

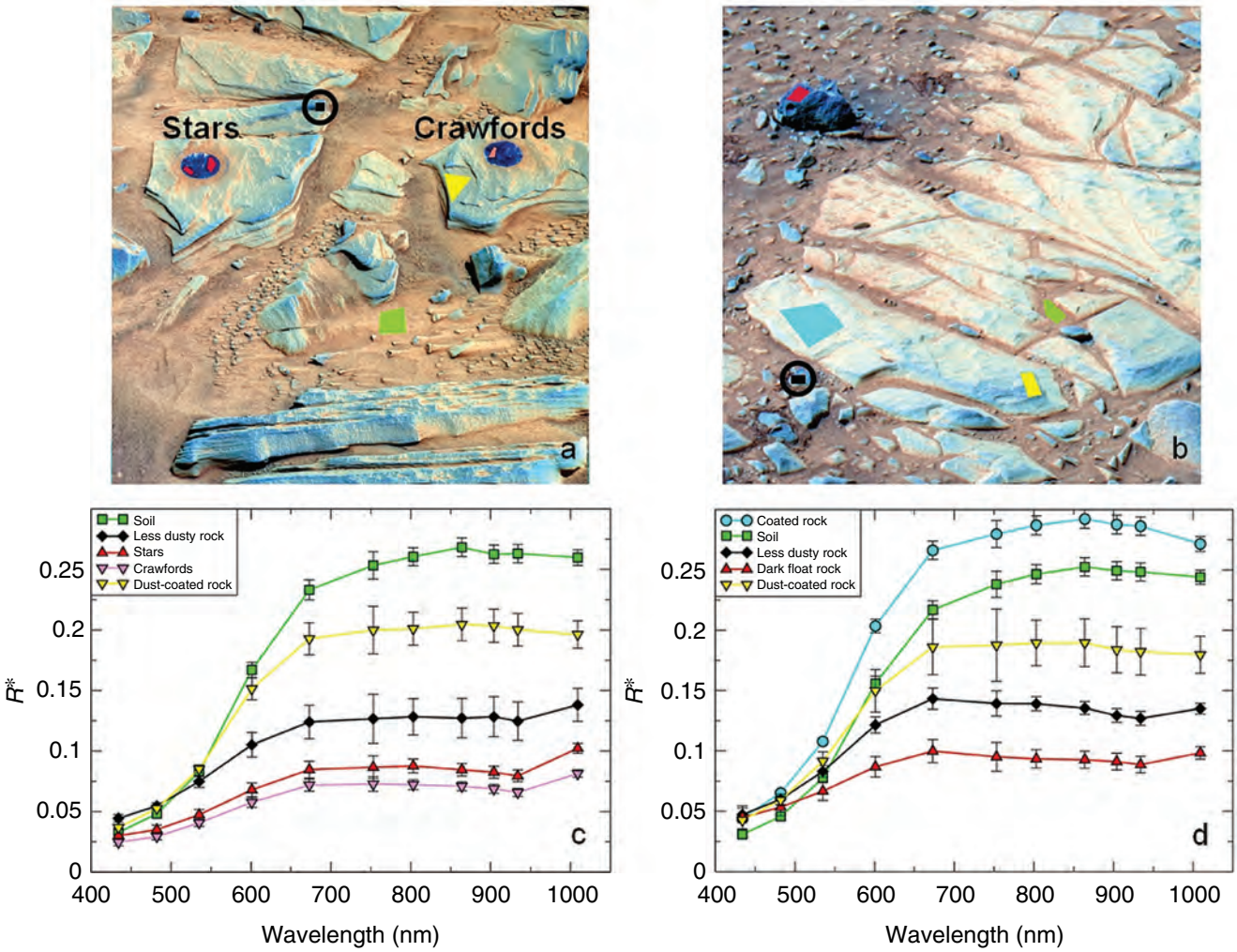

Figure 13.6. Pancam false-color images acquired using 753 nm (L2), 535 nm (L5), and 432 nm (L7) filters, and spectra of Home Plate outcrops. (a) James "Cool Papa" Bell, showing RAT brush locations Stars and Crawfords, acquired on Sol 764 at 11:48 Local True Solar Time (LTST) (P2859). (b) Hilton Smith acquired on Sol 770 at 12:21 LTST (P2591). (c) Spectra derived from color-coded locations shown in (a). (d) Spectra derived from color-coded locations shown in (b). R^* is the radiance factor normalized by the solar elevation angle (Bell *et al.*, 2006b). (For a color version of this figure, please refer to the color plate section or to the e-Book version of this chapter.)

crust that is in direct contact with the (current or past) atmosphere (see Nikiforoff, 1959; Retallack, 1998; Bell *et al.*, 2000), a description that we use throughout this chapter and which also includes "soil" adhering to rock surfaces. In the grain-size scale used by soil scientists (modified from the originally defined scheme of Wentworth [1922]), clay is the size fraction less than about 2 μm, silt is about 2–50 μm, and sand is about 50 μm–2 mm. For Mars, planetary scientists typically define "dust" as the finest-grained component of the soil that easily can become airborne, and this component is known to be less than about 5 μm in diameter from Viking (Pollack *et al.*, 1979), Pathfinder (Markiewicz *et al.*, 1999; Morris *et al.*, 2001) and MER (Lemmon *et al.*, 2004; Morris *et al.*, 2006a) observations. For simplicity, our usage of "sand" includes the sand size fraction used by soil scientists (50 μm to 2 mm) plus the 5–50 μm medium and coarse silt size fractions. Sand and dust that appear to have been concentrated into dunes, ripples, or other bedforms on the surface by the action of wind (Greeley and Iversen, 1985) are often called "drift" or "aeolian drift" (Aeolis was the Greek god of the wind). Collectively, these definitions of "soil," "dust," "drift," and "sand" are often gathered together into the term "fine-grained materials." Examples of the variety of fine-grained materials studied using Pancam in Gusev crater are shown in Figure 13.7. Regardless of the formal definition or planet of interest, soil formation is the result of a combination of many influences, among them parent material composition and climate, and thus the soil provides a window into the past lithologic and environmental history of a planetary surface.

Geomorphology

The current surface of Mars is modified primarily by the action of wind (see, for example, Greeley and Iversen, 1985; Greeley *et al.*, 2004; Sullivan *et al.*, 2005). Dust is carried aloft in suspension, can be transported long distances, and thus is likely to represent a globally homogenized component of

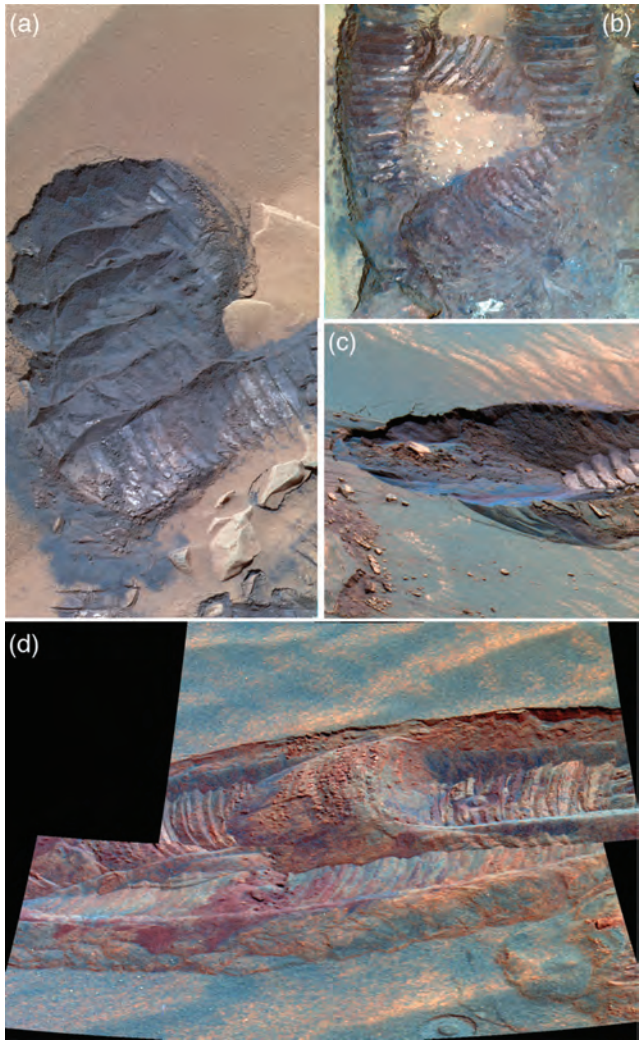

Figure 13.7. Pancam images showing examples of subsurface color variations in soil at Gusev crater. (a) Sol 72 sequence P2352 false-color view of a rover wheel scuff mark into an aeolian bedform near the rim of Bonneville crater. Field of view (FOV) is ~72 cm. (b) Sol 332 sequence P2440 false-color view of rover tracks in West Spur soils. FOV is ~85 cm. (c) Sol 498 sequence P2541 false-color view of rover wheel scuff into an aeolian drift deposit along the "Larry's Lookout" outcrop, visited while ascending Husband Hill. FOV is ~79 cm. (d) Sol 711 sequences P2535 and P2536 false-color mosaic of rover wheel trench dug into the "El Dorado" dune field on the southern flanks of Husband Hill. Different color units appear to have been excavated by the interaction of the rover wheels and the dune sands. FOV is ~83 cm. See also Figures 11.3, 11.11, 11.13, 11.14, and 11.15 for additional morphologic examples of fine-grained materials at Gusev. (For a color version of this figure, please refer to the color plate section or to the e-Book version of this chapter.)

the surface composition anywhere it is found. Sand is transported on or near the ground, can be trapped in craters and dunes, and thus may be more indicative of local and regional compositions. Fine-grained windblown material can also become "plastered" to the surface as soil, forming a thin coating and masking the intrinsic composition of the rock (to which it may or may not have a genetic relationship).

Spirit's traverse path on the floor of Gusev crater has been imaged repeatedly from orbit, allowing changes in surface albedo patterns to be tracked (e.g., Greeley *et al*., 2004, 2005). The most common features observed are dark linear and curvilinear features that appear, disappear, or change orientations with time. Long suspected to be the "tracks" left by the passage of dust devils, observations of active dust devils from *Spirit* confirm this hypothesis (e.g., Lemmon *et al*., 2004; Arvidson *et al*., 2006a; Greeley *et al*., 2006a,b). Vortices in the atmosphere are capable of lifting dust, which is typically "bright," into the atmosphere, leaving coarser-grained materials on the surface, which then appear comparatively dark. *Spirit* MI images show that soils within such a "dark" streak are relatively free of dust, whereas MI images outside the streak appear dustier, confirming this model (Greeley *et al*., 2005, 2006a).

Bright soils occur as organized deposits, including dunes and smaller ripples, and as unorganized patches. Most of these appear to be windblown sand, composed of grains smaller than a millimeter or so (e.g., Herkenhoff *et al*., 2004). In some areas, these deposits have a "lag" layer, or an "armoring," of coarser gains as large as a few millimeters, which has been interpreted to result from the removal of smaller grains by the wind (Herkenhoff *et al*., 2004, 2006).

Dust is observed as mantles on the tops of many rocks and is incorporated in some soil deposits. Its incorporation within some sand dunes suggests that these dunes are not currently active (e.g., Greeley *et al*., 2006a). Over the first 400 to 420 sols of *Spirit*'s mission, dust appears to have settled onto the rover's solar panels and the Pancam calibration target (e.g., Bell *et al*., 2006b). However, on sols 417 and 421, a marked increase in power output from the solar panels combined with images of "wind streaks" of dust on the rover deck indicated that the first of what became several "dust-clearing events" had occurred. This time period marked the initiation of active dust devils in Gusev crater, as seen from *Spirit* (e.g., Greeley *et al*., 2006b), and further emphasized the fact that dust must be treated as an active and variable component in remote-sensing observations of Mars on all spatial scales.

Multispectral properties

Typical soils and dust. Pancam 11-color spectra of a variety of typical soils and rocks are shown in Figure 13.8a (Bell *et al*., 2004a, 2006b). These spectra sample the diversity of visible to NIR units encountered during the early part of *Spirit*'s traverse, from the landing site to the ejecta blanket of Bonneville crater (Figure 13.1); however, they are also representative of typical Pancam spectra encountered along later parts of the traverse in and beyond the Columbia Hills. For comparison, average classical bright and dark region telescopic spectra (Bell *et al*., 1990; Mustard and Bell, 1994), and average bright and dark region spectra from Mars Pathfinder IMP observations (Bell *et al*., 2000; see also Chapter 12) are also plotted in Figure 13.8a.

Pancam spectra of typical bright and dark soils in Gusev crater are consistent with previous average bright and dark region telescopic spectra and IMP multispectral data. Similarity in the bright soil/dust spectra observed by Pancam and remote-sensing signatures of bright/dusty surfaces at much wider spatial scales is not surprising. It has been known for decades that windblown dust is a globally homogenized, ubiquitous component of the soil everywhere

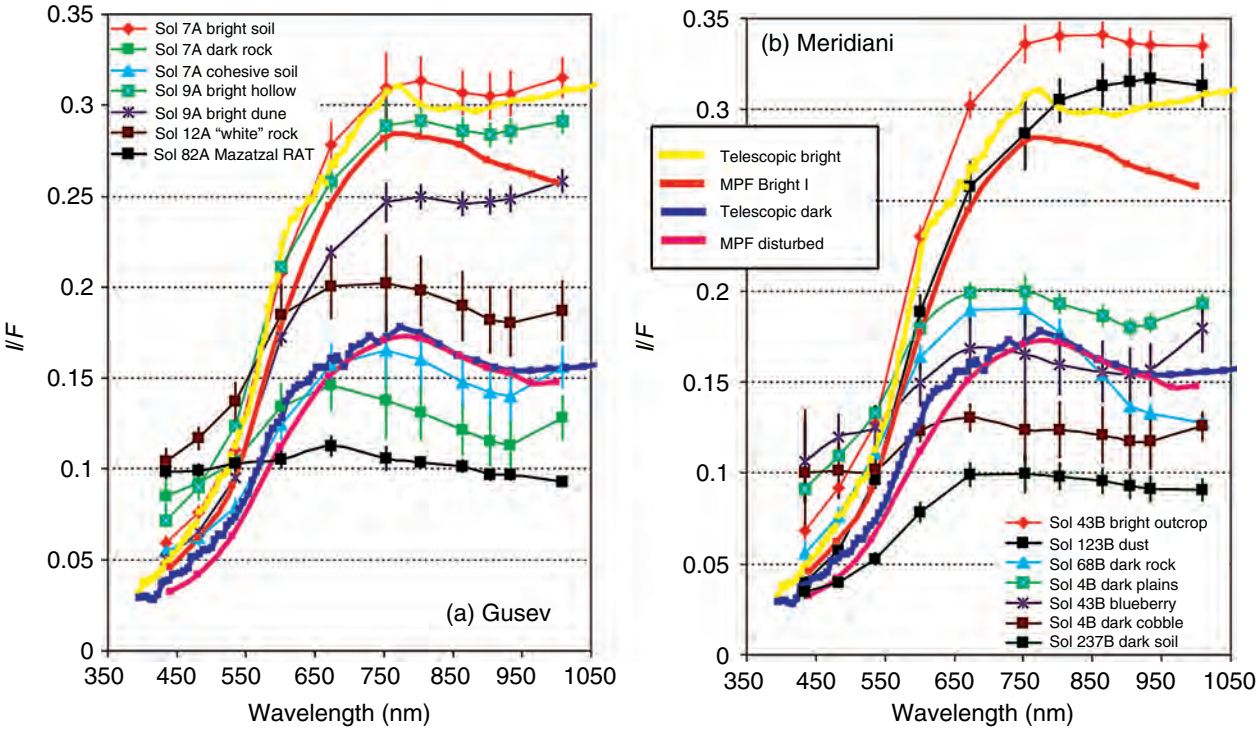

Figure 13.8. (a) Representative Pancam spectra from a variety of materials in Gusev crater, and (b) Meridiani Planum. These are compared to classical telescopic bright and dark region spectra (Bell *et al.*, 1990; Mustard and Bell, 1994), and to Mars Pathfinder Bright I and dark Disturbed Soil spectra of Bell *et al.* (2000). "Sol 68B Dark Rock" is Bounce Rock. (For a color version of this figure, please refer to the color plate section or to the e-Book version of this chapter.)

on Mars, and that its visible-wavelength spectral properties are dominated by the presence of fine-grained (nanophase to poorly crystalline) ferric oxides (see, for example, reviews in Soderblom, 1992; Roush *et al.*, 1993; and Chapter 2). Similarities between telescopic and orbital observations of dust and surface-derived measurements of high-albedo soils and drift had also been noted previously at the Viking and Mars Pathfinder landing sites (e.g., Adams *et al.*, 1986; Arvidson *et al.*, 1989; Bell *et al.*, 2000; Morris *et al.*, 2000).

Observations and modeling of the reflected radiances from the Pancam calibration targets on *Spirit* and *Opportunity*, which became dust-coated with time during the mission (e.g., Bell *et al.*, 2006b), have allowed Kinch *et al.* (2007) to make a direct determination of the spectrum of airfall dust. The derived dust spectrum (Figure 13.9) is comparable to telescopic and IMP spectra of bright regions, and is similar at both landing sites, further confirming the globally mixed nature of the Martian airfall dust signature. In addition, the derived airfall dust spectrum shows little evidence for the kinds of absorption features (e.g., from 800 to 1000 nm) and spectral inflections (e.g., near 535 nm) that would indicate the presence of crystalline ferric (or ferrous) oxides or silicates in the dust, providing further support for nanophase (X-ray amorphous) ferric oxides dominating the dust's spectral behavior. A model of the spectral properties of the dust, combined with knowledge of the reflectance and photometric properties of the calibration target materials, was used to remove the dust contribution from the calibration target reflectance and allow tactical-timescale calibration of Pancam images even using dusty calibration target observations (e.g., Bell *et al.*, 2006b; Kinch *et al.*, 2007).

Inferences about the mineralogy of the dust derived from Pancam spectra are consistent with the thermal infrared spectra of the dust derived by Bandfield *et al.* (2003) from Mars Global Surveyor Thermal Emission Spectrometer (MGS/TES) observations (see also Chapter 9), which also revealed a mineralogy that must be dominated by extremely fine-grained silicates and only small percentages of well-crystalline phases. The nanophase ferric oxides or other fine-grained silicates may just be "chromophore" phases (pigmenting, color-giving, but not volumetrically important) in the dust, however, as Mössbauer measurements of the airfall dust on the rover's Magnetic Properties Experiment surfaces and of bright, undisturbed surface dust have revealed the presence of well-crystalline magnetite, olivine, and perhaps even pyroxene within airfall dust grains (e.g., Goetz *et al.*, 2005; Morris *et al.*, 2006b; see also Chapters 15 and 16). Dust grains appear to be composite particles composed of these ferrous minerals, some probably small fraction of nanophase ferric oxides, and some as-yet uncertain percentage of nonmagnetic phases like feldspars or carbonates.

"Gray" rock grindings and "white" rock coatings. Several new spectral classes unlike those previously seen have been discovered in the Pancam data from Gusev. For example, Pancam spectra of the dust/"soil" created by grinding into Gusev plains basalts like Adirondack, Humphrey, and Mazatzal are dark and remarkably flat, and the spectra of the corresponding RAT-ground rock surfaces are similarly

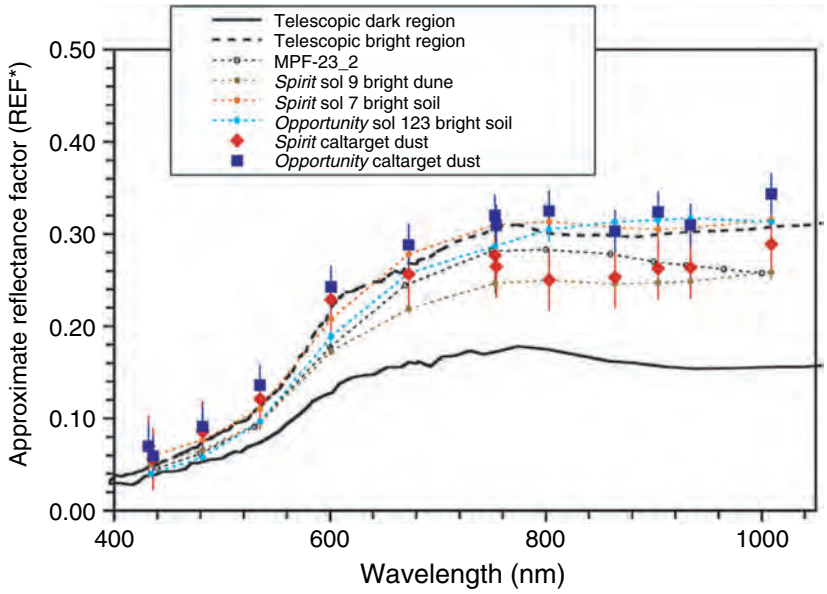

Figure 13.9. Model-derived visible to near-IR spectra of airfall dust on the Pancam calibration targets compared to Martian dust spectra from other sources (telescopic: Mustard and Bell, 1994; Mars Pathfinder bright soil MPF-23_2: Bell *et al.*, 2000; MER bright soils: Bell *et al.*, 2004a,b). Modeling and analysis described in detail in Kinch *et al.* (2007). (For a color version of this figure, please refer to the color plate section or to the e-Book version of this chapter.)

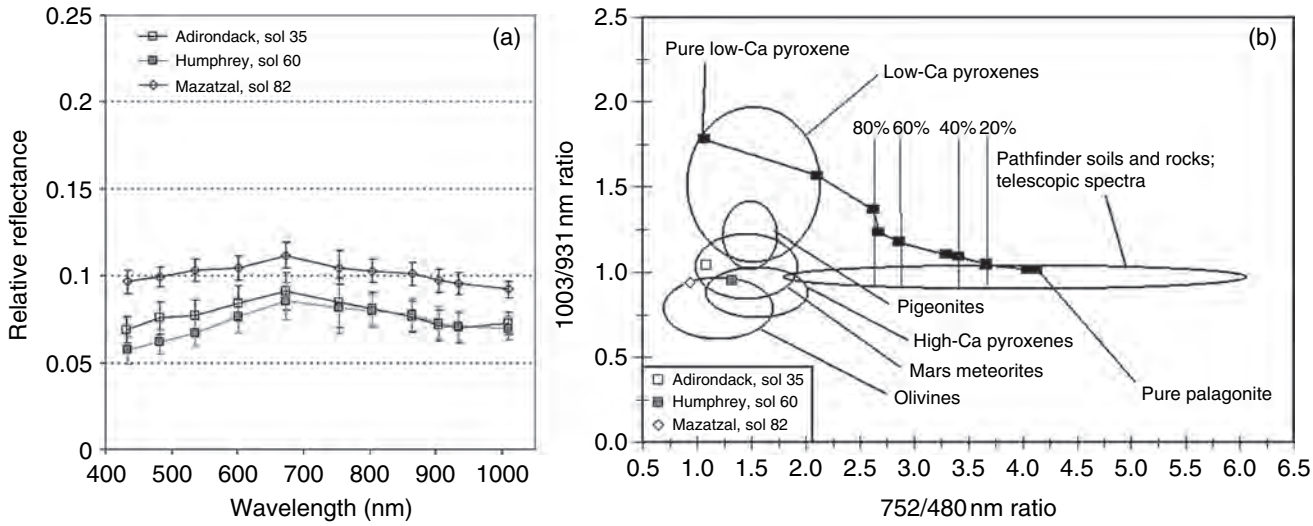

Figure 13.10. (a) Pancam spectra of grinding debris and dark, "pristine" inner rock surfaces exposed by the RAT on the Gusev plains rocks Adirondack, Humphrey, and Mazatzal. (b) Ratios of the spectra in (a) compared to laboratory-derived spectral parameterizations of olivines, pyroxenes, Martian meteorites, and pyroxene-palagonite mixtures studied by Cloutis and Bell (2003). The Gusev rock spectra appear consistent with an olivine- or high-Ca-pyroxene dominated basaltic composition. (Figure after McSween *et al.*, 2006b.)

gray (Figure 13.10a; e.g., McSween *et al.*, 2004, 2006a). In fact, spectra like these are the grayest spectra ever acquired on Mars, and exhibit little to no indication of the presence of ferric iron. The implication from Pancam spectra, comparing them with derived multispectral parameters versus laboratory-derived parameters at comparable wavelengths from minerals and mineral mixtures (Figure 13.10b; e.g., Morris *et al.*, 2000; Cloutis and Bell, 2003), is that the plains rocks in Gusev are ferrous silicate-bearing (olivine-, pyroxene-rich) basalts that have undergone extremely little oxidation and chemical weathering. The flat spectra of these rocks may also result from the presence of opaque magnetite in these rocks. These inferences have been confirmed by more definitive *in situ* APXS and Mössbauer chemistry and mineralogy measurements of these rocks (e.g., McSween *et al.*, 2004, 2006a; see also Chapters 4, 15, and 23). Similarly, pristine basaltic float rocks have also been discovered and characterized by Pancam and other instruments throughout *Spirit*'s traverse, including at high elevations in the Columbia Hills (e.g., McSween *et al.*, 2006b; Ruff *et al.*, 2006; see also Chapter 14).

Another example of a new spectral class was found in Pancam spectra of the so-called "white" (actually quite reddish) rocks seen during the traverse to Bonneville crater (e.g., Bell *et al.*, 2004a; Arvidson *et al.*, 2006a). These surfaces exhibit an anomalously high reflectivity in the blue relative to typical bright reddish soils and dust (Figure 13.8a).

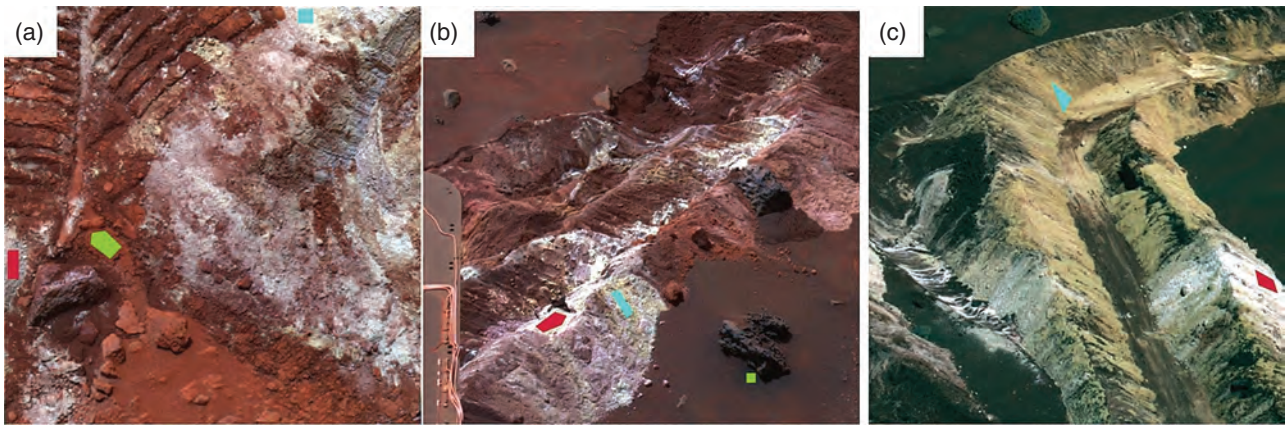

Figure 13.11. False-color RGB (754, 535, 432 nm) images of (a) Paso Robles (Sol 400, P2551); (b) Arad (Sol 721, P2538); and (c) Tyrone (Sol 790, P2531) showing locations from which spectra were acquired. Paso Robles: red = "gray" soil, cyan = "white" soil, green = background soil. Arad: red = "white" soil, cyan = "yellow" soil, green = basaltic soil. Tyrone: red = "white" soil, cyan = "yellow" soil. (Based on Johnson *et al.*, 2007.) (For a color version of this figure, please refer to the color plate section or to the e-Book version of this chapter.)

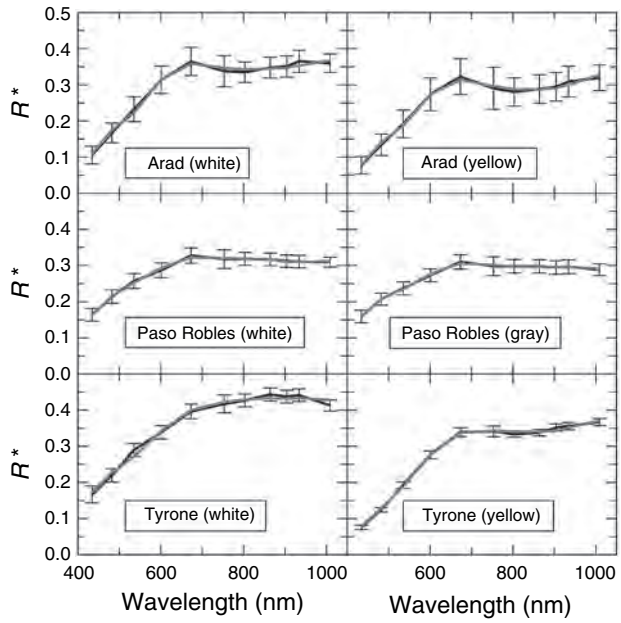

Figure 13.12. Pancam spectra (dark lines) extracted from regions of interest (ROI) shown in Figure 13.11; error bars are standard deviations of pixels selected for each ROI. MESMA model results (gray lines) overlaid. See Table 3 in Johnson *et al.* (2007) for model results. (Based on Johnson *et al.*, 2007.)

These surfaces also exhibit a negative NIR spectral slope, which is also not typical of bright Gusev materials. Combined, the high blue reflectance, negative NIR slope, and knowledge of the dark, grayish spectrum of typical "clean" Gusev plains basalts (e.g., Figure 13.10) support a model of the bright reddish rock surfaces as a thin coating of possibly cemented or duricrusted dust and/or bright soil. In this model, at the shortest wavelengths (400–500 nm), photons appear to be able to penetrate to and interact with the relatively pristine substrate rock. That substrate rock appears to have more than a factor of two greater reflectivity than the dust, which is extremely dark in the blue (Figure 13.8a). At green, red, and short-wave NIR wavelengths (about 500–800 nm), the dust is much more reflective, and so surface scattering appears to dominate over volumetric penetration and interaction with the substrate, yielding a more "dust-like" reflectance spectrum at these wavelengths. At even longer wavelengths, the dust reflectivity remains relatively constant but because it is thin, the coating becomes more transparent to longer-wavelength photons and the spectrum slopes downward toward the much lower NIR reflectance of the relatively pristine rocky substrate. If this model is valid, the coatings must be extremely thin, probably on the order of a few to less than 10 microns, comparable to only a few times the average grain size of typical Martian dust particles. These kinds of spectral effects from thin bright dust coatings over lower albedo rocky or sandy substrates on Mars have also been inferred from previous orbital and Pathfinder remote-sensing observations (e.g., Fischer and Pieters, 1993; Johnson *et al.*, 1999; Bell *et al.*, 2000) and have been directly observed and modeled in laboratory simulations of Mars-like dust covering and coating Mars-like basaltic rocks and other substrates (e.g., Johnson and Grundy, 2001; Johnson *et al.*, 2004, 2006; Kinch *et al.*, 2007; see also Chapter 19).

Whitish/yellowish salty soils. Perhaps the most exciting new spectral class of fine-grained materials discovered by *Spirit* during the traverse within Gusev crater is a set of light-toned soils encountered in three different regions when the action of the rover's wheels excavated subsurface materials (Figure 13.11). The first occurrence of these soils was on the drive toward the summit of Husband Hill near a region named Paso Robles; the second was in the basin south of the Hills at a feature named Arad; and the third was near Home Plate in a region named Tyrone. Where least contaminated by contributions from typical reddish surface soils, these materials exhibited high albedo and white to yellow hues that

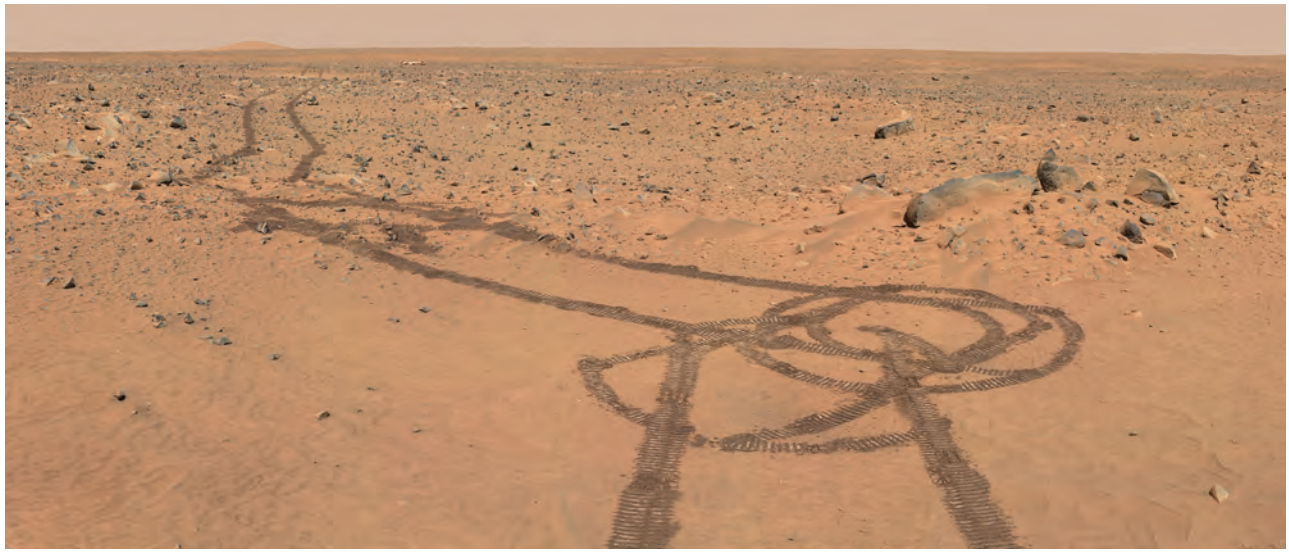

Figure 13.13. Part of the *Spirit* "Legacy" panorama, showing the large albedo and color contrast between the rover's tracks (albedo around 0.20) and the surrounding bright, dusty soils (albedo around 0.30) along the traverse from the landing site to the rim of Bonneville crater. This is an approximate true color rendering generated using Pancam's 753 nm, 535 nm, and 480 nm filters from *Spirit* sols 59–61 Pancam sequences P2211 through P2216. (For a color version of this figure, please refer to the color plate section or to the e-Book version of this chapter.)

varied over small length scales (Figure 13.11). Observations by the APXS instrument at Paso Robles and Arad showed high-sulfur contents (up to 35 wt.% SO_3), and Mössbauer measurements at the same locations suggested that the soils were dominated by Fe^{3+}-bearing sulfates (Gellert *et al.*, 2006; Ming *et al.*, 2006; Morris *et al.*, 2006a). Mini-TES measurements of sulfur-rich soils in Gusev suggested the presence of a 6 μm bound water spectral feature, consistent with the presence of hydrated minerals, particularly for the Tyrone soils (see, for example, Chapter 14). Mini-TES data for Paso Robles have also been shown to be consistent with the presence of Fe^{3+}-bearing sulfates (Lane *et al.*, 2006).

The chemical and mineralogic analyses/inferences from the visibly distinct salt-rich soils in the three Columbia Hills/southern Basin regions noted above are consistent with and an extension of the high Fe^{3+}, Mg, S, Cl, and Br detected in subsurface soils within three shallow trenches dug by *Spirit*'s wheels in the volcanic plains between the landing site and the Columbia Hills (Wang *et al.*, 2006). The sulfur-rich plains trench soils do not exhibit the dramatic Pancam (or Mini-TES) color/spectral differences of the Hills/Basin sulfur-rich soils, suggesting that a larger fraction of spectrally masking "normal" dust/soil is mixed with the high-S soils in the plains trenches than at Paso Robles, Arad, and Tyrone. Still, these trench wall and floor soils exhibit distinctive *in situ* chemical/mineralogic signatures. Wang *et al.* (2006) interpret the APXS and Mössbauer measurements within these trenches to indicate the presence of primarily Mg-rich sulfates, with minor amounts of Ca- and perhaps Fe-sulfates as well. However, Morris *et al.* (2006a) do not report ferric sulfates in the trench soils from their analysis of the Mössbauer data. Perhaps, S-rich subsurface soils in the Gusev plains were formed by a similar, though less efficient or less concentrated, process as the more colorful but chemically similar soils from farther along the traverse.

Pancam spectra of the Paso Robles, Arad, and Tyrone materials are some of the most spectrally diverse of all the fine-grained materials encountered by *Spirit*. All of these whitish to yellowish soils exhibited distinctive reflectance maxima near 670 nm consistent with the presence of hydrated ferric sulfates (and distinct from jarosite and hematite; e.g., Morris *et al.*, 1985; Crowley *et al.*, 2003; Cloutis *et al.*, 2006). Subtle absorptions and inflections near 480 nm (Parente *et al.*, 2007) and between 800 nm and 900 nm (Johnson *et al.*, 2007; Figure 13.12) were also observed in some regions within these soils; these features are consistent with the presence of some Fe^{3+}-bearing sulfate minerals. Analysis by Lane *et al.* (2007) of combined Pancam, Mini-TES, Mössbauer, and APXS data suggests that Fe-bearing phosphates may also be contributing to the observed characteristics of these whitish/yellowish soils.

To systematically model the possible kinds of minerals contributing to the observed Pancam spectra, Johnson *et al.* (2007) used a multiple endmember spectral mixture approach (MESMA) in combination with a spectral reference library composed of laboratory spectra of sulfate minerals plus two Pancam spectra of typical Gusev soil and darker (less dusty) soil (Figure 13.11). Linear mixing models such as MESMA cannot be used to provide absolute abundances of mineral components owing to nonlinear effects induced by intimate mixing (e.g., Clark and Roush, 1984; Mustard and Pieters, 1987; Poulet and Erard, 2004). This is

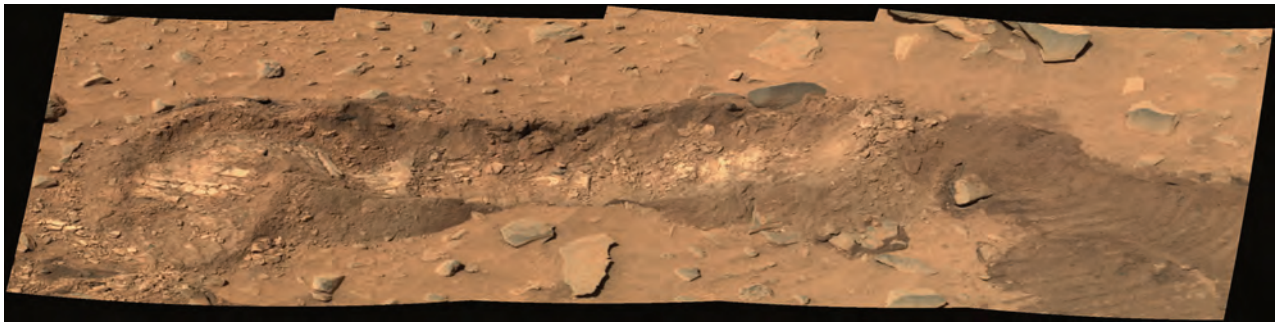

Figure 13.14. Pancam mosaic of "Big Hole Trench," an approximately 50 cm wide by 9 cm deep furrow excavated by one of the rover's wheels in Gusev crater plains materials between Bonneville crater and the Columbia Hills. This is an approximate true color rendering generated using Pancam's 753 nm, 535 nm, and 480 nm filters from *Spirit* sol 116 Pancam sequence P2404. (For a color version of this figure, please refer to the color plate section or to the e-Book version of this chapter.)

especially a problem for the excavated, mixed, light-toned soils analyzed by Johnson *et al*. (2007). Nonetheless, such models can be used to provide first-order mineral detections. Johnson *et al*. (2007) ran the MESMA algorithm for six Pancam spectra extracted from the Paso Robles, Arad, and Tyrone soils (locations shown in Figure 13.11). The modeled spectra are overlain on the Pancam spectra in Figure 13.12, and Table 3 in Johnson *et al*. (2007) lists the major minerals detected by the model as well as the root mean square (RMS) errors. The MESMA results consistently modeled each Pancam spectrum with a large proportion (>50%) of "undisturbed soil." The whitish and yellowish colored soil spectra were modeled using various ferric sulfates hydrated to different degrees (e.g., Kasting *et al*., 1992; Bishop *et al*., 2002). However, the endmember spectral library used by Johnson *et al*. (2007) to model the data may be inadequate, which could possibly lead to incorrect inferences about the mineralogy of the deposits. For example, there is no evidence for hydronium jarosite in the Arad soils from Mössbauer spectroscopy of these materials. Broader, multi-instrument perspectives on these deposits (e.g., Lane *et al*., 2007) may lead to a more accurate understanding of their mineralogy and origin.

Subsurface spectral "stratigraphy". As shown above, multispectral imaging and *in situ* chemical/mineral measurements of soils "disturbed" by the action of the rover's wheels (normal driving, scrambling up hills or down craters, or intentionally or unintentionally digging shallow trenches) or by the landing system's airbags can provide information on the stratigraphy of the near surface. For example, *Spirit*'s wheels typically leave dark tracks after rolling over the relatively high-albedo terrain of the Gusev crater plains (Figure 13.13). The observed drop in approximate Lambert albedo derived from Pancam broadband L1 filter observations (Bell *et al*., 2006b, 2008) is roughly a factor of 2, from typical dusty plains/hills albedo values of 0.20 to 0.30 down to values of 0.10 to 0.12. Multispectral observations of wheel tracks as well as of shallow trenches dug by the rover wheels (Figure 13.14) reveal that the uppermost surface of almost all Gusev plains soils is both brighter and redder than the immediate subsurface (e.g., Bell *et al*., 2004a; Farrand *et al*., 2006; Wang *et al*., 2006), implying an increased ferric mineral content – presumably from a thin layer of windblown and/or airfall dust – in the uppermost surface compared to the subsurface. This inference was confirmed by Mössbauer observations in the floors and walls of several Gusev trenches which showed significantly lower Fe^{3+}/Fe_{total} in the shallow subsurface, consistent with less altered, more "basaltic" materials underlying a thin (few millimeters) dusty uppermost surface (e.g., Morris *et al*., 2006a; Wang *et al*., 2006).

The observed change in albedo between dusty plains (0.20–0.30) and dust devil tracks (about 0.20; Bell *et al*., 2004a) is significantly less than the albedo change associated with plains wheel tracks and trenches. This observation suggests that the rover wheels "scour" and mix the surface and subsurface either more efficiently or more deeply than typical dust devils. There may also be a timescale issue involved, as both dust devil tracks and rover tracks have been observed to brighten with time from the "restorative" action of continual airfall dust deposition brightening these lower albedo surfaces (e.g., Sullivan *et al*., 2005).

The rover wheels sometimes dislodged materials and significantly scoured rock and soil surfaces while climbing the Columbia Hills. In general, there is less contrast between the wheel tracks and the undisturbed soils in the Hills compared to the plains, suggesting either less dust on Hills soils, less efficient surface/subsurface mixing of the soils by normal wheel interactions (perhaps reflecting a harder or more indurated nature to the Hills soils compared to the plains soils), or more dusty or altered subsurface soils in the Hills. In some places, small patches of brighter, bluer, more specularly reflecting fine-grained materials were exposed or exhumed by the action of the wheels (e.g., Figure 13.15). Until arriving at Paso Robles around sol 400 (Figure 13.11), exposures of this kind of material large enough to allow APXS and Mössbauer measurements had not been encountered. These scattered exposures of "shiny soil" may be smaller concentrations

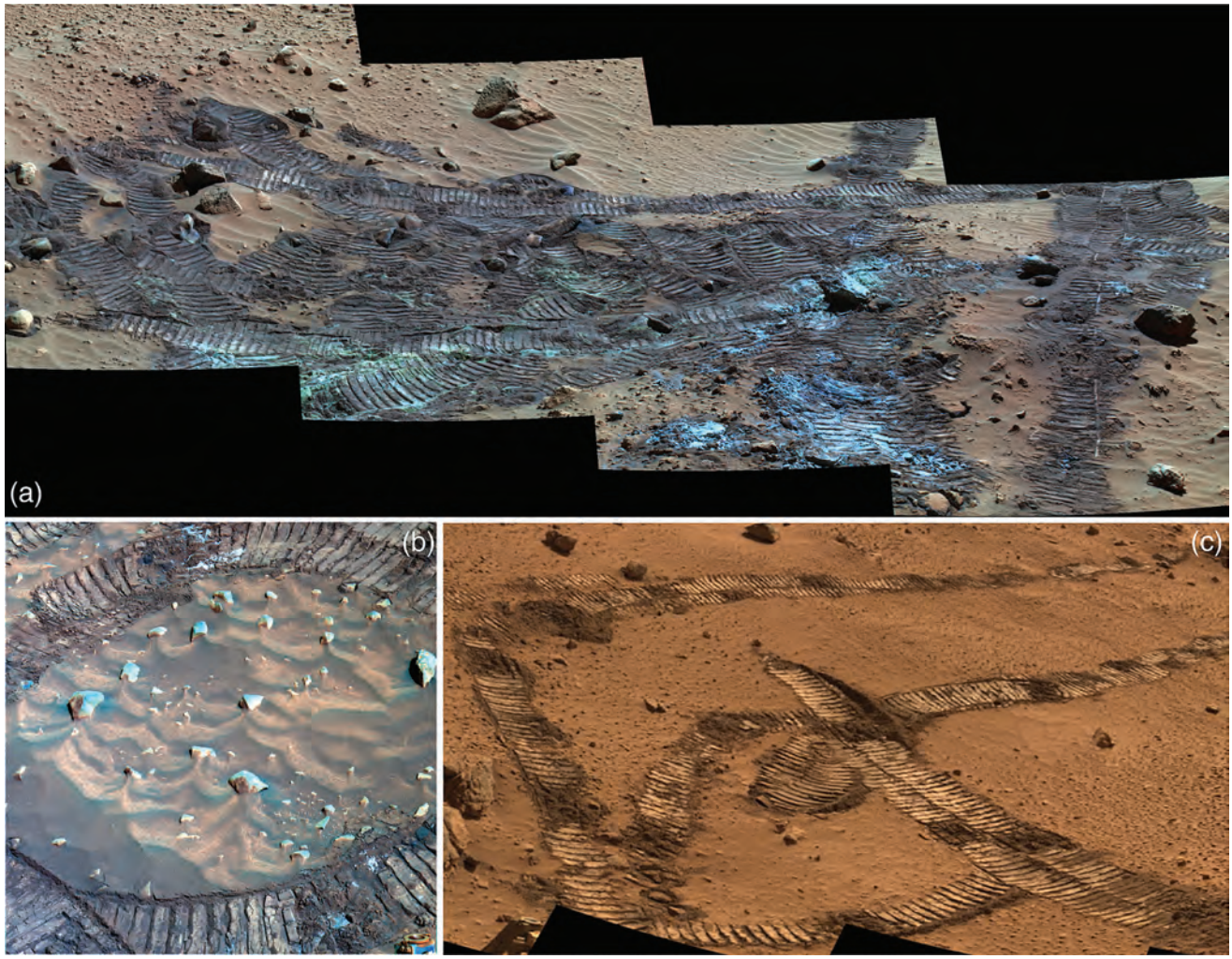

Figure 13.15. (a) False-color Pancam mosaic of disturbed soil and wheel tracks and crushed, "shiny" soils exposed while *Spirit* was scrambling up the West Spur of Husband Hill in a region known as Hank's Hollow. False-color rendering generated using Pancam's 753 nm, 535 nm, and 480 nm filters from *Spirit* sol 170 Pancam sequence P2379. (b) Sol 483 sequence P2594 Pancam view of clasts, wind tails, and rover tracks near the summit of Husband Hill. In general, wheel tracks in the Columbia Hills exhibit less contrast with the surrounding undisturbed soils than wheel tracks in the Gusev plains. (c) Part of the sols 410 to 413 "Lookout" Pancam panorama, showing a natural color view of rover tracks during the traverse from the West Spur to the flanks of Husband Hill. The increased brightness of the tracks in views like this probably represents a photometric effect resulting from compaction of the surface and thus increased specular reflection when viewing the scene in a forward scattering (into the Sun) geometry. (For a color version of this figure, please refer to the color plate section or to the e-Book version of this chapter.)

of the whitish to yellowish sulfur-rich soils described above. For some of these disturbed soils, especially those looking sunward in forward-scattering geometries, the brightness increase may be a physical effect at least partially related to increased specular scattering associated with the compaction of the soils by the rover's wheels (Figure 13.15).

13.3 MULTISPECTRAL AND MORPHOLOGIC PROPERTIES OF SURFACE MATERIALS AT MERIDIANI PLANUM

13.3.1 Overview

As of *Opportunity* sol 810 (May 5, 2006), the second MER rover had traversed roughly 7575 m (odometry based on wheel turns) from her initial landing site (Figure 13.16). The traverse began in the small (20 m diameter) crater called Eagle, where *Opportunity* spent nearly 60 sols investigating the soils and discovering several new classes of Martian surface materials, including small spherules and outcrops of finely laminated sulfur-rich sedimentary rocks. The rover then spent about 30 sols driving across the surface of Meridiani Planum to the larger (160 m diameter) Endurance crater. One goal of going to Endurance was to determine if the spherules and outcrop rocks were geographically extensive and if so, to use them to probe deeper into the layered sedimentary outcrop deposits. The exploration of Endurance proved that the deposits were indeed laterally extensive, and *Opportunity* was able to explore nearly 8 vertical meters of the layered stratigraphic section

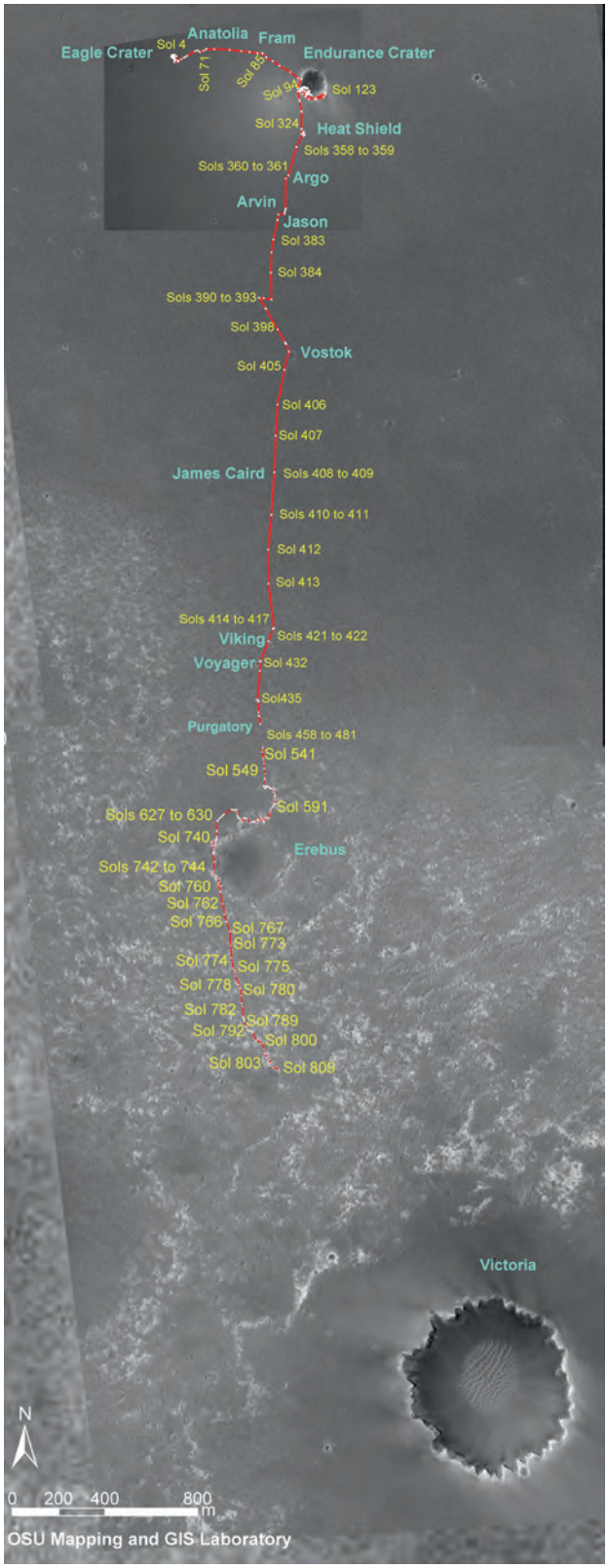

Figure 13.16. *Opportunity*'s traverse in Meridiani Planum as of sol 810 (May 5, 2006). (Base map from MGS/MOC [NASA/JPL/MSSS]. Traverse mapping by T. Parker, R. Li, and the MER/Athena Science Team.) (For a color version of this figure, please refer to the color plate section or to the e-Book version of this chapter.)

exposed within the walls of the crater. From Endurance, the rover began what would be a trek of more than two Earth years across the plains to the south, ultimately arriving at the even larger (800 m diameter) Victoria crater in September, 2006. As of this writing, *Opportunity* has discovered thick, exposed layers of what appear to be sedimentary outcrop rocks at Victoria, and is driving along the rim of the crater searching for a safe entrance and access to those layers. The results described here, however, cover only the part of the plains traverse from Endurance south past a number of plains impact craters and the large (300 m), sand-filled crater Erebus, to a point in the outcrop-rich plains about halfway between Erebus and Victoria (Figure 13.16).

As described in detail in a number of papers (e.g., Squyres *et al*., 2004b, 2006b; Grotzinger *et al*., 2005, 2006; McLennan *et al*., 2005; Morris *et al*., 2006b; see also Chapters 15 and 24), the spherules discovered in Eagle crater and seen along most of *Opportunity*'s traverse have been found to be hematite-rich and have been interpreted as concretions formed from reactions between groundwater and minerals in the sediments. The outcrop rock first seen exposed in the walls of Eagle crater and in the shallow subsurface throughout the plains and studied more deeply at Endurance crater has been found to contain high concentrations of sulfur, chlorine, and bromine as well as the minerals hematite and jarosite (a ferric hydroxosulfate: $(K,Na,H_3O)(Fe,Al)_3(SO_4)_2(OH,Cl)_6$, where $Fe > Al$ and $OH > Cl$). The composition and mineralogy of the outcrop, combined with several key sedimentary features associated with its fine-scale layering, have led to the interpretation that it is a sedimentary sandstone deposit composed of grains of aqueously altered basaltic material and evaporitic sulfate salts, subsequently reworked by aeolian and additional aqueous processes. These features and processes are consistent with origins in a dune- and interdune/playa geologic setting. These interpretations are extremely exciting; if correct, they imply that there were water-saturated near-surface sediments, including some surface water-lain deposits, in this region of Mars early in the planet's history, and that by terrestrial standards, Mars may once have been "habitable" (see Knoll *et al*. [2005] and Chapter 26 for additional discussion of the astrobiological implications). However, there have been initial alternate hypotheses for the formation of the materials observed at Meridiani that do not necessarily involve abundant surface or near-surface liquid water (e.g., Knauth *et al*., 2005; McCollom and Hynek, 2005; Zolotov and Shock, 2005; see also Squyres *et al*., 2006c).

This section of the chapter parallels the sections above for *Spirit* in that we describe the major classes of rocky and fine-grained materials that were characterized by the *Opportunity* Pancams along the Meridiani Planum traverse. Just like at Gusev, Pancam multispectral imaging provides constraints on the composition and mineralogy of these materials that can be used to enhance, augment, or provide context for more diagnostic measurements from other rover and orbital visible and near-infrared (VNIR) instruments.

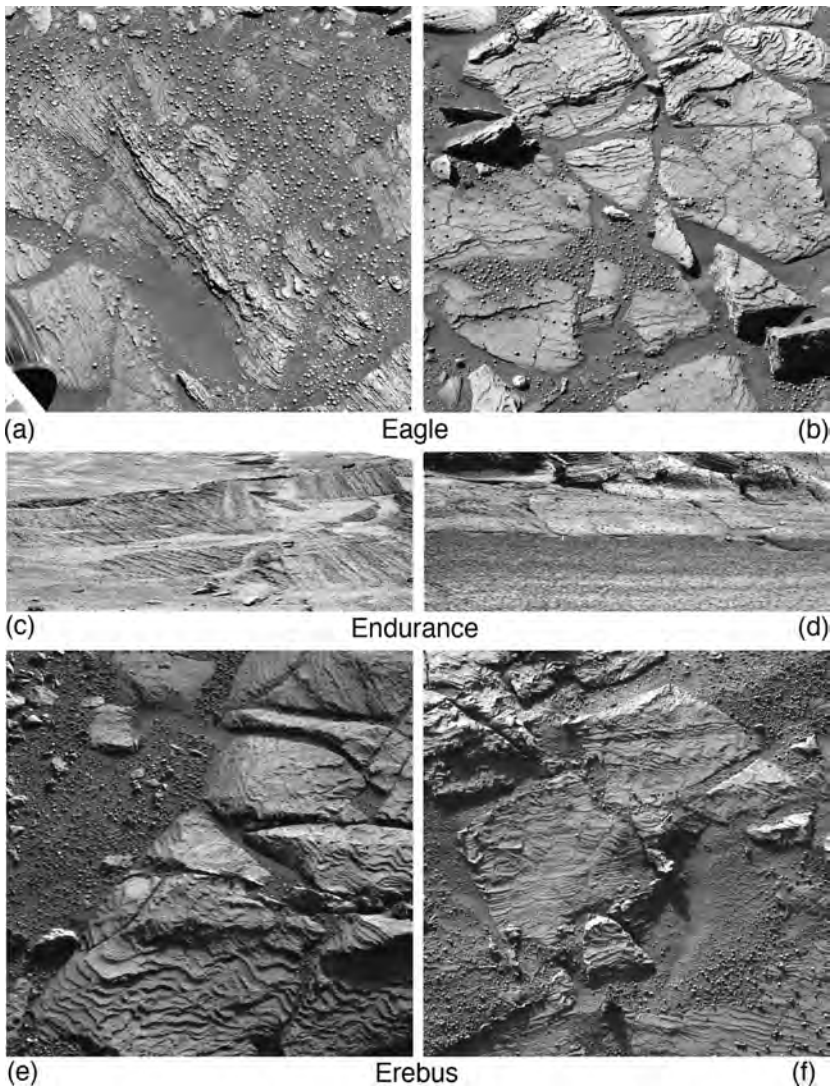

Figure 13.17. Examples showing high-resolution imaging to examine outcrop layering and sedimentary features such as lamination and crossbedding. (a) Sol 43B P2555 R1; (b) Sol 49B P2400 L7; (c) Sol 288B P2544 Super-res L6; (d) Sol 289B P2549 L7; (e) Sol 666B P2589 L7 (16:19 LTST); (f) Sol 690B P2564 L7.

13.3.2 Outcrop rocks and fracture fill

Geomorphology

Pancam monochromatic and stereoscopic observations of rocks and rocky materials at Meridiani Planum, especially at low solar–illumination angles, have played important roles in developing models of the geologic history of the region and in selecting specific targets for detailed *in situ* chemical, mineralogic, and MI investigations. Of particular importance for Meridiani outcrop rocks has been the use of the camera's highest spatial resolution near-UV stereo filter combination (the L7 and R1 filters, with effective wavelengths around 435 nm; Bell *et al.*, 2003), low-solar-illumination-angle-imaging conditions, and image dithering-enhancement techniques ("super resolution"; Bell *et al.*, 2006b) that all maximize the ability to discern and characterize fine textural detail on rocky surfaces.

For example, blue filter imaging observations within Eagle and Endurance craters and along the rim of Erebus crater have revealed spectacular detail within fine-scale (mm- to cm-thickness) laminated outcrop rocks and layered sedimentary deposits (Figure 13.17). The high resolution and textural detail have allowed specific sedimentological features and facies (different depositional environments or units within one or more related formations) to be identified and mapped, including high-angle, likely aeolian crossbed sets (Figure 13.17c; Grotzinger *et al.*, 2005) and trough (festoon) cross-lamination, likely generated by standing waves in shallow surface water (Figure 13.17e,f; Grotzinger *et al.*, 2006). As described in detail by Squyres *et al.* (2004b, 2006b), Grotzinger *et al.* (2005, 2006), and in Chapter 24, these morphologic observations provide evidence for both aeolian and surface liquid-water processes having acted, perhaps episodically or rhythmically, in the near-surface environment at Meridiani Planum. They also provide morphologic indications of diagenetic processes (physical and/or chemical changes in sediments after their deposition) having acted at the site, a hypothesis that has been tested using carefully targeted *in situ* APXS and Mössbauer chemical and mineralogic measurements. High-resolution and multispectral Pancam images provide essential context for the *in situ* chemical and mineralogical measurements, including close-up views made with the MI.

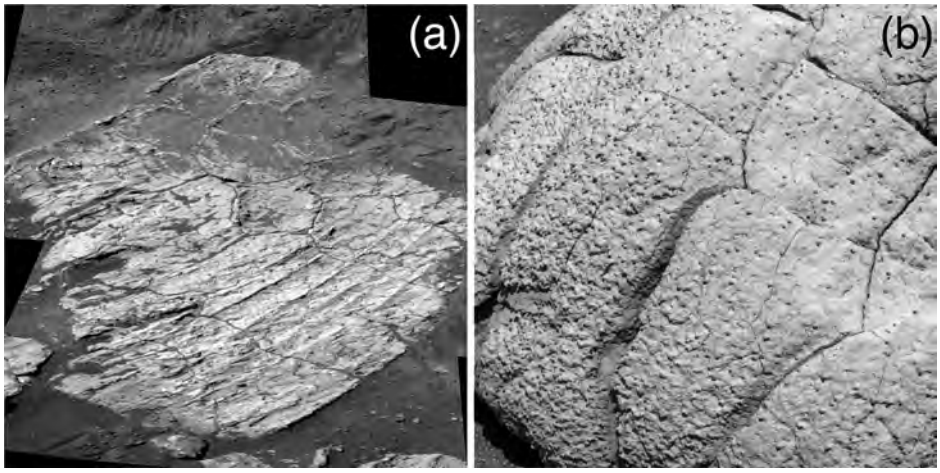

Figure 13.18. Examples of polygonal textures in rock surfaces in Endurance crater. (a) Polygonal desiccation features resembling mud cracks in the rock dubbed "Escher"; Sol 208B P2423 L2. (b) Polygonal texture resembling "septarian" fracture network possibly caused by shrinkage accompanying desiccation in rock dubbed "Wopmay"; Sol 49B P2400 L2.

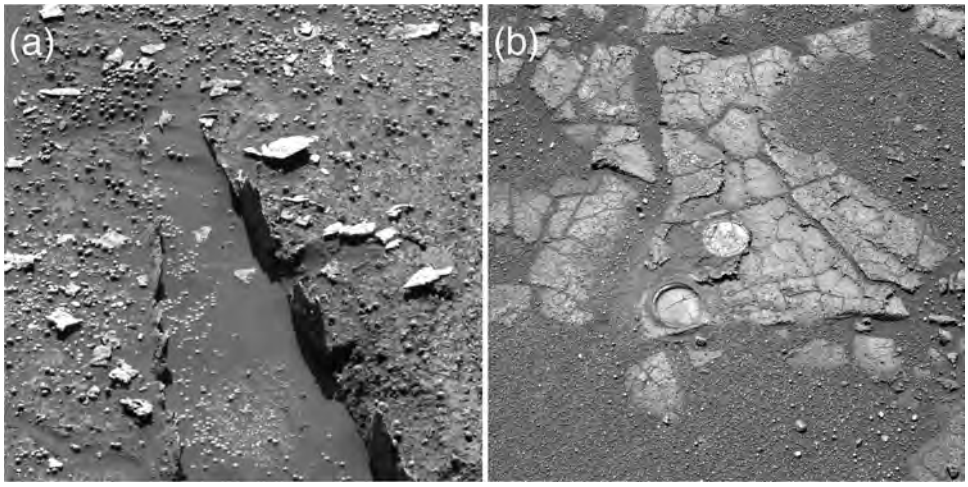

Figure 13.19. (a) Example of a fracture-lining deposit within Endurance crater rock "Razorbacks"; Sol 170B P2598 L7. (b) Example of thick rind developed on the outcrop surface of "Lemon Rind"; Sol 561B P2591 L7. In (b), the upper RAT hole is in the rind whereas the lower RAT hole is in the underlying rock.

A number of other examples of the usefulness of high-resolution morphologic observations in inferring or constraining the composition and/or origin of features have been encountered at Meridiani. For example, the presence of surfaces within Endurance crater that exhibit polygonal fractures (Figure 13.18) have been used to test hypotheses for the origin of these features as (for example) desiccation cracks or a type of "patterned ground" related to freeze-thaw cycling or ice wedging (e.g., McLennan *et al.*, 2005; Jolliff and McLennan, 2006). Thin, apparently fragile rinds and fracture-filling vein-like materials have also been observed in some Meridiani outcrop rocks (Figure 13.19; also discussed below), and models are being developed to test between possible origins of this material from mobile, salt-rich solutions moving up from buried deposits into near-surface fractures in the rock, versus surface aeolian- or perhaps water-transported materials falling down into the fractures (e.g., McLennan *et al.*, 2005; Knoll *et al.*, 2008).

Multispectral properties

Outcrop rocks in Eagle crater and the Meridiani plains. Pancam multispectral observations of rocks in Eagle crater and on the plains and in the rims of craters south of Endurance crater revealed two main color classes of outcrop rocks. In stretched RGB (red, green, and blue) false-color composites generated from Pancam's left eye red-infrared, green, and blue UV filters (Table 13.1), these two color classes appear yellow- to buff-colored and red- to purple-colored (e.g., Figure 13.20). These kinds of false-color composites significantly enhance what are, in reality, only very subtle color differences when viewed in natural or approximate true color (see Figure 13.20c below).

A distinctive spectral parameter that defines the difference between these two classes is the 482–535 nm spectral slope: the "buff-colored" (in false-color composites) surfaces have a higher 482–535 nm slope than the "purple-colored" rock surfaces. Thus, Farrand *et al.* (2007b) referred to these classes as the high 482/535 slope (HFS; buff) and the low 482/535 slope (LFS; purple) classes. Representative spectra of these color units are shown in Figure 13.20d. The HFS surfaces are also generally characterized by a flat to convex NIR spectrum and the LFS surfaces by a flat to concave (shallow absorption centered at 900 nm) NIR spectrum. LFS surfaces are most often associated with steeper faces (such as on the rock "Cathedral Dome" shown in Figure 13.20) and the distal portions of outcrop layers. HFS surfaces are most often flat-lying. Figure 13.20a,b

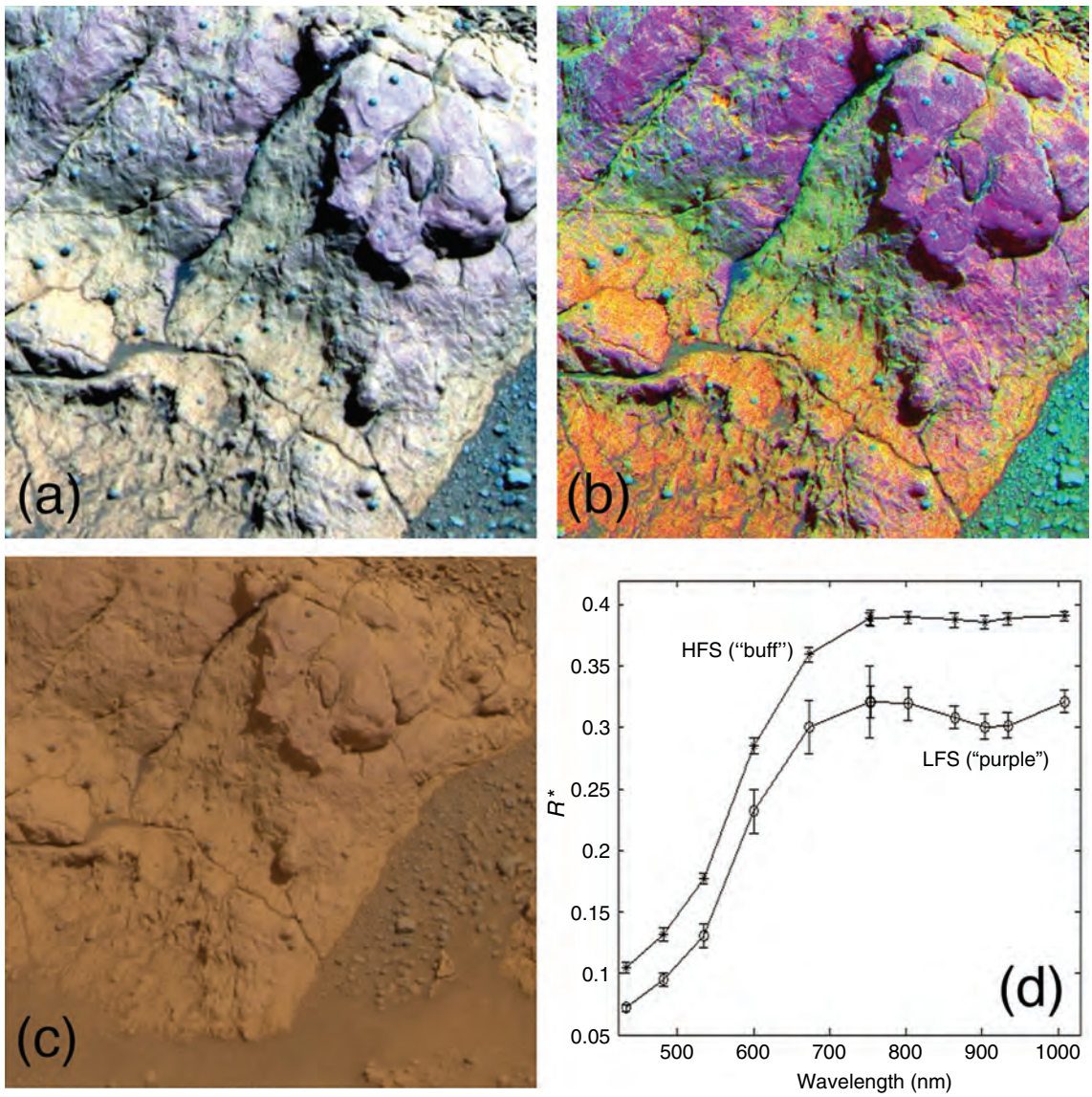

Figure 13.20. (a) Pancam false-color RGB composite from filters L3, L5, and L7 (Table 13.1) from *Opportunity* sol 33 P2589 image sequence on "Cathedral Dome" in Eagle crater. (b) Decorrelation stretch (DCS; see text) version of (a). As described in the text, the purple-colored, massive appearing section is an example of the LFS spectral class. The yellow to buff-colored lower angle portions of outcrop below and above the massive appearing section are examples of the HFS spectral class. (c) Approximate true color rendering of this scene (e.g., Bell *et al.*, 2006b) showing that the color differences exaggerated by the false color and DCS methods in (a) and (b) would be extremely subtle to the unaided human eye. (d) Spectra from Eagle crater of the HFS ("buff-colored") and LFS ("purple-colored") spectral classes. LFS spectrum is from a rock surface in the P2575 image sequence on sol 50. HFS spectrum is from a rock surface in the P2532 image sequence on sol 37. (For a color version of this figure, please refer to the color plate section or to the e-Book version of this chapter.)

shows an L357 composite and a Decorrelation Stretch (DCS: essentially a color composite generated from the top three principal components of variance in a dataset; Gillespie *et al.*, 1987) version of the image sequence on Cathedral Dome in Eagle crater. The flat top of that rock,

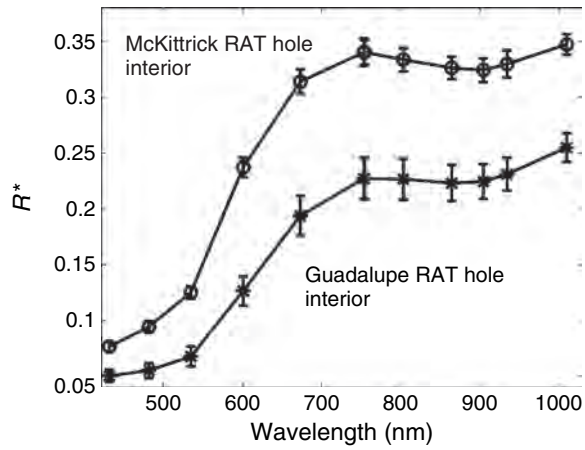

Figure 13.21. Spectra from the interiors of the Guadalupe and McKittrick RAT holes showing inherent spectral differences of different levels of the outcrop at Eagle crater. (From Farrand *et al.*, 2007b.)

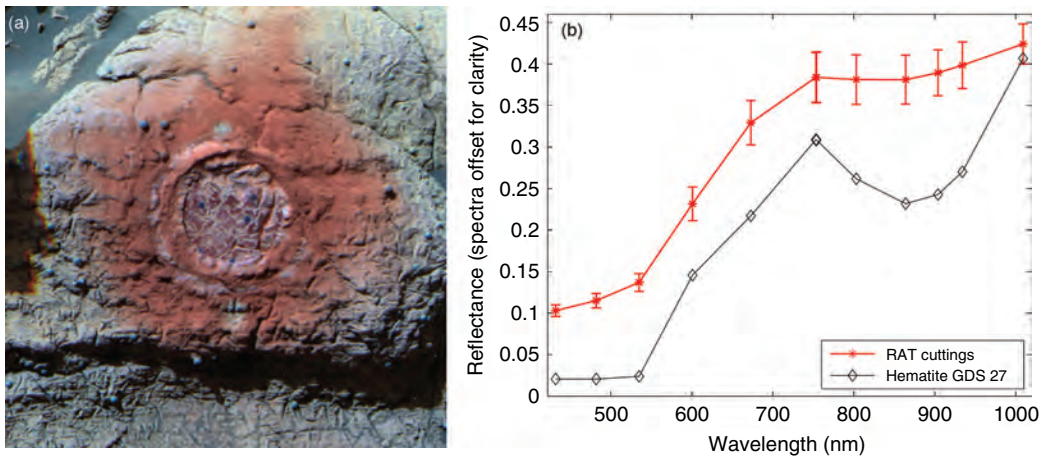

Figure 13.22. (a) False-color composite of the RAT grind into the Guadalupe target in Eagle crater. Note the reddish blanket of RAT cuttings. *Opportunity* Sol 35, Pancam sequence P2598. RGB composite of images at 753, 535, and 432 nm. (b) Comparison of a laboratory spectrum of red hematite, convolved to Pancam bandpasses, and the Guadalupe RAT cuttings. (For a color version of this figure, please refer to the color plate section or to the e-Book version of this chapter.)

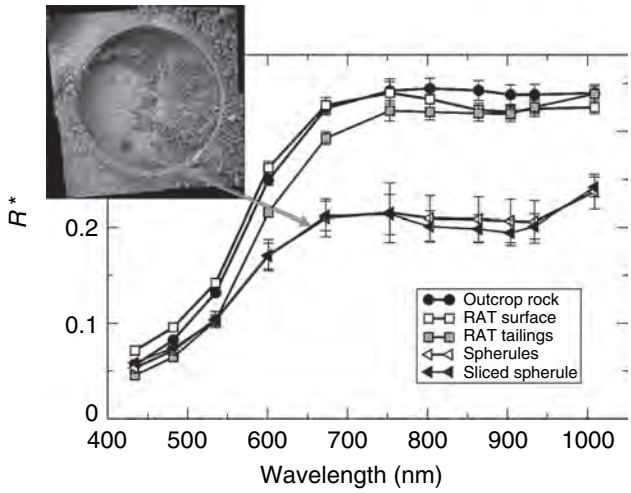

Figure 13.23. Pancam spectra of the Tennessee RAT hole and surrounding materials (Sol 140, P2500). R^* is the radiance factor normalized by the solar elevation angle (Bell *et al.*, 2006b). Inset is Microscopic Imager mosaic (Sol 139) showing 4.2 mm diameter spherule cut into by the RAT, whose Pancam spectrum is nearly identical to that of undisturbed spherules on the nearby soil surface. Also shown are spectra of undisturbed outcrop rock, abraded and brushed surface of the RAT hole, and tailings from the RAT grind.

the lower-angle lower portion, and vugs (small cavities) and other furrows or cracks in the rock are HFS-class materials and the steeper face is LFS-class material. One interpretation relies on the hypothesis that all of these outcrop rocks have an external veneer or rind of more weathered (more Fe^{3+}-rich) HFS-class minerals. The weathered veneer could be partially or wholly stripped away on steeper, wind-scoured LFS-class faces (which have been shown to be more resistant to RAT grinding and thus presumably more resistant to erosion than the weathered veneers; e.g., Arvidson *et al.*, 2004). However, the veneers remain on more flat-lying surfaces and in sheltered vugs and furrows where they are less susceptible to wind-related erosion. Additionally, RAT brushing of some HFS surfaces has also revealed LFS surfaces beneath (Farrand *et al.*, 2007b).

Despite the interpretation of the HFS surfaces as a weathering veneer, Pancam observations have revealed some inherent color differences in rock interiors as well. For example, the McKittrick and Guadalupe RAT hole interiors have distinctly different visible to NIR spectra (Figure 13.21). Some of this difference could be due to slightly differing degrees of brushing and "cleaning" of the RAT holes, however. Pancam spectra also reveal evidence of disseminated, fine-grained crystalline ("red") hematite within the outcrop, because cuttings from RAT grindings have spectral features indicative of fine-grained red hematite (e.g., Figure 13.22; Bell *et al.*, 2004b; Farrand *et al.*, 2007b). While grinding of larger gray-hematite-bearing spherules (discussed below) could produce fine-grained red hematite in some RAT holes, Mössbauer measurements on a number of spherule-free RAT holes also show the presence of hematite not associated with spherules within the sulfate-rich rock (Morris *et al.*, 2006b).

Outcrop rocks in Endurance and Erebus craters. The layers of the Karatepe stratigraphic sequence examined within Endurance crater also exhibited color differences on undisturbed rock surfaces and within RAT hole interiors. As described by Farrand *et al.* (2007b), these differences can be related to subtle variations on the basic HFS and LFS color classes discussed above. Some of the more stark color differences observed between the upper and lower parts of the layered outcrop section exposed at Endurance crater were later determined to be caused largely by rougher textures in the lower part of the section (e.g., Figure 13.23; Grotzinger *et al.*, 2005; Farrand *et al.*, 2007b), which exhibited more shadowing and also appeared to preferentially trap dark basaltic sand. Still there were color differences observed among the undisturbed Karatepe units which, in association with textural differences noted in other Pancam and MI images, were used to establish the stratigraphy of these sedimentary units and to select targets for *in situ* examination.

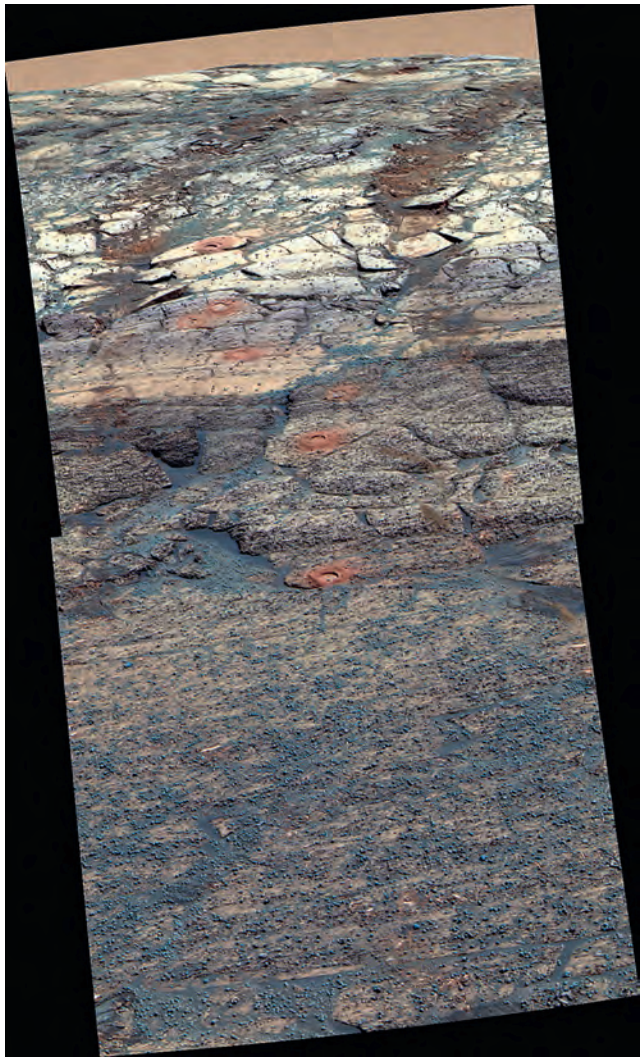

Figure 13.24. Sol 174B Pancam sequence P2401 "Backroads" observation (Farrand *et al.*, 2006). This false color RGB (754, 535, 432 nm) image looks back up the pathway just inside the crater rim on the route taken by *Opportunity* into Endurance crater. RAT hole investigations (bright reddish circular holes here) were made into each of the distinctive strata identified with Pancam color images. (For a color version of this figure, please refer to the color plate section or to the e-Book version of this chapter.)

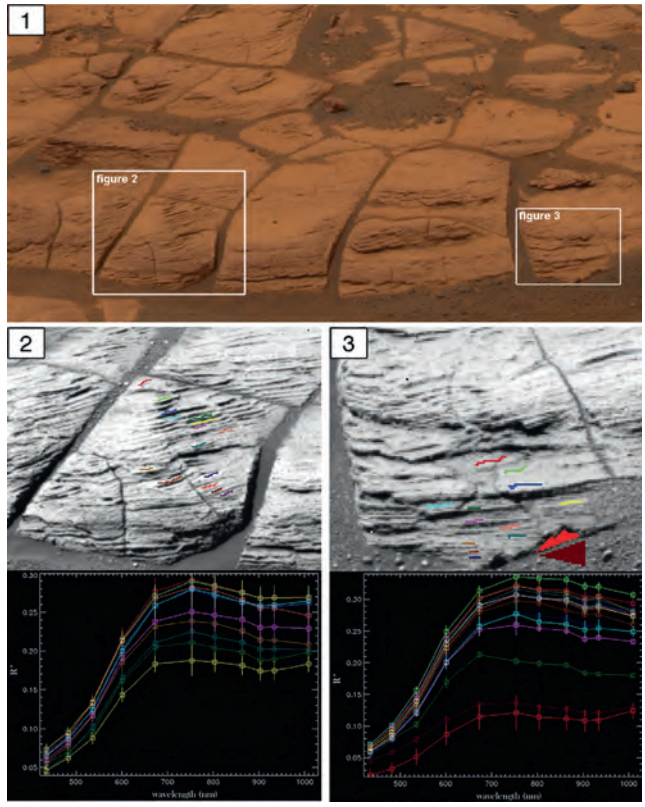

Figure 13.25. Panel (1): Example outcrop material in approximate true color to demonstrate the exposure of sedimentary laminations. Image from sol 648 Pancam sequence P2574. Panels 2 and 3 are denoted by white frames. Panel (2): Closer view of rock fragment in Panel 1 displayed here in the blue filter image (L7, 432 nm). The colors of the spectral profiles plotted correspond to the colors of the selected pixels on the image. Error bars represent standard deviations of pixels in selected regions of interest. Panel (3): Closer view of rock fragment in Panel 1 displayed here in the blue filter image (L7, 432 nm). The colors of the spectral profiles plotted correspond to the colors of the selected pixels on the image. The dark green spectrum is a layer like the others but has a slope sign change from 673 to 753 nm unlike the other lamination plots. The two red shallow profiles are of soil and rind materials near the base of the rock; note the strong positive slope in the longer wavelength region. Error bars represent standard deviations of pixels in selected regions of interest. (For a color version of this figure, please refer to the color plate section or to the e-Book version of this chapter.)

For example, the series of RAT holes created during the entrance into Endurance crater (Figure 13.24) were analyzed by all instruments to provide a suite of geochemical and mineralogical measurements along the stratigraphic sequence of outcrop rocks at Karatepe West (e.g., Clark *et al.*, 2005; McLennan *et al.*, 2005; Morris *et al.*, 2006b). Pancam spectra demonstrated that the abraded and brushed surfaces of the RAT holes were quite similar in their overall high reflectances and weak 900 nm absorption features. RAT tailings exhibited slightly more pronounced absorptions, interpreted to reflect the presence of fine-grained hematite (Farrand *et al.*, 2007b). Pancam spectra of the interior of spherules cut by the RAT were nearly identical to undisturbed spherules present on the surface, consistent with their lack of interior structure in MI images (Figure 13.23). Millimeter-scale nodules and overgrowths on spherules eroded from this section of the outcrop were interpreted by McLennan *et al.* (2005) to represent second generation cements. Pancam spectra of the overgrowths are nearly identical to those of the outcrop rocks.

Many Pancam images of Meridiani outcrop surfaces have sufficient spatial resolution (<10 mm) to allow detailed multispectral studies on individual sedimentary structures as well as erosional and possible secondary diagenetic features (i.e., fracture fill and rind materials, discussed below). For example, Figure 13.25 shows the results of an analysis of fine laminations in outcrop rock near the rim of Erebus crater (Thompson *et al.*, 2006). Typically, from 10 to 30 pixels could be analyzed from individual laminations across approximately 10 cm of vertical stratigraphic section in this region. Nearly all laminations were exposed in direct sunlight, where image quality was sufficient for pixel selections

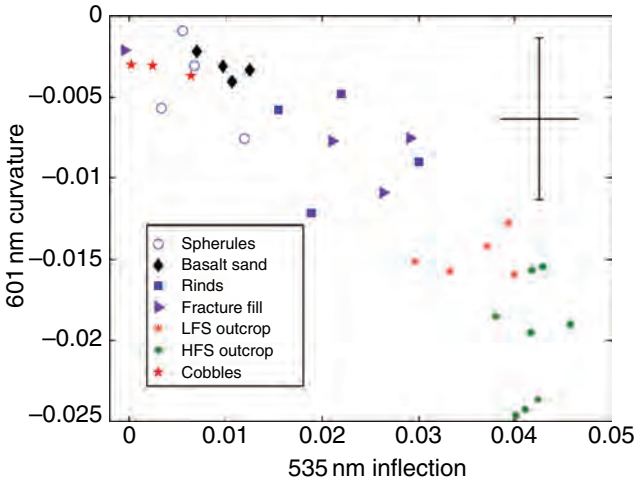

Figure 13.26. Plot of 535 nm band depth versus 601 nm band depth for Meridiani Planum surface materials. (Based on Farrand *et al.*, 2007b.) (For a color version of this figure, please refer to the color plate section or to the e-Book version of this chapter.)

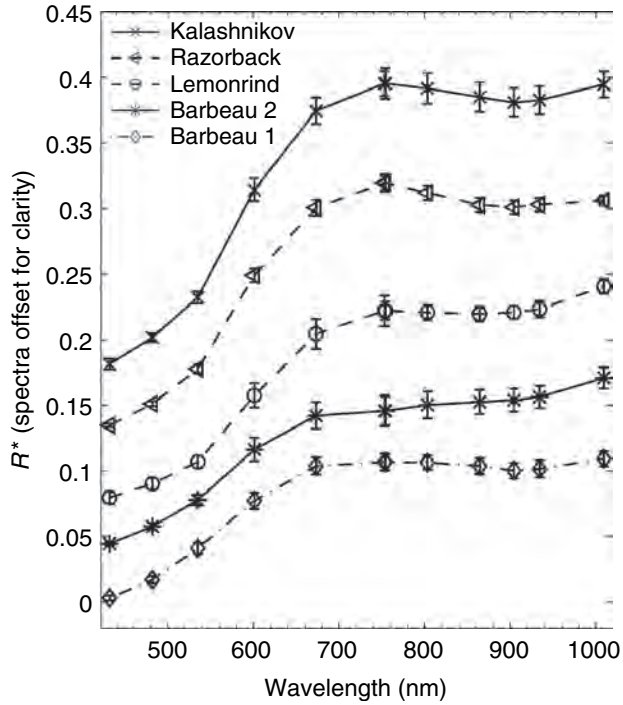

Figure 13.27. Spectra of coating/fracture-fill materials from Endurance crater. An example of the "red rind" material from the Shoemakers Patio area at Eagle crater is also provided, from the target named Kalashnikov. The Barbeau 2 material spectrum is offset upward by 0.02.

in all bands, and where interfering physical effects, such as shadows or changing phase angles due to topography, could be minimized. Example spectra from some of these laminations are also shown in Figure 13.25. Most outcrop spectra at this fine scale exhibit a steep positive slope in the visible region and subtle changes in the NIR (e.g., flat, concave, or convex profiles in the 753–1009 nm region and weak absorption features in the 904 to 934 nm region). Reflectance maxima are typically in the 750–850 nm region but have been observed as low as 673 nm and as high as 1009 nm, with the latter usually related to the presence of the lower albedo materials (i.e., spherules and basaltic sands). A major difference between the specific outcrop layers analyzed here is in the slope of the spectrum in the 934–1009 nm region. Positive slopes at these wavelengths are consistent with the presence of hematite, likely associated with the spherules (e.g., Bell *et al.*, 2004b; Farrand *et al.*, 2007b). Interestingly, the higher albedo surfaces in Figure 13.25 tend to have the strongest negative spectral slopes at the longest wavelengths. This could be an intrinsic characteristic of the outcrop material or could indicate the presence of a thin weathering rind or dust deposit on these surfaces (perhaps consistent with the observation and interpretation of the weathered HFS surfaces noted above and by Farrand *et al.*, 2007b). Rarely, hematite-rich spectral signatures are present in one lamination and not in the adjacent layers. Occurrences like this could be the result of a single iron-rich primary sedimentary episode or a secondary process such as diagenetically related cementation or recrystallization, or could be associated with an invasive vein or fracture fill material. Additional study of these kinds of small-scale spectral variations thus could provide unique insights on the style and extent of the sedimentary depositional events that created the ubiquitous outcrop rocks studied by *Opportunity* in Meridiani Planum.

Rinds and fracture fills. As noted above, examples of rinds and fracture fill materials were encountered in Pancam observations, initially in Eagle crater, but also in Endurance crater and on the plains to the south. For example, during the ingress to Endurance crater, fracture-filling materials were observed coating the broken edges of some outcrop blocks (e.g., Farrand *et al.*, 2007b; Jolliff *et al.*, 2006a). Fracture fill materials appear to have color properties distinct from other parts of the outcrop. For example, in plots of spectral parameters such as the 535 nm band depth versus 601 nm band depth (Figure 13.26), the rind and fracture fill materials plot between the outcrop and other components of the Meridiani surface layer (namely, basaltic sands, hematitic spherules, and dark cobbles). These materials can have variable spectral properties but are often characterized by higher reflectances at the shortest visible wavelengths and a discernable NIR absorption centered at 900 nm (e.g., Figure 13.27; Farrand *et al.*, 2007b). An excellent example was observed along the eastern-most extent of the *Opportunity* traverse, where fracture filling materials extended nearly orthogonally through the Burns Cliff formation (Figure 13.28). Decorrelation stretches of Pancam images showed the surface of these features to exhibit extreme (for Mars) color variations over small length scales, consistent with their inferred emplacement from the presence of intermittent aqueous solutions (e.g., Knoll *et al.*, 2008).

13.3.3 Spherules

Morphology and occurrence

One of the most surprising and exciting findings from *Opportunity*'s exploration of Meridiani Planum was the discovery that the surface, almost everywhere that the rover traversed, was covered by small (1–5 mm), dark, gray to

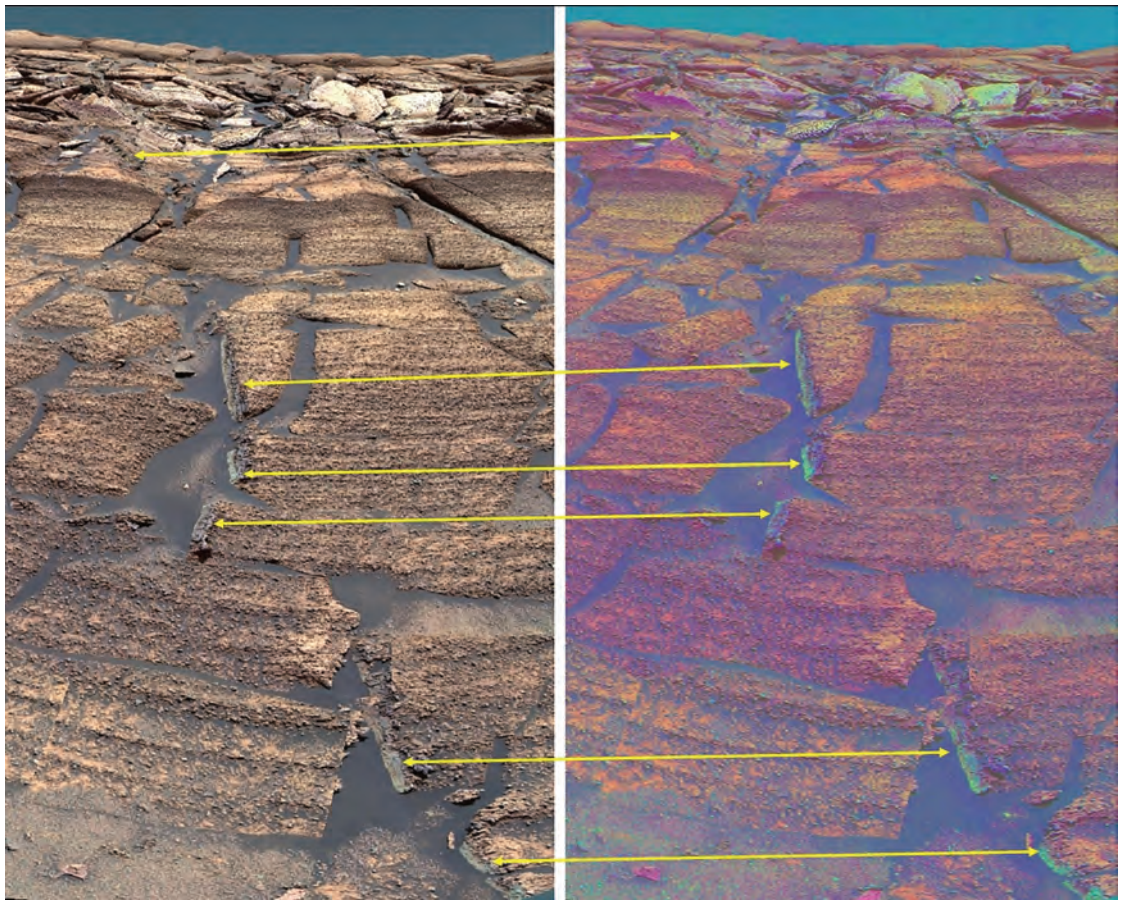

Figure 13.28. (a) Portion of Pancam panorama of Burns Cliff region along southern rim of Endurance crater showing false-color composite (a) created from 754, 535, and 432 nm images, compared to decorrelation stretch (b) from the same images. Yellow arrows point to fracture-fill materials observed here and along the edges of other broken outcrop blocks. (For a color version of this figure, please refer to the color plate section or to the e-Book version of this chapter.)

reddish spherical grains (e.g., Figure 13.29; Soderblom *et al.*, 2004; Weitz *et al.*, 2006). They were given the nickname "blueberries" by the MER science team partly because these spherules are less red than the surrounding soils and outcrop on which they lie (or are embedded), and partly because they light up as garishly blue or purple in false-color Pancam RGB composite images generated using the near-UV (L7, 430 nm), green (L5, 535 nm), and NIR (L2, 750 nm) filters.

The spherules are distinctly harder than the rock in which they occur, hence they stick out on weathered rock surfaces and accumulate as a resistant lag when the other components of the outcrop rocks weather away. They are remarkably spherical and form an "overdispersed" distribution, which is indicative of formation as concretions (e.g., McLennan *et al.*, 2005; see also Chapter 24). That is, they grow by chemical diffusion in an aqueous medium, so they tend to be separated from each other and are not concentrated along primary sedimentary features such as bedding and laminations. This distribution provides strong evidence that the spherules formed in a diagenetic setting, that is, by a reaction after the sediments were buried. In some cases, spherules "inherit" a slight bulge or elongation where they directly intersect a lamination, again consistent with replacive growth after the sediments were buried. Spherules that have been cut by natural processes or ground by the RAT show uniform interiors and lack the concentric zonation commonly seen in terrestrial concretions.

Chemical and mineralogical properties

All of *Opportunity*'s analytical instruments have been used to attempt to determine the mineral and chemical makeup of the spherules. For the Instrument Deployment Device (IDD) instruments and for the Mini-TES, the spherules are always part of a mixed target, either spherules plus rock or spherules plus soil, thus the spherule compositions must be inferred from analyses of the mixtures. Results of chemical analyses clearly reflect enrichment in ferric iron, and modeling the results and chemical trends in terms of mixtures of soil and rock components indicates that the spherules must have at least 50%–60% by weight hematite, and possibly more (Jolliff *et al.*, 2005, 2007; Gellert *et al.*, 2008; Schneider *et al.*, 2007). Results from the Mössbauer spectrometer indicate that among the Fe-bearing phases, hematite is by far the dominant component of the spherules and that they contain no jarosite (Morris *et al.*, 2006b), implying that during growth

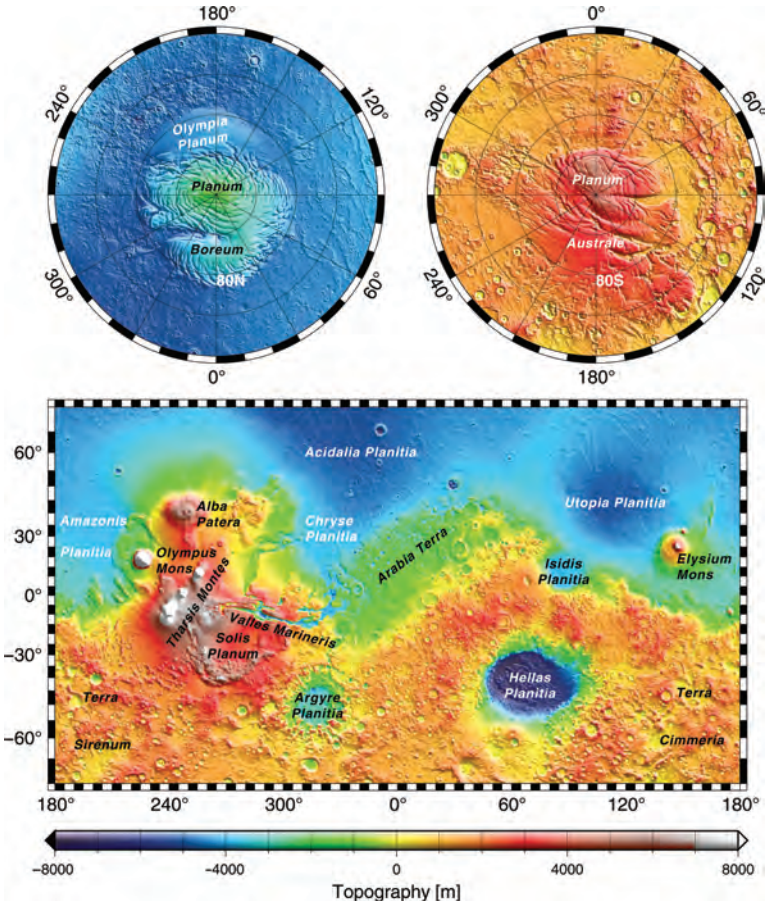

Figure 1.1. Global topography of Mars from the MGS MOLA experiment. (Credit: NASA and the Mars Global Surveyor Mars Orbiter Laser Altimeter Team.)

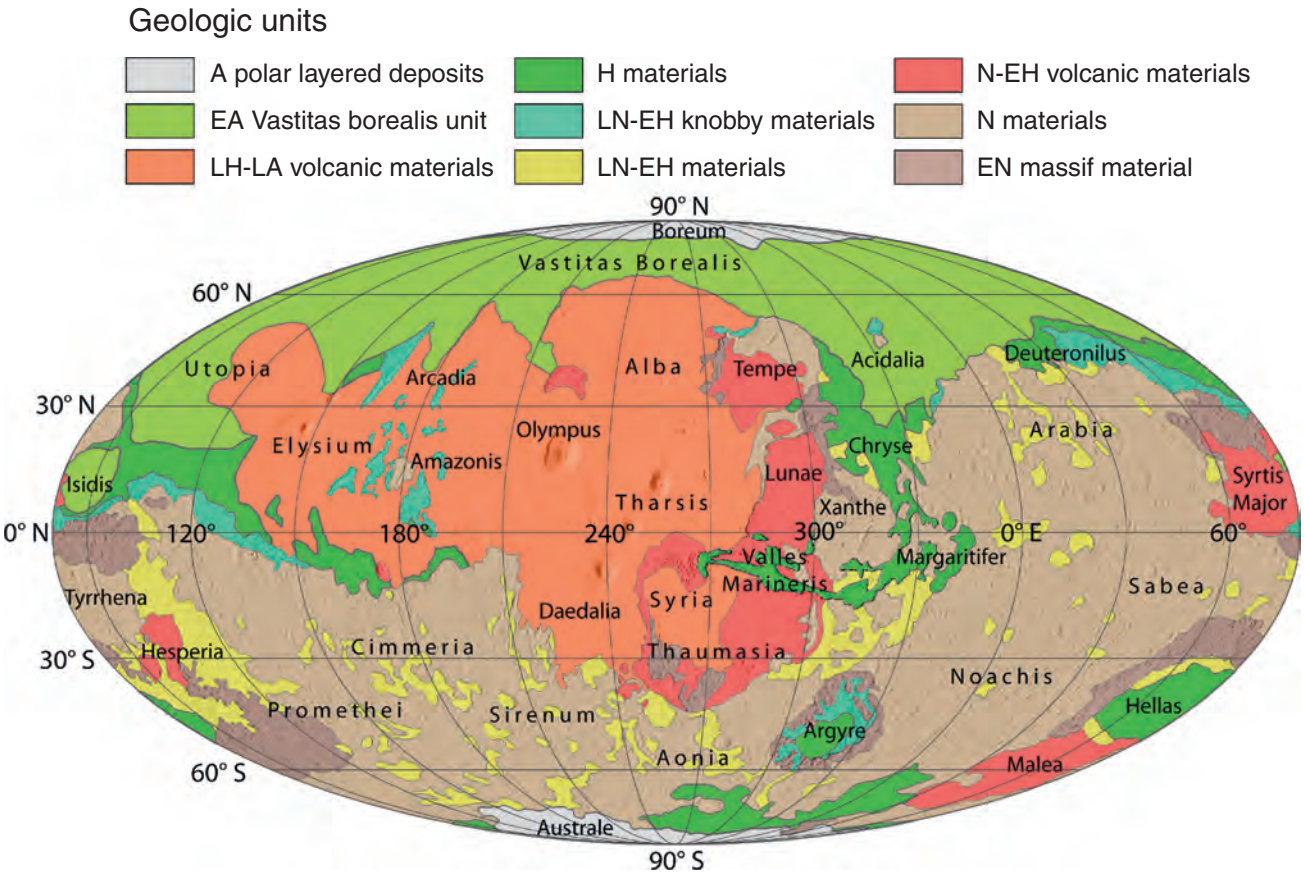

Figure 1.2. (*below*) Generalized global geologic map. Symbols: Early and Late (E and L) Noachian, Hesperian, and Amazonian (N, H, and A). (Credit: Nimmo and Tanaka, 2005, Reprinted, with permission, from the *Annual Review of Earth and Planetary Sciences,* Volume 33; © 2005 by Annual Reviews; www.annualreviews.org.)

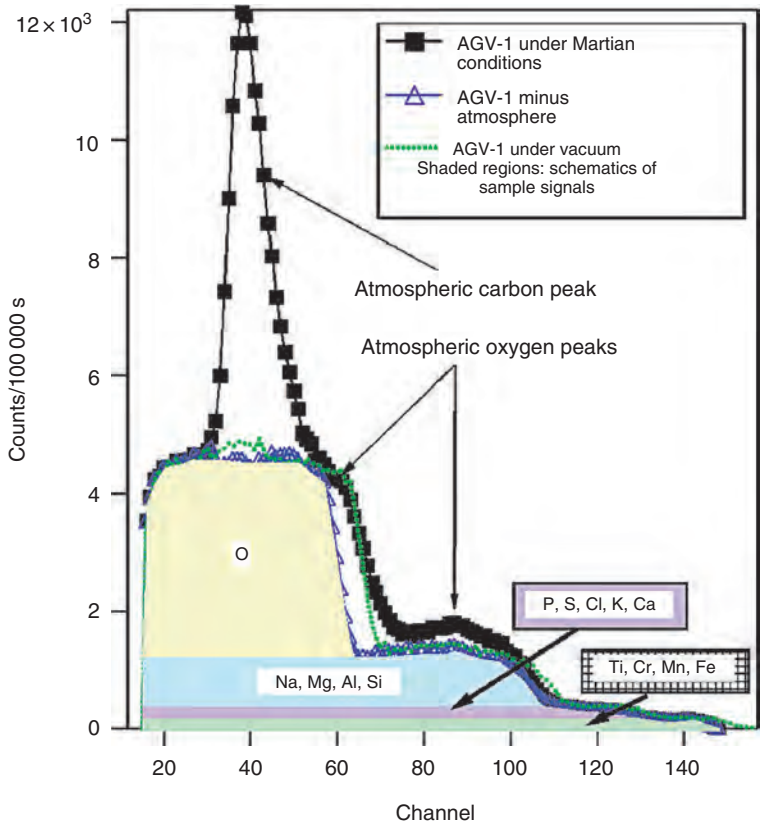

Figure 3.3. Alpha-mode laboratory spectrum of an andesite standard, AGV-1, under Martian conditions. The atmospheric signals from the carbon and oxygen of carbon dioxide form peaks within the AGV-1 sample run. The carbon atmospheric peak is centered at approximately channel 39, while the oxygen atmospheric peaks are centered at approximately channel 60 and 88. Using the atmospheric subtraction technique described within Foley *et al.* (2003a), the atmosphere-free spectrum for AGV-1 has been computed and is plotted here as well. The α spectrum for AGV-1 under vacuum is also shown for comparison. Sample signals for each element are shaded.

Figure 3.9. (*below*) Linear regressions for oxide and element contents, calculated from data in Table 3.1, versus sulfate content for Pathfinder rocks and soils. All of the rocks have considerably less sulfur than the soils and linear trends to no sulfur are made showing that some soil-like component appears to cover the rocks by varying degrees. The linear regressions enable computation of the soil-free rock composition (SFR) and were computed using the technique of Williamson (1968) which takes into account the errors in both the ordinate and the abscissa for each oxide-sulfate pair. Some oxides, such as MgO and SiO_2, show good linear trends to low sulfate content in the rocks. However, other oxides such as Al_2O_3 and CaO, indicate some chemical heterogeneity among the rocks, and the FeO plot illustrates some chemical heterogeneity among the soils.

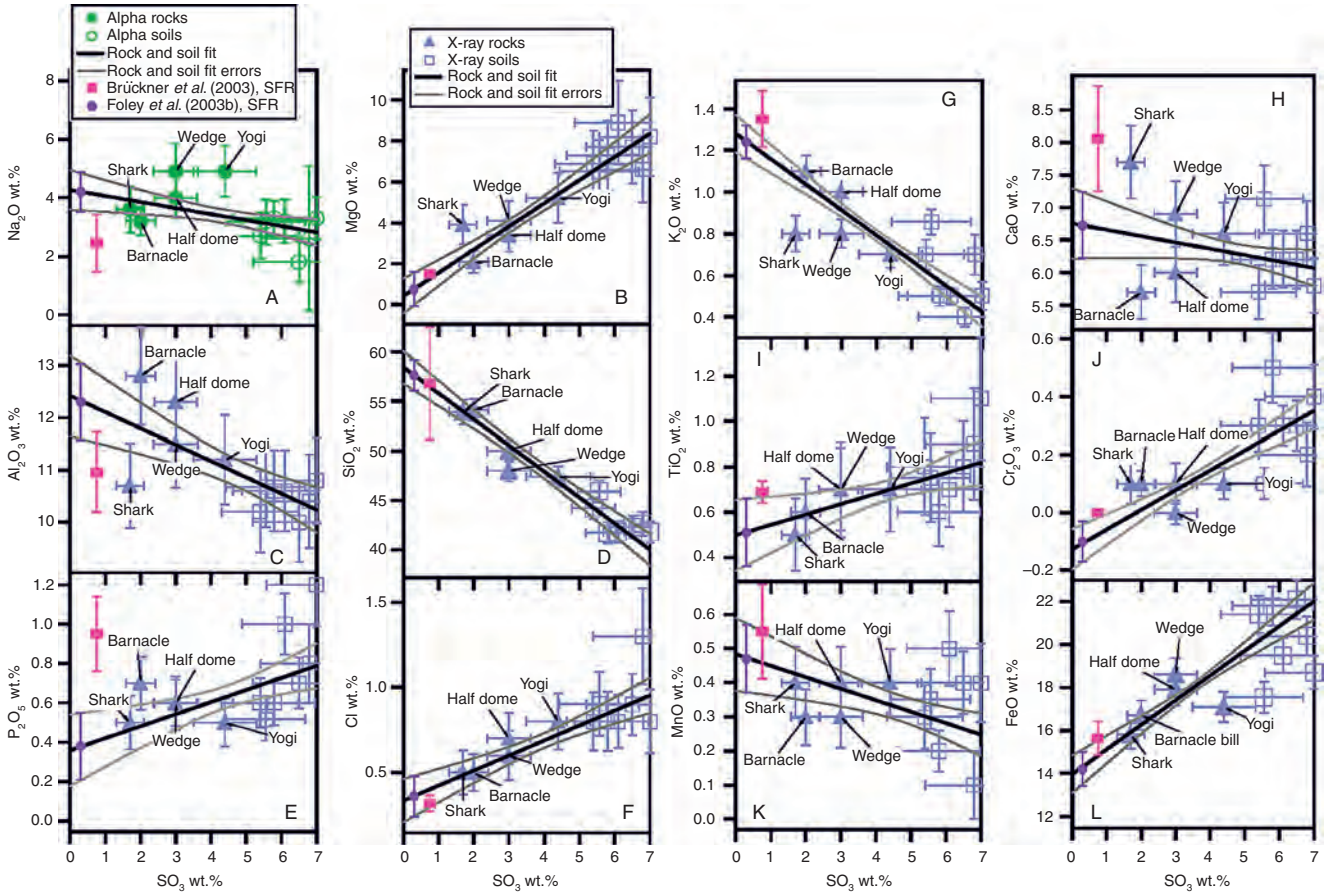

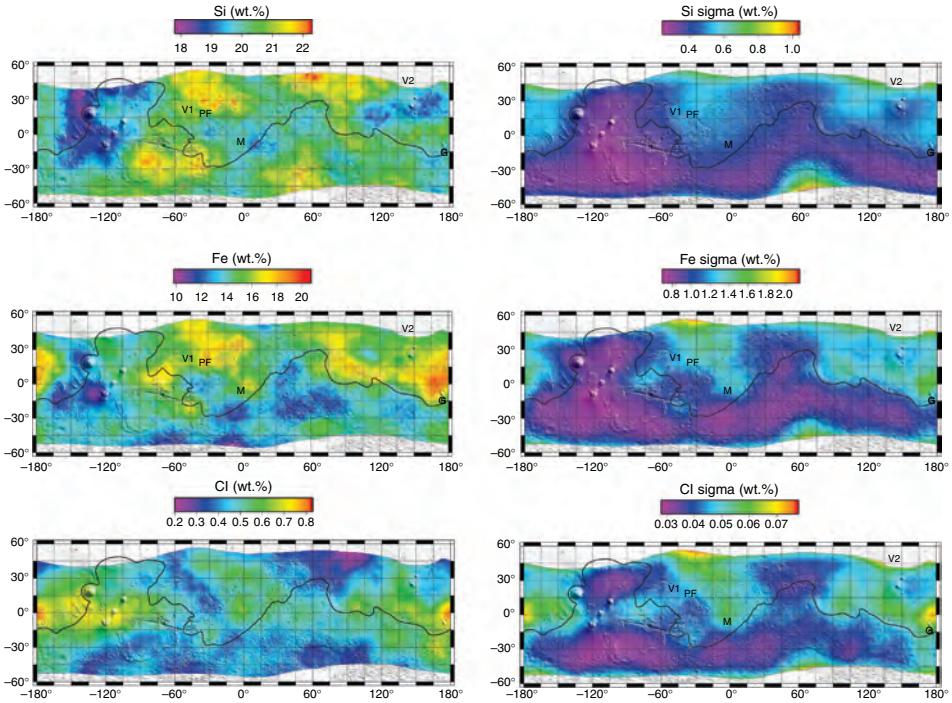

Figure 5.3. Maps of the Si, Fe, and Cl mass fractions (left) and of the $1s_m$ (right) variation at each point on Mars, in the equatorial zone where H concentrations are low enough to allow for ready calculation of elemental abundances. s_m is basically the instrumental uncertainty at each point (as an absolute, not relative, mass fraction) and consequently unrelated to the standard deviation of the sample population. Data have been smoothed using a mean filter. The data are displayed over a shaded relief map of Mars, with mission landing sites indicated (V1: Viking 1 in Chryse Planitia; V2: Viking 2 in Utopia Planitia; PF: Pathfinder in Ares Vallis; M: *Opportunity* in Meridiani Planum; G: *Spirit* in Gusev crater). The black outline is the 0 km contour, which roughly corresponds to the boundary between the southern highlands and northern lowlands.

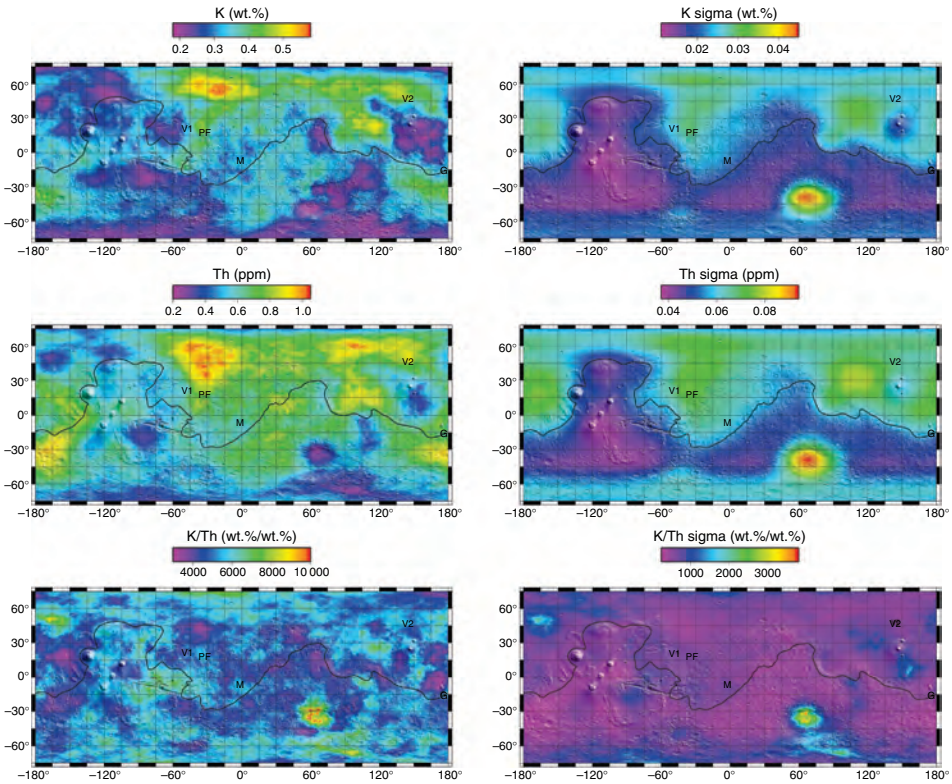

Figure 5.5. Maps (left) of the mass fraction of K (as %), Th (as mg/kg), and K/Th ratio (as ratio of mass fractions) and of the $1s_m$ variation at each point on Mars (right), in the region from 75° S to 75° N, where H concentrations are low enough to allow for ready calculation of elemental abundances; uncertainties are basically the instrumental uncertainty at each point and consequently unrelated to the standard deviation of the sample population. Data have been smoothed using a mean filter. The data are displayed over a shaded relief map of Mars, with mission landing sites indicated (V1: Viking 1 in Chryse Planities; V2: Viking 2 in Utopia Planitia; PF: Pathfinder in Ares Vallis; M: *Opportunity* in Meridiani Planum; G: *Spirit* in Gusev crater). The black outlines are as in Figure 5.3.

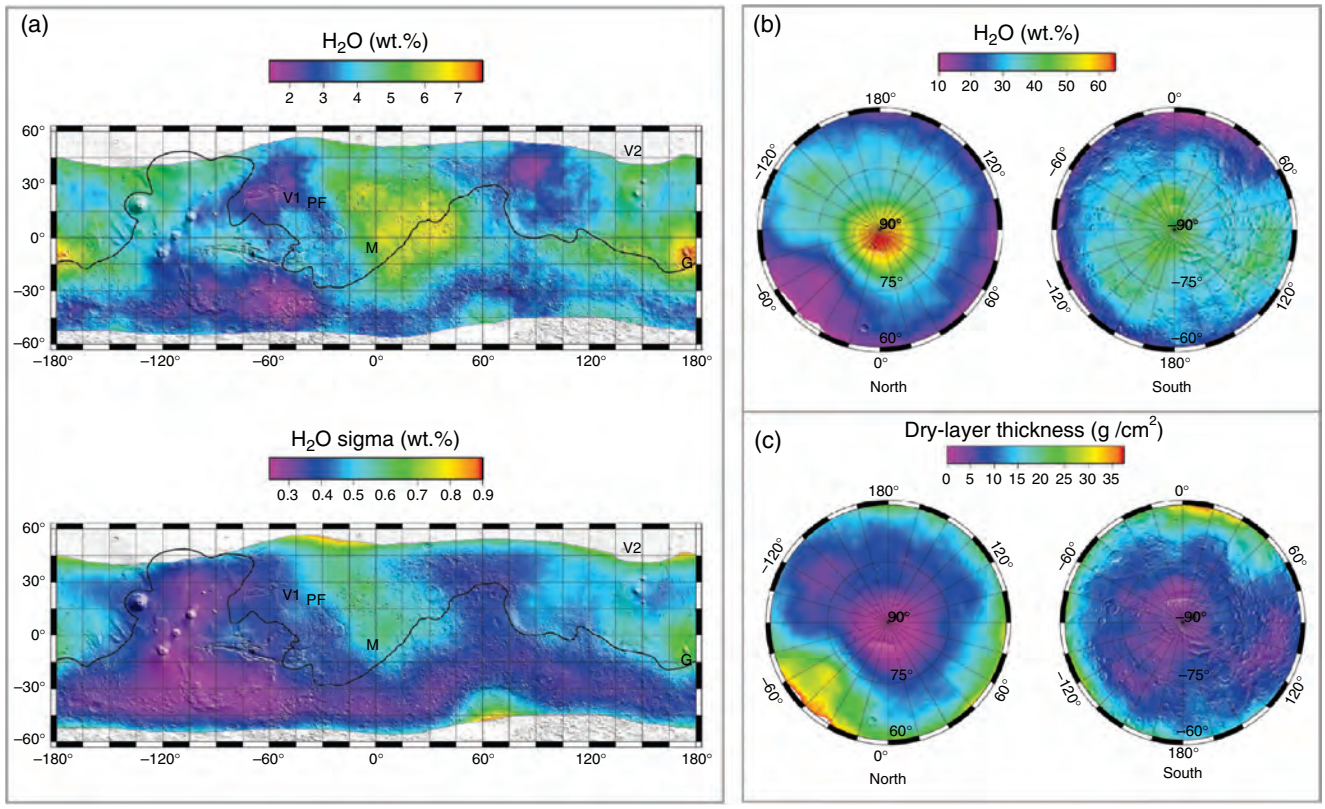

Figure 5.4. (a) Map of the mass fraction (%) of H_2O (stoichiometrically determined from H content) and the $1s_m$ in the equatorial region of Mars. The black outline and letters are as in Figure 5.3. (b) Lower-limit H_2O content in the polar regions based on models shown in Figure 5.7 with the assumption that there is no dry layer, that is, that the H_2O is homogeneously distributed. The high H_2O contents suggest that the ice was deposited on the surface of the soil with modest amounts of dust mixed into the ice as it was being deposited. (c) Map of the maximum dry-layer thickness in the polar regions based on models shown in Figure 5.7, but in this case the assumption is made that the lower layer is actually pure ice, 100% H_2O.

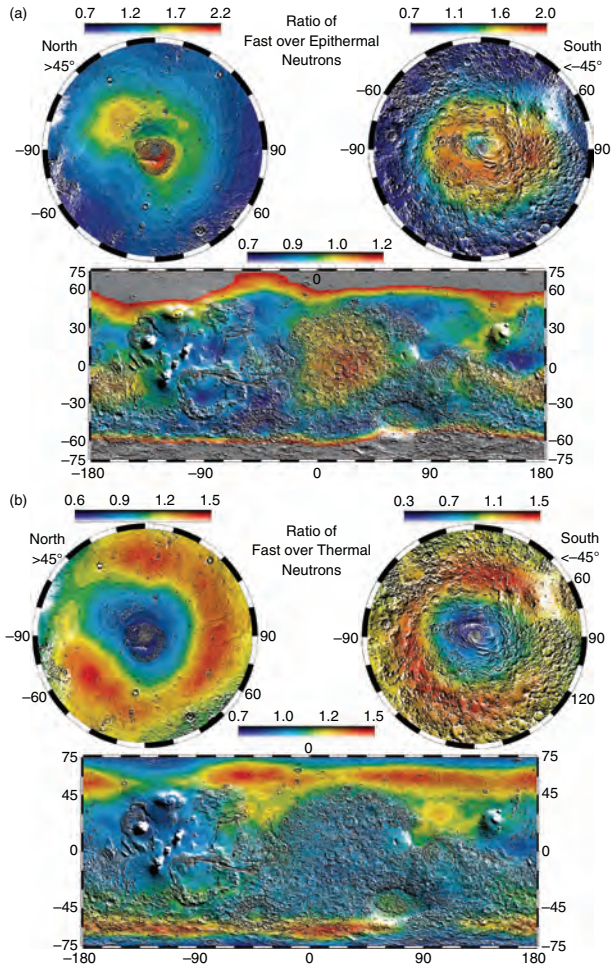

Figure 6.7. (*left*) Maps of the ratios of fast over epithermal (a) and fast over thermal (b) neutron counting rates overlayed on shaded relief maps of Mars. In each set, the top maps are stereographic projections north of +45° latitudes (left) and south of –45° latitudes (right). The bottom maps are cylindrical projections between ±75° latitude.

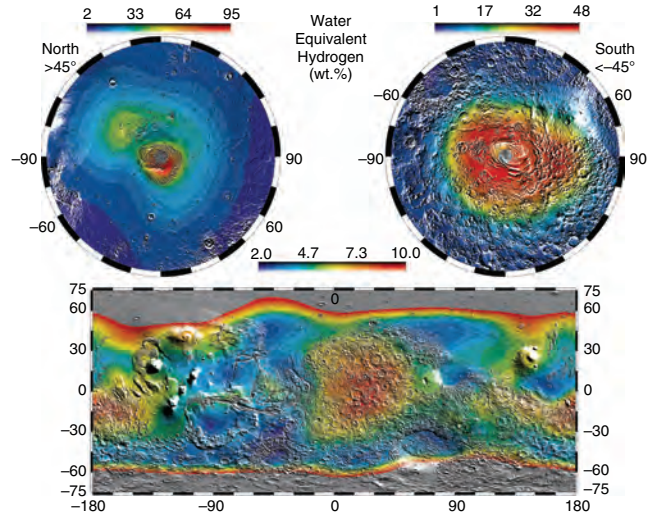

Figure 6.8. (*above*) Maps of water-equivalent hydrogen overlaid on shaded relief maps of Mars. The top maps are stereographic projections north of +45° latitudes (left) and south of –45° latitudes (right). The bottom map is a cylindrical projection between ±75° latitude.

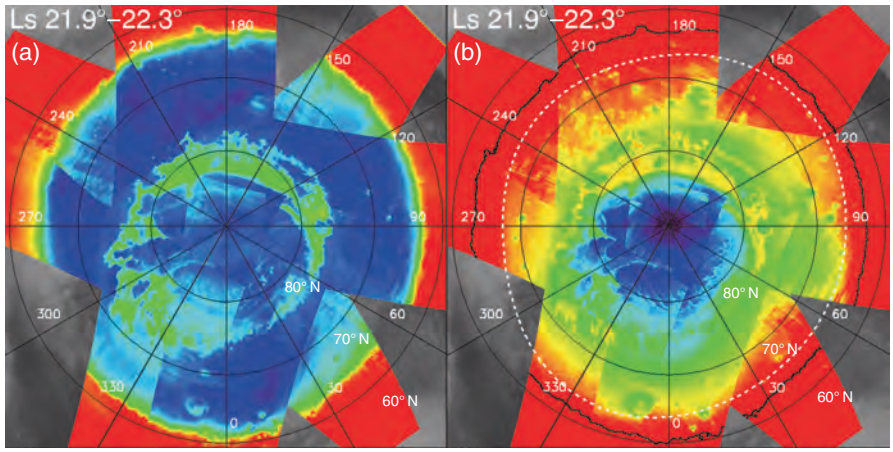

Figure 7.3. Seasonal evolution of the northern polar cap: spatial distribution of spectral signatures of H_2O ice and CO_2 ice observed by OMEGA in early northern spring ($L_s = 22^\circ$, March 2006). (a) Band depth of the H_2O ice absorption feature at 1.5 µm. The rainbow scale covers the range from 60% (black) to 0% (red); (b) band depth of the CO_2 ice absorption feature at 1.43 µm, also from 60% (black) to 0% (red). The annulus observed by TES between the boundary of bright regions (black line on panel (b)) and that of regions at the equilibrium temperature of CO_2 ice (the so-called "crocus line," white dashes, from Titus *et al.*, 2003) is confirmed as being constituted of H_2O frost. At this season, the strongest CO_2 ice signatures (corresponding to large mean grain sizes) are observed over regions corresponding to the central parts of the north permanent cap.

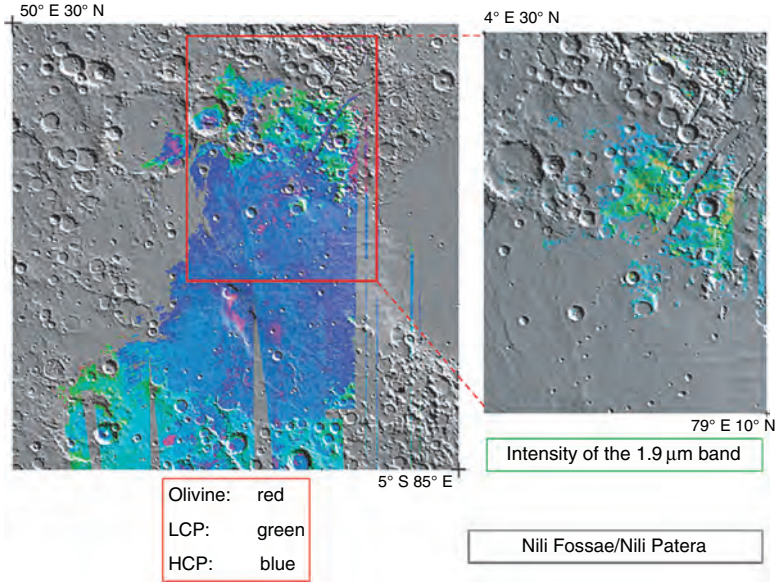

Figure 7.6. OMEGA mineralogical mapping of olivine, pyroxenes, and hydrated clays in the Syrtis Major area. The map at left reveals high-calcium pyroxene (HCP)-bearing lava outflows surrounded by the low-calcium pyroxene (LCP)-bearing Noachian crust and a number of smaller olivine-rich spots. The area in the red box is enlarged on the right and shows the intensity of the 1.93 µm absorption feature interpreted to indicate the location of hydrated clays, found in the ancient terrains and not buried by lava flows.

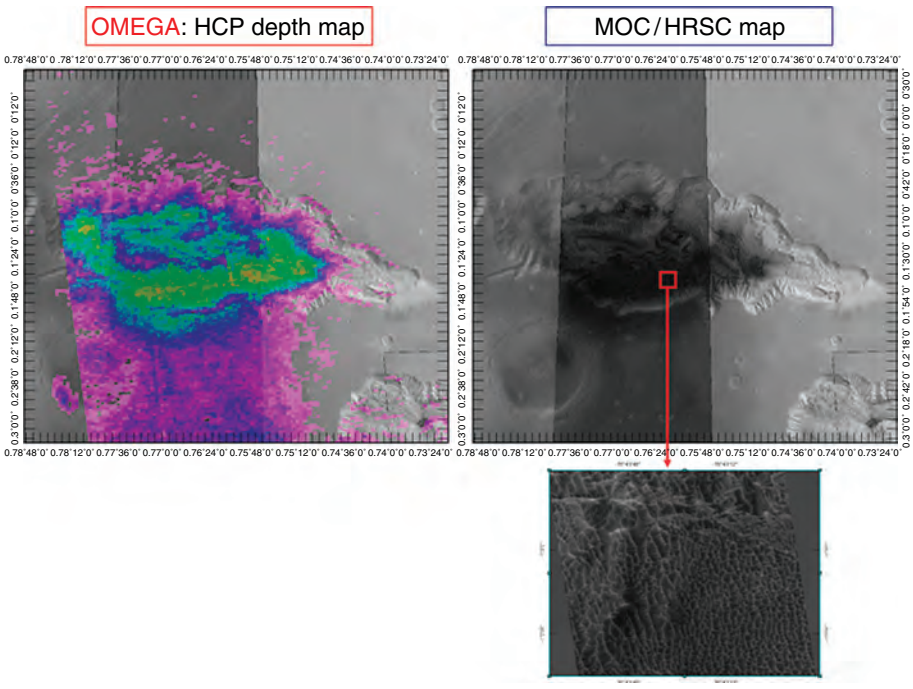

Figure 7.7. Mineralogical (OMEGA) and optical (MOC, HRSC) mapping of Hebes Chasma: HCP band depth (top left) is higher in the dark areas (top right), which appear as sand dunes (bottom right).

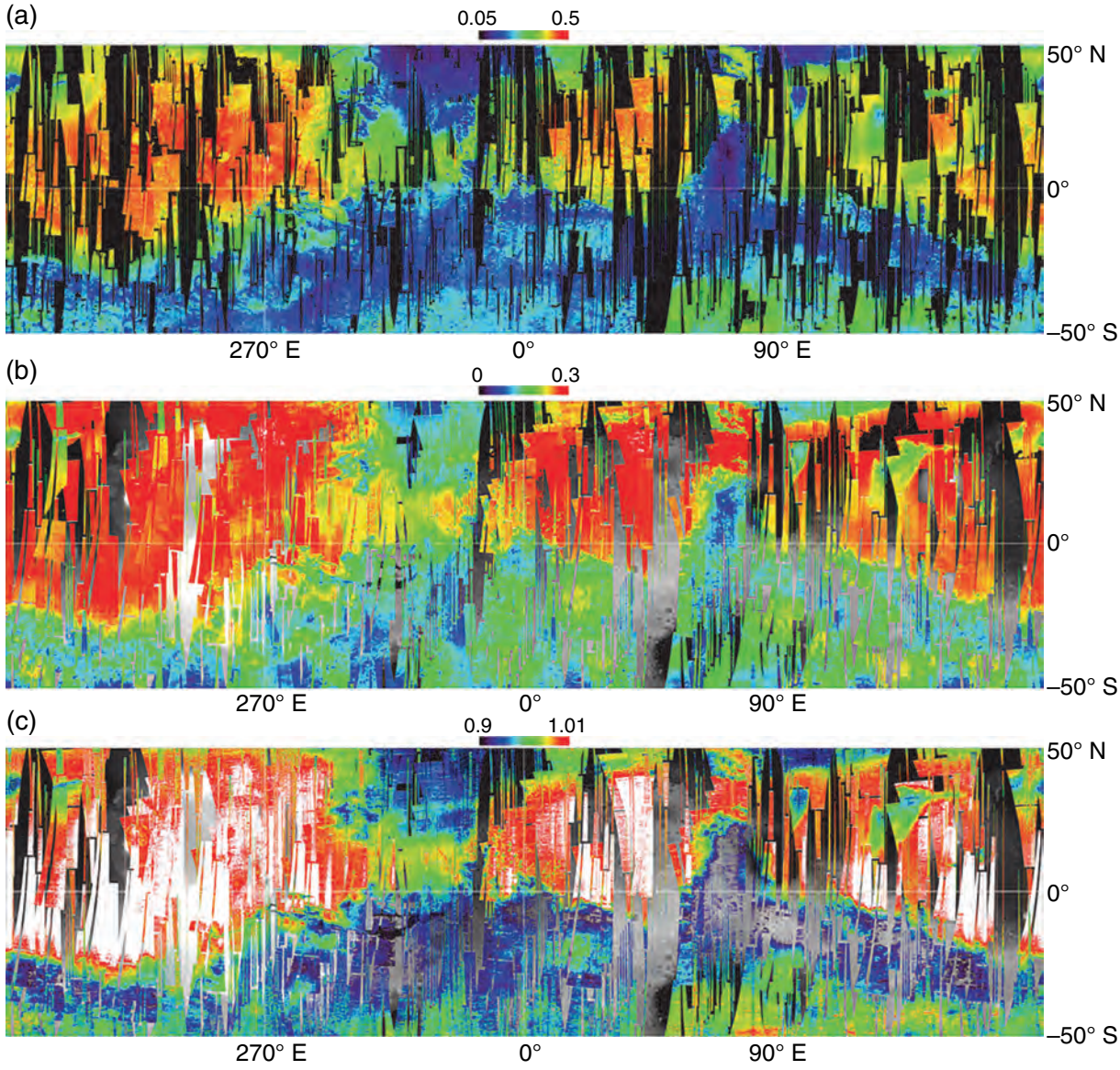

Figure 7.10. Global maps of (a) the NIR albedo; (b) crystalline ferric oxides, and (c) nanophase ferric oxides.

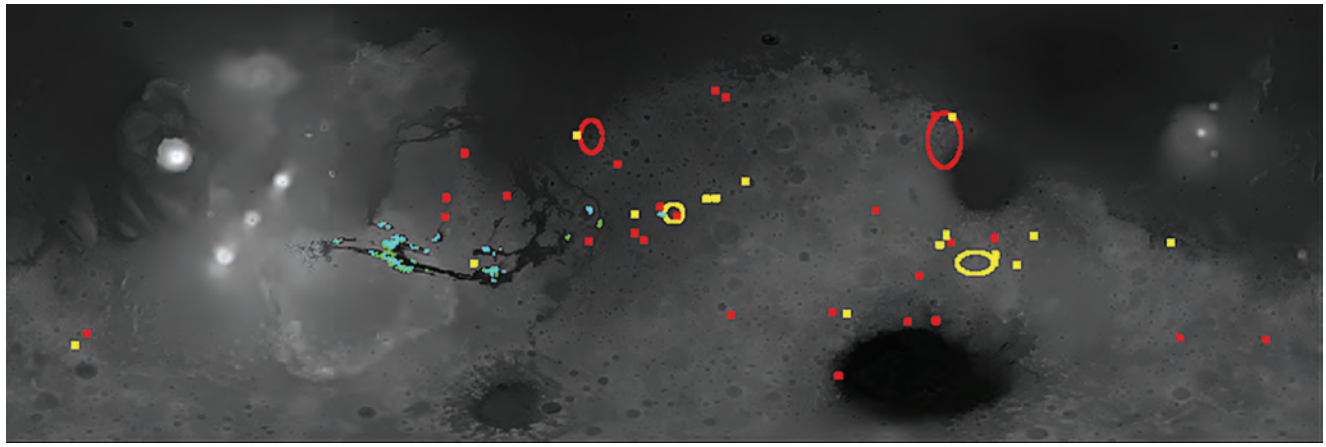

Figure 7.13. Distribution of all hydrated minerals detected so far by OMEGA at the surface of Mars, for latitude from -50° to $+50^{\circ}$. Blue: monohydrated sulfates; green: polyhydrated sulfates; red: phyllosilicates; yellow: other hydrated minerals.

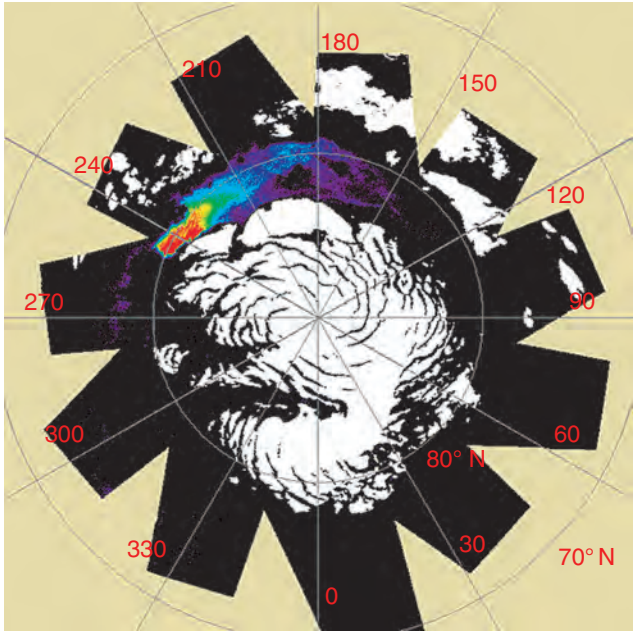

Figure 7.15. Area interpreted to be gypsum-rich within Olympia Planitia, illustrated by a false-color composite showing the distribution of the absorption at 1.93 μm relative to a continuum defined from 1.86 to 2.14 μm. The color code is a rainbow scale from black (<4% band depth) through blue, green, and yellow to red (>25% band depth). A strong absorption at 1.93 μm is observed on an extended dark area centered at 240° E, 80° N. White areas correspond to the regions with permanent water ice at the surface.

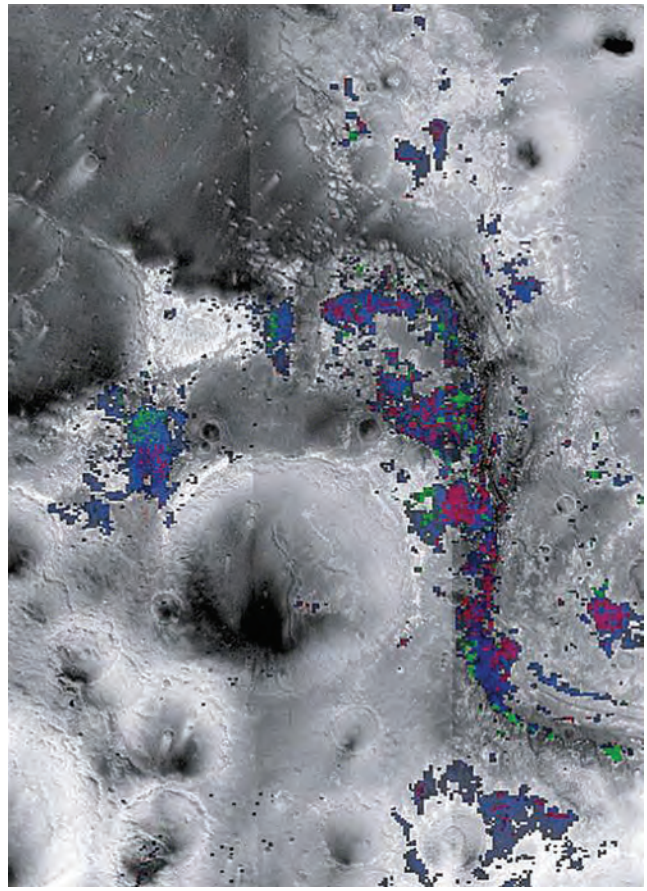

Figure 7.20. Clays in Mawrth Vallis. Distribution, over an HRSC mosaic (3 contiguous maps), of the minerals identified by OMEGA through their 1.93 μm (hydration, blue), 2.20 μm (montmorillonite, green), and 2.30 μm (Mg/Fe-rich smectites, red) features.

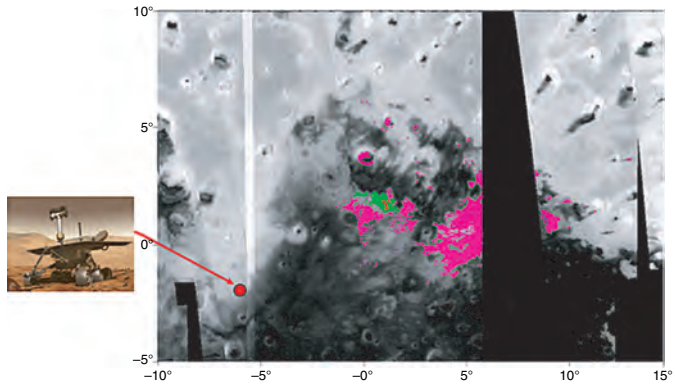

Figure 7.18. Distribution of kieserite (red), polyhydrated sulfates (green), and other hydrated minerals (pink) in Terra Meridiani. *Opportunity* site is shown.

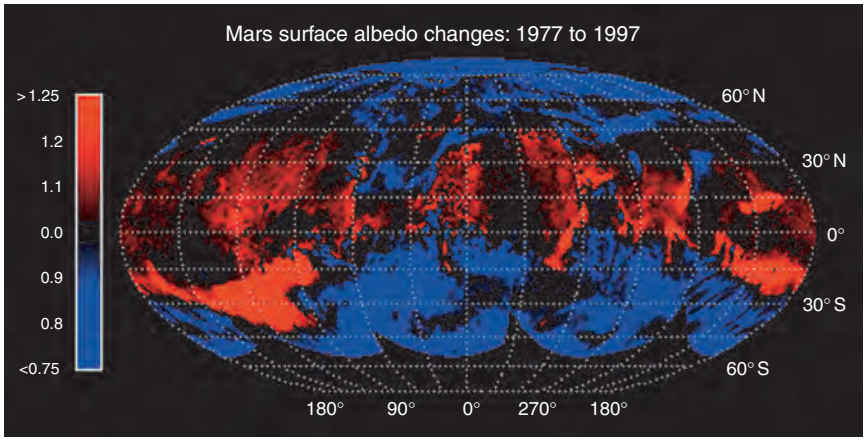

Figure 8.2. Global map of large-scale albedo changes on the Martian surface between the late 1970s and 1997, generated by differencing bolometric albedo maps generated from Viking Orbiter IRTM data (Pleskot and Miner, 1981) and HST (Bell *et al.*, 1999). Redder areas here have brightened since the Viking era, and bluer areas here have darkened. The scale gives the ratio of the IRTM-derived Viking era bolometric albedo to the bolometric albedo from 1997 HST data estimated from 1042 nm global multispectral images (Bell *et al.*, 1999).

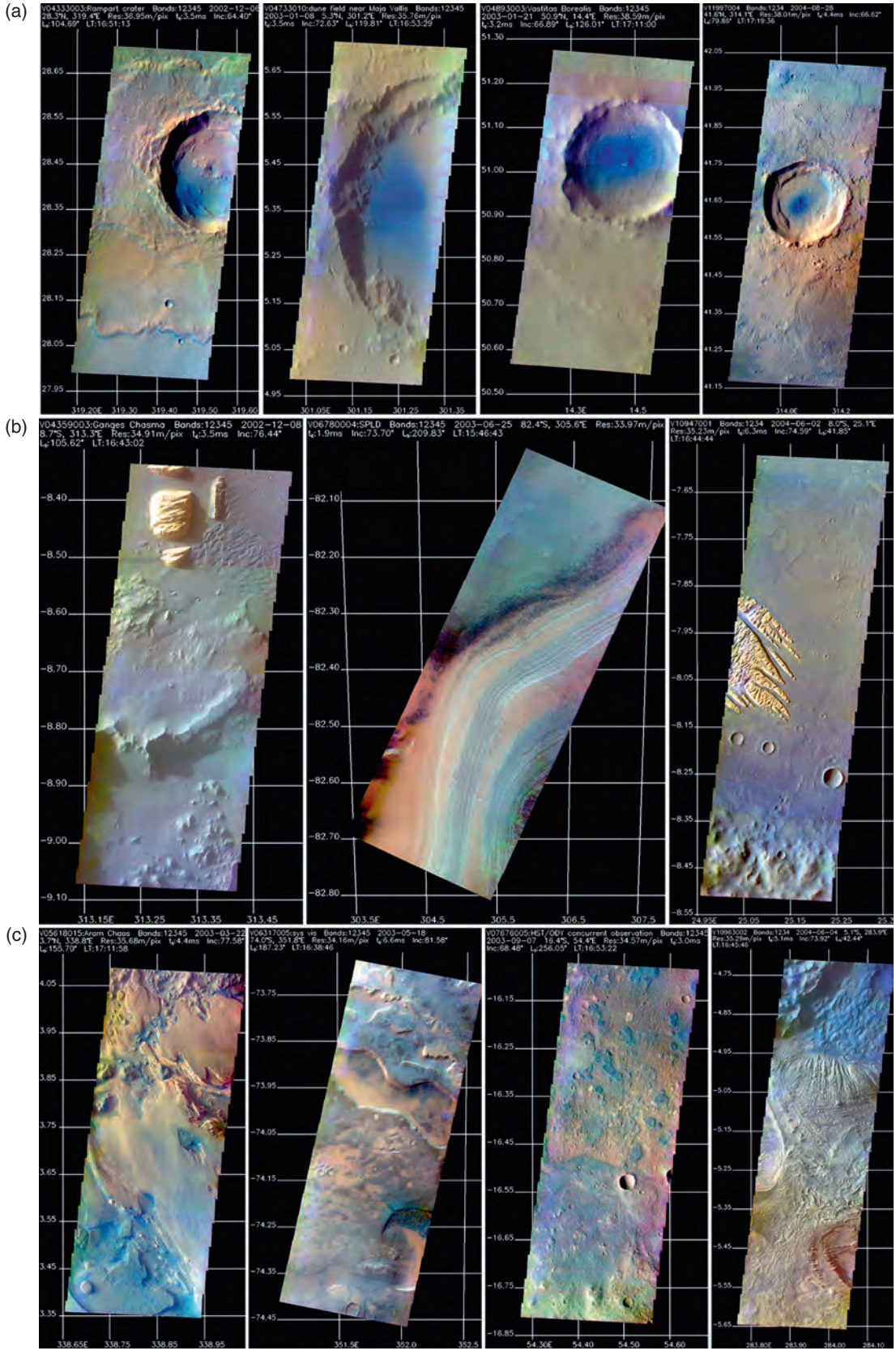

Figure 8.4. (a) Examples of "Blue Crater Materials" observed in false-color THEMIS-VIS images. VIS imaging sequences V04333003, V04733010, V04893003, and V11997004. (b) Examples of "Layered Materials" observed in false color THEMIS-VIS images. VIS imaging sequences V04359003, V06780004, and V10947001. (c) Examples of "Etched Terrain" observed in false-color THEMIS-VIS images. VIS imaging sequences V05618015, V06317005, V07676005, V10963002.

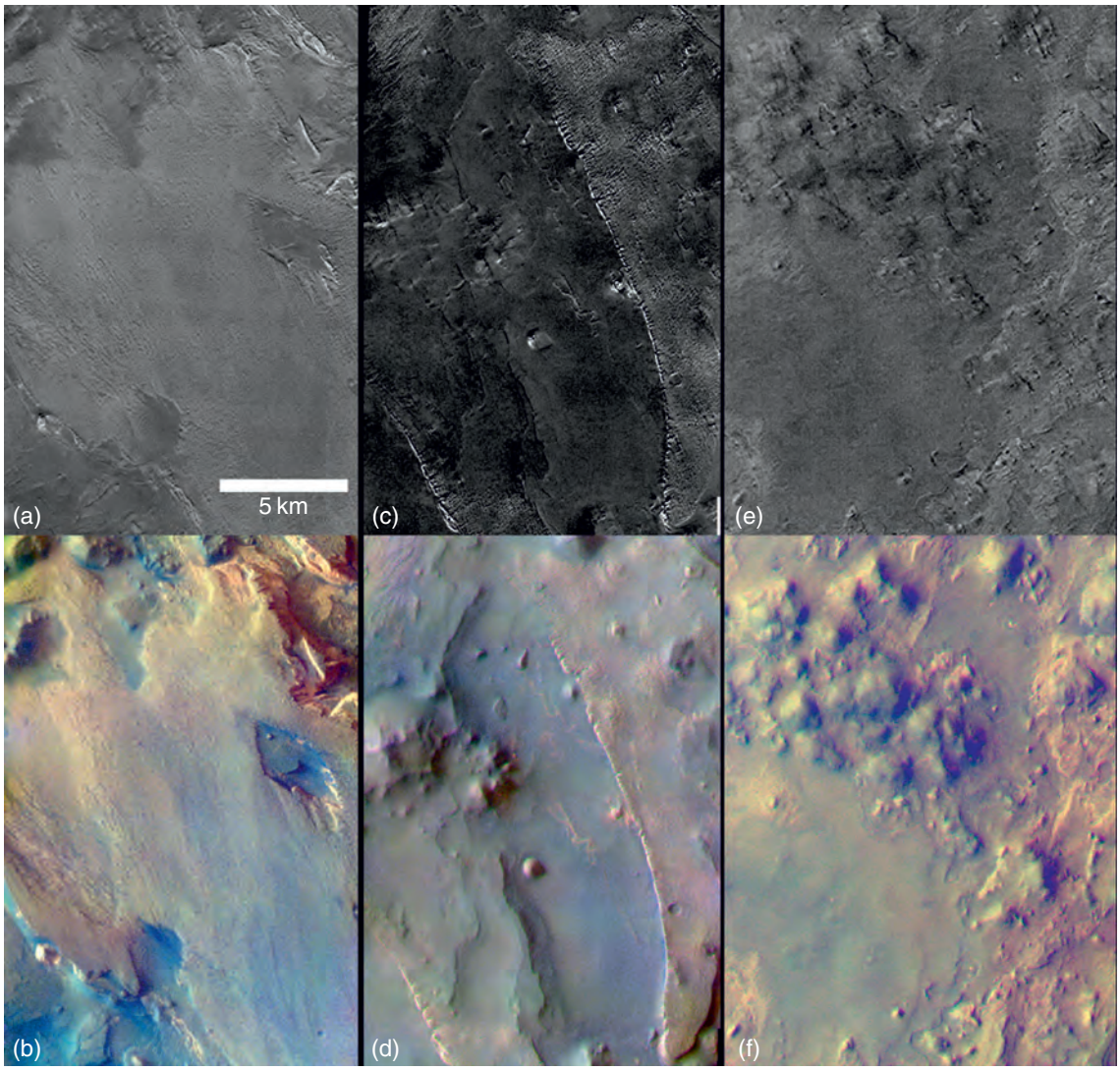

Figure 8.8. Examples of bright, reddish layered units in the equatorial chaotic terrains. Images are THEMIS-VIS 36 m/pixel false-color RGB composites using images at 654, 540, and 423 nm. (a) 540 nm band depth image V05618015 covering Aram Chaos. (b) False-color image V05618015. (c) 540 nm band depth image V10537001 covering Aureum Chaos. (d) False-color image V10537001. (e) 540 nm band depth image V10649001 covering Iani Chaos. (f) False-color image V10649001.

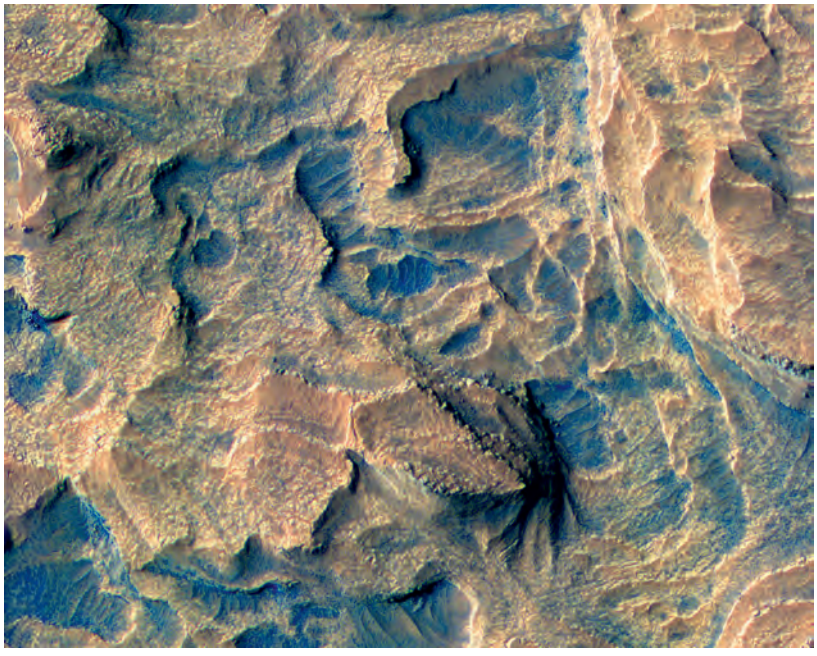

Figure 8.14. Portion of MRO HiRISE image TRA_000873_2015 of light-toned layered deposits on the floor of Bequerel crater. This enhanced RGB color composite was generated from BG, RED, and NIR filter observations (McEwen *et al.*, 2007) acquired on October 3, 2006. The complete image is centered at 21.4° N, 351.9° E, and the segment shown here is about 350 m wide and has a resolution of 25 cm/pixel. Rocky, perhaps dusty outcrop rock is reddish orange in this view, and less dusty, presumably basaltic sand, rocks, and boulders appear as varying shades of blue. Color in scenes like this at such remarkably high spatial resolutions can help establish relationships between geologic units, for example, relating boulders or debris falls back to specific layered units.

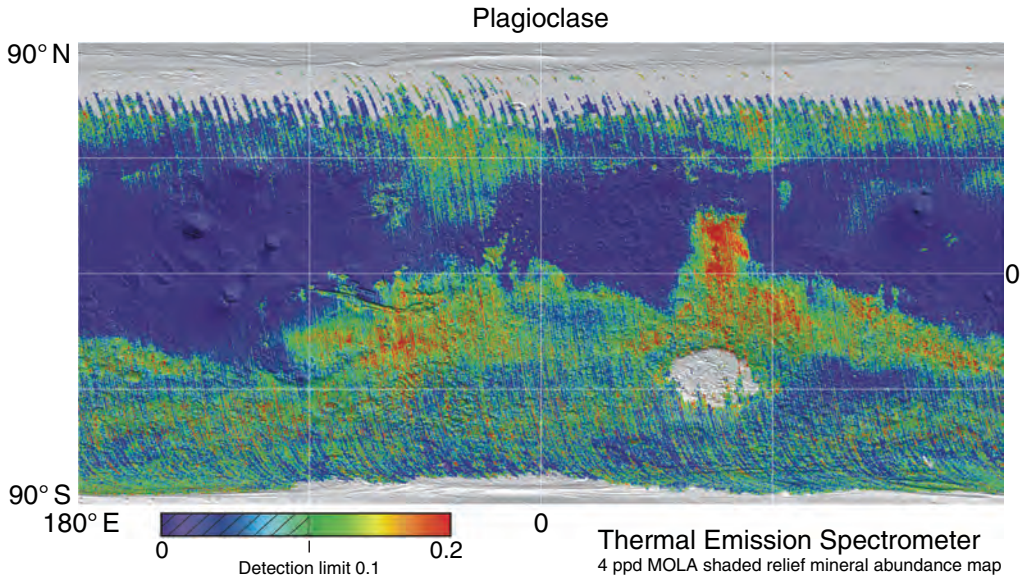

Figure 9.3. TES mineral map of plagioclase superimposed on the MOLA shaded relief map for location. (Based on Bandfield, 2002.)

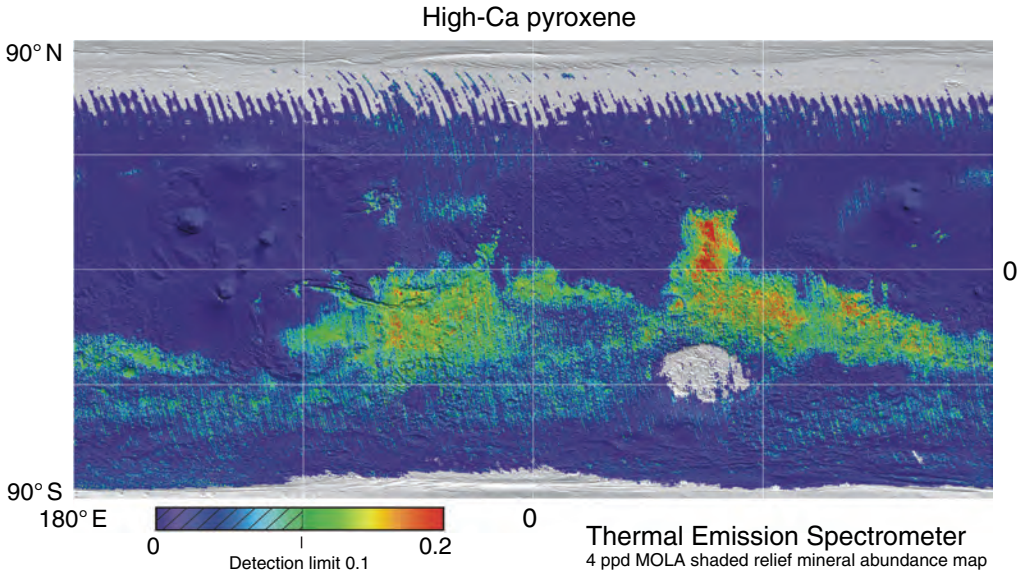

Figure 9.4. TES mineral map of high-Ca pyroxene superimposed on the MOLA shaded relief map for location. (Based on Bandfield, 2002.)

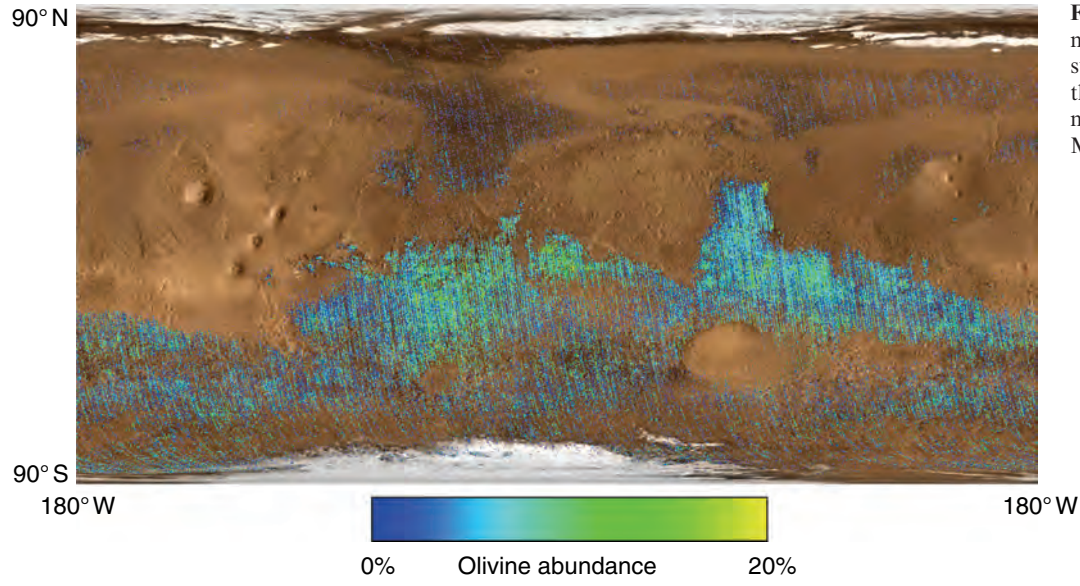

Figure 9.5. TES mineral map of olivine superimposed on the MOLA shaded relief map for location. (Based on McSween *et al.*, 2006.)

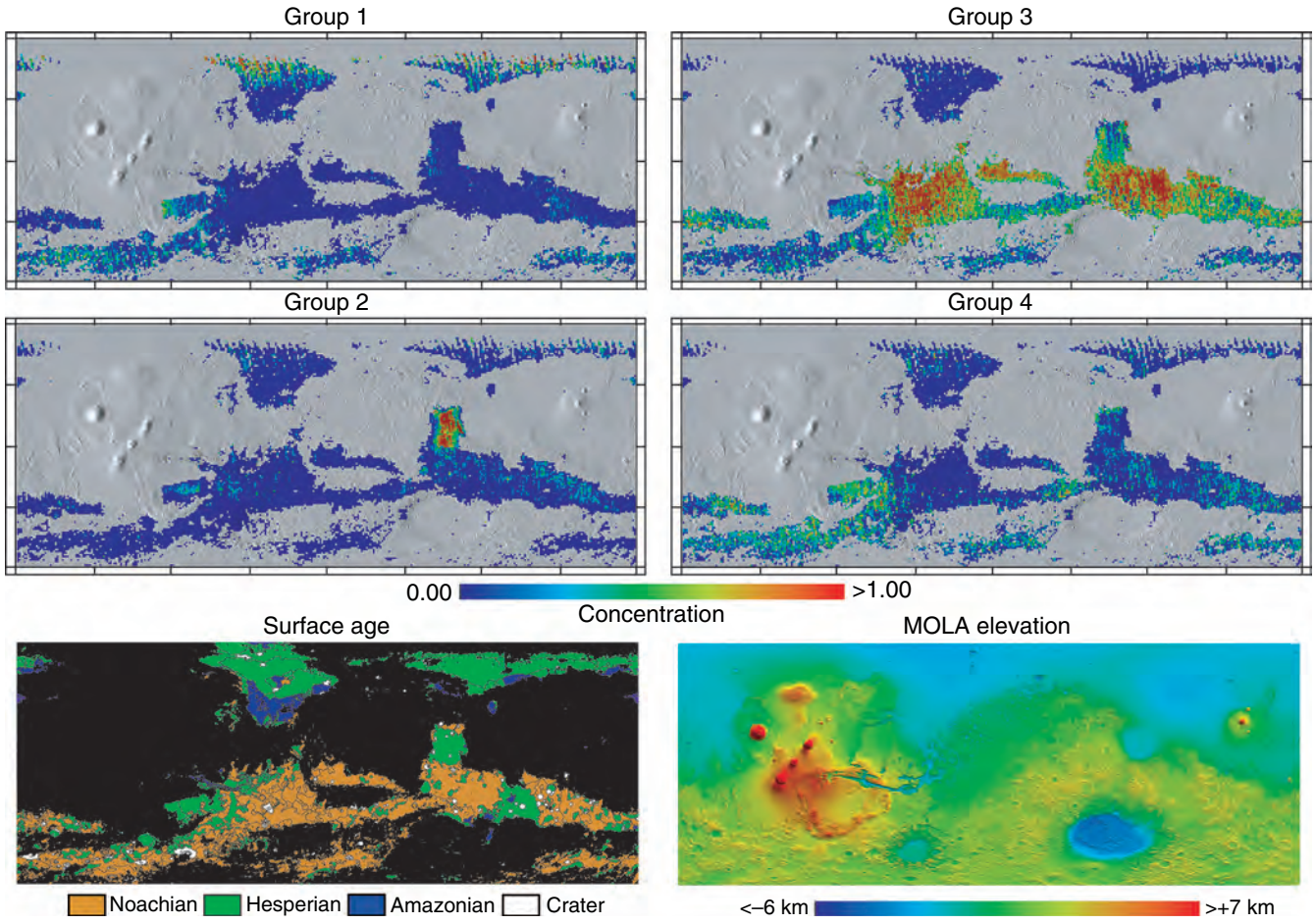

Figure 9.7. (*above*) The spatial distribution of TES volcanic compositional Groups 1–4. The subtle compositional variations are spatially distinct, providing strong evidence that these volcanic terrains reflect differences in primary formation processes. (Based on Rogers *et al.*, 2007.)

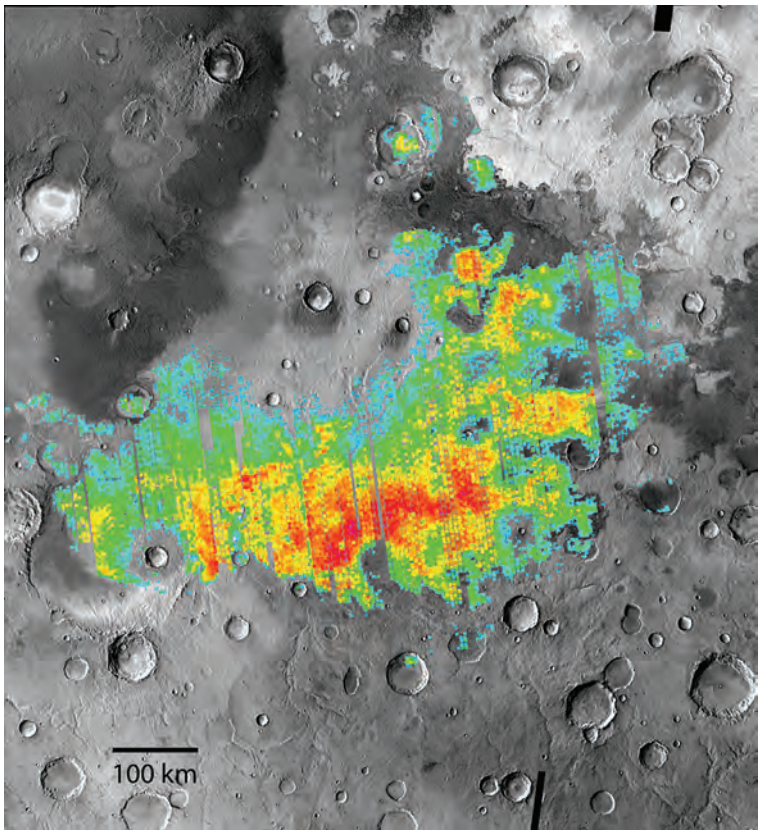

Figure 9.10. The spatial distribution of hematite in Meridiani Planum. The hematite abundance is shown in color, superimposed on a mosaic of THEMIS images of Meridiani Planum and the surrounding region. Red colors correspond to hematite abundances of 20%.

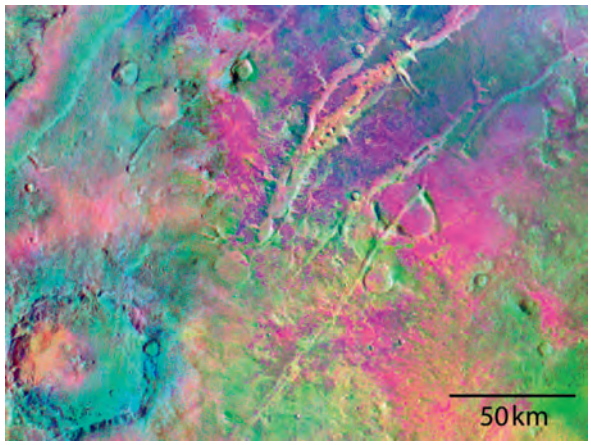

Figure 10.1. Olivine-rich basalts in Nili Fossae. Decorrelation-stretched (DCS) infrared mosaic of Nili Fossae region (20° N to 23.5° N, 75° E to 80° E). DCS bands 9 (12.57 μm), 7 (11.04 μm), and 5 (9.35 μm) are displayed as red, green, and blue, respectively. Olivine exposures are magenta to purple-blue in color. North is to the top in all images. North is up in all figures unless otherwise noted.

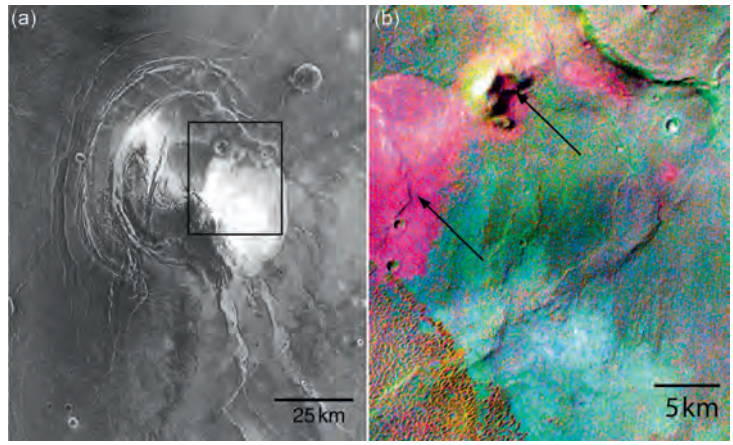

Figure 10.3. Nili Patera. (a) THEMIS nighttime temperature image showing the presence of bedrock, rocky dacite flows, and sand dunes. The bright (warm) surfaces have temperatures of up to 217 K. Box shows the location of Figure (b). (b) THEMIS 3-band multispectral IR DCS mosaic, showing the compositional units, including the dacite flow and cone (arrows), on the floor of the Nili Patera caldera.

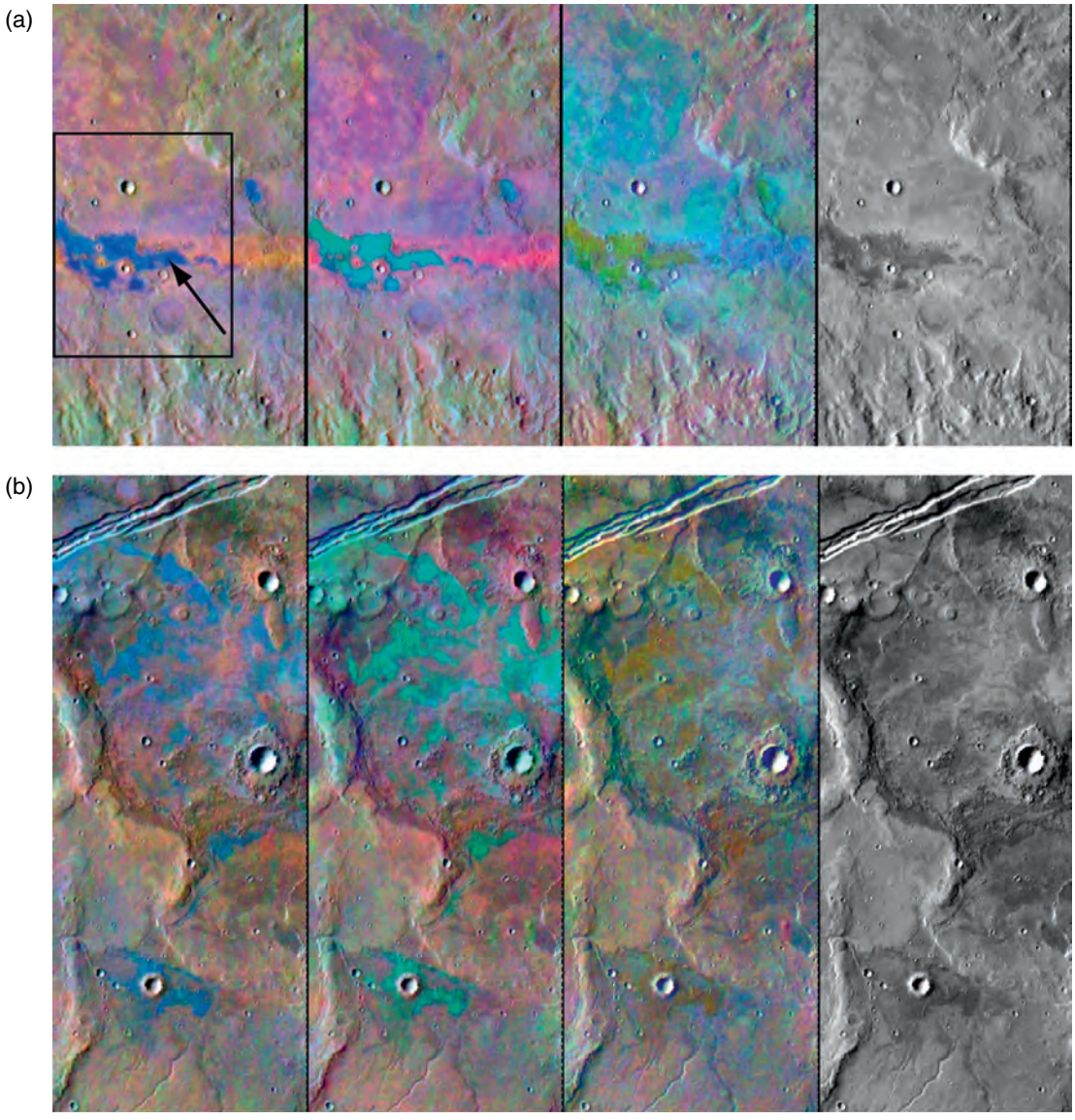

Figure 10.7. THEMIS DCS images for I08831002 (a) and I07734002 (b). The region of interest in these images is displayed as blue/teal/dirty-yellow (arrow) in the three DCS combinations described in the text. Each panel is 32 km wide. Box shows the location of the THEMIS image in Figure 10.8.

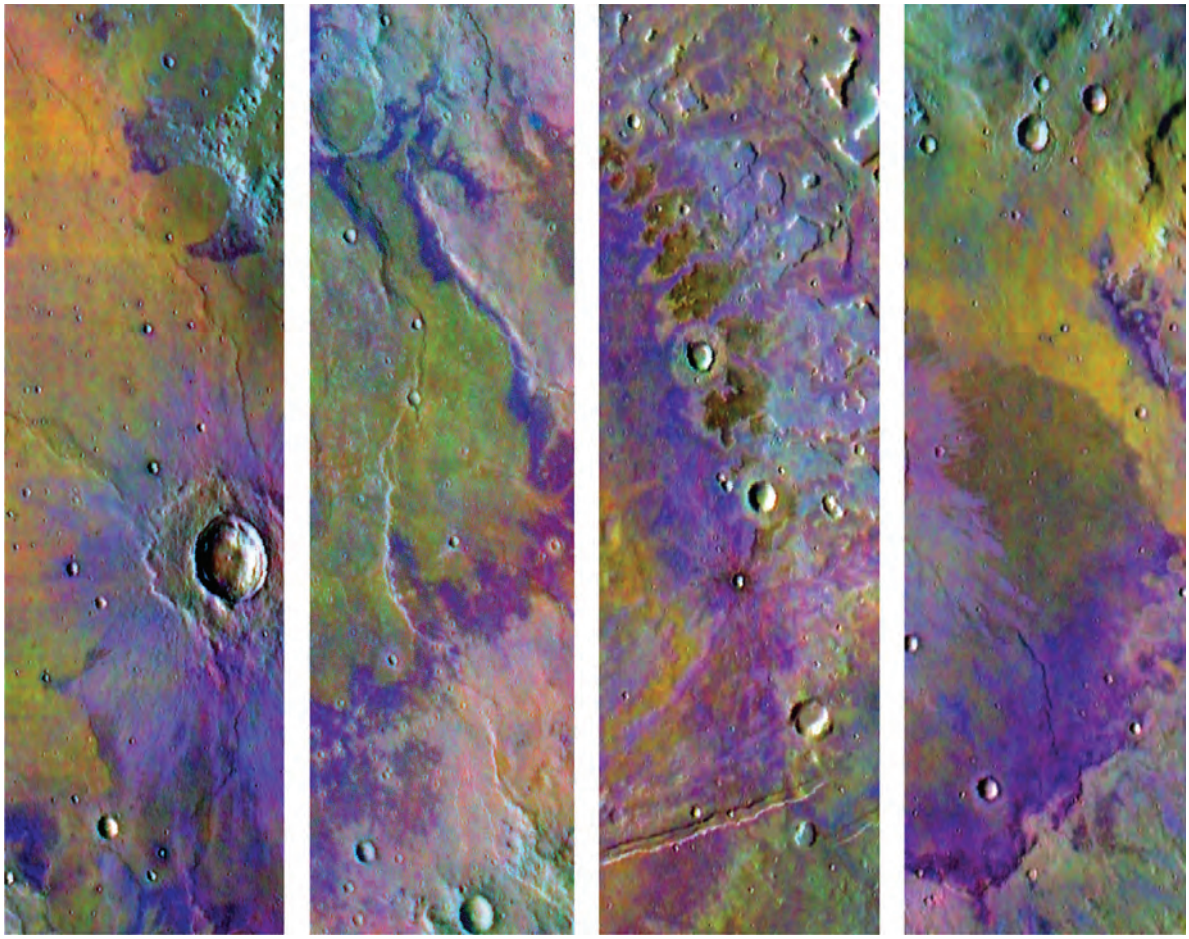

Figure 10.9. Examples of unique surface compositions found in the southern highlands. In THEMIS DCS images using bands 8, 7, 5, a pattern is observed in which a yellow-orange surface unit is often found in association with a purple unit. The purple unit has been determined from TES data to have slightly higher olivine concentrations and the yellow-orange unit contains slightly higher sheet silicate/glass/amorphous silica concentrations. Each panel represents a portion of a different THEMIS daytime IR image and is 32 km wide.

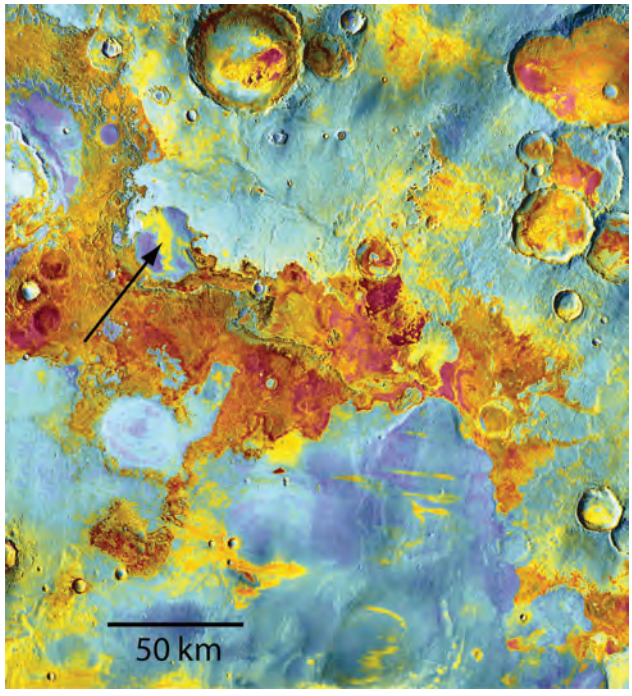

Figure 10.10. THEMIS day/night temperature mosaic of eastern Meridiani. The nighttime temperature data have been colorized and merged with the daytime temperature data. Fine-grained materials have low temperatures (170–190 K; blue) at night; coarser-grained materials are warmer (180–190 K; red). The mesa (arrow) has hematite in the central (yellow-colored) regions, with no hematite in the eastern and western portions.

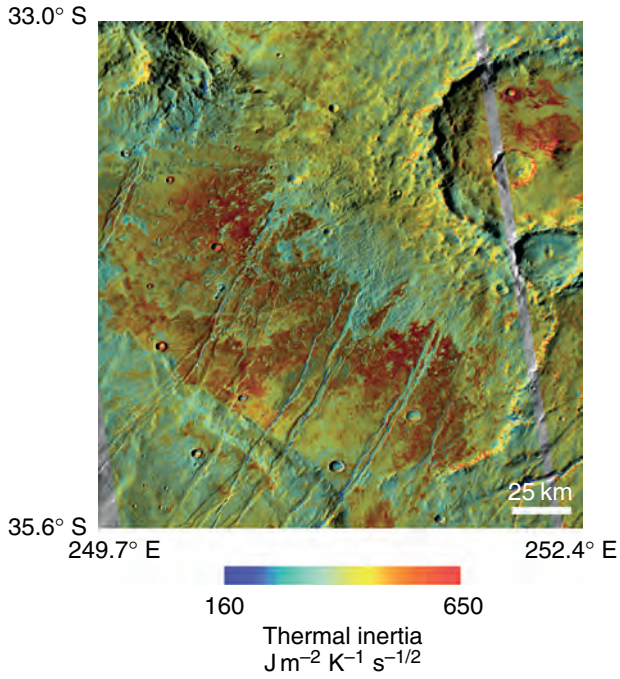

Figure 10.12. Exposed bedrock in the southern highlands. THEMIS thermal inertia mosaic (100 m/pixel resolution) overlaid onto a THEMIS daytime temperature mosaic, centered at 251.0° E, 34.3° S.

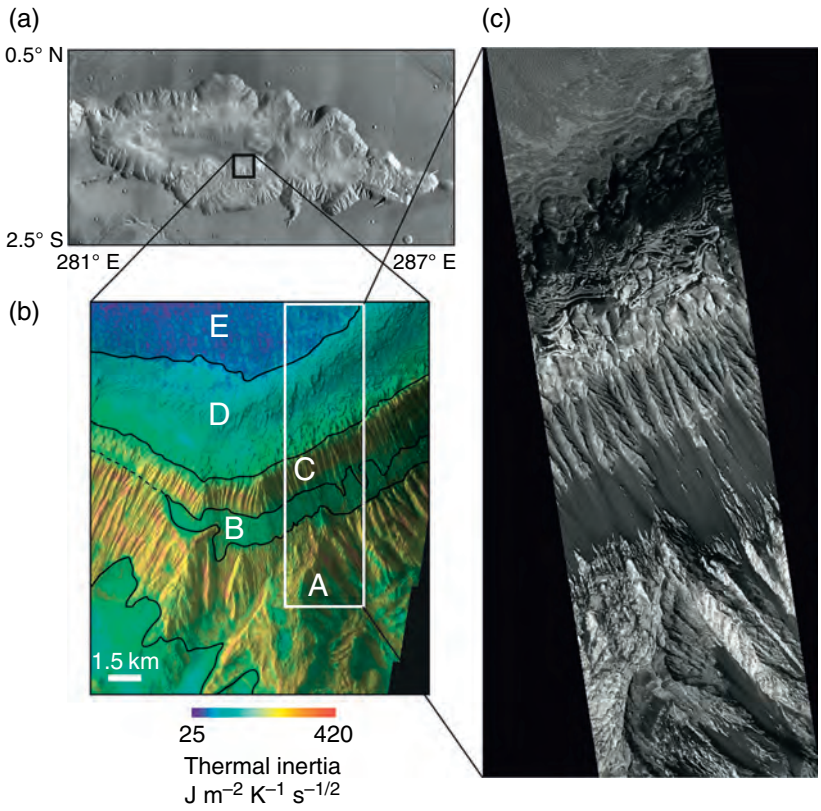

Figure 10.13. (*left*) Hebes Chasma interior layered deposits. (a) THEMIS daytime temperature mosaic of Hebes Chasma. The black box indicates the location of the THEMIS thermal inertia mosaic; (b) THEMIS thermal inertia mosaic (100 m/pixel resolution) overlaid onto a THEMIS visible image V10052001 (18 m/pixel resolution) of Hebes Chasma, centered at 284° E, ~1° N; (c) Portion of MOC Narrow Angle image M0900284, courtesy of Malin Space Science Systems (MSSS/NASA/JPL).

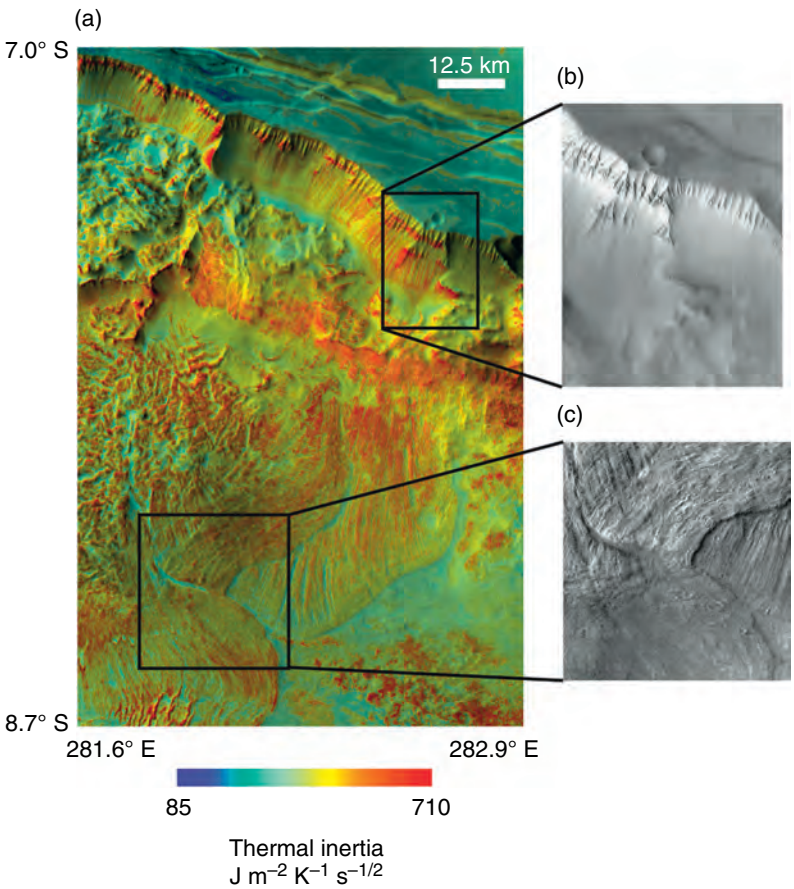

Figure 10.15. Landslide in western Melas Chasma, Valles Marineris. (a) THEMIS thermal inertia mosaic (100 m/pixel resolution) overlaid onto a THEMIS daytime temperature mosaic (100 m/pixel resolution), centered at 282.3° E, 7.9° S, illustrating multiple lobes of landslide deposits; (b) Portion of THEMIS visible image V16816003 (18 m/pixel resolution) of chasma wall material; (c) Portion of THEMIS visible image V02550002 (18 m/pixel resolution) of landslide flow boundaries.

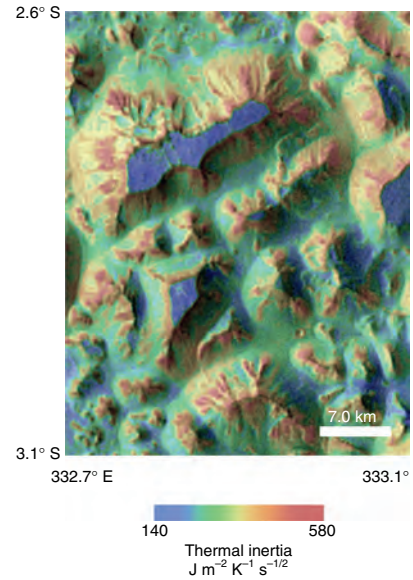

Figure 10.14. (*above*) Rocks and talus on slopes. Rocks are warmer (red) than the colder (blue), dust-covered mesas and fine-sand (green) canyon floor. THEMIS nighttime temperature mosaic (100 m/pixel) overlaid onto THEMIS daytime temperature mosaic (100 m/pixel resolution), centered at 333.0° E, 2.9° S.

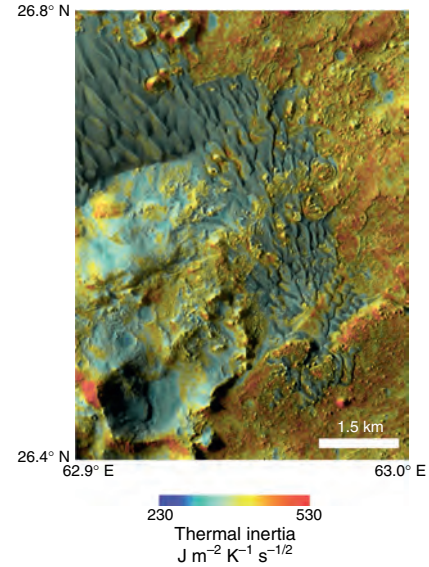

Figure 10.16. Sand dunes. Dunes in unnamed crater centered at ~63° E, 26.6° N. THEMIS thermal inertia (100 m/pixel resolution) overlaid onto THEMIS visible image mosaic (18 m/pixel resolution) showing surfaces that have eroded into mesas, knobs, ridges, and aeolian material.

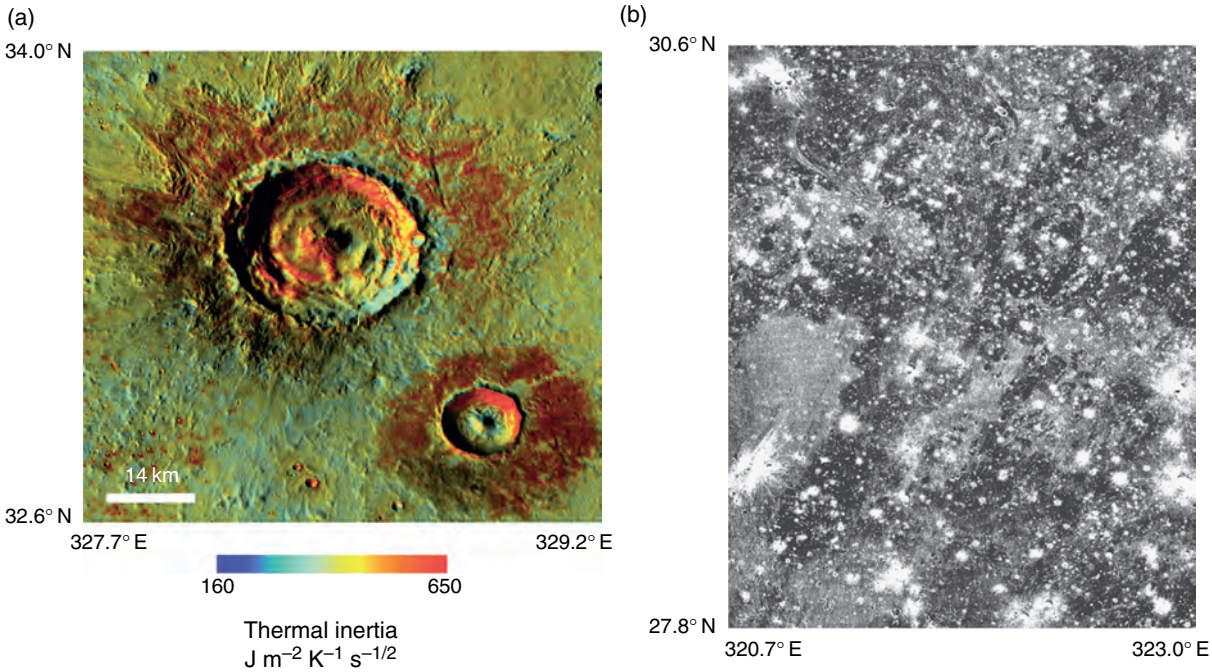

Figure 10.17. Craters. (a) Craters in Acidalia Planitia. THEMIS thermal inertia mosaic (100 m/pixel) overlaid onto a THEMIS daytime temperature mosaic (100 m/pixel resolution) of craters in Acidalia Planitia, centered at 328.5° E, 33.3° N. (b) Nighttime THEMIS temperature image showing rocky (warm) ejecta surrounding numerous small craters in Chryse Planitia. THEMIS nighttime temperature mosaic (100 m/pixel) of craters centered at 321.8° E, 29.2° N that has been stretched to emphasize crater ejecta. Black represents colder temperatures (minimum = 180 K) and white represents warmer temperatures (maximum = 195 K).

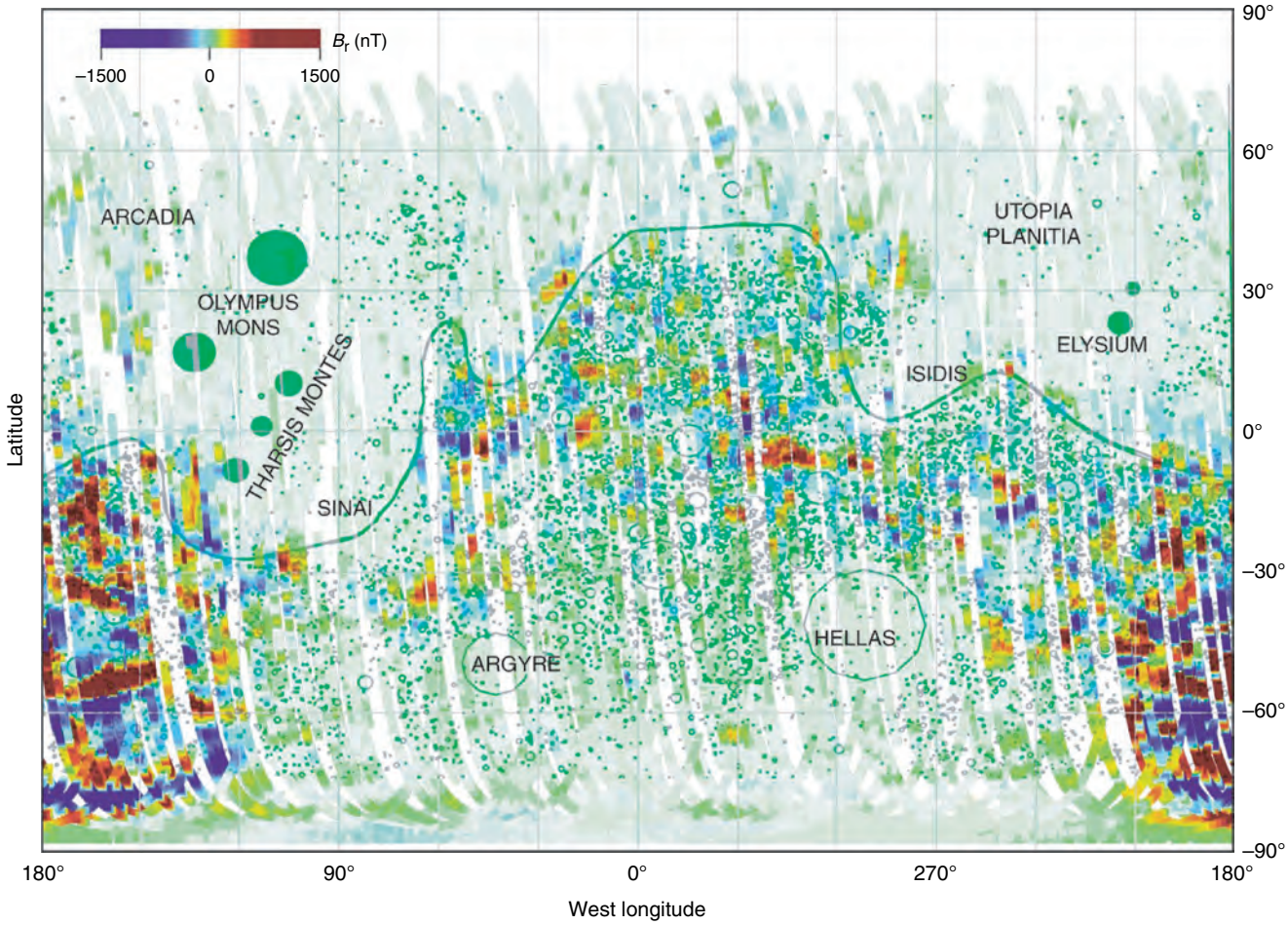

Figure 11.1. Map of the global distribution of Martian crustal magnetization. The intensity of the radial component of the measured magnetic field below 200 km altitude is plotted as a Mercator projection. Note that the majority of the magnetic sources lie south of the dichotomy boundary (solid green line) in the ancient Noachian terrain. The open circles represent craters with diameters >10 km (e.g., Barlow *et al*., 2000); the solid circles represent the location and size of the Martian volcanoes.

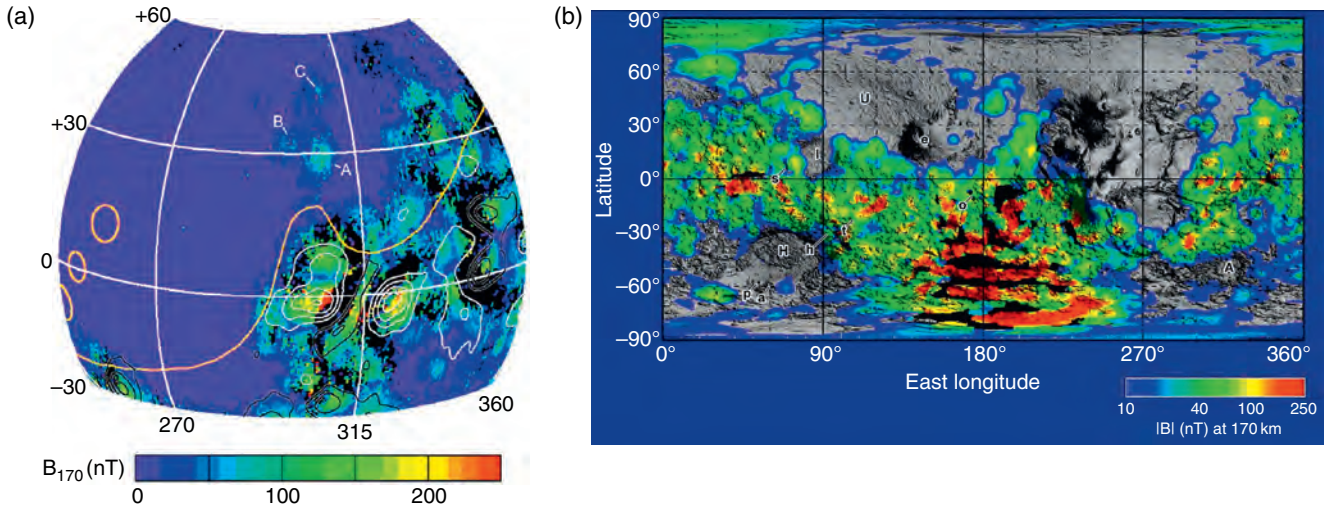

Figure 11.2. (a) The crustal magnetic field strength at 170 km altitude, as inferred from electron reflectometry, is averaged in $0.5^\circ \times 0.5^\circ$ bins (color scale). All data were obtained at 2 a.m. local time. Double-sided loss cones were observed in black regions within 45° of the equator, indicating that the spacecraft was on closed crustal magnetic field lines (miniature magnetospheres – see Figure b). Contours show the radial component of the magnetic field measured by the MAG at 400 km (Connerney *et al.*, 2001) (white: negative; black: positive). The locations of the Tharsis volcanoes and the dichotomy boundary are shown in orange (based on Lillis *et al.*, 2004). (b) A global map of Martian magnetization at 170 km altitude derived from electron reflectometer measurements superimposed on a shaded relief map of MGS MOLA topography (based on Mitchell *et al.*, 2007). Grayscale regions have $B_{170} < 10$ nT. Crustal magnetic field lines form closed loops in the black regions where the electron reflectometer method cannot be used. Labels indicate the centers of the impact basins of Utopia (U), Hellas (H), Argyre (A), and Isidis (I) as well as the volcanoes Elysium (e), Syrtis Major (s), Apollinaris (o), Tyrrhena (t), Hadriaca (h), Peneus (p) and Amphitrites (a).

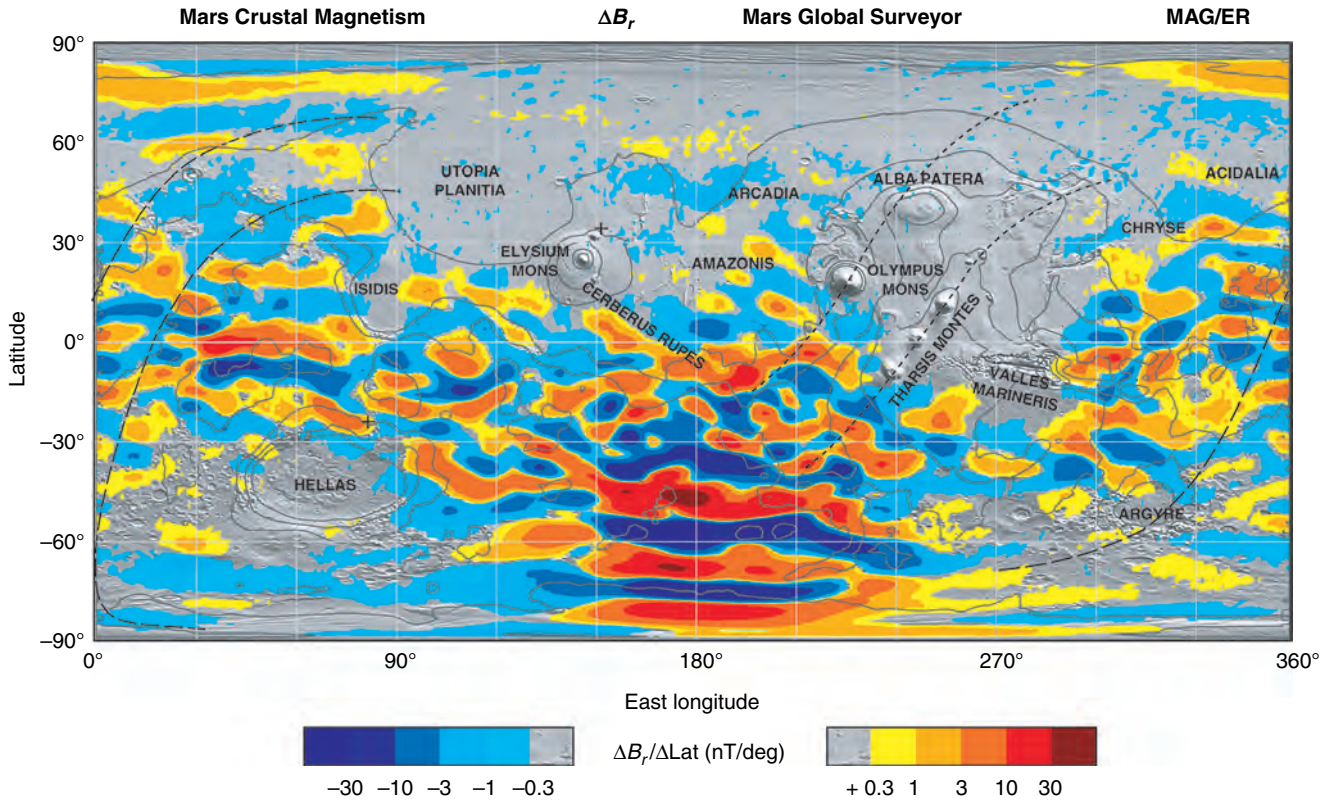

Figure 11.8. Map of the magnetic field of Mars observed by the Mars Global Surveyor satellite at a nominal 400 km altitude. Each pixel is colored according to the median value of the filtered radial magnetic field component observed within the 1° by 1° latitude/longitude range represented by the pixel. Colors are assigned in 12 steps spanning two orders of magnitude variation. Where the field falls below the minimum contour, a shaded MOLA topography relief map provides context. Contours of constant elevation (−4, −2, 0, 2, 4 km elevation) are superimposed, as are dashed lines representing rotations about common axes (short dashes – axis northeast of Elysium Mons; long dashes – axis northeast of Hellas).

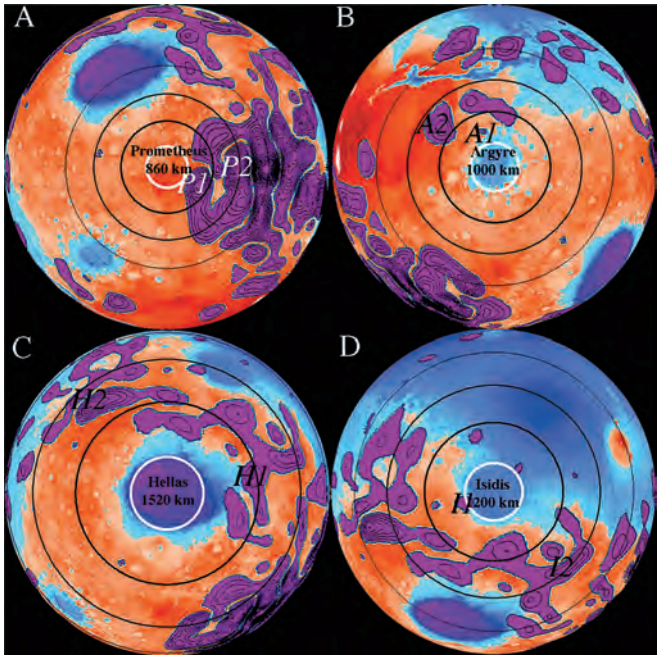

Figure 11.9. Topographic maps (MOLA – dark red is the highest and dark blue is the lowest altitude) compared with magnetic maps (MGS) across large impact basins (A: Prometheus, B: Argyre, C: Hellas, D: Isidis). Purple color indicates absolute values of radial magnetic signature exceeding 10 nT at night side and 400 km satellite altitude. Contour lines have contour interval 10 nT. Heavy white circle is the crater diameter. Circles of increasing diameters indicate the peak pressure exceeding 5, 2, and 1 GPa, respectively, during the impacts (estimated analytically; see text).

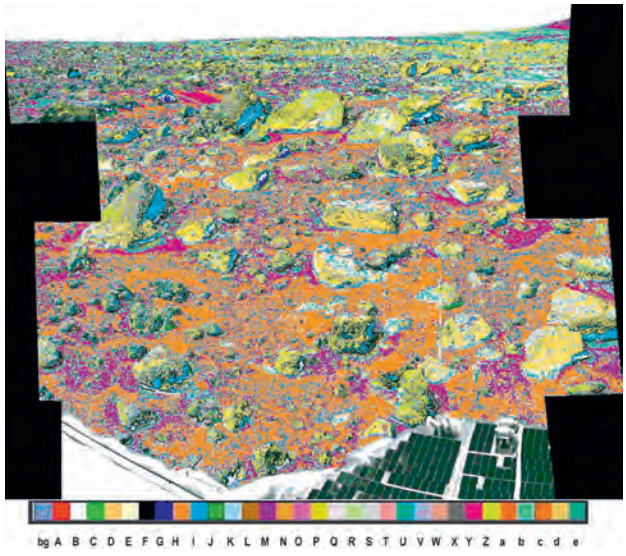

Figure 12.11. Classification map of the right-eye data from the S0184 octant of the SuperPan. Classification was obtained through application of the self-clustering approach of the SOM/ANN method described by Farrand *et al*. (2005) and Merényi *et al*. (2004). Color bar represents key to classes.

(a)

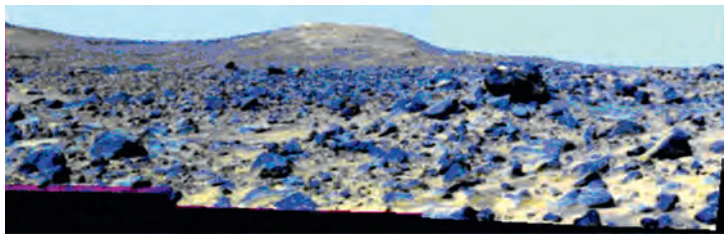

(b)

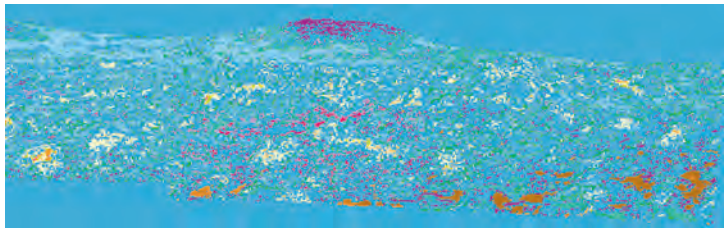

Figure 12.12. (a) Composite of left-eye bands 802, 671, and 443 nm for far field portion of octant S0183. (b) Class map for the far field of S0183 (left-eye data). Note the purple color (class M) associated with the top of North Twin Peak and prevalence of cyan colors of classes b and K in the far field.

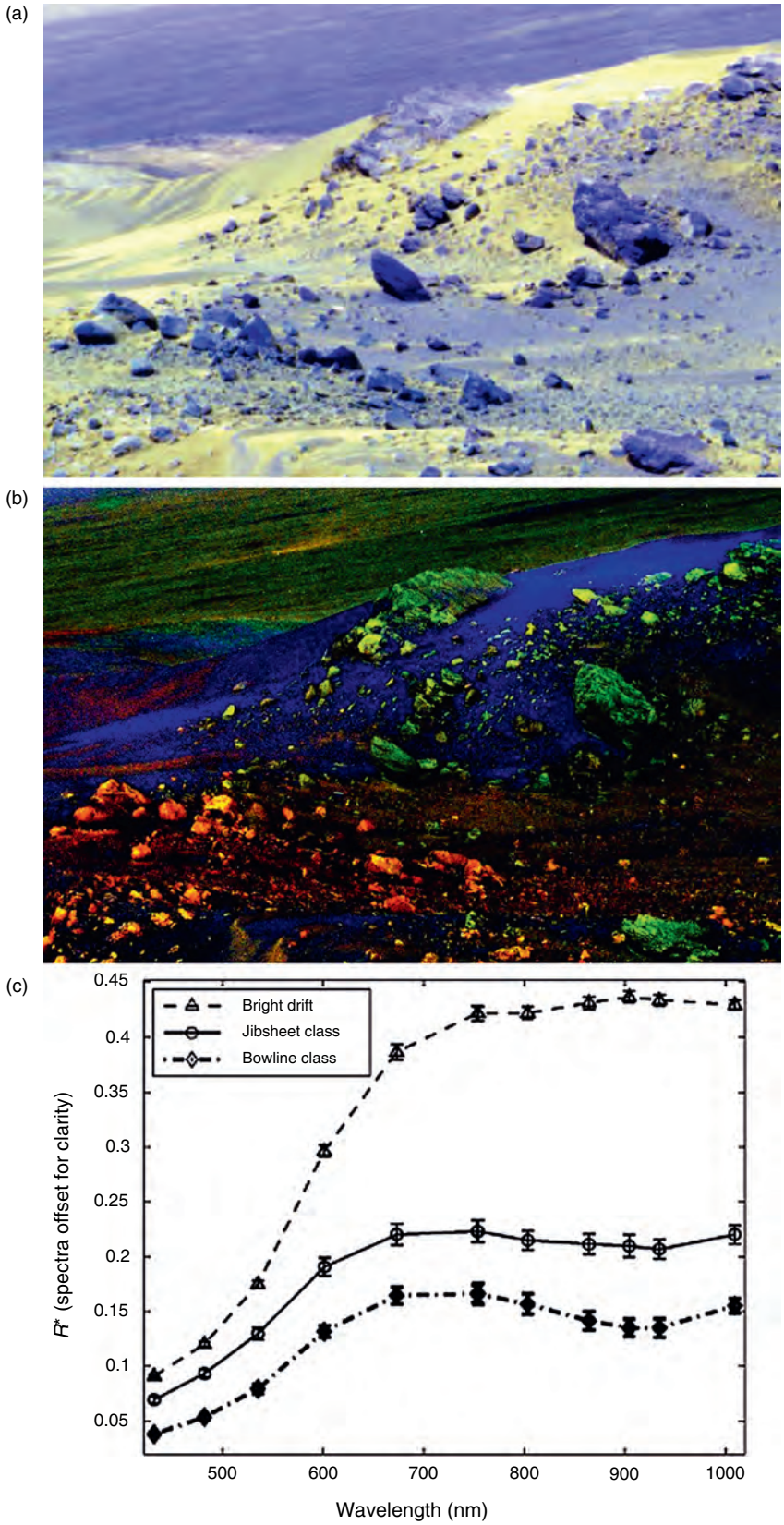

Figure 13.3. (a) False-color composite (red= 673 nm, green= 535 nm, blue= 432 nm) of the sol 608 P2582 Whittaker/Bowline scene. (b) Composite of endmember fraction images of spectrally distinct rock and soil components (red=Bowline type rocks; green=Whittaker/Hillary [Jibsheet class] type rocks; blue=bright drift soil). (c) Spectra of materials mapped out in the fraction image composite image. R^* is the radiance factor normalized by the solar elevation angle (Bell *et al.*, 2006b).

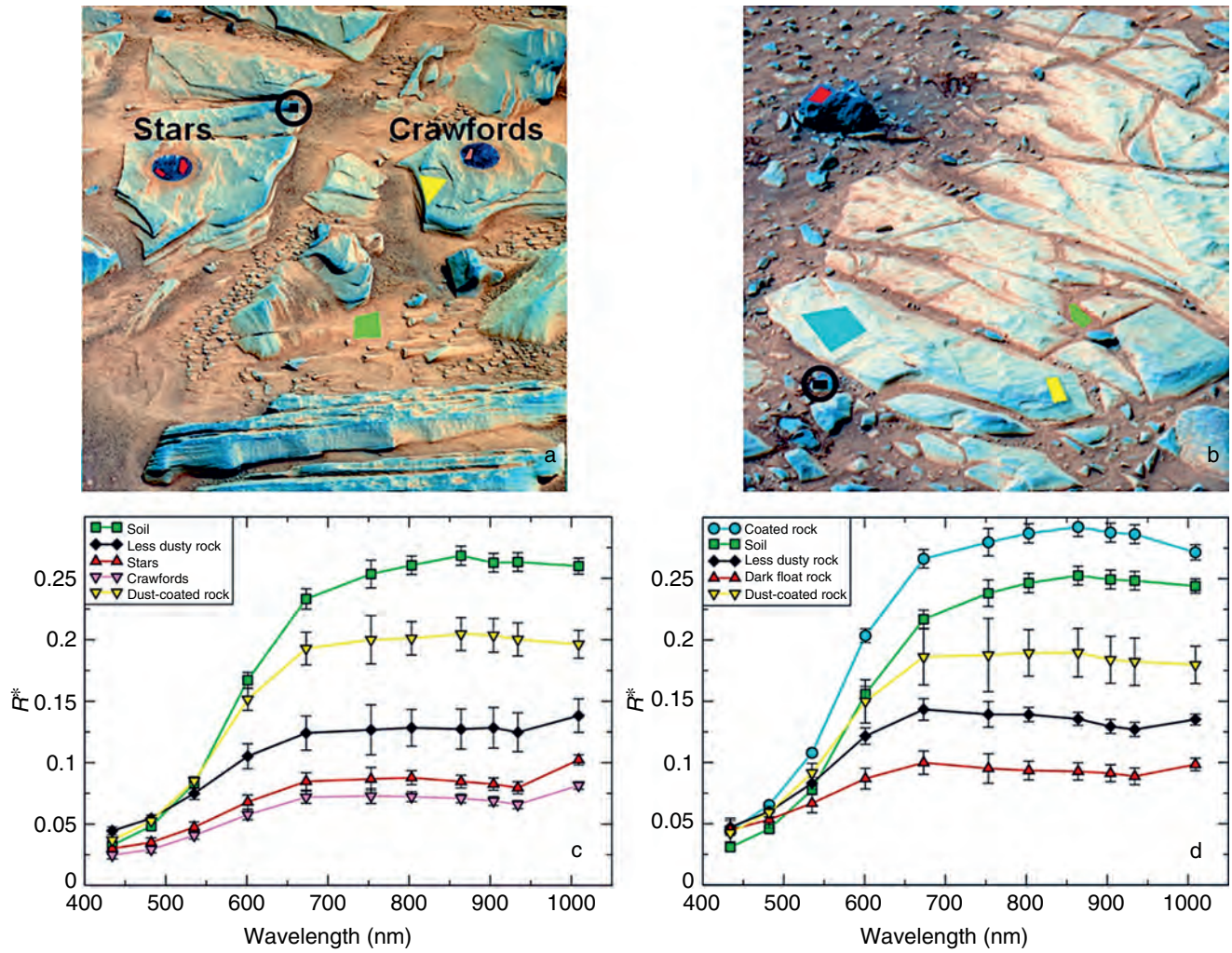

Figure 13.6. Pancam false-color images acquired using 753 nm (L2), 535 nm (L5), and 432 nm (L7) filters, and spectra of Home Plate outcrops. (a) James "Cool Papa" Bell, showing RAT brush locations Stars and Crawfords, acquired on Sol 764 at 11:48 Local True Solar Time (LTST) (P2859). (b) Hilton Smith acquired on Sol 770 at 12:21 LTST (P2591). (c) Spectra derived from color-coded locations shown in (a). (d) Spectra derived from color-coded locations shown in (b). R^* is the radiance factor normalized by the solar elevation angle (Bell *et al*., 2006b).

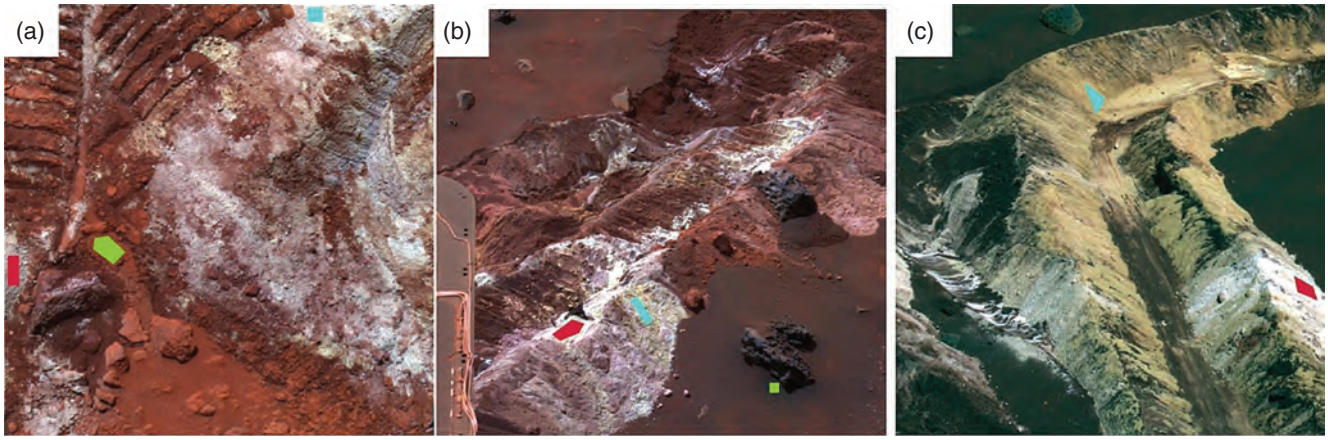

Figure 13.11. False-color RGB (754, 535, 432 nm) images of (a) Paso Robles (Sol 400, P2551); (b) Arad (Sol 721, P2538); and (c) Tyrone (Sol 790, P2531) showing locations from which spectra were acquired. Paso Robles: red = "gray" soil, cyan = "white" soil, green = background soil. Arad: red = "white" soil, cyan = "yellow" soil, green = basaltic soil. Tyrone: red = "white" soil, cyan = "yellow" soil. (Based on Johnson *et al*., 2007.)

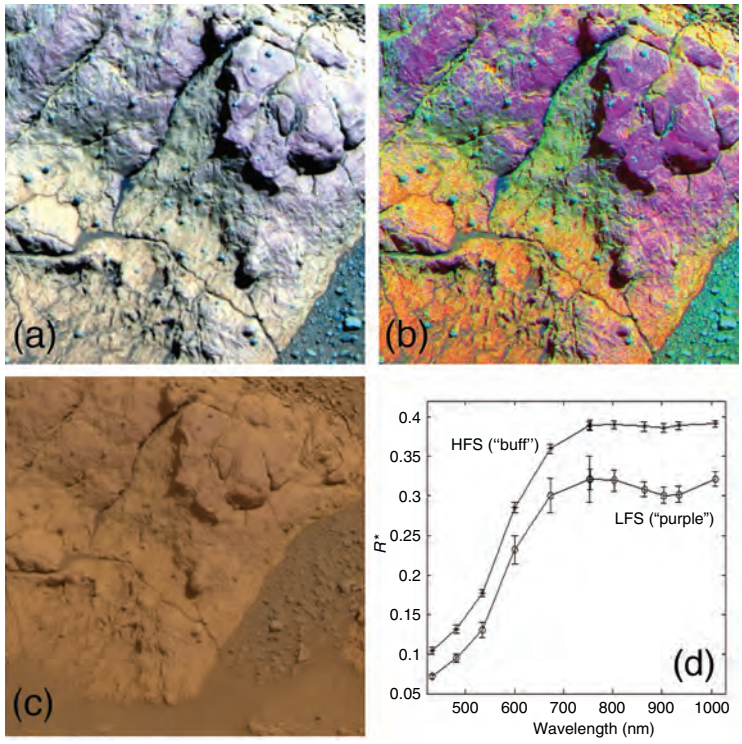

Figure 13.20. (a) Pancam false-color RGB composite from filters L3, L5, and L7 (Table 13.1) from *Opportunity* sol 33 P2589 image sequence on "Cathedral Dome" in Eagle crater. (b) Decorrelation stretch (DCS; see text) version of (a). As described in the text, the purple-colored, massive appearing section is an example of the LFS spectral class. The yellow to buff-colored lower angle portions of outcrop below and above the massive appearing section are examples of the HFS spectral class. (c) Approximate true color rendering of this scene (e.g., Bell *et al*., 2006b) showing that the color differences exaggerated by the false color and DCS methods in (a) and (b) would be extremely subtle to the unaided human eye. (d) Spectra from Eagle crater of the HFS ("buff-colored") and LFS ("purple-colored") spectral classes. LFS spectrum is from a rock surface in the P2575 image sequence on sol 50. HFS spectrum is from a rock surface in the P2532 image sequence on sol 37.

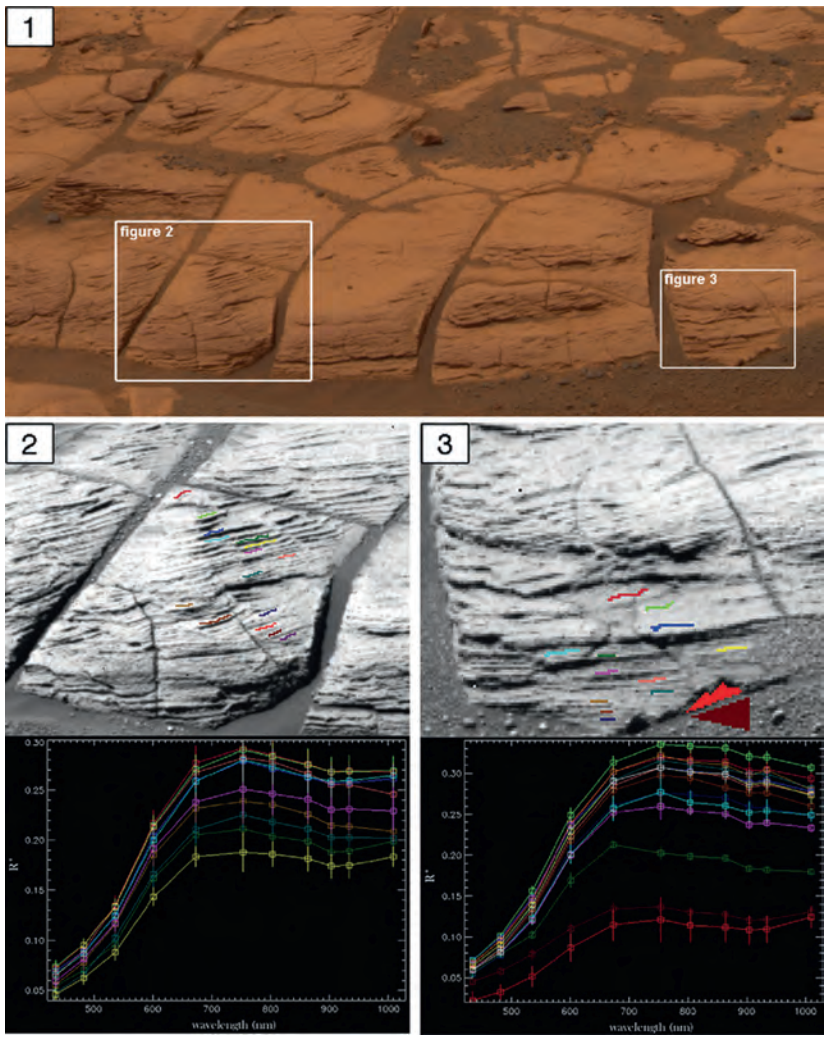

Figure 13.25. Panel (1): Example outcrop material in approximate true color to demonstrate the exposure of sedimentary laminations. Image from sol 648 Pancam sequence P2574. Panels 2 and 3 are denoted by white frames. Panel (2): Closer view of rock fragment in Panel 1 displayed here in the blue filter image (L7, 432 nm). The colors of the spectral profiles plotted correspond to the colors of the selected pixels on the image. Error bars represent standard deviations of pixels in selected regions of interest. Panel (3): Closer view of rock fragment in Panel 1 displayed here in the blue filter image (L7, 432 nm). The colors of the spectral profiles plotted correspond to the colors of the selected pixels on the image. The dark green spectrum is a layer like the others but has a slope sign change from 673 to 753 nm unlike the other lamination plots. The two red shallow profiles are of soil and rind materials near the base of the rock; note the strong positive slope in the longer wavelength region. Error bars represent standard deviations of pixels in selected regions of interest.

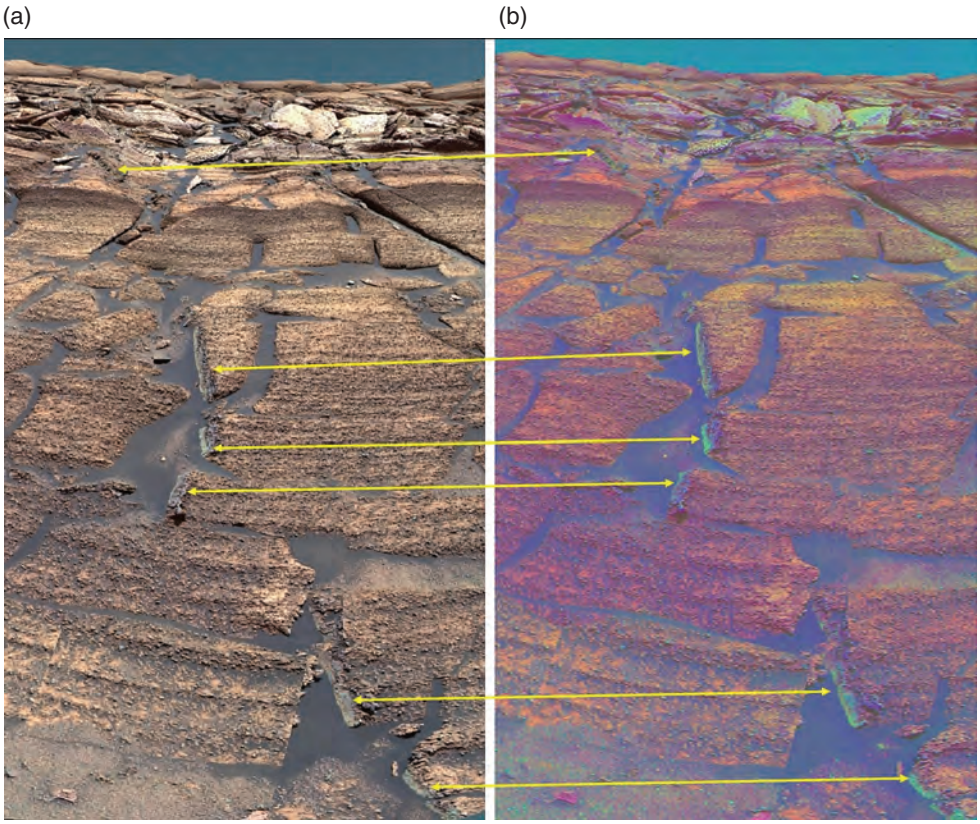

Figure 13.28. (a) Portion of Pancam panorama of Burns Cliff region along southern rim of Endurance crater showing false-color composite (a) created from 754, 535, and 432 nm images, compared to decorrelation stretch (b) from the same images. Yellow arrows point to fracture-fill materials observed here and along the edges of other broken outcrop blocks.

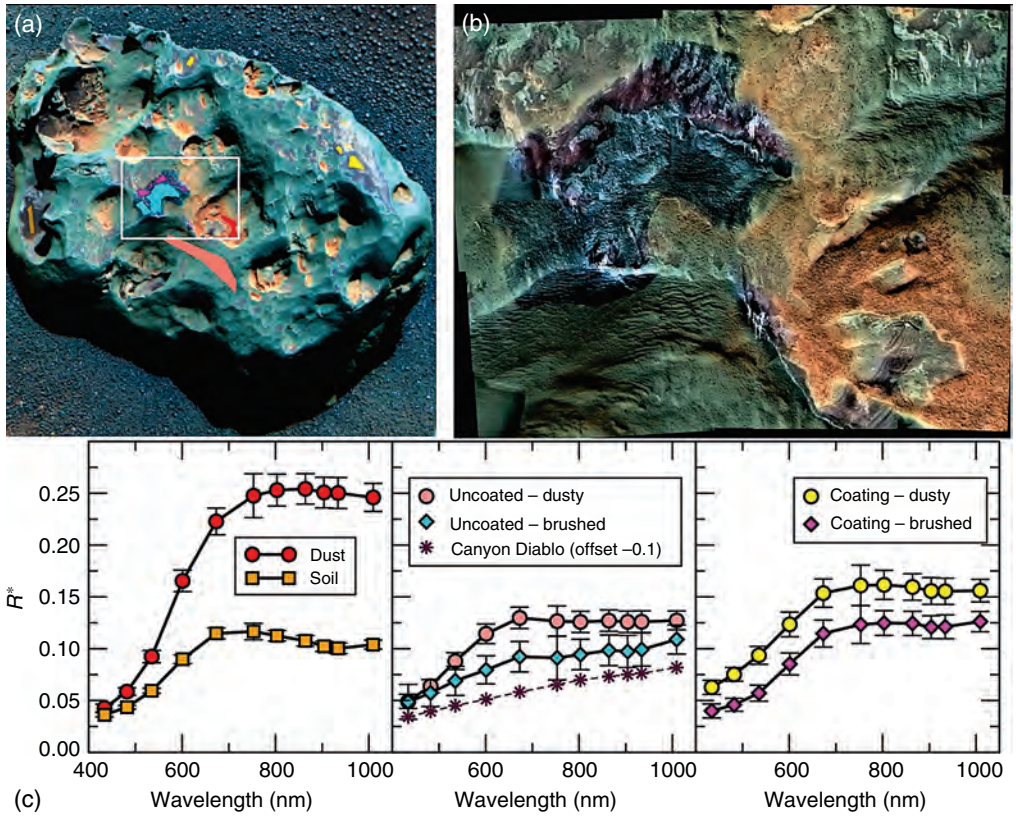

Figure 13.34. (a) Pancam false-color image (sol 352, P2596) of Heat Shield Rock created from 753, 535, and 432 nm images. White box outlines region of Microscopic Imager mosaic acquired after RAT brush (sol 349), shown in (b) with color overlain from the same Pancam false-color images as in (a). (Bright streaks are caused by saturation in MI mosaic.) Colored regions in (a) are regions of interest from which Pancam spectra were extracted as shown in (c). Canyon Diablo laboratory spectrum (RELAB MI-CMP-008, spectrum 001) is vertically offset −0.1.

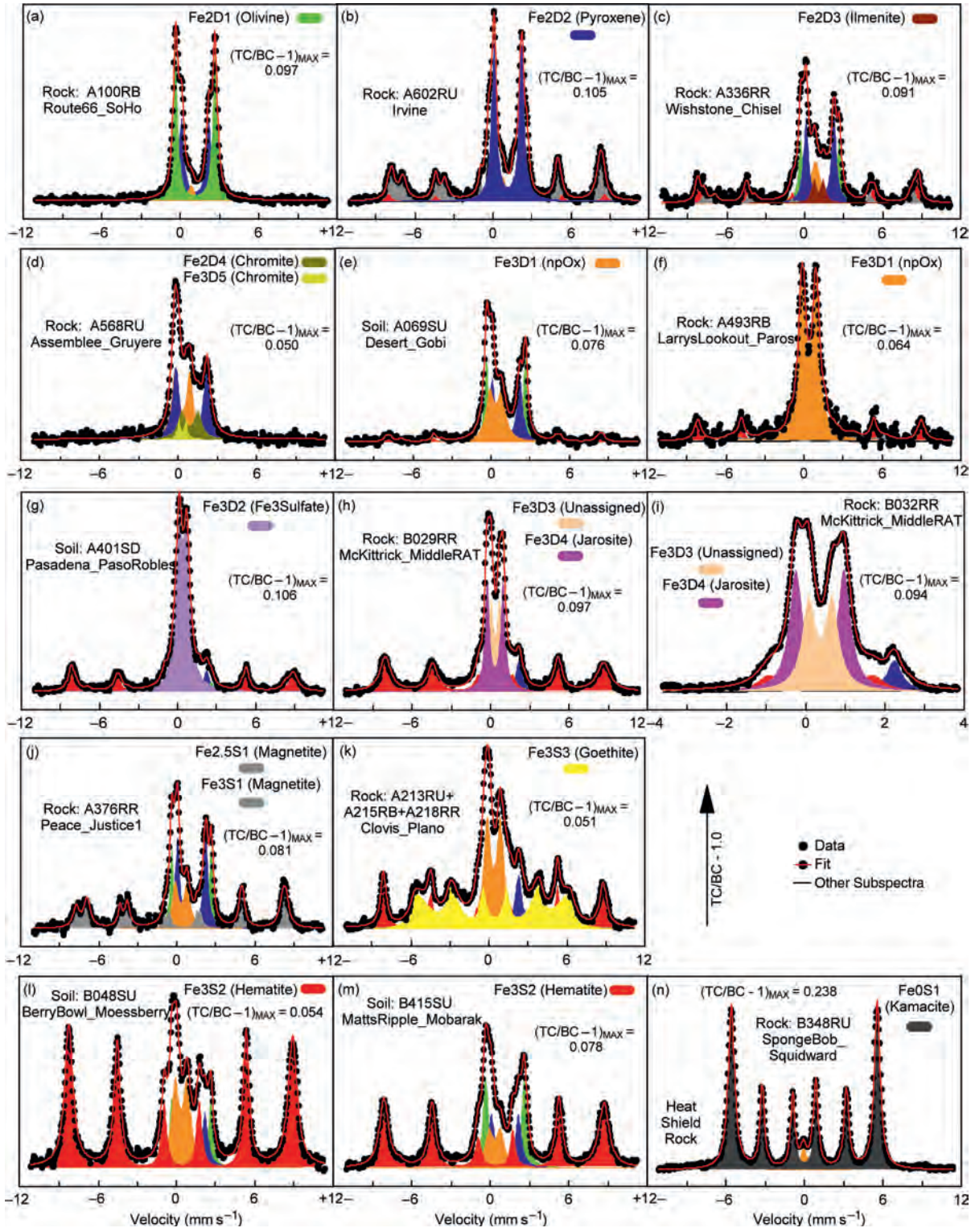

Figure 15.4. Mössbauer spectra that have high proportions of Fe for each of the 14 identified MB doublets and sextets: (a) Fe2D1 (Ol) in Adirondack Class rock Route66; (b) Fe2D2 (Px) in rock Irvine; (c) Fe2D3 (Ilm) in Wishstone Class rock Wishstone; (d) Fe2D4 and Fe3D5 (Chr) in Independence Class rock Assemblee; (e) Fe3D1 (npOx) in Laguna Class undisturbed soil Desert_Gobi; (f) Fe3D1 (npOx) in Watchtower Class rock LarrysLookout; (g) Fe3D2 (Fe3Sulfate) in Paso Robles Class soil Pasadena_PasoRobles; (h) Fe3D3 (unassigned) and Fe3D4 (Jar) in Burns Outcrop Class rock; (i) same as (h) except MB spectrum was acquired over a narrow velocity range; (j) Fe2.5S1 and Fe3S1 (Mt) in Peace Class rock Peace; (k) Fe3S3 (Gt) in Clovis Class rock Clovis; (l) Fe3S2 (Hm) in Berry Class undisturbed soil BerryBowl_Moessberry; (m) Fe3D2 (Hm) in Berry Class undisturbed soil MattsRipple_Mobarak; and (n) Fe0S1 (Kam) in Heat Shield Rock. All MB spectra are the sum of spectra for temperatures between 200 and 270 K. Sample naming convention is Uwwwxyz, where U = A for Gusev crater or U = B for Meridiani Planum, www = sol number, x = R (rock) or S (soil), y = U (undisturbed), D (disturbed), B (RAT brush), or R (RAT grind), and z = 0, 1, 2, . . . as appropriate to keep sample names unique (usually, z = 0). The *y*-axis is TC/BC – 1.0, where TC = total counts and BC = baseline counts. The maximum value of TC/BC – 1.0 for each spectrum is given in the figure as $(TC/BC - 1.0)_{MAX}$.

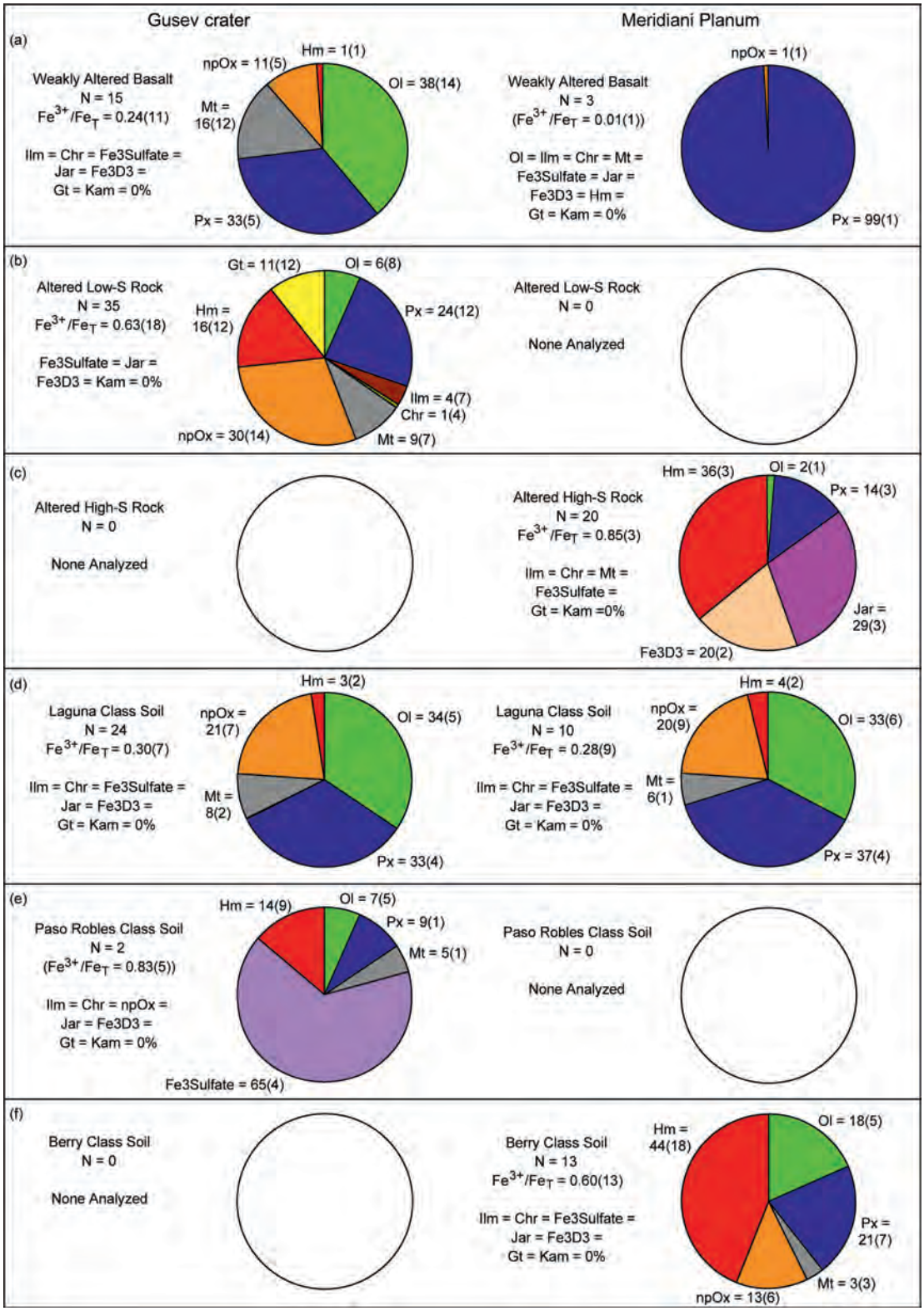

Figure 15.9. Pie diagrams showing the average values (1σ standard deviation in parenthesis) of Fe from Fe-bearing phases (A_x, where x = Ol, Px, Ilm, Chr, Mt, npOx, Fe3Sulfate, Fe3D3, Jar, Hm, and Gt) for rock and soil supergroups at Gusev crater (as of sol 602) and Meridiani Planum (as of sol 557): (a) Weakly Altered Basalt, (b) Altered Low-S Rock, and (c) Altered High-S Rock for RAT-ground surfaces, (d) Laguna Class soil, (e) Paso Robles Class soil, and (f) Berry Class soil. Altered High-S Rock and Berry Class soil are not present at Gusev crater and Altered Low-S Rock and Paso Robles Class soil are not present at Meridiani Planum. The distribution of Fe from Fe-bearing phases for Gusev crater Weakly Altered Basalt (a) is very similar to that for Laguna Class soil (d), except the latter has more Fe from npOx. The meteorite supergroup (not shown), whose distinguishing characteristic is kamacite as an Fe-bearing phase, includes two rocks from Meridiani Planum (Heat Shield and Barberton) and no rocks from Gusev crater. The average concentrations of Fe associated with iron-bearing phases ($A_xFe_T/100$) are given in Table 15.3.

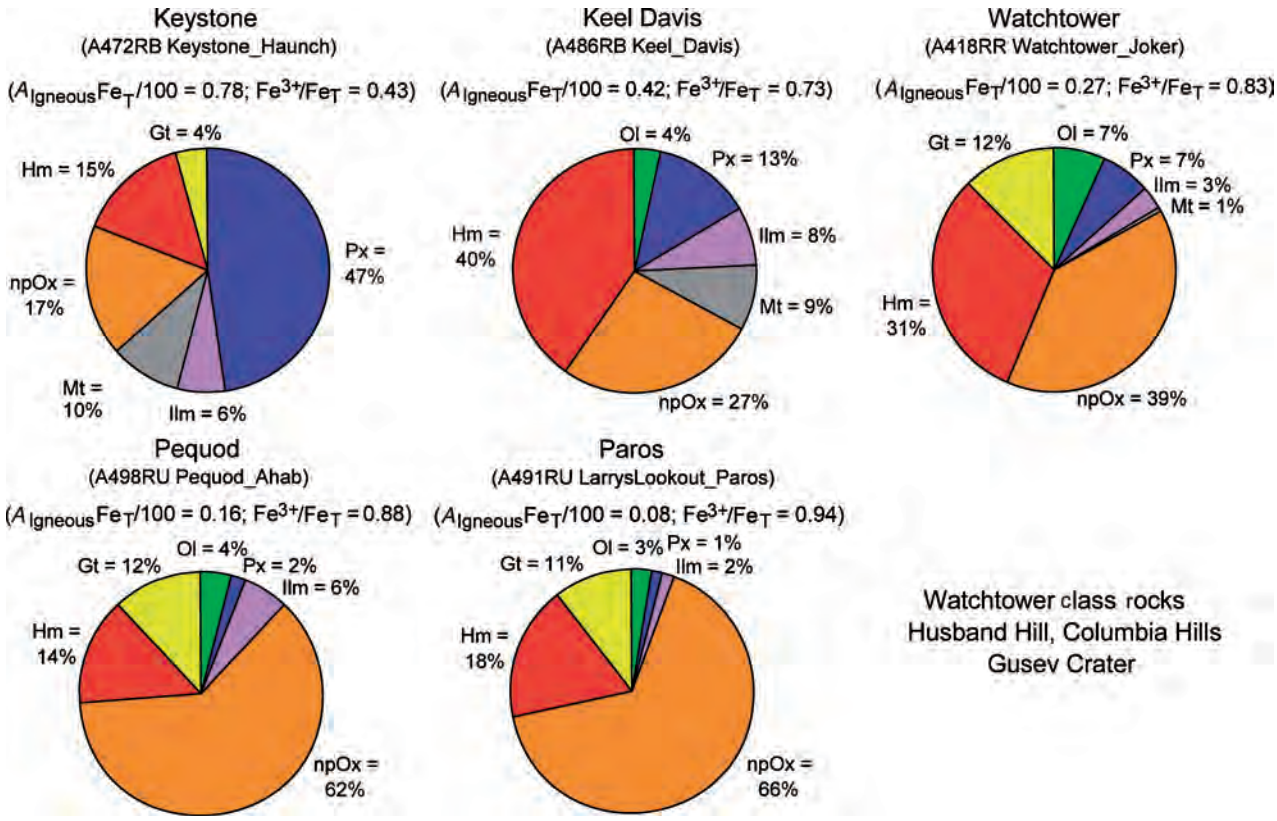

Figure 15.12. Pie diagrams showing Fe mineralogical compositions for Watchtower Class rocks Methusela, Jibsheet, Watchtower, Pequod, and Paros in the Gusev Columbia Hills. These rocks likely have undergone isochemical alteration under low water-to-rock ratio conditions because they have similar chemical compositions but diverse mineralogical compositions ($A_{\text{Ingeous}}\text{Fe}_\text{T}/100 = 0.78$ to 0.08) and Fe oxidations states ($\text{Fe}^{3+}/\text{Fe}_\text{T} = 0.43$ to 0.94).

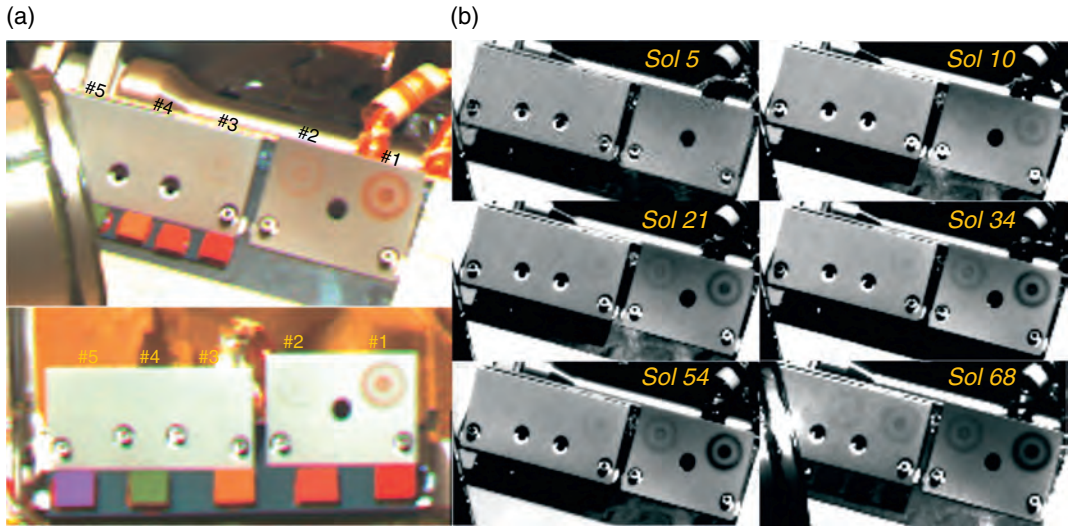

Figure 16.7. (a) Upper magnet array (top) and lower magnet array (bottom) onboard Mars Pathfinder as imaged on sol 64. The magnet array is composed of five permanent magnets. The magnets are labeled from right to left according to decreasing magnetic strength. The strongest (right-most) magnet (magnet #1) is basically identical to the RTC magnet onboard the Viking Landers (see Figure 16.6). Also, the two strongest magnets (#1, #2) are very similar to the backhoe magnets of the Viking soil sampler. Magnet #5 was partially obstructed by the gearbox of the high-gain antenna late in the mission. The colored blocks in front of the array are reference color tiles. The difference between the dust load on the upper and lower magnet array is due to the upper array being exposed to dust arriving from all directions and the lower array being somewhat shielded by the body of the lander. (b) The development of the dust pattern on the upper magnet array over time.

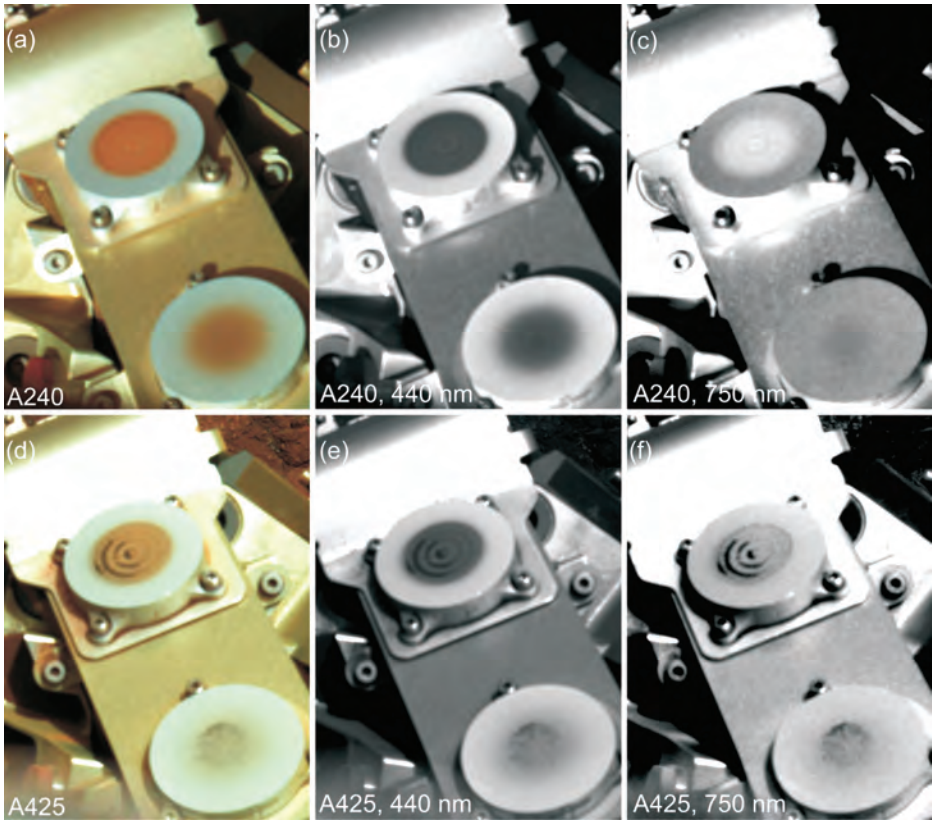

Figure 16.11. Separability of airborne dust as observed on the Mars Exploration Rover *Spirit*. The color images shown are false-color images composed of radiometrically calibrated, equally stretched Pancam L7 (440 nm), L5 (550 nm) and L2 (750 nm) images. Note the change in color between sol 240 and sol 425. A strong wind gust had passed over the rover close to sol 418.

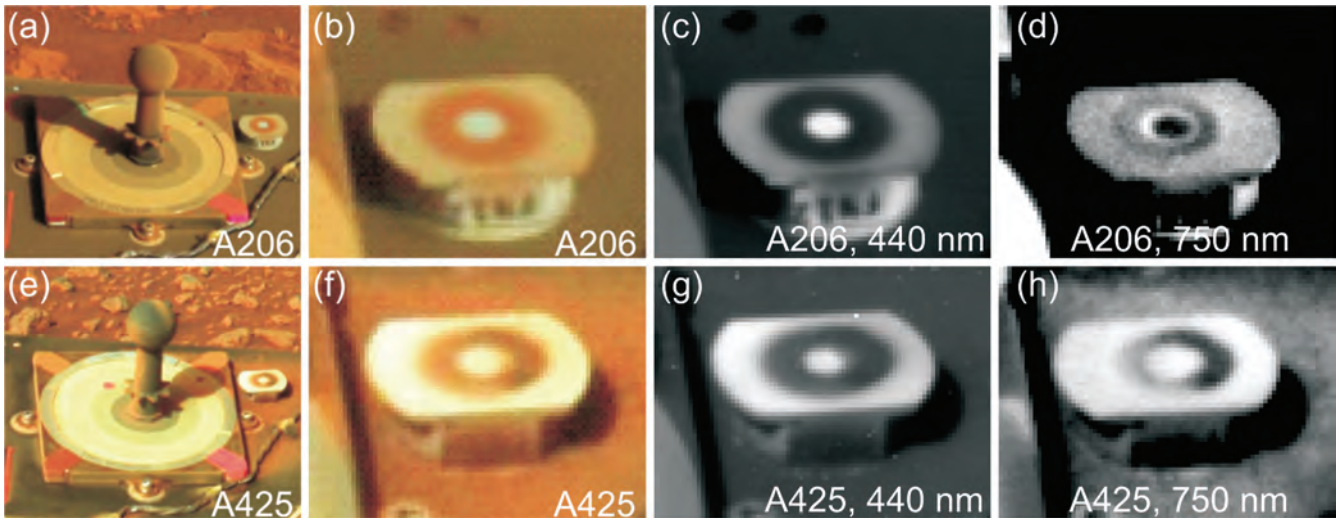

Figure 16.14. Sweep magnet, Mars Exploration Rover *Spirit*, sol 206 (a–d) and sol 425 (e–h). The color images shown are false-color images composed of radiometrically calibrated, equally stretched, images (see, Figure 16.11). Figures (a) and (e) show both the Pancam calibration target and the sweep magnet. The Sun is lower in the sol 206 image and therefore this image appears somewhat darker as compared to sol 425. Episodes of strong winds were observed around sol 418. Note the change in color between sol 206 and sol 425. The black/white images have been acquired through either the blue (c, g) or one of the near-infrared filters (d, h) and have been independently stretched in order to show spectral variations across the magnet surface (in particular in (d) the bright ring around the very center of the magnet surface [see text]).

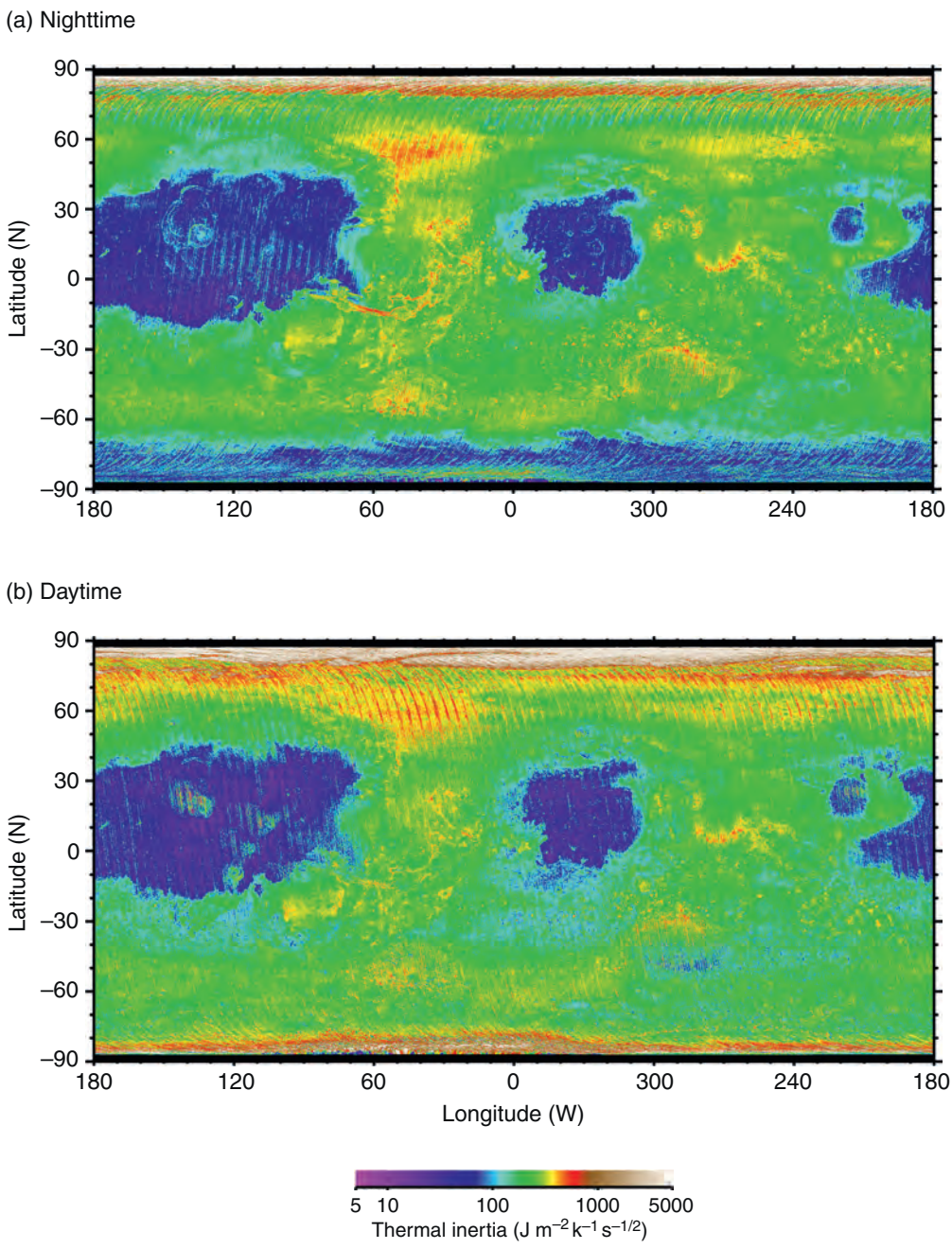

Figure 18.8. Global map of the thermal inertia of Mars based on TES (a) nighttime and (b) daytime bolometric brightness temperature observations (see Putzig and Mellon, 2006b). Maps are generated by a median filter of 36 seasons over 3 Mars years and are binned at 1/20° per pixel. Nighttime and daytime maps cover descending and ascending orbit track of the MGS spacecraft, respectively, and are also referred to nightside and dayside maps (Putzig and Mellon, 2006b). In the polar regions both maps contain thermal inertia results derived from temperature observations of an illuminated surface during polar summer. Local times transition between nighttime hours and daytime hours as the orbit track passes within a few degrees of the pole and transitions between the nightside and dayside orbit tracks. Large low-thermal-inertia regions (shades of blue) are believed to be dominated by surface dust deposits. Higher thermal inertias represent changes in soil grain size, duricrust, rocks, or some combination. Few areas exist indicating bedrock. Differences between nighttime and daytime maps may be related to surface heterogeneity. See text for discussion.

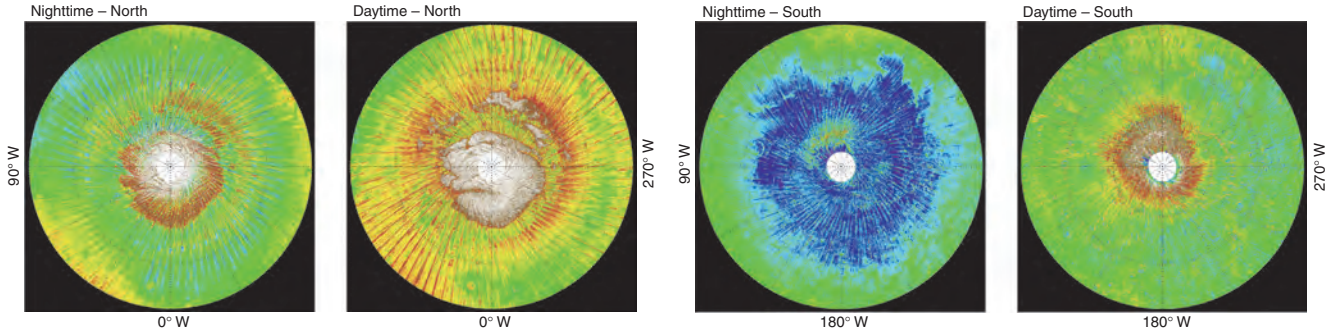

Figure 18.9. Polar orthographic maps of thermal inertia for both northern and southern hemispheres and both dayside and nightside ground tracks. Significant diurnal differences in the apparent thermal inertia are observed, suggesting subsurface layering or ice-rich permafrost beneath a soil veneer (Putzig and Mellon 2006b; see text for additional discussion). Maps are shown between 60° and 90° latitude. Color scale is the same as Figure 18.8.

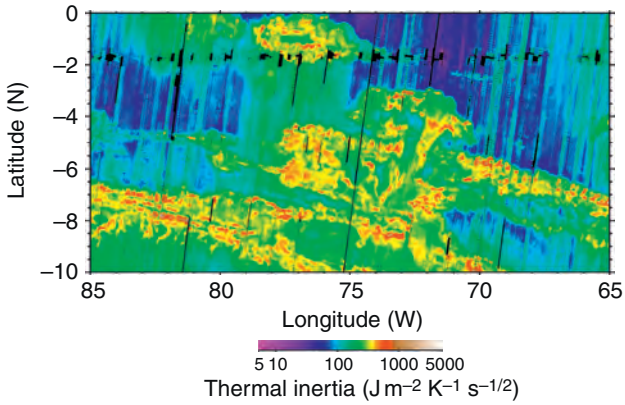

Figure 18.10. A full-resolution TES nighttime bolometric thermal inertia map of Candor Chasma, Melas Chasma, and Ophir Chasma in central Valles Marineris. These regions exhibit some of the most diverse thermal inertia values on Mars for a localized area. Individual 3 km TES footprints are visible. Map width is approximately 120 km. Evident in a number of small multikilometer areas are thermal inertia values in excess of 1200, indicating the presence of clean exposures of bedrock.

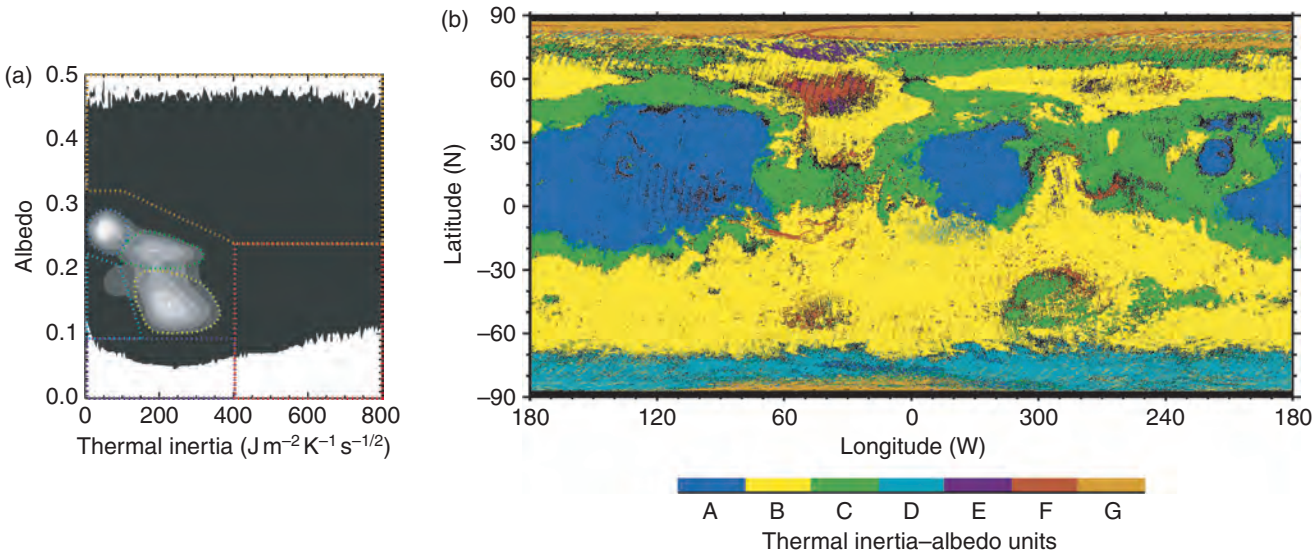

Figure 18.12. (a) A two-dimensional histogram of albedo and nighttime thermal inertia based on the maps shown in Figures 18.8a and 18.11, and (b) a thermophysical unit map based on this histogram (see Putzig, 2006). Shades of gray in the histogram indicate frequency of occurrence, with lighter shades indicating more frequent occurrence. Three major modes are evident: (Unit A) high albedo and low thermal inertia, (Unit B) low albedo and high thermal inertia, and (Unit C) intermediate albedo and high thermal inertia (see Mellon *et al*., 2000; Putzig *et al*., 2005). Other less-dominate units (D–G) are also shown – see text and Table 18.2 for discussion. Histogram bin sizes are 0.01 for albedo and 5 for thermal inertia. Levels are 1 occurrence and 1/20, 1/10, 1/5, 1/3, and 1/2 of the maximum frequency.

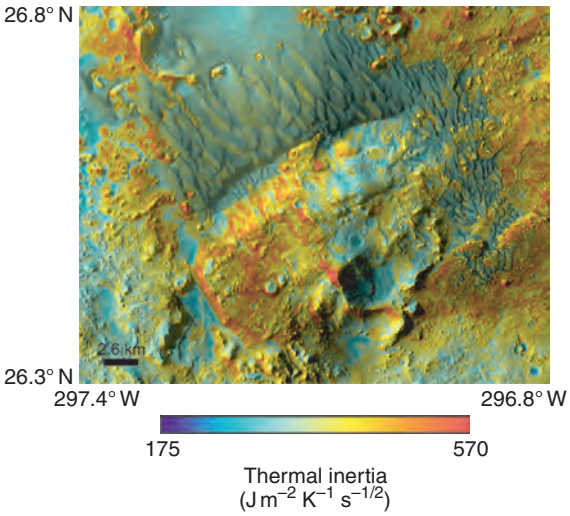

Figure 18.14. THEMIS-based thermal inertia (100 m resolution) superimposed on a THEMIS visible image mosaic (18 m resolution), located near 26.5° N × 357° W. Shown are the thermal inertia contrasts between dune bedforms, sand sheets, and nonaeolian surfaces. These major surface units exhibit thermal inertia values ranging from 230 to 465, although a few outlier surfaces exist with thermal inertia values from 175 to 570. See text and Fergason *et al*. (2006b) for more discussion.

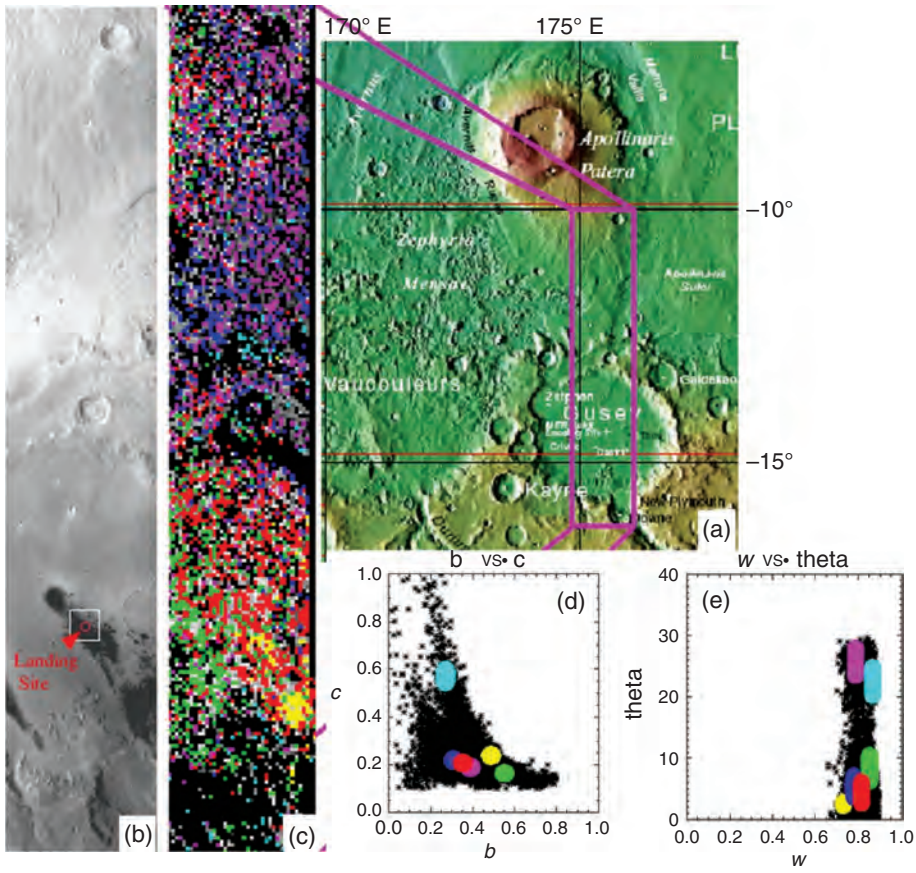

Figure 19.4. (a) Mars Observer Laser Altimeter (MOLA) shaded and color-coded topographic map showing location of HRSC image of Gusev crater and Apollonaris Patera shown in (b), which designates the MER *Spirit* rover landing site. (c) Color-coded map of photometric units modeled by Jehl *et al.* (2006); (d) 2-term Henyey–Greenstein parameters *b* and *c* for all pixels in (c); (e) single-scattering albedo (*w*) and macroscopic surface roughness values ("theta") modeled by Jehl *et al.* (2006). Color regions in (d) and (e) correspond to units in (c) and are arranged as follows: yellow = low-albedo region; red = northern Gusev plains; green = southwestern Gusev plains; pink = rough Apollanaris plains; blue = smooth Apollanaris plains; cyan = topographic highs (see text).

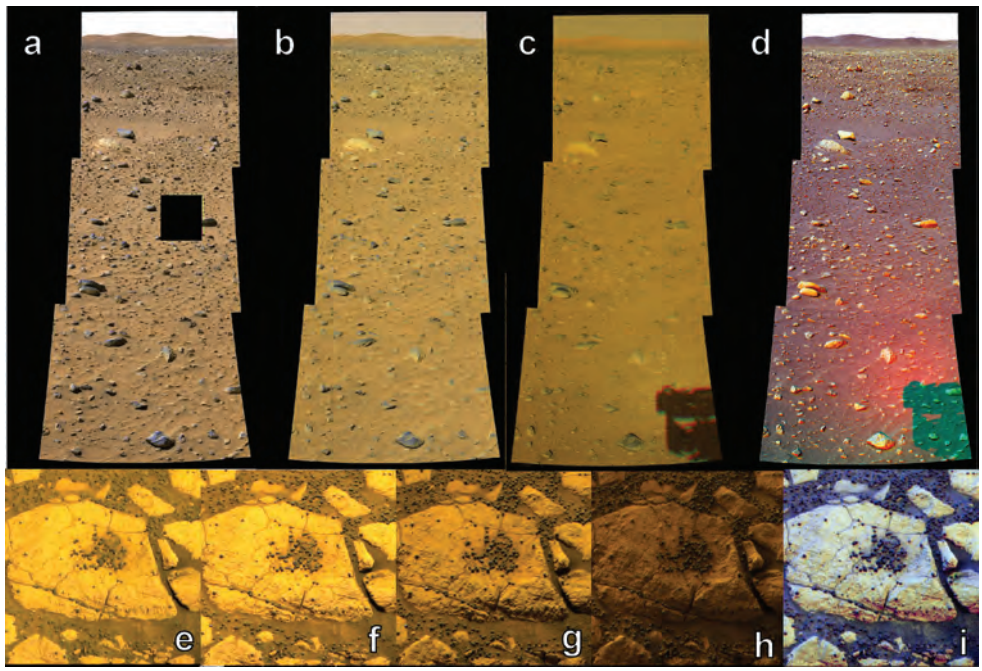

Figure 19.9. Top: False-color *Spirit* Pancam image mosaics acquired on Sols 102–103 pointed east (sequence P2382) acquired at (a) 1024 (the black rectangle represents a missing data packet in the L4 filter), (b) 1308, and (c) 1519 LTST. Images constructed from *I*/*F* data using 753 nm (L2), 601 nm (L4), and 432 nm (L7) filters (identical stretches applied to each mosaic: red = 0.00–0.035, green = 0.00–0.03, blue = 0.00–0.10). Color composite (d) derived from different times of day for the same wavelength (432 nm) using red = 1519 LTST (central phase angle = 15°); green = 1308 LTST (47°); blue = 1023 LTST (88°). Note opposition effect near Pancam Mast Assembly shadow (from Johnson *et al.* [2006a]. Bottom: *Opportunity* Pancam images acquired of the "Berrybowl" in Eagle crater on Sols 42–45 at (e) 1028 (sequence P2556), (f) 1235 (P2552), (g) 1449 (P2548), and (h) 1705 LTST (P2552). All images constructed from *I*/*F* data using 753 nm (L2), 601 nm (L4), and 432 nm (L7) filters; identical stretches applied to each band: 0.00–0.30, except for (d) which is stretched 0.00–0.15. Color composite (i) derived from different times of day for the same wavelength (753 nm) using red = 1027 LTST (central phase angle = 34°); green = 1235 LTST (61°); blue = 1703 LTST (124°).

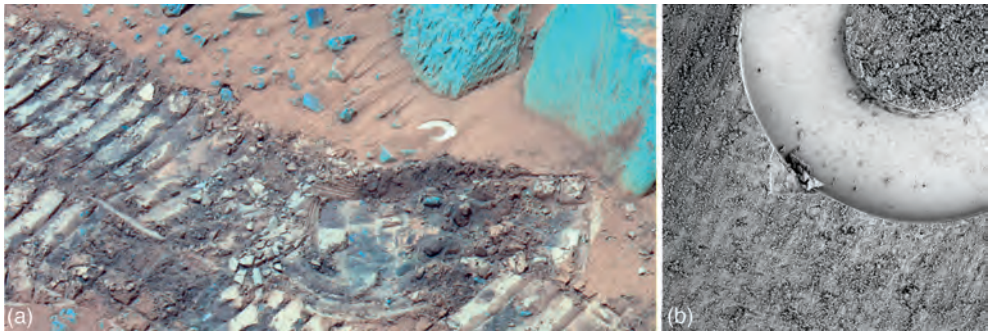

Figure 20.7. (a) *Spirit* Pancam false-color view of tracks and Mössbauer imprint into dusty aeolian drift material, obtained near the summit of Husband Hill on Sol 589. Pancam filters are L2 (753 nm), L5 (535 nm), and L7 (432 nm) stretched into red, green, and blue, respectively. The Mössbauer imprint is the bright, partial ring feature at central upper-right in this view. (b) *Spirit* MI image of the same Mössbauer contact plate imprint, obtained on Sol 588 in full shadow. The MI was rotated at the time of imaging relative to the orientation of (a). MI view is ~31 mm across.

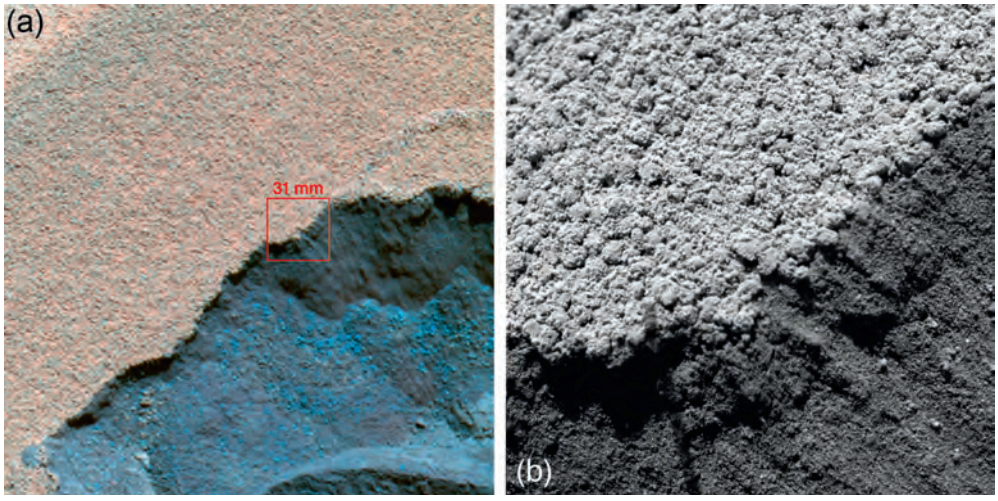

Figure 20.10. (a) *Spirit* Pancam false-color view of the wheel scuff performed on Sol 72 into "Serpent," an aeolian bedform near the rim of Bonneville crater on the plains west of the Columbia Hills. Pancam filters are L2 (753 nm), L5 (535 nm), and L7 (432 nm) stretched into red, green, and blue, respectively. The brighter, redder, dusty exterior contrasts with the darker interior of the feature. Red square shows MI location. (b) MI image 2M132842058IFF2000P2977M2F1 of the edge of the wheel scuff, obtained on Sol 73. A very thin, relatively bright dust layer covers a monolayer of rounded, very coarse sand, which overlies an ~8 mm weakly cohesive layer dominated by finer grains, with similarly fine materials further below (lower right of image). View is about 31 mm across, illuminated from top.

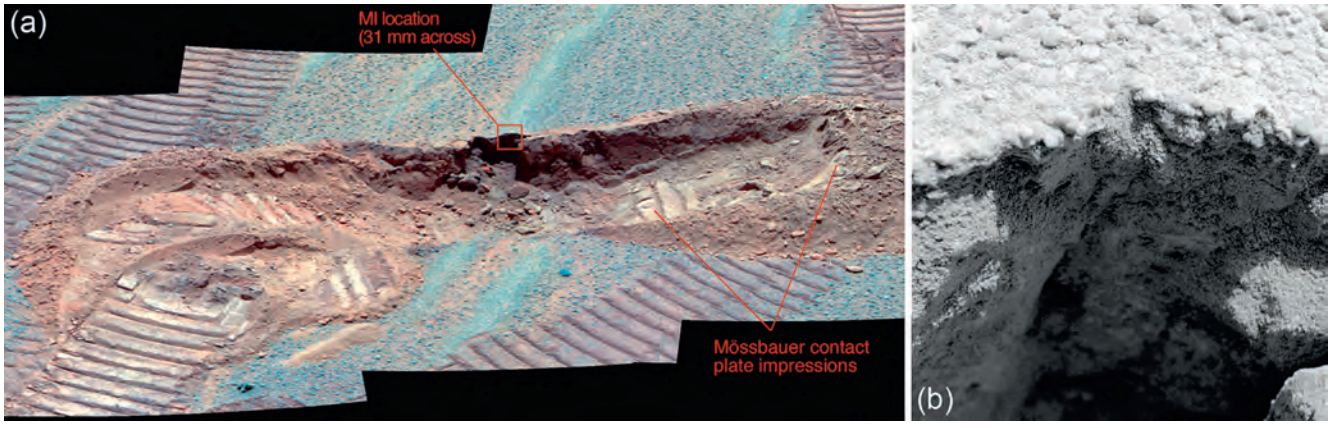

Figure 20.16. (a) *Opportunity* Pancam false-color view of a wheel trench dug on Sol 73 in the Anatolia area on the Meridiani plains between Eagle and Endurance craters. Pancam filters are L2 (753 nm), L5 (535 nm), and L7 (432 nm) stretched into red, green, and blue, respectively. In this view, hematite-enriched spherules several millimeters in diameter are blue, and are scattered across the undisturbed areas between ripples. Low ripples are coated with much smaller ~1 mm rounded hematite grains (also blue, not individually resolved by Pancam). The wheel trench bisected the (blue) ripple extending down the center of this view. The shadowed area on the trench far wall, where the ripple is bisected, is a collapse "cavern" that formed late in the trenching process (as seen in front Hazcam images obtained periodically during trenching), shedding break-away cohesive clods to the base of the trench wall. Maximum trench depth is about 10 cm. Red inset shows MI view location. (b) MI image 1M135284929IFF10CGP2956M2F1 of the rim of the trench. The ripple crest is seen in cross section in the upper middle of this view, where a surface of ~1 mm rounded hematite-enriched spherules form a thin lag. The ripple interior is dominated by ~100 μm sand and even finer, unresolved grains. View is about 31 mm across, illumination from upper right.

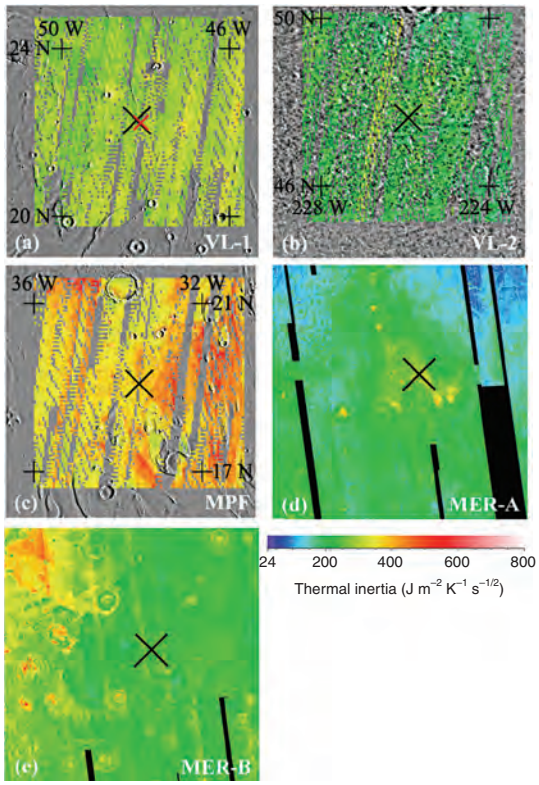

Figure 21.18. TES-based thermal inertia map (5°×5°) over a Viking MDIM 2.0 mosaic (a–c; based on Putzig *et al*., 2005) or 6°×6° THEMIS-based thermal inertia mosaic calibrated to the Putzig *et al*. (2005) TES map (d, e; after Jakosky *et al*., 2006). (a) VL-1, relocated from small red to large black X per Zeitler and Oberst (1999) revised location; (b) VL-2; (c) MPF; (d) MER-A map 182° W to 188° W, 12° S to 18° S; (e) MER-B map 3° W to 9° W, 1° S to 5° N.

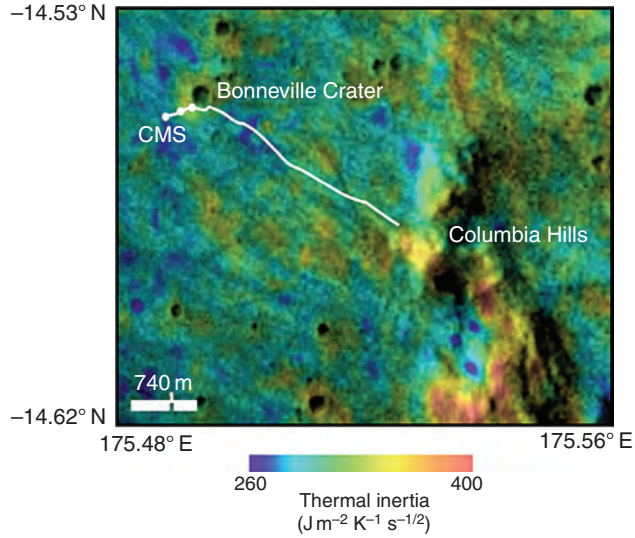

Figure 21.19. THEMIS thermal inertia image in color (100 m/pixel) overlaid on THEMIS visible mosaic (18 m/pixel) of the Gusev crater landing region. *Spirit* landed at Columbia Memorial Station (CMS) in a low albedo, low thermal inertia intercrater plains (southwestern-most white dot: Mission Success panorama location), traversed through the ejecta blanket (middle white dot: Legacy panorama location) to the rim of Bonneville crater about 300 m away (northeastern-most white dot), and then across the low and high thermal inertia plains to the Columbia Hills (with generally higher inertias) to the east and southeast. Thermal inertia (Fergason and Christensen, 2006b) increases from 285 to 330 J m^{-2} K^{-1} s$^{-1/2}$ over the traverse to the rim of Bonneville crater. Rock size frequency distributions are reported at these three locations in Figure 21.12.

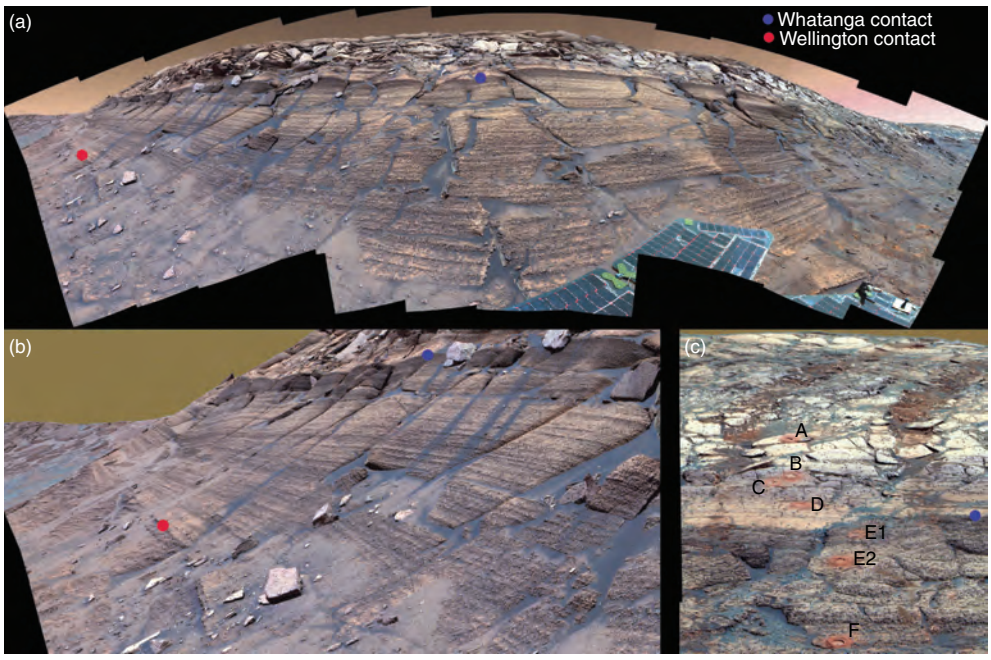

Figure 24.8. Pancam mosaics of the Burns formation exposed at Burns cliff on the southeast rim of Endurance crater. Three units of the Burns formation (Figure 24.9) are visible: the lower unit, beneath the "Wellington" contact, comprises cross-bedded sandstones; the middle unit, above the Wellington contact and beneath the "Whatanga" contact, comprises planar to low-angle cross-stratified sandstone; the upper unit, above the Whatanga contact, comprises light-toned eolian and subaqueous facies. Note the sharp discontinuity along the Wellington contact, interpreted to represent a deflation surface, and the dark tone of rocks beneath the Whatanga contact in panels A and B. In panel C, the location of the RAT holes, used to evaluate mineralogy, geochemistry, and microtextures, are labeled. The scale varies significantly across the area of each image, but the overall exposure at Burns cliff (panel A) is about 7 m and the RAT holes (panel C) are 4.5 cm in diameter. The images are false color-composite Pancam mosaics (see Grotzinger *et al*., 2005, for details).

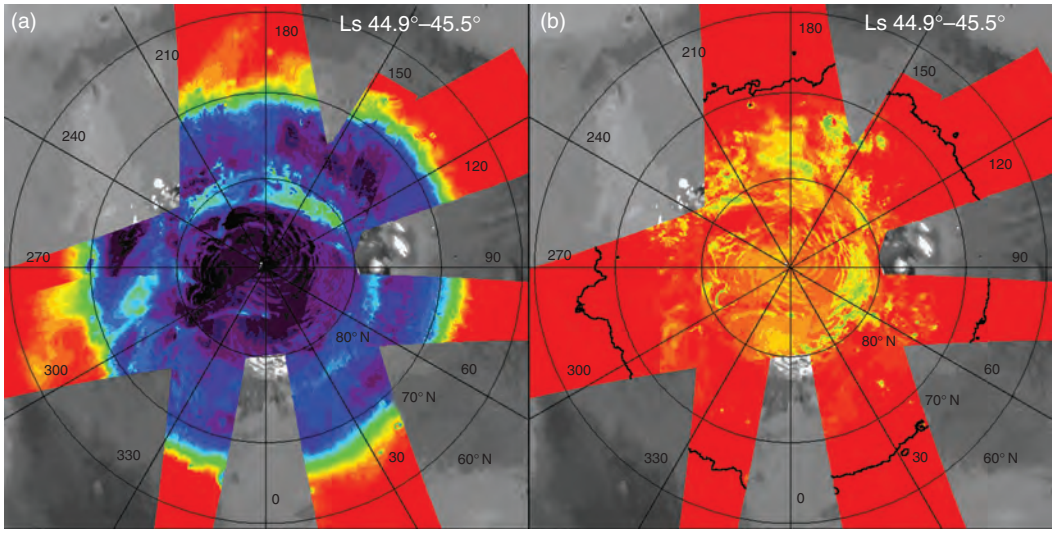

Figure 25.5. Spatial distribution of spectral signatures of CO_2 ice and H_2O ice observed by OMEGA in mid northern spring ($L_s \sim 45^\circ$, April 2006). (a) band depth of the H_2O ice absorption feature at 1.5 μm. The rainbow scale covers the range from 60% (black) to 0% (red). Weak signatures between 60° N and 70° N correspond to water ice clouds; (b) band depth of the CO_2 ice absorption feature at 1.43 μm, also from 60% (black) to 0% (red). The black outline corresponds to the boundary of regions with strong H_2O ice signatures. At this season, H_2O ice dominates the spectral signature of the northern seasonal cap, except for a few regions where strong spectral signatures of CO_2 ice are still observed.

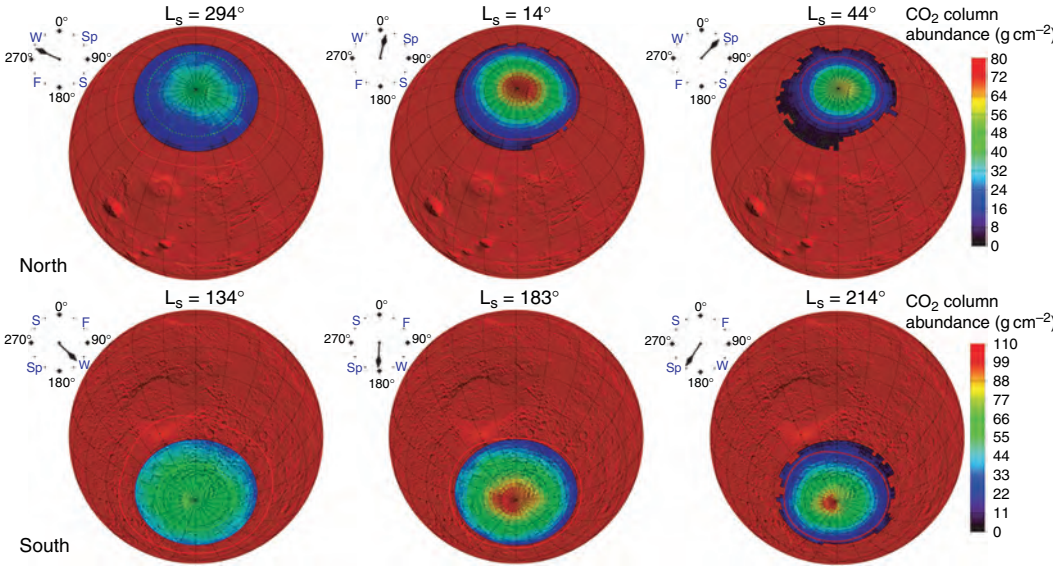

Figure 25.9. Maps of CO_2 column abundance in the northern and southern hemispheres (poleward of 60°) are compared to cap edge functions (solid red line) and the extent of the polar night (dashed green line). In both hemispheres, the maximum column abundance occurs near the pole during the recession. In the southern hemisphere, the distribution is asymmetric, with peak column abundance occurring at the location of the perennial CO_2 cap.

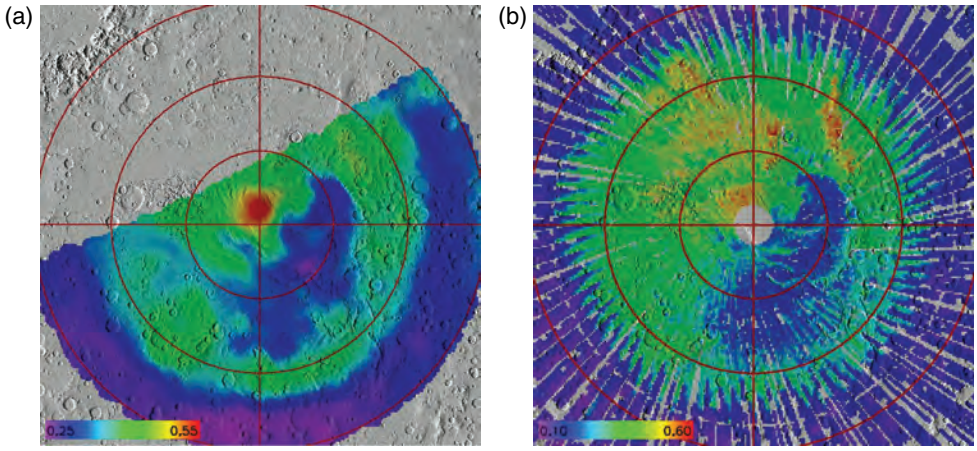

Figure 25.10. Albedo of the cryptic region. (a) The albedo of the southern seasonal cap in 1976 as measured by the Viking IRTM solar channel bolometer. (b) The albedo of the southern seasonal cap in 1999 as measured by the MGS TES solar channel bolometer.

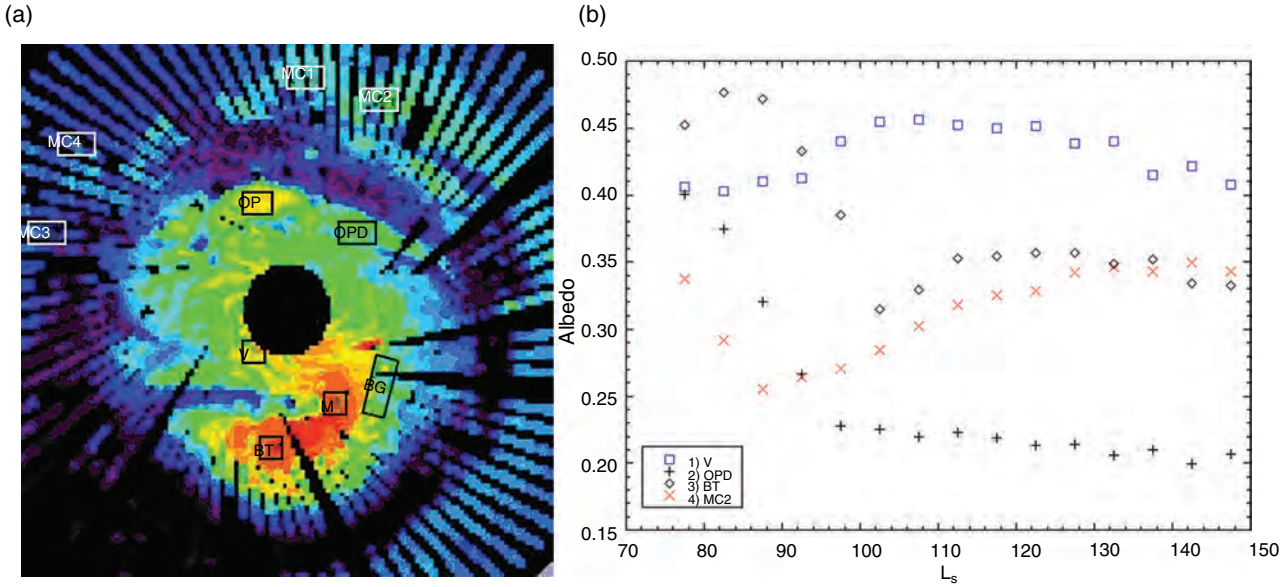

Figure 25.12. (a) Regions identified using TES albedo channels where frost mobility over the summer was noted. Color scale is TES albedo at $L_s = 85$ from 0.15 to 0.5 (purple to red). (b) Seasonal trends in albedo for the four types described in the text.

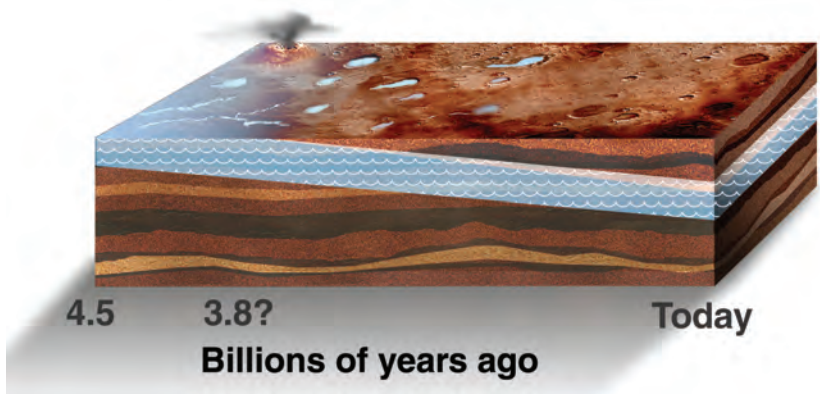

Figure 26.2. Hypothetical distribution of habitable environments, shown in light blue with wavy lines, in the Martian crust during its history. Surface and near-surface environments might have been habitable early in Martian history, whereas any habitable environments today might be restricted to a zone that lies a few kilometers below the surface. Graphics by Cheryse Triano, TopSpin Design Works.

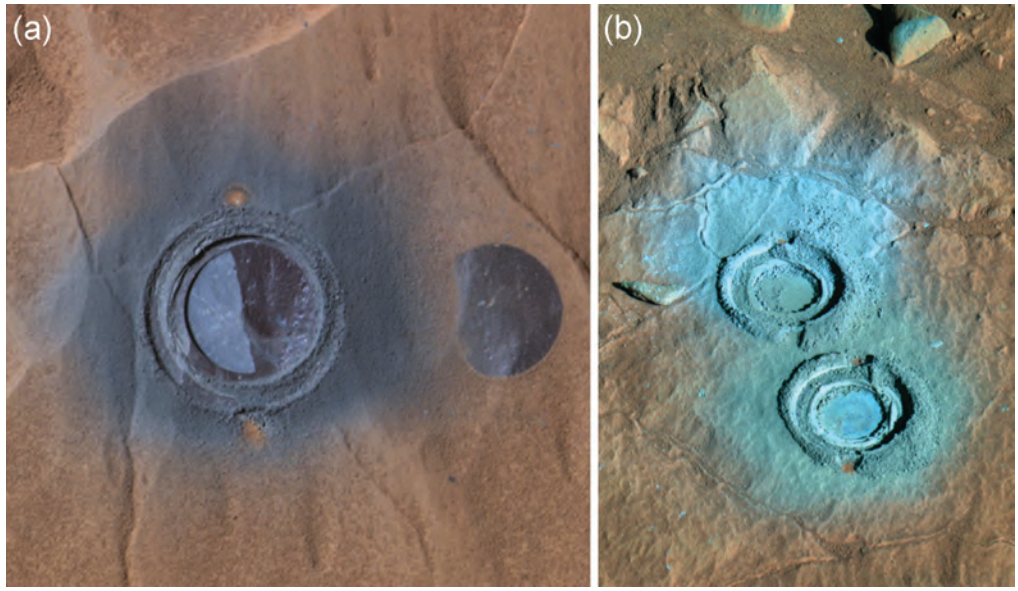

Figure 26.11. (a) Plains basalt "Mazatzal," showing 3 cm diameter brushed area at right and area at left ground by the RAT. Note the dark powder surrounding the 3 cm diameter hole. Part of false color Pancam image from sol 82, sequence P2590, filters 753 nm, 535 nm, and 480 nm. (b) Bedrock outcrop "Wooly Patch," a member of the "Clovis" rock class (see Clovis, Table 26.1), visited by *Spirit* on the West Spur of Husband Hill. The light-toned rock and powder exposed by the two 3 cm diameter RAT holes contrasted strongly with dark-toned basalts (e.g., Mazatzal) and provided evidence that Wooly Patch had sustained extensive aqueous alteration. Part of false color Pancam image from sol 200, sequence P2556, filters 753 nm, 535 nm, and 432 nm.

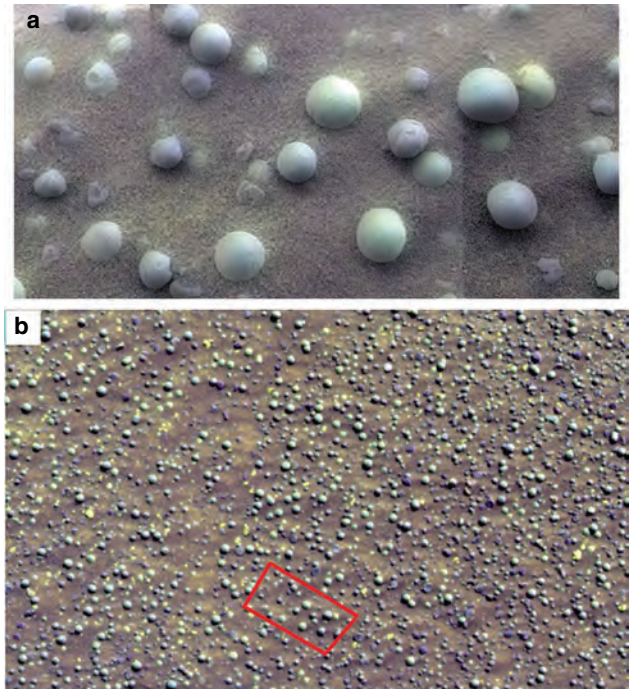

Figure 13.29. (a) Mosaic of 3 MI images (1M129426379, 1M129426503, 1M129426904) from the target "Superwit," merged with false-color Pancam sol 14 sequence P2549 image derived from an RGB composite of the R2 (750 nm), R7 (1009 nm), and R1 (423 nm) filters. (b) Portion of the sol 14 Pancam Superwit observation. Pancam sequence P2549, using the same R2, R7, R1 color scheme as (a). Red box corresponds to location of MI image in part (a). (Figure after Weitz *et al.*, 2006.) (For a color version of this figure, please refer to the color plate section or to the e-Book version of this chapter.)

of the concretions all of the ferric sulfate is converted to hematite. Mini-TES spectra of fields of view dominated by spherules are likewise dominated by the spectral features of well-crystallized hematite (Christensen *et al.*, 2004).

Multispectral properties

The soils of Meridiani Planum display a variety of visible and NIR spectral properties. The upper lag surface of the soils is composed of basaltic sand, dust, millimeter-size hematite-rich spherules interpreted as concretions, spherule fragments, coated and/or partially buried spherules, basalt fragments, sedimentary outcrop fragments, and centimeter-size loose rock fragments (Sullivan *et al.*, 2005; Weitz *et al.*, 2006). Beneath the lag deposit, the soils are dominated by finer-grained basalt sands and dust. The Pancam observations of any given soil patch reflect the variations in the kinds of grains that compose the soil. False-color composites and DCSs of Pancam soil observations are extremely useful for characterizing different spectral properties of millimeter-size and larger grains.

The hematite-rich spherules (Christensen *et al.*, 2004; Klingelhöfer *et al.*, 2004; Morris *et al.*, 2006b) have an absorption around 900 nm and a strong positive inflection from the Pancam's R6 to R7 filters (934–1009 nm). These features have been attributed to hematite in the blueberries (e.g., Bell *et al.*, 2004b; Soderblom *et al.*, 2004). Not all spherules appear blue in Pancam false-color composites, however.

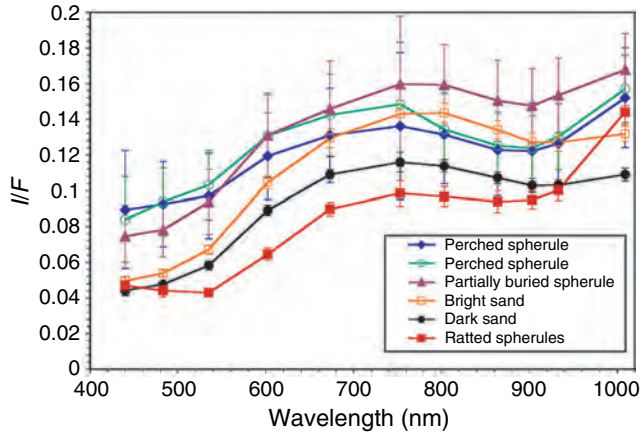

Figure 13.30. Visible to near-IR Pancam spectra of features seen in target Superwit (Figure 13.29). The spectrum of RATed spherules represents an average of two spectra from spherules that were still embedded in the Eagle crater outcrop and had been cut in half by the RAT. (For a color version of this figure, please refer to the color plate section or to the e-Book version of this chapter.)

Many of the partially buried spherules appear yellower, which is consistent with the presence of a dusty coating (Bell *et al.*, 2004b; Soderblom *et al.*, 2004). For example, the Eagle crater spherules shown in Figure 13.29, which have an average major axis of 3.15 ± 1.2 mm, have both bluish and yellowish populations in false color views, suggesting variable degrees of dust covering/coating (Weitz *et al.*, 2006).

Examples of spectra extracted from small numbers of pixels on the various spherules in Figure 13.29 are shown in Figure 13.30. The spectrum of the RAT-ground spherules is an average of two spectra from spherules that were still embedded in the Eagle crater outcrop but which had been ground down to about half their diameter by the RAT to expose a fresh interior. This fresh spherule interior has the strongest upturn between the 933 and 1009 nm filters and exhibits a strong inflection or "kink" in the spectrum around 535 nm. Both of these characteristics are consistent with the presence of hematite within the spherules (see Figure 13.22b). Several spherules perched on the soil also have a strong increase in reflectance between the 933 and 1009 nm filters, in addition to a NIR absorption band centered around 900 nm and shallow spectral slope in the visible. In Figure 13.29, these perched spherules appear lighter blue in color. These spectral characteristics are consistent with the spherules being relatively "clean" (dust-free) and having a surface component of coarser-grained ("gray"), perhaps even specular, hematite compared to the RAT-ground spherule interiors. Those spherules that are partially buried to varying degrees in the soil appear yellower in Figure 13.29 because of a reduced absorption around 900 nm and a steeper red spectral slope in the visible. These spectral characteristics are consistent with dust coating or adhering to the surfaces of these spherules to varying degrees. Even though spherules perched on the soil do not show the dust-like coating seen on the partially buried spherules, they still exhibit different spectra than the fresh RAT-exposed interiors of spherules embedded in the outcrop. One hypothesis is that once spherules erode out of the outcrop rocks in which they formed, they "weather" (either physically as a result of wind-driven sand-blasting, or chemically from

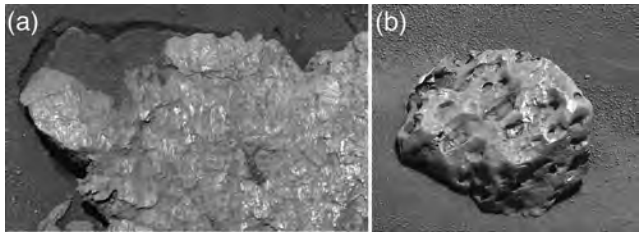

Figure 13.31. Examples of "erratics" at Meridiani Planum. (a) "Bounce Rock" – a pyroxene-rich basaltic rock thrown to its location near Eagle crater by a large impact elsewhere; Sol 65B P2574 L6. (b) "Heat Shield Rock" – an iron meteorite; Sol 346B P2591 R1.

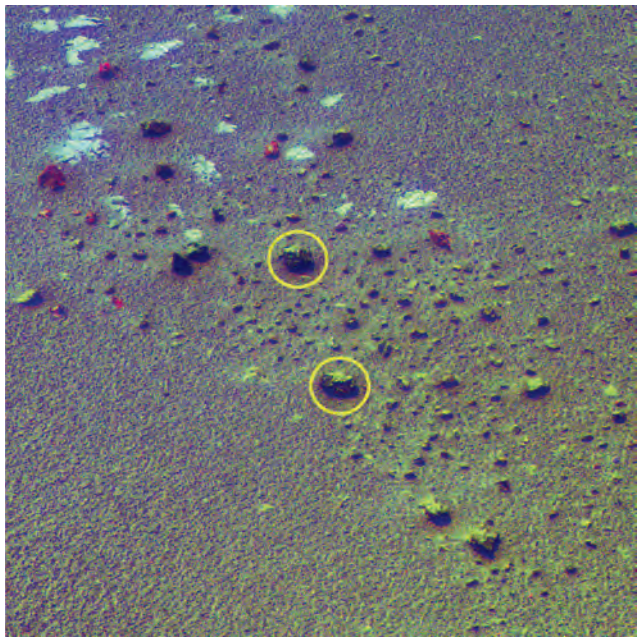

Figure 13.32. Pancam decorrelation stretch using the Right 754 nm, 934 nm, and 1009 nm filters in Red, Green, Blue, respectively. The rocks Arkansas and Perseverance are circled in yellow. The outcrop appears light blue and light green in color compared to the brown and red colors of the rock fragments. The top surfaces of several of the rock fragments appear green, consistent with outcrop spectral properties that could indicate a coating of fine dust derived from erosion of the outcrop. Sol 550 Pancam sequence P2579. (For a color version of this figure, please refer to the color plate section or to the e-Book version of this chapter.)

interactions with minor water vapor) or become covered by fine-grained airfall dust after they fall on the ground or are exposed to the atmosphere (e.g., Weitz *et al.*, 2006).

13.3.4 Cobbles, rock fragments, and meteorites

Geomorphology

Loose, dark, rocky fragments, and cobbles are also visible in Pancam observations of many soils. The fragments are generally just a few centimeters in size, but larger rocks have also been found. The rock fragments tend to concentrate in troughs between ripples and in association with outcrop exposures. There are several types of rocks and rock fragments that have been identified based upon both Pancam observations and geochemical analyses by the APXS and Mössbauer. Two of the best examples are shown in Figure 13.31. Bounce Rock

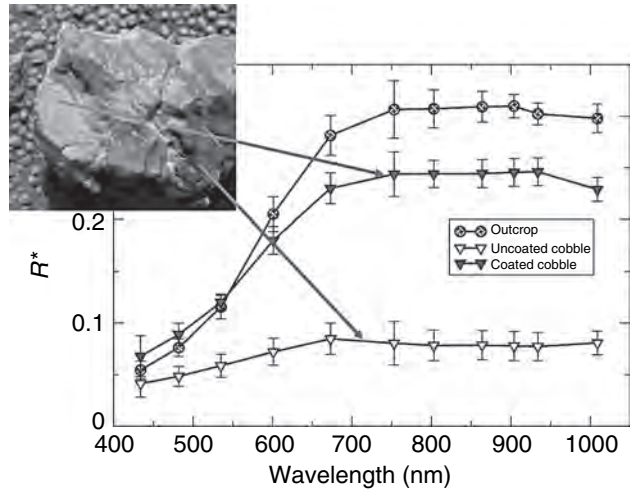

Figure 13.33. Microscopic Imager image from Sol 554 showing Perseverance cobble, with light-toned and dark-toned regions interpreted either as breccia clasts and matrix or as coated and uncoated portions of the cobble, respectively. Pancam spectra of the lighter-toned material appear similar to spectra of nearby outcrop rocks, whereas spectra of darker-toned portions appear more similar to spectra of other basaltic rocks.

(Figure 13.31a), so named because of its location next to an airbag bounce mark made just outside Eagle crater by the rover's landing system, was noticed from a distance to be distinctly different morphologically, texturally, and spectrally from other rocky materials in Meridiani Planum. Pancam, MI, and ultimately *in situ* chemical and mineralogical observations revealed this rock to be rich in pyroxene, and likely a piece of ejecta from a distant impact that sampled surface/subsurface materials not present at the surface where *Opportunity* has traversed (e.g., Figure 13.8b; Bell *et al.*, 2004b; Christensen *et al.*, 2004; Klingelhöfer *et al.*, 2004; Rieder *et al.*, 2004; Morris *et al.*, 2006b). Mineralogical and chemical analyses showed this rock to be very similar in its makeup to one of the basaltic Martian meteorites found previously on Earth (EETA 79001 "Lithology B"; Rieder *et al.*, 2004).

Heat Shield Rock (Figure 13.31b), so named because it was discovered near the debris from the rover landing system's heat shield impact site on the plains south of Endurance crater, exhibits a heavily pitted/eroded morphology and a highly specular surface (Squyres *et al.*, 2006b). The morphology of this rock was immediately suggestive of meteoritic regmaglypts (thumbprint-like indentations), and the specular nature of the surface (in both the visible and the infrared: see Chapter 14) suggested a metallic composition. Pancam multispectral observations (discussed below) were also consistent with a metallic composition. Heat Shield Rock was ultimately shown to be an iron meteorite by APXS and Mössbauer measurements that detected high abundances of Fe and Ni as the meteoritic metallic mineral kamacite (Morris *et al.*, 2006b; Yen *et al.*, 2006). Kamacite has also been identified in the cobble named Barberton (Morris *et al.*, 2006b; Gellert *et al.*, 2008), implicating it as another possible meteorite near the rim of Endurance crater.

Other smaller rock fragments and cobbles, such as Lion Stone and Russet, have been interpreted as ejecta, but they

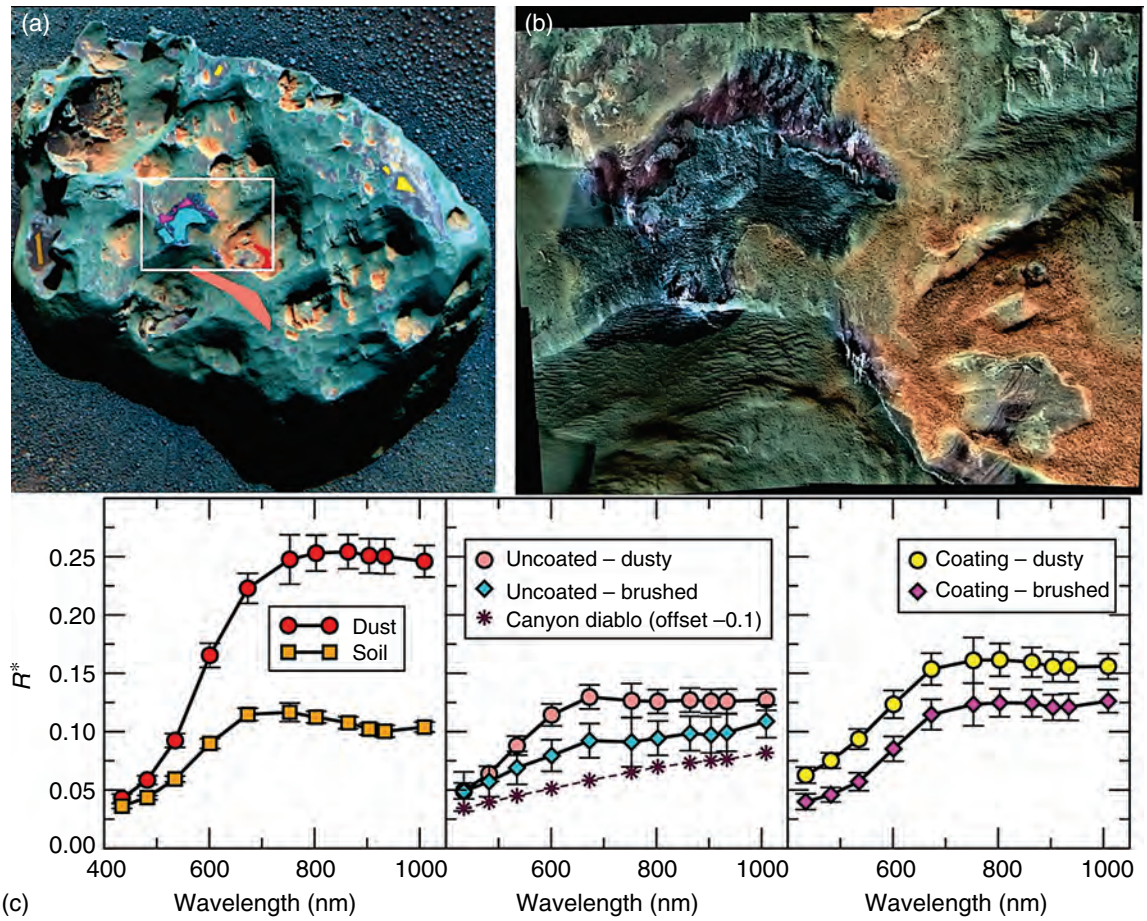

Figure 13.34. (a) Pancam false-color image (sol 352, P2596) of Heat Shield Rock created from 753, 535, and 432 nm images. White box outlines region of Microscopic Imager mosaic acquired after RAT brush (sol 349), shown in (b) with color overlain from the same Pancam false-color images as in (a). (Bright streaks are caused by saturation in MI mosaic.) Colored regions in (a) are regions of interest from which Pancam spectra were extracted as shown in (c). Canyon Diablo laboratory spectrum (RELAB MI-CMP-008, spectrum 001) is vertically offset −0.1. (For a color version of this figure, please refer to the color plate section or to the e-Book version of this chapter.)

have compositions that match the sulfate-rich outcrop rocks and so appear to be locally derived (e.g., Jolliff *et al*., 2006b). Another class of cobbles was found to be abundant near Erebus crater, and several were investigated with the rover's *in situ* arm instruments, including cobbles named Arkansas, Perseverance, and Antistasi (Figure 13.32). These cobbles have chemical compositions (in particular, sulfur contents) that are intermediate between those of the basaltic soils and the outcrop rocks, and they have heterogeneous surface textures that suggest they might be impact breccias or that they have unusual patchy coatings (see below).

Multispectral properties

Pancam and MI studies of cobbles and rocks in Meridiani reveal discontinuous lighter-toned patches across many of their surfaces, as discussed by Weitz *et al*. (2006). The cobbles named Arkansas, Perseverance (Figure 13.32), and Antistasi, as well as hundreds of others resting on soil or low-lying outcrop, have very distinct visible and NIR spectral properties (Figure 13.33) compared to the outcrop. Specifically, these cobbles exhibit low albedo and lower 535 nm and higher 904 nm band depths compared to the outcrop. Spectra extracted from the eight rocks mentioned by name in this section, as well as from numerous other rock fragments not analyzed geochemically with the rover arm instruments, show a great diversity of compositions, and hence potential origins (e.g., Bell *et al*., 2004b; Weitz *et al*., 2006). In addition, several of the rock fragments exhibit apparent coatings, including examples of dust derived from the local outcrop that appears to have become deposited on the loose rock surfaces. As shown in Figure 13.33, Pancam spectra of the lighter-toned patches are more similar to outcrop rock, whereas the darker regions are more like spectra of basaltic materials. The strong tendency for rock fragments to occur on and near outcrop exposures suggests that many rock fragments are either impact ejecta derived from the sulfate-rich outcrop, or from underlying or formerly overlying stratigraphic layers not currently analyzed *in situ* by the *Opportunity* rover, or some combination of both.

Heat Shield rock is one of most intriguing large rocks encountered by *Opportunity*. Figure 13.34 shows Heat Shield rock after the RAT brushed the surface and compares the spectra of brighter dust and darker soil that collected in

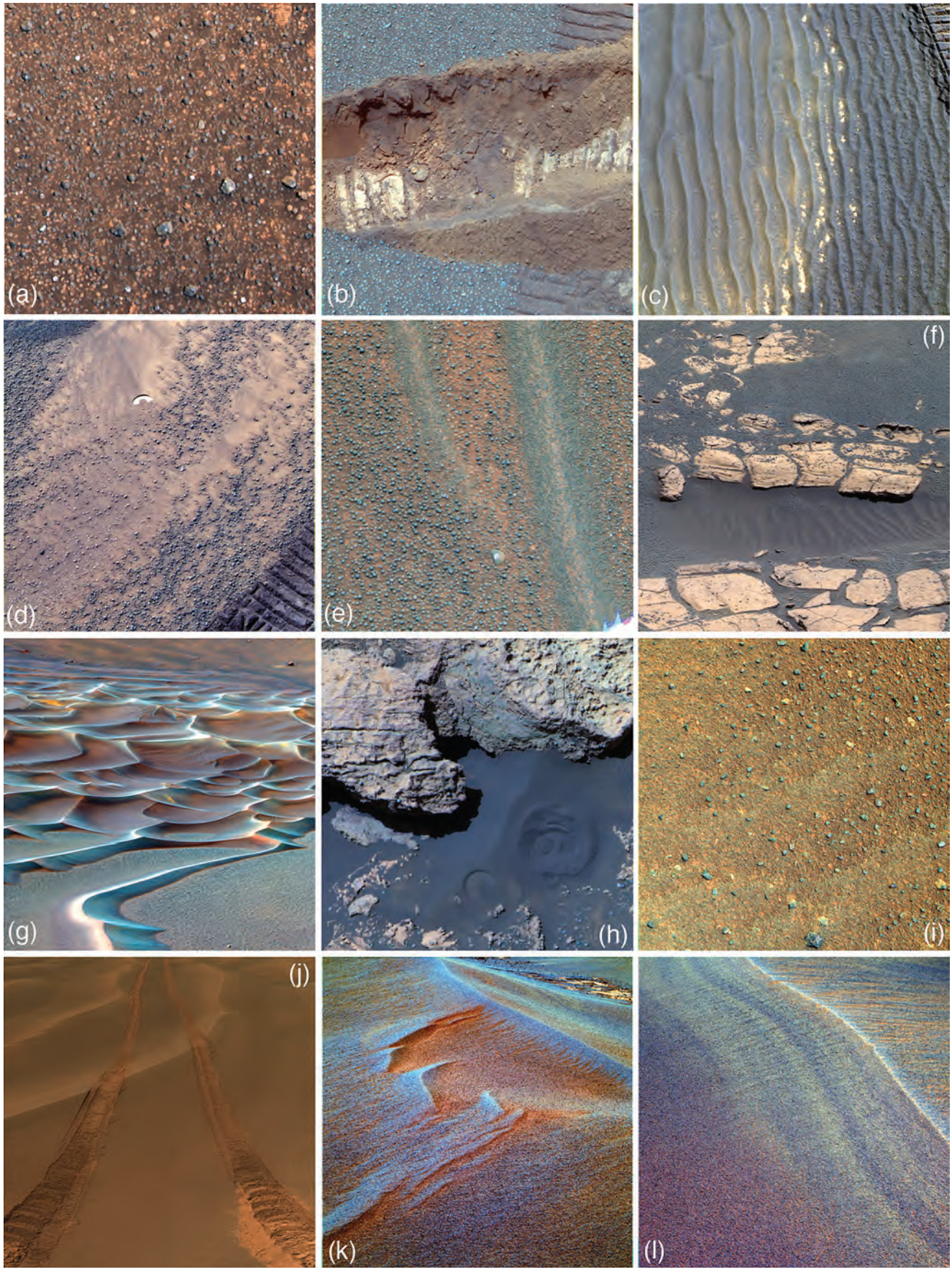
(a)
(b)
(c)
(d)
(e)
(f)
(g)
(h)
(i)
(j)
(k)
(l)

small dimples (possibly regmaglypts) on the surface, as well as dusty and brushed surfaces of the meteorite that appeared coated with a "bluer" material compared to the majority of the surface. The brushed, uncoated material is quite similar to laboratory spectra of the Canyon Diablo meteorite (e.g., Gaffey, 1976; Britt and Pieters, 1987). Heat Shield rock was subsequently determined to be an Fe–Ni meteorite based on APXS and Mössbauer measurements (e.g., Morris *et al.*, 2006b; Yen *et al.*, 2006). Differences in brightness and spectral slope between the spectra of laboratory Fe–Ni meteorites and Heat Shield rock may be related to differences in surface roughness and/or nickel abundance.

13.3.5 Soils and windblown drift deposits

Geomorphology

Examples of different morphologic classes of fine-grained materials encountered during *Opportunity*'s traverse in Meridiani Planum are shown in Figure 13.35.

Soils on the plains of Meridiani appear to be lag deposits that are generally mixtures of basaltic sand, dust, coated and uncoated spherules and their fragments, and fragments of other rocks such as those mentioned in the previous section (e.g., Figure 13.36; Bell *et al.*, 2004b; Soderblom *et al.*, 2004; Morris *et al.*, 2006b; Weitz *et al.*, 2006). Plains soils appear to be more limited in the variety of soil grain sizes and compositions compared to the soils seen in Eagle and Endurance craters (Weitz *et al.*, 2006). Ripples cover the plains and are also seen inside craters. MI images taken on ripple crests along the plains show that they are composed of rounded grains of similar size, with an average grain size smaller than typical spherules seen in Eagle crater (Herkenhoff *et al.*, 2004, 2006; Sullivan *et al.*, 2005; Weitz *et al.*, 2006).

Figure 13.36. Target Panama Canal taken on sol 727. MI image 1M192737103 merged with Pancam sol 729 sequence P2532, false color RGB (753, 1009, 432 nm) composite. The spherules are generally smaller in size than those seen further to the north and in Eagle and Endurance craters. The largest blue grains are more irregular and less rounded in shape compared to typical spherules. The yellow elongate grain near the center of the image is likely a piece of outcrop. Image is 3.2 cm across. (For a color version of this figure, please refer to the color plate section or to the e-Book version of this chapter.)

Multispectral properties

Pancam spectra of typical bright "dusty" and dark "sandy" soils in Meridiani Planum are generally consistent with previous average bright and dark region telescopic spectra and IMP multispectral data (Figure 13.8b) and are similar to those observed in Gusev crater (Figure 13.37; Yen *et al.*, 2005). As discussed previously, bright, reddish spectra in Meridiani like those in Figure 13.37 are consistent with a ferric-iron-rich composition dominated by nanophase, rather than crystalline, ferric oxides (e.g., Morris *et al.*, 1989; Bell *et al.*, 1990). Differences in the absolute reflectivity of the bright, dusty soils between Meridiani (brighter) and Gusev (slightly darker) could result from slightly smaller dust grain sizes at Meridiani relative to Gusev, or to the presence of a locally derived and slightly brighter component in the Meridiani dust (perhaps "outcrop dust"?) and/or the presence of a locally derived and slightly darker component in the Gusev dust (perhaps "rock dust"?). Physical, rather than

Caption for Figure 13.35. Pancam images sampling a range of representative soil morphologies at Meridiani Planum. (a) Sol 20 sequence P2564 natural color view of "clean" and "dusty" blueberries, clasts, outcrop fragments, and soil in the rover's work volume. Field of view (FOV) is ~34 cm. (b) Sol 26 sequence P2385 false-color image of trench in Eagle crater. FOV is ~65 cm. (c) Sol 54 sequence P2540 false-color view of sandy ripples and aeolian dust near the center of Eagle crater. FOV is ~54 cm. (d) Sol 61 sequence P2559 false-color view of dust, sand, and blueberries within the bright wind streak on the rim of Eagle crater. FOV is ~59 cm. (e) Sol 73 sequence P2589 false-color view of ripple crests (covered with very small berries) and troughs (scattered with larger berries) on the plains between Eagle and Endurance craters. FOV is ~52 cm. (f) Sol 81 sequence P2422 false-color view of sandy drift and outcrop deposits within a rift/crack in the plains between Eagle and Endurance craters. FOV is ~192 cm. (g) Sol 211 sequence P2424 false-color view of sand dune field in the center of Endurance crater. For scale, the farthest dunes in this scene are about 50 m from the near-field dunes. (h) Sol 237 sequence P2588 false-color view of dark sand drift next to outcrop blocks within Endurance crater. FOV is ~58 cm. (i) Sol 414 sequence P2583 false-color view of cobble-rich, berry-poor surface in the plains north of Viking crater. FOV is ~45 cm. (j) Part of sols 456–464 sequences P2260 to P2270 natural color mosaic of plains ripples from "Purgatory" near the darker/lighter plains boundary north of Erebus crater. The wheel treads are ~120 cm apart. (k) Sol 749 sequence P2546 false-color view showing airfall dust lingering in the lees of plains ripples just inside the rim of Erebus crater. FOV is ~210 cm. (l) Sol 798 sequence P2393 false-color view of banded ripple structure in the brighter plains materials northwest of Victoria crater. FOV is ~3 m. See also Figures 13.29, 13.31, 13.32, 13.36, and 13.39 for additional morphologic examples of fine-grained materials at Meridiani. (For a color version of this figure, please refer to the color plate section or to the e-Book version of this chapter.)

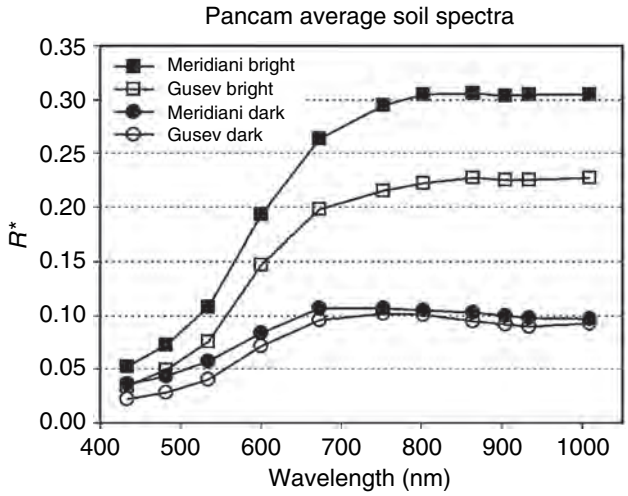

Figure 13.37. Average Pancam spectra from bright (dusty) and dark (sandy) regions in Gusev crater and Meridiani Planum. (Modified from Yen *et al.*, 2005.)

mineralogic or compositional, differences are likely to be contributors to the difference because of the well-mixed and ubiquitous nature of the global dust. A particle size (or other physical) explanation is also supported by the fact that the iron-bearing mineralogy and chemical composition of the dusty soils at Gusev and Meridiani are quite similar (Morris *et al.*, 2006b). However, the presence of a locally derived dark but extremely fine-grained component at Gusev is supported by the identification of fine-grained "rock soil" component to the spectra of several locations at the Mars Pathfinder landing site (Bell *et al.*, 2002). Evidence for a possible "outcrop dust" component to the fine-grained dusty soils at Meridiani comes from the increased reflectance of Meridiani dust at the shortest wavelengths compared to Gusev dust, a spectral characteristic consistent with the most altered Meridiani outcrop surfaces (e.g., the unit HFS spectra in Figure 13.20d and Farrand *et al.*, 2007b).

The dark soils are extremely similar at Gusev and Meridiani (Figure 13.37), and are generally similar to Pathfinder and telescopic dark soil and low-albedo region spectra (Figure 13.8b). MER dark soils exhibit a shallow and broad absorption centered near 900 nm and a negative 900–1000 nm spectral slope that likely results from the presence of ferrous-iron-bearing silicates (e.g., pyroxene, olivine). A similar or stronger band at the same position is seen in Pancam spectra of some of the "cleanest" rock surfaces at Gusev and in spectra of at least one large basaltic rock at Meridiani: Bounce Rock (Figures 13.8 and 13.9). Thus, the dark soils at both MER sites contain a significant component of less altered mafic material, and, by analogy to the dust, this material may represent another "globally homogenized" spectral unit that could be expected to be widespread across the planet (e.g., Yen *et al.*, 2005). Conversely, the global homogeneity of the dark material may simply be a manifestation of the widespread, global availability of relatively homogeneous basaltic, sand- and dust-sized materials on the planet (e.g., Morris *et al.*, 2006a,b).

Figure 13.29b illustrates that the fine-grained, dark, sandy basaltic soils in Meridiani occur in two populations in false-color composites: purplish or yellowish. The main spectral difference between the two soils is shown in Figure 13.30. The "yellower" dark soil appears slightly brighter and redder in Pancam spectra, and with a slightly deeper 535 nm "kink" in the spectrum; there are no significant differences in NIR absorption bands between these populations. This suggests that the brightness differences may result from a fine dust coating on some of the soil grains. This hypothesis is supported by the observation that no morphologic differences can be seen in the associated MI images that correspond to these two soil colors (Soderblom *et al.*, 2004; Weitz *et al.*, 2006).

Pancam spectra of the Meridiani plains ripples have similar shapes to spectra of the spherules, although with a less-pronounced absorption around 900 nm. Mössbauer measurements on the ripple crest target named Aegean Crest and other ripple crests indicated the presence of hematitic soil, with an even higher concentration of hematite than in the plains soils (e.g., Klingelhöfer *et al.*, 2004; Morris *et al.*, 2006b). These high-hematite measurements, along with the Pancam spectral similarity to the spherule signature, support the hypothesis that the grains on the ripples are spherules and/or their broken fragments (e.g., Herkenhoff *et al.*, 2004; Sullivan *et al.*, 2005).

13.4 CORRELATING AND COORDINATING OBSERVATIONS: IMPLICATIONS FOR FUTURE SURFACE AND ORBITAL REMOTE SENSING OF MARS

Mars Exploration Rover observations and results in Gusev crater and Meridiani Planum provide valuable experience with complex, complementary science instrument payload elements (on the surface and in orbit) that can be applied to future surface or orbital remote sensing and *in situ* investigations of Mars. Whenever possible during both *Spirit*'s and *Opportunity*'s traverses, efforts have been made to try to bring as much of the full suite of each rover's science payload (Squyres *et al.*, 2003) to bear as possible for each target of interest, within the real-world constraints on power, data volume, and measurement duration imposed at any given time. In addition, a number of dedicated coordinated/simultaneous observation campaigns have been conducted between instruments on the rovers and those on the Mars Global Surveyor, Mars Odyssey, Mars Express, Mars Reconnaissance Orbiter, and even the Hubble Space Telescope (e.g., Arvidson *et al.*, 2006a; see Chapters 8 and 21 for details).

One example from rover observations is given by Calvin *et al.* (2007) in attempting to seek correlations and complementarity of results between Pancam visible to NIR observations and Mini-TES thermal infrared observations of the same targets. Comparing datasets in these widely different spectral domains provides a way, for example, to test the hypothesis that the only contribution to the strong infrared signature of hematite detected in Meridiani Planum from orbit was from the small hematitic spherules found at the

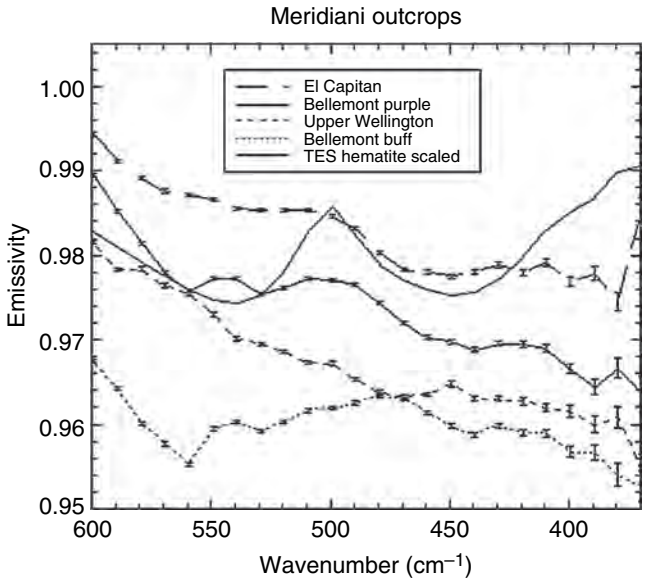

Figure 13.38. Mini-TES signatures of "buff" and "purple" outcrop that show increased hematite in Pancam spectral observations. Upper curves, El Capitan and Bellemont Purple, show increased hematite band strength at 550 and 450 cm^{-1}; lower curves, Upper Wellington and Bellemont Buff, do not show hematite. The solid line is the signature of hematite seen by TES in orbit.

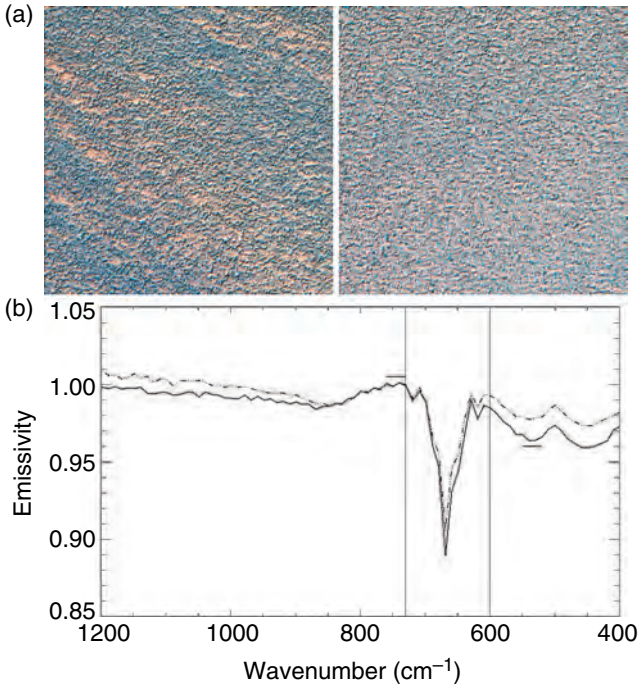

Figure 13.39. (a) Example Pancam images of high (left) and low (right) spherule cover. Left image is from Sol 795 sequence P2577, and right is from Sol 797 sequence P2578. In both cases the image is an RGB composite of bands L2 (753 nm), L5 (535 nm), and L7 (432 nm). (b) Example Mini-TES spectra showing high and low hematite index. The weaker index (dot-dash line) is from Sol 103 (1T137330168EMR2121P3716N0A1.QUB), the stronger (solid line) is from Sol 82 (1T135460592EMR1100P3715N0A1.QUB). The index is derived using a continuum near 750 cm^{-1} and band depth near 550 cm^{-1}, as illustrated by the horizontal lines. Vertical lines show the region obscured by atmospheric CO_2 absorption. (For a color version of this figure, please refer to the color plate section or to the e-Book version of this chapter.)

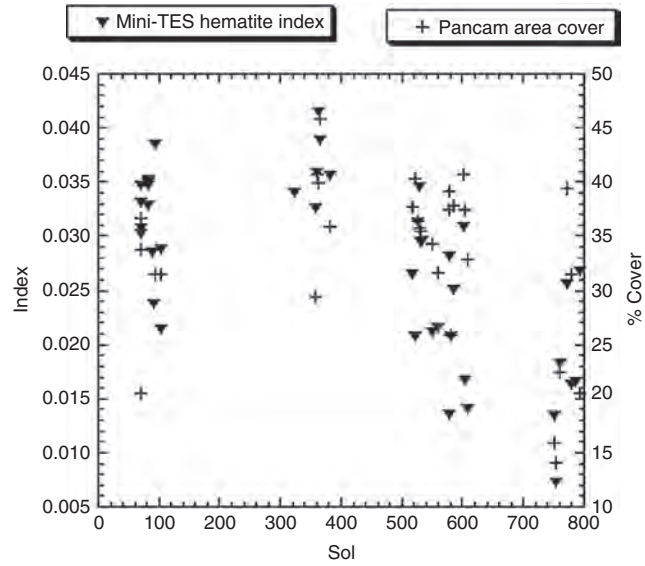

Figure 13.40. Pancam berry cover and Mini-TES hematite index with Sol.

landing site (e.g., Christensen *et al.*, 2000, 2004). Analysis of the sulfate-dominated outcrop has shown that it has a detectable hematite signature in Pancam visible to NIR measurements (see above and Bell *et al.*, 2004b; Farrand *et al.*, 2007b) and that it also exhibits a weak but identifiable feature of "coarse" hematite in Mini-TES spectra (Figure 13.38; Christensen *et al.*, 2004; see also Chapter 14). This suggests that thermal infrared measurements may be sensitive to finer, distributed hematite in addition to the coarser-grained spherules.

Calvin *et al.* (2007) performed an analysis of concurrent Pancam and Mini-TES observations of typical soils taken periodically in the traverse from Endurance crater south toward Victoria crater in order to explore the correlation between the hematite signature observed by Mini-TES and the amount of cover by spherules and their fragments as seen by Pancam. Sixty coordinated observations of soils in the near field were made between sols 70 and 800, and approximately 25 of these were found to have both good Pancam coverage (full 13 filter) and high signal to noise Mini-TES spectra. Typical examples of low- and high-spherule cover and weak and strong Mini-TES hematite signatures are shown in Figure 13.39. Coverage by spherules was determined using unsupervised classification and thresholding on whole-image color ratios or DCSs that enhance the appearance of "berries" against the background soils. Mini-TES band strength was determined using the feature near 550 cm^{-1}, after correcting the spectra for contributions from downwelling sky radiance and dust on the instrument mirror (see Chapter 14 for details). Both berry cover and Mini-TES band strength vary strongly in the dataset (Figure 13.40). Berry cover can vary because of local soil variations (Figure 13.39a), and/or the presence of outcrop, large cobbles, or other atypical "soil" materials present in the scene. Pancam area cover by spherules was estimated to be uncertain by approximately ± 5% because of shadowing and variable quality (bits/pixel) of the images, and the

Mini-TES hematite index was estimated to be accurate to ~0.002. No systematic trend with time (a proxy for position along the traverse) was detected, showing that the Pancam-derived berry cover and the Mini-TES-derived hematite index are sensitive to the heterogeneous nature of the local region where the systematic observations occurred. Although the size of the spherules was observed to decrease significantly in the vicinity of Erebus crater (Weitz *et al.*, 2006), the areal coverage and infrared hematite index do not show any correlated change.

Another example of coordinated observations involving Pancam is the frequent "albedo" observations acquired by both rovers during their respective traverses. Observations using Pancam's broadband L1 filter (739 ± 338 nm), calibrated to radiance factor and then divided by the cosine of the average solar incidence angle at the time of the observation, have been shown to provide a reasonably accurate estimate of the Lambert albedo of the surface, based on comparisons with Viking IRTM and TES bolometric albedos from orbit (Bell *et al.*, 2004b, 2006b, 2008; Golombek *et al.*, 2005). Estimating the broadband albedo of the surface along the traverses provides a way to intercompare (and cross-calibrate) surface and orbital observations at a wide variety of spatial scales, and a way to monitor seasonal and inter-annual variations in albedo from a variety of platforms. Pancam albedo observations also provide key inputs for modeling of the thermal inertia of the surface from Mini-TES observations (e.g., Fergason *et al.*, 2006).

A final example of coordinated Pancam observations is the study by Arvidson *et al.* (2006b), who compared orbital observations from the Mars Express OMEGA (OMEGA – Observatoire pour la Minéralogie, l'Eau, les Glaces et l'Activité) instrument (see Chapter 7) to surface measurements made at Meridiani Planum by the *Opportunity* rover. Of particular interest to this discussion is the comparison of the OMEGA spectra of the Meridiani plains to those collected by *Opportunity*'s Pancam. Mars Express orbit 1183 passed directly over the *Opportunity* landing site. OMEGA data from this orbit had a spatial resolution of approximately 700 m along-track and 500 m cross-track. The OMEGA spectrum for the *Opportunity* landing site shows a red visible to infrared spectrum with a broad reflectance maximum near 1.5 μm and broad absorptions near 1 and 2 μm consistent with the presence of pyroxenes. More detailed comparisons were made over the terrain between Endurance and Erebus craters. Increases in albedo were observed in OMEGA data in regions where *Opportunity* observed greater fractions of outcrop exposed on the plains. Given the relatively large OMEGA pixel size, the OMEGA spectra over *Opportunity*'s traverse path corresponded most closely to Pancam spectra of the ripple and inter-ripple trough features which dominate the plains. Arvidson *et al.* (2006b) also pointed out that results from Pancam, OMEGA, and Mini-TES spectra all indicate or are consistent with the presence of pyroxene, but not olivine, on the Meridiani plains, which contradicts results from the Mössbauer spectrometer which indicated that iron was approximately equivalently split between pyroxene and olivine. They attributed the lack of detection of the olivine signature to the predominance of pyroxene spectral features in nonlinear spectral mixtures (e.g., Singer, 1981) and to the spectral masking effects of nanophase ferric oxides. Chapters 8 and 21 provide additional details and examples on this and other Pancam/orbital data correlated observations.

Given the enormous number of imaging, spectroscopic, chemical, and mineralogic observations in hand from the rovers and the variety and coverage of orbital imaging, compositional, and physical properties datasets either acquired or planned for the near future, these kinds of correlations between and among surface and orbital measurements and investigations represent a fertile area of potential future study. For example, while hundreds of *in situ* MER APXS and Mössbauer measurements have been made on targets of high-scientific interest in both Gusev and Meridiani, many more targets of potential interest could only be analyzed using Pancam or Mini-TES remote-sensing observations. Might there be a way to correlate *in situ* chemistry and/or mineralogy from certain endmember areas with visible/NIR or thermal-IR spectroscopic properties over broader regions, thus enabling the potential to "paint" the chemistry or mineralogy across targets that could not be directly measured *in situ*? As another example, it is possible to use surface Pancam and Mini-TES remote-sensing observations to validate and refine the calibration of orbital visible/NIR and thermal-IR remote-sensing instruments (as has already been done for the Mars Odyssey Thermal Emission Imaging System Visible Subsystem (THEMIS-VIS) camera, for example; McConnochie *et al.*, 2006), as well as to constrain the spectroscopic and radiative properties of atmospheric aerosols by comparing simultaneous measurements acquired through different atmospheric pathlengths (e.g., Wolff *et al.*, 2006). There is significant potential for these and other kinds of coordinated Pancam observations and analysis campaigns to yield new information on the composition, mineralogy, and physical properties of the Martian surface.

13.5 A CLOSING PERSPECTIVE

Pancam observations have provided some of the most dramatic and beautiful views of Mars yet obtained, but as described in this chapter and elsewhere in this book, they have also provided, augmented, or enabled important geologic, compositional, and mineralogic discoveries about the surface of the Red Planet. The ability to obtain high-spatial resolution (comparable to human vision), stereoscopic, multispectral images has been a critical factor in the operational successes and scientific discoveries achieved by the Mars rovers *Spirit* and *Opportunity*. In that vein, Pancam observations have provided an evolutionary step in Martian robotic imaging campaigns, building on and expanding from the previous successes achieved by imaging systems on the Viking and Mars Pathfinder landers. Increased resolution is perhaps the single most important evolutionary step taken as part of the Pancam investigation (Bell *et al.*, 2003), but it is not the only one. Other examples of advances

realized in the Pancam experience include enhanced onboard image acquisition and image processing software, including an extremely robust and efficient data compression scheme that allowed a substantial reduction in the number of bits downlinked to Earth without the introduction of excessive image artifacts (e.g., Maki *et al*., 2003); the ability of the rovers to transmit more than 90% of their data back to Earth through relay satellites like Mars Odyssey rather than Direct-to-Earth (DTE), increasing the total science data return (most of it being Pancam data) by more than an order of magnitude compared to a DTE mission; and the development and optimization of quick-look, tactical-timescale data calibration, mosaicking, and multispectral image analysis software and methods that enabled the best potential *in situ* instrument measurement sites to be selected from images that had often been acquired and downlinked less than one Martian day before. Experience gained, lessons learned, and results obtained from the Pancam investigation are already feeding forward to motivate new evolutionary steps in surface imaging on future Mars lander and rover spacecraft. It is exciting to imagine what new discoveries await.

ACKNOWLEDGMENTS

These spectacular observations of Mars from the *Spirit* and *Opportunity* Pancam instruments have been made possible by the hard work and dedication of a team of many hundreds of scientists, engineers, managers, and administrators at the Jet Propulsion Laboratory, Cornell University, and dozens of other universities, laboratories, and contractor facilities around the world. We owe them all our thanks. This work was supported by NASA Mars Exploration Rover program grants and contracts to Cornell University, JPL, University of Nevada, Space Science Institute, Arizona State University, US Geological Survey, NASA/Johnson Space Flight Center, Washington University, and the Planetary Science Institute.

REFERENCES

Adams, J. B., Visible and near-infrared diffuse reflectance spectra of pyroxenes as applied to remote sensing of solid objects in the solar system, *J. Geophys. Res.* **79**, 4829–36, 1974.

Adams, J. B., M. O. Smith, and P. E. Johnson, Spectral mixture modeling: a new analysis of rock and soil types at the Viking Lander I site, *J. Geophys. Res.* **91**, 8098–112, 1986.

Arvidson, R. E., J. L. Gooding, and H. J. Moore, The Martian surface as imaged, sampled, and analyzed by the Viking Landers, *Rev. Geophys.* **27**, 39–60, 1989.

Arvidson, R. E., R. C. Anderson, P. Bartlett, *et al*., Localization and physical properties experiments conducted by Spirit at Gusev crater, *Science* **305**, 821–4 , 2004.

Arvidson, R. E., S. W. Squyres, R. C. Anderson, *et al*., Overview of the *Spirit* Mars Exploration Rover mission to Gusev crater: landing site to Backstay rock in the Columbia Hills, *J. Geophys. Res.* **111**, E02S01, doi:10.1029/2005JE002499, 2006a.

Arvidson, R. E., F. Poulet, R. V. Morris, *et al*., Nature and origin of the hematite-bearing plains of Terra Meridiani based on analyses of orbital and Mars Exploration Rover data sets, *J. Geophys. Res.* **111**, E12S08, doi:10.1029/2006JE002728, 2006b.

Bandfield, J. L., T. D. Glotch, and P. R. Christensen, Spectroscopic identification of carbonate minerals in the martian dust, *Science* **301**, 1084–7, 2003.

Bell III, J. F., Iron, sulfate, carbonate, and hydrated minerals on Mars. In *Mineral Spectroscopy: A Tribute to Roger G. Burns* (ed. M. D. Dyar, C. McCammon, and M. W. Schaefer), Special Publication No. 5. St. Louis, MO: Geochemical Society, pp. 359–80, 1996.

Bell III, J. F., T. B. McCord, and P. D. Owensby, Observational evidence of crystalline iron oxides on Mars, *J. Geophys. Res.* **95**, 14447–61, 1990.

Bell III, J. F., H. Y. McSween Jr., J. A. Crisp, *et al*., Mineralogic and compositional properties of Martian soil and dust: results from Mars Pathfinder, *J. Geophys. Res.* **105**, 1721–55, 2000.

Bell III, J. F., W. H. Farrand, J. R. Johnson, and R. V. Morris, Low abundance materials at the Mars Pathfinder landing site: an investigation using spectral mixture analysis and related techniques, *Icarus* **158**, 56–71, 2002.

Bell III, J. F., S. W. Squyres, K. E. Herkenhoff, *et al*., The Mars Exploration Rover Athena Panoramic Camera (Pancam) investigation, *J. Geophys. Res.* **108**(E12), doi:10.1029/2003JE002070, 2003.

Bell III, J. F., S. W. Squyres, R. E. Arvidson, *et al*., Pancam multispectral imaging results from the Spirit rover at Gusev crater, *Science* **305**, 800–6, 2004a.

Bell III, J. F., S. W. Squyres, R. E. Arvidson, *et al*., Pancam multispectral imaging results from the Opportunity rover at Meridiani Planum, *Science* **306**, 1703–9, 2004b.

Bell III, J. F., D. Savransky, and M. J. Wolff, Chromaticity of the Martian sky as observed by the Mars Exploration Rover Pancam instruments, *J. Geophys. Res.* **111**, E12S05, doi:10.1029/2006JE002687, 2006a.

Bell III, J. F., J. Joseph, J. N. Sohl-Dickstein, *et al*., In-flight calibration and performance of the Mars Exploration Rover Panoramic Camera (Pancam) Instruments, *J. Geophys. Res.* **111**, E02S03, doi:10.1029/2005JE002444, 2006b.

Bell III, J. F., M. S. Rice, J. R. Johnson, and T. M. Hare, Surface albedo observations at Gusev crater and Meridiani Planum, Mars, *J. Geophys. Res.* doi:10.1029/2007JE002976, in press, 2008.

Bishop, J. L., A. Banin, R. L. Mancinelli, and M. R. Klovstad, Detection of soluble and fixed NH_4^+ in clay minerals by DTA and IR reflectance spectroscopy: a potential tool for planetary surface exploration, *Planet. Space. Sci.* **50**, 11–19, 2002.

Britt, D. T. and C. M. Pieters, Effects of small-scale surface roughness on the bidirectional reflectance spectra of nickel-iron meteorites, *Lunar Planet. Sci. Conf. XVIII*, 131–2, 1987.

Calvin, W. M., J. D. Shoffner, *et al*., Hematite spherules at Meridiani: results from MI, Mini-TES and Pancam, submitted to *J. Geophys. Res*., 2007.

Carr, M. H., *The Surface of Mars*, New Haven, CT: Yale University Press, 1981.

Christensen, P. R. and H. J. Moore, The martian surface layer. In *Mars* (ed. H. H. Kieffer, B. M. Jakosky, C. W. Snyder, and M. S. Matthews), Tucson: University of Arizona Press, pp. 686–729, 1992.

Christensen, P. R., J. L. Bandfield, R. N. Clark, *et al*., Detection of crystalline hematite mineralization on Mars by the Thermal Emission Spectrometer: evidence for near-surface water, *J. Geophys. Res.* **105**(E4), 9623–42, 2000.

Christensen, P. R., M. B. Wyatt, T. D. Glotch, *et al*., Mineralogy at Meridiani Planum from the Mini-TES experiment on the Opportunity Rover, *Science* **306**, 1733–9, 2004.

Clark, B. C., R. V. Morris, S. M. McLennan, *et al*., Chemistry and mineralogy of outcrops at Meridiani Planum, *Earth Planet. Sci. Lett*. **240**, 73–94, 2005.

Clark, R. N. and T. L. Roush, Reflectance spectroscopy: quantitative analysis techniques for remote sensing applications, *J. Geophys. Res*. **89**, 6329–40, 1984.

Cloutis, E. A. and J. F. Bell III, Mafic silicate mapping on Mars: effects of palagonite, multiple mafic silicates, and spectral resolution, *Icarus* **172**, 233–54, 2003.

Cloutis, E. A., M. J. Gaffey, T. L. Jackowski, and K. L. Reed, Calibration of phase abundance, composition, and particle size distribution for olivine-orthopyroxene mixtures from reflectance spectra, *J. Geophys. Res*. **91**, 11641–53, 1986.

Cloutis, E. A., F. C. Hawthorne, S. A. Mertzman, *et al*., Detection and discrimination of sulfate minerals using reflectance spectroscopy, *Icarus* **184**, 121–57, 2006.

Crowley, J. K., D. E. Williams, M. J. Hammarstrom, *et al*., Spectral reflectance properties (0.4–2.5 μm) of secondary Fe-oxide, Fe-hydroxide, and Fe-sulphate-hydrate minerals associated with sulphide-bearing mine wastes, *Geochemistry: Exploration, Environment, Analysis* **3**, 219–28, 2003.

Crumpler, L. S., S. W. Squyres, R. E. Arvidson, *et al*., Mars Exploration Rover geologic traverse by the Spirit rover in the plains of Gusev crater, Mars, *Geology* **33**, 809–12, 2005.

Crumpler, L. S., T. McCoy, M. Schmidt, and the Athena Science Team, Spirit: observations of very vesicular basalts in the Columbia Hills, Mars and significance for primary lava textures, volatiles, and paleoenviroment (abstract). *Lunar Planet. Sci. XXXVIII*, 2007.

Farrand, W. H., J. F. Bell III, J. R. Johnson, *et al*., Spectral variability among rocks in visible and near infrared multispectral Pancam data collected at Gusev crater: examinations using spectral mixture analysis and related techniques, *J. Geophys. Res. – Planets* **111**, E02S15, doi:10.1029/2005JE002495, 2006.

Farrand, W. H., J. F. Bell III, J. R. Johnson, and D. L. Blaney, Multispectral reflectance of rocks in the Columbia Hills examined by the Mars Exploration Rover Spirit: Cumberland Ridge to Home Plate, *Lunar Planet. Sci. Conf. XXXVIII*, Abstract #1338, Houston, TX: Lunar and Planetary Institute, 2007a.

Farrand, W. H., J. F. Bell III, J. R. Johnson, *et al*., Visible and near infrared multispectral analysis of in situ and displaced rocks, Meridiani Planum, Mars by the Mars Exploration Rover Opportunity: spectral properties and stratigraphy, *J. Geophys. Res*. **112**, CiteID E06S02, doi:10.1029/2006JE002773, 2007b.

Fergason, R. L., P. R. Christensen, J. F. Bell III, *et al*., Physical properties of the Mars Exploration Rover landing sites as inferred from Mini-TES derived thermal inertia, *J. Geophys. Res*. **111**, E02S21, doi:10.1029/2005JE002583, 2006.

Fischer, E. and C. Pieters, The continuum slope of Mars: bi-directional reflectance investigations and applications to Olympus Mons, *Icarus* **102**, 185–202, 1993.

Gaffey, M. J., Spectral reflectance characteristics of the meteorite classes, *J. Geophys. Res*. **81**, 905–20, 1976.

Gellert, R., R. Rieder, R. C. Anderson, *et al*., Chemistry of rocks and soils in Gusev crater from the Alpha Particle X-ray Spectrometer, *Science* **305**, 829–32, 2004.

Gellert, R., R. Rieder, J. Brückner, *et al*., Alpha particle X-ray spectrometer (APXS): results from Gusev crater and calibration report, *J. Geophys. Res*. **111**, E02S05, doi:10.1029/2005JE002555, 2006.

Gellert, R., R. Rieder, R. C. Anderson, *et al*., In-Situ Chemistry along the traverse of Opportunity at Meridiani Planum: Sulfate rich outcrops, iron rich spherules, global soils and various erratics, *J. Geophys. Res*. submitted, 2008.

Gillespie, A., A. Kahle, and R. Walker, Color enhancement of highly correlated images: I. Decorrelation and HIS contrast enhancement, *Rem. Sens. Env*. **20**, 209–35, 1987.

Goetz, W., P. Bertelsen, C. S. Binau, *et al*., Chemistry and mineralogy of atmospheric dust at Gusev crater: indication of dryer periods on Mars, *Nature* **436**, 62–5, 2005.

Golombek, M. P., R. C. Anderson, J. R. Barnes, *et al*., Overview of the Mars Pathfinder mission: launch through landing, surface operations, data sets, and science results, *J. Geophys. Res*. **104**, 8523–54, 1999.

Golombek, M. P., R. E. Arvidson, J. F. Bell III, *et al*., Assessment of Mars Exploration Rover landing site predictions, *Nature* **436**, 44–8, 2005.

Golombek, M. P., L. S. Crumpler, J. A. Grant, *et al*., Geology of the Gusev cratered plains from the *Spirit* rover traverse, *J. Geophys. Res*. **111**, E02S07, doi:10.1029/2005JE002503, 2006.

Grant, J. A., R. Arvidson, J. F. Bell III, *et al*., Surficial deposits at Gusev crater along Spirit Rover traverses, *Science* **305**, 807–10, 2004.

Greeley, R. and J. D. Iversen, *Wind as a Geological Process*, New York: Cambridge University Press, 333pp., 1985.

Greeley, R., S. W. Squyres, R. E. Arvidson, *et al*., and the Athena Science Team, Wind-related processes detected by the Spirit Rover at Guzev crater, Mars, *Science* **305**, 810–21, 2004.

Greeley, R., R. Arvidson, J. F. Bell III, *et al*., Martian variable features: new insight from the Mars Express orbiter and the Mars Exploration Rover, Spirit, *J. Geophys. Res*. **110**, doi:10.1029/2005JE002403, 2005.

Greeley, R., R. E. Arvidson, P. W. Barlett, *et al*., Gusev crater: wind-related features and processes observed by the Mars Exploration Rover, Spirit, *J. Geophys. Res*. **111**, doi:10.1029/2005JE002491, 2006a.

Greeley, R., P. L. Whelley, R. E. Arvidson, *et al*., Active dust devils in Gusev crater, Mars: observations from the Mars Exploration Rover, Spirit, *J. Geophys. Res*. **111**, E12S09, doi:10.1029/2006JE002743, 2006b.

Grotzinger, J. P., J. F. Bell III, W. Calvin, *et al*., Stratigraphy, sedimentology and depositional environment of the Burns formation, Meridiani Planum, Mars, *Earth Planet. Sci. Lett*. **240**, 11–72, 2005.

Grotzinger, J., J. F. Bell III, K. Herkenhoff, *et al*., Sedimentary textures formed by aqueous processes, Erebus crater, Meridiani Planum, Mars, *Geology* **34**, 1085–8; doi:10.1130/G22985 A.1, 2006.

Herkenhoff, K. E., S. W. Squyres, R. Arvidson, *et al*., Textures of the soils and rocks at Gusev crater from Spirit's Microscopic Imager, *Science* **305**, 824–6, 2004.

Herkenhoff, K. E., S. W. Squyres, R. Anderson, *et al*., Overview of the Microscopic Imager investigation during *Spirit*'s first 450 sols in Gusev crater, *J. Geophys. Res*. **111**, E02S04, doi:10.1029/2005JE002574, 2006.

Huck, F. O., G. R. Taylor, H. F. McCall, and W. R. Patterson, The Viking Mars lander camera, *Space Sci. Instrum*. **1**, 189–241, 1975.

Johnson, D. L., Lunar soil: should this term be used?, *Science* **160**, 1258, 1968.

Johnson, J. R. and W. M. Grundy, Visible/near-infrared spectra and two-layer modeling of palagonite-coated basalts, *Geophys. Res. Lett*. **28**, 2101–4, 2001.

Johnson, J. R., R. Kirk, L. A. Soderblom, *et al*., Photometric properties of materials at the Sagan Memorial Station, Mars, *J. Geophys. Res.* **104**, 8809–30, 1999.

Johnson, J. R., W. M. Grundy, and M. K. Shepard, Visible/near-infrared spectrogoniometric observations and modeling of dust-coated rocks, *Icarus* **171**, 546–56, 2004.

Johnson, J. R., J. Sohl-Dickstein, W. M. Grundy, *et al*., Radiative transfer modeling of dust-coated Pancam calibration target materials: laboratory visible/near-infrared spectrogoniometry, *J. Geophys. Res.* **111**, E12S07, doi:10.1029/2005JE002658, 2006.

Johnson, J. R., J. F. Bell III, E. A. Cloutis, *et al*., Mineralogic constraints on sulfur-rich soils from Pancam spectra at Gusev crater, Mars, *Geophys. Res. Lett.* **34**, L13202, doi:10.1029/2007GL029894, 2007.

Jolliff, B. L. and S. M. McLennan, Evidence for water at Meridiani, *Elements* **2**, 163–7, 2006.

Jolliff, B. L. and the Athena Science Team, Composition of Meridiani hematite-rich spherules: a mass-balance mixing-model approach, *Lunar Planet. Sci. XXXVI*, Abstract #2269, 2005.

Jolliff, B., A. Knoll, W. Farrand, and R. Sullivan, Rock rinds at Meridiani and surface weathering phenomena, American Geophysical Union Fall Meeting, Abstract #P43A-03, 2006a.

Jolliff, B. L., W. H. Farrand, J. R. Johnson, C. Schröder, and C. M. Weitz, Origin of rocks and cobbles on the Meridiani plains as seen by Opportunity, *Lunar Planet. Sci. XXXVII*, Abstract #2401, 2006b.

Jolliff, B. L., R. Gellert, and D. W. Mittlefehldt, More on the possible composition of the Meridiani hematite-rich concretions, *Lunar Planet. Sci. XXXVIII*, Abstract #2279, 2007.

Kasting, J. F., L. L. Brown, and J. M. Acord, Was early Mars warmed by ammonia?, *Workshop on the Martian Surface and Atmosphere Through Time, Boulder, CO, September 23–25, 1991*. Houston, TX: Lunar and Planetary Institute, pp. 84–5, 1992.

Kinch, K. J., J. Sohl-Dickstein, J. F. Bell III, *et al*., Dust deposition on the Mars Exploration Rover Panoramic Camera (Pancam) calibration targets, *J. Geophys. Res.* **112**, CiteID E06S03, doi:10.1029/2006JE002807, 2007.

Klingelhöfer, G., R. V. Morris, B. Bernhardt, *et al*., Jarosite and hematite at Meridiani Planum from Opportunity's Mössbauer spectrometer, *Science* **306**, 1740–5, 2004.

Knauth, L. P., D. M. Burt, and K. H. Wohletz, Impact origin of sediments at the Opportunity landing site on Mars, *Nature* **438**, 1123–8, 2005.

Knoll, A. H., M. Carr, B. Clark, *et al*., An astrobiological perspective on Meridiani Planum, *Earth Planet. Sci. Lett.* **240**, 179–89, 2005.

Knoll, A., B. L., Jolliff, W. H. Farrand, *et al*., Rinds and fracture fills at Meridiani Planum, Mars, *J. Geophys. Res.* **113**, doi:10.1029/2007JE002949, 2008.

Lane, M. D., J. L. Bishop, M. Parente, *et al*., Determining the chemistry of the bright Paso Robles soils on Mars using multispectral data sets, *Workshop on Martian Sulfates as Recorders of Atmospheric-Fluid-Rock Interactions*, Houston, Texas. LPI Contribution No. 1331, p. 48, 2006.

Lane, M. D., J. L. Bishop, M. D. Dyar, *et al*., Identifying the phosphate and ferric sulfate minerals in the Paso Robles Soils (Gusev crater, Mars) using an integrated spectral approach, *Lunar Planet. Sci. Conf. XXXVIII*, Abstract #1338, 2007.

Lemmon, M. T., M. J. Wolff, M. D. Smith, *et al*., Atmospheric imaging results from the Mars Exploration Rovers: Spirit and Opportunity, *Science* **306**, 1753–6, 2004.

Maki, J. N., J. J. Lorre, P. H. Smith, R. D. Brandt, and D. J. Steinwand, The color of Mars: spectrophotometric measurements at the Pathfinder landing site, *J. Geophys. Res.* **104**, 8781–94, 1999.

Maki, J. N., J. F. Bell III, K. E. Herkenhoff, *et al*., The Mars Exploration Rover Engineering Cameras, *J. Geophys. Res.* CiteID 8071, doi:10.1029/2003JE002077, 2003.

Markewitz, D., Soil without life?, *Nature* **389**, 435, 1997.

Markiewicz, W. J., R. M. Sablotny, H. U. Keller, *et al*., Optical properties of the Martian aerosols derived from Imager for Mars Pathfinder midday sky brightness data, *J. Geophys. Res.* **104**, 9009–17, 1999.

McCollom, T. M. and B. M. Hynek, A volcanic environment for bedrock diagenesis at Meridiani Planum on Mars, *Nature* **438**, 1129–31, doi:10.1038/nature04390, 2005.

McConnochie, T. H., J. F. Bell III, D. Savransky, *et al*., Calibration and in-flight performance of the Mars Odyssey THEMIS Visible Imaging Subsystem (VIS) instrument, *J. Geophys. Res.* **111**, E06018, doi:10.1029/2005JE002568, 2006.

McLennan, S. M., J. F. Bell III, W. M. Calvin, *et al*., Provenance and diagenesis of the evaporite-bearing Burns formation, Meridiani Planum, Mars, *Earth Planet. Sci. Lett.* **240**, 95–121, doi:10.1016/j.epsl.2005.09.041, 2005.

McSween, H. Y., R. E. Arvidson, J. F. Bell III, *et al*., Basaltic rocks analyzed by the Spirit Rover in Gusev crater, *Science* **305**, 842–5, 2004.

McSween, H. Y., M. B. Wyatt, R. Gellert, *et al*., Characterization and petrologic interpretation of olivine-rich basalts at Gusev crater, Mars, *J. Geophys. Res.* **111**, E02S10, doi:10.1029/2005JE002477, 2006a.

McSween, H. Y., S. W. Ruff, R. V. Morris, *et al*., Alkaline volcanic rocks from the Columbia Hills, Gusev crater, Mars, *J. Geophys. Res.* **111**, E09S91, doi:10.1029/2006JE002698, 2006b.

Ming, D. W., D. W. Mittlefehldt, R. V. Morris, *et al*., Geochemical and mineralogical indicators for aqueous processes in the Columbia Hills of Gusev crater, Mars, *J. Geophys. Res.* **111**, E02S12, doi:10.1029/2005JE002560, 2006.

Morris, R., H. Lauer, C. Lawson, *et al*., Spectral and other physicochemical properties of submicron powders of hematite (αFe_2O_3), maghemite (γFe_2O_3), magnetite (Fe_3O_4), goethite (αFeOOH), and lepidocroicite (γFeOOH), *J. Geophys. Res.* **90**, 3126–44, 1985.

Morris, R. V., D. G. Agresti, H. V. Lauer Jr., *et al*., Evidence for pigmentary hematite on Mars based on optical, magnetic, and Mössbauer studies of superparamagnetic (nanocrystalline) hematite. *J. Geophys. Res.* **94**, 2760–78, 1989.

Morris, R. V., D. C. Golden, J. F. Bell III, *et al*., Possible products of hydrolytic, hydrochloric, and sulfuric weathering at the Mars Pathfinder landing site: evidence from multispectral, elemental, and magnetic data on analogue and meteorite samples, *J. Geophys. Res.* **105**, 1757–817, 2000.

Morris, R. V., D. C. Golden, D. W. Ming, *et al*., Phyllosilicate-poor palagonitic dust from Mauna Kea Volcano (Hawaii): a mineralogical analogue for magnetic martian dust?, *J. Geophys. Res.* **106**, 5057–83, 2001.

Morris, R. V., G. Klingelhöfer, C. Schröder, *et al*., Mössbauer mineralogy of rock, soil, and dust at Gusev crater, Mars: Spirit's journey through weakly altered olivine basalt on the plains and pervasively altered basalt in the Columbia Hills, *J. Geophys. Res.* **111**, E02S13, doi:10.1029/2005JE002584, 2006a.

Morris, R. V., G. Klingelhöfer, C. Schröder, *et al*., Mössbauer mineralogy of rock, soil, and dust at Meridiani Planum, Mars: Opportunity's journey across sulfate-rich outcrop, basaltic sand and dust, and hematite lag deposits, *J. Geophys. Res.* **111**, E12S15, doi:10.1029/2006JE002791, 2006b.

Mustard, J. F. and J. F. Bell III, New composite reflectance spectra of Mars from 0.4 to 3.14 μm, *Geophys. Res. Lett.* **21**, 353–6, 1994.

Mustard, J. F. and C. M. Pieters, Quantitative abundance estimates from bidirectional reflectance measurements, *J. Geophys. Res.* **92**, E617–E626, 1987.

Mutch, T. A., R. E. Arvidson, J. W. Head III, K. L. Jones, and R. S. Saunders, The *Geology of Mars*, Princeton, NJ: Princeton University Press, 400pp., 1976.

Nikiforoff, C. C., Reappraisal of the soil, *Science* **129**, 186–96, 1959.

Parente, M., J. L. Bishop, and J. F. Bell III, Spectral unmixing for sulfate identification in Pancam images, *Lunar Planet. Sci. Conf. XXXVIII*, Abstract #1338, 2007.

Patterson III, W. R., F. O. Huck, S. D. Wall, and M. R. Wolf, Calibration and performance of the Viking lander cameras, *J. Geophys. Res.* **82**, 4391–400, 1977.

Pollack, J. B., D. S. Colburn, F. M. Flaser, *et al.*, Properties and effects of dust particles suspended in the Martian atmosphere, *J. Geophys. Res.* **84**, 2929–45, 1979.

Poulet, F. and S. Erard, Nonlinear spectral mixing: quantitative analysis of laboratory mineral mixtures, *J. Geophys. Res.* **109**, E02009, 2004.

Retallack, G. J., Life, love and soil, *Nature* **391**, 12, 1998.

Rieder, R., R. Gellert, R. C. Anderson, *et al.*, Chemistry of rocks and soils at Meridiani Planum from the Alpha Particle X-ray Spectrometer, *Science* **306**, 1746–9, 2004.

Roush, T. L., D. L. Blaney, and R. B. Singer, The surface composition of Mars as inferred from spectroscopic observations. In *Remote Geochemical Analysis: Elemental and Mineralogical Composition* (ed. C. Pieters and P. Englert), Cambridge: Cambridge University Press, pp. 367–93, 1993.

Ruff, S. W., Spirit's home run: more mineralogical diversity as observed by Mini-TES on the traverse to and arrival at home plate in the Columbia Hills of Gusev crater, Mars, AGU Fall Meeting, Abstract #P44A-04, 2006.

Ruff, S. W., P. R. Christensen, D. L. Blaney, *et al.*, The rocks of Gusev crater as viewed by the Mini-TES instrument, *J. Geophys. Res.* **111**, E12S18, doi:10.1029/2006JE002747, 2006.

Schneider, A. L., D. W. Mittlefehldt, R. Gellert, and B. Jolliff, Compositional constraints on hematite-rich spherule (blueberry) formation at Meridiani Planum, Mars, *Lunar Planet. Sci. XXXVIII*, Abstract #1338, 2007.

Sharp, R. P. and M. C. Malin, Surface geology from Viking landers on Mars: a second look, *Geol. Soc. Am. Bull.* **95**, 1398–412, 1984.

Sherman, D. M., R. G. Burns, and V. M. Burns, Spectral characteristics of the iron oxides with application to the martian bright region mineralogy, *J. Geophys. Res.* **87**, 10169–80, 1982.

Singer, R. B., Near-infrared spectral reflectance of mineral mixtures: systematic combinations of pyroxenes, olivine, and iron oxides, *J. Geophys. Res.* **86**, 7967–82, 1981.

Smith, P. H., M. G. Tomasko, D. Britt, *et al.*, The Imager for Mars Pathfinder experiment, *J. Geophys. Res.* **102**, 4003–25, 1997a.

Smith, P. H., J. F. Bell III, N. T. Bridges, *et al.*, First results from the Pathfinder camera, *Science* **278**, 1758–65, 1997b.

Soderblom, L. A. The composition and mineralogy of the martian surface from spectroscopic observations: 0.3–50 μm. In *Mars* (ed. H. Kieffer *et al.*), Tucson: University of Arizona Press, pp. 557–93, 1992.

Soderblom, L. A., R. C. Anderson, R. E. Arvidson, *et al.*, Soils of Eagle crater and Meridiani Planum at the Opportunity Rover landing site, *Science* **306**, 1723–6, 2004.

Soil Science Society of America, *Glossary of Soil Science Terms*, Madison, WI: American Society of Agronomy, 1984.

Squyres, S. W., R. E. Arvidson, E. T. Baumgartner, *et al.*, The Athena Mars Rover science investigation, *J. Geophys. Res.* **108**(E12), 8062, 2003.

Squyres, S. W., R. E. Arvidson, J. F. Bell III, *et al.*, The Spirit Rover's Athena science investigation at Gusev crater, Mars, *Science* **305**, 794–9, 2004a.

Squyres, S. W., J. P. Grotzinger, R. E. Arvidson, *et al.*, In situ evidence for an ancient aqueous environment at Meridiani Planum, Mars, *Science* **306**, 1709–14, 2004b.

Squyres, S. W., R. E. Arvidson, D. L. Blaney, *et al.*, Rocks of the Columbia Hills, *J. Geophys. Res.* **111**, E02S11, doi:10.1029/2005JE002562, 2006a.

Squyres, S. W., R. E. Arvidson, D. Bollen, *et al.*, Overview of the Opportunity Mars Exploration Rover Mission to Meridiani Planum: Eagle crater to Purgatory Ripple, *J. Geophys. Res.* **111**, E12S12, doi:10.1029/2006JE002771, 2006b.

Squyres, S. W., O. Aharonson, R. E. Arvidson, *et al.*, Bedrock formation at Meridiani Planum, *Nature* **443**, E1–E2, 2006c.

Sullivan, R., D. Banfield, J. F. Bell III, *et al.*, Aeolian processes at the Mars Exploration Rover Meridiani Planum landing site, *Nature* **436**, 58–61, 2005.

Thompson, S. D., W. M. Calvin, W. H. Farrand, J. R. Johnson, J. F. Bell III, and the Athena Science Team, Fine scale multispectral features of sedimentary bedrock structures of Meridiani Planum, Mars, *Lunar Planet. Sci. Conf. XXXVII,* Abstract #1938, 2006.

Wang, A., L. A. Haskin, S. W. Squyres, *et al.*, Sulfate deposition in subsurface regolith in Gusev crater, Mars, *J. Geophys. Res.* **111**, E02S17, doi:10.1029/2005JE002513, 2006.

Weitz, C. M., R. C. Anderson, J. F. Bell III, *et al.*, Soil grain analyses at Meridiani Planum, Mars, *J. Geophys. Res.* **111**, E12S04, doi:10.1029/2005JE002541, 2006.

Wentworth, C. K., A scale of grade and class terms for clastic sediments, *J. Geol.* **30**, 377–92, 1922.

Wolff, M. J., M. D. Smith, R. T. Clancy, *et al.*, Constraints on dust aerosols from the Mars Exploration Rovers using MGS overflights and Mini-TES, *J. Geophys. Res.* **111**, E12S17, doi:10.1029/2006JE002786, 2006.

Yen, A. S., R. Gellert, C. Schröder, *et al.*, An integrated view of the chemistry and mineralogy of martian soils, *Nature* **436**, 49–54, doi:10.1038/nature03637, 2005.

Yen, A. S., D. W. Mittlefehldt, S. M. McLennan, *et al.*, Nickel on Mars: constraints on meteoritic material at the surface, *J. Geophys. Res.* **111**, E12S11, doi:10.1029/2006JE002797, 2006.

Zolotov, M. Y. and E. L. Shock, Formation of jarosite-bearing deposits through aqueous oxidation of pyrite at Meridiani Planum, Mars, *Geophys. Res. Lett.* **32**, L21203, doi:10.129/2005GL024253, 2005.

14

The mineralogy of Gusev crater and Meridiani Planum derived from the Miniature Thermal Emission Spectrometers on the *Spirit* and *Opportunity* rovers

S. W. RUFF, P. R. CHRISTENSEN, T. D. GLOTCH, D. L. BLANEY, J. E. MOERSCH, AND M. B. WYATT

ABSTRACT

Two Miniature Thermal Emission Spectrometers (Mini-TES) operated successfully onboard the two Mars Exploration Rovers (MER) on the Martian surface, one at Gusev crater and the other at Meridiani Planum. Designed to provide remotely sensed information on the bulk mineralogy of surface materials, the Mini-TES instruments served to guide the rovers to targets of interest and extrapolate the observations made by the rovers' mechanical-arm-mounted instruments. The Mini-TES on the *Spirit* rover in Gusev crater observed a flat plain covered by rocks with an olivine-rich ($(Mg,Fe)_2SiO_4$) mineralogy and a soil-like unit mantled by airfall dust occurring between the rocks. The dust is a spectral match to dust observed at Meridiani Planum and across the globe. The soil is basaltic in composition, dominated by plagioclase ($NaAlSi_3O_8$–$CaAl_2Si_2O_8$), pyroxene ($Ca(Mg,Fe)Si_2O_6$–$(Mg,Fe)SiO_3$), and olivine that probably was produced in part from the breakdown of local rocks. Approximately 2.5 km from the *Spirit* lander, the Columbia Hills contain a remarkably diverse set of rocks distinct from the plains. Basaltic glass appears to dominate the mineralogy of various outcropping rocks while plagioclase dominates the float rocks that cover most of the north side of Husband Hill, the tallest of the Columbia Hills. Numerous exotic (out of place) rocks dot the hillside that likely were emplaced as impact ejecta in some cases and perhaps as volcanic intrusions in other cases. Onboard the *Opportunity* rover in Meridiani Planum, the Mini-TES observed a nearly rock-free plain covered in hematite (Fe_2O_3) spherules and basaltic sand. Spectrally, the hematite shows evidence for an aqueous origin. The basaltic sand is compositionally similar to the soil found in Gusev crater but no source rocks were identified. The light-toned outcrop that underlies the hematite and sand is dominated by Al-rich amorphous silica, Mg-, Ca-, and Fe-rich sulfates (SO_4), lesser plagioclase, perhaps some phyllosilicates (clay minerals), and minor hematite. The two landing sites present dramatically different views of the geologic environments and processes on early Mars.

14.1 INTRODUCTION

The Miniature Thermal Emission Spectrometer (Figure 14.1) onboard each MER is a Fourier transform interferometer/spectrometer that enabled remote determination of the mineral composition of rocks and soils and provided surface temperatures and atmospheric properties in the scene surrounding the rovers (Christensen *et al.*, 2003). This chapter focuses on the mineralogical observations made through the first 600 sols (Martian days) of the mission. The Mini-TES instruments collected high-resolution infrared spectra over the wavelengths of ~5–29 μm (2000–340 cm^{-1} with ~10 cm^{-1} sampling) (Christensen *et al.*, 2003) where distinctive fundamental vibration spectral bands are best observed, providing a direct means of identifying crystal structure, and hence mineralogy, of nearly all geologic materials including silicates, carbonates, sulfates, phosphates, oxides, and hydroxides (e.g., Coblentz, 1905; Lyon and Burns, 1963; Farmer, 1974; Salisbury *et al.*, 1991). These remote mineralogical measurements, together with the morphologic and color information supplied by the Panoramic Camera (Pancam) (Bell *et al.*, 2003; see also Chapter 13), were used to direct the rovers to specific targets of interest for detailed study by the full suite of rover instruments (e.g., Squyres *et al.*, 2004a; Ruff *et al.*, 2006). The Mini-TES observations also served to extend the range of the rover and its mechanical-arm-mounted instruments by relating the spectra of targets visited by the rover to those more distant and unreachable.

The primary scientific objective for the rovers was to explore two sites on Mars in search of evidence for persistent liquid water in the past that may have led to an environment suitable for life. The two sites, Gusev crater and Meridiani Planum, were selected based upon evidence from orbital datasets for the role of liquid water at sometime in their history (e.g., Golombek *et al.*, 2003). Orbital images of Gusev crater and vicinity provided geomorphic evidence for water in the form of the 900 km long Ma'adim Vallis channel that terminates at the crater, along with a set of eroded mesas at its terminus that were thought to be an eroded delta deposit (e.g., Cabrol *et al.*, 2003). This combination of features suggested that Gusev crater probably hosted a lake sometime in its past. Evidence for persistent liquid water in the past at Meridiani Planum came from thermal infrared (TIR) spectra obtained by the Mars Global Surveyor (MGS) Thermal Emission Spectrometer (TES; Chapter 9). The unambiguous spectral signature of gray, crystalline hematite (Christensen *et al.*, 2000a) was observed over an irregularly shaped, ~300 km by 500 km region of Meridiani Planum that is coincident with a smooth

The Martian Surface: Composition, Mineralogy, and Physical Properties, ed. J. F. Bell III. Published by Cambridge University Press.

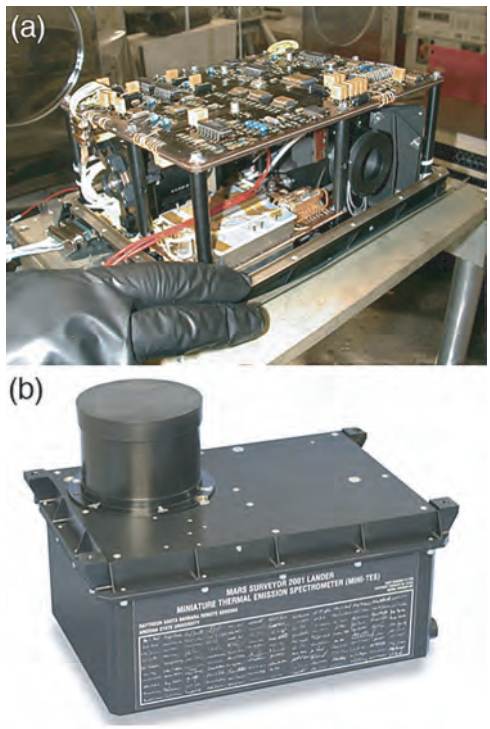

Figure 14.1. The Mini-TES I spectrometer following completion of testing at Santa Barbara Remote Sensing. (a) The Mini-TES with its protective cover off, showing the integrated packaging of the electronics and optics required to meet the size and weight constraints of the rover mission. (b) The instrument with its cover on and the optical aperture facing upward. (For a color version of this figure, please refer to the color plate section or to the e-Book version of this chapter.)

mantle of apparently sedimentary material (e.g., Christensen and Ruff, 2004). The occurrence of hematite in this setting was thought to be the result of aqueous processes either due to standing water or shallow subsurface water, although alternate hypotheses were presented (e.g., Hynek *et al.*, 2002; Knauth *et al.*, 2005)

The *Spirit* rover in Gusev crater and the *Opportunity* rover at Meridiani Planum each were equipped to investigate the role of water in the formation and alteration of materials at the two landing sites (Squyres *et al.*, 2003). Based on results from decades of TIR measurements of geological materials in the laboratory (e.g., Lyon *et al.*, 1959; Salisbury *et al.*, 1987; Lane and Christensen, 1998; Hamilton and Christensen, 2000) and from orbit (e.g., Aronson and Emslie, 1975; Calvin *et al.*, 1994; Christensen *et al.*, 2000b; Bandfield, 2002), the Mini-TES measurements were well suited to assessing the primary and secondary phases in rocks, soils (regolith), and dust, thus contributing to our understanding of the geologic history at each site. Additionally, the spectra from Mini-TES now serve as "ground truth" for orbital TES spectra. In this capacity, Mini-TES spectra likely will improve the interpretation of TES and Thermal Emission Imaging System (THEMIS) (Chapter 10) spectra and any future TIR datasets from Mars.

As one of three "remote-sensing" instruments including the Pancam (Bell *et al.*, 2003; see also Chapter 13) and the navigational (Navcam) and hazard avoidance (Hazcam) cameras (Maki *et al.*, 2003), Mini-TES observations helped to identify targets of interest and eliminate the need to drive to targets that did not warrant further scrutiny by the contact instruments on the rovers' arm-like Instrument Deployment Device (IDD). Given the effort of approaching targets for IDD work and the multiple sols required for such work (Arvidson *et al.*, 2006), the ability to minimize this effort with a degree of confidence was one of the valuable contributions from Mini-TES. This was especially true in Gusev crater where several light-toned rocks aroused interest but were determined simply to be dust covered. The few tens of basaltic exotics (out of place rocks) discovered with Mini-TES spectra in the Columbia Hills of Gusev crater (Section 14.3.6) likely would have been overlooked without the benefit of spectral remote sensing. The much larger populations of rocks in the Columbia Hills that were characterized with Mini-TES spectra further extended this utility by putting into context the rocks measured by the IDD instruments. For example, only 3 members of the Wishstone Class rocks (Section 14.3.3) were measured by the IDD instruments (e.g., Ming *et al.*, 2006), yet at least 95 Mini-TES spectra of this class demonstrated that they are the most ubiquitous rock type on the north side of Husband Hill (Ruff *et al.*, 2006). Much work remains in refining the details of the Mini-TES observations, but as discussed below, sufficient information has emerged to help us better understand the geologic environments explored by both rovers.

14.1.1 Mini-TES instrument and calibration

Details of the Mini-TES design and operation are given elsewhere (Christensen *et al.*, 2003), but here a brief overview is appropriate. The Mini-TES was a Fourier transform infrared spectrometer operating over the spectral range from ~2000 to 340 cm^{-1} (~5–29 μm) with a spectral sampling of ~10 cm^{-1}. It used an uncooled, deuterated triglycene sulfate detector with KBr internal transmissive optics. The spectrometer was mounted inside the warm electronics box (WEB) in the body of the rover to provide a more stable thermal environment and used the periscope-like Pancam Mast Assembly (PMA) to deliver light inward (Squyres *et al.*, 2003). A rotating pointing mirror in the PMA head allowed for a range of elevation angles (−50° to +30°) to be observed and rotation of the entire head allowed a full 360° range of azimuth angles to be viewed. The pointing mirror directed light to an adjacent fixed fold mirror, then down the PMA tube to a primary and secondary mirror system that served as a Cassegrain telescope with a nominal 20 mrad instantaneous field of view (FOV). A CdTe window at the base of the PMA tube separated these four mirrors from the spectrometer inside the WEB. The 20 mrad mode yielded an FOV of ~10 cm in diameter for targets closest to the rover.

A calibration scheme for Mini-TES spectra was developed that relied on the single blackbody calibration target mounted within the head of the PMA. A second calibration target mounted on the rover deck was unusable for standard calibration because of the failure of its two platinum

resistance thermometers within the first few sols of the mission. The basic equation for converting raw voltage spectra to radiance is

$$R_{\text{sample}} = \frac{V_{\text{measured}}}{F} + R_{\text{inst}}, \tag{14.1}$$

where each term is a function of wavenumber, R_{sample} is the radiance of the sample ($\text{W cm}^{-2}\,\text{sr}^{-1}/\text{cm}^{-1}$), which can be either a surface or sky observation, V_{measured} is the Fourier-transformed voltage signal, F is the instrument response function ($\text{V/W cm}^{-2}\,\text{sr}^{-1}/\text{cm}^{-1}$), and R_{inst} is the radiance of the instrument ($\text{W cm}^{-2}\,\text{sr}^{-1}/\text{cm}^{-1}$). With only one blackbody calibration target available, it was not possible to determine F directly. However, because the instrument response function was so well characterized during environmental testing in a thermal vacuum chamber on Earth (Christensen *et al.*, 2003), a set of instrument response functions were available for use in the calibration of Martian spectra. To provide more accurate results, F was interpolated based on the measured detector temperature acquired during each observation. An observation of the calibration target inside the PMA head allowed the instrument energy term (see Equation 14.1) to be determined and removed from each spectrum according to the equation:

$$R_{\text{inst}} = R_{\text{planck}} - \frac{V_{\text{cal target}}}{F}, \tag{14.2}$$

where R_{planck} is the Planck radiance at the measured temperature of the calibration target. Because the calibration target was viewed at least twice during every observation (beginning and end), any change in the instrument energy during the course of an observation was accounted for by interpolation.

The final conversion of sample radiance spectra to unitless, temperature-independent emissivity spectra needs to account for atmospheric contributions. In orbital TES spectra, contributions from the atmosphere are well documented and understood (e.g., Smith *et al.*, 2000; Bandfield *et al.*, 2003). In Mini-TES spectra of the surface, the much shorter atmospheric path lengths of the observations precluded most of the atmospheric contributions that impact TES spectra. Nevertheless, dust in the Martian atmosphere had an impact on Mini-TES spectra. Thermal radiation from the sky illuminating the surface was reflected or possibly scattered into the FOV of the instrument. Known as downwelling radiance, the magnitude of its impact on Mini-TES spectra was dependent on the difference in radiance between the surface target and the atmosphere, which is a function of temperature and atmospheric opacity. Downwelling radiance is a recognized component of TIR emission spectra both in the field (on the ground or from airborne or orbital instruments) (e.g., Hook *et al.*, 1992; Salisbury and D'Aria, 1992; Horton *et al.*, 1998) and in the laboratory (e.g., Ruff *et al.*, 1997). Different methods specific to a given measurement are used to remove the downwelling contribution from the final spectra. For Mini-TES spectra, the routinely collected, upward-looking measurements of atmospheric radiance at $\sim 30^{\circ}$ above the horizon were used to make what is referred to as the "standard downwelling correction" for the downwelling radiance that reflects off the surface target and into the spectrometer (Christensen *et al.*, 2004b; Ruff *et al.*, 2006). The conversion of sample radiance (from a surface target) to emissivity is as follows:

$$\varepsilon_{\text{cor}} = \frac{R_{\text{sample}} - R_{\text{sky}}}{R_{\text{planck}} - R_{\text{sky}}}, \tag{14.3}$$

where R_{sample} is the calibrated radiance spectrum of the surface target from Equation (14.1), R_{sky} is the calibrated radiance of the sky at $\sim 30^{\circ}$ above the horizon, and R_{planck} is the calculated Planck radiance at the maximum brightness temperature of the surface target. It should be noted that the above equation is most strictly valid for controlled laboratory conditions (Christensen and Harrison, 1993; Ruff *et al.*, 1997). It requires the assumption that Kirchhoff's law relating reflectivity and emissivity ($R = 1 - \varepsilon$) is valid, which is strictly true only for lambertian surfaces in isothermal equilibrium with their surroundings (e.g., Badenas, 1997). Mini-TES spectra contain atmospheric features that cannot be accounted for using the standard downwelling correction of Equation (14.3) and that likely are due to some combination of nonlambertian surfaces, nonisotropic scattering by atmospheric dust, and nonisothermal conditions in the atmosphere (Ruff *et al.*, 2006). This additional atmospheric contribution was accounted for using two different strategies that are described in the following section and in Section 14.5.

In Gusev crater on sol 420, a wind event occurred during which dust was cleared from the solar panels (Bell *et al.*, 2006; Greeley *et al.*, 2006) but was deposited on one or more surfaces in the Mini-TES optical path. The most likely surface to be impacted was the pointing (elevation) mirror at the top of the PMA. After sol 420, Mini-TES spectra display features due to dust that vary in intensity. The variability is related to the temperature difference (ΔT) between the target and the pointing mirror. The dust on the mirror was not thick enough to be opaque but it supplied either absorption or emission features, depending on the ΔT, that are most evident in the middle wavenumber range of Mini-TES data ($\sim$800–1300 cm^{-1}). Ruff *et al.* (2006) presented a provisional method to correct for the mirror dust, but without a full validation, avoided using spectra from rocks observed after sol 420 for quantitative mineralogical determinations.

The signal-to-noise ratio (SNR) of Mini-TES spectra is temperature and wavelength dependent. During operations, the SNR was improved by increasing the dwell (the number of spectral scans) for a given observation. It became standard to observe most surface targets using a dwell of 200 and averaging the resulting 200 spectra together. Figure 14.2 shows an example from the rock called Watchtower. It had a derived temperature of $\sim$260 K, which was the approximate median temperature for rocks observed in mid- to late afternoon hours (except during the winter season). The figure shows the average of 200 emissivity spectra from Watchtower along with the standard deviation (1σ) as a proxy for noise. The standard deviation is lowest in the range from $\sim$400 to 1300 cm^{-1}, increasing significantly above 1300 cm^{-1}

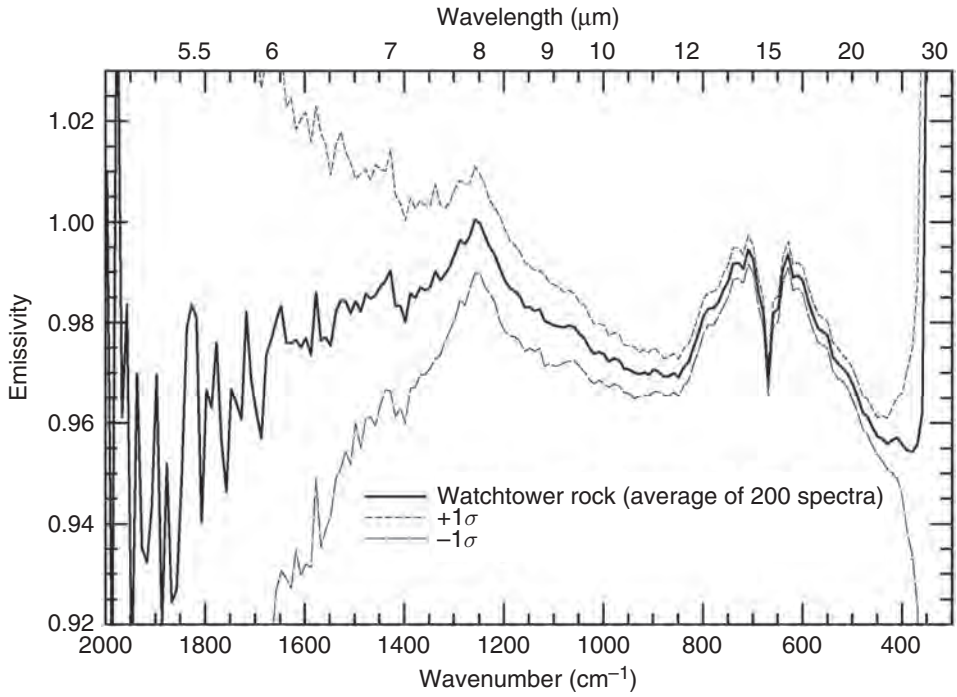

Figure 14.2. An example of the spectral precision of a typical Mini-TES rock "stare" in which 200 spectral scans are averaged together. The Watchtower rock spectrum comes from sol 413 with the sequence identifier p3877.

where the Planck radiance falls off, and increasing sharply below $\sim$380 cm^{-1} where the throughput of the instrument falls off. The features that are present in all three versions of the spectrum give an indication of the precision or reproducibility available in Mini-TES data, that is, the extent to which individual spectral features can be interpreted.

14.1.2 Methodology

The mineralogy of rocks and soils measured by Mini-TES was determined through deconvolution of their emissivity spectra. However, even without deconvolution, many of the spectra display features that can be attributed directly to a particular component phase. For example, the hematite-bearing materials in Meridiani Planum are readily apparent based on distinctive spectral features in the low-wavenumber range (<600) of Mini-TES spectra (Section 14.5.1). In Gusev crater, rocks rich in olivine (Section 14.3.1) or plagioclase (Section 14.3.2) also display distinctive spectral features that are most evident in the low-wavenumber range. It is this portion of the spectrum that is least sensitive to contributions from dust in any form and is host to diagnostic spectral features of many mineral phases. These features also create distinctive spectral signatures that often can be used to group together rocks or soils, allowing for the rapid classification of a given material.

Quantitative mineralogy was obtained using a linear least-squares algorithm and various suites of spectral endmembers to determine the individual phases and their abundance (the areal fraction) in the observed target (e.g., Ramsey and Christensen, 1998; Feely and Christensen, 1999; Hamilton and Christensen, 2000). As shown by an example in Section 14.3.1, multiple endmember sets and multiple deconvolution runs were used because (1) there is a limit on the number of endmembers (N) that can be used at one time imposed by the matrix algebra of the linear deconvolution ($N \leq$ number of spectral points), and (2) the uniqueness of various modeled results can be characterized through multiple trials. The goodness-of-fit of the modeled deconvolution results was quantified using the root mean square (RMS) statistical measure of the difference at each point between the measured and modeled spectra. Root mean square values are dependent on the contrast or magnitude of the features in a given spectrum and thus are not a valid metric that can be used among different modeled spectra. However, they are a valid gauge of the goodness-of-fit of multiple modeled results for a given spectrum, that is, when multiple endmember sets are used (e.g., Hamilton *et al.*, 1997).

The texture or particle size of the various materials observed by Mini-TES impacts the contrast of the resulting spectra (e.g., Hunt and Vincent, 1968; Salisbury and Wald, 1992). As has now become standard in the deconvolution of TIR spectra, a "blackbody" endmember was used to account for contrast differences between the observed target and the endmember spectra (e.g., Hamilton *et al.*, 1997; Ramsey and Christensen, 1998; Feely and Christensen, 1999; Wyatt *et al.*, 2001). Additionally, Mini-TES spectra from both rovers include varying contributions from the sky, surface dust, and spectral slope due to temperature determination error. For the spectra from Gusev crater, additional spectral endmembers (described below) were incorporated into the deconvolution of each spectrum to account for these contributions. An alternative strategy known as "factor analysis/target transformation" (FATT) (Section 14.5) was used for the spectra from Meridiani Planum because the relative homogeneity of the various materials there presented a favorable opportunity to use this technique.

Because the standard downwelling correction (Equation 14.3) does not fully account for the sky component, a

provisional solution was employed in which an emissivity spectrum of the sky was used as an additional endmember in the deconvolution of spectra from Gusev crater. Mini-TES observations of the sky measured at ~30° above the horizon were used for this purpose, incorporating the spectrum of the sky closest in time to that of the surface spectrum to be corrected (Ruff *et al.*, 2006). Although the use of a sky spectrum in deconvolution appears to yield improved results, the accuracy of this approach has not yet been established.

The rocks and soils observed along the *Spirit* rover's traverse were mantled to varying degrees by Fe-oxide-rich dust (Bell *et al.*, 2004a) whose Mini-TES spectrum is similar to the global average dust spectrum measured by TES (Christensen *et al.*, 2004a). The spectrum from a dust-covered surface on the rim of Bonneville crater visited by the *Spirit* rover provided a spectrum that was used as an endmember in spectral deconvolution (Ruff *et al.*, 2006). Based on work by Johnson *et al.* (2002a) and Graff *et al.* (2001), it appears that the spectrum of a dust component combines linearly with the spectral components of the substrate, allowing a dust endmember to be used in deconvolution.

An additional endmember spectrum was added to address the apparent sloping continuum present in some rock spectra (Ruff *et al.*, 2006). This slope is evident as an overall decrease in emissivity from higher to lower wavenumbers that does not conform to the appearance of typical silicate rocks. Such sloping can arise during the conversion of a spectrum from radiance to emissivity. If the radiance of the sample is divided by a Planck curve where the temperature used for the Planck curve is too low, a negative slope will be superimposed on the emissivity spectrum. This is possible if the maximum emissivity of the target is less than one or if temperature errors are present in the initial calibration of the data or when the Mini-TES FOV contains surfaces with different temperatures, including different facets of the same rock. The latter situation is similar to that encountered during the testing-phase of Mini-TES in which a set of rock targets was measured, each of which was smaller than the Mini-TES FOV (Christensen *et al.*, 2003). In this situation, a slope endmember served to account for the variable brightness temperatures of the rocks and mounting hardware within the Mini-TES FOV, producing more accurate results.

The detection limits typically quoted for TES results (10%–15%) (e.g., Bandfield *et al.*, 2000b; Christensen *et al.*, 2000b) likely are higher than can be achieved with Mini-TES spectra because of the much diminished effect of the atmosphere on Mini-TES spectra. Until a more detailed assessment is undertaken, we assume that the Mini-TES detection limits are comparable to those suggested by Christensen *et al.* (2003) based upon laboratory spectra, or about 5%–10% depending on mineral phase.

14.2 GUSEV CRATER PLAINS

14.2.1 Adirondack Class rocks

The *Spirit* rover landed on a broad plain adjacent to a set of low hills ~2.5 km from the lander that were subsequently named the Columbia Hills (Arvidson *et al.*, 2006). *Spirit* spent the first ~160 days exploring the "plains," including a traverse along the rim of the ~200 m diameter Bonneville crater and other smaller and highly eroded craters (Arvidson *et al.*, 2006). The spectra of hundreds of rocks between the lander and the base of the West Spur of the Columbia Hills (Figure 14.3) were acquired both from targeted Mini-TES observations of individual rocks and with multiple-pointing raster observations that included multiple rocks. Images of these rocks acquired with the rover cameras display a range of apparent albedo (hereafter referred to as "tone" to indicate that it is a qualitative brightness assessment). The range from light-toned to dark-toned appears to represent a range of dust coating or mantling as opposed to an intrinsic characteristic of lithology (Bell *et al.*, 2004a; Johnson *et al.*, 2006; Ruff *et al.*, 2006). Most of these rocks were grouped into a single class called Adirondack based on the Alpha Particle X-ray Spectrometer (APXS) data for the rock of this name and other similar ones encountered on the plains (Squyres *et al.*, 2006b).

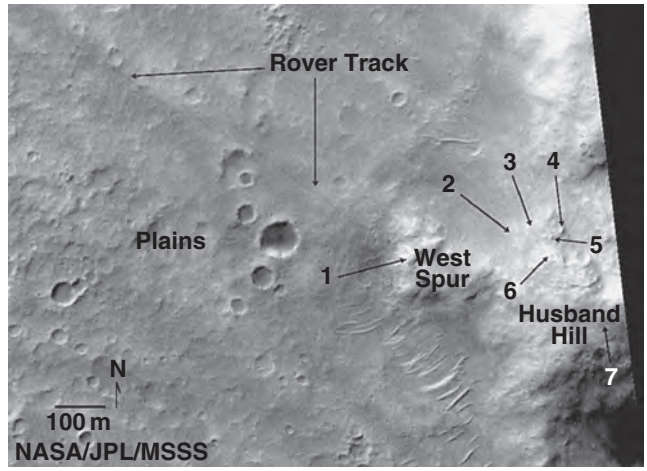

Figure 14.3. Mars Orbiter Camera image (R2001024) showing locations in Gusev crater described in this work. Numbered locations are as follows: (1) Clovis outcrop; (2) Wishstone float rock; (3) Peace/Alligator outcrop; (4) Larry's Lookout; (5) Backstay float rock; (6) Independence outcrop; and (7) Irvine float rock.

Figure 14.4 shows an example of one of the plains rocks to highlight some of the spectral features of the Adirondack Class. All have a prominent local emissivity maximum (hereafter referred to as an "emissivity peak") at ~430 cm^{-1} that is good evidence for an olivine component (Christensen *et al.*, 2004a) and best characterizes the Adirondack Class rocks as a single spectral type. The prominent emissivity minima of olivine at ~900 and 500 cm^{-1} also are evident in Adirondack Class rock spectra. These spectra show some resemblance to MGS TES spectra of olivine-rich surfaces seen elsewhere on the planet (e.g., Hoefen *et al.*, 2003; Hamilton and Christensen, 2005; see discussion in Chapter 9; Figure 14.4). The presence of abundant olivine in the Adirondack Class rocks was confirmed with spectra from the rover's Mössbauer (MB) spectrometer (Morris *et al.*, 2004).

Deconvolution of one of the Adirondack Class rocks called Sarah (Figure 14.4) provided an initial assessment

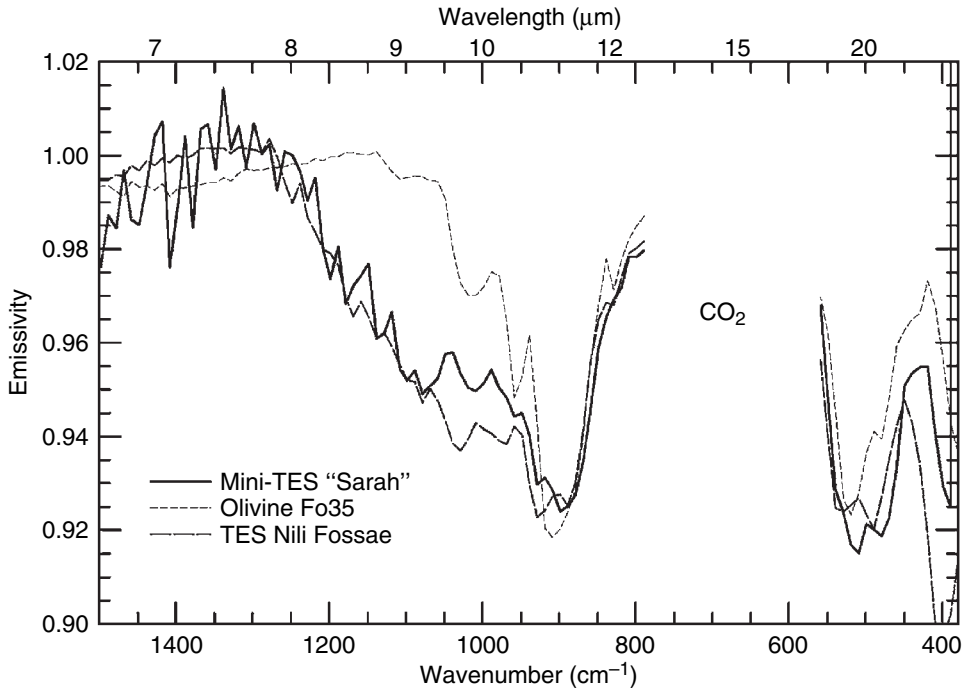

Figure 14.4. Mini-TES, laboratory, and TES spectra highlighting the characteristics of the Adirondack Class rocks of the Gusev crater plains. The Mini-TES spectrum of the Adirondack Class rock called Sarah (p3148, sol 041) following corrections for atmospheric downwelling radiance, temperature-related slope, and surface dust shows an olivine-related emissivity peak at ~430 cm^{-1} and an overall resemblance to an olivine-rich surface in Nili Fossae observed by TES (Hoefen *et al.*, 2003; Hamilton and Christensen, 2005).

of the bulk mineralogy of the plains rocks (Ruff *et al.*, 2006). Refinements to the deconvolution procedure and downwelling correction are still necessary but the initial results demonstrated that the Adirondack Class rocks are consistent with a mineralogy composed of sodic plagioclase, calcium-rich pyroxene, and olivine with an intermediate Fe composition (Fo# ~35–60). Table 14.1 includes a best estimate of the mineralogy of Adirondack Class rocks based on the best-fit deconvolution model of Sarah.

14.2.2 Dust

An optically thick, ferric iron-rich dust mantled many of the surfaces observed on the plains (Bell *et al.*, 2004a). Mini-TES observations of the dustiest surfaces both on the plains as well as in the Columbia Hills and even at the Meridiani Planum landing site (Christensen *et al.*, 2004b) all share a common set of spectral features. These features are remarkably similar to those of the global average surface dust derived from TES observations (Christensen *et al.*, 2004a) (Figure 14.5a), thus supplying ground truth for previous TES-related analyses of the globally distributed dust (Ruff and Christensen, 2002; Bandfield and Smith, 2003; Bandfield *et al.*, 2003; Ruff, 2004). This observation suggests that the dust in Gusev crater is mineralogically equivalent to the bright, fine-grained dust that blankets the low-thermal-inertia regions of Mars such as Tharsis and Arabia. By inference from the analysis of TES spectra, the Mini-TES spectra of dust contain a silicate transparency feature at ~830 cm^{-1} (11.9 μm) that is best matched by plagioclase feldspar (Bandfield and Smith, 2003) and/or zeolite (Ruff, 2004), both tectosilicates (framework silicates). These spectra also exhibit a spectral feature near 1630 cm^{-1} (6.1 μm) of bound water within a transparent silicate matrix (Bandfield and Smith, 2003; Ruff, 2004). The spectral features between ~1300–1600 cm^{-1} are interpreted as due to either minor (2–5 wt.%) carbonate (Bandfield *et al.*, 2003), hydrous iron sulfates (Lane *et al.*, 2004; Lane, 2007), or hydrous iron oxides (Bishop *et al.*, 2007).

14.2.3 Soil

The dark-toned, fine fraction of the surface regolith is termed "soil" to distinguish it from the rocks and dust, although no organic component is implied by this usage. The dark soil on the Gusev plains typically was found underneath a thin (~1 mm) layer of brighter dust (Yen *et al.*, 2005). The darker substrate commonly was exposed in the rover wheel tracks or through trenching operations with one of the rover's wheels. Mini-TES observed these "disturbed" soils throughout *Spirit*'s traverse (Arvidson *et al.*, 2006). Disturbed soil spectra (Figure 14.5b) are similar to low-albedo-surface spectra measured from orbit by TES (Christensen *et al.*, 2000b; Bandfield and Smith, 2003), as well as the basaltic sand at Meridiani Planum (Christensen *et al.*, 2004b; Yen *et al.*, 2005), with only minor added features consistent with airfall dust. The clear spectral differences between dust and soil demonstrate that dust is only a minor component of the bulk soil. Linear deconvolution of Mini-TES spectra of the rover tracks revealed a basaltic soil that, after normalization for the airfall dust component, has a composition of 45% pyroxene (25% pigeonite and 20% clinopyroxene), 35% sodic to intermediate plagioclase, 15% olivine, 5% glass, and less than 5% sulfates or oxides (Christensen *et al.*, 2004a; Yen *et al.*, 2005). The Mini-TES–derived abundances are estimated to have accuracies of ~± 5% to 10% on the basis of similar analyses of laboratory and MGS TES rock and mineral mixtures (Ramsey and Christensen, 1998; Feely and Christensen, 1999; Christensen *et al.*, 2000b; Hamilton *et al.*, 2001;

Table 14.1. *Best-estimate mineralogy of various materials from Gusev crater and Meridiani Planum based on the lowest RMS deconvolutions of Mini-TES spectra. Values are in percent rounded to the nearest 5*

Adirondack Class	
Na-plagioclase	20
Clinopyroxene	30
Olivine ($Fo_{10\&60}$)	40
High-silica glass	10
Clovis Class	
Na-plagioclase	5–10
Pyroxene	5–10
High-silica glass	5
Basaltic glass	40–45
Sulfate	10–25
Goethite	5–10
Secondary silicates	0–20
Wishstone Class	
Ca-plagioclase	55
Olivine ($Fo_{10\&60}$)	15
Basaltic glass	10
Phosphate	10
Sulfate	10
Watchtower Class	
Na-plagioclase	20–25
Orthopyroxene	5
Olivine ($\sim Fo_{60}$)	0–10
High-silica glass	0–15
Basaltic glass	35–50
Phosphate	5
Sulfate	5–15
Secondary silicates	<5
Independence Class	
Independence Outcrop and Float	
Na-plagioclase	20
Olivine ($\sim Fo_{10}$)	10
Aluminous opal	25
Basaltic glass	15
Phosphate	5
Sulfate	25
Independence Class	
Assemblee	
Plag + Pyx + Oliv	10
Aluminous opal	30
Basaltic glass	30
Maskelynite	15
Sulfate	10
Montmorillonite	5
Gusev Disturbed Soil	
Pyroxene	45
Pigeonite	25
Clinopyroxene	20
Plagioclase	35
Olivine	15
Glass	5
Sulfates and oxides	<5
Meridiani Sand	
Pyroxene	35
Plagioclase	40
Olivine	10
Glass	15
Sulfates and oxides	<5
Meridiani Outcrop	
Silica/glass	25
Nontronite	10
Jarosite	10
Mg-sulfate	20
Ca-sulfate	10
Plagioclase	15
Fe-oxides	5
Quartz	5
Bounce Rock	
Pyroxene	60
Clinopyroxene	55
Orthopyroxene	5
Plagioclase	20
Olivine	5
Oxides	10

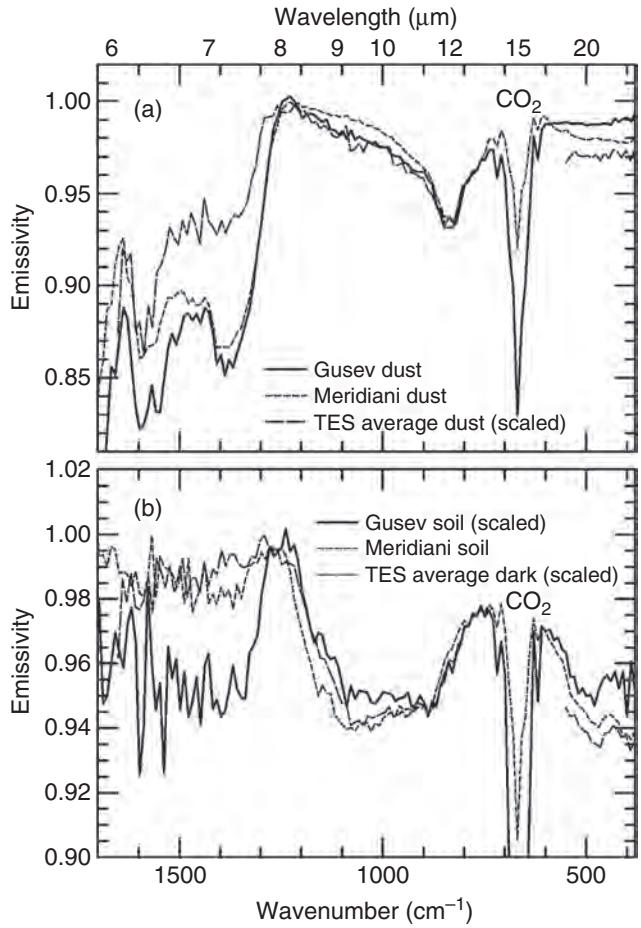

Figure 14.5. The spectra of light-toned dust and dark-toned soil observed by Mini-TES and TES. (a) The light-toned dusty mantle observed at both landing sites is remarkably similar at each and to the average global dust observed by TES (Bandfield and Smith, 2003). (b) Dark-toned soil observed in the rover tracks in Gusev ("Tracks," p3660, sol 89) and in a sand pile in Meridiani ("Auk," p3839, sol 197) (Yen *et al.*, 2005) look similar to the global average dark-toned surfaces observed by TES (Bandfield and Smith, 2003). The Gusev soil has a dust component that causes the mismatch at wavenumbers > 1300.

Wyatt *et al.*, 2001; Bandfield, 2002). The olivine composition of these soils is Fo45 ± 5 to 10, which agrees with APXS-derived normative mineralogy (McSween *et al.*, 2004). This composition is less magnesian than olivine in terrestrial basalts but within the range of Martian meteorites (McSween *et al.*, 2004). Although both the soil and rocks of the Gusev plains are olivine-bearing and basaltic in mineralogy, there is neither a direct spectral nor a mineralogical match between the two materials. This suggests that the soil did not form exclusively from the mechanical disintegration of the local rocks, which also is consistent with results from the APXS-derived chemistry (Yen *et al.*, 2005).

14.3 GUSEV CRATER COLUMBIA HILLS

The notable homogeneity of the rocks on the plains transitioned to a remarkable diversity as *Spirit* made its way through the Columbia Hills. A multitude of different outcrops and float rocks (isolated, nonoutcropping rocks) was observed by Mini-TES that presented a range of spectral variations unlike the plains. Wherever the APXS data demonstrated a distinctive chemical signature, a new rock class was defined (Squyres *et al.*, 2006b). Most of these classes

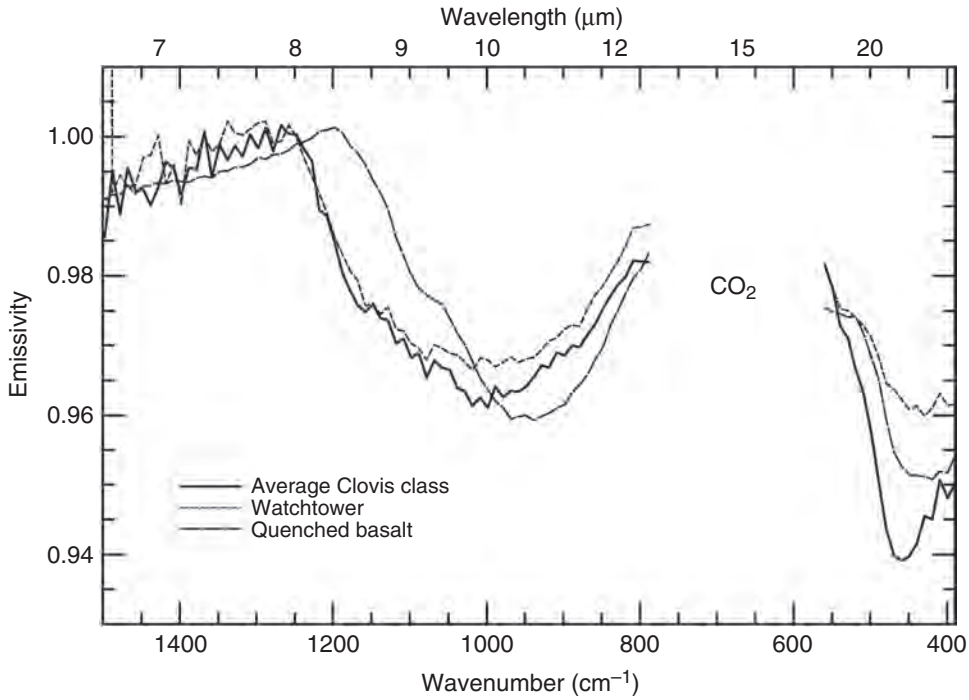

Figure 14.6. Mini-TES and laboratory spectra highlighting the characteristics of Clovis and Watchtower Class rocks on the West Spur and Husband Hill, respectively, of Gusev crater. The Mini-TES spectra of Clovis and Watchtower Class rocks following corrections for atmospheric downwelling radiance, temperature-related slope, and surface dust show a resemblance to a laboratory spectrum of quenched basalt (i.e., basaltic glass, which comes from basaltic lava quenched in air).

were first recognized with Mini-TES spectra and subsequently confirmed using the other instruments. Herein we will review those previously identified classes observed through the 600th sol of the *Spirit* mission.

14.3.1 Clovis Class rocks

Upon reaching the Columbia Hills the rover first encountered the West Spur of Husband Hill (Figure 14.3). Beginning with a collection of rocks named Viera Cairns on the western side of the West Spur and across to its eastern contact with the plains, all of the rocks observed by the Mini-TES displayed a distinctive set of spectral features that readily separates them from the Adirondack Class rocks and allows them to be grouped into one spectral class. The major-element geochemistry of these rocks also supports grouping them into a single class named Clovis after the type outcrop (Squyres *et al.*, 2006b). The Clovis Class rocks have a broad, U-shaped feature in the middle spectral region (~800–1200 cm^{-1}) unlike anything encountered in the spectra of the Adirondack Class rocks (Figure 14.6). But it is the deep, relatively narrow absorption at ~460 cm^{-1} that is so distinctive. This feature persisted with varying spectral contrast in all dark-toned rocks observed by Mini-TES on the West Spur regardless of contributions from downwelling atmospheric radiance (Ruff *et al.*, 2006). It thus served as a discriminator for these rocks compared with the other rock types encountered in Gusev crater.

Deconvolution of the average of six Clovis Class spectra by Ruff *et al.* (2006) proceeded using a varying set of spectral endmembers designed to examine the extent of alteration of these rocks that was evident from the IDD instrument datasets (Ming *et al.*, 2006; Morris *et al.*, 2006; Squyres *et al.*, 2006b). Figure 14.7 shows the results of six different deconvolution runs that began with an endmember set that included only primary igneous minerals (feldspars, pyroxenes, and olivines) and progressed through the addition of amorphous silicate phases (volcanic glasses), sulfates, Fe-oxides, and secondary silicates (alteration phases like clay minerals, zeolites, and serpentine). In this approach, the RMS values served to quantify whether a given model was more accurate than another. The results yielded a picture of the bulk mineralogy in which a component modeled by quenched basaltic glass accounted for ~40% of the total components after normalization for surface dust, slope, sky, and blackbody components. Combined with another ~5% of an obsidian-like glass, these rocks may be composed of nearly half primary glass material. Olivine was notably absent from the best-fit deconvolution results, which is consistent with only a "minor" amount detected by the MB (Morris *et al.*, 2006). Plagioclase and pyroxene components were not uniquely identified but 5%–15% each of sodic plagioclase and either ortho- or clino- pyroxene were permissible components. Sulfates were required to produce the best fits to the Clovis Class average spectrum, with gypsum ($CaSO_4 \cdot 2H_2O$) at ~10% abundance being the most likely candidate but with epsomite ($MgSO_4 \cdot 7H_2O$) and perhaps kieserite ($MgSO_4 \cdot H_2O$) as permissible components at up to ~25% total abundance. Goethite (α-FeOOH) was the only Fe-oxide detected and was required in the amount of 5%–10% to achieve the best fits. It was identified in MB spectra of Clovis (Morris *et al.*, 2006), making goethite one of the few hydrated phases observed in Gusev crater. Finally, secondary silicates such as serpentine, heulandite, and saponite with a combined total of ~20% were permissible components of Clovis Class rocks but were not uniquely identified, that is, the RMS value did not change significantly whether they were included or not. Dioctahedral clay minerals like montmorillonite are unlikely constituents of this rock class due to

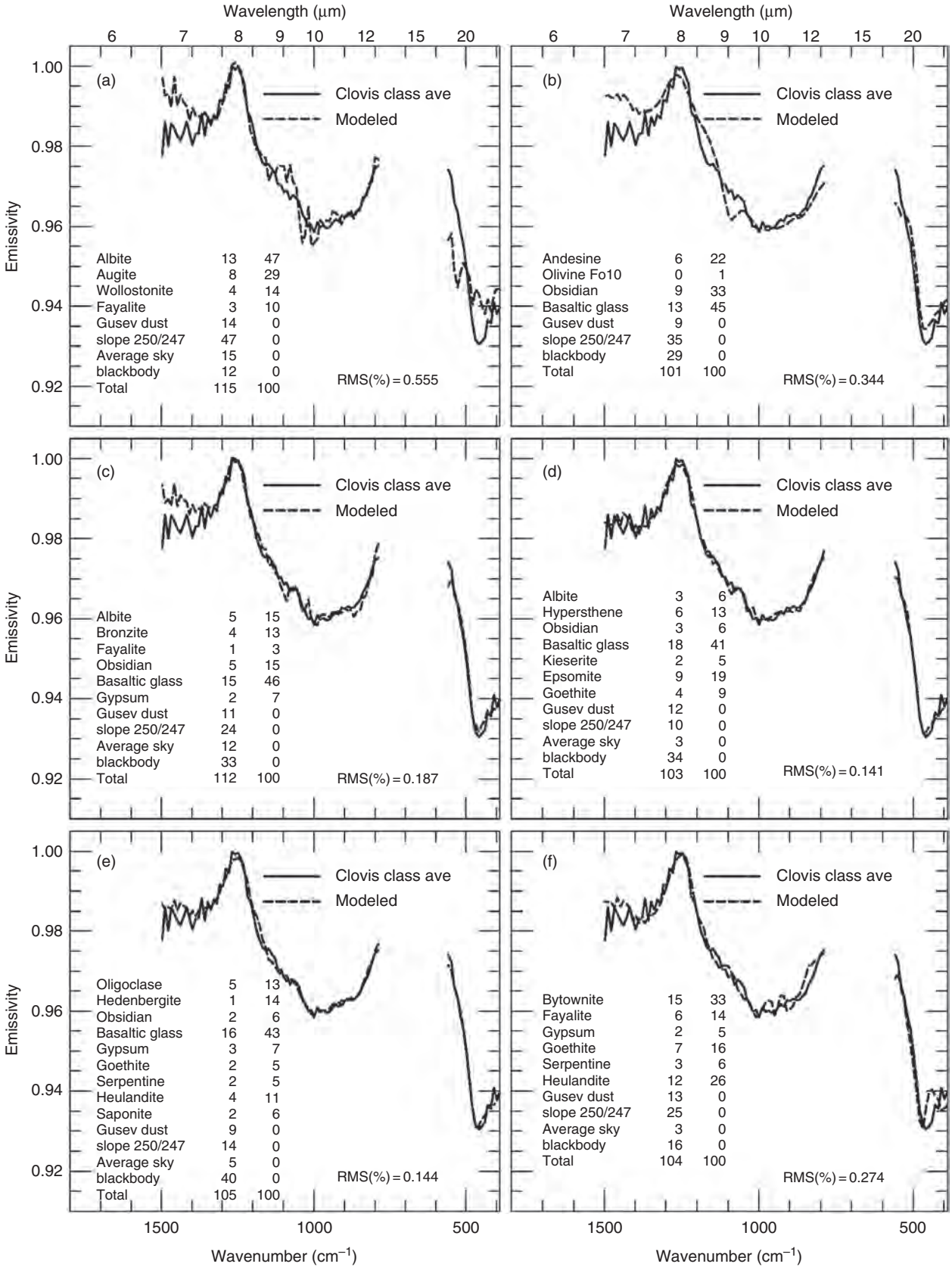
Wavelength (μm)
6 7 8 9 10 12 15 20
Emissivity
1.00 0.98 0.96 0.94 0.92
(a)
Clovis class ave
Modeled
Albite 13 47
Augite 8 29
Wollostonite 4 14
Fayalite 3 10
Gusev dust 14 0
slope 250/247 47 0
Average sky 15 0
blackbody 12 0
Total 115 100
RMS(%) = 0.555
(b)
Clovis class ave
Modeled
Andesine 6 22
Olivine Fo10 0 1
Obsidian 9 33
Basaltic glass 13 45
Gusev dust 9 0
slope 250/247 35 0
blackbody 29 0
Total 101 100
RMS(%) = 0.344
(c)
Clovis class ave
Modeled
Albite 5 15
Bronzite 4 13
Fayalite 1 3
Obsidian 5 15
Basaltic glass 15 46
Gypsum 2 7
Gusev dust 11 0
slope 250/247 24 0
Average sky 12 0
blackbody 33 0
Total 112 100
RMS(%) = 0.187
(d)
Clovis class ave
Modeled
Albite 3 6
Hypersthene 6 13
Obsidian 3 6
Basaltic glass 18 41
Kieserite 2 5
Epsomite 9 19
Goethite 4 9
Gusev dust 12 0
slope 250/247 10 0
Average sky 3 0
blackbody 34 0
Total 103 100
RMS(%) = 0.141
(e)
Clovis class ave
Modeled
Oligoclase 5 13
Hedenbergite 1 14
Obsidian 2 6
Basaltic glass 16 43
Gypsum 3 7
Goethite 2 5
Serpentine 2 5
Heulandite 4 11
Saponite 2 6
Gusev dust 9 0
slope 250/247 14 0
Average sky 5 0
blackbody 40 0
Total 105 100
RMS(%) = 0.144
(f)
Clovis class ave
Modeled
Bytownite 15 33
Fayalite 6 14
Gypsum 2 5
Goethite 7 16
Serpentine 3 6
Heulandite 12 26
Gusev dust 13 0
slope 250/247 25 0
Average sky 3 0
blackbody 16 0
Total 104 100
RMS(%) = 0.274
1500 1000 500
Wavenumber (cm^{-1})

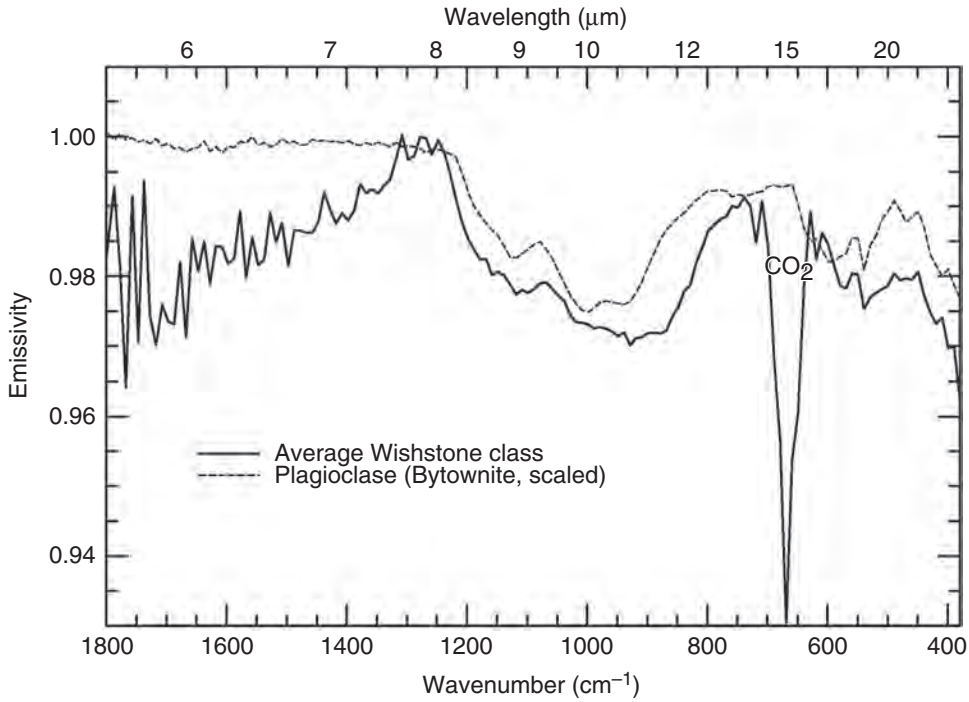

Figure 14.8. Mini-TES and laboratory spectra highlighting the characteristics of Wishstone Class rocks on the Husband Hill of Gusev crater. Wishstone Class rocks are dominated by plagioclase feldspar, whose features are readily apparent in the Mini-TES spectrum.

their low-wavenumber doublet absorption feature that is a poor fit to the pronounced singlet of the Clovis Class spectrum.

In an effort to determine whether the spectra of amorphous silicates could substitute for secondary silicates as has been demonstrated by Wyatt and McSween (2002) for TES spectra, they were excluded from the endmember set in a final deconvolution. In this case (Figure 14.7f), the RMS value was nearly double the RMS value of the best-fit case involving basaltic glass, demonstrating that crystalline secondary silicate minerals cannot substitute for the basaltic glass component. Table 14.1 includes a best estimate of the mineralogy of Clovis Class rocks based on the results from two deconvolution models with the lowest RMS values.

Caption for Figure 14.7. Spectral deconvolution of the average Clovis Class spectrum using various combinations of endmember spectra. The "raw" results with values in percent abundance are shown (see Table 14.1 for the final merged results). The second column of values (in %) represents the modeled components normalized to exclude surface dust, slope, sky, and blackbody components. (a) Using only crystalline, primary igneous minerals, a poor fit is obtained. (b) Adding amorphous phases substantially improves the modeled fit. The feature at ~460 cm^{-1} is better fit by volcanic glasses than by crystalline igneous minerals. (c) An enrichment in sulfur in Clovis Class rocks measured by the APXS prompts the use of sulfate endmembers. The resulting fit has a nearly 50% lower RMS error over the previous iteration and clearly visible improvements to the fit throughout the spectrum. (d) By incorporating the Fe-oxide minerals detected with the Mössbauer instrument into the endmember set, a modest improvement in fit is obtained, reaching the lowest RMS value of any of the iterations. (e) The inclusion of secondary silicates (alteration phases) has no significant impact on the modeled fit but demonstrates that minor abundances of some phyllosilicates and perhaps zeolites are possible. Dioctahedral clay minerals are notably absent from the results. (f) The spectra of all amorphous endmembers were removed in the final iteration to evaluate the potential for crystalline secondary silicates to substitute for them. The result is a near doubling of the RMS error and clear misfit throughout the spectrum.

14.3.2 Wishstone Class rocks

With the completion of the traverse from west to east across the West Spur, the rover passed an apparent lithologic contact manifested by the absence of rocks with Clovis Class spectral character and the presence of rocks with Adirondack Class spectral character (Ruff *et al.*, 2006). But within ~40 m of this contact, a single float rock was observed with a distinctly different spectrum than either Adirondack or Clovis Class (designated as Plymouth, sol 321, sequence identifier p3808). Another ~150 m drive brought the rover to the lower flank of Husband Hill upon which were tens of rocks with similar spectral character. Pancam multispectral observations of these rocks also were distinct from both the Adirondack and Clovis Class rocks (Chapter 13). An IDD campaign on a rock dubbed Wishstone provided the name for this new class of rocks (Squyres *et al.*, 2006b).

Wishstone Class rocks all display a remarkable set of features at low wavenumbers unlike any other rocks observed in the Columbia Hills (Figure 14.8): a narrow emissivity peak at ~560 cm^{-1} followed by a sharp absorption at ~540 cm^{-1} and a notably flat-topped or perhaps double-peaked, relatively wide emissivity peak centered at ~470 cm^{-1} (Ruff *et al.*, 2006). A more subtle but distinctive emissivity peak is evident at ~1070 cm^{-1} that represents a departure from Clovis Class rocks in the middle spectral region (~800–1200 cm^{-1}). All of these features are easily recognized in the spectra of intermediate plagioclase feldspars (Figure 14.8). Although plagioclase has been mapped across the planet through the deconvolution of TES spectra (Bandfield, 2002), the Mini-TES spectra of Wishstone Class rocks represent the first time the spectral features of plagioclase could be observed directly.

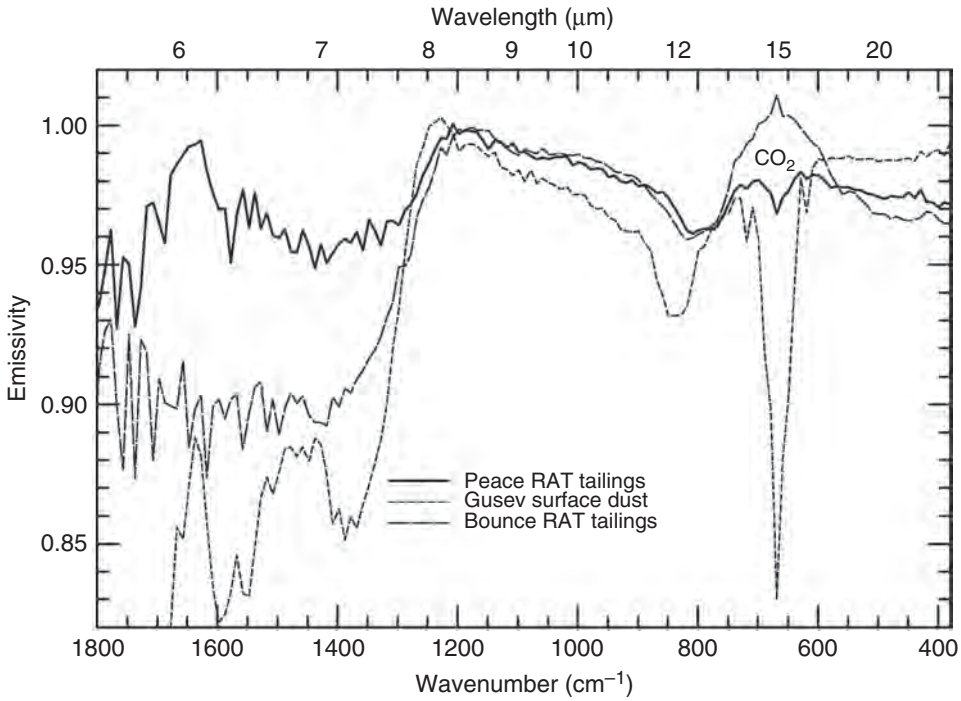

Figure 14.9. Mini-TES spectra comparing fine-particulate materials from both landing sites. A grind by the RAT into a Husband Hill outcrop called Peace produced tailings whose spectrum shows features similar to but distinct from the ubiquitous surface dust. An emissivity peak at ~1630 cm^{-1} is attributed to a water-bearing phase and an absorption feature at ~800 cm^{-1} is almost identical to a pyroxene-related feature observed in the spectrum of RAT tailings from Bounce Rock in Meridiani Planum.

At least 95 rocks with these same spectral features were observed along the traverse up to and including the summit region of Husband Hill (Ruff *et al.*, 2006).

Table 14.1 includes a best estimate of the mineralogy determined from the average of four pre-sol-420 Wishstone Class rocks based on multiple deconvolution models incorporating different endmember libraries (Ruff *et al.*, 2006). Plagioclase was the dominant component at nearly 60% abundance. Olivine was detected but pyroxene was not. A sulfate component (anhydrite – $CaSO_4$) was modeled at a nonnegligible abundance (~10%) as well as a phosphate component (wavellite – $Al_3(PO_4)_2(OH)_3 \cdot 5H_2O$), which is consistent with the elevated P observed by APXS for these rocks (Gellert *et al.*, 2006). Wavellite is a hydrated aluminophosphate of secondary origin and may not represent the actual phosphate component. Additional deconvolution modeling with an expanded set of phosphates is needed before wavellite can be considered a robust detection.

14.3.3 Peace Class rocks

The first outcropping of rock encountered by the rover on Husband Hill was called Peace. A second outcrop called Alligator ~20 m away has similar APXS and MB characteristics that combine to distinguish these rocks from others in the Columbia Hills. Their chemistry measured by APXS serves to group them into a single class called Peace (Squyres *et al.*, 2006b). Although both outcrops were measured prior to the mirror-dusting event on sol 420, their natural surfaces were poor targets for Mini-TES due to an abundance of dust. The Rock Abrasion Tool (RAT) used to grind into the Peace outcrop produced one of the deepest holes of the mission (9.7 mm), an indication of its relative softness compared with other rocks along the rover traverse (Arvidson *et al.*, 2006). The tailings generated by the RAT accumulated in a substantial pile at the front of the rock. The Mini-TES observation of the RAT hole included much of this fine-particulate material. Fine particles produce spectral scattering effects that reduce or eliminate restrahlen (primary) features and introduce transparency features (e.g., Aronson *et al.*, 1966; Hunt and Vincent, 1968; Vincent and Hunt, 1968; Hunt and Logan, 1972; Aronson and Emslie, 1973; Salisbury and Eastes, 1985; Wald and Salisbury, 1995). The Mini-TES spectrum displays these features (Figure 14.9), the most important of which is a pronounced emissivity peak at ~1630 cm^{-1} that typically is attributed to the fundamental bending mode of molecular bound water (e.g., Salisbury *et al.*, 1991; Bishop and Pieters, 1995). It is likely that the ~1630 cm^{-1} feature results from one or more phases in the Peace rock that contain bound water. Based on the high-sulfur content observed by the APXS (Gellert *et al.*, 2006), hydrated sulfate is a likely candidate. Also, Pancam spectra of the Peace RAT tailings exhibit visible-wavelength spectral features similar to those exhibited by some hydrous iron-bearing sulfates (lack of a 535 nm band and maximum reflectance at 673 nm; Lane *et al.*, 2004).

An apparent transparency feature at ~800 cm^{-1} in the spectrum of Peace RAT tailings is notably similar to one observed in the RAT tailings from Bounce rock at the *Opportunity* rover landing site in Meridiani Planum. Mini-TES spectra of Bounce rock prior to grinding, along with MB spectra of it, clearly indicate a dominant pyroxene component (Christensen *et al.*, 2004b; Klingelhöfer *et al.*, 2004). The ~800 cm^{-1} feature in Peace rock was thus inferred to be due to an abundance of pyroxene (Ruff *et al.*, 2006), a result supported by the MB measurements on this rock (Morris *et al.*, 2006).

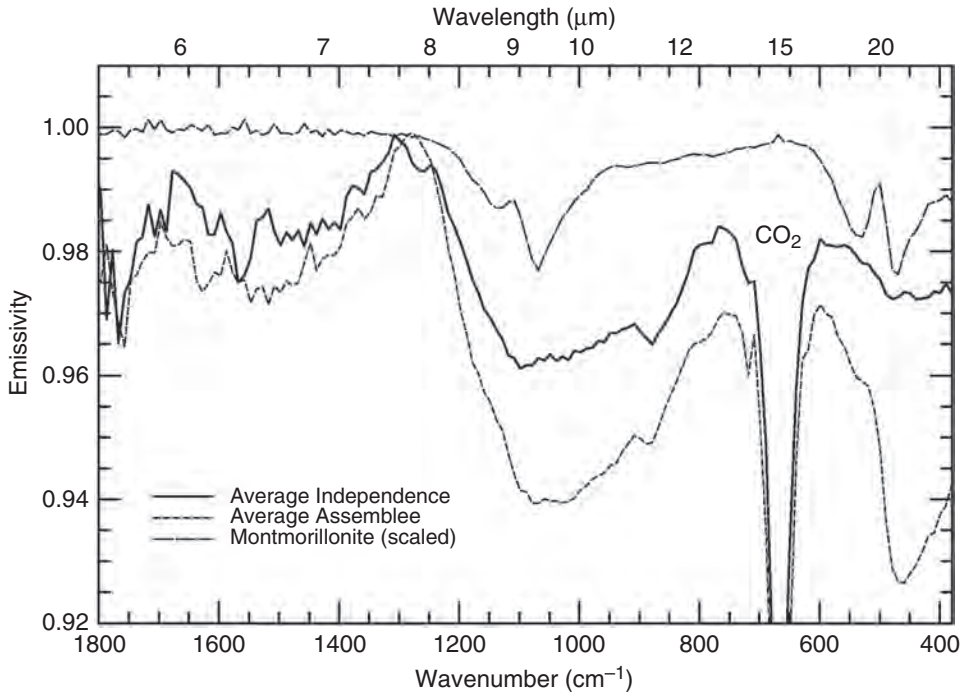

Figure 14.10. Mini-TES and laboratory spectra demonstrating the lack of obvious montmorillonite spectral features in two rocks on Husband Hill. Independence and Assemblee have an elemental chemistry consistent with the clay mineral montmorillonite, yet their emissivity spectra and deconvolved mineralogy do not show this phase.

14.3.4 Watchtower Class rocks

A large outcropping of rock called Larry's Lookout on the crest of the Cumberland Ridge of Husband Hill is the location of the rock Watchtower (Figure 14.3) whose spectral and chemical characteristics define yet another distinctive rock type (Squyres *et al.*, 2006b). Mini-TES observations of rocks at this location and some on the adjacent Jibsheet Ridge outcrop have a common spectral character that allows them to be grouped together (Ruff *et al.*, 2006). As with the Wishstone Class, Mini-TES spectra of these rocks were acquired before and after the sol 420 wind event that deposited dust on the pointing mirror. Only the predusting spectra are described below.

The features in the low-wavenumber region ($< \sim 600$) of Watchtower Class spectra clearly distinguish these rocks from the dominant Husband Hill rock-type Wishstone Class (Figures 14.2 and 14.6). Gone is the distinctive set of plagioclase-related features. Instead, there is a single, relatively deep absorption with an apparent minimum near $\sim 450\,cm^{-1}$. The absence of the plagioclase features as well as any olivine feature gives these spectra an appearance similar to but distinct from Clovis Class rocks (Figure 14.6).

Like Clovis Class rocks, deconvolution of the Watchtower spectrum indicates a significant abundance of basaltic glass with little to no secondary silicates. Silica-rich obsidian glass occurs in small abundance along with the substantial basaltic glass component. In all of the deconvolution models in which glasses were included among the endmember set, they represent at least 45% of the modeled components. Sulfates at 5%–10% abundance are required to achieve a good fit, with gypsum as the favored component. Plagioclase feldspar in the form of the Na-rich oligoclase is the dominant primary igneous mineral that is a persistent component in all of the models, ranging from ~10% to 25% abundance. The results for pyroxene and olivine components are not as clear, but some combination of these minerals totaling ~20% is permissible. Phyllosilicates were not detected. Table 14.1 includes a best estimate of the mineralogy of Watchtower Class rocks based on the results from the three deconvolution models with comparably low-RMS values.

14.3.5 Independence Class rocks

The next outcrop encountered by *Spirit* as it ascended Husband Hill was a low-lying, rough-textured occurrence of light-toned rock called Independence. This was a relatively dusty outcrop but with a dust mantle insufficiently thick to fully obscure the substrate. The IDD instruments were used first and then the rover was backed away to allow Mini-TES observations. APXS measurements revealed that Independence has an Fe content among the lowest of any Martian materials and an Al_2O_3/SiO_2 ratio among the highest. These characteristics along with other chemical indicators led Clark *et al.* (2007) to conclude that Independence is highly altered and is dominated by the phyllosilicate clay mineral montmorillonite ($(Al,Mg)_8(Si_4O_{10})_4(OH)_8 \cdot 12H_2O$) or its compositional equivalent. The rover encountered other examples of materials with similar chemistry including a small clod that was not measured by Mini-TES and a rock first identified by Mini-TES called Assemblee several meters away from Independence that may also be outcrop (Clark *et al.*, 2007).

The Mini-TES spectra of Independence and Assemblee (Figure 14.10) do not contain features readily attributable to montmorillonite or any aluminous, dioctahedral clay minerals as outlined by Michalski *et al.* (2006). A broad absorption between 900 and $1250\,cm^{-1}$ indicates that the rocks contain multiple aluminosilicate components, but the

absence of a doublet in the low-wavenumber range (<600) significantly diminishes the potential for a substantial dioctahedral clay component (Clark *et al*., 2007).

Two Independence spectra along with the spectra of two other spectrally and texturally similar rocks were averaged together for the deconvolution in an effort to minimize the effects of dust and soil contamination (Clark *et al*., 2007). A mix of primary igneous minerals, crystalline phyllosilicates, amorphous silicates, and sulfates was used in the spectral endmember library. Various combinations of this library were used in multiple runs of the deconvolution algorithm. The best-fit results were dominated by amorphous aluminosilicate phases with lesser primary igneous and sulfate phases (Table 14.1). No combination of endmember spectra yielded any phyllosilicate phases in the modeled results. However, there were clear mismatches throughout the full spectral range that indicate that the modeled mineralogy should be interpreted cautiously. Possible causes for the poor fit and the apparent absence of clay minerals include the following: dust and soil contaminants that were not properly modeled; the presence of allophane or other phases that were not included in the spectral library; the possibility that clay-sized particles dispersed throughout a matrix of other grains may be difficult to detect Michalski *et al*., (2006); and possible inaccuracies in the mirror-dust correction (Ruff *et al*., 2006).

Deconvolution of the Assemblee spectrum yielded a much better fit than that achieved with Independence (Clark *et al*., 2007). The quality of the fit suggests that the spectral endmembers used in the deconvolution properly represented the components present in the rock. Amorphous aluminosilicate components dominated the modeled results with lesser sulfate, and only minor primary igneous components (Table 14.1). Clay minerals appeared as only trace components (<5%). It is noteworthy that maskelynite (shocked plagioclase) was one of the modeled amorphous components at ~15%–20% abundance following normalization for dust and the slope component used to account for temperature error (Ruff *et al*., 2006). This suggests the possibility of impact processes in the formation of Assemblee.

Several important conclusions can be drawn from the Mini-TES analysis of Independence and Assemblee (Clark *et al*., 2007). The results do not demonstrate a large component of crystalline clay minerals, including montmorillonite. No Fe-bearing phyllosilicates were observed in the MB spectra either (Clark *et al*., 2007). However, the TIR spectral character and modeled components of both rocks are distinct from typical basaltic materials and the results are consistent with an interpretation of Independence and Assemblee as altered rocks. Modeled amorphous aluminosilicates could correspond to (1) pure aluminous silica (with structural Al^{3+}), (2) an intimate mixture of pure opal ($SiO_2 \cdot nH_2O$) with an aluminous phase like allophane, or (3) primary felsic glass of similar composition (Michalski *et al*., 2005b). The modeled sulfate abundances are consistent with inferred abundances from APXS data. The modeled basaltic glass component could correspond to primary glass, or possibly to an amorphous secondary phase(s) of similar composition that was not present in the endmember library. Mini-TES observations of Independence and Assemblee favor an interpretation of amorphous clay-equivalent mineralogy over crystalline clay mineralogy (Clark *et al*., 2007). The distinction pertains to the fact that the component phase whose chemistry is consistent with montmorillonite lacks its crystalline structure. This may be due to environmental conditions during the time of formation of this phase that prevented it from becoming fully crystalline or, once formed, destroyed its crystalline structure.

14.3.6 Basaltic exotics

Dozens of small (<50 cm), dark-toned, smooth-textured float rocks were observed by Mini-TES beginning at the base of Husband Hill (Ruff *et al*., 2006). These rocks are described as "exotics" because they typically were found as isolated occurrences among rocks with a different lithology. The use of the term "basaltic" acknowledges their texture, dark-tone, and in the case of one of the classes, spectral similarity to the rocks of the Gusev plains. Another feature of these rocks worth noting is that their morphology commonly displays facets and edges that suggest aeolian abrasion.

Three distinct classes of basaltic exotics were identified with Mini-TES spectra (Ruff *et al*., 2006), two of which were confirmed using the IDD instruments (Figure 14.11). Sixteen examples of rocks that are spectrally equivalent to Adirondack Class basaltic rocks from the plains were observed from the base to the summit of Husband Hill. These likely were emplaced onto the hill as ejecta from impacts into the surrounding plains materials. Backstay Class exotics (Figure 14.11) have no known equivalents either on the plains or among the outcrops in the Columbia Hills. Nine examples were observed starting roughly midway up Husband Hill (Figure 14.3) and continuing up to the summit region. Additional examples also were found on Haskin Ridge to the east of the summit. They may represent either the remains of shallow intrusions or impact ejecta from source rock that predates the emplacement of the plains basalts (Grant *et al*., 2006). Their chemistry demonstrates an alkaline affinity, which is distinct from most other volcanic Martian materials (McSween *et al*., 2006). The rocks that became known as Irvine Class were first seen as part of a vague alignment suggestive of an eroded volcanic dike ~2.5 m in length on the south side of the Husband Hill summit (Figure 14.3) (Ruff *et al*., 2006). Additional examples were observed well away from this trend, all with the same spectral and morphological characteristics for a total of at least five occurrences. Spectrally distinct from all the previous basaltic rocks (Figure 14.11), their chemistry suggests that they may be related to Adirondack and Backstay Classes through differentiation of an alkaline parent magma (McSween *et al*., 2006). All of the Backstay and Irvine Class rocks were observed following the sol 420 wind event that left dust on the Mini-TES mirror. Because the mirror-dust correction has not yet been validated, deconvolution of their spectra has been deferred.

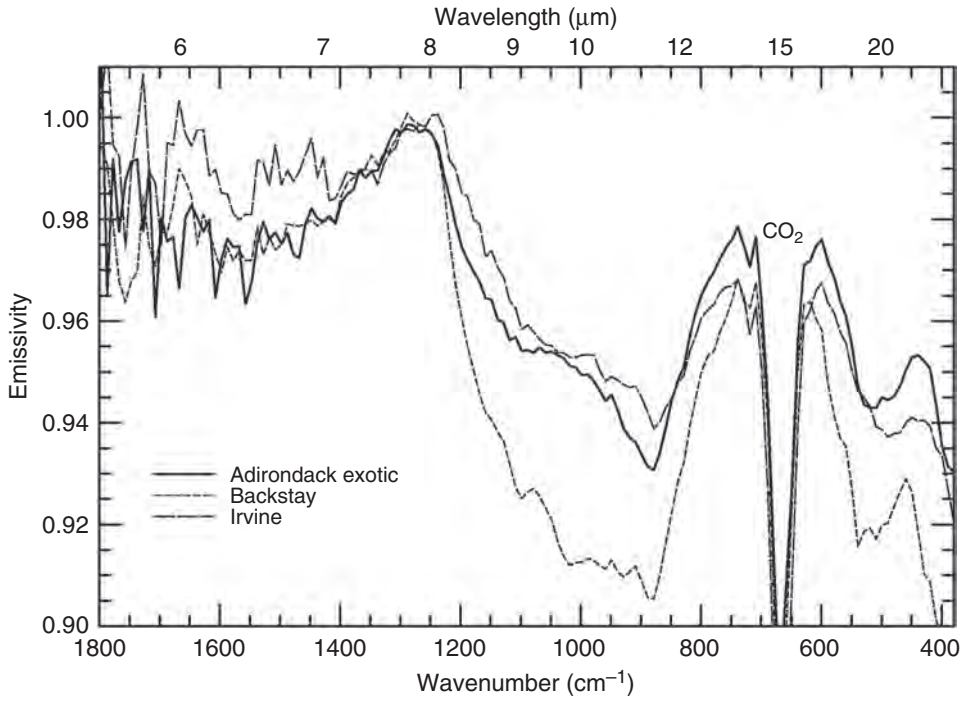

Figure 14.11. Mini-TES spectra of basaltic exotics (out of place rocks) found scattered across Husband Hill. The Adirondack Class exotic represented here by the spectrum of Fountain (p3495, sol 530) is one of fifteen rocks that resemble the rocks on the Gusev plains. Backstay (p3424, sol 482) and Irvine (p3133, sol 590) are the type examples of additional basaltic exotics for which nine and five, respectively, were found using Mini-TES spectra.

14.4 DISCUSSION OF GUSEV CRATER RESULTS

The rocks observed by Mini-TES can be classified generally as olivine-rich, plagioclase-rich, or glass-rich. Each offers insights into the geologic environment through which the *Spirit* rover traversed.

The Adirondack Class rocks that cover the plains of Gusev crater clearly display a significant abundance of olivine and minimal alteration products as seen by both the Mini-TES and MB instruments (e.g., Morris *et al.*, 2004). Additionally, olivine-rich materials have been identified elsewhere using both TES and OMEGA datasets (e.g., Hoefen *et al.*, 2003; Hamilton and Christensen, 2005; Mustard *et al.*, 2005), firmly establishing the ubiquity of this mineral type across the planet. The presence of olivine generally attests to dry conditions that must have prevailed during its exposure to the surface/near-surface environment. However, on the Gusev plains it cannot be used to rule out the presence of a lake in the past given that the plains represent the middle to late history of the crater's stratigraphy (e.g., Milam *et al.*, 2003). Instead, the period during which a lake may have been present mostly likely occurred at a time before the plains basalt was emplaced.

Based on the embayment relationship of the plains basalt to the Columbia Hills, it is clear that the hills predate the emplacement of the basalt (Arvidson *et al.*, 2006; Squyres *et al.*, 2006b). The rocks observed by Mini-TES in the Columbia Hills provide clues to whether the hills experienced the watery environment of an ancient lake in a time predating the plains. The West Spur rocks appear to be a single class, Clovis, and commonly are found in outcrops. Their mineralogy is radically different from the plains basalt, with little to no olivine evident and no dominant crystalline phase apparent. Instead, they appear to be dominated by a component that is best matched by quenched basalt (i.e., basaltic glass). Although data from the rover's other instruments indicate a significant level of alteration of these rocks, based mostly on their high ferric (Fe^{3+}) to total Fe ratio along with minor goethite and elevated S, Cl and Br (e.g., Ming *et al.*, 2006), there is no clear indication of significant alteration products from Mini-TES spectra. Given the susceptibility of basaltic glass to alteration by water (e.g., Bishop *et al.*, 1998), it is unlikely that the rocks of the West Spur have been submerged in a lake. Although they are older than the plains, their placement in the stratigraphy of the Columbia Hills is poorly constrained (Squyres *et al.*, 2006b). It is still possible that the West Spur rocks postdate a putative lake in Gusev crater.

Plagioclase feldspar has been detected across the globe through deconvolution of TES spectra (Bandfield, 2002) and now it is seen to dominate the Wishstone Class rocks of Husband Hill, which are the second most widespread rock type observed by Mini-TES after Adirondack Class rocks. The absence of any outcrop associated with these rocks has led to the suggestion that they may represent impact ejecta strewn across the hill (Grant *et al.*, 2006). However, the presence of clearly identifiable plagioclase spectral features demonstrates that Wishstone Class rocks have not experienced a high level of impact-related shock. In work by Johnson *et al.* (2002b), these features were seen to diminish and go away completely with shock pressures >27 Gpa. This places some constraints on the energy of a possible impact event and, presumably, the distance to the potential source region of these rocks. Similar arguments apply to the hypothesis that Wishstone Class rocks may have been derived

from impact-generated surges, weakening this hypothesis and strengthening that of a pyroclastic origin (Squyres *et al.*, 2006b). Regardless of their origin, Wishstone Class rocks are among the least altered rocks encountered by the *Spirit* rover (e.g., Ming *et al.*, 2006), providing little evidence for exposure to an ancient lake.

The outcrops on the north side of Husband Hill that host the Watchtower and Independence Class rocks also appear to be dominated by basaltic glass according to Mini-TES observations, despite the results from other instruments that indicate that they are significantly altered (Ming *et al.*, 2006; Clark *et al.*, 2007). Like the Clovis Class rocks, there is somewhat of a paradox in these observations. Although basaltic glass is highly susceptible to aqueous alteration, it may be that the elevated oxidation state of the Watchtower Class rocks (Morris *et al.*, 2006) is due to nonaqueous processes (Ruff *et al.*, 2006). Alternatively, the basaltic glass component in all cases may represent the hydrated, amorphous mineraloid known as "palagonite" (e.g., Bishop *et al.*, 1998), which would indicate the role of water in their alteration.

The overall results to date from the Mini-TES experiment in Gusev crater provide no clear mineralogical evidence of the kind expected from the prolonged interaction of abundant water and rock. The presence of an ancient lake has not been confirmed with Mini-TES data.

14.5 MERIDIANI PLANUM

The spacecraft carrying the *Opportunity* rover arrived at Meridiani Planum 20 days after the landing of *Spirit*, coming to rest in a small crater subsequently dubbed Eagle (Squyres *et al.*, 2004b). Outcroppings of light-toned layered rocks exposed along much of the interior wall of the crater lay just a few meters from the lander. Dark-toned, sandy regolith covered both the floor of the crater and the outside plains where a notable paucity of float rocks and dust in the scene provided a remarkable contrast to all of the previous landing sites on Mars. The most unexpected feature of this landing site was the abundant gray, spherical grains a few millimeters in diameter that were contained in the outcrop rock and concentrated as a lag across the surface. Ultimately, these spherules were found to host the hematite that was first observed in orbital TES spectra (Christensen *et al.*, 2000a). Mini-TES observed surfaces that were dominated by each of these components, but given the 20 mrad FOV of the Mini-TES instrument, it was difficult to acquire spectra of the pure components (Christensen *et al.*, 2004b). Spectra of soils and outcrop rocks also were affected by contributions from surface dust (Christensen *et al.*, 2004b) and atmospheric radiance (Smith *et al.*, 2004), complicating the mineralogical interpretation of these surfaces. In response to this problem, Glotch and Bandfield (2006) analyzed over 15 000 individual Mini-TES spectra and applied FATT techniques to isolate the major scene spectral endmembers present at Meridiani Planum. Factor analysis is a technique that can determine the number of independent linear components present in a system of mixed spectra (Malinowski, 1991; Bandfield *et al.*, 2000a, 2002; Glotch and Bandfield, 2006). Target transformation allows for the separation of endmembers from a mixed spectral dataset in which the components combine linearly (Malinowski, 1991; Bandfield *et al.*, 2000a). From this approach, it was determined that the Mini-TES dataset acquired at Meridiani Planum through sol 350 could be modeled accurately using the following seven endmembers: basaltic sand, surface dust similar to the globally homogeneous dust observed by TES, coarsely crystalline hematite, silica/sulfate-rich outcrop rock, two atmospheric shapes, and blackbody (unit emissivity at all wavelengths) (Glotch and Bandfield, 2006). The four surface endmembers are described below. We also present two additional targets of interest in the form of rare float rocks on the plains.

14.5.1 Hematite

The hematite component recovered using FATT was that of pure crystalline hematite comparable to a spectrum of high-grade laboratory material (Glotch and Bandfield, 2006; Figure 14.12a). Although a pure hematite spectrum was apparent in Mini-TES spectra, Jolliff *et al.* (2005) showed through a mass-balance mixing-model approach using APXS data that the spherules at Meridiani Planum are likely composed of 37–60 wt.% hematite. Additionally, MB data (Klingelhöfer *et al.*, 2004) and Pancam spectra (Bell *et al.*, 2004b) showed that hematite also occurs independently of the spherules within the light-toned outcrop matrix. Thus, there are several possible explanations for the recovery of a pure hematite spectrum rather than an average spherule spectrum: (1) the hematite abundance within the spherules varies significantly and independently from the other spherule components; (2) hematite is present not only in the spherules, but in the outcrop rock matrix where its spectral character is comparable to that of the spherules; (3) the hematite is present only in the form of a coating on the spherules; and (4) the other components of the spherules are fine particulates difficult to detect with the Mini-TES. Of these possibilities, choices 1 and 2 are considered to be the most likely (Glotch and Bandfield, 2006).

The recovered hematite spectrum (Figure 14.12a) shows no evidence of a narrow absorption feature at 390 cm^{-1}, as is seen in some terrestrial hematite spectra. This confirms observations made with TES spectra from Meridiani Planum and other hematite-rich locations on Mars (Glotch *et al.*, 2004). The lack of a feature at 390 cm^{-1} is attributable to [001]-dominated emission (Lane *et al.*, 2002), and has been interpreted as due to platy (Lane *et al.*, 2002) or lath-like (Glotch *et al.*, 2004) hematite crystal shapes. Because the spherules exhibit no 390 cm^{-1} feature, they likely are composed of randomly oriented platy or lath-like crystals that are dominated by [001] emission, or an anhedral crystal mass with a preferred [001] orientation radial to the center of the spherules (Glotch *et al.*, 2006b). Additionally, the shapes and positions of the hematite spectral bands are consistent with hematite formed by the low-temperature dehydroxylation of goethite, which produces lath-like hematite crystals (Glotch *et al.*, 2004) as opposed to a magnetite precursor, for example

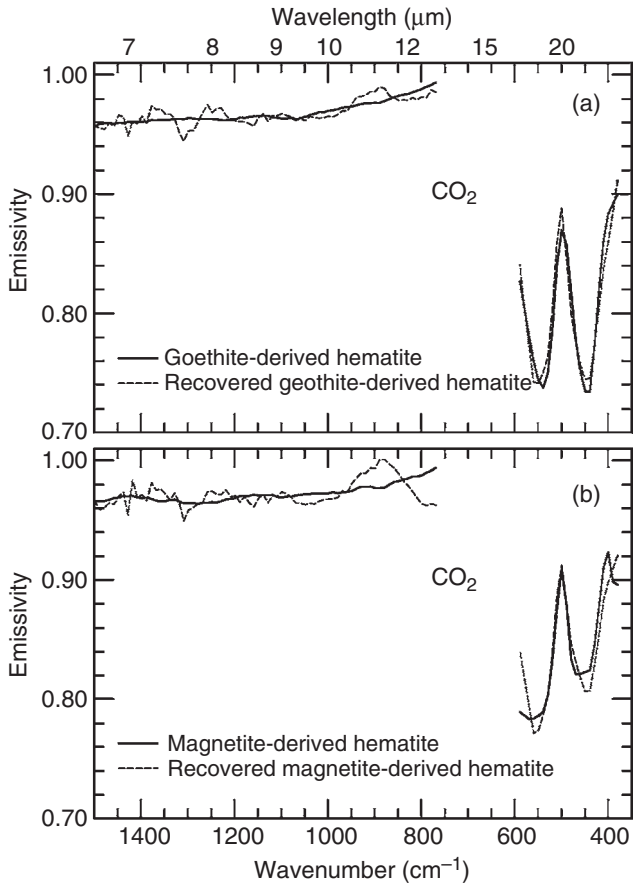

Figure 14.12. Examples of laboratory and target transformation derived hematite spectra. (a) Hematite spectrum derived from Mini-TES data (dashed) using a laboratory goethite-derived hematite as the target spectrum (solid). There is overall good agreement between the target and recovered spectra. (b) Hematite spectrum derived from Mini-TES data (dashed) using a laboratory magnetite-derived hematite as the target spectrum (solid). There is poor agreement between the target and recovered spectra in terms of band shape, position, and depth. The 390 cm^{-1} minimum in the target spectrum is not present in the Mini-TES spectrum and the feature at ~550 cm^{-1} is broader in the target spectrum than in the Mini-TES spectrum.

(Figure 14.12b). This also is consistent with the presence of the Fe-sulfate jarosite $[(K,Na,H_3O)(Fe,Al)_3(SO_4)_2(OH,Cl)_6]$ in the outcrop matrix, as goethite and jarosite are often associated in nature (Herbert, 1995, 1997) and are easily co-precipitated in the laboratory (Brown, 1971; Stahl *et al.*, 1993). Hematite formed by high-temperature processes, such as might be found in a volcanic sulfotara environment (e.g., McCollom and Hynek, 2005), or as the result of formation of volcanic lapilli or impact melt spherules (Knauth *et al.*, 2005), produces a spectrum inconsistent with that seen on Mars (Glotch *et al.*, 2004).

14.5.2 Basaltic sand

Another main component of the Meridiani Planum surface that was isolated using the FATT technique is basaltic sand (Glotch and Bandfield, 2006). The sand has a spectral shape that is similar to the basaltic TES Surface Type 1 (ST1; Chapter 9) as seen from orbit. An acceptable match was not achieved with the TES Surface Type 2 spectrum, which was first interpreted as a basaltic andesite (Bandfield *et al.*, 2000b) and more recently as the product of alteration of basalt (e.g., Wyatt and McSween, 2002). This indicates that the Type 2 composition is not present in appreciable concentrations at Meridiani Planum.

In addition to the spectrum isolated using the FATT technique, basaltic sand was observed in dunes and ripples on the floor of Endurance crater (e.g., Squyres and Knoll, 2005). In these locations, the sand was free of hematite spherules, outcrop rock, and most dust, unlike on the adjacent plains or in Eagle crater. This meant that the sand could be observed by Mini-TES in a purer form. A sand pile in the lee of a rock called Auk has a spectrum notably similar to the global average low-albedo surface derived from TES spectra (Bandfield and Smith, 2003) and is similar to the disturbed soils measured in Gusev crater (Figure 14.5b; Yen *et al.*, 2005). Its mineralogy as determined from spectral deconvolution has a basaltic composition consisting of 35% pyroxene, 40% plagioclase feldspar, 10% olivine, 15% glass, and less than 5% sulfates and oxides (Table 14.1). Within the accuracy of Mini-TES mineral retrievals, these results are of the order of the variation in mineral abundances between the two landing sites and TES data (Yen *et al.*, 2005).

Although multiple lines of evidence strongly suggest aqueous alteration and mineral deposition at Meridiani Planum (Christensen *et al.*, 2000a, 2001; Christensen and Ruff, 2004; Glotch *et al.*, 2004; Klingelhöfer *et al.*, 2004; Rieder *et al.*, 2004; Squyres *et al.*, 2004b; Clark *et al.*, 2005; McLennan *et al.*, 2005; Glotch *et al.*, 2006a; see also Chapters 23 and 24), the presence of a nearly pristine basalt component with appreciable olivine content implies a long period of dry conditions in which significant chemical weathering did not occur. It is also possible that the aqueous activity was relatively short-lived, limiting the chemical alteration of the surface, or that the basalt from which the sands were derived was deposited after the period of aqueous activity and subsequently transported to the region (Glotch and Bandfield, 2006), although basaltic sand transport distances are limited to several hundred kilometers by physical weathering (Edgett and Christensen, 1991; Greeley and Kraft, 2001; Rogers and Christensen, 2003). To date, the source rock from which the basaltic sands at Meridiani Planum were derived has not been found, so it is difficult to ascertain the chronology of events relating the basaltic and aqueously deposited components.

14.5.3 Dust

Although Meridiani Planum is a classic low-albedo region on Mars, the Mini-TES instrument observed light-toned dust in a small wind streak downwind from Eagle crater that is well matched to dust in Gusev crater and the TES global average dust spectrum (Christensen *et al.*, 2004b; Figure 14.5a). Its presence in this location provides support for the model of bright wind streaks forming by deposition of airborne dust in the stagnant air created downwind of topographic obstacles during periods of high-atmospheric

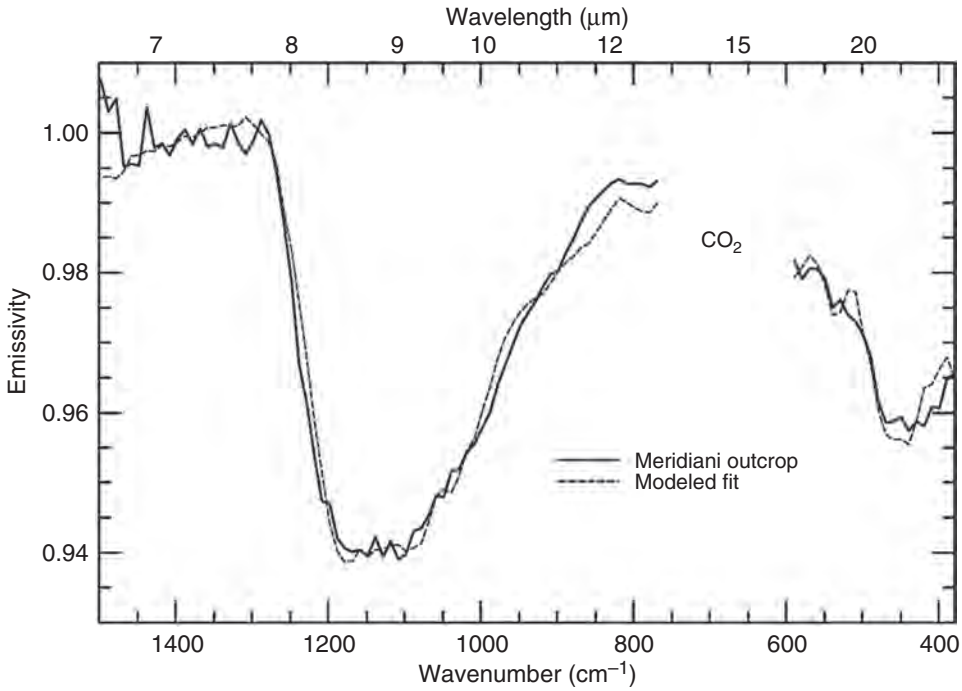

Figure 14.13. The recovered spectrum of outcrop rock in Meridiani Planum along with the model fit from linear deconvolution. There is a good overall fit, although small differences indicate that some components of the outcrop may be absent from the spectral library used for deconvolution.

stability (Veverka *et al.*, 1981). Dust also was widespread enough throughout the rover's traverse that it was identified as a discrete spectral endmember using the FATT technique (Glotch and Bandfield, 2006). The recovered dust spectrum is remarkably similar to the TES global average dust spectrum derived by Bandfield and Smith (2003). The spectral similarity between dust at the Gusev and Meridiani landing sites and the global average dust provides clear indication of its homogeneous bulk mineralogy across the planet, as described in section 14.3.2.

14.5.4 Silica/sulfate-rich outcrop rock

The spectral shape of the light-toned rocky outcrop was more difficult to isolate than that of the other materials because of its limited areal concentration in the analyzed dataset and the ubiquitous contaminants on its surfaces (Glotch and Bandfield, 2006). In an effort to recover a spectral shape representative of the outcrop, Glotch *et al.* (2006a) analyzed a subset of the data that had a larger number of spectra containing the outcrop as a component. Spectra with a greater amount of exposed outcrop in the Mini-TES FOV were chosen based on analysis of accompanying Navcam and Pancam images. The eigenvectors derived from this analysis were fit to 98 terrestrial rock spectra. No direct matches were found, but one spectral shape was consistently observed. Each occurrence of this spectral shape was isolated and about 10 recovered spectra were averaged together (Figure 14.13). This spectrum has realistic emissivity values, is not a combination of any other components, and its presence can be seen in individual spectra in the dataset being examined. Thus it is likely an endmember in the system.

The linear deconvolution was performed with the benefit of information gained from previous analyses of APXS, MB, and Mini-TES data, and removal of any major components from the endmember library that resulted in worse model fits and/or unrealistic modeled mineralogy and chemistry of the outcrop (Glotch *et al.*, 2006a). Results from the best-fit deconvolution model (Figure 14.13) indicate that the outcrop is composed primarily of sulfates and amorphous silica/glass/smectite (Table 14.1). Amorphous silica and glass were modeled at 25% abundance, with the primary contributor from the spectral library being an X-ray amorphous, Al-rich opaline silica (Michalski *et al.*, 2005a). This does not constitute a unique identification of aluminous opal given its spectral similarity to other amorphous silica phases. But it does imply that a particular composition of amorphous silica is present in the outcrop that can be modeled by aluminous opal. In addition, a smectite clay (nontronite – $(Fe_{1.92}Mg_{0.03})(Al_{0.23}Si_{3.76})O_{10}(OH)_2$) (Michalski *et al.*, 2005b) was modeled at 10% abundance. Additional components of plagioclase feldspar (15%) and coarse-grained hematite (5%) also were modeled. Eleven different sulfate spectra were used in the endmember set from which the Mg-bearing sulfate kieserite ($MgSO_4 \cdot H_2O$) was modeled at an abundance of 20%. The Ca-bearing sulfate anhydrite ($CaSO_4$) was modeled at 10% abundance, although preliminary tests with a separate simultaneous least-squares deconvolution model indicated that the Ca-bearing sulfate composition might be composed of both anhydrite and bassanite ($CaSO_4 \cdot 1/2H_2O$).

The Mini-TES observations of the outcrop-derived fines produced from RAT-grinding operations have provided valuable information about the mineralogy of the outcrop at Meridiani Planum (Glotch *et al.*, 2006a). The emissivity peak at $\sim$1630 cm^{-1} seen in the Mini-TES spectrum of the outcrop-derived fines confirms the presence of an H_2O-bearing phase in the outcrop. Conversion of the modeled outcrop mineralogy to chemistry indicates

that the total water content of the outcrop is 5.5 wt.% (Glotch *et al.*, 2006a). The only H_2O-bearing phase in the base deconvolution model results was kieserite, although both jarosite and nontronite were returned by the deconvolution and are OH-bearing. Mg-sulfates with both more and less H_2O than kieserite, and H_2O-bearing Ca-sulfates were not present in the base deconvolution model results although a separate deconvolution model indicated that bassanite, a hydrated Ca-sulfate, may be present in addition to anhydrite. It is possible that other water-bearing sulfates not included in the endmember library also may contribute to this bound water detection. In addition to the confirmation of bound water in minerals contained in the outcrop rock, comparison of the outcrop-derived fines spectrum to the global dust spectrum suggests that carbonate concentration in the outcrop rock is close to zero, and that the plagioclase content of the outcrop rock is likely more sodic than that in the global dust (Glotch *et al.*, 2006a).

The modeled mineralogy, including Na-rich plagioclase, amorphous silica, and the Mg/Ca ratio of the sulfates, is consistent with the weathering and diagenesis of an olivine-bearing basaltic rock (Tosca *et al.*, 2004; McLennan *et al.*, 2005). The experiments of Tosca *et al.* (2004) demonstrate the presence of gypsum as a nearly ubiquitous weathering product of basalts. Although gypsum was not detected in the Mini-TES analysis of the outcrop, the gypsum stability zone transitions to anyhdrite at a temperature of about 60 °C (Catling *et al.*, 2006). Given the diagenetic history of the outcrop (McLennan *et al.*, 2005), it is possible that the outcrop was exposed to such temperatures. Additional results from Tosca *et al.* (2004) indicate that minor Na-sulfates can be produced from the weathering of basalts in certain cases. The spectral library of Glotch *et al.* (2006a) contained only glauberite (a Ca-Na-sulfate), which was not used in the deconvolution.

Chemical weathering products of basalt, rather than unaltered primary igneous minerals, comprise the majority of the silicic components in the outcrop, and thus a volcanic model in which sulfur is added to a basaltic precursor (e.g., McCollom and Hynek, 2005) is not needed to explain the outcrop mineralogy and chemistry (Glotch *et al.*, 2006a; Squyres *et al.*, 2006a). Additionally, the presence of Na-rich plagioclase, the absence of pyroxene and olivine, and the tentative identification of nontronite may indicate that a previous weathering regime was less acidic than that in which jarosite was formed.

14.5.5 Bounce rock

The paucity of float rocks at Meridiani Planum meant that the few that were visible in the images provided by rover cameras typically were the subject of inquiry. The largest and darkest rock present on the exterior rim of Eagle crater was one selected for detailed investigation and named Bounce rock because of its proximity to one of the airbag landing system bounce marks (Squyres *et al.*, 2004b). Bell *et al.* (2004b) analyzed pre- and post-RAT Pancam false-color composite images of Bounce rock (see also Chapter 13). Mini-TES observations of Bounce rock prior to RAT operations did not fully cover the intended target such that portions of the surrounding basalt- and hematite-bearing plains represented a significant spectral contribution. Post-RAT Mini-TES observations of Bounce rock, however, were well targeted, avoiding most of the fine-grained particles produced from RAT-grinding operations on Bounce rock. A spectral component representing the RAT tailings was included as part of the spectral deconvolution (Christensen *et al.*, 2004b).

Deconvolution results from the Bounce rock spectrum show that the rock is unique among those investigated at both the Meridiani and Gusev sites (Christensen *et al.*, 2004b). Figure 14.14 shows the dust-free measured and slope-adjusted Mini-TES spectrum of Bounce rock (Christensen *et al.*, 2004b). Bounce rock has a much higher pyroxene abundance than the basaltic sands and rocks observed at Meridiani Planum and at Gusev crater (except for Peace Class rocks; see Section 14.3.3), with clinopyroxene accounting for ~55% of the rock and orthopyroxene ~5%, followed by ~20% plagioclase, ~5% olivine, and ~10% oxides (Christensen *et al.*, 2004b; Table 14.1). This mineralogy is much closer to that of the Martian basaltic shergottite meteorites (McSween, 1994) than the basaltic components observed at either MER site.

As measured by the APXS instrument, the elemental chemistry of Bounce rock is most similar to that of the basaltic shergottite EETA 79001 lithology B (Rieder *et al.*, 2004), but the infrared spectra of Bounce rock and EETA 79001B differ in the 9 to 12 μm region (Figure 14.14). Christensen *et al.* (2004b) demonstrated that a laboratory spectrum of EETA 79001B can be well modeled using a similar set of spectral endmembers as used in the deconvolution of the Bounce rock spectrum, strengthening the case that the modeled results from Bounce rock represent a distinctive mineralogy compared to that of EETA 79001B. The best fit to the Bounce rock spectrum gives high-Ca clinopyroxene instead of the low-Ca clinopyroxene pigeonite found in EETA 79001B. The overall spectral differences in the 9 to 12 μm region between Bounce rock and EETA 79001B suggest that the structure or composition of the pyroxenes is likely different (Christensen *et al.*, 2004b). However, the four emissivity minima between 850 and 1100 cm^{-1} in the Bounce rock spectrum suggest that some pigeonite may be present but was poorly modeled with the available pyroxene endmembers.

The distinctive mineral composition and chemistry of Bounce rock, together with its isolated occurrence (Squyres *et al.*, 2004b), suggest that this rock may not be derived locally. A possible source region is a relatively unmodified ~25 km crater located ~75 km southwest of Eagle crater, the continuous ejecta of which lies atop the hematite-bearing plains (Christensen *et al.*, 2004b; Squyres *et al.*, 2004b). In this case, Bounce rock may have been derived from materials that are compositionally distinct from the basaltic sands that cover the plains observed by Mini-TES and from regional basaltic surface compositions measured by TES (Bandfield *et al.*, 2000b; Christensen *et al.*, 2000b). The ability of Mini-TES spectra to distinguish between

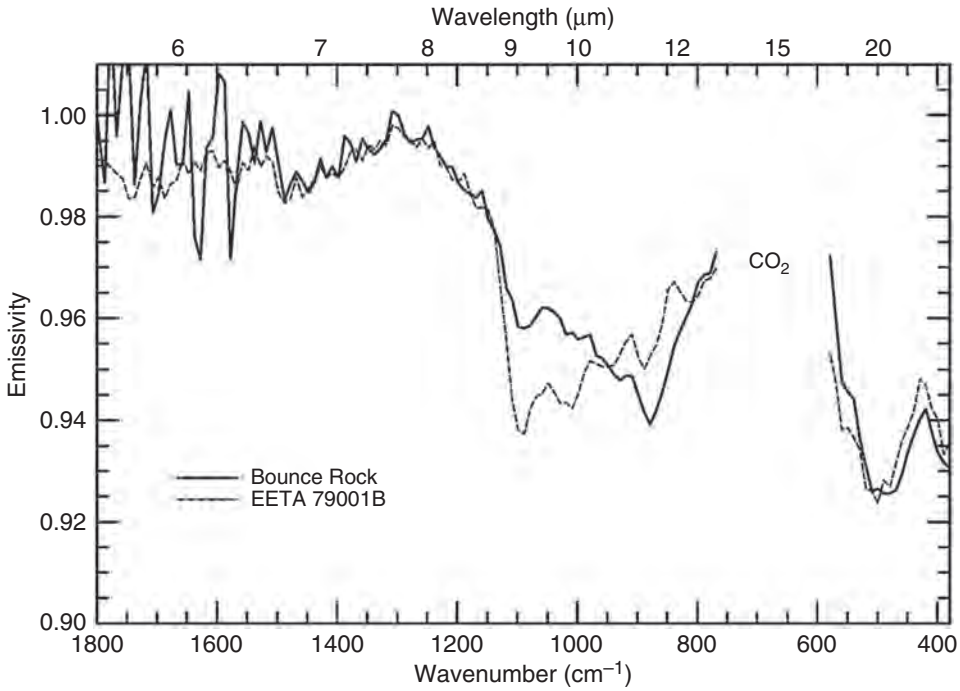

Figure 14.14. Mini-TES and laboratory spectra highlighting the characteristics of Bounce Rock in Meridiani Planum. Bounce Rock is pyroxene-rich and chemically similar to the SNC meteorite EETA 79001 lithology B, but its spectrum departs from that of the meteorite in ways that suggest different pyroxene phases may be present.

Bounce rock and surrounding basaltic sands, and the similarity of Meridiani spectra to the TES orbital spectra, strengthens previous interpretations that use TES data to determine the composition of basalt globally (Christensen *et al.*, 2004b).

14.5.6 Heat Shield rock

So named because of its proximity to the burned and broken heat shield from the descent stage of the *Opportunity* spacecraft, Heat Shield rock was first observed in long-range Pancam images as the rover approached the remnants of the heat shield for an extended investigation (see Chapter 13). Based on its unusual pitted surface and dark tone, speculation arose that this rock, with a long dimension of ~25 cm, might be a meteorite. Mini-TES observations from two different positions provided the first clear indication of its composition and origin. The spectra revealed features that were nearly indistinguishable from those of the atmosphere (Figure 14.15a): a pronounced, rounded emissivity peak centered at ~1075 cm^{-1} analogous to that of atmospheric dust viewed in emission; and a broad, strong peak in the position of atmospheric CO_2 centered at 667 cm^{-1}, which for the first time in any surface spectra, included the side lobes attributable to CO_2 hot bands (e.g., Rothman *et al.*, 1992). The spectral contrast of all these features was several times greater than those of any other surface target observed by the two rovers, approaching the contrast of typical sky observations made with the Mini-TES (Figure 14.15a). Together, these observations indicated that the rock was highly reflective. Because of this, the standard emissivity/temperature separation was not possible. Instead, we modeled the measured radiance of the rock assuming it was a mix of graybody radiance and sky radiance reflecting off its surface. The best-fit combination of rock temperature and emissivity was ~270 K and ~0.3 respectively (Figure 14.15b). Although the quality of fit is good, some remaining misfit suggests that this simplistic modeling strategy is insufficient to accurately model the data. Deconvolution of such low-emissivity spectra will require a different approach than is typically used.

The simplest explanation for the unusual Mini-TES observations and morphology of Heat Shield rock is that it is an iron meteorite. The low emissivity and apparent absence of strong spectral features other than those of the sky is consistent with a material that is highly reflective at TIR wavelengths, a characteristic of metals. Metal-to-metal bonds lack a dipole moment, making them IR inactive, thus providing no absorption features. A subsequent IDD campaign on the rock revealed a bulk composition dominated by Fe and ~7% Ni and an Fe mineralogy dominated by kamacite, an Fe–Ni alloy common in metallic meteorites (Rodionov *et al.*, 2005). The only plausible explanation for such a composition is that Heat Shield rock is an Fe–Ni meteorite. With its low emissivity and apparent lack of spectral features that can be attributed to Fe-oxides, it appears that this meteorite lacks an oxidized coating or other signature of alteration. This can be interpreted in at least three ways: (1) the meteorite is a relatively recent arrival on the Meridiani plains, with insufficient time for alteration to have occurred; (2) alteration has occurred but the evidence for it has been stripped off the rock through the action of wind; or (3) the meteorite arrived on the plains

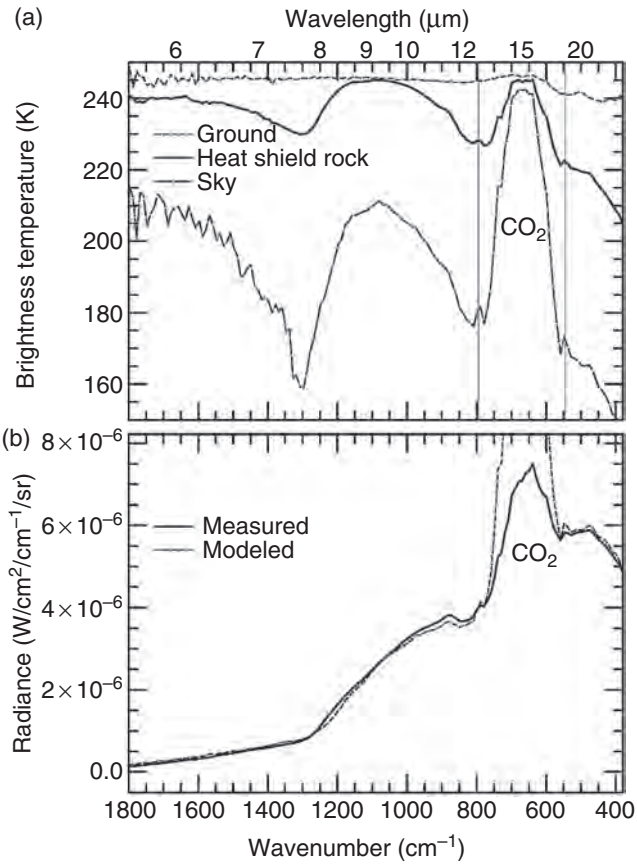

Figure 14.15. Analysis of the Fe-Ni meteorite called Heat Shield Rock from Meridiani Planum. (a) The Mini-TES spectrum shows spectral features very similar to those of the sky in upward-looking Mini-TES observations and completely different from all ground observations. Here, the spectra have been converted from radiance to brightness temperature to avoid the model-dependent emissivity/temperature separation. The vertical lines highlight the two CO_2 "hot bands" that are always found in sky spectra but which had never been seen in surface spectra until Heat Shield Rock. (b) The measured radiance of Heat Shield Rock can be modeled as a 270 K target with a uniform graybody emissivity of 0.3 reflecting the sky. The CO_2 region cannot be modeled properly using this simplified approach.

early in their history, but alteration has been so inefficient that the rock has remained relatively pristine throughout the duration of its presence on the plains.

14.6 CONCLUSIONS AND IMPLICATIONS

The Mini-TES instruments were designed to provide quantitative bulk mineralogy of the rocks and soils at each landing site. Measurement challenges largely attributable to Martian dust were overcome, yielding results that provided both tactical utility in guiding the rovers and a scientific dataset for better understanding the nature of the materials at the two landing sites. The results of the Mini-TES experiment demonstrate the value of rovers equipped with infrared remote-sensing instruments.

The mineralogy of the materials observed by Mini-TES provides insights into global, regional, and local scale geologic processes operating during different epochs on Mars. The dust observed at both sites essentially is spectrally indistinguishable from one site to the other and likely represents material that is actively distributed across the planet in the current Martian environment by aeolian processes. Evidence first seen in TES spectra indicating hydrated and tectosilicate components in the globally distributed dust deposits was confirmed on the ground. The dark-toned soil units at both sites showed notable similarities in mineralogy. In the case of the Gusev crater plains, the soil may contain a substantial contribution from the breakdown of the basaltic rocks that are found there. At Meridiani Planum, no rocks were observed that were comparable in mineralogy to the soil. Transport from an unknown source region is implied although other scenarios are possible.

The rocks at the two sites present very different geologic histories based on evidence from Mini-TES observations. The plains of Gusev crater are covered in olivine-rich basaltic rocks that show no substantial secondary mineralization. An absence of significant aqueous alteration since these volcanic rocks were emplaced is implied by these observations. The Columbia Hills display a remarkable diversity of rock types of which only a partial set (those observed through sol 600) has been presented in this chapter. Despite the diversity, evidence for abundant secondary mineralization is lacking. Minor goethite and sulfates were detected in some of the rocks, but no clear evidence for phyllosilicates was identified with Mini-TES spectra. Instead, both plagioclase-rich and basaltic glass–rich rocks were found. Given the susceptibility of basaltic glass to alteration, it is remarkable that phyllosilicates were not in evidence. Despite the apparent greater age of the Columbia Hills relative to the plains, with Mini-TES spectra it appears that the rocks of the hills have not experienced substantial aqueous alteration throughout their history. Although various scenarios can be invoked to explain the absence of mineralogical evidence for an ancient lake in Gusev crater, there is no clear support for such a lake based on Mini-TES results.

Meridiani Planum presents a different view of the early geologic history of Mars. Sedimentary rocks composed of both hydrous and anhydrous sulfates, amorphous silica and glass, with some plagioclase but no olivine or pyroxene, and possible phyllosilicates indicate an environment where chemical weathering and diagenesis of basaltic materials was possible and at least regionally significant. The hematite that is so dominant in the orbital view was revealed to be only a small component of the rocks, but one that has been concentrated on the surface by erosion to produce a lag deposit. The spectral details of the hematite spherules observed by Mini-TES firmly support a role for water in their production. The once enigmatic combination of unaltered basalt and aqueously derived hematite seen from orbit can now be understood as a mix of an erosional agent (basaltic sand) and a concentrated lag deposit (hematite spherules) that now spans the whole of Meridiani Planum.

REFERENCES

Aronson, J. R. and A. G. Emslie, Spectral reflectance and emittance of particulate materials. 2: Application and results, *Appl. Opt.* **12**, 2573–84, 1973.

Aronson, J. R. and A. G. Emslie, Composition of the martian dust as derived by infrared spectroscopy from Mariner 9, *J. Geophys. Res.* **80**(35), 4925–31, 1975.

Aronson, J. R., A. G. Emslie, and H. G. McLinden, Infrared spectra from fine particulate surfaces, *Science* **152**, 345–6, 1966.

Arvidson, R. E., S. W. Squyres, R. C. Anderson, *et al.*, Overview of the *Spirit* Mars Exploration Rover Mission to Gusev crater: landing site to Backstay Rock in the Columbia Hills, *J. Geophys. Res.* **111**, E02S01, doi:10.1029/2005JE002499, 2006.

Badenas, C., Comments on Kirchhoff's law in thermal-infrared remote sensing, *Int. J. Remote Sens.* **18**, 229–34, 1997.

Bandfield, J. L., Global mineral distributions on Mars, *J. Geophys. Res.* **107**(E6), doi:10.1029/2001JE001510, 2002.

Bandfield, J. L. and M. D. Smith, Multiple emission angle surface-atmosphere separations of Thermal Emission Spectrometer data, *Icarus* **161**, 47–65, 2003.

Bandfield, J. L., P. R. Christensen, and M. D. Smith, Spectral data set factor analysis and end-member recovery: application to analysis of Martian atmospheric particulates, *J. Geophys. Res.* **105**(E4), 9573–87, 2000a.

Bandfield, J. L., V. E. Hamilton, and P. R. Christensen, A global view of Martian volcanic compositions from MGS-TES, *Science* **287**, 1626–30, 2000b.

Bandfield, J. L., K. S. Edgett, and P. R. Christensen, Spectroscopic study of the Moses Lake dune field, Washington: determination of compositional distributions and source lithologies, *J. Geophys. Res.* **107**(E11), doi:10.1029/2000JE001469, 2002.

Bandfield, J. L., T. D. Glotch, and P. R. Christensen, Spectroscopic identification of carbonate minerals in the martian dust, *Science* **301**, 1084–6, 2003.

Bell III, J. F., S. W. Squyres, K. E. Herkenhoff, *et al.*, Mars Exploration Rover Athena Panoramic Camera (Pancam) investigation, *J. Geophys. Res.* **108**(E12), doi:10.1029/2003JE002070, 2003.

Bell III, J. F., S. W. Squyres, R. E. Arvidson, *et al.*, Pancam multispectral imaging results from the *Spirit* Rover at Gusev crater, *Science* **305**, 800–6, 2004a.

Bell III, J. F., S. W. Squyres, R. E. Arvidson, *et al.*, Pancam multispectral imaging results from the Opportunity rover at Meridiani Planum, *Science* **306**, 1703–9, 2004b.

Bell III, J. F., J. Joseph, J. N. Sohl-Dickstein, *et al.*, In-flight calibration and performance of the Mars Exploration Rover Panoramic Camera (Pancam) instruments, *J. Geophys. Res.* **111**, E02S03, doi:10.1029/2005JE002444, 2006.

Bishop, J. L. and C. M. Pieters, Low-temperature and low atmospheric pressure infrared reflectance spectroscopy of Mars soil analog materials, *J. Geophys. Res.* **100**, 5369–79, 1995.

Bishop, J. L., H. Fröschl, and R. L. Mancinelli, Alteration processes in volcanic soils and identification of exobiologically important weathering products on Mars using remote sensing, *J. Geophys. Res.* **103**, 31457–76, 1998.

Bishop, J. L., P. Schiffman, E. Murad, *et al.*, Characterization of alteration products in tephra from Haleakala, Maui: a visible-infrared spectroscopy, Mössbauer spectroscopy, XRD, EPMA, and TEM study, *Clays Clay Miner.*, **55**, 1–17, doi:10.1346/CCMN.2007.0550101, 2007.

Brown, J. B., Jarosite-goethite stabilities at 25 °C, 1 ATM, *Mineral, Deposita* **6**, 245–52, 1971.

Cabrol, N. A., E. A. Grin, M. H. Carr, *et al.*, Exploring Gusev crater with Spirit: review of science objectives and testable hypotheses, *J. Geophys. Res.* **108**(E12), doi:10.1029/2002JE002026, 2003.

Calvin, W. M., T. V. V. King, and R. N. Clark, Hydrous carbonates on Mars? Evidence from Mariner 6/7 Infrared Spectrometer and ground-based telescopic spectra, *J. Geophys. Res.* **99**, 14659–75, 1994.

Catling, D. C., S. E. Wood, C. Leovy, *et al.*, Light-toned layered deposits in Juventae Chasma, Mars, *Icarus* **181**, 26–51, 2006.

Christensen, P. R. and S. T. Harrison, Thermal infrared emission spectroscopy of natural surfaces: application to desert varnish coatings on rocks, *J. Geophys. Res.* **98**(B11), 19819–34, 1993.

Christensen, P. R. and S. W. Ruff, Formation of the hematite-bearing unit in Meridiani Planum: evidence for deposition in standing water, *J. Geophys. Res.* **109**, E08003, doi:10.10292003JE002233, 2004.

Christensen, P. R., J. L. Bandfield, R. N. Clark, *et al.*, Detection of crystalline hematite mineralization on Mars by the Thermal Emission Spectrometer: evidence for near-surface water, *J. Geophys. Res.* **105**(E4), 9623–42, 2000a.

Christensen, P. R., J. L. Bandfield, M. D. Smith, V. E. Hamilton, and R. N. Clark, Identification of a basaltic component on the Martian surface from Thermal Emission Spectrometer data, *J. Geophys. Res.* **105**(E4), 9609–21, 2000b.

Christensen, P. R., R. V. Morris, M. D. Lane, J. L. Bandfield, and M. C. Malin, Global mapping of Martian hematite mineral deposits: remnants of water-driven processes on early Mars, *J. Geophys. Res.* **106**(E10), 23873–85, 2001.

Christensen, P. R., G. L. Mehall, S. H. Silverman, *et al.*, Miniature Thermal Emission Spectrometer for the Mars Exploration Rovers, *J. Geophys. Res.* **108**(E12), 8064, doi:10.1029/2003JE002117, 2003.

Christensen, P. R., S. W. Ruff, R. L. Fergason, *et al.*, Initial results from the Mini-TES Experiment in Gusev crater from the Spirit Rover, *Science* **305**, 837–42, 2004a.

Christensen, P. R., M. B. Wyatt, T. D. Glotch, *et al.*, Mineralogy at Meridiani Planum from the Mini-TES experiment on the Opportunity Rover, *Science* **306**(5702), 1733–9, 2004b.

Clark, B. C., R. V. Morris, S. M. MoLennan, *et al.*, Chemistry and mineralogy of outcrops at Meridiani Planum, *Earth Planet. Sci. Lett.* **240**, 73–94, 2005.

Clark, B. C., R. E. Aravidson, R. Gellert, *et al.*, Evidence for montmorillonite or its compositional equivalent in Columbia Hills, Mars, *J. Geophys. Res.* **112**, CiteID E06S01, doi:10.1029/2006JE002756, 2007.

Coblentz, W. W., *Investigations of Infra-red Spectra: Parts 1 and 2*, Carnegie Institute of Washington, 330pp., 1905.

Edgett, K. S. and P. R. Christensen, The particle size of Martian aeolian dunes, *J. Geophys. Res.* **96**, 22765–76, 1991.

Farmer, V. C., *The Infrared Spectra of Minerals*, London: Mineralogical Society, 539 pp., 1974.

Feely, K. C. and P. R. Christensen, Quantitative compositional analysis using thermal emission spectroscopy: application to igneous and metamorphic rocks, *J. Geophys. Res.* **104**(E10), 24195–210, 1999.

Gellert, R., R. Rieder, J. Brueckner, *et al.*, Alpha Particle X-Ray Spectrometer (APXS): results from Gusev crater and calibration report, *J. Geophys. Res.* **111**, E02S05, doi:10.1029/2005JE002555, 2006.

Glotch, T. D. and J. L. Bandfield, Determination and interpretation of surface and atmospheric Mini-TES spectral end-members at the Meridiani Planum landing site, *J. Geophys. Res.* **111**, E12S06, doi:10.1029/2005JE002671, 2006.

Glotch, T. D., R. V. Morris, P. R. Christensen, and T. G. Sharp, Effect of precursor mineralogy on the thermal infrared emission spectra of hematite: Application to martian hematite mineralization, *J. Geophys. Res.* **109**, E7003, doi:10.1029/2003JE002224, 2004.

Glotch, T. D., J. L. Bandfield, P. R. Christensen, *et al.*, Mineralogy of the light-toned outcrop at Meridiani Planum as seen by the Miniature Thermal Emission Spectrometer and implications for its formation, *J. Geophys. Res.* **111**, E12S03, doi:10.1029/2005JE002672, 2006a.

Glotch, T. D., P. R. Christensen, and R. P. Sharp, Fresnel modeling of hematite crystal surfaces and application to Martian hematite mineralization, *Icarus* **181**, 408–18, 2006b.

Golombek, M. P., J. A. Grant, T. J. Parker, *et al.*, Selection of the Mars Exploration Rover landing sites, *J. Geophys. Res.* **108**(E12), 8072, doi:10.1029/2003JE002074, 2003.

Graff, T. G., R. V. Morris, and P. R. Christensen, Effects of palagonitic dust coatings on thermal emission spectra of rocks and minerals: implications for mineralogical characterization of the Martian surface by MGS-TES, *Lunar Planet. Sci. Conf.* **XXXII**, Abstract #1899, 2001.

Grant, J. A., S. A. Wilson, D. L. Koestler, S. W. Ruff, and M. P. Golombek, The distribution of rocks on the Gusev plains and on Husband Hill, *Geophys. Res. Lett.* **33**, L16202, doi:10.1029/2006GL026964, 2006.

Greeley, R. and M. D. Kraft, Survivability of aggregate sands on Mars, *Lunar Planet. Sci.* **XXXII**, Abstract #1839 (CD-ROM), 2001.

Greeley, R., R. E. Arvidson, P. W. Barlett, *et al.*, Gusev crater: wind-related features and processes observed by the Mars Exploration Rover Spirit, *J. Geophys. Res.* **111**, E02S09, doi:10.1029/2005JE002491, 2006.

Hamilton, V. E. and P. R. Christensen, Determining the modal mineralogy of mafic and ultramafic igneous rocks using thermal emission spectroscopy, *J. Geophys. Res.* **105**, 9717–33, 2000.

Hamilton, V. E. and P. R. Christensen, Evidence for extensive olivine-rich bedrock on Mars, *Geology* **33**(6), 433–6, 2005.

Hamilton, V. E., P. R. Christensen, and H. Y. McSween Jr., Determination of martian meteorite lithologies and mineralogies using vibrational spectroscopy, *J. Geophys. Res.* **102**, 25593–603, 1997.

Hamilton, V. E., M. B. Wyatt, H. Y. McSween Jr., and P. R. Christensen, Analysis of terrestrial and Martian volcanic compositions using thermal emission spectroscopy: 2. Application to Martian surface spectra from the Mars Global Surveyor Thermal Emission Spectrometer, *J. Geophys. Res.* **106**, 14733–46, 2001.

Herbert, R. B., Precipitation of Fe oxyhydroxides and jarosite from acidic groundwater, *GFF* **117**, 81–5, 1995.

Herbert, R. B., Properties of goethite and jarosite precipitated from acidic groundwater, Dalarna, Sweden, *Clays Clay Miner*, **45**, 261–73, 1997.

Hoefen, T. M., R. N. Clark, J. L. Bandfield, *et al.*, Discovery of olivine in the Nili Fossae region of Mars, *Science* **302**, 627–30, 2003.

Hook, S. J., A. R. Gabell, A. A. Green, and P. S. Kealy, A comparison of techniques for extracting emissivity information from thermal infrared data for geologic studies, *Remote Sens. Environ.* **42**, 123–36, 1992.

Horton, K. A., J. R. Johnson, and P. G. Lucey, Infrared measurements of pristine and disturbed soils: 2. Environmental effects and field data reduction, *Remote Sens. Environ.* **64**(1), 47–52, 1998.

Hunt, G. R. and L. M. Logan, Variation of single particle mid-infrared emission spectrum with particle size, *Appl. Opt.* **11**, 142–7, 1972.

Hunt, G. R. and R. K. Vincent, The behavior of spectral features in the infrared emission from particulate surfaces of various grain sizes, *J. Geophys. Res.* **73**, 6039–46, 1968.

Hynek, B. M., R. E. Arvidson, and R. J. Phillips, Geologic setting and origin of Terra Meridiani hematite deposit on Mars, *J. Geophys. Res.* **107**(E10), 5088, doi:10.1029/2002JE001891, 2002.

Johnson, J. R., P. R. Christensen, and P. G. Lucey, Dust coatings on basalts and implications for thermal infrared spectroscopy of Mars, *J. Geophys. Res.* **107**(E6), 5035, doi:10.1029/2000JE001405, 2002a.

Johnson, J. R., F. Horz, P. G. Lucey, and P. R. Christensen, Thermal infrared spectroscopy of experimentally shocked anorthosite and pyroxenite: implications for remote sensing of Mars, *J. Geophys. Res.* **107**, doi:10.1029/2001JE001517, 2002b.

Johnson, J. R., W. M. Grundy, M. T. Leniman, *et al.*, Spectrophotometric properties of materials observed by Pancam on the Mars Exploration Rovers: 1. Spirit, *J. Geophys. Res.* **111**, E02S14, doi:10.1029/2005JE002494, 2006.

Jolliff, B. L. and Athena Science Team, Composition of Meridiani hematite-rich spherules: a mass-balance mixing model approach, *Lunar Planet. Sci.* **XXXVI**, Abstract #2269 (CD-ROM), 2005.

Klingelhöfer, G., R. V. Morris, B. Bernhardt, *et al.*, Jarosite and hematite at Meridiani Planum from the Opportunity's Mössbauer spectrometer, *Science* **306**, 1740–5, 2004.

Knauth, L. P., D. M. Burt, and K. H. Wohletz, Impact origin of sediments at the Opportunity landing site on Mars, *Nature* **438**, 1123–1128, 2005.

Lane, M. D., Midinfrared emission spectroscopy of sulfate and sulfate-bearing minerals, *Am. Mineral.* **92**, 1–18, 2007.

Lane, M. D. and P. R. Christensen, Thermal infrared emission spectroscopy of salt minerals predicted for Mars, *Icarus* **135**, 528–36, 1998.

Lane, M. D., R. V. Morris, S. A. Mertzman, and P. R. Christensen, Evidence for platy hematite grains in Sinus Meridiani, *J. Geophys. Res.* **107**(E12), 5126, doi:10.1029/2001JE001832, 2002.

Lane, M. D., M. D. Dyar, and J. L. Bishop, Spectroscopic evidence for hydrous iron sulfate in the Martian soil, *Geophys. Res. Lett.* **31**, L19702, doi:10.1029/2004GL021231, 2004.

Lyon, R. J. P. and E. A. Burns, Analysis of rocks by reflected infrared radiation, *Econ. Geol.* **58**, 274–84, 1963.

Lyon, R. J. P., W. M. Tuddenham, and C. S. Thompson, Quantitative mineralogy in 30 minutes, *Econ. Geol.* **54**, 1047–55, 1959.

Maki, J. N., J. F. Bell III, K. E. Herkenhoff, *et al.*, Mars Exploration Rover engineering cameras, *J. Geophys. Res.* **108**(E12), 8071, doi:10.1029/2003JE002077, 2003.

Malinowski, E. R., *Factor Analysis in Chemistry*, 2nd edn., New York: John Wiley, 1991.

McCollom, T. M. and B. M. Hynek, A volcanic environment for bedrock diagenesis at Meridiani Planum on Mars, *Nature* **438**, 1129–31, 2005.

McLennan, S. M., J. F. Bell III, W. M. Caluin, *et al.*, Provenance and diagenesis of the evaporate-bearing Burns formation, Meridiani Planum, Mars, *Earth Planet. Sci. Lett.* **240**, 95–121, 2005.

McSween Jr., H. Y., What have we learned about Mars from SNC meteorites, *Meteoritics* **29**, 757–79, 1994.

McSween Jr., H. Y., R. E. Arvidson, J. F. Bell III, *et al*., Basaltic rocks analyzed by the *Spirit* Rover in Gusev crater, *Science* **305**, 842–5, 2004.

McSween Jr., H. Y., S. W. Ruff, R. V. Morris, *et al*., Alkaline volcanic rocks from the Columbia Hills, Gusev crater, Mars, *J. Geophys. Res.* **111**, E09S91, doi:10.1029/2006JE002698, 2006.

Michalski, J. R., M. D. Kraft, R. P. Sharp, and P. R. Christensen, Palagonite-like alteration products on the earth and Mars I: spectroscopy (0.4–25 microns) of weathered basalts and silicate alteration products, *Lunar Planet. Sci.* **XXXVI**, Abstract #1188 (CD-ROM), 2005a.

Michalski, J. R., M. D. Kraft, R. P. Sharp, L. B. Williams, and P. R. Christensen, Mineralogical constraints on the high-silica Martian surface component observed by TES, *Icarus* **174**, 161–77, 2005b.

Michalski, J. R., M. D. Kraft, T. G. Sharp, L. B. Williams, and P. R. Christensen, Emission spectroscopy of clay minerals and evidence for poorly crystalline aluminosilicates on Mars from Thermal Emission Spectrometer data, *J. Geophys. Res.* **111**, E03004, doi:10.1029/2005JE002438, 2006.

Milam, K. A., K. R. Stockstill, J. E. Moersch, *et al*., THEMIS characterization of the MER Gusev crater landing site, *J. Geophys. Res.* **108**(E12), 8078, doi:10.1029/2002JE002023, 2003.

Ming, D. W., D. W. Mittlefehldt, R. V. Morris, *et al*., Geochemical and mineralogical indicators for aqueous processes in the Columbia Hills of Gusev crater, Mars, *J. Geophys. Res.* **111**, E02S12, doi:10.1029/2005JE002560, 2006.

Morris, R. V., G. Klingelhöfer, B. Bernhardt, *et al*., Mineralogy at Gusev crater from the Mössbauer spectrometer on the Spirit Rover, *Science* **305**, 833–6, 2004.

Morris, R. V., G. Klingelhöfer, C. Schröder, *et al*., Mössbauer mineralogy of rock, soil, and dust at Gusev crater, Mars: Spirit's journey through weakly altered olivine basalt on the plains and pervasively altered basalt in the Columbia Hills, *J. Geophys. Res.* **111**, E02S13, doi:10.1029/2005JE002584, 2006.

Mustard, J. F., F. Poulet, A. Gendrin, *et al*., Olivine and pyroxene diversity in the crust of Mars, *Science* **307**, 1594–7, 2005.

Ramsey, M. S. and P. R. Christensen, Mineral abundance determination: quantitative deconvolution of thermal emission spectra, *J. Geophys. Res.* **103**, 577–96, 1998.

Rieder, R., R. Gellert, R. C. Anderson, *et al*., Chemistry of rocks and soils at Meridiani Planum from the Alpha Particle X-ray Spectrometer, *Science* **306**, 1746–9. 2004.

Rodionov, D. S., G. Klingelhofer, D. W. Ming, *et al*., An iron-nickel meteorite on Meridiani Planum: observations by MER Opportunity's Mössbauer spectrometer, *Geophys. Res. Abs.* **7**, 10242, 2005.

Rogers, A. D. and P. R. Christensen, Age relationship of basaltic and andesitic surface compositions on Mars: analysis of high-resolution TES observations of the northern hemisphere, *J. Geophys. Res.* **108**(E4), 5030, doi:10.1029/2002JE001913, 2003.

Rothman, L. S., R. L. Hawkins, R. B. Watson, and R. R. Gamache, Energy levels, intensities, and linewidths of atmospheric carbon dioxide bands, *J. Quant. Spec. Rad. Trans.* **48**(5/6), 537–66, 1992.

Ruff, S. W., Spectral evidence for zeolite in the dust on Mars, *Icarus* **168**, 131–43, 2004.

Ruff, S. W. and P. R. Christensen, Bright and dark regions on Mars: particle size and mineralogical characteristics based on Thermal Emission Spectrometer data, *J. Geophys. Res.* **107**(E12), 5127, doi:10.1029/2001JE001580, 2002.

Ruff, S. W., P. R. Christensen, P. W. Barbera, and D. L. Anderson, Quantitative thermal emission spectroscopy of minerals: a laboratory technique for measurement and calibration, *J. Geophys. Res.* **102**, 14899–913, 1997.

Ruff, S. W., P. R. Christensen, D. L. Blaney, *et al*., The rocks of Gusev crater as viewed by the Mini-TES instrument, *J. Geophys. Res.* **111**, E12S18, doi:10.1029/2006JE002747, 2006.

Salisbury, J. W. and D. M. D'Aria, Emissivity of terrestrial materials in the 8–14 μm atmospheric window, *Remote Sens. Environ.* **42**, 83–106, 1992.

Salisbury, J. W. and J. W. Eastes, The effect of particle size and porosity on spectral contrast in the mid-infrared, *Icarus* **64**, 586–8, 1985.

Salisbury, J. W. and A. Wald, The role of volume scattering in reducing spectral contrast of reststrahlen bands in spectra of powdered minerals, *Icarus* **96**, 121–8, 1992.

Salisbury, J. W., B. Hapke, and J. W. Eastes, Usefulness of weak bands in midinfrared remote sensing of particulate planetary surfaces, *J. Geophys. Res.* **92**, 702–10, 1987.

Salisbury, J. W., L. S. Walter, N. Vergo, and D. M. D'Aria, *Infrared (2.1–25 μm) Spectra of Minerals*, Baltimore and London: The Johns Hopkins University Press, 267 pp., 1991.

Smith, M. D., J. L. Bandfield, and P. R. Christensen, Separation of atmospheric and surface spectral features in Mars Global Surveyor Thermal Emission Spectrometer (TES) spectra, *J. Geophys. Res.* **105**(E4), 9589–607, 2000.

Smith, M. D., M. J. Wolff, M. T. Lenimon, *et al*., First atmospheric science results from the Mars Exploration Rovers Mini-TES, *Science* **306**(5702), 1750–3, 2004.

Squyres, S. W. and A. H. Knoll, Sedimentary rocks at Meridiani Planum: origin, diagenesis, and implications for life on Mars, *Earth Planet. Sci. Lett.* **240**, 1–10, 2005.

Squyres, S. W., R. E. Arvidson, E. T. Baumgartmer, *et al*., Athena Mars rover science investigation, *J. Geophys. Res.* **108**(E12), 8062, doi:10.1029/2003JE002121, 2003.

Squyres, S. W., R. E. Arvidson, J. F. Bell III, *et al*., The *Spirit* Rover's Athena science investigation at Gusev crater, Mars, *Science* **305**(5685), 794–9, 2004a.

Squyres, S. W., R. E. Arvidson, J. F. Bell III, *et al*., The Opportunity rover's Athena science investigation at Meridiani Planum, Mars, *Science* **306**(5702), 1698–703, 2004b.

Squyres, S. W., O. Aharonson, R. E. Arvidson, *et al*., Bedrock formation at Meridiani Planum, *Nature* **443**, E1–E2, 2006a.

Squyres, S. W., R. E. Arvidson, D. L. Blaney, *et al*., The Rocks of the Columbia Hills, *J. Geophys. Res.* **111**, E02S11, doi:10.1029/2005JE002562, 2006b.

Stahl, R. S., D. S. Fanning, and B. R. James, Goethite and jarosite precipitation from ferrous sulfate solutions, *Soil Sci. Soc. Am. J.* **57**, 280–2, 1993.

Tosca, N. J., S. M. McLennan, D. H. Lindsley, and M. A. A. Schoonen, Acid-sulfate weathering of synthetic Martian basalt: the acid fog model revisited, *J. Geophys. Res.* **109**, E05003, doi:10.1029/2003JE002218, 2004.

Veverka, J., P. Gierasch, and P. Thomas, Wind streaks on Mars: meteorological control of occurrence and mode of formation, *Icarus* **45**, 154–66, 1981.

Vincent, R. K. and G. R. Hunt, Infrared reflectance from mat surfaces, *Appl. Opt.* **7**, 53–9, 1968.

Wald, A. E. and J. W. Salisbury, Thermal infrared directional emissivity of powdered quartz, *J. Geophys. Res.* **100**, 24665–75, 1995.

Wyatt, M. B. and H. Y. McSween Jr., Spectral evidence for weathered basalt as an alternative to andesite in the northern lowlands of Mars, *Nature* **417**, 263–6, 2002.

Wyatt, M. B., V. E. Hamilton, H. Y. McSween Jr., P. R. Christensen, and L. A. Taylor, Analysis of terrestrial and Martian volcanic compositions using thermal emission spectroscopy: 1. Determination of mineralogy, chemistry, and classification strategies, *J. Geophys. Res.* **106**, 14711–32, 2001.

Yen, A. S., R. Gellert, C. Schröder, *et al.*, An integrated view of the chemistry and mineralogy of martian soils, *Nature* **436**, 49–54, 2005.

15

Iron mineralogy and aqueous alteration on Mars from the MER Mössbauer spectrometers

R. V. MORRIS AND G. KLINGELHÖFER

ABSTRACT

The twin Mars Exploration Rovers (MER) *Spirit* (Gusev crater) and *Opportunity* (Meridiani Planum) used miniaturized Mössbauer spectrometers (MIMOS II) to analyze Martian surface materials in the first application of extraterrestrial Mössbauer (MB) spectroscopy. The instruments acquired spectra that identified the speciation of Fe according to oxidation state, coordination state, and mineralogical composition and provided quantitative information about the distribution of Fe among oxidation states, coordination states, and Fe-bearing phases. A total of 12 unique Fe-bearing phases were identified: Fe^{2+} in olivine, pyroxene, and ilmenite; Fe^{2+} and Fe^{3+} in magnetite and chromite; Fe^{3+} in nanophase ferric oxide (npOx), hematite, goethite, jarosite, an unassigned Fe^{3+} sulfate, and an unassigned Fe^{3+} phase associated with jarosite; and Fe^0 in kamacite. Weakly altered basalts at Gusev crater (SO_3 = 2.5 ± 1.4 wt.% and $Fe^{3+}/Fe_T = 0.24 \pm 0.11$) are widespread on the Gusev plains and occur in less abundance on West Spur and Husband Hill in the Columbia Hills. Altered low-S rocks ($SO_3 = 5.2 \pm 2.0$ wt.% and $Fe^{3+}/Fe_T = 0.63 \pm 0.18$) are the most common type of rock in the Columbia Hills. Ilm-bearing, weakly altered basalts were detected only in the Columbia Hills, as was the only occurrence of chromite in an altered low-S rock named Assemblee. Altered high-S rocks (SO_3 >14.2 wt.% and $Fe^{3+}/Fe_T = 0.83 \pm 0.05$) are the outcrop rocks of the ubiquitous Burns formation at Meridiani Planum. Two Fe^0-bearing rocks at Meridiani Planum (Barberton and Heat Shield rock) are meteorites. Laguna Class (LC) soil is weakly altered ($SO_3 = 6 \pm 2$ wt.% and $Fe^{3+}/Fe_T = 0.29 \pm 0.08$) and widely distributed at both Gusev crater and Meridiani Planum, implying efficient global mixing processes or a global distribution of precursor rocks with comparable Fe mineralogical compositions. Paso Robles Class (PRC) soil is heavily altered ($SO_3 \sim 31$ wt.% and $Fe^{3+}/Fe_T = 0.83 \pm 0.05$), is relatively uncommon, and occurs as subsurface deposits in the Columbia Hills. Berry Class (BC) soil is also heavily altered ($SO_3 = 5 \pm 1$ wt.% and $Fe^{3+}/Fe_T = 0.60 \pm 0.13$) and occurs at Meridiani Planum as lag deposits, at the crests of aeolian bedforms, and as isolated pockets on outcrop surfaces. Magnetite is identified as the strongly magnetic component in Martian soil. Jarosite (in the Burns outcrop at Meridiani Planum) and goethite (in Clovis Class rocks at Gusev crater) are mineralogical markers for aqueous processes because they contain the hydroxide anion (OH^-) as an essential part of their structure. Each yields ~10 wt.% H_2O upon dehydroxylation. The presence of Fe sulfates on opposite sides of Mars is evidence that aqueous processes under acid sulfate conditions are or were common. Except for Independence Class rocks in the Columbia Hills, the overall Fe mineralogical compositions and similar basaltic bulk chemical compositions (calculated with respect to S = Cl = 0) of the population of altered rocks analyzed by MER imply isochemical alteration of basaltic precursors at low water-to-rock ratios.

15.1 INTRODUCTION

As part of the Athena instrument package, MER carried MB spectrometers to the surface of another planet for the first time. The rover named "*Spirit*" landed at Gusev crater on January 4, 2004, and the rover named "*Opportunity*" landed on the other side of the planet at Meridiani Planum on January 24, 2004 UTC (Squyres *et al.*, 2004a,b, 2006a; Arvidson *et al.*, 2006a). The MER miniature MB spectrometers MIMOS II (Klingelhöfer *et al.*, 2003) detect ^{57}Fe, which has about 2% natural abundance. Mössbauer spectra provide information on the Fe oxidation state (e.g., Fe^0, Fe^{2+}, and Fe^{3+}), the Fe coordination state (e.g., tetrahedral and octahedral coordination), and the relative abundance of Fe among oxidation states, coordination states, and Fe-bearing phases. Identification of oxidation state, coordination state, and Fe-bearing phases is provided by the positions of peaks in an MB spectrum, and the relative distribution of Fe among oxidation state, coordination state, and Fe-bearing phases is calculated by summing the areas of peaks (subspectra associated with particular oxidation states, coordination states, and phases).

Mössbauer spectrometers were sent to Mars because the element Fe, which is multivalent and abundant, provides essential geochemical and mineralogical information. Ferrous iron (Fe^{2+}) is common in many rock-forming minerals (e.g., olivine, pyroxene, ilmenite, (titano)magnetite, and chromite) and secondary minerals (e.g., serpentine and sulfates). The ratio of Fe^{3+} to total Fe (Fe^{3+}/Fe_T) for an igneous assemblage is a measure of the prevailing oxygen fugacity during crystallization. Although present at significant levels in some primary phases (e.g., augite and (titano)magnetite), ferric iron (Fe^{3+}) is commonly a product of oxidative alteration and weathering of primary minerals and often occurs as oxides and oxyhydroxides (e.g., hematite and goethite).

The Martian Surface: Composition, Mineralogy, and Physical Properties, ed. J. F. Bell III. Published by Cambridge University Press.

The speciation and distribution of Fe in Martian rock and soil thus constrain the primary rock type (e.g., olivine- versus pyroxene-bearing basalt), the redox conditions under which primary igneous assemblages crystallize (e.g., presence or absence of magnetite and metallic Fe), the extent of oxidative alteration and weathering (value of Fe^{3+}/Fe_T), the type of alteration and weathering products (e.g., oxides versus sulfates versus phyllosilicates), and the processes and environmental conditions for alteration and weathering (e.g., neutral versus acid-chloride versus acid-sulfate aqueous process under ambient or hydrothermal conditions; Morris *et al*., 2000).

In this chapter, we first review basic principles of MB spectroscopy, and then we review and synthesize MB results and implications from the first 602 sols (Martian days) of *Spirit*'s mission at Gusev crater and the first 557 sols of *Opportunity*'s mission at Meridiani Planum. Additional details, results, and discussion of the implications of the MER MB investigations can be found in Morris *et al*. (2004, 2006a,b), Klingelhöfer *et al*. (2004, 2006), and Clark *et al*. (2007).

15.2 MÖSSBAUER SPECTROSCOPY AND MÖSSBAUER MINERALOGY ON MARS

A full discussion of the MB effect and MB spectroscopy is beyond the scope of this chapter. However, we provide a brief discussion in order to give context for the MER MB results, and the reader is referred to the literature for additional details regarding the MB effect (e.g., Wertheim, 1964; Wegener, 1966; Greenwood and Gibb, 1971; Bancroft, 1973; Gütlich *et al*., 1978; Hawthorne, 1988; Burns, 1993).

The MB effect (also known as "recoil-free nuclear gamma resonance absorption") is the recoil-free emission and absorption of *gamma rays* by nuclei. When the energies of emitting and absorbing nuclei are identical within the line width of the nuclear transition, the resonant absorption process can take place with a certain probability given by the Lamb–Mössbauer factor *f*. The *f*-factor (sometimes called the Debye–Waller factor) is large when the MB nuclei are bound in solid materials and have relatively low ground-state transition energies. Not all elements have suitable nuclear transitions. The isotope ^{57}Fe (2.2% natural abundance) does have a suitable nuclear transition with an energy difference of 14.41 keV between ground and first excited states. An exact energy match between absorbing and emitting ^{57}Fe nuclei would not occur, even if the *f*-factor is close to maximum (1.0), if the nuclei are in different electronic or magnetic environments or if their speciations (e.g., oxidation, coordination, and mineralogical states) are different. An exact energy match can be made, however, by systematically changing the energy of the emitted or absorbed gamma ray. In laboratory MB spectrometers, this "energy scanning" is normally accomplished using the Doppler effect, in which the emitter ^{57}Fe nuclei are set in motion relative to the absorber whose position is fixed.

Energy level diagrams and corresponding MB spectra are shown schematically in Figure 15.1 for typical situations encountered in the ^{57}Fe MB spectroscopy of geological materials. The source is chosen to have an "unsplit" 14.41 keV emission line to minimize the complexity of the MB spectra. A commonly used source and the one selected for the MER MB spectrometers is ^{57}Co incorporated into rhodium metal foil (^{57}Co(Rh)). The ^{57}Co decays in part to the first excited state of ^{57}Fe, which decays to the ground state with emission of the 14.41 keV gamma ray or ejection of an atomic electron. The number and position of absorber lines are determined by the symmetry and nature of the surroundings of the ^{57}Fe nuclei. Only one line is obtained (Absorber 1) if no magnetic field is present and the electric field has cubic symmetry. For example, spinel ($(Mg,Fe^{2+})Al_2O_4$) is a geological material with a singlet MB spectrum. If the symmetry around the ^{57}Fe nuclei is lowered so that an electric field gradient is present, the nuclear energy levels of the excited state are split so that doublet MB spectra are obtained (Absorber 2). Olivine ($(Mg,Fe^{2+})_2SiO_4$; hereafter denoted as Ol), pyroxene ($(Mg,Ca,Fe^{2+})SiO_3$; hereafter denoted as Px), and ilmenite ($Fe^{2+}TiO_3$; hereafter denoted as Ilm) are rock-forming minerals that are characterized by doublet MB spectra. In the presence of a magnetic field, both ground- and excited-state ^{57}Fe nuclear energy levels are completely split, and sextet MB spectra are obtained (Absorber 3). Hematite (α-Fe_2O_3; hereafter denoted as Hm), goethite (α-FeOOH; hereafter denoted as Gt), magnetite (Fe_3O_4; hereafter denoted as Mt), troilite (FeS), and kamacite (α-$(Fe,Ni)^0$ alloy with <8% Ni; hereafter denoted as Kam) are geological materials characterized by sextet MB spectra. Magnetite actually has two sextets, one from Fe^{3+} in the tetrahedral site (tet-Fe^{3+}) and one from $Fe^{2+} + Fe^{3+}$ (denoted as $Fe^{2.5+}$) in the octahedral site (oct-$Fe^{2.5+}$).

Transmission measurement geometry, where the sample is located between source and detector, is implied by diagrams in Figure 15.1. The MB peaks project downward from the baseline (100% transmission) because the absorber in each case is located between the MB source and detector. For planetary exploration, however, backscatter measurement geometry, where source and detector are on the same side of the sample, is a better choice because sample preparation is not required. Backscatter geometry was adopted for the MER MIMOS II MB spectrometers (Klingelhöfer *et al*., 2003), and the instrument sensor head (Figure 15.2a) is simply placed in physical contact with Martian surface targets by the robotic arm on the MERs. Contact is sensed by spring-loaded micro switches that close when the contact plate is depressed as the sensor head encounters the surface. The field of view is 1.5 cm (Figures 15.2a and 15.2h). In backscatter geometry, either the 14.41 keV γ-rays or the fluorescent Fe X-rays may be detected following excited-state decay. Only MB spectra derived from the resonantly scattered 14.41 keV γ-rays are discussed here. The peaks project upward from the baseline because the detected radiation is emitted from the sample, and in the case of resonance conditions the intensity of emitted radiation increases. MIMOS II includes an internal velocity calibration standard (α-Fe metal foil + Hm + Mt) measured in transmission geometry simultaneously with surface samples (Klingelhöfer *et al*., 2003). Fe-bearing phases in rock or soil substrates cannot be detected below ~3 mm of basaltic airfall dust for the

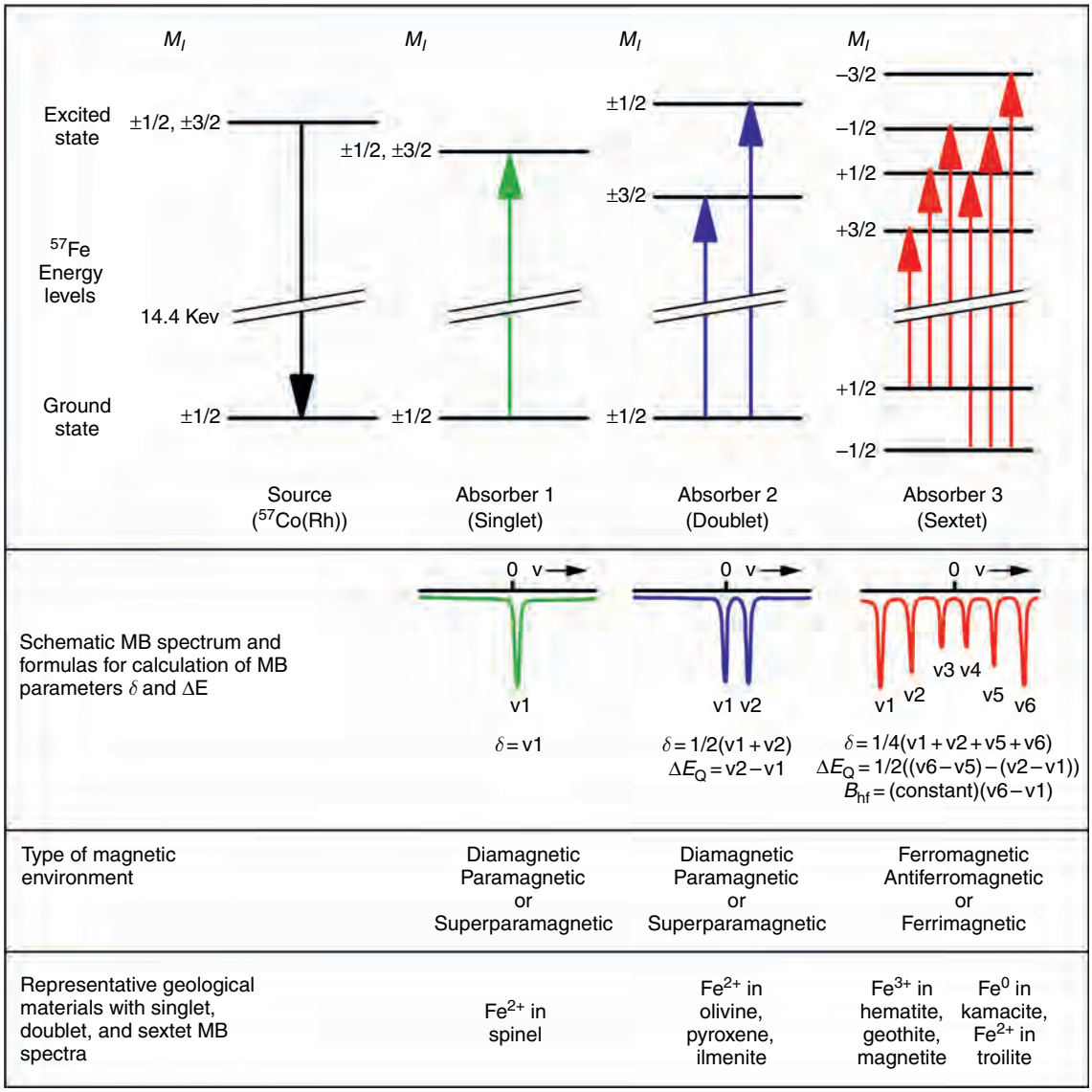

Figure 15.1. Energy level diagrams for ^{57}Fe for the cases of singlet, doublet, and sextet transmission Mössbauer spectra; schematic representation of the corresponding MB spectra and equations used for calculation of MB parameters δ, ΔE_Q, and B_{hf}; and representative geologic materials. MER MB spectra are measured in backscatter geometry, so the MB spectra are emission peaks (i.e., essentially the inverse of the typical laboratory transmission geometry spectra shown here). For MER instruments (Klingelhöfer *et al.*, 2003), δ is measured with respect to the center point of the spectrum of metallic Fe foil at approximately the same temperature as the sample. For peak centers in units of mm/s and B_{hf} in units of tesla (T), the constant in the formula B_{hf} = (constant)(v6−v1) equals 3.101. (For a color version of this figure, please refer to the color plate section or to the e-Book version of this chapter.)

14.41 keV γ-rays (Morris *et al.*, 2001a; Klingelhöfer *et al.*, 2003), and thus brushing or grinding with each rover's Rock Abrasion Tool (RAT) has often been critical in assessing the intrinsic Fe mineralogy at both landing sites.

The peak positions in MB spectra can be described by three parameters arising from hyperfine interactions between atomic electrons and the ^{57}Fe nucleus: (1) the center shift relative to velocity zero, which is the sum of the isomer (or chemical) shift (δ) and the second order Doppler shift (SODS), a relativistic effect resulting from temperature differences between sample and source; (2) the quadrupole splitting (ΔE_Q); and (3) the magnetic hyperfine field (B_{hf}) (Figure 15.1). The value of δ is a relative number between two materials. To compare δ values, the parameter is referenced to a standard material, and, in keeping with standard practice, we use the center point of the spectrum of α-Fe metal foil for MER MB spectra. In terrestrial laboratories, the source is normally kept at ambient temperature. This produces a temperature dependence of the center shift when the sample temperature is varied with respect to the source at ambient temperature. This temperature dependence is not relevant for MER MB measurements because the sample, source, and internal calibration standard are always at approximately the same temperature, as measured by temperature sensors in the contact plate and within the sensor head (Figure 15.2a; Klingelhöfer *et al.*, 2003). The temperature of sample, source, and standard all track each other over the duration of an MB integration in response to the Martian diurnal temperature cycle. The MER MIMOS II

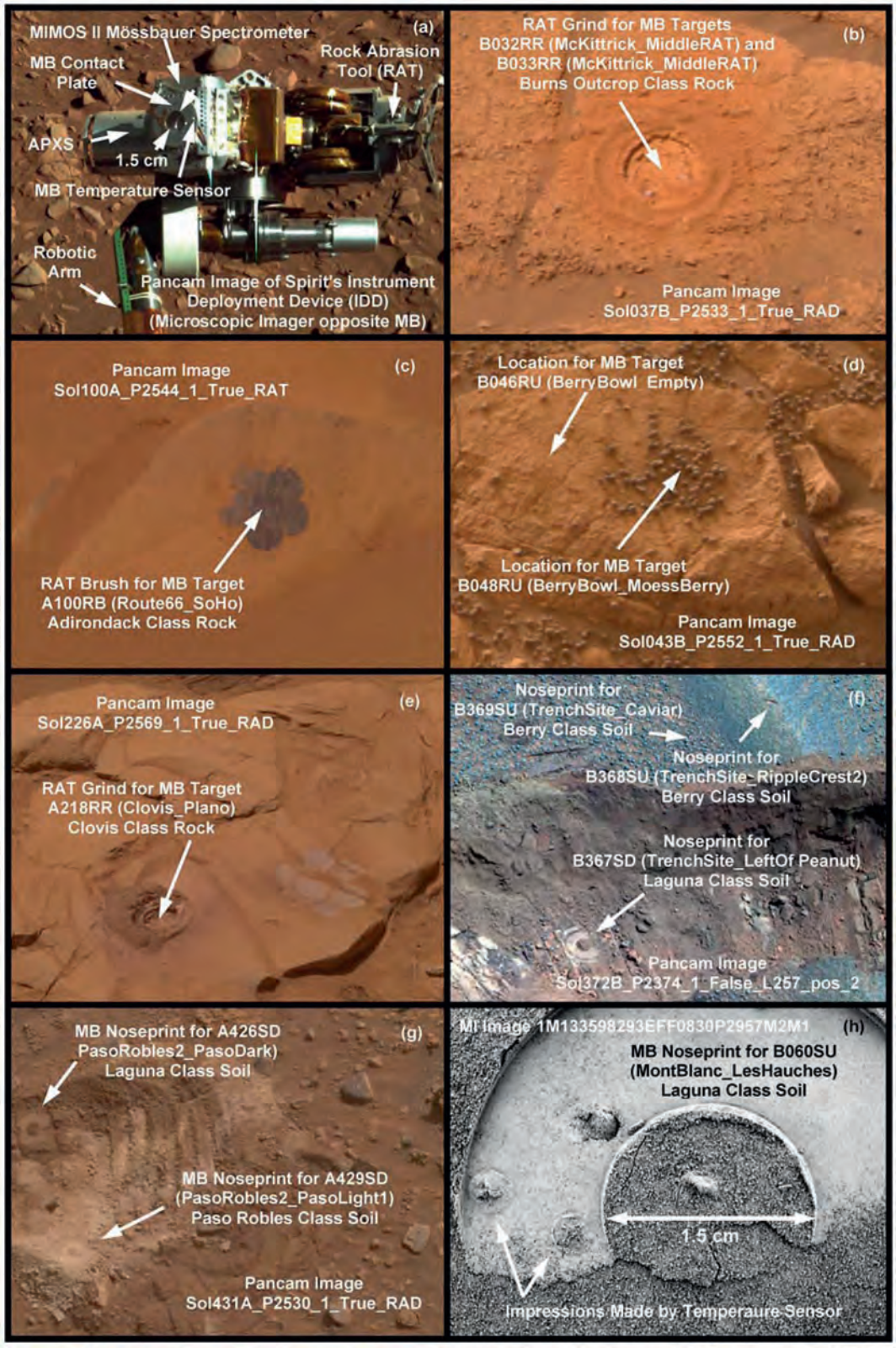
MIMOS II Mössbauer Spectrometer
(a)
MB Contact Plate
Rock Abrasion Tool (RAT)
APXS
1.5 cm
MB Temperature Sensor
Robotic Arm
Pancam Image of Spirit's Instrument Deployment Device (IDD) (Microscopic Imager opposite MB)
RAT Grind for MB Targets B032RR (McKittrick_MiddleRAT) and B033RR (McKittrick_MiddleRAT) Burns Outcrop Class Rock
(b)
Pancam Image Sol037B_P2533_1_True_RAD
Pancam Image Sol100A_P2544_1_True_RAT
(c)
RAT Brush for MB Target A100RB (Route66_SoHo) Adirondack Class Rock
Location for MB Target B046RU (BerryBowl Empty)
(d)
Location for MB Target B048RU (BerryBowl_MoessBerry)
Pancam Image Sol043B_P2552_1_True_RAD
Pancam Image Sol226A_P2569_1_True_RAD
(e)
RAT Grind for MB Target A218RR (Clovis_Plano) Clovis Class Rock
Noseprint for B369SU (TrenchSite_Caviar) Berry Class Soil
(f)
Noseprint for B368SU (TrenchSite_RippleCrest2) Berry Class Soil
Noseprint for B367SD (TrenchSite_LeftOf Peanut) Laguna Class Soil
Pancam Image Sol372B_P2374_1_False_L257_pos_2
MB Noseprint for A426SD PasoRobles2_PasoDark) Laguna Class Soil
(g)
MB Noseprint for A429SD (PasoRobles2_PasoLight1) Paso Robles Class Soil
Pancam Image Sol431A_P2530_1_True_RAD
MI Image 1M133598293EFF0830P2957M2M1
(h)
MB Noseprint for B060SU (MontBlanc_LesHauches) Laguna Class Soil
1.5 cm
Impressions Made by Temperaure Sensor

spectrometers measure temperature during MB experiments and record MB data as a function of temperature in intervals that are 10 K wide (Klingelhöfer *et al*., 2003).

The MB spectrum of a complex geologic material is a sum of MB subspectra from each distinct Fe site, that is sites characterized by different values of the MB parameters. A single Fe-bearing phase can have one or more distinct sites. The subspectra are obtained from the measured MB spectrum using a least-squares fitting procedure. The details of the fitting procedures for MER MB spectra are discussed by Morris *et al*. (2006a,b). Mineralogical assignments are made by comparing the subspectral MB parameters to MB parameters that have been compiled for known mineralogical compositions (e.g., Burns and Solberg, 1990; Burns, 1993; McCammon, 1995; Stevens *et al*., 1998). However, there may be Fe-bearing phases on Mars that are unknown on Earth. Correlations of subspectral areas can also yield clues for mineralogical assignments (e.g., a positive correlation between two subspectral areas might imply that they are present in different sites in the same Fe-bearing phase). In any case, mineralogical assignments on the basis of MB data must be examined within the context of other MER chemical and mineralogical data (e.g., Christensen *et al*., 2004a,b; Gellert *et al*., 2004, 2006; Rieder *et al*., 2004; Ming *et al*., 2006; Yen *et al*., 2006) and what is known about the environment and geochemistry of Mars.

The percentage of total Fe associated with a specific Fe-bearing phase (A_x where $\Sigma A_x = 100\%$) is determined by its subspectral area corrected for the recoil-free fraction (the *f*-factor) of ^{57}Fe in that phase. For MER, we use $f(Fe^{2+})/f(Fe^{3+}) = 1.21$, independent of mineralogical composition (De Grave and Van Alboom, 1991; Morris *et al*., 1995). Note that A_x is the percentage of total iron associated with a particular Fe-bearing phase and not the concentration of the Fe-bearing phase in a sample. Thus, for example, a sample can be 100% Ol as forsterite (Mg_2SiO_4) but have 0% Ol with respect to MB measurements because forsterite contains no Fe.

In summary, the information content of "MB mineralogy" is the oxidation and coordination states of Fe, the mineralogical composition of Fe-bearing phases, and the distribution of Fe among oxidation states, coordination states, and Fe-bearing phases. In practice, it is relatively straightforward to determine the Fe oxidation state (Fe^{3+}/Fe_T) from MB data, but more challenging to assign specific mineralogical compositions to Fe-bearing phases.

15.3 IDENTIFICATION AND MINERALOGICAL ASSIGNMENT OF FE-BEARING PHASES

The MB doublet (δ versus ΔE_Q) and sextet (δ versus ΔE_Q and δ versus B_{hf}) identification diagrams are shown in Figure 15.3 for MER MB data through sols 602 and 575 at Gusev crater and Meridiani Planum, respectively. The parameters were derived from fits of spectra that are the sum of individual spectra from temperature windows between 200 and 270 K (Morris *et al*., 2006a,b). We give each Fe-bearing phase a generic name having the form FeXYZ, where X = Fe oxidation state, Y = D (doublet) or S (sextet), and Z = a sequence number for phases with the same values of X and Y. A total of 9 doublets and 5 sextets, corresponding to 12 distinct Fe-bearing phases, were identified on Mars. We briefly summarize mineralogical assignments next. Additional details can be found in Morris *et al*. (2004, 2006a,b), Klingelhöfer *et al*. (2004), and Clark *et al*. (2007).

Doublets Fe2D1, Fe2D2, and Fe2D3 (Figure 15.3a) are assigned to octahedrally coordinated Fe^{2+} (oct-Fe^{2+}) in Ol, Px, and Ilm, respectively, on the basis of comparison to MB parameters compiled in databases (see, Section 15.2). The assignments for Ol and Px are consistent with MER Mini-TES data (e.g., Christensen *et al*., 2004a). Although the MB parameters for Fe2D1 are consistent with Fe in Ol, an alternate assignment of Fe^{2+}-bearing sulfate was made

Caption for Figure 15.2. Images for the MIMOS II Mössbauer spectrometer and selected surface targets for MB analysis at Gusev crater and Meridiani Planum. Image identifications are given in the figure. Pancam images were downloaded from http://pancam.astro.cornell.edu/ (Bell *et al*., 2006). (a) Approximate true color image of *Spirit*'s Instrument Deployment Device (IDD) showing the sensor head of the MIMOS II Mössbauer spectrometer. The hole in the contact plate (1.5 cm diameter) defines the field of view for the instrument. The contact plate has a temperature sensor for measurement of Martian surface temperatures. Note the small patch of soil adhering to the contact plate. (b) Approximate true color image showing hole ground by the RAT in Burns Outcrop Class rock McKittrick. The hole diameter is ~4 cm. MB spectra from the hole are shown in Figures 15.4 h and 15.4i. (c) Approximate true color image showing the RAT brush "mosaic" on the Adirondack class rock Route66 at Gusev crater. MB spectrum is shown in Figure 15.4a. (d) Approximate true color image showing spherules in the "Blueberry Bowl" at Eagle crater, Meridiani Planum. MB spectra were obtained from a spherule-free region of the outcrop rock and from the spherules that collected in the bowl (sample B048SU0 [BerryBowl_MoessBerry] in Figure 15.4l). (e) Approximate true-color image showing a RAT brush mosaic and a RAT hole in the Clovis class rock Clovis (samples A213RU0, A215RB0, and A218RR [Clovis_Plano] in Figure 15.4k) at West Spur in Gusev crater. (f) False-color image showing trench dug with rover wheels through a ripple on the plains at Meridiani Planum south of Endurance crater. MB spectra were obtained for soils at the ripple crest (Berry Class soil; similar to sample A415SU0 [MattsRipple_Mobarak] in Figure 15.4m), ripple trough (Berry Class soil), and trench bottom (Laguna Class soil). Note that the contact plate creates a "noseprint" in soft soil. (g) Approximate true color image showing a trench dug with rover wheels on the northwestern flank of Husband Hill. As shown by the noseprints, MB spectra were obtained on the "white" soil (Paso Robles Class soil) and on the "dark" soil (Laguna Class soil). The white soil MB spectrum is similar to sample A401SD0 (Pasadena_PasoRobles) in Figure 15.4g. (h) Microscopic Imager (MI) image showing MB noseprint for sample B060SU0 (MontBlanc_LesHauches) in the fine-grained deposit of dust just below the downwind lip of Eagle crater. The spectrum is similar to sample A069SU0 (Desert_Gobi) in Figure 15.4e. (For a color version of this figure, please refer to the color plate section or to the e-Book version of this chapter.)

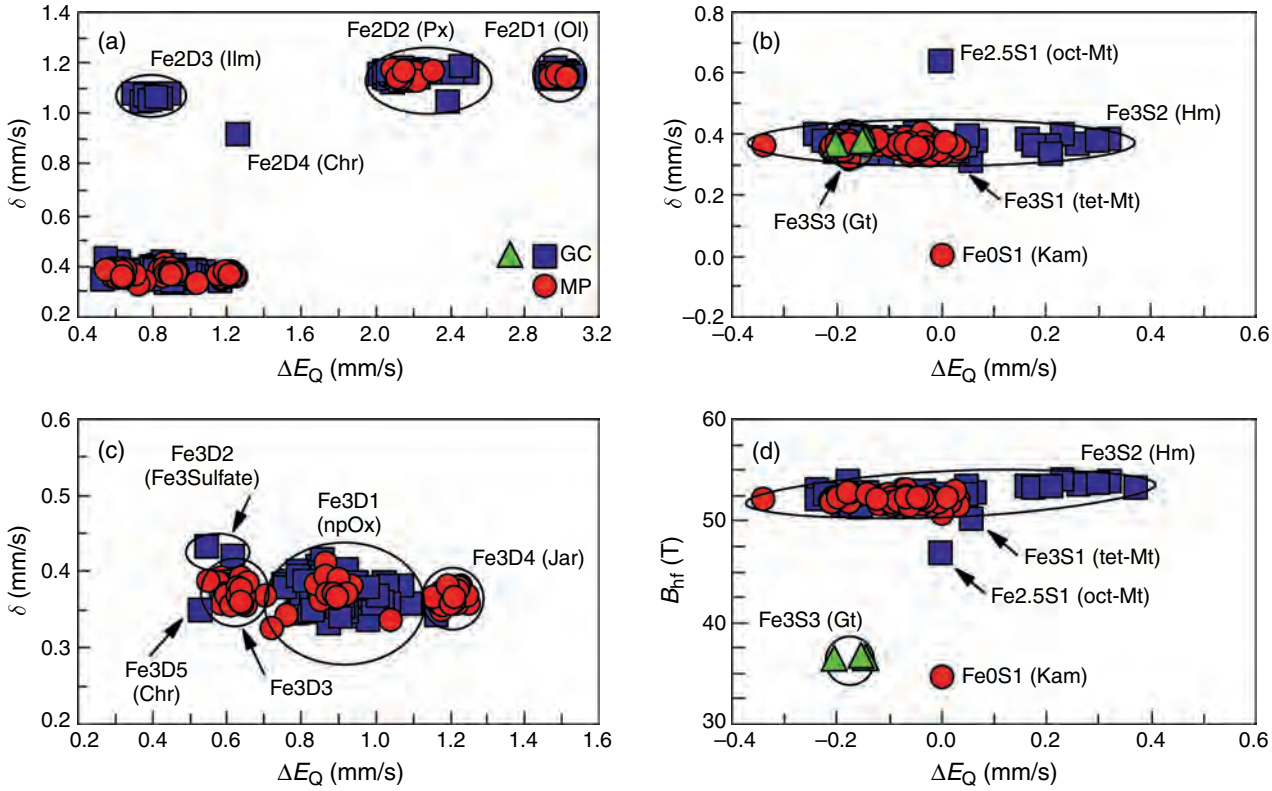

Figure 15.3. Fe-bearing phase identification diagrams for doublet (a and c) and sextet (b and d) spectra acquired at Gusev crater (GC) and Meridiani Planum (MP). Generic names have the form FeXYZ where X = Fe oxidation state, Y = D (doublet) or S (sextet), and Z = a sequence number for phases with the same values of X and Y. Phase assignments are given in parentheses (Ol = olivine, Px = pyroxene, Ilm = ilmenite; Chr = chromite; npOx = nanophase ferric oxide; Fe3Sulfate = ferric sulfate; Jar = jarosite; Mt = magnetite; Hm = hematite; Gt = goethite; Kam = kamacite). Chr has two doublets (Fe2D4 and Fe3D5), and Mt has two sextets (Fe2.5S1 and Fe3S1). One Fe-bearing phase (Fe3D3) was not assigned a mineralogical composition. The large range in values of ΔE_Q for Hm results from a magnetic transition (the Morin transition at ~260 K for pure, well-crystalline bulk hematite) that occurs within the Martian diurnal temperature range (~180 to 300 K). The isomer shift (δ) is measured with respect to the center point of the spectrum of metallic Fe foil at nominally the same temperature as the sample temperature. (For a color version of this figure, please refer to the color plate section or to the e-Book version of this chapter.)

by Lane *et al.* (2004) for Fe2D1, implying that the Fe2D1 parameters are not specific for Ol. As discussed by Yen *et al.* (2005) and Morris *et al.* (2006a), the sulfate assignment is unlikely because of the aforementioned Mini-TES data, the observed decreasing A_{Ol} with increasing SO_3 concentration, and, for rock interiors exposed by grinding with the RAT, SO_3 concentrations that are too low to accommodate all Fe from Fe2D1 as an Fe^{2+}-bearing sulfate. Ilmenite was not detected by Mini-TES, but samples that have Ilm as detected by MB also have higher TiO_2 concentrations as detected by APXS (e.g., Gellert *et al.*, 2004, 2006; Ming *et al.*, 2006). Doublets Fe3D1, Fe3D2, and Fe3D4 (Figure 15.3c) are assigned to oct-Fe^{3+} in npOx, an unidentified Fe^{3+} sulfate (Fe3Sulfate), and Jar, respectively. The Jar ($(K,Na,H_3O)(Fe,Al)_3(SO_4)_2(OH,Cl)_6$, where Fe > Al and OH > Cl) assignment is made on the basis of the unusually high value of ΔE_Q for that phase. The assignment of Fe^{3+}-sulfate is based on the relatively high value of δ and S concentrations that are so high ($SO_3 \sim 31$ wt.%) that they require nearly all cations to occur as sulfates. The npOx refers to a poorly crystalline or amorphous alteration product that can be any combination of superparamagnetic Hm and/or Gt, akaganeite (β-FeOOH), schwertmannite ($\sim Fe_8O_8(OH)_6SO_4$), ferrihydrite ($5Fe_2O_3 \cdot 9H_2O$), iddingsite (a low-temperature alteration product of Ol), and the nanometer-sized ferric oxide particles that pigment palagonitic tephra (e.g., Morris *et al.*, 1993, 2000). Nanophase ferric oxide can also incorporate anions (e.g., SO_4^{2-} and PO_4^{3-}) through specific chemical adsorption (e.g., Borggaard, 1983a,b; Cornell and Schwertmann, 1996; Myneni, 2000). The nature of npOx can change from place to place and time to time, in response to local conditions and processes. Thus, it is possible that the form of npOx on Mars is uncommon or not present on the Earth.

Sextets Fe3S1, Fe2.5S1, Fe3S2, Fe3S3, and Fe0S1 are assigned to tet-Fe^{3+} in Mt, oct-$Fe^{2.5+}$ in Mt, oct-Fe^{3+} in Hm, oct-Fe^{3+} in Gt, and Fe^0 in Kam respectively (Figure 15.3b). The envelope for Hm data is large compared to the other sextet phases because Hm undergoes a magnetic transition (the Morin transition) within the Martian diurnal temperature cycle (~180 to 300 K). For well crystalline and chemically pure Hm, this transition occurs at $T_M \sim 260$ K, where $\Delta E_Q < 0$ for $T > T_M$ and $\Delta E_Q > 0$ for $T < T_M$. For Hm with small particle sizes and/or with substitutional impurities like Al, the Morin transition occurs at lower temperatures and over a wider temperature interval (e.g., De Grave *et al.*, 1983, 2002). Small-particle behavior and/or substitutional

impurities are indicated for most Martian hematites because $\Delta E_Q < 0$ mm/s at Martian diurnal temperatures (Figure 15.3b; Morris *et al.*, 2006a).

In summary, 9 doublets and 5 sextets were identified in MER MB spectra through sols 602 and 557 at Gusev crater and Meridiani Planum, respectively. Specific mineralogical assignments were made for 5 of 9 doublets (Fe^{2+} in Ol, Px, and Ilm; Fe^{3+} in npOx and Jar) and for all 5 sextets ($Fe^{2.5+}$ and Fe^{3+} in Mt; Fe^{3+} in Hm and Gt; Fe^0 in Kam). One doublet (Fe3D2) is associated with oct-Fe^{3+} in a sulfate, but we cannot assign a specific Fe^{3+}-sulfate mineral. Two doublets (Fe2D4 and Fe3D5) are associated with chromite ($Fe^{2+}(Cr,Fe^{3+})_2O_4$ where $Cr > Fe^{3+}$; hereafter denoted as Chr), but this association would not have been possible to make without knowledge of high-Cr concentrations in the sample from APXS measurements. We make no specific mineralogical assignment for the final doublet (Fe3D3), except that it results from a phase with oct-Fe^{3+}. In Figure 15.4, we show MER MB spectra for samples that contain high proportions of each of the 14 doublets and sextets identified in 12 unique Fe-bearing phases. Average values of doublet and sextet MB parameters for individual Fe-bearing phases are summarized in Tables 15.1 and 15.2 respectively.

15.4 SUPERGROUP CLASSIFICATION OF MER ROCKS AND SOILS

In Figure 15.5, we show the frequency of occurrence of the unique 12 Fe-bearing phases for rocks and soils at Gusev crater and Meridiani Planum. The histograms count only those occurrences in MB spectra where the abundance of Fe from an Fe-bearing phase is >10% (i.e., $A_x > 10\%$). We counted all distinct measurements of the same target as separate occurrences. The total number of occurrences of each phase is indicated in the figure.

Five phases have very limited occurrence in MER MB spectra. Chromite is present only in Gusev Columbia Hills rock sample Assemblee_Guryere. Fe^{3+}-sulfate occurs only in two Gusev Columbia Hills soil analyses (Pasadena_PasoRobles and PasoRobles2_PasoLight1). Ilmenite is found in rocks and one soil in the Columbia Hills. Goethite is detected only in rocks from the Columbia Hills. Kamacite occurs only at Meridiani Planum in Heat Shield rock and in the cobble sample Figtree_Barberton.

The Fe mineralogical composition of rocks at Gusev crater is very different from those at Meridiani Planum (Figures 15.5a, 15.5c). Fe-bearing phases associated with igneous rocks (Ol, Px, Mt, Ilm, and Chr) are prevalent at Gusev crater. The Gusev rocks with Hm >10% and Gt >10% are confined to the Columbia Hills and do not occur on the plains. Rock analyses at Meridiani Planum are dominated by measurements of the ubiquitous high-S Burns formation (Rieder *et al.*, 2004; Grotzinger *et al.*, 2005), which is an assemblage of Jar, Hm, and Fe3D3 with respect to Fe-bearing phases (Morris *et al.*, 2006b). The Hm occurs both within the Hm-rich spherules and within the matrix of sulfate-rich rocks at particle diameters below the resolution of the MER Microscopic Imager (Morris *et al.*, 2006b). This result is consistent with Pancam multispectral imaging of the outcrop rocks (Bell *et al.*, 2004b). The high number of Px analyses at Meridiani Planum is inflated by the eight MB analyses of Bounce rock, the most Px-rich sample measured at either MER site.

Compared to rocks, the Fe mineralogical composition of soils at Gusev crater and Meridiani Planum is less variable (Figures 15.5b and 15.5d), although Mt is relatively common compared to Hm at Gusev crater and vice versa for Meridiani Planum. This difference may reflect the prevalence at Gusev and apparent absence at Meridiani of Mt-bearing rocks, and the abundance of Hm-rich spherules at Meridiani Planum. We next consider the distribution of Fe-bearing phases within individual rocks and soils and classify them into supergroups on the basis of chemistry and Fe mineralogy (Table 15.3).

In order to do this classification, we take into account that two or more samples can have identical distributions of Fe among Fe-bearing phases and yet have different bulk elemental compositions. For example, two rocks can both have $A_{Ol} = 40\%$, $A_{Px} = 35\%$, $A_{Mt} = 15\%$, and $A_{npOx} = 10\%$ but very different total Fe concentrations (Fe_T) if they have different proportions of phases that have virtually no Fe (e.g., plagioclase). We use parameters of the form $A_{Ol}Fe_T/100$ (using Ol as an example) to classify soils and rocks into supergroups. The "100" in the denominator is necessary because A_{Ol} is a percentage. We calculate $A_{Ol}Fe_T/100$ in units of moles per 24 moles of oxygen plus chlorine (moles/24(O+Cl)) because stoichiometric information is directly accessible with molar concentration units. We use "24(O+Cl)" because 24 is evenly divisible by the sum of oxygen plus chlorine for many common geological materials (e.g., Fe_2SiO_4, $FeSiO_3$, Fe_3O_4, Fe_2O_3, and $FeTiO_3$). Note that this classification is based on both mineralogical (A_{Ol}, A_{Px}, etc. from MB) and elemental (Fe_T from APXS) data (Gellert *et al.*, 2004; Rieder *et al.*, 2004; Morris *et al.*, 2006a,b; Yen *et al.*, 2006).

We divided the rocks into four supergroups: Weakly Altered Basalt, Altered Low-S Rock, Altered High-S Rock, and Meteorite. The Meteorite supergroup consists of the two rocks from Meridiani Planum that have Kam as an Fe-bearing phase (Heat Shield Rock and the cobble Barberton). We used plots of Fe_T and S as a function of four parameters having the form $A_xFe_T/100$ to classify the remaining MER rocks into supergroups (Figure 15.6). The parameter $(A_{Ol}+A_{Px}+A_{Ilm}+A_{Chr}+A_{Mt})Fe_T/100$ (equivalently $A_{Igneous}Fe_T/100$) is the sum of Fe concentrations from igneous, rock-forming phases. Samples that plot on or near the $y = x$ line in Figure 15.6a are potentially unaltered samples. However, rocks with high concentrations of Fe from Ilm and Chr resulting from alteration of a precursor basalt with those minerals would also plot along this line, except at lower values of Fe_T because of removal of Fe (e.g., by leaching) from Fe-bearing phases that are susceptible to alteration (e.g., Ox and Px). We classify the group of rocks with high values of Fe_T ($Fe_T > 1.2$ moles/24moles(O+Cl)) and $Fe_T \approx A_{Igneous}Fe_T/100$ as "Weakly Altered Basalt" as

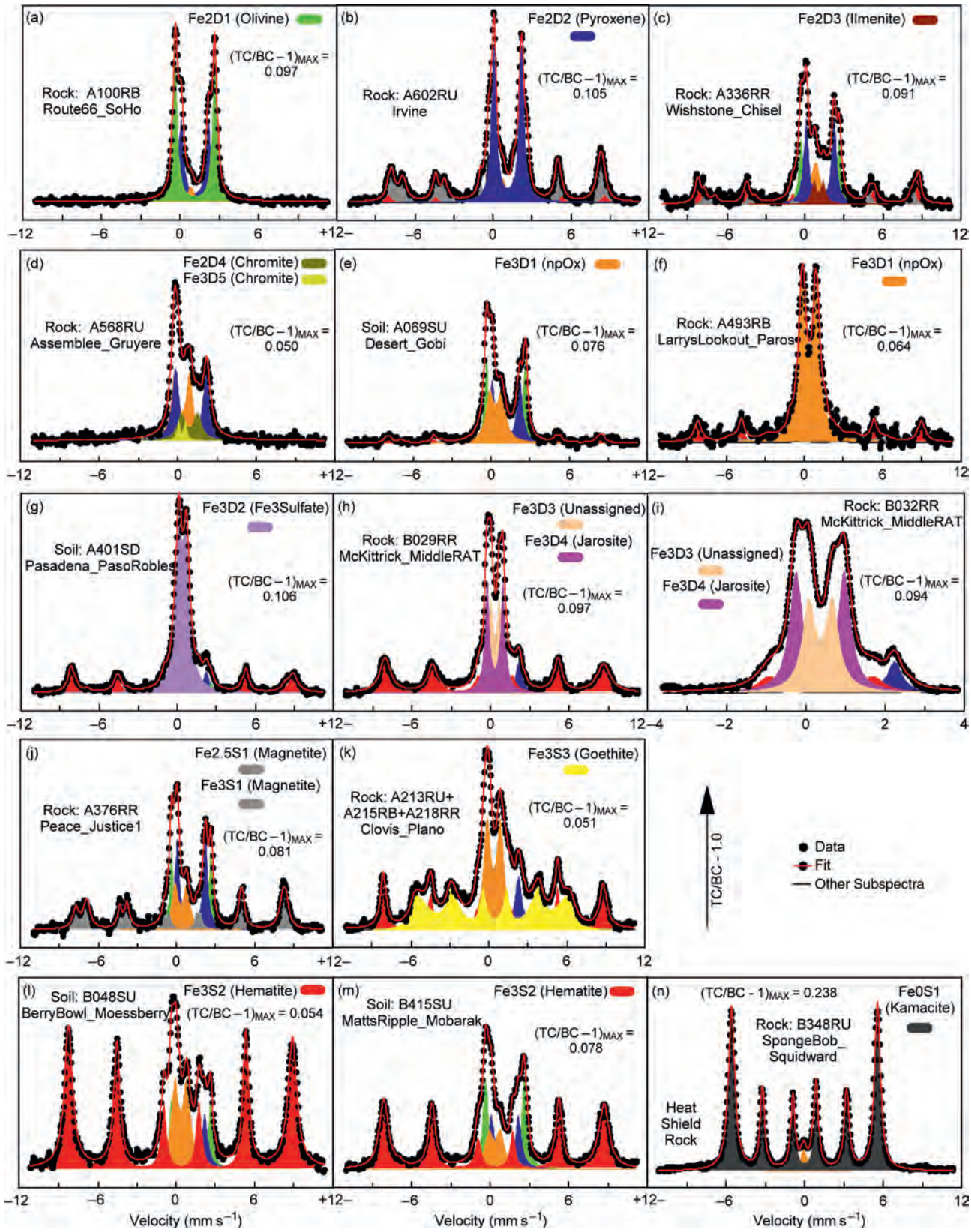
(a)
Fe2D1 (Olivine)
(TC/BC – 1)MAX = 0.097
Rock: A100RB
Route66_SoHo
(b)
Fe2D2 (Pyroxene)
(TC/BC – 1)MAX = 0.105
Rock: A602RU
Irvine
(c)
Fe2D3 (Ilmenite)
(TC/BC – 1)MAX = 0.091
Rock: A336RR
Wishstone_Chisel
(d)
Fe2D4 (Chromite)
Fe3D5 (Chromite)
(TC/BC – 1)MAX = 0.050
Rock: A568RU
Assemblee_Gruyere
(e)
Fe3D1 (npOx)
(TC/BC – 1)MAX = 0.076
Soil: A069SU
Desert_Gobi
(f)
Fe3D1 (npOx)
(TC/BC – 1)MAX = 0.064
Rock: A493RB
LarrysLookout_Paros
(g)
Fe3D2 (Fe3Sulfate)
(TC/BC – 1)MAX = 0.106
Soil: A401SD
Pasadena_PasoRobles
(h)
Fe3D3 (Unassigned)
Fe3D4 (Jarosite)
(TC/BC – 1)MAX = 0.097
Rock: B029RR
McKittrick_MiddleRAT
(i)
Rock: B032RR
McKittrick_MiddleRAT
Fe3D3 (Unassigned)
Fe3D4 (Jarosite)
(TC/BC – 1)MAX = 0.094
(j)
Fe2.5S1 (Magnetite)
Fe3S1 (Magnetite)
(TC/BC – 1)MAX = 0.081
Rock: A376RR
Peace_Justice1
(k)
Fe3S3 (Goethite)
(TC/BC – 1)MAX = 0.051
Rock: A213RU+
A215RB+A218RR
Clovis_Plano
TC/BC - 1.0
Data
Fit
Other Subspectra
(l)
Soil: B048SU
BerryBowl_Moessberry
Fe3S2 (Hematite)
(TC/BC – 1)MAX = 0.054
(m)
Soil: B415SU
MattsRipple_Mobarak
Fe3S2 (Hematite)
(TC/BC – 1)MAX = 0.078
(n)
(TC/BC - 1)MAX = 0.238
Fe0S1
(Kamacite)
Rock: B348RU
SpongeBob_
Squidward
Heat
Shield
Rock
–12 –6 0 6 +12
–4 –2 0 2 4
Velocity (mm s–1)

Table 15.1. *Average Mössbauer parameters* δ *and* ΔE_Q *(210–270 K) for MER doublet spectra*

Name	Cation[a]	Assignment	Location[b]	Type	δ[c] (mm/s)	ΔE_Q (mm/s)	N[d]
Fe2D1	oct-Fe^{2+}	Olivine	GC	Rock	1.16 ± 0.02[e]	3.00 ± 0.04[e]	26, 26
Fe2D1	oct-Fe^{2+}	Olivine	GC	Soil	1.15 ± 0.02	2.98 ± 0.03	26, 26
Fe2D1	oct-Fe^{2+}	Olivine	MP	Rock	1.15 ± 0.02	3.01 ± 0.02	1, 1
Fe2D1	oct-Fe^{2+}	Olivine	MP	Soil	1.15 ± 0.02	3.00 ± 0.03	18, 18
Fe2D2	oct-Fe^{2+}	Pyroxene	GC	Rock	1.16 ± 0.02	2.17 ± 0.10	59, 54
Fe2D2	oct-Fe^{2+}	Pyroxene	GC	Soil	1.15 ± 0.02	2.12 ± 0.04	28, 26
Fe2D2	oct-Fe^{2+}	Pyroxene	MP	Rock	1.15 ± 0.02	2.22 ± 0.04	10, 10
Fe2D2	oct-Fe^{2+}	Pyroxene	MP	Soil	1.15 ± 0.02	2.13 ± 0.02	17, 17
Fe2D3	oct-Fe^{2+}	Ilmenite	GC	Rock	1.07 ± 0.02	0.80 ± 0.06	7, 8
Fe2D3	oct-Fe^{2+}	Ilmenite	GC	Soil	1.05 ± 0.02	0.79 ± 0.02	1, 1
Fe2D4	tet-Fe^{2+}	Chromite	GC	Rock	0.92	1.26	n/a[f]
Fe3D1	oct-Fe^{3+}	npOx	GC	Rock	0.37 ± 0.02	0.92 ± 0.09	55, 57
Fe3D1	oct-Fe^{3+}	npOx	GC	Soil	0.38 ± 0.02	0.86 ± 0.06	18, 25
Fe3D1	oct-Fe^{3+}	npOx	MP	Rock	0.34 ± 0.02	0.84 ± 0.17	3, 3
Fe3D1	oct-Fe^{3+}	npOx	MP	Soil	0.38 ± 0.02	0.88 ± 0.03	16, 17
Fe3D2	oct-Fe^{3+}	Fe3Sulfate	GC	Soil	0.43 ± 0.02	0.58 ± 0.05	2, 2
Fe3D3	oct-Fe^{3+}	None	MP	Rock	0.37 ± 0.02	0.62 ± 0.03	46, 46
Fe3D4	oct-Fe^{3+}	Jarosite	MP	Rock	0.37 ± 0.02	1.20 ± 0.02	46, 46
Fe3D5	oct-Fe^{3+}	Chromite	GC	Rock	0.35	0.53	n/a[f]

[a] oct = octahedral; tet = tetrahedral.
[b] GC = Gusev crater; MP = Meridiani Planum.
[c] δ is measured with respect to metallic Fe foil at the same temperature as the sample.
[d] N = number of analyses used in average calculation for δ and ΔE_Q respectively.
[e] Uncertainty is the larger of the measurement uncertainty and the standard deviation of the average.
[f] n/a = not applicable. Values of δ and ΔE_Q were constrained to values for chromite during the fitting procedures (Morris *et al.*, 2006a).

Caption for Figure 15.4. Mössbauer spectra that have high proportions of Fe for each of the 14 identified MB doublets and sextets: (a) Fe2D1 (Ol) in Adirondack Class rock Route66; (b) Fe2D2 (Px) in rock Irvine; (c) Fe2D3 (Ilm) in Wishstone Class rock Wishstone; (d) Fe2D4 and Fe3D5 (Chr) in Independence Class rock Assemblee; (e) Fe3D1 (npOx) in Laguna Class undisturbed soil Desert_Gobi; (f) Fe3D1 (npOx) in Watchtower Class rock LarrysLookout; (g) Fe3D2 (Fe3Sulfate) in Paso Robles Class soil Pasadena_PasoRobles; (h) Fe3D3 (unassigned) and Fe3D4 (Jar) in Burns Outcrop Class rock; (i) same as (h) except MB spectrum was acquired over a narrow velocity range; (j) Fe2.5S1 and Fe3S1 (Mt) in Peace Class rock Peace; (k) Fe3S3 (Gt) in Clovis Class rock Clovis; (l) Fe3S2 (Hm) in Berry Class undisturbed soil BerryBowl_Moessberry; (m) Fe3D2 (Hm) in Berry Class undisturbed soil MattsRipple_Mobarak; and (n) Fe0S1 (Kam) in Heat Shield Rock. All MB spectra are the sum of spectra for temperatures between 200 and 270 K. Sample naming convention is Uwwwxyz, where U = A for Gusev crater or U = B for Meridiani Planum, www = sol number, x = R (rock) or S (soil), y = U (undisturbed), D (disturbed), B (RAT brush), or R (RAT grind), and z = 0, 1, 2, ... as appropriate to keep sample names unique (usually, z = 0). The *y*-axis is TC/BC – 1.0, where TC = total counts and BC = baseline counts. The maximum value of TC/BC – 1.0 for each spectrum is given in the figure as $(TC/BC - 1.0)_{MAX}$. (For a color version of this figure, please refer to the color plate section or to the e-Book version of this chapter.)

shown in Figure 15.6a. Weakly Altered Basalt at Gusev crater has $S = 0.28 \pm 0.15$ moles/24(O+ Cl) ($SO_3 = 2.5 \pm 1.4$ wt.%) and $Fe^{3+}/Fe_T = 0.24 \pm 0.11$. The values for S and SO_3 exclude the rocks Peace and Alligator, which have a Mg-sulfate coating and/or cement (Ming *et al.*, 2006) but are still Weakly Altered Basalt with respect to Fe-bearing phases.

The parameters $(A_{Jar} + A_{Fe3D3} + A_{Hm})Fe_T/100$ and $A_{Hm}Fe_T/100$ are, respectively, the sum of Fe^{3+}-bearing alteration products associated with the Burns formation and the Fe concentration from Hm. Altered High-S Rock from the Burns formation is distinguished from Altered Low-S Rock and Weakly Altered Basalt in Figures 15.6b and 15.6c. Weakly Altered Basalt and Altered Low-S Rocks have S concentrations between 0 and ~1.5 moles/24(O+ Cl) (equivalently, 0 to ~14.2 wt.% SO_3), and Altered High-S Rock has S concentrations greater than ~1.5 moles/24(O+ Cl) (>14.2 wt.% SO_3) (Figure 15.6c). Altered Low-S basalt has average $S = 0.55 \pm 0.21$ moles/24(O+ Cl) ($SO_3 = 5.2 \pm 2.0$ wt.%) and $Fe^{3+}/Fe_T = 0.63 \pm 0.18$. In general, Altered High-S Rock has higher Hm concentrations than Altered Low-S Rock (Figure 15.6d). In Figures 15.6b, 15.6c, and 15.6d, Weakly Altered Basalt plots on or near the *y*-axis.

As shown in Figure 15.6c, some measurements of Burns outcrop targets have S concentrations less than ~1.5 moles/

Table 15.2. *Average Mössbauer parameters* δ, ΔE_Q, *and* B_{hf} *(210–270 K) for MER sextet spectra*

Name	Cation[a]	Assignment	Location[b]	Type[b]	δ[c] (mm/s)	ΔE_Q (mm/s)	$B^{h,f}$ (T)	N[d]
Fe0S1	Fe^0	Kamacite	MP	Rock	0.00 ± 0.02[e]	0.00 ± 0.02[e]	34.7 ± 0.8[e]	2, 2, 2
Fe2.5S1	oct-$Fe^{2.5+}$	Magnetite	GC	Rock	0.64 ± 0.02	0.00 ± 0.02	46.9 ± 0.8	1, 1, 1
Fe3S1	tet-Fe^{3+}	Magnetite	GC	Rock	0.31 ± 0.02	0.06 ± 0.02	50.1 ± 0.8	1, 1, 1
Fe3S2	oct-Fe^{3+}	Hematite	GC	Rock[f]	0.38 ± 0.02	-0.13 ± 0.07	52.2 ± 0.8	27, 31, 31
Fe3S2	oct-Fe^{3+}	Hematite	GC	Rock[g]	0.37 ± 0.02	0.18 ± 0.12	53.3 ± 0.8	12, 13, 13
Fe3S2	oct-Fe^{3+}	Hematite	GC	LC-soil[h]	0.36 ± 0.02	-0.12 ± 0.05	52.3 ± 0.8	5, 5, 5
Fe3S2	oct-Fe^{3+}	Hematite	GC	PRC-soil[f,i]	0.39 ± 0.02	-0.16 ± 0.05	51.3 ± 0.8	1, 1, 1
Fe3S2	oct-Fe^{3+}	Hematite	GC	PRC-soil[g,i]	0.36 ± 0.02	0.05 ± 0.02	53.3 ± 0.8	1, 1, 1
Fe3S2	oct-Fe^{3+}	Hematite	MP	Rock[j]	0.36 ± 0.02	-0.05 ± 0.06	51.9 ± 0.8	41, 41, 41
Fe3S2	oct-Fe^{3+}	Hematite	MP	BC-soil[k]	0.36 ± 0.02	-0.16 ± 0.05	52.4 ± 0.8	17, 17, 17
Fe3S3	oct-Fe^{3+}	Goethite	GC	Rock	0.38 ± 0.02	-0.17 ± 0.03	35.5 ± 0.8	3, 3, 3

[a] oct = octahedral; tet = tetrahedral.
[b] GC = Gusev crater; MP = Meridiani Planum.
[c] δ is measured with respect to metallic Fe foil at the same temperature as the sample.
[d] N = number of analyses used in average calculation for δ, ΔE_Q, and B_{hf}, respectively.
[e] Uncertainty is the larger of the measurement uncertainty and the standard deviation of the average.
[f] Average of all sextets with $\Delta E_Q < 0$ mm/s. Includes data from one and two Hm sextet fits. Two Hm sextets are required to fit spectra that contain subspectra from Hm above and below the Morin transition (e.g., PotOfGold) at Gusev crater (Morris *et al.*, 2006a).
[g] Average of all sextets with $\Delta E_Q > 0$ mm/s. Includes data from one and two Hm sextet fits.
[h] Laguna Class soil.
[i] Paso Robles Class soil.
[j] Altered High-S Rock (Burns formation).
[k] Berry Class soil.

24(O+Cl), which is in the range for Altered Low-S Rock. The low-S concentrations result from thin coverings of low-S LC soil (discussed below) that are "thick" with respect to APXS analysis and "thin" with respect to MB analysis (Morris *et al.*, 2006b). All APXS measurements of outcrop surfaces exposed by the MER RAT have sulfur concentrations greater than 1.5 moles/24(O+Cl) (Figure 15.6c). Including only analyses of RAT-ground surfaces, Altered High-S Rock has average S = 2.27 ± 0.26 moles/24(O+Cl) (SO_3 = 22 ± 3 wt.%) and $Fe^{3+}/Fe_T = 0.85 \pm 0.03$.

For each rock supergroup, average values of the concentrations of Fe associated with Fe-bearing phases (A_xFe_T/100), Fe_T and S concentrations, Fe^{3+}/Fe_T, and number of targets with both APXS and MB analyses are summarized in Table 15.3. Individual rocks are classified according to supergroup, APXS chemistry (e.g., Squyres *et al.*, 2006b; Ming *et al.*, 2006), and MB mineralogy (Morris *et al.*, 2006a,b) in Table 15.4.

We divided MER soils into three supergroups on the basis of Figure 15.7: Laguna Class (LC) supergroup, Paso Robles Class (PRC) supergroup, and Berry Class (BC) supergroup. Paso Robles Class soils have the lowest values of $A_{Igneous}Fe_T$/100 (Figure 15.7a), and they have the highest S concentrations measured on Mars to date (Figures 15.6c and 15.7c). Paso Robles Class soils have average S = 3.17 ± 0.04 moles/24 moles(O+Cl) (SO_3 = 31.1 ± 0.1 wt.%) and Fe^{3+}/Fe_T = 0.83 ± 0.05. Laguna Class soils plot near the $y = x$ line in Figure 15.7a and thus (for soils) have the highest proportions of igneous rock-forming minerals and are the least altered with average S = 0.66 ± 0.24 moles/24 moles(O+Cl) (SO_3 = 6 ± 2 wt.%) and $Fe^{3+}/Fe_T = 0.29 \pm 0.08$. Comparison of Figures 15.6a and 15.7a shows that the Weakly Altered Basalt rock supergroup and the LC soil supergroup have comparable values of Fe_T and $A_{Igneous}Fe_T$/100. Berry Class soils, which have values of $A_{Igneous}Fe_T$/100 comparable to LC soils (Figure 15.7a), are distinguished by the high values of Fe_T and $A_{Hm}Fe_T$/100 (Figures 15.7a and 15.7d) that result from high concentrations of Hm-rich and Fe-rich spherules and their fragments (Morris *et al.*, 2006b). Note that two BC soils (circled in Figure 15.7a and at the left side of the ellipse enclosing the BC supergroup) are very similar and transitional to LC soil. Berry Class soils have average S = 0.61 ± 0.07 moles/24 moles(O+Cl) (SO_3 = 5 ± 1 wt.%) and $Fe^{3+}/Fe_T = 0.60 \pm 0.13$. Comparison of Figures 15.7b and 15.7d shows that no soil has detectable Fe from Jar and Fe3D3.

Average values of the concentrations of Fe associated with Fe-bearing phases (A_xFe_T/100), Fe_T and S concentrations, Fe^{3+}/Fe_T, and number of targets with both APXS and MB analyses for each soil supergroup are summarized in Table 15.3. Individual soils are classified according to supergroup and APXS chemistry and MB mineralogy in Table 15.5 (after Morris *et al.*, 2006a,b).

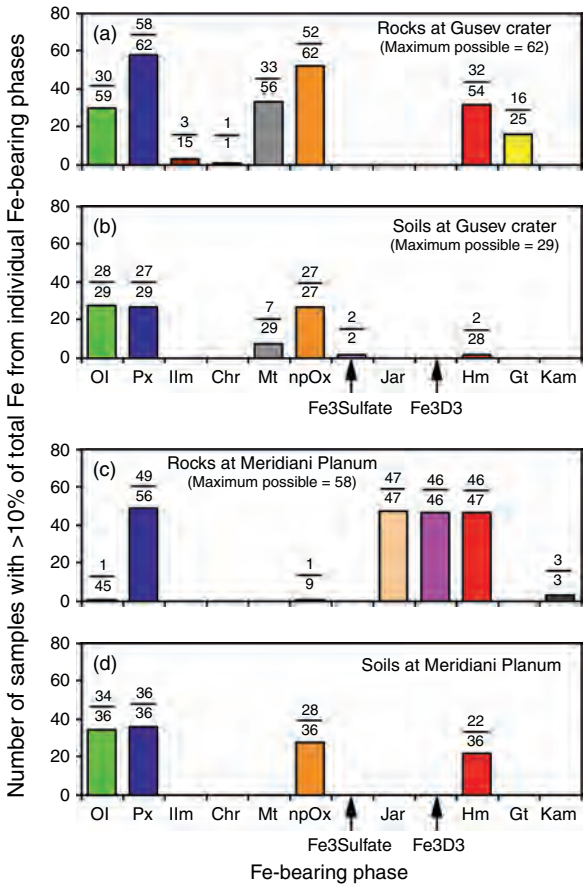

Figure 15.5. Histograms for number of MB analyses having >10% Fe from each of the 12 Fe-bearing phases for rocks (a and c) and soils (b and d) at Gusev crater (a and b) and Meridiani Planum (c and d). The numbers above each non-zero column refer to the number of MB analyses where the Fe percentage from an Fe-bearing phase is >10% (upper) and the total number of MB analyses where the Fe percentage from an Fe-bearing phase is >0% (lower). (For a color version of this figure, please refer to the color plate section or to the e-Book version of this chapter.)

Morris *et al.* (2006a) defined a Mineralogical Alteration Index (MAI = $A_{\text{Alteration}} = A_{\text{npOx}} + A_{\text{Hm}} + A_{\text{Gt}} + A_{\text{Fe3Sulfate}} + A_{\text{Jar}} + A_{\text{Fe3D3}}$) to describe the degree of alteration of Gusev crater rocks. The index, however, is not sensitive to alteration in situations like those for the Independence Class rocks, where alteration and subsequent leaching appear to have resulted in a net loss of Fe from relatively soluble phases (e.g., Ol and Px) and a resulting passive enrichment in Fe associated with less soluble phases (Ilm and Chr). Using data from Clark *et al.* (2007), the values of MAI for the rocks Assemblee and Independence are 32% and 43% respectively. While these values are larger than those for Weakly Altered Basalt (MAI < 22%), they are very low compared to corresponding values for other heavily altered Columbia Hills rocks (e.g., 83%, 88%, and 94% for Watchtower, Pequod, and Paros respectively). One might instead consider using $A_{\text{Alteration}}\text{Fe}_\text{T}/100$ as a measure of alteration because it explicitly takes into account both Fe from alteration phases and Fe loss from leaching. However, this is not a viable alternative because Weakly Altered Basalts and Independence Class rocks have comparable values of $A_{\text{Alteration}}\text{Fe}_\text{T}/100$.

A different way to look at the degree and type of alteration of MER samples is through plots of $A_{\text{Igneous}}\text{Fe}_\text{T}/100$ versus $A_{\text{Alteration}}\text{Fe}_\text{T}/100$ (Figure 15.8). The two solid lines at 2.24 and 1.80 moles/24(O+Cl) are, respectively, the average values of Fe_T for Weakly Altered Basalt from Gusev crater and Meridiani Planum. Isochemical alteration of a basalt with $\text{Fe}_\text{T} = A_{\text{Igneous}}\text{Fe}_\text{T}/100 = 2.24$ (or 1.80) moles/24(O+Cl) and with $A_{\text{Alteration}}\text{Fe}_\text{T}/100 = 0.0$ moles/24(O+Cl) as its initial composition proceeds down the $\text{Fe}_\text{T} = 2.24$ (or 1.80) moles/24(O+Cl) line toward the $A_{\text{Alteration}}\text{Fe}_\text{T}/100$ axis.

Incorporation of SO_3 from acid-sulfate solutions or vapors to form sulfate-bearing phases during alteration would result in rock compositions that plot to the left of the line. Thus, weakly altered Bounce Rock does not appear to be the precursor (by isochemical alteration) of the S-rich outcrop rocks at Meridiani Planum, even though both plot along the line with $\text{Fe}_\text{T} = 1.80$ moles/24(O+Cl) (Figure 15.8a). Incorporation of H_2O or OH^{-1} would not be detected because APXS analyses are calculated on a H_2O-free basis. Alteration of a basalt with an initial composition $\text{Fe}_\text{T} = A_{\text{Igneous}}\text{Fe}_\text{T}/100 = 2.24$ moles/24(O+Cl) in an open system with removal of all oxidized iron (e.g., by leaching) results in a composition on the $A_{\text{Igneous}}\text{Fe}_\text{T}/100$ axis with a value between 0 and 2.24 moles/24(O+Cl). Independence Class rocks are thus likely cases where leaching has been important (Figure 15.8a). Soils at Gusev crater and Meridiani Planum do not appear to be derived directly by isochemical alteration of Weakly Altered Basalt analyzed at the two landing sites (compare Figures 15.8a and 15.8b).

In Figure 15.9, we use pie diagrams to show the average distribution of Fe in Fe-bearing phases for supergroups of rock (Weakly Altered Basalt, Altered Low-S Rock, and Altered High-S Rock) and soil (LC soil, PRC soil, and BC soil) at Gusev crater and Meridiani Planum. The percentages of Fe in Fe-bearing phases can be calculated from the data in Table 15.3. Average Weakly Altered Basalt at Gusev crater ($\text{Fe}^{3+}/\text{Fe}_\text{T} = 0.24$) has nearly equal proportions of Fe from Ol and Px ($A_{\text{Ol}} + A_{\text{Px}} = 71\%$), nearly equal proportions of Fe from Mt and npOx ($A_{\text{Mt}} + A_{\text{npOx}} = 27\%$) and possible minor Fe from Hm (1%). Bounce Rock is the only Weakly Altered Basalt at Meridiani Planum ($\text{Fe}^{3+}/\text{Fe}_\text{T} = 0.01$), and it is essentially monomineralic Px with respect to Fe-bearing phases ($A_{\text{Px}} = 99\%$). Average Altered Low-S Rock at Gusev crater ($\text{Fe}^{3+}/\text{Fe}_\text{T} = 0.63$) has high proportions of Fe^{3+}-only phases (npOx+Hm+Gt = 57%) and much lower Ol+Px ($A_{\text{Ol}} + A_{\text{Px}} = 30\%$) compared to average Weakly Altered Basalt. Altered Low-S Rock has not been analyzed at Meridiani Planum as of sol 557. Average Altered High-S Rock at Meridiani Planum (Burns formation outcrop rock; $\text{Fe}^{3+}/\text{Fe}_\text{T} = 0.85$) is heavily dominated by Fe^{3+}-only phases (Jar+Hm+Fe3D3 = 85%). Altered High-S Rock has not been detected at Gusev crater as of sol 602.

Average LC soil is very similar at Gusev crater ($\text{Fe}^{3+}/\text{Fe}_\text{T} = 0.30$) and Meridiani Planum ($\text{Fe}^{3+}/\text{Fe}_\text{T} = 0.28$) in terms of the mineralogy and abundance of Fe from Fe-bearing phases (Figure 15.9d). This suggests mixing,

Table 15.3. *Average concentration of Fe from individual Fe-bearing phases ($A_xFe_T/100$) in supergroups of Gusev crater and Meridiani Planum rock and soil*

	Gusev crater						Meridiani Planum					
	Weakly Altered Basalt	Altered Low-S Rock	Altered High-S Rock	Laguna Class Soil	Paso Robles Class Soil	Berry Class Soil	Weakly Altered Basalt	Altered Low-S Rock	Altered High-S Rock	Laguna Class Soil	Paso Robles Class Soil	Berry Class Soil
					$\Sigma(A_xFe_T/100) = F_T$; *units = moles/24(O + Cl)*[a]							
$A_{Ol}Fe_T/100$	0.85 ± 0.34[b]	0.10 ± 0.12	—	0.66 ± 0.10	0.13 ± 0.08	—	0	—	0.03 ± 0.02	0.72 ± 0.14	—	0.62 ± 0.13
$A_{Px}Fe_T/100$	0.74 ± 0.14	0.37 ± 0.21	—	0.63 ± 0.08	0.19 ± 0.06	—	1.78 ± 0.11	—	0.24 ± 0.06	0.83 ± 0.13	—	0.71 ± 0.19
$A_{Ilm}Fe_T/100$	0.00 ± 0.01	0.04 ± 0.06	—	0.01 ± 0.03	0	—	0	—	0	0	—	0
$A_{Chr}Fe_T/100$	0	0.01 ± 0.03	—	0	0	—	0	—	0	0	—	0
$A_{Mt}Fe_T/100$	0.39 ± 0.27	0.15 ± 0.13	—	0.16 ± 0.04	0.11 ± 0.01	—	0	—	0	0.13 ± 0.02	—	0.11 ± 0.11
$A_{npOx}Fe_T/100$	0.23 ± 0.10	0.44 ± 0.19	—	0.41 ± 0.14	0	—	0.01 ± 0.02	—	0.03 ± 0.17	0.43 ± 0.18	—	0.44 ± 0.11
$A_{Fe3Sulfate}Fe_T/100$	0	0	—	0	1.35 ± 0.17	—	0	—	0	0	—	0
$A_{Fe3D3}Fe_T/100$	0	0	—	0	0	—	0	—	0.34 ± 0.04	0	—	0
$A_{Jar}Fe_T/100$	0	0	—	0	0	—	0	—	0.51 ± 0.06	0	—	0
$A_{Hm}Fe_T/100$	0.03 ± 0.03	0.28 ± 0.21	—	0.05 ± 0.04	0.31 ± 0.25	—	0	—	0.63 ± 0.08	0.09 ± 0.04	—	1.62 ± 0.79
$A_{Gt}Fe_T/100$	0	0.18 ± 0.20	—	0	0	—	0	—	0	0	—	0
Fe_T	2.24 ± 0.22	1.56 ± 0.38	—	1.91 ± 0.11	2.07 ± 0.40	—	1.80 ± 0.09	—	1.75 ± 0.10	2.21 ± 0.18	—	3.49 ± 0.60
S[c]	0.28 ± 0.15[d]	0.55 ± 0.21	—	0.68 ± 0.24	3.17 ± 0.04	—	0.06 ± 0.01	—	2.27 ± 0.26	0.64 ± 0.11	—	0.61 ± 0.07
					Other parameters							
Fe^{3+}/Fe_T	0.24 ± 0.11	0.63 ± 0.18	—	0.30 ± 0.07	0.83 ± 0.05	—	0.01 ± 0.01	—	0.85 ± 0.03	0.28 ± 0.09	—	0.60 ± 0.13
N[e]	15	35	0	24	2	0	3[f]	0	20[g]	10	0	13

[a] MB and APXS data from Morris *et al.* (2006a,b), Gellert *et al.* (2004), Rieder *et al.* (2004), and Yen *et al.* (2006). Pie diagrams showing distribution of Fe among Fe-bearing phases (values of A_x) are shown in Figure 15.9.
[b] Average concentration and 1σ standard deviation of the average.
[c] Excludes analyses of undisturbed surfaces when analyses of RAT-brushed or RAT-ground surfaces are available.
[d] Excludes Peace and Alligator, which have a Mg-sulfate cement (Ming *et al.*, 2006) but are Weakly Altered Basalt with respect to Fe-bearing phases.
[e] Number of targets with both MB and APXS data.
[f] All analyses are for Bounce Rock. S concentration is from one analysis of a RAT-ground surface; uncertainty is measurement uncertainty.
[g] Includes only analyses for RAT-ground surfaces.

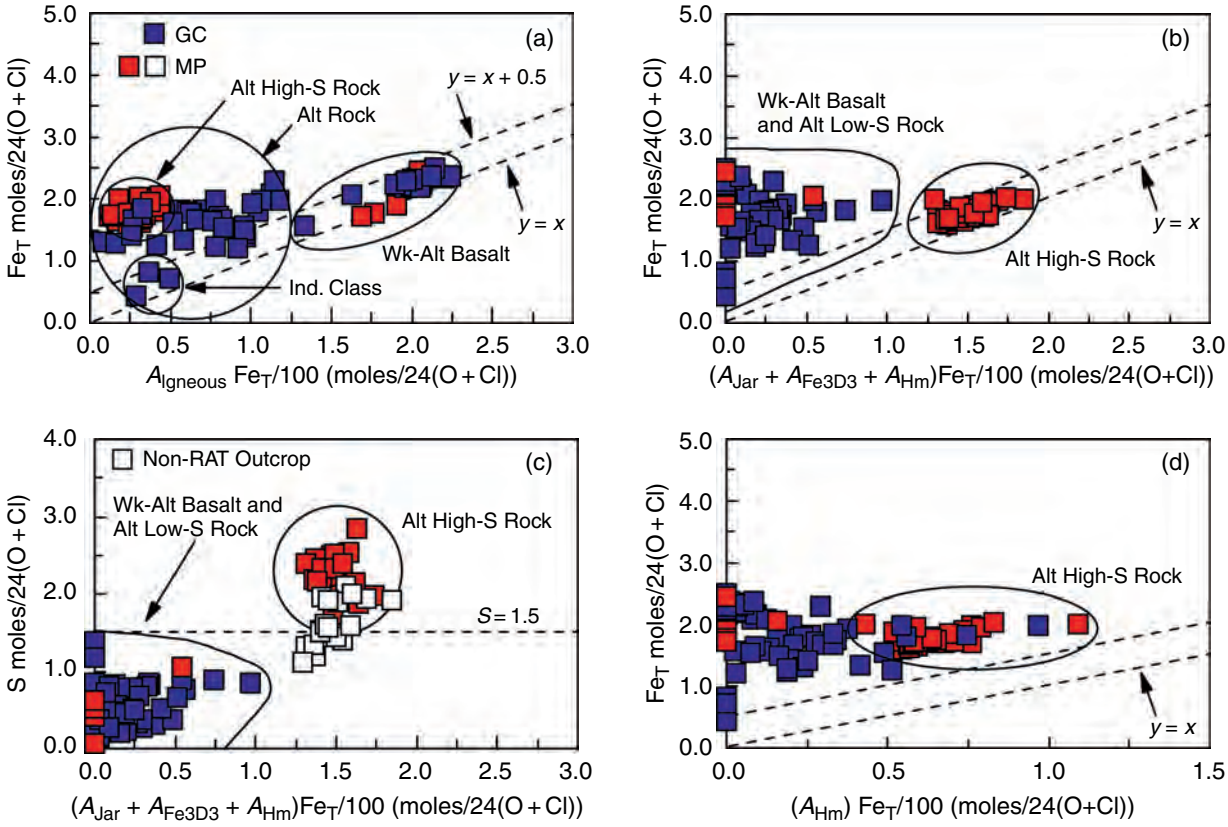

Figure 15.6. Diagrams for assignment of MER nonmeteorite rock samples to supergroups (Weakly Altered Basalt, Altered Low-S Rock, and Altered High-S Rock). (a) Fe_T versus $A_{Igneous}Fe_T/100$, where $A_{Igneous} = A_{Ol} + A_{Px} + A_{Ilm} + A_{Chr} + A_{Mt}$. Weakly Altered Basalts are distinguished from altered rocks by high values of Fe_T and $Fe_T \sim A_{Igneous}\ Fe_T/100$ (dashed line with labeled "$y = x$"). Independence Class rocks (Ind. Class), having $Fe_T \sim A_{Igneous}Fe_T/100$ and low Fe_T, are Altered Low-S Rocks. (b) Fe_T versus $(A_{Jar} + A_{Fe3D3} + A_{Hm})Fe_T/100$. Altered High-S Rocks are distinguished from Altered Low-S Rocks, because Jar, Fe3D3, and Hm are the dominant Fe-bearing phases in the former but not in the latter. (c) S versus $(A_{Jar} + A_{Fe3D3} + A_{Hm})Fe_T/100$. Altered High-S Rocks have S concentration greater than ~1.5 moles/24(O+Cl) (equivalently, ~14.2 wt.% SO_3). Outcrop surfaces not exposed by grinding with the RAT (open square symbols) tend to have lower concentrations of S because the analysis volumes include contributions from soil and dust coatings that have low-S concentrations. (d) Fe_T versus $A_{Hm}Fe_T/100$. High concentrations of Fe from Hm are found in rocks from both Gusev crater and Meridiani Planum. (For a color version of this figure, please refer to the color plate section or to the e-Book version of this chapter.)

presumably by aeolian processes, on a global scale and/or similar precursor rocks on a global scale. Laguna Class soil is similar in mineralogical composition to Weakly Altered Basalt at Gusev crater. Average PRC soil ($Fe^{3+}/Fe_T = 0.83$) has high proportions of Fe from Fe3Sulfate ($A_{Fe3D2} = 65\%$) plus Hm ($A_{Hm} = 14\%$) and silicates ($A_{Ol} + A_{Px} = 16\%$). Paso Robles Class soil has not been detected at Meridiani Planum. Average BC soil ($Fe^{3+}/Fe_T = 0.60$) has high proportions of Fe from Hm ($A_{Hm} = 44\%$) plus Fe from silicates ($A_{Ol} + A_{Px} = 39\%$) and Mt and npOx ($A_{Mt} + A_{npOx} = 16\%$). Berry Class soil is likely a mechanical mixture of Hm-rich spherules (and their fragments) and LC soil. Setting A_{Hm} to 4% for BC soil and recalculating to 100% gives a composition ($A_{Ol} = 32\%$, $A_{Px} = 37\%$, $A_{Mt} = 5\%$, $A_{npOx} = 23\%$, and $A_{Hm} = 4\%$) that is nearly the same as the average for LC soil at Meridiani Planum (Figure 15.9d). Berry Class soil has not been detected at Gusev crater as of sol 602.

15.5 SPATIAL DISTRIBUTION OF ROCK AND SOIL SUPERGROUPS

Together with the Fe^{3+}/Fe_T ratio, the analysis locations for the four rock and three soil supergroups are shown in Figure 15.10 using sol number as a proxy for location. For Gusev crater (Figures 15.10a and 15.10c), Weakly Altered Basalt was analyzed on the Gusev plains (rocks Adirondack, MimiShoe, Humphry, Mazatzal, Route66, and Joshua) and on Husband Hill in the Columbia Hills (rocks Peace, Alligator, Backstay, and Irvine). All these rocks are float (i.e., delivered to their present location rather than formed in place), except for Peace and Alligator which are outcrop rocks. Although Peace and Alligator are Weakly Altered Basalt according to MB analyses, they are enriched in Mg and S suggesting that they were invaded and cemented by Mg-sulfate solutions after formation (e.g., Ming *et al.*, 2006; Squyres *et al.*, 2006b). The oxidation state (Fe^{3+}/Fe_T) of Weakly Altered Basalt is largely controlled by Mt. The rock Route66, with no detectable Mt, has $Fe^{3+}/Fe_T = 0.07$, and the rocks MimiShoe, Peace, and Irvine, which have

Table 15.4. *Classification, target name, location, oxidation state (Fe^{3+}/Fe_T), and $A_{Igneous}$ of rocks at Gusev crater and Meridiani Planum*

Rock name	Class[a]	Subclass[a]	Mössbauer target name[b]	Location[c]	Fe^{3+}/Fe_T	$A_{Igneous}$ (%)
			Rock Supergroup: Weakly Altered Basalt[d]			
Adirondack	Adirondack	—	A034RR0 (Adirondack_Blue)	GC Pl	0.16[e]	93[f]
Humphrey	Adirondack	—	A060RR0 (Humphrey Heyworth2)	GC Pl	0.15	93
Mazatzal	Adirondack	—	A084RR0 (Mazatzal_Brooklyn)	GC Pl	0.10	95
PaperBack	Adirondack	—	A076RU0 (PaperBack_Appendix)	GC Pl	0.23	80
Route66	Adirondack	—	A100RB (Route66_SoHo)	GC HH	0.07	93
Backstay	Backstay	—	A510RB0 (Backstay_Scuppler)	GC HH	0.23	82
Bounce Rock	Bounce Rock	—	B067RR0 (BounceRock_Case)	MP Pl	0.00	100
Irvine	Irvine	—	A602RU0 (Irvine)	GC HH	0.36	90
Alligator	Peace	—	A385RB0 (Alligator_Jambalaya)	GC HH	0.31	86
Peace	Peace	—	A379RR0 (Peace_Justice2)	GC HH	0.37	86
Joshua	Other Rock	Joshua	A150RU0 (Mohave_Joshua)	GC Pl	0.26	87
MimiShoe	Other Rock	Joshua	A042RU0 (MimiShoe_Lace)	GC Pl	0.43	77
			Rock Supergroup: Altered Low-S Rock[d]			
Clovis	Clovis	Clovis	A218RR0 (Clovis_Plano)	GC WS	0.84	17
Ebenezer	Clovis	Clovis	A233RR0 (Ebenzer_Ratchit2)	GC WS	0.83	31
Lutefisk	Clovis	Clovis	A303RB0 (Lutefisk_Roe)	GC WS	0.65	49
Temples	Clovis	Clovis	A269RU (Temples_Dwarf)	GC WS	0.74	33
Tetl	Clovis	Clovis	A275RU0 (Tetle_Clump)	GC WS	0.70	47
Uchben	Clovis	Clovis	A288RR0 (Uchben_Koolik)	GC WS	0.79	31
Wooly Patch	Clovis	Wooly Patch	A200RR0 (WoolyPatch_Mastadon)	GC WS	0.61	50
Assemblee	Independence	—	A568RU0 (Assemblee_Gruyere)	GC HH	0.37	91
Independence	Independence	—	A542RS0 (Independence_Penn2)	GC HH	0.25	32
BreadBox	Other Rock	PotOfGold	A176RU0 (Breadbox_Sourdough)	GC WS	0.47	58
Fork Knox	Other Rock	PotOfGold	A166RU0 (FortKnox_Goldbar)	GC WS	0.52	49
Keel Davis	Watchtower	Keel	A486RB0 (Keel_Davis)	GC HH	0.73	25
Keel Reef	Watchtower	Keel	A483RU0 (Keel_Reef)	GC HH	0.64	43
Keystone	Watchtower	Keystone	A472RB0 (Keystone_Haunch)	GC HH	0.43	57
Paros	Watchtower	Watchtower	A493RB0 (LarrysLookout_Paros)	GC HH	0.94	4
Pequod	Watchtower	Watchtower	A498RU0 (Pequod_Ahab)	GC HH	0.88	6
Watchtower	Watchtower	Watchtower	A418RR0 (WatchTower_Joker)	GC HH	0.83	14
Champagne	Wishstone	—	A358RR0 (Champagne_RAT2)	GC HH	0.45	56
WishingWell	Wishstone	—	A350RU0 (WishingWell_Dreaming)	GC HH	0.41	63
Wishstone	Wishstone	—	A336RR0 (Wishstone_Chisel)	GC HH	0.40	62
PotOfGold	Other Rock	PotOfGold	A173RR0 (HanksHollow_PotOfGold)	GC WS	0.62	39
StringOfPearls	Other Rock	PotOfGold	A178RU (StringOfPearls_Pearl)	GC WS	0.43	59
			Rock Supergroup: Altered High-S Rock[g]			
Blackcow	Burns Outcrop	—	B308RR0 (Blackcow_Wharenhui)	MP-End	0.81	19
Bylot	Burns Outcrop	—	B196RR0 (Bylot_Aktineq3)	MP-End	0.85	15
Diamond Jenness	Burns Outcrop	—	B179RR0 (DiamondJenness_Holeman3)	MP-End	0.88	12
Escher	Burns Outcrop	—	B219RR0 (Escher Kirchner)	MP-End	0.84	16
Flatrock	Burns Outcrop	—	B045RR0 (FlatRock_Mojo2)	MP Eag	0.85	25

Table 15.4. (*cont.*)

Rock name	Class[a]	Subclass[a]	Mössbauer target name[b]	Location[c]	Fe^{3+}/Fe_T	$A_{Igneous}$ (%)
Guadalupe	Burns Outcrop	—	B035RR0 (Guadalupe_King3)	MP Eag	0.90	10
IceCream	Burns Outcrop	—	B548RR0 (IceCream_Onescoop)	MP Pl	0.87	13
Inuvik	Burns Outcrop	—	B188RR0 (Inuvik_Tuktoyaktuk)	MP-End	0.84	16
Lionstone	Burns Outcrop	—	B108RR0 (LionStone_NummaNewNormal)	MP-End	0.86	14
Kentucky	Burns Outcrop	—	B144RR0 (Kentucky_CobbleHill)	MP-End	0.84	16
Mackenzie	Burns Outcrop	—	B183RR0 (Mackenzie_Campbell2)	MP-End	0.84	16
Manitoba	Burns Outcrop	—	B152RR0 (Manitoba_Grindstone)	MP-End	0.82	19
McKittrick	Burns Outcrop	—	B032RR0 (McKittrick_MiddleRAT)	MP Eag	0.87	13
Millstone	Burns Outcrop	—	B163RR0 (Millstone_Drammensfjord)	MP-End	0.78	22
Ontario	Burns Outcrop	—	B150RR0 (Ontario_London)	MP-End	0.81	19
Pilbara	Burns Outcrop	—	B088RR0 (Pilbara_Golf)	MP-Frm	0.90	10
Tennessee	Burns Outcrop	—	B1400RR (Tennessee_Vols)	MP-End	0.85	15
Virginia	Burns Outcrop	—	B148RR0 (LayerC_Virginia)	MP-End	0.82	18
Yuri	Burns Outcrop	—	B404RR0 (Yuri_Gagarin)	MP Pl	0.92	8
			Rock Supergroup: Meteorite[d]			
Barberton	Meteorite	—	B121RU0 (FigTree_Barberton2)	MP End	0.06	83
Heat Shield Rock	Meteorite	—	B351RB0 (SpongeBob_Squidward)	MP Pl	0.06	0

[a] Rock classes Gusev crater from Squyres *et al.* (2006), except for Independence Class. Rock subclass for Gusev crater from Morris *et al.* (2006a).
[b] Target naming convention: Mwwwxyz (Feature-name_Target-name). M = A for MER-A (Gusev crater) or B for MER-B (Meridiani Planum); www = sol number that data product was returned to Earth. For integrations covering multiple sols, the sol of the first returned data product is used. x = R (rock) or S (soil); y = U (undisturbed), D (disturbed), T (trench), B (RAT-brushed surface), R (RAT-ground surface), S (scuff of rock surface by rover wheel), or G (RAT grindings); z = 0 by default; z = 1, 2, 3 . . . for multiple analyses of the same target on the same sol. For MxxxSTz, z = 1, 2, 3 . . . with increasing number corresponding to increasing depth. Alphanumeric strings before parentheses are unique target identifiers.
[c] GC = Gusev crater; Pl = Plains; WS = West Spur; HH = Husband Hill; MP = Meridiani Planum; Eag = Eagle crater; End = Endurance crater.
[d] Includes only the first target for a rock in the order RAT-grind (RR), RAT-brushed (RB), and undisturbed (RU).
[e] Uncertainty = ±0.03.
[f] $A_{Igneous} = A_{Ol} + A_{Px} + A_{Ilm} + A_{Chr} + A_{Mt}$. Note that $A_{Igneous} = (1.0 - MAI)$, where MAI = Mineralogical Alteration Index (Morris *et al.*, 2006a).
[g] Includes only targets of Burns Outcrop exposed by RAT-grinding.

significant concentrations of Mt, have $Fe^{3+}/Fe_T = 0.30–0.43$ (Morris *et al.*, 2006a). CIPW normative mineral calculations for Weakly Altered Basalt from APXS chemistry and MB Fe^{3+}/Fe_T are discussed by McSween *et al.* (2004, 2006). Normative minerals represent the minerals that might crystallize if a rock cooled under equilibrium and anhydrous conditions.

Altered Low-S Rock was analyzed throughout the Columbia Hills. For the most part, the rocks are outcrops (e.g., Wooly Patch, Clovis, and Ebenezer; Squyres *et al.*, 2006b). Clovis at West Spur has the highest measured concentration of Gt ($A_{Gt} = 37\%$). Other Gt-bearing rocks with $A_{Gt} > 10\%$ are Ebenezer, Temples, Tetl, Uchben, Lutefisk, Champagne, Watchtower, Paros, and Pequod. Altered Low-S Rock tends to have higher values of Fe^{3+}/Fe_T compared to Weakly Altered Basalt (0.87 and 0.94 for Clovis and Watchtower respectively), but this is not always the case. For example, Altered low-S outcrop rocks Independence and Assemblee have low values of Fe^{3+}/Fe_T (0.30 and 0.35 respectively) because the Fe associated with primary silicate minerals was removed (presumably by leaching), leaving the oxides Ilm and Chr (Clark *et al.*, 2007).

Laguna Class soil was analyzed throughout the Gusev plains and the Columbia Hills (average $Fe^{3+}/Fe_T = 0.30$) as undisturbed surface soils and as subsurface soils revealed by trenching or other rover wheel actions. The two PRC soils were detected and analyzed on Husband Hill; they are very oxidized ($Fe^{3+}/Fe_T = 0.83$). Paso Robles Class soil occurs in the subsurface, under a thin overburden of LC soil

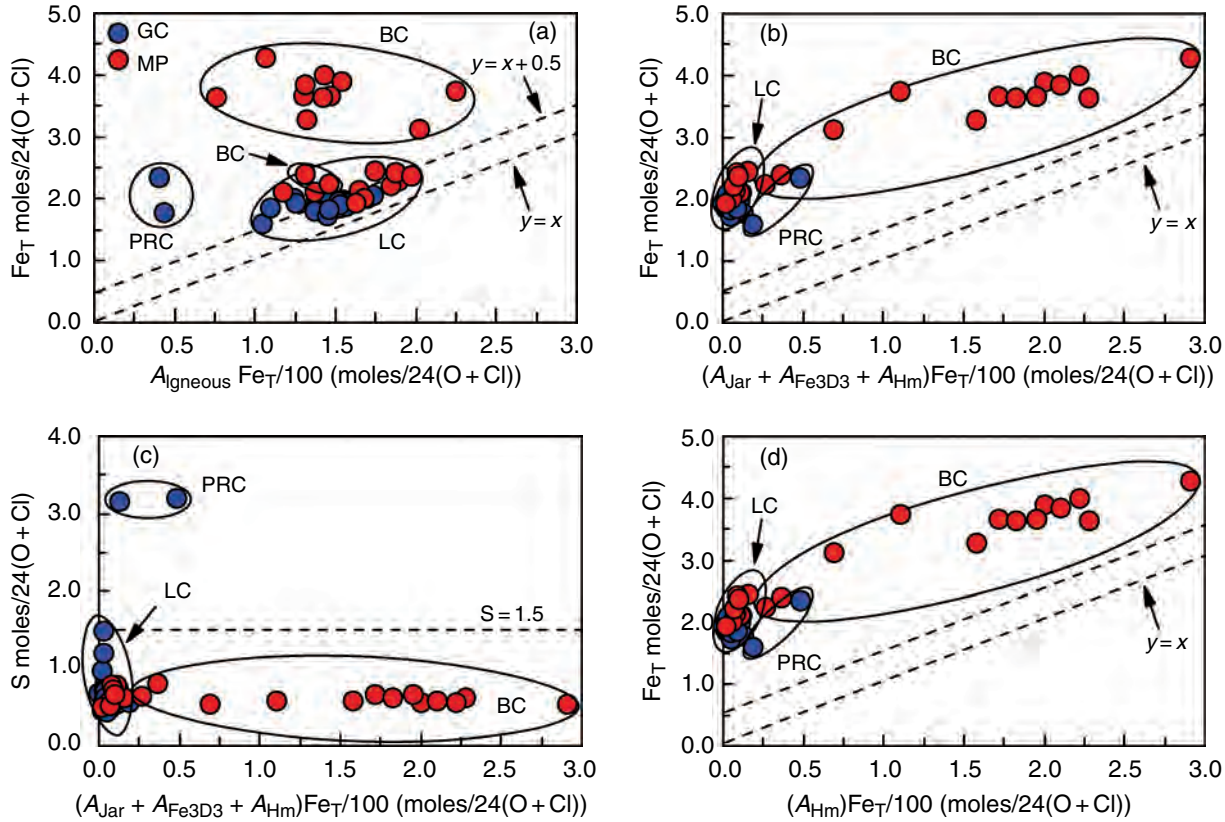

Figure 15.7. Diagrams for assignment of MER soil samples to supergroups (Laguna Class soil, Paso Robles Class soil, and Berry Class soil). (a) Fe_T versus $A_{Igneous}Fe_T/100$. Soils form into Laguna Class (LC), Paso Robles Class (PRC) and Berry Class (BC) supergroups, except for two BC soils that have LC affinities. (b) Fe_T versus $(A_{Jar} + A_{Fe3D3} + A_{Hm})Fe_T/100$. BC soils are distinguished from LC soils. (c) S versus $(A_{Jar} + A_{Fe3D3} + A_{Hm})Fe_T/100$. The three soil supergroups form into different regions. LC and BC supergroups have S concentrations within the range for Altered Low-S Rock (Figure 15.6c). PRC soils at Gusev crater have the highest S concentrations measured on Mars. (d) Fe_T versus $A_{Hm}Fe_T/100$. Soils do not have detectable concentrations of Jar and Fe3D3 (compare with (b)). (For a color version of this figure, please refer to the color plate section or to the e-Book version of this chapter.)

(see, e.g., Chapter 13). Thus, its overall geographic extent is unknown because it cannot be detected from Martian orbit or by *Spirit* without disturbing the surface layer.

For Meridiani Planum (Figures 15.10b and 15.10d), the rock population is dominated by Altered High-S Rock belonging to Burns Outcrop Class (the Burns formation). The Burns formation rocks are highly oxidized and have Hm-rich spherules dispersed throughout the S-rich rock. The spherules are popularly known as "blueberries" and have been interpreted to be concretions (Squyres *et al.*, 2004b, 2006a; Grotzinger *et al.*, 2005). The oxidation state ($Fe^{3+}/Fe_T = 0.85$) and the Fe mineralogical composition of the outcrop (Figure 15.9c) actually pertain to "interspherule" regions, because spherules were not present in the MB analysis volume. No Altered Low-S Rock and only one Weakly Altered Basalt (Bounce Rock) have been identified by the *Opportunity* rover at Meridiani Planum through sol 557. An iron meteorite with Kam (Heat Shield Rock) was analyzed, and Barberton is also a meteorite based on the presence of Kam (Morris *et al.*, 2006b). Bounce Rock, Heat Shield Rock, and Barberton are regarded as "erratics" within the part of Meridiani Planum explored to date by the rover.

Laguna Class soil at Meridiani Planum (average $Fe^{3+}/Fe_T = 0.28$) covers the surface of the Burns formations as aeolian bedforms (small ripples and dunes), except for areas of outcrop exposed by impact events (e.g., Eagle, Fram, and Endurance craters) and in scattered exposed patches in shallow fractures and between bedforms. Berry Class soil, which is composed of basaltic clasts, spherules, and spherule fragments, primarily occurs as a lag deposit at ripple crests or in topographic lows. The cover of LC and BC soils over the Burns formation masks its detection from Martian orbit (e.g., Bell *et al.*, 2004b; Arvidson *et al.*, 2006b). Berry Class soil is the source of the coarse-grained "gray" Hm first detected from Martian orbit by the Mars Global Surveyor Thermal Emission Spectrometer (Christensen *et al.*, 2000, 2001) and is thus the mineralogical beacon that focused attention on Meridiani Planum as an MER landing site (e.g., Golombek *et al.*, 2003).

15.6 NPOX, S, AND CL IN MARTIAN SOIL AND DUST

We discussed earlier the assignment of the oct-Fe^{3+} doublet Fe3D1 to npOx, which is a generic name for a poorly

Table 15.5. *Classification, target name, location, oxidation state (Fe^{3+}/Fe_T), and $A_{Igneous}$ of soils at Gusev crater and Meridiani Planum*

Soil name	Subclass[a]	Mössbauer target name[b]	Location[c]	Fe^{3+}/Fe_T	$A_{Igneous}$ (%)
		Soil Supergroup: Laguna Class[a]			
Auk	Panda	B237SB0 (Auk_AukRAT)	MP End	0.20[d]	84[e]
BearPaw Panda	Panda	A073SD0 (BearPaw_Panda)	GC Pl	0.25	84
Big Hole May Fly	Boroughs	A113ST1 (BigHole_MayFly)	GC Pl	0.26	82
Big Hole RS2	Boroughs	A114ST2 (Bighole_RS2)	GC Pl	0.44	62
Brians Choice	Liberty	B056SU0 (BlackForest_BriansChoice)	MP Eag	0.27	78
Coffee	Liberty	A281SD0 (TakeABreak_Coffee)	GC WS	0.31	78
Cookie Cutter	Gobi	A182SU0 (CookieCutter_Shortbread)	GC WS	0.38	71
Conjunction	Gobi	A260SD0 (Conjunction_Disturbance)	GC WS	0.31	75
Crumble	Panda	A459SU0 (Crumble_Almonds)	GC HH	0.21	84
Cutthroat	Gobi	A122SD0 (Cutthroat_Owens)	GC Pl	0.34	75
Dahlia	Panda	B165SU0 (Millstone_Dahlia)	MP End	0.20	83
Desert Gobi	Gobi	A069SU0 (Desert_Gobi)	GC Pl	0.36	70
Fine soil	Panda	B038SU0 (FineSoil_Paydirt)	MP Eag	0.22	83
First soil	Gobi	A014SU0 (FirstSoil)	GC Pl	0.29	75
Goldfinger	Panda	A167SU0 (Goldfinger_Jaws)	GC WS	0.26	82
Hells Kitchen	Boroughs	A141ST2 (Boroughs_HellsKitchen)	GC Pl	0.42	65
Hema Trench Bottom	Gobi	B025ST2 (BigDig HemaTrench1)	MP Eag	0.48	55
Hema Trench Wall	Gobi	B026ST1 (BigDig_HemaTrenchWall2)	MP Eag	0.32	72
Jeffs Choice	Liberty	B078ST1 (DogPark_JeffsChoice)	MP Pl	0.27	78
Laguna Hollow Floor	Panda	A049ST2 (LagunaHollow_Floor3)	GC Pl	0.23	84
Laguna Hollow Trout	Liberty	A047SU0 (LagunaHollow_Trout1)	GC Pl	0.30	76
Laguna Hollow Wall	Panda	A050ST1 (LagunaHollow_WallMIonly)	GC Pl	0.23	83
Left of Peanut	Liberty	B367ST1 (TrenchSite_LeftOfPeanut)	MP Pl	0.27	77
Les Hauches	Gobi	B060SU0 (MontBlanc_LesHauches)	MP Eag	0.39	65
Liberty	Liberty	A479SU0 (Liberty_Bell)	GC HH	0.25	79
McDonnell	Liberty	B123SU0 (HillTop_McDonnell)	MP End	0.28	77
Mazatzal Flats	Liberty	A077SU0 (MazatzalFlats_Soil1)	GC Pl	0.30	79
Meringue	Liberty	B055SU0 (Meringue_MBone)	MP Eag	0.24	80
Merlot	Panda	B011SU0 (Merlot_Tarmac)	MP Eag	0.22	82
Mill Basin	Boroughs	A140ST1 (Boroughs_MillBasin)	GC Pl	0.36	69
Mimi Tracks	Panda	A043SD0 (MimiTracks_Middle)	GC Pl	0.27	78
Mount Hillyer	Liberty	A135SD0 (MountHillyer_HorseFlats)	GC Pl	0.26	80
Paso Dark	Liberty	A426SD0 (PasoRobles2_PasoDark)	GC HH	0.27	80
Penny	Panda	A342SD0 (Penny_DS1)	GC HH	0.22	84
Rocknest	Panda	B246SU0 (Rocknest_VoidMod)	MP End	0.21	84
Scruffy	Panda	B373SD0 (Trench_Scruffy)	MP Pl	0.21	83
Shreaded	Panda	A158SD0 (Shreaded_Dark4)	GC WS	0.22	83
Waffel Flats	Gobi	A110SU0 (WaffelFlats_Soil1)	GC Pl	0.40	75
Yams	Liberty	A316SD0 (Yams_Turkey)	GC WS	0.30	76
		Soil Supergroup: Paso Robles Class			
Paso Light	—	A429SD0 (PasoRobles2_PasoLight1)	GC HH	0.79	24
Paso Robles	—	A401SD0 (Pasadena_PasoRobles)	GC HH	0.86	17

Table 15.5. (*cont.*)

Soil name	Subclass[a]	Mössbauer target name[b]	Location[c]	Fe^{3+}/Fe_T	$A_{Igneous}$ (%)
		Soil Supergroup: Berry Class			
Aegean Crest	Moessberry	B073SU0 (Seas_AegeanCrest)	MP Pl	0.76	30
Berry Stop	Moessberry	B097SU0 (BerryStop_LeahsChoice)	MP Pl	0.63	40
Berry Survey	Moessberry	B222SU0 (BerrySurvey_Cluster3)	MP End	0.64	37
Cavair	Nougat	B369SU0 (TrenchRipple_Cavair_Tweaked)	MP Pl	0.45	60
Cleo	Moessberry	B063SU0 (Whitestreak_Cleo3)	MP Pl	0.67	36
Freckles	Nougat	B017SU (BerryFlats_Freckles)	MP Eag	0.46	54
Fred Ripple	Moessberry	B091RU0 (PhotoTIDD_FredRipple)	MP Pl	0.66	39
Hematite Slope	Nougat	B023SU0 (HematiteSlope_Hema2)	MP Eag	0.39	65
Jack Russell	Moessberry	B080SU0 (DogPark_Jack Russell)	MP Pl	0.64	36
Mayberooz	Moessberry	B420SU0 (Ripple Mayberooz)	MP Pl	0.66	34
Mobarak	Moessberry	B415SU0 (MattsChoice_Mobarak)	MP Pl	0.61	40
MoessBerry	Moessberry	B048SU0 (BerryBowl_MoessBerry)	MP Eag	0.79	21
Mud Pie	Nougat	B054SU0 (MudPie_Coconut2)	MP Eag	0.30	75
Munter	Nougat	B062SU0 (BlackPatch Munter)	MP Pl	0.40	66
Norooz	Moessberry	B419SU0 (Ripple_Norooz)	MP Pl	0.65	35
Nougat	Nougat	B090SD0 (PhotoTIDD_Nougat)	MP Pl	0.40	65
Nullarbor	Moessberry	B084SU0 (Nullarbor_GreatSandy)	MP Pl	0.70	33
Panaluu	Moessberry	B052SU (Goal5WorkVolume_Panaluu)	MP Eag	0.78	28
Purgatory	Nougat	B509SD0 (Purgatory_Track2)	MP Pl	0.49	55
Recovery Soil	Moessberry	B445SU0 (RecoverySoil_Cure)	MP Pl	0.63	39
Ripple Crest	Moessberry	B368SU0 (TrenchRipple_RippleCrest2b)	MP Pl	0.75	25
Vanilla	Nougat	B053SU0 (Goal3Field_Vanilla)	MP Eag	0.35	70
		Unclassified soil			
Doubloon	Doubloon	A502SU0 (Pequod_Doubloon)	GC HH	0.38	66

[a] Soil classes and subclasses from Morris *et al.* (2006a,b).
[b] See Table 15.4 footnote for target naming convention.
[c] GC = Gusev crater; Pl = Plains; WS = West Spur; HH = Husband Hill; MP = Meridiani Planum; Eag = Eagle crater; End = Endurance crater.
[d] Uncertainty = ± 0.03.
[e] $A_{Igneous} = A_{Ol} + A_{Px} + A_{Ilm} + A_{Chr} + A_{Mt}$. Note that $A_{Igneous} = (1.0 - MAI)$, where MAI = Mineralogical Alteration Index (Morris *et al.*, 2006a).

crystalline (probably X-ray amorphous) alteration product with oct-Fe^{3+} as the Fe cation. The concentration of Fe from npOx ($A_{npOx}Fe_T/100$) in LC and BC Martian soils is highly variable (Figure 15.11), ranging from ~0.2 moles/24(O+ Cl) at one extreme (e.g., samples BearPaw_Panda and Crumble_Almonds at Gusev crater) to ~0.8 moles/24(O+ Cl) at the other extreme (e.g., samples Desert_Gobi, Bighole_RS2, and Wymper at Gusev crater and MontBlanc_LesHauches, Pergatory_Track2, and BigDig_HemaTrench1 at Meridiani Planum). Undisturbed (by rover wheels) surface soils that are bright (high albedo) in Pancam observations (Bell *et al.*, 2004a) and have high-dust signatures according to Mini-TES (Christensen *et al.*, 2004a) characteristically have high values of $A_{npOx}Fe_T/100$ (e.g., samples Desert_Gobi, Wymper, MontBlanc_LesHauches, and Pergatory_Track2). Disturbed soils (except PRC soil) and undisturbed soils that are dark and have low-dust signatures characteristically have low values of $A_{npOx}Fe_T/100$ (e.g., sample BearPaw_Panda). These associations imply that Martian dust, in addition to being bright and fine grained, has high concentrations of npOx, perhaps higher than for any soil that has been analyzed by MB to date (Morris *et al.*, 2006a,b).

In Figure 15.11a, we plot the concentration of S as a function of $A_{npOx}Fe_T/100$ for LC and BC soils (after Yen *et al.*, 2005; Morris *et al.*, 2006a,b). We also include analyses for two thick dust coatings on the Gusev crater rock Mazatzal (samples Mazatzal_NewYork and Mazatzal_Oregon) (Morris *et al.*, 2006a). The solid line is the linear least-squares fit of the data excluding the two analyses of subsurface soils from the Boroughs trench. The trench

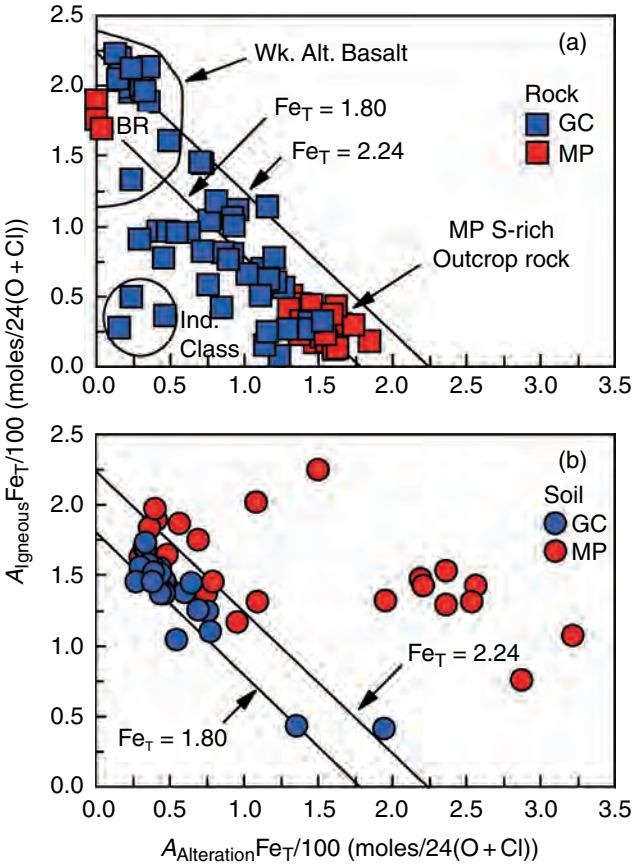

Figure 15.8. Plots of $A_{\text{Igneous}}\text{Fe}_T/100$ versus $A_{\text{Alteration}}\text{Fe}_T/100$ for (a) rock and (b) soil at Gusev crater (GC) and Meridiani Planum (MP). Solid lines correspond to $\text{Fe}_T = 2.24$ and 1.80 moles/24(O+ Cl). Weakly Altered Basalts (Wk. Alt. Basalt) plot near the upper left corner of (a). Assuming that all unaltered Martian rocks have $\text{Fe}_T > 1.0$ moles/24(O+ Cl) and $A_{\text{Alteration}}\text{Fe}_T/100 \sim 0$ moles/24(O+ Cl), compositions that plot on the *y*-axis of (a) with $\text{Fe}_T < 1.0$ moles/24(O+ Cl) are rocks altered in an open system without retention of Fe-bearing alteration products. Independence Class (Ind. Class) rocks, for example, are examples of rocks that show evidence for alteration in an open system. Samples that plot along a line of constant Fe_T (e.g., $\text{Fe}_T = 2.24$ and 1.80 moles/24(O+ Cl)) are only potentially related by isochemical alteration (on an H_2O-free basis), because all elemental concentrations must be considered to validate isochemical alteration. For example, in (a), Bounce Rock (BR) and MP S-rich outcrop rocks plot along the line with $\text{Fe}_T = 1.80$ moles/24(O+ Cl) but are not related by isochemical alteration because of differences in major element chemistry (e.g., Rieder *et al.*, 2004). (For a color version of this figure, please refer to the color plate section or to the e-Book version of this chapter.)

analyses were excluded because they have anonymously high concentrations of Mg and S, indicating the presence of a Mg-sulfate that is not present in the other soils (Wang *et al.*, 2006a). Figure 15.11b is the corresponding plot for Cl, and the solid line is the linear least-squares fit for all the data. The equations for the fits are given in Figure 15.11.

A simple explanation of the data in Figure 15.11 is that the soils are binary mixtures of two endmembers. One endmember, which has the lowest concentrations of $A_{\text{npOx}}\text{Fe}_T$, S, and Cl, is the composition represented by the *y*-intercepts of the linear least-squares fits ($A_{\text{npOx}}\text{Fe}_T/100 = 0.0$ moles/24(O+ Cl)), i.e., 0.37 and 0.12 moles/24(O+ Cl) for S and Cl, respectively. The second endmember is an altered soil having concentrations of S, Cl, and $A_{\text{npOx}}\text{Fe}_T/100$ extrapolated along the least squares lines to a value of $A_{\text{npOx}}\text{Fe}_T/100$ greater than 0.84 moles/24(O+ Cl), the highest value observed for that parameter. The upper limit for $A_{\text{npOx}}\text{Fe}_T/100$ is Fe_T, which is ~2.0 moles/24(O+ Cl) for LC soil at Gusev crater (Figure 15.7a). The corresponding upper limit concentrations for S and Cl are 1.6 and 0.36 moles/24(O+ Cl) respectively. The molar S/Cl ratio depends on $A_{\text{npOx}}\text{Fe}_T/100$, ranging from 3.1 for $A_{\text{npOx}}\text{Fe}_T/100 = 0$ moles/24(O+ Cl) to 4.4 for $A_{\text{npOx}}\text{Fe}_T/100 = 2.0$ moles/24(O+ Cl).

The slopes in Figure 15.11 give molar S/($A_{\text{npOx}}\text{Fe}_T/100$) and Cl/($A_{\text{npOx}}\text{Fe}_T/100$) ratios (0.62 and 0.12 respectively) that are potentially characterizing parameters for npOx. Molar S/Fe ratios for typical terrestrial ferric sulfates are 0.13–0.25 for schwertmannite, 0.67 for Jar, 1.5 for binary Fe-sulfates ($Fe_2(SO_4)_3 \cdot nH_2O$), and 1.3 for ferricopiapite ($Fe_{4.67}(SO_4)_6(OH)_2 \cdot 20H_2O$). Although the observed value of the S/Fe molar ratio for npOx is comparable to the value for Jar, we believe that the correspondence is a coincidence and not causative evidence for Jar because (a) the quadrupole splitting (average ± 1σ) for npOx in soils is too low (0.91 ± 0.07 mm/s) compared to 1.20 ± 0.02 mm/s for Meridiani Planum Jar (Morris *et al.*, 2006b); (b) the molar S/Fe and Cl/Fe ratios are actually upper limits; and (c) reflectivity spectra do not provide a mineralogical constraint for Jar. With regard to (b), the previous discussion assumes that all S and Cl are associated with npOx. The actual S/Fe and Cl/Fe ratios for npOx would be lower in a scenario where npOx and one or more S- and Cl-bearing and Fe-free phases are formed contemporaneously in fixed proportions during weathering. With regard to (c), multispectral Pathfinder IMP (IMP – Imager for Mars Pathfinder) and MER Pancam visible to near-IR data (0.40–1.1 μm) and hyperspectral OMEGA (OMEGA – Observatoire pour la Minéralogie, l'Eau, les Glaces et l'Activité) near-IR data (1.0–2.5 μm) for Martian bright regions show a relatively featureless ferric absorption edge extending from ~0.40 to ~0.75 μm and relative constant reflectivity from ~0.75 to 2.5 μm. These spectral characteristics imply npOx and not a Jar-like phase (e.g., Bell *et al.*, 2000, 2004a,b; Morris *et al.*, 2000; Bibring *et al.*, 2006). According to Bibring *et al.* (2006), the absence of detectable spectra features near 1.4, 1.9, and 2.1–2.4 μm in OMEGA spectra imply that the surface material in Martian bright regions (dust or bright soil) is anhydrous. Specifically, a spectral feature associated with the Fe-OH vibration of Jar (or any other phase with the Fe-OH functional group) was not detected, although the presence of a spectral feature near 3 μm implies that some H_2O/OH must be present (e.g., Yen *et al.*, 1998).

Would we expect to find surface deposits of dust (bright soil) with $A_{\text{npOx}}\text{Fe}_T/100 = \text{Fe}_T$? That is, might there be a high-albedo soil with npOx as the only Fe-bearing phase, with Fe, S, and Cl concentrations of ~2.0, 1.6, and 0.36

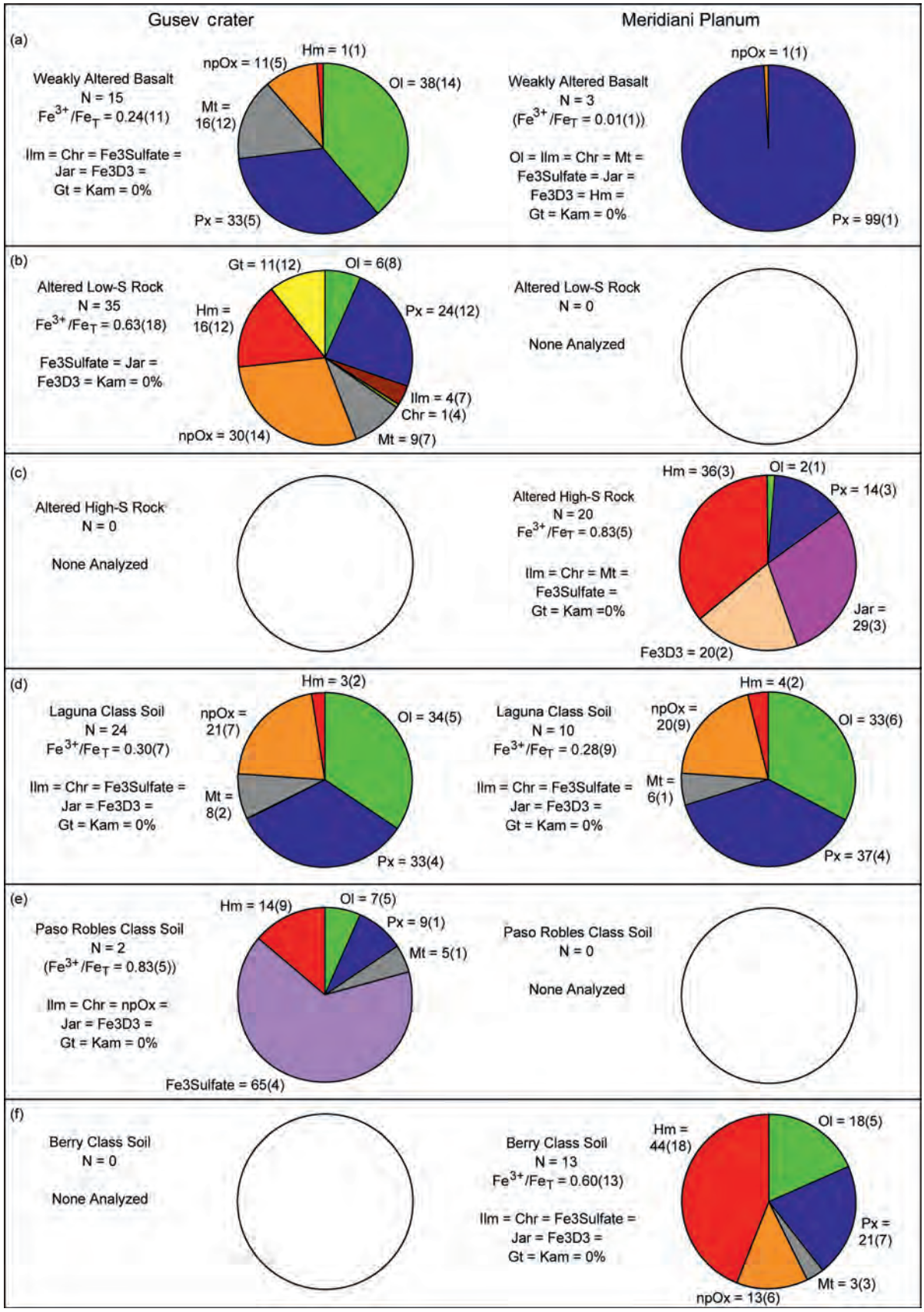
Gusev crater
Meridiani Planum
(a)
Weakly Altered Basalt
N = 15
Fe3+/FeT = 0.24(11)
Ilm = Chr = Fe3Sulfate = Jar = Fe3D3 = Gt = Kam = 0%
Hm = 1(1)
npOx = 11(5)
Ol = 38(14)
Mt = 16(12)
Px = 33(5)
Weakly Altered Basalt
N = 3
(Fe3+/FeT = 0.01(1))
Ol = Ilm = Chr = Mt = Fe3Sulfate = Jar = Fe3D3 = Hm = Gt = Kam = 0%
npOx = 1(1)
Px = 99(1)
(b)
Altered Low-S Rock
N = 35
Fe3+/FeT = 0.63(18)
Fe3Sulfate = Jar = Fe3D3 = Kam = 0%
Gt = 11(12)
Ol = 6(8)
Hm = 16(12)
Px = 24(12)
Ilm = 4(7)
Chr = 1(4)
npOx = 30(14)
Mt = 9(7)
Altered Low-S Rock
N = 0
None Analyzed
(c)
Altered High-S Rock
N = 0
None Analyzed
Altered High-S Rock
N = 20
Fe3+/FeT = 0.83(5)
Ilm = Chr = Mt = Fe3Sulfate = Gt = Kam =0%
Hm = 36(3)
Ol = 2(1)
Px = 14(3)
Jar = 29(3)
Fe3D3 = 20(2)
(d)
Laguna Class Soil
N = 24
Fe3+/FeT = 0.30(7)
Ilm = Chr = Fe3Sulfate = Jar = Fe3D3 = Gt = Kam = 0%
Hm = 3(2)
npOx = 21(7)
Ol = 34(5)
Mt = 8(2)
Px = 33(4)
Laguna Class Soil
N = 10
Fe3+/FeT = 0.28(9)
Ilm = Chr = Fe3Sulfate = Jar = Fe3D3 = Gt = Kam = 0%
Hm = 4(2)
npOx = 20(9)
Ol = 33(6)
Mt = 6(1)
Px = 37(4)
(e)
Paso Robles Class Soil
N = 2
(Fe3+/FeT = 0.83(5))
Ilm = Chr = npOx = Jar = Fe3D3 = Gt = Kam = 0%
Hm = 14(9)
Ol = 7(5)
Px = 9(1)
Mt = 5(1)
Fe3Sulfate = 65(4)
Paso Robles Class Soil
N = 0
None Analyzed
(f)
Berry Class Soil
N = 0
None Analyzed
Berry Class Soil
N = 13
Fe3+/FeT = 0.60(13)
Ilm = Chr = Fe3Sulfate = Jar = Fe3D3 = Gt = Kam = 0%
Hm = 44(18)
Ol = 18(5)
Px = 21(7)
Mt = 3(3)
npOx = 13(6)

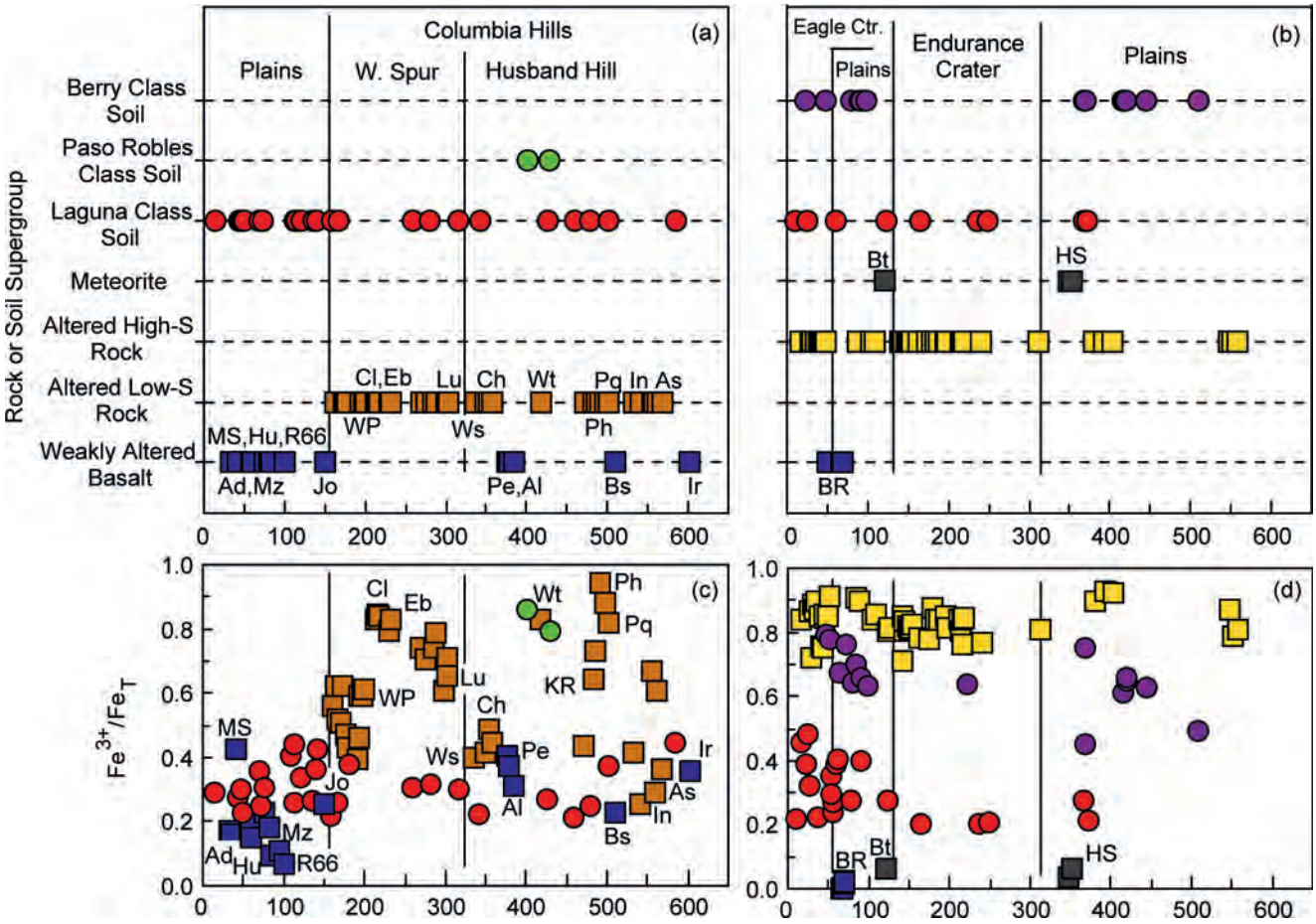

Figure 15.10. Supergroup membership of rock and soil analyses and Fe^{3+}/Fe_T as a function of sol number for Gusev crater (a and c) and Meridiani Planum (b and d). Sol number is a proxy for location, and general location names are shown in the figures. The Weakly Altered Basalts are Adirondack (Ad), Mimi Shoe (MS), Humphrey (Hu), Mazatzal (Mz), Route66 (R66), Joshua (Jo), Peace (Pe), Alligator (Al), Backstay (Bs), Irvine (Ir), and Bounce Rock (BR). The significant range in Fe^{3+}/Fe_T for Weakly Altered Basalt results from variable contributions from magnetite which has $Fe^{3+}/Fe_T = 0.67$ for the stoichiometric composition (Fe_3O_4). The Altered Low-S Rocks are Wooly Patch (WP), Clovis (Cl), Ebenezer (Eb), Wishstone (Ws), Champagne (Ch), Watchtower (Wt), Pharos (Ph), Pequod (Pq), Independence (In), and Assemblee (As). Barberton (Bt) and Heat Shield (HS) rocks are meteorites at Meridiani Planum. (For a color version of this figure, please refer to the color plate section or to the e-Book version of this chapter.)

moles/24(O+ Cl), and with a featureless ferric absorption edge at visible wavelengths? Although possible, such an occurrence is unlikely based on MB spectra of atmospheric dust collected by the MER permanent magnets, which revealed Fe from Ol, Px, and Mt, as well as npOx, in the airborne dust (e.g., Goetz *et al.*, 2005).

Caption for Figure 15.9. Pie diagrams showing the average values (1σ standard deviation in parenthesis) of Fe from Fe-bearing phases (A_x, where x = Ol, Px, Ilm, Chr, Mt, npOx, Fe3Sulfate, Fe3D3, Jar, Hm, and Gt) for rock and soil supergroups at Gusev crater (as of sol 602) and Meridiani Planum (as of sol 557): (a) Weakly Altered Basalt, (b) Altered Low-S Rock, and (c) Altered High-S Rock for RAT-ground surfaces, (d) Laguna Class soil, (e) Paso Robles Class soil, and (f) Berry Class soil. Altered High-S Rock and Berry Class soil are not present at Gusev crater and Altered Low-S Rock and Paso Robles Class soil are not present at Meridiani Planum. The distribution of Fe from Fe-bearing phases for Gusev crater Weakly Altered Basalt (a) is very similar to that for Laguna Class soil (d), except the latter has more Fe from npOx. The meteorite supergroup (not shown), whose distinguishing characteristic is kamacite as an Fe-bearing phase, includes two rocks from Meridiani Planum (Heat Shield and Barberton) and no rocks from Gusev crater. The average concentrations of Fe associated with iron-bearing phases ($A_xFe_T/100$) are given in Table 15.3. (For a color version of this figure, please refer to the color plate section or to the e-Book version of this chapter.)

15.7 MINERALOGICAL EVIDENCE FOR AQUEOUS ACTIVITY ON MARS

Although the MER MB spectrometers are not directly sensitive to either the H_2O molecule or the OH^{-1}, they did identify two Fe-bearing phases that have OH^{-1} as a part of their structure and thus did provide direct mineralogical evidence for aqueous activity on Mars. First, Gt (α-FeOOH) is present at Gusev crater in a series of outcrop rocks (Clovis Class) on Husband Hill (Morris *et al.*, 2006a). The rock Clovis

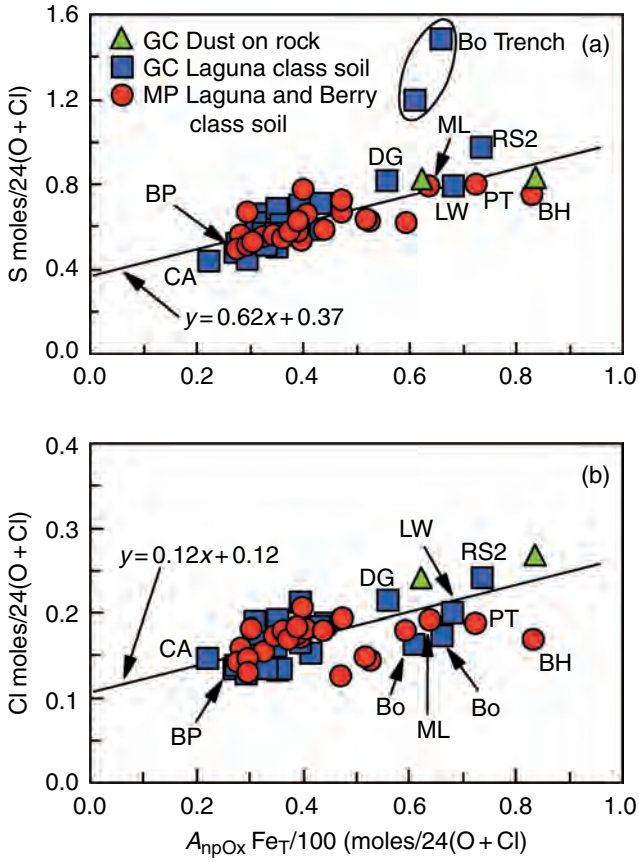

Figure 15.11. Molar concentrations of (a) S and (b) Cl versus the molar concentration of Fe from npOx ($A_{npOx}Fe_T/100$) for Laguna and Berry Class soils and two analyses of thick dust coatings on the Gusev crater rock Mazatzal. The solid lines are linear least squares fits, excluding the subsurface Boroughs trench (Bo Trench) samples in (a). The slopes of the lines are upper limits for the molar ratios of S/Fe (0.62) and Cl/Fe (0.12) for npOx (see text). Specific soil samples labeled on the graph are Crumble_Almond (CA), BearPaw Panda (BP), Desert_Gobi (DG), Boroughs_MillBasin and Boroughs_HellsKitchen (Bo), MontBlanc_LesHauches (ML), Lambert_Whymper (LW), BigHole_RS2 (RS2), Purgatory_Track2 (PT), and BigDig_HemaTrench1 (BH). (For a color version of this figure, please refer to the color plate section or to the e-Book version of this chapter.)

has the highest Gt concentration (A_{Gt} ~37%). The detection of Gt in multiple outcrop rocks implies an extensive occurrence at Husband Hill in particular and perhaps in the Columbia Hills in general. And second, Jar ($(K,Na,H_3O)(Fe,Al)_3(SO_4)_2(OH,Cl)_6$, where Fe > Al and OH > Cl) is present throughout Meridiani Planum in the S-rich outcrop (Burns formation) (Morris *et al.*, 2006b). The Jar concentration is remarkably constant throughout the Burns formation (A_{Jar} ~29%). Both Gt and Jar yield ~10 wt.% H_2O upon dehydroxylation, so that Clovis and the Burns formation have the equivalent of ~1–2 wt.% H_2O based on just their Gt and Jar contents respectively. On the basis of elemental data and mineralogical compositions constrained by MB data, Clark *et al.* (2005) estimated that the Burns formation might have the equivalent of ~6–20 wt.% H_2O overall.

The Jar detection is also important because its formation is constrained to acid-sulfate environments (pH <4 at room temperature; e.g., Dutrizac and Jambor, 2000; Stoffregen *et al.*, 2000). Under hydrothermal conditions, Jar can form at pH = 1 to 2, and Hm instead of Gt is the favored hydrolysis product (Stoffregen *et al.*, 2000). The alteration of a basaltic precursor resulting in the S-rich Burns formation could have occurred under oxidizing, acid-sulfate conditions provided by interactions with acid-sulfate (possibly hydrothermal) waters (Burns, 1988; Burns and Fisher, 1990; McLennan *et al.*, 2005) and/or condensation of SO_2-rich volcanic emanations (Clark and Baird, 1979; Settle, 1979; Banin *et al.*, 1997). Jarosite is a known product of alteration of basaltic/andesitic precursors in association with acid-sulfate volcanic activity on the Earth (e.g., Johnson, 1977; Morris *et al.*, 1996, 2000; Bishop *et al.*, 1998). Interestingly, on Mauna Kea volcano (Hawaii), small Hm-rich spherules are also found in S-rich basaltic material (Morris *et al.*, 2005).

Other evidence based on Fe mineralogical compositions point to aqueous activity. The Independence Class rocks (Independence and Assemblee) have a Fe^{2+} mineral assemblage that is atypical for unaltered igneous rocks ($A_{Ilm} + A_{Chr} > A_{Ol} + A_{Px}$). This result, plus their low-Fe_T concentrations (<1.0 moles/24(O+ Cl); Figure 15.6a), suggests dissolution of Ol and Px and subsequent leaching of Fe. The residual rock has an elemental composition that suggests the presence of the phyllosilicate montmorillonite or its compositional equivalent (Clark *et al.*, 2007). The high concentration of Fe^{3+} sulfate in PRC soil and its bulk elemental composition point to alteration of basaltic precursors under acid-sulfate and oxidizing conditions. Additional evidence for aqueous alteration in the Columbia Hills is developed in more detail by Ming *et al.* (2006; also see Chapter 23), and further details and models for the aqueous alteration history of Meridiani Planum are described by McLennan *et al.* (2005), Grotzinger *et al.* (2005), Squyres *et al.* (2005), Knauth *et al.* (2005), McCollom and Hynek (2005a,b), and Zolotov and Shock (2005). Also see Chapter 24.

15.8 MINERALOGICAL AND OXIDATION STATE DIVERSITY DURING ISOCHEMICAL ALTERATION

The Watchtower Class rocks on Husband Hill in the Columbia Hills of Gusev crater are a group of chemically similar but mineralogically diverse outcrop rocks (Ming *et al.*, 2006; Morris *et al.*, 2006a; Squyres *et al.*, 2006b). The mineralogical diversity of their Fe-bearing phases is shown in Figure 15.12. When available, we used APXS and MB analyses for surfaces brushed or ground by the RAT. The values of $A_{Igneous}Fe_T/100$ range from 0.78 moles/24(O+ Cl) for Keystone, the least oxidized rock ($Fe^{3+}/Fe_T = 0.43$), to 0.08 moles/24(O+ Cl) for Paros, the most oxidized rock at Gusev crater ($Fe^{3+}/Fe_T = 0.94$). Keystone has ~63% of its iron from primary igneous phases (Px, Ol, Ilm, and Mt) and Paros has only ~6%.

How can such extreme diversity in mineralogical composition and oxidation state be achieved relatively isochemically?

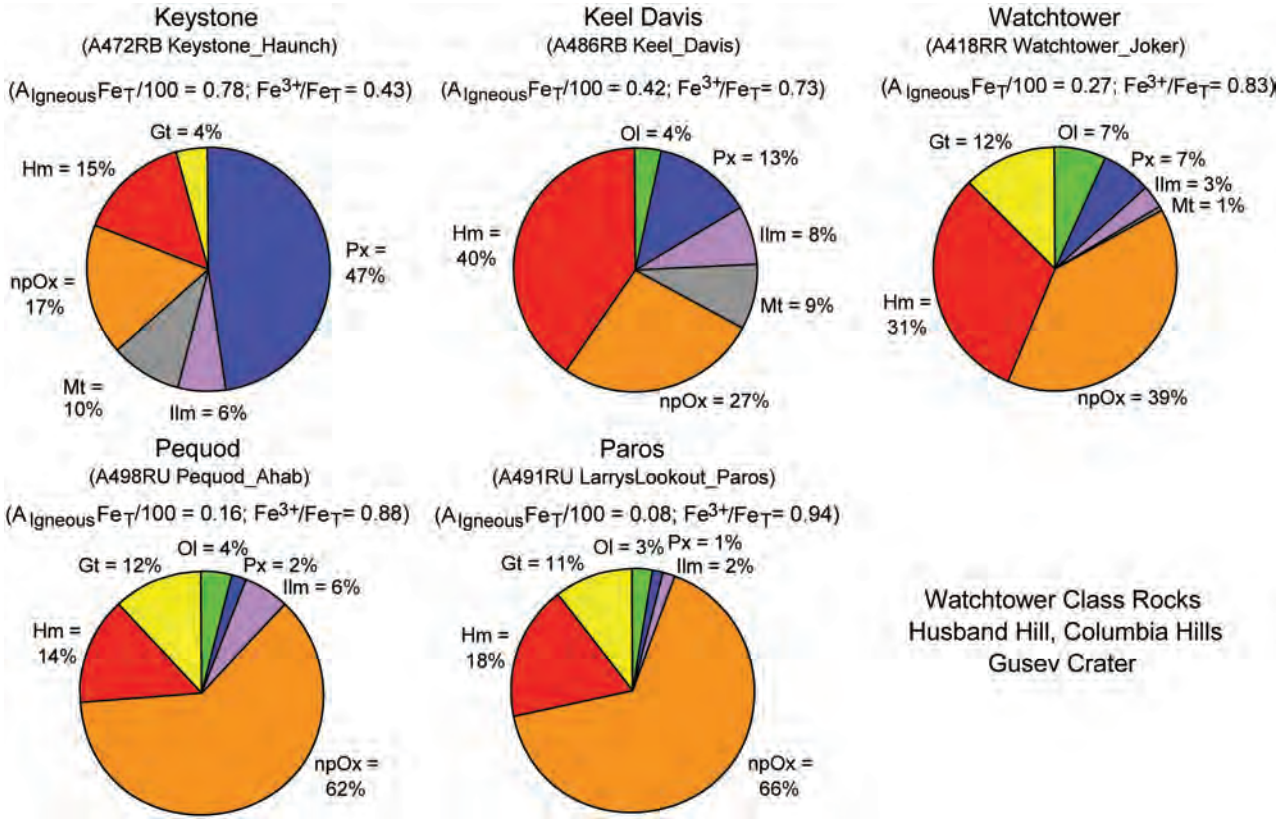

Figure 15.12. Pie diagrams showing Fe mineralogical compositions for Watchtower Class rocks Methusela, Jibsheet, Watchtower, Pequod, and Paros in the Gusev Columbia Hills. These rocks likely have undergone isochemical alteration under low water-to-rock ratio conditions because they have similar chemical compositions but diverse mineralogical compositions ($A_{\text{Ingeous}}\text{Fe}_\text{T}/100 = 0.78$ to 0.08) and Fe oxidations states ($\text{Fe}^{3+}/\text{Fe}_\text{T} = 0.43$ to 0.94). (For a color version of this figure, please refer to the color plate section or to the e-Book version of this chapter.)

However, the presence of Gt in most of the rocks implies aqueous alteration. The nearly constant chemical composition implies low water-to-rock ratios to prevent or minimize chemical fractionation by transport of elements as dissolved species in aqueous solutions. A terrestrial example of isochemical alteration resulting in mineralogical and oxidation state diversity can be found in the 230 m thick, 55 km diameter melt sheet of the Manicouagan impact structure (Quebec, Canada) (Floran *et al.*, 1976, 1978; Simonds *et al.*, 1978; Morris *et al.*, 1995). There are no statistically significant vertical, horizontal, or radial differences in the regional chemical composition of the melt sheet (Floran *et al.*, 1978), and yet the mineralogical diversity of Manicouagan impact melt rocks is as extreme as for Watchtower Class rocks. Considering just MB mineralogy (Morris *et al.*, 1995), the values of $\text{Fe}^{3+}/\text{Fe}_\text{T}$ for Manicouagan rocks range from ~0.32 to ~0.92 for rocks whose Fe-bearing phases are dominated by Px and by Hm+ npOx, respectively. Oxidative alteration of Manicouagan impact melt rocks is considered to have occurred after the impact event by (hydrothermal) interaction with oxidizing vapors and/or fluids while the rocks were still hot but below solidus temperatures (~915 °C) (Floran *et al.*, 1978; Simonds *et al.*, 1978). For example, petrographic studies of Manicouagan and West Clearwater Lake (also in Quebec, Canada) impact melt rocks show that Hm forms by oxidative (subsolidus) alteration of primary titanomagnetite, mafic minerals, and Fe-bearing glass (Floran *et al.*, 1978; Phinney *et al.*, 1978). In laboratory experiments, Straub *et al.* (1991) produced nanophase Hm as the alteration product of Px under similar oxidative and subsolidus conditions.

Although the Watchtower Class rocks are located in Gusev impact crater, the evidence is equivocal as to whether they are actually a product of target homogenization (by the impact event), crystallization of the impact melt, and subsequent isochemical alteration in a manner analogous to Manicouagan impact melt rocks. The important implication of Manicouagan for alteration processes on Mars is that hydrothermal subsolidus alteration as a regional process can occur isochemically, resulting in the formation of rocks with diverse mineralogical compositions and Fe oxidation states.

An important generalization from Watchtower Class rocks and Manicouagan impact melt rocks is that mineralogical interpretations based solely on chemical data (such as from CIPW normative calculations) are equivocal. Recognizing this, Clark *et al.* (2007) inferred the presence of montmorillonite or its compositional equivalent for an endmember composition derived using chemical mixing models for the highly altered Independence Class rocks (Independence and Assemblee) in the Columbia Hills. In fact, Mini-TES data for the same rocks are not consistent with the presence of phyllosilicates like montmorillonite

(Clark *et al.*, 2007). Similarly, Wang *et al.* (2006b) used chemical mixing models to infer the presence of the phyllosilicate kaolinite in the Columbia Hills rock Wooly Patch. In the absence of corroborative mineralogical data, this assignment is also equivocal.

15.9 MAGNETIC PROPERTIES OF MARTIAN SOIL AND ROCK

The magnetic properties experiments on the Viking Landers, the Mars Pathfinder rover, and the two MER rovers have shown that Martian soil and dust has a strongly magnetic component (e.g., Hargraves *et al.*, 1979; Madsen *et al.*, 1999; Goetz *et al.*, 2005; also see Chapter 16). Pre-MER estimates for the saturation magnetization of bulk Martian soil were 1–4 A m^2/kg (Morris *et al.*, 2001b; Madsen *et al.*, 2003). The Viking and Pathfinder mission teams concluded that the strongly magnetic component was maghemite (γ-Fe_2O_3) produced as a weathering product (e.g., Hargraves *et al.*, 1979; Posey-Dowty *et al.*, 1986; Madsen *et al.*, 1999). Other phases advocated pre-MER as the strongly magnetic component included (titano)Mt as a product of igneous activity (Morris *et al.*, 1990, 2001b), titanomaghemite as a product of igneous activity and subsequent titanomagnetite oxidation (Coey *et al.*, 1990), and δ-δ'-FeOOH assemblages (Burns, 1980a,b; Towe, 1980) and nanophase Hm (Morris *et al.*, 1989) as products of weathering.

The identification of Mt in surface rocks and soils by the MER MB instruments firmly establishes that oxide as one of and perhaps the dominant strongly magnetic component on the Martian surface. The concentration of Fe from Mt ($A_{Mt}Fe_T/100$) is shown as a function of Fe_T in Figure 15.13. The horizontal dashed lines are the values of the saturation magnetization (J_s) as a function of Mt concentration using 92 A m^2 kg^{-1} for bulk Mt. The samples with the most Mt are the rocks Peace and Irvine on Husband Hill (J_s~4 A m^2/kg). The range of J_s for LC soil is ~0.4–1.2 A m^2/kg, which is at the low end of the range estimated by the magnetic properties experiments.

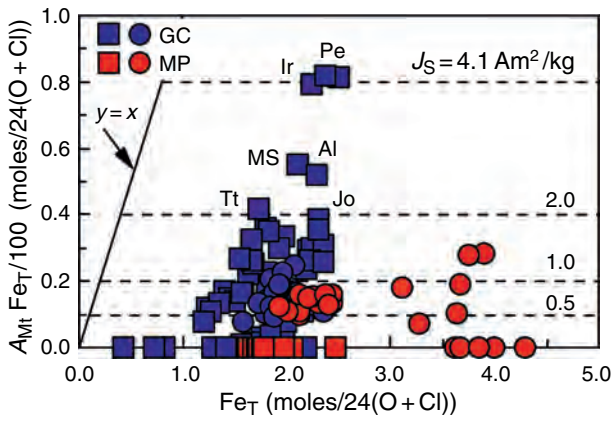

Figure 15.13. $A_{Mt}Fe_T/100$ versus Fe_T for Gusev crater (dark symbols) and Meridiani Planum (light symbols) rock (squares) and soil (circles) samples. The solid line refers to $A_{Mt}Fe_T/100 = Fe_T$. The horizontal dashed lines correspond to values for the saturation magnetization using 92 Am^2/kg for stoichiometric bulk magnetite. Named rocks are Irvine (Ir), Peace (Pe), MimiShoe (MS), Alligator (Al), Tetle (Tt), and Joshua (Jo). (For a color version of this figure, please refer to the color plate section or to the e-Book version of this chapter.)

15.10 SUMMARY

The MB spectrometers on the MER rovers *Spirit* and *Opportunity* have provided detailed information on the mineralogical composition and spatial distribution of Fe-bearing phases on opposite sides of Mars at Gusev crater and Meridiani Planum. As of sol 602 at Gusev crater and sol 557 at Meridiani Planum, a total of 12 Fe-bearing phases were identified, and mineralogical assignments were made for 10 of them: Ol, Px, and Ilm as Fe^{2+}-bearing phases; npOx, Jar, Hm, and Gt as Fe^{3+}-bearing phases; Mt and Chr as Fe^{2+}- and Fe^{3+}-bearing phases; and Kam as an Fe^0-bearing phase. An octahedrally coordinated Fe^{3+}-sulfate phase was identified, but a more specific assignment could not be made. Another unidentified oct-Fe^{3+} phase (Fe3D3) appears to be associated with Jar. These phases occur within four rock supergroups (Weakly Altered Basalt, Altered Low-S Rock, Altered High-S Rock, and Meteorite) and three soil supergroups (LC soil, PRC soil, and BC soil).

The Fe from igneous minerals (Ol, Px, Ilm, Chr, and Mt) is primarily associated with Weakly Altered Basalt, which occurs primarily as float and occasionally as outcrop rocks in Gusev crater, and with LC (basaltic) soil that is ubiquitous at both MER landing sites. Altered Low-S Rock occurs as outcrop and float rocks in the Gusev Columbia Hills. Compared to Weakly Altered Basalt, these rocks have minor to undetectable Fe from Ol and significant concentrations of Fe from npOx, Hm, and Gt. Altered High-S Rock is the ubiquitous outcrop rock at Meridiani Planum (the Burns formation), with Jar, Hm, and Fe3D3 being the important Fe-bearing phases. Berry Class soil, which is composed of Hm-rich spherules, spherule fragments, and basaltic clasts, occurs at Meridiani Planum primary as lag deposits on ripple crests. Paso Robles Class soil, which has high concentration of an Fe^{3+}-bearing sulfate (not Jar), occurs as subsurface deposits at isolated locations in the Columbia Hills. It is possible that this soil class is significantly more widespread, but hidden from view by overlying LC soil except when churned up by rover wheels.

On the basis of MER MB spectra, the strongly magnetic mineral (titano)Mt is present in LC soil and in both Weakly Altered Basalt (e.g., Adirondack Class and Irvine Class) and Altered Low-S Rock (e.g., Clovis Class) at Gusev crater. This result is direct mineralogical evidence that the strongly magnetic phase in Martian soil and dust is predominantly Mt formed as a result of igneous processes and not, as generally advocated pre-MER, maghemite (γ-Fe_2O_3) formed during alteration processes.

The Fe mineralogy provides abundant evidence for aqueous alteration on Mars. The most compelling evidence is the

identification of two Fe-bearing minerals (Jar and Gt) that have hydroxide as a part of their crystal structure. Both minerals yield ~10–12 wt.% H_2O when dehydroxylated. It is difficult to estimate the regional extent of the Gt occurrence, because there has been no observed spectral signature for the mineral and no associated morphological unit discernable from orbital observations. This situation is not the case for the Jar-containing Burns formation. On the basis of Hm detections and morphological observations from Martian orbit, the Burns formation is laterally extensive (~10^5 km^2; Christensen *et al.*, 2001) with a thickness of ~600 m (Hynek *et al.*, 2002). Jarosite at Meridiani Planum and Fe3Sulfate at Gusev crater are evidence for aqueous processes under acid-sulfate conditions on a planetary scale.

The basaltic bulk chemical composition of the Burns formation and of the highly altered rocks in the Columbia Hills (calculated to a chemical composition with S = Cl = 0) suggests that the alteration occurred at low water-to-rock ratios to prevent or minimize removal of soluble components by leaching (isochemical alteration). The exception to this observation is the Independence Class rocks on Husband Hill, which show evidence of aqueous leaching on the basis of low Fe concentrations and anomalously high concentrations of Ilm or Chr. The Wishstone Class rocks are evidence that isochemical alteration can result in mineralogical diversity, implying variable local conditions but still low water-to-rock ratios.

ACKNOWLEDGMENTS

R. V. Morris acknowledges support of the NASA Mars Exploration Rover Project and the NASA Johnson Space Center. Development of the MIMOS II Mössbauer spectrometer was directed by G. Klingelhöfer and funded by the German Space Agency under contract 50QM 99022 and supported by the Technical University of Darmstadt and the University of Mainz. Part of the work described in this chapter was conducted at the Jet Propulsion Laboratory, California Institute of Technology, under a contract with the National Aeronautics and Space Administration. This chapter benefitted from the careful reviews of D. Agresti, D. Ming, and C. Schröder.

REFERENCES

Arvidson, R. E., S. W. Squyres, R. C. Anderson, *et al.*, Overview of the Spirit Mars Exploration Rover Mission to Gusev crater: landing site to the Methuselah Outcrop in the Columbia Hills, *J. Geophys. Res.* **111**, E02S01, doi:10.1029/2005JE002499, 2006a.

Arvidson, R. E., F. Poulet, R. V. Morris, *et al.*, Nature and origin of the hematite-bearing plains of Terra Meridiani based on analysis for orbital and Mars Exploration Rover data sets, *J. Geophys. Res.* **111**, E12S08, doi:10.1029/2006JE002728, 2006b.

Bancroft, G. M., *Mössbauer Spectroscopy: An Introduction for Inorganic Chemists and Geochemists*, New York: McGraw-Hill, 1973.

Banin, A., F. X. Han, I. Kan, and A. Cicelsky, Acidic volatiles and the Mars soil, *J. Geophys. Res.* **102**, 13341–56, 1997.

Bell III, J. F., H. Y. McSween Jr., J. A. Crisp, *et al.*, Mineralogic and compositional properties of Martian soil and dust: results from Mars Pathfinder, *J. Geophys. Res.* **105**, 1721–55, 2000.

Bell III, J. F., S. W. Squyres, R. E. Arvidson, *et al.*, Pancam multispectral imaging results from the Spirit rover at Gusev crater, *Science* **305**, 800–6, 2004a.

Bell III, J. F., S. W. Squyres, R. E. Arvidson, *et al.*, Pancam multispectral imaging results from the Opportunity rover at Meridiani Planum, *Science* **306**, 1703–9, 2004b.

Bell III, J. F., J. Joseph, J. N. Sohl-Dickstein, *et al.*, In-flight calibration and performance of the Mars Exploration Rover Panoramic Camera (Pancam) instruments, *J. Geophys. Res.* **111**, E02S03, doi:10.1029/2005JE002444, 2006.

Bibring, J.-P., Y. Langevin, J. F. Mustard, *et al.*, Global mineralogical and aqueous Mars history derived from OMEGA/Mars Express data, *Science* **312**, 400–4, 2006.

Bishop, J. L., H. Froschl, and R. L. Mancinelli, Alteration processes in volcanic soils and identification of exobiologically important weathering products on Mars using remote sensing, *J. Geophys. Res.* **103**, 31457–76, 1998.

Borggaard, O. K., Effect of surface area on mineralogy of iron oxides on their surface charge and anion-adsorption properties, *Clays Clay Miner.* **31**, 230–2, 1983a.

Borggaard, O. K., The influence of oxides on phosphate adsorption by soil, *J. Soil Sci.* **34**, 333–41, 1983b.

Burns, R. G., Does feroxyhyte occur on the surface of Mars?, *Nature* **285**, 467, 1980a.

Burns, R. G., Feroxyhte on Mars?, *Nature* **288**, 196, 1980b.

Burns, R. G., Gossans on Mars, *Proc. Lunar Planet. Sci. Conf. XVIII*, 713–21, 1988.

Burns, R. G., Mossbauer spectral characterization of iron in planetary surface materials. In *Remote Geochemical Analysis: Elemental and Mineralogical Composition* (ed. C. M. Pieters and P. A. J. Englert), Cambridge: Cambridge University Press, pp. 539–56, 1993.

Burns, R. G. and D. S. Fisher, Iron-sulfur mineralogy of Mars: magmatic evolution and chemical weathering products, *J. Geophys. Res.* **95**, 14415–21, 1990.

Burns, R. G. and T. C. Solberg, 57Fe-bearing oxide, silicate, and aluminosilicate minerals, crystal structure trends in Mössbauer spectra, *Spectroscopic Characterization of Minerals and Their Surfaces*, Washington, DC: American Chemical Society, pp. 262–83, 1990.

Christensen, P. R., J. L. Bandfield, R. N. Clark, *et al.*, Detection of crystalline hematite mineralization on Mars by the Thermal Emission Spectrometer, *J. Geophys. Res.* **105**, 9623–42, 2000.

Christensen, P. R., J. L. Bandfield, V. E. Hamilton, *et al.*, Mars Global Surveyor Thermal Emission Spectrometer experiment: investigation description and surface science results, *J. Geophys. Res.* **106**, 23823–71, 2001.

Christensen, P. R., S. W. Ruff, R. L. Fergason, *et al.*, Initial results from the Mini-TES experiment in Gusev crater from the Spirit rover, *Science* **305**, 837–42, 2004a.

Christensen, P. R., M. B. Wyatt, T. D. Glotch, *et al.*, Mineralogy at Meridiani Planum from the Mini-TES experiment on the Opportunity rover, *Science* **306**, 1733–9, 2004b.

Clark, B. C. and A. K. Baird, Is the Martian lithosphere sulfur rich?, *J. Geophys. Res.* **84**, 8395–403, 1979.

Clark, B. C., R. V. Morris, S. M. McLennan, *et al*., Chemistry and mineralogy of outcrops at Meridiani Planum, *Earth Planet. Sci. Lett*. **240**, 73–94, 2005.

Clark, B. C., R. E. Arvidson, R. Gellert, *et al*., Evidence for montmorillonite or its compositional equivalent in the Columbia Hills, Mars, *J. Geophys. Res*. **112**, E06S01, doi:10.1029/2006JE002756, 2007.

Coey, J. M. D., S. Morup, M. B. Madsen, and J. M. Knudsen, Titanomaghemite in magnetic soils on Earth and Mars, *J. Geophys. Res*. **95**, 14423–5, 1990.

Cornell, R. and U. Schwertmann, *The Iron Oxides: Structure, Properties, Reactions, Occurrences, and Uses*, New York: VHC, 1996.

De Grave, E. and A. Van Alboom, Evaluation of ferrous and ferric Mossbauer fractions, *Phys. Chem. Miner*. **18**, 337–42, 1991.

De Grave, E., D. Chambaere, and L. H. Bowen, Nature on the Morin transition in Al-substituted hematite, *J. Magn. Magn. Mater*. **30**, 349–54, 1983.

De Grave, E., C. A. Barrero, G. M. Da Costa, R. E. Vandenberghe, and E. Van San, Mössbauer spectra of α- and γ-FeOOH and Fe_2O_3: effects of poor crystallinity and Al-for-Fe substitution, *Clay Miner*. **37**, 591–606, 2002.

Dutrizac, J. E. and J. L. Jambor, Jarosites and their application in hydrometallurgy. In *Reviews in Mineralogy and Geochemistry*, Vol. 40*: Sulfate Minerals – Crystallography, Geochemistry, and Environmental Significance* (ed. C. N. Alpers, J. L. Jambor, and D. K. Nordstom), Washington, DC: Mineralogical Society of America & Geochemical Society, pp. 454–79, 2000.

Floran, R. J., C. H. Simonds, R. A. F. Grieve, *et al*., Petrology, structure and origin of the Manicouagan melt sheet, Quebec, Canada: a preliminary report, *Geophys. Res. Lett*. **3**, 49–52, 1976.

Floran, R. J., R. A. F. Grieve, W. C. Phinney, *et al*., Manicouagan impact melt, Quebec, 1, Stratigraphy, petrology, and chemistry, *J. Geophys. Res*. **83**, 2737–59, 1978.

Gellert, R., R. Rieder, R. C. Anderson, *et al*., Chemistry of rocks and soils in Gusev crater from the Alpha Particle X-ray Spectrometer, *Science* **305**, 829–32, 2004.

Gellert, R., R. Rieder, J. Brückner, B. C. Clark, *et al*., Alpha Particle X-Ray Spectrometer (APXS): results from Gusev crater and calibration report, *J. Geophys. Res*. **111**, E02S05, doi:10.1029/2005JE002555, 2006.

Goetz, W., P. Bertelsen, C. S. Binau, *et al*., Indication of drier periods on Mars from the chemistry and mineralogy of atmospheric dust, *Nature* **436**, 7, doi:10.1038/nature03807, 2005.

Golombek, M. P., J. A. Grant, T. J. Parker, *et al*., Selection of the Mars Exploration Rover landing sites, *J. Geophys. Res*. **108**, 8072, doi:10.1029/2003JE002074. 2003.

Greenwood, N. N. and T. C. Gibb, *Mössbauer Spectroscopy*, London: Chapman and Hall Ltd., 1971.

Grotzinger, J. P., R. E. Arvidson, J. F. Bell III, *et al*., Stratigraphy and sedimentology of a dry to wet eolian depositional system, Burns formation, Meridiani Planum, Mars, *Nature* **240**, 11–72, 2005.

Gütlich, P., R. Link, and A. Trautwein, *Mössbauer Spectroscopy and Transition Metal Chemistry*, Inorganic Chemistry Concepts, Vol. 3, New York: Springer-Verlag, 1978.

Hargraves, R. B., D. W. Collinson, R. E. Arvidson, and P. M. Cates, Viking magnetic properties experiment: extended mission results, *J. Geophys. Res*. **84**, 8379–84, 1979.

Hawthorne, F. C., Mossbauer spectroscopy. In *Reviews in Mineralogy*, Vol. 18*: Spectroscopic Methods in Mineralogy and Geology* (ed. F. C. Hawthorne), Chantilly, VA: Mineralogical Society of America, pp. 255–340, 1988.

Hynek, B. M., R. E. Arvidson, and R. J. Phillips, Geologic setting and origin of Terra Meridiani hematite deposit, *J. Geophys. Res*. **107**, 5508, doi:10.1029/2002JE001891, 2002.

Johnson, J. H., Jarosite and akaganeite from White Island volcano, New Zealand: an X-ray and Mössbauer study, *Geochem. Cosmochem. Acta* **41**, 539–44, 1977.

Klingelhöfer, G., R. V. Morris, B. Bernhardt, *et al*., Athena MIMOS II Moessbauer spectrometer investigation, *J. Geophys. Res*. **108**, 8067, doi:10.1029/2003JE002138, 2003.

Klingelhöfer, G., R. V. Morris, B. Bernhardt, *et al*., Jarosite and hematite at Meridiani Planum from Opportunity's Mössbauer spectrometer, *Science* **306**, 1740–5, 2004.

Klingelhöfer, G., E. DeGrave, R. V. Morris, *et al*., Mössbauer spectroscopy of Mars: goethite in the Columbia Hills at Gusev crater, *Hyperfine Interact*, **166**, 549–554, doi:10.1007/s110751–006–9329-y, 2006.

Knauth, L. P., D. M. Burt, and K. H. Wohletz, Impact origin of sediments at the Opportunity landing site on Mars, *Nature* **438** (22/29), 1123–8, doi:10.1038/nature04383, 2005.

Lane, M. D., M. D. Dyar, and J. L. Bishop, Spectroscopic evidence for hydrous iron sulfate in the Martian soil, *Geophys. Res. Lett*. **31**, L19702, doi:10.1029/20–04GL021231, 2004.

Madsen, M. B., S. F. Hviid, H. P. Gunnlaugsson, *et al*., The magnetic properties experiments on Mars Pathfinder, *J. Geophys. Res*. **104**, 8761–79, 1999.

Madsen, M. B., P. Bertelsen, W. Goetz, *et al*., Magnetic properties experiments on the Mars Exploration Rover mission, *J. Geophys. Res*. **108**, 8069, doi:10.1029/2002JE002029, 2003.

McCammon, C., Mössbauer spectroscopy of minerals. In *Mineral Physics and Crystallography: A Handbook of Physical Constants* (ed. T. J. Ahrens), Washington, DC: American Geophysical Union, pp. 332–47, 1995.

McCollom, T. M. and B. M. Hynek, A volcanic environment for bedrock diagenesis at Meridiani Planum on Mars, *Nature* **438**(22/29), 1129–31, doi:10.1038/nature04390, 2005a.

McCollom, T. M. and B. M. Hynek, McCollom & Hynek reply, *Nature* **433**(7), E2, doi:10.1038/nature05213, 2005b.

McLennan, S. M., J. F. Bell III, W. M. Calvin, *et al*., Provenance and diagenesis of the evaporite-bearing Burns formation, Meridiani Planum, Mars, *Earth Planet. Sci. Lett*. **240**, 95–121, 2005.

McSween, H. Y., R. E. Arvidson, J. F. Bell III, *et al*., Basaltic rocks analyzed by the Spirit rover in Gusev crater, *Science* **305**, 842–5, 2004.

McSween, H. Y., M. B. Wyatt, R. Gellert, *et al*., Characterization and petrologic interpretation of olivine-rich basalts at Gusev crater, Mars, *J. Geophys. Res*. **111**, E02S10, doi:10.1029/2005JE002477, 2006.

Ming, D. W., D. W. Mittlefehldt, R. V. Morris, *et al*., Geochemical and mineralogical indicators for aqueous processes in the Columbia Hills of Gusev crater, Mars, *J. Geophys. Res*. **111**, E02S12, doi:10.1029/2005JE002560, 2006.

Morris, R. V., D. G. Agresti, H. V. Lauer Jr., *et al*., Evidence for pigmentary hematite on Mars based on optical magnetic and Mössbauer studies of superparamagnetic (nanocrystalline) hematite, *J. Geophys. Res*. **94**, 2760–78, 1989.

Morris, R. V., J. J. Gooding, H. V. Lauer Jr., and R. B. Singer, Origins of Marslike spectral and magnetic properties of a Hawaiian palagonitic soil, *J. Geophys. Res*. **95**, 14427–34, 1990.

Morris, R. V., D. C. Golden, J. F. Bell III, H. V. Lauer Jr., and J. B. Adams, Pigmenting agents in Martian soils: inferences from spectral, Mossbauer, and magnetic properties of nanophase and other iron oxides in Hawaiian palagonitic soil PN-9, *Geochim. Cosmochim. Acta* **57**, 4597–609, 1993.

Morris, R. V., D. C. Golden, J. F. Bell III, and H. V. Lauer Jr., Hematite, pyroxene, and phyllosilicates on Mars: implications from oxidized impact melt rocks from Manicouagan crater, Quebec, Canada, *J. Geophys. Res.* **100**, 5319–28, 1995.

Morris, R. V., D. W. Ming, D. C. Golden, and J. F. Bell III, An occurrence of jarositic tephra on Mauna Kea, Hawaii: implications for the ferric mineralogy of the Martian surface. In *Mineral Spectroscopy: A Tribute to Roger G. Burns* (ed. M. D. Dyar, C. McCammon, and M. W. Schaefer), Houston: The Geochemical Society, Special Publication No. 5, pp. 327–36, 1996.

Morris, R. V., D. C. Golden, J. F. Bell III, *et al.*, Mineralogy, composition, and alteration of Mars Pathfinder rocks and soils: evidence from multispectral, elemental, and magnetic data on terrestrial analogue, SNC meteorite, and Pathfinder samples, *J. Geophys. Res.* **105**, 1757–817, 2000.

Morris, R. V., T. G. Graff, T. D. Shelfer, and J. F. Bell III, Effect of palagonitic dust coatings on visible, near-IR and Mossbauer spectra of rocks and minerals: implications for mineralogical remote sensing of Mars, *Lunar Planet. Sci. XXXII*, Houston, TX, Abstract #1912 (CD-ROM), March 12–16, 2001a.

Morris, R. V., D. C. Golden, D. W. Ming, *et al.*, Phyllosilicate-poor palagonitic dust form Mauna Kea Volcano (Hawaii): a mineralogical analogue for magnetic martian dust?, *J. Geophys. Res.* **106**, 5057–83, 2001b.

Morris, R. V., G. Klingelhöfer, B. Bernhardt, *et al.*, Mössbauer mineralogy on Mars: first results from the *Spirit* landing site in Gusev crater, *Science* **305**, 833–6, 2004.

Morris, R. V., D. W. Ming, T. G. Graff, *et al.*, Hematite spherules in basaltic tephra altered under aqueous, acid-sulfate conditions on Mauna Kea volcano, Hawaii: possible clues for the occurrence of hematite-rich spherules in the Burns formation at Meridiani Planum, Mars, *Earth Planet. Sci. Lett.* **240**, 168–78, 2005.

Morris, R. V., G. Klingelhöfer, C. Schröder, *et al.*, Mössbauer mineralogy of rock, soil, and dust at Gusev crater, Mars: Spirit's journey through weakly altered olivine basalt on the plains and pervasively altered basalt in the Columbia Hills, *J. Geophys. Res.* **111**, E02S13, doi:10.1029/2005JE002584, 2006a.

Morris, R. V., G. Klingelhöfer, C. Schröder, *et al.*, Mössbauer mineralogy of rock, soil, and dust at Meridiani Planum, Mars: Opportunity's journey across sulfate-rich outcrop, basaltic sand and dust, and hematite lag deposits, *J. Geophys. Res.* **111**, E12S15, doi:10.1029/2006JE00279, 2006b.

Myneni, S. C. B., X-ray and vibrational spectroscopy of sulfate in Earth materials. In *Reviews in Mineralogy and Geochemistry*, Vol. 40: *Sulfate Minerals – Crystallography, Geochemistry, and Environmental Significance* (ed. C. N. Alpers, J. L. Jambor, and D. K. Nordstom), Washington, D. C: Mineralogical Society of America & Geochemical Society, pp. 113–72, 2000.

Phinney, W. C., C. H. Simonds, A. Cochran, and P. E. McGee, West Clearwater, Quebec impact structure, Part II: Petrology, *Proc. Lunar Planet. Sci. Conf. IX*, 2659–93, 1978.

Posey-Dowty, J., B. Moskowitz, D. Crerar, *et al.*, Iron oxide and hydroxide precipitation from ferrous solutions and its relevance to martian surface mineralogy, *Icarus* **66**, 105–16, 1986.

Rieder, R., R. Gellert, R. C. Anderson, *et al.*, Chemistry of rocks and soils at Meridiani Planum from the Alpha Particle X-ray Spectrometer, *Science* **306**, 1746–9, 2004.

Settle, M., Formation and deposition of volcanic sulfate aerosols on Mars, *J. Geophys. Res.* **84**, 8343–54, 1979.

Simonds, C. H., R. J. Floran, P. E. McGee, W. C. Phinney, and J. W. Warner, Petrogenesis of melt rocks, Manicouagan impact structure, Quebec, *J. Geophys. Res.* **83**, 2773–88, 1978.

Squyres, S. W., R. E. Arvidson, J. F. Bell III, *et al.*, The Spirit rover's Athena science investigation at Gusev crater, Mars, *Science* **305**, 794–9, 2004a.

Squyres, S. W., R. E. Arvidson, J. F. Bell III, *et al.*, The Opportunity rover's Athena science investigation at Meridiani Planum, Mars, *Science* **306**, 1698–703, 2004b.

Squyres, S. W., O. Aharonson, R. E. Arvidson, *et al.*, Bedrock formation at Meridiani Planum, *Nature* **443**(7), E1–E2, doi:10.1038/nature05212, 2005.

Squyres, S. W., R. E. Arvidson, D. Bollen, *et al.*, Overview of the Opportunity Mars Exploration Rover Mission to Meridiani Planum: Eagle crater to Purgatory Ripple, *J. Geophys. Res.* **111**, E12S12, doi:10.1029/2006JE002771, 2006a.

Squyres, S. W., R. E. Arvidson, D. L. Blaney, *et al.*, Rocks of the Columbia Hills, *J. Geophys. Res.* **111**, E02S11, doi:10.1029/2005JE002562, 2006b.

Stevens, J. G., A. M. Khasanov, J. W. Miller, H. Pollak, and Z. Li, *Mössbauer Mineral Handbook*, Ashville, NC: Biltmore Press, 1998.

Stoffregen, R. E., C. N. Alpers, and J. L. Jambor, Alunite-jarosite crystallography, thermodynamics, and geochemistry. In *Reviews in Mineralogy and Geochemistry,* Vol. 40*: Sulfate Minerals – Crystallography, Geochemistry, and Environmental Significance* (ed. C. N. Alpers, J. L. Jambor, and D. K. Nordstom), Washington, DC: Mineralogical Society of America & Geochemical Society, pp. 453–80, 2000.

Straub, D. W., R. G. Burns, and S. F. Pratt, Spectral signature of oxidized pyroxenes: implications to remote sensing of terrestrial planets, *J. Geophys. Res.* **96**, 18819–30, 1991.

Towe, K. M., Feroxyhyte on Mars?, *Nature* **288**, 196, 1980.

Wang, A., L. A. Haskin, S. W. Squyres, *et al.*, Sulfate deposition in subsurface regolith exposed in trenches at the plains traversed by Spirit rover in Gusev crater, Mars, *J. Geophys. Res.* **111**, E02S17, doi:10.1029/2005JE002513, 2006a.

Wang, A., R. L. Korotev, B. L. Jolliff, *et al.*, Evidence of phyllosilicates in Wooly Patch, an altered rock encountered at West Spur, Columbia Hills, by the Spirit rover in Gusev crater, Mars, *J. Geophys. Res.* **111**, E02S16, doi:10.1029/2005JE002516, 2006b.

Wegener, H., *Der Mössbauer-Effect und Seine Anwendungen in Physik und Chemie*, 2nd edn., Mannheim, Germany: Bibliographisches Institute, 1966.

Wertheim, G. K., *Mössbauer Effect: Principles and Applications*, San Diego, CA: Academic, 1964.

Yen, A. S., B. C. Murray, and G. R. Rossmann, Water content of the Martian soil: laboratory simulations of reflectance spectra, *J. Geophys. Res.* **103**, 11125–33, 1998.

Yen, A. S., R. Gellert, C. Schröder, *et al.*, An integrated view of the chemistry and mineralogy of martian soils, *Nature* **436**(7), doi:10.1038/nature03637, 2005.

Yen, A. S., D. W. Mittlefehldt, S. M. McLennan, *et al.*, Nickel on Mars: constraints on meteoritic material at the surface, *J. Geophys. Res.* **111**, E12S11, doi:10.1029/2006JE002797, 2006.

Zolotov, M. Y. and E. L. Shock, Formation of jarosite-bearing deposits through aqueous oxidation of pyrite at Meridiani Planum, Mars, *Geophys. Res. Lett.* **32**, L21203, doi:1029–2005GL024253, 2005.

16

Magnetic properties of Martian surface materials

W. GOETZ, S. F. HVIID, K. M. KINCH, AND M. B. MADSEN

ABSTRACT

The surface and aeolian dust on Mars is rich in iron compounds, and significant quantities of dust have been observed to stick to permanent magnets that are either exposed to the dusty atmosphere, exposed to dust released by grinding into rocks, or inserted into the soil. All successful lander missions to Mars so far have carried permanent magnets of various designs for the purpose of studying dust magnetic properties. The magnetism of the aeolian dust is the result of the presence of magnetite, which apparently derives from mechanical weathering of magnetite-rich surface rocks. A strong correlation between the elements titanium and iron is observed in elemental abundance spectra of dust attracted to permanent-magnet surfaces, suggesting that the magnetite responsible for the magnetization of the dust is actually titanomagnetite. Overall, the dust can be shown to have a saturation magnetization of less than $2\,A\,m^2\,kg^{-1}$. However, some grains are significantly more magnetic, and by interaction with a permanent magnet it is possible to separate the airborne dust into populations of more and less magnetic grains. Subpopulations attracted to a magnet have been seen to have magnetizations above $7\,A\,m^2\,kg^{-1}$. The widespread presence of magnetite and other easily oxidized minerals like olivine in rocks and in the global Martian dust imply that the Martian surface has been largely devoid of liquid water for a very long time.

16.1 INTRODUCTION

A characteristic feature of the Martian surface environment is the ubiquitous presence of minerals containing the element iron in various states of oxidation (Knudsen *et al.*, 1991, Klingelhöfer *et al.*, 2004; Morris *et al.*, 2004, 2006; Chapter 15). In particular, the Martian aeolian dust contains a significant amount of ferric iron, which contributes to the reddish-brown color of the dust and indeed of the planet as a whole. Because many Fe-bearing minerals are magnetic to some degree (see, e.g., Table 16.1), investigating the magnetic properties of the Martian dust provides a useful source of information about dust mineralogy.

Inspired by a similar instrument on the Surveyor mission to the Moon (de Wys, 1969), a set of permanent magnets designed to attract magnetic particles on the surface of Mars was integrated into the science payload of the two Viking Landers (VL1, 1976–82; VL2, 1976–80; Hargraves *et al.*, 1976a,b). Since then, permanent-magnet experiments have been carried on the Mars Pathfinder Lander (MPF, July to September 1997; Hviid *et al.*, 1997; Gunnlaugsson *et al.*, 1998; Madsen *et al.*, 1999; Gunnlaugsson, 2000), the Mars Polar Lander (MPL, lost December 1999; Mogensen *et al.*, 2001) as well as the Mars Exploration Rovers (MER, surface mission ongoing since January 2004; Madsen *et al.*, 2003; Bertelsen *et al.*, 2004; Goetz *et al.*, 2005). Table 16.2 provides a summary of and list of references for these investigations. The Viking permanent-magnet experiment was named the Magnetic Properties Investigation (MPI). Later experiments on the MPF and MER missions carried a different name (Magnetic Properties Experiments, MPE), but are nevertheless conceptual descendants of the Viking MPI. In the following the acronym MPE will be used to refer collectively to all of these experiments, including the Viking MPI.

Figure 16.1 shows the location of the MPEs on the various landers/rovers. On the VLs MPE (Hargraves *et al.*, 1977), a pair of magnets were incorporated in the backhoe of the robotic arm so that magnetic soil particles could be captured during soil insertions. Another magnet was incorporated into the cameras' Reference Test Charts (RTCs) on the lander deck. The MPF Lander carried two magnet arrays, each composed of five magnets of differing strengths (Smith *et al.*, 1997). One of them was mounted on the lander deck about 70 cm above the surface and is referred to as the "upper magnet array" (UMA). The other one, called the "lower magnet array" (LMA), was mounted near one of the solar panels at about 20 cm above ground. The design of these magnet arrays was inherited from the Viking MPE and is illustrated in Figure 16.2. Another magnet onboard the MPF Lander, called the "Tip-Plate Magnet," was placed at about 10 cm from the right camera eye in order to acquire high-resolution images of accumulated magnetic material through a close-up lens. Flexibly constructed magnetic plates were also mounted at the outer end of both of the ramps for the rover's descent from the lander onto the Martian surface. These magnets are referred to as "Ramp Magnets," and they were positioned such that they could have been accessed by the rover's Alpha Proton X-ray Spectrometer (APXS) for chemical analysis of magnetic dust. Finally, the MERs also carried a series of magnets (Squyres *et al.*, 2003). Two of these magnet instruments were mounted in front of the camera mast, allowing the attracted dust to be investigated by all the robotic-arm instruments (Alpha Particle X-ray Spectrometer,

The Martian Surface: Composition, Mineralogy, and Physical Properties, ed. J. F. Bell III. Published by Cambridge University Press.

Mössbauer spectrometer, and Microscopic Imager) and by each rover's high-resolution Pancam color imaging system. Small magnets called the "RAT Magnets" were mounted near the grinding bit of the Rock Abrasion Tool (RAT) in order to capture magnetic grains that might be liberated during grinding into rocks. The final MER magnet was the so-called "Sweep Magnet," designed for the search for and characterization of nonmagnetic airborne particles and mounted on the rover deck's rear solar panel near the Pancam calibration target.

Table 16.1. *Saturation magnetizations of selected minerals*

Mineral	Formula	σ_s ($A\,m^2\,kg^{-1}$)
Magnetite	Fe_3O_4 as $Fe^{2+}\,Fe_2^{3+}O_4$	92
Titanomagnetite	$Fe_{3-x}Ti_xO_4$	<92
Maghemite	γ-Fe_2O_3	70
Pyrrhotite	Fe_7S_8	~20
Feroxyhite	δ-FeOOH	<10
Hematite	α-Fe_2O_3	0.4
Nanophase hematite	Fe_2O_3	<5

Source: Data from Madsen *et al.* (1999).

In each case the permanent magnets served as platforms for accumulation of magnetic particles throughout the lifetime of the mission. For most of the experiments listed above, particles falling out of atmospheric suspension were allowed to land onto the magnets. The presence of permanent magnets led to a significant attraction of particles containing magnetizable material. Particles extracted from the dust-laden atmosphere (VL, MPF, MER), from soil (VL), or from rocks (MER) were investigated by the onboard science instruments, at least (and most often) by one or several cameras on each spacecraft. Data acquired during these missions has provided constraints on the magnetic properties and mineralogy of these particles. Monitoring the accumulation of magnetic particles over time has also provided information on the dynamics of the Martian atmospheric environment, in particular about dust settling rates and wind regimes.

The basic physical process at work in these experiments is simple: When a dust grain containing magnetic minerals is exposed to the magnetic field from a permanent magnet, it will become magnetized according to the details of its intrinsic magnetic properties (i.e., the hysteresis curve) and the strength of the field from the magnet. The magnetic force acting on a free floating dust particle is given by (Jackson, 1999)

$$\vec{F} = m\sigma\vec{\nabla}B, \tag{16.1}$$

Table 16.2. *Missions to Mars carrying magnetic properties experiments*

Mission	Name of experiment	Additional tool used for the experiment
Viking Landers 1 & 2	Reference Test Chart (RTC) Magnet[a] for studies of airborne dust	Cameras of the mission
Viking Landers 1 & 2	Surface Sampler Backhoe Magnets[a]	Cameras and a magnifying mirror[a,b]
Mars Pathfinder	Upper Magnet Array[c]	Imager for Mars Pathfinder (IMP), the stereo camera of the mission
Mars Pathfinder	Lower Magnet Array[c]	IMP
Mars Pathfinder	Tip Plate Magnet[c]	IMP
Mars Pathfinder	Ramp Magnet (2 units)[c,d,e]	IMP and APXS (basically an X-ray fluorescence spectrometer)
Mars Polar Lander	Upper Magnet Array[f]	Surface Stereo Imager (SSI), the stereo camera of the mission.
Mars Polar Lander	Tip Plate Magnet[f]	SSI
Mars Polar Lander	TEGA Magnets[f] (3 units – TEGA is a Thermal Evolved Gas Analyzer instrument)	SSI, Robotic Arm Camera (RAC)
Mars Exploration Rovers	Capture Magnet[g]	Panoramic Camera (Pancam), Microscopic Imager, APXS, Mössbauer spectrometer, Navigation Camera (Navcam)
Mars Exploration Rovers	Filter Magnet[g]	Pancam, Microscopic Imager, APXS, Mössbauer spectrometer, Navcam
Mars Exploration Rovers	Sweep Magnet[g]	Pancam
Mars Exploration Rovers	RAT Magnets[g] (RAT is a Rock Abrasion Tool)	Pancam, Front Hazard Avoidance Cameras (Hazcams)

[a] Hargraves and Petersen (1972).
[b] Hargraves *et al.* (1976a).
[c] Gunnlaugsson *et al.* (1998).
[d] Hviid *et al.* (1997).
[e] Hviid *et al.* (1998).
[f] Mogensen *et al.* (2001).
[g] Madsen *et al.* (2003).

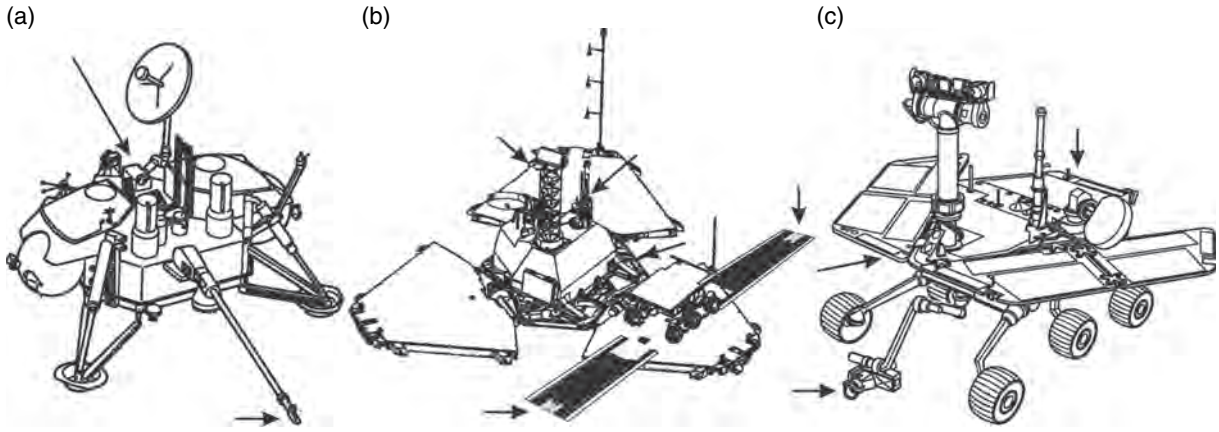

Figure 16.1. The three missions that have included magnetic properties experiments to date; (a) The Viking mission (two landers); (b) The Mars Pathfinder Lander; (c) The Mars Exploration Rover mission (two rovers). The arrows indicate the location of the magnetic properties experiments on the landers/rovers. The different spacecraft are not shown at their correct relative scales.

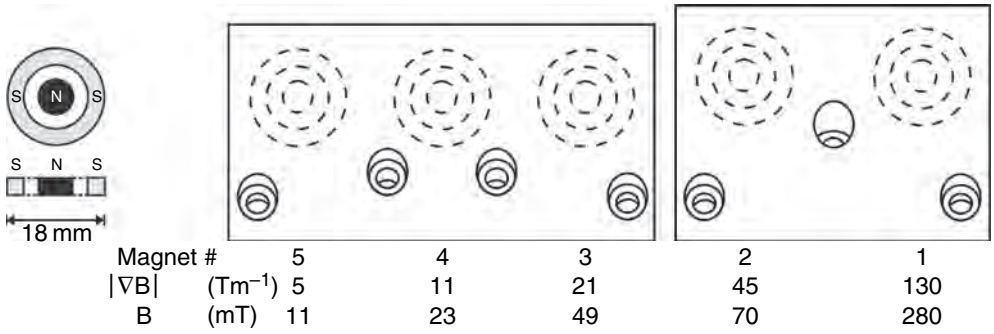

Figure 16.2. Structural diagram of the Mars Pathfinder magnet array experiment. The left figure illustrates the historic "bull's eye" magnet design used for the Viking MPE and the Mars Pathfinder MPE. The magnet is composed of a ring and a cylinder magnet mounted with opposite magnetization direction. The right figure shows the two elements of a Mars Pathfinder magnet array and the associated maximum surface magnetic field properties of the five "bull's eye" magnets mounted in the magnet array. Two such magnet arrays were mounted on the Mars Pathfinder lander.

where m is the mass of the dust grain, σ is the specific magnetization of the particle (which depends on the magnetic field) and B is the magnitude of the magnetic field. Thus, a magnetized dust grain in a nonuniform magnetic field will be subjected to a force directed along the gradient of the magnitude of the magnetic field. The grain will be attracted toward the regions where the magnetic force is strongest, which will generally be near the surface of the permanent magnet. The specific details of the capture of magnetic particles can be complex, however. In particular, the above formula neglects dynamic effects, assuming alignment of the specific magnetization of the particle with the local magnetic field. The microscopic origin of the magnetic properties of materials is described in many solid state physics textbooks (e.g., Ashcroft and Mermin, 1976) and the magnetism in natural soils and rocks is also described in detail in, for example, O'Reilly (1976, 1984), Coey (1988), and Dunlop and Özdemir (1997).

Because Martian dust is magnetic, a permanent magnet exposed to the dusty Martian atmosphere will gradually accumulate a layer of dust grains on its surface. This accumulation will happen more quickly on a stronger magnet. Relative deposition rates on different strength magnets, as well as dust patterns that develop on the surfaces of the magnets, are determined by magnet design, dust grain magnetic properties, and other factors such as dust grain size and the aerodynamic environment. Magnets exposed to a cloud of dust from brushing or grinding of rocks or magnets being pressed into the Martian soil will likewise attract material according to magnet design, soil/rock magnetic properties, and other factors.

These types of experiments have a substantial sensitivity for detection of various iron oxides and oxyhydroxides, as well as native iron. Moreover, these experiments come with advantages of simplicity and low cost. However, in terms of quantitative precision of the results, they have their limitations. This is especially true if conclusions must be drawn based only on camera images of dust patterns on magnets. When results from other types of measurements are also available, especially composition or mineralogy data, more firm conclusions can be drawn.

The MPEs together have imposed constraints on the magnetic properties of particles or particulate material that has

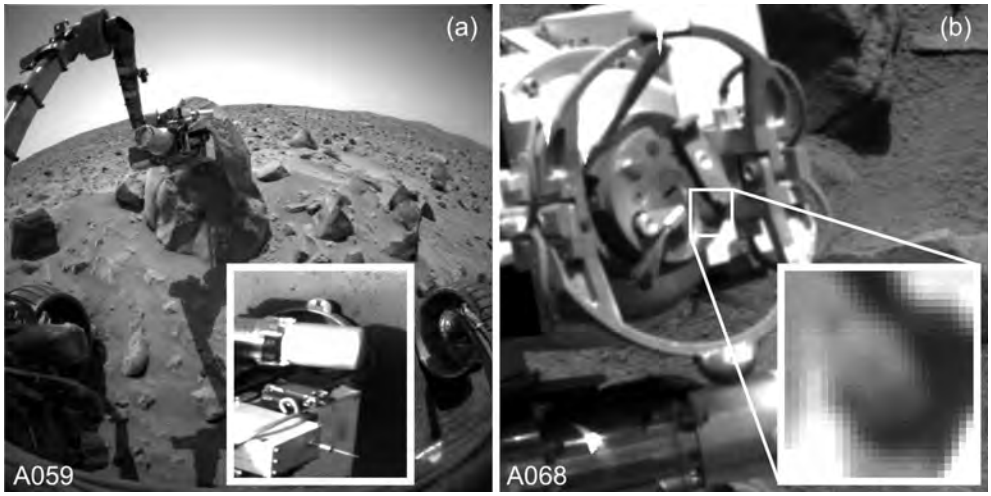

Figure 16.3. Mars Exploration Rover *Spirit* RAT magnet experiment on the rock Humphrey, Gusev crater, around mission sol 60. (a) Grinding into Humphrey: RAT contact documentation images as acquired by the Front Hazcam (large image) and Pancam (inset). (b) RAT magnet observation as acquired by Pancam. The inset shows an enlargement of the magnetic particle accumulation (top height $\sim$ 1.0 mm) on one of the strong RAT magnets.

been found on the surface of Mars. Among the relevant magnetic parameters that influence the magnetic hysteresis curve, the strongest constraints have been applied on the saturation magnetization of magnetized surface and airborne dust grains. A table of the saturation magnetization, σ_s, of selected minerals is shown in Table 16.1. In addition, MPE observations have provided constraints on the separability of magnetic particles, which in turn provides clues on the way the magnetic minerals may be intergrown with nonmagnetic minerals in dust grains, thereby indirectly constraining their mode of formation.

The following sections describe the findings from the various lander and rover MPEs on Mars with respect to rocks, soils, and airborne dust. In particular, it will be shown how the combination of results from optical reflectance, APXS, and Mössbauer spectroscopy can be used to narrow the constraints on the magnetic properties of Martian dust and soil.

16.2 MAGNETIC PROPERTIES OF ROCKS

As mentioned earlier, one of the MPEs on board the MERs focused specifically on the magnetic properties of Martian rocks. Four permanent magnets of different strengths are built into the "revolve housing" near the grinding end of the RAT (Gorevan *et al.*, 2003; Madsen *et al.*, 2003; Squyres *et al.*, 2003; Goetz *et al.*, 2007). Apart from the RAT magnets, the revolve housing contains the mechanisms associated with the tool's spinning grinding bits and brush. Thus, a small fraction of any magnetic grains liberated during the grinding process hits the active surface of these magnets and is accumulated there. The amount and the multispectral properties of the accumulated particles provide constraints on the magnetic phase(s) present in the rock.

In general, the magnetic properties of rocks are correlated with the presence of iron-bearing oxides. For this reason, some of these properties (like the saturation magnetization) can be inferred from or strongly constrained by APXS and Mössbauer data. However, the RAT magnet experiment has a much larger sensitivity for the *detection* of strongly magnetic phases as compared to Mössbauer spectroscopy, and was intended to (and indeed has turned out to) complement Mössbauer and APXS data in the case of rocks containing only minute amounts of (strongly) magnetic minerals. Of course, a complete identification of the mineral cannot be performed without Mössbauer and APXS analysis, but nevertheless information about saturation magnetization of the material on the RAT magnets can be deduced from the images as shown below.

An example from *Spirit* RAT grinding into the Gusev crater rock named Humphrey is shown in Figure 16.3. Note the accumulation of magnetic particles on one of the strong RAT magnets. Based on APXS and Mössbauer data of the grinding hole, as well as Pancam visible/near-infrared (NIR) spectra, the RAT magnet material was identified as magnetite-rich basalt (e.g., Goetz *et al.*, 2007; McSween *et al.*, 2006; Morris *et al.*, 2006). A substantial accumulation of magnetic particles has also been observed on the RAT magnets during grinding into Eagle crater outcrops at the Meridiani Planum landing site. According to Mössbauer and APXS data, these outcrops contain ample amounts of hematite, both as part of hematitic concretions (nicknamed "blueberries") and as part of the rock matrix. However, no strongly magnetic phase has been identified by Mössbauer spectroscopy or APXS. Goetz *et al.* (2007) have hypothesized the possible existence of an additional but still as-yet unidentified ferrimagnetic phase that may occur at low abundance in these outcrops.

16.3 MAGNETIC PROPERTIES OF SOILS

During the VL missions a set of two permanent magnets built into the backhoe of the soil sampler were inserted into soils

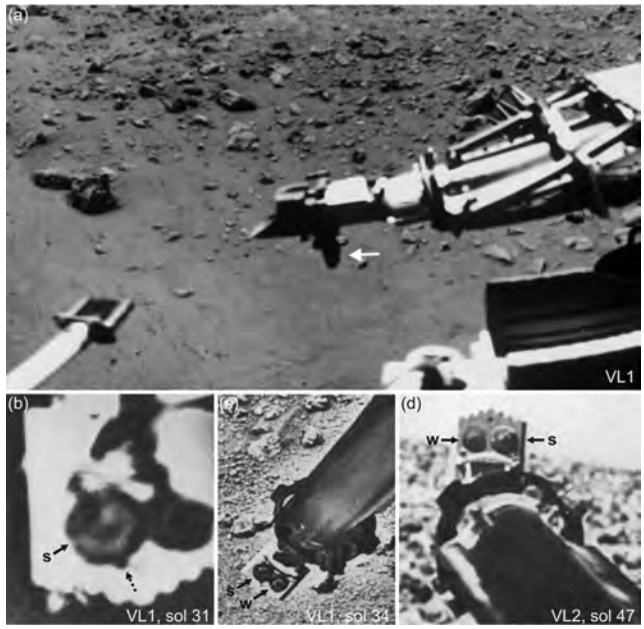

Figure 16.4. Magnets (arrows) on the backhoe of the Viking Lander soil sampler. (a) Location of the backhoe on the Viking Lander 1 sampling arm. (b–d) View of backhoe and backhoe magnets at different times during the mission. Weak (w) and strong (s) magnets hold similar amounts of material. Viking Lander 1 images (b, c) were acquired after six insertions into the soil. Note the protrusion (dotted arrow) near the periphery of the particle accumulation likely caused by an ~2 mm large magnetic particle. Viking Lander 2 image (d) was acquired after eleven insertions into the soil. The height of the particle accumulations on both magnets is estimated to be 2–4 mm.

around each lander. The two magnets on each backhoe were similar to the two strongest MPF magnets (magnet #1 and #2 in Figure 16.2). After a few insertions into the soil, these magnets were saturated with magnetic material. The amount of material adhering to the magnets was almost similar on both magnets, but depended somewhat on the sampling site (Figure 16.4; Hargraves *et al.*, 1976a). By comparison with simulation experiments, it was concluded that the soils contain 3–7 wt.% of a strongly magnetic phase, which in turn translates into a saturation magnetization of 2–6 $A\,m^2\,kg^{-1}$, depending on the nature of the magnetic phase. In a subsequent paper (Hargraves *et al.*, 1977) the estimate of the amount of the strongly magnetic phase was extended slightly in the direction downward to between 1 and 7 wt.%. The saturation magnetizations as inferred for Viking soils are thus very close to the values for airborne dust inferred from analysis of the MPF MPEs. As discussed in Section 16.4, the preferred interpretation of the Viking and Pathfinder magnetic properties teams was that the mineral maghemite (γ-Fe_2O_3) is the strongly magnetic phase in the soil and dust. However, other studies favored magnetite ($Fe^{2+}Fe_2^{3+}O_4$), based on different datasets or analysis methods (Pollack *et al.*, 1979; Morris *et al.*, 2000, 2001). Based on the results of Mössbauer data returned by MER, it has eventually become the consensus that the strongly magnetic phase in the dust and soil is indeed nonstoichiometric magnetite of basaltic origin.

For comparison, it may be noted that Morris *et al.* (2006) estimated the saturation magnetization of typical Gusev crater soils from Mössbauer and APXS data to be ~0.8 $A\,m^2\,kg^{-1}$. This magnetization may not necessarily be inconsistent with the Viking soil value of 2–6 $A\,m^2\,kg^{-1}$, given the uncertainties in the Viking and MER MPE and chemical/mineralogical results and/or possible regional variations in soil magnetic properties.

Simulation experiments performed with a full-size model of the Viking backhoe on different magnetic samples are presented in Figure 16.5. Synthetic hematite (from Merck, Inc.) and Mars regolith simulant JSC-Mars-1 (Allen *et al.*, 1998) have almost the same saturation magnetization (0.4 and 0.6 $A\,m^2\,kg^{-1}$, respectively), but stick in different ways to the magnets after insertion into these materials (Figure 16.5). In fact, well crystalline hematite does not stick at all to either magnet as a result of magnetic forces. The difference between the behavior of these samples is due to the fact that JSC-Mars-1 contains easily separable strongly magnetic (magnetite-rich) grains.

Another material studied as a potential regolith simulant is a strongly magnetic soil found near Salten Skov, Denmark (Salten soil). This soil contains about 60 wt.% iron oxides (hematite, maghemite, and goethite in roughly equal amounts), the rest being quartz and feldspars (Nørnberg *et al.*, 2004). Its saturation magnetization is mainly caused by maghemite and is ~5 $A\,m^2\,kg^{-1}$. Each Salten soil particle is a composite such that the strongly magnetic phase cannot be separated out by means of a permanent magnet. Figure 16.5c shows that Salten soil is effectively held by both of the Viking backhoe magnets after one insertion. By comparison with Viking images, Salten soil seems to be slightly more magnetic than the investigated Martian soils. The comparison of hematite, JSC-Mars-1, and Salten soil simulation experiment results shows clearly the importance of the separability of strongly magnetic grains in the interpretation of MPE results. In fact, it is this unresolved issue of the separability of magnetic grains in Martian soils that is responsible for some of the large uncertainty in the magnetization of these soils as inferred from the MPEs.

16.4 SATURATION MAGNETIZATION OF AIRBORNE DUST

One of the RTCs for the cameras on board each VL carried a single magnet assembly, the so-called "RTC magnet" (Hargraves *et al.*, 1976a). The structural design of this magnet was similar to the backhoe magnets (Figure 16.2), with the anti-parallel alignment of cylinder and ring magnet resulting in a "bull's eye" pattern of attracted aeolian dust. Immediately after touchdown and again on sol 3 a low-resolution image of the RTC magnet revealed adhesion of magnetic material on its surface (Hargraves *et al.*, 1976a). High-resolution images acquired on sols 15 and 31 (Figure 16.6) showed a clear bull's eye pattern, confirming the presence of a strongly magnetic phase in the airborne dust. While this pattern was very sharp early in the mission, contrast was gradually reduced on later sols due to fill-in of

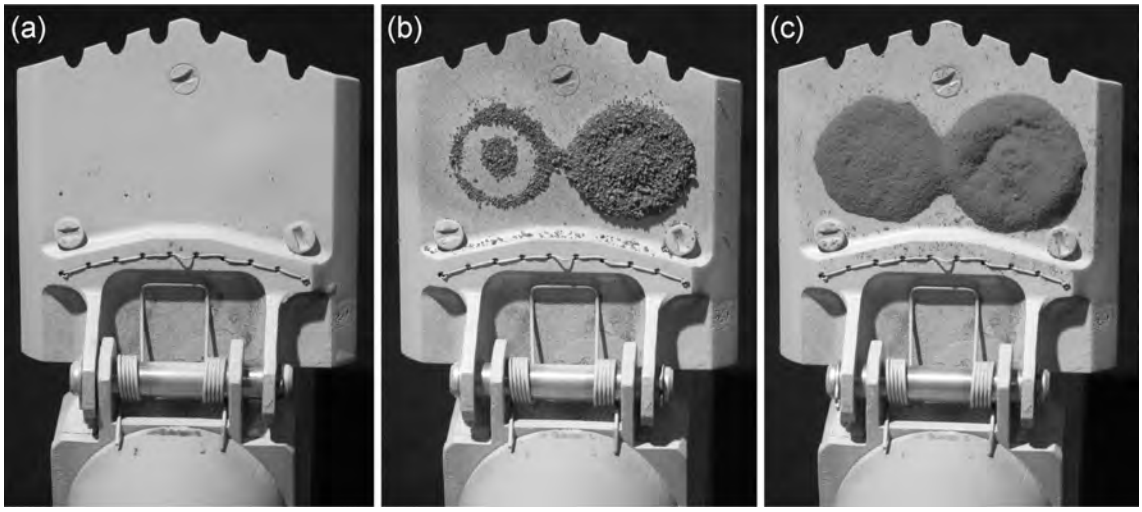

Figure 16.5. Insertion of a Viking backhoe model into particulate magnetic materials: (a) Synthetic hematite; (b) "JSC-Mars-1" Mars regolith simulant; and (c) Salten soil. The stronger of both magnets is located to the right in figures (a) to (c).

weakly or nonmagnetic material of similar spectral properties in between the central dust spot and the ring (Figure 16.6; Hargraves *et al.*, 1979).

The Viking discovery of a strongly magnetic phase in the airborne dust motivated further studies as opportunities arose with later landed missions. Thus, almost twenty years later, two sets of permanent magnets were implemented into the science payload of MPF (from hereon referred to as the MPF magnet arrays; Smith *et al.*, 1997). These arrays each consisted of five permanent magnets, labeled by numbers from one through five according to decreasing magnetic strength (Figure 16.2). The two strongest magnets (#1 and #2) were very similar to the Viking bull's eye RTC and backhoe magnets. The remaining three magnets (#3, #4, and #5) were substantially weaker, somewhat more complex in construction, but also designed to produce a dust pattern of similar bull's eye geometry (Hviid *et al.*, 1997; Gunnlaugsson *et al.*, 1998; Madsen *et al.*, 1999). While the bull's eye pattern on magnet #1 was visible already on MPF sol 2, similar patterns on magnets #2, #3, and #4 did not appear until sol 5, 20, and ~50, respectively (Figure 16.7). The formation of a pattern on magnet #5 before the end of the mission (sol 84) remains controversial. From the gradual accumulation of magnetic particles on these magnets as monitored by the camera and by comparison with simulation experiments, the saturation magnetization of airborne dust was estimated to be $4 \pm 2\,\mathrm{A\,m^2\,kg^{-1}}$ (Hviid *et al.*, 1997; Madsen *et al.*, 1999).

A remodeling of the results from the Pathfinder magnet arrays (Gunnlaugsson, 2000) led to a lowering of its lower bound to $1\,\mathrm{A\,m^2\,kg^{-1}}$, while the dust accumulated on the weakest magnet seen to capture dust (magnet #4), presumably then the most strongly magnetic subset of the airborne dust, was estimated to have a mean saturation magnetization of $5\,\mathrm{A\,m^2\,kg^{-1}}$. Subsequent simulation experiments performed under Martian conditions in a recirculating, depressurized wind tunnel made it apparent that aerodynamic

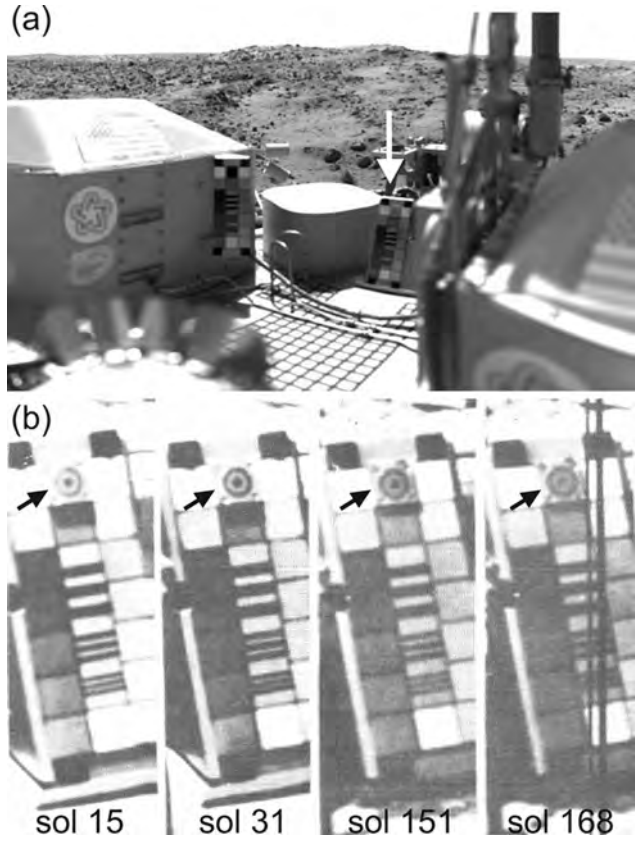

Figure 16.6. Bull's-eye magnet (arrow) on one of the Reference Test Charts (RTC) for the cameras onboard Viking Lander 1. (a) Location of RTC on lander deck. (b) Accumulation of magnetic, wind-blown dust over time.

parameters such as pressure and wind speed have a significant influence on the capture rates of magnetic dust on permanent magnets like these (Merrison *et al.*, 2002a,b; Kinch *et al.*, 2006), and thus on the patterns formed on such magnets. Based on that work as well as on analysis of dust optical spectra (Goetz, 2002), the estimate of the saturation magnetization of the airborne dust was adjusted downward to $2.5 \pm 1.5\,\mathrm{A\,m^2\,kg^{-1}}$ (Madsen *et al.*, 2003).

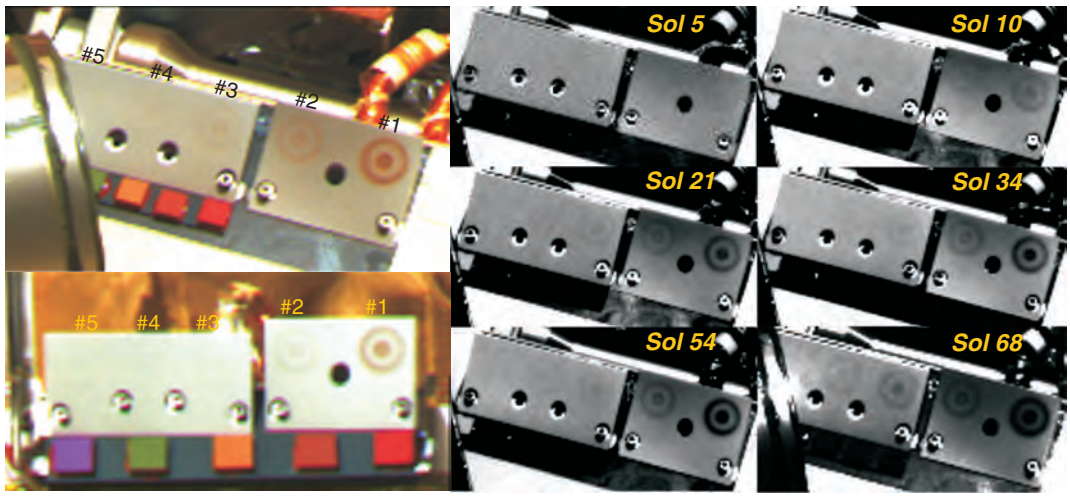

Figure 16.7. (a) Upper magnet array (top) and lower magnet array (bottom) onboard Mars Pathfinder as imaged on sol 64. The magnet array is composed of five permanent magnets. The magnets are labeled from right to left according to decreasing magnetic strength. The strongest (right-most) magnet (magnet #1) is basically identical to the RTC magnet onboard the Viking Landers (see Figure 16.6). Also, the two strongest magnets (#1, #2) are very similar to the backhoe magnets of the Viking soil sampler. Magnet #5 was partially obstructed by the gearbox of the high-gain antenna late in the mission. The colored blocks in front of the array are reference color tiles. The difference between the dust load on the upper and lower magnet array is due to the upper array being exposed to dust arriving from all directions and the lower array being somewhat shielded by the body of the lander. (b) The development of the dust pattern on the upper magnet array over time. (For a color version of this figure, please refer to the color plate section or to the e-Book version of this chapter.)

Several formation pathways might explain the observed high-saturation magnetization of Martian aeolian dust: The model generally favored by the Viking and MPF magnetic properties teams was that the dust was magnetic due to the presence of substantial amounts of maghemite, pointing to an origin of the dust in past oxidative weathering processes, likely involving the action of liquid water (Hargraves *et al.*, 1977, 1979, 2000; Hviid *et al.*, 1997; Madsen *et al.*, 1999). However, other studies interpreted the dust magnetic properties as deriving mainly from the presence of (titano)magnetite inherited directly from igneous rocks by mechanical weathering (Coey *et al.*, 1990; Morris and Singer, 1990; Morris *et al.*, 2000, 2001). These divergent interpretations were ultimately resolved in favor of the latter view by results from the MER Mössbauer Spectrometer and the MER Magnetic Properties Experiment.

A strongly modified version of the MPF MPE was developed for MER. A very strong magnet and a weaker one with very different properties (from hereon referred to as the "Capture Magnet" and the "Filter Magnet" respectively; see Figure 16.8) were mounted obliquely in front of the camera mast with the surface tilted 45° with respect to horizontal (Madsen *et al.*, 2003; Squyres *et al.*, 2003); the accumulation of dust on these magnets was monitored by the MER Panoramic Camera (Pancam) (see Section 16.5). These magnets were designed to accumulate a reasonably homogeneous layer of dust optimized for investigation by the MER Alpha Particle X-Ray Spectrometer and Mössbauer Spectrometer (Madsen *et al.*, 2003).

After several hundred sols of the MER mission, satisfactory Mössbauer spectra of dust on the Capture Magnet of both rovers were obtained. Figure 16.9 shows the Mössbauer spectrum that was acquired on the *Opportunity* rover from sol 328 through sol 330. Approximately, half of the spectral area of this spectrum can be ascribed to non-stoichiometric magnetite, while the remaining half is interpreted to result from olivine, pyroxene, and some unidentified paramagnetic, possibly superparamagnetic, ferric compounds (Goetz *et al.*, 2005). In other words, about half of the iron atoms in the dust on the *Opportunity* Capture Magnet are present in magnetite. Mössbauer spectra from the *Spirit* Capture Magnet likewise show a large fraction of magnetite. Magnetite was also found in significant amounts in many rocks and in soils at the *Spirit* landing site (Morris *et al.*, 2006; see also Chapter 15).

It is thus evident that the magnetic nature of the Martian airfall dust derives mainly from the presence of a significant amount of magnetite in the dust. The presence of relatively unoxidized magnetite and primary minerals such as olivine that are known to be easily reworked by the action of liquid water were interpreted as an indication of long-lasting dry periods on the surface of Mars (see Section 16.6; Goetz *et al.*, 2005).

Mössbauer spectra and APXS chemical composition together provide constraints on the saturation magnetization of the airborne dust. Assuming that average Gusev soil is representative for a large portion of the Martian surface and assuming furthermore that this soil has the same chemical composition as the global airborne dust, an estimate of the saturation magnetization of that dust can be obtained. Average Gusev soil contains 15 wt.% FeO or 11.7 wt.% Fe (Gellert *et al.*, 2004), and we assume similar iron abundance for the airborne dust. However, the iron abundance of dust on the Capture Magnet must be higher because of magnetic

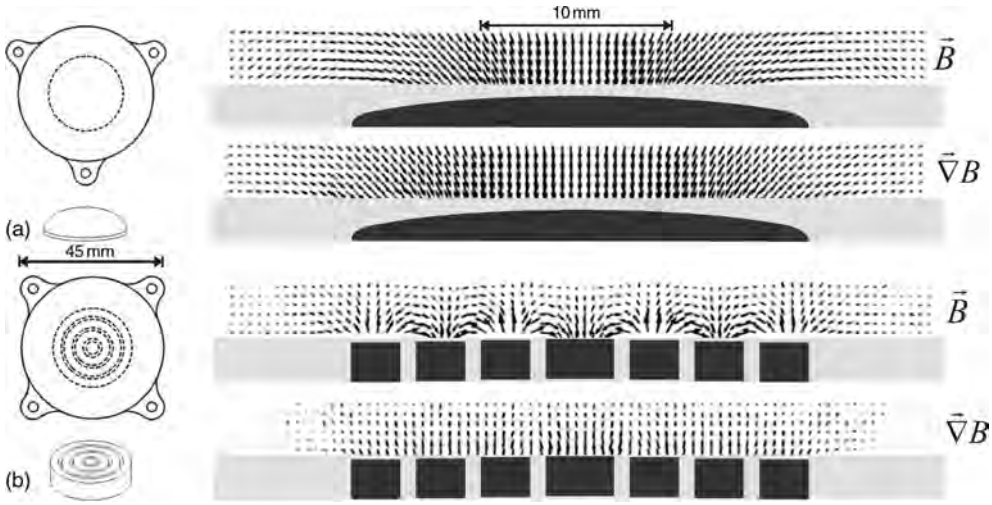

Figure 16.8. Design and magnetic field properties of the MER filter magnet (a) and capture magnet (b). Left side: Top view of the outer appearance of these magnets. Positions of the samarium-cobalt magnetized material are indicated by dash-dotted circles. The differing shapes of these magnets are shown below each magnet top view as (correctly sized) 3D drawings. Right side: Vector fields of the magnetic field and field gradient at distances up to 3 mm from the top surface of the magnets. The filter magnet is the weaker of the two magnets and is designed to retain only the strongest magnetic particles. The capture magnet is the stronger of the two magnets and is designed to also capture and retain the weaker magnetic particles. Note that the magnetic capture volume of the filter magnet extends much further out into space (as compared to the capture magnet).

separation, given that all strongly magnetic mineral phases are iron-bearing. As to the occurrence of magnetite we can make the following statement: About 50% of the Mössbauer spectral signature of dust on the magnet is due to magnetite, and a smaller amount would likely be measured in an average sample of airborne dust, given that the magnet will – at least to some degree – preferentially pick out the dust particles that are richer in magnetite.

A hypothetic sample that contained 11.7 wt.% iron with half of these iron atoms belonging to a magnetite phase would have a saturation magnetization of $7.2\,\mathrm{A\,m^2\,kg^{-1}}$. We can conclude that the airborne dust must have a lower overall saturation magnetization, since the magnetite fraction would be smaller than the 50% fraction found on the magnets. On the other hand, the magnetic extract of airborne dust as accumulated on the Capture Magnet must have a higher saturation magnetization (larger than $7.2\,\mathrm{A\,m^2\,kg^{-1}}$) because of higher iron abundance in this sample than the 11.7 wt.% seen in surface soil.

We therefore conclude that the dust on the Capture Magnet must have a saturation magnetization larger than $7.2\,\mathrm{A\,m^2\,kg^{-1}}$, while the airborne dust as a whole must have a saturation magnetization below that value. We can further constrain the latter quantity by introducing the optical properties of airborne dust.

A close relationship must exist between fine-grained bright reddish soil and airborne dust, given the observed exchange between the two units by various mechanisms, such as gravitational fall-out from the atmosphere (Landis and Jenkins, 2000; Johnson *et al.*, 2003; Landis *et al.*, 2006; Kinch *et al.*, 2007) or turbulent uplift of soil particles (Schofield *et al.*, 1997; Metzger *et al.*, 1999; Greeley *et al.*, 2006). Hereafter, we use the term "martian dust" as a generic term for representative, reddish particulate material with grain sizes in the micrometer range. A large number of previous studies have shown that typical Martian reflectance spectra have a maximum near 750 nm, be they spectra of classical bright or dark regions recorded from orbit or from Earth, or *in situ* spectra of bright soils and dusty, flat-topped rocks or hardpans as recorded by the Imager for Mars Pathfinder (IMP) or MER's Pancam. This common spectral reflectance maximum near 750 nm implies that, intrinsically, Martian dust must also have a minimum absorption at (or near) that wavelength (Hapke, 1993).

Magnetite is one of the most strongly magnetic oxide minerals found in nature, and is also one of the most strongly optically absorbing minerals to occur naturally. In particular, the imaginary index of refraction for pure magnetite (denoted $k_{\mathrm{magnetite}}$; Figure 16.10) varies in the range ~0.3–~1.1 in the UV/VIS/NIR (VIS – Visible Imaging Subsystem) region (200–1200 nm), with a weakly pronounced minimum around 800 nm (Huffmann and Stapp, 1973; Schlegel *et al.*, 1979; Tanaka, 1979). At 750 nm $k_{\mathrm{magnetite}}$ is in the range ~0.35–~0.55. Pollack *et al.* (1977, 1979) used the spectral dependence of $k_{\mathrm{magnetite}}$ to tentatively identify this mineral as the principal absorbant in Martian dust, an interpretation that was later confirmed by Mössbauer spectroscopy (Morris *et al.*, 2004, 2006). Following a method similar to Pollack *et al.* (1977, 1979), we can estimate the maximum possible abundance of magnetite in airborne Martian dust by comparison with the literature values of $k_{\mathrm{magnetite}}$. A series of workers (Pollack *et al.*, 1977, 1979, 1995; Ockert-Bell *et al.*, 1997; Markiewicz *et al.*, 1999; Tomasko *et al.*, 1999; Lemmon *et al.*, 2004) have estimated the imaginary index of refraction for airborne dust from Viking, MPF, and MER light scattering data as acquired by the respective multispectral cameras. In particular, the imaginary index of refraction for Martian airborne dust was

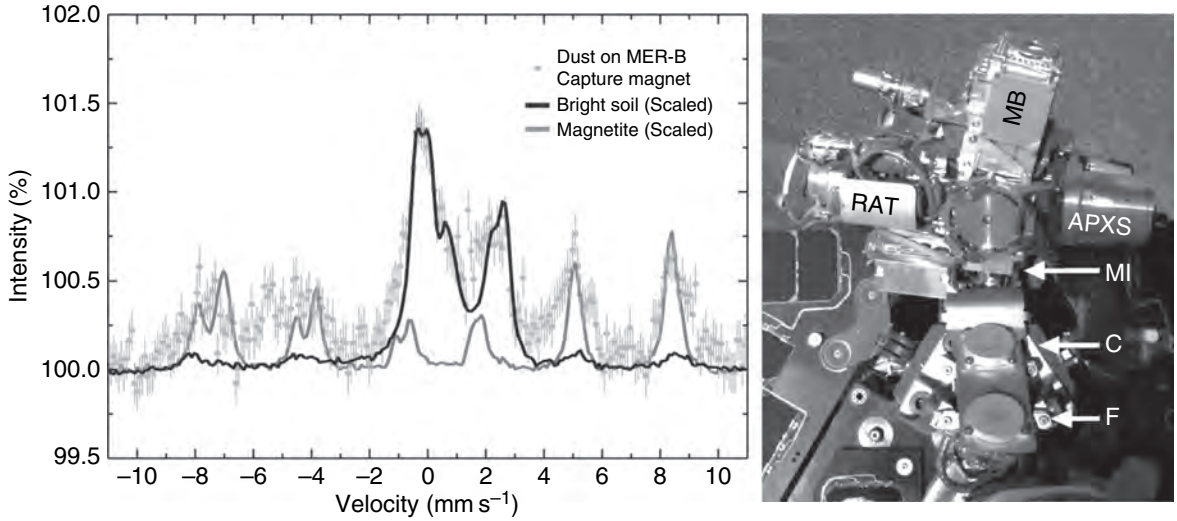

Figure 16.9. Mars Exploration Rover *Opportunity* Mössbauer spectrum (sols 328–330) of Martian airborne dust as attracted to the capture magnet. To the right, a navigation camera context image from sol 328 showing the Microscopic Imager (MI) in position for imaging of the capture magnet (C). Following MI imaging, the turret of the robotic arm was turned by approximately 180° for placing the Mössbauer (MB) spectrometer on the capture magnet. Also labeled in the figure is the filter magnet (F), as well as the remaining IDD instruments (RAT, APXS). (For a color version of this figure, please refer to the color plate section or to the e-Book version of this chapter.)

determined to be ~0.002–~0.004 at wavelengths around 750 nm, where the absorption is minimum.

Assuming that the absorption of Martian airborne dust at 750 nm is *exclusively* due to magnetite, we can infer an upper bound on the abundance of magnetite in the dust. This abundance can be converted into saturation magnetization. Let us denote the fractional abundance of iron oxides in Martian dust particles by X and distinguish between the fractional abundance by weight (X_{wt}) or by volume (X_{vol}). The imaginary index of refraction is denoted by k and the saturation magnetization by σ. The above assumptions lead to the following expression:

$$\sigma_{\text{Mars dust}} < \left(\frac{K_{\text{Mars dust}}}{K_{\text{magnetite}}}\right)_{750\text{nm}} \cdot \frac{X_{\text{wt}}(\text{Fe-oxides})}{X_{\text{vol}}(\text{Fe-oxides})} \cdot \sigma_{\text{s(magnetite)}}$$
$$\approx \frac{0.003}{0.45} \cdot 2 \cdot 92\,\text{A m}^2/\text{kg} \approx 1.2\,\text{A m}^2/\text{kg}. \quad (16.2)$$

Here we assume that a Martian dust particle is composed of silicates and small amounts of iron oxides (<10% assumed here; this assumption would be too simplistic in most contexts, but is sufficient for this particular application, where we try to convert volume abundances into weight abundances). From this assumption, it is possible to show that

$$\frac{X_{\text{wt}}(\text{Fe-oxides})}{X_{\text{vol}}(\text{Fe-oxides})} \approx \frac{\rho(\text{Fe-oxides})}{\rho(\text{silicates})} \approx 2. \quad (16.3)$$

Following Pollack *et al.* (1977, 1979), we assumed above that the imaginary index of refraction of a given dust particle scales linearly with the fractional abundance by volume for some absorbing mineral that may be present in that particle. In particular, this assumption requires that the interfaces between several inter-grown mineral grains do not give rise to much internal scattering. We thus estimate that the saturation magnetization of airborne dust (as a whole) cannot exceed ~1.2 A m^2 kg^{-1}. In fact, it must be smaller to the extent that other NIR-absorbing minerals are present apart from magnetite. This estimate is fully consistent with the magnetization of ~0.8 A m^2 kg^{-1} as inferred by Morris *et al.* (2006a) for typical Gusev soils, and provides additional support for the assumption made above of mineralogical similarity between airborne dust and bright soils on the surface of Mars.

We conclude that the optical properties provide much narrower constraints on the saturation magnetization of airborne dust than the Mössbauer spectra recorded on the MER Capture Magnet. The saturation magnetization of airborne dust (as a whole) is likely to be below 1.2 A m^2 kg^{-1} (or at least below 2 A m^2 kg^{-1}, using extreme values for both $k_{\text{Mars dust}}$ and $k_{\text{magnetite}}$), while the saturation magnetization of the dust on the Capture Magnet exceeds 7.2 A m^2 kg^{-1} based on the measured Mössbauer spectrum.

On the basis of results of the MPE on MPF, Hviid *et al.* (1997) and Madsen *et al.* (1999) proposed a somewhat higher average saturation magnetization of the Martian airborne dust caught by the magnets (~4 A m^2 kg^{-1}, later revised to ~2.5 A m^2 kg^{-1}) and suggested that maghemite was the dominant magnetic mineral. Although the properties of maghemite are not as well represented in the literature as those of magnetite, a rough idea on the imaginary index of refraction can be inferred from its diffuse reflectance spectrum. As in the case of hematite, this spectrum depends on grain size. The important point is that in contrast to relatively opaque magnetite, maghemite is brownish/reddish like Martian dust, with a strong drop-off in absorption within a characteristic wavelength interval (~500–600 nm; e.g., Morris *et al.*, 1985). Obviously, relative to magnetite, a much larger maghemite abundance would be compatible with the data for the imaginary index of airborne dust as

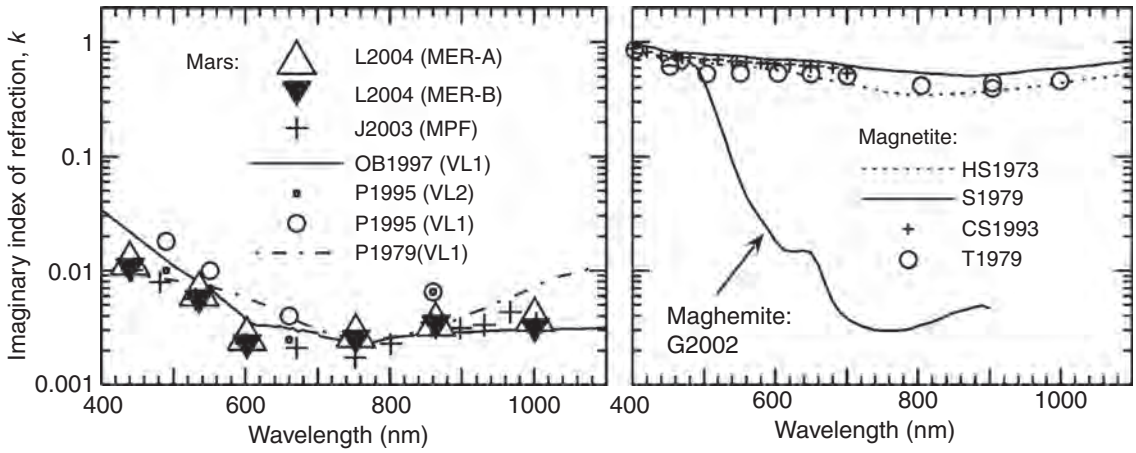

Figure 16.10. Imaginary index of refraction as a function of wavelength for Martian airborne dust, magnetite, and maghemite. Magnetite and Martian airborne dust have an absorption minimum at around 800 nm. The airborne dust may contain no more than 0.002/0.4 • 100 vol.% = ~0.5 wt.% magnetite, assuming that magnetite is the only mineral species absorbing at that wavelength. Acronyms in the legend: L2004 = Lemmon *et al.* (2004); J2003 = Johnson *et al.* (2003); OB1997 = Ockert-Bell *et al.* (1997); P1979 and P1995 = Pollack *et al.* (1979, 1995); HS1973 = Huffmann and Stapp (1973); S1979 = Schlegel *et al.* (1979); CS1993 = Criddle and Stanley (1993); T1979 = Tanaka (1979); G2002 = Goetz (2002).

inferred from light scattering. By the same arguments as the ones presented above, we would arrive at a somewhat higher upper bound for the saturation magnetization (Goetz, 2002). However, the MER Mössbauer results indicate clearly that a significant fraction of the magnetic mineral in the Martian dust is magnetite, and so the limit $\sigma_s < 2\,\mathrm{A\,m^2\,kg^{-1}}$ for the overall dust magnetization should hold firm.

16.5 MAGNETIC SEPARABILITY OF AIRBORNE DUST

It was shown in the previous section that the saturation magnetization of the population of aeolian dust particles attracted to a magnet is likely to be higher than the saturation magnetization of the entire population of dust particles as observed in dusty areas on the ground. In other words, the airborne Martian dust is not magnetically homogeneous, but can be separated into more and less magnetic grains by the presence of a permanent magnet.

Limited separability was observed during the Viking mission (see, previous section). Probably as a result of the short mission lifetime, it was not possible to make any firm conclusions about separability from the results obtained during the MPF mission, either on the magnet array (limited by the camera's resolution and by the low thickness of the dust layer) or on the Tip Plate Magnet (Figure 16.12; Hviid *et al.*, 1997; Madsen *et al.*, 1999).

The first clear evidence for magnetic separation of airborne dust was provided by MER data. Figure 16.11 shows images of the Capture and Filter magnets acquired on *Spirit* sols 240 and 425. These false-color composites have been generated from blue (440 nm), green (532 nm) and near-infrared (750 nm) radiometrically (RAD) calibrated images (Bell *et al.*, 2006), where equal weight has been given to each component. Comparison of sol 240 to sol 425 images shows clear differences in texture and color. The sol 425 image was acquired after a strong wind gust had been observed on approximately sol 418. This event had noticeable impact on the Pancam (Kinch *et al.*, 2007) and Mini-TES calibration targets and it cleaned some of the dust off the solar panels, providing a substantial increase of the available electric power. Figure 16.11c shows that in the NIR region airborne dust can be brighter than the almost pure aluminum surfaces near the borders of the magnets. The strong wind gust around sol 418 removed preferentially some of the weakly magnetic particles, whereby the dust on the magnets was enriched in magnetite. Accordingly, on sol 425, the dust on the magnets was darker as compared to the border of the magnet (Figure 16.11f) and MI (MI – Microscopic Imager) images of the magnets show the formation of magnetic particle chains, features that are diagnostic of material rich in strongly magnetic phases (Figure 16.12). Similar features have been seen on the *Opportunity* rover Capture Magnet, where chain formations after strong wind events around sol 331 became particularly prominent (Figure 16.13).

A detailed analysis of color variations across the Capture Magnet surface early in the mission revealed the dust to be darker around the edge of the magnetic region and redder and brighter in the central region. Numerical modeling of the dust grain capture process and its dependence on factors such as wind speed, grain size, and dust magnetic properties shows that highly magnetic dust grains will preferably stick to the edge of the magnetic region, whereas less magnetic grains will be more likely to stick to the center. Thus, the observation of color variations supports a model of the Martian airborne dust grains as widely varying in magnetic properties, with the more magnetic grains also being darker, consistent with a larger magnetite content (Kinch *et al.*, 2006).

Magnetic separability of airborne dust has also been observed on the Sweep Magnet (Figure 16.14). This small ring magnet was designed to keep even slightly magnetic dust away from its central region (Figure 16.15; Madsen

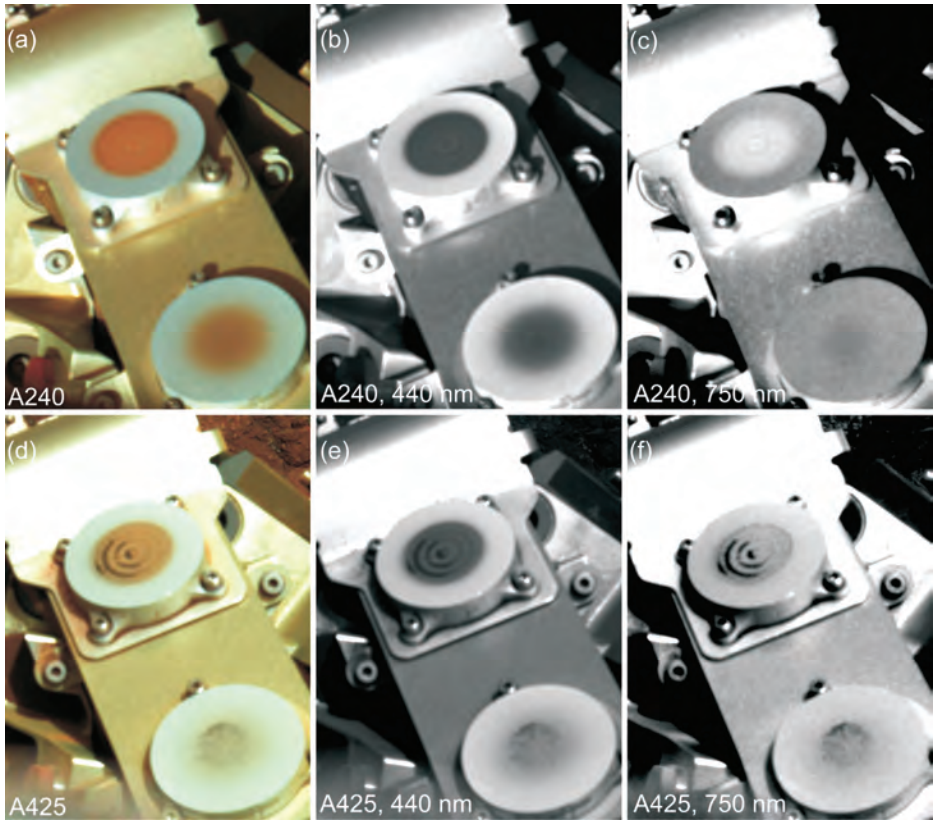

Figure 16.11. Separability of airborne dust as observed on the Mars Exploration Rover *Spirit*. The color images shown are false-color images composed of radiometrically calibrated, equally stretched Pancam L7 (440 nm), L5 (550 nm) and L2 (750 nm) images. Note the change in color between sol 240 and sol 425. A strong wind gust had passed over the rover close to sol 418. (For a color version of this figure, please refer to the color plate section or to the e-Book version of this chapter.)

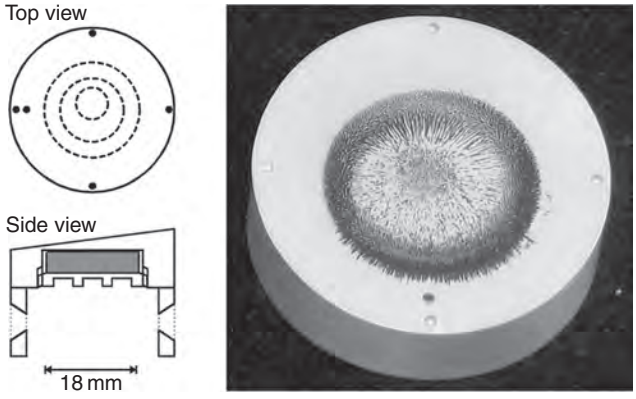

Figure 16.12. Spontaneous formation of magnetic chains in the laboratory with a sample of synthetic magnetite (BASF black pigment). The magnet shown is the Mars Pathfinder tip plate magnet. This magnet was designed to create a range of magnetic field gradients across the surface of the magnet by an asymmetric position of the central disk magnet and a wedged surface of the aluminum structure. On the image (right) this variation of magnetic fields can be seen reflected in the varying separation between the particle chains particularly along the inner rim of the ring on the surface of the magnet. The small dots in the surface of the structure serve as orientation markers. (For a color version of this figure, please refer to the color plate section or to the e-Book version of this chapter.)

et al., 2003). The center of the Sweep Magnet remained rather clean during the entire MER mission (up to the time of this writing) indicating a very low abundance of completely nonmagnetic dust. Whether any nonmagnetic dust at all has settled in the center of this magnet is still an open issue.

Note the bright ring around the darker center in the L2 (750 nm) image (Figure 16.14c). This image has been

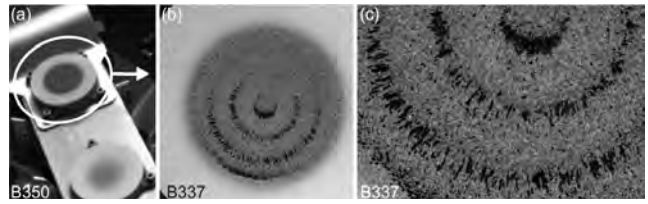

Figure 16.13. Separability of airborne dust, as observed on the Mars Exploration Rover *Opportunity* Capture Magnet. (a) Pancam image acquired on sol 350. (b) MI image acquired on sol 337, a few sols after a strong wind gust that was observed on sol 331. (c) Zoom of (b).

stretched heavily to bring out the (small) contrast between dust and the aluminum magnet surface at this wavelength. The dark magnet center is a rather clean patch of aluminum, presumably in almost the same condition as it was on its first day on Mars. Near the center of the magnet, strong attractive magnetic forces act on any iron-containing particle and move such particles outward, away from the central area, and toward the ring magnet. As was the case for the Capture Magnet, color variations can be seen in the dust settled on the Sweep Magnet: A layer of bright dust settles in a specific ring region of the Sweep Magnet and makes it appear bright, but only in that particular narrow region. Going further out from the center toward the border of the instrument, the dust is much darker. Given the previous discussions, the darker color likely results from enrichment in the opaque mineral magnetite. The darker region is certainly the one that holds the most material. Beyond this region we encounter a region with an almost negligible magnetic field, where basically any airfall dust can settle and stick to the surface by nonmagnetic forces.

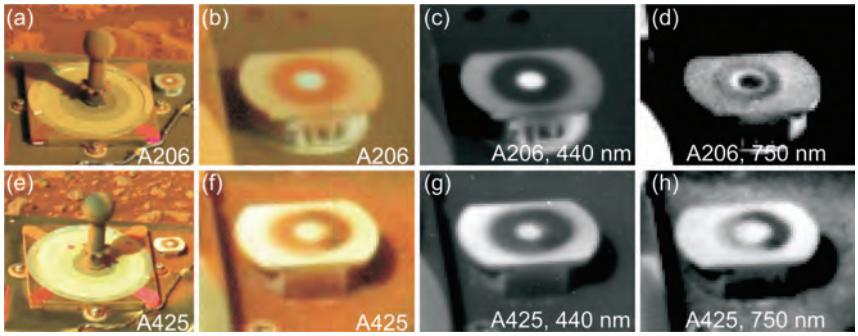

Figure 16.14. Sweep magnet, Mars Exploration Rover *Spirit*, sol 206 (a–d) and sol 425 (e–h). The color images shown are false-color images composed of radiometrically calibrated, equally stretched, images (see, Figure 16.11). Figures (a) and (e) show both the Pancam calibration target and the sweep magnet. The Sun is lower in the sol 206 image and therefore this image appears somewhat darker as compared to sol 425. Episodes of strong winds were observed around sol 418. Note the change in color between sol 206 and sol 425. The black/white images have been acquired through either the blue (c, g) or one of the near-infrared filters (d, h) and have been independently stretched in order to show spectral variations across the magnet surface (in particular in (d) the bright ring around the very center of the magnet surface [see text]). (For a color version of this figure, please refer to the color plate section or to the e-Book version of this chapter.)

Figure 16.15. The principle of the Sweep Magnet experiment on MER. (left) A vector field illustrating the magnetic field gradient (effectively the magnetic force) as a function of radial distance from the center of the magnet. The gray box illustrates the aluminum structure of the magnet and the dark gray boxes embedded in the structure illustrate the samarium-cobalt (Sm_2Co_{17}) magnetic material. Note that the force is slightly repulsive in the center of the magnet. (top right) A figure illustrating how the paths of magnetic dust grains settling out of the atmosphere are deflected as a result of interaction with the magnet and (bottom right) how nonmagnetic dust grains settle on the magnet. (For a color version of this figure, please refer to the color plate section or to the e-Book version of this chapter.)

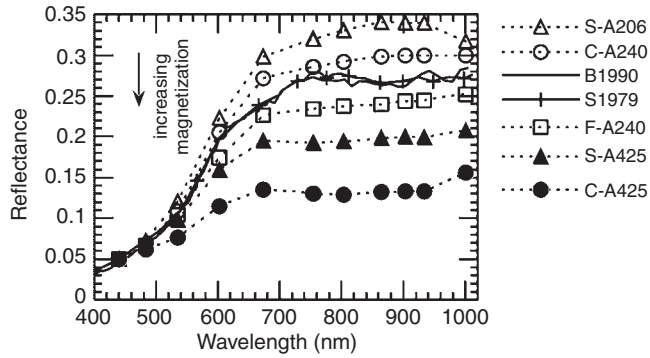

Figure 16.16. Reflectance (I/F) spectra (scaled to 0.05 at 440 nm) of different magnetic subsets of the airborne dust that have been accumulated on the Mars Exploration Rover *Spirit* magnets (S = sweep magnet, C = capture magnet, F = filter magnet). Also shown are representative spectra of classical bright Martian regions (Singer *et al.*, [1979] and Bell *et al.*, [1990] referred to as S1979 and B1990, respectively). These magnetic subsets of dust can be prepared either by exposing several magnets of strongly different properties to the Martian atmosphere (such as the filter and capture magnets; see, Figure 16.8) and/or by leaving the magnetic selection to the Martian winds. Lower reflectance is systematically correlated with stronger magnetization. Episodes of strong winds were observed around sol 418. Open and filled symbols refer to observations before and after this sol, respectively. Corresponding color images can be found in Figures 16.11 and 16.14.

As was the case for the Capture Magnet, we observed a tendency for darker, presumably more magnetite-rich and hence more magnetic, material to settle closer to the edge of the magnet. The bright, inner ring likely represents an accumulation of paramagnetic (or more generally, very weakly magnetic) particles, which only react weakly to the central repulsive forces of the Sweep Magnet.

As in the case of the Capture Magnet, the dominant ring structure appearing in the 440 nm (L7) filter images appears to be built up of both strongly (magnetite-rich) and weakly magnetic (including paramagnetic) particles, since episodes of strong winds (such as the event around *Spirit* sol 418) are able to remove substantial amounts of material (Figure 16.14e–h).

The ability of the Sweep Magnet to keep its central area clean of magnetic Martian dust will be utilized on the optical calibration targets for the Surface Stereo Imager (SSI) on board the Phoenix mission (launch scheduled for late 2007), and possibly also for the Mast Camera (Mastcam) on board the Mars Science Laboratory mission (launch scheduled for late 2009).

The magnetic separability of airborne dust can be illustrated by the diffuse reflectance spectra of the various magnetic subsets (Figure 16.16). These subsets can be prepared either by exposing very different kinds of magnets to the Martian environment or by waiting for periods of strong winds. In fact, the MER Capture and Filter magnets differ strongly in their magnetic properties: While the Capture Magnet captures any magnetic particle from a small volume above the magnet, the Filter Magnet attracts only the most strongly magnetic particles from a much larger volume above its surface (Figure 16.8). Early on during both MER missions, the dust on the Filter Magnet was observed to be substantially darker than that on the Capture Magnet. We conclude that albedo anti-correlates with magnetization of the material sticking to the magnets, an observation that is fully consistent with magnetite being the dominant magnetic phase in Martian airborne dust. Based on Figure 16.16 we

expect the following sequence of *Spirit* rover measured magnetic subsets in terms of saturation magnetization (or abundance of magnetite): sol 206, Sweep < sol 240, Capture < sol 240, Filter < sol 425, Sweep < sol 425, Capture (< sol 425, Filter). The last mentioned magnetic subset, "sol 425, Filter" is not shown in Figure 16.16, because the amounts of material accumulated on the Filter Magnet after the sol 418 dust event were too small to extract a reasonable reflectance spectrum. Note how the shape of the NIR part of the spectrum changes as the magnetization increases. However, even the most magnetic fraction of the airborne dust (here sol 425, Capture) still has a strongly reddish reflectance spectrum that is very different from that of magnetite. The optical appearance of any magnetic subset appears to be dominated by the presence of some ferric oxide(s) that may occur as thin, poorly crystallized coating on the surface of a more magnetic (magnetite-rich) composite mineral grain.

Figure 16.16 also presents telescopic (Earth-based) reflectance spectra of typical bright Martian regions. All spectra shown in Figure 16.16 have a similar ferric absorption edge. Despite the well-known pitfalls that appear when comparing Earth-based to *in situ* reflectance spectra, a few substantial differences may be noted: All magnet dust spectra have a clear slope change at around 680 nm and none of them have a significant slope change around 750 nm, which is a prominent feature in the telescopic spectra. In addition, the telescopic spectra seem to have a weak (though clearly identifiable) dip in the wavelength range ~870–~900 nm, while such a dip is absent in most magnet dust spectra, and in particular Capture Magnet dust spectra. This dip in reflectance has generally been attributed to the presence of crystalline ferric oxides (Bell *et al.*, 1990), and we might conclude that airborne dust is the spectral unit on the surface of Mars that is least crystalline from an optical point of view. Similar conclusions were made based on data from earlier missions (see Morris *et al.*, 2000, for a summary).

16.6 SUMMARY AND CONSTRAINTS ON THE FORMATION OF AIRBORNE DUST AND SOILS

We have described a series of experiments performed with permanent magnets on the surface of Mars. It was found that Martian airborne dust (as a whole) and its magnetic part (more specifically, the subset accumulated on the MER Capture Magnet) have a saturation magnetization below $2\,A\,m^2\,kg^{-1}$ and above $7\,A\,m^2\,kg^{-1}$ respectively. The dominant ferrimagnetic phase in the dust particles has been identified as (nonstoichiometric) magnetite. In this section, we will try to assess what these findings might reveal about the evolution of the Martian surface environment.

In Figure 16.17, the amount of titanium is plotted versus the amount of iron in the dust accumulated on the *Opportunity* Capture Magnet from sols 53 through sol 335. The last of these data points coincides with the acquisition of the Mössbauer spectrum shown in Figure 16.9. A word of caution: The data presented in Figure 16.17 are raw APXS

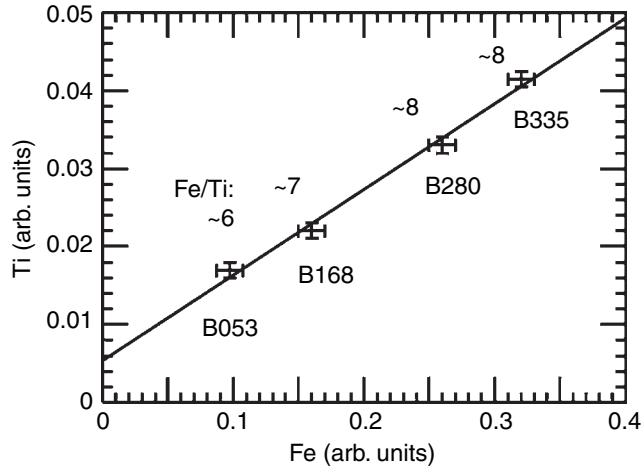

Figure 16.17. Elemental composition (Fe, Ti) of dust on the *Opportunity* capture magnet (APXS data). The amount of Fe and Ti increases over time (sol numbers ranging from 53 through 335), while the ratio Fe/Ti remains essentially constant.

data and have *not* been corrected for the small sample thickness. In any case we may postulate a linear relationship between the number of atoms accumulated on the active surface of the magnet and the APXS signal. However, the APXS sampling depth is different for Fe and Ti. As a result, the ratio between Fe- and Ti-peak deviates from the ratio of Fe- to Ti-abundance in the sample, and this deviation varies with sample thickness.

Given these limitations, the following conclusions can be drawn from Figure 16.17:

(1) In APXS spectra, the signal from iron increases continuously with time because more and more (magnetic) dust is accumulated on the Capture Magnet. The element iron is associated with all naturally occurring magnetic phases and it is therefore not surprising that the iron-peak increases as the dust layer accumulates; and (2) The APXS lines from both iron and titanium seem to be very well correlated even though no correction was made for the (slightly) different thickness effect for these two elements. The fact that the fitted straight line does not intersect the origin is most likely a calibration issue, but also can have a more subtle explanation, namely that strong gusts of wind interacting through time with the dusty surface of the magnet has a tendency to preferentially remove dust particles with more strongly Ti-substituted magnetite (slightly less magnetic) than those with more pure magnetite; and (3) The ratio Fe/Ti is almost constant over time, but may be growing slightly. Note again that the particular value for this ratio (in the range 6 to 8 according to Figure 16.17) cannot be simply translated into the ratio between abundances of the two elements, because the ratio will depend on both the dust layer thickness and the particular data reduction model used.

All three points nevertheless do support a very important conclusion: The concentration of Ti seems to be very well correlated with the concentration of Fe, which is so closely associated with the magnetic phase. This is a very strong

indication that the ferrimagnetic mineral identified in the Mössbauer spectrum (Figure 16.9) is actually titanomagnetite rather than pure magnetite. Also, the Mössbauer spectrum itself may point in this direction because the ratio between the areas of the two magnetite sextets in the spectrum is not exactly what is usually found for pure magnetite. Titanomagnetite is most probably inherited directly from basaltic rocks, which are known to be common on the surface of Mars and, in particular, have been frequently encountered at the *Spirit* landing site (Morris *et al*., 2006).

Here it should be emphasized that the Mössbauer spectrum presented in Figure 16.9 does also contain (besides the strong titanomagnetite sextets) one or more lower intensity sextet(s) that may be assigned to traces of hematite and possibly one more mineral. And, finally, it is also relevant to note that the prominent Mössbauer doublets have been assigned to a ferric paramagnetic or superparamagnetic oxide or oxyhydroxide, pyroxene, and olivine (Goetz *et al*., 2005). Both the moderate degree of oxidation of iron in Martian airborne dust (substantially below the oxidation state 3) and the presence of small particles of a mineral species such as olivine that over geologic time is relatively easily reworked or dissolved by liquid water at postulated Martian environmental conditions are interpreted as a strong indicator of long arid periods on the surface of Mars (Goetz *et al*., 2005). The admixture of small amounts of a secondary iron oxide (such as hematite and possibly other ferric oxyhydroxides) may be indicative of the action of liquid water over a limited amount of time, possibly early in the history of the planet.

REFERENCES

Allen, C. C., R. V. Morris, K. M. Jager, *et al*., JSC-Mars-1: Martian regolith simulant, *Proc. Lunar Planet. Sci. Conf. IXXX*, Abstract #1690, 1998.

Ashcroft, N. W. and N. D. Mermin, *Solid State Physics*, Philadelphia, PA: Saunders College Publishing, 1976.

Bell III, J. F., T. B. McCord, and P. D. Owensby, Observational evidence of crystalline iron oxides on Mars, *J. Geophys. Res.* **95**, 14447, 1990.

Bell III, J. F., J. Joseph, J. N. Sohl-Dickstein, *et al*., In-flight calibration and performance of the Mars Exploration Rover Panoramic Camera (Pancam) instruments, *J. Geophys. Res.* **111**, E02S03, doi:10.1029/2005JE002444, 2006.

Bertelsen, P., W. Goetz, M. B. Madsen, *et al*., Magnetic properties experiments on the Mars Exploration Rover Spirit at Gusev crater, *Science* **305**, 827–9, 2004.

Coey, J. M. D., Magnetic properties of iron in soil iron oxides and clay minerals. *Iron in Soils and Clay Minerals* (ed. J. W. Strucki *et al*.), Dordrecht: D. Reidel Publishing Company, pp. 397–466, 1988.

Coey, J. M. D., S. Morup, M. B. Madsen, and J. M. Knudsen, Titanomaghemite in magnetic soils on Earth and Mars, *J. Geophys. Res.* **95**, 14423–5, 1990.

Criddle, A. J. and C. J. Stanley, *Quantitative Data File for Ore Minerals (QDF3)*, 3rd edn., London: Chapmann & Hall, 1993.

de Wys, J. N., Magnet Data, In Surveyor: Program Results, *NASA SP-184*, **223**, 1969.

Dunlop, D. J. and Ö. Özdemir, *Rock Magnetism, Fundamentals and Frontiers*, Cambridge University Press, 1997.

Gellert, R., R. Rieder, R. C. Anderson, *et al*., Chemistry of rocks and soils in Gusev crater from the Alpha Particle X-ray Spectrometer, *Science* **305**, 829–32, 2004.

Goetz, W., The optical properties of Martian dust, Ph.D. thesis, Center for Planetary Science, University of Copenhagen, 2002.

Goetz, W., P. Bertelsen, C. S. Binau, *et al*., Chemistry and mineralogy of atmospheric dust at Gusev crater: indication of dryer periods on Mars, *Nature* **436**, 62–5, 2005.

Goetz, W., K. Leer, H. P. Gunnlaugsson, *et al*., Overview of the RAT Magnet Investigation on Spirit and Opportunity, *J. Geophys. Res.* doi:10.1029/2006JE002819, 2007.

Gorevan, S. P., T. Myrick, K. Davis, *et al*., Rock abrasion tool: Mars Exploration Rover mission, *J. Geophys. Res.* **108**, 8068, 2003.

Greeley, R., R. E. Arvidson, P. W. Barlett, *et al*., Gusev crater: wind-related features and processes observed by the Mars Exploration Rover Spirit, *J. Geophys. Res.* **111**, 2006.

Gunnlaugsson, H. P., Analysis of the magnetic properties experiment data on Mars: results from Mars Pathfinder, *Planet. Space Sci.* **48**, 1491–504, 2000.

Gunnlaugsson, H. P., S. F. Hviid, J. M. Knudsen, and M. B. Madsen, Instruments for the magnetic properties experiments on Mars Pathfinder, *Planet. Space Sci.* **46**, 449, 1998.

Hapke, B., *Theory of Reflectance and Emittance Spectroscopy*, Cambridge: Cambridge University Press, 1993.

Hargraves, R. B. and N. Petersen, Magnetic properties investigation: the Viking Mars lander, *Icarus* **16**, 223–7, 1972.

Hargraves, R. B., D. W. Collinson, and C. R. Spitzer, Viking magnetic properties investigation: preliminary results, *Science* **194**, 84–6, 1976a.

Hargraves, R. B., D. W. Collinson, R. E. Arvidson, and C. R. Spitzer, Viking magnetic properties investigation: further results, *Science* **194**, 1303, 1976b.

Hargraves, R. B., D. W. Collinson, R. E. Arvidson, and C. R. Spitzer The Viking magnetic properties experiment: primary mission results, *J. Geophys. Res.* **82**, 4547–58, 1977.

Hargraves, R. B., D. W. Collinson, R. E. Arvidson, and P. M. Cates, Viking magnetic properties experiment: extended mission results, *J. Geophys. Res.* **84**, 8379–84, 1979.

Hargraves, R. B., J. M. Knudsen, P. Bertelsen, *et al*., Magnetic enhancement on the surface of Mars?, *J. Geophys. Res. – Planets* **105**, 1819–27, 2000.

Huffmann, D. R. and J. L. Stapp, Optical measurements on solids of possible interstellar importance. In *Interstellar Dust and Related Topics* (ed. Greenberg and V. d. Hulst), Boston, MA: D. Reidel Co., p. 297, 1973.

Hviid, S. F., M. B. Madsen, H. P. Gunnlaugsson, *et al*., Magnetic properties experiments on the Mars Pathfinder lander: preliminary results, *Science* **278**, 1768–70, 1997.

Hviid, S. F., M. B. Madsen, J. M. Knudsen, *et al*., Results of the magnetic properties experiment on the Mars Pathfinder lander, *Lunar Planet. Sci.* **XXIX**, 1605–6, 1998.

Jackson, J. D., *Classical Electrodynamics*, 3rd edn., New York, NY: John Wiley & Sons, 189pp., 1999.

Johnson, J. R., W. M. Grundy, and M. T. Lemmon, Dust deposition at the Mars Pathfinder landing site: observations and modeling of visible/near-infrared spectra, *Icarus* **163**, 330–46, 2003.

Kinch, K. M., *et al*. Preliminary analysis of the MER magnetic properties experiment using a computational fluid dynamics model, *Planet. Space Sci.* **54**, 28–44, 2006.

Kinch, K. M., *et al*., Dust deposition on the Mars Exploration Rover Panoramic Camera (Pancam) calibration targets, *J. Geophys. Res*., **112**, Cite ID E06S03, doi:10.1029/2006JE002807, 2007.

Klingelhöfer, G., R. V. Morris, B. Bernhardt, *et al*., Jarosite and hematite at Meridiani Planum from Opportunity's Mössbauer spectrometer, *Science* **306**, 1740–5, 2004.

Knudsen, J. M., M. B. Madsen, M. Olsen, *et al*., Mössbauer spectroscopy on the surface of Mars: Why?, *Hyperfine Interactions* **68**, 83–94, 1991.

Landis, G. A. and P. J. Jenkins, Measurement of the settling rate of atmospheric dust on Mars by the MAE instrument on Mars Pathfinder, *J. Geophys. Res.* **105**, 1855–7, 2000.

Landis, G. A., K. Herkenhoff, R. Greeley, *et al*., Dust and sand deposition on the MER solar arrays as viewed by the Microscopic Imager, *Proc. Lunar Planet. Sci. Conf. XXXVII*, 2006.

Lemmon, M., M. J. Wolff, M. D. Smith, *et al*., Atmospheric imaging results from the Mars Exploration Rovers: Spirit and Opportunity, *Science* **306**, 1753–6, 2004.

Madsen, M. B., S. F. Hviid, H. P. Gunnlaugsson, *et al*., The magnetic properties experiments on Mars Pathfinder, *J. Geophys. Res.* **104**, 8761–79, 1999.

Madsen, M. B., P. Bertelsen, W. Goetz, *et al*., The magnetic properties experiments on the Mars Exploration Rover mission, *J. Geophys. Res.* **108**, 8069, 2003.

Markiewicz, W. J., R. M. Sablotny, H. U. Keller, *et al*., Optical properties of the Martian aerosols as derived from imager for Mars Pathfinder midday sky brightness data, *J. Geophys. Res.* **104**, 9009–17, 1999.

McSween, H. Y., M. B. Wyatt, R. Gellert, *et al*., Characterization and petrologic interpretation of olivine-rich basalts at Gusev crater, Mars, *J. Geophys. Res.* **111**, E02S10, doi:10.1029/2005JE002477, 2006.

Merrison, J. P., H. Gunnlaugsson, L. Mossin, *et al*., Capture of magnetic dust in a simulated Martian aerosol: the importance of aerodynamics, *Planet. Space Sci.* **50**, 371–4, 2002a.

Merrison, J. P., P. Bertelsen, C. Frandsen, *et al*., Simulation of the Martian dust aerosol at low wind speeds, *J. Geophys. Res.* **107**, 5133, 2002b.

Metzger, S. M., J. R. Carr, J. R. Johnson, T. J. Parker, and M. T. Lemmon, Dust devil vortices seen by the Mars Pathfinder camera, *Geophys. Res. Lett.* **26**, 2781–4, 1999.

Mogensen, C. T., J. M. Knudsen, M. B. Madsen, *et al*., Magnetic properties experiments on the Mars polar lander, *J. Geophys. Res.* **106**, 17579–88, 2001.

Morris, R. V. and R. Singer, Origins of Marslike spectral and magnetic properties of a Hawaiian Palagonitic soil, *J. Geophys. Res.* **95**, 14427–34, 1990.

Morris, R. V., H. V. Lauer Jr., C. A. Lawson, *et al*., Spectral and other physiochemical properties of submicron powders of hematite (α-Fe_2O_3), maghemite (γ-Fe_2O_3), magnetite (Fe_3O_4), goethite (α-FeOOH), and lepidocrocite (γ-FeOOH), *J. Geophys. Res.* **90**, 3126–44, 1985.

Morris, R. V., D. C. Golden, J. F. Bell III, *et al*., Mineralogy, composition, and alteration of Mars Pathfinder rocks and soils: evidence from multispectral, elemental, and magnetic data on terrestrial analogue, SNC meteorite, and Pathfinder samples, *J. Geophys. Res.* **105**, 1757–818, 2000.

Morris, R. V., T. G. Graff, and S. A. Mertzman, Phyllosilicate-poor palagonitic dust from Mauna Kea Volcano (Hawaii): a mineralogical analogue for magnetic Martian dust?, *J. Geophys. Res.* **106**, 5057–84, 2001.

Morris, R. V., G. Klingelhöfer, B. Bernhardt, *et al*., Mineralogy at Gusev crater from the Mössbauer spectrometer on the Spirit Rover, *Science* **305**, 833–6, 2004.

Morris, R. V., G. Klingelhöfer, C. Schröder, *et al*., Mössbauer mineralogy of rock, soil, and dust at Gusev crater, Mars: Spirit's journey through weakly altered olivine basalt on the plains and pervasively altered basalt in the Columbia Hills, *J. Geophys. Res.* **111**, 2006.

Nørnberg, P., U. Schwertmann, H. Stanjek, T. Andersen, and H. P. Gunnlaugsson, Mineralogy of a burned soil compared with four anomalously red Quaternary deposits in Denmark, *Clay Miner.* **39**, 85–98, 2004.

Ockert-Bell, M. E., J. F. Bell III, C. P. Mckay, J. B. Pollack, and F. Forget, Absorption and scattering properties of the Martian dust in the solar wavelengths, *J. Geophys. Res.* **102**, 9039–50, 1997.

O'Reilly, W., Magnetic minerals in the crust of Earth, *Rep. Prog. Phys.* **39**, 857–908, 1976.

O'Reilly, W., *Rock and Mineral Magnetism*, Glasgow: Blackie and son Ltd., 1984.

Pollack, J. B., D. Colburn, R. A. Kahn, *et al*., Properties of aerosols in the Martian atmosphere as inferred from Viking Lander imaging data, *J. Geophys. Res.* **82**, 4479–96, 1977.

Pollack, J. B., D. S. Colburn, F. M. Flaser, *et al*., Properties and effects of dust suspended in the Martian atmosphere, *J. Geophys. Res.* **84**, 2929–45, 1979.

Pollack, J. B., M. E. Ockert-Bell, and M. K. Shepard, Viking Lander image analysis of Martian atmospheric dust, *J. Geophys. Res.* **100**, 5235, 1995.

Schlegel, A., S. F. Alvarado, and P. Wachter, Optical properties of magnetite (Fe_3O_4), *J. Phys. C: Solid State Phys.* **12**, 1157–64, 1979.

Schofield, J. T., J. R. Barnes, D. Crisp, *et al*., The Mars Pathfinder Atmospheric Structure Investigation/Meteorology (ASI/MET) experiment, *Science* **278**, 1752–8, 1997.

Singer, R. B., T. B. McCord, and R. N. Clark, Mars surface composition from reflectance spectroscopy: a summary, *J. Geophys. Res.* **84**, 8415–26, 1979.

Smith, P. H., M. G. Tomasko, D. Britt, *et al*., The Imager for Mars Pathfinder experiment, *J. Geophys. Res.* **102**, 4003–25, 1997.

Squyres, S. W., R. E. Arvidson, E. T. Baumgartner, *et al*., The Athena Mars Rover science investigation, *J. Geophys. Res.* **108**, 8062, doi:10.1029/JE002121, 2003.

Tanaka, T., Optical constants of polycrystalline 3d transition metal oxides in the wavelength region 350 to 1200 nm, *Japanese J. Appl. Phys.* **18**, 1043, 1979.

Tomasko, M. G., L. R. Doose, M. Lemmon, P. H. Smith, and E. Wegryn, Properties of dust in the Martian atmosphere from the imager on Mars Pathfinder, *J. Geophys. Res.* **104**, 8987–9007, 1999.

PART III.D

Martian Meteorites as Crustal Samples

17

Martian meteorites as crustal samples

H. Y. McSWEEN JR.

ABSTRACT

Times of impact ejection of Martian meteorites occur in clusters and correlate with petrographic classifications. The clustered or unique ejection ages apparently sample as many as seven distinct locations on Mars. All these sites, as yet not identified unambiguously, are dominated by basaltic flows or cumulate rocks formed from basaltic magmas. Except for ALH 84001, a 4.5 Ga sample of the Noachian crust, all SNCs were extracted from Amazonian volcanic terrains. Lithologies identified by landed or orbiting spacecraft are generally different from SNCs, although the distinctive mineralogic characteristics of SNCs (ferroan olivine and pyroxenes, sodic plagioclase) are commonly indicated by remote-sensing data. Aqueous alteration of SNC meteorites is limited, and light stable isotopic fractionations suggest hydrologic cycling. These meteorites reveal many geochemical, mineralogical, and chronological properties of the crust that cannot yet be measured by remote sensing.

17.1 INTRODUCTION

Martian meteorites include Shergottites, Nakhlites, and Chassignites (SNCs), as well as the unique meteorite ALH 84001. These achondrites are thought to have been derived from Mars, based a variety of observations (e.g., Treiman *et al*., 2000, and references therein). All are basalts or ultramafic rocks exhibiting various degrees of shock metamorphism. The most telling evidence linking SNCs to Mars is the presence in them of shock-implanted gases with distinctive elemental and isotopic compositions that match those of the Martian atmosphere (Figure 17.1). These meteorites also share similarities in their geochemistry, including a common oxygen isotopic fingerprint, and their mineralogies are distinctive from other extraterrestrial materials (McSween and Treiman, 1998).

Martian meteorites, all igneous rocks (so far), provide critical information about the deep mantle source regions that melted to produce their parent magmas (McSween, 2002); they can also inform our understanding of the mineralogy, geochemistry, chronology, and petrogenesis of the Martian *surface*. If SNCs are to serve as indicators of surface minerals or as ground truth for remote-sensing observations, it is fair to ask how representative of the exposed crust they really are.

Most Martian meteorites are lavas that erupted onto the planet's surface, but a few are plutonic rocks that crystallized within the crust. All of these meteorites, even the plutonic rocks, probably were located on or very near the surface at the time of their extraction. The only plausible model for liberating rocks from Mars involves large impacts. Models suggest that spalls of surface or near-surface materials around craters are the only target rocks accelerated to Martian escape velocity (Melosh, 1984; Artemieva and Ivanov, 2002; Head *et al*., 2002); rocks excavated by impacts from deeper levels are not ejected at the requisite velocities to become meteors.

As explained below, the present collection of SNC meteorites probably represents as many as seven different sites on the planet's surface. These launch sites are not randomly distributed among the various kinds of surface materials inferred from remote sensing, or among crustal materials of different ages. Even though they appear to constitute a biased sample of the crust, they nonetheless comprise a wider sampling of igneous terrains than has been studied by landed spacecraft. This chapter describes evidence for the number and possible locations of launch sites, characterizes the rocks at each launch site, and compares their properties to those inferred from orbital spectroscopy or measured by landers.

17.2 NUMBER AND POSSIBLE LOCATIONS OF SAMPLING SITES

17.2.1 Ejection events

Rocks ejected from Mars and orbiting as small (meter-sized) objects in space are irradiated by cosmic rays, producing cosmogenic nuclides. Measurement of these nuclides allows the *cosmic-ray exposure age* to be determined. Once a meteorite falls to Earth, the atmosphere shields it from further exposure and short-lived cosmogenic nuclides begin to decay. Comparison of the abundances of short-lived and longer-lived cosmogenic nuclides allows the meteorite's residence time on Earth, its *terrestrial age*, to be estimated. The sum of the cosmic-ray exposure age and the terrestrial age is the *Mars ejection age*.

Ejection ages for SNC meteorites (Nyquist *et al*., 2001; Christen *et al*., 2005, and references therein) are summarized in Figure 17.2 and Table 17.1. Well-defined clusters containing 4–5 meteorites each occur at 1.16 ± 0.6, 2.8 ± 0.3, 4.1 ± 0.4, and 10.8 ± 0.7 millions of years ago (Ma) (boxes in Figure 17.2). Three isolated meteorites occur at younger or older ages.

The Martian Surface: Composition, Mineralogy, and Physical Properties, ed. J. F. Bell III. Published by Cambridge University Press.

Table 17.1. *Chronology and properties of individual SNC meteorites*

	Crystallization age (Ma or Ga)	Mars ejection age (Ma)	Descriptive reference
Basaltic shergottites			
Los Angeles	170 ± 7 Ma	3.0 ± 0.3	Rubin *et al.* (2000)
NWA 480		2.4 ± 0.2	Barrat *et al.* (2002a)
NWA 856	170 ± 19 Ma	2.6 ± 0.2	Jambon *et al.* (2002)
QUE 94201	327 ± 10 Ma	2.8 ± 0.3	McSween *et al.* (1996)
Shergotty	165 ± 11 Ma	3.0 ± 0.3	Stöffler *et al.* (1986)
Zagami	169 ± 7 Ma	3.0 ± 0.3	McCoy *et al.* (1992)
Olivine-phyric shergottites			
DAG 476/489[a]	474 ± 11 Ma	1.25 ± 0.12	Zipfel *et al.* (2000)
NWA 1068		1.14 ± 0.17	Barrat *et al.* (2002b)
NWA 1195	348 ± 19 Ma	1.1 ± 0.2	Irving *et al.* (2002)
SAU 005/094/150[a]		1.2 ± 0.3	Goodrich (2003)
Y-980459	290 ± 40 Ma	1.1 ± 0.2	Greshake *et al.* (2004)
EET 79001	173 ± 3 Ma	0.73 ± 0.15	McSween and Jarosewich (1983)
DHO 019	575 ± 7 Ma	19.8 ± 2.3	Taylor *et al.* (2002)
Lherzolitic shergottites			
ALH 77005	177 ± 6 Ma	3.8 ± 0.7	McSween *et al.* (1979)
LEW 88516	178 ± 9 Ma	3.9 ± 0.4	Harvey *et al.* (1993)
NWA 1950		4.1 ± 1.4	Gillet *et al.* (2005)
Y-793605	212 ± 62 Ma	4.7 ± 0.5	Mikouchi and Miyamoto (1996)
Nakhlites/chassignites			
Chassigny	1.36 ± 0.06 Ga	11.3 ± 0.6	Floran *et al.* (1978)
NWA 2737	~1.38 Ga	11.1 ± 1.0	Mikouchi (2005)
Governador Valadares	1.37 ± 0.02 Ga	10.0 ± 2.1	Berkley *et al.* (1980)
Lafayette	1.32 ± 0.05 Ga	11.9 ± 2.2	Boctor *et al.* (1976)
Nakhla	1.26 ± 0.07 Ga	10.8 ± 0.8	Treiman (1990)
NWA 817		10.0 ± 1.3	Sautter *et al.* (2002)
Y-000593/749/802[a]	1.31 ± 0.03 Ga	12.1 ± 7	Mikouchi *et al.* (2003)
Orthopyroxenite			
ALH 84001	4.50 ± 0.13 Ga	14.7 ± 0.9	Mittlefehldt (1994)

Crystallization ages summarized by Borg and Drake (2005), plus Misawa *et al.* (2005).
Mars ejection ages summarized by Christen *et al.* (2005), plus Marty *et al.* (2005).
[a] Paired meteorites.

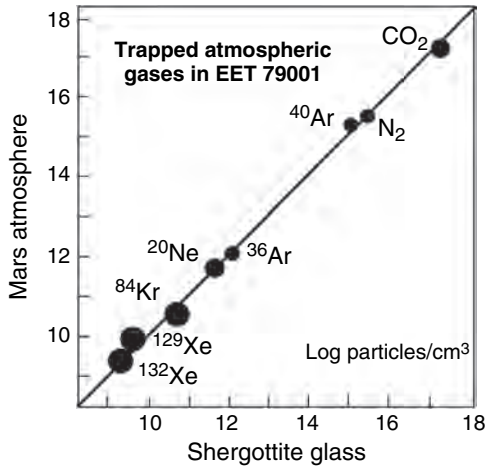

Figure 17.1. Comparison of molecular and isotopic abundances of the Mars atmosphere with shock-implanted gases in the EET 79001 shergottite. This correspondence provides the best evidence for the Martian origin of SNC meteorites.

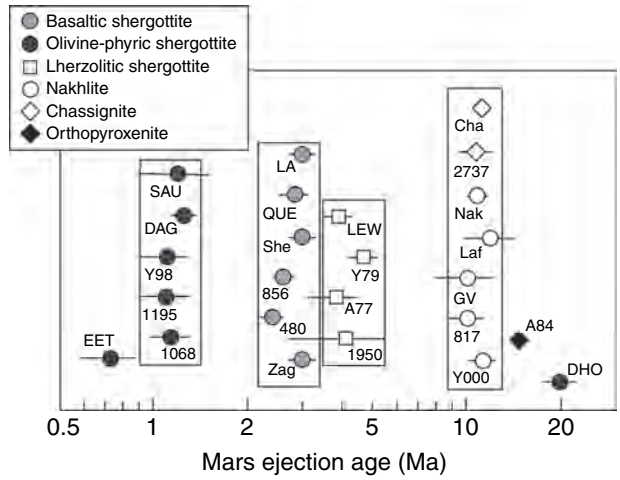

Figure 17.2. Mars ejection ages, data sources listed in Table 17.1.

Each of these ejection ages presumably corresponds to an individual impact event at a different site (Christen *et al.*, 2005). This hypothesis is bolstered by the uniformity in meteorite petrography (classifications are indicated in Figure 17.2) within each ejection age cluster. The meteorites for which ejection ages are available thus may represent as many as seven sampling sites (assuming the chassignites and nakhlites are from the same location). This compares with only five landing sites visited by spacecraft (two Viking, Mars Pathfinder, and two Mars Exploration Rovers [MERs]).

17.2.2 Sampling sites

The specific locations of SNC launch sites remain conjectural. The young crystallization ages for all but one Martian meteorite (Nyquist *et al.*, 2001; Borg and Drake, 2005, and references therein) demand that they are samples of late Hesperian or Amazonian igneous units. Mouginis-Mark *et al.* (1992) and Barlow (1997) identified several possible large source craters, based on crater density ages of their host terrains. Originally, only large (~100 km diameter) impact craters were thought to be plausible launch sites (Melosh, 1984; Vickery and Melosh, 1987), but that constraint has been progressively whittled down to craters of only ~3 km diameter (Head *et al.*, 2002). Plausible launch sites lie on young volcanic units, such as those on Tharsis and Elysium. Unfortunately, these sparsely cratered units are thickly covered with dust, eliminating the possibility of determining launch sites by spectroscopic comparisons with meteorites.

Searches for other, less dusty terrains with similar Mars Global Surveyor thermal emission spectra to SNCs were initially unsuccessful, except for a few localized olivine-, orthopyroxene-, and clinopyroxene-bearing regions (Hamilton *et al.*, 2003). Clinopyroxene-bearing localities in Syrtis Major have been suggested as the launch site for nakhlites and chassignites (Harvey and Hamilton, 2005). However, the Hesperian crater-density age for Syrtis Major is inconsistent with the younger 1.3 billions of years ago (Ga) crystallization ages of nakhlites and chassignites and would require a substantial (and controversial) revision of the Martian stratigraphic timescale. An orthopyroxene-rich locality on the floor of Eos Chasma (Valles Marineris) has a spectrum similar to ALH 84001, and has been proposed as its launch site (Hamilton, 2005).

Using nighttime thermal infrared images from the Mars Odyssey THEMIS instrument, Tornabene *et al.* (2006) discovered seven fresh, rayed craters (2–10 km diameter), thought to be among the youngest craters on Mars (as required by the Mars ejection ages for SNCs). Five of these craters are located within recent (as determined from crater densities) volcanic regions in Elysium, consistent with the young crystallization ages of SNCs. Two rayed craters in older terrains might be the launch sites for nakhlites/chassignites and ALH 84001. The rays, formed by chains of secondary craters, are themselves evidence of spallation, and calculations suggest that ejecta at the ends of the longest rays approached the Martian escape velocity (5 km s^{-1}). Unfortunately, the rays are too thin for measurements of their thermal emission spectra, but the CRISM (CRISM – Compact Reconnaissance Imaging Spectrometer for Mars) instrument on Mars Reconnaissance Orbiter (MRO) might be able to obtain visible/near-infrared (NIR) spectra for comparison with meteorite spectra.

17.3 MINERALOGY/PETROLOGY/GEOCHEMISTRY OF SNC SAMPLING SITES

Based on the plausible assumption that each cluster of Mars ejection ages corresponds to a distinct sampling site, it is instructive to summarize the petrologic and geochemical characteristics of each of these sites. The focus here is on geologic properties that might be determined by remote-sensing methods. Preterrestrial alteration of these igneous rocks was very limited in extent and will be considered in a later section. Petrologic classifications, chronologies, and representative descriptive references for individual SNC meteorites are given in Table 17.1. Additional SNCs having the same petrographic classifications as these meteorites are known but their Mars ejection ages have not yet been determined, so they cannot be assigned confidently to specific sites and are not included in Table 17.1. Table 17.2 summarizes the mineralogy of rocks at each site, divided into major minerals that might be detected by remote-sensing methods and accessory igneous and secondary minerals in low abundances. A detailed summary of the mineralogy of individual Martian meteorites was provided by McSween and Treiman (1998), which can be supplemented with data for newly discovered meteorites from references in Table 17.1. Table 17.3 gives the ranges in the bulk chemical compositions of multiple meteorite samples from each site. A summary of the geochemistry of individual Martian meteorites was given by Lodders (1998), and geochemical data for more recently described meteorites can be found in references in Table 17.1.

17.3.1 Basaltic shergottites

Basaltic shergottites ejected at ~2.8 Ma have crystallization ages of ~170 Ma, except for one sample (QUE 94201) that is 327 Ma old (Table 17.1). The initial Sr and Nd isotopic compositions of these samples suggest that none represent the same magma (Borg and Drake, 2005), so this site is likely to contain a series of volcanic flows ranging over 150 Ma. QUE 94201 represents a melt composition, but the younger basaltic shergottites contain accumulated pyroxene crystals (now the cores of zoned crystals) that were apparently entrained and aligned in the flows (McCoy *et al.*, 1992; Hale *et al.*, 1999).

The various shergottite samples were derived from two distinct sources: a reduced, depleted source and an oxidized, enriched source (Herd *et al.*, 2001). The former source resides in the mantle, but the latter could indicate mantle heterogeneity or assimilation of crust. On Earth, oxidation

Table 17.2. *Mineralogy of SNC meteorite classes*

Basaltic shergottites	Olivine-phyric shergottites	Lherzolitic shergottites	Nakhlites	Chassignites	ALH 84001
Major minerals (igneous)					
Pigeonite	Pigeonite	Orthopyx	Augite	Olivine	Orthopyx
Augite	Augite	Olivine	Olivine	Augite	
Maskelynite	Maskelynite	Pigeonite			
Accessory minerals (igneous)					
Magnetite	Chromite	Augite	Orthopyx	Orthopyx	Maskelynite
Ilmenite	Ilmenite	Maskelynite	Plagioclase	Plagioclase	Chromite
Merrillite	Merrillite	Chromite	K-feldspar	Sanidine	Apatite
Apatite	Apatite	Ilmenite	Magnetite	Chromite	
Pyrrhotite	Pyrrhotite	Sulfides	Ilmenite	Apatite	
Fayalite		Merrillite	Apatite	Sulfides	
Quartz			Silica		
Pyroxferroite			Sulfides		
Baddeleyite			Baddeleyite		
Secondary minerals (Mars alteration or shock)					
Calcite		Sulfate	Iddingsite	Carbonates	Carbonates
Gypsum		Clay	Siderite	Sulfate	Magnetite
Clays		Silica	Sulfates		Sulfides
Stishovite		Phosphate	Halite		Silica
Ringwoodite					
Majorite					

Source: Mineralogy summarized by McSween and Treiman (1998).

Table 17.3. *Geochemistry of SNC meteorite classes*

Oxides (wt.%)	Basaltic shergottites	Olivine-phyric shergottites	Lherzolitic shergottites	Nakhlites
SiO_2	51.5–46.0	51.7–45.5	45.5–41.3	50.8–48.2
TiO_2	1.98–0.67	1.67–0.33	0.46–0.19	0.47–0.07
Al_2O_3	12.0–3.53	7.71–4.17	3.86–1.28	3.59–1.45
Cr_2O_3	0.58–0.01	0.83–0.52	1.21–0.83	0.41–0.19
FeO*	21.4–14.2	24.3–15.4	20.9–17.9	21.7–19.2
MnO	0.62–0.20	0.54–0.45	0.53–0.44	0.67–0.45
MgO	12.3–3.53	20.8–11.9	29.7–22.7	12.9–9.33
CaO	11.5–6.57	9.42–5.18	4.54–2.66	15.8–13.1
Na_2O	2.24–1.25	1.14–0.51	0.60–0.20	1.01–0.41
K_2O	0.36–0.04	0.16–0.02	0.06–0.01	0.32–0.10
P_2O_5	1.28–0.50	0.66–0.31	0.40–0.39	0.45–0.10

Source: Compositional ranges for shergottites from Shirai and Ebihara (2004), for nakhlites from Treiman (2005).
* Standard geochemical notation meaning all iron reported as FeO.

and enrichment in incompatible trace elements and some radiogenic isotopes characterize the crust and parts of the mantle that have undergone metasomatic alteration. Most of these meteorites contain very little water, suggesting a dry mantle source. However, the meteorites containing a significant enriched source component, like Shergotty, may have contained dissolved water that was lost during ascent, as inferred from depletions in water-soluble elements like boron and lithium (McSween *et al.*, 2001). Trapped melt inclusions in pyroxene cores contain kaersutitic amphibole (Treiman, 1985), signaling different (hydrous?) crystallization conditions at depth.

Basaltic shergottites consist primarily of clinopyroxenes (pigeonite and augite), plus intermediate plagioclase that has been converted to maskelynite by shock (Figure 17.3a). The compositions of coexisting titanomagnetite and ilmenite indicate crystallization under variable redox conditions. High-pressure polymorphs of pyroxene and silica have also been identified. Accessory igneous minerals, alteration minerals, and shock polymorphs are listed in Table 17.2. Mineral compositions and zoning patterns are described by McSween and Treiman (1998).

The major element compositions of basaltic shergottites (Table 17.3) are characterized by high FeO/MgO (reflected

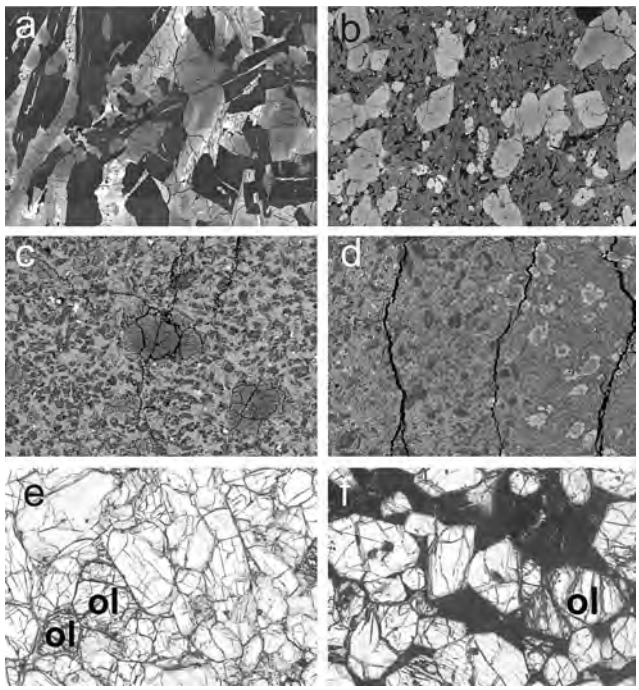

Figure 17.3. Photomicrographs of shergottites and nakhlites. (a) Backscattered electron (BSE) image of basaltic shergottite QUE 94201, 6 mm across. (b) Olivine-phyric shergottite SAU 005; BSE image, 5.5 mm across. (Reprinted from Geochimica et Cosmochimica Acta, **67** (19), Goodrich, C. A., Petrogenesis of olivine-phyric shergottites Sayh al Uhaymir 005 and Elephant Moraine A79001 lithology A, © 2003 with permission from Elsevier.) (c) Olivine-phyric shergottite Y-980459; BSE image, 10 mm across, courtesty of C. Goodrich. (d) Contact in EET 79001, showing olivine-phyric lithology A on the right and basaltic lithology B on the left; BSE image, 12 mm across, courtesy of A. Krot. (e) Nakhlite Lafayette; plane polarized light, 2.1 mm across, courtesy of A. Treiman. (f) Nakhlite NWA 817; plane polarized light, 2.1 mm across, courtesy of A. Treiman.

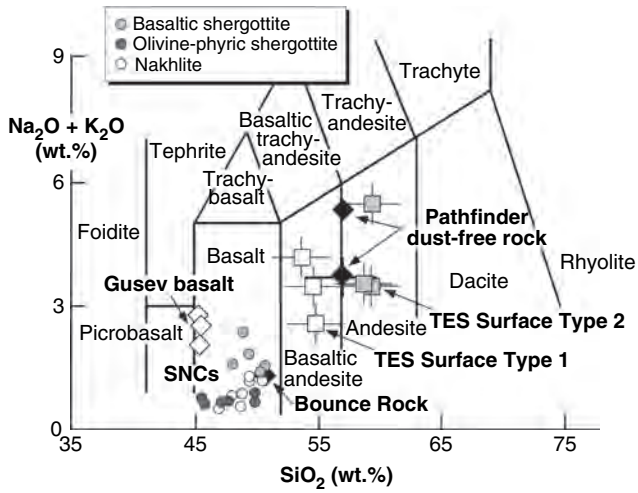

Figure 17.4. Total alkalis versus silica classification diagram for volcanic rocks, showing the compositions of basaltic and olivine-phyric shergottites and nakhlites (references in Table 17.3), two calibrations of the Mars Pathfinder dust-free rock (Wänke *et al.*, 2001; Foley *et al.*, 2003), Gusev basalts (McSween *et al.*, 2006), and MGS TES-derived chemical compositions for Surface Types 1 and 2 (Bandfield *et al.*, 2000; Hamilton *et al.*, 2001; McSween *et al.*, 2003).

in ferroan pyroxene compositions), high P_2O_5 (reflected in abundant merrillite), and low Al_2O_3 (reflected in small proportions of maskelynite), relative to terrestrial basalts. They are silica-saturated, containing fayalitic olivine only as a late-stage phase in mesostasis. On an alkalis-silica diagram used to classify volcanic rocks (Le Bas *et al.*, 1986), these meteorites plot within the basalt field (Figure 17.4). Rare earth element patterns are either flat or light rare earth depleted.

17.3.2 Olivine-phyric shergottites

A cluster of olivine-phyric (containing large crystals of olivine) shergottites ejected at ~1.2 Ma comprises volcanic rocks with crystallization ages that overlap but are mostly older than basaltic shergottites, ranging over 185 Ma (Table 17.1). Like the basaltic shergottites, these meteorites had either depleted or enriched sources, and their launch site contains multiple flows formed over a protracted time period.

The groundmass of these meteorites is mineralogically similar to basaltic shergottites (Table 17.2), but is generally finer-grained – even vitrophyric (glassy with skeletal crystals) in one sample (Y-980459). Thus these rocks cooled more rapidly than basaltic shergottites, perhaps in thinner flows. Their most distinctive textural feature is the presence of large olivine and sometimes orthopyroxene crystals (Figure 17.3b). Olivine abundances range from 7 to 29 vol.%. These megacrysts are generally too Fe-rich to have been in equilibrium with the groundmass, which leads to the hypothesis that they are xenocrysts (foreign crystals incorporated into magma). However, the olivines in Y-980459 (Figure 17.3c) and DHO 019 have Mg-rich cores that indicate they are phenocrysts (crystals that formed early during magma solidification; Taylor *et al.*, 2002; Mikouchi *et al.*, 2004), and other observations suggest that most megacrysts in other olivine-phyric shergottites are probably re-equilibrated phenocrysts (Goodrich, 2003). Olivine-phyric shergottites also contain chromite as an early crystallizing phase.

Based on their alkalis-silica contents, olivine-phyric shergottites are basalts (Figure 17.4) with element abundances similar to those of basaltic shergotittes (Table 17.3). However, they tend to have higher MgO, Ni, and Cr concentrations and lower silica concentrations, reflecting the abundances of olivine and chromite in these meteorites. Olivine-phyric shergottites also share the Al_2O_3 depletion seen in basaltic shergottites. Y-980459 appears to be multiply saturated with olivine and pyroxene at mantle pressures (Musselwhite and Treiman, 2005), suggesting that it represents a primitive magma composition. Rare earth element patterns are flat or light rare earth depleted.

17.3.3 Shergottites with unique ejection ages

Two shergottites have ejection ages that distinguish them from other meteorites, likely requiring separate ejection events and sites. Both sites are characterized by basaltic flows.

EET 79001 has a Mars ejection age of ~0.73 Ma, distinctly younger than the ejection events for other shergottites. If a

large fragment was excavated and achieved escape velocity, the interior would not have recorded cosmic ray exposure until it was broken into meter-size pieces in space, so this meteorite could conceivably have been launched from either the basaltic or olivine-phyric shergottite localities. However, launch of such large rocks is thought to be difficult, so this meteorite may represent a distinct launch event and site.

EET 79001 contains both an olivine-phyric member (lithology A) and a basaltic shergottite member (lithology B) joined along a planar contact. The two lithologies (Figure 17.3d) are commonly thought to represent multiple flows (McSween and Jarosewich, 1983), although Mittlefehldt *et al.* (1999) suggested that lithology A might be a shock melt. In any case, this meteorite clearly demonstrates that basaltic and olivine-phyric shergottites occurred at the same locality. The crystallization age of both lithologies is ~173 Ma, identical to those of most basaltic shergottites but younger than other olivine-phyric shergottites (Table 17.1). Its mineralogy (McSween and Jarosewich, 1983; Goodrich, 2003) resembles other meteorites of these groups. EET 79001 is heavily shocked, and contains veins and pockets of impact-melted glass.

Dhofar 019 resembles other olivine-phyric shergottites in its mineralogy, petrography, and geochemistry, but it was ejected from Mars ~19 Ma earlier (Table 17.1). Unlike EETA 79001, this older ejection age could not result from breakup of a large fragment in space.

Some features distinguishing DHO 019 from other shergottites are a lack of orthopyroxene megacrysts and somewhat greater compositional ranges for its minerals, indicative of fairly rapid crystallization (Taylor *et al.*, 2002). Spinel chemistry indicates that it crystallized under reducing conditions. Its magma formed by melting a highly depleted mantle source at ~575 Ma. Its chemical composition is similar to other shergottites (Taylor *et al.*, 2002), but has been compromised by terrestrial weathering.

17.3.4 Lherzolitic shergottites

Mars ejection ages for the lherzolitic (ultramafic) shergottites form a distinct cluster at ~4.1 Ma, and their crystallization ages are also uniform at ~180 Ma. Although these are plutonic rocks, they are clearly related to the volcanic members of the shergottite clan and formed by accumulation of mafic cumulus minerals from shergottite-like magmas. Their launch site must have exposed plutonic rocks, perhaps excavated by a large crater or landslide.

Portions of these meteorites are truly lherzolite, consisting of cumulus olivine and chromite enclosed by low-Ca pyroxene; however, other portions are more properly called "gabbro," composed of olivine with interstitial plagioclase (converted to maskelynite by shock), pyroxenes (orthopyroxene, pigeonite, and augite), ilmenite, merrillite, and other accessory phases (Table 17.2). As in olivine-phyric shergottites, the olivines are Fe-rich and are thought to have undergone subsolidus re-equilibration (Harvey *et al.*, 1993; Mikouchi and Miyamoto, 1996). The olivine's distinctive brown coloration is thought to result from oxidation during shock. The meteorites contain pockets of impact-melted glass with skeletal olivine and chromite (McSween *et al.*, 1979), and tiny amounts of alteration minerals (sulfates, clay, silica, and phosphate) have been noted. Mineral compositions are described by McSween and Treiman (1998).

Chemical compositions of lherzolitic shergottites (Table 17.3) have higher MgO and FeO and lower Al_2O_3 and SiO_2 than basaltic shergottites, reflecting the higher abundance of olivine and low amount of feldspar. Bulk meteorites analyses show light rare earth depletions. Incompatible trace element concentrations are lower than in shergottite lavas, as appropriate for cumulate rocks (McSween *et al.*, 1979).

17.3.5 Nakhlites and chassignites

The nakhlites and chassignites were ejected at ~10–11 Ma. These two classes of meteorites are thought to be related, although the exact petrologic relationship is obscure. All have crystallization ages of ~1.3 Ga, and formed by accumulation of pyroxene and olivine within a differentiated flow or shallow sill (Friedman-Lentz *et al.*, 1999). At ~620 Ma, the nakhlites were infiltrated by aqueous fluids which produced alteration minerals (Treiman, 2005).

The nakhlites are clinopyroxenites comprised primarily of subcalcic augite with lesser amounts of olivine, and various accessory and alteration minerals (Table 17.2). The pyroxenes have thin, Fe-rich rims, consistent with igneous fractionation in a cumulate pile (Treiman, 1990). Olivines are Fe-rich and presumably re-equilibrated after accumulation. Plagioclase and alkali feldspar occur as radiating sprays in mesostasis, and the compositions of titanomagnetite and ilmenite indicate crystallization under oxidizing conditions. Solidification at different rates produced varying textures in interstitial materials, ranging from glassy to crystalline (Figure 17.3e,f). Mineral abundances and compositions are described by Treiman (2005). The nakhlites show the least shock effects of all the SNC meteorites.

Chassigny is a dunite composed of cumulus olivine and chromite, with minor amounts of augite, pigeonite, plagioclase and alkali feldspar, and other phases (Table 17.2). Kaersutite and mica occur in trapped melt inclusions (Floran *et al.*, 1978).

The chemical compositions of nakhlites plot within the basalt field (Figure 17.4), as do estimates of their parental magmas (e.g., Longhi and Pan, 1989; Stockstill *et al.*, 2005). These meteorites share the high-FeO/MgO and low-Al_2O_3 abundance that is characteristic of other Martian meteorites, and are relatively enriched in incompatible elements including light rare earths. As befits olivine cumulates, the compositions of chassignites are rich in Mg and Fe and low in incompatible elements like Al and Ti. Estimates of the chassignite parent magma (Johnson *et al.*, 1991; Longhi and Pan, 1989) indicate that it was a low-Al ferroan basalt as well.

17.3.6 Allan Hills 84001

This ancient (~4.5 Ga crystallization age) rock was ejected from Mars at ~14.7 Ma (Table 17.1), identifying it as the

only available sample of the Noachian crust. ALH 84001 is an ultramafic cumulate rock that must have formed in a plutonic setting. Originally misclassified as a diogenite, it was recognized as a unique Martian meteorite by Mittlefehldt (1994). It has a complex shock history that predates ejection, including resetting the $^{40}Ar/^{39}Ar$ age at 4.0 Ga (Ash *et al.*, 1996), and multiple shock events (just how many is contested) and formation of shock-melted veins that permeate the sample (Treiman, 1998; Greenwood and McSween, 2001). It is likely that the launch site includes craters that have excavated subsurface rocks.

ALH 84001 is an orthopyroxenite, composed of coarse, homogeneous orthopyroxene grains with various accessory phases, including augite, olivine, maskelynite, and chromite (Table 17.2). Alteration phases include zoned carbonate rosettes of varying composition – now famous for the suggestion that they contain evidence, in the form of magnetite inclusions with peculiar morphologies and hydrocarbons, for extraterrestrial life (McKay *et al.*, 1996). Most workers (e.g., Treiman, 2003, and references therein) now accept other nonbiologic explanations for all the observations used to support a biologic origin for the carbonate and magnetite.

The chemical composition of ALH 84001 is ultramafic, as appropriate for a cumulate orthopyroxenite. It is light rare earth depleted with a negative Eu anomaly (Mittlefehldt, 1994; Warren and Kallemeyn, 1996).

17.4 COMPARISONS WITH ORBITAL REMOTE SENSING AND LANDER DATA

The mineralogy, petrology, and geochemistry of rocks at the SNC launch sites provide interesting comparisons for Mars surface compositions determined by orbital remote sensing or measurements made by landed spacecraft.

17.4.1 Dominance of basaltic or basalt-derived igneous rocks

All SNC meteorites are basalts or cumulate rocks formed by fractional crystallization of basaltic magmas. There are no highly differentiated rocks. The presence of olivine-phyric shergottites and closely related lherzolitic shergottites from four separate launch sites (if each Mars ejection age cluster represents a separate event) suggests that this magma type may be widespread, at least within Amazonian terrains.

In situ analyses of rocks by the *Spirit* rover at Gusev crater reveal olivine-rich basalts similar in mineralogy to olivine-phyric shergottites (McSween *et al.*, 2006). However, the Gusev basalts are more picritic (Figure 17.4). Bounce Rock, an isolated sample thought to be ejecta from a distant impact crater, was studied by the *Opportunity* rover at Meridiani (Squyres *et al.*, 2004). The chemical composition of this rock (Zipfel *et al.*, 2004) is virtually identical to basaltic shergottites (Figure 17.4) and, like the shergottites, its mineralogy is dominated by pyroxenes and plagioclase. In contrast, the composition of rocks analyzed by Mars Pathfinder at Ares Vallis (McSween *et al.*, 1999) is andesitic

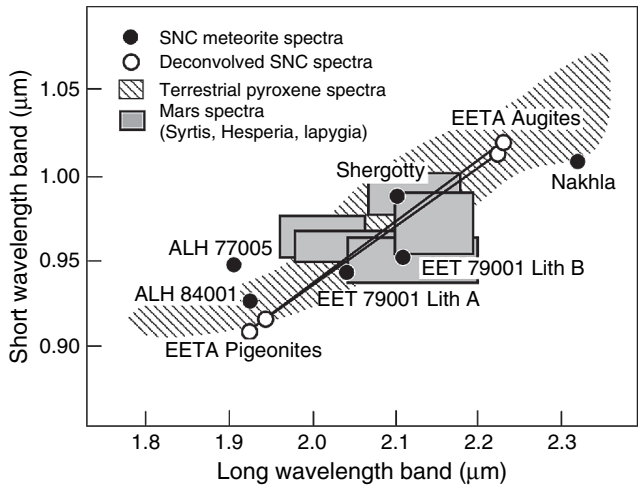

Figure 17.5. Long- and short-wavelength band positions for terrestrial pyroxenes (Cloutis and Gaffey, 1991), SNC meteorites (McFadden, 1987; Sunshine *et al.*, 1993; Bishop *et al.*, 1994), and dark regions of Mars (Singer *et al.*, 1980; Mustard *et al.*, 1993). Deconvolved spectra for EET 79001 shergottite (Sunshine *et al.*, 1993) are from separate pigeonite and augite phases.

(Figure 17.4). Unlike the MER rovers, Pathfinder could not access rock interiors, so its Alpha Proton X-ray Spectrometer (APXS) analysis is of the rock surface, albeit dust-covered. Given the discovery of alteration rinds on Gusev basalts, it is possible that the andesitic composition represents a silica-rich coating, a possibility reinforced by rock photometric properties (Johnson *et al.*, 1999) and the high abundance of H_2O inferred from alpha mode measurement of oxygen (Foley *et al.*, 2003).

Visible/NIR reflectance spectra of Martian dark regions contain two absorption bands that indicate the presence of pyroxenes with variable Ca and Fe contents, as appropriate for coexisting augite and pigeonite. Figure 17.5 shows a crosshatched field representing the long- and short-wavelength positions for pyroxene absorption bands in terrestrial rocks. Reflectance data for various Martian meteorites (McFadden, 1987; Sunshine *et al.*, 1993; Bishop *et al.*, 1994) are also shown. ALH 84001 and ALH 77005 plot near the low-wavelength end of this distribution, as appropriate for orthopyroxene-dominated rocks, and Nakhla plots at the opposite end, reflecting its high augite content. Basaltic shergottites (Shergotty) and olivine-phyric shergottites (EET 79001) contain both augite and pigeonite and plot in the middle, as do telescopic spectra of three dark regions (Hesperia, Iapygia, and two spectra from Syrtis Major) on Mars. Deconvolution of overlapping absorption bands for pigeonite and augite in EET 79001 are also shown (Sunshine *et al.*, 1993). The spectral similarities support the contention that basaltic rocks mineralogically similar to shergottites may be widespread on Mars.

Global mapping by the Mars Global Surveyor Thermal Emission Spectrometer (TES) indicates that basaltic rocks (Surface Type 1; Figure 17.4) dominate the ancient southern highlands (e.g., Christensen *et al.*, 2000). Rocks interpreted to be andesitic (Surface Type 2; Figure 17.4) occur in the northern lowlands and at high latitudes in the south

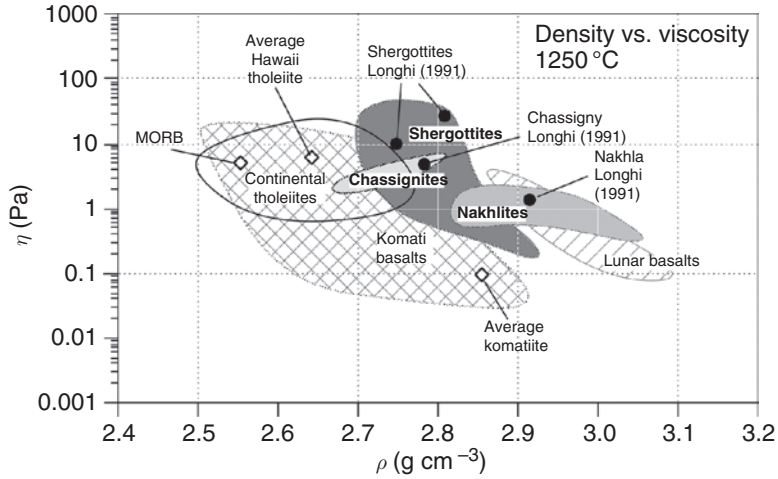

Figure 17.6. Comparison of viscosity and density calculations for SNC parent magmas with those of terrestrial and lunar basalts (Longhi, 1991; McSween, 1994).

(Bandfield *et al.*, 2000; Hamilton *et al.*, 2001). The chemical compositions of these rocks, estimated from deconvolved TES data, suggest that they are calc-alkaline (McSween *et al.*, 2003). If correct, that would imply early melting of a hydrous mantle to form calc-alkaline magmas, followed by later remelting of the ensuing dry mantle to form SNC parental magmas. An alternative interpretation is that Surface Type 2 materials are partly altered basalts (Wyatt and McSween, 2002; Kraft *et al.*, 2003; Michalski *et al.*, 2005), an idea bolstered by geomorphic interpretations of these areas as sites where rocks interacted with water (Wyatt *et al.*, 2004). Visible/NIR measurements by the OMEGA (Observatoire pour la Minéralogie, l'Eau, les Glaces et l'Activité) spectrometer do not reveal the presence of either pyroxene or clays in the lowlands (Mustard *et al.*, 2005), supporting neither interpretation. Instead, Surface Type 2 materials may be coated with alteration rinds, like those on basalts at Gusev crater (Herkenhoff *et al.*, 2004; Haskin *et al.*, 2005). In that case, the composition of Surface Type 2 rocks remains undetermined.

17.4.2 Magma physical properties

Eruptive styles are functions of magma rheology and gravity. Lower Mars gravity encourages more rapid effusion of magma, and very long lava flows on Mars have been attributed to high effusion rates rather than rheology. Consequently, rheologies (and magma compositions) are difficult to constrain from Martian flow morphologies (Mouginis-Mark *et al.*, 1992). The compositions of Martian meteorites, however, can provide useful data on magma rheology.

Estimates of the density and viscosity of SNC parent magmas are shown in Figure 17.6. The results calculated by Longhi (1991) for dry magmas plot within the larger fields calculated for hydrous magmas (McSween, 1994). These densities are generally higher than for terrestrial basaltic rocks (except komatiites, Figure 17.6) and reflect the higher Fe contents of Martian basaltic meteorites. The viscosities are similar, but highly uncertain because the presence of phenocrysts can increase viscosity significantly.

17.4.3 Timing and duration of magmatic events

With the exception of ALH 84001, all SNC meteorites represent Amazonian magmatism (Nyquist *et al.*, 2001; Borg and Drake, 2005). These young ages are distinct from the ancient ages for most of the crust estimated from crater densities (Hartmann and Neukum, 2001). This curious sampling bias may be a consequence of the impact launch mechanism. Strong, coherent surface rocks may be required to transmit the requisite seismic waves that can accelerate spalls to escape velocity, and recent volcanic rocks would seem to meet that requirement (McSween, 2002). In addition, young basaltic terrains are commonly elevated >5km above the datum, resulting in lower atmospheric density and shorter trajectory lengths, which may assist launch (Fritz *et al.*, 2005). If launch sites could be confidently identified, the radiometric crystallization ages of SNCs would provide calibrations for crater density ages. ALH 84001 is the only meteorite sample of the ancient crust. This meteorite is a thermally annealed breccia, and its coherent character may account for its successful launch.

Different crystallization ages for petrologically similar SNC meteorites in the same ejection age group (Table 17.1) suggest that some Martian magmatic centers were volcanically active for long periods of time. For example, the olivine-phyric shergottites define an eruption interval spanning 185 Ma, although several groups have uniform crystallization ages (Table 17.1). The 4.5 Ga age of ALH 84001 confirms that Noachian igneous activity was initiated soon after planet formation.

17.4.4 Distinctive igneous mineral compositions

A comparison of SNC mineral compositions with corresponding igneous minerals from the Earth, Moon, and asteroid 4 Vesta (Papike, 1998) delineates some clear differences. Plagioclase in Martian meteorites is more sodic (generally $An_{30–70}$, expressed as mole fraction of anorthite, the Ca endmember) than in basalts from other Solar System bodies.

Olivine and pyroxene are more FeO-rich than terrestrial minerals but not lunar minerals. Expressed as mole fraction of forsterite, the Mg endmember, olivines in olivine-phyric shergottites are $Fo_{30–80}$, in lherzolitic shergottites are $Fo_{60–75}$, and in nakhlites are $Fo_{40–23}$ (Taylor *et al.*, 2002). The Mn/Fe ratios of olivine and pyroxene in SNCs are distinctive (Papike, 1998) and serve as a fingerprint for Martian samples.

Sodic plagioclase and ferroan olivine and pyroxene are also inferred from the calculated compositions of normative minerals in Gusev basalts (McSween *et al.*, 2006). Ferroan pyroxenes are indicated by VIS/NIR (VIS – Visible Imaging Subsystem) spectra of Mars surface materials (Mustard *et al.*, 1997), and ferroan olivines are indicated by deconvolved TES spectra of Mars surface materials (Hoefen *et al.*, 2003; Hamilton and Christensen, 2005).

Geochemistry

The most notable geochemical features of SNC meteorites are low-MgO/FeO ratios and Al_2O_3 contents, as visualized in a plot of Mg/Si versus Al/Si (Figure 17.7). The high FeO is interpreted to reflect mantle sources more oxidized than that of the Earth, and the low Al_2O_3 is thought to reflect melt extraction to form the voluminous crust. Oxidation of the Martian mantle is also reflected in the concentrations of P, Mn, Cr, and W, which are moderately siderophile on Earth but more lithophile on Mars (Halliday *et al.*, 2001). The Mg/Si versus Al/Si ratios have been cited as geochemical fingerprints for Mars (Wänke and Dreibus, 1988). However, Gusev basalts do not plot with SNC meteorites in Figure 17.7, nor do surface compositions calculated from TES data (McSween *et al.*, 2003). Although these materials do show consistently high FeO/MgO ratios, relative to terrestrial basalts, they are not depleted in Al_2O_3.

The various Martian meteorite groups can be readily distinguished from each other based on their atomic, Si-normalized concentrations of Ca and Mg (Ouri *et al.*, 2003). Figure 17.8 illustrates this geochemical classification, and shows how the meteorite compositions relate to those of Gusev basalts analyzed by the *Spirit* rover and Bounce Rock analyzed by the *Opportunity* rover.

Another general geochemical characteristic of Mars, inferred from SNCs, is enrichment in volatile elements, relative to the Earth (Dreibus and Wänke, 1985). This enrichment is seen in ratios of volatile to refractory trace elements with similar incompatible behavior during igneous processes, such as K/U or Rb/Sr which are roughly twice as high as the values for the Earth (Halliday *et al.*, 2001). Other element ratios (Fe/Mn, Cr/Mg, Al/Ti, Na/Al) appear to be nearly uniform in SNCs and have been suggested to be characteristic for Mars (Wänke and Dreibus, 1988). The validity of these geochemical signatures for older Martian rocks must await *in situ* or remote-sensing measurements of these elements.

SNC meteorites are exceedingly dry, and Dreibus and Wänke (1985) estimated the water content of their mantle source to be low, in spite of evidence for abundant water on the planet's surface in the past. McSween *et al.* (2001) questioned this estimate, and interpreted zoning of water-soluble trace elements in some shergottites as evidence that the magmas had lost water on ascent and eruption.

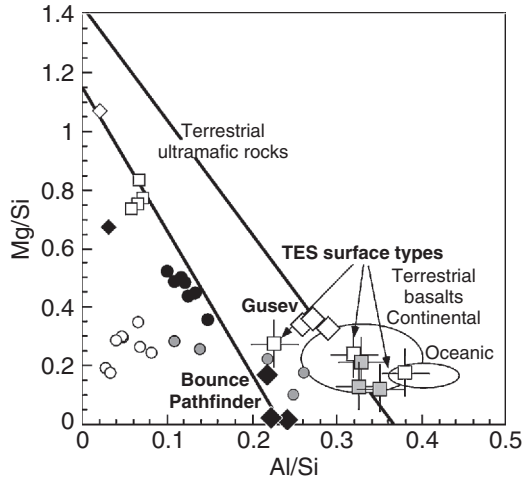

Figure 17.7. Mg/Si versus Al/Si diagram, illustrating compositional differences between SNC meteorites and other Mars samples. Meteorite symbols as in Figure 17.2, and data from McSween *et al.* (2003).

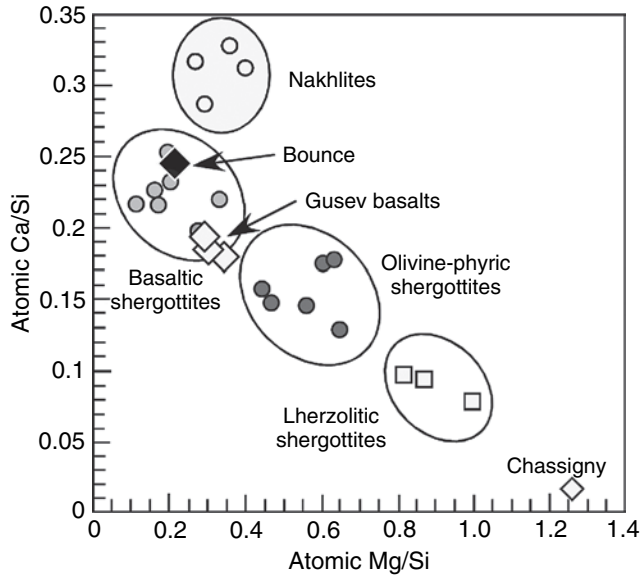

Figure 17.8. Geochemical classification diagram for SNC meteorites (Ouri *et al.*, 2003), also showing compositions of Gusev basalts and Bounce Rock analyzed by the Mars Exploration Rovers.

17.4.5 Alteration

The Amazonian SNC meteorites show only minimal effects of aqueous alteration, but the alteration minerals are revealing. Small quantities of carbonates, sulfates, halite, Fe oxides, clays, and iddingsite (e.g., Bridges and Grady, 2000, and references therein) demonstrate that brines have permeated even these young rocks, probably in the subsurface. The alteration mineral assemblages in SNC meteorites

are distinct from those documented at the *Opportunity* landing site in ancient Meridiani Planum, which was apparently too acidic for carbonate precipitation (Squyres *et al*., 2004). It is tempting to interpret this difference as reflecting temporal changes in the acidity of the alteration environment. However, carbonate globules in ALH 84001 formed at ~4 Ga (Borg *et al*., 1999) and indicate alteration by nonacid aqueous fluids in the Noachian. Oxygen and carbon isotopic measurements on these carbonates (Romanek *et al*., 1994; Valley *et al*., 1997) are compatible with alteration by low-temperature fluids.

Isotopically heavy oxygen and hydrogen in bulk shergottites (Leshin *et al*., 1996; Eiler *et al*., 2002) reveal interactions between the lithosphere and the atmosphere, suggesting that a hydrologic cycle operated even in recent times. D/H values are much higher than expected for solid-water fractionations, confirming spacecraft spectroscopic results that the Martian atmosphere has very high D/H that likely implies extensive loss of hydrogen to space (Owen *et al*., 1988). The D-enriched water was then cycled into rocks, producing phases with high D/H ratios (Leshin, 2000; Boctor *et al*., 2003). Anomalies in oxygen and sulfur isotopes measured in bulk SNCs suggest atmospheric chemistry that resulted in mass-independent isotope effects (Farquhar and Thiemens, 2000; Farquhar *et al*., 2000), also providing a strong constraint on volatile cycling.

17.4.6 Limitations of SNC: remote-sensing comparisons

Viking, Pathfinder, and MER observations indicate that the mineralogical and geochemical signatures of all these sites are not dominated by rocks, but by soils that are not derived from local rocks (e.g., Yen *et al*., 2005). Certainly, there are significant surfaces on Mars dominated by bedrock (Christensen *et al*., 2005), but much of the planet is covered to varying degrees by eolian sand and globally distributed dust. Comparisons of SNC mineralogy and geochemistry with data obtained from orbiting spacecraft will likely be limited by their dilution with soils. To date, no Martian meteorites are regolith breccias.

Another factor is that all Martian meteorites experienced shock metamorphism during excavation and launch, with pressures ranging from 5 to 55 GPa and postshock temperature increases of as much as 1000 °C (Fritz *et al*., 2005). The resulting mineralogical changes may limit comparisons with remote-sensing data.

17.5 SUMMARY

Clusters of Mars ejection ages for SNC meteorites correlate with sample petrology and geochemistry. Assuming that each cluster or unique ejection age represents a distinct sampling site, we can infer that these meteorites represent as many as seven locations – a larger sampling than has been provided so far by Mars landed spacecraft. However, all but one SNC have young (<1.3Ga) crystallization ages, indicating that their sampling by impacts is biased toward Amazonian terrains. Some specific launch sites have been suggested, but they remain controversial. Ranges in the crystallization ages of meteorites from several launch sites suggest that volcanism was long-lived. ALH 84001 is 4.5 Ga old, a sample of the early Noachian crust.

All SNC meteorites are basalts or cumulates derived from basaltic magmas. Most are compositionally distinct from the rocks analyzed by Mars rovers, although olivine-phyric shergottites are chemically identical to Bounce Rock at Meridiani and are similar in many respects to olivine-rich basalts at Gusev crater. These meteorites are also distinct from igneous surface compositions estimated from deconvolved VIS/NIR and thermal emission spectra, although basalts are commonly observed from orbital spacecraft. Most orbital remote-sensing data are dominated by soils, limiting the degree to which SNC data can be compared. The mineralogic characteristics of SNCs that distinguish them from terrestrial basalts (ferroan olivine and pyroxenes, sodic plagiclase) are also seen in remote-sensing data of surface materials. Some bulk geochemical characteristics of SNC meteorites, such as aluminum depletion, are not generally observed, and current remote-sensing techniques cannot measure the enrichment in volatile/refractory element ratios revealed by SNCs. Alteration in SNCs is pervasive but of limited extent, suggesting that exposure to aqueous fluids occurred but was limited in volume and duration. Fractionations in stable isotopic data for SNCs indicate that the fluids were cycled through the atmosphere before interacting with the crust.

REFERENCES

Artemieva, N. and B. A. Ivanov, Ejection of Martian meteorites: can they fly?, *Lunar Planet. Sci. Conf. XXXIII*, Abstract #1113 (CD-ROM), 2002.

Ash, R. D., S. F. Knott, and G. Turner, A 4-Gyr shock age for a Martian meteorite and implications for the cratering history of Mars, *Nature* **380**, 57–9, 1996.

Bandfield, J. L., V. E. Hamilton, and P. R. Christensen, A global view of Martian surface compositions from MGS-TES, *Science* **301**, 1084–7, 2000.

Barlow, N. G., Identification of possible source craters for the Martian meteorites ALH84001, *Proc. SPIE Annu. Meeting*, 26–35, 1997.

Barrat, J. A., P. Gillet, V. Sautter, *et al*., Petrology and chemistry of the basaltic shergottite North West Africa 480, *Meteorit. Planet. Sci.* **37**, 487–99, 2002a.

Barrat, J. A., A. Jambon, B. Bohn, *et al*., Petrology and chemistry of the picritic shergottite North West Africa 1068 (NWA1068), *Geochim. Cosmochim. Acta* **66**, 3505–18, 2002b.

Berkley, J. L., K. Keil, and M. Prinz, Comparative petrology and origin of Governador Valadares and other nakhlites, *Proc. Lunar Planet. Sci. Conf. XI*, 1089–102, 1980.

Bishop, J., C. Pieters, J. Mustard, S. Pratt, and T. Hiroi, Spectral analyses of ALH 84001, a meteorite from Mars, *Meteoritics* **29**, 444–5, 1994.

Boctor, N. Z., A. Ho, and G. Kullerud, Lafayette meteorite: petrology and opaque mineralogy, *Earth Planet. Sci. Lett.* **32**, 69–76, 1976.

Boctor, N. Z., C. M. O. Alexander, J. Wang, and E. Hauri, The sources of water in Martian meteorites: clues from hydrogen isotopes, *Geochim. Cosmochim. Acta* **67**, 3971–89, 2003.

Borg, L. and M. J. Drake, A review of meteorite evidence for the timing of magmatism and of surface or near-surface liquid water on Mars, *J. Geophys. Res.* **110**, E12S03, doi:10.1029/2005JE002402, 2005.

Borg, L. E., J. N. Connelly, L. E. Nyquist, *et al.*, The age of the carbonates in Martian meteorite ALH84001, *Science* **286**, 90–4, 1999.

Bridges, J. C. and M. M. Grady, Evaporite mineral assemblages in the nakhlite (Martian) meteorite, *Earth Planet. Sci. Lett.* **176**, 267–79, 2000.

Christen, R., O. Eugster, and H. Busemann, Mars ejection times and neutron capture effects of the nakhlites Y000593 and Y000749, the olivine-phyric shergottite Y980459, and the lherzolite NWA1950, *Antarct. Meteorite Res.* **18**, 117–32, 2005.

Christensen, P. R., J. L. Bandfield, M. D. Smith, V. E. Hamilton, and R. N. Clark, Identification of a basaltic component on the Martian surface from Thermal Emission Spectrometer data, *J. Geophys. Res.* **105**, 9609–22, 2000.

Christensen, P. R., H. Y. McSween, J. L. Bandfield, *et al.*, Evidence for magmatic evolution and diversity on Mars from infrared observations, *Nature* **436**, 504–9, doi:10.1038/nature03639, 2005.

Cloutis, E. A. and M. J. Gaffey, Pyroxene spectroscopy revisited: spectral-compositional correlations and relationships to geothermometry, *J. Geophys. Res.* **96**, 22809–26, 1991.

Dreibus, G. and H. Wänke, Mars: a volatile rich planet, *Meteoritics* **20**, 367–82, 1985.

Eiler, J. M., J. W. Valley, C. M. Graham, and J. Fournelle, Two populations of carbonate in ALH84001: geochemical evidence for discrimination and genesis, *Geochim. Cosmochim. Acta* **66**, 1285–303, 2002.

Farquhar, J. and M. H. Thiemens, Oxygen cycle of the Martian atmosphere-regolith system: D17O of secondary phases in Nakhla and Lafayette, *J. Geophys. Res.* **195**(E5), 11991–7, 2000.

Farquhar, J., J. Savarino, T. L. Jackson, and M. H. Thiemens, Evidence of atmospheric sulphur in the Martian regolith from sulphur isotopes in meteorites, *Nature* **404**, 50–2, 2000.

Floran, R. J., M. Prinz, R. F. Hlava, *et al.*, The Chassigny meteorite: a cumulate dunite with hydrous amphibole-bearing melt inclusions, *Geochim. Cosmochim. Acta* **42**, 1213–29, 1978.

Foley, C. N., T. E. Economou, and R. N. Clayton, Final chemical results from the Mars Pathfinder alpha proton X-ray spectrometer, *J. Geophys. Res.* **108**(E12), 8096, doi:10.1029/2002JE002019, 2003.

Friedman-Lentz, R. C., G. J. Taylor, and A. H. Treiman, Formation of a Martian pyroxenite: a comparative study of the nakhlite meteorites and Theo's Flow, *Meteorit. Planet. Sci.* **34**, 919–32, 1999.

Fritz, J., N. Artemieva, and A. Greshake, Ejection of Martian meteorites, *Meteorit. Planet. Sci.* **40**, 1393–411, 2005.

Gillet, P., J. A. Barrat, P. Beck, *et al.*, Petrology, geochemistry, and cosmic-ray exposure age of lherzolitic shergottite Northwest Africa 1950, *Meteorit. Planet. Sci.* **40**, 1175–84, 2005.

Goodrich, C. A., Petrogenesis of olivine-phyric shergottites Sayh al Uhaymir 005 and Elephant Moraine A79001 lithology A. *Geochim. Cosmochim. Acta* **67**, 3735–71, 2003.

Greenwood, J. P. and H. Y. McSween, Petrogenesis of Allan Hills 84001: constraints from impact-melted feldspathic and silica glass, *Meteorit. Planet. Sci.* **36**, 43–61, 2001.

Greshake, A., J. Fritz, and D. Stöffler, Petrology and shock metamorphism of the olivine-phyric shergottite Yamato 980459: evidence for a two-stage cooling and a single-stage ejection history, *Geochim. Cosmochim. Acta* **68**, 2359–77, 2004.

Hale, V. P. S., H. Y. McSween, and G. McKay, Re-evaluation of intercumulus liquid composition and oxidation state for the Shergotty meteorite, *Geochim. Cosmochim. Acta* **63**, 1459–70, 1999.

Halliday, A. N., H. Wanke, J.-L. Birck, and R. N. Clayton, The accretion, composition and early differentiation of Mars, *Space Sci. Rev.* **96**, 197–230, 2001.

Hamilton, V. E., A source region for Martian meteorite ALH84001: Eos Chasma, Mars (abstract), *Meteorit. Planet. Sci.*, **40** (Suppl.), A63, 2005.

Hamilton, V. E. and P. R. Christensen, Evidence for extensive, olivine-rich bedrock on Mars, *Geology* **33**, 433–6, 2005.

Hamilton, V. E., M. B. Wyatt, H. Y. McSween, and P. R. Christensen, Analysis of terrestrial and Martian volcanic compositions using thermal emission spectroscopy: 2. Application to Martian surface spectra from the Mars Global Surveyor Thermal Emission Spectrometer, *J. Geophys. Res.* **107** (E6), 14733–46, 2001.

Hamilton, V. E., P. R. Christensen, H. Y. McSween, and J. L. Bandfield, Searching for the source regions of Martian meteorites using MGS TES: integrating Martian meteorites in to the global distribution of igneous materials on Mars, *Meteorit. Planet. Sci.* **38**, 871–86, 2003.

Hartmann, W. K. and G. Neukum, Cratering chronology and the evolution of Mars. *Space Sci. Rev.* **96**, 165–94, 2001.

Harvey, R. P. and V. E. Hamilton, Syrtis Major as the source of the nakhlite/chassignite Martian meteorites (abstract), *Meteorit. Planet. Sci.* **40** (Suppl.), A64, 2005.

Harvey, R. P., M. Wadhwa, H. Y. McSween, and G. Crozaz, Petrography, mineral chemistry, and petrogenesis of Antarctic shergottite LEW88516, *Geochim. Cosmochim. Acta* **56**, 4769–83, 1993.

Haskin, L. A., A. Wang, B. L. Jolliff, *et al.*, Water alteration of rocks and soils on Mars at the Spirit rover site in Gusev crater, *Nature* **436**, 66–9, doi:10.1038/nature03640, 2005.

Head, J. N., H. J. Melosh, and B. A. Ivanov, Martian meteorite launch: high-speed ejecta from small craters, *Science* **298**, 1752–6, 2002.

Herd, C. D. K., J. J. Papike, and A. J. Brearley, Oxygen fugacity of Martian basalts from electron microprobe, oxygen, and TEM-EELs analyses of iron-titanium oxides, *Am. Mineral.* **86**, 1015–24, 2001.

Herkenhoff, K. E., S. W. Squyres, R. Arvidson, *et al.*, Textures of soils and rocks at Gusev crater from Spirit's Microscopic Imager, *Science* **305**, 824–6, 2004.

Hoefen, T. M., R. N. Clark, J. L. Bandfield, *et al.*, Discovery of olivine in the Nili Fossea region of Mars, *Science* **302**, 627–30, 2003.

Irving, A. J., S. M. Kuehner, A. C. Hupe, and G. M. Hupe, Olivine-phyric basaltic shergottite NWA 1195: a very primitive Martian lava (abstract), *Meteorit. Planet. Sci.* **37** (Suppl.), A69, 2002.

Jambon, A., J. A. Barrat, V. Sautter, *et al.*, The basaltic shergottite North West Africa 856: petrology and chemistry, *Meteorit. Planet. Sci.* **37**, 1147–64, 2002.

Johnson, J. R., R. Kirk, L. A. Soderblom, *et al.*, Preliminary results on photometric properties of materials at the Sagan Memorial Station, Mars, *J. Geophys. Res.* **104**(E4), 8809–30, 1999.

Johnson, M. C., M. J. Rutherford, and P. C. Hess, Chassigny petrogenesis: melt compositions, intensive parameters, and water

contents of Martian(?) magmas, *Geochim. Cosmochim. Acta* **55**, 349–66, 1991.

Kraft, M. D., J. R. Michalski, and T. G. Sharp, Effects of pure silica coatings on thermal emission spectra of basaltic rocks: considerations for Martian surface mineralogy, *Geophys. Res. Lett.* **30**, 2288, doi:10.1029/2003GL018848, 2003.

Le Bas, M. J., R. W. Le Maitre, A. Streckeisen, and B. Zanettin, A chemical classification of volcanic rocks based on the total alkali-silica diagram, *J. Petrol.* **27**, 745–50, 1986.

Leshin, L. A., Insights into Martian water reservoirs from analyses of Martian meteorite QUE 94201, *Geophys. Res. Lett.* **27**, 2017–20, 2000.

Leshin, L. A., S. Epstein, and E. M. Stolper, Hydrogen isotope geochemistry of SNC meteorites, *Geochim. Cosmochim. Acta* **60**, 2635–50, 1996.

Lodders, K., A survey of shergottite, nakhlite and chassigny meteorites whok-rock compositions, *Meteoritics Planet. Sci.*, **33** 183–90, 1998.

Longhi, J., Complex magmatic processes on Mars: inferences from the SNC meteorites, *Proc. Lunar Planet. Sci. Conf. XXI*, 695–709, 1991.

Longhi, J. and V. Pan, The parent magmas of the SNC meteorites, *Proc. Lunar Planet. Sci. Conf. XIX*, 451–64, 1989.

Marty, B., A. Grimberg, V. S. Heber, and R. Wieler, Noble gases in the newly found NWA 2737 chassignite (abstract), *Meteorit. Planet. Sci.* **40** (Suppl.), A98, 2005.

McCoy, T. J., G. J. Taylor, and K. Keil, Zagami: product of a two-stage magmatic history, *Geochim. Cosmochim. Acta* **56**, 3571–82, 1992.

McFadden, L. A., Spectral reflectance of SNC meteorites: relationships to Martian surface composition, *Lunar Planet. Inst. Tech. Rept.* **88-05**, 88–90, 1987.

McKay, D. S., E. K. Gibson, K. L. Thomas-Keprta, *et al.*, Search for past life on Mars: possible relic biogenic activity in Martian meteorite ALH 84001, *Science* **273**, 924–30, 1996.

McSween, H. Y., What we have learned about Mars from SNC meteorites, *Meteoritics* **29**, 757–79, 1994.

McSween, H. Y., The rocks of Mars, from far and near, *Meteorit. Planet. Sci.* **37**, 7–25, 2002.

McSween, H. Y. and E. Jarosewich, Petrogenesis of the Elephant Moraine A79001 meteorite: multiple magma pulses on the shergottite parent body, *Geochim. Cosmochim. Acta* **47**, 1501–13, 1983.

McSween, H. Y. and A. H. Treiman, Martian meteorites. In *Planetary Materials* (ed. J. J. Papike), *Reviews in Mineralogy* **36**, Mineralogical Society of America, 6–1 to 6–53, 1998.

McSween, H. Y., L. A. Taylor, and E. M. Stolper, Allan Hills 77005: a new meteorite type found in Antarctica, *Science* **204**, 1201–3, 1979.

McSween, H. Y., D. D. Eisenhour, L. A. Taylor, M. Wadhwa, and G. Crozaz, QUE94201 shergottite: crystallization of a Martian basaltic magma, *Geochim. Cosmochim. Acta* **60**, 4563–9, 1996.

McSween, H. Y., S. L. Murchie, J. A. Crisp, *et al.*, Chemical, multispectral, and textural constraints on the composition and origin of rocks at the Mars Pathfinder landing site, *J. Geophys. Res.* **104**(E4), 8679–715, 1999.

McSween, H. Y., T. L. Grove, R. C. F. Lentz, *et al.*, Geochemical evidence for magmatic water within Mars from pyroxenes in the Shergotty meteorite, *Nature* **409**, 487–90, 2001.

McSween, H. Y., T. L. Grove, and M. B. Wyatt, Constraints on the composition and petrogenesis of the Martian crust, *J. Geophys. Res.* **108**(E12), 5135, doi:10.1029/2003JE002175, 2003.

McSween, H. Y., M. B. Wyatt, R. Gellert, *et al.*, Characterization and petrologic interpretation of olivine-rich basalts at Gusev crater, Mars, *J. Geophys. Res.* **110**, E12S39, doi:10.1029/2005JE002477, 2006.

Melosh, J. J., Impact ejection, spallation, and the origin of meteorites, *Icarus* **59**, 234–60, 1984.

Michalski, J. R., M. D. Kraft, T. G. Sharp, L. B. Williams, and P. R. Christensen, Mineralogical constraints on the high-silica Martian surface component observed by TES, *Icarus* **174**, 161–77, doi:10.1016/j.icarus.2004.10.022, 2005.

Mikouchi, T., Comparative mineralogy of Chassigny and NWA 2737: implications for the formation of chassignite igneous body(s) (abstract), *Meteorit. Planet. Sci.* **40** (Suppl.), A102, 2005.

Mikouchi, T. and M. Miyamoto, Comparative mineralogy of Antarctic Iherzolitic shergottites Allan Hills 77005, Lewis Cliff 88516 and Yamoto 793605, *Meteorit. Planet. Sci.*, **31**, A89–A90, 1996.

Mikouchi, T., E. Koizumi, A. Monkawa, Y. Ueda, and M. Miyamoto, Mineralogy and petrology of Yamato 000593: comparison with other Martian nakhlite meteorites, *Antarct. Meteorite Res.* **16**, 34–57, 2003.

Mikouchi, T., T. Koizumi, G. McKay, *et al.*, Yamato 980459: mineralogy and petrology of a new shergottite-related rock from Antarctica, *Antarct. Meteorite Res.* **17**, 13–34, 2004.

Misawa, K., C.-Y. Shih, Y. Reese, L. E. Nyquist, and J. A. Barrat, Rb-Sr and Sm-Nd isotopic systematics of the NWA 2737 chassignite (abstract), *Meteorit. Planet. Sci.* **40** (Suppl.), A104, 2005.

Mittlefehldt, D. W., ALH84001, a cumulate orthopyroxenite member of the Martian meteorite clan, *Meteoritics* **29**, 214–21, 1994.

Mittlefehld, D. W., D. J. Lindstrom, M. M. Lindstrom, and R. R. Martinez, An impact-melt origin for lithology A of Martian meteorite Elephant Moraine A79001, *Meteorit. Planet. Sci.*, **34**, 357–67, 1999.

Mouginis-Mark, P. J., T. J. McCoy, G. J. Taylor, and K. Keil, Martian parent craters for the SNC meteorites, *J. Geophys. Res.* **97**, 10213–55, 1992.

Musselwhite, D. S. and A. H. Treiman, Experimental petrology of olivine-phyric shergottites: primary mantle melts? (abstract), *Meteorit. Planet. Sci.* **40** (Suppl.), A109, 2005.

Mustard, J. F., S. Erard, J.-P. Bibring, *et al.*, The surface of Syrtis Major: composition of the volcanic substrate and mixing with altered dust and soil, *J. Geophys. Res.* **98**(E2), 3387–400, 1993.

Mustard, J. F., A. Murchie, S. Erard, and J. M. Sunshine, In situ compositions of Martian volcanics: implications for the mantle, *J. Geophys. Res.* **102**, 25605–15, 1997.

Mustard, J. F., F. Poulet, A. Gendrin, *et al.*, Olivine and pyroxene diversity in the crust of Mars, *Science*. **307**, 1594–7, 2005.

Nyquist, L. E., D. D. Bogard, C.-Y. Shih, *et al.*, Ages and history of Martian meteorites, *Space Sci. Rev.* **96**, 105–64, 2001.

Ouri, Y., N. Shirari, and M. Ebihara, Chemical composition of Yamato (Y)980459 and Y000749: neutron-induced prompt gamma-ray analysis study, *Antarct. Meteorite Res.* **16**, 80–93, 2003.

Owen, T., J. P. Maillard, C. DeBergh, and B. L. Lutz, Deuterium on Mars: the abundance of HDO and the value of D/H, *Science*. **240**, 1767–70, 1988.

Papike, J. J., Comparative planetary mineralogy: chemistry of melt-derived pyroxene, feldspar, and olivine. In *Planetary Materials* (ed. J. J. Papike), *Reviews in Mineralogy* 36, Mineralogical Society of America, 7–1 to 7–11, 1998.

Romanek, C. S., M. M. Grady, I. P. Wright, *et al*., Record of fluid-rock interactions on Mars from the meteorite ALH 84001, *Nature* **372**, 655–7, 1994.

Rubin, A. E., P. H. Warren, J. P. Greenwood, *et al*., Petrology of Los Angeles: a new basaltic shergottite find, *Geology* **28**, 1011–14, 2000.

Sautter, V., J. A. Barrat, A. Jambon, *et al*., A new Martian meteorite from Morocco: the nakhlite North West Africa 817, *Earth Planet. Sci. Lett*. **195**, 223–38, 2002.

Shirai, N. and M. Ebihara, Chemical characteristics of a Martian meteorite, Yamato 980459, *Antarct. Meteorite Res*. **17**, 55–67, 2004.

Singer, R. B., R. N. Clark, and P. D. Owensby, Mars: new regional near-infrared spectrophotometry (0.65–2.50 μm) obtained during the 1980 apparition, *Bull. Am. Astron. Soc*. **12**, 680, 1980.

Squyres, S. W., R. E. Arvidson, J. F. Bell III, *et al*., The Opportunity rover's Athena science investigation at Meridiani Planum, Mars, *Science* **306**, 1698–703, 2004.

Stockstill, K. R., H. Y. McSween, and R. J. Bodnar, Melt inclusions in augite of the Nakhla Martian meteorite: evidence for basaltic parental melt, *Meteorit. Planet. Sci*. **40**, 377–96, 2005.

Stöffler, D., R. Ostertag, C. Jammes, *et al*., Shock metamorphism and petrography of the Shergotty achondrite, *Geochim. Cosmochim. Acta* **50**, 889–913, 1986.

Sunshine, J. M., L. A. McFadden, and C. M. Pieters, Reflectance spectra of the Elephant Moraine A79001 meteorites: implications for remote sensing of planetary bodies, *Icarus* **105**, 79–91, 1993.

Taylor, L. A., M. A. Nazarov, C. K. Shearer, *et al*., Martian meteorite Dhofar 019: a new shergottite, *Meteorit. Planet. Sci*. **37**, 1107–28, 2002.

Tornabene, L. L., J. E. Moersch, H. Y. McSween, *et al*., Identification of large (2–10 km) rayed craters on Mars in THEMIS thermal infrared images: implications for possible Martian meteorite source regions, *J. Geophys. Res*. **111**(E10), 2006.

Treiman, A. H., Amphibole and hercynite spinel in Shergotty and Zagami: magmatic water, depth of crystallization, and metasomatism, *Meteoritics* **20**, 229–43, 1985.

Treiman, A. H., Complex petrogenesis of the Nakhla (SNC) meteorite: evidence from petrography and mineral chemistry, *Proc. Lunar Planet. Sci. Conf. XX*, 273–80, 1990.

Treiman, A. H., The history of ALH 84001 revised: multiple shock events, *Meteorit. Planet. Sci*. **33**, 753–64, 1998.

Treiman, A. H., Submicron magnetite grains and carbon compounds in Martian meteorite ALH84001: inorganic, abiotic formation by shock and thermal metamorphism, *Astrobiology* **3**, 369–92, 2003.

Treiman, A. H., The nakhlite meteorites: augite-rich igneous rocks from Mars, *Chem. Erde* **65**, 203–70, 2005.

Treiman, A. H., J. D. Gleason, and D. D. Bogard, The SNC meteorites are from Mars, *Planet. Space Sci*. **48**, 1213–30, 2000.

Valley, J. W., J. M. Eiler, C. M. Graham, *et al*., Low-temperature carbonate concretions in the Martian meteorite ALH 84001: evidence from stable isotopes and mineralogy, *Science* **275**, 1633–8, 1997.

Vickery, A. M. and H. J. Melosh, The large crater origin of the SNC meteorites, *Science* **237**, 738–43, 1987.

Wänke, H. and G. Dreibus, Chemical composition and accretion history of terrestrial planets, *Philos. Trans. R. Soc. Lond. A* **325**, 545–57, 1988.

Wänke, H., J. Brückner, G. Dreibus, R. Rieder, and I. Ryabchikov, Chemical composition of rocks and soils at the Pathfinder site, *Space Sci. Rev*. **96**, 317–30, 2001.

Warren, P. H. and G. W. Kallemeyn, Siderophile trace elements in ALH 84001, other SNC meteorites and eucrites: evidence of heterogeneity, possibly time-linked, in the mantle of Mars, *Meteorit. Planet. Sci*. **31**, 97–105, 1996.

Wyatt, M. B. and H. Y. McSween, Spectral evidence for weathered basalt as an alternative to andesite in the northern lowlands of Mars, *Nature* **417**, 263–6, 2002.

Wyatt, M. B., H. Y. McSween, K. L. Tanaka, and J. W. Head, Global geologic context for rock types and surface alteration on Mars, *Geology* **32**, 645–8, doi:10.1130/G20527.1, 2004.

Yen, A. S., R. Gellert, C. Schröder, *et al*., An integrated view of the chemistry and mineralogy of Martian soils, *Nature* **436**, 49–54, doi:10.1038/nature03637, 2005.

Zipfel, J., P. Scherer, B. Spettel, G. Dreibus, and L. Schultz, Petrology and chemistry of the new shergottite Dar al Gani **476**, *Meteorit. Planet. Sci*. **35**, 95–106, 2000.

Zipfel, J., R. Anderson, J. Brückner, *et al*., APXS analyses of Bounce Rock: the first shergottite on Mars (abstract), *Meteorit. Planet. Sci*. **39** (Suppl.), A118, 2004.

PART IV

PHYSICAL PROPERTIES OF SURFACE MATERIALS

18

The thermal inertia of the surface of Mars

M. T. MELLON, R. L. FERGASON, AND N. E. PUTZIG

ABSTRACT

The thermal inertia of Mars is a physical property that controls the diurnal and seasonal cycles in surface temperature. It is defined as a function of the thermal conductivity, heat capacity, and density, all of which depend primarily on the physical structure of the surface layer. As such, thermal inertia provides information about the nature of the surface of Mars and the types of materials from which it is composed. Interpreting thermal inertia can be complicated by the variety of structures and material properties that result in the same thermal inertia value. In general, variations in the thermal conductivity have the greatest influence on the thermal inertia. Factors such as soil grain size, cementing or induration, rock abundance, the presence of bedrock, and surface heterogeneity all play an important role. The physical processes that effect the thermal conductivity are discussed to provide a framework from which thermal inertia of the Martian surface may be better understood.

Over the years, thermal inertia has been derived from numerous Earth-based and spacecraft temperature observations of Mars. In particular, thermal inertia from Viking, Mars Global Surveyor (MGS), and Mars Odyssey data has been derived and mapped with increasing spatial resolution, in each case providing an improved understanding of the surface layer. In addition, local-scale observations from the Mars Exploration Rovers (MERs) have provided *in situ* thermal inertia ground truth of characteristic soils and rocks. Overall, the surface of Mars is dominated by soils to a depth of a few centimeters or more. Large continental-scale expanses of low thermal inertia are indicative of extensive dust deposits. Other regions exhibit higher thermal inertia values, suggesting some combination of variations in particle size, rock abundance, and induration of soils. While rocks on Mars are widespread, the soil component between the rocks dominates the bulk thermal inertia as observed from orbit. Indurated soils are also believed to be widespread, based on analysis of multiple datasets. By examining the thermal inertia of the surface of Mars, a deeper understanding can be obtained regarding the physical structure of the surface and the geologic processes that have formed and shaped it.

18.1 INTRODUCTION

The ability of the surface of Mars to conduct and store heat throughout the day offers a unique window into the small-scale physical characteristics of the materials that make up the surface layer. Visible images typically reveal morphologic features that provide insight into decameter- to kilometer-scale structures and geologic processes. Spectroscopic data provides compositional and mineralogical information of the upper tens to hundreds of micrometers of the regolith. However, thermophysical data reveals the microscopic to decimeter-scale structure of the soils and rocks that blanket the Martian surface. Thermal inertia is a key composite parameter that incorporates subsurface heat conduction and the heat-storage capacity of the surface layer, to define the diurnal and seasonal temperature response to solar heating. While it varies little with mineralogy, thermal inertia varies greatly with the physical structure of the surface material, with factors such as grain size, the presence and degree of cementation, and the abundance of rocks or presence of bedrock each playing a role. All of these factors influence the surface temperatures throughout the day and the overall thermal signature of the surface. As such, observations of surface temperature either *in situ* or from orbit allow the thermal inertia to be determined. In conjunction with other datasets, thermal inertia allows for a more complete interpretation of the physical, structural, and compositional makeup of the Martian surface layer.

Thermal inertia differences between, for example, rock, sand, and dust are distinct and can be identified from orbit by analysis of observed thermal radiation and inferred brightness temperatures. Local- and global-scale derivation and mapping of the thermal inertia of the Martian surface at ever-increasing resolution has revealed a wide range of surface types from continental-scale dust deposits to local exposures of bedrock. A variety of soil surfaces also cover Mars at all scales. Thermal inertia is commonly used to infer a typical or effective particle size of the soil. While most soils contain a distribution of grain sizes that is not well represented by a single diameter, under specific geologic conditions that naturally sort grains, such as with aeolian or fluvial processes, the inferred particle size can provide insight into these erosional or depositional environments. The presence of surface rocks are often inferred from thermal inertia observations, which may shed light on characteristics such as the extent of impact ejecta or mass wasting features, the erosion or deposition of fine-grained particles, and the general production and development of soils. The hunt for exposures of bedrock peeking through the soil layer is facilitated by examining thermal inertia. Often, morphologic features that appear as extensive bedrock are shown

The Martian Surface: Composition, Mineralogy, and Physical Properties, ed. J. F. Bell III. Published by Cambridge University Press.

from thermal inertia to be blanketed by soils centimeters or more deep.

In addition to its use in geologic interpretation and for understanding the processes responsible for developing the surface, thermal inertia is used extensively in theoretical and physical studies. As a boundary condition for Martian climate and global-circulation models, thermal inertia controls the temperature of the surface which acts to heat or cool the lowest layers of the atmosphere. Similarly, calculating seasonal surface and subsurface temperatures are necessary for understanding the behavior of volatiles and chemistry within the regolith. For example, subsurface water-ice stability and water migration within the Martian permafrost are largely controlled by thermal inertia, through the resulting seasonal mean temperatures and cycles of temperature gradients in the subsurface. Thermal inertia is also used in engineering both landed and orbiting spacecraft, to determine the exterior thermal environment in which these spacecraft must function, and to assess the surface texture on which a spacecraft might land.

In this chapter we describe the processes and physical structure of the regolith that influence thermal inertia and surface temperatures, focusing mostly on thermal conductivity, to provide a framework for interpreting derived thermal inertia values. We will describe how thermal inertia is determined from remotely sensed temperature observations. A review of Martian thermal inertia observations and interpretations will reveal the nature of the surface and some of the processes responsible for forming and modifying surface soils. While our discussion will focus on understanding the physical character of the Martian surface, the value and uses of thermal inertia in understanding the Martian environment and climate are more far reaching. Throughout this chapter, SI thermal inertia units of $\mathrm{J\,m^{-2}\,K^{-1}\,s^{-1/2}}$ are assumed when not specified.

18.2 THE PHYSICS OF TEMPERATURE AND THERMAL INERTIA

18.2.1 What is thermal inertia and how does it relate to temperature?

As with any rotating planet, Mars experiences surface temperature cycles, the amplitude of which depends on the relative magnitude of solar heating and radiative cooling processes, and on the efficiency of the subsurface at storing heat energy. The instantaneous thermal energy balance at the surface is commonly described by (see also Wesselink, 1948; Sinton and Strong, 1960).

$$\varepsilon\sigma T_s^4 = (1-A)S_m\cos(i) + F_{IR} + L\frac{\partial m}{\partial t} + k\left.\frac{\partial T}{\partial z}\right|_{z=0}. \tag{18.1}$$

The left side of the equation represent the loss of heat energy from the surface, while terms on the right represent sources of heat to the surface. The term on the left accounts for heat lost by thermal emission, where ε is the bolometric emissivity, σ is the Stefan–Boltzmann constant, and T_s is surface temperature. The first term on the right represents solar heating, where S_m is the solar flux at the Martian surface, which may include the effects of atmospheric extinction. A is the Bond albedo of the surface (assumed to follow a Lambertian reflectance law), and i is the solar incidence angle which changes with time of day, season, and location on Mars. F_{IR} is the downwelling thermal radiation from the atmosphere that is absorbed by the surface. The third term on the right accounts for the release of latent heat of sublimation, L, in winter that results when the surface cools enough to allow seasonal CO_2 frost mass to accumulate at the rate $\partial m/\partial t$. Finally, the last term represents conduction of heat into and out of the subsurface, where T is the subsurface temperature and z is the depth below the surface. Additional terms are sometimes added to include the effects of sensible-heat exchange between the surface and atmosphere, the diffuse sky illumination that results from the scattering of sunlight by airborne dust, and the reduction of solar flux by scattering and absorption of sunlight by atmospheric dust (e.g., Haberle and Jakosky, 1991; Pollack *et al*., 1990).

Thermal inertia, I, is defined as $\sqrt{k\rho c}$, a composite of the thermal conductivity, k, the density, ρ, and the specific heat capacity, c. It represents the ability of the subsurface to conduct and store heat energy away from the surface during the daytime and to return that heat energy to the surface at night. Physical properties of the surface strongly affect the thermal inertia through variations in the thermal conductivity and the heat capacity of the bulk material. Soil temperature and the gas pressure in the soil pore space can also play a role. For most geologic materials, the product ρc can vary by roughly a factor of 2–4, while k can vary by several orders of magnitude. Table 18.1 shows typical values for some geologic materials.

In the last term of Equation (18.1), $\partial T/\partial z$ also depends on the thermal properties of the surface layer. This dependence is eliminated by substituting $\delta\partial z'$ for ∂z, where z' is a unitless depth and δ is the thermal skin depth or e-folding depth of the subsurface thermal wave,

$$\delta \equiv \sqrt{\frac{k}{\rho c}\frac{P}{\pi}}, \tag{18.2}$$

and P is the diurnal period. Therefore, Equation (18.1) can be expressed as

$$\varepsilon\sigma T_s^4 = (1-A)S_m\cos(i) + F_{IR} + L\frac{\partial m}{\partial t} + I\sqrt{\frac{\pi}{P}}\left.\frac{\partial T}{\partial z'}\right|_{z'=0}, \tag{18.3}$$

where all the thermal properties of the surface layer are contained in I (e.g., Wesselink, 1948; Kieffer *et al*., 1977). It is therefore evident that the thermal inertia is the relevant physical property controlling surface temperature, rather than the thermal conductivity or the thermal diffusivity. While albedo and emissivity are important radiative properties that control the magnitude of heating and cooling forces

Table 18.1. *Typical thermophysical properties of some geological materials*

Material	Density ($kg\ m^{-3}$)	Heat capacity ($J\ kg^{-1}\ K^{-1}$)	Thermal conductivity ($W\ m^{-1}\ K^{-1}$)	Thermal inertia ($J\ m^{-2}\ K^{-1}\ s^{-1/2}$)
Volatiles and ices				
Water, ice[a]	915	1960	2.3–3.6	2030–2540
Water, liquid[b]	999.8	4217	0.56	1536
New snow	200[c]	1962[a]	0.078[c]	174
Ice-saturated soil[d]	2018	1040	2.5	2290
CO_2 ice (150 K)[e]	1560[b]	1083[f]	0.6[g]	1006
Methane clathrate[h]	1100[i]	1800[j]	0.45[k]	943
Rocks and mineral cements				
Andesite	2870[l]	450[m]	1.35–4.86[m]	1320–2505
Basalt	2900[l]	830–900[m]	1.12–2.38[m]	1642–2492
Granite	2650[l]	900[m]	1.78–5.02[m]	2060–3460
Sandstone	2310[l]	850[n]	2.15–3.80[m]	2054–2731
Calcite	2710[b]	780[m]	0.37[m]	884
Gypsum	2320[b]	1010[m]	2.1[m]	2218
Halite	2170[b]	850[m]	6.0[m]	3326
Tuff	1980[l]	850[n]	0.91–3.20 (1.8)[m]	1237–2320
Terrestrial and Mars analog soils				
Sand (20% moisture)	1650[o]	850[n]	1.76[p]	1571
Dry sand	1650[o]	850[n]	0.29[p]	637
200 μm sand @ 1 bar	1650[o]	850[n]	0.25[o]	592
Birch Hill Loess[q]	1130	650	0.15	332
Permafrost Tunnel[q]	480–880	650	0.07–0.18	148–320
Antarctic Till	1430[r]	850[n]	0.1[r]	348
JSC Mars 1[s]	1910[s]	850[n]	0.07[t]	337
200 μm sand @ 6 mb	1650[o]	850[n]	0.044[o]	248
10 μm dust @ 6 mb	1375[o]	850[n]	0.01[o]	108
1 μm dust @ 6 mb	1100[o]	850[n]	0.004[o]	61
1% Gypsum Duricrust[u]	1400	853	0.325	623

[a] Hobbs (1974); Petrenko and Whitworth (1999); with conductivity given for a range of Mars-like temperatures.
[b] Weast (1986).
[c] Strum *et al*. (2002).
[d] Assuming ice saturated soil (see Mellon *et al*., 2004).
[e] Because the temperature of CO_2 ice on Mars is buffered by latent heat release, derived thermal inertia is not meaningful.
[f] Value at 150 K (Giauque and Egan, 1937).
[g] Krovchenko and Krupskii (1986).
[h] Common values among clathrates suggest CO_2 clathrate would exhibit similar values (see also Mellon, 1996).
[i] Holder *et al*. (1995).
[j] Heat capacities of clathrates are typically similar to, but slightly less than, that of water ice (e.g., Leaist *et al*., 1982).
[k] Cook and Leaist (1983).
[l] Average values from Judd and Shakoor (1989).
[m] Range (modal) or average values from Roy *et al*. (1989).
[n] Approximate values assuming basaltic grains.
[o] Using Equation (18.9) for thermal conductivity and assuming a porosity of 40%, 50%, and 60% for 200, 10, and 1 μm soil grains respectively, with an intrinsic grain density of $2750\ kg\ m^{-3}$, and assuming interstitial CO_2.
[p] Hillel (1980).
[q] Example of low-thermal-conductivity desiccated loess, from Birch Hill and the Fox Permafrost Tunnel, Alaska (Johnson and Lorenz, 2000).
[r] Sublimation till from Beacon Valley, Antarctica (Putkonen *et al*., 2003).
[s] Weathered volcanic ash commonly used as a Martian soil simulant (Allen *et al*., 1998).
[t] Thermal conductivity measured at 6 mb of CO_2, similar to 500 μm sand via Equation (18.9) (Presley and Craddock, 2006).
[u] Assuming 1% of the soil volume is occupied by gypsum, about 40 μm basaltic grains, and 50% porosity.

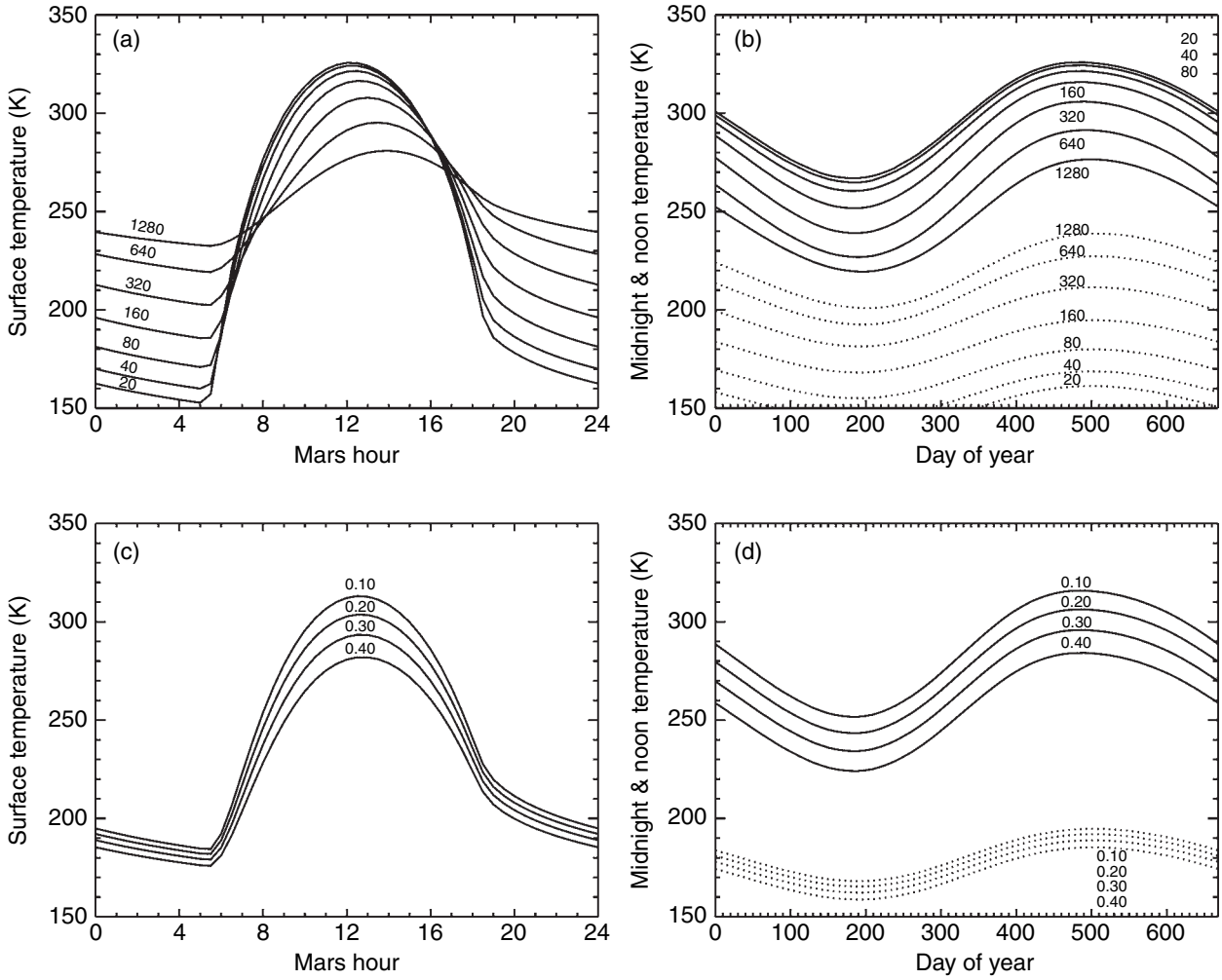

Figure 18.1. Surface temperature behavior of Mars as a function of thermal inertia and albedo. Shown are (a) diurnal temperatures for a range of thermal inertia during the summer (day 500); (b) minimum and maximum daily temperatures as a function of season for the same range of thermal inertia as in (a); (c) diurnal temperatures for a range of albedo during the summer (day 500); (d) minimum and maximum daily temperatures as a function of season for the same range of albedo as in (c). Minimum daily temperatures are shown as dotted lines, and maximum daily temperatures are shown as solid lines. Generally, thermal inertia controls the amplitude and the phase of the diurnal temperature cycle and the albedo controls the mean. All kinetic surface temperatures are generated by a numerical thermal model (e.g., Mellon *et al.*, 2000), assuming 6 mb atmospheric pressure and a visible dust opacity of 0.2 at 20° S latitude. A constant albedo of 0.10 is assumed for (a) and (b), and thermal inertia values are shown for each curve ranging from 20 to 1280 J m^{-2} K^{-1} s$^{-1/2}$. A constant thermal inertia of 160 J m^{-2} K^{-1} s$^{-1/2}$ is assumed for (c) and (d), and albedo values are shown for each curve ranging from 0.1 to 0.4. The term "day" is used here to describe a Mars solar day (a sol, 88775 s) and Mars hours are 1/24th of a Mars solar day.

on the surface (i.e., incoming and outgoing energy), it is thermal inertia alone that controls the magnitude of the surface temperature response to these thermal forces.

Subsurface heat conduction is described by the thermal diffusion equation,

$$\rho c \frac{\partial T}{\partial t} = \nabla \cdot k \nabla T. \tag{18.4}$$

We can solve Equation (18.4) for the temperature T as a function of time t and depth z within the Martian subsurface using Equation (18.3) to define a periodic surface boundary condition, assuming a lower boundary condition of either nonconducting zero flux or the geothermal heat flux, and assuming an initial condition. In three dimensions additional boundary conditions are needed, typically nonconducting or mirrored edges. Due to the nonlinearity of Equation (18.3), a numerical solution is usually employed, in which case an arbitrary initial condition is assumed, the effects of which dissipate over several cycles. Figure 18.1 shows typical diurnal and seasonal temperature cycles on Mars as a function of thermal inertia and albedo, based on a numerical solution to Equations (18.3) and (18.4). As the thermal inertia increases, the diurnal temperature oscillations become subdued, because the solar energy absorbed during the daytime is distributed over more thermal mass at depth and this energy is returned to the surface at night. Throughout this chapter, time measurement in days refers to the Martian solar day. Variations in albedo affect the overall quantity of energy being absorbed by the surface, but do not

strongly affect the amplitude of the temperature oscillations as does thermal inertia.

18.2.2 What controls thermal inertia?

The thermal inertia is a material property that depends strongly on the composition and physical structure of the Martian surface layer with thermal conductivity playing by far the largest role. Many factors can affect the thermal conductivity of a soil including composition, particle size, porosity, density, interstitial gas pressure, soil temperature, and the presence of cementing agents. Heterogeneity of the bulk soil is also important. The particle size distribution (including the presence of rocks and bedrock), as well as the presence of subsurface layers and horizontal mixtures of soils, all influence the bulk thermal inertia of the surface layer. Naturally occurring terrestrial soils are complicated by the omnipresence of liquid water (e.g., Hillel, 1980), which is generally absent on Mars. With the exception of some dry Antarctic soils (Putkonen *et al*., 2003) and desiccated Arctic loess (Johnson and Lorenz, 2000), terrestrial analogs for the thermal properties of soils on Mars are limited. High atmospheric pressure relative to that on Mars also complicates terrestrial comparisons (see below). Therefore, most analog studies have focused on theory and laboratory measurements.

In a dry, unconsolidated soil the heat flow is controlled by a combination of conduction through and between the soil grains. While heat conduction through the soil grains depends on the grain mineralogy, conduction between the grains depends on heat flow across the grain-to-grain contacts and through the void space between the grains. Heat flow through the void space consists of a combination of heat transported by gas conduction and by thermal radiation. Assuming a simple model of in-series heat conductors across the grains and the interstice, the bulk thermal conductivity k_b can be expressed as

$$k_b = \frac{k_p k_v}{\alpha k_p + (1-\alpha)k_v}, \tag{18.5}$$

where the subscripts p represents the solid particle conduction and v represents that of both the void space and grain contacts. The porosity α gives an approximate measure of the relative path lengths through the soil particles and the void space. Combining heat transported across the grain contacts and the void space and assuming a simple model where all grain-to-grain conduction processes operate in parallel,

$$k_v = k_c + k_g + k_r, \tag{18.6}$$

where the subscripts c, g, and r represent contact, gas, and radiative conduction components respectively (Wechsler *et al*., 1972). Other approaches of combining parallel and series conduction paths have been proposed (e.g., Masamune and Smith, 1963), which differ mainly in the relative consideration of microscopic and macroscopic conduction processes in a bulk soil while still capturing the bulk behavior. In a real soil the particle size distribution, grain shapes, and packing result in a complex three-dimensional structure, with smaller particles occupying the void space between larger ones and with complex contacts between soil grains. The resulting three-dimensional flow of heat energy can be equally complex. However, Equations (18.5) and (18.6) provide a simple framework in which many of the aspects of thermal conductivity and thermal inertia in Martian soils may be understood.

In the case of unconsolidated soils on Mars, the thermal conductivity within soil grains is typically very large in comparison to that of the interstices between the grains, and Equation (18.5) reduces to $k_b \cong k_v/\alpha$. Essentially, the soil grains are nearly isothermal and relatively large temperature gradients exist at the grain contacts and across the void space. In a vacuum, grain-contact and radiative conduction $k_c + k_r$ has been shown to be approximated well by $A_o + BT^3$ (Fountain and West, 1970). A_o and B are constants that depend on factors such as composition, density, particle shape, packing, and the degree of lithostatic compression of the soil grains (Wechsler *et al*., 1972). Over most of the Martian surface, this temperature dependence is minimal relative to gas conduction, and indeed gas conduction effects can dominate the bulk conductivity (Fountain and West, 1970; Wechsler *et al*., 1972).

From kinetic theory, gas conduction in the soil pore space follows two regimes (see also Woodside and Messmer, 1961a; Wechsler *et al*., 1972; Jakosky, 1986). At higher pressures where the mean free path of the gas is much smaller than the pore size and gas–gas collisions dominate the heat transfer, the pressure effects on the mean free path and on the gas density cancel and the conductivity is independent of gas pressure:

$$k_{gg} = e\beta\eta c_g \tag{18.7a}$$

and

$$\eta = \frac{aT^{1/2}}{1 + b/T}, \tag{18.7b}$$

where β is a gas constant (1.64 for CO_2), η is the gas dynamic viscosity, c_g is the specific heat of the gas at constant volume, and e is an efficiency of energy exchange between the gas and soil grains, nominally less than unity (see also Kennard, 1938; Present, 1958). For the dynamic viscosity of CO_2 (Equation 18.7b), a is $1.65 \times 10^{-6}\,\mathrm{N\,s\,m^{-2}\,K^{-1/2}}$ and b is 269 K (Kennard, 1938). At lower pressures where the pore size is smaller than the mean free path of the gas and gas–soil collisions dominate the heat transfer, the effective mean free path becomes the pore diameter and thermal conductivity of the gas is proportional to the gas pressure:

$$k_{gs} = \frac{1}{2}(\gamma + 1)c_g\ \Psi\ (2\pi RT)^{-1/2}\overline{X}, \tag{18.8}$$

where γ is the specific heat ratio, Ψ is the gas pressure, R is the ideal gas constant, and $\overline{X}$ represents the mean distance between soil grains. For spherical grains in contact the mean distance between grains is 1/3 the diameter of the grains. In real soils, complex grain shapes, packing, porosity, and grain-size mixtures will change the mean distance.

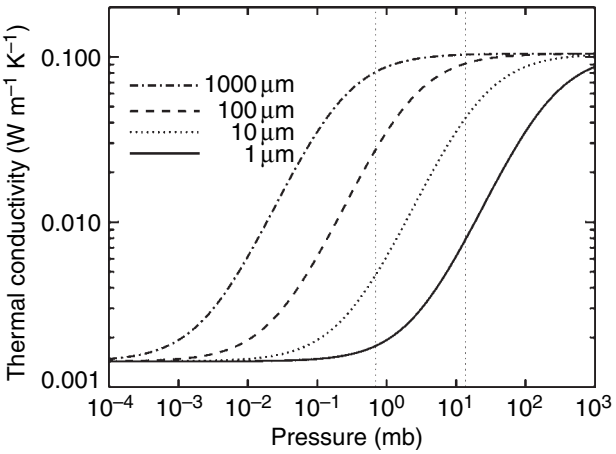

Figure 18.2. Bulk thermal conductivity of unconsolidated soil as a function of interstitial CO_2 pressure, utilizing Equations (18.5), (18.6), (18.7), and (18.8). Curves are shown for a range of particle sizes from 1 to 1000 μm. At high pressure bulk thermal conductivity is dominated by CO_2 gas conduction, while at the lowest pressures radiative conduction and grain to grain contact dominate the heat flow (see also Fountain and West, 1970). Vertical dotted lines indicate 0.7 and 13.7 mb, the range of atmospheric pressures expected on Mars. At Mars pressures both the conductivity and thermal inertia are very sensitive to the soil particle size.

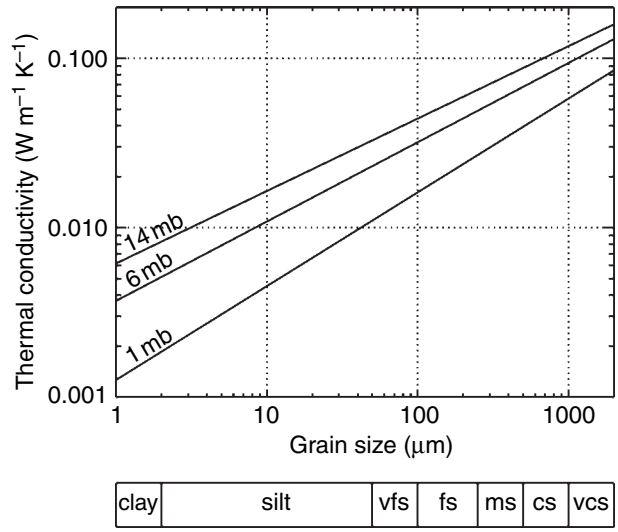

Figure 18.3. An empirical fit to thermal conductivity measurements as a function of grain size and CO_2 gas pressure, based on the results of Presley and Christensen (1997a). Differences in conductivity between Figures 18.2 and 18.3 can be attributed to the different functional forms (see text for additional discussion). The US Department of Agriculture standard soil grain diameter designations are shown for clay, silt, very fine sand (vfs), fine sand (fs), medium sand (ms), coarse sand (cs), and very coarse sand (vcs) (see Hillel, 1980).

Combining these effects at intermediate pressures and assuming series conduction between Equations (18.7a) and (18.8), Figure 18.2 shows an example of the bulk thermal conductivity as a function of gas pressure for a selection of soil particle sizes. This theory is in good agreement with laboratory measurements (Wechsler and Glaser, 1965; Wechsler *et al.*, 1972; Presley and Christensen, 1997a). At very low pressures the contact and radiative conduction pathways dominate the bulk thermal conductivity. At high gas pressures comparable to those on Earth, the gas conduction dominates. For these endmembers, factors such as temperature, soil density, and mechanical loading result in variation in bulk conductivity from soil to soil. Mars's atmospheric surface pressure ranges between about 0.7 and 13.7 mb depending on elevation and season (see also Tillman *et al.*, 1993). At these pressures, the thermal conductivity is the most sensitive to the particle size (Figure 18.2).

Using powdered-rock data from Wechsler and Glaser (1965), Kieffer *et al.* (1973) estimated a relationship between the particle size and the thermal conductivity and thermal inertia for the Martian surface. Presley and Christensen (1997a) measured the thermal conductivity for a range of sizes of glass beads over a range of CO_2 pressures, and found an empirical relationship:

$$k_b = C\Psi^{0.6} d^{-0.11\,\log(\Psi/K)}, \tag{18.9}$$

where C and K are constants equal to 0.0015 and 8.1×10^4 respectively, with pressure given in torr, particle diameter d in μm, and conductivity in W m^{-1} K^{-1}. This relation agrees roughly with the "hand-plotted" results of Kieffer *et al.* (1973) with the advantage of being based on measurements at (rather than extrapolated to) CO_2 pressures typical of the Martian surface. While this relationship is extremely useful, it should be noted that the functional dependence of pressure is nonlinear in Equation (18.9), but linear in Equation (18.8). This difference can be explained by the additional effects of contact and radiative conduction and the combination of gas conduction processes at intermediate pressures (Jakosky, 1986), all approximated empirically by Equation (18.9). Figure 18.3 shows the relationship between thermal conductivity and particle size from Equation (18.9). In addition, Presley and Christensen (1997b) found that increasing the packing density of soil grains increases the conductivity, interpreted as due to increased grain-to-grain contacts. While real soils are infrequently of a single grain size, the relationship illustrated in Figure 18.3 is valuable in understanding the relative coarseness or fineness of Martian soils, and has specific applications in geologic settings where particle sorting is expected, such as sand dunes and wind streaks. When mixtures of particle sizes were considered, Presley and Craddock (2006) found that the larger grains tended to dominate the bulk thermal conductivity.

Jakosky (1986) noted that for larger particles the thermal conductivity reached a maximum under Mars-like pressures (see Figure 18.2). This effect is the result of the voids between the particles being much larger than the mean free path of CO_2 under Mars conditions and conduction being completely dominated by gas–gas collisions. Thus, for particles on Mars larger than roughly 1 mm particle-size effects do not influence the thermal conductivity, and the resulting thermal inertia will plateau around 400 J m^{-2} K^{-1} s$^{-1/2}$ regardless of particle size above ~1 mm. As particle sizes approach the dimensions of a thermal skin depth (a few centimeters), the bulk soil can no longer be considered statistically homogeneous and this relationship begins to break down.

Thus far, we have considered unconsolidated soils. Bonding of soil grains by mineral deposits or ice commonly occurs on Earth. Indeed, duricrusts (weakly salt-cemented soils) have been observed at all of the existing Mars landing sites (Binder *et al.*, 1977; Mutch *et al.*, 1977; Moore *et al.*, 1999; Arvidson *et al.*, 2004a,b) and have been proposed to be widely distributed over the globe (e.g., Jakosky and Christensen, 1986a; Arvidson *et al.*, 1989; Christensen and Moore, 1992; Mellon *et al.*, 2000; Putzig and Mellon, 2007b). Additionally, ice-rich permafrost has been predicted and observed to be dominating the high latitude soil (e.g., Leighton and Murray, 1966; Farmer and Doms, 1979; Fanale *et al.*, 1986; Paige, 1992; Mellon and Jakosky, 1993; Boynton *et al.*, 2002; Feldman *et al.*, 2004; Chapter 6). Mellon *et al.* (1997) developed a model of the thermal conductivity of subsaturated icy soil. They recognized that, thermodynamically, ice (as with liquid water) will preferentially collect at the grain contacts, minimizing its Gibbs free energy and thus increasing the size of the conductive bridge across the grain contacts. A similar process of sintering occurs between ice grains and in snow (e.g., Hobbs, 1974). Through examining a variety of soil-particle geometries, Mellon *et al.* (1997) found the relationship

$$k_v = (1 - f)k_{v0} + fk_i, \tag{18.10}$$

where k_{v0} is the cement-free thermal conductivity of the interstitial void and k_i is the conductivity of pure-ice cement. The fraction of the cross-sectional area of the pore space occupied by the cement, f, is a function of the fraction of the porosity occupied by the cement α_i relative to the cement-free porosity α_0;

$$f = \sqrt{\frac{(\alpha_0 - \alpha_i)}{\alpha_0}}. \tag{18.11}$$

This relation works well for a wide range of soil grain shapes and is independent of particle size (Mellon *et al.*, 1997). Assuming that salt cements are mobilized by water and will become similarly concentrated at the grain contacts, Equations (18.10) and (18.11) can be applied to duricrust deposits. Because solid conduction in the cement is far more efficient than that of the gas and radiative components in the cement-free pore space ($k_i \gg k_{v0}$), it can quickly dominate the bulk conductivity with only a small amount of cement. In this instance the conductivity of the soil particles becomes important (see Equation 18.5) as the particles become less isothermal. Figure 18.4 shows examples of the thermal conductivity as a function of the amount of cement between soil grains for some common cements. As little as 1% by volume of a cementing agent can increase the thermal conductivity by 5–50 times depending on the cement species, a roughly 2–7 times increase in thermal inertia.

Solid rock, ice, or densely ice-cemented soils all have a very high thermal conductivity and high thermal inertia relative to unconsolidated soils (see Table 18.1). Variability exists due to mineralogy, porosity, and some of the same processes that affect soils. For example, porous rocks and sandstones exhibit some variability with pore-space gas pressure and lithostatic compression (Woodside and Messmer, 1961b). The thermal conductivity of water ice is similar to that of most rock-forming minerals (Hobbs 1974; Petrenko and Whitworth, 1999), making it difficult to discriminate between the thermal inertia signatures of bedrock, surface ice, and densely ice-cemented soil. CO_2 ice and clathrate hydrates exhibit intermediate conductivities, about 5–6 times smaller than that of water ice (e.g., Cook and Leaist, 1983; Dharma-wardana, 1983; Krovchenko and Krupskii, 1986; Honda and Cook, 1987). Surface rocks and rock outcrops are observed at every landing site in some abundance (e.g., Moore and Keller, 1990; Golombek *et al.*, 2003; Arvidson *et al.*, 2004a,b) and are believed to be widespread on Mars (Christensen, 1986a). When rocks much larger than a few centimeters (i.e., larger than a thermal skin depth) are mixed with surface soils, a heterogeneous surface results (discussed below).

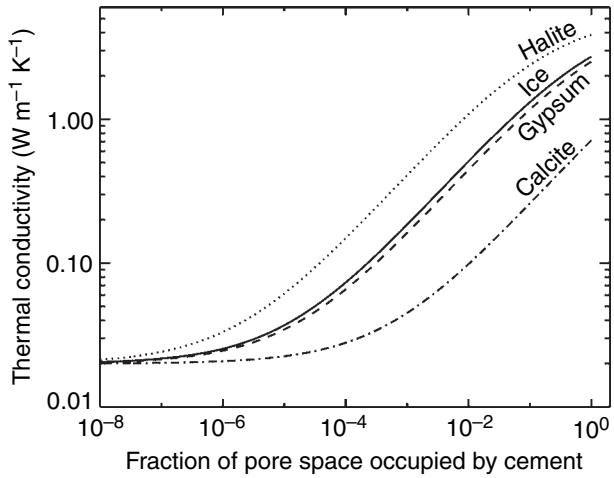

Figure 18.4. Thermal conductivity of duricrust or permafrost assuming a halite, water ice, gypsum, or calcite cement between the soil grains, utilizing Equations (18.5), (18.6), (18.10), and (18.11) (see also Mellon *et al.*, 1997). Very little cement will dramatically increase the conductive bridge between soil grains and dominate the heat flow pathways (see text). Cement-free soil assumed here is consistent with 40 μm grains. See Table 18.1 for cement properties.

In addition to thermal conductivity, specific heat capacity and density also play a role in thermal inertia variations. For most rock-forming minerals and typical geologic materials, however, these variations are small, typically a factor of 2–4 (see also Table 18.1). The specific heat capacity is dependent on the mineralogical makeup of the soil grains and rocks. Most minerals also exhibit a temperature-dependent heat capacity, but for the range of temperatures encountered on Mars, this effect is small, less than a factor of 2 (e.g., Urquhart and Jakosky, 1997). The density and porosity of soils and rocks can vary depending on the packing of soil grains, the grain size distribution, cementing, or lithification. For most terrestrial soils porosities range from about 25% to 60% with 40%–50% being most common (e.g., Brady, 1974). Assuming an intrinsic density (soil grain density) of 2750 kg m^{-3}, the bulk soil density can range from 1100 to 2060 kg m^{-3}. Estimates of soil densities at the Viking landing sites ranged from 1400 to 1700 kg m^{-3} (Moore and Jakosky, 1989) with drift material bulk density being closer to 1200 kg m^{-3} (Moore *et al.*, 1987). Appropriate densities for

rocks depend strongly on lithology and porosity; most terrestrial dense igneous rock ranges from 2650 to 2900 $kg\,m^{-3}$ (Judd and Shakoor, 1989). Combining thermal conductivity, specific heat capacity, and density, the thermal inertia for likely geologic materials on Mars may range from less than 50 $J\,m^{-2}\,K^{-1}\,s^{-1/2}$ for fine-grained dust to more than 2500 $J\,m^{-2}\,K^{-1}\,s^{-1/2}$ for solid rock (see also Table 18.1). The term "dust" refers to airborne particles tens of micrometers or smaller in diameter (silt and clay size) and their unconsolidated surficial deposits.

18.2.3 Methods of deriving thermal inertia

Historically, thermal inertia of the Martian surface has been derived primarily using one of two methods, depending on the type of observational data and physical assumptions being made. In every study, a common thread has been to compare an observed surface brightness temperature (the temperature of a black body that produces an equivalent radiant infrared flux) to a numerical-model-based temperature, varying the model thermal inertia to find the best-fitting value. This comparison is usually accomplished through a suite of numerical simulations and various degrees of interpolation. Since surface temperatures vary throughout the day and day-to-day throughout the seasons, these numerical thermal models need to account for the cycles in insolation (incident solar radiation) that drive these variations. In the first method, brightness temperatures are observed at multiple times of day at one location (during only a few days at the same season) and fit to the diurnal temperature curves (e.g., Figure 18.1a) by simultaneously varying the thermal inertia to match the amplitude of the temperature cycle, and varying the albedo to match the mean temperature (e.g., Kieffer *et al.*, 1977; Palluconi and Kieffer, 1981; Paige *et al.*, 1994; Fergason *et al.*, 2006a). In the second method, brightness temperature is observed only at one time of day the albedo is fixed based on the observed bolometric reflectance of sunlight and only thermal inertia is varied to find a best-fitting model temperature (e.g., Jakosky *et al.*, 2000; Mellon *et al.*, 2000; Fergason *et al.*, 2006b; Putzig and Mellon, 2007b). The latter method works best during the nighttime or mid-day hours, as temperature as a function of thermal inertia near dusk and dawn are generally not single-valued and a unique solution is not forthcoming (Figure 18.1a). A third special-case approach that has been employed is to examine the decay of the surface temperature perturbation due to a solar eclipse by the moon Phobos (Betts *et al.*, 1995), which is sensitive to a shallower depth scale because of the short duration of the perturbation.

Numerical thermal models play a central role in deriving thermal inertia. Most numerical models used today follow a solution to Equations (18.3) and (18.4) with appropriate boundary conditions, components of which can be traced back to Kieffer *et al.* (1977). Divergence between models comes from an assortment of improvements to the represented physics with the goal of obtaining higher accuracy or to adapt the models to special applications. For example, Kieffer *et al.* (1977) in the analysis of Viking Infrared Thermal Mapper (IRTM) data used a simple atmospheric model, wherein downwelling thermal radiation (F_{IR} in Equation 18.3) was assumed to be equivalent to 2% of either the peak insolation or the CO_2 frost emission in polar night (Neugebauer *et al.*, 1971). Haberle and Jakosky (1991) examined this approximation using a multilayer radiative–convective atmospheric model originally developed for a Mars atmosphere general circulation model (Pollack *et al.*, 1990) and found the downwelling flux to be a factor of several larger, depending on the dust opacity, and to vary significantly with time of day and season. Paige *et al.* (1994) evaluated polar thermal inertia, adapting a thermal model by incorporating a version of a radiative-convective atmosphere tuned to polar conditions, and reported reasonable agreement with Haberle and Jakosky (1991). Jakosky *et al.* (2000) used the radiative–convective model of Haberle and Jakosky (1991) for derivation of thermal inertia from MGS Thermal Emission Spectrometer (TES) observations. Putzig *et al.* (2004) and Jakosky *et al.* (2006) used the same model to derive thermal inertia from Mars Odyssey Thermal Emission Imaging System (THEMIS) data. An improved version of the original Kieffer *et al.* (1977) model, with a tuned one-layer radiative atmosphere, was used to derive THEMIS-based thermal inertia values (Christensen *et al.*, 2003a; Fergason and Christensen, 2003; Fergason *et al.*, 2006b) and Mini-TES-based thermal inertia (Christensen *et al.*, 2004a; Fergason *et al.*, 2006a). Numerous other small differences in model technique exist, including variations in methods for handling of surface frosts, assumptions about atmospheric parameters and vertical structure, numerical methods and convergence schemes, photometric functions, etc. Ideally, a single perfect model would be used to derive thermal inertia from all datasets, so that thermal inertia results would be completely comparable and independent of numerical approach, but in practice differences occur, particularly when models are adapted to special cases. While the various thermal models generally agree well (e.g., Haberle and Jakosky, 1991; Mellon and Jakosky, 1993; Mellon *et al.*, 2000; Fergason *et al.*, 2006b), small temperature differences can result in small thermal inertia differences. For example, a 1 K difference in instantaneous model temperature corresponds to about a 10% difference in derived thermal inertia over a wide range of conditions. However, despite the differences in numerical methods, the global scale trends in thermal inertia and resulting interpretations remain largely unchanged from model to model.

Surface temperature at any instant depends on the time history of heating and cooling processes. As these oscillations propagate into the subsurface they dissipate with depth and time (see Equation 18.2). Thus, surface temperature at a given time of day is more influenced by the magnitude of solar heating from hours earlier than from weeks earlier. Low-thermal-inertia soils, which store heat less effectively than high-thermal-inertia soils, respond more quickly to changes in diurnal cycles and "remember" less of the seasonal changes. High-thermal-inertia soils and rock, which store heat more efficiently, tend to be influenced by slightly longer timescales. In addition, the magnitude of oscillations in the solar flux are generally larger for diurnal cycles than they are for seasonal cycles. Therefore, diurnal cycles tend to

influence the temperature at any instant more than seasonal cycles and the thermal inertia is largely a measure of the properties of the upper diurnal skin depth of soil. Seasonal cycles are still present; however, the thermal inertia is less sensitive on annual skin-depth scales. Complications to this generalization can arise when subsurface layers are present, but instantaneous temperatures are still influenced largely by diurnal cycles over an effective skin depth. For a diurnal cycle the skin depth varies from a few millimeters to a few decimeters, depending on the thermal properties of the soil, being shallower for low-thermal-inertia soils.

Measurements of brightness temperature used in deriving thermal inertia have come from mainly two types of remote-sensing sources. Bolometric brightness temperatures are determined by measuring the total thermal-infrared flux emitted by the surface at all wavelengths and then calculating the corresponding brightness temperature using the Stefan–Boltzmann law (e.g., Christensen *et al*., 1992). Measured from orbit, bolometric temperature includes contributions from the atmosphere (both absorption and emission), which must be accounted for in the thermal models. Spectral brightness temperatures are determined within selected thermal-infrared spectral bands using the Planck function (e.g., Kieffer *et al*., 1977; Christensen *et al*., 1992). If chosen in an atmospheric window, the atmospheric contributions are largely negligible, but the temperature and derived thermal inertia are sensitive to the spectral emissivity of the surface, and thus are sensitive to geographic variations in the surface mineralogy. Bolometric temperature and associated thermal inertia are almost entirely insensitive to the emissivity, so long as the thermal model and the measured flux assume the same bolometric emissivity when calculating the brightness temperature (Mellon *et al*., 2000).

Uncertainties in deriving thermal inertia result from several sources: (1) accuracy of the observed brightness temperature; (2) uncertainty in the thermal model physics, assumptions, and numerical techniques; (3) uncertainty in the other assumed physical properties, such as albedo, atmospheric dust opacity, surface topography, etc.; and (4) error in subsequent interpolations (e.g., Palluconi and Kieffer, 1981; Mellon *et al*., 2000; Fergason *et al*., 2006b). In some cases estimates of uncertainty from these sources can be made based on the partial derivative of thermal inertia with respect to each source. For example, if we know the temperature measurement accuracy and $\partial I / \partial T$, we can estimate the resulting uncertainty in thermal inertia. In other cases the uncertainty results from a lack of knowledge of a particular parameter, such as dust opacity or surface slope. While estimates can be made of these parameters, a limited knowledge of their accuracy can lead to a weakly constrained uncertainty in the thermal inertia. Numerical thermal models used to derive thermal inertia can generally predict temperatures to within a small fraction of a degree given the physical processes included (e.g., Mellon and Jakosky, 1993). However, these numerical models assume that all the physical processes which control surface temperature have been properly captured. The fact that the observed albedo is frequently insufficient to describe the temperatures at multiple times of day for a given thermal inertia (Palluconi and Kieffer, 1981; Fergason *et al*., 2006a) strongly suggests that something remains missing from these models.

Given the errors induced by instrument uncertainty, numerical model accuracy, and interpolation, Mellon *et al*. (2000) estimated the uncertainty for TES-bolometer-based nighttime thermal inertia to be around 6% and uncertainty for thermal inertia based on the 20 μm spectral band to be closer to 17%, for a surface temperature of 180 K and assuming as a worst case that errors are systematic and cumulative. Comparable estimates for TES-based daytime thermal inertia (assuming a surface temperature of 270 K) are 15% (bolometer) and 8% (20 μm spectral band); the difference relative to the nighttime thermal inertia is mainly due to lower measurement uncertainty at higher daytime temperatures offset by increased daytime sensitivity to albedo and modeled temperatures. An absolute uncertainty of 20% was estimated for THEMIS-based thermal inertia determined by a root sum squared (RSS) method, assuming random uncorrelated errors and including estimated uncertainties in interpolation parameters (Fergason *et al*., 2006b). In addition, Putzig *et al*. (2004) noted a systematic offset between TES-based and THEMIS-based nighttime thermal inertia as large as 25%. Fergason *et al*. (2006a) estimated an RSS uncertainty of 12% for Mini-TES thermal inertias derived from single temperature observations. In practice, differences in the methods and assumptions used between investigations to quantify uncertainty make direct comparison difficult. However, the repeatability of thermal inertia values at a particular location suggests that at least the secular components of the uncertainty are small and that the overall uncertainty is typically smaller than reported.

18.2.4 Ideal models and nonideal surfaces

Thus far, an underlying assumption in deriving thermal inertia has been that on the spatial scale of the temperature observation the surface of Mars is homogeneous. This assumption is necessitated by the need to constrain the thermal inertia with a limited amount of observational data. However, Mars exhibits heterogeneities on a number of spatial scales, from rocks and soil distributions to layers of duricrust and permafrost. These departures from the homogeneous assumption can have a pronounced effect on the derived thermal inertia values and how we interpret them.

Surface rocks have been observed at each landing site (Moore and Keller, 1990; Golombek *et al*., 2003; Arvidson *et al*., 2004a,b). Rocks and soils will exhibit different temperatures throughout the day, due to differences in their thermal properties (see Table 18.1). Therefore, an observation of thermal emission from a rocky surface will comprise a mixture of thermal infrared emission from each component of that surface. Since no orbital brightness-temperature observations can yet resolve decimeter-scale rocks, the observed temperature must result from a linear mixture of emitted thermal energy from rock and soil surface components. Depending on the nature of the observation, a generalized heterogeneous mixture can be examined by bolometric mixing,

$$\sigma T_{\text{eff}}^4 = \sum_j a_j \varepsilon_j \sigma T_j^4, \tag{18.12}$$

or spectral mixing,

$$B(T_{\text{eff}}, \lambda) = \sum_j a_j \, \varepsilon(\lambda)_j B(T_j, \lambda), \tag{18.13}$$

where σ is the Stefan–Boltzmann constant and T_{eff} is the effective brightness temperature (with the effective emissivity assumed to be unity). For each component j, a is its fractional surface area, ε is its bolometric emissivity (or spectral emissivity at wavelength λ), T is its kinetic temperature, and B is the Planck function. Equations (18.12) and (18.13) represent a nonlinear dependence of T_{eff} on the component temperatures.

From a single bolometric brightness-temperature observation, it is not possible to separate the temperatures of each component. However, Equation (18.12) helps to understand how horizontally heterogeneous surfaces can affect the apparent bulk thermal inertia derived using the homogeneous assumption. For a simple two-component mixture of rocks and soil, Figure 18.5 shows how rocks can increase the bulk thermal inertia of the surface (Putzig and Mellon, 2007a; see also Golombek *et al*., 2003). It is evident from this figure that for moderate-to-low rock abundances, the bulk thermal inertia is dominated by the soil component (see also Christensen, 1982). From Figure 18.5 we can also estimate that for an average soil with a thermal inertia of 250, the addition of 10% rocks would increase the bulk thermal inertia to about 300 (see also Christensen, 1986a).

On the basis of Equation (18.13) and IRTM multispectral data, Christensen (1986a) derived the global distribution of rocks by examining the spectral contrast between the 7 μm and 20 μm bands in IRTM data. A thermal model (Kieffer *et al*., 1977) was used to calculate the brightness temperatures for rock and soil components of the surface separately, and the thermal infrared flux in each spectral band was mixed correcting for the emissivity of each component. The rock abundance and the thermal inertia of the soil were then varied to obtain a best fit to the IRTM data. Rocks were assumed to have a thermal inertia of about 1250 and an albedo of 0.1, and assumed to be 15 cm or larger in diameter (see Christensen, 1986a). Rocks larger than a few centimeters exhibit values of thermal inertia much higher than those of unconsolidated soils, while rocks larger than a thermal skin depth exhibit values of thermal inertia closer to that of bedrock (Jakosky, 1986). Christensen (1986a) found that rock abundances on Mars at a $1^\circ \times 1^\circ$ (latitude × longitude) scale averaged 6%, but ranged as high as 25% in some areas. The resulting thermal inertia values of the soil component by this method are similar in spatial distribution to those derived utilizing a homogeneous model, but are generally lower by about 40 J m^{-2} K^{-1} s$^{-1/2}$; for these low-to-moderate rock abundances, the soil component dominates the bulk thermal inertia (see also Figure 18.5).

Other horizontal mixtures can also be explored. Rock, dust, soil, and duricrust, as well as hills and other slopes, are all observed in lander images (e.g., Binder *et al*., 1977; Mutch *et al*., 1977; Ward *et al*., 1999; Squyres *et al*., 2004a,b). Each component will exhibit a different thermal inertia and a distinct temperature signature. For a mixture of surface types and slope facets within the instrument's field of view, all of these components will contribute to the total thermal emission (e.g., Equations (18.12) and (18.13)). To quantify the effects of horizontal heterogeneity for selected mixtures, Putzig and Mellon (2007a) used a numerical model to estimate the diurnal and seasonal temperatures for each component. Equation (18.12) then gave an effective temperature from which an apparent bulk thermal inertia was derived. A similar approach was employed by Golombek *et al*. (2003) specifically to examine the effects of rock abundance. Figure 18.6a shows an example of the diurnal cycle in temperature for an areal mixture of sand and duricrust, assuming that each component is vertically uniform. Figure 18.6b shows the resulting apparent thermal inertia from 2 a.m. and 2 p.m. temperatures throughout the year for various binary mixtures. A substantial diurnal and seasonal signature is seen in the apparent bulk thermal inertia, with a seasonal amplitude up to about 90 J m^{-2} K^{-1} s$^{-1/2}$ (about 15%–20%) and a smaller but comparable diurnal amplitude. The larger the thermal inertia contrast between surface components, the larger the seasonal and diurnal effects (Putzig and Mellon, 2007a), with the contrast between rock and dust being the largest. Mixtures of sloped surfaces also influence the apparent thermal inertia with north–south slopes playing a larger role. The apparent thermal inertia of a surface sloped just 5° northward can differ from that of a level surface by as much as 60% (see Putzig and Mellon, 2007a).

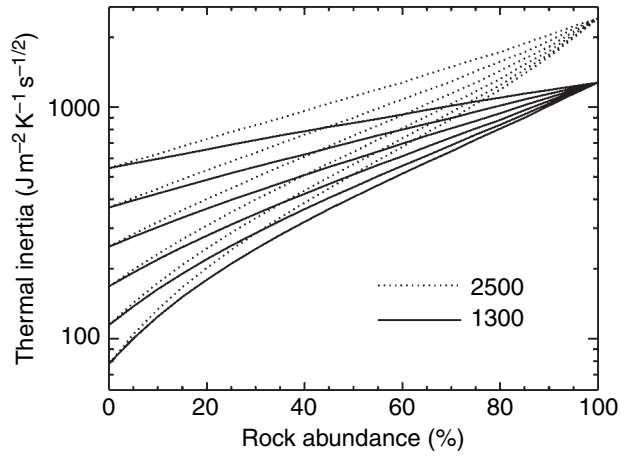

Figure 18.5. Bulk thermal inertia as a function of rock abundance (Putzig and Mellon, 2007a). Based on Equation (18.12), results are shown for a range of soil thermal inertia values and rock thermal inertia values of 1300 and 2500, 5 a.m. local time, and 10° N. For low-to-moderate rock abundances expected on Mars, the bulk thermal inertia is dominated by the soil component. For an increase of 0% to 10% rock abundance, the thermal inertia typically increases by only 40 to 50. Soil thermal inertia values are 77, 114, 168, 249, 367, and 542. Results are similar to that of Golombek *et al*. (2003), but differ in that Equation (18.12) assumes bolometric mixing, while Golobek *et al*. assumed 20-μm spectral mixing. In addition, these results will vary with time of day, season, latitude, and other conditions.

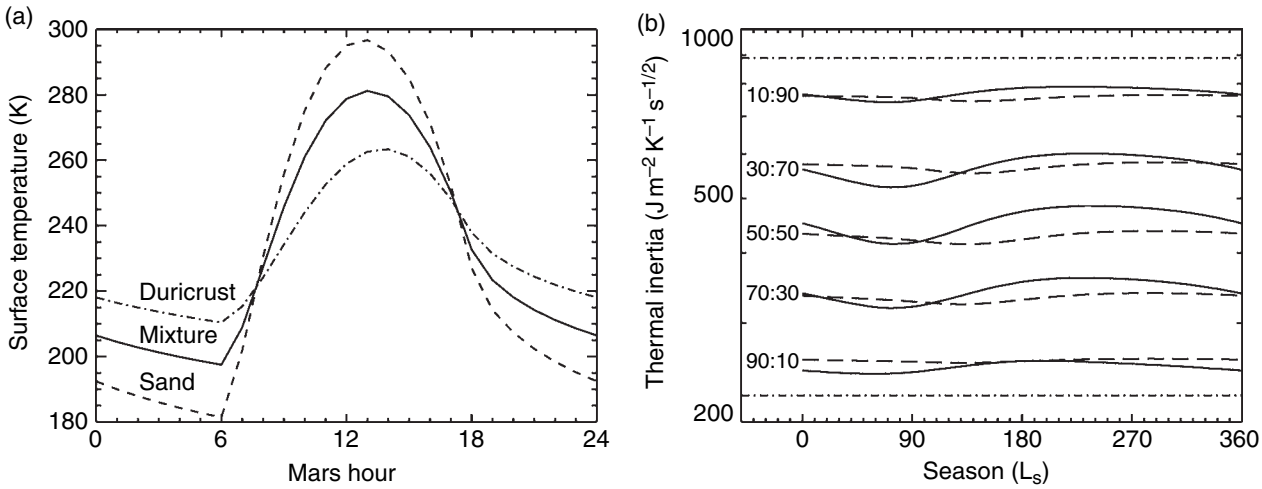

Figure 18.6. Diurnal temperature (a) and apparent seasonal thermal inertia (b) for a horizontally mixed surface of sand (thermal inertia of 223) and duricrust (thermal inertia of 889). Horizontal dot-dashed lines indicate component thermal inertia. Areal mixtures of 10%, 30%, 50%, 70%, and 90% are shown for seasonal thermal inertia. In (b) 2 a.m. and 2 p.m. thermal inertia values are shown as dashed and solid lines, respectively. Diurnal temperature curves are shown for a 50% mixture. See also Putzig and Mellon (2007a). Models assume 20° S latitude.

Similarly, subsurface layers with contrasting thermal properties can substantially affect the apparent bulk thermal inertia relative to that of a homogeneous soil by causing perturbations to the diurnal and seasonal temperatures (Jakosky, 1979; Ditteon, 1982). Examples of subsurface layers include surface dust coatings on rock, buried ice-rich permafrost, duricrust, and desert pavement. The former two examples comprise lower-thermal-inertia material over a higher-thermal-inertia substrate, while the latter two examples are the reverse.

Subsurface layers have been found at every landing site and are expected to be widespread on Mars. Subsurface ice is believed to occur stably over much of the high latitude regions in both hemispheres and to persist beneath a veneer of ice-free soil (e.g., Leighton and Murray, 1966; Mellon and Jakosky, 1993; Boynton *et al.*, 2002; Feldman *et al.*, 2004; Chapter 6). If this veneer is sufficiently thin, it will have a pronounced effect on the mean annual temperature (Mellon *et al.*, 2004) and on the seasonal and diurnal signatures from which thermal inertia is derived (Titus *et al.*, 2006). Air-fall dust deposits are also commonplace, coating rocks, soils, and spacecraft alike. Surface rocks and exposures of bedrock can potentially be masked by a layer of dust, making their thermal identification difficult. Modification of Equation (18.4) to account for such subsurface vertical structure allows us to incorporate this effect into a numerical thermal model (e.g., Mellon *et al.*, 2004; Mellon and Putzig, 2007), which may be used to predict brightness temperatures and to derive the apparent bulk thermal inertia for various layered structures (e.g., Putzig and Mellon, 2007b; Mellon and Putzig, 2007). Figures 18.7a and 18.7b show an example of these effects for the case of a low-thermal-inertia dust coating on a high-thermal-inertia bedrock (see also Mellon and Putzig, 2007).

Similar results occur for the case of ice-rich permafrost, where low-thermal-inertia dust or soil overlies ice-cemented soil, which exhibits similar thermal properties to that of bedrock (Table 18.1). In Figure 18.7a the diurnal temperature signature of bedrock is substantially affected by even a thin 250 μm coating of dust, because the dust insulates the rock from surface temperature cycles. The diurnal signature of the rock is completely masked by about 1 cm (one diurnal skin depth) of dust. Thermal inertia derived from these temperatures at noon and midnight are shown in Figure 18.7b. While the diurnal temperature curves shown in Figure 18.7a appear similar to those in Figure 18.1a for a homogeneous soil, there is a notable daytime-to-nighttime difference (up to ~75%) in the apparent thermal inertia derived for this surface. Significant seasonal variability is also observed, similar to that of the horizontally mixed surface in Figure 18.6, but with considerably larger amplitude (typically 40%–50% of the average) due to the higher thermal contrast. This seasonal behavior does not become masked until the layer thickness approaches a seasonal skin depth. For a 1 cm layer of dust (just over a diurnal skin depth) the apparent thermal inertia periodically falls below that of pure dust, a result of differences in the phase of seasonal heat storage between dust and rock components which dies out as the dust layer becomes thicker.

A layered structure of higher-thermal-inertia material over a lower-thermal-inertia substrate displays a different behavior. As discussed above, duricrust has a higher thermal conductivity and thermal inertia than unconsolidated soil when formed with only a modest amount of salt cement (see Figure 18.4). Additionally, desert pavements are common in terrestrial polar and nonpolar deserts, forming a surface layer of interlocking coarse sand or gravel by aeolian deflation. Such structure is observed at the Meridiani Planum landing site in the form of a lag of hematite spherules over a fine-grained basaltic sand (e.g., Squyres *et al.*, 2004b). These larger surface particles will also tend to exhibit higher thermal inertia than the fine-grained substrate, especially in the case of an interlocking monolayer of dense rock cobbles. Figure 18.7c shows

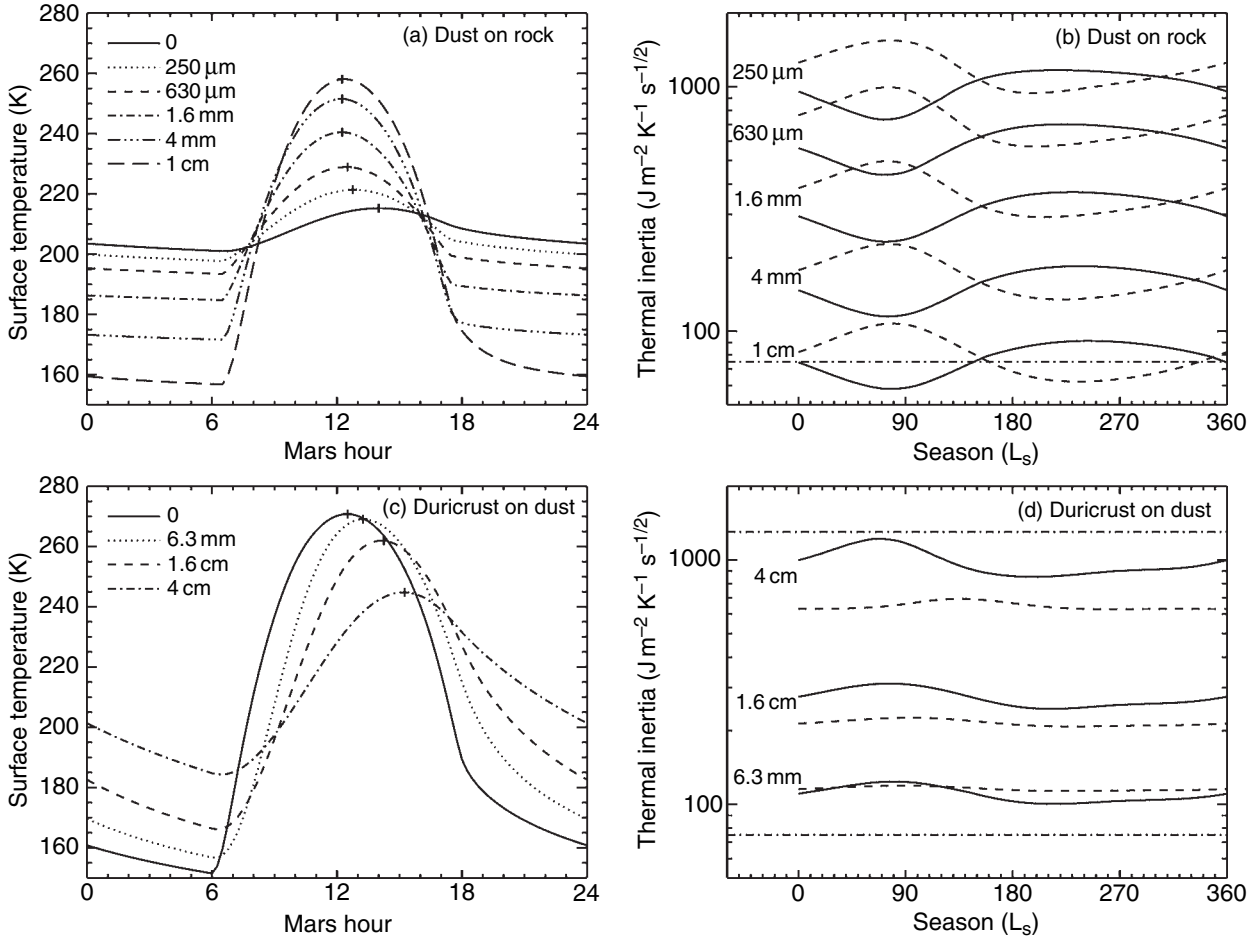

Figure 18.7. Diurnal temperature (a and c) and apparent seasonal thermal inertia (b and d) for a level rock surface coated with a layer of dust, and a layer of duricrust overlying dust. Layer thermal inertia values are assumed for rock (2250), dust (75), and duricrust (1300). Horizontal dot-dashed lines indicate component thermal inertia. Dust coating or duricrust thicknesses are shown. Dust-coating results are shown for 15° S latitude. Duricrust results are shown for the equator. In all cases albedo is assumed to be 0.25. Midnight and noon thermal inertia are shown as dashed and solid lines, respectively. Diurnal temperatures are shown for Ls 90, summer solstice. The diurnal skin depth of the dust is about 8 mm, while a seasonal skin depth is about 21 cm. For duricrust the diurnal skin depth is about 19 cm, while the seasonal skin depth is nearly 5 m. The relative magnitude of these effects vary with latitude, albedo, and other assumed parameters, but are representative of the behavior. See also Putzig and Mellon (2007b) and Mellon and Putzig (2007).

the diurnal temperatures for a high-thermal-inertia surface layer of duricrust over a dust substrate. The diurnal signature changes dramatically with layer thickness, where afternoon temperatures remain warm and the rise in post dawn temperatures is delayed. This result stems from the high thermal mass of the thin surface layer responding more slowly to changes in solar heating, combined with the inability of the substrate to conduct much of the day's solar energy to greater depth. Figure 18.7d shows the seasonal trends in the apparent thermal inertia at noon and midnight. Of particular interest is that the seasonal trends are nearly opposite to those of the dust-coating results in Figure 18.7b. This difference in behavior can allow separation of surface structure from observed thermal inertia signatures (Putzig and Mellon, 2007b). The amplitude of the apparent thermal inertia oscillations (about 10%–20% seasonally and 20%–60% between noon and midnight) is smaller than the case shown in Figure 18.7b, largely due to the smaller thermal contrast between layers.

18.2.5 Thermal inertia derivation

Previous thermal inertia analysis

There have been a number of studies to determine the thermal inertia of the Martian surface from both spacecraft and telescopic observations of brightness temperature, each with increasing resolution and precision. Sinton and Strong (1960) estimated the diurnal cycle in surface temperature from Earth-based telescopic limb-to-limb scans. They derived a global thermal inertia of 170 $J\,m^{-2}\,K^{-1}\,s^{-1/2}$ to match the diurnal phase and about 420 to match the amplitude of the diurnal cycle, the difference being attributed to the lack of an atmosphere in their model. Both Leovy (1966) and Morrison *et al.* (1969), while incorporating atmospheric effects on the surface temperature, reanalyzed the data of Sinton and Strong. They derived values similar to the diurnal-phase result and suggested that the upper 3 cm of the regolith consists of a range of 20–300 µm particles.

Analyzing Mariner 6, 7, and 9 radiometer data, Neugebauer *et al.* (1971) and Kieffer *et al.* (1973) estimated regional thermal inertia values ranging from 210 to 500, with a global average around 290. Moroz and Ksanfomaliti (1972) and Moroz *et al.* (1976) used Mars-3 data to estimate the thermal inertia for various light and dark regions over the surface. They found that thermal inertia values of 170–340 were consistent with the temperature data, and higher-thermal-inertia values were appropriate for darker regions. Ksanfomaliti and Moroz (1975) reached similar conclusions from Mars-5 radiometer data. Selivanov *et al.* (1998) derived thermal inertia from the Phobos-2 TERMOSCAN thermal images, at a maximum spatial resolution of 1.8 km. While the geographic coverage was limited, their results indicated a great deal of variability of the surface at this smaller scale. Betts *et al.* (1995) derived thermal inertia from TERMOSCAN temperature measurements of eclipse cooling in the shadow of the moon Phobos. They found thermal inertia values mostly in the range from 38 to 59 in the region of Arsia Mons, representing the upper 1 mm of the surface.

Detailed geographic mapping of thermal inertia began with Kieffer *et al.* (1977), who reported a preliminary map at a resolution of 2° in latitude and longitude (~120 km at the equator) from Viking IRTM data. Their map included thermal inertia values from about 70 to 500. They also noted a strong bimodal inverse correlation with albedo. Palluconi and Kieffer (1981) reported a refined 2° thermal-inertia map covering 60° N to 60° S latitude, about 81% of the planet, with values ranging from about 40 to 630. In a later reanalysis of the IRTM data, Hayashi *et al.* (1995) included the effects of a dusty, radiative–convective atmosphere and found that thermal inertia values were typically 50 lower than previously reported. Paige *et al.* (1994) and Paige and Keegan (1994) mapped IRTM thermal inertia for the polar regions and found values as high as 2000 for the north polar cap, consistent with surface water ice. Christensen and Malin (1988) and Christensen and Moore (1992) reported a 1/2° resolution IRTM thermal inertia map, with a wider range of thermal inertia values (20–1050).

New views of the thermal inertia of the Martian surface have come from the TES on the MGS spacecraft, the THEMIS on Mars Odyssey, and Mini-TES on the MERs. Increasing resolution, global- and local-scale orbital mapping, and lander-scale ground truth have all led to an improved understanding of the physical nature of the Martian surface layer. These data and their analysis will be the primary focus of the remainder of this chapter.

MGS TES thermal inertia derivation

The MGS spacecraft began its mapping mission after the completion of aerobraking in early 1999. From a near-circular, near-polar orbit of about 400 km altitude with equator crossings at approximately 2 a.m. and 2 p.m. local Mars time, the MGS TES instrument observed the Martian surface every 2 s using 6 detectors arranged in a 2 × 3 array. Each detector provided a nominal 3 km × 3 km surface resolution; however, due to aerobraking difficulties, MGS orbited opposite to the original design, leading to a downtrack smear of 5.4 km (full width at half maximum) for each detector. The TES platform included three boresighted instruments: a 6–50 μm spectrometer, a 5.5–100 μm thermal bolometer, and a 0.3–2.7 μm visible bolometer used to determine albedo (see Christensen *et al.*, 1992, 2001). The observed radiances from the first two instruments were used to calculate spectral and bolometric brightness temperatures of the surface from which thermal inertia values were derived (Jakosky *et al.*, 2000).

Thermal inertia from TES-based temperatures were derived using a seven-dimensional lookup table of numerically modeled brightness temperatures for broad ranges of season (L_S), time of day, latitude, albedo, surface pressure, dust opacity, and thermal inertia (Jakosky *et al.*, 2000; Mellon *et al.*, 2000; Putzig *et al.*, 2005; Putzig and Mellon, 2007b). For each observed brightness temperature, correlated values for each of the first six dimensions were obtained from other sources (spacecraft ephemeris, other MGS measurements, etc.), and the temperature was then interpolated through the lookup table to find the best-fitting thermal inertia. Initially, thermal inertia values were derived between 24 and 800, though a few surfaces outside of this range exist on Mars. Later, this range was expanded to 5–5000 (Putzig and Mellon, 2007b). Results included thermal inertia derived from both daytime and nighttime temperature observations and from both bolometer and spectrometer instrument components. Uncertainty estimates from sources discussed above are 6% and 15% for bolometer-based thermal inertia and 17% and 8% for spectrometer-based thermal inertia, derived using nighttime and daytime temperatures respectively. Most TES thermal inertia analysis to date has tended to focus on nighttime bolometer-based values, due in part to the lower overall uncertainty and sensitivity to uncertainties in albedo and slope, and in part to a greater familiarity within the scientific community.

Thermal inertia values were mapped and analyzed at up to 3 km resolution (Jakosky *et al.*, 2000; Mellon *et al.*, 2000; Putzig *et al.*, 2005; Putzig and Mellon, 2007b). In the two most recent studies, a series of filters were employed to remove the residual effects of temporal variations in the atmosphere, which were not sufficiently accounted for in the numerical thermal model. Thermal inertia values from times and locations of high infrared atmospheric dust opacity (>0.2), surface temperatures below 160 K, and high water-ice opacity (>0.1) were discarded and the remaining values were mapped at 36 seasonal intervals by averaging or median filtering at 1/20° bining (3 km at the equator). Figure 18.8 shows the resulting TES-based median maps from the 36 seasonal nighttime and daytime thermal inertia maps (Putzig and Mellon, 2007b). Approximately, 93% coverage was obtained using data from TES orbits 1583 to 24, 346 (covering approximately 3 Mars years beginning in February 1999), with the remaining locations filled by interpolation between 87° S and 87° N. Additionally, high latitude and polar coverage is limited in season, due to the presence of CO_2 surface frost during much of the year. Surface frost maintains the temperature at the CO_2 frost point and thus no diurnal temperature cycles occur (see also Equation 18.3). Elsewhere, gaps in geographic coverage occur during calibration and limb observations.

Mars Odyssey THEMIS thermal inertia derivation

The Mars Odyssey spacecraft is in a near-polar sun synchronous orbit with a drifting equator-crossing local time, ranging from 3–6 a.m. and p.m. The THEMIS infrared data are acquired using a multispectral microbolometer array that consists of 10 infrared spectral channels between about 6 and 15 μm. The instrument provides 100 m/pixel spatial resolution on the surface, 30 times higher resolution than TES. A unique advantage to THEMIS infrared data is that the 32 km wide field of view allows for the derivation of thermal inertia images, where the same season and climate conditions apply to every pixel within the image. The approach to deriving thermal inertia from THEMIS data is similar to that used for TES (e.g., Christensen *et al.*, 2003a, 2004a; Putzig *et al.*, 2004; Fergason *et al.*, 2006b; Jakosky *et al.*, 2006). Key differences lie in the style of measurement, temperature accuracy, and the resolution of interpolated parameters. For example, at 100 m resolution, local slope effects can be more apparent than at lower resolution and the surface temperatures are sensitive to albedo variations not resolved in available TES albedo data. In addition, THEMIS measurements provide only spectral brightness temperature and are therefore sensitive to surface emissivity variations.

To maximize the signal-to-noise ratio and to minimize emissivity and atmospheric-dust effects, thermal inertia values were derived from THEMIS band 9 (12.57 μm) nighttime temperature data (Christensen *et al.*, 2003a, 2004a; Putzig *et al.*, 2004; Fergason *et al.*, 2006b; Jakosky *et al.*, 2006). The THEMIS band 9 temperatures were converted to a thermal inertia by interpolation through a seven-dimensional lookup table, similar to that used for TES thermal inertia derivation (e.g., Putzig *et al.*, 2004; Fergason *et al.*, 2006b). The TES-based albedo and atmospheric dust opacity were used as input parameters to the lookup table, as well as MGS Mars Orbiter Laser Altimeter (MOLA) elevation values, all at a coarser resolution than that of the temperature data. The lower resolution in these parameters may alias THEMIS-scale variability. However, atmospheric pressure (derived from elevation) has only a second-order effect on the thermal inertia, and the atmospheric dust opacity is not expected to vary significantly over the area of a single THEMIS image (Clancy *et al.*, 2000; Smith *et al.*, 2001). Sub-pixel variations in TES-based albedo may affect the accuracy of individual thermal inertia values, and caution should be used when interpreting regions where albedo may be varying over short distances (less than 3 km). The effects of local slopes are not typically considered (Christensen *et al.*, 2003a, 2004a; Putzig *et al.*, 2004; Fergason *et al.*, 2006b) and may play a substantial role (Putzig and Mellon, 2007a). However, by including local slopes in the THEMIS thermal inertia calculations in a nonautomated manner, the accuracy of these calculations can be improved (Fergason *et al.*, 2006b).

The absolute accuracy of the THEMIS thermal inertia was estimated at 20% (Fergason *et al.*, 2006b) to 25% (Jakosky *et al.*, 2006). Comparisons between TES and THEMIS thermal inertia values have revealed not only random variations, but also systematic offsets of 10%–30% (Putzig *et al.*, 2004; Fergason *et al.*, 2006b). Random variations are easily explained by the scale difference, where higher resolution discerns larger local extremes that are washed out in a lower resolution areal average. Additionally, the noise equivalent delta temperature (NEΔT) is approximately 5 times larger for THEMIS than for TES (Christensen *et al.*, 1992, 2004a), and will contribute to random error. The systematic offsets are harder to explain. As with TES, uncertainties in the THEMIS-based thermal inertia values are primarily due to (1) instrument calibration, (2) uncertainties in assumed or interpolated parameters, such as albedo, and (3) numerical model uncertainties (Fergason *et al.*, 2006b; Jakosky *et al.*, 2006). Band-9 emissivity variations due to local changes in mineralogy may also play a role. Factors such as atmospheric pressure and dust opacity will affect all pixels in a THEMIS temperature image similarly. The systematic differences may be related to such atmospheric conditions or differences in instrument design, but may also be an indication of regionally distributed subpixel heterogeneity made apparent by observations at different times of day between THEMIS and TES (Putzig *et al.*, 2004; Fergason *et al.*, 2006b; Putzig, 2006).

Thermal inertia from the Mars Exploration Rovers

The MERs *Spirit* and *Opportunity* landed on Mars in January 2004, each carrying a Miniature Thermal Emission Spectrometer (Mini-TES; Christensen *et al.*, 2003b). Mini-TES is a 5–29 μm thermal-infrared spectrometer with 8 and 20 mrad fields of view. Spatial resolution depends on distance from the rover to the target and can be as small as 12 cm (Christensen *et al.*, 2004b). One goal of Mini-TES is to derive targeted thermal inertia values of rocks and soils at the landing sites to aid in operational decisions for further analysis and in science interpretations (Christensen *et al.*, 2003b). There are several advantages to Mini-TES thermal inertia over orbital observations. Surface temperatures can be recorded over most of a diurnal cycle on the same day, eliminating the effects of changing atmospheric conditions. In addition, Mini-TES provides an opportunity to validate orbital datasets and offers *in situ* insight regarding the interpretation of orbital thermal inertia data. With its ability to target observations, direct separation of soil types and rock components is possible at the highest resolution. Finally, direct imaging observations of soil particle size by the MER Microscopic Imager (MI) (Herkenhoff *et al.*, 2004a,b) and of rock textures by MER Panoramic Camera (Bell *et al.*, 2004a,b) can be compared with the derived thermal inertia of each target.

Thermal inertia values were derived from Mini-TES temperature data (Christensen *et al.*, 2003b) at the MERs landing sites at both Gusev crater and Meridiani Planum (Fergason *et al.*, 2006a). Both previously described methods of deriving thermal inertia were employed, fitting each to the diurnal cycle and to a single temperature observation, depending on the availability of temperature data. In the

case of fitting a diurnal cycle, temperatures were compared with a numerical thermal model varying thermal inertia and albedo to find a least-squares fit. In the case of a single temperature observation, more often acquired, a similar approach to that used for TES and THEMIS analysis was employed.

Uncertainties in Mini-TES thermal inertia have been estimated independently for the two methods used. For the case of single temperature observations, a total minimum uncertainty of 12% includes the RSS of uncertainties due to instrument accuracy, sensitivity to associated parameters (e.g., dust opacity), and surface slopes (Fergason *et al.*, 2006a). Additional uncertainties may occur in the atmospheric extinction of sunlight and downwelling thermal radiance. For the case of fitting to a diurnal cycle, uncertainties were estimated from the RMS residuals occurring in the diurnal fit. These uncertainties typically range from 14% to 23% (Fergason *et al.*, 2006a). However, since the method includes deriving an albedo that often departs slightly from the observed value in order to obtain a best fit (see also Palluconi and Kieffer, 1981), some of these errors are contained within the derived albedo. Another key difference between Mini-TES and other thermal inertia derivations is that the Mini-TES thermal inertia calculations utilize the highest value of spectral brightness temperature (outside of the atmospheric CO_2 absorption region), and thus spectral emissivity variation may play a role. In contrast, TES thermal inertia calculations reported here utilize bolometric temperatures, that are insensitive to emissivity (Mellon *et al.*, 2000), and THEMIS thermal inertia calculations utilize 12.57 μm (Band 9) temperatures where only spatial emissivity variations may play a role (Putzig *et al.*, 2004; Fergason *et al.*, 2006b).

18.5.5 Interpretations of thermal inertia

In this section we describe analysis of thermal inertia derived from TES, THEMIS, and Mini-TES temperature data on a variety of spatial scales. Mapping TES thermal inertia provides nearly global coverage on a 3 km scale. THEMIS thermal inertia, determined image-by-image has not yet been derived for global coverage, but supports local-scale interpretations at 100 m resolution. Mini-TES observations are limited to the two MER landing and roving regions; at the highest resolution they provide thermal inertia values of specific targets for comparison and extrapolation to global scales using orbital-based thermal inertia values.

Global view from TES

Figure 18.8 shows maps of thermal inertia derived from TES nighttime and daytime observations covering nearly 3 Mars years (Putzig and Mellon, 2007b). Clearly evident in the equatorial and middle latitudes are several large, continent-scale regions of low thermal inertia (<150), near Amazonis, Tharsis, Arabia Terra, and Elysium. An additional large expanse of low thermal inertia occurs in the south polar region nighttime map (Figure 18.8a). Encompassing most of the Martian surface are regions of moderate thermal inertia (150–400) which surround the low-thermal-inertia areas. Smaller, discontinuous patches of high thermal inertia (>400) include the floors or rims of several large impact basins (Hellas, Isidis, and Argyre), Valles Marineris and associated outflow channels, a large portion of Acidalia Planitia, numerous smaller impact craters, and the northern residual polar cap. These TES results are largely consistent with previous global-scale analysis of IRTM thermal inertia (see Palluconi and Kieffer, 1981; Paige and Keegan, 1994; Paige *et al.*, 1994; Jakosky *et al.*, 2000; Vasavada *et al.*, 2000). Weak north–south trending streak-like artifacts are evident in Figure 18.8 aligned with MGS orbital tracks (see Mellon *et al.*, 2000; Putzig *et al.*, 2005; Putzig and Mellon, 2007b). These patterns are the result of seasonal variations in apparent thermal inertia as orbit tracks from differing seasons cover adjacent terrain, and may be related to near-surface layering or sub-pixel horizontal mixing of materials (Putzig and Mellon, 2007b). Regardless of these effects, track-to-track repeatability and year-to-year repeatability are extremely good and the great deal of detailed geographic structure observed in Figure 18.8 well represents the Martian surface. While daytime thermal inertia values are similar in geographic distribution to the nighttime values, there are significant systematic offsets in thermal inertia between the daytime and nighttime maps that cover large contiguous regions. Equatorial and mid-latitude regions more often exhibit lower daytime thermal inertia values (up to a factor of 2), while polar regions typically exhibit significantly lower nighttime thermal inertia values (up to a factor of 10). In both regions offsets are much larger than the uncertainty in the thermal inertia derivation. In combination with seasonal patterns, these offsets are thought to indicate complex surface heterogeneity (see Putzig and Mellon, 2007b; Figures 18.6 and 18.7). Over much of the equatorial and mid-latitude regions, thermal inertia patterns suggest that the surfaces are dominated by layering with higher-thermal-inertia material on top, such as duricrust or desert pavements (see Putzig and Mellon, 2007b).

Figure 18.9 shows north and south polar orthographic projections for both daytime and nighttime maps. Two patterns are clearly evident. First, the occurrence of streak-like artifacts is most pronounced in the northern high-latitude regions relative to other locations around the planet, reflecting a stronger seasonal variation than in other regions. Second, the difference between daytime and nighttime thermal inertia values (in some locations exceeding $600\,J\,m^{-2}\,K^{-1}\,s^{-1/2}$) are greater in the high-latitude regions than elsewhere on the planet. Both of these observations may be due to layered heterogeneity such as near-surface water ice overlain by a thin veneer of ice-free soil (Putzig and Mellon, 2007b). Ice-cemented soil is expected to dominate the near-surface soils at these high latitudes based on the theoretical studies of ice stability (e.g., Leighton and Murray, 1966; Mellon and Jakosky, 1993; Mellon *et al.*, 2004) and on spacecraft observations of subsurface hydrogen (Boynton *et al.*, 2002; Feldman *et al.*, 2004; Chapter 6). Relative to unconsolidated soil, ice-cemented soil exhibits a

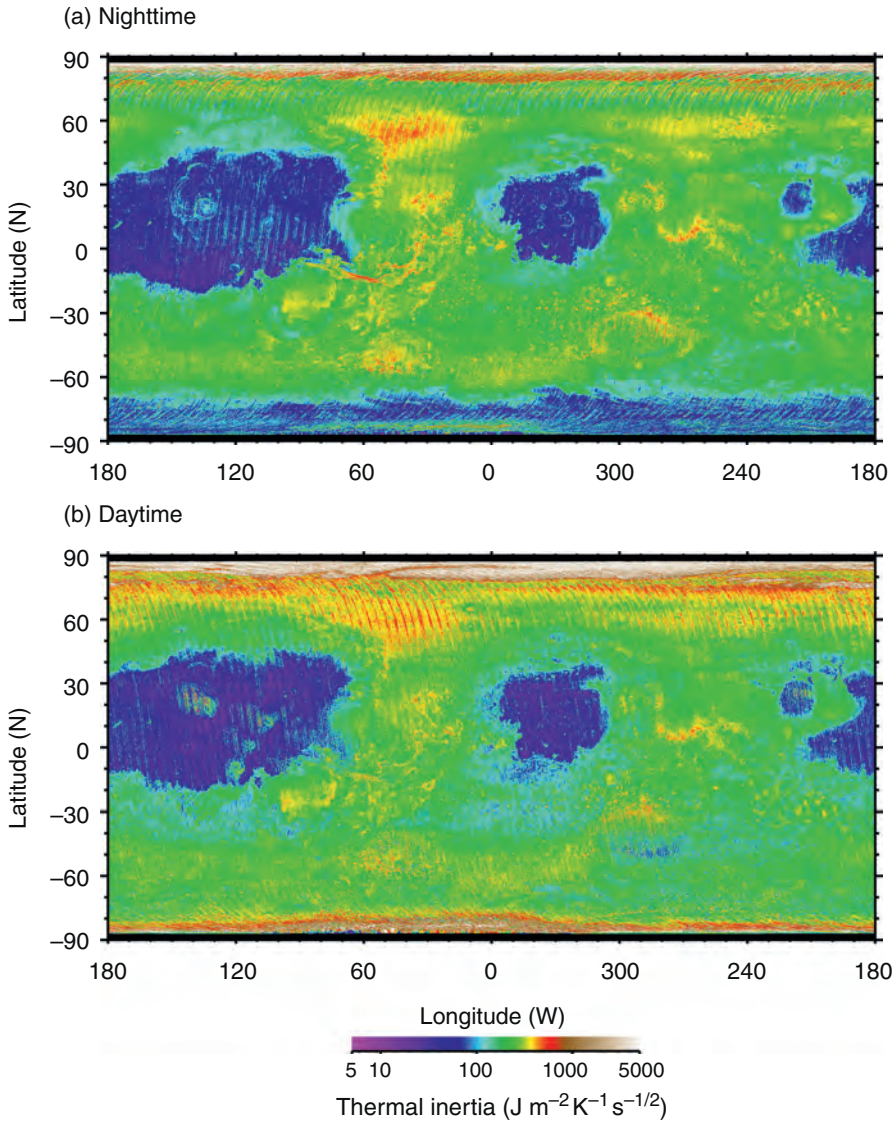

Figure 18.8. Global map of the thermal inertia of Mars based on TES (a) nighttime and (b) daytime bolometric brightness temperature observations (see Putzig and Mellon, 2007b). Maps are generated by a median filter of 36 seasons over 3 Mars years and are binned at 1/20° per pixel. Nighttime and daytime maps cover descending and ascending orbit track of the MGS spacecraft, respectively, and are also referred to nightside and dayside maps (Putzig and Mellon, 2007b). In the polar regions both maps contain thermal inertia results derived from temperature observations of an illuminated surface during polar summer. Local times transition between nighttime hours and daytime hours as the orbit track passes within a few degrees of the pole and transitions between the nightside and dayside orbit tracks. Large low-thermal-inertia regions (shades of blue) are believed to be dominated by surface dust deposits. Higher thermal inertias represent changes in soil grain size, duricrust, rocks, or some combination. Few areas exist indicating bedrock. Differences between nighttime and daytime maps may be related to surface heterogeneity. See text for discussion. (For a color version of this figure, please refer to the color plate section or to the e-Book version of this chapter.)

significantly higher thermal inertia (similar to that of rock) and if the ice-free soil veneer is shallower than a seasonal skin depth (a few centimeters to a few tens of centimeters), the apparent thermal inertia will be higher than that of unconsolidated soil and vary strongly with season and time of day (see, for example, Figure 18.7; Mellon and Putzig, 2007). Other forms of heterogeneity (surface rocks, slopes, and duricrust layers) can also play a role. Although examination of the seasonal variations in apparent thermal inertia is limited by the winter CO_2 frost at these latitudes, a low-thermal-inertia ice-free soil over an ice table is most consistent with these observations (Putzig and Mellon, 2007b).

Figure 18.10 shows an example of the full resolution of the TES nighttime thermal inertia (Figure 18.8a) for the central region of Valles Marineris, including Candor Chasma, Melas Chasma, and Ophir Chasma. Distinct thermal inertia differences are seen between the surrounding low-thermal-inertia plateau to the north (typically less than 120) and the higher-thermal-inertia values of the valley floor deposits (typically in the range of 200–400). Mellon *et al.* (2000) and Jakosky and Mellon (2001) examined the thermal inertia in this region and noted that, while this terrain exhibits some of the most diverse thermal inertia distributions on Mars, no obvious relationship between thermal inertia units and particular types of geologic units was found, aside from the gross contrast between the canyon interior and adjacent plateau. However, Chojnacki *et al.* (2006) observed that thermal inertia tends to be anticorrelated with elevation (see also elevation discussion below) within the canyon system, suggesting that focused winds and higher pressures have preferentially scoured the low elevations of dust, possibly forming a desert pavement (Mellon *et al.*, 2000). Close examination of some of the major landslide units in Ophir Chasma found that their associated TES thermal inertia is mostly consistent with a variety of unconsolidated debris (Chojnacki *et al.*, 2006). The highest thermal inertia values in Figure 18.10 are consistent with a number of small, multi-kilometer exposures of bedrock with thermal inertia values over 1200, and as high as 2700. These exposures occur in a variety of contexts from valley floor deposits as in western Melas Chasma, to spur and gully outcrops at the boundary between Melas and central Candor Chasma, to a number of

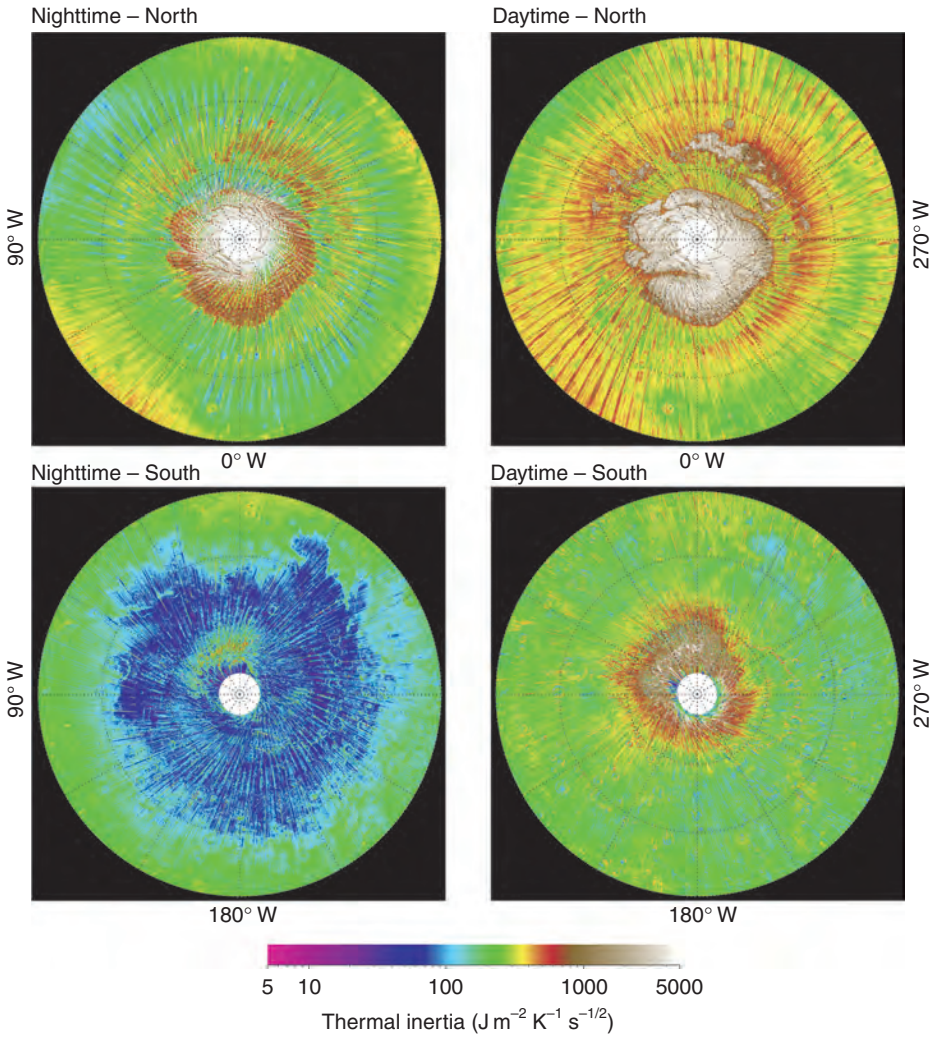

Figure 18.9. Polar orthographic maps of thermal inertia for both northern and southern hemispheres and both dayside and nightside ground tracks. Significant diurnal differences in the apparent thermal inertia are observed, suggesting subsurface layering or ice-rich permafrost beneath a soil veneer (Putzig and Mellon, 2007b; see text for additional discussion). Maps are shown between 60° and 90° latitude. See also Figure 18.8. (For a color version of this figure, please refer to the color plate section or to the e-Book version of this chapter.)

the smaller landslide deposits and exposures of wall rock. The high-thermal-inertia values suggest that these bedrock exposures are devoid of soil or air-fall dust over kilometers of terrain.

While surface properties such as thermal inertia are often considered independently, a better understanding of Martian surface materials can be obtained by comparing different types of data. For example, correlations of albedo or elevation with thermal inertia have been shown to provide useful constraints on interpretations of surface materials and geologic processes (Kieffer *et al*., 1977; Jakosky, 1979; Palluconi and Kieffer, 1981; Christensen, 1986b; Christensen and Moore, 1992; Mellon *et al*., 2000; Putzig *et al*., 2005). Comparisons of two datasets may be performed quantitatively by creating two-dimensional histograms to delineate areas with common features and to assign thermophysical units, which may then be mapped back to their surface locations.

Thermal inertia–albedo units. Analysis of Viking-based thermal inertia and albedo (Kieffer *et al*., 1977; Palluconi and Kieffer, 1981) revealed an inverse correlation, where regions of high albedo and low thermal inertia were proposed to be dominated by bright dust and regions of low albedo and high thermal inertia were dominated by less dust and more

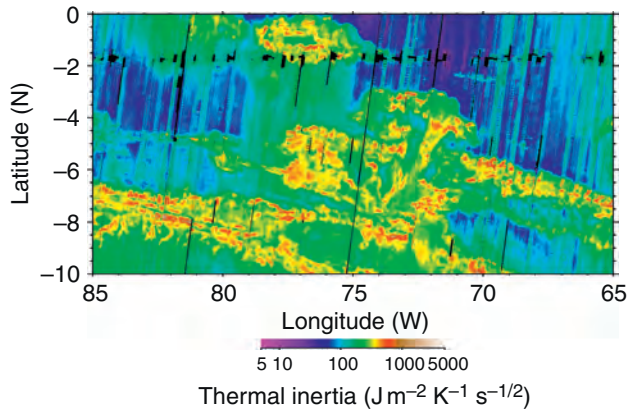

Figure 18.10. A full-resolution TES nighttime bolometric thermal inertia map of Candor Chasma, Melas Chasma, and Ophir Chasma in central Valles Marineris. These regions exhibit some of the most diverse thermal inertia values on Mars for a localized area. Individual 3 km TES footprints are visible. Map width is approximately 120 km. Evident in a number of small multikilometer areas are thermal inertia values in excess of 1200, indicating the presence of clean exposures of bedrock. (For a color version of this figure, please refer to the color plate section or to the e-Book version of this chapter.)

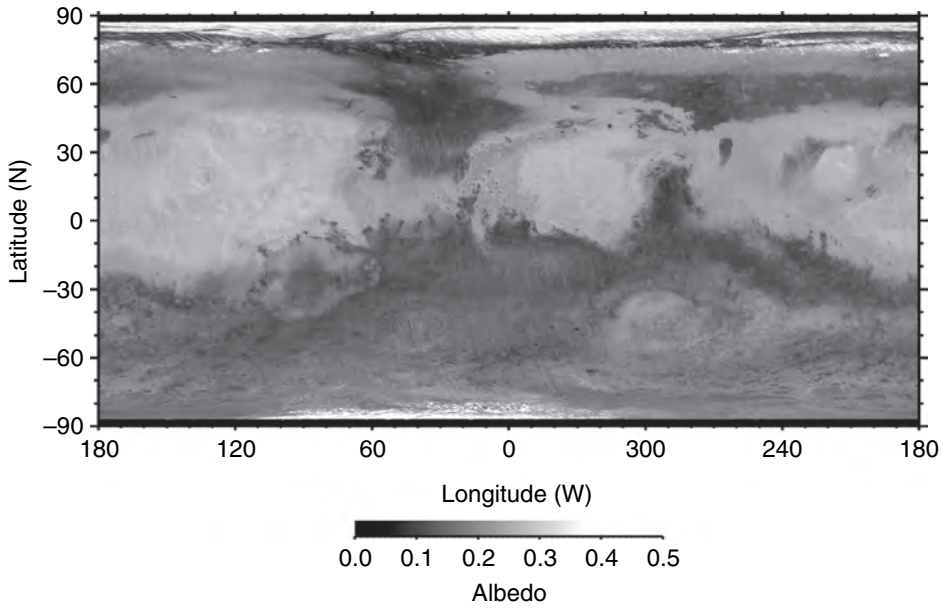

Figure 18.11. A global map of Mars albedo from TES visible bolometer observations during the third year of the MGS mapping mission (see Putzig and Mellon, 2007b). Fine-grained dust generally exhibit higher albedo than coarse-grained soils or rocks.

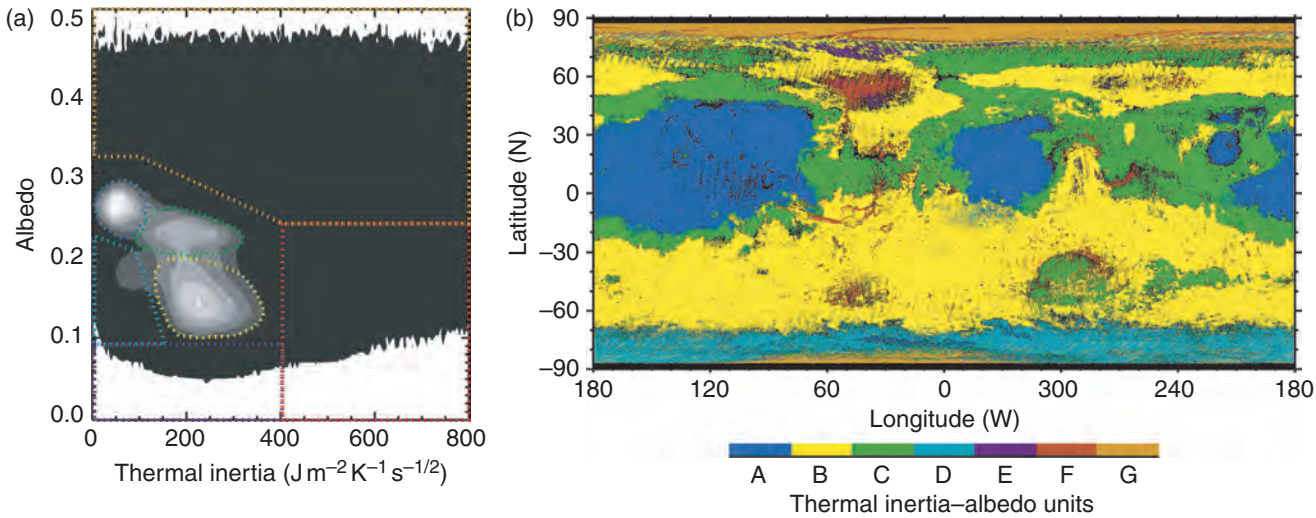

Figure 18.12. (a) A two-dimensional histogram of albedo and nighttime thermal inertia based on the maps shown in Figures 18.8a and 18.11, and (b) a thermophysical unit map based on this histogram (see Putzig, 2006). Shades of gray in the histogram indicate frequency of occurrence, with lighter shades indicating more frequent occurrence. Three major modes are evident: (Unit A) high albedo and low thermal inertia, (Unit B) low albedo and high thermal inertia, and (Unit C) intermediate albedo and high thermal inertia (see Mellon *et al.*, 2000; Putzig *et al.*, 2005). Other less-dominate units (D–G) are also shown – see text and Table 18.2 for discussion. Histogram bin sizes are 0.01 for albedo and 5 for thermal inertia. Levels are 1 occurrence and 1/20, 1/10, 1/5, 1/3, and 1/2 of the maximum frequency. (For a color version of this figure, please refer to the color plate section or to the e-Book version of this chapter.)

rocks (see also Christensen and Moore, 1992). Mellon *et al.* (2000) compared TES thermal inertia with TES-based Lambert albedo (Christensen, 1999), confirmed the bimodal inverse correlation, and identified a third pronounced mode of intermediate albedo and high thermal inertia (Unit C discussed below) that was not apparent in Viking data at lower resolution, partly due to clearer atmospheric conditions during the TES observations. Mapping these thermophysical units showed that they fell in distinct geographic regions suggesting distinct soil surfaces. Putzig *et al.* (2005), incorporating significantly more geographic coverage in the TES-based thermal inertia map and a higher resolution albedo map (e.g., Figure 18.11; Pelkey and Jakosky, 2002), mapped seven global thermal inertia–albedo units. They confirmed the three major modes of distinct albedo and thermal inertia characteristics identified previously and further delineated four minor units. Figure 18.12 shows the current version of this histogram and unit map, utilizing data from Figures 18.8 and 18.11.

The major thermophysical units in Figures 18.12a and 18.12b are regions of (A) low thermal inertia and high albedo, (B) high thermal inertia and low albedo, and (C) high thermal inertia and intermediate albedo (Table 18.2). Together, these units compose about 78% of the Martian surface. Unit A has been proposed to be composed primarily

Table 18.2. *Thermophysical units*

Unit	Inertia ($J\,m^{-2}\,K^{-1}\,s^{-1/2}$)	Albedo	Coverage[a] (%)	Interpretation
A	Low (5–116)	High (0.22–0.29)	18	Bright unconsolidated fines
B	High (134–364)	Low (0.10–0.20)	39	Sand, rocks, and bedrock; some duricrust
C	High (93–320)	Med. (0.20–0.26)	21	Duricrust; some sand, rocks, and bedrock
D	Low (5–154)	Low–med. (0.09–0.22)	2.6	Low density mantle
E	High (5–403)	Very low (<0.09)	0.2	Similar to B, but little or no fines
F	Very high (>403)	Low–med. (<0.24)	3.3	Rocks, bedrock, duricrust, and polar ice
G	Low–high (>5)	Very high (>0.24)	1.1	Similar to A, possibly thin and discontinuous with higher thermal inertia

[a] Coverage includes only areas that fall within the unit boundaries as defined in Figure 18.12a.

of fine-grained unconsolidated material (e.g., Kieffer *et al.*, 1977; Zimbelman and Kieffer, 1979; Palluconi and Kieffer, 1981; Christensen, 1982). Dust with a mean particle size of <40 μm is consistent with the low thermal inertia; larger particles, more than a few rocks, or any degree of consolidation would raise the thermal inertia above that which is observed (Christensen, 1986a; Jakosky and Christensen, 1986a). The depth of these deposits would need to exceed at least a thermal skin depth or more, else the surface temperatures and derived thermal inertia values would be higher due to influences of subsurface layers or buried rocks. For an intermediate thermal inertia of 75 and assuming nominal density and heat capacity, a diurnal skin depth for these deposits would be about 1.2 cm. Alternatively, a lower-thermal-inertia finer dust could more thinly blanket the surface, resulting in an observed apparent thermal inertia that is intermediate (see nonideal surface discussion above). Radar data also suggest a 1–2 m thick, low-density material blankets these regions (Christensen, 1986a; Christensen and Moore, 1992), suggesting thick deposits of dust. In addition, a thin deposit (high thermal contrast layered structure) would exhibit large seasonal variability in apparent thermal inertia (e.g., Figure 18.7b), while only small variability is observed (Putzig and Mellon, 2007b). However, it remains possible that very fine dust blankets moderately fine dust in these regions, which would be consistent with the low eclipse-based thermal inertia determined by Betts *et al.* (1995).

The higher thermal inertia, Unit B, is more complex, as many factors can act to raise the thermal inertia. Researchers have proposed this unit to be composed of some combination of additional surface rocks or exposures of bedrock, larger particle sizes, and/or indurated fines forming a duricrust (e.g., Kieffer *et al.*, 1977; Palluconi and Kieffer, 1981; Christensen, 1986a; Jakosky and Christensen, 1986a; Christensen and Moore, 1992). Rock abundance analysis (Christensen, 1986a) showed that, while there is a correlation between thermal inertia and rock abundance, the fine component dominates the bulk thermal inertia of the field of view, particularly for the generally low rock abundances that were observed. Therefore, the fine component or nonrock component is primarily distinguished in the bulk thermal inertia. While higher thermal inertia values may indicate the presence of rock, other soil textures (e.g., larger particles and induration) are playing a dominant role.

The high-thermal-inertia and intermediate albedo unit, Unit C, represents a distinct surface unit (Mellon *et al.*, 2000). As seen in Figure 18.12b, the geographic distribution of Unit C tends to form a transitional band between the low thermal inertia of Unit A and the high thermal inertia of Unit B. While this proximity suggests a genetic relationship, such as a gradual thinning of dust making up Unit A and exposing Unit B soils, a closer inspection of the clustering of Unit C in the histogram (Figure 18.12a) indicates a distinct type of surface separate from Units A and B. An alternative hypothesis is that Unit C is partly or entirely composed of a thicker dust or soil deposit that has become cemented and darkened by the cementing process. Other studies have suggested such indurated soils dominate these same regions based on thermal inertia, color, and the sparseness of aeolian geomorphology (e.g., Presley and Arvidson, 1988; Arvidson *et al.*, 1989; Christensen and Moore, 1992; Merényi *et al.*, 1996). The dark red color in these regions differs from the bright red color of Unit A dust or the dark gray color of high-thermal-inertia regions, Unit B. The average thermal inertia of Unit C, if interpreted as unconsolidated particles, would indicate a particle size easily mobilized by wind; yet there is a general absence of aeolian landforms, suggesting a resistance to erosion due to cementing of soil particles (Presley and Arvidson, 1988). The boundaries of these study areas in Oxia Palus, Lunae Planum, Xanthe Terra, and Deucalionis Regio (Presley and Arvidson, 1988; Arvidson

et al., 1989; Christensen and Moore, 1992; Merényi *et al.*, 1996) correspond well to Unit C boundaries (Mellon *et al.*, 2000).

The minor units in Figure 18.12 represent outliers of thermal inertia and albedo which are subdivided into regions of (D) low thermal inertia and low-to-intermediate albedo, (E) very low albedo, (F) very high thermal inertia, and (G) very high albedo (Putzig *et al.*, 2005). In the south polar region, Unit D dominates the terrain (see also Figure 18.9c). It exhibits relatively sharp thermal inertia boundaries with Units B and C, suggesting that it represents a distinct type of surface. Based on nighttime thermal inertia alone, there is little to distinguish Unit D from Unit A. However, fine-grained materials on Mars normally exhibit high albedo (typified by Unit A), whereas Unit D exhibits a lower albedo, similar to that of Unit B. The most plausible physical explanation is that Unit D represents a surface of either coarse materials or duricrust in which the bulk thermal conductivity has been lowered. From Equation (18.9), Putzig *et al.* (2005) found that the 2-fold reduction in thermal inertia from Unit B to Unit D requires a 2.5-fold reduction in bulk density. Recent estimates from Mars Odyssey Neutron Spectrometer data indicate 75% by volume of ice occurs within the top meter of the Martian surface in the south polar region (e.g., Boynton *et al.*, 2002) and within ~10 cm of the surface (e.g., Prettyman *et al.*, 2004). Present-day ice instability in the upper few centimeters (Mellon and Jakosky, 1995; Mellon *et al.*, 2004) may have allowed once stable ice from a period of high obliquity to sublimate away in the present epoch, leaving an extremely porous soil structure. Analogous sublimation processes found on Earth result in filamentary sublimate residues (very-high-porosity phyllosilicates with relatively high tensile strength) that exhibit similar reductions in density, both in laboratory experiments (Storrs *et al.*, 1988) and at field locations in Alaskan permafrost (Johnson and Lorenz, 2000). Mars Orbiter Camera images showing terrain softening within Unit D and a dissected near-surface layer to the north of Unit D (Mustard *et al.*, 2001) lend support to this concept of a low-density mantle. Similar interpretations have also been suggested by previous workers using lower-resolution IRTM-based thermal inertia results (Paige and Keegan, 1994; Vasavada *et al.*, 2000). The strong diurnal signature apparent in Figures 18.9c and 18.9d also suggests that a relatively thin mantle overlies a high-thermal-inertia substrate, consistent with buried ice beneath a desiccated layer (Putzig and Mellon, 2007b).

The other outlying units (E–G) have relatively simple interpretations. Unit E has very low albedo, with thermal inertia values similar to those in Unit B. Geographically, it is found in moderate- to small-sized regions which are almost exclusively surrounded by Unit B (see Figure 18.12). Thus, Unit E is interpreted as representing the near-absence of unconsolidated fines in these areas (i.e., a higher proportion of dark coarse materials, such as bedrock and duricrust). Unit F, defined by very high thermal inertia, is found in Valles Marineris and nearby outflow channels, parts of Acidalia, within several large impact basins (Argyre, Hellas, Isidis) and smaller intercrater deposits, near-surface water ice in Vastitas Borealis, and on the exposed water ice of the residual polar caps. Unit F is generally surrounded by Units B and C and has thermal inertia values suggestive of surfaces dominated by very coarse-grained or highly indurated materials and bedrock or water-ice exposures. Unit G has very high albedo and occurs predominantly in areas flanking the large volcanic structures (Tharsis, Olympus Mons, and Elysium), in association with Unit A. Its high albedo suggests that Unit G represents deposits of the finest dust, which may be thin or horizontally discontinuous where its thermal inertia is high.

Thermal inertia–elevation units. Studies of thermal inertia and elevation have shown a weak correlation (Jakosky, 1979; Palluconi and Kieffer, 1981; Mellon *et al.*, 2000). Over much of Mars, the distribution of thermal inertia over elevation is similar, with both low- and high-thermal inertia terrains occurring at all elevations except the highest and lowest. At the highest elevations, the surface is dominated by low-thermal-inertia values, while at the lowest elevations the surface is dominated by the highest thermal inertia values. The high-elevation trend may be partly related to the dependence of thermal inertia on pressure (e.g., Wechsler and Glaser, 1965; Jakosky, 1986; Bridges, 1994; Presley and Christensen, 1997a), where lower atmospheric pressures result in lower thermal conductivity, and to the potential for dust settling out of the atmosphere to become trapped on high-elevation surfaces (Zimbelman and Kieffer, 1979; Christensen, 1986b). Conversely, at the lowest elevations winds at higher atmospheric pressures can cause surface sand to more easily saltate, and thereby preferentially strip the surface of loose dust (Christensen and Moore, 1992). Putzig *et al.* (2005) conducted a quantitative comparison of thermal inertia with elevation (Figure 18.13; see also

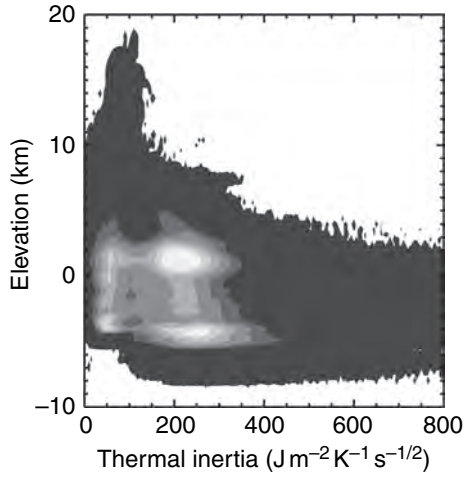

Figure 18.13. A 2D histogram of TES-based nighttime thermal inertia (Figure 18.8a) and MGS MOLA elevation (see Putzig, 2006). Shades of gray indicate frequency of occurrence. Over most of Mars high and low thermal inertia values occur at all elevations. Exceptions are that the highest elevations (mountain peaks) are dominated by lower thermal inertia values and that the lowest elevations are dominated by higher thermal inertia values. See text for additional discussion. Histogram bin sizes are 400 m for elevation and 5 for thermal inertia. Levels are 1 occurrence and 1/20, 1/10, 1/5, 1/3, and 1/2 of the maximum frequency.

Putzig, 2006). The histogram shows four nearly aligned modes, indicating a bimodal distribution of both parameters and demonstrating that the vertical distribution of thermal inertia is fairly uniform, consistent with earlier analyses. However, the very lowest thermal inertia values (<30) occur only at lower elevations (between −5 and 3 km), indicating that atmospheric pressure is not the only factor controlling the bulk conductivity and vertical distribution of fine particles.

In comparison of the elevation analysis with the albedo and thermal inertia units, Mellon *et al*. (2000) found that all three major thermophysical units (A–C) occur at all elevations between −4 and 6 km, covering the majority of the Martian surface. A large portion of Unit C occurs at lower elevations, −5 to −1 km, suggesting that atmospheric processes or conditions may influence its formation. Putzig *et al*. (2005) showed that the mode of low elevation and low-thermal-inertia mode (Figure 18.13) often occurs westward of more elevated features such as Tharsis, Arabia, and Elysium, which also exhibit low thermal inertia, supporting suggestions based on Viking data and atmospheric models that these regions may act as atmospheric dust sinks (Christensen, 1986b; Kahn *et al*., 1992; Zurek *et al*., 1992).

Comparisons with other data. Correlations between thermal inertia and other datasets were examined using IRTM thermal inertia to gain deeper insight into the Martian surface layer (see Christensen and Moore, 1992). While rock abundance is not the primary factor controlling thermal inertia (e.g., Golombek *et al*., 2003), a weak correlation was observed with rock abundance as determined from spectral contrast in the brightness temperature (Christensen, 1986a). In general, darker regions with higher thermal inertia tend to have more rocks, though some regions such as Syrtis Major are an exception, while brighter regions of low thermal inertia tend to be more rock-free (Christensen, 1986b). Earth-based radar measurements of the reflectivity and dielectric constant of the Martian surface at wavelengths between 3.8 and 70 cm correlate with thermal inertia in the majority of regions (Jakosky and Muhleman, 1981). Since the dielectric constant is strongly density-dependent, this correlation could indicate the degree of packing, cementation of the soil grains and pore filling, or a relationship with near-surface rocks (Jakosky and Christensen, 1986a, 1986b). However, some of the weaknesses in the correlation could result from differences in sensing depth (Jakosky and Christensen, 1986b), with thermal inertia being mostly sensitive to the upper diurnal skin depth (a few millimeters to a few centimeters) and radar most sensitive to the upper wavelength (a few centimeters to about 1 m). Color correlations were also done, noting that Mars is dominated by bright-red, dark-red, and dark-gray color units (Arvidson *et al*., 1982). Bright-red regions tend to cluster with low thermal inertia, indicative of regional dust deposits (Unit A discussed above). Dark-red surfaces appear to correlate with intermediate-thermal-inertia Unit C and may be indicative of duricrust (Presley and Arvidson, 1988; Arvidson *et al*., 1989).

Regional view from THEMIS

THEMIS thermal inertia images enable an improved quantification of fine-scale geomorphic detail observed in high-resolution visible images, and offer near-global coverage at 100 m/pixel resolution. While global 100 m coverage of derived thermal inertia has not yet been accomplished, local THEMIS-based thermal inertia images provide insight into geologic structures and processes seen in high-resolution visible images. To highlight some of the thermophysical units discussed above, example of dust-mantled surfaces, bedform material, and local outcrops of bedrock are examined by 100 m resolution thermal inertia data.

Unit A: dust-mantled surfaces in Tharis Montes. The Tharsis region is part of the largest low-thermal-inertia expanse on Mars. Fergason *et al*. (2006b) examined a portion of this region (near 99.5° W, 7° N) and found it to have both a uniform low thermal inertia of 90–115 and high albedo of 0.29–0.31, corresponding to thermophysical Unit A (discussed above). The combination of thermal inertia and albedo and their uniformity indicates that a layer of dust greater than a few centimeters thick dominates the surface. A dust cover index (DCI) of 0.93–0.94 also indicates that fine, unconsolidated material is present on the surface (Ruff and Christensen, 2002); the DCI represents the average TES emissivity in the 9 μm dust band and globally ranges from about 0.9 to 1.0, with lower values indicating a stronger dust spectral signature. Visible images from the Mars Orbiter Camera on MGS show lava flow textures, such as flow fronts and variable amounts of surface degradation (Malin and Edgett, 2001). However, the uniformity of thermal inertia at THEMIS resolution suggests a minimum dust thickness sufficient to thermally mask the underlying material (one to a few centimeters). Since geomorphic textures are still visible, such as 10–500 m craters, unconsolidated dust is not more than 1 or 2 m thick, consistent with previous estimates (e.g., Christensen, 1986b), and is potentially thinner in many locations (Fergason *et al*., 2006b).

Unit B: bedform material. Aeolian activity currently dominates the Martian surface (e.g., Malin and Edgett, 2001). Fergason *et al*. (2006b) examined aeolian bedforms and consolidated surface material within a crater centered at about 357° W, 26.5° N (Figure 18.14). The aeolian material occurs as low-albedo sand sheets and dune bedforms, or between otherwise inactive, nonaeolian surfaces. Nonaeolian surface material may consist of partially indurated soils (dust or sand), and may contain smaller bedrock exposures intermixed with unconsolidated soil resulting in a lower thermal inertia than expected for bedrock alone (see Figure 18.5); the thermal inertia of these surfaces does not exceed 465 indicating an absence of clean bedrock outcrops at the 100 m scale. The aeolian bedforms have the lowest thermal inertia values within the studied region, from 230 to 340. While the large scale sand sheet and bedform features are resolved in TES-based 3 km thermal inertia maps, the smaller scale bedforms and the juxtaposition between bedforms, sand sheets, and nonaeolian surfaces becomes clearly apparent in THEMIS

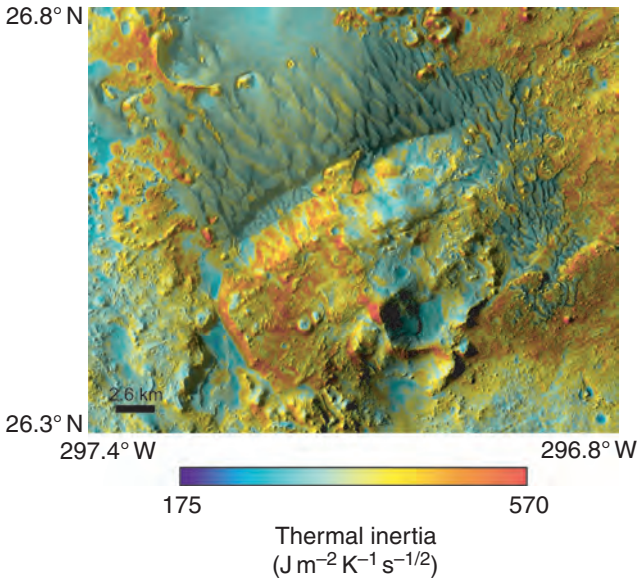

Figure 18.14. THEMIS-based thermal inertia (100 m resolution) superimposed on a THEMIS visible image mosaic (18 m resolution), located near 26.5° N × 357° W. Shown are the thermal inertia contrasts between dune bedforms, sand sheets, and nonaeolian surfaces. These major surface units exhibit thermal inertia values ranging from 230 to 465, although a few outlier surfaces exist with thermal inertia values from 175 to 570. See text and Fergason *et al.* (2006b) for more discussion. (For a color version of this figure, please refer to the color plate section or to the e-Book version of this chapter.)

data. The sand sheet at the north end of the deposit exhibits a thermal inertia of 230–270, suggesting particle diameters of ~290–575 μm corresponding to medium to coarse sand (Fergason *et al.*, 2006b; see also Equation (18.9); correlation between particle size and thermal inertia depends slightly on assumptions about density and heat capacity). The bedforms have a low albedo of 0.11–0.12 and a high DCI of 0.98 (Ruff and Christensen, 2002), suggesting that little dust is present. Although there is currently no direct evidence that these aeolian bedforms are presently active, the active migration of bedform features and sand saltation would prevent dust accumulation on their surface (Greeley *et al.*, 1992), consistent with the thermal inertia and DCI observations. The sand and small bedforms between the nonaeolian surfaces exhibit thermal inertia values between 230 and 340, suggesting particle diameters of ~290–1500 μm (Fergason *et al.*, 2006b). The higher thermal inertia range of smaller bedforms may also be due to duricrust-cementing of smaller grains of an otherwise inactive dune (e.g., Malin and Edgett, 2001; Wilson and Zimbelman, 2004). Alternatively, consolidated soils, rocks, and bedrock may be exposed between the smallest dunes on a scale smaller than 100 m.

Unit F: exposed bedrock. The identification of bedrock provides an opportunity to study the chemical and physical characteristics of *in situ* rock and rock-forming minerals, and to better constrain the geologic history. The thermal inertia of common volcanic rock materials ranges from approximately 1300 to more than 2500 (see Table 18.1). At TES 3 km resolution, very few locations on Mars exhibit thermal inertia values indicative of expanses of exposed bedrock (Mellon *et al.*, 2000; Putzig *et al.*, 2005), limited largely to regions in Valles Marineris (see also Figure 18.10). However, at THEMIS 100 m resolution the identification of smaller bedrock exposures becomes possible. High-thermal-inertia surfaces (greater than ~1200), indicating potential exposed bedrock, have been identified with THEMIS data (e.g., Christensen *et al.*, 2003a; Rogers *et al.*, 2003; Edwards *et al.*, 2005), ranging in size and exposed in a variety of geologic settings.

Christensen *et al.* (2003a) and Fergason *et al.* (2006b) examined the THEMIS thermal inertia in Nili Patera (293° W, 9° N), which forms the northern-most caldera on the summit of Syrtis Major. This feature is near the limit of TES resolution, but exhibits higher than average thermal inertia values. Of particular interest, THEMIS thermal inertia values as high as 1180 are observed in the eastern portion of the caldera. Rogers *et al.* (2005) and Fergason *et al.* (2006b) examined potential bedrock exposures in Ares Valles, about 250 km downstream of the Pathfinder landing site. While reported thermal inertia values are as high as 950, these values fall just under their ~1200 definition of bedrock, suggesting that bedrock is present, but that any clean bedrock exposures exist at lower spatial resolution. Hynek (2004) reported extensive bedrock in Terra Meridiani; however, his reported THEMIS thermal inertia of ~360 falls far short of that of rock and is more consistent with a variety of soil surfaces with little areal exposure of bedrock (Jakosky *et al.*, 2006). Rogers *et al.* (2003) and Edwards *et al.* (2005) surveyed inertia THEMIS thermal images for temperatures consistent with exposed bedrock. They found numerous potential bedrock locations planet wide ranging in size from hundreds of meters to kilometers. Typically, these locations included valley and crater walls and floors consistent with exposed wall rock and impact melt sheets, within chaotic terrain, and in a number of otherwise largely featureless plains.

Combined regional studies

Polar ices are an important component of the Martian climate. Included in Unit F described above, the polar caps exhibit some of the highest thermal inertia values on the planet, indicative of surface water ice. The surface of the residual north polar cap is known to consist of water ice based on warm temperatures and high humidity in the summer (Farmer *et al.*, 1976, Kieffer *et al.*, 1976). Based on IRTM seasonal temperature data, Paige and Ingersoll (1985) estimated the polar cap thermal inertia to be around 1250 ± 400. Paige *et al.* (1994), Paige and Keegan (1994), and Vasavada *et al.* (2000) derived and mapped polar thermal inertia from IRTM data at ½° spatial resolution. On both residual polar caps, they reported high-thermal-inertia values. At the north residual cap, believed to be exposed water ice, the thermal inertia values were as high at 2000, also consistent with solid water-ice deposits at the surface. The south residual cap, however, is covered mostly by CO_2 frost at these resolutions, which experiences no significant diurnal

temperature cycles, and the resulting high apparent thermal inertia values were attributed to the presence of frost (Paige and Keegan, 1994). Latent heat released by CO_2 frost buffers the surface temperature at the frost point, preventing diurnal or seasonal temperature cycles, and resulting in artificially high thermal inertia. However, analysis of TES seasonal temperature data along the edge of the south residual cap indicates thermal inertia values between 1600 and 2000, and in conjunction with THEMIS temperature observations well above the CO_2 frost point indicates water ice may be exposed at the surface (Titus *et al.*, 2003). Similar arguments were made by Armstrong *et al.* (2005) that deposits within Korolev crater in the northern polar regions are largely ice-rich, with thermal inertia values in excess of 1000.

Aeolian processes are perhaps the most active geologic process on Mars today. Aeolian features such as intracrater dune deposits, crater-related wind streaks, sand sheets and dune fields, and the north polar erg are observed to be widespread and varied in form and size (Greeley *et al.*, 1992; Malin and Edgett, 2001). The observed movement of sand-size particles at the MER-*Spirit* landing site in Gusev crater (e.g., Arvidson *et al.*, 2006; Greeley *et al.*, 2005), dust devil activity (e.g., Thomas and Gierasch, 1985; Malin and Edgett, 2001; Fisher *et al.*, 2005), and wind streak variability (e.g., Sagan *et al.*, 1972; Thomas *et al.*, 1981; Pelkey *et al.*, 2001) all suggest the presence of a wind regime favorable to aeolian activity. Indeed, particles of order 100 μm in diameter are most easily moved by the low-pressure atmosphere observed on Mars (Greeley *et al.*, 1980), and corresponds to a thermal inertia of about 200 (see Equation 18.9 and assuming a density of $1500\,kg\,m^{-3}$ and a heat capacity of $850\,J\,kg^{-1}\,K^{-1}$, see also Table 18.1). Aeolian deposits are commonly observed in topographic hollows (e.g., Malin and Edgett, 2001; Arvidson *et al.*, 2006). In addition, continental-scale dust deposits (e.g., Unit A discussed above) suggest widespread trapping of fine-grained material with particles sizes smaller than 40 μm (Zimbelman and Kieffer, 1979; Palluconi and Kieffer, 1981; Christensen, 1982).

Since aeolian processes naturally sort particles sizes, some aeolian landforms allow consideration of a direct relationship between thermal inertia and particle size (e.g., Kieffer *et al.*, 1973; Presley and Christensen, 1997a; see also the bedform discussion above). Intracrater dark "splotch" deposits were found to exhibit visible bedforms and high IRTM thermal inertia suggesting fine- to medium-sand-sized particles (~160–360 μm), also easily moved by wind (Christensen and Kieffer, 1979; Zimbelman and Greeley, 1982; Edgett and Christensen, 1994). Fenton *et al.* (2003), Fenton and Fergason (2004), and Fenton and Mellon (2006) examined TES and THEMIS data specifically for Proctor crater dunes and found higher thermal inertia values indicative of particles twice as large. Zimbelman (1986) examined the IRTM thermal inertia of the Pettit wind streak and associated intracrater deposits, suggesting bedforms composed of 250–350 μm sand; Mellon *et al.* (2000) examining TES-based thermal inertia of Pettit and suggested particles as large as 900 μm, with this larger-size estimate believed to be a result of the higher resolution of TES data relative to IRTM. Pelkey *et al.* (2001) examined the TES-based thermal inertia of Type I and Type II wind streaks (as classified by Thomas *et al.*, 1981). They found that Type 1 bright and dark streaks are not distinguishable in thermal inertia, suggesting that they are very thin, while Type II dark streaks are thermally distinct and must be thicker than a few centimeters. The north polar erg exhibits lower IRTM thermal inertia than other dune fields on Mars suggesting smaller particles (Paige *et al.*, 1994; Herkenhoff and Vasavada, 1999). These anomalous values may be related to atmospheric effects not fully modeled (Paige *et al.*, 1994), or to the formation of low-density sublimation residues (Herkenhoff and Vasavada, 1999). Similarly, low-density sublimation residues (Storrs *et al.*, 1988) were also suggested for TES-based low-thermal-inertia deposits (of nonbedform surfaces) in the southern high latitudes (Putzig *et al.*, 2005). However, subsurface layering and other heterogeneity may also play a role at these latitudes.

The view from the ground (Mini-TES). Thermal inertia values were derived from Mini-TES temperature observations of selected dust deposits, dune bedforms, and rock targets at both of the MER landing sites, representing a variety of the surface types observed during the primary mission. Mini-TES-based thermal inertia provides an excellent opportunity to validate inferences about thermal inertia of different materials. Thermal inertia derived *in situ* also provides ground truth for orbital observations and interpretations, such as those from IRTM, TES, and THEMIS.

The MER Lander *Spirit* at Gusev crater encountered a rock-strewn plain with ubiquitous soils, aeolian drifts, and near-circular impact hollows containing mostly fines (Arvidson *et al.*, 2004a; Grant *et al.*, 2004; Squyres *et al.*, 2004a). Thermal inertia values of about 150 were derived from Mini-TES temperature observations of the interior soils of the hollows implying that they contain fine material (Fergason *et al.*, 2006a). These hollows contain some of the finest material observed by *Spirit*, interpreted as a combination of air-fall dust and locally derived or locally transported fines (e.g., Grant *et al.*, 2004). Bedforms observed on the floors of craters exhibit thermal inertia values closer to 200, consistent with particles approaching 160 μm in diameter (Fergason *et al.*, 2006a). Since particles near 100 μm in size are most easily moved by wind in the current atmosphere (see Greeley *et al.*, 1980), these bedforms may have formed under present-day atmospheric conditions. The thermal inertia of the Gusev-plains rock-target Bonneville Beacon is about 1200, consistent with a dense, basaltic rock (Fergason *et al.*, 2006a). The rocks at the lower Columbia Hills exhibit lower thermal-inertia values (average ~620). These rocks have physical characteristics consistent with volcaniclastic sediments, ash flow deposits, or impact debris, suggesting a volcaniclastic origin (e.g., Arvidson *et al.*, 2006). This consistency with morphologic textures demonstrates that thermal inertia can be used to differentiate between rocks of different types and formation histories.

Microscopic Imager data were acquired for Mini-TES soil targets allowing a direct comparison between the effective particle sizes derived from thermal inertia values (Fergason *et al.*, 2006a) and sizes measured directly using MI images

(Herkenhoff *et al.*, 2004a). Effective particle sizes can be determined from Mini-TES-derived thermal inertia by inverting Equation (18.9) (Fergason *et al.*, 2006a). Uncertainty in this approach was estimated at 10%–15% (Presley and Christensen, 1997a). However, Equation (18.9) was empirically derived from measurements of uniform glass beads, and real soils are typically composed of irregular grains with complex grain-to-grain contacts and mixtures of particle sizes unless well sorted by geologic processes. Assumptions about density, heat capacity, uncertainty in atmospheric pressure, and uncertainty in the derived thermal inertia also have some effect on effective particle size estimates. Likewise, particle sizes determined from MI images are limited by the resolution of the MI camera (31 μm), the need for at least 3–4 pixels to identify a grain, and ±1 pixel uncertainty in the grain measurement (Herkenhoff *et al.*, 2004a). Soil grains can be measured down to diameter of 100–120 ± 31 μm.

At Gusev crater, MI images in the hollows indicated that the majority of the particles were at or below 100 μm (Herkenhoff *et al.*, 2004a). In comparison, particle sizes of ~45 μm (very fine sand to silt size) were estimated from Mini-TES thermal inertia (Fergason *et al.*, 2006a). Gusev plains soil is generally very fine grained or conglomerates of grains at the margin of MI resolution (Herkenhoff *et al.*, 2004a). Mini-TES estimates of the grain size of these soils, ~160 μm, are also in general agreement with the MI results. Two aeolian bedforms, Saber and Serpent, were observed near the rim of Bonneville crater at Gusev (Squyres *et al.*, 2004a; Greeley *et al.*, 2004). Rover-wheel excavation of Serpent revealed a layered stratigraphy, with a coarse outer armor over finer-grained particles (Greeley *et al.*, 2004). The bedform Saber likely has a similar subsurface because of the similar appearance, temperature, morphology, and proximity of these bedforms. Mini-TES-based thermal inertia of the undisturbed Saber bedform is 250, corresponding to a particle diameter of ~420 μm, medium sand (Fergason *et al.*, 2006a). MI images of Serpent indicate a tri-modal distribution of particle sizes of 1–2 mm, 250–500 μm, and below 210 μm (Herkenhoff *et al.*, 2004a). While the presence of a coarse outer armor of 1–2 mm particles will increase the bulk thermal inertia, the armor is thin and the finer-grained substrate tends to dominate the Mini-TES thermal inertia signature. In contrast, when a material with a range of particle sizes is uniformly mixed, laboratory measurements show that the bulk thermal conductivity and thermal inertia are dominated by the largest grains (Presley and Christensen, 1997b; Presley and Craddock, 2006).

Comparison of lander-based thermal inertia and that derived from orbit can yield insight about the nature of remotely sensed data and allow extrapolation of the inferred properties over the globe. While a wide range of thermal inertia values exist over the Gusev crater region from roughly 100 to 500 (Jakosky and Mellon, 2001; Martinez-Alonso *et al.*, 2005), the TES- and THEMIS-based thermal inertia at the *Spirit* landing site is 280–320, suggesting that the surface is dominated by cemented soil, noncohesive coarse sand, or a combination (Christensen *et al.*, 2004b;

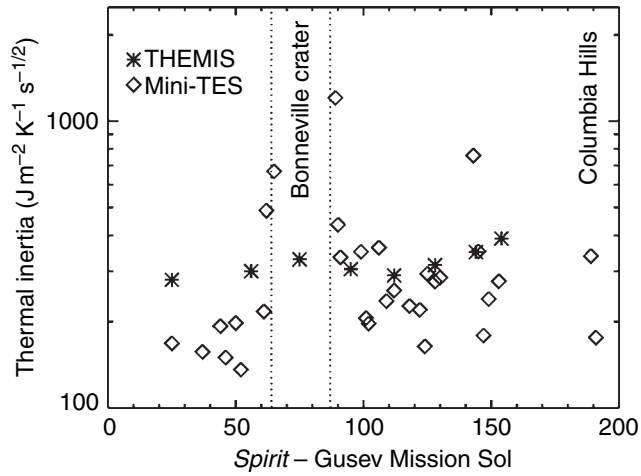

Figure 18.15. Comparison of thermal inertia derived from THEMIS and Mini-TES temperature observations for the MER Gusev landing site and rover traverse (Fergason *et al.*, 2006a). Thermal inertia in both datasets generally increases along the traverse and in the ejecta of Bonneville crater. Uncertainty of Mini-TES values is estimated to be around 12%. See text for more discussion.

Golombek *et al.*, 2005; Martinez-Alonso *et al.*, 2005; Fergason *et al.*, 2006a; Jakosky *et al.*, 2006). These thermal inertia values are consistent with the variety of surface types observed by the *Spirit* rover (Fergason *et al.*, 2006a). Comparison of Mini-TES-based thermal inertia at points along the rover traverse with THEMIS-based thermal inertia at roughly the same points along the traverse shows a similar trend between datasets (Figure 18.15). The thermal inertia in both datasets generally increases along the traverse from the landing site to Bonneville crater and decrease again leaving from Bonneville crater. This trend is likely due to an increase in small-scale rocky material as the crater ejecta material is approached and traversed (Christensen *et al.*, 2004a,b; Golombek *et al.*, 2005). In contrast, thermal inertia is slightly more variable (by about ±35) along the traverse from Bonneville crater to the Columbia Hills, but the average values of each dataset are similar.

Overall, the range of orbit-based thermal inertia values (280–320) and of lander-based thermal inertia values (150–430) over the entire region are in approximate agreement (Golombek *et al.*, 2005; Fergason *et al.*, 2006a); the wider range of values observed at the lander scale is not surprising, given a greater variability in surface material is observed at the smaller scale. However, while the two ranges overlap, point-to-point thermal inertia values along the traverse measured at the surface are typically lower than values determined from orbit-based data. The lower Mini-TES thermal inertia values may result from a sampling bias, as observations were taken directly in front of the rover during the traverse, and obstacles such as bedforms or large rocks, which exhibit higher thermal inertia, were avoided (Fergason *et al.*, 2006a). The difference may also be due to inherent differences in the instruments and thermal inertia derivation techniques. For example, THEMIS-based thermal inertia is derived from band 9 (12.57 μm) brightness temperatures (Christensen *et al.*, 2003a; 2004a; Putzig *et al.*,

2004), while Mini-TES thermal inertia is derived from the warmest spectral temperature, and are thus determined at different wavelengths (Christensen *et al*., 2003a; Fergason *et al*., 2006a). In general, rocky material from crater ejecta, aeolian bedforms, and rock fragments control the thermal inertia at local meters to tens-of-meter scales (e.g., Fergason *et al*., 2006a), whereas regional processes such as dust deposition, erosion or deposition of soils by wind or mass wasting (or even fluvial processes in the past), and large-scale volcanic or impact processes, influence the thermal inertia at kilometers to tens-of-kilometer scales.

The MER lander *Opportunity* at Meridiani Planum encountered a less rocky plain dominated by fine-grained basaltic sand, numerous well-sorted ripples and dunes, and outcrops of bedrock within craters (Arvidson *et al*., 2004b; Squyres *et al*., 2004b). Based on RMS errors in this region, the modeled diurnal temperature behavior did not well represent the measured Mini-TES temperatures (Fergason *et al*., 2006a). The best-fit Mini-TES thermal-inertia values range between 100 and 150, indicating an average particle diameter of $<45\,\mu m$ (silt and clay size), smaller than the particle size capable of being measured using MI images. MI data indicates a bimodal distribution of 0.6–6 mm particles and smaller than 125 μm grains (Herkenhoff *et al*., 2004b), while numerically modeled and observed temperatures produced larger RMS residuals relative to observations in other regions. The cause of this discrepancy between Mini-TES and MI particle size estimates is not understood, but may be related to the layering of hematite spherules on the surface (see Figure 18.7 and nonideal surface discussion above). In other cases, particle sizes estimated from thermal inertia agree well with MI observed size distributions (discussed above; see Fergason *et al*., 2006a), suggesting that this relationship as observed *in situ* by the rovers is similar to that derived from laboratory measurements (Presley and Chirstensen, 1997a), within the uncertainties in density and heat capacity.

Comparisons between TES and THEMIS orbit-based thermal inertia and *in situ* observations from Mini-TES at Meridiani Planum are complicated by the inconsistency between Mini-TES thermal-inertia-based and MI-based particle sizes. As measured from orbit, the landing site region exhibits a TES thermal inertia of 220 (Jakosky *et al*., 2006) and a THEMIS thermal inertia of 190–220 (Golombek *et al*., 2005; Fergason *et al*., 2006a; Jakosky *et al*., 2006), implying a particle size of fine sand (Golombek *et al*., 2005). Golombek *et al*. (2005) reported a thermal inertia of 225 based on Mini-TES nighttime-only data, in excellent agreement with the orbit-based values. Similarly, nighttime temperatures were used in deriving TES and THEMIS thermal inertia values. As discussed above, thermal inertias from combined Mini-TES nighttime and daytime diurnal temperatures result in lower thermal-inertia values of 100–150. These diurnal fit thermal inertias are notably lower and imply particle sizes of only 45 μm, which is inconsistent with the observed aeolian bedforms (Fergason *et al*., 2006a). Potential explanations for this discrepancy include a non-Lambertian surface phase function, inadequacies in the thermal model potentially related to heterogeneities in the particle distribution such as a surface layer of hematite spherules (see discussion above on nonideal surfaces), or differences in thermal inertia derivation between single-point measurements and fits to diurnal cycles. The cause of this discrepancy is not well understood.

18.5 SUMMARY

Thermal inertia is a key parameter for a wide array of topics in Mars exploration. In addition to geologic studies, thermal inertia is also an important component for studies of the Martian climate, the behavior of surface and subsurface volatiles, and in the design and operation of spacecraft missions. The seasonal cycles of CO_2 frost are controlled largely by the thermal inertia of the underlying soil surface. Because low-thermal-inertia surfaces store little heat during the daytime and summer, they cool more quickly at night and in the winter, and thus are the first to collect frost. These cool surfaces also accumulate thicker deposits of winter CO_2 frost and are the last to become frost-free in the spring. In permafrost studies, low-thermal-inertia surfaces are generally colder than their high-thermal-inertia counterparts on an annual average; low-thermal-inertia soils reach higher peak daytime temperatures and more efficiently radiate energy to space than do high-thermal-inertia soils. As a result, these cooler soils are preferred locations for stable ground ice in middle and high latitudes. Indeed, geographic variations in ice stability resulting from geographic variations in soil temperature (controlled by thermal inertia and albedo) agree well with the gamma-ray and neutron-spectrometer inferences of the distribution of ice in the Martian subsurface (e.g., Mellon *et al*., 2004). In climate studies thermal inertia (along with albedo) controls the diurnal and seasonal surface temperatures, and is important to the exchange of heat with the atmosphere through direct contact or thermal radiation. While the thermal mass of the atmosphere is very low relative to that of the soil and sensible heat exchange from the air temperature has little effect on the surface energy balance, the soil surface can cause large perturbations to the air temperature in the boundary layer. Upwelling thermal radiation from the surface is also partly absorbed by dust and CO_2 and is an important component of the atmosphere's energy budget. Finally, thermal inertia is heavily utilized in the design of spacecraft and in the selection of suitable and safe landing sites. For example, orbiting spacecraft experience temporal variations in thermal heating from upwelling surface radiation due to geographic variations in the thermal inertia of the surface. In landed spacecraft missions, the type of surface and potential for rock hazards is critical to mission success, and analysis of thermal inertia is a major component of landing site selection (see Chapter 21).

Thermal inertia is a physical property of the Martian surface that provides a window into the geologic structure of surface materials and the nature of geologic processes that shape the Martian surface. Many factors control thermal inertia, including but not limited to, particle size, packing, induration, density, interstitial gas pressure, and large scale

heterogeneity such as layering and horizontally mixed materials. Interpreting thermal inertia can be complicated by the variety of structures and properties that can result in the same value. Interpretations are relatively clear for the lowest and highest thermal inertia values. The lowest values are limited to highly porous, fine-grained dust deposits at least several centimeters deep. The highest thermal inertia values are limited to consolidated rock or dense ice deposits. In some cases the geologic context, such as aeolian or fluvial landforms where natural particle sorting can occur, may help to constrain the interpretations and support a relationship between thermal inertia and grain size.

The surface of Mars is almost entirely covered by soil to a depth of a few centimeters or more. Few exposures of bedrock are apparent at kilometer scales, though bedrock can nominally be obscured by a thin coating of dust. The constant deposition and removal of dust by present-day aeolian activity, combined with the absence of significant interannual variability in thermal inertia (e.g., Jakosky *et al*., 2000; Putzig and Mellon, 2007b), suggests that such a thin obscuring layer would be limited in geographic extent. Overall, the surface soil layer of Mars as inferred from thermal inertia is quite varied in physical composition and structure, ranging from dust deposits to coarse soils and mixed rocky surfaces. On a sub-kilometer scale some bedrock exposures are also observed. Variations in particle size, rock abundance, and induration account for much of the global scale variability. Ever-improving instrument resolution, modeling techniques, and analysis will continue to expand our understanding of the Martian surface and its physical structure. Together with other remote-sensing techniques, thermal inertia will continue to be a valuable tool in understanding the surface of Mars.

REFERENCES

Allen, C. C., R. V. Morris, K. M. Jager, *et al*., Martian regolith simulant JSC Mars-1, *Lunar Planet. Sci. Conf. XXIX*, Houston, 1998.

Armstrong, J. C., T. N. Titus, and H. H. Kieffer, Evidence for subsurface water ice in Korolev crater, Mars, *Icarus* **174**, 360–72, 2005.

Arvidson, R. E., E. A. Guinness, and A. P. Zent, Classification of surface units in the equatorial region of Mars based on Viking Orbiter color, albedo and thermal data, *J. Geophys. Res.* **87**, 10149–57, 1982.

Arvidson, R. E., E. A. Guinness, M. A. Dale-Bannister, *et al*., Nature and distribution of surficial deposits in Chryse Planitia and vicinity, Mars. *J. Geophys. Res.* **94**, 1573–87, 1989.

Arvidson, R. E., R. C. Anderson, P. Bartlett, *et al*., Localization and physical property experiments conducted by Opportunity at Meridiani Planum, *Science* **306**, 1730–3, 2004a.

Arvidson, R. E., R. C. Anderson, P. Bartlett, *et al*., Localization and physical property experiments conducted by Spirit at Gusev crater, *Science* **305**, 821–4, 2004b.

Arvidson, R. E., S. W. Squyres, R. C. Anderson, *et al*., Overview of the Spirit Mars Exploration Rover mission to Gusev crater: landing site to Backstay Rock in the Columbia Hills, *J. Geophys Res.* **111**, E02S01, 2006.

Bell III, J. F., S. W. Squyres, R. E. Arvidson, *et al*., Pancam multispectral imaging results from the Spirit rover at Gusev crater, *Science* **305**, 800–6, 2004a.

Bell III, J. F., S. W. Squyres, R. E. Arvidson, *et al*., Pancam multispectral imaging results from the Opportunity rover at Meridiani Planum, *Science* **306**, 1703–9, 2004b.

Betts, B. H., B. C. Murray, and T. Svitek, Thermal inertias in the upper millimeter of the martian surface derived using Phobos' shadow. *J. Geophys. Res.* **100**, 5285–96, 1995.

Binder, A. B., R. E. Arvidson, E. A. Guinness, *et al*., The geology of the Viking Lander 1 site, *J. Geophys. Res.* **82**, 4439–51, 1977.

Boynton, W. V., W. C. Feldman, S. W. Squyres, *et al*., Distribution of hydrogen in the near surface of Mars: evidence for subsurface ice deposits, *Science* **297**, 81–5, 2002.

Brady, N. C., *The Nature and Properties of Soils*, Old Tappan, NJ: Macmillan, 1974.

Bridges, N. T., Elevation-corrected thermal inertia and derived particle size on Mars and implications for the Tharsis Montes. *Geophys. Res. Lett.* **21**, 785–8, 1994.

Chojnacki, M., B. M. Jakosky, and B. M. Hynek, Surficial properties of landslides and surrounding units in Ophir Chasma, Mars, *J. Geophys. Res.* **111**, E040005, 2006.

Christensen, P. R., Martian dust mantling and surface composition: interpretation of thermophysical properties, *J. Geophys. Res.* **87**, 9985–98, 1982.

Christensen, P. R., The spatial distribution of rocks on Mars, *Icarus* **68**, 217–38, 1986a.

Christensen, P. R., Regional dust deposits on Mars: physical properties, age, and history, *J. Geophys Res.* **91**, 3533–45, 1986b.

Christensen, P. R., Global view of surface materials, *5th Int. Conf. Mars*, Lunar Planetary Institute Contribution 972, Pasadena, 1999.

Christensen, P. R. and H. H. Kieffer, Moderate resolution mapping of Mars: the channel terrain around the Chryse basin, *J. Geophys. Res.* **84**, 8233–8, 1979.

Christensen, P. R. and M. C. Malin, High resolution thermal imaging of Mars. *Proc. Lunar Planet. Sci. Conf. XIX*, 180–1, 1988.

Christensen, P. R. and H. J. Moore, The martian surface layer. In *Mars* (ed. H. H. Kieffer, B. M. Jakosky, C. W. Snyder, and M. S. Matthews), Tucson: University of Arizona Press, 1992.

Christensen, P. R., D. L. Anderson, S. C. Chase, *et al*., Thermal emission spectrometer experiment: Mars Observer, *J. Geophys. Res.* **97**, 7719–34, 1992.

Christensen, P. R., J. L. Bandfield, V. E. Hamilton, *et al*., The Mars Global Surveyor Thermal Emission Spectrometer experiment: investigation description and surface science results, *J. Geophys. Res.* **106**, 23823–71, 2001.

Christensen, P. R., J. L. Bandfield, J. F. Bell, *et al*., Morphology and composition of the surface of Mars: Mars Odyssey THEMIS results, *Science* **300**, 2056–61, 2003a.

Christensen, P. R., G. L. Mehall, S. H. Silverman, *et al*., Miniature Thermal Emission Spectrometer for the Mars Exploration Rovers, *J. Geophys. Res.* **108**(8064), 1–23, 2003b.

Christensen, P. R., B. M. Jakosky, H. H. Kieffer, *et al*., The Thermal Emission Imaging System (THEMIS) for the Mars 2001 Odyssey Mission, *Space Sci. Rev.* **110**, 85–130, 2004a.

Christensen, P. R., S. W. Ruff, R. L. Fergason, *et al*., Initial results from the Mini-TES experiment in Gusev crater from the Spirit Rover, *Science* **305**, 837–42, 2004b.

Clancy, R. T., B. J. Sandor, M. J. Wolff, *et al*., An intercomparison of ground-based millimeter, MGS TES, and Viking atmospheric temperature measurements: seasonal and

interannual variability of temperatures and dust loading in the global Mars atmosphere, *J. Geophys. Res.* **105**(E4), 9553–71, 2000.

Cook, J. G. and D. G. Leaist, An exploratory study of the thermal conductivity of methane hydrate. *Geophys. Res. Lett.* **10**, 397–9, 1983.

Dharma-wardana, M. W. C., Thermal conductivity of the ice polymorphs and the ice clathrates. *J. Phys. Chem.* **87**, 4185–90, 1983.

Ditteon, R., Daily temperature variations on Mars, *J. Geophys. Res.* **87**, 10197–214, 1982.

Edgett, K. S. and P. R. Christensen, Mars aeolian sand: regional variations among dark-hued crater floor features, *J. Geophys. Res.* **99**, 1997–2018, 1994.

Edwards, C. S., J. L. Bandfield, P. R. Christensen, and R. L. Fergason, Global distribution of bedrock on Mars using THEMIS high resolution thermal inertia, *EOS Trans. AGU*, **86**(52), Fall Meeting Suppl., Abstract P21C-0158, 2005.

Fanale, F. P., J. R. Salvail, A. P. Zent, and S. E. Postawko, Global distribution and migration of subsurface ice on Mars, *Icarus* **67**, 1–18, 1986.

Farmer, C. B. and P. E. Doms, Global seasonal variations of water vapor on Mars and the implications for permafrost, *J. Geophys. Res.* **84**, 2881–8, 1979.

Farmer, C. B., D. W. Davies, and D. D. LaPorte, Mars: northern summer ice cap – water vapor observations from Viking 2, *Science* **194**, 1339–41, 1976.

Feldman, W. C., T. H. Prettyman, S. Maurice, *et al.*, Global distribution of near-surface hydrogen on Mars, *J. Geophys. Res.* **109**, E09006, 2004.

Fenton, L. K. and R. L. Fergason, Thermal properties of sand from TES and THEMIS: do martian dunes make a good control for thermal inertia calculations?, *Lunar Planet. Sci. Conf. XXXV*, Houston, 2004.

Fenton, L. K. and M. T. Mellon, Thermal properties of sand from Thermal Emission Spectrometer (TES) and Thermal Emission Imaging System (THEMIS): spatial variations within the Proctor crater dune field on Mars, *J. Geophys. Res.* **111**, E06014, 2006.

Fenton, L. K., J. L. Bandfield, and A. W. Ward, Aeolian processes in Proctor crater on Mars: sedimentary history as analyzed from multiple data sets, *J. Geophys. Res.* **108**, 5129, 2003.

Fergason, R. L. and P. R. Christensen, Thermal inertia using THEMIS infrared data, *Lunar Planet. Sci. Conf. XXXIV*, Houston, 2003.

Fergason, R. L., P. R. Christensen, J. F. Bell, *et al.*, Physical properties of the Mars Exploration Rover landing sites as inferred from Mini-TES derived thermal inertia, *J. Geophys. Res.* **111**, E02S21, 2006a.

Fergason, R. L., P. R. Christensen, and H. H. Kieffer, High resolution thermal inertia derived from THEMIS: thermal model and applications, *J. Geophys. Res.* **111**, E12004, 2006b.

Fisher, J. A., M. I. Richardson, C. E. Newman, *et al.*, A survey of Martian dust devil activity using Mars Global Surveyor Mars Orbiter Camera images, *J. Geophys. Res.* **110**, E03004, 2005.

Fountain, J. A. and E. A. West, Thermal conductivity of particulate basalt as a function of density in simulated lunar and martian environments, *J. Geophys. Res.* **75**, 4063–9, 1970.

Giauque, W. F. and C. J. Egan, Carbon dioxide; The heat capacity and vapor pressure of the solid; The heat of sublimation; Thermodynamic and spectroscopic values of the entropy, *J. Chem. Phys.* **5**, 45–54, 1937.

Golombek, M. P., A. F. C. Haldemann, N. K. Forsberg-Taylor, *et al.*, Rock size-frequency distributions on Mars: at the Pathfinder landing site, in boulder fields, thermal inertia of rock populations, and rock shape and burial, and implications for Mars Exploration Rover landing safety and operations, *J. Geophys. Res.* **108**, 8086, 2003.

Golombek, M. P., R. E. Arvidson, J. F. Bell, *et al.*, Assessment of Mars Exploration Rover landing site predictions, *Nature* **436**, 44–8, 2005.

Grant, J. A., R. Arvidson, J. F. Bell, *et al.*, Surficial deposits at Gusev crater along Spirit Rover traverses, *Science* **305**, 807–10, 2004.

Greeley, R., R. Leach, B. White, J. Iversen, and J. Pollack, Threshold windspeeds for sand on Mars: wind tunnel simulations, *Geophys. Res. Lett.* **7**, 121–4, 1980.

Greeley, R., N. Lancaster, S. Lee, and P. Thomas, Mars aeolian processes, sediments, and features. In *Mars* (ed. H. H. Kieffer, B. M. Jakosky, C. W. Snyder, and M. S. Matthews), Tucson: University of Arizona Press, pp. 730–66, 1992.

Greeley, R., S. W. Squyres, R. E. Arvidson, *et al.*, Wind-related processes detected by the Spirit Rover at Gusev crater, *Science* **305**, 810–21, 2004.

Greeley, R., R. Arvidson, J. F. Bell, *et al.*, Martian variable features: new insight from the Mars Express Orbiter and the Mars Exploration Rover Spirit, *J. Geophys. Res.* **110**, E06002, 2005.

Haberle, R. M. and B. M. Jakosky, Atmospheric effects on determination of thermal inertia on Mars, *Icarus* **90**, 187–204, 1991.

Hayashi, J. N., B. M. Jakosky, and R. M. Haberle, Atmospheric effects on the mapping of martian thermal inertia and thermally derived albedo, *J. Geophys. Res.* **100**, 5277–84, 1995.

Herkenhoff, K. E. and A. R. Vasavada, Dark material in the polar layered deposits and dunes on Mars, *J. Geophys. Res.* **104**, 16487–500, 1999.

Herkenhoff, K. E., S. W. Squyres, R. Arvidson, *et al.*, Textures of the soils and rocks at Gusev crater from Spirit's Microscopic Imager, *Science* **305**, 824–6, 2004a.

Herkenhoff, K. E., S. W. Squyres, R. Arvidson, *et al.*, Evidence from Opportunity's Microscopic Imager for water on Meridani Planum, *Science* **306**, 1727–30, 2004b.

Hillel, D., *Fundamentals of Soil Physics*, New York: Academic Press, 1980.

Hobbs, P. V., *Ice Physics*, London: Oxford University Press, 1974.

Holder, G. D., A. V. Cugini, and R. P. Warzinski, Modeling clathrate hydrate formation during carbon dioxide injection into the ocean, *Environ. Sci. Tech.* **29**, 276–8, 1995.

Honda, Y. P. and J. G. Cook, Thermal conductivity of xenon hydrate. *J. Phys. Chem.* **91**, 6327–8, 1987.

Hynek, B. M., Implications for hydrologic processes on Mars from extensive bedrock outcrops throughout Terra Meridiani, *Nature* **431**, 156–9, 2004.

Jakosky, B. M., The effects of nonideal surfaces on the derived thermal properties of Mars. *J. Geophys. Res.* **84**, 8252–62, 1979.

Jakosky, B. M., On the thermal properties of martian fines. *Icarus* **66**, 117–24, 1986.

Jakosky, B. M. and P. R. Christensen, Global duricrust on Mars: analysis of remote-sensing data. *J. Geophys. Res.* **91**, 3547–59, 1986a.

Jakosky, B. M. and P. R. Christensen, Are the Viking Lander sites representative of the surface of Mars?, *Icarus* **66**, 125–33, 1986b.

Jakosky, B. M. and M. T. Mellon, Thermal inertia of Mars: sites of exobiological interest, *J. Geophys. Res.* **106**, 23887–908, 2001.

Jakosky, B. M. and D. O. Muhleman, A comparison of the thermal and radar characteristics of Mars, *Icarus* **45**, 25–38, 1981.

Jakosky, B. M., M. T. Mellon, H. H. Kieffer, *et al.*, The thermal inertia of Mars from the Mars Global Surveyor Thermal Emission Spectrometer, *J. Geophys. Res.* **105**, 9643–52, 2000.

Jakosky, B. M., B. M. Hynek, S. M. Pelkey, *et al*., Thermophysical properties of the MER and Beagle II landing site regions on Mars, *J. Geophys Res*. **111**, E08008, 2006.

Johnson, J. B. and R. D. Lorenz, Thermophysical properties of Alaskan loess: an analog material for the martian polar layered terrain?, *Geophys. Res. Lett*. **27**, 2769–72, 2000.

Judd, W. R. and A. Shakoor, *Density in Physical Properties of Rocks and Minerals* (ed. C. Y. Ho *et al*.), Philadelphia, PA: Taylor and Francis, pp. 409–502, 1989.

Kahn, R. A., T. Z. Martin, and R. W. Zurek, The martian dust cycle. In *Mars* (ed. H. H. Kieffer, B. M. Jakosky, C. W. Snyder, and M. S. Matthews), Tucson: University of Arizona Press, pp. 1017–53, 1992.

Kennard, E. H., *Kinetic Theory of Gases, with an Introduction to Statistical Mechanics*, New York: McGraw-Hill, 1938.

Kieffer, H. H., S. C. Chase, E. Miner, G. Münch, and G. Neugebauer, Preliminary report on infrared radiometric measurements from the Mariner 9 spacecraft. *J. Geophys. Res*. **78**, 4291–312, 1973.

Kieffer, H. H., S. C. Chase, T. Z. Martin, E. D. Miner, and F. D. Palluconi, Martian north pole summer temperatures: dirty water ice, *Science*, **194**, 1341–4, 1976.

Kieffer, H. H., T. Z. Martin, A. R. Peterfreund, *et al*., Thermal and albedo mapping of Mars during the Viking primary mission, *J. Geophys. Res*. **82**, 4249–91, 1977.

Krovchenko, Yu. G. and I. N. Krupskii, Thermal conductivity of solid N_2O and CO_2, *Sov. J. Low Temp. Phys*. **12**, 46–8, 1986.

Ksanfomaliti, L. V. and V. I. Moroz, Infrared radiometry on board Mars-5, *Cosmic Res*. **13**, 65–7, 1975.

Leaist, D. G., J. J. Murray, M. L. Post, and D. W. Davidson, Enthalpies of decomposition and heat capacity of ethylene oxide and tetrahydrofuran hydrates, *J. Phys. Chem*. **86**, 4175–8, 1982.

Leighton, R. B. and B. C. Murray, Behavior of carbon dioxide and other volatiles on Mars, *Science* **153**, 136–44, 1966.

Leovy, C., Note on thermal properties of Mars, *Icarus* **5**, 1–6, 1966.

Malin, M. C. and K. S. Edgett, Mars Global Surveyor, Mars Orbiter Camera: interplanetary cruise through primary mission, *J. Geophys. Res*. **106**, 23429–570, 2001.

Martinez-Alonso, S., B. M. Jakosky, M. T. Mellon, and N. E. Putzig, A volcanic interpretation of Gusev crater surface materials from thermophysical, spectral, and morphological evidence, *J. Geophys. Res*. **110**, E01003, 2005.

Masamune, S. and J. M. Smith, Thermal conductivity of beds of spherical particles, *I & EC Fundamentals* **2**(2), 136–43, 1963.

Mellon, M. T., Limits on the CO_2 content of the martian polar deposits, *Icarus* **124**, 268–79, 1996.

Mellon, M. T. and B. M. Jakosky, Geographic variations in the thermal and diffusive stability of ground ice on Mars, *J. Geophys. Res*. **98**, 3345–64, 1993.

Mellon, M. T. and B. M. Jakosky, The distribution and behavior of martian ground ice during past and present epochs, *J. Geophys. Res*. **100**, 11781–99, 1995.

Mellon, M. T. and N. E. Putzig, The apparent thermal inertia of layered surfaces on Mars, *Lunar Planet. Sci. Conf. XXXVIII*, Houston, 2007.

Mellon, M. T., B. M. Jakosky, and S. E. Postawko, The persistence of equatorial ground ice on Mars, *J. Geophys. Res*. **102**, 19357–69, 1997.

Mellon, M. T., B. Jakosky, H. Kieffer, and P. Christensen, High resolution thermal inertia mapping from the Mars Global Surveyor Thermal Emission Spectrometer, *Icarus* **148**, 437–55, 2000.

Mellon, M. T., W. C. Feldman, and T. H. Prettyman, The presence and stability of ground ice in the southern hemisphere of Mars, *Icarus* **169**, 324–40, 2004.

Merényi, E., K. S. Edgett, and R. B. Singer, Deucalionis Regio, Mars: evidence for a new type of immobile weathered soil unit, *Icarus* **124**, 296–307, 1996.

Moore, H. J. and B. M. Jakosky, Viking landing sites, remote sensing observations, and the physical properties of Martian surface materials, *Icarus* **81**, 164–84, 1989.

Moore, H. J. and J. M. Keller, Surface-material maps of the Viking landing sites on Mars (abstract), in *Rep. Planet. Geol. Geophys. Prog*. – 1990, NASA Technical Memorandum, 4210, 160–2, 1990.

Moore, H. J., R. E. Hutton, G. D. Clow, and C. R. Spitzer, Physical properties of the surface materials at the Viking landing sites on Mars, *US Gs. Prof. Paper*, 1389, 1987.

Moore, H. J., D. B. Bickler, J. A. Crisp, *et al*., Soil-like deposits observed by Sojourner, the Pathfinder rover, *J. Geophys. Res*. **104**, 8729–46, 1999.

Moroz, V. I. and L. V. Ksanfomaliti, Preliminary results of astrophysical observations of Mars from Mars-3, *Icarus* **17**, 408–22, 1972.

Moroz, V. I., L. V. Ksanfomaliti, G. N. Krasovskii, *et al*., Infrared temperatures and thermal properties of the martian surface measured by the Mars 3 Orbiter, *Cosmic Res*. **13**, 346–56, 1976.

Morrison, D., C. Sagan, and J. B. Pollack, Martian temperatures and thermal properties, *Icarus* **11**, 36–45, 1969.

Mustard, J. F., C. D. Cooper, and M. K. Rifkin, Evidence for recent climate change on Mars from the identification of youthful near-surface ground ice, *Nature* **412**, 411–14, 2001.

Mutch, T. A., R. E. Arvidson, A. B. Binder, E. A. Guinness, and E. C. Morris, The geology of the Viking Lander 2 site, *J. Geophys. Res*. **82**, 4452–67, 1977.

Neugebauer, G., G. Münch, H. Kieffer, S. C. Chase, and E. Miner, Mariner 1969 infrared radiometer results: temperatures and thermal properties of the martian surface, *Astron. J*. **76**, 719–28, 1971.

Paige, D. A., The thermal stability of near-surface ground ice on Mars, *Nature* **356**, 43–5, 1992.

Paige, D. A. and A. P. Ingersoll, Annual heat balance of martian polar caps: Viking observations, *Science* **228**, 1160–8, 1985.

Paige, D. A. and K. D. Keegan, Thermal and albedo mapping of the polar regions of Mars using Viking thermal mapper observations: 1. South polar region, *J. Geophys. Res*. **99**, 25992–6013, 1994.

Paige, D. A., J. E. Bachman, and K. D. Keegan, Thermal and albedo mapping of the polar regions of Mars using Viking thermal mapper observations: 1. North polar region, *J. Geophys. Res*. **99**, 25959–91, 1994.

Palluconi, F. D. and H. H. Kieffer, Thermal inertia mapping of Mars from 60° S to 60° N, *Icarus* **45**, 415–26, 1981.

Pelkey, S. M. and B. M. Jakosky, Surficial geologic surveys of Gale crater and Melas Chasma, Mars: integration of remote sensing data, *Icarus* **160**, 228–57, 2002.

Pelkey, S. M., B. M. Jakosky, and M. T. Mellon, Thermal in inertia of crater-related wind streaks on Mars, *J. Geophys. Res*. **106**, 23909–20, 2001.

Petrenko, V. F. and R. W. Whitworth, *Physics of Ice*, New York: Oxford University Press, 1999.

Pollack, J. B., R. M. Haberle, J. Schaffer, and H. Lee, Simulations of the general circulation of the martian atmosphere: 1. Polar processes, *J. Geophys. Res*. **95**, 1447–73, 1990.

Present, R. D., *Kinetic Theory of Gases*, New York: McGraw-Hill, 1958.

Presley, M. A. and R. E. Arvidson, Nature and origin of materials exposed in Oxia Palus – Western Arabia – Sinus Meridiani Region of Mars, *Icarus* **75**, 499–517, 1988.

Presley, M. A. and P. R. Christensen, Thermal conductivity measurements of particulate materials: 2. Results, *J. Geophys. Res.* **102**, 6551–66, 1997a.

Presley, M. A. and P. R. Christensen, The effect of bulk density and particle size sorting on the thermal conductivity of particulate materials under martian atmospheric pressures, *J. Geophys. Res.* **102**, 9221–9, 1997b.

Presley, M. A. and R. A. Craddock, Thermal conductivity measurements of particulate materials: 3. Natural samples and mixtures of particle sizes, *J. Geophys Res.* **111**, E09013, 2006.

Prettyman, T. H., W. C. Feldman, M. T. Mellon, *et al.*, Composition and structure of the martian surface in the high southern latitudes from neutron spectroscopy, *J. Geophys. Res.* **109**, E05001, 2004.

Putkonen, J., R. S. Sletten, and B. Hallet, Atmosphere/ice energy exchange through thin debris cover in Beacon Valley, Antarctica, *Proc. 8th Intern. Conf.* (ed. M. Phillips, S. M. Springman, and L. U. Arenson), Permafrost, Zurich, Switzerland, pp. 913–28, July 21–25, 2003.

Putzig, N. E., Thermal inertia and surface heterogeneity on Mars, Ph.D. dissertation, University of Colorado, Boulder, 2006.

Putzig, N. E. and M. T. Mellon, Thermal behavior of horizontally mixed surfaces on Mars, *Icarus*, **191**, 52–67, 2007a.

Putzig, N. E. and M. T. Mellon, Apparent thermal inertia and the surface heterogeneity of Mars, *Icarus*, **191**, 68–94, 2007b.

Putzig, N. E., M. T. Mellon, B. M. Jakosky, *et al.*, Mars thermal inertia from THEMIS data, *Lunar Planet. Sci. Conf. XXXV*, Houston, 2004.

Putzig, N. E., M. T. Mellon, K. A. Kretke, and R. E. Arvidson, Global thermal inertia and surface properties of Mars from the MGS mapping mission, *Icarus* **173**, 325–41, 2005.

Rogers, A. D., J. L. Bandfield, and P. R. Christensen, Global bedrock composition mapping on Mars using THEMIS and TES data, *Lunar Planet. Sci. Conf. XXXIV*, Houston, 2003.

Rogers, A. D., P. R. Christensen, and J. L. Bandfield, Compositional heterogeneity of the ancient Martian crust: analysis of Ares Vallis bedrock with THEMIS and TES data, *J. Geophys. Res.* **110**, E05010, 2005.

Roy, R. F., A. E. Beck, and Y. S. Touloukian, Thermophysical properties of rocks. In *Physical Properties of Rocks and Minerals* (ed. C. Y. Ho, *et al.*), Philadelphia, PA: Taylor and Francis, pp. 409–502, 1989.

Ruff, S. W. and P. R. Christensen, Bright and dark regions on Mars: particle size and mineralogical characteristics based on Thermal Emission Spectrometer data, *J. Geophys. Res.* **107**, 5127, 2002.

Sagan, C., B. A. Smith, J. Veverka, *et al.*, Variable features on Mars: preliminary Mariner 9 Television results, *Icarus* **17**, 346–72, 1972.

Selivanov, A. S., Yu. M. Gektin, N. K. Naraeva, *et al.*, Atlas of Mars by the TERMOSCAN Radiometer data, *Assoc. Adv. Space Sci. Tech.*, Moscow, 1998.

Sinton, W. M. and J. Strong, Radiometric observations of Mars, *Astrophys. J.* **131**, 459–69, 1960.

Smith, M. D., J. C. Pearl, B. J. Conrath, and P. R. Christensen, One martian year of atmospheric observations by the Thermal Emission Spectrometer, *Geophys. Res. Lett.* **28**(22), 4263–55, 2001.

Squyres, S. W., R. E. Arvidson, J. F. Bell, *et al.*, The Spirit Rover's Athena *Science* investigation at Gusev crater, Mars, *Science* **305**, 794–9, 2004a.

Squyres, S. W., R. E. Arvidson, J. F. Bell, *et al.*, The Opportunity Rover's Athena *Science* investigation at Meridiani Planum, Mars, *Science* **306**, 1698–703, 2004b.

Storrs, A. D., F. P. Fanale, R. S. Saunders, and J. B. Stephens, The formation of filamentary sublimate residues (FSR) from mineral grains, *Icarus* **76**, 493–512, 1988.

Strum, M., D. K. Perovich, and J. Holmgren, Thermal conductivity and heat transfer through the snow on the ice of Beaufort Sea, *J. Geophys. Res.* **107**, 8043, 2002.

Thomas, P. and P. J. Gierasch, Dust devils on Mars, *Science* **230**, 175–7, 1985.

Thomas, P., J. Veverka, S. Lee, and A. Bloom, Classification of wind streaks on Mars, *Icarus* **45**(1), 124–53, 1981.

Tillman, J. E., N. C. Johnson, P. Guttorp, and D. B. Percival, The martian annual atmospheric pressure cycle: years without great dust storms, *J. Geophys. Res.* **98**, 10963–71, 1993.

Titus, T. N., H. H. Kieffer, and P. R. Christensen, Exposed water ice discovered near the south pole of Mars, *Science* **299**, 1048–51, 2003.

Titus, T. N., T. H. Prettyman, and A. Colaprete, Thermal characterization of the three proposed Phoenix Landing sites, *Lunar Planet. Sci. Conf. XXXVII*, Houston, 2006.

Urquhart, M. L. and B. M. Jakosky, Lunar thermal emission and remote determination of surface properties, *J. Geophys. Res.* **102**, 10959–69, 1997.

Vasavada, A. R., J. P. Williams, D. A. Paige, *et al.*, Surface properties of Mars' polar layered deposits and polar landing sites. *J. Geophys. Res.* **105**, 6961–9, 2000.

Ward, A. W., L. R. Gaddis, R. L. Kirk, *et al.*, General geology and geomorphology of the Pathfinder landing site, *J. Geophys. Res.* **104**, 8555–71, 1999.

Weast, R. C. (ed.), *CRC Handbook of Chemistry and Physics*, 67th edn., Boca Raton, FL: CRC Press, p. B-82, 1986.

Wechsler, A. E. and P. E. Glaser, Pressure effects on postulated lunar materials, *Icarus* **4**, 335–52, 1965.

Wechsler, A. E., P. E. Glaser, A. D. Little, and J. A. Fountain, Thermal properties of granulated materials. In *Thermal Characteristics of the Moon* (ed. J. W. Lucas), Cambridge, MA: MIT Press, pp. 215–41, 1972.

Wesselink, A. F., Heat conductivity and nature of the lunar surface material, *Bull. Astr. Insts. Netherlands* **10**, 351–63, 1948.

Wilson, S. A. and J. R. Zimbelman, Latitude-dependent nature and physical characteristics of transverse aeolian ridges on Mars, *J. Geophys. Res.* **109**, E10003, 2004.

Woodside, W. and J. H. Messmer, Thermal conductivity of porous media: I. Unconsolidated sands, *J. Appl. Phys.* **32**, 1688–99, 1961a.

Woodside, W. and J. H. Messmer, Thermal conductivity of porous media: I. Consolidated rock. *J. Appl. Phys.* **32**, 1699–706, 1961b.

Zimbelman, J. R., Surface properties of the Pettit wind streak on Mars: implications for sediment transport, *Icarus* **66**, 83–93, 1986.

Zimbelman, J. R. and R. Greeley, Surface properties of ancient cratered terrain in the northern hemisphere of Mars, *J. Geophys. Res.* **87**, 10181–9, 1982.

Zimbelman, J. R. and H. H. Kieffer, Thermal mapping of the northern equatorial and temperate latitudes of Mars, *J. Geophys. Res.* **84**, 8239–51, 1979.

Zurek, R. W., J. R. Barnes, R. M. Haberle, *et al.*, Dynamics of the atmosphere of Mars. In *Mars* (ed. H. H. Kieffer, B. M. Jakosky, C. W. Snyder, and M. S. Matthews), Tucson: University of Arizona Press, pp. 835–933, 1992.

19

Physical properties of the Martian surface from spectrophotometric observations

J. R. JOHNSON, J. F. BELL III, P. GEISSLER, W. M. GRUNDY, E. A. GUINNESS, P. C. PINET, AND J. SODERBLOM

ABSTRACT

The reflection of visible and near-infrared light from Mars can vary significantly depending on the directional scattering characteristics of surface materials. Observations acquired under a range of illumination and viewing angles can be input to radiative transfer models to constrain the albedo, surface roughness, grain size, and/or porosity of these materials. This chapter reviews multiangular measurements of Mars obtained by Earth-based telescopes (including the Hubble Space Telescope), orbiters (Mariner, Viking, Mars Express), landers (Viking, Mars Pathfinder), and rovers (Mars Exploration Rovers), and how the photometric analyses of these datasets have been used to understand the surface properties of local and regional geologic units and terrain types. Although acquisition of data covering sufficient incidence, emission, or phase angles to fully constrain all parameters within photometric models is challenging, a common theme among these studies is the dominantly backscattering nature of the Martian surface, the magnitude of which is often related to the presence of high-albedo aeolian dust. The local and regional photometric variability observed in these data encourages further refinement of radiative transfer methods and atmospheric correction algorithms to provide additional tools with which to categorize and map distinct photometric units on Mars, particularly to provide support for ongoing and upcoming orbital and landed missions.

19.1 INTRODUCTION

The manner in which visible and near-infrared light reflects from the Martian surface depends on the viewing geometry and solar illumination angle. Apparent surface brightness can vary substantially not only as a function of wavelength and composition but also as a result of differences in surface roughness (at scales ranging from microns to meters), internal heterogeneities, grain size, and porosity of the constituent particles (Figure 19.1). Surface and orbital observations acquired at a variety of emission, solar incidence, and phase angles provide the data necessary to model these properties and allow refined interpretations of the microphysical characteristics of different geologic materials. The photometric properties of local and regional terrains can be used to normalize multispectral observations to common illumination geometries. This allows equivalent comparisons of data obtained at different times of day or from laboratory measurements and improves interpretations of compositional and mineralogical information gleaned from multispectral imaging. The combination of photometric and multispectral analyses is thus a powerful tool to deduce the formation and distribution of Martian geologic materials.

In this chapter, we first present some of the common photometric functions used to describe scattering from planetary surfaces. We then provide a short background on Earth-based telescopic observations of the photometric variability of Mars, followed by descriptions of the orbital investigations conducted by the Mariner, Viking, and Mars Express (MEx) missions, as well as observations by the Hubble Space Telescope (HST). We then summarize investigations of the photometric properties of the Martian surface determined by imaging systems at the Viking Lander, Mars Pathfinder (MPF), and Mars Exploration Rover (MER) landing sites. Photometric studies regarding Phobos and Deimos are not discussed here, although interested readers are referred to the works of Simonelli *et al.* (1998), Clancy *et al.* (1995), Thomas *et al.* (1996), and Cantor *et al.* (1999).

In the discussions below, we use the term "soil" in its traditional planetary context to imply unconsolidated materials that can be discriminated from rock or bedrock, with no implication for the presence or absence of organic materials. Also, we note that some names used here for landforms, rocks, and soils have not been approved by the International Astronomical Union and are intended to be informal references to specific features or targets.

19.2 COMMON PHOTOMETRIC FUNCTIONS

The simplest empirical expression used to describe the scattering behavior of particulate surfaces is Lambert's law (Lambert, 1760), which defines the bidirectional reflectance (r_L) of a surface at given angles of incidence (i), emission (e), and phase (g) as

$$r_L(i, e, g) = K_L \cos(i), \tag{19.1}$$

where K_L is a constant equal to A_L/π, where A_L is the Lambert albedo (the total power scattered per unit area by a Lambert surface divided by the incident power per unit area). A perfectly diffuse surface has $A_L = 1.0$ (Hapke, 1993). In practice, Lambert's law tends to describe

The Martian Surface: Composition, Mineralogy, and Physical Properties, ed. J. F. Bell III. Published by Cambridge University Press.

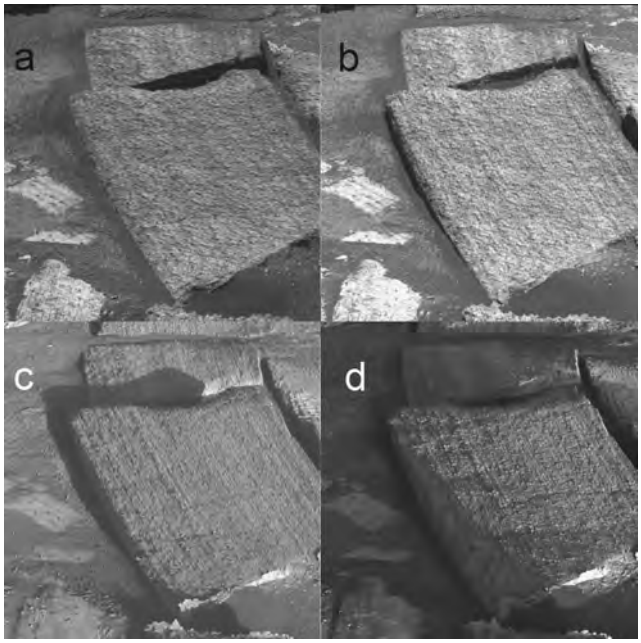

Figure 19.1. Mars Exploration Rover Pancam images of "Tipuna" rock acquired in Endurance crater at 753 nm on Sols 306–307 at (a) 0906, (b) 1142, (c) 1608, (d) 1705 LTST demonstrating variations in small-scale surface roughness as a function of illumination conditions.

high-albedo surfaces better than dark surfaces (Hapke, 1993), although no planetary surface has been shown to scatter as a Lambert body, including the icy satellites (e.g., Buratti, 1984; Domingue and Verbiscer, 1997).

Minnaert (1941) generalized this relation to a bidirectional reflectance function that was used widely for photometric analyses of Mars because it describes brightness variations relatively well over the limited range of phase angles obtainable from Earth (<48°). It has the form:

$$r_{\mathrm{M}}(i,e,g) \;=\; A_{\mathrm{M}}\cos(i)^{k}\cos(e)^{(k-1)}, \tag{19.2}$$

where r_{M} is the Minnaert bidirectional reflectance, and k (the Minnaert index) and A_{M} are both empirical "constants," whose values actually vary with wavelength, phase, albedo, and azimuth angle (Hapke, 1981, 1993).

In cases where the single scattering albedos are sufficiently small to neglect multiple scattering (e.g., portions of the Moon and Mercury), the Lommel–Seeliger law is applicable (Chandrasekhar, 1960; Hapke, 1993) and has the form:

$$I(i,e,g) \;=\; \frac{(Jw/4\pi)P(g)\cos(i)}{\cos(i)+\cos(e)}\,, \tag{19.3}$$

where I is the total radiance observed from the scene ($\mathrm{W\,m^{-2}\,sr^{-1}}$) and J is the irradiance on the scene ($\mathrm{W\,m^{-2}}$) (Slater, 1980, p. 90; Hapke, 1993, p. 64). $P(g)$ is an arbitrary function describing the phase dependence of the single particle surface scattering function, and w is the single-scattering albedo (Hapke, 1993). A simple function that adequately models the photometric properties of most surfaces as a linear combination of a Lambert function (Equation 19.1) and the Lommel–Seeliger lunar function (Equation 19.3) is the Lunar–Lambert function (Meador and Weaver, 1975):

$$\frac{I(i,e,g)}{F} \;=\; \frac{\mathrm{A}\,P(g)\cos(i)}{\cos(i)+\cos(e)+\mathrm{B}\cos(i)}\,, \tag{19.4}$$

where I is the radiance observed from the scene and πF is the incident solar irradiance at the top of the Martian atmosphere, A and B are empirical parameters that determine the relative lunar-like and Lambert contributions to the scattering function. $I(i, e, g)/F$ is the "radiance factor" of Hapke (1993, p. 262) and is equal to the bidirectional reflectance multiplied by π.

Comparisons of the above photometric functions have shown that both the Lunar–Lambert and the Minnaert functions can provide satisfactory photometric fits for most surfaces observed in the Solar System, albeit under a limited range of geometries (Gradie and Veverka, 1984; McEwen, 1991; Hapke, 1993). The Lunar–Lambert function provides a superior fit compared to a Minnaert function for surfaces with a macroscopic surface roughness of <30° (McEwen, 1991). However, none of the above photometric functions incorporate a term for macroscopic roughness, which is the average of surface facet tilts at scales from the wavelength of light to the centimeter-scale (often below the resolution limit of an imaging system) (Hapke, 1993; Shepard and Campbell, 1998; Helfenstein and Shepard, 1999, 2003; Cord *et al.*, 2005).

Hapke's photometric model (Hapke, 1993) includes parameters for the macroscopic roughness ($\bar{\theta}$), the single scattering albedo (w), the single scattering phase function P(g) (directional scattering behavior of an individual particle), and the magnitude ($B0$) and width (h) of the opposition effect (the nonlinear increase in brightness observed near zero phase angle). The $B0$ parameter is physically related to the opacity of particles, where a value of 1.0 implies that all light is scattered at the surface and the particle is opaque (e.g., Domingue *et al.*, 1997). The parameter h is physically related to porosity (P) and particle size distribution function $Y(r)$ of the optically active layer through the approximate relation

$$h \;\simeq\; -(3/8)\ln(P)\;Y(r). \tag{19.5}$$

Less porous materials or those that have lower ratios of largest-to-smallest particle size, depending on $Y(r)$, have large values of h. Grain size distributions characteristic of lunar or asteroidal regolith have typically been used to estimate surface porosities (Hapke, 1986, 1993; Helfenstein and Veverka, 1987, 1989; Domingue *et al.*, 1995, 2002; Helfenstein *et al.*, 1997), although this can lead to overestimates of porosity for some surfaces (e.g., Hendrix *et al.*, 2005).

The opposition effect has been studied extensively for surfaces throughout the Solar System, and is comprised of two physical mechanisms described as "shadow hiding" (where shadows from individual grains are progressively minimized with smaller phase angle) and "coherent backscatter" (where constructive interference between incoming and outgoing photons increases with smaller phase angle). Coherent backscatter mainly occurs at phase angles <1–2° and is particularly dominant for very bright materials (e.g., $w > 0.95$; see Nelson *et al.*, 1998). Because most Martian

observations are acquired at phase angles >2°, and albedos for nonpolar regions on Mars are usually <0.40, the shadow-hiding effect dominates the opposition effect for Mars. Equation (19.5) therefore represents only the shadow-hiding portion of the opposition effect width (see Helfenstein *et al.*, 1997).

Some workers have used a series of Legendre polynomials to represent $P(g)$ (Hapke, 1993). For example, in their laboratory study of scattering behaviors of minerals Mustard and Pieters (1989) used a two-term Legendre polynomial suggested by Hapke (1981) of the form

$$P(g) = 1 + b_1 \cos(g) + b_2(1.5\cos^2(g) - 0.5) \tag{19.6}$$

where b_1 described the magnitude of forward and backward scattering and b_2 represented the broadness of the scattering lobe.

Henyey and Greenstein (1941) proposed a single-particle phase function $P(g)$ of the form

$$P(g) = \frac{(1-\xi^2)}{(1+2\xi\cos(g) + \xi^2)^{3/2}} \tag{19.7}$$

where ξ is the phase function asymmetry parameter (constrained to be between −1 and 1). Values of $\xi = 0$ imply isotropic grains (those that scatter equally in both forward and backward directions) whereas forward scattering (relatively transparent) grains exhibit $\xi > 0$, and backscattering (relatively opaque) grain are characterized by $\xi < 0$ (Hapke, 1993; Pappalardo *et al.*, 2004). Although this phase function was originally formulated to model light scattering from interstellar dust, it has since been widely applied to planetary surface photometric studies.

The two-term Henyey–Greenstein (HG) phase functions are useful to characterize surface particles that exhibit both forward and backscattering. This function is represented by the asymmetry parameter (b) and forward scattering fraction (c'). The form of the two-term HG phase function used here is:

$$P(g) = \frac{c'\,(1-b^2)}{(1+2b\cos(g)+b^2)^{3/2}} + \frac{(1-c')(1-b^2)}{(1-2b\cos(g)+b^2)^{3/2}} \tag{19.8}$$

Other workers define the two-term HG function somewhat differently such that their c parameter represents the *backward* scattering fraction (e.g., Hartmann and Domingue, 1998; Cord *et al.*, 2003). To be consistent with those studies, we convert our forward fraction parameter c' to a backward fraction c via $c = (1 - c')$. Historically, a different version of the two-term HG function was used by Hapke (1993; Eqn. 6.18a) and McGuire and Hapke (1995) in which their "c" parameter is related to c by the relation "c" $= (2c - 1)$.

In their study of the photometric properties of centimeter-scale artificial particles, McGuire and Hapke (1995) found that particles with different degrees of heterogeneity exhibited discrete b and c values related to deviations from a particle's internal and spherical perfection. Particles with greater roughness, microcracks, or inclusions exhibit more pronounced backscattering (large c values) but with low and broad scattering lobes (small b values). Smooth, clear spheres exhibit greater forward scattering (small c values) and larger asymmetry in their scattering lobes (large b values). Hartmann and Domingue (1998) noted that centimeter-sized particles are not typical of most planetary regoliths, but also showed that the McGuire and Hapke (1995) scattering functions are not significantly different from the behavior of the larger particles when scaled to smaller particle sizes. The McGuire and Hapke (1995) measurements are used here for comparison to results from photometric models of the Martian surface.

As discussed by several workers (e.g., Helfenstein and Veverka, 1987, 1989; Mustard and Pieters, 1989; McEwen, 1991; Cord *et al.*, 2003; Johnson *et al.*, 2006a), the parameters in the Hapke model are strongly coupled and can provide mathematically reasonable solutions even for parameters that are poorly constrained by the data. This can result in nonunique solutions, especially when data are only available at limited illumination or observation geometries. For example, Helfenstein (1988) demonstrated that changes in the particle phase function influence the shape of the phase curve most acutely at small (<50°) and large (>130°) phase angles. For comparison, the effects of macroscopic surface roughness are less important when viewed at small phase angles. In situations where model results are underconstrained, the number of fitted parameters must be reduced, if all remaining fitted parameters are to be meaningfully constrained by the data. As discussed below, this strategy usually involves assuming constant values for particular parameters during model runs. In reality, few photometric datasets collected for Mars sample a sufficient angular range of incidence, emission, and phase to completely constrain all model parameters used to describe global, regional, or local surface scattering properties. Nonetheless, the studies summarized below have increased our understanding of the photometric properties of Martian terrains by providing useful constraints on the relative scattering differences among varied geologic materials on Mars.

19.3 HISTORICAL WORK

19.3.1 Early telescopic observations

Visual estimates of the photometric properties of Mars date back to as far as 1865 by Zöllner (de Vaucouleurs, 1964). Between 1887 and 1889, Muller made extensive observations of Mars and reported a phase coefficient (α, the slope of the phase curve plotted on a magnitude scale, see. Veverka *et al.*, 2000) of about +0.015 mag/deg (de Vaucouleurs, 1964). De Vaucouleurs (1964) compiled photographic observations by King (1923) and Livlander (1933) and photoelectric observations by Johnson and Gardiner (1955), de Vaucouleurs (1960), and Harris (1961) to determine that the mean visual phase curve was well described by a linear phase law. De Vaucouleurs (1964) reported a reduced magnitude $V = -1.52 \pm 0.01$ and a phase coefficient $\alpha = +0.015$ mag/deg.

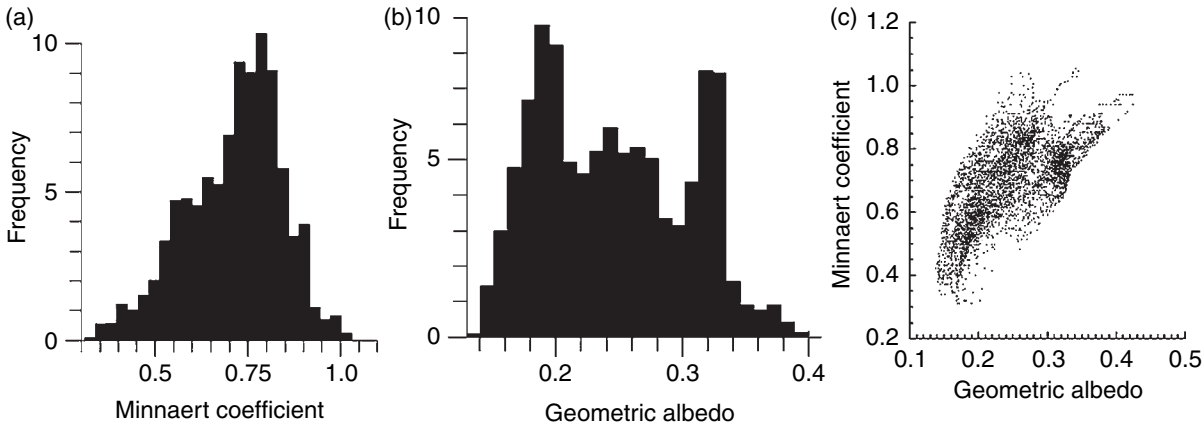

Figure 19.2. Results of Minnaert models applied to 1988 opposition measurements acquired at 0.98 μm (Pinet and Rosemberg, 2001). (a) Histogram of Minnaert coefficient k parameters; (b) Histogram of geometric albedo values; (c) Scatter plot of k versus geometric albedo.

De Vaucouleurs (1967) compiled observations acquired in unfiltered (white) light and using green and red filters to create a low resolution (~600 km) photometric map of relative luminance values of Mars near opposition. He estimated absolute radiometric albedos (integrated over all wavelengths) ranging from ~0.08 for the darkest regions (e.g., Syrtis Major) to ~0.30 in the brightest regions (e.g., Arabia Terra).

O'Leary (1967) detected a nonlinear increase in brightness near zero phase angle indicating an opposition effect in the Martian phase curve. O'Leary and Rea (1968) used the same data to determine that the opposition effect scales inversely with wavelength and albedo. They concluded that the pronounced opposition effect of the classically bright Martian surface regions meant that these areas must be physically different than any lunar surfaces. They further suggested that because the opposition effect of the lunar highlands is close to the upper limit of the opposition effect reported for the dark surfaces on Mars, it was improbable that these two surfaces were similar in nature. O'Leary and Rea (1968) and Mead (1970) suggested that scattering, particularly Mie scattering, in the Martian atmosphere may contribute to the opposition effect. Unfortunately, O'Leary (1967) selected a variable star for his standard and as such his results have relatively larger uncertainties (Young 1975).

Egan (1969) compared measurements of the albedo, phase curve, limb darkening, and polarimetric properties of laboratory samples to results from previous studies of Mars to constrain the composition and structure of the Martian surface. Limonite (any one of a number of hydrated forms of iron oxide, $Fe_2O_3 \cdot nH_2O$) with median particle size of 1–2 mm and a minor component of <1 μm limonite or <37 μm siderite (an iron-bearing carbonate, $FeCO_3$) was determined to provide the best match to the observed Martian photometric and polarimetric properties. However, O'Leary and Pollack (1969) concluded that the mean particle size was probably an order of magnitude smaller than Egan's 1–2 mm estimate. By comparing the reflectance values of typical bright and dark areas across visible wavelengths, Pollack and Sagan (1968) concluded that the pronounced increase in brightness between 450 and 650 nm is due to multiple scattering of light in powdered iron oxides. They postulated that the composition of the dark regions was similar to that of the bright regions but that the decrease in brightness in the dark regions is caused by a larger mean particle size.

Binder and Jones (1972) acquired multispectral data in 10 bands from 595 to 2270 nm over phase angles from 2° to 26° during the 1969 opposition. They used a Minnaert function to model data acquired in the "uniform deserts" (e.g., Chryse, Tharsis, and Amazonis) and reported results for k that suggested these regions became more like Lambertian surfaces ($k \sim 1.0$) at longer wavelengths and larger phase angles, although this was potentially a consequence of diminishing Martian atmospheric contributions to their observations at longer wavelengths.

During the 1988 opposition, visible/near-infrared multispectral imaging data of the Martian eastern hemisphere at 100–300 km spatial resolution were obtained at phase angles from 3.0° to 5.5° (de Grenier and Pinet, 1995). Minnaert's equation was used to approximate the photometric behavior, which limited analyses to incidence and emergence angles <60° (e.g., McEwen *et al.*, 1991). Regional variations of the Minnaert coefficient and geometric albedo were mapped by Pinet and Rosemberg (2001; Figure 19.2) using the procedure developed by de Grenier and Pinet (1995). The modal value for k was ~0.75, although a wide range of values were modeled. Values <0.50 were more evident in low-albedo terrains compared to larger, more variable k values for intermediate/high-albedo terrains (Figure 19.2c; see Tejfel *et al.*, 1992). Although atmospheric multiple scattering longward of 0.70 μm could easily contribute to uncertainties in the model results (e.g., Combes *et al.*, 1991; Drossart *et al.*, 1991; Erard *et al.*, 1994), the 1988 observations were acquired under low opacity (~0.5) conditions (Pinet and Chevrel, 1990).

19.3.2 Mariner spacecraft observations

The advent of spacecraft observations expanded available data to larger phase angles than obtainable from Earth-based observations. A combination of these datasets and telescopic observations was used to quantify the apparent

surface brightness variations across the surface and infer surface properties such as porosity and grain size.

Young (1969) modeled the Martian surface photometric properties using Mariner 4 television data by fitting a Minnaert function to the surface. By extrapolating to the expected surface brightness of the limb, he modeled the residual observed brightness as atmospheric scattering, yielding an optical depth profile of the Martian atmosphere. However, the Mariner 4 data were significantly affected by stray light, leading Young and Collins (1971) to use Mariner 6 and 7 data to analyze five regions on Mars over a narrow phase angle range (20°–24°). Although the analyses were mainly performed to compare the performance of the Mariner 6 versus 7 cameras, the resulting k and A_M values varied substantially among the different regions studied, which Young and Collins attributed to variations in albedo and porosity of surface materials.

Pleskot and Kieffer (1977) expanded on these studies by using the Mariner 6 and 7 infrared spectrometer (IRS) data to analyze observations of several regions at four phase angles from 39° to 84° over three wavelengths from 1850 to 3500 nm. They combined their infrared results with those of Binder and Jones (1972) to determine that bright regions scatter according to Minnaert's law and have similar Minnaert indices, but that darker regions (e.g., Sinus Meridiani) do not follow Minnaert's law as well. They also noted that Hellas Basin exhibited notably lower Minnaert indices and suggested this was a result of a more powdery, porous surface than typical bright "deserts." All their Minnaert indices were ~1.0, although they noted that their phase coverage was insufficient to determine the Minnaert index very well.

Pang and Hord (1971) used Mariner 7 near-ultraviolet data to model the photometric properties of Mars' polar cap to constrain the surface roughness of the south polar cap. They found that the polar cap exhibits varying degrees of specular scattering during different seasons and used this to develop a model for the formation of the seasonal polar cap. Hord *et al*. (1972) used the Mariner 9 ultraviolet spectrometer dataset covering phase angles from 15° to 84° to study variations in atmospheric pressure across the Martian surface and to construct a rudimentary topographic map of the surface. They also demonstrated that a Minnaert function was not sufficient to adequately describe the surface reflectance at ultraviolet wavelengths.

Thorpe (1973) used Mariner 9 television data to model the photometric properties of the Martian surface and atmosphere over phase angles from 20° to 80°. Although he emphasized that the photometric variability of the vidicon cameras used on the Mariner missions made analyses difficult, he found that a Minnaert function was required to model the data at phase angles >40° or at large emission and/or incidence angles.

19.4 VIKING ORBITERS

The Viking Orbiter (VO) missions (1976–80) contributed much to our understanding of the diversity of scattering behavior on Mars' surface. The Orbiters' steerable scan platforms, changes in the orbital elements and the longevity of the missions combined to produce a rich dataset of repeated observations with a wide variety of incidence, emergence, and phase angles, ideal for photometric studies. On the other hand, the large (~15%) uncertainties in absolute calibration inherent in the imagers' vidicon technology combined with the day-to-day changes in atmospheric opacity made photometric analyses of the VO images challenging. The earliest studies of these data aimed to derive a globally averaged photometric model for Mars, valid for phase angles unobservable from Earth, that could be used to correct imaging observations for variations in illumination and viewing geometry and to construct global mosaics (e.g., Thorpe, 1977; Soderblom *et al*., 1978).

The first disk-resolved photometric studies were performed by Thorpe (1978, 1979, 1982), using low phase angle (0°–7°) images from Syrtis Major, Arabia, and Chryse, supplemented by low phase images of a dust storm in Mare Erythraeum and slightly higher phase (5°–15°) images of Elysium. Thorpe found that pronounced, narrow opposition surges were ubiquitous among bright, dust-covered surfaces. The zero phase brightness of such regions was enhanced by ~10% in the VO red filter, and the angular width of the opposition spike was ~3°. The surges were more pronounced (narrower and larger) with increasing albedo. In contrast, opposition surges were either absent from the dark, dust-free Syrtis Major region or their widths were so broad as to be indistinguishable. Thorpe presented quantitative analyses of these measurements that included considerations of atmospheric scattering (constrained by opposition effect measurements of the dust storm at Erythraeum), surface roughness, and linear mixing of two components with different scattering behaviors. He interpreted the results in terms of porosity (opposition effect width), particle size, and roughness (both related to the slope of the phase curve outside of the opposition spike).

The problems surrounding the use of high phase angle data continued to daunt investigators until the late 1980s, when two crucial facts were pointed out. First, Arvidson *et al*. (1989a) showed that uncorrected (exoatmospheric) VO data closely matched the predictions of a photometric model derived from surface observations made from Viking Lander 1, suggesting that atmospheric and roughness effects could be neglected under certain circumstances (atmospheric opacity $\tau < 0.47$, $\bar{\theta} < 10°$). Second, large-scale differences were seen between the high phase (106°) VO 2 approach mosaic and the lower phase (47°) VO 1 apoapsis mosaic that were attributed by Strickland (1989) to surface roughness variations. Thus encouraged, two separate studies were initiated to derive surface photometric parameters from VO images using the full range of available phase angles, acquired during various seasons, times of day, and atmospheric conditions throughout the mission.

Regner (Regner *et al*., 1998; Regner, 1990) selected 325 training sites in Oxia Palus, including Chryse, and extracted radiance factor estimates from images ranging in phase from 0.2° to 107°. These measurements were inverted for five of Hapke's (1986) parameters: single scattering albedo (w), single scattering phase function asymmetry factor (ξ),

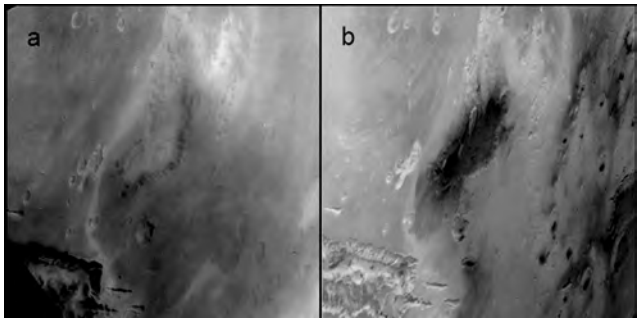

Figure 19.3. Images of Juvente Chasma (looking to the northeast) acquired by Viking Orbiter 1 under different phase angles (g): (a) Image 759A67 ($g = 113°$); (b) Image 334S41/43 ($g = 37°$). At high phase angles the strongly forward-scattering sand deposits in the interior of Juvente are brighter than the neighboring plains, whereas at lower phase angles, the low-albedo sand deposits are darker than the plains.

opposition effect amplitude (*B0*), opposition compaction parameter (h), and average macroscopic roughness ($\bar{\theta}$). In addition, three additional parameters were solved using a modified version of the Hapke scattering model to account for atmospheric scattering: the aerosol single scattering albedo, aerosol single scattering phase function asymmetry factor, and optical depth, bringing the total number of unknowns to eight. Regner found that the atmospheric opacity calculated in this way was very small ($\tau < 0.05$). He found that all terrains were forward scattering, becoming more forward scattering with increasing albedo. He found that for a given wavelength the opposition effect amplitude increased and width diminished with increasing albedo. He also found no significant change in opposition width between VO red and blue filters.

Geissler (1992; Geissler and Singer, 1992) analyzed images from the Juventae Chasma area of Coprates (Figure 19.3) that spanned a range of phase angles from 20° to 120°, precluding any estimation of the opposition effect. These data were analyzed on a pixel-by-pixel basis, so that spatial continuity of the results could be examined. Atmospheric effects and calibration uncertainties were included together in multiplicative and additive terms that were required to be consistent across the whole of each individual image, and were derived in an earlier iteration of the calculation and subsequently held constant. Hence, the photometric inversion solved for only four unknowns: single scattering albedo w, the terms b and c of a two-term HG single scattering phase function, and average macroscopic roughness $\bar{\theta}$. Surprisingly, even this reduced set of unknowns could not be uniquely derived. Geissler found that values for the single scattering albedo, phase function, and roughness varied wildly from one pixel to the next when solving for the parameters simultaneously. Only by holding the roughness constant could he obtain spatially coherent results. After the albedo and phase function were established, macroscopic roughness could then be estimated. This behavior was attributed to the strong mathematical coupling between macroscopic roughness and both single scattering albedo and single scattering phase function (e.g., Helfenstein and Veverka, 1987), allowing multiple combinations of the parameters to fit the data equally well. The maps of photometric parameters ultimately produced by this analysis correlated well with the observed geology. The bright red (dust) and dark red (indurated dust) units in the area showed differences in single scattering albedo but identical phase functions, isotropic to slightly backscattering. In contrast, the dark sand deposits inside Juventae Chasma were markedly forward-scattering, consistent with the curious contrast reversal seen in high phase images of the sand deposits, when they appear brighter than their surroundings.

19.5 MARS EXPRESS

The High Resolution Stereo Camera (HRSC) and the Observatoire pour la Minéralogie, l'Eau, les Glaces et l'Activité (OMEGA) instruments on board the MEx spacecraft have been used to derive surface photometric characteristics for Martian regions. The HRSC camera is a pushbroom imaging system containing nine parallel Charge-coupled device (CCD)–line detectors. Five of the nine detectors have the same panchromatic filters that are nominally directed toward nadir. Two photometric channels (directed 12.9° in both directions from nadir) and two stereo channels (directed 18.9° from nadir) provide five overlapping images that can be used to extract photometric information. However, the narrow range of photometric angles in a single HRSC image set does not contain enough information to constrain the photometric function (Pinet *et al*., 2005a, 2006; Jehl *et al*., 2006). Further, atmospheric contributions of ~10%–20% in apparent surface brightness complicate models of the surface. Kreslavsky *et al*. (2006) proposed a method to compensate for these issues by mapping an interpretable photometric parameter from a single HRSC image set that is sensitive to the relative changes in the steepness of the phase function slope, with steeper slopes indicating a rougher surface. Application of this procedure to HRSC images taken over Hesperia Planum revealed several anomalous areas (including bright and dark wind streaks) related to variations in surface structure (e.g., Dao Vallis, Niger Vallis; Kreslavsky *et al*., 2006).

Greater phase angle coverage was possible by combining HRSC observations acquired at different times under varying illumination geometries. Up to four sets of images covering Gusev crater and the south flank of Apollinaris Patera were combined to extend the phase angle coverage to 25°–95° (Pinet *et al*., 2005a; Jehl *et al*., 2006). Jehl *et al*. (2006) applied the Hapke inversion procedure of Cord *et al*. (2003) to these data using a two-term HG function. Figure 19.4 illustrates the result of this work, including the surface properties associated with the dark wind streaks in the low-albedo region where *Spirit* landed (yellow), the northern part of the crater (red), the southwestern Gusev plains (green), the rough ($\bar{\theta} = 17°$–$27°$) southern Apollanaris terrain (pink) and smoother ($\bar{\theta} < 10°$) patches (blue), and a distinct terrain with low b (0.20–0.30), high c (0.5–0.65), and high $\bar{\theta}$ (25°–30°) values (cyan), whose distribution is limited to topographic highs (e.g., the Columbia Hills). The

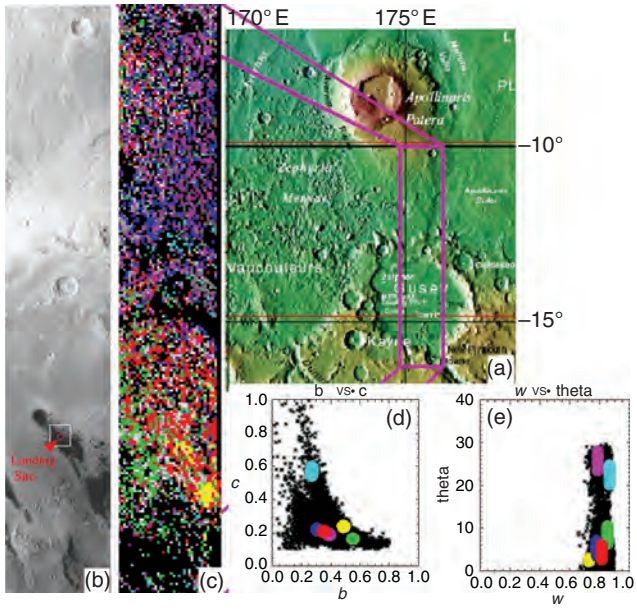

Figure 19.4. (a) Mars Observer Laser Altimeter (MOLA) shaded and color-coded topographic map showing location of HRSC image of Gusev crater and Apollonaris Patera shown in (b), which designates the MER *Spirit* rover landing site. (c) Color-coded map of photometric units modeled by Jehl *et al.* (2006); (d) 2-term Henyey–Greenstein parameters *b* and *c* for all pixels in (c); (e) single-scattering albedo (*w*) and macroscopic surface roughness values ("theta") modeled by Jehl *et al.* (2006). Color regions in (d) and (e) correspond to units in (c) and are arranged as follows: yellow = low-albedo region; red = northern Gusev plains; green = southwestern Gusev plains; pink = rough Apollanaris plains; blue = smooth Apollanaris plains; cyan = topographic highs (see text). (For a color version of this figure, please refer to the color plate section or to the e-Book version of this chapter.)

photometric contrast observed between the Gusev plains and the Columbia Hills is consistent with *in situ* and other orbital photometric surveys (Johnson *et al.*, 2006a) and studies of surface textures (e.g., Martinez-Alonso *et al.*, 2005).

Emission phase function (EPF) spacecraft observations allow extensive angular coverage and allow assessment and separation of surface and aerosol scattering phase functions. By rotating the MEx spacecraft during orbit 604 in 2004, the OMEGA instrument obtained an EPF over a homogeneous equatorial region in Medusae Fossae, covering phase angles 60°–95° and emission angles 2°–58°. Pinet *et al.* (2005b) modeled these data to determine that the two-term phase function parameters (*b*, *c*) for most surface units displayed coherent spatial variations. As of this writing, OMEGA EPF observations are underway over low-albedo areas (e.g., Meridiani, Syrtis Major) to document their surface/aerosol scattering properties.

19.6 HUBBLE SPACE TELESCOPE

Photometric analysis of data acquired using the 1042 nm filter of Wide Field/Planetary Camera 2 (WFPC2) on board the HST between 1995 and 1997 was performed by Bell *et al.* (1999). These data spanned phase angles from 10° to 40° and covered latitudes from 60° S to 90° N. After applying a Minnaert correction to the images, they reported little correlation between phase coefficient and normal albedo, which they attributed to the diffusely scattering nature of the Martian atmosphere even during low opacity conditions.

Subsequent work by Soderblom *et al.* (2006a) included WFPC2 data acquired between 1996 and 2005 as part of a long-term observing campaign. Images were acquired in five bands between 400 and 1050 nm and modeled using a series of photometric functions including Lambert, Minnaert, Lunar–Lambert, and Hapke. The data were processed and calibrated to units of flux or radiance (e.g., $W\,cm^{-2}\,nm^{-1}\,sr^{-1}$) and then to radiance factor or I/F (where I is the radiance observed from the scene and πF is the incident solar irradiance at the top of the Martian atmosphere at the time of the observation and convolved to the bandpass of the relevant filter), as described in Bell *et al.* (1999) and Wolff *et al.* (1999). No attempts were made to model the scattering by atmospheric dust, although errors were minimized by selecting data with low dust opacities as retrieved from the Thermal Emission Spectrometer (TES) aboard the Mars Global Surveyor spacecraft (Smith *et al.*, 2000). Phase coefficients varied from 0.014 ± 0.002 mag/deg (at 502 nm) to 0.0094 ± 0.0035 mag/deg (at 1042 nm). Visibly opaque water-ice clouds were excluded from the analysis by identifying all pixels with a reflectance at 410 nm above a threshold after applying a Minnaert correction.

Data were extracted for several geographic regions representing endmembers of albedo and thermal inertia (Syrtis Major, Arabia Terra, Isidis, and Amazonis Planitia). Among the photometric models used, Soderblom *et al.* (2006a) preferred the empirical Lunar–Lambert model, despite limitations on its suitability to model data acquired under periods of low atmospheric opacity and for phase angles between 3° and 40°. They suggested that the particles that comprise the high-albedo surfaces are more loosely packed and/or have a nonuniform grain size distribution compared to lower albedo surfaces. The Hapke models were underconstrained by the available data. Indeed, the lack of high phase data made it difficult to constrain the forward-scattering nature of the surface for all explicit single scattering phase functions.

19.7 VIKING LANDERS

The Viking Landers were two identical spacecraft that landed on the surface of Mars in 1976 and operated on the surface for several years (Soffen, 1977; Moore *et al.*, 1987). Viking Lander 1, which was renamed as the Mutch Memorial Station, touched down on Chryse Planitia in an area dominated by a rock-strewn surface, along with exposed bedrock and loose and partially indurated soils. Soil material was also found in drifts within a few meters of the spacecraft. Individual rocks were sitting on top of and partially buried within the soil material (Binder *et al.*, 1977). Viking Lander 2, which was renamed as the Soffen

Memorial Station, landed on Utopia Planitia and also found a soil-covered surface with abundant rocks on the surface and partially buried within the soil (Mutch *et al.*, 1977). Many of the rocks at both landing sites had a combination of bright surfaces and darker facets, particularly at their edges. Both Landers were equipped with an imaging system consisting of 2 stereo cameras with 6 multispectral filters covering wavelengths from 400 to 1100 nm. There were three color filters: blue, green, and red filters with bandwidths of 400–520, 500–590, and 600–740 nm, respectively. Each camera also had three near-infrared filters that have not been used in any photometric analysis because they had significant out-of-band responses. Moreover, the response functions and calibrations of the infrared filters likely degraded during the mission due to neutron radiation from the radioisotope thermoelectric generators that powered the Landers (Huck *et al.*, 1975; Patterson *et al.*, 1977).

Several imaging sequences were acquired by the Viking Lander cameras in order to investigate the photometric properties of rock and soil materials seen near the Landers (Figure 19.5). These sequences typically viewed the same area on the surface at multiple times within a single sol. Photometric sequences were acquired early in the mission and then again nearly 1 Mars year later after a thin dust layer was deposited on the surface at both landing sites (Guinness *et al.*, 1979). These specially designed photometric sequences provided data where individual surface features were seen at a single viewing geometry and with multiple illumination angles. In order to view rock and soil materials at multiple emission angles, images covering different areas of the landing site were also used in photometric modeling with the assumption that the material seen at those separate locations have uniform photometric properties.

Radiance factor values were computed from Viking Lander image data using preflight calibration parameters whose accuracy was verified by analysis of images of the Reference Test Charts mounted on the Landers. The estimated uncertainty in computed radiance factor values was about ±10% (Guinness *et al.*, 1987). Calibrated radiance factor values were corrected for diffuse illumination based on the camera response for shadows in the scene. Adjustments to radiance factor values for attenuation of the incoming illumination were based on optical depth measurements made using the camera's specialized solar filter (e.g., Pollack *et al.*, 1979).

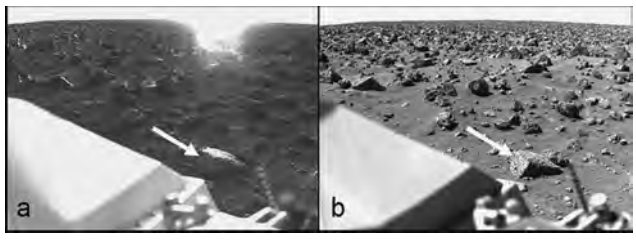

Figure 19.5. Viking Lander 2 red filter image pairs. (a) Portion of 21B124 acquired on Sol 045 at high phase angle (~18:30 local solar time, incidence = 85.1°) showing pronounced specular reflection in ~20 cm rock designated with arrow. (b) Portion of 21A213 image acquired on Sol 025 at intermediate phase angle showing same rock (~1200 local solar time, incidence = 29.1°).

Several photometric studies have been published that applied a variety of photometric models to Viking Lander image data. Photometric observations of soil-covered areas acquired during the primary phase of the mission were modeled with the initial version of the Hapke photometric function (Hapke, 1981), which did not include a macroscopic roughness term (Guinness, 1981). The Hapke models of these soil areas showed a prominent opposition effect at phase angles less than about 20°. The soil models also had phase functions that were backscattering. In addition, the shape of the photometric functions was different for the three color filters. As a result, a ratio computed from two filters, such as a red/blue ratio, will systematically vary as a function of phase angle. The soil red/blue ratio increases as the phase angle increases from near zero phase, reaches a maximum at about 75°, and then begins to decline at even larger phase angles (Guinness, 1981). This effect was also seen in images acquired after the deposition of dust on the surface at the Viking Lander 2 site (Guinness *et al.*, 1979). Photometric observations of soil-covered areas acquired after the deposition of a thin dust layer at the Viking 1 landing site were modeled with the Hapke (1984) function, which included the macroscopic roughness term (Arvidson *et al.*, 1989a). Single scattering albedo values for the dust deposit are shown in Figure 19.6. The macroscopic roughness parameter was modeled at about 5°–6°. The opposition effect *h* parameter, which governs the width of the opposition effect, ranged from 0.13 to 0.17 in the three color filters (Table 19.1). The modeled phase function was generally backscattering at all three wavelengths, consistent with previous photometric modeling of soils at the landing site. The derived Hapke photometric parameters of the dust-covered soil were used to compute a reflectance that corresponded to lighting and viewing geometries for VO images of the landing site. Results of the comparison suggested that the color of the dust-covered soil dominated the color of the site seen from orbit (Arvidson *et al.*, 1989a,b).

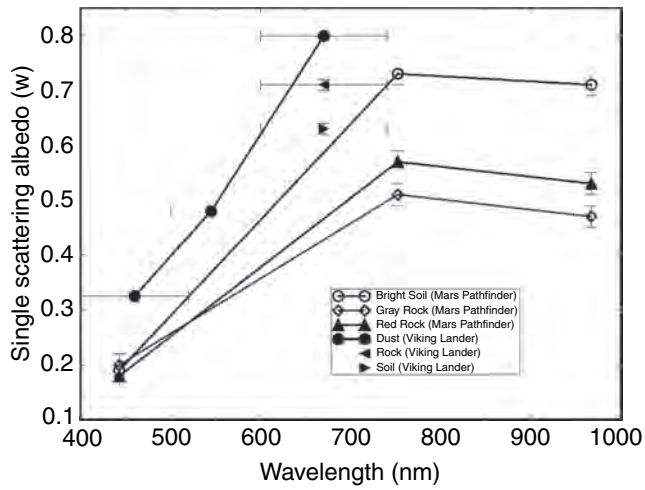

Figure 19.6. Single scattering albedos derived for Mars Pathfinder Gray rock, Red rock, and Soil units (Johnson *et al.*, 1999), Viking Lander dust (Arvidson *et al.*, 1989a), and rock and soil units (Guinness *et al.*, 1997). Vertical error bars are standard deviations of *w* values.

Table 19.1. *Representative Hapke model parameters from orbiter and landed missions*

Mission	Unit type/area	λ (nm)	w	$\bar{\theta}$	ξ	b	c	h	$B0$	g	Reference
Viking Lander 1	Dust	465	0.33	6.4°	−0.066	—	—	0.125	0.397	6°–130°	Arvidson *et al.* (1989a)
		545	0.48	5.3°	−0.089			0.136	0.629		
		670	0.80	5.4°	−0.101			0.173	1.090		
Viking Landers 1, 2	Rocks	670	0.71	8.9°	—	—	—	0.13	2.00	1°–169°	Guinness *et al.* (1997)
Viking Landers 1, 2	Soils	670	0.63	26.8°	—	—	—	0.14	2.00	1°–169°	Guinness *et al.* (1997)
Viking Orbiter	Arabia	443	0.41	—	—	—	—	0.17	—	0°–19°	Thorpe (1982)
		592	0.76					0.13			
Viking Orbiter	Chryse	443	0.41	—	—	—	—	0.25	—	0°–19°	Thorpe (1982)
		592	0.68					0.26			
Viking Orbiter	Syrtis Major	443	0.41	—	—	—	—	0.45	—	0°–19°	Thorpe (1982)
		592	0.51					0.4			
Viking Orbiter	Elysium Planitia	443	0.41	—	—	—	—	0.25	—	0°–19°	Thorpe (1982)
		592	0.60					0.25			
Viking Orbiter	Mare Erythraeum	443	0.41	—	—	—	—	0.25	—	0°–19°	Thorpe (1982)
		592	0.68					0.12			
Viking Orbiter	Oxia Palus	440	0.29–0.64	1°–8°	0.345–0.990	—	—	0.01–0.33	0.17–0.63	0°–107°	Regner *et al.* (1988)
		592	0.53–0.81	1°–8°	0.152–0.834			0.01–0.35	0.36–0.91		
Viking Orbiter	Juventae Chasma sands	592	0.58	—	—	0.283	0.117	—	—	19°–116°	Geissler (1992)
Viking Orbiter	V. Marineris plains	592	0.64	—	—	0.173	0.596	—	—	19°–116°	Geissler (1992)
Mars Pathfinder	Bright soil	443	0.19		—	0.285	0.522	0.062	1.00	2°–177°	Johnson *et al.* (1999)
		752	0.73	4°		0.113	0.997	0.062	0.37		
		967	0.71			0.095	1.000	0.062	0.24		
Mars Pathfinder	Dark soil	443	0.16		—	0.200	0.925	0.100	1.00	4°–135°	Johnson *et al.* (1999)
		752	0.53	2°		0.178	1.000	0.100	0.73		
		967	0.50			0.183	1.000	0.100	0.66		
Mars Pathfinder	Red rock	443	0.18		—	0.205	0.870	0.068	1.00	5°–178°	Johnson *et al.* (1999)
		752	0.57	4°		0.178	1.000	0.068	0.38		
		967	0.53			0.173	1.000	0.068	0.18		
Mars Pathfinder	Gray rock	443	0.20		—	0.348	0.432	0.054	0.99	5°–137°	Johnson *et al.* (1999)
		752	0.51	4°		0.375	0.367	0.054	0.41		
		967	0.47			0.363	0.397	0.054	0.16		
Mars Express	Gusev plains	679	0.80–0.85	2°–10°	—	0.37–0.58	0.12–0.26	—	—	25°–95°	Jehl *et al.* (2006)
Mars Express	Columbia Hills	679	0.75–0.85	20°–30°	—	0.15–0.30	0.48–0.75	—	—	25°–95°	Jehl *et al.* (2006)

MER – *Spirit*	Drift[a]	432/436	0.29 ± 0.01		−0.021 ± 0.008			—	—	65°–122°	Johnson *et al.* (2006a)
		601	0.62 ± 0.01	2°	+0.025 ± 0.010	0.245 ± 0.013	0.583 ± 0.062				
		753/754	0.75 ± 0.01		−0.046 ± 0.007						
		1009	0.75 ± 0.01		−0.058 ± 0.007						
MER – *Spirit*	Soil[a]	432/436	0.25 ± 0.12		−0.127 ± 0.043						Johnson *et al.* (2006a)
		601	0.58 ± 0.08	14° ± 7°	−0.125 ± 0.032	0.346 ± 0.155	0.416 ± 0.246	0.094 ± 0.030	U.C.	4°–125°	
		753/754	0.71 ± 0.07		−0.141 ± 0.040						
		1009	0.72 ± 0.04		−0.115 ± 0.044						
MER – *Spirit*	Red rock[a]	432/436	0.24 ± 0.08		−0.110 ± 0.054						Johnson *et al.* (2006a)
		601	0.64 ± 0.07	19° ± 5°	−0.124 ± 0.040	0.332 ± 0.122	0.429 ± 0.242	0.115 ± 0.045	U.C.	4°–125°	
		753/754	0.77 ± 0.06		−0.169 ± 0.074						
		1009	0.75 ± 0.06		−0.139 ± 0.074						
MER – *Spirit*	Gray rock[a]	432/436	0.30 ± 0.09		−0.063 ± 0.075						Johnson *et al.* (2006a)
		601	0.65 ± 0.06	18° ± 7°	−0.072 ± 0.060	0.497 ± 0.165	0.184 ± 0.109	0.118 ± 0.024	U.C.	2°–118°	
		753/754	0.75 ± 0.06		+ 0.168 ± 0.461						
		1009	0.74 ± 0.06		−0.061 ± 0.093						
MER – *Opportunity*	Soil[a,b]	432/436	0.17 ± 0.02		−0.114 ± 0.032						Johnson *et al.* (2006b)
		601	0.40 ± 0.02	8° ± 2°	−0.156 ± 0.041	0.264 ± 0.073	0.592 ± 0.167	0.067 ± 0.020	U.C.	∼0°–150°	
		753/754	0.48 ± 0.03		−0.155 ± 0.043						
		1009	0.48 ± 0.03		−0.113 ± 0.059						
MER – *Opportunity*	Outcrop[a]	432/436	0.44 ± 0.10		−0.086 ± 0.060			—	—		Johnson *et al.* (2006b)
		601	0.75 ± 0.05	22° ± 6°	−0.126 ± 0.046	0.453 ± 0.192	0.291 ± 0.272			15°–124°	
		753/754	0.84 ± 0.06		−0.131 ± 0.062						
		1009	0.83 ± 0.05		−0.154 ± 0.044						

λ = wavelength; w = single scattering albedo; $\bar{\theta}$ = average macroscopic roughness; ξ=1-term Henyey–Greenstein single scattering phase function asymmetry factor, b = two-term Henyey–Greenstein asymmetry factor; c = backward scattering fraction; h = opposition compaction parameter; *B0* = opposition effect amplitude; g = phase angle coverage. U.C. = parameter was underconstrained by the model.

Note that because of variations in (1) incidence, emission, and phase angle coverage, (2) type(s) of atmospheric correction applied, (3) forms of (and constraints applied to) the photometric functions used in the Hapke models, direct comparison among these model results is inadvisable, and individual references should be consulted for details.

[a] All values except ω and ξ are averages of all wavelengths. All values derived from two-term HG models except h and ξ.

[b] Soil average values are for plains units only (excludes data from impact craters Eagle, Endurance, and Vostok).

Reflectance data from bright and dark facets on a large boulder seen at Viking Lander 2 were modeled with a single scattering model that used an empirical exponential phase function (sometimes referred to as a "Hapke–Irvine function"; Guinness *et al*., 1987). This relatively simple model was applied to the dataset because the observations were all made at fairly large phase angles so that the opposition effect was not a factor and because the overall dark tone of the rock suggested that single scattering was the dominant scattering factor. The intent of the study was to investigate whether the brightness variations on the rock were due to lighting and viewing differences versus an inherent difference in the materials exposed in the bright and dark areas. Model results showed that different photometric parameters were needed to properly model the bright and dark areas and that the two areas would have different reflectance values when viewed at a common geometry. The darker facet was shown to have a color similar to laboratory data for mafic rocks that were thinly coated with nanophase ferric oxide material, whereas the color of the brighter facet was consistent with a thicker coating of the same nanophase ferric oxide material (Guinness *et al*., 1987). A more recent study of the photometric properties of rocks and soils at the Viking landing sites used a model that combined the current Hapke model (Hapke, 1993) with a specular scattering model of Shepard *et al*. (1993) to investigate possible specular reflections observed for forward-scattering geometries (Guinness *et al*., 1997). Model single scattering albedos for the red filter (the only filter used) are shown in Figure 19.6. Both rocks and soils showed a strong opposition effect with a Hapke *h* parameter about 0.13–0.14 and had backscattering phase functions over the 1°–169° phase angle range studied (Table 19.1). Rock surfaces were found to have lower values of the roughness parameter, which implies smoother surfaces and stronger specular reflections at forward-scattering geometries. These results are consistent with rocks being abraded by wind and/or coated with atmospheric dust to produce smoother surfaces (Guinness *et al*., 1997).

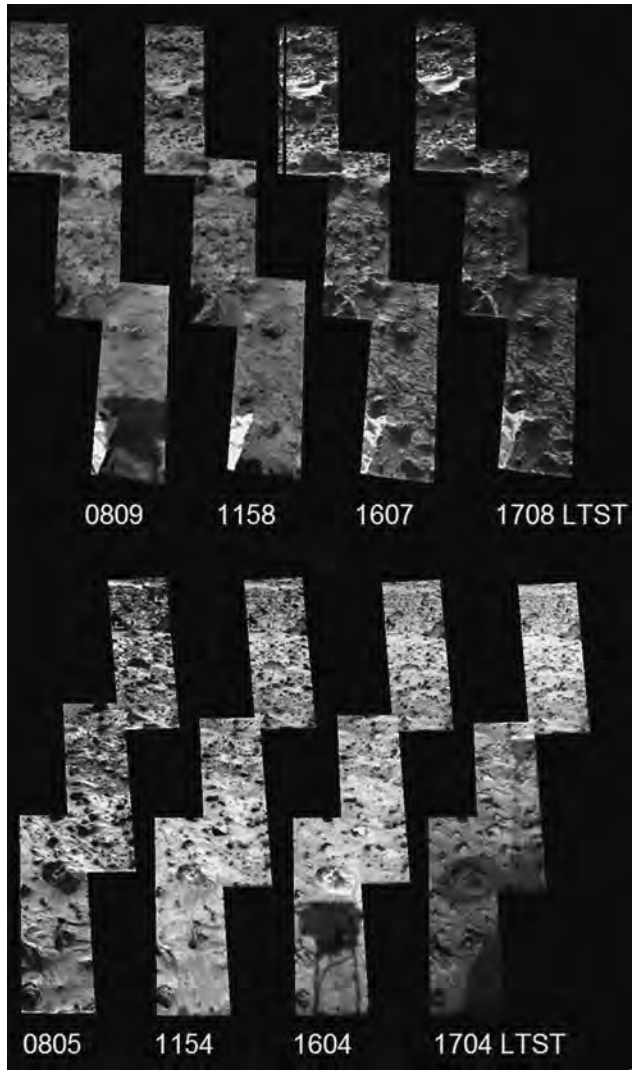

Figure 19.7. Image for Mars Pathfinder (IMP) mosaics (acquired at 752 nm) of photometric equator sequences of (top) anti-sunrise and (bottom) anti-sunset directions used by Johnson *et al*. (1999). Acquisition times (Local True Solar Time, LTST) shown below each image. Images at 0809, 1604, and 1704 LTST show shadow of IMP camera head; image at 1704 LTST also shows shadow of high gain antenna.

19.8 MARS PATHFINDER

19.8.1 Data and methods

Portions of the MPF landing site were imaged by the Imager for Mars Pathfinder (IMP) stereo camera at multiple times of day throughout the mission. The IMP was composed of two eyes, each of which illuminated one-quarter of a single 512-pixel square CCD detector (Smith *et al*., 1997) with a field-of-view of 14°. A total of 24 filters were available (12 for each eye), of which 15 were designed for imaging geologic materials from 440 to 1000 nm. Johnson *et al*. (1999) described five IMP sequences that provided multispectral reflectance measurements of rocks and soils over a wide range of phase angles. The primary sequences were obtained in three filters at four times of day ($g \sim 0°$–$155°$) and were composed of two image strips of three sub-framed, losslessly compressed images located in the principal plane along the anti-sunrise and anti-sunset lines (the so-called "photometric equator"; Figure 19.7).

IMP images were radiometrically calibrated to a quantity referred to as R^* using onboard calibration targets imaged at or near the same time of day (Reid *et al*., 1999). R^* was defined as the total radiance of the sunlit scene relative to the total radiance of the calibration targets, scaled by their "known" laboratory reflectances. In this sense, R^* is approximately equivalent to the reflectance factor (coefficient) of Hapke (1993, p. 262), defined as the ratio of the surface reflectance to that of a Lambertian surface under the same conditions of illumination and measurement. The non-Lambertian nature of the calibration targets was not accounted for in the IMP calibration algorithm (Reid

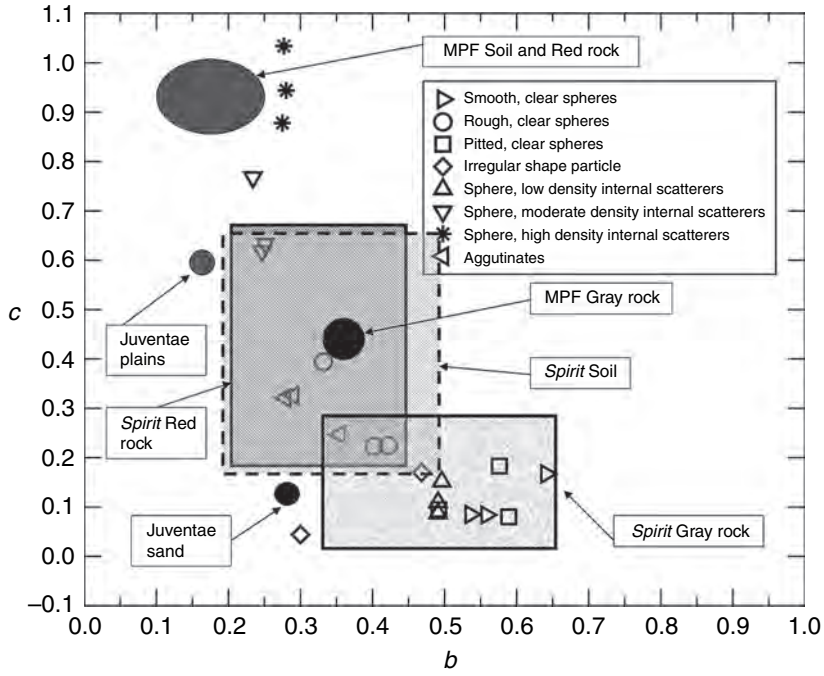

Figure 19.8. Asymmetry parameters, *b*, versus backward-scattering fraction parameters, *c*, for artificial particle types from McGuire and Hapke (1995) overlain by average regions occupied by Mars Pathfinder (MPF) Gray rock unit (solid black circle), Red rock and Soil units (gray oval) from Johnson *et al.* (1999); MER *Spirit* Gray rock, Red rock, and Soil units from Johnson *et al.* (2006a) (Table 19.1); and Juventae dark sands and brighter plains units derived from Viking Orbiter data by Geissler (1992). Gray rock units have more overall forward scattering, narrower phase functions than the more broad, backscattering nature of the Soil and Red rock units, although overlap between regions is apparent.

et al., 1999). Neither was a detailed atmospheric model used to correct for the effects of reddened diffuse skylight on the image scene (Thomas *et al.*, 1999, 2001a,b). However, atmospheric contributions were minimized by obtaining calibration target and scene images close in time under similar illumination geometries, particularly for relatively flat surfaces. Typical uncertainties on the absolute reflectance derived in the calibration were ~10% (Reid *et al.*, 1999).

The Hapke model used by Domingue *et al.* (Hapke, 1984, 1986; Domingue and Hapke, 1992; Domingue *et al.*, 1997) was slightly modified to permit use of the radiance coefficient R^* instead of radiance factor (Hapke, 1993). This model used a grid search algorithm to minimize the least-squares residual between the model and data. The search used the parameters w (single-scattering albedo), $\bar{\theta}$ (macroscopic roughness), b and c (single particle scattering parameters used in a two-term HG function), $B0$ (opposition effect amplitude), and h (opposition effect width). Error estimates for each parameter represented their variations in the ten best-fits to the model.

Material units were defined on the basis of multispectral classification work of landing site materials (McSween *et al.*, 1999; Bell *et al.*, 2000) and spectra were extracted and combined for each unit following the methods used on Viking lander multispectral images (Guinness *et al.*, 1997). "Bright soil" materials appeared brighter and redder than "dark soil" materials, whereas "gray" rocks were interpreted to be relatively less dust-covered than "red" rocks (McSween *et al.*, 1999). The phase curves derived from these data suggested a dominantly backscattering function for the rocks and soils, although a strong forward-scattering component was also observed for the gray rock materials.

19.8.2 Results

Johnson *et al.* (1999) noted that although the photometric parameters they modeled included uncertainties owing to a combination of limited phase angle coverage and residual instrument calibration uncertainties, preliminary conclusions could be made regarding the photometric properties of rocks and soils. The materials they studied were dominantly backscattering, in agreement with results from Viking lander data (e.g., Guinness, 1981; Guinness *et al.*, 1987, 1997; Arvidson *et al.*, 1989a,b). Some materials exhibited an additional forward-scattering component, particularly the gray rock unit, and the soil units demonstrated less photometric variability than the rock units. The single scattering albedo (w) was the most well-constrained parameter in the Hapke model results. The bright soils exhibited the highest albedo in the red and near-infrared, the gray rocks had the highest 443 nm albedo, and the red rock albedos were intermediate (Figure 19.6; Table 19.1).

The McGuire and Hapke (1995) artificial particle types are plotted as a function of the single particle scattering function parameters b and c in Figure 19.8 along with the scattering parameters from MPF red rocks, soils, and gray rocks, as well as results from the MER *Spirit* rover (see Section 19.9.3). Also shown are the b and c parameters derived by Geissler (1992) from VO images (converted from Legendre polynomial coefficients; see Hapke, 1993; Table 19.1) for the dark sands and brighter plains in Juventae Chasma. Soils and red rocks cluster at high c values, near materials with a high density of internal scatterers. The gray rock points plot at lower c values in the region characterized by agglutinates and rough, clear spheres. This is consistent with the theory that most rocks free from major dust contamination at the Mars Pathfinder site reveal a smooth surface (possibly a coating) similar to terrestrial varnished rock surfaces (Guinness *et al.*, 1996, 1997; Israel *et al.*,

1997). Alternatively, such a coating could be indicative of an impact-derived glassy rind, similar to that postulated by Schultz and Mustard (1998) based on laboratory reflectance spectra of terrestrial impact melts. This impact glass hypothesis is also consistent with results from the Alpha Proton X-ray Spectrometer (APXS) data (see Chapter 3).

Although the opposition width parameter h was weakly constrained by the Hapke scattering model in the IMP datasets, it appeared to increase on average from gray rock to bright soil/red rock to dark soil units. Because large values of h correspond to a less porous material and/or to lower ratios of largest-to-smallest particle size (see Helfenstein and Veverka, 1987; Hapke, 1993), the relatively larger h values for the dark soils ($h = 0.100 \pm 0.004$) implied materials with lower porosity and/or a more uniform particle size distribution. Conversely, the gray rocks' low h values ($h = 0.054 \pm 0.005$) suggested materials with higher porosity and/or a broader particle size distribution, potentially consistent with the vesicular texture observed on many gray rock surfaces or a wide range of mineral grain sizes in the rock (see McSween *et al.*, 1999). Opposition effect widths for red rocks ($h = 0.068 \pm 0.006$) suggested that their surfaces were less porous than gray rocks. The opposition effect amplitude (*B0*) decreased with increasing wavelength for materials studied by Johnson *et al.* (1999), which suggested that these materials were more opaque (more surface scattering) in the blue wavelengths, and become more transparent (more internal scattering) in the red (see Domingue and Hapke, 1992).

Johnson *et al.* (2003) analyzed IMP images of the radiometric calibration targets (RCTs) on the MPF lander acquired during the mission under a variety of illumination conditions to study the photometric properties of airfall-deposited dust on the lander deck. They implemented a version of the two-layer radiative transfer model derived by Hapke (1993), but ignored the opposition effect and macroscopic surface roughness parameters because no IMP observations were acquired at appropriate phase angles. Using this model in combination with sky brightness models, Johnson *et al.* (2003) estimated changes in the dust opacity on the RCTs throughout the mission. Their results suggested that for plausible values of effective dust grain size (10 μm) and porosity (0.8), about 5–10 μm of dust was deposited on the RCTs during the 83-sol mission. Single scattering albedo values of the deposited dust were derived for 8 wavelengths from 443 to 1003 nm, and were consistent with spectra of bright soils (Bell *et al.*, 2000) and spectra acquired of dust adhered to the magnets on the lander (Madsen *et al.*, 1999; Hviid *et al.*, 2000).

19.9 MARS EXPLORATION ROVERS

Spectrophotometric observations were acquired throughout the MER missions by the Panoramic Cameras (Pancam) to investigate the surface scattering properties of the rocks and soils encountered in the plains and hills in Gusev crater (*Spirit*) and the sulfate-rich outcrop rocks, hematite-bearing spherules and basaltic sands in Meridiani Planum (*Opportunity*). These measurements also provided ground truth for orbital measurements to better characterize regional photometric properties (e.g., Martin *et al.*, 2005; Pinet *et al.*, 2005a,b; Arvidson *et al.*, 2006a). Johnson *et al.* (2006a,b) analyzed these data using a Hapke radiative transfer model (Hapke, 1993) in combination with corrections for diffuse sky illumination (see Thomas *et al.*, 1999; Thomas, 2001b; Lemmon *et al.*, 2004) and local surface facet orientations (Soderblom *et al.*, 2004). They derived Hapke parameters of different rock and soil units that included the single scattering albedo, phase function, macroscopic roughness, and opposition effect parameters. Seelos *et al.* (2005) analyzed a subset of these data using an alternative atmospheric correction algorithm to provide a synoptic view of the landing sites for comparison to orbital datasets. The data, methods, and results from those studies are summarized below.

19.9.1 Pancam datasets

The Pancam stereo camera system is composed of two 1024×1024-pixel active area CCD cameras, each of which provide 0.27 mrad per pixel resolution and a field-of-view of 16°. A total of 16 filters were available (8 for each eye), of which 13 were designed for imaging geologic materials from 440 to 1000 nm in 11 distinct bands. Images were radiometrically calibrated using a combination of preflight and onboard measurements, and estimated uncertainties were <7% (Bell *et al.*, 2003, 2004a,b, 2006; Bell, 2004). Calibrated data were converted to radiance factor (I/F) using measurements of an RCT acquired at or near the same time of day. Absolute calibration accuracy was estimated to be ~10% or better and relative band-to-band precision was 1% to 5%.

Photometric sequences used filters that covered wavelengths of 432 nm (L7 filter), 601 nm (L4), 753 nm (L2), and 1001 nm (R7), with the stereo filter selected as either 436 nm (R1) or 754 nm (R2). Observations were most often acquired toward the east and west (along the photometric equator) to maximize phase angle coverage, although operational constraints owing to power, data volume, or duration limited phase coverage to <130° for *Spirit* datasets and to <150° for *Opportunity*. Johnson *et al.* (2006a) reported results obtained for *Spirit* up to Sol 426A, comprising three photometry sequences in the Gusev plains and five in the Columbia Hills (Table 19.2a). Johnson *et al.* (2006b) reported on results for *Opportunity* up to Sol 473B, including 4 photometry sequences acquired in Eagle crater, 2 in Endurance crater, and 11 more in the plains west and south of Endurance (Table 19.2b).

19.9.2 Methods

Johnson *et al.* (2006a,b) analyzed each of the datasets using a four-step procedure: (1) Analysis of spectral variability within the scenes and selection of regions of interest (ROIs) representative of the spectrophotometric and/or geomorphologic endmember rocks and soils; (2) Creation of "Photometry QUBs" described below; (3) Application of

Table 19.2a. Spirit *Pancam photometry sequences*

Sol	Location	Site(s)	Position(s)	Filters	Local Azimuths	Phase range (°)
13	Landing site	03	09	L247R27	West	~30–120
87–88	Bonneville rim	23	00	L247R27	West, east	~25–120
102–103	NW of Missoula	29	00	L247R17	North, south, east, west	~0–125
212–225	Cahokia	85	00,22	L247R17	East, west	~0–125
284–286	Palenque 1	89	87	L247R17	West, southeast	~0–100
291–295	Palenque 2	89	87,92	L247R17	East	~0–100
401–404	Paso Robles 1	106	00	L247R17	East, southeast, northeast	~0–70
425–426	Paso Robles 2	108	139	L247R17	East, southeast, northeast	~10–110

Source: Johnson *et al.* (2006a).

Table 19.2b. Opportunity *Pancam photometry sequences*

Sols	Location	Site(s)	Position(s)	Filters	Local Azimuths	Phase range (°)
11	Eagle crater (Landing site)	02	04	L247R27	West, east	40–115
29–33	Eagle crater (McKittrick/Guadalupe/ Tamanend Park)	04	54	All	North, east-northeast	30–90
38–39	Eagle crater (Last Chance)	05	44	L247R27	North, east	20–105
42–45	Eagle crater (Berrybowl)	05	106	All	West	30–125
89–91	Plains NW of Endurance	15	00	L247R17	North, south, west, east	~0–150
261–262	Endurance: Wopmay	36	193	L27R12	East	20–80
306–307	Endurance: Tipuna	38	275	L247R17	Southeast	25–75
328–329	Westpoint (Heatshield)	40	103	L247R17	East-southeast	~0–75
335–336	Heatshield	40	144	L247R17	West	~0–150
339–352	Heatshield Rock	40	170/226/ 233/265	L247R17	West	40–100
363	Plains S of Endurance (near Alvin crater)	42	3	L247R17	East, west	25–110
367–374	Trench site (near Alvin crater)	42	217, 231	L247R17	North, south, west, east	~0–150
403–404	Valentina (Vostok crater)	50	0	L247R17	East-southeast	30–90
437–439	Plains S of Voyager	55	3	L247R17	East, west	~5–140
449–455	Purgatory Ripple	55	226	L247R27	North, south, west, east	~0–135
473	Purgatory Ripple	55	383	L247R27	East, west	52–115

Source: Johnson *et al.* (2006b).

the sky radiance model of Lemmon *et al.* (2004) to compensate for the effects of reddened diffuse skylight for a given sol, local time, and ROI; and (4) Derivation of Hapke scattering parameters at a given wavelength for each endmember unit using bidirectional reflectance observations corrected for diffuse skylight and incorporating local facet tilts for ROIs.

To increase the phase angle sampling of particular geologic materials, distinct units were defined in each Pancam dataset on the basis of experience gained from classification work of rocks and soils from Pancam multispectral imaging (Bell *et al.*, 2004a,b, 2006; Farrand *et al.*, 2006; McSween *et al.*, 2006), Miniature Thermal Emission Spectrometer (Mini-TES) observations (Christensen *et al.*, 2004; Ruff *et al.*, 2006), and geomorphologic characteristics (e.g., Crumpler *et al.*, 2005; Golombek *et al.*, 2005; Grant *et al.*, 2004). This classification method was similar to those used for photometry studies of the Viking Lander and MPF sites (Guinness *et al.*, 1997; Johnson *et al.*, 1999) and resulted in typical unit classes such as "Gray" rocks (those inferred to be relatively free of airfall-deposited dust or other coatings), "Red" rocks (those with greater amounts of coatings), and

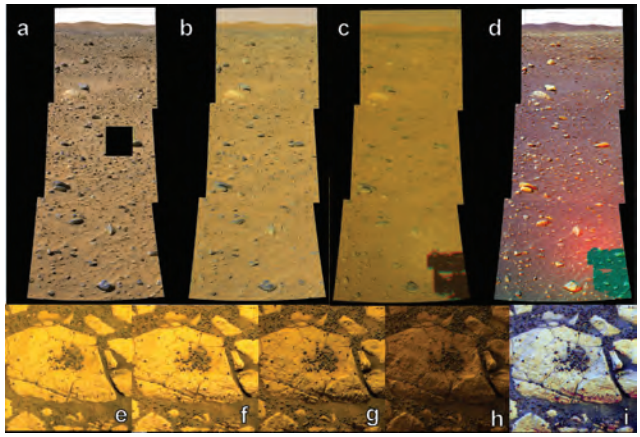

Figure 19.9. Top: False-color *Spirit* Pancam image mosaics acquired on Sols 102–103 pointed east (sequence P2382) acquired at (a) 1024 (the black rectangle represents a missing data packet in the L4 filter), (b) 1308, and (c) 1519 LTST. Images constructed from I/F data using 753 nm (L2), 601 nm (L4), and 432 nm (L7) filters (identical stretches applied to each mosaic: red = 0.00–0.035, green = 0.00–0.03, blue = 0.00–0.10). Color composite (d) derived from different times of day for the same wavelength (432 nm) using red = 1519 LTST (central phase angle = 15°); green = 1308 LTST (47°); blue = 1023 LTST (88°). Note opposition effect near Pancam Mast Assembly shadow (from Johnson *et al.* [2006a]). Bottom: *Opportunity* Pancam images acquired of the "Berrybowl" in Eagle crater on Sols 42–45 at (e) 1028 (sequence P2556), (f) 1235 (P2552), (g) 1449 (P2548), and (h) 1705 LTST (P2552). All images constructed from I/F data using 753 nm (L2), 601 nm (L4), and 432 nm (L7) filters; identical stretches applied to each band: 0.00–0.30, except for (d) which is stretched 0.00–0.15. Color composite (i) derived from different times of day for the same wavelength (753 nm) using red = 1027 LTST (central phase angle = 34°); green = 1235 LTST (61°); blue = 1703 LTST (124°). (For a color version of this figure, please refer to the color plate section or to the e-Book version of this chapter.)

different types of "Soil" units. An additional means of discriminating units involved using images acquired at the same wavelength but different times of day to create color composite images. Figure 19.9i shows an example of this procedure from the *Opportunity* images of the Berrybowl outcrop area in Eagle crater using 753 nm filter images at low (red), intermediate (green), and high (blue) phase angles. Over the available ~34°–124° phase angle range, this processing makes backscattering materials appear redder (outcrop rocks) and forward-scattering materials bluer (spherules).

Multiband cubes containing both image and photometric angle data (referred to as "Photometry QUBs"; Soderblom *et al.*, 2004) were created using a modified version of the image processing pipeline that was used for normal MER operations (Alexander *et al.*, 2006). Regions of interest were selected for the specific geologic units and radiance data extracted from the Photometry QUBs.

Spectrophotometry of surface observations on Mars is complicated by the effects of diffuse skylight in the atmosphere (e.g., Guinness *et al.*, 1987; Tomasko *et al.*, 1999; Thomas, 2001b; Lemmon *et al.*, 2004). Johnson *et al.* (2006a,b) treated illumination onto the Martian surface as being composed of two separate components: (1) direct sunlight and (2) diffuse illumination. Their goal was to estimate and remove the amount of diffuse skylight present for a given ROI observation, thereby isolating the direct sunlight component for subsequent radiative transfer modeling (Hapke, 1993). To accomplish this, Johnson *et al.* (2006a) developed an iterative procedure that incorporated the atmospheric radiative transfer models of Lemmon *et al.* (2004) and a Hapke radiative transfer model for surface scattering. This iterative sky model was run for a given ROI set of radiance measurements and the atmospherically corrected bidirectional reflectances were input to the Hapke scattering model. Models were run to determine the photometric parameters using 1-term and 2-term HG phase functions. All models included the single scattering albedo (w) and the macroscopic roughness ($\bar{\theta}$), and produced a reduced chi-square (χ_v^2) estimate of their goodness of fit. For datasets lacking observations at phase angles <20°, the opposition effect parameters h and $B0$ were set to zero. Johnson *et al.* (2006a,b) estimated one-sigma confidence limits on each of their fitted Hapke parameters by testing how a given model's χ_v^2 value varied when a particular parameter was purposely varied from its original best-fit value (see Cord *et al.*, 2003). This method helped demonstrate that model fits for some datasets were unable to fully constrain certain parameters when using a given phase function.

A complementary photometric study was performed by Seelos *et al.* (2005) using the *Spirit* dataset from Sols 102 to 103 and the *Opportunity* data from Sols 089 to 091. In that work a customized version of the Discrete Ordinate Radiative Transfer (DISORT) package (Stamnes *et al.*, 1988) was used to calculate the radiance-on-sensor. A plane-parallel model of the Martian atmosphere accounted for direct and diffuse skylight components by combining TES and Pancam atmospheric measurements acquired close in time to the Pancam surface observations (e.g., Lemmon *et al.*, 2004). After spatially resampling the Pancam 754 nm radiance images from the *Opportunity* dataset, a two-term HG function was used to model single scattering albedo ($w = 0.60$) and the macroscopic roughness ($\bar{\theta} = 15°$), and phase functions parameters ($b = 0.243$, $c = 0.624$).

19.9.3 Summary of results: *Spirit*

Johnson *et al.* (2006a) found that despite variations in photometric parameter values both within and among the main unit types, some consistent trends were observed in the *Spirit* Pancam datasets. For example, Gray rocks usually exhibited the highest single scattering albedos at 432, 436, and 601 nm (consistent with their less dusty nature). Gray rocks were typically more forward-scattering than Red rocks and soils. Gray rocks also generally exhibited macroscopic roughness values greater than or equal to Red rocks and soils. Gray rocks were also less porous (or exhibited a more uniform grain size) than most Red rocks or soils. The fortuitous acquisition of data before and after strong winds lifted dust from the soils and rocks at the Paso Robles site between Sols 404 and 425 provided the opportunity to study changes in surface albedo as a result of the "wind-cleaning" event.

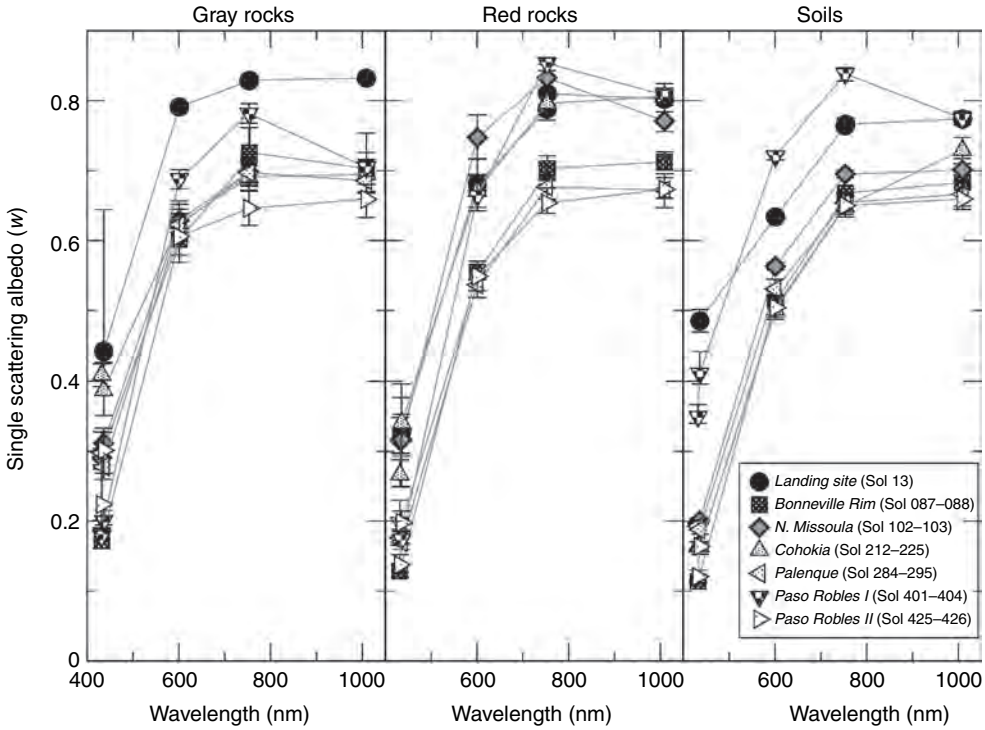

Figure 19.10. Single scattering albedo (w) spectra derived from 2-term HG models for Gray rock, Red rock, and Soil units encountered at Gusev crater by *Spirit*. (After Johnson *et al.*, 2006a.)

Single scattering albedo

Figure 19.10 shows the single scattering albedo spectra for the Gray rock, Red rock, and Soil units derived from the two-term HG models. The similarities between the Gray and Red rock w spectra suggested that the spectral differences between the two rock types were often based on relatively subtle differences likely related to variations in dust-coating thicknesses and/or areal distribution. For example, the 432 and 436 nm w values were most often larger for the Gray rocks than Red rocks, indicative of a lower red/blue ratio that is consistent with thinner dust coatings (e.g., McSween *et al.*, 1999; Farrand *et al.*, 2006). Also, the decrease in 601 nm w values from Gray to Red rocks to Soils is a result of the increasing effect of the ferric absorption band at 535 nm in the Red rocks and Soils (see Farrand *et al.*, 2006; Chapter 13).

Two distinct groups of Red rocks appear in Figure 19.10: (1) a higher albedo suite including the Sol 013 and 102–103 plains sites, the Sol 212–225 Cahokia site, and the prewind event Sol 401–404 Paso Robles site; and (2) a lower albedo suite including the Sol 087 Bonneville Rim site, the Sol 284–295 Palenque site, and the postwind event Sol 425–426 Paso Robles site. The second group can be interpreted as less affected by dust coatings than the first group, as discussed further below. For comparison, the Soil units exhibit the same general w spectrum with the exception of the Sol 013 and Sol 401–404 sites, suggesting that those two sites may have been intrinsically dustier than the "average" spectral albedo at the Gusev site.

Macroscopic roughness

Average macroscopic roughness $\bar{\theta}$ values ranged from 2° to 25°, as derived from the two-term HG models. The roughest surfaces observed were the Gray rocks at the Sol 087–088 Bonneville site, consistent with the more rugged morphology observed in the ejecta blocks near the crater rim compared to other plains units and materials in the Columbia Hills (Grant *et al.*, 2004; Crumpler *et al.*, 2005; Ward *et al.*, 2005). The Sol 013 Gray rocks were the smoothest rocks, consistent with their very forward-scattering nature. Surface roughness values for the Red and Gray rocks were significantly dissimilar in the plains units, but were more equal in the Columbia Hills.

The smoothest unit overall was the Bright soil (hollows) at the Sol 013 landing site. The roughest Soil unit was the Sol 013 landing site Soil, likely as a result of the abundance of fine-grained clasts in the soils (e.g., Ward *et al.*, 2005). The smoothest Soil unit was the prewind event Paso Robles soils, consistent with the interpretation that these surfaces were heavily dust-coated prior to the aeolian event. The increase in roughness of the Paso Robles Soils after the wind event is an indication of the erosive nature of the aeolian activity that occurred between acquisitions of the two datasets.

Phase function parameters

The 1-term HG phase function asymmetry parameter (ξ) provided a useful description of the phase function behavior (although some surfaces were better described by the two-term HG phase function). All asymmetry parameters for the Soil units were relatively backscattering ($\xi < 0.0$) except the postwind event Soil unit at Paso Robles, which was the least backscattering ($\xi \sim 0.0$), consistent with the loss of fine,

backscattering grains from those surfaces. Among the Red rocks unit, the Sol 425–426 Paso Robles rocks were the most forward-scattering and the Sol 401–404 and Sol 087–088 were the most backscattering. The Sol 013 and Sol 087–088 Red rocks both demonstrated increasing backscatter with w, suggesting that the scattering nature of these surfaces is wavelength-dependent. The most backscattering Gray rocks were those from the prewind event Paso Robles site (Sol 401–404), consistent with their inferred dust-coated surfaces. The most forward-scattering surfaces of all units were the Gray rocks after the aeolian event at Paso Robles (Sol 425–426). The moderate inverse correlation between ξ and w observed particularly for the Sol 425–426 Paso Robles and Sol 087–088 Bonneville rim Gray rocks suggested that scattering behavior is wavelength-dependent, perhaps an indication of the greater penetration and multiple scattering of longer-wavelength photons within very thin or discontinuous coatings on these rocks, consistent with Pancam and Microscopic Imager (MI) imaging evidence of Rock Abrasion Tool (RAT) holes on some of these rocks (Bell *et al.*, 2004a; Herkenhoff *et al.*, 2006).

The two-term HG asymmetry parameter (b) and backward-scattering fraction (c) provided a more complete (although not always well constrained) view of the single particle phase function behavior. Figure 19.8 shows the regions covered in b versus c space for the Gray rock, Red rock, and Soil units compared to the McGuire and Hapke (1995) artificial particles, along with the MPF VO units (Geissler, 1992; Johnson *et al.*, 1999). All Gray rocks exhibited c values less than 0.5. The most backscattering Gray rocks were those from the Sol 087–088 Bonneville rim region. These rocks also had the highest $\bar{\theta}$ values, which may influence the derived phase function properties because at high phase angles macroscopically rougher surfaces cast more shadows than smoother surfaces, causing a decrease in forward-scattering (see McGuire and Hapke, 1995). Red rocks had dominantly greater backscattering behavior than Gray rocks, although the Red rocks at the Sol 102–103 Missoula area and the Sol 212–225 Cahokia region fell well within the Gray rock–scattering region. This may represent rocks with relatively thinner or more discontinuous dust coatings. At the Sol 087–088 site the soils are the least forward-scattering and exhibited the broadest scattering lobes, whereas the most forward-scattering soils are those from the Sol 425–426 Paso Robles area, consistent with the removal of fine-grained deposits after the wind event. Johnson *et al.* (2006a) noted that the largest b values for the *Spirit* Soils in Figure 19.8 (from the Sol 401–404 Paso Robles soils) were not well-constrained because of the limited phase angle coverage.

Opposition effect parameters

The only plains unit with sufficient phase angle coverage to allow modeling of h values was the Sol 102–103 dataset, for which the opposition widths were similar for all units. In the West Spur datasets, the Sol 212–225 Cahokia Gray rocks exhibited substantially greater h values than the Red rocks or Soils, which suggested that their surfaces are less porous or have a more uniform grain size distribution. However, whereas the Sol 284–295 Palenque Gray rocks had comparable h values to the Cahokia Gray rocks, the Palenque Red rocks exhibited even greater h values (albeit with large error bars) which may reflect a much less porous surface (or one with much more uniform grain size) than the Red or Gray rocks at the Cahokia site. Johnson *et al.* (2006a) discussed the possibility that the Palenque Red rocks had an optically thicker coating and/or one with more uniform grain size distribution than the Cahokia rocks, despite little variations between these rock types in their textures (as revealed by MI images) or mineralogy- and composition-derived Mini-TES, Pancam, Mössbauer, or APXS results (Farrand *et al.*, 2006; Gellert *et al.*, 2006; Morris *et al.*, 2006; Ruff *et al.*, 2006). The opposition amplitude parameter *B0* was underconstrained in nearly all model results (Table 19.1).

19.9.4 Summary of results: *Opportunity*

Johnson *et al.* (2006b) found that outcrop rocks at *Opportunity* exhibited the highest single scattering albedos at all wavelengths, whereas spherule-rich soil albedos varied substantially. Macroscopic roughness values varied substantially within and among soil and outcrop units, as did phase function parameters. Rover tracks and bounce marks showed the lowest $\bar{\theta}$ values and the most forward-scattering surfaces observed, except for the enigmatic Heat Shield rock, the Fe–Ni meteorite that exhibited a broad forward-scattering lobe.

Single scattering albedo

Figure 19.11 shows representative spectral albedos derived from two-term HG models for several units by Johnson *et al.* (2006b). The outcrop rocks exhibited the highest albedos, with subtle variations that may be related to differences in spherule content and/or siliciclastic components (e.g., Grotzinger *et al.*, 2005; McLennan *et al.*, 2005). Greater albedo variations were observed in the spherule-rich soils, likely related to differences in spherule abundance and presence of high albedo, fine-grained dust derived from atmospheric fallout and/or eroded outcrop materials. However, Johnson *et al.* (2006b) also reported that higher single scattering albedo values modeled for some spherule soils (e.g., Eagle crater) may have resulted from interplay between Hapke parameters that was exacerbated by insufficient data.

Macroscopic roughness

Among the outcrop rocks, Johnson *et al.* (2006b) modeled the highly laminated Tipuna rock to have the roughest surface ($\bar{\theta}\sim30^\circ$), whereas Valentina was the smoothest ($\bar{\theta}\sim13^\circ$). Heat Shield rock $\bar{\theta}$ values were $\sim17^\circ$, and Spherule-rich soils had $\bar{\theta}$ values upward of 28°, although those near Alvin crater were lower ($\bar{\theta}\sim11^\circ$), perhaps also as a result of the decreasing spherule size in the plains along the southerly traverse of *Opportunity* (Weitz *et al.*, 2006). For

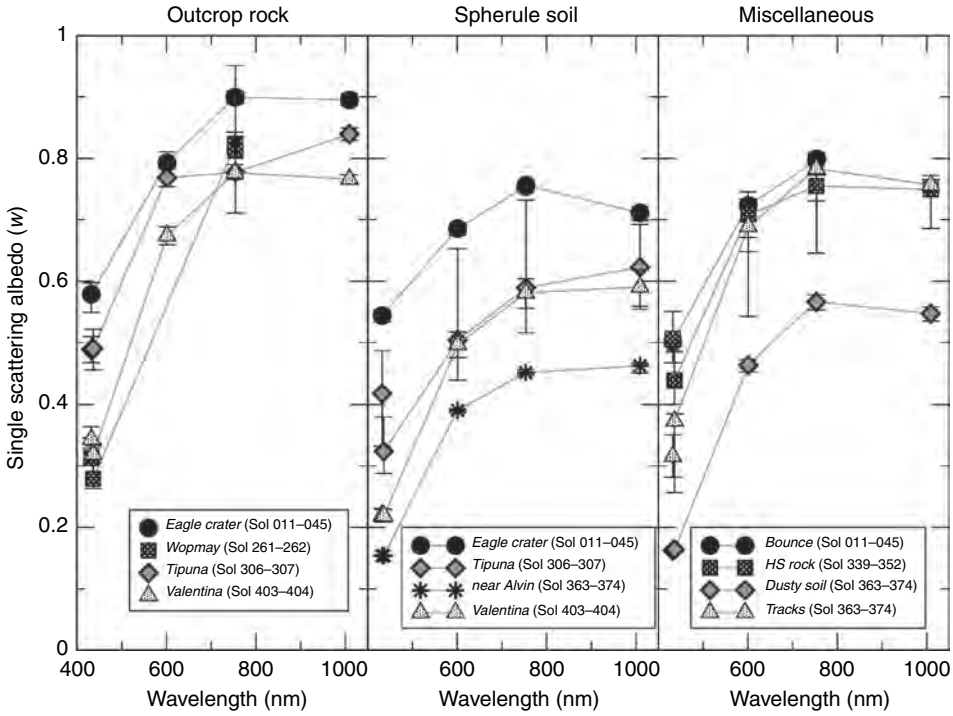

Figure 19.11. Single scattering albedo (w) spectra derived from 2-term HG models for Outcrop rock, Spherule-rich soil, Tracks and Bounce mark units and Heat Shield rock encountered by *Opportunity*. (After Johnson *et al.*, 2006b.)

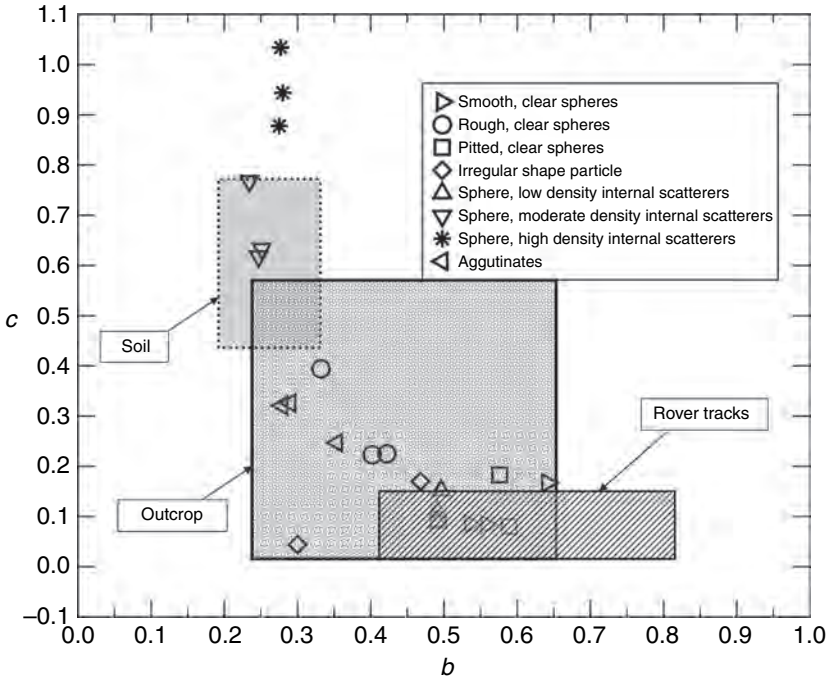

Figure 19.12. Asymmetry parameters, b, versus backward-scattering fraction parameters, c, for artificial particle types from McGuire and Hapke (1995) overlain by average regions occupied by MER *Opportunity* Outcrop rock, Spherule-rich soil, and Rover tracks units from Johnson *et al.* (2006b; Table 19.1). Spherule soil data excludes model results from Eagle, Endurance, and Vostok craters (see text). Rover tracks exhibit narrow forward-scattering lobes. Outcrop rocks vary significantly in their scattering properties, potentially caused by variations in airfall dust deposits or spherule abundances.

comparison, $\bar{\theta}$ values for the bounce marks at the landing site and rover track compressed soils near Alvin crater were 17°–20°.

Phase function parameters

For the 1-term HG function models run by Johnson *et al.* (2006b), the only positive asymmetry parameter values ($\xi >$ 0.0, forward scattering) were for Heat Shield rock, although the airbag bounce marks and some rover tracks were only mildly backscattering ($\xi > -0.07$). Outcrop rocks were slightly more backscattering overall, although Tipuna rock was the most backscattering outcrop material observed. Most spherule-rich soil backscattering properties were similar to the outcrop rocks except for the highly backscattering ($\xi < -0.15$) soils near Tipuna and Valentina.

Two-term HG phase functions are summarized in Figure 19.12, where rover tracks exhibit narrow, forward-scattering lobes compared to the more broad, backscattering characteristics of spherule soils. The b versus c region covered

by outcrop rocks varies significantly. This may be caused by variations in airfall dust deposits or spherule abundances. For example, the spherules shown in Figure 19.9i are relatively forward-scattering at 753 nm compared to all outcrop materials and some of the basaltic sands. Hence the abundance of spherules can alter the overall scattering characteristics of particular units. The *b* versus *c* values for the spherule soils also varied, although the average value shown in Figure 19.12 excludes the data in Eagle, Endurance, and Vostok craters, whose limited datasets resulted in somewhat less well-constrained model results (Johnson *et al.*, 2006b).

Opposition effect parameters

In the photometry sequences analyzed by Johnson *et al.* (2006b), the lack of near-zero phase angle coverage precluded modeling the opposition effect parameters for the outcrop rocks. However, values were modeled for several of the plains units. Although the *B0* values were most often near 1.0, *h* values ranged from 0.040 to 0.100 depending on the surface type (and the phase function used) and possibly on the degree to which airfall-deposited dust coated the soil surfaces during the course of the mission. Some rover tracks (e.g., near Alvin crater) exhibited *h* values up to 0.266, implying a less porous surface (or one with a relatively uniform distribution of particle sizes), which is intuitive for a compressed soil surface (see Weitz *et al.*, 2006).

MER photometric studies of dust deposition

The Pancam calibration targets (Bell *et al.*, 2003) and other selected structures on the decks of the *Spirit* and *Opportunity* rovers (e.g., the Mini-TES external calibration target, particular solar cells used for monitoring energy production levels) were observed as "reference surfaces" under a variety of illumination conditions throughout each rover mission. Over time, these surfaces accumulated airfall dust and were occasionally "cleaned" of some of that dust by wind events (Bell *et al.*, 2006). Bell *et al.* (2006) implemented a preliminary two-layer bidirectional reflectance model (Hapke, 1993) to characterize the spectral properties of dust deposition on the cal targets and enable rapid I/F calibration of Pancam images for tactical-timescale rover operations. Kinch *et al.* (2007) implemented a similar diffusive reflectance version of this model to derive the opacity of the airfall dust layer and its estimated thickness on the cal targets. Their results indicated that for plausible values of dust porosity (0.8) one monolayer of dust built up by Sol 100 on the *Spirit* target and by Sol 125 on the *Opportunity* target before the wind events. The airfall dust deposition rates on the rover decks were found to be consistent with MPF deposition rates (Johnson *et al.*, 2003), when scaled for differences in atmospheric dust opacity among the missions.

19.10 CONCLUSIONS

Observations of visible and near-infrared light reflected from the Martian surface under different illumination and viewing angles can be used to reveal the albedo and scattering characteristics of discrete geologic terrains. By extending radiative transfer modeling of laboratory measurements to data acquired by telescopic, orbital, and landed multispectral imaging instruments, constraints on parameters such as grain size distribution, porosity, internal heterogeneity, and macroscopic roughness of surface particles are possible. In this chapter, we reviewed multiangular measurements of Mars acquired from Earth-based and orbital instruments, the models used to analyze the data, and how those studies have complemented analyses of observations from landed instruments on the Viking, MPF, and MER missions.

Photometric models using multiangular observations have revealed that variations in scattering properties, particularly at the scale of lander and rover observations, are controlled as much by local environments as regional geologic terrains. For example, photometric differences between the plains and Columbia Hills terrains at the *Spirit* landing site were less pronounced than differences related to local (and temporally variable) dust concentrations and surface roughness variations induced by geologic processes such as impact cratering and aeolian weathering.

As of this writing, the MERs *Spirit* and *Opportunity*, and the HRSC and OMEGA instruments on board the MEx continue to collect photometric observations, and analyses of those data are ongoing. The local photometric variability observed from these data encourages additional analyses to constrain geology-driven photometric information, particularly in regard to the potential implications for spectroscopic interpretation, atmospheric compensation, and sequence preparation for Compact Reconnaissance Imaging Spectrometer for Mars (CRISM) observations on the Mars Reconnaissance Orbiter (MRO). Continued photometric observations will serve to test the trends observed in the current datasets and provide additional ground truth for ongoing orbital observations (e.g., Arvidson *et al.*, 2006b). Future work will also include modeling the broadband photometric properties of the surface materials at the MER landing sites using the Navcam images (Soderblom *et al.*, 2006b).

Although practical difficulties often restrict acquisition of data covering sufficient incidence, emission, or phase angles to fully constrain parameters within photometric models, it is clear that even rudimentary modeling of available datasets has provided useful estimates of the relative variations in important surface properties. Table 19.1 summarizes the Hapke model parameters fit by assorted authors using diverse orbital and landed datasets. It is apparent that disparities in data coverage affect the model results, as do differences in the formulations, constraints, and applications of the Hapke models among various workers. Nonetheless, as radiative transfer methods and atmospheric correction algorithms steadily advance, photometric studies using data supplied by upcoming orbital and landed missions will continue to provide additional tools with which to categorize and map distinct units on Mars and assist in reconstructing their geologic formation and evolutionary histories.

ACKNOWLEDGMENTS

A portion of the research described in this chapter was carried out at the Jet Propulsion Laboratory, California Institute of Technology, under a contract with the National Aeronautics and Space Administration. J. R. Johnson and W. Grundy gratefully acknowledge partial support from NASA Planetary Geology and Geophysics grants. We thank K. Kinch for providing model results prior to publication. Valuable discussions with D. Domingue and P. Helfenstein on radiative transfer modeling and sequence design improved the work presented here. We thank B. Buratti for an extremely helpful review that improved the clarity of the chapter.

REFERENCES

Alexander, D. A., R. G. Deen, P. M. Andres, *et al*., Processing of Mars Exploration Rover Imagery for science and operations planning, *J. Geophys. Res.* **111** (E2), E02S02, doi:10.1029/2005JE002462, 2006.

Arvidson, R. E., E. A. Guinness, M. A. Dale-Bannister, *et al*., Nature and distribution of surficial deposits in Chryse Planitia and vicinity, Mars, *J. Geophys. Res.* **94**, 1573–87, 1989a.

Arvidson, R. E., J. L. Gooding, and H. J. Moore, The Martian surface as imaged, sampled, and analyzed by the Viking landers, *Rev. Geophys.* **27**, 39–60, 1989b.

Arvidson, R. E., S. W. Squyres, R. C. Anderson, *et al*., Overview of the *Spirit* Mars Exploration Rover Mission to Gusev crater: landing to the crest of Husband Hill, *J. Geophys. Res.* **111**, E02S01, doi:10.1029/2005JE002499, 2006a.

Arvidson, R. E., J. F. Bell III, R. V. Morris, *et al*., Martian surface properties as inferred from joint analyses of Earth-based, orbital, and surface observations, Ch. 22. In *The Martian Surface: Composition, Mineralogy, and Physical Properties*, Cambridge University Press, 2006b.

Bell III, J. F., *MER 1 Mars Panoramic Camera EDR Ops V1.0*, NASA Planetary Data System, MER1-M-PANCAM-2-EDR-OPS-V1.0, 2004.

Bell III, J. F., M. J. Wolff, T. C. Daley, *et al*., Near-infrared imaging of Mars from HST: surface reflectance, photometric properties, and implications for MOLA data, *Icarus* 138, 25–35, 1999.

Bell III, J. F., H. Y. McSween Jr., S. L. Murchie, *et al*., Mineralogic and compositional properties of Martian soil and dust: preliminary results from Mars Pathfinder, *J. Geophys. Res*, **105**, 1721–55, 2000.

Bell III, J. F., S. W. Squyres, K. E. Herkenhoff, *et al*., The Mars Exploration Rover Athena panoramic camera (Pancam) investigation, *J. Geophys. Res.* **108**(E12), doi:10.1029/2003JE002070, 2003.

Bell III, J. F., S. W. Squyres, R. E. Arvidson, *et al*., Initial Pancam multispectral imaging results from the Mars Exploration Rover Gusev landing site, *Science* **305**, 800–6, 2004a.

Bell III, J. F., S. W. Squyres, R. E. Arvidson, *et al*., Pancam multispectral imaging results from the *Opportunity* rover at Meridiani Planum, *Science* **306**, 1703–9, 2004b.

Bell III, J. F., J. Joseph, J. N. Sohl-Dickstein, *et al*., In-flight calibration and performance of the Mars Exploration Rover Panoramic Camera (Pancam) instruments, *J. Geophys. Res.* **111**, E02S03, doi:10.1029/2005JE002444, 2006.

Binder, A. B. and J. C. Jones, Spectrophotometric studies of the photometric function, composition, and distribution of the surface materials of Mars, *J. Geophys. Res.* **77**, 3005–20, 1972.

Binder, A. R., R. Arvidson, E. Guinness, *et al*., The geology of the Viking Lander 1 site, *J. Geophys. Res*., **82**, 4439–51, 1977.

Buratti, B. J., Voyager disk resolved photometry of the Saturnian satellites, *Icarus* **59**, 392–405, 1984.

Buratti, B. J., J. K. Hillier, and M. Wang, The lunar opposition surge: observations by Clementine, *Icarus* **124**, 490–9, 1996.

Cantor, B. A., M. J. Wolff, P. C. Thomas, P. B. James, and G. Jensen, Phobos disk-integrated photometry: 1994–1997 HST observations, *Icarus* **142**, 414–20, 1999.

Chandrasekhar, S., *Radiative Transfer*, New York: Dover, 1960.

Christensen, P. R., S. W. Ruff, R. L. Jergason, *et al*., Initial results from the Miniature Thermal Emission Spectrometer experiment at the *Spirit* landing site in Gusev crater, *Science* **305**, 837–42, 2004.

Clancy, R. T., S. W. Lee, G. R. Gladstone, W. W. McMillan, and T. Roush, A new model for Mars atmospheric dust based upon analysis of ultraviolet through infrared observations from Mariner 9, Viking, and Phobos, *J. Geophys. Res.* **100**, 5251–63, 1995.

Combes, M., C. Cara, P. Drossart, *et al*., Martian atmosphere studies from the ISM experiment, *Planet. Space Sci.* **39**, 189–98, 1991.

Cord, A. M., P. C. Pinet, Y. Daydou, and S. D. Chevrel, Planetary regolith surface analogs: optimized determination of Hapke parameters using multi-angular spectro-imaging laboratory data, *Icarus* **165**, 414–27, 2003.

Cord, A. M., P. C. Pinet, Y. Daydou, and S. D. Chevrel, Experimental determination of the surface photometric contribution in the spectral reflectance deconvolution processes for a simulated Martian crater-like regolithic target, *Icarus* **175**, 78–91, 2005.

Crumpler, L. S., S. W. Squyres, R. E. Arvidson, *et al*., Mars Exploration Rover Geologic traverse by the Spirit rover in the plains of Gusev crater, Mars, *Geology* **33**(10), 809–12, 2005.

de Grenier, M. and P. C. Pinet, Near-opposition Martian limb darkening: quantification and implication for visible-near-infrared bidirectional reflectance studies, *Icarus* **115**, 354–68, 1995.

de Vaucouleurs, G., Multicolor photometry of Mars in 1958, *J. Planet. Space Sci.* **2**, 26–32, 1960.

de Vaucouleurs, G., Geometric and photometric parameters of the terrestrial planets, *Icarus* **3**, 187–237, 1964.

de Vaucouleurs, G., A low-resolution photometric map of Mars, *Icarus* **7**, 310–49, 1967.

Domingue, D. and B. Hapke, Disk-resolved photometric analysis of Europan terrains, *Icarus* **99**, 70–81, 1992.

Domingue, D. and A. Verbiscer, Re-analysis of the solar phase curves of the icy Galilean satellites, *Icarus* **128**, 49–74, 1997.

Domingue, D., G. W. Lockwood, and D. T. Thompson, Surface textural properties of icy satellites: a comparison between Europa and Rhea, *Icarus* **115**, 228–49, 1995.

Domingue, D., B. Hartmann, and A. Verbiscer, The scattering properties of natural terrestrial snows versus icy satellite surfaces, *Icarus* **128**, 28–48, 1997.

Domingue, D. L., M. Robinson, B. Carcich, *et al*., Disk-integrated photometry of 433 Eros, *Icarus* **155**, 205–19, 2002.

Drossart, P., J. Rosenqvist, S. Erard, *et al*., Martian aerosols properties from the Phobos/ISM experiment, *Ann. Geophys.* **9**, 754–60, 1991.

Egan, W. G., Polarimetric and photometric simulation of the Martian surface, *Icarus* **10**, 223–7, 1969.

Erard, S., J. F. Mustard, S. Murchie, *et al*., Martian aerosols: near-infrared spectral properties and effects on the observation of the surface, *Icarus* **111**, 313–37, 1994.

Farrand, W., J. F. Bell III, J. R. Johnson, *et al*., Spectral variability in visible and near infrared multispectral Pancam data collected at Gusev crater: examinations using spectral mixture analysis and related techniques, *J. Geophys. Res.* **111**, E02S15, doi:10.1029/2005JE002495, 2006.

Geissler, P. E., Spectrophotometric mapping of Coprates Quadrangle, Mars. Ph.D. thesis, University of Arizona, 1992.

Geissler, P. E. and R. B. Singer, Spectrophotometric mapping of Coprates Quadrangle, Mars. *Lunar Planet. Inst. Conf.*, Abstract 23, 403, 1992.

Gellert, R., R. Rieder, J. Brückner, *et al*., Alpha Particle X-Ray Spectrometer (APXS): results from Gusev crater and calibration report, *J. Geophys. Res.* **111**, E02S05, doi:10.1029/2005JE002555, 2006.

Golombek, M. P., R. E. Arvidson, J. F. Bell III, *et al*., Assessment of Mars Exploration Rover landing site predictions, *Nature*, **436**, 44–8, 2005.

Gradie, J. and J. Veverka, Photometric properties of powered sulfur, *Icarus* **58**, 227–45.

Grant, J. A., R. Arvidson, J. F. Bell III, *et al*., Surficial deposits at Gusev crater along Spirit Rover traverses, *Science*, **305**, 807–10, 2004.

Grotzinger, J. P., R. E. Arvidson, J. F. Bell III, *et al*., Stratigraphy and sedimentology of a dry to wet eolian depositional system, Burns formation, Meridiani Planum, Mars, *Earth Planet. Sci. Lett.* **240**, 11–72, 2005.

Guinness, E. A., Spectral properties (0.40 to 0.75 microns) of soils exposed at the Viking 1 landing site, *J. Geophys. Res.* **86**, 7983–92, 1981.

Guinness, E. A., R. E. Arvidson, D. C. Gehret, and L. K. Bolef, Color changes at the Viking landing sites over the course of a Mars year, *J. Geophys. Res.* **84**, 8355–64, 1979.

Guinness, E. A., R. E. Arvidson, M. A. Dale-Bannister, R. B. Singer, and E. A. Bruckenthal, On the spectral reflectance properties of materials exposed at the Viking landing sites, *J. Geophys. Res.* **92**, E575–E587, 1987.

Guinness, E. A., R. E. Arvidson, and M. K. Shepard, Specular scattering from rock surfaces at the Viking lander sites, *Lunar Planet. Sci. Conf. XXVII*, 471–2, 1996.

Guinness, E. A., R. E. Arvidson, I. H. D. Clark, and M. K. Shepard, Optical scattering properties of terrestrial varnished basalts compared with rocks and soils at the Viking Lander sites, *J. Geophys. Res.* **102**, 28687–703, 1997.

Hapke, B., Bi-directional reflectance spectroscopy: 1. Theory, *J. Geophys. Res.* **86**, 3039–54, 1981.

Hapke, B., Bidirectional reflectance spectroscopy: 3. Correction for macroscopic roughness, *Icarus* **59**, 41–59, 1984.

Hapke, B., Bidirectional reflectance spectroscopy: 4. The extinction coefficient and the opposition effect, *Icarus* **67**, 264–80, 1986.

Hapke, B., *Theory of Reflectance and Emittance Spectroscopy*, Cambridge University Press, 455pp., 1993.

Harris, D. L., Photometry and colorimetry of planets and satellites. In *Planets and Satellites*, (ed. G. P. Kuiper and B. M. Middlehurst), Chicago, IL: University of Chicago Press, p. 272, 1961.

Hartmann, B. and D. Domingue, Scattering of light by individual particles and the implications for models of planetary surfaces, *Icarus* **131**, 421–48, 1998.

Helfenstein, P., The geological interpretation of photometric surface roughness, *Icarus* **73**, 462–81, 1988.

Helfenstein, P. and M. K. Shepard, Submillimeter-scale topography of the lunar regolith, *Icarus* **141**, 107–31, 1999.

Helfenstein, P. and M. Shepard, A blind test of Hapke's photometric model, *Lunar Planet. Sci. Conf. XXXIV*, Abstract 1968, 2003.

Helfenstein, P. and J. Veverka, Photometric properties of lunar terrains derived from Hapke's equation, *Icarus* **72**, 342–57, 1987.

Helfenstein, P. and J. Veverka, Physical characterization of asteroid surfaces from photometric analysis. In *Asteroids II* (ed. R. P. Binzel, T. Gehrels, and M. S. Matthews), University of Arizona Press, pp. 557–93, 1989.

Helfenstein, P., J. Veverka, and J. Hillier, The lunar opposition effect: a test of alternative models, *Icarus* **128**, 2–14, 1997.

Hendrix, A. R., D. L. Domingue, and K. King, The icy Galilean satellites: ultraviolet phase curve analysis, *Icarus* **173**, 29–49, 2005.

Henyey, L. G. and J. Greenstein, Diffuse radiation in the galaxy, *Astrophys. J.* **93**, 70–83, 1941.

Herkenhoff, K. E., *et al*., Overview of the Microscopic Imager Investigation during Spirit's first 450 sols in Gusev crater, *J. Geophys. Res.* **111**, E02S04, doi:10.1029/2005JE002574, 2006.

Hord, C. W., Mariner 6 and 7 ultraviolet spectrometer experiment: photometry and topography of Mars, *Icarus* **16**, 253–80, 1972.

Hord, C. W., C. A. Barth, A. I. Stewart, and A. L. Lane, Mariner 9 ultraviolet spectrometer experiment: photometry and topography of Mars, *Icarus* **17**, 443–56, 1972.

Huck, F. O., H. F. McCall, W. R. Patterson, and G. R. Taylor, The Viking Mars lander camera, *Space Sci. Instr.* **1**, 189–241, 1975.

Hviid, S. F., J. M. Knudsen, M. B. Madsen, R. B. Hargraves, Spectroscopic investigation of the dust attracted to the magnetic properties experiments on the Mars Pathfinder lander, *Lunar Planet. Sci. Conf. XXXI*, Abstract #1641, 2000.

Israel, E. J., R. E. Arvidson, A. Wang, J. D. Pasteris, and B. L. Jolliff, Laser Raman spectroscopy of varnished basalt and implications for *in situ* measurements of Martian rocks, *J. Geophys. Res.* **102**, 28705–16, 1997.

Jehl, A., P. C. Pinet, A. Cord, *et al*., Improved surface photometric mapping across Gusev and Apollinaris from an HRSC/Mars Express integrated multi-orbit dataset: implication on Hapke parameters determination, *Lunar Planet. Sci. Conf. XXXVII* Houston, Abstract #1219, 2006.

Johnson, H. L. and A. J. Gardiner, The magnitude and color of Mars during the 1954 opposition. *Publs. Astron. Soc. Pacific* **67**, 74–7, 1955.

Johnson, J. R., R. Kirk, L. A. Soderblom, *et al*., Preliminary results on photometric properties of materials at the Sagan Memorial Station, Mars, *J. Geophys. Res.*, **104**, 8809–30, 1999.

Johnson, J. R., W. M. Grundy, and M. T. Lemmon, Dust deposition at the Mars Pathfinder landing site: observations and modeling of visible/near-infrared spectra, *Icarus* **163**, 330–46, 2003.

Johnson, J. R., W. M. Grundy, M. T. Lemmon, *et al*., Spectrophotometric properties of materials observed by Pancam on the Mars Exploration Rovers: 1. Spirit, *J. Geophys. Res.* **111**, E02S14, doi:10.1029/2005JE002494, 2006a.

Johnson, J. R., W. M. Grundy, M. T. Lemmon, *et al*., Spectrophotometric properties of materials observed by Pancam on the Mars Exploration Rovers: 2. Opportunity, *J. Geophys. Res.* **111**(E12), doi:10.1029/2006JE002762, 2006b.

Kinch, K. M., J. Sohl-Dickstein, J. F. Bell III, *et al*., A preliminary radiative transfer analysis of dust deposition on the Mars Exploration Rover Panoramic Camera (Pancam) calibration

targets, *J. Geophys. Res.*, **112**, Cite ID E06S03, doi:10.1029/2006JE002807, 2007.

King, E. S., Revised magnitudes and color indices of the planets, *Ann. Harvard Obs.* **85**, 63–72, 1923.

Kreslavsky, M. A., N. V. Bondarenko, P. C. Pinet, J. Raitala, G. Neukum, and The Mars Express HRSC Co-Investigator Team, Mapping of photometric anomalies of martian surface with HRSC data, *Lunar Planet. Sci. Conf. XXXVII*, Houston, Abstract #2211 2006.

Lambert, J. H., *Photometria Sive de Mensura et Gradibus Luminis, Colorum et Umbrae*. Augsburg: Detleffsen, 1760.

Lemmon, M. T., M. J. Wolff, M. D. Smith, *et al.*, Atmospheric imaging results from the Mars Exploration Rovers: *Spirit* and *Opportunity*, *Science* **306**, 1753–6, 2004.

Livlander, R., *Publ. Obs. Astron.* Universiti de Tartu **27** (6), 1933.

Madsen, M. B., S. F. Hviid, H. P. Gunnlaugsson, *et al.*, The magnetic properties experiment on Mars Pathfinder, *J. Geophys. Res.* **104**, 8761–79, 1999.

Martin, P. D., A. Cord, B. Foing, *et al.*, Photometric and compositional surface properties of the Gusev crater region, Mars, as derived from multi-angle, multi-spectral investigation of Mars Express HRSC data, *Lunar Planet. Sci. Conf. XXXVI*, Abstract #1687, 2005.

Martinez-Alonso, S., B. M. Jakosky, M. T. Mellon, and N. E. Putzig, A volcanic interpretation of Gusev crater surface materials from thermophysical, spectral, and morphological evidence, *J. Geophys. Res.* **110**, E01003, doi:10.1029/2004JE002327, 2005.

McLennan, S. M., J. F. Bell, W. M. Calvin, *et al.*, Provenance and diagenesis of the evaporite-bearing Burns formation, Meridiani Planum, Mars, *Earth Planet. Sci. Lett.* **240**, 95–121, 2005.

McEwen, A. S., Photometric functions for photoclinometry and other applications, *Icarus* **92**, 298–311, 1991.

McGuire, A. F. and B. W. Hapke, An experimental study of light scattering by large, irregular particles, *Icarus* **113**, 134–55, 1995.

McSween Jr., H. Y., S. L. Murchie, J. A. Crisp, *et al.*, Chemical, multispectral, and textural constraints on the composition and origin of rocks at the Mars Pathfinder landing site, *J. Geophys. Res.* **104**, 8679–715, 1999.

McSween Jr., H. Y., M. B. Wyatt, R. Gellert, *et al.*, Characterization and petrologic interpretation of olivine-rich basalts at Gusev crater, Mars, *J. Geophys. Res*, **111**, E02S10, doi:10.1029/2005JE002477, 2006.

Mead, J. M., The contribution of atmospheric aerosols to the Martian opposition effect, *Icarus* **13**, 82–95, 1970.

Meador, W. E. and W. R. Weaver, A photometric function for diffuse reflection by particulate materials, *NASA Tech. Note*, D-7903, 1975.

Minnaert, M., The reciprocity principle in lunar photometry, *Astrophys. J.* **93**, 403–10, 1941.

Moore, H. J., R. E. Hutton, G. D. Clow, and C. R. Spitzer, Physical properties of the surface materials at the Viking landings sites on Mars, *USGS Prof. Paper*, 1389, 1987.

Morris, R. V., G. Klingelhöfer, C. Schröder, *et al.*, Spirit's Journey through weakly altered olivine basalt on the plains and pervasively altered basalt in the columbia Hills, *J. Geophys. Res.*, **111**, E02S13, doi:10.1029/2005JE002584, 2006.

Mustard, J. F. and C. M. Pieters, Photometric phase functions of common geologic minerals and applications to quantitative analysis of mineral mixture reflectance spectra, *J. Geophys. Res.* **94**, 13619–34, 1989.

Mutch, T., R. Arvidson, A. Binder, E. Guinness, and E. Morris, The geology of the Viking Lander 2 site, *J. Geophys. Res.* **82**, 4452–67, 1977.

Nelson, R. M., B. W. Hapke, W. D. Smythe, and L. J. Horn, Phase curves of selected particulate materials: the contribution of coherent backscattering to the opposition surge, *Icarus* **131**, 223–30, 1998.

O'Leary, B. T., The opposition effect of Mars, *Astrophys. J.* **149**, L147–L149, 1967.

O'Leary, B. T. and J. B. Pollack, A critique of the paper by Walter G. Egan, "Polarimetric and photometric simulation of the Martian surface," *Icarus* **10**, 228–40, 1969.

O'Leary, B. T. and D. G. Rea, The opposition effect of Mars and its implications, *Icarus* **9**, 405–28, 1968.

Pang, K. and C. W. Hord, Mariner 7 ultraviolet spectrometer experiment: photometric function and roughness of Mars' polar cap surface, *Icarus* **15**, 443–53, 1971.

Pappalardo, R. T., G. C. Collins, J. W. Head III, *et al.*, Geology of Ganymede, Ch. 16, *Jupiter: The Planet, Satellites and Magnetosphere*, Cambridge University Press, 2004.

Patterson, W. R., F. O. Huck, S. D. Wall, and M. R. Wolf, Calibration and performance of the Viking Lander cameras, *J. Geophys. Res.* **82**, 4391–400, 1977.

Pinet, P. C. and S. D. Chevrel, Spectral identification of geological units on the surface of Mars related to the presence of silicates from earthbased near-infrared telescopic CCD imaging, *J. Geophys. Res.* **95** (B9), 14435–46, 1990.

Pinet, P. C. and C. Rosemberg, Regional photometry and spectral albedo of the eastern hemisphere of Mars in the 0.7–1 micron domain, *Lunar Planet. Sci. XXXII*, Houston, Abstract #1640, 2001.

Pinet, P. C., A. Cord, A. Jehl, *et al.*, Mars Express imaging photometry and surface geologic processes at Mars: what can be monitored within Gusev crater?, *Lunar Planet. Sci. Conf. XXXVI*, Abstract #1721, 2005a.

Pinet, P. C., Y. Daydou, A. Cord, *et al.*, Derivation of mars surface scattering properties from OMEGA spot pointing observations, *Lunar Planet. Sci. Conf. XXXVI*, Abstract #1694, 2005b.

Pinet, P. C., A. Jehl, A. Cord, *et al.*, Mars Express/HRSC Imaging photometry and MER Spirit/PANCAM in situ spectrophotometry within Gusev, *Lunar Planet. Sci. Conf. XXXVII*, Houston, Abstract #1220, 2006.

Pleskot, L. K. and H. H. Kieffer, The infrared photometric function of Mars and its bolometric albedo, *Icarus* **30**, 341–59, 1977.

Pollack, J. B. and C. Sagan, An analysis of Martian photometry and polarimetry, *Space Sci. Rev.* **9**, 243–99, 1968.

Pollack, J. B., D. Colburn, F. M. Flasar, *et al.*, Properties and effects of dust particles suspended in the Martian atmosphere, *J. Geophys. Res.* **84**, 2929–45, 1979.

Regner, P., Photometric analyses for the determination of physical and structural properties of the Martian surface in the Oxia Palus region, Ph.D. thesis, Ludwig-Maximilians-University, 1990.

Regner, P., L. Kamp, and G. Neukum, Multispectral photometric classification and mapping of the Martian surface in the Oxia Palus region, *Lunar Planet. Inst. Conf.*, Abstracts 19, 968, 1988.

Reid, R. J., P. H. Smith, M. Lemmon, *et al.*, Imager for Mars Pathfinder (IMP) image calibration, *J. Geophys. Res.* **104**, 8907–26, 1999.

Ruff, S., P. R. Christensen, D. L. Blaney, *et al.*, The rocks of Gusev crater as viewed by Mini-TES, *J. Geophys. Res.* **111** (E12), 2006.

Schultz, P. H. and J. F. Mustard, Martian impact glass: generation and evidence, *Lunar Planet. Sci. Conf. XXIX*, Abstract #1847 (CD-ROM), 1998.

Seelos, F. P., R. E. Arvidson, E. A. Guinness, M. J. Wolff, and the Athena Science Team, Radiative transfer photometric

analyses at the Mars Exploration Rover landing sites, *Lunar Planet. Sci. Conf. XXXVI*, Abstract #2054, 2005.

Shepard, M. K. and B. A. Campbell, Shadows on a planetary surface and implications for photometric roughness, *Icarus* **134**, 279–91, 1998.

Shepard, M. K., R. E. Arvidson, and E. A. Guinness, Specular scattering on a terrestrial playa and implications for planetary surface studies, *J. Geophys. Res.* **98**, 18707–18, 1993.

Simonelli, D. P., M. Wisz, A. Switala, *et al*., Photometric properties of Phobos surface materials from Viking images, *Icarus* **131**, 52–77, 1998.

Slater, P. N., *Remote Sensing, Optics and Optical Systems*, ISBN 0–201–07250–5, Reading, Massachusetts, USA: Addison-Wesley Publishing Company, 575pp., 1980.

Smith, M. D., J. C. Pearl, B. J. Conrath, and P. R. Christensen, Mars Global Surveyor Thermal Emission Spectometer (TES) observations of dust opacity during aerobraking and science phasing, *J. Geophys. Res.* **105**, 9539–52, 2000.

Smith, P. H., M. G. Tomasko, B. Britt, *et al*., The imager for Mars Pathfinder experiment, *J. Geophys. Res.* **102**, 4003–26, 1997.

Soderblom, J. M., J. F. Bell, R. E. Arvidson, *et al*., Mars Exploration Rover Pancam photometric data QUBs: definition and example uses, *EOS Trans. AGU* **85**(47), Fall Meeting Suppl., Abstract P21A-0198, 2004.

Soderblom, J. M., J. F. Bell III, M. Y. Hubbard, and M. J. Wolff, Martian phase function: modeling the visible to near-infrared surface photometric function using HST-WFPC2 data, *Icarus* **2**, 401–23, 2006a.

Soderblom, J. M., J. F. Bell III, J. R. Johnson, J. N. Maki, and M. J. Wolff, Photometry of the Martian surface using data from the Navigation Cameras on the Mars Exploration Rovers *Spirit* and *Opportunity*, *Lunar Planet. Sci. Conf. XXXVII*, Abstract #1935, 2006b.

Soderblom, L. A., K. Edwards, E. M. Eliason, E. M. Sanchez, and M. P. Charette, Global color variations on the Martian surface, *Icarus* **34**, 446–64, 1978.

Soffen, G. A., The Viking Project, *J. Geophys. Res.* **82**, 3959–70, 1977.

Strickland, E. L., Surface photometric properties and albedo changes in the central equatorial of Mars, *Lunar Planet. Inst. Conf.*, Abstracts 20, 1081, 1989.

Tejfel, U. G., N. U. Shinyaeva, A. N. Aksenov, and G. Kharitonova, The experience of the Mars normal albedo and limb darkening coefficient from the observations during 1990 opposition, *Proc. Lunar Planet. Sci. Conf. XXIII*, 1417–18, 1992.

Thomas, N., Photometry of resolved planetary surfaces. In *Solar and Extra-Solar Planetary Systems* (ed. I. P. Williams and N. Thomas), *Lect. Notes Phys.* **577**, 153, 2001a.

Thomas, N., Light scattering in the Martian atmosphere: effects on surface photometry. In *Solar and Extra-Solar Planetary Systems* (ed. I. P. Williams and N. Thomas), *Lect. Notes Phys.* **577**, 191, 2001b.

Thomas, N., W. J. Markiewicz, R. M. Sablotny, *et al*., The color of the Martian sky and its influence on the illumination of the Martian surface, *J. Geophys. Res.* **104**, 8795–808, 1999.

Thomas, P. C., D. Adinolfi, P. Helfenstein, D. Simonelli, and J. Veverka, The surface of Deimos: contribution of materials and processes to its unique appearance, *Icarus* **123**, 536–56, 1996.

Thorpe, T. E., Mariner 9 photometric observations of Mars from November 1971 through March 1972, *Icarus* **20**, 482–9, 1973.

Thorpe, T. E., Viking Orbiter photometric observations of the Mars phase function: July through November 1976, *J. Geophys. Res.* **82**, 4161–5, 1977.

Thorpe, T. E., Viking Orbiter observations of the Mars opposition effect, *Icarus* **36**, 204–15, 1978.

Thorpe, T. E., The Mars opposition effect at 20 deg N. latitude and 20 deg W. longitude, *Icarus* **37**, 389–98, 1979.

Thorpe, T. E., Martian surface properties indicated by the opposition effect, *Icarus* **49**, 398–415, 1982.

Tomasko, M. G., L. R. Doose, M. T. Lemmon, P. H. Smith, and E. Wegryn, Properties of dust in the Martian atmosphere from the imager on Mars Pathfinder, *J. Geophys. Res.* **104**, 8987–9007, 1999.

Veverka, J., M. Robinson, P. Thomas, *et al*., NEAR at Eros: imaging and spectral results, *Science* **289**, 2088–97, 2000.

Ward, J. G., R. E. Arvidson, and M. Golombek, The size-frequency and areal distribution of rock clasts at the *Spirit* landing site, Gusev crater, Mars, *Geophys. Res. Lett.* **32**, L11203, doi:10.1029/2005GL022705, 2005.

Weitz, C. M., R. C. Anderson, J. F. Bell III, *et al*., Soil grain analyses at Meridian Planum, Mars, *J. Geophys. Res.* **111** (E12), 2006.

Wolff, M. J., J. F. Bell III, P. B. James, R. T. Clancy, and S. W. Lee, Hubble Space Telescope Observations of the Martin aphelion could belt prior the Pathfinder mission: Seasonal and interannual variations, *J. Geophys. Res.*, 98JEO1967, **104**, E4, 9027, 1999.

Young, A. T., High-resolution photometry of a thin planetary atmosphere, *Icarus* **11**, 1–23, 1969.

Young, A. T., UBV photometry of Mars. In *Exploration of the Planetary System* (ed. A. Woszczyk and C. Iwaniszewska), Boston, Massachusetts: D. Reidel Publishing Co., pp. 253–85, 1975.

Young, A. T. and S. A. Collins, Photometric properties of the Mariner cameras and of selected regions on Mars, *J. Geophys. Res.* **76**, 432–7, 1971.

20

In situ observations of the physical properties of the Martian surface

K. E. HERKENHOFF, M. P. GOLOMBEK, E. A. GUINNESS, J. B. JOHNSON, A. KUSACK, L. RICHTER, R. J. SULLIVAN, AND S. GOREVAN

ABSTRACT

The physical properties of rocks and soils on the surface of Mars have been investigated by several landed spacecraft. Studies of these physical properties constrain interpretation of Martian geologic processes and provide engineering data for future mission planning. As on Earth, these properties vary considerably from place to place, and provide constraints on the origin and evolution of the surface materials. Martian soils commonly have thin surface crusts that may be caused by salts cementing grains together. Estimates of soil physical properties at the various landing sites are generally comparable, but rather uncertain in many cases. Rock physical properties, based on abrasion by the Mars Exploration Rover (MER) Rock Abrasion Tool (RAT) and other experiments, vary widely.

20.1 INTRODUCTION

Martian surface rocks and soils record the most recent history of physical and chemical modifications of the surface, perhaps including the effects of climate variations. In some instances, physical properties relate to soil cementation and thereby to diagenesis and chemical deposition. This chapter summarizes the physical and mechanical properties of the Martian surface inferred from landed spacecraft (Viking Landers, Mars Pathfinder, MERs). Knowledge of these surface properties helps to constrain the origin of the surface materials and the processes that have affected them. In addition, information regarding physical and mechanical properties is useful in planning future spacecraft exploration of the surface of Mars.

Soil physical properties of prime interest are grain characteristics, as well as estimates of soil-bearing strength and shear strength. Soil compaction state affects overall strength, and thus (with certain assumptions) derived soil strength allows estimates of other parameters such as bulk density and thermophysical properties. Variations in soil strength can indicate the degree of any postdepositional induration that has occurred. Grain shapes in sedimentary deposits, commonly described in terms of roundness and sphericity, are controlled by mineralogy as well as the type and duration of transport processes. Roundness is a measure of the regularity of the two-dimensional margin of a grain, in terms of the average radius of curvature of all convex sections of the margin (McLane, 1995). Sphericity is the ratio of the diameter of a sphere of the same volume as the particle to the diameter of the smallest circumscribed sphere. The relative abundances of various sizes of grains in a deposit (the degree of sorting) can sometimes be an indicator of grain transport distance. Rock physical properties of interest include hardness and bulk density – properties that generally have been difficult or impractical to evaluate on the Martian surface. Neither magnetic nor electrostatic properties are discussed in this chapter (see, instead, Chapter 16 and Ferguson *et al.*, 1999, respectively).

All five successful Mars lander missions returned data that have been used to infer physical properties of the Martian surface: two Viking Landers (1976–82), the Mars Pathfinder lander with Sojourner rover (1997), and two MERs (2004–present). All of these spacecraft carried imaging systems that returned information about natural surfaces and disturbed materials (Huck *et al.*, 1975; Smith *et al.*, 1997; Moore *et al.*, 1999; Bell *et al.*, 2003; Herkenhoff *et al.*, 2003; Maki *et al.*, 2003; Table 20.1). All of these spacecraft also included mechanical devices (wheels, arms, grinding tools) that interacted with soils and rocks, allowing physical properties to be constrained from reactive forces and torques and from the associated responses of the target materials.

Studies of Mars's soil physical properties help to interpret Martian geologic processes and to provide engineering data for future mission planning. The goals of soil physical properties studies are therefore supplementary to the primary objectives of past and planned landed missions, which focus on Mars geology and its evolution, investigating the possibility of life, and finding evidence of water and its effects on the Martian landscape. Instruments for examining the grain size, texture, and mineralogy of rocks and soils have been limited to the surface or near-subsurface, however, thus reducing the ability to characterize soil stratigraphy and rock interiors. Soil scoops/backhoes (Moore *et al.*, 1979, 1982) and wheels (Moore *et al.*, 1999) allow access to only the nearest subsurface (less than 30 cm; Figures 20.2 and 20.9). Few instruments (all of them on Soviet lunar missions) have been deployed to directly assess soil physical properties like density, soil strength (internal friction and cohesion), and rheology.

Without specialized apparatus designed for measuring soil or rock physical properties, special methods involving adapting available equipment (primarily scoops and wheels) have instead been developed. This approach typically has been complicated by sparse experiment time and data return, low resolution, and complex soil/mechanism

The Martian Surface: Composition, Mineralogy, and Physical Properties, ed. J. F. Bell III. Published by Cambridge University Press.

interface geometry and interactions. For example, the forces required to push a scoop into soil or for a wheel to dig into soil are not directly measured, but are instead estimated from currents drawn by motors during scoop or wheel motions.

Earth-based laboratory tests using Mars soil simulants and flight-identical equipment have been used to "calibrate" the interpretation of experiments conducted on the Martian surface. Soil–machine interaction models that assume homogeneous soils are also used to simulate soil failure and soil properties (Moore *et al.*, 1982). Actual Martian soils commonly are more complex and less homogeneous than soil simulants, further complicating interpretation of test results and model calculations (Figures 20.2, 20.7, and 20.9). Remotely sensed data on soil thermal inertia and dielectric properties have also been used to limit the range of possible soil properties like density and the qualitative degree of induration (cementation between soil grains). Data derived using these methods have a high degree of variability, including unrealistic negative cohesion values, and differences of as much as 10° for internal friction angles (ϕ) for similar Mars soils (Table 20.2).

Table 20.1. *Resolution of cameras on Mars landers/rovers*

Camera	IFOV[a] (mrad)	Best resolution[b] (mm)	Comment
Viking Landers	0.7	1.5	High-resolution mode
Mars Pathfinder	1.0	3.0	Before mast deploy
Sojourner	2.9–3.4	2.0	Rectangular pixels
MER Pancam	0.27	1.4	After mast deploy
MER MI	N/A	0.1	At best focus

[a]Instantaneous Field of View; the angular resolution of each pixel.
[b]Size of smallest object that can be recognized (typically 3 pixels across).

20.2 DATA AND INFERENCES

This section describes observations and interpretations of Martian soil and rock strength characteristics, soil grain sizes/shapes, and particle sorting. Implications for the origin and evolution of surface materials are discussed at the end of this section.

20.2.1 Soils

The term "soil" is used here to denote any loose, unconsolidated materials that can be distinguished from rocks, bedrock, or strongly cohesive sediments. No implication of the presence or absence of organic materials or living matter is intended. Martian soils have been observed remotely and *in situ*, and their physical properties can be inferred from analysis of both kinds of data. Remote observations of soil physical properties are summarized elsewhere in this book, for example in Chapters 12, 13, 16, 18, 19, and 21, including analysis of spectrophotometric data acquired by lander instruments. In this section, soil physical properties derived from morphologic and grain size-frequency analyses of Mars landed spacecraft images and from their observed deformation behavior are summarized.

Table 20.2. *Mars soil cohesion (C), internal friction (ϕ), and bulk density (ρ) as inferred from landed missions prior to MER*

C (kPa)	ϕ (°)	ρ (kg m^{-3})	Soil type	Measurement method	Source
−0.34–0.57	31.4–42.2	2000–2200	Cloddy	Wheel dig trenching	MPF Sojourner[a]
0.18–0.53	15.1–33.1	1066–1269	Drift	Wheel dig	MPF Sojourner[a]
1.6 ± 1.2 0–3.7	18 ± 2.4	1150 ± 150	Drift	Scoop trenching and landing pad sinkage	Viking Lander 1[b,c,d]
5.1 ± 2.7 2.2–10.6	30.8 ± 2.4	1600 ± 400	Blocky	"	Viking Lander 1[b,c,d]
1000–10 000	40–60	2600	Rocks	"	Viking Lander 1 and 2[b,c,d]
1.1 ± 0.8 0–3.2	34.5 ± 4.7	1400 ± 200	Crusty to cloddy	"	Viking Lander 2[b,c,d]
2.7–3.4	22.0–27.0		Lunar intercrater terrain	Vane shear tester	Lunokhod 1 and 2[e]

[a]Moore *et al.* (1999).
[b]Moore *et al.* (1982).
[c]Moore *et al.* (1987).
[d]Moore and Jakosky (1989).
[e]Kemurdzhian *et al.* (1978).
Note that Viking-based rock properties actually were unmeasured; these were simply broad estimates based on assumed similitude with many terrestrial silicate rocks. Lunar regolith properties along Lunokhod rover traverses are shown for comparison.

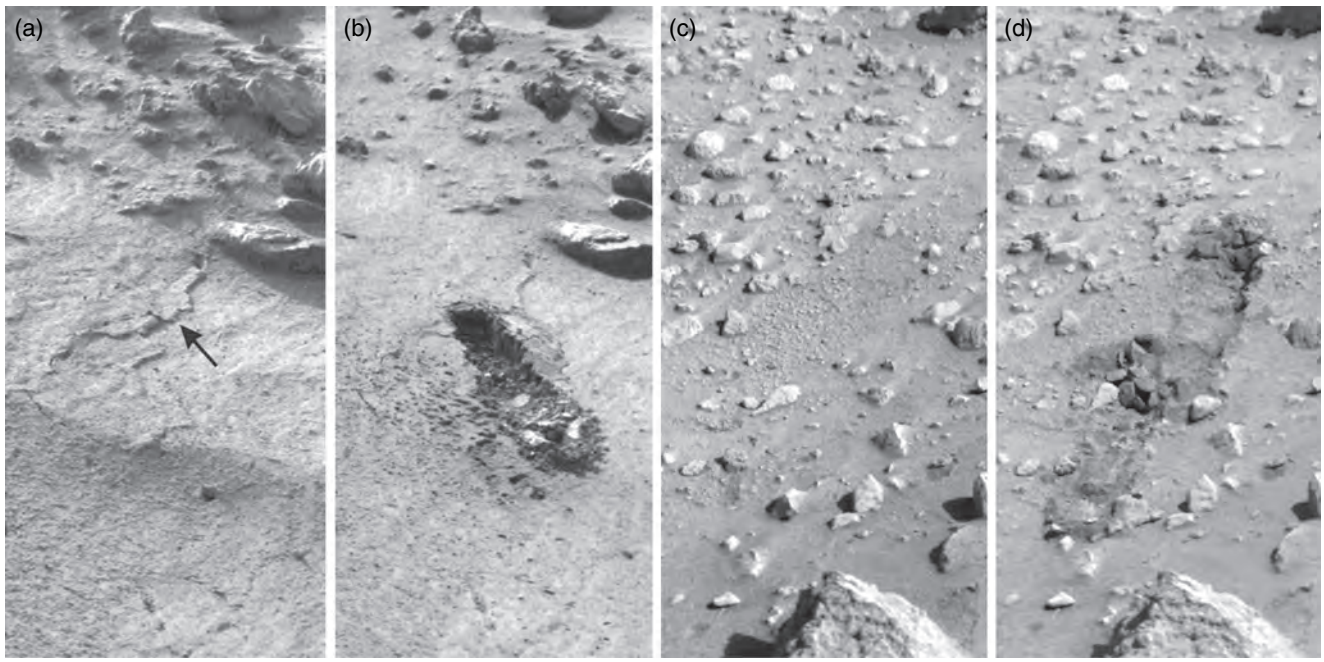

Figure 20.1. Example Viking Lander 1 images of the drift and blocky material soil classes, shown for the natural surfaces and after trenching into the materials. (a) Natural surface of drift material from Sandy Flats at VL1 is exposed from near the center to bottom of the frame (Viking Lander Image ID: 11A055/008). The sinuous pattern at the surface (indicated by arrow) could be an expression of cross laminations in the subsurface. (b) Same area of drift material is shown after trenching during sample acquisition (Image ID: 11A058/008). The trench exhibits steep walls, along with a domed and fractured surface surrounding the far end of the trench. The trench is about 8 cm wide, 45 cm long, and 5 cm deep. (c) At the center of the frame is an area of blocky material at VL1 known as Rocky Flats, which shows a characteristic pebbly texture (Image ID: 12A140/024). (d) Trenches into the Rocky Flats area are seen after several sample collection activities (Image ID: 12B163/073). The disrupted areas at the far ends of the trenches clearly show the blocky nature of this material. Multiple trenching sequences excavated down to a maximum depth of about 5 cm. The upper trench is about 9 cm wide.

Viking Landers

Physical properties investigations were conducted by the two identical Viking Lander spacecraft that operated on the surface of Mars for several Earth years between 1976 and 1982. The Viking Lander 1 (VL1) landing site is located in Chryse Planitia on a surface that includes drifts superimposed on a rocky substrate (Binder *et al*., 1977; Arvidson *et al*., 1989; see also Chapter 21). Viking Lander 2 (VL2) landed on the opposite side of Mars in Utopia Planitia. The VL2 site is characterized by lower relief, but is littered with centimeter- to meter-sized rocks perched on the surface and partially buried in soil (Mutch *et al*., 1977; see also Chapter 21). The objectives of the Viking physical properties investigation were to determine soil-bearing strengths, cohesions, angles of internal friction, porosities, thermal properties, grain sizes, and adhesions (Moore *et al*., 1987). However, there were no Viking Lander instruments designed to directly measure any of these parameters. Instead, information on material physical properties was derived from imaging observations of the interactions between surface materials and spacecraft components, such as footpad penetration and erosion by descent rocket exhaust during landing. In addition, the behavior of materials was interpreted from electro-mechanical resistances during surface sampler arm activities while collecting samples, trenching, sieving, and pushing rocks. Moore *et al*. (1987) provide a detailed description of the surface sampler system used in many of the physical properties experiments. Moore *et al*. (1987) also give a complete catalog of the types of experiments done and a chronology of the lander activities associated with the physical properties investigations.

The surface sampler arm on each Viking Lander consisted of an extendable boom that pivoted in both azimuth and elevation. At the end of the surface sampler arm was a collector head that had a fixed lower jaw with a backhoe underneath and a movable upper jaw that had a grating with 2 mm holes for sieving. Sieving was done by inverting the collector head and vibrating. Motor currents from the arm were recorded during sample collection to provide additional data on surface material properties. The area accessible to the surface sampler arm was located in front of each lander and was referred to as the sample field, which comprised an annular area about 1.5 m across. Analyses of physical properties experiments produced a classification of sample field materials at the two sites that included three types of soil-like materials, and rocks. The soil materials listed in order of increasing strength are drift material, crusty to cloddy material, and blocky material (Moore *et al*., 1977, 1987).

Drift material, which is found only at the VL1 site, is the weakest of the soil materials studied by Viking. It covers about 14% of the sample field (Moore and Jakosky, 1989). Its name derives from several locations outside the sample field where this material is seen in drift forms that cover areas from 1 to 10 m across. Some of the drifts in the midfield are eroded and expose crosslaminations. Closer to the VL1, drift material appears smooth, suggesting unresolved, very fine-grained silt to clay-size particles (Figures 20.1a and b).

During the VL1 landing, footpad number 2 penetrated 16.5 cm into drift material and became partially buried. Experiments known as "backhoe touchdowns" were conducted to help determine the cohesion of the material. In a backhoe touchdown experiment, the collector head was positioned over a target with the backhoe pointing down toward the surface. The arm was then lowered onto the surface. As the backhoe penetrated into the surface material, the collector head would rotate about 10° until a contact switch stopped the arm motion. Backhoe touchdown sequences into drift material generated penetration depths of 3–4 cm (Moore *et al.*, 1987).

Excavation of a deep hole into an area of drift material known as Sandy Flats was accomplished by pushing the backhoe into the surface and retracting the arm. The deep hole trench sequence at Sandy Flats retracted the backhoe 48 times and produced a trench that was 23 cm deep with average wall slopes of 68°. By the end of the mission, these trench walls had remained unchanged for over 1000 sols (Moore *et al.*, 1987). Drift material has the lowest angle of friction (18°) among the three soil materials based on analyses of trenches. The slope stability of trench walls suggests low cohesion (less than 3.7 kPa with an average of 1.6 kPa; Moore *et al.*, 1982, 1987) for drift material. These cohesion values are smaller than most dry, fine-grained terrestrial sediments. Drift material appears to have the consistency of loose baking flour (Arvidson *et al.*, 1989). The bulk density of the drift material was estimated from X-ray Fluorescence Spectrometer (XRFS) data to be $1150 \pm 150\ \mathrm{kg\,m^{-3}}$ (Clark *et al.*, 1977). Thus, drift material is also likely to be porous, given its low bulk density.

Crusty to cloddy material covers about 86% of the VL2 sample field, occurring between individual rocks (Moore and Jakosky, 1989). Crusty to cloddy material is characterized by relatively smooth and fractured surfaces (Figure 20.2a). It also tends to break up into small 0.5–1 cm sized clods. Crusty to cloddy material occurs at or near the surface and appears to be underlain by less cohesive material (Moore *et al.*, 1982). Disrupted areas of crusty to cloddy material around trenches tend to have broken, platy slabs of crust (Figure 20.2b). A deep trenching sequence using 47 backhoe retractions reached a depth of 11–12 cm into crusty to cloddy material. In addition, backhoe touchdown experiments into the surface of crusty to cloddy material produced penetration depths of only about 0.9–1.4 cm (Moore *et al.*, 1979). These observations suggest that crusty to cloddy material is stronger than drift material based on shallower trenches and backhoe penetrations. However, numerous sieving operations with the collector head easily disaggregated clods of this material, with the loose particles passing through the 2 mm holes in the sieve. Deformations around the edges of trenches and the stability of trench walls suggest that crusty to cloddy material has an angle of internal friction of around 35° and cohesions <3.2 kPa, with an average of 1.1 kPa (Moore *et al.*, 1982) – still low when compared to dry, fine-grained terrestrial soils. Several failed attempts to collect rock fragments from areas of crusty to cloddy material suggest that millimeter- to centimeter-size rock fragments or strong clods do not commonly occur within this material (Moore *et al.*, 1987). Overall, the observations suggest that the crusty to cloddy material consists of fine-grained material that is weakly cemented together by salts (Clark *et al.*, 1982; Arvidson *et al.*, 1989).

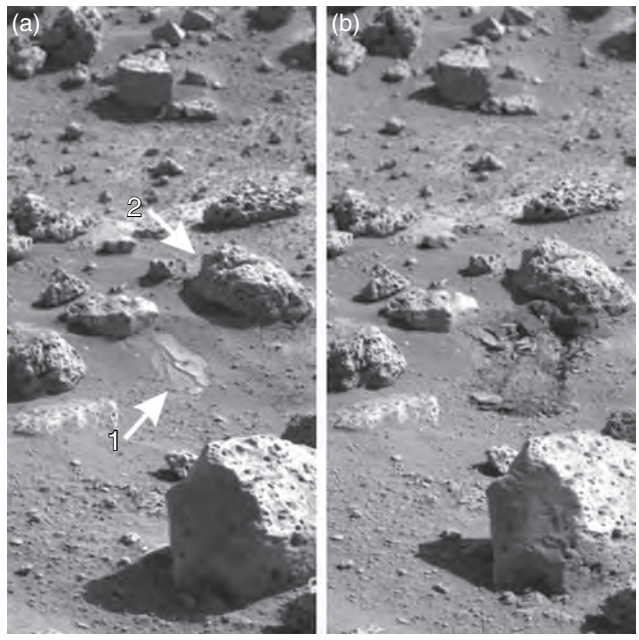

Figure 20.2 Example Viking Lander 2 images of the crusty to cloddy soil class, shown before and after trenching into the materials. (a) A region of crusty to cloddy material from VL2 is shown before any disturbance by trenching (Image ID: 22A007/001). Note the relatively smooth crusty area cut by fractures located near the center of the image and indicated with the arrow labeled 1. The rock labeled with arrow 2 is about 25 cm across. (b) The same area is seen after two sample acquisitions produced a trench into the crusty material (Image ID: 22A247/030). Trenching disrupted the surface to form plates of crusty material several centimeters across and about 1 cm thick. The first sample acquisition reached a depth of about 2–3 cm, whereas the second one excavated down to about 4–5 cm. The overall length of the trench is about 29 cm.

The blocky material found at the VL1 site is the strongest of the soil materials at the two Viking lander sites. Blocky material occurs between rocks and drift material at the VL1 site, and covers about 78% of the VL1 sample field (Moore and Jakosky, 1989). Blocky material is characterized by centimeter-sized prismatic clods (Figure 20.1c). When disrupted by trenching, it forms 2–4 cm sized fragments (Figure 20.1d). The descent engines eroded into the blocky material during landing to expose a fractured material that appears to be cohesive or indurated. Footpad number 3 of the VL1 landed on top of blocky material and only penetrated 3.6 cm, as opposed to the 16.5 cm of penetration of footpad 2 into nearby drift material. Similarly, backhoe penetration depths into blocky material of 0.5–1.4 cm were less than that for drift material (Moore *et al.*, 1987). Trenching using 48 backhoe retractions to dig into the surface excavated to a depth of about 13 cm into blocky material (Moore *et al.*, 1979) and required large forces by the surface sampler arm (Moore *et al.*, 1982). Sieving and purging sequences while collecting samples of blocky material yielded millimeter- to centimeter-sized rock fragments or strong clods. Analyses of trenches dug into blocky material suggest an angle of internal friction of 31° and cohesions

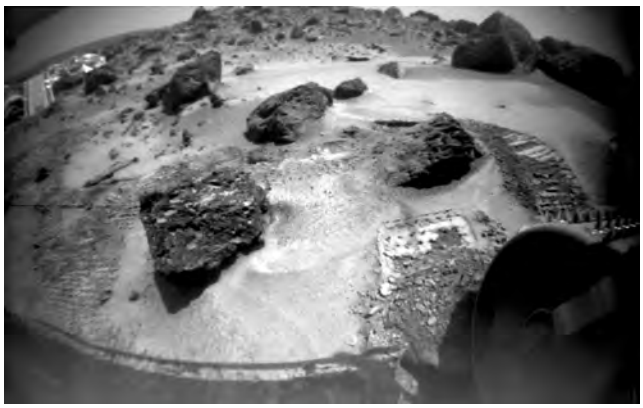

Figure 20.3. Sojourner rover camera image of wheel tracks showing bright reflective molds of cleats, flakes of compressed drift deposits, and darker, less-well-sorted underlying soil deposits.

between 2.2 and 10.6 kPa, with an average of 5.5 kPa (Moore *et al*., 1982). The measurements got from XRFS show that these coarse clods are enriched in S and Cl (Clark *et al*., 1982), which suggests that the cohesion of blocky material is related to cementation by salts (Moore and Jakosky, 1989).

Sojourner/Mars Pathfinder

The Sojourner rover, carried aboard the Mars Pathfinder lander, was the first successful wheeled vehicle to interact with the Martian surface, allowing soil physical properties to be studied at multiple locations at the landing site near the mouth of the Ares Vallis catastrophic outflow channel. Pathfinder lander airbag bounce and retraction marks also provided information on disturbed surface materials before the rover was deployed. Airbag bounce and retraction marks appear darker than undisturbed soil, suggesting the presence of a thin, bright surface layer. Airbag retraction marks are shallow trenches radial from the lander, with pebbles and rocks entrained in the nearby soil (Golombek *et al*., 1999a). Rover tracks also generally appear dark except in locations where the bright surface material is compressed into smooth, reflective bright clods that carry imprints of the rover wheel cleats (Figure 20.3; Moore *et al*., 1999). The bright surface material is the same color as the dust in the atmosphere (light yellowish brown), and drift material at least on the surface of wind tails behind rocks and within the wheel tracks appears to be very fine-grained, porous, and compressible. These observations argue that this material is micron-sized dust that has settled from the atmosphere. Beneath the bright, fine-grained drift is darker, poorly sorted soil composed of unresolved fine-grained material mixed with pebbles, cobbles, and rock fragments. This cloddy soil is similar to moderately dense soils on Earth.

More diagnostic in understanding the mechanical properties of the soil than simply imaging the wheel tracks were the 14 special soil mechanics tests performed by the Sojourner rover over its ~100 m traverse. These tests were performed by locking 5 wheels and rotating the 6th wheel in quarter-revolution steps while measuring the rocker bogie differential angle (wheel depth with time) and the motor current, which was converted to wheel torque (during revolutions

Figure 20.4. IMP image of Sojourner rover performing APXS measurement of "Scooby Doo," a hard, indurated, soil-like deposit whose elemental composition is similar to other soils but which was not noticeably scratched or marked during "road warrior" rock wheel scratch tests.

and no-load "wheelies") and shear and tractive forces using the results of a series of tests on a variety of soil types on Earth. Derived normal and shear stresses were used to iteratively solve a standard Mohr Coulomb failure criterion that included cohesion and friction angle (angle of internal friction) or coefficient of friction. The angle of internal friction was estimated from the angle of repose of excavated piles of material that had low cohesion (Moore *et al*., 1999). Estimates of the angle of internal friction are believed to be better constrained than cohesion (which is very small) by the experiments. The abrasiveness of the Martian dust was measured from the wear on a thin metal film mounted on one of the rover wheels (Ferguson *et al*., 1999).

Results of the Sojourner soil mechanics experiments are consistent with soil simulants tested on Earth and suggest that cloddy soil behaves like moderately dense soils on Earth, with friction angles near 34°–39°, low cohesion of 0.0–0.42 kPa, and angle of repose of 33°–38° (Moore *et al*., 1999). Scooby Doo, a bright patch of cohesive soil or rock that had a chemical composition similar to other soils, was undeformed by the rover wheel cleats during a scratch test, indicating that it was well-indurated, resembling hardpan on Earth (Figure 20.4). Mechanically, cloddy soils at the Pathfinder site resemble the crusty to cloddy soils at VL2, albeit with lower cohesion. Scooby Doo resembles blocky material at VL1, and the drift deposits at the Pathfinder site are like very porous and weak drift deposits at VL1. Inferred bulk densities of cloddy soils estimated from their friction angles (Moore *et al*., 1999), assuming they behave like lunar soil simulants (Mitchell *et al*., 1972), are 1285–1518 kg m^{-3} for average friction angles of 34°–37°; higher bulk densities of 2000–2200 are likely for well-indurated materials such as Scooby Doo at Pathfinder and blocky soils at VL1. These

Figure 20.5. Sojourner rover wheel tracks in "Cabbage Patch" showing cloddy deposits and at least one rounded pebble.

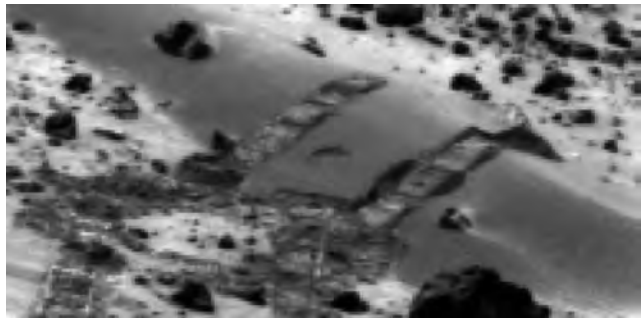

Figure 20.6. IMP image of "Mermaid" duneform showing reflective rover tracks, darker subsurface soils, pile of material excavated by a rover wheel, and circular spot where APXS disturbed soil during measurement. Pile of material allowed measurement of angle of repose, and close-up rover images show the dark, poorly sorted substrate.

bulk densities are also similar to those estimated from the radar reflectivity of the surface (Golombek *et al*., 1999b; see also Chapter 21) via extrapolation of a radar echo model (Hagfors, 1964; Evans and Hagfors, 1968) and a relation between bulk density and normal reflectivity (Olhoeft and Strangway, 1975). Cloddy soils at the Pathfinder site, many of which contain pebbles (Figure 20.5), may be poorly sorted fluvial materials deposited by the Ares and Tiu catastrophic floods (Golombek *et al*., 1999a; Moore *et al*., 1999); the finer fractions may have been reworked via eolian activity (Greeley *et al*., 1999, 2000). Drift deposits may be dust deposited from atmospheric suspension, and in the case of bright dust covering at least the surface of wind tails, may be sculpted by the wind (Moore *et al*., 1999). Sojourner tracks in the "Mermaid" duneform appear bright, suggesting a significant fraction of fine-grained (dusty) material there (Figure 20.6). Comparison of wear results of thin metal films shows that the Martian dust is comparable to fine-grained soils of limited hardness (Ferguson *et al*., 1999).

Mars Exploration Rovers

As of early 2007, the two MERs *Spirit* and *Opportunity* have each traversed distances of more than 6 and 10 km at their respective landing sites in more than three years of surface operations. Each rover carries an identical science payload of remote-sensing and arm-mounted, surface-contact instruments. Both MER vehicles performed the following investigations related to physical properties (Arvidson *et al*., 2003): (i) quantification of dust accumulation and dispersal dynamics by periodically monitoring the rover decks with the Pancam (Bell *et al*., 2003) and Miniature Thermal Emission Spectrometer (Mini-TES) (Christensen *et al*., 2003); (ii) inference of soil properties from analyses of wheel track patterns, wheel sinkage, and wheel slippage during traverses; (iii) extraction of along-track terrain topography and physical properties from rover wheel and suspension telemetry recorded during traverses; (iv) excavation of trenches using rover wheels to characterize mechanical properties of soils with depth; (v) analysis of rock grind telemetry from the RAT (Gorevan *et al*., 2003) to infer rock strength; and (vi) observations of the Mössbauer Spectrometer (Klingelhöfer *et al*., 2003) and Microscopic Imager (MI) (Herkenhoff *et al*., 2003) contact sensor interactions with surface materials. Initial results of the MER physical properties investigations covering the primary missions of both rovers were reported by Arvidson *et al*. (2004a,b).

The ring-shaped Mössbauer contact plate applied a force of ~1 N (1 N is about the weight of a 102 g apple in Earth's gravity, or 0.225 lb) to soils at both landing sites to refine knowledge of instrument arm positioning relative to a surface target and/or to specifically observe the effect of slight pressure applied to the soil. MI images of Mössbauer contact plate soil impressions show that the natural texture of fine-grained soils typically is obliterated on contact (Figures 20.7 and 20.8). The observed molding behavior under pressure, exhibited by most soils at both MER sites, suggests that some soils include weak particles that are easily crushed, and/or a significant fraction of unresolved very fine particles is present that reconfigures among voids between larger particles under applied pressure.

Soils at the Gusev site generally are covered by a layer of dust typically less than 1 mm thick that was easily disturbed by *Spirit*'s landing system and wheels (see also Chapter 13). Darker soils beneath this surface layer commonly showed evidence of cohesion when disturbed by the rover wheels or lander airbags. A weak surface crust a few millimeters thick (including the dust layer) was easily crushed by the rover wheels or Mössbauer contact plate. MI images of crushed soils show that fine grains are molded to form casts that are smooth at sub-millimeter scales, implying a significant fraction of fine-grained material (Figure 20.9). Some of the fine particles may be agglomerates of dust grains that are held together by electrostatic cohesion or minor cementation (Herkenhoff *et al*., 2004a).

The aeolian bedform dubbed "Serpent" was disturbed by *Spirit*'s wheels, exposing weakly cohesive, fine-grained material beneath a surface layer of very coarse sand and granules (Figure 20.10). Larger wheel trenches dug into other soils on the plains between the lander and the Columbia Hills all retained wall slopes greater than typical angles of repose. They also yielded break-away clods from the walls, indicating that some minor cohesion is pervasive with depth, although it must be even weaker than that of the

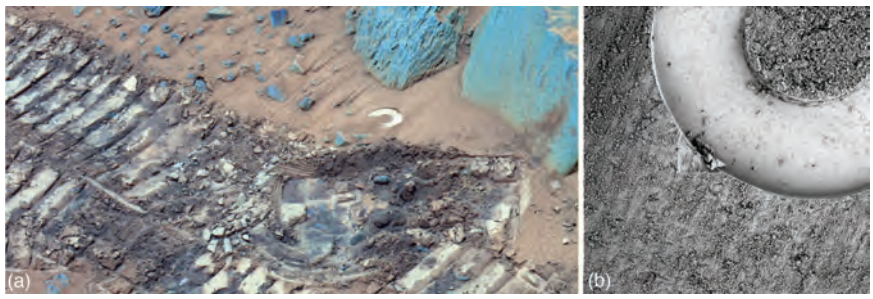

Figure 20.7. (a) *Spirit* Pancam false-color view of tracks and Mössbauer imprint into dusty aeolian drift material, obtained near the summit of Husband Hill on Sol 589. Pancam filters are L2 (753 nm), L5 (535 nm), and L7 (432 nm) stretched into red, green, and blue, respectively. The Mössbauer imprint is the bright, partial ring feature at central upper-right in this view. (b) *Spirit* MI image of the same Mössbauer contact plate imprint, obtained on Sol 588 in full shadow. The MI was rotated at the time of imaging relative to the orientation of (a). MI view is ~31 mm across. (For a color version of this figure, please refer to the color plate section or to the e-Book version of this chapter.)

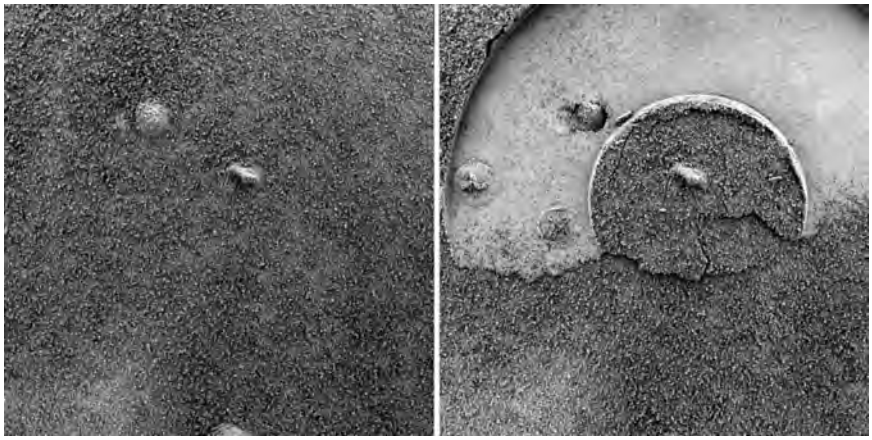

Figure 20.8. *Opportunity* MI images of a relatively rare (at Meridiani Planum) bright, dusty soil before (left) and after Mössbauer contact. Dust-sized particles (seen clumped into resolved agglomerates) allow the soil to accurately mold the Mössbauer contact plate, including screw heads on the left. Fissures near the center indicate small amounts of surface cohesion. Images 1M133421996IFF0830P2957M2F1 and 1M133598234IFF0830P2957M2F1 were obtained on Sols 59 and 61, respectively. Both views are about 31 mm across. Compare this pair of images with Figure 20.9 (Gusev).

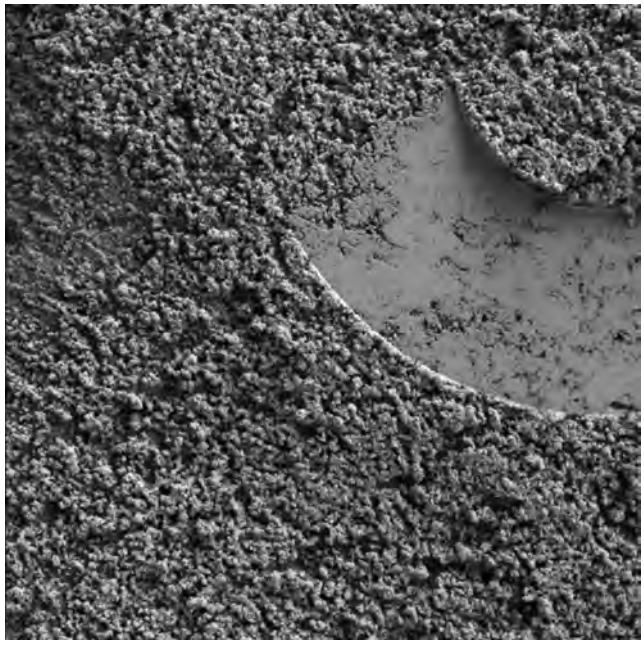

Figure 20.9. *Spirit* MI image 2M147677362IFF8800P2976M2F1 of a Mössbauer plate impression into dusty soil. Unresolved dust particles apparently have clumped together into irregularly shaped, resolved agglomerates that are easily crushed and molded by the ~1 N contact force. The image, spanning about 31 mm, was obtained on Sol 240 when the target was fully shadowed by the instrument, with diffuse illumination from top.

fragile ~1 mm surface crust (Figure 20.11). Trenching depths achieved varied between ~6 and 10 cm. A soil crust on the flank of Husband Hill showed evidence for cementation of well-sorted sand grains (Figure 20.12). Visual measurements of wheel rut depths in various soils (Figure 20.13) yielded preliminary estimates of bearing strength from about 15 to 130 kPa, cohesive strength of ~1–7 kPa, and angle of internal friction of ~20°–25°, using semi-empirical wheel–soil interaction theory calibrated to the shape of the MER wheel (Richter *et al.*, 2006).

The upper ~1 mm of soil at Meridiani Planum also commonly appears to be weakly cohesive in MI images of soil disturbed by the Mössbauer contact plate or rover wheels (Figure 20.14; Herkenhoff *et al.*, 2004b). The cohesion may be due to the presence of chloride and/or sulfate salts, a conclusion that is consistent with Alpha Particle X-Ray Spectrometer (APXS) observations of soils at the *Opportunity* landing site (Rieder *et al.*, 2004). These salts may have precipitated from thin films of water that formed during warmer periods and that dissolved salts in dust particles. In places, the cohesion appears to be minor and easily destroyed (Figure 20.15). The Meridiani soil surfaces typically have a bimodal size distribution, with very coarse sand grains and granules up to 6 mm in diameter, along with very fine (<125 microns) dark sand (Soderblom *et al.*, 2004; Weitz *et al.*, 2006; see also Chapter 13). Trenches dug into soils by *Opportunity*'s wheels showed that the coarser grains are concentrated at the surface, likely by aeolian removal of the finer particles (Figure 20.16), forming a lag that

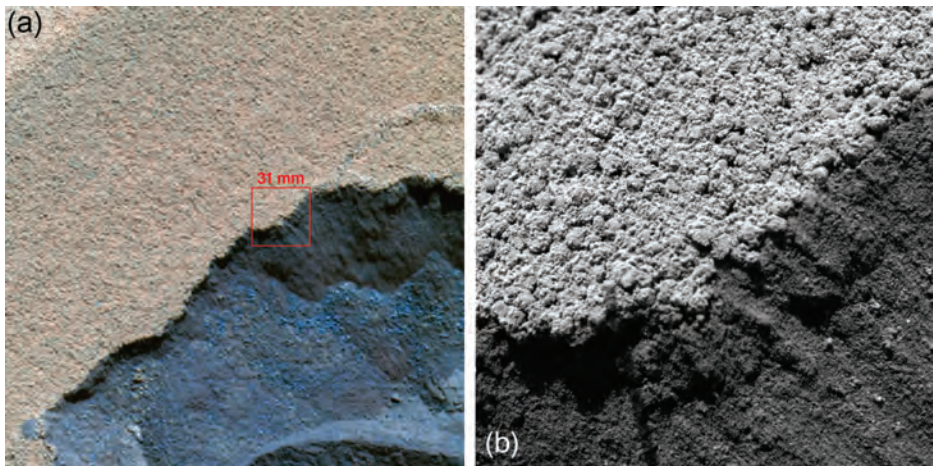

Figure 20.10. (a) *Spirit* Pancam false-color view of the wheel scuff performed on Sol 72 into "Serpent," an aeolian bedform near the rim of Bonneville crater on the plains west of the Columbia Hills. Pancam filters are L2 (753 nm), L5 (535 nm), and L7 (432 nm) stretched into red, green, and blue, respectively. The brighter, redder, dusty exterior contrasts with the darker interior of the feature. Red square shows MI location. (b) MI image 2M132842058IFF2000P2977M2F1 of the edge of the wheel scuff, obtained on Sol 73. A very thin, relatively bright dust layer covers a monolayer of rounded, very coarse sand, which overlies an ~8 mm weakly cohesive layer dominated by finer grains, with similarly fine materials further below (lower right of image). View is about 31 mm across, illuminated from top. (For a color version of this figure, please refer to the color plate section or to the e-Book version of this chapter.)

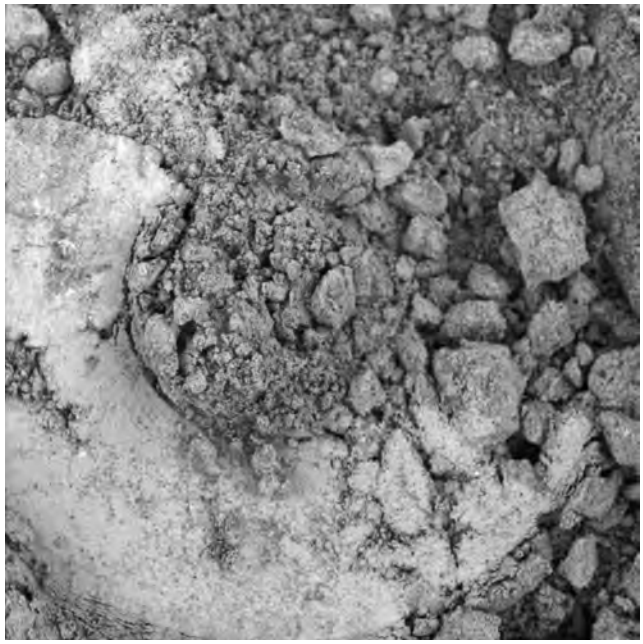

Figure 20.11. *Spirit* MI image 2M136501952IFF37CAP2957M2F1 of a Mössbauer imprint into debris on the floor of the Sol 113 wheel trench. Soil clods are easily compressed and molded by the ~1 N contact force of the contact plate, implying relatively weak cohesion. The image spans about 31 mm and was obtained on Sol 114 when the target was fully shadowed by the instrument.

Figure 20.12. *Spirit* MI image of a disrupted soil crust containing well-sorted 200–300 μm grains, overlying finer material (darker zones in image). Weak soil crusts of varying thicknesses and strengths are common at both MER landing sites. Image 2M170218789IFFAAEEP2976M2F1, obtained on Sol 494 with direct illumination from the upper left, spans about 31 mm.

protects finer grains in the subsurface from further erosion (Arvidson *et al.*, 2004b; Soderblom *et al.*, 2004; Sullivan *et al.*, 2005; Jerolmack *et al.*, 2006; Weitz *et al.*, 2006). Trench walls steeper than the angle of repose and the presence of break-away clods from the walls are additional evidence for soil cohesion extending to maximum trench depths of about 10 cm. Wheel tracks, Mössbauer contact plate impressions, and airbag bounce marks showed that the soil can be finely molded, indicating the presence of a substantial fraction of very fine particles, unresolved by the MI, that fill voids during compression and remolding. Soil physical properties estimated from wheel rut depths exhibited similar values as those inferred for the Gusev site (Arvidson *et al.*, 2004a,b).

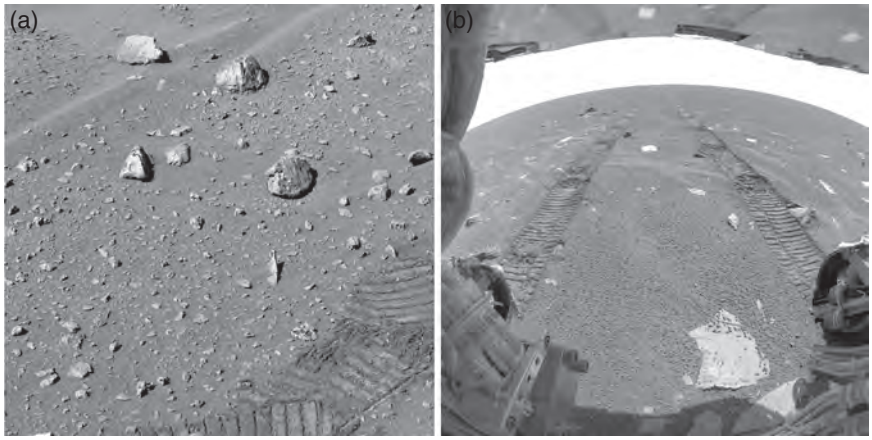

Figure 20.13. Examples of MER wheel tracks. (a) *Spirit* Pancam R1 (436 nm) frame 2P129996790RAD0506P2599R1C4 (Sol 41), showing wheel track with comparatively small rut depth on plains surface between the landing site and Bonneville crater. (b) *Opportunity* Rear Hazcam frame 1R135651546 (Sol 84), showing wheel tracks with comparatively large rut depth on Meridiani plains surface close to Fram crater.

Figure 20.14. *Opportunity* MI image 1M173457602IFF55W4P2936M2F1 obtained where *Opportunity* became severely bogged (embedded) while climbing an unusually large ripple, informally dubbed "Purgatory." This view, about 31 mm across, shows part of a tablet of soil compacted and remolded by the wheel cleats, then deposited alongside a track. Hematitic spherules (interpreted as concretions) 1–2 mm in diameter have been incorporated into this wheel-made, molded clod. They were mixed with and embedded within a finer, poorly sorted soil matrix that acquired slightly cohesive properties when compacted by the wheel. After creation, the tablet was subjected to aeolian erosion of the matrix, exposing the 1–2 mm concretions, particularly along the tablet's lower edge (note pedestals). During *Opportunity*'s ~40 sol stay in this area, wind events were seen to affect only areas disturbed by the rover, such as this example viewed on Sol 510.

Soil thermal inertia was derived using the relations proposed by Presley and Christensen (1997), which link bulk thermal conductivity of soils at Martian atmospheric pressure to soil bulk density, with the density estimated from wheel rut depth analysis. The resultant estimates range between 130 and 150 $J\,m^{-2}\,K^{-1}\,s^{-1/2}$ and are lower bounds because the effect of soil cohesion on the thermal inertia is not included in the Presley and Christensen model.

Discussion

The mechanical properties of soils at the landing sites are consistent with inferences made from orbital thermal inertia measurements (see Chapters 9, 18, and 21). Thermal inertia is a measure of the resistance of surface materials to a change in temperature that can be related to particle size, bulk density, and cohesion (Kieffer *et al*., 1977; Christensen and Moore, 1992). The fine component thermal inertia is the thermal inertia of the soil after the thermal radiance of the rocky component has been factored out (Kieffer *et al*., 1977; Christensen, 1986). Because rocks consist of <20% of the surface of the landing sites, their effect on the bulk inertia can be factored out via simple models of the effective thermal inertia of the rock population based on their diameter (Golombek *et al*., 1999b, 2003). For the bulk thermal inertia of the Pathfinder site of 435 $J\,m^{-2}\,K^{-1}\,s^{-1/2}$ and the estimated effective inertia of the measured rock size-frequency distribution of 1700 $J\,m^{-2}\,K^{-1}\,s^{-1/2}$, a fine component thermal inertia of about 320 $J\,m^{-2}\,K^{-1}\,s^{-1/2}$ was derived (Golombek *et al*., 2003), which is consistent with that expected for the observed poorly sorted, moderately dense, cloddy soils (Moore *et al*., 1999). Lower fine component thermal inertias at VL1 (240 $J\,m^{-2}\,K^{-1}\,s^{-1/2}$) and VL2 (170 $J\,m^{-2}\,K^{-1}\,s^{-1/2}$) derived in a similar way (Golombek *et al*., 2003) are consistent with the greater drift coverage at VL1 (18%–30%) and at VL2 (40%) (Moore *et al*., 1999). The fine component thermal inertia derived from rock abundance counts along *Spirit*'s traverse from the landing site to the rim of Bonneville crater similarly varies from 240 to 140 $J\,m^{-2}\,K^{-1}\,s^{-1/2}$ and can be related to the increased coverage of very-low-thermal-inertia dust (Golombek *et al*., 2005). In the case of Meridiani Planum, the bulk and fine component thermal inertia are effectively the same due to the lack of rocks, and the orbital thermal inertia of 200 $J\,m^{-2}\,K^{-1}\,s^{-1/2}$ corresponds directly to that expected (Presley and Christensen, 1997) from a surface dominated by the ubiquitous 0.2 mm fine sand observed by the rover (Herkenhoff *et al*., 2004b).

Estimates of the thermal inertia based on MER Mini-TES observations and soil physical properties (including cohesion) are presented in Chapter 21. The Mini-TES results, corrected for observed rock and clast abundances (Fergason *et al*., 2006) (150–200 $J\,m^{-2}\,K^{-1}\,s^{-1/2}$ for Gusev soils and 100–150 $J\,m^{-2}\,K^{-1}\,s^{-1/2}$ for Meridiani Planum soils), are

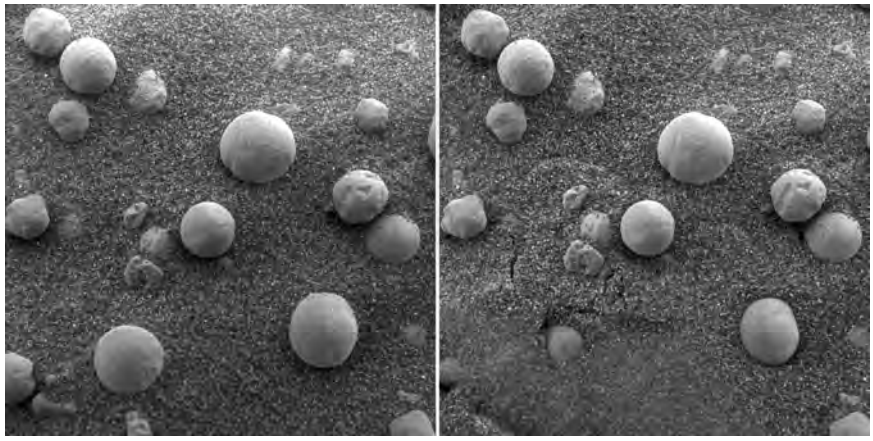

Figure 20.15. *Opportunity* MI images of hematitic concretions and mafic sand in Eagle crater, before (left) and after (right) being touched with the ring-shaped Mössbauer contact plate. Minor fissures opening in slightly distorted soil (right) indicate slight original cohesion. This cohesion is destroyed where more aggressive distortion occurs under the contact plate itself, resulting in self-burial of one of the larger concretions by effectively cohesionless sand. MI images 1M129426966IFF0300P2932M1F1 and 1M129430301IFF0300P2932M1F1 were obtained on Sol 14 in the shadow of the instrument, with diffuse illumination from the top. Each image is about 31 mm across.

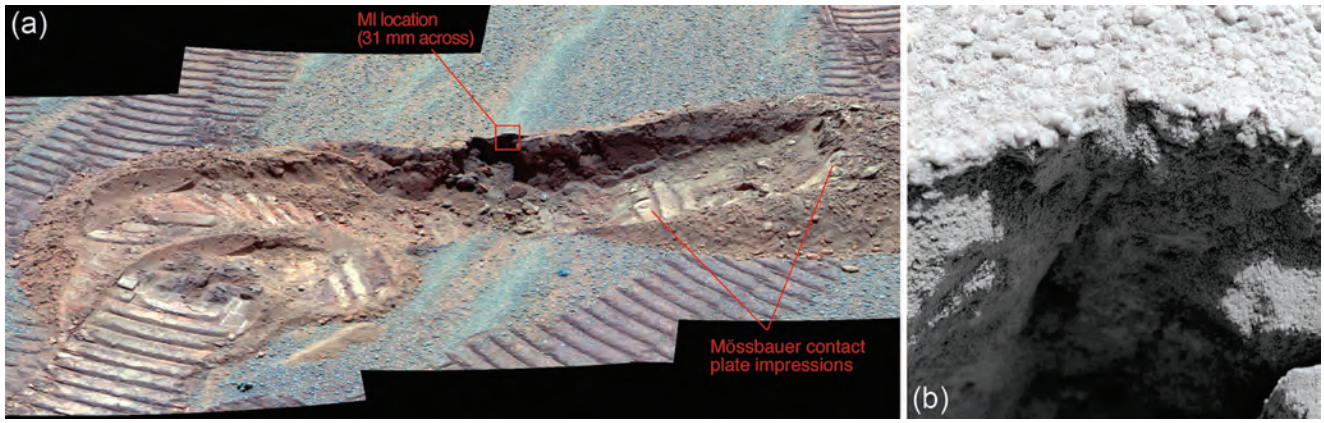

Figure 20.16. (a) *Opportunity* Pancam false-color view of a wheel trench dug on Sol 73 in the Anatolia area on the Meridiani plains between Eagle and Endurance craters. Pancam filters are L2 (753 nm), L5 (535 nm), and L7 (432 nm) stretched into red, green, and blue, respectively. In this view, hematite-enriched spherules several millimeters in diameter are blue, and are scattered across the undisturbed areas between ripples. Low ripples are coated with much smaller ~1 mm rounded hematite grains (also blue, not individually resolved by Pancam). The wheel trench bisected the (blue) ripple extending down the center of this view. The shadowed area on the trench far wall, where the ripple is bisected, is a collapse "cavern" that formed late in the trenching process (as seen in front Hazcam images obtained periodically during trenching), shedding break-away cohesive clods to the base of the trench wall. Maximum trench depth is about 10 cm. Red inset shows MI view location. (b) MI image 1M135284929IFF10CGP2956M2F1 of the rim of the trench. The ripple crest is seen in cross section in the upper middle of this view, where a surface of ~1 mm rounded hematite-enriched spherules form a thin lag. The ripple interior is dominated by ~100 μm sand and even finer, unresolved grains. View is about 31 mm across, illumination from upper right. (For a color version of this figure, please refer to the color plate section or to the e-Book version of this chapter.)

similar to the fine-component thermal inertias derived from TES and THEMIS data (140–200 $J\,m^{-2}\,K^{-1}\,s^{-1/2}$) (Golombek *et al*., 2005).

Minimum thermal inertias inferred from MER wheel rut depth analysis (~130–150 $J\,m^{-2}\,K^{-1}\,s^{-1/2}$) are somewhat lower than those obtained from orbital observations. This may be explained by the presence of cements interspersed in the soils that would enhance thermal conductivity (and thus thermal inertia) over that predicted by the empirical relation of Presley and Christensen (1997), which assumes loose, noncemented particulate materials. MER APXS and Viking Lander XRFS data are consistent with the presence of such ubiquitous, dispersed cements in the form of sulfates (Clark *et al*., 1982; Wänke *et al*., 2001; Rieder *et al*., 2004).

From a strength perspective, MER soils most resemble the VL1 "blocky" soil type, although larger soil deformations by the wheels and Mössbauer spectrometer contact plate in some places suggest locally weaker deposits. Preliminary cohesion estimates obtained from the MER wheel rut depth analyses (Arvidson *et al*., 2004a,b) are similar to results of Viking Lander sample trench analyses but higher than those derived from the Pathfinder Sojourner soil mechanics investigations (although large uncertainties were assigned to the Pathfinder soil cohesion retrievals by the investigators themselves) (Moore *et al*., 1999).

Several empirical relations have been proposed between the shear strength of soils and their bulk density, such as those of Mitchell *et al*. (1972) which relate soil void ratio to internal friction angle and to cohesion respectively, assuming that the material physically behaves like lunar regolith. For a mineral density of 2900 $kg\,m^{-3}$ (the range of mineral densities in the lunar soil is 2300–3200 $kg\,m^{-3}$ [Carrier *et al*., 1991]), these relations were applied to the inferred MER soil strengths to produce corresponding estimates for bulk density, which was found to range from ~1200 to ~1400 $kg\,m^{-3}$. A simpler approach, perhaps justified by

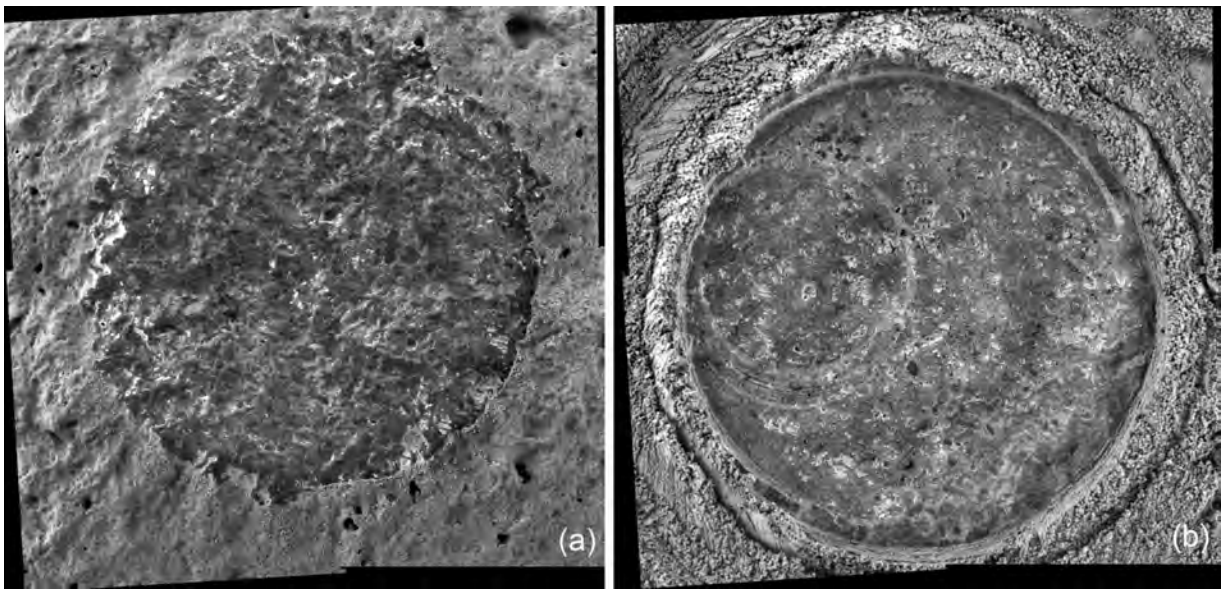

Figure 20.17. *Spirit* MI mosaics of target "Chisel" on rock "Wishstone" before ((a) acquired on Sol 333) and after ((b) acquired on Sol 334) RAT grinding. Each mosaic is about 5 cm across; all images taken while target was fully shadowed.

observed lateral and depth-dependent soil heterogeneities (e.g., coarse particle lags and slightly cohesive soil crusts), involves assuming a typical porosity of around 50% applied to a mineral density of 2700–2900 kg m^{-3} yielding a similar range of bulk densities. These bulk densities are similar to those inferred from measured radar reflectivities of Gusev and Meridiani of 1200 kg m^{-3} (Gusev) and 1500 kg m^{-3} (Meridiani) (Golombek *et al.*, 2003). Elevated radar reflectivities of 0.05 across Meridiani Planum may be caused partly by the observed lag deposit of hematite-rich spherules.

20.2.2 Rocks

Rocks are abundant at both Viking Lander sites. Rocks larger than 3.5 cm cover about 8% of the sample field at the VL1 site and about 16% at the VL2 site (Moore and Jakosky, 1989; Moore and Keller, 1991). Some rocks near the landers are meter-scale in size. For example, at the VL1 site there is a 2 m wide sediment-capped boulder named Big Joe within 10 m of the lander. Little is known about the composition or physical properties of rocks at the two landing sites. Despite several attempts, rock samples were never successfully collected for measurement by either lander's analytical instruments. However, rocks appear to be relatively strong, given that they were never chipped, scratched, or spalled while being pushed with the sampler arm or scraped by the backhoe. These observations also suggest that the rocks are not likely to have weak rinds (Moore *et al.*, 1987). It is estimated that rocks at the Viking sites have cohesions in the range of 10^3–10^4 kPa and angles of internal friction of 40°–60° based on analogy to crystalline terrestrial rocks (Moore *et al.*, 1987; Moore and Jakosky, 1989).

Similarly, rocks at the Mars Pathfinder landing site were never chipped nor scraped by rover wheels when driven onto or over during surface operations (see Chapter 21). The chemical composition of rocks analyzed by the Pathfinder Alpha Proton X-ray Spectrometer are all consistent with the rocks being dense, fine-grained volcanic rocks with weathering rinds or dust coatings (McSween *et al.*, 1999). Therefore, the physical properties of rocks at the Pathfinder landing site are similar to those estimated for rocks at the Viking landing sites (Moore and Jakosky, 1989).

As of early 2007, the MER RATs had been used to grind into 15 rocks in Gusev crater, and 30 rocks on Meridiani Planum (both outcrop and float; e.g., Figure 20.17). Energy expended during the deepest 0.25 mm of each grind can be calculated from instrument telemetry and compared with the volume removed. This calculation was used to obtain a measurement of each rock's resistance to grinding, which has been termed the "specific grind energy" (SGE; Myrick *et al.*, 2004):

$$\mathrm{SGE} = \frac{\mathrm{Energy}}{\mathrm{Volume}} = \frac{N\Delta t(\bar{I}_{\mathrm{grind}} - I_{\mathrm{noload}})V_{\mathrm{grind}}}{A_{\mathrm{abraded}}\Delta Z}, \qquad (20.1)$$

where N is the number of samples in the dataset, Δt is the sampling period, $\bar{I}_{\mathrm{grind}}$ is the mean current drawn by the grind motor, I_{noload} is an estimate of the current required to drive the mechanism without load, V_{grind} is the mean voltage applied to the grind motor, A_{abraded} is the grind area (measured from MI mosaics), and ΔZ is the overall change in depth across the dataset. Results from the *Spirit* rover are summarized in Table 20.3 and results from the *Opportunity* rover in Table 20.4.

Although SGE is not readily separated into constituent physical properties, initial investigations with testing on Earth indicated that grind energy is loosely correlated with unconfined compressive strength; rocks with higher grind energies typically have higher unconfined compressive strength (Myrick *et al.*, 2004). On Mars, the rocks that the *Spirit* RAT encountered at Gusev generally had much higher SGE values than the rocks that the *Opportunity* RAT encountered at Meridiani Planum.

Table 20.3. *Specific grind energy ($J\,mm^{-3}$) for rocks abraded by the* Spirit *RAT in Gusev crater*

Sol	Rock (target)	SGE
34	Adirondack (Prospect)	53.2
59	Humphrey (Heyworth)	49.2
81	Mazatzal (New York)	55.7
83	Mazatzal (Brooklyn)	49.7
195	Wooly Patch (Sabre)	5.15
198	Wooly Patch (Mastadon)	4.11
216	Clovis (Plano Spot)	8.26
231	Ebenezer (Cratchit 2)	8.92
285	Uchben (Koolik)	7.32
334	Wishstone (Chisel)	22.4
355	Champagne (Bubbles)	14.0
374	Peace (RAT Justice–1)	1.76
377	Peace (RAT Justice–2)	2.08
416	Watchtower (Joker)	30.6

Table 20.4. *Specific grind energy ($J\,mm^{-3}$) for rocks abraded by the* Opportunity *RAT in Meridiani Planum*

Sol	Rock (target)	SGE
30	McKittrick (Middle RAT)	1.67
34	Guadalupe (King 3)	46.2
44	Flatrock (Mojo 2)	1.14
66	Bouncerock (Case)	4.19
86	Pilbara (Golf)	1.25
107	Lion Stone (Puma)	18.1
138	Tennessee, a.k.a. Layer A (Vols)	0.332
143	Kentucky, a.k.a. Layer B (Cobble Hill)	1.41
145	Virginia, a.k.a. Layer C	0.775
148	London, a.k.a. Layer D, Ontario	0.183
151	Manitoba (Grindstone, a.k.a. Layer E1)	0.406
153	Manitoba (Kettlestone, a.k.a. Layer E2)	0.676
161	Millstone (Drammensfjord, a.k.a. Layer F)	0.145
177	Diamond Jenness (Holman 3–1)	0.149
178	Diamond Jenness (Holman 3–2)	−0.403
182	Mackenzie (Cambell 2)	−0.016
186	Inuvik (Tuktoyuktuk 2)	0.037
194	Bylot (Atkineq)	0.446
218	Escher (Kirchner)	4.69
311	Black Cow (Wharenhui)	0.567
402	Yuri (Gagarin)	1.22
545	IceCream (OneScoop)	0.683
558	FruitBasket(LemonRind)	0.507
633	Olympia (Kalavrita)	0.782
691	Rimrock (Ted)	0.928

However, the negative SGE values measured by *Opportunity* on Sol 178 and 182 highlight the practical uncertainties in SGE calculations from available telemetry; these uncertainties are present to some extent in all values of SGE. I_{noload} was calculated from postgrind RAT brushings (for those grind events which were immediately followed by a brushing, otherwise I_{noload} was estimated), and in this time period the grind motor and its transmission may have cooled sufficiently to increase the no-load current to the extent that it was larger than the grind current (on *Opportunity* Sols 178 and 182). Mechanism health otherwise may also affect SGE, as particulate matter caught in the seals of the RAT grind head may increase mechanical load and thus I_{noload}. Additionally, there is uncertainty regarding the forces at the grinding interface, where different rocks may provide different proportions of cutting and frictional resistance, when the cutting resistance is the only component that should be measured to assess rock grind energy.

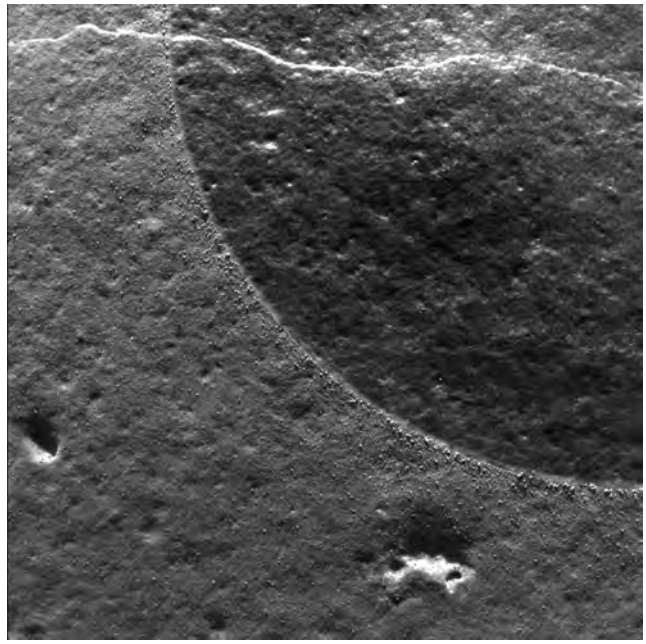

Figure 20.18. *Spirit* MI image 2M171727520IFFAAJCP2936M2F1 showing an area on the rock "Backstay" where RAT brushing of a dusty coating has occurred. Note that detailed rock relief is present in both brushed (darker) and unbrushed surfaces, implying that the dust coating is very thin ($\ll$ 1 mm). The image spans about 31 mm and was obtained on Sol 511 with illumination from the top. The dusty coating removed by the RAT brush appears to be ubiquitous in Gusev crater, and probably at many other places on Mars as well.

The grind energies required for abrading rocks at the Gusev crater and Meridiani sites can be compared to other chemical, mineralogical, and thermal data from the rovers to categorize their physical properties (summarized in Chapter 21). Extensive chemical composition and mineralogy investigations of rocks on the Gusev cratered plains indicate that they are olivine basalts with thin weathering rinds (McSween *et al.*, 2004). Gusev rock surfaces that have been brushed but not abraded by the RAT show evidence for a thin dust coating (Figure 20.18). Mini-TES measurements of thermal inertia are also high (Fergason *et al.*, 2006). These measurements suggest that Gusev plains rocks are fine-grained, dense volcanic rocks with high density, high cohesion, and high angle of internal friction (all of which are also consistent with the high grind energies [50–60] needed to abrade these rocks). Rocks in the Columbia Hills are mostly clastic rocks formed by volcanic or impact processes, with varying degrees of aqueous alteration (Squyres *et al.*, 2006). They have a different chemical composition and physical

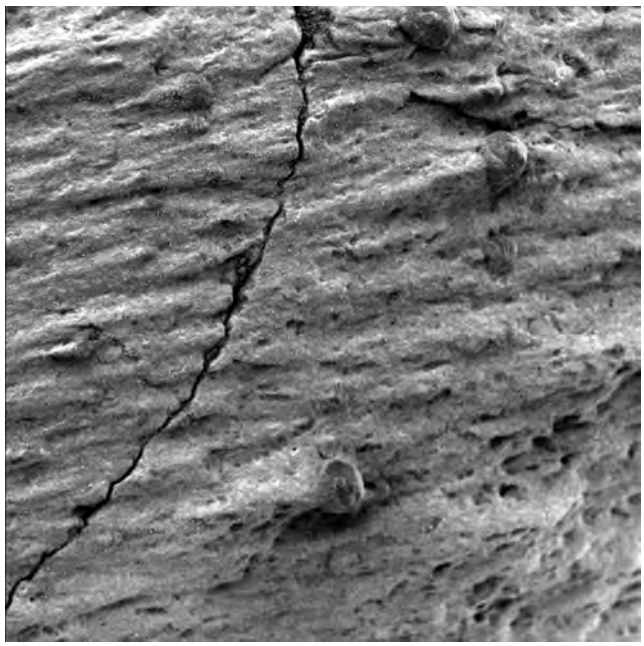

Figure 20.19. *Opportunity* MI image 1M162982683IFF4705P2977-M2F1 of sulfate-enriched bedrock abraded by wind-driven impacts of fine grains. The abrading grains were most likely similar to the ~100 μm mafic sand grains seen nearby (e.g., Figure 20.15). Hematite-enriched concretions are weathering out of this rock (~2 mm diameter examples are most obvious). The concretions are more resistant to abrasion, protecting streamlined "wind tails" of sulfate-enriched bedrock immediately downwind (toward left). This view is an example of the range of hardness of grains present in the same rock, revealed by differential erosion. The image is about 31 mm across, and was obtained on Sol 392 in the shadow of the instrument; diffuse illumination is from the top.

appearance than rocks observed on the plains, with lower Mini-TES thermal inertias and much lower grind energies of 2–24 J mm^{-3}. These results suggest that Columbia Hills rocks have reduced densities as well as cohesion and angle of internal friction compared with the denser volcanic rocks of the Gusev cratered plains. Layered evaporites at Meridiani Planum have very-low grind energies (0.1–2 J mm^{-3}), and the easily eroded nature of these outcrops by saltating basaltic sand suggests that they likely have even lower density and cohesion than the Columbia Hills rocks (Figure 20.19).

20.3 SUMMARY

Physical properties of Martian surface materials generally are not investigated as ends in themselves, but are evaluated to help address larger, science-driven questions or engineering needs. Soil and rock physical properties augment other information to help determine the origins and histories of surface materials, and can influence designs of future spacecraft mechanisms intended to interact with the Martian surface (e.g., landing systems, wheels, scoops, drills). For Viking, Pathfinder/Sojourner, and MER, the pursuit of this knowledge has been carried out according to the capabilities and limitations of each mission payload. These capabilities have changed dramatically from Viking to MER.

The Viking Landers, developed for investigating the possibility of life on Mars, were extremely ambitious machines for their time but had few tools for developing a "feel" for the surface materials at their landing sites. Compared with later missions, important limitations were lack of mobility, limited imaging resolution, and no capability for measurements below rock surfaces. Cameras could not resolve individual soil particles, so basic information on grain sizes, shapes, and sorting could not be measured. This was problematic in view of the significant aeolian-related bedforms observed at both sites. The unknown particle sizes of these bedforms left open questions about whether these features were composed of once-saltating, sand-sized grains, airfall dust, or a mixture (are they ripples, or dunes, or drift?). In the absence of definitive information, it was speculated that sand-sized grains might have short residence times on the Martian surface due to very high-speed saltation trajectories (Mutch *et al.*, 1976; Sagan *et al.*, 1977; Smalley and Krinsley, 1979; Sharp and Malin, 1984), and that if the aeolian features at the Viking sites were formed at least partly by saltation, grains of the expected saltation size might be assembled from smaller particles by electrostatic or other forces (Sagan *et al.*, 1977; Greeley, 1979). The Viking surface sampler arms were too delicate to manipulate all but the weakest materials, allowing only approximate lower limits of rock hardness to be estimated. And without mobility, distinct soil units seen by the cameras out beyond the range of the sampler arm could not be investigated. Any additional nearby soil or rock units just out of view of the cameras at each site remained hidden.

Pathfinder/Sojourner offered improved capabilities for physical properties investigations, but in most respects the investigations were similar in approach to those of Viking. The Imager for Mars Pathfinder (IMP) had significantly greater spectral discriminability for identifying distinct soil, crust, and rock units (Smith *et al.*, 1997), although resolution of individual soil grains still was not possible, leading to uncertainties about the nature and origin of the aeolian wind tails and bedforms observed there. Pathfinder had no sampler arm, but Sojourner rover wheel motor currents offered an analogous capability of inferring soil strength from electromechanical resistances. Unlike Viking, the Sojourner wheel/suspension system could be guided to different soil and crust targets over a larger area around the Pathfinder lander than could be reached by the Viking surface sampler arms. Sojourner was restricted to exploring only short distances from Pathfinder, however, but this was enough to reveal some terrain (including a different type of aeolian bedform) blocked from view of the lander (Matijevic *et al.*, 1997; Rover Team, 1997). Like the Vikings, little could be measured or even inferred about hardness of the rocks at the Pathfinder landing site.

The two MER rovers have a much greater capability than previous missions for investigating soil and rock physical properties. Both MER vehicles are still operating as of this writing, and comprehensive analyses of physical properties

of materials encountered along each of their multikilometer traverses have not yet been completed. It is clear at this stage, however, that the greater capability of the MERs for determining physical properties has begun to change the way this information is pursued and considered. As with previous missions, the strength of soil and rock materials is estimated indirectly from current drawn by electric motors driving mechanisms in contact with surface materials; for MER, these mechanisms are the six wheels and the RAT. Similar to Pathfinder's Sojourner rover, motor currents during MER wheel digging activities have been analyzed to distinguish stronger soils from weaker soils. While the MER arm is a relatively delicate device unsuitable for scratching or impacting rock by its own motions, the RATs carried on these arms have revealed a wide range of resistances to grinding, with some correlation to rock type and degree of aqueous alteration. Variations in soil and rock strength revealed by each rover are more likely to be encountered and to be recognized over distances longer than the reach of a Viking sampler arm, or even the range of a Sojourner-class rover. This extended mobility of the MER vehicles, combined with much better imaging of tracks and airbag bounce/retraction marks than was possible with Pathfinder/Sojourner, has allowed more informative analysis of track and bounce/retraction mark morphology and sinkage, another indicator of soil strength and its variation at the landing sites and along traverses. However, the most significant improvement of MER over previous missions for assessing physical properties of materials is the capability to resolve fine particles and textural features with the MI. For the first time, sand-sized and larger soil grains can be resolved directly (although roundness and other shape properties are measurable only for the larger grains). One of the most significant discoveries regarding Martian soils and the role of wind currently shaping these deposits has been the direct imaging of sand-sized grains at both MER sites (even – perhaps surprisingly – on the rover deck, 66 cm above the surface), and their association with saltation of these grains to form the bedforms where they are found, helping to resolve uncertainties about particle movement on Mars (Greeley *et al.*, 2004; Herkenhoff *et al.*, 2004a,b; Sullivan *et al.*, 2005).

20.4 FUTURE NEEDS AND DIRECTIONS

Uncertainties associated with determining some soil properties limit their usefulness in bounding engineering properties and geological processes. Actions that can be undertaken to reduce uncertainty in determining soil properties fall into three categories:

(1) Improve simulation models of machine/soil interactions.
(2) Design and fly instrumentation that directly measures load and torque during interactions with rocks and soil.
(3) Develop and deploy instruments specific to achieving soil study goals.

New approaches to simulating machine/soil interactions have been developed using the discrete (or distinct) element method (DEM) to represent granular media and soil particles (Tanaka *et al.*, 2000; Momozua *et al.*, 2003; Nakashima and Oida, 2004; Zhang and Li, 2006). These have been extended to analyze lunar microrover wheel performance (Nakashima *et al.*, 2007) and to develop a simulation capability for the MER wheel (Figure 20.20). The DEM is a technique for explicitly modeling the dynamics of assemblies of particles and is useful when a material undergoes large-scale discontinuous deformations that depend on micro-scale contact processes, internal breakage of contact bonds, and compaction of broken fragments (Cundall and Strack, 1979; Hopkins, 2004; Johnson and Hopkins, 2005). The simulations of DEM are numerical experiments of complex machine/soil interactions that can be compared to measured forces and observed three-dimensional soil deformation.

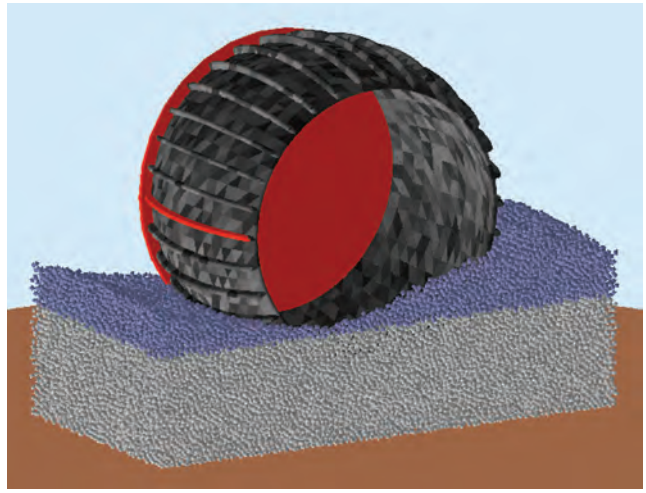

Figure 20.20. Discrete Element Method (DEM) computer simulation of an MER wheel digging in soil. (For a color version of this figure, please refer to the color plate section or to the e-Book version of this chapter.)

Equipment modifications to reduce uncertainty in determining Mars soil strength and heterogeneity consist primarily of adding force and torque sensors to wheels and probes to allow higher resolution measurements during interactions with soil. For example, the addition of a ranging/motion laser pointed toward ground next to a wheel would allow direct measurement of rover velocity, and wheel slip and sinkage during travel or during wheel trenching operations. Such additions, and wheel rotation monitoring, could allow the robot wheel to act as a mobile terrain characterization tool (Iagnemma *et al.*, 2004; Ojeda *et al.*, 2005) to estimate soil strength and its variation. Wheel force and torque measurements can also be used to implement optimizing criteria to minimize the occurrence of terrain failure and gross wheel slip, by monitoring the ratio of wheel tractive force (torque) to the normal force (Iagnemma and Dubowsky, 2004). Terrain failure detection methods that compare wheel and rover speeds could be used, for example, to prevent rover embedment from occurring. The addition of force sensors to scoops or other objects pressed into the soil could provide additional machine/soil data at higher resolution than is currently achieved by analyzing machine motor currents for later analysis and simulation.

Surface and subsurface access could be achieved using a dedicated instrumented digging bucket or an instrumented penetrometer. An instrumented digging bucket could serve dual purposes of digging trenches to expose soil layers to rover instruments and acting as a platform for soil properties measurement tools. These tools could include, for example, two force-sensitive indenters of different areas for pressure/sinkage measurements, a force-sensitive skid plate to measure soil/metal friction and abrasion, and a direct shear blade to measure soil strength. With some creative design, the bucket could apply varying normal loads during shear tests to determine both soil internal friction and cohesion.

An instrumented penetrometer might consist of a cone mounted on a hollow rod that is pushed or hammered into the soil. Instruments or fiber optics that transmit laser light to interrogate soil properties could be inserted into the core of the rod. The depth of penetration and the force, momentum, or energy required to insert the penetrometer into the soil could be measured to estimate soil strength, layering, compaction, and density. Instruments to measure density, mineralogy, grain size and shape, and texture as a function of depth have been developed for both Earth and space applications (e.g., Ball *et al*., 1998, 2001; Lieberman and Knowles, 1998; Rossabi *et al*., 2000; Mungas *et al*., 2007). A penetrometer could also make bevameter-like measurements of steel/soil friction and shear strength by using in-line cone sections. The lower section could be smooth and rotate, providing a friction versus normal load measurement. The upper section could contain shear vanes that would produce a shear failure in the soil when rotated (Garciano *et al*., 2006). Self-propelled penetrometers are devices equipped with an internal hammering mechanism that transfers the recoil force to the medium surrounding the penetrometer. One such instrument has already been developed for flight (Richter *et al*., 2002) and instrumented ones are currently under technology development (e.g., Stoker *et al*., 2003).

REFERENCES

Arvidson, R. E., J. L. Gooding, and H. J. Moore, The martian surface as imaged, sampled and analyzed by the Viking Landers, *Rev. Geophys.* **27**, 39–60, 1989.

Arvidson, R. E., R. C. Anderson, A. F. C. Haldemann, *et al*., Physical properties and localization investigations associated with the 2003 Mars Exploration Rovers, *J. Geophys. Res.* **108** (E12), 8070, doi:10.1029/2002JE002041, 2003.

Arvidson, R. E., R. C. Anderson, P. Bartlett, *et al*., Localization and physical properties experiments conducted by Spirit at Gusev crater, *Science* **305**, 821–4, 2004a.

Arvidson, R. E., R. C. Anderson, P. Bartlett, *et al*., Localization and physical properties experiments conducted by Opportunity at Meridiani Planum, *Science* **306**, 1730–3, 2004b.

Ball, A. J., C. J. Solomon, and J. C. Zarnecki, The response of gamma backscatter density gauges to spatial inhomogeneity: an extension of the single scattering model, *Nucl. Instrum. Meth. Phys. Res. B* **140**(3/4), 449–62, 1998.

Ball, A. J., S. Gadomski, M. Banaszkiewicz, *et al*., An instrument for in situ comet nucleus surface density profile measurement by gamma ray attenuation, *Planet. Space Sci.* **49**(9), 961–76, 2001.

Bell III, J. F., S. Squyres, K. Herkenhoff, *et al*., Mars Exploration Rover Athena Panoramic Camera (Pancam) investigation, *J. Geophys. Res.* **108**(E12), 8063, doi:10.1029/2003JE002070, 2003.

Binder, A. B., R. E. Arvidson, E. A. Guinness, *et al*., The geology of the Viking Lander 1 site, *J. Geophys. Res.* **82**, 4439–51, 1977.

Carrier III, W. D., G. R. Olhoeft, and W. Mendell, Physical properties of the lunar surface. In *Lunar Sourcebook* (ed. G. H. Heiken, D. T. Vaniman, and B. M. French), Cambridge University Press, pp. 475–594, 1991.

Christensen, P. R., The spatial distribution of rocks on Mars, *Icarus* 68, 217–38, 1986.

Christensen, P. R. and H. J. Moore, The Martian surface layer. In *Mars* (ed. H. H. Kieffer, B. M. Jakosky, C. W. Snyder, and M. S. Matthews), Tucson: University of Arizona Press, pp. 686–727, 1992.

Christensen, P. R., G. L. Mehall, S. H. Silverman, *et al*., Miniature thermal emission spectrometer for the Mars Exploration Rovers, *J. Geophys. Res.* **108** (E12), 8064, doi:10.1029/2003JE002117, 2003.

Clark, B. C., A. K. Baird, H. J. Rose Jr., *et al*., The Viking X-ray fluorescence experiment: analytical methods and early results, *J. Geophys. Res.* **82**, 4577–94, 1977.

Clark, B. C., A. K. Baird, R. J. Weldon, *et al*., Chemical composition of martian fines, *J. Geophys. Res.* **87**, 10059–67, 1982.

Cundall, P. A. and O. D. L. Strack, A discrete numerical model for granular assemblies, *Geotechnique* **29**, 47–65, 1979.

Evans, J. V. and T. Hagfors, *Radar Astronomy*, New York: McGraw-Hill, 620pp., 1968.

Fergason, R. L., P. R. Christensen, J. F. Bell III, *et al*., Physical properties of the Mars Exploration Rover landing sites as inferred from Mini-TES derived thermal inertia, *J. Geophys. Res.* **111**(E2), E02S21, doi:10.1029/2005JE002583, 2006.

Ferguson, D. C., J. C. Kolecki, M. W. Siebert, D. M. Wilt, and J. R. Matijevic, Evidence for martian electrostatic charging and abrasive wheel wear from wheel abrasion experiment on the Pathfinder Sojourner rover, *J. Geophys. Res.* **104**, 8747–89, 1999.

Garciano, L. O., S. K. Upadhyaya, R. A. Jones, and S. R. Jersy, *Development of an Instrumented Portable Device that Measures Shear, Sinkage and Friction Properties of Soil in-situ*, American Society of Agricultural and Biological Engineers meeting presentation paper No. 061093, 14pp., 2006.

Golombek, M. P., and the Mars Pathfinder science team, Overview of the Mars Pathfinder mission: launch through landing, surface operations, data sets, and science results, *J. Geophys. Res.* **104**, 8523–53, 1999a.

Golombek, M. P., H. J. Moore, A. F. C. Haldemann, T. J. Parker, and J. T. Schofield, Assessment of Mars Pathfinder landing site predictions, *J. Geophys. Res.* **104**, 8585–94, 1999b.

Golombek, M. P., A. F. C. Haldemann, N. K. Forsberg-Taylor, *et al*., Rock size-frequency distributions on Mars and implications for MER landing safety and operations, *J. Geophys. Res.* **108**(E12), 8086, doi:10.1029/2002JE002035, 2003.

Golombek, M. P., R. E. Arvidson, J. F. Bell III, *et al*., Assessment of Mars Exploration Rover landing site predictions, *Nature* **436**, 44–8, 2005.

Gorevan, S. P., T. Myrick, K. Davis, *et al*., Rock Abrasion Tool: Mars Exploration Rover mission, *J. Geophys. Res.* **108**, 8068, doi:10.129/2003JE002061, 2003.

Greeley, R., Silt-clay aggregates on Mars, *J. Geophys. Res.* **84**, 6248–54, 1979.

Greeley, R., M. Kraft, R. Sullivan, *et al*., Aeolian features and processes at the Mars Pathfinder landing site, *J. Geophys. Res.* **104**, 8573–84, 1999.

Greeley, R., M. D. Kraft, R. O. Kuzmin, and N. T. Bridges, Mars Pathfinder landing site: evidence for a change in wind regime and climate from lander and orbiter data, *J. Geophys. Res.* **105**, 1829–40, 2000.

Greeley, R., S. W. Squyres, R. E. Arvidson, *et al*., Wind-related processes detected by the Spirit rover at Gusev crater, Mars, *Science* **305**, 810–21, 2004.

Hagfors, T., Backscattering from an undulating surface with applications to radar returns from the Moon, *J. Geophys. Res.* **69**, 3779–84, 1964.

Herkenhoff, K. E., S. W. Squyres, J. F. Bell III, *et al*., Athena Microscopic Imager investigation, *J. Geophys. Res.* **108**, 8065, doi:10.1029/2003JE002076, 2003.

Herkenhoff, K. E., S. W. Squyres, R. Arvidson, *et al*., Textures of the soils and rocks at Gusev crater from Spirit's Microscopic Imager, *Science* **305**, 824–6, 2004a.

Herkenhoff, K. E., S. W. Squyres, R. Arvidson, *et al*., Evidence for ancient water on Meridiani Planum from Opportunity's Microscopic Imager, *Science* **306**, 1727–30, 2004b.

Hopkins, M. A., Discrete element modeling with dilated particles, *J. Eng. Comput.* **21**(2), 422–30, doi:10.1108/02644400410519866, 2004.

Huck, F. O., H. F. McCall, W. R. Patterson, and G. R. Taylor, The Viking Mars lander camera, *Space Sci. Instrum.* **1**, 189–241, 1975.

Iagnemma, K. and S. Dubowsky, Traction control of wheeled robotic vehicles in rough terrain with application to planetary rovers, *Int. J. Robot. Res.* **23**, 1029–40, doi:10.1177/0278364904047392, http://ijr.sagepub.com/cgi/content/abstract/23/10-11/1029, 2004.

Iagnemma, K., S. Kang, H. Shibly, and S. Dubowsky, On-line terrain parameter estimation for planetary rovers, *IEEE Trans. Robot.*, **20**(2), 921–7, 2004.

Jerolmack, D. J., D. Mohrig, J. P. Grotzinger, D. A. Fike, and W. A. Watters, Spatial grain size sorting in eolian ripples and estimation of wind conditions on planetary surfaces: application to Meridiani Planum, Mars. *J. Geophys. Res.* **111**, E12S02, doi:10.1029/2005JE002544, 2006.

Johnson, J. B. and M. A. Hopkins, Identifying microstructural deformation mechanisms in snow using discrete element modeling, *J. Glaciology* **51**, 432–42, 2005.

Kemurdzhian, A. L., O. G. Ivanov, P. S. Pavlov, *et al*., The self-propelled chassis of Lunokhod-1 as an instrument for investigating the lunar surface. In *Mobile Laboratory on the Moon* (ed. V. L. Barsukov), Lunokhod-1, Moscow: Nauka, Vol. 2, pp. 25–66, 1978.

Kieffer, H. H., T. Z. Martin, A. R. Peterfreund, *et al*., Thermal and albedo mapping of Mars during the Viking Primary Mission, *J. Geophys. Res.* **82**, 4249–91, 1977.

Klingelhöfer, G., R. V. Morris, B. Bernhardt, *et al*., Athena MIMOS II Mössbauer spectrometer investigation, *J. Geophys. Res.* **108**, 8067, doi:10.1029/2003JE002138, 2003.

Lieberman, S. H. and D. S. Knowles, Cone penetrometer deployable *in situ* video microscope for characterizing sub-surface soil properties, *Field Analyt. Chem. & Technol.* **2**(2), 127–32, 1998.

Maki, J. N., J. F. Bell III, K. E. Herkenhoff, *et al*., The Mars Exploration Rover engineering cameras, *J. Geophys. Res.* **108**, doi:10.1029/2003JE002077, 2003.

Matijevic, J. R., J. Crisp, D. B. Bickler, *et al*., Characterization of the Martian surface deposits by the Mars Pathfinder rover, Sojourner, *Science* **278**, 1765–8, 1997.

McLane, M., *Sedimentology*, New York: Oxford University Press, 1995.

McSween Jr., H. Y., S. L. Murchie III, D. T. Britt, *et al*., Chemical, multispectral, and textural constraints on the composition and origin of rocks at the Mars Pathfinder landing site, *J. Geophys. Res.* **104**, 8679–716, doi:10.1029/98JE02551, 1999.

McSween, H. Y., R. E. Arvidson, J. F. Bell III, *et al*., Basaltic rocks analyzed by the Spirit rover in Gusev crater, *Science* **305**, 842–5, 2004.

Mitchell, J. K., W. N. Houston, R. F. Scott, *et al*., Mechanical properties of lunar soils: density, porosity, cohesion, and angle of internal friction, *Proc. Lunar Sci. Conf. III, Sup. 3, Geochim. Cosmochim. Acta* **3**, 3235–53, 1972.

Momozua, M., A. Oidaa, M. Yamazakib, and A. J. Koolenc, Simulation of a soil loosening process by means of the modified distinct element method, *J. Terramechanics* **39**, 207–20, 2003.

Moore, H. J. and B. M. Jakosky, Viking landing sites, remote-sensing observations, and physical properties of martian surface materials, *Icarus* **81**, 164–84, 1989.

Moore, H. J. and J. M. Keller, Surface-material maps of Viking landing sites on Mars, *Reports of Planetary Geology and Geophysics Program – 1990*, NASA Technical Memorandum **4300**, 160–2, 1991.

Moore, H. J., R. E. Hutton, R. F. Scott, C. R. Spitzer, and R. W. Shorthill, Surface materials of the Viking landing sites, *J. Geophys. Res.* **82**, 4497–523, 1977.

Moore, H. J., C. R. Spitzer, K. Z. Bradford, *et al*., Sample fields of the Viking landers, physical properties, and aeolian processes, *J. Geophys. Res.* **84**, 8365–77, 1979.

Moore, H. J., G. D. Clow, and R. E. Hutton, A summary of Viking sample-trench analyses for angles of internal friction and cohensions, *J. Geophys. Res.* **87**, 10043–50, 1982.

Moore, H. J., R. E. Hutton, G. D. Clow, and C. R. Spitzer, *Physical Properties of the Surface Materials of the Viking Landing Sites on Mars*, *USGS Prof.* Paper, 1389, 222pp., 1987.

Moore, H. J., D. Bickler, J. Crisp, *et al*., Soil-like deposits observed by Sojourner, the Pathfinder rover, *J. Geophys. Res.* **104**, 8729–46, 1999.

Mungas, G., C. Sepulveda, K. Johnson, *et al*., *Raman/CHAMP Instrument for Lunar in-situ Resource Prospecting I–Imager Design*, IEEEAC paper #1554, 2007.

Mutch, T. A., R. E. Arvidson, A. B. Binder, *et al*., Fine particles on Mars: observations with the Viking 1 Lander cameras, *Science* **194**, 87–91, 1976.

Mutch, T. A., R. E. Arvidson, A. B. Binder, E. A. Guinness, and E. C. Morris, The geology of the Viking Lander 2 site, *J. Geophys. Res.* **82**, 4452–67, 1977.

Myrick, T. M., P. Bartlett, L. Carlson, *et al*., The RAT as a Mars Rock Physical Properties Tool, *Space 2004 Conference and Exhibit*, San Diego, CA, AIAA-2004–6096, American Institute of Aeronautics and Astronautics, Reston, VA, September 28–30, 2004.

Nakashima, H. and A. Oida, Algorithm and implementation of soil–tire contact analysis code based on dynamic FE–DE method, *J. Terramechanics* **41**, 127–37, 2004.

Nakashima, H., H. Fujii, A. Oida, *et al*., Parametric analysis of lugged wheel performance for a lunar microrover by means of DEM, *J. Terramechanics* **44**, 153–62, 2007.

Ojeda, L., J. Borenstein, and G. Witus, Terrain trafficability characterization with mobile robot, *Proc. SPIE Defense and Security Conf., Unmanned Ground Vehicle Technology VII*, Orlando, FL, March 28–April 1, 2005.

Olhoeft, G. R. and D. W. Strangway, Dielectrical properties of the first 100 meters of the Moon, *Earth Planet. Sci. Lett.* **24**, 394–404, 1975.

Presley, M. A. and P. R. Christensen, Thermal conductivity measurements of particulate materials: 2. Results, *J. Geophys. Res.* **102**, 6551–66, 1997.

Richter, L., P. Coste, V. V. Gromov, *et al.*, Development and testing of subsurface sampling devices for the Beagle 2 lander, *Planet. Space Sci.* **50**, 903–13, 2002.

Richter, L., A. Ellery, Y. Gao, *et al.*, A predictive wheel-soil interaction model for planetary rovers validated in testbeds and against MER Mars Rover performance data, *Proc. 10th European Conf. Int. Soc. Terrain-Vehicle Systems (ISTVS)*, Budapest, October 3–6, 2006.

Rieder, R., R. Gellert, R. C. Anderson, *et al.*, Chemistry of rocks and soils at Meridiani Planum from the Alpha Particle X-ray Spectormeter, *Science* **306**, 1746–9, 2004.

Rossabi, J., B. D. Riha, J. W. Haas, *et al.*, Field tests of a DNAPL characterization system using cone penetrometer-based Raman spectroscopy, *Ground Water Monit. Rem.* **20**(4), 72–81, 2000.

Rover Team, The Pathfinder microrover, *J. Geophys. Res.* **102**, 3989–4001, 1997.

Sagan, C., D. Pieri, P. Fox, R. E. Arvidson, and E. A. Guinness, Particle motion on Mars inferred from the Viking Lander cameras, *J. Geophys. Res.* **82**, 4430–8, 1977.

Sharp, R. P. and M. C. Malin, Surface geology from Viking landers on Mars: a second look, *Geol. Soc. Am. Bull.* **95**, 1398–412, 1984.

Smalley, I. J. and D. H. Krinsley, Eolian sedimentation on Earth and Mars: some comparisons, *Icarus* **40**, 276–88, 1979.

Smith, P., M. Tomasko, D. Britt, *et al.*, The imager of Mars Pathfinder experiment, *J. Geophys. Res.* **102**, 4003–25, 1997.

Soderblom, L. A., R. C. Anderson, R. E. Arvidson, *et al.*, Soils of Eagle crater and Meridiani Planum at the Opportunity rover landing site, *Science* **306**, 1723–6, 2004.

Squyres, S. W., R. E. Arvidson, D. L. Blaney, *et al.*, Rocks of the Columbia Hills, *J. Geophys. Res.* **111**, E02S11, doi:10.1029/2005JE002562, 2006.

Stoker, C. R., L. Richter, W. H. Smith, *et al.*, The Mars Underground Mole (MUM): a subsurface penetration device with in situ infrared reflectance and Raman spectroscopic sensing capability, *6th Int. Mars Conf.*, Abstract #3007, 2003.

Sullivan, R., D. Banfield, J. F. Bell III, *et al.*, Aeolian processes at the Mars Exploration Rover Meridiani Planum landing site, *Nature* **436**, 58–61, 2005.

Tanaka, H., M. Momozua, A. Oida, and M. Yamazaki, Simulation of soil deformation and resistance at bar penetration by the Distinct Element Method, *J. Terramechanics* **37**, 41–56, 2000.

Wänke, H., J. Brückner, G. Dreibus, R. Rieder, and I. Ryabchikov, Chemical composition of rocks and soils at the Pathfinder site, *Space Sci. Rev.* **96**, 317–30, 2001.

Weitz, C. M., R. C. Anderson, J. F. Bell III, *et al.*, Soil grain analyses at Meridiani Planum, Mars, *J. Geophys. Res.* **111**, E12S04, doi:10.1029/2005JE002541, 2006.

Zhang, R. and J. Li, Simulation on mechanical behavior of cohesive soil by distinct element method, *J. Terramech.* **43**, 303–16, 2006.

21

Martian surface properties from joint analysis of orbital, Earth-based, and surface observations

M. P. GOLOMBEK, A. F. C. HALDEMANN, R. A. SIMPSON, R. L. FERGASON, N. E. PUTZIG, R. E. ARVIDSON, J. F. BELL III, AND M. T. MELLON

ABSTRACT

Surface characteristics at the five sites where spacecraft have successfully landed on Mars can be related favorably to their signatures in remotely sensed data from orbit and from the Earth. Comparisons of the rock abundance, types and coverage of soils (and their physical properties), thermal inertia, albedo, and topographic slope all agree with orbital remote-sensing estimates and show that the materials at the landing sites can be used as "ground truth" for the materials that make up most of the equatorial and mid-latitude regions of Mars. The five landing sites sample two of the three dominant global thermal inertia and albedo units that cover ~80% of the surface of Mars. The Viking Landers 1 and 2, *Spirit*, and Mars Pathfinder landing sites are representative of the moderate-to-high thermal inertia and intermediate-to-high albedo unit that is dominated by crusty, cloddy, and blocky soils (duricrust) with various abundances of rocks and bright dust. The *Opportunit*y landing site is representative of the moderate-to-high thermal inertia and low-albedo surface unit that is relatively dust-free and composed of dark eolian sand and/or increased abundance of rocks. Interpretation of radar data confirms the presence of load bearing, relatively dense surfaces controlled by the soil type at the landing sites, regional rock populations from diffuse scattering similar to those observed directly at the sites, and root-mean-squared (RMS) slopes that compare favorably with 100 m scale topographic slopes extrapolated from altimetry profiles and meter scale slopes from high-resolution stereo images. The third global unit has very low thermal inertia and very high albedo, indicating that it is dominated by meter thick deposits of bright red atmospheric dust that may be neither load-bearing nor trafficable. The landers have thus sampled the majority of likely safe and trafficable surfaces that cover most of Mars and shown that remote-sensing data can be used to infer the surface characteristics, slopes, and surface materials present at other locations.

21.1 INTRODUCTION

Understanding the relationship between orbital remote-sensing data and the surface is essential for safely landing spacecraft and for correctly interpreting the surfaces and materials globally present on Mars. Understanding the surfaces and materials globally present on Mars is also fundamentally important for inferring the erosional, weathering, and depositional processes that create and modify the Martian surface layer (Christensen and Moore, 1992). Although relatively thin, this surface layer or regolith, composed of rocks and soils, represents the key record of geologic processes that have shaped it, including the interaction of the surface and atmosphere through time via various chemical alteration, weathering, and eolian (wind-driven) processes.

Most of our detailed information about the specific materials that make up the Martian surface comes from the *in situ* investigations accomplished by the five successful landers. The first successful landings were the Viking landers in 1976, part of two orbiter/lander pairs that were launched in 1975 (Soffen and Young, 1972). Although the overriding impetus for the Viking Landers was to determine if life existed on Mars, both stationary landers carried imagers, seismometers, atmospheric science packages, and magnetic and physical properties experiments as well as the sophisticated life detection experiments. The Viking Landers imaged the landing sites, determined the chemistry of soils at the surface and in shallow trenches, and determined physical properties of surface materials by digging trenches with their sampling arms (Soffen, 1977).

The Mars Pathfinder (MPF) mission, launched 20 years later in 1996, was an engineering demonstration of a low-cost lander and small mobile rover (Golombek, 1997). The lander carried a stereoscopic color imager, which included a magnetic properties experiment and wind sock, and an atmospheric structure and meteorology experiment. The 10 kg rover (Sojourner) carried engineering cameras, ten technology experiments, and an Alpha Proton X-ray Spectrometer for measuring the elemental composition of surface materials. The MPF rover traversed about 100 m around the lander, exploring the landing site and characterizing surface materials in a few hundred square meter area (Golombek *et al*., 1999a; see also Chapters 3 and 12).

The Mars Exploration Rovers (MERs) *Spirit* and *Opportunity* landed twin moderate-sized rovers in early 2004 which have explored over 7 and 10 km, respectively, of the surface at two locations. Each rover carries a payload that includes multiple imaging systems consisting of stereo Navigation Cameras (Navcam), the color stereo Panoramic Cameras (Pancam), and the Miniature Thermal Emission Spectrometer (Mini-TES), all on a 1.5 m high mast. The rovers also carry an arm that can brush and grind away the outer layer of rocks (the Rock Abrasion Tool or RAT) and can place an Alpha Particle X-Ray Spectrometer (APXS),

The Martian Surface: Composition, Mineralogy, and Physical Properties, ed. J. F. Bell III. Published by Cambridge University Press.

Mössbauer Spectrometer (MB), and Microscopic Imager (MI) against rock and soil targets (Squyres *et al*., 2003; see also Chapters 4, 13, 15, and 20). These rovers have returned measurements of the elemental composition, mineralogy, and physical properties of rocks and soils encountered along their traverses (Squyres *et al*., 2004a,b). The inclusion of Mini-TES on the two rovers allows direct correlation of thermophysical properties of surface materials from the ground with those inferred from orbit (Christensen *et al*., 2004b; see also Chapters 9 and 14).

This chapter focuses on the relationship between the physical properties of materials investigated at the landing sites and their remote-sensing signatures from orbit and Earth. The chapter complements the chapters on physical properties of surface materials derived by the interaction of the landers and rovers with surface materials (Chapter 20) and global thermophysical properties derived from orbit (Chapter 18). This chapter begins by introducing the five sites where spacecraft have successfully landed on Mars and the remote-sensing data used in their selection to estimate surface properties from orbit. Next, the surfaces, landforms, and geologic materials – including their distributions observed at the landing sites – are discussed, along with their physical properties (density, cohesion, angle of internal friction, and thermal inertia estimated from these properties or directly measured). The thermophysical properties of the landing sites and their relationships to global thermophysical units defined by thermal inertia and albedo are discussed, as are local variations in thermophysical properties and the soils and rocks observed at the landing sites. Finally, radar data of the landing sites and their implications for surface roughness, dielectric constant, and surface density are compared with the *in situ* observations at the landing sites and the topographic slopes determined from altimetry and stereo image data. This chapter shows that the soils and rocks observed at the landing sites and their relative abundances can be related directly to their orbital signatures in thermophysical and radar data, and that remote-sensing data can thus be confidently used to infer the surface characteristics, slopes, and surface materials present at other locations on Mars.

21.2 LANDING SITES AND THEIR SELECTION ON MARS

The five landing sites that constitute the "ground truth" for orbital remote-sensing data on Mars were all selected primarily on the basis of safety considerations, in which surface characteristics interpreted from orbit were consistent with the engineering constraints based on the designed entry, descent and landing system, with scientific desires being secondary (although the scientific objectives became more important as the size of the landing "uncertainty ellipse" decreased, allowing more sites to be considered initially). The most important factor controlling the selection of the five landing sites is elevation (Figure 21.1), as all landers used an aeroshell and parachute to slow them down and thus a sufficient atmospheric density column and time were required to carry out entry and descent before landing. Other important engineering constraints are: (1) equatorial latitudes for solar-powered landers; (2) low winds and low-atmospheric turbulence for stability and reduced horizontal velocity on the parachute; (3) low-surface slopes for nominal landing system radar performance, for stability at touchdown, to reduce airbag bounce and spinup for airbag-encased landers, and for trafficability (relative ease of rover driving); (4) few rocks that could impact the bottom of a lander or abrade or puncture airbags; and (5) a radar-reflective, load-bearing, and trafficable surface.

Landing site selection for the five landers included intense periods of data analysis of preexisting and incoming information. Because the selection of a landing site is a mission critical decision (landing safely is obviously required for mission success), enormous effort has been put into certifying that the surface and atmosphere are within specifications of the entry, descent, and landing system, and are therefore safe for the lander (and trafficable for rovers). These landing site selection efforts and the assessment of predictions after landing form the basis for much of our knowledge about how surface materials investigated by the landers and rovers relate to their remote-sensing signatures. Furthermore, comparison of surface characteristics after landing with predictions made prior to landing have substantially changed views on the correlation of orbital remote-sensing data with surface materials on Mars.

The Viking lander/orbiter pairs were captured into Mars orbit and the orbiter cameras started a concentrated campaign to image prospective landing sites (at tens to hundreds of meters per pixel) that had been selected on the basis of previous Mariner 9 images (Soffen and Young, 1972; Soffen, 1977). A large site selection science group assembled mosaics in real time and waived off several landing sites on the basis of rough-appearing terrain and radar scattering results. Viking Lander 1 (VL1) landed on Late Hesperian ridged plains in Chryse Planitia at 22.27° N, 312.05° E, downstream from Maja Valles, and thus was expected to be a lava flow surface similar to mare ridged plains on the Moon (e.g., Christensen and Moore, 1992), perhaps modified by flooding from Maja Valles (Craddock *et al*., 1997). Its low elevation and proximity to the channels suggested that water and near-surface ice might have accumulated there (along with flood sediments), possibly leading to the development/evolution of organic molecules and life (Masursky and Crabill, 1976a, 1981). Viking Lander 2 (VL2) was sent to the middle northern latitudes (47.62° N, 134.23° E) where larger amounts of atmospheric water vapor existed, thereby ostensibly improving the chance for the development and discovery of life. The site selection team analyzed images and thermal observations before choosing to land in Utopia Planitia, just west of Mie crater (Masursky and Crabill, 1976b, 1981). The mapped surface at VL2 is Early Amazonian in age (Tanaka *et al*., 2005) with ejecta lobes from Mie and pedestal craters nearby suggesting a deflated surface (Arvidson *et al*., 1979; Jakosky and Christensen, 1986; Christensen and Moore, 1992). The predictions made for the types of

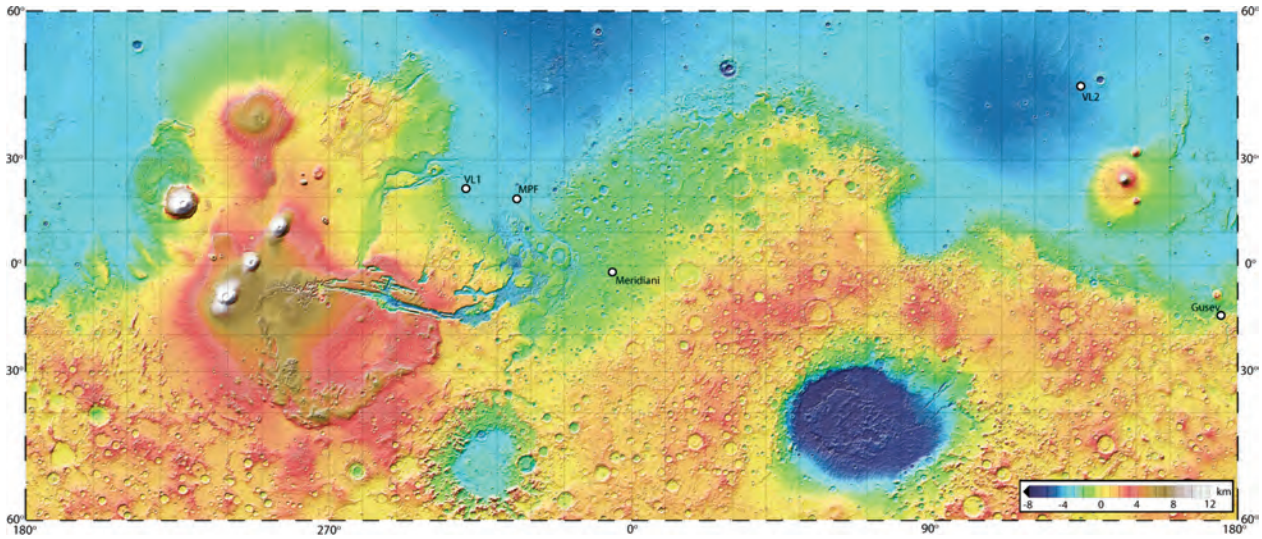

Figure 21.1. MOLA (Mars Orbiter Laser Altimeter on Mars Global Surveyor) topographic map of Mars showing the five successful landing sites. The first three landing sites (VL1, VL2, MPF) were located in the northern plains to take advantage of the lower elevation (all are below −3.6 km) and thus more atmosphere for aeroshell entry and parachute descent. The two MER spacecraft were capable of landing on surfaces with elevations up to −1.3 km, and so locations near the highlands–lowlands boundary could be considered. Meridiani Planum is located in western Arabia Terra, a portion of the highlands that was lowered by flexing from the Tharsis load and by extensive erosion in the Noachian. VL1 is located in Chryse Planitia on the ridged plains near the mouths of Kasei (to the west) and Maja Valles (to the southwest). MPF is located in Chryse Planitia near the mouth of Ares Vallis (to the southeast). VL2 is in Utopia Planitia near the crater Mie (to the northeast). Gusev crater is located on the northern edge of the highlands, south of Elysium Planitia. Elevations are reported with respect to the geopotential surface (geoid) derived from the average equatorial radius extrapolated to the rest of the planet via a high order and degree gravity field. (For a color version of this figure, please refer to the color plate section or to the e-Book version of this chapter.)

surfaces and materials that would be present at the Viking landing sites were incorrect, likely due to the newness of the data and the coarse resolution of the orbital images. Subsequent analysis indicated that geologic units defined in Viking resolution orbital images (average ~230 m/pixel) had little to do with the characteristics of the thin regolith or surface layer at the two landing sites (rock abundance, soils, and drifts), but that the nature of the surface layer could be more closely related to orbital thermal inertia and albedo characteristics. Most importantly, however, the atmosphere was within predicted specifications, and both VL1 and VL2 landed successfully.

The MPF site selection effort involved little new data since the Viking mission 20 years earlier, but there was a much better understanding of how the surface characteristics of the two Viking landing sites related to the remote-sensing data (particularly thermal inertia and albedo; e.g., Christensen and Moore, 1992). The site selection effort took place over a two-and-a-half-year period prior to launch and included extensive analysis of all existing data, as well as the acquisition of new Earth-based radar data (Golombek *et al.*, 1997). Important engineering constraints, in addition to the required low elevation, were the narrow latitudinal band ($15^\circ \pm 5^\circ$ N) for adequate solar power, and the large landing ellipse (300 km by 100 km), which required a relatively smooth surface over a large area. This and the requirement to have the landing area covered by high-resolution Viking Orbiter images (<50m/pixel) severely limited the number of possible sites that could be considered to ~7. The landing site selected for MPF was near the mouth of the catastrophic outflow channel Ares Vallis, which drains into Chryse Planitia (Figure 21.2) from the highlands to the southeast (Golombek *et al.*, 1997). An Earth analog (the Ephrata fan near the mouth of a catastrophic outflow channel in the Channeled Scabland of western and central Washington State) was identified and studied as an aid to understanding the predicted surface characteristics of the selected site. The Late Hesperian cratered surface at the MPF site appeared acceptably safe, and the site offered the prospect of analyzing a variety of rock types from the ancient cratered terrain and intermediate-aged ridged plains. Pathfinder landed safely; predictions of the characteristics of the surface layer based on thermal inertia and albedo were correct, the atmosphere was within expectations, and for the first time the nature of the surface matched that expected from geologic mapping of features at kilometer scale, which suggested that the site would be a plain composed of materials deposited by the catastrophic floods (Golombek *et al*, 1999b).

Landing site selection for the MERs *Spirit* and *Opportunity* took place over a two-and-a-half-year period and involved an unprecedented profusion of new information from the Mars Global Surveyor (MGS, launched in 1996) and Mars Odyssey (launched in 2001) orbiters. These orbiters supplied targeted remote-sensing data of the prospective sites that made them the best-imaged, best-studied locations in the history of Mars exploration (Golombek *et al.*, 2003a). For comparison, most of the potential MER landing ellipses were covered by ~3 m/pixel MGS Mars Orbiter Camera (MOC) images, whereas the MPF ellipse had been covered only by ~40 m/pixel Viking Orbiter images. All of the major engineering constraints were

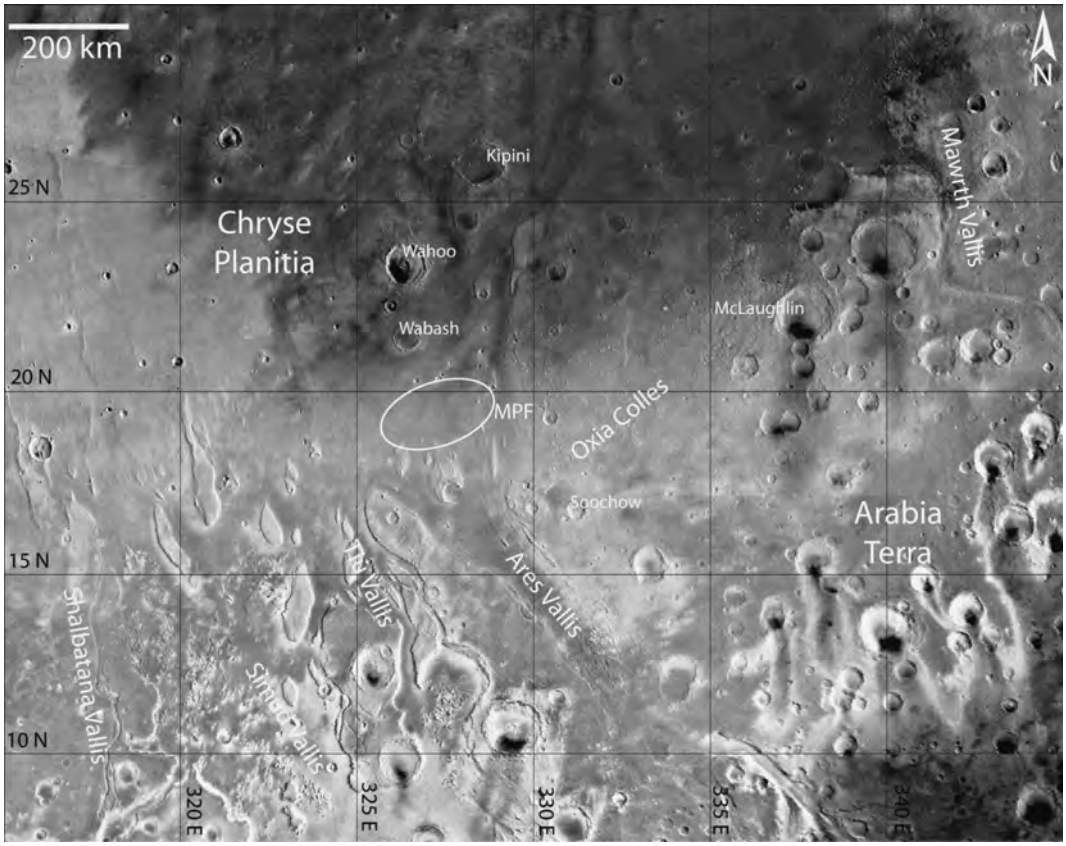

Figure 21.2. Regional mosaic of Chryse Planitia, Ares Vallis, and the Mars Pathfinder landing ellipse. Mosaic shows catastrophic outflow channels cutting the heavily cratered (ancient) terrain to the south and flowing to the lower northern plains. Ares Vallis is about 100 km wide and 2 km deep. Streamlined islands produced during the flooding are located throughout the scene. The Mars Pathfinder landing ellipse shown is 200 km by 100 km and lies about 100 km north of the mouth of the channel where it exits the highlands, and thus was interpreted to be a depositional plain composed of materials deposited by the floods. Characterization of the surface after landing supports this interpretation.

addressed by data and scientific analyses that indicated that the selected sites were safe. Important engineering requirements for landing these rovers included relatively low elevation (below −1.3 km), a latitude band of 10° N to 15° S for adequate solar power, low rock abundance, low winds, and ellipse sizes that were ultimately less than 100 km long and 15 km wide. Because of the smaller ellipse size, ∼150 sites were identified as initially possible, from which high science priority sites were selected for further investigation.

Both sites selected for MER showed strong evidence for surface processes involving water, which was consistent with the science goal to determine the aqueous, climatic, and geologic history of sites where conditions may have been favorable to the preservation of prebiotic or biotic processes. The site selected for the *Spirit* rover (MER-A) was within Gusev crater, an ancient 160 km diameter impact crater at the edge of the cratered highlands in the eastern hemisphere (Golombek *et al.*, 2003a). The southern rim of Gusev is breached by Ma'adim Vallis, an 800 km long branching valley network that drains the ancient cratered highlands to the south (Figure 21.3). The smooth, flat, Late Hesperian cratered floor of Gusev (Figure 21.4) was interpreted by some researchers to be sediments deposited in a crater lake, raising the possibility that the rover could analyze fluvial sediments deposited in a lacustrine environment. Although the physical characteristics of the surface inferred from orbital data were correct, the interpretation of lacustrine surface materials deposited from Ma'adim Vallis available for study by the rover was incorrect (materials studied by *Spirit* do not appear to have been deposited in a lake fed by Ma'adim Vallis; Golombek *et al.*, 2005).

The site selected for the *Opportunity* rover (MER-B) is in Meridiani Planum (Golombek *et al.*, 2003a), where MGS thermal emission spectra from orbit indicated an abundance (somewhat unique) of dark, gray, coarse-grained hematite (α-Fe_2O_3) similar to that which typically forms on Earth in the presence of liquid water (see Chapter 9). Layers associated with the hematite deposit in Meridiani Planum suggested a sequence of Late Noachian sedimentary rocks that could be interrogated by the rover. Images of Meridiani Planum indicated a young, lightly cratered (Figure 21.5) Late Amazonian plain (as opposed to the moderately cratered Hesperian surfaces of the other landing sites). The atmospheric and surface characteristics inferred from the extensive remote-sensing data were essentially correct, and *Opportunity* landed safely (Golombek *et al.*, 2005). In addition, the hematite detected from orbit was found at the surface, and it correctly indicated the presence of rocks

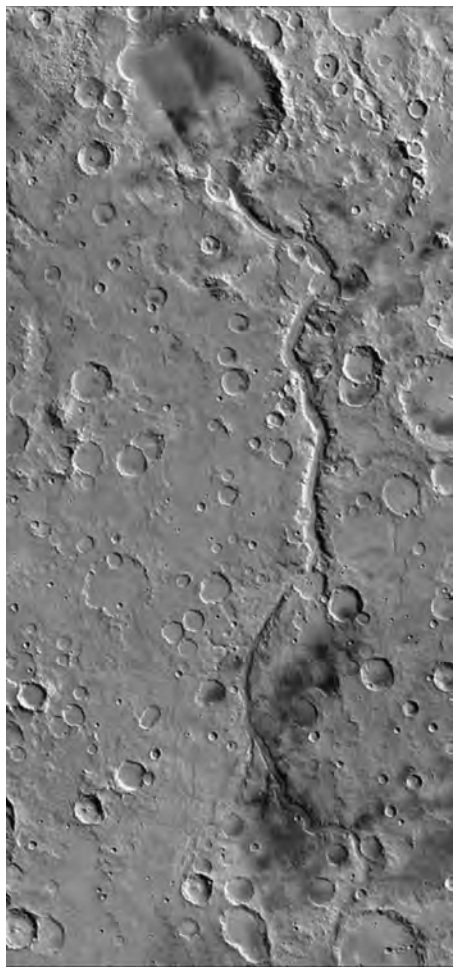

Figure 21.3. Regional mosaic of Ma'adim Vallis and Gusev crater. The 800 km long Ma'adim Vallis, one of the largest branching valley networks on Mars, drains the heavily cratered terrain to the south and breaches the southern rim of Gusev crater. Gusev crater, which formed in the Noachian, is 160 km diameter and the smooth flat floor suggests it was a crater lake that filled with water and sediments. *Spirit* has yet to identify sediments associated with Ma'adim Vallis. The cratered plains that *Spirit* traversed are best explained as impacted basalt flows and so represent a late volcanic cover. Rocks in the Columbia Hills have been altered by water, but have not been related to deposition in a lake associated with Ma'adim discharge.

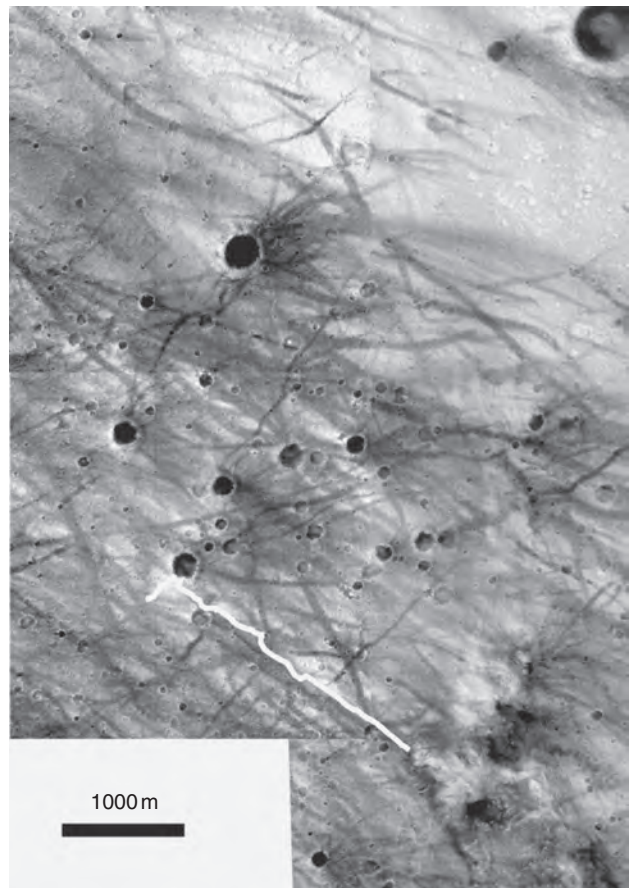

Figure 21.4. MOC images of the *Spirit* landing and traverse area. Image shows cratered plains with most crater interiors darker than the plains as well as dark dust-devil tracks (darker from the removal of dust). *Spirit* landed southwest of Bonneville in a dark dust-devil track, traversed to the southern rim of Bonneville crater and then roved 2 km to the southeast to the Columbia Hills (traverse across the cratered plains shown in white). MOC images R07–01606 and R13–01467; north is up.

deposited in an aqueous environment (Christensen and Ruff, 2004; see also Chapters 9, 13, 14, 15, 23, and 24) that were studied by the rover.

21.3 REMOTE-SENSING DATASETS

Remote-sensing data available for selecting landing sites have varied for each of the landed missions, but most used are visible images of the surface, thermal inertia and albedo, radar data, and altimeter data to infer elevation and slopes (see detailed review and description of data used for the recent MER site selection in Golombek *et al.* [2003a] and references therein). Because many of the remote-sensing datasets do not extend into the polar regions, our treatment in this chapter will focus on the equatorial and mid-latitude regions on Mars ($\pm 60^\circ$ latitude), where successful landing sites are located. Images of Mars used in site selection include a wide variety of data from multiple spacecraft: (1) Mariner 9 images (many hundreds of meters per pixel); (2) Viking Orbiter images (tens of meters to hundreds of meters per pixel; global mosaic at 230 m/pixel); (3) MGS/MOC high-resolution images (several meters per pixel; Malin and Edgett, 2001); and (4) Mars Odyssey Thermal Emission Imaging System (THEMIS) 100 m/pixel thermal and 18 m/pixel visible images (Christensen *et al.*, 2004a). Images from (1) and (2) factored into the site selection for the Viking landers; MPF site selection dominantly used images from (2) and MER site selection used images from (2) to (4). Slopes at the scale of a lander or rover (1–3 m) are important for landing and traversing safely and have been evaluated using MOC stereo images and photoclinometery (or shape from shading; Beyer *et al.*, 2003; Kirk *et al.*, 2003).

Prior to the return of high-quality elevation data from the MGS Mars Orbiter Laser Altimeter (MOLA), surface

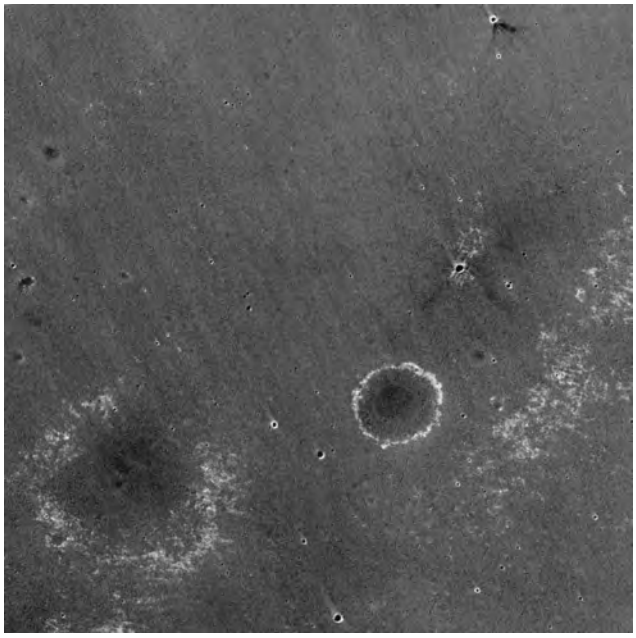

Figure 21.5. MOC image showing typical dark, smooth, basaltic sand surface and underlying light-toned sulfate evaporites in Meridiani Planum. Lightly cratered surface is Late Amazonian in age and a population of much older, highly degraded craters (bright rings) that date back to the Late Noachian is also present. Relatively fresh, small craters, as well as more degraded, dark-floored small craters, likely correspond to the eroded and degraded Late Amazonian craters documented by the *Spirit* rover. Saltating sand appears to have easily eroded the weak sulfates. MOC image E22–01660 is about 30 km west of the landing site and is about 2.6 km wide (north is up).

elevations for Viking and MPF site selections were estimated from radar data, spacecraft occultation data, and atmospheric pressure estimates. MOLA data have provided definitive global elevation information (Figure 21.1; Smith *et al*., 2001) that, when combined with gravity data, has defined the geoid and its relationship with atmospheric pressure (Smith and Zuber, 1998). MOLA data also allow evaluation of the long baseline slopes (~1 km) that are important for the airbag-encased landers (MPF and MER) as well as slopes on the hundreds of meters scale that are important for landing radar system performance. The returned spread of the MOLA laser pulse also provided a measure of the roughness within each ~75 m laser surface spot (Neumann *et al*., 2003). Gridded MOLA elevation data were also used to make shaded relief maps (Smith *et al*., 2001) that have been particularly useful in areas with poor imaging data, such as the northern plains, and have resulted in improved mapped ages for three of the landing sites (VL1, VL2, MPF; Tanaka *et al*., 2003, 2005).

Thermophysical properties have been an important discriminator of potential landing sites and a tool for global extrapolation of what we learn at each landing, because thermal inertia measurements (a composite of thermal conductivity and heat capacity, and a measure of the resistance of surface materials to changes in temperature over the upper thermal skin depth of several centimeters; see Chapter 18) can be related to particle size, bulk density, and cohesion. Bulk thermal inertia observations (the representative thermal inertia over an observational footprint) of Mars used in landing site selection studies include values derived from (1) Viking Infrared Thermal Mapper (IRTM) data at ~60 km per pixel (Kieffer *et al*., 1977; Palluconi and Kieffer, 1981), (2) MGS Thermal Emission Spectrometer (TES) data (Christensen *et al*., 1992) at ~3 km/pixel (Mellon *et al*., 2000; Putzig *et al*., 2005), and (3) Mars Odyssey THEMIS data at ~100 m/pixel (Christensen *et al*., 2004a; Fergason *et al*., 2006b; Jakosky *et al*., 2006). In addition, the contrast between measurements of thermal emission from the surface at different wavelengths using IRTM and TES data has been used to determine the rock abundance (the fractional area covered by high thermal inertia rocky material) at about 60 and 8 km/pixel scales (Christensen, 1986; Nowicki and Christensen, 2007). With the rock abundance and the bulk thermal inertia, the thermal inertia of the remaining soil, referred to as the fine-component thermal inertia (Kieffer *et al*., 1977), was also determined (Christensen, 1986). The Lambert albedo (the brightness of reflected solar energy from the surface in which the viewing geometry has been taken into account) was also available as measured by both IRTM and TES (e.g., Pleskot and Miner, 1981; Christensen *et al*., 2001). The albedo can, for example, be used to infer the dustiness of the surface, as very dusty areas exhibit very high albedo (and, in addition, very low-thermal inertia). The amount of dust cover at the landing sites was also evaluated using the TES dust index, which includes a more explicit measure of the particle size (Ruff and Christensen, 2002).

Radar data have been used to infer surface roughness at the scale of the radar wavelength (diffuse scattering), as well as at 10–100 times the radar wavelength (specular reflection; Simpson *et al*., 1992; Haldemann *et al*., 1997). Specular and diffuse radar data are available at 3.5 cm wavelength for many equatorial areas and some 12.6 cm data also exist (see Section 21.6 for further discussion of radar data). RMS slopes at the 10–100 times radar wavelength scale compare favorably with those determined from MOC images. Slopes at the scale of the lander are important for evaluating lander stability and rover traversability. Radar reflectivity is important for the radar altimeter on a lander to accurately measure the descent of the spacecraft. Radar reflectivity can be related to the bulk density of the surface materials, which can be used to infer whether the surface is load-bearing and trafficable.

21.4 LANDING SITES AND SURFACE MATERIALS: PHYSICAL PROPERTIES AND THERMAL INERTIA

21.4.1 Introduction

The surface materials at the five landing sites have been investigated using color, stereo, panoramic imaging that provides information on the morphology of the landing sites, and on the lithology, texture, distribution, and shape of rocks and eolian and soil deposits and other local geologic

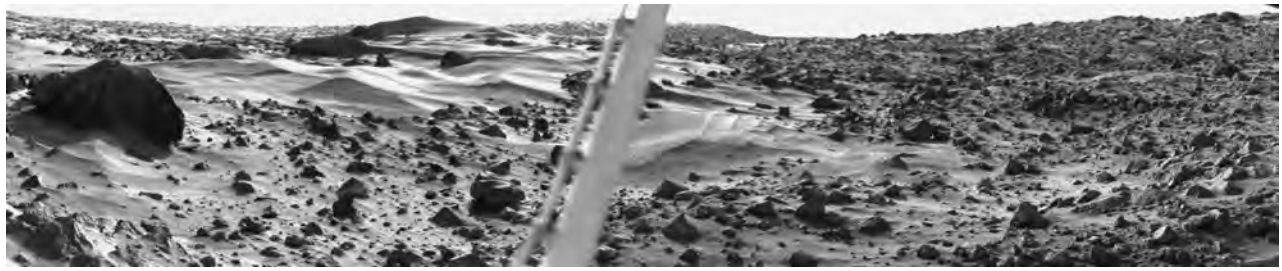

Figure 21.7. Mosaic of the Viking 1 landing site showing dusty bright surface, darker pitted rocks nearby, and the rim of a crater on the left horizon. Jointed, slightly lighter-toned low rock mass in the middle distance appears to be outcrop. The location of the site on ridged plains suggests that the outcrop is basalt, with angular rocks as ejecta and drift materials deposited by either the wind or floodwaters from Maja or Kasei Valles. Mosaic shows moderately rough terrain at 1 km, 100 m, and several meter length scales, consistent with MOLA-derived slopes and radar roughness. (For a color version of this figure, please refer to the color plate section or to the e-Book version of this chapter.)

features. Our knowledge of the physical properties of surface materials has been particularly enhanced by the interaction of arms and rover wheels with these materials, which has enabled the derivation of basic soil mechanics parameters (Moore *et al.*, 1987, 1999; Arvidson *et al.*, 2004a,b; Chapter 20). The MER rovers also included Mini-TES instruments that acquired thermophysical measurements of surface materials that could be compared with their characteristics determined by the rover payload, and with thermophysical properties from orbit (Section 21.5). These investigations and their relation to remote-sensing data have been dramatically improved by the mobility of rovers to traverse the terrain and characterize diverse surface materials. All landing sites that have been investigated on Mars are composed of rocks, outcrops, eolian bedforms, and soils, many of which have been cemented. Craters and eroded crater forms and distant hills have also been observed at almost all of the landing sites. This section provides a brief

Figure 21.6. Mosaic of the Viking Lander 1 site showing relatively thick bright drifts and dark rocks. The large (~1 m tall) rock to left is Big Joe and is subrounded. Smaller angular dark rocks are sitting on soil and have been interpreted as impact ejecta blocks. Bright drift in the center of the image shows layers, and some particles may be large enough to require deposition by running water rather than the wind in some interpretations.

description of each of the landing sites and their geologic setting, and then describes the common features and materials at the sites, with special reference to their physical properties and remote-sensing signatures (mostly thermal inertia and albedo).

21.4.2 Viking Lander 1

Panoramic images of the VL1 landing site show a moderately rocky plain, with substantial soil and drift deposits (Figure 21.6) atop local flat lying bedrock (Figure 21.7) of suspected volcanic origin (Binder *et al.*, 1977; Christensen and Moore, 1992). Soil materials are blocky when disturbed by the sample arm (indicating cohesion likely due to cementation) and have soil mechanics properties that are broadly similar to moderately dense soils on Earth (Moore *et al.*, 1987). Some drifts appear crosslaminated, suggesting eolian or fluvial deposition (Figure 21.6). Blocky crater rims give the site moderate relief (Figure 21.7). The site appears to be consistent with a volcanic substrate (ridged plains) impacted by craters with ejected fragments and eolian and/or fluvial deposits (Binder *et al.*, 1977; Garvin *et al.*, 1981; Christensen and Moore, 1992; Craddock *et al.*, 1997).

21.4.3 Viking Lander 2

VL2 is on a uniformly rocky plain with very little relief (Figure 21.8; Mutch *et al.*, 1977). Soil surfaces between the rocks are covered with fines or small clods. Drifts are scarce within the sample field of the lander arm, but thin drift deposits cover 40% of the far field (Moore and Keller, 1990) and, along with crusty soil materials, are exposed in troughs that may be the surface expressions of ice wedge polygons (Mutch *et al.*, 1977). The rocky plain is consistent with impact ejecta (perhaps with contributions from nearby Mie crater) that has been deflated and concentrated (Christensen and Moore, 1992).

21.4.4 Mars Pathfinder

The MPF landing site is a rocky plain that is more rugged (more relief) than previous landing sites (Figure 21.9). The site appears consistent with expectations that it would be

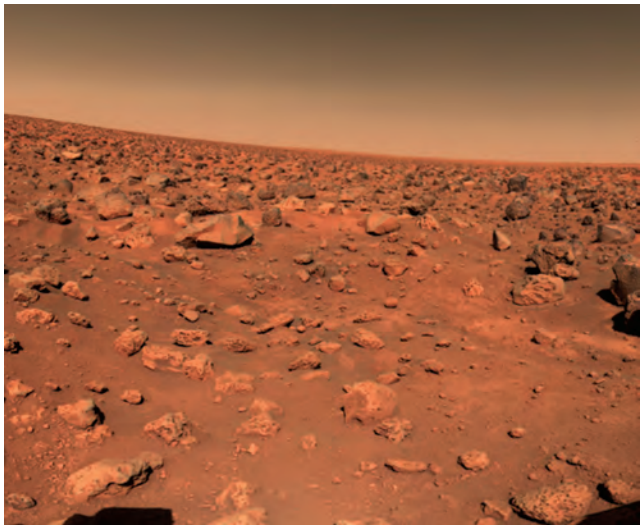

Figure 21.8. Mosaic of the Viking 2 landing site showing a flat, rocky, and dusty plain. Pitted rocks in the foreground suggest that they are volcanic basalts and the angular homogeneous rock field suggests that they are distal ejecta, perhaps from the fresh crater Mie to the east of the landing site. The lighter-toned trough in the middle of the image, in front of the large rocks, has been interpreted as an ice wedge polygon. Mosaic shows flat terrain at 1 km and 100 m scales, but rougher at the several meter length scale, consistent with MOLA-derived slopes and radar results. (For a color version of this figure, please refer to the color plate section or to the e-Book version of this chapter.)

shaped and deposited by catastrophic floods (Golombek *et al.*, 1997, 1999a,b). Large rocks are tabular and sub-rounded, and imbricated or stacked rocks are all similar to those found in terrestrial catastrophic flood deposits (Golombek *et al.*, 1999a,b). Streamlined islands are visible in the far field and troughs are visible throughout the scene. Wind tails, drifts, ripples, and other eolian duneforms are present and the rover discovered many ventifacts (Bridges *et al.*, 1999; Greeley *et al.*, 1999). The rover documented cloddy soils composed of fine-grained material mixed with pebbles, cobbles, and rock fragments that behave like moderately dense soils on Earth (Moore *et al.*, 1999). Rover wheel tracks in bright drift deposits indicate that it is very fine-grained, porous, and compressible, arguing that this material is micron-sized dust that has settled from the atmosphere. Very cohesive soil-like deposits like Scooby Doo (Chapter 20) appeared well cemented and indurated because rover wheel cleats did not dig into or scratch these materials during rover soil mechanics tests (Moore *et al.*, 1999).

21.4.5 *Spirit*

Although the Gusev crater landing site was selected to sample sediments deposited in a lake setting, the cratered plains traversed by *Spirit* show no evidence that they were deposited or modified by water (Grant *et al.*, 2004; Golombek *et al.*, 2006a). Conversely, direct evidence indicates that the surface is composed of basalt flows that have been modified by impact and eolian activity (Figure 21.10). The low-relief rocky plains are dominated by soil-filled circular depressions or "hollows" that are impact craters filled in with eolian sediment. A large fresh crater visited by *Spirit* (Bonneville) shows an impact-generated regolith up to 10 m thick; other large craters are filled with sediment. Most bedforms are eolian ripples; dust devils were observed and produced the lower albedo tracks (Greeley *et al.*, 2006) crossed by the rover and observed in orbital images (Figures 21.4 and 21.10; see also Chapter 13). Weakly cemented soils were found near the top of trenches dug into the surface with the wheels. Older rocks in the Columbia Hills (likely Noachian), a promontory within Gusev crater that *Spirit* climbed, are a mix of clastic and igneous rocks, some of which may be pyroclastic debris or impact ejecta deposits that show substantial evidence for processing by water, including cementation that is unrelated to flooding associated with a possible lake (Squyres *et al.*, 2006; see also Chapters 23 and 24).

21.4.6 *Opportunity*

Opportunity landed on a very smooth, flat plain (Figure 21.11) composed of basaltic sand arranged in ripples and exhibiting a surface lag of hematitic granular spherules several millimeters in diameter (Soderblom *et al.*, 2004; Sullivan *et al.*, 2005; see also Chapters 13 and 24). The hematite spherules are interpreted as concretions derived from saltating basaltic sand eroding the underlying weak, layered, light-toned sulfate-rich evaporites (Squyres *et al.*, 2004c; Chapter 24). In some locations, bright dust is trapped below the hematitic granules. The saltating sand has eroded and filled in young impact craters, implying that the sandy surface is Late Amazonian, even though the sulfate sedimentary rocks that document a wet past at the site are Late Noachian (e.g., Golombek *et al.*, 2006b).

21.4.7 Rocks and outcrops

Rocks are common at all of the landing sites except Meridiani (*Opportunity*). At most sites, they are distinct dark, angular to sub-rounded clasts that range in size from several meters diameter down to small pebbles that are a centimeter or less in diameter. Most appear as float – individual rocks not associated with a continuous outcrop or a body of rock. Many appear dust-covered and there is evidence at Gusev for some surface chemical alteration, where rocks exposed to the atmosphere develop a thin outer rind of weathered material (McSween *et al.*, 1999, 2004). Rocks making up the cratered plains on which *Spirit* landed and traversed for the first few kilometers are clearly made up of basalts (McSween *et al.*, 2006). The distribution and shape of many of the rocks at the VL1 and VL2 sites and the Gusev cratered plains are all consistent with a surface that has experienced impact cratering, with the rocks constituting the ejected fragments (Garvin *et al.*, 1981; Grant *et al.*, 2004, 2006a,b). Many subrounded rocks at the MPF and VL1 sites have been attributed to deposition in catastrophic floods, during which rock–rock impacts in the flowing water partially rounded the clasts (Golombek *et al.*, 1999a;

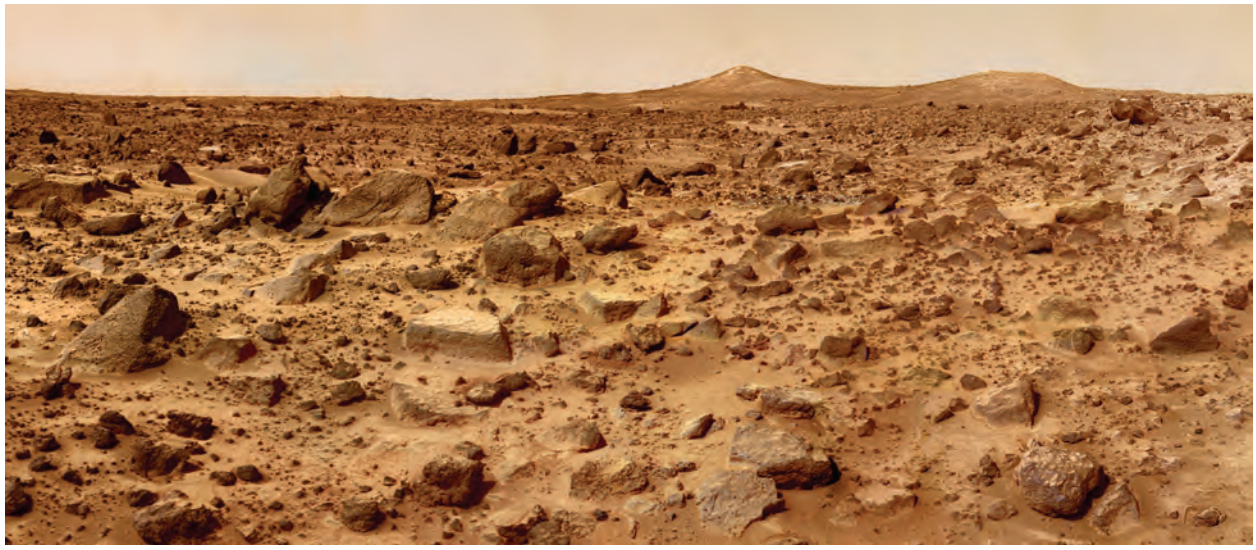

Figure 21.9. Mosaic of the Mars Pathfinder landing site showing an undulating, ridge-trough, moderately dusty and rocky plain. Large rocks in the middle left of the image appear stacked or imbricated on a ridge, with a trough behind it that trends toward the northeast. Streamlined hills on the horizon, the ridge-trough topography, and angular to subrounded boulders are consistent with depositional plains deposited by catastrophic floods, as expected from the setting of the site downstream from the mouth of the Ares Valles outflow channel. Note dust coating the tops of rocks. Mosaic shows this site to have the roughest terrain at 1 km, 100 m, and several-meter length scales, consistent with MOLA-derived slopes, radar roughness, and MOC stereogrammetry and photoclinometry results. (For a color version of this figure, please refer to the color plate section or to the e-Book version of this chapter.)

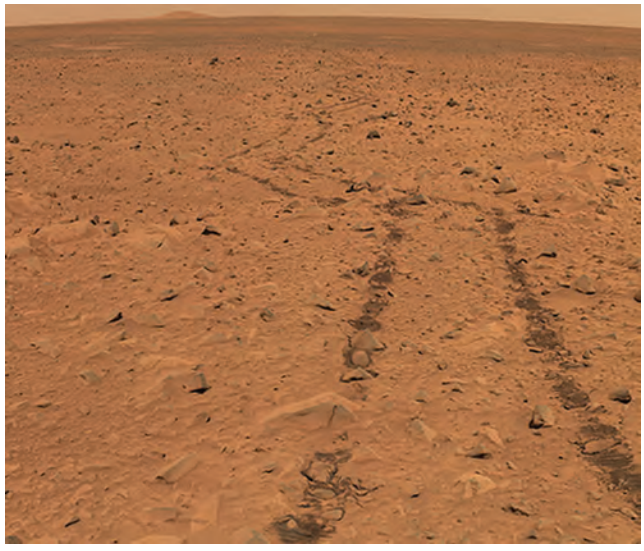

Figure 21.10. Pancam mosaic obtained by *Spirit* looking back at the lander from her traverse toward Bonneville crater. The nearfield is bright, dusty, and moderately rocky and the farfield is darker and corresponds to a dust-devil track where some of the dust has been removed. Grissom Hill is on the horizon 7.5 km away. Mosaic shows moderately smooth terrain at 1 km, 100 m, and several meter length scales, consistent with MOLA-derived slopes, radar roughness, and MOC stereogrammetry and photoclinometry results. (For a color version of this figure, please refer to the color plate section or to the e-Book version of this chapter.)

Craddock *et al*., 1997). Some rocks at most of the landing sites appear polished, fluted, and grooved and are interpreted as ventifacts in which sand-sized grains, entrained by the wind, impact and erode the rocks (Bridges *et al*., 1999; Greeley *et al*., 2004).

Continuous expanses of rocks typically referred to as outcrop (or bedrock) have been observed at three of the five landing sites. An area of continuous jointed rocks has been observed at the VL1 site (Figure 21.7), but little else is known about it (Moore and Jakosky, 1989). Outcrop has been discovered on Husband Hill in the Columbia Hills by *Spirit*, where there may be coherent stratigraphic layers in and nearby the region known as Cumberland Ridge (Arvidson *et al*., 2006; Squyres *et al*., 2006). In some places the rocks are finely layered, and in other places they appear massive, implying different modes of deposition. At Meridiani Planum light-toned outcrops are exposed in crater walls and areas where the dark, basaltic sand observed throughout the plains is thin (Squyres *et al*., 2004b).

The size-frequency distributions of rocks measured at the landing sites all show a characteristic exponential decrease in fractional area covered by larger rocks when cumulative fractional area is plotted against diameter (Figure 21.12). The cumulative fractional area covered by all rocks varies from about 7% at VL1 (not counting the ~5% covered by outcrop or the ~4% covered by assumed rocks <0.25 m diameter in the far field), to 16% at VL2 (Moore and Keller, 1990, 1991), to 19% at MPF (Golombek *et al*, 2003b), to 7%, 7%, and 20% at the *Spirit* landing site (Columbia Memorial Station, CMS), Legacy, and Bonneville panorama sites respectively. The shape of these curves is similar to those found at rocky sites on Earth (Golombek and Rapp, 1997) and has been ascribed to fracture and fragmentation theory (e.g., Rosin and Rammler, 1933; Gilvarry, 1961; Gilvarry and Bergstrom, 1961), which predicts that ubiquitous flaws or joints will lead to exponentially fewer blocks with increasing size during ejection and transport (e.g., Wohletz *et al*., 1989; Brown and Wohletz, 1995; see Golombek and Rapp,

Figure 21.11. Mosaic of the *Opportunity* landing site showing dark, basaltic sand plain and the rim of Eagle crater in the foreground (brighter). Light-toned pavement outcrop near the rim is slightly brighter and dustier than the plains. Parachute and 1 m high backshell that *Opportunity* used to land are 450 m away and demonstrate the exceptionally smooth, flat surface as expected from orbital data at all length scales. The dust-free surface of the plains is in agreement with their very low albedo from orbital data. Even though dust has rapidly fallen on the solar panels, the basalt surface is relatively dust-free, indicating that the dust is being swept off the surface at a rate that must be roughly equal to its deposition. (For a color version of this figure, please refer to the color plate section or to the e-Book version of this chapter.)

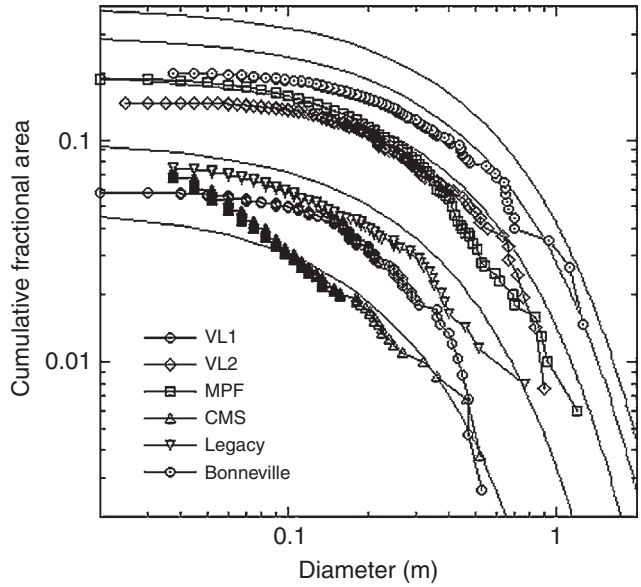

Figure 21.12. Cumulative fractional area versus diameter plots of rocks counted in portions of the Mission Success (Columbia Memorial Station; CMS), Legacy, and Bonneville panoramas; VL (Viking Lander), MPF (Mars Pathfinder) landing sites and model distributions (solid lines) based on VL sites and rocky location on Earth (Golombek and Rapp, 1997) shown for reference. Model distributions are for 5%, 10%, 20%, 30%, and 40% total rock abundance and can be distinguished based on where the curves intersect the ordinate, which is the cumulative fractional area covered by all rocks.

1997, for further discussion). Equations of the form $F_k(D) = k \exp[-q(k)\ D]$ were derived from the VL1 and VL2 sites that also generally fit the Pathfinder and Gusev rock distributions (Golombek *et al.*, 2003b, 2005, 2006a), where $F_k(D)$ is the cumulative fractional area covered by rocks of diameter D or larger, k is the total area covered by all rocks, and $q(k)$ is the exponential that governs how abruptly the area covered by rocks decreases with increasing diameter (Golombek and Rapp, 1997; Figure 21.12). Plots of the cumulative number of rocks per area versus diameter tend to show a slightly more power law-like behavior (expected if they are equivalent to the cumulative area versus diameter plots [Golombek and Rapp, 1997; Golombek *et al.*, 2003b, 2006a]), which has been used to distinguish multiple versus single fragmentation processes and the minimal gradation of the cratered plains and Husband Hills surfaces (e.g., Grant *et al.*, 2006b).

No chemical measurements were made of rocks at the Viking landing sites; but the rocks are hard (not chipped or scratched by the arm), dark (those not covered by dust), angular, and pitted (perhaps vesicular), and they resemble dense mafic volcanic rocks (Garvin *et al.*, 1981; Moore and Jakosky, 1989; Christensen and Moore, 1992). The outcrop observed at VL1 covers about 4.5% of the surface (Moore and Keller, 1990, 1991) and on the basis of morphology and regional setting is likely dense, ridged plains basalt (Christensen and Moore, 1992). Although a variety of rock types was inferred from rock texture and color at the MPF landing site, the elemental composition of rocks analyzed by the APXS is consistent with their being volcanic rocks (either andesite or weathered basalt) with weathering rinds

Table 21.1. *Estimated physical properties and thermal inertia of surface materials at the five successful landing sites on Mars*

Surface material	Bulk density ($kg\,m^{-3}$)	Grain size (mm)	Cohesion (kPa)	Angle of internal friction (°)	Thermal inertia ($J\,m^{-2}\,K^{-1}\,s^{-1/2}$)
Drift	1000–1300	0.001–0.01	0–3	15–21	40–125
Sand	1100–1300	0.06–0.2	0–1	30	60–200
Crusty to cloddy soil	1100–1600	0.005–0.5	0–4	30–40	200–326
Blocky, indurated soil	1200–2000	0.05–3	3–11	25–33	368–410
Dense float rock, volcanic	2600–2800	2–2000	1000–10 000	40–60	>1200–2500
Clastic rock, Columbia Hills	~2000				620–1100
Sulfate rock, Meridiani	<2000				>400–1100

Source: Data derived from Moore *et al.* (1987, 1999), Moore and Jakosky (1989), Christensen and Moore (1992), Arvidson *et al.* (2004a,b), Christensen *et al.* (2004a,b), Herkenhoff *et al.* (2004a,b), Fergason *et al.* (2006a), and Chapter 20.

and/or dust coatings (McSween *et al.*, 1999). As a result, rocks at the Viking and MPF landing sites are likely dense volcanic rocks (density ~2600 $kg\,m^{-3}$) with high cohesion and angle of internal friction (Moore and Jakosky, 1989; Christensen and Moore, 1992; Table 21.1).

Rocks at the Gusev crater landing site were analyzed by *Spirit*; weathering rinds were evaluated directly using the RAT, MB, and APXS, and their thermal inertias were measured directly with the Mini-TES. Rocks on the cratered plains are olivine basalts with thin weathering rinds (McSween *et al.*, 2004). The basaltic rock on the cratered plains informally named Bonneville Beacon has a Mini-TES derived thermal inertia of 1200 $J\,m^{-2}\,K^{-1}\,s^{-1/2}$ (after incorporating slopes in the thermal modeling [Fergason *et al.*, 2006a]). This and other results that account for observational effects and coatings correspond to the thermal inertia expected for a dense, basaltic rock this size with density ~2800 $kg\,m^{-3}$ and an effective thermal inertia of about 2500 $J\,m^{-2}\,K^{-1}\,s^{-1/2}$ (Table 21.1).

Rocks in the Columbia Hills studied by *Spirit* are mostly clastic rocks formed by pyroclastic ash fall or impact processes with varying degrees of aqueous alteration (Squyres *et al.*, 2006). They have a different elemental composition and physical appearance than rocks observed on the plains, and in places appear as outcrop (Squyres *et al.*, 2006). The average Mini-TES thermal inertia of 11 selected rock targets is ~620 $J\,m^{-2}\,K^{-1}\,s^{-1/2}$ (the maximum was 1100 ± 130 $J\,m^{-2}\,K^{-1}\,s^{-1/2}$). This average thermal inertia value is lower than the Bonneville Beacon thermal inertia on the Gusev plains (1200 $J\,m^{-2}\,K^{-1}\,s^{-1/2}$), and suggests that thermal inertia can be used to discriminate differences in the density or porosity of rocks at different locations, and differentiate between dense and friable, weathered rocks (Fergason *et al.*, 2006a). Based on the amount of energy necessary to grind rocks using the RAT, the rocks at the lower Columbia Hills are easier to grind (average energy per volume of rock removed of 2 –24 $J\,mm^{-3}$) than rocks on the Gusev plains (average energy per volume of rock removed of 50–60 $J\,mm^{-3}$; (Squyres *et al.*, 2006). Since the energy required relates directly to rock density, among other properties, these results corroborate the thermal inertia differences and suggest reduced densities of the Columbia Hills rocks (~2000 $kg\,m^{-3}$; Fergason *et al.*, 2006a). Thermal inertia measurements of layered evaporites at Meridiani Planum have not been made, but on the basis of the easily eroded nature of these outcrops by the saltating sand and the very low-grind energy required by the *Opportunity* RAT (0.1–2 $J\,mm^{-3}$; Arvidson *et al.*, 2004b), they likely have even lower density and thermal inertia than the Columbia Hills rocks (Table 21.1).

21.4.8 Craters

Impact craters are ubiquitous on Mars, so it is no surprise that craters have been imaged at most of the landing sites. At VL1 (Figure 21.7) and the MPF landing sites the uplifted rims of craters have been imaged from the side (Arvidson *et al.*, 1979; Golombek *et al.*, 1999a). At Gusev and Meridiani (Figure 21.11), craters of various sizes and degradation state have been imaged during the rover traverses. At Gusev, most small craters have been filled in by sediment, and appear as hollows (Grant *et al.*, 2004, 2006a; Golombek *et al.*, 2006a). The freshest impact crater, Bonneville, has a well-preserved continuous ejecta sheet (Crumpler *et al.*, 2005) with increasing rock abundance toward the rim (Crumpler *et al.*, 2005; Grant *et al*, 2006a; Golombek *et al.*, 2006a). Fresh impact craters into sulfate sedimentary rocks were also visited by *Opportunity* (e.g., Fram and Vega), although most have been eroded by saltating sand and partially or completely filled (Golombek *et al.*, 2006b; Grant *et al.*, 2006a). Because fresh impact craters have a well-understood geometry, their degradation provides clues to the geomorphologic changes that have occurred at the site, such as the amount of erosion and/or deposition (Golombek *et al.*, 2006b; Grant *et al.*, 2006b).

21.4.9 Soils

All of the landing sites have soils composed of generally small fragments of pebbles, granules, sand, and finer materials (our use of the term "soils" implies no organic component as is common on Earth, but instead refers to the upper regolith of unconsolidated or poorly consolidated material). Soils at the landing sites have been divided into crusty to cloddy and blocky to indurated types based on their soil mechanics properties (e.g., Moore *et al.*, 1987, 1999). Surface materials sorted by wind have been divided into drift, sand (including sand dunes), and granules (generally ripples formed by saltation-induced creep). Most soils have a variety of physical characteristics due to grain size and degree of cohesion, even though their composition appears remarkably similar at all of the landing sites (dominantly basaltic), suggesting some global homogenizing process (e.g., Yen *et al.*, 2005).

Crusty to cloddy soils

Crusty to cloddy soils are present at most of the landing sites. They have weak cohesion (1–4 kPa) and moderate angles of internal friction (30°–40°), likely due to mild cementation. Crusty and cloddy soils make up most of the VL2 sample field where they tended to break up into platy slabs of crust when investigated with the robotic arm (Moore *et al.*, 1987; Moore and Jakosky, 1989; Christensen and Moore, 1992). At the MPF site, cloddy soils observed in rover wheel tracks are poorly sorted (Figure 21.13) with rounded pebbles (Moore *et al.*, 1999). Larger particles in the Viking soils were cloddy aggregates of fine particles that disaggregated in the sample sieve. Steeper upper slopes in trenches dug by the MERs at Meridiani (Figure 21.14) and Gusev crater also have small cohesions (Arvidson *et al.*, 2004a,b; see also Chapters 13 and 20) and data from MER and VL suggest cementation by sulfur and chlorine compounds likely involving small amounts of water (Yen *et al.*, 2005; Wang *et al.*, 2006). Grain sizes in crusty to cloddy material range from very fine dust to sand, granule, and pebble-sized materials. The bulk density of crusty to cloddy soils estimated from their friction angles is 1100–1600 $kg\,m^{-3}$ (Moore and Jakosky, 1989; Moore *et al.*, 1999; Chapter 20). Thermal inertia estimates from bulk density, particle size, and cohesion for crusty to cloddy material at the VL2 site are 200–326 $J\,m^{-2}\,K^{-1}\,s^{-1/2}$ (Moore and Jakosky, 1989); if the soil is cohesionless, such thermal inertias correspond to soils with average particle sizes of 0.16–0.5 mm (medium sand; Presley and Christensen, 1997; Table 21.1).

Blocky, indurated soils

More cemented soils have also been characterized at VL1, MPF, and the MER sites. At VL1, blocky material makes up most of the sample field explored by the arm; it broke into 2–4 cm fragments when trenched (Moore *et al.*, 1987; Moore and Jakosky, 1989). Larger fragments of rock are present in blocky material than cloddy material as determined by Viking, and overall soil cohesion is greater (~5 kPa). Well-cemented soils were also found at the MPF site (Figure 21.15), where rover wheel cleats failed to scratch the material, but its composition matched soil deposits elsewhere (Scooby Doo; see image in Chapter 20). The densest soils derived from wheel rut depth and slip analysis of MER tracks are also consistent with blocky or indurated material.

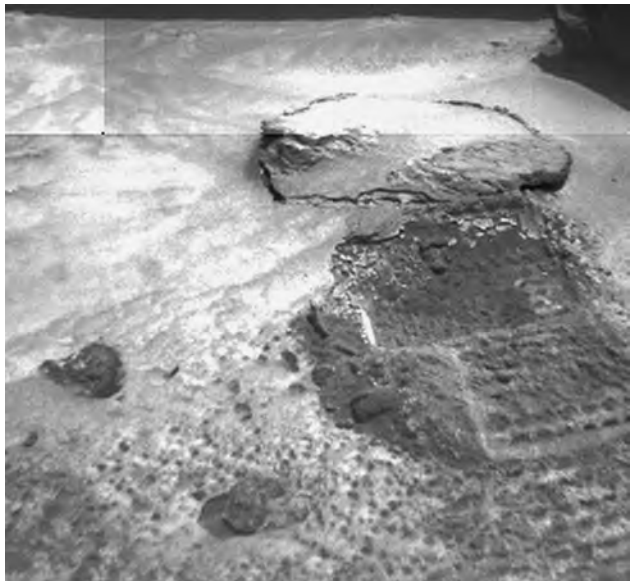

Figure 21.13. Image acquired by the Mars Pathfinder rover Sojourner, showing soils near the base of the rock Yogi. Sojourner bulldozed the tabular rock or indurated crust target called "Pop Tart" out of the ground here after partially burying the right front wheel and then driving the other 5 wheels forward. Image shows the poorly sorted cloddy and pebbly soil and bright drift material. Fine-grained drift material becomes cohesive when compressed, breaking into clods at the base of Pop Tart.

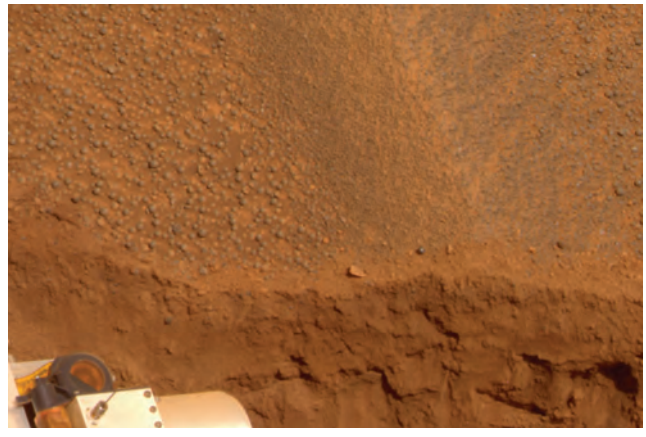

Figure 21.14. Pancam image of trench through ripple crest by *Opportunity* on Meridiani Planum. Image shows the granule-rich surface lag of blueberries (hematite concretions) that has weathered out of the sulfates and a more poorly sorted, dominantly sand interior. The steep upper portion of the trench indicates weak cementation in the surface's crusty soils. (For a color version of this figure, please refer to the color plate section or to the e-Book version of this chapter.)

Figure 21.15. Image of Bakers Bench, far field light-toned area of cohesive or cemented soil at the Mars Pathfinder landing site. Similar soils such as the target known as "Scooby Doo" were not scratched by the rover wheel cleats. This observation and the fact that its composition is similar to loose soil suggests that these kinds of materials are well-cemented, indurated soils or duricrust. These somewhat extensive deposits of duricrust at the Pathfinder site likely are responsible for the higher bulk thermal inertia of this site compared to other landing sites. (For a color version of this figure, please refer to the color plate section or to the e-Book version of this chapter.)

As a class, blocky material has relatively high cohesion (3–10 kPa) and moderate friction angles (25°–33°; Moore and Jakosky, 1989; Moore *et al.*, 1999; Chapter 20). In general, crusty to cloddy and blocky materials correspond to the cemented soils or duricrust that appears to control most of the high-thermal-inertia but low-rock-abundance regions on Mars (see discussion in Section 21.5). Bulk densities for blocky material have been estimated to be greater than cloddy and crusty material (1200–2000 $kg\,m^{-3}$) and thermal inertia has been estimated at 368–410 $J\,m^{-2}\,K^{-1}\,s^{-1/2}$ (Moore and Jakosky, 1989; Table 21.1), which if cohesionless corresponds to soils with average particle size of 0.6–3 mm (coarse sand to granules; Presley and Christensen, 1997).

21.4.10 Eolian deposits

Drift deposits

Drift material is weak, porous, high-albedo material that is characterized by small angles of internal friction (15°–21°) and very low bulk densities (1000–1300 $kg\,m^{-3}$). Its high albedo, low bulk density, and distribution as rock coatings and wind tails behind rocks at all of the landing sites (Figures 21.7–21.11) suggest that it is likely atmospheric dust that has settled onto the surface. Drift material was investigated with the sample arm at VL1, and was driven over at the Pathfinder and MER sites. It is very fine-grained, has very low-bearing strength (e.g., VL1 footpad 2 sank out of sight into it) and is compressible (e.g., perfectly preserving rover wheel tracks at the Pathfinder site and airbag bounce marks at Meridiani). Estimates of grain size at the VL1 site are roughly micron size (clay size; Moore *et al.*, 1987; Moore and Jakosky, 1989) and correspond to the 2–4 μm diameter size of dust in the atmosphere derived from optical scattering (e.g., Toon *et al.*, 1977; Pollack *et al.*, 1979; Tomasko *et al.*, 1999; Lemmon *et al.*, 2004).

By analogy with very dusty surfaces on Mars that have very low thermal inertia and high albedo (such as Tharsis, Arabia Terra, and Elysium [Chapter 18]), drift deposits should have very low thermal inertias of 40–125 $J\,m^{-2}\,K^{-1}\,s^{-1/2}$ (Table 21.1). Mini-TES measurement of fine-grained bright material in a sediment-filled depression (hollow) called Middle Ground visited by *Spirit* is ~150 $J\,m^{-2}\,K^{-1}\,s^{-1/2}$, which corresponds to ~45 μm diameter particles (silt; Fergason *et al.*, 2006a). A similar hollow, Laguna (~40 m from Middle Ground), was trenched with the rover wheel to expose cohesive material to a depth of 6–7 cm (Squyres *et al.*, 2004a), and is likely filled with material analogous to that of Middle Ground. MI images of the Laguna trench indicate that grains are sometimes clumped together, but individual particles are too small (less than 100 μm) to measure with the MI instrument (Herkenhoff *et al.*, 2004a). This observation is consistent with the thermal inertia values and particle sizes derived from Mini-TES. Although these measured thermal inertias are higher than that expected for very fine-grained dust (clay-sized particles) alone, mixtures of more cohesive substrate and rock fragments likely produce the measured Mini-TES thermal inertias.

Sand and eolian bedforms

Sand dunes have been identified at the MPF landing site, where a barchanoid dune was discovered in a trough by the rover, and at Meridiani Planum, where dune fields were found at the bottom of Endurance (Figure 21.16) and Victoria craters. Bedforms of sandy deposits were also observed inside Bonneville crater and at El Dorado on the southern flanks of Husband Hill by *Spirit*. Dunes identified by their morphology indicate sand-sized grains that have been moved by saltation and sorted by the wind, and thus represent an important pure component of soils.

The bedforms on the floor of Endurance crater at Meridiani Planum (Figure 21.16) were also observed by the *Opportunity* Mini-TES. These bedforms have sharp crests and a Pancam albedo of ~0.12, suggesting a relatively dust-free surface. The average Mini-TES thermal inertia of the entire bedform is 200 $J\,m^{-2}\,K^{-1}\,s^{-1/2}$ (Table 21.1), corresponding to a particle diameter of ~160 μm (fine sand; Fergason *et al.*, 2006a). The rover did not traverse to these bedforms because the area surrounding them was untrafficable, and thus an MI measurement of the same surface observed by the Mini-TES was not acquired. However, an MI image of a patch of similar dark sand near the wall of the crater was acquired. The average measured particle size of this bedform was ~130 μm, which corresponds well with the particle diameter derived from the Mini-TES thermal inertia value (Fergason *et al.*, 2006a) and to the typical sizes of sand grains that saltate to form dunes.

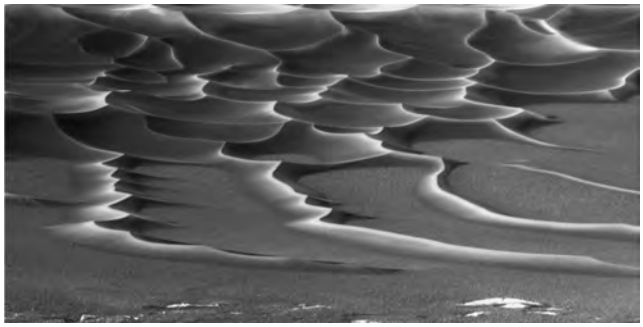

Figure 21.16. Mosaic of sand dunes in the bottom of Endurance crater. Dark surface is basalt with a surface lag of hematitic spherules. Lighter sides of dunes are likely dust that has settled from the atmosphere. Light-toned outcrop is in the foreground. Thermal inertia measurements by Mini-TES confirm that the dunes are composed of basaltic, sand-sized particles.

An extensive eolian bedform observed at the *Spirit* site is located in Bonneville crater. Mini-TES-derived thermal inertia was determined for two sections of this bedform: (1) an upper section that climbs the north crater wall (modeled slope of 11° [Grant *et al*., 2004]) and has a lower Pancam albedo (∼0.18); and (2) a lower portion that occurs on the crater floor and has a higher Pancam albedo (∼0.23). The Mini-TES thermal inertia for the upper bedform section is $200\,J\,m^{-2}\,K^{-1}\,s^{-1/2}$, which corresponds to a particle diameter of ∼160 μm (fine sand). The bedform section on the crater floor has a thermal inertia of $160\,J\,m^{-2}\,K^{-1}\,s^{-1/2}$, suggesting ∼60 μm diameter particles (silt to very fine sand; Fergason *et al*., 2006a). The aeolian sediment on the crater floor and wall may be of the same origin, and a thin layer (≤1 cm) of dust may be causing the increased Pancam albedo and lower thermal inertia on the crater floor. The coarser, darker grains of the upper bedform section are consistent with bedforms that have been active more recently than the lower bedform section, because they presumably have less dust mantling their surfaces (Fergason *et al*., 2006a).

Ripples are eolian bedforms formed by saltation-induced creep of granules (Figure 21.17), which are millimeter-sized particles. They typically have a coarse fraction of granules at the crest and poorly sorted interiors, indicating a lag of coarser grains after the sand-sized particles have been removed (Figure 21.14). Ripples have been observed at the MPF, *Spirit*, and *Opportunity* sites.

The surface at Meridiani Planum is dominated by centimeters-high ripples spaced an average of 10 m apart, and is covered with 0.6–6 mm diameter hematite spherules (Herkenhoff *et al*., 2004b; Soderblom *et al*., 2004; Sullivan *et al*., 2005; Figure 21.17). Measured Mini-TES thermal inertia of Meridiani plains soil is $100–150\,J\,m^{-2}\,K^{-1}\,s^{-1/2}$, corresponding to a particle diameter of ∼45 μm (silt). However, a single thermal inertia does not fit the entire diurnal curve. Thus, there is a phase lag in which measured temperatures cool more slowly in the afternoon than modeled temperatures, relative to the best fit thermal inertia for mid-day observations. This complex behavior suggests that this surface is retaining more heat in the afternoon than the thermal model predicts and that the processes operating at this site are not adequately represented in current thermal models (e.g., Fergason *et al*., 2006a). In addition, the Mini-TES thermal inertia is lower than that implied by MI particle size measurements, which observed a bi-modal particle size distribution of 0.6–6 mm diameter particles set in fine sand with particle sizes <125 μm (Herkenhoff *et al*., 2004b). The *Opportunity* landing site at Meridiani has a TES thermal inertia of $\sim 200\,J\,m^{-2}\,K^{-1}\,s^{-1/2}$ and a THEMIS thermal inertia of $190 \pm 30\,J\,m^{-2}\,K^{-1}\,s^{-1/2}$, implying a particle size of fine sand (Golombek *et al*., 2005); these values are consistent with particle sizes estimated from Pancam and MI imagery (Bell *et al*., 2004b; Herkenhoff *et al*., 2004b). The Mini-TES-derived thermal inertias, however, are $100–150\,J\,m^{-2}\,K^{-1}\,s^{-1/2}$, which are lower than the orbital values, and imply particle sizes (10–45 μm) that are lower than expected for the observed ripples. A possible explanation for the lower surface thermal inertia measurements is that they are responding to a trapped layer of atmospheric dust beneath the granule surface (indicated, for example, by the perfect imprints of the airbag bounce marks in Eagle crater; Bell *et al*., 2004b).

Figure 21.17. Navcam image of ripples covering Meridiani Planum. Image obtained by the *Opportunity* rover on sol 439. Ripples are formed by saltation-induced creep of granules. Bright reflective patches in the rover tracks are likely fine-grained, compressible dust.

21.5 THERMOPHYSICAL PROPERTIES

21.5.1 Introduction: relationship to global thermophysical units

A general relationship has been found between kilometer-scale global thermal inertia and albedo data and specific materials found in the surface layer at the Viking, Pathfinder, and MER landing sites (e.g., Moore and Jakosky, 1989; Christensen and Moore, 1992; Golombek

et al., 1999b, 2005; Mellon *et al.*, 2000; Putzig *et al.*, 2005; Fergason *et al.*, 2006b). Global thermal inertia and albedo data show that the surface of Mars exhibits three "units" that cover most of the surface (units A, B, and C in Putzig *et al.*, 2005; Chapter 18). Regions of high albedo and very low thermal inertia (unit A) are believed to be dominated by bright red dust and have low rock abundance. Such dusty areas have been eliminated as possible landing sites for solar-powered or rover missions due to concerns that the dust would coat the solar panels (reducing power) and that the spacecraft would sink if the material were not load-bearing (Golombek *et al.*, 1997, 2003a). Regions of moderate-to-high thermal inertia and low albedo (unit B) are likely to be relatively dust-free and composed of dark eolian sand and/or an increased abundance of rock (Christensen and Moore, 1992). Regions of moderate-to-high thermal inertia and intermediate-to-high albedo (unit C) are likely to be dominated by crusty, cloddy, and blocky soil materials, often referred to as duricrust, with some dust and various abundances of rocks (Jakosky and Christensen, 1986; Moore *et al.*, 1987; Mellon *et al.*, 2000; Putzig *et al.*, 2005). The range of high and low thermal inertias observed on Mars occurs over most elevations. Exceptions are that the very lowest elevations tend to exhibit higher thermal inertia values, and the very highest elevations tend to exhibit lower thermal inertias (Putzig *et al.*, 2005; Chapter 18).

The five landing sites sample two of the three dominant surface units of thermal inertia and albedo (B and C) discussed above that cover most of Mars. Although rock abundances vary in these units (and can be high), they are considered generally safe for landing spacecraft (Golombek *et al.*, 2005; Table 21.2). The Viking landing sites (both in unit C) have high rock abundances (~17%), relatively high albedo, and intermediate thermal inertia. As seen from the surface, these sites are consistent with their orbital-derived characteristics; both are rocky and somewhat dusty plains with a variety of soils, some of which are cohesive and cemented.

Prior to landing, the MPF site was expected to be a rocky plain composed of materials deposited by the Ares Vallis catastrophic flood that was safe for landing and roving and was less dusty than the Viking landing sites (Golombek *et al.*, 1997). These predictions were based on the site's high rock abundance (18%), intermediate-to-high thermal inertia, slightly lower albedo (in material similar to unit C, except with higher thermal inertia), and relation to an analogous catastrophic outflow depositional plain in the Channeled Scabland of Washington State (Golombek *et al.*, 1997). These predictions were confirmed by data gathered by the MPF lander and rover (Golombek *et al.*, 1999b; Figure 21.9).

The *Spirit* landing site in Gusev crater has bulk and fine-component thermal inertia and albedo comparable to the two Viking sites, and thus was expected to be similar to these locations (all are in unit C), but with fewer rocks (8%) (Golombek *et al.*, 2003a; Table 21.2). Dark dust-devil tracks in orbital images (Figure 21.4) suggested that some of the surfaces would have lower albedo, where dust has been preferentially removed. *Spirit* traversed across both dusty and relatively less dusty surfaces and found that the average rock abundance was similar to expectations. In darker dust-devil tracks, *Spirit* found that the albedo is lower and the surface is relatively less dusty (e.g., at the landing site) and in areas outside of dust-devil tracks the albedo is higher (e.g., at the rim of Bonneville crater) and the surface is more heavily coated with bright airfall atmospheric dust (Figure 21.10; Bell *et al.*, 2004a; Golombek *et al.*, 2005).

The Meridiani Planum site has moderate thermal inertia, and in contrast to the other sites, very low albedo and few rocks. This site was expected to look very different from the Viking and MPF landing sites because of its dark surface, low abundance of bright red dust, and few rocks (in unit B). *Opportunity* has indeed traversed across a dark, basaltic sand surface (Figure 21.11) with very few rocks and almost no dust (Golombek *et al.*, 2003a, 2005; Bell *et al.*, 2004b), consistent with the surface properties inferred from orbital data.

21.5.2 Orbital thermal inertia

For remotely studying the physical properties of the Martian surface, thermal inertia is a uniquely suitable tool due to its dependence on bulk thermal conductivity, which is most dependent on the physical characteristics of materials in the range of temperatures and pressures currently found at the surface of Mars. These dependencies allow us to make inferences about the grain size of soils and their degree of cementation or induration, to assess rock abundance and detect the presence of bedrock or surface ices, and to evaluate the physical heterogeneity of surface materials, all either from thermal inertia alone or by considering it together with other surface properties. The lowest thermal inertia values observed on Mars can only be explained by the presence of fine-grained, unconsolidated dust (silt and clay-sized particles), at least a few centimeters thick. The highest thermal inertias observed can only be explained by the presence of exposed soil-free bedrock (or surface ice in the polar regions). For intermediate thermal inertia values, many different materials or combinations of different materials can produce the same value of thermal inertia, and therefore many nonunique interpretations of results derived solely from remotely sensed observations are possible. Data acquired at the surface from landed spacecraft provide "ground truth," which may be used to resolve the ambiguity inherent in the remote observations, and thereby provide a greater level of confidence in extrapolating properties observed *in situ* to broader areas using data acquired by orbiting spacecraft. A thorough discussion of thermal inertia in a global context may be found in Chapter 18. Here, we focus on landing site thermal inertia results and their relationship to other data from orbiting and landed spacecraft.

A variety of studies have included an assessment of the relationship between thermophysical properties determined from orbiter instruments and observations made from landers and rovers (e.g., Moore and Jakosky, 1989; Christensen and Moore, 1992; Golombek *et al.*, 1999b, 2005; Putzig *et al.*, 2005; Fergason *et al.*, 2006a, 2006b; Jakosky *et al.*,

Table 21.2. *Landing site location, elevation, thermal inertia, albedo, global thermophysical units, and rock abundances*

Lander	Location		MOLA	TES[a]		Unit[b], Inertia vs.		Rock abund. (%)			IRTM[c]	
	Latitude (°)	Longitude (°E)	Elevation (km)	Inertia ($J\,m^{-2}K^{-1}\,s^{-1/2}$)	Albedo	Albedo	Elevation	IRTM[c]	TES[d]	Lander[e]	Bulk inertia ($J\,m^{-2}\,K^{-1}\,s^{-1/2}$)	Fine-component inertia ($J\,m^{-2}\,K^{-1}\,s^{-1/2}$)
VL1	22.27	312.05	−3.63	283	0.22	C	3	16		16	355	284
VL2	47.62	134.23	−4.50	234	0.24	C	3	17	13 ± 4	16	338	260
MPF	19.09	326.74	−3.68	386	0.19	F	3	18	12 ± 4	19	434	338
Spirit	−14.57	175.47	−1.94	300[f]	0.19, 0.26	C	4	8	11 ± 4	7	284	248
Opportunity	−1.95	354.47	−1.39	222[f]	0.12	B	4	∼3		∼3	315	307

[a] Values from Putzig *et al*. (2005). TES data from 6×6 map pixels (∼18×18 km).
[b] Map units of Putzig *et al*. (2005). See Table 18.2 and Figures 18.10 and 18.11.
[c] Data from Christensen (1986), Golombek *et al*. (1999b, 2003a, 2005), selected point for MPF, *Spirit*, and *Opportunity*.
[d] From Nowicki and Christensen (2007).
[e] From Moore and Jakosky (1989), Moore and Keller (1990, 1991), Golombek *et al*. (2003b, 2005). For the Viking sites, low values are from near-field data and high values include far-field estimates and VL1 outcrops.
[f] Individual TES pixel values from Jakosky *et al*. (*2006*).

2006). Table 21.2 summarizes the thermal inertia, albedo, elevation, and rock abundance in the vicinity of each landing site. Also included in the table are thermophysical surface units, derived from quantitative comparisons of thermal inertia with albedo and elevation (Putzig *et al.*, 2005; see also Chapter 18, Table 18.2, and Figures 18.10 and 18.11). In Figure 21.18, regional ($5° \times 5°$ and $6° \times 6°$) maps of thermal inertia derived from observations by TES (for Viking and Pathfinder sites) or THEMIS (for MER sites) are provided that can be compared with panoramic images and mosaics from each landed spacecraft (Figures 21.7–21.11).

In the Viking regions, the thermal inertia is relatively uniform at 3 km scale, while the regions around the MPF and MER sites show greater range and spatial variability of thermal inertia. Ground-based observations of rock abundance (Golombek *et al.*, 2003b, 2005) also show greater variability for the MPF and MER sites, although these characteristics may be unrelated, given the substantial difference in scale of the observations. At the MPF site, apparent erosional remnants from catastrophic flooding (Baker *et al.*, 1992) show generally lower thermal inertia than the surrounding terrain. Also, the interiors of several craters show elevated thermal inertia, which may be indicative of coarse-grained intracrater, possibly eolian, deposits (e.g., Pelkey *et al.*, 2001). The higher-resolution THEMIS results at the MER sites show greater detail and a broader range of thermal inertia values. Many of the crater rims explored by the rovers have elevated thermal inertia values due to high rock abundances or outcrop exposures, and some have high thermal inertia values in their interiors, corroborating expectations from orbital data (Figure 21.18).

The Viking, Pathfinder, and *Spirit* image mosaics in Figures 21.7 to 21.9 show rock-strewn surfaces with varying characteristics. Rock abundances have been estimated from IRTM and TES data by Christensen (1986) and Nowicki and Christensen (2007) using a thermal emission spectral differencing technique, and from surface imagery by Moore and Jakosky (1989), Moore and Keller (1990, 1991), and Golombek *et al.* (1999b, 2003b, 2005, 2006a). As is evident in the images, the VL2 and MPF surfaces contain a higher percentage of large rocks than VL1 (Moore and Keller, 1990; Golombek *et al.*, 2003b), even though the total area covered by rocks is fairly similar (due to the outcrop at VL1). The MER landing sites are nearly devoid of large boulders and have substantially lower overall rock abundances (Golombek *et al.*, 2005, 2006a). The relationship between thermal inertia as derived from orbital observations and rock abundance as observed from the landers is complex (Mellon *et al.*, 2000; Jakosky and Mellon, 2001; Golombek *et al.*, 2003b; Putzig *et al.*, 2005; Jakosky *et al.*, 2006). The VL1 and VL2 thermal inertia values derived from TES are, respectively, about 100 and 150 $J\,m^{-2}\,K^{-1}\,s^{-1/2}$ lower than that of MPF, whereas the lander-observed rock abundances are similar for all three sites (within 3% when including far-field rock estimates and outcrops). Relative to the *Spirit* site, the VL1 and VL2 TES thermal inertia values are, respectively, about 15 and 65 $J\,m^{-2}\,K^{-1}\,s^{-1/2}$ lower, but the rock abundances are 10% or more higher. This lack of correlation indicates that rock abundance is not the most important factor controlling

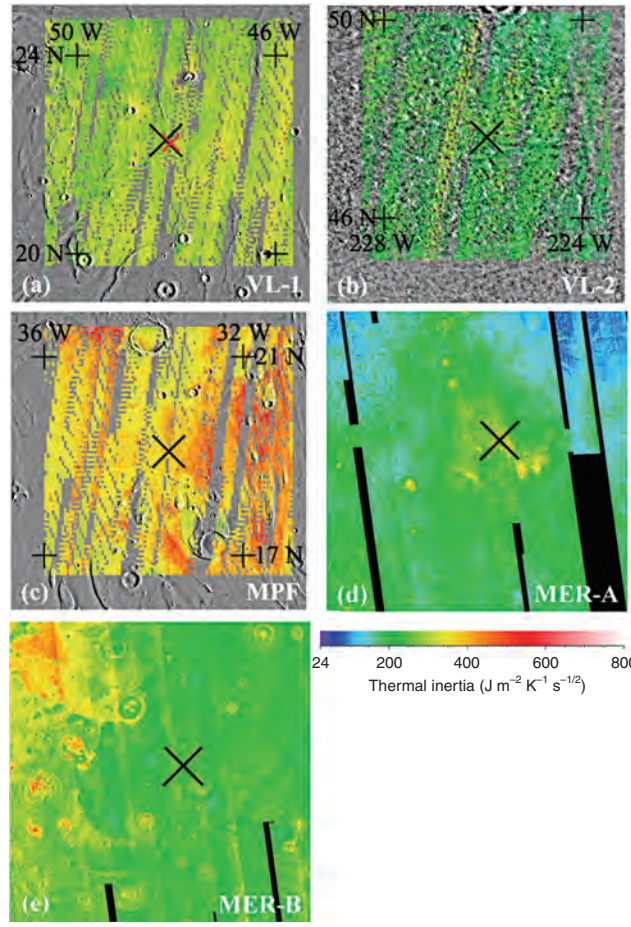

Figure 21.18. TES-based thermal inertia map ($5° \times 5°$) over a Viking MDIM 2.0 mosaic (a–c; based on Putzig *et al.*, 2005) or $6° \times 6°$ THEMIS-based thermal inertia mosaic calibrated to the Putzig *et al.* (2005) TES map (d, e; after Jakosky *et al.*, 2006). (a) VL-1, relocated from small red to large black X per Zeitler and Oberst (1999) revised location; (b) VL-2; (c) MPF; (d) MER-A map 182° W to 188° W, 12° S to 18° S; (e) MER-B map 3° W to 9° W, 1° S to 5° N. (For a color version of this figure, please refer to the color plate section or to the e-Book version of this chapter.)

thermal inertia in these regions (Jakosky and Mellon, 2001; Golombek *et al.*, 2003b; Putzig *et al.*, 2005; Jakosky *et al.*, 2006), supporting a similar conclusion for global data reached by Christensen (1982, 1986) that was based solely on Viking orbiter data. Clearly, the distribution of fines, degree of induration, or other characteristics are more important than rock abundance in determining the bulk thermal properties of these regions, and by extension, likely much of the Martian surface. Jakosky and Christensen (1986) proposed that dominance of the thermal properties by variations in the degree of induration and spatial distribution of duricrust could reconcile most of these apparent conflicts between the distribution of rocks and remotely derived thermal inertia, as well as explain Earth-based radar data (compare thermal inertia of soils in Table 21.1).

In an analysis of three Mars years of TES thermal inertia results, Putzig and Mellon (2007) have found large (100–200 $J\,m^{-2}\,K^{-1}\,s^{-1/2}$) seasonal and diurnal variations in apparent thermal inertia at each landing site that appear

to be consistent with model results for layered surfaces with ~20–30 mm of duricrust over dust at VL1, VL2, and MPF, and with ~3 mm of dust over rock at the *Spirit* site. Results for the *Opportunity* site did not correspond to any of the simple two-component models considered by Putzig and Mellon (2007), but were suggestive of more complex surface heterogeneity. It is important to note that even the highest estimates of rock abundance (19%) at the landing sites leave over 80% of the surface rock-free, and thus all of the landing-site observations are consistent with a model wherein the fines (whether unconsolidated, cemented, horizontally mixed, or layered) dominate the thermal signature.

21.5.3 Comparison of surface to orbital thermal inertia

At Gusev crater, *Spirit* conducted a campaign to systematically monitor properties of the soil along the traverse from CMS to Bonneville crater and the Columbia Hills (Figure 21.4) using Navcam, Pancam, and Mini-TES observations. The Mini-TES-derived thermal inertia values along this traverse provide an opportunity to compare with TES (Christensen *et al.*, 1992) and THEMIS (Christensen *et al.*, 2004a) (Figure 21.19) orbital thermophysical data at a spatial resolution of ~3 km × ~6 km per pixel and ~100 m per pixel respectively.

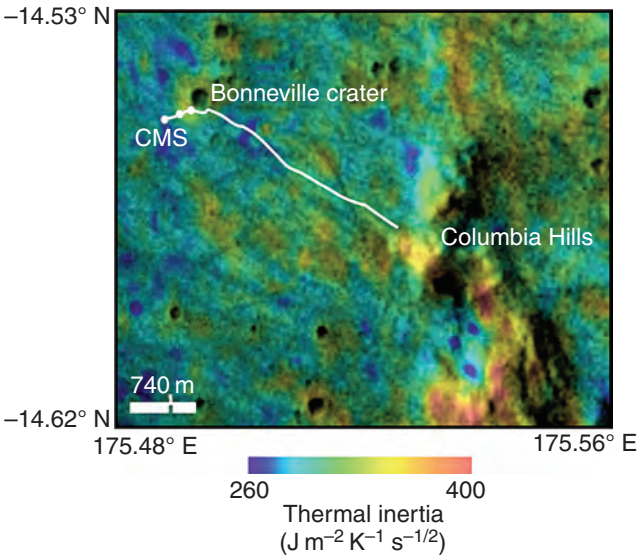

Figure 21.19. THEMIS thermal inertia image in color (100 m/pixel) overlaid on THEMIS visible mosaic (18 m/pixel) of the Gusev crater landing region. *Spirit* landed at Columbia Memorial Station (CMS) in a low albedo, low thermal inertia intercrater plains (southwestern-most white dot: Mission Success panorama location), traversed through the ejecta blanket (middle white dot: Legacy panorama location) to the rim of Bonneville crater about 300 m away (northeastern-most white dot), and then across the low and high thermal inertia plains to the Columbia Hills (with generally higher inertias) to the east and southeast. Thermal inertia (Fergason *et al.*, 2006b) increases from 285 to 330 J m^{-2} K^{-1} s$^{-1/2}$ over the traverse to the rim of Bonneville crater. Rock size frequency distributions are reported at these three locations in Figure 21.12. (For a color version of this figure, please refer to the color plate section or to the e-Book version of this chapter.)

The *Spirit* landing site at Gusev has an average TES-based thermal inertia of ~290 J m^{-2} K^{-1} s$^{-1/2}$ (Christensen *et al.*, 2004b), suggesting that the surface is dominated by duricrust, cemented soil, noncohesive coarse sand, or a combination of these materials. This value is consistent with the variety of surface types observed by the *Spirit* rover. The comparison of THEMIS-based thermal inertia (Fergason *et al.*, 2006b) with Mini-TES thermal inertia along the traverse from the CMS to Bonneville crater and the Columbia Hills (Fergason *et al.*, 2006a) shows that the general trends match between datasets. The thermal inertia increases along the traverse from CMS (THEMIS: 280 ± 40 J m^{-2} K^{-1} s$^{-1/2}$; Mini-TES: 175 ± 20 J m^{-2} K^{-1} s$^{-1/2}$) to Bonneville crater (THEMIS: 330 ± 50 J m^{-2} K^{-1} s$^{-1/2}$; Mini-TES: 380 ± 45 J m^{-2} K^{-1} s$^{-1/2}$) in both datasets (Figure 21.19), and reflects the greater number or size of clasts or rocks in the Mini-TES field of view (Christensen *et al.*, 2004a; Golombek *et al.*, 2005, 2006a; Moersch *et al.*, 2005). The Mini-TES thermal inertia is more variable along the traverse from Bonneville crater to the Columbia Hills, but increasing and decreasing thermal inertia patterns are similar to those determined from orbit, and the average value of each dataset along this traverse differs by only ~35 J m^{-2} K^{-1} s$^{-1/2}$. Generally, the thermal inertia measured from the surface is lower than that observed from orbit. These lower surface values may indicate a data bias because the Mini-TES observations were taken directly in front of the rover and during the rover traverse, obstacles such as bedforms or large rocks were avoided. However, it has been documented that there is variability and mixing of particle sizes along the traverse at Gusev crater that is not resolved in the THEMIS thermal inertia (Fergason *et al.*, 2006b).

The thermal inertia along the Gusev plains traverse varies by less than 90 J m^{-2} K^{-1} s$^{-1/2}$, and these changes can typically be attributed to the presence of rock fragments or eolian material in the Mini-TES field of view (Fergason *et al.*, 2006a). Navcam and Pancam images taken of the same location as the Mini-TES observations show that the variations in thermal inertia correlate with the percentage of rock fragments in the area, where the number and size of rock fragments increase in higher thermal inertia regions (Moersch *et al.*, 2005; Ward *et al.*, 2005). An increase in thermal inertia and rock abundance is also associated with crater ejecta (e.g., Golombek *et al.*, 2005; 2006a; Figures 21.19 and 21.20). These observations suggest that at meter scales, variations in thermal inertia are controlled by the local physical abundance of drift material, rocks, and rock fragments, all of which are controlled by local processes that redistribute grains and rocky material (Fergason *et al.*, 2006a). In contrast, Christensen (1982) examined the relationship between rock abundance and the fine-component thermal inertia with global thermal inertia patterns and concluded that at global scales the variations in the fine-component properties and resulting thermal inertia, rather than the abundance of rocks, produce much of the variation in thermal inertia. These observations imply that different processes are affecting the physical surface characteristics at different scales. Rocky material from crater ejecta, the presence of eolian

bedforms, and rock fragment concentrations control the thermal inertia variations at meter to tens-of-meter scales. Regional processes, such as the induration of soils, deposition of airfall dust, deflation or deposition of wind-blown sand, or large-scale volcanic processes, control the major thermal inertia variations at kilometer to tens-of-kilometers scales (Fergason *et al.*, 2006b).

The *Opportunity* landing site in Meridiani Planum has a TES and THEMIS bulk thermal inertia of ~200 and 190 $J\,m^{-2}\,K^{-1}\,s^{-1/2}$, respectively, although Viking IRTM–derived thermal inertia values are higher (~315 $J\,m^{-2}\,K^{-1}\,s^{-1/2}$). The TES and THEMIS thermal inertia values correspond to surfaces dominated by ~0.2 mm sand-size particles (Presley and Christensen, 1997), which is consistent with the ubiquitous fine sand observed at Meridiani Planum (Herkenhoff *et al.*, 2004b). Mini-TES-measured thermal inertia values are somewhat lower (see Section 4.10.2) and likely record a complex interplay among surface granules, trapped dust, and the sand.

21.5.4 Relationship of thermophysical properties to surface materials at the landing sites

The soils at the landing sites and their physical properties can also be related to orbital thermal inertia measurements. Because rocks consist of <20%–30% of the surface of the landing sites, their effect on the bulk thermal inertia can be factored out via simple models of the effective thermal inertia of the rock population based on their diameter (Golombek *et al.*, 1999b, 2003b). For the IRTM bulk thermal inertia of the Pathfinder site of 435 $J\,m^{-2}\,K^{-1}\,s^{-1/2}$ and the estimated effective thermal inertia of the measured rock size-frequency distribution of 1700 $J\,m^{-2}\,K^{-1}\,s^{-1/2}$, a fine-component thermal inertia of about 320 $J\,m^{-2}\,K^{-1}\,s^{-1/2}$ is derived (Golombek *et al.*, 2003b), which is consistent with that expected for the observed poorly sorted moderately dense cloddy to blocky soils (Moore *et al.*, 1999; Table 21.1). Lower fine-component thermal inertias at VL1 (240 $J\,m^{-2}\,K^{-1}\,s^{-1/2}$) and VL2 (170 $J\,m^{-2}\,K^{-1}\,s^{-1/2}$), derived in a similar way (Golombek *et al.*, 2003b), are consistent with the greater areal coverage of thick drift coverage at VL1 (18%–30%) and thin drift coverage at VL2 (40%; Moore and Keller, 1990; Moore *et al.*, 1999). Using this method (Golombek *et al.*, 1999b, 2003b), effective thermal inertia values of the rock populations of 1125, 1590, and 1870 $J\,m^{-2}\,K^{-1}\,s^{-1/2}$ were derived at 3 locations along *Spirit*'s traverse where rocks were counted (Golombek *et al.*, 2005, 2006a), from the landing site to the rim of Bonneville crater (Figures 21.19 and 21.20). The fine-component thermal inertia derived from these effective rock inertia values are 240, 250, and 140 $J\,m^{-2}\,K^{-1}\,s^{-1/2}$, which can be related to the increased coverage of very-low-thermal-inertia dust at the crater rim (Golombek *et al.*, 2005; Figure 21.20). In the case of Meridiani Planum, the bulk and fine-component thermal inertia are effectively the same due to the lack of rocks, and the orbital thermal inertia of 200 $J\,m^{-2}\,K^{-1}\,s^{-1/2}$ corresponds directly to that expected (Presley and Christensen, 1997) from a surface dominated by the ubiquitous 0.2 mm fine sand observed on the surface (Herkenhoff *et al.*, 2004b).

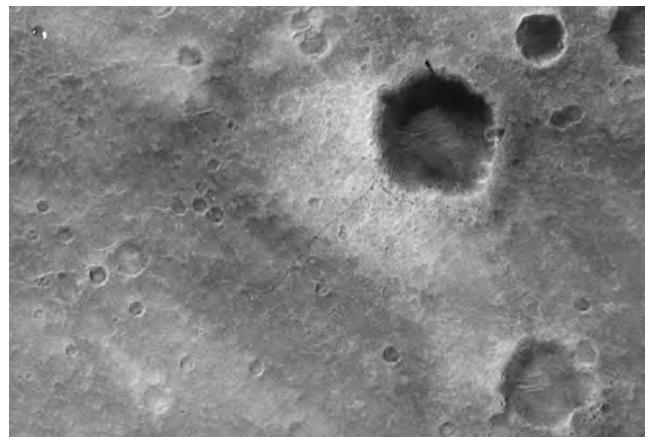

Figure 21.20. MOC image showing the Columbia Memorial Station lander and the *Spirit* rover's tracks to Bonneville crater. The lander (bright spot) is in relatively low albedo dust-devil track; the albedo increases around Bonneville crater. The difference in albedo is produced by the deposition of atmospheric dust, so that albedo is a proxy for dustiness in this region. Note also the landing system's backshell and parachute in the upper left corner of the image, the dark smudge on the north rim of Bonneville which is the heat shield, and the rover itself (dark spot at end of rover track near the rim of Bonneville crater). Rock abundance counts in Figure 21.12 were done at the landing site, at the edge of the continuous ejecta (edge of bright area) and at the rim of Bonneville. Compare this image with the thermal inertia data shown in Figure 21.19.

The above discussion shows a good correspondence between materials at the landing sites, their physical and mechanical properties, and their thermophysical properties derived from orbit. The five landing sites sample two of the thermal inertia and albedo units (units B and C) that account for most of the surfaces on Mars that are likely to be safe and trafficable. Four of the landing sites (VL1, VL2, MPF, and *Spirit*) are in terrains with moderate-to-high thermal inertia and intermediate-to-high albedo. The bulk thermal inertia of these sites appears dominated by their fine-component thermal inertia rather than by their rock abundance. The MPF site, with the highest overall thermal inertia, also has the highest fine-component thermal inertia due to the preponderance of pebble-rich, cloddy, blocky, and indurated soils. The bulk thermal inertia of VL1 and *Spirit* are lower due to the greater amounts of low-inertia drift deposits, and VL2 is lower still due to extensive areas covered by thin drift deposits and the lower thermal inertia of its cloddy soils (compared to the higher thermal inertia blocky soils at VL1 and *Spirit*). The bulk thermal inertia at the *Opportunity* site has very little rocky fraction and is dominated by cohesionless and uncemented (or very poorly cemented) sand and granule ripples, likely with some dust beneath the granules.

The influence of dust and drift deposits at the landing sites (and their impact on thermal inertia) can also be related to the albedo of the sites (Table 21.2). The site with the highest albedo, VL2, also has the greatest area (~40%) covered by drift deposits (Moore and Keller, 1990), followed by VL1 with 18%–30% of the surface covered by drifts (Moore and Keller, 1990). Dustier areas, such as the rim of Bonneville

crater at Gusev crater (Figure 21.20), have high albedo (~0.30) in surface measurements from Pancam (Bell *et al.*, 2004a) that is comparable to the orbital TES-derived albedo of 0.26 (and its corresponding low fine-component inertia). Areas in dust-devil tracks in Gusev crater that have been "swept" cleaner of dust have much lower albedo (~0.20 from Pancam [Bell *et al.*, 2004a] and 0.19 from TES) and higher fine-component thermal inertia (Golombek *et al.*, 2005). The MPF landing site has relatively little dust, and its albedo is comparable to the less dusty areas of Gusev crater. The *Opportunity* rover in Meridiani Planum was the first to land in a low-albedo region of Mars (~0.12 from both TES and Pancam of the plains [Bell *et al.*, 2004b]) and the site is essentially dust-free, with the plains surface dominated by dark, basaltic sand (although several brighter, dustier wind streaks have been identified with higher albedo).

Finally, rock abundances derived from orbit essentially match those determined from rock counts at the surface (Table 21.2). This is somewhat surprising given the large differences in scale. Orbital IRTM-derived values are averaged over $1^\circ \times 1^\circ$ pixels (~60 km or 3600 km^2; Christensen, 1986) and TES values are averaged over 8 pixels per degree (Nowicki and Christensen, 2007). In contrast, surface measurements of rocks cover only tens to several hundred square meters (Moore and Keller, 1990, 1991; Golombek *et al.*, 2003b, 2005, 2006a). IRTM-estimated rock abundances (Christensen, 1986) are 18%, 17%, 16%, 8%, and ~3% at the MPF, VL2, VL1, *Spirit*, and *Opportunity* sites, respectively. TES rock abundances are 13±4%, 12±4%, and 11±4% at VL2, MPF, and *Spirit*, respectively. These estimates compare favorably with surface measurements of 19%, 16%, 16%, 7% (average), and ~3% (Moore and Keller, 1990, 1991; Golombek *et al.*, 2003b, 2005, 2006a), respectively, at the MPF, VL2, VL1, *Spirit*, and *Opportunity* sites. Substantial variability in rock abundance has been observed at Gusev crater (5%–30%) and these variations correlate well with differences in bulk thermal inertia determined from the surface and from orbit. Taken together, the landing sites characterize most of the range in rock abundance on Mars as determined from orbit (1%–30%; Christensen, 1986; Nowicki and Christensen, 2007).

21.6 RADAR DATA: SURFACE SLOPES, SMALL-SCALE ROUGHNESS, AND DIELECTRIC CONSTANT

Radar remote sensing actively probes targets of interest at discrete frequencies using circularly polarized waves in the range of 400–8500 MHz for Mars. The response of a target is the coherent sum of many individual electromagnetic interactions in which the relationship among radar wavelength λ and dimensions and orientations of surface structures is important. For gently rolling terrain, where undulations occur over horizontal scales of tens to hundreds of λ (or more), the surface behaves as though it were covered with mirrors, each tilted at the local mean slope. The echo is dispersed, but is generally in the direction predicted for a perfectly smooth sphere; rougher surfaces will spread the echo into a larger solid angle than smoother surfaces. The strength of these "quasi-specular" echoes is proportional to the Fresnel reflectivity of the surface material. For surfaces that are rough on scales of the wavelength (e.g., a'a lavas), the electromagnetic interactions are more complicated; however, empirically derived expressions can still be used to model the amplitude, angular distribution, and polarization of such "diffuse" echoes. The challenge at Mars is to invert radar measurements to infer large-and small-scale roughness and dielectric constant using the models and comparisons with terrestrial analogs.

21.6.1 Radar scattering

Specific radar cross section σ^0 describes the echo power from a unit surface in terms of viewing geometry, roughness, reflectivity, and polarization. For radar observations with a co-located (monostatic) transmitter and receiver illuminating the surface at an angle θ from the local normal, the specific cross section is

$$\sigma^0 = \sigma^0_{\mathrm{Q}} + \sigma^0_{\mathrm{D}} = \left(\frac{\rho_0\, C}{2}\right)\left(\cos^4\theta + C\sin^2\theta\right)^{-3/2} + A\cos^n\theta. \tag{21.1}$$

The first term represents the quasi-specular reflection from gently rolling terrain. The expression was derived by Hagfors (1964) and has become a de facto standard for radar interpretation; ρ_0 is the Fresnel power reflection coefficient and the RMS surface slope ζ is tied to the Hagfors shape parameter through $C = \zeta^{-2}$, when ζ is expressed in radians. The second term describes the diffuse echo from small-scale structure such as rocks, sharp edges, cracks, voids, and inhomogeneities either on or within the surface. Typical values for the exponent are $1 < n < 2$. The subscripts "SC" and "OC" can be added to σ^0, A, and n to indicate whether the echo has the same sense of circular polarization as the transmitted wave or the opposite sense. Electromagnetic theory predicts no SC quasi-specular echo, so σ^0_{Q} (the Hagfors expression) appears only in the OC version of Equation (21.1), where it is typically dominant for $\theta < 15^\circ - 30^\circ$. When the transmitter and receiver are separated, as has been the case for some spacecraft studies, additional dependencies are required. For more background, see Evans and Hagfors (1968), Simpson *et al.* (1992), and references therein.

Interpreting radar data is not straightforward. A reduced σ^0_{Q} component can be caused by greater RMS roughness, a decrease in ρ_0, or a reduction in the fraction of illuminated surface that behaves quasi-specularly. A decrease in ρ_0 may result from reduced density of the surface material, a change in composition, or blanketing by a thin veneer of soil or dust which can mask the dielectric constant of denser material if the veneer is more than a few tenths of a wavelength thick. Sometimes the circular polarization ratio of the diffuse echo components is useful in understanding the wavelength-scale structure:

$$\mu_C = \frac{C_{SC}}{C_{OC}}, \tag{21.2}$$

where $C_{SC} = A_{SC}/(n_{SC}+1)$ and $C_{OC} = A_{OC}/(n_{OC}+1)$. The relationships among parameter values, physical properties of the surface, and λ have been debated for years. Recent advances in describing surfaces with self-similar statistical properties show promise (Franceschetti *et al.*, 1999; Sultan-Salem and Tyler, 2006).

21.6.2 Radar and topographic data

The radar data discussed here include both published and unpublished results. Most of the quasi-specular measurements at landing sites (which are infrequent) are from older Earth-based experiments and are documented in the literature. Newer data include results from the Goldstone Solar System Radar (GSSR) at $\lambda = 3.5$ cm. Some of these have been averaged over regions on Mars that have been photogeologically mapped and appear to be similar to the existing landing sites; these average results are provided for context. Other data collected using Goldstone and the Very Large Array (G-VLA; Butler, 1994) have been processed to characterize the diffuse component of the scattering function at the landing sites. The spatial resolution over which these measurements apply is variable. It is important to remember that although the radar resolution is on the order of tens to hundreds of kilometers, the structures responsible for the scattering typically have dimensions in the range λ–100λ (where $\lambda = 3.5$–13 cm), and that there will be considerable averaging over the resolution elements.

We also present data from spacecraft instruments, partly to constrain the issue of scale. MOLA on MGS measured range from the spacecraft to the surface approximately every 300 m along a ground track. These data were used to determine bidirectional and adirectional kilometer scale slopes at the MER landing sites (Anderson *et al.*, 2003; Golombek *et al.*, 2003a). In addition, under the assumption of self-affine statistics for height deviations, 100 m slopes in the landing site regions were determined via extrapolation (Anderson *et al.*, 2003). Statistical robustness of the extrapolation process (Campbell *et al.*, 2003) can be achieved by binning all MOLA tracks in a 12–15 km pixel on Mars. Separately, MOLA pulse widths are a measure of the height variance within the laser shot footprint, which is ~75 m in size (Neumann *et al.*, 2003). Pulse widths can be corrected for regional slope effects based on differences among the measurements at 300 m spacing. An equivalent slope can be determined by dividing the corrected pulse width by the spot size to obtain a lower limit for the decameter slopes within the spot. We also include 5 m adirectional slopes derived from MOC (Malin and Edgett, 2001) stereo images (Golombek *et al.*, 2003a; Kirk *et al.*, 2003).

21.6.3 Viking Lander 1 site: Chryse Planitia

In preparation for the descent of VL1, near real-time radar analysis was integrated with the study of the first images from orbit and previous knowledge of the surface (Masursky and Crabill, 1976a). Through an unusual coincidence, Earth-based observations of Chryse Planitia were possible during the weeks leading up to the landing, and data were collected by both the GSSR at $\lambda = 3.5$ cm and Arecibo Observatory at $\lambda = 12.6$ cm. The new measurements confirmed surprisingly high values of RMS surface slope ($\zeta \sim 6^\circ$) derived from earlier, less sophisticated, measurements. When the Viking orbital images also suggested a much rougher surface than had been inferred from Mariner 9 images, the landing target was relocated at least twice (Tyler *et al.*, 1976). Using new data collected in 1978, Simpson and Tyler (1980) reported $\zeta = 4^\circ$–5°, confirming the high values seen prior to the Viking landing.

The radar properties at VL1 are strongly influenced by the rock population. Whereas the analyses performed before the landing were based almost entirely on quasi-specular scattering functions, the high rock population (Figure 21.7) meant that adjustments for the diffuse component should have been included. Table 21.3 summarizes the results from all GSSR quasi-specular and G-VLA measurements for all landing sites; parameters for both the quasi-specular and diffuse terms are included where the quasi-specular parameters are averages from apparently similar geologic surfaces.

Table 21.4 lists quasi-specular parameters derived from measurements at the landing sites themselves; the RMS

Table 21.3. *Regional Mars radar properties near landing sites*

		Goldstone radar ($\lambda = 3.5$ cm) results								
	Geologic unit	Quasi-specular (average over unit)		Diffuse scattering (~60 km resolution)						
Landing site		ρ_0	ζ (°)	A_{SC}	n_{SC}	C_{SC}	A_{OC}	n_{OC}	C_{OC}	μ_C
Viking Lander 1 (VL1)	Hchp	0.04 ± 0.03	4.7 ± 1.8	0.062	1.76	0.022	0.078	1.12	0.037	0.60
Viking Lander 2 (VL2)	Hvk	N/A	N/A	0.041	1.03	0.020	0.161	1.14	0.075	0.27
Pathfinder (MPF)	Hch	0.04 ± 0.02	4.7 ± 1.6	0.038	1.20	0.017	0.085	1.17	0.039	0.43
Gusev crater	Hch	0.04 ± 0.02	4.7 ± 1.6	0.082	1.78	0.029	0.149	2.07	0.029	0.61
Meridiani Planum	Npl2	0.05 ± 0.03	3.2 ± 1.1	0.028	1.18	0.013	0.064	1.47	0.026	0.50

Source: Diffuse scattering portion from Haldemann and Butler (2006). Geologic units from Scott and Tanaka (1986) and Greeley and Guest (1987).

Table 21.4. *Mars landing site local quasi-specular radar results and slopes at three scales*

Landing site	Radar ($\lambda = 3.6$ cm)		Radar ($\lambda = 12.6$ cm)		MOLA			MOC stereo
	ρ_0	Hagfors RMS slope, ζ (°)	ρ_0	Hagfors RMS slope, ζ (°)	1.2 km slope[a,b] bidirectional (°); adirectional (°)	Pulse width raw (m)[a,c]; slope equivalent (°); [slope corrected] (m)[c]	100 m slope from self-affine extrapolation[a] (°)	5 m adirectional slope[b] (°)
Viking (VL1)			0.20 ± 0.05[d]	6.0 ± 0.5[d] 3.5–5.5[e]	0.26 ± 0.96 0.33 ± 0.95	$2.1 \pm 3.7; \geq 1.6$ [1.7 ± 2.9]	1.3	
Viking (VL2)					0.29 ± 0.29 0.28 ± 0.21	$1.1 \pm 0.4; \geq 0.8$ [1.1 ± 0.4]	0.7	
Pathfinder (MPF)	0.05 ± 0.01[f]	4.7 ± 1.6[f]	0.16 ± 0.03[d]	$\leq 8.0 \pm 0.5$[d]	0.25 ± 0.66 0.30 ± 0.51	$2.0 \pm 3.6; \geq 1.5$ [2.0 ± 4.1]	1.4	4.9
Gusev crater	0.05 ± 0.02[g]	1.4 ± 0.2[g]	0.02 ± 0.01[h]	1.7 ± 0.2[h]	0.20 ± 0.44 0.19 ± 0.29	$1.5 \pm 1.3; \geq 1.1$ [1.1 ± 1.0]	1.1	4.1–16.9
Meridiani Planum	0.06 ± 0.02[i]	0.9 ± 0.2[i]			0.15 ± 0.18 0.24 ± 0.47	$0.8 \pm 0.9; \geq 0.6$ [0.8 ± 0.8]	0.8	1.7–4.0

[a] Slope values at 100 m for 12 km pixels that contain each site (Anderson *et al.*, 2003). Slope at 1.2 km also reported in Golombek *et al.* (2003a).
[b] From Kirk *et al.* (2003) as reported in Golombek *et al.* (2003a).
[c] Raw pulse width and pulse width corrected for slope (Slope Corrected) from Neumann *et al.* (2003). Equivalent slope determined by dividing the corrected pulse width (in meters) by the spot size (75 m) as lower limit for the decameter slopes within the spot. The pulse-width slope at 75 m length scale should be similar to or slightly greater than the extrapolated MOLA interspot slope if roughness is increasing at shorter length-scales.
[d] From Harmon (1997).
[e] from Tyler *et al.* (1976) and Simpson *et al.* (1978).
[f] Average of Hagfors model fits from three 1995 delay-Doppler tracks that cover the site.
[g] Interferometric delay-Doppler measurements made in 2003.
[h] Data described by Downs *et al.* [1975], although Gusev is not mentioned explicitly.
[i] Average of Hagfors model fits from two 2001 delay-Doppler tracks that cover the site.

Table 21.5. *Landing site SC specific radar cross section*[a]

Landing site	Incidence angle	σ^0_{SC}
Viking 1 (VL1)	29°	0.0316 ± 0.0024
	36°	0.0191 ± 0.0015
Viking 2 (VL2)	47°	0.0130 ± 0.0035
	51°	0.0141 ± 0.0057
	54°	0.0184 ± 0.0024
	61°	0.0115 ± 0.0018
Pathfinder (MPF)	34°	0.0144 ± 0.0015
	42°	0.0208 ± 0.0024

[a] Arecibo data ($\lambda = 12.6$ cm) from Harmon (1997); resolution is $3° \times 3°$.

slopes ($3.5° < \zeta < 6.5°$) should apply on horizontal scales of 1–100λ, or 3.5–12.6 m. The MOLA pulse-width data listed in Table 21.4 are consistent with the values for ζ at VL1. The pulse-width relief of 2 m over the MOLA spot size of ~75 m implies that slopes within the pulse spot are = 1.6°.

Table 21.5 contains specific SC cross sections measured at Arecibo during the 1990 and 1992/3 oppositions (Harmon, 1997). The VL1 $\lambda = 12.6$ cm cross sections are lower than their 3.5 cm counterparts, evaluated at the same angles, which is consistent with the notion that diffuse scattering is controlled by wavelength scale roughness and that, for the same rock distribution, the surface should appear smoother at longer wavelengths.

Models of diffuse scattering due to rocks set σ^0_D proportional to the surface rock coverage. Calvin *et al.* (1988) modeled isotropic scattering from a population of either flat rock exposures or of rocks exposed above the surface. The Calvin *et al.* (1988) total cross sections were reasonable, but the variation with incidence angle and the relative polarization behavior was not reproduced. Baron *et al.* (1998) used Finite Difference Time Domain (FDTD) numerical scattering modeling with a real rock shape scaled to the VL1 rock size distribution, including both buried and partly buried rocks in addition to surface rocks. They synthesized the cross section rock by rock from the actual rock size distribution observed at VL1, making reasonable assumptions about the buried rock population, and obtained agreement for the angular and polarization dependencies of the VL1 site's radar properties. A notable disagreement is a peak from surface rock backscatter around $\theta = 70°$, which is not observed in the G-VLA data. Baron *et al.* (1998) found that *buried* rock scatterers could explain about one-third of the VL1 site backscatter at $\theta = 30°$ and about one-fifth at $\theta = 60°$. For VL1 the surface rock areal coverage is 16%, of which 4.5% is due to outcrops (Moore and Keller, 1990).

The FDTD scattering model by Baron *et al.* (1998) also reproduced the $\sigma^0_{SC}(\theta) \sim 0.6\sigma^0_{OC}(\theta)$ behavior that is observed at the VL1 site, and over most of Mars (e.g., Moore and Thompson, 1991). Indeed, average Mars values of the G-VLA total cross section can be ratioed to produce the global circular polarization ratio

$$\mu_C = \frac{C_{SC}}{C_{OC}} = \frac{0.024}{0.039} = 0.61 \quad (21.3)$$

which is exactly the value found at VL1 (Table 21.3), suggesting that the decimeter-scale surface roughness, and general geomorphic character, of VL1 is common on the planet.

Earth-based observations of the quasi-specular reflectivity have been used to infer the regolith dielectric constant. Downs *et al.* (1973) estimated a global average $\rho_0 = 0.06 - 0.08$ at $\lambda = 12.6$ cm, consistent with a density around 1500 kg m^{-3}. Where there are no $\lambda = 3.5$ cm data directly over a landing site, our approach has been to report the average σ^0_Q model parameters for all data for the same photogeologic unit (e.g., VL1; Unit Hchp [Scott and Tanaka, 1986]). As listed in Table 21.3, at VL1 ($\lambda = 3.5$ cm) the reflectivity is $\rho_0 = 0.04 \pm 0.03$, where the mean value translates to a dielectric constant $\varepsilon \sim 2.3$. At $\lambda = 12.6$ cm Harmon (1997) obtained the much higher $\rho_0 = 0.20 \pm 0.05$ (Table 21.4), and noted generally that "Chryse's quasi-specular reflectivity is strongly wavelength-dependent (being higher at the longer wavelength), suggesting a rapid density increase within the top decimeter of regolith."

The VL1 dielectric constant $\varepsilon = 3.3 \pm 0.7$ from orbiter-to-lander bistatic observations at $\lambda = 12.6$ cm (Tang *et al.*, 1977) is consistent with the 16% rock coverage (including 4% flat bedrock), where rocks and powdered rocks have dielectric constants of 6 and 2.5, respectively. This dielectric constant suggests a density of the surface of 1600 kg m^{-3}, which is consistent with estimated densities of blocky soil and drift at the VL1 site (Moore and Jakosky, 1989).

21.6.4 Viking Lander 2 site: Utopia Planitia

Because of its relatively high northern latitude, VL2 is outside the range of Earth-based radar systems for quasi-specular studies, and so no values for ρ_0 or ζ are shown in Table 21.3. The MOLA landing site pulse widths (Table 21.4) indicate that VL2 is smoother than VL1 at decameter and hectometer scales, which is confirmed by the lander images (Figures 21.7 and 21.8). A pair of dual-frequency Mars Express bistatic experiments were conducted near VL2 in late 2005 and returned the unexpected result that the dielectric constant is larger at $\lambda = 3.6$ cm ($\varepsilon_x = 3.2–3.6$) than at 13 cm ($\varepsilon_s = 2.3–2.4$) (Simpson *et al.*, 2006). The bistatic radar dielectric constants are derived from echo power ratios and do not depend on any assumed scattering function; these results are consistent with the conclusion in the paragraph immediately above if one more constraint is added: the denser, more perched population must be concentrated in a surface "crust" having an average thickness of no more than 1–2 cm. This configuration is also implied by the deflated appearance of the landing site (Arvidson *et al.*, 1979; Christensen and Moore, 1992), the perched rock population (Garvin *et al.*, 1981), and modeling of thermophysical results (Putzig and Mellon, 2007) discussed in Section 5.2 and in Chapter 18.

Deviations of μ_C from the planetary average value ($\mu_C = 0.61$) imply a different diffuse scattering process, or a

different diffuse scattering population. This appears to be the case at the VL2 site, where $\mu_C = 0.27$ at $\lambda = 3.5$ cm. The average shape and angularity of a rock population should affect μ_C; purely spherical scatterers do not depolarize and have $\mu_C = 0$ while elliptical scatterers, depending on their axial ratio and orientation with respect to the radar wave, can approach $\mu_C = 1$. Garvin *et al.* (1981) noted that the population at VL2 (relative to VL1) has more cobble-sized members, fewer wind-fluted members, and more angular rocks (even though the total rock abundance is about the same [Moore and Keller, 1990, 1991]). Although there were few rocks smaller than 1 cm at either site, the number of small rocks (diameter $D > 1$ cm) was higher at VL1 while the number of large rocks was higher at VL2 (the distribution crossover is at $D \sim 9.5$ cm). Finally, Garvin *et al.* (1981) and Golombek *et al.* (2003b) observed that VL2 had more rocks perched on the surface (particularly the larger rocks), in agreement with the Baron *et al.* (1998) modeling that showed that the backscatter from "perched" rocks is stronger than from partially or deeply buried rocks.

In terms of the data, VL2 $\lambda = 12.6$ cm observations show an increase in σ^0_{SC} over the range $45^\circ < \theta < 55^\circ$ (Table 21.5) which cannot be modeled by functions of the form $A\cos^n\theta$ unless the exponent is negative. There is no comparable trend at either site at $\lambda = 3.5$ cm, though the VL2 diffuse exponent $n_{SC} = 1.03$ is the smallest shown in Table 21.3. The modeling by Baron *et al.* (1998) does show a peak in scattering by *surface* rocks near $\theta_i = 70^\circ$. This is also consistent with a denser, more spherical, and more "perched" rock population in the area contributing to the VL2 radar echo. Happily, the diameter and height data for the rock populations (Moore and Keller, 1990, 1991) indicate that large rocks are higher at VL2 than VL1 (Golombek and Rapp, 1997).

21.6.5 Mars Pathfinder landing site: Ares Vallis, Chryse Planitia

The MPF landing site is very similar in its radar properties to the VL1 site, especially regarding its quasi-specular behavior. Regionally, Ares Vallis has a Hagfors RMS slope of $4.8 \pm 1.1^\circ$ when observed using a range-Doppler radar and an RMS slope of $6.4 \pm 0.6^\circ$ when observed using a radar without modulation (Haldemann *et al.*, 1997), both at $\lambda = 3.5$ cm. At the landing site itself, $\zeta = 4.7 \pm 1.6^\circ$ at $\lambda = 3.5$ cm (Haldemann *et al.*, 1997) and $\zeta = 8.0^\circ$ at $\lambda = 12.6$ cm (Harmon, 1997). Harmon (1997) pointed out that, in general, "quasi-specular roughness across Chryse is considerably higher than the Martian average and shows strong spatial variation." In particular, he noted a correlation of increased meter-scale roughness at the distal ends of outflow channels in Chryse Planitia. The MPF landing site (Figure 21.9) roughness similarity with VL1 also holds for the hectometer-length scales as determined from MOLA pulse widths and by the self-affine extrapolation of MOLA topography to 100 m length-scale slopes (Table 21.4), both of which are consistent with MOC stereo results (Kirk *et al.*, 2003). Slopes at the 1 km length scale from MOLA are generally similar at VL1 and MPF and also, perhaps surprisingly given the visual impression of the horizon, at VL2 (Table 21.4).

The presence of near-surface layers at the MPF site (Moore *et al.*, 1999) and of well-cemented soil (Scooby Doo) may be responsible for the region's strong dependence of the quasi-specular reflectivity on wavelength. As is the case at VL1, ρ_0 is much larger at 12.6 cm than at 3.5 cm. Christensen and Moore (1992) have pointed out that quasi-specular reflectivity may include a scattering contribution from the near-subsurface. The value $\rho_0 = 0.20$ suggests a dielectric constant $\varepsilon \sim 7$, or a density like that of rock, which is consistent with the abundance of indurated soil deposits at the Pathfinder site (see Section 4.9.2 and Figure 21.15).

MPF's diffuse scattering properties are also very similar to those of VL1. Harmon (1997) observed that Chryse diffuse scattering shows "modest enhancements", which he associated with Maja and Kasei Valles; however, he concurred that the similarity of MPF and VL1 diffuse cross sections (Table 21.3) indicates similar rock coverages (MPF rock coverage is 19% versus 16% for VL1).

21.6.6 *Spirit* Landing site: Gusev crater

Regional quasi-specular GSSR radar data for the Gusev crater site are associated with the Hch geologic unit (Table 21.3), described as older channel material of the plateau and high plains assemblage by Greeley and Guest (1987). The quasi-specular ρ_0 and ζ for Gusev are almost identical to the values for VL1 and MPF, suggesting a surface similar in its regional 35 cm to 3.5 m roughness and bulk dielectric properties. However, in the $\lambda = 12.6$ cm data from GSSR (Table 21.4), the Gusev site exhibits lower roughness in the 1.2 m–12 m length-scale range than the other Mars landing sites considered so far. Delay-Doppler interferometry data acquired at $\lambda = 3.5$ cm in 2003 prior to *Spirit*'s landing confirmed a smooth surface: $\zeta = 1.6^\circ$ at the rover location. The view on the ground (Figure 21.10) is consistent; there are fewer swales than at the Viking sites or MPF. The lower values of radar slopes are also consistent with lower hectometer (and, coincidentally, kilometer) slopes from analysis of MOLA data (Table 21.4).

Quasi-specular properties that are distinct in Gusev are the lower reflectivities at both 3.5 and 12.6 cm (Downs *et al.*, 1973, 1975). The shoulder of the quasi-specular peak is fit in this case to determine the Hagfors model parameters that are listed in Table 21.3. The lack of a strong wavelength dependence in scattering at Gusev suggests a surface and subsurface homogeneity at the decimetric scale, consistent with the lack of obvious subsurface structure in 10 cm deep trenches dug with *Spirit*'s wheels (Arvidson *et al.*, 2004a).

Gusev's diffuse scattering cross section is generally like VL1 (Table 21.3). The landscape at decimeter scales resembles the VL1 view, although with fewer rocks (Figure 21.10). The fact that a surface at Gusev, with fewer rocks, is producing $\mu_C \sim 0.6$ suggests that volume scattering is occurring at Gusev. The diffuse scattering behavior at high-incidence angles at Gusev is also consistent with this model: multiple surface scattering at VL1 from its higher rock population

raises the diffuse cross section at grazing incidence angles. This appears consistent with the observation by Golombek *et al*. (2006a) that the Gusev plains away from fresh crater rims are dominantly covered with pebbles rather than large blocks.

21.6.7 *Opportunity* landing site: Meridiani Planum

Meridiani Planum is unusually smooth and there are almost no rocks (Figure 21.11). However, the regional radar properties and the parameter values for both the diffuse and quasi-specular models at $\lambda = 3.5$ cm are reminiscent of the properties of the Pathfinder site (Table 21.1), which has similarities to VL1 and Gusev. The most distinctive radar properties of the *Opportunity* landing site are its quasi-specular cross section and low-RMS slope at $\lambda = 3.5$ cm (Table 21.4; Larsen *et al*., 2002). Values for the four delay-Doppler cells that contained *Opportunity*'s landing site were $\rho_0 = 0.06 \pm 0.02$ and $\zeta = 0.9 \pm 0.2^\circ$. The average reflectivity along track for the 100 km length of the original MER landing ellipse was $\rho_0 = 0.08 \pm 0.01$. Prior to discovery of the hematite spherules in Meridiani, Larsen (2003) proposed a radar scattering model that included the TES hematite abundance to explain the slightly (for Mars) elevated reflectivities, especially east of the MER landing ellipse. The MOLA pulse width and self-affine slopes are very close to ζ as well as the MOC-derived slopes (Kirk *et al*., 2003), suggesting that there is little roughness added as one changes scales from hundreds of meters to tens of centimeters. Slopes at the kilometer scale are also very low (Table 21.4). In general, RMS slope versus baseline distributions derived from MOC stereogrammetry and photoclinometry (Kirk *et al*., 2003) are consistent with RMS slopes at kilometer scale from MOLA, 100 m scale from MOLA pulse spread and extrapolation, and at the meter scale from radar RMS slope at all of the landing sites.

21.7 SUMMARY AND CONCLUSIONS

The investigations of the surfaces and materials at the five successful Mars landing sites provide the "ground truth" for remote-sensing observations of the surface. Understanding the relationship between orbital remote-sensing data and the surface is essential for safely landing spacecraft and for correctly interpreting the surfaces and kinds of materials globally present on Mars. These surfaces are dominated by the regolith of rock and soils that make up the Martian surface layer, which has resulted from the geologic materials at the surface and their interaction with the atmosphere through time via various alteration (weathering) and eolian (wind-driven) processes. Because the selection of a landing site is a mission critical decision, enormous effort has been put into certifying that the surface and atmosphere are within specifications of the entry, descent, and landing system, and therefore safe for landers and trafficable for rovers. These landing site selection efforts and the assessment of predictions after landing form the basis for much of our knowledge about how surface materials investigated by the landers and rovers relate to their remote-sensing signatures.

The five landing sites that constitute the "ground truth" for orbital remote-sensing data on Mars were all selected primarily on the basis of safety considerations, in which surface characteristics appeared to match the engineering constraints based on the designed entry, descent and landing system, with scientific desires being subsidiary. Site selection efforts for the 5 landings varied according to the remote-sensing data available, but all depended on (1) elevation, which is important to provide enough atmosphere for aeroshell entry and parachute descent; (2) latitude, to insure adequate solar insolation for solar-powered landers and rovers; (3) low surface slopes, for lander stability; (4) few large rocks to impinge on the lander during touchdown or to abrade or puncture airbags; and (5) a radar reflective and load-bearing surface that is not dominated by fine-grained dust that could coat solar panels, cover materials of interest to study, or not support a lander or rover. Remote-sensing data used to evaluate the safety and scientific potential of landing sites include visible, near-infrared, and thermal images at a variety of resolutions, altimetry data, thermophysical data (including bulk thermal inertia, fine-component thermal inertia, and rock abundance), albedo, and Earth-based and spacecraft bistatic radar data.

All landing sites that have been investigated on Mars are composed of rocks, outcrops, eolian bedforms, and soils, many of which have been cemented to varying degrees. Investigations by lander and rover instruments allow the derivation of physical and mechanical properties as well as their thermal inertia, which can be related to orbital thermophysical properties. Rocks are common at all of the landing sites except Meridiani, and typically appear as float. At most sites, they are distinct dark, angular to sub-rounded clasts that range in size from several meters diameter down to small pebbles that are a centimeter or less in diameter. Outcrop (or bedrock) has been observed at three of the landing sites. The cumulative fractional area covered by rocks varies from about 7% to 20% at VL1, VL2, MPF, and different portions of the cratered plains investigated by *Spirit*. The size-frequency distributions of rocks measured at the landing sites all show a characteristic exponential decrease in fractional area covered by larger rocks (in accord with fracture and fragmentation theory), when cumulative fractional area is plotted against diameter. These rocks appear as dense volcanic rocks ($\sim$2800 kg m^{-3}) and have an effective thermal inertia of about 2500 J m^{-2} K^{-1} s$^{-1/2}$. Clastic rocks in the Columbia Hills and layered sulfate evaporites at Meridiani have lower thermal inertia and likely lower density based on their RAT-grind energy, Mini-TES measurements, and susceptibility to erosion.

Soils that have been studied at the five landing sites can be distinguished by their mechanical properties, which are generally similar to moderately dense soils on Earth. Crusty and cloddy soils are distinguished by their weak cohesion (1–4 kPa) and moderate angles of internal friction (30°–40°), likely due to mild cementation. Blocky and indurated soils have higher cohesion (3–10 kPa) and moderate friction angles (25°–33°). The bulk densities inferred from their friction

angles are 1100–1600 $kg\,m^{-3}$ and 1200–2000 $kg\,m^{-3}$, and thermal inertia estimates from their bulk densities, particle sizes, and cohesions are 200–326 $J\,m^{-2}\,K^{-1}\,s^{-1/2}$ and 368–410 $J\,m^{-2}\,K^{-1}\,s^{-1/2}$ for crusty to cloddy and blocky-indurated soils, respectively. Eolian deposits at the landing sites include drift, sand dunes, ripples, and wind tails. Drift material is weak, porous, high albedo, very fine-grained dust (3–4 μm) that has settled out of the atmosphere. It has very low-bearing strength, small angles of internal friction (15°–21°), very low bulk densities (1000–1300 $kg\,m^{-3}$), and very low thermal inertias (40–125 $J\,m^{-2}\,K^{-1}\,s^{-1/2}$). Sand dunes and other sandy eolian bedforms are dominantly fine sand (160 μm), with mechanical properties (friction angle 30°), densities (1100–1300 $kg\,m^{-3}$), and thermal inertia (200 $J\,m^{-2}\,K^{-1}\,s^{-1/2}$) consistent with values expected for wind-sorted cohesionless sand.

Soils and rocks observed at the landing sites and their relative abundances can be related to their orbital (generally kilometer scale) signatures in thermal inertia and albedo data. Successful landers have sampled two of the three units of combined thermal inertia and albedo that cover most of Mars. Moderate-to-high thermal inertia and low-albedo regions are relatively dust-free and composed of dark eolian sand and/or rock (*Opportunity*). Moderate-to-high thermal inertia and intermediate-to-high albedo regions are dominated by crusty, cloddy, and blocky soil units that have been referred to as duricrust, with some dust and various abundances of rocks (VL1, VL2, *Spirit*, and MPF, which has higher thermal inertia). Along with variations in their rock abundances, they sample the majority of likely safe surfaces that are available for landing spacecraft on Mars (the third combination of thermal inertia and albedo is likely dominated by potentially meter-thick deposits of bright red atmospheric dust that may be neither load-bearing nor trafficable). Comparisons of soils and rocks covering the landing sites indicate that the main contributor to the bulk thermal inertia globally is the degree of induration or cementation of the soils or fine component, rather than the rock abundance that generally covers less than one quarter of the surface. At a scale of 100 m, however, orbital thermal images of the Gusev cratered plains show variations in thermal inertia that scale directly with observed variations in rock abundance (with higher rock abundance yielding higher bulk thermal inertia).

The highest thermal inertia landing site, MPF, has the highest fine-component thermal inertia due to the preponderance of pebble-rich, cloddy, blocky, and indurated soils. The bulk thermal inertia of VL1 and *Spirit* are lower due to the greater amounts of low thermal inertia drift deposits, and VL2 is lower still due to extensive areas covered by thin drift deposits and the lower thermal inertia of its cloddy soils (compared to the higher inertia blocky soils at VL1 and *Spirit*). The bulk thermal inertia at *Opportunity* has very little rocky fraction and is dominated by uncemented (or very poorly cemented) sand and granule ripples, with some dust likely beneath the granules. The influence of dust and drift deposits at the landing sites (and their impact on thermal inertia) can also be related to the albedo of the sites. The site with the highest albedo, VL2, also has the greatest area (~40%) covered by drift deposits, followed by VL1 with 18%–30% of the surface covered by drifts. At the *Spirit* site, dusty areas, such as the rim of Bonneville crater, have high albedo, and areas in dust-devil tracks in Gusev crater that have been swept cleaner of dust have lower albedo. The *Opportunity* landing site in Meridiani Planum has the lowest albedo of any landing site and is essentially dust-free. Finally, rock abundance derived from orbital thermal differencing techniques essentially matches that determined from rock counts at the surface and varies from ~3% at Meridiani, to 7% at Gusev, to 16%–19% at VL1, VL2, and MPF.

Radar data have been used to infer surface roughness at the scale of the radar wavelength (diffuse scattering) as well as at 10 to 100 times the radar wavelength (specular). They have been compared favorably with stereogrammetry- and photoclinometry-derived slopes from MOC images and estimates of relief within the returned MOLA pulse over the 75 m laser spot. Radar reflectivity has also been used to estimate the bulk density of the surface materials, which can be used to infer whether the surface is load-bearing and trafficable. The diffuse scattering data measured at wavelength scales at the VL1 and VL2 sites have been successfully modeled using the observed rock populations. Radar reflectivity suggested a bulk density of 1500 $kg\,m^{-3}$, consistent with the blocky soil at VL1, and RMS slopes of 4.5°, which are consistent with relatively high (for the landing sites) MOLA pulse spread and interpolated 100 m slopes. MPF radar results are similar to VL1. The cratered plains at Gusev crater have lower radar-derived RMS slopes than VL1 or MPF, correspondingly lower MOLA pulse spread and interpolated 100 m slopes, and comparable diffuse scattering from the moderately rocky but pebble-rich surface. The low-radar-RMS slope at Meridiani Planum agrees with the low slopes estimated from MOLA altimetry and pulse spread.

The slopes and relief at three length scales important to landing safely (1 km, 100 m, several meters) were also estimated and compared at the 5 landing sites using MOLA altimetry, MOC stereo images and photoclinometry (shape from shading), and radar backscatter methods. Results estimated from these data are in accord with each other and what was found at the surface. Of the 5 landing sites, Meridiani Planum was judged to be the smoothest, flattest location investigated to date at 1 km, 100 m, and several-meter length scales, which is in agreement with the incredibly smooth flat plain traversed by *Opportunity*. On the other extreme, the MPF landing site was expected to be the roughest at all three of these length scales, which agrees with the undulating ridge and trough terrain and the more distant streamlined islands with greater relief visible from the lander. The other 3 landing sites are in between these extremes at the 3 length scales, with Viking 2 and portions of Gusev fairly smooth at the 100 m and 1 km scales, Viking 1 slightly rougher at all 3 length scales, and Viking 2 and portions of Gusev (such as the Columbia Hills) intermediate in roughness at the several-meter length scale. All of these observations are consistent with the relief observed at the surface.

Linking the five landing sites to their remote-sensing signatures suggests that they span many of the important surfaces available for landing present spacecraft designs on Mars. Such surfaces have moderate-to-high thermal inertia with low-to-high albedo (but not low albedo and low thermal inertia) and constitute almost 80% of the planet, suggesting that to first order most of Mars is likely safe for suitably engineered landers. The close correspondence between surface characteristics inferred from orbital remote-sensing data and those found at the landing sites argues that future efforts to select safe landing sites will also be successful. These results also show that basic engineering parameters important for safely landing spacecraft (such as elevation, atmospheric profile, bulk density, rock distribution, and slope) can be adequately constrained using available and targeted remote-sensing data.

REFERENCES

Anderson, F. S., A. F. C. Haldemann, N. T. Bridges, *et al*., Analysis of MOLA data for the Mars Exploration Rover landing sites, *J. Geophys. Res.* **108**(E12), 8084, doi:10.1029/2003JE002125, 2003.

Arvidson, R., E. Guiness, and S. Lee, Differential aeolian redistribution rates on Mars, *Nature* **278**, 533–5, 1979.

Arvidson, R. E., R. C. Anderson, P. Bartlett, *et al*., Localization and physical properties experiments conducted by Spirit at Gusev crater, *Science* **305**, 821–4, doi:10.1126/science.1099922, 2004a.

Arvidson, R. E., R. C. Anderson, P. Bartlett, *et al*., Localization and physical properties experiments conducted by *Opportunity* at Meridiani Planum, *Science* **306**, 1730–3, doi:10.1126/science.1104211, 2004b.

Arvidson, R. E., S. W. Squyres, R. C. Anderson, *et al*., Overview of the Spirit Mars Exploration Rover mission to Gusev crater: landing site to Backstay rock in the Columbia Hills, *J. Geophys. Res.* **111**, E02S01, doi:10.1029/2005JE002499, 2006.

Baker, V. R., M. H. Carr, V. C. Gulick, C. R. Williams, and M. S. Marley, Channels and valley networks. In *Mars* (ed. H. H. Kieffer, B. M. Jakosky, C. W. Snyder, M. S. Matthews), Tucson: University of Arizona Press, pp. 493–522, 1992.

Baron, J. E., R. A. Simpson, G. L. Tyler, H. J. Moore, and J. K. Harmon, Estimation of Mars radar backscatter from measured surface rock populations, *J. Geophys. Res.* **103**, 22695–712, 1998.

Bell III, J. F., S. W. Squyres, R. E. Arvidson, *et al*., Pancam multispectral imaging results from the Spirit rover at Gusev crater, *Science* **305**(5685), 800–6, doi:10.1126/science.1100175, 2004a.

Bell III, J. F., S. W. Squyres, R. E. Arvidson, *et al*., Pancam multispectral imaging results from the *Opportunity* Rover at Meridiani Planum, *Science* **306** (5702), 1703–9, 2004b.

Beyer, R. A., A. S. McEwen, and R. L. Kirk, Meter-scale slopes of candidate MER landing sites from point photoclinometry, *J. Geophys. Res.* **108**(E12), 8085, doi:10.1029/2003JE002120, 2003.

Binder, A. B., R. E. Arvidson, E. A. Guinness, *et al*., The geology of the Viking Lander 1 site, *J. Geophys. Res.* **82**, 4439–51, 1977.

Bridges, N. T., R. Greeley, A. F. C. Haldemann, *et al*., Ventifacts at the Pathfinder landing site, *J. Geophys. Res.* **104**(E4), 8595–615, 1999.

Brown, W. K. and K. H. Wohletz, Derivation of the Weibull distribution based on physical principles and its connection to the Rosin-Rammler and lognormal distributions, *J. Appl. Phys.* **78**, 2758–63, 1995.

Butler, B. J., The 3.5-cm radar investigation of Mars and Mercury: planetological implications, Ph.D. thesis, California Institute of Technology. Pasadena, CA, 28, 1994.

Calvin, W. M., B. M. Jakosky, and P. R. Christensen, A model of diffuse radar scattering from Martian surface rocks, *Icarus* **76**, 513–24, 1988.

Campbell, B. A., R. R. Ghent, and M. Shepard Limits on inference of Mars small-scale topography from MOLA data, *Geophys. Res. Lett.* **30**, CiteID 1116, doi:10.1029/2002GL016550, 2003.

Christensen, P. R., Martian dust mantling and surface composition: interpretation of thermophysical properties, *J. Geophys. Res.* **87**(B12), 9985–98, 1982.

Christensen, P. R., The spatial distribution of rocks on Mars, *Icarus* **68**, 217–38, 1986.

Christensen, P. R. and H. J. Moore, The martian surface layer. In *Mars* (ed. H. H. Kieffer, B. M. Jakosky, C. W. Snyder, and M. S. Matthews), Tucson: University of Arizona Press, pp. 686–727, 1992.

Christensen, P. R. and S. W. Ruff, Formation of the hematite-bearing unit in Meridiani Planum: evidence for deposition in standing water. *J. Geophys. Res.* **109**, E08003, doi:10.1029/2003JE002233, 2004.

Christensen, P. R., D. L. Anderson, S. C. Chase, *et al*., Thermal Emission Spectrometer experiment: Mars Observer mission, *J. Geophys. Res.* **97**(E5), 7719–34, 1992.

Christensen, P. R., J. L. Bandfield, V. E. Hamilton, *et al*., Mars Global Surveyor Thermal Emission Spectrometer experiment: investigation description and surface science results, *J. Geophys. Res.* **106**, 23823–71, 2001.

Christensen, P. R., B. M. Jakosky, H. H. Kieffer, *et al*., The Thermal Emission Imaging System (THEMIS) for the Mars 2001, *Space Sci. Rev.* **110**, 85–130, 2004a.

Christensen, P. R., S. W. Ruff, R. L. Fergason, *et al*., Initial results from the Mini-TES experiment in Gusev crater from the Spirit Rover, *Science* **305** (5685), 837–42, 2004b.

Craddock, R. A., L. S. Crumpler, J. C. Aubele, and J. R. Zimbelman, Geology of the Chryse Planitia and the Viking 1 landing site: implications for the Mars Pathfinder mission, *J. Geophys. Res.* **102**(E2), 4161–83, 1997.

Crumpler, L. S., S. W. Squyres, R. E. Arvidson, *et al*., Mars Exploration Rover geologic traverse by the Spirit rover in the plains of Gusev crater, Mars, *Geology* **33**, 809–12, doi:10.1130/G21673.1, 2005.

Downs, G. S., R. M. Goldstein, R. R. Green, G. A. Morris, and P. E. Reichly, Martian topography and surface properties as seen by radar: the 1971 opposition, *Icarus* **18**, 8–21, 1973.

Downs, G. S., P. E. Reichley, and R. R. Green, Radar measurements of Martian topography and surface properties: the 1971 and 1973 oppositions, *Icarus* **26**, 273–312, 1975.

Evans, J. V. and T. Hagfors, *Radar Astronomy*, New York: McGraw-Hill, 620pp., 1968.

Fergason, R. L., P. R. Christensen, J. F. Bell III, *et al*., Physical properties of the Mars Exploration Rover landing sites as inferred from Mini-TES derived thermal inertia, *J. Geophys. Res.* **111**(E2), E02S21, doi:10.1029/2005JE002583, 2006a.

Fergason, R. L., P. R. Christensen, and H. H. Kieffer, High resolution thermal inertia derived from the Thermal Emission

Imaging System: thermal model and applications, *J. Geophys. Res.* **111**, E12004, doi:10.1029/2006JE002735, 2006b.

Franceschetti, G., A. Iodice, M. Migliaccio, and D. Riccio, Scattering from natural rough surfaces modeled by fractional Brownian motion two-dimensional processes, *IEEE Trans. Antennas and Propagation* **47**, 1405–15, 1999.

Garvin, J. B., P. J. Mouginis-Mark, and J. W. Head, Characterization of rock populations on planetary surfaces: techniques and a preliminary analysis of Mars and Venus, *Moon and Planets* **24**, 355–87, 1981.

Gilvarry, J. J., Fracture of brittle solids: I. Distribution function for fragment size in single fracture (theoretical), *J. Appl. Phys.* **32**, 391–9, 1961.

Gilvarry, J. J. and B. H. Bergstrom, Fracture of brittle solids: II. Distribution function for fragment size in single fracture (experimental), *J. Appl. Phys.* **32**, 400–10, 1961.

Golombek, M. P., The Mars Pathfinder mission, *J. Geophys. Res.* **102**, 3953–65, 1997.

Golombek, M. and D. Rapp, Size-frequency distributions of rocks on Mars and Earth analog sites: implications for future landed missions, *J. Geophys. Res.* **102**, 4117–29, 1997.

Golombek, M. P., R. A. Cook, H. J. Moore, and T. J. Parker, Selection of the Mars Pathfinder landing site, *J. Geophys. Res.* **102**, 3967–88, 1997.

Golombek, M. P. and the Mars Pathfinder science team, Overview of the Mars Pathfinder mission: launch through landing, surface operations, data sets, and science results, *J. Geophys. Res.* **104**, 8523–53, 1999a.

Golombek, M. P., H. J. Moore, A. F. C. Haldemann, T. J. Parker, and J. T. Schofield, Assessment of Mars Pathfinder landing site predictions, *J. Geophys. Res.* **104**, 8585–94, 1999b.

Golombek, M. P., J. A. Grant, T. J. Parker, *et al.*, Selection of the Mars Exploration Rover landing sites, *J. Geophys. Res.*, **108**(E12), 8072, doi:10.1029/2003JE002074, 48pp., 2003a.

Golombek, M. P., A. F. C. Haldemann, N. K. Forsberg-Taylor, *et al.*, Rock size-frequency distributions on Mars and implications for MER landing safety and operations, *J. Geophys. Res.* **108**(E12), 8086, doi:10.1029/2002JE002035, 2003b.

Golombek, M. P., R. E. Arvidson, J. F. Bell III, *et al.*, Assessment of Mars Exploration Rover landing site predictions, *Nature* **436**, doi:10.1038/nature03600, 2005.

Golombek, M. P., L. S. Crumpler, J. A. Grant, *et al.*, Geology of the Gusev cratered plains from the Spirit rover transverse, *J. Geophys. Res.* **111**, E02S07, doi:10.1029/2005JE002503, 2006a.

Golombek, M. P., L. S. Crumpler, J. A. Grant, *et al.*, Erosion rates at the Mars Exploration Rover landing sites and long-term climate change on Mars: *J. Geophys. Res.* **111**, E12S10, doi:10.1029/2006JE002754, 2006b.

Grant, J. A., R. Arvidson, J. F. Bell III, *et al.*, Surficial deposits at Gusev crater along Spirit rover traverses, *Science* **305**, 807–10, 2004.

Grant, J. A., R. Arvidson, L. S. Crumpler, *et al.*, Crater gradation in Gusev crater and Meridiani Planum, Mars, *J. Geophys. Res.* **111**, E02S08, doi:10.1029/2005JE002465, 2006a.

Grant, J. A., S. A. Wilson, S. W. Ruff, M. P. Golombek, and D. L. Koester, The distribution of rocks on the Gusev plains and on Husband Hill, *Geophys. Res. Lett.* **33**, L16202, doi:10.1029/2006GL026964, 2006b.

Greeley, R. and J. E. Guest, Geologic map of the eastern equatorial region of Mars, *USGS Misc. Inv. Map*, I-1802B, 1987.

Greeley, R., M. Kraft, R. Sullivan, *et al.*, Aeolian features and processes at the Mars Pathfinder landing site, *J. Geophys. Res.* **104**, 8573–84, 1999.

Greeley, R., S. W. Squyres, R. E. Arvidson, *et al.*, Wind-related processes detected by the Spirit rover at Gusev crater, Mars, *Science* **305**(5685), 810–13, doi:10.1126/science.1100108, 2004.

Greeley, R., R. E. Arvidson, P. W. Bartlett, *et al.*, Gusev crater: wind-related features and processes observed by the Mars Exploration Rover Spirit, *J. Geophys. Res.* **111**, E02S09, doi:10.1029/2005JE002491, 2006.

Hagfors, T., Backscattering from an undulating surface with applications to radar returns from the Moon, *J. Geophys. Res.* **69**, 3779–84, 1964.

Haldemann, A. F. C. and B. J. Butler, Evaluating the Phoenix region B landing site rock coverage from available radar data, *4th Int. Conf. Mars Polar Sci. Explor.*, Houston: Lunar and Planetary Institute, Abstract #8057 (CD-ROM), 2006.

Haldemann, A. F. C., D. L. Mitchell, R. F. Jurgens, M. A. Slade, and D. O. Muhleman, Mars Pathfinder landing site assessment with Goldstone delay-Doppler and CW radar experiments, *J. Geophys. Res.* **102**, 4097–106, 1997.

Harmon, J. K., A radar study of the Chryse region, Mars, *J. Geophys. Res.* **102**, 4081–96, 1997.

Herkenhoff, K. E., S. W. Squyres, R. Arvidson, *et al.*, Textures of the soils and rocks at Gusev crater from Spirit's Microscopic Imager, *Science* **305**(5685), 824–6, 2004a.

Herkenhoff, K. E., S. W. Squyres, R. Arvidson, *et al.*, Evidence from *Opportunity*'s Microscopic Imager for water on Meridiani Planum, *Science* **306**(5702), 1727–30, 2004b.

Jakosky, B. M. and P. R. Christensen, Global duricrust on Mars: analysis of remote-sensing data, *J. Geophys. Res.* **91**, 3547–59, 1986.

Jakosky, B. M. and M. T. Mellon, High-resolution thermal inertia mapping of Mars: sites of exobiological interest, *J. Geophys. Res.* **106**, 23887–907, 2001.

Jakosky, B. M., B. M. Hynek, S. M. Pelkey, *et al.*, Thermophysical properties of the MER and Beagle II landing site regions on Mars, *J. Geophys. Res.* **111**, E08008, doi:10.1029/2004JE002320, 2006.

Kieffer, H. H., T. Z. Martin, A. R. Peterfreund, *et al.*, Thermal and albedo mapping of Mars during the Viking Primary Mission, *J. Geophys. Res.* **82**, 4249–91, 1977.

Kirk, R., E. Howington-Kraus, B. Redding, *et al.*, High-resolution topomapping of candidate MER landing sites with Mars Orbiter Camera narrow angle images, *J. Geophys. Res.* **108**(E12), 8088, doi:10.1029/2003JE002131, 2003.

Larsen, K. W., Terrestrial quadstatic interferometric radar observations of Mars, Ph.D. thesis, Washington University, St. Louis, 2003.

Larsen, K. W., A. F. Haldemann, R. F. Jurgens, R. E. Arvidson, and M. A. Slade, Radar observations of Mars, 2001 opposition, *Lunar Planet. Sci. XXXIII*, Houston: Lunar and Planetary Institute, Abstract #1800 (CD-ROM), 2002.

Lemmon, M. T., M. J. Wolff, M. D. Smith, *et al.*, Atmospheric imaging results from the Mars Exploration Rovers: Spirit and Opportunity, *Science* **306**, 1753–6, 2004.

Malin, M. C. and K. S. Edgett, Mars Global Surveyor Mars Orbiter Camera: interplanetary cruise through primary mission, *J. Geophys. Res.* **106**, 23429–570, 2001.

Masursky, H. and N. L. Crabill, The Viking landing sites: selection and certification, *Science* **193**, 809–12, 1976a.

Masursky, H. and N. L. Crabill, Search for the Viking 2 landing site, *Science* **194**, 62–8, 1976b.

Masursky, H. and N. L. Crabill, Viking site selection and certification, *NASA SP-429*, 34pp., 1981.

McSween Jr., H. Y., S. L. Murchie, J. Crisp, *et al*., Chemical, multispectral, and textural constraints on the composition and origin of rocks at the Mars Pathfinder landing site, *J. Geophys. Res.* **104**, 8679–715, 1999.

McSween, H. Y., R. E. Arvidson, J. F. Bell III, *et al*., Basaltic rocks analyzed by the Spirit rover in Gusev crater, *Science* **305**, 842–5, 2004.

McSween, H. Y., M. B. Wyatt, R. Gellert, *et al*., Characterization and petrologic interpretation of olivine-rich basalts at Gusev crater, Mars, *J. Geophys. Res.* **111**, E02S10, doi:10.1029/2005JE002477, 2006.

Mellon, M. T., B. M. Jakosky, H. H. Kieffer, and P. R. Christensen, High-resolution thermal inertia mapping from the Mars Global Surveyor Thermal Emission Spectrometer, *Icarus* **148**, 437–55, 2000.

Moersch, J. E., L. Crumpler, R. Arvidson, *et al*., Comparison of orbital infrared observations and surface measurements by the Mars Exploration Rover Spirit at Gusev crater, *Lunar Planet. Sci. Conf. XXXVI*, Houston: Lunar and Planetary Institute, Abstract #2020 (CD-ROM), 2005.

Moore, H. J. and B. M. Jakosky, Viking landing sites, remote-sensing observations, and physical properties of martian surface materials, *Icarus* **81**, 164–84, 1989.

Moore, H. J. and J. M. Keller, Surface-material maps of Viking landing sites on Mars. Reports of Planetary Geology and Geophysics Program – 1989, *NASA Tech. Memo*., **4210**, 533–5 (Abstract), 1990.

Moore, H. J. and J. M. Keller, Surface-material maps of Viking landing sites on Mars. Reports of Planetary Geology and Geophysics Program – 1990, *NASA Tech. Memo*., **4300**, 160–2 (Abstract), 1991.

Moore, H. J. and T. W. Thompson, A radar-echo model for Mars, *Proc. Lunar Planet. Sci. Conf. XXI*, 457–72, 1991.

Moore, H. J., R. E. Hutton, G. D. Clow, and C. R. Spitzer, Physical properties of the surface materials of the Viking landing sites on Mars, *USGS Prof. Paper*, **1389**, 222pp., 2 plates. 1987.

Moore, H. J., D. Bickler, J. Crisp, *et al*., Soil-like deposits observed by Sojourner, the Pathfinder rover, *J. Geophys. Res.* **104**, 8729–46, 1999.

Mutch, T. A., R. E. Arvidson, A. B. Binder, E. A. Guinness, and E. C. Morris, The geology of the Viking Lander 2 site, *J. Geophys. Res.* **82**, 4452–67, 1977.

Neumann, G. A., J. B. Abshire, O. Aharonson, *et al*., Mars Orbiter Laser Altimeter pulse width measurements and footprint scale roughness, *Geophys. Res. Lett.* **30**, 1561–5, 2003.

Nowicki, S. A. and P. R. Christensen, Rock abundance on Mars from the Thermal Emission Spectrometer, *J. Geophys. Res.* **112**, EO5007, doi:10.1029/2006JE002798, 2007.

Palluconi, F. D. and H. H. Kieffer, Thermal inertia mapping from 60°S to 60°N, *Icarus* **45**, 415–26, 1981.

Pelkey, S. M., B. M. Jakosky, and M. T. Mellon, Thermal inertia of crater-related wind streaks on Mars, *J. Geophys. Res.* **106**, 23909–20, 2001.

Pleskot, L. K. and E. D. Miner, Time variability of Martian bolometric albedo, *Icarus* **45**, 179–201, 1981.

Pollack, J. B., D. S. Colburn, F. M. Flasar, Properties and effects of dust particles suspended in the martian atmosphere, *J. Geophys. Res.* **84**(B6), 2929–45, 1979.

Presley, M. A. and P. R. Christensen, Thermal conductivity measurements of particulate materials. 2. Results, *J. Geophys. Res.* **102**, 6551–66, 1997.

Putzig, N. E. and M. T. Mellon, Apparent thermal inertia and the surface heterogeneity of Mars, *Icarus* **191**, 68–94, 2007.

Putzig, N. E., M. T. Mellon, R. E. Arvidson, and K. A. Kretke, Global thermal inertia and surface properties of Mars from the MGS mapping mission, *Icarus* **173**, 325–41, 2005.

Rosin, P. and E. Rammler, The laws governing the fineness of powdered coal, *J. Inst. Fuel* **7**, 29–36, 1933.

Ruff, S. W. and P. R. Christensen, Bright and dark regions on Mars: particle size and mineralogical characteristics based on Thermal Emission Spectrometer data, *J. Geophys. Res.* **107** (E12), 5127, doi:10.1029/2001JE001580, 2002.

Scott, D. H. and K. L. Tanaka, Geologic map of the western equatorial region of Mars, *USGS Map*, I–1802–A, 1986.

Simpson, R. A. and G. L. Tyler, Radar measurements of heterogeneous small-scale surface texture on Mars Chryse, *J. Geophys. Res.* **85**, 6610–14, 1980.

Simpson, R. A., G. L. Tyler, and D. B. Campbell, Arecibo radar observations of Mars surface characteristics in the Northern Hemisphere, *Icarus* **36**, 153–73, 1978.

Simpson, R. A., J. K. Harmon, S. H. Zisk, T. W. Thompson, and D. O. Muhleman, Radar determination of Mars surface properties. In *Mars* (ed. H. H. Kieffer, B. M. Jakosky, C. W. Snyder, and M. S. Matthews), Tucson: University of Arizona Press, pp. 652–85, 1992.

Simpson, R. A., G. L. Tyler, M. Pätzold, and B. Häusler, Mars Express bistatic radar observations in Northern Mars plains with possible application to PHOENIX landing site characterization. *Lunar Planet. Sci.* XXXVII, Houston: Lunar and Planetary Institute, Abstract #1862, 2006.

Smith, D. E. and M. T. Zuber, The relationship between MOLA northern hemisphere topography and the 6.1-Mbar atmospheric pressure surface of Mars, *Geophys. Res. Lett.* **25**, 4397–400, 1998.

Smith, D. E., M. J. Zuber, H. V. Frey, *et al*., Mars Orbiter Laser Altimeter (MOLA): experiment summary after the first year of global mapping of Mars, *J. Geophys. Res.* **106**, 23689–722, 2001.

Soderblom, L., R. C. Anderson, R. E. Arvidson, *et al*., Soils of Eagle crater and Meridiani Planum at the Opportunity Rover landing site, *Science* **306**(5702), 1723–6, 2004.

Soffen, G. A., The Viking project, *J. Geophys. Res.* **82**, 3959–70, 1977.

Soffen, G. A. and A. T. Young, The Viking missions to Mars, *Icarus* **16**, 1–16, 1972.

Squyres, S. W., R. E. Arvidson, E. T. Baumgartner, *et al*., Athena Mars rover science investigation, *J. Geophys. Res.* **108** (E12), 8062, doi:10.1029/2003JE002121, 2003.

Squyres, S. W., R. E. Arvidson, J. F. Bell III, *et al*., The Spirit Rover's Athena science investigation at Gusev crater, Mars, *Science* **305**(5685), 794–9, doi:10.1126/science.1100194, 2004a.

Squyres, S. W., R. E. Arvidson, J. F. Bell III, *et al*., The Opportunity Rover's Athena science investigation at Meridiani Planum, Mars, *Science* **306**(5702), 1698–703, doi:10.1126/science.1106171, 2004b.

Squyres, S. W., J. P. Grotzinger, R. E. Arvidson, *et al*., In-Situ evidence for an ancient aqueous environment on Mars, *Science* **306**, 1709–14, 2004c.

Squyres, S. W., R. E. Arvidson, D. L. Blaney, *et al*., Rocks of the Columbia Hills, *J. Geophys. Res.* **111**, E02S11, doi:10.1029/2005JE002562, 2006.

Sullivan, R., D. Bandfield, J. F. Bell III, *et al*., Aeolian processes at the Mars Exploration Rover Meridiani Planum landing site, *Nature* **436**, 58–61, doi:10.1038/nature03641, July 7, 2005.

Sultan-Salem, A. K. and G. L. Tyler, Generalized fractal-based laws for scattering from planetary surfaces: a unifying scale-explicit paradigm, *J. Geophys. Res.* **111**(E06), doi:10.1029/2005JE002540, 2006.

Tanaka, K. L., J. A. Skinner Jr., T. M. Hare, T. Joyal, and A. Wenker, Resurfacing history of the northern plains of Mars based on geologic mapping of Mars Global Surveyor data, *J. Geophys. Res.* **108**(E4), 8043, doi:10.1029/2002JE001908, 2003.

Tanaka, K. L., J. A. Skinner Jr., and T. M. Hare, Geologic map of the northern plains of Mars, *USGS Sci. Inv. Map*, SIM 2888, 2005.

Tang, C. H., T. I. S. Boak III, and M. D. Grossi, Bistatic radar measurements of electrical properties of the Martian surface, *J. Geophys. Res.* **82**, 4305–15, 1977.

Tomasko, M. G., L. R. Doose, M. Lemmon, P. H. Smith, and E. Wegryn, Properties of dust in the Martian atmosphere from the Imager for Mars Pathfinder, *J. Geophys. Res.* **104**, 8987–9007, 1999.

Toon, O. B., J. B. Pollack, and C. Sagan, Physical properties of the particles comprising the Martian dust storm of 1971–1972, *Icarus* **3**, 633–96, 1977.

Tyler, G. L., D. B. Campbell, G. S. Downs, R. R. Green, and H. J. Moore, Radar characteristics of Viking 1 landing sites, *Science* **193**, 812–815, 1976.

Wang, A., L. A. Haskins, S. W. Squyres, *et al.*, Sulfate deposition in the subsurface regolith of Gusev crater, Mars, *J. Geophys. Res.* **111**, E02S17, doi:10.1029/2005JE002513, 2006.

Ward, J. G., R. E. Arvidson, and M. Golombek, The size-frequency and areal distribution of rock clasts at the Spirit landing site, Gusev crater, Mars, *Geophys. Res. Lett.* **32**, L11203, doi:10.1029/2005GL022705, 2005.

Wohletz, K. H., M. F. Sheridan, and W. K. Brown, Particle size distributions and the sequential fragmentation/transport theory applied to volcanic ash, *J. Geophys. Res.* **94**, 15703–21, 1989.

Yen, A. S., R. Gellert, C. Schröder, *et al.*, An integrated view of the chemistry and mineralogy of Martian soils, *Nature* **436**, 49–54, doi:10.1038/nature03637, 2005.

Zeitler, W. and J. Oberst, The Mars Pathfinder landing site and the Viking control point network, *J. Geophys. Res.* **104**, 8935–41, 1999.

PART V

SYNTHESIS

22

Implications of observed primary lithologies

G. J. TAYLOR, S. M. McLENNAN, H. Y. McSWEEN JR.,
M. B. WYATT, AND R. C. F. LENTZ

ABSTRACT

Data from Martian meteorites, orbital remote-sensing instruments, and *in situ* measurements at robotic landing sites reveal that Mars has a heterogeneous surface composition. We use these data to infer the compositional and mineralogical nature of Martian igneous rocks. Basaltic rocks dominate, but highly mafic magmas also formed, producing cumulate rocks inside lava flows. Cumulate rocks also formed in intrusions. Evolved, silicic rocks occur, but are not abundant. The diversity of igneous rocks indicates several distinctive source regions in the Martian mantle. These sources probably formed early in Martian history as the result of crystallization in a magma ocean followed by overturn of an unstable cumulate pile. Shergottites alone represent at least two distinct mantle sources (assuming no crustal assimilation), with mixing between them, but could represent several distinct sources on the basis of initial Sr-isotopic compositions. The nakhlites may represent a somewhat complementary source, but there is clearly an additional source with subchondritic Ba/La. Surface Types 1 and 2 are probably composed of multiple types of igneous rock, possibly mixed with altered materials, and on average are different in trace element (K, Th) and Fe abundances. They may be derived from distinct mantle source regions. The crust appears to have been constructed by basaltic magmatism, some associated with primary differentiation (probably a magma ocean), the rest formed by partial melting during mantle overturn and other dynamic processes. A small amount of partial melting of the crust driven by intrusion of basaltic magma may have formed the rare silicic rocks observed. Water was delivered from the mantle to the surface as magmas exsolved their complement of volatiles. The bulk composition of Mars, specifically K/Th and total oxidized iron, is distinctly different from that of the Earth. This argues that the feeding zones during planetary accretion were relatively narrow, precluding widespread mixing throughout the inner solar system.

22.1 INTRODUCTION

The Martian crust is voluminous, comprising >4 vol.% of the planet (Earth's crust comprises <1 vol.% of the planet). It was constructed by igneous processes and modified by hydrothermal alteration, weathering, and sedimentary processes. The rocky products of this complicated history contain the record of the early differentiation of Mars, the evolution of magma compositions (hence mantle source region compositions) through time, the nature of interactions among the atmosphere, hydrosphere, and lithosphere, and possibly the history of microbial life. In this chapter we focus on the nature and evolution of igneous rocks on Mars.

Magmatic activity built the crusts of all differentiated bodies in the Solar System. There are several interrelated, first-order issues about Martian magmatism. The composition of the oldest crust contains a record of the primary differentiation of Mars, which, isotopic data on Martian meteorites indicate, occurred very early in the planet's history. Whether primary differentiation of Mars developed through a magma ocean or by serial magmatism, much of the crust was constructed by igneous activity following the primary differentiation event, and mostly during the Noachian. The nature of the primary magmas and the igneous rocks they produced involved many factors: mantle composition and dynamics, degrees of partial melting, depths (pressures) of melting, oxygen fugacity, and water abundance. Once magmas were produced, they could have fractionally crystallized, forming cumulates and evolved liquids, or interacted with pre-existing crust, changing their composition, oxidation state, and water contents, which could lead to a large array of potential products. The Earth has produced a vast array of rocks, from ultramafic magmas to extreme differentiates, but basaltic, andesitic, and granitic rocks are dominant. How extreme was igneous differentiation on Mars? We explore these issues here, beginning with an assessment of the chemical and mineralogical composition of igneous rocks on Mars.

22.2 SYNTHESIS OF PRIMARY LITHOLOGIES ON MARS

The information summarized in other chapters in Parts II and III shows clearly that there is a wide range of igneous rocks identifiable on Mars. We summarize the general mineralogical and chemical characteristics of these lithologies in this section and in Table 22.1. Diverse as it is, the observed variety of igneous rocks is almost certainly a fraction of what is present on Mars. Nevertheless, as we show in Section 22.3, it allows us to address significant questions about the

The Martian Surface: Composition, Mineralogy, and Physical Properties, ed. J. F. Bell III. Published by Cambridge University Press.

Table 22.1. *Summary of chemical and mineralogic characteristics of igneous rock types on Mars (total Fe reported as FeO)*

	Locale	Abundance	Major minerals (vol.%)	Age	SiO_2 (wt.%)	FeO (wt.%)	K_2O (wt.%)	K/Th[a]
Basalts								
Shergottites[b]	Unknown	Low	Augite + Pigeonite (43–70) Maskelynite (22–47)	~170–320 Myr	45–52	14–21	0.04–0.4	2700–7200
Olivine basalts								
Olivine-phyric shergottites[b]	Unknown	Unknown	Pigeonite (48–63) Olivine (7–29) Maskelynite (12–26)	~170–580 Myr	45–52	15–24	0.02–0.2	3900–4100
MER[c,d]	Gusev crater Meridiani Planum	Local Landing sites	Plagioclase (40–50) Pyroxene (25–40) Olivine (10–30)	Hesperian–Noachian	45–49	16–19	0.03–0.11	—
TES Surface Type 1[e,f,g] OMEGA[h]	Low albedo, equatorial to mid latitude southern hemisphere	Widespread	Plagioclase (35–50) Pyroxene (25–40) Olivine (10–15)	Hesperian–Noachian	52–55	5–17	0.1–1.8	5000
Andesitic								
Pathfinder[i,j]	Chryse Planitia	Local Landing site	Plagioclase (~50) Pyroxene (~35) Quartz (~10)	Hesperian–Noachian	56–59	13–15	1.1–1.3	—
TES Surface Type 2[f,g]	Low albedo, northern plains and high latitudes	Widespread	Plagioclase (20–50) High-silica phases (30–45) Pyroxene (10–15)	Amazonian–Noachian	57–59	4–11	2–3	4600
Dacitic								
TES[k]	Nili Patera, Syrtis Major	Local, minor	Plagioclase (~35) High-silica phases (~30) Pyroxene (~20)	Hesperian	60–63	—	—	—
Quartzofeldspathic								
TES[l]	Northern Syrtis Major	Local, minor	High-silica Phases (~30) Feldspars (~40) Pyroxene (~10) Quartz (~10)	Hesperian	—	—	—	—
Clinopyroxenite								
Nakhlites[b,m]	Unknown	Low	Augite + Pigeonite (69–85) Olivine (5–20)	~1.3 Gyr	48–51	19–22	0.1–0.3	4500–6000

TES[n]	Nili Fossae, Syrtis Major	Local, minor	—	Hesperian	—	—	—	—
Orthopyroxenite								
ALH 84001[b]	Unknown	Low	Orthopyroxene (97)	~4.5 Gyr	53	17	0.02	4000
TES[n]	Highlands; Eos Chasma	Local, minor	—	Hesperian	—	—	—	—
Dunites								
Chassigny[b]	Unknown	Unknown	Olivine (92) Augite + Pigeonite (5)	~1.3 Gyr	37	27	0.04	5260
TES[n]	Nili Fossae, Syrtis Major	Local, minor	—	Hesperian	—	—	—	—
Trachybasalt-tephrite								
MER[o]	Columbia Hills, Gusev crater	Local Landing site	Plagioclase (56–57) Pyroxene (13–17) Olivine (0–16) Apatite (3–12)	Noachian	44–50	12–19	0.5–1.1	—

[a] Our data compilation from the literature (see caption for Figure 22.5);
[b] Bridges and Warren (2006) and references therein;
[c] Squyres *et al*. (2004a) and references therein;
[d] Squyres *et al*. (2004b) and references therein;
[e] Christensen *et al*. (2000);
[f] Bandfield *et al*. (2000);
[g] McSween *et al*. (2003);
[h] Mustard *et al*. (2005);
[i] McSween *et al*. (1999);
[j] Foley *et al*. (2003);
[k] Christensen *et al*. (2005);
[l] Bandfield *et al*. (2004);
[m] Treiman (2005);
[n] Hamilton *et al*. (2003);
[o] McSween *et al*. (2006).

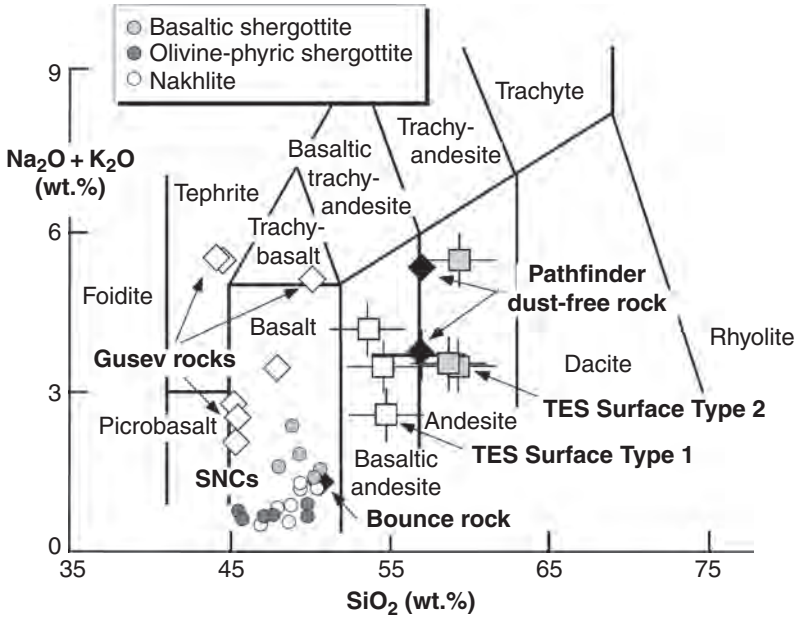

Figure 22.1. Total alkalis versus silica classification diagram for volcanic rocks, showing the compositions of Gusev basalts (McSween *et al.*, 2004), two calibrations of the Mars Pathfinder dust-free rock (Brückner *et al.*, 2003; Foley *et al.*, 2003), basaltic and olivine-phyric shergottites and nakhlites (McSween *et al.*, 2003), and MGS TES-derived chemical compositions for ST1 and ST2 (Bandfield *et al.*, 2000; Hamilton *et al.*, 2001; McSween *et al.*, 2003).

composition of the Martian mantle, the abundance of water in it and how it is transferred to the crust, and the bulk composition of the planet.

In constructing our synthesis of igneous lithologies on Mars we used data from diverse sources: Martian meteorites, orbital observations, and landing site analyses. Martian meteorites provide detailed information about rocks from unknown places on Mars. Orbital thermal-infrared emission measurements provide bulk modal mineral abundances and chemical information of the upper few hundreds of microns. The Thermal Emission Spectrometer (TES) has a spatial resolution of about 3 km and the Thermal Emission Imaging System (THEMIS) a spatial resolution of 100 m, but with fewer measured wavelength bands. Orbital near-infrared reflectance measurements provide mineralogical and chemical information of iron-bearing mineral phases in the upper few tens of microns. The Observatoire pour la Minéralogie, l'Eau, les Glaces, et l'Activité (OMEGA) has a spatial resolution that varies from 300 m to 4.8 km (Bibring *et al.*, 2005). The Mars Odyssey Gamma Ray Spectrometer (GRS) provides elemental concentrations and samples much deeper than do TES, THEMIS, and OMEGA, the upper few tens of centimeters, but with a nominal spatial resolution of 450 km. Data from landed missions are quantitative and have very high-spatial resolution, but represent only a few places on the Martian surface.

The different analytical uncertainties, sampling depths, and spatial resolutions of these measurements make it a challenge to combine them to characterize different igneous rock types. This may lead to some ambiguity in the summary characterizations given in Table 22.1. However, some of these differences, such as sampling depth, may also provide new insight to the vertical distribution of surface mineral phases. The addition of different datasets and development of new integrated models is critical to our understanding the range of igneous composition on Mars.

22.2.1 Basaltic shergottites

The basaltic shergottites (olivine-free volcanic rocks; see Chapter 17) do not appear to be abundant on the surface, and they make up less than half of the shergottite group of Martian meteorites. All are young (<327 Myr), high in FeO, generally low in K, and variable in K/Th. They are composed of two clinopyroxenes (68–75 vol.%) with lesser amounts (20–25 vol.%) of late-stage, interstitial plagioclase (now converted by shock to maskelynite), and variable amounts of minor igneous phases. In spite of their young crystallization ages, their mantle source regions formed 4.5 Ga (Borg *et al.*, 2003; Foley *et al.*, 2005). On a plot of total alkalis versus silica (Figure 22.1), the shergottites plot in the basalt field, but with low alkalis. Initial Sr and Nd isotopic compositions correlate with oxygen fugacity, indicating several distinct magma types.

Near-infrared remote-sensing observations indicate the presence of low- and high-calcium pyroxene basalt on the Martian surface (Mustard and Sunshine, 1995; Mustard *et al.*, 2005). The two-pyroxene composition is best expressed in Syrtis Major, which is also the locality of the TES Surface Type 1 (ST1) basalt spectral endmember (Bandfield *et al.*, 2000). TES data analyses reveal the presence of two pyroxenes (augite and pigeonite), but an overall dominance of plagioclase in bulk modal mineralogy (e.g., McSween *et al.*, 2003). Results from the different wavelength regions are consistent as thermal-infrared data reveal bulk modal abundances, including plagioclase, while near-infrared data are sensitive to iron-bearing phases, which plagioclase is not. TES modeled abundances of pyroxene/plagioclase (0.5–1.2) generally differ from that of the basaltic shergottites (0.9–2.6) (McSween *et al.*, 2003). Furthermore, thermal-infrared remote-sensing observations have not identified any specific localities in which basaltic shergottites occur (Hamilton *et al.*, 2003), so we infer that their exposed abundance is low. Their young ages and

absence in the TES dataset suggest that they occur in young volcanic areas, such as Tharsis, hidden beneath a layer of high-albedo dust.

The Mars Exploration Rover (MER) *Opportunity* may have found a rock similar to the shergottites. It landed in Meridiani Planum, a region selected on the basis of strong mineralogical and geomorphological evidence that the area had been subjected to interactions with water. *Opportunity* focused on outcrops of sedimentary rocks containing appreciable quantities of evaporite minerals and diagenetic hematite concretions (Squyres *et al.*, 2004a). However, it did encounter one rock that may represent a primary crustal sample. Bounce Rock, so named because of its proximity to an airbag bounce mark, is unlike any other rock found at Meridiani (Squyres *et al.*, 2004b). The rock is weak and friable, as demonstrated by its low Rock Abrasion Tool (RAT) grinding energy per unit volume. Microscopic images reveal a fine-grained texture with some features suggesting brecciation (Bell *et al.*, 2004; Herkenhoff *et al.*, 2004). The distinct appearance and composition of Bounce Rock suggest that it is not locally derived. Rays of blocky ejecta from a fresh crater located 75 km to the southwest are observed within 10 km of the site (Christensen *et al.*, 2004). This probably heavily shocked rock may have been excavated from this crater, and thus may represent older plains material interpreted to underlie the Meridiani Formation.

The APXS analysis of Bounce Rock (Zipfel *et al.*, 2004) indicates that its composition is virtually indistinguishable from those of basaltic shergottites (Figure 22.1). The normative mineralogy is dominated by high- and low-calcium pyroxenes, with plagioclase (An_{63}), Fe-Ti-Cr oxides, and apatite. The high abundance of pyroxene is confirmed by its Mössbauer spectrum (Klingelhöfer *et al.*, 2004), which shows only pyroxene. Miniature Thermal Emission Spectrometer (Mini-TES) spectra also indicate that the rock consists primarily of pyroxenes and lesser amounts of plagioclase (Christensen *et al.*, 2004).

22.2.2 Olivine basalts

Basalts with significant amounts of olivine appear to be common on the Martian surface. Although somewhat variable in composition, they occur among Martian meteorites, igneous rocks at the MER *Spirit* (Gusev) landing site, and within the TES ST1 regions. They are all rich in FeO and have typical basaltic concentrations of SiO_2 (Figure 22.1). Olivine basalts in the Martian meteorite collection exhibit a groundmass similar to, although finer grained than, the basaltic shergottites, with cumulus grains of two pyroxenes (51–64 vol.%) with interstitial plagioclase (15–24 vol.%). However, picritic shergottites are also characterized by megacrysts of olivine (7–24 vol.%), and sometimes orthopyroxene (up to 5 vol.%; see Chapter 17).

Visible/near-infrared (Pancam) and thermal emission Mini-TES spectra of ground or brushed rocks at the Gusev crater plains site indicate the presence of olivine and possibly pyroxene (McSween *et al.*, 2004). Mössbauer spectra confirm that the rocks contain olivine, pyroxene, and magnetite. Microscopic images of the RATed rocks show that

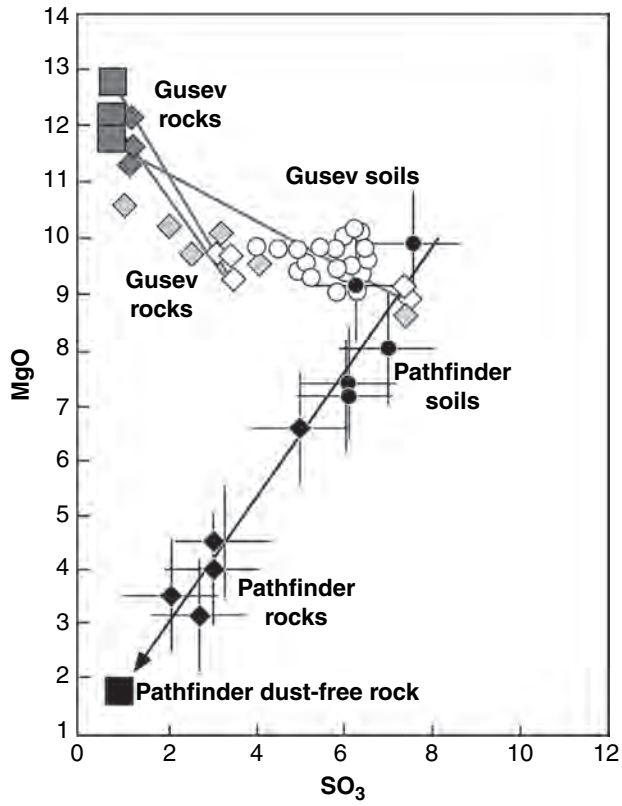

Figure 22.2. MgO versus SO_3 (wt.%) for APXS-analyzed rocks and soils from the Mars Pathfinder site (McSween *et al.*, 1999) and the *Spirit* landing site in Gusev crater (McSween *et al.*, 2004). Extrapolation of the trend of Pathfinder dust-covered rocks to 0.3 wt.% S (0.75% SO_3) gives the composition of the dust-free rock. Gusev rock compositions (large symbols) were determined by extrapolating through the compositions of surface and brushed rocks to 0.75% SO_3.

the rocks have porphyritic textures, with dark, anhedral crystals interpreted to be olivine (McSween *et al.*, 2004, 2005). APXS analyses of rock interiors were determined by extrapolating through surface coating compositions (Figure 22.2) to 0.3 wt.% sulfur, as in Pathfinder rocks (see below). Three analyzed rocks contain ~46 wt.% SiO_2, classifying them as basalts (Figure 22.1). These rocks are picritic (olivine-rich), with high alkali contents (Figure 22.1). A revised APXS calibration of rock compositions was given by Gellert *et al.* (2006). In spite of high Na_2O, K_2O concentrations are low (0.06 wt.%), in the range of olivine-phyric shergottites. Their normative mineralogy consists of olivine, pyroxenes, plagioclase, Fe-Ti-Cr oxides, and apatite (McSween *et al.*, 2005). The olivine (Fo51–55) is relatively iron-rich and the plagioclase (An40–45) is relatively sodic – both similar to the compositions of those phases in Martian meteorites. The high proportion of magnetite and Mössbauer-determined Fe^{3+}/Fe_{Total} (Morris *et al.*, 2004) indicates that these basalts are relatively oxidized.

Soils for both sites are indicated by circles and rocks by diamonds. Only dust-coated rock surfaces were analyzed by Pathfinder. Rock analyses by *Spirit* include dust-coated surfaces (open diamonds), brushed surfaces (light gray diamonds), and RAT-abraded surfaces (dark gray

diamonds). Extrapolation of the trend of Pathfinder dust-coated rocks to 0.3 wt.% S (0.75% SO_3) gives the composition of the dust-free rock (large black square). Gusev rock compositions (large gray squares) were determined by extrapolating through the compositions of brushed and RATed rocks to 0.75% SO_3.

Material comprising TES ST1, found primarily in equatorial regions and the mid latitudes of the southern hemisphere, has been interpreted to be dominated by minimally weathered basalt (Bandfield *et al*., 2000). Spectral deconvolution indicates that ST1 contains olivine, pyroxene, and plagioclase, broadly consistent with olivine-phyric shergottites and Gusev basalts. GRS data (Chapter 5) show that ST1 averages 0.3 wt.% K_2O, substantially more than Gusev basalts or olivine-phyric shergottites. Olivine-phyric shergottites have K/Th in the range 3200–4000, but ST1 averages 5000 (Karunatillake *et al*., 2006), with much of the area up to 6000. The difference between olivine-phyric shergottites and ST1 in K/Th indicates that a variety of magmas make up this category, representing a variety of source regions in the mantle (see Section 22.3.1). This is consistent with observations by Rogers and Christensen (2003, 2007), which show a diversity of basaltic rocks within regions dominated by ST1. Olivine basalts have also been observed in a number of areas, including a large occurrence surrounding the Nili Fossae (Hamilton *et al*., 2003; Hoefen *et al*., 2003). Thus, olivine basalts constitute a diverse, abundant rock type on the Martian surface.

22.2.3 Andesitic rocks

Since the discovery by the TES team of a Surface Type 2 (ST2) spectral endmember on Mars (Bandfield *et al*., 2000), there has been a continuing debate about the petrologic nature of the rocks comprising it. Bandfield *et al*. (2000) proposed that the rocks could be andesites or basaltic andesites, on the basis of the modal mineralogy derived from spectral deconvolutions. This was supported by the high-SiO_2 concentration (62 wt.%) in the calculated Pathfinder soil-free rock. APXS X-ray mode analyses for sulfur in five rocks at the Pathfinder landing site in Ares Vallis showed strong correlations with spectral redness (750/440 nm ratios), with high-sulfur soils defining the red end of this trend (McSween *et al*., 1999). Various oxides in rocks plotted against sulfur defined linear arrays (Figure 22.2), supporting the hypothesis that the rock analyses represented mixtures of rock and adhering dust (Rieder *et al*., 1997). APXS analyses determine the composition of only the outermost surface, generally just a few tens of microns, depending on the element. New APXS calibrations (Brückner *et al*., 2003; Foley *et al*., 2003) confirm these linear trends. Extrapolation of oxide-sulfur regression lines to low sulfur (0.3 wt.%, the sulfur occurring as troilite in shergottites) gives the composition of the dust-free rock (Figure 22.2). This rock has 62 wt.% SiO_2 (McSween *et al*., 1999; Brückner *et al*., 2003), corresponding to its classification as andesite (Figure 22.1). The calculated normative mineralogy consists of feldspars, pyroxenes, and quartz; however, the norm is provisional because no information on iron oxidation state was available.

McSween *et al*. (1999) also note an alternative interpretation for Pathfinder rocks by suggesting that APXS-measured chemical abundances may reflect resistant coatings of siliceous weathering rinds formed by chemical alteration of basalt. The formation of, and likelihood of, sedimentary silica phases existing on Mars is also described by McLennan (2003a). In addition, Foley *et al*. (2003) note that the inferred high-water content from the APXS α-mode may be due to palagonitization of igneous rocks and that some Pathfinder rocks may not be unaltered volcanics. The chemical alteration of basalt and formation of secondary minerals is suggested by Wyatt and McSween (2002) as an alternative interpretation for describing the spectral character of TES ST2. They suggest that the high-silica glass modeled by Bandfield *et al*. (2000) and interpreted as a primary volcanic interstitial phase may also represent secondary amorphous silica coatings. Laboratory work by Michalski *et al*. (2005) support this interpretation. Additional secondary phases such as palagonite (Morris *et al*., 2003) and zeolite (Ruff, 2004) have also been suggested as possible components in ST2 materials.

Karunatillake *et al*. (2006) used GRS data (Chapter 5) to show that there is not a significant difference in SiO_2 concentrations between ST1 and ST2, but that ST2 was richer in K and Th (but have the same K/Th). They concluded that it is most likely that ST2 is a different igneous rock than ST1, but probably not andesitic. The TES and GRS observations are not necessarily in conflict. TES senses the upper few hundred microns while GRS senses the upper few tens of centimeters. It is possible that ST2 rocks are basaltic and have been chemically weathered (Wyatt and McSween 2002; Morris *et al*., 2003; Ruff, 2004; Michalski *et al*., 2005) as an altered or silicic rind could influence both the TES spectra and APXS analyses, indicating higher silica in both, while not affecting the much larger analytical volume sampled by the GRS. This debate will not be settled easily. Nevertheless, it is clear that ST2 is distinctive, no matter how it is classified, and even if weathered, its basaltic protolith was likely different than that of ST1.

22.2.4 Dacitic and granitic rocks

At local scales, there have been reports of even more evolved igneous rocks than andesites. Christensen *et al*. (2005) and Rogers *et al*. (2005) show that there is a thick (80 m) lobate flow inside the Nili Patera caldera (Syrtis Major) with TES spectral characteristics of a dacite (plagioclase, silicic glass rich in K). The smooth outline of its margin is consistent with a silicic composition (Bruno *et al*., 1994). Bandfield *et al*. (2004) used TES data to identify a quartz-bearing lithology in central uplifts of two craters (both 30 km in diameter) on the northern flank of Syrtis Major. Although the dacite and quartz-bearing (granitic) rocks are rare on the surface of Mars, their presence implies either that extensive magmatic fractionation took place, at least locally, or that there was remelting of the basaltic crust to produce evolved liquids.

22.2.5 Clinopyroxenites

The nakhlite group of Martian meteorites (Treiman, 2005) are dominated by clusters of subcalcic augite (68–81 vol.%) and Fe-rich olivine (3–17 vol.%). Interstitial to these cumulus phases is a fine-grained mesostasis of plagioclase laths and other late stage phases (8–21 vol.%). TES data suggest that similar rocks may outcrop in a region of northern Syrtis Major (Harvey and Hamilton, 2005), but the Syrtis occurrence may be much older (>3 Gyr) than the nakhlites (1.3 Gyr). K/Th is 4500–6000 in the nakhlites; the occurrence in Syrtis is too small to allow measurement of K/Th by GRS. The nakhlites are likely to be highly mafic lava flows (Friedman Lentz *et al.*, 1999), but could be near-surface intrusions.

22.2.6 Orthopyroxenites

ALH 84001 is an ancient (4.5 Gyr crystallization age) orthopyroxenite. It has 97 vol.% orthpyroxene, 1 vol.% plagioclase, and 2 vol.% assorted minor minerals. ALH 84001 is clearly a cumulate rock, where the primary phase reached such high proportions by accumulation from the magma by crystal settling. However, its multiple-shock history suggests that it was exposed at the surface for launch by a previous impact (Mittlefehldt, 1993). It presumably hails from the Martian highlands. TES data show that there are also patches of orthopyroxene-rich rocks on the floor of Eos Chasma (Hamilton *et al.*, 2003; Hamilton and Schneider, 2005). Although detected on the valley floor, the unit most likely formed as an intrusive rock, which was later exposed in the valley wall and eventually deposited on the floor by mass wasting. The abundance of orthopyroxene in the original igneous rock is unknown, but could have been greater than the maximum abundance measured in the floor deposits in Eos Chasma, 60 vol.% (Hamilton and Schneider, 2005). ALH 84001 and the Eos Chasma rocks are cumulates from basaltic magma that crystallized only orthopyroxene for at least some period of its crystallization history.

22.2.7 Dunites and other olivine-rich cumulate rocks

There are two Martian meteorites, the chassignites, that are clearly cumulate rocks and their high-olivine contents (90–92 vol.%) indicate that they are dunites (Chapter 17). They also contain 4–5 vol.% clinopyroxene and nearly 2 vol.% plagioclase. The chassignites have the same crystallization (1.3 Gyr) and cosmic ray exposure ages (11 Myr) as the nakhlites, suggesting a relationship between them. TES data show that there may also be olivine-rich outcrops on Mars, but none has been proven to consist of cumulate rocks (Hamilton *et al.*, 2003; Hoefen *et al.*, 2003; Hamilton and Christensen, 2005).

Other, unrelated cumulate rocks are the lherzolitic shergottites, containing olivine, orthopyroxene, and pigeonite. This meteorite group is typified by large poikilitic, low-Ca pyroxene grains (30–65 vol.%) enclosing smaller olivine (21–53 vol.%) and chromite grains, with minor interstitial plagioclase (4–11 vol.%). The large poikilitic grains (i.e., those enclosing smaller, randomly oriented grains of a different phase) of this lithology indicate that the rocks are intrusive, not lava flows. Similarities in mineral chemistry suggest that they may have formed from magmas like those that produced the olivine-phyric shergottites.

22.2.8 Trachybasalts and tephrites

Mini-TES observations in the Columbia Hills of Gusev crater have identified three classes of fine-grained or fragmented, relatively unaltered rocks with distinct thermal emission spectral signatures (Ruff *et al.*, 2006). The type specimens for these rock classes are named Irvine, Backstay, and Wishstone. APXS chemical analyses indicate that these rocks are mildly alkaline basalt, trachybasalt, and tephrite, respectively (McSween *et al.*, 2006). Their mineralogy consists of Na- and K-rich feldspars, low- and high-Ca pyroxenes, ferroan olivine, Fe-Ti (and possibly Cr) oxides, phosphate, and possibly glass (McSween *et al.*, 2006). The compositions of these rocks are distinct from the subalkaline volcanic rocks thought to dominate the Martian surface (Figure 22.2). The textures of Irvine and Backstay are consistent with lavas or possibly dike rocks, whereas Wishstone likely has a pyroclastic origin. McSween *et al.* (2006) infer that the three classes of alkaline volcanic rocks may have formed by fractionation of primitive, oxidized basaltic magma similar to the olivine-rich rocks found in the plains of Gusev crater.

22.2.9 Poorly characterized low-Si rocks

GRS data show that Si is low (<39 wt.% SiO_2) over much of the Tharsis Montes and particularly west of Olympus Mons (see Chapter 5). If silica is not low because of dilution with other elements such as Cl, S, and Mg, then it is possible that the low-silica areas contain low-silica lava flows, perhaps similar to rejuvenation stage Hawaiian lavas (e.g., Clague and Frey, 1982). These regions appear to be covered with dust, masking the primary mineralogy of the young lavas, but low-silica (38–41 wt.% SiO_2) mafic rocks have been described in craters in Amazonis Planitia (Schneider and Hamilton, 2006), slightly to the west (18° N, 170° W) of the anomalously low-silica region.

22.3 DISCUSSION

22.3.1 Distinct mantle reservoirs

Both short-lived (e.g., ^{182}Hf-^{182}W, $t_{1/2}$~9 Myr; ^{146}Sm-^{142}Nd, $t_{1/2}$~103 Myr) and long-lived (e.g., ^{147}Sm-^{143}Nd, ^{87}Rb-^{87}Sr, ^{235,238}U-^{207,206}Pb, ^{176}Lu-^{176}Hf, ^{187}Re-^{187}Os) radiogenic isotope systems in Martian meteorites provide compelling evidence that Mars differentiated into core, mantle, and crust very early in its history, likely within a few tens of million years after accretion (e.g., Chen and Wasserburg, 1986; Jagoutz 1991; Harper *et al.*, 1995; Nyquist *et al.*, 1995, 2001; Blichert-Toft *et al.*, 1999; Brandon *et al.*, 2000;

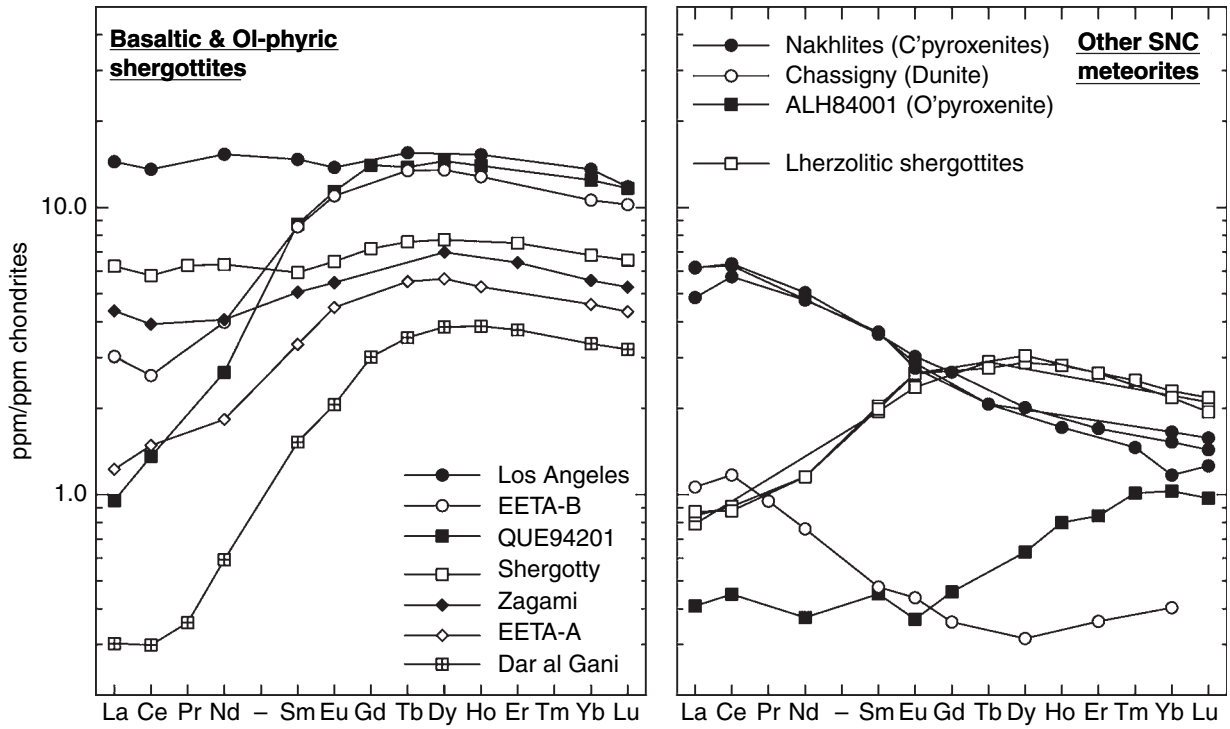

Figure 22.3. REE concentrations in Martian meteorites. Shergottite patterns (left) may reflect two distinct endmember mantle compositions: a depleted one (represented by Dar al Gani at the extreme) and an enriched ("crustal") one represented by Los Angeles and Shergotty. The nakhlites (right) have distinctive, light-enriched REE patterns. Data from references cited in Meyer (2006).

Halliday *et al.*, 2001; Borg *et al.*, 2005; Foley *et al.*, 2005). The core appears to have formed within about 12 Myr of the formation of the Solar System and the nakhlite, shergottite, and possibly ALH 84001 source regions were established within about 25 Myr of the formation of the Solar System (Foley *et al.*, 2005). There is growing experimental and isotopic evidence that during this period of early differentiation, Mars possessed a magma ocean, broadly analogous to that of the Moon's (Borg and Draper, 2003; Elkins-Tanton *et al.*, 2003, 2005), but of unknown dimension and duration. Geophysical modeling of an early Martian magma ocean and lunar analogies predict both formation of an early enriched crust and the likelihood of multiple chemically distinct mantle reservoirs (e.g., Borg and Draper, 2003; Elkins-Tanton *et al.*, 2005). Although some controversy remains about the apparent young crystallization ages of both the 1.3 Ga nakhlite and 0.47–0.16 Ga shergottite meteorites (e.g., Bouvier *et al.*, 2005), it is very likely that mantle-derived magmatism continued sporadically throughout Martian history (Nyquist *et al.*, 2001; Hauck and Phillips, 2002; Kiefer, 2003).

On Earth, the long geological history of mantle differentiation, plate tectonics, and crust–mantle interaction has resulted in a planet with numerous fundamental geochemical and isotopic heterogeneities on all scales: from mantle reservoirs on the scale of mantle convection through to distinct mantle sources on the scale of individual ocean ridge segments and lava flows (e.g., Hofmann, 1997; Klein, 2003). Although the geological and tectonic history of Mars is generally thought to be less complex and the available record is seriously incomplete, there is nevertheless compelling evidence for mantle heterogeneity and multiple geochemical reservoirs within the crust–mantle system.

A simple approach to evaluating planetary scale geochemical reservoirs in the crust–mantle system using trace elements can be adapted from that used for the Earth by Hoffman and co-workers (Hofmann *et al.*, 1986; Hofmann, 1989, 1997; Jochum *et al.*, 1991). In spite of igneous processing (e.g., partial melting, fractional crystallization, assimilation) that can cause significant changes in most trace element ratios, for incompatible lithophile trace elements, there should be a simple mass balance among the various major crust and mantle reservoirs and the primitive mantle composition (Hofmann *et al.*, 1986; Hofmann, 1989). For the refractory lithophile elements, the primitive mantles of the terrestrial planets are generally accepted to have chondritic ratios (Taylor, 2001). For Mars, there is added uncertainty for volatile elements (e.g., K, Rb, Cs) because it is likely that they are enriched in the Martian primitive mantle compared to the Earth (Dreibus and Wänke, 1985; Wänke and Dreibus, 1988; Wänke, 1991; Halliday *et al.*, 2001; Taylor *et al.*, 2006a).

Shergottites source regions

The shergottite meteorites are generally accepted to be young (Nyquist *et al.*, 2001; but see Bouvier *et al.*, 2005 for an alternative view) and exhibit a large range in geochemical and isotopic composition. This is well illustrated in their rare earth element (REE) patterns that range from severely light REE (LREE) depleted with low abundances through to very slightly LREE-enriched with high abundances (Figure 22.3). The variations in REE patterns correlate with a variety of

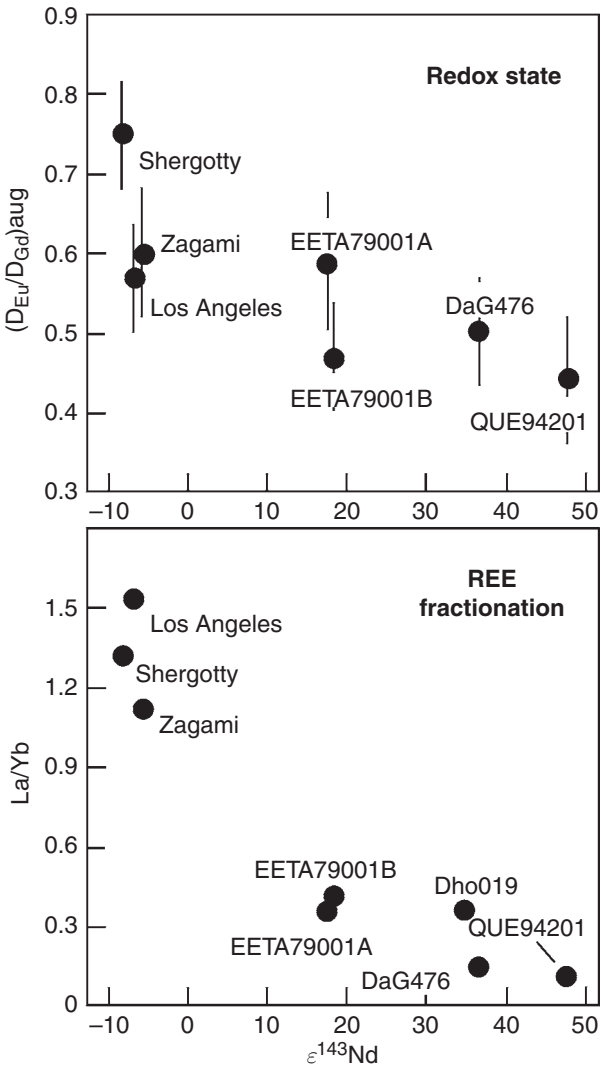

Figure 22.4. Chemical and isotopic correlations among shergottites, arising from incorporation of an enriched crustal or mantle component. Decreasing values of ε^{143}Nd indicate increasing amounts of enrichment. This parameter correlates with magma redox state, indicated by size of the Eu anomaly in pyroxenes (Wadhwa, 2001), and ratio of light to heavy REEs.

isotopic characteristics such as $^{87}Sr/^{86}Sr$ and $^{143}Nd/^{144}Nd$ (e.g., Norman, 1999, 2002) and geochemical features such as ratios among incompatible elements (e.g., McLennan, 2003b) and apparent magmatic oxygen fugacity (e.g., Wadhwa, 2001; Herd *et al.*, 2002). These variations (Figure 22.4) have been interpreted to indicate that the shergottites represent a mixture of two distinctive sources. One source is generally agreed to be an ancient long-term highly LREE-depleted mantle source (Longhi and Pan, 1989; Longhi, 1991). However, the nature of the second source is less well-constrained. Most workers have suggested that the second component is the ancient Martian crust, which is enriched in large-ion lithophile (LIL) elements, that was assimilated to varying degrees during magma ascent and emplacement (e.g., Longhi and Pan, 1989; Longhi, 1991; Norman, 1999; Wadhwa, 2001; McSween, 2002, 2003; McLennan, 2003b). However, suggestions of an early Martian magma ocean have given rise to the possibility that the second component is a minor ancient LIL-enriched late stage mantle-derived liquid, comparable to the sources of lunar KREEP basalts (high in Potassium, Rare Earth Elements, and Phosphorus; e.g., Borg and Draper, 2003; Bridges and Warren, 2006). The crustal assimilation interpretation also fell out of favor because it does not explain the lack of correlation between indices of differentiation (e.g., Mg/Fe) and the concentrations of incompatible trace elements (e.g., Borg and Draper, 2003). The difficulty of distinguishing ancient LIL-enriched mantle components from crustal contamination in mantle-derived igneous rocks has long plagued the study of terrestrial mantle-derived basalts (e.g., McLennan, 1988; Hofmann, 1997) and so this controversy is unlikely to be readily resolved. Both alternatives have important implications for understanding the evolution of Mars.

Trace element data provide interesting insights. Some caution is warranted in interpreting the Martian meteorite data, especially for samples from desert environments (NWA, Dhofar, SaU meteorites), where in some samples terrestrial weathering has affected the distribution of some key trace elements, such as K, U, and Ba (e.g., Barrat *et al.*, 2001; Dreibus *et al.*, 2001). The influence of contamination is generally most striking in samples with low trace element abundances (McLennan, 2003b). In the diagrams below, samples with clear evidence for terrestrial weathering (e.g., Th/U <1) are excluded and other desert meteorites are labeled.

Figure 22.5 plots K/Th versus K abundances for Martian meteorites and selected regions mapped by the Mars Odyssey GRS. The GRS data are generally thought to be broadly representative of the Martian upper crust (Taylor *et al.*, 2006a). The basaltic and olivine-phyric basaltic shergottites appear to form a scattered negative correlation consistent with mixing between two geochemically distinct components (McLennan, 2003b). The depleted (low K) endmember has K/Th ratios of 6000 or more, consistent with the suggestion that Mars is a moderately volatile-enriched planet compared to the Earth (K/Th = 2800 for primitive mantle of Earth). However, the K-enriched endmember appears to have a lower K/Th of about 3000, similar to typical terrestrial values (Taylor and McLennan, 1985). This K/Th value is significantly less than the ratio measured at the Martian surface by GRS, which is essentially uniform at about 5300. Several possibilities arise from these relationships:

1. The enriched component in shergottites is indeed of mantle origin. One implication of this is that ratios among highly incompatible elements may be severely fractionated during mantle differentiation and, depending on the size of the enriched reservoir, the degree of volatile element enrichment in the Martian primitive mantle is less certain.
2. The Martian crust is vertically stratified by igneous processes such that the surface has a much higher K/Th ratio than the crust as a whole. The petrologically evolved continental crust of the Earth is vertically stratified

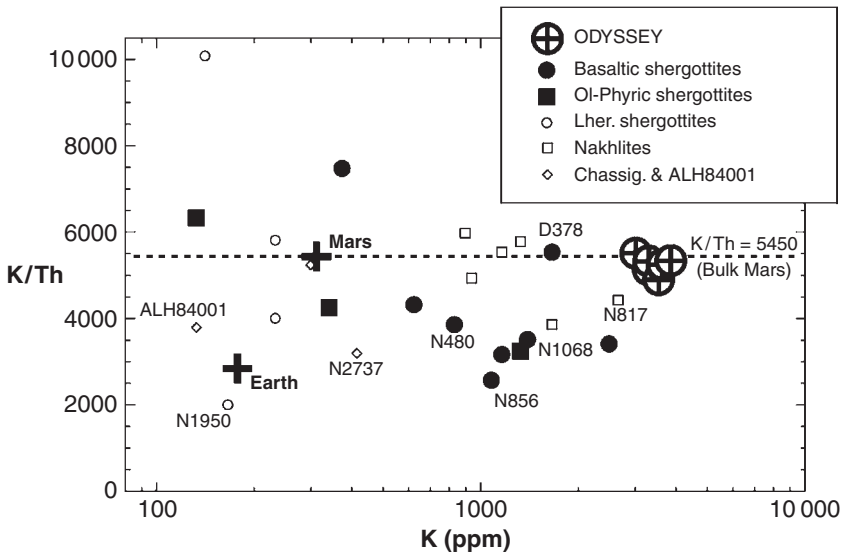

Figure 22.5. Plot of K/Th versus K abundances for Martian meteorites and selected Odyssey GRS regions. Shown for reference are the primitive mantle compositions for Earth (Taylor and McLennan, 1985) and Mars (Halliday *et al*., 2001) and the K/Th ratio of the Martian primitive mantle. Note the olivine-phyric and other basaltic shergottites form a scattered negative correlation and that shergottites with high K abundances have low K/Th ratios. The high-K shergottite end member appears to have a lower K/Th ratio that typical Martian crust reflected in the Odyssey GRS data. Martian data from compilation of Meyer (2006) with recent additions (Beck *et al*., 2006; Day *et al*., 2006) and Odyssey data from Taylor *et al*. (2006a). Martian meteorite samples that have clear evidence for substantial terrestrial weathering have been excluded.

largely due to intracrustal differentiation processes to produce granites (Taylor and McLennan, 1985) but such extreme differentiation is less likely to have occurred in a basaltic crust and in the apparent absence of plate tectonics (Taylor, 1989).

3. The high K/Th ratio of the Martian surface measured by GRS is due to secondary aqueous alteration processes and similarly this ratio is not reflective of the bulk crust. Taylor *et al*. (2006b) explored this possibility and although plausible, a specific mechanism giving rise to a planetary scale change in K/Th ratio of surficial materials has not been identified.

There are significant differences in the ratios among refractory lithophile trace elements Ba, Th, Hf, and REE that provide additional constraints. This can be seen in Figure 22.6, which plots La/Th, Sm/Hf and Ba/La versus incompatible element abundances for the Martian meteorites. For the various classes of shergottites, there are correlations among these ratios consistent with the two-component system described above. However, for essentially all shergottites, La/Th and Sm/Hf ratios are subchondritic and Ba/La ratios are superchondritic. Assuming that Mars has chondritic ratios for these refractory lithophile elements, such relationships suggest that at least one additional major geochemical reservoir is required (low Ba/La). This is discussed in greater detail below.

Nakhlite and chassignite source regions

Treiman (2005) exhaustively reviewed the petrology and geochemistry of the ~1.3 Ga nakhlites and the reader is referred to this publication for details. The nakhlites appear to represent a single suite of cumulate igneous rocks derived from basalts and are possibly cogenetic. The ~1.3 Ga chassignites (Chassigny and NWA 2737) are cumulate dunites and although not identical to each other, may be petrogenetically related (Beck *et al*., 2006). Trace element characteristics of the chassignites are distinct from nakhlites, suggesting that they are not cogenetic, although again they may be broadly related (Nyquist *et al*., 2001). Both nakhlites and chassignites have similar radiogenic isotope characteristics and exposure ages suggesting they were ejected from Mars during the same event.

Nakhlites are enriched in incompatible elements (Figure 22.3), but long-lived radiogenic isotopes (e.g., $^{87}Sr/^{86}Sr$, $^{143}Nd/^{144}Nd$) clearly indicate that they were derived from an ancient moderately LIL-depleted (compared to the highly depleted shergottite end-member) mantle source (see Treiman, 2005, for review). Although the nakhlite mantle source region represents a distinctive geochemical reservoir (e.g., Foley *et al*., 2005), its size and relationship to other mantle reservoirs is less clear. Longhi (1991) noted that high field strength elements (Ta, Nb, Zr, Hf) in Martian meteorites exhibit anomalous distributions and suggest a possible complementary relationship between nakhlites and shergottites, although ^{182}W and ^{142}Nd systematics show that nakhlites and shergottites originated in separate mantle reservoirs (Foley *et al*., 2005). Jones (2003; also see Bridges and Warren, 2006) suggested that the nakhlite source region was representative of the lower mantle whereas the shergottite source region was representative of the upper mantle. Such a model implies that the overall Martian mantle is depleted to a far greater degree than the terrestrial mantle (i.e., Martian upper mantle more depleted than terrestrial MORB source and Martian lower mantle comparably depleted to MORB source) and the voluminous Martian crust is highly enriched in incompatible elements, for which there is some evidence.

The refractory lithophile elements suggest that the mantle may indeed be even more complex than the two-reservoir model of Jones (2003). The La/Th and Sm/Hf ratios of nakhlites are superchondritic and thus could be interpreted to be complementary to the shergottite source regions. On the other hand, all of the Martian meteorites have superchondritic Ba/La ratios suggesting that there is at least one major "missing" reservoir.

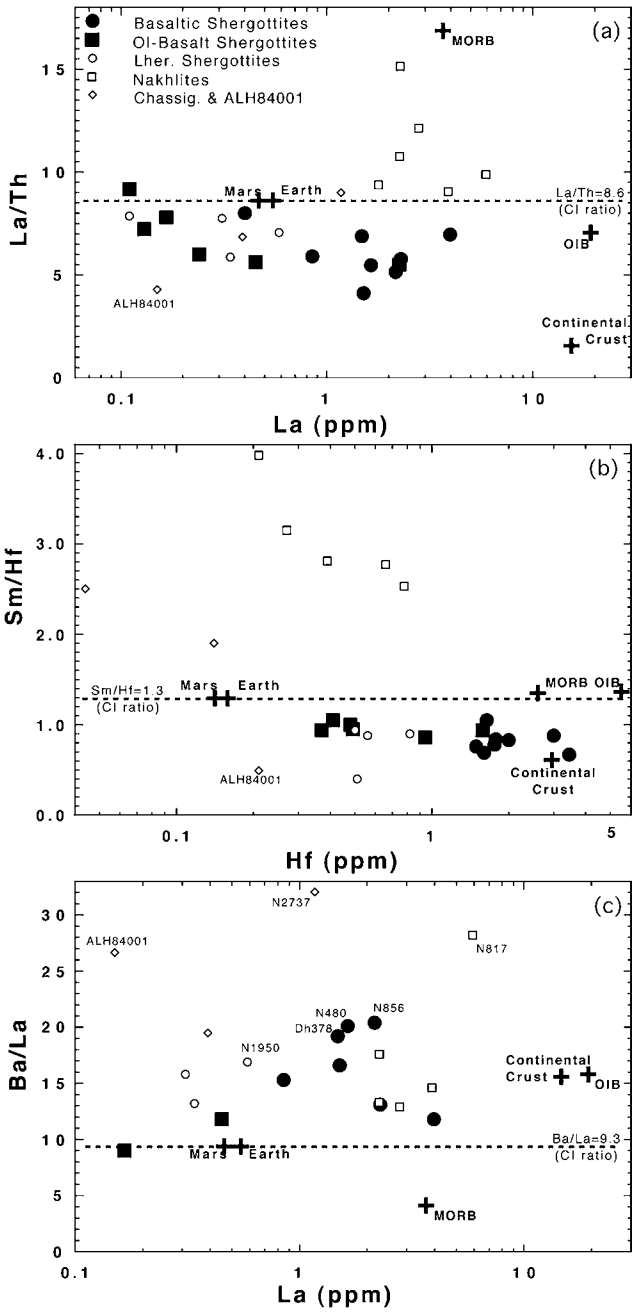

Figure 22.6. Plots of La/Th versus La, Sm/Hf versus Hf, and Ba/La versus La for Martian meteorites. Note that olivine-phyric and other basaltic shergottites form linear trends, consistent with mixing of distinct reservoirs and are all subchondritic with respect to La/Th and Sm/Hf ratios. For La/Th and Sm/Hf, the nakhlites and chassignites are plausible complementary reservoirs. However Ba/La is superchondritic for all Martian meteorites, including the sole sample of Noachian crust ALH 84001, suggesting an additional reservoir. Data sources the same as Figure 22.5 and terrestrial geochemical reservoirs (crust, mid-ocean ridge basalts [MORB], ocean island basalts [OIB]) from Taylor and McLennan (2002).

ALH 84001

The ~4.5 Ga cumulate orthopyroxenite ALH 84001 appears to be the only available remnant of the Noachian crust. Its REE pattern (Figure 22.3) is slightly LREE-depleted with approximately chondritic abundance levels. The current best estimate of its crystallization age comes from an Sm/Nd bulk rock – pyroxene isochron of 4.50 ± 0.13 Ga (Nyquist *et al.*, 1995). The isochron and pyroxene model age ($T_{CHUR} = 4.57 \pm 0.03$ Ga) are consistent with extraction from a near chondritic (possibly slightly depleted) Nd/Sm reservoir. Similarly, the ε^{182}W (0.49 ± 0.33, where $\varepsilon^{182}W = [(^{182}W/^{180}W)_{sample} / (^{182}W/^{180}W)_{standard} - 1] \times 10\,000$) is indistinguishable from the estimated Martian primitive mantle ($\varepsilon^{182}W = 0.34 \pm 0.07$), again consistent with a near-chondritic (possibly slightly elevated) Hf/W reservoir (Foley *et al.*, 2005).

Crustal dichotomy and mantle reservoirs

The infrared spectral characteristics of ST1 are best described by basalt and ST1 lies mostly in the Noachian southern highlands. Surface Type 2 is found primarily in the northern lowlands and its origin is more controversial, as discussed in Section 22.2. Bandfield *et al.* (2000) interpreted ST2 to represent a petrologically evolved "andesitic" composition whereas Wyatt and McSween (2002) and Michalski *et al.* (2005) suggested that a surface veneer of partly altered basalt would also explain the spectral features of ST2.

The regions of distinctive TES surface types are also characterized by differences in surface chemical compositions determined by the Odyssey GRS, notably for iron (Taylor *et al.*, 2006a). Karunatillake *et al.* (2006) examined the GRS data binned specifically to separate regions characterized by ST1 and ST2 and noted that ST2 was enriched in K and Th (but with indistinguishable K/Th) but showed no significant enrichment in Si. From these results, Karunatillake *et al.* (2006) suggested that the results were more consistent with ST2 fundamentally being an igneous signature and thus consistent with derivation from a compositionally distinct mantle source. Taylor *et al.* (2006a) also noted that the northern lowlands on average had about 2%–3% higher FeO_T than the southern highlands (17.6% vs. 20.1%), consistent with distinctive average surface magmatic compositions.

Rogers and Christensen (2003) examined in some detail the geological relationships of ST1 and ST2 and suggested that ST2 was younger and perhaps related to a resurfacing of Noachian terrains in the northern regions of Mars by more evolved magmatic compositions. Such an interpretation is complicated by recent discovery of large circular depressions in the northern plains that likely reflect the presence of large "ghost" impact craters just below the surface (e.g., Frey *et al.*, 1999; Frey, 2006). The northern plains may in fact be as old as or older than the southern highlands but with only a thin veneer of younger material on top. Whether or not these hemispheric-scale differences in TES and GRS compositions reflect differences in magmatic composition and hence mantle sources, differences in surficial processes, or some combination must be considered an outstanding issue.

22.3.2 Magmatic evolution

The Martian crust

The crust of Mars is mostly ancient and was largely in place by about 3.5 Ga (Jacobsen and Yin, 2002). Most workers

consider the crust to be basaltic in character and thus an example of "secondary crust" (Taylor, 1989) formed by partial melting of the planetary interior. On the other hand, if Mars was differentiated by an early magma ocean, there could be remnants of early primary crust preserved. There is also spectral evidence for segments of relatively differentiated crust (Table 22.1). Such features are not areally extensive and are more likely the localized end products of basalt differentiation rather than examples of evolved crust analogous to the Earth's continents.

Recent attempts to constrain the bulk composition of the Martian crust have been provided by McLennan (2001), McSween *et al*. (2003), and Taylor *et al*. (2006a). Four approaches have been adopted and each appears to provide generally similar results. The fine Martian soils are broadly similar in their composition at each landing site (Viking 1 and 2, Pathfinder, *Spirit*, *Opportunity*) and have led to suggestions that they sample the Martian upper crust in a manner comparable to terrestrial sedimentary rocks (Taylor and McLennan, 1985). A second approach has been to reconstruct the composition using the mineralogical distributions determined from orbit by thermal-infrared spectroscopy (McSween *et al*., 2003). Estimates of the density of the crust by modeling the relationship between gravity and topography also constrain crustal composition (McSween *et al*., 2003). Most recently, surface mapping by GRS has provided elemental maps for a number of key elements, including Si, Fe, K, and Th (see Chapter 5).

Each of these approaches lead to a crustal composition that is basically basalt. However, the levels of incompatible elements (K, Th, U) appear to be significantly higher than currently seen in the vast majority of available Martian meteorites. McLennan (2001) suggested an LIL-enriched crust with about 5000 ppm K, 0.9 ppm Th and 0.25 ppm U. Recent GRS mapping of the Martian surface provides more robust estimates and suggests about two-thirds of these values: 3300 ppm K, 0.62 ppm Th, and 0.16 ppm U (for Th/U = 3.8). For a crust on the order of 50–60 km thick (Wieczorek and Zuber, 2004) this implies that the Martian crust contains roughly 50% of the planetary complement of highly incompatible elements (Taylor *et al*., 2006a). For comparison, the concentration of heat-producing elements in the terrestrial crust is <40% of the bulk planetary inventory (McLennan, 2001).

Fractional crystallization

The degree to which Martian basaltic magmas have undergone fractional crystallization is unclear. Most of the surface appears to be composed of olivine-bearing basalts (Table 22.1). Variations in incompatible element concentrations suggest variations in mantle source compositions, the percentage of partial melting, and the extent of fractional crystallization. Some Martian meteorites show that they have undergone fractional crystallization because they contain cumulus phases. The nakhlites (Treiman, 2005), chassignites (Floran *et al*., 1978), lherzolitic shergottites (Harvey *et al*., 1993), and ALH 84001 (Mittlefehldt, 1993) are cumulate rocks, and some basaltic shergottites like QUE 94201 have fractionated liquid compositions (McSween *et al*., 1996). The absence of magnesian olivine phenocrysts in olivine-phyric shergottites suggests that they may have been separated through fractional crystallization (Goodrich, 2003). However, samples of the ancient crust are needed to evaluate the extent of fractional crystallization throughout the crustal system.

If the northern lowlands are composed of andesite (Section 22.2.3), then Mars has experienced a profound fractionation event of global proportions. The FeO/MgO versus SiO_2 compositions of ST2 materials, if they are interpreted as igneous, suggest hydrous melting and fractionation, producing magmas with calc-alkaline affinities (McSween *et al*., 2003). However, there are no areas with very large K/Th that would be indicative of subduction zone magmatism, suggesting that primary calc-alkaline rocks are not abundant on Mars (Taylor *et al*., 2006a; Chapter 5). Wyatt *et al*. (2004) have argued that the geologic context for ST2 materials is more consistent with weathered basalt. It is, therefore, unclear whether ST2 materials are evolved igneous rocks or weathered basaltic rocks.

Spectroscopic searches for quartz, an unambiguous indicator of fractionation, have largely been unrewarded, except for one location (see Section 22.2.4 and Table 22.1). Dacite was identified spectrally at another location (Table 22.1; Christensen *et al*., 2005). These observations suggest that quartzofeldspathic and other evolved rocks do occur, but they are exceedingly rare. An origin by fractional crystallization of basaltic magma is possible, but large volumes of mafic cumulates would be produced by the same source. Such geographically associated cumulates have not been identified. A more likely origin is by partial melting of the basaltic crust (Bandfield *et al*., 2004).

In situ analyses of rocks on the Martian surface only cloud the issue. Rocks at the Mars Pathfinder site have andesitic compositions, but it is unclear whether these rocks are really andesites or have been compromised by silica-rich weathering rinds. Igneous rocks on the Gusev crater plains analyzed by *Spirit* and Bounce Rock in Meridiani Planum analyzed by *Opportunity* are generally basaltic, and weathering rinds on them are clearly visible. The Gusev plains basalts appear to be primitive basalts that have undergone no fractionation en route to the surface (McSween *et al*., 2005), but other volcanic rocks in the Columbia Hills may be related to the plains basalts through fractional crystallization (McSween *et al*., 2006).

Magmatic mixing and assimilation processes

Varying trace element and radiogenic isotope compositions of basaltic shergottites and olivine-phyric shergottites result from mixing different geochemical components (section "Shergottites source regions" and Figures 22.3 and 22.4). One component is depleted in incompatible trace elements and radiogenic isotopes. The other, enriched component has the opposite geochemical signature. Some shergottites like QUE 94201 formed from the depleted mantle source. In other cases, incorporation of varying amounts of the enriched component produced hybrid shergottite magmas

with varying trace element patterns, radiogenic isotopic compositions, and oxidation states. Correlations between some of these geochemical signatures are illustrated in Figure 22.4. The depleted, reduced component is certainly from a mantle source region. The source of the enriched, oxidized component is unclear. It could be the Martian crust, which has been assimilated by mantle-derived magmas to varying degrees (Jones, 1989; Longhi, 1991). Alternatively, the enriched component could reflect a metasomatized (chemically altered by fluids) mantle source (Borg *et al.*, 1997), implying mantle heterogeneity in shergottite source regions, as discussed above.

22.3.3 Water in Martian magmas and mantle

There is abundant geomorphic and geochemical evidence for the interaction of water with the surface, and near subsurface, of Mars throughout its history (e.g., Carr and Wänke, 1992; Bridges and Grady, 2000; Malin and Edgett, 2000; Baker, 2001). However, there is still great uncertainty in the volume of water included in the bulk planet during accretion, residing in the current mantle, or carried to the surface by erupted magmas through time. Understanding the volatile inventory of Mars is essential to understanding how planets form and evolve.

The eruption of volatile-rich magmas is the primary conduit for transporting water and other volatiles from the mantle to the surface and atmosphere. Results from the Odyssey GRS and measurements by landers (Pathfinder, MER) show high levels of volatile elements such as S, Cl, K, and even Br in the soil and rock weathering rinds (e.g., Gellert *et al.*, 2004; Haskin *et al.*, 2005; Chapters 3–5), and GRS indicates several percent of H_2O in equatorial regions and very substantial amounts in polar regions (Chapter 5). These data imply substantial volcanic degassing of volatile-rich magmas through time. The presence at multiple landing sites of vesicular basaltic rocks (e.g., McSween *et al.*, 2004) supports the idea of volatile-bearing magmas. Atmospheric ratios of D/H were measured at five times the terrestrial value (Owen *et al.*, 1988), which has been interpreted as showing the loss of a large proportion of atmospheric water through sputtering by the solar wind and thermal escape of H. This in turn implies a larger volume of water cycling between the near subsurface and atmosphere of ancient Mars that has since disappeared.

The only hand samples of Mars that we have for detailed study are the Martian meteorites, which unfortunately give a limited temporal view of Martian evolution, since all but one are 1.3 Gyr old or younger (see Chapter 17). The rocks themselves are mostly dry (130–350 ppm H_2O; Karlsson *et al.*, 1992), except for water associated with hydrous secondary alteration minerals, which are interpreted as evidence for recent (<200 Ma) subsurface brine interactions (Bridges and Grady, 2000). However, indirect signs of magmatic water in these young meteorites suggest that geologically, recently, there was still water in the Martian mantle, too.

Chassigny and Zagami, in particular, contain magmatic inclusions within olivine that include minerals typically considered hydrous (e.g., kaersutite [Ti-rich amphibole], apatite [Ca-phosphate]). Originally, the presence of these minerals was interpreted as reflecting significant magma water contents at mantle pressures (Floran *et al.*, 1978; McSween and Harvey, 1993). However, when the actual H abundances in kaersutite were measured (Watson *et al.*, 1994) the implied water abundances were lower than expected. Laboratory experiments have since suggested that the kaersutite compositions can be grown under rather dry conditions (e.g., Popp *et al.*, 1995). However, King *et al.* (1999) suggested that the amphiboles might have undergone oxidation and dehydrogenation, which would mask the true crystallization conditions. Despite the ultimate uncertainty of how much water was in the parental source regions of Zagami and Chassigny, there is still the implication that the mantle had some amount of water that was delivered to the surface by these magmas.

Two other approaches have been used to investigate whether the Martian basaltic meteorites came from water-rich magmas: controlled crystallization experiments and light lithophile element distribution patterns. Several attempts have been conducted over the years to reproduce the simultaneous crystallization of two pyroxenes matching the compositions found in Shergotty and Zagami (Stolper and McSween, 1979; McCoy and Lofgren, 1996; McKay *et al.*, 2000). In these nonaqueous experiments, pigeonite crystallizes alone for a long temperature interval before augite joins the liquidus, even under variable pressure and oxidation conditions. Dann *et al.* (2001) had similar results with dry experiments, but then introduced an aqueous component and found that at a moderate pressure (55 MPa) and 1.8 wt.% H_2O, they could reproduce the co-crystallization and compositions of two pyroxenes in Shergotty. However, Jones (2004) and Treiman *et al.* (2006) argue that this water component is not strictly necessary as Stolper and McSween (1979) also produced a good match to the Shergotty pyroxenes under anhydrous conditions, once they added an extra augite component to the assumed parental magma composition.

Several studies have now been conducted investigating light lithophile elements as tracers of magmatic water in the shergottites (Lentz *et al.*, 2001; Beck *et al.*, 2004; Herd *et al.*, 2005; Treiman *et al.*, 2006). Lentz *et al.* (2001) measured the light lithophile element abundances in Shergotty and Zagami pyroxenes and presented evidence of depletion of Li and B from cores to rims, in contrast to increases of other nonsoluble incompatible elements. They interpreted these patterns as indicating the depletion of the soluble lithophiles by dissolution in an aqueous fluid exsolved by the magma at depth and lost upon eruption at the surface. Beck *et al.* (2004) came to a similar conclusion after investigating Li abundances and isotopic distributions in NWA 840, another basaltic shergottite. However, Herd *et al.* (2005) and Treiman *et al.* (2006) argue against the loss of Li and B to an aqueous fluid, since their modeling suggests fluid:magma distribution coefficients that are unrealistically high. Instead, Treiman *et al.* (2006) proposes that late-stage diffusion, or the presence of a more Li-compatible mineral, better accounts for the flat profiles that they

measured. There are complexities with this suggestion, too; first, diffusion rates for Li in pyroxene are faster than other elements, but may be temperature-dependent (Coogan *et al*., 2005); and second, if Li diffuses out of the pyroxenes, as in the case of depleted distribution profiles, it must be moving preferentially into another phase. But such a phase has not been documented or suggested, and for the shergottites it may prove difficult to find one that Li prefers to pyroxene. To resolve this quandary, more experimental work needs to be done on water-magma distribution coefficients and mineral diffusion coefficients for the light lithophile elements.

If the water estimates based on the meteorites are correct, equivalent water contents for the shergottite (McSween *et al*., 2001) and chassignite (Jones, 2004) source regions would be on the order of 0.01 wt.% (Solomon *et al*., 2005). Note that this would only represent the contents of a recent, depleted Martian mantle. The ancient Martian mantle would likely have been wetter.

Geophysical modeling results seem to support the idea of a wet mantle. Recent accretion simulations suggest incorporation of outer solar system water-rich planetary embryos would give bulk water abundances of 0.01–0.1 wt.% (Lunine *et al*., 2003; Solomon *et al*., 2005). Thermal evolution models attempting to detail crustal thickness distributions (Hauck and Phillips, 2002; Guest and Smrekar, 2005) require similar water abundances to produce low enough mantle viscosities to allow for convection and ductile flow of mantle materials. Modeling of processes in a Martian magma ocean (Elkins-Tanton and Parmentier, 2005) suggests beginning with a bulk water content up to 2 wt.% and after substantial degassing during magma ocean crystallization, finishing with 0.05–0.25 wt.% water in the mantle.

All these estimates are in contrast to the venerable bulk composition model of Dreibus and Wänke (1985), which concluded that the Martian mantle was (and is) quite dry, with only 36 ppm of water. However, this estimate was based on the relative solubilities of Cl and H_2O in basaltic magma and the abundance of Cl calculated on the basis of the Cl concentration in the Shergotty meteorite, about 0.01 wt.% (Lodders, 1998). Global measurements by GRS (Chapter 5; Keller *et al*., 2006) suggest that the average surface materials on Mars contain 0.5 wt.% Cl. This suggests that the bulk Cl abundance is substantially higher than Dreibus and Wänke's estimate, implying a bulk H_2O content also much greater.

22.3.4 Bulk composition of Mars and implications for planetary accretion

Igneous rocks record the chemical and mineralogical composition of the planetary interior where their primary magmas formed. In the case of Mars, the mantle is clearly heterogeneous, as described in Section 3.1. Nevertheless, there are overall trends that can be used to assess the bulk compositional features of the planet for comparison with other terrestrial planets. These features, in turn, can be informative about the dynamics of planetary accretion. Two particularly useful parameters for which global data exist are the K/Th ratio and the FeO concentration (Taylor *et al*., 2006a).

There is a clear difference in the abundance of moderately volatile elements in Mars compared to Earth, as shown by K/Th in Mars' crust being double that in Earth's (Figure 22.5; also see Chapter 5). This implies that on average Mars accreted from materials that were richer in volatiles than the average of the materials that formed the Earth. In turn, this suggests that mixing among planetesimals was not extensive during the formation of the two planets, as argued on different grounds by Drake and Righter (2002). In other words, there was not widespread mixing of material throughout the inner Solar System during accretion and that accretion zones were relatively narrow. This conclusion contrasts with calculations of the dynamics of planet formation, which suggest that there was considerable mixing of planetary embryos during the final stage of accretion (Wetherill and Stewart, 1993; Wetherill, 1994; Chambers, 2001).

Assuming that the FeO measured for the surface and in Martian meteorites reflects the FeO in the mantle, the much higher FeO abundance in Mars (18 wt.%) shows that the planet is more oxidized than Earth (8 wt.%). Robinson and Taylor (2001) argue that Venus has roughly the same FeO as Earth and that Mercury has only 2–3 wt.%, suggesting a trend of increasing FeO with heliocentric distance. The trend even includes 4Vesta, which resides in the inner asteroid belt and is often viewed as a small terrestrial planet. Vesta, however, has much lower K/Th, 1050 (Mittlefehldt and Lindstrom, 1993; Kitts and Lodders, 1998), than does Mars, accompanied by about the same concentration of FeO, ~20 wt.% (Warren, 1997). The higher FeO in Mars may have been caused by oxidation of metallic iron by H_2O during accretion of Mars, as hypothesized by Wänke and Dreibus (1994). Whatever the cause of the variation of FeO in the inner Solar System, comparison of the compositions of Mars and Vesta indicates that there is not a simple correlation of FeO and K/Th with heliocentric distance: both bodies have high FeO, but very different K/Th.

22.4 SUMMARY AND CONCLUSIONS

Data from Martian meteorites, orbital remote sensing, and *in situ* surface analyses indicate that the Martian crust contains a variety of igneous rocks. The crust is largely basaltic, but several types of basalts have been identified, possibly including more evolved basaltic andesite and andesite. Some magmas were highly mafic, giving rise to cumulate lava flows such as the nakhlites and many shergottites. Intrusive cumulates also occur, represented by cumulate lherzolitic shergottites, chassignites, and orthopyroxenite ALH 84001. Rare silicic rocks have also been identified, probably representing partial melts of the largely basaltic crust.

Meteorites and surface compositions indicate that the Martian mantle is heterogeneous. Shergottites alone represent at least two distinct mantle sources, with mixing between

them, but could represent several distinct sources on the basis of initial Sr-isotopic compositions (e.g., Borg *et al.*, 2003). The nakhlites may represent a somewhat complementary source, but there is clearly an additional source with subchondritic Ba/La. Surface Types 1 and 2 are probably composed of multiple types of igneous rock (e.g., Rogers and Christensen, 2003, 2007), possibly mixed with weathered materials, and on average are different in trace element (K, Th) and Fe abundances. They may be derived from distinct mantle source regions. Meteorite isotopic data suggest that the shergottite and nakhlite sources formed 4.5 Gyr ago and were unaltered until partial melting to produce the shergottites began about 600 Myr ago. If this is any indication of when the other source regions formed, it suggests that they were established at the time of primary differentiation, probably in a magma ocean or soon thereafter during magma ocean overturn, and that the mantle has not been mixed since.

The crust appears to have been constructed by basaltic magmatism, some associated with primary differentiation (probably a magma ocean), the rest formed by partial melting during mantle overturn and other dynamic processes. A small amount of partial melting of the crust driven by intrusion of basaltic magma may have formed the rare silicic rocks observed. Water was delivered to the surface as magmas exsolved their complement of volatiles. Water was also remobilized by the intrusion of magma at depth, forming hydrothermal systems.

The bulk composition of Mars, specifically K/Th and total oxidized iron, is distinctly different from that of the Earth. This argues that the feeding zones during planetary accretion were relatively narrow, precluding widespread mixing throughout the inner solar system.

REFERENCES

Baker, V. R., Water and the Martian landscape, *Nature* **412**, 228–36, 2001.

Bandfield, J. L., V. E. Hamilton, and P. R. Christensen, A global view of Martian surface compositions from MGS-TES, *Science* **287**, 1626–30, 2000.

Bandfield, J. L., V. E. Hamilton, P. R. Christensen, and H. Y. McSween, Identification of quartzofeldspathic materials on Mars, *J. Geophys. Res.* **109**, E10009, doi:10.1029/2004JE002290, 2004.

Barrat, J. A., J. Blichert-Toft, R. W. Nesbitt, and F. Keller, Bulk chemistry of Saharan shergottite Dar al Gani 476, *Meteorit. Planet. Sci.* **36**, 23–9, 2001.

Beck, P., J.-A. Barrat, M. Chaussidon, Ph. Gillet, and M. Bohn, Li isotopic variations in single pyroxenes from the Northwest Africa 480 shergottite (NWA 480): a record of degassing of Martian magmas?, *Geochim. Cosmochim. Acta* **68**, 2925–33, 2004.

Beck, P., J. A. Barrat, Ph. Gillet, *et al.*, Petrography and geochemistry of the chassignite Northwest Africa 2737 (NWA 2737), *Geochim. Cosmochim. Acta* **70**, 2127–39, 2006.

Bell III, J. F., S. W. Squyres, R. E. Arvidson, *et al.*, Pancam multispectral imaging results from the Opportunity rover at Meridiani Planum, *Science* **305**, 1703–9, 2004.

Bibring, J. P., Y. Langevin, A. Gendrin, *et al.*, Mars surface diversity as revealed by the OMEGA/Mars Express observations, *Science* **307**, 1576–81, 2005.

Blichert-Toft, J., J. D. Gleason, P. Télouk, and F. Albarède, The Lu-Hf isotope geochemistry of shergottites and the evolution of the Martian mantle-crust system, *Earth Planet. Sci. Lett.* **173**, 25–39, 1999.

Borg, L. E. and D. S. Draper, A petrogenetic model for the origin and compositional variation of the Martian basaltic meteorites, *Meteorit. Planet. Sci.* **38**, 1713–31, 2003.

Borg, L. E., L. E. Nyquist, L. A. Taylor, H. Wiesmann, and C.-Y. Shih, Constraints on Martian differentiation processes from Rb-Sr and Sm-Nd isotopic analyses of the basaltic shergottite QUE94201, *Geochim. Cosmochim. Acta* **61**, 4915–31, 1997.

Borg, L. E., L. E. Nyquist, H. Weissman, C.-Y. Shih, and Y. Reese, The age of Dar al Gani 476 and the differentiation history of the Martian meteorites inferred from their radiogenic isotopic systematics, *Geochim. Cosmochim. Acta* **67**, 3519–36, 2003.

Borg, L. E., J. E. Edmunson, and Y. Asmerom, Constraints on the U-Pb isotopic systematics of Mars inferred from a combined U-Pb, Rb-Sr, and Sm-Nd isotopic study of the Martian meteorite Zagami, *Geochim. Cosmochim. Acta* **69**, 5819–30, 2005.

Bouvier, A., J. Blichert-Toft, J. D. Vervoort, and F. Albarède, The age of Martian meteorites and the antiquity of the Martian surface, *Earth Planet. Sci. Lett.* **240**, 221–33, 2005.

Brandon, A. D., R. J. Walker, J. W. Morgan, and G. G. Goles, Re-Os isotopic evidence for early differentiation of the Martian mantle, *Geochim. Cosmochim. Acta* **64**, 4083–95, 2000.

Bridges, J. C. and M. M. Grady, Evaporite mineral assemblages in the nakhlite (Martian) meteorites, *Earth Planet. Sci. Lett.* **176**, 267–79, 2000.

Bridges, J. C. and P. H. Warren, The Martian meteorites: basaltic igneous processes on Mars, *J. Geol. Soc. Lond.* **163**, 229–51, 2006.

Brückner, J., G. Dreibus, R. Rieder, and H. Wänke, Refined data of Alpha Proton X-ray Spectrometer analyses of soils and rocks at the Mars Pathfinder site: implications for surface chemistry, *J. Geophys. Res.* **108**(E12), 8094, doi:10.1029/2003JE002060, 2003.

Bruno, B. C., G. J. Taylor, S. K. Rowland, and S. M. Baloga, Quantifying the effect of rheology on lava-flow margins using fractal geometry, *Bull. Volc.* **56**, 193–206, 1994.

Carr, M. H. and H. Wänke, Earth and Mars: water inventories as clues to accretional histories, *Icarus* **98**, 61–71, 1992.

Chambers, J. E., Making more terrestrial planets, *Icarus* **152**, 205–24, 2001.

Chen, J. H. and G. J. Wasserburg, Formation ages and evolution of Shergotty and its parent planet from U-Th-Pb systematics, *Geochim. Cosmochim. Acta* **50**, 955–68, 1986.

Christensen, P. R., J. L. Bandfield, M. D. Smith, V. E. Hamilton, and R. N. Clark, Identification of a basaltic component on the Martian surface from Thermal Emission Spectrometer data, *J. Geophys. Res.* **105**, 9609–21, 2000.

Christensen, P. R., M. B. Wyatt, T. D. Glotch, *et al.*, Mineralogy at Meridiani Planum from the Mini-TES experiment on the Opportunity rover, *Science* **306**, 1733–9, 2004.

Christensen, P. R., H. Y. McSween Jr., J. L. Bandfield, *et al.*, Evidence for magmatic evolution and diversity on Mars from infrared observations, *Nature* **436**, 504–9, 2005.

Clague, D. A. and F. A. Frey, Petrology and trace element geochemistry of the Honolulu Volcanics, Oahu: implications for the oceanic mantle below Hawaii, *J. Petrol.* **23**, 447–504, 1982.

Coogan, L. A., S. A. Kasemann, and S. Chakraborty, Rates of hydrothermal cooling of new oceanic upper crust derived from lithium-geospeedometry, *Earth Planet. Sci. Lett.* **240**, 415–24, 2005.

Dann, J. C., A. H. Holzheid, T. L. Grove, and H. Y. McSween Jr., Phase equilibria of the Shergotty meteorite: constraints on pre-eruptive water contents of Martian magmas and fractional crystallization under hydrous conditions, *Meteorit. Planet. Sci.* **36**, 793–806, 2001.

Day, J. M. D., L. A. Taylor, C. Floss, and H. Y. McSween Jr., Petrology and chemistry of MIL 03346 and its significance in understanding the petrogenesis of nakhlites on Mars, *Meteorit. Planet. Sci.* **41**, 581–606, 2006.

Drake, M. J. and K. Righter, Determining the composition of the earth, *Nature* **416**, 39–44, 2002.

Dreibus, G. and H. Wänke, Mars: a volatile rich planet, *Meteoritics* **20**, 367–82, 1985.

Dreibus, G., W. Huisl, R. Haubold, and E. Jagoutz, Influence of terrestrial desert weathering in Martian meteorites (abst.), *Meteorit. Planet. Sci.* **36** (Suppl.), A50–A51, 2001.

Elkins-Tanton, L. T. and E. M. Parmentier, The fate of water in the Martian magma ocean and the formation of an early atmosphere, *Lunar Planet. Sci. Conf. XXXVI*, Houston: Lunar and Planetary Institute, Abstract #1906, (CD-ROM), 2005.

Elkins-Tanton, L. T., E. M. Parmentier, and P. C. Hess, Magma ocean fractional crystallization and cumulate overturn in terrestrial planets: implications for Mars, *Meteorit. Planet. Sci.* **38**, 1753–71, 2003.

Elkins-Tanton, L. T., P. C. Hess, and E. M. Parmentier, Possible formation of ancient crust on Mars through magma ocean processes, *J. Geophys. Res.* **110**, E12S01, doi:10.1029/2005JE002480, 2005.

Floran, R. J., M. Printz, P. F. Hlava, *et al.*, The Chassigny meteorite: a cumulate dunite with hydrous amphibole-bearing melt inclusions, *Geochim. Cosmochim. Acta* **42**, 1213–29, 1978.

Foley, C. N., T. Economou, and R. N. Clayton, Final chemical results from the Mars Pathfinder alpha proton X-ray spectrometer, *J. Geophys. Res.* **108**(E12), 8096, doi:10.1029/2005JE002555, 2003.

Foley, C. N., M. Wadhwa, L. E. Borg, *et al.*, The early differentiation history of Mars from 183W-142Nd isotope systematics in the Martian meteorites, *Geochim. Cosmochim. Acta* **69**, 4557–71, 2005.

Frey, H. v., Impact constraints on the age and origin of the lowlands of Mars, *Geophys. Res. Lett.* **33**, L08S02, doi:10.1029/2005GL024484, 2006.

Frey, H. V., S. E. H. Sakimoto, and J. H. Roark, Discovery of a 450 km diameter multi-ring basin on Mars through analysis of MOLA data, *Geophys. Res. Lett.* **26**, 1657–60, 1999.

Friedman Lentz, R. C., G. J. Taylor, and A. H. Treiman, Formation of a Martian pyroxenite: a comparative study of the nakhlite meteorites and Theo's flow, *Meteorit. Planet. Sci.* **34**, 919–32, 1999.

Gellert, R., R. Rieder, R. C. Anderson, *et al.*, Chemistry of rocks and soils in Gusev crater from the Alpha Particle X-ray Spectrometer, *Science* **305**, 829–32, 2004.

Gellert, R., R. Rieder, J. Brückner, *et al.*, The Alpha Particle X-ray Spectrometer (APXS): results from Gusev crater and calibration report, *J. Geophys. Res.* **111**, E02S05, doi: 10.1029/2005 JE 002555, 2006.

Goodrich, C. A., Petrogenesis of olivine-phyric shergottites Sayh al Uhaymir 005 and Elephant Moraine A79001 lithology A, *Geochim. Cosmochim. Acta* **67**, 3735–71, 2003.

Guest, A. and S. E. Smrekar, Relaxation of the Martian dichotomy and elastic thickness estimates as constraints on the thermal and volatile evolution of Mars, *AGU fall meeting*, Abstract #P51B-0918, 2005.

Halliday, A. N., H. Wänke, J.-L. Birck, and R. N. Clayton, The accretion, composition and early differentiation of Mars, *Space Sci. Rev.* **96**, 197–230, 2001.

Hamilton, V. E. and P. R. Christensen, Evidence for extensive, olivine-rich bedrock on Mars, *Geology* **33**, 433–6, 2005.

Hamilton, V. E. and R. D. Schneider, Alteration phases associated with high concentrations of orthopyroxene and olivine on Mars, *Lunar Planet. Sci. Conf. XXXVI*, Houston: Lunar and Planetary Institute, Abstract #2212, (CD-ROM), 2005.

Hamilton, V. E., M. B. Wyatt, H. Y. McSween, and P. R. Christensen, Analysis of terrestrial and Martian volcanic compositions using thermal emission spectroscopy: 2. Application to Martian surface spectra from the Mars Global Surveyor Thermal Emission Spectrometer, *J. Geophys. Res.* **107**(E6), 14733–46, 2001.

Hamilton, V. E., P. R. Christensen, H. Y. McSween Jr., and J. L. Bandfield, Searching for the source regions of Martian meteorites using MGS TES: integrating Martian meteorites into the global distribution of volcanic materials on Mars, *Meteorit. Planet. Sci.* **38**, 871–86, 2003.

Harper, C. L., L. E. Nyquist, B. Bansal, H. Wiesmann, and C. Y. Shih, Rapid accretion and early differentiation of Mars indicated by $^{142}Nd/^{144}Nd$ in Martian meteorites, *Science* **267**, 213–17, 1995.

Harvey, R. P. and V. E. Hamilton, Syrtis Major as the source region for the nakhlite/Chassigny group of Martian meteorites: implications for the geological history of Mars, *Lunar Planet. Sci. Conf. XXXVI*, Houston: Lunar and Planetary Institute, Abstract #1019, (CD-ROM), 2005.

Harvey, R. P., M. Wadhwa, H. Y. McSween Jr., and G. Crozaz, Petrography, mineral chemistry, and petrogenesis of Antarctic shergottite LEW88516, *Geochim. Cosmochim. Acta* **56**, 4769–83, 1993.

Haskin, L. A., A. Wang, B. L. Jolliff, *et al.*, Water alteration of rocks and soils from the Spirit rover site, Gusev crater, Mars, *Nature* **436**, 66–9, doi:10.1038/nature03640, 2005.

Hauck II, S. A. and R. J. Phillips, Thermal and crustal evolution of Mars. *J. Geophys. Res.* **107**(E7), 5052, 10.1029/2001JE001801, 2002.

Herd, C. K., L. E. Borg, J. H. Jones, and J. J. Papike, Oxygen fugacity and geochemical variations in the Martian basalts: implications for Martian basalt petrogenesis and the oxidation state of the upper mantle of Mars, *Geochim. Cosmochim. Acta* **66**, 2025–36, 2002.

Herd, C. K., A. H. Treiman, G. A. McKay, and C. K. Shearer, Light lithophile elements in Martian basalts: evaluating the evidence for magmatic water degassing, *Geochim. Cosmochim. Acta* **69**, 2431–40, 2005.

Herkenhoff, K. E., S. W. Squyres, R. Arvidson, *et al.*, Evidence from Opportunity's microscopic imager for water on Meridiani Planum, *Science* **306**, 1727–30, 2004.

Hoefen, T. M., R. N. Clark, J. L. Bandfield, *et al.*, Discovery of olivine in the Nili Fossae region of Mars, *Science* **302**, 627–30, 2003.

Hofmann, A. W., Geochemistry and models of mantle circulation, *Philos. Trans. R. Soc. Lond.* **A328**, 425–439, 1989.

Hofmann, A. W., Mantle geochemistry: the message from oceanic volcanism, *Nature* **385**, 219–29, 1997.

Hofmann, A. W., K. P. Jochum, M. Seufert, and W. M. White, Nb and Pb in oceanic basalts: new constraints on mantle evolution, *Earth Planet. Sci. Lett.* **79**, 33–45, 1986.

Jacobsen, S. B. and Q.-Z. Yin, The mean age of mantle and crustal reservoirs for the planet Mars, *Lunar Planet. Sci. Conf. XXXIII*, Houston: Lunar and Planetary Institute, Abstract #1940 (CD-ROM), 2002.

Jagoutz, E., Chronology of Martian meteorites, *Space Sci. Rev.* **56**, 13–22, 1991.

Jochum, K. P., N. T. Arndt, and A. W. Hofmann, Nb-Th-La in komatiites and basalts: constraints on komatiite petrogenesis and mantle evolution, *Earth Planet. Sci. Lett.* **107**, 272–89, 1991.

Jones, J. H., Isotopic relationships among the shergottites, the nakhlites and Chassigny, *Proc. Lunar Planet. Sci. Conf. XIX*, 465–74, 1989.

Jones, J. H., Constraints on the structure of the Martian interior determined from the chemical and isotopic systematics of Martian meteorites, *Meteorit. Planet. Sci.* **38**, 1807–14, 2003.

Jones, J. H., The edge of wetness: the case for dry magmatism on Mars, *Lunar Planet. Sci. Conf. XXXV*, Houston: Lunar and Planetary Institute, Abstract #1798 (CD-ROM), 2004.

Karlsson, H. R., R. N. Clayton, E. K. Gibson Jr., and T. K. Mayeda, Water in Martian meteorites: evidence for a Martian hydrosphere, *Science* **255**, 1409–11, 1992.

Karunatillake, S. K., S. W. Squyres, G. J. Taylor, *et al.*, Composition of northern low albedo regions of Mars: insights from the Mars Odyssey Gamma Ray Spectrometer, *J. Geophys. Res.* **111**, E03S05, doi:10.1029/2006 JE002675, 2006.

Keller, J., W. V. Boynton, S. Karunatillake, *et al.*, Equatorial and midlatitude distribution of chlorine measured by Mars Odyssey GRS, *J. Geophys. Res.* **111**, E03S08, doi:10.1029/2006 JE002679, 2006.

Kiefer, W. S., Melting in the Martian mantle: shergottite formation and implications for present-day mantle convection on Mars, *Meteorit. Planet. Sci.* **38**, 1815–32, 2003.

King, P. L., R. L. Hervig, J. R. Holloway, T. W. Vennemann, and K. Righter, Oxy-substitution and dehydrogenation in mantle-derived amphibole megacrysts, *Geochim. Cosmochim. Acta* **63**, 3635–51, 1999.

Kitts, K. and K. Lodders, Survey and evaluation of eucrite bulk compositions, *Meteorit. Planet. Sci.* **33**, A197–A213, 1998.

Klein, E. M., Geochemistry of the igneous oceanic crust, *Treatise on Geochemistry* **3**, 433–63, 2003.

Klingelhöfer, G., R. V. Morris, B. Beruhardt, *et al.*, Jarosite and hematite at Meridiani Planum from Opportunity's Mössbauer spectrometer, *Science* **306**, 1740–5, 2004.

Lentz, R. C. F., H. Y. McSween Jr., J. G. Ryan, and L. R. Riciputi, Water in the Martian mantle: clues from light lithophile elements in shergottite and nakhlite pyroxenes, *Geochim. Cosmochim. Acta* **65**, 4551–65, 2001.

Lodders, K., A survey of shergottites, nakhlite and chassigny meteorites whole-rock compositions, *Meteorit. Planet. Sci.* **33**, A183–A190, 1998.

Longhi, J., Complex magmatic processes on Mars: inferences from the Martian meteorites, *Proc. Lunar Planet. Sci. Conf. XXI*, 695–709, 1991.

Longhi, J. and V. Pan, The parent magmas of the Martian meteorites, *Proc. Lunar Planet. Sci. Conf. XIX*, 451–464, 1989.

Lunine, J. I., J. Chambers, A. Morbidelli, and L. A. Leshin, The origin of water on Mars, *Icarus* **165**, 1–8, 2003.

Malin, M. C. and K. S. Edgett, Evidence for recent groundwater seepage and surface runoff on Mars, *Science* **288**, 2330–5, 2000.

McCoy, T. J. and G. E. Lofgren, The crystallization of the Zagami shergottite: a 1 atm. experimental study, *Lunar Planet. Sci. Conf. XXVII*, 839–40, 1996.

McKay, G., T. Mikouchi, L. Le, C. Schwandt, and M. Hashimoto, The Shergotty paradox: an experimental perspective on intercumulus melt compositions, *Lunar Planet. Sci. Conf. XXXI*, Houston: Lunar and Planetary Institute, Abstract# 2000 (CD-ROM), 2000.

McLennan, S. M., Recycling of continental crust, *Pure Appl. Geophys.* **128**, 683–724, 1988.

McLennan, S. M., Crustal heat production and the thermal evolution of Mars, *Geophys. Res. Lett.* **28**, 4019–22, 2001.

McLennan, S. M., Sedimentary silica on Mars, *Geology* **31**, 315–18, 2003a.

McLennan, S. M., Large-ion lithophile element fractionation during the early differentiation of Mars and the composition of the Martian primitive mantle, *Meteorit. Planet. Sci.* **38**, 895–904, 2003b.

McSween, Jr. H. Y., The rocks of Mars, from far and near, *Meteorit. Planet. Sci.* **37**, 7–25, 2002.

McSween Jr., H. Y., Mars, *Treatise on Geochemistry* **1**, 601–21, 2003.

McSween Jr., H. Y. and R. P. Harvey, Outgassed water on Mars: constraints from melt inclusions in Martian meteorites, *Science* **259**, 1890–2, 1993.

McSween Jr., H. Y., D. D. Eisenhour, L. A. Taylor, M. Wadhwa, and G. Crozaz, QUE 94201 shergottite: crystallization of a Martian basaltic magma, *Geochim. Cosmochim. Acta* **60**, 4563–9, 1996.

McSween Jr., H. Y., S. L. Murchie, J.Crisp, *et al.*, Chemical, multispectral, and textural constraints on the composition and origin of rocks at the Mars Pathfinder landing site, *J. Geophys. Res.* **104**(E4), 8679–715, 1999.

McSween Jr., H. Y., T. L. Grove, R. C. F. Lentz, *et al.*, Geochemical evidence for magmatic water within Mars from pyroxenes in the Shergotty meteorite, *Nature* **409**, 487–90, 2001.

McSween Jr., H. Y., T. L. Grove, and M. B. Wyatt, Constraints on the composition and petrogenesis of the Martian crust, *J. Geophys. Res.* **108**(E12), 5135, doi:10.1029/2003JE002175, 2003.

McSween Jr., H. Y., R. E. Arvidson, J. F. Bell III, *et al.*, Basaltic rocks analyzed by the Spirit rover in Gusev crater, *Science* **305**, 842–5, 2004.

McSween Jr., H. Y., M. B. Wyatt, R. Gellert, *et al.*, Characterization and petrologic interpretation of olivine-rich basalts at Gusev crater, Mars, *J. Geophys. Res.* **110**, E12S39, doi:10.1029/2005JE002477, 2005.

McSween, H. Y., S. W. Ruff, R. V. Morris, *et al.*, Alkaline volcanic rocks from the Columbia Hills, Gusev crater, Mars, *J. Geophys. Res.* **111**, E09S91, doi:10.1029/2006JE002698, 2006.

Meyer Jr., C., Mars Meteorite Compendium, JSC#27672 Revision C, NASA Johnson Space Center, Houston, Texas (Available at http://curator.jsc.nasa.gov/antmet/mmc/index.cfm), 2006.

Michalski, J. R., M. D. Kraft, T. G. Sharp, L. B. Williams, and P. R. Christensen, Mineralogical constraints on the high-silica Martian surface component observed by TES, *Icarus* **174**, 161–77, doi:10.1016/j.icarus.2004.10.022, 2005.

Mittlefehldt, D. W., ALH 84001, a cumulate orthopyroxenite member of the Martian meteorite clan, *Meteoritics* **29**, 214–21, 1993.

Mittlefehldt, D. and M. Lindstrom, Geochemistry and petrology of a suite of ten Yamato HED meteorites, *Proc. NIPR Symp. Antarct. Meteor.* **6**, 268–92, 1993.

Morris, R. V., T. G. Graff, S. A. Mertzman, M. D. Lane, and P. R. Christensen, Palagonitic (not andesitic) Mars: evidence from Thermal Emission and VNIR spectra of palagonitic

alteration rinds on basaltic rock, *6th Int. Conf. on Mars*, Abstract #3211, 2003.

Morris, R. V., G. Klingelhöfer, B. Bernhardt, *et al*., Mineralogy at Gusev crater from the Mössbauer Spectrometer on the Spirit rover, *Science* **305**, 833–6, 2004.

Mustard, J. F. and J. M. Sunshine, Seeing through the dust: Martian crustal heterogeneity and links to the SNC meteorites, *Science* **267**, 1623–6, 1995.

Mustard, J. F., F. Poulet, A. Gendrin, *et al*., Olivine and pyroxene diversity in the crust of Mars, *Science* **307**, 594–7, 2005.

Norman, M. D., The composition and thickness of the crust of Mars estimated from rare earth elements and neodymium-isotopic composition of Martian meteorites, *Meteorit. Planet. Sci.* **34**, 439–49, 1999.

Norman, M. D., Thickness and composition of the Martian crust revisited: implications of an ultradepleted mantle with a Nd isotopic composition like that of QUE 94201, *Lunar Planet. Sci. XXXIII*, Houston: Lunar and Planetary Institute, Abstract #1175 (CD-ROM), 2002.

Nyquist, L. E., B. M. Bansal, H. Wiesmann, and C.-Y. Shih, "Martians" young and old: zagami and ALH 8400 1 (abstract), *Lunar Planet. Sci. Conf. XXVI*, 1065–66, 1995.

Nyquist, L. E., D. D. Bogard, C.-Y. Shih, *et al*., Ages and geologic histories of Martian meteorites, *Space Sci. Rev.* **96**, 105–64, 2001.

Owen, T., J. P. Maillard, C. de Bergh, and B. L. Lutz, Deuterium on Mars: the abundance of HDO and the value of D/H, *Science* **240**, 1767–70, 1988.

Popp, R. K., D. Virgo, H. S. Yoder Jr., T. C. Hoering, and M. W. Phillips, An experimental study of phase equilibria and Fe oxy-component in kaersutitic amphibole: implications for the f_{H2} and a_{H2O} in the upper mantle, *Am. Miner* **80**, 534–48, 1995.

Rieder, R., T. Economou, H. Wänke, *et al*., The chemical composition of Martian soil and rocks returned by the mobile Alpha Proton X-ray Spectrometer: preliminary results from the x-ray mode, *Science* **278**, 1771–4, 1997.

Robinson, M. S. and G. J. Taylor, Ferrous oxide in Mercury's crust and mantle, *Meteorit. Planet. Sci.* **36**, 841–7, 2001.

Rogers, A. D. and P. R. Christensen, Age relationship of basaltic and andesitic surface compositions on Mars: analysis of high-resolution TES observations of the northern hemisphere, *J. Geophys. Res.* **108**(E4), 5030, doi:10.1029/2002JE001913, 2003.

Rogers, A. D. and P. R. Christensen, Surface mineralogy of martian low-albedo regions from MGS-TES data: implications for upper crustal evolution and surface alteration, *J. Geophys. Res.* **112**, E01003, doi:10.1029/2006JE002727, 2007.

Rogers, A. D., P. R. Christensen, and J. L. Bandfield, Compositional heterogeneity of the ancient Martian crust: analysis of Ares Vallis bedrock with THEMIS and TES data, *J. Geophys. Res.* **110**, doi:10.1029/2005/JE002399, 2005.

Ruff, S. R., Spectral evidence for zeolite in the dust on Mars, *Icarus* **168**, 131–43, 2004.

Ruff, S. W., P. R. Christensen, D. L. Blaney, *et al*., The rocks of Gusev crater as viewed by the Mini-TES instrument, *J. Geophys. Res.* **111**(E12), doi:10.1029/2006JE002747, 2006.

Schneider, R. D. and V. E. Hamilton, Evidence for locally-derived, ultramafic intracrater materials in Amazonis Planitia, Mars, *J. Geophys. Res.* **111**(E9), 2006.

Solomon, S. C., O. Aharonson, J. M. Aurnou, *et al*., New perspectives on ancient Mars, *Science* **307**, 1214–20, 2005.

Squyres, S. W., R. E. Arvidson, J. F. Bell III, *et al*., The Opportunity rover's Athena science investigation at Meridiani Planum, Mars, *Science* **306**, 1698–703, 2004a.

Squyres, S. W., J. P. Grotzinger, R. E. Arvidson, *et al*., In situ evidence for an ancient aqueous environment at Meridiani Planum, Mars, *Science* **306**, 1709–14, 2004b.

Stolper, E. M. and H. Y. McSween Jr., Petrology and origin of the shergottite meteorites, *Geochim. Cosmochim. Acta* **43**, 1475–98, 1979.

Taylor, G. J., W. Boynton, J. Brückner, *et al*., Bulk composition and early differentiation of Mars, *J. Geophys. Res.* **111**, E03S10, doi: 10.1029/2005JE002645, 2006a.

Taylor, G. J., J. D. Stopar, W. V. Boynton, *et al*., Variations in K/Th on Mars, *J. Geophys. Res.* **111**, E03S06, doi:10.1029/2006JE002676, 2006b.

Taylor, S. R., Growth of planetary crusts, *Tectonophysics*. **161**, 147–56, 1989.

Taylor, S. R., *Solar System Evolution: A New Perspective*, 2nd edn., Cambridge: Cambridge University Press, 460pp., 2001.

Taylor, S. R. and S. M. McLennan, *The Continental Crust: Its Composition and Evolution*. Oxford: Blackwell, 312pp., 1985.

Taylor, S. R. and S. M. McLennan, Chemical composition and element distribution in the Earth's crust, *Encyclopedia of Physical Science and Technology*, (3rd edn.) Academic Press, **2**, pp. 697–719, 2002.

Treiman, A. H., The nakhlite meteorites: augite-rich igneous rocks from Mars, *Chem. Erde* **65**, 203–70, 2005.

Treiman, A. H., D. S. Musselwhite, C. D. K. Herd, and C. K. Shearer Jr., Light lithophile elements in pyroxenes of Northwest Africa (NWA) 817 and other Martian meteorites: implications for water in Martian magmas, *Geochim. Cosmochim. Acta* **70**, 2919–34, 2006.

Wadhwa, M., Redox state of Mars' upper mantle and crust from Eu anomalies in shergottite pyroxenes, *Science* **291**, 1527–30, 2001.

Wänke, H., Chemistry, accretion, and evolution of Mars, *Space Sci. Rev.* **56**, 108, 1991.

Wänke, H. and G. Dreibus, Chemical composition and accretion history of terrestrial planets. *Philos. Trans. R. Soc. Lond.* **A325**, 545–57, 1988.

Wänke, H. and G. Dreibus, Chemistry and accretion history of Mars. *Philos. Trans. R. Soc. Lond.* **A349**, 285–93, 1994.

Warren, P. H., MgO-FeO mass balance constraints and a more detailed model for the relationship between eucrites and diogenites, *Meteorit. Planet. Sci.* **32**, 945–63, 1997.

Watson, L. L., I. D. Hutcheon, S. Epstein, and E. M. Stolper, Water on Mars: clues from deuterium/hydrogen and water contents of hydrous phases in Martian meteorites, *Science* **265**, 86–90, 1994.

Wetherill, G. W., The provenance of the terrestrial planets, *Geochem. Cosmochem. Acta* **58**, 4513–20, 1994.

Wetherill, G. W. and G. R. Stewart, Formation of planetary embryos: effects of fragmentation, low relative velocity, and independent variation of eccentricity and inclination, *Icarus* **106**, 190–209, 1993.

Wieczorek, M. A. and M. T. Zuber, Thickness of the Martian crust: improved constraints from geoid-to-topography ratios, *J. Geophys. Res.* **109**, E01009, doi:10.1029/2003JE002153, 2004.

Wyatt, M. B. and H. Y. McSween Jr., Spectral evidence for weathered basalt as an alternative to andesite in the northern lowlands of Mars, *Nature* **417**, 263–6, 2002.

Wyatt, M. B., H. Y. McSween, K. L. Tanaka, and J. W. Head, Global geologic context for rock types and surface alteration on Mars, *Geology* **32**, 645–8, doi:10.1130/G20527.1, 2004.

Zipfel, J., R. Anderson, J. Brückner, *et al*., APXS analyses of Bounce Rock: the first shergottite on Mars (abstract), *Meteorit. Planet. Sci.* **39** (Suppl)., A118, 2004.

23

Aqueous alteration on Mars

D. W. MING, R. V. MORRIS, AND B. C. CLARK

ABSTRACT

Aqueous alteration is the change in composition of a rock, produced in response to interactions with H_2O-bearing ices, liquids, and vapors by chemical weathering. A variety of mineralogical and geochemical indicators for aqueous alteration on Mars have been identified by a combination of surface and orbital robotic missions, telescopic observations, characterization of Martian meteorites, and laboratory and terrestrial analog studies. Mineralogical indicators for aqueous alteration include goethite (lander), jarosite (lander), kieserite (orbiter), gypsum (orbiter) and other Fe-, Mg-, and Ca-sulfates (landers), halides (meteorites, lander), phyllosilicates (orbiter, meteorites), hematite and nanophase iron oxides (telescopic, orbiter, lander), and Fe-, Mg-, and Ca-carbonates (meteorites). Geochemical indicators (landers only) for aqueous alteration include Mg-, Ca-, and Fe-sulfates, halides, and secondary aluminosilicates such as smectite. Based upon these indicators, several styles of aqueous alteration have been suggested on Mars. Acid-sulfate weathering (e.g., formation of jarosite, gypsum, hematite, and goethite) may occur during (1) the oxidative weathering of ultramafic igneous rocks containing sulfides, (2) sulfuric acid weathering of basaltic materials, and (3) acid-fog (i.e., vapors rich in H_2SO_4) weathering of basaltic or basaltic-derived materials. Near-neutral or alkaline alteration occurs when solutions with pH near or above 7 move through basaltic materials and form phases such as phyllosilicates and carbonates. Very low water:rock ratios appear to have been prominent at most of the sites visited by landed missions because there is very little alteration (leaching) of the original basaltic composition (i.e., the alteration is isochemical or in a closed hydrologic system). Most of the aqueous alteration appears to have occurred early in the history of the planet (3–4.5 Ga); however, minor aqueous alteration may be occurring at the surface even today (e.g., in thin films of water or by acid fog).

23.1 INTRODUCTION

The geologic processes responsible for aqueous alteration on Mars are modeled beginning with our knowledge of analog processes on Earth; i.e., characterization of elemental and mineralogical composition of terrestrial environments where the alteration and weathering pathways related to aqueous activity are better understood. A key ingredient to successful modeling of aqueous processes on Mars is identification of phases that have formed by those processes. The purpose of this chapter is to describe what is known about the elemental and mineralogical composition of products of aqueous weathering and alteration on Mars and their implications for specific aqueous environments. The environmental conditions for aqueous alteration and the epoch in which they occurred are critical for assessing the extent and the timing for possible life on Mars.

23.2 DEFINITIONS AND TERMINOLOGY

23.2.1 Aqueous alteration

Aqueous alteration is the change in chemical and/or mineralogical composition of a rock, produced in response to interactions with H_2O-bearing ices, liquids, and vapors by chemical weathering at ambient or hydrothermal (above ambient) temperatures. In general, weathering is the chemical and physical breakdown of rocks upon exposure to atmospheric agents under ambient temperatures at or near the surface (e.g., Gooding *et al*., 1992).

Chemical alteration is the process by which chemical reactions (e.g., hydrolysis, hydration, oxidation, carbonation, ion exchange, and solution) transform rocks into new chemical combinations. Hydrolysis is a decomposition reaction involving water and the subsequent formation of metal-hydroxyl ion pairs and metal polynuclear complexes (e.g., iron oxyhydroxides). Hydration is the chemical combination of water with another substance. Oxidation is a reaction where an ion or molecule loses one or more electrons, and the process can happen in aqueous and nonaqueous systems (e.g., thermal oxidation). Carbonation is a reaction that transforms minerals or phases containing Ca, Mg, Fe, K, Na, etc. into carbonates or bicarbonates of these metals by CO_2-containing (or CO_3-containing) water. Ion exchange is a reversible processes where ions in a crystal are exchanged with ions in solution (e.g., ion exchange in the interlayers of smectites). Solution chemical weathering is a process where a mineral or phase is removed into solution (e.g., salts dissolving in passing waters). In contrast to these chemical processes, physical weathering occurs when mechanical processes (e.g., abrasion, freeze-thaw, and salt-crystal growth) fragment a rock without a chemical change.

The Martian Surface: Composition, Mineralogy, and Physical Properties, ed. J. F. Bell III. Published by Cambridge University Press.

Aqueous alteration without subsequent removal of elements from the precursor rock is referred to as isochemical (or closed system) aqueous alteration. In the strictest sense, only energy (and not matter) is exchanged with its surroundings in a closed system; however, a system may be closed (i.e., no removal of the original elements during alteration) but open with respect to the addition of acidic, neutral, or basic water and gases (e.g., O_2, CO_2, Cl_2, and SO_x). Aqueous alteration with subsequent removal of elements from the precursor rock (e.g., by leaching) is referred to as open-system aqueous alteration. In an open system both energy and matter are exchanged with the surroundings. The style and extent of aqueous alteration on Mars can vary in time and/or location in response to changes in local conditions (e.g., meteoritic impact into volatile-rich material or invasion by hydrothermal fluids associated with volcanism) and/or global conditions (e.g., climate change). Diagenesis is the change in physical and chemical properties of a sediment after its initial deposition. Diagenetic processes are those that occur under conditions of pressure and temperature in the outer part of the crust, including processes such as cementation, replacement, and compaction. Aqueous processes may be key factors in the diagenetic alteration of a sedimentary deposit.

23.2.2 Style of aqueous alteration

The style of aqueous alteration depends on the chemical composition of the H_2O-bearing fluids or gases that interact with the host rock or material. For example, hydrolytic, acid-sulfate, and acid-chloride aqueous alterations cause the breaking of chemical bonds in solid materials and adding of the elements of H_2O (H^+ and OH^-), H_2SO_4 (H^+ and SO_4^{-2}), and HCl (H^+ and Cl^-), respectively, to the weathering products (e.g., Morris *et al.*, 2000). The breaking of bonds most commonly involves H^+ reacting with and breaking M-O-Si bonds (where M = Si, Al, Mg, Ca, Fe, etc.). These three styles of alteration have been suggested as generating aqueous solutions that have interacted with Martian host rocks, most likely basaltic in composition (see discussion in Section 23.6).

23.2.3 Extent of aqueous alteration

The extent of aqueous alteration is governed by many factors, including temperature, time, alteration style, parent rock mineralogy, H_2O to rock ratio, and rock permeability. Two indices have been used to evaluate the extent of alteration/weathering based upon measurements made at Mars. The Mineralogical Alteration Index (MAI) is based upon the percentage of total Fe (Fe_T) present as Fe^{3+} in alteration products (Morris *et al.*, 2006a; Chapter 15; see Figure 23.1a). However, magnetite, which contains Fe^{3+}, is considered to be a product of igneous activity and not an alteration product. Unaltered to weakly altered rocks have values of MAI in the range 0%–20%, and pervasively altered rocks have values in the range of 80%–100%. Although the MAI indicates the extent of alteration, it does not distinguish between aqueous and nonaqueous processes. For example, it is possible that primary magnetite in the host basalt can be converted to hematite by dry, thermal processes (possibly associated with igneous or impact processes) and not aqueous processes.

In contrast, the Chemical Index of Alteration is based upon the chemical composition of the basaltic material that has been weathered (Nesbitt and Young, 1982, 1984, 1989; Nesbitt and Wilson, 1992). The Chemical Index of Alteration provides information on the extent to which elements have been removed from the host rock and the likely formation of secondary phases (see Nesbitt and Young, 1982, 1984, 1989, for details). For the purposes of this chapter, we have adopted the ternary diagrams used by Nesbitt and Wilson (1992) to evaluate the extent that elements are removed or leached away from the reaction front (see Hurowitz *et al.*, 2006, for examples of this method used for Mars). Basaltic compositions lie along the olivine to feldspar join (Figure 23.1b). As weathering of bulk rock proceeds, the primary minerals are destroyed and secondary minerals (such as smectite) form and the composition of the resulting secondary phases are more aluminum-rich than the original basalt. Care must be taken, however, when interpreting such plots because small changes in composition resulting from weathering or leaching are not necessarily apparent. In such cases, additional techniques such as basalt normative calculations (standard normative calculations for rocks and soils on a S-, Cl-, and Br-free basis with an assumed Fe^{3+}/Fe_T) may add information on the extent that a material has been altered from the original basaltic composition (e.g., Ming *et al.*, 2006). For example, corundum normative mineralogies (i.e., enriched in Al compared to that accommodated by feldspar) can indicate weathering and removal of mobile elements during aqueous alteration (see Section "Normative versus actual mineralogical composition").

23.2.4 Nomenclature for H_2O and OH speciation in solid phases

For purposes of discussion, it is useful to have specific working definitions for the ways the H_2O molecule is incorporated into solid geologic materials. We will use the following nomenclature: adsorbed H_2O, trapped H_2O, solvation H_2O, and crystal H_2O. Adsorbed H_2O is physically held to surfaces by either weak Van der Waals type forces because of the dipolar nature of the water molecule or by hydrogen bonding to acid sites on mineral surfaces. Adsorbed H_2O can usually be removed by decreasing pressure or heating the material to about 110 °C under ambient pressures. Trapped H_2O is a general term we use for H_2O physically confined into interstices, pore space, fluid/vapor inclusions, and/or grain boundaries during or subsequent to rock formation. Solvation H_2O (sometimes referred to as exchange cation water or zeolitic water) is H_2O that is coordinated with a cation on the exchange sites in the interlayers of phyllosilicates and within the cages of zeolites. Crystal H_2O is part of the unit cell and cannot be removed without changing the structure (although the dehydration of exchangeable or extraframework cations in zeolites and smectites may cause only very slight changes to unit cell parameters; e.g., Brown

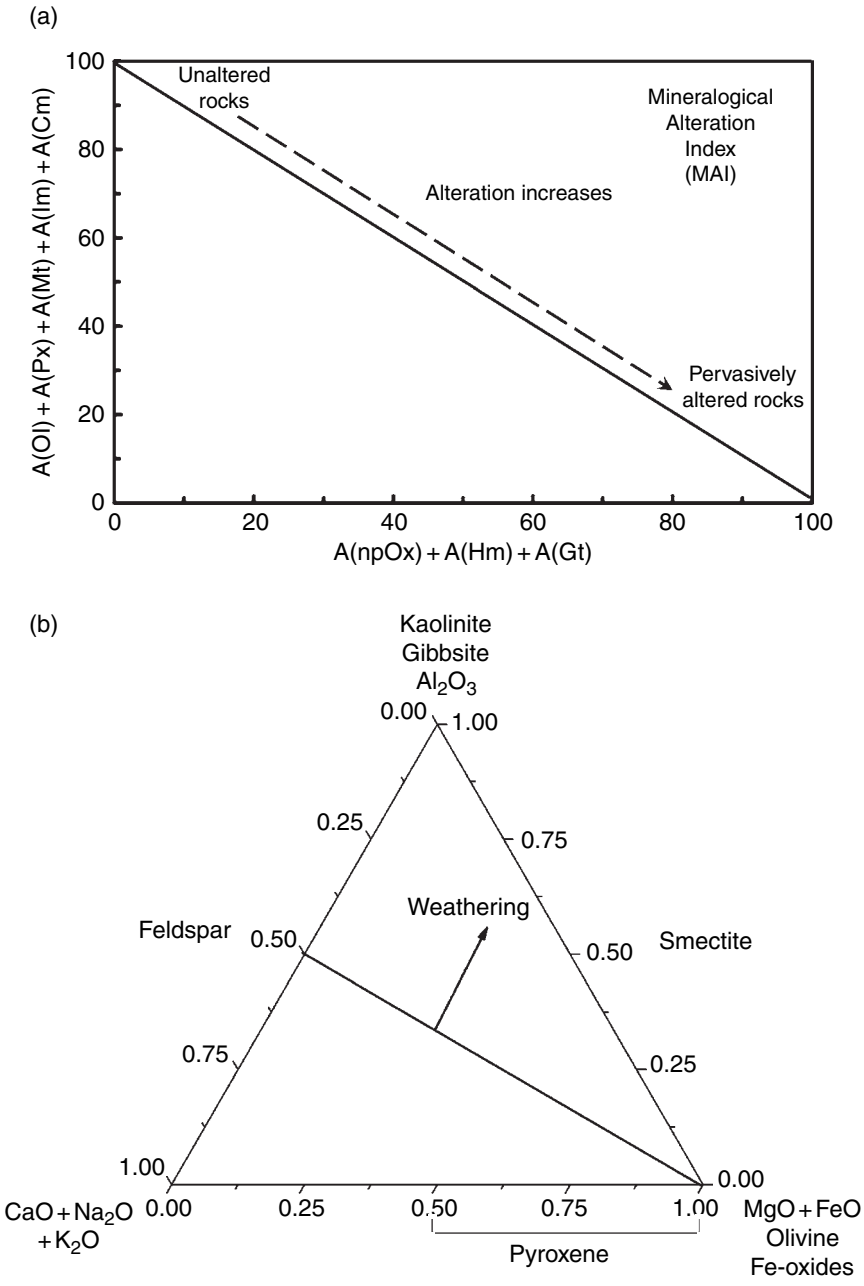

Figure 23.1. Chemical and mineralogical indices to evaluate alteration on Mars. (a) Mineralogical Alteration Index (MAI) established by the mineralogy of iron-bearing phases (Morris *et al.*, 2006a, b). Alteration trends are based on the area (spectral area [A] of each phase determined by Mössbauer spectroscopy) of primary phases (olivine [Ol], pyroxene [Px], magnetite [Mt], ilmenite [Im], chromite [Cm]) compared to the area of the secondary phases (nanophase oxide [npOx], hematite [Hm], and goethite [Gt]). (b) Compositional trends for basaltic materials (molar %). Unaltered basaltic materials will lie under the olivine–feldspar join. Weathered basaltic materials where leaching has taken place will fall upward from the olivine–feldspar join to more Al-rich composition (after Nesbitt and Wilson, 1992).

and Brindley, 1980; Bish and Carey, 2001; Bish *et al.*, 2003). In some cases (e.g., in the sulfate hexahydrite–epsomite system), the rehydration of these phases is reversible and results in reconstituting the mineral. Phases with solvation and crystal H_2O are collectively referred to as either "hydrous minerals" or "hydrated minerals." However, the phrase "waters of hydration" refers only to crystal water. The removal of adsorbed H_2O is called desorption, and the removal of trapped, solvated, and crystal H_2O is dehydration. Minerals that contain only OH^- (hydroxide anion) in their structures are, technically, anhydrous minerals containing hydroxyls (Dana's New Mineralogy; Gaines *et al.*, 1997), although they are formed as a product of aqueous activity and will decompose with evolution of H_2O when heated (i.e., dehydroxlyation).

23.3 PRE-MER MINERALOGICAL AND GEOCHEMICAL INDICATORS FOR AQUEOUS ALTERATION

A thorough characterization of the elemental and mineralogical composition of alteration phases and their precursors is required in order to fully evaluate the style and extent of aqueous alteration. Our knowledge of the occurrence of aqueously altered materials on Mars is limited to *in situ* and remote-sensing data returned by robotic missions (orbiters and landers/rovers), remote-sensing data by Earth-based telescopes, and laboratory analyses of the small number of Martian meteorites that have been discovered on Earth. The style and extent of aqueous alteration can

be addressed by comparing the Martian materials to terrestrial analogs that have similar phases of alteration. For purposes of discussion, we divide data for Martian surface materials into pre-Mars Exploration Rover (MER) orbital and lander missions (Telescopic, Mariner, Viking, Phobos, Pathfinder, and Mars Global Surveyor), Martian meteorites, and MER-era orbital and lander missions (MER, Mars Odyssey, and Mars Express).

23.3.1 Telescopic, Mariner, Viking, Phobos 2, and MGS Orbiters: "bound" water, hematite, and ice

Results from these earlier observations are discussed in detail elsewhere in this book (see, for example, Chapters 2, 7, 8, and 9). The intent of this section is to briefly point out major scientific findings that have suggested materials that might have formed on Mars by aqueous processes. IR spectrometry from telescopes and instruments on board the Mariner spacecraft detected possible water-bearing phases including frost, ice, or hydrated minerals such as montmorillonite along with mixtures of silicate minerals (e.g., Hanel *et al*., 1972; Houck *et al*., 1973; Hunt *et al*., 1973; Pimental *et al*., 1974; Toon *et al*., 1977; Clark and McCord, 1982; Bell and Crisp, 1993; Calvin, 1997). Visible multispectral imaging on board the Viking orbiters suggested the presence of amorphous Fe oxides (Evans and Adams, 1980). The presence of these hydrated phases and amorphous Fe oxides established that Mars has likely seen some extent of aqueous processes during its history. A distinct 3 μm water band was detected by the ISM (ISM – Imaging Spectrometer for Mars) instrument on board the Phobos-2 orbiter (Murchie *et al*., 2000), confirming the presence of water-bearing phases as indicated on earlier orbiting missions and telescopic observations.

The next major step forward in understanding alteration materials on the surface was the discovery of coarse-grained "gray" hematite by the Thermal Emission Spectrometer (TES) on board the Mars Global Surveyor (Christensen *et al*., 2000, 2001a,b). Several hypotheses were put forth for the formation of the gray hematite (Christensen *et al*., 2001b). One was hematite formation via precipitation of ferric iron oxides (e.g., ferrihydrite and goethite) from water on early Mars, followed by subsequent burial and recrystallization to platy hematite particles and later re-exposure at the surface (Lane *et al*., 2002). Since that time, the MERs have shown that water was indeed involved in the formation of the hematite and the sulfate-rich siliciclastic sediments at Meridiani Planum, and that the hematite is associated with a lag deposit of iron-rich spherules (see Chapter 24). Other minor abundances of secondary phases have been suggested based upon TES spectral data, including carbonates (e.g., Bandfield *et al*., 2003) and zeolites (Ruff, 2004). However, with the exception of the discovery of gray hematite by the MGS TES, our knowledge of the specific elemental and mineralogical composition of the phases that might have formed by aqueous processes is extremely limited from these earlier telescopic observations and orbiting missions.

23.3.2 Viking and Pathfinder Landers: sulfates? clays?

The Viking Lander missions significantly improved our understanding of the chemical composition of the Martian surface. The data returned by the X-ray Fluorescence Spectrometers (XRFSs) provided the first geochemical information on surface materials (Clark *et al*., 1977, 1982). However, the mineralogy of these phases was not determined by any definitive mineralogical method (e.g., X-ray Diffraction, Raman, or Mössbauer). Comparing explicit models with chemical data via multiple variation diagrams, it was inferred that Viking soils can be explained by two chemical components, one of which is restricted to contain S, Cl, and most of the Mg (Clark, 1993). The high Mg-S component occurs in what appeared to be duricrusted samples, suggesting cementation by Mg-sulfates. The Alpha Proton X-ray Spectrometer (APXS) on the Mars Pathfinder Sojourner microrover also found systematic variation between Mg and S (see Chapter 3). However, that trend is evident mainly in diagrams which include both soils and rocks, and could also be explained as a correlation simply resulting from Mg-S rich soil coating Mg-S poor rock surfaces to varying degrees (Pathfinder had no capability to clean or grind the rock targets, and Viking was unsuccessful in finding small rocks which could be delivered to the analytical instruments). The Martian soils analyzed by Viking and Pathfinder did not show positive correlations between Ca and S, in agreement with all later MER results. Using an X-ray backscatter standard, it was deduced that the Viking samples contained an additional 9 to 10 wt.% of undetectable components, which could include Na_2O, carbonates, and H_2O. Applying the typical Na_2O value of 3 wt.% for Martian soils (Yen *et al*., 2005) and allowing for 0–2 wt.% of CO_2 (as carbonate), these results indicate a possible H_2O content of 4–7 wt.%.

Pathfinder analyses using the Rutherford scattering alpha backscatter technique placed the strongest upper limit on carbon in the soils and rocks, at a value corresponding to less than 2.5 wt.% of CO_2 equivalent (Brückner *et al*., 1999). These measurements also indicate some H_2O content in some of the local K-rich rocks but less in soils (see Chapter 3).

23.4 MARTIAN METEORITES: SULFATES, HALIDES, CARBONATES, OXIDES, AND "CLAY MINERALS"

Laboratory analyses of Martian meteorites have greatly improved our knowledge of the geochemical, mineralogical, and chronological characteristics of materials from the Martian crust (see Chapter 17). Although these meteorites exhibit primary lithologies, several contain minerals strongly indicating indigenous aqueous processes on Mars, showing that water did at least have some influence on Martian crustal materials. The lack of evidence for extensive alteration in the Martian subsurface as represented by the Martian meteorites suggests that acidic weathering on Mars

is restricted to the surface or uppermost crust (e.g., Newsom, 2005). The intent of this section is to survey the phases that likely formed by aqueous processes in the Martian meteorites; a detailed review of the alteration assemblages in Martian meteorites is provided by Bridges *et al.* (2001).

The secondary phases that have been identified in Martian meteorites include sulfates, carbonates, iron oxides, sulfides, and poorly crystalline silicates/aluminosilicates (Table 23.1). The ALH84001 Martian meteorite, which is the oldest and is also known for the possibility that it harbors relicts of life (McKay *et al.*, 1996), contains mixed Fe-Mg-Ca carbonates, magnetite, and Fe sulfides (Mittlefehldt, 1994). A plausible model for the formation of this secondary mineral suite was that carbonate globules in ALH 84001 first formed as a hydrothermal precipitation product from CO_2-rich fluids whose composition changed with time and temperature, producing globules with ankeritic (Fe-Mg-Ca-carbonate) cores and concentric zones of Fe-rich carbonate (siderite) plus Fe disulfide (pyrite), magnesite (Mg-carbonate), and another Fe-rich carbonate plus Fe sulfide outer zone. During a subsequent thermal event initiated by impact or volcanic events, the ALH 84001 globules were sufficiently heated to form magnetite and pyrrhotite as decomposition products of siderite and pyrite, respectively (Golden *et al.*, 2001, 2004).

Minor amounts of Ca-rich sulfate (and other sulfates), halite (and other chlorides), and possibly phyllosilicates are present in Shergotty meteorite (Table 23.1). Solutions may have passed through the Shergotty precursor, periodically resulting in episodic alteration (Wentworth and Gooding, 2000). The Nakhlites (Lafeyette, Governador Valadares, Nakhla) contain a variety of secondary phases, including Fe-rich carbonates, Ca-sulfates, poorly crystalline aluminosilicates and iron oxides (e.g., iddingsite in Lafeyette), and halite (see Table 23.1). The recently discovered Nakhlite MIL 03346 has jarosite veins running through the meteorite's mesostasis (glassy and/or microcrystalline interstitial material); however, it is not clear whether the jarosite is indigenous to Mars or formed as the meteorite was weathered on Earth (Herd, 2006). Water appears to have reacted with the Nakhlites' host rocks (probably at low temperature), releasing ions into solution; the secondary phases likely formed during the evaporation of the solutions (Bridges and Grady, 1999, 2000). Chassigny contains minor amounts of Ca- and Mg-rich carbonates and Ca-rich sulfates. One possible scenario for their formation is percolation of briny water through the host rock and subsequent precipitation during evaporation of solutions (Wentworth and Gooding, 1994).

In summary, aqueous fluids have interacted with the host rocks of the Martian meteorites, and the interaction has resulted in low levels of alteration. No known Martian meteorite has been pervasively altered. It appears that in most instances briny waters have passed through the host rock and the secondary phases (salts) formed during evaporation of the solutions. With the exception of ALH 84001, these host materials are relatively young (by Martian standards); hence, these solutions must have interacted with the host rock during the late stages of the Amazonian period (recent to 1.8 Ga). The oldest Martian meteorite (ALH 84001), however, may have experienced hydrothermal fluids moving through its host rock during the Noachian period (3.5 Ga to around 4.54 Ga).

23.5 MER-ERA MINERALOGICAL AND GEOCHEMICAL INDICATORS FOR AQUEOUS ALTERATION

The four most recent spacecraft to arrive at Mars (the MERs *Spirit* and *Opportunity*, and the Mars Odyssey and Mars Express orbiters) have provided several positive mineralogical identifications of phases that formed as products of aqueous alteration. The most important mineralogical and geochemical markers for aqueous processes by the four spacecraft are briefly summarized below. The recent arrival of the Mars Reconnaissance Orbiter (MRO) will provide additional information on the mineralogical composition of the Martian surface.

23.5.1 Mineralogical markers

Mars Odyssey: water ice, hydrated minerals, adsorbed water, OH-bearing phases

One of the most significant discoveries by the Mars Odyssey Gamma Ray Spectrometer (GRS) and Neutron Spectrometers is the occurrence of near-surface H that is thought to be in the form of water ice, water associated with solid phases (i.e., crystal, solvation, trapped, and adsorbed water) and/or OH-bearing phases. Surface and subsurface ice is the most probable candidate for the high H signatures observed by GRS at high latitudes and near the polar regions (Boynton *et al.*, 2002; see Chapter 5). The Neutron Spectrometer also indicated H enrichments in low to middle latitude areas that may indicate chemically and/or physically bound water and/or OH (Feldman *et al.*, 2002; see Chapter 6). Water ice indicates that liquid water was available to play a significant role in surface processes (e.g., diffusion of water into regolith materials, atmospheric exchange, thin water films, and adsorbed water). The H signals in areas where ice is not thermodynamically favored, that is, at low to mid latitudes, suggest that earlier aqueous processes once interacted with solid materials to form hydrated and OH-bearing phases.

MER: goethite, jarosite, hematite, hydrated Fe-sulfates, and npOx

The Athena science payload on board the MERs *Spirit* and *Opportunity* has provided new insights into the aqueous history at their respective landing sites in Gusev crater and Meridiani Planum (Squyres *et al.*, 2004a,b). Aqueous alteration in Gusev crater ranges from minor alteration on the surfaces and interiors of rocks and within the regolith on the basaltic plains, to highly altered outcrops and rocks in the Columbia Hills (e.g., McSween *et al.*, 2004;

Table 23.1. *Aqueous alteration phases in Martian materials*

Mineralogy	Location/material	Mission/method	References
Sulfates			
Mg-rich sulfates	CP and UP duricrusts[a]	Viking XRFS	Clark (1993)
	GC soils, GC and MP outcrops[a]	MER APXS	Clark *et al.* (2005); Haskin *et al.* (2005); Ming *et al.* (2006); Wang *et al.* (2006a)
	MM (Nakhla, Chassigny)	Laboratory analysis	Gooding *et al.* (1991); Wentworth and Gooding (1994)
Kieserite	Layered terrians	MEx OMEGA	Gendrin *et al.* (2005)
Ca-rich sulfates	GC and MP outcrops; GC rocks[a]	MER APXS	Clark *et al.* (2005); Ming *et al.* (2006)
	MM (Chassigny, Nakhla, Shergotty, Governador Valadares, Layafette)	Laboratory analysis	Wentworth and Gooding (1994); Bridges and Grady (2000); Wentworth *et al.* (2005)
Gypsum	Layered terrians, north polar region	MEx OMEGA	Gendrin *et al.* (2005); Langevin *et al.* (2005)
Anhydrite	MM (Nakhla)	Laboratory analysis	Bridges and Grady (2000)
Fe-rich sulfates			
Jarosite	MP outcrops	MER MB	Klingelhöfer *et al.* (2004)
	MM (Mil 03346 Nakhalite[b])	Laboratory analysis	Fries *et al.* (2006); Herd (2006)
Ferric sulfate	GC soils	MER MB	Morris *et al.* (2006a)
Carbonates			
Fe-rich carbonates	MM (Lafayette, Governador Valadares, Nakhla)	Laboratory analysis	Bridges and Grady (1999, 2000)
Mg-rich carbonates	MM (ALH 84001, Chassigny)	Laboratory analysis	Mittlefehldt (1994); Wentworth and Gooding (1994)
	Martian dust (minor[c])	MGS TES	Bandfield *et al.* (2003)
	GC dust and surface soils (minor[c])	MER Mini-TES	Christensen *et al.* (2004b)
Mg-Ca-Fe carbonates	MM (ALH 84001)	Laboratory analysis	Dreibus *et al.* (1994); Romanek *et al.* (1994); Harvey and McSween (1996)
Ca-rich carbonates	MM (Chassigny, EETA 79001, ALH 84001)	Laboratory analysis	Gooding *et al.* (1988); Wentworth and Gooding (1994); Harvey and McSween (1996)
Oxides/oxyhydroxide			
Goethite	GC outcrops and rocks	MER MB	Morris *et al.* (2006a)
	MM (Nakhla, Lafayette, Governador Valadares)	Laboratory analysis	Bridges and Grady (2000)
Hematite	MP soils	MGS TES	Christensen *et al.* (2001a,b)
	GC outcrops and rocks, MP outcrops and soils	MER MB and Mini-TES	Christensen *et al.* (2004a,b); Klingelhöfer *et al.* (2004); Morris *et al.* (2006a)
npOx	GC soils, outcrops, and rocks	MER MB	Morris *et al.* (2004, 2006a)
	Mars bright and dark regions	Telescopic	Singer (1982); Bell *et al.* (1990); Morris *et al.* (2000)
Iddingsite ferrihydride	MM (Lafayette)	Laboratory analysis	Treiman *et al.* (1993)
Magnetite[d]	GC rocks, outcrops, and soils	MER MB	Morris *et al.* (2004, 2006a)
	MM (ALH 84001)	Laboratory analysis	McKay *et al.* (1996)
Chromite[e]	GC outcrop	MER MB and APXS	Morris *et al.* (2006a); Clark *et al.* (2007)

Silicates			
Amorphous silica	GC soils[a]	MER APXS	Haskin *et al.* (2005); Ming *et al.* (2006)
Phyllosilicates			
Smectite			
Montmorillonite-like[c]	GC outcrop[a]	MER APXS	Clark *et al.* (2007)
Al-rich (montmorillonite[c])	Mawrth Vallis	MEx OMEGA	Poulet *et al.* (2005)
Fe-rich (nontronite[c])	Nili Syrtis Mensae	MEx OMEGA	Poulet *et al.* (2005)
Fe-rich (nontronite[c])	CP and UP	Viking Labeled Release	Banin and Margulies (1983)
Iddingsite (smectite[c])	MM (Lafayette)	Laboratory analysis	Gooding *et al.* (1991); Treiman *et al.* (1993)
Chlorite[c]			
Fe/Mg-rich (chamosite[c])	Northern Syrtis Major	MEx OMEGA	Poulet *et al.* (2005)
Mica (phlogopite)	MM (ALH 84001)	Laboratory analysis	Brearley (1998, 2000)
Kaolinite/serpentine/1:1 phyllosilicate[c]	GC outcrop[a]	MER APXS	Wang *et al.* (2006b)
Zeolites[c]	Martian dust	MGS TES	Ruff (2004)
Salts of Cl and Br			
Cl salts	GC and MP soils, rocks, and outcrops[a]	MER APXS	Gellert *et al.* (2004, 2006); Rieder *et al.* (2004); Clark *et al.* (2005); Ming *et al.* (2006).
Halite	MM (Nakhla, Shergotty)[b] MP outcrop	Laboratory analysis MER APXS	Gooding *et al.* (1991); Wentworth and Gooding (2000) Yen *et al.* (2006)
Br salts[a]	GC and MP soils, rocks, and outcrops[a]	MER APXS	Gellert *et al.* (2004, 2006); Rieder *et al.* (2004); Clark *et al.* (2005); Ming *et al.* (2006)
Phosphates			
Brushite[c]	GC outcrops, rocks, and soils	MER APXS	Ming *et al.* (2006)
Others			
Pyrite[d]	MM (ALH 84001)	Laboratory analysis	Mittlefehldt (1994)
Pyrrhotite	MM (ALH 84001)	Laboratory analysis	Weiss *et al.* (2002)

Key: CP = Chryse Planitia; UP = Utopia Planitia; MPF = Mars Pathfinder; MER = Mars Exploration Rovers; MGS = Mars Global Surveyor; MEx = Mars Express; GC = Gusev crater; MP = Meridiani Planum; XRFS = X-ray Fluorescence Spectrometer; APXS = Alpha Particle X-ray Spectrometer; MB = Mössbauer Spectrometer; Mini-TES = Minature Thermal Emission Spectrometer; TES = Thermal Emission Spectrometer; OMEGA = Observatoire pour la Minéralogie, l'Eau, les Glaces et l'Activité; MM = Martian meteorite.

[a] Implied phase from elemental chemistry measurements on the surface of Mars.

[b] Possible terrestrial contamination.

[c] Questionable phase.

[d] Primary or secondary phase.

[e] Residual primary phase after aqueous alteration.

Haskin *et al*., 2005; Hurowitz *et al*., 2006; Ming *et al*., 2006; Morris *et al*., 2006a; Wang *et al*., 2006a). Some outcrops (layered and massive) and rocks on the Colombia Hills appear to be extensively altered as suggested by their relative "softness" as compared to crater floor basalts, high Fe^{3+}/Fe_T ratios, iron mineralogy dominated by nanophase Fe^{3+} oxides, hematite, and goethite, and high Br, S, and Cl concentrations in rock interiors exposed by grinding with the Rock Abrasion Tool (RAT; Gellert *et al*., 2006; Ming *et al*., 2006, Morris *et al*., 2006a; Squyres *et al*., 2006a; see Chapters 4 and 15). The discovery of goethite in Columbia Hills rocks is very important to understanding the history of water in Gusev crater, because this mineral can only form in the presence of water, in contrast to hematite that can form by either aqueous or nonaqueous processes (Morris *et al*., 2006a). Mössbauer measurements also detected the presence of a ferric-sulfate in a surface soil named Paso Robles (Morris *et al*., 2006a). Observations by Mini-TES (Mini-TES – Miniature Thermal Emission Spectrometer) suggest that the sulfate is hydrated (see Chapter 14). The extreme mineralogical and chemical compositions of Paso Robles soil very strongly implicate aqueous processes that involved the movement of liquid water (highly acidic) through the host material (Ming *et al*., 2006). Nanophase Fe-oxides (npOx) are also detected by the MB in soils and rocks at Gusev crater (Morris *et al*., 2004, 2006a; see Chapter 15); these npOx phases may include one or more superparamagnetic forms of hematite and goethite, lepidocrocite, akaganéite, schwertmannite, hydronium jarosite, ferrihydrite, iddingsite, and the Fe^{3+} pigment similar to that found in palagonitic tephra (Morris *et al*., 1989, 2000, 2004, 2006a; Bishop and Murad, 1996). Some of these phases contain H_2O and/or OH, but we do not have independent observational evidence that Martian npOx contains H_2O/OH. However, the concentration of Fe associated with npOx increases as the concentration of S + Cl increases, showing that npOx is an alteration product (Yen *et al*., 2005; Morris *et al*., 2006a; see Chapter 15).

The occurrence of jarosite, other sulfates (e.g., Mg- and Ca-sulfates), and hematite along with siliciclastic materials in outcrops of sedimentary materials at Meridiani Planum are strong indicators of aqueous processes (Christensen *et al*., 2004a; Klingelhöfer *et al*., 2004; Squyres *et al*., 2004c; Clark *et al*., 2005; McLennan *et al*., 2005; Morris *et al*. 2006b; see Chapters 15 and 24). Jarosite can only form by aqueous processes under very acidic conditions (van Breeman, 1980; Bigham and Nordstrom, 2000); for example, acid-sulfate weathering conditions resulting from the aqueous oxidation of Fe sulfides (e.g., Fernández-Remolar *et al*., 2005) or by sulfuric acid alteration of basalts by solutions associated with SO_2-rich volcanic gases (e.g., Morris *et al*., 1996). Hematite occurs as small particles (below MI [MI – Microscopic Imager] resolution of ~30 μm/pixel) embedded within the outcrop, as spherules embedded in the Meridiani outcrop, and a lag deposit where the hematite has physically weathered out of the outcrop and concentrated at the surface. The hematite-rich spherules have been interpreted to be concretions that have formed in the outcrop during a complex diagenetic history, as suggested by episodes of cementation and recrystallization, formation of the hematite-rich spherules, and dissolution and formation of crystal mold vugs in outcrops (McLennan *et al*., 2005; see Chapter 24).

The identification of jarosite and goethite was made on the basis of Mössbauer data along with supportive elemental data by the APXS. Hematite in the lag deposits was identified by both the Mössbauer Spectrometer and the Mini-TES. Details on the identification of these phases by Mössbauer and Mini-TES are presented in Chapters 14 and 15.

Mars Express OMEGA: kieserite, gypsum, M-OH (possible phyllosilicates)

The Observatoire pour la Mineralogie, l'Eau, les Glaces et l'Activité (OMEGA) instrument on board the Mars Express orbiter has returned visible/near-IR hyperspectral reflectance image data suggesting a diverse and complex surface mineralogy on Mars (see Chapter 7). Hydrated sulfates have been identified in some layered terrains on Mars. Kieserite ($MgSO_4 \cdot H_2O$) has been mapped at Candor, Melas, and Terra Meridiani and a few other locations; gypsum has been mapped in locations such as Iani Chaos and the northern polar dune regions; and a polyhydrated sulfate of unknown mineralogy has been identified in such locations such as Candor, Melas, and Terra Meridiani (Bibring *et al*., 2005, Gendrin *et al*., 2005, Langevin *et al*., 2005). One of the most exciting discoveries by the OMEGA instrument is the occurrence of phyllosilicate or phyllosilicate-like phases (based on metal-OH vibrations) associated with some Noachian outcrops. These iron-rich (possibly nontronite), Fe-, Mg-rich (possibly chamosite), and Al-rich (possibly montmorillonite) phyllosilicates appear to be associated with older terrains, suggesting that they formed by more neutral-pH aqueous processes during the very early history of the planet (Poulet *et al*., 2005; Bibring *et al*., 2006).

23.5.2 Geochemical inferences: element correlations and mineralogical mixing models

Except for Fe-bearing sulfates, hematite, and goethite identified by the MER Mössbauer instrument and hematite and sulfates suggested in Mini-TES spectra, there have been no other alteration phases such as halides, secondary aluminosilicates, and amorphous silica unambiguously detected by *in situ* instruments that are sensitive to mineralogical composition. The abundances of various phases have been estimated using elemental associations obtained from analysis of XRFS (Viking) and APXS (MER and Pathfinder) elemental data. Only MER chemical datasets are discussed here; XRFS and Pathfinder APXS data are discussed and reviewed by Clark *et al*. (1977, 1982), and in Chapter 3.

The mineralogical modeling of chemical data can vary significantly depending on the assumptions made in the mixing models. For example, S is assumed to be present in the form of a sulfate because of the highly oxidized nature of the Martian surface materials. The mineralogical composition of Columbia Hills outcrops, rocks, and soils was estimated from Fe mineralogy established by MB and mass balance calculations based upon APXS (Ming *et al*., 2006, Table 23.2). Somewhat arbitrary chemical compositions

Table 23.2. *Mineralogy of Columbia Hills outcrops, rocks, and soils estimated from Fe mineralogy established by MB, whole rock mineralogy by Mini-TES, and mass balance calculations based upon APXS compositions (see Ming* et al., *2006)*

	Rock classes											
	Clovis class				Wishstone class		Watchtower class		Peace class		Soil class	
	Clovis outcrop		Ebenezer rock		Wishstone rock		Watchtower outcrop		Peace outcrop		Paso Robles class	
Mineralogy	Case 1	Case 2	Case 1	Case 2	Case 1	Case 2	Case 1	Case 2	Case 1	Case 2	Paso Robles[a] Case 1	Paso Robles[b] Case 1
	%											
Primary phases												
Olivine	tr	tr	tr	tr	7	6	4	4	15	14	[c]	[c]
Pryoxene	12	33	9	42	11	12	5	22	24	48	[c]	[c]
Feldspar	0	34	0	21	13	52	0	30	0	7	[c]	[c]
Apatite	0	2	0	2	11	11	7	10	1	1	[c]	[c]
TiO_2	1	1	tr	tr	1	1	1	1	tr	tr	[c]	1[c]
Other metal oxides	tr	tr	tr	tr	tr	tr	tr	tr	1	1	[c]	[c]
Magnetite[d]	tr	tr	2	2	1	1	tr	tr	5	5	[c]	[c]
Ilmenite	0	0	0	0	1	1	1	1	0	0	0	0
Secondary phases												
npOx	3	3	4	4	1	1	4	4	2	2	[c]	[c]
Hematite	2	2	2	2	1	1	3	3	0	0	4	1
Goethite	5	5	2	2	0	0	1	1	0	0	0	0
Ferric sulfate	0	0	0	0	0	0	0	0	0	0	29	25
Mg-sulfate	tr	1	0	tr	2	1	5	5	9	10	10	10
Ca-sulfate	11	10	5	4	1	2	0	0	6	6	3	4
Other sulfates	0	0	0	0	0	0	0	0	0	0	2	5
Brushite ($CaH(PO_4) \cdot 2H_2O$)	2	0	2	0	0	0	0	0	0	0	10	8
Halides	2	2	1	1	1	1	1	1	1	1	1	1
Secondary aluminosilicates[e]	62	—	71	—	47	—	67	—	35	—	—	—
Allophane[e]	—	7	—	12	—	8	—	13	—	tr	5	7
Amorphous SiO_2[e]	—	0	—	5	—	0	—	5	—	4	10	11
Soil component[f]	NA	NA	NA	NA	NA	NA	NA	NA	NA	NA	27	27

The mineralogic modeling of these rocks and outcrops can vary significantly depending on the assumptions made for minerals used in the mixing models. Two extreme cases (Case 1 and Case 2) are provided to constrain the possible degree of alteration. Case 1 is modeled for pervasively altered materials assuming secondary phases (i.e., sulfates, aluminosilicates) are present. Case 2 is for least altered materials where primary phases are assumed present.

[a] Feature/Target = Paso Robles/Light Soil.

[b] Feature/Target = Pasadena/Paso Robles.

[c] Phase is calculated as part of the soil component listed below.

[d] Magnetite may be secondary phase.

[e] Secondary aluminosilicates include allophane and amorphous silica for the pervasive alteration case. Allophane and amorphous silica are listed for the minimal alteration case.

The dash mark (—) indicates that these phases were not modeled for that case.

[f] NA = not applicable. Soil component is the average composition of Gusev surface soils that has been mixed with the Paso Robles materials.

must sometimes be chosen for the Fe-bearing phases (e.g., the Fe/Mg ratio for olivine and pyroxene, the K/Na ratio for jarosite, npOx, etc.). Two extreme alteration cases (pervasive versus minimal) are presented to constrain the possible degrees of alteration among these materials. On the basis of these calculations, a variety of alteration phases were modeled in rocks and outcrops, including npOx, goethite, hematite, Ca- and Mg-sulfates, halides, and secondary

aluminosilicates. The altered aluminosilicate phases are grouped into a generic "secondary aluminosilicates" category because there is no direct mineralogical evidence for phases like phyllosilicates, allophane, zeolites, or other poorly crystalline phases.

Another example of an inferred mineralogy from geochemical data is the possible occurrence of montmorillonite or a montmorillonite-like phase in the Independence class outcrops on the upper slopes of Husband Hill in Gusev crater (Clark *et al.*, 2007). Compared to other Martian rocks and soils, these materials are characterized by their very low Fe content and high Al abundances as measured by their Al/Si ratios. Their major component (80 wt.%), after allowing for minor but significant levels of $MgSO_4$, Ca-phosphate, and ilmenite, is quartz normative (i.e., excess Si, suggesting quartz in an idealized mineral abundance calculation from a bulk chemical analysis of a rock). Associated with several of these samples are trace elements at elevated concentrations, including Cu, Sr, Y, and Cr. The elemental profile of the major component is well within the range of terrestrial montmorillonites or possibly a fortuitous mixture of certain zeolites. There is no indication of smectite phyllosilicates or zeolites from the IR spectra taken by the Mini-TES instrument, however (see Chapter 14). This major component therefore may be amorphous, resulting from an incomplete formation process or a structural degradation process acting on the material.

Only part of the sulfate occurring in the outcrops at Meridiani Planum is in the form of the Fe-rich sulfate jarosite. Other sulfates (Mg- and Ca-bearing) are inferred from the geochemical data obtained by the APXS on numerous holes ground by the RAT on *Opportunity* (Clark *et al.*, 2005; Table 23.3, see also Chapter 4) and Mini-TES spectra suggested the possibility of Mg- and Ca-bearing sulfates (Christensen *et al.*, 2004a; see also Chapter 14). Over a significant portion of the outcrop sequence, MgO correlates stoichiometrically with SO_3 (for $MgSO_4$) while CaO has no clear correlation with SO_3; this correlation suggests the presence of Mg-sulfates in the outcrop. However, to balance cations with sulfate anions, a portion of the Ca in these samples can be assigned to sulfate, after apportioning Ca also to phosphate and pyroxene. No definitive evidence is available to indicate the presence of carbonates in these samples, but a small amount could be present if the pH conditions at the time of formation or emplacement were much higher than that required for the initial jarosite formation. Multiple episodes of diagenetic modification have overprinted an earlier mineral assemblage (McLennan *et al.*, 2005). Chlorides are present, but at a low abundance relative to sulfate salts, and the predominant cation(s) could be Mg or Na. The element assemblage also is consistent with excess Si (one-fifth to one-fourth of the sample by weight as SiO_2), so that one or more of the likely weathering forms of silica and/or an aluminosilicate such as allophane may be present.

Upper limits for crystal water

The crystal water content of a bulk material (such as the Meridiani outcrop) can be estimated from its mineralogical

Table 23.3. *Mineralogical composition of Meridiani Planum outcrop inferred by modeling of geochemical data (Clark* et al.*, 2005)*

	Case 1 (SO_3 = 20%) wt.%	Case 2 (average) wt.%
Rock components		
Basaltic rock	0.0	16.2
Pyroxene[a]	4.6	0.0
Feldspar (Ab= 79 wt.%, Or=21%, An=0%)[b]	16.7	0.0
Sum rock components	21.3	16.2
Oxide components		
Hematite, Fe_2O_3	6.0	6.0
Anatase, TiO_2	(0.7)	0.6
Pyrolusite, MnO_2	(0.3)	0.3
Np-Ox, $(Fe_{0.94}Cr_{0.06})_2O_3$ (Fe3D3)	3.7	2.7
Sum oxide components	10.7	9.6
Sulfate components		
Jarosite, $(K_{0.51}Na_{0.49})(Fe_{0.91}Al_{0.09})_3S_2O_{11}(H_2O)_3$	0.0	9.9
H-Jarosite, $(H_3O)_3S_2O_{11}(H_2O)_3$	9.9	0.0
Schwertmannite, (Fe3D3), $(Fe_{0.94}Cr_{0.06})_{32}O_{69}S_7(H_2O)_9$	0.0	1.0
Kieserite, $(Mg_{0.99}Ni_{0.01})SO_4(H_2O)$	17.3	17.6
Bassanite, $Ca(SO_4)(H_2O)_{0.5}$	8.8	7.4
Thenardite, Na_2SO_4	0.0	0.5
Sum sulfate components	36.0	36.5
Chloride components		
Bischofite $(MgCl_2)(H_2O)_6$	2.4	0.0
Halite (NaCl)	0.0	1.9
Phosphate components		
Ca-phosphate	2.4	0.0
Variscite, $(Al_{0.90}Fe_{0.10})PO_4(H_2O)_2$	0.0	1.2
Aluminosilicate components		
Allophane, halloysite, and/or kaolinite, $Al_2Si_2O_7(H_2O)_2$	7.4	8.9
Opalline Silica, $SiO_2(H_2O)_{0.2}$	21.5	25.8
Sum aluminosilicate components	28.9	34.7
Carbonate component		
$CaCO_3$	0.2	0.0

Note: An aluminosilicate is advocated as feldspar in Case 1. A basaltic rock composition similar to Bounce rock is used for the rock component in Case 2. The principle difference between the two cases is that alkali elements and Al are modeled in the feldspar for Case 1 and these elements are modeled as alteration phases in Case 2.

[a] Tentatively identified as pyroxene by the Mössbauer spectrometer.

[b] Ab = albite; Or = orthoclase, An = anorthite.

composition. The water content cannot be determined from MER APXS data because the element totals are normalized on a water-free basis (Gellert *et al*., 2004, 2006; Rieder *et al*., 2004). The content of H_2O (as OH) associated with jarosite and goethite is known by stoichiometry, but the number of crystal waters associated with other Fe-bearing sulfates and the Ca- and Mg-sulfates at the MER landing sites is not well-constrained. For example, the binary Fe-sulfate, $Fe_2(SO_4)_3 \cdot nH_2O$, has values of n ranging from 1 to 9. Because the mineralogical composition of secondary phases is poorly constrained, only ranges of the amount of crystal water can be derived for surface materials by assuming limiting cases for crystal water contents.

Jarosites, along with Ca- and Mg-sulfates, have been suggested as the sulfur-bearing phases in Meridiani Planum outcrop (Klingelhöfer *et al*., 2004; Clark *et al*., 2005; Morris *et al*., 2006b). A survey of common evaporites, including mixed salt compounds with more than one cation, shows that about one-half of all candidate salts for Meridiani outcrops can be hydrated. Magnesium sulfate is particularly versatile, with minerals ranging from 1 water of hydration (i.e., kieserite) up through 2, 4, 6 (hexahydrite), and even 7 (epsomite) water molecules per unit cell. Calcium sulfate occurs commonly as gypsum, bassanite, or anhydrite, only the last of which is not hydrated. Hydrated sulfates are expected in Meridiani Planum outcrops as modeled during the evaporation of sulfate-rich chloride brines (Tosca *et al*., 2005). Based upon these models, the possible hydration levels for the outcrop in Meridiani Planum are shown in Table 23.4 (hydroxides in oxyhydroxides and hydration in possible phyllosilicates, allophane, or silica are not included in this analysis). These models reveal that from 6 to 22 wt.% of the outcrop may occur as crystal H_2O and/or OH. The estimate of water in Meridiani outcrop is consistent with measurements from the Odyssey orbiter, where the GRS has detected an average concentration of 7% H_2O-equivalent H down to a depth of approximately 1 m for the Meridiani Planum region (Feldman *et al*., 2004).

Another example of the crystal H_2O and OH content of a rock material is shown in Table 23.5 for rocks (Clovis, Ebenezer, Wishstone, Watchtower, and Peace) and a soil (Paso Robles) from West Spur and the northwest slope of Husband Hill in Gusev crater. A range of water content is estimated from the least and most hydrated sulfate, phosphate, and halide phases that may be present in these materials. Unfortunately, the mineralogical composition of the secondary aluminosilicate phases and npOx is unknown, and thus the crystal water content contributed by these phases cannot be included in this estimate. A variety of secondary aluminosilicates may be present in these materials, including phyllosilicates, allophane, amorphous silica, and other poorly crystalline aluminosilicate phases. It is highly likely that the ranges listed in Table 23.5 are higher than indicated because of contributions of hydrated aluminosilicates to the bulk water contents of these materials. Nonetheless, the Peace outcrop materials exhibited the highest water content (1.2–6.9 wt.% H_2O) of the rocks and outcrops encountered on Husband Hill. The Mini-TES spectra for Peace outcrop have a pronounced emissivity peak at

Table 23.4. *Inferred salt hydration content for the average composition of Meridiani Planum outcrop material for Case 1 mineralogy listed in Table 23.3 (Clark* et al.*, 2005)*

Salt	Min. H_2O (wt.%)	Max. H_2O (wt.%)
$MgSO_4 \cdot 7H_2O$ (epsomite)	—	14.5
$MgSO_4 \cdot H_2O$ (kieserite)	2.8	—
$MgSO_4$ adsorbed[a]	2.2	—
$CaSO_4$ (bassanite)	0.0	—
$CaSO_4 \cdot 2H_2O$ (gypsum)	0.0	
$MgCl_2 \cdot 6H_2O$	—	2.2
Na-jarosite	0.9	—
H_3O-jarosite	—	1.3
Hydroxylapatite	—	0.04
Chloroapatite	0.0	—
Total H_2O	5.9	22.2

Minimum (Min.) and maximum (Max.) water contents are provided to bracket the possible water content. The estimate for the minimum and maximum H_2O contents used minerals that would satisfy the composition with the lowest and highest possible water contents in their structures, respectively.
[a] $MgSO_4$ adsorbed is the amount of water assumed to be adsorbed on the surfaces of the sulfate.

$\sim 1630\,cm^{-1}$ that typically is attributed to the bending mode of molecular bound water (Ruff *et al*., 2006). Peace outcrop appears to be composed of basaltic sands that have been cemented by Mg- and Ca-sulfates and possibly amorphous silica (Ming *et al*., 2006), and the high water content results from the hydrated Mg- and Ca-sulfates.

The derived water content of the unique Paso Robles soil ranges from 2.4 to 16.9 wt.%. Paso Robles soil is extensively altered. The most notable characteristic of Paso Robles light-colored material is its high concentration of S, one of the highest contents measured on Mars at any location (Gellert *et al*., 2006). Paso Robles consists of Fe^{3+}-, Mg-, Ca-bearing and other sulfates, Ca-phosphates, hematite, halite, allophane, and amorphous silica (Ming *et al*., 2006). The hydration state of the ferric sulfate is not currently constrained by Mössbauer parameters, but if the sulfate is a simple ferric sulfate ($Fe_2(SO_4)_3 \cdot nH_2O$), the hydration state (n) is between 1 and 9. Thus, the majority of the water in Paso Robles is likely tied up in hydrated Fe^{3+}- and Mg-sulfates and perhaps hydrous forms of silica.

Normative versus actual mineralogical composition (norm calculations on a S-, Cl-, and Br-free basis)

Normative mineral calculations based upon the MER APXS elemental composition for relatively unaltered basaltic rocks

Table 23.5. *Inferred water content (wt.%) of several outcrops, rocks, and soils in the Columbia Hills, Gusev crater*

	Clovis outcrop		Ebenezer rock		Wishstone rock		Watchtower outcrop		Peace outcrop		Paso Robles soil	
Mineralogy	Min. H_2O	Max. H_2O	Min. H_2O	Max. H_2O	Min. H_2O	Max. H_2O	Min. H_2O	Max. H_2O	Min. H_2O	Max. H_2O	Min. H_2O	Max. H_2O
npOx	?	?	?	?	?	?	?	?	?	?	?	?
Hematite Fe_2O_3	0	0	0	0	0	0	0	0	0	0	0	0
Goethite FeOOH	0.5	0.5	0.2	0.2	0	0	0.1	0.1	0	0	0	0
Ferric sulfate												
$Fe_2(SO_4)_3 \cdot H_2O$	0	0	0	0	0	0	0	0	0	0	1.1	0
$Fe_2(SO_4)_3 \cdot 9H_2O$	0	0	0	0	0	0	0	0	0	0	0	8.4
Mg-sulfate												
$MgSO_4 \cdot H_2O$	0.1	0	0	0	0.2	0	0.7	0	1.2	0	1.3	0
$MgSO_4 \cdot 7H_2O$	0	0.5	0	0	0	1	0	2.6	0	5.1	0	5.1
Ca-sulfate												
$CaSO_4$	0	0	0	0	0	0	0	0	0	0	0	0
$CaSO_4 \cdot 2H_2O$	0	2.1	0	1.0	0	0.4	0	0	0	1.3	0	0.8
Other sulfates	0	0	0	0	0	0	0	0	0	0	?	?
Ca-phosphate												
Chloroapatite (or fluoro)[a]	0	0	0	0	0	0	0	0	0	0	0	0
Hydroxyapatite $Ca_5(PO_4)_3OH$[a]	0	tr	0	tr	0	0.2	0	0.2	0	tr	NM	NM
brushite $CaH(PO_4) \cdot 2H_2O$	NM	NM	NM	NM	NM	NM	NM	NM	NM	NM	?	2.1
Halides												
Halite NaCl	0	0	0	0	0	0	0	0	0	0	0	0
Mirabalite $MgCl_2 \cdot 6H_2O$	0	1.1	0	0.5	0	0.5	0	0.5	0	0.5	0	0.5
Secondary aluminosilicates[b]	?	?	?	?	?	?	?	?	?	?	?	?
Soil component[c]	NM	NM	NM	NM	NM	NM	NM	NM	NM	NM	?	?
Total H_2O	0.6	4.2	0.2	1.7	0.2	2.1	0.8	3.4	1.2	6.9	2.4	16.9

Note: Minimum (Min.) and maximum (Max.) water contents are provided to bracket the possible water content. The estimate for the minimum and maximum H_2O contents used minerals that would satisfy the elemental composition with the lowest and highest, respectively, water contents in their structures.
? Denotes H_2O content unknown and not modeled (i.e., H_2O content is assumed to be 0). npOx may include nanophases of goethite and other iron oxyhydroxides.
NM = phase not modeled for this case.
[a] Primary phase.
[b] Secondary aluminosilicates may include phyllosilicates, allophone, amorphous SiO_2, or other poorly crystalline aluminosilicates.
[c] Gusev basaltic soil component mixed in with Paso Robles light-toned soil. Water content of Gusev basaltic soils is unknown.
Source: Data taken from Ming *et al.* (2006).

in Gusev crater compare very well with the mineralogy indicated by the Mössbauer and Mini-TES instruments (McSween *et al.*, 2004, 2006). These same calculations on a S-, Cl-, and Br-free basis, with an assumed Fe^{3+}/Fe_T (see Section 23.2), performed on altered materials may be used to evaluate the hydrologic system in which they were altered (i.e., closed or isochemical versus open). The Wishstone, Watchtower, and Independence Class rocks in the Columbia Hills have corundum normative mineralogies (i.e., excess Al suggesting corundum in an idealized mineral abundance calculation from a bulk chemical analysis of a rock), although the Wishstone and Watchtower rocks are only slightly corundum normative (Ming *et al.*, 2006; Clark *et al.*, 2007). Terrestrial igneous rocks are rarely corundum normative. Therefore, the corundum normative rocks in the Columbia Hills have likely had their original igneous compositions changed by an alteration processe under an open hydrologic system where some of the original basaltic elements were removed from the system. However, with the exception of Independence, the elemental compositions of these rocks have not been substantially changed, suggesting minimal leaching from the system (see Section 23.6.1).

23.6 MODELS FOR AQUEOUS ALTERATION PROCESSES

Our knowledge of the types of aqueous alteration that are or have been active on Mars is limited by the small number of sites examined and by the small number of phases definitively identified to date that have formed by aqueous processes. The previous sections of this chapter focused on summarizing what is known about the mineralogical composition of secondary phases on Mars. In this section, styles of aqueous alteration are described based upon our current best estimates of the alteration mineralogy at the surface.

23.6.1 Isochemical versus open-system alteration

Mars is a basaltic planet and the surface is dominated by basaltic elemental and mineralogical compositions (Christensen *et al.*, 2000; McSween *et al.*, 2004, 2006; Rieder *et al.*, 2004; see also Chapters 3, 4, 9, 10, 14, 15, 22, and 24). Weathering or the removal of soluble species from the reaction front is expected if water freely moved on the surface of Mars similar to the way it moves in open hydrologic systems on Earth. For example, elements such as the alkali and alkaline earth cations and Si are removed from reaction fronts under near-neutral pH conditions; altered or precipitated phases that remain behind after weathering of basaltic materials are enriched in Al (see Figure 23.1; Nesbitt and Wilson, 1992). The MER mission has significantly enhanced our understanding of the extent of alteration and weathering because of the mobility of the rovers, the resulting ability to characterize the geochemistry of rocks, outcrops, and soils at numerous locations, and the ability to identify minerals by the MB and Mini-TES instruments. The geochemistry of the major rock classes encountered in Gusev crater is illustrated on the ternary diagram in Figure 23.2a. Four of the major rock classes (Adirondack, Clovis, Wishstone, and Watchtower) fall along the olivine–feldspar join. The geochemistry of these four rock classes suggests that they have not been extensively altered by open-system aqueous processes; that is, they have not been extensively leached of mobile elements. Independence Class rocks, on the other hand, show trends toward Al-enrichments, suggesting that this material has undergone weathering with leaching and may contain a smectite-like phase or its compositional equivalent (Clark *et al.*, 2007).

Although leaching is not prominent in most Gusev crater rocks and outcrops (Figure 23.2a), the iron mineralogy suggests that some materials have been extensively altered by aqueous processes (Figure 23.2b). Adirondack Class basalt has undergone minimal alteration according to the MAI discussed above; however, the weathering trend in Figure 23.2b suggests that Clovis and Watchtower class rocks range from moderately to pervasively altered materials (i.e., highest Fe^{3+}/Fe_T). The more altered outcrops and rocks on the West Spur of Husband Hill contain goethite (Ming *et al.*, 2006; Morris *et al.*, 2006a). Although the Watchtower outcrop has several compositional similarities to Wishstone class rock targets (Wishstone and Champagne), it is highly altered compared to the other targets. Interestingly, Independence class rocks appear to be among the least altered rock in the classes shown on Figure 23.2b. One reason for its moderate-to-low MAI is that most of the iron has been weathered or removed from the material, except that fraction most resistant to weathering (e.g., chromite; Clark *et al.*, 2007). It is therefore likely that the MAI does not adequately represent the actual degree of alteration in Independence class rocks because of the low iron content and the likely removal of Fe-bearing phases by alteration.

The combination of the two alteration/weathering indices presented here (Chemical Alteration Index and MAI) suggest that most rocks and outcrops in the Columbia Hills have not undergone extensive leaching in an open hydrolytic system. The extensively altered rocks (e.g., Watchtower and Clovis class), with the exception of Independence class rocks as discussed above, appear to have undergone alteration under isochemical or nearly isochemical conditions. Most likely they have been altered by water, where the water/rock ratio is very low. Because these extensively altered materials contain sulfates (possibly hydrated as illustrated earlier), these systems are likely open in the sense that they received additions of S, Cl, and water, but they are closed in the sense that there is very little or no leaching of major elements away from reaction fronts. With the exception of Independence and Peace Class rocks, aqueous alteration in the Columbia Hills appears to be isochemical, with only the addition of the volatile phases most likely from volcanic emissions.

Jarosite, hematite, and other sulfates (e.g., Mg-bearing sulfates) occur along with siliciclastic sediments in outcrops at Meridiani Planum. A leading candidate for the formation of these sediments is the evaporation of acid fluids that have interacted with and altered olivine-bearing basaltic materials (Tosca *et al.*, 2005). A key but reasonable assumption is that waters rich in sulfuric acid interacted with precursor basaltic sediments in Meridiani Planum. Alternatively, sulfuric acid waters could form by the interaction of volcanic emissions (i.e., SO_2, Cl, Br) with water vapor or liquid or by reaction of H_2O and sulfides under oxidizing conditions. Key questions on the formation of these sulfate-rich sediments are how much acidic water interacted with the basaltic sediments and whether solutions moved through these sediments and removed soluble constituents (i.e., open hydrologic system) or if these sediments were altered under isochemical conditions (i.e., closed hydrologic system with the additions of water, S, Cl, and other volatiles from volcanic emissions). The bulk chemical composition of the Meridiani outcrop materials does not deviate substantially from what would be expected for basalt weathered under isochemical conditions (Figure 23.3). It thus appears that there was very little movement of soluble components out of the Meridiani "basin" during the formation of the bedrock. Although the alteration of the original basaltic sediments is extensive, the weathering or leaching of soluble components out of the system was minimal. An alternative hypothesis is that the sulfates, chlorides, and possibly other phases were brought into Meridiani as sediments by water and then precipitated to form the sulfate-rich siliciclastic sediments (e.g., Newsom *et al.*, 2003). For example, the composition of the siliciclastic

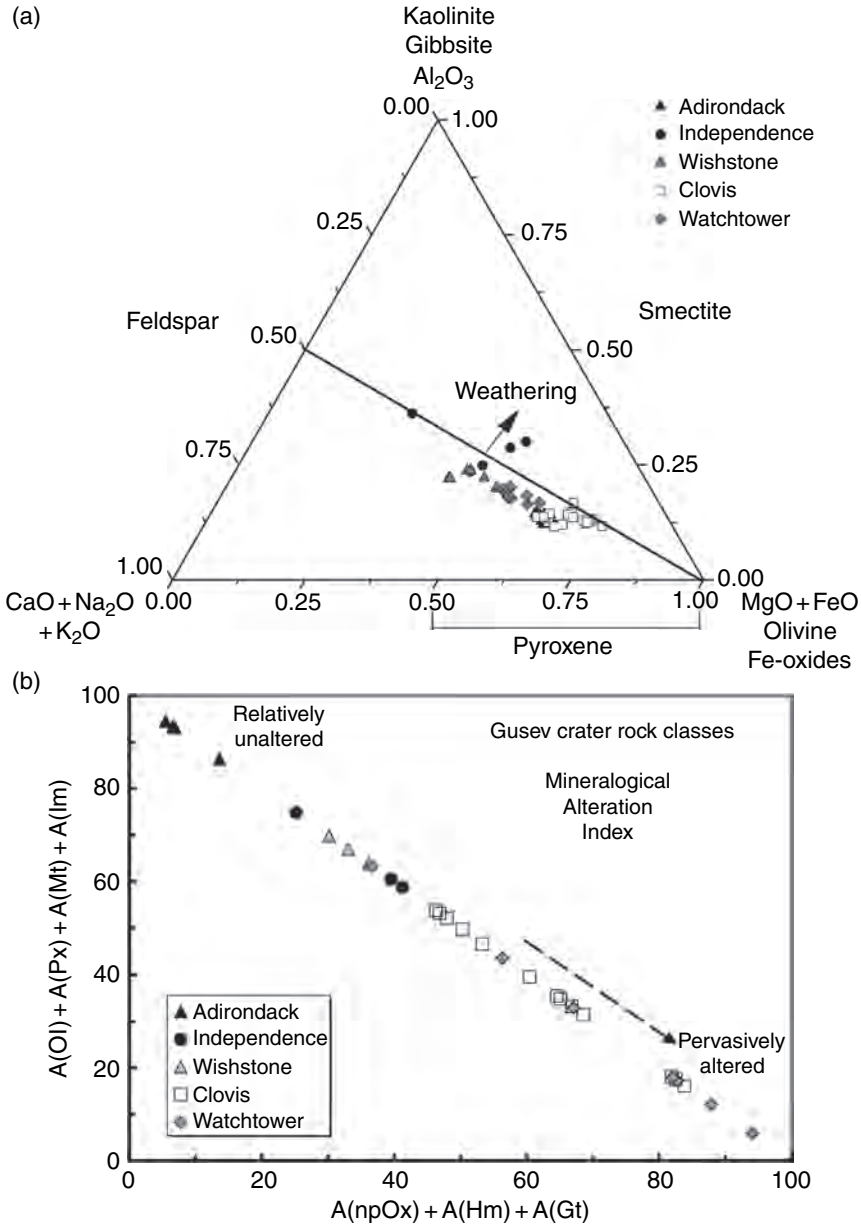

Figure 23.2. Chemical and mineralogical alteration indices for rock classes in the Columbia Hills, Gusev crater. (a) Mineralogical Alteration Index (MAI). (b) Compositional trends (see Figure caption 23.1 for definition of terms).

component begins to trend toward a smectite-like composition if the composition of the sulfates and that of halides are extracted from the average composition of the Meridiani bedrock (Figure 23.3). However, this hypothesis is somewhat suspect if the compositional sums of the siliciclastic sediments and sulfates resemble a basaltic composition similar to basaltic sands in the Meridiani area.

Several hypotheses on the formation processes for Meridiani outcrop materials have been put forth, including aqueous, volcanic, and impact processes. Squyres *et al.* (2006b) suggested that the outcrops formed when ancient Meridiani once had abundant acidic groundwater, arid and oxidizing surface conditions, and occasional liquid flow on the surface. Another hypothesis is that regional heating caused a release of sulfide-rich hydrothermal waters that formed pyrite-rich deposits, and the subsequent aqueous oxidation of these deposits formed the sulfates and hematite in Meridiani outcrops (Zolotov and Shock, 2005). On the other hand, McCollom and Hynek (2005) and Knauth *et al.* (2005) have suggested that the aqueous alteration occurred during flows induced by volcanic and impact base surges, respectively.

23.6.2 Acid-sulfate alteration

The high elemental abundance of S in surface materials is obvious evidence that sulfate has played a major role in aqueous processes at all landing sites on Mars. The sulfate-rich outcrop at Meridiani Planum contains jarosite and Ca-Mg-sulfates and has an SO_3 content of up to 25 wt.% (Rieder *et al.*, 2004; Clark *et al.*, 2005). The interiors of rocks and outcrops on the Columbia Hills have up to 8 wt.% SO_3 (Ming *et al.*, 2006). Soils at both sites generally have between 5 to 14 wt.% SO_3 (Haskin *et al.*, 2005; Gellert

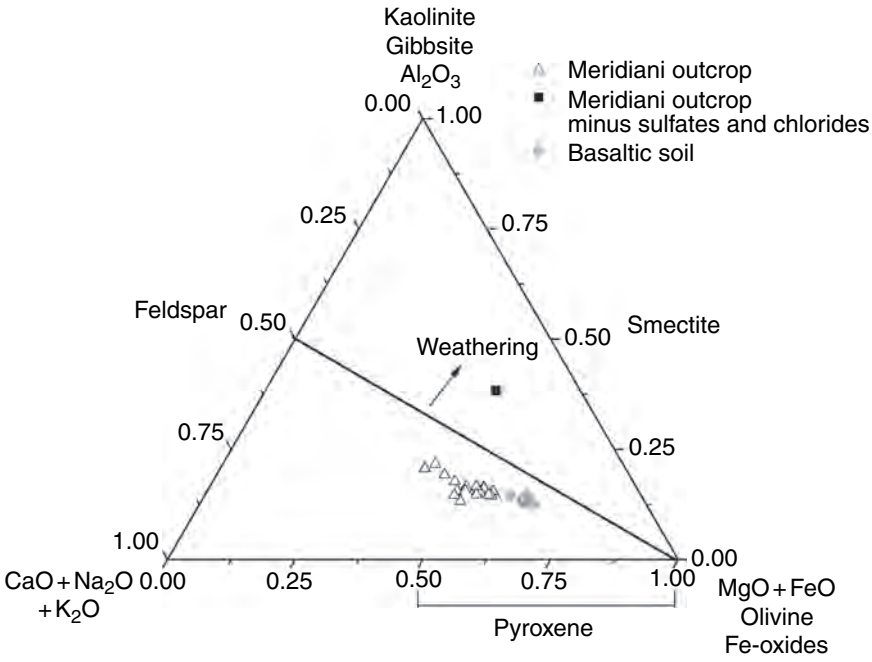

Figure 23.3. Compositional trends for Meridiani Planum outcrop materials. The composition for the point marked Outcrop minus sulfates & chlorides has been corrected for Fe, Mg, and Ca sulfates and chlorides (data from Clark *et al.*, 2005).

et al., 2006) and one soil (Paso Robles) on Husband Hill contains around 31 wt.% SO_3 (Gellert *et al.*, 2006). After normalization of major element compositions to a SO_3-free basis, the bulk compositions of these materials are basaltic, with a few exceptions in the Columbia Hills (e.g., Watchtower and Independence Class rocks, along with certain other outcrops such as Wooly Patch; Ming *et al.*, 2006). These observations suggest that the surface materials were derived from basaltic precursors by acid-sulfate alteration under nearly isochemical conditions and/or very low water:-rock ratios with minimal leaching.

Several hypotheses have been suggested for the aqueous formation of sulfate-bearing phases on the surface of Mars including (1) oxidative weathering of ultramafic igneous rocks containing sulfides (Burns, 1988; Burns and Fisher, 1990); (2) sulfuric acid weathering of basaltic materials (Morris *et al.*, 1996, 2000); and (3) acid-fog (i.e., vapors rich in H_2SO_4) weathering of basaltic or basaltic-derived materials (Clark and Baird, 1979; Banin *et al.*, 1997). All three processes involve acid-sulfate alteration environments. Other candidate processes not involving acid-sulfate conditions might include the dissolution and movement of soluble components by water (e.g., groundwater, water in thin films, flowing or standing water) and the subsequent formation of evaporitic mineral deposits (e.g., Mg- and Ca-sulfates and chlorides; Moore *et al.*, 1978, 1987; Clark *et al.*, 1982).

Sulfuric acid solutions from volcanic processes

The formation of jarosite in Meridiani Planum outcrops is strong evidence for the aqueous alteration of basaltic materials under acid-sulfate conditions and may be analogous to the formation of jarosite in basaltic materials on Mauna Kea volcano in Hawaii under oxidizing, hydrothermal conditions (Morris *et al.*, 1996, 2000). The Mauna Kea sulfuric acid solutions are the result of interactions of SO_2-rich volcanic gases with water. Acid-sulfate solutions percolated up through the basaltic tephra, dissolved Fe and other cations, and precipitated jarosite when environmental conditions permitted its formation (see Golden *et al.* [2005] for detailed discussion on environmental conditions necessary for formation of jarosite). The pH of the system plays a major role in defining the stability field between jarosite and hematite (or goethite) formation. Jarosite is stable in the pH range ~0.75–3.5; below this range jarosite dissolves and above this range it hydrolyzes to form hematite and/or goethite (e.g., see the stability diagram in Burns and Fisher, 1990). The sulfuric acid solutions in Meridiani were apparently not sufficiently "neutralized" by the basaltic sediments, and thus the pH was low enough to favor precipitation of jarosite.

Although jarosite was not identified in the rocks and soils of the Columbia Hills of Gusev crater, the mineralogy and chemistry of ferric sulfates in Paso Robles soil are still very strong indicators of aqueous processes. Ming *et al.* (2006) suggested that Paso Robles is an evaporite deposit that formed from solutions rich in Fe, Mg, Ca, S, P, and Si. The occurrence of ferric sulfates and not jarosite constrains the solution Eh and pH to a highly oxidized, extremely low pH solution. Support for this scenario comes from the high Fe^{3+}/Fe_T and the lack of goethite, jarosite, and abundant hematite. Ferric sulfates are predicted in acid-sulfate weathering environments when solution pH is <1 (Burns and Fisher, 1990; Bigham and Nordstrom, 2000; Madden *et al.*, 2004). As noted above, the stability field for jarosite is between pH ~0.75 and 3.5, and Fe-oxides/oxyhydroxides form in acid-sulfate solutions with pH >3.5 (e.g., Nordstrom, 1982; Tosca *et al.*, 2005). Golden *et al.* (2005) showed that Ca-, Mg- and Al-sulfates form by the alteration of olivine-rich and plagioclase-rich basaltic materials in very-acidic (sulfuric acid), oxidizing solutions (pH <1) with a very low level of water activity. The high Mg, Fe,

and P in Paso Robles may reflect the nature of the host material that was altered by sulfuric acid. For example, it is reasonable to assume that the high Fe and Mg are the result of sulfuric-acid solutions reacting with the source materials of the Peace basalt source and the P and Ca are the result of these caustic solutions reacting with a Wishstone-like source material (Ming *et al*., 2006). Paso Robles soil appears to be localized in a small area. This may indicate that volcanic vents with SO_2-rich vapors were present in the Husband Hill area, similar to alteration vents seen on cinder cones on Mauna Kea (e.g., Morris *et al*., 2000). Other soils similar to Paso Robles have been located elsewhere on Husband Hill and in the Inner Basin (Yen *et al*., 2007). The possibility that Paso Robles materials are more widespread cannot be ruled out because of its occurrence in the subsurface (only exposed in certain places by the action of the rover wheels). Another confounding problem with unraveling the genesis of this material is the impact history of the Columbia Hills. Materials may have been reworked and possibly overturned by impact (Arvidson *et al*., 2006), so it is difficult to place this material into a stratigraphic sequence.

Sulfuric acid solutions from sulfides

Acid-sulfate weathering on Earth, in general, results from processes that release sulfuric acid into a soil or sediment. Nearly all of the occurrences of acid-sulfate soils and sediments on Earth have resulted from the oxidative weathering of sulfidic materials (i.e., materials containing sulfides such as pyrite) and are often the culmination of complex biogeochemical processes (Nordstrom, 1982). Acid-sulfate minerals (e.g., jarosite) form during the oxidation of sulfides (e.g., pyrite) when the quantity of sulfuric acid exceeds the acid neutralizing capacity of adsorbed bases and weatherable minerals to the extent that the solution pH drops below 3.5 (Pons *et al*., 1982). Under terrestrial conditions, acid-sulfate production is generally observed in freshly exposed sediments that contain sulfidic materials (e.g., mine spoils) and in sediments that undergo a change in hydrology that produces oxidizing conditions (e.g., drying of a lake bed, sea line regression, draining of lagoons). Major products of acid-sulfate weathering include jarosite, barite, and gypsum (Carson *et al*., 1982); hydrated ferrous sulfates (melanterite, rozenite, szomolnokite) and copiapite (hydrated ferrous/ferric sulfate) in coal deposits (Nuhfer, 1967); oxyhydroxysulfates like schwertmannite and ferrihydrite (Bigham *et al*., 1990); goethite (van Breeman, 1980); hematite (Kevie and Yenmanas, 1972); nontronite (van Breeman, 1980); amorphous silica (van Breeman, 1980); and ferric sulfates (copiapite, coquimbite, jarosite, schwertmannite) in acid river sediments (Hudson-Edwards *et al*., 1999; Buckby *et al*., 2003).

Burns (1988) suggested that oxidative weathering of sulfides might be a significant process on the surface of Mars. In his model, iron-rich ultramafic igneous rocks containing pyrrhotite–pentlandite contacted aerated groundwater, generating strongly acidic, sulfate-rich solutions. In the oxidized section above the groundwater table, sulfates (e.g., jarosite) and hydrated ferric oxides are precipitated from solution by the oxidation of the sulfide and dissolution of Fe. In a follow-up study, Burns and Fisher (1990) proposed that massive and disseminated iron-sulfide mineralization might have occurred near the Martian surface based upon the probable presence of komatiitic igneous rocks, as suggested by geochemical evidence from SNC (SNC – Shergottite, Nakhlite, and Chassignite) meteorites and the Viking XRFS analyses (Baird and Clark, 1984). As described above, these deposits would then be postulated to have undergone oxidative weathering near the Martian surface and result in the formation of Fe-rich sulfates and hydrated Fe-oxides.

Perhaps the basaltic sediments at Meridiani Planum initially contained sulfides (e.g., pyrite) as a major component; however, there are no indicators (e.g., framboidal growth and/or cubic morphology of jarosite) that suggest a sulfide precursor.

Acid fog on rock/soil surfaces

Acid-fog alteration on rock and soil surfaces has been suggested as an acid-sulfate weathering process for surface materials (Clark and Baird, 1979; Banin *et al*., 1997; Tosca *et al*., 2004; Golden *et al*., 2005; Hurowitz *et al*., 2006). The acid-sulfate reactions are driven by acidic volatiles (e.g., SO_2, HCl, H_2O) deposited from the atmosphere and then reacted with the mineral surfaces in the dry Mars environment. Laboratory-simulated acid weathering of palagonitic tephra by Banin *et al*. (1997) resulted in the formation of gypsum and alunogen; those authors hypothesized that the top layer of Mars "soil" may have formed by extremely slow ongoing weathering interactions at the atmosphere–rock interfaces. Tosca *et al*. (2004) subjected synthetic basaltic analogs derived from Mars Pathfinder soil and rock compositions to various acidic solutions and subsequent evaporation. Crystalline Mg-, Fe-, Ca-, and Al-sulfates (but not jarosite) were identified as reaction products, along with secondary ferric-oxide phases, which formed via rapid Fe oxidation under relatively high pH levels buffered by basalt dissolution. Amorphous silica was also identified as a ubiquitous product on particle surfaces. Golden *et al*. (2005) subjected basaltic tephra materials to acid-fog conditions in the laboratory and found that Al-, Fe-, and Ca-sulfates and amorphous silica formed from plagioclase-rich tephra, and Mg- and Ca-sulfates and amorphous silica formed from the olivine-rich sand.

Hurowitz *et al*. (2005) have presented evidence for very low pH (pH = 0–1) alteration at rock and outcrop surfaces in Gusev crater based upon laboratory experiments. They suggest that there is a leached layer where, for example, Clovis outcrops and rocks are depleted in Mg and Fe at their surfaces compared to their interiors (i.e., holes created by grinding with the RAT), probably as a result of pyroxene and/or basaltic glass dissolution by acidic fluids (e.g., sulfuric acid fog). Under this process, acidic vapors reacted only at the surfaces of rocks and outcrops, leaching some elements (i.e., Fe and Mg) and resulting in the observed depletion trends of Mg and Fe from the rock's interior.

23.6.3 Neutral and alkaline pH hydrolytic alteration

The geochemistry and mineralogy of surface materials analyzed by MER instruments are consistent with aqueous alteration under acid-sulfate conditions, with the possible exception of the Independence class rocks. However, recent near-IR spectral data returned by the OMEGA instrument on Mars Express suggests the presence of phyllosilicates such as smectites that potentially formed under near neutral or even slightly basic conditions (Bibring *et al.*, 2006).

The formation of smectites in the terrestrial environment requires aqueous environments where solutions have high Si and Mg activity and neutral-to-alkaline pH conditions (Jackson, 1965; Kittrick, 1971; Weaver *et al.*, 1971; Kloprogge *et al.*, 1999). Although smectites can form under low-temperature and hydrothermal conditions, smectite formation in laboratory experiments has been most successful under hydrothermal conditions (see review by Kloprogge *et al.*, 1999). The OMEGA instrument detected IR spectral features from Fe-OH, Fe/Mg-OH, and Al-OH functional groups that may suggest a range of smectite compositions from nontronite (Fe-rich) to montmorillonite (Al-rich). Numerous starting materials may result in the formation of smectites and other phyllosilicates (including volcanic materials; Kloprogge *et al.*, 1999), so it is reasonable to expect smectite formation by aqueous alteration of basaltic materials especially under neutral-to-alkaline pH, hydrothermal conditions.

A potential terrestrial analog for the formation of smectites and other phyllosilicates on Mars are several altered cinder cones (Puu Poliahu and Puu Waiau) near the summit of Mauna Kea volcano in Hawaii. Deposits on these cones have been significantly altered under hydrothermal conditions to produce well-developed crystalline sulfates (alunite and jarosite), phyllosilicates (smectites and kaolinite), and zeolites (Ugolini, 1974; Golden *et al.*, 1993; Morris *et al.*, 1996, 2000; Wolfe *et al.*, 1997). Visible and near-IR spectra suggest that the smectite endmembers are montmorillonite and saponite (Guinness *et al.*, 2007). The mineralogy of Puu Poliahu is dominated by four types of alteration processes: (1) Hydrolytic, low temperature alteration of basaltic tephra to form palagonite and nanophase Fe-oxides; (2) Hydrothermal, sulfatetic/hydrochloric acid alterations of basaltic tephra to form sulfates (jarosite, alunite) and kaolinite; (3) Hydrothermal neutral-to-alkaline pH alterations of basaltic tephra to smectites (saponite and montmorillonite) and zeolites; and (4) Thermal, oxidative alteration of fresh basaltic tephra to form concentrically zoned hematite units on cinder cones (Morris *et al.*, 2000; Guinness *et al.*, 2007). The processes observed and described on Mauna Kea may not only be analogs for smectite formation on Mars, but also analog processes for the formation of sulfates, Fe-oxides, and other poorly crystalline phases on Mars in general.

Another potential aqueous process that may form smectites and other secondary phases under neutral or alkaline conditions is hydrothermal aqueous alteration associated with an impact event (e.g., Newsom, 1980; Allen *et al.*, 1982; Morris *et al.*, 1995; Newsom *et al.*, 1999, 2001; Naumov, 2002). Large impacts will generate a thermal pulse through the host material. Hydrothermal aqueous alteration can thus occur in these large impact events if the host materials contain water and/or other volatile phases.

23.6.4 Style and timing of aqueous alteration

The existence of sulfates and probably phyllosilicates on the Martian surface suggests that it has experienced very different aqueous conditions over time. Although carbonates are not thought to persist at the surface (Clark and Baird, 1979), their presence in Martian meteorites suggests that crustal materials have been influenced by aqueous processes that favored carbonate formation in some epoch. The general conditions and possible styles of alteration on Mars are shown in Figure 23.4. Fe-sulfates detected by the MERs suggest that acid-sulfate weathering has played a major role in the alteration process on Mars as discussed in Section 23.6.2. Other sulfates that are common products during acid-sulfate alteration (e.g., Ca- and Mg-bearing sulfates) are also being detected in large areas by Mars Express (see Section "Mars Express OMEGA: kieserite, gypsum, M-OH" and also Chapter 7). The OMEGA instrument on Mars Express is also detecting possible phyllosilicates that most likely formed under neutral to more alkaline hydrolytic conditions (see Sections "Mars Express OMEGA: kieserite, gypsum, M-OH" and 23.6.3, as well as Chapter 7). The occurrence of apparently secondary carbonates in the Martian meteorites also suggests alteration and precipitation in neutral-to-alkaline conditions in crustal materials.

The occurrence of phyllosilicates suggests the presence of neutral to slightly alkaline hydrolytic conditions very early in the planet's history (Noachian) and that the sulfates may have formed later under acid-sulfate conditions during the Hesperian (Bibring *et al.*, 2006). Also during the Noachian, alkaline conditions in crustal waters would have been favorable, at least locally, for the formation of carbonates as suggested by the 3.9-Gyr-old carbonates in the

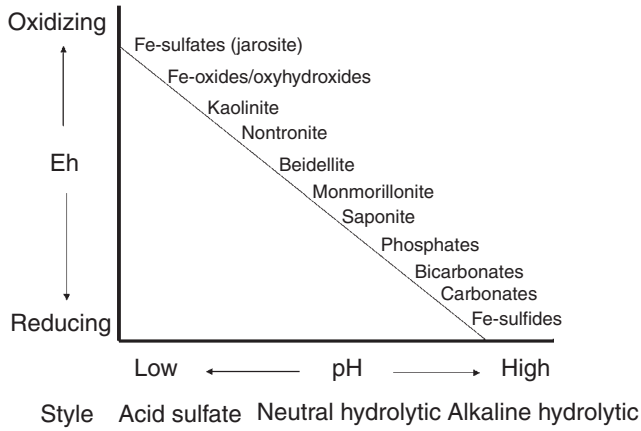

Figure 23.4. General environmental conditions and styles of weathering for the formation of secondary phases that might be present on Mars. *Note:* These conditions are provided only in a general sense. Formation conditions vary substantially for these phases.

ALH 84001 Martian meteorite (Golden *et al.*, 2001). Conditions at the surface were either unfavorable for the formation of carbonates, or the carbonates have since been destroyed (Clark *et al.*, 1979), because there is only minor orbital or *in situ* evidence for their existence on the surface and in the airborne dust (e.g., Bandfield *et al.*, 2003; see also Chapter 9). Thus, most of the aqueous alteration appears to have occurred early in the history of the planet (3–4.5 Ga). While aqueous alteration may still be occurring at the surface today (e.g., thin films of water, acid fog, etc.), no evidence has yet been found of substantial alteration at the surface for the past 3 Gyr.

Some of the Martian meteorites are relatively young (e.g., 1.26–1.38 Ga for Nakhlites) and have evidence for minor secondary phases such as carbonates. Although the alteration of these crustal materials is minor, it does suggest that solutions have moved through these materials in Amazonian times and that aqueous processes may indeed still be active in the subsurface on Mars.

23.7 SCIENCE NEEDS AND FUTURE MISSIONS

Our understanding of aqueous processes on Mars will be significantly enhanced by additional definitive mineralogical identification of phases that form by one or a limited number of pathways. Mars Reconnaissance Orbiter data will enhance our understanding of the occurrence and distribution of sulfates and secondary aluminosilicates on the surface, but it may not be able to provide definitive mineralogy of those phases. The next landed mission on Mars is the 2007 Mars Phoenix Scout Mission, which does not have instruments on board that will provide definitive mineralogical identifications. However, the Phoenix payload will provide unique new information on the volalite-bearing content of regolith materials (Thermal Evolved Gas Analyzer, TEGA) and the chemistry of soluble components (Microscopy, Electrochemistry, Conductivity Analyzer, MECA; Smith, 2006). The 2009 Mars Science Laboratory (MSL) will provide an instrument suite that should significantly improve our understanding of the mineralogical composition of secondary phases (Blaney, 2006). For example, the CheMin instrument is primarily an X-ray diffraction instrument that should provide definitive mineralogical data. The Sample Analysis at Mars (SAM) instrument should provide chemistry of the volatile-bearing phases (i.e., carbonates, sulfates, hydrated minerals). Along with the APXS and ChemCam element analyzers on the MSL payload, our new knowledge about the secondary phases on Mars should allow significant enhancements in our understanding of the aqueous processes at work there. Ultimately, sample return missions will provide suites of samples from specific locations with known geologic context.

The continuation of both laboratory experimental and terrestrial analog studies will also be needed to understand and interpret the data returned by the missions described above. Aqueous processes on Mars can only be understood to the degree that we understand those processes on Earth.

23.8 SUMMARY

Aqueous alteration has substantially shaped the geologic history of Mars. A key requirement to model aqueous alteration is the identification of phases that have formed by these processes. Our knowledge on the style and extent of aqueous alteration on Mars is based upon our understanding of terrestrial environments where these phases have formed.

A variety of mineralogical and chemical indicators for aqueous alteration on Mars have been identified by a combination of surface and orbital robotic missions, telescopic observations, characterization of Martian meteorites, and laboratory and terrestrial analog studies. Phases that have formed by aqueous alteration such as sulfates (polyhydrated sulfates, kieserite, and gypsum), phyllosilicates (smectites), hematite, and nanophase iron oxides (e.g., palagonite) have been identified by Earth-based telescopic and Mars orbital observations. Jarosite, Fe-Mg-Ca-bearing sulfates, goethite, hematite, nanophase iron oxides, halides, and possibly secondary aluminosilicates have been identified by landers and rovers. Analyses of Martian meteorites in terrestrial laboratories have led to the identification of minor amounts of phases that have formed by aqueous alteration, such as Fe-Ca-Mg-bearing carbonates, Ca-bearing sulfates, goethite, iddingsite, halite, and pyrrhotite.

Based upon these phases, several styles of alteration have been proposed for the surface of Mars. Mars is a basaltic planet, so most of the styles involve the alteration of basaltic precursors. The high sulfur content and the occurrence of jarosite suggest that one style of aqueous alteration on Mars (especially at Meridiani Planum) is acid-sulfate alteration. There may be several pathways for materials to be altered in acid-sulfate environments including (1) oxidative aqueous alteration of ultramafic igneous rocks containing sulfides; (2) sulfuric acid alteration of basaltic materials; and (3) acid-fog (i.e., vapors rich in H_2SO_4) alteration of basaltic or basaltic-derived materials. Another possible style is the alteration of basaltic materials by near-neutral or alkaline pH solutions. This type of alteration may result in the formation of smectites like those observed by the Mars Express OMEGA instrument.

The extent of alteration will depend on whether the material is altered in a closed or open hydrologic system and the rock:water ratio. Reactants are not displaced from the reaction front in a closed system (i.e., isochemical alteration) whereas in an open system soluble phases are removed as water moves through the host material. The Mössbauer spectrometer on board the MERs indicated that the extent of alteration varies substantially from rocks that are relatively unaltered to rocks and outcrops that appear to be pervasively altered. In most cases, the pervasively altered materials still had essentially basaltic compositions,

suggesting that the alteration was isochemical (i.e., closed hydrologic system) and/or low rock:water ratios. On the other hand, in several instances the altered materials were enriched in Al (e.g., Independence outcrop on the Columbia Hills), suggesting that alteration occurred in an open hydrologic system where soluble phases were removed from the host rock.

Future missions, observations, and laboratory and terrestrial analog studies will no doubt advance our understanding of the phases, styles, and extent of aqueous alteration on Mars.

ACKNOWLEDGMENTS

D. W. Ming and R. V. Morris acknowledge support of the NASA Mars Exploration Rover Project, NASA Mars Fundamental Research Program, and the NASA Johnson Space Center. We thank H. Newsom, D. C. Golden, and J. F. Bell III for their insightful reviews of this chapter.

REFERENCES

Allen, C. C., J. L. Gooding, and K. Keil, Hydrothermally altered impact melt rock and breccia: contributions to the soil of Mars, *J. Geophys. Res.* **87**, 10083–101, 1982.

Arvidson, R. E., S. W. Squyres, R. C. Anderson, *et al.*, Overview of the Spirit Mars Exploration Rover mission to Gusev crater: landing site to the Methuselah Outcrop in the Columbia Hills, *J. Geophys. Res.* **111**, E02S01, doi:10.1029/2005JE002499, 22, 2006.

Baird, A. K. and B. C. Clark, Did komatiitic lavas erode channels on Mars?, *Nature* **311**, 18–19, 1984.

Bandfield, J. L., T. D. Glotch, and P. R. Christensen, Spectroscopic identification of carbonate minerals in the Martian dust, *Science* **301**, 1084–7, 2003.

Banin, A. and L. Margulies, Simulation of Viking biology experiment suggests smectites not palagonite, as Martian soil analogs, *Nature* **305**, 523–6, 1983.

Banin, A., F. X. Han, I. Kan, and A. Cicelsky, Acidic volatiles and the Mars soil, *J. Geophys. Res.* **102**, 13341–56, 1997.

Bell III, J. F. and D. Crisp, Groundbased imaging spectroscopy of Mars in the near-infrared: preliminary results, *Icarus* **104**, 2–19, 1993.

Bell III, J. F., T. B. McCord, and P. D. Owensby, Observational evidence of crystalline iron oxides on Mars, *J. Geophys. Res.* **95**, 14447–61, 1990.

Bibring, J.-P., Y. Langevin, A. Gendrin, *et al.*, Mars surface diversity as revealed by the OMEGA/Mars Express observations, *Science* **307**, 1576–81, 2005.

Bibring, J.-P., Y. Langevin, J. F. Mustard, *et al.*, Global mineralogy and aqueous Mars history derived from OMEGA/Mars Express data, *Science* **312**, 400–4, 2006.

Bigham, J. M. and D. K. Nordstrom, Iron and aluminum hydroxysulfates from acid sulfate waters. In Sulfate Minerals: Crystallography, Geochemistry, and Environmental Significance, (ed. C. N. Alpers, J. L. Jambor, and D. K. Nordstom), *Rev. Mineral. Geochem., Mineral. Soc. Amer. & Geochem. Soc.* **40**, 351–403, 2000.

Bigham, J. M., U. Schwertman, L. Carlson, and E. Murad, A poorly crystalline oxyhydroxysulfate of iron formed by bacterial oxidation of Fe(II) in acid mine waters, *Geochim. Cosmochim. Acta* **54**, 2743–58, 1990.

Bish, D. L. and J. W. Carey, Thermal behavior of natural zeolites. In *Natural Zeolites: Occurrence Properties, Applications* (ed. D. L. Bish and D. W. Ming), *Rev. Min. Geochem.* 45, 403–52, 2001.

Bish, D. L., J. W. Carey, D. T. Vaniman, and S. J. Chipera, Stability of hydrous minerals on the martian surface, *Icarus* **164**, 96–103, 2003.

Bishop, J. L. and E. Murad, Schwertmannite on Mars? Spectroscopic analyses of schwertmannite, its relationship to other ferric minerals, and its possible presence in the surface material on Mars. In *Mineral Spectroscopy: A Tribute to Roger G. Burns* (ed. M. D. Dyar, C. McCammon, and M. W. Schaefer), Houston: The Geochemical Society, Special Publication No. 5, 337–58, 1996.

Blaney, D. L., *The Mars Science Laboratory (MSL) Mission, Workshop on Martian Sulfates as Recorders of Atmospheric-Fluid-Rock Interactions*, LPI Contribution No. 1331, Houston, Texas: Lunar and Planetary Institute, Abstract #7034, 2006.

Boynton, W. V., W. C. Feldman, S. W. Squyres, *et al.*, Distribution of hydrogen in the near surface of Mars: evidence for subsurface ice deposits, *Science* **297**, 81–5, 2002.

Brearley, A. J., Magnetite in ALH84001: product of decomposition of ferroan carbonate, *Lunar Planet. Sci. XXIX*, Houston: Lunar and Planetary Institute, Abstract #1451 (CD-ROM), 1998.

Brearley, A. J., Hydrous phases in ALH84001: further evidence for preterrestrial alteration and a shock-induced thermal overprint, *Lunar Planet. Sci. XXXI*, Houston: Lunar and Planetary Institute, Abstract #1203 (CD-ROM), 2000.

Bridges, J. C. and M. M. Grady, A halite-siderite-anhydrite-chlorapatite assembalage in Nakhla: mineralogical evidence for evaporates on Mars, *Meteorit. Planet. Sci.* **34**, 407–16, 1999.

Bridges, J. C. and M. M. Grady, Evaporite mineral assemblages in the Nakhlite (Martian) meteorites. *Earth Planet. Sci. Lett.* **176**, 267–79, 2000.

Bridges, J. C., D. C. Catling, J. M. Saxton, *et al.*, Alteration assemblages in Martian meteorites: implications for near-surface processes, *Space Sci. Rev.* **96**, 365–92, 2001.

Brown, G. and G. W. Brindley, X-ray diffraction procedures for clay mineral identification. In *Crystal Structures of Clay minerals and Their X-ray Identification*, (ed. G. W. Brindley and G. Brown), Mineralogical Society Monograph No. 5, Washington, DC: Mineralogical Society, pp. 305–60, 1980.

Brückner, J., G. Dreibus, G. W. Lugmair, *et al.*, Chemical composition of the martian surface as derived from Pathfinder, Viking, and martian meteorite data, *Lunar Planet. Sci. XXX*, Houston: Lunar and Planetary Institues, Abstract #1250, 1999.

Buckby, T., S. Black, M. L. Coleman, and M. E. Hodson, Fe-sulfate-rich evaporative mineral precipitates from the Rio Tinto, southwest Spain, *Mineral. Mag.* **67**, 263–78, 2003.

Burns, R. G., Gossans on Mars, *Proc. Lunar Planet. Sci. XVIII*, 713–21, 1988.

Burns, R. G. and D. S. Fisher, Iron-sulfur mineralogy of Mars: magmatic evolution and chemical weathering products, *J. Geophys. Res.* **95**, 14169–73, 1990.

Calvin, W. M., Variation of the 3-μm absorption feature on Mars: observations over eastern Valles Marineris by the Mariner 6 infrared spectrometer, *J. Geophys. Res.* **102**, 9097–107, 1997.

Carson, C. D., D. S. Fanning, and J. B. Dixon, Alfisols and Ultisols with acid sulfate weathering features in Texas. In *Acid Sulfate Weathering* (ed. J. A. Kittrick, D. S. Fanning, and L. R. Hossner), SSSA Special Publication No. 10, Madison, WI, pp. 127–46, 1982.

Christensen, P. R., J. L. Bandfield, M. D. Smith, V. E. Hamilton, and R. N. Clark, Identification of a basaltic component on the Martian surface from Thermal Emission Spectrometer data, *J. Geophys. Res.* **105**, 9609–22, 2000.

Christensen, P. R., J. L., Bandfield, V. E. Hamilton, *et al.*, Mars Global Surveyor Thermal Emission Spectrometer experiment: investigation description and surface science results, *J. Geophys. Res.* **106**, 23823–71, 2001a.

Christensen, P. R., R. V. Morris, M. D. Lane, J. L. Bandfield, and M. C. Malin, Global mapping of Martian hematite deposits: remnants of water-driven processes on early Mars, *J. Geophys. Res.* **106**, 23873–86, 2001b.

Christensen, P. R., M. B. Wyatt, T. D. Glotch, *et al.*, Mineralogy at Meridiani Planum from the Mini-TES experiment on the Opportunity rover, *Science* **306**, 1733–9, 2004a.

Christensen, P. R., S. W. Ruff, R. L. Fergason, *et al.*, Initial results from the Mini-TES experiment in Gusev crater from the Spirit Rover, *Science* **305**, 837–42, 2004b.

Clark, B. C., Geochemical components in Martian soil, *Geochem. Cosmochim. Acta* **57**, 4575–81, 1993.

Clark, B. C. and A. K. Baird, Is the Martian lithosphere sulfur rich?, *J. Geophys. Res.* **84**, 8395–402, 1979.

Clark III, B. C., A. K. Baird, H. J. Rose Jr., *et al.*, The Viking X-ray fluorescence experiment: analytical methods and early results, *J. Geophys. Res.* **82**(28), 4577–94, 1977.

Clark, B. C., S. L. Kenley, D. L. O'Brien, *et al.*, Heterogeneous phase reactions of Martian volatiles with putative regolith minerals, *J. Mol. Evol.* **14**, 91–102, 1979.

Clark, B. C., A. K. Baird, R. J. Weldon, *et al.*, Chemical composition of Martian fines, *J. Geophys. Res.* **87**, 10059–67, 1982.

Clark, B. C., R. V. Morris, S. M. McLennan, *et al.*, Chemistry and mineralogy of outcrops at Meridiani Planum, *Earth Planet. Sci. Lett.* **240**, 73–94, 2005.

Clark, B. C., R. E. Arvidson, R. Gellert, *et al.*, Evidence for montmorillonite or its compositional equivalent in Columbia Hills, Mars, *J. Geophys. Res.* **112**, E06501, doi:10.1029/2006JE002756, 2007.

Clark, R. N. and T. B. McCord, Mars residual north polar cap: earth-based spectroscopic confirmation of water ice as a major constituent and evidence for hydrated minerals, *J. Geophys. Res.* **87**, 367–70, 1982.

Dreibus, G., A. Burghele, K. P. Jochum, *et al.*, Chemical and mineral composition of ALH84001: a Martian orthopyroxenite (abs), *Meteoritics* **29**, 461, 1994.

Evans, D. L. and J. B. Adams, Amorphous gels as possible analogs to Martian weathering products. *Proc. Lunar Planet. Sci. Conf. X*, 1829–34, 1980.

Feldman, W. C., W. V. Boynton, R. L. Tokar, *et al.*, Global distribution of neutrons from Mars: results from Mars Odyssey, *Science* **297**, 75–8, 2002.

Feldman, W. C., T. H. Prettyman, S. Maurice, *et al.*, Global distribution of near-surface hydrogen on Mars, *J. Geophys. Res.* **109**, E09006, doi:10.1029/2003JE002160, 2004.

Fernández-Remolar, D. C., R. V. Morris, J. E. Gruener, R. Amils, and A. H. Knoll, The Rio Tinto Basin Spain, Mineralogy, sedimentary geobiology, and implications for interpretation of outcrop rocks at Meridiani Planum, Mars, *Earth Planet. Sci. Lett.* **240**, 149–67, 2005.

Fries, M., D. Rost, E. Vicenzi, and A. Steele, Raman imaging analysis of jarosite in MIL 03346, *Workshop on Martian Surfaces as Recorders of Atmospheric-Fluid-Rock Interactions*, Houston, TX: Lunar Planetary Institute, Abstract #7060, 2006.

Gaines, R. V., H. C. Skinner, E. E. Foord, *et al.*, *Dana's New Mineralogy*, New York: John Wiley & Sons, Inc., 1819pp., 1997.

Gellert, R., R. Rieder, R. C. Anderson, *et al.*, Chemical composition of Martian rocks and soils at the Spirit landing site in Gusev crater: initial results of the Alpha Particle X-ray Spectrometer, *Science* **305**, 829–32, 2004.

Gellert, R., R. Rieder, J. Brückner, *et al.*, Alpha Particle X-Ray Spectrometer (APXS): results from Gusev crater and calibration report, *J. Geophys. Res.* **111**, E02S05, doi:10.1029/2005JE002555, 2006.

Gendrin, A., N. Mangold, J.-P. Bibring, *et al.*, Sulfates in Martian layered terrains: the OMEGA/Mars Express view, *Science* **307**, 1587–91, 2005.

Golden, D. C., R. V. Morris, D. W. Ming, H. V. Lauer Jr., and S. R. Yang, Mineralogy of three slightly palagonitized soils from the summit of Mauna Kea, Hawaii, *J. Geophys. Res. – Planets*, **98**(E2), 3401–11, 1993.

Golden, D. C., D. W. Ming, C. S. Schwandt, *et al.*, A simple inorganic process for formation of carbonates, magnetite and sulfides in Martian meteorite ALH84001, *Am. Mineral.* **86**, 370–5, 2001.

Golden, D. C., D. W. Ming, R. V. Morris, *et al.*, Evidence for exclusively inorganic formation of magnetite in Martian meteorite ALH84001, *Am. Mineral.* **89**, 681–95, 2004.

Golden, D. C., D. W. Ming, R. V. Morris, and S. A. Mertzman, Laboratory simulated acid-sulfate weathering of basaltic materials: implications for formation of sulfates at Meridiani Planum and Gusev crater, Mars, *J. Geophys. Res.*, **110** E12S07, 15, doi:10.1029/2005JE002451, 2005.

Gooding, J. L., S. J. Wentworth, and M. E. Zolensky, Calcium carbonate and sulfate of possible extraterrestrial origin in the EETA79001 meteorite, *Geochim. Cosmochim. Acta* **50**, 1049–59, 1988.

Gooding, J. L., S. J. Wentworth, and M. E. Zolensky, Aqueous alteration of the Nakhla meteorite, *Meteoritics* **26**, 135–43, 1991.

Gooding, J. L., R. E. Arvidson, and M. Y. Zolotov, Physical and chemical weathering. In *Mars* (ed. H. H. Kielffer, B. M. Jakosky, C. W. Snyder, and M. S. Matthews), Tucson: The University of Arizona Press, 626–51, 1992.

Guinness, E. A., R. E. Arvidson, B. L. Jolliff, *et al.*, Hyperspectral reflectance mapping of cinder cones at the summit of Mauna Kea and implications for equivalent observations on Mars, *J. Geophys. Res.* **112**, E08511, doi:10.1029/2006JE002822, 2007.

Hanel, R. A., B. J. Conrath, W. Hovis, *et al.*, Investigation of the Martian environment by infrared spectroscopy on Mariner 9, *Icarus* **17**, 423–42, 1972.

Harvey, R. P. and H. Y. McSween Jr., A possible high-temperature origin for the carbonates in the Martian meteorite ALH84001, *Nature* **382**, 49–51, 1996.

Haskin, L. A., A. Wang, B. L. Jolliff, *et al.*, Water alteration of rocks and soils from the Spirit rover site, Gusev crater, Mars, *Nature* **436**, 66–9, 2005.

Herd, C. D. K., An occurrence of jarosite in Mil 03346: implications for conditions of Martian aqueous alteration, *Meteorit. Planet. Sci.* **41**, A74, 2006.

Houck, J. R., J. B. Pollack, C. Sagan, D. Schaack, and J. Decker, High altitude infrared spectroscopic evidence for bound water on Mars, *Icarus* **18**, 470–80, 1973.

Hudson-Edwards, K. A., C. Schell, and M. G. Macklin, Mineralogy and geochemistry of alluvium contamination by

metal mining in the Rio Tinto area, southwest Spain, *App. Geochem.* **14**, 1015–30, 1999.

Hunt, G. E., L. M. Logan, and J. W. Salisbury, Mars: component of infrared spectra and composition of the dust cloud, *Icarus* **18**, 459–69, 1973.

Hurowitz, J. A., S. M. McLennan, D. H. Lindsley, and M. A. A. Schoonen, Experimental epithermal alteration of synthetic Los Angeles meteorite: implications for the origin of Martian soils and identification of hydrothermal sites on Mars, *J. Geophys. Res.* **110**, E07002, doi:10.1029/2004JE002391, 2005.

Hurowitz, J. A., S. M. McLennan, N. J. Tosca, *et al.*, In-situ and experimental evidence for acidic weathering of rocks and soils on Mars, *J. Geophys. Res.* **111**(16), E02S19, doi:10.1029/2005JE002515, 2006.

Jackson, M. L., Clay transformations in soil genesis during the Quaternary, *Soil Sci.* **99**, 15–22, 1965.

Kevie, W. and B. Yenmanas, Detailed reconnaissance soil survey of southern central plain area, *Report SSR-89*. Soil Survey Division & Land Development Department, Bangkok, India, 187pp., 1972.

Kittrick, J. A., Montmorillonite equilibria and the weathering environment, *Soil Sci. Soc. Am. J.* **35**, 815–20, 1971.

Klingelhöfer, G., R. V. Morris, B. Bernhardt, *et al.*, Jarosite and hematite at Meridiani Planum from the Mössbauer Spectrometer on the Opportunity Rover, *Science* **306**, 1740–5. 2004.

Knauth, L. P., D. M. Burt, and K. H. Wohletz, Impact origin of sediments at the Opportunity landing site on Mars, *Nature* **438**, 1123–8, 2005.

Kloprogge, J. T., S. Komarneni, and J. E. Amonette, Synthesis of smectite clay minerals: a critical review, *Clays Clay Miner.* **47**, 529–54, 1999.

Lane, M. D., R. V. Morris, S. A. Mertzman, and P. R. Christensen, Evidence for platy hematite grains in Sinus Meridiani, Mars, *J. Geophys. Res.* **106**, 5126, doi:10.1029/2001JE001832, 2002.

Langevin, Y., F. Poulet, J-.P. Bibring, and B. Gondet, Sulfates in the North Polar region of Mars detected by OMEGA/Mars Express, *Science* **307**, 1584–6, 2005.

Madden, M. E. E., R. J. Bodnar, and J. D. Rimstidt, Jarosite as an indicator of water limited chemical weathering on Mars, *Nature*, **431**, 821–3, 2004.

McCollom, T. M. and B. M. Hynek, A volcanic environment for bedrock diagenesis at Meridiani Planum on Mars, *Nature* **438**, 1129–31, 2005.

McKay, D. S., E. K. Gibson Jr., K. L. Thomas-Keprta, *et al.*, Search for past life on Mars: possible relic biogenic activity in Martian meteorite ALH84001, *Science* **273**, 924–30, 1996.

McLennan, S. M., J. F. Bell III, W. M. Calvin, *et al.*, Provenance and diagenesis of the Burns formation, Meridiani Planum, Mars, *Earth Planet. Sci. Lett.* **30**, 95–121, 2005.

McSween, H. Y., R. E. Arvidson, J. F. Bell III, *et al.*, Basaltic rocks analyzed by the Spirit Rover in Gusev crater, *Science* **305**, 842–5, 2004.

McSween, H. Y., M. B. Wyatt, R. Gellert, *et al.*, Characterization and petrologic interpretation of olivine-rich basalts at Gusev crater, Mars, *J. Geophys. Res.* **111**(17), E02S10, doi:10.1029/2005JE002477, 2006.

Ming, D. W., D. W. Mittlefehldt, R. V. Morris, *et al.*, Geochemical and mineralogical indicators for aqueous processes in the Columbia Hills of Gusev crater, Mars, *J. Geophys. Res.* **111**, E02S12, doi:10.1029/2005JE002560, 2006.

Mittlefehldt, D. W., ALH84001, a cumulate orthopyroxenite member of the martian meteorite clan, *Meteoritics* **29**, 214–21, 1994.

Moore, H. J., S. Liebes Jr., D. S. Crouch, and L. V. Clark, Rock pushing and sampling under rocks on Mars, *USGS Prof. Paper*, 1081, 1978.

Moore, H. J., R. M. Hutton, G. D. Clow, and C. R. Spitzer, Physical properties of surface materials at the Viking landing sites on Mars, *USGS Prof. Paper*, 1389, 1987.

Morris, R. V., D. G. Agresti, H. V. Lauer Jr., *et al.*, Evidence for pigmentary hematite on Mars based on optical, magnetic, and Mossbauer studies of superparamagnetic (nanocrystalline) hematite, *J. Geophys. Res.* **94**, 2760–78, 1989.

Morris, R. V., D. C. Golden, J. F. Bell III, and H. V. Lauer Jr., Hematite, pyroxene, and phyllosilicates on Mars: implications from oxidized impact melt rocks from Manicouagan crater, Quebec, Canada, *J. Geophys. Res.* **100**, 5319–28, 1995.

Morris, R. V., D. W. Ming, D. C. Golden, and J. F. Bell III, An occurrence of jarositic tephra on Mauna Kea, Hawaii: implications for the ferric mineralogy of the martian surface. In *Mineral Spectroscopy: A Tribute to Roger G. Burns* (ed. M. D. Dyer, C. McCammon, and M. W. Schaefer), Special Publication No. 5, Houston, TX: The Geochemical Society, pp. 327–36, 1996.

Morris, R. V., D. C. Golden, J. F. Bell III, *et al.*, Mineralogy, composition, and alteration of Mars Pathfinder rocks and soils: evidence from multispectral, elemental, and magnetic data on terrestrial analogue, SNC meteorite, and Pathfinder samples, *J. Geophys. Res. – Planets* **105**, 1757–817, 2000.

Morris, R. V., G. Klingelhöfer, B. Bernhardt, *et al.*, Mössbauer mineralogy on Mars: first results from the Spirit landing site in Gusev crater, *Science* **305**, 833–6, 2004.

Morris, R. V., G. Klingelhöfer, C. Schröder, *et al.*, Mössbauer mineralogy of rock, soil, and dust at Gusev crater, Mars: Spirit's journey through weakly altered olivine basalt on the plains and pervasively altered basalt in the Columbia Hills, *J. Geophys. Res.* **111**, E02S13, doi:10.1029/2005JE002584, 2006a.

Morris, R. V., G. Klingelhöfer, C. Schröder, *et al.*, Mössbauer mineralogy of rock, soil, and dust at Meridiani Planum, Mars: Opportunity's journey across sulfate-rich outcrop, basaltic sand and dust, and hematite lag deposits, *J. Geophys. Res.* **111**, E12S15, doi:10.1029/2006JE002791, 2006b.

Murchie, S., L. Kirkland, S. Erard, J. Mustard, and M. Robinson, Near-infrared spectral variations of Martian surface materials from ISM imaging spectrometer data, *Icarus* **147**, 444–71, 2000.

Naumov, M. V., Impact-generated hydrothermal systems: data from Popigai, Kara, and Puchezh-Katunki impact structures. In *Impacts in Precambian Shields: Impact Studies* (ed. J. Plado and L. J. Pesonen), Berlin: Springer, pp. 117–72, 2002.

Nesbitt, H. W. and G. M. Young, Early Proterozoic climates and plate motions inferred from major element chemistry of lutites, *Nature* **279**, 715–17, 1982.

Nesbitt, H. W. and G. M. Young, Prediction of some weathering trends of plutonic and volcanic rocks based on thermodynamic and kinetic considerations, *Geochem. Cosmochem. Acta* **48**, 1523–34, 1984.

Nesbitt, H. W. and G. M. Young, Formation and diagenesis of weathering profiles. *J. Geol.* **97**, 129–47, 1989.

Nesbitt, H. W. and R. E. Wilson, Recent chemical weathering of basalts, *Am. J. Sci.* **292**, 740–77, 1992.

Newsom, H. E., Hydrothermal alteration of impact melt sheets with implications for Mars, *Icarus* **44**, 207–16, 1980.

Newsom, H., Clays in the history of Mars, *Nature* **438**, 570–1, 2005.

Newsom, H. E., J. J. Hagerty, and F. Goeff, Mixed hydrothermal fluids and the origin of the Martian soil, *J. Geophys. Res.* **104**, 8717–28, 1999.

Newsom, H. E., J. J. Hagerty, and I. E. Thorsos, Location and sampling of aqueous and hydrothermal deposits in Martian impact craters, *Astrobiology* **1**, 71–88, 2001.

Newsom, H. E., C. A. Barber, T. M. Hare, *et al*., Paleolakes and impact basins in southern Arabia Terra, including Meridiani Planum: implications for the formation of hematite deposits on Mars, *J. Geophys. Res.* **108** (E12), 8060, E02S12, doi:10.1029/2003JE002072, 2003.

Nordstrom, D. K., Aqueous pyrite oxidation and the consequent formation of secondary iron minerals. In *Acid Sulfate Weathering* (ed. J. A. Kittrick, D. S. Fanning, and L. R. Hossner), SSSA Special Publication No. 10, pp. 37–56, 1982.

Nuhfer, E., Efflorescent minerals associated with coal, Master's thesis, West Virginia University, Morgantown, WV, 1967.

Pimental, G. C., P. B. Forney, and K. C. Herr, Evidence about hydrate and solid water in the Martian surface from the 1969 Mariner infrared spectrometer, *J. Geophys. Res.* **79**, 1623–34, 1974.

Pons, L. J., N. van Breeman, and P. M. Driesen, Physiography of coastal sediments and development of potential soil acidity. In *Acid Sulfate Weathering* (ed. J. A. Kittrick, D. S. Fanning, and L. R. Hossner), SSSA Special Publication No. 10, Madison, WI, 1982.

Poulet, F., J.-P. Bibring, J. F. Mustard, *et al*., Phyllosilicates on Mars and implications for early martian climate, *Nature* **438**, 623–7, 2005.

Rieder, R., R. Gellert, R. C. Anderson, *et al*., Chemistry of rocks and soils at Meridiani Planum from the Alpha Particle X-ray Spectrometer, *Science* **306**, 1746–9, 2004.

Romanek, C. S., M. M. Grady, I. P. Wright, *et al*., Record of fluid-rock interactions on Mars from the meteorite ALH84001, *Nature* **372**, 655–7, 1994.

Ruff, S., Spectral evidence for zeolite in the dust on Mars, *Icarus* **168**, 131–43, 2004.

Ruff, S., P. R. Christensen, D. L. Blaney, *et al*., The rocks of Gusev crater as viewed by the Mini-TES instrument, *J. Geophys. Res.* **111**, 36, doi:10.1029/2006JE002747, 2006.

Singer, R. B., Spectral evidence for the mineralogy of high-albedo soils and dust on Mars, *J. Geophys. Res.* **87**, 10159–68, 1982.

Smith, P. H., Overview of the Phoenix Mars Lander Mission, *Workshop on Martian Sulfates as Recorders of Atmospheric-Fluid-Rock Interactions*, LPI Contribution No. 1331, Houston, TX: Lunar and Planetary Institute, Abstract #7069, 2006.

Squyres, S. W., R. Arvidson, J. F. Bell III, *et al*., Initial results from the Athena Science Investigation at Gusev crater, Mars, *Science* **305**, 794–9, 2004a.

Squyres, S. W., R. E. Arvidson, J. F. Bell III, *et al*., The Opportclassy Rover's Athena Science Investigation at Meridiani Planum, Mars, *Science* **306**, 1698–703, 2004b.

Squyres, S. W., J. P. Grotzinger, R. E. Arvidson, *et al*., In situ evidence for an ancient aqueous environment on Mars, *Science* **306**, 1709–14, 2004c.

Squyres, S. W., R. E. Arvidson, B. C. Clark, *et al*., The rocks of the Columbia Hills, *J. Geophys. Res.* **111**, E02S11, doi:10.1029/2005JE002562, 2006a.

Squyres, S. W., A. H. Knoll, R. E. Arvidson, *et al*., Two years at Meridiani Planum: results from the Opportunity rover, *Science* **313**, 1403–7, 2006b.

Toon, O. B., J. B. Pollack, and C. Sagan, Physical properties of the particles composing the Martian dust storm of 1971–1972, *Icarus* **30**, 663–96, 1977.

Tosca, N. J., S. M. McLennan, D. H. Lindsley, and M. A. A. Schoonen, Acid-sulfate weathering of synthetic Martian basalt: the acid fog model revisited, *J. Geophys. Res.* **109**, E05003, doi:10.1029/2003JE002218, 2004.

Tosca, N. J., S. M. McLennan, B. C. Clark, *et al*., Geochemical modeling of evaporation processes on Mars: insight from the sedimentary record at Meridiani Planum, *Earth Planet. Sci. Lett.* **240**, 122–48, 2005.

Treiman, A. H., R. A. Barrett, and J. L. Gooding, Preterrestrial alteration of the Lafayette (SNC) meteorite, *Meteoritics* **28**, 86–97, 1993.

Ugolini, F. C., Hydrothermal origin of the clays from the upper slopes of Mauna Kea, Hawaii, *Clays Clay Miner.* **22**, 189–94, 1974.

van Breeman, N., Acid sulfate soils, *Land Reclamation and Water Management*, ILRI Publication No. 27, Waganingan, The Netherlands, pp. 53–7, 1980.

Wang, A., L. A. Haskin, S. W. Squyres, *et al*., Sulfate deposition in subsurface regolith in Gusev crater, Mars, *J. Geophys. Res.* **111**, E02S17, doi:10.1029/2005JE002513, 2006a.

Wang, A., R. L. Korotev, B. L. Jolliff, *et al*., Evidence of phyllosilicates in Wooly Patch, an altered rock encountered at West Spur, Columbia Hills, by Spirit Rover, *J. Geophys. Res.* **111**, E02S16, doi:10.1029/2005JE002516, 2006b.

Weaver, R. M., M. L. Jackson, and J. K. Syers, Magnesium and silicon activities in matrix solutions of montmorillonite-containing soils in relation to clay mineral stability, *Soil Sci. Soc. Am. J.* **35**, 823–30, 1971.

Weiss, B. P., H. Vali, H. J. Baudenbacher, *et al*., Records of an ancient Martian magnetic field in ALH 84001, *Earth Planet. Sci. Lett.* **201**, 449–63, 2002.

Wentworth, S. J. and J. L. Gooding, Carbonates and sulfates in the Chassigny meteorite: further evidence for aqueous chemistry on the SNC parent body, *Meteoritics* **29**, 861–3, 1994.

Wentworth, S. J. and J. L. Gooding, Weathering and secondary minerals in the Martian meteorite Shergotty, *Lunar Planet. Sci. Conf.*, Abstract #1888 (CD-ROM), 2000.

Wentworth, S. J., E. K. Gibson, M. A. Velbel, and D. S. McKay, Antarctica Dry Valleys and indigenous weathering in Mars meteorites: implications for water and life on Mars, *Icarus* **174**, 383–95, 2005.

Wolfe, E. W., W. S. Wise, and G. B. Dalrymple, The geology and petrology of Mauna Kea Volcano, Hawaii: a study of post-shield volcanism, *USGS Prof. Paper*, **1557**, 1997.

Yen, A. S., R. Gellert, C. Schröder, *et al*., An integrated view of the chemistry and mineralogy of martian soils, *Nature* **436**, 49–69, doi:10.1038/nature03637, 2005.

Yen, A. S., J. Grotzinger, R. Gellert, *et al*., Evidence for halite at Meridiani Planum, *Lunar Planet. Sci. XXXVII*, Houston, TX: Lunar and Planetary Institute, Abstract #2128, 2006.

Yen, A. S., R. V. Morris, R. Gellert, *et al*., Composition and formation of the "Paso Robles" class soils at Gusev crater, *Lunar Planet. Sci XXXVIII*, Houston, TX: Lunar and Planetary Institute, Abstract #2030, 2007.

Zolotov, M. Y. and E. L. Shock, Formation of jarosite-bearing deposits through aqueous oxidation of pyrite at Meridiani Planum, Mars, *Geophys. Res. Lett.* **32** (5), L21203, doi:10.1029/2005FL024253, 2005.

24

The sedimentary rock cycle of Mars

S. M. McLENNAN AND J. P. GROTZINGER

ABSTRACT

Orbital and landed missions have demonstrated that Mars possesses an extensive and diverse sedimentary rock record that is mostly ancient. Many observed or inferred processes appear familiar to sedimentary geologists but, in detail, the sedimentary record of Mars differs in fundamental ways from the terrestrial record. Mars is a basaltic planet and accordingly, the provenance of sedimentary material, including particulate debris and aqueous fluids from which chemical constituents precipitate, is composed of basalt rather than intermediate to felsic igneous compositions characteristic of terrestrial upper continental crust. Aqueous alteration, observed on Mars and studied experimentally, indicates surficial processes dominated by low pH; under acidic conditions, many chemical relationships that are characteristic of terrestrial weathering do not apply. Aluminum and Fe are far more soluble and mobile, Si mobility is limited by fluid/rock ratio and iron oxidation rates are sluggish. Low fluid/rock ratios are indicted by the observation that only the most soluble minerals (olivine, Fe-Ti oxides, phosphates, possibly pyroxene) appear to be widely involved in surface alteration with little evidence for involvement of relatively insoluble plagioclase. An intriguing result, from both global-scale orbital and detailed surface spectroscopy, and geochemistry obtained by rovers, is that evaporitic processes, leading to a wide variety of Ca-, Mg- and Fe-bearing sulfates in sedimentary rocks, alteration profiles, and soils, appear to have been common throughout Martian geological history. Investigations by *Spirit* and *Opportunity* demonstrate that classical stratigraphy and sedimentology can be accomplished on the Martian surface using remote techniques. On the Meridiani plains, *Opportunity* has documented a late Noachian to early Hesperian wetting-upwards eolian dune/sand sheet/interdune sedimentary succession, derived largely from recycled impure playa evaporites. The sequence exhibits a strong groundwater diagenetic overprint resulting in multiple generations of evaporitic cements, recrystallization, formation of hematitic concretions, and development of extensive secondary porosity. Periodically, the groundwater table breached the surface, leading to localized subaqueous deposition. In the Columbia Hills of Gusev crater, a variety of sedimentary lithologies have been observed that are volcaniclastic and/or impact-derived and in places, such as Home Plate, may have been reworked by eolian processes. Sulfate cements are present in some of these deposits. Widespread occurrence of sulfates and the dearth of carbonate minerals suggest that the sulfur cycle, rather than the carbon cycle, dominates surficial processes. Resulting acidic waters, derived from basaltic sources, were enriched in Fe, Mg, and Al and depleted in K and Na compared to terrestrial seawater. Evaporite assemblages were dominated by Mg-, Fe-, and Ca-sulfates with carbonates possibly being restricted to local environments where acidity was buffered by water–rock interaction, leading to increased alkalinity. The gravity of Mars is only about 0.4 times that of Earth. However, this has only a modest effect on sediment transport, so the well-understood relationships between sedimentary structures and depositional environment, known for Earth, can be readily applied to Mars with only minor modification. The apparent absence of plate tectonics on Mars leads to critical differences in the development of the Martian sedimentary rock record. For example, on Earth, plate tectonic forces provide for most of the subsidence responsible for basin development. Plate tectonic processes also profoundly influence large-scale sediment transport, the broad architecture of sedimentary deposits (e.g., development of clastic wedges), and sedimentary recycling processes. Instead, on Mars the formation, transport, and deposition of sedimentary rocks are likely dominated by a combination of impact, volcanic, and eolian processes. Thus, even the enormous Valles Marineris rift system appears to lack thermal subsidence on the flanks. On the other hand, it is likely that flexural basins developed on Mars in response to large-scale volcanic loading. Impact structures are also an important focus for sediment deposition at a wide variety of scales. Recent experience clearly demonstrates that subaqueous processes (e.g., fluvial, lacrustrine) also play a role in generating the Martian sedimentary record, although the overall extent of such processes remains to be determined.

24.1 INTRODUCTION

The surface of Mars possesses a dynamic sedimentary environment (e.g., Head *et al.*, 2001). For example, eolian processes largely sculpt the present-day surface of the planet. Exquisitely layered deposits in the polar regions, observed from orbit, bear witness to a fluctuating climate. In the absence of a large moon, the climate of Mars is likely to respond to orbital forcing in a far more dramatic manner than is observed on Earth where Milankovich climate forcing is heavily modulated by Earth–Moon gravitational

The Martian Surface: Composition, Mineralogy, and Physical Properties, ed. J. F. Bell III. Published by Cambridge University Press.

interaction. For example, obliquity likely averaged about 40° over the history of the planet and may have reached in excess of 60° during the early Noachian (e.g., Haberle *et al.*, 2003; Armstrong *et al.*, 2004; Laskar *et al.*, 2004). Orbital images show unambiguous geomorphological evidence for the occurrence of flowing water at the surface sometime in the past, although the detailed mechanisms and timescales of such flow remain uncertain and controversial. Among the nonmutually exclusive possibilities are groundwater sapping, catastrophic outflow associated with meteorite impact, volcanic eruption or hydrous mineral dewatering, glacial meltwater systems, long-lived fluvial and lacustrine systems, and ocean-scale reservoirs.

Over the past few years, the acquisition of high-resolution orbital images (Malin and Edgett, 2000, 2003; Edgett and Malin, 2002; Edgett, 2005) and *in situ* investigations by the Mars Exploration Rovers (MERs) *Spirit* and *Opportunity* (Squyres *et al.*, 2004a,b; Grotzinger *et al.*, 2005, 2006) have demonstrated the presence of widespread sedimentary layering in the oldest geological terrains of Mars. These discoveries have ignited a new era of understanding of the potential richness of the Martian stratigraphic record, especially early in the planet's history. At Meridiani Planum and in the Columbia Hills of Gusev crater, ancient stratigraphic sequences have been examined at meter to millimeter scales and, in large part, with fidelity that is comparable to many of the detailed stratigraphic studies that have been carried out on Earth.

In this chapter we review some of the recent work devoted to understanding the sedimentary history of Mars by direct observation, both from orbit and on the surface, as well as from recent experimental and theoretical modeling studies. Our principal objective is to discuss the implications of these studies for understanding the basic controls on sedimentation and sedimentary processes, including basin evolution, sediment provenance, weathering, transport, deposition, and diagenesis, that may have operated during the early history of Mars when much of the sedimentary rock record appears to have accumulated. In particular, we are concerned with what these studies may reveal about fundamental differences that exist in the sedimentary rock cycle and the sedimentary evolution of Mars compared to Earth. Our focus is on the ancient sedimentary record; more recent sedimentary processes, dominated by eolian, glacial, and periglacial activity, have already received considerable attention (e.g., Greeley *et al.*, 1993, 2006; Head *et al.*, 2001; Sullivan *et al.*, 2005).

24.2 ORBITAL CONTEXT FOR ANCIENT LAYERED ROCKS

Occurrences of Amazonian layered sedimentary terrains in the north and south polar regions of Mars are well documented, dating back to the Mariner 9 mission (Thomas *et al.*, 1992). These deposits represent a complex and variable mixture of ice and mainly fine-grained terrigenous (derived from land) debris, dominated by eolian dust. The specific origin of these deposits remains under debate (Clifford *et al.*, 2000). However, their deposition in response to orbital forcing and associated variations in climate-related controls (such as mass balances between cryosphere and hydrosphere, dust storm intensity and atmosphere composition), with superimposed processes of volcanism and meteorite impact, is reasonably well established (e.g., Thomas *et al.*, 1992; Clifford *et al.*, 2000; Head *et al.*, 2001; Kolb and Tanaka, 2001; Laskar *et al.*, 2002). The virtual absence of absolute age constraints prohibits a more detailed understanding of the relationship between climate and layering in these relatively young sediments.

Outside the polar regions, the existence of older layered deposits also has been known since the Mariner 9 mission, notably where these rocks are exposed in the walls of the Martian canyon systems (e.g., Lucchitta *et al.*, 1992). More recently, however, the Mars Orbiter Camera (MOC) on the Mars Global Surveyor spacecraft has revealed the remarkable aerial extent and great thickness of the Noachian and Hesperian layered deposits. These have been interpreted as mostly indurated sedimentary rocks exposed across the Martian surface (Malin and Edgett, 2000, 2003; Edgett and Malin, 2002). Most exposures are at mid latitudes but also can be found locally at much higher latitudes. Layering is present at all scales down at least to the 0.5–1.5 m/pixel resolution of the MOC. Considerable improvement in our understanding of these layered deposits is likely to come as the next generation of high resolution imaging, such as HiRISE (HiRISE – High Resolution Imaging Science Experiment), begins to return data in earnest. Figure 24.1 shows some orbital images of ancient layered terrains.

Although there are few absolute age constraints on these layered deposits, there is considerable potential for building local to regional stratigraphic frameworks. For example, the occurrence of impact craters and their ejecta can be used to provide timelines around which local stratigraphic relations may be built (e.g., Edgett and Malin, 2002).

Sedimentary rocks examined thus far on Mars are essentially flat lying; significant tilting, where it exists, appears to be associated with impact processes or with deposition draped over preexisting topography (Malin and Edgett, 2000). The large-scale geometry of most of the deposits studied from orbit is relatively simple, and often reminiscent of the layering preserved in flat-lying terrestrial sedimentary packages such as the Grand Canyon sequence. In some places, geomorphological evidence is distinctive enough to provide some constraints on the origin of the sedimentary rocks. For example, in Holden NE crater, large-scale fan-shaped geometry has been used to suggest the presence of an ancient drainage network (Malin and Edgett, 2003; also see Moore *et al.*, 2003). However, in most cases there is no unambiguous evidence preserved, at the currently available scale, resolution, and coverage of orbital images, for either the source of sediment or the sedimentological controls on deposition, burial, and preservation. Indeed, when examined in detail, the exact nature of such deposits is debated (e.g., compare Moore *et al.*, 2003 and Lewis and Aharonson, 2004), as are estimates of how much time and how much water were required to form the deposits (e.g., compare Jerolmack *et al.*, 2004 and Bhattacharya *et al.*, 2005).

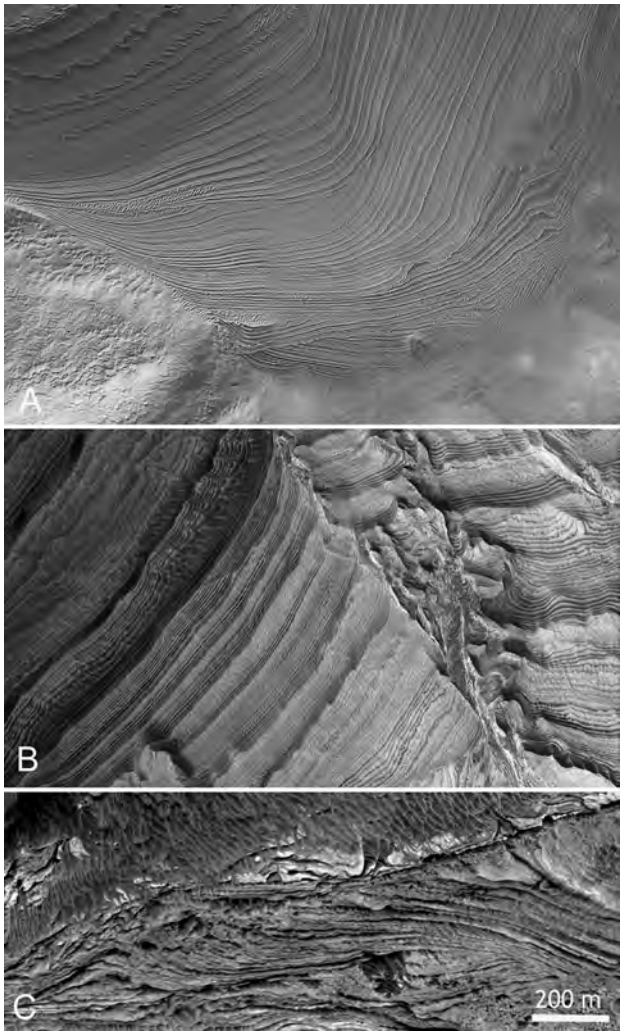

Figure 24.1. (a) Mosaic showing a paleotopographic depression infilled by layered sedimentary deposits. Note thinning and onlap of strata onto margin, represented by massive rocks. Repeated events of progradation and truncation of strata suggest infill by eolian or fluvial processes; absence of overlapping, draping stratal geometries excludes fallout as a mode of deposition. Three MOC images, E22–01557, M14–02055, and R11–04138 were stitched together to create the mosaic. Location is near 52.3° S, 30.1° W. Mosaic is about 4 km across. (b) Light-toned sedimentary rocks in Becquerel crater, in the western Arabia region. Note distinct bedding, and intervals marked by bundles of strata that progress from less well-defined strata to well-defined strata, suggesting sedimentary cyclicity. Location is near 21.5° N, 8.2° W. MOC image R1800383. Field of view is about 3 km across. (c) Mosaic showing complex stratal geometries in sedimentary strata, in southwest Melas Chasma. The image shows left-to-right progradation of steeply dipping strata over flat-lying to gently dipping strata. In terrestrial strata these geometries are consistent with subaqueous sedimentation in sites such as deltas. Location is near 9.9° S, 76.5° W. Scale is 200 m. Two MOC images, R1200541 and R2001281, were stitched together to create the mosaic.

Accordingly, just like the vast majority of ancient sedimentary sequences on Earth, outcrop-scale stratigraphic analysis would be required before the sedimentary history of such deposits could be understood with any confidence. Such *in situ* investigations obviously are not possible, apart from those studies at the rare landing sites that will be visited over the coming decades. In spite of the wealth of detailed information, at the time of this writing, it is important to recall that the MERs combined have traversed only a total of less than 17 km and have studied less than about 50 m of total stratigraphic section of sedimentary rocks.

24.3 WEATHERING AND SURFICIAL ALTERATION PROCESSES

There is abundant evidence to suggest that surficial processes on Mars have occurred under rather low pH conditions over much of the planet's history. The first chemical analyses of Martian soils at the two Viking landing sites revealed unexpectedly high sulfur and chlorine abundances, and these characteristics have been found in all soils at the subsequent three landing sites. Mars Odyssey Gamma Ray Spectrometer (GRS) mapping of the planet confirmed high levels of Cl across the surface (Keller *et al.*, 2006; see also Chapter 5; GRS sulfur data have not yet been reported). High S and Cl contents in soils have led to suggestions that low-pH acid-sulfate alteration has been an important process at the Martian surface. The absence of any carbonate minerals at the surface has also been taken to be consistent with acidic near-surface conditions (e.g., Morse and Marion, 1999). Geological models that provide for the low pH conditions that could give rise to high-sulfur soils and rock surfaces include acid fog vapor alteration processes (e.g., Settle, 1979; Banin *et al.*, 1997; Tosca *et al.*, 2004), low-temperature weathering (e.g., McSween and Keil, 2000), palagonitization (e.g., Gooding and Keil, 1978; Morris *et al.*, 2000), volcanic and/or impact hydrothermal processes (e.g., Griffith and Shock, 1997; Newsom and Hagerty, 1997; Baker *et al.*, 2000), crater lakes or other acid lakes (e.g., Newsom *et al.*, 1996; Benison and LaClair, 2003), impact recycling of preexisting sulfate deposits (McLennan *et al.*, 2006), and evaporative processes (e.g., Clark and Van Hart, 1981; Catling, 1999; Tosca *et al.*, 2005; Tosca and McLennan, 2006).

Recent experimental results provide important constraints on the nature of primary basalt compositions, alteration products, and fluids that are likely to be associated with low pH alteration. A number of workers have conducted H_2SO_4–HCl fluid alteration experiments on synthesized basalts of known Martian composition (Tosca *et al.*, 2004; Hurowitz *et al.*, 2005) and aqueous and vapor alteration experiments on carefully selected Martian basalt analogs (Golden *et al.*, 2005). Results confirm many of the original suggestions of Roger Burns (1993) that at low pH (i.e., <4) and moderate-to-high fluid/rock ratios ($>10^2$), basalt alteration differs in many significant ways to basalt weathering at more modest pH ~5–8, typically encountered on Earth (e.g., White and Brantley, 1995):

1. Al and Fe(III) are essentially soluble elements and are less likely to form residual clays and oxides at the sites of alteration (Figure 24.2a,b);

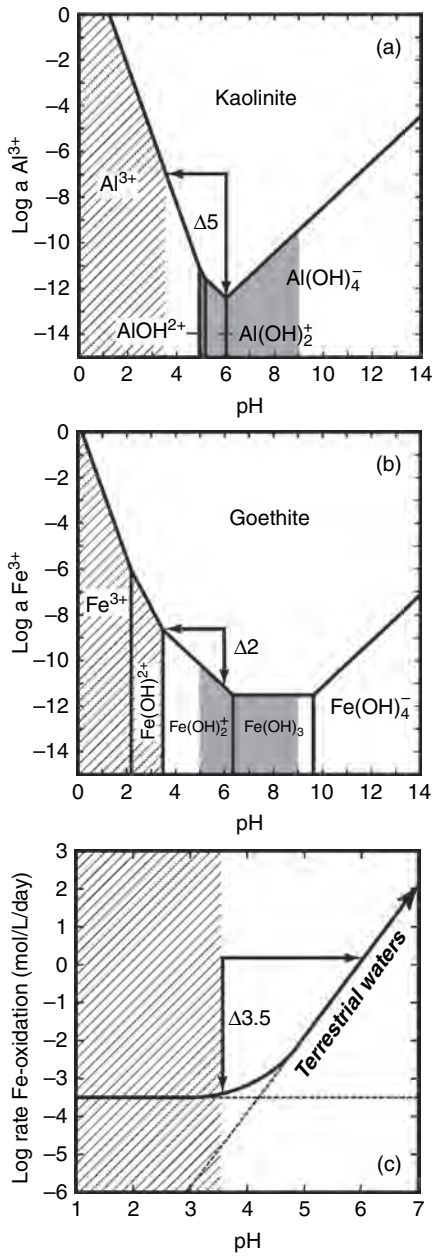

Figure 24.2. (a) Plot of log activity of Al^{3+} versus pH showing the speciation of Al with respect to kaolinite. (b) Plot of log activity of Fe^{3+} versus pH showing the speciation of ferric iron in equilibrium with goethite. (c) Plot of log iron oxidation rate as a function of pH. In all diagrams, the diagonal hatched region shows the low pH regions suggested for Mars, and in (a) and (b) the shaded region shows the pH range typical of most terrestrial conditions (pH = 5 to 9). Note that Al and Fe^{3+} solubilities are at a minimum at intermediate pH and that they increase by many orders of magnitude with decreasing pH. Also note that iron oxidation rates are sluggish and pH-independent at pH < 4, but increase logarithmically with pH at pH > 4. (From Hurowitz *et al*., 2006).

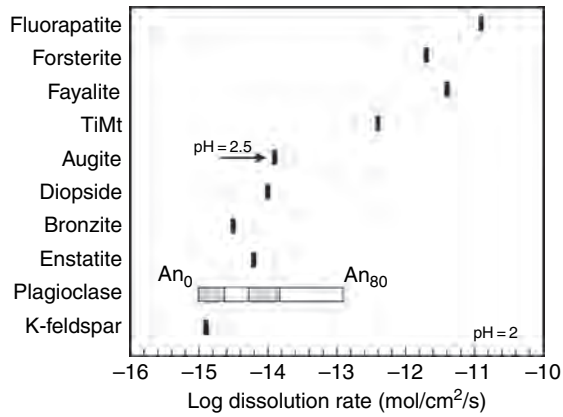

Figure 24.3. Plot of dissolution rates of selected basaltic minerals determined experimentally at pH = 2 to 2.5 and $T = 25\,^{\circ}C$ (see Hurowitz *et al*. [2006]. for data sources). Note that Ca-phosphates and olivine have between 2 and 3 orders of magnitude higher dissolution rates than plagioclase of intermediate An content ($An_{50–80}$). (From Hurowitz *et al*., 2006).

2. Olivine ($(Mg,Fe)_2SiO_4$) dissolves stoichiometrically, and residual alteration products, such as ferric clays and iddingsite ($MgFe^{2+}{}_2Si_3O_{10}{\cdot}4H_2O$), are more likely to be restricted to relatively low water/rock ratios (e.g., fractures in altered SNC [SNC – Shergottite, Nakhlite, and Chassignite] meteorites);
3. Fe-Ti oxides dissolve more readily and Fe is more soluble than Ti (e.g., Arlauckas *et al*., 2006);
4. Pyroxene ($XY(Si,Al)_2O_6$, where X can be Ca, Na, Fe^{2+}, Mg, Zn, Mn, and Li and Y can be Al, Fe^{3+}, Mg, Mn, Cr, Sc, Ti, V, and Fe^{2+}) M2 sites dissolve more readily than M1 sites and at overall rates that overlap plagioclase ($NaAlSi_3O_8$-$CaAl_2Si_2O_8$) dissolution rates (Figure 24.3);
5. Iron oxidation rates are very sluggish (Figure 24.2c) and pH-independent at pH < 4;
6. Amorphous silica is a ubiquitous product of acid alteration of basaltic rocks (McLennan, 2003) and is relatively insoluble up to a pH of about 9. Accordingly, Si mobility would be effectively governed by fluid/rock ratio.

Although there is growing evidence for the presence of clay minerals on the Martian surface (Poulet *et al*., 2005; Bibring *et al*., 2006) that would be consistent with intermediate pH conditions for surficial processes (see below), the available data strongly suggest that acidic conditions have generally prevailed throughout recorded Martian history. Figure 24.4 plots ternary diagrams of mole fraction $Al_2O_3 - (CaO + Na_2O + K_2O) - (FeO_T + MgO)$, or abbreviated as A-CNK-FM (Hurowitz and McLennan, 2007). Such diagrams effectively capture the composition of the major basalt minerals (i.e., olivine, pyroxene, plagioclase, Fe-Ti oxides) and clay and oxide mineral weathering products (e.g., kaolinite ($Al_2Si_2O_5(OH)_4$), smectite/montmorillonite ($(Ca,Na,H)(Al,Mg,Fe)_2(Si,Al)_4O_{10}(OH)_2{\cdot}nH_2O$), Fe-oxide) and have been used successfully in terrestrial basalt weathering studies to evaluate mineralogical and mass balance controls (e.g., Nesbitt and Wilson, 1992). On this diagram, the diagonal line between plagioclase compositions and the $FeO_T + MgO$ apex (i.e., olivine, Fe-Ti-oxides) separates

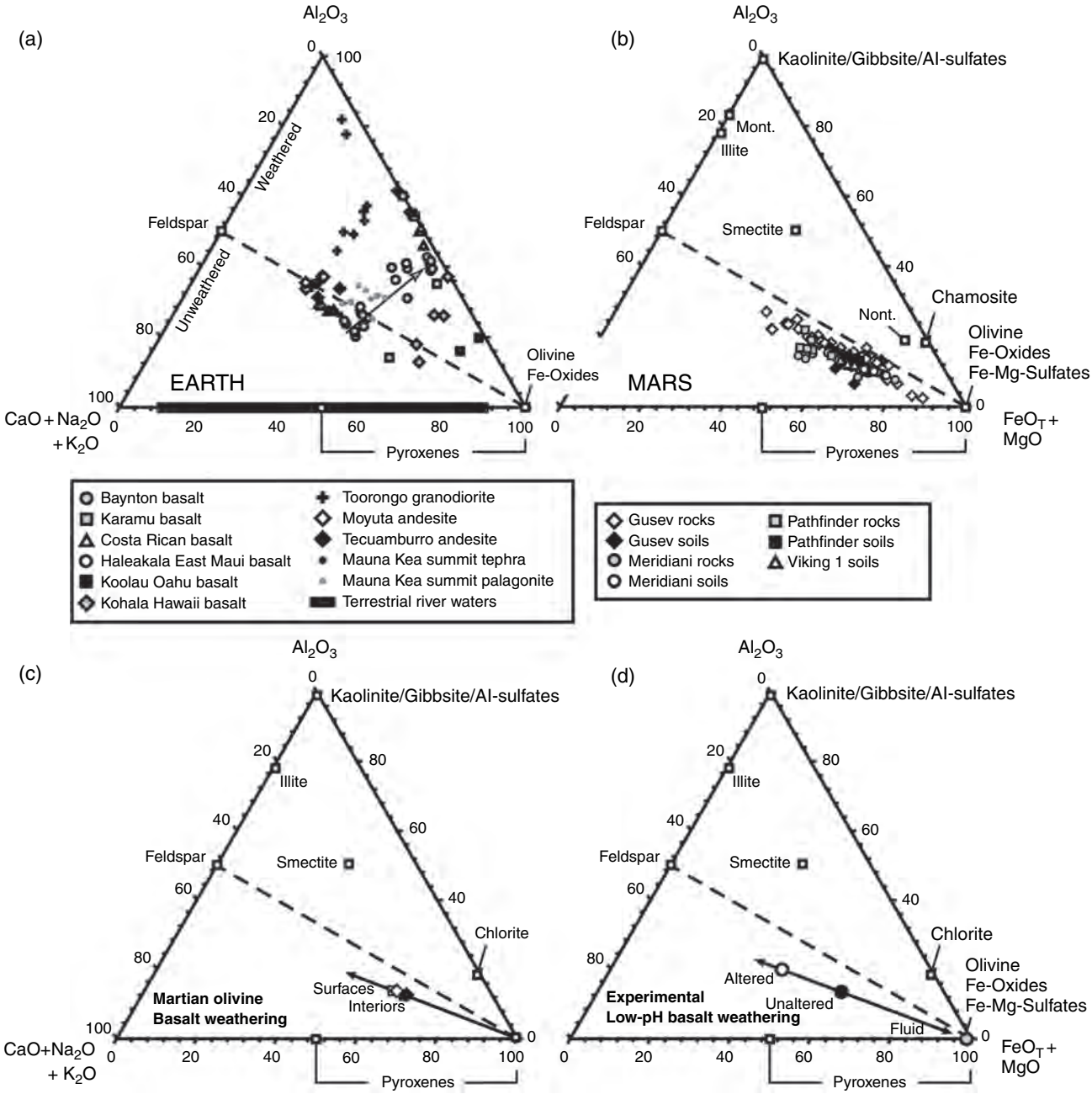

Figure 24.4. Ternary plots of molar proportions Al_2O_3 – $(CaO + Na_2O + K_2O)$ – $(FeO_T + MgO)$. Position of selected mineral compositions are shown in (b)–(d). (a) Selected data for terrestrial weathering profiles and other alteration products are mainly for basaltic rocks. Note that in all cases, increased alteration results in enrichment of Fe and Al due to the insoluble nature of these elements during terrestrial weathering (i.e., at intermediate pH). (b) All available Martian soil and rock data (Viking, Pathfinder, *Spirit*, *Opportunity*). Note that the Martian data all fall below and parallel to the line joining feldspar and the $FeO_T + MgO$ apex (olivine, Fe-oxides, Fe-Mg-sulfates) in spite of evidence for alteration in many of the samples. (c) Data for altered (brushed) surfaces (open symbols) and RATed rock interiors (closed symbols) for basalts on Gusev plains showing that chemical variations induced by surface alteration are consistent with dissolution of olivine. (d) Experimental data for altered (open symbol) and unaltered (closed symbol) olivine basalt showing that most primary igneous rock compositions that lie just below the diagonal line, and Al±Fe(III)-enriched residual clays and oxides that lie on or above the line. Note that Fe-Mg-sulfates would also plot at this apex.

In Figure 24.4a, a wide variety of typical terrestrial basalt weathering and alteration profiles are plotted (Hurowitz and McLennan, 2007). Note that primary igneous compositions vary sub-parallel to the plagioclase-olivine diagonal line, with more evolved (felsic) compositions plotting closer to

Caption for Figure 24.4. (cont.)
olivine ± Fe-Ti oxide dissolution dominates the alteration of olivine basalts under conditions of low pH. Fluid composition shown as gray circle at the $FeO_T + MgO$ apex. See text for further discussion. (Adapted from Hurowitz and McLennan, 2007.)

the plagioclase end. The weathering trends are consistent with the relatively insoluble nature and residual behavior of Al and Fe(III) at intermediate pH (Figure 24.2) and the formation of secondary clays and oxides at the expense of primary igneous minerals. Extrapolation of weathering trends through the original igneous compositions to the CNK–FM join gives the composition of the altering aqueous fluid. In terrestrial settings, such fluids are essentially devoid of Al and, unless highly reducing or unusually acidic, also of Fe (consistent with Figure 24.2).

In striking contrast, Figure 24.4b plots all geochemical analyses available for all Martian rocks and soils measured by Viking, Pathfinder, *Spirit*, and *Opportunity*. Included are surface and subsurface soils, undisturbed rock surfaces, "brushed" rock surfaces, and abraded rock surfaces, including basaltic rocks and sedimentary rocks preserved both in the Columbia Hills and in the Burns formation – all data from the surface of Mars available at the time of this writing. Although there is clear independent evidence for aqueous alteration and the presence of secondary minerals in many of these samples (e.g., high and variable Fe^{3+}/Fe_T [where Fe_T is total Fe], sulfates±chlorides, nanophase iron oxides, hematite [Fe_2O_3], amorphous silica, chemical-mineralogical depth profiles on rock surfaces – see Figure 24.4c), to a first order the trend cannot be distinguished from variations in primary basalt composition on this diagram.

The likely explanation for this different chemical behavior can be gleaned from low-pH basalt alterations experiments (Figure 24.4d). Acid alteration trends for various synthetic Martian basalts determined from experimental studies are also essentially parallel to the Mars data trend (Tosca *et al.*, 2004; Hurowitz *et al.*, 2005, 2006). This is because dissolution processes involving olivine, Fe-Ti oxides, pyroxene, and plagioclase do not result in selective elemental leaching because the relatively high solubility of Al and Fe(III) at low pH inhibit the formation of residual aluminous and ferric clays and oxides. Thus, from a purely geochemical perspective, it is impossible to distinguish olivine dissolution from olivine igneous crystal fractionation. Precipitation of dissolved Mg^{2+}, Ca^{2+}, and $Fe^{2+,3+}$ as chemical constituents (i.e., sulfates) within the soils and rocks further re-homogenize their bulk chemical compositions (e.g., Hurowitz *et al.*, 2005, 2006).

The composition of fluids that are involved in acid alteration do not lie along the CNK–FM join but rather plot in a field also broadly parallel to the plagioclase–FM tie line. This is both predicted from the Martian rock and soil data (e.g., Hurowitz *et al.*, 2006; Figure 24.4c) and consistent with low pH alteration experiments (e.g., Tosca *et al.*, 2004; Hurowitz *et al.*, 2005, 2006; Figure 24.4d). These relationships provide compelling evidence that low pH conditions have dominated during alteration of materials that have been studied thus far on the surface of Mars.

These relationships also suggest that large-scale Al mobility is largely absent on the Martian surface samples that have been examined to date. At low pH, both Fe and Al should be relatively soluble and carried in solution when released during rock alteration (Figure 24.2). There is abundant evidence in Martian soils and rocks for Fe mobility in the form of hematite, goethite (FeOOH), jarosite ($(K,Na,H_3O)Fe^{3+}{}_3(SO_4)_2(OH)_6$), and poorly crystalline iron phases. However, no such evidence exists for large-scale Al mobility and no evidence has yet been found for the occurrence of Al-sulfates, such as alunite ($(K,Na)Al_3(SO_4)_2(OH)_3$). The reasons for this are not entirely clear but one possibility, suggested by Hurowitz and McLennan (2007), is that at low water/rock ratios, dissolution of only the most soluble minerals (olivine, Fe-Ti oxides) dominates fluid chemistry, with the less soluble Al-bearing minerals (mainly plagioclase) being relatively unaffected (Figure 24.3). If this is the case, then it suggests that the currently available regions of Mars for which there are geochemical data have been altered in "rock-dominated" (i.e., low fluid/rock ratios) aqueous systems (Hurowitz and McLennan, 2007).

The nature and fate of the dissolved constituents derived from acid alteration also can be evaluated from field and experimental results. Sulfate components found in Martian soils are thought to be dominated by Mg- and Ca-sulfates of unknown hydration state. At Meridiani Planum, the chemical composition and Mössbauer- and thermal infrared-derived mineralogy of sulfate-rich sandstones of the Burns formation are best interpreted as having chemical constituents composed of a combination of Mg-, Ca-, and Fe(III)-sulfates and hematite. Halite (NaCl) and possibly Mg-, Fe-, and Ca-chlorides have also been suggested on a local scale both within the sandstones (Clark *et al.*, 2005; Squyres *et al.*, 2006a) and as later coatings and fracture fillings on outcrop surfaces (that could form by remobilization of soluble components from within the sandstones; Yen *et al.*, 2006; Knoll *et al.*, 2008). Ferrous sulfates have not been confirmed but have been suggested to have perhaps been once present on the basis of textural evidence (McLennan *et al.*, 2005) and are predicted from evaporation modeling and experiments (see below).

The occurrence of abundant Mg-sulfates, in addition to Ca-sulfates – which completely dominate sulfate deposits on Earth – appears to be a critical observation in terms of constraining the nature of the source basaltic rocks from which the aqueous fluids were derived. In a series of low pH aqueous alteration experiments in a variety of low-temperature to hydrothermal conditions (Tosca *et al.*, 2004; Golden *et al.*, 2005, Hurowitz *et al.*, 2005, 2006) the production of significant amounts of Mg-sulfates as alteration products or fluid evaporation products was restricted to olivine-bearing basalt or olivine-normative (i.e., Mg-rich) basaltic glass. In cases where olivine is absent, fluids tend to have high Ca/Mg ratios because plagioclase dissolution does not produce any dissolved Mg and pyroxene dissolution tends to liberate more Ca from M2 sites, thus leading to the early precipitation of abundant Ca-sulfates (Tosca *et al.*, 2005).

Although available evidence suggests that low pH conditions have prevailed over much of geological time and that large-scale Al-mobility is limited, there is growing evidence for the formation of clay minerals, suggestive of more modest pH conditions on at least local or temporally distinct scales (Poulet *et al.*, 2005; Bibring *et al.*, 2006). Mars Express OMEGA spectral data have shown evidence for phyllosilicates on the Martian surface, although the distribution is limited and the overall concentrations are not well constrained. Bibring *et al.* 2006 (see also Chapter 7) have

suggested that such minerals are restricted mainly to ancient Noachian terrains and that the nature of surface alteration processes changed through time, from relatively water-rich moderate pH during the early Noachian to water-rich low pH during the late Noachian/Hesperian to water-poor low pH during the late Hesperian/Amazonian. Although age-related distributions of sedimentary minerals (sulfates, phyllosilicates) are an intriguing suggestion, confirmation of such a relationship must await further and more quantitative spectral mapping of the Martian surface.

The possible presence of clay minerals has also been suggested in local alteration surfaces for rocks in the Columbia Hills of Gusev crater. Although there is no spectral identification, chemical mass balance calculations are suggestive of the presence of aluminous phyllosilicates (Wang *et al.*, 2006a).

24.4 EVAPORITES ON MARS

Most of the occurrences of sulfate minerals observed in stratified bedrock by the MER *Opportunity* appear to have formed originally by evaporation processes and subsequently reworked by a variety of eolian, groundwater, and other diagenetic processes. If the layered sedimentary rocks observed at Meridiani are representative of the layered terrains observed by OMEGA (OMEGA – Observatoire Pour la Minéralogie, l'Eau, les Glaces et l' Activité), it is likely that evaporites may have been common on Mars throughout its history (Bibring *et al.*, 2005; Gendrin *et al.*, 2005; Squyres and Knoll, 2005; Wang *et al.*, 2006b). An important caveat is that both freezing and evaporation can result in the formation of brines from which carbonate, sulfate, and chloride minerals can precipitate. In the case of the Burns formation at Meridiani, the overall sedimentological setting, sedimentary structures, and microtextural relationships are most consistent with processes that involve evaporation of significant amounts of water, analogous to formation of sedimentary evaporites in terrestrial settings (e.g., Hardie and Eugster, 1970; Eugster and Hardie, 1978; Hardie *et al.*, 1985; Hardie, 1991; Schrieber and El Tabakh, 2000). On the other hand, in Martian soils observed by the MER *Spirit* (such as at the target named Arad) and other surface sulfate deposits recognized from orbit, the actual mechanism of brine formation is less clear. In these cases, it is possible that sulfate formation may be related to condensation of only small amounts of water vapor. Evidence for evaporites on Mars can be summarized as follows:

1. As described above, high S and Cl in Martian soils, correlations between Mg and S, bright regions in soils exposed by trenching (with exceptionally high-S and locally high-Br contents) all are consistent with evaporative processes giving rise to Mg- and Ca-sulfates (e.g., Wang *et al.*, 2006b).
2. The Burns formation sandstones studied by *Opportunity* are characterized by exceptionally high sulfur and chlorine content. Detailed chemical characterization, Mössbauer and thermal infrared spectroscopy, and microtextural analysis indicate that the rocks were strongly influenced by evaporative processes both prior to and during deposition (see summary in Squyres and Knoll, 2005). A more detailed description of the Burns formation is given elsewhere (e.g., Grotzinger *et al.*, 2005; McLennan *et al.*, 2005; Squyres *et al.*, 2006a) and summarized below. Sand grains are interpreted to be sulfate-cemented altered basaltic mud and there is textural evidence for syndepositional evaporite mineral growth and formation of evaporite cements. The mineral assemblage includes Mg- and Ca-sulfates of unknown hydration state and possibly rare halite (Squyres *et al.*, 2006a). Jarosite has also been identified and, as described below, is a plausible evaporite mineral in this geochemical system.
3. The Peace Class sedimentary rocks preserved in the Columbia Hills of Gusev crater appear to be well-sorted basalt-ultramafic sands that have been cemented by Mg- and Ca-sulfates. The preferred model is that the sands were saturated with groundwater and sulfates precipitated during evaporation (Squyres *et al.*, 2006b; see also Chapter 23).
4. Within SNC meteorites, notably the nakhlites, mineral assemblages are recognized that have been interpreted to represent low-temperature evaporites (Bridges and Grady, 1999, 2000; Bridges *et al.*, 2001; see also Chapter 17). The evaporite assemblage that appears to be represented in the nakhlites consists of siderite ($Fe^{2+}CO_3$; an expected evaporite mineral in carbonate- and Fe-rich aqueous systems; see below), gypsum ($CaSO_4 \cdot 2H_2O$; and anhydrite, $CaSO_4$), epsomite ($MgSO_4 \cdot 7H_2O$), and halite. Also associated with these minerals are goethite and some clays.
5. The orbiting OMEGA visible through infrared spectrometer on Mars Express has identified gypsum, kieserite ($MgSO_4 \cdot H_2O$), and undetermined polyhydrated sulfates over a number of regions on Mars (Bibring *et al.*, 2005; Gendrin *et al.*, 2005; see also Chapter 7). The absolute abundances of these minerals are not well constrained and because of the shallow sensing depth of this instrument ($\sim$ upper few microns), it is not possible to determine which fraction of these minerals may be a surface coating, perhaps associated with a crust or soil, and which fraction records the composition of bedrock as has been determined by the MERs.

Expected evaporation sequences for a wide variety of freshwater and seawater brines on Earth are reasonably well understood from field studies, experiments, and theoretical modeling. Modeling evaporation is relatively complex in very high-ionic strength brines because of nonideal behavior of dissolved constituents. The method most commonly used to estimate activity coefficients in these brine systems is the Pitzer ion interaction approach (e.g., Pitzer, 1991). The necessary thermodynamic datasets are well characterized for terrestrial systems and a number of workers have attempted to apply these models to Martian conditions (e.g., Catling, 1999; King *et al.*, 2004; Marion and Kargel, 2005). Some workers have extended the modeling to include Fe(II) species (Marion *et al.*, 2003). Until recently, however, available evaporation models did not include thermodynamic data for both Fe(II) and Fe(III) species that are extremely rare during evaporation processes on Earth but could be important on Mars where low pH conditions prevail.

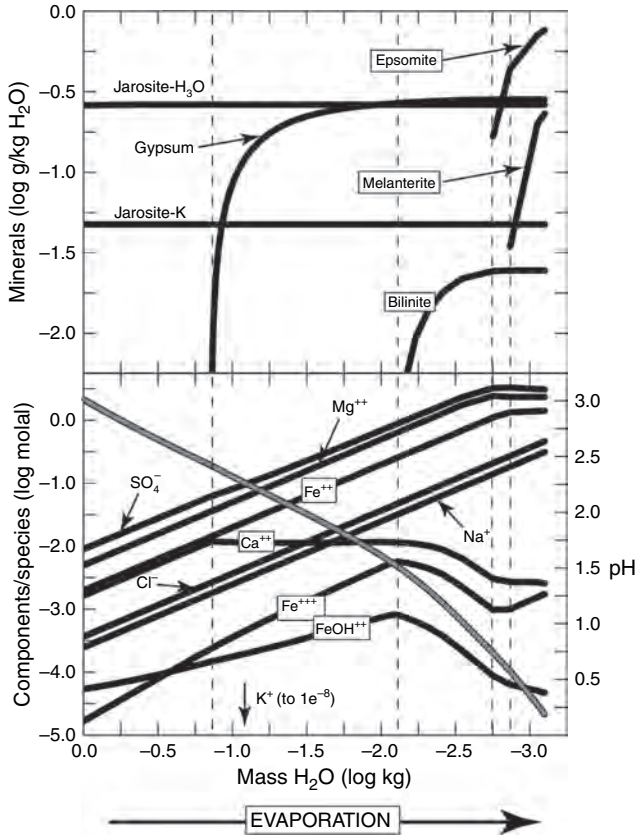

Figure 24.5. Geochemical model of the evaporation of a brine derived from the experimental low pH alteration of an olivine-bearing Martian basalt. Top panel shows the accumulation of evaporite minerals with increasing evaporation and the lower panel shows the evolution of the brine composition. Note that jarosite is an early-forming evaporite mineral (the amount depends of the Fe^{2+}/Fe_T ratio of the initial brine; in this case, $Fe^{2+}/Fe_T = 0.5$) and that significant amounts of ferrous sulfates and Mg-sulfate also precipitate (Tosca *et al.*, 2005). (Figure adapted from Tosca *et al.*, 2005.)

Tosca *et al.* (2005, 2007) compiled a complete thermodynamic dataset that includes Fe(II) and Fe(III) and other species that are possible evaporite phases from fluids derived from basalt at low pH. Results of one typical evaporation sequence using a low-pH Mg-, Fe- and Ca-rich brine as a starting fluid are shown in Figure 24.5. Among the significant findings that are applicable to Mars in general and the Burns formation in particular (Tosca *et al.*, 2005) are that Mg-, Fe-, and Ca-sulfates are all predicted (with the former two dominating), and that the ferric sulfate jarosite is a plausible early evaporite phase under low pH conditions (although it could also form by diagenetic oxidation mechanisms) as are ferrous sulfates, such as melanterite ($Fe^{2+}SO_4 \cdot 7H_2O$).

The exact evaporation pathway is largely controlled by the initial brine composition and accordingly will be strongly influenced by the cation/anion ratios due to the development of chemical divides within the brine as evaporation proceeds (e.g., Hardie and Eugster, 1970; Eugster and Hardie, 1978). Tosca and McLennan (2006) modeled the chemical divides that could be expected from the evaporation of brines derived by low pH alteration of typical Martian upper crust. In this modeling, the relative cation composition of the Mg-, Fe-, and Ca-rich brine was fixed at values expected for acid alteration of olivine-bearing basalt, and pH was varied by varying the HCO_3^-/SO_4^{2-} mole ratio and thus the cation/anion mole ratios (i.e., $(Mg,Ca,Fe)/SO_4^{2-}$, $(Mg,Ca,Fe)/HCO_3^-$). The results are summarized in Figure 24.6. Although more than 20 different evaporation sequences are possible, they result in only 5 distinct late stage brine compositions and thus a limited number of evaporite assemblages. All of the late stage brines are characterized by acidic composition and have pH $\leq$4 with four out of the five late stage brines having pH $\leq$2. It is especially notable that it is possible to generate all of the known evaporite assemblages on Mars (SNC meteorites, Meridiani, OMEGA) from a single brine composition by simply varying the initial pH (HCO_3^-/SO_4^{2-} ratio) of the starting brine (Tosca and McLennan, 2006).

Although low pH conditions appear to dominate, at least locally that may not always be the case. As discussed above, phyllosilicates have been identified associated with Noachian outcrops (Poulet *et al.*, 2005) and have been inferred for some rocks in the Columbia Hills of Gusev crater. In SNC meteorites, minor amounts of carbonate-sulfate-chloride assemblages, interpreted as evaporite assemblages, are found in veins, suggesting a relatively well-buffered system in which intermediate pH prevailed (Bridges *et al.*, 2001). Since SNC meteorites are likely derived from some depth within the Martian crust, Tosca and McLennan (2006) suggested that the Nakhlite evaporite assemblage may have evolved out of contact with the SO_2-rich atmosphere and thus were more readily buffered by low water/rock ratio basaltic weathering reactions, leading to increased carbonate alkalinity.

24.5 SEDIMENTATION AT MERIDIANI PLANUM

The occurrence of ancient sedimentary rock outcrops at Meridiani Planum, observed by the *Opportunity* rover, stands as one of the great discoveries by any planetary mission. The investigation of these deposits has demonstrated that the basic stratigraphic and sedimentological tools that have been used to elucidate the geological history of Earth may be applied to Mars with surprising rigor. At the time of this writing, *Opportunity* has traversed about 10 km (Figure 24.7) and has investigated in excess of 8 m of stratigraphic section. Although this represents only a tiny fraction of the Meridiani sedimentary rock record, it has revealed many remarkable characteristics that provide new insight into the types of processes that shaped the ancient Martian surface. As has been shown for Earth, even a small volume of sedimentary rock can provide significant insight into regional and global processes.

Traditionally, terrestrial sedimentary rocks have been used as "remote-sensing" tools to understand tectonic, climatic, and paleobiologic processes in a first pass interpretation, to help provide a framework to focus more topical analysis (e.g., Pettijohn, 1943; Walker, 1965; Hoffman,

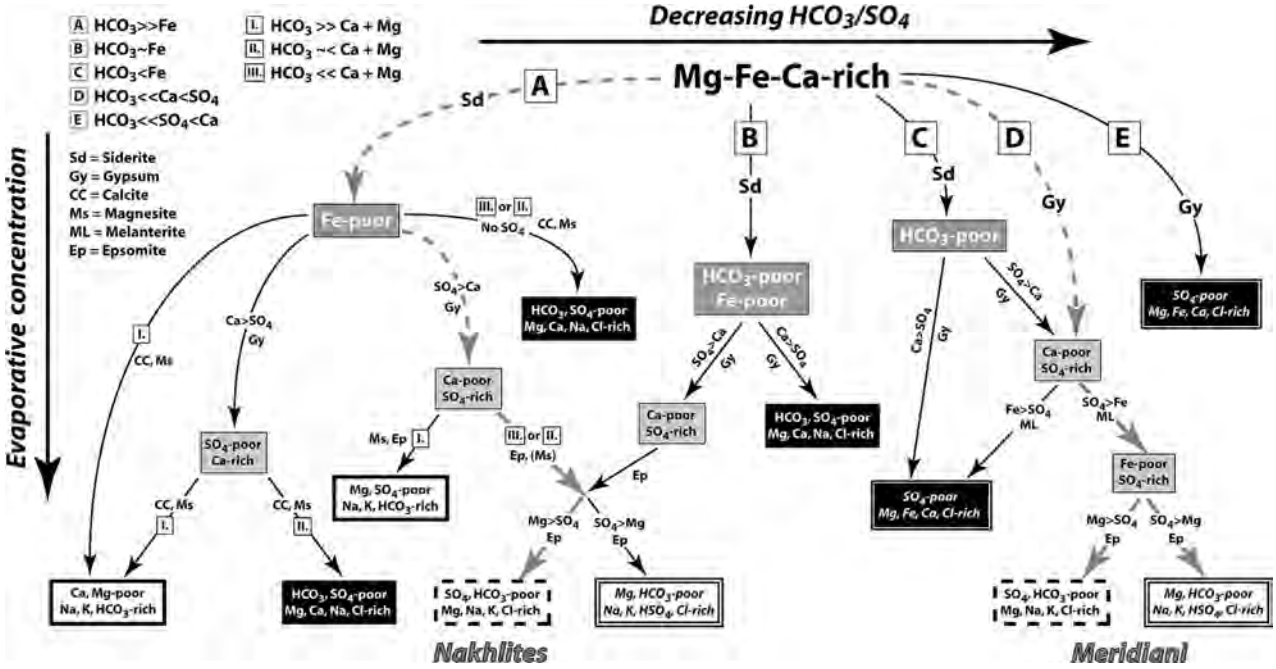

Figure 24.6. Chemical divide flow-chart showing chemical evolution of evaporating fluids derived by weathering of olivine-bearing basalt. The ratio of HCO_3^-/SO_4^{2-} decreases to the right and evaporative concentration increases downward. Resulting late-stage brines and their chemical characteristics are described in boxes that terminate each evaporation pathway. Note that only five distinctive brines result from the numerous possible evaporation pathways. Possible evaporation/mineral precipitation pathways for assemblages preserved in Nakhla meteorites (heavy-dashed gray lines on the left-hand side of the figure) and at Meridiani Planum evaporite mineralogy (heavy-dashed gray lines on the right-hand side) are shown. (Figure adapted from Tosca and McLennan, 2006.)

1968, 1973; Walker and Pettijohn, 1971; Henderson, 1975). More detailed studies of terrestrial sedimentary rocks provide insight into the nature of surface processes and environments. For example, studies of ancient siliciclastic depositional systems were used to first demonstrate the existence of flowing water and its environmental stability on the young (early Archean) Earth (e.g. McGlynn and Henderson, 1970; Eriksson, 1978). Studies of Archean chemical sedimentary systems demonstrated environmental change on the early Earth, including the chemical evolution of seawater (e.g., Grotzinger, 1989; Buick and Dunlop, 1990; Sumner and Grotzinger, 1996; Grotzinger and James, 2000). Chemical sedimentary rocks also provided the material for early paleontological discoveries (e.g., Schopf, *et al.*, 1971; Buick, *et al.*, 1981; Hofmann, *et al.*, 1985; Schopf and Packer, 1987; also see Buick, 2001). Thermodynamic studies of evaporite mineral stability have helped to constrain the surface temperature of the early Earth (e.g., Hardie, 1967).

The first observations of sedimentary processes at Meridiani have similarly helped to define the early history of surface processes on Mars. Detailed observations and measurements related to the sedimentology, stratigraphy, mineralogy, provenance, and diagenesis of these rocks have been reported elsewhere (Squyres *et al.*, 2004a, 2006a; Clark *et al.*, 2005; Grotzinger *et al.*, 2005, 2006; McLennan *et al.*, 2005; Squyres and Knoll, 2005) and will not be repeated here. Instead, we briefly summarize the history of deposition and diagenesis and comment on some of the broad implications for understanding the sedimentary record of Mars. The geological history of the Burns formation is summarized in Table 24.1 (from McLennan *et al.*, 2005).

24.5.1 Stratigraphy and sedimentology of the Burns formation

The Burns formation is the informal name given to the sequence of well-sorted, moderately indurated sandstones (Grotzinger *et al.*, 2005) preserved immediately beneath the surface of the Meridiani plains and examined in most detail at exposures in the vicinity and within Eagle, Endurance, Erebus, and Victoria craters (Figure 24.8). Regional geology suggests that the deposit is of late Noachian age and thus is likely in excess of 3.5 Ga. Detailed stratigraphic measurements (Figure 24.9) and sedimentological observations (Figure 24.10) indicate that eolian and locally subaqueous processes deposited these sedimentary rocks as part of a "wetting upward" dune–sand sheet–interdune depression sequence (Figure 24.11). The Burns formation has been divided into three stratigraphic units (lower, middle, and upper) and three major sedimentary facies associations have been identified:

1. Eolian dune facies are characterized by the occurrence of large-scale cross-bedded well-sorted sandstones. This facies is interpreted to represent a migrating dune system of unknown extent that was deposited under dry conditions such that the sediment was noncohesive and thus transported in migrating dune fields. Bed set thicknesses suggest moderately large dunes in excess of 2 m.
2. Eolian sand sheet facies are characterized by planar-laminated to low-angle cross-stratified, well-sorted

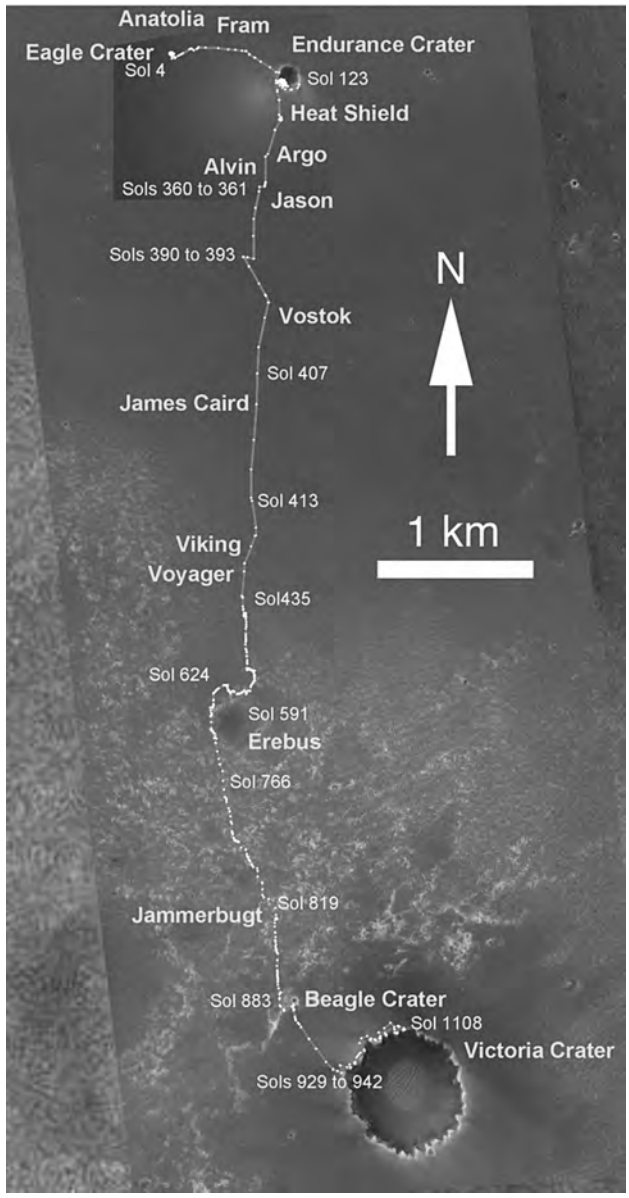

Figure 24.7. Mars Orbiter Camera image of Meridiani Planum in the region between the *Opportunity* landing site at Eagle crater and Victoria crater. Also shown is the traverse of *Opportunity* through to sol 1108 with major locations visited. The Olympia outcrop (Grotzinger *et al*., 2006) is located along the northwest margin of Erebus crater. (Figure courtesy of Ron Li [Ohio State University]. Image sources: NASA/JPL/MSSS.)

sandstones. This type of stratification results from sediment limitation, forming low-relief bedforms produced by migrating impact ripples (where the "impact" is related to the collisions of small saltating grains, not macroscopic impact cratering processes). In Endurance crater, the contact between the dune and overlying sand sheet facies marks the boundary between the lower and middle stratigraphic units. This important stratigraphic boundary, termed the Wellington contact, is interpreted to be a deflation surface formed where the groundwater capillary fringe limited erosion of previously deposited dune sediments.

3. Wet to evaporitic interdune facies characterized by centimeter-scale trough (or "festoon") ripple cross-lamination (e.g., Figure 24.10d), diagnostic of subaqueous current transport in the lower flow regime. At Endurance and Eagle craters, this facies is found in the upper part of the upper unit of the Burns formation and marks where the groundwater table breached the surface and wind-driven subaqueous currents transported the sediment. Centimeter-scale trough cross-lamination is particularly well developed at Erebus crater, where additional features suggestive of desiccation also are present (Grotzinger *et al*., 2006; Metz *et al*., 2008). Prism cracks are interpreted to have formed during multiple wetting and drying events, and soft sediment deformation features are consistent with sediment liquefaction.

Alternative Interpretations

Two alternative depositional models have been suggested for the Burns formation. McCollom and Hynek (2005) argue that the sequence was a volcanic base surge deposit that experienced *in situ* isochemical acid-sulfate alteration in an acid-fog-like setting. Knauth *et al*. (2005) suggested that the Meridiani strata were formed by an impact-induced base surge, whereby an iron meteorite struck an area with buried sulfate-rich evaporite deposits. Both of these models were proposed before the entire set of observations was available (e.g., Clark *et al*., 2005; Grotzinger *et al*., 2005, 2006; McLennan *et al*., 2005; Tosca *et al*., 2005; Squyres *et al*., 2006a). Furthermore, these alternative models are inconsistent with the regional geological context, which provides no evidence for contemporaneous sources of volcanism or age-appropriate impacts of sufficient size. Knauth *et al*. (2005) argue that the Schiaparelli impact basin may have been the target site for materials ejected to the *Opportunity* landing site. However, the Meridiani layered deposits disconformably overlie the dissected cratered terrain, including Schiaparelli crater. Thus, the Meridiani deposits are younger than the Schiaparelli impact event (Arvidson *et al*., 2006a).

Furthermore, Knauth *et al*. (2005) contend that the Burns spherules are iron condensation spherules – not diagenetic concretions. However, the Fe/Ni ratios are inconsistent with such an impact origin. In addition, if the spherules are accretionary lapilli or impact condensation spherules, as Knauth *et al*. (2005) argue, they should show concentrations along bedding planes. In all outcrops observed to date by *Opportunity*, spherules are always highly dispersed relative to bedding (McLennan *et al*., 2005). Hydraulic segregation of particles with different settling velocities is why sorting occurs, and why out-sized particles (e.g., lapilli) are commonly concentrated along bedding planes in successions of flow-emplaced strata (Lowe *et al*., 2003). The bedding planes observed at Meridiani represent surfaces formed during reconfiguration of the bed in response to scouring during flow bursting, migration of 3D bedforms with frontal scour pits, and/or decreases in the sediment concentration of the flow. Note that this conclusion is independent of flow mechanism. However, spherules are dispersed across all

Table 24.1. *Geologic history of the Burns formation from oldest to youngest*

Depositional stage	Event
Predepositional *(Playa lake facies)*	1. Deposition and evaporative cementation of basaltic mud, likely near margin of playa lake. Erosion to produce sand-sized grains.
Depositional *(Dune–sand sheet–interdune facies)*	2. Aeolian transport of impure evaporitic sand grains within dune–sand sheet–interdune depositional environment under a range of dry to wet conditions. Periodic rise of groundwater table results in shallow subaqueous conditions in interdune setting.
Diagenetic *(Related to syndepositional evaporation and fluctuating groundwater table)*	3. Syndepositional formation of small (mm-scale) cross-cutting crystals of an evaporite mineral more soluble than Mg-sulfates, likely during evaporation of near-surface water table or capillary fringe of water table.
	4. Syndepositional to very early diagenetic formation of fine-grained ($<100\,\mu m$) cement filling primary porosity, likely caused by evaporation of near-surface water table or capillary fringe of water table.
	5. Rapid formation of hematitic concretions likely during a chemically distinct groundwater recharge event. A thermodynamically plausible model is that hematite (or hematite precursor) forms by the breakdown of jarosite or other iron sulfate such as melanterite.
	6. Formation of secondary porosity by dissolution of small tabular crystals (crystal molds) and dissolution of earlier cements to form elongate to sheet-like vugs. Possible that the secondary porosity forms as a result of concretion growth.
	7. Formation of overgrowth cements around concretions under fluid-saturated conditions. In the lower and middle units (dune, lower part of sand sheet facies), this cement is more abundant and forms at nucleation sites in addition to concretions. Contact between the middle and upper units, interpreted to be a diagenetic front, is marked by a dark-colored zone where primary stratification is obscured by recrystallization and secondary porosity is especially abundant.
"Postdiagenetic" *(Impact, erosion)*	8. Formation of fractures, fracture fillings, veins, and polygonal features likely associated with impact processes. May also involve very late diagenetic processes, such as minor dissolution/reprecipitation.
	9. Erosion of units above outcrop to produce lag of concretions on plains.

Source: Adapted from McLennan *et al.* (2005).

strata, even at obvious erosional surfaces such as the lower–middle unit boundary (Wellington contact) at Burns Cliff (Grotzinger *et al.*, 2005). They are not concentrated along these surfaces, despite clear evidence that the surfaces truncate spherule-bearing strata and represent erosion of spherule-bearing sediments. The spherules therefore must have developed *in situ*, after deposition of the sediments.

Both McCollom and Hynek (2005) and Knauth *et al.* (2005) argue that cross-bedding may be developed in base-surge deposits, and that this discounts its diagnostic value in constraining the sediment transport mechanism. Indeed, a particular type of cross-bedding associated with migrating "sand waves" has been observed in terrestrial volcanic base surge deposits. Arguments of hydrodynamic similitude between volcanic and impact-generated gravity flows presume that the flow conditions required to produce cross-bed-generating bedforms should also be present in impact-generated base-surge deposits (Knauth *et al.*, 2005). However, cross-bedding has not been observed in terrestrial examples of impacts (e.g., Shoemaker and Kieffer, 1974; Dressler *et al.*, 2004).

Nevertheless, a more general point can be made which is relevant to any discussion of Martian sedimentary rocks: if all geometrically discordant strata are grouped together using the term "cross-bedding," we agree that the term loses interpretive value. Therefore, our conclusions about the mechanisms of deposition at Meridiani (Squyres *et al.*, 2004a; Grotzinger *et al.*, 2005, 2006) were based on the *particular properties* of cross-stratification, including geometry, scale, and sediment grain size and sorting, and not simply its presence or absence. At Meridiani, we observe both centimeter-scale trough ("festoon") cross-laminae at Eagle and Erebus craters and meter-scale cross-beds at Endurance (Grotzinger *et al.*, 2005; 2006) and, most recently, Victoria craters. In all cases studied in detail so far, grain sizes are fine to medium, occasionally coarse, and sediments are well sorted, even on a lamina-by-lamina basis.

Knauth *et al.* (2005) provided no illustration of analogous cross-stratification, either as evidence of migrating centimeter-scale ripples, or as larger meter-scale dunes. Instead, Knauth *et al.* (2005) illustrate (their Figure 24.3b) a single *low-angle* scour and fill structure, rather than a series of high-angle trough cross-laminae, that show multiple sets and multiple truncation surfaces (compare with Grotzinger

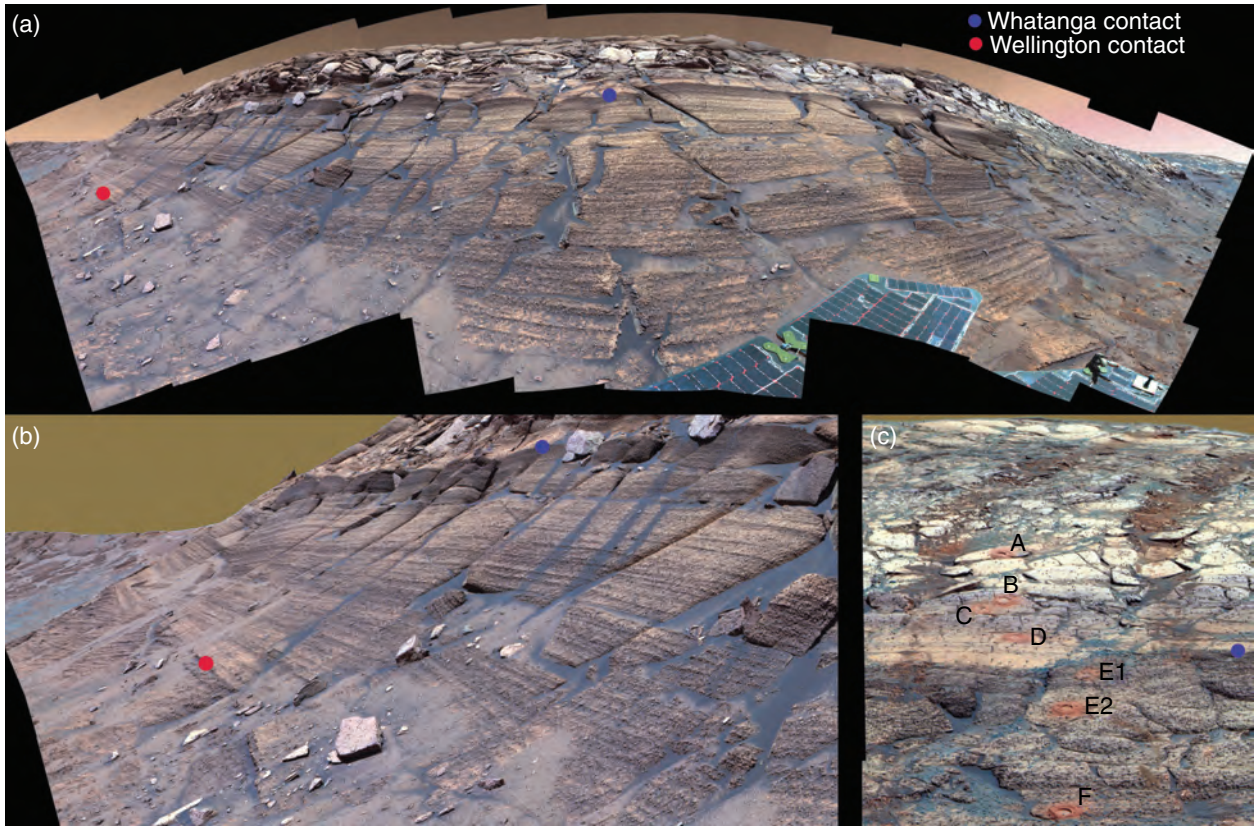

Figure 24.8. Pancam mosaics of the Burns formation exposed at Burns cliff on the southeast rim of Endurance crater. Three units of the Burns formation (Figure 24.9) are visible: the lower unit, beneath the "Wellington" contact, comprises cross-bedded sandstones; the middle unit, above the Wellington contact and beneath the "Whatanga" contact, comprises planar to low-angle cross-stratified sandstone; the upper unit, above the Whatanga contact, comprises light-toned eolian and subaqueous facies. Note the sharp discontinuity along the Wellington contact, interpreted to represent a deflation surface, and the dark tone of rocks beneath the Whatanga contact in panels A and B. In panel C, the location of the RAT holes, used to evaluate mineralogy, geochemistry, and microtextures, are labeled. The scale varies significantly across the area of each image, but the overall exposure at Burns cliff (panel A) is about 7 m and the RAT holes (panel C) are 4.5 cm in diameter. The images are false color-composite Pancam mosaics (see Grotzinger *et al.*, 2005, for details). (For a color version of this figure, please refer to the color plate section or to the e-Book version of this chapter.)

et al., (2005), Figure 24.16). These latter stratification styles are most consistent with low velocity, subcritical flows that are characteristic of fluvial and eolian transport. Similarly, Figures 3a and 4b in Knauth *et al.* (2005) illustrate low-angle cross-stratification formed by low-relief scour and fill in the upper flow regime, or possibly as antidunes formed in supercritical flows. Such high velocity, rapidly fluctuating flows are typical of the hydrodynamic setting of a base-surge deposit (Branney and Kokelaar, 2002), for which there is no evidence at Meridiani. Centimeter-scale trough cross-lamination is notably absent in their figures, and to our knowledge has not been described from an impact-generated base-surge deposit. Similarly, we are not aware of centimeter-scale cross-lamination described from terrestrial volcanic base-surge deposits. If volcanogenic centimeter-scale cross-lamination does occur, then the conditions leading to this must be very rare. However, because meteoric precipitation is common on Earth, care should be taken to insure that centimeter-scale cross-lamination did not result from fluvial reworking of pyroclastic particles (see White, 1990, for description of fluvial reworking of base-surge and other pyroclastic deposits). Finally, to the extent that cross-bedding does form in volcanic (and possibly impact) base-surge deposits, it is generally formed under conditions of high sediment fallout, leading to supercritical angles of climb. In contrast, the bedforms indicated by the cross-stratification observed by *Opportunity* all suggest development under conditions of low sediment fallout and subcritical angles of climb.

Taken individually, and out of context, multiple interpretations are possible for the origin of the varied geochemical and textural features at Meridiani. However, when considered collectively, and in context, or even individually but in detail, many of the key observations are best explained using a sedimentary model of deposition and diagenesis. All available data, from the smallest scale physical textures of lamination and sorting, through the regional stratigraphic relationships, favor the sedimentary origin of the rocks exposed at the *Opportunity* landing site. Observations from orbit suggest that sedimentary rocks probably characterize the bulk of the Meridiani succession (Edgett, 2005). We therefore accept this as a firm constraint, and now consider the broader scale implications of this sedimentary model for the early evolution of the Martian crust and surface environment.

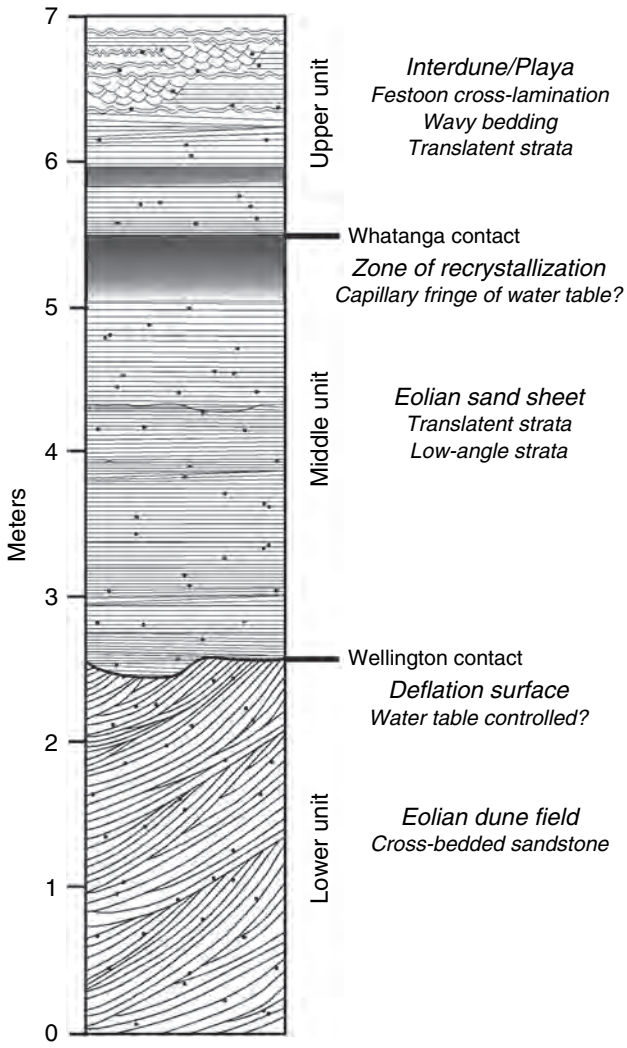

Figure 24.9. Stratigraphy of the Burns formation exposed at Burns cliff and within Eagle crater, Meridiani Planum. Key stratigraphic boundaries and sedimentological interpretations of the three stratigraphic units are shown on the right-hand side of the column. See text for further discussion. (Modified from Grotzinger *et al.*, 2005.)

24.5.2 Burns formation composition, sediment sources, and evaporative processes

The Burns formation is composed of fine- to coarse-grained sandstones with grain sizes mostly in the range of 200–1000 μm (the effective resolution of the microscopic imager [MI] is about 100 μm – about 3 MI pixels – and so any grains smaller than this cannot be unambiguously recognized). Where examined with the MI, sandstones are well sorted and individual laminae are very well sorted. It is difficult to confidently evaluate the original shape of all grains because of postdepositional corrosion and recrystallization (their mineralogy is highly labile; see below). Nevertheless, where grain boundaries appear reasonably intact, grains appear subrounded to well-rounded and accordingly, the formation is most likely texturally mature to supermature, consistent with an eolian influence on sediment transport.

The Burns sandstones have highly unusual chemistry (e.g., $SO_3 = 18\%$ to 25%), and considerable effort has gone into evaluating their bulk mineralogy using a combination of Mössbauer (Klingelhöfer *et al.*, 2004; Morris *et al.*, 2006; see also Chapter 15), visible through near-infrared spectroscopy (Bell *et al.*, 2004; Farrand *et al.*, 2007; see Chapter 13), thermal-infrared spectroscopy (Christensen *et al.*, 2004; Glotch *et al.*, 2006; see Chapter 14), and chemical mass balance calculations (Clark *et al.*, 2005; McLennan *et al.*, 2005; see also Chapters 4 and 23). Table 24.2 provides the most recent evaluation of the overall mineralogy of the Burns formation. The Burns formation has been described as a "dirty evaporite" (Squyres *et al.*, 2004a) but perhaps is more accurately characterized as an evaporitic sandstone (see below).

The chemically inferred and spectrally documented mineralogy of the siliciclastic components indicate an origin from altered basaltic rocks (Figure 24.12). Original Mössbauer determinations were seen to be consistent with a complete absence of unaltered basaltic material (Klingelhöfer *et al.*, 2004), but the most recent mineralogical assignments, coupled with recent thermal-infrared mineral deconvolutions, are consistent with the siliciclastic components being composed of substantially altered basaltic material but with some primary igneous mineralogy (pyroxene, possibly plagioclase, and trace olivine) remaining intact (Morris *et al.*, 2006).

The mineralogy and distribution of the chemical constituents is complex. No more than about half of the hematite ($\leq$3% of the bulk mineralogy) occurs as hematitic spherules that in turn contain 50%–100% hematite. The remaining hematite is distributed throughout the rocks in an unknown pattern. Identification of secondary (amorphous) silica comes from thermal-infrared deconvolutions (Glotch *et al.*, 2006) and is consistent with chemical mass balance (Clark *et al.*, 2005; McLennan *et al.*, 2005). Such a component is most likely the result of basalt weathering processes at low pH (McLennan, 2003). Whether silica is present within sand grains, as intergranular cements, or both, is not known. However, if the pH of the aqueous environment within which the Burns formation accumulated was low, silica transport would have been limited. Accordingly, it is most likely that the secondary silica is more closely associated with the altered basalt components and thus contained substantially within grains, but could have been remobilized into the later cements. Depending on the exact structure, amorphous silica (e.g., opal-A) could contain up to 10%–12% H_2O (e.g., Jones and Renaut, 2004).

The remaining chemical constituents are composed of sulfate minerals (±minor chlorides) and include Mg-sulfates (18%), jarosite (ferric sulfate; 10%), and most likely Ca-sulfates (~10%). Abundances are estimated on an anhydrous basis, but sulfate minerals typically have significant amounts of structural water (i.e., $MgSO_4 \cdot nH_2O$, $n = 1$–12; $(H_3O,K,Na)Fe_3(SO_4)_2(OH)_6$; $CaSO_4 \cdot 2H_2O$) and accordingly the total sulfate mineralogy volume fraction may be up to a factor of 2 higher than listed on Table 24.2 (and thus the amount of siliciclastics could be as little as 20% by volume). Of these sulfate minerals, Mg- and Ca-sulfates

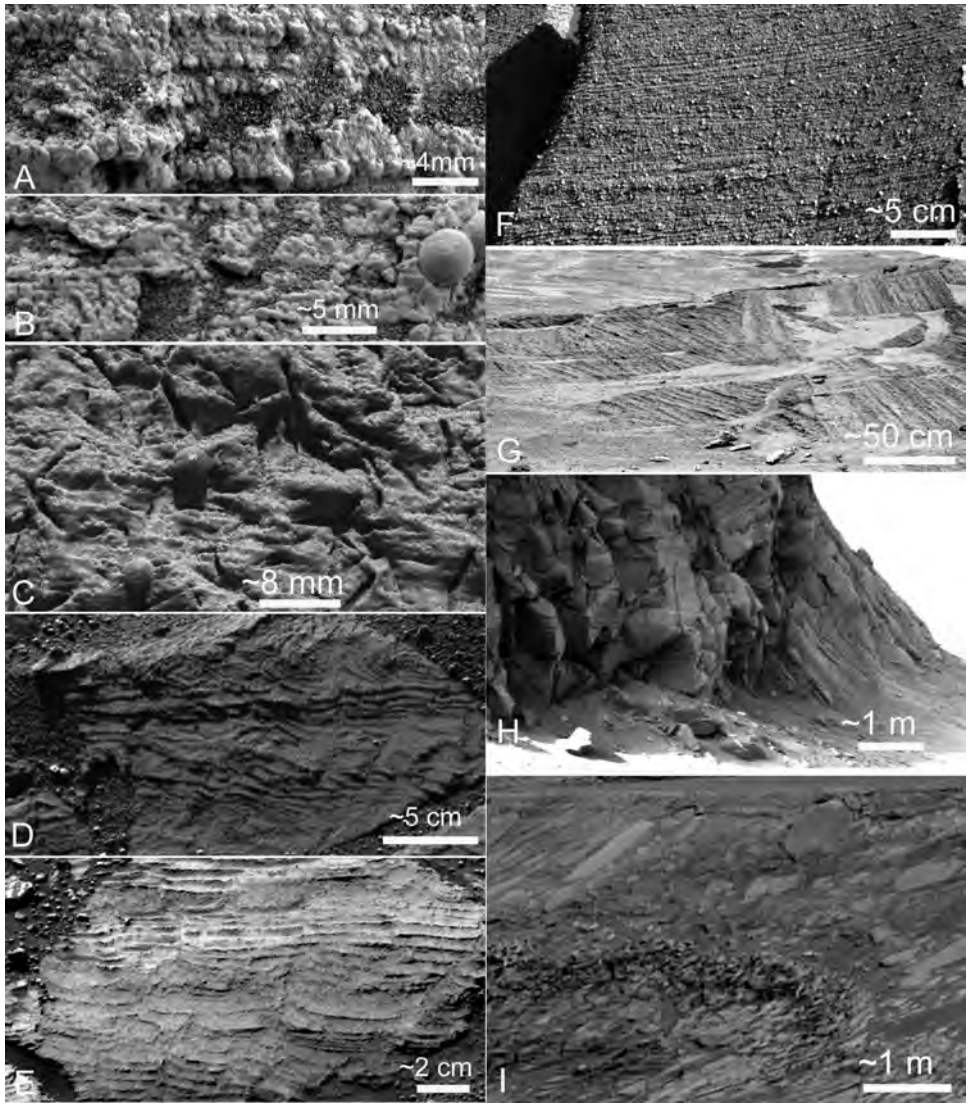

typically form as evaporites. On the other hand, in terrestrial settings, jarosite is typically formed by pyrite alteration in acid mine drainage systems, in acid lakes, and as an acid-sulfate alteration product in volcanic settings. However, under low pH conditions water derived from basalt alteration could also produce jarosite by evaporation processes (Tosca *et al.*, 2005) or by secondary oxidation of ferrous sulfates (N. Tosca, pers. comm.).

The simplest interpretation is that the entire sulfate assemblage formed by evaporative processes with later diagenetic mineral transformations (see below). However, it is equally clear that the sulfate minerals do not represent a primary evaporite sequence assemblage, having been reworked by eolian and subaqueous transport and having experienced diagenetic mineral growth, transformation, and dissolution. Furthermore, there is insufficient volume of siliciclastic material and amorphous silica to account for all of the sand grains. At the available level of MI resolution, the sand grains are of uniform character with no evidence for individual volcanic clasts, rock fragments, or composite

Figure 24.10. (a) MI image showing distinct grains that form lamination ("Flatrock," Eagle crater), indicating that most of the Burns formation was composed of sandstones, whose grains were derived from reworked evaporites. Grains range in size from 0.1 to 1.0 mm, are moderately well rounded, and are well sorted into discrete laminae. The excellent size sorting on the scale of individual laminae is strongly suggestive of "translatent" strata, formed by sediment transport within migrating eolian impact (saltation) ripples (see Grotzinger *et al.*, 2005, for more details). Fabric preservation, which reveals discrete grains, is rare due to cementation recrystallization; preservation is best where early cementation was minimal, permitting grains to weather in positive relief. Compare with Figure (b), which shows the effects of increasing cementation. The image (1M131912465) was acquired on Sol 42. (b) MI image showing effects of early cementation and recrystallization, visible in the center left ("Algerita," Eagle crater). Note set of 3 or 4 laminae, expressed by fused grains. The lack of expression of individual grains, as compared to Figure (a), is interpreted to reflect the greater extent of early cementation. At center right, the effects of recrystallization on destruction of primary fabrics are well illustrated by a halo which envelops a hematitic concretion. Note complete loss of primary fabric and development of blocky, interlocking crystals (see McLennan *et al.*,

grains formed of finer particles within the grains themselves. Accordingly, the grains have been interpreted to represent reworked sulfate-cemented altered basaltic mud (McLennan *et al.*, 2005; Squyres *et al.*, 2006a). Material such as this is produced in great abundance in terrestrial playa lake settings associated with eolian depositional systems (Grotzinger *et al.*, 2005).

24.5.3 Role of groundwater diagenesis and history of groundwater recharge

Terrestrial eolian depositional environments are commonly influenced by groundwater during both deposition and later diagenesis (e.g., Fryberger *et al.*, 1983; Hardie *et al.*, 1985; Schenk and Fryberger, 1988). The sulfate-rich sandstones of the Burns formation similarly contain abundant evidence for the influence of groundwater, and several distinct episodes of groundwater-mediated diagenetic changes have been documented (Squyres *et al.*, 2004a, 2006a; McLennan *et al.*, 2005; Squyres and Knoll, 2005). Using the well-established concepts of cross-cutting relationships it is also possible to place many diagenetic features into an approximate paragenetic sequence (e.g., Choquette and Pray, 1970; Meyers, 1974), and this has also been done for the Burns formation (McLennan *et al.*, 2005).

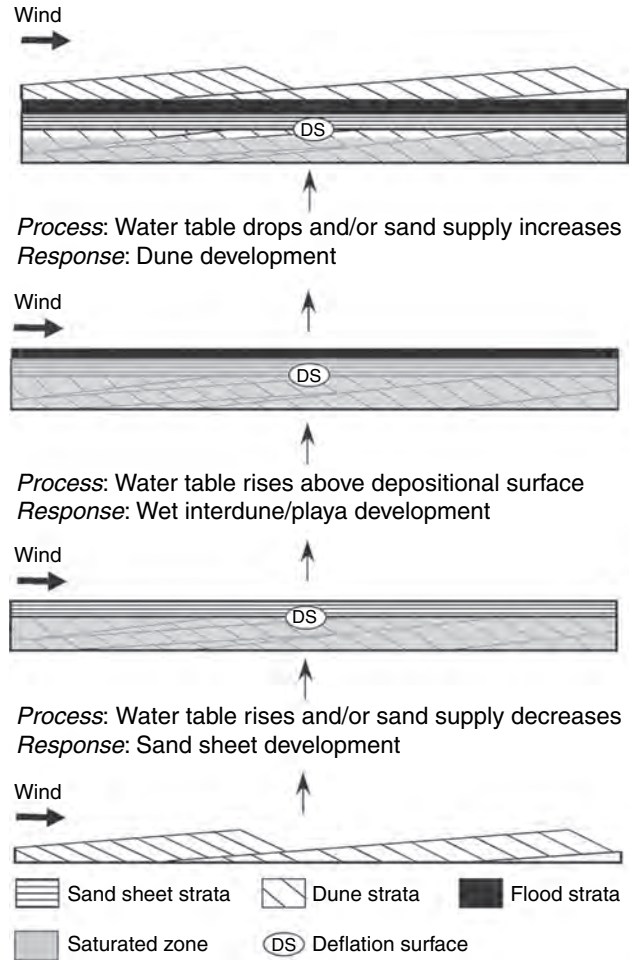

Figure 24.11. Depositional model for the Burns formation in the region of Eagle and Endurance craters (from Grotzinger *et al.*, 2005) documenting a "wetting upward" eolian system. The lower unit accumulates by migration of eolian dunes composed of sulfate-cemented altered basalt sand grains. Elevation of the water table (or decrease in sediment flux) results in the formation of a deflation surface (DS) down to the level of the capillary fringe of the water table. Sand sheet strata are deposited above the deflation surface. At some point, the groundwater table breaches the surface, resulting in deposition of subaqueous interdune sandstones ("Flood Strata"). To date, only one such cycle has been confirmed by *Opportunity*, but such a model predicts that the cycle would be repeated as the level of the groundwater table fluctuated.

The major diagenetic features that have been observed (Figure 24.13) in their approximate paragenetic sequence (Figure 24.14) can be summarized as follows:

1. Syndepositional crystallization of millimeter-scale, highly soluble (comparable to Mg-sulfate solubility), lozenge- to tabular-shaped (possible monoclinic) evaporite crystals (Figures 24.13h,i) analogous to halite crystals that precipitate from groundwater capillary fringes in sabkha-like environments on Earth (Fryberger *et al.*, 1983). Rarely, and notably in the vicinity of Erebus crater, pseudomorphs of cubic hopper crystals may be present, suggesting the precipitation of halite (Squyres *et al.*, 2006a).

Caption for Figure 24.10. (cont.)
2005, for more details). The image was acquired on Sol 28. (c) MI mosaic showing both diagenetic concretions (positive relief), and molds after diagenetic minerals (negative relief). Note distinct geometric shapes of crystal molds, which cross-cut primary lamination. The images were acquired on Sol 29. (d) Pancam image of trough (or "festoon") cross-lamination (upper "Overgaard," Erebus crater). Small-scale trough cross-lamination is interpreted to have formed in low-velocity subaqueous flows (see Grotzinger *et al.*, 2006, for further discussion). This image was acquired on Sol 716. (e) Pancam image of probable desiccation cracks and soft-sediment deformation features ("Skull Valley," Erebus crater). Cracks cross-cut lamination, some obliquely to bedding. Note characteristic upward-deflected laminae along crack margins, termination of prominent crack in center of rock at a discrete bedding plane, and truncation of upward-deflected laminae along discrete bedding planes in center and upper parts of rock. This image was acquired on Sol 713 (see Grotzinger *et al.*, 2006, for further details). (f) Pancam image of low-angle cross-stratification featuring well-developed pinstripe texture which has likely formed due to differential cementation of eolian translatent strata ("Tipuna," Endurance crater). The Tipuna outcrop represents the uppermost 30–40 cm of the Burns middle unit. The image was obtained on Sol 307. (g) Pancam image of the contact between the lower and upper units of the Burns formation. Below the contact, large-scale cross-bedding forms a bedset at least 2 m thick that was likely formed by migrating eolian dunes. The contact – a truncation surface – is interpreted to represent deflation of the dune field down to the level of the groundwater table (see Grotzinger *et al.*, 2006, for further details). The image was acquired on Sol 288. (h) Pancam image of large-scale cross-bedding in the cliffs of Victoria crater, along the west-facing wall of Cape St. Mary. This cross-stratification is also diagnostic of migrating eolian dunes, as indicated by the presence of meter-scale scours and wedge-shaped sets. The image is part of a mosaic acquired during Sols 970–991. (i) Pancam image of ejecta blanket deposited on Burns formation bedrock at Victoria crater, along the east face of Cabo Frio. The blanket consists of coarse block breccia and is capped by a stratified upper unit, which drapes protruding breccia blocks. The image is part of a mosaic acquired on Sol 952.

Table 24.2. *Constraints on mineralogy of the Burns formation*

Mineral[a]	Weight%	Comment
Chemical constituents	***60 ± 10***	Consistent with S, Cl, and Fe mass balance
Hematite	6	36% of iron as hematite from Mössbauer. At least one-half of hematite is in spherules
Jarosite[b]	10	29% of iron as jarosite from Mössbauer
Mg-sulfate[b]	18 ± 5	From variation associated with Mg and S correlation; Mini-TES spectrum best fit with Mg- and Ca-sulfates
Other sulfates[b]	10 ± 5	From S mass balance; likely to be mainly Ca- sulfates; Mini-TES spectrum best fit with Mg- and Ca-sulfates
Chlorides	≤2	Possible presence based on Cl abundance; Cl may not be separate mineral but solid solution with sulfate or mixed anion salt
Secondary silica	22 ± 3	Presence is inferred from geochemical mass balance (e.g., Si/Al ratios) which indicates as much as 25%; Recent Mini-TES deconvolutions also suggest 20%–25%
Siliciclastic constituents	***40 ± 10***	Consistent with S, Cl, and Fe mass balance and Al abundance
Olivine	~1	2% of iron as olivine from Mössbauer
Pyroxene	6 ± 3	14% of iron as pyroxene from Mössbauer; assumes Fe contents typical of pyroxenes in SNC meteorites The mineral assignment of pyroxene was not considered to be a unique interpretation for octahedrally coordinated Fe(II) by Klingelhöfer *et al*. (2004) but further refinement suggests an assignment as pyroxene (Morris *et al*., 2006).
Plagioclase	10 ± 10	Mini-TES deconvolution suggests 15%–20% depending on remaining mineralogy, and chemical mass balance is consistent with up to ~15% but does not require any
Other	23 ± 10	Includes other igneous and altered igneous components and possibly sheet silicates (e.g., nontronite); remaining 20% of iron as Fe_3D_3 component (i.e., nanophase Fe^{3+}) and so likely altered.

[a] All mineralogical constraints are on a volatile-free basis. Chemical constituents likely are hydrated and so their proportions could accordingly be far greater than indicated above.
[b] Total sulfate mineralogy is constrained to be about 35% to 40% on an anhydrous basis based on SO_3 content, with exact amounts depending on the mineralogy.
Source: Updated from McLennan *et al*. (2005).

2. Syndepositional formation of prism cracks and soft sediment deformation features suggestive of cyclical wetting/drying and sediment liquifaction, respectively (Figure 24.10e; Grotzinger *et al*., 2006).
3. Syndepositional to postdepositional crystallization of intergranular pore-filling cement (Figure 24.13a). In many places, primary grain boundaries are obscured and appear to be corroded during the formation of cements, suggesting that the grains are composed of chemically and mineralogically labile components.
4. Crystallization of millimeter-scale, highly spherical and over-dispersed hematitic spherules (50%–100% crystalline hematite), interpreted to be replacive sedimentary concretions (Figures 24.13b,c,e,f,j). These concretions constitute about 3% (but with considerable variability) of the outcrop in the vicinity of the Eagle–Endurance craters. Further south, in the vicinity of Erebus crater, the concretions are locally smaller, numerically more abundant (but with similar overall volume) and more irregularly shaped (Figure 24.13g), suggesting local, possibly facies-controlled, variations in hydrological conditions (Squyres *et al*., 2006a). Although such concretion occurrences have not been reported on Earth, Morris *et al*. (2005) noted that much smaller but chemically and mineralogically similar hematitic spherules form during aqueous acid-sulfate alteration of basaltic tephra on Mauna Kea.
5. Development of secondary porosity due to dissolution of relatively soluble components of the sediment. Two dominant types of secondary porosity are recognized, including crystal mold porosity formed from the dissolution of the early syndepositional crystals described in stage 1 above (Figures 24.13h,i), and elongate to sheet-like porosity that forms both parallel to and cutting across primary laminations (Figure 24.13j).
6. Formation of later generations of cements. Higher in the sequence, zones of pervasive recrystallization occur, notably around concretions (Figure 24.13b). These are significant because the zone of recrystallization obliterates the primary grains, strongly suggesting that grains are composed of highly labile material. Lower in the section, zones of pervasive cementation and recrystallization in contact with concretions (Figure 24.13c) and as nodules composed of cemented sandstone (Figure 24.13d)

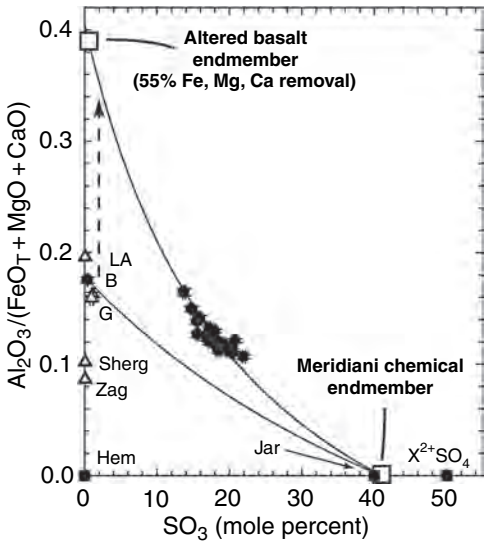

Figure 24.12. Plot of molar $(Al_2O_3/(FeO_T + MgO + CaO)$ versus SO_3 for the abraded portions of the Burns formation outcrop. Also plotted are the compositions of Martian meteorites (LA – Los Angeles; Sherg – Shergotty; Zag – Zagami), Martian surface basalts (B – Bounce Rock; G – Gusev crater plains basalts), selected mineral compositions (Hem – hematite; Jar – jarosite; various Ca-, Mg- and Fe^{2+}-sulfates as $X^{2+}SO_4$). The composition of the Burns formation is consistent with mixing between an "altered" Martian basalt and a chemical endmember consisting of a variety of sulfate minerals and hematite. Variations in the Burns formation composition are in part stratigraphically controlled (SO_3 decreases down section) and result mainly from variations in Mg and Al and are interpreted to be due to diagenetic redistribution of soluble salts (e.g., Clark *et al.*, 2005). (Adapted from Squyres *et al.*, 2006a.)

occur. Geochemical evidence is also consistent with vertical diagenetic redistribution of sulfates and chlorides (Clark *et al.*, 2005; Squyres *et al.*, 2006a). At about the same time, decimeter-scale stratigraphically controlled zones of greatly enhanced secondary porosity formed, notably at the Whatanga contact. These stratigraphic horizons and enhanced zones of recrystallization in the lower part of the Burns formation section are interpreted to represent a period of enhanced groundwater interaction, possibly associated with the stagnation of the groundwater table at or below the Whatanga contact (Grotzinger *et al.*, 2005; McLennan *et al.*, 2005).

The depositional and diagenetic histories of the Burns formation at Meridiani Planum appear to record a dynamic fluctuating groundwater table and at least four distinct episodes of groundwater recharge appear to be recorded. The most likely source of evaporite-cemented sand grains is from pene-contemporaneous desiccating playa lakes and, if so, an early recharge event that breaches the surface can be inferred. A second recharge is required to explain the deflation surface represented by the Wellington contact that separates the lower dune facies from the middle sand sheet facies of the Burns formation (Grotzinger *et al.*, 2005). The subaqueous interdune sediments preserved in the upper unit at Eagle crater represents a third recharge that is about 7 m above the base of Burns Cliff. At Eagle and Endurance

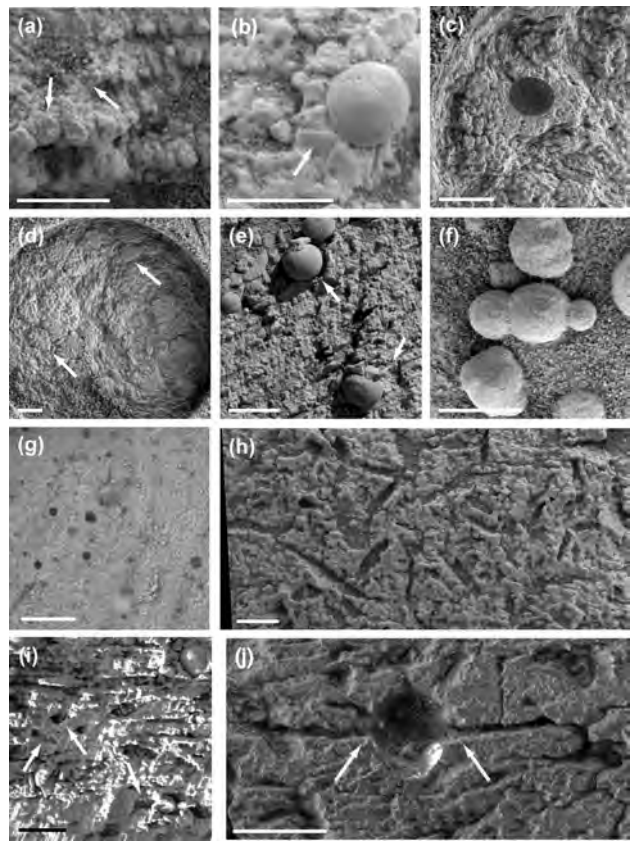

Figure 24.13. Selected Microscopic Imager images illustrating diagenetic textures within the Burns formation (adapted from McLennan *et al.*, 2005 and Squyres *et al.*, 2006a). In all cases, scale bars are 5 mm. (a) Close up of MI image taken on Sols 42 (Flatrock) showing early pore-filling cement. Note that the grain boundaries are obscured due to cementation and recrystallization. (b) Close up of MI taken in upper unit on Sol 28 (Algerita) showing isopachous blocky cements, about 2 mm thick, around spherules (also see Figure 24.10b for context). (c) MI image of abraded surface taken on Sol 177 (Diamond Jenness) showing grain-cemented overgrowths on spherule in lower part of the section. Note that this second generation of cement differs from that shown in Figure (b). (d) MI of abraded rock surface (Diamond Jenness, RAT-2) taken on Sols 178–9. Note the nodular texture. Cementation that gives rise to this texture is likely associated with the same diagenetic process that caused the later overgrowths (Figure c) on the spherules but centered on different, indistinct nucleation sites. (e) MI taken on Sol 144 showing the lack of disruption of bedding by spherules, consistent with concretionary growth. (f) MI taken on Sol 48 of weathered-out spherules on soil surface. Note the spherule "triplet" with the central spherule being larger than the other two. (g) MI of Kalavrita at the Olympia outcrop near Erebus crater, taken on Sol 633, showing the numerous, small, and irregular-shaped nature of spherules in this part of the Burns formation. (h) MI mosaic taken on Sol 27 (El Capitan) showing crystal molds in the upper interdune facies. Note that pores are elongate, with sharply defined margins and angular terminations. The pores are interpreted to represent secondary crystal moldic porosity. The site of the molds is interpreted to have been the original location of a highly soluble, near-euhedral evaporitic mineral that formed within the sediment during or shortly after deposition. (i) MI mosaic taken on Sol 151 (Kettlestone) showing crystal molds that have similar shapes as seen in Figure (h); however, many are smaller and have lower length/width ratios (arrows). (j) MI taken on Sol 152 (Grindstone)

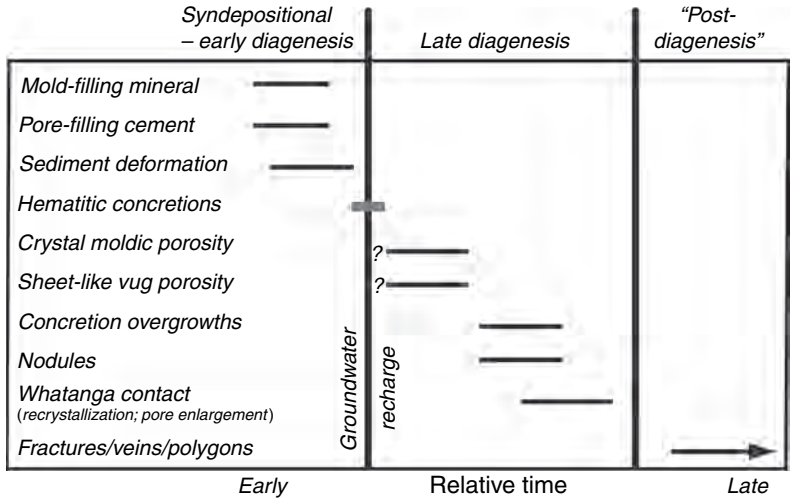

Figure 24.14. Paragenetic sequence of diagenetic events observed in the Burns formation. The boundary between early and late digenesis is arbitrary and set at the time of formation of the concretions, because this appears to have been a relatively rapid event associated with a chemically distinct groundwater recharge event. (From McLennan *et al.*, 2005.)

craters and across the Meridiani plains, concretions are found uniformly across all facies, and thus represent a fourth distinctive recharge event that reached at least as high as the highest stratigraphic level examined by the *Opportunity* rover.

In terrestrial eolian settings, highly dynamic groundwater systems are typical and fluctuate in response to tectonic, eustatic, and climatic influences. The origin of groundwater fluctuations within the Burns formation is not well understood. However, during the Noachian, regional tilting of Meridiani Planum, associated with loading of the Tharsis plateau, could have created sufficient topography to provide the hydrostatic head necessary to initiate and sustain large-scale groundwater flow (Arvidson *et al.*, 2006a; also see Andrews-Hanna *et al.*, 2007), assuming that liquid water was available. The origin of higher-order fluctuations in the level of the groundwater table, such as those that may be recorded within the depositional and diagenetic history of the Burns formation, could be related to a variety of processes, including groundwater flux, sediment flux, subsidence and, perhaps less likely, tectonic fluctuations. Some of the possible implications for climate change on Mars are discussed in the next section.

24.5.4 Climate and climate change

On earth, hydrologically closed basins are very sensitive to fluctuations in climate, which controls the composition of sediments deposited in those basins (Eugster, 1982) and their stratigraphic architecture (Ahlbrandt and Fryberger, 1981; Kocurek and Havholm, 1993). Changes in climate lead to variability in surface runoff and fluctuations in water table elevation. Surface runoff will directly affect sedimentation patterns, whereas changes in the elevation of the groundwater table serve to mostly affect the preservation of eolian strata. The exceptions to this are when the capillary zone reaches the surface to induce the formation of crusts, or when the water table rises fully above the surface to form a lake. The stratigraphic architecture of the Burns formation at Meridiani Planum preserves a rich record of interactions between eolian and fluvial (possibly lacustrine) processes that controlled transport and deposition, and water table fluctuations which controlled preservation of strata and diagenesis.

The Burns formation is interpreted to record gradual wetting of the Martian surface, very likely related to a relative rise in the water table (Figure 24.11). The rise can be absolute, perhaps associated with climate change, or relative, due to subsidence of the sediment column through a fixed water table (Kocurek and Havholm, 1993). On Earth, absolute changes in the groundwater table of intracontinental basins reflect climatically driven changes in meteoric precipitation. However, the spectacular preservation of Burns outcrops and apparent lack of karst despite the likely presence of extremely soluble minerals (Clark *et al.*, 2005; Tosca *et al.*, 2005) suggest that meteoric precipitation did not occur – at least at the site of deposition and subsequent exhumation. Thus, models that suggest that groundwater recharge is driven by precipitation require a significant time interval between recharge and evaporative water loss during groundwater upwelling (Andrews-Hanna *et al.*, 2007). Another mechanism for climate-driven changes in the water table may involve thermal fluctuations of the land surface, which could influence partial melting of permafrost in distant recharge regions. In this manner, water may have been released to the phreatic (saturated) zone where it migrated from the basin margins toward the basin center to collect and rise, occasionally above the surface, to form the sediments that compose the Burns formation.

At other locations on Mars, enclosed basins such as the Valles Marineris system may have formed traps for emerging groundwater that could have pooled to form playas and evaporite-dominated eolian sediments that may have become widely distributed throughout the valley network.

Caption for Figure 24.13. (cont.)
illustrating elongate to sheet-like vugs. The circular feature in the center is the location of a spherule that has fallen out during the RATing operation. Although the original shape of the spherule is not known, there is no suggestion from its mold that the shape was influenced by the presence of the sheet-like vug porosity and thus the porosity likely post-dates formation of the spherules.

The remarkably regular banding present in outcrops within closed basins such as Juventae Chasma is reminiscent of the regular banding in ancient Precambrian chemical sediments on Earth, interpreted to record climate-driven changes in sedimentation (Grotzinger, 1986). Recently, the layered ice-rich deposits at high latitudes on Mars have been interpreted to record climatic variability driven by changes in the obliquity of Mars' pole of rotation (e.g., Head *et al*., 2003). The accumulation of sedimentary rocks on Mars may also have been driven by variations in obliquity; variations in planetary orbital parameters have long been invoked to explain the highly cyclic nature of terrestrial sedimentary rocks, even for strata as old as 2 Gyr (Grotzinger, 1986). However, it is difficult to speculate further on the nature of any sedimentary cycles on Mars due to the absence of methods to measure sediment accumulation rates. We simply note that the amplitude of obliquity-related climate forcing is much greater for Mars as compared to Earth (Laskar *et al*., 2002), and therefore that where climate is invoked to explain sedimentary cyclicity on Earth, it makes sense to seriously consider it as a mechanism for cyclic sedimentation on Mars.

24.6 SEDIMENTATION AT GUSEV CRATER

The *Spirit* rover landed at Gusev crater anticipating the possible presence of a large ancient lake-bed (e.g., Cabrol *et al*., 2003). Instead, the Gusev plains in the vicinity of the *Spirit* landing site are characterized by blocks of impact ejecta composed primarily of olivine-bearing basalt (e.g., Arvidson *et al*., 2006b). It was not until *Spirit* traversed to the Columbia Hills that it discovered a complex layered sequence that includes sedimentary rocks, likely dominantly of impact and/or pyroclastic origin (Arvidson *et al*., 2006b; Squyres *et al*., 2006b; Figure 24.15).

The evaluation of the sedimentary rocks exposed in the Columbia Hills is not as comprehensive as the study of the Burns formation at Meridiani for a number of reasons. In the Gusev Hills, there is considerable lithological diversity and structural complexity; accordingly, each rock type has not received as much attention as has the relatively uniform, flat-lying lithologies preserved at Meridiani. In addition, the RAT (Rock Abrasion Tool) grinding bits on *Spirit* wore out around Sol 416, precluding the study of microtextures on fresh surfaces and chemical analyses on fresh rock exposures after this sol.

Nevertheless, there is abundant textural, mineralogical, and geochemical evidence indicating that many of the layered rocks exposed in the Columbia Hills are of sedimentary origin (Figure 24.15). Squyres *et al*. (2006b) reviewed the textural, chemical, and mineralogical characteristics of the lithologies encountered up to sol 512 and evaluated their origin. Sedimentary lithologies that have been recognized to that date include the following:

1. *Clovis Class*. Possibly laminated (millimeter- to centimeter-scale), poorly sorted clastic sedimentary rocks containing millimeter- to centimeter-scale angular fragments with a basaltic bulk chemical composition (Figure 24.15a). Primary igneous phases include basaltic glass, plagioclase, and pyroxene. Iron mineralogy is dominated by secondary phases (goethite, hematite) with Fe^{3+}/Fe_T of 0.5–0.8, suggesting some degree of alteration. These rocks also include a 10%–20% component of Mg- and Ca-sulfate, possibly as a cementing agent. These rocks are interpreted to represent impact ejecta or possibly tephra.
2. *Wishstone Class*. Found only as float (delivered to their present location rather than formed in place), this class of rocks consists of poorly sorted sediments with millimeter-scale irregular clasts in a fine-grained matrix (Figure 24.15b) and a Ti- and P-rich basaltic bulk composition, possibly indicating a provenance from alkali basaltic terrains. Primary igneous phases include plagioclase, olivine, pyroxene Fe-Ti-oxides and Ca-phosphates. Iron mineralogy indicates lesser alteration than Clovis Class rocks, with Fe^{3+}/Fe_T of 0.3–0.5 and minor nanophase iron oxides and goethite. These rocks are interpreted to represent pyroclastics but an origin by impact processes cannot be ruled out.
3. *Peace Class*. This is a tens of meter thick, poorly exposed unit of laminated, moderately sorted sulfate-cemented fine-to-medium sandstone (Figure 24.15c). Its bulk chemistry and Mini-TES and Mössbauer-derived mineralogy suggest a slightly altered ultramafic sandstone cemented by about 15%–20% Ca- and Mg-sulfates. Insufficient data exist to usefully constrain the depositional environment (e.g., eolian versus subaqueous) of Peace Class rocks.
4. *Watchtower Class*. This is texturally diverse, millimeter-scale parallel laminated rock with a "globular" texture suggestive of lapilli (Figure 24.15d). These rocks have chemical and mineralogical characteristics similar to Wishstone Class, but are more heavily altered (e.g., variable and higher Fe^{3+}/Fe_T). These rocks are interpreted as either pyroclastic- or impact-related, with relatively high Ni content favoring the latter.

Although considerably more work is needed to better constrain the origin of sedimentary rocks preserved in the Columbia Hills of Gusev crater, available data appear to support an origin dominated by either pyroclastic or impact processes (or both).

24.6.1 Stratigraphy and sedimentology of Home Plate

Spirit was able to study a well-preserved outcrop called "Home Plate," southward and downslope of the Columbia Hills. Home Plate appears to be a small layered butte, approximately 90 m in diameter, with relief of up to about 2 m, and exposes several depositional units that likely contain pyroclastic volcanics, possibly reworked by eolian processes (Squyres *et al*., 2007a). Scoriaceous basalt clasts are abundant close to Home Plate, suggesting that Home Plate strata may have accumulated atop older lava flows.

Textural observations show that Home Plate contains at least two units (Figure 24.16). The lower unit is coarse-grained, poorly sorted, and contains a possible bomb sag (Figure 24.17a). Most evidence points to this facies being

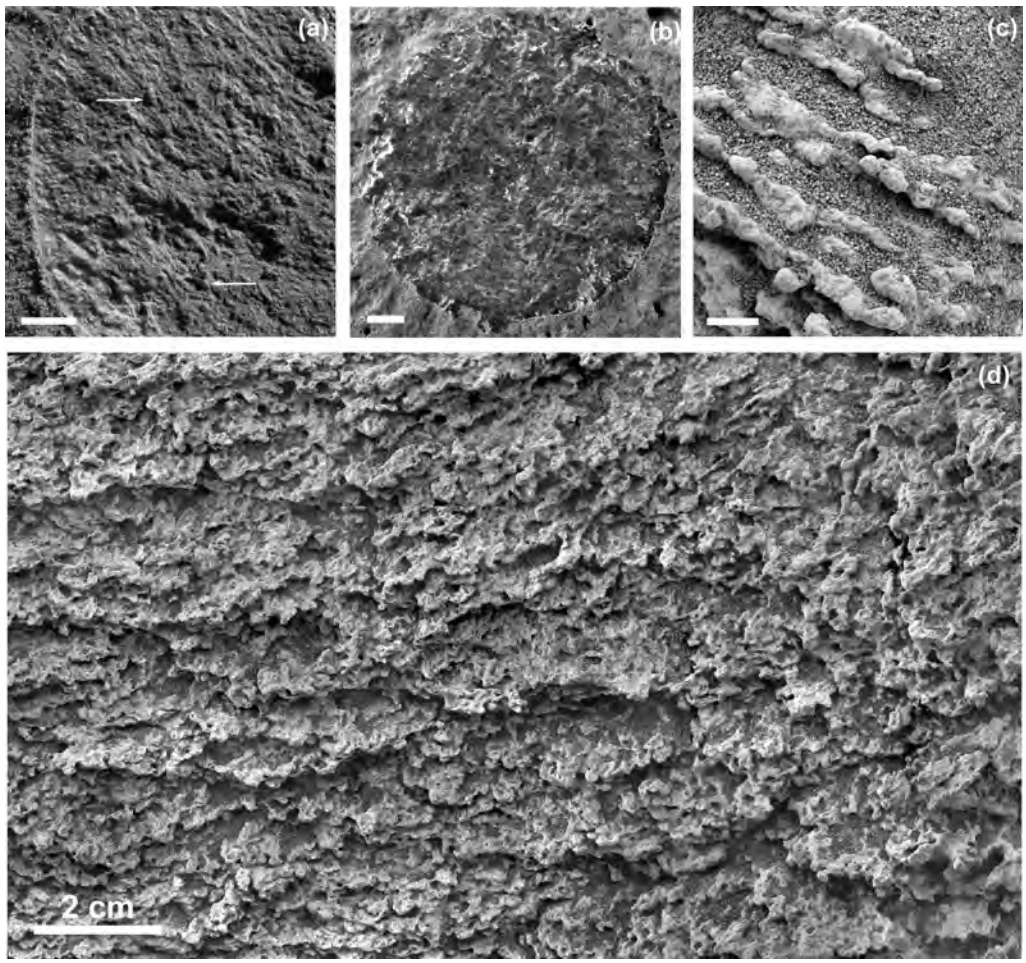

Figure 24.15. Selected MI images of sedimentary rocks from the Columbia Hills (adapted from Herkenhoff *et al*., 2006; Squyres *et al*., 2006b). Scale bars are 5 mm except Figure (d) where the scale bar is 2 cm. (a) Merge of five MI images, taken on Sol 299, of Lutefisk, a Clovis class rock. Note poorly sorted sedimentary texture with examples of relatively large subangular clasts indicated with arrows. (b) Part of an MI mosaic of the brushed surface of the rock Wishstone, taken on Sol 333. Note the presence of angular clasts, in places reaching up to 2 mm diameter, set in a finer-grained matrix. These rocks are interpreted to have been deposited by either pyroclastic or impact processes. (c) MI image (2M159478927) of the rock Peace, taken on Sol 373, showing millimeter-scale layering of this moderately sorted fine-to-medium-grained sulfate-cemented ultramafic sandstone. (d) Part of a 4×6 MI mosaic taken on Sols 469–470 of Keystone, a Watchtower class rock. This class of rocks on Husband Hills is texturally diverse, with this example being finely laminated at the millimeter-scale.

emplaced as a pyroclastic deposit. The lower unit displays crude, parallel stratification, formed of granules that range in diameter from 0.5 to 3 mm in size. This stratification grades upward into a massive facies which is fine-grained and cross-cut by a network of diffuse fractures. These fractures do not extend into the overlying upper unit, and may represent elutriation pipes formed during deflation of a sediment–gas mixture. The close association of the Home Plate strata and scoriaceous basalt supports the inference of an origin by volcanic processes.

The upper unit rests on the lower unit with a sharp contact and, in contrast, consists of finely laminated, fine-grained (0.2–0.4 mm), well-rounded (Figure 24.17b), well-sorted sediments (Squyres *et al*., 2007a; Lewis *et al*., 2008). These sediments display ubiquitous high-angle cross-stratification, expressed as wedge sets (up to several tens of centimeters thick) of distinctly trough-shaped cross-strata (Figure 24.17c). Foresets in the thicker bedsets are marked by continuous laminae that tend to rise in the apparent downcurrent direction. Internal stratification ranges from finely laminated to more thickly laminated. Cross-strata also preserve evidence of reactivation surfaces, cut at variable angles and generally backfilled by cross-strata concordant with the scour surface. Bedding planes of the type observed in the upper unit represent surfaces formed during reconfiguration of the bed in response to scouring during flow bursting, migration of 3D bedforms with frontal scour pits, and times when the sediment concentration of the flow was decreased. A second facies is preserved as bedsets with planar to low-angle cross-stratification. Associated features include gently dipping, curved or irregular surfaces of erosion, small-scale cut-and-fill structures, convex-upward laminations, and occasional intercalation of thin beds of high-angle cross-bedding.

A base-surge origin is not obvious for the upper unit due to the absence of other vent-proximal indicators, including coarse layering, coarse particles, poor sorting, and the

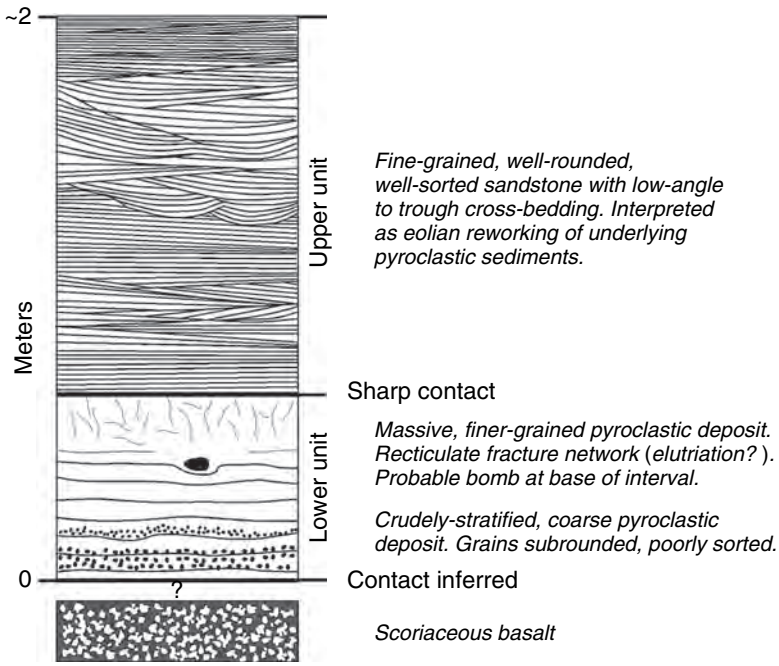

Figure 24.16. Stratigraphic column for Home Plate. Note subdivision into two units: the lower unit consists of probable pyroclastic deposits and the upper unit may represent eolian reworking of those deposits. The lower unit may have been deposited on underlying scoriaceous basalt; however, at the time of this writing, the contact was inferred based on the close proximity of scoria rubble and the lowest outcrops of the lower unit. (Modified from Lewis *et al*., 2008.)

presence of bombs (Squyres *et al*., 2007a; Lewis *et al*., 2008). Furthermore, the cross-strata of surge deposits are dominated by supercritical angles of climb; in contrast, the cross-strata preserved at Home Plate are dominated by subcritical angles of climb (only one observed set shows critical climb) indicating little deposition from fallout.

The combined characteristics of the upper unit are perhaps more consistent with eolian transport, which would increase the textural maturity of the sediments. The planar to low-angle stratification would have formed by the migration of impact ripples over a sand sheet surface, while the high-angle cross-stratification would have been produced by migration of dunes. This interpretation is consistent with the lack of interbedding of lower unit facies with upper unit facies. The geometry of the upper unit cross-beds indicates that most bedforms were truncated during migration, suggesting only a small component of suspended sediment deposition relative to the bedload fraction. Again, this is typical of eolian transport and contrasts with surge transport where deposition of suspended particles is a substantial or even dominant component of bedform development.

In the eolian interpretation, the basaltic composition of the upper unit sediment would be explained by reworking of pyroclastic debris derived from the same source as the lower unit. Eolian reworking of pyroclastic deposits is common on Earth (White, 1990; Smith and Katzman, 1991) and should be expected for Mars where wind velocities are sufficiently high to transport sand-sized particles of basaltic density (Greeley and Iverson, 1985).

24.6.2 Chemistry and mineralogy of Home Plate

The chemistry and mineralogy of sedimentary rocks preserved at Home Plate are also consistent with a mixed pyroclastic-reworked eolian origin (Squyres *et al*., 2007a). Overall chemistry is basaltic and mildly alkaline (SiO_2 ~49%, $Na_2O + K_2O$ ~3.5%–4.0%; on a S- and Cl-free basis); Mössbauer and infrared spectroscopy indicate mineralogy consisting of olivine, pyroxene, plagioclase, and significant amounts of magnetite. Small amounts of nanophase iron oxide (~30% of Fe) and Fe^{2+}/Fe_T ~0.5 indicate that the rocks are mildly altered. Chemical analyses are only available on brushed and untouched surfaces, although effort was made to analyze the cleanest available regions (Squyres *et al*., 2007a). Accordingly, the high levels of SO_3 (3.5%–5.5%) may suggest a sulfate-cementing agent, although surface coatings cannot be excluded. These rocks are also enriched in chlorine and "volatile" trace elements Zn, Ge, and Br that do not appear to correlate with igneous fractionation trends, possibly suggesting subsurface magma–brine interaction, a plausible trigger for a hydromagmatic eruption. Although analyses are few, another interesting observation is that the two analyzed samples from the lower unit are variable in composition, whereas the three analyses from the upper unit are chemically distinct from the lower unit (e.g., higher Ti, P, Na) but very uniform in composition (see Table 24.1 in Squyres *et al*., 2007a). These features are consistent with the suggested pyroclastic origin for the lower unit and the eolian reworking of the upper unit, where increased sedimentary reworking would tend to homogenize the sediment.

24.7 THE SEDIMENTARY ROCK CYCLE ON A BASALTIC PLANET

Much of what has been observed thus far in the ancient sedimentary rock record found at the surface of Mars, including stratigraphic relationships, bedforms, sedimentary

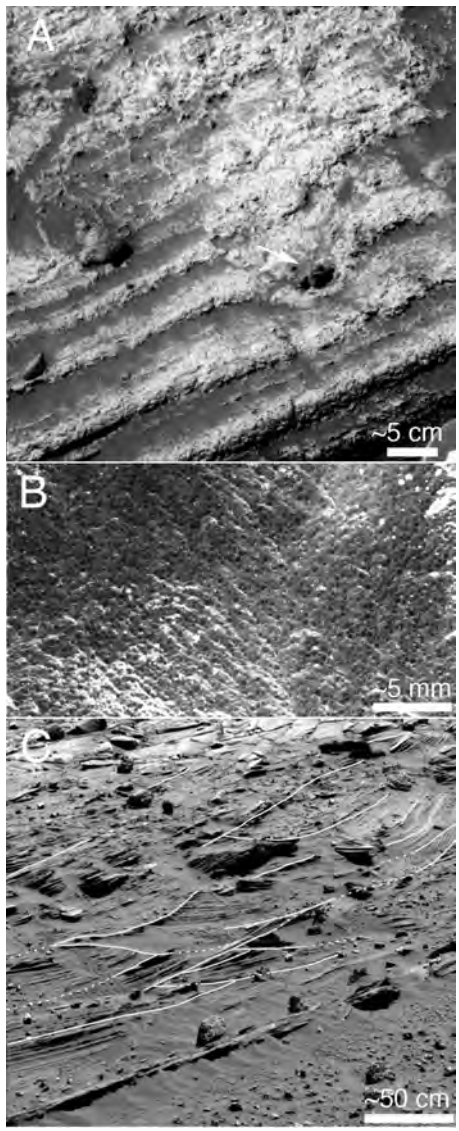

Figure 24.17. Home Plate depositional facies. (a) Lower unit, showing coarse clastic sediments that grade up into poorly stratified to massive bedding that is pierced by at least one bomb (arrow) and overprinted by a recticulate fracture network. This network is restricted to the upper part of the bed and may represent gas escape (elutriation) from compacting pyroclastic sediments. Image was obtained using Pancam's L2 filter on Sol 751. (b) Upper unit, showing fine-grained, well-rounded, well-sorted sediments of basaltic composition. Textural maturity suggests eolian reworking of underlying pyroclastic sediments. MI image 2M194100679 taken on Sol 763. (c) High-angle trough cross-bedding exposed along the northeast edge of Home Plate. Bounding surfaces of cross-bed sets have been interpreted to emphasize trough geometry and general occurrence of subcritical angles of climb (a single exception is present at the center left part of the image). Such stratification is produced under conditions of limited sediment fallout from suspension, as is characteristic for eolian environments. Image was obtained using Pancam's L2 filter on Sol 774.

structures, and microtextural relationships, would be very familiar to most terrestrial sedimentary geologists. On the other hand, there are also abundant physical, chemical, and mineralogical observations that suggest that the Martian sedimentary rock cycle, involving weathering and erosion, transport, deposition, burial, lithification, and a variety of sedimentary and crustal recycling processes, differs from Earth in many profound ways. Understanding these differences may well be critical for interpreting the Martian sedimentary rock record in terms of the prevailing hydrological, climatic, and tectonic regimes that would have existed at the time of sedimentation. In these final sections, we discuss the broad nature of the Martian sedimentary rock cycle and explore some of these differences.

24.7.1 Lithological diversity

The lithological diversity of the Earth's sedimentary mass is reasonably well understood (e.g., Garrels and Mackenzie, 1971; Ronov, 1983). The common lithologies and their proportions reflect both the fundamental upper continental crust and continental margin volcanic provenance from which most sediment is derived and the dominant regime of chemical weathering that converts igneous/metamorphic rocks and minerals into sediments. The proportions in the terrestrial sedimentary mass are as follows: 53% fine-grained siliciclastic sediments dominated by clays and very fine-grained quartz (e.g., shales, mudstones), 27% "volcanogenic" sediments, which mostly include relatively unweathered first-cycle sediments deposited at tectonically active continental margins and other volcanically active tectonic settings, 11% carbonates dominated by limestones, 8% sandstones dominated by quartz and to a lesser extent K-feldspar ($KAlSi_3O_8$) and rock fragments, <2% evaporites dominated by gypsum/anhydrite and halite, and <1% siliceous sediment, mainly cherts. Lithological diversity also varies with plate tectonic setting and with geological age (Veizer and Jansen, 1979, 1985; Ronov, 1983; Veizer and Mackenzie, 2003). Crustal evolution processes, different weathering regimes, and differences in sedimentary recycling rates among different tectonic settings and lithologies ultimately control the variations (e.g., Taylor and McLennan, 1985).

Of the surface sediments and ancient sedimentary rocks that have been studied on Mars, the lithological components that have been identified or strongly inferred include relatively unweathered basaltic detritus with a wide range of grain size (e.g., on surface dunes and ripples; certain sedimentary rocks in the Columbia Hills of Gusev crater), both weathered and unweathered very fine-grained debris of basaltic provenance (e.g., modern global dust; siliciclastic components in the Burns formation sandstones; certain sedimentary rocks in the Columbia Hills), Mg-, Ca-, and possibly Fe-bearing evaporite minerals at all locations and possibly covering a broad age range, secondary iron oxides, poorly crystalline nanophase iron components, and amorphous silica. Hematitic concretions, locally weathered from outcrops, may form rare but locally important accumulations as lag deposits (Jerolmack *et al.*, 2006). Notably, carbonate minerals are restricted to trivial occurrences in Martian meteorites and, although suggested to be present in Martian dust at very low levels based on orbital thermal emission data (Bandfield *et al.*, 2003), none have been

Table 24.3. *Mineralogical composition of igneous/metamorphic terrestrial and Martian upper crust and sedimentary mass*

	Continental upper crust[a]	Martian upper crust – expt.[b]	Martian upper crust – norm[c]	Terrestrial sedimentary mass[d]	Martian sedimentary mass[e]
Quartz	20	—	—	34	—
Plagioclase	35	29	40	3	X
K-feldspar	11	<1	4	3	—
Sheet silicates	12	—	—	tr.	?
Chlorite	1.9	—	—	tr.	—
Amphibole	1.8	—	—	—	—
Pyroxene	1.2	22	22	—	X
Olivine	0.2	17	29	—	X
Oxides	1.4	10	2	tr.	X
Glass	13	21	—	—	?
Phyllosilicates	—	—	—	41	X
Carbonates	—	—	—	14	?tr.
Lithic fragments	—	—	—	6	X
Sulfates/chlorides	—	—	—	1–2	X
Amorphous silica	—	—	—	tr.	X

[a] From Nesbitt and Young (1984).
[b] Based on derived mineralogy of synthesized olivine-bearing "Martian" basalt of average Pathfinder soil composition (on S-, Cl-free basis) and used for low alteration experiments by Tosca *et al*. (2004).
[c] Based on normative mineralogy of synthesized olivine-bearing "Martian" basalt used for low alteration experiments by Tosca *et al*. (2004). Also includes 2.8% apatite.
[d] From Garrels and Mackenzie (1971) and Blatt (1989). Note that terrestrial sedimentary mass excludes volcanogenic sediments, which are largely unweathered.
[e] Tabulation only of the detection of major sedimentary minerals that have been either directly identified on Mars or strongly inferred from geochemical relationships.

unambiguously identified in surface sediments or ancient sedimentary rocks. Accordingly, although we are only beginning to tabulate the types of sedimentary lithologies that exist and are far from understanding the full lithological diversity and lithological proportions, there are clear suggestions that the nature and proportions of Martian sedimentary lithologies differ greatly from that seen on Earth. Of special note is that among the chemical sediments, the role of carbonates versus sulfate-rich evaporites (and possibly amorphous silica deposits) appear to be completely reversed for Earth versus Mars.

24.7.2 Ultimate provenance: basalt versus granite

The average composition of the terrestrial upper continental crust approximates to granodiorite (Taylor and McLennan, 1985). Igneous rocks preserved in the upper crust are mostly petrologically evolved and range from diorites through granites and their volcanic equivalents. Plate tectonic processes continually uplift crustal rocks to high elevation, providing the potential energy required for physical erosion and mass wasting to proceed. Chemical weathering of the exposed crust, even under the most extreme circumstances found in tropical environments, leads to abundant residual solid particles. The vast majority of sediments on Earth are ultimately derived from these petrologically evolved rocks of the upper continental crust through a combination of physical and chemical weathering that gives rise to particulates and chemical precipitates from a variety of aqueous fluids (e.g., groundwater, seawater).

The particulate fraction of terrestrial sediment is derived by a combination of physical and chemical denudation either as relatively unweathered components (e.g., volcanic and metamorphic rock fragments, quartz, feldspar, heavy minerals) or as residual alteration products of weathering (clays, oxides). With increased sedimentary reworking during repeated cycles of uplift, erosion, and sedimentation (see below), the proportion of nonsedimentary rock fragments and feldspar decreases and the ratio of K-feldspar/plagioclase increases. Chemical constituents (carbonates, sulfates, chlorides, secondary silica) make up approximately 15% of the sedimentary rock record (Garrels and Mackenzie, 1971; Ronov, 1983) and are mostly derived from the cations released during upper crustal weathering, with a lesser proportion coming from submarine hydrothermal interactions.

The long-term result of tectonic and sedimentary cycling of the "granitic" upper crustal sources is to produce a terrestrial sedimentary mass dominated by quartz and clays. This result is illustrated in Table 24.3 where the average mineralogical composition of the upper continental crust is tabulated (Nesbitt and Young, 1984) and compared to the bulk mineralogical composition of the terrestrial sedimentary mass (excluding "volcanogenic" sediments).

The partitioning of components between solution and particulates during chemical weathering is greatly influenced by plate tectonic processes. For example, in order to achieve

an intensely weathered soil mantle, such as that preserved in laterites, very long-lived subdued topography is required to inhibit physical mass wasting and enhance dissolution. Under such conditions, surficial deposits quickly (on geological timescales) become depleted in soluble components but often with limited overall mass loss, leading to thick residual deposits. On the other hand, in order to produce high volumes of siliciclastic sedimentary rock, substantial topography is required to enhance mass wasting, erosion, and transport to sedimentary basins. Thus the effects of chemical weathering on sediment composition are diminished, but the overall mass loss to the sedimentary record both as particulates and in solution can be large.

On Earth, there is a link between the rates of chemical (R_{chem}) and physical (R_{phys}) weathering, estimated on a global scale to be (Millot *et al.*, 2002)

$$R_{chem} = 0.39(R_{phys})^{0.66} \quad (24.1)$$

This relationship appears to apply to both granitic and basaltic terrains on Earth (Millot *et al.*, 2002). The expected dominance of terrigenous over chemical sedimentary rocks that this relationship would imply is observed in the global sedimentary mass, where the ratio of terrigenous/chemical sedimentary rocks is about 6.5 (Garrels and Mackenzie, 1971).

Although there is growing evidence that the exposed Martian crust may include components of relatively evolved igneous rocks including granitoids (e.g., Christensen *et al.*, 2005; Taylor *et al.*, 2006; see also Chapters 9, 10, and 22), the ultimate source of Martian sediments is almost certainly dominated by basalt (e.g., Taylor *et al.*, 2006). Thus, olivine, pyroxene, plagioclase, Fe-Ti oxides, and perhaps mafic glass will dominate the primary mineralogical components. A very approximate estimate, designed more for illustrative purposes than as a truly quantitative estimate, is tabulated on Table 24.3 and is derived from the "Pathfinder Soil" composition that Tosca *et al.* (2004) used to synthesize typical Martian upper crust basalt for low pH alteration experiments. Two compositions are shown: the modal mineralogy derived from the basalt synthesis obtained by Tosca *et al.* (2004) and the normative mineralogy determined from the bulk chemical composition.

What are some of the effects of these differences for the Martian sedimentary rock record? On Mars, siliciclastic sedimentary rocks are likely to be composed mainly of basaltic rock fragments and minerals that form phenocryst assemblages. In the absence of chemical weathering or if such effects are limited due to low water/rock ratios in the Martian near surface, production of sedimentary particles would be dominated by purely physical processes such as fragmentation due to thermal cycling and eolian (saltation) impact, supplemented by the accumulation of pyroclastic deposits and impact-generated debris. Under such circumstances, terrigenous sedimentary rocks should dominate the sedimentary rock record. On the other hand, dissolution processes rather than formation of residual clays and oxides would largely govern an active chemical weathering regime, especially one operating at low pH. Accordingly, for a given volume of igneous rock that is "processed" by chemical weathering, the ratio of chemical/terrigenous sediment that is produced would likely be higher than on Earth. In other words, basalt weathering under low pH conditions, at a given fluid/rock ratio, is far more efficient and produces far fewer particulates than does granite weathering at modest pH. During any cannibalistic sedimentary recycling, for a given degree of chemical weathering (i.e., an equal amount of fluid interaction), there should be fewer residual constituents (analogous to terrestrial quartz, stable clays, and oxides), and thus the susceptibility of recycled sediment to chemical destruction would be greater.

24.7.3 Composition of the Martian hydrosphere

The composition of the terrestrial hydrosphere is extremely variable from place to place. The chemistry of dilute waters on the continents and ocean islands is governed largely, but complexly, by the composition of the crustal terrains with which they are in contact. Terrestrial seawater composition is governed by a complex combination of fresh water input, terrigenous sediment input from fluvial, glacial, and eolian processes, hydrothermal interaction (exchange) of oceanic crust, chemical sedimentation, seawater–particle interaction, biological activity, and other minor factors (Broecker and Peng, 1982). There is every reason to believe that the composition of any Martian hydrosphere will also be similarly variable and complex. Its composition is not readily constrained by current knowledge.

On the other hand, it is also likely that a Martian hydrosphere derived largely from low pH aqueous interaction with a basaltic upper crust will have a composition that differs from that observed at most places on Earth. Some sense of these possible differences is revealed in Figure 24.18 which compares the composition of terrestrial seawater to a fluid composition experimentally derived by low pH alteration of a synthesized olivine-bearing Martian basalt composition (adapted from Tosca *et al.*, 2005). Both compositions are normalized to total dissolved solids to eliminate possible differences related to total ionic strength. The exact anion content in the basaltic fluid is contrived since it is governed by the starting pH and relative proportions of H_2SO_4–HCl acids used in the alteration experiments (Tosca *et al.*, 2004) and thus are not considered. The cation abundances in terrestrial seawater and basaltic fluid differ significantly, with the Martian low-pH basalt fluid being greatly enriched in Fe and Al, significantly enriched in Si and Mg (but note in terrestrial seawater Si is strongly depleted by biogenic processes), and depleted in K and Na. If the Martian hydrosphere composition is produced even in part by low pH weathering conditions, then it is likely that it would be enriched in Fe, Al and Mg, and depleted in Na and K due to a combination of the increased solubility of Fe(III) and Al at low pH (Figure 24.2) and the contrasting compositions of terrestrial granodioritic upper crust versus Martian basaltic upper crust (Table 24.3). The exact composition of the fluid would depend on both the composition of the starting basalt being altered and the conditions of alteration (e.g., pH, temperature). In the case shown (Figure 24.18), the basalt

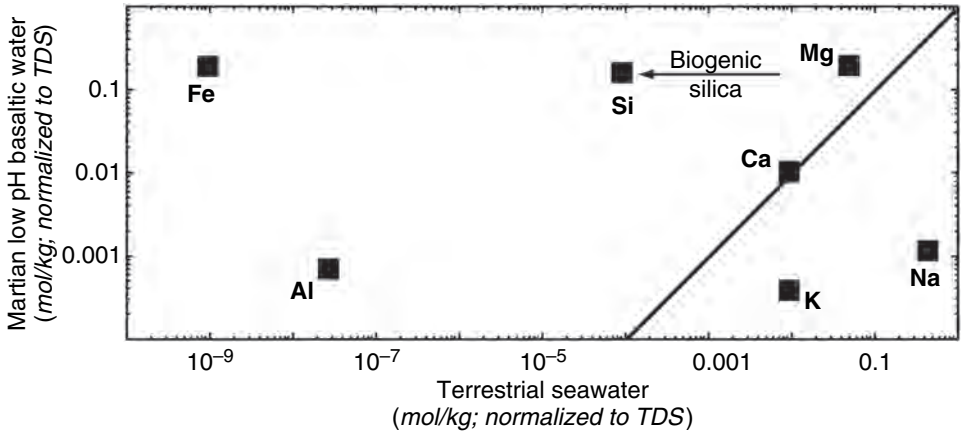

Figure 24.18. Comparison of terrestrial seawater to experimentally derived "basaltic" fluid normalized to total dissolved solids (TDS; adapted from Tosca *et al*., 2005). Diagonal line denotes equal compositions. Note that the exact composition of the basaltic fluid would depend on the composition of the altered basalt and the conditions of alteration. In this particular case, the basaltic fluid was derived from low pH alteration experiments on olivine-bearing basalt and thus is particularly Mg- and Fe-rich and Al-poor. A fluid derived from a plagioclase-rich, olivine-poor basalt would be expected to have higher abundances of Al and lower abundances of Fe. Note that in terrestrial seawater, Si is greatly undersaturated due to the extraction of silica by silica-secreting organisms.

was olivine-bearing and thus the fluid was especially enriched in Fe and Mg. In cases where olivine is absent and plagioclase is dominant, the fluid would likely have higher Al contents (e.g., Hurowitz *et al*., 2005).

24.7.4 Controls on global weathering: carbonate Earth versus sulfate Mars?

Surficial processes on Earth are controlled primarily by the long-term and short-term carbon cycles. Early in Earth history, the bulk of the planet's complement of surficial CO_2 was sequestered into carbonate rocks and other reduced carbon-rich sediments (e.g., Garrels and Mackenzie, 1971; Morse and Marion, 1999; Grotzinger and James, 2000) thus avoiding a Venus-like greenhouse. Tectonic processes, which provide CO_2 sources from associated volcanism as well as mechanisms for the continual recycling of ancient carbon-bearing rocks (carbonates and reduced carbon-bearing sediments), allow for a small amount of CO_2 to remain within the ocean–atmosphere system and thus provide the acidity necessary for rock weathering.

CO_2 provides the dominant acid consumed in terrestrial rock weathering, in the form of relatively weak carbonic acid (H_2CO_3) and various organic acids. The pH levels associated with carbonate equilibria are controlled by the equilibrium constants (K) of the various carbonate dissociation reactions, and are modest. For example, the pH of water in equilibrium with the modern terrestrial atmosphere ($p(CO_2) = 3.6 \times 10^{-4}$ atm) is about 5.6, and the pH of the ocean mass is strongly buffered to a value of about 8 by atmospheric CO_2 content and carbonate equilibria involving

$$CO_2 + H_2O \Leftrightarrow H^+ + HCO_3^- \quad (24.2)$$

$$Ca^{2+} + HCO_3^- \Leftrightarrow H^+ + CaCO_3 \quad (24.3)$$

Accordingly, the pH range of common natural waters on Earth lies between about 5 and 9. Low pH aqueous environments are restricted to relatively exotic geological settings such as crater lakes, acid mine drainage systems, and acid lakes, typically where sulfur rather than carbon cycling locally dominates (see below), or in weathering profiles where pyrite oxidation is prevalent (such as black shale weathering) and gives rise to sulfuric acid-bearing fluids (e.g., Chigira and Oyama, 1999). At moderate pH values, quartz is relatively insoluble, Al and Fe(III) are at their solubility minima, and iron oxidation is extremely rapid and efficient (Figure 24.2). These geochemical characteristics lead to abundant residual quartz, aluminous clays, and Fe-oxides produced during extreme weathering (Garrels and Mackenzie, 1971). On a continental scale, chemical weathering rates can be correlated to the average bicarbonate concentration in stream waters (e.g., Garrels and Mackenzie, 1971); thus, the erosion of carbonate rocks greatly influences the overall rate of weathering.

Weathering reactions of various rocks and minerals are numerous and complex, but carbon, in the form of carbonic acid and a variety of organic acids, again dominates and the basic processes can be simplified into the following reactions (adapted from Berner, 1995):

For silicate weathering (simplified as wollastonite and enstatite):

$$CaSiO_3 + 2H_2CO_3 + H_2O \Leftrightarrow Ca^{2+} + 2HCO_3^- + H_4SiO_4 \quad (24.4)$$

$$MgSiO_3 + 2H_2CO_3 + H_2O \Leftrightarrow Mg^{2+} + 2HCO_3^- + H_4SiO_4. \quad (24.5)$$

For carbonate weathering:

$$CaCO_3 + H_2CO_3 \Leftrightarrow Ca^{2+} + 2HCO_3^- \quad (24.6)$$

$$CaMg(CO_3)_2 + 2H_2CO_3 \Leftrightarrow Ca^{2+} + Mg^{2+} + 4HCO_3^- \quad (24.7)$$

For Fe-silicate (simplified as ferrosilite) and organic matter oxidative weathering:

$$2FeSiO_3 + 4H_2O + 1/2\,O_2 \Leftrightarrow Fe_2O_3 + 2H_4SiO_4 \quad (24.8)$$

$$CH_2O + O_2 \Leftrightarrow H_2O + CO_2 \quad (24.9)$$

One of the most perplexing questions about Mars is the fate of CO_2. It is widely accepted that Mars, like Earth and Venus, should have degassed significant amounts of CO_2 into its early atmosphere. However, apart from minor secondary carbonates preserved in fractures in a few SNC meterorites, no unambiguous evidence has been found for any carbonate deposits on the Martian surface or in the subsurface. This absence has led to suggestions that there may be abundant carbonates at depth or that CO_2 was lost to space by impact processes or upper atmosphere ablation by solar winds (e.g., Pollack *et al.*, 1987; Melosh and Vickery, 1989; Morse and Marion, 1999; Jakosky and Phillips, 2001). Of course, these options are not mutually exclusive.

Regardless of the ultimate fate of CO_2 on Mars, the absence of carbonate minerals and the apparent abundance of sulfate minerals in the available geological record suggests that perhaps the sulfur cycle, rather than the carbon cycle, dominates surficial processes on Mars, at least in the sedimentary systems that have been examined so far (e.g., McLennan *et al.*, 2006; Halevy *et al.*, 2007). Note that in a CO_2-bearing atmosphere, even small amounts of SO_2 could lead to the sulfur cycle dominating the chemistry of weathering. The Henry's Law solubility and equilibrium constants for SO_2 dissociation are orders of magnitude greater than for CO_2 dissociation and, accordingly, resulting aqueous systems are much more likely to have substantially lower pH. For example, pure water in equilibrium with an atmosphere containing SO_2 that is more than an order of magnitude less than terrestrial CO_2 levels (i.e., $pSO_2 = 10^{-5}$ atm versus $pCO_2 = 3.6 \times 10^{-4}$ atm in the terrestrial atmosphere) would have a pH of 2.9 rather than 5.6. Under such conditions, weathering reactions analogous to those that have been used to describe weathering on Earth might take the form:

For silicate weathering:

$$CaSiO_3 + 2H_2SO_4 + H_2O \Leftrightarrow Ca^{2+} + 2HSO_4^- + H_4SiO_4 \quad (24.10)$$

$$MgSiO_3 + 2H_2SO_4 + H_2O \Leftrightarrow Mg^{2+} + 2HSO_4^- + H_4SiO_4 \quad (24.11)$$

$$FeSiO_3 + 2H_2SO_4 + H_2O \Leftrightarrow Fe^{2+} + 2HSO_4^- + H_4SiO_4. \quad (24.12)$$

For sulfate weathering:

$$CaSO_4 + H_2SO_4 \Leftrightarrow Ca^{2+} + 2HSO_4^- \quad (24.13)$$

$$MgSO_4 + H_2SO_4 \Leftrightarrow Mg^{2+} + 2HSO_4^- \quad (24.14)$$

$$FeSO_4 + H_2SO_4 \Leftrightarrow Fe^{2+} + 2HSO_4^-. \quad (24.15)$$

If carbonate rocks have been involved in weathering reactions:

$$CaCO_3 + H_2SO_4 \Leftrightarrow CaSO_4 + H_2CO_3 \quad (24.16)$$

$$MgCO_3 + H_2SO_4 \Leftrightarrow MgSO_4 + H_2CO_3 \quad (24.17)$$

$$FeCO_3 + H_2SO_4 \Leftrightarrow FeSO_4 + H_2CO_3. \quad (24.18)$$

These reactions point out an apparent paradox: how can aqueous fluids on Mars maintain low pH, given that a highly reactive basaltic planet should rapidly titrate and neutralize the acid by weathering reactions? Several factors may be involved. Many of the sulfate minerals that have been suggested for Mars are highly soluble (e.g., Mg- and Fe(II)-sulfates) and their presence within sedimentary rocks that maintain primary sedimentary features suggests that aqueous fluids are at persistently high ionic strength (McLennan *et al.*, 2005). At very high ionic strength, the activity coefficient of H^+ goes up dramatically (Pitzer, 1991) and thus the number of H^+ ions available for reaction may be as much as an order of magnitude less than the pH might otherwise imply. In the presence of excess sulfuric acid during evaporation, minerals such as rhomboclase ($(H_5O_2)Fe(SO_4)_2 \cdot 2H_20$) may form (e.g., Tosca *et al.*, 2004; Hurowitz *et al.*, 2005) and effectively sequester acid. Accordingly, on Mars it is possible that considerable amounts of excess SO_2 are stored in sulfate deposits through silicate weathering processes, analogous to the vast carbonate deposits on Earth. In this case, more recent acid alteration could be accomplished by younger additions of SO_2 through volcanism and weathering (or impact recycling) of ancient sulfate deposits (McLennan *et al.*, 2006). Hurowitz *et al.* (2006) examined the surface alteration of basalt cobbles examined by the *Spirit* rover in Gusev crater in an attempt to understand aqueous alteration processes. The amount of basalt that could react is a function of both pH and total water volume and, accordingly, another factor is that the sedimentary systems may be rock-dominated rather than water-dominated (see also Hurowitz and McLennan, 2007).

24.7.5 Sedimentary silica

Much of the silica in terrestrial upper crustal rocks is in the form of quartz and potassium feldspar, both of which are relatively resistant to chemical weathering. In contrast, silica in basalts is mostly sequestered in minerals that are relatively labile during aqueous alteration, including olivine, pyroxene, and plagioclase. Accordingly, even incipient aqueous alteration of basaltic lithologies invariably releases significant quantities of free silica (McLennan, 2003), thereby making amorphous silica a ubiquitous component of altered basaltic rocks on Earth. Although attempts to evaluate the presence and amount of amorphous silica on Mars by spectroscopic techniques are at an early stage, where careful analyses have been carried out, such as at the Burns formation (Glotch *et al.*, 2006), significant amounts of secondary silica are indicated. Recent orbital spectral observations from Valles Marineris identified laterally continuous amorphous silica deposits, possibly associated with hydronium jarosite, suggestive of a low temperature sedimentary origin (Milliken *et al.*, 2008). In the vicinity of Home Plate in the Columbia Hills, high-silica rocks and soils (up to 90% SiO_2) of likely hydrothermal origin have been identified (e.g., Squyres *et al.*, 2007b).

Mobility of silica is controlled almost exclusively by pH and temperature. At low pH and 25 °C, silica in dilute aqueous solutions is in the form of orthosilicic acid (H_4SiO_4)

and its activity is pH-independent at $10^{-2.7}$ moles/liter (~120 ppm). At increasing pH, silicic acid dissociates:

$$H_4SiO_4 \Leftrightarrow H_3SiO_4^- + H^+ \qquad K_1 = 10^{-9.9} \tag{24.19}$$

$$H_3SiO_4^- \Leftrightarrow H_2SiO_4^{2-} + H^+ \qquad K_2 = 10^{-11.7} \tag{24.20}$$

These species are far more soluble and begin to dominate the silica speciation mass balance at about pH > 9. Accordingly, silica solubility increases by orders of magnitude over the pH range of 9–14. For Mars, where low pH conditions appear to dominate, silica is likely to be produced by basalt alteration but its mobility will be restricted by its low solubility. Under these conditions, silica concentration in the fluid is more or less fixed and, at a given temperature, silica mobility will be controlled by the effective water/rock ratio and flow rate of transporting fluids.

24.7.6 Lithification of Martian sedimentary rocks

Following deposition, most particulate sediments are loosely packed, often with high porosities. The process of converting unconsolidated sediment into lithified sedimentary rock is accomplished during sediment burial with accompanying changes in pressure, temperature, and interstitial fluid chemistry affecting mineral stability and the physical properties of grains. Thus, lithification is accomplished by some combination of mechanical compaction, intergranular pressure solution, cementation, and recrystallization. In terrestrial sedimentary sequences, burial depths required for lithification can be highly variable. For chemical sediments, such as carbonates and evaporites, cementation can occur essentially synchronous with deposition, whereas for terrigenous sediments, such as quartz sandstones, cementation may not be complete before several kilometers of burial.

Ancient sedimentary sequences on Mars appear to have been largely lithified into sedimentary rocks (e.g., McLennan *et al.*, 2005; Squyres *et al.*, 2006b). Malin and Edgett (2000) argued that the presence of steep cliffs, ridges, fault contacts and offsets, sharp stratigraphic boundaries, and evidence for hard surfaces all argued for the ancient sedimentary terrains being indurated sedimentary rocks rather than unconsolidated sediment. At both Meridiani Planum (Burns formation) and Gusev crater (e.g., Peace Class rocks), the dominant form of lithification appears to be the formation of syn- to postdepositional intergranular sulfate cements, suggesting relatively early timing. Indeed, a wide variety of plausible sedimentary sulfate minerals (which are typically hydrated) could also generate fluids by dehydration reactions that transport cementing agents (e.g., Montgomery and Gillespie, 2005). Another possible early cementing agent is secondary silica, which is a common sedimentary cementing agent on Earth and likely to be ubiquitous during chemical weathering on Mars.

24.7.7 Effect of reduced gravity on Martian sediment transport

Sediment transport across planetary surfaces is dependent on several important variables, including mean flow velocity U, mean flow depth d, sediment size D, fluid density ρ, fluid viscosity μ, grain density ρ_s, and submerged weight per unit volume of the sediment γ' (Southard, 1973). These variables can be used to describe the organization of loose sediment to form various bedforms, including the small-scale 3D ripples in the upper unit of the Burns formation (Grotzinger *et al.*, 2005):

$$\text{Bed configuration} = f(U, d, D, \rho, \mu, \rho_s, \gamma') \tag{24.21}$$

Note that the influence of the acceleration of gravity is specified in γ'. Although all these variables can influence bed configurations for different situations on Earth or Mars, the only one that is required to change between Earth and Mars is the acceleration of gravity. Therefore, it is important to consider what effect this may have on the initial entrainment of sediment in subaqueous and eolian flows, and how bedforms which appear to uniquely constrain subaqueous flows might differ on Mars.

Sediment transport: first motion

The initial motion of sediment particles in the presence of moving fluids is controlled by several forces (Wiberg and Smith, 1987). These include: drag, lift, bed resistance, and gravity. Only the last of these is required to change for Mars. A summary of relevant forces includes:

- F_g = total gravitational force:

$$F_g = (\rho_s - \rho)gV, \tag{24.22}$$

where ρ_s is sediment density, ρ is fluid density, g is gravitational acceleration, and V is the volume of the particle. Lift can be accounted for by defining the *net gravitational force*, $F_N = F_g - F_L$.

- F_L = the lift force caused by pressure differences around the particle due to velocity shear across it:

$$F_L = \rho \frac{C_L}{2}\left(u_T^2 - u_B^2\right)A, \tag{24.23}$$

where $C_L \sim 0.2$ is a lift coefficient, u_T and u_B are the velocities at the top and bottom of the particle, and A is the horizontal cross-sectional area.

- F_D = drag force that the particle is subjected to as it projects up into the boundary layer flow:

$$F_D = \frac{1}{2}\rho C_D u_D^2 A, \tag{24.24}$$

where C_D is the drag coefficient, u_D is the velocity of the flow if the particle were absent, and A is the vertical cross-sectional area.

- F_R = the resistance of the particle to motion, and has vertical ($(F_R)_y$) and horizontal ($(F_R)_x$) components. Here, the difference in g again plays an important role because the vertical component of the resisting force imparted by adjacent, constricting grains must balance the net gravitational force ($(F_R)_y = F_N$). The horizontal component also depends on g because the resisting force depends on the net weight of the particle and its angle of rest on the adjacent constricting particle (ϕ, the particle angle of repose):

$$\begin{aligned} (F_R)_y &= (\rho_s - \rho)gV - F_L; \\ (F_R)_x &= [(\rho_s - \rho)gV - F_L]\tan\phi. \end{aligned} \tag{24.25}$$

These forces, which must balance at the threshold for particle motion, show that for the lower g of Mars, the lifting force required to cause first motion of a particle is smaller for Mars by a factor of $g_{mars}/g_{earth} \sim 0.4$. This also applies for the drag force, which must balance the resistance provided by adjacent grains. Therefore, all other factors being equal, it should be easier to initiate sediment transport on Mars as compared to Earth. For example, for fixed grain size, grain density, and fluid density, lower velocity flows should be more effective on Mars. However, it is currently not possible to fix these other important variables in order to, for example, solve for current velocity; though we can measure grain size (at least above particles sizes of ~100 microns, for MER MI data), we can only guess at grain density and fluid density.

Sediment transport: development of bedforms

It has long been observed that eolian bedforms, which result from sediment transport, are present on the modern surface of Mars. The presence of these bedforms provides unambiguous evidence for sediment transport through saltation, an important sediment transport mechanism. Traditionally, in the study of terrestrial sedimentary systems, analysis of the sediment transport mechanism is often the starting point for more refined interpretations of depositional processes and reconstruction of ancient environments (Harms *et al*., 1975). Therefore, it was of considerable importance when evidence of cross-stratification was discovered in the sedimentary rocks at Meridiani (Squyres *et al*., 2004a; Grotzinger *et al*., 2005, 2006). Cross-stratification provides evidence of past bedforms in ancient rocks, and its analysis can reveal much about both bedform geometry and transport mechanisms. The sequences that are formed of cross-stratification can also be used to infer past environments and to distinguish, for example, between eolian and fluvial processes.

The analysis of cross-stratification at the *Opportunity* landing site has been used to infer the presence of both eolian and fluvial depositional environments on the past surface of Mars (Grotzinger *et al*., 2005, 2006). Two scales are present: meter-scale cross-bedding is regarded as evidence for past sand dunes formed by eolian transport, yet centimeter-scale trough cross-lamination is regarded as evidence for subaqueous, fluvial transport. Scale is not the only important parameter. Geometry also matters, and the occurrence of centimeter-scale cross-lamination with trough geometry is regarded to have a uniquely subaqueous origin.

Given its importance in the search for signs of past water on the surface of Mars, one may ask what role gravity plays in the formation of bedforms and, by consequence, cross-bedding. These arguments are more fully developed in Grotzinger *et al*. (2005), but are summarized here.

Small-scale (ripple) bedforms of the type observed in the Burns formation have been well studied in laboratory and natural systems on Earth (Southard, 1973; Harms *et al*., 1975, 1982; Middleton and Southard, 1984; Hunter, 1985), as well as theoretically for both Earth (Rubin, 1987) and Mars (Southard and Boguchwal, 1990a). The festoon cross-lamination observed in the Burns formation, implying highly sinuous bedform crestlines, is known to develop only in subaqueous ripples. In contrast, eolian impact ripples have very straight crestlines and their migration generally does not produce festoon cross-lamination. Indeed, the tabular-planar cross-lamination which is produced is often not well expressed and is inclined at angles much lower than the angle of repose (Sharp, 1963; Hunter, 1977). Instead, the "pinstripe" lamination defined by inversely graded millimeter-thick layers is often the diagnostic attribute of eolian wind-ripple migration (Hunter, 1977; Fryberger and Schenk, 1988). Based on analogy to Earth, volcanic or impact-generated base-surge transport has been suggested to account for the cross-stratification observed at Meridiani (Knauth *et al*., 2005; McCollom and Hynek, 2005). However, centimeter-scale bedforms, with trough (or "festoon") geometry developed by base-surge deposits, have never been observed in terrestrial environments (Fisher and Waters, 1970; Branney and Kokelaar, 2002). Furthermore, based on analogy to subaqueous flows it seems unlikely that ripple bedforms (a subcritical flow phenomena; Froude number <1) would develop in base-surge flows, which are regarded to deposit sediment under supercritical flow conditions (Froude number >1). Consequently, they are not considered further here. The principle issue that needs to be discussed is the effect of g on the stability of subaqueous ripples and, if present, what do they indicate about sediment transport.

The variables in Equation 24.21 can be used to describe bed configurations, including the development of the 3D ripples inferred to have produced the festoon cross-lamination in the Burns formation. Note that the influence of the acceleration of gravity is specified in γ', which will be discussed further below as it relates to changes in the physical interpretation of open-channel flow on Mars as compared to Earth. By dimensional analysis, the variables in Equation 24.21 can be grouped into dimensionless variables that characterize the flow (Southard, 1973; Southard and Boguchwal, 1990b). The sedimentologically most interesting set isolates d, U, and D:

$$\begin{aligned}&\text{Dimensionless flow velocity } U^0 = U(\rho^2/\mu\gamma')^{1/3};\\ &\text{Dimensionless flow depth } d^0 = d(\rho\gamma'/\mu^2)^{1/3};\\ &\text{Dimensionless grain size } D^0 = D(\rho\gamma'/\mu^2)^{1/3};\\ &\text{Density ratio } \rho_s/\rho.\end{aligned} \tag{24.26}$$

This set of dimensionless variables provides a complete set of scale-modeling parameters that can take into account a wide range of sedimentologically interesting behaviors such as the effects of changing grain size, current velocity, flow depth, fluid viscosity (via temperature change), grain density, and the acceleration of gravity. Although all these effects can logically vary for different situations on Earth or Mars, or between Earth and Mars, only the last of these effects is *required* to change for flows on Mars versus Earth. Fortunately, the change in the acceleration of gravity is known; other variables are imprecisely known, or worse yet, unknown. Therefore, it is important that we consider here what can be determined and what must be assumed. The good news is that in several cases the influence of these unknowns is small.

For the purpose of this analysis, we will assume reasonable values for the unknowns. This includes fluid viscosity

and density (assume water at 10 °C), grain density (assume quartz), and flow depth (likely to have been shallow). We know a priori that g is contained in γ', and that $g_M \sim 0.4 g_E$ (where g_M and g_E are the values of the acceleration of gravity on Mars and on the Earth, respectively). Therefore, the actual values of d, U, and D would be different in two dynamically similar flows on Mars and Earth even if the water viscosity (mostly affected by temperature) were the same (Southard and Boguchwal, 1990a). Scale factors, which relate the sense and magnitude of the effects of Mars' different gravitational constant, are considered later.

The initiation of sediment motion and the bedforms which develop as a result of grain–fluid interactions can be displayed on multidimensional graphs which show the stability of the various bedforms based on terrestrial observational data (Southard, 1973; Boguchwal and Southard, 1990). The observational data – collected during careful experiments – are then plotted so that the various bedforms occupy contiguous stability fields, with boundary surfaces separating the fields (Boguchwal and Southard, 1990). A 3D graph of flow depth, bed shear stress, and grain size is most commonly used to illustrate the effects of these most important parameters. However, the effects of flow depth may be neglected if only shallow flows are considered, which is appropriate for the inferred interdune depositional environment of the Burns formation upper unit. Furthermore, since the velocity of most natural flows is the most important component of bed shear stress, then we can accept flow velocity as a surrogate for bed shear stress. Thus, the simplest representation of the system is provided by a 2D graph (Figure 24.19), which relates the bed configuration to flow velocity and grain size, normalized to 10 °C water temperature and flow depth of 0.25–0.40 m.

This velocity-size graph provides some guidance to the likely range of flow velocities, given a particular bed configuration and grain size. Since we have reconstructed the bed to have consisted of 3D ripples, we need only obtain an estimate of grain size. The lower range is difficult to obtain because of diagenetic effects associated with recrystallization, and because the lower limit of resolution of the MI is 30 microns/pixel, which means that the smallest resolvable grains would have a diameter of about 0.1 mm. However, as Figure 24.19 illustrates, it is the upper limit that is more important because above a certain limit, ripples do not develop. Our measurements of grain size in the Burns formation indicate that most sediment has a grain size finer than 0.3–0.8 mm, and the coarsest particles observed are up to 1.0 mm. This upper limit is close to the no-ripple boundary, but the finer-grained particles could have formed ripples. Indeed, the evidence for 3D ripples having actually formed in the Burns formation is not precluded by any of these terrestrial experimental data. Assuming a lower grain size of silt, this generates a range of possible flow velocities of 0.1–1.0 m s^{-1} for the currents that formed the 3D ripples of the Burns formation. If larger grains were involved, then the maximum velocities would have been a bit slower.

The estimates for flow velocity obtained above are subject to adjustment as a result of the different acceleration of gravity for Mars. Southard and Boguchwal (1990a) have considered how this difference may influence resulting bed configurations, assuming cohesionless quartz-density sediment. (This assumption is clearly incorrect for the Burns formation, but its effect on the density ratio ρ_s/ρ may be small; the density of quartz is 2.65 g cm^{-3} and the densities of the likely mixture of sulfate evaporite minerals thought to partially compose the Burns formation range from 1.9 to 3.2 g cm^{-3}, so perhaps the mean density of the Burns mineral assemblage in water is not significantly different from the density of quartz in water.) Equation (24.26) shows that each axis of the dimensionless velocity-size graph contains g via γ', but because $g_M \sim 0.4 g_E$ the actual values of U and D would be different in two dynamically similar flows on Mars and Earth if the water temperature was the same. To provide an idea of these effects, Southard and Boguchwal (1990a) computed the scale factors by which the axes of the velocity-size graph standardized for some temperature on Mars are multiplied relative to the velocity-size graph standardized for the same temperature on Earth. To obtain the scale factors, they solved for the ratios U_M/U_E and D_M/D_E:

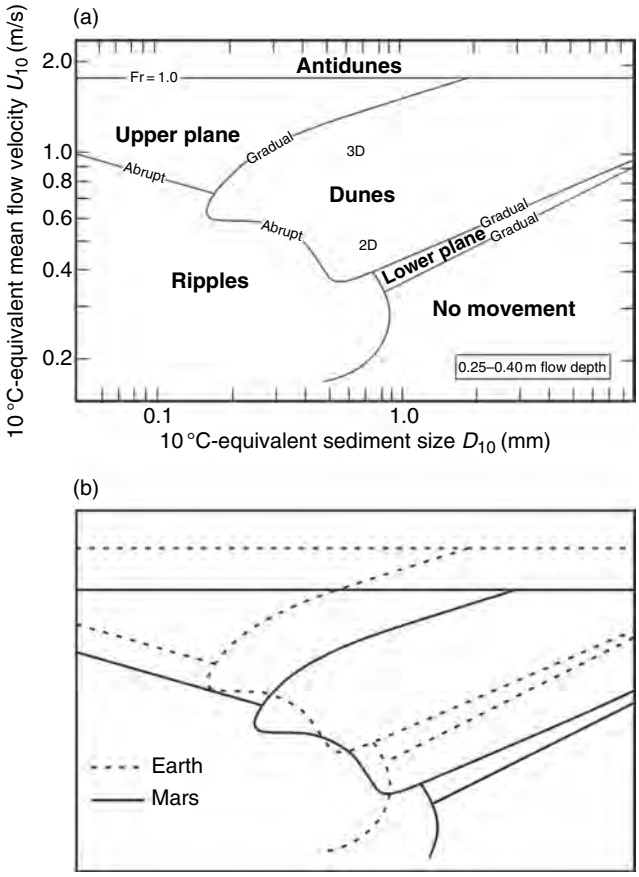

Figure 24.19. (a) Plot of dimensionless velocity versus grain size for 10 °C-equivalent flow depths of 25–40 cm. Note that neither ripples nor dunes form in the "upper plane" and "lower plane" regions of the diagrams. (b) Rescaling of Figure (a) for the effect of reduced acceleration of gravity (g) on Mars. Note that the fields shift slightly toward larger grain size and/or slower velocities as a consequence of reduced g but that the shapes of the fields remain the same. (From Grotzinger *et al.*, 2005.)

$$U_M\left(\frac{\rho^2}{\mu\gamma'_M}\right)^{1/3} = U_E\left(\frac{\rho^2}{\mu\gamma'_E}\right)^{1/3};$$
$$\frac{U_M}{U_E} = \left(\frac{\gamma'_M}{\gamma'_E}\right)^{1/3} = \left(\frac{g_M}{g_E}\right)^{1/3} = 0.74;$$

$$D_M\left(\frac{\rho\gamma'_M}{\mu}\right)^{1/3} = D_E\left(\frac{\rho\gamma'_E}{\mu}\right)^{1/3};$$
$$\frac{D_M}{D_E} = \left(\frac{\gamma'_E}{\gamma'_M}\right)^{1/3} = \left(\frac{g_E}{g_M}\right)^{1/3} = 1.36; \quad (24.27)$$

where U_E, D_E, and γ'_E are the velocity, grain size, and submerged weight per unit volume of the sediment in the terrestrial flow and U_M, D_M, and γ'_M are the respective variables in the Martian flow.

The first set of equations indicate that a given transition between bedforms, for example ripples to upper plane bed, at constant grain size and flow depth, occurs at a lower velocity on Mars as compared to Earth, by a factor of 0.74. The second set of equations indicate that a similar transition between bedforms, at constant velocity and flow depth, occurs at a larger grain size on Mars as compared to Earth, by a factor of 1.36. This small, but nonnegligible effect is shown in Figure 24.19b. The important point is that ripples should be easily formed in shallow subaqueous flows on the surface of Mars given the observed range of grain size. The change in g, as well as potential changes in grain density or even water temperatures (Southard and Boguchwal, 1990a), poses little challenge to this prediction.

24.7.8 Formation of sedimentary basins

Most sedimentary basins on Earth are aerially extensive systems owing to the lithospheric scale of basin-forming processes. They are filled with thick successions of strata owing to the effectiveness of the hydrologic cycle in assuring general continuity of sediment availability to fill the basin. Sediments tend to accumulate in depressions in the Earth's crust that are formed by subsidence, in which a broad area of the crust sinks relative to the surrounding crust. Subsidence is induced partly by the additional weight of sediments on the crust but is caused mostly by tectonic forces.

In contrast, most sedimentary basins on Mars are likely to have been created as impact-generated depressions and rift systems such as the Valles Marineris. However, the apparent absence of lithospheric plates floating atop a convecting asthenosphere imparts significant differences between sedimentary basins on Earth and Mars. The largest terrestrial basins form due to two principal processes, both dependent on the unique mechanical and thermal properties of lithospheric plates. First, extension of the lithosphere leads to stretching, heating, and then cooling to develop rifts and overlying thermal sag basins. Isostatic considerations demand that the ultimate thickness of basin-filling sediments be on the order of 10 km or more where the continental lithosphere is extended to the point of ocean basin development. Initial rifting results in accumulation of thick successions of terrestrial (generally nonmarine) sedimentary rocks, which commonly are interspersed with bimodal suites of basaltic and granitic extrusive igneous rocks. Subsequently, during cooling of stretched continental crust, subsidence below sea level insures that thick successions of marine strata are formed. The depth and width of extensional basins primarily depend on the degree of lithospheric thinning, and the area over which it is thinned.

The second important terrestrial basin type develops along zones of plate convergence, where the overriding plate creates a load on the underlying plate and causes it to bend, producing a flexural basin. The depth and width of these basins depend on the magnitude of the load, and the flexural rigidity of the bending plate. These basins tend to be cool compared to extensional basins and therefore lack volcanism except for pyroclastic deposits. Because of the strength of the continental lithosphere, it is rare to see accumulations of strata in excess of several kilometers formed in flexural basins, except where antecedent continental margin topography has been involved.

In both basin types, buried strata become subjected to regional to continental scale groundwater flow typically resulting in pervasive cementation as described above. Compaction during basin filling leads to expulsion of sediment pore fluids, which migrate across pressure gradients within permeable zones. As the fluids interact with the sediments they may become saturated with certain mineral phases which then, because of changes in physical parameters (such as temperature and pressure), may become oversaturated and consequently precipitate as cements.

On Mars, the same physical and chemical principles of basin development apply. However, the likely absence of plate tectonics, even early on in Martian history, results in some substantial differences. For example, rifting to produce the enormous Valles Marineris system occurred at a scale unknown on Earth. However, whatever extension of the crust occurred to produce the Valles Marineris apparently was not accompanied by subsequent thermal subsidence of the flanking regions. If these thermal subsidence basins were ever formed, then they have been inverted to the level of preexisting rift basins, and in turn those rift basins have been significantly exhumed. Though a case can be made for eolian deflation of pre-existing strata, which accumulated in local topographic depressions such as impact craters, it is not obvious that this mechanism can account for the paucity of fill in the Valles Marineris. Furthermore, such a mechanism could not account for basin inversion required to restore rift-related structures and strata to the current surface of Mars. The simplest conclusion is that rifting was not accompanied by attenuation of the crust to the extent observed on Earth for rifts of similar magnitude.

Similarly, the absence of plate tectonics leaves Mars devoid of linear mountain belts flanked by linear flexural basins. However, previous work has shown that the Martian crust does behave elastically when stressed; it seems likely that a flexural basin was developed in association with the loading created by the growth of Olympus Mons and associated Tharsis volcanos (Phillips *et al.*, 2001). Indeed, the very gentle northward tilt of the strata at Meridiani may

reflect deformation associated with loading of the Martian crust. However, if so, then these strata would have to predate loading or at most be equivalent to the earliest stages of basin development, so that additional loading would result in rotation of earlier-formed strata. Future high-resolution mapping may help to identify sites where onlap of older rocks by younger rocks could demonstrate the cogenetic relationship between loading, subsidence, and sedimentation.

Sedimentary basin fill facies

Substantial evidence supports transport of particulate sediments across Mars over distances similar to the scale of Earth's great rivers (thousands of kilometers). However, transport may have been short-lived, though intense (Baker, 2001). In some cases, more mature drainage networks are developed (e.g., Hynek and Phillips, 2003; Irwin *et al*., 2005); however, there is no evidence for the thick clastic wedges that accumulate over hundreds of millions of years and form along the margins of continents on Earth. Neverthess, large and abundant alluvial fans are often preserved in craters at middle-to-low southern latitudes, and they appear to have been formed dominantly by fluvial processes (Moore and Howard, 2005). Locally, deltas appear to have developed within crater lakes (Malin and Edgett, 2003; Lewis and Aharonson, 2004). These observations suggest that the flux of sediment appears to have been into local depressions rather than regional basins. Exceptions may include the parts of the Northern plains (Carr and Head, 2003) and Elysium Planitia (Murray *et al*., 2005) where sediments may have been deposited in a large water body. However, if this did in fact occur, there is no evidence for deposition of thick clastic wedges along the topographic margins of these basins. In fact, even the presence of possible geomorphic shorelines (Clifford and Parker, 2001) is debated (Carr and Head, 2003; Webb, 2004). Thus, even if the "accommodation space" may have been present due to regional geodynamic processes, it seems unlikely that regional basins may ever have been significantly filled on Mars, as often occurs on Earth.

Mars is often regarded as a planet dominated by volcanic or impact processes (Kieffer *et al*., 1992) and there can be no doubt that their history is recorded in the Martian stratigraphic record. But it must also be recognized that eolian processes, which are dominant on the modern surface of Mars (Greeley and Iverson, 1985; Greeley *et al*., 1993; Sullivan *et al*., 2005), were likely to have also been important in the past (Armstrong and Leovy, 2005). It is possible that ancient eolian deposits were widespread across the early surface of Mars, and Grotzinger *et al*. (2005) provide evidence for eolian transport of sediments across the *Opportunity* landing site. Particles generated through weathering, erosion, mineral precipitation in aqueous environments, volcanism, and impact gardening would have been reworked by winds with velocities above the saltation threshold. If atmospheric pressure were higher on early Mars, then eolian processes would have been even more effective (Armstrong and Leovy, 2005). Eolian transport would have been a ubiquitous process whereby extensive sheets of sediments could have been dispersed over hundreds to thousands of square kilometers, forming substantial (kilometers thick) sequences whose thickness would have been limited mostly by the availability of sediment. As on Earth, it seems reasonable to expect that their composition would have been dependent on the composition of source materials. Thus, it is possible to imagine an eolian stratigraphy consisting of compositionally varied units derived from weathered basalts derived from older terrains, unweathered basalts derived from reworking of fresh volcaniclastic detritus, altered basalts (and other sediments) derived from rocks at impact targets, and varied minerals formed by reworking sites of subaqueous mineral precipitation.

24.7.9 The role of recycling

On Earth, the stratigraphic age of the sedimentary mass is significantly younger than the ages of their crustal sources, and this appears in stark contrast to Mars, where the ages of sedimentary terrains are only slightly younger than their crustal sources (Figure 24.20). On Earth, the sedimentary mass has been approximately constant over the past 2.5 Ga and is largely cannibalistic, with 70% of eroding sediment being derived from preexisting sedimentary rocks (Veizer and Jansen, 1979). Mechanisms for sedimentary recycling on Earth are complex and can be accomplished in a number of ways (e.g., Veizer and Jansen, 1979, 1985; McLennan, 1988; Veizer and Mackenzie, 2003):

1. *Sediment–sediment recycling*. Plate tectonic processes (mainly subduction and collision) preferentially elevate continental margins where sediment tends to accumulate, thus preferentially causing the erosion of ancient sedimentary terrains. This controlling mechanism imposes a strong control on recycling rates by the tectonic setting. Thus, sedimentary recycling rates in tectonically stable continental cratons are orders of magnitude slower than rates at volcanically active island arcs (Veizer and Jansen, 1985).
2. *Intracrustal recycling*. Sediments are commonly buried deep within the crust, causing metamorphism and melting; such material may be returned to the surface and form the source of new sediment. Such processes may be "invisible" to petrographic and many geochemical techniques but may be clearly visible to certain isotopic tracers (e.g., Nd isotopes).
3. *Crust–mantle recycling*. In some cases, subduction may return sediments to the mantle where they can be reincorporated and essentially "lost" from the geological record. Thus, in order to maintain the volume of the sedimentary mass these losses are replaced by sediments derived from "new" crustal sources.

The overall effect has been quantified by a number of workers (Figure 24.21). The terrestrial sedimentary mass likely evolved as a substantially "open" system during the early history of the Earth and grew as the continental crust grew. Sedimentary recycling no doubt took place but was largely overwhelmed by new additions to the sedimentary

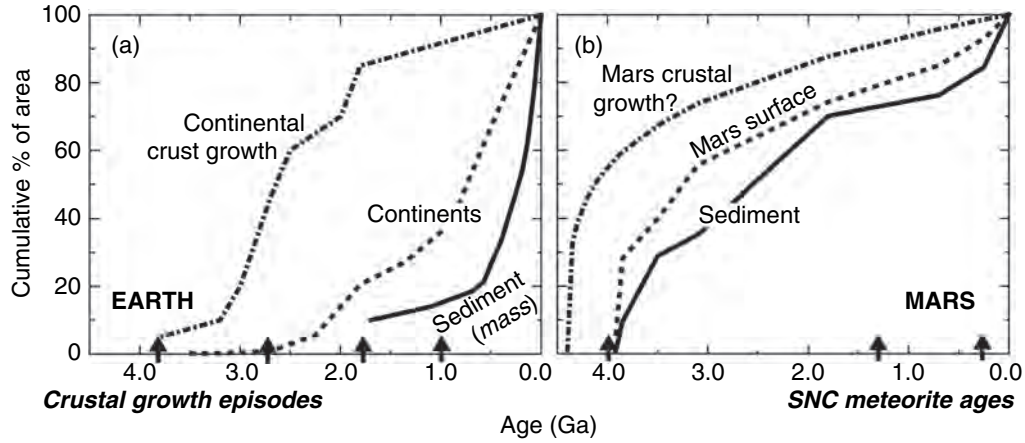

Figure 24.20. Plots of cumulative area versus age for (a) continental crustal growth (based on Nd model ages), continental Rb-Sr crystallization ages, and sediment distribution (from Veizer and Jansen, 1979, 1985); and (b) Mars surface ages and sediment terrain ages from crater counts (Tanaka *et al.*, 1988). The concave up, exponential shape of the terrestrial sediment curve is a result of intracrustal (sedimentary) recycling processes (Garrels and Mackenzie, 1971). Such processes do not appear to be significant on Mars, especially after about 2 to 3 Ga. On the bottom of the diagrams are ages of major crust forming events on Earth (*left*) and ages of SNC meteorites (*right*).

mass. However, over the past 2–3 Ga, the sedimentary mass has been substantially "closed" and represents a system in which >70%–75% of the sediment is derived from preexisting sediment, with only the remaining 25%–30% derived from new crustal additions.

Although suggestions of an early phase of plate tectonics on Mars continue to appear (e.g., Connerney *et al.* [1999]; also see Chapter 11; Sleep [1994]; and especially Nimmo and Tanaka [2005] for recent discussions of the issue), our judgment is that the evidence is not compelling. There is certainly no evidence to suggest that plate tectonics have been operating any time during the past 3–4 Ga. In the absence of plate tectonics, the processes that control sedimentary recycling on Earth are largely absent on Mars. Very early in the history of both planets, impact processes may have been a reasonably significant way to recycle sediment, but such processes become exponentially less efficient over geological time. In addition, although magmatism on Mars has continued sporadically through to at least 0.2–0.4 Ga (age of basaltic shergottites), the vast majority of the Martian crust appears to be ancient (Figure 24.20). Thus, the Martian sedimentary system may have become substantially closed to new additions much earlier in its history (Figure 24.21).

24.8 CONCLUDING REMARKS

From a sedimentological point of view, perhaps the greatest achievement of the MERs has been the exquisite detail and fidelity with which stratigraphic and sedimentological measurements have been made. As the analytical tools that are sent to Mars on landed missions improve, *in situ* sedimentological measurements will become ever more sophisticated. The potential for understanding the sedimentary record of Mars goes far beyond the few meters of stratigraphic section that have been evaluated thus far by *Spirit* and *Opportunity*. Just as on Earth, careful evaluation of even a few stratigraphic sections can guide us into a position to be able to pose sensible questions that in turn address the most fundamental issues of sedimentology, such as the basic controls on the formation and history of sedimentary basins, the nature and relative proportions of sedimentary lithologies, and the various processes of sediment formation, transport, deposition, diagenesis, and recycling: in short, the fundamental nature of the Martian sedimentary rock cycle. In addition, even a few detailed studies provide for a far more constrained framework within which to design laboratory experiments and theoretical models of the physical and chemical nature of the Martian sedimentary record.

Landed missions to Mars are necessarily rare, and for a planet that we now understand to have a diverse and complex geological record, only a few of the many geological settings can be evaluated at a comparable scale in the coming decades. Nevertheless, these few studies will engender much greater confidence in interpreting and integrating into a global stratigraphic framework the new generation of high-resolution orbital images and spectroscopy. Finally, it cannot go without comment that the full power of sedimentary rocks to elucidate the environmental conditions within which they form can come only through intense laboratory study of the physical, chemical, and isotopic character of the sediment and its components. Some of these measurements can be achieved by "laboratories" that will be sent to Mars, but others will have to await the return to Earth of Martian sedimentary rocks.

ACKNOWLEDGMENTS

We are extremely grateful to the entire Mars Exploration Rover science and engineering team for making so much of

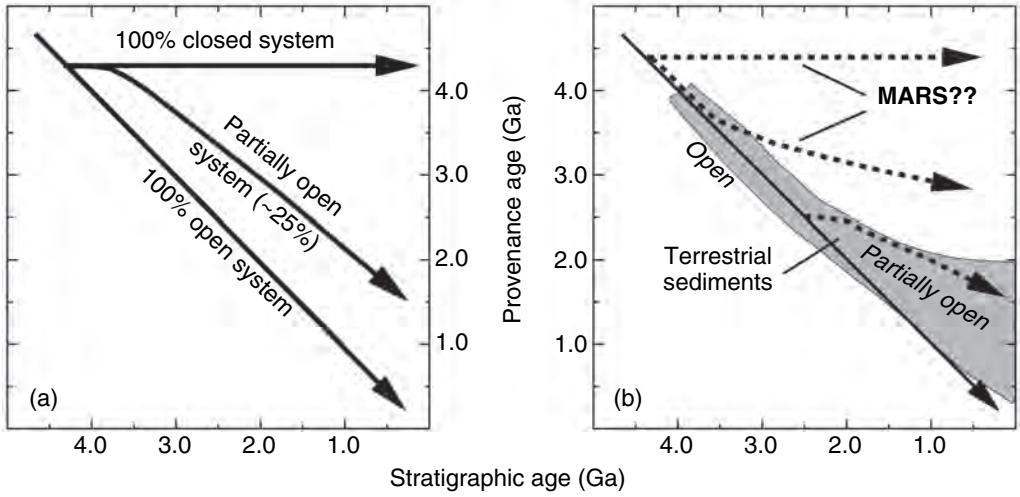

Figure 24.21. Plots of provenance age versus stratigraphic age for terrestrial sediments. For the Earth, sedimentary provenance age is estimated from their Nd-isotopic compositions. Nd-model ages estimate the mean age of separation of sedimentary crustal sources from the mantle and thus effectively define provenance age as the age of crust–mantle fractionation of the provenance components (adapted from Veizer and Jansen, 1985; McLennan, 1988). Also shown are models illustrating that the terrestrial sedimentary system is partially open to new crustal additions from the mantle during the sedimentary recycling process. Dashed arrows show a possible evolution of a Martian sedimentary mass that formed early in Martian history with relatively little addition since.

the material discussed in this chapter possible. We also thank Jim Bell, Ross Taylor, Nick Tosca, and an anonymous referee for very helpful comments on the chapter.

REFERENCES

Ahlbrandt, T. S. and S. G. Fryberger, Sedimentary features and significance of interdune deposits. In *Recent and Ancient Nonmarine Depositional Environments: Models for Exploration* (ed. F. G. Ethridge and R. M. Flores), Special Publication No. 31, Tulsa: Society of Economic Mineralogists and Paleontologists, pp. 293–314, 1981.

Andrews-Hanna, J. C., R. J. Phillips, and M. T. Zuber, Meridiani Planum and the global hydrology of Mars, *Nature* **446**, 163–6, 2007.

Arlauckas, S. M., S. M. McLennan, and D. H. Lindsley, The effect of low-temperature acidic weathering on the magnetic signature of primary Fe-Ti oxides on Mars, *Lunar Planet. Sci. XXXVII*, Houston: Lunar and Planetary Institute, Abstract #1609 (CD-ROM), 2006.

Armstrong, J. C. and C. B. Leovy, Long term wind erosion on Mars, *Icarus* **176**, 57–74, 2005.

Armstrong, J. C., C. B. Leovy, and T. Quinn, A 1 Gyr climate model for Mars: new orbital statistics and the importance of seasonally resolved polar processes, *Icarus* **171**, 255–71, 2004.

Arvidson, R. E., F. Poulet, R. V. Morris, *et al.*, Nature and origin of the hematite-bearing plains of Terra Meridiani based on analyses of orbital and Mars Exploration rover data sets, *J. Geophys. Res.* **111**, E12S08, doi:10.1029/2006JE002728, 2006a.

Arvidson, R. E., S. W. Squyres, R. C. Anderson, *et al.*, Overview of the Spirit Mars Exploration Rover mission to Gusev crater: landing site to Backstay rock in the Columbia Hills, *J. Geophys. Res.* **111**, E02S01, doi:10.1029/2005JE002499, 2006b.

Baker, L. L., D. J. Agenbroad, and S. A. Wood, Experimental hydrothermal alteration of a Martian analog basalt: implications for Martian meteorites, *Meteorit. Planet. Sci.* **35**, 31–8, 2000.

Baker, V. R., Water and the Martian landscape, *Nature* **412**, 228–36, 2001.

Bandfield, J. L., T. D. Glotch, and P. R. Christensen, Spectroscopic identification of carbonate minerals in the martian dust, *Science* **301**, 1084–7, 2003.

Banin, A., F. X. Han, I. Kan, and A. Cicelsky, Acidic volatiles and the Mars soil, *J. Geophys. Res.* **102**, 13341–56, 1997.

Bell III, J. F., S. W. Squyres, R. E. Arvidson, *et al.*, Pancam multispectral imaging results from the Opportunity rover at Meridiani Planum, *Science* **306**, 1703–9, 2004.

Benison, K. C. and D. A. LaClair, Modern and ancient extremely acid saline deposits: terrestrial analogs for Martian environments?, *Astrobiology* **3**, 609–18, 2003.

Berner, R. A., Chemical weathering and its effect on atmospheric CO_2 and climate, *Rev. Mineral.* **31**, 565–83, 1995.

Bhattacharya, J. P., T. H. D. Payenberg, S. C. Lang, and M. Bourke, Dynamic river channels suggest a long-lived Noachian crater lake on Mars, *Geophys. Res. Lett.* **32**(10), L10201, 2005.

Bibring, J.-P., Y. Langevin, A. Gendrin, *et al.*, Mars surface diversity as revealed by the OMEGA/Mars Express observations, *Science* **307**, 1576–81, 2005.

Bibring, J.-P., Langevin, Y., Mustard, J. F., *et al.*, Global mineralogical and aqueous Mars history derived from OMEGA/Mars Express data, *Nature* **312**, 400–4, 2006.

Blatt, H., Flux of siliciclastic grains in sediments, *J. Geol. Education* **37**, 243–9, 1989.

Boguchwal, L. A. and J. B. Southard, Bed configurations in steady unidirectional flows. Part 1. Scale model using fine sands, *J. Sediment. Petrol.*, **60**, 649–57, 1990.

Branney, M. J. and P. Kokelaar, *Pyroclastic Density Currents and the Sedimentation of Ignimbrites*, London: The Geological Society, 142pp., 2002.

Bridges, J. C. and M. M. Grady, A halite-siderite-anhydrite-chlorapatite assemblage in Nakhla: mineralogical evidence for evaporites on Mars. *Meteorit. Planet. Sci.* **34**, 407–15, 1999.

Bridges, J. C. and M. M. Grady, Evaporite mineral assemblages in the nakhlites (martian) meteorites, *Earth Planet. Sci. Lett.* **176**, 267–79, 2000.

Bridges, J. C., D. C. Catling, J. M. Saxton, *et al*., Alteration assemblages in martian meteorites: implications for near-surface processes, *Space Sci. Rev*. **96**, 365–92, 2001.

Broecker, W. S. and T.-H. Peng, *Tracers in the Sea*, Palisades, NY: Eldigio Press, 690pp., 1982.

Buick, R., Life in the Archaean. In *Palaeobiology II* (ed. D. E. G. Briggs and P. R. Crowther), Oxford: Blackwell, pp. 13–21, 2001.

Buick, R. and J. S. R. Dunlop, Evaporitic sediments of early Archean age from the Warrawoona Group, North Pole, Western Australia, *Sedimentology* **37**, 247–78, 1990.

Buick, R., J. S. R. Dunlop, and D. I. Groves, Stromatolite recognition in ancient rocks: an appraisal of irregularly laminated structures in an early Archean chert-barite unit from North Pole, Western Australia, *Alcheringa* **21**, 161–81, 1981.

Burns, R. G., Rates and mechanisms of chemical weathering of ferromagnesian silicate minerals on Mars, *Geochim. Cosmochim. Acta* **57**, 4555–74, 1993.

Cabrol, N. A., E. A. Grin, M. H. Carr, *et al*., Exploring Gusev crater with Spirit: review of science objectives and testable hypotheses, *J. Geophys. Res*. **108**, E128076, doi:10.1029/2002JE002026, 2003.

Carr, M. H., J. W. Head III, Oceans on Mars: an assessment of observational evidence and possible fate, *J. Geophys. Res*. **108**(E5), 5042, doi 10.1029/2002JE001963, 2003.

Catling, D. C., A chemical model for evaporites on early Mars: possible sedimentary tracers of the early climate and implications for exploration, *J. Geophys. Res*. **104**, 16453–69, 1999.

Chigira, M. and T. Oyama, Mechanism and effect of chemical weathering of sedimentary rocks, *Eng. Geol*. **55**, 3–14, 1999.

Choquette, P. W. and L. C. Pray, Geologic nomenclature and classification of porosity in sedimentary carbonates, *Am. Assoc. Pet. Geol. Bull*. **54**, 207–50, 1970.

Christensen, P. R., M. B. Wyatt, T. D. Glotch, *et al*., Mineralogy at Meridiani Planum from the mini-TES experiment on the Opportunity rover, *Science* **306**, 1733–9, 2004.

Christensen, P. R., H. Y. McSween Jr., J. L. Bandfield, *et al*., Evidence for magmatic evolution and diversity on Mars from infrared observations, *Nature* **436**, 504–9, 2005.

Clark, B. C. and D. C. Van Hart, The salts of Mars, *Icarus* **45**, 370–8, 1981.

Clark, B. C., R. V. Morris, S. M. McLennan, *et al*., Chemistry and mineralogy of outcrops at Meridiani Planum, *Earth Planet. Sci. Lett*. **240**, 73–94, 2005.

Clifford, S. M. and T. J. Parker, The evolution of the Martian hydrosphere: implications for the fate of a primordial ocean and the current state of the northern plains, *Icarus* **154**, 40–79, 2001.

Clifford, S. M., D. Crisp, D. A. Fisher, *et al*., The state and future of Mars polar science and exploration, *Icarus* **144**, 210–42, 2000.

Connerney, J. E. P., M. H. Acuña, P. J. Wasilewski, *et al*., Magnetic lineation in the ancient crust of Mars, *Science* **284**, 794–8, 1999.

Dressler, B. O., V. L. Sharpton, C. S. Schwandt, and D. Ames, Impactites of the Yaxcopoil-1 drilling site, Chicxulub impact structure: petrography, geochemistry, and depositional environment, *Meteorit. Planet. Sci*. **39**, 857–78, 2004.

Edgett, K. S., The sedimentary rocks of Sinus Meridiani: five key observations from data acquired by Mars Global Surveyor and Mars Odyssey orbiters, *Mars* **1**, 5–58, 2005.

Edgett, K. S. and M. C. Malin, Martian sedimentary rock stratigraphy: outcrops and interbedded craters of northwest Sinus Meridiani and southwest Arabia Terra, *Geophys. Res. Lett*. **29**(24), 2179, doi:10.1029/2002GL016515, 2002.

Eriksson, K. A., Alluvial and destructive beach facies from the Archean Moodies Group, Barberton Mountain Land, South Africa and Swaziland, *Canadian Soc. Petrol. Geol. Mem*. **5**, 287–311, 1978.

Eugster, H. P., Climatic significance of lake and evaporite deposits, *Climate in Earth History, Studies in Geophysics*, Washington, DC: National Academy Press, pp. 105–11, 1982.

Eugster, H. P. and L. A. Hardie, Saline lakes. In *Lakes: Chemistry, Geology, Physics* (ed. A. Lerman), New York: Springer-Verlag, pp. 237–93, 1978.

Farrand, W. H., J. F. Bell III, J. R. Johnson, *et al*., Visible and near infrared multispectral analysis of rocks at Meridiani Planum, Mars, by the Mars Exploration Rover Opportunity, *J. Geophys. Res*. **112**, E06S02, doi:10.1029/2006JE002773, 2007.

Fisher, R. V. and A. C. Waters, Base surge bed forms in maar volcanoes, *Am. J. Sci*. **268**, 157–80, 1970.

Fryberger, S. G. and C. J. Schenk, Pin stripe lamination: a distinctive feature of modern and ancient eolian sediments, *Sediment. Geol*. **55**, 1–55, 1988.

Fryberger, S. G., A. M. Al-Sarl, and T. J. Clisham, Eolian dune, interdune, sand sheet, and silicilcastic sabkha sediments of an off-shore prograding sand sea, Dhahran area, Saudi Arabia, *Am. Assoc. Pet. Geol. Bull*. **67**, 280–312, 1983.

Garrels, R. M. and F. T. Mackenzie, *Evolution of Sedimentary Rocks*, New York: W. W. Norton, 397pp., 1971.

Gendrin, A., N. Mangold, J.-P. Bibring, *et al*., Sulfates in martian layered terrains: the OMEGA/Mars Express view, *Science* **307**, 1587–91, 2005.

Glotch, T. D., J. L. Bandfield, P. R. Christensen, *et al*., Mineralogy of the light-toned outcrop rock at Meridiani Planum as seen by the Miniature Thermal Emission Spectrometer and implications for its formation, *J. Geophys. Res*. **111**, E12S03, doi:10.1029/2005JE002762, 2006.

Golden, D. C., D. W. Ming, R. V. Morris, and S. A. Mertzman, Laboratory-simulated acid-sulfate weathering of basaltic materials: implications for formation of sulfates at Meridiani Planum and Gusev crater, Mars, *J. Geophys. Res*. **110**, E12S07, 2005.

Gooding, J. L. and K. Keil, Alteration of glass as a possible source of clay minerals on Mars, *Geophys. Res. Lett*. **5**, 727–30, 1978.

Greeley, R. and J. Iverson, *Wind as a Geological Process on Earth, Mars, Venus and Titan*, New York: Cambridge University Press, 333 pp., 1985.

Greeley, R., A. Skypeck, and J. B. Pollack, Martian aeolian features and deposits: comparisons with general circulation model results, *J. Geophys. Res*. **98**, 3183–93, 1993.

Greeley, R., R. E. Arvidson, P. W. Bartlett, *et al*., Gusev crater: wind-related features and processes observed by the Mars Exploration Rover Spirit, *J. Geophys. Res*. **111**, E02S09, doi:10.1029/2005JE002491, 2006.

Griffith, L. L. and E. L. Shock, Hydrothermal hydration of martian crust: illustration via geochemical model calculations, *J. Geophys. Res*. **102**, 9135–43, 1997.

Grotzinger, J. P., Cyclicity and paleoenvironmental dynamics, Rocknest Platform, northwest Canada, *Geol. Soc. Am. Bull*. **97**, 1208–31, 1986.

Grotzinger, J. P., Facies and evolution of Precambrian carbonate depositional systems: emergence of the modern platform archetype, *Soc. Econ. Paleontol. Mineral. Spec. Publ*. **44**, 79–106, 1989.

Grotzinger, J. P. and N. P. James, Carbonate sedimentation and diagenesis in the evolving Precambrian world, *Soc. Econ. Paleontol. Mineral. Spec. Publ*. **67**, 365, 2000.

Grotzinger, J. P., J. F. Bell III, W. Calvin, *et al*., Stratigraphy and sedimentology of a dry to wet eolian depositional system, Burns formation, Meridiani Planum, Mars, *Earth Planet. Sci. Lett*. **240**, 11–72, 2005.

Grotzinger, J. P., J. F. Bell III, K. E. Herkenhoff, *et al*., Sedimentary textures formed by aqueous processes, Erebus crater, Meridiani Planum, Mars, *Geology* **34**, 1085–8, 2006.

Haberle, R. M., J. R. Murphy, and J. Schaeffer, Orbital change experiments with a Mars general circulation model, *Icarus* **161**, 66–89, 2003.

Halevy, I., M. T. Zuber, and D. P. Schrag, A sulfur dioxide feedback on early Mars, *Science* **318**, 1903–07, 2007.

Hardie, L. A., Gypsum: anhydrite equilibrium at one atmosphere pressure, *Am. Mineral*. **52**, 171–200, 1967.

Hardie, L. A., On the significance of evaporites, *Annu. Rev. Earth Planet. Sci*. **19**, 131–68, 1991.

Hardie, L. A. and Eugster, H. P., The evolution of closed-basin brines, *Mineral. Soc. Am. Spec. Paper* **3**, 273–90, 1970.

Hardie, L. A., T. K. Lowenstein, and R. J. Spencer, The problem of distinguishing between primary and secondary features in evaporites. In *Sixth International Symposium on Salt* (ed. B. C. Schrieber and H. L. Harner), Alexandria, VA: Salt Institute, **1**, 11–39, 1985.

Harms, J. C., J. B. Southard, D. R. Spearing, and R. G. Walker, *Depositional Environments as Interpreted from Primary Sedimentary Structures and Stratification Sequences*, Tulsa: Society of Economic Mineralogists and Paleontologists, 161pp., 1975.

Harms, J. C., J. B. Southard, R. G. Walker, *Structures and Sequences in Clastic Rocks*, Tulsa: Society of Economic Mineralogists and Paleontologists, 253pp., 1982.

Head, J. W., R. Greeley, M. P. Golombek, *et al*., Geological processes and evolution, *Space Sci. Rev*. **96**, 263–92, 2001.

Head, J. W., J. F. Mustard, M. A. Kreslavsky, R. E. Milliken, and D. R. Marchant, Recent ice ages on Mars, *Nature* **426**, 797–802, 2003.

Henderson, J. B., Sedimentology of the Archean Yellowknife Supergroup at Yellowknife, District of Mackenzie, *Geol. Surv. Canada Bul*. **246**, **62**, 1975.

Herkenhoff, K. E., S. W. Squyres, R. Anderson, *et al*., Overview of the Microscopic Imager investigation during Spirit's first 450 sols in Gusev crater, *J. Geophys. Res*. **111**, E02S04, doi:10.1029/2005JE002574, 2006.

Hoffman, P. F., Stratigraphy of the Lower Proterozoic (Aphebian), Great Slave Supergroup, East Arm of Great Slave Lake, District of Mackenzie, *Geol. Surv. Canada Paper* **68**–42, 93pp., 1968.

Hoffman, P. F., Evolution of an early Proterozoic continental margin: the Coronation Geosyncline and associated aulacogens of the northwestern Canadian Shield, *Philos. Trans. R. Soc. Lond*., **A273**, 547–81, 1973.

Hofmann, H. J., P. C. Thurston, and H. Wallace, Archean stromatolites from Uchi greenstone belt, northwestern Ontario, *Geol. Assoc. Canada Spec. Paper* **28**, 125–32, 1985.

Hunter, R. E., Basic types of stratification in small eolian dunes, *Sedimentology* **24**, 361–87, 1977.

Hunter, R. E., Subaqueous sand-flow cross strata, *J. Sediment. Petrol*. **55**, 886–94, 1985.

Hurowitz, J. A. and S. M. McLennan, A ~3.5 Ga record of water-limited, acidic weathering conditions on Mars, *Earth Planet. Sci. Lett*. **260**, 432–43, 2007.

Hurowitz, J. A., S. M. McLennan, D. H. Lindsley, and M. A. A. Schoonen, Experimental epithermal alteration of synthetic Los Angeles meteorite: implications for the origin of Martian soils and the identification of hydrothermal sites on Mars, *J. Geophys. Res*. **110**, E07002, doi:10.1029/2004JE002391, 2005.

Hurowitz, J. A., S. M. McLennan, N. J. Tosca, *et al*., In-situ and experimental evidence for acidic weathering on Mars, *J. Geophys. Res*. **111**, E02S19, doi:10.1029/2005JE002515, 2006.

Hynek, B. M. and R. J. Phillips, New data reveal mature integrated drainage systems on Mars indicative of past precipitation, *Geology* **31**, 757–60, 2003.

Irwin III, R. P., R. A. Craddock, and A. D. Howard, Interior channels in Martian valley networks: discharge and runoff production, *Geology* **33**, 489–92, 2005.

Jakosky, B. M. and R. J. Phillips, Mars' volatile and climate history, *Nature* **412**, 237–44, 2001.

Jerolmack, D. J., D. Mohrig, M. T. Zuber, and S. Byrne, A minimum time for the formation of Holden Northesast fan, Mars, *Geophys Res. Lett*. **31**(21), L21701, doi:10.1029/2004GL021326, 2004.

Jerolmack, D. J., D. Mohrig, J. P. Grotzinger, D. A. Fike, and W. A. Watters, Spatial grain size sorting in eolian ripples and estimation of wind conditions on planetary surfaces: application to Meridiani Planum, Mars, *J. Geophys. Res*. **111**, E12S02, doi:10.1029/2005JE002544, 2006.

Jones, B. and R. W. Renaut, Water content of opal-A: implications for the origin of laminae in geyserite and sinter, *J. Sediment. Res*. **74**, 117–28, 2004.

Keller, J. M., W. V. Boynton, S. Karunatillake, *et al*., Equatorial and midlatitude distribution of chlorine measured by Mars Odyssey GRS, *J. Geophys. Res*. **111**, E03S08, doi:10.1029/2006JE002679, 2006.

Kieffer, H. H., B. M. Jakosky, C. W. Snyder, and M. S. Matthews (eds.), *Mars*, Tucson: Arizona University Press, 1498pp., 1992.

King, P. L., D. T. Lescinsky, and H. W. Nesbitt, The composition and evolution of primordial solutions on Mars, with application to other planetary bodies, *Geochim. Cosmochim. Acta* **68**, 4993–5008, 2004.

Klingelhöfer, G., R. V. Morris, B. Bernhardt, *et al*., Jarosite and hematite at Meridiani Planum from Opportunity's Mössbauer spectrometer, *Science* **306**, 1740–5, 2004.

Knauth, L. P., D. M. Burt, and K. H. Wohletz, Impact origin of sediments at the Opportunity landing site on Mars, *Nature* **438**, 1123–8, 2005.

Knoll, A. H., B. L. Jolliff, W. H. Farrand, *et al*., Late diagenetic veneers, rinds, and fracture fill at Meridiani Planum, Mars, *J. Geophys. Res*. in press, 2008.

Kocurek, G. and K. G. Havholm, Eolian sequence stratigraphy: a conceptual framework. In *Siliciclastic Sequence Stratigraphy, Am. Assoc. Pet. Geol. Memoir* 58 (ed. P. Weimer and H. W. Posamentier), pp. 393–409, Tulsa, OK. 1993.

Kolb, E. J. and K. L. Tanaka, Geologic history of the polar regions of Mars based on Mars Global Surveyor data: II. Amazonian Period, *Icarus* **154**, 22–39, 2001.

Laskar, J., B. Levrard, and J. F. Mustard, Orbital forcing of the martian polar layered deposits, *Nature* **419**, 375–7, 2002.

Laskar, J., A. C. M. Corrieia, M. Gastineau, *et al*., Long term evolution and chaotic diffusion of the insolation quantities of Mars, *Icarus* **170**, 343–54, 2004.

Lewis, K. and O. Aharonson, Characterization of the distributary fan in Holden NE crater using stereo analysis, *Lunar Planet. Sci. XXXV*, Houston: Lunar and Planetary Institute, Abstract #2083 (CD-ROM), 2004.

Lewis, K., O. Aharonson, J. P. Grotzinger, *et al*., Stratigraphy and structure of Home Plate from the Spirit Mars Exploration Rover, *J. Geophys. Res*. (Submitted), 2008.

Lowe, D. R., G. R. Byerly, F. T. Kyte, *et al*., Spherule beds 3.47–3.24 billion years old in the Barberton Greenstone Belt, South Africa: a record of large meteorite impacts and their influence on early crustal and biological evolution, *Astrobiology* **3**, 7–48, 2003.

Lucchitta, B. K., A. S. McEwen, G. D. Clow, *et al*., The canyon system on Mars. In *Mars* (ed. H. H. Kieffer, B. M. Jakosky, C. W. Snyder, and M. S. Matthews), Tucson: University of Arizona Press, pp. 453–92, 1992.

Malin, M. C. and K. S. Edgett, Sedimentary rocks of early Mars, *Science* **290**, 1927–37, 2000.

Malin, M. C. and K. S. Edgett, Evidence for persistent flow and aqueous sedimentation on early Mars, *Science* **302**, 1931–4, 2003.

Marion, G. M. and J. S. Kargel, Stability of magnesium sulfate minerals in martian environments, *Lunar Planet. Sci. XXXVI*, Houston: Lunar and Planetary Institute, Abstract #2290 (CD-ROM), 2005.

Marion, G. M., D. C. Catling, and J. S. Kargel, Modeling aqueous ferrous iron chemistry at low temperatures with application to Mars, *Geochim. Cosmochim. Acta* **67**, 4251–66, 2003.

McCollom, T. M. and B. M. Hynek, A volcanic environment for bedrock diagenesis at Meridiani Planum on Mars, *Nature* **438**, 1129–31, 2005.

McGlynn, J. C. and J. B. Henderson, Archean volcanism and sedimentation in the Slave structural province, *Geol. Surv. Canada Paper* **70**–40, 31–44, 1970.

McLennan, S. M., Recycling of the continental crust, *Pure Appl. Geophys. (PAGEOPH)* **128**, 683–724, 1988.

McLennan, S. M., Sedimentary silica on Mars, *Geology* **31**, 315–18, 2003.

McLennan, S. M., J. F. Bell III, W. Calvin, *et al*., Provenance and diagenesis of the evaporite-bearing Burns formation, Meridiani Planum, Mars, *Earth Planet. Sci. Lett*. **240**, 95–121, 2005.

McLennan, S. M., J. P. Grotzinger, J. A. Hurowitz, and N. J. Tosca, Sulfate geochemistry and the sedimentary rock record of Mars, *Workshop on Martian Sulfates as Records of Atmospheric-Fluid-Rock Interactions*, LPI Contribution No. 1331, Houston: Lunar and Planetary Institute, p. 54, 2006.

McSween Jr., H. Y. and K. Keil, Mixing relationships in the Martian regolith and the composition of globally homogeneous dust, *Geochim. Cosmochim. Acta* **64**, 2155–66, 2000.

Melosh, H. J. and A. M. Vickery, Impact erosion of the primordial atmosphere of Mars, *Nature* **338**, 487–9, 1989.

Metz, J. M., J. P. Grotzinger, D. M. Rubin, *et al*., Sulfate-rich eolian and wet interdune deposits, Erebus crater, Meridiani Planum, Mars, *J. Sediment. Petrol*. (submitted), 2008.

Meyers, W. J., Carbonate cement stratigraphy of the Lake Valley Formation, Mississippian, Sacramento mountains, New Mexico, *J. Sediment. Petrol*. **44**, 837–61, 1974.

Middleton, G. V. and J. B. Southard, *Mechanics of Sediment Movement*, Tulsa: Society of Economic Mineralogists and Paleontologists, 401pp., 1984.

Milliken, R. E., G. Swayze, R. Arvidson, *et al*., Spectral evidence for sedimentary silica on Mars, *Lunar Planet. Sci. XXXIX*, Houston: Lunar and Planetary Institute, Abstract #2025 (CD-ROM), 2008.

Millot, R., J. Gaillardet, B. Dupre, and C. J. Allègre, The global control of silicate weathering rates and the coupling with physical erosion: new insights from rivers on the Canadian Shield, *Earth Planet. Sci. Lett*. **196**, 83–98, 2002.

Montgomery, D. R. and D. R. Gillespie, Formation of Martian outflow channels by catastrophic dewatering of evaporite deposits, *Geology* **33**, 625–8, 2005.

Moore, J. M. and A. D. Howard, Large alluvial fans on Mars, *J. Geophys. Res*. **110**, E04005, 2005.

Moore, J. M., A. D. Howard, W. E. Dietrich, and P. M. Schenk, Martian layered fluvial deposits: implications for Noachian climate scenarios, *Geophys. Res. Lett*. **30**(24), 2292, doi:10.1029/2003GL019002, 2003.

Morris, R. V., D. C. Golden, J. F. Bell III, *et al*., Mineralogy, composition, and alteration of Mars Pathfinder rocks and soils: evidence from multispectral, elemental, and magnetic data on terrestrial analogue, SNC meteorite, and Pathfinder samples, *J. Geophys. Res*. **105**, 1757–817, 2000.

Morris, R. V., D. W. Ming, T. G. Graff, *et al*., Hematite spherules in basaltic tephra altered under aqueous, acid-sulfate conditions on Mauna Kea volcano, Hawaii: possible clues for the occurrence of hematite-rich spherules in the Burns formation at Meridiani Planum, Mars, *Earth Planet. Sci. Lett*. **240**, 168–78, 2005.

Morris, R. V., G. Klingelhöfer, C. Schröder, *et al*., Mössbauer mineralogy of rock, soil, and dust at Meridiani Planum, Mars: Opportunity's journey across sulfate-rich outcrop, basaltic sand and dust, and hematite lag deposits, *J. Geophys. Res*. **111**, E12S15, doi:10.1029/2006JE002791, 2006.

Morse, J. W. and G. M. Marion, The role of carbonates in the evolution of early martian oceans, *Am. J. Sci*. **299**, 738–61, 1999.

Murray, J. B., J. P. Muller, G. Neukum, *et al*., Evidence from the Mars Express High Resolution Stereo Camera for a frozen sea close to Mars' equator, *Nature* **434**, 352–6, 2005.

Nesbitt, H. W. and R. E. Wilson, Recent chemical weathering of basalts, *Am. J. Sci*. **292**, 740–77, 1992.

Nesbitt, H. W. and G. M. Young, Prediction of some weathering trends of plutonic and volcanic rocks based on thermodynamic and kinetic considerations, *Geochim. Cosmochim. Acta* **48**, 1523–34, 1984.

Newsom, H. E. and J. J. Hagerty, Chemical components of the martian soil: melt degassing, hydrothermal alteration, and chondritic debris, *J. Geophys. Res*. **102**, 19345–55, 1997.

Newsom, H. E., G. E. Brittelle, C. A. Hibbitts, *et al*., Impact crater lakes on Mars, *J. Geophys. Res*. **101**, 14951–5, 1996.

Nimmo, F. and K. Tanaka, Early crustal evolution of Mars, *Annu. Rev. Earth Planet. Sci*. **33**, 133–61, 2005.

Pettijohn, F. J., Archean sedimentation, *Geol. Soc. Am. Bull*. **54**, 925–72, 1943.

Phillips, R. J., M. T. Zuber, S. C. Solomon, *et al*., Ancient geodynamics and global-scale hydrology on Mars, *Science* **291**, 2587–91, 2001.

Pitzer, K. S., Ion interaction approach: theory and data correlation. In *Activity Coefficients in Electrolyte Solutions* (ed. K. S. Pitzer), Boca Raton: CRC Press, pp. 75–154, 1991.

Pollack, J. B., J. F. Kasting, S. M. Richardson, and K. Polliakoff, The case for a warm, wet climate on early Mars, *Icarus* **71**, 203–24, 1987.

Poulet, F., J.-P. Bibring, J. F. Mustard, *et al*., Phyllosilicates on Mars and implications for early martian climate, *Nature* **438**, 623–7, 2005.

Ronov, A. B., *The Earth's Sedimentary Shell: Quantitative Patterns of its Structure, Compositions, and Evolution*, Reprint Series V, Falls Church, VA: American Geological Institute, 80pp., 1983.

Rubin, D. M., Formation of scalloped cross-bedding without unsteady flows, *J. Sediment. Res*. **57**, 39–45, 1987.

Schenk, C. J. and S. G. Fryberger, Early diagenesis of eolian dune and interdune sands at White Sands, New Mexico, *Sediment. Geol*. **55**, 109–20, 1988.

Schopf, J. W. and B. M. Packer, Early Archean (3.3-billion-year-old) microfossils from Warrawoona Group, Australia, *Science* **237**, 70–3, 1987.

Schopf, J. W., D. Z. Oehler, R. J. Horodyski, and K. A. Kvenvolden, Biogenecity and significance of the oldest known stromatolites, *J. Paleontol.* **45**, 477–85, 1971.

Schrieber, B. C. and M. El Tabakh, Deposition and early alteration of evaporites, *Sedimentology* **47**(Suppl. 1), 215–38, 2000.

Settle, M., Formation and deposition of volcanic sulfate aerosols on Mars, *J. Geophys. Res.* **84**, 8343–54, 1979.

Sharp, R. P., Wind ripples, *J. Geol.* **71**, 617–36, 1963.

Shoemaker, E. M. and S. W. Kieffer, *Guidebook to the Geology of Meteor Crater, Arizona*, Tempe, Arizona State University, Center for Meteorite Studies, 66pp., 1974.

Sleep, N. H., Martian plate tectonics, *J. Geophys. Res.* **99**, 5639–56, 1994.

Smith, G. A. and D. Katzman, Discrimination of eolian and pyroclastic-surge processes in the generation of cross-bedded tuffs, Jemez Mountains volcanic field, New Mexico, *Geology* **19**, 465–8, 1991.

Southard, J. B., Flume experiments on transition from ripples to lower flat bed with increasing sand size, *J. Sediment. Petrol.* **43**, 1114–21, 1973.

Southard, J. B. and L. A. Boguchwal, Bed configurations in steady unidirectional flows. Part 3. Effects of temperature and gravity, *J. Sediment. Petrol.* **60**, 680–6, 1990a.

Southard, J. B. and L. A. Boguchwal, Bed configurations in steady unidirectional flows. Part 2. Synthesis of flume data, *J. Sediment. Petrol* **60**, 658–79, 1990b.

Squyres, S. W. and A. H. Knoll, Sedimentary rocks at Meridiani Planum: origin, diagenesis, and implications for life on Mars, *Earth Planet. Sci. Lett.* **240**, 1–10, 2005.

Squyres, S. W., R. Arvidson, J. F. Bell III, *et al.*, The Opportunity rover's Athena science investigation at Meridiani Planum, Mars, *Science* **306**, 1698–703, 2004a.

Squyres, S. W., R. Arvidson, J. F. Bell III, *et al.*, The Spirit rover's Athena science investigation at Gusev crater, Mars, *Science* **305**, 794–9, 2004b.

Squyres, S. W., A. N. Knoll, R. E. Arvidson, *et al.*, Two years at Meridiani Planum: Results from the Opportunity rover, *Science* **313**, 1403–7, 2006a.

Squyres, S. W., R. E. Arvidson, D. L. Blaney, *et al.*, Rocks of the Columbia Hills, *J. Geophys. Res.* **111**, E02S11, doi:10.1029/2005JE002562, 2006b.

Squyres, S. W., O. Aharonson, B. C. Clark, *et al.*, Pyroclastic activity at Home Plate in Gusev crater, *Science*, **316**, 738–42, 2007a.

Squyres, S. W. and the Athena Science Team, Recent results from the Spirit rover at Home Plate and "Silica Valley", *EOS Trans. AGU* **88**(52), Fall Meeting, Suppl., Abstract P21C-01, 2007b.

Sullivan, R., D. Banfields, J. F. Bell III, *et al.*, Aeolian processes at the Mars Exploration Rover Meridiani Planum landing site, *Nature* **436**, 58–61, 2005.

Sumner, D. Y. and J. P. Grotzinger, Were kinetics of Archean calcium carbonate precipitation related to oxygen concentration?, *Geology* **24**, 119–22, 1996.

Tanaka, K. L., N. K. Isbell, D. H. Scott, R. Greeley, and J. E. Guest, The resurfacing history of Mars: a synthesis of digitized, Viking-based geology, *Proc. Lunar Sci. Conf. XVIII*, 665–78, 1988.

Taylor, S. R. and S. M. McLennan, *The Continental Crust: Its Composition and Evolution*, Oxford: Blackwells, 312pp., 1985.

Taylor, G. J., W. Boynton, J. Brückner, *et al.*, Bulk composition and early differentiation of Mars, *J. Geophys. Res.* **111**, E03S10, doi:10.1029/2005JE002645, 2006.

Thomas, P., S. Squyres, K. Herkenhoff, A. Howard, and B. Murray, Polar deposits of Mars. In *Mars* (ed. H. H. Kieffer, B. M. Jakosky, C. W. Snyder, and M. S. Matthews), Tucson: University of Arizona Press, pp. 767–95, 1992.

Tosca, N. J. and S. M. McLennan, Chemical divides and evaporite assemblages on Mars, *Earth Planet. Sci. Lett.* **241**, 21–31, 2006.

Tosca, N. J., S. M. McLennan, D. H. Lindsley, and M. A. A. Schoonen, Acid-sulfate weathering of synthetic Martian basalt: the acid fog model revisited, *J. Geophys. Res.* **109**, E05003, doi:10.1029/2003JE002218, 2004.

Tosca, N. J., S. M. McLennan, B. C. Clark, *et al.*, Geochemical modeling of evaporation processes on Mars: insight from the sedimentary record at Meridiani Planum, *Earth Planet. Sci. Lett.* **240**, 122–48, 2005.

Tosca, N. J., A. Smirnov, and S. M. McLennan, Application of the Pitzer ion interaction model to isopiestic data for the $Fe_2(SO_4)_3$–H_2SO_4–H_2O system at 298.15 K and 323.15 K, *Geochim. Cosmochim. Acta* **71**, 2680–98, 2007.

Veizer, J. and S. L. Jansen, Basement and sedimentary recycling and continental evolution, *J. Geol.* **87**, 341–70, 1979.

Veizer, J. and S. L. Jansen, Basement and sedimentary recycling: 2. Time dimension to global tectonics, *J. Geol.* **93**, 625–43, 1985.

Veizer, J. and F. T. Mackenzie, Evolution of sedimentary rocks, *Treatise on Geochemistry* **7**, 369–407, 2003.

Walker, R. G., The origin and significance of the internal sedimentary structures of turbidites, *Proc. Yorkshire Geol. Soc.* **35**, 1–32, 1965.

Walker, R. G. and F. J. Pettijohn, Archaean sedimentation: analysis of Minnitaki Basin, Northwestern Ontario, Canada, *Geol. Soc. Am. Bull.* **82**, 2099–130, 1971.

Wang, A., R. L. Korotev, B. L. Jolliff, *et al.*, Evidence of phyllosilicates in Wooly Patch, an altered rock encountered at West Spur, Columbia Hills, by the Spirit rover in Gusev crater, Mars, *J. Geophys. Res.* **111**, E02S16, doi:10.1029/2005JE002516, 2006a.

Wang, A., L. A. Haskin, S. W. Squyres, *et al.*, Sulfate deposition in subsurface regolith in Gusev crater, Mars, *J. Geophys. Res.* **111**, E02S17, doi:10.1029/2005JE002513, 2006b.

Webb, V. E., Putative shorelines in northern Arabia Terra, Mars, *J. Geophys. Res.* **109**, E09010, doi 10.1029/2004JE002205, 2004.

White, A. F. and S. L. Brantley (eds.), Chemical weathering rates of silicate minerals, *Rev. Mineral.* **31**, 583pp., 1995.

White, J. D. L., Depositional architecture of a maar-pitted playa: sedimentation in the Hopi Buttes volcanic field, northeastern Arizona, U.S.A., *Sediment. Geol.* **67**, 55–83, 1990.

Wiberg, P. L. and J. D. Smith, Calculations of the critical shear stress for motion of uniform and heterogeneous sediments, *Water Resour. Res.* **23**, 1471–80, 1987.

Yen, A. S., J. P. Grotzinger, R. Gellert, *et al.*, Evidence for halite at Meridiani Planum, *Lunar Planet. Sci. XXXVII*, Houston: Lunar and Planetary Institute, Abstract #2128, (CD-ROM), 2006.

25

Martian polar processes

T. N. TITUS, W. M. CALVIN, H. H. KIEFFER, Y. LANGEVIN, AND T. H. PRETTYMAN

ABSTRACT

The polar caps are the most active regions on Mars. The annual cycling of atmospheric CO_2 into the seasonal CO_2 ice caps is a driving force of the Martian climate. The polar layered deposits (PLDs), with thousands of layers whose thickness is only resolvable with sub-meter spatial resolution from orbit, may contain a record of past climates. The polar regions contain the majority of known H_2O ice deposits, distributed between the residual caps and near-surface ice in the regolith. In this chapter, we synthesize results from missions and instruments largely presented in detail elsewhere in this book, and consider the implications for Martian polar processes and the areas for future research. The focus here is on presenting evidence for and interpretations concerning the CO_2 cycle and other related polar processes. Implications for water-ice in the subsurface are examined with respect to its effects on the CO_2 cycle. Comparisons of water-ice abundance to the mass and distribution of seasonal CO_2 ice are also explored. While the amount of available data has increased exponentially, our knowledge and understanding of Martian polar processes has increased much more gradually. As each question about the polar regions of Mars is answered, several new questions are brought to light. Many of the processes that occur in the polar regions of Mars do not have direct analogs on Earth, but do have analogs in other parts of the Solar System. If we are to understand the history of Mars, and by association, the evolution of Earth within our Solar System, we must understand the polar regions. We conclude the chapter with a review of those questions that have at least been partially answered since 1992, as well as those questions where the answers still elude us.

25.1 INTRODUCTION

25.1.1 Historical overview

The history of Mars polar cap observations through the Viking era, with the now well-known seasonal deposition of CO_2 ice, is summarized in *Mars*, the University of Arizona Press book, in chapters by James *et al*., (1992) and Jakosky and Haberle (1992). Briefly, a long history of telescopic observations of the polar regions of Mars showed that the seasonal cycle, as expressed by the location of the cap edge, closely repeats from year to year. The caps were assumed to be water ice until shortly before the era of spacecraft observations. Prediction that the CO_2 atmosphere should condense in the winter (Leighton and Murray, 1966) was confirmed by Mariner 7 infrared spectrometer observations that recorded the appearance of forbidden transitions of CO_2 ice (Herr and Pimentel, 1969) and telescopic spectral observations by Larson and Fink (1972). It is this process of the CO_2 atmosphere condensing out as snow and ice onto the surface during autumn and winter and then subliming back into the atmosphere in the spring that drives the current Martian climate. Roughly 25% of the atmosphere, which is 95% CO_2 by volume, is cycled through the seasonal caps annually (Tillman *et al*., 1993; Forget and Pollack, 1996; Kelly *et al*., 2006). This CO_2 cycle dominates atmospheric circulation on Mars and must be thoroughly understood before the fundamental questions about Mars' climate history and the global distribution of near-surface water can be addressed.

25.1.2 Nomenclature

As observations of Mars expand to higher spatial resolutions and to a wider range of data types (e.g., radar, neutrons, gamma rays), conflicting or vague terminology may lead to confusion with regard to surface features and phenomena. Throughout this chapter, we will use the commonly used nomenclature and terminology as laid out by the US Geological Survey (Herkenhoff *et al*., 2006), in which seasonal deposits overlie residual or permanent ice. In both the northern and southern hemispheres, layered deposits, which include non-ice materials, underlie the icy caps and separate them from the surrounding plains.

25.2 THE POLAR ENERGY BALANCE

The amount, rate, and distribution of CO_2 condensation/sublimation is determined by the balance of several energy sources and sinks, including insolation (exposure to sunlight), net radiative loss to space, the latent heat of fusion, summertime heat storage in the regolith, and atmospheric storage and transport of energy. Mars climate models attempt to replicate this energy balance through a variety of physical processes. For recent summaries and detailed physical descriptions, see Pollack *et al*. (1993), Hourdin *et al*. (1995), and Forget *et al*. (1998, 1999). We only briefly

The Martian Surface: Composition, Mineralogy, and Physical Properties, ed. J. F. Bell III. Published by Cambridge University Press.

summarize the various contributions to the energy balance here.

25.2.1 Albedo effects and feedback

Surface albedo is inversely proportional to energy absorbed; hence, sublimation depends on surface processes such as ice grain size, water and dust contamination, and photometric effects (solar illumination and surface scattering function). As a general rule, the seasonal caps are brighter in late spring than they are in early spring. This is true for both the northern and the southern caps, with the notable exception of the so-called "cryptic region" (discussed in Section 25.5.3 below) located within the southern seasonal cap (Kieffer *et al.*, 2000). Possible causes include seasonal brightening with increased solar insolation (and other photometric effects), and cold trapping of water vapor into frost (Paige, 1985; Houben *et al.*, 1997). The north polar region is generally richer in water ice than the south polar region; migration of H_2O is observed along the edge of the retreating northern seasonal cap (Kieffer and Titus, 2001; Schmitt *et al.*, 2005a,b; Titus, 2005a; Wagstaff *et al.*, 2007). While the Mars Express Observatoire pour la Minéralogie, l'Eau, les Glaces et l'Activité (OMEGA) near-infrared (NIR) imaging spectrometer observed H_2O as a component of the southern retreating seasonal cap (e.g., Langevin *et al.*, 2005), those observations do not reveal large scale H_2O ice lags on the edge of the cap. Possible ice lags are seen at the end of the southern cap retreat, but these could also be an artifact of subpixel mixing of remnant CO_2 ice and dust (Titus, 2005b; Douté *et al.*, 2007). The third possible process, photometric effects, has not been fully explored. For most studies, CO_2 ice has simply been assumed to be Lambertian (Paige, 1985; Paige and Ingersoll, 1985; James *et al.*, 2005).

25.2.2 Atmospheric effects, clouds, and surface emissivity

In addition to surface albedo, the temperatures observed by orbiting spacecraft reflect surface temperature, surface emissivity, and the atmospheric temperature and opacity profiles. A hot and dusty or warm and cloudy atmosphere will increase both the radiative losses to space as well as increase the downwelling radiation on the surface. During the polar night, when the insolation is zero, both surface emissivity and atmospheric opacity can significantly modify the energy budget. The primary factors that influence surface emissivity are CO_2 grain size and purity. The major influence from the atmosphere is that an increase in aerosol opacity can reduce the radiative losses to space.

Results from the Mars Global Surveyor (MGS) Mars Orbiter Laser Altimeter (MOLA; Neumann *et al.*, 2003), Thermal Emission Spectrometer (TES; Pearl *et al.*, 2001), and Radio Science experiments (Tyler *et al.*, 2001; Hinson and Wilson, 2002) all indicate that there is significant CO_2 cloud cover during the polar night at both poles. Much of the cloud cover is in the form of dust-free haze, often with a component of H_2O ice, as opposed to stratified clouds (Pearl *et al.*, 2001). Supercooled conditions can arise, causing instability and strong convection currents (Colaprete *et al.*, 2008). The exact effects of this process on the energy balance are still poorly constrained. Nonetheless, these new observations do provide a context for many previous observations, dating back to the first spacecraft to observe the polar night.

Early spacecraft observations of the polar regions revealed brightness temperatures significantly lower than the expected kinetic temperature (~140 K) for CO_2 ice in equilibrium with a CO_2 atmosphere (Kieffer *et al.*, 1976). These cold areas or cold spots were typically a few hundred kilometers in diameter, with 20 μm brightness temperatures as low as 130 K and typical lifetime of a few days (Kieffer *et al.*, 1976). Plausible suggestions for the cause of the cold spots included high-altitude CO_2 clouds (Hunt, 1980), surface CO_2 snow, and low partial pressures of CO_2. Hess (1979) showed that low partial pressure (i.e., an increase in the mixing ratio of inert gases) at the surface was dynamically unstable and would mix to the top of the atmosphere. Forget *et al.* (1995) were able to fit Mariner 9 IRIS spectra with a combination of fine-grained CO_2 snow and a thin layer of warmer water clouds. They suggested that the cold spots were freshly deposited CO_2 snow or perhaps CO_2 condensates high in the atmosphere. More recently, instruments on board MGS, Mars Odyssey, and Mars Express have all observed high-altitude clouds (Ivanov and Muhleman, 2001; Montmessin *et al.*, 2006). While a small fraction of the cold spots could be "dry-ice blizzards" in progress, these snow storms are short-lived, perhaps only a few hours. Condensation models instead suggest that most of the cold spots observed are the result of surface emissivity effects that appear to be a result of these storms (Hansen, 1999; Titus *et al.*, 2001). Because the snow that remains once the storms pass can be observed as cold spots for up to several weeks, they can affect the long-term energy balance within the polar night.

25.2.3 Regolith and near-surface ice

Most energy balance studies have followed the example of Leighton and Murray (1966) and ignored the contribution of the regolith (e.g., Kieffer *et al.*, 2000). The discovery of high concentrations of near-surface H_2O ice at high latitudes (see Chapters 5 and 6) has brought into question this assumption. Studies (e.g., Paige and Ingersoll, 1985; Haberle *et al.*, 2004; Kieffer, 2007) have shown that the energy balance, and thus the accumulation of seasonal CO_2, can be greatly affected by the presence of ice. H_2O ice can strongly influence the surface thermal inertia (see Chapter 18), delaying the formation of seasonal CO_2 frost and reducing net accumulation.

25.2.4 Atmospheric transport

The final contribution to the atmosphere energy balance discussed here is heat capacity and lateral transport. The heat capacity of the atmosphere is small, and thus its contribution can generally be neglected. However, the lateral transport of heat is not well constrained and could be quite large, depending on the location and season. For example, a study by Haberle *et al.* (2004) suggests that the atmospheric

transport contribution may be the same order of magnitude as the heat storage contribution from an icy regolith.

A quantitative analysis of the abundance of noncondensable gases has been carried out by Prettyman *et al.* (2004) using neutron spectroscopy (thermal- and epithermal-counting data) and by Sprague *et al.* (2004) using gamma ray spectroscopy. The abundance of noncondensable gases increases rapidly as CO_2 is deposited at high latitudes. This is likely the result of the formation of a strong polar vortex accompanying the condensation flow and inhibiting meridional mixing of the polar atmosphere with lower latitudes. The magnitude of the enrichment observed during the advance was used to estimate coefficients for eddy diffusion by Sprague *et al.* (2004). During the recession, CO_2 subliming from the cap mixes with the atmosphere, resulting in depletion of noncondensable gases. While one of the early hypotheses of cold spot formation was the reduction of the CO_2 partial pressure (or an increase in the mixing ratio of inert gases like Ar), the observed enhancement of Ar (approximately a factor of 6 in the south) is only sufficient to depress the CO_2 frost temperature by $\sim 2^\circ$. The effects of inert gas enrichments in the north are even smaller, due to a weaker polar vortex. Observations such as these, along with additional modeling, may provide insights and constraints on atmospheric dynamics and transport.

25.3 SPECTRAL PROPERTIES OF MARTIAN ICES

As described in Chapter 2, both water and CO_2 ice have strongly varying spectroscopic properties with wavelength. Small amounts of water or dust in CO_2 ice can dramatically change the reflectivity and emissivity, thus modifying the energy balance of the seasonal frost cap.

The optical constants for CO_2 ice have been measured over the solar reflectance and thermal emission ranges by Hansen (1997, 2005), and measurements of the strong lines have been made by Quirico and Schmitt (1997). Laboratory measures of the spectral properties of H_2O over a wide wavelength range were compiled by Warren (1984), and important spectral variations with temperature were measured by Grundy and Schmitt (1998). In addition, optical constants for Martian dust have been derived from both down-looking satellite observations (Clancy *et al.*, 1995; Clancy *et al.*, 2003; Wolff and Clancy, 2003; Wolff *et al.*, 2006) and landed observations of both the surface and atmosphere (Pollack *et al.*, 1995; Ockert-Bell *et al.*, 1997; Markiewicz *et al.*, 1999; Tomasko *et al.*, 1999; Bell *et al.*, 2000; Lemmon *et al.*, 2004). While these dust spectral shapes appear to be adequate for modeling dirty ice deposits, one must be careful. For example, there is an order of magnitude difference between the VIS/NIR (VIS – Visible wavelengths) optical constants of Lemmon *et al.* (2004) and the commonly used optical constants of Clancy *et al.* (1995). Nonetheless, many spectral modeling efforts have taken advantage of these recently derived optical constants, combined with modern scattering models (Hapke, Mie, delta-Eddington), and the models often match well with observations (e.g., Calvin, 1990; Grundy *et al.*, 1999; Kieffer *et al.*, 2000; Glenar *et al.*, 2005; Hansen *et al.*, 2005; Langevin *et al.*, 2006).

Example spectra of CO_2 ice, H_2O ice, dust, and mixtures of these components are shown in Figures 25.1 and 25.2. Particle scattering properties were computed from Mie theory (intimate mixtures), and the surface reflectance was computed using a two-stream delta-Eddington model (Kieffer *et al.*, 2000). Pure CO_2 has low absorption coefficients in the solar reflected wavelength region, so that small amounts of H_2O or dust have a large effect on the reflectance. For example, in the 1.5–2.5 μm region, only 0.1% fine dust or 1% fine H_2O will lower the reflectance about 25%; at visible wavelengths only dust can darken CO_2 frosts. In the thermal IR, CO_2 grain size has a large effect on emissivity. For example, fine dust (typical atmospheric-particle sized) at the 0.1% level will raise the emissivity in the 25 μm band to 0.85, and sand-sized (0.25 mm) particles of either rock or H_2O can dominate the spectrum of coarse-grained CO_2.

Both the OMEGA instrument and the Compact Reconnaissance Imaging Spectrometer for Mars (CRISM) on the Mars Reconnaissance Orbiter observe these polar deposits in the wavelength range where multiple, diagnostic features can separate H_2O and CO_2 ices. Initial analyses have shown evidence for the evolution of water frost grain size in the residual ice cap (Langevin *et al.*, 2005) and allow the determination of effective grain size and level of ice and dust contamination. Using the full spectral capabilities of these instruments is an area of active research and study that has only just begun.

25.4 ACTIVE PROCESSES: THE ANNUAL CYCLE

Because the Martian atmosphere is so thin, its heat capacity and thermal-transport capability compared to the Earth's atmosphere and ocean is miniscule. That fact and the planet's greater distance from the Sun result in the cooling of the Martian winter atmosphere to its condensation point. The resulting condensation of CO_2 near the poles (in seasonal amounts up to six times the columnar mass of the atmosphere) drives a net CO_2 circulation, with concomitant zonal transport of H_2O and dust. The result of a full annual cycle is quite different for these three materials: CO_2 processes are reversible and the cycle is virtually closed; H_2O and dust can form condensation nuclei for CO_2 and be carried into the seasonal cap; H_2O returns to the vapor state and becomes mobile after all the CO_2 is gone. Dust probably becomes partially trapped and is included in the PLDs by as-yet unknown processes. The CO_2 condensation rates and the transport of H_2O and dust are becoming treated by increasingly competent and complex General Circulation Models (GCMs).

There is the potential for many positive and negative feedback processes in these annual cycles (some of which we discuss here). Presumably, natural processes would drive

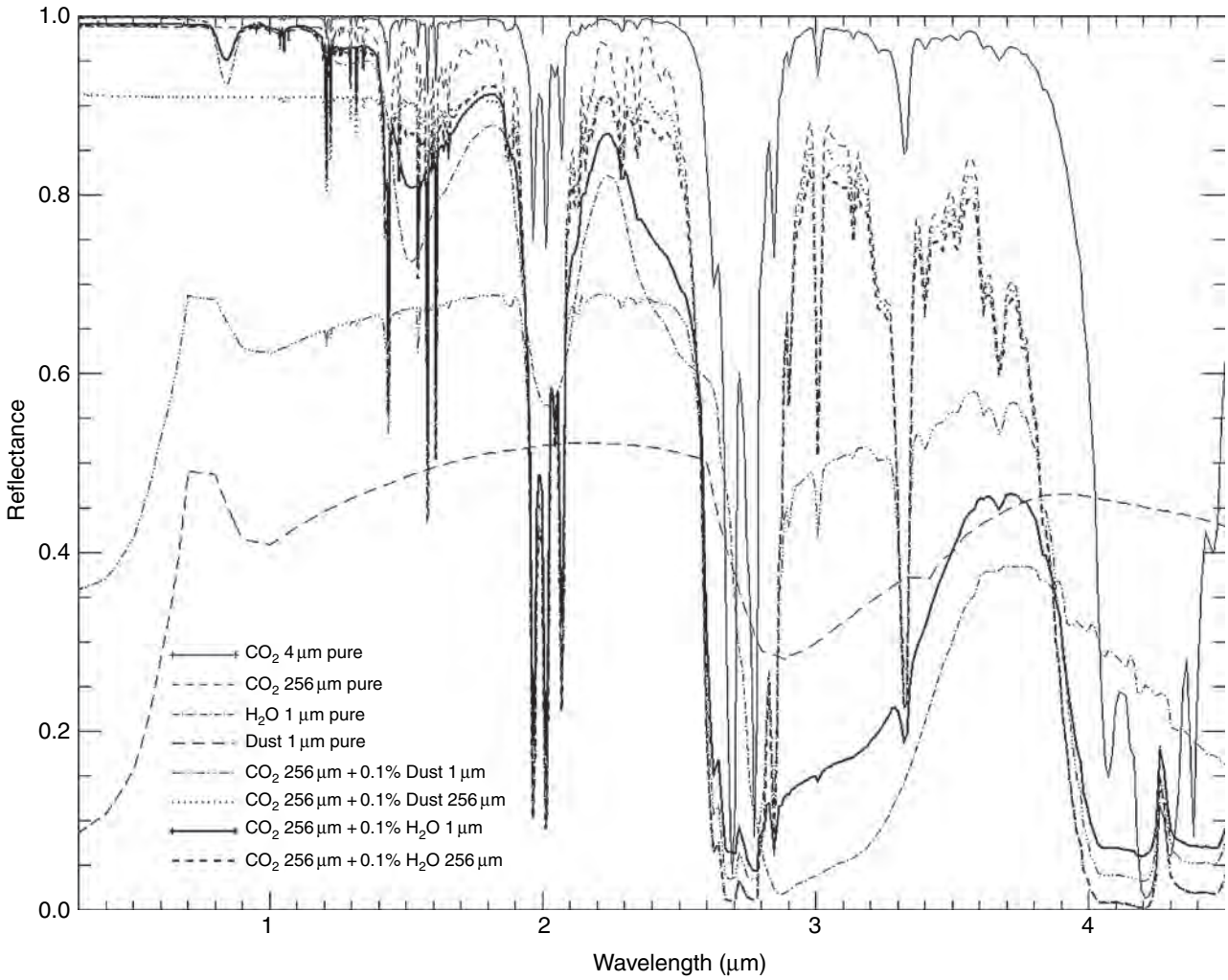

Figure 25.1. Computed spectra of polar ice components and mixtures, in the solar reflected wavelength region. Values are the Bond albedo for thick materials computed using Mie theory and a delta-Eddington radiative transfer model. Complex indices of refractions for CO_2 ice are based on Hansen (1997, 2005); for H_2O on Warren (1984), with the near-IR replaced with the temperature-dependent measurements of Grundy and Schmitt (1998) at 190 K and for dust (Wolff *et al.*, 2006). The solar incidence angle was set to 60°. The compositions, minor mass fractions, and grain radii in μm are listed in the legend. Pure CO_2 is shown for grain radii of 4 and 256 μm; pure H_2O and pure dust each are for radii of 1 μm, representative of atmospheric values. The large effects of admixtures of 0.1% (by mass) dust and H_2O of these size aerosols are shown for 256 μm-sized grains of CO_2. The effects for larger grains of dust and H_2O are considerably less at the same mass fractions.

Mars to a state where these all balance and the net effect of a mean annual cycle is virtually zero. However, the presence of major changes in the insolation cycle due to periodic changes in Mars spin orientation and orbital parameters (e.g., Ward and Rudy, 1991) may result in a continuing imbalance. It is difficult for us to estimate the magnitude of this imbalance because although we know the period and magnitude of the driving insolation variations (at least for the last few million years), we know little about the timescales of the equilibrating processes.

Given the finely layered appearance of the PLDs, the large exchange of carbon dioxide between the atmosphere and the seasonal caps, and the known presence of water in both seasonal and residual caps, three major components appear to control the current Martian climate and have influenced the formation and evolution of the ice caps and their underlying layered terrains. These are the carbon dioxide, water, and dust cycles. These are often treated separately in GCMs, but all contribute to evolution of the polar regions as observed. While we will not explicitly discuss the dust cycle in this chapter, the reader should be aware that the dust cycle impacts the polar regions by changing the albedo and emissivity of CO_2 ice and by changing the energy balance of the planet by scattering solar insolation back into space during global and regional dust storms. Also, some of the dust that is incorporated into the seasonal caps may eventually become part of the PLDs. For more summaries and details about the dust cycle, see Kahn *et al.* (1992), Basu *et al.* (2004), and Kahre *et al.* (2006).

25.4.1 CO_2 transport

Mars' northern and southern seasonal polar caps are formed during their respective autumn and winter seasons both by

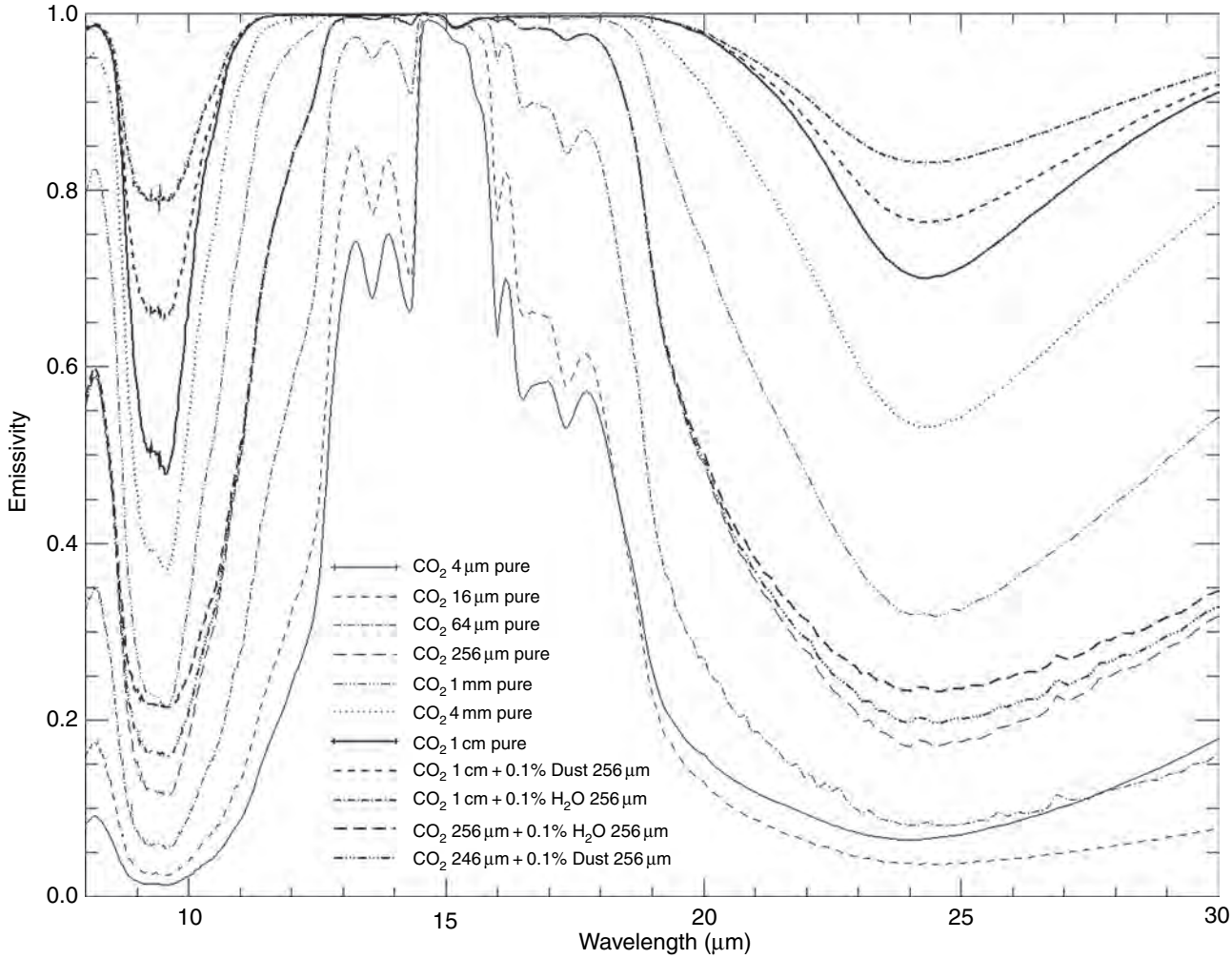

Figure 25.2. Computed spectra of polar ice components and mixtures in the thermal emission wavelength region. Values are the zenith emissivity (1 – Bond albedo); otherwise conditions are as stated in Figure 25.1. The progression of the 25 μm band as a function of grain size is shown for pure CO_2; the similar feature at 9.5 μm is difficult to utilize on Mars because of the strong spectral absorption of dust in the atmosphere. The effect of admixtures of 0.1% (by mass) dust and H_2O are shown for 1 cm-sized CO_2 (uppermost three curves: top is with H_2O, middle is with dust, bottom is pure CO_2); the three curves with minima near 0.2 that converge on both sides of the strong CO_2 bands near 15 μm show the effect of the same admixtures for CO_2 grain sizes of 256 μm.

condensation of atmospheric CO_2 directly onto the surface and through atmospheric precipitation in the form of CO_2 snow. During the polar spring and summer, the seasonal ice sublimes, returning CO_2 to the atmosphere. James *et al.* (1992) summarized the seasonal flow of carbon dioxide between the north and south polar caps based mainly on Mariner and Viking data. Considerable amounts of new data from MGS, Mars Odyssey, and Mars Express have added to our understanding of the CO_2 cycle, which is discussed in Section 25.5.

25.4.2 H_2O transport

Water is currently known to reside in the residual ice caps, at shallow depth in the regolith, and in the atmosphere. Among the major unresolved questions is the exchange of water between these reservoirs; what amounts and timescales are involved? Water is known to occur as both vapor and ice clouds (e.g., Jakosky, 1985), and was seen to condense at lower latitudes at the Viking landing site (Jones *et al.*, 1979; Wall, 1981; Svitek and Murray, 1990). An annulus of water ice follows the retreat of the northern seasonal cap (Kieffer and Titus, 2001; Langevin *et al.*, 2006), and water-ice lags may also persist after the retreat of CO_2 frost in the south (Titus, 2005b). Water ice at the edges of the re-entrant valleys of the south residual cap has been mapped by OMEGA (Bibring *et al.*, 2004). Water-ice clouds form the north polar hood, which can extend as far south as 48° N (Zasova *et al.*, 2005) and can begin to obscure the residual cap as early as L_s ~167° (L_s is the heliocentric longitude of Mars in its orbit measured from Vernal Equinox; Wang and Ingersoll, 2002) with the onset of seasonal CO_2 frost deposition. Clouds and other weather are seen to form repeatable patterns from year to year (Cantor *et al.*, 2002).

Smith (2002) presented the MGS-TES view of water vapor in the atmosphere. Peak atmospheric water vapor is noted in the north at L_s ~120°, with consistent values over two Martian northern summers. In contrast, water over the southern cap is highly variable (as seen by Smith [2004], and inferred from earlier observations [Barker *et al.*, 1970;

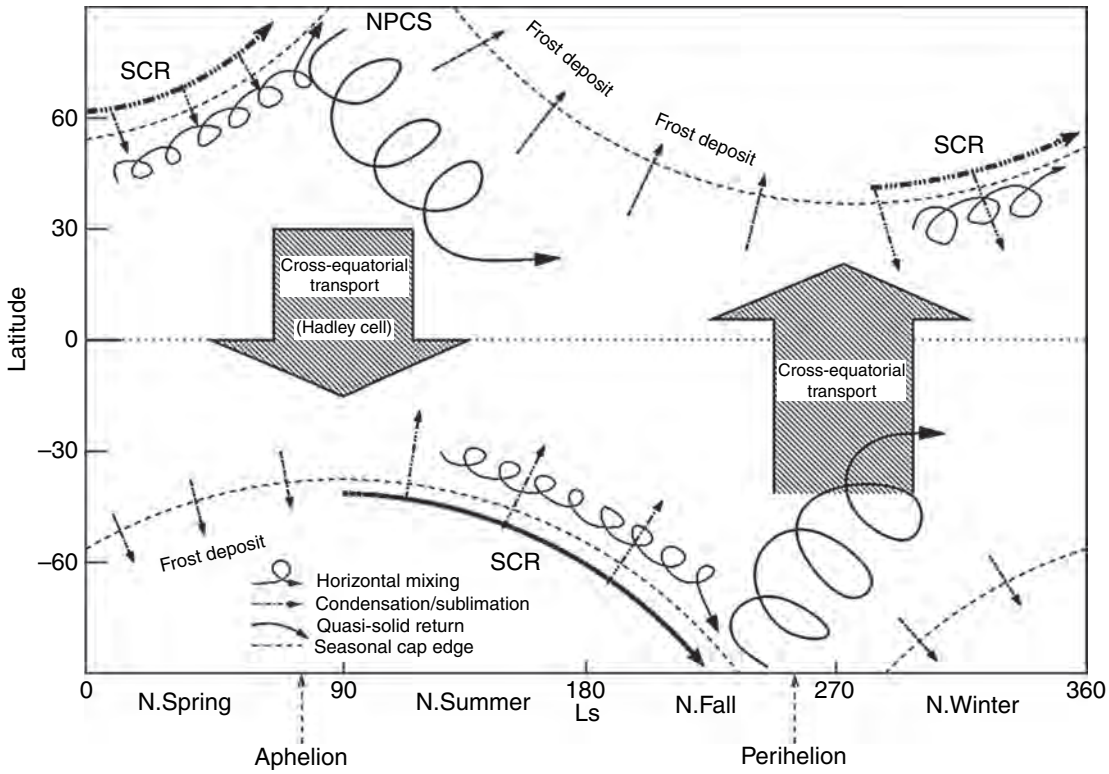

Figure 25.3. The components of the H_2O cycle, including the migration of H_2O ice along the edge of the retreating seasonal caps (Montmessin *et al.*, 2004). SCR: Seasonal Cap Retreat; NPCS: North Polar Cap Sublimation.

Jakosky and Haberle, 1990; Titov, 2002]). This suggests that a water cap underlies the residual CO_2 ice in the south, with a highly variable history of exposure and sublimation. Models suggest that the amount of water sublimated from the north residual cap is insufficient to account for the peak amounts seen in the atmosphere (100 precipitable μm in the north and 50 precipitable μm in the south), and that regolith exchange must also contribute to the observed atmospheric reservoir in the northern summer (Jakosky, 1983a,b; Jakosky *et al.*, 1997). The Mars Odyssey Gamma Ray Spectrometer/Neutron Spectrometer (GRS/NS) results have been interpreted to indicate a vast mid- to high-latitude subsurface reservoir of ice-permeated ground, supporting this view (Boynton *et al.*, 2002; Feldman *et al.*, 2004; see also Chapters 5 and 6), yet the amount of ice actively in exchange with the atmosphere has not been well constrained. While GRS/NS results show large amounts of subsurface ice in both the north and the south, the fact that the southern hemisphere lacks a large water-vapor peak implies that the ground ice in the southern hemisphere is not in exchange with the atmosphere and may thus be more deeply buried, as inferred from thermal inertia data (Paige *et al.*, 1994).

General Circulation Models have been used extensively to understand the water cycle, especially the role of clouds, which can impact the radiation budget of the planet (e.g., Houben *et al.*, 1997; Richardson and Wilson, 2002; Montmessin *et al.*, 2004; see Figure 25.3). Recently, Tyler and Barnes (2005) have used a high resolution GCM to model water transport and winds in the north polar region, noting eddies consistent with repeated cloud patterns observed by the Mars Orbiter Camera (MOC) on MGS, and strong circulation variability with season during the northern summer. They note a "storm track" linking the polar regions with Tharsis Montes and Alba Patera, suggesting that this corridor may be responsible for transport of water away from the pole, and supporting the observation of Smith (2002) that water from the north crosses the equator as the seasonal vapor maximum decays.

25.5 SEASONAL SURFACE DEPOSITS

The growth and recession of the seasonal caps are the most dynamic processes on Mars and were first recorded in the drawings of Cassini in 1666. In the late eighteenth century, Herschel (1784) was the first to observe the dynamic nature of the polar caps and believed that the polar caps were composed of H_2O; this was the popular belief for almost two centuries. Near the end of the nineteenth century, there were a few dissenters. For example, A. C. Ranyard and G. J. Stoney believed that Mars was too small to gravitationally hold onto H_2O. They believed that the polar caps must be dry ice, not wet ice (e.g., Stoney, 1898). It was not until 1966 that Leighton and Murray (1966) determined from models and observations of surface temperatures and pressures that the seasonal caps must be composed of CO_2. Even then, the idea that the polar caps were composed of anything besides H_2O ice was not popular (Bruce Murray, 2006, pers. comm.). Mariners 6 and 7 flew past Mars in 1969 and firmly established that the surface temperatures of the seasonal caps were indeed consistent with the presence of CO_2 ice (Neugebauer *et al.*, 1971).

Just as terrestrial oceans control the climate on Earth, the seasonal polar caps control the climate on Mars, with 25% of the atmosphere being cycled from vapor to ice and back to vapor annually (Tillman *et al.*, 1993). While there seems to be little annual variation of global properties (e.g., atmospheric pressure), there are regional and local variations in the cap's recession (e.g., James *et al.*, 1992; Bonev *et al.*, 2002). Global dust storms do not appear to have a major impact on the global rate at which the polar caps advance and recede, but apparently they can affect regional and local rates of CO_2 condensation and sublimation, such as an early disappearance of the "Mountains of Mitchel" (e.g., James *et al.*, 1992; Martin *et al.*, 1992).

25.5.1 Seasonal cap edges

The most observable parameter that describes the polar seasonal caps is their size. The size of the caps has been measured since the days of Herschel. Telescopic observations of the dynamic nature of the seasonal caps have been restricted to the recession phase of the caps, however. During the period of growth, Mars is tilted away from the Earth, thus placing the cap edge at unfavorable viewing angles. In addition, the cap edge is close to the terminator and is often obscured by clouds or haze. Fischbacher *et al.* (1969) compiled recession curves for the polar caps from 1905 to 1965, using photographic material archived at the Lowell Observatory. A number of other observers used telescopic data to characterize the cap recessions in the early 1960s through the present. Spacecraft observations began in 1969 with Mariner 7 and continue to the present day. A compilation of both telescopic and spacecraft observations of the polar caps can be found in James *et al.* (1992), Hansen (1999), and Benson and James (2005).

The advance and retreat of the polar cap from year to year may contain many clues to help elucidate little understood physical processes. For example, summertime heat storage in the regolith could delay the onset of the seasonal CO_2 cap. The onset of the seasonal cap could also be directly affected by the thermal inertia of the near-surface regolith and place constraints on the depth of the ice table.

Parameterizations of the seasonal cap edges provide useful constraints on atmospheric GCMs and mesoscale models. Longitudinally resolving the cap edges as they advance and retreat constrains the times when zonal means are appropriate and when longitudinal asymmetries make zonal means invalid. Figure 25.4 illustrates one such parameterization, where both the advance and the retreat of the seasonal caps have been modeled as a series of sines and cosines. These same kinds of parameterizations can also be used when modeling other data that have large spatial resolutions, such as GRS and NS data. By knowing where the cap edge should be, coarse spatial resolution instruments can correct for subpixel mixing caused by their large instrument point spread functions convolving both frosted and frost-free areas.

Northern seasonal cap edge

The northern seasonal cap has been less well studied than the south, both because Mars is typically farther from Earth

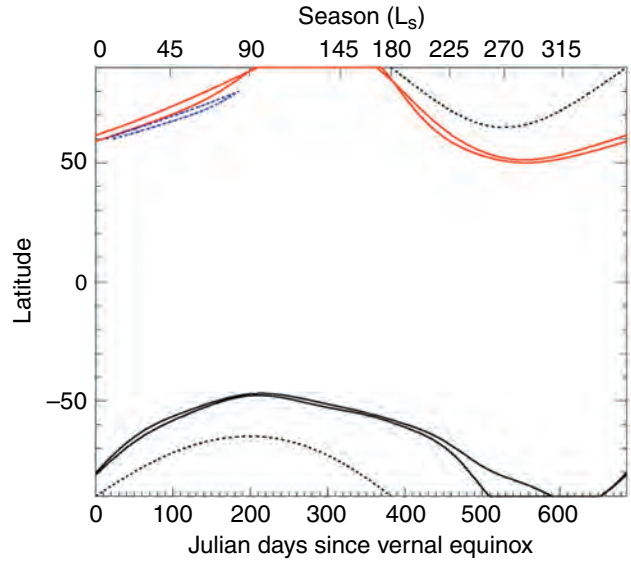

Figure 25.4. Polar cap edge behavior. The solid red and black lines indicate the best-fit sine-cosine function for the northern cap edge at 0° E, 180° E and the southern cap edge at 45° E, 135° E. The two dotted black lines are the edge of polar night. The dotted blue line indicates the edge of visual cap at 0° E and 180° E. (For a color version of this figure, please refer to the color plate section or to the e-Book version of this chapter.)

during Martian northern winter and due to the consistent formation of the north "polar hood." The north cap exhibits a near-symmetric retreat, which has been well characterized at visible wavelengths by both telescopic and spacecraft observations. However, the advance of the cap has not been well characterized until recently. Kieffer and Titus (2001) have used zonal means to observe surface temperature and visible bolometric albedo with season using MGS TES. The TES thermal observations show a nearly perfect symmetric advance; that is, condensation at consistent latitude across all longitudes, with the most northern edge of the seasonal cap occurring between longitudes 245° E and 265° E and the most southern edge of the seasonal cap occurring between 280° E and 30° E (Titus, 2005a). The advance of the northern cap typically leads the advance of the edge of polar night by 10° of latitude (Figure 25.3). The northern spring retreat is also nearly symmetric in both visual and thermal observations, and follows the same small asymmetries as seen in the advance. The latitude difference between the maximum and minimum extent of the thermal cap is generally between 3° and 5°, regardless of whether the cap is advancing or retreating. Benson and James (2005) saw changes in the recession rates between 2000 and 2002. The changes occurred in the same longitude ranges as Titus (2005a) saw the asymmetries, with the slower retreat occurring between longitudes 300° E and 30° E and the faster retreat between 230° E and 270° E.

In addition to four Martian years of seasonal observations by TES and MOC, the north seasonal cap was observed in detail with OMEGA in 2004 and 2006. The bright ring at intermediate temperatures (~180 K) observed by TES (Kieffer and Titus, 2001) in early spring is confirmed by OMEGA as resulting from H_2O ice frost, with a sublimation front which lags by up to 4° in latitude south of the CO_2 ice

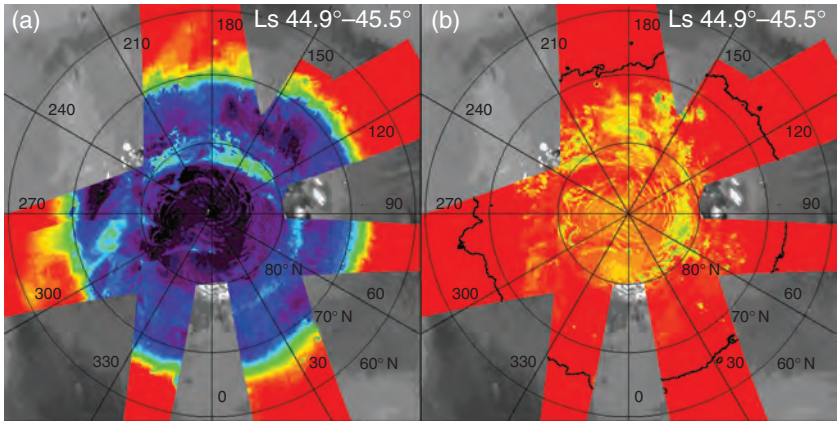

Figure 25.5. Spatial distribution of spectral signatures of CO_2 ice and H_2O ice observed by OMEGA in mid northern spring (L_s ~45°, April 2006). (a) band depth of the H_2O ice absorption feature at 1.5 μm. The rainbow scale covers the range from 60% (black) to 0% (red). Weak signatures between 60° N and 70° N correspond to water ice clouds; (b) band depth of the CO_2 ice absorption feature at 1.43 μm, also from 60% (black) to 0% (red). The black outline corresponds to the boundary of regions with strong H_2O ice signatures. At this season, H_2O ice dominates the spectral signature of the northern seasonal cap, except for a few regions where strong spectral signatures of CO_2 ice are still observed. (For a color version of this figure, please refer to the color plate section or to the e-Book version of this chapter.)

sublimation front. H_2O ice contamination of CO_2 ice is ubiquitous in the northern seasonal cap at all stages of its evolution. H_2O ice dominates the spectral signatures over most of the seasonal cap after mid-spring (L_s ~45°, see Figure 25.5).

In addition to the presence of an H_2O ice annulus that tracks the seasonal cap retreat, occasional brightening of the entire seasonal cap will occur (Kieffer and Titus, 2001). This temporary brightening of the cap (referred to as "flashing") typically lasts for a day, and then returns to normal. This type of flashing is most likely due to a sudden cold trapping of water vapor across the entire cap, resulting in a thin and temporary layer of bright water frost. This relatively slow type of flashing should not be confused with the "flashing" observed by many amateur astronomers (e.g., Wilson, 1937; Wells and Hale, 1971; Haas, 2003), which occurs very quickly and is probably the reflection of sunlight off of ice crystals in high-altitude Martian clouds, or possibly specular reflections off of isolated pockets of surface ice.

South polar seasonal cap edge

During the southern fall, the advance of the southern seasonal cap is nearly symmetric, just as in the case of the northern seasonal cap. Only a 2°–4° difference in the latitude of the cap edge has been observed, with the most northern extension generally occurring near longitude 300° E. This symmetry remains until L_s ~220°, which corresponds to the season when the cryptic region (Section 25.5.3) has maximum albedo contrast with the rest of the seasonal cap.

The retreat of the southern cap has been known to be asymmetric since early telescopic observations. It was observed frequently by TES during the MGS aerobraking phase as an offshoot of atmospheric monitoring for engineering purposes, during which the cryptic region was identified (Kieffer *et al.*, 2000) as a dramatic discrepancy between the visual and thermal retreat. Continuing observations by TES, The Mars Odyssey Thermal Emission Imaging System (THEMIS), MOC, and OMEGA have shown that the asymmetric sequence repeats consistently.

MOC observations of the global recession in 1999, 2001, and 2003 suggest that the overall seasonal cap is insensitive to global-scale dust storms. However, Bonev *et al.* (2005) showed evidence for local variations due to the redistribution of absorbed solar energy. During large dust storms, when the direct absorption of solar energy is reduced and thermal downwelling radiation is increased due to increased atmospheric opacity, bright regions of the cap have higher sublimation rates, while darker regions have lower sublimation rates. Inevitably, this means that the cryptic region lasts longer and features like the "Mountains of Mitchel" disappear earlier.

The southern seasonal cap has been observed by OMEGA from its maximum extent, close to the southern winter solstice, to the end of the retreat at L_s ~325°. It is spectrally dominated by CO_2 ice, consistent with previous temperature measurements by TES and THEMIS. During winter, the longitudinal distribution of CO_2 ice is relatively symmetric, in agreement with previous observations. H_2O ice, initially limited to regions close to the Hellas basin, extends eastward due to the sublimation–recondensation process initially proposed by Houben *et al.* (1997). The OMEGA observations are consistent with circulation models which demonstrate the major role of Hellas on weather patterns in the south (Colaprete *et al.*, 2003; Montmessin *et al.*, 2004). In early southern spring, the brightening of central regions of the seasonal cap is associated with a decrease in grain size and dust contamination. The development of a dark and cold region within the seasonal cap (the cryptic region) corresponds to extensive dust contamination at the surface of CO_2 ice (Langevin *et al.*, 2006). At the time of maximum extent (L_s ~225°), the seasonal cap is very complex in terms of spectral signatures, with a few regions spectrally dominated by H_2O ice and a wide range of grain sizes and levels of dust contamination. From late southern spring to mid summer, most of the seasonal cap appears to be remarkably clean CO_2 ice with grain sizes ranging from a few millimeters to a few centimeters. During this season, H_2O ice appears to play very little role, either as frost on the surface or as icy aerosols (Langevin *et al.*, 2007). The sublimation–recondensation process of H_2O ice, which is so effective in the north and in southern winter, is also not observed, most likely due to the very low amounts of available H_2O. Although the overall agreement with general circulation models is satisfactory (Montmessin *et al.*, 2004; Langevin

et al., 2007), there are a few discrepancies (e.g., the extent of ice aerosols close to equinox, the lack of H_2O recondensation in late spring) that will help to further constrain climate models.

25.5.2 Seasonal cap mass and density

The mass of the polar caps is an important parameter in understanding the Martian climate. The distribution of seasonal CO_2 ice provides information about the interaction between the atmosphere, topography, and surface properties. The density of the CO_2 ice constrains several important polar processes, including deposition mechanisms and densification. Calculations and remote-sensing data that have been analyzed to determine seasonal cap characteristics are reviewed here, as is the use of neutron spectroscopy to determine CO_2 cap thickness.

Several approaches have been used to estimate the amount of CO_2 that condenses into the seasonal cap (see James *et al.* [1992] for earlier estimates). The most robust have been GCMs tuned to match the atmospheric pressure curves from the Viking landers (Tillman *et al.*, 1993). While these models often use unrealistic albedo and emissivity for the seasonal caps, they do match the pressure curves, and therefore must match the net global accumulation; however, they do not necessarily match local distributions. Other methods use energy balance considerations. For example, Kieffer *et al.* (2000) computed the annual southern mass at several locations from thermal and albedo observations throughout the sublimation season, yielding 800 to 1200 $kg\,m^{-2}$ (polar cap sublimation and accumulation budgets are often expressed in mass per unit area; e.g., for an assumed density of 1000 $kg\,m^{-3}$, a budget of 1200 $kg\,m^{-2}$ would correspond to a thickness of 1.2 m). Kieffer and Titus (2001) used energy balance during both condensation and sublimation seasons in the north to estimate the zonal distribution of cap mass, not only finding peak budgets of $\sim$1100 $kg\,m^{-2}$ near the pole, but also finding the condensation budget several hundred $kg\,m^{-2}$ larger than the sublimation budget near 70° N, suggesting substantial zonal heat transport in the spring. This analysis, however, neglected the effects of heat storage in the regolith. The polar CO_2 condensation creates an observable increase in the planet's rotation rate by conservation of angular momentum (Folkner *et al.*, 1997; Yoder and Standish, 1997). A combination of gravity and differential elevation measurements were used to estimate a seasonal cap density of $910 \pm 230\,kg\,m^{-3}$ (Smith *et al.*, 2001a).

Nuclear spectroscopy measurements made by Mars Odyssey are sensitive to the column abundance ($kg\,m^{-2}$) of CO_2 surface ice, which has been monitored for over two Mars years. The GRS, NS, and High Energy Neutron Detector (HEND) instruments provide signatures that can be analyzed to map the distribution and mass of seasonal ice, with a spatial resolution of approximately 600 km (see Chapters 5 and 6). Signals from neutrons and gamma rays have different sensitivities to ice depth and are thus complementary. Gamma ray transmission measurements were used to map the column abundance of CO_2 ice in the northern and southern hemispheres (Kelly *et al.*, 2006). The leakage flux of neutrons is sensitive to surface CO_2 ice because the ice does not strongly absorb neutrons and is a poor moderator in comparison to H. Therefore, neutron counting rates generally increase monotonically as ice is added to the surface (e.g., see Figure 25.6). Initial results were obtained from NS measurements, in which the data were analyzed to determine the column abundance poleward of 85° N. The column abundance was compared to GCM estimates of the mass (Feldman *et al.*, 2003) and combined with MOLA thickness data to estimate density (Aharonson *et al.*, 2004). The data were subsequently analyzed to determine the spatial distribution of ice in the north and south for two Mars years (Prettyman *et al.*, 2005). HEND data have also been analyzed to determine the local column abundance, mass, and density (in combination with MOLA data) of the seasonal caps in both hemispheres (e.g., Litvak *et al.*, 2007). All of these techniques give results that are consistent with GCM predictions (tuned to Viking pressure data) of mass, to within the limits of their systematic and statistical errors. In addition, the mass and distribution of CO_2 were found to be consistent between the two years for which data have been acquired. The strength of the measurements is their ability to determine spatial distributions of CO_2, which can be used to further understand polar circulation and dynamics, as well as to constrain the polar energy balance and to improve physical models of condensation and cap properties for GCMs.

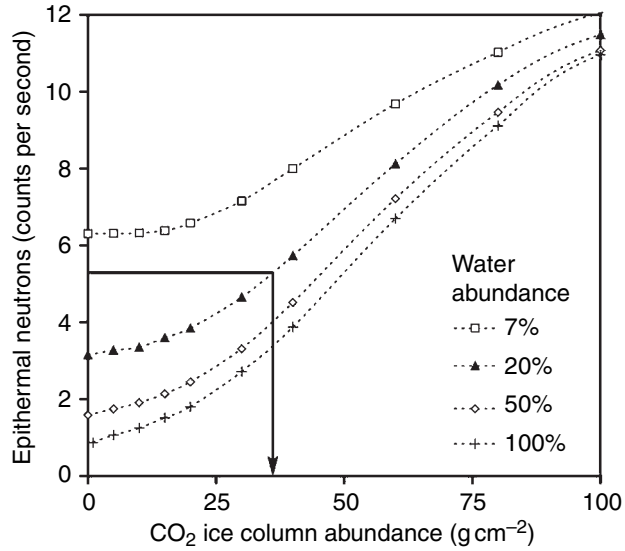

Figure 25.6. Epithermal neutron counting rate as a function of CO_2 ice column abundance. The CO_2 ice covers four different homogeneous regolith materials, consisting of soil mixed with water ice. The abundance of water ice for each material is indicated in the legend. If the abundance and stratigraphy of water equivalent hydrogen is known, then the column abundance of CO_2 ice can be uniquely determined, as indicated by the arrow.

To illustrate the information provided by nuclear spectroscopy, counting rates measured by the NS poleward of 60° show a strong seasonal variation (Figure 25.7). Counting rates for three distinct energy ranges measured by the spectrometer (fast, epithermal, and thermal) are shown. The observed variations are caused primarily by changes in the

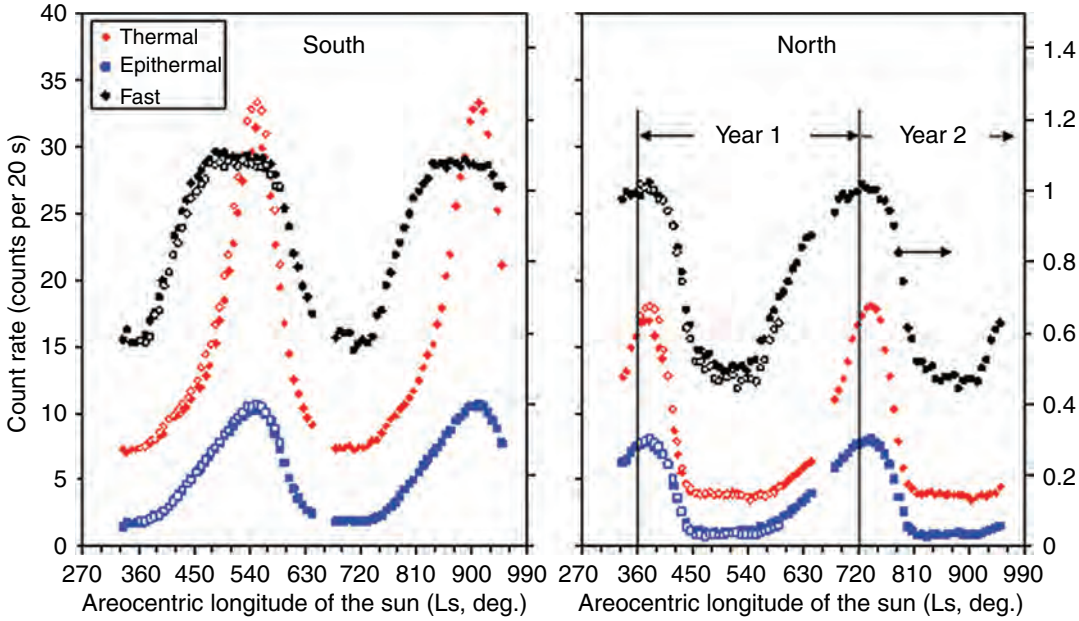

Figure 25.7. Time series Mars Odyssey NS instrument neutron counting data binned poleward of 85° S (left) and 85° N (right) from February 2002 to July 2005. Time is given in terms of the areocentric longitude of the Sun (L_S), or season. Each point is averaged over roughly 7° of L_S. $L_S = 0°, 360°, 720°, \ldots$ corresponds to the vernal equinox in the northern hemisphere. $L_S = 90°, 450°, 810°, \ldots$ corresponds to the northern summer solstice. Successive years are arbitrarily labeled "Year 1" and "Year 2." Data from the second year (shown as open symbols) were shifted and superimposed on the first year to show the level of inter-annual variations. (For a color version of this figure, please refer to the color plate section or to the e-Book version of this chapter.)

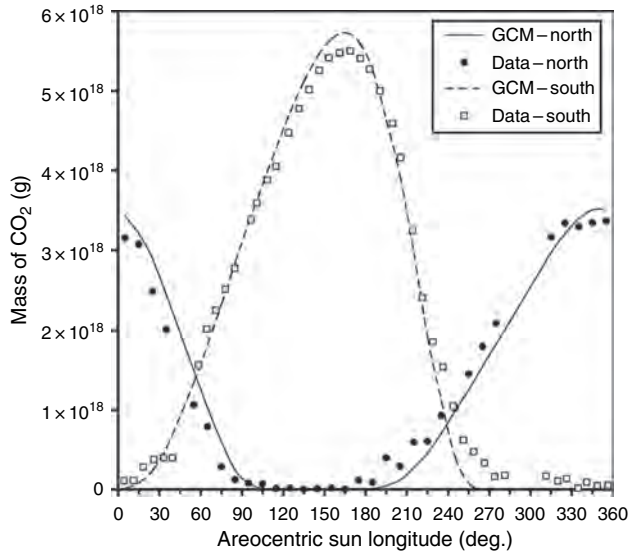

Figure 25.8. The total mass of seasonal CO_2 ice poleward of 60° is shown for the northern and southern hemispheres, determined from epithermal neutron counting data (points) and estimated by a GCM calculation (lines). In the GCM calculation, the seasonal cap albedo and emissivity were adjusted to match the seasonal pressure variation observed at the Viking landing sites. (The GCM results are courtesy of NASA Ames Research Center and the New Mexico State University Department of Astronomy.)

polar surface and atmosphere as CO_2 ice condenses onto and sublimes from the surface. For all three energy ranges, the counting rate begins to increase in the fall during the polar night as CO_2 ice forms on the surface, achieving a maximum in the winter, and decreasing again during spring as the CO_2 sublimes. Each energy range has a unique time profile, which reflects their different sensitivities to CO_2 ice. Generally, the counting rates do not vary between Years 1 and 2, which implies that the polar inventory of CO_2 ice does not vary significantly from year to year. The counting rates are converted into CO_2 ice column abundance using the relationships shown in Figure 25.6, which were determined by modeling cosmic ray interactions with the Martian surface and atmosphere.

The total mass of seasonal CO_2 ice poleward of 60° was determined for Year 1 from the epithermal counting data for the northern and southern hemispheres and is compared to a GCM calculation in Figure 25.8. For the GCM calculation, the emissivity and albedo of the seasonal frost, which were assumed to be uniform, were adjusted so that the results of the calculation matched the seasonal pressure variation measured by the Viking landers in the 1970s (Hourdin *et al.*, 1995; Haberle *et al.*, 1999). Differences between the GCM calculations and the GRS/NS/HEND estimates are relatively small, which suggests that the seasonal cap evolution has not varied significantly over thirty years. Estimates of the total cap mass varied between 3 to 4×10^{15} kg for the northern cap and 3 to 6×10^{15} kg for the southern seasonal cap. Local variations in CO_2 column abundance are shown in Figure 25.9 for the northern and southern hemispheres.

Measurements of density are more reliable than measurements of mass, probably owing to uncertainties in linear thickness measurements and comparisons between regionally averaged frost values (from nuclear spectroscopy) and local measurements provided by MOLA. Density estimates for the northern seasonal cap vary from 500 to 1100 kg m^{-3} (e.g., Smith *et al.*, 2001a; Aharonson *et al.*, 2004; Smith and

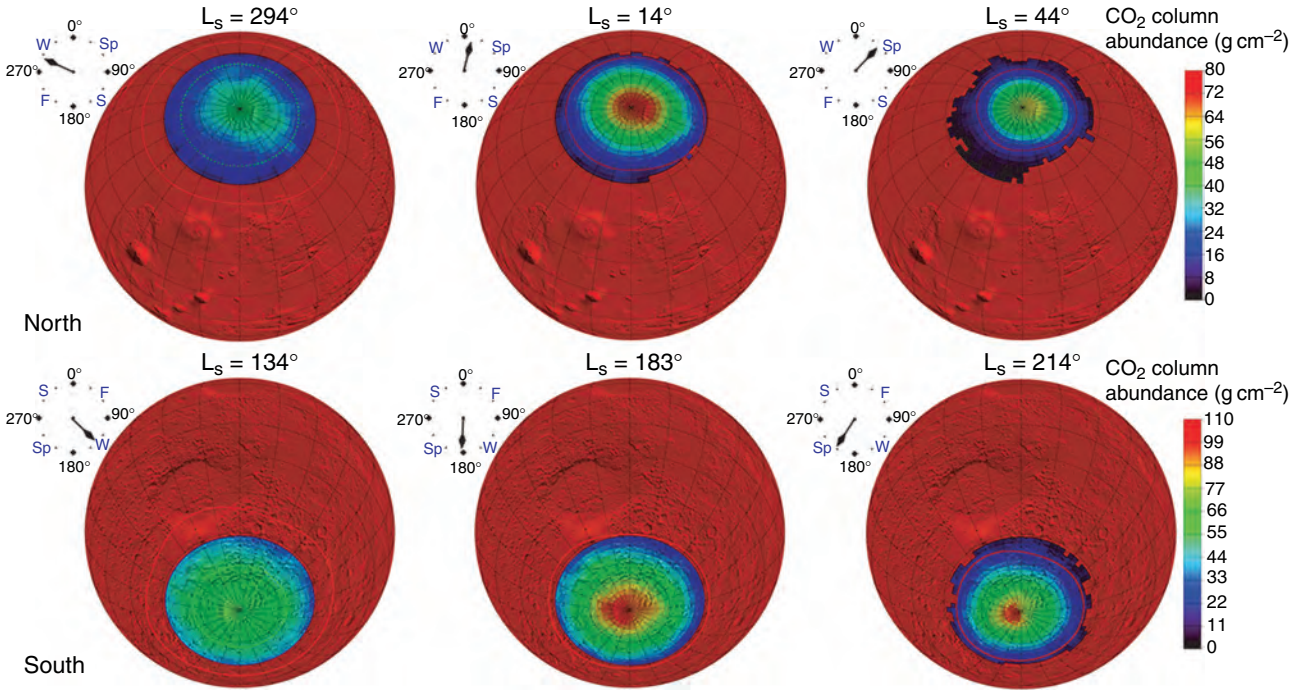

Figure 25.9. Maps of CO_2 column abundance in the northern and southern hemispheres (poleward of 60°) are compared to cap edge functions (solid red line) and the extent of the polar night (dashed green line). In both hemispheres, the maximum column abundance occurs near the pole during the recession. In the southern hemisphere, the distribution is asymmetric, with peak column abundance occurring at the location of the perennial CO_2 cap. (For a color version of this figure, please refer to the color plate section or to the e-Book version of this chapter.)

Zuber, 2005) depending on how the estimate was determined and over which latitude region. The southern seasonal cap appears to have a density of ~1000 kg m^{-3}. The density of the seasonal cap may not be constant, but may vary over latitude and season. The density can vary due to the mechanism of deposition (e.g., direct condensation versus snowfall). The density of the CO_2 ice can also change over time due to densification. Impurities, such as dust or H_2O, can also affect density. Finally, the presence of noble gases can create bubbles inside the CO_2 ice, thus increasing its porosity.

25.5.3 The cryptic region

The cryptic (meaning obscure or camouflaged) region, a dark and cold region within the southern seasonal cap, has been identified as "dark and dirty" dry ice (Titus *et al.*, 1998, Kieffer *et al.*, 2000). While these authors were the first to recognize the cryptic region as dark CO_2 ice, they were not the first to have observed the region. Observations of this dark seasonal feature date back to 1845, when first seen by the American astronomer Ormsby MacKnight Mitchel (Blunck, 1982).

This southern springtime phenomenon was also observed by several astronomers through the late nineteenth and early twentieth centuries. In 1892, Barnard, Hussey, Schaeberle, and Young observed the cryptic region from L_s ~210° to 229°. The cryptic region was again observed in 1894 by Barnard, Pickering, and Lowell (L_s ~ 206°–237°). Fournier observed and drew an illustration (L_s ~235°) of the cryptic region in 1909. In 1924, Antoniadi (1930) observed this region, which he called *Depressio Magna* (~80° S, 270° W), or Big Depression. Antoniadi even speculated that this dark region inside the bright seasonal cap might be a polar lake. In addition to the observation of *Depressio Magna*, Antoniadi also observed a smaller dark patch, which he referred to as *Depressio Parva* (Little Depression). These two dark patches correlate with the location of the cryptic region as observed by both the Viking Orbiter Infrared Thermal Mapper (IRTM) and MGS TES. *Depressio Magna*, or what is presently referred to as the cryptic region, can still be seen in the best ground-based images taken of Mars around favorable oppositions.

The two Viking Orbiter IRTM instruments were the first thermal IR instruments to observe the southern retreating cap (Kieffer, 1979). While observed by the IRTM (Figure 25.10a), the cryptic region was not fully recognized as a region of dark CO_2 ice and was relegated to a footnote in a paper by Kieffer (1979).

With the arrival of MGS, three new instruments were observing the cryptic phenomenon: a high resolution optical camera (MOC), a thermal IR spectrometer (TES, a thermal spectrometer and bolometer and a solar bolometer with ~3 × 6 km resolution), and MOLA, which, when operated as a reflectometer, could map the cap albedo at a wavelength near 1 μm.

The TES bolometers revealed a region of the springtime southern cap that was cold and dark (Figure 25.10b). Spectra from TES did not show the 25 μm transparency band, typical of fine-grained CO_2 frost and snow, suggesting that the cryptic region was composed of either coarse-grained

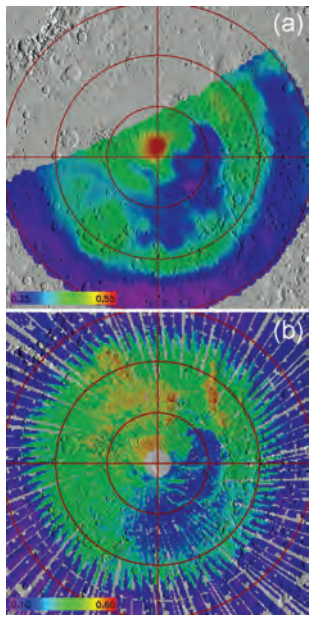

Figure 25.10. Albedo of the cryptic region. (a) The albedo of the southern seasonal cap in 1976 as measured by the Viking IRTM solar channel bolometer. (b) The albedo of the southern seasonal cap in 1999 as measured by the MGS TES solar channel bolometer. (For a color version of this figure, please refer to the color plate section or to the e-Book version of this chapter.)

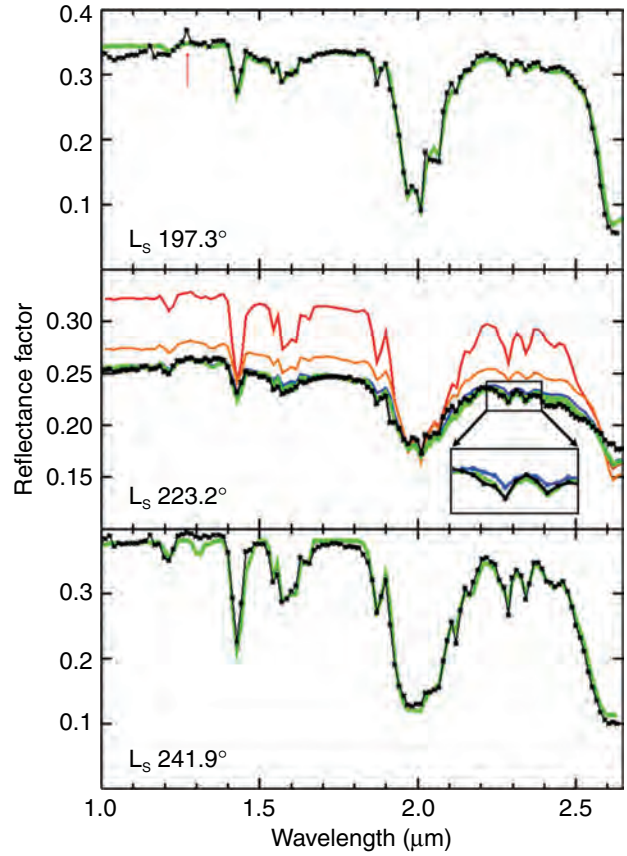

Figure 25.11. The black lines correspond to observed OMEGA reflectance spectra of the cryptic region (82° E, 85° S) at three values of L_s (197.3°, 223.2°, 241.9°). The thick green lines correspond to best fit model spectra, including dust, water ice, and CO_2. In the middle panel ($L_s = 223.2°$), the sensitivity of the models to different parameters is examined, in particular to the dust contamination within surface layers (red: 50% less dust) and the thickness of the CO_2 layer (blue curve in the insert: 7.5 cm instead of 15 cm). (Reprinted by permission from Nature Publishing Group: *Nature*, Langevin, Y., S. Douté, M. Vincendon, *et al.,* No signature of clear CO_2 ice from the "cryptic" regions in Mars' south seasonal cap, **442**, 790–2, © 2006.) (For a color version of this figure, please refer to the color plate section or to the e-Book version of this chapter.)

or slab CO_2, or dirty dry ice. While thermal IR spectral observations could not determine the form of CO_2 ice that composed the cryptic region, other observations provided indirect evidence that supported the concept of a coarse-grained translucent slab. For example, MOC images, with resolution as high as ~1.5 m/pixel, revealed that the cryptic region had a cornucopia of bizarre albedo features that have been referred to as a "zoo" (Kieffer *et al.*, 2000, 2006; Kieffer, 2007). Subkilometer dark areas were observed within the seasonal frost. Also discovered were fields of dark, round spots with parallel-oriented tails ("fans"), fields of spots with individual or collective medium-toned halos, and fields of dark (later to become relatively light) radial and ragged branching patterns ("black spiders"), usually centered on the narrow ends of fans (Piqueux *et al.*, 2003). Some of the spots must form in the dark, as they are observed in prepolar-dawn images (Aharonson *et al.*, 2004).

The initial interpretations, based solely on imaging, of these dark surfaces within the polar frost were that they were defrosted surfaces and should be warm (Malin *et al.*, 1998). However, the TES instrument observed low temperatures in the cryptic region for weeks and months after the formation of the spots and fans, indicating that solid CO_2 was still present at the surface. A small diurnal temperature variation (~5 K) suggested the possible presence of either a thin layer of surface dust or a layer of near-surface atmospheric dust (Kieffer *et al.*, 2000; Titus and Kieffer, 2001). THEMIS simultaneous visual and thermal imaging of these features with 100 m resolution or better confirmed the TES inference that they were entirely at solid CO_2 temperatures for much of the spring. Once the spots begin to warm, however, they grow and coalesce quickly, forming large defrosted regions (Kieffer *et al.*, 2006). All the albedo features disappear when the ground warms, except the "spiders," which are observed as depressions when the cap is gone.

With the arrival of Mars Express, NIR and short wave mid-IR hyperspectral imaging observations became available. The OMEGA spectrometer has provided additional information about the cryptic region through the analysis of H_2O and CO_2 ice absorption features. Spectral modeling has proven very successful for the interpretation of OMEGA observations. As an example (Figure 25.11), the evolution of the observed spectrum from the cryptic region during the southern spring (L_s ~197°) can be interpreted first as an intimate mixture of dust (0.7 wt.%) and H_2O ice (0.06 wt.%) within CO_2 ice. Later (L_s ~223°), there is evidence for extensive contamination of the surface layers by ~7 wt.% of dust. Finally, two weeks before the area becomes completely free of ices (L_s ~242°), the spectra are consistent with areal mixing of 25% ice-free areas and 75% ice-covered areas within each pixel. Such subkilometer-scale ice-free and ice-covered areas are a consistent feature of regions

close to the sublimation front at all stages of the retreat of the southern seasonal cap.

Hypotheses

A series of unanticipated observations by the MGS TES and MOC, with confirmation by THEMIS (Kieffer *et al*., 2006), has led to a complex model for surface processes in the seasonal polar cap. All of the cryptic region features described above were observed by THEMIS to occur at solid CO_2 temperatures and to stay that cold for weeks to months. A possible explanation pivots on the physical and optical properties of solid CO_2, which has a very small absorption coefficient in the solar wavelength region and becomes opaque to thermal radiation within a few millimeters thickness (Hansen, 1997, 2005; Kieffer, 2007). H_2O and dust are also involved in this proposed explanation that is summarized by a brief description of the annual sequence based on the discussion by Kieffer (2007).

Deep in the Martian polar night, there is some CO_2 snowfall, but most of the solid CO_2 takes the form of a uniform, continuous, nonscattering slab with embedded dust (and H_2O ice) grains. Predawn seasonal heat flow sublimes CO_2 and some "vents" form to release this gas. Following seasonal sunrise, in some areas the ice brightens due to fracture or surficial frosting, but in other areas the slab persists to form the dark, cold cryptic region. Here, the solar energy is largely absorbed by embedded dust grains (which either burrow downward or escape upward), cleaning the CO_2 slab and annealing small holes near its surface. Sunlight then penetrates to the bottom of the slab, warming the soil and subliming ice from the bottom. Some unidentified process causes a slight uniform darkening of the slab around vents to form "halos." The CO_2 at the bottom of the slab sublimes and forces gas into the subsurface. Additional vents develop that allow this gas to escape. As the sub-slab gas converges toward the vents, it scours the soil surface along ragged channels (spiders). Dust entrained in the jetting gas falls out downwind to form "fans." As the slab thins and the sub-slab pressure drops, gas enriched in water vapor is released from the subsurface to cool and deposit water frost in the channels, brightening the spiders. As soon as the CO_2 slab is gone, the water frost warms and evaporates. Only the topographic ghosts of the spiders persist through the summer. Thus, seasonal reworking of the soil below the ice slab may help to explain the uniformity and youthful appearance of the terrain upon which the vents form.

This venting model is mainly based on visible and thermal IR observations. The results of OMEGA spectroscopy presented by Langevin *et al*. (2006) raised major questions, however, as most of the cryptic region in mid spring ($L_s \sim 220^\circ$) did not exhibit the spectral signature of a clear slab of CO_2 ice, which is the most favorable configuration for the venting model. Instead, the surface of the CO_2 ice appeared strongly contaminated by dust, with few photons making it to the underlying surface. These observations led to a hypothesis in which dust could be deposited on the surface shortly after equinox by storm systems originating from the Hellas region (Colaprete *et al*., 2005). Additional surface dust could be provided by dust initially embedded with the CO_2 ice slab. Dust trapped within the ice would warm under sunlight, subliming the ice and allowing the dust particles to escape. The largest dust grains would burrow down to the surface underlying the ice, while the smallest dust grains would blow away with the sublimation winds (Kieffer, 2007).

These hypotheses are not mutually exclusive. The venting model is the best candidate to explain the spots, fans, and spiders observed at different times and places in the seasonal cap. However, heavy contamination by surficial dust (either due to venting or due to other dust sources) markedly decreases the proportion of solar photons reaching the underlying surface, thereby reducing the efficiency of the venting process. One of the possibilities to be considered is that the venting process is mainly active very soon after sunrise at high southern latitudes, close to equinox. Another source of dust may play a role either simultaneously with venting or at a later stage, as large areas in the cryptic region do not exhibit features such as spiders, spots, and fans that would indicate that the venting process had been active. New high resolution observations by CRISM and HiRISE (HiRISE – High Resolution Imaging Science Experiment), new observations and modeling from OMEGA, and more laboratory work will all be needed to improve our understanding of the wide diversity of processes at work at high southern latitudes.

Cryptic region location

Why is the cryptic region located where it is on the seasonal cap? Initial attempts to find correlations of the cryptic region's location with local geologic features failed (Kieffer *et al*., 2000). A majority of the cryptic region lies over the PLDs, but it also extends over other geologic units. Intraseasonal and interannual variations in the shape of the cryptic region suggested that atmospheric dynamics might play a role. Indeed, this hypothesis has gained additional support from mesoscale modeling that has demonstrated that regional topography (primarily the Hellas basin), sets up an $N = 1$ standing wave during the southern winter (Colaprete *et al*., 2005). The standing wave appears to cause two distinct microclimates to form over the southern polar region: the western hemisphere (longitudes 210° E–30° E, south and southwest of Argyre) is colder, cloudier, and has more snowfall, while the eastern hemisphere (longitudes 30° E–210° E, south and southeast of Hellas) is slightly warmer and wetter (higher water-vapor abundance). The cryptic region lies in the "warmer and wetter" microclimate, where there is less snowfall and enhanced radiative loss to space.

25.6 PERMANENT DEPOSITS

25.6.1 Residual caps

Viking observations of large increases of atmospheric water after seasonal cap sublimation (Farmer *et al*., 1976) and

temperatures well above those possible for CO_2 ice (Kieffer *et al.*, 1976) led to the conclusion that the north residual cap is water ice, while the persistently low temperature of the south residual cap (Kieffer, 1979) showed that to be CO_2. This was a surprising conclusion of disparate surface compositions! However, during one season (in 1969), enhanced atmospheric water observations over the South Pole suggested that a CO_2 cover over the south cap may have sublimed (Jakosky and Haberle, 1990).

Thus, the Viking era view of the Mars residual caps was one with a large H_2O ice cap in the north and a smaller CO_2 cap in the south. Since the arrival of MGS, however, this view has changed. Specifically, now the south polar residual cap (SPRC) is also believed to be an H_2O ice cap, but with a decameter-scale veneer of CO_2 ice that remains through most southern summers.

Observations in the era between Viking and MGS are summarized in Chapter 2 of this book. More recent observations by Thomas *et al.* (2000) using MOC imagery show that the north cap grades into the underlying layered materials while the south cap appears as a distinct geologic unit with very different topography than the surrounding layered terrains. Observations by MOLA (Zuber *et al.*, 1998; Smith *et al.*, 2001b) provided estimates of total residual cap plus polar layered deposits volumes but did not constrain relative proportions of dust and ice within the caps.

Dark and layered markings in the interior of the residual caps were noted in Mariner 9 observations and subsequently mapped in detail with Viking (e.g., Cutts and Smith, 1973; Soderblom *et al.*, 1973; Cutts *et al.*, 1976; Tanaka and Scott, 1987; Thomas *et al.*, 1992). These features include troughs, scarp faces, and the large and broad re-entrant valleys Chasma Boreale and Chasma Australe. Exposures in these regions are finely layered and generally much darker than the surrounding ice surfaces. Zuber *et al.* (1998) showed that the troughs and chasmata are quite deep, cutting up to 1 km into the ice surface. Models for formation and migration have variously included accumulation, wind ablation, glacial flow, and sublimation; the history and arguments for all these processes have been recently summarized by Howard (2000), Ivanov and Muhleman (2000), and Fisher (2000). The study by Durham *et al.* (1997) on ice rheology revived the glacial flow hypothesis; however, current deformation rates from glacial flow may be minimal at present polar temperatures. Even if the trough surfaces migrate poleward, timescales for migration remain uncertain. It is generally presumed that the layers exposed in the troughs provide a record of cap evolution or climate history. In the north, the layered deposits cover nearly the same area as the residual cap, while in the south the layered terrains are much more extensive than the permanent ice deposit (e.g., Thomas *et al.*, 1992). Among geologists, the layered terrains are often discussed as including the overlying permanent ice as part of the unit. Paige *et al.* (1994) found that both the permanent ice cap and the layered deposits in the north had very high thermal inertias, which they interpreted as indicating coarse-grained or solid water ice for at least 1 m under the residual cap and also underlying the layered deposits. In contrast, the South PLDs show a systematic poleward decrease in thermal inertia, interpreted as aeolian deposits, while the south residual cap again had very high thermal inertia (Paige and Keegan, 1994). Zuber *et al.* (1998) suggested that polar outliers in the north are likely soil-covered ground ice and that the north permanent cap was previously larger in spatial extent.

North polar residual cap

Examination of the northern residual ice cap showed a change in albedo in a number of north polar bright ice outliers and in the overall coverage by bright ice deposits between Viking and Mariner 9 and between Viking Orbiter summers (Kieffer, 1990; Paige *et al.*, 1994; Bass *et al.*, 2000). These changes were attributed to the possible effects of global dust storms (Paige *et al.*, 1994); however, Bass *et al.* (2000) showed that significant variations occurred within the summer season among Viking images. Cantor *et al.* (2002) also examined such variations in MOC images and noted brightening at the cap edges within a given Mars summer season as well as changes in the cap appearance at the same L_s (areocentric longitude) between the first two MGS years. The early season appearance was possibly attributed to the occurrence of a large dust storm the previous year, and it was noted that late season ice extent recovers to Viking levels but exhibits small-scale inter-year variations that may not be related to globally repeated weather events.

The evolution of the north perennial cap was monitored with OMEGA in late 2004 (Langevin *et al.*, 2005). These observations confirmed that the north perennial cap consisted of H_2O ice. Imaging spectroscopy in the NIR range provides strong constraints on ice grain sizes. The OMEGA observations demonstrated that the albedo of the ice-covered regions is controlled by a combination of all the parameters which had been considered as potentially contributing to albedo changes by Kieffer and Titus (2001): (1) Seasonal frost, with grain sizes $<100\,\mu m$, is brighter than permanent ice, with grain sizes up to 1 mm in mid summer; (2) Dust contamination in surface layers lowers the albedo; and (3) When the optical thickness of aerosols is large, albedo contrasts decrease because the apparent albedo of bright ice-covered regions decreases while that of the dark surrounding regions increases.

In the central part of the cap, the decrease in albedo observed during early summer ($L_s = 93^\circ$–110°) is a result of the sublimation of fine-grained seasonal frost, exposing coarser-grained permanent ice underneath. Patches a few tens of kilometers in extent at the edge of the permanent cap remain bright throughout summer, most likely corresponding to accumulations of small ice grains. In the outlying regions, defrosting occurs before solstice, and the albedo and band strengths increase in early summer due to a combination of a decrease in surface dust contamination and a decrease in aerosol opacity in early summer.

Calvin and Titus (2008) used TES observations from three Martian years to monitor large-scale variations in the north residual ice cap (Figure 25.12). These observations monitor the defrosting process during spring and early summer, confirming that the central parts of the cap undergo a period of

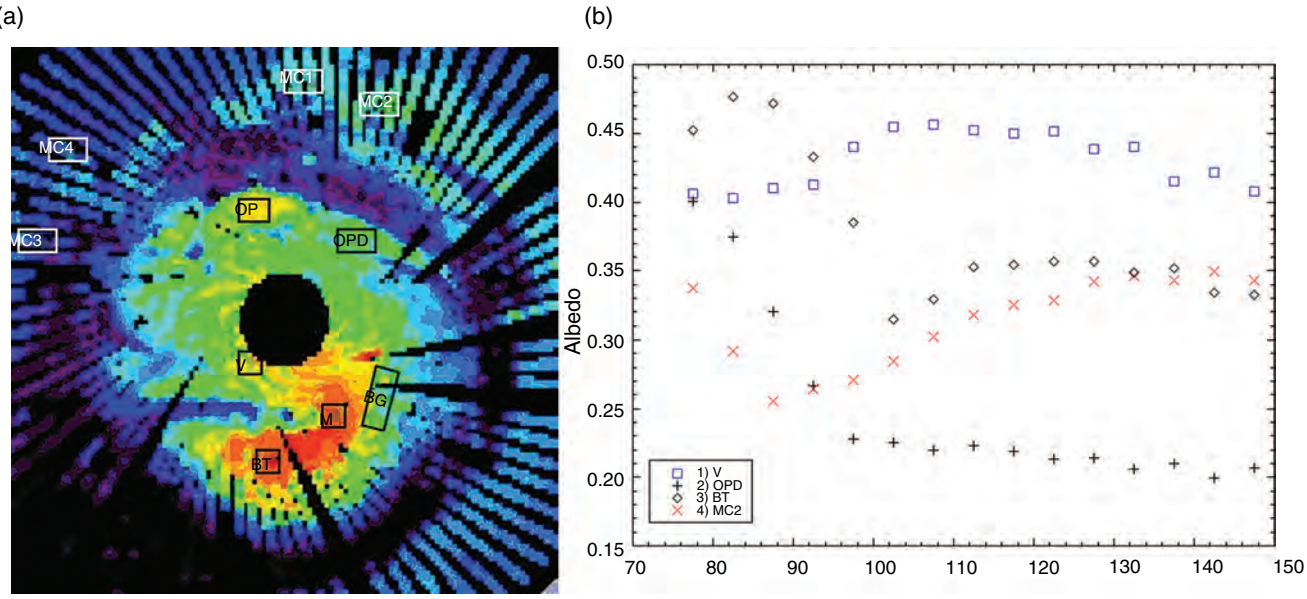

Figure 25.12. (a) Regions identified using TES albedo channels where frost mobility over the summer was noted. Color scale is TES albedo at $L_s = 85$ from 0.15 to 0.5 (purple to red). (b) Seasonal trends in albedo for the four types described in the text. (For a color version of this figure, please refer to the color plate section or to the e-Book version of this chapter.)

defrosting up to L_s ~100° to 105° as temperatures warm. Then, as temperatures begin to cool, higher elevations cold-trap new frost. Outlier ice deposits also preferentially cold-trap frosts later in the summer, although coarse-grained ice continues to dominate the ice spectra. Processes involved in frost mobility are as varied as the terrains in the north polar region, but albedo, temperature, and elevation appear to exert the strongest controls. While large scale patterns remain the same, there is some amount of interannual variability in both the persistence and location of the highest albedo deposits. Over the course of the summer season, four major trends were observed: (1) Two odd patches stayed bright throughout the summer; (2) Peripheral areas defrosted to non-ice material and stayed thereafter at a low albedo; (3) Cap materials defrosted to icy material that is coarser or dirtier than early spring ice; and (4) Outlier deposits defrosted early but then re-accumulated bright frost late in the summer season. The location and persistence of cold and bright patches may depend on heterogeneous deposition in the previous winter, or on the locations of cold spots influenced by winds or precipitation during the polar night (e.g., Titus *et al.*, 2001).

South polar residual cap

The disaggregated appearance of the SPRC and a single ground-based observation of unusually high water-vapor abundance in the southern hemisphere (Barker *et al.*, 1970) lead many to speculate that the southern CO_2 ice residual cap might only be a "thin" veneer covering an H_2O cap, and that in some years the CO_2 ice completely sublimes, exposing the underlying H_2O ice (Jakosky and Haberle, 1990).

While the complete disappearance of the CO_2 ice veneer has never been directly observed, there are several observations indicating that the SPRC is mainly H_2O ice. The flood of evidence started with MGS observations and continues with Mars Express observations. One of the clues from the post-Viking era was topographical modeling conducted by Nye *et al.* (2000) with MOLA elevation data. They showed that the SPRC could not retain its current shape if it was composed of CO_2, but would be stable if composed of dirty H_2O ice. Warm temperatures (<200 K) were observed by THEMIS in the interior of the cap (Byrne and Ingersoll, 2003) and around the edge of the cap (Titus *et al.*, 2003). MGS TES confirmed that the thermal inertia of the warm temperature regions at the edge of the SPRC was consistent with high thermal inertia material, presumably H_2O ice. Neutron spectroscopy data from the Mars Odyssey GRS/NS/HEND are consistent with an H_2O cap covered by CO_2 ice.

The south perennial cap was first observed by OMEGA at a relatively low resolution (3 km) in January 2004, shortly after the orbit insertion of Mars Express, then at a higher resolution (300 to 500 m) in early 2006. These observations revealed a widespread contamination of the dominant CO_2 ice component by H_2O ice and dust, and patches of H_2O ice heavily contaminated by dust have been observed around the perennial cap (Bibring *et al.*, 2004; Douté *et al.*, 2007).

Swiss cheese and CO_2 veneer thickness

With the advent of high resolution imaging of the SPRC came the discovery of a new terrain type, dubbed "Swiss cheese" terrain (Figure 25.13; Thomas *et al.*, 2000) because it consists of a network of swirl-covered mesas and circular pits that cover much of the SPRC. Both thermal and NIR imaging has shown that many of these pits reach to an underlying H_2O ice unit (Byrne and Ingersoll, 2003; Bibring *et al.*, 2004), presumably an H_2O ice cap similar to, but smaller than, the north polar residual cap (NPRC). Early measurements (Malin *et al.*, 2001) concluded that some scarps were retreating at ~2 m/Mars year. A more

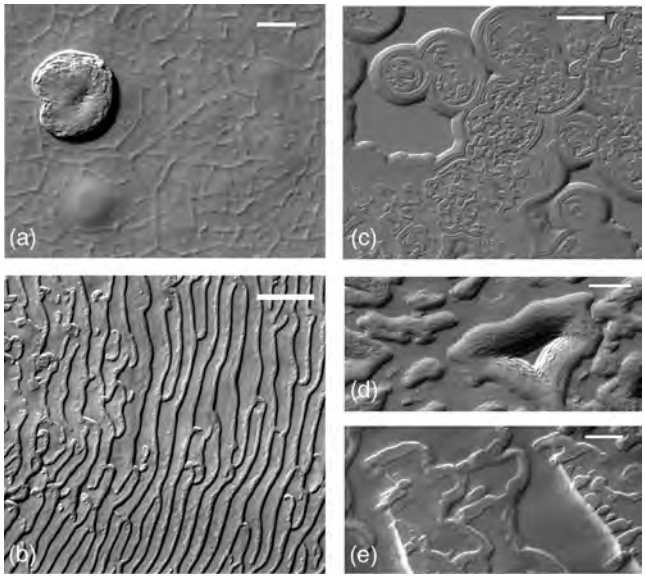

Figure 25.13. Examples of south polar residual cap "Swiss cheese" topography. (a) Nearly circular depression and polygonally cracked sag surface on top layer. Portion of MOC image M09-000609; 87.0° S, 5.9° W, acquired at $L_s = 237.3°$; Scale bar is 100 m and illumination is from the lower right. (b) "Fingerprint" pattern of depressions. Portion of MOC image M03-06756; 86.0°S, 53.9°W, acquired at $L_s = 182.4°$; Scale bar is 500 m and illumination is from lower right. (c) Circular collapse features, leaving mesas on upper surface with debris aprons and moats. Largest scarps here are about 4 m high. Portion of MOC image M03-06646; 85.6° S, 74.4° W, acquired at $L_s = 181.3°$; Scale bar is 500 m and illumination is from lower right. (d) Residual mesa exposing four layers and surrounding moat. Portion of MOC image M07-02129; 86.9° S, 78.5° W, acquired at $L_s = 204°$; Scale bar is 100 m and illumination is from bottom right. (e) Complex covering of depressions which suggest burial and exhumation of topography on part of the southern residual cap area. Portion of MOC image M04-03877; 84.6° S, 45.1° W, acquired at $L_s = 196°$; Scale bar is 200 m and illumination is from the lower right. (Figure from Thomas *et al.*, 2000.)

detailed study by Thomas *et al.* (2005) concluded that there were two types of Swiss cheese, an older thicker unit and a younger thinner unit. The older unit, which is typically less than 15 m thick and composed of several layers ~2 m thick, is backwasting at a rate of ~3.6 m/Mars year. The younger unit, which is composed of 1 to 3 layers, each ~1 m thick, is backwasting at a rate of ~2.2 m/Mars year. Other studies (e.g., Titus *et al.*, 2003; Winfree and Titus, 2006), have suggested that the residual cap may actually be getting larger in at least a few locations and that the circumpolar exposed water ice and outliers may mark the location of the SPRC in the not-to-distant geologic past.

The rheology of solid CO_2 at temperatures slightly higher (150 to 190 K) than the Martian polar caps was measured by Durham *et al.* (1999); deformation followed $\varepsilon' = A\ \sigma e^{Q/RT}$ where R is the gas constant, A is $10^{3.86}\,\mathrm{MPa}^{-n}\,\mathrm{s}^{-1}$, $n = 5.6$, and $Q = 33\,\mathrm{kJ\,mol}^{-1}$. This is much weaker than solid H_2O; the regional profiles and probable age of the perennial south cap are thus not compatible with a bulk composition of CO_2. High resolution imaging suggests that the perennial CO_2 is only a few meters thick; the underlying material is probably ice-saturated PLDs.

How thick is this "thin" veneer of CO_2 ice? What percentage of the H_2O ice is covered and how much is exposed? Tokar *et al.* (2002) and Prettyman *et al.* (2004) tried constraining the answers by using variations in the neutron flux as Mars Odyssey flew over the SPRC. They were able to constrain the answers between two endmembers: a cap completely covered by a uniform veneer of CO_2 ice $160\,\mathrm{g\,cm}^{-2}$ thick, or a cap partially covered by thick CO_2 ice (greater than $1000\,\mathrm{g\,cm}^{-2}$). If one assumes a density of $1\,\mathrm{g\,cm}^{-2}$, then the column density estimates from their analysis are equivalent to either a cap completely covered by a veneer 1.6 m thick or a partially covered water-ice cap where the CO_2 cover is at least 10 m thick over 45% of the cap. Analyses of Swiss cheese terrain within the cap interior (Byrne and Ingersoll, 2003; Thomas *et al.*, 2005) suggest that the CO_2 cover is between 8 and 11 m thick, more consistent with the thick partial coverage endmember. However, thermal observations during the mid summer would suggest a cap with a lower percentage of exposed ice, thus supporting the thin uniform layer endmember. The actual thickness of the CO_2 veneer is an important parameter in determining the current stability of the CO_2 SPRC (Jakosky and Haberle, 1990).

The offset of the SPRC from the geographical pole has been an outstanding mystery. But recent studies (Colaprete *et al.*, 2005) suggest that the same atmospheric dynamics that may cause the deposition of dry ice that remains dark throughout the spring (the cryptic region, see Section "Cryptic region location") may also preferentially deposit snow at the present location of the SPRC.

25.6.2 North polar erg

Surrounding the north PLDs is a vast unit of dark dunes sometimes called a "sand sea" or "erg" (Tsoar *et al.*, 1979). The dunes are inferred to form, at least in part, from material eroded from the layered deposits, and volume estimates support this view (e.g., Lancaster and Greeley, 1990). In contrast to the layered deposits, however, the dunes were found to have very low thermal inertias (Paige *et al.*, 1994) and their inertias are much lower than dark dunes elsewhere on the planet (Herkenhoff and Vasavada, 1999). Bell *et al.* (1997) noted that the dunes also have a different short-wave NIR spectral signature in images from the Hubble Space Telescope. The dunes appear to have a surface coating of gypsum as identified by OMEGA (Langevin *et al.*, 2005). The gypsum deposits appear to have the largest concentrations near the mouth of Chasma Boreale, decreasing toward the west. Recent CRISM observations imply that the gypsum is concentrated along the dune crests rather than in the troughs (Roach *et al.*, 2007). Both CRISM and OMEGA observations suggest that the basal unit of the PLD is not the source of the gypsum. However, CRISM has identified small outcrops of bedrock that do contain gypsum (Roach *et al.*, 2007), and thus the bedrock is a possible source.

25.7 CURRENT STATE OF KNOWLEDGE

25.7.1 How far have we come?

At the end of Chapter 27 of the 1992 University of Arizona Press book *Mars*, James *et al*. (1992) presented several outstanding questions regarding Martian polar cycles and studies. In light of recent discoveries since then, here we consider how much our understanding has advanced, but also what old problems remain and new enigmas have emerged.

Suppression of winter condensation. Comparisons of Viking pressure curves to energy budget considerations suggested that the condensation of CO_2 was being suppressed either by cloud effects or low emissivity. The recent discovery of near-surface H_2O ice in the high latitudes suggests that autumnal sublimation occurs, thus reducing the net accumulation of CO_2 ice throughout the fall and into the winter. Fall and early winter upward flow of heat from the regolith has now been modeled to have a significant effect, especially at latitudes where water ice is near the surface.

Significant spatial inhomogeneity of the seasonal caps. Lateral differences in the surface properties of the CO_2 ice certainly play a role. The driving force may be standing waves in the atmosphere set up by the large southern basins.

Differences in the spring regression curves. Seasonal pressure curves which are similar from year to year even with vastly different climate conditions have perplexed modelers. Recent analyses suggest that interannual weather (e.g., large-scale dust storms) affects the sublimation rate of the seasonal cap, but in such a way that local effects cancel out on the global scale.

Different natures of the residual caps. The two residual polar caps are not as different as was believed in 1992. Both caps are water-ice caps. The southern cap retains a thin veneer of CO_2 ice throughout most summers. The other major difference that remains is that of the size of the caps, with the northern cap significantly larger.

The offset of the SPRC from the pole. The driving force may be low-order standing waves in the atmosphere, set up by the large southern basins.

The stability of the residual CO_2. The stability of the SPRC remains an outstanding mystery. Several studies have suggested that the SPRC is thinning in the Swiss cheese regions. Other studies have suggested that the cap may be growing in places. With the arrival of Mars Reconnaissance Orbiter and its high-resolution VIS and NIR cameras and spectrometer, a dedicated polar monitoring campaign is underway to try to address this question.

25.7.2 Unresolved issues

There are as many unresolved issues in Martian polar science as ever, and new data seem to only deepen certain enigmas. Outstanding questions include:

- What is the nature of the CO_2 ice deposits ("Swiss cheese," "slab ice," "cryptic regions," etc.), and the detailed processes responsible for their evolution?
- What are the seasonal and longer timescale variations in water-ice properties (e.g., grain size, compaction, accumulation, and loss zones in the northern residual cap)?
- What is the composition and amount of non-ice material in the residual caps?
- How much water ice underlies the southern residual cap, and how often is it exposed?
- What is the relationship of dark materials in the wind-swept lanes and re-entrant valleys of the polar caps to the surrounding dark dune and surface materials?
- What is the relationship of the ice deposits to the underlying layered units, and why do they differ from the north to the south?
- What is the nature of seasonal and longer timescale obliquity variations, and what are their connections to the fine laminations of the PLDs?

ACKNOWLEDGMENTS

We acknowledge the extremely useful comments of Gary Hansen, Larry Soderblom, Kenneth Herkenhoff, and Jim Bell in the review of this chapter.

APPENDIX: INFORMATION ON PHYSICAL PROPERTIES OF MARTIAN ICES

H_2O ice

Physical property values for water ice are widely available, although commonly under terrestrial conditions; compilations can be found in the treatise by Hobbs (1974) and on the web at http://www.lsbu.ac.uk/water/data.html and http://skua.gps.caltech.edu/hermann/ice.table2.html.

CO_2

Physical property values for CO_2 are dispersed throughout the literature and are largely oriented toward commercial use. No compilation appropriate for Mars beyond that in James *et al*. (1992) has been assembled. Some additional information and values are summarized here.

There have been no recent measurements of the CO_2 saturation relation; the Clausius–Clapeyron relation is within 1% in pressure and 0.1 K in temperature of observations over Martian polar conditions (120 to 160 K) (James *et al*., 1992) and is adequate for most uses: $\mathrm{Log}(p) = a - b/T$; with $a = 27.9546$ and $b = 3182.48$, p is in Pascal, T is in Kelvin.

The thermal conductivity of CO_2 gas can be fit by an empirical formulation as

$k_g = -12.0817 + 1.39898\,T$; the value is $\sim 0.006\,\mathrm{W\,s^{-1}\,m^{-1}\,K^{-1}}$ at 145 K.

Although the kinetic theory of gases yields viscosity to be proportional to $\sqrt{T}$, experimental data available over the temperature range from 190 K to 290 K (Lange, 1967; Weast, 1970) more closely follow $\nu = \exp(1.4326 + 0.004404\ T)$. The extrapolated value at 145 K is 8 μPa s.

Solid carbon dioxide at Martian pressures forms a cubic crystal lattice. The latent heat of sublimation is $6.52308 \times 10^5 - 371.28\ T\ \mathrm{J\,kg^{-1}}$.

Thermal conductivity of the solid from 120 to 150 K in $\mathrm{W\,s^{-1}\,m^{-1}\,K^{-1}}$ follows closely the equation $k = 93.4/T$ (Kravchenko and Krupskii, 1998).

The heat capacity of the solid is $459.6 + 1.3585\ T\ \mathrm{kJ\,kg^{-1}\,K^{-1}}$

The density of solid CO_2 is $1606\ \mathrm{kg\,m^{-3}}$. However, estimates of the bulk density of CO_2 ice deposits on Mars suggest a range of $\sim 600\ \mathrm{kg\,m^{-3}}$ (Haberle *et al*., 2004) to $\sim 1000\ \mathrm{kg\,m^{-3}}$ (Smith *et al*., 2001a; Prettyman *et al*., 2004).

REFERENCES

Aharonson, O., M. T. Zuber, D. E. Smith, *et al*., Depth, distribution, and density of CO_2 deposition on Mars, *J. Geophys. Res.* **109**, E05004, doi:10.1029/2003JE002223, 2004.

Antoniadi, E. M., 1930, *The Planet Mars*, Trans. Patrick Moore, Devon, UK: Keith Reid Ltd., 1975.

Barker, E. S., R. A. Schorn, A. Woszczyk, R. G. Tull, and S. J. Little, Mars: detection of atmospheric water vapor during the southern hemisphere spring and summer season, *Science* **170**, 1308–10, 1970.

Bass, D. S., K. E. Herkenhoff, and D. A. Paige, Variability of Mars' north polar water ice cap. 1. Analysis of Mariner 9 and Viking Orbiter imaging data, *Icarus* **144**, 382–96, 2000.

Basu, S., M. I. Richardson, and J. R. Wilson, Simulation of the Martian dust cycle with the GFDL Mars GCM, *J. Geophys. Res.* **109**, E11006, doi:10.1029/2004JE002243, 2004.

Bell III, J. F., P. C. Thomas, M. J. Wolff, S. W. Lee, and P. B. James, Mineralogy of the north polar sand sea from 1995 Hubble Space Telescope near-IR observations. *Lunar Planet. Sci. Conf. XXVIII*, Abstract #1757, 1997.

Bell III, J. F., H. Y. McSween, J. A. Crisp, *et al*., Mineralogic and compositional properties of Martian soil and dust: results from Mars Pathfinder, *J. Geophys. Res.* **105**, 1721–55, 2000.

Benson, J. L. and P. B. James, Yearly comparisons of the martian polar caps: 1999–2003 Mars Orbiter Camera observations, *Icarus* **174**, 513–23, 2005.

Bibring, J.-P., Y. Langevin, F. Poulet, *et al*., Perennial water ice identified in the South polar cap of Mars, *Nature* **428**, 627–30, 2004.

Blunck, J., *Mars and Its Satellites: A Detailed Commentary on the Nomenclature*, 2nd rev edn., Smithtown, NY: Exposition Press, 1982.

Bonev, B. P., P. B. James, J. E. Bjorkman, and M. J. Wolff, Regression of the Mountains of Mitchel polar ice after the onset of a global dust storm on Mars, *Geophys. Res. Lett.* **29**, doi:10.1029/2002GL015458, 2002.

Bonev, B. P., J. E. Bjorkman, G. B. Hansen, P. B. James, and M. J. Wolff, Effects of atmospheric dust on residual south polar cap stability, *Annu. Lunar Planet. Conf. XXXVI*, Houston, TX: Lunar and Planetary Institute, Abstract #1101, March 14–18, 2005.

Boynton, W., W. C. Feldman, S. W. Squyres, *et al*., Distribution of hydrogen in the near surface of Mars: evidence for subsurface ice deposits, *Science* **297**, 81–5, 2002.

Byrne, S. and A. P. Ingersoll, A sublimation model for Martian south polar ice features, *Science* **299**, 1051–3, 2003.

Calvin, W. M., Additions and corrections to the absorption coefficients of CO_2 ice: applications to the martian south polar cap, *J. Geophys. Res.* **95**, 14743–50, 1990.

Calvin, W. M. and T. N. Titus, Summer season variability of the north residual cap of Mars as observed by the Mars Global Surveyor Thermal Emission Spectrometer (MGS-TES), *Planet. Space Sci.* **56**, 212–26, doi:10.1016/j.pss.2007.08.005, 2008.

Cantor, B., M. Malin, and K. S. Edgett, Multiyear Mars Orbiter Camera (MOC) observations of repeated Martian weather phenomena during the northern summer season, *J. Geophys. Res.* **107**, CiteID 5014, doi:10.1029/2001JE001588, 2002.

Clancy, R. T., S. W. Lee, G. R. Gladstone, W. W. McMillan, and T. Roush, A new model for Mars atmospheric dust based upon analysis of ultraviolet through infrared observations from Mariner 9, Viking, and Phobos, *J. Geophys. Res.* **100**, 5251–63, 1995.

Clancy, R. T., M. J. Wolff, and P. R. Christiansen, Mars aerosol studies with the MGS TES emission phase function observations: Opacities, particle sizes, and ice cloud types versus latitude and solar longitude, *J. Geophys. Res.* **108**, 5098, doi:10.1029/2003JE002058, 2003.

Colaprete, A., R. M. Haberle, and O. B. Toon, Formation of convective carbon dioxide clouds near the south pole of Mars, *J. Geophys. Res.* **108**, CiteID 5081, doi:10.1029/2003JE002053, 2003.

Colaprete, A., J. R. Barnes, R. M. Haberle, *et al*., Albedo of the south pole on Mars determined by topographic forcing of atmosphere dynamics, *Nature* **435**, 184–8, 2005.

Colaprete, A., J. R. Barnes, R. M. Haberle, and F. Montmessin, CO_2 clouds, CAPE and convection on Mars: observations and general circulation modeling, *Planet. Space Sci.* **56**, 150–80, doi:10.1016/j.pss.2007.08.010, 2008.

Cutts, J. A. and R. S. U. Smith, Eolian deposits and dunes on Mars, *J. Geophys. Res.* **78**, 4139–54, 1973.

Cutts, J. A., K. R. Blasius, G. A. Briggs, *et al*., North polar region of Mars: imaging results from Viking 2, *Science* **194**, 1329–37, 1976.

Douté, S., B. Schmitt, Y. Langevin, J. -P. Bibring, *et al*., South pole of Mars: nature and composition of the icy terrains from Mars Express OMEGA observations, *Planet. Space Sci.* **55**, 113–33, 2007.

Durham, W. B., S. H. Kirby, and L. A. Stern, Creep of water ices at planetary conditions: a compilation, *J. Geophys. Res.* **102**, 16293–302, 1997.

Durham, W. B., S. H. Kirby, and L. A. Stern, Steady-state flow of solid CO_2: preliminary results, *Geophys. Res. Lett.* **26**, 3493–6, 1999.

Farmer, C. B., D. W. Davies, and D. D. LaPorte, Mars: northern summer ice cap water vapor observations from Viking 2, *Science* **194**, 1339–41, 1976.

Feldman, W. C., T. H. Prettyman, W. V. Boynton, *et al*., CO_2 frost cap thickness on Mars during northern winter and spring, *J. Geophys. Res.* **108**, CiteID 5103, doi:10.1029/2003JE002101, 2003.

Feldman, W. C., T. H. Prettyman, S. Maurice, *et al*., Global distribution of near-surface hydrogen on Mars, *J. Geophys. Res.* **109**, CiteID E09006, doi:10.1029/2003JE002160, 2004.

Fischbacher, G. E., L. J. Martin, and W. A. Baum, *Martian Polar Cap Boundaries*. Final Report A, Contract 951547, Jet Propulsion Laboratory, Pasadena, CA. Planetary Research Center, Lowell Observatory, Flagstaff, AZ, 1969.

Fisher, D. A., Internal layers in an "accublation" ice cap: a test for flow, *Icarus* **144**, 289–94, 2000.

Folkner, W. M., R. D. Kahn, R. A. Preston, *et al*., Mars dynamics from Earth-based tracking of the Mars Pathfinder lander, *J. Geophys. Res*. **102**, 4057–64, 1997.

Forget, F. and J. B. Pollack, Thermal infrared observations of the condensing Martian polar caps: CO_2 ice temperatures and radiative budget, *J. Geophys. Res*. **101**, 16865–79, 1996.

Forget, F., G. B. Hansen, and J. B. Pollack, Low brightness temperatures of Martian polar caps: CO_2 clouds or low surface emissivity, *J. Geophys. Res*. **100**, 21219–34, 1995.

Forget, F., F. Hourdin, and O. Talagrand, CO_2 snowfall on Mars: simulation with a general circulation model, *Icarus* **131**, 302–16, 1998.

Forget, F., F. Hourdin, R. Fournier, *et al*., Improved general circulation models of the Martian atmosphere from the surface to above 80 km, *J. Geophys. Res*. 104, 24155–76, 1999.

Glenar, D. A., G. Hansen, G. Bjoraker, *et al*., Bright-region radiative properties within the Mars south polar cap ($L_s = 231^\circ$) from near-infrared spectroscopic imaging, *Icarus* **174**, 600–3, 2005.

Grundy, W. M. and B. Schmitt, The temperature-dependent near-infrared absorption spectrum of hexagonal H_2O ice, *J. Geophys. Res*. **103**, 25809–22, 1998.

Grundy, W. M., M. W. Buie, J. A. Stansberry, J. R. Spencer, and B. Schmitt, Near-infrared spectra of icy outer Solar System surfaces: remote determination of H_2O ice temperatures, *Icarus* **142**, 536–49, 1999.

Haberle, R. M., M. M. Joshi, J. R. Murphy, *et al*., General circulation model simulations of the Mars Pathfinder atmospheric structure investigation/meteorology data, *J. Geophys. Res*. **104**, 8957–74, 1999.

Haberle, R. M., B. Mattingly, and T. N. Titus, Reconciling different observations of the CO_2 ice mass loading of the Martian north polar cap, *Geophys. Res. Lett*. **31**, CiteID L05702, 2004.

Hansen, G. B., The infrared absorption spectrum of carbon dioxide ice from 1.8 to 333 micrometers, *J. Geophys. Res*. **102**, 21569–87, 1997.

Hansen, G. B., Control of the radiative behavior of the Martian polar caps by surface CO_2 ice: evidence from Mars Global Surveyor measurements, *J. Geophys. Res*. **104**, 16471–86, 1999.

Hansen, G. B., Ultraviolet to near-infrared absorption spectrum of carbon dioxide ice from 0.174 to 1.8 μm, *J. Geophys. Res*. **110**, CiteID E11003, doi:10.1029/2005JE002531, 2005.

Hansen, G. B., W. Giuranna, V. Formisano, *et al*., PFS-MEX observation of ices in the residual south polar cap of Mars, *Planet. Space Sci*. **53**, 1089–95, 2005.

Haas, W. H., Flashes on Mars observed in 1937 and some random remarks, *J. Assoc. Lunar Planet. Observers, The Strolling Astronomer* **45**, 43–5, 2003.

Herkenhoff, K. E. and A. R. Vasavada, Dark material in the polar layered deposits and dunes on Mars, *J. Geophys. Res*. **104**, 16487–500, 1999.

Herkenhoff, K. E., S. Byrne, and K. L. Tanaka, Mars polar geologic nomenclature: what are the caps? *4th Int. Conf. Mars Polar Sci. Explor*., Davos, Switzerland, LPI Contribution No. 1323, p. 8034, October 2–6, 2006.

Herr, K. C. and G. C. Pimentel, Infrared absorptions near 3 microns recorded over the polar cap of Mars, *Science* **166**, 496–9, 1969.

Herschel, W., On the remarkable appearances at the polar regions of the planet mars, the inclination of its axis, the position of its poles, and its spheroidical figure; with a few hints relating to its real diameter and atmosphere, *Philos. Trans. R. Soc. Lond*. **74**, 233–73, 1784.

Hess, S. L., Static stability and thermal wind in an atmosphere of variable composition: application to Mars, *J. Geophys. Res*. 84, 2969–73, 1979.

Hinson, D. P. and R. J. Wilson, Transient eddies in the southern hemisphere of Mars *Geophys. Res. Lett*. **29**, CiteID 1154, doi:10.1029/2001GL014103, 2002.

Hobbs, P. V., *Ice Physics*, Oxford: Clarendon Press, 837pp., 1974.

Houben, H., R. M. Haberle, R. E. Young, and A. P. Zent, Modeling the Martian seasonal water cycle, *J. Geophys. Res*. **102**, 9069–84, 1997.

Hourdin, F., F. Forget, and O. Talagrand, The sensitivity of the Martian surface pressure and atmospheric mass budget to various parameters: a comparison between numerical simulations and Viking observations, *J. Geophys. Res*. **100**, 5501–23, 1995.

Howard, A. D., The role of eolian processes in forming surface features of the martian polar layered deposits, *Icarus* **144**, 267–88, 2000.

Hunt, G. E., On the infrared radiative properties of CO_2 ice clouds: application to Mars, *Geophys. Res. Lett*. **7**, 481–4, 1980.

Ivanov, A. B. and D. O. Muhleman, The role of sublimation for the formation of the northern ice cap: results from the Mars Observer Laser Altimeter, *Icarus* **144**, 436–8, 2000.

Ivanov, A. B. and D. O. Muhleman, Cloud reflection observations: results from the Mars Orbiter Laser Altimeter, *Icarus* **154**, 190–206, 2001.

Jakosky, B. M., The role of seasonal reservoirs in the Mars water cycle: 1. Seasonal exchange of water with the regolith, *Icarus* **55**, 1–18, 1983a.

Jakosky, B. M., The role of seasonal reservoirs in the Mars water cycle: 2. Coupled models of the regolith, the polar caps, and atmospheric transport, *Icarus* **55**, 19–39, 1983b.

Jakosky, B. M., The seasonal cycle of water on Mars, *Space Sci. Rev*. **41**, 131–200, 1985.

Jakosky, B. M. and R. M. Haberle, Year-to-year instability of the Mars south polar cap, *J. Geophys. Res*. **95**, 1359–65, 1990.

Jakosky, B. M. and R. M. Haberle, The seasonal behavior of water on Mars. In *Mars* (ed. H. H. Kieffer *et al*.), University of Arizina Press, pp. 969–1016, 1992.

Jakosky, B. M., A. P. Zent, and R. W. Zurek, The Mars water cycle: determining the role of exchange with the regolith, *Icarus* **130**, 87–95, 1997.

James, P. B., H. H. Kieffer, and D. A. Paige, Seasonal cycle of carbon dioxide on Mars. In *Mars* (ed. H. H. Kieffer *et al*.), University of Arizona Press, pp. 934–68, 1992.

James, P. B., B. P. Bonev, and M. J. Wolff, Visible albedo of Mars' south polar cap: 2003 HST observations, *Icarus* **174**, 596–9, 2005.

Jones, K. L., R. E. Arvidson, E. A. Guinness, *et al*., One Mars year: Viking lander imaging observations, *Science* **204**, 799–806, 1979.

Kahn, R., T. Z. Martin, R. W. Zurek, and S. W. Lee, The Martian dust cycle. In *Mars* (ed. H. H. Kieffer *et al*.), University of Arizona Press, pp. 1017–53, 1992.

Kahre, M. A., J. R. Murphy, and R. M. Haberle, Modeling the Martian dust cycle and surface dust reservoirs with the NASA Ames general circulation model, *J. Geophys. Res*. **111**, E06008, doi:10.1029/2005JE002588, 2006.

Kelly, N. J., W. V. Boynton, K. Kerry, *et al*., Seasonal polar carbon dioxide frost on Mars: CO_2 mass and columnar thickness distribution, *J. Geophys. Res*. **111**, E03S07, doi:10.1029/2006JE002678, 2006.

Kieffer, H. H., Mars south polar spring and summer temperatures: A residual CO_2 frost, *J. Geophys. Res.* **84**, 8263–88, 1979.

Kieffer, H. H., H_2O grain-size and the amount of dust in Mars residual north polar-cap, *J. Geophys. Res.* **95**, 1481–93, 1990.

Kieffer, H. H., Cold jets in the martian polar caps, *J. Geophys. Res.* **112**, E08005, doi:10.1029/2006JE002816, 2007.

Kieffer, H. H. and T. Titus, TES mapping of Mars' north seasonal cap, *Icarus* **154**, 162–80, 2001.

Kieffer, H. H., S. C. Chase Jr., T. Z. Martin, E. D. Miner, and F. D. Palluconi, Martian north pole summer temperatures: dirty water ice, *Science* **194**, 1341–4, 1976.

Kieffer, H. H., T. N. Titus, K. F. Mullins, and P. R. Christensen, Mars south polar spring and summer behavior observed by TES: seasonal cap evolution controlled by frost grain size, *J. Geophys. Res.* **105**, 9653–99, 2000.

Kieffer, H. H., P. R. Christensen, and T. N. Titus, CO_2 jets formed by sublimation beneath translucent slab ice in Mars' seasonal south polar ice cap, *Nature* **442**, 793–6, 2006.

Kravchenko, Y. and I. Krupskii, Thermal conductivity of solid N_2O and CO_2, *Sov. J. Low Temp. Phys.* **12**, 46–8, 1998.

Lancaster, N. and R. Greeley, Sediment volume in the north polar sand sea of Mars, *J. Geophys. Res.* **95**, 10921–7, 1990.

Lange, N. A., *Lange's Handbook of Chemistry*, 10th edn., revised. New York: McGraw-Hill, 1967.

Langevin, Y., F. Poulet, J.-P. Bibring, *et al.*, Summer evolution of the north polar cap of Mars as observed by OMEGA/Mars Express, *Science* 307, 1581–3, 2005.

Langevin, Y., S. Douté, M. Vincendon, *et al.*, No signature of clear CO_2 ice from the "cryptic" regions in Mars' south seasonal cap, *Nature* **442**, 790–2, 2006.

Langevin, Y., J.-P. Bibring, F. Montmessin, *et al.*, Observations of the south seasonal cap of Mars during recession in 2004–2006 by the OMEGA visible/near-infrared imaging spectrometer on board Mars Express, *J. Geophys. Res.* **112**, E08S12, doi:10.1029/2006JE002841, 2007.

Larson, H. P. and U. Fink, Identification of carbon dioxide on the Martian polar caps, *Astrophys. J.* **171**, L91–L95, 1972.

Lemmon, M. T., M. J. Wolff, M. D. Smith, *et al.*, Atmospheric imaging results from the Mars exploration rovers: Spirit and opportunity, *Science* **306**, 1753–6, 2004.

Leighton, R. R. and B. C. Murray, Behavior of carbon dioxide and other volatiles on Mars, *Science* **153**, 136–44, 1966.

Litvak, M. L., I. G. Mitrofanov, A. S. Kozyrev, *et al.*, Long-term observations of southern winters on Mars: estimations of column thickness, mass, and volume density of the seasonal CO_2 deposit from HEND/Odyssey data, *J. Geophys. Res.* **112**, E03S13, doi:10.1029/2006JE002832, 2007.

Malin, M. C., M. H. Carr, G. E. Danielson, *et al.*, Early views of the Martian surface from the Mars orbiter camera of Mars global surveyor, *Science* **279**, 1681–5, 1998.

Malin, M. C., M. A. Caplinger, and S. D. Davis, Observational evidence for an active surface reservoir of solid carbon dioxide on Mars, *Science* **294**, 2146–8, 2001.

Markiewicz, W. J., R. M. Sablotny, H. U. Keller, *et al.*, Optical properties of the Martian aerosols as derived from Imager for Mars Pathfinder midday sky brightness data, *J. Geophys. Res.* **104**, 9009–17, 1999.

Martin, L. J., P. B. James, A. Dollfus, K. Iwasaki, and J. D. Beish, Telescopic observations: visual, photographic, polarimetric. In *Mars* (ed. H. H. Kieffer *et al.*), Tucson: University of Arizona Press, pp. 34–70, 1992.

Montmessin, F., F. Forget, P. Rannou, M. Cabane, and R. M. Haberle, Origin and role of water ice clouds in the Martian water cycle as inferred from a general circulation model, *J. Geophys. Res.* **109**, E10004, doi:10.1029/2004JE002284, 2004.

Montmessin, F., J. L. Bertaux, E. Quemerais, *et al.*, Subvisible CO_2 ice clouds detected in the mesosphere of Mars, *Icarus* **183**, 403–10, 2006.

Neugebauer, G., G. Miinch, H. H. Kieffer, S. C. Chase Jr., and E. Miner, Mariner, 1969 Infrared Radiometer results: temperatures and thermal properties of the Martian surface, *Astron. J.* **76**, 719, 1971.

Neumann, G. A., D. E. Smith, and M. T. Zuber, Two Mars years of clouds detected by Mars Orbiter Laser Altimeter, *J. Geophys. Res.* **108**, doi:10.1029/2002JE001849, 2003.

Nye, J. F., W. B. Durham, P. M. Schenk, and J. M. Moore, The instability of a south polar cap on Mars composed of carbon dioxide, *Icarus* **144**, 449–55, 2000.

Ockert-Bell, M. E., J. F. Bell III, J. B. Pollack, C. P. McKay, and F. Forget, Absorption and scattering properties of the Martian dust in the solar wavelengths, *J. Geophys. Res.* **102**, 9039–50, 1997.

Paige, D. A., The annual heat balance of the Martian polar caps from Viking observations, Ph.D. thesis, California Institute of Technology, 1985.

Paige, D. A. and A. P. Ingersoll, Annual heat-balance of Martian polar caps: Viking observations, *Science* **228**, 1160–8, 1985.

Paige, D. A. and K. D. Keegan, Thermal and albedo mapping of the polar regions of Mars using Viking thermal mapper observations. 2. South polar region, *J. Geophys. Res.* **99**, 25993–26013, 1994.

Paige, D. A., J. E. Bachman, and K. D. Keegan, Thermal and albedo mapping of the polar regions of Mars using Viking thermal mapper observations: 1. North polar region, *J. Geophys. Res.* **99**, 25959–91, 1994.

Pearl, J. C., M. D. Smith, B. J. Conrath, and P. R. Christensen, Observations of Martian ice clouds by the Mars Global Surveyor Thermal Emission Spectrometer, *J. Geophys. Res.* **106**, 12325–38, 2001.

Piqueux, S., S. Byrne, and M. I. Richardson, Sublimation of Mars's southern seasonal CO_2 ice cap and the formation of spiders, *J. Geophys. Res.* **108**, CiteID 5084, doi:10.1029/2002JE002007, 2003.

Pollack, J. B., R. M. Haberle, J. R. Murphy, J. Schaeffer, and H. Lee, Simulations of the general circulation of the Martian atmosphere: 2. Seasonal pressure variations, *J. Geophys. Res.* **98**, 3149–81, 1993.

Pollack, J. B., M. E. Ockert-Bell, and M. K. Shepard, Viking lander image analysis of Mar, tian atmospheric dust, *J. Geophys. Res.* **100**, 5235–50, 1995.

Prettyman, T. H., W. C. Feldman, M. T. Mellon, *et al.*, Composition and structure of the Martian surface at high southern latitudes from neutron spectroscopy, *J. Geophys. Res.* **109**, E05001, doi:10.1029/2003JE002139, 2004.

Prettyman, T. H., R. C. Elphic, W. C. Feldman, *et al.*, Spatial deconvolution of Mars Odyssey neutron spectroscopy data: analysis of Mars southern seasonal cap, *Lunar Planet. Sci. XXXVI*, Abstract #1384, 2005.

Quirico, E. and B. Schmitt, Near-infrared spectroscopy of simple hydrocarbons and carbon oxides diluted in solid N_2 and as pure ices: implications for Triton and Pluto, *Icarus* **127**, 354–78, 1997.

Richardson, M. I. and R. J. Wilson, Investigation of the nature and stability of the Martian seasonal water cycle with a general circulation model, *J. Geophys. Res.* **107**, 5031, doi:10.1029/2001JE001536, 2002.

Roach, L. H., J. F. Mustard, S. Murchie, *et al.*, CRISM spectral signatures of the north polar gypsum dunes, *Lunar Planet. Sci.*

Conf. XXXVIII, League City, Texas, LPI Contribution No. 1338, p. 1970, March 12–16, 2007.

Schmitt, B., S. Douté, Y. Langevin, *et al.*, *Northern seasonal condensates on Mars by OMEGA/Mars Express, Annu. Lunar Planet. Sci. Conf. XXXVI*, League City, Texas, Abstract #2326, March 14–18, 2005a.

Schmitt, B., S. Douté, Y. Langevin, *et al.*, Spring sublimation of the seasonal condensates on Mars from OMEGA/Mars Express, *Fall AGU Meeting*, Abstract #P23C-02, 2005b.

Smith, D. E., M. T. Zuber, and G. A. Neumann, Seasonal variations of snow depth on Mars, *Science* **294**, 2141–6, 2001a.

Smith, D. E., M. T. Zuber, H. V. Frey, *et al.*, Mars Orbiter Laser Altimeter: experiment summary after the first year of global mapping of Mars, *J. Geophys. Res.* **106**, 23689–722, 2001b.

Smith, D. E. and M. T. Zuber, Variation in the masses of the seasonal martian icecaps, Fall AGU Meeting, Abstract #P23C-01, 2005.

Smith, M., Interannual variability in TES atmospheric observations of Mars during 1999–2003, *Icarus* **167**, 148–65, 2004.

Smith, M. D., The annual cycle of water vapor on Mars as observed by the Thermal Emission Spectrometer, *J. Geophys. Res.* **107**, CiteID 5115, doi:10.1029/2001JE001522, 2002.

Soderblom, L. A., M. C. Malin, J. A. Cutts, and B. C. Murray, Mariner 9 observations of the surface of Mars in the north polar region, *J. Geophys. Res.* **78**, 4197–210, 1973.

Sprague, A. L., W. V. Boynton, K. E. Kerry, *et al.*, Mars' south polar Ar enhancement: a tracer for south polar seasonal meridional mixing, *Science* **306**, 1364–7, 2004.

Stoney, G. Jo, Of atmospheres upon planets and satellites, *Astrophys. J.* **7**, **25**, 1898.

Svitek, T. and B. Murray, Winter frost at Viking Lander 2 site, *J. Geophys. Res.* **95**, 1495–510, 1990.

Tanaka, K. L. and D. H. Scott, Geologic map of the polar regions of Mars, Scale 1:15,000,000. *USGS Misc. Inv. Ser. Map*, I-1802 C, 1987.

Thomas, P., K. E. Herkenhoff, A. D. Howard, B. C. Murray, and S. L. Squyres, Polar deposits of Mars. In *Mars* (ed. H. H. Kieffer *et al.*), University of Arizona Press, pp. 767–95, 1992.

Thomas, P. C., M. C. Malin, K. S. Edgett, *et al.*, North-south geological difference between the residual polar caps on Mars, *Nature* **404**, 161–4, 2000.

Thomas, P. C., M. C. Malin, P. B. James, *et al.*, South polar residual cap of Mars: features, stratigraphy, and changes, *Icarus* **174**, 535–59, 2005.

Tillman, J. E., N. C. Johnson, P. Guttorp, and D. B. Percival, The Martian annual atmospheric-pressure cycle: years without great dust storms, *J. Geophys. Res.* **98**, 10963–71, 1993.

Titov, D. V., Water Vapour in the atmosphere of Mars, *Adv. Space. Res.* **29**, 183–91, 2002.

Titus, T. N. and H. H. Kieffer, IR spectral properties of dust and ice at the mass south polar cap, American Astronomical society, DPS Meeting #33, Abstract #19.15, *Bull. Am. Astron. Soc.* **33**, 1071, 2001.

Titus, T. N., Mars polar cap edges tracked over 3 full Mars years, *Annu. Lunar Planet. Sci. Conf. XXXVI*, Houston, TX: Lunar and planetary Institute, Abstract #1993, March 14–18, 2005a.

Titus, T. N., Thermal infrared and visual observations of a water ice lag in the Mars southern summer, *Geophys. Res. Lett.* **32**, L24204, doi:10.1029/2005GL024211, 2005b.

Titus, T. N., Kieffer, H. H., Mullins, K. F., TES observations of the south pole, American Astronomical Society, DPS meeting #30, #20.05, *Bull. Amer. Astron. Soc.* **30**, 1049, 1998.

Titus, T., H. H. Kieffer, K. F. Mullins, and P. R. Christensen, TES premapping data: slab ice and snow flurries in the Martian north polar night, *J. Geophys. Res.* **106**, 23181–96, 2001.

Titus, T. N., H. H. Kieffer, and P. R. Christensen, Exposed water ice discovered near the south pole of Mars, *Science* **299**, 1048–51, 2003.

Tokar, R. L., W. C. Feldman, T. H. Prettyman, *et al.*, Ice concentration and distribution near the south pole of Mars: synthesis of Odyssey and global surveyor analyses, *Geophys. Res. Lett.* **29**, 1904, doi:10.1029/2002GL015691, 2002.

Tomasko, M. G., L. R. Doose, M. Lemmon, P. H. Smith, and E. Wegryn, Properties of dust in the Martian atmosphere from the Imager on Mars Pathfinder, *J. Geophys. Res.* **104**, 8987–9007, 1999.

Tsoar, H., R. Greeley, and A. R. Peterfreund, Mars: the north polar sand sea and related wind patterns, *J. Geophys. Res.* **84**, 8167–80, 1979.

Tyler, D. and J. R. Barnes, A mesoscale model study of summertime atmospheric circulations in the north polar region of Mars, *J. Geophys. Res.* **110**, CiteID E06007, doi:10.1029/2004JE002356, 2005.

Tyler, G. L., G. Balmino, D. P. Hinson, *et al.*, Radio science observations with Mars Global Surveyor: orbit insertion through one Mars year in mapping orbit, *J. Geophys. Res.* **106**, 23327–48, 2001.

Wagstaff, K. L., T. N. Titus, A. B. Ivanov, R. Castaño, and J. L. Bandfield, Stratigraphic analysis of the northern polar layered deposits of Mars: implications for recent climate history, *Planet. Space Sci.* **56**, 256–65, doi:10.1016/j.pss.2007.08.008, 2008.

Wall, S. D., Analysis of condensates formed at the Viking-2 Lander site: the 1st winter, *Icarus* **47**, 173–83, 1981.

Ward, W. R. and D. J. Rudy, Resonant obliquity of Mars? *Icarus* **94**, 160–4, 1991.

Wang, H. and A. P. Ingersoll, Martian clouds observed by Mars Global Surveyor Mars Orbiter Camera, *J. Geophys. Res.* **107**, CiteID 5078, doi:10.1029/2001JE001815, 2002.

Warren, S. G., Optical constants of ice from the ultraviolet to the microwave, *Appl. Opt.* **23**, 1206–25, 1984.

Weast, R. C. (ed.), *Handbook of Chemistry and Physics*, 51st edn., Cleveland: Chemical Rubber Co., 1970.

Wells, E. H. and D. P. Hale, Flashes on Mars observed in 1937 and some random remarks, *Nature* **232**, 324–5, 1971.

Wilson, L. J., Apparent flashes seen on Mars, *Pop. Astron.* **45**, 430, 1937.

Winfree, K. W. and T. N. Titus, Estimation of CO_2 coverage on Mars' south pole: an interannual assessment, *Annu. Lunar Planet. Sci. Conf. XXXVII, League City, Texas*, Abstract #2283, March 13–17, 2006.

Wolff, M. J. and R. T. Clancy, Constraints on the size of Martian aerosols from Thermal Emission Spectrometer observations, *J. Geophys. Res.* **108**, 5097, doi:10.1029/2003JE002057, 2003.

Wolff, M. J., M. D. Smith, R. T. Clancy, *et al.*, Constraints on dust aerosols from the Mars Exploration Rovers using MGS overflights and Mini-TES, *J. Geophys. Res.* **111**, E12S17, doi:10.1029/2006JE002786, 2006.

Yoder, C. F. and E. M. Standish, Martian precession and rotation from Viking lander range data, *J. Geophys. Res.* **102**, 4065–80, 1997.

Zasova, L., V. Formisano, V. Moroz, *et al.*, Water clouds and dust aerosols observations with PFS MEX at Mars, *Planet. Space Sci.* **53**, 1065–77, 2005.

Zuber, M. T., D. E. Smith, S. C. Soloman, *et al.*, Observations of the north polar region of Mars from the Mars Observer Laser Altimeter, *Science* **282**, 2053–60, 1998.

26

Astrobiological implications of Mars' surface composition and properties

D. J. DES MARAIS, B. M. JAKOSKY, AND B. M. HYNEK

ABSTRACT

A central goal in Mars exploration is to determine whether life has ever existed there and, whether it did or not, the degree to which the Mars environment could have sustained life. To attain this goal, we can characterize the environmental context, identify places most likely to have sustained life and retained evidence of its presence, and search for "biosignatures," namely features created only by life and that can persist long after they were formed. Life as we know it requires liquid water, source(s) of energy to sustain metabolism, and chemical building blocks for its cellular constituents. The availability of liquid water appears to be the primary limiting factor in near-surface Martian environments. Liquid water apparently was more widespread on the surface in ancient times and it has occurred within the crust at various times. Oscillations in the orbital obliquity of Mars probably influenced the distribution of water, and some evidence hints of recent liquid water. Observations by the Mars Exploration Rover (MER) *Spirit* in Gusev crater are consistent with the possibility that liquid water, nutrients and sources of chemical energy were simultaneously available to sustain habitable conditions in subsurface Columbia Hills materials at least some time in the distant (Noachian?) past. As of this writing *Spirit* rover has not yet determined that these conditions ever existed in a surface environment. MER *Opportunity* revealed that habitable environments might have persisted for an extended period of time in the Meridiani Planum region at some time in the distant past. If these ancient aqueous environments had been highly acidic, this acidity might have inhibited prebiotic chemical reactions leading to the origins of life at those locations. But we must admit that the attributes of any Martian life might differ in fundamental ways from life on Earth. We must be prepared to explore a "gray zone" that extends beyond the characteristics or limits of life as inferred from our terrestrial example. The Martian meteorite ALH 84001 might be an example of such a "gray zone." Mars exploration will engender years of continuing analysis, debate and, perhaps eventually, profound insights about the potential for life in the universe.

26.1 INTRODUCTION

A central goal in Mars exploration is to determine whether life has ever existed there. A closely related goal is to determine whether Mars could have been habitable anytime during its history, even if life never existed there. To address this goal we must know the conditions that are required to support an origin or persistence of life as well as the conditions that have occurred on Mars throughout its history. We also must understand the nature of the Martian atmosphere and how it has evolved through time, the interactions with the surface and subsurface, and the geological and geochemical environment of the surface and subsurface. Although these goals were identified at the time of the Viking mission three decades ago, some of the key measurements that bear directly on them have been identified or made only recently.

The composition, mineralogy, and geology of the surface have played central roles in determining the habitability of Mars. They have defined the environmental niches that might exist and their distribution in space and time. We will explore those aspects of the surface and near-surface region that determine habitability and discuss the overall potential for Martian life to exist or have existed. Clearly, we cannot determine from only this information whether life ever existed on Mars – that will require measurements specific to the detection of life or fossil life – but we can describe the environmental context, identify places most likely to have sustained life and retained some evidence of its presence, and discuss ways in which a search for life might be carried out in order to have the greatest possibility of success.

We discuss certain fundamental attributes of life on Earth and some general environmental characteristics that it requires, the regional and global characteristics of Mars that constrain habitability, and the local characteristics of two regions that have recently been explored in detail by the MERs. We finish with a synthesis of the question of the potential for life on Mars and a brief discussion of how to go about searching for evidence of present or past life.

Several highly informative books and articles provide more general overviews of astrobiology and the exploration of other planetary environments. For example, Jakosky (1998) describes the science and the strategies involving the search for evidence of life beyond Earth. An excellent overview of the history of Earth also addresses the factors that influence its habitability as well as its cosmic context (Lunine, 1998). Ward and Brownlee (2000) evaluate in detail the probability that a biosphere with complex life (e.g., plants and animals) might arise on other planets. Selected journal articles also provide key perspectives on astrobiology exploration. For example, studies of the environmental

The Martian Surface: Composition, Mineralogy, and Physical Properties, ed. J. F. Bell III. Published by Cambridge University Press.

limitations to life on Earth provide guidance to our search for life on Mars (Nealson, 1997). Nonphotosynthetic ecosystems on Earth give examples of sites that we might explore for life on Mars and also key features that we might find (Shock, 1997). Jakosky and Shock (1998) address potential amounts of chemical energy available to any life on Mars. And finally, NASA's Astrobiology Roadmap outlines the goals, objectives, and strategies of NASA's astrobiology program (Des Marais *et al*., 2003).

26.2 LIFE AND HABITABLE ENVIRONMENTS

26.2.1 Attributes and signatures of life

A search for evidence of life requires a working concept of life's fundamental attributes. Such a concept helps to identify and interpret features on Mars that might be indicative of life, hereafter called "biosignatures." The concept also identifies the "services" that an environment must provide in order to sustain life. This in turn helps to identify either ancient or present-day potentially habitable environments that are promising candidates for exploration.

Our approach must provide for the possibility that life on Earth and Mars might differ in fundamental ways. Indeed, some have argued that without a second, independent example of life, it is not possible to determine which characteristics are unique to terrestrial life and which are common or required for life in general, and that this precludes our enunciating a unique definition of life (Cleland and Chyba, 2007). For example, given the enormous diversity of organic chemistry, life elsewhere may not utilize DNA and RNA molecules to perform genetic and self-replicative functions. Thus we should not simply equate the search for life with a search for specific Earthly biochemicals. Astrobiology must blaze the path that leads from our incomplete Earth-centric concept of life to a more universal one. We have little choice but to begin our search with fundamental attributes of living systems as we know them and then strive to discern those characteristics shared by all life.

In his book *Beginnings of Cellular Life*, H. Morowitz identified several attributes, shown within quotation marks below, which are universal to life on Earth (Morowitz, 1992). The examples listed below seem particularly relevant to astrobiology.

1. "*The chemistry of life is carried out in aqueous solutions or at water interfaces. Cells can survive the removal and restoration of cellular water, but water is essential to cellular function*." Water is therefore essential to ensure life's long-term survival. Although other liquids potentially could serve similar functions, we will discuss below that water is likely to have been abundant on Mars throughout its history and that other liquids are not.
2. "*The major atomic components in the covalently bonded portions of all functioning biological systems are C, H, N, O, P and S*." The distribution and chemical compounds of these elements therefore deserve particular attention.
3. "*A cell is the most elementary unit that can sustain life*." Single-celled organisms are by far the most diverse and most ancient forms of life known. Microorganisms can tolerate greater environmental extremes than can plants and animals.
4. "*There is a universal set of small organic molecules that constitutes the total mass of all cellular systems*." The array of organic molecules utilized by life on Earth represents an infinitesimally small subset of all possible organic molecules. A remarkably small number of key molecules participate in intermediary metabolism and serve as the building blocks of cellular structures and macromolecules. This small number perhaps reflects an evolutionary selection for speed and efficiency. Living systems maintain high information contents at molecular and structural levels.
5. "*Those reactions that proceed at appreciable rates in living cells are catalyzed by enzymes*." Catalysis enables cells to maintain their metabolism and to repair damage caused by environmental challenges such as radiation. Cellular enzymes also enable life to acquire essential energy by harvesting sunlight and by accelerating reactions between oxidized and reduced chemical species in the environment.
6. "*Sustained life is a property of an ecological system rather than a single organism or species*." For example, biofilms are byproducts of highly successful ecological systems and have an ancient fossil record.
7. "*All populations of replicating biological systems give rise to altered phenotypes that are the result of mutated genotypes*." All known living systems evolve by Darwinian-like natural selection and survival. "Phenotype" is a cell's molecular and structural "machinery"; genotype is the information preserved in genomic molecules (DNA and RNA are examples in our biosphere).

These basic attributes of life have allowed biochemists, paleontologists, and astrobiologists to identify and interpret categories of biosignatures in ancient geologic deposits on Earth. Categories of biosignatures that might also be applicable to Mars include the following:

1. *Organic compounds having certain molecular structures*. "Unusually" high relative abundances of specific organic molecules in a rock *might* constitute evidence of a biological origin. Molecules such as porphyrins, fatty acids, amino acids, and polysaccharides help to sustain key biochemical functions and therefore can be relatively abundant. Some of these molecules are relatively robust and can survive burial and storage in sedimentary rocks. For example, 2.7 Gyr old ancient sediments contain higher molecular weight hydrocarbons having molecular structures that reveal their ancestry as hopanoid, isoprenoids, and steroids (Brocks *et al*., 2003). These compounds are key constituents of cellular membranes and they can even be diagnostic for particular groups of microorganisms.
2. *Cellular fossils*. Microorganisms have been preserved as micrometer-scale spheres, rods, and filaments in fine-grained mineral and sedimentary deposits as old as 3.5 Gyr (Schopf *et al*., 1992). Their biological origin

can be demonstrated by the presence of cellular structures or particular chemical compositions. Their size distributions might match those of modern microbial populations.

3. *Stable isotopic patterns*. Both the biosynthesis of organic matter and biologically catalyzed oxidation–reduction reactions can discriminate against the heavier isotopes of carbon or sulfur to create patterns that indicate biological origins. For example, the bimodal distribution of $^{13}C/^{12}C$ abundances in ancient sedimentary reservoirs of carbonates and reduced carbon indicate that our biosphere existed since at least 3.5 Ga (Des Marais, 2001). The geologic record of sedimentary sulfides reveals a comparable antiquity for sulfate reducing microorganisms (Canfield, 2001).
4. *Fabrics and structures*. Biofilms can permeate and stabilize accreting sediment surfaces and create distinctive fabrics. For example, ancient rocks can preserve curved and/or contorted sheet-like structures indicating the former presence of flexible organic biofilms. Stacks of laminations can accumulate in aqueous sedimentary environments to form stromatolites, which are microbial reef-like structures that represent the oldest, most widespread fossil evidence of early microbial communities (Walter, 1976).
5. *Minerals*. Microorganisms can precipitate minerals such as magnetite, sulfides, or phosphates during their metabolic or energy-harvesting activities. The crystal morphology and chemical composition of such minerals can indicate their biological origins (e.g., Bazylinski and Moskowitz, 1997).
6. *Energy harvesting and storage*. Life processes energy by promoting reactions between reduced and oxidized compounds. Products of these reactions can become biosignatures. For example, atmospheric O_2 is a biosignature on Earth because its high abundance requires both a photosynthetic source and the burial in sediments of a substantial quantity of photosynthetically produced organic matter (Des Marais, 2001). This sedimentary organic matter and its oxidized equivalents in the atmosphere and elsewhere are biosignatures. They are stored energy that we exploit when we burn fossil fuels. Microorganisms can harvest chemical energy either by reducing sulfate or by oxidizing Fe^{2+}, creating sulfide (Canfield, 2001) and iron oxide mineral products (e.g., Bazylinski and Moskowitz, 1997) that can become biosignatures in sedimentary rocks.

But biosignatures must not only be produced to be useful, they also must be preserved in geologic deposits. In sedimentary deposits that consist of detritus (e.g., sands, silts, and clays), preservation is favored by rapid burial in fine-grained, clay-rich sediments (Farmer and Des Marais, 1999). In chemically precipitated sediments, preservation is enhanced by rapid entombment in fine-grained, stable minerals. Biosignatures are better preserved in deposits that resist weathering and alteration by permeating gases and fluids. Host rocks composed of silica (e.g., chert rocks), phosphates (e.g., phosphorite rocks) afford excellent preservation. Although carbonates and shales are less resistant, they are far more abundant and therefore they have preserved the bulk of the geologic record of Earth's early biosphere.

26.2.2 Environmental requirements

We can categorize the range of environmental conditions in which life on Earth can exist and discuss those aspects of the environment that allow life to exist and that provide support for the metabolic pathways actually utilized by life. We will focus on the presence of liquid water, access to the biogenic elements in a useful form, and a source of energy that can support the metabolism of microorganisms (see Jakosky, 2006). Recognizing that we have only one example of a biosphere that might indeed be unique in fundamental ways, we wish to extrapolate from our one example to understand the conditions suitable for life anywhere. This is a more difficult problem and, of necessity, involves speculation and uncertainty.

A liquid is required in order to provide a medium through which nutrients can diffuse to an organism and through which waste products can diffuse away. This process is facilitated if molecules can dissolve in the liquid. Based on our terrestrial example and based on general chemical principles, liquid water is an excellent medium for life (Pohorille, 2006). It may not be the only possible medium in which life can exist, given both the tremendous versatility of life and the potential and actual occurrence of other liquids elsewhere in our Solar System or beyond. However in the case of Mars, the evidence that liquid water has been widespread is compelling, and there is little or no evidence for other liquids.

Temperature must be within the range that allows liquid water and the biomolecules necessary to support life to exist. At the cold end, liquid water can exist at temperatures below 0 °C either as thin films at grain contacts or when dissolved salts depress the freezing point (Jakosky *et al*., 2003). Cellular growth has been measured at temperatures below −10 °C, and metabolic activity normally associated with growth has been detected down to −20 °C (Bakermans *et al*., 2003; Figure 26.1). There is no inherent reason why

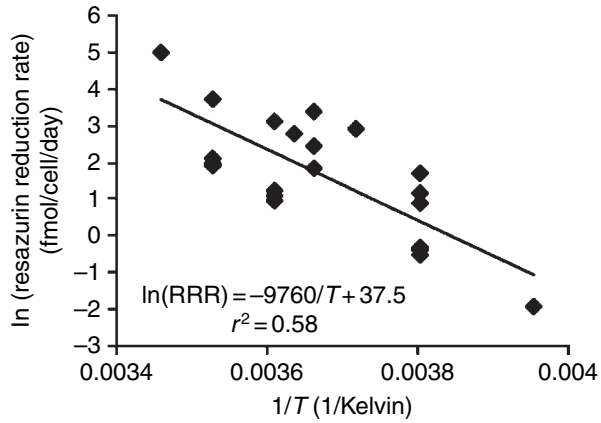

Figure 26.1. Measured reduction rate for one biochemical, resazurin, for organisms derived from Siberian permafrost, showing clear evidence of ongoing metabolism at temperatures as low as −20 °C ($1/T$ = 0.00395; Jakosky *et al*., 2003).

life could not exist at lower temperatures, although the potential absence of liquid water at colder temperatures and the much slower pace of chemical reactions at those temperatures probably limit the distribution of any such habitable environments. Of course, organisms can survive long periods at lower temperatures without growth, as we observe when storing microorganisms at liquid nitrogen temperatures or in spore generation and survival.

At higher temperatures, organisms isolated from hot springs have demonstrated growth at temperatures above 120 °C and possibly approaching 130 °C (e.g., Stetter, 1990). Water is kept liquid at these temperatures by higher pressures that occur beneath the surface or at the bottom of the ocean. The temperature at which DNA and other biomolecules break apart might set the ultimate upper temperature limit for terrestrial life. This is thought to be in the range 125–150 °C (Brock *et al.*, 1994). Although other molecules could be used to carry out the same functions, and it is conceivable that they have higher denaturation temperatures, the complexity of the required molecules suggests that the upper temperature would not be too different from the limit for DNA. However, the incredible adaptivity of organisms precludes our knowing this upper limit with any certainty.

Access to the biogenic elements is required to support life. Life could make use of a different set of elements on Mars than it does on Earth, so we look for evidence that Mars has a diverse suite of elements, starting with C, H, N, and O, and that they are accessible at and near the surface. Mars certainly has abundant H, C, and O, which are central to terrestrial life. These are contained in atmospheric CO_2 and H_2O, and there is evidence for subsurface CO_2 (as carbonates, and it also could be dissolved in subsurface water) and H_2O (Owen, 1992). The global abundance of C is uncertain, however. There is evidence for nonatmospheric C in the form of carbonates in the dust (Bandfield *et al.*, 2000) and in the Martian meteorites, with the abundance being as much as a few percent in ALH 84001 (Mittlefehldt, 1994). However, the total amount of C sequestered in the crust is unknown and could be sufficiently small as to make life problematic. Presumably, the isotopic evidence for loss of C to space (Jakosky and Phillips, 2001) means that the C abundance must have been greater during earlier times. The global inventory of N also is unknown, however; the amount of N_2 gas in the atmosphere is low, and N compounds have not been detected on the surface. The N inventory could be low enough to be problematic for life. Life on Earth utilizes about two dozen additional elements, including P, S, Ca, Mg, Fe, and so on. In general, these elements are thought to be available in any geologically active environment. *In situ* measurements from landed spacecraft and analyses of Martian meteorites collected here on Earth indicate that, in fact, these elements are available and accessible on Mars (e.g., McSween, 1994; see also Chapters 3, 4, and 17).

Energy is required in order to drive metabolism, whether it be utilized to repair damaged cellular structures, to drive motion or reproduction, or to create new cellular material. On Earth, most energy derives from sunlight via photosynthesis. Mars, orbiting at an average of 1.4 times the Earth's distance from the Sun, still has access to abundant sunlight at the surface. Sunlight also should be accessible beneath the surface in limited regions, such as at shallow depths within the polar ice. Sunlight may be a problematic source of energy today, though, given the difficulty that organisms would have surviving at the surface in the present environment; and it may be problematic in the earliest times when the surface was more conducive to life, given that photosynthesis is a sophisticated source of energy utilization and may not have evolved early. A plausible source of energy for potential Martian organisms, though, is via chemical reactions at and beneath the surface (Shock, 1997). Some terrestrial organisms make use of such chemical reactions. The reactions take advantage of the chemical disequilibrium that exists in many environments. For example, rocks emplaced by geological processes often find themselves out of chemical equilibrium with water. Useful reactions can include those between water and rock (equivalent to geochemical weathering reactions) or involving oxidation or reduction of Fe, Mn, or C, and can occur in aqueous systems that are at relatively low-temperature conditions (as long as liquid water is available) or that have been heated by nearby volcanic or impact activity (Nealson, 1997). An inventory of the energy available via such reactions indicates that there is sufficient energy to support a Martian biosphere (Jakosky and Shock, 1998; Varnes *et al.*, 2003; Link *et al.*, 2005).

The radiation environment at the Martian surface is often mentioned as being problematic to either an origin of life or its continued evolution. High-energy galactic and solar cosmic rays and solar ultraviolet radiation have sufficient energy to break molecular bonds in cellular components, and can damage or kill living organisms (Brock *et al.*, 1994). These processes have the potential to affect life at the Martian surface, although subsurface life (shielded beneath only millimeters of regolith for ultraviolet light or decimeters to meters for cosmic rays) would be protected. However, it is not clear what the real impact would be on surface life. Surface life would have been most likely during the early, wetter epochs. At this time, a thicker atmosphere would have provided substantial protection (as it does on Earth today). In addition, the presence of an intrinsic magnetic field early on (e.g., Solomon *et al.*, 2005), and of localized crustal magnetism that would create "mini-magnetospheres" subsequently (Brain *et al.*, 2003), would provide significant protection. Also, some organisms on Earth have developed the capability to survive in high-radiation environments (likely as a side benefit of living in very dry, desiccating environments), and might be able to do so on Mars as well (Ghosal *et al.*, 2005). The key is whether the constructive processes of metabolism in organisms occurred more quickly than the destructive processes involving radiation; it is unknown which would win out on Mars.

In summary, the constraints placed on a Martian environment that would allow it to support life are straightforward (Chang, 1988). There is strong evidence that the biogenic elements are adequately available, with the possible exception of N. The other requirements both hinge on the availability of liquid water, to act as a medium in which life resides and to support the types of chemical weathering

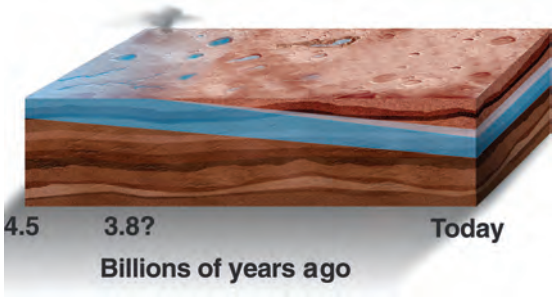

Figure 26.2. Hypothetical distribution of habitable environments, shown in light blue with wavy lines, in the Martian crust during its history. Surface and near-surface environments might have been habitable early in Martian history, whereas any habitable environments today might be restricted to a zone that lies a few kilometers below the surface. Graphics by Cheryse Triano, TopSpin Design Works. (For a color version of this figure, please refer to the color plate section or to the e-Book version of this chapter.)

reactions that can support life. Thus, the ability of Mars to support life depends on the availability and distribution of water, which we will discuss in the next section.

26.3 GLOBAL CHARACTERISTICS OF MARS

Do conditions exist on Mars at the present, or did they at some time in the past, which are conducive to the existence of life (Figure 26.2)? We will focus primarily on the availability of water, as that appears to be the primary limiting factor. We will discuss the occurrence of water on the surface in ancient times, within the crust at various times, the potential to produce liquid water by the oscillations in obliquity, and the evidence and potential for recent liquid water.

26.3.1 Ancient surface water

Evidence that liquid water has flowed over the Martian surface and that Mars may have had a thicker atmosphere in its early history has been available since the days of the Mariner 9 spacecraft. There are three pertinent observations.

First is the occurrence of valley networks. These consist of integrated dendritic (branching) systems of valleys averaging 2 km across (Carr and Clow, 1981; Carr and Malin, 2000; Williams and Phillips, 2001) that have an appearance reminiscent of water drainage systems on Earth. These occur primarily on the ancient highlands, surfaces dated by crater counting as being older than about 3.7 Gyr (Carr, 1995). In addition, a small number of valleys occur on the boundary between the highlands and lowlands, or on the flanks of younger volcanoes; some of the latter might be associated either with the thermal or water environment associated with volcanic activity, and may not be related directly to the extant climate (e.g., Gulick and Baker, 1990). Many tributaries of the valley network systems have their heads near topographic divides, suggestive of precipitation and runoff (Craddock and Howard, 2002; Hynek and Phillips, 2003).

Second is the removal of impact craters smaller than about 15–20 km diameter on these same ancient surfaces, along with

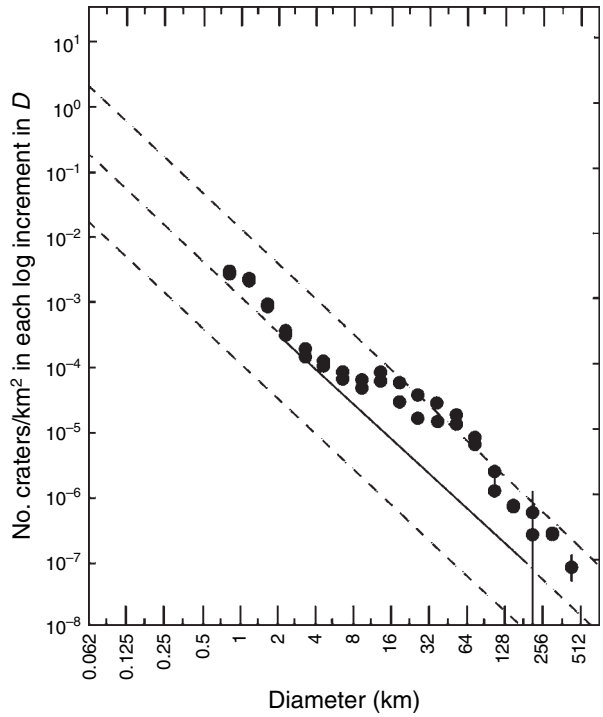

Figure 26.3. Crater size-frequency distribution for heavily cratered terrain on Mars, showing the sharp decline in the number of craters at sizes smaller than about 15 km diameter (Basaltic Volcanism Study Project, 1981).

the severe degradation of larger craters (Chapman and Jones, 1977). Craters smaller than 15 km are present in reduced numbers, and these are thought to be younger in age. The crater size-frequency distribution is most easily interpreted as indicating the removal of the smaller craters, followed by the production of new craters in subsequent years; the number of younger craters is what allows us to date the end of the erosion event as being approximately 3.7 Ga (Figure 26.3).

Third is degradation in the appearance of impact craters that remained. The larger remaining craters have lost their distinct ejecta blankets, raised rims, and central peaks. Many of them show just a round, flat-floored depression remaining on the surface. Some craters appear to have been only partially degraded. Many of these show a spur-and-gully topography on the interior rim that is reminiscent of similar features here on Earth that were formed by erosion by flowing water (Craddock and Maxwell, 1993; Figure 26.4). Degraded craters are generally at least 500 m to as much as 3000 m shallower than fresh craters at equivalent diameters, indicative of copious erosion (Craddock and Howard, 2002).

The general (but not unanimous) consensus has been that these characteristics are most consistent with the erosion of surface materials by flowing water (e.g., Pollack *et al.*, 1987; Carr, 1996). The widespread occurrence of the erosion, and the fact that the style of erosion probably required relatively long periods of time (rather than, say, a single, short-lived, catastrophic event), suggested that the liquid water must have been present for relatively long periods. This would have been possible if liquid water was more stable than at present, and is most readily explained if the ancient

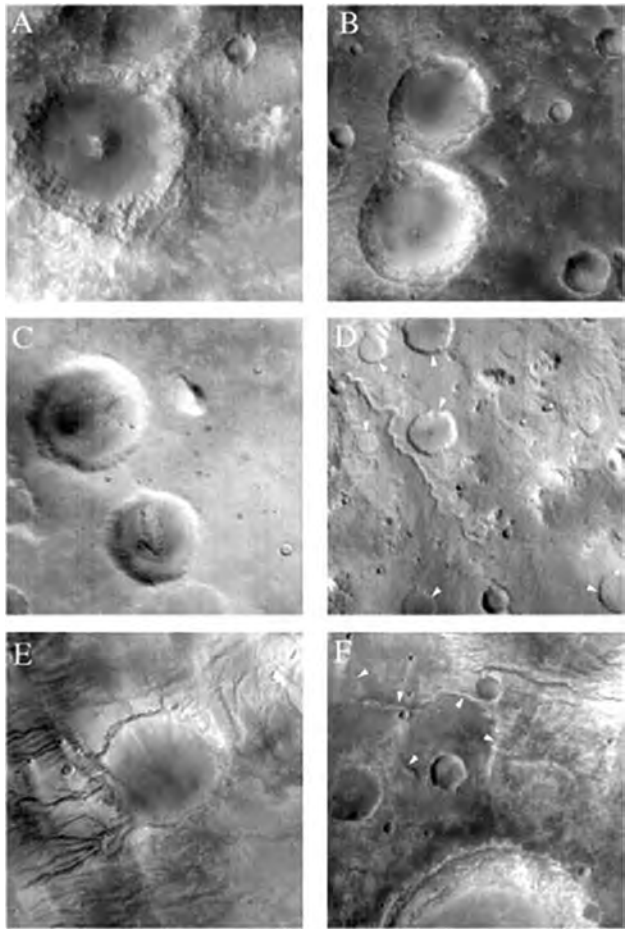

Figure 26.4. Sequence of partially degraded craters, showing the transition from fresh appearing crater to crater heavily degraded by runoff (Craddock and Maxwell, 1993).

atmosphere contained abundant greenhouse gases that would raise surface temperatures enough to allow liquid water to be stable. The change in the nature of surface erosion, with these features being absent from most surfaces younger than 3.7 Gyr in age, would then be explained by the disappearance of the greenhouse atmosphere and the cooling of the environment at that time (Pollack *et al*., 1987).

Models for the thermal evolution of the Martian mantle are also consistent with a substantial crustal reservoir of water on ancient Mars. Hauck and Phillips (2002) stated:

> The importance of a wet mantle in satisfying the basic constraints of Mars' thermal and crustal evolution suggests (independently from traditional geomorphology or meteorite geochemistry arguments) that early Mars had a wet environment. Extraction of water from the mantle of a one-plate planet such as Mars is found to be extremely inefficient, such that 90–95% of all water present in the mantle after the initial degassing event should still reside there currently. Yet extraction of even 5% of a modestly wet mantle (≈36 ppm water) would result in a significant amount (6.4 m equivalent global layer) of water available to influence the early surface and climate evolution of the planet.

Carbon dioxide has been suggested as being the most plausible greenhouse gas, especially because the amounts required to raise the temperature to the melting point of ice, perhaps several bars, are consistent with estimates of how much CO_2 might have been available on the planet. The amounts are uncertain for several reasons, however. First is that, although the Sun likely was about 30% dimmer at that time than it is at present, the exact amount is unknown due to the possibility that the Sun has lost mass and changed its luminosity (Sagan and Mullen, 1972; Sackman and Boothroyd, 2003). Second, models of greenhouse warming produce saturation of the atmosphere at high altitudes that might limit the total amount of CO_2 that the atmosphere could hold (Kasting, 1991). Additional warming due to clouds, dust, or other greenhouse gases might offset this effect, however (Forget and Pierrehumbert, 1997). Third, it is not clear how warm the surface must have been to allow liquid water to erode the surface. Liquid water can flow over the surface even when average temperatures are below freezing, perhaps protected by a thin covering of ice or with freezing temperatures depressed by small amounts of dissolved salts (e.g., McKay *et al*., 1992).

If the early atmosphere did, in fact, contain several bars of CO_2, it might have been removed from the atmosphere by several mechanisms. Impacts during the tail end of accretion and the late-heavy bombardment may have ejected gas from the atmosphere (Melosh and Vickery, 1989; Brain and Jakosky, 1998). Formation of carbonate minerals within the subsurface could provide a sink for atmospheric CO_2 (Pollack *et al*., 1987). And interactions with solar ultraviolet light and with the impinging solar wind could have stripped off much of the atmosphere (Luhmann *et al*., 1992). There is compelling observational evidence that each of these processes has happened. We see carbonate minerals in at least some Martian meteorites (Mittlefehldt, 1994), and there is remote-sensing evidence for its occurrence at the few percent level in Martian dust (Bandfield, *et al*., 2000); we know that impacts that formed the observed impact craters would have ejected atmospheric gas to space; and we see an enrichment in heavier stable isotopes that is a unique indicator of the removal of the lighter isotopes to space (Jakosky *et al*., 1994). Although we do not at present know the relative importance of each of these processes, together they likely can account for loss of the bulk of a thick, early greenhouse atmosphere. (We did not include early hydrodynamic escape of hydrogen, with its ability to drag along other molecules, on our list of loss processes. This process would have occurred very early in Martian history [Pepin, 1994], prior to the earliest remaining geologic record; thus, while potentially important as a process by which planetary volatiles would have been lost, it would not have been important in driving any change in the climate as inferred from that geologic record [Brain and Jakosky, 1998].)

An alternative scenario has been suggested recently by Segura *et al*. (2002). They point out that large impacts associated with the oldest remaining geological record would have heated the surface and mobilized any subsurface water or ice. This water would drive a transient greenhouse atmosphere that could have provided a short-lived increase in temperature. The water also would have precipitated out of the atmosphere in a relatively short-lived (hundreds of years) rainfall and runoff event that could have formed the

geological features described above. In theory, enough water could have been mobilized in this way to account for the observed features.

However, there are concerns with this model as well. The timing of the large impacts that would have mobilized water is not consistent with the timing of formation of the valley networks. While later, smaller impacts also would have mobilized water (Segura, 2005), the decline in the rate of impact is gradual enough that it would continue to produce valleys for a much longer time than is observed. This latter problem could be resolved if the atmospheric thickness were also declining throughout this same period; it is unclear, however, how the declining atmospheric thickness and impact rate would play off against each other, and whether they could produce the observed cutoff in the formation of the geologic features.

The two different scenarios have very different ramifications for the potential for life to be able to exist at the Martian surface. In the first case, temperatures would have been clement for a relatively long period of time, presumably from the time of onset of the Martian geological record about 4.4 Ga (Nimmo and Tanaka, 2005) up to the time of loss of the atmosphere centered roughly at about 3.7 Ga. Having long periods of surface and near-surface liquid water, and temperatures consistent with liquid water, allows the possibility that life could have originated independently on Mars; or, if life had been brought from Earth on a meteorite (Melosh, 1988), it could have gained a foothold on Mars and continued to exist. In the second case, typical ambient surface temperatures would have been subfreezing, perhaps even colder than the present-day average of around 220 K. At intermittent times, following a large impact, water would have been mobilized from the atmosphere and would rain down globally or quasi-globally. This water likely would have been superheated to temperatures well above those at which life could possibly exist, and would not have been conducive to the existence of life. Unfortunately, we are not able to determine which of these scenarios actually occurred.

26.3.2 Surface and subsurface water throughout Martian history

The nature of ongoing geological processes changed significantly about 3.7 Ga. On younger surfaces, there is little evidence to indicate that liquid water was stable and persisted at the surface (Carr, 1996). However, there is evidence for short-lived surface liquid water and for long-lived subsurface liquid water. We will discuss the catastrophic outflow channels, lakes in impact craters, layered sedimentary deposits and sulfate deposits, and the potential for volcanically heated hydrothermal systems. A more speculative issue is whether there could have been ancient oceans on Mars.

There are perhaps a dozen occurrences of what are interpreted as large-scale catastrophic flood channels that are dated to the middle to recent epochs of Martian history (Baker *et al*., 1992; Figure 26.5). The downstream portions of these channels clearly show morphologies indicative of the flow of a large quantity of liquid over the surface. The source typically consists of a region of chaotic debris suggesting that the liquid emanated from the subsurface. The width of the channels, their depth, and the flow indicators suggest the catastrophic release of large quantities of liquid from a stable reservoir. Combined, the evidence suggests that the source of the fluid was a subsurface aquifer, and that release to the surface was triggered by some discrete event that allowed a catastrophic drainage, such as the thickening of the frozen cryosphere due to secular cooling of the surface (Carr, 1979; Baker *et al*., 1992). Although most scientists believe that the liquid was water, there is little direct evidence to support this. Liquid CO_2 has been suggested (Hoffman, 2000), but is less plausible physically. Perhaps the strongest evidence for liquid H_2O is the appearance of the flood features being very similar to terrestrial features that were carved by liquid water, the direct detection of water ice and vapor in the Martian environment, the likely abundances of outgassed water that would support formation of the channels (Tanaka *et al*., 1988; Greeley and Schneid, 1991; McSween *et al*., 2001), and the existence of a plausible physical mechanism for emplacing and confining liquid water beneath the surface (Carr, 1996). If indeed the outflow channels were due to liquid water, then liquid water must have been widespread throughout the Martian crust and throughout geological history.

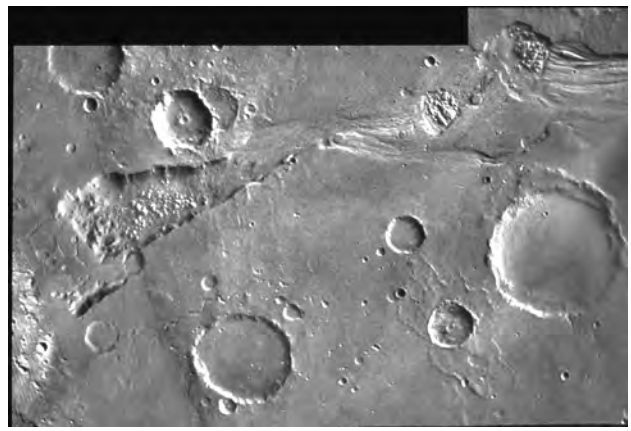

Figure 26.5. Ravi Vallis catastrophic outflow channel. Source region at left suggests eruption of liquid water from the subsurface. Well-defined channel and erosion features indicate flow of liquid water over the surface toward the upper right.

There are numerous impact craters on Mars that show evidence for the past existence of interior lakes (Cabrol *et al*., 1998; Cabrol and Grin, 1999). Many of these features show notches cut into the crater walls where water flowed into or out of the crater. Thinly bedded friable deposits have been observed in dozens of crater basins on Mars and a number of researchers have interpreted these materials as lacustrine deposits formed in the bottom of a persistent lake. Furthermore, a few deposits within craters have an appearance similar to deltas, sedimentary terraces, and shorelines, as might be formed by flowing water or within standing bodies of water. Although most of the impact craters that have these features are themselves relatively old, the age of the lakebed deposits is uncertain. There are few impact

craters superposed on the lakebed deposits, which indicates either that they are very young or that they were buried for long periods and exhumed only recently. Also, the length of time that water was present as a standing lake within the crater was uncertain. The observed morphological features characterize the results of the flow of water, and not its longevity, and there are no chemical or mineralogical effects that have been identified (such as carbonate or sulfate deposits associated with these features). Some, but not all, of the craters are associated with the catastrophic flood features, and the standing water may have been relatively short-lived. Caution must be employed when interpreting orbiter geomorphic observations related to water, as was the case in Gusev crater. Strong evidence of a paleolake was inferred from orbit and was a major factor in the locale being chosen as the *Spirit* rover landing site. Yet to date, rover observations have not uncovered any evidence for lacustrine deposits at the surface and it is likely that any paleolake deposits in Gusev crater may have been buried by younger volcanics (Martínez-Alonso *et al.*, 2005).

The best presently known "smoking gun" for existence of an ancient crater lake on Mars is located in NE Holden crater (Malin and Edgett, 2003; Moore, 2003) (now named Eberswalde crater). A layered apron of debris is observed at an inlet to a large enclosed basin and the inlet is down-slope from an integrated fluvial drainage network. Sinuous ridges reside on the digitate apron and are interpreted as former fluvial channel beds that have been preserved while surrounding materials eroded away, forming inverted topography (Figure 26.6). The fan deposit is strikingly similar to deltaic deposits found on Earth and is thought to have had a similar origin. In the 155 km diameter NE Holden crater example, the lake is required to have been 50 m deep and flow must have persisted long enough to form meandering channels on the deposit. Unfortunately, the duration of surface flow to form this feature is poorly constrained and estimates range from thousands to millions of years. However, a number of researchers have suggested a minimum duration of about 10^5 years, thus making the apron inconsistent with an origin by precipitation from a large impact event and thus requiring a substantially different climate than at present (Moore 2003; Bhattacharya *et al.*, 2005).

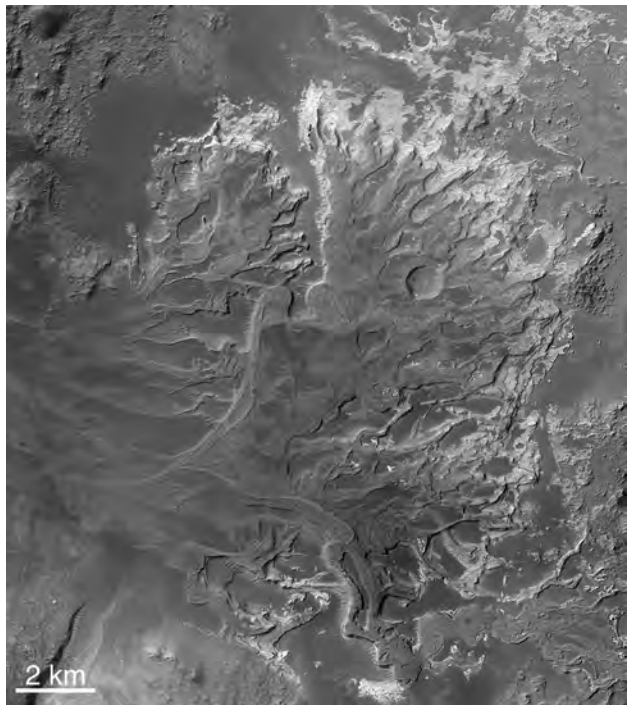

Figure 26.6. Ancient delta deposit in NE Holden crater (now Eberswalde crater). The meandering channel forms and multiple flow paths imply water was present for extended periods of time at this location. (Image modified from Malin and Edgett, 2003).

Ancient surface or near-surface water has also been inferred from hydrated minerals detected by spectroscopic observations from orbiting spacecraft. The Thermal Emission Spectrometer (TES) on the Mars Global Surveyor detected coarse-grained gray hematite over the Sinus Meridiani region of Mars (Christensen *et al.*, 2001). On Earth, this mineral typically forms in association with water and for this reason the area became the landing site of the *Opportunity* rover (discussed below). More recently, the OMEGA (OMEGA – Observatoire pour la Minéralogie, l'Eau, les glaces et l'Activité) instrument aboard the Mars Express spacecraft has revealed a few geographically small locales containing phyllosilicates (clays) on some of the most ancient terrains on Mars, indicative of extensive aqueous chemical weathering of igneous rocks (Bibring *et al.*, 2006). Sulfate-bearing minerals, including Ca and Mg sulfates, are also evident in discrete layered deposits scattered around the globe (e.g., Bibring *et al.*, 2005; Gendrin *et al.*, 2005; see Chapter 7). The layered sulfate terrains have an unknown age owing to substantial resurfacing that has affected crater populations, but it is likely that most date from the Hesperian epoch or older (pre-3.0 Ga). The sulfate minerals identified on Mars typically form in wet acidic conditions, thus giving a clue about the conditions of formation (see Chapters 23 and 24); however, the temperature and duration of formation is poorly constrained. Regardless, the presence of gray hematite, phyllosilicates, and sulfates on Mars implies that significant amounts of water were available. This could occur at the surface in a warmer and wetter ancient Mars or, alternatively, in the subsurface even under present conditions.

With the abundant evidence for both volcanic activity and crustal liquid water throughout time, there is every reason to expect that hydrothermal activity would have occurred and that this might manifest itself in the form of hot springs at the surface (Walter and Des Marais, 1993). There are a small number of instances in which volcanic and water-related features occur together on the surface in a way that suggests a genetic connection. For example, the occurrence of the Dao Vallis flood channel on the flanks of Hadriaca Patera volcano suggests (but does not uniquely prove) that heat and water from the volcanic eruptions combined to produce the flood features. Athabasca Valles, on the slopes of the Elysium Mons volcano, is another example of a spatial and temporal relation between volcanics and catastrophic floods. There, at least three separate flood events emanated from Cerberus Fossae, a large volcanotectonic fissure (Burr *et al.*, 2002). Interspersed with the flood deposits are lavas

and other volcanic features including rootless cones, which form when lava flows over water- or ice-rich ground causing phreatic explosions that form cones. Some of the youngest known lava flows on Mars (perhaps 10 Ma) occur in this region (Berman and Hartmann, 2002; Burr *et al*., 2002) and the flood features (mega-ripples, streamlined islands, etc.) around Athabasca Valles exhibit pristine morphology. Both lava and water are thought to have repeatedly flowed from the fissure system, which shows evidence of subsequent reactivation. Burr *et al*. (2002) concluded that a deep subsurface regional or global aquifer was required, and not simply melting of ice through magmatic heating.

Other evidence also indicates that volcano/water interactions occurred throughout Mars' history and into recent times. Through detailed crater density analyses with high-resolution images, Neukum *et al*. (2004) examined the Hecates Tholus volcano which is heavily dissected by channels that were potentially carved by water mobilized from episodes of volcanism. They found that the volcano and associated channel formation were active episodically over the past 3.4 Ga, with the most recent episode occurring around 5 Ma. There is some uncertainty in the absolute ages of any crater-dated terrain on Mars because of a lack of consideration of secondary impacts in the lunar crater densities, which are the basis for the extrapolation to the Martian impact flux. As such, the impact rate of small bodies is currently poorly understood for the Moon and Mars, and absolute ages derived from small diameter (<1km) crater counts have significant uncertainties (e.g., Bierhaus *et al*., 2005). Regardless, it is thought that volcanically induced heating of a water- or ice-rich surface or near subsurface occurred at this particular locale, and at least episodically, for billions of years. This contrasts with any volcanic setting on Earth, which typically has active heat sources that last for up to a few million years. Athabasca Valles and Hecates Tholus are just two examples of persistent volcanic and aqueous interactions that continued to recent times.

To date, however, no observations have yet been made that allow identification of any specific active or ancient hydrothermal systems or hot springs. Such evidence might take the form of the presence of minerals or small-scale morphology associated with such systems. It is not clear whether their absence reflects a lack of the appropriate measurements (in the proper wavelength range and at the right spatial resolution) or a true absence of these features.

Were there ever global or global-scale oceans on Mars? The issue was raised initially based on the inference from Viking images that the northern lowlands were "ringed" by two sharp boundaries that were in places reminiscent of a shoreline and that each appeared to be at a constant altitude (Parker *et al*., 1989). The source of water for such an ocean was not identified, nor was its sink (Baker *et al*., 1991). Subsequent analysis showed that the constant-altitude ring was not actually at a constant altitude, nor could the variations in altitude be easily understood by a combination of additional processes (Carr and Head, 2003). Higher-resolution data demonstrated that some of the "shoreline" features are clearly volcanic in origin. An additional argument for an ocean was the very flat surface in the northern lowlands. On Earth, the only feature that is this flat is the sea floor. However, the flatness of the lowlands may be more closely related to their nature as volcanic deposits, with very fluid basaltic volcanism similar to the kind that formed the terrestrial sea floor (Head *et al*., 2002). There are no observations either that require the presence of an ocean or for which the presence of an ocean is the best explanation.

However, there is an important point that should not be lost. The catastrophic flood channels presumably each released large quantities of liquid water (totaling $\sim 2.3 \times 10^7\,\mathrm{km}^3$; Baker, 2001; Phillips, *et al*., 2001; Carr and Head, 2003) within a short time span. These all debouched into the northern lowlands, and probably would have resulted in at least short-lived bodies of water until the water either evaporated into the atmosphere (and was transported elsewhere on the planet), froze in place and eventually either sublimated away or became covered with later deposits, or percolated into the regolith where it might reside today. Baker *et al*. (1991) have proposed that the release of water to the surface via the catastrophic flooding also released other gases into the atmosphere that could have created a short-lived greenhouse atmosphere that allowed the water to persist as a liquid for a longer period of time.

The evidence for water during the middle and late epochs in Martian history is very strong. Although some of the water would have been present at the surface, at least for short periods of time, it is clear that there must have been abundant subsurface water present for much of Martian history. The presence of water in the pore spaces within the crust, and the potential for the types of geochemical reactions that could release energy, provides the opportunity for life to exist; this is the case whether the water is at ambient temperatures or has been heated geothermally. Certainly, life exists in just this type of environment on Earth.

26.3.3 Obliquity-driven movement of water

Gravitational forcing by Jupiter and the other planets causes the Martian orbital elements to change on timescales longer than $\sim 10^4$ years (Ward, 1974; Toon *et al*., 1980). These changes redistribute incoming sunlight with respect to latitude and season, with consequent changes in the climate and in the response by volatile species. One possible outcome is the production of transient or steady state liquid water at or near the surface, at both low and high latitudes (albeit for different reasons).

The primary dynamical response of Mars involves a change in the eccentricity of its orbit around the Sun, a precession of its spin axis, and a change in the axial obliquity (tilt of the spin axis with respect to the orbit normal). The first results in Mars being significantly closer to the Sun at some seasons than others. The second results in the season at which Mars is closest to the Sun moving from, for example, southern-hemisphere summer to northern-hemisphere summer. The third results in a redistribution of sunlight either from low to high latitudes or vice versa; this is the primary driver in changes in the climate, due to its ability to cool the low latitudes and heat the polar regions or vice versa (Toon *et al*., 1980).

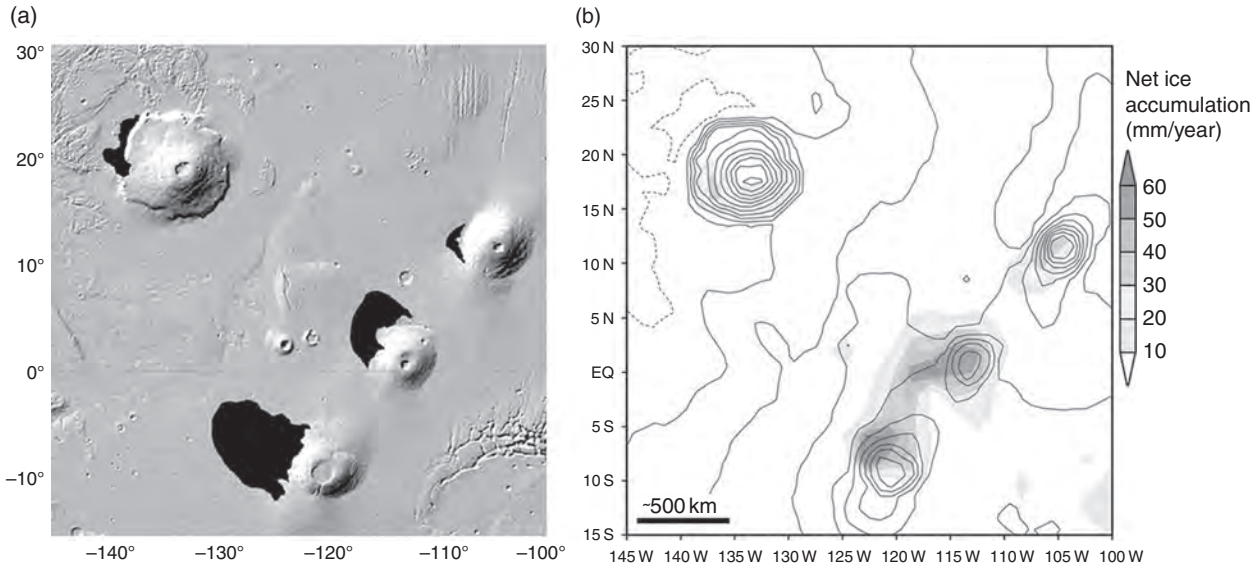

Figure 26.7. Correlation of models of ice accumulation at high obliquities with fan-shaped deposits interpreted by some as relict glacial deposits. (a) Geologic map modified from Scott and Tanaka (1986) of the Tharsis region showing the location of fan-shaped deposits of Amazonian age (black) located on the northwest slopes of the Tharsis Montes and Olympus Mons. (b) Net surface water ice accumulation in the Tharsis region simulated with 45° obliquity and assuming that surface water ice is present on the northern polar cap. Superimposed MOLA topography contours are at 2000 m intervals. (Figure modified from Forget *et al.*, 2006).

The obliquity varies on a timescale of about 10^5 years, with the amplitude of the oscillations changing on a timescale of about 10^6 years. On timescales longer than about 10^7 years, the system is chaotic (Touma and Wisdom, 1993). Combined with the multiple frequencies of forcing, this means that the obliquity cannot be predicted and that it can only be determined on a statistical basis (Laskar *et al.*, 2004). On the long timescales, the obliquity is thought to have varied from as low as nearly 0° to as high as 70° or more. The most likely value is near 40°, as compared with the present-day value of 25.2° (Laskar *et al.*, 2004).

At low obliquity, the polar caps become colder. It is likely that more CO_2 could condense onto the cap in the winter, and that the atmospheric pressure would drop compared to today. At higher obliquity, the polar caps would become warmer. The absence of a large reservoir of polar cap CO_2 ice means that the atmospheric pressure would not go up significantly in response (Kieffer and Zent, 1992).

However, the cooling or heating of the poles would also allow them to act as either sinks or sources for water vapor. At low obliquity, more water from the atmosphere would freeze onto the polar cap, and water also would be drawn from low- and middle-latitude sources of ground ice. At high obliquity, the polar caps would warm up, pumping additional water vapor into the atmosphere. This water could exchange between the polar caps seasonally, could diffuse into the regolith and condense out as additional ground ice, or could even saturate the atmosphere at low latitudes and result in the condensation of ice onto the surface. In an extreme scenario, all of the water ice in the polar deposits could move to low latitudes, covering the surface globally with up to tens of meters of ice (Jakosky *et al.*, 1995; Mellon and Jakosky, 1995; Levrard *et al.*, 2004).

Possibly of more interest, any surface ice during high obliquity might be deposited preferentially at low latitudes in places determined by the global and local circulation patterns. Models of the circulation suggest that the ice might deposit on the flanks of the large volcanoes and on the eastern edge of the Hellas basin. If deposits occurred in only these locations, they could be kilometers thick (Jakosky and Carr, 1985; Jakosky *et al.*, 1995; Levrard *et al.*, 2004).

There are two types of observations that are consistent with these scenarios and appear to confirm at least parts of them. They deal with the occurrence of ground ice and surface ice.

Ground ice occurs in the top few meters of the surface at intermediate and high latitudes where temperatures are below the frost-point temperature of the atmosphere. Water vapor will diffuse into the subsurface and condense as ice. If ice is already present, it will continue to be stable. The occurrence of ice was predicted theoretically (Mellon and Jakosky, 1995), and maps of subsurface hydrogen abundance derived from measurements of neutrons and gamma rays indicate that ice is present in just those places where it is predicted to be stable (Boynton *et al.*, 2002; Feldman *et al.*, 2002; see also Chapters 5 and 6).

Images show a terrain that is interpreted as a remnant of desiccation, in which ice has become unstable in response to the changing obliquity, has been removed by diffusion of vapor to the atmosphere, and has left behind a porous terrain that has collapsed. The latitudes at which this terrain occurs are the same as those at which water would exchange in response to the changing obliquity (Mustard *et al.*, 2001).

Surface ice, if deposited in layers a kilometer thick at high obliquity, could flow as a glacier, and we might expect to see glacial morphologies. Such features are observed, and at the same locations where ice is predicted to deposit preferentially during the periods of high obliquity (Head and Marchant, 2003; Shean *et al.*, 2005; Forget *et al.*, 2006; Figure 26.7).

Thus, we have apparently identified a self-consistent thread of changes in the orbital elements driving changes in the solar forcing, with the response of the atmosphere and climate system resulting in deposition of ice and the formation of glacial features.

Although the obliquity driving can result in deposition and removal of ice, can it produce the liquid water that might be relevant for potential organisms?

Polar surface temperatures at moderate and high obliquity can rise to the melting point of ice and give rise to liquid water directly. At slightly lower obliquity, temperatures beneath a thin covering of ice can reach the melting point, or liquid water could occur where the proximity to grain boundaries depresses the melting temperature (Jakosky *et al*., 1995, 2003). Geological evidence for liquid water has been seen associated with the polar deposits, suggesting that such a melting process might, in fact, have occurred (Fishbaugh and Head, 2002).

At lower latitudes, the occurrence of deposits of ice thick enough to allow glacial movement opens up the possibility of melting to form water. Temperatures at a depth of one to several tens of centimeters can be tens of degrees warmer than at the surface, allowing ice to melt (Clow, 2003). Where surface ice is absent but subsurface ice is present, peak daily and annual temperatures could allow small quantities of ice to melt.

In either case, the amounts of liquid water may or may not be sufficient to create large-scale geological evidence of its existence, but this water would still be able to support microorganisms.

26.3.4 Potential for recent water

Most of the evidence described so far for liquid water relates to the ancient and middle epochs. There is evidence for more recent liquid water, however. That evidence exists as geologically recent gullies (discussed here) and volcanic activity that might have water associated with it (discussed above).

Small channels, termed "gullies," have been identified in high-resolution imaging of the flanks of valley and crater slopes (Malin and Edgett, 2000; Figure 26.8). They occur preferentially at middle latitudes. It was thought initially that these features were oriented preferentially on poleward-facing slopes in a way that indicated a connection to solar heating and melting of ice, but those patterns were later determined to be an artifact of a relatively limited number of observations. More detailed analysis indicated that there is no strong preferred orientation (Heldmann and Mellon, 2004).

The gullies are channels that are roughly 10 m across cut into steep slopes. Aprons occur at the bottoms of the gullies where the debris removed from them has accumulated. The debris aprons often are incised by channels, suggesting that multiple episodes of erosion and deposition had occurred. Many of the gullies appear to emanate from regions situated tens to hundreds of meters below the top of the slopes, with all of the gullies in a particular location having a source at the same depth but with the depth varying from one location to another. However, some of the gullies appear to have sources all the way at the top of the slope (Malin and Edgett, 2000).

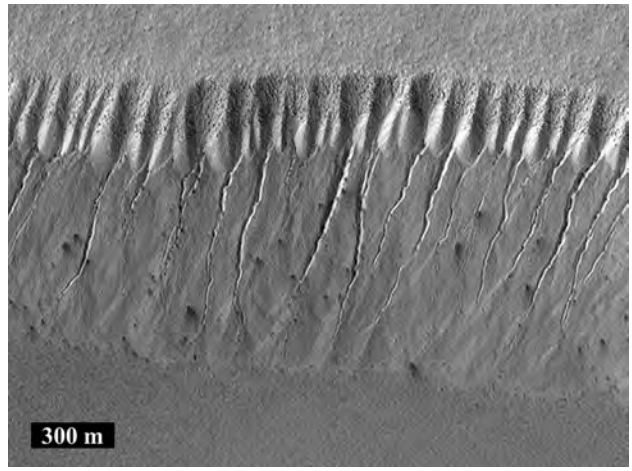

Figure 26.8. Gullies carved in the side of a scarp. From the top of the scarp down, features consist of collapse channels formed by undercutting of the slope, gullies carved into the side of the slope, debris aprons deposited at the bottom of the slope, and the flat bottom of the valley below the slope. These particular gullies appear to emanate from a uniform depth beneath the surface at the top of the slope, but all gullies might not share the same mechanism of formation.

It was proposed initially that the gullies were formed by liquid water held in a subsurface aquifer and released laterally where the slope had been cut into the bedrock (Malin and Edgett, 2000; Mellon and Phillips, 2001). Alternative mechanisms have been proposed that also involve liquid water, but that rely on melting of ice at the bottom of a surface snow pack under a variety of different conditions (Costard *et al*., 2002; Christensen, 2003). Liquid CO_2 also has been proposed as the carving agent, also emanating from a confined aquifer (Musselwhite, *et al*., 2001); this explanation has problems, though, in terms of the thermodynamics and physics of release of liquid CO_2 and the difficulty of forming a subsurface, liquid-CO_2 aquifer (Stewart and Nimmo, 2002).

An additional explanation has been put forward involving dry avalanches, in which the gravity-fed debris flows are lubricated only by entrainment of atmospheric gas (e.g., Treiman, 2003). It is not clear, though, that this process could produce the features that are observed.

In the end, it is not at all clear how the gullies formed (Heldmann and Mellon, 2004). While it is generally (but not unanimously) accepted that their formation involved liquid water, the details of the mechanism are unclear. This means also that the implications for astrobiology are unclear. One possible mechanism would suggest the long-term stability of a near-surface aquifer that would be conducive to supporting life. At the other extreme, the liquid water could be a relatively short-lived surface phenomenon that would have difficulty supporting life as anything but a transient occurrence.

26.3.5 Local characteristics of Mars at the MER landing sites

The two MERs were targeted to sites at which there was evidence of liquid water, with the goal of understanding the

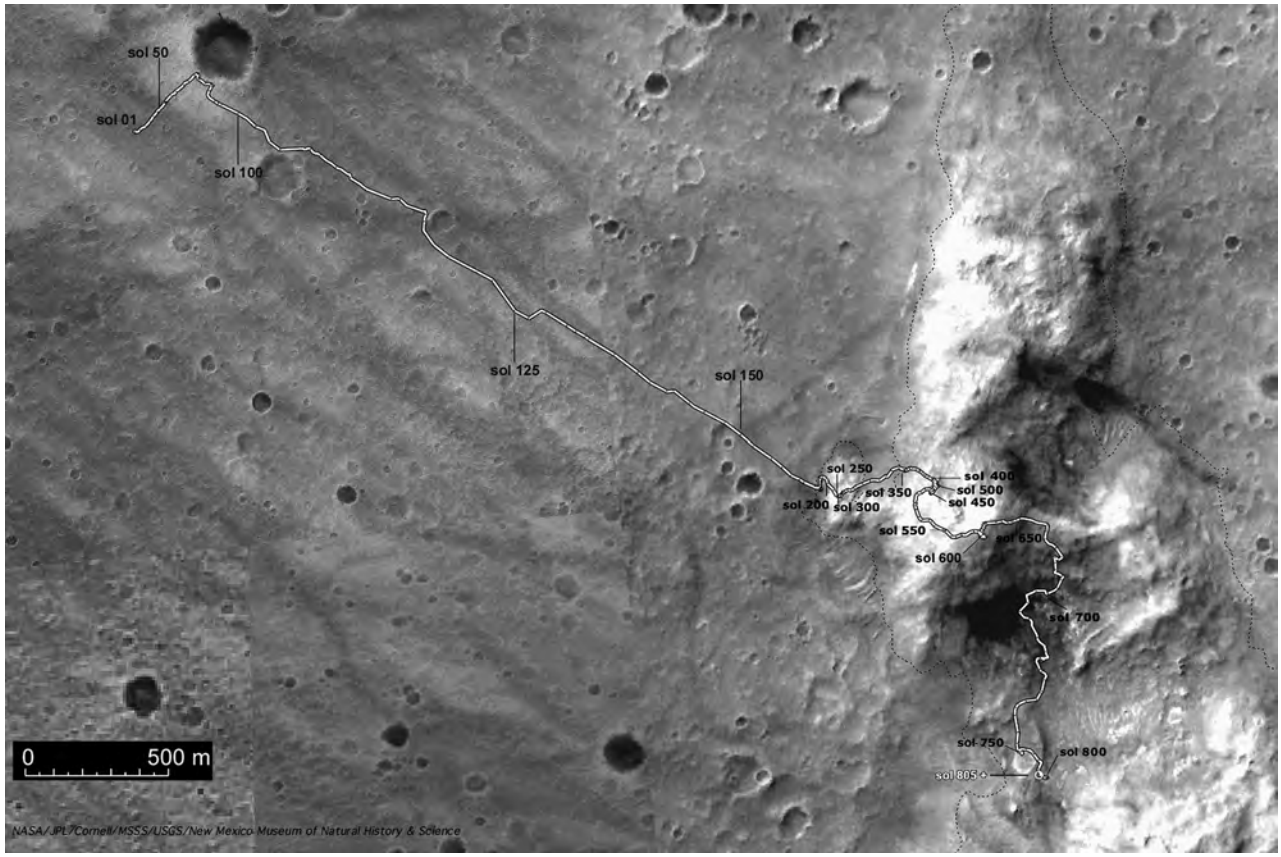

Figure 26.9. View from orbit of Columbia Memorial Station, basaltic plains and Columbia Hills region, Gusev crater. The broken yellow line shows the traverse of the Mars Exploration Rover *Spirit*. Numbers adjacent to this line give the numbers of the sols since *Spirit* landed. *Spirit* was situated in certain areas during the corresponding time periods, as follows: Basaltic plains – Sols 1 to 156, West Spur – 156 to 316, Blue Valley – 316 to 329, Cumberland Ridge (NW flank of Husband Hill) – 329 to 526, Husband Hill summit area – 526 to 650, Haskin Ridge – 650 to 700, Inner basin – 700 to 960. (Image was obtained by the Mars Global Surveyor orbiter, Mars Observer Camera, Malin Space Science Systems. *Spirit* route and annotations by L. Crumpler, New Mexico Museum of Natural History and Science.)

role that liquid water played at each site. The Gusev crater landing site for *Spirit* was chosen based on morphological evidence suggesting that it had been a crater lake. The Meridiani site for *Opportunity* was selected based on spectroscopic evidence for coarse-grained hematite that would have required liquid water to form. Discussion of these sites in detail allows us to make the connection between what is observed globally from orbit and what is observed locally (and at very different physical scales) from the ground.

26.3.6 Gusev crater

Gusev crater is of Noachian age, as evidenced by its highly degraded rim and the abundance of ancient degraded impact craters in its interior. The extensive branching valley network Ma'adim Vallis breaches the crater's southern rim. The water that formed Ma'adim is expected to have delivered vast amounts of sediments to a lake in Gusev crater before it overflowed and drained into the northern lowlands through a gap in the northern rim of the crater. Although orbiters had detected no evidence of minerals that might have formed in water, the geography of the Gusev crater region presented a compelling case that the sediments filling the crater had preserved a long record of ancient, potentially habitable environments (Cabrol *et al.*, 1996).

The elemental and mineral contents of rocks can record the extent to which water affected their development. For example, water can alter minerals in a volcanic rock to form alteration products such as clays, iron oxides, and soluble salts. Mobile fluids can selectively remove relatively soluble cations such as Ca^{2+} and Mg^{2+} and add soluble species such as sulfates, halides, and silica. Because abundant water promotes the development of habitable environments, evidence of more extensive aqueous alteration of rocks would be consistent with the former presence of habitable environments.

Spirit landed on basalt-rich plains that represent a major component of the floor of Gusev crater (Figure 26.9). It soon became apparent that volcanism, impacts, aeolian activity, and a dry cold climate had shaped the terrane surrounding the landing site, perhaps for 3 Gyr or longer (Golombek *et al.*, 2006). Evidence that the basalts had sustained at least limited aqueous alteration included chemically altered coatings and void fills, and their softness and anomalously high contents of sulfur, chlorine, and bromine, relative to basalts on Earth (Haskin *et al.*, 2005). However, the elemental abundances and most of the minerals were identical to those of the original unaltered basalts. Therefore,

the water that partially altered these rocks must have been very limited in its abundance relative to the quantity of rock and it did not even remove a significant fraction of any soluble alteration products. Well-developed soils on the plains exhibited positively correlated concentrations of magnesium and sulfate, consistent with limited mobilization by water (Haskin *et al*., 2005). However, this water might have occurred ephemerally and sparingly as brine saturated with respect to magnesium sulfate. Such brine was unlikely to have sustained habitable conditions (Des Marais *et al*., 2005). Apparently, little aqueous activity had occurred in Gusev crater since the basaltic plains were emplaced in Hesperian times (Golombek *et al*., 2005).

The Columbia Hills, located ~3 km southeast of the landing site (Figure 26.9) are older than the surrounding basaltic plains and therefore might be Noachian in age (Squyres *et al*., 2004a). The hills might be remnants of volcanic deposits and/or lakebed sediments that were subsequently exposed by erosion and/or uplifted as part of an ancient crater rim or by movement along a fault. Accordingly, hills materials were assessed for any evidence of aqueous processes, nutrient contents (e.g., Ca, Fe, K, Mg, P, and S), and potential sources of energy for metabolism.

Aqueous processes have extensively altered bedrock in the Columbia Hills, in contrast to the minimal alteration observed for rocks on the basaltic plains (Figures 26.10 and 26.11). Table 26.1 lists some of the key indicators of the effects of alteration on rock composition and mineralogy. Ferrous iron in the original, unaltered parent rock (the "protolith") of hills materials has typically been oxidized extensively to form ferric oxides, hydroxides, other ferric minerals and ultra-fine grained materials (Morris *et al*., 2006). Migrating fluids have removed Ca and other cations, allowing residual Al to become relatively more abundant, and fluids added sulfates and chlorides (Ming *et al*., 2006; see also Chapter 23). These patterns indicate that fluids ranging from highly acidic to near-neutral pH values had migrated through and altered these rocks. Evidence of fluid flow contributes significantly to an assessment of potentially habitable environments. Not only do migrating fluids sustain alteration reactions that can release nutrients from the rocks, they can also deliver exogenous nutrients to and remove waste products from microbial communities living in rock fractures and voids. The evidence that Columbia Hills rocks had both gained and lost elemental constituents as a direct consequence of aqueous alteration is consistent with the presence of at least one key attribute of subsurface habitable environments.

It remains uncertain whether the chemical activity of the waters that altered Columbia Hills rocks had ever attained the values required to sustain active metabolism in earthly microorganisms. Nor can it yet be determined whether any Martian microbiota could have adapted to even lower water activity levels. (The "chemical activity" of water is a measure of its "availability" for chemical interactions, where distilled water has an activity of 1.0. For example, because some of the water in a saline brine is coordinated with cations and anions, its activity lies between 1.0 and 0.) The minimum water activity that is necessary to sustain microbial processes on Earth (Grant, 2004) is ~0.75 for haloarchea in NaCl brines and ~0.61 for fungi in high-sugar media. Organisms can maintain a viable but dormant state for extended periods at even lower water activities, but they must become active at least periodically in order to repair cellular damage caused by radiation and other environmental challenges. This would be particularly true for life in the modern Martian near-surface

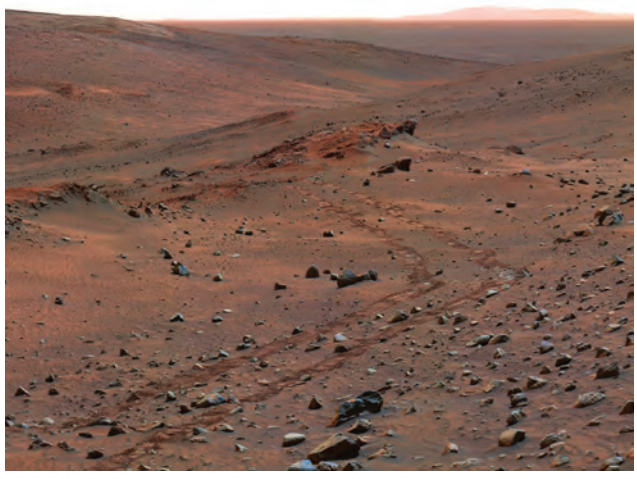

Figure 26.10. View from *Spirit* Rover on Sol 454, looking the northwest across bedrock outcrops at the summit of Cumberland ridge. Note rover tracks in foreground. The sample "Watchtower" (Table 26.1) is located in the prominent outcrop at upper right center. These outcrops provided evidence of extensive aqueous alteration and iron oxidation. Pancam false color composite mosaic from sequence P2402, filters 753 nm, 535 nm, and 432 nm. (For a color version of this figure, please refer to the color plate section or to the e-Book version of this chapter.)

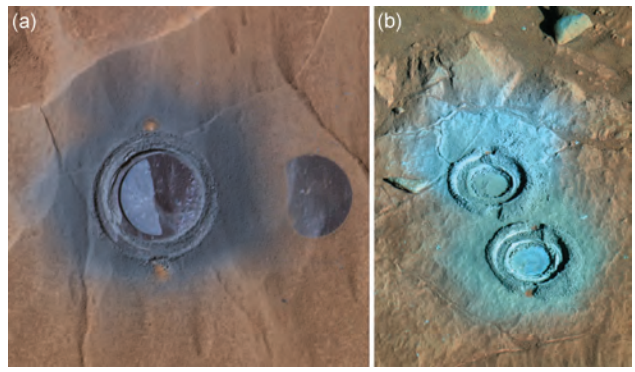

Figure 26.11. (a) Plains basalt "Mazatzal," showing 3 cm diameter brushed area at right and area at left ground by the RAT. Note the dark powder surrounding the 3 cm diameter hole. Part of false color Pancam image from sol 82, sequence P2590, filters 753 nm, 535 nm, and 480 nm. (b) Bedrock outcrop "Wooly Patch," a member of the "Clovis" rock class (see Clovis, Table 26.1), visited by *Spirit* on the West Spur of Husband Hill. The light-toned rock and powder exposed by the two 3 cm diameter RAT holes contrasted strongly with dark-toned basalts (e.g., Mazatzal) and provided evidence that Wooly Patch had sustained extensive aqueous alteration. Part of false color Pancam image from sol 200, sequence P2556, filters 753 nm, 535 nm, and 432 nm. (For a color version of this figure, please refer to the color plate section or to the e-Book version of this chapter.)

Table 26.1. *Abundances of elements (wt.%) and certain minerals (%) in some rocks and a light-toned deposit in the Columbia Hills*

Elements	Backstay	Clovis	Wishstone	Watchtower	Paso Robles
Si	23.1	21.4	20.3	19.8	10.9
Ti	0.56	0.51	1.71	1.33	0.45
Al	6.9	5.4	7.9	6.5	2.7
Fe	10.3	12.5	9.5	10.3	14.4
Mn	0.19	0.14	0.19	0.17	0.21
Mg	5.0	7.6	2.5	6.0	3.2
Ca	4.3	3.0	6.3	5.3	4.9
Na	3.0	2.2	3.7	2.0	1.1
K	0.85	0.19	0.45	0.62	0.25
P	0.59	0.47	2.23	1.97	2.25
Cr	0.11	0.13	0.00	0.00	0.14
Cl	0.4	1.4	0.5	0.8	0.6
S	0.7	1.7	0.8	1.4	12.7
Major primary mineral phases[a]					
Olivine	23.18	trace	6 to 7	4	0[b]
Pyroxene	13.39	33 to *12*	12 to 11	22 to *5*	0[b]
Feldspar	50.37	34 to *0*	52 to 13	30 to *0*	0[b]
Apatite	3.29	2 to *0*	11	10 to *7*	0[b]
Key secondary mineral phases[a]					
npOx[c]		3	1	4	0[b]
Hematite		2	1	4	0[b]
Goethite		5	0	1	0
Ferric sulfate		0	0	0	25 to *29*
Mg sulfate		1 to trace	1 to 2	5	10
Ca sulfate		10 to *11*	2 to 1	0	4 to *3*
Halides		2	1	1	1
Al- and Si-containing phases		7 to *62*	8 to 47	18 to *67*	-[d] to *17*

[a] Mineral abundances are based upon whole rock mineralogy inferred from Mini-TES observations, iron minerals established by Mössbauer analyses, and mass balance calculations that utilize elemental abundances measured by APXS and that consider potential primary and secondary mineral phases. Pairs of values indicated for Clovis, Wishstone, and Watchtower indicate possible mineral abundances predicted by two models that assume less altered and more altered rocks, respectively. Italicized numbers are interpreted to lie closer to the actual mineral abundances, based upon various indicators of the degree of alteration (Ming *et al*., 2006; see also Chapter 14).
[b] Values estimated for the Paso Robles light-toned deposit have been adjusted by subtracting contributions attributed to admixed local soil.
[c] "Nanophase" (very fine-grained; nanometer-sized) iron oxides.
[d] No estimate was made for a less-altered assemblage.
Source: Ming *et al*. (2006).

environment, which experiences much higher exposure to UV radiation and cosmic rays than the Earth's surface.

Living organisms require certain key elements in order to synthesize cellular components and to maintain key functions such as enzymatic processes and self-replication. In subsurface environments on Earth, microorganisms can obtain key nutrients from the weathering of basalts (Ehrlich, 1996). Typical Mid-Oceanic Ridge Basalt (MORB) has the following abundances of key nutrients (Fisk *et al*., 1982): calcium (8.7 wt.%), iron (6.6 wt.%), potassium (0.05 wt.%), magnesium (5.8 wt.%), phosphorus (0.03 wt.%), and sulfur (0.07 wt.%). Materials examined in the Columbia Hills have comparable or greater abundances of these elements (Table 26.1) than do MORB. Wishstone rock and Watchtower outcrop have very high contents of phosphorous (2.23 and 1.97 wt.%, respectively). The *Spirit* rover could not measure abundances of carbon and nitrogen. However, if the circulating fluids that altered these rocks had exchanged with the atmosphere, they might have contained dissolved CO_2 and N_2. Thermodynamic calculations indicate that if acidic CO_2-bearing fluids equilibrated with Martian crustal rocks, carbonates might have formed and been sequestered within the crust (Griffith and Schock, 1995). Martian landers have not yet detected nitrogen compounds in Martian rocks and soils, however fixed nitrogen compounds might have been sequestered in the regolith (Mancinelli, 1996); some of these might have been delivered by circulating fluids to the subsurface.

Following the example of our own biosphere, any Martian organisms conceivably might have obtained their energy from sunlight and/or from redox chemical reactions. The surface environment must have been habitable to allow any phototrophs ("light-feeders") in Gusev crater to exploit sunlight. Although the Ma'adim Vallis system might have maintained a body of standing water in Gusev crater sometime in the distant past, the *Spirit* Rover has not yet obtained (at the time of this writing) evidence indicating that liquid water necessarily existed at the surface. Chemoautotrophs ("chemical-feeders" that can grow exclusively on inorganic chemicals) do not necessarily require sunlight; therefore they can thrive in subsurface environments where conditions are otherwise favorable. For example, *Thiobacillus ferrooxidans* obtains energy by oxidizing reduced iron and sulfur compounds. Microbial oxidation of sulfur compounds is a very important biogeochemical process (Canfield, 2001). Mixing oxidized constituents from surface environments with generally more reduced constituents from subsurface rocks and thermal emanations provides non-equilibrium conditions that can sustain microorganisms.

Observations by the *Spirit* rover indicate that ferrous iron in parent materials in the Columbia Hills has been oxidized to form a variety of ferric minerals (Table 26.1). For example, the abundances of several of the elements in Wishstone and Watchtower are similar, indicating perhaps that the abundances of the iron containing olivine and pyroxene were similar in these two rocks before they were altered. Of these two rocks, Watchtower (Figure 26.10) was altered to a greater extent than Wishstone, as indicated by its lower olivine and pyroxene contents and greater abundances of nanophase oxides, hematite, and goethite (Table 26.1). The mineral jarosite was not detected, indicating that these alteration reactions occurred under pH conditions that were mildly acidic to neutral. Microbial processes have been documented to contribute to the production of goethite, hematite, and other iron oxides in terrestrial environments (Brown *et al*., 1994). Evidence for the dissolution of olivine in rock rinds (Hurowitz *et al*., 2006) indicates that geologically recent climate regimes were accompanied by weathering under more acidic conditions.

Materials that contain a larger percentage of their iron as ferric minerals also have greater abundances of sulfur, indicating that migrating fluids containing sulfur were responsible for the oxidation of the iron. The Paso Robles soil contains abundant ferric sulfate (Ming *et al*., 2006), indicating that strongly acidic solutions having pH values ≤ 1 had contributed to the Paso Robles deposit. The abundant sulfate indicates that sulfuric acid was the source of the acidity in the Paso Robles fluids and perhaps also in the fluids that altered other materials in the Columbia Hills. Sulfuric acid typically forms by the oxidation of reduced sulfur compounds, elemental sulfur, or sulfur dioxide. Microorganisms can utilize these oxidation reactions in habitable environments.

In summary, observations by the *Spirit* rover are consistent with the possibility that liquid water, nutrients, and sources of chemical energy were simultaneously available to sustain habitable conditions in subsurface Columbia Hills materials at least some time in the distant (Noachian?) past. There is as yet no evidence that these conditions ever existed at the surface. Habitable conditions probably have not occurred near the surface since the time that the basalts were emplaced in the plains surrounding the Columbia Hills. It remains unknown whether the aqueous alteration processes occurred episodically or were sustained over periods sufficiently long to sustain habitable environments. Early in its history, the floor of Gusev crater received large impacts that might have sustained hydrothermal activity for extended periods of time. Newsom estimated that large impacts could have sustained hydrothermal systems that persisted for thousands of years or longer (Newsom, 1980). It remains unresolved whether the ancient migrating fluids revealed by *Spirit*'s observations ever achieved the activity of water needed to sustain active metabolism (Grant, 2004).

26.3.7 Meridiani Planum

The landing site in the Meridiani Planum region addressed the objectives of the MER mission in several ways. The site is situated within southern highland terrane, therefore it provided access to a rock record of ancient Martian environments that might have been habitable. The extensive flat-lying rock layers might represent very ancient (approximately 4 to 3 Gyr-old) sedimentary deposits that became exposed and accessible when overlying deposits were stripped away (Hynek *et al*., 2002; Arvidson *et al*., 2003). The TES on NASA's Mars Global Surveyor orbiter discovered coarse-grained deposits of the mineral hematite. On Earth, coarse-grained hematite (grains many tens of microns or larger in diameter) typically forms in aqueous environments such as aqueous sediments or hydrothermal systems (Christensen *et al*., 2001). Conceivably, the hematite at Meridiani was a "beacon" that signaled the presence of water-lain deposits. The Meridiani region harbored extensive, rich deposits of coarse-grained hematite, indicating that the *Opportunity* rover should be able to access it.

Soon after it landed in 20 m diameter Eagle crater (Figure 26.12), *Opportunity* found that liquid water had influenced the composition of the rocks and soils. The Miniature Thermal Emission Spectrometer (Mini-TES) instrument observed that the abundance of coarse-grained hematite that had been detected from orbit was greater on the soil surface covered with a litter of millimeter-size rounded grains than it was in places where the lander's airbags had pressed these grains into the surrounding soil. The grains' shapes resembled those of concretions that develop in water-saturated sediments on Earth. However volcanic, aeolian, and other processes also can form similarly rounded shapes, therefore additional observations were required.

Opportunity analyzed the 30–50 cm high bedrock bench that lined nearly half of the crater perimeter. The energy expended to grind a shallow hole in the bedrock was only a few percent of that required to grind a comparable hole in fresh basalt (Squyres *et al*., 2004b). Elemental analyses (Table 26.2) of the freshly exposed surface by the APXS instrument indicated that the rock contained up to 25

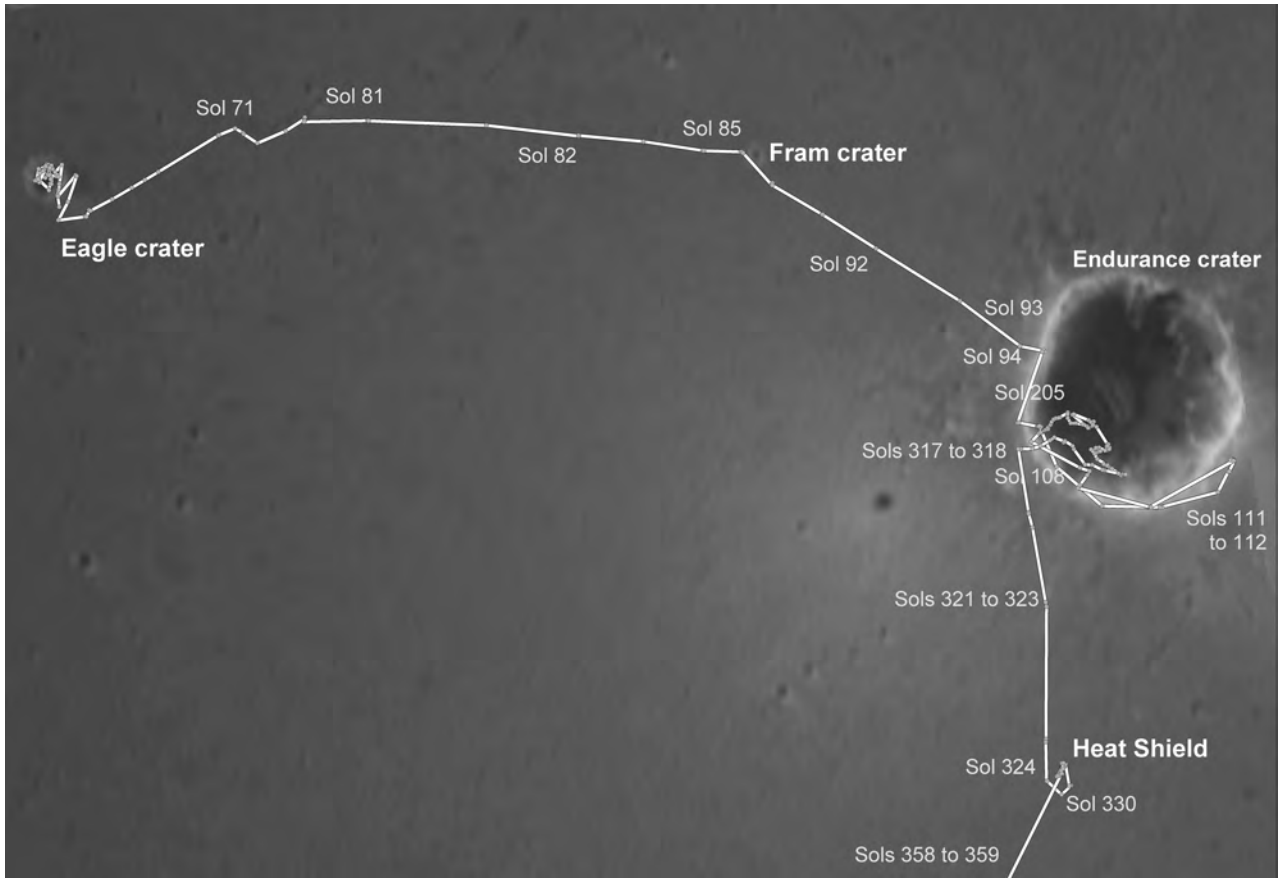

Figure 26.12. View from orbit of Eagle and Endurance craters and the surrounding plains in Meridiani Planum. The broken red line shows the traverse of the Mars Exploration Rover *Opportunity*. Numbers adjacent to this line give the numbers of the sols since *Opportunity* landed. The uppermost bedrock layers in Endurance crater were observed to correlate with the bedrock outcrop in Eagle crater. (Image was obtained by the Mars Global Surveyor orbiter, Mars Observer Camera, Malin Space Science Systems. *Opportunity* route and annotations provided by R. Li, Ohio State University.)

percent by weight sulfur as SO_3 (Rieder *et al*., 2004). Chlorine and bromine also were observed and Cl/Br ratios varied by more than an order of magnitude across the outcrop (Rieder *et al*., 2004). Mini-TES detected Mg and Ca sulfates at abundances of a few tens of percent (Christensen *et al*., 2004), indicating that most of the sulfur occurred as sulfate salts. The Mössbauer instrument detected the minerals hematite (Fe_2O_3) and jarosite ($[K,Na][Fe,Al]_3[SO_4]_2[OH]_6$) (Klingelhöfer *et al*., 2004). The Pancam camera and the microscopic imager observed rounded grains within the bedrock that were identical to the grains that littered the soil surface (Bell *et al*., 2004; Herkenhoff *et al*., 2004). Hematite was found to comprise more than 50% of these grains (Klingelhöfer *et al*., 2004). The bedrock consists of silicate minerals, sulfate and halide salts, and oxidized iron-bearing phases that apparently derived from essentially complete weathering of an olivine basalt protolith by sulfuric acid (McLennan *et al*., 2005; Tosca *et al*., 2005).

Rock textures observed at Eagle crater provided additional clues about the environment in which the bedrock had formed. Cemented grains formed finely laminated, millimeter-scale textures that exhibited, in some places, wavy bedding and low-angle festoon cross-lamination. Such textures are interpreted to develop from ripple migration induced by shallow liquid water flowing over a sandy sediment surface (Grotzinger *et al*., 2005). Both textural and geochemical evidence indicated that the bedrock is "dirty evaporite" sandstone that developed in shallow, acidic bodies of water under oxidizing and arid conditions (Squyres *et al*., 2004b). The acidity apparently arose from sulfuric acid that might have been produced during volcanism or hydrothermal activity.

Subsequent observations by *Opportunity* of a several meters thick bedrock exposure in 170 m diameter Endurance crater (Figure 26.12) provided important additional information about ancient depositional environments. Trends in texture and composition indicated that water played an increasingly important role as this sequence of layers was deposited. Meter-scale, crossbedded aeolian sand dunes in the deeper strata are overlain by finely laminated sediments that were formed by the migration of eolian rippled sands over a flat to undulating sand sheet surface (Figures 26.13 and 26.14; Grotzinger *et al*., 2005). The boundary between these two units was interpreted to be an erosional surface that had developed at the upper capillary fringe of a water table. The topmost units in Endurance crater were correlative with those observed previously in Eagle crater. The

Table 26.2. *Abundances of elements (wt.%) in Eagle crater bedrock*[a] *and model-based estimates of minerals (%) in Endurance crater bedrock*[b]

Elements[a]	Eagle crater Guadalupe RAT	Karatepe Case 1a[c]	Karatepe Case 2[d]
Si	17.1		
Ti	0.4		
Al	3.0		
Fe	12.3		
Mn	0.25		
Mg	4.7		
Ca	3.6		
Na	0.74		
K	0.45		
P	0.5		
Cr	0.13		
Cl	0.33		
S	9.8		
Modeled mineral components[b]			
Silica		22	26
Feldspar mix		17	~1
Allophane		7	9
Mg sulfate		17	18
Ca sulfate		9	7
Jarosite		10	10
Hematite		6	6
Basalt		—	16
Pyroxene mix		5	—
Phosphate		2	1
Mg chloride		2	—
Halite		—	2
Schwertmanite		1	—
Np-Ox[e]		—	3
Ferric iron ("Fe_3D_3" Mössbauer doublet)		4	—

[a] Rieder *et al*. (2004).
[b] Mineral models by Clark *et al*. (2005).
[c] "Model 1a" assumes presence of an aluminosilicate and pyroxene, that S not in jarosite and Mg sulfate is in Ca sulfate, that Cl is in either Mg or Ca chloride, and that P is in Ca phosphate. Pyroxene composition is then varied empirically to achieve best overall match for the candidate cations.
[d] "Model 2" assumes that jarosite contains only K and Na cations (no H), that Na not in jarosite is in Na chloride and Na sulfate, that the ferric doublet observed by Mössbauer represents Np-Ox and schwertmanite, that P is in Al phosphate, and that there is a basaltic component that resembles Bounce Rock, a basalt found near Eagle crater.
[e] "Nanophase" (very fine-grained; nanometer-sized) iron oxides.

Endurance crater units exhibited wavy bedding, irregular lamination with convolute bedding, and centimeter-scale festoon crosslamination indicating shallow water with current flows of a few tens of cm s^{-1} (Grotzinger *et al*., 2005). The sulfate-rich sands in the lower, middle, and water-deposited upper bedrock units indicated an evaporative depositional environment. Evidence observed in Endurance crater regarding both the nature of the depositional environment and the composition of the bedrock indicates that groundwater played critical roles both in producing the sandy sediment and in controlling the sedimentary architecture of the deposits.

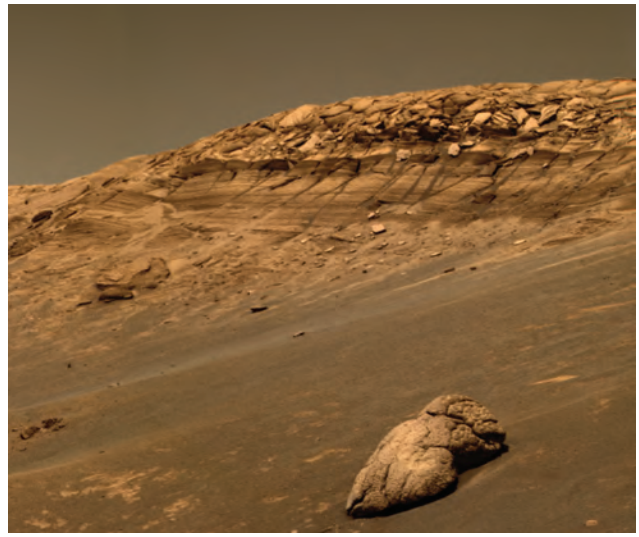

Figure 26.13. View eastward across Endurance crater to Burns Cliff. Eolian dune field deposits occur as tilted beds located in lower part of the cliff at left. Finely layered eolian sand sheet strata comprise the middle of the cliff, and the interdune/playa lake strata form the uppermost part of the cliff. Approximate true color Pancam image from sol 248, sequence P2269, filters 753 nm, 535 nm, and 480 nm. (For a color version of this figure, please refer to the color plate section or to the e-Book version of this chapter.)

Groundwater substantially modified the bedrock after it had been deposited (a process known as "diagenesis"). Perhaps as many as four episodes of cementation occurred (McLennan *et al*., 2005). Some of the primary minerals, possibly sulfates, were later dissolved to produce millimeter-scale vugs and crystal-shaped voids (Figure 26.15). Rounded millimeter-size hematitic concretions precipitated within the sediment pore spaces (Figure 26.15). These concretions displayed internal laminations that were aligned with laminations in the surrounding matrix. The concretions are very evenly spaced within the bedrock, indicating that as they grew they competed with each other for Fe^{3+} dissolved in the sediment pore waters. Ferric iron is more soluble in more acidic waters. The mineral jarosite was observed; it is stable in the pH range 1 to 5. The bedrock experienced acidic conditions during its formation and/or later diagenesis. The bedrock at the Meridiani site had been modified over an extended period of time by slowly fluctuating, chemically evolving groundwater system having fluids that persistently maintained relatively high ionic strengths (McLennan *et al*., 2005).

An alternative view about formation of the Meridiani deposits was put forward by McCollom and Hynek (2005). They proposed that the composition could have been produced by hydrothermal alteration of basalt in a volcanic environment rather than by low-temperature processes in a surface and near-surface environment. The authors of this

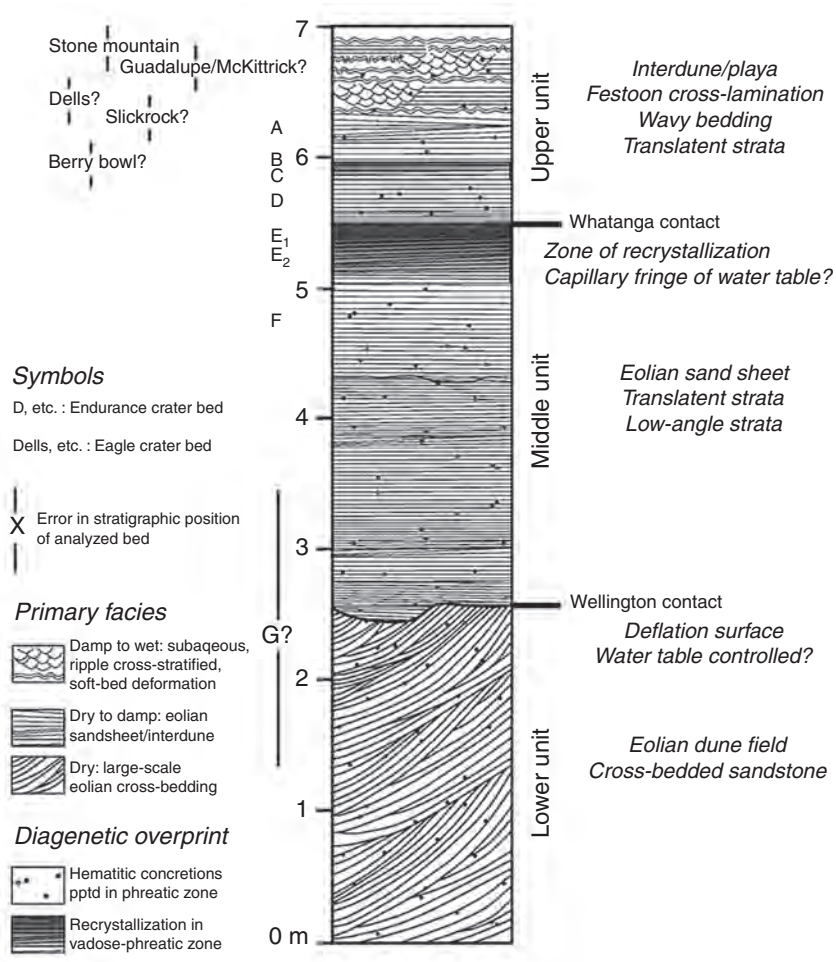

Figure 26.14. Schematic cross section of bedrock units exposed at Burns cliff, Endurance crater. The sedimentary structures and textures are consistent with a "wetting upward" transition from an eolian dune field (bottom) to eolian sheet sands to interdune/playa lake rippled sands (top). (Illustration from Grotzinger *et al*., 2005. Reproduced with permission from Elsevier.)

chapter agree that volcanic processes probably played a role, for example by producing sulfur compounds that altered volcanic rocks somewhere within the Meridiani region. The authors disagree as to whether low-temperature processes in a surface environment or volcanic base surges are consistent with the observations by the *Opportunity* rover (McCollom and Hynek, 2006; Squyres *et al*., 2006). Regardless, and importantly, either scenario involves conditions that would be capable of supporting life.

Some microorganisms have adapted to environments on Earth that resemble the ancient aqueous environments at Meridiani described above. In order to mitigate detrimental effects of certain dissolved salts, microorganisms can maintain organic "compatible solutes" and/or compatible salts inside their cells in order to exclude disruptive solutes and to solve the challenges of osmoregulation (Galinski and Trueper, 1994). Organisms can persist in seasonally or episodically dry environments by developing strategies to survive periods of prolonged dryness. However, all organisms require that a minimum level of water activity (Grant, 2004) be maintained at least intermittently so that they can become active metabolically and repair damage caused by radiation, chemical degradation, or physical disruption that might have occurred during their dormancy. Because the evolving Martian groundwater fluids apparently maintained relatively high ionic strengths (McLennan *et al*., 2005), it is not clear whether the water activities required to sustain metabolic activity ever were achieved after the bedrock had been deposited.

Microorganisms can thrive under highly acidic conditions such as those inferred for the deposits at the Meridiani site. Acid-mine drainage sites occur worldwide where iron oxides, jarosite, and other sulfate minerals have precipitated abundantly (Knoll, 2005). Some acid-tolerant eukarya, bacteria, and archea can maintain their cell interiors at near-neutral pH values by utilizing membrane-bound pumps to export hydrogen ions (e.g., Booth, 1985). Acidic solutions impose additional challenges by mobilizing toxic metals (Rothschild and Mancinelli, 2001) and by limiting certain sources of essential nutrients. For example, biological nitrogen fixation has not yet been observed to occur within environments such as acid-mine drainages that exhibit very low pH values (Baker and Banfield, 2003). On the other hand, commonly occurring phosphates such as apatite are more soluble in acidic waters. Phosphate is apparently relatively abundant in Martian olivine basalts (e.g., Table 26.1; Fisk and Giovannoni, 1999).

It is important to consider potential sources of energy that would have been required to sustain primary production in this ancient aqueous environment. Both phototrophic and

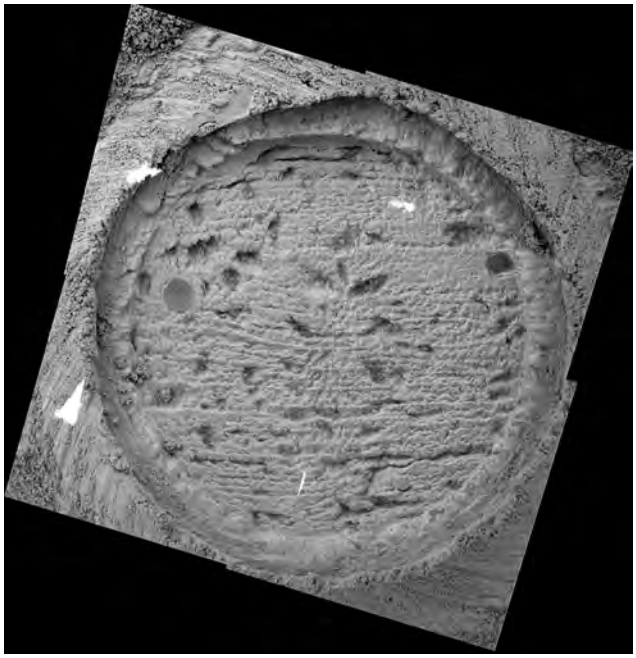

Figure 26.15. Microscopic imager mosaic image of "Ontario" RAT hole, obtained on Sol 149 during the Karetepe ingress into Endurance crater, Meridiani Planum. This 3 cm diameter hole shows sedimentary laminations (that locally exhibit ripples), the granular nature of these sedimentary laminations, blade-shaped vugs created by the dissolution of a soluble mineral, and a cross section of a hematite-rich concretion (upper left-center). These features are consistent with "dirty evaporite" sediment that was altered subsequent to its deposition by fluids that dissolved some minerals and precipitated others.

chemotrophic microorganisms can withstand moderately acidic conditions. The evidence that standing bodies of water existed at least intermittently at the Meridiani site is consistent with the possibility that phototrophic microorganisms could have thrived there. However, bacterial photosynthesis is strongly inhibited at pH values below 4 (Knoll, 1989). Accordingly, eukaryotic algae are the principal phototrophs in strongly acidic lakes and streams. Conceivably, any Martian life forms might have evolved forms of photosynthesis that tolerated highly acidic environments.

Chemotrophic microorganisms require redox gradients where oxidized and reduced constituents can react to provide energy. For example, the weathering of olivine basalt by acidic fluids readily releases Fe^{2+} and makes it available for oxidation by microorganisms. Aqueous alteration of olivine-rich rocks also can release H_2 (Sleep *et al.*, 2004), which is utilized by virtually all microorganisms as a substrate to produce energy and to synthesize organic matter. These and other sources of reduced compounds will diminish as weathering reactions exhaust the supply of unaltered rocks. Chemotrophs require that reduced materials be provided at the minimum rate needed to maintain their viability. All of the sulfur and iron in the Meridiani bedrock apparently resides in oxidized forms as sulfates and ferric minerals. Therefore once these bedrock materials achieved their current state of alteration, they probably no longer provided the redox gradient necessary to support chemotrophic microorganisms. However, both sulfur and the olivine basalts clearly could have been available in the source regions of these deposits. Examples of such regions include volcanic vents, hydrothermal systems, and basalts subjected to acidic weathering.

Although it seems possible that microorganisms could have existed at Meridiani for an extended period of time at some time in the distant past, it seems less certain whether life could have originated there (Knoll, 2005). On Earth, certain key prebiotic chemical reactions might have occurred along a chemical boundary between alkaline submarine seepages and mildly acidic seawater (Russell and Hall, 1997). However, proteins and nucleic acids are rapidly degraded in strongly acidic solutions. Furthermore, acidic conditions tend to inhibit HCN condensation reactions to form purines as well as the strecker synthesis of amino acids. These two processes are considered to be crucial in certain scenarios for prebiotic chemistry and the origins of life (Miller and Orgel, 1974). However, the acidic highly oxidizing environment at Meridiani might represent the waning stages of an earlier period where conditions might have been more favorable for life to begin (Knoll, 2005; Bibring *et al.*, 2006).

In summary, a habitable environment probably could have existed in the Meridiani Planum region at some time in the past and might have persisted for an extended period of time. No evidence has yet been obtained that demonstrates the presence of life. If these ancient aqueous environments had been highly acidic, this acidity might have inhibited prebiotic chemical reactions leading to the origins of life.

26.4 THE POTENTIAL FOR LIFE ON MARS

We have discussed the global perspective of life on Mars as derived from remote sensing and from analyses of meteorites and from the local and regional perspective as inferred especially from the two MERs. Here, we would like to address specific questions that provide a synthesis relative to the potential for life on Mars. Throughout the discussion, we want to address the two separate questions of whether Mars has conditions that allow it to be habitable by microorganisms and whether, in fact, organisms are or were present. Each of these is an important issue, and together they describe the astrobiology of Mars.

Does Mars meet the environmental requirements that would allow either an origin or the continued existence of life on Mars?

Based on the available evidence, as summarized throughout this discussion, Mars could have sustained life at least for some period of time at some time in the past. Current evidence is consistent with the possibility that subsurface environments can support life today. Although the apparently acidic ancient waters inferred at the Meridiani Planum landing site seem unfavorable for the origins of life (Knoll, 2005), environmental conditions at other places and times

might have been more favorable. Even if life could not have originated on Mars, it could exist there if it had been transferred from Earth by hitchhiking on a meteorite (e.g., Melosh, 1988).

Do we have definitive answers about the occurrence of life from either the Viking missions or the analyses of the ALH 84001 Martian meteorite?

The Viking missions indeed conducted life-detection experiments, but only in two (similar) localities on the surface and using methods that might not have detected many kinds of microorganisms as we know them. Analyses of the ALH 84001 Martian meteorite revealed several features consistent with the former presence of microbial life (discussed further, below), but nonbiological processes have since emerged as more consistent and compelling sources of these features. Therefore, neither Viking nor ALH 84001 have provided definitive answers regarding Martian life. It is valuable to understand why not, given that these represent our only efforts to date to try to identify life in another planetary environment, and revisiting those analyses can provide guidance in subsequent searches.

The two Viking landers in 1976 each included three experiments designed to search for evidence of metabolism in Martian soil samples, and an additional experiment that looked for organic molecules (e.g., Klein, 1979). The three metabolism experiments each took a different approach as to how metabolism might operate. In each, though, water was added (either as liquid or vapor, and either containing or not containing nutrients) to the soil, and the nature of reactions was analyzed. One experiment (the Gas Exchange experiment) looked for release of gases that might be byproducts of metabolic reactions. A second (Pyrolitic Release) looked for the uptake of organic molecules in the nutrients by possible organisms in the soil. The final experiment (Labeled Release [LR]) looked for gaseous CO or CO_2 that might be given off by metabolism.

Each experiment showed an initial positive reaction that might be consistent with life. For each, a control experiment was run subsequently, in which the sample was first heated to temperatures high enough that survival of life would be unlikely. In two of the three experiments, the heating did not affect the result, suggesting that nonbiological reactions were involved. In the third, the LR experiment, the response was substantially diminished by heating, and might have been consistent with life (Levin and Straat, 1977; see, however, Klein *et al*., 1992; Klein, 1999).

However, the Gas Chromatograph/Mass Spectrometer (GCMS) indicated that no organics were present at the ppb level (Biemann *et al*., 1977). This absence of organics suggested that the LR experiment was unlikely to represent a biological reaction. The absence of organics has been questioned recently, however, Martian organics could have been reduced to a nonvolatile form that would not have been detected by the GCMS (Benner *et al*., 2000). Even were this the case, however, the LR results probably would not be consistent with life – there being a biological response would have required that the organics be present in a labile form.

With 30 years' hindsight, it is likely that the Viking experiments were ill conceived, for several reasons: (i) On Earth, more than 99% of organisms cannot be cultured in the lab. It would be remarkable if Martian organisms could be cultured, especially with a very nonspecialized collection of nutrients. (ii) The Viking experiments were not carried out under Martian conditions, but were done inside the spacecraft with different temperatures, pressures, and in particular the presence of liquid water that would not be stable at the surface. (iii) The surface of Mars appears to be an inhospitable place for life. Liquid water is not stable, both due to the low pressure and low temperature (it would either freeze or sublimate/evaporate into the atmosphere). Any organisms would be subject to strong ultraviolet light that likely would be harmful. And average temperatures are extremely low, so that biochemical reactions would proceed very slowly. A search for life today should, rather, look in environments that would be likely to be more conducive to the presence of life; these are discussed below.

The meteorite ALH 84001 was collected in Antarctica in 1984 and eventually recognized as Martian based on its isotopic abundances and similarity to other Martian meteorites. It stands out by virtue of its crystallization age of 4.5 Gyr, meaning that it was present on Mars during the early epoch of more clement climate and during the subsequent change in climate. It also has several percent of carbonate minerals as weathering product within the rock (e.g., Mittlefehldt, 1994; see also Chapter 17). This carbonate could represent a sink for gas from the atmosphere, and its presence also suggested that liquid water had been present. Both points make this an interesting rock from an astrobiological perspective.

McKay *et al*. (1996) examined the rock with this in mind. They identified several characteristics of the rock that could be consistent with the presence of fossil evidence for life. These included polycyclic aromatic hydrocarbons (PAHs), which are a particular form of reduced organic molecules, minerals out of equilibrium with their environment as might be produced by life, small magnetite grains that were similar to those produced by organisms here on Earth, and morphological entities reminiscent of fossilized organisms. While each of these pieces of evidence could have geological mechanisms for their formation, McKay *et al*. suggested that biological processes could be responsible.

Their results triggered an intense period of analysis of ALH 84001. While there still is not unanimity in the Mars community, there is a general consensus regarding this rock. First, demonstrably terrestrial organisms were found in the rock, and clearly had infiltrated after the rock landed on Earth (Steele *et al*., 2000). Interestingly, this meant that the rock could, in fact, support life. But it also meant that any evidence for possible life had to consider the possibility of terrestrial contamination. Second, several lines of evidence were found to be artifacts of the sample preparation or analysis technique, rather than indigenous to the rock. Third, the key aspects of the remaining characteristics (see Friedmann *et al*., 2001) were shown to be capable of being produced by very straightforward geological processes involving multiple events of infiltration by heated water;

these processes are common in terrestrial rocks, and also should have occurred in Martian rocks (Golden *et al.*, 2001, 2002).

The ALH 84001 analyses demonstrated that we were very ill prepared to consider the issues of possible Martian life and how to distinguish biological from geological processes. While we are better prepared today, the lesson we need to learn is that we have to keep an open mind in analyzing samples. While any evidence truly suggestive of life may be obvious, ambiguous evidence likely will end up still being ambiguous even after years of analysis.

What issues still remain regarding Martian planetary habitability?

Although the general characteristics of Mars that might allow habitability have been identified, both locally and globally, there are major questions still to be addressed before we understand the issues. Of particular interest is the question of relating the local and regional properties as derived from the MERs with the global perspective. While it is easy to say that the global evidence appears to support habitability, the more difficult question is what the geochemical environment was globally. Was the surface water for which there is evidence at the *Opportunity* landing site widespread geographically? Was it present for a long period of time? How does it relate to the evidence for surface water seen at global scales? Are the acidic conditions seen at the *Opportunity* landing site representative of global conditions over a long period of time? Is the evidence for aqueous processes typical of what would be found globally? These questions do not have easy answers.

More broadly, we can ask questions about the distribution of liquid water through time, both at the surface and within the crust; the chemical properties of the water (e.g., salinity, acidity, etc.) that are pertinent to biological processes; the processes that allowed liquid water to be stable at the surface and that changed the surface climate to the cold, dry environment we see today; and the availability of chemical resources to support life, including nitrogen and carbon in particular. Of particular interest is the question of determining the Martian climate through time, the conditions that allowed liquid water to be present early on, and the changes that produced an environment that precluded stable liquid water at later epochs. The processes that drove the climate change are of special importance for understanding the general nature of planetary habitability as well as the specific instance of Mars.

In addition, there are abundant questions about Mars that relate to its evolution as a planet and which, in essence, control habitability. These include the history of geological processes at the surface (e.g., the history of volcanism and its relation to liquid water), the thermal history and interior composition and structure that drive surface and crustal processes such as volcanism, and the initial volatile inventory of Mars and its subsequent evolution.

How can we search for life on Mars?

Our search for life must consist of incremental steps that orbiters, landers and, ultimately, sample return missions can achieve. Key observations include evidence of environments that might be habitable today or were likely to have been habitable some time in the past, biosignatures, or direct observations of living organisms. The Viking mission taught us that the present surface environment of Mars is inhospitable to life and therefore that direct observations of active metabolism are highly improbable if not impossible in the near-term except in isolated (and as yet undiscovered) locations. However, observations of accessible crustal materials might allow us to discover geologic records of habitable environments and biosignatures. And we can apply valuable perspectives gained from Mars exploration, from studies of Earth's early biosphere as recorded in rocks and in living microorganisms, and from an appreciation of the diversity of modern microbial life and its habitats.

Given the harsh conditions on the surface of Mars today, any modern habitable environments are probably restricted to the deep subsurface where liquid water is present. Spacecraft will not be able to obtain samples directly from such regions in the foreseeable future. But spacecraft outfitted with geophysical sounders are beginning to explore the subsurface. MARSIS on ESA's Mars Express orbiter and SHARAD on NASA's Mars Reconnaissance Orbiter are searching for aquifers and other evidence of subsurface water. Recent reports of methane in the Martian atmosphere are also intriguing (e.g., Allen *et al.*, 2006). Microorganisms and plants produce methane, but nonbiological sources also exist. However, water is involved in virtually all methane-producing reactions. In any case, future efforts to confirm the presence of methane and localize its potential sources will contribute to the search for extant life on Mars.

The long-term stability of the Martian crust probably has allowed it to preserve an excellent record of its early history. Cameras and spectrometers on the orbiters from NASA, ESA, and other space agencies will continue to map the surface of Mars for evidence of liquid water and geologic processes that might have sustained habitable environments. Examples of past habitable environments that might be detected from orbit include: paleolake basins, springs, hydrothermal systems, indurated soils, and ice derived from subsurface discharges (Farmer and Des Marais, 1999). These orbiters will search for clays, silica, carbonates, sulfates, and other materials that can preserve biosignatures. Such global mapping will contribute substantially to the selection of sites for landers and rovers. Rovers will perform definitive analyses of the composition and mineralogy of surface materials in order to determine their environments of origin and to search for potential biosignatures. Rovers will analyze volatile materials, including any organic carbon, in order to define further their environments of origin and to search for biosignatures. NASA's Mars Science Laboratory mission (http://marsprogram.jpl.nasa.gov/msl/) will perform these and other key observations. Concepts for landed missions in the following decade include life-detection experiments that will search for chemical species that might indicate extant life (http://mars.jpl.nasa.gov/missions/future/).

As we proceed with the search for evidence of life, we must keep in mind that the attributes of any Martian life might

differ in fundamental ways from life on Earth. We need to keep an open mind as to what constitutes life and what constitutes evidence for life. We must be prepared to explore a "gray zone," a continuum between the nonliving and the living. It will not be easy to know uniquely whether something is alive in the middle of this zone, and in which otherwise reasonable people will disagree as to whether something is biological or not.

At Mars, it seems likely that one of three outcomes will occur. We may see evidence that is truly compelling for the presence of life and a consensus will develop relatively quickly. We may see evidence that clearly requires only nonbiological planetary processes and therefore we did not find life. Or the evidence will be ambiguous and engender years of continuing analysis, debate and, perhaps eventually, profound insights about life in the universe. Let us go and find out.

ACKNOWLEDGMENTS

D. J. Des Marais and B. M. Jakosky acknowledge support from the NASA Astrobiology Institute, which provided support for B. M. Jakosky through a Cooperative Agreement with the University of Colorado.

REFERENCES

Allen, M., B. Sherwood-Lollar, B. Runnegar, *et al*., Is Mars alive?, *EOS* **87**(41), 433, 439, 2006.

Arvidson, R. E., F. P. Seelos, K. S. Deal, *et al*., Mantled and exhumed terrains in Terra Meridiani, Mars. *J. Geophys. Res. – Planets* **108**, 8073, 2003.

Baker, B. J. and J. F. Banfield, Microbial communities in acid mine drainage, *FEMS Microb. Ecol.* **44**, 139–52, 2003.

Baker, V. R., Water and the Martian landscape, *Nature* **412**, 228–36, 2001.

Baker, V. R., R. G. Strom, V. C. Gulick, *et al*., Ancient oceans, ice sheets and the hydrological cycle on Mars, *Nature* **352**, 589–94, 1991.

Baker, V. R., M. H. Carr, V. C. Gulick, C. R. Williams, and M. S. Marley, Channels and valley networks. In *Mars* (ed. H. H. Kieffer, B. M. Jakosky, C. W. Snyder, and M. S. Matthews), Tucson: University of Arizona Press, pp. 493–522, 1992.

Bakermans, C., A. I. Tsapin, V. Souza-Egipsy, D. A. Gilichinisky, and K. H. Nealson, Reproduction and metabolism at −10 degrees C of bacteria isolated from Siberian permafrost. *Environ. Microbiol.* **5**, 321–6, 2003.

Basaltic Volcanism Study Project, *Basaltic Volcanism on the Terrestrial Planets* (ed. W. M. Kaula *et al*.), New York: Pergamon Press, 1981.

Bandfield, J. L., T. D. Glotch, and P. R. Christensen, Spectroscopic identification of carbonate minerals in the martian dust, *Science* **301**, 1084–7, 2000.

Bazylinski, D. A. and B. M. Moskowitz, Microbial biomineralization of magnetic iron minerals: microbiology, magnetism and environmental significance. In *Geomicrobiology: Interactions between Microbes and Minerals* (ed. J. F. Banfield and K. H. Nealson), Washington, DC: Mineralogical Society of America, pp. 181–223, 1997.

Bell III, J. F., S. W. Squyres, R. E. Arvidson, *et al*., Pancam multispectral imaging results from the Opportunity rover at Meridiani Planum, *Science* **306**, 1703–9, 2004.

Benner, S. A., K. G. Devine, L. N. Matveeva, and D. H. Powell, The missing organic molecules on Mars, *Proc. Natl. Acad. Sci.* **97**, 2425–30, 2000.

Berman, D. C. and W. K. Hartmann, Recent fluvial, volcanic and tectonic activity on the Cerberus plains of Mars, *Icarus* **159**, 1–17, 2002.

Bhattacharya, J. P., T. H. D. Payenberg, S. C. Lang, and M. Bourke, Dynamic river channels suggest a long-lived Noachian crater lake on Mars, *Geophys. Res. Lett.* **32**, L10201, 2005.

Bibring, J. -P., Y. Langevin, A. Gendrin, *et al*., Mars surface diversity as revealed by the OMEGA/Mars Express observations, *Science* **307**, 1576–81, 2005.

Bibring, J. -P., Y. Langevin, J. F. Mustard, *et al*., Global mineralogical and aqueous Mars history derived from OMEGA/Mars express data, *Science* **312**, 400–4, 2006.

Biemann, K., J. Oro, P. Toulmin III, *et al*., The search for organic substances and inorganic volatile compounds in the surface of Mars, *J. Geophys. Res.* **82**, 4641–58, 1977.

Bierhaus, E. B., C. R. Chapman, and W. J. Merline, Secondary craters on Europa and implications for cratered surfaces, *Nature* **437**, 1125–7, 2005.

Booth, I. R., Regulation of cytoplasmic pH in bacteria, *Microbiol. Rev.* **49**, 359–78, 1985.

Boynton, W. V., W. C. Feldman, S. W. Squyres, *et al*., Distribution of hydrogen in the near surface of Mars: evidence for subsurface ice deposits, *Science* **297**, 81–4, 2002.

Brain, D. A. and B. M. Jakosky, Atmospheric loss since the onset of the martian geologic record: combined role of impact erosion and sputtering, *J. Geophys. Res.* **103**, 22698–94, 1998.

Brain, D. A., F. Bagenal, M. H. Acuna, and J. E. P. Connerney, Martian magnetic morphology: contributions from the solar wind and crust, *J. Geophys. Res.* **108**, doi:10.1029/2002JA009482, 2003.

Brock, T. D., M. T. Madigan, J. M. Martinko, and J. Parker, *Biology of Microorganisms*, New Jersey: Prentice Hall, 1994.

Brocks, J. J., R. Buick, R. E. Summons, and G. A. Logan, A reconstruction of Archean biological diversity based on molecular fossils from the 2.78–2.45 billion year old Mount Bruce Supergroup, Hamersley Basin, Western Australia, *Geochim. Cosmochim. Acta* **67**, 4321–35, 2003.

Brown, D. A., D. C. Kamineni, J. A. Sawicki, and T. J. Beveridge, Minerals associated with biofilms occurring on exposed rock in a granite underground research laboratory, *Appl. Environ. Microbiol.* **60**, 3182–91, 1994.

Burr, D. M., J. A. Grier, A. S. McEwen, and L. P. Keszthelyi, Repeated aqueous flooding from the Cerberus Fossae: evidence for very recently extant, deep groundwater on Mars, *Icarus* **159**, 53–73, 2002.

Cabrol, N. A. and E. A. Grin, Distribution, classification, and ages of Martian impact crater lakes, *Icarus* **142**, 160–72, 1999.

Cabrol, N. A., E. A. Grin, and G. Dawidowicz, Ma'adim-Vallis revisited through new topographic data: evidence for an ancient intravalley lake, *Icarus* **123**, 269–83, 1996.

Cabrol, N. A., E. A. Grin, R. Landheim, R. O. Kuzmin, and R. Greeley, Duration of the Ma'adim Vallis/Gusev crater hydrogeologic system, *Icarus* **133**, 98–108, 1998.

Canfield, D. E., Biogeochemistry of sulfur isotopes. In *Stable Isotope Geochemistry* (ed. J. W. Valley and D. R. Cole),

Washington, DC: Mineralogical Society of America, pp. 607–36, 2001.
Carr, M. H., Formation of martian flood features by release of water from confined aquifers, *J. Geophys. Res.* **84**, 2995–3007, 1979.
Carr, M. H., The Martian drainage system and the origin of valley networks and fretted channels, *J. Geophys. Res.* **100**, 7479–507, 1995.
Carr, M. H., *Water on Mars*, Oxford University Press, 1996.
Carr, M. H. and G. D. Clow, Martian channels and valleys: their characteristics, distribution, and age, *Icarus* **48**, 91–117, 1981.
Carr, M. H. and J. W. Head III, Oceans on Mars: an assessment of the observational evidence and possible fate, *J. Geophys. Res.* **108**, 5042, doi:5010,1029/2002JE001963, 2003.
Carr, M. H. and M. C. Malin, Meter scale characteristics of martian channels and valleys. *Icarus* **146**, 366–86, 2000.
Chang, S., Planetary environments and the conditions of life, *Philos. Trans. R. Soc. Lond.* **325**, 601–10, 1988.
Chapman, C. R. and K. L. Jones, Cratering and obliteration history of Mars, *Annu. Rev. Earth Planet. Sci.* **5**, 515–40, 1977.
Christensen, P. R., Formation of recent martian gullies through melting of extensive water-rich snow deposits, *Nature* **422**, 45–8, 2003.
Christensen, P. R., R. V. Morris, M. D. Lane, J. L. Bandfield, and M. C. Malin, Global mapping of Martian hematite mineral deposits: remnants of water-driven processes on early Mars, *J. Geophys. Res. – Planets* **106**, 23873–85, 2001.
Christensen, P. R., M. B. Wyatt, T. D. Glotch, *et al.*, Mineralogy at Meridiani Planum from the Mini-TES Experiment on the Opportunity Rover, *Science* **306**, 1733–9, 2004.
Clark, B. C., R. V. Morris, S. M. McLennan, *et al.*, Chemistry and mineralogy of outcrops at Meridiani Planum, *Earth Planet. Sci. Lett.* **240**, 73–94, 2005.
Cleland, C. E. and C. F. Chyba, Does life have a definition? In *Planets and Life* (ed. W. Sullivan and J. Baross), Cambridge: Cambridge University Press, pp. 119–3, 2007.
Clow, G. D., Generation of liquid water on Mars through melting of a dusty snowpack, *Icarus* **72**, 95–127, 2003.
Costard, F., F. Forget, N. Mangold, and J. P. Peulvast, Formation of recent Martian debris flows by melting of near surface ground ice at high obliquity, *Science* **295**, 110–13, 2002.
Craddock, R. A. and A. D. Howard, The case for rainfall on an early warm, wet Mars, *J. Geophys. Res.* **107**, doi:10.1029/2001JE001505, 2002.
Craddock, R. A. and T. A. Maxwell, Geomorphic evolution of the Martian highlands through ancient fluvial processes, *J. Geophys. Res.* **98**, 3453–68, 1993.
Des Marais, D. J., Isotopic evolution of the biogeochemical cycle during the Precambian. In *Stable Isotope Geochemistry* (ed. J. W. Valley and D. R. Cole), *Rev. Mineral.* **43**, 555–78, 2001.
Des Marais, D. J., L. J. Allamandola, S. A. Benner, *et al.*, The NASA astrobiology roadmap, *Astrobiology* **3**(2), 219–35, 2003.
Des Marais, D. J., B. C. Clark, L. S. Crumpler, *et al.*, Astrobiology and the basaltic plans in Gusev crater, paper presented at *Lunar Planet. Sci. XXXVI*, Houston, TX: Lunar and Planetary Institute, Abstract #2353, March 14–18, 2005.
Ehrlich, H. L., How microbes influence mineral growth and dissolution, *Chem. Geol.* **132**, 5–9, 1996.
Farmer, J. D. and D. J. Des Marais, Exploring for a record of ancient Martian life, *J. Geophys. Res.* **104**, 26977–95, 1999.
Feldman, W. C., W. V. Boynton, R. L. Tokar, *et al.*, Global distribution of neutrons from Mars Odyssey, *Science* **297**, 75–8, 2002.
Fishbaugh, K. E. and J. W. Head III, Topographic characterization from Mars Orbiter Laser Altimeter data and implications for mechanisms of formation, *J. Geophys. Res.* **107**, 5013, doi:5010.1029/2000JE001351, 2002.
Fisk, M. R. and S. J. Giovannoni, Sources of nutrients and energy for a deep biosphere on Mars, *J. Geophys. Res.* **104**, 11805–15, 1999.
Fisk, M. R., A. E. Bence, and J. G. Schilling, Major-element chemistry of Galapagos Rift Zone magmas and their phenocrysts, *Earth Planet. Sci. Lett.* **61**, 171–89, 1982.
Forget, F. and R. T. Pierrehumbert, Warming early Mars with carbon dioxide clouds that scatter infrared radiation, *Science* **278**, 1273–6, 1997.
Forget, F., R. M. Haberle, F. Montmessin, B. Levrard, and J. W. Head, Formation of glaciers on Mars by atmospheric precipitation at high obliquity, *Science* **311**, 368–71, 2006.
Friedmann, E. I., J. Wierzchos, and M. Winkelhofer, Chains of magnetite crystals in the meteorite ALH84001: evidence of biological origin, *Proc. Natl. Acad. Sci.* **98**, 2176–81, 2001.
Galinski, E. A. and H. G. Trueper, Microbial behaviour in salt-stressed ecosystems, *FEMS Microb. Rev.* **15**, 95–108, 1994.
Gendrin, A., N. Mangold, J.-P. Bibring, *et al.*, Sulfates in martian layered terrains: the OMEGA/Mars Express view, *Science* **307**, 1587–91, 2005.
Ghosal, D., M. V. Omelchenko, E. K. Gaidamakova, *et al.*, How radiation kills cells: survival of *Deinococcus radiodurans* and *Shewanella oneidensis* under oxidative stress, *FEMS Microbiol. Rev.* **29**, 361–75, 2005.
Golden, D. C., D. W. Ming, C. S. Schwandt, *et al.*, A simple inorganic process for formation of carbonates, magnetite, and sulfides in martian meteorites, *Am. Mineral.* **86**, 370–5, 2001.
Golden, D., D. W. Ming, R. Morris, G. Lofgren, and G. A. McKay, Inorganic formation of "truncated hexa-octahedral" magnetite: implications for inorganic processes, in Martian meteorite ALH84001, paper presented at *Lunar Planet. Sci Conf. XXXIII*, 2002.
Golombek, M. P., R. E. Arvidson, J. F. Bell III, *et al.*, Assessment of Mars exploration Rover landing site predictions, *Nature* **436**, 44–8, 2005.
Golombek, M. P., L. S. Crumpler, J. A. Grant, *et al.*, Geology of the Gusev cratered plains from the Spirit rover traverse, *J. Geophys. Res. – Planets* **111**, doi:10:1029/2005/JEO02503, 2006.
Grant, J. A., Life at low water activity, *Philos. Trans. R. Soc. Lond.* Series B – Biological Sciences **359**, 1249–66, 2004.
Greeley, R. and B. D. Schneid, Magma generation on Mars: amounts, rates, and comparisons with Earth, Moon, and Venus, *Science* **254**, 996–8, 1991.
Griffith, L. L. and E. L. Schock, A geochemical model for the formation of hydrothermal carbonate on Mars, *Nature* **377**, 406–8, 1995.
Grotzinger, J. P., R. E. Arvidson, J. F. Bell III, *et al.*, Stratigraphy and sedimentology of a dry to wet eolian depositional system, Burns formation, Meridiani Planum, Mars, *Earth Planet. Sci. Lett.* **240**, 11–72, 2005.
Gulick, V. C. and V. R. Baker, Origin and evolution of valleys on Martian volcanoes, *J. Geophys. Res.* **95**, 14325–44, 1990.
Haskin, L. A., A. Wang, B. L. Jolliff, *et al.*, Water alteration of rocks and soils on Mars at the Spirit rover site in Gusev crater, *Nature* **436**, 66–9, 2005.
Hauck II, S. A. and R. J. Phillips, Thermal and crustal evolution of Mars, *J. Geophys. Res.* **107**(E7), doi:10.1029/2001JE001801, 2002.
Head, J. W. and D. R. Marchant, Cold-based mountain glaciers on Mars: Western Arsia Mons. *Geology* **31**, 641–4, 2003.
Head, J. W., M. A. Kreslavsky, and S. Pratt, Northern lowlands of Mars: evidence for widespread volcanic flooding and tectonic deformation in the Hesperian Period, *J. Geophys. Res.* **107**, doi:10.1029/2000JE001445, 2002.
Heldmann, J. L. and M. T. Mellon, Observations of martian gullies and constraints on potential formation mechanisms, *Icarus* **168**, 285–304, 2004.

Herkenhoff, K. E., S. W. Squyres, R. Arvidson, *et al*., Evidence from Opportunity's Microscopic Imager for water on Meridiani Planum, *Science* **306**, 1727–30, 2004.

Hoffman, N., White Mars: a new model for Mars' surface and atmosphere based on CO_2, *Icarus* **146**, 326–42, 2000.

Hurowitz, J. A., S. M. McLennan, and H. Y. McSween Jr., Mixing relationships and the effects of secondary alteration in the Wishstone and Watchtower Classes of Husband Hill, Gusev crater, Mars, *J. Geophys Res*. **111**(E12), 2006.

Hynek, B. M. and R. J. Phillips, New data reveal mature, integrated drainage systems on Mars indicative of past precipitation, *Geology* **31**, 757–60, 2003.

Hynek, B. M., R. E. Arvidson, and R. J. Phillips, Geologic setting and origin of Terra Meridiani hematite deposit on Mars, *J. Geophys. Res*. **107**, 5088, doi:10.1029/2002JE001891, 2002.

Jakosky, B. M., *Search for Life on Other Planets*, Cambridge: Cambridge University Press, 1998.

Jakosky, B. M., *Science, Society, and the Search for Life in the Universe*, Tuscon: University of Arizona Press, 2006.

Jakosky, B. M. and M. H. Carr, Possible precipitation of ice at low latitudes of Mars during periods of high obliquity, *Nature* **315**, 559–61, 1985.

Jakosky, B. M. and R. J. Phillips, Mars' volatile and climate history, *Nature* **412**, 237–44, 2001.

Jakosky, B. M. and E. L. Shock, The biological potential of Mars, the early Earth, and Europa, *J. Geophys. Res*. **103**, 19359–64, 1998.

Jakosky, B. M., R. O. Pepin, R. E. Johnson, and J. L. Fox, Mars atmospheric loss and isotopic fractionation by solar-wind-induced sputtering and photochemical escape, *Icarus* **111**, 271–88, 1994.

Jakosky, B. M., B. G. Henderson, and M. T. Mellon, Chaotic obliquity and the nature of the martian climate, *J. Geophys. Res*. **100**, 1579–84, 1995.

Jakosky, B. M., K. H. Nealson, C. Bakermans, R. E. Ley, and M. T. Mellon, Sub-freezing activity of microorganisms and the potential hability of Mars' polar regions, *Astrobiology* **3**, 343–50, 2003.

Kasting, J. F., CO_2 condensation and the climate of early Mars, *Icarus* **94**, 1–13, 1991.

Kieffer, H. H. and A. P. Zent, Quasi-periodic climate change on Mars. In *Mars* (ed. H. Kieffer, B. Jakosky, C. Snyder, M. Matthews), Tucson: University of Arizona Press, pp. 1180–218, 1992.

Klein, H. P., The Viking mission and the search for life on Mars, *Rev. Geophys. Space Phys*. **17**, 1655–62, 1979.

Klein, H. P., Did Viking discover life on Mars?, *Orig. Life Evol. Biosphere* **29**, 625–31, 1999.

Klein, H. P., N. H. Horowitz, and K. Biemann, The search for extant life on Mars. In *Mars* (ed. H. H. Kieffer, B. M. Jakosky, C. W. Snyder, and M. S. Matthews), Tucson: University of Arizona Press, pp. 1221–33, 1992.

Klingelhöfer, G., R. V. Morris, B. Bernhardt, *et al*., Jarosite and hematite at Meridiani Planum from Opportunity's Mössbauer spectrometer, *Science* **306**, 1740–5, 2004.

Knoll, A. H., The evolution of ecological tolerance in prokaryotes, *Trans. R. Soc. Edinburgh Earth Sci*. **80**, 209–23, 1989.

Knoll, A. H., An astrobiological perspective on Meridiani Planum, *Earth Planet. Sci. Lett*. **240**, 179–89, 2005.

Laskar, J., A. C. M. Correia, M. Gastineau, *et al*., Long term evolution and chaotic diffusion of the insolation quantities of Mars, *Icarus* **170**, 343–64, 2004.

Levin, G. V. and P. A. Straat, Recent results from the Viking labeled release experiment on Mars, *J. Geophys. Res*. **82**, 4663–8, 1977.

Levrard, B., F. Forget, F. Montmessin, and J. Laskar, Recent ice-rich deposits formed at high latitudes on Mars by sublimation of unstable equatorial ice during low obliquity, *Nature* **431**, 1072–5, 2004.

Link, L. S., B. M. Jakosky, and G. D. Thyne, Biological potential of low-temperature aqueous environments on Mars, *Int. J. Astrobiol*. **4**, 155–64, 2005.

Luhmann, J. G., R. E. Johnson, and M. H. G. Zhang, Evolutionary impact of sputtering of the martian atmosphere by O+ pickup ions, *Geophys. Res. Lett*. **19**, 2151–4, 1992.

Lunine, J. I., *Earth: Evolution of a Habitable World*, Cambridge: Cambridge University Press, 344pp., 1998.

Malin, M. C. and K. S. Edgett, Evidence for recent ground water seepage and surface runoff on Mars, *Science* **288**, 2330–5, 2000.

Malin, M. C. and K. S. Edgett, Evidence for persistent flow and aqueous sedimentation on early Mars, *Science* **302**, 1931–4, 2003.

Mancinelli, R. L., The search for nitrogen compounds on the surface of Mars, *Adv. Space Res*. **18**, 241–8, 1996.

Martínez-Alonso, S., B. M. Jakosky, M. T. Mellon, and N. E. Putzig, A volcanic interpretation of Gusev crater surface materials from thermophysical, spectral, and morphological evidence, *J. Geophys. Res*. **110**, E01003, doi:10.1029/2004JE002327, 2005.

McCollom, T. M. and B. M. Hynek, A volcanic environment for bedrock diagenesis at Meridiani Planum on Mars, *Nature* **438**, 1129–31, 2005.

McCollom, T. M. and B. M. Hynek, Planetary science: bedrock formation at Meridiani Planum (Reply), *Nature* **443**, 2, 2006.

McKay, C. P., R. L. Mancinelli, C. R. Stoker, and J. R. A. Wharton, The possibility of life on Mars during a water-rich past. In *Mars* (ed. B. M. Jakosky, H. H. Kieffer, C. W. Snyder, and M. S. Matthews), Tucson: University of Arizona Press, pp. 1234–45, 1992.

McKay, D. S., E. K. Gibson Jr., K. L. Thomas-Keprta, *et al*., Search for past life on Mars: Possible relic biogenic activity in martian meteorite ALH84001, *Science* **273**, 24–30, 1996.

McLennan, S. M., J. F. Bell III, W. M. Calvin, *et al*., Provenance and diagenesis of the evaporite-bearing Burns formation, Meridiani Planum, Mars, *Earth Planet. Sci. Lett*. **240**, 95–121, 2005.

McSween Jr., H. Y., What have we learned about Mars from SNC Meteorites, *Meteoritics* **29**, 757–79, 1994.

McSween Jr., H. Y., T. L. Grove, R. C. F. Lentz, *et al*., Geochemical evidence for magmatic water within Mars from pyroxenes in the Shergotty meteorite, *Nature* **409**, 487–90, 2001.

Mellon, M. T. and B. M. Jakosky, The distribution and behavior of martian ground ice during past and present epochs, *J. Geophys. Res*. **100**, 11781–99, 1995.

Mellon, M. T. and R. J. Phillips, Recent gullies on Mars and the source of liquid water, *J. Geophys. Res*. **106**, 23165–79, 2001.

Melosh, H. J., The rocky road to Panspermia, *Nature* **332**, 687–8, 1988.

Melosh, H. J. and A. M. Vickery, Impact erosion of the primordial atmosphere of Mars, *Nature* **338**, 487–9, 1989.

Miller, S. L. and L. E. Orgel, *The Origins of Life on the Earth*, Englewood Cliffs, NJ: Prentice-Hall, 1974.

Ming, D. W., D. W. Mittlefehldt, R. V. Morris, *et al*., Geochemical and mineralogical indicators for aqueous processes in the Columbia Hills of Gusev crater, Mars, *J. Geophys. Res. – Planets* **11**, E02S12, 2006.

Mittlefehldt, D. W., ALH84001, a cumulate orthopyroxenite member of the martian meteorite clan, *Meteoritics* **29**, 214–21, 1994.

Moore, J. M., Martian layered fluvial deposits: implications for Noachian climate scenarios. *Geophys. Res. Lett*. doi:10.1029/2003GL019002, 2003.

Morowitz, H., *Beginnings of Cellular Life*, New Haven, CT: Yale University Press, 1992.

Morris, R. V., G. Klingelhöfer, C. Schröder, *et al*., Mössbauer mineralogy of rock, soil, and dust at Guesev crater, Mars: Spirit's journey through weakly altered olivine basalt on the plains and pervasively altered basalt in the Columbia Hills, *J. Geophys. Res.* **111**, E02S13, doi:10.1029/2005JE002584, 2006.

Musselwhite, D. S., T. D. Swindle, and J. L. Lunine, Liquid CO_2 breakout and the formation of recent gullies on Mars, *Geophys. Res. Lett.* **28**, 1283–5, 2001.

Mustard, J. F., C. D. Cooper, and J. F. Rifkin, Evidence for recent climate change on Mars from the identification of youthful near-surface ground ice, *Nature* **412**, 411–14, 2001.

Nealson, K. H., The limits of life on Earth and searching for life on Mars, *J. Geophys. Res.* **102**, 23675–86, 1997.

Neukum, G., R. Jaumann, H. Hoffmann, *et al*., Recent and episodic volcanic and glacial activity on Mars revealed by the High Resolution Stereo Camera, *Nature* **432**, 971–9, 2004.

Newsom, H. E., Hydrothermal alteration of impact melt sheets with implications for Mars, *Icarus* **44**, 207–16, 1980.

Nimmo, F. and K. L. Tanaka, Early crustal evolution of Mars, *Annu. Rev. Earth Planet. Sci.* **33**, doi:10.1146/annurev.earth.1133.092203.122637, 2005.

Owen, T., The composition and early history of the atmosphere of Mars. In *Mars* (ed. H. H. Kieffer, B. M. Jakosky, C. W. Snyder, and M. S. Matthews), Tucson: University of Arizona Press, pp. 818–34, 1992.

Parker, T. S., R. S. Saunders, and D. M. Schneeberger, Transitional morphology in the west Deuteronilus Mensae region of Mars: implications for modification of the lowland/upland boundary, *Icarus* **82**, 111–45, 1989.

Pepin, R. O., Evolution of the Martian atmosphere, *Icarus* **111**, 289–304, 1994.

Phillips, R. J., M. T. Zuber, S. C. Solomon, *et al*., Ancient geodynamics and global-scale hydrology on Mars, *Science* **291**, 2587–91, 2001.

Pohorille, A., Protocells as universal ancestors of living systems. In *Protocells: Bridging Nonliving and Living Matter* (ed. S. Rasmussen, M. Bedau, L. Chen, *et al*.), Cambridge, MA: MIT Press, 2006.

Pollack, J. B., J. F. Kasting, S. M. Richardson, and K. Poliakoff, The case for a warm, wet climate on early Mars, *Icarus* **71**, 203–24, 1987.

Rieder, R., R. Gellert, R. C. Anderson, *et al*., Chemistry of rocks and soils at Meridiani Planum from the alpha particle X-ray spectrometer, *Science* **306**, 1746–9, 2004.

Rothschild, L. J. and R. L. Mancinelli, Life in extreme environments, *Nature* **409**, 1092–101, 2001.

Russell, M. J. and A. J. Hall, The emergence of life from monosulphide bubbles at a submarine hydrothermal redox and pH front, *J. Geol. Soc. Lond.* **154**, 377–402, 1997.

Sackman, I. J. and A. I. Boothroyd, Our Sun: V. A bright young Sun consistent with helioseismology and warm temperatures on ancient Earth and Mars, *Astrophys. J.* **583**, 1024–39, 2003.

Sagan, C. and G. Mullen, Earth and Mars: evolution of atmospheres and surface temperatures, *Science* **177**, 52–6, 1972.

Schopf, J. W., S. Chang, W. G. Ernst, *et al*., Geology and paleobiology of the Archean Earth. In *The Proterozoic Biosphere* (ed. J. W. Schopf and C. Klein), Cambridge: Cambridge University Press, pp. 5–42, 1992.

Scott, D. H. and K. L. Tanaka, Geologic map of the western equatorial region of Mars, 1:15,000,000 geologic map, *Map I-1802-A* USGS, Reston, VA, 1986.

Segura, T. L., Impact-triggered greenhouses on Mars, Ph.D. dissertation, University of Colorado, 2005.

Segura, T. L., O. B. Toon, A. Colaprete, and K. Zahnle, Environmental effects of large impacts on Mars, *Science* **298**, 1977–80, 2002.

Shean, D. E., J. W. Head, and D. R. Marchant, Origin and evolution of a cold-based tropical mountain glacier on Mars: the Pavonis Mons fan-shaped deposit, *J. Geophys. Res.* **110**, CiteID E05001, doi:10.1029/2004JE002360, 2005.

Shock, E. L., High-temperature life without photosynthesis as a model for Mars, *J. Geophys. Res.* **102**, 23687–94, 1997.

Sleep, N. H., A. Meibom, Th. Fridriksson, R. G. Coleman, and D. K. Bird, H_2-rich fluids from serpentinization: geochemical and biotic implications, *Proc. Natl. Acad. Sci.* **101**, 12818–23, 2004.

Solomon, S. C., O. Aharonson, J. M. Aurnou, *et al*., New perspectives on ancient Mars, *Science* **307**, 1214–20, 2005.

Squyres, S. W., R. E. Arvidson, J. F. Bell III, *et al*., The Spirit Rover's Athena science investigation at Gusev crater, Mars, *Science* **305**, 794–9, 2004a.

Squyres, S. W., R. E. Arvidson, J. F. Bell III, *et al*., The Opportunity Rover's Athena science investigation at Meridiani Planum, Mars, *Science* **306**, 1698–703, 2004b.

Squyres, S. W., O. Aharonson, R. E. Arvidson, *et al*., Planetary science: bedrock formation at Meridiani Planum, *Nature* **443**, E1–E2, 2006.

Steele, A., D. T. Goddard, D. V. Stapleton, *et al*., Investigations into an unknown organism on the martian meteorite Allan Hills 84001, *Meteorit. Planet. Sci.* **35**, 237–41, 2000.

Stetter, K. O., Hyperthermophilic microorganisms, *FEMS Microb. Rev.* **75**, 117–24, 1990.

Stewart, S. T. and F. Nimmo, Surface runoff features on Mars: testing the carbon dioxide formation hypothesis, *J. Geophys. Res.* **107**, 5069, doi:5010.1029/2000JE001465, 2002.

Tanaka, K. L., N. K. Isbell, D. H. Scott, R. Greeley, and J. E. Grant, The resurfacing history of Mars: a synthesis of digitized, Viking-based geology, *Proc. Lunar Planet. Sci. Conf. XVIII*, Cambridge University Press, pp. 665–78, 1988.

Toon, O. B., J. B. Pollack, W. Ward, J. A. Burns, and K. Bilski, The astronomical theory of climatic change on Mars, *Icarus* **44**, 552–607, 1980.

Tosca, N. J., S. M. McLennan, B. C. Clark, *et al*., Geochemical modeling of evaporation processes on Mars: insight from the sedimentary record at Meridiani Planum, *Earth Planet. Sci. Lett.* **240**, 122–48, 2005.

Touma, J. and J. Wisdom, The chaotic obliquity of Mars, *Science* **259**, 1294–7, 1993.

Treiman, A. H., Geologic setting of martian gullies: implications for their origins, *J. Geophys. Res.* **108**, doi:10.1029/2002JE001900, 2003.

Varnes, E. S., B. M. Jakosky, and T. M. McCollom, Biological potential of Martian hydrothermal systems, *Astrobiology* **3**, 407–14, 2003.

Walter, M. R., *Stromatolites*, Amsterdam: Elsevier, 790pp., 1976.

Walter, M. R. and D. J. Des Marais, Preservation of biological information in thermal spring deposits: developing a strategy for the search for fossil life on Mars, *Icarus* **101**, 129–43, 1993.

Ward, P. D. and D. Brownlee, *Rare Earth: Why Complex Life is Uncommon in the Universe*, New York: Springer-Verlag, 2000.

Ward, W. R., Astronomical theory of insolation, *J. Geophys. Res.* **79**, 3375–86, 1974.

Williams, R. M. and R. J. Phillips, Morphometric measurements from Mars Orbital Laser Altimeter (MOLA) measurements, *J. Geophys. Res.* **106**, 23737–51, 2001.

PART VI

SUMMARY, UPCOMING MISSIONS, AND NEW MEASUREMENT NEEDS

27

The future of Mars exploration

J. F. BELL III

27.1 INTRODUCTION

The information, interpretations, and speculations in this book represent a snapshot in time. Planetary scientists are in the midst of what is – despite the cliché – truly a golden age of Mars exploration. Most of us hardly have time to catch our breath before some new, exciting image or spectrum or model result pops up on our computer screens – or, many times, in our newspapers and TV screens.

Trying to summarize the state of a rapidly moving scientific field such as the current exploration of Mars is challenging at best, futile at worst. However, the authors of the preceding chapters of this book have risen to the challenge admirably and have provided outstanding, timely summaries of the specific aspects of Mars science that are the main focus of this book: the composition, mineralogy, and physical properties of the surface. If this book had been written five years ago, it would have presented an entirely different perspective. It is humbling to also realize that if we had all waited to write this book five years from now, the data, interpretations, and speculations would also almost certainly again be significantly different from what is summarized here. Mars is a moving target, but at some point one has to let the arrow fly.

27.2 ENDINGS

If there ever were an optimal time to try to stop for a moment and grasp the implications of the stunning observations and discoveries of the past 15 years in Mars science, now might arguably be that time. In late 2006, while many of the chapters in this book were being drafted, edited, and finalized, the Mars Global Surveyor (MGS) mission came to an abrupt end after a long and successful nine-year career. MGS was launched in 1996 in an attempt to recover some of the science measurements lost by the failure of the Mars Observer mission in 1993. MGS arrived at Mars in Fall of 1997 and proceeded to spend more than an Earth year slowly aerobraking into its final mapping orbit by early 1999. MGS scientific observations started during aerobraking in 1997, and continued during primary and extended missions for nine Earth years (more than four Mars years), until contact was lost with the spacecraft in November of 2006. During that time, the observations acquired by MGS, and the interpretations of those observations made by the MGS science team, completely revolutionized our view of the red planet. Indeed, it can be safely stated that it was MGS that catalyzed the aggressive scientific trajectory that emerged in early 2000 as the NASA Mars Exploration Program was totally restructured.

Many of the discoveries enabled by MGS involve the composition, mineralogy, and physical properties of the Martian surface, and thus they are the subject of many of the chapters in this book. While researchers will no doubt re-analyze, re-interpret, and plumb the MGS data for new discoveries about Mars for decades to come, many of the "greatest hits" discoveries so far from the mission's extensive global datasets are described, illustrated, and debated here in these pages. The loss of MGS was unfortunate; even after nearly a decade of service, exciting new mission results were still being frequently announced (most recently the discovery, announced only a month after the mission ended, of contemporary impact cratering events and possibly contemporary subsurface liquid water in gullies, both by means of MGS Mars Orbiter Camera time-series observations; Malin *et al.*, 2006). Thus, here at the MGS mission's end, much of this book serves as part of a lasting tribute to all of the scientists, engineers, technicians, managers, students, administrators, and others who were involved in what has arguably been the most successful, prolific, and scientifically rewarding Mars exploration mission completed to date.

Furthermore, MGS embodied the concept of "faster-better-cheaper" that was in vogue during the 1990s at NASA, and its contribution on the basis of science per dollar is arguably amongst the greatest in history.

27.3 BEGINNINGS

This book is ultimately just as much about beginnings as endings, however. For example, the Mars Reconnaissance Orbiter's (MRO) mission has only just begun, and even the initial results are extremely exciting (e.g., Smrekar *et al.*, 2007; see also, for example, Figure 27.1 and also Figures 8.14 and 8.15 in Chapter 8). Launched in 2005, MRO arrived at Mars in March 2006 and began its primary science mission in November of that year, coincidentally in the same month that MGS was lost. MRO results are only briefly touched on in this book, however. The data are still fresh, "hot off the spacecraft" results, many of them confusing, conflicting, and challenging our prior

The Martian Surface: Composition, Mineralogy, and Physical Properties, ed. J. F. Bell III. Published by Cambridge University Press.

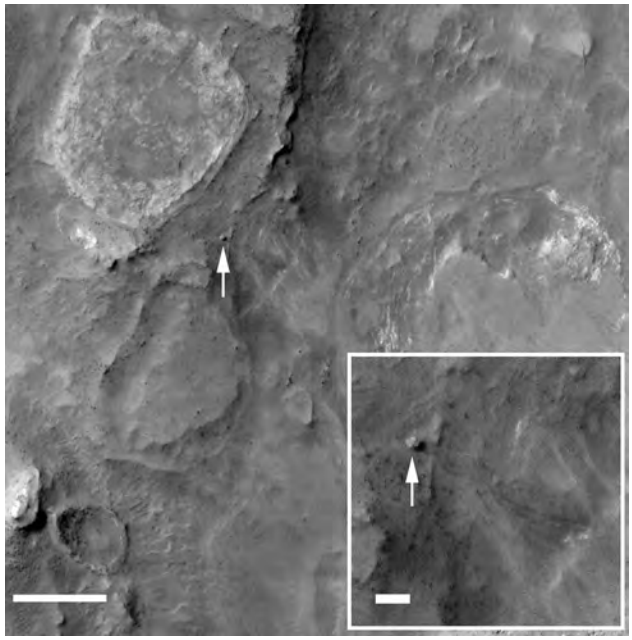

Figure 27.1. Mars Reconnaissance Orbiter (MRO) HiRISE image of the Mars Exploration Rover *Spirit* (arrowed) and the "Home Plate" feature (upper left), in the southern basin of the Columbia Hills, Gusev crater. The image was acquired in November 2006, shortly after MRO began its primary science mission. It is a dramatic example of the image quality and resolution now being routinely acquired from MRO. The scalebar at lower left is 40 m. The inset shows the *Spirit* rover (about 2 m across) and its tracks, near the "Tyrone" bright soil deposit. The scalebar in the inset is 5 m. (Photo credit: NASA/JPL-Caltech/University of Arizona.)

conceptions of what to expect at Mars. Indeed, they are arriving in unprecedented detail and in unimaginable torrents of bits that promise to eventually dwarf the data return of all previous Mars missions combined. MRO has us drinking from a fire hose, and it seems as though yet another Mars revolution may be in the making. Check back in five years and see what is ultimately written about it . . .

More broadly, though, the results discussed in this book are about the beginnings of a deeper understanding of the processes that have shaped our planetary neighbor Mars. Missions such as MGS, MRO, Mars Odyssey, and Mars Express are enabling us to look at and think about Mars from orbit in the same ways that we use remote sensing to study and understand the Earth from orbit and aircraft. Global maps, regional context, local landform details – all of these steps represent a continuum familiar to Earth scientists trying to piece together the complex history of our own planet. Missions such as Mars Pathfinder and the twin Mars Exploration Rovers (MERs) *Spirit* and *Opportunity* take the exploration experience down to the mobile, *in situ* level. Ground truthing, unit mapping, direct chemical/mineralogical sampling, walking the outcrop – these are the methods of the field geologist, and for the first time they are being used in conjunction with advanced robotics capabilities to enable virtual (and vicarious) field work on another planet. It would be the pinnacle of hubris to imagine that we will "figure Mars out" any time soon, however. After all, look at the trouble that we have figuring out our own planet, with essentially infinite access in comparison to our level of access to Mars' surface. Still, it is hard to escape the feeling that the methods and capabilities being pioneered for Mars exploration today represent the beginning of a very special, new era of planetary exploration.

Figure 27.2. Artist's rendering of the *Phoenix* lander, a low-cost "Scout" class mission to the high northern latitudes of Mars that launched in 2007 and is scheduled to land in 2008. The lander's large robotic arm will search for evidence of subsurface ice at the landing site. (This rendition was generated by artist Corby Waste of the Jet Propulsion Laboratory.) (For a color version of this figure, please refer to the color plate section or to the e-Book version of this chapter.)

27.4 THE NEAR FUTURE

It is also hard to escape the urge to be excited about the potential for the future of Mars exploration. MRO has just begun, and the early results are exciting. Mars Odyssey, Mars Express, and (still, incredibly, as of this writing) the *Spirit* and *Opportunity* rovers continue to return remarkable images and other data. And now, two new NASA missions are working their way through design, fabrication, and mission operations.

First will be *Phoenix*, a low-cost "Scout" class lander (Figure 27.2) that launched in August 2007 and will land on the Martian surface in 2008 in the high northern latitudes. *Phoenix* carries cameras, chemical analysis instruments (including a mass spectrometer), and meteorological instruments that are all designed to characterize the geology of the Martian north polar region, to study the history of water on Mars, and to begin the task of assessing the biological potential and habitability of the surface and shallow subsurface (Smith *et al.*, 2006). A powerful and robust 2.35 m long robotic arm will enable trenching down to perhaps 50 cm, and will deliver several key instruments and experiments to the subsurface for direct analyses. While the mission may be short-lived (i.e., after its 90–120 sol primary mission, the static lander is not predicted to be able to survive during the Martian polar night) and will lack the mobility of other recent Mars surface missions, there is still great potential for *Phoenix* to make discoveries about the current and past

Figure 27.3. Artist's rendering of the Mars Science Laboratory rover, scheduling for launch in 2009 and landing in 2010. The rover is about twice the size of the Mars Exploration Rovers *Spirit* and *Opportunity*, and is being designed to drive farther and survive longer than any of the predecessor Mars rovers. (This rendition was generated by artist Corby Waste of the Jet Propulsion Laboratory.) (For a color version of this figure, please refer to the color plate section or to the e-Book version of this chapter.)

climate of Mars by directly sampling surface and subsurface volatiles. Indeed, the lander will be at a prime field site for directly witnessing geologic and meteorologic processes that result from the major cycles of dust, water, and CO_2 that dominate the planet's present climate. These cycles also frame our understanding of potential past climate change on Mars.

The next planned NASA mission to Mars after *Phoenix* will be the Mars Science Laboratory (MSL), a large and capable rover (Figure 27.3) scheduled to be launched in 2009 and to land in 2010 at a site (not yet chosen) identified as a potential *habitat* for past or present life (e.g., Vasavada and the MSL Science Team, 2006). MSL is being designed to be a long-lived, highly mobile field station on Mars. Nominally, the mission should last at least a Mars year, and the rover should be capable of driving 10–20 km from its initial landing site. Having this kind of long duration, "go to" capability on a rover mission opens up a large number of new potential landing sites, and the Mars community is currently in the midst of identifying potential sites and acquiring and analyzing images and other data of these areas from the MGS, Odyssey, Mars Express, and MRO orbiters (details and summaries of the MSL landing site workshops can be found in Golombek *et al.*, 2007, and online at http://marsoweb.nas.nasa.gov/landingsites/index.html). The MSL rover will be able to make many of the same kinds of geological and elemental chemistry observations as the MER and Mars Pathfinder rovers (see Chapters 3, 4, 12, and 13). However, it will enhance previous rover capabilities by acquiring X-ray diffraction and X-ray fluorescence mineralogy and elemental chemistry measurements, as well as mass spectroscopy, isotopic measurements, and gas chromatography measurements of well-selected samples of soils and (ground up) rocks. These data and their subsequent analysis and interpretation will significantly enhance the potential for the mission to assess the biologic and "habitability" potential of what will hopefully be aqueous sedimentary rocks explored during a long and exciting traverse. The rover will also acquire detailed meteorological observations to provide new data on the current climate of Mars. MSL will also hopefully open up far more of the surface of Mars to science-driven robotic exploration by virtue of its advanced entry–descent–landing (EDL) system. This EDL capability could allow access to more than 50% of the Martian surface, including portions of the southern highlands and northern lowland plains not accessible previously. As such, MSL will demonstrate technologies that "feed forward" to more capable mobile analytical exploration systems, including, perhaps, robotic sample return.

27.5 AND BEYOND

The future of Mars exploration beyond *Phoenix* and MSL is less certain, and will depend critically on the stability of funding for NASA's science and exploration programs in what are difficult fiscal times. Still, NASA's plans are beginning to be formulated for at least the next decade or so (e.g., Beebe, 2006; NASA, 2006). NASA may utilize the 2011 or 2013 launch opportunity to send a new "Scout" class orbiter to Mars to study the planet's atmosphere in more detail, especially the upper atmosphere, to learn more about the way the solar wind influences (and has influenced in the past) the planet's climate. Plans for 2013 and beyond include a possible combined science–telecommunications orbiter, perhaps optimized for the study of trace atmospheric gases like methane, or for more in-depth studies of volatile cycles and the planet's energy balance, or for other high-priority science objectives that arise in response to discoveries being made by current and near-future missions. Studies are also being conducted to explore the feasibility of sending a network of landers to Mars in 2013 or thereafter, in order to enable global seismic studies of the interior and/or global monitoring of atmospheric and surface-atmospheric cycles. Another option being considered is sending more so-called "mid-range" rovers similar in capability to *Spirit* and *Opportunity*, to study more of the many different places on Mars that may once have been habitable. In the meantime, it is hoped that Mars Odyssey, MRO, and MSL can continue returning high-quality science data as part of extended missions well into the decade of the 2010s.

The exploration of Mars has truly become an international endeavor, as evidenced by the success of the Mars Express mission and of the international experiments and science team collaborations that have been carried out on many past and current NASA Mars missions. Thus, it should not be surprising that other space agencies besides NASA are formulating plans for future Mars exploration. For example, the Russian Space Agency is planning a 2009 or 2011 launch of a mission called *Phobos-Grunt* (Phobos-soil) that would acquire and return to Earth a sample from the Martian moon Phobos (Marov *et al.*, 2004). Mars remote-sensing observations would also be conducted as part of the mission, which would be the first Russian-led Mars mission since the failed Mars-96 orbiter and Phobos-88 orbiter-landers, and which would also include a variety of scientific instruments and other systems to be provided by the China National Space Administration and perhaps the European Space Agency (ESA). ESA, meanwhile, is considering its own plans for a launch of an ambitious Mars rover

called *ExoMars* (Vago *et al*., 2006) in 2013 or beyond. ExoMars as currently envisioned would focus on exploring a site chosen for its biologic potential, and could include the capability to drill into the subsurface and perform detailed organic chemistry measurements on those materials to search for signs of past or present life. Its powerful astrobiology-oriented payload (Pasteur) would complement the pathfinding observations planned for the NASA MSL mission.

Looking beyond the decade of the 2010s, there is as yet only a vague idea of how Mars exploration should – or could – proceed. Most planetary scientists studying Mars agree that the next important big leap to take, probably in the late 2010s or early 2020s, should be a series of robotic missions that will return to Earth Martian rock and soil samples from several carefully selected sites. However, robotic Mars sample return missions will be expensive (compared to past robotic Mars missions) and technically challenging endeavors. From the vantage point of the latter part of the first decade of this new century, the fiscal and engineering hurdles to bringing back samples from Mars appear almost insurmountable to many people who are carefully studying the problem. Still, it seems likely that studying samples returned from Mars for radiometric age dating and geochemical, isotopic, and biologic analyses in the best-available terrestrial laboratories could be easier, less expensive, and more scientifically robust than assembling such laboratories on Mars itself. The need for such missions to be international in scope also seems apparent, not only from the standpoint of decreasing the financial burden on any one nation, but also in terms of tapping into the best possible engineering solutions, scientific minds and instruments, and laboratory analysis facilities across our own planet. If we take such a perspective, the challenge may not be insurmountable after all.

Another reason to conduct robotic Mars sample return missions, of course, is to prepare for eventual human missions to Mars. Samples will provide critical information needed to assess the engineering issues and biologic potential of Martian surface materials, as well as any potential health hazards (from, for example, the micron-sized nature of Martian dust). Since 2004, NASA has been steadily embarking upon a so-called "Vision for Space Exploration" that is designed to recreate much of the heavy-lift and beyond low-Earth-orbit rocket capability that was abandoned when the Apollo missions ended in the 1970s. As presently imagined, this capability could first be used to return humans to the Moon in a series of Apollo-like (though longer) sortie missions in the 2020s or so, ideally followed by the establishment of a lunar outpost by the middle to end of that decade. Going back to the Moon has been justified as a necessary first step to Mars, in order to enable the development of the technical and engineering infrastructure and the human experience/expertise required for more complex, expensive, and more risky voyages to Mars. Human missions to Mars are presently only a fuzzy goal, however, with no firm timelines or dedicated budgets established for such missions by any of the world's space agencies. In the meantime, we can only wish Godspeed to our robotic emissaries. They go where, so far, we can only dream of going ourselves.

27.6 SUMMARY

Despite continuous uncertainty about funding and some significant technical hurdles that need to be overcome, it appears that the future of Mars exploration will continue to be exciting and rewarding. The rewards will be partly scientific – with new data about the geology, geochemistry, meteorology, and habitability of Mars (past and present) streaming in from planned orbiters, landers, and rovers for the next several decades. But there will also be less tangible rewards, including educating and inspiring teachers and the next generation of explorers. A generation of scientists and engineers (and politicians) were inspired to change the world when *Sputnik* rocketed into orbit 50 years ago. These people took us to the Moon, and then trained a new generation of people who are building – literally and figuratively – a technological web that is slowly connecting all humans to each other, to our past, and to our future. Exploring Mars provides a new, distant strand for that web, and a window to the past, present, and future of our own planet. At Mars, we also have an opportunity to study another of the rare places in our Solar System where life may once have been, and perhaps could still be.

REFERENCES

Beebe, R., Chair, *Assessment of NASA's Mars Architecture: 2007–2016*, National Research Council, National Academy of Sciences, Washington DC, 2006 (available online at www.nap.edu/catalog/11717.html).

Golombek, M., J. Grant, A. R. Vasavada, and M. Watkins, Landing sites proposed for the Mars science laboratory mission, *Lunar Planet. Sci. Conf. XXXVIII*, League City, Texas, LPI Contribution No. 1338, p. 1392, March 12–16, 2007.

Malin, M. C., K. S. Edgett, L. V. Posiolova, S. M. McColley, and E. Z. Noe Dobrea, Present-day impact cratering rate and contemporary gully activity on Mars, *Science* **314**, 1573–7, 2006.

Marov, M. Ya., V. S. Avduevskyb, E. L. Akima, *et al*., Phobos-Grunt: Russian sample return mission, *Adv. Space Res.* **33**, 2276–80, 2004.

NASA, Solar System Exploration Division Roadmap for NASA's Science Mission Directorate, Jet Propulsion Laboratory Technical Report CL#06–1867-A, Pasadena, CA, 2006 (available online at http://science.hq.nasa.gov/strategy/comm.html).

Smith, P. H. and the Phoenix Science Team, Overview of the Phoenix Mars Lander Mission, *4th Int. Conf. Mars Polar Sci. Explor*., Davos, Switzerland. LPI Contribution No. 1323, p. 8010, 2006.

Smrekar, S. E., R. W. Zurek, G. M. Keating, *et al*., Mars Reconnaissance Orbiter's first look at Mars, *Lunar Planet. Sci. Conf. XXXVIII*, League City, Texas, LPI Contribution No. 1338, p. 2126, March 12–16, 2007.

Vago, J. L., B. Gardini, P. Baglioni, *et al*., ExoMars: ESA's mission to search for signs of life on the Red Planet, *Annu. Lunar Planet. Sci. Conf. XXXVII*, League City, Texas, Abstract #1871, March 13–17, 2006.

Vasavada, A. R. and the MSL Science Team, NASA's 2009 Mars science laboratory: an update, *Annu. Lunar Planet. Sci. Conf. XXXVII*, League City, Texas, Abstract #1940, March 13–17, 2006.

INDEX

S